SCHOLARLY PUBLICATIONS

A CURRENT AWARENESS BULLETIN
OF RESEARCH OUTPUT

@DTU

(124th Edition)

APRIL 2023

BY: CENTRAL LIBRARY

DELHI TECHNOLOGICAL UNIVERSITY
(FORMERLY *DELHI COLLEGE OF ENGINEERING)*
GOVT. OF N.C.T. OF DELHI
SHAHBAD DAULATPUR, MAIN BAWANA ROAD
DELHI 110042

PREFACE

This is the **One Hundred Twenty Fourth** Issue of Current Awareness Bulletin started by Delhi Technological University, Central Library. The aim of the bulletin is to compile, preserve and disseminate information published by the faculty, students and alumni for mutual benefits. The bulletin also aims to propagate the intellectual contribution of Delhi Technological University (DTU) as a whole to the academia.

The bulletin contains information resources available in the internet in the form of articles, reports, presentations published in international journals, websites, etc. by the faculty and students of DTU. The publications of faculty and student which are not covered in this bulletin may be because of the reason that the full text either was not accessible or could not be searched by the search engine used by the library for this purpose.

The learned faculty and students are requested to provide their uncovered publications to the library either through email or in CD, etc. to make the bulletin more comprehensive.

This issue contains the information published during **April, 2023**. The arrangement of the contents is alphabetical. The full text of the article which is either subscribed by the university or available in the web is provided in this bulletin.

Central Library

CONTENTS

1. 5G AND MODULATION SCHEMES, ***6.Rahul Singh***, Environmental, DTU

2. A hybrid Firefly and Particle Swarm Optimized FOF-PID Strategy for Interconnected Multi-area Power System with Renewable Energy Sources, Gomaa Haroun A. H, Khaled Eltag and ***7.Mustafa Eltigani I. M.***, Electrical, DTU

3. A New Three-Phase Eleven Level Packed E-Cell Converter for Solar Grid-Tied Applications, SANJAY UPRETI, BHIM SINGH and ***3.NARENDRA KUMAR***, Electrical, DTU

4. A novel cloud model based on multiplicative unbalanced linguistic term set, ***6.Parul Chauhan***, ***3.Anjana Gupta*** and ***6.Tanya Malhotra***, Applied Mathematics, DTU

5. A novel reduced nano- phase change material based absorber for enhancing the water productivity and performance of solar desalination system, ***3.Anil Kumar***, ***6.Anand Kushwah*** and ***3.Anil Kumar***, Mechanical and Environment, DTU

6. A Practical PHEV Charging Polic y to Improve Performance of Power Distribution Systems, ***7.Divyanshu Khandelwal***, ***6.Shefali Painuli***, ***3.Suman Bhowmick*** and ***3.Radheshyam Saha***, Electrical, DTU

7. A study on Holographic dark energy model with adiabatic matter creation, ***6.Simran Kaur*** and ***3.C.P. Singh***, Applied Physics, DTU

8. A systematic review of the methodologies for the processing and enhancement of the underwater images, ***8.Nishant Singh*** and ***3.Aruna Bhat***, CSE, DTU

9. AGC of 2-Area Restructured Power System using Polar Fuzzy Controller and Energy Storage Units, ***6.Ram Naresh Mishra***, ***3.Narendra Kumar***, and Mohd. Zuhaib, Electrical, DTU

10. Air quality changes in Delhi due to open waste burning: an accidental fire in Bhalswa landfill, ***6.M. Sharma***, M. Khare and ***3.R. K. Mishra***, Environmental, DTU

11. An Effective Technique for Single Image Haze Removal using MSMO, ***6.Vikas Varshney***, ***3.Jeebananda Panda*** and ***3.Rashmi Gupta***, Electronics, DTU

12. An iterative analytic approximation for a class of nonlinear singularly perturbed parabolic partial differential equations, ***6.Kartikay Khari*** and ***3.Vivek Kumar***, Applied Mathematics, DTU

13. Analysis of Differential Privacy and study of its variation with privacy budget using real-world data, ***8.Rakshit Chauhan***, ***8.Pooja Narula***, ***8.Shaurya Shekhar*** and ***3.Manoj Kumar***, CSE, DTU

14. Analysis of Shapes of Centrifugal Force-Generating Rod in Centrifugal Force-Assisted Abrasive Flow Machining Process, ***6.A. Bhardwaj***, ***3.K. Srinivas*** and ***3.R. Chaudhary***, Mechanical, DTU

15. Analytical Modelling and Simulation of a Junctionless Accumulation-Mode Tube (JLAMT) Field-Effect Transistor (FET) for Radiation Sensing Dosimeter Applications, Sia Batra and ***3.Sonam Rewari***, Electronics, DTU

16. Aromatic plants: a multifaceted asset, ***6.Anuradha*** and ***3.Navneeta Bharadvaja***, Biotechnology, DTU

17. Autonomous Active Grid islanding and DGs outage detection in a μG utilizing Goertzel Algorithm in collaboration with Fuzzy Inferencing System, ***7.Samavedam Swetha*** and ***3.Vishal Verma***, Electrical, DTU

18. Axis Control of a Nonlinear Helicopter Model Using Intelligent Controller, ***3.Abhishek Chaudhary***, Electrical, DTU

19. CAT-CapsNet: A Convolutional and Attention Based Capsule Network to Detect the Driver's Distraction, Himanshu Mittal and ***3.Bindu Verma***, IT, DTU

20. Chalcogenide glass-based Low Loss Graded Index Photonic Crystal Fiber for Non-linear applications in the Mid-IR regime, ***6.Jyoti Chauhan***, ***3.Yogita Kalra*** and ***3.Ravindra Kumar Sinha***, Physics, DTU

21. Chlorella minutissima-assisted silver nanoparticles synthesis and evaluation of its antibacterial activity, ***6.Lakhan Kumar***, ***6.Lalit Mohan***, ***7.Raksha Anand*** and ***3.Navneeta Bharadvaja***, Biotechnology, DTU

22. CLOUD COMPUTING AND ITS IMPLEMENTATION CHALLENGES, Zalmai Zormatai, ***6.Samiullah Mehraban***, Hameed Yousof and Shafiullah Shinwari, CSE, DTU

23. Combined effects of high voltage gradient and electrolyte conditioning on electrokinetic remediation for chromium (VI)-contaminated soils, ***6.Sonam Taneja***, Oznur Karaca and ***3.A. K. Haritash***, Environmental, DTU

24. Comparative Performance Analysis of Mamdani and Sugeno Fuzzy Controller using Application on 2DoF Ball Balancer System, ***6.Nikita Nikita***, ***3.Bharat Bhushan*** and ***3.Abhishek Chaudhary***, Electrical, DTU

25. Computation of energy across the type-C piano key weir using gene expression programming and extreme gradient boosting (XGBoost) algorithm, ***3.Nipun Bansal***, ***8.Deepak Singh*** and ***3.Munendra Kumar***, CSE and Civil, DTU

26. Conductive Ink-Coated Paper-Based Supersandwich DNA Biosensor for Ultrasensitive Detection of Neisseria gonorrhoeae, ***6.1.Niharika Gupta***, ***3.D. Kumar***, ***3.Asmita Das***, Seema Sood and ***3.Bansi D. Malhotra***, Biotechnology and Applied Chemistry, DTU

27. Congestion Aware Data Transmission in Mobile and Constrained IoT Network, ***6.Aastha Maheshwari***, ***3.Rajesh Kumar Yadav*** and Prem Nath, CSE, DTU

28. Cosmological test of $\sigma\ \theta$ as function of scale factor in $f(R,\ T\ )$ framework, ***7.Himanshu Chaudhary***, ***3.Aditya Kaushik*** and ***7.Ankita Kohli***, Applied Mathematics, DTU

29. COVID-19 Detection using Inception V3: A Deep Learning Approach, ***8.Adithya Krishnan*** and ***8.Akhilesh Gautam***, Software Engineering, DTU

30. CovSumm: an unsupervised transformer-cum-graph-based hybrid document summarization model for CORD-19, ***6.Akanksha Karotia*** and ***3.Seba Susan***, IT, DTU

31. Current Feedback Operational Amplifier Based Active Filter Configuration, ***3.Ram Bhagat***, ***7.Monika Kumari***, ***8.Nilesh Kumar Jha*** and ***7.Rishabh Yadav***, Electrical, DTU

32. Data Analysis of three parameter models of deceleration parameter in FRW Universe, Amine Bouali, ***7.Himanshu Chaudhary***, Ujjal Debnath, Alok Sardar and G.Mustafa, Applied Mathematics, DTU

33. Deception Detection using a Multimodal Stacked Bi-LSTM Model, ***8.Puneet Kumar Sehrawat***, ***8.Rajat Kumar***, ***8.Nitish Kumar*** and ***3.Dinesh Kumar Vishwakarma***, IT, DTU

34. Deep Learning-based Advancement in Fuzzy Logic Controller, ***6.Supriya Kaul***, Shekhar Yadav, Nitesh Tiwari and Amit Singh, Electrical, DTU

35. Design and analysis of questionnaire on coach skill set for effective sports management, ***6.Subodh Mor***, ***3.Shikha N. Khera*** and ***3.G. C. Maheshwari***, DSM, DTU

36. Design and Dynamic Response of FOGI-FLL Based Controller in Grid Tied Solar PV System, ***6.Sukhbir Singh*** and ***3.J N Rai***, Electrical, DTU

37. Design and Evaluation of a Water-Based, Semitransparent Photovoltaic Thermal Trombe Wall, ***8.Sheel Bhadra***, Niloy Sen, Akshay K K, Harmeet Singh and Paul G. O'Brien, Mechanical, DTU

38. Design and Performance Evaluation of Three-Phase Grid-Tied Solar Power Generation System Using STF based Algorithm, ***6.Ranjeet Singh***, ***3.Vinod Kumar Yadav*** and ***3.Madhusudan Singh***, Electrical, DTU

39. Determination of endogenous concentration of Sodium potassium Cadmium Lead and Cadaverine correlating with physio-chemical parameters in Lycopersicon esculentum under multiple stress conditions, CHARU RAJPAL, ***6.SUMIT DAGAR*** and PUSHPA C. TOMAR, Environmental, DTU

40. Development of Brake System Plausibility Device of an FSAE Race Car, ***3.D.C Meena***, ***8.Aryan Motla***, ***8.Anuj Majumdar*** and ***8.Aatish Kumar Ghosh***, Electrical, DTU

41. Dynamic Performance Assessment of Power System Interconnected via Asynchronous Transmission Link in Reorganized Configuration, Ram Naresh Mishra and ***3.Narendra Kumar***, Electrical, DTU

42. Email Spam Detection Using Naïve Bayes, ***8.Hrithik Vohra*** and ***3.Manoj Kumar***, CSE, DTU

43. Empirical Study of Integrating Social Sustainability Factors: an Organizational Perspective, ***6.Deepak Sharma***, ***3.Pravin Kumar*** and Rajesh Kumar Singh, Mechanical, DTU

44. Energy Efficient Cluster-Based Routing Protocol for WSN Using Nature Inspired Algorithm, ***6.1.Rashmi Mishra*** and ***3.Rajesh K. Yadav***, CSE, DTU

45. Energy Use Patterns of Pearl Millet (Pennisetumglaucum (L.)) Production in Haryana, India, Raveena Kargwal, Yadvika, Vijay Kumar Singh and ***3.Anil Kumar***, Mechanical and Environmental, DTU

46. Enhanced structural, dielectric, ferroelectric and piezoelectric properties of (1-x)Ba0.9Sr0.1TiO3 – (x)Ba0.7Ca0.3TiO3 ceramics derived using mechanochemical activation technique, ***6.Aditya Jain***, ***3.Amrish K. Panwar***, ***6.Rakesh Saroha***, A. K. Jha, Applied Physics, DTU

47. Face Manipulation Detection in Images using Inception Layers and Graph Convolutional Networks, ***8.Aman Mahendroo***, ***8.Aaradhya Beri*** and ***3.Anukriti Kaushal***, CSE, DTU

48. Fault classification using deep learning based model and impact of dust accumulation on solar photovoltaic modules, ***6.Rahma Aman***, ***3.M. Rizwan*** and ***6.1.Astitva Kumar***, Electrical, DTU

49. Flying Squirrel Search Optimization based MPPT Controller for Stand-Alone PV System, ***6.Atul Avasthi***, ***3.Rachana Garg*** and ***3.Priya Mahajan***, Electrical, DTU

50. Game theory and MCDM-based unsupervised sentiment analysis of restaurant reviews, ***Neha Punetha*** and ***3.Goonjan Jain***, Applied Mathematics, DTU

51. High Performance CMOS Voltage Level Shifters Design for Low Voltage Applications, ***8.Ananya Kapoor***, ***8.Chaitanya Shanker Jha***, ***8.Ayush Thapar*** and ***3.Chaudhry Indra Kumar***, Electrical, DTU

52. IMPACT AND BENEFITS OF SOFTWARE DEFINED NETWORK ON THE CLOUD NETWORK INFRASTRUCTURE, Zalmai Zormatai, ***6.Samiullah Mehraban***, Hameed Yousof and Shafiullah Shinwari, CSE, DTU

53. Impact of impurity on the non-linear and linear optical properties of InxGa1-xAs Quantum Dot, ***6.Priyanka*** and ***3.Rinku Sharma***, Applied Physics, DTU

54. Integrating Solar Photovoltaic Power Source and Biogas Energy-Based System for Increasing Access to Electricity in Rural Areas of Tanzania, ***6.Isaka J. Mwakitalima***, ***3.Mohammad Rizwan*** and ***3.Narendra Kumar***, Electrical, DTU

55. IntelliCode: A speech-based programming environment, Dr. Manoj Kumar*, Hitesh Yadav*, Jayant Yadav*, Mayank Jha,

56. KL Grade Classification of Knee Osteoarthritis using Convolutional Neural Networks and CBAM, ***8.Pragya Gupta***, ***8.Raghav Gupta***, ***8.Ram Aggarwal*** and ***3.Manoj Kumar***, CSE, DTU

57. Lower hybrid wave nonlinear saturation and turbulence in the magnetopause, Manoj K. Upadhyay, ***6.Neha Pathak***, R. Uma and R.P. Sharma, Applied Physics, DTU

58. Lumino-structural properties of Dy3+ activated Na3Ba2LaNb10O30 phosphors with enhanced internal quantum yield for w-LEDs, Kanishk Poria, Ravina Lohan, Sanjana Bhatia, Amit Kumar, Rajwinder Singh, Nisha Deopa, Rajesh Punia, Jangvir Singh Shahi and ***3.A. S. Rao***, Applied Physics, DTU

59. MANUFACTURING MACHINE- A REVIEW PAPER, ***8.Satyendra Kumar Pandey***, ***8.Vansh Baliyan***, ***8.Vishal Singh*** and ***3.Dr. Ashok Kumar Madan***, Mechanical, Production And Industrial Engineering, DTU

60. Model-independent study for a quintessence model of dark energy: Analysis and Observational constraints, © Amine Bouali,, ***7.Himanshu Chaudhary***, Amritansh Mehrotra, and S. K. J. Pacif, Applied Mathematics, DTU

61. Multilayer Convolutional Neural Network Based Approach to Detect Apple Foliar Disease, ***7.Barsha Biswas*** and ***3.Rajesh Kumar Yadav***, CSE, DTU

62. Multi-response mathematical model for optimization of process parameters in CMT welding of dissimilar thickness AA6061-T6 and AA6082-T6 alloys using RSM-GRA coupled with PCA, ***6.Yashwant Koli***, ***3.N. Yuvaraj*** and S. Aravindan, ***3.Vipin***, Mechanical, DTU

63. Natural polymers used in the dressing materials for wound healing: Past, present and future, Bharti Sheokand, Monika Vats, Anand Kumar, Chander ***6.1.Mohan Srivastava***, Indra Bahadur and Seema R. Pathak, Chemistry, DTU

64. Numerical Evaluation of the Gate Stacked GNR FET for improved Device Switching, ***6.Anshul*** and ***3.Rishu Chaujar***, Applied Physics, DTU

65. On a Class of Non-Univalent functions Associated with a Parabolic Region, ***7.Mridula Mundalia*** and ***3.S. Sivaprasad Kumar***, Applied Mathematics, DTU

66. Performance Analysis of Dual-HopaMixed RF/FSO Systemaover Nakagami-m/Fisher Snedecor Fading Channels, ***6.Rekha Rani***, ***3.Gurjit Kaur***, Shubham Gautam, Lakshmanan. M and Shubham Kumar, Electronics, DTU

67. Performance analysis of Linear Quadratic Regulator for DC-DC Converter Systems, ***6.Soni Kumari***, ***3.Dr. Madan Mohan Rayguru*** and ***3.Shreyansh Upadhyaya***, Electrical, DTU

68. Performance assessment of hydrogen-based commercial hybrid renewable energy power generation system, ***8.Rishabh Kumar***, ***8.Vishvender Kumar Dheer***, ***8.Piyush Sharma***, ***8.Nishant*** and ***3.Anil Kumar***, Mechanical and Environment, DTU

69. Physical and numerical modelling of single tunnels under static loading conditions, ***6.Parvesh Kumar*** and ***3.Amit Kumar Shrivastava***, Civil, DTU

70. Power Quality Improvement using Hopfield Neural Network in Grid Distribution System, ***8.Pranshu Bansal***, ***8.Prashant Bharati***, ***8.Sambhav Jeswani*** and ***3.Ankita Arora***, Electrical, DTU

71. Prospective applications of thermally stable Dy3+ doped potassium zinc strontium borate (KZSB) glasses in w-LEDs, ***6.Sheetal Kumari***, ***7.Anu***, Aman Prasad, ***7.Pooja Rohilla*** and ***3.A. S. Rao***, Applied Physics, DTU

72. Rare deleterious mutations in Bruton's tyrosine kinase as biomarkers for ibrutinib-based therapy: an in silico insight, ***6.Jaishree Meena*** and ***3.Yasha Hasija***, Biotechnology, DTU

73. Redefining Industry 5.0 in Ophthalmology and Digital Metrology: A Global Perspective, ***8.S. Chourasia***, ***3.S. M. Pandey***, ***3.Q. Murtaza***, ***3.S. Agrawal*** and ***6.K. Gupta***, Mechanical and DSM, DTU

74. Review—Advancements and Perspectives of Organic LED: In Depth Analysis of Architectural Design, Characteristics Parameters, Fabrication Techniques and Applications, ***6.Sugandha Yadav***, ***3.Poornima Mittal*** and Shubham Negi, Electronics, DTU

75. Sign Language to Text Classification using One-Shot Learning, ***8.Sourav Pal***, ***8.Sparsh Sinha***, ***8.Sourabh Ruhella*** and ***3.Anurag Goel***, CSE, DTU

76. Simultaneous Seismic Data Denoising and Reconstruction with Attention based Wavelet-Convolutional Neural Network, Vineela Chandra Dodda, Lakshmi Kuruguntla, ***3.Anup Kumar Mandpura*** and Karthikeyan Elumalai, Electrical, DTU

77. SOME DIFFERENTIAL SUBORDINATION RESULTS FOR A CLASS OF STARLIKE FUNCTIONS, ***7.MRIDULA MUNDALIA*** AND ***3.S. SIVAPRASAD KUMAR***, APPLIED MATHEMATICS, DTU

78. SupRes: Facial Image Upscaling Using Sparse Denoising Autoencoder, ***8.Manan Agrawal***, ***8.Mohd Ayaan Anwar***, ***8.Nakul Saroha*** and ***3.Anurag Goel***, CSE, DTU

79. Switched Capacitor Based High Gain Boost Converter for Renewable Energy Application, Manikant Kumar, ***3.Vinod Kumar Yadav*** and Arun Kumar Verma, Electrical, DTU

80. SYNTHESIS AND EFFECT OPTIMIZATION OF M R FLUID COMPOSITION FOR REDUCTION IN INDUCED RESIDUAL STRESS, Anil Kumar, Neeraj Kumar and ***3.M.S. Niranjan***, Mechanical, DTU

81. Technology enabled communication during COVID 19: analysis of tweets from top ten Indian IT companies using NVIVO, Swati Chawla, Puja Sareen, Sangeeta Gupta, ***3.Meha Joshi*** and Ritu Bajaj, DSM, DTU

82. The Role of Deep Learning in Diagnosis and Grading of Diabetic Retinopathy: A Review, ***8.Samarpit Minz***, ***8.Saarthak Seth***, ***8.Sarvesh Tiwari*** and ***3.Rahul Katarya***, CSE, DTU

83. Theoretical modeling and numerical simulation of enhanced graphene growth under the influence of oxidizers in RF-PECVD plasma using finite element method, ***6.Sagar Khanna*** and ***3.Suresh C. Sharma***, Applied Physics, DTU

84. Zinc Oxide incorporated Molybdenum Diselenide Nanosheets for Chemiresistive Detection of Ethanol Gas, ***6.Nikita Jain*** and ***3.Nitin K. Puri***, Applied Physics, DTU

1. *Vice Chancellor*
2. *Pro Vice Chancellor*
3. *Faculty*
4. *Teaching-cum-Research Fellow*
5. *Asst. Librarian*
6. *Research Scholar*
7. *PG Scholar*
8. *Undergraduate Student*

1.1. *Ex Vice chancellor*
2.1. *Ex Pro Vice Chancellor*
3.1. *Ex Faculty*
4.1. *Alumni*
5.1 *Others*
6.1. *Ex Research Scholar*
7.1. *Ex PG Scholar*
8.1. *Ex Undergraduate Student*

e-ISSN: 2582-5208
International Research Journal of Modernization in Engineering Technology and Science
(Peer-Reviewed, Open Access, Fully Refereed International Journal)
Volume:05/Issue:03/March-2023 Impact Factor- 7.868 www.irjmets.com

5G AND MODULATION SCHEMES

Rahul Singh[*1]

[*1]Department Of Environmental Engineering, Delhi Technological University

Bawana Delhi-110042, India.

DOI : https://www.doi.org/10.56726/IRJMETS35172

ABSTRACT

This paper discusses from the ground up; the origin, need, evolution, and various new modulation techniques for 5G communication. From the advent of the first automated mobile network, 1G to ushering in the era of 5G, the ever-increasing need for robust and advanced communication has pushed forward the research and development of the next big communication technology. 5G introduces the internet of things in the equation and solves various requirements all at once.

Keywords: 5G, Modulation, Communication, Iot, Multiplexing.

I. INTRODUCTION

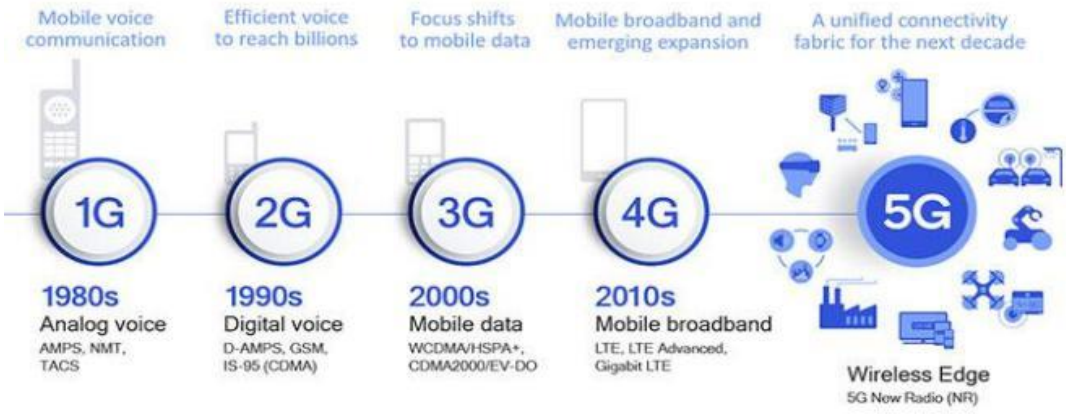
The first commercially automated mobile network was 1G, or the first "Generation." Nippon Telegraph and Telephone (NTT) launched it in Tokyo, and it quickly grew to reach the whole population of Japan by 1979.

In 1991, Finland was the birthplace of the second generation of mobile networks. 2G was introduced under the Global System for Mobile Communication (GSM) and provided a wireless technology that was significantly superior to 1G.

NTT DoCoMo launched 3G in 2001, effectively ushering in the 'packet-switching' revolution by assuring significantly greater connectivity for the 'data packets' that drive internet connectivity. Standardization was a major driving force behind 3G. In a market cluttered with numerous suppliers and protocols, 3G intended to deliver a single network standard.

In 2009, the first commercial deployments of the Long Term Evolution (LTE) 4G technology took place in Oslo and Stockholm. Since then, it has rapidly spread around the world, including the United States. With theoretical data rates of 200Mbps, this network generation ushers in a new era of high-quality streaming.

The greater range of frequency spectrum that 4G employs addresses one of the previously limiting limitations of 2G and 3G. This is a theme that will continue throughout the 5G era.



The fifth-generation mobile network is referred to as 5G. After 1G, 2G, 3G, and 4G networks, it is a new global wireless standard. 5G allows for the creation of a new type of network that connects nearly everyone and everything, including machines, objects, and gadgets.

5G wireless technology is designed to provide multi-gigabit per second peak data speeds, ultra-low latency, greater dependability, huge network capacity, increased availability, and a more consistent user experience to a larger number of users. Higher performance and efficiency allow for new user experiences and industry connections. It is a more capable and unified air interface. It has been built with increased capacity to support next-generation user experiences, new deployment patterns, and service delivery.

e-ISSN: 2582-5208
International Research Journal of Modernization in Engineering Technology and Science
(Peer-Reviewed, Open Access, Fully Refereed International Journal)
Volume:05/Issue:03/March-2023 Impact Factor- 7.868 www.irjmets.com

While previous generations of cellular technology (such as 4G LTE) concentrated on ensuring connectivity, 5G takes connectivity to the next level by providing customers with connected experiences via the cloud. Virtualized and software-driven 5G networks make use of cloud technology.

With seamless open roaming capabilities between cellular and Wi-Fi connectivity, the 5G network will also simplify mobility. Without user involvement or the need to reauthenticate, mobile users can stay connected as they travel between outside wireless connections and wireless networks inside buildings.

A. Need for Modulation of Signals

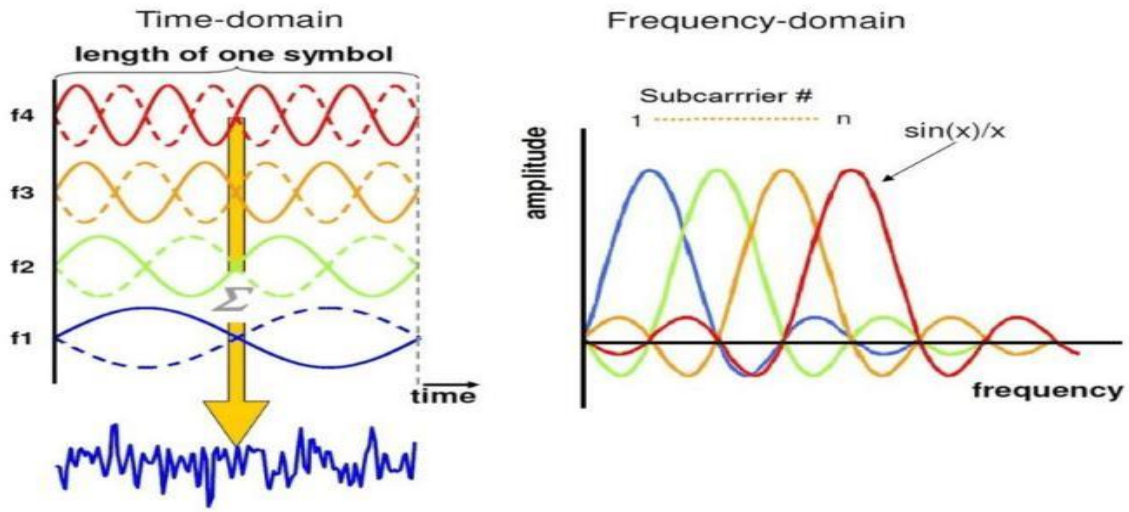
1) Increase the strength of the signal: The sender's baseband signals aren't capable of being transferred directly. The message signal's power should be raised to allow it to reach longer distances. Modulation is crucial in this situation. The most important requirement of modulation is to increase the signal's strength without changing the carrier signal's properties.

2) System of Wireless Communication: In communication systems, modulation has eliminated the need for wires. It's because modulation is extensively utilized to send signals at a higher rate from one site to another. As a result, the modulation method has aided in the advancement of wireless communication systems.

3) Mixing Of Message Signals Is Prevented: Modulation and its various variants prevent extraneous signals from interfering with the message signal. It's because a person delivering a message signal over the phone won't be able to distinguish between them. As a result, they'll get in each other's way. The mixing of the signals can be avoided by utilizing carrier signals with a high frequency. As a result, modulation guarantees that the signals received by the receiver are flawless.

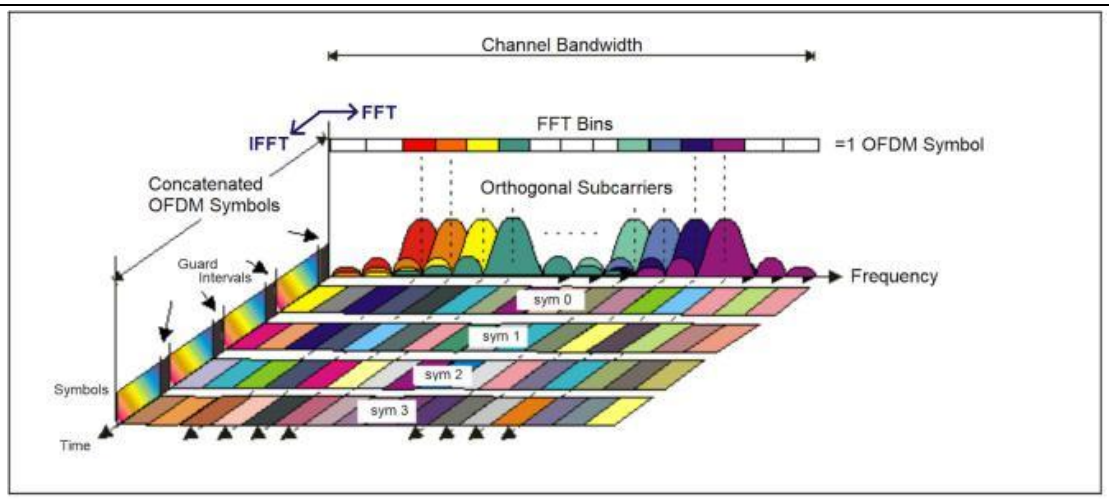
B. Modulation for 5G

For 4G LTE, orthogonal frequency division multiplexing has proven to be an excellent waveform. It has outstanding spectrum efficiency, can be processed and handled with current mobile device processing levels, and works well with high data rate streams occupying large bandwidths. It works well in situations when selective fading is present.



Orthogonal Frequency Division Multiplexing (OFDM) is a new wireless communication system modulation scheme that includes 5G. OFDM is a high-data-rate communication method that combines the advantages of Quadrature Amplitude Modulation (QAM) with Frequency Division Multiplexing (FDM). BPSK (Binary Phase Shift Keying), QPSK (Quadrature Phase Shift Keying), 16QAM (16-state QAM), 64QAM (64-state QAM), and so on are all examples of QAM modulation.

e-ISSN: 2582-5208
International Research Journal of Modernization in Engineering Technology and Science
(Peer-Reviewed, Open Access, Fully Refereed International Journal)
Volume:05/Issue:03/March-2023 Impact Factor- 7.868 www.irjmets.com



II. MODULATION

High-speed, high-resolution streaming video, devices with artificial intelligence, network availability everywhere and at all times, high-speed gaming, a revolution in manufacturing, automation, healthcare, and energy would be some of the potential 5G uses. The most difficult task is to handle a large number of devices that require quick network access to send minor data. Low-end sensor traffic is also latency-sensitive, necessitating an ultra-resilient communication link. Users will be able to access extremely high data rates while machines would have minor latency. Orthogonal Frequency Division Multiplexing (OFDM) is used in fourth-generation communications [2]. Single-frequency networks such as Digital Video Broadcast (DVB), Digital Audio Broadcast (DAB), and indoor wireless systems use OFDM. The fifth-generation (5G) modulation scheme addresses critical requirements such as the ability to use signals with high data rates, the ability to provide minimal delay for long and concise data, the ability to exchange data quickly in the uplink and downlink, and the option of cost-effective broadcasting by reducing the on-time of devices with low data rates. Various waveforms and modulation techniques were proposed during the development phase for 5G technology, but for 5G New Radio (5G NR), Cyclic Prefix OFDM (CP-OFDM) was chosen as the main candidate, with DFT-s-OFDM, discrete Fourier transform spread orthogonal frequency division multiplexing being used in some areas.

High-speed video downloads, gaming, car-to-car / car-to-infrastructure communications, general cellular communications, IoT / M2M communications, and other uses for 5G mobile communications all impose demands on the type of 5G waveform scheme that can deliver the requisite performance.

The modulation method and overall waveform must support a number of critical requirements, including

1) Signals with a high data rate and a broad bandwidth can be handled.

2) Very short Transmission Tine Intervals, or TTIs, are required to offer low latency transmissions for long and brief data bursts.

3) For TDD systems that are likely to be employed, the ability to quickly switch between uplink and downlink is required.

4) Reduce the on-times for low-data-rate devices, allowing for more energy-efficient communications.

5) These are only a few of the specifications that 5G waveforms must meet in order to support the necessary facilities.

A. Current Methods

1) Cyclic Prefix OFDM: The cyclic prefix OFDM, or CP-OFDM, variant of OFDM used in 5G NR downlink is the same waveform used by LTE for the downlink signal.

The final half of an OFDM frame's data is added to the beginning of an OFDM frame in CP OFDM, and the length of the cyclic prefix is selected to be bigger than the channel delay spread. This eliminates the inter-symbol interference that delays and reflections might cause. Furthermore, the channel delay spread is frequency dependent, with the cyclic prefix length being set to account for both interferences. As a result, the CP length varies depending on the connection circumstances.

e-ISSN: 2582-5208
International Research Journal of Modernization in Engineering Technology and Science
(Peer-Reviewed, Open Access, Fully Refereed International Journal)
Volume:05/Issue:03/March-2023 Impact Factor- 7.868 www.irjmets.com

The uplink format for 5G NR is different from that of 4G LTE. In the uplink, CP-OFDM and DFT-S-OFDM waveforms are employed. Furthermore, 5G NR allows for the usage of variable subcarrier spacing. LTE subcarriers were formerly spaced at 15 kHz, while 5G NR allows for 15 kHz x 2s spacing with a maximum spacing of 240 kHz. To keep the carriers orthogonal, integral s carrier spacing is necessary rather than fractional carrier spacing.

When compared to some of the other waveforms explored for 5G, the usage of OFDM waveforms has a reduced implementation complexity. Furthermore, OFDM is well-known, having been employed in 4G and a variety of other wireless systems.

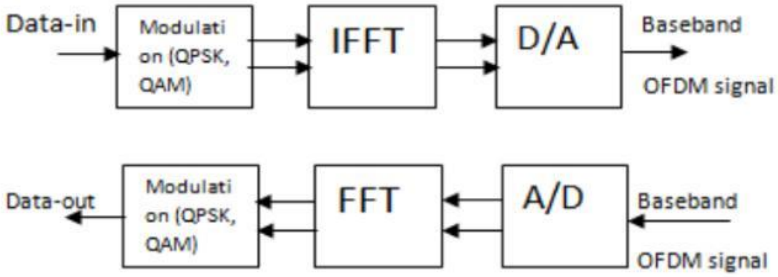


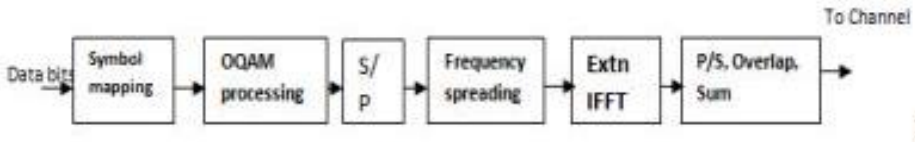
Fig. 1: OFDM Transmitter and Receiver

2) DFT-s-OFDM: Spread of the Direct Fourier Transform OFDM, also known as DFT-s-OFDM, is a single carrier-like transmission technique that may be used with OFDM to provide mobile communications systems like 5G a lot of flexibility. SC-FDMA is the most frequent name for it.

SC-FDMA transmission processing is quite similar to OFDM transmission processing. The transmission of bits is translated to a complicated constellation of symbols for each user (BPSK, QPSK, or M-Quadrature amplitude modulation). Then various Fourier coefficients are assigned to distinct transmitters (users). This task is completed in the mapping and demapping sections. For each user signal to be received, the receiver side comprises one de-mapping block, one IDFT block, and one detection block. Guard intervals (called cyclic prefixes) with cyclic repetition are placed between blocks of symbols, similar to how they are in OFDM, to effectively minimize intersymbol interference caused by temporal spreading (produced by multi-path propagation) among the blocks.

B. New and Interesting methods

The fifth-generation (5G) modulation scheme addresses several important requirements, including the ability to use signals with high data rates, the ability to provide minimal delay for long and concise data, the ability to exchange data quickly in the uplink and downlink, and the option of cost-effective broadcasting by reducing the on time of devices with low data rates. Filter Bank Multi-Carrier (FBMC), Universal Filtered Multi-Carrier (UFMC), Generalized Frequency Division Multiplexing (GFDM), and Filtered OFDM are some of the 5G modulation methods (fOFDM).



F

ig. 2: a) FBMC Transmitter

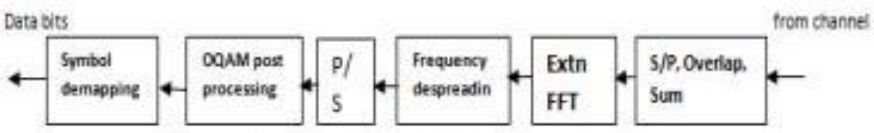


Fig. 2: b) FBMC Receiver

e-ISSN: 2582-5208
International Research Journal of Modernization in Engineering Technology and Science
(Peer-Reviewed, Open Access, Fully Refereed International Journal)
Volume:05/Issue:03/March-2023 Impact Factor- 7.868 www.irjmets.com

1) FBMC-Filter Bank Multi-Carrier: FBMC does not employ a cyclic prefix and instead filters each sub-carrier separately. This strategy emphasizes spectrum efficiency. The subcarriers' tapered filters require stretched time constants. This is over four times the length of the principal multiple carrier sign. The symbols will overlap in time as a result of this.

2) UFMC-Universal Filtered Multi-Carrier: Filtered OFDM and FBMC (Filter Bank Multi-carrier) modulations are considered as a generalization of UFMC. Individual subcarriers and groups of subcarriers (sub-bands) are in filtered OFDM, whereas the entire band is filtered in UFMC.

This subcarrier grouping allows the filter length to be reduced (when compared with FBMC). In addition, as compared to FBMC, UFMC may still employ QAM since it preserves the complex orthogonality that works with existing MIMO schemes.

UFMC is a better waveform technique for 5G communication when compared to OFDM and FBMC which will have less PAPR and the PAPR is further reduced by applying the optimization techniques.

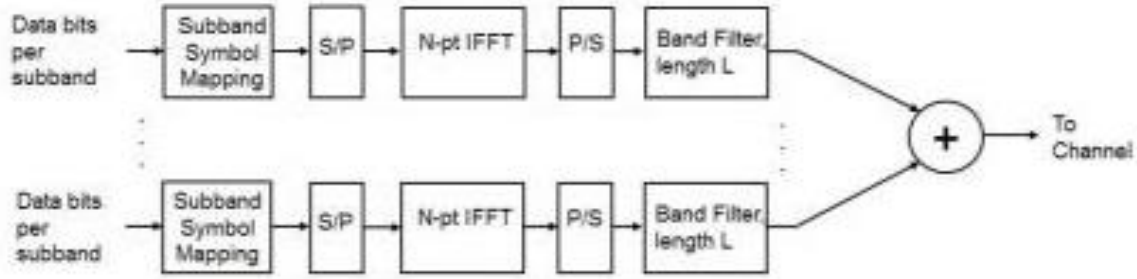


Fig. 3: a) UFMC Transmitter

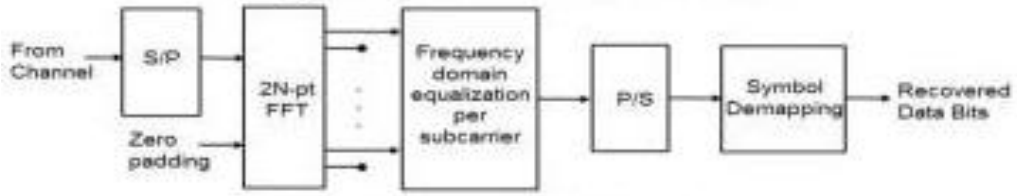


Fig. 3: b) UFMC Receiver

3) GFDM-Generalized Frequency Division Multiplexing: GFDM is an adaptable multiple carrier transmission method. Unlike the other schemes, the carrier Orthogonality is not maintained. The out-of-band emissions can be managed in a better way and the Peak to Average Power Ratio (PAPR) can be lowered.

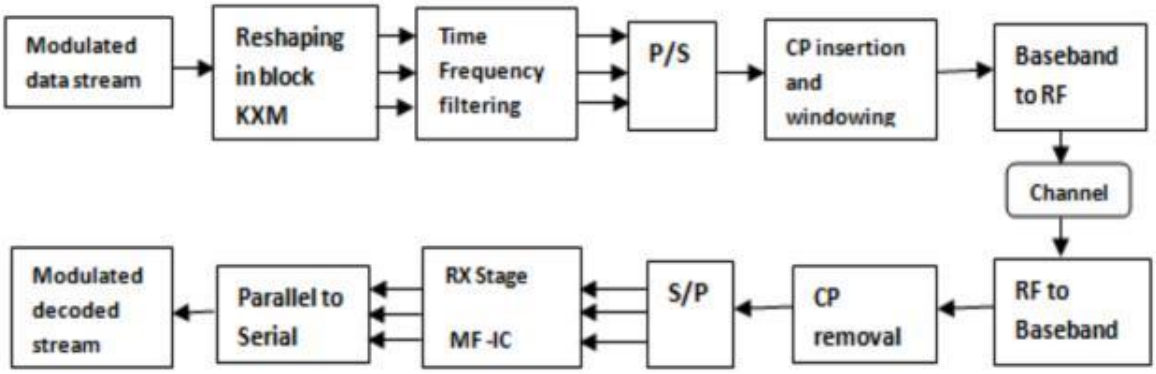


Fig. 4: GFDM transceiver

e-ISSN: 2582-5208
International Research Journal of Modernization in Engineering Technology and Science
(Peer-Reviewed, Open Access, Fully Refereed International Journal)
Volume:05/Issue:03/March-2023 Impact Factor- 7.868 www.irjmets.com

Waveform	LTE (scrambler ON)	LTE (scrambler OFF)	FBMC	UFMC	GFDM
PAPR for PN9	12.15 dB	10.13 dB	8.14 dB	10.44 dB	13.24 dB
PAPR for PN15	11.34 dB	12.89 dB	13.25 dB	14.02 dB	13.17 dB
PAPR for PN20	11.18 dB	17.18 dB	17.36 dB	14.63 dB	17.13 dB
PAPR for PN23	11.11 dB	17.56 dB	17.27 dB	14.74 dB	17.76 dB

Fig. 5: Experimental values for PAPR

III. CONCLUSION

5G is progressively becoming a part of people's daily lives. It is crucial in many areas, including communication and the use of large-scale machines. Users demand better and more varied services as mobile and wireless communications develop in terms of data volume, number of users, and investment in communications infrastructure, while network operators expect bigger profitability.

IV. REFERENCES

[1] S. Nagul, "A review on 5G modulation schemes and their comparisons for future wireless communications," 2018 Conference on Signal Processing And Communication Engineering Systems (SPACES), 2018, pp. 72-76, doi: 10.1109/SPACES.2018.8316319.

[2] Dimitrios Karampatsis and Izzat Darwazeh, "OFDM; A Possible Technology for 4th Generation Mobile Systems?", International Symposium on Telecommunication (IST 2001), Tehran, Iran.

[3] L. Chettri and R. Bera, "A comprehensive survey on Internet of Things (IoT) toward 5G wireless systems," in IEEE Internet of Things Journal, vol. 7, no. 1, pp. 16-32, Jan. 2020.

[4] Y. Yifei and Z. Longming, "Application scenarios and enabling technologies of 5G," in China Communications, vol. 11, no. 11, pp. 69- 79, Nov. 2014.

[4] C. Wang, "Cellular architecture and key technologies for 5G wireless communication networks," in IEEE Communications Magazine, vol. 52, no. 2, pp. 122-130, February 2014.

[5] C.-X. Wang et al., ''Cellular architecture and key technologies for 5G wireless communication networks,'' IEEE Commun. Mag., vol. 52, no. 2,pp. 122-130, Feb. 2014.

ResearchGate

See discussions, stats, and author profiles for this publication at: https://www.researchgate.net/publication/361228741

A hybrid Firefly and Particle Swarm Optimized FOF-PID Strategy for Interconnected Multi-area Power System with Renewable Energy Sources

Article *in* IOSR Journal of Electrical and Electronics Engineering · June 2022

CITATIONS
0

READS
69

3 authors:



Gomaa Haroun Ali
University of Nyala
12 PUBLICATIONS **107** CITATIONS
SEE PROFILE



Mustafa Eltigani I. M
Delhi Technological University
8 PUBLICATIONS **2** CITATIONS
SEE PROFILE



Khaled Eltag
Nanjing University of Science and Technology
5 PUBLICATIONS **86** CITATIONS
SEE PROFILE

Some of the authors of this publication are also working on these related projects:

Frequency stabilization for large scale hybrid power systems. View project

Optimization of Microgrid Protection System View project

All content following this page was uploaded by Gomaa Haroun Ali on 16 August 2022.

The user has requested enhancement of the downloaded file.

IOSR Journal of Electrical and Electronics Engineering (IOSR-JEEE)
e-ISSN: 2278-1676, p-ISSN: 2320-3331, Volume 17, Issue 3 Ser. I (May. – June. 2022), PP 23-42
www.iosrjournals.org

A hybrid Firefly and Particle Swarm Optimized FOF-PID Strategy for Interconnected Multi-area Power System with Renewable Energy Sources

Gomaa Haroun A. H.[1,*], Khaled Eltag[2], Mustafa Eltigani I. M.[3]
[1] *College of Engineering Sciences, Department of Electrical and Electronics Engineering, University of Nyala, South Darfur, Nyala, Sudan*
[2]*Electrical Engineering Department, Omdurman Islamic University, Omdurman, Sudan*
[3] *Department of Electrical Engineering, Delhi Technological University, Delhi, India*
** Corresponding author: Gomaa Haroun (E-mail: gomaaharoun1982@yahoo.com)*

Abstract:
This article presents optimal load frequency control (LFC) designed by a hybrid fractional order fuzzy PID (FOF-PID) controller trained via a hybrid firefly and particle swarm optimization (hFA-PSO) algorithm for multi-interconnected power system be made up of renewable energy sources (RESs). Four-area interconnected power systems comprising from hydro, thermal, photovoltaic (PV) and wind power plants are considered. A hFA-PSO is employed to explore the optimal gains of fractional order fuzzy PID (FOF-PID) controller such that the integral time square error (ITSE) criteria of frequency and tie line power deviations is diminished. Different simulations are carried out and the results are compared with the proposed controller optimized via hFA-PSO, craziness particle swarm optimization (CPSO), PSO and firefly algorithm (FA). It is observed that the suggested controller optimized via hFA-PSO techniques is robust and achieves satisfactorily results even if the plant including nonlinearity as well as varying in operating load condition and plant parameters. The obtained results confirmed the accuracy and reliability of the proposed FOF-PID controller-based hFA-PSO in designing LFC for multi-interconnected power systems compared to others.

Key Word*: Load frequency control (LFC), Interconnected multi-area power systems, fractional order fuzzy PID controller, Firefly algorithm.*

Date of Submission: 28-05-2022 Date of Acceptance: 10-06-2022

I. Introduction

The main aim of the power system (PS) utility is to maintain continuous supply of electrical power within an acceptable quality, to all the consumers in the network. The PS will be in equilibrium, when there is a balance between electrical power demand and the power generated. Load frequency control (LFC) is an external strategy used in an interconnected system to maintain the frequency and tie-line power within their specified limits in case of load perturbation [1]. LFC is continuously observing the system frequency and calculate the net deviations of same from their prescribed values of the area control error (ACE), and accordingly adjust the valve settings of generators so as to maintain ACE to its minimum value [2,3]. It is observed from the literature that there are countless classical and advanced controllers have been approved for LFC problem [1-8]. In [4], the authors designed structure of fuzzy PID controller for an interconnected complex PS, in which the controller gains are tuned using Firefly algorithm (FA). In [5], fuzzy-PI controller is proposed for load frequency control of a hybrid system comprising from PV and thermal generator to improve the dynamic performance. Recently, fractional Order PID (FOPID) is introduced in the control system, which is a generalized type of the classical PID controller [7]. Regarding this controller, the derivative and integrator parts have non-integer orders; therefore the order should be determined by the designer.

This article presents a hybrid fractional order fuzzy PID (FOF-PID) controller for interconnected complex-area power system, where each control area made up of different generation units such as; thermal, hydro, and renewable energy sources (RESs). RESs interconnected power plant may be wind turbine (WT), photovoltaic (PV), and fuel cell (FC), these energies has gained a great attention and have widely prevalence in electrical power plants due to the harmful effects of fossil fuels [8]. The controller gains of the proposed strategy are optimized via a hybrid firefly and particle swarm optimization (hFA-PSO) algorithm.

The following are the main contributions of this article:

1. A new structure of fractional order based hybrid fuzzy PID controller is proposed for LFC of interconnected multi-area power system,
2. A hybrid firefly and particle swarm optimization (hFA-PSO) algorithm is adopted to optimize the controller gains,
3. The effectiveness of the proposed controller is assessed by comparing the results with different optimization techniques; hFA-PSO, CPSO, and PSO.
4. Sensitivity analysis is carried out to prove the robustness of the advocated strategy.

The remainder sections of this article are prepared as follows: The mathematical modeling of the proposed system is addressed in Section 2, followed by wind turbine and PV system modeling. Controller structure is elaborated in Section 3. The overview of hFA-PSO is stated in Section 4 followed by the objective function. Simulation results and comparative analysis are presented in Section 5. Finally, the conclusion of the article was presented in Section 6.

II. System Modelling

2. System under study

Two types of power system configurations have been studied in this article: Configuration 1: Two-area interconnected power systems; area-1 comprises from thermal power plant and area-2 comprises from photovoltaic (PV) power plant. Configuration 2: Four-area interconnected power plants; every area comprises from multi-source; namely: thermal, hydro, wind and photovoltaic (PV) power plants.

2.1. Nonrenewable energy sources

Figs. 1 and 2 show the dynamic structures of nonrenewable energy sources represented in thermal and hydro power plants; respectively. The thermal power plant as offered in Fig. 1, is composed from speed governing, reheat time delay, turbine system, and power plant unit. So, the state space model of the plant can be directly derived from the block diagram. The turbine system can be derived as:

$$\Delta \dot{P}_{gi} = -\frac{1}{T_{ti}}\Delta P_{gi} + \frac{1}{T_{ti}}\Delta P_{ri} \quad (1)$$

where, T_{ti} denotes the reheat turbine time constant (s); ΔP_{gi} is the generator output power error (p.u. MW). The linearization of the speed governing can be derived as:

$$\Delta \dot{X}_{gi} = -\frac{1}{T_{gi}R_i}\Delta f_i - \frac{1}{T_{gi}}\Delta X_{gi} + \frac{1}{T_{gi}}\Delta P_{ci} \quad (2)$$

where, ΔX_{gi} designates as the governor valve position error (p.u), ΔP_{ci} is the control signal, T_{gi} implies the thermal governor time constant, and R_i signifies the speed drop (Hz/p.u. MW). The linearization of the reheat time delay can be derived as:

$$\Delta \dot{P}_{ri} = -\frac{K_{ri}}{T_{gi}R_i}\Delta f_i + \left(\frac{1}{T_{ri}} - \frac{K_{ri}}{T_{gi}}\right)\Delta X_{gi} - \frac{1}{T_{ri}}\Delta P_{ri} \quad (3)$$

The hydro-power system as displayed in Fig. 2, is constructed from speed governing, hydraulic turbine unit, water dynamic system, and power system unit. Thus, the state space model of the plant can be directly derived from the block diagram. The linearization model of water dynamic can be derived as:

$$\Delta \dot{P}_{gi} = 2\left\lfloor\frac{T_{Ri}}{T_{1i}T_{2i}R_i}\right\rfloor\Delta f_i - \frac{2}{T_{wi}}\Delta P_{gi} + 2\left\lfloor\frac{T_{2i}+T_{wi}}{T_{2i}T_{wi}}\right\rfloor\Delta X_{gi} + 2\left\lfloor\frac{T_{Ri}-T_{1i}}{T_{1i}T_{2i}R_i}\right\rfloor\Delta X_{gi} \quad (4)$$

The linearization model of the speed governing can be modeled as:

$$\Delta \dot{X}_{gi} = -\left\lfloor\frac{T_{Ri}}{T_{1i}T_{2i}R_i}\right\rfloor\Delta f_i - \frac{1}{T_{2i}}\Delta X_{gi} - \frac{T_{Ri}-T_{1i}}{T_{1i}T_{2i}R_i}\Delta X_{ghi} \quad (5)$$

The linearization model of the turbine unit can be expressed as:

$$\Delta \dot{X}_{ghi} = -\frac{1}{T_{1i}R_i}\Delta f_i - \frac{1}{T_{1i}}\Delta X_{ghi} \quad (6)$$

The frequency deviation (Δf_i) for each control area $i(i = 1, 2, 3, 4)$ can be expressed as:

$$\Delta \dot{f}_i = -\frac{1}{T_{pi}}\Delta f_i - \frac{K_{pi}}{T_{pi}}\Delta P_{tie,i} + \frac{K_{pi}}{T_{pi}}\Delta P_{gi} - \frac{K_{pi}}{T_{pi}}\Delta P_{Li} \quad (7)$$

where, Δf_i denotes the frequency error (Hz); $\Delta P_{tie,i}$ is the tie-line power deviation (p.u. MW); ΔP_{Li} is the load perturbation (p.u. MW); T_{pi} is the power system time constant (s) and K_{pi} is the power plant gain (Hz/p.u. MW).

The transmission-line power interchange between areas i and j can be describe as

$$\Delta \dot{P}_{tie,ij} = 2\pi T_{ij}\left(\Delta f_i - \Delta f_j\right), \qquad \Delta P_{tie,ij} = -\Delta P_{tie,ji} \tag{8}$$

The total transmission-line power between area-i and the other areas can be formulated as:

$$\Delta \dot{P}_{tie,i} = \sum_{\substack{j=1 \\ j\neq i}}^{4} \Delta P_{tie,ij} = 2\pi \sum_{\substack{j=1 \\ j\neq i}}^{4} T_{ij}\left(\Delta f_i - \Delta f_j\right) \tag{9}$$

The linearized mathematical modeling of each of the 4-areas can be described with following two equations:

$$\begin{cases} \dot{x}_i(t) = A_i x_i(t) + B_i u_i(t) + \mathrm{D}_i w_i(t) + \sum_{\substack{i\neq j \\ j=1}} \left(A_{ij} x_j(t)\right) \\ y_i(t) = C_i x_i(t) \end{cases} \tag{10}$$

The state space model for thermal plant as highlighted in Fig. 1 can be formulated as:

$$x_i(t) = \begin{bmatrix} \Delta f_i(t) \\ \Delta P_{tie,i}(t) \\ \Delta P_{gi}(t) \\ \Delta X_{gi}(t) \\ \Delta P_{ri}(t) \end{bmatrix}, A_i = \begin{bmatrix} -\frac{1}{T_{pi}} & -\frac{K_{pi}}{T_{pi}} & \frac{K_{pi}}{T_{pi}} & 0 & 0 \\ 2\pi\sum_j T_{ij} & 0 & 0 & 0 & 0 \\ 0 & 0 & -\frac{1}{T_{ti}} & 0 & \frac{1}{T_{ti}} \\ -\frac{1}{T_{gi}R_i} & 0 & 0 & -\frac{1}{T_{gi}} & 0 \\ -\frac{K_{ri}}{T_{gi}R_i} & 0 & 0 & \frac{1}{T_{ri}} - \frac{K_{ri}}{T_{gi}} & -\frac{1}{T_{ri}} \end{bmatrix}, B_i = \begin{bmatrix} 0 \\ 0 \\ 0 \\ \frac{1}{T_{gi}} \\ 0 \end{bmatrix}, D_i = \begin{bmatrix} -\frac{K_{pi}}{T_{pi}} \\ 0 \\ 0 \\ 0 \\ 0 \end{bmatrix}$$ and $C_i = [B_i \quad 1 \quad 0 \quad 0 \quad 0]$

The state space model for hydro plant as highlighted in Fig. 2 can be formulated as:

$$x_i(t) = \begin{bmatrix} \Delta f_i(t) \\ \Delta P_{tie,i}(t) \\ \Delta P_{gi}(t) \\ \Delta X_{gi}(t) \\ \Delta X_{ghi}(t) \end{bmatrix}, A = \begin{bmatrix} -\frac{1}{T_{pi}} & -\frac{K_{pi}}{T_{pi}} & \frac{K_{pi}}{T_{pi}} & 0 & 0 \\ 2\pi\sum_j T_{ij} & 0 & 0 & 0 & 0 \\ 2\left[\frac{T_{Ri}}{T_{1i}T_{2i}R_i}\right] & 0 & -\frac{2}{T_{wi}} & 2\left[\frac{T_{2i}+T_{wi}}{T_{2i}T_{wi}}\right] & 2\left[\frac{T_{Ri}-T_{1i}}{T_{1i}T_{2i}R_i}\right] \\ -\left[\frac{T_{Ri}}{T_{1i}T_{2i}R_i}\right] & 0 & 0 & -\frac{1}{T_{2i}} & -\left[\frac{T_{Ri}-T_{1i}}{T_{1i}T_{2i}R_i}\right] \\ -\frac{1}{T_{1i}R_i} & 0 & 0 & 0 & -\frac{1}{T_{1i}} \end{bmatrix}, B_i = \begin{bmatrix} 0 \\ 0 \\ -2R_i\left[\frac{T_{Ri}}{T_{1i}T_{2i}R_i}\right] \\ R_i\left[\frac{T_{Ri}}{T_{1i}T_{2i}R_i}\right] \\ \frac{1}{T_{1i}} \end{bmatrix}, D_i = \begin{bmatrix} -\frac{K_{pi}}{T_{pi}} \\ 0 \\ 0 \\ 0 \\ 0 \end{bmatrix}$$ and

$C_i = [B_i \quad 1 \quad 0 \quad 0 \quad 0]$

where, $x_i \in R^{n_i}$, $u_i \in R^{m_i}$, and $w_i(t) = \Delta P_{Li} \in R^{r_i}$ represent, respectively, the state vector, input vector, and load disturbance in control area i. Matrices A_i, B_i, and D_i represent appropriate system matrices of the control area i.

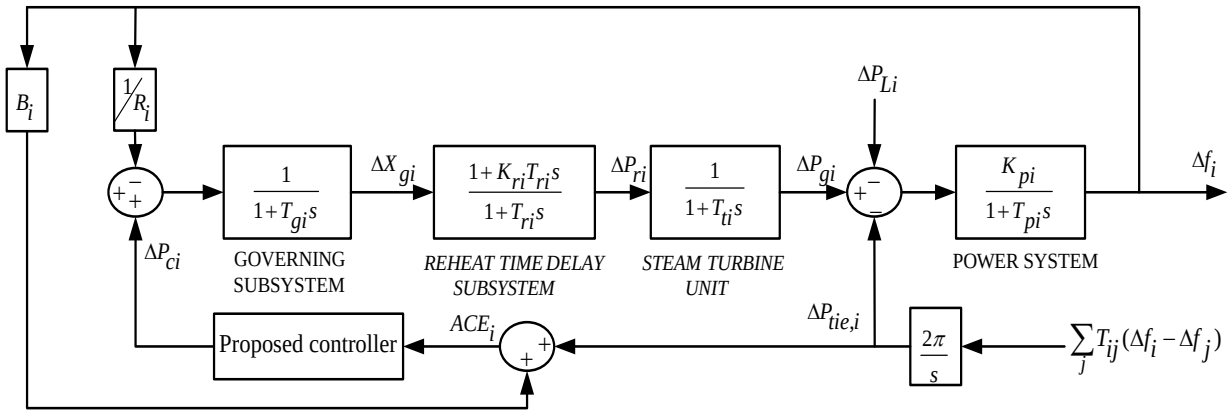


Fig. 1. Block diagram of thermal power plant.

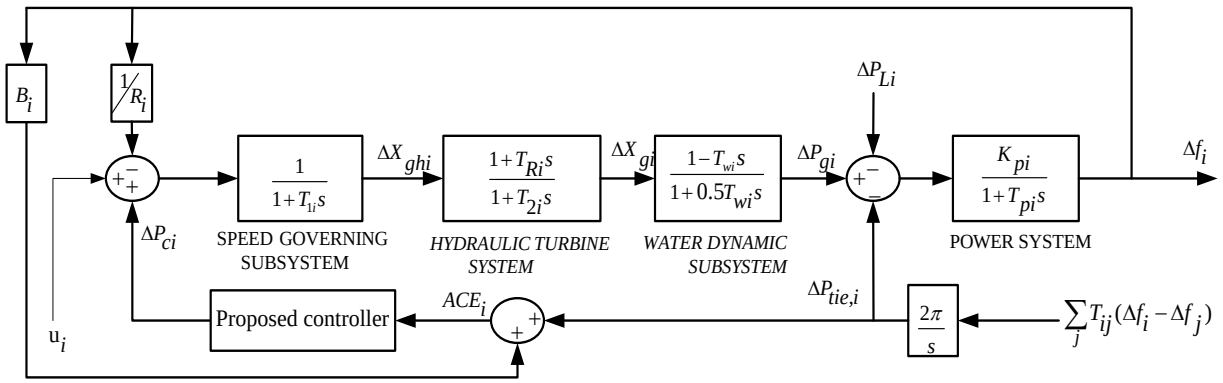


Fig. 2. Block diagram of hydro power plant.

2.2. Renewable energy sources

2.2.1. LFC-based DFIG wind turbine

Currently, the doubly-fed induction generator (DFIG), is widely used in power system in which the power electronic interface controls the rotor currents to generate the variable speed for maximum available energy capture in variable-speed turbines [9]. The variable speed wind energy conversion (WECS) system can extract kinetic energy stored in the mechanical plant of wind turbines which can be utilized to support the frequency regulation. Several frequency control structures like droop control, inertia control, etc. are introduced with these strategy to make DFIGs behave like classical generators.

2.2.1.1. Wind turbine aerodynamic model

This article presents the frequency regulation with variable speed wind turbines employing inertia control strategy and coordinated operation of wind turbine and classical generators. The maximum mechanical power that can be provided from the wind by wind turbine is elaborated by Eq. (11) below [10]:

$$P_{opt} = \frac{1}{2}\rho C_{opt}(\lambda_{opt}, \beta) A V_m^3 \tag{11}$$

where, C_{opt} signifies the optimal power coefficient of the wind turbine modeled as a function of tip speed ratio (λ_{opt}) and pitch angle (β), A is the effective swept area in m^2, V_m is the wind speed in m/s and ρ is the air density in kg/m^3. The optimal power coefficient C_{opt} is given by the following function [10]:

$$C_{opt}(\lambda_{opt}, \beta) = 0.22\left(\frac{116}{\lambda_i} - 0.4\beta - 5\right)e^{-\frac{12.5}{\lambda_i}} \tag{12}$$

$$\frac{1}{\lambda_i} = \frac{1}{\lambda_{opt} + 0.08\beta} - \frac{0.035}{\beta^3 + 1} \tag{13}$$

where the optimal tip speed ratio (λ_{opt}) is given as:

$$\lambda_{opt} = \frac{\omega_{opt} R}{V_m} \tag{14}$$

in which R denotes the blade radius in m and ω_{opt} signifies the optimal wind turbine rotor speed in rad/s .

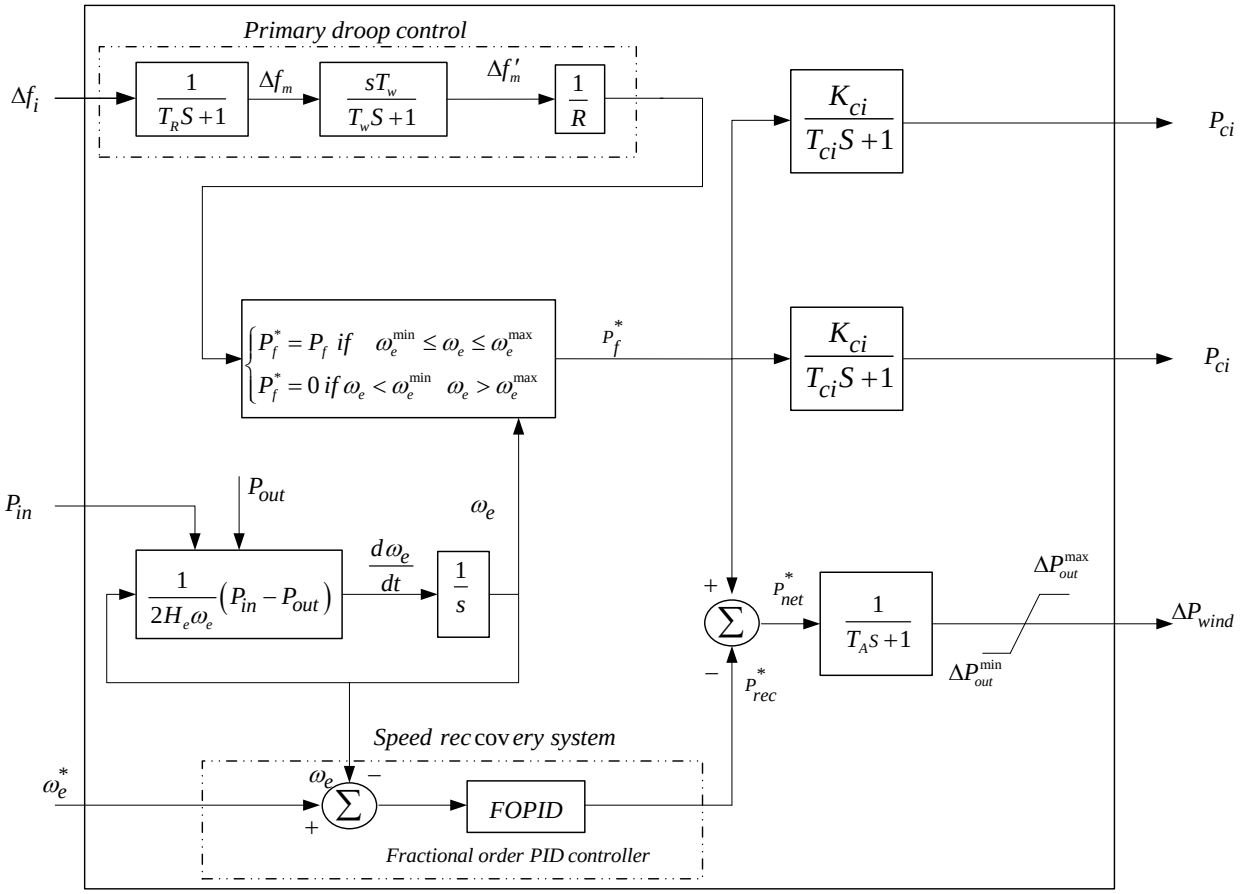


Fig. 3: Block diagram of DFIG based wind turbine model.

2.2.1.2. Strategies employed for frequency regulation of wind turbines

The primary droop and speed recovery strategies are proposed for the frequency regulation of the wind turbine power plant as displayed in Fig. 3. The load perturbations can causes of large frequency oscillations in the power plant, thus in order to handle this effect a droop based control strategy has been employed to assist the primary frequency control for a short period of time after the load change as shown in Fig. 3. In this strategy, the filter is employed in loop to cancel the steady state frequency deviation, and the injected power can be expressed as:

$$P = \frac{1}{R}\Delta f \tag{15}$$

in which P_f signifies the signal given to power electronics scheme and Δf_m denotes the filter frequency error.

Due to an unexpected rate of the stored kinetic energy from the wind turbine generator rotor, the primary droop control strategy gets activated resulting in declining of the rotor speed. To bring the wind turbine generator rotor speed back to its optimal rated value, a fractional order PID (FOPID) controller as presented in Eq. (16) is initiated quickly after the occurrence of load perturbation. This strategy absorbs energy from the network when the frequency error settles down to zero and is relatively slow in comparison with the previous strategy. This strategy avoids the negative influence on the WECS performance.

$$P_{rec} = FOPID = \tilde{K}_p e(t) + \tilde{K}_i \frac{d^{-\eta} e(t)}{dt^{-\eta}} + \tilde{K}_d \frac{d^{\delta} e(t)}{dt^{\delta}} \tag{16}$$

where $e(t) = (\omega_e^* - \omega_e)$, where, $\tilde{K}_p$, $\tilde{K}_i$, $\tilde{K}_d$ are the gains of the controller, η and δ the order of integration and differentiation, respectively.

2.2.2. LFC-based photovoltaic (PV) modeling

Photovoltaic (PV) power system comprises of solar cells it may be arranged in series or in parallel fashion to provide the desired power required by the load demand. The photovoltaic (PV) is modeled and demonstrated as nonlinear voltage-current characteristic relies on the solar radiation as follows [11]:

$$V_{PV} = \left(\frac{N_s \varepsilon Z T_a}{Q}\right) \ln\left(\frac{G I_{ph} N_p - I_{PV} + N_p I_0}{N_p I_0}\right) - I_{PV} R_s \left(\frac{N_s}{N_p}\right) \tag{17}$$

where V_{PV} and I_{PV} represent the PV voltage and current; respectively, T_a is the cell temperature, more detail about the system parameter discussed in [11,12]. The transfer functions of the photovoltaic (PV) system and dc-dc converter with maximum power point tracker algorithm (MPPT) connected to the inverter can be formulated in the following equations [12]:

$$G_1 = \left(\frac{s^2}{s^2 + \omega^2}\right)\left(\frac{V(s^2 + \omega^2)(s^2 + 2\omega^2)}{k s^2 (s^2 + 4\omega^2)}\right)\left(\frac{1 - e^{-sT_s}}{sT_s}\right) \tag{18}$$

$$G_2 = \left(\frac{M_1 / LC}{s^2 + \left(\frac{1}{RC}\right)s + \frac{1}{LC}}\right)\left(\frac{1 - e^{-\frac{sT_s}{2}}}{1 + e^{-\frac{sT_s}{2}}}\right)\left(\frac{M_2}{1 + sT_s}\right) \tag{19}$$

where ω denotes the angular frequency of the grid voltage, R, L and C signify the resistance, inductance and capacitance output of the converter respectively. M_1, M_2 are the dc-dc converter and inverter voltage gain; respectively, T_s denotes the time period.

III. Controller structures

3.1 Fractional order concept

Fractional order (FO) is generally defined by the operator ${}_aD_t^{\alpha}$ which is composed of integer order integral and differential parts, a and t denote the confines of the operation and α is the FO which is a complex number [13].

$${}_aD_t^{\alpha} = \begin{cases} d^{\alpha}/dt^{\alpha}, & \Re(\alpha) > 0 \\ 1, & \Re(\alpha) = 0 \\ \int_a^t (d\tau)^{\alpha}, & \Re(\alpha) < 0 \end{cases} \tag{20}$$

Based on the Riemann-Liouville (R-L) approach, the FO differential and FO integral can be stated as in Eq. (21) and (22) respectively:

$${}_aD_t^{\alpha} f(t) = \frac{1}{\Gamma(n-\alpha)} \frac{d^n}{dt^n} \int_a^t (t-\tau)^{n-\alpha-1} f(\tau) d\tau \tag{21}$$

Where $n-1 > \alpha \geq n$; n is an integer number, and $\Gamma(\cdot)$ signifies the Euler's gamma function.

$${}_aD_t^{\alpha} f(t) = \frac{1}{\Gamma(\alpha)} \int_a^t (t-\tau)^{\alpha-1} f(\tau) d\tau \tag{22}$$

where α $(0 < \alpha < 1)$ in general, the Laplace transformation (LT) of the R-L fractional derivative or integral is modeled by:

$$L\left\{{}_aD_t^{\alpha} f(t)\right\} = s^{\alpha} F(s) - \sum_{k=0}^{n-1} s^k \, {}_aD_t^{\alpha-k-1} f(t)\big|_{t=0} \tag{23}$$

Under zero initial conditions for $n-1 \geq \alpha < n$:

$$L\left\{{}_aD_t^{\pm\alpha} f(t)\right\} = s^{\pm\alpha} F(s) \tag{24}$$

where s signifies the Laplace operator.

3.2. Fractional order PID (FOPID) controller

Fractional order PID (FOPID) or $PI^{\lambda}D^{\mu}$ controller can be formulated as in Eq. (25):

$$u_{FOPID}(t) = K_p e(t) + K_i \frac{d^{-\lambda} e(t)}{dt^{-\lambda}} + K_d \frac{d^{\mu} e(t)}{dt^{\mu}} \tag{25}$$

where, K_p, K_i, K_d represent the gains, λ and μ are the integration and differentiation of fractional order. Hence, the architecture of $PI^{\lambda}D^{\mu}$ controller has five independent knobs to be optimized.

3.3. Fractional order hybrid fuzzy intelligent PID controller design

In this part, the FOF-PID strategy as presented as shown in Fig. 4 which is designed from the fractional order fuzzy PI controller integrated with the fractional order PD controller. In Fig. 4, K_{e1}, K_{e2}, K_{d1}, K_{d2} denote the input factors and K_{pi}, K_{pd} are the output factors. The output signal of the fractional order fuzzy PID (FOF-PID) can be highlighted as in Eq. (26):

$$u_{FOF-PID}(t) = u_{FOF-PI}(t) + u_{FOF-PD}(t) = K_{pi} \frac{d^{-\lambda} u_{FLC-1}(t)}{dt^{-\lambda}} + K_{pd} \, u_{FLC-2}(t) \tag{26}$$

where, $u_{FOF-PI}(t)$ represent the fractional order fuzzy PI controller, $u_{FOF-PD}(t)$ represents the fractional order fuzzy PD controller, and $u_{FOF-PID}(t)$ represents the proposed controller structure output.

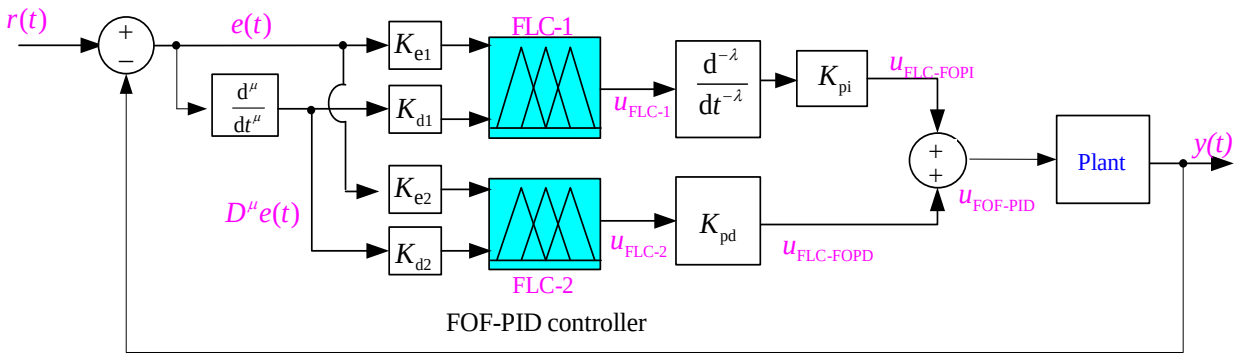


Fig. 4: Fraction order hybrid fuzzy PID controller architecture.

The error $(e(t))$ and its fractional derivative $(D^{\mu}e(t))$ are selected as input variables of the proposed controllers, and $(u_{FLC-1}), (u_{FLC-2})$ is selected as the output variables of the fuzzy controller. These variables are fuzzified into 7 triangular membership functions which are characterized by linguistic variables, and then the rule base associated with the fuzzy controller are furnished in Table 1. Finally, the output of the proposed controller (u_{FOiPID_FOFPID}) is subjected to the interconnected multi-source power system. In doing so, the associated gains and the scaling parameters are optimized by employing hFA-PSO algorithm.

Table 1: Fuzzy rule base.

$\frac{d^{\mu}e(t)}{dt^{\mu}}$ \ $e(t)$	NL	NM	NS	Z	PS	PM	PL
PL	Z	PS	PM	PL	PL	PL	PL
PM	NS	Z	PS	PM	PL	PL	PL
PS	NM	NS	Z	PS	PM	PL	PL
Z	NL	NM	NS	Z	PS	PM	PL
NS	NL	NL	NM	NS	Z	PS	PM
NM	NL	NL	NL	NM	NS	Z	PS
NL	NL	NL	NL	NL	NM	NS	Z

IV. A hybrid firefly and particle swarm optimization algorithm:

4.1. Firefly optimization algorithm:

Firefly algorithm (FA) is one of the most lately developed swarm intelligence technique, which introduced by Yang [14]. The technique is motivated by flashing characteristic of the fireflies. Flashing light fashioned by the firefly in the bio-inspired meta-heuristics process is the motive behind the development of the algorithm. This flashing light gives out courtship signals for mating. Modern research demonstrates that the FA is very efficient and may provide better results than other similar approaches [15].

For proper designed of firefly algorithm (FA), a number of important issues such as the change in light intensity, the attractiveness of fireflies, number of population and generation are to be appropriately chosen [15]. While the brightness of fireflies depends on the function to be tuned, their attractiveness is adjusted by its light intensity. Light intensity $I_{(r)}$ relies on distance as presented below:

$$I_{(r)} = I_0 e^{-\gamma r} \tag{27}$$

where, I_0 signifies the intensity of flight at original, and γ represent the light absorption factor. As a firefly's attractiveness is proportional to the light intensity seen by neighboring fireflies, the attractiveness β of a firefly is derived as:

$$\beta = \beta_0 e^{-\gamma r^2} \tag{28}$$

in which β_0 denotes the attractiveness at $r = 0$.

The distance between any two fireflies s_i and s_j is modeled by Euclidean distance as:

$$r_{ij} = \left\| x_i - x_j \right\| = \sqrt{\sum_{k=1}^{k=n} (x_{i,k} - x_{j,k})^2} \tag{29}$$

where n signifies the dimensionality of the issue. The movements of fireflies comprise of three terms: the present location of ith firefly, attraction to another more attractive firefly, and stochastic walk that comprises of a randomization parameter Ξ and the stochastic produced number $\Upsilon_i \in [0;\ 1]$. The movement is derived as:

$$x_i = x_i + \beta_0 e^{-\gamma r_{ij}^2}(x_i - x_j) + \Xi \Upsilon_i \tag{30}$$

The flowchart of firefly is shown in Fig. 5.

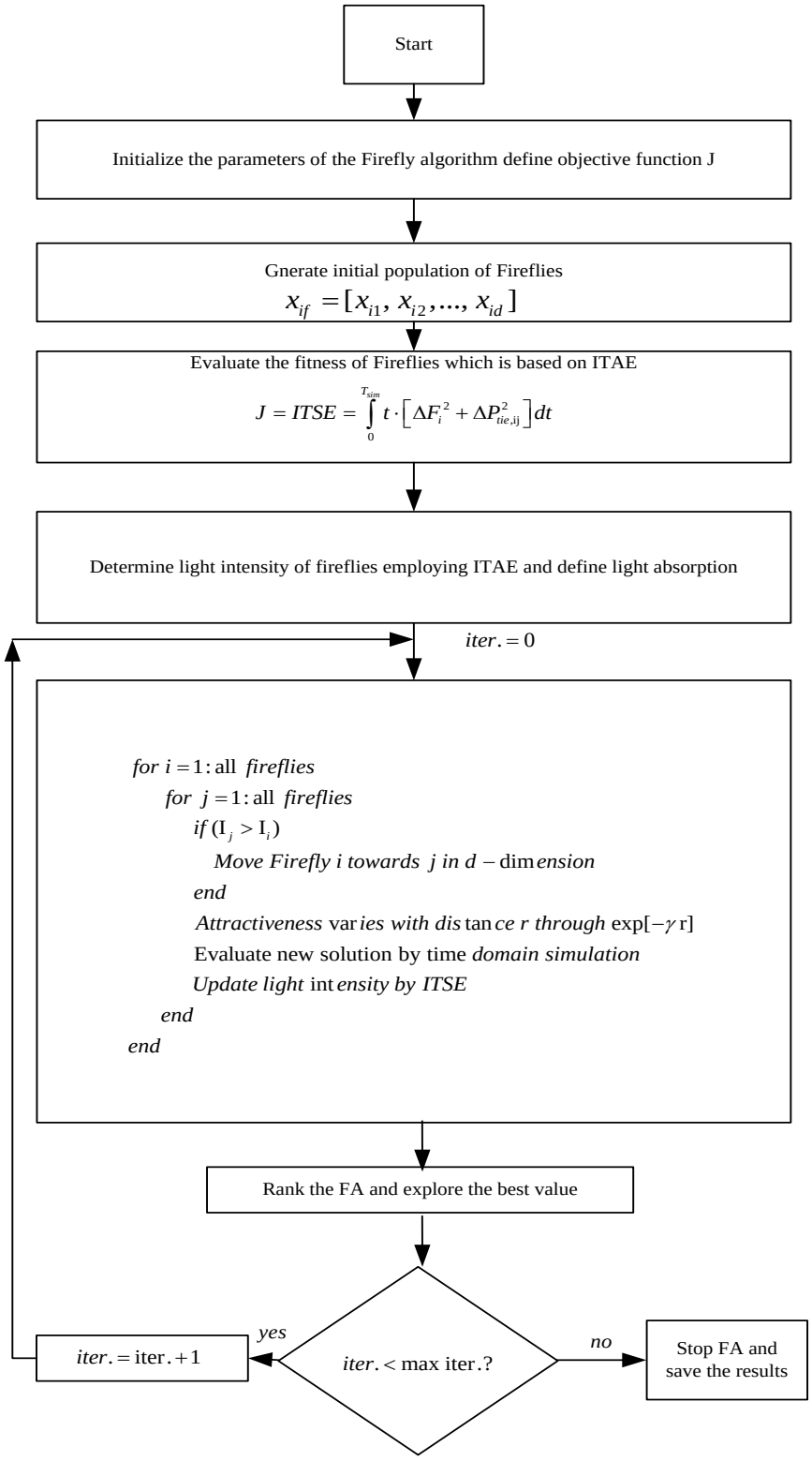


Fig. 5: Flowchart of the FA algorithm.

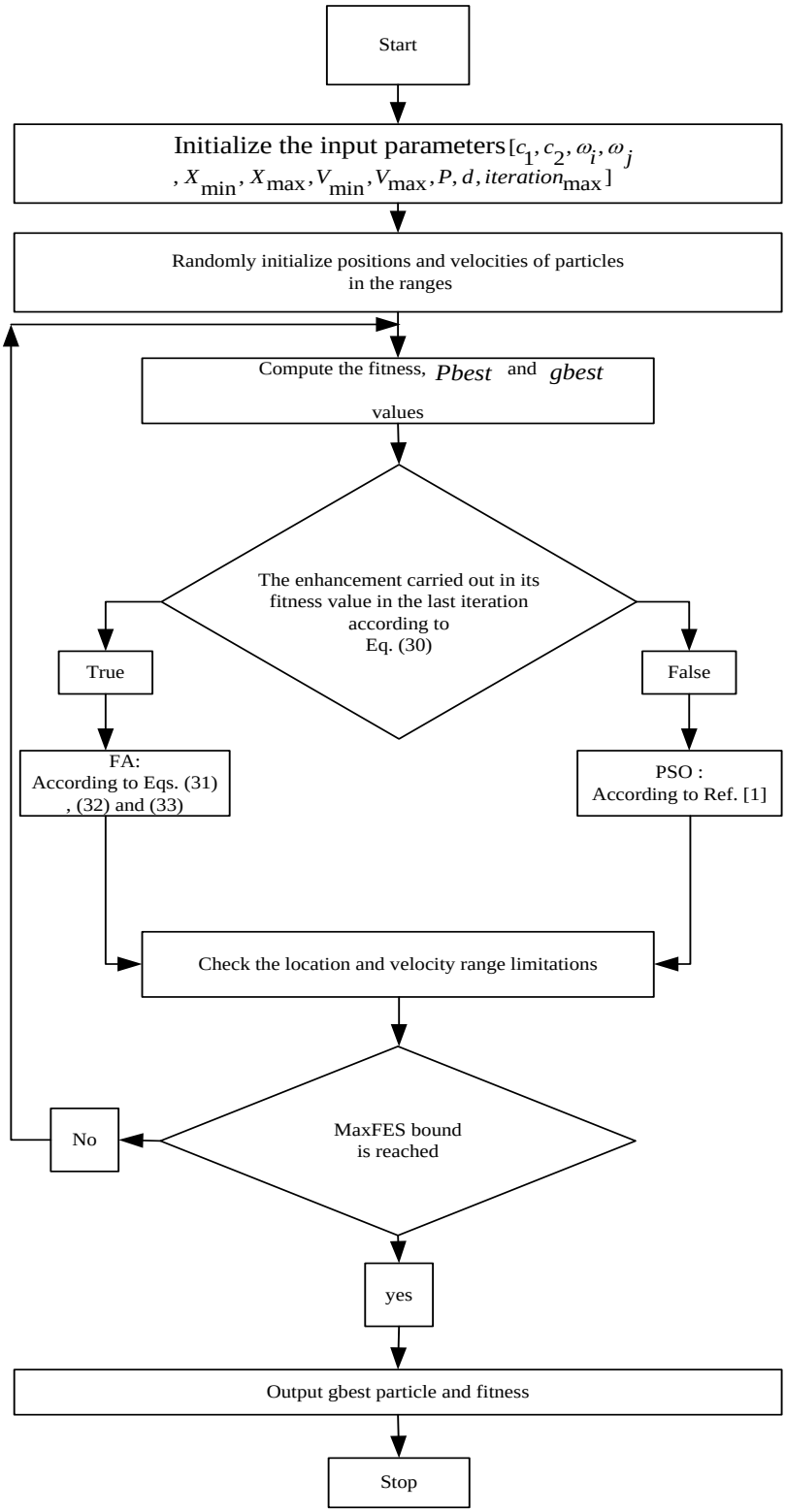


Fig. 6: Flowchart of the proposed hFA-PSO algorithm.

4.2. Proposed a hybrid firefly and particle swarm optimization (hFA-PSO) algorithm:

Realizing a reliable success in assessing a limited number of functions is the main objective of the suggested hFA-PSO algorithm. Therefore, the speed of convergence is significant in the early phase of iterations. PSO technique has faster convergence capability rather than several other techniques in certain problems, as introduced in [1]. This fast convergence ability in the PSO local search phase, decreases and decelerates down especially when searching in the solution space near to a global optimal solution. The Equilibrium between exploration and exploitation in the PSO technique can be efficiently handled by

employing control parameters of the PSO: inertia weight (ω), acceleration coefficients (c_1, c_2). Velocity of a particle (v) can be computed by utilizing these control parameters. The value of particle velocity is important in local search, but calculating the appropriate velocity can be a defying task through local search, as incorrect values can cause particles to fluctuate around optimal solution. These fluctuation cause some delays in the whole optimization issue. As a result of this problem, velocity can be ignored in exploitation phases. In the other hand, FA technique does not have a velocity (v) characteristic [16]. In addition, there have no parameters in FA technique to utilize preceding best location of each firefly. Therefore, fireflies can move regardless of their preceding best locations.

In this article, an optimization technique that combines search capability of FA and PSO algorithms has been proposed. Thus, the equilibrium between exploration and exploitation is intended to establish and it benefits supports of both algorithms. Since in fireflies have not velocity (v) and personal best position ($pbest$) memories in comparison to particles. In the suggested hybrid combination of two techniques: PSO is generally employed in the global search, because it provides fast convergence in exploration as well as FA is used in local search, because it provides well-tuning in exploitation. The flowchart of the proposed hybrid firefly and particle swarm optimization (hFA-PSO) algorithm is highlighted in Fig. 6. The input parameters that are employed by both algorithms in the proposed algorithm are inserted and the uniform particle vectors are stochastically prepared in the pre-defined search and velocity ranges. the global ($gbest$) and personal best ($pbest$) particles are computed and assigned. In the subsequent comparing phase, it is compared that if particle has an enhancement in its fitness value in the previous iteration according to Eq. (31). Then present location is reserved in a temp variable (X_{i-temp}) and the new location and velocity are computed according to Eqs. (32) and (33).

$$f(i,t) = \begin{cases} T, if \ \ fitness\,(particle_i^t) \le gbest^{t-1} \\ F, if \ \ fitness\,(particle_i^t) > gbest^{t-1} \end{cases} \tag{31}$$

where, T mean true, F mean false

$$X_i(t+1) = X_i(t) + \beta_0 e^{-\gamma r_{ij}^2}\left(X_i(t) - gbest^{t-1}\right) + \Xi \Upsilon_i \tag{32}$$

$$V_i(t+1) = X_i(t+1) - X_{i-temp} \tag{33}$$

According to above, if a particle has an improved or equal fitness value than preceding global best, it is expected that local search starts and particle is controlled by FA technique, otherwise particle will be controlled by PSO technique and PSO continues its standard procedures with this particle. In the following subsequent comparing phase, fitness function assessments and range limitations are checked for all particles and fireflies. If the maximum repetition limit is reached, hybrid algorithm will be ended, whereas $gbest$ and its fitness value will be specified as output of suggested hybrid algorithm. The pseudo code of the suggested hFA-PSO technique is well-demonstrated in algorithm 1. In an evolutionary calculating the maximum number of fitness function evaluation (MaxFES) is a popular termination benchmark that allowed the maximum computation of objective functions. The inertia weight (ω) parameter helps to equilibrium between exploration and exploitation in PSO technique, which can be derived it according to Eq. (34). The Maximum and minimum velocities of a particle ($V_{\max}$, $V_{\min}$) are utilized to confine the next distance in a direction.

$$\omega = \omega_i - ((\omega_i - \omega_f) / iteration_{\max}) * iteration \tag{34}$$

To compensate the imbalance between generation and load demand of a power plant, the area control error (ACE) should be derived to zero by appropriate adjustment of the regulator parameters. In a well-restructured LFC, the system performance in the transient state should basically be at a satisfactory level of responsiveness, fast, damped oscillations, and simultaneously the dynamic stability of the plant guaranteed. Thus, to achieve the design objectives of power plants by inspired algorithms, a suitable objective function it essentials to be selected so that the desired outcomes of the transient response in terms of settling time, rise time, peak overshoot and steady-state error be obtained. In this article, PSO, FA and hybrid firefly-based particle swarm optimization (hFA-PSO) algorithm are employed in this article to optimize the parameter of proposed controller. For which the integral of time multiplied squared error (ITSE) as presented in Eq. (35) is designated as the performance index to assess the performance of the multi-area power system.

$$J = ITSE = \int_0^{T_{sim}} t \cdot \left[\Delta F_i^{\,2} + \Delta P_{tie,ij}^{\,2}\right] dt \tag{35}$$

where, T_{sim} signifies the simulation time. In this study, the minimum and maximum parameters for the proposed controller are designated in the range [0 3].

Table 2: System parameters

Hydro-thermal parameters					
Parameter	Unit	Value	Parameter	Unit	Value
T_{pi}	[s]	20	T_{2i}	[s]	10
T_t	[s]	0.3	T_{Ri}	[s]	0.513
T_{r1}	[s]	10	T_{1i}	[s]	48.7
K_{r1}	[Hz/ p.u.MW]	0.5	T_{wi}	[s]	1.0
T_g	[s]	0.08	B_i	[p.u.MW/ Hz]	0.425
R	[Hz/ p.u.MW]	2.4	T_{ij}	[p.u.MW]	0.08674
B	[p.u.MW/ Hz]	0.425	a_{ij}		1.0
	Notice: $i = 1, 2, 3$ *and* 4.				

V. Simulation results and discussion

5. Simulation results

To validate the effectiveness of the proposed LFC of the interconnected power system in the presence of RESs two cases are studied; the first one comprises from thermal and photovoltaic interconnected power plants while the second case comprises four-area, every area have multi-source power plants namely: thermal, hydro, PV and wind turbine generating units. The corresponding parameters for the proposed system is furnished in Table 2. The modeling of the systems under study are carried out using MATLAB/SIMULINK platform. The controller gains of the simulations procedure are regulated via PSO, CPSO, FA and hybrid firefly-particle swarm optimization (hFA-PSO) algorithms. Maximum iteration size is designated equal in entirely experiments, while the controller parameters of the algorithms are selected as: In PSO algorithm: $c_1 = c_2 = 1.759$, $\omega_i = 0.85$, $\omega_f = 0.55$ are used. In FA algorithms, $\Xi = 0.43$, $\beta_0 = 1.95$, $\gamma = 0.75$. The simulation procedure of the proposed strategy can be divided into following subsections:

1- Two-area interconnected power systems,
2- Multi-area multi-source interconnected systems:
   - Case 1: Performance analysis considering 10% step load perturbation,
   - Case 2: Sensitivity analysis,
   - Case 3: Performance analysis under step load change with wind turbine and PV system.

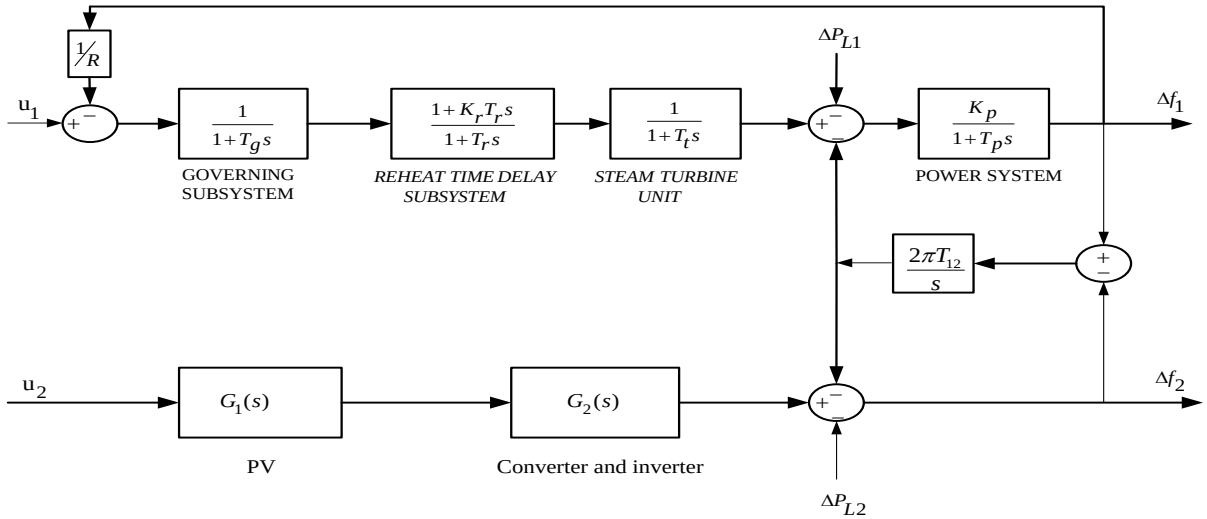


Fig. 7. Block diagram of Thermal/PV interconnected power plant.

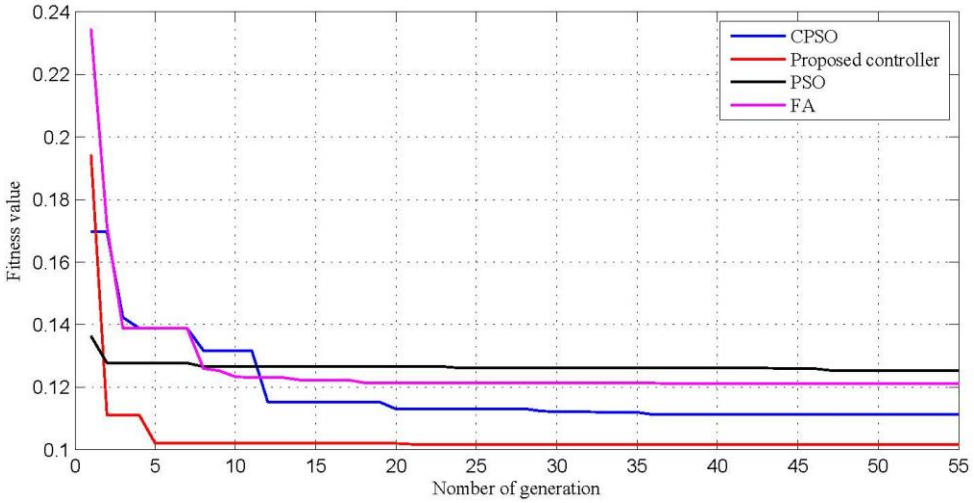
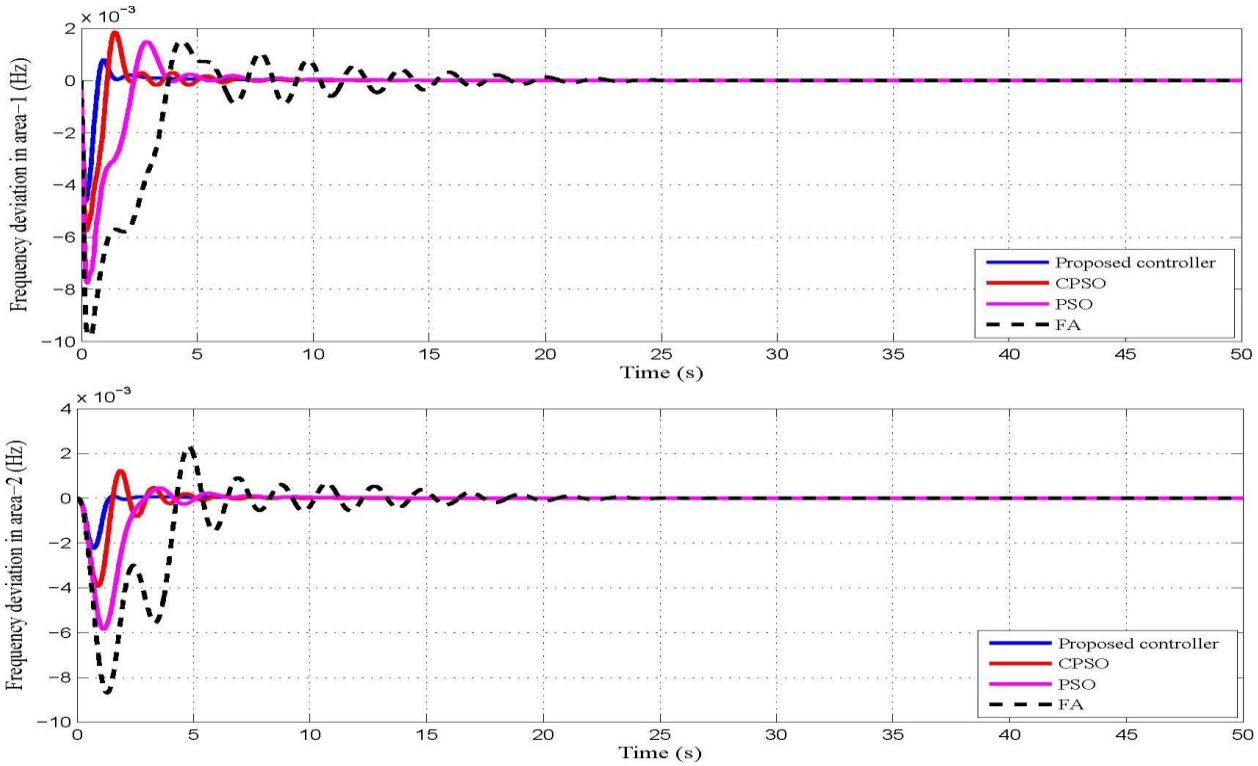


Fig. 8: Convergence characteristics.

Table 3: Controlling parameters of CPSO, PSO, and FA and the proposed hFA-PSO optimized FOF-PID controller.

Controllers	Controller gains							
	K_{e1}	K_{e2}	K_{d1}	K_{d2}	K_{pi}	K_{pd}	λ	μ
FOF-PID optimized via FA	-2.056	-1.765	1.876	-0.654	1.876	1.765	0.765	0.987
FOF-PID optimized via PSO	1.654	1.875	-1.765	0.543	-1.654	-1.765	0.997	0.8765
FOF-PID optimized via CPSO	-0.678	-1.005	-1.876	-1.654	-1.123	1.765	0.654	0.876
Proposed controller	1.097	-2.765	2.065	2.765	-3.432	-1.875	0.543	0.998



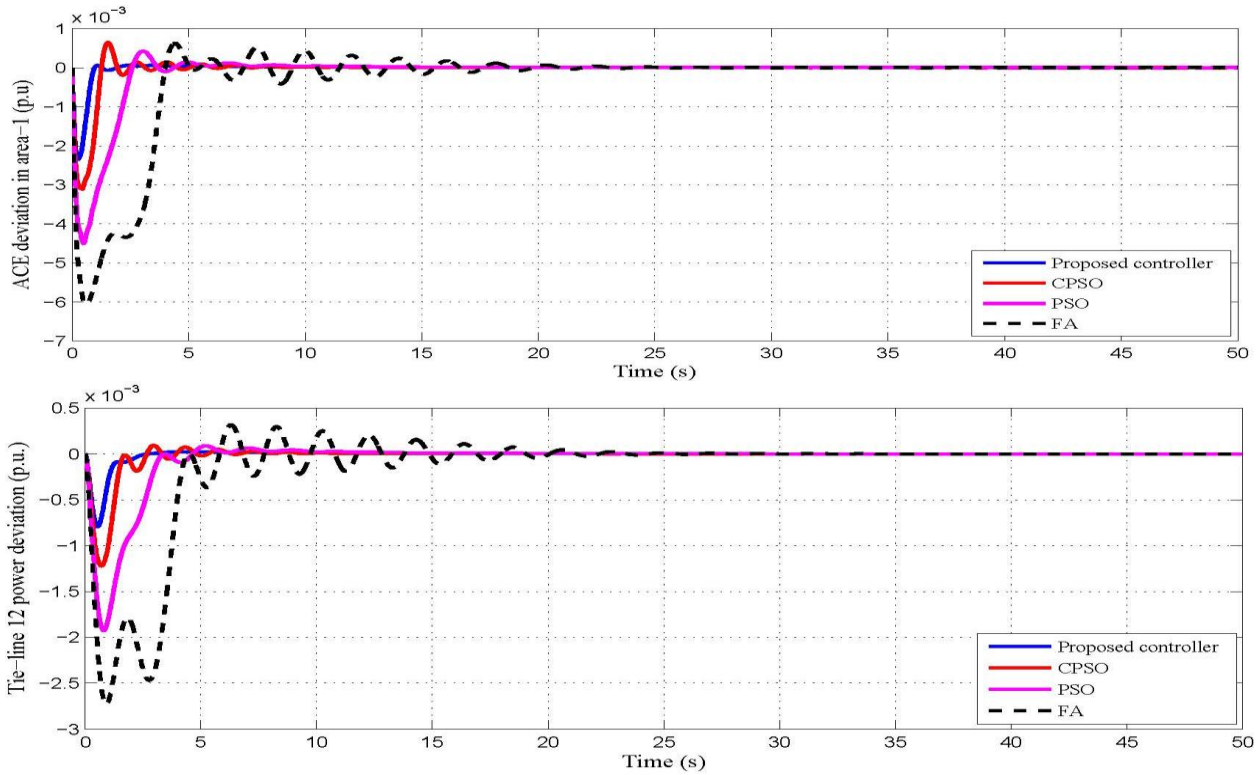


Fig. 9. Time responses of the frequency, area control error and tie-line power deviations for the plant after 10% step load perturbation.

5.1. Two-area interconnected power system:

In this scenario two-area interconnected power plant as displayed in Fig. 7 has been considered for study; where area-1 comprises reheat thermal power generation system and area-2 comprises photovoltaic (PV) system. The suggested system incorporated with 10% step load perturbation in area-1, while the system parameters of each unit are furnished in Table 2. The obtained results of the proposed strategy are compared with those attained by particle swarm optimization (PSO), CPSO, and firefly algorithm (FA). The optimal gains of FOF-PID controller, obtained via a hybrid hFA-PSO optimizer compared to PSO, CPSO, and FA results are tabulated in Table 3. Fig. 8 shows the convergence response of hFA-PSO compared to CPSO, PSO, and FA algorithms for the best objective function. It is clear that the convergence of hFA-PSO is faster and the objective function of the hFA-PSO decreases over the generations comparing to CPSO, PSO, and FA algorithms. The hFF-PSO optimizer succeeded in achieving the optimum solution after 7.192 s while the CPSO consumes 21.7 s, PSO consumes 21.7 s, FA consumes 21.7 s to get the optimum solution. One can conclude that, the obtained results via the proposed strategy are the best with short time convergence compared to the others. Fig. 9 and Table 4 shows the performance specifications (settling time, over shoot, under shoot, and ITSE) of frequency error, area control error and tie-line power deviation obtained by the proposed FOF-PID controller in comparison with those obtained via CPSO, PSO, and FA algorithms. It is clear that, the specifications obtained via hFA-PSO optimized FOF-PID controller are the best compared to CPSO, PSO, and FA approaches, the proposed strategy is superior in obtaining the steady state performance of the proposed interconnected power systems.

Table 4: The optimal results obtained by hFA-PSO optimized FOF-PID compared with CPSO, PSO, and FA.

Controller	Settling time (s)				Peak overshoot				Peak undershoot (-ve)				ITSE
	Δf_1	Δf_2	ACE_1	$\Delta P_{tie,12}$	Δf_1	Δf_2	ACE_1	$\Delta P_{tie,12}$	Δf_1	Δf_2	ACE_1	$\Delta P_{tie,12}$	Value
FOF-PID optimized via FA	4.61	7.01	9.13	10.01	0.0015	0.0023	0.0006	0.0003	0.0097	0.0087	0.0059	0.0027	0.0267
FOF-PID optimized via PSO	3.10	2.35	2.44	2.94	0.0014	0.0005	0.0004	0.00002	0.0076	0.0058	0.0044	0.0018	0.0131
FOF-PID optimized via CPSO	1.72	1.45	1.56	1.44	0.0018	0.0012	0.0006	0.00001	0.0059	0.0037	0.0030	0.0012	0.0081
Proposed controller	0.73	1.15	0.84	1.06	0.0007	0.0	0.0	0.0	0.0044	0.0021	0.0021	0.0008	0.0048

5.2. Multi-area multi-source interconnected systems:

5.2.1. Case I: Performance analysis under step load perturbation:

In this case a four-area interconnected power system as highlighted in Fig. 10 have being proposed for study; where every control area has thermal/hydro power plants. The system is incorporated with the proposed FOF-

PID controller optimized via hFA-PSO technique, under 10% step load perturbation in area-1. Optimal setting of the controller parameters are optimized via CPSO, PSO, FA, hFA-PSO techniques and listed in Table 5. The effectiveness of the suggested approach is compared with CPSO, PSO and FA algorithms. Fig. 11 show the frequency errors, area control errors and tie-line power deviations of the proposed system. The dynamic specifications of the plant in terms of ITSE, settling time, and peak overshoot/undershoot are gathered in Tables 6 and 7. It is noted from Tables 6 that the hFA-PSO optimized FOF-PID controller provides a smaller objective function (ITSE = 0.0228) than CPSO optimized FOF-PID controller (ITSE = 0.0258), PSO optimized FOF-PID controller (ITSE = 0.0289), FA optimized FOF-PID controller (ITSE = 0.0332). It can be summarized from Tables 6, 7 and Fig. 11, that the performance oscillations are properly settled down to the steady value in a small time by the proposed control technique. Thus the desirable dynamic stability for sudden change in the load demand is accomplished by FOF-PID controller optimized via hFA-PSO algorithm and the proposed technique is outperforms the other techniques.

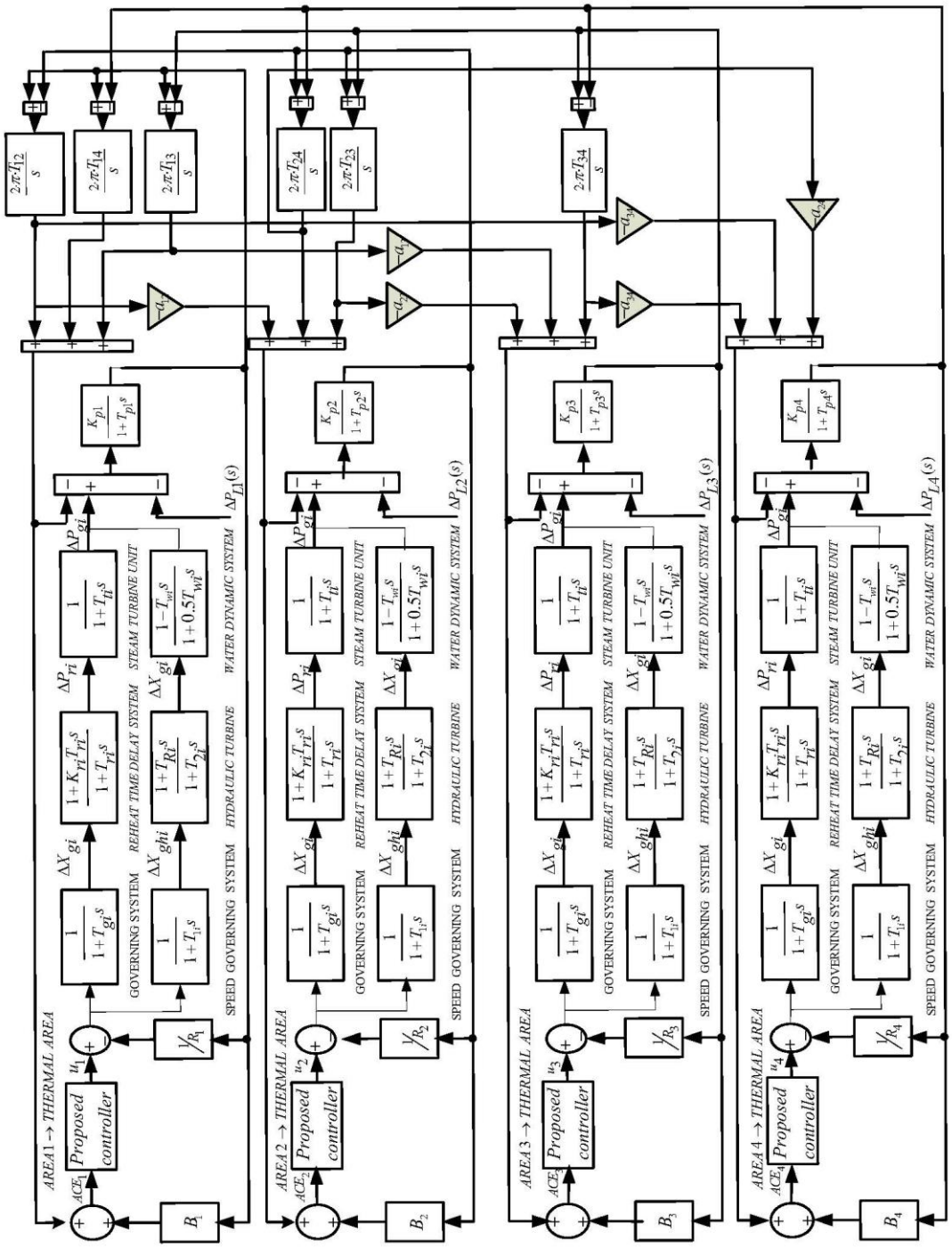
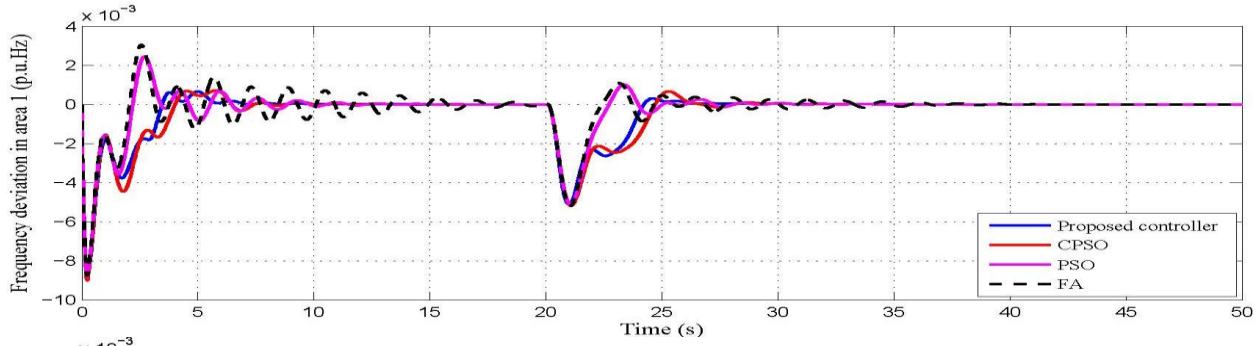
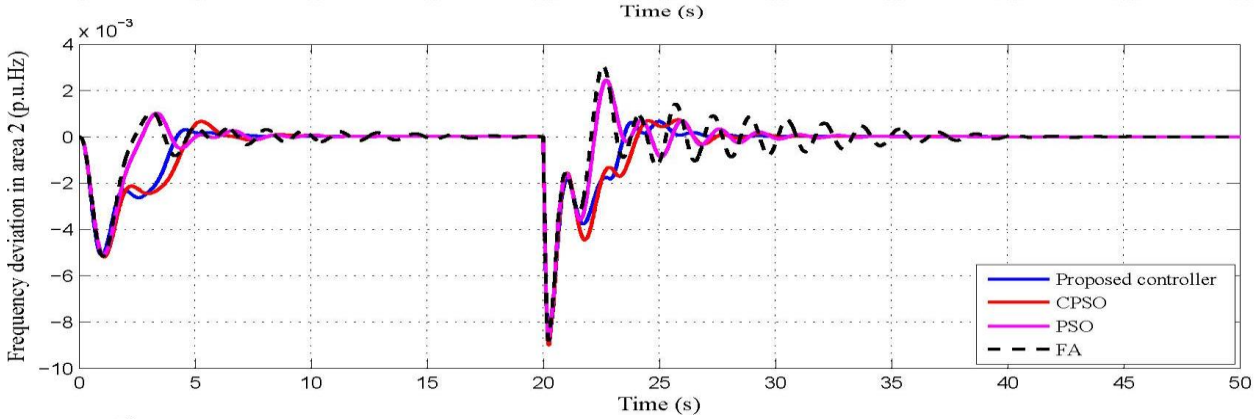
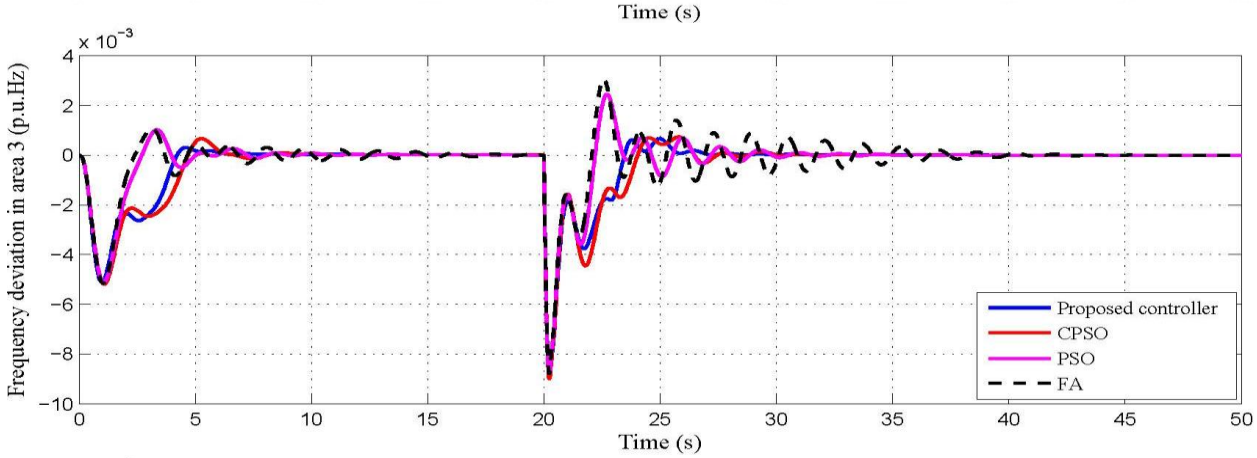
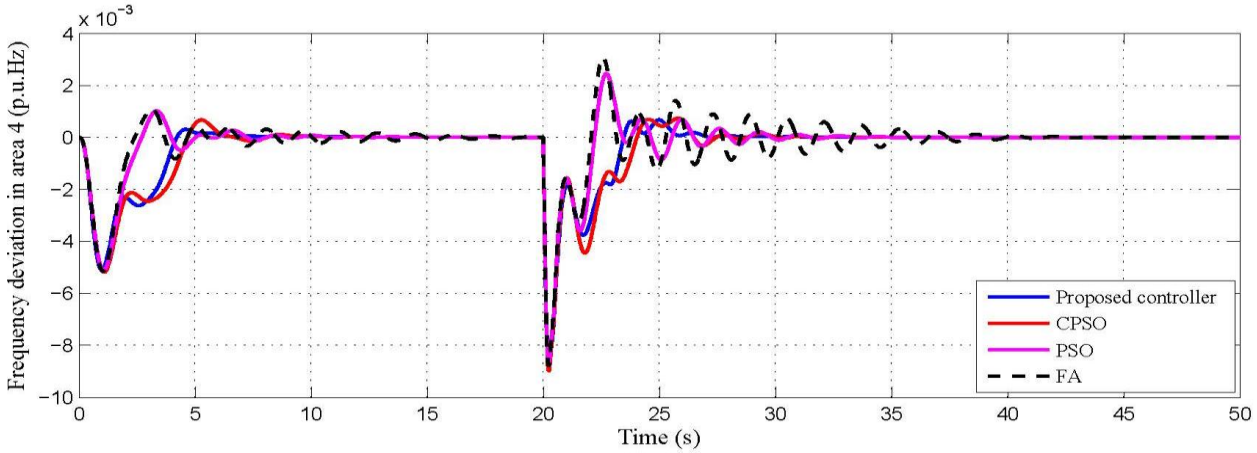


Fig. 10: Four area power system under investigation for case I.


x 10^-3
Frequency deviation in area 1 (p.u.Hz)
Time (s)
Proposed controller
CPSO
PSO
FA


x 10^-3
Frequency deviation in area 2 (p.u.Hz)
Time (s)
Proposed controller
CPSO
PSO
FA


x 10^-3
Frequency deviation in area 3 (p.u.Hz)
Time (s)
Proposed controller
CPSO
PSO
FA


x 10^-3
Frequency deviation in area 4 (p.u.Hz)
Time (s)
Proposed controller
CPSO
PSO
FA

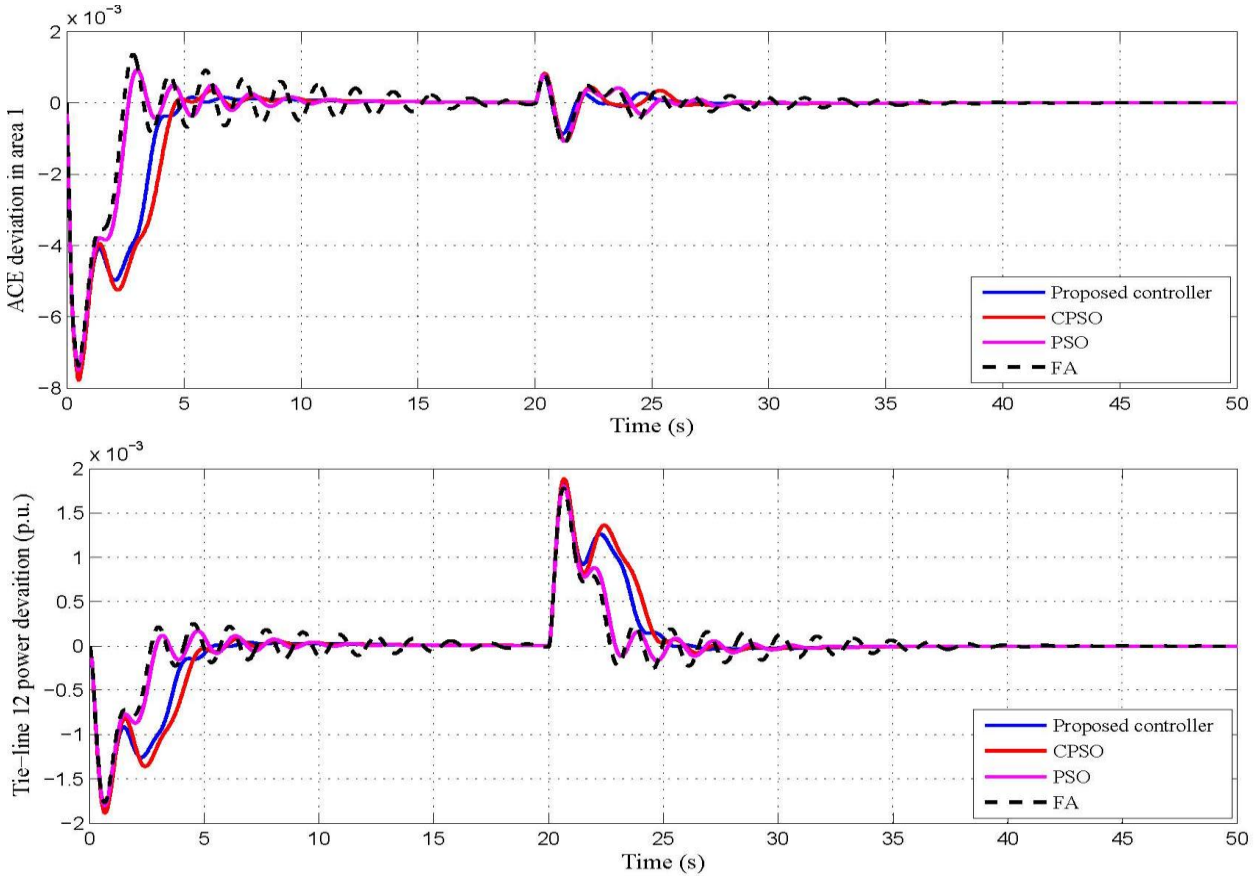


Fig. 11. Comparative dynamic performances of the plant in term of frequency, area control error, and tie-line power deviations for case I.

Table 5: Optimized controllers parameters for case I.

Controllers	Controller gains							
	K_{e1}	K_{e2}	K_{d1}	K_{d2}	K_{pi}	K_{pd}	λ	μ
FOF-PID optimized via FA	0.235	2.345	0.365	-0.067	-0.543	-2.765	0.765	0.876
FOF-PID optimized via PSO	0.363	-0.254	-2.872	0.187	0.654	0.564	0.675	0.763
FOF-PID optimized via CPSO	-1.548	1.654	1.653	-0.654	-2.765	-0.6538	0.876	0.762
Proposed controller	1.064	-0.987	-3.570	0.563	1.654	2.765	0.905	0.998

Table 6: Comparative analysis of the system in terms of ITSE and settling time for case I.

Controller	ITSE	Settling time (s)					
	Value	Δf_1	Δf_2	Δf_3	Δf_4	$\Delta P_{tie,12}$	ACE_1
FOF-PID optimized via FA	0.0332	8.99	4.27	4.27	4.27	6.19	10.54
FOF-PID optimized via PSO	0.0289	5.11	4.18	4.18	4.18	4.92	6.42
FOF-PID optimized via CPSO	0.0258	3.76	4.15	4.15	4.15	4.47	4.44
Proposed controller	0.0228	3.29	3.72	3.72	3.72	3.84	3.79

Table 7: Comparative analysis of the system in terms of peak over/undershoot for case I.

Controller	Peak undershoot (-ve)						Peak overshoot					
	Δf_1	Δf_2	Δf_3	Δf_4	$\Delta P_{tie,12}$	ACE_1	Δf_1	Δf_2	Δf_3	Δf_4	$\Delta P_{tie,12}$	ACE_1
FOF-PID optimized via FA	0.0086	0.0052	0.0052	0.0052	0.0018	0.0076	0.0031	0.0011	0.0011	0.0011	0.0003	0.0013
FOF-PID optimized via PSO	0.0079	0.0051	0.0051	0.0051	0.0017	0.0073	0.0025	0.0010	0.0010	0.0010	0.0002	0.0009
FOF-PID optimized via CPSO	0.0085	0.0051	0.0051	0.0051	0.0018	0.0077	0.0007	0.0006	0.0006	0.0006	0.0001	0.0003
Proposed controller	0.0073	0.0050	0.0050	0.0050	0.0016	0.0072	0.0005	0.0002	0.0002	0.0002	0.0	0.0001

Table 8: Sensitivity analysis of the plant with the proposed FOF-PID optimized via hFA-PSO.

Parameter variation	% Change	ITSE	Settling time (Sec) for 5% band						Peak undershoot (−ve)					
		Value	Δf_1	Δf_2	Δf_3	Δf_4	$\Delta P_{tie,12}$	ACE_1	Δf_1	Δf_2	Δf_3	Δf_4	$\Delta P_{tie,12}$	ACE_1
Nominal	No change	0.0228	3.29	3.72	3.72	3.72	3.84	3.79	0.0073	0.0050	0.0050	0.0050	0.0016	0.0072
Loading condition	+50	0.0467	4.89	5.32	5.32	5.32	5.73	5.94	0.0123	0.0102	0.0102	0.0102	0.0045	0.0131
	+25	0.0332	3.56	3.89	3.89	3.89	4.56	3.89	0.0100	0.0092	0.0092	0.0092	0.0032	0.0101
	-25	0.0201	2.92	3.43	3.43	3.43	3.52	3.23	0.0056	0.0042	0.0042	0.0042	0.0010	0.0053
	-50	0.0200	2.67	3.32	3.31	3.31	3.32	3.01	0.0050	0.0040	0.0040	0.0040	0.0098	0.0050
T_g	+50	0.0230	3.3	3.74	3.74	3.74	3.85	3.81	0.0076	0.0054	0.0054	0.0054	0.0018	0.0075
	+25	0.0229	3.29	3.73	3.73	3.73	3.85	3.80	0.0074	0.0052	0.0052	0.0052	0.0017	0.0074
	-25	0.0227	3.28	3.71	3.71	3.71	3.82	3.77	0.0072	0.0050	0.0050	0.0050	0.0015	0.0071
	-50	0.0226	3.27	3.70	3.70	3.70	3.82	3.76	0.0071	0.0049	0.0049	0.0049	0.0014	0.0070
T_r	+50	0.0232	3.34	3.92	3.92	3.92	3.91	3.81	0.0081	0.0054	0.0054	0.0054	0.0018	0.0076
	+25	0.0231	3.32	3.75	3.75	3.75	3.88	3.80	0.0079	0.0052	0.0052	0.0052	0.0018	0.0076
	-25	0.0226	3.27	3.70	3.70	3.70	3.81	3.76	0.0071	0.0048	0.0048	0.0048	0.0014	0.0070
	-50	0.0224	3.25	3.68	3.68	3.68	3.80	3.74	0.0070	0.0046	0.0046	0.0046	0.0013	0.0068
T_{12}	+50	0.0222	3.23	3.64	3.64	3.64	3.77	3.74	0.0067	0.0046	0.0046	0.0046	0.0012	0.0069
	+25	0.0226	3.27	3.71	3.71	3.71	3.82	3.77	0.0071	0.0049	0.0049	0.0049	0.0015	0.0070
	-25	0.0231	3.33	3.75	3.75	3.75	3.89	3.81	0.0082	0.0056	0.0056	0.0056	0.0021	0.0078
	-50	0.0235	3.36	3.79	3.79	3.79	3.92	3.84	0.0086	0.0059	0.0059	0.0059	0.0025	0.0081

5.2.2. Case II: Sensitivity analysis.

The performance evaluating of the interconnected complex power plant against wide variations in system parameters is a typical measure to appraise the robustness of the close-loop system. Generally, the robust structure designed for LFC mechanism must have sufficient ability versus the plant uncertainties to preserve the frequency and transmission-line power oscillations in a desired level of deviations. Therefore, to validate the advantages of the suggested FOF-PID controller optimized via hFA-PSO algorithm versus robustness analysis, we take the same the plant as in case I with the same regulated gains (Table 5). Then, the interconnected complex power plant is examined by changing the operating load condition and some critical parameters of the plant such as T_g, T_r, and T_{12} in the range of ±40% from the nominal values. The lowest ITSE values, settling time and peak undershoot of the proposed plant under the aforesaid uncertainties are furnished in Table 8 . It is inspected from Table 8 that the impact of uncertainties on fitness value, settling time and peak undershoot derived by the hFA-PSO based FOF-PID controller in nominal condition is insignificant. Having knowledge of the above analysis, it can be inferred that the suggested FOF-PID controller optimized via hFA-PSO algorithm are quite robust and perform satisfactory results even against the uncertainties.

5.2.3. Case III: Performance analysis under step load change with RESs.

For the time being, most of power plants have more than one generation utility as hydro, thermal, gas, nuclear, wind, photovoltaic. Therefore, to deal with real power plant model, different generation utility multi-interconnected power plants are studied. In order to assess the reliability of the proposed load frequency controller, a four-area interconnected power system have being considered; where every control area have multi-source generation units namely: Thermal, hydro, photovoltaic and wind power generations have being considered in this work. The data of wind turbine system is taken from [17], the data of PV system is taken from [11]. The interconnected power system incorporated with the proposed controller under step load perturbation $\Delta P_{L1} = 0.01$ in area-1 and the optimal gains of the controllers are furnished in Table 9. The obtained results of Δf_1, Δf_2, Δf_3, Δf_4, $\Delta P_{tie,12}$ and ACE_1 are shown in Figs. 12 in comparison with hFA-PSO, CPSO, PSO, and FA optimized FOF-PID controller. From the simulation results one can get that, the suggested FOF-PID controller optimized via hFA-PSO succeeded in obtaining the best performances than those obtained via CPSO, PSO and FA. The performance specifications of the frequency, area control error and tie line power errors are presented in Tables 10 and 11 in comparison with hFA-PSO, CPSO, PSO, and FA optimized FOF-PID controller. From the Table 10, it can observe that the proposed controller optimized via hFA-PSO gives the optimal ITSE function of 0.0059, while CPSO gives ITSE index of 0.0106, PSO gives ITSE index of 0.0088, FA gives ITSE index of 0.0217. Finally, one can get that the proposed controller regulated via hFA-PSO succeeded in obtaining zero frequency and tie line power deviations for interconnected multi-utilities system subjected to load perturbation.

Table 9: Optimized controllers parameters for case 4.

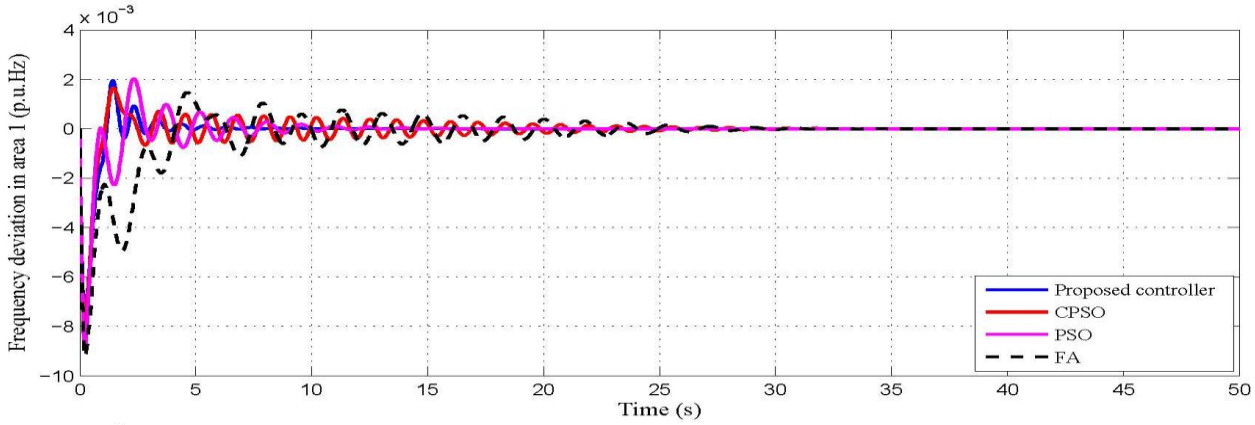
Controllers	Controller gains							
	K_{e1}	K_{e2}	K_{d1}	K_{d2}	K_{pi}	K_{pd}	λ	μ
FOF-PID optimized via FA	-2.654	1.764	1.564	-1.452	-1.531	1.543	0.654	0.915
FOF-PID optimized via PSO	4.763	-2.043	-0.654	1.760	0.654	-1.954	0.153	0.786
FOF-PID optimized via CPSO	-2.065	1.764	1.543	-0.754	-0.431	0.546	0.653	0.876
Proposed controller	0.572	-2.785	-1.065	0.543	0.542	-0.342	0.543	0.987

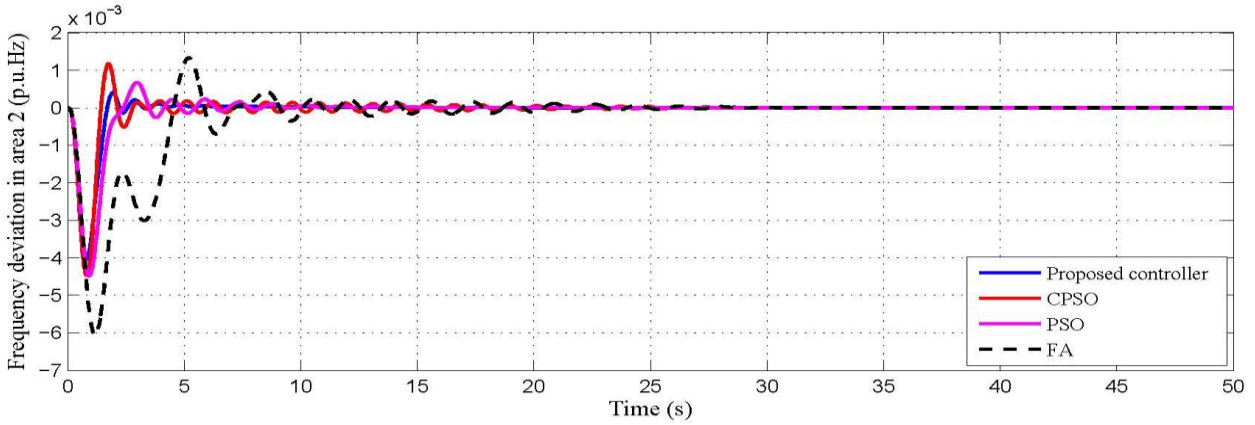
Table 10: Comparative analysis of the system in terms of ITSE and settling time case 4

Controller	ITSE	Settling time (s)					
	Value	Δf_1	Δf_2	Δf_3	Δf_4	$\Delta P_{tie,12}$	ACE_1
FOF-PID optimized via FA	0.0217	9.02	8.84	8.84	8.84	15.41	15.19
FOF-PID optimized via PSO	0.0088	3.58	2.54	2.54	2.54	5.76	5.56
FOF-PID optimized via CPSO	0.0106	3.91	3.26	3.26	3.26	4.81	3.75
Proposed controller	0.0059	1.86	1.56	1.56	1.56	2.41	2.18

Table 11: Comparative analysis of the system in terms of peak over/undershoot case 4.

Controller	Peak undershoot (*-ve*)						Peak overshoot					
	Δf_1	Δf_2	Δf_3	Δf_4	$\Delta P_{tie,12}$	ACE_1	Δf_1	Δf_2	Δf_3	Δf_4	$\Delta P_{tie,12}$	ACE_1
FOF-PID optimized via FA	0.0092	0.0060	0.0060	0.0060	0.0021	0.0083	0.0015	0.0013	0.0013	0.0013	0.0002	0.0007
FOF-PID optimized via PSO	0.0077	0.0045	0.0045	0.0045	0.0016	0.0064	0.0016	0.0007	0.0007	0.0007	0.0001	0.0005
FOF-PID optimized via CPSO	0.0086	0.0043	0.0043	0.0043	0.0014	0.0061	0.0021	0.0011	0.0011	0.0011	0.0	0.0006
Proposed controller	0.0069	0.0039	0.0039	0.0039	0.0013	0.0060	0.0020	0.0004	0.0004	0.0004	0.0	0.0001





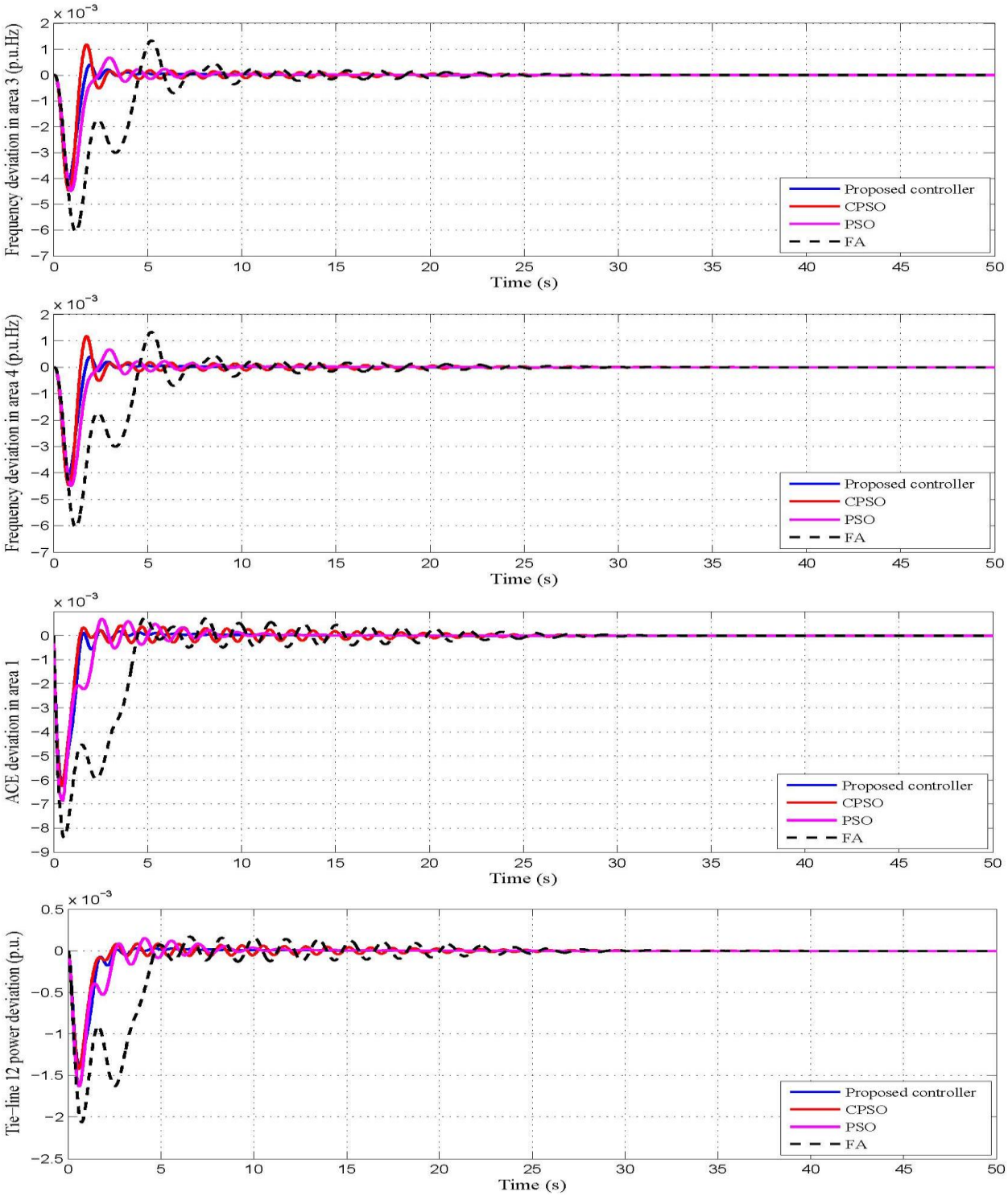


Fig. 12. Comparative dynamic performances of the plant with nonlinearities after 10% SLP in area-1 frequency deviations in area 1, 2, 3, 4 respectively, area control error deviation in area-1, and tie-line power $\Delta P_{tie,12}$ deviation.

VI. Conclusion

In this article, a hybrid firefly and particle swarm optimization (hFA-PSO) is employed for training fractional order fuzzy PID (FOF-PID) controller based LFC of interconnected multi-area power plants. A hFA-PSO is used for regulating the optimal gains of the proposed controller such that minimizing the ITSE of the frequency and tie-line power deviations. Then, the proposed controller is incorporated to an interconnected complex power system comprising nonrenewable and renewable energy sources. The obtained results via hFA-

PSO optimized FOF-PID controller is compared with the other reported techniques such as CPSO, PSO, FA for the same interconnected power system. The proposed hFA-PSO technique takes merit of global exploration competences of FA and local exploitation capability of PSO algorithm. The performance specifications, settling time and over shoot/under shoot of the frequency and tie line power deviations are recorded and compared with others. It is observed that the results of the proposed controller based hFA-PSO is preeminence to others techniques. Also, robustness analysis is performed by varying the loading conditions and plant parameters in the range of +50% to -50% from their nominal values. It is shown that the proposed controller optimized via hFA-PSO approach outperforms to the others approaches. Finally, the obtained results performed that the proposed hFA-PSO optimized FOF-PID controller based LFC of interconnected power systems is meaningfully robust in spite considered wide variation in loading conditions and system parameters.

Acknowledgments: This work was supported by the University of Nyala. The authors wish to thank the anonymous reviewers and the editors for providing valuables comments to improve the quality of the manuscript.

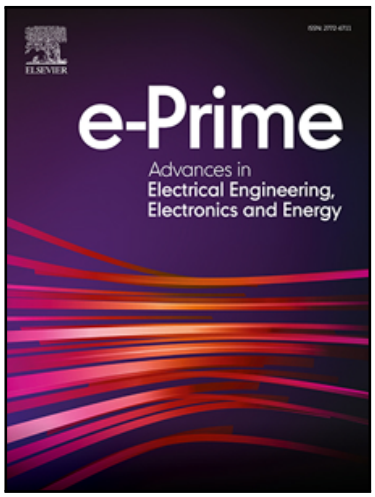
References:

[1]. Gomaa Haroun A. H. and Li Y. Y., A novel optimized hybrid fuzzy logic intelligent PID controller for an interconnected multi-area power system with physical constraints and boiler dynamics, ISA Transactions, , 2017, vol. 71, pp. 364-379.
[2] Gomaa Haroun AH, Yin-Ya L. A novel optimized fractional-order hybrid fuzzy intelligent PID controller for interconnected realistic power systems. Transactions of the Institute of Measurement and Control. 2019; 41(11):3065-80.
[3] Gomaa Haroun A. H., and Li Y.Y. Ant lion optimized fractional order fuzzy pre-compensated intelligent pid controller for frequency stabilization of interconnected multi-area power systems. Applied System Innovation. 2019; 2(2):17.
[4]. P. C. Pradhan, R. K. Sahu, and S. Panda, Firefly algorithm optimized fuzzy PID controller for AGC of multi-area multi-source power systems with UPFC and SMES, Engineering Science and Technology, an International Journal, 2016, vol. 19, pp. 338-354.
[5]. T. Santy and R. Natesan, Load frequency control of a two area system consisting of a grid connected PV system and diesel generator, Int J Emerg Technol Comput Electron, 2015, vol. 13, pp. 456-461.
[6]. S. M. Abd-Elazim and E. S. Ali, Firefly algorithm-based load frequency controller design of a two area system composing of PV grid and thermal generator, Electrical Engineering, 2018, vol. 100, pp. 1253-1262.
[7]. Y. Arya and N. Kumar, BFOA-scaled fractional order fuzzy PID controller applied to AGC of multi-area multi-source electric power generating systems, Swarm and Evolutionary Computation, 2017, vol. 32, pp. 202-218.
[8]. L. Liu, H. Matayoshi, M. Lotfy, M. Datta, and T. Senjyu, Load frequency control using demand response and storage battery by considering renewable energy sources, Energies, 2018, vol. 11, pp. 3412.
[9]. P. Dahiya, V. Sharma, and R. N. Sharma, Optimal generation control of interconnected power system including DFIG-based wind turbine, IETE Journal of Research, 2015, vol. 61, pp. 285-299.
[10]. J. P. Lopes, R. Almeida, and E. Castronuovo, Optimum generation control in wind parks when carrying out system operator requests, 2006.
[11]. S. Abd-Elazim and E. Ali, Load frequency controller design of a two-area system composing of PV grid and thermal generator via firefly algorithm, Neural Computing and Applications, 2018, vol. 30, pp. 607-616.
[12]. M. K. Alam and F. H. Khan, Transfer function mapping for a grid connected PV system using reverse synthesis technique, in Control and Modeling for Power Electronics (COMPEL), 2013 IEEE 14th Workshop on, 2013, pp. 1-5.
[13]. V. Çelik, M. T. Özdemir, and G. Bayrak, The effects on stability region of the fractional-order PI controller for one-area time-delayed load–frequency control systems, Transactions of the Institute of Measurement and Control, 2016.
[14]. X.-S. Yang, Nature-inspired metaheuristic algorithms: Luniver press, 2010.
[15]. P. Kora and K. S. Rama Krishna, Hybrid firefly and Particle Swarm Optimization algorithm for the detection of Bundle Branch Block, International Journal of the Cardiovascular Academy, 2016, vol. 2, pp. 44-48.
[16]. K. S. Rajesh, S. S. Dash, and R. Rajagopal, Hybrid improved firefly-pattern search optimized fuzzy aided PID controller for automatic generation control of power systems with multi-type generations, Swarm and Evolutionary Computation, 2018.
[17]. S. Ali, G. Yang, and C. Huang, Performance optimization of linear active disturbance rejection control approach by modified bat inspired algorithm for single area load frequency control concerning high wind power penetration, ISA Transactions, 2018, vol. 81, pp. 163-176.

Gomaa Haroun A. H, et. al. "A hybrid Firefly and Particle Swarm Optimized FOF-PID Strategy for Interconnected Multi-area Power System with Renewable Energy Sources." *IOSR Journal of Electrical and Electronics Engineering (IOSR-JEEE)*, 17(3), (2022): pp. 23-42.

View publication stats

Journal Pre-proof



A New Three-Phase Eleven Level Packed E-Cell Converter for Solar Grid-Tied Applications

SANJAY UPRETI , BHIM SINGH , NARENDRA KUMAR

PII: S2772-6711(23)00047-5
DOI: https://doi.org/10.1016/j.prime.2023.100152
Reference: PRIME 100152

To appear in: *e-Prime - Advances in Electrical Engineering, Electronics and Energy*

Received date: 8 October 2022
Revised date: 22 March 2023
Accepted date: 6 April 2023

Please cite this article as: SANJAY UPRETI , BHIM SINGH , NARENDRA KUMAR , A New Three-Phase Eleven Level Packed E-Cell Converter for Solar Grid-Tied Applications, *e-Prime - Advances in Electrical Engineering, Electronics and Energy* (2023), doi: https://doi.org/10.1016/j.prime.2023.100152

This is a PDF file of an article that has undergone enhancements after acceptance, such as the addition of a cover page and metadata, and formatting for readability, but it is not yet the definitive version of record. This version will undergo additional copyediting, typesetting and review before it is published in its final form, but we are providing this version to give early visibility of the article. Please note that, during the production process, errors may be discovered which could affect the content, and all legal disclaimers that apply to the journal pertain.

© 2023 Published by Elsevier Ltd.
This is an open access article under the CC BY-NC-ND license
(http://creativecommons.org/licenses/by-nc-nd/4.0/)

Journal Pre-proof

.

A New Three-Phase Eleven Level Packed E-Cell Converter for Solar Grid-Tied Applications

SANJAY UPRETI*, BHIM SINGH and NARENDRA KUMAR
Electrical and Electronics Engineering Department, Bhagwan Parsuram Institute of Technology Delhi 110089, Indian Institute of Technology Delhi, New Delhi 110016, Delhi Technological University Delhi 110042 India e-mail: supreti223@gmail.com; bsingh@ee.iitd.ac.in; narendrakumar@dtu.ac.in
*Corresponding author

Abstract. A new three-phase eleven-level packed E-Cell (PEC11) converter is formed by selecting a quintuple ratio (1:5) between the voltages of solar photovoltaic arrays. The converter consists of three solar panels per phase, highest level of staircase voltage is achieved by the top solar panel. The subsequent voltage levels are obtained using an algebraic formulation with lower two solar panels. The operating modes to get each level are explained. The mathematical modeling is presented with voltage and current equations of three-phase grid. PEC11 converter feeds the current to the grid with closed-loop proportional-resonant (PR) controllers. The nearest level modulation (NLM) technique generates the gating pulses for PEC converter. It provides minimum switching loss and simple control in grid tied mode. This system is simulated in MATLAB/SIMULINK platform, and the power is fed smoothly in both steady-state and dynamic conditions. These results are validated in the real-time simulator (OPAL-RT), which makes this converter ideal for solar applications.

Keywords. Solar Photovoltaic, Packed E Cell, Power quality, Renewable Energy, Nearest Level Modulation

1. Introduction

The power electronic device, an inverter is used for conversion of power with high efficiency. When an inverter generate voltage and current between equal positive and negative levels it is known as two level inverter. The high voltage applications, it is difficult to use the two level inverter due to requirement of high rating of power switches. With the introduction of three level multilevel inverter (MLI) in 1975, it has become possible to increase the power and voltage rating of inverters by lower rating of the power switches. Nowadays MLIs have an important role to play in the medium to high voltage industrial and solar-grid applications. The electrical power quality improves due to its simplicity in generating higher voltage levels. The MLI has the advantage of maintaining the power quality by offering low harmonics distortion. It is a preferred choice in electric vehicles, high voltage DC transmission, renewable energy sources etc. The lesser level MLI is difficult to use in medium and high voltage applications as the power rating requirement of switching devices is high. The MLI of a high number of levels needs low power rating devices, which improves the life and reliability of the converter [1]. Moreover, voltage output is more closure to sinusoidal wave shape resulting in lower size of harmonic filter [2].

Few conventional MLI uses more number of devices, which means complex control for gate driver circuit for logical switching of all switches. So the research in MLI area is focused on reduction in power semiconductor switches and simplification in the control circuit. The basic classification of MLI topologies is of three types: diode clamped, flying capacitors, and cascaded H-bridge (CHB) [3-6]. In the diode clamped inverter, the diode is used to clamp the DC bus voltage to generate the levels at the inverter output. By connection of the phases to a series of capacitor, diode clamped inverter can provide multiple levels [7]. The flying capacitor inverter, which is basically capacitor clamped configuration is a alternate topology to the diode clamped inverter. The flying capacitor is a switching cell clamping by the series connection of capacitor [8]. This topology is better than diode-clamped as clamping diode are not required and there is switching redundancy within the phase, which is used to balance the capacitors. CHB is formed by the series connection of four switch two leg bridge and each full bridge can have three states $+V_{dc}$, 0, $-V_{dc}$. The power and voltage of CHB can easily be scaled since power conversion cells are series connected. The DC link supply is separate for each full bridge inverter. CHB based configuration has high leakage current due to isolated solar PV arrays. The common advantage is that all the MLI configurations can be extended to many voltage steps in the expansion process. Researchers have explored the hybrid configurations of basic topologies to achieve more levels without an increase in a number of switches. Packed U-cell (PUC), packed E-cell (PEC) topologies are created by modification in multilevel converter (MLC) structures. The PUC converter is the result of optimization of MLC topologies to generate more voltage levels with a single voltage source, lesser count of switches, and floating capacitors as auxiliary voltage sources [9]. However, floating capacitor voltage control at high voltage levels, is a complication associated with the PUC. Eventually, PEC topology with one E-cell in place of two U-cell is suggested to overcome these drawbacks [10-14]. The main advantage of PEC is generating the nine levels with fewer switches and DC link capacitors. Moreover, it can be operated at five or seven levels with proper switching sequence. In [15], a nine-level grid-tied packed E-cell, referred to as PEC9, is proposed with a single DC source and two capacitors as auxiliary sources with the advantage of simple control of capacitor voltage. However, power capability of this system is limited due to a single source, which can be increased by the addition of DC sources in place of capacitors.

Owing to capability of MLI to increase the power and voltage, there is a significant development in the reliability

.
of these inverters. The control of inverter for switching, converter voltage, grid injected current and DC link voltage are very important, which ensure the smooth and reliable operation of inverter. Modulation technique in MLI plays a vital role as switching frequency and sequence affect the inverter in terms of efficiency and harmonics spectra of output voltage. The level shifted-sinusoidal pulse width modulation (LS-SPWM) technique is the one of the carrier switching method applied for level generation in inverters. In this modulation, the pulse width is varied, while magnitude of pulse is constant. The reference wave and carrier wave are compared to generate the gating pulses. Reference wave is pure sinusoidal of fundamental frequency and carrier wave is a triangular shape, whose frequency is several times of fundamental frequency. There are total (m-1) number of carrier wave where m is the number of level of MLI. The LS-SPWM is proposed in [16-18], which improves the power quality, however it becomes complex with rise in voltage levels and efficiency of inverter reduced due to high switching loss. The modulation technique of low frequency is more suited for MLIs of more number levels and nearest level modulation (NLM) offers a very viable option as it is independent of number of levels of the MLI and have simple implementation. In [19], NLM is successfully tested for eleven levels for high power applications. The controlled flow of power to the grid is a key feature of a solar system. The closed-loop control of inverter ensures the maximum PV power from solar arrays, DC link balancing and sinusoidal grid current injection in both steady and dynamic conditions. Model predictive control (MPC) is preferred by researchers, which is formulated by the full steady state information in terms of output current and voltage. Value prediction is done at each sampling instant The MPC is proposed in [20], and MPC based direct power control is used in [21]. The reference current is obtained by grid voltage measurement and its decomposition into direct quadrature (D-Q) frame. Most of the research on PEC is carried at nine levels with one DC source and two floating capacitors. Researchers have reported various eleven level converter topologies [22-28].
This paper presents the grid-tied solar fed PEC11 without changing the topology configuration and count of switches of PEC9. Three solar PV arrays feed the PEC11. Moreover, it presents the NLM technique for switching converter and PR controller to regulate flow of active power with current tracking in steady state and dynamic conditions.

The proposed work offers the following advantages.

- The eleven-level PEC with new quintuple voltage progression is used for solar applications for the first time.
- The application to NLM is done, which is easy to implement and operate with minimum switching stress.
- It implements a PR controller for each cluster, which smoothly controls the power fed to the grid without any complex implementation.
- This work provides a new solar photovoltaic (SPV) system and tests the close loop control in real-time mode.

2. System configuration

A new three phase solar photovoltaic (SPV) system consisting of PEC11 converter is shown in Fig 1. Each phase of this system has six unidirectional and one bidirectional switches, it is fed by one main photovoltaic array PV_{1a} and two similar arrays PV_{2a} & PV_{3a} which act as the auxiliary DC sources in the phase a. The voltage of PV_1 (370V) is five times of the voltage of $PV_{2\text{-}3}$ (74V). Each PV array has maximum power point tracker (MPPT) that ensures maximum solar power extraction. R-L filter for harmonics mitigation is connected between the converter output and power grid. The switching state and mode of operation to generate all the voltage levels are depicted in Table I. The voltage output equation for positive upper half of phase 'A' is expressed as,

$$v_{AO} = \begin{Bmatrix} V_{PV1A} = +5V_{PV} \\ V_{PV1A} - V_{PV3A} = +4V_{PV} \\ V_{PV1A} - V_{PV2A} - V_{PV3A} = +3V_{PV} \\ V_{PV2A} + V_{PV3A} = +2V_{PV} \\ V_{PV2A} = +V_{PV} \end{Bmatrix} \quad (1)$$

Similarly negative half cycle is represented as,

$$v_{AO} = \begin{Bmatrix} -V_{PV1A} = -5V_{PV} \\ -V_{PV1A} + V_{PV3A} = -4V_{PV} \\ -V_{PV1A} + V_{PV2A} + V_{PV3A} = -3V_{PV} \\ -V_{PV2A} - V_{PV3A} = -2V_{PV} \\ -V_{PV2A} = -V_{PV} \end{Bmatrix} \quad (2)$$

Where v_{AO} is the PEC-11 phase-voltage of phase 'A', V_{PV1A} represents the voltage of top solar array, V_{PV2A} & V_{PV3A} is the voltage of bottom solar arrays. These voltage values are at the maximum power point condition. The voltage ratio of bottom and top solar array is 1:5, one can write as,

Journal Pre-proof

.

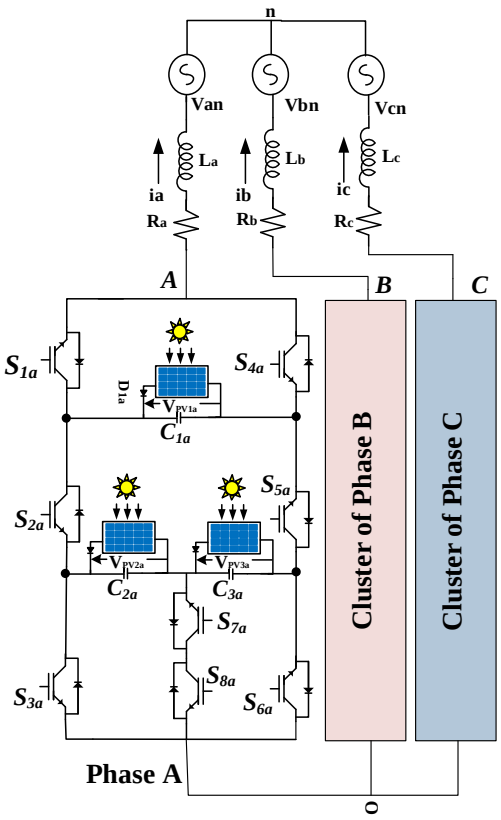


Fig. 1. Eleven level PEC SPV system

Table I. PEC11 switching states.

Switching Logic and Desired Levels								
S_{1a}	S_{2a}	S_{3a}	S_{4a}	S_{5a}	S_{6a}	S_{7a}	S_{8a}	V_{out}(V)
1	0	0	0	1	1	0	0	$+5V_{PV}$
1	0	0	0	1	0	1	1	$+4V_{PV}$
1	0	1	0	1	0	0	0	$+3\ V_{PV}$
1	1	0	0	0	1	0	0	$+2\ V_{PV}$
1	1	0	0	0	0	1	1	$+\ V_{PV}$
1	1	1	0	0	0	0	0	0
0	0	0	1	1	1	0	0	0
0	0	0	1	1	0	1	1	$-\ V_{PV}$
0	0	1	1	1	0	0	0	$-2\ V_{PV}$
0	1	0	1	0	1	0	0	$-3\ V_{PV}$
0	1	0	1	0	0	1	1	$-4\ V_{PV}$
0	1	1	1	0	0	0	0	$-5\ V_{PV}$

$$v_{PV2A} = v_{PV3A} = v_{PV}, \quad v_{PV1A} = 5v_{PV} \qquad (3)$$

Grid voltage KVL expression is presented as,

$$v_{conp(abc)} = R\,i_{abc} + L\,\frac{d\,i_{abc}}{dt} + v_{gabc} \qquad (4)$$

Where $v_{conp(abc)}$ is the converter phase voltages of phase A, B and C, i_{abc} are the grid currents and v_{gabc} are grid voltages. R and L are the resistance and inductance of converter-grid interface harmonic filter of each phase.

In Figs. 2-3. all the modes of operation of PEC11 for phase 'a' are depicted. Fig. 2 displays positive half cycle of eleven level converter output voltage. Fig. 2a shows the peak step of $+5V_{PV}$ by turning ON switches S_{1a}, S_{5a} and S_{6a} connects the top solar panel PV_{1a} to the converter output. Fig. 2(b) shows the $+4V_{PV}$ step by turning ON appendix$_a$, S_{5a} , S_{7a} and S_{8a}, in this combination PV_{3a} and PV_{1a} give resulting output voltage of $+4V_{PV}$ ($+5V_{PV}$-V_{PV}). Fig. 2(c) shows level $+3V_{PV}$ is obtained by turning ON S_{1a}, S_{3a} and S_{5a} that connects both PV_{2a} and PV_{3a} opposite to PV_{1a} that results $+3V_{PV}$ (($+5V_{PV}$-$2V_{PV}$). Fig. 2(d) shows the $+2V_{PV}$, which is obtained by the connection of PV_{2a} and PV_{3a} in series, which is done by the switching ON S_{1a}, S_{2a} and S_{6a}. Fig. 2(e) shows $+V_{PV}$ level by connecting the PV_{2a} through S_{1a}, S_{2a} S_{7a} and S_{8a}. Fig. 3 shows the states for the negative cycle of converter output. Fig. 3(a) shows level $-V_{PV}$ achieved by connecting positive terminal of PV_{3a} to neutral point 'O' of converter through S_{7a} and S_{8a} while negative terminal is connected to output by S_{4a} and S_{5a}. Fig. 3(b) shows the level of $-2V_{PV}$ by series connection of PV_{2a} and PV_{3a} by switching ON S_{3a}, S_{4a} and S_{5a}. Fig. 3(c) shows the $-3V_{PV}$ level is obtained through S_{2a}, S_{4a} and S_{6a} that connects negative terminal of PV_{1a} through S_{4a} to the converter output while PV_{2a} and PV_{3a} are connected in series opposes the PV_{1a} which results in net converter voltage of $-3V_{PV}$. Fig. 3(d) shows that level of $-4V_{PV}$ obtained by series connection PV_{1a} and PV_{2a} through switches S_{2a}, S_{4a} S_{7a} and S_{8a}. Fig. 3(e) shows $-5V_{PV}$ is obtained by turning ON switches S_{2a}, S_{3a} and S_{4a} that connects negative terminal to converter output and positive terminal to the neutral 'O'.

3. Grid-tied control strategy

The DC-link voltage control, power control and NLM are part of the control structure of PEC11. Fig. 4 depicts complete scheme. The MPPT controller of each solar array generates reference voltage by using the perturb and observe (P&O) method. Phase 'a' reference voltages V_{REF1a}, V_{REF2a} and V_{REF3a} of PV_{1a}, PV_{2a}, PV_{3a} respectively are compared with actual DC-link voltages V_{C1a}, V_{C2a} and V_{C3a} in phase 'a'. Similarly, DC-link voltages of phase 'b' & 'c' are compared with reference voltages of the respective charge controllers. The PI controllers are employed to minimize the difference between reference and actual DC-link voltages. PI controller expression for the first solar panel of phase 'a' is presented as,

$$W_{1a}(k+1) = W_{1a}(k) + k_{p(PV1a)}\{e_{PV1a}(k+1) - e_{PV1a}(k)\} + k_{i(PV1a)}T_S\,e_{PV1a}(k+1) \qquad (5)$$

Here e_{PV1a}, $k_{p(PV1a)}$, $k_{i(PV1a)}$ are error, proportional gain and integral gain of PI_{1a}. Similarly PI controller expression for bottom solar panels of phase 'a' are presented as,

$$W_{2a}(k+1) = W_{2a}(k) + k_{p(PV2a)}\{e_{PV2a}(k+1) - e_{PV2a}(k)\} + k_{i(PV2a)}T_S\,e_{PV2a}(k+1) \qquad (6)$$

$$W_{1a}(k+1) = W_{1a}(k) + k_{p(PV3a)}\{e_{PV3a}(k+1) - e_{PV3a}(k)\} + k_{i(PV3a)}T_S e_{PV3a}(k+1) \qquad (7)$$

Here e_{PV2a}, $k_{p(PV2a)}$, $k_{i(PV2a)}$, e_{PV3a}, $k_{p(PV3a)}$, $k_{i(PV3a)}$ are error, proportional gain and integral gain of PI_{2a} and PI_{3a}.

Journal Pre-proof

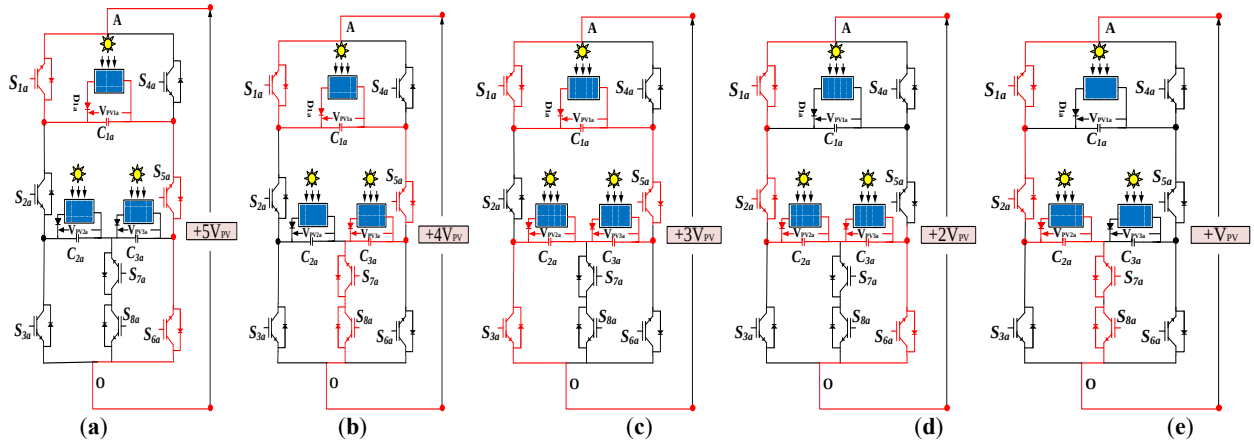


Fig. 2. Positive cycle operating path

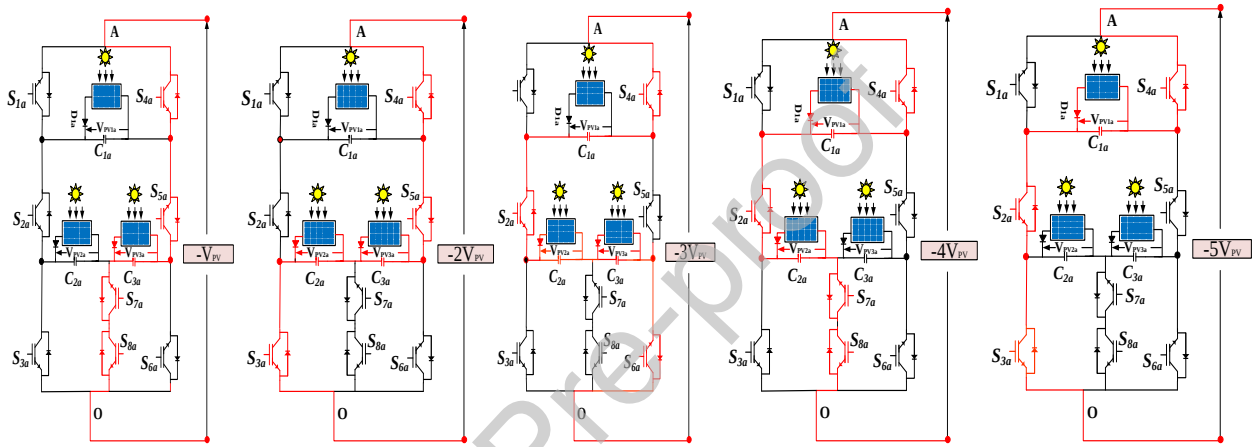


Fig. 3. Negative cycle operating path.

The comparison of DC-link and reference voltage gives the reference DC currents of all solar PV arrays, which are added to find the total reference DC current I^*_d. It is given as,

$$I^*_d = \sum_{k=1}^{n} W_{ka} + \sum_{k=1}^{n} W_{kb} + \sum_{k=1}^{n} W_{kc} \quad (8)$$

Where n is a number of solar panels in each phase. I^*_d decomposed by the dq-abc transformation that gives three reference phase currents i_{aref} i_{bref} and i_{cref}. The reference quadrature axis current I^*_q is kept zero to feed only active power to the grid and phase locked logic (PLL) is employed to match the phase of grid voltage with converter voltage. The grid currents i_a, i_b and i_c are compared to reference values by proportionate-resonant (PR) controllers, which gives modulate signals m_a, m_b and m_c. The ideal PR controllers are mathematically represented as,

$$F(s) = K_p + K_i \frac{s}{s^2 + (2\pi f_0)^2} \quad (9)$$

The PR controller used for this work, which involves damping also, is represented for phase 'a', 'b' & 'c' as,

$$G_{PRa}(s) = K_{pa} + K_{ia} \frac{4\pi f_c s}{s^2 + 4\pi f_c s + (2\pi f_0)^2} \quad (10)$$

$$G_{PRb}(s) = K_{pb} + K_{ib} \frac{4\pi f_c s}{s^2 + 4\pi f_c s + (2\pi f_0)^2} \quad (11)$$

$$G_{PRc}(s) = K_{pc} + K_{ic} \frac{4\pi f_c s}{s^2 + 4\pi f_c s + (2\pi f_0)^2} \quad (12)$$

Where K_{pabc} and K_{iabc} are control inputs for phase 'a', 'b' and 'c', f_o is system frequency and f_c is bandwidth. The carrier-less NLM technique is implemented for the generation of switching pulses of inverter. Fig. 4 depicts the code for each phase. Reference signal m_{abc} is divided into five levels in the positive half denoted by FL. Quotient (Q) is defined by division of m_a with FL, which divides running reference wave. The reference wave vary

Journal Pre-proof

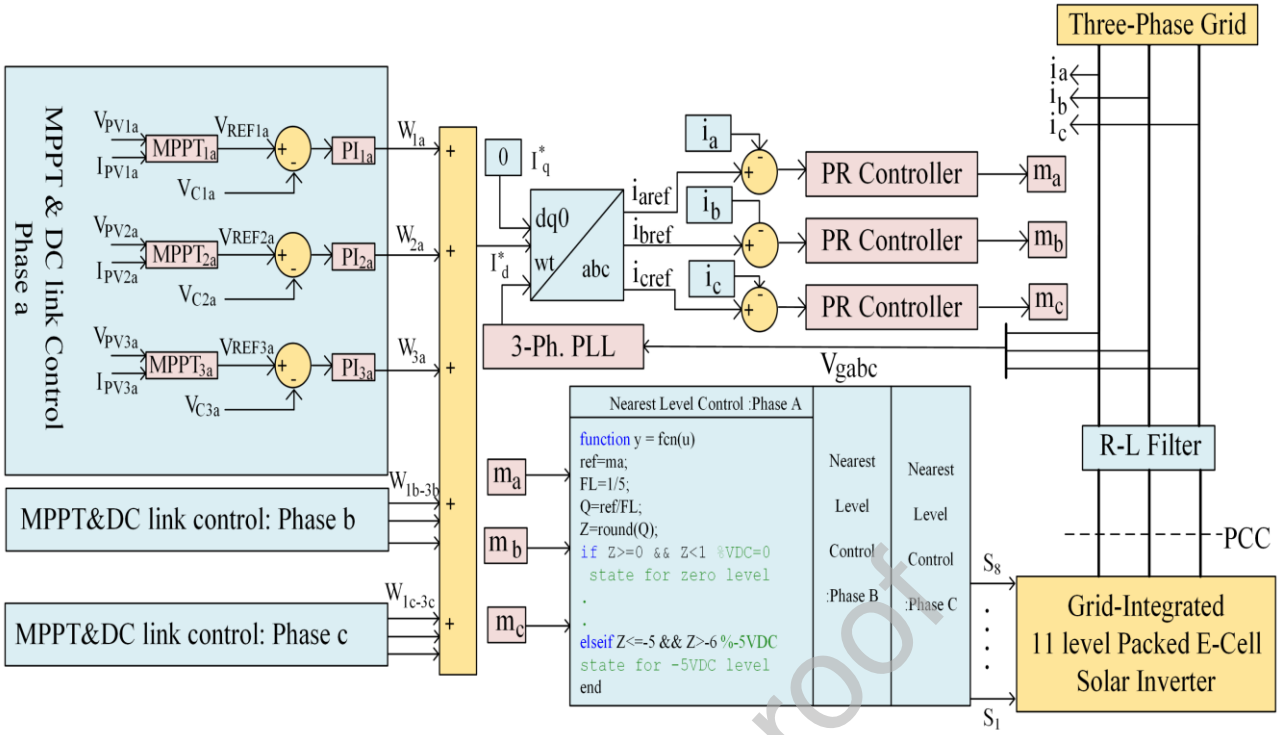


Fig. 4. Control structure of PEC11

0 to 1 for positive half and 0 to -1 for negative half. As the value of FL is 1/5, the value of Q carries from 0 to 5 and 0 to -5 for positive and negative half respectively. Z is determined by rounding off the Q, give five integer values for each half. Five levels in each half cycle are generated from Z as,

$$NLM_{Logic} = \begin{cases} for\ 0 \le Z < 1 \Rightarrow trigger\ level\ 0 \\ for\ 1 \le Z < 2 \Rightarrow trigger\ level\ 1 \\ for\ 2 \le Z < 3 \Rightarrow trigger\ level\ 2 \\ for\ 3 \le Z < 4 \Rightarrow trigger\ level\ 3 \\ for\ 4 \le Z < 5 \Rightarrow trigger\ level\ 4 \\ for\ 5 \le Z < 6 \Rightarrow trigger\ level\ 5 \end{cases} \quad (13)$$

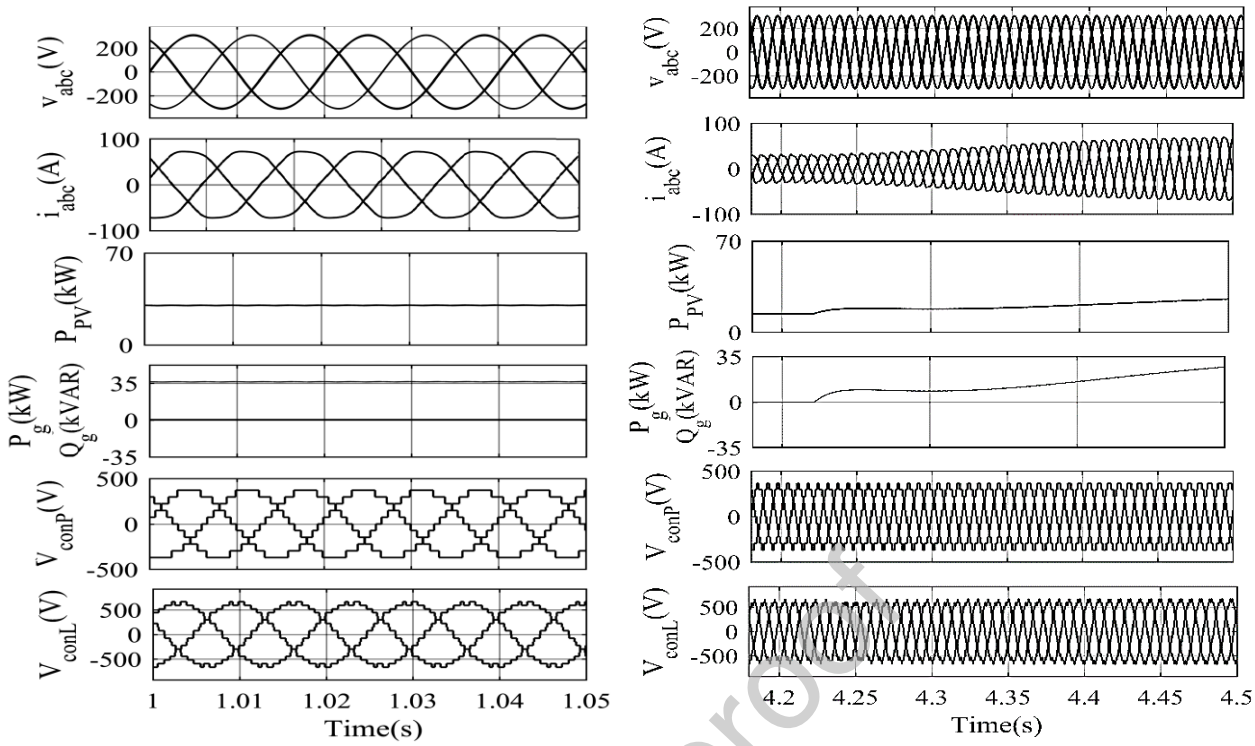
The quintuple operation is maintained in between the reference output voltages of the MPPT controller blocks. The proper trackings of actual voltages with the reference provide a perfect eleven level generation. Similarly, each phase controls the power keeping the quintuple progression.

4. Results and discussion

The PEC11 converter is simulated in grid-solar integrated mode. The system is operated at solar irradiation of 1000W/m^2 with NLM technique. For steady state condition, the converter voltage (Line and phase), active and reactive power fed by converter and grid voltage and current are measured and monitored. These results are presented in Fig. 5(a). V_{conp} & V_{conl} are maintained at designed values with eleven levels of V_{conp}. Active power transferred to the grid is equal to 36.50 kW, which means the power is transferred at 97% efficiency and no reactive power is transferred. The 50.5 A (RMS) grid current is injected at 415 V grid voltage. Performance of PEC11 is analyzed for varying solar irradiation. Fig. 5(b) shows dynamic response when solar irradiation rises to 1000W/m^2 from 500W/m^2. The solar power gets doubled to 36.5 kW and the grid current increases to twice from 25.25 A (rms). The converter voltages V_{conp} and V_{conl} remain same. Fig. 6(a) shows the dynamic response when solar irradiation falls to the 500W/m^2 from 1000W/m^2. The dynamic response is similar to that of rise of irradiation. The injected power decreases to half of power, corresponding to 1000W/m^2 while converter phase voltages V_{conp} maintain the voltage profile of eleven level. The PEC11 is analyzed for harmonic response and results are shown in Fig. 6(b). In top section of Fig. 6(b), current THD is shown which is 2.92% below the 5% limit set by the IEEE-519 standard. The peak value of the fundamental grid current is 71.4 A. In bottom section of Fig. 6(b), the line voltage THD is shown, which is 7.96% and fundamental voltage is 370V. Table II shows the system specifications. Table III shows the detailed comparison of presented converter with existing eleven level configurations [22]-[28]. This converter proposes new voltage ratios (5:1:1) for successful power conversion.

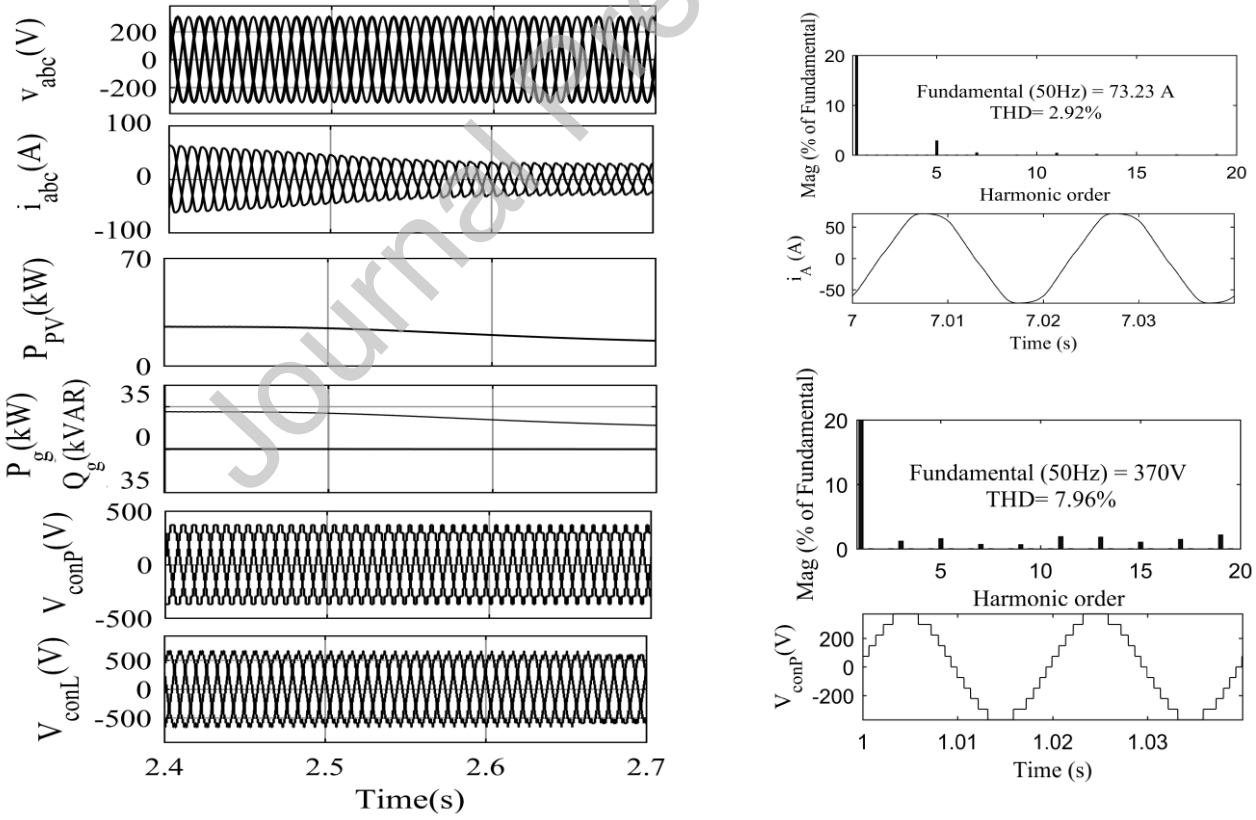
Journal Pre-proof

.



(a) **(b)**

Fig. 5. Simulation results set I (**a**) Steady-state response of PEC11 (**b**) Dynamic response of PEC11 during the rise of irradiation.



(a) **(b)**

Fig. 6. Simulation results set II (**a**) Dynamic response of PEC11 during irradiation fall. (**b**) Grid current and converter voltage THD

Journal Pre-proof

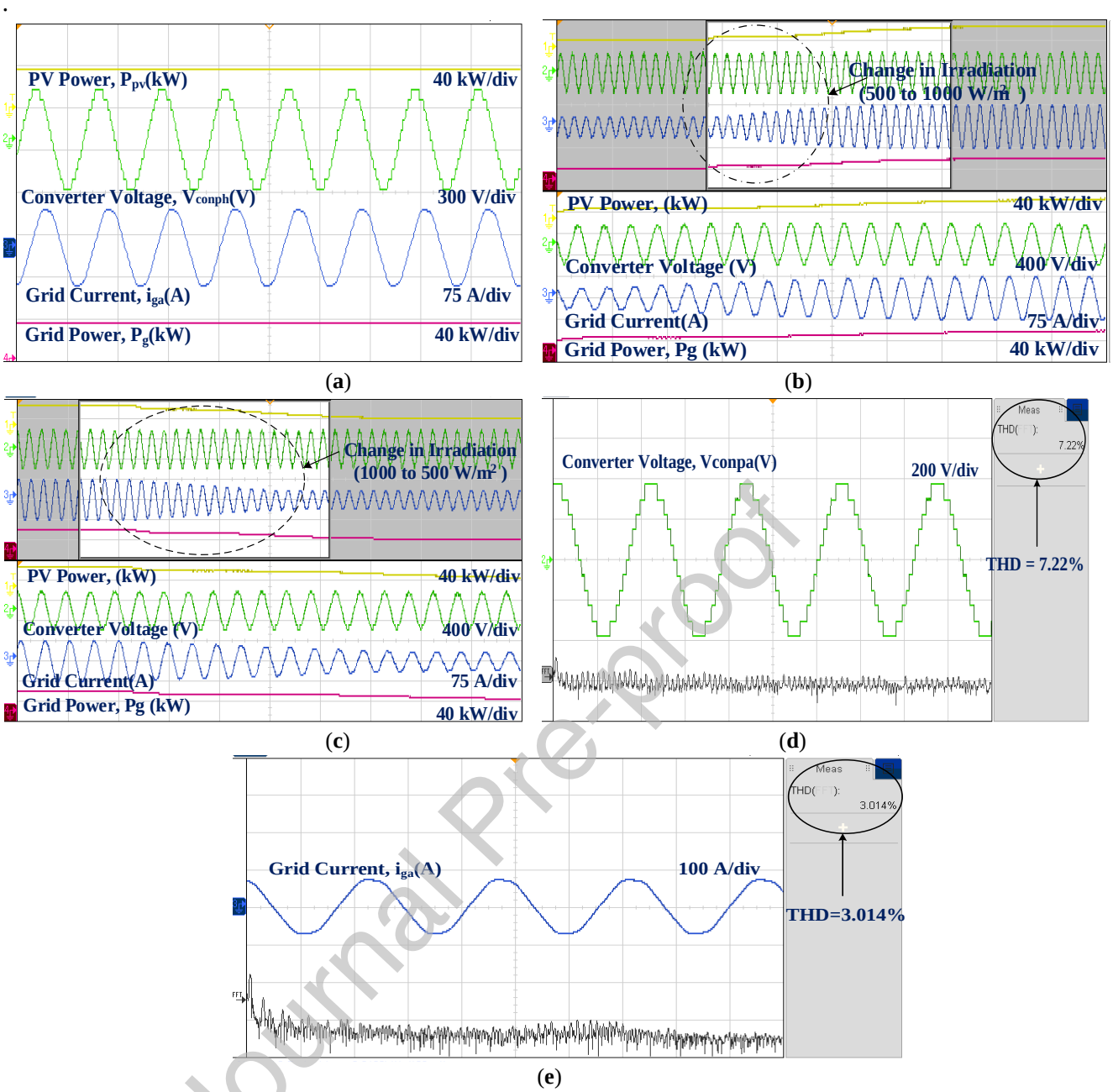


Fig. 7. PEC11 response in Real-time simulator; (**a**) Steady state, **(b)** Rise in irradiation, (**c**) Fall in irradiation, (**d**) Voltage harmonic distortion and (**e**) Current harmonic distortion

The solar powered PEC11 is verified in real-time simulator OPAL-RT. Fig. 7(a) shows the steady response for solar irradiation of 1000 W/m^2. The dynamic responses are shown in the Fig. 7(b), which is observed when solar power increases to 1000 W/m^2 from 500 W/m^2. Similarly, the real-time system dynamics when solar power falls to 500 W/m^2 from 1000 W/m^2 are shown in Fig. 7(c). These real-time results validate the results of MATLAB/SIMULINK, which excellent performance of the PEC11. The harmonic response of converter voltage and injected current is displayed in Fig. 7 (d)-(e) as THD, which are 7.22% and 3.014% for voltage and current, respectively. The harmonic response of PEC11 by OPAL-RT validates the improved power quality.

Table II. PEC11 Specifications

S.N.	Parameter	Value
1	V_{MPP} (V)	37.01
2	I_{MPP} (A)	7.47
3	No. of series modules in main solar panel	10
4	No. of series modules in auxiliary solar panel	2
5	No. of parallel modules in all solar panels	10
6	Grid voltage (V)	415
7	L_{abc} of harmonic filter (mH)	2.0
8	K_p, K_i (AC side control parameters)	0.002,0.0015
9	K_p, K_i (DC side control parameters)	2.1, 0.35

Table III. PEC11 Comparative Analysis for Three-Phase SPV System

Journal Pre-proof

.

Parameter	[22] HI	[23] MMLI	[24] HC-MLI	[25] Cascaded MLI	[26] PUC11	[27] UXE11	[28] H-NPC-HB	Proposed PEC11
No. of levels	11	11	11	11	11	11	11	11
No. of Switches	36	36	36	18	24	36	30	24
No. of Sources	3	15	9	9	9	3	6	9
No. of diodes	Nil	12	Nil	Nil	Nil	Nil	12	Nil
No. of Capacitors	6	Nil	Nil	Nil	Nil	6	3	Nil
Voltage ratio	1:1:1	1:1:1:1:1	2:2:1	1:2:2	5:3:1	4:1:1	2:1:1	5:1:1
Closed/Open Loop Control	Closed Loop	Closed Loop	Closed Loop	Open Loop	Closed Loop	Open Loop	Open Loop	Closed Loop
PWM Technique	Carrier	Carrier	SHE-PSO	SHE	Carrier	Carrier	Carrier	NLM
Switching Frequency	2 kHz	10 kHz	50 Hz	50 Hz	1 kHz	5 kHz	10 kHz	50 Hz
Control Method	dSpace PI	dSpace PI	DSP	DSP	RT-PI	DSP	DSP	PI
Grid Tied Implementation	Discussed	Not Discussed	Not Discussed	Not Discussed	Discussed	Not Discussed	Not Discussed	Discussed

Fig. 8 shows the converter voltage waveform with switching technique of carrier and NLM. It is seen that the switching is reduced for NLM, which makes it simple and efficient technique for the presented PEC-11 level topology. Moreover, the number of switching instants for each technique for different modulation index are recorded and tabulated in Table IV. NLM reduces the stress on the switches and improves the converter lifetime. Fig. 9(a) shows the test platform with real-time results recorder. The irradiance/temperature is regulated from G1 to G2 and vice versa using the logic of OPALRT blocks as shown in in Fig. 9(b).

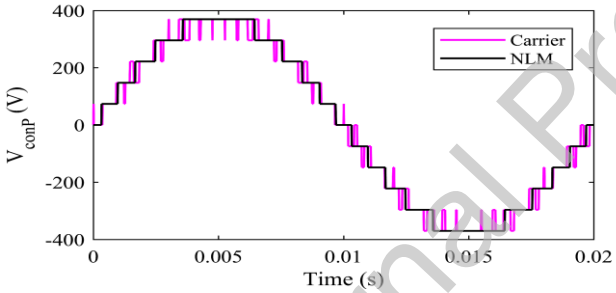


Fig. 8 Converter voltage switching in carrier and NLM modulation

Table IV. Switching instants comparison for Carrier and NLM

m	Carrier PWM (Total Switching Instants)	NLM Technique (Total Switching Instants
0.2	42	4
0.4	42	8
0.6	42	12
0.8	40	16
1.0	35	20

5. Conclusion

The selection of quintuple voltage ratio among the voltage sources has given a new 11 level PEC based new solar PV system. The count of switches and PV arrays remains same like PEC9. The converter voltage is expressed by relevant equations. The switching states of the converter are tabulated and the operating modes for each state are explained by the

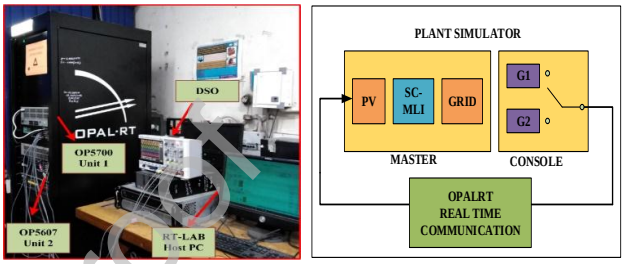


Fig. 9. Test platform (a) OPAL-RT (b) Change in irradiance for real-time mode.

PEC11 diagrams. The PR controllers are used to track grid currents, and governing mathematical equations are provided. The complete control scheme with DC-link voltage of top and bottom PV arrays, resonant current controllers, and code of NLM is shown for PEC11. The simulated results of DC and AC side of the PEC11 in steady and varying solar conditions are demonstrated. The harmonic performance (THD) is determined by FFT and shown in the results. The performance of the new PEC11 is verified on real-time OPALRT, which have given a new improved solution to solar-grid systems.

Acknowledgments

The authors acknowledge "SERB National Science Chair Fellowship" and are also grateful to Department of Science and Technology for expediting research in Electrical Department at IIT, Delhi under: RP03195 and thanks OPALRT to fund under grant number: RP03253.

References

[1] S.K. Yadav, N. Mishra, B. Singh, Multilevel Converter with Nearest Level Control for Integrating Solar Photovoltaic System, IEEE Trans. on Ind. App. 58 (4) (2022) 5117-5126, https://doi.org/10.1109/TIA.2022.3177399

[2] Marif Daula Siddique, Saad Mekhilef, A New Configuration of Nine-Level Boost Inverter with Reduced Component Count, e-Prime Adv. in Electrical Engg, Electron. and Energy, 1 (2021) 100010, https://doi.org/10.1016/j.prime.2021.100010

Journal Pre-proof

[3] Sangeetha S and Jeevananthan S 2015 Influence of crossover methods used by genetic algorithm-based heuristic to solve the selective harmonic equations (SHE) in multi-level voltage source inverter. *Sadhana* 40(8): 2389–2410, https://doi.org/10.1007/s12046-015-0422-2

[4] M. Nguyen, T, Tran, Quasi Cascaded H-Bridge Five-Level Boost Inverter, IEEE Trans. on Ind. Electron., 64(11) (2017) 8525-8533, https://doi.org/10.1109/TIE.2017.2701770

[5] W. Zhang, H. Wang, X. Zhu, H. Wang, X. Deng, X. Yue, A Three-Phase Five-Level Inverter With High DC Voltage Utilization and Self-Balancing Capacity of Floating Capacitor, IEEE Trans. on Power Electron, 37(9) (2022) 10609-10619, https://doi.org/10.1109/TPEL.2022.3163158

[6] W. Song, M.S.R. Saeed, M.B. Yu, J. Li, Y. Guo, Model Predictive Current Control With Reduced Complexity for Five-Phase Three-Level NPC Voltage-Source Inverters, IEEE Trans. on Transport. Electrific. 8(2) (2022) 1906-1917, https://doi.org/10.1109/TTE.2021.3131420

[7] J. Amini, A.H. Viki, A. Radan, M. Moallem, 2016 A General Active Capacitor Voltage Regulating Method for L-Level M-Cell N-Phase Flying Capacitor Multilevel Inverter With Arbitrary DC Voltage Distribution, IEEE Trans. on Ind. Electron, 63(5) (2016) 2659-2668, https://doi.org/10.1109/TIE.2016.2517058

[8] A. Sadigh, V. Dargahi, R.R. Khorasani, K.A. Corzine, E. Babaei, Simple Active Capacitor Voltage Balancing Method Without Cost Function Optimization for Seven-Level Full-Bridge Flying-Capacitor-Multicell Inverters, IEEE Trans. on Ind. App. 57(2) (2021) 1629-1643, https://doi.org/10.1109/TIA.2021.3052155

[9] M. Tariq, M. Meraj, M.A. Azeem, A.I. Maswood, A. Iqbal, B. Chokkalingam, Evaluation of level-shifted and phase-shifted PWM schemes for seven level single-phase packed U cell inverter, CPSS Trans. on Pow. Electron. and App. 3(3) (2018) 232-242, https://doi.org/10.24295/CPSSTPEA.2018.00023

[10] A. Kaymanesh, M. Babaie, A. Chandra, K. Al-Haddad, PEC Inverter for Intelligent Electric Spring Applications Using ANN-Based Controller, IEEE J. of Emerg. and Sel. Top. in Ind. Electron. 3(3) (2022) 704-714, https://doi.org/10.1109/JESTIE.2021.3095018

[11] M.S. Sadabadi, M. Sharifzadeh, M. Mehrasa, H. Karimi, K. Al-Haddad, 2022 Decoupled dq Current Control of Grid-tied Packed E-Cell Inverters in Vehicle-to-Grid Technologies. IEEE Trans. on Ind. Electron,70(2) (2023) 1356-1366, https://doi.org/10.1109/TIE.2022.3156160

[12] M. Sharifzadeh, K. Al-Haddad, Packed E-Cell (PEC) Converter Topology Operation and Experimental Validation, IEEE Access. 7 (2019) 93049-93061, https://doi.org/10.1109/ACCESS.2019.2924009

[13] H. Shutari, N. Saad, N. B. M. Nor, M. F. N. Tajuddin, A. Alqushaibi, M. A. Magzoub, Towards Enhancing the Performance of Grid-Tied VSWT via Adopting Sine Cosine Algorithm-Based Optimal Control Scheme, in IEEE Access, vol. 9 (2021) 139074-139088, https://doi.org/10.1109/ACCESS.2021.3119019

[14] S. A. Saleh, A. S. Aljankawey, M. S. Abu Khaizaran, B. Alsayid, Influences of power electronic converters on current-voltage behaviors during faults in DGUs-Part I: Wind energy conversion systems, 2014 IEEE Ind. Application Society Annual Meeting, (2014) 1-8, https://doi.org/10.1109/IAS.2014.6978504

[15] M. Sharifzadeh, M. Khenar, K. Al-Haddad, Grid-Tied Packed E-Cell Inverter with Active Capacitor Voltage Balancing, IECON 2020 The 46th Annual Conference of the IEEE Ind. Electron. Society, (2020) 2338-2343, https://doi.org/10.1109/IECON43393.2020.9255311

[16] M. Ahmadijokani, M. Sharifzadeh, M. Mehrasa, F. Sebaaly, K. Al-Haddad, Modified Level-Shifted PWM Technique With Active DC Capacitors Voltages Balancing for Nine-level Packed E-Cell (PEC9) Inverter, 2020 IEEE Int. Conf. on Ind. Tech. (ICIT) (2020) 843-848, https://doi.org/10.1109/ICIT45562.2020.9067245

[17] Y. Wang, C. Hu, R. Ding, L. Xu, C. Fu, E. Yang, A Nearest Level PWM Method for the MMC in DC Distribution Grids, IEEE Trans. on Pow. Electron., vol. 33(11) (2018) 9209-9218, https://doi.org/10.1109/TPEL.2018.2792148

[18] K. Shen, S. Wang, D. Zhao, G. Zhao, A Discrete-Time Low-Frequency-Ratio Nearest Level Modulation Strategy for Modular Multilevel Converters With Small Number of Power Modules, IEEE Access, 7 (2019) 25792-25803, https://doi.org/10.1109/ACCESS.2019.2900488

[19] S. Jain, M. B. Shadmand, R. S. Balog, Decoupled Active and Reactive Power Predictive Control for PV Applications Using a Grid-Tied Quasi-Z-Source Inverter, IEEE J. of Emerg. and Selected Topics in Pow. Electron., 6(4) (2018) 1769-1782, https://doi.org/10.1109/JESTPE.2018.2823904

[20] M. Babaie, M. Mehrasa, K. Al-Haddad, Direct Active and Reactive Power Control for Grid-Connected PEC9 Inverter

.

Using Finite Control Set Model Predictive Method, 2021 22nd IEEE Int. Conf. on Ind. Tech. (ICIT), (2021) 1371-1376, https://doi.org/10.1109/ICIT46573.2021.9453660

[21] M. Moranchel, E. J. Bueno, F. J. Rodriguez, I. Sanz, Implementation of nearest level modulation for Modular Multilevel Converter, 2015 IEEE 6th Int. Symp. on Pow. Electron. for Distrib. Generation Sys. (PEDG) (2015) 1-5, https://doi.org/10.1109/PEDG.2015.7223079

[22] N. Panda, B. Das, A. Chakrabarti, P. R. Kasari, A. Bhattacharya, D. Chatterjee, A New Grid Interactive 11-Level Hybrid Inverter Topology for Medium-Voltage Application, in IEEE Trans. on Industry Appl. 57(1) (2021) 869-881, https://doi.org/10.1109/TIA.2020.3040204

[23] A. M. M. Hassan, X. Yang, A. I. M. Ali, T. A. Ahmed, A. M. Azmy, A Study of Level-Shifted PWM Single-phase 11-Level Multilevel Inverter, 2019 21st Int. Middle East Pow. Sys Conf. (MEPCON), (2019) 170-176, https://doi.org/10.1109/MEPCON47431.2019.9008015

[24] A. Routray, R. Kumar Singh, R. Mahanty, Harmonic Minimization in Three-Phase Hybrid Cascaded Multilevel Inverter Using Modified Particle Swarm Optimization, in IEEE Trans. on Ind. Informatics, 15(8) (2019) 4407-4417, https://doi.org/10.1109/TII.2018.2883050

[25] M. D. Siddique, S. Mekhilef, N. M. Shah, A. Sarwar, A. Iqbal, M. A. Memon, A New Multilevel Inverter Topology With Reduce Switch Count, in IEEE Access, 7 (2019) 58584-58594, https://doi.org/10.1109/ACCESS.2019.2914430

[26] N. Mishra, S. K. Yadav, B. Singh, M. Tariq, S. Padmanaban, F. Blaabjerg, Performance Assessment of Eight-Switch 11-Level Packed U Cell Converter Under Dynamic Solar Photovoltaic Environment, in IEEE Journ. of Emerg. and Selected Topics in Pow. Electron. 10(4) (2022) 3851-3860, https://doi.org/10.1109/JESTPE.2021.3098828

[27] M. Ali, M. Tariq, A. Sarwar, B. Alamri, A 13-, 11-, and 9-Level Boosted Operation of a Single-Source Asymmetrical Inverter With Hybrid PWM Scheme, in IEEE Trans. on Ind. Electron.69(12) 12817-12828 (2022), https://doi.org/10.1109/TIE.2022.3144576

[28] Q. Ren, A. Chen, J. Chen, C. Zhang, A Novel Neutral-Point-Clamped Half-Bridge Eleven-level Inverter With High DC Voltage Utilization Ratio and Fewer Switches," 2020 IEEE Applied Power Electronics Conference and Exposition (APEC), 1148-1153 (2020), https://doi.org/10.1109/APEC39645.2020.9124074

Author-bio



Sanjay Upreti has done his B.Tech. from G. B. Pant University of Agriculture and Technology, Pantnagar, Udham Singh Nagar, Uttarakhand, India in 1989, M.Tech. from IIT Delhi in 2012, and pursuing Ph.D. in Electrical Engineering from Department of Electrical Engineering, Delhi Technological University, Delhi, India. He has worked in the electrical maintenance department of the chemical process industry from 1990 to 1993. He worked in a PCB manufacturing unit from 1994 to 2008 as a factory manager. He joined academics in 2008 as an Assistant Professor in Al-Falah school of engineering and technology (AFSET), Faridabad, Haryana, and worked till 2010. Since then, he is associated with Bhagwan Parshuram Institute of Technology (BPIT), Delhi, India, as an Assistant Professor in the electrical and electronics engineering (EEE) department. His research area is power quality, renewable energy, multilevel converter, and its applications.

Corresponding author. E-mail: supreti223@gmail.com



Bhim Singh Bhim Singh (SM'99, F'10) has received his B.E. (Electrical) from University of Roorkee (Now IIT Roorkee), India, in 1977 and his M.Tech. (Power Apparatus & Systems) and Ph.D. from IIT Delhi, India, in 1979 and 1983, respectively. In 1983, Dr. Singh joined Department of Electrical Engineering, University of Roorkee, as a Lecturer. He became a Reader there in 1988. In December 1990, he joined the Department of Electrical Engineering, IIT Delhi, India, as an Assistant Professor, where he has become an Associate Professor in 1994 and a Professor in 1997. He has been ABB Chair Professor from September 2007 to September 2012. He has been Head of the Department of Electrical Engineering at IIT Delhi from July 2014 to August 2016. He has been the Dean, Academics at IIT Delhi from August 2016 to August 2019. He has been JC Bose Fellow of DST from December 2015 to June 2021. He is the SERB National Science Chair Professor at IIT Delhi since July 2021. Prof. Singh has guided 114 Ph.D. dissertations, and 176 M.E./M.Tech./M.S.(R) theses. He has filed 105 patents. He has executed ninety sponsored and consultancy projects. He has co-authored a textbook on power quality: *Power Quality Problems and Mitigation Techniques* published by John Wiley &

Journal Pre-proof

Sons Ltd. 2015. His areas of interest include solar PV grid interface systems, microgrids, power quality mitigation, solar PV water pumping, improved power quality AC-DC converters and electric vehicles.**E-mail:** bsingh@ee.iitd.ac.in



Narendra Kumar has done his B.E. from IIT-Roorkee in 1985, M.E. from P.E.C. Chandigarh in 1987 and Ph.D. from Delhi College of Engineering (Now known as Delhi Technological University), Delhi in 2003 in Electrical Engineering. He is currently a Professor with the Department of Electrical Engineering, Delhi Technological University, and Delhi, India. His current area of interest is Power Electronics applications in Power Systems, Instrumentation and Control.

E-mail: narendrakumar@dtu.ac.in

Declaration of Competing Interest

The authors declare that they have no known competing financial interests or personal relationships that could have appeared to influence the work reported in this paper.

Journal Pre-proof

The Journal of Supercomputing
https://doi.org/10.1007/s11227-023-05295-z

A novel cloud model based on multiplicative unbalanced linguistic term set

Parul Chauhan[1] · **Anjana Gupta**[1] · **Tanya Malhotra**[1]

Accepted: 11 April 2023
© The Author(s), under exclusive licence to Springer Science+Business Media, LLC, part of Springer Nature 2023

Abstract
The cloud decision support model is an effective technique for describing an ambiguous mapping between qualitative notions and their quantitative manifestations. However, the existing research on cloud models is based on balanced linguistic term set and cannot address information in an unbalanced linguistic form. Henceforth, to thoroughly capture the intrinsic fuzziness and vagueness of decision information an accurate decision model is required to acquire good solution. In this direction, the proposed work aims to introduce a cloud model based on multiplicative unbalanced linguistic term sets. To match our research requirements, we initially propose a multiplicative unbalanced point-based cloud model. The innovation of the model overcomes the inherent limitation of the existing cloud and is competent of producing new solution according to the cloud model theory. Furthermore, a generalized multiplicative unbalanced linguistic scale function is introduced. The proposed generalized function creates a map between the linguistic data and numerical interval values. Based on this rational conversion method, interval cloud variables are transformed, which overcomes the loss of information existing in the point-based cloud models where linguistic variables are transformed into a specific numerical value. The process is then used to demonstrate the accuracy and efficacy of the suggested model using a numerical example, which is then followed by a comparison study. The overall results typically show that the cloud model has excellent performance and provides better solutions.

Keywords Normal cloud model · Asymmetric trapezoidal clouds · Multiplicative unbalanced interval cloud · Unbalanced linguistic term set

✉ Anjana Gupta
anjanagupta@dce.ac.in

[1] Department of Applied Mathematics, Delhi Technological University, Bawana Road Rohini, Delhi, India

Published online: 27 April 2023

1 Introduction

Several decision analysis problems under uncertain conditions encounter the challenge of ultimately representing decision-makers' (DMs) opinions and preferences. Given the vague information incorporated within those problems or the high computational cost required to express precise numerical data, the DMs do not describe their evaluations in terms of quantitative descriptors but rather in linguistic form. The requirement for linguistic data is excellently suited because it is simple to distinguish uncertainty with a non-probabilistic nature. As a result, numerous researchers have researched it [1, 2]. In order to demonstrate a pertinent idea involved in expressing issues in terms of natural languages, Zadeh [3] introduced linguistic variables. As the basis of human thought and the embodiment of human intellect, natural languages are crucial to understanding difficulties. In the present specialized literature on linguistic decision analysis and Computing with Words (CWW)-related approaches, the utility of linguistic ideas implies a broad outlook. Many linguistic computational models [4, 5] were created based on symmetrical and balanced linguistic data to prevent the information loss occurring in CWW operations.

Nevertheless, as the complications within the practical decision-making issues increase, it is arduous to reflect the qualitative information in a balanced linguistic term set. Taking investment returns as an example where investors care about the distribution of investment return data. Empirically, the investment return data follow an asymmetric distribution scheme. This is because investment performance is usually skewed by periods of high market volatility or unusual fiscal and monetary policies during which returns growth are abnormally high or low. Considering the irregularity of the data, it is envisioned that the existing linguistic models are not capable enough to represent asymmetric information effectively. To resolve this issue, a series of research is conducted, for instance, [6–14] to proficiently describe qualitative concept having an irregular spacing of linguistic labels. Henceforth, the developed content related to unbalanced linguistic information has made a significant impact on linguistic decision-making theories. As a popular tool for modelling the qualitative assessment information, the theories [15–21] allow the decision makers to work under uncertain linguistic environment. The use of uncertain linguistic information enriches the flexibility of DMs in decision-making [22–25] scenarios. Considering the existing literature of unbalanced linguistic computational models, it is identified that the representation of unbalanced information is presented in terms of a uniformly distributed set of linguistic terms. A new consensus-reaching approach for MCGDM with multi-granular unbalanced linguistic information, for instance, is developed by Zhang et al. [26] that simultaneously takes into account the adjustment amount and limited confidence levels of DMs. To do this, the authors first use the model provided in [9] to determine the numerical scales of multi-granular unbalanced linguistic terms, and then, they convert these terms into linguistic 2-tuples defined on the same balanced linguistic term set. A clustering approach based on LDAs is subsequently developed to categorize decision-makers in the paper [27], which also converts all multi-granular unbalanced hesitant fuzzy linguistic data into

LDAs defined on a balanced linguistic word set. The results are then used to compute the overall ratings for each cluster. In this way, the accurate sense of "unbalanced" is not well represented. To remedy this, Malhotra and Gupta [28] introduced a novel 2-tuple multiplicative unbalanced linguistic computational model addressing a substantial amount of linguistic information in terms of a globally inconsistent multiplicative unbalanced linguistic scale set. This set is primarily based on the notion of minimum distance measure. It is anticipated that under complicated decision-making circumstances, the proposed model is computationally less expensive and reduces time complexity.

Addressing decision-making issues with linguistic information to apprehend the uncertainty has received much interest. However, with rapid societal development, linguistic decision-making problems have become increasingly complex and challenging. In such a scenario, the cognitive cloud models proposed by Li et al. [29–31] are lucrative for defining linguistic labels as they can synthetically explain the notion of randomness and fuzziness of the decision information simultaneously.

Since the introduction of cloud models, several researchers have devoted their efforts to enhance cloud specialized studies such as integrated cloud [32], risk assessment [33, 34], water quality assessment [35] along with more wide-ranging applications [36–43]. The experts introduce some methods for applying cloud models to MCDM [44–49]. The cloud models outline a linguistic concept using three numerical properties, namely *EX* (expectation), *EN* (entropy), and *HE* (hyper-entropy). To realize the bidirectional cognitive transformation of a notion [50–52], two cloud transformations, forward cloud transformation and backward cloud transformation, are used. In addition to propose a second-order generic forward normal cloud transformation technique, Wang et al. [53] provided a generic cloud model that established a connection between the normal cloud and the normal distribution. This transformation algorithm reveals that the second-order normal cloud [54] and the normal distribution are both special cases of the second-order generic normal cloud. A linguistic assessment scale is defined by Wang et al. [49] to perform the transformation among the clouds and the linguistic variables. Although it is envisioned that the existing cloud models can retain the original information as much as possible, they still cannot create a good representation for the concepts where linguistic labels are asymmetrically distributed. To resolve this issue, Wang et al. [55] proposed an extended cloud model, namely the Asymmetric Trapezoidal Clouds (ATCs) model. The *EN* and *HE* of the ATCs are different on the left and right sides in this model; thus, the authors gave expectation as an interval rather than a precise number. The authors claim that ATCs are excellent quantitative information representations. However, unlike unbalanced linguistic assessments, ATCs are not promptly used in decision-making due to their non-existence in a practical scenario. Consequently, the authors link ATCs to unbalanced linguistic distribution assessments (ULDAs). The authors also provided an extended linguistic scale function (LSF), which indicates variations in spacing rather than symmetrical spacing among linguistic terms, to map linguistic terms to interval values. The expectation interval value of ATCs can be computed using the extended LSF. Also, a method is suggested for calculating the entropy and hyper-entropy values of ATCs developed using the 3σ concept.

Throughout the past, researchers working on cloud models representing balanced concepts were acknowledged for enhancing the literature on cloud models. As a kind of uncertain information representation in complex decision-making issues, these models are not competent to express unbalanced concepts well. In the light of the latter point, a number of computationally challenging unbalanced linguistic models have been proposed in the literature; as a result, solving complex decision problems becomes more time-consuming. Henceforth, the primary purpose of this current study is to develop an accurate and innovative cloud decision support model to address unbalanced linguistic concepts by emphasizing the succeeding momentous research gaps.

1.1 Research gap

- The ULDA utilized in the existing ATC model is primarily based on the hierarchical unbalanced linguistic model which is a very complex and computationally expensive approach.
- The existing theories apply to additive linguistic data only.
- It is crucial to choose a string of appropriate linguistic cardinalities in real fuzzy decision-making problems using linguistic variables. To the best of our knowledge, the majority of the existing literature uses linguistic cardinality with a uniformly distributed scale pattern, which means that any two neighbouring linguistic cardinalities have the same level of granularity. A symmetrically distributed linguistic term (LT) set, thus, provides the representation of the unbalanced linguistic judgements. As a result, the uneven linguistic information lacks its literal meaning.
- The use of the translation function to convert a balanced LT set into an unbalanced LT set leads to the complexity of the model.

To address above-mentioned practical issues, in our research, we provide two kinds of cloud models, i.e. point based and generalized interval cloud models where linguistic information is defined on a multiplicative scale set. The advantage of using a multiplicative scale set is that the set perfectly maintains unbalanced information throughout the process. As a result, it is computationally cheaper and simpler than other linguistic computational models [1, 9]. Further, the proposed model manages the linguistic information effortlessly, reducing the time and cost complexity. Additionally, the innovative model proposed in this paper reduces the risk of information loss occurring in the process of unbalanced decision-making. We next summarize the differences and similarities of the uncertain cloud models, and the characteristics of a few existing models in Table 1.

1.2 Contribution

The key contributions of this work can be summed up as follows in order to fulfil the aforementioned objectives.

Table 1 A summary of similarity and differences of various cloud models

Paper	Linguistic model implemented	Multiplicative	Unbalanced	Point based/interval
[29]	N/A	No	No	Point based
[49]	N/A	No	No	Point based
[47]	N/A	No	No	Point based
[44]	N/A	No	No	Partially interval (Expectation values are interval based, rest values point based)
[55]	Hierarchy model [1]	No	Yes	Both
Current paper	Unbalanced 2-tuple linguistic model [28]	Yes	Yes	Both

- The research gap is filled by introducing a multiplicative unbalanced linguistic point-based and interval cloud model that makes use of an unbalanced LT set which is computationally less expensive than other existing computational models.
- Extended multiplicative unbalanced linguistic scale functions have been developed to transform an unbalanced linguistic term into an interval value. The so-developed extended multiplicative unbalanced linguistic scale function efficiently embodies the differences in spacing of linguistic terms, both in terms of representation and meaning.
- A method based on the 3σ principle is provided to determine entropy and hyper-entropy of the extended multiplicative unbalanced interval cloud model. The entropy and hyper-entropy thus defined differ from the ones defined in [49] as the former is based on multiplicative unbalanced linguistic data.
- Based on the concept of generalized multiplicative unbalanced linguistic interval cloud, our research develops the comparison method to rank the cloud variables.
- The proposed theory contributes to the existing decision-making theories [48, 56, 57] by solving a decision-making real-life problem.

The rest of the paper is organized as follows. Section 2 introduces some basic concepts related to normal cloud model and unbalanced linguistic computational model. In Sect. 3, a method for transformation between the unbalanced linguistic terms and clouds is proposed. Section 4 introduces the generalized multiplicative unbalanced interval cloud model. In Sect. 5, some numerical example along with comparison analysis is given to demonstrate the consistency of the defined model. Section 6 offers the conclusions of the paper.

Before proceeding further in this article, we introduce some common abbreviations used in the paper in Table 2.

2 Preliminaries

In this section, we first review some basic concepts of the normal cloud model along with the transformation of linguistic variables into normal clouds. Then, we outline the ATC model and some essential LSFs that are required in our paper. Finally, the multiplicative unbalanced linguistic term set is presented along with its properties.

2.1 Basic concepts of the normal cloud model

The normal cloud model, as described by Li et al. [29], is a cognitive model that implements the uncertain translation between linguistic concepts and quantitative values and describes the uncertainties of linguistic concepts, particularly the randomness and fuzziness.

Table 2 Abbreviation and symbols used throughout the paper

Abbreviation/ Symbol	Definition/Meaning	Characteristic
CWW	Computing with Words	A methodology in which words are used in place of numbers for computing & reasoning
DM	Decision maker	Anybody who makes decisions or takes part in decision making process
MCDM	Multi-Criteria Decision Making	Decision-making problems based on multiple criteria
MCGDM	Multi-Criteria Group Decision Making	Decision-making problems based on multiple criteria involving multiple groups
LDA	Linguistic Distribution Assessments	Linguistic information represented in terms of symbolic proportions assigned to all linguistic terms
EX	Expectation	Mathematical expectation of the cloud drops belonging to a concept in the universe
EN	Entropy	The uncertainty measurement of a qualitative concept
HE	Hyper-entropy	The uncertain degree of entropy EN
ATC	Asymmetric Trapezoidal Cloud	A numerical concept developed to describe linguistic information
LSF	Linguistic Scale Function	A function that maps linguistic terms to numerical values
MULSF	Multiplicative Unbalanced Linguistic Scale Function	A function that maps multiplicative unbalanced linguistic terms to numerical values
LT	Linguistic Term	A term whose value is not number but words or sentences in a natural or artificial language
ULTS	Unbalanced Linguistic Term Set	A set whose members are linguistic terms distributed in an unbalanced or asymmetric manner
2-TLCM	2-tuple linguistic computational model	A novel 2-tuple model for unbalanced linguistic information based upon a notion of minimum distance measures
MUIC	Multiplicative Unbalanced Interval Cloud	A cloud in interval form transformed from multiplicative unbalanced linguistic terms
t_{a^i}	Multiplicative Unbalanced Linguistic Term	Notation of LT
δ_{a^i}	A numerical value corresponding to t_{a^i}	Belongs to the interval $[0, \frac{1}{\log a}]$
$\widetilde{\mathbb{g}}$	LSF	A function that transforms t_{a^i} to δ_{a^i}
$\underline{\delta}_{a^i}$	Lower value of δ_{a^i} in the interval $[\underline{\delta}_{a^i}, \overline{\delta}_{a^i}]$	–
$\overline{\delta}_{a^i}$	Upper value of δ_{a^i} in the interval $[\underline{\delta}_{a^i}, \overline{\delta}_{a^i}]$	–
$\widetilde{\mathbb{G}}$	LSF	A function that transforms t_{a^i} to $\underline{\delta}_{a^i}, \overline{\delta}_{a^i}$
$\underline{EX}_{a^i}$	Lower value of expectation (Entropy/ hyper-entropy) in	–

Table 2 (continued)

Abbreviation/ Symbol	Definition/Meaning	Characteristic
$(\underline{EN}_{a^i}/\underline{HE}_{a^i})$	the expectation (entropy/ hyper-entropy) interval	
$\overline{EX}_{a^i}$	Upper value of expectation (entropy/hyper-entropy)	–
$(\overline{EN}_{a^i}/\overline{He}_{a^i})$	in the expectation (entropy/hyper-entropy) interval	
var_{Int}	Variance of interval cloud droplets	Given by a formula
sd_{Int}	Standard deviation of interval cloud droplets	Given by a formula
sc_{Int}	Interval score function	A coefficient to capture the attitude towards standard deviation

Definition 1 [29] Let U be the universe of discourse, and $\widetilde{T}$ be a qualitative concept defined over U. If $x \in U$ is a random instantiation of the concept $\widetilde{T}$ that satisfies $x \sim N(EX, EN'^2)$, $EN' \sim N(EN, HE^2)$, and $y \in [0, 1]$ defined as

$$y = e^{-\frac{(x-EX)^2}{2(EN')^2}}$$

be the certainty degree of x, then the distribution of x in the universe U is called as a normal cloud and (x, y) is called a normal cloud drop. Here,

- EX is the mathematical expectation of the cloud drops.
- Entropy EN represents the uncertainty measurement of the qualitative concept.
- Hyper-entropy HE is the uncertain degree of entropy EN.

Given the numerical attributes (EX, EN, HE) of a cloud, the forward generator of this cloud is given in the following algorithm:

Forward normal cloud generator

Input: three parameters EX, EN, HE and the number of cloud drops c.

Output: c cloud drops and their certainty degree.

Steps:

1. Generate a normally distributed random number EN'_i with expectation EN and variance HE^2.
2. Generate a normally distributed random number x_i with expectation EX and variance EN'_i.
3. Calculate $y_i = e^{-\frac{(x_i-EX)^2}{2(EN'_i)^2}}$.
4. x_i is a cloud drop in the universe, and y_i is the degree of certainty of x_i belonging to the concept $\widetilde{T}$.
5. Repeat steps 1–4 until c cloud drops have been generated.

Next, the transformation between linguistic variables and clouds is presented by Wang et al. in [49]. The challenging problem of transforming the linguistic variables into normal clouds was first dealt with by Wang et al. [48] based on the golden ratio. But this method had a limitation associated that it could transform an LT set possessing five labels only. To overcome this limitation, Wang et al. [49] introduced a new method as given below.

Definition 2 [49] Let $\mathbb{T} = \{t_i | i = -n, \ldots, 0, \ldots, n, n \in N^*\}$ be a finite subscript-symmetric LT set with odd cardinality, where N^* =the set of positive integers, t_i denotes the value of a linguistic variable, t_{-n} and t_n are the lower and upper limits of LT set. The LSF running the mapping from t_i to θ_i $(i = -n, \ldots, 0, \ldots, n)$ is given as:

$$f : t_i \to \theta_i$$

$$\theta_i = \begin{cases} \frac{a^n - a^{-i}}{2a^n - 2}, & -n \le i \le 0 \\ \frac{a^n + a^i - 2}{2a^n - 2}, & 0 < i \le n \end{cases} \tag{1}$$

Here, $\theta_i \in [0, 1]$ is a numeric value. Also, the value of a can be calculated with the help of experiments. Based on various experimental studies, the value of a is mostly obtained in the interval [1.36, 1.4]. The procedure for transforming linguistic labels into $2n + 1$ number of clouds is given as follows. Assume the subscript-symmetric LT set to be $\mathbb{T} = \{t_i | i = -n, \ldots, 0, \ldots, n, n \in N^*\}$, and a valid universe $[X_{\min}, X_{\max}]$ as provided by the experts. When the cloud model is used to express linguistic values, a corresponding cloud variable $Y_i(EX_i, EN_i, HE_i)$ is formulated for each arbitrary $t_i \in \mathbb{T}$. The following is the process for creating cloud variables.

1. Calculate θ_i. Map t_i to θ_i using Equation (1).
2. Calculate EX_i as $EX_i = X_{\min} + \theta_i(X_{\max} - X_{\min})$.
3. Calculate EN_i as

$$EN_{-i} = EN_i = \begin{cases} \frac{(\theta_{|i-1|}+\theta_{|i|}+\theta_{|i+1|})(X_{\max}-X_{\min})}{9} & 0 < |i| \leq n-1 \\ \frac{(\theta_{|i|}+\theta_{|i-1|})(X_{\max}-X_{\min})}{6} & |i| = n \\ \frac{(\theta_i+2\theta_{i+1})(X_{\max}-X_{\min})}{9} & i = 0 \end{cases}$$

4. Calculate HE_i. Due to $EN'_i \sim N(EN_i, HE_i^2)$, the hyper-entropy must follow the 3σ principle of the normal distribution curve. Hence, $HE_{-i} = HE_i = (EN'^{+} - EN_i)/3$, where $EN'^{+} = \max_k\{EN'_k\}$.

Next, we introduce the asymmetric trapezoidal cloud (ATC) method as defined by Wang et al. [55] in which the authors describe the values of expectation, entropy, and hyper-entropy as interval values instead of specific ones. Moreover, this model bridges ULDAs (common information representations in group decision-making) and ATCs. Also, the ATC model overcomes the limitations of the normal cloud model.

Definition 3 [55] The ATC model is denoted by $\mathbb{z}$ and is given by

$$\mathbb{z} = (\underline{HE}, \underline{EN}, \underline{EX}, \overline{EX}, \overline{EN}, \overline{HE})$$

The expectation interval $[\underline{EX}, \overline{EX}]$, the left half cloud $(\underline{HE}, \underline{EN}, \underline{EX}, 0, 0)$, and the right half cloud $(0, 0, \overline{EX}, \overline{EN}, \overline{HE})$ constitute this model. $\underline{EX}, \underline{EN}, \underline{HE}$ and $\overline{EX}, \overline{EN}, \overline{HE}$ are the expectation, entropy and hyper-entropy of the left and right half cloud, respectively. Also, the range of the qualitative notions is explained by the interval $[\underline{EX}, \overline{EX}]$ explains the range of the qualitative notions. The level of uncertainty of a qualitative concept is shown by the $\underline{EN}$ and $\overline{EN}$, respectively, while the entropies' level of uncertainty is shown by $\underline{HE}$ and $\overline{HE}$.

In comparison with the normal cloud model, the ATC model has novel advantages instinctively represented in Fig. 1. For detailed knowledge of the ATC model, one can refer to the paper [55].

It is well known that the operations cannot be carried out directly when numbers combine with linguistic terms. So there is a need to define LSFs that assign

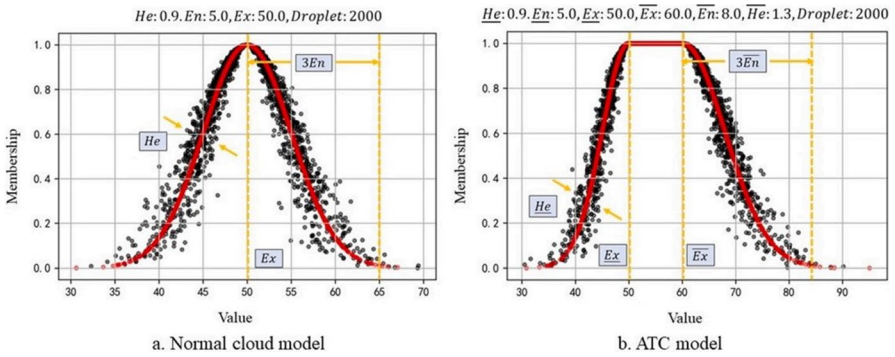


Fig. 1 Comparison between normal cloud model and ATC model [55]

different semantic values to linguistic terms under certain situations. Wang et al. [43] defined different LSFs for different cases, but their research includes a transformation from a linguistic term to a single number. However, it does not sufficiently outline the uncertain information in some conditions. Hence, to avoid this information loss, Wang et al. [42] defined some LSFs that convert linguistic variables to interval numbers. These LSFs are described below.

Definition 4 [42] Let $\mathbb{L} = \{t_i | i = 0, 1, \ldots, 2n, n \in \mathbb{N}\}$ be an LT set and $t_i \in \mathbb{L}$ be a linguistic variable. When $[\underline{\theta}_i, \overline{\theta}_i]$ is an interval fuzzy number, the LSF runs a mapping given as:

$$f : t_i \to [\underline{\theta}_i, \overline{\theta}_i],\ i = 0, 1, \ldots, 2n$$

$[\underline{\theta}_i, \overline{\theta}_i]$ satisfies the relationship $0 \le \underline{\theta}_0 \le \overline{\theta}_0 \le \underline{\theta}_1 \le \overline{\theta}_1 \le \cdots \le \underline{\theta}_{2n} \le \overline{\theta}_{2n} \le 1$. To meet this property, the mapping rule is improved and shown below:

$$\begin{aligned} H :& t_0 \to [\underline{\theta}_0, \overline{\theta}_0]; \\ & t_i \to [\max\{\overline{\theta}_{i-1}, \underline{\theta}_i\}, \overline{\theta}_i],\ i = 1, 2 \ldots, n; \\ & t_i \to [\underline{\theta}_i, \min\{\overline{\theta}_i, \underline{\theta}_{i+1}\}],\ i = n+1, \ldots, 2n-1; \\ & t_{2n} \to [\underline{\theta}_{2n}, \overline{\theta}_{2n}]. \end{aligned}$$

Hence, the improved LSF is:

$$LSF : H_2(t_i) = [\underline{\theta}_i, \overline{\theta}_i]$$

$$\underline{\theta}_i = \begin{cases} \frac{(a^n - a^{n-i})}{2(a^n - 1)}, & i = 0, 1, \ldots, n \\ \frac{(a^n + a^{i-n} - 2 - \lambda_3(i-n))}{2(a^n - 1)}, & i = n+1, \ldots, 2n \end{cases} \tag{2}$$

$$\overline{\theta}_i = \begin{cases} \frac{(a^n - a^{(}n-i) + \lambda_4(n-i))}{2(a^n-1)}, & i = 0, 1, \ldots, n \\ \frac{(a^n + a^{i-n} - 2)}{2(a^n-1)}, & i = n+1, \ldots, 2n \end{cases} \tag{3}$$

where λ_3 and λ_4 are adjustable parameters. Based on the above-mentioned LSF, the transformation method is conducted to map linguistic information into numerical values. For detailed understanding of the given transformation procedure, one may refer to the corresponding paper [55].

2.2 The unbalanced 2-tuple linguistic computational model (2-TLCM)

The unbalanced 2-TLCM is introduced by Malhotra, and Gupta [28] to cope with unbalanced linguistic information. To do so, an efficient method is designed to characterize the interpretation of the linguistic terms belonging to the unbalanced LT set.

Definition 5 [28] Let $\mathbb{LS} = \{t_{a^{-n}}, t_{a^{-(n-1)}}, \ldots, t_{a^0}, \ldots, t_{a^m}\}$, $a > 1$, $n, m \in \mathbb{Z}^+$ be a multiplicative unbalanced LT set having cardinality $n + m + 1$ such that n and m may not be equal. Moreover, the set $\mathbb{LS}$ is ordered if the given properties hold:

- $\mathbb{LS}$ is an ordered set: $t_{a^i} \geq t_{a^j}$ for $i \geq j$;
- $\max(t_{a^i}, t_{a^j}) = t_{a^i}$ for $i \geq j$;
- $\min(t_{a^i}, t_{a^j}) = t_{a^i}$ for $i \leq j$.

Further, the negation operator for such 2-tuples is defined as:

$$Neg(t_{a^i}, \phi) = (Neg(t_{a^i}), -\phi)$$

where $Neg(t_{a^i})$ is defined as follows:

- If $n = m$, then $Neg(t_{a^i}) = t_{a^{-i}}$
- If $n < m$, then $Neg(t_{a^i}) = t_{a^{-i}}$, for $i \leq n$ and $Neg(t_{a^i}) = t_{a^{m-i}}$ otherwise.
- If $n > m$, then $Neg(t_{a^{-i}}) = t_{a^i}$, if $i \leq m$ and $Neg(t_{a^{-i}}) = t_{a^{i-n}}$ otherwise.

For further explanation of the operators, one may refer to Algorithm 2 of Malhotra and Gupta [28].

Definition 6 [28] Let $\mathbb{LS}$ be the multiplicative unbalanced LT set as defined above and $\mathbb{R}$ be the set of real numbers. Then the numerical scale function

$$NS : \mathbb{LS} \to \mathbb{R}$$

such that

$$NS(t_{a^i}) = a^i$$

In the practical world scenario, several situations exist involving imprecise information. The uncertainty of such information is too complicated to explain with the help of quantitative expressions, but linguistic descriptors describe reality much better. However, the transformation between quantitative and qualitative concept values has always been a hurdle in developing linguistic decision-making methods. Modern researchers need a perfect way for CWWs. Our next section introduces a novel transformation method between the quantitative and unbalanced qualitative concept.

3 Method for transformation between multiplicative unbalanced linguistic variables and clouds

The present section introduces a novel multiplicative unbalanced linguistic scale function to transform multiplicative unbalanced linguistic variables into point-based unbalanced clouds.

Definition 7 Let $\mathbb{LS} = \{t_{a^i} | i = -n, \ldots, 0, \ldots, m\}$, $a > 1$ (n and m may or may not be equal) be any finite ordered multiplicative unbalanced LT set,

and a valid universe $[X_{\min}, X_{\max}]$. When the defined cloud model is applied to represent the multiplicative unbalanced linguistic variables, the corresponding clouds are represented as follows:

$$\begin{aligned} t_{a^{-n}} &\rightarrow (EX_{a^{-n}}, EN_{a^{-n}}, HE_{a^{-n}}) \\ &\vdots \\ t_{a^0} &\rightarrow (EX_{a^0}, EN_{a^0}, HE_{a^0}) \\ &\vdots \\ t_{a^m} &\rightarrow (EX_{a^m}, EN_{a^m}, HE_{a^m}) \end{aligned}$$

Definition 8 Let $\mathbb{LS} = \{t_{a^i} | i = -n, \ldots, 0, \ldots, m\}$, $a > 1$ (n and m may or may not be equal) be any finite ordered multiplicative unbalanced LT set. The LSF converting a linguistic term t_{a^i} to a certain number δ_{a^i}, $(i = -n, \ldots, 0, \ldots, m)$ can be expressed as follows:

$$\widetilde{\mathfrak{g}} : t_{a^i} \rightarrow \delta_{a^i} \, (i = -n, \ldots, 0, \ldots, m)$$

where

$$\delta_{a^i} = \begin{cases} \left(\frac{b^n - b^{-i}}{2b^n - 2}\right) \frac{1}{\log a}, & -n \leq i \leq 0 \\ \left(\frac{b^n + b^i - 2}{2b^n - 2}\right) \frac{1}{\log a}, & 0 < i \leq n \end{cases} \tag{4}$$

Here, $\delta_{a^i} \in [0, 1/\log a] \subseteq [0, 1]$ is a numeric value. The value of the parameter b can be obtained through experiments such as $b \in [1.36, 1.4]$ [58].

We next describe the following theorem giving the specific properties of the above-mentioned multiplicative unbalanced LSF.

Theorem 1 *Based on the multiplicative unbalanced linguistic scale function* (*MULSF*), *the following properties hold*:

1. *If* $-n \leq i \leq 0$, *then* $0 \leq \delta_{a^i} \leq \frac{1}{2\log a}$
2. *If* $0 < i \leq n$, *then* $\frac{1}{2\log a} < \delta_{a^i} \leq \frac{1}{\log a}$
3. *If* $i + j = 0$, *then* $\delta_{a^i} + \delta_{a^j} = \frac{1}{\log a}$.

Proof

1. For given $-n \leq i \leq 0$, we have

$$\delta_{a^i} = \left(\frac{b^n - b^{-i}}{2b^n - 2}\right)\frac{1}{\log a}$$

By setting $i = -n$ in the above equation, we have

$$\delta_{a^{-n}} = \left(\frac{b^n - b^n}{2b^n - 2}\right)\frac{1}{\log a} = 0 \text{ as } n \to \infty$$

By setting $i = 0$, we have

$$\delta_{a^0} = \left(\frac{b^n - b^0}{2b^n - 2}\right)\frac{1}{\log a} = \frac{1}{2\log a} \text{ as } n \to \infty$$

Next, by setting $-n < i < 0$, we have

$$\delta_{a^i} = \left(\frac{b^n - b^{-i}}{2b^n - 2}\right)\frac{1}{\log a}$$

Taking limits on both sides, we get

$$\lim_{n\to\infty} \delta_{a^i} = \lim_{n\to\infty} \left(\frac{b^n - b^{-i}}{2b^n - 2}\right)\frac{1}{\log a} = \frac{1}{2\log a}$$

Therefore, the limiting value of the function δ_{a^i} is obtained as

$$\lim_{n\to\infty} \delta_{a^i} = \begin{cases} 0, & i = -n \\ \frac{1}{2\log a}, & -n < i \leq 0 \end{cases}$$

2. Based on Definition 8, for $0 < i \leq n$, we have

$$\delta_{a^i} = \left(\frac{b^n + b^i - 2}{2b^n - 2}\right)\frac{1}{\log a}$$

By setting $i = 0$,

$$\delta_{a^0} = \left(\frac{b^n + 1 - 2}{2b^n - 2}\right)\frac{1}{\log a} = \frac{1}{2\log a} \text{ as } n \to \infty.$$

By setting $i = n$

$$\delta_{a^n} = \left(\frac{b^n + b^n - 2}{2b^n - 2}\right)\frac{1}{\log a} = \frac{1}{\log a} \text{ as } n \to \infty.$$

By setting $0 < i < n$, then

$$\delta_{a^i} = \left(\frac{b^n + b^i - 2}{2b^n - 2}\right)\frac{1}{\log a}$$

On rearranging the terms and taking limit on both sides, we get

$$\lim_{n\to\infty} \delta_{a^i} = \frac{1}{2\log a}$$

3. Based on Definition 8,

$$\delta_{a^i} = \begin{cases} \left(\frac{b^n - b^{-i}}{2b^n - 2}\right)\frac{1}{\log a}, & -n \le i \le 0 \\ \left(\frac{b^n + b^i - 2}{2b^n - 2}\right)\frac{1}{\log a}, & 0 < i \le n \end{cases}$$

For $i + j = 0$, we have $j = -i$. Therefore,

$$\delta_{a^i} + \delta_{a^j} = \left(\frac{b^n - b^{-i}}{2b^n - 2}\right)\frac{1}{\log a} + \left(\frac{b^n + b^j - 2}{2b^n - 2}\right)\frac{1}{\log a}$$

Adding and subtracting the term b^{-i} in the above expression, and by rearranging the terms, we obtain

$$\delta_{a^i} + \delta_{a^j} = \frac{1}{\log a}$$

Hence the proof.

□

We will next introduce the process of generating cloud droplets based on the rational transformation method of unbalanced linguistic variables into clouds.

Let $t_{a^i} \in \mathbb{LS}$ be any arbitrary unbalanced linguistic term corresponding to the cloud drop $z_{a^i}(EX_{a^i}, EN_{a^i}, HE_{a^i})$. Then, the working cloud generation procedure is given as follows:

Step 1: Calculate δ_{a^i} using Eq. 4.

Step 2: Calculate EX_{a^i}.

$$EX_{a^i} = X_{\min} + \delta_{a^i}(X_{\max} - X_{\min})$$

Step 3: Calculate EN_{a^i}. Let us represent a cloud droplet as (x, y), since $x \sim N(EX_{a^i}, {EN'_{a^i}}^2)$, then as per the 3σ principle of the normal distribution curve, we have

$$3EN'_{a^i} = \max(X_{\max} - EX_{a^i}, EX_{a^i} - X_{\min})$$

Because of $EN' \sim N(EN, HE^2)$, EN_{a^i} may be considered the mean value of EN'_{a^i} corresponding to the clouds in consideration and their adjacent clouds.

$$EN_{a^{-i}} = EN_{a^i} = \frac{EN'_{a^{i-1}} + EN'_{a^i} + EN'_{a^{i+1}}}{3\log a} \text{ for } |i| = 0, 1, \ldots, n-1, \tag{5}$$

and for $|i| = n$,

$$EN_{a^{-n}} = EN_{a^n} = \frac{EN'_{a^n} + EN'_{a^{n-1}}}{2\log a} \tag{6}$$

These calculations may be rewritten as the following formulas:

$$EN'_{a^i} = \begin{cases} \frac{(1-\delta_{a^i})(X_{\max}-X_{\min})}{3\log a}, & -n \le i \le 0 \\ \frac{\delta_{a^i}(X_{\max}-X_{\min})}{3\log a}, & 0 < i \le n \end{cases} \tag{7}$$

$$EN_{a^{-i}} = EN_{a^i} = \begin{cases} \frac{(\delta_{a|i-1|}+\delta_{a|i|}+\delta_{a|i+1|})(X_{\max}-X_{\min})}{9\log a}, & 0 < |i| < n-1 \\ \frac{(\delta_{a|i|}+\delta_{a|i-1|})(X_{\max}-X_{\min})}{6\log a}, & |i| = n \\ \frac{(\delta_{a^i}+2\delta_{a^{i+1}})(X_{\max}-X_{\min})}{9\log a}, & i = 0 \end{cases} \tag{8}$$

Step 4: Calculate HE_{a^i}. Due to $EN'_{a^i} \sim N(EN_{a^i}, {HE_{a^i}}^2)$, the hyper-entropy satisfies the 3σ principle. In particular,

$$HE_{a^{-i}} = HE_{a^i} = \frac{EN'^{+} - EN_{a^i}}{3\log a} \tag{9}$$

where, $EN'^{+} = \sup_k\{EN'_k\}$.

Next, we present the working example to explain the methodology mentioned above.

Example 1 Consider the universe $[X_{\min}, X_{\max}] = [0, 9]$ and let the unbalanced LT set can be given as

$$\begin{aligned}\mathbb{LS} = \{&t_{2^{-4}} : \text{None}, t_{2^{-3}} : \text{extremely poor}, t_{2^{-2}} : \text{very poor},\\ &t_{2^{-1}} : \text{poor}, t_{2^0} : \text{avg}, t_{2^1} : \text{good}, t_{2^2} : \text{very good},\\ &t_{2^3} : \text{extremely good}, t_{2^4} : \text{excellent}\}\end{aligned}$$

The procedure of transforming unbalanced linguistic variables into clouds is presented in the following manner:

1. Based on Definition 8, setting $b = 1.4$, the value for $\delta_{2^i}(i = -4, -3, \ldots, 0, 1, 2, \ldots, 4)$ can be computed as

$$\begin{aligned}&\delta_{2^{-4}} = 0,\ \delta_{2^{-3}} = 0.6416,\ \delta_{2^{-2}} = 1.0998,\ \delta_{2^{-1}} = 1.4271,\\ &\delta_{2^0} = 1.6609,\ \delta_{2^1} = 1.8948,\ \delta_{2^2} = 2.2221,\\ &\delta_{2^3} = 2.6804,\ \delta_{2^4} = 3.3219\end{aligned}$$

2. $$\begin{aligned}&Ex_{2^{-4}} = 0.0625,\ Ex_{2^{-3}} = 10.2875,\ Ex_{2^{-2}} = 17.5910,\\ &Ex_{2^{-1}} = 22.8078,\ Ex_{2^0} = 26.5341,\ Ex_{2^1} = 30.2604,\\ &Ex_{2^2} = 35.4772,\ Ex_{2^3} = 42.7808,\ Ex_{2^4} = 53.0057\end{aligned}$$

3. $$\begin{aligned}&En'_{2^{-4}} = 1.5992,\ En'_{2^{-3}} = 0.5732,\\ &En'_{2^{-2}} = -0.1596,\ En'_{2^{-1}} = -0.6831,\ En'_{2^0} = -1.0570,\\ &En'_{2^1} = 3.0302,\ En'_{2^2} = 3.5536,\ En'_{2^3} = 4.2865,\ En'_{2^4} = 5.3125\end{aligned}$$

4. $$\begin{aligned}&En_{2^{-4}} = 4.7995 \quad En_{2^{-3}} = 4.042 \quad En_{2^{-2}} = 3.3791\\ &En_{2^{-1}} = 2.9056 \quad En_{2^0} = 0.6840 \quad En_{2^1} = 2.9056\\ &En_{2^2} = 3.3791 \quad En_{2^3} = 4.042 \quad En_{2^4} = 4.7995\end{aligned}$$

5. $$\begin{aligned}&He_{2^{-4}} = 0.0515 He_{2^{-3}} = 0.1275\\ &He_{2^{-2}} = 0.1940 He_{2^{-1}} = 0.2415 He_{2^0} = 0.4644\\ &He_{2^1} = 0.2415 He_{2^2} = 0.1940\\ &He_{2^3} = 0.1275 He_{2^4} = 0.0515\end{aligned}$$

Thus, the 9-asymmetric linguistic clouds obtained are given as follows:
$t_{2^{-4}} \longrightarrow (0.0625, 4.7995, 0.0515)$, $t_{2^{-3}} \longrightarrow (10.2875, 4.042, 0.1275)$, $t_{2^{-2}} \longrightarrow (17.5910, 3.3791, 0.1940)$, $t_{2^{-1}} \longrightarrow (22.8078, 2.9056, 0.2415)$, $t_{2^0} \longrightarrow (26.5341, 0.684, 0.4644)$, $t_{2^1} \longrightarrow (30.2604, 2.9056, 0.2415)$, $t_{2^2} \longrightarrow (35.4772, 3.3791, 0.1940)$, $t_{2^3} \longrightarrow (42.7808, 4.042, 0.1275)$, $t_{2^4} \longrightarrow (53.0057, 4.7995, 0.0515)$. Figure 2 presents the graphical representation of the obtained nine asymmetric clouds. Here, *EN* and *HE* reflect the extent of dispersion of the cloud droplets.

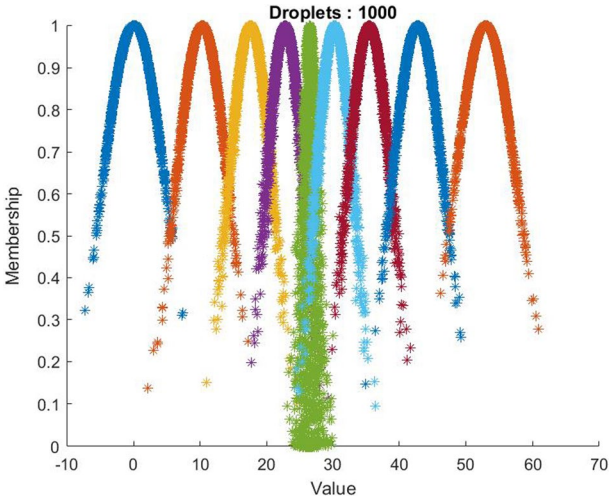


Fig. 2 Evaluation information for asymmetric point-based cloud model with respect to unbalanced linguistic terms

Note 1 It should be noted that the point-based cloud-generating procedure described above can be used in the scenario $n \neq m$ if dummy variables are added to the multiplicative unbalanced linguistic term set in a way that $n = m$.

Although the above-defined methodology is a well-defined model; it has some limitations associated, as the expected value of the unbalanced linguistic term is a single numeric value. This causes information loss in representing the semantics of linguistic terms to an extent. Thus, to overcome this information loss, we define a generalized multiplicative unbalanced interval cloud model in the next section, to effectively describe unbalanced linguistic terms that entail interval concepts instead of specific ones.

4 Generalized multiplicative unbalanced interval cloud model

In this section, we first develop a generalized MULSF to transform an unbalanced linguistic variable into an interval numerical value. Then, we provide a detailed procedure to generate a generalized multiplicative unbalanced interval cloud, followed by suggesting a novel interval score function to rank interval clouds.

Definition 9 Let $\mathbb{LS} = \{t_{a^i} | i = -n, -(n-1), \ldots, 0, \ldots, m, a > 1, n, m \in \mathbb{Z}^+\}$ (where n and m may or may not be equal) be a finitely ordered unbalanced LT set. Then, the extended MULSF can be conducted as a mapping from unbalanced linguistic label t_{a^i} to interval numbers $[\underline{\delta}_{a^i}, \overline{\delta}_{a^i}]$ and the mapping can be expressed as below

$$\widetilde{\mathbb{G}} : t_{a^i} \to [\underline{\delta}_{a^i}, \overline{\delta}_{a^i}], i = -n, \ldots, 0, \ldots, m$$

where $[\underline{\delta}_{a^i}, \overline{\delta}_{a^i}] \in [0, 1/\log a] \subseteq [0, 1]$.

Usually, the correspondence between unbalanced linguistic term t_{a^i} and the subscript a^i, $a > 1$ is strictly increasing, and therefore, $[\underline{\delta}_{a^i}, \overline{\delta}_{a^i}]$ needs to satisfy

$$0 \le \underline{\delta}_{a^{-n}} < \overline{\delta}_{a^{-n}} \le \cdots \le \underline{\delta}_{a^0} < \overline{\delta}_{a^0} \le \cdots \le \underline{\delta}_{a^m} < \overline{\delta}_{a^m} \le 1/\log a$$

To strictly meet this property, an improved mapping rule is defined below

$$\begin{aligned}
\widetilde{\mathbb{G}} : & t_{a^{-n}} \to [\underline{\delta}_{a^{-n}}, \overline{\delta}_{a^{-n}}]; \\
& t_{a^i} \to [\sup\{\overline{\delta}_{a^{i-1}}, \underline{\delta}_{a^i}\}, \overline{\delta}_{a^i}], \ i = -n, \ldots, 0; \\
& t_{a^i} \to [\underline{\delta}_{a^i}, \inf\{\overline{\delta}_{a^i}, \underline{\delta}_{a^{i+1}}\}], \ i = 1, 2, \ldots, m-1; \\
& t_{a^m} \to [\underline{\delta}_{a^m}, \overline{\delta}_{a^m}]
\end{aligned}$$

Here, t_{a^0} is the mid-term of the set $\mathbb{LS}$ and $I(t_{a^i}) = a^i$.

The preceding mapping rules state that $\widetilde{\mathbb{G}}$ is a strictly and monotonically increasing function with respect to a^i. Based on the knowledge of function translation, the extended MULSF is represented as follows:

$$MULSF : \widetilde{\mathbb{G}}(t_{a^i}) = [\underline{\delta}_{a^i}, \overline{\delta}_{a^i}]$$

where

$$\underline{\delta}_{a^i} = \begin{cases} \dfrac{1}{\log a}\left|\dfrac{b^{\#\mathbb{LS}_{left}} - b^{\left(\#\mathbb{LS}_{left} - a^i\right)}}{2\left(b^{\#\mathbb{LS}_{left}} - 1\right)}\right|, & -n \le i \le 0 \\ \dfrac{1}{\log a}\left|\dfrac{b^{\#\mathbb{LS}_{right}} + b^{\left(a^i + C - \#\mathbb{LS}_{right}\right)} - 2 - \lambda_3\left(a^i + C - \#\mathbb{LS}_{right}\right)}{2\left(b^{\#\mathbb{LS}_{right}} - 1\right)}\right|, & 0 < i \le m \end{cases} \tag{10}$$

And,

$$\overline{\delta}_{a^i} = \begin{cases} \dfrac{1}{\log a}\left|\dfrac{b^{\#\mathbb{LS}_{left}} - b^{\left(\#\mathbb{LS}_{left} - a^i\right)} + \lambda_4\left(\#\mathbb{LS}_{left} - a^i\right)}{2\left(b^{\#\mathbb{LS}_{left}} - 1\right)}\right|, & -n \le i \le 0 \\ \dfrac{1}{\log a}\left|\dfrac{b^{\#\mathbb{LS}_{right}} + b^{\left(a^i + C - \#\mathbb{LS}_{right}\right)}}{2\left(b^{\#\mathbb{LS}_{right}} - 1\right)}\right|, & 0 < i \le m \end{cases} \tag{11}$$

The meaning of other symbols remains the same, where λ_3 and λ_4 are adjustable parameters. Further, $C = |\#\mathbb{LS}_{right} - \#\mathbb{LS}_{left}|$. We define the adjustable parameters λ_3 and λ_4 for the sake of calculation convenience as follows:

$$\lambda_3 = \frac{1}{a^i + C - \#\mathbb{LS}_{right} + 1}$$

and,

$$\lambda_4 = \frac{1}{\#\mathbb{LS}_{left} - a^i + 1}$$

For a fit with the psychological value during the evaluation process, *MULSF* makes use of the bidirectional rise in the geometric progression of the scale value to accurately depict the cognitive behaviour of experts. In this situation, the absolute deviation between adjacent linguistic subscripts increases with an extension from the central portion of linguistic terms to both ends. After considerable experiments, parameter 'b' is demonstrated to belong to the interval [1.36, 1.4] [58]. Without loss of generality, b is taken to be equal to 1.4 throughout the paper for numerical computation.

Next, we proceed to define the concept of the multiplicative unbalanced interval cloud model.

Definition 10 The multiplicative unbalanced interval cloud (MUIC) model, denoted by A, is defined as

$$A = (\underline{HE}, \underline{EN}, \underline{EX}, \overline{EX}, \overline{EN}, \overline{HE})$$

The MUIC model involves three numerical sections, i.e. the expectation interval $[\underline{EX}, \overline{EX}]$, left half cloud $(\underline{HE}, \underline{EN}, \underline{EX}, 0, 0)$ and right half cloud $(0, 0, \overline{EX}, \overline{EN}, \overline{HE})$. Here, $\underline{EX}$, $\underline{EN}$, $\underline{HE}$ are the expectation, entropy, and hyper-entropy of the left half cloud, also known as lower expectation, lower entropy, and lower hyper-entropy, respectively. On the other hand, $\overline{EX}$, $\overline{EN}$, $\overline{HE}$ are the expectation, entropy, and hyper-entropy of the right half cloud, also called upper expectation, upper entropy, and upper hyper-entropy, respectively.

We next proceed to present the procedure proficient in converting unbalanced linguistic term into unbalanced linguistic interval cloud variables based on the aforementioned MULSF.

Let $\mathbb{LS} = \{t_{a^i} | i = -n, \ldots, 0, 1, \ldots, m \text{ and } a > 1, n, m \in \mathbb{Z}^+\}$ be a multiplicative unbalanced LT set, where t_{a^i} is plausible unbalanced linguistic term. The relationship between the unbalanced linguistic term and MUIC is presented in the following steps.

Step 1: Initially calculate $[\underline{\delta}_{a^i}, \overline{\delta}_{a^i}]$ using *MULSF* defined earlier, over the universe $[X_{\min}, X_{\max}]$.

Step 2: Determine the expectation interval $[\underline{EX}_{a^i}, \overline{EX}_{a^i}]$ where $\underline{EX}_{a^i}$ and $\overline{EX}_{a^i}$ are calculated as

$$\begin{aligned} \underline{EX}_{a^i} &= X_{\min} + \underline{\delta}_{a^i}(X_{\max} - X_{\min}) \\ \overline{EX}_{a^i} &= X_{\min} + \overline{\delta}_{a^i}(X_{\max} - X_{\min}) \end{aligned} \tag{12}$$

Step 3: Determine the entropy $\underline{EN}_{a^i}$ and $\overline{EN}_{a^i}$. Based on the 3σ principle,

$$\begin{aligned} \underline{EN}_{a^{-n}} &= 0 \\ \underline{EN}_{a^i} &= \left| \frac{\underline{EX}_{a^i} - \overline{EX}_{a^{i-1}}}{3 \log a} \right|, -(n-1) \le i \le m \\ \overline{EN}_{a^i} &= \left| \frac{\underline{EX}_{a^{i+1}} - \overline{EX}_{a^i}}{3 \log a} \right|, -n \le i \le m-1 \\ \overline{EN}_{a^m} &= 0 \end{aligned} \tag{13}$$

Step 4: Determine the hyper-entropies $\underline{HE}_{a^i}$ and $\overline{HE}_{a^i}$. Since $EN' \sim N(EN, HE^2)$, $\underline{HE}$ also satisfies the 3σ principle. Hence, the hyper-entropies $\underline{HE}_{a^i}$ and $\overline{HE}_{a^i}$ of MUIC may be obtained using the formulas:

$$\begin{aligned} \underline{HE}_{a^{-n}} &= 0 \\ \underline{HE}_{a^i} &= \frac{\max\{\max\{\underline{EN}_{a^i}\} - \underline{EN}_{a^i}, \underline{EN}_{a^i} - \min\{\underline{EN}_{a^i}\}\}}{3 \log a}, -(n-1) \le i \le m \\ \overline{HE}_{a^i} &= \frac{\max\{\max\{\overline{EN}_{a^i}\} - \overline{EN}_{a^i}, \overline{EN}_{a^i} - \min\{\overline{EN}_{a^i}\}\}}{3 \log a}, -n \le i \le m-1 \\ \overline{HE}_{a^m} &= 0 \end{aligned} \tag{14}$$

In the literature, Li et al. [29] proposed the concept of variance of a normal cloud. Analogously, we introduce the notion of variance for MUIC.

Definition 11 Let $A = (\underline{HE}, \underline{EN}, \underline{EX}, \overline{EX}, \overline{EN}, \overline{HE})$ be a MUIC with c generated interval cloud droplets, the variance of c interval cloud droplets can be calculated as follows:

$$var_{Int} = [\underline{EN}, \overline{EN}] \times [\underline{EN}, \overline{EN}] + [\underline{HE}, \overline{HE}] \times [\underline{HE}, \overline{HE}]$$

then, the standard deviation of c interval cloud droplets is

$$sd_{Int} = \sqrt{[\underline{EN}, \overline{EN}] \times [\underline{EN}, \overline{EN}] + [\underline{HE}, \overline{HE}] \times [\underline{HE}, \overline{HE}]}$$

Here, the standard deviation sd_{Int} estimates the dispersal of interval cloud droplets that can be utilized to address the existing uncertainty and alteration of an unbalanced qualitative concept. A low sd_{Int} specifies that an unbalanced linguistic label tends to be relatively stable. In contrast, a high sd_{Int} implies the existence of a high level of uncertainty and alteration about the linguistic label. In this scenario, the

relationship between $EX_{Int} = [\underline{EX}, \overline{EX}]$ and sd_{Int} can be considered as the expected utility and the utility dispersion in the utility theory [59]. Then, the preference made for a choice can be presented by a linear trade-off between expected utility and utility dispersal. Motivated by the notion, we define an interval score function below to rank MUICs.

Definition 12 Given a MUIC $A = (\underline{HE}, \underline{EN}, \underline{EX}, \overline{EX}, \overline{EN}, \overline{HE})$, an interval score function can be stated as

$$sc_{Int} = EX_{Int} - \gamma.sd_{Int}$$

where $\gamma \in [0, 1]$ reflects a coefficient to capture the attitude towards the standard deviation.

The γ value is estimated based on the real-world decision-making scenario. If $\gamma = 0$, it means that the DMs simply take into account the EX_{Int} and ignore uncertainty and informational modification.

The monotonicity property is satisfied by the defined interval score function. When compared to EX_{Int}, the score function increases, but when compared to EN_{Int} or HE_{Int}, it decreases.

Next, based on Definition 12, the following method can be proposed to rank two MUICs.

Definition 13 Let A_1 and A_2 be any two MUICs, then

- If $sc_{Int1} > sc_{Int2}$, then $A_1 > A_2$;
- If $sc_{Int1} = sc_{Int2}$, then $A_1 = A_2$;
- If $sc_{Int1} < sc_{Int2}$, then $A_1 < A_2$.

Note 2 It is noted that the inequality stated in the above definition is crisply defined. Henceforth, the case of a nested interval is neglected.

5 Illustrative example and comparative analysis

This section demonstrates the complete process of transforming unbalanced linguistic variables into MUICs via numerical illustration. Subsequently, the feasibility and rationality of the proposed methodology are given via comparative analyses from existing studies in the literature.

5.1 Illustrative example

Here, we propose a practical decision-making example to demonstrate the feasibility and advantages of the developed methodology for both the cases, $n = m$ and $n \neq m$.

Table 3 Five IT companies considered for investing purpose

IT1	IT2	IT3	IT4	IT5
Infosys	Wipro	TCS	HCL Technologies	Larsen & Toubro Infotech

Table 4 The assessment representation of the linguistic terms by MUICs for case $n = m$

Linguistic terms	MUICs
$t_{2^{-2}}$	$A_1 = (0, 0, 1.3675, 6.873, 4.7032, 2.1314)$
$t_{2^{-1}}$	$A_2 = (2.1314, 3.2918, 2.626, 7.817, 4.7032, 3.6454)$
t_{2^0}	$A_3 = (1.563, 0.9584, 4.8445, 9.171, 3.2918, 2.5841)$
t_{2^1}	$A_4 = (2.1314, 0.9584, 8.3055, 8.3055, 2.7785, 2.5841)$
t_{2^2}	$A_5 = (0, 0, 10.8145, 16.611, 2.7785, 3.6454)$

Example 2 We first consider the case where $n = m$, i.e. $\mathbb{LS} = \left\{t_{a^{(-n)}}, \ldots, t_{a^0}, \ldots, t_{a^{(n)}}\right\}$.

Suppose there is a DM who is willing to invest his sum of money in IT companies by carefully observing the average closing stock values for the past 5 consecutive year, i.e. 2017-21. There are five possible alternatives DM is considering for investing the money. Table 3 shows the alternatives of the IT companies.

Since the stock values of companies get affected by linguistic factors. Henceforth, it facilitates to evaluate stock prices for the IT companies in terms of the predefined unbalanced linguistic scale set given as:

$$\mathbb{LS} = \{t_{2^{-2}} : \text{Very Low (VL)}, t_{2^{-1}} : \text{Low (L)},$$
$$t_{2^0} : \text{Average (Avg)}, t_{2^1} : \text{High (H)}, t_{2^2} : \text{Very High (VH)}\}$$

The variations incurred in the companies' average stock values for the past five years are expressed in an unbalanced linguistic scale set $\mathbb{LS}$. In this scenario, analysing the uncertainty and fluctuation of stock values expressed by the dispersion of cloud drops is significant. Henceforth, we utilize our methodology to transform unbalanced linguistic variables into clouds so that the preference for selecting a particular alternative is possible. To do this, we follow similar steps 1–4 as given in the last section.

Based on the defined methodology in Steps, 1–4, the assessment information presented by MUICs is shown in Table 4 and their graphical representation is illustrated in Figs. 3 and 4. Next, based on Definition 12, the scoring values obtained are given as follows: $sc_{Int1} = [1.3675, 1.7094]$, $sc_{Int2} = [-1.2956, 1.8665]$,

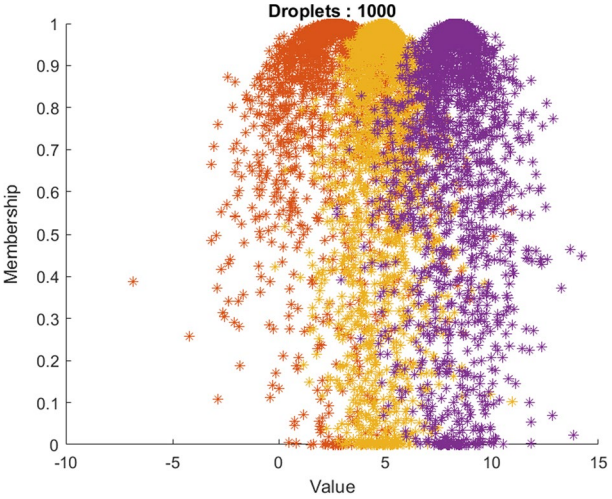


Fig. 3 Evaluation information for asymmetric lower half cloud with respect to unbalanced linguistic terms for Case $n = m$

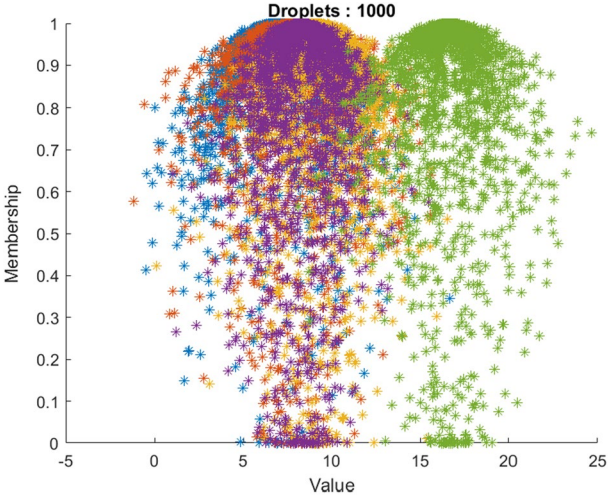


Fig. 4 Evaluation information for asymmetric upper half cloud with respect to unbalanced linguistic terms for Case $n = m$

$sc_{Int3} = [3.0111, 4.9861]$, $sc_{Int4} = [4.5111, 5.9685]$ and $sc_{Int5} = [10.8145, 12.0274]$. According to the score values, the ranking scheme of the alternatives can be fixed, and they are obtained as follows: $A_5 > A_4 > A_3 > A_1$. Hence, IT5 has a stable cloud and is preferred over other alternatives.

Table 5 The assessment representation of the linguistic terms by MUICs for the case $n \neq m$

Linguistic terms	MUICs
$t_{2^{-2}}$	$A_1 = (0, 0, 1.9145, 9.6222, 6.5853, 31.234)$
$t_{2^{-1}}$	$A_2 = (5.1017, 4.6069, 3.6757, 10.9424, 6.5853, 31.234)$
t_{2^0}	$A_3 = (3.6166, 1.3411, 6.7823, 12.838, 4.6069, 33.425)$
t_{2^1}	$A_4 = (3.6166, 1.3411, 11.627, 11.627, 2.14, 36.1572)$
t_{2^2}	$A_5 = (2.7319, 2.14, 13.5597, 18.0264, 34.79, 36.1572)$
t_{2^3}	$A_6 = (3.6454, 0, 49.4424, 55.1565, 34.79, 0)$

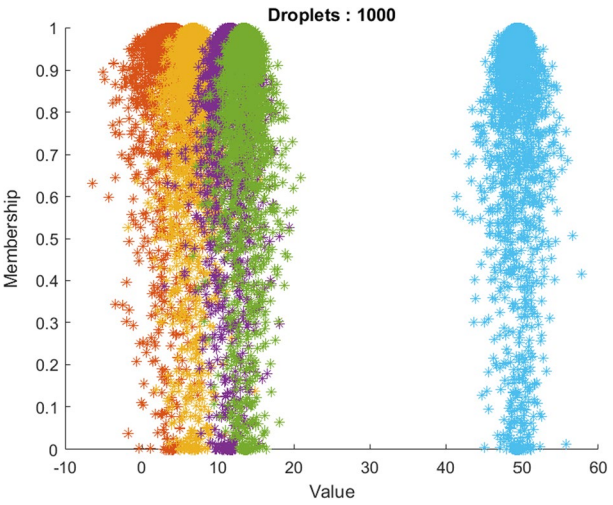


Fig. 5 Evaluation information for asymmetric lower half cloud with respect to unbalanced linguistic terms for Case $n \neq m$

Example 3 Next, we discuss the case where $n \neq m$, i.e. $\mathbb{LS} = \left\{t_{a^{(-n)}}, \ldots, t_{a^0}, \ldots, t_{a^{(m)}}\right\}$. Consider a multiplicative unbalanced set

$$\mathbb{LS} = \{t_{a^{-2}} : \text{Terrible}, t_{a^{-1}} : \text{Poor}, t_{a^0} : \text{Middle},$$
$$t_{a^1} : \text{Satisfactory}, t_{a^2} : \text{Good}, t_{a^3} : \text{Excellent}\}$$

In this particular instance, $\#\mathbb{LS}_{left} = n = 2$, $\#\mathbb{LS}_{right} = m = 3$. Let $a = 2$, $b = 1.4$, $[X_{\min}, X_{\max}] = [0, 7]$. The assessment representation of linguistic terms by MUICs is given in Table 5, and their graphical representation is illustrated in Figs. 5 and 6.

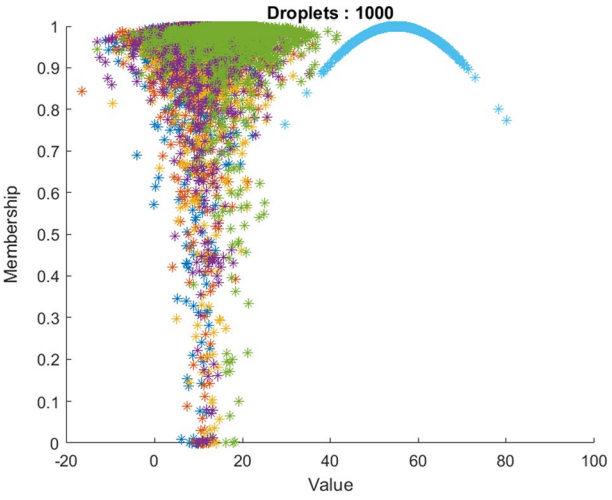


Fig. 6 Evaluation information for asymmetric upper half cloud with respect to unbalanced linguistic terms for Case $n \neq m$

5.2 Comparative analysis

Here, we analyse the numerical results presented in the previous subsection and demonstrate the viability and superiority of the proposed cloud model by comparing it to the existing studies from [55] and [44].

To confirm that the ranking outcomes are comparable, numerical example 3 given in the previous subsection is taken from the paper [55]. Since the final ranking outcome obtained is the same as that of the ATC model [55], therefore the proposed model offers analogous results. However, the difference lies in the information representation and the evaluation method to solve decision problems. The unbalanced linguistic computational model put forth by Herrera et al. [11] serves as the foundation for the model proposed by Wang et al. [55]. The scale values could be mapped to a number of hierarchically constructed uniformly distributed scale sets, which is effective for unbalanced linguistic cardinalities. Then, in information aggregation procedures, the uniformly dispersed scale values are used to replace the original imbalanced ones. This whole process altogether increases the complexity of the ATC model. Moreover, the unbalanced linguistic information presented in the model is given by a symmetrically distributed LT set. Consequently, the literal meaning of the unbalanced LT set is missing. On the contrary, the superiority of our work lies in the fact that it develops a new concept, namely a multiplicative unbalanced linguistic cloud model, to overcome the limitation of the existing cloud model as a qualitative information representation model. Our proposed model is based on the multiplicative unbalanced linguistic

model developed by Malhotra and Gupta [28] which is computationally less expensive and preserves the literal meaning of the unbalanced LT set. In addition, the existing ATC cloud model has difficulty describing Type II unbalanced linguistic concepts; however, our proposed model is suitable for both Type I and Type II unbalanced LT sets. The MULSF proposed in our work is based on a multiplicative scale set and improves the related mapping rules. Moreover, the existing cloud model [55] has difficulty in describing a continuous concept. Taking the concept of investment return, where the data distribution of investment return follows an irregular pattern, our proposed model is more suitable for description as it preserves the meaning and prevents information loss.

In the literature, the Fuzzy Trapezium Cloud model [44] is a subjective and effective cloud model that transforms different types of linguistic fuzzy sets and trapezium clouds. Calculations of weights for decision-making problems are also done by some defined operations. However, this model has a limitation that an optimization method is used for solving weight vectors which is a very complex and time taking procedure. Moreover, the model is based on a linguistic term set which is a purely balanced and symmetric term set. On the contrary, our model defined in the paper works for unbalanced linguistic data along with balanced linguistic data. Furthermore, the unbalanced linguistic set used in our paper is not transformed from a balanced linguistic set. This property reduces the time and evaluation steps of the transforming method. Taking the example picked in the Fuzzy Trapezium Cloud model [44], the battlefield situation is analysed and expressed in terms of different levels. Further, these levels correspond to linguistic terms that are symmetrically distributed. Nevertheless, in a real-life scenario, this situation might occur irregularly and the level of performance may not be symmetrically distributed. Hence, multiplicative unbalanced information could provide improved results.

Apart from the aforementioned examples, there are various real-life examples such as picking a multiplicative unbalanced cloud model in paper [38] for improving power grid failures analysis of the shortage of power supply and the pressure of dual control of energy consumption in [46], etc., provides significant results. Finally, on calculating the complexity of the proposed model given in Table 6, it is foreseen that the complexity of the defined model is linear, i.e. $4\mathcal{O}(n+m+1) \equiv \mathcal{O}(n+m+1)$, whereas other existing cloud model [55] has a nonlinear complexity. Hence, our model is applicable to handle complex decision problems.

Table 6 Computation complexity of the defined methodology

Step	Complexity
δ_{a^i}	$\mathcal{O}(n+m+1)$
EX_{a^i}	$\mathcal{O}(n+m+1)$
EN_{a^i}	$\mathcal{O}(n+m+1)$
HE_{a^i}	$\mathcal{O}(n+m+1)$

where $n+m+1$ is the cardinality of the multiplicative ULTS

6 Conclusions

The normal cloud model is an excellent tool for converting qualitative concepts to quantitative information in linguistic decision-making problems. But the existing cloud models either cannot adequately describe the linguistic concepts or include information loss in the conversion process. Our work defines a comprehensive information representation model, the MUIC model, that can handle the multiplicative unbalanced data well. This model forms a bridge enabling efficient conversions between unbalanced linguistic information and clouds. A MULSF has been defined for this purpose. However, the LSFs existing in the literature map only a linguistic term to a particular specific value, thus creating information loss in the transformation process. To overcome this defect, we have defined a generalized MULSF that can convert the unbalanced linguistic data into an interval rather than a specific point. Thus, the advantage of a MUIC model is that it overcomes the loss of information persisting in converting the unbalanced linguistic data to a specific value. Rather it maps an unbalanced linguistic term to a continuous interval. The generalized MULSF is thus stated to efficiently incorporate the disparities in spacing of LTs in terms of representation and meaning by making a mapping from unbalanced LTs to interval values. Also, a method based on the 3σ principle is proposed to determine the values of entropy and hyper-entropy of the generalized MUIC. Lastly, this research provides a comparison method to rank the MUICs. The defined methodology has been implicated practically with the help of some examples.

Our method effectively addresses the linguistic imbalance, but it also has some limitations. It is noted that one must add a dummy variable to the set $\mathbb{LS}$ to proceed with calculations for the point-based unbalanced cloud model for the case where the unbalanced LT set has an unequal number of linguistic terms spread on each side of the central term. Some multi-criteria decision-making problems may not have an accurate solution after adding this dummy variable. Therefore, further extension of this model is required to get over the corresponding limitation. Moreover, to enhance the continuity of our work, we also plan to improve the proposed cloud model's efficacy and attempt to create a decision support model based on cloud variables to resolve complex decision issues and deliver efficient outcomes in fewer computation times.

Author Contributions Parul Chauhan, Tanya Malhotra were involved in conceptualization, methodology, writing and editing, and Anjana Gupta contributed to methodology, formal analysis and review.

Funding The authors did not receive support from any organization for the submitted work.

Data availability Data sharing not applicable to this article as no datasets were generated or analysed during the current study.

Declarations

Conflicts of interest The authors have no competing interests to declare that are relevant to the content of this article.

Ethical approval This article does not contain any studies with human participants or animals performed by any of the authors.

Code availability Not applicable.

References

1. Martínez L, Liu J, Yang JB, Herrera F (2005) A multigranular hierarchical linguistic model for design evaluation based on safety and cost analysis. Int J Intell Syst 20(12):1161–1194
2. Martínez L, Ruan D, Herrera F, Herrera-Viedma E, Wang PP (2009) Linguistic decision making: tools and applications. Inform Sci 179(14):2297–2298
3. Zadeh LA (1975) The concept of a linguistic variable and its application to approximate reasoning, I–III. Inf Sci 8:301–357
4. Herrera F, Martínez L (2000) A 2-tuple fuzzy linguistic representation model for computing with words. IEEE Trans Fuzzy Syst 8(6):746–752
5. Herrera F, Martínez L (2001) The 2-tuple linguistic computational model, advantages of its linguistic description, accuracy and consistency. Int J Uncertain Fuzziness Knowl Based Syst 9:33–48
6. Bartczuk L, Dziwínski P, Starczewski JT (2012) A New Method for Dealing with Unbalanced Linguistic Term Set. ICAISC 2012. Part I, LNCS 7267:207–212
7. Abchir MA, Truck I (2013) Towards an extension of the 2-tuple linguistic model to deal with unbalanced linguistic term sets. arXiv:1304.5897v1:1-17
8. Cai M, Gong Z, Yu X (2016) A method for unbalanced linguistic term sets and its application in group decision making. Int J Fuzzy Syst 19(3):671–682. https://doi.org/10.1007/s40815-016-0209-6
9. Dong Y, Xu Y, Yu S (2009) Computing the numerical scale of the linguistic term set for the 2-tuple fuzzy linguistic. IEEE Trans Fuzzy Syst 17(6):1366–1378
10. Fu Z, Liao H (2019) Unbalanced double hierarchy linguistic term set: The TOPSIS method for multi-expert qualitative decision making involving green mine selection. Inf Fus 51:271–286
11. Herrera F, Viedma E-H, Martínez L (2008) A fuzzy linguistic methodology to deal with unbalanced linguistic term sets. IEEE Trans Fuzzy Syst 16(2):354–370
12. Wang JH, Hao J (2006) A new version of 2-tuple fuzzy linguistic representation model for computing with words. IEEE Trans Fuzzy Syst 14(3):435–445
13. Zhang G, Dong Y, Xu Y (2014) Consistency and consensus measures for linguistic preference relations based on distribution assessments. Inf Fus 17:46–55
14. Zou L, Pei Z, Karimi HR, Shi P (2012) The Unbalanced Linguistic Aggregation Operator in Group Decision Making. IEEE International Symposium on Intelligent Control (ISIC), pp 703–707
15. Lin M, Chen Z, Chen R, Fujita H (2021) Evaluation of startup companies using multicriteria decision making based on hesitant fuzzy linguistic information envelopment analysis models. Int J Intell Syst 36(5):2292–2322. https://doi.org/10.1002/int.22379
16. Lin M, Wang H, Xu Z (2020) TODIM-based multi-criteria decision-making method with hesitant fuzzy linguistic term sets. Artif Intell Rev 53:3647–3671. https://doi.org/10.1007/s10462-019-09774-9
17. Lin M, Huang C, Xu Z, Chen R (2020) Evaluating IoT platforms using integrated probabilistic linguistic MCDM method. IEEE Internet Things J 7(11):11195–11208
18. Lin M, Wang H, Xu Z, Yao Z, Huang J (2018) Clustering algorithms based on correlation coefficients for probabilistic linguistic term sets. Int J Intell Syst. https://doi.org/10.1002/int.22040
19. Lin M, Chen Z, Liao H, Xu Z (2019) ELECTRE II method to deal with probabilistic linguistic term sets and its application to edge computing. Nonlinear Dyn 96:2125–2143. https://doi.org/10.1007/s11071-019-04910-0
20. Lin M, Li X, Chen L (2019) Linguistic q-rung orthopair fuzzy sets and their interactional partitioned Heronian mean aggregation operators. Int J Intell Syst 35(2):217–249. https://doi.org/10.1002/int.22136
21. Lin M, Xu Z, Zhai Y, Yao Z (2017) Multi-attribute group decision-making under probabilistic uncertain linguistic environment. J Oper Res Soc 69(2):157–170. https://doi.org/10.1057/s41274-017-0182-y

22. Song Y, Li G, Ergu D, Liu N (2021) An optimisation-based method to conduct consistency and consensus in group decision making under probabilistic uncertain linguistic preference relations. J Oper Res Soc 1–15. https://doi.org/10.1080/01605682.2021.1873079
23. Song Y, Li G (2018) A large-scale group decision-making with incomplete multi-granular probabilistic linguistic term sets and its application in sustainable supplier selection. J Oper Res Soc 1–15. https://doi.org/10.1080/01605682.2018.1458017
24. Li Y, Kou G, Li G, Hefni MA (2022) Fuzzy multi-attribute information fusion approach for finance investment selection with the expert reliability. Appl Soft Comput 126:109270
25. Li G, Kou G, Peng Y (2022) Heterogeneous large-scale group decision making using fuzzy cluster analysis and its application to emergency response plan selection. IEEE Trans Syst Man Cybern: Syst 52(6):3391–3403
26. Zhang Z, Li Z, Gao Y (2021) Consensus reaching for group decision making with multi-granular unbalanced linguistic information: A bounded confidence and minimum adjustment-based approach. Inf Fus 74:96–110. https://doi.org/10.1016/j.inffus.2021.04.006
27. Zhang Z, Yu W, Martínez L, Gao Y (2020) Managing multigranular unbalanced hesitant fuzzy linguistic information in multiattribute large-scale group decision making: a linguistic distribution-based approach. IEEE Trans Fuzzy Syst 28(11):2875–2889
28. Malhotra T, Gupta A (2021) A new 2-tuple linguistic approach for unbalanced linguistic term sets. IEEE Trans Fuzzy Syst 29(8):2158–2168. https://doi.org/10.1109/TFUZZ.2020.2994987
29. Li D, Liu C, Gan W (2009) A new cognitive model: cloud model. Int J Intell Syst 24:357–375
30. Li DY, Du Y (2007) Artificial intelligence with uncertainty. Chapman and Hall/CRC, London
31. Li DY, Liu CY, Du Y, Han X (2004) Artificial intelligence with uncertainty. J Softw 15:1583–1594
32. Li DY, Han JW, Shi XM, Man CC (1998) Knowledge representation and discovery based on linguistic atoms. Knowl Based Syst 10:431–440
33. Song W, Zhu J (2019) A multistage risk decision making method for normal cloud model considering behavior characteristics. Appl Soft Comput 78:393–406
34. Song W, Zhu J, Wang H, Chang A (2020) Multistage risk assessment of direct delivery business from local oil refineries in Sinopec Group based on normal cloud model. Int J Prod Res 58(18):5624–5650
35. Wang D, Zeng D, Singh VP, Xu P, Liu D et al (2016) A multidimension cloud model-based approach for water quality assessment. Environ Res 149:113–121
36. Li LL, Liu LX, Yang CW, Li ZG (2012) The comprehensive evaluation of smart distribution grid based on cloud model. Energy Proc 17:96–102
37. Liao LC, Guo WW (2012) Incorporating utility and cloud theories for owner evaluation in tendering. Expert Syst Appl 39:5894–5899
38. Liu W, Zhu Z (2021) A multistage decision-making method for multi-source information with Shapley optimization based on normal cloud models. Appl Soft Comput 111(107716)
39. Meng XY, Zhang GW, Kang JC, Li HS, Li DY (2008) A new subjective trust model based on cloud model. IEEE International Conference on Networking, Sensing and Control, ICNSC '08:1125-1130
40. Meng QH, Lei LY, Kong AX (2012) Study on immune cloud model adapted to complex mechanical system diagnosis. Proc Eng 29:2167–2171
41. Wang P, Huang S, Cai C (2021) Dual linguistic term set and its application based on the normal cloud model. IEEE Trans Fuzzy Syst 29(8):2180–2194. https://doi.org/10.1109/TFUZZ.2020.2994994
42. Wang XK, Wang SH, Zhang HY, Wang JQ, Li L (2021) The Recommendation Method for Hotel Selection Under Traveller Preference Characteristics: A Cloud-Based Multi-Criteria Group Decision Support Model. Group Decision and Negotiation. https://doi.org/10.1007/s10726-021-09735-0
43. Wang JQ, Wu JT, Wang J, Zhang HY, Chen XH (2014) Interval-valued hesitant fuzzy linguistic sets and their applications in multi-criteria decision-making problems. Inf Sci 288:55–72. https://doi.org/10.1016/j.ins.2014.07.034
44. Jia Q, Hu J, Zhang W, Zhai S, Li Z (2023) A new situation assessment method for aerial targets based on linguistic fuzzy sets and trapezium clouds. Eng Appl Artif Intell 117:105610. https://doi.org/10.1016/j.engappai.2022.105610
45. Liu W, Zhu J (2022) A multistage decision-making method with quantum-guided expert state transition based on normal cloud models. Inf Sci 615:700–730
46. Liu W, Zhu J, Chiclana F (2023) Large-scale group consensus hybrid strategies with three-dimensional clustering optimisation based on normal cloud models. Inf Fus 94:66–91

47. Wang P, Xu X, Huang S, Cai C (2018) A linguistic large group decision making method based on the cloud model. IEEE Trans Fuzzy Syst 26(6):3314–3326
48. Wang HL, Feng YQ (2005) On multiple attribute group decision making with linguistic assessment information based on cloud model. Control Decis 20(6):679–685
49. Wang JQ, Peng L, Zhang HY, Chen XH (2014) Method of multi-criteria group decision-making based on cloud aggregation operators with linguistic information. Inf Sci 274:177–191
50. Liu CY, Feng M, Dai XJ, Li DY (2004) A new algorithm of backward cloud. J Syst Simul 16:2417–2420
51. Wang GY, Xu CL (2012) Cloud model-a bidirectional cognition model between concept's extension and intension. Proceeding of 1st International Conference on Advanced Machine Learning Technologies and Applications, CCIS 322:391–400
52. Wang GY, Xu CL, Zhang QH, Wang XR (2012) A multi-step backward cloud generator algorithm. Proceeding of 8th Internaltional Conference on Rough Sets and Current Trends in Computing, LNAI 7413:313–322
53. Wang G, Xu C, Li D (2014) Generic normal cloud model. Inf Sci 280:1–15
54. Wang GY, Xu CL, Zhang QH, Wang XR (2013) p-Order normal cloud model recursive definition and analysis of bidirecional cognitive computing. Chin J Comput 36:2316–2329
55. Wang X, Wang Y, Zhang H, Wang J, Li L, Goh M (2021) An asymmetric trapezoidal cloud-based linguistic group decision-making method under unbalanced linguistic distribution assessments. Comput Ind Eng 160:107457
56. Li CC, Dong Y, Liang H, Pedrycz W, Herrera F (2022) Data-driven method to learning personalized individual semantics to support linguistic multi-attribute decision making. Omega 111:102642. https://doi.org/10.1016/j.omega.2022.102642
57. Yang Y, Gai T, Cao M, Zhang Z, Zhang H, Wu J (2023) Application of group decision making in shipping industry 40: bibliometric analysis, trends, and future directions. Systems 11(2):69. https://doi.org/10.3390/systems11020069
58. Bao G, Lian X, He M, Wang L (2010) Improved two-tuple linguistic representation model based on new linguistic evaluation scale. Control Decis 25(5):780–784
59. Blavatskyy PR (2010) Modifying the mean-variance approach to avoid violations of stochastic dominance. Manage Sci 56(11):2050–2057

Publisher's Note Springer Nature remains neutral with regard to jurisdictional claims in published maps and institutional affiliations.

Springer Nature or its licensor (e.g. a society or other partner) holds exclusive rights to this article under a publishing agreement with the author(s) or other rightsholder(s); author self-archiving of the accepted manuscript version of this article is solely governed by the terms of such publishing agreement and applicable law.

Materials Letters 341 (2023) 134298

Contents lists available at ScienceDirect

Materials Letters

journal homepage: www.elsevier.com/locate/matlet

A novel reduced nano- phase change material based absorber for enhancing the water productivity and performance of solar desalination system

Anil Kumar [a], Anand Kushwah [a], Anil Kumar [a,b,*]

[a] Department of Mechanical Engineering, Delhi Technological University, Delhi 110042, India
[b] Centre for Energy and Environment, Delhi Technological University, Delhi 110042, India

ARTICLE INFO

Keywords:
Solar still
PCM
Nanoparticles
Yield
Water

ABSTRACT

In present research work, two different types solar stills - conventional solar still and advanced solar still (ASS) have been studied. To enhance the yield (productivity) of ASS a nano-phase change material (ZnO-PCM) has been used. Conventional and advanced solar still performance is compared under same climatological conditions in two investigation sets. Maximum thermal efficiency and improved yield are obtained as 51% and 6600 ml/m^2 for ASS-ZnO-PCM, respectively. Thus, cmulative yield of ASS-ZnO/PCM (6600 ml/m^2) was nearly 113% more than conventional SS (3090 ml/m^2.day). As a result, the productivity of ASS-ZnO/PCM has increased by about 36% employing the PCM.

1. Introduction

Water is one of the amplest resources on earth, making up around 75% of the earth. However, a major crisis in many nations is inadequate water. Choosing a suitable and affordable desalination process is necessary to address the fresh water shortage. Sun's power is a more important renewable energy source and plays a significant role in solar water heating, cooking, drying, air heating, cooling, power generation, and water desalination. Among the earlier solar energy methods, solar water desalination is an efficient and attractive technique for providing drinkable water, which is the life of all living being [1]. Several techniques of solar water desalination have been studied and put for experiments. Amongst them, solar stills (SS) are more common, lower price, small scale, and existing system, which can be used to drinkable stock water for humans in arid regions. Number of studies have been carried out to improve productivity and thermal efficiency of SS systems. In addition, the performance of solar still systems has been improved by introducing reflectors, nanoparticles [2], phase change solar still. Among the aforementioned factors, applying nanoparticles to a brine has attracted much attention for enhancing solar intensity adsorption [3]. Different nanoparticles have been used for this purpose i. e. SiO_2, ZnO, CuO, Al_2O_3, CuO_2, TiO_2, Fe_2O_3, SnO_2, graphite, and SiC [4]. Sharshir et al. used graphite and CuO nanoparticles in SS to increase its yield. Productivity improved as 44.91% and 53.95% for CuO and graphite nanoparticles, respectively [5]. Elango et al. studied the effect of ZnO, SnO_2, and Al_2O_3 in single basin SS. Their findings revealed that productivity was 18.63%, 12.67%, and 29.95% more than without nanoparticle use [6]. Madhu et al. evaluated the performance analysis of CSS using CuO, TiO_2, and Al_2O_3 nanoparticles in brine water. The results indicated that solar still achieved maximum efficiency (50%) using Al_2O_3 nanoparticles [7]. Hasanianpour and Ameri developed a single slope SS and tested the performance of system using γ-Al_2O_3 nanoparticles in base fluid. It was observed from the findings that productivity of fresh water had increased up to 61% [8]. Recently, a variety of nanoparticles, namely Al_2O_3/Cu, Fe_3O_4/carbon, TiO_2/Cu, TiO_2/Ag, and CuO/graphene oxide (GO), have been synthesised and used to improve heat transfer rate in heat exchangers, solar stills, and other heat transfer equipment [9].

In current work, effect of nano-phase change material name paraffin wax (ZnO-PCM) on yield of advanced solar still (ASS) by adding a 20 mm ZnO-PCM nano-particle layer underneath the absorber plate and an external condenser with an electric fan was examined. The influence of different parameters, such as nano-phase change material concentration in base fluid and volume ratio of ZnO and PCM in hybrid nanocomposite, were also experimentally analyzed.

2. Materials and methods

The fabrication, installation, and procedure for the experiment are

Abbreviations: BWT, Basin Water Temperature; SS, Solar Still.

* Corresponding author at: Department of Mechanical Engineering, Delhi Technological University, Delhi 110042, India.
E-mail address: anilkumar76@dtu.ac.in (A. Kumar).

https://doi.org/10.1016/j.matlet.2023.134298
Received 7 February 2023; Received in revised form 15 March 2023; Accepted 25 March 2023
Available online 28 March 2023
0167-577X/© 2023 Elsevier B.V. All rights reserved.

Nomenclature

P_F	DC fan power
m_{np}	Mass of nanoparticles (gm)
η_d	Daily thermal efficiency (%)
A	Area of the system (m^2)
m_w	Mass of water (ml)
T_w	Temperature of water (℃)

discussed in this section.

2.1. Material used

A stainless steel sheet of 2 mm thickness (thermal conductivity 58 W/m^2K and density 7.80 g/cm^3), plywood of thickness 20 mm, and polystyrene (thermocol) of thickness 20 mm were brought from local market of Gwalior (India). Toughened glass of 4 mm thickness was used to enclose the system. Copper tube of 5 mm diameter was used to make a condenser on the back walls of solar still.

i.

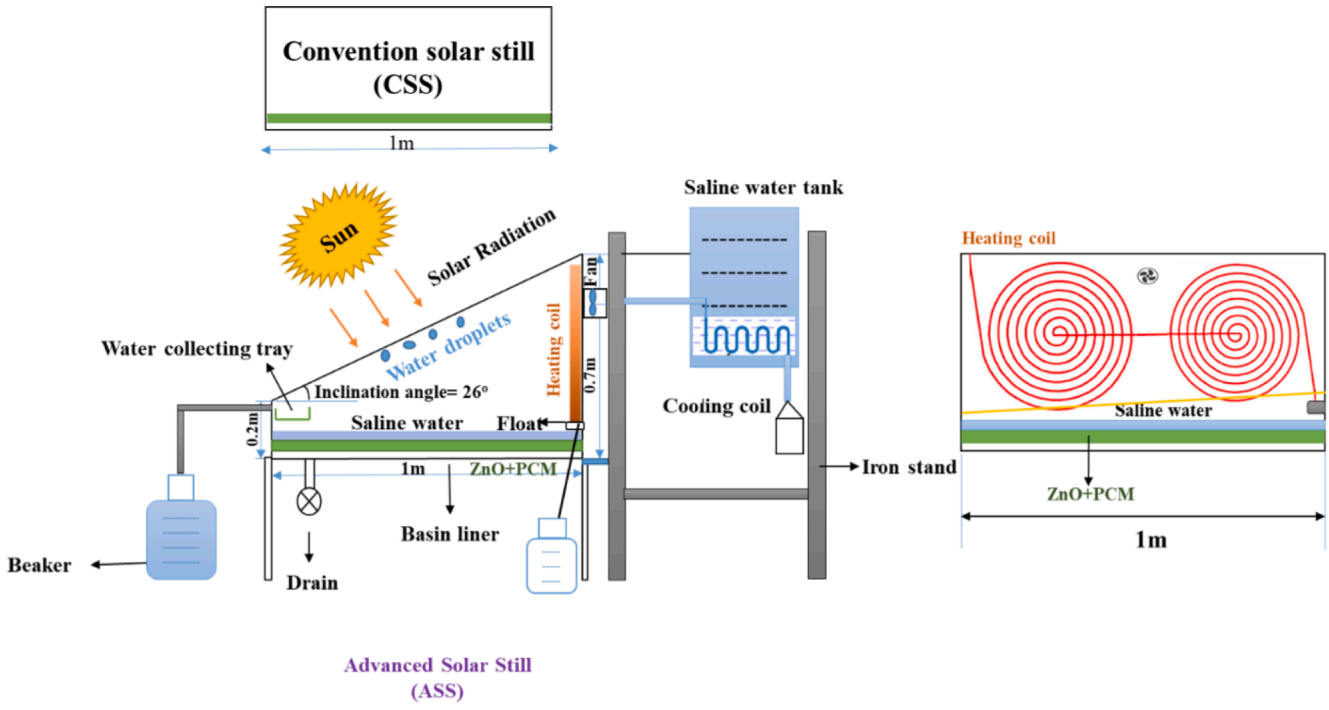


Fig. 1. Schematic view of experimental setup.

Table 1
Detailed description of experimental setup.

Component	Description
Solar still	
Plywood	20 mm (Thickness)
Thermocol (Polystyrene)	20 mm (Thickness)
Steel sheet	2 mm (Thickness)
Glass cover	4 mm (Thickness)
Iron stand	02 ((Thickness 5 mm)
Basin area	1 m × 1 m
Lower height	0.2 m
Height of back wall	0.7 m
Inclination angle	26°
Latitude of site location	26.2183° N, 78.1828° E
DC fan	
Types	06 W DC solar powered
Copper tube	
Length of copper tube heater	4 m
Diameter of copper tube	5 mm
Thickness of PCM-ZnO layer	20 mm

2.2. Methodology

In current research, two types of SS systems have been fabricated in the Madhav Institute of Science and Technology, Gwalior (India) solar energy lab. The first is considered a CSS, while the second is an advanced SS, as shown in Fig. 1. The CSS is used to build a stainless steel sheet of 2 mm thickness. A detailed description of CSS and ASS is discussed in Table 1. A toughened glass of 4 mm thickness enclosed the system and acted as a condensing surface. An inclined trough was attached to the lower edge of solar still for collecting the condensates water. In ASS, a 20 mm ZnO/PCM nano-particle layer is underneath the absorber plate.

2.3. Instrumentation for recording observations

i. Data-logger (Data Taker DT85 series 3, Australia) is installed and records relative humidity (Rh) and ambient air temperature. Experimentation work is carried out from 8:00 to 20:00hr.
ii. Anemometer (Dynalab DLAW 8701) measures airflow rate (m/s) over the glass cover of CSS and ASS.
iii. Solarimeter (Megger PVM 210) is mounted and used to record direct beam radiations and diffused solar radiations at regular intervals.

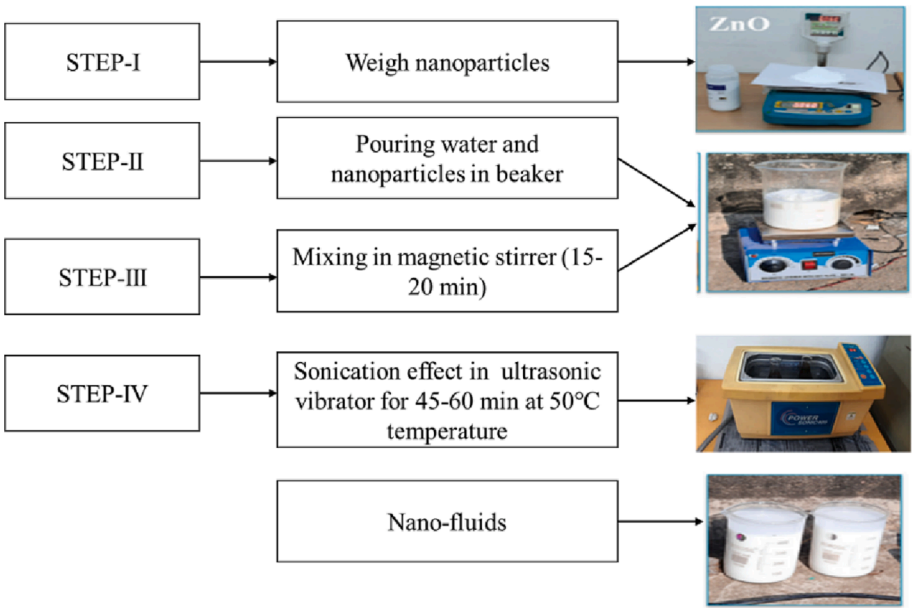


Fig. 2. Nano fluids preparation.

iv. K-type thermocouples are used to record the temperature.

2.4. Thermal efficiency of system

Thermal efficiency of solar still system can be calculated using the following relations [9]:

$$\eta_d = \frac{\sum m \cdot \times h_{fg}}{\sum A \times I + P_F} \tag{1}$$

Latent heat of vaporization (h_{fg}) according to water temperature can be evaluated as [9]:

$$h_{fg} = 3.1625 \times 10^6 + \left[1 - \left(7.1616 \times 10^{-4} \times T_w\right)\right] \text{for } T_w > 70\,^{\circ}\text{C} \tag{2}$$

$$h_{fg} = 2.4935 \times 10^6 \left[1 - \left(9.4779 \times 10^{-4} \times T_w\right) + \left(1.3131 \times 10^{-7} \times T_w^2\right) - \left(4.7974 \times 10^{-9} \times T_w^3\right)\right] \text{for } T_w < 70\,^{\circ}\text{C} \tag{3}$$

2.5. Nano-fluid preparation

Nanoparticles ZnO are hydrophobic in nature. To make nanoparticles hydrophilic some methodologies have been implemented. Fig. 2 demonstrate the step involved in preparation of Nano-fluids. Usually, it was observed that most researchers had adopted surfactants and dispersants to make nanoparticles solvable in water.

Boiling point temperature of water increases due to surfactants and dispersants, under which water will evaporate slowly. Concentration of nanoparticles is determined using Eq. (4) [9].

$$\varphi_{np} = \left(\frac{m_{np}}{m_{np} + m_w}\right) \times 100 \tag{4}$$

3. Results and discussion

3.1. Performance analysis of ASS with heating coil and ZnO + PCM (ASS-PCM)

A mixture of phase change material (PCM) and ZnO nanoparticles, which act as thermal storage bed, was employed underneath the absorber plate of ASS to enhance productivity. The experiment was conducted on ASS employing a heating coil and PCM to reduce the glass cover temperature by storing energy during high solar intensity and temperature periods and then releasing it again. Temperature plays a significant role in PCM during charging and discharging process. Energy is stored as sensible and latent heat, depending on whether the PCM temperature is outside or inside the melting temperature limit. Energy is stored and released during charging and discharging processes, respectively. The variation of PCM and water temperature for ASS-ZnO/PCM and CSS are demonstrated in Fig. 3(a). PCM with ZnO nanoparticles has superior thermal conductivity and lower melting and solidification temperatures than PCM without nanoparticles. Curve trends indicate that the temperature of water for ASS-PCM & CSS and temperature of PCM progressively increased from the early morning until about 13:00 h and then began to reduce. Heat transmitted from absorber to PCM before 13:00 h and heat transmitted from PCM to absorber later. It is because, after 13:00 h, PCM temperature begins to drop until it achieves the atmospheric temperature. The difference in water temperature between ASS-ZnO/PCM and conventional SS was more during the discharging than during the charging period (Fig. 3(a). It is because heat is transmitted from PCM to ASS-ZnO/PCM absorber.

Fig. 3(b) shows the hourly and cumulative productivities for ASS-ZnO/PCM and CSS. The curve trends indicate that ASS-ZnO/PCM constantly performs more efficiently than CSS in terms of yield during the experimentation. It is because of high BWT, evaporation, and condensation rates for ASS-ZnO/PCM compared to conventional SS. The cumulative yield of ASS-ZnO/PCM (6600 ml/m^2) was nearly 113% more than that of conventional SS (3090 ml/m^2), as presented in Fig. 3(b). As a result, the productivity of ASS-ZnO/PCM has increased by about 36% employing the PCM.

3.2. Thermal efficiency and increased yield of ASS

Thermal efficiency and freshwater yield play a significant role in the evaluation of thermal performance of SS system. Productivity improvement for ASS compared to CSS is shown in Fig. 3(b) as a percentage increase. Therefore, the representation of thermal efficiency for each case is discussed. Maximum thermal efficiency and improved yield are calculated as 51% and 113% for ASS-ZnO/PCM, respectively.

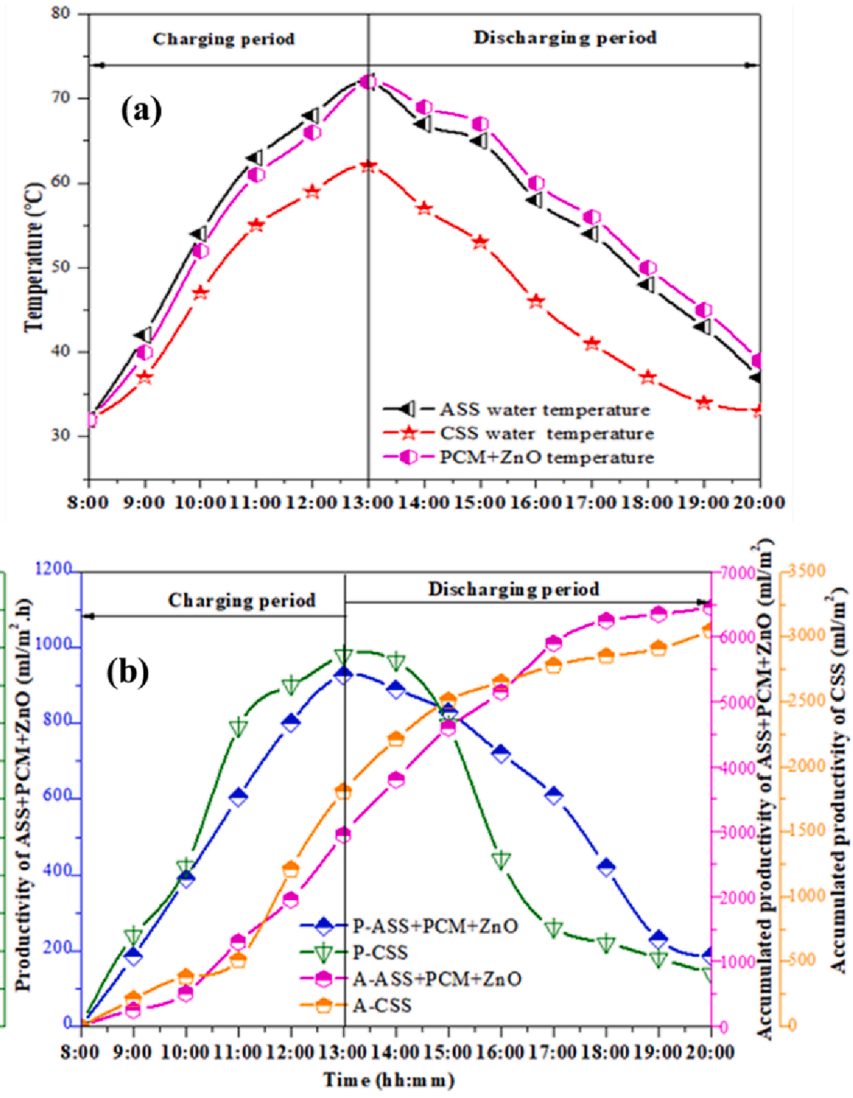


Fig. 3. **(a)** Variation in temperature for ASS, CSS, and ASS-ZnO/PCM, **(b)** Representation of productivity and accumulated productivity.

4. Conclusions

The experiment was performed to compare the thermal performance, efficiency, and productivity of fresh water in CSS and ASS (for ZnO/PCM) under identical metrological conditions. The results demonstrate the following conclusions:

- Cumulative yield of ASS (5500 ml/m^2.day) was nearly 77% more than conventional SS (3090 ml/m^2.day).
- Cumulative yield of ASS-ZnO/PCM (6600 ml/m^2) was attained nearly 113% more than conventional SS (3090 ml/m^2.day). The productivity of ASS-ZnO/PCM has increased by about 36% employing the PCM.
- Maximum thermal efficiency and improved yield are obtained as 51% and 113% for ASS-ZnO/PCM, respectively.

CRediT authorship contribution statement

Anil Kumar: Methodology, Writing – original draft, Investigation. **Anand Kushwah:** Investigation, Conceptualization, Formal analysis, Validation. **Anil Kumar:** Conceptualization, Writing – review & editing, Visualization, Supervision.

Declaration of Competing Interest

The authors declare that they have no known competing financial interests or personal relationships that could have appeared to influence the work reported in this paper.

Data availability

Data will be made available on request.

Acknowledgment

The authors thank MITS, Gwalior (India) and Centre for Energy and Environment, Delhi Technological University, for providing basic infrastructure for compiling this work.

References

[1] A.E. Kabeel, Z.M. Omara, M.M. Younes, Techniques used to improve the performance of the stepped solar still-a review, Renew. Sustain. Energy Rev. 46 (2015) 178–188, https://doi.org/10.1016/j.rser.2015.02.053.
[2] M.M. Younes, A.S. Abdullah, F.A. Essa, Z.M. Omara, Half barrel and corrugated wick solar stills – Comprehensive study, J. Energy Storage 42 (2021), 103117, https://doi.org/10.1016/j.est.2021.103117.

[3] A.K. Thakur, R. Sathyamurthy, S.W. Sharshir, A. Elnaby Kabeel, M. Shamsuddin Ahmed, J.Y. Hwang, A novel reduced graphene oxide based absorber for augmenting the water yield and thermal performance of solar desalination unit, Mater. Lett. 286 (2021), 128867, https://doi.org/10.1016/j.matlet.2020.128867.
[4] A. Sampathkumar, S.K. Natarajan, Experimental investigation on productivity enhancement in single slope solar still using Borassus Flabellifer micro-sized particles, Mater. Lett. 299 (2021), 130097, https://doi.org/10.1016/j.matlet.2021.130097.
[5] S.W. Sharshir, G. Peng, L. Wu, N. Yang, F.A. Essa, A.H. Elsheikh, S.I.T. Mohamed, A. E. Kabeel, Enhancing the solar still performance using nanofluids and glass cover cooling: experimental study, Appl. Therm. Eng. 113 (2017) 684–693.
[6] T. Elango, A. Kannan, K. Kalidasa Murugavel, Performance study on single basin single slope solar still with different water nanofluids, Desalination 360 (2015) 45–51, https://doi.org/10.1016/j.desal.2015.01.004.
[7] B. Madhu, E. Bala Subramanian, P.K. Nagarajan, R. Sathyamurthy, D. Mageshbabu, Improving the yield of freshwater and exergy analysis of conventional solar still with different nanofluids, FME Trans. 45 (4) (2017) 524–530, https://doi.org/10.5937/fmet1704524M.
[8] Z. Hasanianpour Faridani, A. Ameri, Performance enhancement of a basin solar still using γ-Al2O3 nanoparticles and a mixer: an experimental approach, J. Therm. Anal. Calorim. 147 (3) (2022) 1919–1931, https://doi.org/10.1007/s10973-021-10564-1.
[9] R. Anshika, S. Suresh, K. Anil, Review on thermal modeling of solar desalination systems, Res. J. Chem. Environ. 23 (4) (2019) 90–102.

A Practical PHEV Charging Policy to Improve Performance of Power Distribution Systems

Divyanshu Khandelwal
Department of Electrical Engineering
Delhi Technological University
New Delhi, India
divyanshudeutsch@gmail.com

Shefali Painuli
Department of Electrical Engineering
Delhi Technological University
New Delhi, India
shefalipainuli28@gmail.com

Suman Bhowmick
Department of Electrical Engineering
Delhi Technological University
New Delhi, India
suman.bhowmick@dce.ac.in

Radheshyam Saha
Department of Electrical Engineering
Delhi Technological University
New Delhi, India
rshahacno@yahoo.com

2023 International Conference on Power, Instrumentation, Energy and Control (PIECON) | 979-8-3503-9976-9/23/$31.00 ©2023 IEEE | DOI: 10.1109/PIECON56912.2023.10085850

***Abstract*— Continuously dwindling fossil fuel reserves, high fuel costs, greenhouse gas (GHG) emissions and global warming has led to increased penetration of electric vehicles (EVs) in the transportation sector. However, EV charging increases the system load with high peak and off-peak demand ratio in the daily load profile, thereby causing increased system losses, poor bus voltages and power quality issues in power distribution systems. Adoption of a suitable electric vehicle charging policy can minimize this load profile distortion and reduce the maximum load. In this paper, a study on the charging effects of about 3000 electric vehicles in more than 800 residents is carried out on a 240-bus real distribution grid located in the Midwest U.S. Multiple case studies were carried out to investigate the profiles of the network demand and bus voltages without and with EV charging, vis-à-vis implementation of a practical PHEV charging policy. The results confirm the improvement of load and bus voltage profiles, thus validating the proposed EV charging guidelines.**

Keywords*— charging policies, daily load profile, distribution system, EVs, NHTS.

I. INTRODUCTION

About ninety percent energy for the world's transportation comes from petroleum based fuels, mostly gasoline and diesel. This fact is observed from the 2017 data of transportation energy resources in the U.S. which includes 55% gasoline (petroleum), 22% distillate (petroleum), 12% jet fuel (petroleum), 5% biofuel, 3% natural gas, and 3% others [1]. Therefore, transportation sector is considered as one of the major user of greenhouse gas emitting fossil fuels. Also, the use of fossil fuels in transportation has been deteriorating the environment. For revitalizing ecological balance, fossil fuel consumption should be eliminated [2].

Electric vehicles (EVs) have noticeably evolved as an alternative to internal combustion engine (ICE) vehicles [3]-[5]-[6]. However, with increase in the level of EV penetration, the existing distribution network configuration will be affected in terms of demand profile distortion, increased line losses, voltage dip, power quality, loss of transformer life and grid stability issues [7]-[9].

Presently, there are various types of EVs available in the market which can be broadly categorized as: Battery Electric Vehicles (BEVs), Hybrid Electric Vehicles (HEVs) and Plug-in Hybrid Electric Vehicles (PHEVs) [10]. The description of the same is given in Table I.

EVs consume a significant amount of electrical power which is being supplied by the distribution grid [10]-[11]. Therefore, in order to investigate the impacts of EV charging on power distribution systems, efficient modelling of EV charging is necessary. Commonly, charging of PHEVs can be divided into two broad scenarios - smart and non-smart charging [12]. In the former, the power rate and the time of PHEV charging is optimally adjusted, whereas, in the latter, the PHEV owners charge their vehicles right after arriving home with a fixed power rate, which has adverse impacts on the distribution network [10]. Therefore, for the worst-case scenario, non-smart or uncoordinated charging is considered in our study.

TABLE I. CLASSIFICATION OF EVS

BEV	HEV	PHEV
Battery is fully charged by electricity.	Battery can be charged by gasoline engine and regenerative braking.	Battery can be charged by gasoline engine, power grid and regenerative braking.
Can be plugged into an external power grid for charging battery.	Cannot be charged by power grid.	Can be plugged into an external power grid for charging battery.

In this paper, a study on the charging effects of about 3000 electric vehicles in more than 800 residents is carried out on a 240-bus real distribution network [13] in the Midwest U.S.A. The real system belongs to a municipal utility and has smart meters installed at all customer premises. This network is supplied by a 69-kV substation, with the three-phase substation transformer used to supply the feeders at 13.8 kV. Further, three-phase and single-phase secondary distribution transformers are used to supply the commercial and residential customers at 240 V and 240 V/120 V, respectively. Unlike most of the IEEE standard distribution test systems, this 240-bus network contains hourly real and reactive power demand of all customers. The hourly demand profile due to PHEV charging is constructed for residential customers on the basis of details like vehicle type, distance travelled and starting time of charging based on the realistic U. S. national household travel survey (NHTS) data of 2009 [14]. These generated demand profiles are then analyzed with respect to the base demand profile of the 240-bus network. A practical charging policy is adopted to minimize the distortion of the demand profile due to the PHEV charging. The policy is used to achieve two objectives – reduce the peak demand and flatten the demand

979-8-3503-9976-9/23/$31.00 ©2023 IEEE

Authorized licensed use limited to: DELHI TECHNICAL UNIV. Downloaded on April 10,2023 at 07:26:30 UTC from IEEE Xplore. Restrictions apply.

profile. Multiple case studies are carried out in the MATLAB platform to investigate the profiles of the total demand and the bus voltages in the 240-bus network, without and with PHEV charging, vis-à-vis adoption of the proposed charging policy. Results demonstrate that adoption of the PHEV charging policy results in reduced system losses and marked improvements in the profiles of the network demand and bus voltages.

II. Charging Model of a PHEV

PHEVs can completely drive in electric mode at full power but for a specific range. The PHEV charging influences the distribution network since they consume large amount of electrical power which leads to unpleasant peaks in the network demand profile. This section illustrates the parameters used in the charging model of a PHEV which is described in the following subsections.

A. PHEV Battery Capacity

Knowing the fact that PHEVs runs on blended mode (either using battery or by using gasoline), they are defined by their All-Electric-Range (AER). AER is the distance covered by a PHEV with a completely charged battery. In general, PHEVs are stated in the format 'PHEVx'. Here, 'x' represents the AER of the PHEV. For example, PHEV30 indicates a PHEV having an AER of 30 miles i.e., this PHEV can travel 30 miles in the electric mode with a fully charged battery.

Table II (columns 1-2) details the battery capacity and the electrical energy consumption per mile (ECPM) for PHEV33 of different types as per the study by Pacific Northwest National Laboratory (PNNL) [15]. This calculation can be further extended for PHEV40 as shown in column 3 of Table II.

TABLE II. PHEV33 and PHEV40 Battery Capacities and ECPM for Different Types of Vehicles

Vehicle Type	ECPM (kWh/mile)	PHEV33 Battery Capacity (kWh)	PHEV40 Battery Capacity (kWh)
1. Compact Sedan	0.26	8.6	10.4
2. Mid-size Sedan	0.30	9.9	12.0
3. Mid -size SUV	0.38	12.5	15.2
4. Full-size SUV	0.46	15.2	18.4

Therefore, the formulation of PHEV usable battery capacity (C) is as follows,

$$C = AER \times ECPM \tag{1}$$

B. State of Charge (SOC)

SOC is defined as the amount of stored energy in a battery. In this study, SOC is considered as the residual energy in the battery of a PHEV when it arrives home. The expression for the SOC of a PHEV is given as

$$SOC = \left(1 - \frac{\alpha * d}{AER}\right) 100 \tag{2}$$

where 'α' is a factor representing the percentage of distance travelled by a PHEV in electric mode, 'd' is the total travelled distance and 'α*d' is the distance travelled by a PHEV in electric mode. In this paper, α and AER is taken as 0.6 and 40 respectively. It should be noted that (2) is valid only when 'α*d' is less than AER else SOC will be zero or negligible.

C. Energy Required for PHEV battery charging

The energy required by a PHEV for charging the battery depends on the battery capacity and its SOC. Therefore, the amount of electrical energy 'E_g' required by a PHEV for charging is a function of the battery capacity 'C' and 'SOC' which is depicted in (3) as,

$$E_g = \frac{\left(1 - \frac{SOC}{100}\right) C}{\eta} \tag{3}$$

where 'η' is PHEV battery efficiency.

In literature, 'η' is selected as 90% [16] and 88% [17]. In this study, efficiency is taken as 90% i.e., η = 0.9.

D. Charging Time (T_{ch})

The time required for charging a PHEV depends on certain parameters like its AER, C, SOC and the charging level (Table IV). Therefore, the charging time required by a PHEV (T_{ch}) is decided on the basis of 'E_g' and the charging level ('ch level') as given in (4),

$$T_{ch} = \frac{E_g}{ch\ level} \tag{4}$$

III. Assumptions and Input Data

This section describes the data and the assumptions which are utilized in the study of this paper.

A. Filtering NHTS 2009 Data

In this study, NHTS 2009 data is used for extracting the trip characteristics of the vehicles. NHTS furnishes an encyclopedic travel pattern data in the U.S [14]. The database contains two Microsoft Excel files, VEHV2PUB.csv and DAYV2PUB.csv.

(a) VEHV2PUB.csv: This file demonstrates vehicle's characteristics and provides information related to more than three lakh vehicles. Eight attributes for each vehicle are used in this paper. They are: HOUSEID, TDAYDATE, TRAVDAY, PERSONID, VEHID, VEHTYPE, HHVEHCNT, BESTMILE. HOUSEID, PERSONID provides the trip characteristics covered by a specific member of a particular house. TDAYDATE and TRAVDAY stands for the date of travel and the day of the week respectively. HHVEHCNT indicates the count of vehicles in a household. Since BESTMILE is the best estimation of annual miles of each vehicle therefore, it is divided by 365 to extract daily miles travelled (DailyMile). VEHTYPE and VEHID indicates the type of the vehicle and the particular vehicle of a house used in a specific trip respectively.

(b) DAYV2PUB.csv: This file demonstrates trip characteristics and consists of more than 10 lakh trips. Nine attributes of each trip are used in this paper. They are: HOUSEID, TDAYDATE, TRAVDAY, PERSONID, VEHID, VEHTYPE, ENDTIME, TDTRPNUM and HHVEHCNT. ENDTIME indicates the time at which the trip ends. It is considered as the charging start time in this paper. TDTRPNUM indicates travel day trip number which is the number of trips covered by a vehicle in a day. VEHV2PUB.csv and DAYV2PUB.csv are merged to form a common file containing the required data. Table III presents

Authorized licensed use limited to: DELHI TECHNICAL UNIV. Downloaded on April 10,2023 at 07:26:30 UTC from IEEE Xplore. Restrictions apply.

TABLE III. FILTERED NHTS 2009 DATA

HOUSEID	TDAYDATE	TRAVDAY	PERSONID	VEHID	VEHTYPE	ENDTIME	TDTRPNUM	HHVEHCNT	BESTMILE
20005517	200809	2	1	1	1	1800	1	1	10967.11
20006381	200804	2	3	1	1	2120	4	3	22183
20008273	200806	2	2	1	4	1845	6	2	18792.09
20024170	200808	2	1	1	1	1705	2	2	9192.44
20026482	200808	2	1	1	3	1745	4	3	24509.68
. .	. .	. .	. .	. .	. .	. .	. .	. .	. .

a small portion of the filtered data.

B. Charging Standards and Strategy

There are various charging standards (both AC and DC) for EVs as presented in Table IV [17]-[19]. SAE J1772 and IEC 62196 Type 1 couplers are used in Japan and US for residential and public charging by AC while IEC 62196 Type 2 is employed in the European market [20]. Generally, rapid DC charging circuit includes CHAdeMO (Charge de Move) and CCS (Combined Charging System) which are extensively used in charging or parking stations and in highways [21].

TABLE IV. DIFFERENT CHARGING STANDARDS FOR EVS

SAEJ1772			**IEC**			
AC Charging			***AC Charging***			
Level 1	***Level 2***	***Level 3***	***Level 1***	***Level 2***	***Level 3***	
Single Phase 120 V 12 A 1.44 kW	Single Phase (208-240) V 32 A (6.66-7.68) kW	Three Phase (208-600)V 400 A >7.68 kW	Single Phase 16 A (4-7.5) kW	Single /Three Phase 32 A (8-15) kW	Three Phase 250 A (60-120) kW	
DC Charging			***DC Charging***			**CHAdeMO** ***DC Charging***
Level 1	***Level 2***	***Rapid Charging***	***Rapid Charging***			***Rapid Charging***
(200-450) V 80 A 40 kW	(200-450) V 200 A 90 kW	125 A 62.5 kW	400 A (1000-2000) kW			125 A 62.5 kW

In this paper, residential charging (120 V) in U.S. is considered and hence, level 1 SAEJ1772 standard is used, with 120 V AC, 12 A, 1.4 kW outlet. The modelling of PHEVs is done using (1) to (4).

The total number of customers in the system are 1079 [22] and each customer is considered as a household receiving single phase 120 V supply. The 240-bus system has 139 load buses which are single phase and customers allotted to each of them pertain to the phase (A, B or C) of that particular bus. The number of three phase load buses are 55 and customers allotted to each of them are distributed equally among the three single phases (A, B and C), in order to minimize phase unbalance. It is assumed in this paper that all customers charge their EVs from the confines of their home at 120 V, following the last trips of the vehicles.

C. Load Profile

For obtaining the daily load curve, the smart meter data of all the customers is taken into account [22]. On this basis, a 24-hour demand curve is plotted which is the base case for this study.

D. Charging Policy

To minimize the effect of PHEV charging on the profiles of the system demand and the bus voltages, a practical charging policy is proposed in this work. As per this policy, all vehicles arriving home for charging between the interval 16:00 hrs to 03:00 hrs (next day) will be allowed to charge only if their SOC is below 50%. Otherwise, they will be allowed to charge after 3 AM only. The proposed policy is aimed to flatten the daily load profile, improve the bus voltage profile and reduce the system losses.

IV. RESULTS AND DISCUSSIONS

Fig. 1. details the distribution system used in the study. It represents a residential network, having a secondary side low voltage of 120V for single phase customers and 208 V for three phase customers [13]. The complete table for the same is available in the load data provided in [22].

To compute the charging demand due to the PHEVs, the following methodology is adopted:

1. Each household (from the NHTS 2009 data) represents a single-phase customer. The number of customers allocated to the buses are carried out as per table V.
2. The charging demand of each household (customer) is computed based on the number of PHEVs, type of the PHEV and its mileage using (1)-(3) and Table IV.
3. The allocation of number of customers to each individual phase (‘a’, ‘b’ or ‘c’) is carried out using the customer data provided in Table V and as already detailed in Section III.
4. Finally, the charging demand of each phase is computed by summing the demands of all the customers pertaining to that phase. This is carried out for all the buses.

Fig. 2 shows the total hourly demand (three-phase) of the 240-bus network, on a typical summer weekday. The plot in blue colour shows the base load demand (without any PHEV). The red one presents the total network demand with PHEV charging.

From Fig. 2, it can be observed that the demand starts increasing from 3 p.m. onwards as residential customers start to plug in their vehicles after arriving home. Therefore, in order to counter this peak charging demand, a practical charging policy is adopted which doesn’t allow the charging of vehicles between 16:00 to 03:00 hrs (next day). The network demand with the charging policy is shown in green colour. It can be observed that with the charging policy, the total network demand (in green) with PHEV charging has substantially flattened than that without any policy (in red).

Authorized licensed use limited to: DELHI TECHNICAL UNIV. Downloaded on April 10,2023 at 07:26:30 UTC from IEEE Xplore. Restrictions apply.

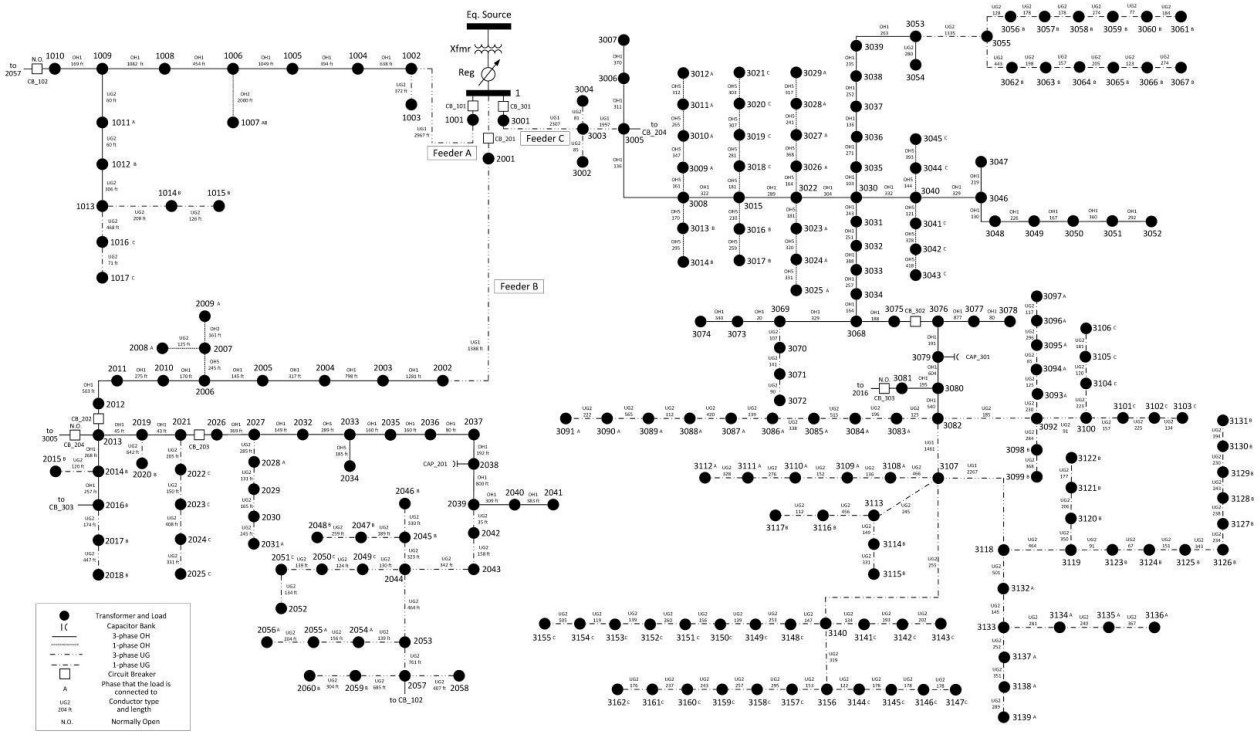


Fig. 1. 240-Bus Distribution Test System [13]

Figs. 3-5 shows the bus voltage profiles of the distribution network without and with PHEV charging at 18:00 hrs for phases A, B and C, respectively. It can be observed from all the plots that the bus voltage profiles with PHEV charging have deteriorated as compared to the cases without PHEV. The system losses (at 18:00 hrs) for the base case (without any PHEV) and with PHEV (without any charging policy) are 31.06 kW and 71.43 kW, respectively. Thus, with PHEV charging, the system losses have increased substantially.

TABLE V. CUSTOMER DATA

Bus Number	Transformer Type	Voltage (V)	Connection & Load Model	Number of customers
1003	3Ø-T	208	wye-PQ	4
.	.	.	.	.
1010	3Ø-T	208	wye-PQ	4
1011	1Ø-CT	120	wye-PQ	13
1012	1Ø-CT	120	wye-PQ	7
1013	3Ø-T	208	wye-PQ	3
.	.	.	.	.
3034	3Ø-T	208	wye-PQ	9
.	.	.	.	.
3147	1Ø-CT	120	wye-PQ	17
.	.	.	.	.
3162	1Ø-CT	120	wye-PQ	3

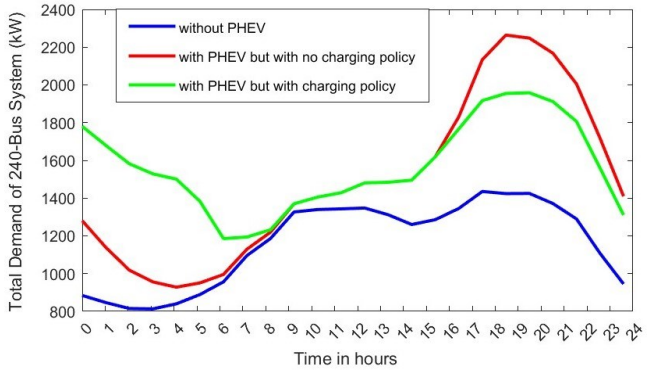


Fig. 2. Total Demand Profile for 240-Bus Distribution System for Different Scenarios

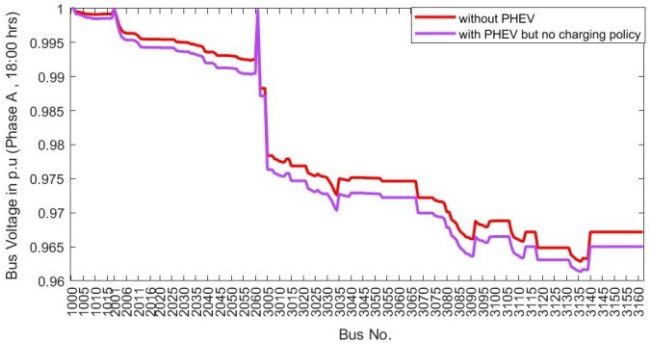


Fig. 3. Bus Voltage for 240-Bus Distribution System without and with PHEV Charging for Phase-A at 18:00 hrs

Authorized licensed use limited to: DELHI TECHNICAL UNIV. Downloaded on April 10,2023 at 07:26:30 UTC from IEEE Xplore. Restrictions apply.

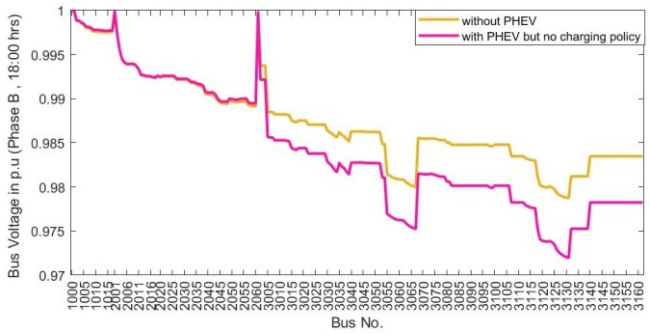


Fig. 4. Bus Voltage for 240-Bus Distribution System without and with PHEV Charging for Phase-B at 18:00 hrs

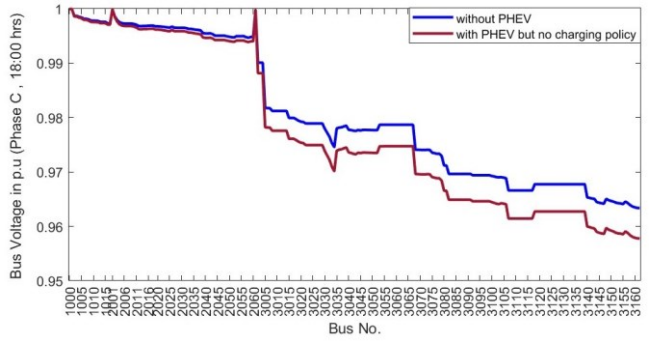


Fig. 5. Bus Voltage for 240-Bus Distribution System without and with PHEV Charging for Phase-C at 18:00 hrs

The bus voltage profiles of the network (at 18:00 hrs) pertaining to phases A, B and C without and with PHEV charging policy is shown in Figs. 6-8 respectively. It can be observed from the plots that the network bus voltage profile after adoption of PHEV charging has improved substantially than that without any policy.

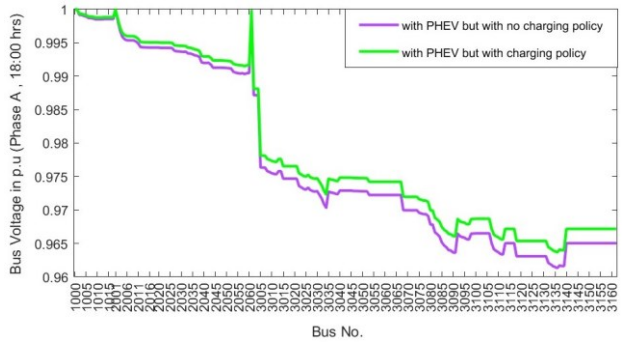


Fig. 6. Bus Voltage for 240-Bus Distribution System with PHEV Charging and Charging Policy for Phase-A at 18:00 hrs

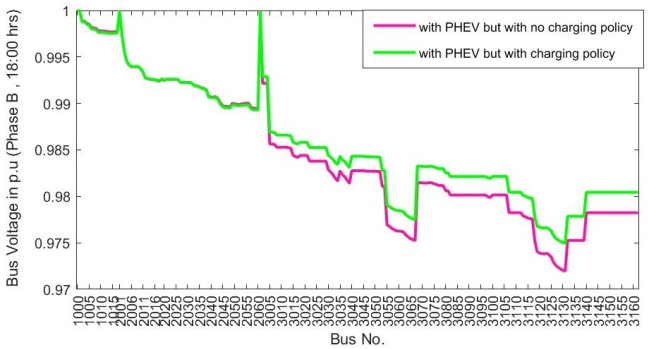


Fig. 7. Bus Voltage for 240-Bus Distribution System with PHEV Charging and Charging Policy for Phase-B at 18:00 hrs

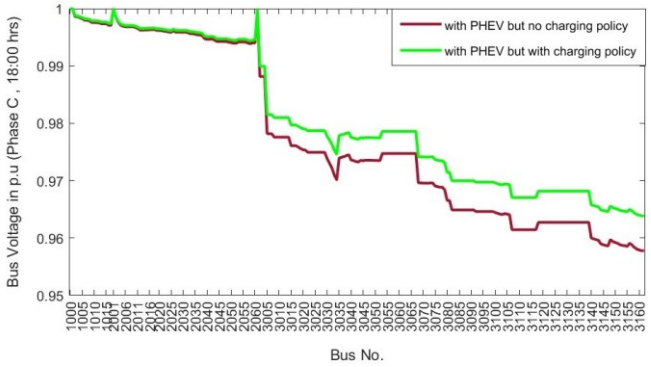


Fig. 8. Bus Voltage for 240-Bus Distribution System with PHEV Charging and Charging Policy for Phase-C at 18:00 hrs

The system losses (at 18:00 hrs) with PHEVs but without any charging policy and with the proposed PHEV charging policy are 71.43 kW and 56.53 kW, respectively. Thus, after the adoption of the PHEV charging policy, the system losses have decreased substantially.

Bus no. 3147 is a single-phase bus (Phase-C) with 17 connected customers and bus no. 3034 is a three-phase bus with 9 connected customers. These two buses are targeted for further investigations as they have the maximum number of customers (and hence PHEVs) connected.

Fig. 9 shows both the 24-hour voltage profile for single phase bus 3147 with PHEV charging, without and with charging policy. From Fig. 9, it is observed that adoption of the proposed charging policy substantially improves the voltage profile during peak charging hours (1600-2100 hrs).

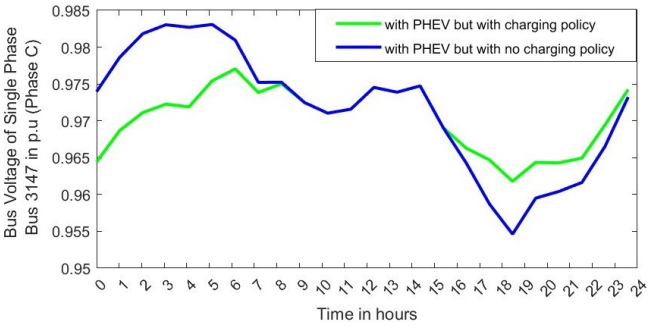


Fig. 9. 24-hour Voltage Profile for Single Phase Bus 3147 without and with PHEV Charging Policy

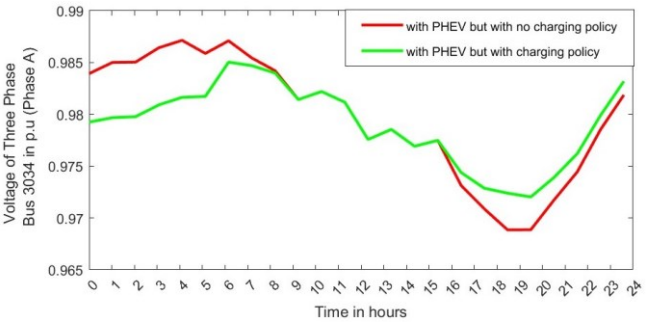


Fig. 10. 24-hour Voltage Profile for Single Phase Bus 3034 without and with PHEV Charging Policy for Phase A

Authorized licensed use limited to: DELHI TECHNICAL UNIV. Downloaded on April 10,2023 at 07:26:30 UTC from IEEE Xplore. Restrictions apply.

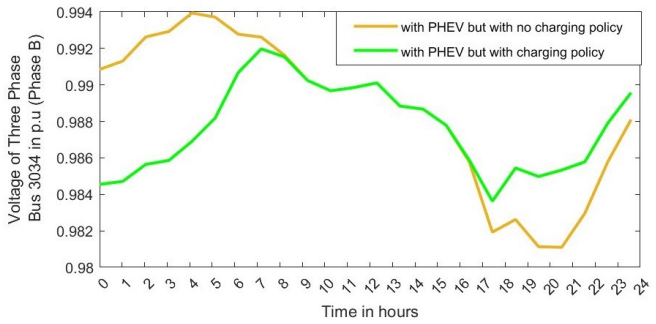


Fig. 11. 24-hour Voltage Profile for Three Phase Bus 3034 without and with PHEV Charging Policy for Phase B

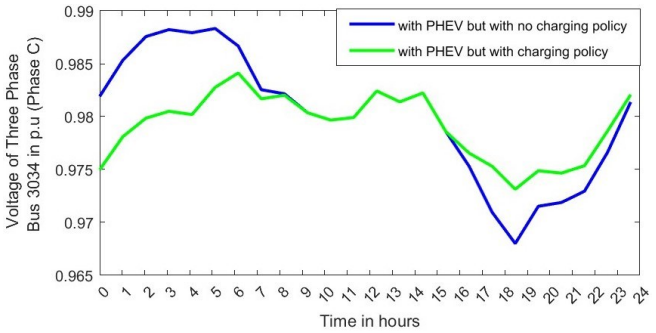


Fig. 12. 24-hour Voltage Profile for Three Phase Bus 3034 without and with PHEV Charging Policy for Phase C

Subsequently, bus no. 3034 is considered, which is a three-phase bus with 9 customers (3 customers each for phase 'a', 'b' and 'c'). Figs. 10-12 presents the 24-hour voltage profile for bus no. 3034 without and with PHEV charging policy for phases A, B and C, respectively. From Figs. 10-12, it is again observed that adoption of the proposed charging policy substantially improves the bus voltage profile for all the three phases during peak charging hours (1600 - 2100 hrs).

V. Challenges for Adoption of the Proposed Charging Policy

The qualitative and quantitative benefits of the proposed EV charging policy should be worked out in detail before introducing the policy. Regulatory approval may require to be obtained from the state-owned regulators in this context, if needed.

VI. Conclusions

PHEVs have evolved as an alternative to internal combustion engine (ICE) vehicles. PHEVs have the proficiency to either charge from an electrical plug outlet or charging via on-board electricity generation. However, PHEV charging consumes large amount of power which is being supplied by the distribution utility. In order to examine the consequences of residential PHEV charging, the effect of the charging of more than 3000 PHEVs pertaining to 800 households on the network demand and the bus voltage profiles of a 240-bus Midwest U.S. distribution utility is investigated, based on the realistic U.S. NHTS 2009 data. Multiple case studies carried out with the 240-bus distribution network demonstrates that adoption of the proposed PHEV charging policy substantially improves the network demand and bus voltage profiles, thereby reducing the system losses and enhancing the voltage stability of the distribution network.

References

[1] U.S. Energy Information Administration, Monthly Energy Review, Tables 2.5, 3.8c, and 10.2b, Apr. 2018.

[2] Ouyang X, Lin B. Impacts of increasing renewable energy subsidies and phasing out fossil fuel subsidies in China. Renew Sustain Energy Rev 2014;37:933–42.

[3] S. Painuli, M. S. Rawat, and D. R. Rayudu, "A Comprehensive Review on Electric Vehicles Operation, Development and Grid Stability.," in 2018 International Conference on Power Energy, Environment and Intelligent Control (PEEIC), 2018, pp. 807–814, doi: 10.1109/PEEIC.2018.8665643.

[4] W. Tushar, C. Yuen, S. S. Huang, D. B. Smith, and H. V. Poor, "Cost minimization of charging stations with photovoltaics: an approach with EV classification," IEEE Transactions on Intelligent Transportation Systems, vol. 17, no. 1, pp. 156–169, Jan. 2016.

[5] Q. Zhang, T. Tezuka, K. N. Ishihara, and B. C. McLellan, "Integration of PV power into future low-carbon smart electricity systems with EV and HP in Kansai Area, Japan," Renewable Energy, vol. 44, pp. 99–108, 2012.

[6] IEA. (2020, May). Global EV Outlook 2019–Analysis-IEA, [Online]. Available: https://www.iea.org/reports/global-ev-outlook-2019

[7] D. Wu, D. Aliprantis, and K. Gkritza, "Electric energy and power consumption by light-duty plug-in electric vehicles," IEEE Trans. Power Syst., vol. 26, no. 2, pp. 738–746, May 2011.

[8] U. Eberle and R. von Helmolt, "Sustainable transportation based on electric vehicle concepts: A brief overview," Roy. Soc. Chem., vol. 3, pp. 689–699, May 2010.

[9] J. T. Salihi, "Energy requirements for electric cars and their impact on electric power generation and distribution systems," IEEE Trans. Ind. Appl., vol. IA-9, no. 5, pp. 516–532, Sep. 1973.

[10] U. S. Department of Energy (2019, May). [Online]. Available: https://www. fueleconomy. gov/feg/Find. do? action=sbs&id=40080&id=40228 &id=40346.

[11] Ali Ahmadian, Behnam Mohammadi-Ivatloo, and Ali Elkamel. "A Review on Plug-in Electric Vehicles: Introduction, Current Status, and Load Modeling Techniques". JOURNAL OF MODERN POWER SYSTEMS AND CLEAN ENERGY, VOL. 8, NO. 3, May 2020. p. 412-425.

[12] Abulawafa AR, Elagarably A, Mohamed WAF. Impacts of uncoordinated and coordinated integration of electric vehicles on distribution systems performance. 2017 19th Int Middle-East Power Syst Conf MEPCON 2017 - Proc 2018;2018February:33746. doi:10.1109/MEPCON.2017.8301203.

[13] F. Bu, Y. Yuan, Z. Wang, K. Dehghanpour, and A. Kimber, "A timeseries distribution test system based on real utility data," in Proc. North Amer. Power Symp. (NAPS), 2019, pp. 1–6.

[14] National Household Travel Survey [Online]. Available: http://nhts. ornl.gov

[15] M. Kintner-Meyer, K. Schneider, and R. Pratt, "Impacts assessment of plug-in hybrid vehicles on electric utilities and regional U.S. power grids part 1: Technical analysis," PNNL Rep., Nov. 2007. Available: http://www.pnl.gov/energy/eed/etd/pdfs/phev_feasibility_analysis_combined.pdf.

[16] W. Su and M. Y. Chow, "Performance evaluation of an eda-based large-scale plug-in hybrid electric vehicle charging algorithm," IEEE Trans. Smart Grid, vol. 3, no. 1, pp. 308–315, Mar. 2012.

[17] SAE Electric Vehicle and Plug-in Hybrid Electric Vehicle Conductive Charge Coupler, SAE Standard J1772, Jan. 2010.

[18] CHAdeMO Association, "Desirable characteristics of public quick charger," Tokyo Electric Power Company, Tokyo, Japan, Jan. 2011.

[19] SAE Electric Vehicle and Plug-in Hybrid Electric Vehicle Conductive Charge Coupler, SAE Standard J1772, Jan. 2010.

[20] Anamika Dubey and Surya Santoso, "Electric Vehicle Charging on Residential Distribution Systems: Impacts and Mitigations", IEEE Access, Vol. 3, 2015, DOI: 10.1109/ACCESS.2015.2476996, pp. 1871-1893.

[21] Electric Vehicle Conductive Charging System, IEC Standard 61851, 2011.

[22] http://wzy.ece.iastate.edu/Testsystem.html

Authorized licensed use limited to: DELHI TECHNICAL UNIV. Downloaded on April 10,2023 at 07:26:30 UTC from IEEE Xplore. Restrictions apply.

A study on Holographic dark energy model with adiabatic matter creation

Simran Kaur and C.P. Singh

Department of Applied Mathematics
Delhi Technological University
New Delhi - 110 042, India.

Abstract

- We explore the adiabatic matter creation process in holographic dark energy (HDE) to explain the observed accelerated expansion of the Universe.
- The field equations are solved analytically for cosmological parameters, like Hubble parameter, deceleration parameter and equation of state parameter in terms of redshift by assuming a generalized form of the matter creation rate.
- The evolution of such model is tested by the latest observational datasets.
- It is found that the HDE model with matter creation achieves the phase transition when the Hubble horizon is taken as an IR cut-off.
- Finally, we perform geometrical and cosmographic analyses in order to elucidate the differences and advantages of our model with the other dark energy models like ΛCDM model.

Holographic dark energy model with adiabatic matter creation

- Let us start with the homogeneous and isotropic flat Friedmann-Robertson - Walker(FRW) line element

$$ds^2 = -dt^2 + a^2(t)\left[dr^2 + r^2(d\theta^2 + sin^2\theta d\phi^2)\right], \tag{1}$$

  where $a(t)$ is the scale factor of the universe.

- In the background of FLRW metric, the Einstein's Field Equations (EFEs) are given by

$$R_{\mu\nu} - \frac{1}{2}R\, g_{\mu\nu} = T_{\mu\nu}, \tag{2}$$

  where $T_{\mu\nu}$ is the energy-momentum tensor of the cosmic fluid and concerning to matter fluids. Notice, that in order to simplify our formalism we use geometrical units $8\pi G = c = 1$. The other symbols have their usual meaning.

- In this work, we assume that the Universe is filled with HDE and pressureless dark matter. In open thermodynamical systems, the matter creation processes can be included phenomenologically in the energy-momentum tensor, which can be written as [I. Prigogine, et al., *Proc. Natl. Acad. Sci.* **85**, 7428 (1988), I. Prigogine, et al., *Gen. Relativ. Grav.* **21**, 8 (1989)].

$$T_{\mu\nu} = (\rho + \bar{P})u_\mu u_\nu + \bar{P}\, g_{\mu\nu}, \tag{3}$$

- where $\rho = \rho_m + \rho_h$ is the total energy density and $\bar{P}$ is the effective pressure which is the sum of pressures of HDE fluid and matter creation, i.e., $\bar{P} = p_h + p_c$.
- Here, ρ_m is the energy density of dark matter, ρ_h the energy density of HDE, while p_h and p_c are the corresponding pressures due to HDE and matter creation.
- In the framework of line element (1) and energy-momentum tensor (3), the basic equations of (2) which govern the global dynamics of the Universe in the matter dominated epoch ($p_m = 0$), are given by

$$3H^2 = \rho = \rho_m + \rho_h, \tag{4}$$

$$\dot{\rho_m} + \dot{\rho_h} + 3H(\rho_m + \rho_h + p_h + p_c) = 0, \tag{5}$$

where $H = \dot{a}/a$ is the Hubble parameter.

- The particle flux vector N^μ is introduced via the definition $N^\mu = nu^\mu$, which obeys the general balance equation $\nabla_\mu N^\mu = \Gamma$, where Γ is the matter production rate, $n = N/V$ is the particle number density and u^μ is the usual particle four velocity.
- Using FLRW metric and comoving observer, $u^\mu = \delta^\mu_i$, in which $u^\mu u_\mu = -1$, we obtain a new balance equation

$$\dot{n} + 3nH = n\Gamma, \tag{6}$$

where the comoving volume is $V = a^3$.

- Let us consider the scenarios driven by adiabatic particle production. In this case, particles and entropy are generated but the entropy per particle does not vary.
- Under such circumstances, Eq.(6) with the second law of thermodynamics, naturally leads to the appearance of a negative pressure associated to the creation rate which is given by [J.A.S. Lima, F.E. Silva and R.C. Santos, *Class. Quantum Grav.* **25**, 205006 (2008), G. Steigman, R.C. Santos and J.A.S. Lima, *J. cosmol. Astropart. Phys.* **06**, 033 (2009) , C.P. Singh and A. Kumar, *Eur. Phys. J. C* **80**, 106 (2020)]

$$p_c = -\frac{\rho_m}{3H}\Gamma. \tag{7}$$

- We suppose that there is no interaction between the two fluids. Therefore, the energy conservation equation (5) for dark matter and HDE conserve separately, which are given by

$$\dot{\rho_m} + 3H\left(1 - \frac{\Gamma}{3H}\right)\rho_m = 0, \tag{8}$$

$$\dot{\rho_h} + 3(\rho_h + p_h)H = 0. \tag{9}$$

- HDE model depends on the choices of IR cutoff L.
- We propose the HDE model with matter creation with same Hubble horizon as an IR cutoff, i.e., assuming the IR cut-off as the inverse of Hubble scale ($L = H^{-1}$).
- Thus, the HDE energy density is given by

$$\rho_h = 3b^2 H^2. \tag{10}$$

- By assuming the usual equation of state for HDE, $p_h = \omega_h \rho_h$, where ω_h is the equation of state parameter of HDE, it is readily checked from Eqs. (4) and (8)- (10) that the Hubble function is governed by the differential equation

$$\dot{H} + \frac{3}{2}\left[(1-b^2)\left(1-\frac{\Gamma}{3H}\right) + (1+\omega_h)b^2\right] H^2 = 0. \tag{11}$$

- We can observe that the above evolution equation will be fully determined once Γ is specified.
- In this paper, we consider a more generalized form of Γ which is a linear combination of three terms: first term is constant, second term is proportional to Hubble parameter and the third term as the combination of Hubble parameter and it's derivative [C.P. Singh and A. Kumar, *Eur. Phys. J. C* **80**, 106 (2020)], that is,

$$\Gamma = 3\left[\alpha H_0 + \beta H + \gamma\left(\frac{\dot{H}}{H} + H\right)\right] \tag{12}$$

where the parameters α, β and γ are dimensionless parameters lying in the interval $[0, 1]$ and H_0 is the present value of Hubble parameter.

- Using (12), the dynamical equation (11) becomes

$$H' + 3k\frac{H}{a} = \frac{3\alpha(1-b^2)H_0}{[2-3(1-b^2)\gamma]a} \tag{13}$$

where $k = \frac{3\left((1-\beta-\gamma)+(\beta+\gamma+\omega_h)b^2\right)}{2-3(1-b^2)\gamma}$ and a prime denotes the derivative with respect to lna.

- On solving (13), we get the Hubble parameter as

$$H = H_0\left[\frac{3\alpha(1-b^2)}{k[2-3\gamma(1-b^2)]} + \left(1 - \frac{3\alpha(1-b^2)}{k[2-3\gamma(1-b^2)]}\right)a^{-k}\right] \tag{14}$$

- We can find the solution of matter-dominated epoch $H = H_0 a^{-3/2}$ by setting all the parameters equal to zero.

- The solution for the scale factor is given by

$$a(t) = \left[1 + \frac{(2 - 3(1-b^2)\gamma)k}{3\alpha(1-b^2)}\{e^{\frac{3\alpha(1-b^2)H_0}{2-3(1-b^2)\gamma}(t-t_0)} - 1\}\right]^{1/k} \tag{15}$$

- From (15)), it can be noticed that the scale factor varies as a power-law $a(t) \propto [1 + kH_0(t - t_0)]^{1/k}$ in early time where as it varies as an exponential form $a(t) \propto e^{\frac{(1-b^2)\alpha}{k(2-3(1-b^2)\gamma)}H_0(t-t_0)}$ in late epoch, which corresponds to de Sitter universe.
- Thus, the HDE model with matter creation shows transition from decelerated epoch to late time accelerated expansion.
- Now, by considering a well-known relation between the scale factor and redshift, $a = (1 + z)^{-1}$, Eq. (14) can be rewritten as

$$H(z) = H_0 \left[\frac{3\alpha(1-b^2)}{k(2-3\gamma(1-b^2))} + \left(1 - \frac{3\alpha(1-b^2)}{k(2-3\gamma(1-b^2))}\right)(1+z)^k\right] \tag{16}$$

Observational Analysis

- For the estimation of parameters of the model (16), we briefly present a statistical analysis of HDE model parameters using observational data obtained from Type Ia Supernovae (Pantheon data), Hubble parameter $H(z)$ observation, baryon acoustic oscillations/cosmic microwave background and latest local H_0 by SHOES.
- We use the Markov Chain Monte Carlo (MCMC) package EMCEE to perform the numerical analysis of our model [D. Foreman-Mackey, D. Hogg, D. Lang, *J. Goodman, Publ. Astron. Soc. Pac.* **125**, 306 (2012)] to put constraints on the free parameters.

- The most probable values of the model free parameters are estimated correspond to the minimal χ^2_{total} values of the three different combined datasets, namely

  1. DS1: $\chi^2_{DS1} = \chi^2_{SNe} + \chi^2_{H(z)} + \chi^2_{BAO/CMB} + \chi^2_{H_0}$,
  2. DS2: $\chi^2_{DS2} = \chi^2_{SNe} + \chi^2_{H(z)} + \chi^2_{H_0}$ and
  3. DS3: $\chi^2_{DS3} = \chi^2_{SNe} + \chi^2_{H(z)} + \chi^2_{BAO/CMB}$.

Table 1: The best-fit results of different model parameters obtained from joint analysis of different data sets.

Parameters	$DS1$	$DS2$	$DS3$
H_0	$70.880^{+0.996}_{-1.038}$	$70.586^{+1.382}_{-0.902}$	$68.646^{+1.250}_{-1.669}$
α	$0.452^{+0.067}_{-0.126}$	$0.392^{+0.101}_{-0.116}$	$0.441^{+0.087}_{-0.107}$
β	$0.054^{+0.085}_{-0.033}$	$0.085^{+0.078}_{-0.052}$	$0.071^{+0.060}_{-0.060}$
γ	$0.310^{+0.099}_{-0.079}$	$0.391^{+0.106}_{-0.104}$	$0.283^{+0.103}_{-0.074}$
ω_h	$-0.793^{+0.534}_{-0.671}$	$-0.790^{+1.030}_{-0.826}$	$-0.807^{+2.008}_{-1.690}$
b	$0.097^{+0.105}_{-0.064}$	$0.075^{+0.140}_{-0.133}$	$0.012^{+0.075}_{-0.070}$

Table 2: The values of z_{tr}, q_0, $\omega_{\rm eff}(z=0)$ and t_0 (Gyr) using different combinations of data sets.

Values	DS1	DS2	DS3
z_{tr}	$0.94^{+0.479}_{-0.937}$	$0.90^{+0.503}_{-0.892}$	$0.97^{+0.231}_{-0.681}$
q_0	$-0.51^{+0.053}_{-0.045}$	$-0.48^{+0.061}_{-0.047}$	$-0.51^{+0.043}_{-0.036}$
$\omega_{\rm eff}(z=0)$	$-0.77^{+1.7}_{-1.6}$	$-0.73^{+1.9}_{-1.4}$	$-0.75^{+1.9}_{-1.5}$
t_0 (Gyr)	14.27	14.10	14.40

Deceleration Parameter & Equation of state parameter

- We know that a cosmological parameter is required to describe the transition from decelerated phase to accelerated phase.
- In this context, the first cosmological parameter is the deceleration parameter, which is a dimensionless measure of the cosmic acceleration of the Universe, plays an important role in describing the transition phase.
- It is defined as $q = \frac{-a\ddot{a}}{\dot{a}^2}$. which takes the form in terms of redshift for our model as

$$q(z) = -1 + \frac{k - \frac{3\alpha(1-b^2)}{2-3(1-b^2)\gamma}}{1 + \frac{3\alpha(1-b^2)}{(2-3(1-b^2)\gamma)k}\{(1+z)^{-k} - 1\}}. \tag{17}$$

- The transition redshift z_{tr}, which is defined at $q = 0$, is given by

$$z_{tr} = -1 + \left[\frac{3\alpha(1-b^2)}{3\alpha(1-b^2) + k(1-3\alpha-3\beta+3\alpha b^2+3\beta b^2+3\omega_h b^2)}\right]^{1/k} \tag{18}$$

- It is noted that if $\alpha = 0$, there is no transition from an early decelerating to a late time accelerating Universe. The present value of q at $z = 0$ is

$$q_0 = \frac{\left(1-3\alpha-3\beta+3\alpha b^2+3\beta b^2+3b^2\omega_h\right)}{(2-3(1-b^2)\gamma)}. \tag{19}$$

- The second cosmological parameter is the equation of state (EoS) parameter which is used to describe the evolution of the Universe filled with matter.
- It is defined as $\omega = \bar{P}/\rho$. This can also be represented as $\omega = -1 - \frac{2a}{3H}\frac{dH}{da}$. In this we calculate the effective EoS ω_{eff}, which is given by

$$\omega_{eff} = -1 + \frac{2}{3}\left[\frac{k - \frac{3\alpha(1-b^2)}{2-3(1-b^2)\gamma}}{1 + \frac{3\alpha(1-b^2)}{(2-3(1-b^2)\gamma)k}\{(1+z)^{-k} - 1\}}\right] \tag{20}$$

- The present value of ω_{eff} is calculated as

$$\omega_{eff}(z=0) = -1 + \frac{2}{3}\left(k - \frac{3\alpha(1-b^2)}{2-3(1-b^2)\gamma}\right) \tag{21}$$

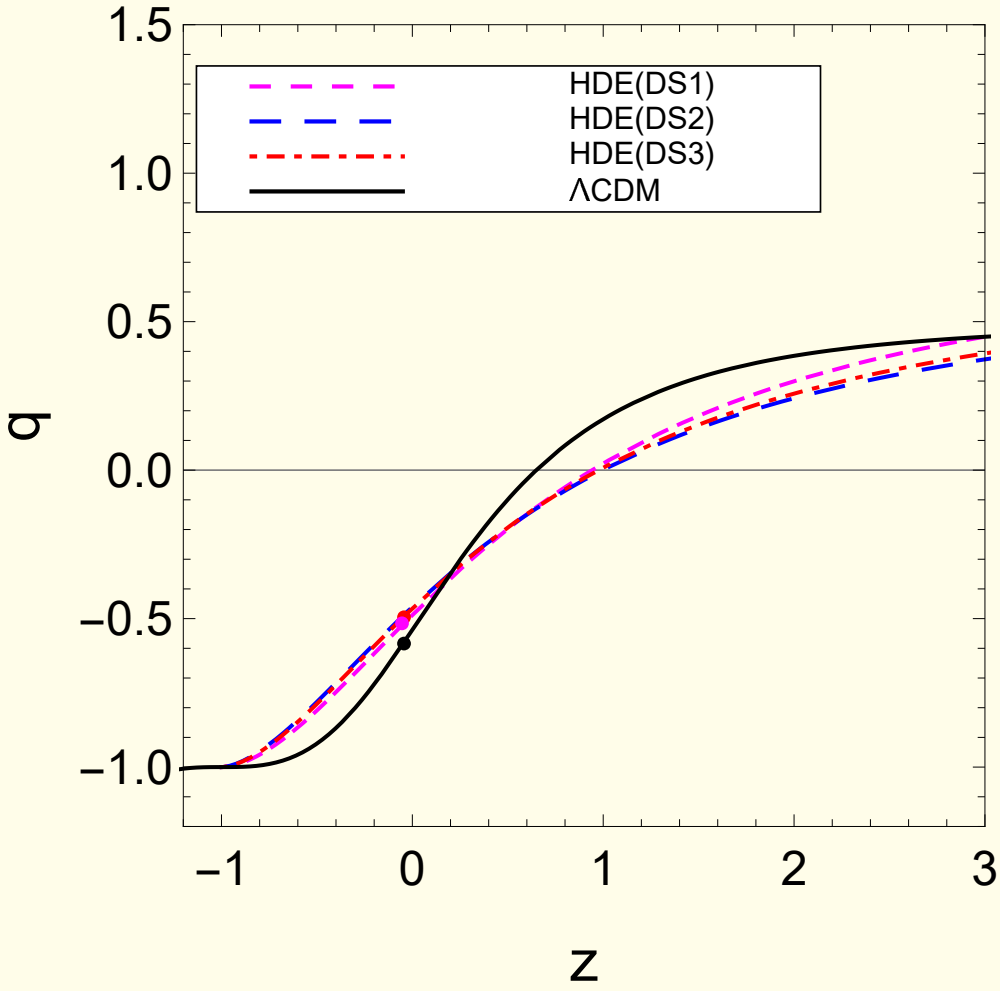


Figure 1: Plot of the deceleration parameter q as a function of redshift z for best-fit values of parameters obtained from DS1, DS2 and DS3 data sets.

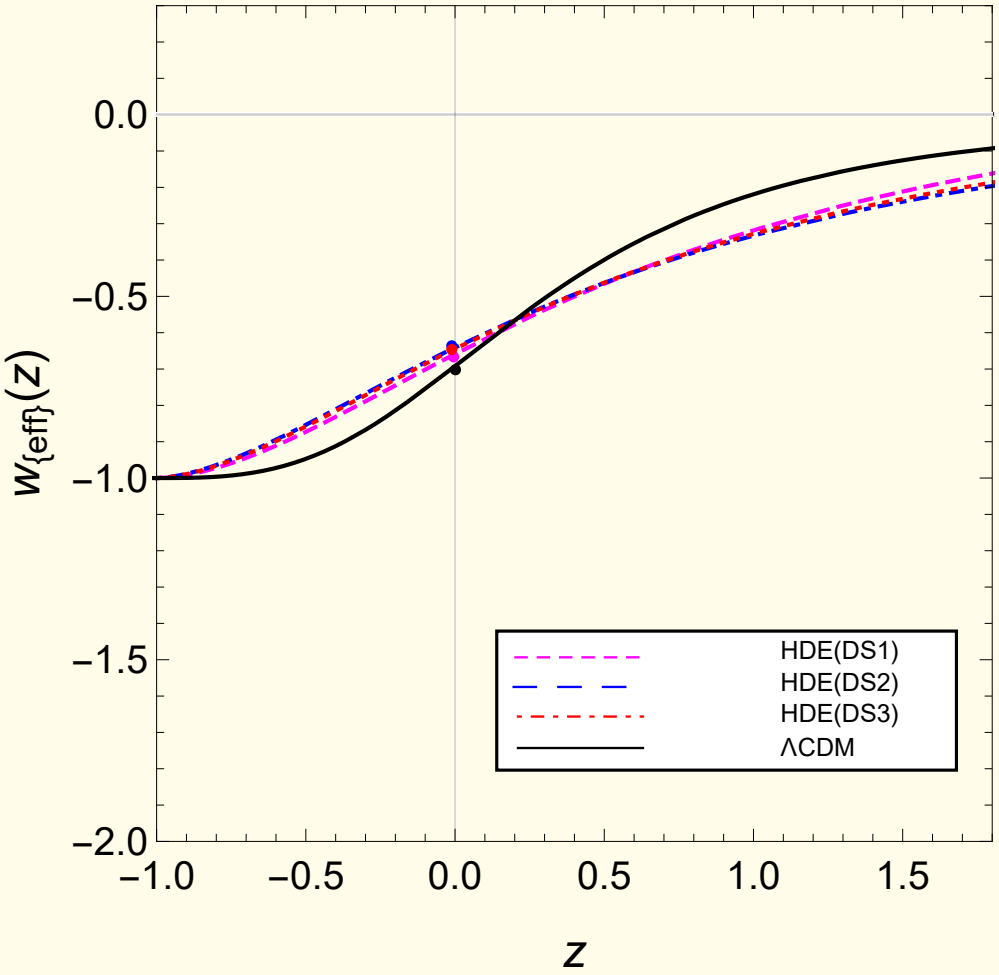


Figure 2: The evolution of effective EoS parameter ω_{eff} with respect to the redshift z for best-fit values of parameters obtained from DS1, DS2 and DS3 data sets.

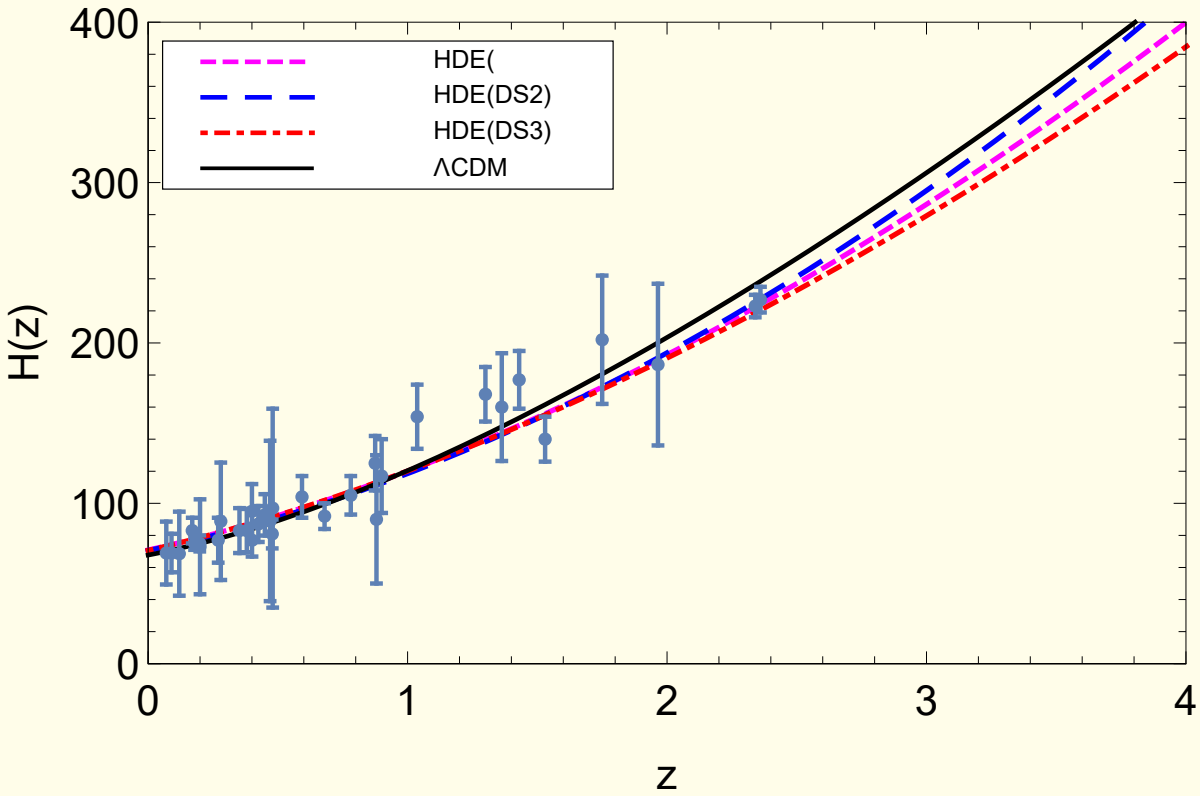


Figure 3: The Hubble function as a function of redshift for HDE model with matter creation from DS1, DS2 and DS3 data sets. The solid curve corresponds to the ΛCDM model. The $H_{obs}(z)$ data are also plotted with their error bars.

Geometric and Cosmographic Analyses

- We study various geometric and cosmographic parameters which are used to discriminate between the various contenders of DE models.
- Firstly, we discuss geometrical analysis of our model.[V. Sahni, et al., *JETP Lett.* **77**, 201 (2003), U. Alam, et al., *Mon. Not. R. Astron. Soc.* **344**, 1057 (2003)] proposed two geometrical diagnostic parameters $\{r, s\}$, called statefinder parameters, defined as

$$r = \frac{1}{aH^3}\frac{d^3a}{dt^3} \quad \text{and} \quad s = \frac{r-1}{3(q-1/2)}. \tag{22}$$

- The fixed points $\{r, s\} = \{1, 0\}$ represents the ΛCDM model of the Universe where as $\{r, s\} = \{1, 1\}$ represents the standard cold dark matter (SCDM) model.
- We plot the $\{r, s\}$ and $\{r, q\}$ evolutions of trajectory in $s - r$ and $q - r$ planes for the best fit values of parameters obtained by observational data sets DS1, DS2 and DS3 which are shown in Figs. 4 and 5, respectively.

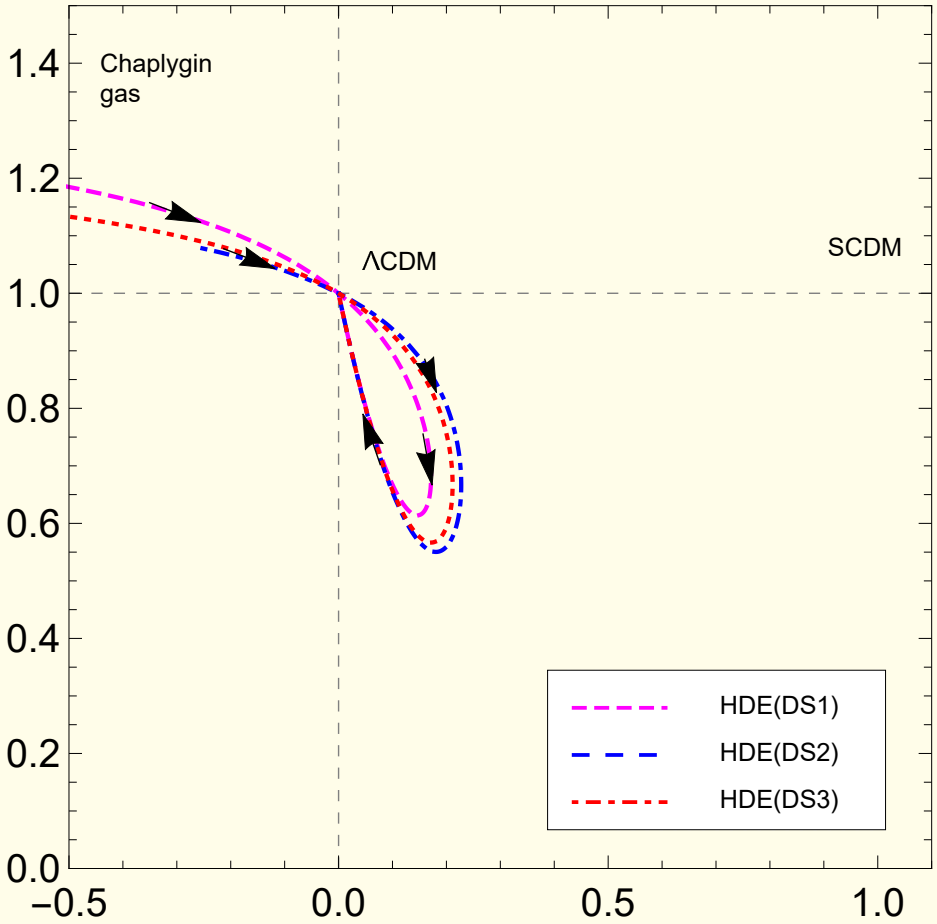


Figure 4: The evolutions of $\{r, s\}$ in $s - r$ plane corresponding to best fit values of model parameters obtained from data sets DS1, DS2 and DS3. The arrow shows the direction of the evolution of each trajectory.

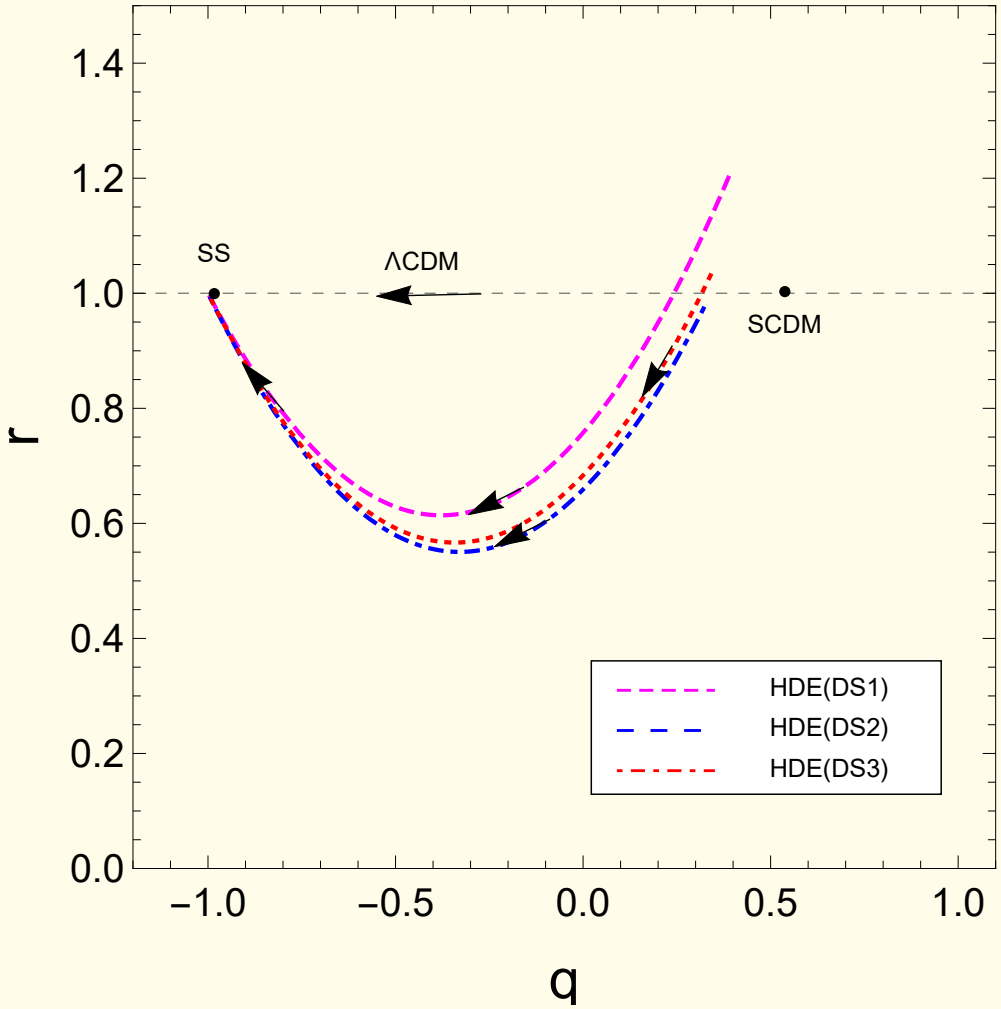


Figure 5: The evolutions of $\{r, q\}$ in $q - r$ plane corresponding to best fit values of model parameters for data sets DS1, DS2 and DS3. The arrow shows the direction of the evolution of each trajectory.

- We plot the $\{r, s\}$ and $\{r, q\}$ evolutions of trajectory in $s - r$ and $q - r$ planes for the best fit values of parameters obtained by observational data sets DS1, DS2 and DS3 which are shown in Figs. 4 and 5, respectively.
- It can be observed that the all the trajectory of $\{r, s\}$ begin from chaplygin gas type DE ($r > 1$, and $s < 0$) [Y.-B. Wu, S. Li, M.-H. Fu and J. He, *Gen. Relativ. Grav.* **39**, 653 (2007)] in early times and go to the quintessence region ($r < 1$ and $s > 0$) [V. Sahni, et al., *JETP Lett.* **77**, 201 (2003)], U. Alam, et al., *Mon. Not. R. Astron. Soc.* **344**, 1057 (2003)] in intermediate phase, and finally approach to ΛCDM model ($r = 1$ and $s = 0$) in late time.
- In Fig. 5, the fixed point $\{r, q\} = \{1, 0.5\}$ corresponds to standard cold dark matter (SCDM) and $\{r, q\} = \{1, -1\}$ to steady state (SS) or de Sitter.
- The horizontal line $r = 1$ corresponds to the trajectory of ΛCDM model.

- The evolutions of the trajectory corresponding to data sets $DS1$, $DS2$ and $DS3$ show that the model starts from decelerated phase in early time and after transition to accelerated phase, the model with each data sets approach to de Sitter model.
- Apart from the above mentioned two geometric parameters, the comparing of models can also be extracted by cosmography.
- The fundamental rule of cosmography is based on the Taylor series expansion of the scale factor about the present time [M. Visser, *Class. Quantum. Grav.* **21**, 2603 (2004), M. Visser, *Class. Quantum Grav.* **37**, 1541 (2005).].
- From it one obtains the cosmographic parameter (CP) usually referred to as *jerk* (j), *snap* ($\mathbf{s}$), *lerk* (l) and m parameters which are respectively defined as (see, [M. Dunajski, G. Gibbons, *Class. Quantum Grav.* **25**, 235012 (2008)]).

$$j = \frac{1}{aH^3}\frac{d^3a}{dt^3}\ ,\ \mathbf{s} = \frac{1}{aH^4}\frac{d^4a}{dt^4}\ ,\ l = \frac{1}{aH^5}\frac{d^5a}{dt^5}\ ,\ m = \frac{1}{aH^6}\frac{d^6a}{dt^6} \quad (23)$$

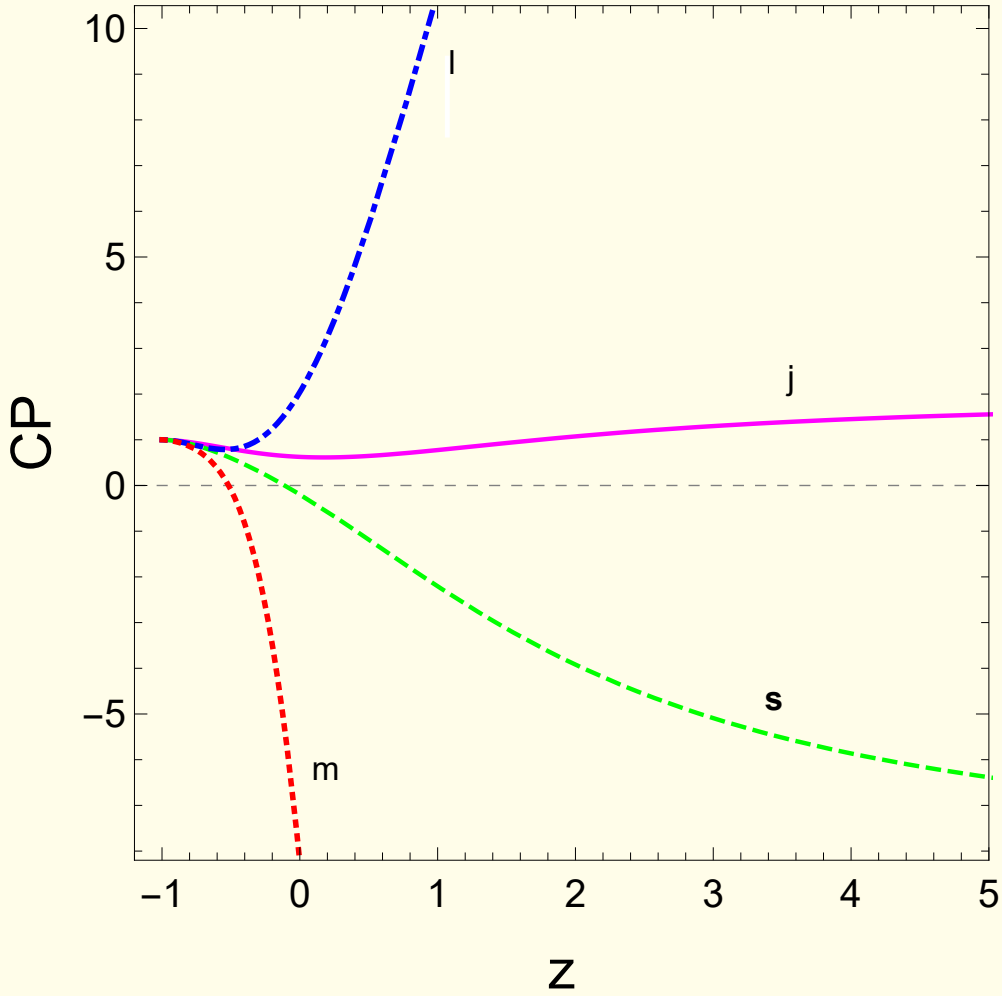


Figure 6: The cosmographic parameters j, $\mathbf{s}$, l and m are plotted for best fit values of model parameters for DS1.

- We find that j, $\mathbf{s}$, l and $m \to 1$ as $z \to -1$, i.e., in late time evolution, which is in good agreement with the observations of standard ΛCDM model.
- It is also observed that $jerk$ and $lerk$ parameters are positive throughout the cosmic evolution. The jerk parameter gives information about inflection points in the expansion history of the Universe.
- A positive $jerk$ and $lerk$ implies that the Universe has gone through a change of sign of the acceleration parameter in the past, which means that there has been a transition from deceleration to acceleration.
- On the other hand, it is well known that the $snap$ and m parameters do not have a well established physical meaning, however they are important part of the Taylor series of the Hubble parameter in cosmography, giving us more precision in the preferred model.
- Figure 6 shows that $snap$ and m transit from initial negative values to later positive ones.

Conclusion

- HDE model with Hubble horizon as an IR cutoff does not explain the transition phase.
- In order to overcome this drawback we have presented the HDE model using same IR cutoff but with gravitationally induced matter creation mechanism to observe the possible transition during the evolution of the Universe.
- We have considered the most general phenomenological form of Γ in terms of H and $\dot{H}$ and investigated the evolution equation by three different latest observational data sets; DS1 (SNe Pantheon, $H(z)$, BAO/CMB and local H_0 by SH0ES), DS2 (SNe Pantheon, $H(z)$ and local H_0) and DS3 (SNe Pantheon, H(Z) and BAO/CMB) to observe how they depict present scenario of the Universe.
- We have plotted the trajectories of Hubble parameter and other cosmographic parameters like deceleration parameter, effective EoS parameter, $jerk$, $snap$, $lerk$ and m parameters with respect to the redshift.

- We know that the current observational data seem to favour an EoS for DE greater than -1.
- The present values q_0 and $\omega_{eff}(z=0)$ for HDE model are very much compatible with the present value of these parameters of ΛCDM model.
- The evolutions of these parameters almost match with the evolution of the ΛCDM from the data sets of DS1, DS2 and DS3.
- We find that the evolution of the Universe begins from higher redshift, from a decelerating phase to low redshift, i.e. to accelerating phase. In late time, the HDE model with matter creation approaches to standard ΛCDM model.
- The present values of effective EoS parameter are comparatively higher than that predicted by the joint analysis of WMAP, BAO, H_0 and SNe [E. Komatsu, et al., *Astrophys. J. Suppl.* **192**, 18 (2011)]. The age of Universe with each data set is found to be slightly higher than that of ΛCDM model.

- We have calculated the chi-squared minimum and reduced chi-squared for the model using DS1, DS2 and DS2 data sets. We have observed that the χ^2_{red} is less than unity with each data set which shows that the model gives the best fit values of model parameters and shows the good support to ΛCDM model.
- We have also discussed the statefinder parameters and have plotted the trajectories of {r, s} in $s - r$ plane and {r, q} in $q - r$ plane using best fit values of model parameters for all three combination of data sets.
- It can be observed that the each trajectory starts from chaplygin gas region in early times, enters into quintessence region in medieval time and finally approaches to ΛCDM in late times.

- In conclusion, we have investigated (analytically and numerically) the overall dynamics of HDE model with matter creation along with the Hubble horizon as an IR cutoff.
- This dynamical HDE model provides a transition phase from decelerating to accelerating phase of the cosmic expansion. The HDE model with matter creation provides good quality fits of the cosmological parameters at all redshifts and it resembles the global dynamics of the standard ΛCDM model.

References

- I. Prigogine, et al., *Proc. Natl. Acad. Sci.* **85**, 7428 (1988).
- I. Prigogine, et al., *Gen. Relativ. Grav.* **21**, 8 (1989).
- J.A.S. Lima, F.E. Silva and R.C. Santos, *Class. Quantum Grav.* **25**, 205006 (2008).
- G. Steigman, R.C. Santos and J.A.S. Lima, *J. cosmol. Astropart. Phys.* **06**, 033 (2009).
- C.P. Singh and A. Kumar, *Eur. Phys. J. C* **80**, 106 (2020).
- C.P. Singh and A. Kumar, *Phys. Rev. D* **102**, 123537 (2020).
- D. Foreman-Mackey, D. Hogg, D. Lang, *J. Goodman, Publ. Astron. Soc. Pac.* **125**, 306 (2012).

- T. Harko, F.S.N. Lobo, J.P. Mimoso and D. Pavon, *Eur. Phys. J. C* **75**, 386 (2015).
- S. Basilakos and J.A.S. Lima, *Phys. Rev.D* **82**, 023504 (2010).
- J.A.S. Lima, J.F. Jesus and F.A. Oliveira, *J. Cosmol. Astropart. Phys.* **11** 27 (2010).
- J.A.S. Lima, S. Basilakos and F.E.M. Costa, *Phys. Rev.D* **86**, 103534 (2012).
- J.A.S. Lima, L.L. Graef, D. Pavon and S. Basilakos, *J. Cosmol. Astropart. Phys.* **10**, 42 (2014).
- R.O. Ramos, et al., *Phys. Rev.D* **89**, 083524 (2014).
- S. Pan and S. Chakraborty, *Adv. High Energy Phys.* **201**, 654025 (2015).
- S. Pan, et al., *Mon. Not. R. Astron. Soc.* **460**, 1445 (2016).

- V. Sahni, et al., *JETP Lett.* **77**, 201 (2003).
- U. Alam, et al., *Mon. Not. R. Astron. Soc.* **344**, 1057 (2003).
- Y.-B. Wu, S. Li, M.-H. Fu and J. He, *Gen. Relativ. Grav.* **39**, 653 (2007).
- M. Visser, *Class. Quantum. Grav.* **21**, 2603 (2004).
- M. Visser, *Class. Quantum Grav.* **37**, 1541 (2005).
- M. Dunajski, G. Gibbons, *Class. Quantum Grav.* **25**, 235012 (2008).
- E. Komatsu, et al., *Astrophys. J. Suppl.* **192**, 18 (2011).

THANKYOU!

Multimedia Tools and Applications
https://doi.org/10.1007/s11042-023-15156-9

A systematic review of the methodologies for the processing and enhancement of the underwater images

Nishant Singh[1] · Aruna Bhat[1]

Received: 1 September 2021 / Revised: 29 September 2022 / Accepted: 13 March 2023
© The Author(s), under exclusive licence to Springer Science+Business Media, LLC, part of Springer Nature 2023

Abstract
Underwater image processing has received tremendous attention in the past few years. The reason for increased research in this area is that the process of taking images underwater is very difficult. Images obtained underwater frequently suffer from quality deterioration issues such as poor contrast, blurring features, colour variations, non-uniform lighting, the presence of dust particles, noise at the bottom of the sea, different properties of the water medium, and so on. The improvement of underwater images is a critical problem in image processing and computer vision for a variety of practical applications. To address this problem, we need to find some other methods to increase the quality of the image while capturing it underwater. But capturing the image in normal circumstances as well as underwater is the same, so once we get an image, some mechanism to increase the quality of the captured image will also be required. A complete and in-depth study of relevant accomplishments and developments, particularly the survey of underwater image methods and datasets, which are a critical issue in underwater image processing and intelligent application, is still lacking. In this paper, we first provide a review of more than 85 articles on the most recent advancements in underwater image restoration methods, underwater image enhancement methods, and underwater image enhancement using deep learning and machine learning methods, along with the techniques, data sets, and evaluation criteria. To provide a thorough grasp of underwater image restoration, enhancement, and enhancement using deep learning and machine learning, we explore the strengths and limits of existing techniques. Additionally, we offer thorough, unbiased reviews and evaluations of the representative methodologies for five distinct types of underwater situations, which vary their usefulness in various underwater circumstances. Two main evaluations, subjective image quality evaluation and objective image quality evaluation; are used for evaluating the quality of images. These evaluations are useful to determine the efficiency of the predefined methods. With

✉ Aruna Bhat
aruna.bhat@dtu.ac.in

[1] Department of Computer Science & Engineering, Delhi Technological University, Delhi, Delhi 110042, India

Published online: 28 March 2023

the help of these image quality evaluations, we come to the conclusion that the image enhancement methods and image enhancement methods using deep learning and machine learning are superior in comparison to the image restoration methods. As deep learning and machine learning based enhancement methods are newer and give far better results in comparison to the other two methods, lots of researchers are moving towards these methods. Finally, we also explore the potential difficulties and unresolved problems associated with underwater image enhancement and offer potential future research areas.

Keywords Underwater image enhancement · Underwater image restoration · Deep learning · Image quality evaluation · Image dehazing · Image datasets

1 Introduction

There is a different world under the ocean, and nowadays there are many ways available to explore it. In today's world, there is a very high level of technology which has attracted attention to carry high and useful information [52, 68]. Researchers are capturing a very high quality underwater image for enormous purposes and applications like robotics, ecological monitoring, tracking of sea organisms, artefact inspection, which are present underwater, rescue missions, and various real-time navigation [16, 57, 74, 78].

The underwater images are difficult to capture; the main constraints are light issues, capturing phenomena, dust particles, etc. An artificial mechanism which consists of an optical camera or some methods like spectral imaging, panoramic and polarization [1, 13, 64, 71] is required, as under the sea light is not that much visible as it is in the normal environment. Other than optical cameras, each of these techniques has its own limitations, such as narrow field of view, complex and professional operation, limited depth, etc.

What happens when an image is captured underwater - The immensity of the underwater image has been observed to diminish because of the nature of light. Light is made up of numerous wavelengths of different hues, including red, green, and blue. It has been discovered that, depending on light attenuation, blue and green color wavelengths reach deeper lengths than red color wavelengths, which vanish beyond 5 m, resulting in images with mostly blue and green tones [70]. Because water is a thick content, when we snap a photo in it light propagates underwater, becomes refracted, and consumed by the surrounding water, resulting in hazy pictures.

Underwater images get affected by poor visibility of light, which significantly fades while travelling in the water, thus impacting the result in terms of haziness and poor contrast. The visibility of light gets affected underwater by the distance travelled, i.e., around twenty meters in the case of clear water and approximately five meters or less in the case of cloudy water. Scattering and absorption affect the travel of light in water. In scattering, the direction of the light path is changed, while in absorption, light energy is reduced. Hence, scattering and absorption influence the overall performance of an underwater imaging system.

Scattering is basically of two types i.e. forward scattering and backward scattering. A light deviating randomly while travelling from an object to the camera creates blurriness in the image is featured in forwarding scattering while in the case of backward scattering contrast of an image is impacted. The scattering and absorption effect increases with water itself but is also affected by some other components like small dust particles, organic particles, tiny observable floating particles, etc. The presence of all these particles will increase the effect of scattering and absorption.

As light propagates in the sea its amount is reduced and the color present in light gets decreased sequentially, depending on the color wavelength. The shorter the wavelength, the higher the range or distance it covers in the sea, similarly higher the wavelength, and the shorter the range or distance it covers in the sea. We all know that in comparison to other colors, the wavelength of blue color is the shortest thus it travels the longest in the sea. Hence, the impact of blue color on objects in the sea is higher than any other colors. Therefore, the images on which we are interested to work can be affected by any one of the reasons: dull contrast, constant range visibility, blurring, haziness, non-uniform light, color diminished, bluish appearance, and various types of noise. To work on these captured images we require some mechanism so that we can increase the quality of these images.

Image processing is categorized on the basis of three viewpoints: first as an image enhancement technique, second as an image restoration method and third as image enhancement using deep learning and machine learning techniques.

Image enhancement in image processing techniques depends on subjective photo exceptional criteria. No mathematical criteria are used for optimizing processing outcomes. Image enhancement depends mainly on quality subjective criteria in order to generate an image which is of good quality. The generation of images, they are independent of any concrete model. These techniques are generally faster and easier in comparison to others.

Using various models of degradation and of the original image construction, the image restoration recovers the degraded image and it is basically a reverse process. These methods are very specific; however, they require different parameters like depth estimation, attenuation and diffusion coefficient, etc.

Deep learning techniques have rapidly evolved over the last several decades, and they have been widely utilized in a variety of computer vision and image processing applications. Deep learning has considerably enhanced the accuracy of high-level vision tasks such as object identification. Furthermore, low-level vision tasks like image super-resolution and image denoising benefit from deep network benefits and offer state-of-the-art performance. Fortunately, we have seen the convincing quality of deep learning-based underwater image improvement. Because of that, many researchers have used deep learning approaches to improve underwater image enhancement [7].

Underwater image processing is also categorized into three parts based on the model free methods, model based methods and data driven methods. Although the techniques which have been used either in restoration and enhancement methods or in model free and model based methods are the same. But the differentiation between model free and model based depends on their physical properties. Model-free approaches often redistribute the pixel values of a given image to improve contrast or color correction without simulating the image generation process underwater. Many common model-free approaches, such as histogram equalization, contrast limited adaptive histogram equalization, gray-world assumption, color constancy and automatic white balance, attempted to adjust underwater image pixels in the subspace. Model-based techniques often create physics models that take into consideration the mechanics of image processing and light transmission. People may get essential parameters of the deterioration model based on previous assumptions and observations, and then invert the model to obtain the desired outcomes. Many techniques have been proposed using model based approaches like dark channel prior, underwater dark channel prior, red channel prior, maximum attenuation identification etc. Deep learning has made significant progress in recent years, particularly in the field of vision, because of its immense potential in dealing with non-linear issues. Modern learning-based algorithms give a cutting-edge performance for image

enhancing tasks. Normally, these data driven models need a significant amount of information paired with ground truth to achieve the desired results; however, for underwater image enhancement, this is a major impediment to effectively applying a supervised learning method to this specific task, because it is hard to procure numerous quality images of the same scenes in a real-world underwater environment. Several underwater image enhancement researchers have studied the utilization of synthetic images to solve the problem of a lack of matched training data and claimed fair effectiveness. WaterGAN, UnderwaterGAN, CycleGAN, etc. are some methods which are based on data driven approach [69].

1.1 Study selection

The selection procedure identified items that were most related to the purpose of this systematic literature review. According to our research, if the same article appeared in more than one domain, it was only examined once. The content of the publications chosen for the final study was examined to ensure that the outcomes of the current systematic literature review generated clear and non-biased conclusions. We completed the examination in order to obtain a decision on ultimate inclusion or exclusion. Following this, individual assessment inconsistencies were resolved through discussion. When the articles were discovered, the first step was to remove duplicate titles and those that were not related to the study. The inclusion criteria (IC) were confined to the search for String, and a study done by at least one of the exclusion criteria (EC) is removed.

1.1.1 Inclusion criteria (IC)

IC1: The studies are available before September 2021.
IC2: Only workshop, report, symposium, conference and journal publication are studied.
IC3: Complete texts are available in a digital database.
IC4: Models or frameworks that have been proposed are present.

1.1.2 Exclusion criteria (EC)

EC1: Duplicate research has been avoided.
EC2: Remove previews, book chapters, periodicals, theses, monographs, and interviews based papers.
EC3: Studies relying on quality rating standards should be excluded.
EC4: Different from English, studies are written in other languages.

The selection of articles was based on the above-mentioned explicit criteria for inclusion and disqualification. Figure 1 was created using the information from the PRISMA model. Figure 1 depicts the study selection procedure.

The focus of this paper is as follows: (i) about eighty-five research papers have been reviewed and their existing methodology, data set and evaluation process is summarized, which will help the researcher to understand the progress in this field; (ii) clear evaluation of target and complete analysis of the methods of underwater enhancement is performed, so a researcher can select the suitable method for practical case; (iii) Dataset which is one of the major concern in underwater image enhancement is explained and (iv) further, some of the open issues and challenges of underwater image enhancement and restoration will be discussed, which will provide some research direction for future.

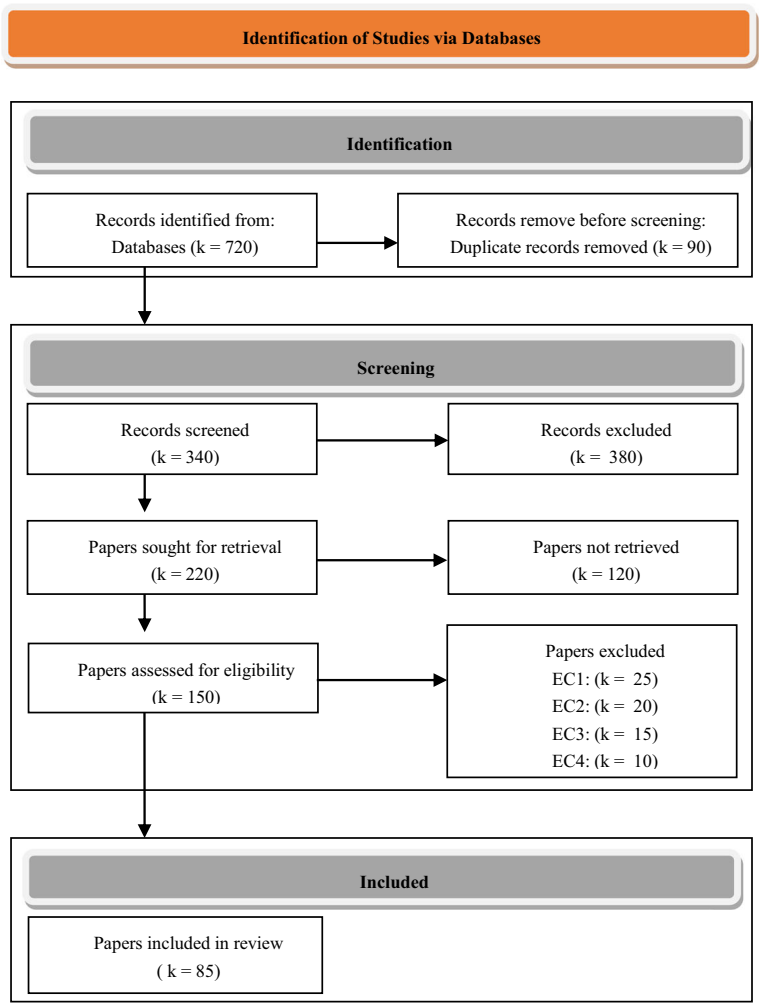


Fig. 1 PRISMA flow chart based studies selection procedure

Under section 2 of this paper, there is a literature survey on recent underwater image restoration and enhancement methods. In section 3, underwater image enhancement is evaluated and the dataset is recorded, subsequently experimental results on some groups related to the underwater image are discussed. Section 4 contains the result analysis of various methods with specific parameters. Section 5 discusses open challenges and issues in the processing of underwater images so that a researcher can identify the new research objection in this domain. In the last section 6, the conclusion of the paper is given and then publications.

2 Underwater image processing algorithm

The Underwater Image Processing algorithms are broadly classified into three parameters, first parameter is based on the image restoration method. The second parameter is based on the

image enhancement method. The third parameter is based on the newer concept of underwater image enhancement with the help of machine learning and deep learning [84]. Hence, in our study, all these three parameters will be discussed. All the literature survey is based on these parameters, so here we are going to discuss the various papers with methods that have been used with their objectives.

2.1 Underwater image restoration method

In detail, underwater image restoration method is classified in four main groups

(i) Turbulence degradation model
(ii) Jaffe-McGlamery model
(iii) Point spread function (PSF) model
(iv) Image dehazing based model

2.1.1 Turbulence degradation model

Turbulence generates a non-uniform switch in the refractive index of the atmosphere; it resembles light propagation in water. Degradation model A designed by Hufnagel and Stanley [44] is totally based on the atmospheric turbulence properties. On the basis of frequency domain (u, v) it is defined by Eq. (1):

$$A\left(u,v\right)=\exp\left[-k\left(u^2+v^2\right)^{5/6}\right] \tag{1}$$

Here, k represents the magnitude of turbulence. The underwater image restoration is realized by merging the degradation model with the evaluation function. Yang and Gong [82] also designed an underwater image restoration method on the basis of turbulence, where the weighted contrast average grads (WCAG) are applied in determining the standard of underwater images.

2.1.2 Jaffe-McGlamery model

This method of underwater image restoration [17, 39, 56] is one of the most widely used models, in which the light E_T coming from the camera is divided into the following divisions: (i) reflected light from an object E_d, (ii) light which is emulated from a target known as forward scattered light E_f and (iii) the non-target reflected light known as back scattered light E_b, as given in Eq. (2).

$$E_T=E_d+E_f+E_b \tag{2}$$

Based on the simplified model by Jaffe McGlamery model; Trucco and Olmos [73] designed a self-calibrated filter. The filter designed in this method is based on two presumptions: (i) lighting (direct sunlight) underwater is consistent, and (ii) forward scattering is an important component whereas other components like direct component and backscattering were neglected.

Few researchers not only focused on backscattering in the Jaffe McGlamery model but also used the Dark Channel Prior (DCP). Here in this method, it was presumed that backscattering did not affect a high contrast region in an image. The parameters of this model were evaluated on the basis of this presumption.

2.1.3 Point spread function model

The imaging process in seawater with the help of a linear system was introduced by Hou et al. [40–42]. They also introduced optical properties of water under the standard underwater image restoration system. Various parameters like attenuation, volume scattering function, absorption, and particle distribution were measured with some specific instruments. Grosso [23], Voss [35] and Chapin [77] also used some specific instruments to measure the PSF. However, the instruments were too complicated and expensive.

2.1.4 Image Dehazing based model

This model is divided into two parts: (i) classical DCP based underwater image restoration model and (ii) learning DCP based underwater image restoration model. Table 1 is representing these methods, where in model column R is restoration, C is color correction, ML is machine learning, and DL is deep learning. In the Hypothesis priori column, DCP is dark channel prior, DBGR is the difference between blue green and red channels, RDCP is red dark channel prior, UDCP is underwater dark channel prior, and CDCP is color corrected images of dark channel prior. In the background light column, GB is global background light estimation and LB is local background light estimation. In the transmission map (TM) estimation column DEP is depth, AP is attenuation prior, FDC is from the dark channel, RET is Retinex, BM is blurring map, and MIL is minimum information loss.

In previous years DCP based underwater image restoration model has gained attention [3–5, 14, 18, 19, 24–27, 31, 38, 43, 48, 49, 53, 58–60, 80, 81, 83]. In it, there is a presumption that red debilitation is agile as compared to other attenuation colors, which is absolutely true in the case of open water and is used for calculating dark channel images in both DCP based restoration models.

Table 1 DCP based underwater image restoration models

#	Publication	Model	Hypothesis Priori	Background Light	Color correction	TM estimation	Year
25	OCEANS	R	DBGR	GB	N	FDC	2010
23	PAMI	R	DCP	GB	N	FDC	2011
26	TIP	R	DCP	GB	N	DEP+AP	2012
28	JCCV	R	UDCP	GB	N	FDC	2013
27	JVCIR	R	RDCP	GB	N	FDC	2015
29	ICIP	R+C	DCP	GB	Y	BM	2015
30	BMVC	R	UDCP	GB	N	FDC	2015
31	ICIP	R+C	DCP	GB	Y	DEP	2016
32	OCEANS	R+C+ML	DCP	GB	Y	DEP	2016
33	ICIP	R+C	DCP	GB	Y	MIL+FDC	2016
34	ICPR	R	DCP	LB	Y	FDC	2016
35	TIP	R+C	DCP	GB	Y	DEP+AP	2017
36	PRL	R+C+ML	CDCP	GB	Y	ML+AP	2017
37	OCEANS	R+C+DL	DCP	GB	Y	DL+DEP	2017
38	ICIP	R+C	CDCP	GB	Y	FDC	2017
39	CVPR	R+C	CDCP	GB	Y	FDC	2017
40	ISCAS	R+ML	DCP	GB	N	DEP+AP	2017
41	TCSI	R+ML	DCP	GB	N	DEP+AP	2018
42	CVIU	R+C	UDCP	GB	Y	FDC	2018
43	ICIP	R+C+DL	DCP	GB	Y	DL+DEP	2018
44	JOE	R+C	DCP	LB	Y	RET+AP	2019

Carlevaris et al. [14] initially computed the highest variation in red and blue–green channels. Thereafter, the transmission map is evaluated by setting the maximum variation till it becomes one. Whatever is the least value of the transmission map, it is considered background light. Now, the posterior probability is maximized and the final image is evaluated. The transmission map is further studied by Chiang and Chen [18] in terms of the ratio of residual energy of the input image to the camera after reflection. The average brightness difference between foreground and background is compared to estimate an artificial light source. The red channel was taken as underwater prior by Galdran et al. [31]. Here using the highest value of the red channel the background light was computed. The red channel was considered as the fasted attenuated channel by P. Drews, Jr., et al. [25], because of which any information related to field depth was not provided. Therefore one new method having an underwater dark channel prior (UDCP) was proposed. This dark channel image was computed after calculating the smallest difference between green and blue channels and from the highest value which was obtained from the dark channel image the background light was estimated.

When light is absorbed through water, it causes scattered color projection which generally causes dark channels prior to failing to identify the transmission map more precisely. Furthermore, an underwater scenario is generally defined by a limited or inappropriate light. There will be no change in the dark scene area even after imaging. In some previous work, fuzzy image and field depth is used for enhancing the transmission map estimation [19, 24, 58–60] and color correction has been added to adjust the uneven projection occurred by absorption [4, 5, 19, 24, 27, 43, 48, 49, 58–60, 83]. Ancuti et al. [3] used the local highest value of dark channels for evaluating background light.

Background's light whether global or local is also defined as flat area [48, 49] or blurry region [26, 27]. In order to compute the blurry area in an underwater image and identify the background light, Emberton et al. [26] designed a hierarchical model. While the color of the underwater target was near to blur area, this model became unreliable. Emberton et al. [27] again dissolved the underwater image into; (i) greenish, (ii) bluish and (iii) blue greenish, based on the hierarchy technique. Before the DCP based restoration, different white balance procedures were gained for each part. Whereas, if the theoretical highest merit of background light was applied as a denominator for evaluating the transmission map, then this resulted in over saturation phenomenon leading to the appearance of artefacts in the background area [79].

In existing approaches, the maximum of learning used in DCP based restoration models is based on supervised scenarios [49]. Whereas in some of the approaches, unsupervised methods were used. With respect to the statistical distribution of color images, authors [80, 81] combined the colors present in original images in 500 types. Every pixel present in color image was presented with the cluster centre. In clustering space, color pixel shows a line segment based on distance with respect to the camera. Clustering with the logarithmic of the RGB value, an attenuation curve is obtained using the k dimension (KD) tree. After identifying the pixel value that has a maximum variation between RGB channels in the image, background light has been evaluated. To correct the transmission map simultaneously, the saturation constraint is applied; still, the restored image remained over saturated and dark.

2.2 Underwater image enhancement method

In this method, information related to the image is extracted even in absence of prior knowledge of the environment. Hence these methods are more generalized compared to the restoration method. In underwater image processing and analysis, many underwater

enhancements are combined which are taken from methods directly applied to natural images [37, 65, 76]. Here we are discussing the main aspects of underwater image enhancement methods in which they focus on contrast stretching, merged improvement along with multi information and noise removal. All these methods have been listed in Table 2.

2.2.1 Filter based method

Arnold-Bos et al., [8] designed a pre processing model for luminance components in the underwater image. This model identified a specific noise range in the underwater image by combining enhancement and deconvolution methods. Log Gabor wavelet is used for denoising, decreasing various quantization errors and also to suspend particle noise. This system increases the effect of edge detection. A model designed by Bazeille [9] contains various filtering steps which enhance the quality of non-uniform illumination, increase contrast, decrease noise, and update color of an underwater image. In order to minimize the noise in the underwater image, a non-sub sampled contourlet transform (NSCT) which depends on adaptive total variation was designed by Jia and Ge [46]. A partial differential equation (PDE) was also used by the authors to reduce noise in an image and construct frequency components. The quality of enhancement of underwater images was examined by using the sharpness and PSNR i.e. peak signal to noise ratio.

2.2.2 Color correction based method

A model was proposed by Chambah et al. [15] in which automatic color equalization (ACE) was applied on each channel of RGB separately and adjusted the outputs of all three channels to increase the efficiency of identifying the fish recognition from an aquarium. ACE algorithm's various parameters were adjusted internally. A model based on Rayleigh distribution which contains a sequence of color correction schemes was designed by Ghani and Isa [32,

Table 2 Underwater image enhancement techniques

#	Publication	Technique	Quality	Fusion	Year
52	ISOP	ACE	None	N	2003
49	EuCPS	Gaussian filter, Contrast Stretch	None	N	2005
55	Emmcvpr	MRF	None	N	2005
50	CMM'06	Homomorphic filtering, Wavelet Transform, Anisotropic filtering, Contrast Stretch	Distribution of gradient histogram	N	2006
56	IJCS	Integrated color model	None	N	2007
57	ICASSP	Quaternion's rotation	None	N	2009
48	Acta Phot Sin	Morphological filter	None	N	2011
58	CVPR	White Balance, Bilateral Filter, Histogram equalization	None	Y	2012
51	CSIP	NSCT, ATV	PSNR and Sharpness	N	2012
53	Springer Plus	Rayleigh stretching	None	N	2014
54	Applied Soft Computing	Rayleigh stretching	None	N	2015
59	ICIP	Retibex, color correct	None	N	2015
60	TIP	Gray World, Gamma Correction, High Pass Filter	PCQI	Y	2017
47	OE	Wavelet	SSIM, PSNR, Entropy	N	2017
61	Neurocomputing	Retinex	MSE, UIQM, UCIQE	Y	2017

33]. An underwater image was taken by Torres-Méndez and Dudek [72], which was treated like a Markov random field (MRF) and in it, nodes evident in random fields indicated the poor quality of color values while those which were not visible indicated the true color values in the underwater image. It explained the relationship between the pixels and their neighborhood by training the true color of sample pixels. Iqbal et al. [45] designed an underwater image enhancement model for the marine environment using the integrated color model. In this model, an RGB color space is used and it depends on the sequence of sliding stretching like contrast stretching whereas in HSI color space it depends on brightness and saturation stretching. An underwater image color enhancement model, designed by Petit et al. [62] was based on optical attenuation inversion.

The variational Retinex model was designed by Fu et al. [29] that were on the basis of Retinex theory and herein using the linear domain variational Retinex the spatial luminance parameter of color corrected underwater image was disintegrated through 4–6 iterations. In [30], triangular and bilateral filters were used on a, b and L components in place of the Gaussian filter, and then they were combined based on the ratio of values present in the RGB space.

2.2.3 Image fusion based method

There are many methods and model based on observation which plays an important role in improvement. Gradually, the fusion process was also considered under image enhancement. A fusion based underwater image enhancement model was designed by Ancuti et al. [2], here white balance color improvement and the output of bilateral filtering were weighted using the outcome of histogram equalization. In order to get a pixel level fusion output, four types of fusion weights having Gaussian, local, sensitometry and saliency contrast were calculated. However, under the consideration that fast attenuation was of the red channel, they increased the white balance processing in [6].

2.3 Comparison between image restoration and image enhancement methods

Comparison of various techniques used in the image restoration method and image enhancement method with their advantage and disadvantage has been shown in Tables 3 and 4.

2.4 Deep learning based method

Based on deep learning, underwater image enhancement has challenges like labeling of images, difficulty to collect practically etc. Some of the approaches are discussed in Table 5 wherein training images column N stands for normal images and U stands for underwater images.

A collection of color corrected underwater images [12] has been used as a training data set in [61], in which based on a CNN an underwater image enhancement method is constructed. In this model, 55 elements are used following which a three-D enhanced underwater image is achieved. In [50] WaterGAN network was designed for underwater image color alteration enhancement which is used to simulate the attenuation caused by the water body. This is similar to the Generative Adversarial Networks (GAN) [34], where two training sets were taken into consideration, one containing normal images and their relative depth maps in air and another one containing underwater images that are taken from simulated underwater and laboratory images referred by Jaffe- McGlamery model.

Table 3 Comparison of various techniques used in image restoration method

Image Restoration Methods	
Techniques	Advantages (A) and Disadvantages (D)
Blind Deconvolution Approach with Wells' Approximation Theory	A: applicable to stripe image D: no guarantee for good result by iteration
Homomorphic Filtering	A: betterment on inhomogeneous illumination D: double time-consuming Fourier transform
Inverse Wavelet Transformation	A: decrease the noise of bright spot in ultrasound images D: restrict application scope
Light Channel Prior Model Calculation	A: artificial light source is taken into account D: few shadow or dark images have no bright channel
Modelling of Point Spread Function	A: determine medium attenuation in detail D: applicable to polarized laser image
Model Calculation and Wiener Filter	A: improvement on inhomogeneous illumination D: recurrent parameter calculation generate difficulty of time control
Model Calculation	A: good restoration for low contrast ratio image D: noise points on result image
Stereo RANSAC	A: depth information restoration for 3 dimensional image D: very time consuming
Unsupervised ColorCorrection Model	A: lager color fidelity and clarity D: high time consuming and computation overhead
Self-Tuning Model Calculation	A: coefficient self-adaption D: high time consuming and computation overhead
Wiener Filter & Adaptive Contrast Stretch	A: comprehensive enhancement and restoration algorithms D: can't applied to different noise situation

Table 4 Comparison of various techniques used in image enhancement method

Image Enhancement Methods	
Techniques	Advantages (A) and Disadvantages (D)
Automatic Color Correction	A: accurate than auto enhanced technique D: not applicable to remove noise
Brightness Preserving Histogram Equalization with Maximum Entropy	A: save the average brightness with maximum entropy D: not suitable for some dark or shadow image
Fuzzy Histogram Equalization	A: improved image contrast, good equalization D: not applicable for single image
Fusion Method	A: improved considerably the visibility range D: distant region in the image is not considering
RGB and HSV Contrast Limited Adaptive Histogram Equalization	A: generate the lower MSE and the higher PSNR values D: less comparison with other color models
Partial Differential Equation of Histogram Equalization	A: improved interpretability or perception of information in images D: cannot automatic enhance image
RGB Tone Vector Quaternion Transformation	A: improve contrast and color restoration D: saturation decreases
Remainder Energy Ratio Estimate Water Depth, Reductive Color Balance Compensation Change	A: effectively restore image color balance and remove haze D: highly computing overhead
Two-Dimension Empirical Mode Decomposition	A: widely Encountered low contrast problem D: low Color Correction
Unsupervised Color Correction Method	A: improve the lower red color and lower illumination D: cannot suitable for low blue color image

Table 5 Deep learning based underwater image enhancement models

#	Publication	Model	Source of training sets	Training Images	Effects	Year
63	IWINAC	CNN	Corrected Underwater Images	Not mentioned	Color Correction	2017
34	IEEERAL	GAN [34]	Tank and Simulated underwater images	5348 N+7000 U	Color Correction	2018
66	SPL	CycleGAN [85]	online underwater images	3800 N+3800 U	Color Correction	2018

Inspired by the cycle consistent adversarial network (CycleGAN) [85] a weakly supervised color migration model was proposed by Lie et al. [51], to provide accuracy in color deformation in deep sea underwater images. Herein between the underwater and normal images, forward and backward mapping and also adversarial discriminators were incorporated. Several distortion functions like adversarial losses LossGAN, Structural similarity LossSSIM, and periodic continuity LossCyc were used in the forward mapping and backward mapping generator. All useful information of underwater images was the same while the color was improved.

3 Underwater image dataset and evaluation

3.1 Underwater image dataset

The underwater image dataset is very useful in the evolution of underwater image processing techniques. Here various underwater image datasets that have been used by several authors for image enhancement and image restoration have been summarized, in Table 6.

In Fig. 2, images for these datasets are recorded. Due to the difficulty in the collection of datasets, we cannot confirm that this dataset is the complete dataset. Few problems like low accuracy labelling information, small category and single target object hamper the development of underwater image enhancement techniques.

3.2 Evaluation of underwater image quality

There are some parameters such as image restoration, image enhancement, image classification, image retrieval, image transmission, and optimization in optical image systems where the assessment of image quality plays a vital role. Two main methods i.e., subjective image quality evaluation (IQE) and objective image quality evaluation are used for evaluating the quality of images. Classification of objective IQE is independent of the reference image. If a reference image for any underwater image is not found, then to obtain the image quality we need a no-reference image metric.

We can use a number of quantitative metrics to assess the restoration and enhancement performance of different types of underwater images. These are (i) global contrast dealing with a grayscale underwater image quality; (ii) weighted gray scale angle (WGSA) metrics to evaluate the improvement of restored image, and (iii) robustness index to identify the proximity of gray scale histogram to their exponential distribution. Some papers also defined a method to assess the robustness of underwater image noise removal.

In color based underwater images, two important no reference evaluation metrics were used. One is underwater image quality measure (UIQM) in which the following three methods were combined to assess the quality of underwater images, (i) underwater image sharpness measure UISM, (ii) underwater image contrast measure UIConM and (iii) underwater image colorfulness measure UICM.

Table 6 Underwater Images Datasets

Dataset	Objects	Souce	Images	Resolution	Annotation	Year
Wild Fish Marker Dataset [20]	Fishes and other species in seabed	NOAA Fisheries	1934 in +ve, 3167 in –ve image set,	Variable	Y	2015
Port Royal Underwater Image database [63]	Natural and Artificial structures	Real scientific surveys in Port Royal	18,091	1360*1024	N	2015
OUCVISION Underwater Image dataset [47]	Rocks and artificial targets in the pool	Ocean University of China	4400	2592*1944	Y	2017
Underwater Photography Fish Database [75]	Coral, reef fishes and other underwater creatures	Amateur contribution	8644 (variables)	Variable	N	2018
Underwater Rock Image Database [63]	Rocks in the pool	University of Michigan	15,057	1360*1024	N	2018
HabCam Underwtaer Image Dataset [21, 22, 36]	Scallops, sand dollars, rocks and occasional fishes	Integrated and Provided by CVPR and AAMVEM Workshop	10,465	2720*1024	Y	2019
MOUSS underwater image dataset [21, 22]	Fishes	Integrated and Provided by CVPR and AAMVEM Workshop	159	968*728	Y	2019
AFSC underwater image dataset [21, 22]	Fishes and other relates species	Integrated and Provided by CVPR and AAMVEM Workshop	571	2112*2816	Y	2019
MBARI underwater image dataset [21, 22, 55]	Fishes	Monterey Bay Aquarium Research Institute	666	1920*1080	Y	2019
NWFSC underwater image dataset [21, 22]	Fishes and other relates species near the seabed	Integrated and Provided by CVPR and AAMVEM Workshop	123	2448*2050	Y	2019
RUIE Dataset [54, 67]	Scallops, sea cucumbers & sea urchins	Dalian University of Technology	4000	400*300	Partially	2019
RGBD underwater image dataset [10, 66]	Waterproof color charts in underwater environment	Tel Aviv University	1100+	1369*914	N	2018
Fish4Knoeledge [11, 28]	Marine environment and marine life	The Fish4knowledge Team	Images taken from video	Variable	Partially	2010

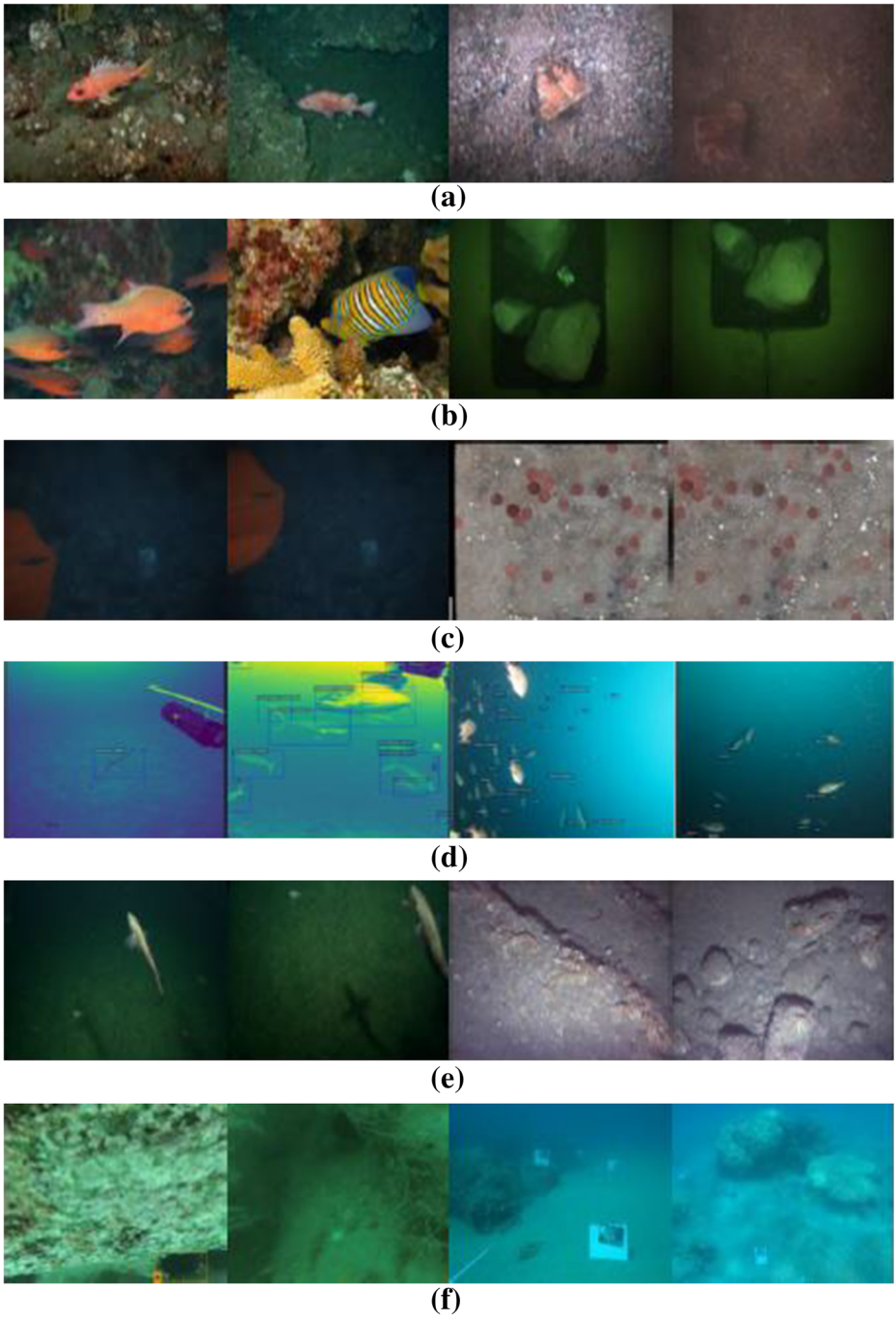


Fig. 2 Some images from different dataset. **a** Wild Fish Marker [20] and OUCVISION Dataset [47] **b** Underwater Photography-Fish [75] and Rock Database [63] **c** Port Royal [50, 63] and HabCam Underwater dataset [21, 22, 36] **d** MOUSS [21, 22] and AFSC Underwater dataset [21, 22] **e** MBARI [21, 22, 55] and NWFSC Underwater Dataset [21, 22] (f) RUIE [54, 67] and RGBD Underwater Dataset [10, 28, 53]

The other reference metric is the underwater color image quality evaluation (UCIQE) metric which is widely used to evaluate the quantity of non uniform color cast, enhance the quality of the image and quantify the blur and noise in the underwater image.

In subjective evaluation, some methods are defined to evaluate the quality of natural images like patch based contrast quality index (PCQI), mean square error (MSE), global contrast factor (GCF), structural similarity index measure (SSIM), average execution, peak signal to noise ratio (PSNR), entropy, a contrast to noise ratio (CNR), visibility metrics based on CNR (VM-CNNR), discrete entropy and contrast measure (DECM) and gradient ration in visible edge (GAVE).

The overall deterioration dominates all underwater images, including chroma reduction, poor contrast, nonuniform light, blurring, nonuniform color casts, and noise from numerous parameters. Because of the various distortions present in underwater images, it is difficult to develop a standard image quality metric which can be applied to all kinds of underwater conditions. Using the existing underwater image quality criteria, an incorrect score was given for an underwater image containing dark areas, oversaturation, and non-uniform brightness.

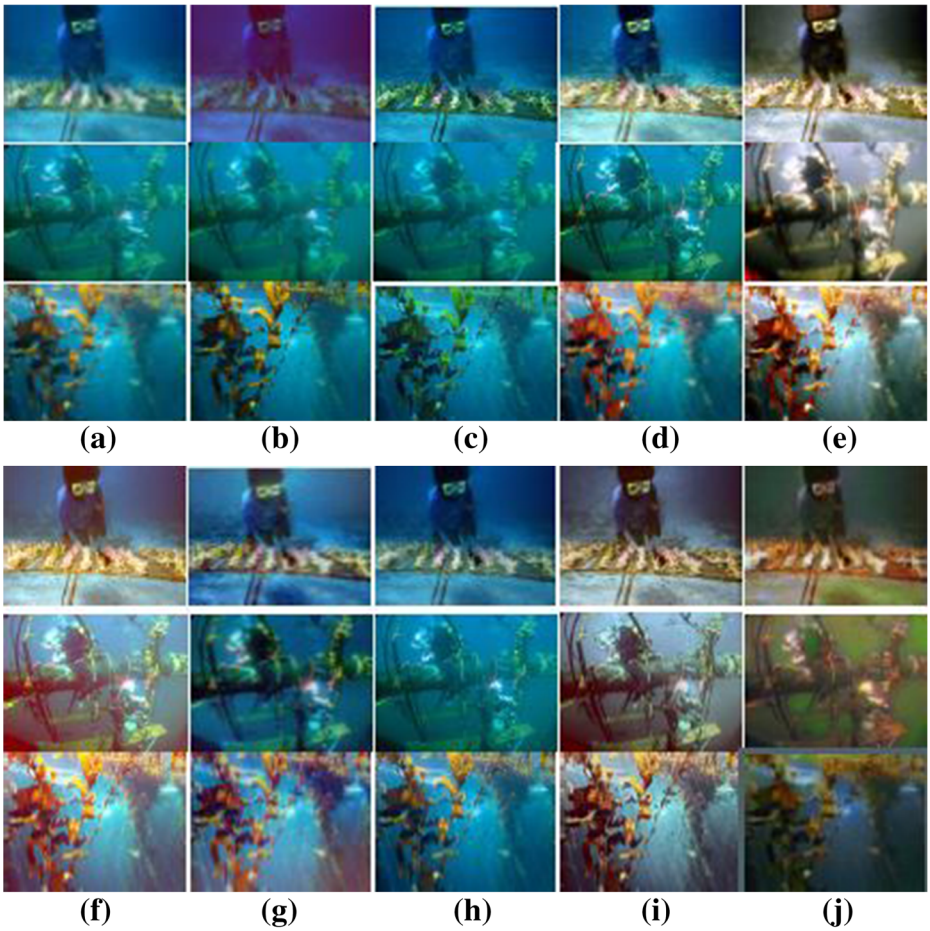


Fig. 3 Bluish Underwater images results comparison. **a** Original Images **b** He model results [38] **c** Galdran model results [31] **d** Peng model results [59] **e** Li model results [49] **f** Yang model results [83] **g** ACE model results [11] **h** Iqbal model results [45] **i** Fu model results [29] **j** Li model results [51]

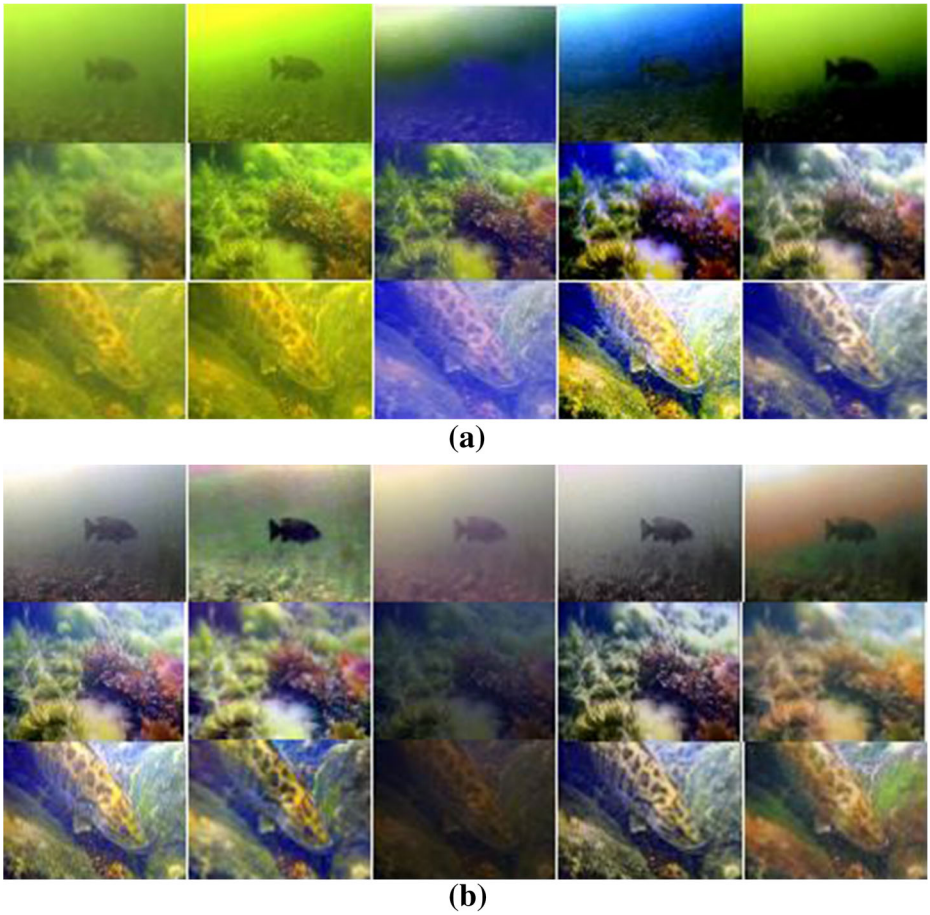


Fig. 4 Yellowish Underwater images results comparison. **a** Original Images **b** He model results [38] **c** Galdran model results [31] **d** Peng model results [59] **e** Li model results [49] **f** Yang model results [83] **g** ACE model results [11] **h** Iqbal model results [45] **i** Fu model results [29] **j** Li model results [51]

4 Result evaluation and analysis

Various types of techniques for underwater image restoration and enhancement were tested in this section to identify their subjective and objective performance. The images were classified into five parts: bluish, greenish, yellowish, whitish and deep sea underwater images. Various underwater image dehazing methods were analyzed as given by He et al. [38], and Galdran et al. [31]. Moreover, techniques using DCP with color correction like those given by Yang et al. [83], Peng et al. [59], Le et al. [49], tested color enhancement method used in ACE [11], by Iqbal et al. [45], a method based on Retinex [29] and deep learning model based method [51] were studied and analyzed.

4.1 Subjective evaluation

The experimental results of various methods have been shown in Figs. 3, 4, 5, 6 and 7. In this, it is observed that the output of the technique by Galdran et al. [31], Peng et al. [59],

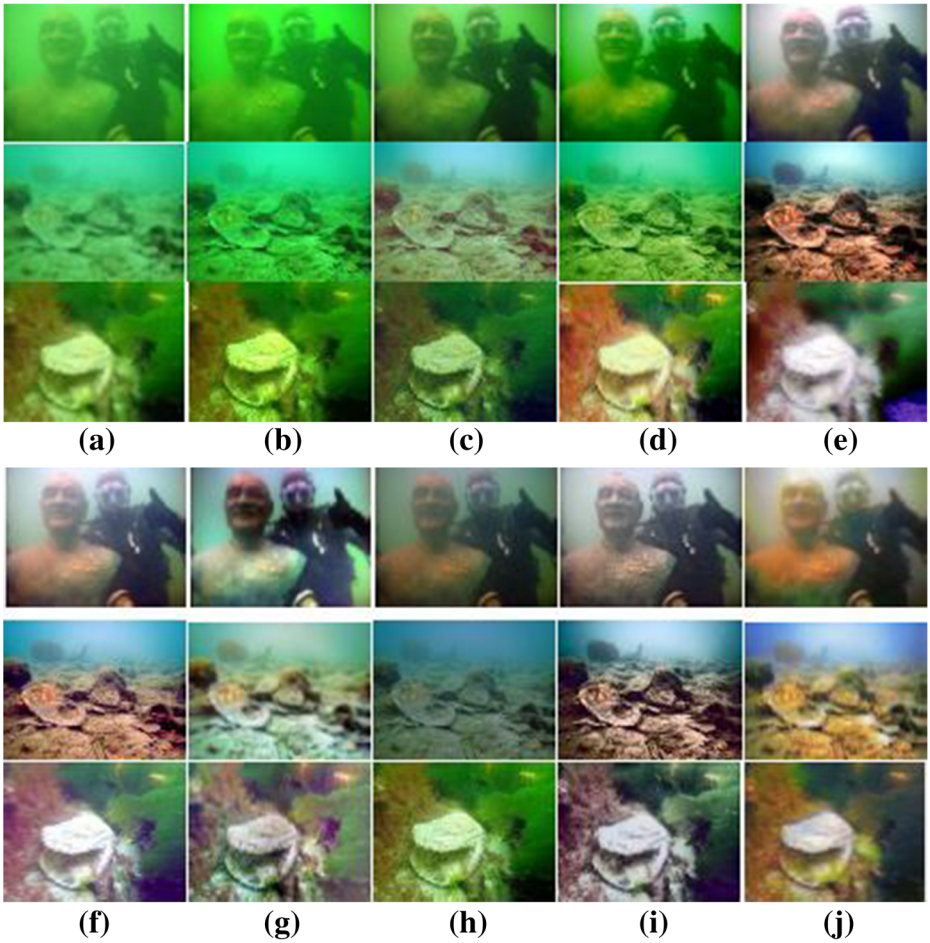


Fig. 5 Greenish Underwater images results comparison. **a** Original Images **b** He model results [38] **c** Galdran model results [31] **d** Peng model results [59] **e** Li model results [49] **f** Yang model results [83] **g** ACE model results [11] **h** Iqbal model results [45] **i** Fu model results [29] **j** Li model results [51]

ACE [11], Le et al. [49], Yang et al. [83], Fu et al. [29], enhances color visibly up to an optimum level in different parts of the underwater image. Among all, the ACE method [11], method of Le et al. [49], Yang et al. [83], and Fu et al. [29]; recorded fine performance. Fu et al. also enhanced the color congestion but in the output image, it generated blurred details. Difficulties in developing the bright targeted images were generated by various other DCP based underwater image restoration methods. The method of Yang et al. [83], generally experienced superior color restoration effects for every type of underwater image. It helped in increasing divergence of the dark region but also simplified technicalities in underwater images.

4.2 Objective evaluation

The result of restoration has been assessed by UCIQE, UIQM and PCQI metrics; because these metrics have been largely used to evaluate the execution of underwater images. To

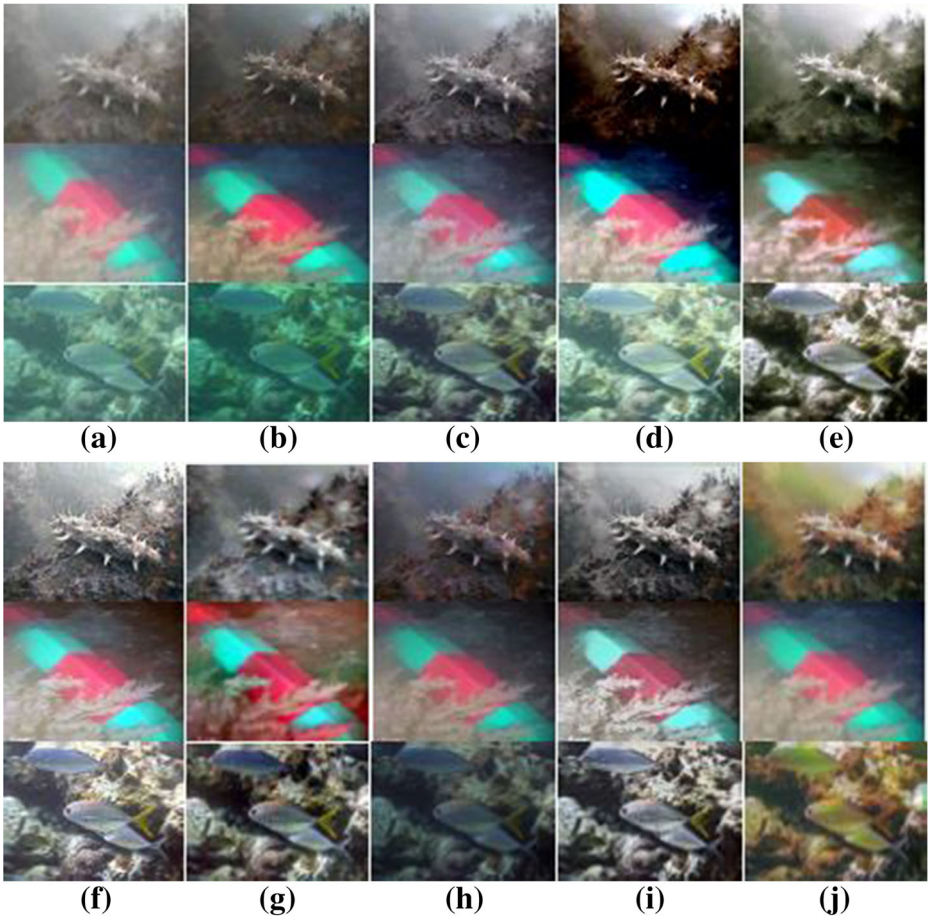


Fig. 6 Whitish Underwater images results comparison. **a** Original Images **b** He model results [38] **c** Galdran model results [31] **d** Peng model results [59] **e** Li model results [49] **f** Yang model results [83] **g** ACE model results [11] **h** Iqbal model results [45] **i** Fu model results [29] **j** Li model results [51]

evaluate the difference between the original and the enhanced gray scale images, the PCQI has been used. If we get 1, it shows no change between both of the input and evaluated images whereas a value less than or more than 1, signifies a change. This significant change doesn't essentially mean up-gradation of image quality.

In order to amplify the quality of images, higher values in UIQM and UCIQE of underwater images were observed. Tables 7 and 8 represents the five groups having ten methods each with their numeric values of three metrics. The variation between the original image and the processed image was observed to be less; when the value of PCQI was closer to 1. The reason is no information to evaluate the color involved in PCQI. In Tables 7 and 8, the lower values of output images indicate that the overall brightness of these images has changed significantly. These images are shown in Figs. 3, 4, 5e, 6j and 7g. The images given in Figs. 4, 5 and 6d and in Fig. 7j have extremely dark regions in output images that include an average saturation, and peculiarly high global contrast, causing larger values in UCIQE. This data is presented in Tables 7 and 8. In Tables 7 and 8, the UIQM image value attained by model Li et al. is affected

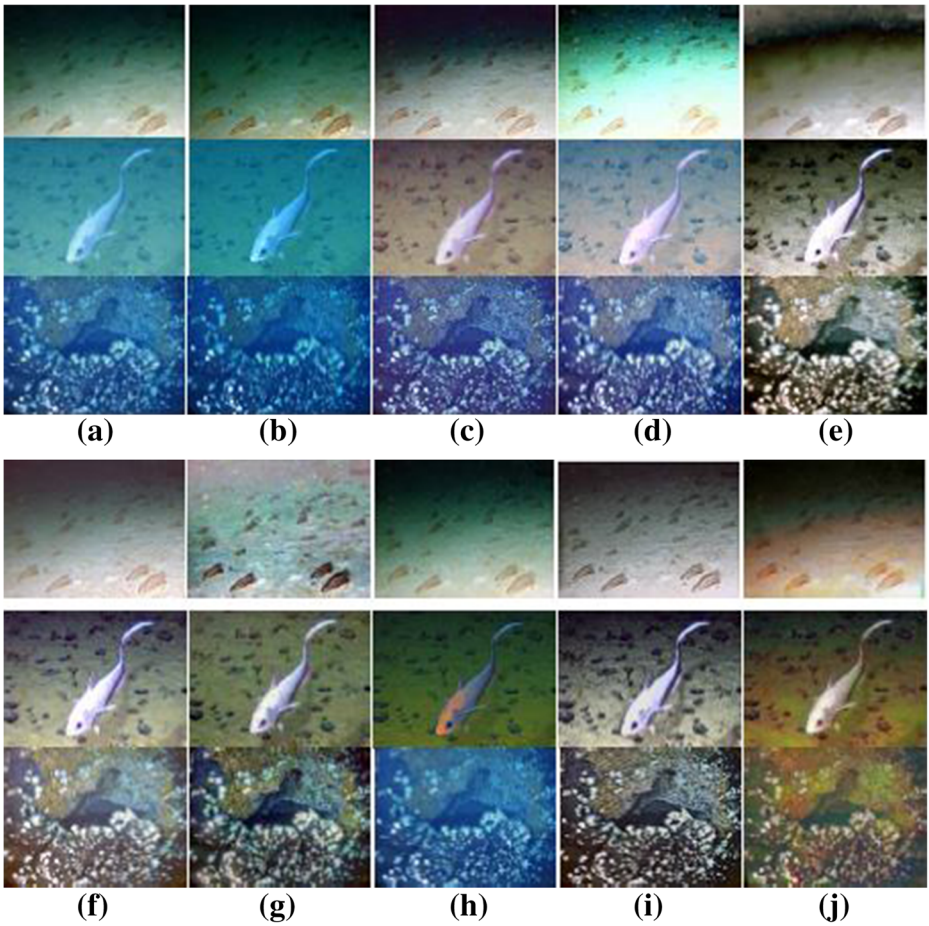


Fig. 7 Deep sea underwater images results comparison. **a** Original Images **b** He model results [38] **c** Galdran model results [31] **d** Peng model results [59] **e** Li model results [49] **f** Yang model results [83] **g** ACE model results [11] **h** Iqbal model results [45] **i** Fu model results [29] **j** Li model results [51]

through color deviation in output images that can be represented by high chroma variance and local contrast.

In conclusion, the accuracy of state-of-the-art underwater image quality evaluation techniques was not appropriate owing to the complexity of the underwater imaging environment and degradation categories (low contrast, color deviation, noise, blurring, etc.). The validity of color restoration and the amount of detail restoration in dark regions, particularly, did not meet the quality evaluation requirements of subjective visual assessment. The UCIQE has the shortest processing time among the PCQI, UCIQE, and UIQM average processing times and it is also suitable for real-time underwater applications.

If we compare the image restoration method and the image enhancement method based on the objective and subjective evaluations, then we find that the values of these evaluations are more appropriate in techniques that use enhancement methods rather than the restoration method. But if we compare the enhancement method with deep learning and machine learning enhancement techniques, then we get better results in deep learning and machine learning

Table 7 Bluish, Yellowish and Greenish underwater images quality evaluation in Figs. 3, 4 and 5 respectively

Methods	Bluish underwater images quality evaluation			Yellowish underwater images quality evaluation			Greenish underwater images quality evaluation		
	PCQI	UCIQE	UIQM	PCQI	UCIQE	UIQM	PCQI	UCIQE	UIQM
DCP [38]	0.9998	0.5753	0.7331	0.9997	0.5220	1.0030	0.9998	0.4662	1.3590
	0.9999	0.5373	0.6543	0.9999	0.5495	2.0703	0.9999	0.4601	1.1571
	0.9997	0.6206	1.3922	1.0000	0.5120	1.6096	0.9999	0.6153	1.4145
Carlevaris et al. [14]	0.9996	0.6617	1.2793	0.9998	0.5168	0.9297	0.9998	0.4662	1.2963
	0.9993	0.6723	−9.8942	0.9999	0.5612	2.3912	0.9999	0.5305	1.3641
	0.9996	0.7001	7.3351	0.9996	0.4788	1.9463	0.9998	0.6090	1.3012
Galdran et al. [31]	0.9995	0.5095	1.0839	0.9992	0.5759	1.1584	0.9995	0.5502	1.1036
	0.9999	0.5427	0.7909	0.9996	0.6116	2.1556	0.9999	0.4926	1.3740
	0.9998	0.5640	1.6841	0.9998	0.4664	2.4878	0.9996	0.5753	1.5394
Peng et al. [59]	0.9997	0.6506	1.2415	0.9990	0.6647	1.1260	0.9990	0.6647	1.1260
	1.0000	0.6080	0.8416	0.9996	0.6867	2.6617	1.0000	0.5499	1.6100
	0.9999	0.6974	1.9013	0.9995	0.6842	2.3114	0.9998	0.6580	2.2868
Li et al. [49]	0.9984	0.6438	1.3415	0.9991	0.6693	1.7985	0.9985	0.6109	1.0522
	0.9983	0.6349	1.4812	0.9986	0.6392	2.9309	0.9986	0.6030	3.0888
	0.9984	0.6996	1.6962	0.9984	0.5813	2.2163	0.9983	0.6310	2.5077
Yang et al. [83]	0.9995	0.6281	1.0638	0.9997	0.5265	0.7070	0.9997	0.5953	1.1409
	0.9994	0.6173	1.1396	0.9999	0.6283	2.3095	0.9992	0.5574	1.5148
	0.9995	0.6606	1.7997	0.9998	0.6312	2.0441	0.9997	0.5968	2.1840
ACE [11]	0.9990	0.6363	3.1240	0.9985	0.5631	3.0004	0.9984	0.6010	1.8157
	0.9990	0.6175	1.7808	0.9988	0.6216	4.5135	0.9986	0.5924	2.9807
	0.9988	0.6617	3.1858	0.9986	0.6255	4.6322	0.9991	0.5679	5.2560
Iqbal et al. [45]	0.9998	0.5900	0.0951	0.9999	0.4787	1.0029	0.9993	0.5324	1.0550
	0.9999	0.5502	0.7017	0.9996	0.5399	2.2466	1.0000	0.5374	1.4593
	0.9988	0.6208	1.6988	0.9992	0.5499	1.7704	1.0000	0.5996	2.1166
Fu et al. [29]	0.9989	0.6048	2.6445	0.9986	0.5146	0.5483	0.9985	0.5635	1.3496
	0.9985	0.6039	2.3926	0.9986	0.6028	3.3883	0.9988	0.5611	3.4128
	0.9987	0.6431	2.5730	0.9985	0.6029	3.7813	0.9987	0.5687	3.5260
Li et al. [51]	0.9985	0.6187	2.8621	0.9984	0.6055	0.8810	0.9985	0.6225	1.8308
	0.9986	0.5268	2.5723	0.9986	0.5899	3.7556	0.9986	0.6372	4.1197
	0.9985	0.6450	2.7541	0.9981	0.6051	3.3028	0.9998	0.6330	1.7280

techniques. But to conclude this, we need some more research on deep learning and machine learning enhancement techniques.

5 Discussion on future work

The comparison and assessment provided in this research demonstrate that by using an appropriate enhancement technique for various underwater activities and situations, a satisfying outcome may be attained. To satisfy the needs of complicated circumstances, the optimal algorithm should be capable of automatically assessing the information in the input underwater image and make adaptive adjustments for diverse scenarios and lighting conditions. There is currently a lack of knowledge on the best underwater enhancement technique. Furthermore, the impact of uneven illumination from artificial lighting sources is a little bit discussed. Furthermore, motion blurring is a deterioration that occurs in practically every underwater image, although it is hardly taken into account in enhancement or restoration procedures.

Table 8 Whitish and Deep sea underwater images quality evaluation in Figs. 6 and 7 respectively

Methods	Whitish underwater images quality evaluation			Deep sea underwater images quality evaluation		
	PCQI	UCIQE	UIQM	PCQI	UCIQE	UIQM
DCP [38]	0.9991	0.4868	0.9216	0.9995	0.5621	1.3005
	0.9995	0.6332	1.5901	0.9996	0.3875	1.8184
	0.9994	0.4506	1.5081	0.9995	0.5267	1.7723
Carlevaris et al. [14]	0.9998	0.4936	1.6122	0.9997	0.5907	1.6579
	0.9994	0.6570	1.5804	0.9998	0.4124	2.0374
	0.9998	0.4687	1.6462	1.0002	0.6052	2.4124
Galdran et al. [31]	0.9997	0.5086	1.6818	0.9999	0.5570	1.5566
	0.9996	0.5810	1.7226	0.9999	0.4918	1.8768
	0.9996	0.5173	1.5890	1.0000	0.5161	2.4359
Peng et al. [59]	0.9991	0.6435	1.5226	0.9990	0.5865	1.9853
	0.9994	0.6644	1.6376	0.9996	0.4871	2.0641
	0.9997	0.5009	1.8489	1.0001	0.5637	2.5266
Li et al. [49]	0.9985	0.5662	1.7145	0.9989	0.5800	0.7010
	0.9985	0.6348	0.5088	0.9985	0.5784	2.8738
	0.9985	0.5861	2.5875	0.9986	0.6207	4.0225
Yang et al. [83]	1.0000	0.5395	1.4461	0.9997	0.5251	1.8474
	0.9998	0.6145	2.0333	0.9999	0.5786	2.2721
	0.9999	0.5673	1.7655	0.9998	0.5627	2.4049
ACE [11]	0.9987	0.5610	4.1327	0.9980	0.5351	4.2408
	0.9981	0.6152	1.2117	0.9987	0.5602	4.2793
	0.9986	0.5868	3.2399	0.9996	0.6153	4.7435
Iqbal et al. [45]	0.9992	0.5242	1.5409	0.9999	0.5638	1.5289
	0.9994	0.5781	1.6597	0.9991	0.4921	1.7773
	0.9990	0.4759	1.5078	0.9999	0.5156	2.2373
Fu et al. [29]	0.9986	0.5241	2.3631	0.9990	0.5100	1.6565
	0.9985	0.5819	0.7441	0.9984	0.5491	3.4114
	0.9987	0.5513	3.5733	0.9993	0.5736	4.6958
Li et al. [51]	0.9984	0.6017	2.2486	0.9988	0.6084	1.5257
	0.9985	0.5966	1.2255	0.9981	0.6234	2.3039
	0.9985	0.5770	4.1733	0.9990	0.5448	5.5620

Most studies concentrate on a single underwater image and spend little emphasis to underwater video processing; yet underwater video processing is critical relevance in practical applications. At the moment, there are several issues that require immediate attention, such as underwater pollution, video processing efficiency and inter-frame uniformity is required.

The available underwater image quality evaluation methods cannot accurately assess contrast and partial color improvements. It is difficult to build a significant standardized objective assessment approach for underwater image improvement. Although present natural image databases contribute significantly to the advancement of image quality assessment, image deformation in these datasets is either single deformation created manually or deformation of an image obtained by mobile devices. Furthermore, when applied to another database, the accuracy of an image quality assessment approach based on training with only one database is frequently poor.

With respect to future work, the researcher may contemplate the following features to carry out the relevant work: (i) by comparing and analyzing various methods present in the present study, we needed more appropriate underwater image enhancement methods which focus on adaptive adjustment for various scene and lightening issue in the deep sea, (ii) uneven

availability of external light source in underwater sea, (iii) motion blurring also is one parameter for improvement in underwater image enhancement and restoration, (iv) researcher should not only focus on underwater image processing but also focus on underwater video processing.

6 Conclusion

The difficulty of achieving visibility of things at long or short distances in underwater environments is a challenge for the image analysis community. Even while there is various image enhancing techniques available, they are mostly confined to regular images, and only a handful have been created expressly for underwater images. We evaluated some of them in this paper to bring the facts together for a deeper understanding and evaluation of the approaches. We outlined the existing approaches for image restoration, enhancement and enhancement using deep learning and machine learning, concentrating on the conditions under which each algorithm was initially designed. We also examined the methods used to assess the efficacy of the algorithms, highlighting studies that employed a quantitative quality score.

According to our research findings, a shared acceptable dataset of test images for varied imaging situations, as well as standard criteria for qualitative and quantitative evaluation of the results, is still necessary to improve underwater imaging processing.

Emerging underwater photography techniques and technologies necessitate the adaptation and extension of the methods described above, for example, to handle data from numerous sources which can collect 3-dimensional scene information. However, investigating the visual systems of underwater creatures will undoubtedly provide us with clean perspectives into the knowledge extraction of underwater images.

This paper introduced various predefined models of underwater image enhancement and restoration. Some common issues present are outlined. Results from various underwater image restoration and enhancement techniques on yellow, green, blue, white, and deep sea images are correlated, which is helpful to identify the most suitable methods under various constraints. Other than this the accuracy and limitation of various underwater image quality evaluation metrics are analyzed. In this, we also summarized various underwater image datasets and provided future research directions for researchers in this area.

Funding Any agency does not fund this study.

Data availability Data sharing not applicable to this article as no datasets were generated or analyzed during the current study.

Declarations Author 1 declares that he/she has no conflict of interest.
Author 2 declares that he/she has no conflict of interest.
This article does not contain any studies with human participants or animals performed by any of the authors.

Ethical approval This article does not contain any studies with human participants or animals performed by any of the authors.

Conflict of interest All the authors of this paper declare that he/she has no conflict of interest.

References

1. Almabouada F, Abreu MA, Coelho JMP, Aiadi KE (2019) Experimental and simulation assessments of underwater light propagation. Front Optoelectron 12(4):405–412
2. Ancuti C, Ancuti CO, Haber T et al (2012) Enhancing underwater images and videos by fusion. Proceeding IEEE conference on computer vision and pattern recognition (CVPR 2012) pp 81–88
3. Ancuti C, Ancuti CO, De C et al (2016) Multi-scale underwater descattering. Procceding of 23rd international conference on pattern recognition (ICPR 2016) pp 4202–4207
4. Ancuti CO, Ancuti C, De C et al (2017) Color transfer for underwater dehazing and depth estimation. Proceeding IEEE international conference on image processing (2017) pp 695–699
5. Ancuti CO, Ancuti C, De C et al (2017) Locally adaptive color correction for underwater image dehazing and matching, proceeding on IEEE computer vision and pattern recognition. Workshops pp 1–9
6. Ancuti CO, Ancuti C, De Vleeschouwer C et al (2018) Color balance and fusion for underwater image enhancement. IEEE Trans Image Process 27(1):379–393
7. Anwar S, Li C (2020) Diving deeper into underwater image enhancement: A survey. *Signal Process Image Commun* 89:115,978–115,978
8. Arnold-Bos A, Malkasse JP, Kervern G (2005) A preprocessing framework for automatic underwater images denoising, european conference on propagation and systems. pp 15–18
9. Bazeille S, Quidu I, Jaulin L et al (2006) Automatic underwater image pre-processing. Proceeding Caracterisation Du Milieu *Marin*. pp 16–19
10. Berman D, Levy D, Avidan S et al (2018) Underwater single image color restoration using haze-lines and a new quantitative dataset. URL: https://arxiv.org/abs/1811.01343
11. Boom BJ, He J, Palazzo S, Huang PX, Beyan C, Chou HM, Lin FP, Spampinato C, Fisher RB (2014) A research tool for long term and continuous analysis of fish assemblage in coral-reefs using underwater camera footage. Ecol Inform 23:83–97
12. Bryson M, Johnson-Roberson M, Pizarro O, Williams SB (2016) True color correction of autonomous underwater vehicle imagery. J Field Robot 33(6):853–874
13. Caimi FM, Dalgleish FR, Giddings TE et al (2007) Pulse versus CW laser line scan imaging detection methods: simulation results. Europe 18:1–4
14. Carlevaris-Bianco N, Mohan A, Eustice RM (2010) Initial results in underwater single image dehazing, Oceans Mts/IEEE Seattle pp 1–8
15. Chambah M, Semani D, Renouf A et al (2003) Underwater color constancy: enhancement of automatic live fish recognition, Color Imaging IX: Processing, Hardcopy, and Applications pp 157–168
16. Chen CLP, Zhou J, Zhao W (2012) A real-time vehicle navigation algorithm in sensor network environments. IEEE Trans Intell Transp Syst 13(4):1657–1666
17. Chiang JY, Chen YC (2011) Underwater image enhancement by wavelength compensation and dehazing. IEEE Trans Image Process 21(4):1756–1769
18. Chiang JY, Chen YC, Chen YF (2011) Underwater image enhancement: using wavelength compensation and image dehazing (WCID). In International conference on advanced concepts for intelligent vision systems pp 372–383
19. Cho Y, Shin YS, Kim A (2016) Online depth estimation and application to underwater image dehazing. Proceeding of IEEE Oceans pp 1–7
20. Cutter G, Stierhoff K, Zeng J et al (2015) Automated detection of rocks in unconstrained underwater videos using Haar cascades and a new image dataset: labelled fishes in the wild. IEEE Winter Appl Comput Vis Workshops 1:57–62
21. CVPR 2018 Workshop and Challenge (AAMVEM) (n.d.) Available: http://www.viametoolkit.org/cvpr-2018-workshop-data-challenge/challenge-data-description/
22. CVPR 2019 Workshop and Challenge (AAMVEM) (n.d.) Available: https://www.aamvem.com/datachallenge
23. Del Grosso VA (1975) Modulation transfer function of water. Oceans 75 Conference pp 331–347
24. Ding X, Wang Y, Zhang J (2017) Underwater image dehaze using scene depth estimation with adaptive color correction, Procceding of IEEE Oceans pp 1–5
25. Drews P, Nascimento E, Moraes F et al (2013) Transmission estimation in underwater single images. Proceedings of the IEEE international conference on computer vision workshops pp 815–830
26. Emberton S, Chittka L, Cavallaro A (2015) Hierarchical rank-based veiling light estimation for underwater dehazing. Proceedings of the British machine vision conference pp 1–12
27. Emberton S, Chittka L, Cavallaro A (2018) Underwater image and video dehazing with pure haze region segmentation. Comput Vis Image Underst 168:145–156

28. Fish4Knowledge (n.d.) Available: http://homepages.nf.ed.ac.uk/rbf/Fish4Knowledge/?tdsourcetag=s_pcqq_aiomsg.
29. Fu X, Zhuang P, Huang Y et al (2014) A Retinex-based enhancing approach for single underwater image. Proceeding IEEE international conference on image processing, (ICIP 2014) pp 4572–4576
30. Fu X, Zhuang P, Huang Y et al (2014) A retinex-based enhancing approach for single underwater image. IEEE international conference on image processing (ICIP 2014) pp 4572–4576
31. Galdran A, Pardo D, Picón A et al (2015) Automatic red channel underwater image restoration. J Vis Commun Image Represent 26:132–145
32. Ghani ASA, Isa NAM (2014) Underwater image quality enhancement through composition of dual-intensity images and Rayleigh-stretching. Springer Plus 3(1):757
33. Ghani ASA, Isa NAM (2015) Underwater image quality enhancement through integrated color model with Rayleigh distribution. Appl Soft Comput 27:219–230
34. Goodfellow I, Pouget-Abadie J, Mirza M et al Generative adversarial nets. Proceeding International Conference on Neural Information Processing Systems pp 2672–2680
35. Grosso VAD (1978) Optical transfer function measurements in the Sargasso Sea. International Society for Optics and Photonics pp 74–101
36. HabCam Underwater Image Dataset. (n.d.) Available: https://habcam.whoi.edu/
37. Han HW, Zhang XH, Ge WL et al (2011) A mixed noise reduction algorithm for underwater laser images based on soft-morphological filter. Acta Photonica Sinica 40(1):136–141
38. He K, Sun J, Tang X (2011) Single image haze removal using dark channel prior. IEEE Trans Pattern Anal Mach Intell 33(12):2341–2353
39. Honjo S, Doherty KW, Agrawal YC (1984) Direct optical assessment of large amorphous aggregates (marine snow) in the deep ocean. Deep Sea Res Part A Oceanogr Res Pap 31(1):67–76
40. Hou W, Gray DJ, Weidemann AD (2007) Automated underwater image restoration and retrieval of related optical properties. IEEE International Geoscience and Remote Sensing Symposium pp 1889–1892
41. Hou W, Weidemann D, Gray DJ (2007) Imagery derived modulation transfer function and its applications for underwater imaging. Int Soc Optics Photonics 6696:707–714
42. Hou W, Gray DJ, Weidemann AD, Arnone RA (2008) Comparison and validation of point spread models for imaging in natural waters. Opt Express 16(13):9958–9965
43. Hou M, Liu R, Fan X et al (2018) Joint residual learning for underwater image enhancement. Proceeding IEEE international conference on image processing pp 4043–4047
44. Hufnagel RE, Stanley NR (1964) Modulation transfer function associated with image transmission through turbulent media. J Opt Soc Am 54(1):52–60
45. Iqbal K, Salam RA, Osman A et al (2007) Underwater image enhancement using an integrated color model. Int J Comput Sci 34(2):1–6
46. Jia DX, Ge YR (2012) Underwater image de-noising algorithm based on non sub sampled contour let transform and total variation. International conference on computer science and information processing (CSIP 2012) pp 76–80
47. Jian M, Qi Q, Dong J et al (2017) The OUCvision large-scale underwater image database. IEEE international conference on multimedia and expo (ICME 2017) pp 1297–1302
48. Li C, Guo J, Chen S et al (2016) Underwater image restoration based on minimum information loss principle and optical properties of underwater imaging, proceeding IEEE international conference on image processing, (ICIP 2016) pp 1993–1997
49. Li C, Guo J, Guo C, Cong R, Gong J (2017) A hybrid method for underwater image correction. Pattern Recogn Lett 94:62–67
50. Li J, Skinner KA, Eustice RM et al (2018) Water-GAN: unsupervised generative network to enable real-time color correction of monocular underwater images. IEEE Robot Autom Lett 3(1):387–394
51. Li C, Guo J, Guo C et al (2018) Emerging from water: underwater image color correction based on weakly supervised color transfer. IEEE Signal Process Lett 25(3):323–327
52. Li Y, Takahashi S, Serikawa S (2019) Cognitive Ocean of things: a comprehensive review and future trends. Wirel Netw. pp 1–10
53. Li C, Guo C, Ren W, Cong R, Hou J, Kwong S, Tao D (2019) An underwater image enhancement benchmark dataset and beyond. IEEE Trans Image Process 29:4376–4389
54. Liu R, Fan X, Zhu M et al (2019) Real-world underwater enhancement: Challenges, benchmarks, and solutions, (2019), Available: https://arxiv.org/abs/1901.05320
55. MBARI Underwater Image Dataset (n.d.) Available: https://www.mbari.org
56. McGlamery BL (1980) A computer model for underwater camera systems. International Society for Optics and Photonics (208)

57. Nery MS, Machado AM, Campos MFM et al (2005) Determining the appropriate feature set for fish classification tasks. XVIII Brazilian symposium on computer graphics and image processing (SIBGRAPI'05) pp 173–180
58. Peng YT, Cosman PC (2016) Single image restoration using scene ambient light differential. Proceeding IEEE international conference on image processing (ICIP 2016) pp 1953–1957
59. Peng YT, Cosman PC (2017) Underwater image restoration based on image blurriness and light absorption. IEEE Trans Image Process 26(4):1579–1594
60. Peng YT, Zhao X, Cosman PC (2015) Single underwater image enhancement using depth estimation based on blurriness. Proceeding IEEE international conference on image processing pp 4952–4956
61. Perez J, Attanasio AC, Nechyporenko N et al (2017) A deep learning approach for underwater image enhancement. International work-conference on the interplay between natural and artificial computation pp 183–192
62. Petit F, Capelle-Laize AS, Carre P (2009) Underwater image enhancement by attenuation inversion with quaternions. IEEE international conference on acoustics, speech and signal processing, (ICASSP 2009) pp 1177–1180
63. Port Royal Underwater Image Database and Underwater Rock Image Database (n.d.) Available: https://github.com/kskin/WaterGAN/
64. Qin D, Yue G, Yeqiu L, Le Z et al (2013) High-precision measurement technology of laser pulse flight time based on TDC-GP21. Infrared Laser Eng 42(7):1706–1709
65. Rai KR, Gour P, Singh B (2012) Underwater image segmentation using CLAHE enhancement and thresholding. Int J Emerg Technol Adv Eng 2(1):118–123
66. RGBD Underwater Image Dataset (n.d.) Available: http://csms.haifa.ac.il/proles/tTreibitz/datasets/ambient_forwardlooking/index.html
67. RUIE Dataset (n.d.) Available: https://github.com/dlut-dimt/Realworld-Underwater-Image-Enhancement-RUIEBenchmark
68. Sahoo A, Dwivedy SK, Robi PS (2019) Advancements in the field of autonomous underwater vehicle. Ocean Eng 181:145–116
69. Singh N, Bhat A (2021) A detailed understanding of underwater image enhancement using deep learning. In: 2021 5th International Conference on Information Systems and Computer Networks (ISCON 2021). IEEE, pp 1–6
70. Soni OK, Kumar JS et al (2020) A survey on underwater images enhancement techniques. IEEE 9th international conference on communication systems and network technologies (CSNT 2020) pp 333-338
71. Tan CS, Sluzek A, G. Seet GL, Jiang TY (2006) Range gated imaging system for underwater robotic vehicle. In: OCEANS 2006-Asia Pacific. IEEE, pp 1–6
72. Torres-Méndez LA, Dudek G (2005) Color correction of underwater images for aquatic robot inspection. In: Energy Minimization Methods in Computer Vision and Pattern Recognition: 5th International Workshop, EMMCVPR 2005, St. Augustine, FL, USA, November 9-11, 2005. Proceedings 5. Springer Berlin Heidelberg, pp 60–73
73. Trucco E, Olmos-Antillon AT (2006) Self-tuning underwater image restoration. IEEE J Ocean Eng 31(2): 511–519
74. Uemura T, Lu H, Kim H (2020) Marine organisms tracking and recognizing using yolo. In: 2nd EAI International Conference on Robotic Sensor Networks: ROSENET 2018. Springer International Publishing, pp 53–58
75. Underwater Photography Fish Database (n.d.) Available: http://www.fishdb.co.uk/. Accessed 27 Aug 2019
76. Vasamsetti S, Mittal N, Neelapu BC, Sardana HK (2017) Wavelet based perspective on variational enhancement technique for underwater imagery. Ocean Eng 141:88–100
77. Voss KJ, Chapin AL (1990) Measurement of the point spread function in the ocean. Appl Opt 29(25):3638–3642
78. Wang M, Wu Y, Li J et al (2010) Object recognition via adaptive multi-level feature integration. 12th international Asia-Pacific web conference pp 253–259
79. Wang K, Dunn E, Tighe, Frahm JM (2014) Combining scene priors and haze removal for single image depth estimation. In: IEEE Winter Conference on Applications of Computer Vision. IEEE, pp 800–807
80. Wang Y, Liu H, Chau LP (2017) Single underwater image restoration using attenuation-curve prior. In: 2017 IEEE International Symposium on Circuits and Systems (ISCAS). IEEE, pp 1–4
81. Wang Y, Liu H, Chau LP (2018) Single underwater image restoration using adaptive attenuation-curve prior. IEEE Trans Circuits Syst I Reg Pap 65(3):992–1002
82. Yang M, Gong C et al (2012) Underwater image restoration by turbulence model based on image gradient distribution. 2nd international conference on uncertainty reasoning and knowledge engineering pp 296–299

83. Yang M, Sowmya A, Wei Z et al (2019) Offshore underwater image restoration using reaction-decomposition-based transmission map estimation. IEEE J Ocean Eng 45(2):521–533
84. Yang M, Hu J, Li C, Rohde G, du Y, Hu K (2019) An in-depth survey of underwater image enhancement and restoration. IEEE Access 7:123638–123657
85. Zhu JY, Park T, Isola P et al (2017) Unpaired image-to-image translation using cycle-consistent adversarial networks. Proceeding IEEE international conference on computer vision (ICCV 2017) pp 2223–2232

Publisher's note Springer Nature remains neutral with regard to jurisdictional claims in published maps and institutional affiliations.

Springer Nature or its licensor (e.g. a society or other partner) holds exclusive rights to this article under a publishing agreement with the author(s) or other rightsholder(s); author self-archiving of the accepted manuscript version of this article is solely governed by the terms of such publishing agreement and applicable law.

2023 2nd International Conference for Innovation in Technology (INOCON)
Bangalore, India. Mar 3-5, 2023

AGC of 2-Area Restructured Power System using Polar Fuzzy Controller and Energy Storage Units

Ram Naresh Mishra[1, 2], Narendra Kumar[2], and Mohd. Zuhaib[1]
[1]Department of Electrical Engineering, GLA University, Mathura-281406, U P, India
[2]Department of Electrical Engineering, Delhi Technological University, Delhi-110042, India
ramnaresh.mishra@gla.ac.in,dnk_1963@yahoo.com, mohd.zuhaib@gla.ac.in

2023 2nd International Conference for Innovation in Technology (INOCON) | 979-8-3503-2092-3/23/$31.00 ©2023 IEEE | DOI: 10.1109/INOCON57975.2023.10101346

***Abstract* —A comprehensive and accurate knowledge base is necessary for a fuzzy logic controller to function well. The complexity of a knowledge base increases with the number of rules in it, which in turn influences the computation time and memory needs. In order to solve these issues, a Polar Fuzzy logic controller is proposed to automatically control the generation of two-area restructured thermal (non-reheat) power system interconnected via AC tie-line. So that deviation in frequency and tie-line power due to load disturbance in any area can be restored quickly. To further enhance the functionality of the polar fuzzy controller, an energy storage unit is provided to each control region. When system is subjected to 3% step load perturbation (SLP) in each area. To produce different dynamic responses for the system under study, SIMULINK models and program codings are done using MATLAB software version R2021a.**

Keywords— AC tie line, automatic generation control (AGC), dynamic stability, polar fuzzy logic controller (PFC) proportional integral derivative (PID). redox flow batteries (RFB).

I. INTRODUCTION

AGC is crucial to the power system's operation and design. Since they have an impact on the machine's performance and dependability, frequency changes that go beyond the established limit may cause a volatile state in the system. The preservation of tie line strength interchanges and scheduled frequency values is one of the main objectives of AGC. The literature reports a variety of intelligent control methods for AGC [1, 2].

Major structural changes have been made to the current electricity system in order to increase its operational efficiency. The distribution companies (DISCOs), transmission companies (TRANSCOs), and generation companies (GENCOs) all have specific roles to play. Any GENCO may be chosen by a DISCO for a power deal. For the system to run safely and steadily, the independent system operator (ISO) offers one of the supplementary services termed AGC. AGC's role is to re-dispatch GENCOs in accordance with the area participation factor (apfs). Area control error determines steady-state, relatively inelastic demand..AGC system deregulation plans are described in [3]. AGC of the deregulated power system was offered by Donde et al. [4], where the idea of DPM is applied to allow bilateral contracts. For both traditional and restructured thermal power systems, Y. Arya et al [5] analysis the performance of the efficient controller in comparison to I/PI controllers tuned using some heuristic optimization techniques. AGC simulation analysis for a 2-area deregulated power system utilizing an integral control strategy was presented by Rajan et al. [6]. In real environment, a control region may also feature a variety of energy resources, including hydro, thermal, gas, renewable energy, and so forth. Challenges and potential of Load Frequency Control (LFC) in traditional, present day systems are described in [7, 8]. Several electrical transactions may happen at once in a competitive electricity market. The work of AGC/LFC in a restructured setting without and with RFB is documented in [9-11]. In comparison to classical logic systems, the fuzzy logic system on which the fuzzy logic controller (FLC) is based is significantly more akin to human reasoning and natural language. How well FLC performs, is determined by the knowledge base, which includes the quantity of rules, diversity of membership functions, overlap of those functions, etc. To solve these problems, a Polar Fuzzy Controller is presented [12-13].

In this study, polar fuzzy technique is employed in an interconnected two area non-reheat thermal system under deregulated environment .Three GENCOs, two DISCOs, and one RFB are taken into account in each control area with numerous electricity transactions using PID as well as PFC control schemes without and with RFB for the proposed system's AGC under 3% SLP in each control zone. This is the way the paper has been put-up. In segment two, the proposed system's mathematical modeling is shown. PFC is discussed in section III and segment IV highlights the simulation results and discussion. Phase V is dedicated to wrapping up the suggested work.

II. MODEL UNDER INVESTIGATION

The system studied comprise of two control areas of same size. Area-l and Area-2 have non-reheat thermal system with three GENCOs and two DISCOs. Fig. 5 displays the block diagram for the system under investigation. DISCOs have choice to agreement of power with any GENCOs. DISCOs' contracted power is shown in Fig. 6. Figure 7 displays the RFB system's block diagram. The RFB are devices for electro-chemical energy storage with rechargeable features that are designed for extensive utility applications. When power is needed, RFBs use a reduction-oxidation cycle to transform and store electrical energy into chemical energy; this means that when the system encounters peak or abrupt load needs, the battery quickly recharges itself during routine load requirements. A dual converter converts between AC and DC or DC and AC (i.e. power generation and demand are out of balance, RFB offers an alternative solution). Therefore, they can be recommended for AGC systems that are deregulated. The proposed system is meant to have RFB provided in both areas, and the input command for the RFB in AGC is directly derived from the Delta F_i signal [10]. apf_{ij} = Area (i) participation factor of GENCO-j

$$\Delta P_{tie}^{Scheduled} = \sum_{i=1}^{3}\sum_{j=3}^{4} Cpf_{ij}\,\Delta P_{Lj} - \sum_{i=4}^{6}\sum_{j=1}^{2} Cpf_{ij}\,\Delta P_{Lj}$$

Authorized licensed use limited to: DELHI TECHNICAL UNIV. Downloaded on April 24,2023 at 04:29:35 UTC from IEEE Xplore. Restrictions apply.

(1)

$$\Delta P_{tie}^{actual} = \frac{2\pi T_{12}}{S}\left(\Delta F_1 - \Delta F_2\right) \quad (2)$$

$$\Delta P_{tie}^{Error} = \Delta P_{tie}^{Actual} - \Delta P_{tie}^{Scheduled} \quad (3)$$

ΔP_{tie}^{Error} , drops to zero in stable zones .Following are two areas' area control errors (ACEs).

$$ACE_1 = B_1\Delta F_1 + \Delta P_{tie}^{Error} \quad (4)$$

$$ACE_2 = B_2\Delta F_2 + \alpha_{12}\Delta P_{tie}^{Error} \quad (5)$$

ΔP_1 , ΔP_2 , ΔP_3 , ΔP_4 , ΔP_5 , ΔP_6 , ΔP_{L1LOC} , ΔP_{L2LOC} demonstrates signals from the power market.

$$\Delta P_{L1LOC} = \Delta P_{L1} + \Delta P_{L2} \quad (6)$$

$$\Delta P_{L2LOC} = \Delta P_{L3} + \Delta P_{L4} \quad (7)$$

DISCO Participation Matrix (DPM) is given below:

$$\begin{pmatrix} Cpf_{11} & Cpf_{12} & Cpf_{13} & Cpf_{14} \\ Cpf_{21} & Cpf_{22} & Cpf_{23} & Cpf_{24} \\ Cpf_{31} & Cpf_{32} & Cpf_{33} & Cpf_{34} \\ Cpf_{41} & Cpf_{42} & Cpf_{43} & Cpf_{44} \\ Cpf_{51} & Cpf_{52} & Cpf_{53} & Cpf_{54} \\ Cpf_{61} & Cpf_{62} & Cpf_{63} & Cpf_{64} \end{pmatrix} \quad (8)$$

Where, $\Delta P_{Li,\ LOC}$ = Deviation in contracted local load demand in i^{th} area; ΔP_{Li}= a change in the area's demand for electricity in i^{th} area. The ΔP_{UCi} is the deviation for the area's un-contracted load demand. When there is no un-contracted load, ΔP_{UC1} and ΔP_{UC2} are both equal to zero.

III. Polar Fuzzy Controller

The variance in system frequency (ΔF) and its integral (ΔF′) are the two inputs used by fuzzy controllers to determine the control action. These inputs are translated into polar coordinates in the case of PFC, and only one input (angle) is required to compute, as illustrated in Fig. 1. Consequently, PFC is relatively simple and just uses two rules. The PFC only utilizes one input, the angle, which is dependent on the ratio of the appropriately scaled inputs, so it is not essential to employ two distinct input gains for variation in system frequency and it's integral. Thus, while calculating the integral of frequency variation or variance in the system frequency, only one gain, K, is considered [12-13]. The origin "0" in Figure 2 represents the ideal equilibrium position, and all control efforts should be focused on moving the vector R in that direction. The output of the PFC is formed angle directly using the fuzzy input. Figures 3 and 4 demonstrate the input and output variables for fuzzy sets, respectively.

- FLC controls for sector A (0°–90°) should be significant positives because both ΔF and ΔF′ (integrals of variations in system frequency) are positives.
- Sector B (315°–360°) should get a low-positive FLC control signal as scaled ΔF is great positive and ΔF′ is small negative.
- Sector C (270°-315°) should get a low negative control signal from FLC thus scaled ΔF is small positive and ΔF′ is great negative.
- Sectors D, E, and F are entirely different from sectors A, B, and C, respectively.

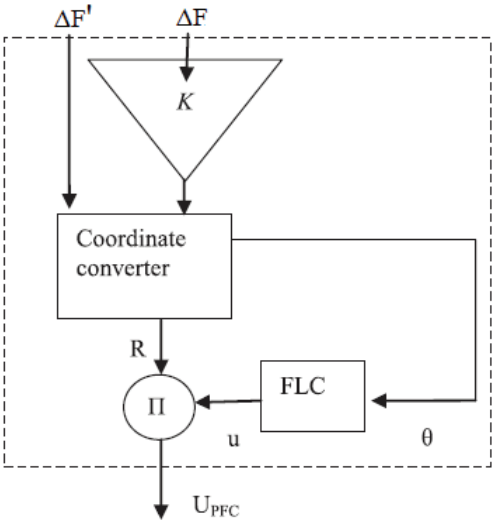


Fig 1 Block diagram of PFC

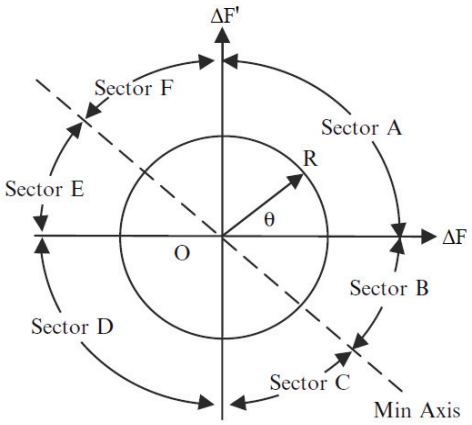


Fig.2 Plan for Six Sectors

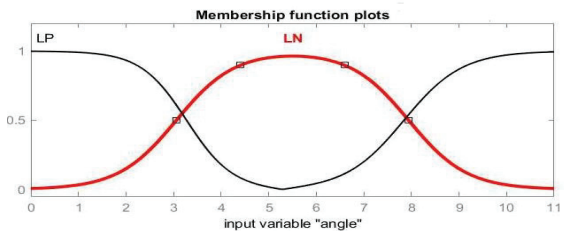


Fig. 3 Fuzzy sets for input variable

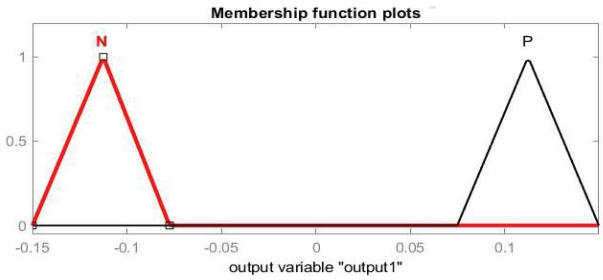


Fig.4: Fuzzy sets for output variable

Authorized licensed use limited to: DELHI TECHNICAL UNIV. Downloaded on April 24,2023 at 04:29:35 UTC from IEEE Xplore. Restrictions apply.

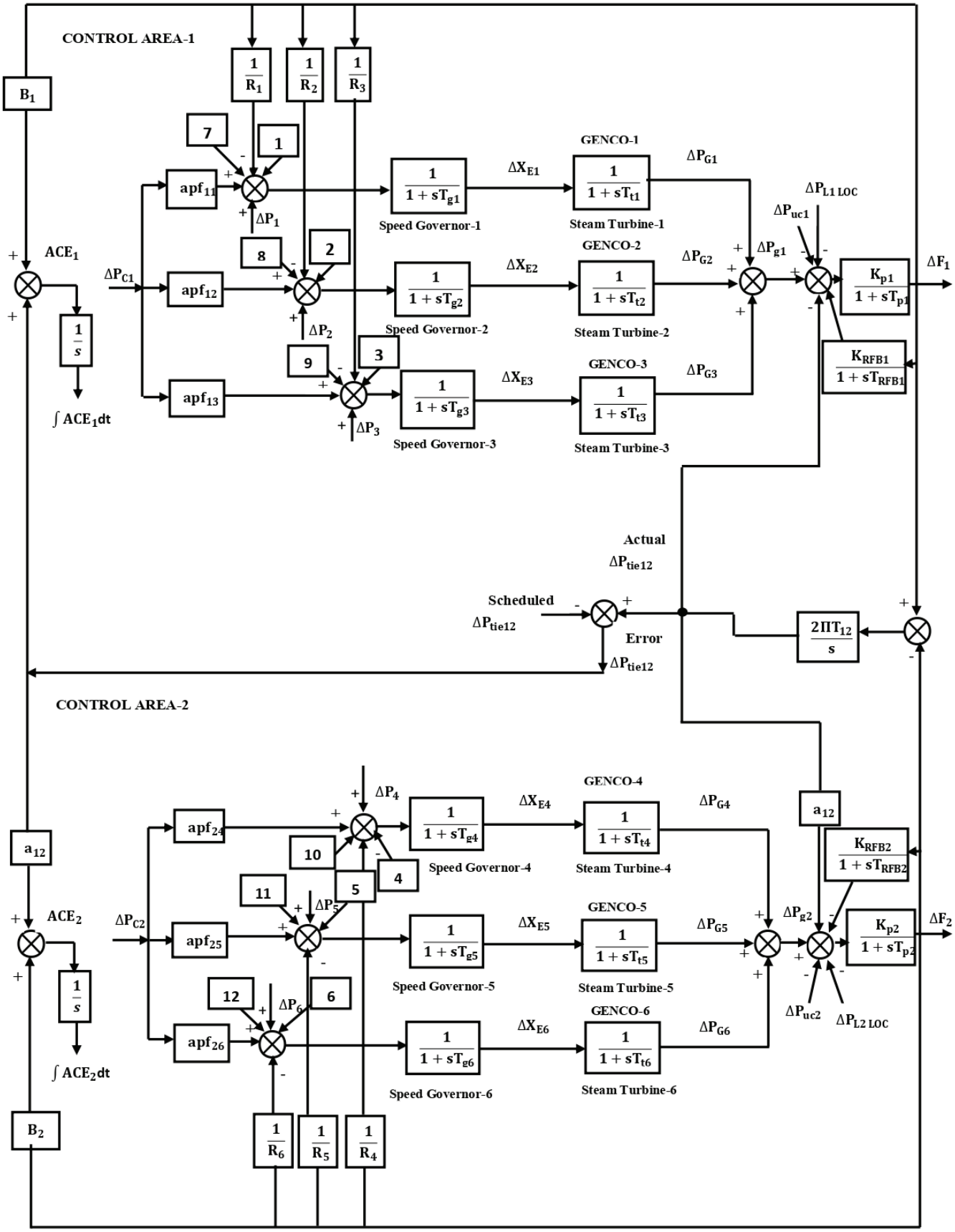


Fig.5. Transfer function block diagram

Authorized licensed use limited to: DELHI TECHNICAL UNIV. Downloaded on April 24,2023 at 04:29:35 UTC from IEEE Xplore. Restrictions apply.

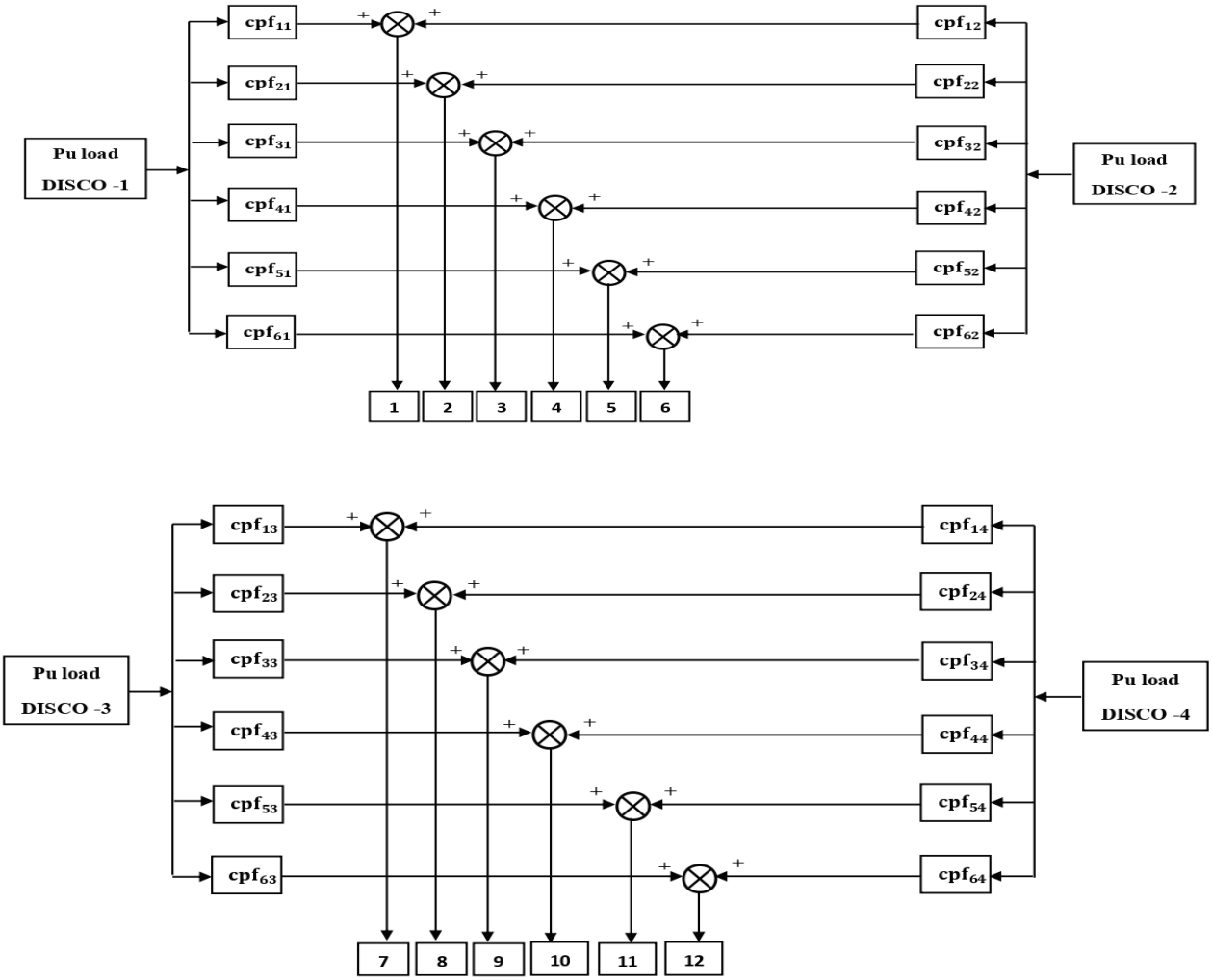


Fig.6. Contracted power of DISCOs

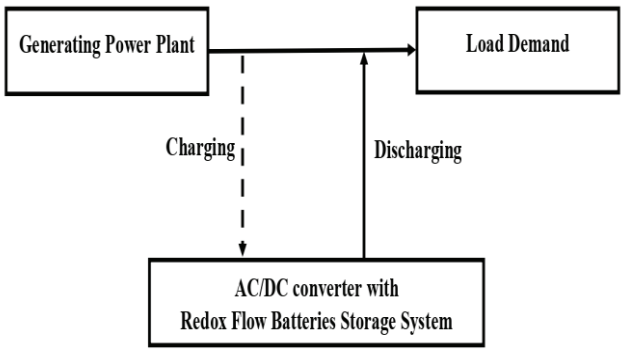


Fig.7. Block diagram of RFB

IV. RESULTS AND DISCUSSION

The contribution of GENCOs in each segment is as follows. $apf_{11}=apf_{12}=apf_{21}=apf_{22}=0.33$ and $apf_{13}=apf_{23}=0.34$.

The different cases are discussed below.

Case A: Poolco-bilateral transaction (PBT)

In this case, as per agreement of contract GENCOs can distribute power to any DISCO. GENCOs distribute 0.005 Hence the SLP is 0.03pu in each area. The simulation study for PBT reveals that achievement in the phrases of apex overshoot, undershoot and time of settling using PID control scheme and PFC without / with RFB is validated as proven in Fig. 8 to 9 . Proposed system with RFB performs significantly better. DPM for PBT is mentioned below.

$$\begin{pmatrix} 0.2 & 0.1 & 0.3 & 0 \\ 0.2 & 0.2 & 0.1 & 0.1666 \\ 0.1 & 0.3 & 0.1 & 0.1666 \\ 0.2 & 0.1 & 0.1 & 0.3336 \\ 0.2 & 0.2 & 0.2 & 0.1666 \\ 0.1 & 0.1 & 0.2 & 0.1666 \end{pmatrix}$$

Case B: Contract Violation (CV)

In this case, load demand of area-1 becomes 0.033 pu MW due to un-contracted DISCOs power of 0.003 pu MW, where SLP is 0.03 pu MW in each area. The simulation study reveals that achievement in the phrases of apex overshoot, undershoot and time of settling using PID control scheme to meet the objectives of AGC for proposed system without and with RFB is validated as proven in Figures 10 and 11 .

Authorized licensed use limited to: DELHI TECHNICAL UNIV. Downloaded on April 24,2023 at 04:29:35 UTC from IEEE Xplore. Restrictions apply.

pu MW power to each DISCO of its area according to cpfs.

Frequency deviations are greater in control zones, and tie-line power deviation reaction has gotten worse when DISCOs break power contract terms. Proposed system with RFB performs significantly better.

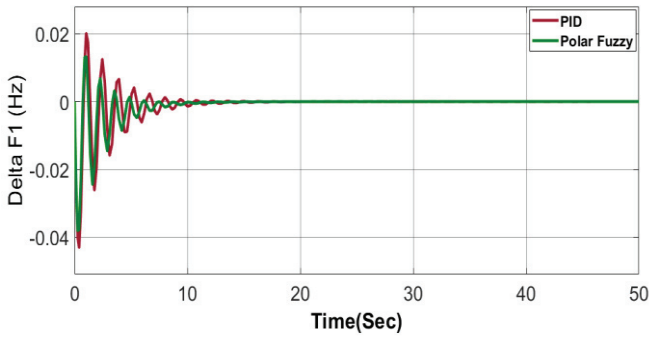


Fig.8(a) Dynamic responses of ΔF_1 for PBT

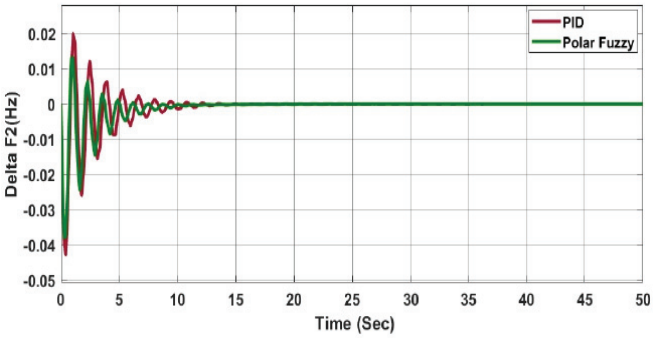


Fig.8(b) Dynamic responses of ΔF_2 for PBT

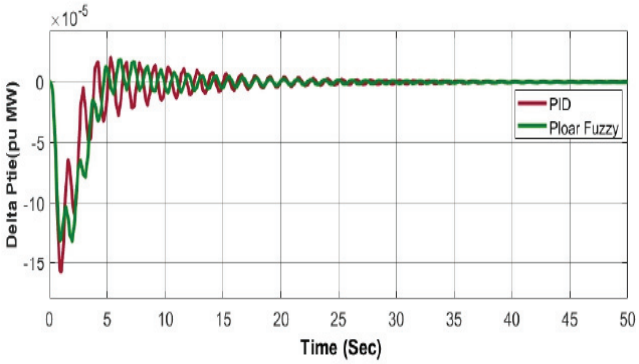


Fig.8(c) Dynamic responses of ΔP_{tie} for PBT

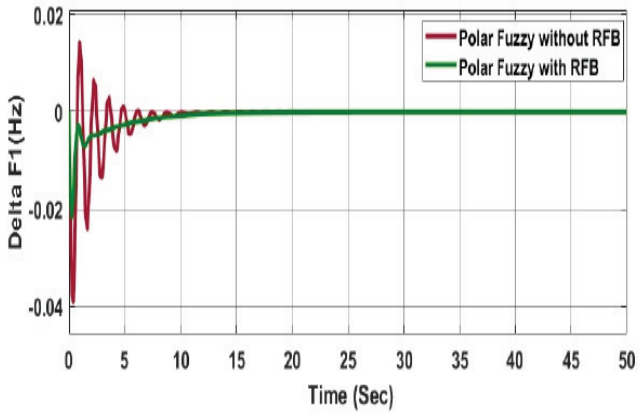


Fig.9.(a) Dynamic responses of ΔF_1 for PBT without /with RFB

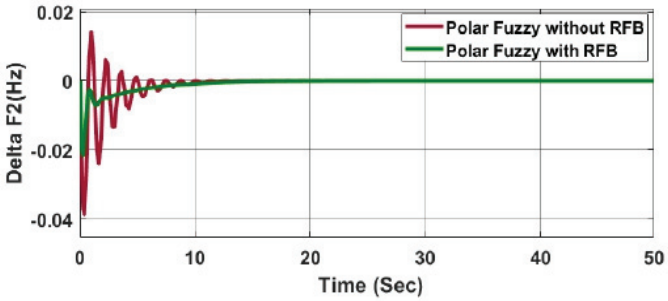


Fig.9.(b) Dynamic responses of ΔF_2 for PBT without /with RFB

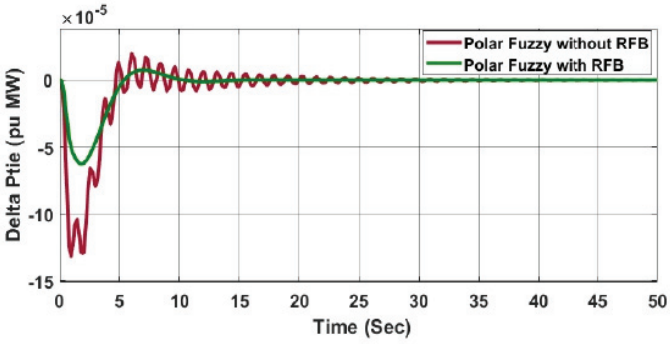


Fig.9.(c) Dynamic responses of ΔPtie for PBT without /with RFB

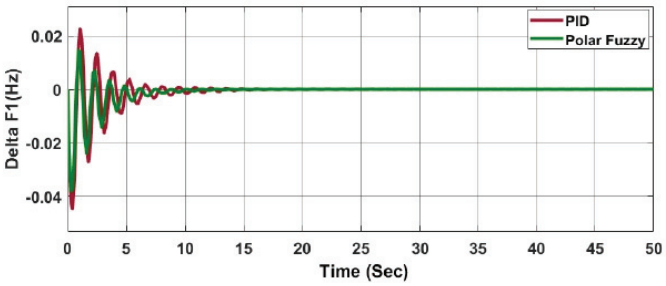


Fig.10(a) Dynamic responses of ΔF_1 for CV

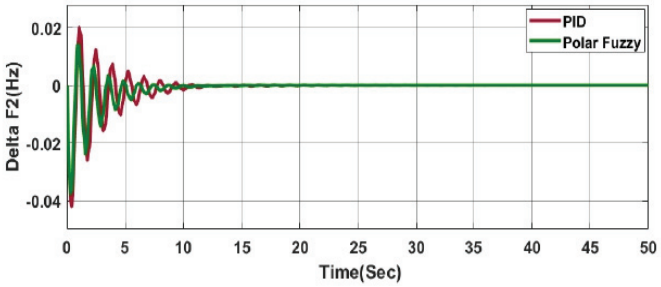


Fig.10(b) Dynamic responses of ΔF_2 for CV

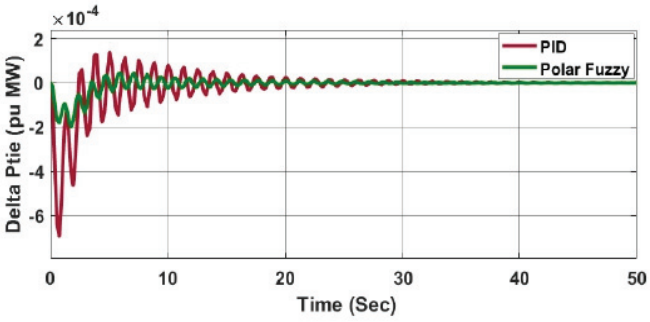


Fig.10(c) Dynamic responses of ΔP_{tie} for CV

Authorized licensed use limited to: DELHI TECHNICAL UNIV. Downloaded on April 24,2023 at 04:29:35 UTC from IEEE Xplore. Restrictions apply.

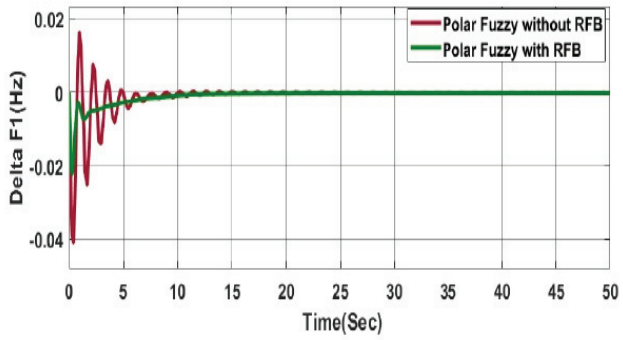


Fig.11.(a) Dynamic responses of ΔF_1 for CV without /with RFB

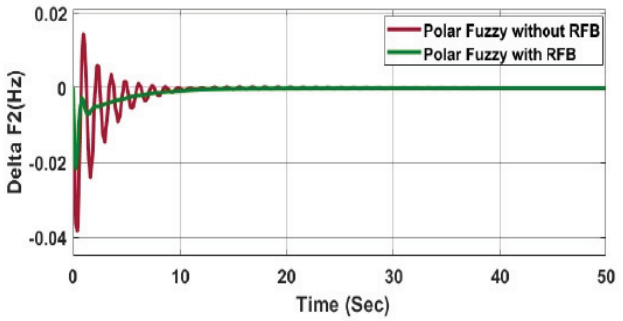


Fig.11.(b) Dynamic responses of ΔF_2 for CV without /with RFB

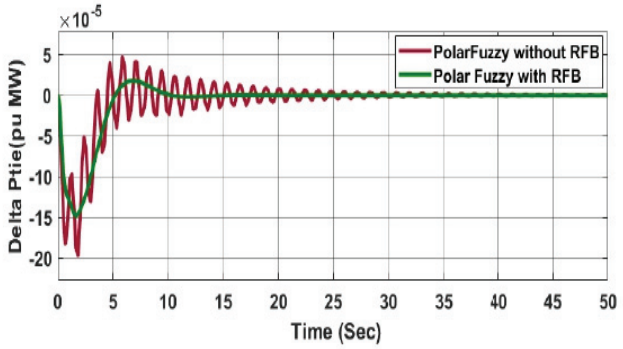


Fig.11.(c) Dynamic responses of ΔP_{tie} for CV without /with RFB

IV. CONCLUSION

In this study, a two-area restructured non-reheat thermal power system is used to create and evaluate the polar fuzzy logic controller. The suggested system undergoes 3% step load perturbation in each region; the performance of PFC is compared with that of a classical PID controller. PFC performed better in terms of apex undershoot, overshoot, and time to settle. To further enhance the system's performance for various power transactions, an energy storage unit is incorporated to each control area.

SIMULINK model and program codes in MATLAB version R2021a provide varied dynamic responses for the system under investigation.

REFERENCES

[1] Fosha C.E., and Elgerd 0.I., "The megawatt-frequency control problem: a new approach via optimal control theory", *IEEE Trans., PAS-89,, pp.563-577,1970.*

[2] Ibraheem, Kumar, P., and Kothari, D. P., "Recent philosophies of automatic generation control strategies in power systems," IEEE Trans. Power Syst., Vol. 20, No. 1, pp. 346–357, 2005.

[3] Ram Naresh Mishra, D.K. Chaturvedi and Prabhat Kumar, "Recent Philosophies of AGC Techniques in Deregulated Power Environment", J. Inst. Eng. India Ser. B, https://doi.org/10.1007/s40031-020-00463-8, 2020.

[4] Donde, V., Pai, M. A., and Hiskens, I. A., "Simulation and optimization in a AGC system after deregulation," IEEE Trans. Power Syst., Vol. 16, No. 3, pp. 481–489, 2001.

[5] Arya Y, Kumar N. Optimal control strategy–based AGC of electrical power systems: A comparative performance analysis. Optimal Control Appl Meth. 2017. doi: 10.1002/oca.2304

[6] Rajan Kumar and Lal Bahadur Prasad: Performance Analysis of Automatic Generation Control of Multi-Area Restructured Power System, ICAECT, DOI: 10.1109/ ICAECT49130.2021.9392417 , 2021.

[7] H. Haes Alhelou, Mohd-Esmail Hamedani-Golshan, R. Zamani, Ehsan Heydarian-Forushani and Pierluigi Siano: Challenges and Opportunities of Load Frequency Control in Conventional, Modern and Future Smart Power Systems: A Comprehensive Review, Energies 11, 2497;doi:10.3390/en11102497 ,2018.

[8] Christie, R. D., and Bose, A., "Load frequency control issues in power system operations after deregulation," IEEE Trans. Power Syst., Vol. 11, No. 3, pp. 1192–1200, 1996.

[9] P. Bhatt, S. P. Ghoshal, R. Roy, and S. Ghosal, "Load frequency control of interconnected restructured power system along with DFIG and coordinated operation of TCPS-SMES,"*IEEE Conf proc.,PEDES*, 2010.

[10] Mandeep Sharma, Sandeep Dhundhara and Yogendra Arya: Frequency stabilization in deregulated energy system using coordinated operation of fuzzy controller and redox flow battery, International Journal of Energy Research Wiley, 7457-7473, 2020.

[11] M. R. Chakraborty, S. Dawn, P. K. Saha, J. B. Basu and T. S. Ustun, "A Comparative Review on Energy Storage Systems and Their Application in Deregulated Systems'', *Batteries,8,124.https*://doi.org/10.3390/batteries8090124, (2022).

[12] Rahul Umrao and Chaturvedi D K, "Load Frequency control using Polar Fuzzy Controller," IEEE Tencon 2010, pp 557-562.

[13] D.K. Chaturvedi, Rahul Umrao, O.P. Malik, Adaptive Polar Fuzzy logic based Load Frequency Controller, Electrical Power and Energy Systems 66 (2015) 154–159.

Authorized licensed use limited to: DELHI TECHNICAL UNIV. Downloaded on April 24,2023 at 04:29:35 UTC from IEEE Xplore. Restrictions apply.

International Journal of Environmental Science and Technology
https://doi.org/10.1007/s13762-023-04921-w

ORIGINAL PAPER

Air quality changes in Delhi due to open waste burning: an accidental fire in Bhalswa landfill

M. Sharma[1] · M. Khare[2] · R. K. Mishra[1]

Received: 28 November 2022 / Revised: 31 January 2023 / Accepted: 25 March 2023
© The Author(s) under exclusive licence to Iranian Society of Environmentalists (IRSEN) and Science and Research Branch, Islamic Azad University 2023

Abstract

Open waste burning is a significant contributor to air pollution in urban cities. The contribution includes sources from local and centralized waste burning. This paper focuses on the air quality changes in the surrounding regions of the Bhalswa landfill in the north-west part of Delhi, India, where a fire broke out accidentally in the landfill from 20 April 2022 to 8 May 2022. Bhalswa landfill is one among the three major landfills in Delhi, and during the waste burning, $PM_{2.5}$ shows a maximum average concentration of about 107.32 and 338 μg/m^3 for $PM_{10.}$ The average $PM_{2.5}$ concentration increment was around 45–55%, and for PM_{10}, it was 40–50% during the fire. Apart from particulate matter, fumes generated during open waste burning emit gaseous and toxic substances. Dispersion of pollutants was less during low (< 3 m/s) and calm winds (< 1 m/s) and more during high winds (> 3 m/s). The correlation value (R^2) of gaseous pollutants with $PM_{2.5}$ was significant and exhibited a moderate correlation (R^2 around 0.5–0.6). It is high time for residents, government authorities and various other stack holders to be aware and implement policies and adopt technologies for segregation and processing. Identifying potential reuse of waste in energy and volume reduction forms should be encouraged to avoid further accidents/incidents related to open waste burning. The study's outcomes indicate the potential changes that occurred in regional air quality during the open waste burning in a short period.

Keywords Landfill · Open waste burning · Particulate matter · Urban air pollution

Abbreviations

CPCB	Central Pollution Control Board
CO	Carbon monoxide
CO_2	Carbon dioxide
DPCC	Delhi Pollution Control Committee
E-Waste	Electronic waste
Hrs	Hours
IGP	Indo-Gangetic Plain
IMD	India Meteorological Department
Km	Kilometre
Km^2	Per square kilometre
m	Metre
mm	Millimetre
m/s	Metre per second
MSW	Municipal Solid Waste
NCR	National Capital Region
NDMC	New Delhi Municipal Committee
NO	Nitric oxide
NO*x*	Nitrogen oxides
NO_2	Nitrogen dioxide
O_3	Ozone
PM	Particulate matter
$PM_{2.5}$	Particulate matter with a diameter of 2.5 μm
PM_{10}	Particulate matter with a diameter of 10 μm
SF	Supplementary figure
SO_2	Sulphur dioxide
ST	Supplementary table
WD	Wind direction
WS	Wind speed
μg/m^3	Microgram per metre cube

Editorial responsibility: U.W. Tang.

✉ R. K. Mishra
rajeevkumarmishra@dtu.ac.in

[1] Department of Environmental Engineering, Delhi Technological University, Delhi 110042, India

[2] Department of Civil Engineering, Indian Institute of Technology, Delhi, New Delhi 110016, India

Published online: 10 April 2023

Introduction

The national capital of India, Delhi, is home to more than 26 million inhabitants and is growing in terms of industrialization, population and vehicle fleet (Nagar et al. 2017; Yadav et al. 2020). It is encountering frequent events of air quality degradation episodes, and most of the time, the air quality consistently exceeds the national permissible limit (Sharma et al. 2022). Around 3000 metric tonnes of air pollutants is released into the atmosphere in Delhi. The major contributor is vehicular pollution, followed by power plants and municipal solid waste burning (Kumar 2018). Air pollution and its control measures are a major concern for governing agencies and environmental scientists globally. The focus on measurements, reduction and health impacts of particulate matter (PM_{10} and $PM_{2.5}$) is increasing day by day (Nagpure et al. 2015; Kumar et al. 2015a, b; Somvanshi et al. 2020). Exposure to particulate matter is associated with various human health threats, especially premature deaths (Agarwal et al. 2020; Cash et al. 2021; Hama et al. 2021). Handling and processing municipal solid waste are another big issue in urban regions and globally; every day, 2.01 billion tonnes of municipal solid waste is generated. It is estimated that by 2050, it will be around 3.40 billion tonnes (Krecl et al. 2021). Delhi generates around 1,11,44 tonnes of MSW per day (www.dpcc.delhigovt.nic.in). The process of MSW cycle includes collection, segregation, composting, recycling, dumping and incinerating. Every day about a certain percentage of MSW in both cities and towns is left uncollected, which leads to the accumulation of waste in the nook and corner of the streets (Nagpure 2019; Peter and Nagendra 2021; Ray et al. 2005). The collection efficiency in urban cities ranges from 70 to 90%, whereas in small towns, it ranges from 50 to 70%. Burning waste on a small scale or dumping it in landfills is the most commonly used and cheapest method for developing countries. It is estimated that globally around 41% of the waste is treated by open burning (Agarwal et al. 2020) and it leads to a significant source of air pollution caused by particulate matter emissions (Kumari et al. 2019; Ramaswami et al. 2016). Burning of biomass generates particulate matter along with gaseous pollutants. Dioxin/furans are released due to the open burning of wastes (Kumari et al. 2019). Open waste burning contributes to around 8% of direct PM emissions in India and 22% in China (Kumar et al. 2015a, b; Lal et al. 2016). The governing body CPCB reports the range of contribution from 5 to 11% in Indian cities (CPCB 2010) (Nagpure et al. 2015; Ramaswami et al. 2016). Burning of MSW openly acts as a non-point source for pollutants (Park et al. 2013; Kumari et al. 2019; Okedere et al. 2019). A study in Mexico shows that burning of waste contributes to around 3–30% of $PM_{2.5}$ and a sudden increase of 40–80% in aerosol emissions during waste burning activities (Agarwal et al. 2020). However, many countries, including India, banned the open burning of MSW (Estrellan and Iino 2010). The study area Delhi has three major dump yards for the disposal of MSW, namely Ghazipur (70 acres, 56 m height), Bhalswa (36 acres, 54 m height) and Okhla (46 acres, 40 m height). Densely populated residents surround the Bhalswa landfill in the northern part of Delhi. It is considered for the study due to an accidental fire breakout in the landfill from 26 April 2022 to 8 May 2022. The study period is classified into three types: before, during and after the fire accident, which helps analyse the changes in the landfill's nearby regions. This study analyses the air quality changes due to open waste burning and its impact on the surrounding areas. The study's outcomes help in analysing the effects on air quality due to open waste burning, public health and necessary mitigation measures for reducing the open waste burning. This will also helpful in policy formulation and fighting climate change.

Selection of study area

The study area is located in the northern part of Delhi (28.7395° N, 77.1573° E, Fig. 1). The landfill site comes under NDMC administration. Delhi is the national capital of India and its area is 1483 km^2, with a density of about 11,297 persons per km^2. This urban city comes in the territory of the Indo-Gangetic Plain (IGP) region. This IGP region is considered the country's largest river basin area. Delhi has extreme climatic conditions, which are very hot in summer from April to July and cold in winter from December to January. The average temperature ranges from 25 to 45 ºC during summer and during winter, it ranges from 22 to 5 ºC. The annual average rainfall of the city was around 714 mm. The monitoring locations are adjacent to the Bhalswa landfill regions (< 5 km aerial distance). The name of the locations and coordinates are shown in Table 1.

Materials and methods

The continuous ambient air quality monitoring stations in Ashok Vihar, Burari Crossing, Rohini, Sonia Vihar, Wazirpur and Jahangirpuri were selected to carry out this study. These six locations were selected based on

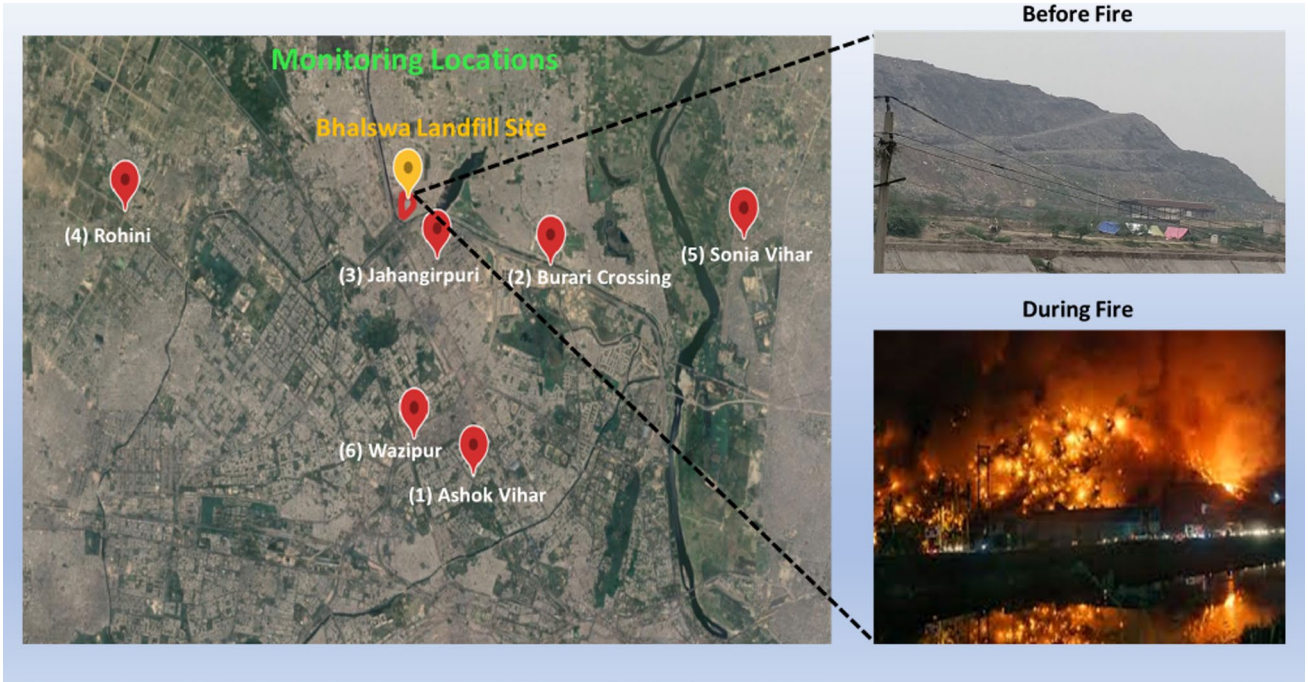


Fig. 1 Map displaying the monitoring stations

Table 1 Details of monitoring locations selected for study

Location name	Coordinates	
	Longitude	Latitude
Ashok Vihar, Delhi—DPCC	77.176524	28.690979
Burari Crossing, Delhi—IMD	77.160724	28.75513
Jahangirpuri, Delhi—DPCC	77.166631	28.729617
Rohini, Delhi—DPCC	77.082215	28.738268
Sonia Vihar, Delhi—DPCC	77.249589	28.733247
Wazirpur, Delhi—DPCC	77.16044	28.697544

the distance from the landfill out of 45 continuous ambient air quality monitoring stations in the city. The data were taken for a period of 19 days from 20 April 2022 to 08 May 2022 in which the total time period is classified into three different periods such as before fire (20 to 25 April), during fire (26 April to 1 May) and after fire (2 May to 8 May). The parameters such as PM_{10}, $PM_{2.5}$, NO, NO_2, NO*x*, SO_2, CO, O_3 and meteorological parameters such as wind speed (WS), wind direction (WD)) at a resolution of 1 h are taken from the CPCB live air quality data monitoring stations (https://app.cpcbccr.com/ccr/#/caaqm-dashboard-all/caaqm-landing/data). The data are analysed using RStudio version 1.3.1093.

Result and discussion

Box whisker plot analysis

The landfill fires emit different types of pollutants, majorly particulate matter such as PM_{10} and $PM_{2.5}$. The city's national ambient air quality 24 h standard for PM_{10} is 100 µg/m^3, and for $PM_{2.5}$, it is 60 µg/m^3 (ST.1). The fire event caused an increase in $PM_{2.5}$ concentration by around 60–70% in Ashok Vihar and Sonia Vihar locations and regions like Jahangirpuri and Rohini; the range was from 50 to 60% increase. The impact of $PM_{2.5}$ due to the landfill fire has a low impact on Burari Crossing region, which is the lowest percentage increase of about 28% (ST.2) among these six study sites. A percentage reduction of about 40–50% (ST.2) was observed in the $PM_{2.5}$ concentration at almost all the locations except Sonia Vihar. At Sonia Vihar, the reduction was observed only 28% after the landfill fire was eliminated (Fig. 2). The difference in scenarios such as before and after fire conditions was equal to ± 20%. The PM_{10} concentration shows an increase of about 10–20% at all the locations during the fire events except for Burari Crossing and Jahangirpuri, where the increase was seen about < 10%). After the fire event, it was around 25–40% (ST.2) reduction in $PM_{2.5}$ at all locations. This is due to the contribution of

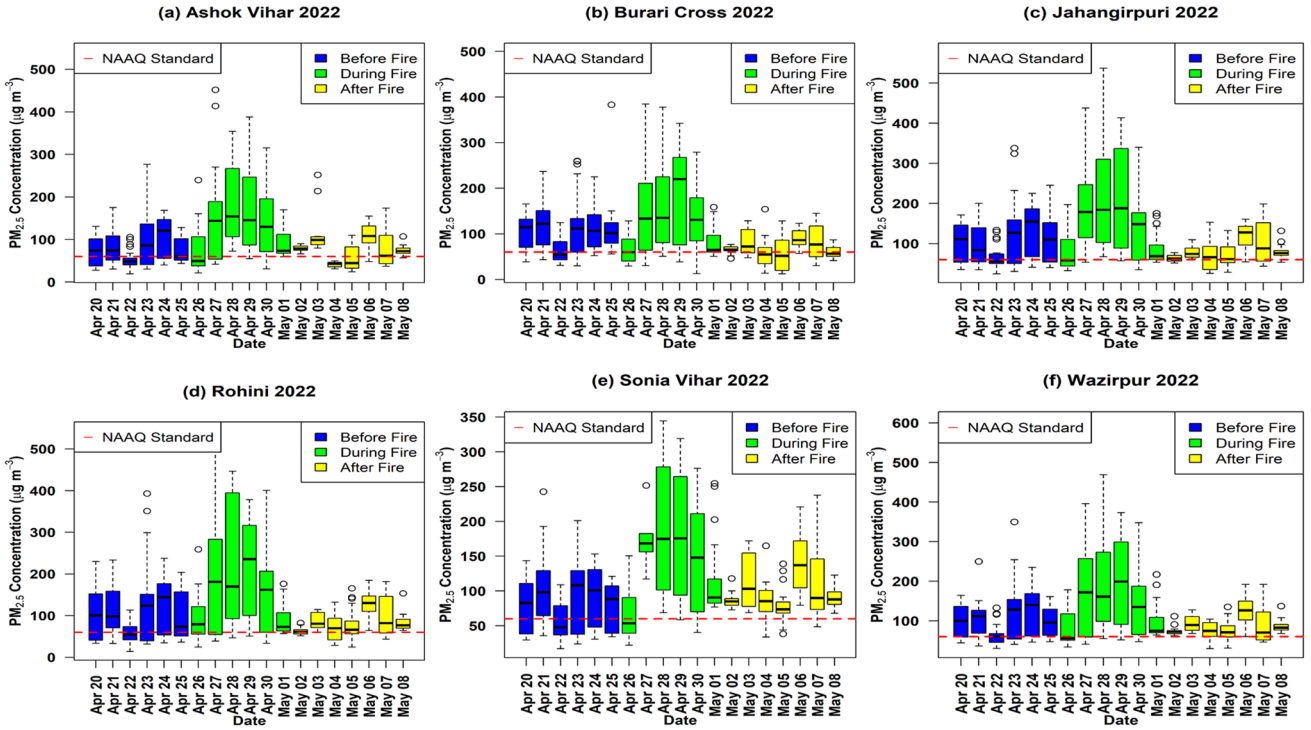


Fig. 2 $PM_{2.5}$ concentration in **a** Ashok Vihar, **b** Burari Crossing, **c** Jahangirpuri, **d** Rohini, **e** Sonia Vihar and **f** Wazirpur during different phases of the fire event

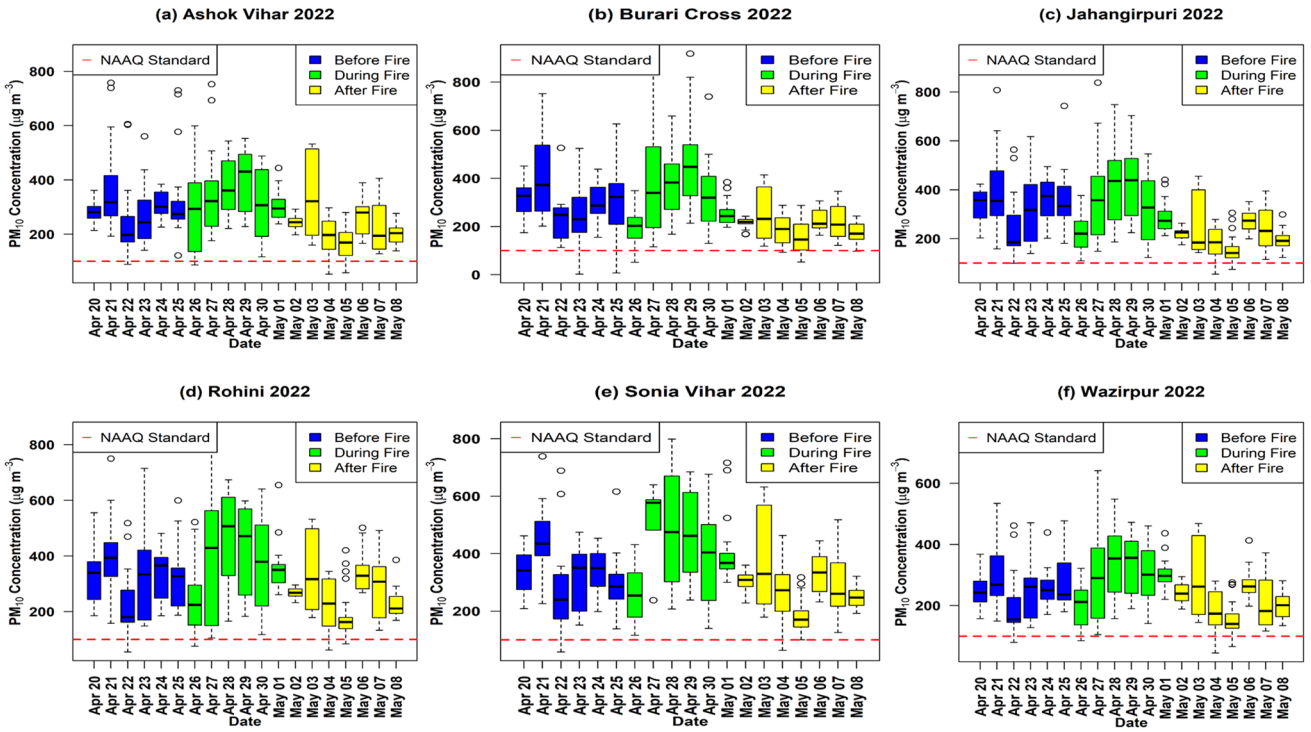


Fig. 3 PM_{10} concentration in **a** Ashok Vihar, **b** Burari Crossing, **c** Jahangirpuri, **d** Rohini, **e** Sonia Vihar and **f** Wazirpur during different phases of fire event

$PM_{2.5}$ to the overall mass of PM_{10}. As the concentration of smaller size particles ($PM_{2.5}$) reduces, a subsequent reduction in larger size PM_{10} concentration shows the contribution of smaller size particles ($PM_{2.5}$) in the overall particulate matter concentration (PM_{10}) (Fig. 3). The emission from the open biomass burning contributes to particulate matter and emits a series of gaseous pollutants. The concentration of NO, NO*x*, SO_2 and CO also increased significantly during the fire, and the maximum change was observed in NO and NO*x* components. The concentration of NO increases by more than 100% in majority of the location and NO*x* increases by 50–100%, whereas the concentration of CO and SO_2 increased from 25 to 50% and 50 to 100%, respectively.

The average concentration of $PM_{2.5}$ and PM_{10} at different locations shows the effect of open biomass burning. In Ashok Vihar, the concentration of $PM_{2.5}$ was 81.2 ± 67.7 µg/m^3; during the fire, it was 137.3 ± 106.6 µg/m^3, and after the fire event, the concentration resumed to 83.4 ± 78.7 µg/m^3. Similarly, at Burari Crossing, the concentration was 105.7 ± 104.0, 135.3 ± 114.5 and 72.1 ± 68.1 µg/m^3. In Jahangirpuri, it was 107 ± 94.5, 160.7 ± 125.7 and 82.6 ± 73.7 µg/m^3. The statistical summary of various pollutants at different locations during the monitoring period is provided in Table 2. Similarly, the concentration increased during the open waste burning accident at all the other three locations. The spatiotemporal variation study on the waste burning site in the Bhalswa landfill shows the impact of open burning sites on the local and regional air quality. The people living in the vicinity of the region are prone to various health-related issues due to the hazardous emission. Globally open waste burning leads to 24–29% of total anthropogenic emissions yearly (Agarwal et al. 2020). The materials like plastic wastes and e-wastes found in the solid waste dump yards on burning release toxic and harmful fumes that may cause serious illness when inhaled in larger quantities. The incomplete combustion of carbonaceous material in the waste, when not oxidized fully into CO_2, increases CO concentration in the nearby regions. Apart from health issues, open waste burning will also lead to reduced visibility and helpful in forming photochemical smog (Lal et al. 2016).

Polar cluster analysis

The relationship between the emitting sources and their impact on air pollutants such as particulate matter and gaseous pollutants can be understood using the local meteorological condition, specifically wind speed and wind direction (Nagar et al. 2017). The polar cluster analysis depicts the local sources of pollutants that contribute to pollution with respect to the wind direction and wind speed. The wind direction data are unavailable in the Burari Crossing location, so all the other five locations are considered for the analysis. Ashok Vihar is located south-east of the Bhalswa landfill, and the air masses from the waste burning site under low wind speed (< 1.5 m/s) in the south direction show more concentration contribution from waste burning sites for $PM_{2.5}$ (Fig. 4). The PM_{10} at the same location does not show much dispersion of particles under wind speed till 3 m/s. The wind speed can be classified into three categories based on their speed such as calm < 1 m/s, low wind speed 1–3 m/s and high wind speed > 3 m/s (Mohan and Mishra 2022) (Fig. 4). The wind speed determines the concentration of the pollution dispersion from source to various places. The monitoring stations are located in different zones where the Ashok Vihar and Jahangirpuri are located south-west of the landfill, such as Rohini in the west and Sonia Vihar

Table 2 Statistical summary of PM_{10}, $PM_{2.5}$, NO, NO_2, NO*x*, SO_2, CO and O_3

Location	Parameter	$PM_{2.5}$	PM_{10}	NO	NO_2	NO_x	SO_2	CO	O_3
Ashok Vihar	Mean	101.86	287.7	25.4	40.46	43.11	25.17	1.40	44.08
	SD	73.479	124.5	40.31	28.15	43.65	17.91	0.9	42.50
Burari Crossing	Mean	104.11	280.1	56.3	13.77	61.79	NA*	1.12	34.02
	SD	69.853	140.1	76.647	1.62	69.75	NA*	0.5	11.83
Jahangirpuri	Mean	115.9	297.21	NA*	61.56	67.43	31.51	1.72	50.38
	SD	85.93	142.5	NA*	54.87	68.84	22.03	0.8	47.41
Rohini	Mean	116.96	319.3	32.51	27.05	59.39	9.88	1.19	29.27
	SD	88.253	145.5	66.25	19.84	80.79	7.06	1	29.71
Sonia Vihar	Mean	107.32	338.0	41.64	44.32	57.51	22.02	2.01	54.7
	SD	61.377	145.2	76.734	33	75.21	11.37	0.9	47.42
Wazirpur	Mean	112.78	255.2	35.51	38.13	73.47	10.46	1.05	31.0
	SD	78.923	105.1	56.092	21.42	70.87	7.63	1.2	28.96

*NA** represents missing data points

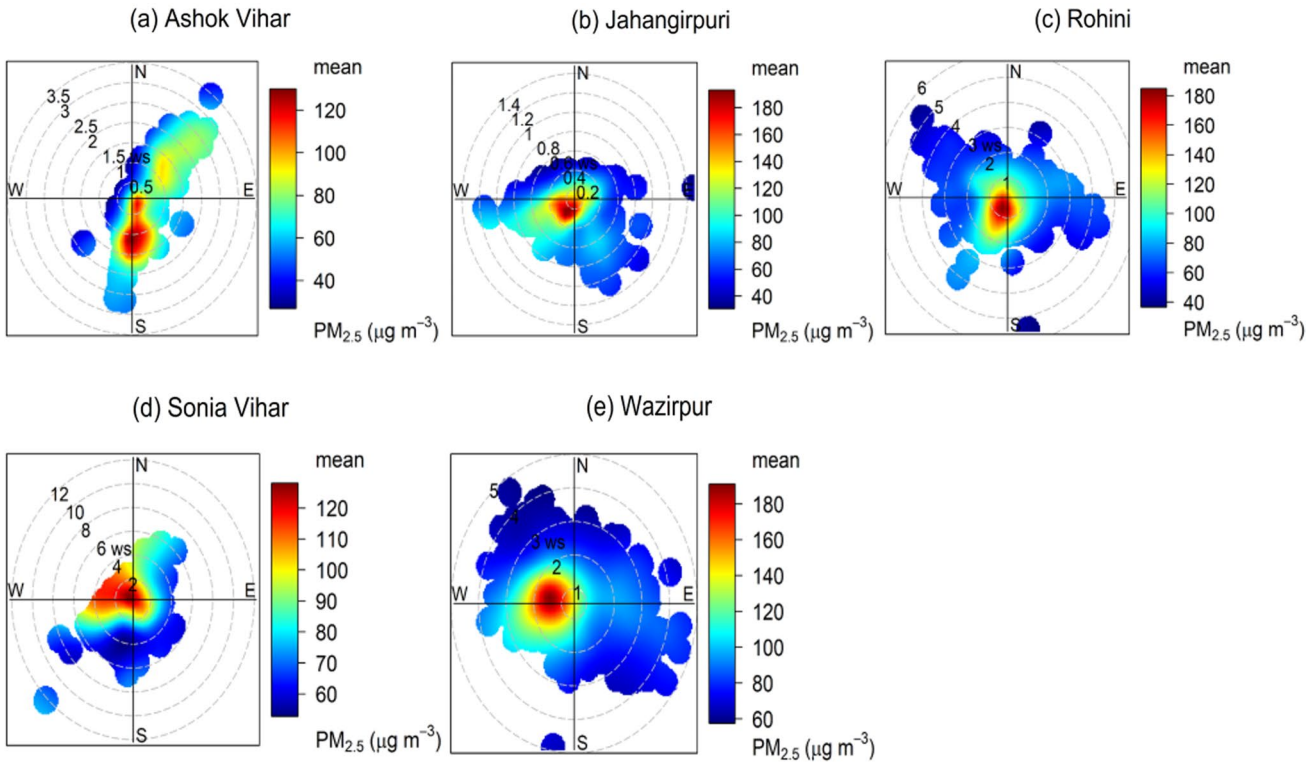


Fig. 4 $PM_{2.5}$ concentration in **a** Ashok Vihar, **b** Jahangirpuri, **c** Rohini, **d** Sonia Vihar and **e** Wazirpur during different phases of fire event

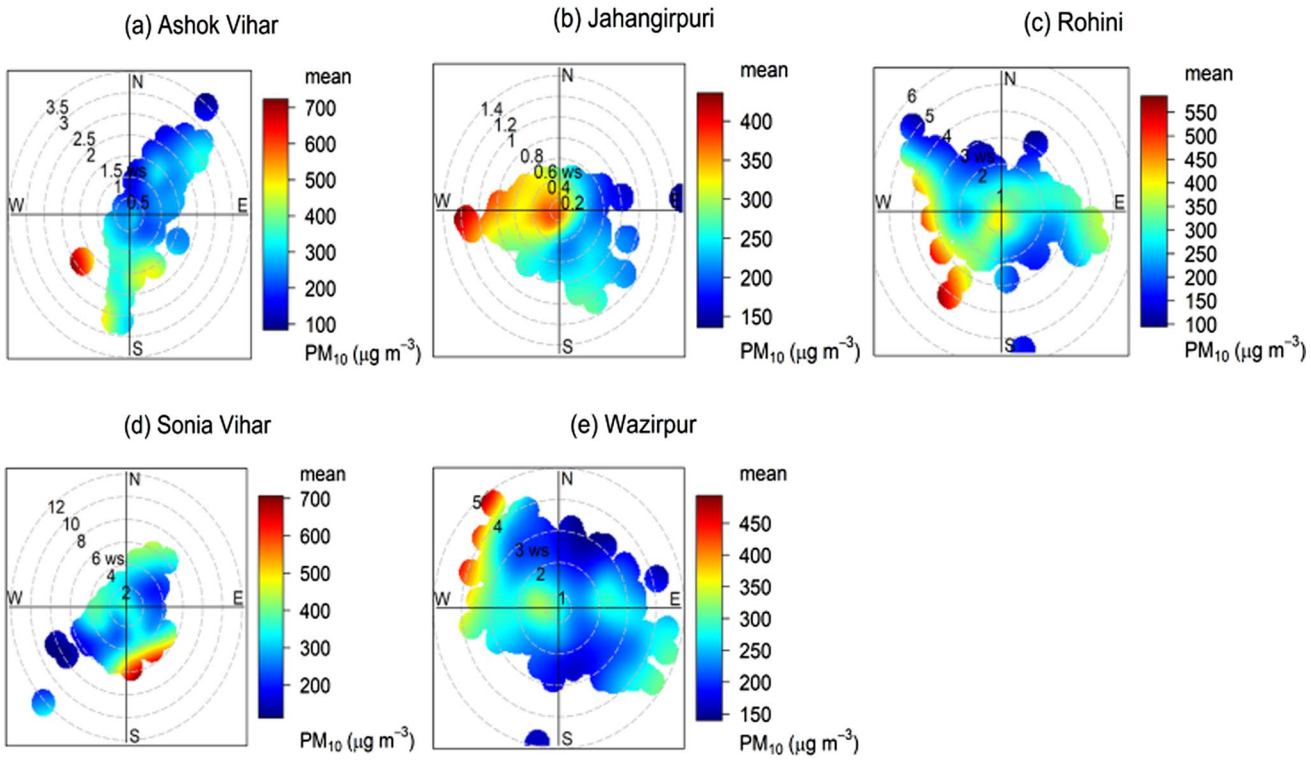


Fig. 5 PM_{10} concentration in **a** Ashok Vihar, **b** Jahangirpuri, **c** Rohini, **d** Sonia Vihar and **e** Wazirpur during different phases of fire event

in the east. Wazirpur is located in the south-west direction. The lower wind and calm wind conditions favour higher particle concentration since it does not favour the particles' dispersion.

The different locations of sources, along with the favouring wind direction, especially the downwind conditions from the source to the monitoring location, recorded higher concentration of pollutants. $PM_{2.5}$ shows more fluctuations with fluctuating wind speed due to their lower mass than PM_{10} (Fig. 5). Meteorology also plays a significant role in the dispersion of the gaseous pollutants as well. The pollutants such as CO and SO_2 concentration also recorded higher concentration under low and calm winds (Figs. S1–S2). Combustion and biomass burning are considered major sources of organic carbon (Hama et al. 2021). In November 2016, because of biomass burning in NCR region, it was recorded as a highly polluted city worldwide. It also created pressure on the government authorities to declare an air pollution emergency due to increased pollution levels. The scenario continues in the next years, and the reason behind this is favouring meteorological conditions such as wind direction and the boundary layer condition. Apart from inhalation of pollution, ingestion is another mechanism in which the pollutants are entered into living things through bioaccumulation and biomagnification and cause health effects.

Contribution analysis

The contribution of open landfill burning was higher when compared to the before and after fire events. The nearest location Jahangirpuri shows the highest contribution of landfill fire emission in the total concentration of $PM_{2.5}$ (54.48%) since it was the closest location to the landfill (Fig. 6). At all the remaining locations, the range of contribution of $PM_{2.5}$ during fire event to the overall percentage of $PM_{2.5}$ monitored was from 43 to 46% (Fig. 6). Similarly, PM_{10} concentration in Jahangirpuri shows 51.88%, and in remaining all other locations, the range is from 28 to 29% (Fig. S4). Fire events such as biomass and open waste burning contribute to significant air pollutants in urban regions. Open waste burning is recognized as a major source of $PM_{2.5}$ and PM_{10} in cities of developing countries (Nagpure et al. 2015). Open waste burning is not only associated with air pollution issues but also with urban health. Since open waste burning is not only a biomass substance, it can also be carcinogenic, as estimated by the Global Burden of Disease study.

Correlation analysis

SO_2 is a major gaseous pollutant that combines with water vapour in the atmosphere and causes acid rain, affecting humans, animals, plants and monuments. It can create

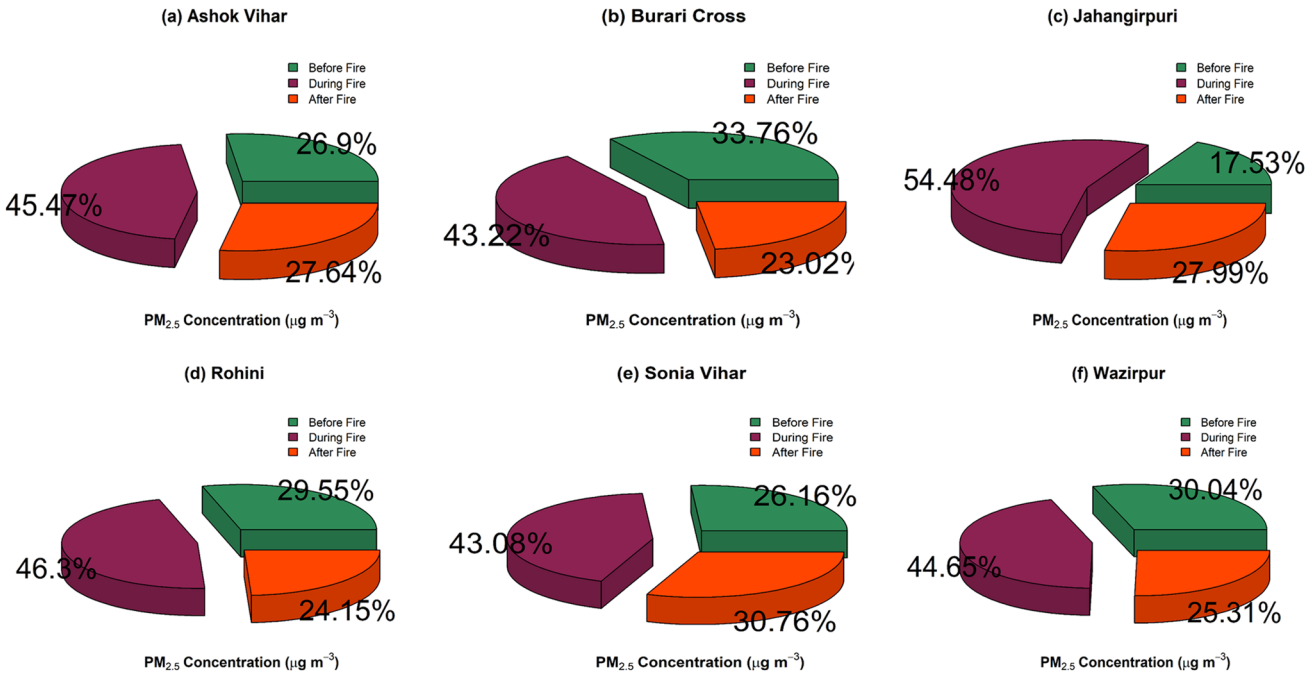


Fig. 6 $PM_{2.5}$ concentration in **a** Ashok Vihar, **b** Burari Crossing, **c** Jahangirpuri, **d** Rohini, **e** Sonia Vihar and **f** Wazirpur during different phases of fire event

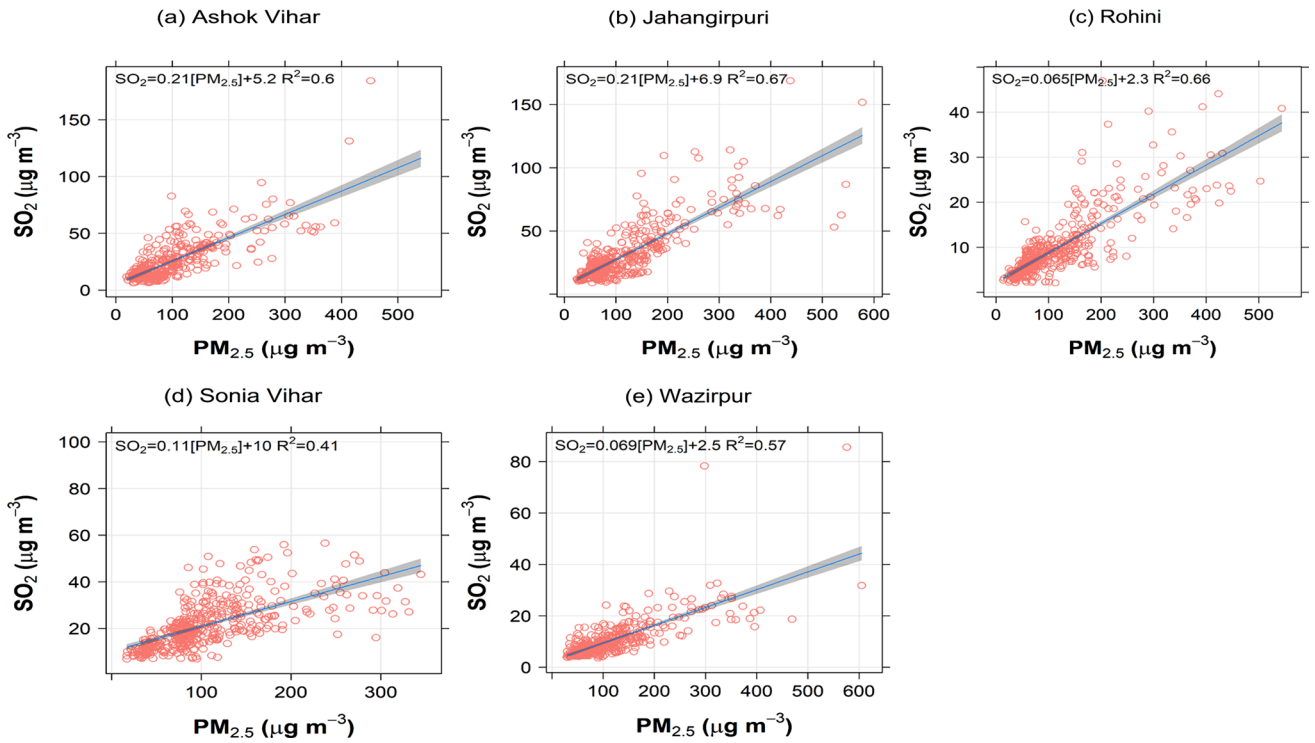


Fig. 7 Correlation of SO_2 and $PM_{2.5}$ in **a** Ashok Vihar, **b** Jahangirpuri, **c** Rohini, **d** Sonia Vihar and **e** Wazirpur during different phases of fire event

serious issues for the person with asthma, bronchitis, lung disease and cardiac problems (Okedere et al. 2019). During the study, SO_2 shows a moderate correlation with $PM_{2.5}$. In Ashok Vihar, Jahangirpuri and Rohini, the correlation value (R^2) was found > 0.6 (Fig. 7). In contrast, Wazirpur and Sonia Vihar showed a correlation value of 0.57 and 0.41, respectively (Fig. 7). The correlation value shows the influence of SO_2 with the $PM_{2.5}$ with the open waste burning. They are moderately related and show a positive correlation. The correlation of $PM_{2.5}$ and SO_2 shows that the source for this factor is mainly open waste burning in landfills. However, the concentration of SO_2 or CO may vary according to the composition of waste as well as in urban and rural regions where the characteristics of waste generation are different. The landfill consists of different kinds of waste, including biomass, biomedical waste, e-waste and a large number of fumes, and different compositions of gases are produced. The SO_2 emissions responsible for acid rain formation in urban regions and health issues such as skin irritation and cancer create aesthetic problems in the areas where it corrodes important monuments like the Taj Mahal in Agra near the city of Delhi, India.

Conclusion

Open waste burning is a serious issue in urban regions, especially in developing countries like India. The study analysed the impacts on regional air quality due to open waste burning of MSW (an accidental fire) in Delhi. The MSW dump yards can catch fire during summer due to the presence of various combustible materials found along with the waste materials. The fire outbreak in Delhi was from 26 April 2022 to 8 May 2022, which falls under the summer season. The fire releases a large number of fumes, including various types of pollutants.

This study analysed the major pollutants, such as particulate matter and gaseous pollutants. During fire event, $PM_{2.5}$ concentration shows an increase of about 60–70% at Ashok and Sonia Vihar sites located away from other monitoring stations. The highest concentration in these regions is due to the influence of wind speed, which causes the fumigation of pollutants. In Jahangirpuri and Rohini, the percentage increase in the $PM_{2.5}$ concentration was around 50–60%. Burari Crossing site records the lowest increase in the concentration (28%) of $PM_{2.5}$. During fire, the concentration of both $PM_{2.5}$ and PM_{10} shows a significant increase of about 40–50% of particles. Along with particulate matter, gaseous

pollutants such as CO increased by about 25–50% and SO_2 by 50–100%. The influence of meteorology (wind speed and direction) is significant for the dispersion of pollutants. The region located in the downwind conditions receives maximum concentration. The correlation coefficient of $PM_{2.5}$ and SO_2 concentration shows a medium correlation, in almost all regions. The R^2 value ranges from 0.5 to 0.6, indicating that the potential sources are due to emissions from open waste burning of MSW.

Open waste burning emits a large amount of air pollutants and increases potential health impacts. Handling open waste is a significant issue in developed and developing countries. Proper utilization of resources such as waste-to-energy conversion can help to extract valuable resources, and manage MSW and preventive measures for climate change initiatives.

Supplementary Information The online version contains supplementary material available at https://doi.org/10.1007/s13762-023-04921-w.

Acknowledgements The authors thank the Central Pollution Control Board (CPCB) for providing a platform for accessing data of various locations; also other agencies such as the Delhi Pollution Control Committee (DPCC), India Meteorological Department (IMD) and Indian Institute of Tropical Meteorology (IITM) for providing data facility; and members of the Advanced Air and Acoustics Research Laboratory, Department of Environmental Engineering, Delhi Technological University (DTU), for their support to conduct this study.

Author's contribution statement MS was involved in conceptualization, visualization, data compilation and formal analysis. MK was responsible for framework, discussion and reviewing the manuscript. RKM took part in investigation, discussion, reviewing and editing.

Funding Not applicable.

Availability of data and material Data are taken from public domain resources (CPCB website).

Code availability Not applicable.

Declarations

Conflict of interest The authors declare that they have no known competing financial interests or personal relationships that could have appeared to influence the work reported in this paper.

Consent for publication The work has not been published anywhere previously in any form and it is not in consideration for publication elsewhere. The publication is approved by all authors.

References

Agarwal R, Shukla K, Kumar S, Aggarwal SG, Kawamura K (2020) Chemical composition of waste burning organic aerosols at landfill and urban sites in Delhi. Atmos Pollut Res 11(3):554–565. https://doi.org/10.1016/j.apr.2019.12.004

Cash JM, Langford B, Di Marco C, Mullinger NJ, Allan J, Reyes-Villegas E, Joshi R, Heal MR, Acton WJF, Hewitt CN, Misztal PK, Drysdale W, Mandal TK, Shivani GR, Gurjar BR, Nemitz E (2021) Seasonal analysis of submicron aerosol in Old Delhi using high-resolution aerosol mass spectrometry: chemical characterisation, source apportionment and new marker identification. Atmos Chem Phys 21(13):10133–10158. https://doi.org/10.5194/acp-21-10133-2021

CPCB (2010) Air quality monitoring, emission inventory and source apportionment study for Indian cities. Central Pollution Control Board (CPCB), 2010, 39(8):483–490.

Estrellan CR, Iino F (2010) Toxic emissions from open burning. Chemosphere 80(3):193–207. https://doi.org/10.1016/j.chemosphere.2010.03.057

Hama S, Kumar P, Alam MS, Rooney DJ, Bloss WJ, Shi Z, Harrison RM, Crilley LR, Khare M, Gupta SK (2021) Chemical source profiles of fine particles for five different sources in Delhi. Chemosphere 274. https://doi.org/10.1016/j.chemosphere.2021.129913

Krecl P, de Lima CH, Dal Bosco TC, Targino AC, Hashimoto EM, Oukawa GY (2021) Open waste burning causes fast and sharp changes in particulate concentrations in peripheral neighborhoods. Sci Total Environ 765:142736. https://doi.org/10.1016/j.scitotenv.2020.142736

Kumar J (2018) Haze formation during winter in Delhi. EnvironmentAsia 11(3):213–220. https://doi.org/10.14456/ea.2018.49

Kumar P, Khare M, Harrison RM, Bloss WJ, Lewis AC, Coe H, Morawska L (2015a) New directions: air pollution challenges for developing megacities like Delhi. Atmos Environ 122:657–661. https://doi.org/10.1016/j.atmosenv.2015.10.032

Kumar S, Aggarwal SG, Gupta PK, Kawamura K (2015b) Investigation of the tracers for plastic-enriched waste burning aerosols. Atmos Environ 108:49–58. https://doi.org/10.1016/j.atmosenv.2015.02.066

Kumari K, Kumar S, Rajagopal V, Khare A, Kumar R (2019) Emission from open burning of municipal solid waste in India. Environ Technol (United Kingdom) 40(17):2201–2214. https://doi.org/10.1080/09593330.2017.1351489

Lal RM, Nagpure AS, Luo L, Tripathi SN, Ramaswami A, Bergin MH, Russell AG (2016) Municipal solid waste and dung cake burning: discoloring the Taj Mahal and human health impacts in Agra. Environ Res Lett 11(10). https://doi.org/10.1088/1748-9326/11/10/104009

Mohan V, Mishra RK (2022) A picture of Delhi's regional air quality during diminished anthropogenic activities in the COVID-19 era. Arab J Geosci 15(15):1–14. https://doi.org/10.1007/s12517-022-10567-8

Nagar PK, Singh D, Sharma M, Kumar A, Aneja VP, George MP, Agarwal N, Shukla SP (2017) Characterization of PM2.5 in Delhi: role and impact of secondary aerosol, burning of biomass, and municipal solid waste and crustal matter. Environ Sci Pollut Res 24(32):25179–25189. https://doi.org/10.1007/s11356-017-0171-3

Nagpure AS (2019) Assessment of quantity and composition of illegal dumped municipal solid waste (MSW) in Delhi. Resources Conserv Recycling 141(July 2018):54–60. https://doi.org/10.1016/j.resconrec.2018.10.012

Nagpure AS, Ramaswami A, Russell A (2015) Characterizing the spatial and temporal patterns of open burning of Municipal Solid Waste (MSW) in Indian cities. Environ Sci Technol 49(21):12911–12912. https://doi.org/10.1021/acs.est.5b03243

Okedere OB, Olalekan AP, Fakinle BS, Elehinafe FB, Odunlami OA, Sonibare JA (2019) Urban air pollution from the open burning of municipal solid waste. Environ Qual Manage, pp 1–8. https://doi.org/10.1002/tqem.21633

Park YK, Kim W, Jo YM (2013) Release of harmful air pollutants from open burning of domestic municipal solid wastes in a metropolitan area of Korea. Aerosol Air Qual Res 13(4):1365–1372. https://doi.org/10.4209/aaqr.2012.10.0272

Peter AE, Nagendra SMS (2021) Dynamics of PM2.5 pollution in the vicinity of the old municipal solid waste dumpsite. Environ Monit Assess 193(5):1–16. https://doi.org/10.1007/s10661-021-09052-8

Ramaswami A, Baidwan NK, Nagpure AS (2016) Exploring social and infrastructural factors affecting open burning of municipal solid waste (MSW) in Indian cities: a comparative case study of three neighborhoods of Delhi. Waste Manage Res 34(11):1164–1172. https://doi.org/10.1177/0734242X16659924

Ray MR, Roychoudhury S, Mukherjee G, Roy S, Lahiri T (2005) Respiratory and general health impairments of workers employed in a municipal solid waste disposal at an open landfill site in Delhi. Int J Hyg Environ Health 208(4):255–262. https://doi.org/10.1016/j.ijheh.2005.02.001

Sharma G, Annadate S, Sinha B (2022) Will open waste burning become India's largest air pollution source? Environ Pollut 292(PA):118310. https://doi.org/10.1016/j.envpol.2021.118310

Somvanshi SS, Vashisht A, Chandra U (2020) Handbook of environmental materials management. Handbook of Environmental Materials Management, April. https://doi.org/10.1007/978-3-319-58538-3

Yadav A, Behera SN, Nagar PK, Sharma M (2020) Spatio-seasonal concentrations, source apportionment and assessment of associated human health risks of pm2.5-bound polycyclic aromatic hydrocarbons in delhi, india. Aerosol Air Qual Res 20(12):2805–2825. https://doi.org/10.4209/aaqr.2020.04.0182

Springer Nature or its licensor (e.g. a society or other partner) holds exclusive rights to this article under a publishing agreement with the author(s) or other rightsholder(s); author self-archiving of the accepted manuscript version of this article is solely governed by the terms of such publishing agreement and applicable law.

An Effective Technique for Single Image Haze Removal using MSMO

Vikas Varshney
Department of Electronics and Communication Engineering
Delhi Technological University
Delhi, India
vksvar@gmail.com

Jeebananda Panda
Department of Electronics and Communication Engineering
Delhi Technological University
Delhi, India
jpanda@dce.ac.in

Rashmi Gupta
Department of Electronics and Communication Engineering
Netaji Subhas University of Technology
Delhi, India
rashmi.gupta@nsut.ac.in

2023 International Conference on Communication System, Computing and IT Applications (CSCITA) | 978-1-6654-5987-7/23/$31.00 ©2023 IEEE | DOI: 10.1109/CSCITA55725.2023.10104784

***Abstract*— Due to scattering of light in an atmosphere, hazy images along with noise, color distortions, block artifacts and low intensity are obtained during the image capturing process. The paper proposes a new approach to deal with the problems as mentioned to achieve a better dehazed image. The methodology involves the Dark Channel Prior (DCP) algorithm followed by multi-scale switching morphological operator (MSMO) and contrast limited adaptive histogram equalization (CLAHE). The two inputs are derived by applying MSMO and CLAHE techniques on DCP algorithm based output image and then final dehazed image is obtained through linear fusion. Extensive experiments have been done on various images collected from BeDDE dataset. Results achieved by the proposed approach demonstrate that the quality of dehazed images have significant improvements in terms of better color preservation, reduced noise and blocking artifacts.**

Keywords—Haze removal, contrast enhancement, fusion, color preservation, denoisung, contrast enhancement, morphological.

I. FRAMEWORK

Haziness is a type of atmospheric occurrence that is resulting from the scattering of light by small particles in the air [1]-[2]. It can diminish the objects visibility and make them appear hazy or blurry. Single image haze removal is a technique used to restore the clarity and visibility of an image that has been affected by haze. It is a significant assignment in image processing and computer vision, as it could enhance the image quality and cause the quality images more useful for various applications [3]-[5]. There are several methods that can be used for an image dehazing, including physical models, image restoration techniques and machine learning approaches. These methods can be useful in removing haze from a hazy image or a series of hazy images, and they can be carried out to variety of purposes that include medical imaging, vigilance and environmental monitoring [6]-[8].

There has been plenty of research on single image dehazing, and several methodologies have been proposed inside the literature. He *et al.* [9] proposed the dark channel prior (DCP) method that is a physical model-based method for removing haze in an image. The DCP technique works by constructing a dark channel image, which is a grayscale image where the intensity of each pixel is the minimal intensity value in the three color channels (Red, Green and Blue) at that pixel. Then, the dark channel image is used to estimate the transmission map of the captured scene, which indicates an amount of light that is transmitted through the atmosphere at each pixel. This map is used to restore the flawless image via atmospheric scattering model (ASM).

In the context of haze elimination in an image, a color attenuation prior (CAP), proposed by Zhu *et al.* [10], has been used in estimating the haze thickness. Intensity of the colors in the image is expected to change due to haze and using this information, the original intensities of the colors in the image can be restored. He *et al.* [11] has proposed the difference-structure-preservation prior-based haze removal method. The key point about this technique is to preserve the structural information (or small-scale details) of the image while removing the haze. In multi-scale fusion strategy proposed by Ancuti *et al.* [13], the transmission map is estimated by combining the information at different scales of the hazy image obtained through white-balancing and contrast enhacement. Guo *et al.* [14] fused the information from the manifold foggy images of the similar scene, taken beneath distinct situations, in order to estimate the transmission map. With this map, fog-free image can be restored but with high computational cost. The method of Kim *et al.* [15] combined the information obtained from DWT and CLAHE on the haze-free image restored from DCP algorithm. In the haze removal method of Liu *et al.* [16], the input hazy image is passed through a gamma correction (GC) to generate the pseudo-exposure images and on the other hand, same input image is passed through color preserving adaptive histogram equalization (CP-AHE). Then, these derived inputs are blended using a patch based fusion strategy for haze removal.

In recent times, the deep learning has gain much importance in almost every field. Many researchers has develop convolution neural network (CNN) based haze removal methods for getting the better visual quality of the image. A model, called as DehazeNet, has been proposed by Cai *et al.* [17] to estimate the transmission map. This CNN based network has shown improvements in dehazing effects due to first layer followed by maxout unit and last layer activation function but the method avoids structural attributes. AOD-Net presented by Li *et al.* [18] is based on reformulated ASM but the method visually darkens the image. Santra *et al.* [19] presented a new way of achieving transmission map through patch quality comparator (PQC) based on CNN followed by binary search for determining good or bad dehazed patch to train the classifier. However, the method suffers from high computation costing. In general, CNN based approaches [20], [21], [22] for an image haze elimination suffer from the problem of large amount of training data and high computational complexity.

After preforming intense literature survey, it is observed that a suitable and efficient approach is still required in the field of haze removal. The challenges need to be addressed involve robust method, improvement in accuracy, and reduction in the computation time. In the paper, a new fusion approach based on MSMO and CLAHE techniques has been proposed. Following segments of the paper are structured as: Background study for the proposed approach is described in segment II. In segment III, a new fusion approach for single image dehazing is presented. In segment IV, result analysis is shown to evaluate the performance of the proposed approach. In addition, conclusion is discussed in segment V.

978-1-6654-5987-7/23/$31.00 ©2023 IEEE

Authorized licensed use limited to: DELHI TECHNICAL UNIV. Downloaded on April 26,2023 at 10:21:57 UTC from IEEE Xplore. Restrictions apply.

II. BACKGROUND

In this paper, we have applied MSMO and CLAHE on the output of DCP algorithm to get the two derived inputs for fusion process. These methods are described in this section.

A. DCP Technique

As per the theory given via He *et al.* [9], DCP algorithm is built on the remark that the transmission of light through the atmosphere is typically very low. The method works by first identifying the dark channel of the image, which is the least intensity value of RGB channels at each pixel. Mathematical expression for dark channel is given as:

$$I^{dark}(x) = \min_{y\epsilon\Omega(x)}\left(\min_{c\epsilon\{R,G,B\}} I_c(y)\right) \tag{3}$$

where I^c is an intensity of a color channel $\{R, G, B\}$ of the image, and $\Omega(x)$ represents a local patch centered at pixel x.

The dark channel of a hazy image is expressed as:

$$\min_{y\epsilon\Omega(x)}\left(\min_{c\epsilon\{R,G,B\}} \frac{I_c(y)}{A^c}\right) = \tilde{t}(x) \min_{y\epsilon\Omega(x)}\left(\min_{c\epsilon\{R,G,B\}} \frac{J_c(y)}{A_c}\right) + [1 - \tilde{t}(x)] \tag{4}$$

The transmission map can be estimated from the dark channel as:

$$\tilde{t}(x) = 1 - \min_{y\epsilon\Omega(x)}\left(\min_{c\epsilon\{R,G,B\}} \frac{I_c(y)}{A_c}\right) \tag{5}$$

The atmospheric light, A_c can be estimated by taking the average of top 0.1% brightest pixels of the dark channel in color channels of $I_c(x)$. A dehazed image can be obtained by reversing Eq. (1) as:

$$J_c(x) = \frac{I_c(x) - A_c}{\max(\tilde{t}(x), t_0)} + A_c \tag{6}$$

where, t_0, denotes the least periphery of the transmission. The range of t_0 would be from 0.1–0.03.

B. MSMO Technique

A MSMO is an image processing technique that is used to perform morphological operations, such as erosion and dilation, on an image at multiple scales. In case of SMO, these two operations are performed on grey-scale image 'G' using structuring element 'S' of appropriate size. Mathematically, dilation and erosion are described as [23]:

$$D = G \oplus S = \{(a, b) + (c, d) : a, b \in G; c, d \in S\} \tag{7}$$

$$E = G \ominus S = \{(a, b) - (c, d) : a, b \in G; c, d \in S\} \tag{8}$$

SMO is a morphological operator that is used to smooth regions of an image by altering the minute regions of the image as per the size of structuring element. The morphological operator, SMO is defined as:

$if\ \big((D - G) < (G - E)\big)\ then$

$SMO = D;$

$else\ if\ \big((D - G) > (G - E)\big)\ then$

$SMO = E;$

$else$

$SMO = G;$

$end\ if$

Here, the key point of SMO operation is that in the improved image obtained from SMO, each image pixel is replaced by that pixel in the outcome of dilation or erosion with a gray value which is found nearer to gray value of identical pixel in the real image. However, improper size of the structuring element yields poor results as small size provides less efficient results while large size provides more noise in the image. To deal with these problems of SMO, multi-scale SMO (i.e. MSMO) is applied in the paper. Basically, MSMO involves the implementation of SMO at several stages with varying size of structuring elements. The structuring element typically uses the following shapes: circle, rectangle, square and hexagon. Except circle shape, remaining structuring element shapes with large size produces block-effects in the output image due to having rough edges, whereas, circle shape structuring element produces very less block-effect due to smooth edges. Therefore, structuring element of circle shape is selected in the paper.

C. CLAHE Technique

Instead of working on the entire image, the CLAHE technique works on small areas called tiles. With a view to eliminate unnatural boundaries, bi-linear interpolation is used to group the adjacent tiles. The main purpose of CLAHE algorithm is in improving the image contrast. The technique is able to process variety of images such as heterogeneous, homogeneous, color, gray-scale and uneven distribution of intensity.

Contrast is restricted in CLAHE, which is different from standard AHE. The CLAHE implements a trimming limit to solve the problem of noise intensification. The CLAHE restricts the intensification by trimming the histogram at a predetermined value prior to computing the Cumulative Distribution Function (CDF). The CLAHE approach separates an input image into contextual sub-images or tiles that do not overlap [24]. Here, Block Size (BS) and Clip Limit (CL) serve as the parameters that define the CLAHE and also determines the improved quality of the image. Because the input image contains a very small value of intensity and a greater CL flattens its histogram, the image gets brighter with the increasing CL. Also, the image contrast is increased when BS is increased.

D. Linear Fusion

In the linear fusion process, two or more than two images are derived from the actual image and then, a weighting parameter is utilized to combine the two derived images linearly. For the paper, we have derived the two images, I_{MSMO} and I_{CLAHE} by applying MSMO and CLAHE techniques separately on the output image obtained from implementation of DCP algorithm. Mathematical expression for an output image, I_{Lf} obtained by linear fusion is:

$$I_{Lf} = \gamma I_{MSMO} + (1 - \gamma) I_{CLAHE} \tag{9}$$

Authorized licensed use limited to: DELHI TECHNICAL UNIV. Downloaded on April 26,2023 at 10:21:57 UTC from IEEE Xplore. Restrictions apply.

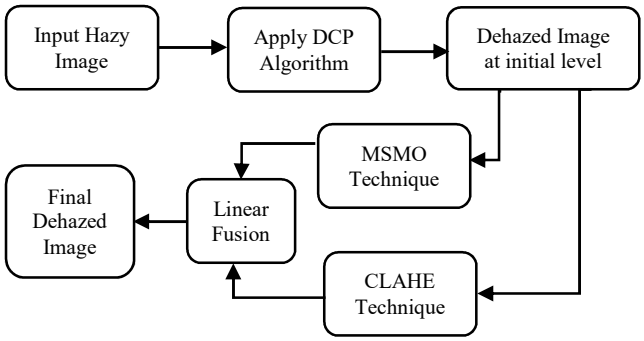


Fig. 1. Proposed methodology with block diagram

where, γ denotes the weighting parameter and grid search [25] is carried out to attain the optimum value of γ.

III. Approach for Haze Removal

This segment describes the simple approach for single image haze removal involving DCP, MSMO and CLAHE algorithms. Here, the output images obtained through MSMO and CLAHE implemented on DCP based dehazed image are combined linearly. The methodology along with algorithm have been described as follows:

A. Proposed Method

In the paper, a different blending approach is proposed with the help of DCP, MSMO and CLAHE algorithms. The illustration of proposed technique is shown in Fig. 1. In order to apply MSMO technique, the DCP based output color image is first converted into the gray-scale image by using either Principal Component Analysis (PCA) or the command COLOR_BGR2GRAY in openCV library of Python platform. For better quality of gray-scale image with the preservation of discriminable color and texture features, PCA is selected over COLOR_BGR2GRAY. However, if we use PCA to convert the gray-scale image back to color image, the resulted image could not obtained that looks natural. Therefore, after applying MSMO technique on PCA output, a command COLOR_GRAY2BGR is adopted for color conversion process.

In this methodology, first DCP algorithm is applied to obtain the dehazed output at initial level. Then, PCA is applied on the resulting image so that MSMO technique can be implemented on gray-scale image generated by PCA technique. Then, the multi-scale outputs produced by MSMO technique are transformed in to color images to obtain

TABLE I. Comparison of PSNR, SSIM and Computation Time (seconds) values using two approcahes on ten images of BeDDE dataset. Here ⊕ denotes the Fusion Process.

Image	(BGR2GRAY+MSMO+ GRAY2BGR)⊕ CLAHE			(PCA+MSMO+ GRAY2BGR)⊕ CLAHE		
	PSNR	*SSIM*	*Time*	*PSNR*	*SSIM*	*Time*
beijing_3	20.23	0.5358	12.57	19.45	0.8665	16.42
hefei_1	19.95	0.6826	11.43	19.83	0.7621	15.37
lanzhou_6	20.13	0.6725	11.52	19.67	0.8163	14.54
sian_1	20.76	0.4391	10.34	21.28	0.5519	16.08
taiwan_2	20.52	0.7513	10.39	18.65	0.8801	12.38
guilin_4	19.64	0.8026	11.16	18.59	0.8614	13.48
xining_4	19.23	0.7635	10.55	18.64	0.8204	14.03
nanjing_1	20.43	0.7006	12.61	20.56	0.7912	14.47
chengdu_21	19.11	0.7801	11.51	19.06	0.8019	13.36
wuhan_1	20.27	0.8629	12.03	19.48	0.8920	16.29
Average	**20.02**	**0.6991**	**11.41**	**19.52**	**0.8043**	**16.34**

TABLE II. Quantitative Comparison (PSNR, SSIM and Computation Time (seconds)) of the Proposed Method with other Dehazing Methods.

Dehazing Technique	Quantitative Parameters		
	PSNR	*SSIM*	*Time*
DCP [9]	22.39	0.9504	18.39
CAP [10]	21.57	0.8629	10.44
LGIA [12]	21.26	0.9953	8.27
Multi-scale fusion [13]	21.13	0.8327	10.52
DCP+CLAHE+DWT [15]	22.19	0.8207	12.61
CEEF [16]	20.68	0.8216	9.49
Proposed Method	**19.52**	**0.8043**	**16.34**

another input is derived by applying CLAHE technique on the DCP based output image. Next, both the derived input images are combined linearly to obtain the final dehazed image with more enhanced details and better visual quality.

B. Algorithm

Final dehazed image as an output image can be obtained by following the steps as:

1) Read the hazy image, I.

2) Obtain the dehazed image at initial level with the implementation of DCP algorithm. This image needs to be enhanced with contrast adjustment, texture details and color preservation.

3) Obtain the gray-scale image by applying PCA on dehazed image.

4) Obtain the multi-scale images using the circle shaped structuring element with varied sizes.

5) Then, apply the gray-scale to RGB command to obtain the colored image as the output of MSMO technique. This ouput is the first derived input image for linear fusion.

6) Obtain the second derived input image by applying CLAHE technique on the DCP based output image for contrast enehancement.

7) Obtain the final dehazed image by combining the results of step 5 and 6.

IV. Result Anaysis

The proposed method has been evaluated on outdoor Benchmark Dataset for Defogging Evaluation (BeDDE) [26]. This dataset contains 208 pairs of hazy images and ground truth images. The implementation of the proposed method has been performed on Python software on HP desktop with configuration 4GB RAM, Intel(R) Core(TM) i5-4200U CPU @ 1.60GHz, 2.30 GHz processor and 64-bit operating system.

In the paper, 10 images (refer to Table I) from the dataset BeDDE are selected for the evaluation purpose. It is evident from the Table I that on an average, the proposed method attains lower PSNR value and higher SSIM value if implementing the proposed method using PCA as compared with same technique using BGR2GRAY command for generating the gray-scale image as the input image for applying MSMO. Table II provides the quantitative comparison of the proposed approach with other dehazing approaches in terms of PSNR, SSIM and computation time in seconds. From the Table II, it has been observed that the proposed method has comparable values of PSNR and SSIM.

However, the computation time of the proposed method is comparatively on higher side, hence good results are observed

Authorized licensed use limited to: DELHI TECHNICAL UNIV. Downloaded on April 26,2023 at 10:21:57 UTC from IEEE Xplore. Restrictions apply.

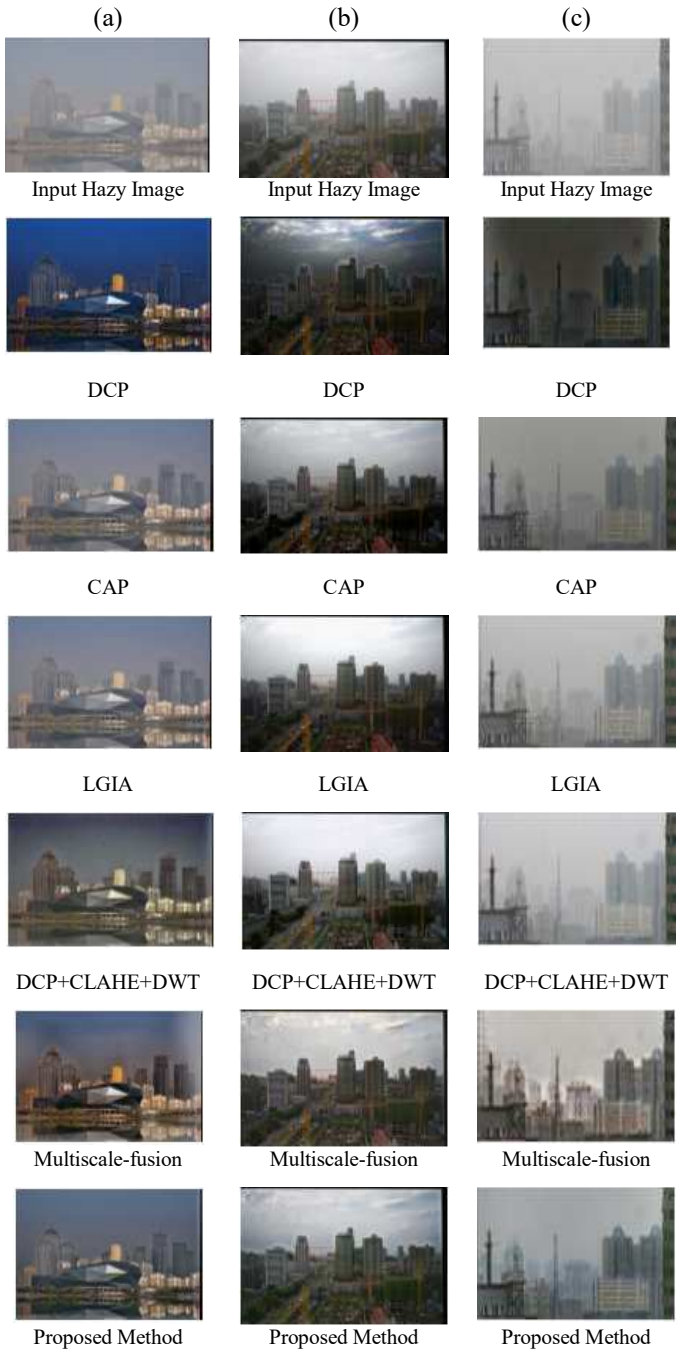


Fig. 2. Visual quality assessment over hazy images collected from BeDDE database. File name of the input hazy images in the database are as: (a) shenyang_14 (b) wuhan_1 (c) chengdu_8

at the expense of processing time. The high computation time is probably due to the structuring element of varied sizes applied on an image.

Fig. 2 shows the images dehazed by different techniques such as DCP [9], CAP [10], LGIA [12], multi-scale fusion [13], DCP+CLAHE+DWT [15], CEEF [16] and proposed method for qualitative comparison. By observing the images in Fig. 2, the image enhanced by the proposed approach has better quality in terms of objects visibility, rich texture details and color information.

V. Conclusion

The images with high quality are always desired in various applications such as computer vision, surveillance system, object recognition, and other real time models. And for the images captured under unusual atmospheric conditions i.e. haze, an efficient approach is required to remove haze and noise present in those images. This paper has suggested a fusion based approach utilizing two different approaches applied on a specific image. The two derived input images obtained from implementation of MSMO and CLAHE on DCP technique based output image are passed through linear fusion process. The paper also discusses about the reason of utilizing PCA instead of BGR2GRAY command for obtaining gray-scale image. On the basis of result analysis on the images of BeDDE dataset, the qualitative and quantitative comparisons demonstrate that the quality of dehazed images processed by the proposed method has significant improvements in terms of contrast enhancement and color preservation. Moreover, the proposed approach is better than other existing methods as depicted from Table II. However, the proposed method is still lacking in removing the haze completely and struggling from high computation complexity.

References

[1] S. G. Narasimhan and S. K. Nayar, “Vision and the atmosphere,” Int. J. Comput. Vis., vol. 48, no. 3, pp. 233–254, 2002.

[2] L. J. Wang and R. Zhu, “Image defogging algorithm of single color image based on wavelet transform and histogram equalization,” Appl. Math. Sci., vol. 7, no. 79, pp. 3913–3921, 2013.

[3] P. Pandey, R. Gupta, and N. Goel, “A fast and effective vision enhancement method for single foggy image”, Engineering Science and Technology, Elsevier, vol. 24, issue 6, pp. 1478-1489, May 2021.

[4] P. Pandey, N. Goel, R. Gupta, “Signal Image Defogging Algorithm Based on Modified Haze Line Prior”, Proceedings of Academia-Industry Consortium for Data Science (AICDS 2020), pp. 229-240, Feb 2022.

[5] P. Pandey, R. Gupta, and N. Goel, “Morphological Map based Single Image Defogging”, 8th International Conference on Signal Processing and Integrated Networks (SPIN), IEEE, pp. 1-5, Aug 2021.

[6] P. Pandey, R. Gupta, N. Goel, "Recognition of Foggy Image for Surveillance Application", Book Chapter in Multimodal Biometric System, CRC Press, Taylor & Francis, pages 13, 2021.

[7] R. Gupta, M. Khari,V. Gupta, E. Verdú, X. Wu, and R. G. Crespo, “Fast Single Image Haze Removal Method for Inhomogeneous Environment Using Variable Scattering Co-efficient”, CMES-Computer Modeling in Engineering & Sciences, Tech Science Press, 123(3): 1175-1195, May 2020.

[8] R. Kapoor, R. Gupta, L. H. Son, R. Kumar, and S. Jha “Fog Removal in Imag-es using Improved Dark Channel Prior and Contrast Limited Adaptive Histogram Equalization", Mul-timedia Tools and Applications, Springer, vol.78, pp 23281–23307, Aug 2019.

[9] K. He, J. Sun and X. Tang, “Single Image Haze Removal Using Dark Channel Prior”, in IEEE Transactions on Pattern Analysis and Machine Intelligence, Vol. 33, No. 12, Dec 2011, pp. 2341-2353.

[10] Q. Zhu, J. Mai, and L. Shao, “A fast single image haze removal algorithm using color attenuation prior,” IEEE Trans. Image Process., vol. 24, no. 11, pp. 3522–3533, Nov. 2015.

[11] L. He, J. Zhao, N. Zheng, and D. Bi, “Haze removal using the difference structure-preservation prior,” IEEE Trans. Image Process., vol. 26, no. 3, pp. 1063–1075, Mar. 2017.

[12] H.-M. Hu, H. Zhang, Z. Zhao, B. Li, and J. Zheng, “Adaptive Single Image Dehazing Using Joint Local-Global Illumination Adjustment”, IEEE Transactions on Multimedia, Vol. 22, No. 6, June 2020, pp. 1485-1495.

[13] C. O. Ancuti and C. Ancuti, “Single image dehazing by multi-scale fusion,” IEEE Trans. Image Process., vol. 22, no. 8, Aug. 2013, pp. 3271–3282.

[14] J.-M. Guo, J.-Y. Syue, V. R. Radzicki, and H. Lee, “An efficient fusion-based defogging,” IEEE Trans. Image Process., vol. 26, no. 9, pp. 4217–4228, Sep. 2017.

[15] K. Kim, S. Kim, and K. Kim, “Effective image enhancement techniques for fog-affected indoor and outdoor images,” IET Image Process., vol. 12, no. 4, pp. 465–471, Apr. 2018.

Authorized licensed use limited to: DELHI TECHNICAL UNIV. Downloaded on April 26,2023 at 10:21:57 UTC from IEEE Xplore. Restrictions apply.

[16] X. Liu, H. Li, and Ce Zhu, "Joint Contrast Enhancement and Exposure Fusion for Real-World Image Dehazing", IEEE Transactions on Multimedia, Vol. 24, 2022, pp. 3934-3946.

[17] B. Cai, X. Xu, K. Jia, C. Qing, and D. Tao, "DehazeNet: An End-to-End System for Single Image Haze Removal", IEEE Transactions on Image Processing, vol. 25, no. 11, Nov. 2016, pp. 5187 – 5198.

[18] B. Li, X. Peng, and Z. Wang, J. Xu, and D. Feng, "AOD-Net: All-in-One dehazing network", in Proc. IEEE Conf. Comput. Vis., Oct. 2017, pp. 4780-4788.

[19] S. Santra, R. Mondal, and B. Chanda, "Learning a Patch Quality Comparator for Single Image Dehazing", IEEE Transactions on Image Processing, vol. 27, no. 9, pp. 4598-4607. Sep. 2018.

[20] C. Li, J. Guo, F. Porikli, H. Fu, and Y. Pang, "A Cascaded Convolutional Neural Network for Single Image Dehazing", IEEE Access, vol. 6, pp. 24877-24887, May 2018.

[21] C.-H. Yeh, C.-H. Huang, and L.-W. Kang, "Multi-Scale Deep Residual Learning-Based Single Image Haze Removal via Image Decomposition", IEEE Transactions on Image Processing, vol. 29, pp. 3153-3167, 2020.

[22] X. Zhang, J. Wang, T. Wang, and R. Jiang, "Hierarchical Feature Fusion with Mixed Convolution Attention for Single Image Dehazing", IEEE Transactions on Circuits and Systems for Video Technology, Vol. 32, No. 2, pp. 510-522, Feb 2022.

[23] S. K. Saroj, R. Kumar, and N. P. Singh, "An Efficient Hybrid Approach for Medical Image Enhancement," Electronics Letter on Computer Vision and Image Analysis, vol. 21, no. 2, pp. 62-76, 2022.

[24] A. M. Reza, "Realization of the contrast limited adaptive histogram equalization (CLAHE) for real-time image enhancement," J. VLSI signal Process. Syst. Signal, Image Video Technol., vol. 38, no. 1, pp. 35–44, 2004.

[25] C.-H. Hsieh, B.-C. Chen, C.-M. Lin, and Q. Zhao, "Detail aware contrast enhancement with linear image fusion," vol. 126, 11 2010.

[26] S. Zhao, L. Zhang, S. Huang, Y. Shen, S. Zhao, and Y. Yang, "Evaluation of defogging: A real-world benchmark dataset, a new criterion and baselines," in Proc. IEEE Int. Conf. Multimedia Expo (ICME), Jul. 2019, pp. 1840–1845.

Authorized licensed use limited to: DELHI TECHNICAL UNIV. Downloaded on April 26,2023 at 10:21:57 UTC from IEEE Xplore. Restrictions apply.

Soft Computing
https://doi.org/10.1007/s00500-023-08057-4

APPLICATION OF SOFT COMPUTING

An iterative analytic approximation for a class of nonlinear singularly perturbed parabolic partial differential equations

Kartikay Khari[1] · **Vivek Kumar**[1]

Accepted: 7 March 2023
© The Author(s), under exclusive licence to Springer-Verlag GmbH Germany, part of Springer Nature 2023

Abstract
In this article, a closed-form iterative analytic approximation to a class of nonlinear singularly perturbed parabolic partial differential equation is developed and analysed for convergence. We have considered both parabolic reaction diffusion and parabolic convection diffusion type of problems in this paper. The solution of this class of problem is polluted by a small dissipative parameter, due to which solution often shows boundary and interior layers. A sequence of approximate analytic solution for the above class of problems is constructed using Lagrange multiplier approach. Within a general frame work, the Lagrange multiplier is optimally obtained using variational theory. The sequence of approximate analytical solutions so obtained is proved to converge the exact solution of the problem. To demonstrate the proposed method's efficiency and accuracy, linear and nonlinear test problems have been taken into account. From numerical experiments, it is observed that the proposed method is highly accurate, straightforward.

Keywords Singular perturbation · Nonlinear parabolic · Reaction–diffusion · Convection–diffusion · Liouville–Green transform · Lagrange multiplier

1 Introduction

The nonlinear singularly perturbed parabolic partial differential equations (NSPPPDEs) play an essential role in converting a real life phenomenon into a mathematical model. The dynamics of NSPPPDEs are utterly different from the conventional nonlinear partial differential equations. These types of problems depend on a small positive parameter, which makes the solution varies rapidly in narrow regions of the domain and changes slowly in rest parts of the domain. This behaviour of the solution in narrow regions is called layer phenomena and this class of problem is known as singularly perturbed problems. The problem is singular in such a way that when $\varepsilon \to 0$ changes the order of the differential equation, but the number boundary conditions remain the same, causing the problem ill-posed. This type of problems occurs in oceanography, population dynamic, generic repression, size dependent cell growth, division modelling, ecology, quantum physics, chemistry, finance (Black–Scholes Equation) and material science.

The fundamental equations that describe the kinematic and dynamic interactions among flow parameters, fluid and medium at any location within the flow domain under consideration are nonlinear singularly perturbed problems such as nonlinear singularly perturbed reaction diffusion, singularly perturbed convection diffusion and Navier–Stokes equations. The NSPPPDEs are crucial in understanding the mechanics of transport phenomena in permeable mediums. One of the most remarkable examples of NSPPDES that occurs in fluid dynamics is the Navier–Stokes equation with a higher Reynolds number. Considering the following Navier–Stokes equation that governs unsteady incompressible viscous fluids flow problem.

$$\frac{\partial \upsilon_\varepsilon}{\partial t} + \upsilon_\varepsilon.\Delta\upsilon_\varepsilon + \Delta\rho = \frac{1}{\Re e}\Delta^2\upsilon_\varepsilon, \tag{1.1}$$

$$\Delta\upsilon_\varepsilon = 0, \tag{1.2}$$

where ρ signifies pressure and $\upsilon = (\upsilon_1, \upsilon_2)$ denotes the velocity, with velocity components υ_1 and υ_2 along with x and y directions. The parameter $\Re e$ represents Reynold num-

✉ Kartikay Khari
kartikay_phd2k17@dtu.ac.in; kartikaybharadwaj@gmail.com

Vivek Kumar
vivekkumar.ag@gmail.com

[1] Department of Applied Mathematics, Delhi Technological University, Delhi 11004, India

Published online: 09 April 2023

ber which is directly proportional to the velocity scale, length scale and inversely proportional to the kinematic viscosity of the fluid. Equation (1.1) behaves as a singularly perturbed PDE if the Reynold number $\Re e >> 1$ is large enough.

The designing of computational algorithms for such types of problems is burdened with difficulties because the solution of the proposed problem is contaminated by a small positive parameter ε and nonlinear term simultaneously, due to which so-called boundary layer and shock layer arises (Das and Natesan 2013, 2014; Kumar and Leugeringb 2021; Chandru et al. 2018). One needs to employ locally refined meshes that are standard on the outside and fine in the layer regions in order to obtain consistent numerical approximations of layer solutions effectively (Shakti et al. 2022; Das et al. 2019; Das 2019). One can use this knowledge to design suitable layer-adapted meshes if the positions and widths of the layers are known in advance. Since only few nonlinear systems can be solved explicitly, we rely on numerical techniques by linearizing the nonlinear problems.

In recent years, the researchers have made efforts to provide consistent numerical techniques to solve NSPPPDEs. In Khari and Kumar (2022a), Kartikay and Vivek deal with the nonlinear singularly perturbed reaction diffusion problem and implemented an operational matrix method based on Bernstein polynomials. In Boglaev (2004), Igor Boglaev presented a monotone iterative algorithm for nonlinear singularly perturbed parabolic problem, and then in Boglaev (2012), Igor Boglaev presented an inexact monotone iterative method based on method of upper and lower solution for a class of semi-linear parabolic singularly perturbed problem. In Kopteva and Linß (2012); Kopteva and Linss (2013), Kopteva and Linß used an elliptic reconstruction approach and provided the error estimate in maximum norm using Green's function. In Kabeto and Duressa (2021), authors provide a consistent finite difference method for singularly perturbed semi-linear parabolic differential difference equation. In Cheng et al. (2021), Yao Cheng, Chuanjing Song and Yanjie Mei used a discontinuous Galerkin finite element method along with backward-Euler method for our proposed problem. In Amrein and Wihler (2017), Mario Amrein and Thomas P. Wihler proposed an adaptive space-time Newton–Galerkin method which is consisted of a linearization technique using Newton's method along with finite element for spatial variable and backward-Euler for time variable and others (Kumar et al. 2021; Khari and Kumar 2022b; Das and Natesan 2012; Kumar and Leugeringb 2023).

To best of our knowledge, till date no analytic method (exact or approximate) is developed to solve the NSPPPDEs. The novelty of this paper is the development of an iterative analytic method based on variation of iteration approach to find the approximate solution of the NSPPPDEs. The variation of iteration method (VIM) was first developed by J. H. He (1999) in 1999. The VIM is based on a Lagrange's multiplier developed by Inokuti et al. (1978) in which they constructed adjoint operators and stated that Lagrange multiplier λ is regarded as a Green's function rather than a constant. Ramos Ramos (2008) proves that the claim made by Inokuti et al. is indeed correct.

We can drive the VIM method by using variation theory, method of weighted residuals and using integration by parts. The best property of VIM method is to drive a closed-form solution of a nonlinear problem without any need of linearization and discretization. Due to the flexibility and ability, the VIM has emerged as a promising tool to solve nonlinear or complex systems. Consequently, this method was successfully implemented to find the approximate solution of Hilfer fractional advection diffusion equations with power law initial condition (Ali and Malik 2014), of reaction diffusion system with fast reversible reaction (Al-Sawoor and Al-Amr 2014), of wave-like and heat-like equations in large domains (Ghaneai and Hosseini 2015), of delay differential equations (He 1997), of nonlinear singular boundary value problems (Kanth and Aruna 2010), of the time fractional Fornberg–Whitham equation (Sakar and Ergören 2015), of Burger's flow with fractional derivatives (Wu and Baleanu 2013), of non-isothermal reaction diffusion model equations in a spherical catalyst (Wazwaz 2017), of optical bright and dark soliton solutions for coupled nonlinear Schrödinger (CNLS) equations (Wazwaz 2020), to Bratu-like equation arising in electrospinning (He et al. 2014), to free vibration analysis of a tapered beam mounted on two-degree of freedom subsystems (El-Sayed and El-Mongy 2018), to fuzzy fractional differential equation (Kumar and Gupta 2021) and to others (Doeva et al. 2021; Das and Rana 2021; Das et al. 2022; Kumar et al. 2020; Mohammadi et al. 2021; Alshabanat et al. 2020; Veeresha et al. 2020).

The paper is organized as follows: The continuous model problem is defined in Sect. 2. In Sect. 3, a brief sketch of the method is given. Section 4 contains the solution methodology and optimal value of Lagrange multiplier is evaluated. In Sect. 5, the convergence analysis is carried out. In Sect. 6, linear and nonlinear test problems are taken into account to validate theoretical results obtained in Sect. 5. Finally, Sect. 7, contains a conclusion.

2 Preliminary results

2.1 Variation of iteration method

In this section, we have given a brief sketch of variation of iteration method. Consider a general class nonlinear parabolic partial differential equation.

$$Dv(x,t) = \mathcal{L}(v(x,t)) + \mathcal{N}(v(x,t)) = \mathcal{F}, \tag{2.1}$$

where $\mathcal{L}$ and $\mathcal{N}$ are the linear and nonlinear operator, respectively, and $\mathcal{F}(x,t)$ be the force term or inhomogeneous term. Then, the correction functional associated with (2.1) is defined as:

$$v_{n+1}(x,t) = v_n(x,t) + \int_0^t \lambda(s)\{\mathcal{L}v_n(x,s) + \mathcal{N}\tilde{v_n}(x,s) - \mathcal{F}(x,s)\}ds \qquad n \geq 0, \tag{2.2}$$

where λ be the general Lagrange's multiplier, which is evaluated optimally (He 1999) by using variational theory and Liouville–Green transformation. Furthermore, v_n denotes the nth iterative approximation of v and $\tilde{v}_n$ denotes the restricted variation, i.e. $\delta\tilde{v}_n = 0$. After evaluating the Lagrange's multiplier λ and choosing an appropriate initial condition v_0, and using (2.2), one obtains the successive approximations v_n of solution $v(x,t)$. Hence, the exact solution of the problems (2.1) is obtained as

$$v(x,t) = \lim_{n\to\infty} v_n(x,t).$$

2.2

Theorem 1 *Let us suppose that χ be a Banach space such that $\boldsymbol{A} : \chi \to \chi$ be the nonlinear mapping and suppose*

$$\|\boldsymbol{A}[v] - \boldsymbol{A}[\bar{v}]\| \leq \varrho\|v - \bar{v}\|, \qquad v, \bar{v} \in \chi \tag{2.3}$$

then $\boldsymbol{A}$ has a unique fixed point for $\varrho < 1$. Moreover

$$v_{n+1} = \boldsymbol{A}[v_n] \tag{2.4}$$

Sequence converges to a fixed point $\boldsymbol{A}$ for any arbitrary choice of $v_0 \in \chi$,

$$\|v_k - v_l\| \leq \|v_1 - v_0\| \sum_{j=l-1}^{k-2} \varrho^j \tag{2.5}$$

Proof See (Odibat 2010) □

3 Statement of problem

3.1 Parabolic reaction diffusion problem

Consider the following class of nonlinear singularly perturbed parabolic problem of reaction diffusion type.

$$(v_\varepsilon)_t(x,t) - \varepsilon(v_\varepsilon)_{xx}(x,t) + v_\varepsilon(x,t) - f(x,t,v) = 0, \tag{3.1}$$

where $(x,t) \in (0,1)\times(0,1)$, subject to the initial condition and boundary conditions prescribed as:

$$\begin{cases} v_\varepsilon(x,0) = & \psi_b(x), \\ v_\varepsilon(0,t) = & \psi_l(t), \\ v_\varepsilon(1,t) = & \psi_r(t). \end{cases} \tag{3.2}$$

where $0 < \varepsilon \ll 1$ is a small positive parameter known as singular perturbation parameter. Let $f(x,t,v)$ be sufficiently smooth and ϱ,$\bar{\varrho}$ be some constant satisfies,

$$0 \leq \varrho^2 \leq f_v(x,t,v) \leq \bar{\varrho}^2 \quad \forall (x,t,v) \in [0,1] \times [0,1] \times \mathbf{R} \tag{3.3}$$

3.2 Parabolic convection diffusion problem

Consider the following class of singularly perturbed parabolic convection dominated problem.

$$(v_\varepsilon)_t(x,t) - \varepsilon(v_\varepsilon)_{xx}(x,t) + (v_\varepsilon)_x(x,t) - f(x,t,v_\varepsilon) = 0, \tag{3.4}$$

where $(x,t) \in (0,1)\times(0,1)$, subject to the initial condition and boundary conditions prescribed as:

$$\begin{cases} v_\varepsilon(x,0) = & \psi_b(x), \\ v_\varepsilon(0,t) = & \psi_l(t), \\ v_\varepsilon(1,t) = & \psi_r(t), \end{cases} \tag{3.5}$$

where $0 < \varepsilon \ll 1$ is a small positive parameter known as singular perturbation parameter. Let $f(x,t,v)$ be sufficiently smooth and ϱ,$\bar{\varrho}$ be some constant satisfies,

$$0 \leq \varrho^2 \leq f_v(x,t,v) \leq \bar{\varrho}^2 \quad \forall (x,t,v) \in [0,1] \times [0,1] \times \mathbf{R} \tag{3.6}$$

4 Solution methodology

4.1 Lagrange's multiplier for parabolic reaction diffusion problem

Taking the correction functional in $t-$direction, the problem (3.1) can be expressed as:

$$v_{n+1}(x,t) = v_n(x,t) + \int_0^t \lambda(s)\left(\frac{\partial v_n(x,s)}{\partial s} - \varepsilon\frac{\partial^2 v_n(x,s)}{\partial x^2} + f_n(x,s,v)\right)\mathrm{d}s, n \geq 0. \tag{4.1}$$

Now let $\delta\tilde{v_n}$ be the restricted variation and the restricted variation of nonlinear source term is denoted by $\tilde{f_n}(x, s, v)$.

$$v_{n+1}(x,t) = v_n(x,t) + \int_0^t \lambda(s)\left(\frac{\partial v_n(x,s)}{\partial s} - \varepsilon\frac{\partial^2 \tilde{v_n}(x,s)}{\partial x^2} + \tilde{f_n}(x,s,v)\right)\mathrm{d}s. \tag{4.2}$$

Using integration by part and restricting the restricted variation term,

$$v_{n+1}(x,t) = v_n(x,t) + [\lambda(s)v_n(x,s)]_{s=0}^t - \left[\frac{\mathrm{d}\lambda(s)}{\mathrm{d}s}v_n(x,s)\right]_{s=0}^t. \tag{4.3}$$

We recall the variational theory for evaluating Lagrange's multiplier optimally and applying variation corresponding to v_n and making correction functional stationary, i.e. $\delta v_{n+1} = 0$.

$$\delta v_{n+1}(x,t) = \delta v_n(x,t) + \lambda(s)\delta v_n(x,t) - \frac{\mathrm{d}\lambda(s)}{\mathrm{d}s}\delta v_n(x,t) = 0. \tag{4.4}$$

We obtain the following Euler–Lagrange equation and stationary conditions as:

$$\left[\frac{\mathrm{d}\lambda(s)}{\mathrm{d}s}\right]_{s=t} = 0; \qquad [1-\lambda(s)]_{s=t} = 0. \tag{4.5}$$

From stationary condition (4.5), we obtain the optimal value of Lagrange's multiplier

$$\lambda(s) = -1 \tag{4.6}$$

Now the iteration formulae are written as

$$v_{n+1}(x,t) = v_n(x,t) - \int_0^t \left(\frac{\partial v_n(x,s)}{\partial s} - \varepsilon\frac{\partial^2 v_n(x,s)}{\partial x^2} + f_n(x,s,v)\right)\mathrm{d}s. \tag{4.7}$$

4.2 Lagrange's multiplier for parabolic convection diffusion problem

Taking the correction functional in $t-$direction, the problem (3.4) can be expressed as:

$$v_{n+1}(x,t) = v_n(x,t) + \int_0^t \lambda(s)\left(\frac{\partial v_n(x,s)}{\partial s} - \varepsilon\frac{\partial^2 v_n(x,s)}{\partial x^2} + \frac{\partial v_n(x,s)}{\partial x} + f_n(x,s,v)\right)\mathrm{d}s, n \geq 0. \tag{4.8}$$

Now let $\delta\tilde{v_n}$ be the restricted variation and the restricted variation of nonlinear source term is denoted by $\tilde{f_n}(x, s, v)$.

$$v_{n+1}(x,t) = v_n(x,t) + \int_0^t \lambda(s)\left(\frac{\partial v_n(x,s)}{\partial s} - \varepsilon\frac{\partial^2 \tilde{v_n}(x,s)}{\partial x^2} + \frac{\partial \tilde{v_n}(x,s)}{\partial x} + \tilde{f_n}(x,s,v)\right)\mathrm{d}s. \tag{4.9}$$

Using integration by part and restricting the restricted variation term,

$$v_{n+1}(x,t) = v_n(x,t) + [\lambda(s)v_n(x,s)]_{s=0}^t - \left[\frac{d\lambda(s)}{\mathrm{d}s}v_n(x,s)\right]_{s=0}^t. \tag{4.10}$$

We recall the variational theory for evaluating Lagrange's multiplier optimally and applying variation corresponding to v_n and making correction functional stationary, i.e. $\delta v_{n+1} = 0$.

$$\delta v_{n+1}(x,t) = \delta v_n(x,t) + \lambda(s)\delta v_n(x,t) - \frac{\mathrm{d}\lambda(s)}{\mathrm{d}s}\delta v_n(x,t) = 0. \tag{4.11}$$

We obtain the following Euler–Lagrange equation and stationary conditions as:

$$\left[\frac{\mathrm{d}\lambda(s)}{\mathrm{d}s}\right]_{s=t} = 0; \qquad [1-\lambda(s)]_{s=t} = 0. \tag{4.12}$$

From stationary condition (4.12), we obtain the optimal value of Lagrange's multiplier

$$\lambda(s) = -1 \tag{4.13}$$

Now the iteration formulae are written as

$$v_{n+1}(x,t) = v_n(x,t) - \int_0^t \left(\frac{\partial v_n(x,s)}{\partial s} - \varepsilon\frac{\partial^2 v_n(x,s)}{\partial x^2} + \frac{\partial v_n(x,s)}{\partial x} + f_n(x,s,v)\right)\mathrm{d}s. \tag{4.14}$$

5 Convergence

The above iteration formulae (4.7) generate a sequence $< v_n(x,t) >$. Now we construct the series from variational iteration formulae (4.7) as,

$$v_0(x,t) + [v_1(x,t) - v_0(x,t)] + [v_2(x,t) - v_1(x,t)] + \cdots + [v_n(x,t) - v_{n-1}(x,t)] + \cdots. \tag{5.1}$$

Now let

$$S_{n+1}(x,t) = v_0(x,t) + [v_1(x,t) - v_0(x,t)] + [v_2(x,t) - v_1(x,t)] + \cdots + [v_n(x,t) - v_{n-1}(x,t)] = v_n(x,t), \tag{5.2}$$

then we have the following bounds.

Theorem 2 *Let $v_n(x,t) \in [0,1]$ be the sequence generated by (5.1) with $v_0 = q(x)c$, where $q(x) \in C^2[0,1]$ bounded in interval $[0,1]$ and c is an arbitrary constant. Let the optimal value of Lagrange's multiplier corresponding to the stationary conditions (4.5) belong to $C^\infty[0,1]$. Then, the sequence v_n converges to the exact solution to $v(x,t)$ of the problem.*

Proof

$$|v_1(x,t) - v_0(x,t)| = |\int_0^t \lambda(s)\left(\frac{\partial v_0(x,s)}{\partial s} - \varepsilon\frac{\partial^2 v_0(x,s)}{\partial x^2} + \tilde{f_n}(x,s,v_0)\right)\mathrm{d}s|, \tag{5.3}$$

$$\leq \int_0^t |\lambda(s)|\left(\|\frac{\partial v_0(x,s)}{\partial s} - \varepsilon\frac{\partial^2 v_0(x,s)}{\partial x^2}\| + \|\tilde{f_n}(x,s,v_0)\|\right)\mathrm{d}s, \tag{5.4}$$

$$\leq \int_0^t |A_i|\left(\|B_i\|_\infty + \|C_i\|_\infty\right)\mathrm{d}s \tag{5.5}$$

$$\leq M\int_0^t \mathrm{d}s, \tag{5.6}$$

$$\leq Mt. \tag{5.7}$$

where $|A_i| = \max_{s\in[0,1]}|\lambda(s)|$; $\|B_i\|_\infty \leq \max_i |B_i|$ and $\|C_i\|_\infty \leq \max_i |C_i|$,

$$M = \max\{|A_i|\left(\|B_i\|_\infty + \|C_i\|_\infty\right), \|B_i\|_\infty\}. \tag{5.8}$$

Similarly,

$$|v_2(x,t) - v_1(x,t)| = |\int_0^t \lambda(s)\left(\frac{\partial v_1(x,s)}{\partial s} - \varepsilon\frac{\partial^2 v_1(x,s)}{\partial x^2} + \tilde{f}(x,s,v_1)\right)\mathrm{d}s|, \tag{5.9}$$

$$\leq \int_0^t |\lambda(s)|\left(\|\frac{\partial v_1(x,s)}{\partial s} - \varepsilon\frac{\partial^2 v_1(x,s)}{\partial x^2}\| + \|\tilde{f}(x,s,v_1)\|\right)\mathrm{d}s, \tag{5.10}$$

$$\leq \int_0^t |A_i|\left(\|B_i\|_\infty + \|C_i\|_\infty\right)\mathrm{d}s, \tag{5.11}$$

$$\leq M^2\int_0^t s\mathrm{d}s, \tag{5.12}$$

$$\leq \frac{M^2t^2}{2!}. \tag{5.13}$$

By mathematical induction,

$$|v_{n+1}(x,t) - v_n(x,t)| = |\int_0^t \lambda(s)\left(\frac{\partial v_n(x,s)}{\partial s} - \varepsilon\frac{\partial^2 v_n(x,s)}{\partial x^2} + \tilde{f}(x,s,v_n)\right)\mathrm{d}s|, \tag{5.14}$$

$$\leq \int_0^t |\lambda(s)|\left(\|\frac{\partial v_n(x,s)}{\partial s} - \varepsilon\frac{\partial^2 v_n(x,s)}{\partial x^2}\| + \|\tilde{f}(x,s,v_n)\|\right)\mathrm{d}s, \tag{5.15}$$

$$\leq \int_0^t |A_i|\left(\|B_i\|_\infty + \|C_i\|_\infty\right)\mathrm{d}s, \tag{5.16}$$

$$\leq M^{n+1}\int_0^t s^n\mathrm{d}s, \tag{5.17}$$

$$\leq \frac{M^{n+1}t^{n+1}}{(n+1)!}. \tag{5.18}$$

Hence, for $t \in [0,1]$ the series $\frac{M^nt^n}{n!}$ is uniformly convergent and converges to 0 as $n \to \infty$. Therefore, we conclude that the sequence $< v_n >$ is uniformly convergent and converges to the exact solution $v(x,t)$. From above convergence analysis, it is concluded that the proposed method is parameter uniform convergent, i.e. independent of singular perturbation parameter ε. □

Theorem 3 *Let $v_n(x,t) \in [0,1]$ be the sequence generated by (4.14) with $v_0 = q_1(x)c_1$, where $q_1(x) \in C^2[0,1]$ bounded in interval $[0,1]$ and c_1 is an arbitrary constant. Let the optimal value of Lagrange's multiplier corresponding to the stationary conditions (4.12) belong to $C^\infty[0,1]$. Then, the sequence v_n converges to the exact solution to $v(x,t)$ of the problem.*

Proof The proof is similar to theorem (2). □

6 Numerical discussion

In this section, linear and nonlinear test problems are taken into account, to validate the theoretical finding and to check the proposed method's efficiency. The maximum absolute error is calculated by using the following:

$$\eta = \|v - v_n\| \tag{6.1}$$

The approximate solution at the nth iteration is symbolized by v_n. We define

$$\hat{\eta} = \max_{x=0.1,0.2\cdots,0.9}\|\eta\| \tag{6.2}$$

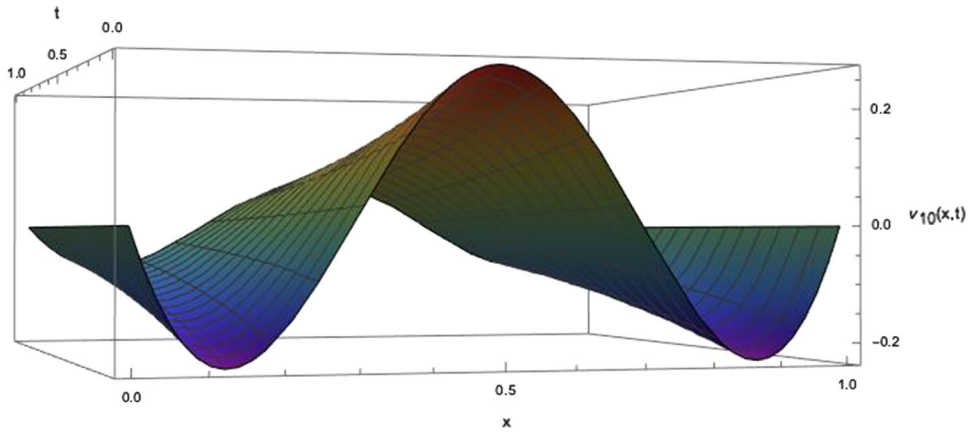


Fig. 1 Solution obtained by VIM method at 10th iteration for $\varepsilon = 2^{-4}$ for example (6.1)

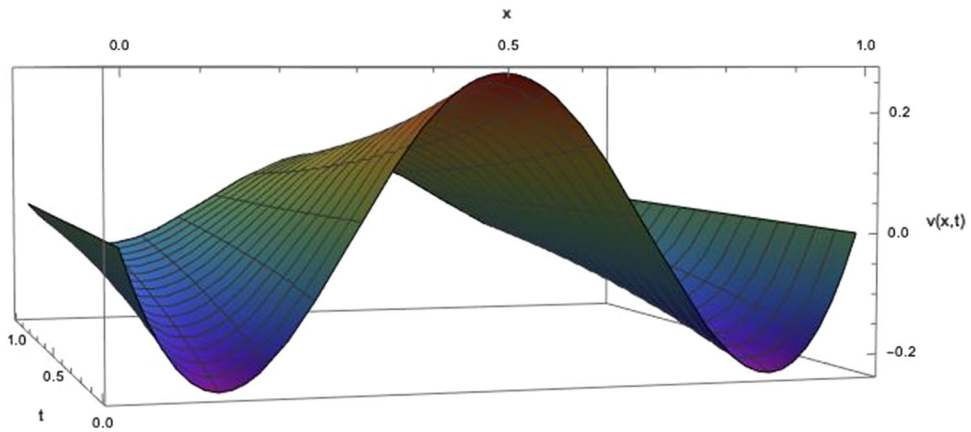


Fig. 2 Exact solution for $\varepsilon = 2^{-4}$ for example (6.1)

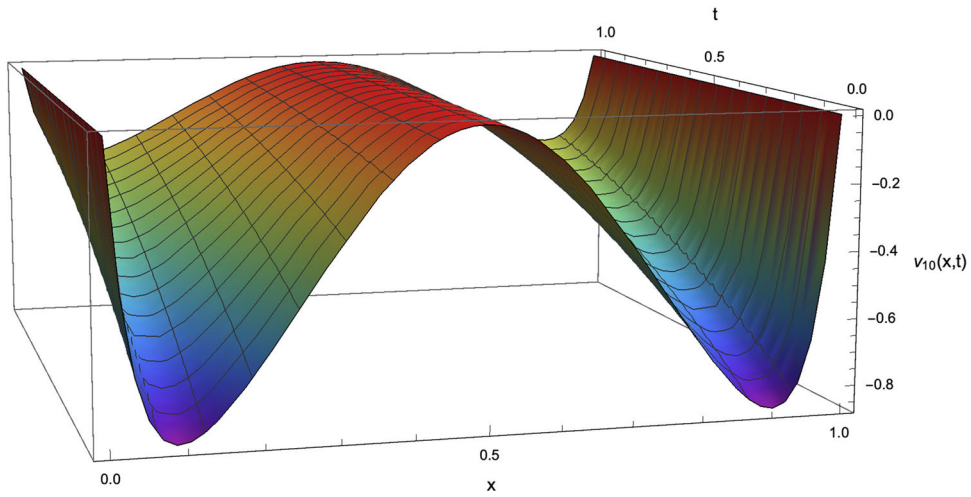


Fig. 3 Solution obtained by VIM method at 10th iteration for $\varepsilon = 2^{-10}$ for example (6.1)

The approximate solution obtained by proposed method for example (6.1) and example (6.2) with $\varepsilon = 2^{-4}$ and 2^{-6} at 10th and 4th iteration is plotted in Figs. 1 and 6, respectively, which coincide with the exact solutions plotted in Figs. 2 and 7, respectively. The approximate solution computed by proposed method for example (6.1) and example (6.2) with $\varepsilon = 2^{-10}$ at 10th and 4th iteration is plotted in Figs. 3 and 8, respectively, which coincide with the exact solutions plotted in Figs. 4 and 9, respectively. From Figs. 1 to 3, it is clear that the solution exhibits the boundary layers at the both boundaries, which corroborate the theoretical property of the considered test problem (6.1). The example (6.2) is a time-dependent second-order differential equation; therefore, the basic theory of singularly perturbed problem says that there should be two boundary layers at both the boundaries of spatial domain but contrarily the graphs of the solution of the example (6.2) in Figs. 6 and 9 show one boundary layer at $x = 0$. This is happened because the exact solution of

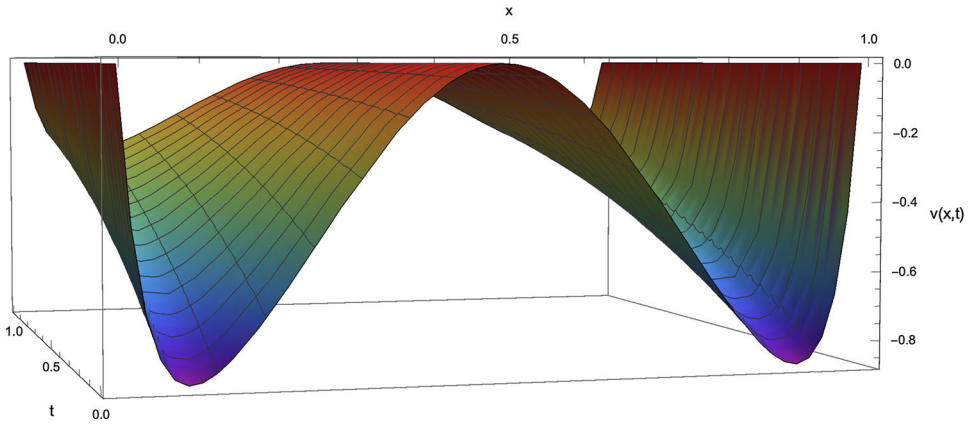


Fig. 4 Exact solution for $\varepsilon = 2^{-10}$ for Example (6.1)

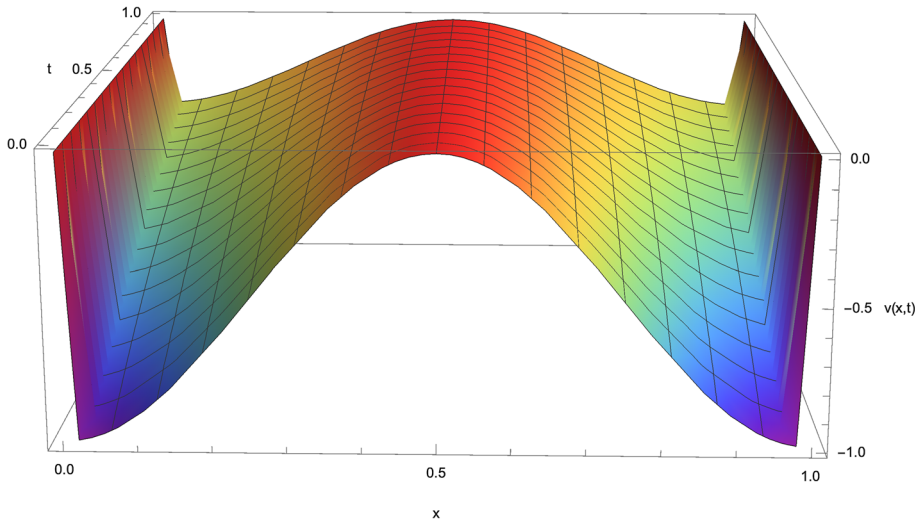


Fig. 5 Solution obtained by VIM method at 10th iteration for $\varepsilon = 10^{-9}$ for example (6.1)

the example (6.2) $v(x,t) = e^{-t-\frac{x}{\sqrt{\varepsilon}}}$ satisfies the boundary condition $v(1,t) = e^{\left(-t-\frac{1}{\sqrt{\varepsilon}}\right)}$ at $x = 1$ (Figs. 5, 6, 7, 8, 9, 10, 11, 12, 13, 14, 15 and 16).

The computed results are tabulated in Table 1 for example (6.1) and in Table 1and 2 for example (6.2). Therefore, from Tables 2 and 1 we observe that after further increasing the number of iteration the error term decreases. Hence, it is concluded that the proposed method is convergent and converges to the exact solution.

6.1 Reaction–diffusion problem

Example 6.1 "Consider the following linear parabolic singularly perturbed reaction diffusion problem.

$$\begin{cases} \frac{\partial v(x,t)}{\partial t} - \varepsilon \frac{\partial^2 v(x,t)}{\partial x^2} + v(x,t) = f(x,t), \\ v(x,0) = \left(\dfrac{e^{-\frac{x}{\sqrt{\epsilon}}} + e^{-\frac{1-x}{\sqrt{\epsilon}}}}{e^{-\frac{1}{\sqrt{\epsilon}}} + 1} - \cos^2(\pi x) \right), \quad x \in [0,1], \\ v(0,t) = 0, \quad v(1,t) = 0, \quad t \in [0,1] \end{cases} \tag{6.3}$$

with exact solution

$$v(x,t) = e^{-t} \left(\frac{e^{-\frac{x}{\sqrt{\epsilon}}} + e^{-\frac{1-x}{\sqrt{\epsilon}}}}{e^{-\frac{1}{\sqrt{\epsilon}}} + 1} - \cos^2(\pi x) \right).'' \tag{6.4}$$

Example 6.2 "Consider the following nonlinear parabolic singularly perturbed reaction diffusion equation.

$$\begin{cases} \frac{\partial v(x,t)}{\partial t} - \varepsilon \frac{\partial^2 v(x,t)}{\partial x^2} + v(x,t) + (v(x,t))^2 \\ \quad = e^{-2t-\frac{2x}{\sqrt{\varepsilon}}} - e^{-t-\frac{x}{\sqrt{\varepsilon}}}, \\ v(x,0) = e^{\left(-\frac{x}{\sqrt{\varepsilon}}\right)}, \qquad x \in [0,1], \\ v(0,t) = e^{(-t)}, \quad v(1,t) = e^{\left(-t-\frac{1}{\sqrt{\varepsilon}}\right)}, \quad t \in [0,1] \end{cases} \tag{6.5}$$

with exact solution

$$v(x,t) = e^{-t-\frac{x}{\sqrt{\varepsilon}}}.'' \tag{6.6}$$

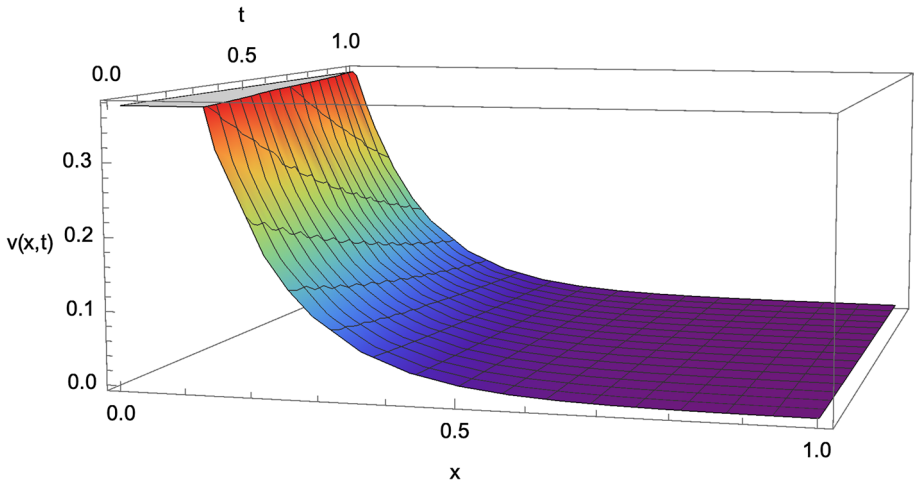


Fig. 6 Exact solution $v(x,t)$ for $\varepsilon = 2^{-6}$ for example (6.2)

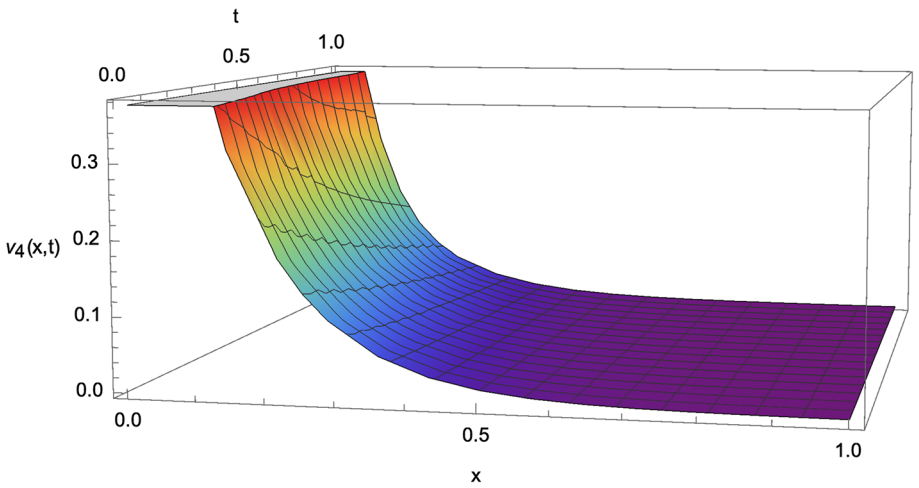


Fig. 7 Solution obtained by VIM method at 4th iteration for $\varepsilon = 2^{-6}$ for example (6.2)

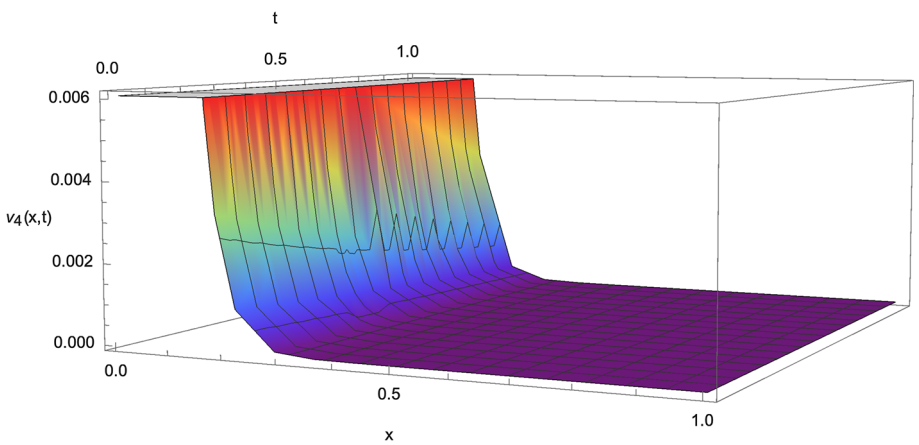


Fig. 8 Solution obtained by VIM method at 4th iteration for $\varepsilon = 2^{-10}$ for example (6.2)

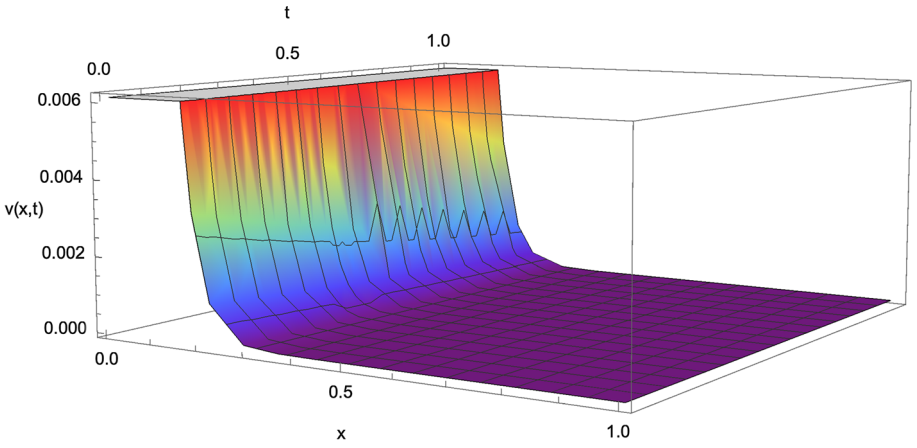


Fig. 9 Exact solution for $\varepsilon = 2^{-10}$ for Example (6.2)

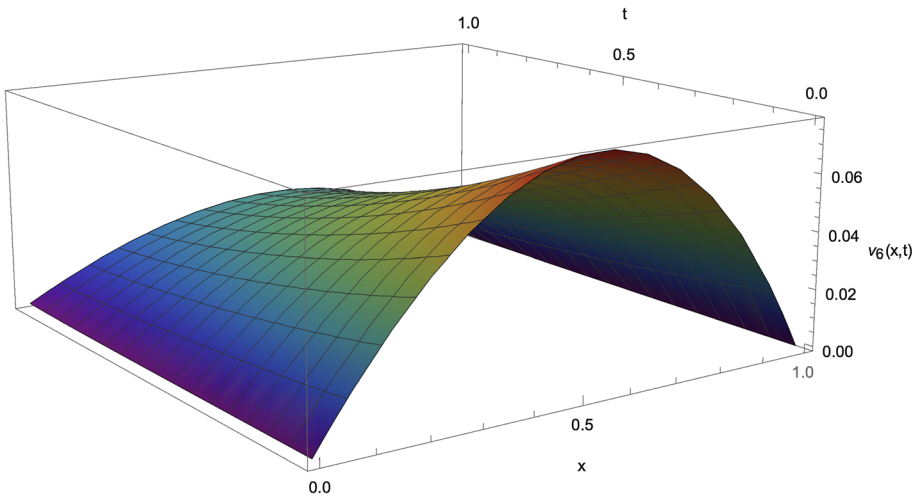


Fig. 10 Solution obtained by VIM method at 6th iteration for $\varepsilon = 2^{0}$ for example (6.3)

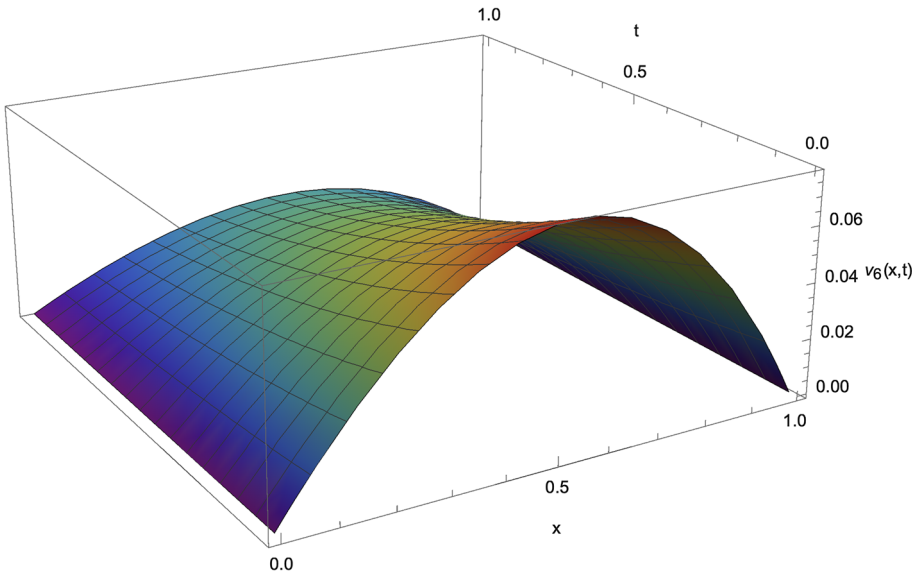


Fig. 11 Exact solution for $\varepsilon = 2^{0}$ for Example (6.3)

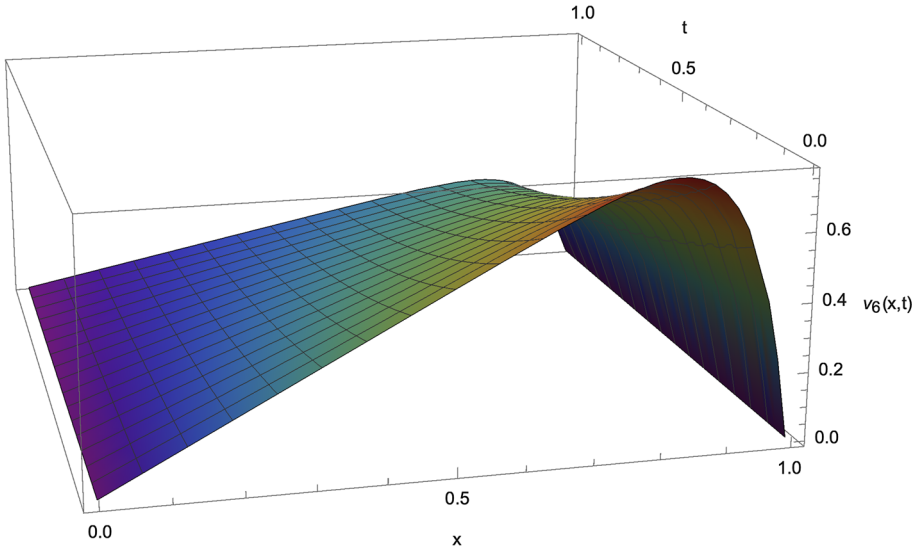


Fig. 12 Solution obtained by VIM method at 6th iteration for $\varepsilon = 2^{-4}$ for example (6.3)

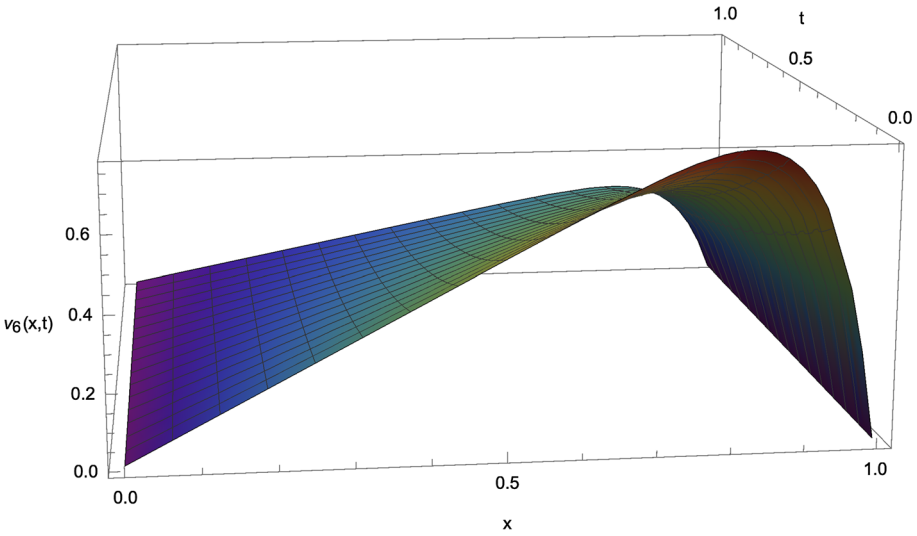


Fig. 13 Exact solution for $\varepsilon = 2^{-4}$ for example (6.3)

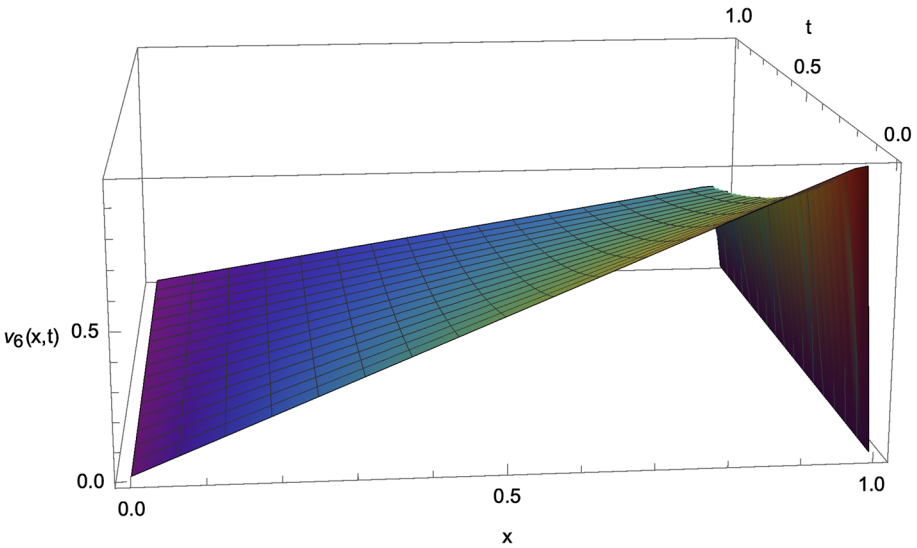


Fig. 14 Solution obtained by VIM method at 6th iteration for $\varepsilon = 2^{-8}$ for example (6.3)

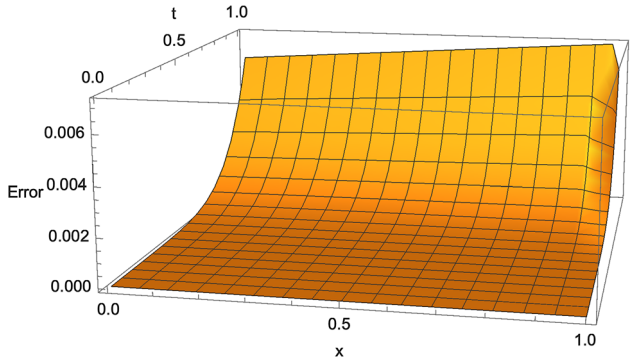


Fig. 15 Error at v_5 for $\varepsilon = 2^{-8}$ for Example (6.3)

6.2 Convection reaction–diffusion problem

Example 6.3 "Consider the following nonlinear parabolic singularly perturbed convection–reaction diffusion problem.

$$\begin{cases} \frac{\partial v(x,t)}{\partial t} - \varepsilon \frac{\partial^2 v(x,t)}{\partial x^2} + \frac{\partial v(x,t)}{\partial x} + v(x,t) + (v(x,t))^2 \\ \quad = f(x,t), \\ v(x,0) = e^{\left(-\frac{x}{\sqrt{\varepsilon}}\right)}, \qquad x \in [0,1], \\ v(0,t) = e^{(-t)}, \quad v(1,t) = e^{\left(-t-\frac{1}{\sqrt{\varepsilon}}\right)}, \quad t \in [0,1] \end{cases} \tag{6.7}$$

with exact solution

$$v(x,t) = e^{-t}\left(x\left(1-e^{-1/\epsilon}\right) - e^{-\frac{1-x}{\epsilon}} + e^{-1/\epsilon}\right)." \tag{6.8}$$

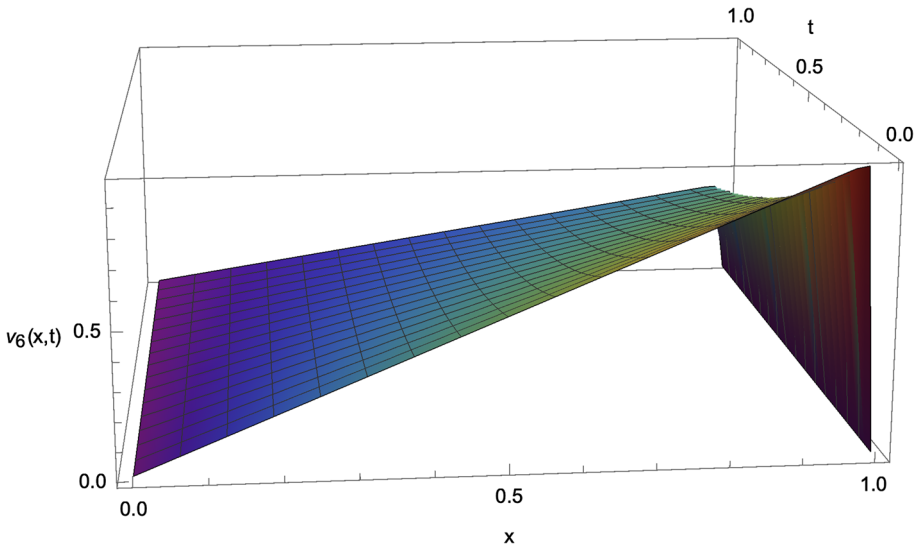


Fig. 16 Solution obtained by VIM method at 6th iteration for $\varepsilon = 2^{-8}$ for example (6.3)

Table 1 Maximum absolute error $\hat{\eta}$ of proposed method for Example (6.2) solved for third iteration v_3.

t	$\varepsilon = 2^{-2}$	$\varepsilon = 2^{-4}$	$\varepsilon = 2^{-6}$	$\varepsilon = 2^{-8}$	$\varepsilon = 2^{-10}$
0.2	3.85497×10^{-4}	1.3886×10^{-4}	2.40926×10^{-5}	2.62891×10^{-5}	1.68401×10^{-6}
0.4	3.56725×10^{-3}	8.5865×10^{-4}	7.28079×10^{-4}	4.24775×10^{-4}	2.53068×10^{-5}
0.6	5.11157×10^{-3}	5.11257×10^{-3}	5.11157×10^{-3}	2.15044×10^{-3}	1.20588×10^{-4}
0.8	2.26075×10^{-2}	2.19989×10^{-2}	1.98954×10^{-2}	6.7509×10^{-3}	3.59495×10^{-4}

Table 2 Maximum absolute error $\hat{\eta}$ of proposed method for Example (6.1) solved for fifth iteration v_5

t	$\varepsilon = 2^{-4}$	$\varepsilon = 2^{-6}$	$\varepsilon = 2^{-8}$	$\varepsilon = 2^{-12}$	$\varepsilon = 2^{-16}$
0.2	2.6148×10^{-12}	2.1399×10^{-13}	1.3250×10^{-13}	3.1572×10^{-15}	1.2101×10^{-14}
0.4	6.8904×10^{-10}	4.6791×10^{-10}	2.0960×10^{-10}	8.5420×10^{-13}	9.40137×10^{-13}
0.6	5.9053×10^{-8}	3.9830×10^{-8}	1.7842×10^{-8}	7.2197×10^{-11}	7.8050×10^{-11}
0.8	1.3761×10^{-6}	9.2819×10^{-7}	4.1580×10^{-7}	1.6825×10^{-9}	1.8193×10^{-9}

7 Conclusion

In this article, we have successfully developed the variational iteration method for solving NSPPPDEs. The convergence analysis is carried out and method is found to be convergent. In nonlinear problems, one often uses a quasi-linearization technique to linearize the problem and then solve the linearized problem by numerical or other existing techniques. Due to the linearization of the nonlinear problem, the approximated solution's accuracy somehow degenerates, which leads to deceptive solutions. In this paper, an attempt has been made to address such types of issues associated with NSPPPDEs. The method presented in this paper seems to be robust, as it maintains high accuracy concerning the perturbation parameter ε. Unlike numerical approaches, the proposed method is simple to implement because it does not require either linear or nonlinear systems of equations. It eliminates the need for time-consuming algebraic equations, prior simplification, discretion or linearization, allowing it to greatly reduce the size of the calculation while maintaining excellent accuracy. We obtain a higher level of precision just in few iterations without any limiting assumption. The obtained numerical results appear to be promising and justify the efficiency of the proposed method. The proposed method is easy to implement. With some modification, the technique can readily be extended to even more general problems like singularly perturbed problems with discontinuous source terms, singularly perturbed problems with time and advance delay, and the evolution equations of mathematical physics.

Author Contributions KK helped in conceptualization, methodology, writing—original draft, supervision

Funding VK would like to acknowledge the National board of higher mathematics (NBHM) for research Grant No.–Ref. No. 2/48(6)/2016/NBHM(R.P.)/R D II /15455.

Data availability This manuscript has no associated data.

Declarations

Conflict of interest The authors declare no conflict of interest.

References

Ali I, Malik N (2014) Hilfer fractional advection diffusion equations with power law initial condition: a numerical study using variational iteration method. Comput Math Appl 68:1161–1179. https://doi.org/10.1016/j.camwa.2014.08.021

Al-Sawoor A, Al-Amr M (2014) A new modification of variational iteration method for solving reaction diffusion system with fast reversible reaction. J Egypt Math Soc 22:396–401. https://doi.org/10.1016/j.joems.2013.12.011

Alshabanat A, Jleli M, Kumar S, Samet B (2020) Generalization of caputo-fabrizio fractional derivative and applications to electrical circuits. Front Phys 8:64. https://doi.org/10.3389/fphy.2020.00064

Amrein M, Wihler TP (2017) An adaptive space-time newton-galerkin approach for semilinear singularly perturbed parabolic evolution equations. IMA J Numer Anal 37(4):2004–2019. https://doi.org/10.1093/imanum/drw049

Boglaev I (2004) Monotone iterative algorithms for a nonlinear singularly perturbed parabolic problem. J Comput Appl Math 172(2):313–335. https://doi.org/10.1016/j.cam.2004.02.010

Boglaev I (2012) An inexact monotone method for solving semilinear parabolic problems. Appl Math Comp 219(6):3253–3263. https://doi.org/10.1016/j.amc.2012.09.067

Chandru M, Das P, Ramos H (2018) Numerical treatment of two-parameter singularly perturbed parabolic convection diffusion problems with non-smooth data. Math Meth Appl Sci 14:5359–5387. https://doi.org/10.1002/mma.5067

Cheng Y, Song C, Mei Y (2021) Local discontinuous galerkin method for time-dependent singularly perturbed semilinear reaction-diffusion problems. Comput Methods Appl Math 21(1):31–52. https://doi.org/10.1515/cmam-2019-0185

Das P (2019) An a posteriori based convergence analysis for a nonlinear singularly perturbed system of delay differential equations on an adaptive mesh. Numer Algor 81:465–487. https://doi.org/10.1007/s11075-018-0557-4

Das P, Natesan S (2012) Higher order parameter uniform convergent schemes for Robin type reaction diffusion problems using adaptively generated grid. Int J Comput Methods 9:125–152

Das P, Natesan S (2013) A uniformly convergent hybrid scheme for singularly perturbed system of reaction-diffusion robin type boundary-value problems. J Appl Math Comput 41:447–471. https://doi.org/10.1007/s12190-012-0611-7

Das P, Natesan S (2014) Optimal error estimate using mesh equidistribution technique for singularly perturbed system of reaction diffusion boundary value problems. Appl Math Comput 249:265–277

Das P, Rana S (2021) Theoretical prospects of fractional order weakly singular volterra integro differential equations and their approximations with convergence analysis. Math Meth Appl Sci 44(3):9419–9440. https://doi.org/10.1002/mma.7369

Das P, Rana S, Ramos H (2019) Homotopy perturbation method for solving caputo-type fractional-order volterra-fredholm integro-differential equations. Comp Math Methods 1:2577–7408. https://doi.org/10.1002/cmm4.1047

Das P, Rana S, Ramos H (2022) On the approximate solutions of a class of fractional order nonlinear volterra integro-differential initial value problems and boundary value problems of first kind and their convergence analysis. J Comput Appl Math 404:0377–0427. https://doi.org/10.1016/j.cam.2020.113116

Doeva O, Masjedi PK, Weaver PM (2021) A semi-analytical approach based on the variational iteration method for static analysis of composite beams. Compos Struct 257:113110. https://doi.org/10.1016/j.compstruct.2020.113110

El-Sayed T, El-Mongy H (2018) Application of variational iteration method to free vibration analysis of a tapered beam mounted on two-degree of freedom subsystems. Appl Math Model 58:349–364. https://doi.org/10.1016/j.apm.2018.02.005

Ghaneai H, Hosseini M (2015) Variational iteration method with an auxiliary parameter for solving wave-like and heat-like equations in large domains. Comput Math Appl 69:363–373. https://doi.org/10.1016/j.camwa.2014.11.007

He J (1997) Variational iteration method for delay differential equations. Commun Nonlinear Sci Numer Simul 2:235–236. https://doi.org/10.1016/S1007-5704(97)90008-3

He J (1999) Variational iteration method - a kind of non-linear analytical technique: some examples. Int J Non Linear Mech 34:699–708. https://doi.org/10.1016/S0020-7462(98)00048-1

He J-H, Kong H-Y, Chen R-X, Hu M-s, Chen Q-l (2014) Variational iteration method for bratu-like equation arising in electrospinning. Carbohydr Polym 105:229–230. https://doi.org/10.1016/j.carbpol.2014.01.044

Inokuti M, Sekine H, Mura T (1978) General use of the Lagrange multiplier in non-linear mathematical physics. Pergamon Press, Oxford

Kabeto MJ, Duressa GF (2021) Robust numerical method for singularly perturbed semilinear parabolic differential difference equations. Math Comput Simul 188:537–547. https://doi.org/10.1016/j.matcom.2021.05.005

Kanth AR, Aruna K (2010) He's variational iterational method for treating nonlinear singular boundary value problems. Comput Math Appl 60:821–829. https://doi.org/10.1016/j.camwa.2010.05.029

Khari K, Kumar V (2022) An efficient numerical technique for solving nonlinear singularly perturbed reaction diffusion problem. J Math Chem 60:1356–1382. https://doi.org/10.1007/s10910-022-01365-4

Khari K, Kumar V (2022) Finite element analysis of the singularly perturbed parabolic reaction-diffusion problems with retarded argument. Numer Methods Partial Differ Eq 38:997–1014. https://doi.org/10.1002/num.22785

Kopteva N, Linss T (2012) Maximum norm a posteriori error estimation for a time-dependent reaction-diffusion problem. Comput Methods Appl Math 12:189–205. https://doi.org/10.2478/cmam-2012-0013

Kopteva N, Linss T (2013) Maximum norm a posteriori error estimation for parabolic problems using elliptic reconstructions. SIAM J Numer Anal 51(3):1494–1524. https://doi.org/10.1137/110830563

Kumar S, Gupta V (2021) An application of variational iteration method for solving fuzzy time-fractional diffusion equations. Neural Comput Applic 33:17659–17668. https://doi.org/10.1007/s00521-021-06354-3

Kumar V, Leugeringb G (2021) Singularly perturbed reaction-diffusion problems on a k-star graph. Math Meth Appl Sci 44:14874–14891. https://doi.org/10.1002/mma.7749

Kumar V, Leugeringb G (2023) Convection dominated singularly perturbed problems on a metric graph. J Comput Appl Math. https://doi.org/10.1016/j.cam.2023.115062

Kumar S, Nisar KS, Kumar R, Cattani C, Samet B (2020) A new rabotnov fractional-exponential function-based fractional derivative for diffusion equation under external force. Math Meth Appl Sci 43(7):4460–4471. https://doi.org/10.1002/mma.6208

Kumar K, Podila P, Das P, Ramos H (2021) A graded mesh refinement approach for boundary layer originated singularly perturbed time-delayed parabolic convection diffusion problems. Math Meth Appl Sci 44:12332–12350. https://doi.org/10.1002/mma.7358

Mohammadi H, Kumar S, Rezapour S, Etemad S (2021) A theoretical study of the caputo-fabrizio fractional modeling for hearing loss due to mumps virus with optimal control, Chaos. Solitons Fractals 144:110668. https://doi.org/10.1016/j.chaos.2021.110668

Odibat ZM (2010) A study on the convergence of variational iteration method. Math Comput Model 51(9):1181–1192. https://doi.org/10.1016/j.mcm.2009.12.034

Ramos J (2008) On the variational iteration method and other iterative techniques for nonlinear differential equations. Appl Math Comp 199:39–69. https://doi.org/10.1016/j.amc.2007.09.024

Sakar M, Ergören H (2015) Alternative variational iteration method for solving the time fractional Fornberg-Whitham equation. Appl Math Model 14:3972–3979. https://doi.org/10.1016/j.apm.2014.11.048

Shakti D et al (2022) A moving mesh refinement based optimal accurate uniformly convergent computational method for a parabolic system of boundary layer originated reaction-diffusion problems with arbitrary small diffusion terms. J Comput Appl Math 404(3):0377–0427. https://doi.org/10.1016/j.cam.2020.113167

Veeresha P, Prakasha DG, Kumar S (2020) A fractional model for propagation of classical optical solitons by using nonsingular derivative. Math Meth Appl Sci. https://doi.org/10.1002/mma.6335

Wazwaz A-M (2017) Solving the non-isothermal reaction-diffusion model equations in a spherical catalyst by the variational iteration method. Chem Phys Lett 679:132–136. https://doi.org/10.1016/j.cplett.2017.04.077

Wazwaz A-M (2020) Optical bright and dark soliton solutions for coupled nonlinear schrödinger (cnls) equations by the variational iteration method. Optik 207:164457. https://doi.org/10.1016/j.ijleo.2020.164457

Wu G-C, Baleanu D (2013) Variational iteration method for the Burger's flow with fractional derivatives: New Lagrange multipliers. Appl Math Model 37:6183–6190. https://doi.org/10.1016/j.apm.2012.12.018

Publisher's Note Springer Nature remains neutral with regard to jurisdictional claims in published maps and institutional affiliations.

Springer Nature or its licensor (e.g. a society or other partner) holds exclusive rights to this article under a publishing agreement with the author(s) or other rightsholder(s); author self-archiving of the accepted manuscript version of this article is solely governed by the terms of such publishing agreement and applicable law.

Analysis of Differential Privacy and study of its variation with privacy budget using real-world data.

Rakshit Chauhan
Department of Computer Science and Engineering, Delhi Technological University

Pooja Narula
Department of Computer Science and Engineering, Delhi Technological University

Shaurya Shekhar
Department of Computer Science and Engineering, Delhi Technological University

Manoj Kumar
Department of Computer Science and Engineering, Delhi Technological University

***Abstract*-** The privacy of data is one of the most essential topics in the world of privacy and security. All the advancement in technology is rendered non-essential if the data cannot be secured and be protected from various organisations. Every person or organisation desires privacy, be it technological or otherwise. It is getting more and more complicated to preserve one's privacy and maintain the confidentiality of data due to numerous policies put forth by almost every organisation to exist. Differential privacy, which makes very careful assumptions about the adversary's past knowledge, has recently become a powerful element for privacy protection. Differential privacy has received attention ever since it was initially proposed and put forth, and it is now considered to be among the most potential concepts for privacy-preserving data release and analysis in many computer science and information technology domains. In this paper, we discuss the motivation for its introduction as a tool to replace other privacy methods, use databases and datasets for the comparison of data before and after using differential privacy on it. We also explore deep into differential privacy and replicate an attack on the data by an outsider to see if the data secured by differential privacy really is protected. Comparison of the probability distributions of data before and after applying differential privacy and the variation of these distributions is also reflected in this report.

***Index Terms*-** Differential privacy, data privacy, smart noise, data analysis, privacy preserving

I. INTRODUCTION

Data privacy refers to the protection of sensitive or confidential information contained in datasets from unauthorized access, use, or disclosure. Names, addresses, Social Security numbers, and financial details are all part of this information, as well as private company information like secrets of trade and client information. Data privacy is important for several reasons. First and foremost, it helps to protect the privacy rights of individuals by preventing unauthorized access to their personal information. This can help to prevent identity theft, financial fraud, and other forms of harm that can result from the misuse of personal information. [1]

In addition to protecting individuals, data privacy is also important for businesses and organizations. Data breaches and other privacy violations can result in significant financial and reputational damage, as well as legal liability. By implementing strong data privacy policies and practices, businesses can protect themselves from these risks and ensure that they are in compliance with relevant laws and regulations.

Data privacy is also important for maintaining trust and transparency in the digital age. As more and more personal and sensitive information is collected and stored online, individuals are becoming increasingly concerned about the security and privacy of their data. By prioritizing data privacy and using better methods of practicing privacy and its policies, organizations can demonstrate their commitment to protecting the privacy of their customers and stakeholders.

Overall, data privacy is an essential component of responsible data management and is critical for protecting the rights and interests of individuals and organizations alike. By prioritizing data privacy and taking steps to safeguard sensitive information, businesses and organizations can build trust and demonstrate their commitment to responsible data stewardship.

Differential privacy [2] is a privacy-preserving technique that can help to protect the privacy of individuals whose data is contained in datasets. It accomplishes this by carefully introducing noise into the data while concealing any information about specific data points, preserving the data's statistical features. By doing so, differential privacy helps to protect the privacy of individuals by ensuring that their data is indistinguishable from other data points in the dataset.

There are several ways in which differential privacy helps to improve data privacy:

1. Protection against re-identification attacks: One of the main risks to data privacy is re-identification, where an attacker is able to link an individual to their data within a dataset. Differential privacy helps to protect against this type of attack by making it more difficult to identify individual data points within the dataset.
2. Protection against inference attacks: Another risk to data privacy is inference attacks, where an attacker is able to infer sensitive information about an individual from their data within a dataset. Differential privacy helps to protect against this type of attack by ensuring that the data released from the dataset is statistically similar irrespective of whether a specific individual's data is included or excluded.
3. Protection against membership attacks: Membership attacks involve an attacker trying to determine whether a specific individual's data is contained in a dataset. Differential privacy helps to protect against this type of attack by ensuring that the statistical properties of the data are consistent regardless of whether a specific individual's data is included or excluded.

Overall, differential privacy is an important tool for protecting the privacy of individuals whose data is contained in datasets. By incorporating differential privacy techniques into data analysis and sharing processes, organizations can help to ensure that sensitive information remains protected while still enabling meaningful analysis of the data.

II. THEORETICAL FRAMEWORK

Differential privacy is a concept in data privacy that provides a way to protect sensitive information while still allowing useful statistical analysis to be performed on the data. The idea behind differential privacy is to add random noise to the data in such a way that the statistical properties of the data are preserved, while the individual data points are protected. The fundamental theoretical foundation of differential privacy entails the definition of a privacy budget, which denotes the greatest amount of data an adversary can gather about a person by looking at the results of a computation. The privacy budget is often calculated using a factor known as epsilon, which reflects the most data an attacker may discover about a person by looking at a computation's result.

To achieve differential privacy, a randomized algorithm is used to compute a noisy version of the data that satisfies the privacy budget constraint. The randomized algorithm adds random noise to the data in a way that is calibrated to the privacy budget, so that the amount of noise added increases as the privacy budget decreases. The key property of differential privacy is that it provides strong privacy guarantees even in the presence of a powerful adversary who has access to auxiliary information. In particular, differential privacy ensures that the probability of learning any specific piece of information about an individual is only slightly increased by the presence of that individual's data in the dataset. There are several different mechanisms that can be used to achieve differential privacy, including randomized response [3], Laplace noise, and Gaussian noise [4]. These mechanisms are designed to add noise to the data in a way that is calibrated to the privacy budget, so that the level of noise added increases as the privacy budget decreases.

Overall, the theoretical framework of differential privacy provides a powerful tool for protecting sensitive information while still allowing useful statistical analysis to be performed on the data. By adding carefully calibrated noise to the data, differential privacy ensures that individual data points are protected while statistical properties of the data are preserved.

III. LITERATURE REVIEW

Practising Differential Privacy in Health Care: A Review [Dankar et Amam, 2013 TDP] [5]

Through the review paper, authors alluded to multiple interpretations of Differential Privacy, specifically referring to the epsilon as the "knowledge gain ratio from one data set over the other" to the power of the Euler's number. It further makes the assertion that the values used in the literature generally are 0.01, 0.1, ln(2), and ln(3) respectively. As a compendium of the various techniques used to conceal private data, the review paper highlights the various limitations, and contemporaneous models implementing differential privacy. An interesting element of the work done by Dankar et Amam is the inter-disciplinary approach to differential privacy and its limitations especially with respect to the legality and its efficacy as a privacy tools. Alternatives to the traditional differential privacy methods, such as (ε,τ)-Differential Privacy and (ε,δ)-Differential Privacy methods. Further the review work highlights mechanisms used for achieving the conditions for differential privacy. Intertwined with a specialized approach to the healthcare industry, the review examines the feasibility of the achieving total privacy and whether it's as necessary as posited.

Differential Privacy [Cynthia Dwork, ICALP 2006] [2]

In this landmark paper, Cynthia et al. brought to the table the "Dream" of differential privacy, as a useful notion to codify the meaning of privacy and to ensure analyses of the datasets aren't compromised in quality all the while protecting the individual privacy. Here Cynthia presents a simple method to ensuring Differential Privacy by the use of additive noise mechanisms, where the additive noise is bounded by the largest difference a particular entry could make on the result of a query function. Further the paper delves into the mathematical framework for Differential privacy and the core observations made therein, including the observation of adding symmetric exponential noise to each coordinate of the query function and the importance of choosing noise as a function of the sensitivity.

Differential Privacy: What is all the noise about? [Roxana Danger, arXiv 2022] [6]

In this paper, the author examines the concepts of Differential Privacy as it relates to ML, the use of GANs to generate synthetic data, which accords to the definition of Differential Privacy and various mechanism involved to achieve the same. The author then delves into the various DP techniques in ML and makes the mention of Ensemble-DP and DP-SGD, with the special mention of the PATE algorithm, which combines the elements of both the aforementioned techniques. Finally, the paper goes to explore the concerns for privacy in Federated Learning (FL), taking a closer look at the types of FL, and specifically focusing on the aspect of privacy as it relates to the Centralized and Decentralized FL (Using Blockchain for the Decentralized aspect)

IV. WORKFLOW

The project utilises two datasets, one for the application of differential privacy and is a census dataset while the second dataset is for the attack analysis in order to check the efficiency of differential privacy over varied value of epsilons. The Adult Census Dataset [7] has been formed with the data collected from the 1994 Census database. It contains 32561 instances, with

fifteen attributes. The dataset which was used to demonstrate the attack was collected from the synthetic random data generator. The dataset contains 10000 instances and six attributes. In order to apply differential privacy on the adult census data, we have pre-processed the data by assigning unique numeric identification to every different option for the following attributes- 1) Age, 2) Gender, 3) Race, 4) Country.

The workflow can be broadly categorised into two parts- Applying differential privacy to various attributes of the dataset, and launching an attack or trying to read the dataset after adding SmartNoise.

A. Applying differential privacy to various attributes of the census dataset

Firstly, the dataset has been pre-processed, that is, the required attributes have been assigned integral records through Excel functions. The resultant data is then read as the csv file via the Python Pandas. For different attributes, the categories array has been created of the unique numerical values the particular attribute stores. The differential privacy has been implemented for various attributes using the SmartNoise library of the OpenDP framework of Python. For each of the attributes, a dp_histogram has been created which takes the data and results into an array of categories distribution, with each index of the array storing the noisy value for that particular value of the attribute. Thereafter, the true distribution array is formed for various attributes using the actual data in the Excel and comparison has been made between the true distribution and the noisy distribution using Python Pandas library for creating pie charts. The above process of comparison using pie charts has been carried out for different values of epsilon (0.01, 0.1, ln2, ln3) to observe the variety of deviation from true distribution.

B. Launching an attack on the dataset value after the smart noise has been added.

Random data is generated for the purpose of launching an attack and a person of interest is chosen, in our case it is the 10th record of the dataset. We print the true income value of the person of interest and calculate the true mean of income of the dataset by calculating the sum of income of all the records and dividing it with the number of records.

V. OUTCOME & ANALYSIS

Thereafter, the modified data is created by adding noise via OpenDP framework to each record and through this data, we access the income attribute of the person of interest in order to observe the deviation in the values. We also find the new mean of modified data in order to notice the deviation in mean values. The mentioned process of modifying the data is repeated for different values of epsilon- 0.01, 0.1, 1, ln2, ln3 and the income value is recorded and the mean value is calculated.

Upon categorising the various attributes into different groups and applying differential privacy on the same using different values of epsilons, we were able to generate the results in the form of pie charts of the distribution of the attribute data. Each attribute has five pie charts distribution corresponding to them- based on true values, for epsilon with value 0.01, 0.1, ln 2 and ln 3. The results for the age attributes are shown as follows-

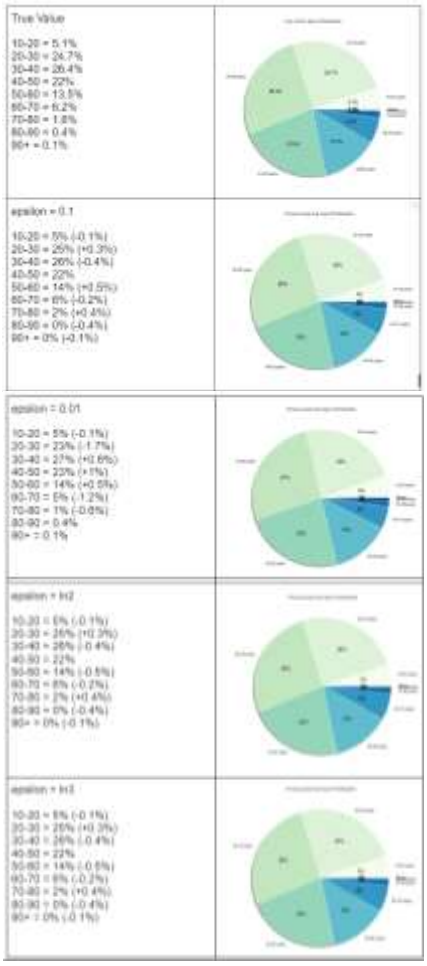


Figure 1: Distribution of various attributes

Similar comparisons have been done for other attributes namely salary, gender, country, race and marital status. The table for the same is below as follows.

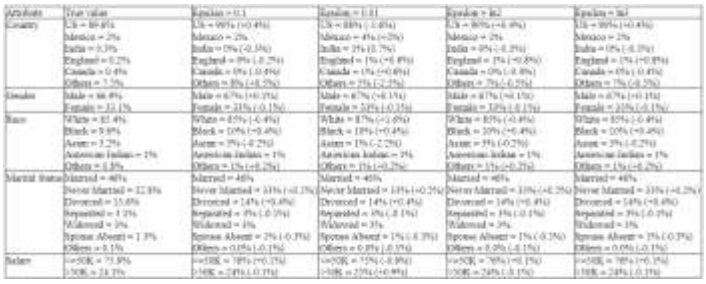


Table 1:Compiled Result for Country, Gender, Race, Marital Status and Salary

The second part of the project was to launch an attack on the data after the noise has been added to it. The attack has been launched

using five different values of epsilon, i.e 1, 0.01, 0.1, ln 2 and ln 3, to compare and contrast the variance in the actual value and the deviated value. The person of interest that is the record on which the attack has been launched is the tenth record of the dataset.

```
person of interest:

sex          0.0
age         45.0
educ         6.0
income    6000.0
married      1.0
race         1.0
Name: 0, dtype: float64
```

Figure 2: A sample person of interest

The attack has been launched on the income attribute of the person of interest. The true value of the income is 6000 and the overall mean of the incomes of the dataset is 30943.45. These values have been compared to the results after applying the differential privacy, which have been accumulated in the table mentioned below.

Epsilon Value	New Mean	New Income	Difference in Mean (New Mean - 30943)	Difference in Income (New Income - 6000)
ln 3	26883	230	-4060	-5770
1	26884	6710	-4059	+710
ln 2	26884	5330	-4059	-670
0.1	26884	8326	-4059	+2326
0.01	26888	43030	-4055	+37030

Table 2: Comparison between the Mean and Individual values

As it can be deduced from the table that as the value of epsilon deviates farther away from 1, the new calculated value of the income inculcates more noise and therefore, the actual value is difficult to find after the data has been treated with the differential privacy. As the epsilon approaches 1, the deviation in the income's value reduces. It is also noticeable that even though the true value of an attribute, here income, varies greatly with the change in epsilon, the variation in the mean value of the attribute over the whole data stays the same for all cases and doesn't deviate much from the actual figure.

To sum up, this quality of the differential privacy helps in adding the smart noise through which the actual information of each record is not available but the crux of the overall data is maintained which can be utilised by the receiver of the data.

VI. LIMITATIONS

Differential privacy is an approach of safeguarding people's privacy when gathering, analysing, and exchanging data. By introducing random noise to the data to mask individual data points, it tries to offer strong privacy assurances. Yet, while applying differential privacy in practise, it is important to take into account a number of its drawbacks [8]. The main drawbacks of differential privacy are as follows:

1. Utility versus privacy trade-off: One of the main obstacles to differential privacy is the utility versus privacy trade-off. The level of privacy protection is determined by the quantity of noise added to the data, which also has an impact on the precision of the data analysis. While too little noise can jeopardise people's privacy, too much noise can render the data unusable for study. To prevent the privacy protection offered by differential privacy from detracting from the usefulness of the data, this trade-off must be carefully weighed.

2. Limited protection against inference attacks: Differential privacy is intended to defend against direct attacks that seek to identify specific data points, but it offers only limited defence against inference assaults. The protection it offers against inference attacks, which utilise statistical methods to infer private information about specific people, is, however, somewhat restricted. When the data collection is tiny or the attacker has access to additional information not present in the data set, inference assaults can be especially potent.

3. Data perturbation sensitivity: Differential privacy is sensitive to the type of data perturbation. To effectively preserve privacy, the quantity of noise that is introduced to the data must be precisely adjusted. Yet, even little data modifications might significantly affect how much privacy is protected by differential privacy.

4. Limitations of the Laplace mechanism: The Laplace mechanism is an amazing tool to achieve differential privacy, but it comes with its own cons. It uses a Laplace distribution to choose data, adding random noise to the data. The Laplace mechanism, however, has a number of drawbacks. For instance, it makes the assumption that the data is continuous and quantitative, which may not be true for all data sets. Choosing a good noise parameter can also prove to be a strenuous task while using the Laplace mechanism.

5. Difficulty of implementing differential privacy: Achieving differential privacy can be difficult, especially for firms without a strong background in data privacy and security. A thorough understanding of statistical procedures, data analysis methodologies, and privacy-preserving algorithms is necessary for the design and implementation of a differentially private system. To ensure that differential privacy offers the necessary level of privacy protection, the implementation must also be rigorously evaluated and tested.

To conclude, differential privacy is a potent instrument for safeguarding people's privacy when gathering, analysing, and

exchanging data. But, while putting it into effect, there are a number of restrictions that must be properly taken into account.

VII. SCOPE OF STUDY

The current research figures out the significance of applying differential privacy to the data and the impact of privacy budget values to the smart noise. The research can be further expanded to understand the importance and use cases of applying differential privacy over data which gets used in the training of various machine learning models.

Depending on whether the job at hand requires supervised learning or unsupervised learning, several methods can be used to include differential privacy into machine learning algorithms. The primary idea of focus is to randomize part of the mechanism's behaviour to provide privacy, where mechanism refers to a learning algorithm, but the differential privacy framework can be further expanded and applied to study any algorithm ensuring privacy.

The target is to train the various models with both the raw data as well as the differentially private data and subsequently compare the results of statistical analysis, which should ideally remain similar. In contrary to this, the comparison of results of data prediction of individual records must give wrong results for the differentially private data, thus protecting the individual's data and ensuring data privacy.

VIII. CONCLUSION

The "concept of differential privacy" has brought a revolution in the data privacy sector. This non-conventional technique of protecting data of individuals yet conveying the essence and the crux of data is significantly useful in the field of data analysis.

Through the project, we tried to understand the application of differential privacy on various data of individuals and compared the results of deviation for various epsilon values. As it can be noted from the results, the differential privacy adds the "smart noise" to the data, which barely disturbs the overall distribution of data into various categories, but at the same time prevents any kinds of breaching of individual records of the data through attacks.

Although the mean and the categorical distribution of the modified data remains the same for analytical studies by any third party or other organisations, the individual record values change highly, especially when the value of epsilon deviates far from 1, like in the case of 0.01 as epsilon values. This helps in simultaneous data protection as well as analysis.

The application of the project holds a special importance when the census data is required to be sent to various agencies or municipal corporations to analyse the data in order to understand the possible ideologies, needs and demands of the population. This understanding is required to prepare the propagandas for future projects in an area.

ACKNOWLEDGMENT

We would like to express our sincere gratitude to all of the individuals and organizations who supported us during the course of this research project. First and foremost, we would like to thank our supervisor, Prof. Manoj Kumar, for his guidance, support, and encouragement throughout the project. His insights and expertise were invaluable in helping us to design and carry out our research. In addition, we are grateful to Delhi Technological University for their support and assistance with various aspects of the research, including provision of required hardware and software. Their help was essential to the success of the project. Finally, we would like to thank our families and friends for their unwavering support and encouragement throughout the project. Their patience and understanding were critical to our ability to complete this work. Once again, we would like to express our deepest gratitude to all of those who supported us during this research project.

REFERENCES

[1] E. Aïmeur and D. Schőnfeld, "The ultimate invasion of privacy: Identity theft," in *Ninth Annual International Conference on Privacy, Security and Trust*, Montreal, 2011.

[2] C. Dwork, "Differential privacy," in *Automata, Languages and Programming: 33rd International Colloquium, ICALP*, Venice, Italy, 2006.

[3] S. L. Warner, "Randomized response: A survey technique for eliminating evasive answer bias.," *Journal of the American Statistical Association*, pp. 63-69, 1965.

[4] A. Nikolov, K. Talwar and L. Zhang, "The geometry of differential privacy: the sparse and approximate cases," in *Proceedings of the forty-fifth annual ACM symposium on Theory of computing*, Palo Alto, USA, 2013.

[5] F. K. Dankar and K. E. Imam, "Practicing Differential Privacy in Health Care: A Review," *Transactions on Data Privacy*, vol. 6, no. 1, p. 35–67, 2013.

[6] R. Danger, "Differential Privacy: What is all the noise about? " *arXiv preprint arXiv:2205.09453*, 2022.

[7] D. Dua and C. Graff, *Adult Census Income Dataset, UCI Machine Learning Repository*, Irvine, CA: the University of California, School of Information and Computer Science, 2019.

[8] K. Nissim, T. Steinke, A. Wood, M. Bun, M. Gaboardi, D. R. O'Brien and S. Vadhan, "Differential Privacy: A Primer for a Non-technical Audience" 3 March 2017. [Online]. Available: https://privacytools.seas.harvard.edu/files/privacytools/files/pedagogical-document-dp_0.pdf.

AUTHORS

First Author – Rakshit Chauhan, Bachelor of Technology, Delhi Technological University,
Second Author –Pooja Narula, Bachelor of Technology, Delhi Technological University,
Third Author –Shaurya Shekhar, Bachelor of Technology, Delhi Technological University,
Fourth Author – Manoj Kumar, Professor , Delhi Technological University,

MAPAN-Journal of Metrology Society of India
https://doi.org/10.1007/s12647-023-00626-0

ORIGINAL PAPER

Analysis of Shapes of Centrifugal Force-Generating Rod in Centrifugal Force-Assisted Abrasive Flow Machining Process

A. Bhardwaj*, K. Srinivas and R. Chaudhary

Department of Mechanical Engineering, Delhi Technological University, New Delhi, India

Received: 14 September 2022 / Accepted: 02 March 2023

© Metrology Society of India 2023

Abstract: Centrifugal force-assisted abrasive flow machining (CFAAFM) is a hybrid of abrasive flow machining (AFM) that clubs the advantage of centrifugal force with media extrusion for improving the efficiency and enhancing material removal of AFM. In the present investigation, three differently shaped rods (triangular, circular and rectangular) are rotated in the CFAAFM set-up to analyse their effect on percentage improvement in the surface finish ($\%\Delta R_a$) and material removal (MR); also, ANSYS FLUENT 22.0 is used to analyse the effect of flow parameters on the workpiece during the media flow. In this investigation, the Taguchi method was used for optimising the process parameters, including the rod's shape, the rotational speed of the centrifugal force-generating (CFG) rod and the number of extrusions cycles of media. The other machining parameters were kept constant during the machining. The experiments were performed using DOE (L_9 orthogonal array), and the simulation was performed for the process. The simulation showed rectangular rod generates maximum pressure over the workpiece surface among the three differently shaped rods. The streamline showed a higher concentration of abrasive particles at the wall of the workpiece during the machining process, indicating an effective machining process. The optimal value of parameters for MR was 15.54 mg at 300 RPM of rectangular rod at 6 extrusions of media. The optimum value for $\%\Delta R_a$ is 28.97% at 200 RPM of the triangular rod at 9 extrusions of media. The rotational speed was the primary factor that contributed 22.53% for MR and 58.32% for $\%\Delta R_a$. The number of extrusions is the least contributing factor contributing 15.23% in MR and 4.86% in $\%\Delta R_a$. The experimental results validate the simulation results, and the optical micrographs and SEM images justify the machining process. The increase in the value of microhardness with the rotation of the CFG rod justifies the work hardening of the workpiece at the higher rotation of the CFG rod.

Keywords: Abrasive flow machining; Material removal; Surface finish; CFAAFM

1. Introduction

The growth of industrialisation and a fast-growing economy has opened a new scope for the industry to develop enduring products with high utilitarian values, which tend to innovate new processes with optimal parameters synchronising with the environment and at a lower cost. CFAAFM is one process that improves the workpiece quality in the case of mechanical and functional properties. The process is non-hazardous and economical in operation.

AFM is a non-conventional machining process that uses a non-Newtonian abrasive laden media containing polymer, gel and abrasive for machining internal surfaces of hollow and hard-to-reach intrinsic surfaces of the workpiece. The process finds its application in biomedical, automobile, aerospace, semiconductors, shipbuilding and defence manufacturing sectors [1]. Due to its wide application and uses, there is a constant need for the improvement and development of the AFM process as its MR is low, which is the major limitation of the conventional AFM process. Various hybrids of conventional AFM have been developed to cater for the limitations and improve efficiency [2]. The various hybrids developed so far are based on the relative motion of the electrode and the workpiece (CFAAFM [3–5], drill bit-guided abrasive flow machining [6], helical abrasive flow machining [7], rotational abrasive flow machining [8]) and some based on the source of energy input and mechanism of material removal such as magnetic force-assisted AFM (MFAFM) [9], ultrasonic-force-assisted AFM [10], electrochemical-force-

*Corresponding author, E-mail: anant5892@gmail.com

Published online: 02 April 2023

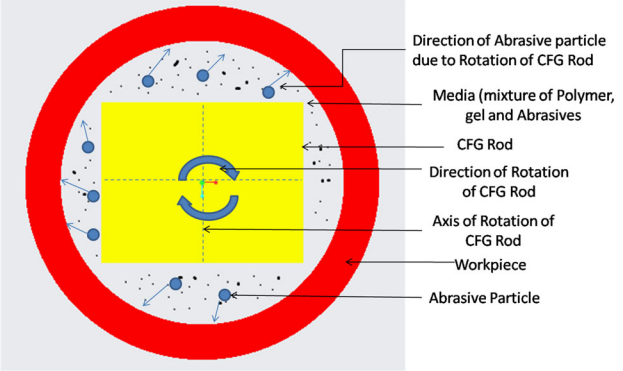


Fig. 1 Mechanism of CFAAFM process

assisted AFM (ECMAFM) [11], hybrid of MFAFM and CFAAFM [12] and hybrid of ECMAFM and CFAAFM process [13]. Thermal additive centrifugal abrasive flow machining is a new name on the list that uses the advantage of spark energy along with the combination of centrifugal and reciprocation of the media [14–16].

With the continuous development of hybridisation, there is an improvement in various process parameters targeting the lower MR and higher machining time. To improve the machining efficiency of media, many researchers worked on the mathematical and simulations model to enhance the productivity of AFM. The property of media is varied by improving the flow parameters through the requisite boundary conditions and equations [17–21].

Consistent efforts were made to enhance the machining capability of media by either improving the chemical composition of the media, changing the abrasive type and size or changing the composition of media constituent (polymer, gel and abrasive). Ali et al. [22] used CNT particles to enhance the machining capability of media and reported a significant improvement in the MR and surface finish. Dixit et al. [23] synthesised a new media based on xanthan gum and observed its material removal characteristics. Zhenzhong et al. [24] developed a water-based viscoelastic fluid for the polishing surface of monocrystalline silicon, which is used in the manufacturing of biological microelectromechanical systems using the AFM process.

The abrasive present in the media plays a significant role in machining in the AFM process as they act as a cutting tool. Many researchers worked on applying abrasives in the modern machining process and highlighted their application in modern abrasive-based machining [25–27].

The application of the AFM process and its hybrids are in recent trends as it is used in various industrial applications. Manjunath et al. [28] applied the AFM process for the surface roughness improvement of the aluminium propeller, which was made of aluminium (6061-T6). The surface finish reaches up to 0.035 mm from 0.712 mm and 3.057 mm from 4.952 mm, and 2.241 mm from 4.952 mm. Baraiya et al. [29] investigated the cylindrical ring shape of aluminium alloy, which has applications in medical, defence, automobile, aerospace and manufacturing ventures. Han et al. [30] experimented on the conformal cooling channel of selected laser melting technology and highlighted the drastic improvement in the surface roughness area. Han et al. [31] highlighted the application of the AFM process in achieving the desired R_a and compressive residual stress. Kuma et al. [32] opened a new area in the scope of the AFM process. The researchers experimented with additive manufacturing and suggested improvement in the AFM to compensate for the loss of dimensional tolerances.

Hence, there is a need for continuous development of the AFM process in terms of hybridisation, functioning, costing and green energy inclusion. As a result, the present investigation deals with improving the CFAAF process efficiency.

2. Materials and Methods

The requirement to cater for the low material removal and higher machining time has prompted the researchers for an improved hybridisation of AFM, which could optimise the cost, energy and productivity with the product's aesthetic value. The CFAAFM process is one of the significant hybridisation processes as it enhances the effective contact of the workpiece and abrasives. Also, the centrifugal force provided due to the rotation of the rod results in proper mixing of the media resulting in the enhanced MR with an improved surface finish. The present investigations include the different shapes of the CFG rod (circular, triangular and rectangular) to study their effect on material removal and surface finish in the CFAAFM process. The geometry of the CFG rod is a significant factor in the CFAAFM process as it controls the concentration of media flowing towards the constrictive passage between the workpiece and the CFG rod.

2.1. Principal for CFAAFM Process

The process involves rotating the CFG rod coaxially between the hollow workpiece and the media flowing through it. The CFG rod generates a centrifugal force on the media particles that pushes the media (mixture of gel, abrasive particles and polymer) towards the wall of the workpiece. The CFG rod also constricts the passage of media as it is placed coaxially between the hollow workpiece increasing the concentration of the abrasive near the wall of the workpiece. Thus, the process efficiently

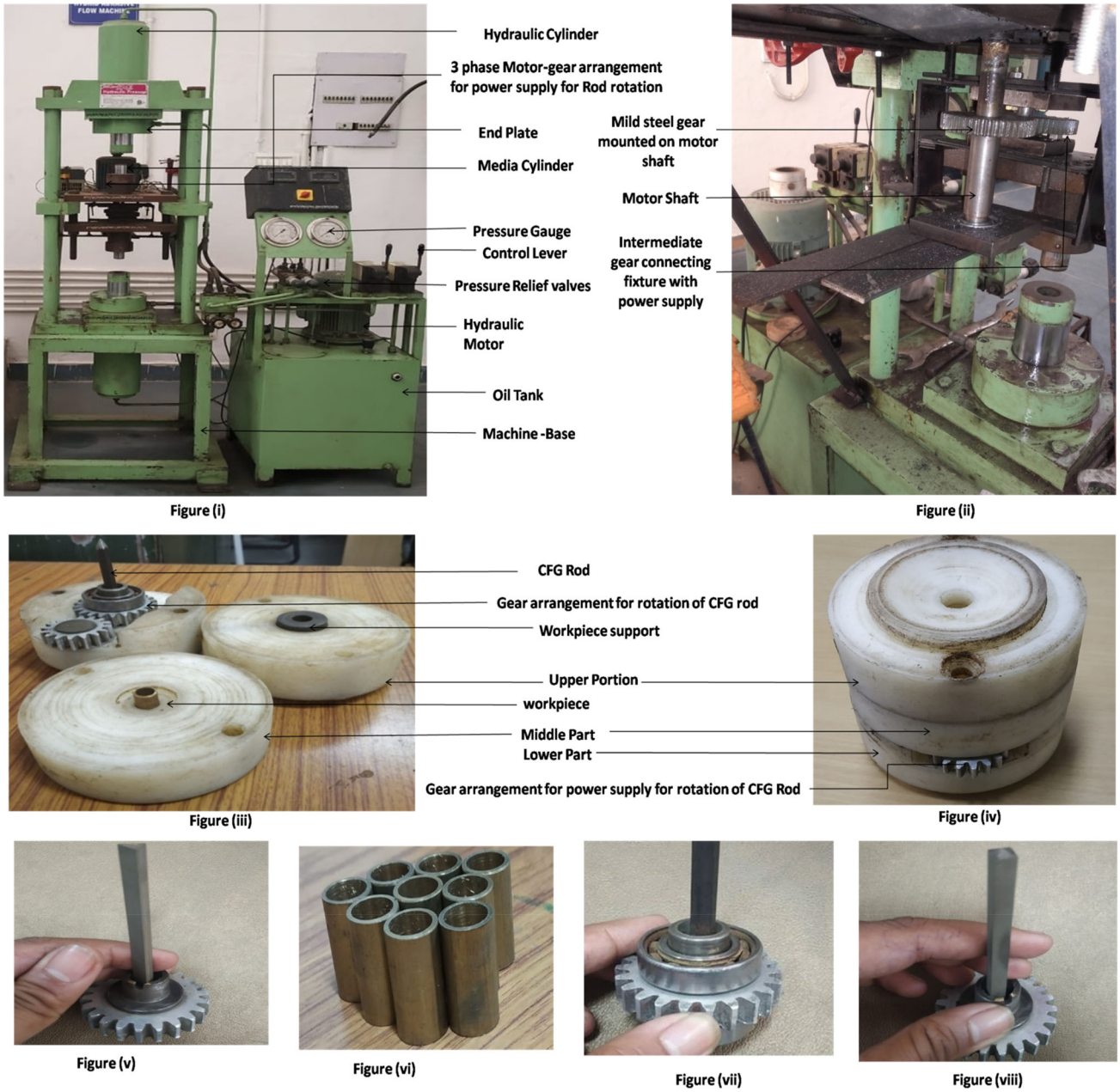


Fig. 2 Experimental set-up. **i** CFAAFM set-up, **ii** side view of CFAAFM set-up, **iii** components of fixture assembly, **iv** fixture used in CFAAFM process, **v** triangular CFG rod, **vi** workpiece, **vii** circular CFG rod, **viii** rectangular CFG rod

improves the machining capability of AFM as the machining occurs due to the extrusion of media through a conventional process and the centrifugal action of the rotating CFG rod. Figure 1 shows the mechanism of the CFAAFM process. The figure shows a CFG rod placed coaxially with the workpiece in the media and rotated clockwise. Due to the rotation of the rod, the abrasive particles present in the media are directed towards the wall of the workpiece, which increases the concentration of the abrasive towards the inner surface. The direction of the abrasive particle is also affected by the Coriolis effect as there is extrusion of media due to the pressure difference and rotation of the rod as well.

2.2. Experimental Set-up

The experimentation was done on the brass workpiece because brass is a prominent component in the electric and precision industries with a wide application in manufacturing gears, bearings, springs, hinges, ammunition casing, locks, zippers and plumbing. Moreover, the alloy possesses excellent mechanical properties like ductility, wear

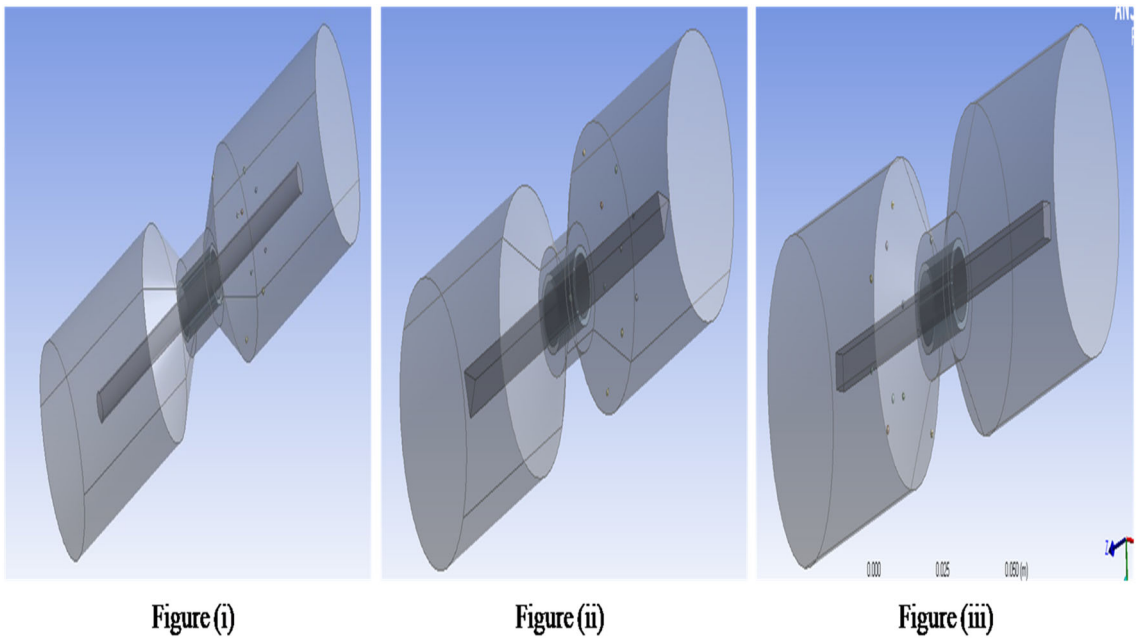


Fig. 3 Simulation set-up for various rods. **i** Circular rod geometry, **ii** triangular rod geometry, **iii** rectangular rod geometry

resistance, strength, machinability, corrosion resistance and hardness which is a prominent factor in choosing brass as a workpiece material. Three different shapes of the CFG rods were rotated within the internal surface of the workpiece, and the MR and $\%\Delta R_a$ was calculated. The set-up consists of the two-way conventional AFM set-up with the motor arrangement for the rotation of the CFG rod. Figure 2 shows the experimental set-up with the required accessories. Figure 2i shows the conventional AFM set-up in which a provision of gear and 3-phase induction motor arrangement was made for providing the rotation to the CFG rod. Figure 2ii shows the side view of the CFAAFM set-up containing the intermediate gear arrangement for rod rotation.

The media is extruded between the upper and lower cylinder with a pressure difference of 20 MPa. The media is a non-Newtonian liquid containing silicon oil-based polymer, hydrocarbon-based gel and alumina as the abrasive particles. For the experimentation, the media flow rate was 290 cm^3/min. The abrasive-to-media concentration was taken fifty per cent by weight, and the polymer-to-gel ratio was taken as 1:1. The abrasive mesh size was 300. The experimentations were done at room temperature to eliminate the effect of temperature on the viscosity of the media.

The fixture was specifically designed for holding the CFG rod coaxially with the workpiece and for the requisite rotation arrangement. The fixture was made of nylon and contained three parts (Fig. 2iii, iv). The lower part contains a gear arrangement for the rotation of the rod. This gear is coupled with the main gear attached to three phase induction motor, which results in the rotation of the rod. The middle part contains the workpiece, supported by the lower and upper parts. Figure 2v shows the triangular rod used in the investigation. The cross section of the triangular rod is an equilateral triangle with sides equal to 5 mm. The dimension of the rod is selected by considering the maximum length of the side that could be fitted in the circle of a given radius, so that area for the media flow is minimised. Figure 2vi shows the brass workpiece used for the investigations. The workpiece was taken from a large piece of extruded brass, and thus, a very narrow range of initial surface roughness of the test specimens was considered to eliminate the effect of initial roughness. The workpiece dimensions were 10 mm OD and 8 mm ID, and the workpiece's height was taken as 16 mm.

Figure 2vii shows the circular-shaped rod. The material of the rod was taken as mild steel, and the dimensions of the rod were taken (6 mm diameter) so that the area for the media flow is minimised so that maximum abrasive concentration would occur at the inner surface of the workpiece. Figure 2viii shows the rectangular-shaped rod used in the experiment. The rod dimensions were taken as 5.70 mm × 4.50 mm. Similar criteria of minimum area of flow for media and maximum concentration of abrasives near the wall were considered for the computation of dimensions for the rectangular rod. The reason for selecting the rod's regular shape geometry is their ease in manufacturing as they can be prepared on simple machine tools without any complex process.

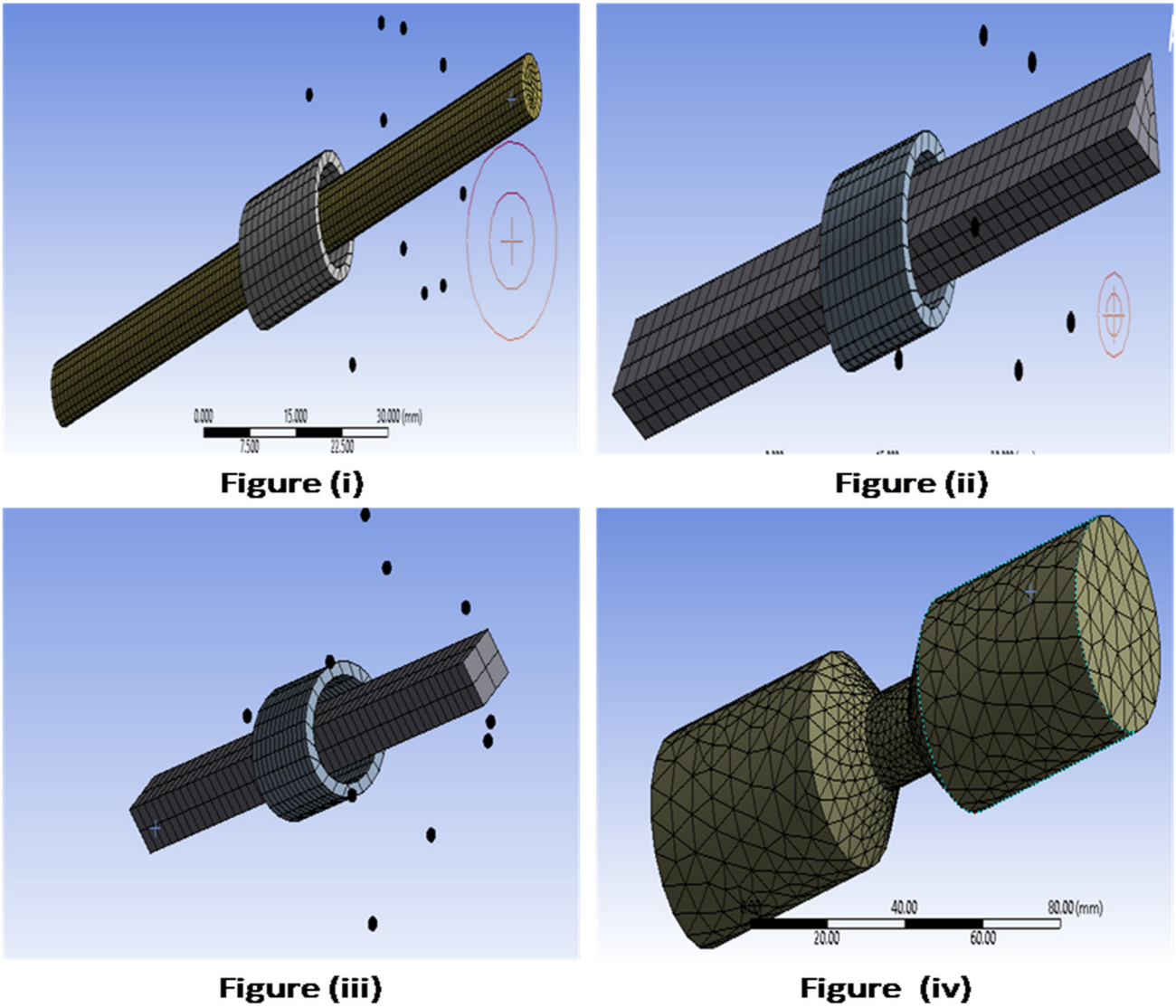


Fig. 4 Meshing of simulation set-up. **i** Meshing of circular rod, **ii** meshing of triangular rod, **iii** meshing of rectangular rod, **iv** messing fluid domain

2.3. Modelling of CFAAFM Process

Simulations were performed to study the effect of pressure and to trace the media path during the CFAAFM process. The three rods were modelled CREO parametric and then analysed in ANSYS FLUENT. The geometry of each rod was prepared using Boolean operation, and proper name selection was given to compute the resultant values at the desired locations. The mesh is prepared for each rod separately with the same parameters. The size of the element was kept as 3×10^{-6} m, and the shape of the maximum elements was tetragonal. The skewness and sizing of the mesh were adequately checked, and the corners were prepared properly. The total number of nodes for the assembly was 2,180,493, and the total number of elements was 2,159,633. The grid test for the mesh was done for each rod, and the result obtained was independent of the mesh size. Figure 3 shows the geometry of the three different shapes of the rod, and Fig. 4 shows the meshing of the rod and the combined model.

The next step was the analysis in fluent set-up. The laminar model was put on with an energy equation. The fluid was assigned the property of silicon-based media. The density of the fluid was 1219 kg/m^3, with a thermal conductivity of 0.22 w/m-k. The specific heat of fluid is 20.25 J/kg-K with a viscosity of 0.789 kg/m-s. The property of alumina and brass was given from the ANSYS FLUENT database. The boundary condition given at the inlet was the pressure inlet at 40 MPa, and the pressure at the outlet was 20 MPa. The workpiece was fitted inside the

Table 1 Process parameters and levels

Symbols	Process parameters	Unit	First level	Second level	Third level
S	Rotational speed	rpm	100	200	300
P	Shape of the rod		Rectangular	Triangular	Circular
N	Number of extrusions		3	6	9

Polymers-to-gel ratio—1:1
Workpiece—brass
Abrasive—alumina
Mesh size—300
Extrusion pressure—20 MPa
Media flow—290 cm^3/min
Temperature—32 ± 2 °C
Initial R_a variations—1.1–2.96 microns

Table 2 Orthogonal array

Exp. no	Running order	Trials for parameters			Signal-to-noise ratio (db)
		S RPM	P Shape	N Extrusions	
1	1	100	R	3	s_1
2	4	100	T	6	s_2
3	7	100	C	9	s_3
4	2	200	R	6	s_4
5	5	200	T	9	s_5
6	8	200	C	3	s_6
7	3	300	R	9	s_7
8	6	300	T	3	s_8
9	9	300	C	6	s_9

S_i—Signal-to-noise ratio at ith experiment number
Rectangular rod—R
Triangular rod—T
Circular rod—C

fixture, and the rotation of 100 RPM was given to the CFG rod. The solutions were initialised for analysis. The conversion curve and the result are discussed in the result section.

2.4. Design of Experiments

Taguchi method was used to study the effect of process parameters on the material removal and percentage improvement in surface finish. The working parameters were the rod's rotation speed, shape, and the number of extrusion cycles. The process parameters were selected based on the literature review and available set-up. Taguchi method was applied to optimise MR and surface $\%\Delta R_a$ separately, and the results were analysed. Surface roughness for all the specimens was measured by Taylor Hobson precision machine (TAYLOR HOBSON SURTRONIC 3+) having resolution of 0.01 μm. Weight of the workpiece was measured by precision weighing machine (SHIMADZU AUX220) having 0.1 mg resolution. Microhardness of the workpiece was measured by FISCHERSCOPE microhardness tester (HM 2000S) having test force range between 0.1–2000 mN. The percentage improvement in surface roughness is given by the ratio of the difference between surface roughness before and after machining to the surface roughness before machining. The data were listed according to the DOE. The difference in weight before and after the machining is taken to measure the MR. A relevant orthogonal array was made for this task, with the L_9 array having 8 DOF. The three levels are tabulated in Table 1. The L_9 (3^3) orthogonal array (parameters assigned) with the response is tabulated in Table 2. The larger, the better approach is considered for the analysis.

The experiments were performed based on Table 3, and the response values are put in Table 6. Three workpieces were taken for each trial, conforming to 27 workpiece. The overall mean value for MR is calculated by adding all the value corresponding to responses (89.45, 80.57 and 88.21) and dividing it by 27 (the total number of experiments), which gives 9.56 mg. A similar procedure was applied to compute the total mean value for percentage improvement in surface roughness and got 17.01% from Table 6.

Figure 5 shows the surface roughness computation of the single workpiece. The surface roughness was computed at five different locations, and the average value was considered in the response table. Material removal and percentage improvement in surface roughness were calculated by the following expressions.

Table 3 The L9(3^3) orthogonal array (parameters assigned) with response

Exp. no	Run order	Parameters trial conditions			Response (raw data)			S/N ratio (db)
		S 1	P 2	N 3	R1	R2	R3	
1	1	1	1	1	A_{11}	A_{12}	A_{13}	S_1
2	4	1	2	2	A_{21}	A_{22}	A_{23}	S_2
3	7	1	3	3	A_{31}	A_{32}	A_{33}	S_3
4	2	2	1	2	A_{41}	A_{42}	A_{43}	S_4
5	5	2	2	3	A_{51}	A_{52}	A_{53}	S_5
6	8	2	3	1	A_{61}	A_{62}	A_{63}	S_6
7	3	3	1	3	A_{71}	A_{72}	A_{73}	S_7
8	6	3	2	1	A_{81}	A_{82}	A_{83}	S_8
9	9	3	3	2	A_{91}	A_{92}	A_{93}	S_9
Total				Σ		Σ	Σ	

R_i—response value for ith trial repetitions

1's, 2's, 3's—levels 1,2,3 of the parameters (top of the column)

(—)—no assignment

A_{ij}—response values (quality characteristics)

$$\% \text{ improvement in } R_a = [(\text{Initial roughness} - \text{Final Roughness})/(\text{initial roughness})] * 100$$

Material Removal = Weight of the workpiece before machining − Weight of the workpiece after machining.

The signal-to-noise ratio was calculated based on the higher, the better approach and is given by

$$(S/N)\text{HB} = -10 \log \frac{1}{n} \sum_{jas=1}^{R} \frac{1}{y_j^2}$$

The data for the weights and surface roughness of the workpiece are shown in Tables 4 and 5, respectively. Table 6 shows the combined response table for both material removal and percentage change in surface roughness.

The data were analysed using Taguchi's recommended standard approach. From the stated experiment data, the approach entails computing the average values and the S/N ratio characteristics (usually taken for quality and response) for each parameter and at each level. The primary effects determined by the data of the S/N ratio and the raw data were then plotted. ANOVA (analysis of variance) is used to determine the significant parameters and how much they influence the process parameters and response characteristic values.

The responses for microhardness at different conditions according to L_9 OA are discussed in Table 7.

3. Results and Discussion

The simulation and experimental results were separately analysed in the following sections. Three different models with sample parametric and boundary conditions were made for three different shapes of the rod.

3.1. Simulation Results

The simulations were done to predict the effect of flow parameters on the workpiece under the machine parameters. The media is extruded inside the workpiece surface at a pressure difference, and the pressure extruded over the workpiece during the process is analysed for three different geometries of the rods. Figure 6 shows the simulation results and distributions of parameters on the media flow path. Figure 6i shows the conversion curve representing the energy line below the continuity, X, Y and Z velocity line, representing the smooth conversion. Figure 6ii shows the pressure variation on the brass workpiece (8 mm ID, 10 mm OD and 16 mm length) when the rectangular rod is subjected to 100 rpm. A pressure of 40 MPa is supplied at the inlet and 20 MPa at the outlet.

Similar conditions were given to the triangular rod in Fig. 6iii and the circular rod in Fig. 6iv. The result showed a maximum pressure of 33.54 MPa on the circular rod and 33.59 MPa on the triangular rod, and 38.53 MPa on the Rectangular rod.

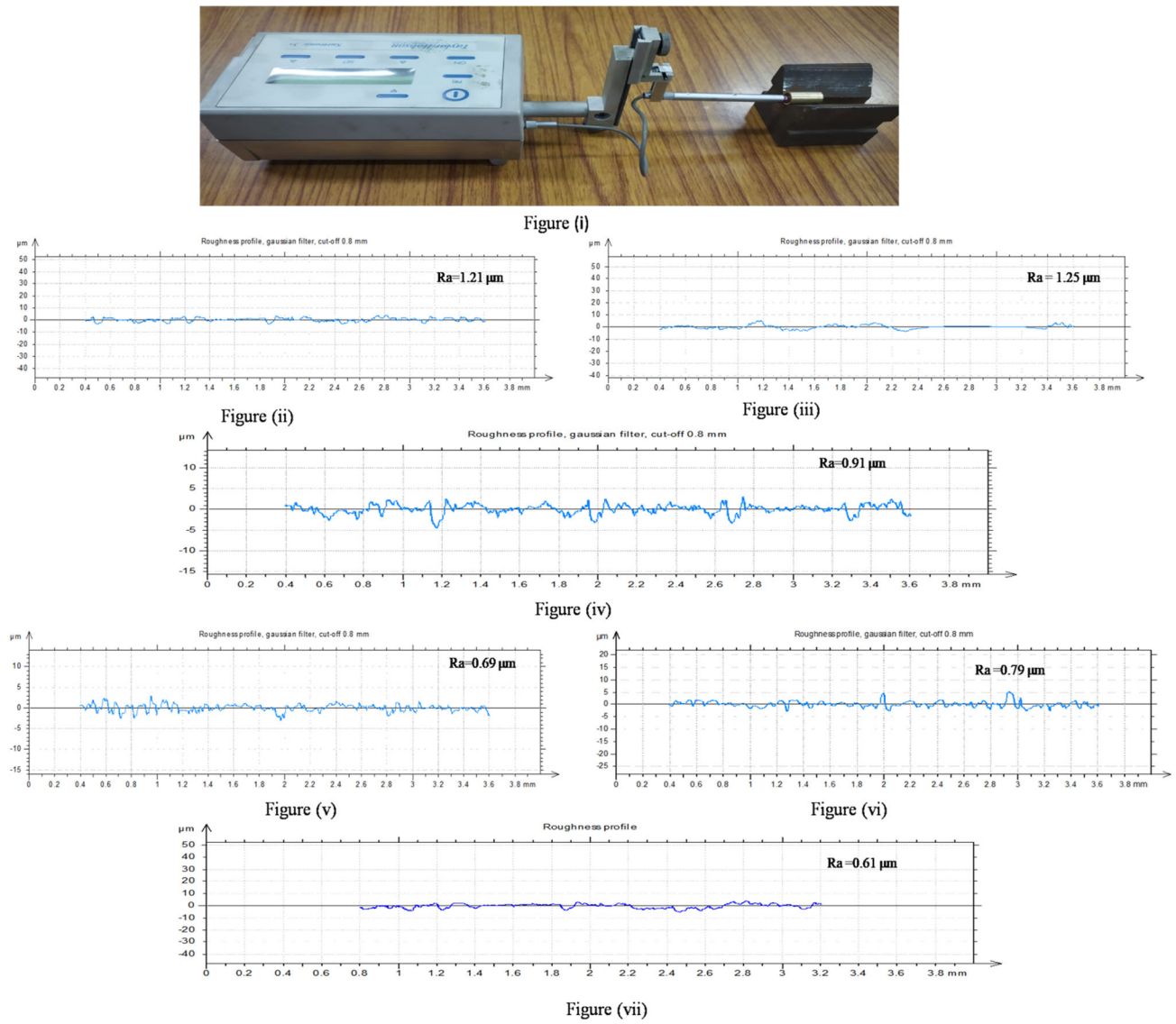


Fig. 5 Surface roughness measurement. **i** Measurement of surface roughness using Taylor Hobson Talysurf, **ii**, **iii** and **iv** surface roughness of the workpiece at different points before machining, **v**, **vi** and **vii** surface finish of the workpiece after machining

The simulation results for the pressure distributions justify that the media exerts a cutting force on the workpiece, which results in the material removal through the abrasion mechanism of the workpiece. Also, the maximum pressure obtained for the simple AFM process [18] between the same pressure ranges was about 25–30 MPa. But the value of the maximum pressure in the case of CFAAFM for the three rods ranges between 30 and 35 MPa (Fig. 6). This is due to the coaxial placement of the CFG rod between the workpiece, the effective concentration of the abrasive particles increases near the workpiece wall as the flow area is constricted due to the rod. Also, due to the rotation of the rod, the dynamic number of the abrasive particle increases near the workpiece's wall due to Coriolis's action and centrifugal force acting on the abrasive particles, which results in the increase in pressure at the workpiece surface [19].

Another observation point is that the maximum pressure is shown by the rectangular rod among the three used in the simulation. So it can be inferred that the cutting force would be maximum in the case of the rectangular rod as compared to the other rod, which results in the enhancement of material removal under identical conditions, compared to other rods.

Figure 7i–iii shows the streamlined variation of fluid during CFAAFM. The pattern of a fluid streamline (media) is similar due to the rotation of the rod in a circular- and rectangular-shaped rod, as the equal rotation of 100 rpm is given to the rod. Also, the shape is symmetrical, whereas, in a triangular rod, the pattern is different due to the

Table 4 Response characteristics (for material removal)

Exp no	RO	Material removal (mg)									Signal-to-noise ratio db
		Workpiece 1			Workpiece 2			Workpiece 3			
		$W_{specimen}$ Before machining (g)	$W_{specimen}$ After machining (g)	R_1 (mg)	$W_{specimen}$ Before machining (g)	$W_{specimen}$ After machining (g)	R_2 (mg)	$W_{specimen}$ Before machining (g)	$W_{specimen}$ After machining (g)	R_3 (mg)	
1	1	4.1842	4.1761	8.10	4.2317	4.22136	10.34	5.0123	5.0045	7.75	18.62
2	4	4.3432	4.3357	7.50	4.4123	4.4035	8.80	4.6721	4.665	7.10	17.73
3	7	4.5123	4.5031	9.20	4.2543	4.2515	2.80	4.2315	4.2239	7.60	12.821
4	2	5.7321	5.7185	13.60	4.9875	4.9744	13.10	4.5324	4.5148	17.60	23.16
5	5	4.1835	4.17515	8.35	5.0123	5.00642	5.88	4.5324	4.52304	9.36	17.39
6	8	4.1624	4.15528	7.12	5.9654	5.95497	10.43	4.3216	4.31334	8.26	18.37
7	3	5.7635	5.75226	11.24	5.2314	5.22251	8.89	4.5623	4.55177	10.53	20.06
8	6	4.9721	4.9599	12.20	4.2315	4.22139	10.11	4.6324	4.62026	12.14	21.10
9	9	4.6317	4.61956	12.14	4.7643	4.75408	10.22	4.1342	4.12633	7.87	19.651
Total				89.45			80.57			88.21	

T_{MR} = Overall mean of MR = 9.56 mg

$W_{specimen}$ = Weight of the specimen

$R_{1,2,3}$ = Responses (material removal)

Table 5 Response characteristics (for percentage improvement in surface roughness)

Exp no	RO	% Improvement in R_a									Signal-to-noise ratio db
		Workpiece 1			Workpiece 2			Workpiece 3			
		Average R_a Before machining (μm)	Average R_a After machining (μm)	R_1 (%)	Average R_a Before machining (μm)	Average R_a After machining (μm)	R_2 (%)	Average R_a Before machining (μm)	Average R_a After machining (μm)	R_3 (%)	
1	1	1.41	1.30	7.89	1.38	1.26	8.32	1.21	1.10	8.81	18.42
2	4	1.46	1.22	16.40	1.51	1.25	17.10	1.43	1.08	17.88	24.67
3	7	1.39	1.18	15.31	1.62	1.35	16.71	1.54	1.30	15.60	24.01
4	2	1.55	1.29	16.42	1.31	1.07	18.11	1.26	1.04	17.23	24.73
5	5	1.46	1.04	29.04	1.14	0.78	31.86	1.09	0.74	31.90	29.80
6	8	1.23	0.97	20.84	1.07	0.82	23.74	1.02	0.73	28.29	27.70
7	3	1.39	1.26	9.54	1.34	1.20	10.44	1.51	1.35	10.85	20.23
8	6	1.48	1.27	13.94	1.59	1.35	15.37	1.61	1.39	13.31	23.04
9	9	1.64	1.40	14.51	1.58	1.35	14.25	1.29	1.09	15.68	23.40
Total				143.89			155.90			159.53	

$T_{\%\Delta Ra}$ = Overall mean of ΔRa = 17. 01%

$R_{1,2,3}$ = Responses (% improvement in R_a)

unsymmetrical shape of the rod, which is evident from Fig. 7iii. The streamlined plots of the CFAAFM process justify the bell effects on the workpiece. The velocity value is higher, and the pressure is low at the lower part of the workpiece [20]. Also, the path of the particle can be traced using the streamlined plots. Another point of observation is that the streamline is very closed near the workpiece and passes between the minimum area between the workpiece wall and the CFG rod resulting in the dynamic increase in the number of abrasives at the workpiece wall [4].

3.2. Effect on Material Removal

Table 8 gives the MR and S/N ratio values for each parameter at three levels specified by L, followed by the subscript representing the number of levels.

Table 6 Combined response characteristics for MR and % improvement in R_a

Experiment number	RO	MR (mg)			Signal-to-noise ratio db	% Improvement in Ra			Signal-to-noise ratio db
		R1	R2	R3		R1	R2	R3	
1	1	8.10	10.34	7.75	18.62	7.89	8.32	8.81	18.42
2	4	7.50	8.80	7.10	17.73	16.40	17.10	17.88	24.67
3	7	9.20	2.80	7.60	12.821	15.31	16.71	15.60	24.01
4	2	13.60	13.10	17.60	23.16	16.42	18.11	17.23	24.73
5	5	8.35	5.88	9.36	17.39	29.04	31.86	31.90	29.80
6	8	7.12	10.43	8.26	18.37	20.84	23.74	28.29	27.70
7	3	11.24	8.89	10.53	20.06	9.54	10.44	10.85	20.23
8	6	12.20	10.11	12.14	21.10	13.94	15.37	13.31	23.04
9	9	12.14	10.22	7.87	19.651	14.51	14.25	15.68	23.40
Total		89.45	80.57	88.21		143.89	155.90	159.53	
		T_{MR} = Overall mean of MR = 9.56 mg				$T_{\%\Delta Ra}$ = Overall mean of $\%\Delta R_a$ = 17.01%			

Table 7 Responses for microhardness

Exp. no	RO	Trials for parameters			Microhardness (HV)
		S RPM	P Shape	N Extrusions	
1	1	100	R	3	244.27
2	4	100	T	6	248.89
3	7	100	C	9	250.43
4	2	200	R	6	288.67
5	5	200	T	9	291.65
6	8	200	C	3	284.12
7	3	300	R	9	378.69
8	6	300	T	3	360.54
9	9	300	C	6	371.23

Rectangular rod—R

Triangular rod—T

Circular rod—C

Figure 8 highlights the proportional increase in MR with the rotational speed at initial phase, but a marginal decrease is observed in MR after 200 rpm of the CFG rod. The abrasive particles are under the action of centrifugal and the Coriolis force due to rotation and extrusion of media [14]; as a result, a high-resultant force acts on the abrasive particles pertaining to the initial increase in MR. As the rotational speed increases continuously, the abrasive–work surface interaction increases continuously resulting in the bunting of sharp cutting edges due to which the cutting edges becomes dull and MR decreases [22].

Figure 9 demonstrates the significance of shape of CFG rod on the centrifugal force generated by CFG rod inside the media, as it depicts the throwing ability of media on the work surface. The figure shows the dominance of the rectangular-shaped rod over the other two CFG rods. This is evident from the simulation results as well, as the maximum pressure is possessed by the rectangular rod at similar conditions resulting in high cutting force over the workpiece, thus enhancing the MR [18]. Also, the throwing capability of rectangular rod is higher than the other two CFG rod. The circular rod shows the lowest throwing ability as the edges are absent pertaining to lowest MR among the three rods used [3].

It is evident from Fig. 10 that the MR increases up to six extrusions cycles and then shows a decreasing trend. With the increase in extrusions cycles, the abrasive–workpiece surface interaction increases resulting in more MR. As the

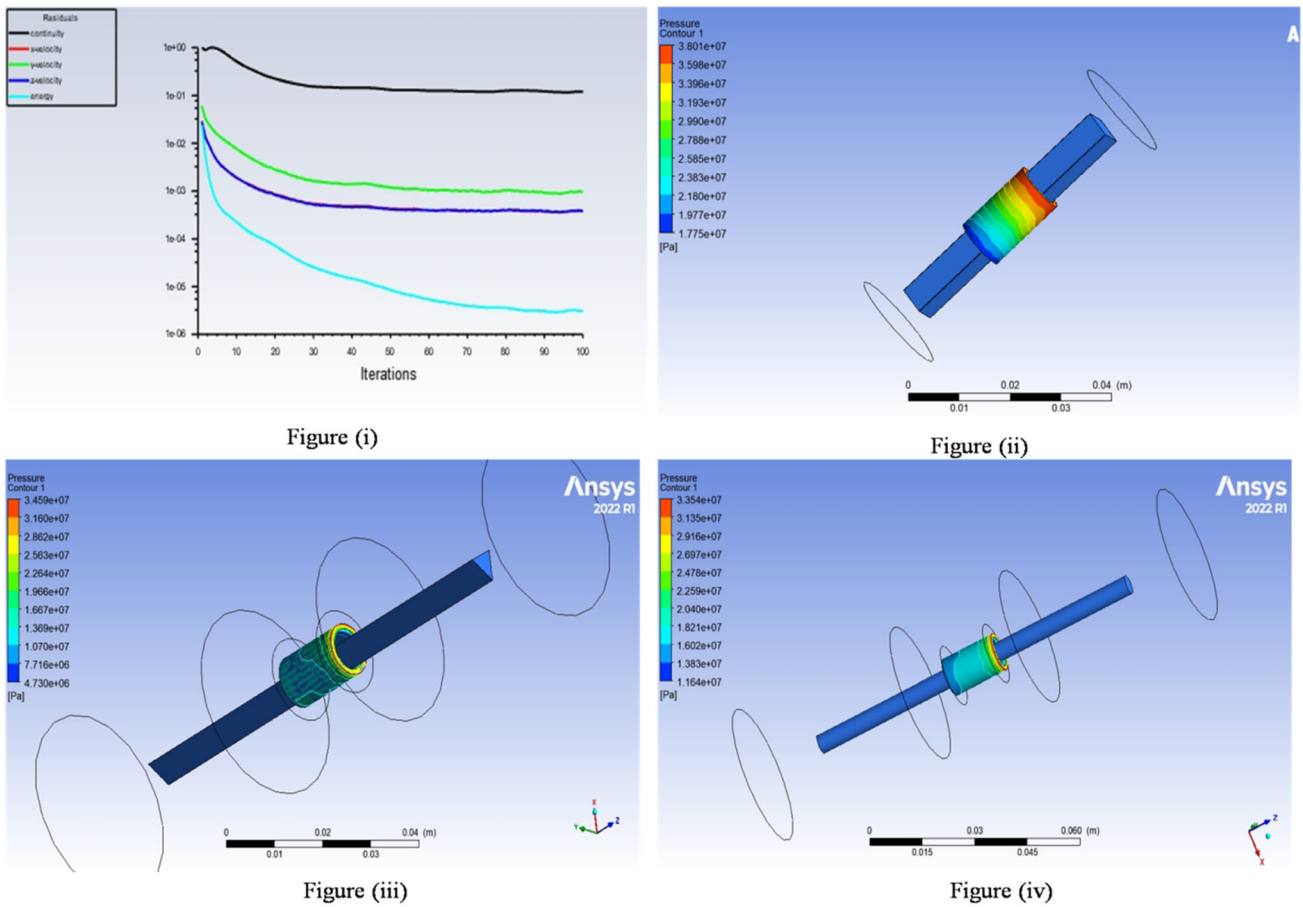


Fig. 6 Simulation results. **i** Conversion curve, **ii** pressure distribution over the workpiece by rectangular rod, **iii** pressure distribution over the workpiece by triangular rod, **iv** pressure distribution over the workpiece by circular rod

extrusion cycles increase, the media temperature also increases, affecting the viscosity of the media. The decrease in the viscosity of media results in a decrease in the dynamic number of abrasives as the abrasive holding capacity of media is reduced. This results in a significant decrease in MR at higher extrusion [18, 22].

The effects of significant parameters which affect MR are studied with ANOVA. Tables 9 and 10 show the data of ANOVA analysis on S/N and the raw data. The table indicates the parameters of rotational speed, the shape of the rod and the number of extrusion cycles majorly affect both MR and Ra values.

3.3. Effect on Percentage Improvement in Surface Roughness

Table 11 gives values of $\%\Delta R_a$ and S/N ratio for each parameter at three levels specified by L_9 orthogonal array, followed by the subscript representing the number of levels.

Figure 11 depicts that on increasing the rotational speed, $\%\Delta R_a$ increases, but the value of $\%\Delta R_a$ decreases after further raising the rotational speed. This is because, on increasing the rotational speed initially, the resultant force on abrasive particle was increased which results in enhancing MR, corresponding to an improved R_a. The value of R_a decreases with the increase in the rotational speed as the sharp cutting edges of the abrasive get dull which reduces MR and deteriorates the surface quality [22].

Figure 12 shows that the maximum $\%\Delta R_a$ occurs for a triangular-shaped rod and is the minimum for a rectangular rod. The rectangular-shaped rod has the largest throwing ability; as a result, the MR in the rectangular-shaped rod significantly increases resulting in degradation of the surface. The circular-shaped rod does not possess edges; as a result, the throwing ability is least due to which the abrasive–work surfaces interaction is less pertaining to less degradation of surface compare to the rectangular rod. The $\%\Delta R_a$ is maximum in case of triangular rod as the intermixing of abrasive laden media with polymer, gel and abrasive is better in the triangular-shaped rod as compared to the other shaped rod [18].

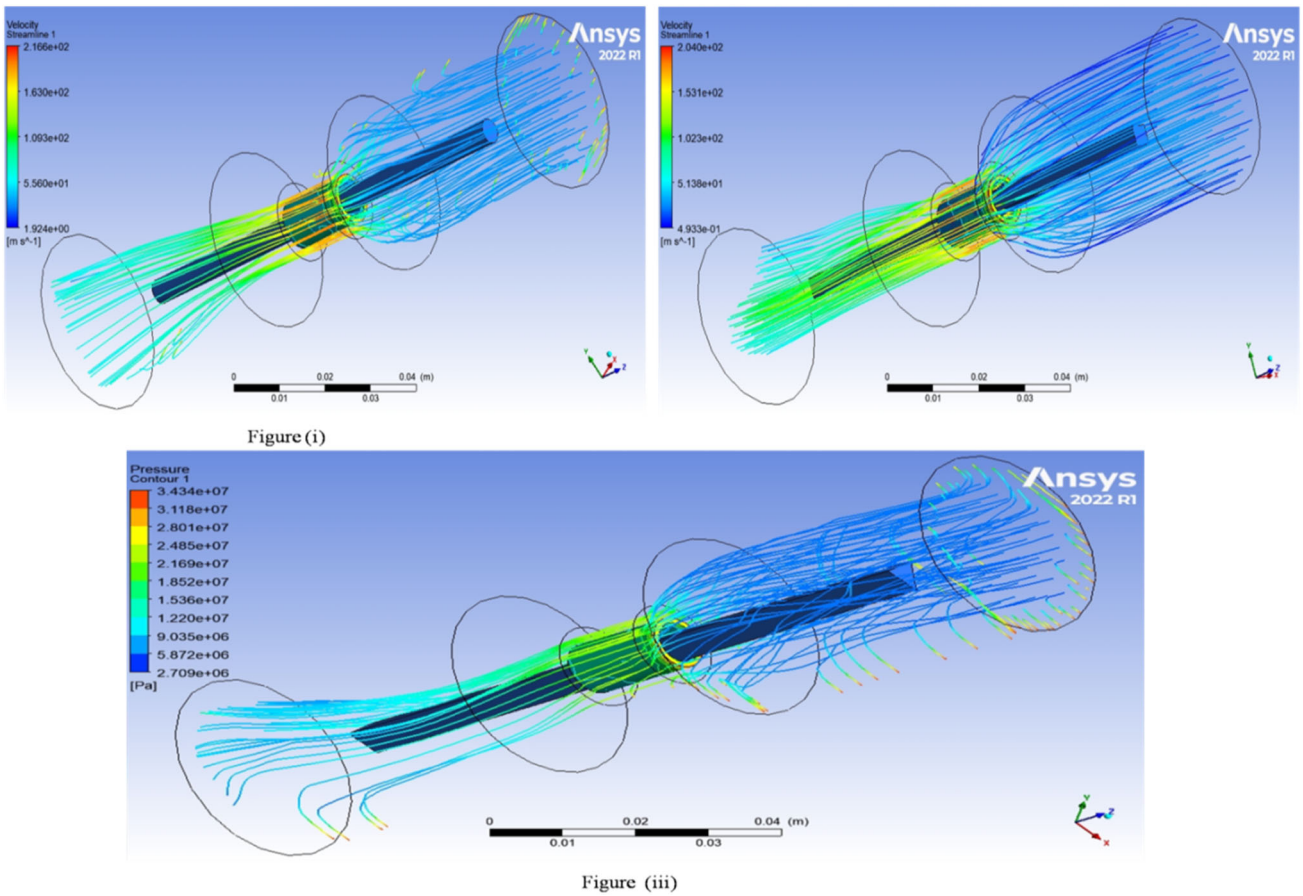


Fig. 7 Streamline plots. **i** Streamline plot of the rectangular rod, **ii** streamline plot of the circular rod, **iii** streamline plot of the triangular rod

Table 8 Average values and main effects: material removal, MR (in mg)

Process parameters	Level	Rotational speed (s)		The shape of rod (P)		No. of extrusions(N)	
Type of data		Raw data	S/N ratio	Raw data	S/N ratio	Raw data	S/N ratio
Average values (%Ra)	L1	7.68	16.39	11.23	20.61	9.60	19.36
	L2	10.41	19.64	9.04	18.74	10.88	20.18
	L3	10.59	20.27	8.40	16.95	8.20	16.75
Main effects (%Ra)	L2–L1	2.72	3.25	− 2.19	− 1.87	1.27	0.82
	L3–L2	0.18	0.62	− 0.64	− 1.79	− 2.67	− 3.42
Difference (L3–L2)–(L2–L1)		− 2.54	− 2.63	− 1.54	− 0.08	− 3.95	− 4.24

L_i—level i of a parameter

(L_j–L_i) is the average main effect when the corresponding parameter changes from level i to level j

Figure 13 shows that with the rise in extrusion, $\%\Delta R_a$ increases. The reason may be that, on raising the number of extrusion cycles, more abrasive particles contact the inner surface of the workpiece. This corresponds to an increase in the shear energy required to remove the material from the surface, increasing both MR and R_a [22]. The raw data and signal-to-noise ratio for pooled ANOVA are shown in Tables 12 and 13.

3.4. Computation of Optimum Response Characteristics

To forecast the ideal response characteristics at corresponding confidence intervals, the following steps were followed.

- The conformation experiment data were first given for verification of the best outcomes.

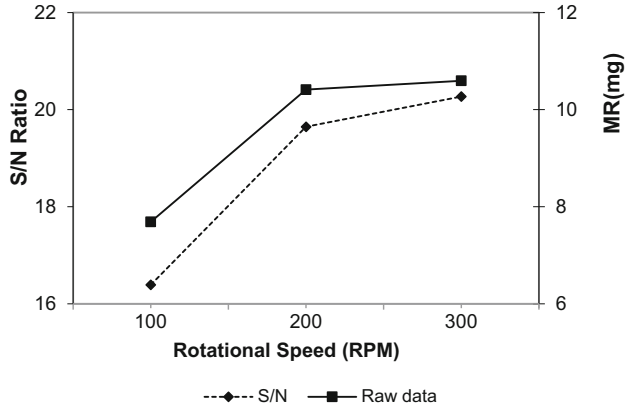


Fig. 8 Effect of rotational speed on material removal

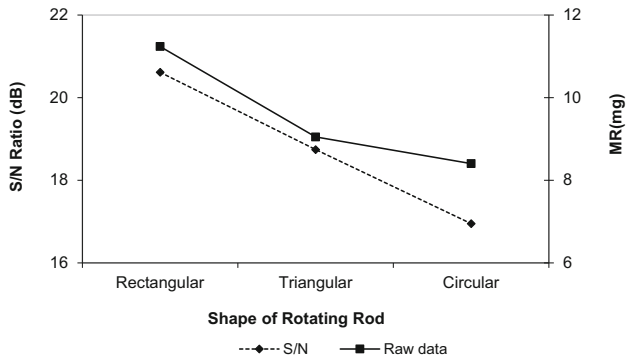


Fig. 9 Effect of shape of rotating rod on material removal

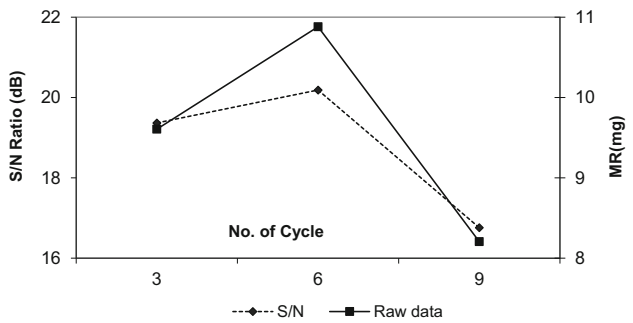


Fig. 10 Effect of number of extrusions on material removal

- Based on certain response characteristics, the ideal level of the process parameters was found.
- Each response characteristic's ideal value is anticipated using important parameters.
- CI_{CE} for CI_{POP} may or may not be 95%, according to the 95% confidence level.

$S_3P_1N_2$ are the ideal numbers for the maximum MR in both signal-to-noise ratio data and raw data. Additionally, $S_2P_2N_3$ is the optimal value for the largest per cent improvement in R_a for both raw and signal-to-noise ratio data.

3.4.1. Material Removal (MR)

The mean value for the optimal condition for MR is given by

$$\mu = \overline{S}_3 + \overline{P}_1 + N_2 - 2\overline{T} \tag{1}$$

$\overline{T}$ = 9.56 mg (mean value for overall response), $\overline{S}_3$ = 10.59 mg (MR value of the rod's RPM at level 3), $\overline{P}_1$ = 11.23 mg (MR value of Rod shape at level 1), $\overline{N}_2$ = 10.88 mg (MR value of the number of extrusions at level 2).

With these numbers, mean MR equals 13.58 mg.

The computation of the both-type confidence level is addressed in the following equations (CI_{CE} and CI_{POP}).

$$CI_{CE} = \sqrt{F_a(1, f_e)V_e\left[\frac{1}{n_{eff}} + \frac{1}{R}\right]} \tag{2}$$

$$CI_{POP} = \sqrt{\frac{F_a(1, f_e)V_e}{n_{eff}}} \tag{3}$$

The Fischer ratio corresponding to the level of confidence of (1–α) with 1 DOF is represented by F_α (1, f_e). The value of the error degree of freedom represented by f_e is 3.4928 (tabulated value)

$$n_{eff} = \frac{N}{1 + [\text{DOF associated in the estimate of mean response}]} = 3.86 \tag{4}$$

The value of F_e is taken as 20, the value of total results (represented by N in Eq. 4) is taken as 27, and the value of R (sample size) is taken as 3. The error in variance (V_e) is 4.59. The value of n_{eff} is 3.86, given by Eq. 4. The value of CI_{CE} and CI_{POP} is $\pm$ 3.08 and $\pm$ 4.15, respectively, computed using Eq. 2 and Eq. 3, respectively. The value of the optimal range at a 95 per cent confidence level using confidence interval for confirmation experiment is given by [(average M.R. $-$ CI_{CE}) $<$ M.R. $<$ (M.R. $+$ CI_{CE})] which is 10.5 $<$ MR $<$ 16.66. Similarly the value of the optimal range at a 95 per cent confidence level using confidence interval for population is given by [(average M.R. $-$ CI_{POP}) $<$ M.R. $<$ (M.R. $+$ CI_{POP})] which is 9.43 $<$ MR $<$ 17.73.

3.4.2. Percentage Improvement in $\%\Delta R_a$

The mean value for the optimal condition for $\%\Delta R_a$ is given by

Table 9 Raw data for MR pooled ANOVA

Source	Sum of square	Degree of freedom	Variance	Fischer ratio	Pure sum of square	Probability%
S	47.67	2	23.83	5.18	691.32	22.53
P	39.73	2	19.86	30.54	368.75	18.78
N	32.23	2	16.11	9.76	23.04	15.23
E	91.93	20	4.59		119.52	43.45
Total (T)	211.58	26			211.58	100

95% confidence level

F critical represents the 3.4928

S—Rotational speed

P—Shape of the rod

N—number of extrusions cycles

Table 10 S/N data material removal pooled ANOVA

Source	Sum of square	Degree of freedom	variance	Fischer ratio	Pure sum of square	Probability%
Rotational speed	26.03	2	13.01	74.64	25.68	39.59
Shape of electrode	20.15	2	10.07	57.78	19.80	30.64
No. of extrusions	19.21	2	9.60	55.10	18.86	29.22
E	0.34	2	0.17		1.39	0.53
Total (T)	65.75	8			65.75	100

95% confidence level

The value of F_{critical} is 19

Table 11 Average values and main effects: %age improvement in Ra

Process parameters	Level	Rotational speed		Shape of rod		No. of cycles	
Type of data		Raw data	Signal-to-noise ratio	Raw data	Signal-to-noise ratio	Raw data	Signal-to-noise ratio
Average values ($\%R_a$)	First level	14.78	21.95	12.03	21.10	16.61	21.96
	Second level	23.16	27.34	21.75	24.81	16.79	23.25
	Third level	13.09	21.9	18.32	25.01	18.99	24.65
Main effects (%Ra)	L2–L1	8.38	5.39	9.72	3.61	0.18	1.29
	L3–L2	− 10.07	− 6.15	− 3.43	− 0.20	2.20	1.40
Difference (L_3–L_2)–(L_2–L_1)		− 18.45	− 11.54	− 13.15	− 3.81	2.02	0.11

L_1, L_2, L_3—levels at a subsequent stage

(L_j–L_i)—Main effect for parameter change from level i to level j

$$\mu = \overline{S}_2 + \overline{P}_2 + \overline{N}_3 - 2\overline{T} \tag{5}$$

$\overline{T}$ = 17.01% (mean value for overall response), $\overline{S}_2$ = 24.16% ($\%\Delta R_a$ value of rpm at second level), $\overline{P}_2$ = 20.75% ($\%\Delta R_a$ value of shape of rod at second level), $\overline{N}_3$ = 19.03% ($\%\Delta R_a$ value of number of extrusions at third level).

With the above values, the mean value for $\%\Delta R_a$ is 29.92%. The value of F_e is taken as 20, the value of total results (represented by N in Eq. 4) is taken as 27, and the value of R (sample size) is taken as 3. The error in variance (V_e) is 3.26. The value of n_{eff} is 3.86, given by Eq. 4. The value of CI_{CE} and CI_{POP} are ± 2.59 and ± 2.94, respectively, computed using Eqs. 2 and 3, respectively.

The value of the optimal range at a 95 per cent confidence level using confidence interval for confirmation experiment is given by [(average $\%\Delta R_a - CI_{CE}) < \%\Delta R_a < (\%\Delta R_a + CI_{CE})$] which is $27.33 < \%\Delta R_a < 32.51$. Similarly the value of the optimal range at a 95 per cent confidence level using confidence interval for population is given by [(average $\%\Delta R_a - CI_{POP}) < \%\Delta R_a < \%\Delta R_a + CI_{POP})$] which is $26.98 < \%\Delta R_a < 32.86$.

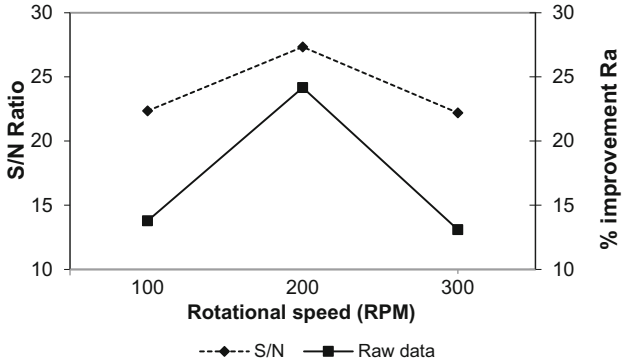


Fig. 11 Effect of rotational speed on percentage improvement in surface roughness

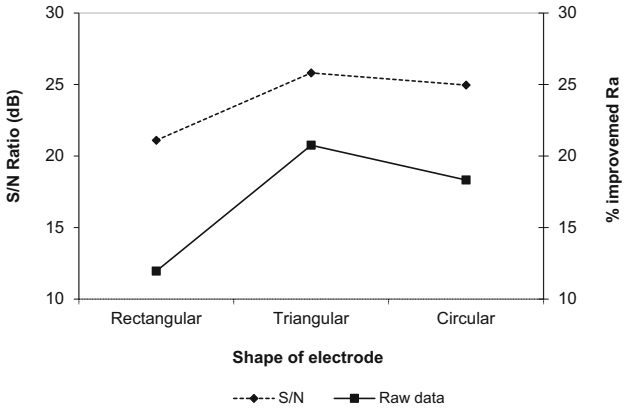


Fig. 12 Effect of shape of rod on $\%\Delta R_a$

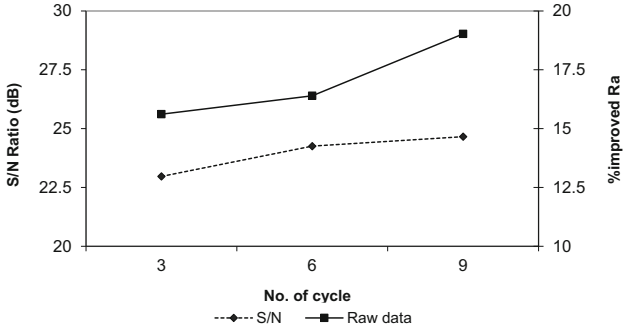


Fig. 13 Effect of number of extrusion cycle over $\%\Delta R_a$ in surface roughness

3.5. Confirmation Experiments

The optimal values for MR are $S_3P_1N_2$ and for $\%\Delta R_a$ is $S_2P_2N_3$, where S_3 is 300 rpm of CFG rod, P_1 is the rectangular shape of CFG rod and N_2 represents 6 number of extrusion cycles, S_2 represents 200 rpm of the CFG rod, P_2 represents triangular shape of CFG rod, and N_3 represents 9 number of extrusions cycles. The obtained MR and $\%\Delta R_a$ values are within 95% of the relevant response characteristics' CI_{CE}. As a result, the obtained values fall within the process parameter's specified range, as shown in Table 14.

3.6. Morphology of Finished Surface

The optical microscope is used to observe the finished workpiece after the CFAAFM process. Figure 14 shows the optical graph of the finished workpiece at 200 and 100 microns, respectively. The microimage shows the abrasion

Table 12 Raw data ($\%\Delta R_a$) pooled ANOVA

Source	Sum of squares	Degree of freedom	Variance	Fischer ratio	Pure sum of square	Probability%
Rotational speed	691.84	2	345.92	105.95	685.31	58.32
Shape of electrode	371.56	2	185.78	56.90	365.03	31.32
No. of extrusions	57.60	2	28.80	8.82	51.07	4.86
E	65.29	20	3.26		84.88	5.50
Total (T)	1186.31	26			1186.31	100

Significant at 95% confidence level, $F_{critical} = 3.4928$

Table 13 Signal-to-noise ratio data ($\%\Delta R_a$) pooled ANOVA

Source	Sum of squares	Degree of freedom	Variances	Fischer ratio	Pure sum of squares	Probability%
Rotational speed	51.30	2	25.65	429.45	51.18	54.63
Shape of electrode	37.79	2	18.90	316.43	37.68	40.25
No. of extrusions	4.67	2	2.34	39.09	4.55	4.97
E	0.1194	2	0.059		0.47	0.12
Total (T)	93.88	8			3.88	100

Significant at 95% confidence level, $F_{critical} = 19$

Table 14 Confirmation of experiments

Response characteristic	Optimal process parameters	Predicted optimal value	Confidence intervals 95%	Actual value (Average of confirmation experiments)
MR	$S_3P_1N_2$	13.58 mg	CI_{CE}: $10.5 < MR < 16.66$	15.54 mg
			CI_{POP}: $9.43 < MR < 17.73$	
$\%\Delta R_a$	$S_2P_2N_3$	29.92%	CI_{CE}: $27.33 < \%\Delta R_a < 32.51$	28.97%
			CI_{POP}:$26.98 < \%\Delta R_a < 32.86$	

CI_{CE}—confidence interval for the mean of the confirmation experiments

CI_{POP}—confidence interval for the mean of the population

MR—material removal

% ΔR_a—percentage improvement in surface finish

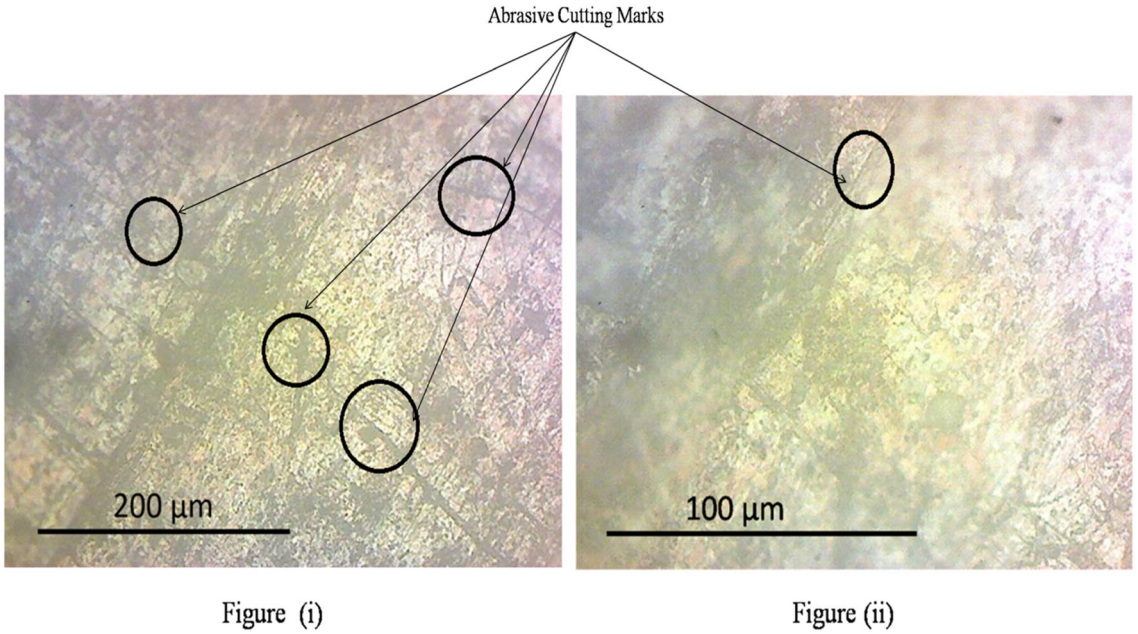


Fig. 14 Optical microscope image with abrasive marks at **i** 200× , **ii** 100×

marks produce during the media action over the workpiece. The purpose was to show the abrasive marks over the finished surface; as a result, polishing and etchant are not used for viewing the microimage. The abrasive present in the media is under the action of Coriolis and centrifugal force, due to which the action of abrasive on the surface is not uniform. As a result, the workpiece randomly strikes the surface by the action of the resultant force due to rotation and reciprocation.

Figure 15 shows the SEM images of unfinished and finished surfaces. In Fig. 15i, it is visible that irregularities occur over the surface, but as the finishing process continues, abrasive particles remove the material in the form of chips from the surface and the surface irregularities disappear after a certain number of cycles. Figure 15ii–iv clearly shows the SEM of the finished surface, which is achieved at a lesser number of cycles. Figure 15ii–iv also shows the cutting marks of abrasive particles over the surface.

Figure 16 shows the microhardness of the workpiece. The microhardness value was found 236 HV when the rod was stationary. As the rotational speed increased, microhardness of the workpiece was increased due to strain hardening. The values for microhardness at 100 rpm, 200 rpm and 300 rpm were found 250.43 HV, 291.65 HV and 378.69 HV, respectively. The increase in microhardness value may be attributed to the strain hardening of the workpiece surface. When the CFG rod rotates, the abrasive

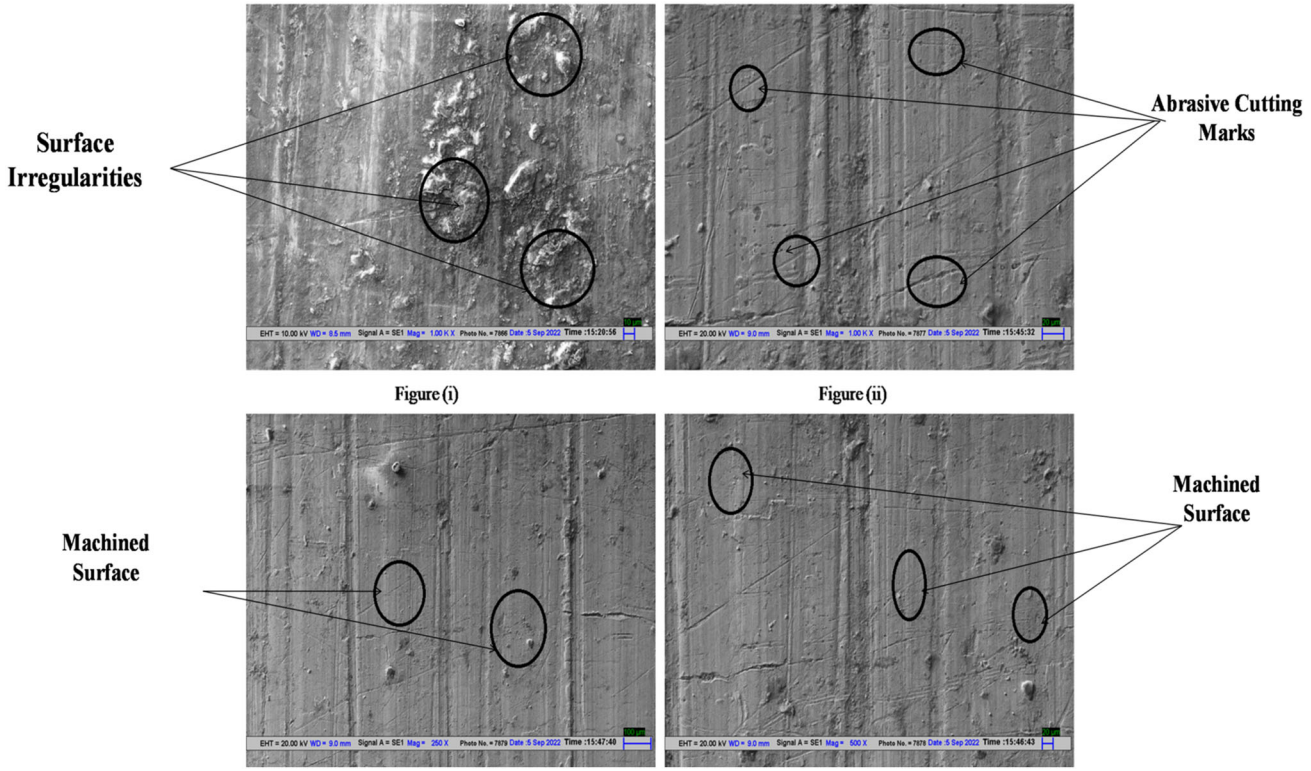


Fig. 15 SEM images. **i** Unmachined surface at 1000× magnification. **ii** Machined surface at 1000× magnification. **iii** Machined surface at 500× magnification. **iv** Machined surface at 250× magnification

particles strike the work piece's surface due to the resultant action of the centrifugal and Coriolis force, and due to this, an effect similar to shot peening occurs in the workpiece which increases the microhardness and work hardening of the workpiece surface. Evidently, with the increase in rotational speed of CFG rod, the resultant force on the abrasive would increase, resulting in higher work hardening.

Also, at zero rpm, there is no rotation of the CFG rod. The centrifugal action of the CFG rod would decrease, resulting in the abrasive rolling action over the workpiece's surface, due to which axial scouring of the work surface takes place [5].

4. Conclusions

In this research work, an effort has been made to simulate the CFAAFM through three-rod geometry. After critically analysing the results, the following conclusion can be drawn.

1. It is evident from the literature review and the experimental results that the material removal for conventional AFM is low, and hybridisation is needed to improve MR. With the improvement in material removal, there is a requirement for the optimum surface finish value, which needs to cater. Thus, a suitable hybridisation process is required to be chosen. CFAAFM is a suitable process in this regard.
2. The pressure distribution on the workpiece obtained from the simulation result for different geometry is between 16 and 35 MPa, which is in the higher range compared to the pressure distribution on the workpiece compared to the conventional AFM process, which ranges from 16 to 25 MPa, resulting in the higher cutting force and thus aiming to higher MR in case of CFAAFM process.
3. The streamlines plots obtained from the simulations results show a more significant number of streamline concentrating between the workpiece and the CFG rod, as the CFG rod constricts the passage of the media, which increases the media concentration near the wall of the workpiece, increasing the dynamic number of abrasives which enhances the material removal process.
4. The simulation result shows that the rectangular rod possesses the largest value of the maximum pressure among the three rods selected, with a value of 38.54 MPa, indicating higher cutting force and the highest MR. The experimental results validate that a

		HM	EIT/ (1-vs^2)	HV
Mean value	x. :	1964.63 N/mm²	115.39 GPa	236.33
Confid.interval	q :	------ N/mm²	------ GPa	------
Standard. Dev.	s :	------ N/mm²	------ GPa	------
No of Readings	n :	1	1	1
Min. Reading	:	1964.6 N/mm²	115.4 GPa	236.3
Max. Reading	:	1964.6 N/mm²	115.4 GPa	236.3
Range	R :	------ N/mm²	------ GPa	------
Range/%	R/%:	0.00	0.00	0.00

Test parameter

F = 300.000mN/20s
C = 5.0s
R = Same as load increase
C = ---
T = ---

Designations of the Test Parameters described in ISO 14577-1

HM	0.300 / 20.0 / 0.0
EIT/(1-vs^2)	0.300 / 20.0 / 5.0 / 11.2
HV	0.031

Calculation of tangent with Power Law Method
20.00% - 100.00% Fmax Epsilon = 0.750

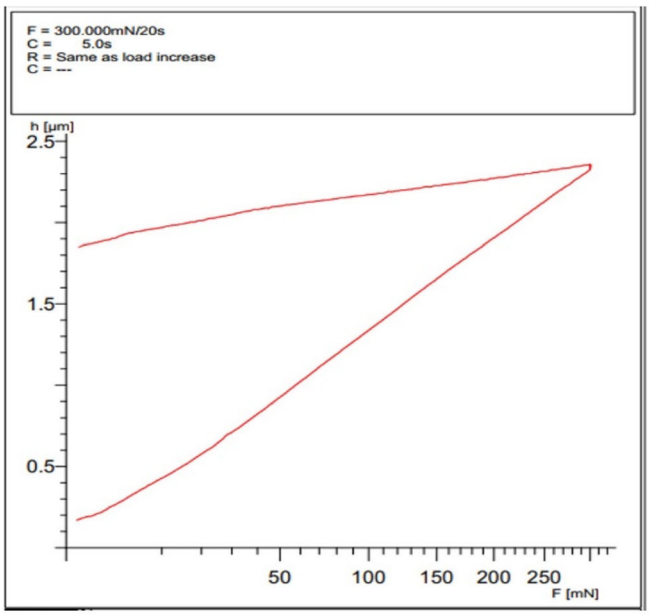


Figure (i)

WIN-HCU® DIN 50 359 / ISO 14577 fischer®

Block No: 1 B L O C K R E S U L T 19-04-2018 12:48:31
Application: 38.hap Operator: administrator

		HM	EIT/ (1-vs^2)	HV
Mean value	x. :	2014.23 N/mm²	96.35 GPa	250.43
Confid.interval	q :	------ N/mm²	------ GPa	------
Standard. Dev.	s :	------ N/mm²	------ GPa	------
No of Readings	n :	1	1	1
Min. Reading	:	2014.2 N/mm²	96.4 GPa	250.4
Max. Reading	:	2014.2 N/mm²	96.4 GPa	250.4
Range	R :	------ N/mm²	------ GPa	------
Range/%	R/%:	0.00	0.00	0.00

Test parameter

F = 500.000mN/20s
C = 5.0s
R = Same as load increase
C = ---
T = ---

Designations of the Test Parameters described in ISO 14577-1

HM	0.500 / 20.0 / 0.0
EIT/(1-vs^2)	0.500 / 20.0 / 5.0 / 11.1
HV	0.051

Calculation of tangent with Power Law Method
20.00% - 100.00% Fmax Epsilon = 0.750

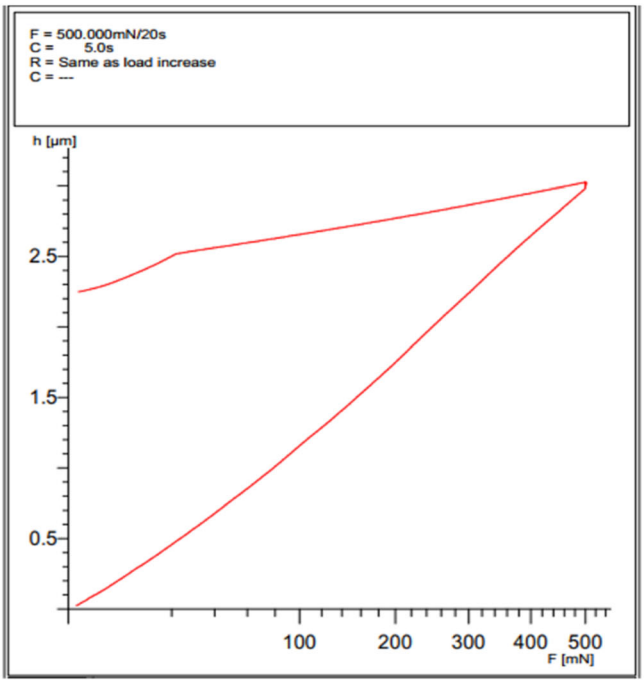


Figure (ii)

Fig. 16 Microhardness, **i** microhardness at zero RPM of CFG rod, **ii** microhardness at 100 RPM of CFG rod, **iii** microhardness at 200 RPM of CFG rod, **iv** microhardness at 300 RPM of CFG rod

rectangular-shaped rod is an optimised parameter for MR.

5. The experimental results show that for the material removal, machining with the rectangular rod rotating at 300 rpm and with media oscillating six times between the pressure differences of 20 MPa would give an optimal value of 15.54 mg.
6. For the percentage improvement in surface finish, it is observed that rotating a triangular-shaped rod at 200 rpm with nine oscillating cycles between the pressure differences of 20 MPa would serve the

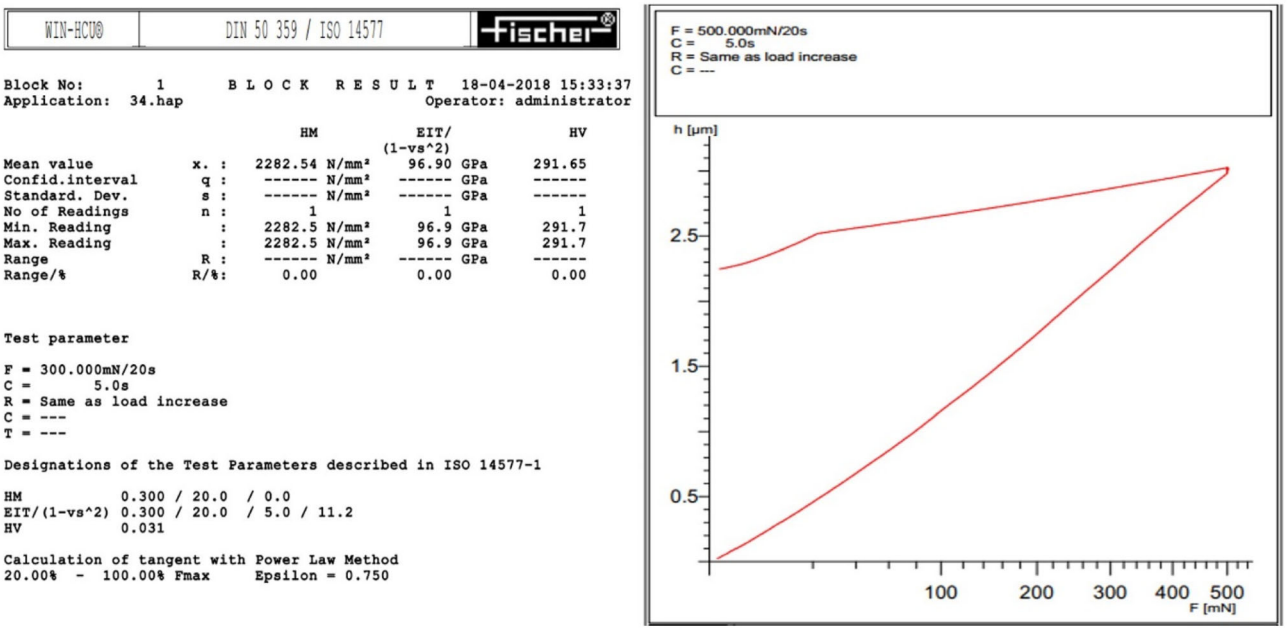


Figure (iii)

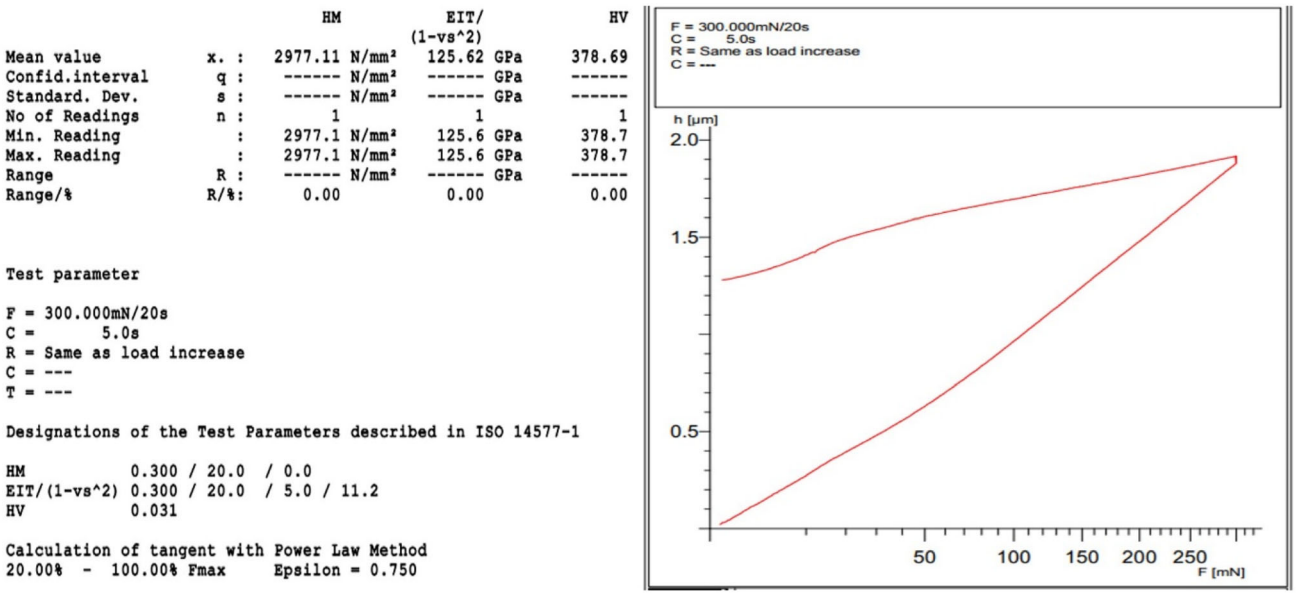


Figure (iv)

Fig. 16 continued

optimal finishing result, with the optimal value of 28.97 per cent.

7. The value of MR obtained from the model is 12.61 per cent higher than the experimental values, whereas the difference in modelled and actual value is 3.17 per cent for percentage roughness in surface finish.
8. For MR and percentage improvement in surface finish, rotational speed is the primary contributing parameter, with 22.53 per cent for MR and 58.32 for % ΔR_a. The shape of the electrode contributes 18.78 per cent in MR and 31.32 per cent % ΔR_a. The number of extrusions contributes the least, with 15.23 per cent in MR and 4.86 per cent in % ΔR_a.

9. The predicted optimal for the material removal is $10.5 < \text{MR} < 16.66$, and the percentage improvement in the surface roughness is $27.33 < \%\ \Delta R_a < 32.51$. The range for MR at a ninety-five per cent interval is $9.43 < \text{MR} < 17.73$ and for $\%\ \Delta R_a$ is $26.98 < \%\ \Delta R_a < 32.86$.
10. The SEM images and optical micrograph validate the work surface's machining process with abrasive marks highlighting the abrasion process.
11. The microhardness value was found 236 HV when the rod was stationary. As the rotational speed increased, microhardness of the workpiece was increased due to strain hardening. The values for microhardness at 100 rpm, 200 rpm and 300 rpm were found 250.43 HV, 291.65 HV and 378.69 HV respectively. The increase in microhardness with the RPM corresponds to the work hardening of the workpiece due to the action of abrasive on the work surface under the centrifugal and Coriolis force.

Acknowledgements The authors thank the Delhi Technological University for providing a Research fellowship to cater for the financial requirement.

References

[1] P. Ali, S. Dhull, R.S. Walia, Q. Murtaza and M. Tyagi, Hybrid abrasive flow machining for nano finishing—a review. Mater. Today Proc., *4*(8) (2017) 7208–7218. https://doi.org/10.1016/j.matpr.2017.07.048.

[2] A. Bhardwaj, P. Ali, R.S. Walia, Q. Murtaza and S.M. Pandey, Development of hybrid forms of abrasive flow machining process: a review. In: K. Shanker et al (eds) Advances in industrial and production engineering lecture notes in mechanical engineering, Springer, Berlin (2019), pp. 41–67.

[3] R.S. Walia, H.S. Shan and P. Kumar, Parametric optimisation of centrifugal force-assisted abrasive flow machining (CFAAFM) by the Taguchi method. J. Mater. Manuf. Process. (2006). https://doi.org/10.1080/10426910500411645.

[4] R.S. Walia, H.S. Shan and P.K. Kumar, Determining dynamically active abrasive particles in the media used in centrifugal force assisted abrasive flow machining process. Int. J. Adv. Manuf. Technol., *38* (2008) 1157–1164. https://doi.org/10.1007/s00170-007-1184-8.

[5] R.S. Walia, H.S. Shan and P. Kumar, Morphology and integrity of surfaces finished by centrifugal force assisted abrasive flow machining. Int. J. Adv. Manuf. Technol., *39*(11) (2008) 1171–1179. https://doi.org/10.1007/s00170-007-1301-8.

[6] M.R. Sankar, S. Mondal, J. Ramkumar and V.K. Jain, Experimental investigations and modelling of drill bit guided abrasive flow finishing (DBG-AFF) process. Int. J. Adv. Manuf. Technol., *42*(7–8) (2009) 678–688. https://doi.org/10.1007/s00170-008-1642-y.

[7] B.S. Barr, R.S. Walia, V.P. Singh and M. Sharma, A robust helical abrasive flow machining process (HLX-AFM). J. Inst. Eng. India Ser. C, *94*(1) (2013) 21–29. https://doi.org/10.1007/s40032-012-0054-9.

[8] M.K. Sankar, V.K. Jain and J. Ramkumar, Rotational abrasive flow finishing process and its effects on a finished surface. Int. J. Mach. Tools Manuf., *50*(7) (2010) 637–650. https://doi.org/10.1016/j.ijmachtools.2010.03.007.

[9] S. Singh and H.S. Shan, Development of magneto abrasive flow machining process. Int. J. Mach. Tools Manuf., *42* (2002) 953–959. https://doi.org/10.1016/S0890-6955(02)00021-4.

[10] A.K. Sharma, P. Kumar and S. Rajesh (2011) An improved ultrasonic abrasive flow machining. Patent number 3578/DEL/201, India.

[11] L. Dabrowski, M. Marciniak, W. Wieczarek and A. Zygmunt, Advancement of abrasive flow machining using an anodic solution. J. New Mater. Electrochem. Syst., *9* (2006) 439–445.

[12] R. Singh, R.S. Walia and N.M. Suri, Parametric optimisation of a centrifugal-magnetic force assisted abrasive flow machining process using utility concept. Int. J. Res. Eng. Technol., *4*(8) (2015) 2321–2730.

[13] R. Vaishya, R.S. Walia and P. Kalra, Design and development of hybrid electrochemical and centrifugal force assisted abrasive flow machining. In 4th international conference on materials processing and characterisation. Mater Today Proc (2015) 2:3327–3341. https://doi.org/10.1016/j.matpr.2015.07.158.

[14] P. Ali, R.S. Walia, Q. Murtaza and R.M. Singari, Material removal analysis of hybrid EDM-assisted centrifugal abrasive flow machining process for performance enhancement. J. Braz. Soc. Mech. Sci. Eng., *42* (2020) 302. https://doi.org/10.1007/s40430-020-02375-6.

[15] P. Ali, R.S. Walia, Q. Murtaza and M.S. Ranganath, Modeling and analysis of developed thermal additive centrifugal abrasive flow machining process. Surf. Topogr. Metrol. Prop., *8* (2020) 035013. https://doi.org/10.1088/2051-672X/abaffe.

[16] P. Ali, R.S. Walia, Q. Murtaza and R.M. Singari, Characterisation of finished surface through thermal additive centrifugal abrasive flow machining for better surface integrity. Indian J. Eng. Mater. Sci., *29* (2022) 29–44.

[17] A. Bhardwaj, S. Krovvidi and R. Chaudhary, Modelling of wind turbine magnet for magnetic abrasive finishing and magnetic force assisted abrasive flow machining process. J. Eng. Res. ICARI Spec. Issue (2021). https://doi.org/10.36909/jer.ICARI.15291.

[18] A. Bhardwaj, Computational and experimental analysis of parameters in centrifugal force assisted abrasive flow machining process, Diss. Delhi Technological University (2019)

[19] A. Bhardwaj, S. Krovvidi and R. Chaudhary, Modelling and simulation of abrasive flow machining. IJAPIE, *6*(2) (2021) 01–09. https://doi.org/10.35121/ijapie202104251.

[20] K. Srinivas and A. Bharadwaj, Pressure variation in abrasive flow machining: modelling and simulation. IJAPIE, *3*(4) (2018) 15–19.

[21] Y. Seifu, S.S. Kumar and S.S. Hiremath, Modelling and simulation: machining of mild steel using indigenously developed abrasive flow machine global colloquium in recent advancement and effectual researches in engineering. Science and Technology (RAEREST 2016). Procedia Technol., *25* (2016) 1312–1319. https://doi.org/10.1016/j.protcy.2016.08.230.

[22] P. Ali, S.M. Pandey, M.S. Ranganath, R.S. Walia and Q. Murtaza, Experimentation and modelling of CNT additive abrasive media for microfinishing. Measurement, *151* (2020) 107–133. https://doi.org/10.1016/j.measurement.2019.107133.

[23] N. Dixit, V. Sharma and P. Kumar, Development and characterisation of Xanthan Gum based abrasive media and performance analysis using abrasive flow machining. J. Manuf. Process., *67* (2021) 101–115. https://doi.org/10.1016/j.jmapro.2021.04.053.

[24] Z. Zhenzhong, Z. Xianpeng, L. Xiao, Z. Peifa, Y. Peng, H. Chuanzhen, L. Hanlian, Z. Hongtao, B. Zoua, Preparation and

application of a novel water-based viscoelastic polishing fluid for abrasive flow machining. In: CIRP biomanufacturing conference (2019). https://doi.org/10.1016/j.procir.2020.05.153.

[25] A. Chaudhari, A. Sharma, A.S. Awale, M.Z.Y. Khan and M. Vashista, Modeling and simulation study of dry ultrasonic vibration-assisted grinding of tool steel with single alumina abrasive grit. ASME J. Manuf. Sci. Eng., *144*(11) (2022) 111001. https://doi.org/10.1115/1.4054602.

[26 K. Srinivas, Q. Murtaza and A.K. Aggarwal, Modelling of viscoelastic fluid in finishing processes. Int. J. Sci. Technol. Res., *8*(09) (2019) 2277–8616.

[27] A. Chaudhari, A. Sharma, A.S. Awale, M.Z.Y. Khan and M. Vashista, Experimental analyses into dry ultrasonic vibration-assisted grinding of difficult-to-machine tool steel with alumina wheel. J. Mater. Eng. Perform. (2022). https://doi.org/10.1007/s11665-022-07444-6.

[28] M.A. Manjunath, V. Prakash, N. Balashanmugam and M.R. Sankar, Abrasive flow finishing for surface roughness improvement of aluminium propeller: a case study. Mater. Today Proc., *26* (2020) 1113–1118. https://doi.org/10.1016/j.matpr.2020.02.223.

[29] R. Baraiya, A. Babbar, V. Jain and D. Gupta, In-situ simultaneous surface finishing using abrasive flow machining via novel fixture. J. Manuf. Process., *50* (2020) 266–278. https://doi.org/10.1016/j.jmapro.2019.12.051.

[30] S. Han, F. Salvatore, J. Rech and J. Bajolet, Abrasive flow machining (AFM) finishing of conformal cooling channels created by selective laser melting (SLM). Precis. Eng. (2020). https://doi.org/10.1016/j.precisioneng.2020.03.006.

[31] S. Han, F. Salvatore, J. Rech, J. Bajolet and J. Courbon, Effect of abrasive flow machining (AFM) finish of selective laser melting (SLM) internal channels on fatigue performance. J. Manuf. Process. (2020). https://doi.org/10.1016/j.jmapro.2020.09.065.

[32] C.W. Kuma, C.H. Wu, S. Wan and C.W. Kang, Prediction and compensation of material removal for abrasive flow machining of additively manufactured metal components. J. Mater. Process. Technol. (2020). https://doi.org/10.1016/j.jmatprotec.2020.116704.

Publisher's Note Springer Nature remains neutral with regard to jurisdictional claims in published maps and institutional affiliations.

Springer Nature or its licensor (e.g. a society or other partner) holds exclusive rights to this article under a publishing agreement with the author(s) or other rightsholder(s); author self-archiving of the accepted manuscript version of this article is solely governed by the terms of such publishing agreement and applicable law.

Journal of Electronic Materials
https://doi.org/10.1007/s11664-023-10240-0

ORIGINAL RESEARCH ARTICLE

Analytical Modelling and Simulation of a Junctionless Accumulation-Mode Tube (JLAMT) Field-Effect Transistor (FET) for Radiation Sensing Dosimeter Applications

Sia Batra[1] · **Sonam Rewari**[2]

Received: 30 July 2022 / Accepted: 10 January 2023
© The Minerals, Metals & Materials Society 2023

Abstract
In this paper, an analytical model for a junctionless accumulation-mode-based nanotube field-effect transistor (JLAM-NT-FET) is proposed for radiation sensing dosimeter applications. The drift in electrical parameters including potential, threshold voltage (V_{th}), drain current (I), and subthreshold slope (SS) for different values of interface trap charge is studied in depth. The numerical findings accord well with the those of the simulation, and the numerical/analytical results are also validated at different channel lengths. The sensitivity of the proposed design is compared with the conventional junctionless FET for dosimeter applications by analysing the differences in I_{ds}, I_{ON}/I_{OFF} ratio, g_m, SS, V_{th} and sensitivity. The results indicate that the JLAM-FET demonstrates better radiation sensing than the conventional junctionless FET.

Keywords Silicon · dosimeter · trap charges · radiation · dielectric engineered · FET · transconductance

Introduction

Devices that are aggressively scaled have a variety of issues, including drain-induced barrier lowering, short-channel effects (SCE), and hot carrier effects.[1] The SCEs can be reduced to a great extent using surrounding-gate (SG) and multi-gate metal–oxide–semiconductor field-effect transistors (MOSFETs).[2–5] The most efficient device architecture among them is that of the SG MOSFET, which improves gate dominance over the channel, reduces corner effects, and indeed modulates the threshold voltage but with less current driving. Because of the increased current, ideal off-state properties, high-density integration, and restricted area compensation, nanotubes have recently attained substantial relevance.[6] When compared at the chip level with the SG MOSFET, nanotube field-effect transistors (NFET) have an output that is 13 times greater[6–9] and have a multi-fold gain in performance. The dual cylindrical gate effect produced by the presence of a core gate and a shell gate in NFETs increases the gate control. However, a number of devices have been developed to address the scaling-related issues. The junctionless transistor stands out among these devices as having the highest potential for gradient-free doping concentration and the best high thermal annealing for dopant activation. However, there are certain drawbacks to junctionless transistors, including reduced mobility and high metal work function.[10,11] The junctionless accumulation-mode FET (JLAM-FET) was proposed to overcome these limitations. Strongly doped source and drain regions reduce mobility deterioration while also simplifying fabrication.[12]

Ionizing radiation negatively affects the performance of Si microelectronic devices by trapping charge in oxides and causing the formation of interface traps.[13] Radiation has many different uses, and is obtained from many sources; radiation therapy is one such application. Calculating the radiation emitted by a source and the radiation absorbed by a substance is therefore essential. The threshold voltage changes as the ionizing radiation permeates the oxide and generates a charge that is trapped permanently. The MOSFET dosimeter uses the threshold voltage theory to function; although it is less sensitive, it is linear in relation to absorbed dosage.[14] A dosimeter sensor for measuring absorbed dose according to the radiation dose induced on the interface of

✉ Sonam Rewari
rewarisonam@gmail.com

Sia Batra
siabatra@gmail.com

[1] Delhi Public School, Vasant Kunj, Delhi, India

[2] Department of Electronics and Communication Engineering, Delhi Technological University, Delhi, India

Published online: 04 April 2023

SiO2/Si was developed using a junctionless accumulation-mode-based field-effect transistor for radiation sensing dosimeter applications due to the highly sensitive surface. AlGaN MOS high-electron-mobility transistor (HEMT)-based dosimeters were also developed by Ruby et al. for the detection of radiation[15] by varying the concentration of trap charges.

JLAMT-FET Structure and Simulation

The three-dimensional cylindrical structure and two-dimensional cross-sectional view of the JLAMT-FET dosimeter are shown in Fig. 1a and b, respectively. A cavity of 1 nm is embedded inside the gate oxide layer of the JLAMT-FET dosimeter for inserting the radiation and thereby carrying out radiation detection. Using the findings from our Silvaco ATLAS device simulator[13] for identical device dimensions, we calibrated the experimental work of Fan et al.[14] to ensure that our simulation was accurate. The results are displayed in Fig. 1c. It was found that the results are quite similar to those from our simulation. The simulations are performed on an ATLAS Silvaco 3D device simulator.[16] The parametric values of the devices are given in Table I and the device parameters are given in Table II. The variation in trap charge is directly related to the change in the radiation. This is because, to realize the MOSFET as a radiation sensor (RADFET), the RADFET can be biased or unbiased during irradiation. With some biasing at the gate terminal, electron–hole pairs are generated in the oxide by the radiation, and further increasing the biasing at the gate terminal will increase the density of the trap charges.[17] These electron–hole pairs are transported to the interface of Si/SiO_2 and will result in either an increase or a decrease in the flat-band voltage of the device, and this change will shift the threshold voltage accordingly.[18]

$$V_{\text{fbeff}} = V_{\text{fb}} \pm \frac{qN_{\text{f}}}{C_{\text{ox}}} \tag{1a}$$

Radiation Sensing Dosimeter Analytical Model

By resolving the two-dimensional Poisson equation in cylindrical coordinates, it is possible to realize the mathematical interpretations of the subthreshold current (I_{sub}) and potential. The formulas for surface potential and I_{sub} are generated using the superposition approach[19] and appropriate boundary constraints. According to Trivedi et al.,[20] the two-dimensional Poisson equation is as follows:

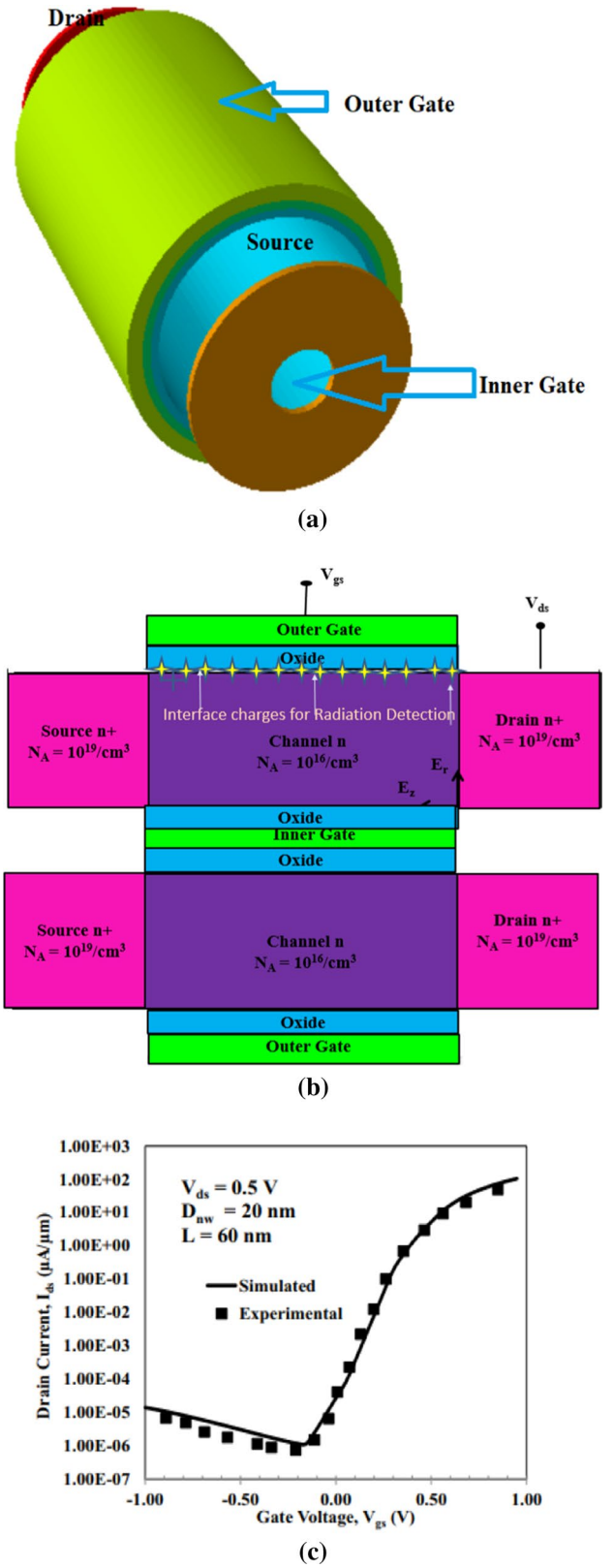


Fig. 1 (a) 3D device structure of the JLAMT-FET dosimeter, (b) 2D device structure of the JLAMT-FET dosimeter, (c) calibration.

$$\frac{1}{r}\frac{\partial}{\partial r}\Phi(r,z)+\frac{\partial}{\partial r^2}\Phi(r,z)+\frac{\partial}{\partial z^2}\Phi(r,z)=-\frac{qN_{\mathrm{D}}}{\varepsilon_{\mathrm{si}}} \tag{1b}$$

where N_{D} is the doping concentration, and $\Phi(r,z)$ gives the potential distribution in the channel region. The definitive potential solution can be broken down into the following by using the superposition technique: $V(r)$ is a one-dimensional long-channel solution, and $U(r, z)$ is a two-dimensional short-channel solution.

$$\Phi(r,z)=V(z)+U(r,z) \tag{2}$$

The 1D Poisson equation and 2D Laplace equation can now be used to rewrite Eq. 1:

$$\frac{1}{r}\frac{\partial}{\partial r}(V(r))+\frac{\partial^2}{\partial r^2}V(r)=\frac{-qN_{\mathrm{D}}}{\varepsilon_{\mathrm{si}}} \tag{3}$$

$$\frac{1}{r}\frac{\partial}{\partial r}(U(r,z))+\frac{\partial^2}{\partial r^2}U(r,z)+\frac{\partial^2}{\partial z^2}U(r,z)=0 \tag{4}$$

The boundary conditions used to solve the 2D potential are as follows:

$$\Phi(t,z)=\Phi_{\mathrm{os}}(z) \tag{5}$$

$$\Phi(t-t_{\mathrm{si}},z)=\Phi_{\mathrm{is}}(z) \tag{6}$$

Table I Parametric values of the devices

Device specification	JLAMT-FET-based dosimeter	JLAM-FET-based dosimeter
Length of the channel (nm)	30	30
Doping of the channel region (cm^3)	1×10^3	1×10^{19}
Thickness of silicon (nm)	20	20
Metal gate work function (eV)	5.2	5.0
Source/drain length (nm)	15	15
Permittivity of silicon, $\varepsilon_{\mathrm{si}}$	$3.9_{\varepsilon 0}$	$3.9_{\varepsilon 0}$
Thickness of silicon oxide, t_{SiO2} (nm)	5	5
Thickness of interface trap charges (nm)	1	1

$$\left.\frac{\partial\Phi(r,z)}{\partial r}\right|_{r=t_{\mathrm{eff}}}=-\Delta(V_{\mathrm{gs}}-\Phi_{0\mathrm{s}}(z)) \tag{7}$$

$$\left.\frac{\partial\Phi(r,z)}{\partial r}\right|_{r=t_{\mathrm{eff}}-t_{\mathrm{si}}}=-\Delta(V_{\mathrm{gs}}-\Phi_{\mathrm{is}}(z)) \tag{8}$$

$$\Phi(r,L)=V_{\mathrm{bi}} \tag{9}$$

$$\Phi(r,L)=V_{\mathrm{bi}}+V_{\mathrm{ds}} \tag{10}$$

$$C_{\mathrm{ax}}=\frac{2\varepsilon_{\mathrm{ax}}}{\left(t_{\mathrm{m}}+t_{t_{\mathrm{ax}}}\right)\ln\left(1+\frac{2t_{\mathrm{ax}}}{\left(t_{\mathrm{m}}+t_{t_{\mathrm{ax}}}\right)}\right)} \tag{11}$$

$\Phi_{\mathrm{os}}(z)\rightarrow$ consistent outer surface potential, $\Phi_{\mathrm{is}}(z)\rightarrow$ consistent inner surface potential, t_{ox} is the thickness of the oxide, $\varepsilon_{\mathrm{ox}}$ is the dielectric permittivity of the oxide, and $\varepsilon_{\mathrm{bio}}$ is the dielectric permittivity of the biomolecules.

The solution of Eq. 3 can now be realized as a parabolic approximation:

$$V(r)=P_0+P_1r+P_2r^2 \tag{12}$$

where $P_0=V_{\mathrm{gseff}}-P_1\left(t+\frac{1}{\Delta}\right)-P_2\left(t^2+\frac{2t}{\Delta}\right)$, $P_1=-\delta\left(t_{\mathrm{eff}}-\frac{t_{\mathrm{si}}}{2}\right)$ $P_2=\delta/2$, $\delta=\frac{-qN_{\mathrm{d}}}{\varepsilon_{\mathrm{si}}}$, $V_{\mathrm{gseff}}=V_{\mathrm{gs}}-V_{\mathrm{fb}}+\frac{qN_{\mathrm{f}}}{C_{\mathrm{ox}}}$ $V_{\mathrm{fb}}=\phi_{\mathrm{m}}$ $-(\chi_{\mathrm{Si}}-q\phi_{\mathrm{f}})\rightarrow$ flat-band voltage, $V_{\mathrm{gs}}\rightarrow$ applied gate-to-source voltage, $N_{\mathrm{f}}\rightarrow$ biomolecule charged density, $\chi_{\mathrm{Si}}\rightarrow$ electron affinity of silicon, $q\phi_{\mathrm{f}}\rightarrow$ channel Fermi potential.

The solution of Eq. 4 can be obtained as:

$$U(r,z)=\sum_{n=1}^{\infty}J_0(\alpha_n r)(M_n\exp(\alpha_n z)+N_n\exp(-\alpha_n z)) \tag{13}$$

with J_0 and $J_1\rightarrow$ Bessel functions of order 0 and 1, respectively, M_n and N_n are constants calculated using boundary conditions (9) and (10) and are given in the Appendix, α_n is the eigenvalues of:

$$J_1\left(\frac{t_{\mathrm{eff}}}{\alpha_{\mathrm{n}}}\right)=\frac{\mathrm{C}_{\mathrm{ox}}}{\alpha_{\mathrm{n}}\varepsilon_{\mathrm{si}}}J_0\left(\frac{t_{\mathrm{eff}}}{\alpha_{\mathrm{n}}}\right) \tag{14}$$

The 2D potential can be given as:

Table II Models used for simulation

Simulation model	Type	Description
Mobility model	Lombardi-CVT model	Appropriate for non-planar structures along with inversion region modelling
Recombination model	SRH (Schottky–Read–Hall) model	Appropriate for carrier lifetimes
Concentration-dependent model		Appropriate for SRH recombination with their lifetimes
Energy transport model	Drift–diffusion model	Appropriate for numerical techniques
Statistics	Boltzmann model	Appropriate for considering carrier statistics

$$\Phi(r,z) = \mathrm{V}(r) + \sum_{n=1}^{\infty} J_0(\alpha_n r)(M_n \exp(\alpha_n z) + N_n \exp(-\alpha_n z)) \tag{15}$$

where $\alpha_n = {}^1/_{\eta_n}$.

I_{sub}[21] is:

$$I_{sub} = 2R\pi\mu kT\eta_i \frac{1 - e^{\frac{-qV_{ds}}{kT}}}{\int_0^L 1 \Big/ \int_0^{t_{eff}} e^{\frac{q\Phi(r,z)}{kT}} dr\,dz} \tag{16}$$

where the Boltzmann constant $k = 1.38 \times 10^{-23}$ J/K, $T = 300$ K, intrinsic carrier density $\eta_i = 1.45 \times 10^{10}$ cm^{-3}, and electron mobility $\mu = 1300$ cm^2/Vs.

Results and Discussion

Figure 2 shows the electron velocity (E_v) across the channel. At the beginning of the gate (the end of the source region), E_v increases sharply; thereafter, it increases progressively across the channel. The acceleration of electrons at the gate along with an extremely strong fringing electric field is responsible for this increase.

Figure 3 shows the impact of tap charges (-1×10^{-12}, no trap charges, 1×10^{-12}) on the drain characteristics (I_{ds} w.r.t. V_{gs}) for dosimeter applications for the JLAM-FET and JLAMT-FET. The trap charges are inserted into the gate oxide, and by varying the concentration of the trap charges, the change in the drain current is analysed in depth. It can be clearly understood from the figure that the JLAMT-FET shows a larger deviation in I_{ds} than the JLAM-FET for detecting the change in radiation. Because the tube structure possesses two gates, the drain current undergoes a greater amount of variation. The potential improves the I_{ds} and radiation detection by increasing the transverse electric field and gate transfer efficiency.

Figure 4 shows the impact of trap charges (-1×10^{-12}, no trap charges, 1×10^{-12}) on the I_{ON}/I_{OFF} ratio for dosimeter applications for the JLAM-FET and JLAMT-FET. A device must effectively function as a switch in order to be used for digital applications, making switching speed a critical criterion for assessing the device performance, which can be expressed as:

$$\frac{I_{ON}}{I_{OFF}} = \frac{I_{ds(ON)atVgs} = 1.0\ \mathrm{V}}{I_{ds(OFF)atVgs} = 0.0\ \mathrm{V}} \tag{17}$$

As can be seen from the figure, the greater regulation along the channel increases the sensitivity of the JLAMT-FET, and therefore the change in the I_{ON}/I_{OFF} ratio is greater in the JLAMT-FET than in the JLAM-FET. It is evident from the figure that a higher drift in the ratio is obtained

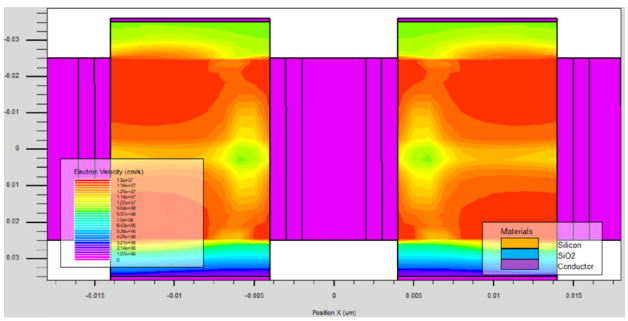


Fig. 2 Electron velocity across the channel.

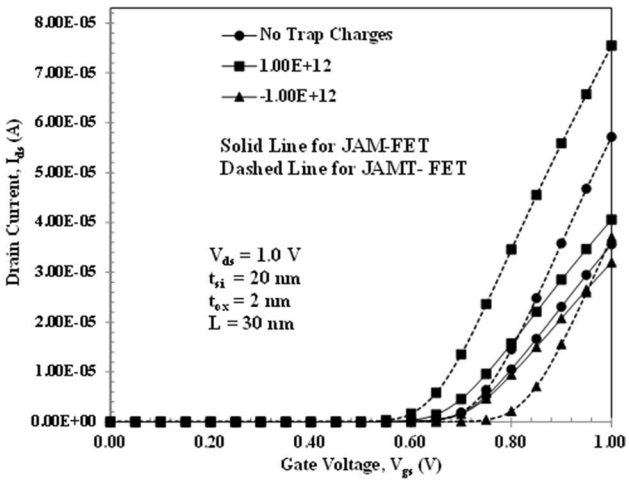


Fig. 3 Impact of trap charges on drain characteristics for dosimeter applications.

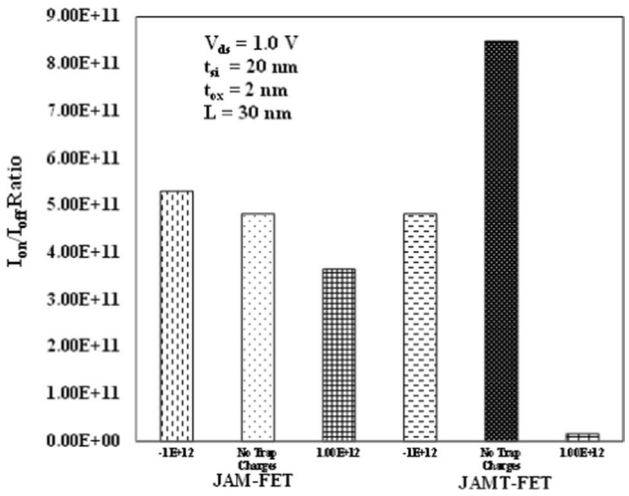


Fig. 4 Impact of trap charges on the I_{ON}/I_{OFF} ratio for dosimeter applications.

when the JLAM-FET is utilized for detecting various radiation because of a supplemental inner core gate that shows effective performance by the charge carriers across the channel.

Figure 5 shows the impact of trap charges (-1×10^{-12}, no trap charges, 1×10^{-12}) on the conductance characteristics (g_m w.r.t. V_{gs}) for dosimeter applications for the JLAM-FET and JLAMT-FET. The trap charges are inserted into the gate oxide, and by varying the concentrations of the trap charges, the change in the conductance is analysed in depth. It can be clearly understood from the figure that the JLAMT-FET shows a larger deviation in conductance characteristics (g_m w.r.t. V_{gs}) for dosimeter applications than the JLAM-FET for detecting the change in radiation. Because the tube structure possesses two gates, the drain current undergoes a greater amount of variation. The potential improves I_{ds} and radiation detection by increasing the transverse electric field and gate transfer efficiency.

Figure 6 shows the impact of trap charges on the SS for dosimeter applications for the JLAM-FET and JLAMT-FET. The theoretical value of the subthreshold slope (SS) is around 60 mV/decade, and it also regulates the switching capacity of a device. The greater regulation along the channel increases the sensitivity of the JLAMT-FET, and therefore the change in SS is higher in the JLAMT-FET than in the JLAM-FET. It is evident from the figure that there is a higher drift in the ratio when the JLAM-FET is utilized for detecting various radiation because of a supplemental inner core gate that shows effective performance by the charge carriers across the channel. It should be highlighted that due to the reduced screening of carriers in nanowires, the sensitivity of tube FET sensors may be exponentially improved in the subthreshold region where the gating action of molecules bonded to a surface is most effective.

A device's V_{th} (threshold voltage) is defined as the lowest V_{gs} at which a MOSFET switches ON and begins conduction. Figure 7 shows the impact of trap charges (-1×10^{-12}, no trap charges, 1×10^{-12}) on V_{th} for dosimeter applications for the JLAM-FET and JLAMT-FET. The trap charges are inserted into the gate oxide, and by varying the concentrations of the trap charges, the change in the threshold voltage is analysed in depth. It can be clearly understood from the figure that the JLAMT-FET exhibits a larger deviation in V_{th} for dosimeter applications than the JLAM-FET for detecting the change in radiation. Because the tube structure possesses two gates, the drain current undergoes a greater amount of variation.

Figure 8 shows the impact of trap charges (-1×10^{-12}, no trap charges, 1×10^{-12}) on sensitivity for dosimeter

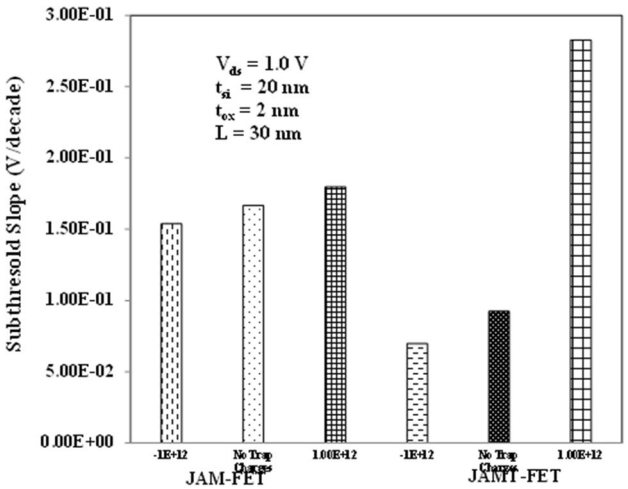


Fig. 6 Impact of trap charges on SS for dosimeter applications.

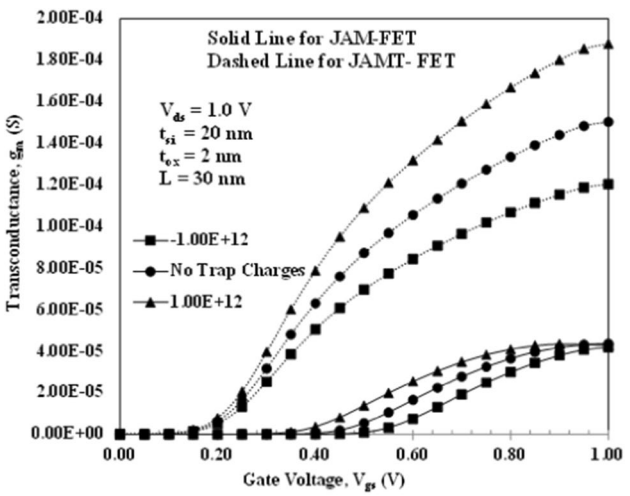


Fig. 5 Impact of trap charges on g_m for dosimeter applications.

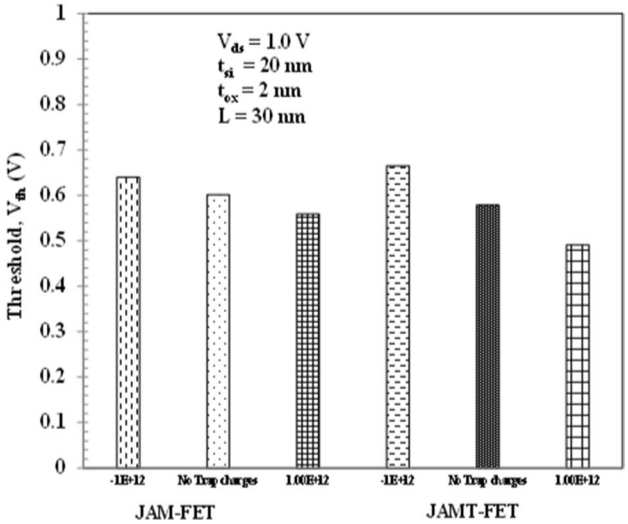


Fig. 7 Impact of trap charges on V_{th} for dosimeter applications.

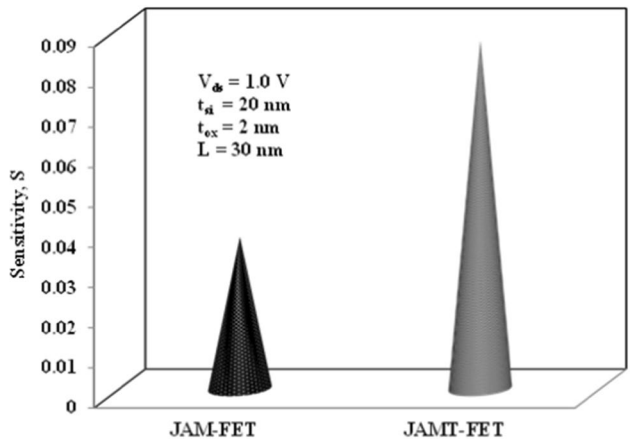


Fig. 8 Impact of trap charges on sensitivity for dosimeter applications.

applications for the JLAM-FET and JLAMT-FET. The trap charges are inserted into the gate oxide, and by varying the concentrations of the trap charges, the change in the sensitivity is analysed in depth by studying the change in the threshold voltage. It can be clearly understood from the figure that the JLAMT-FET exhibits a larger deviation in sensitivity for dosimeter applications than the JLAM-FET for detecting the change in radiation. Because the tube structure possesses two gates, the drain current undergoes a greater amount of variation.

Figure 9 shows the potential distribution for the JLAMT-FET dosimeter for (a) negatively charged trap charges, (b) no charges, and (c) positively charged trap charges. The reduction in the charge control linear region, which results in the potential shift towards the source region, causes the minimum potential at the centre of the channel to increase as the channel length decreases, as can be clearly seen.[22] This source potential then influences the minimum potential at the centre of the channel. The numerical findings accord well with those of the simulation. It can be inferred from the figures that there is a considerable change in potential on changing the concentration of trap charges.

Figure 10 shows the subthreshold current for the JLAMT-FET dosimeter for (a) negatively charged trap charges, (b) no charges, and (c) positively charged trap charges. It should be noted that the I_{OFF} increases as the channel length decreases. SCEs, which appear as the channel length decreases,[22] are the cause of this increase in I_{OFF}. The numerical findings accord well with those of the simulation. It can be inferred from the figure that there is a considerable change in current on changing the concentration of trap charges.

Figure 11 shows the subthreshold slope for the JLAMT-FET dosimeter for negatively charged trap charges, no charges,

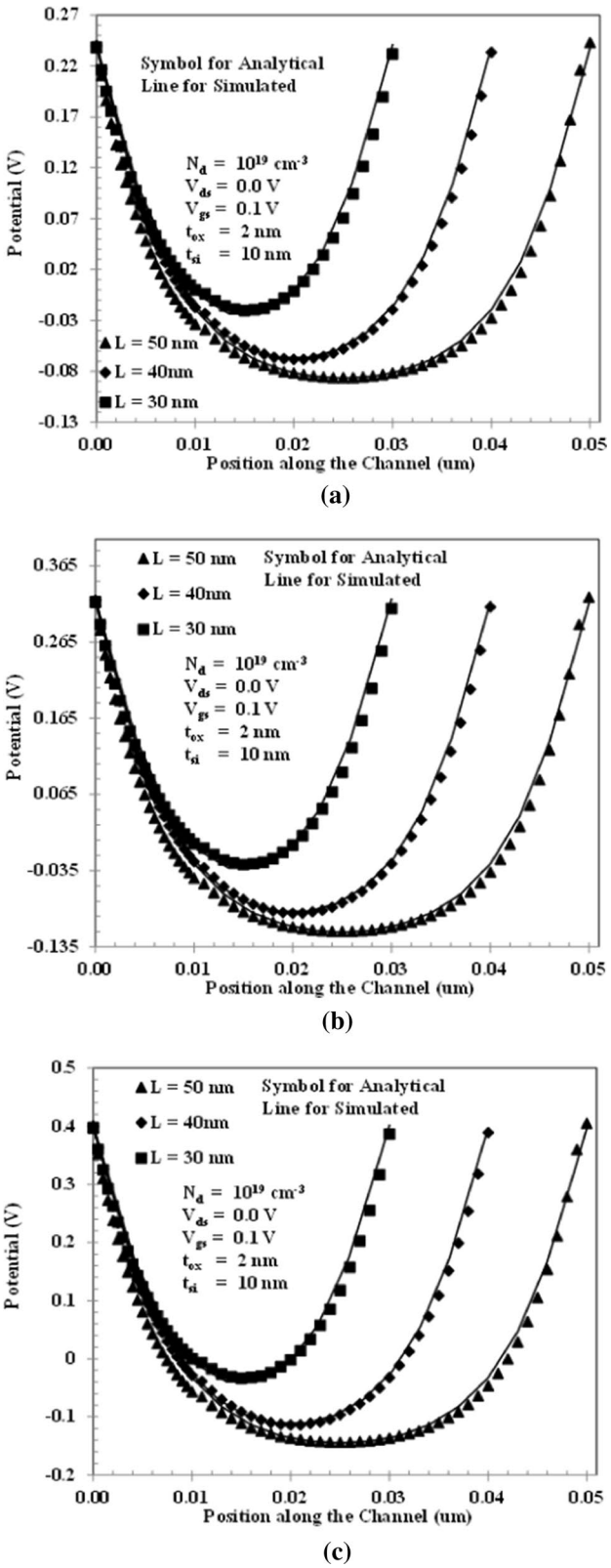


Fig. 9 Potential distribution for the JLAMT-FET dosimeter for (a) negatively charged trap charges, (b) no charges, (c) positively charged trap charges.

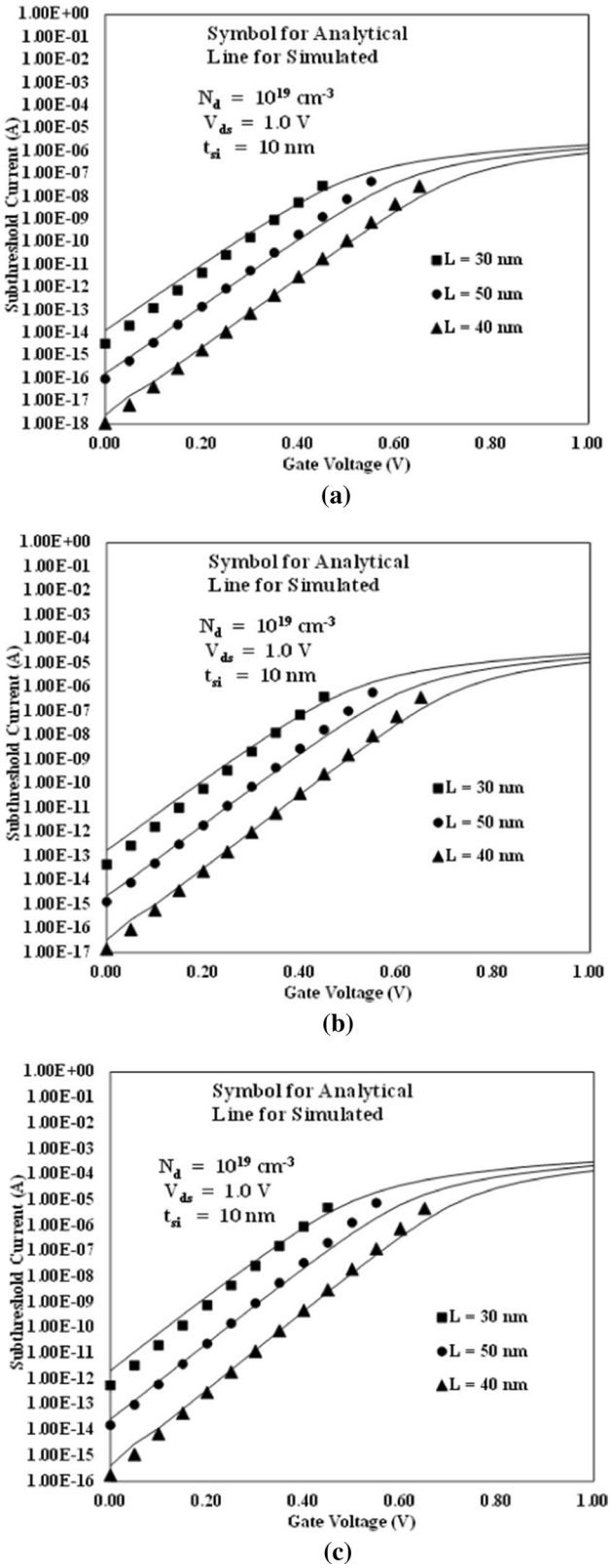


Fig. 10 Subthreshold current for the JLAMT-FET dosimeter for (a) negatively charged trap charges, (b) no charges, (c) positively charged trap charges.

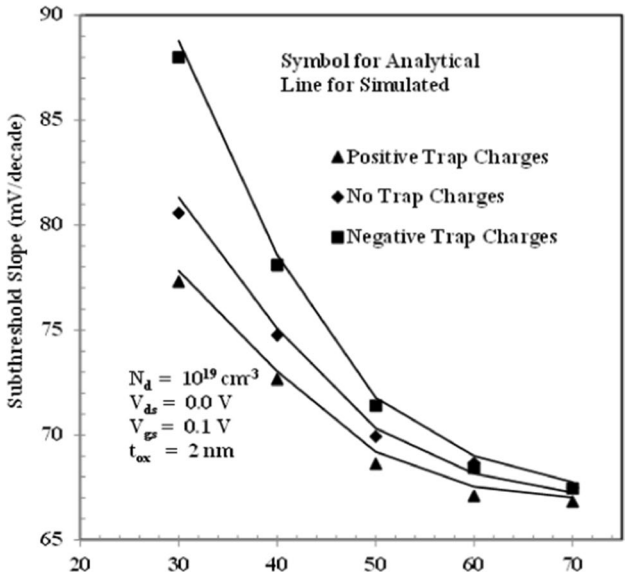


Fig. 11 Subthreshold slope for the JLAMT-FET dosimeter for negatively charged trap charges, no charges, positively charged trap charges.

and positively charged trap charges. It can be clearly seen that there is considerable deviation in current on changing the concentration of trap charges, owing to the change in the potential across the channel.

Conclusion

An analytical model has been proposed for a junctionless accumulation-mode-based nanotube field-effect transistor (JLAM-NT-FET) for radiation sensing dosimeter applications. The drift in electrical parameters including potential, threshold voltage (V_{th}), drain current (I_{ds}), and subthreshold slope (SS) for different values of interface trap charges was studied in depth. The numerical findings accord well with those of the simulation, and the numerical/analytical results were validated at different channel lengths. The sensitivity of the proposed design was compared with a conventional junctionless FET for dosimeter applications by analysing the difference in I_{ds}, I_{ON}/I_{OFF} ratio, g_m, SS, V_{th}, and sensitivity. The results indicate that the JLAM-FET shows better radiation sensing than the conventional junctionless FET.

Appendix 1

$$M_n = \frac{L_{2n} - L_{1n}\exp\left(-\eta_n L\right)}{2\sinh\left(\eta_n L\right)} \tag{A1}$$

$$N_{\mathrm{n}} = \frac{L_{1\mathrm{n}} \exp\left(\eta_{\mathrm{n}} L\right) - L_{2\mathrm{n}}}{2 \sinh\left(\eta_{\mathrm{n}} L\right)} \tag{A2}$$

$$L_{1\mathrm{n}} = \frac{2}{t^2 J_1^2\left(\eta_{\mathrm{n}} t_{\mathrm{eff}}\right)} \left[\left(V_{\mathrm{bi}} - V_{\mathrm{gseff}} + \frac{t_{\mathrm{si}}}{2} \right) \frac{t_{\mathrm{eff}} J_1\left(\eta_{\mathrm{n}} t_{\mathrm{eff}}\right)}{\eta_{\mathrm{n}}} + \frac{\wp t_{\mathrm{eff}}}{\eta_{\mathrm{n}}^2} \left\{ t_{\mathrm{eff}} J_2\left(\eta_{\mathrm{n}} t_{\mathrm{eff}}\right) - \left(t_{\mathrm{eff}} - \frac{t_{\mathrm{eff}}}{2} \right) \left(\frac{J_1\left(\eta_{\mathrm{n}} t_{\mathrm{eff}}\right)}{\eta_{\mathrm{n}} t_{\mathrm{eff}} - 1} - J_0\left(\eta_{\mathrm{n}} t_{\mathrm{eff}}\right) \right) \right\} \right] \tag{A3}$$

$$L_{2\mathrm{n}} = \frac{2}{t^2 J_1^2\left(\eta_{\mathrm{n}} t_{\mathrm{eff}}\right)} \left[\left(V_{\mathrm{bi}} + V_{\mathrm{ds}} - V_{\mathrm{gseff}} + \frac{t_{\mathrm{si}}}{2} \right) \frac{t_{\mathrm{eff}} J_1\left(\eta_{\mathrm{n}} t_{\mathrm{eff}}\right)}{\eta_{\mathrm{n}}} + \frac{\wp t_{\mathrm{eff}}}{\eta_{\mathrm{n}}^2} \left\{ t_{\mathrm{eff}} J_2\left(\eta_{\mathrm{n}} t_{\mathrm{eff}}\right) - \left(t_{\mathrm{eff}} - \frac{t_{\mathrm{eff}}}{2} \right) \left(\frac{J_1\left(\eta_{\mathrm{n}} t_{\mathrm{eff}}\right)}{\eta_{\mathrm{n}} t_{\mathrm{eff}} - 1} - J_0\left(\eta_{\mathrm{n}} t_{\mathrm{eff}}\right) \right) \right\} \right] \tag{A4}$$

Author Contributions The authors have contributed equally regarding this paper.

Funding None.

Conflict of interest There are no conflicts of interest amongst the authors.

Consent for Publication All the authors have complete consent for publication.

Ethical Approval All the ethics have been followed.

Human or Animal Rights Research involving human participants and/or animals. No animals or humans were harmed during this research.

Informed Consent All the authors have informed consent.

Consent to Participate All the authors have complete consent to participate.

References

1. N. Mendiratta and S.L. Tripathi, A review on performance comparison of advanced MOSFET structures below 45 nm technology node. *J. Semicond.* (2020). https://doi.org/10.1088/1674-4926/41/6/061401.
2. B. Yu, H. Lu, M. Liu, and Y. Taur, Explicit continuous model for double gate and surrounding gate MOSFET. *IEEE Trans. Electron Device* 54(10), 2715 (2007). https://doi.org/10.1109/TED.2007.904410.
3. P. Kumar, D. Joy, and B.K. Jeblin, Nanoscale tri-gate MOSFET for Ultra low power applications using high-k dielectrics, Nanoelectronics, in *2013, INEC 2013, 5th IEEE International Conference on 2e412–19*. (2013).
4. D. Jimenez, J.J. Saenz, B. Iniguez, J. Sune, L.F. Marsal, and J. Pallares, Modeling of nanoscale gate-all-around MOSFETs. *IEEE Electron Device Lett.* 25(5), 314 (2004). https://doi.org/10.1109/LED.2004.826526.
5. K.H. Yeo, S.D. Suk, M. Li, Y. Yeoh, K.H. Cho, K.-H. Hong, S. Yun, M.S. Lee, N. Cho, K. Lee, D. Hwang, B. Park, D.W. Kim, D. Park, and B.-I. Ryu, Gate-All-Around (GAA) Twin Silicon Nanowire MOSFET (TSNWFET) with 15 nm Length Gate and 4 nm Radius Nanowires. International Electron Devices Meeting https://doi.org/10.1109/IEDM.2006.346838. (2006), pp. 1–4.
6. V.M. Srivastava, K.S. Yadav, and G. Singh, Drain current and noise model of cylindrical surrounding double gate MOSFET for RF switch. *Procedia Eng.* 38, 517 (2012). https://doi.org/10.1016/j.proeng.2012.06.064.
7. S. Rewari, V. Nath, S. Haldar, S.S. Deswal, and R.S. Gupta, Improved analog and AC performance with increased noise immunity using nanotube junctionless field effect transistor (NJLFET). *Appl. Phys. A* 122, 1049 (2016). https://doi.org/10.1007/s00339-016-0583-9.
8. A. Goel, S. Rewari, S. Verma, and R.S. Gupta, Novel dual-metal junctionless nanotube field-effect transistors for improved analog and low-noise applications. *J. Electron. Mater.* 50, 108 (2021). https://doi.org/10.1007/s11664-020-08541-9.
9. A. Goel, S. Rewari, S. Verma, and R.S. Gupta, Dielectric modulated junctionless biotube FET (DM-JL-BT-FET) bio-sensor. *IEEE Sens. J.* 21(15), 16731 (2021). https://doi.org/10.1109/JSEN.2021.3077540.
10. S. Sahay and M.J. Kumar, Fundamentals of Junctionless Field-Effect Transistors, *Junctionless Field-Effect Transistors*. (Wiley, 2019), pp. 67–123. https://doi.org/10.1002/9781119523543.ch3.
11. A. Nowbahari, A. Roy, and L. Marchetti, Junctionless transistors: state-of-the-art. *Electronics* 9(7), 1 (2020). https://doi.org/10.3390/electronics9071174.
12. T.K. Kim, D.H. Kim, Y.G. Yoon, J.M. Moon, B.W. Hwang, D.I. Moon, G.S. Lee, D.W. Lee, D.E. Yoo, H.C. Hwang, J.S. Kim, Y.-K. Choi, B.J. Cho, and S.-H. Lee, First demonstration of junctionless accumulation-mode bulk FinFETs with robust junction isolation. *IEEE Electron Device Lett.* 34(12), 1479 (2013). https://doi.org/10.1109/LED.2013.2283291.
13. M. Soubra, J. Cygler, and G. Mackay, Evaluation of a dual bias dual metal oxide-silicon semiconductor field effect transistor detector as radiation dosimeter. *Med. Phys.* 21(4), 567 (1994). https://doi.org/10.1118/1.597314.
14. T. Cheung, M.J. Butson, and K.N. Peter, Effects of temperature variation on MOSFET dosimetry. *Phys. Med. Biol.* 49(13), N191 (2004). https://doi.org/10.1088/0031-9155/49/13/n02.
15. R. Mann, S. Rewari, P. Pal, S. Sharma, and R.S. Gupta, Radiation-sensitive AlGaN/GaN MOS-HEMT-based dosimeter. *J. Electron. Mater.* 51, 5609 (2022). https://doi.org/10.1007/s11664-022-09795-1.
16. ATLAS: 3D Device Simulator, SILVACO International, (2022)
17. A.B. Rosenfeld, Semiconductor detectors in radiation medicine: radiotherapy and related applications, *Radiation detectors for medical applications, NATO Security through Science Series*. (Dordrecht: Springer, 2006), pp. 111–147.
18. A. Dubey, M. Gupta, R. Narang, and M. Saxena, Comparative Study of CMOS based Dosimeters for Gamma Radiation, in *2018 4th International Conference on Devices, Circuits and Systems (ICDCS)*, pp. 117–120, https://doi.org/10.1109/ICDCSyst.2018.8605158. (2018).
19. A. Goel, S. Rewari, S. Verma, and R.S. Gupta, Temperature-dependent gate-induced drain leakages assessment of dual-metal nanowire field-effect transistor—analytical model. *IEEE Trans. Electron Devices* 366(5), 2437 (2019). https://doi.org/10.1109/TED.2019.2898444.
20. N. Trivedi, M. Kumar, S. Haldar, S.S. Deswal, M. Gupta, and R.S. Gupta, Analytical modelling of junctionless accumulation mode MSOFET (JAM-CSG). *Int. J. Numer. Modell Electron. Netw. Devices Fields* 29(6), 1036 (2016). https://doi.org/10.1002/jnm.2162.
21. J.P. Colinge, C.W. Lee, A. Afzalian, N.D. Akhavan, R. Yan, I. Ferain, P. Razavi, B. O'Neill, A. Blake, M. White, A. Kelleher, B. McCarthy, and R. Murphy, Nanowire transistors without

junctions. *Nat. Nanotechnol.* 5(3), 225 (2010). https://doi.org/10.1038/nnano.2010.15.
22. C. Jiang, R. Liang, J. Wang, and J. Xu, A two dimensional numerical model for short channel junctionless double gate MOSFET. *AIP Adv.* 5, 057122 (2015). https://doi.org/10.1063/1.4921086.

Publisher's Note Springer Nature remains neutral with regard to jurisdictional claims in published maps and institutional affiliations.

Springer Nature or its licensor (e.g. a society or other partner) holds exclusive rights to this article under a publishing agreement with the author(s) or other rightsholder(s); author self-archiving of the accepted manuscript version of this article is solely governed by the terms of such publishing agreement and applicable law.

Brazilian Journal of Botany
https://doi.org/10.1007/s40415-023-00882-z

BIOCHEMISTRY & PHYSIOLOGY - REVIEW ARTICLE

Aromatic plants: a multifaceted asset

Anuradha.[1] · **Navneeta Bharadvaja**[1]

Received: 7 November 2022 / Revised: 7 March 2023 / Accepted: 10 April 2023
© The Author(s), under exclusive licence to Botanical Society of Sao Paulo 2023

Abstract
Aromatic plants are utilised as traditional medicines in many cultures, but they are also traded as goods that satisfy the needs of frequently far-off marketplaces. The term "medicinal and aromatic plant" (MAP) is used in this study to refer to the entire range of plants utilised not only for medicinal purposes but also in the closely related and frequently converging fields of condiments, food, and cosmetic. Essential oil-based products are growing in popularity in various industries such as pharmaceuticals, cosmetics, food and beverage, colorants, and biopesticides and are slowly marking the realm of nanotechnology for the betterment of mankind. Due to their natural, eco-friendly, and generally accepted safety as products, these plants and the derivatives they produce are currently in higher demand. As a result, extracts from aromatic plants have the potential to develop into novel types of foods and medicines for both human and animal nutrition and health. The usage of new ideas like nutraceuticals, cosmeceuticals, phytotherapy, and aromatherapy is expanding, and there are new developments in functional foods, animal husbandry, and agricultural pest management. Aside from their possible advantages for human health, fragrant plants are also esteemed for their ecological and advantage by being an eco-friendly phytostabilizer and thus removing the heavy metal toxicity from soils. Aromatic plants are truly human assets that add value to our daily lives.

Keywords Aromatherapy · Essential oils · Food industry · Natural dye · Nutraceuticals · Pharmaceutical industry

1 Introduction

For chiliads, humans have relied significantly on plants for both nourishment and illness prevention (Sen and Samanta 2014). For thousands of years, aromatic herbs have been utilised in traditional medicine in many forms, ranging from the fresh plant and its natural secretions through extracts and oils. There are 18,000 different varieties of plants distributed in 15 agroclimatic zones in India, with 6000–7000 of them having therapeutic characteristics. Medicinal and aromatic plants are plants that have medicinal or aromatic characteristics and are used in pharmacy and/or perfumery apart from these aromatic plants are popular among cosmetic sector (Samarth et al. 2017).While these plants have been used for a number of applications throughout recorded history, they have been referred to as medicinal herbs, culinary herbs, potherbs, spices, seasonings, essential oil plants, or other words to identify plant use (Barata et al. 2016). Before the advent of pharmaceutical research and development, there was a time when civilizations have relied on their traditional knowledge, skills, and customary practises to prevent, diagnose, and cure health problems, utilizing the numerous resources offered by nature (Dixon and Aldous 2014). Different types of seeds, roots, leaves, fruit, skin, flowers, and even the entire plant may be utilised as therapeutic plant components (Jamshidi-Kia et al. 2018). According to the WHO, traditional medications, mostly plants, are now used by more than 80% of the world's population as their primary source of health care (Farnsworth et al. 1985). Around 12.5 per cent of the 422,000 plant species identified globally are said to have therapeutic properties, yet only a few hundred are known to be grown commercially (Lakey 2016).

Allopathic medications, phytotherapeutic goods, botanical supplements, cosmetics and personal care products, paints and dyes, insecticides, and other intermediate or final products can be made utilizing MAPs as raw ingredients (Cadar et al. 2021). Bioactive chemicals from medicinal and aromatic plants have been shown to have key qualities that make them attractive candidates for industrial applications in addition to medical applications (Fierascu et al. 2021). Many plants are used as a traditional formulation, traditional food, as well as perfumers and cosmetics (Ribeiro-Santos

✉ Navneeta Bharadvaja
navneeta@dtu.ac.in

[1] Delhi Technological University, New Delhi, India

Published online: 21 April 2023

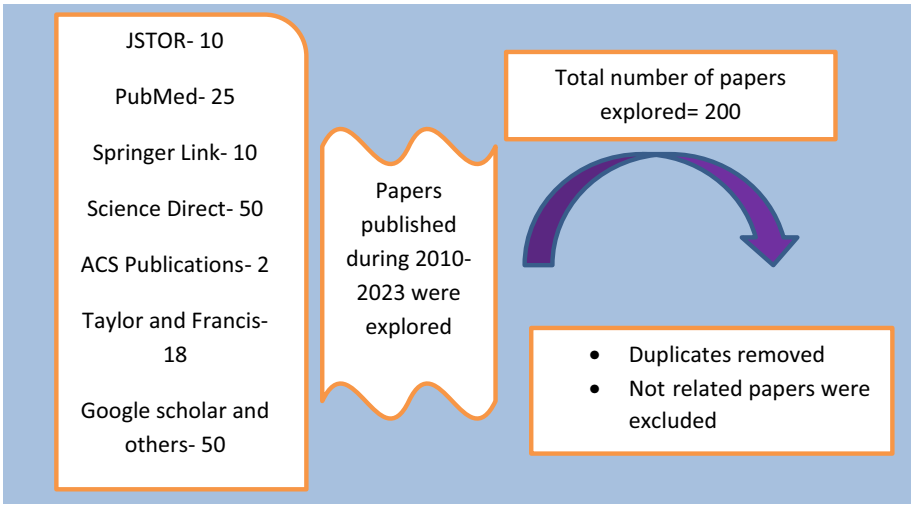


Fig. 1 Flow of methodology

et al. 2015). Essential oils (EOs) are complex blends of tens to hundreds of volatile molecules, including terpenes and terpenoids, as well as aliphatic and phenol-derived aromatic components, found in aromatic plants (Calvo-Irabien 2018). Essential oils (EOs) are complex blends of tens to hundreds of volatile molecules, including terpenes and terpenoids, as well as aliphatic and phenol-derived aromatic components, found in aromatic plants (Kumar et al. 2018). Essential oils are beneficial substances for human health that are employed as natural essences and aromas (Rehman et al. 2016). Aromatic and medicinal plants planted in the field require less energy to thrive, can help agroecosystems become more diverse, and can be utilised to repair degraded areas (Kumar and Jnanesha 2016). This review summarizes the use of aromatic plants for different industries as per the data available on different search engines as shown in Fig. 1. The aim of this paper is to explore the wide potential of aromatic plants for different arena of industries such as cosmetic, pharmaceuticals, aromatherapy, and many more. Also, aromatic plants are prized for their economic and environmental advantages in addition to any potential health advantages. In order to promote local economies and lessen agriculture's negative environmental effects such as phytoremediation, aromatic plants must be cultured on a large scale. The review gives an insight into different industrial and eco-friendly potential, which will lead into fresh discoveries and improvements in a variety of fields, including medicine, agriculture, cosmetics, and more.

2 Market scenario of medicinal and aromatic plants globally

Aromatics are highly versatile and offer safety, high performance, and a wide range of benefits to products. Due to their versatile properties, nanoparticles find applications in numerous fields, including pharmaceuticals, automotive, paints and coatings, oil and gas, chemicals, and more. The aromatic sector is mainly concentrated in the regions of the world mainly—Europe, North America, Asia Pacific, Middle East, North America, Latin America & Africa. The largest share of the global market is held by Asia Pacific, which is expected to maintain its dominance due to the growing demand for aromatics in various industries such as automotive, pharmaceuticals, paints & coatings, chemicals, and others. According to precedence research 2022 report, the market is expected to experience significant growth in the paints and coatings segment, mainly because of the increasing use of organic compounds. This trend is driven by the desire to enhance product performance and prolong its lifespan. As a result, the market is projected to see a high CAGR. Furthermore, the beverage industry has also been driving the demand for aromatic plants, especially for herbs and spices. The worldwide market for herbs and spices is predicted to reach USD 10.7 billion by 2026, rising at a CAGR of 5.1% over the forecast period, according to a report by research and markets.

The Asia–Pacific region is anticipated to experience a compelling growth in requirement of toluene due to its various applications in the production of products such as paint thinners, nail polish removers, and glues. China, India, and Japan are the main contributors to this growth as they are the leading players in the region. The use of aromatics in various industries such as paints & coatings, oil & gas, and chemicals is expected to increase in the North American market, leading to a higher compound annual growth rate (CAGR). The USA, Canada, and Mexico are important players in this market due to their substantial investments in these industries. As a result, the demand for synthetic rubber and plastics produced from aromatics is expected to rise, contributing to market growth over the forecast period (Graphical research 2021). Europe has made significant progress

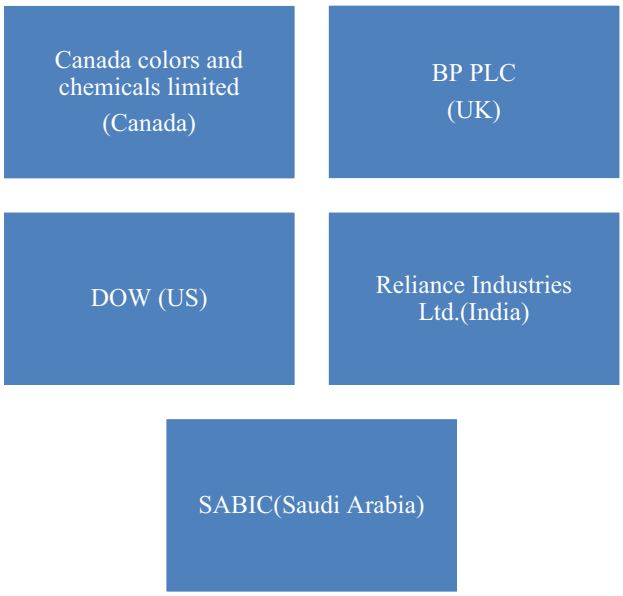


Fig. 2 Major aromatic plant-based companies distributed globally

Table 1 A worldwide market survey of aromatic plant-based industries

Industry	CAGR (%)	2020	2028202820282028(Expected)
1. Food and Beverage	3.0	USD 17.9 billion	USD 22.8 billion
2. Pharmaceutical	3.2	USD 1.25 trillion	USD 1.6 trillion
3. Cosmetic	5.9	USD 532.4 billion	USD 784.6 billion
4. Fragrance	4.0	USD 52.6 billion	USD 72.3 billion

in meeting the rising demand for lightweight materials in various industries such as electrical and electronics, packaging, and others. The market has seen remarkable growth due to technological advancements and innovations. Germany, the United Kingdom, and Italy are the main players in this market (Data bridge market research 2021). Significant progress is anticipated in several Latin American countries, including Brazil, Uruguay, and Argentina, as a result of the rising demand for hydrocarbons in major industries (Fig. 2). Similarly, rapid growth is projected in the Middle East and Africa, particularly in Qatar, the U.A. E, and other countries, due to the expanding production of aromatics within refineries (Market Research Survey 2023). The aromatic market share is predicted to achieve a global worth of USD 323.88 billion by the end of 2030, with an estimated growth rate of 5.6% (Market Research Future 2023). Rising demand from numerous industries has been fuelling the expansion of the aromatic plant industry world widely over the past ten years as depicted in Table 1. Its expansion has been facilitated due to rising interest in natural and organic items as well as herbal-based medications.

3 Essential oils derived from aromatic plants

Aromatic plants extracts are extracted in different forms with multiple uses as depicted in Fig. 3. Aromatic and therapeutic plants produce secondary metabolites known as essential oils (Falleh et al. 2019). Essential oils have a variety of biological effects, including antioxidant, antibacterial, and anti-inflammatory properties (Falleh et al. 2020). Generally, essential oils constitute to a minor portion of a plant's entire makeup, accounting for less than 5% of the vegetable dry matter (Valderrama and Ruiz 2018). Around 17% of the global flavour and fragrance market is made up of essential oils. Essential oil production varies between 40,000 and 60,000 tonnes per year around the world. Two thousand tonnes of spice oils are needed each year (Riaz et al. 2021). Essential oils are a complex assemblage constituting a variety of polar and non-polar components at various concentrations (Raut and Karuppayil 2014). EOs are renowned for having a wide range of biological actions (Dhifi et al. 2016). Essential oil can be found in many sections of the plant; however, it is most commonly collected from the leaves due to its high phytoconstituent content (Dutta et al. 2018). Major formulation of essential oils comprises of monoterpene compounds, which are constituted by ten carbon atoms often arranged in a ring or in acyclic form in addition to sesquiterpenes, which are hydrocarbons comprising of fifteen carbon atoms (Matsumura 1997).

Essential oils have a wide range of uses. They are widely used in cosmetics and perfumes, but they also have medicinal and agro-alimentary applications due to their antibacterial and antioxidant qualities (Ríos 2016). According to a recent bibliometric review, insecticidal effect of plant essential oils has been a focus of research in the new millennium (Isman 2020). Even EOs have the potential to be developed as multi-potent treatments for neurological illnesses with improved efficacy, safety, and cost-effectiveness (Ayaz et al. 2017). The synergy between aromatic plant components is frequently important in the effectiveness and reduction of pathogenic microorganism resistance development (Elshafie and Camele 2017).

EOs has been shown to have antimicrobial effects, which are evident from number of investigations (Bajpai et al. 2012). The antibacterial activity of EOs having aldehydes or phenols as significant components, such as cinnamaldehyde, citral, carvacrol, eugenol, and thymol, has been reported to be effective, followed by EOs containing terpene alcohols (Bassolé and Juliani 2012). Many in vitro and in vivo studies

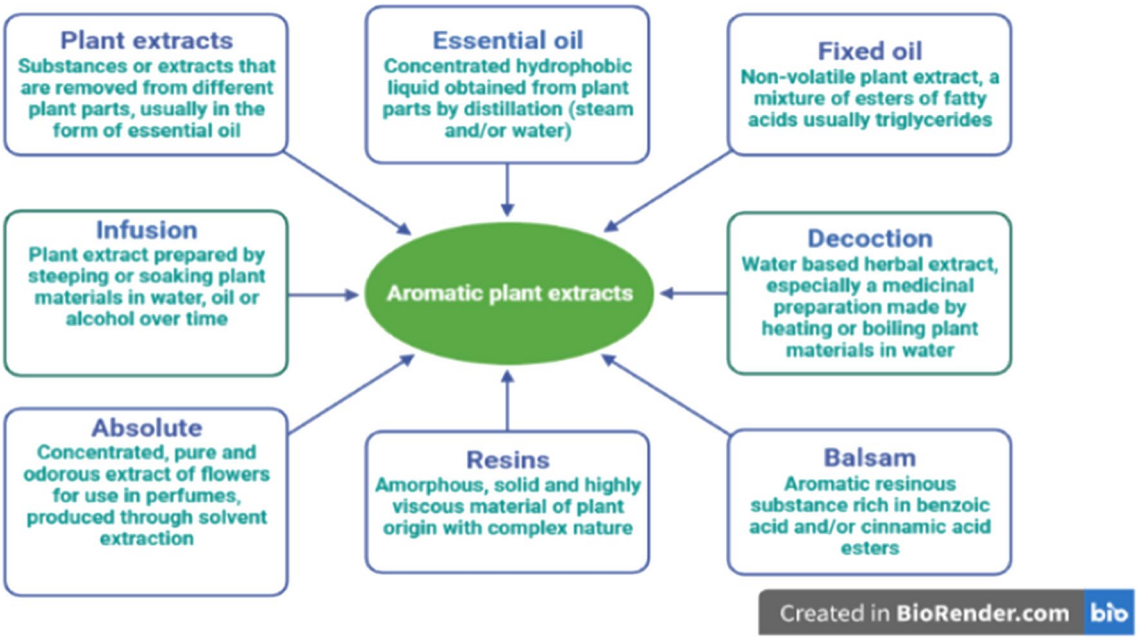


Fig. 3 Role of different form of aromatic extracts

have been carried out to assess the overall antimicrobial properties such as antibacterial, antiviral, and antifungal properties of essential oils (Leyva-López et al. 2017). EOs can be successfully used in various aspects of health care, according to the current chemical, medical, and pharmacological literature (Palazzolo et al. 2013). The beneficial use of essential oils in clinical operations has recently received a lot of attention (Watanabe et al. 2015).

EOs are widely employed in the cosmetics arena due to their well-known fragrance attribute (Carvalho et al. 2016). Essential oils (EOs) derived from plants including rose, tuberose, narcissus, gardenia, jasmine, and Lavandula officinalis are still the most popular fragrance exhibiting components in cosmetics (Aburjai and Natsheh 2003). Plants like Artemisia afra, Pteronia incana, and Rosmarinus officinalis are employed as preservation constituent in cosmetics arena due to their essential oils exhibiting antimicrobial property against a wide range of bacterial strain (Bakkali et al. 2008). The essential oils of chamomile, rosemary, and West Indian bay assist to condition and promote healthy hair development, whereas dandruff can be effectively controlled with the use of bergamot and tea tree essential oils (Lall and Kishore. 2014). The use of essential oils in the creation of cosmetics and associated goods may have a number of benefits, including improving dermato-cosmetic characteristics and preservation, as well as the finished product's marketing image (Muyima et al. 2002).

Aromatherapy, which uses blended essential oils as therapeutically active agents, has lately gained a lot of popularity (Hongratanaworakit 2011). Essential oils are generally constituted of terpenes, which combine with a variety of organic molecules such as alcohols, hydrocarbons, esters, ketones, phenols, and their substituents in aromatherapy (Joseph Mari and Faller 2021). Aromatherapy has relied on a variety of products including essential oils to treat physical and emotional ailments, thus contributing to well-being of human race (Sawamura et al. 2004). Aromatherapy, which is practised using essential oils from plants via both direct interventions on the skin and inhalation, which is a more effective method, is one of the non-pharmacological treatments utilised for sleep disturbances (Karadag et al. 2017). PMS, vaginal infections, menopausal symptoms, cystitis, infertility, and lichen sclerosis are some of the women's health issues that can be treated using essential oils (Tillett and Ames 2010).

3.1 Essential oils for food industry

Due to the existence of essential oils, aromatic plants have been employed in food flavouring, medicinal, cosmetic, and perfumery since ancient times (Ayadi et al. 2009). Culinary herbs and spices have recently been discovered to be a dietary source of bioactive polyphenols, prompting research into their phenolic content and antioxidant capabilities (Park 2011). Mint, basil, lavender, rosemary, and laurel are some of the herbs used to flavour sweet meals. Zingiberaceae are used in Asian cuisine because of their distinct flavour and scent, and of their various bioactive constituents. Piper species are aromatic herbs used in cooking, and their secondary metabolites have also been found to have biological effects

Table 2 Aromatic plants as a healthy ingredient for variety of dishes

Plant	Dish	Quantity	References
1. *Coriandrum sativum*	Sweet Chili Tofu Stir-Fry	1 Tbsp,5 mL	(Dietitians of Canada from simply Great food. 2007)
2. *Cymbopogon citratus*	Khao Tom (Thai rice soup)	1–2 (5 cm)	(Heart and stroke Foundation of Canada. 2007)
3. *Laurus nobilis*	Curried Cream of Parsnip and Carrot Soup	1 Leaf	(Foodland Ontario. 2009)
4. *Petroselinum crispum*	Chicken Bulgur Salad		
5.		½ Tbsp, 250 mL	(Foodland Ontario. 2009)
6. *Anethum graveolens*	Mustard Beet And Apple Salad	Garnishing	(Foodland Ontario. 2010)
7. *Ocimum basilicum*	Tomato Salad with Basil Vinaigrette	2 Tbsp, 25 mL	(Foodland Ontario, 2010)
8. *Origanum majorana*	Ontario Winter Vegetable Soup	½ Tbsp, 2 mL	(Foodland onatario. 2010)
9. *Origanum vulgare*	Mediterranean Zucchini and Eggplant	2 Tbsp, 10 mL	(Foodland Ontario. 2010)
10. *Salvia rosmarinus*	Pork Tenderloin with Cider-Glazed Carrots	1 Tbsp, 5 mL	(Foodland Ontario. 2010)
11.*Withania somnifera*	Ashwagandha Banana Smoothie	1 Tbsp, 5 gms	(Regi George Jenarius. 2017)

on human health (Salehi et al. 2019). Aromatic halophyte plants are a prominent source of bioactive chemicals and natural products that have applications in the food sector (Pereira et al. 2017). Garlic (*Allium sativum L.)* is a fragrant herbaceous plant that is used as a food and a traditional medicine for a variety of disorders as it exhibits properties such as anti-carcinogenic, antioxidant, anti-diabetic, renoprotective, anti-atherosclerotic, antibacterial, antifungal, and antihypertensive (Batiha et al. 2020).

The consumers and the food sector are increasingly concerned about food safety. The European Spice Association and the European Commission are two among many organisations that set limitations, regulations, and standards for the spices and aromatic herbs business (Cilak et al. 2021). Innumerable EOs inherit the capability to be used as a preservative for meal products or dairy products and even for the greens and fruits (Falleh et al. 2020). Different forms of EOs including tea tree oil, lemon oil, clove oil, cinnamon oil, and thyme oil from numerous conventional plants, have substantially confirmed higher antimicrobial and antioxidant activities, and additionally correctly accelerated the shelf lives of the cereal merchandise and accelerated the nice of meals safety (Bhavaniramya et al. 2019). Plant essential oils (EOs) have a high antibacterial efficiency and so have a lot of potential as a healthier alternative to toxic synthetic preservatives (Kumar et al. 2018). When it comes to essential oils with a high percentage of volatile components, the vapour phase has a far stronger effect than contact application (Mugao et al. 2020). Besides this, plenty of plants are available as food with different nutrients as shown in Table 2.

Essential oils for pharmaceutical industry. Currently, an emphasis on integrated medicine has bought plant and plant-based options as therapy in limelight for curing plenty of diseases (Inoue et al. 2019). Attributes such as therapeutic and pharmacological quality' aromatic herbs popularize them as natural remedies (Samarth et al. 2017). Sustainable techniques have been proposed to combat overexploitation of natural resources and the resulting dangers to biodiversity, and various international organisations have produced recommendations for the gathering and sustainable production of medicinal plants. Aromatic plants can be an affordable and easy source of promising therapeutic compounds for deadly diseases like cancer and other infectious disorders caused by drug-resistant microbes (Ahmad Ganaie 2021). For instance, Curcuma species essential oils have anti-inflammatory, anti-proliferative, hypocholesterolemic, antidiabetic, antihepatotoxic, antidiarrheal, carminative, diuretic, antirheumatic, hypotensive, antioxidant, antimicrobial, antiviral, insecticidal, larvicidal, antivenomous, antithrombotic, antityrosinase, and cyclooxyglutamate properties (Dosoky and Setzer 2018). Bioactive compounds found in essential oils generated from aromatic plants, such as phenylpropanoids, have anticancer therapeutic potential and can be used in cancer treatment (Carvalho et al. 2015). Besides this, many plants are there with different bioactive constituent which at different doses are beneficial against various ailments as shown in Table 3.

Essential oils for cosmetic industry There is a constant developing interest in cosmetics and cosmeceuticals employing plant substances, according to complementary and alternative medicine, which is based mostly on traditional or folklore treatments of various world cultures. Skincare products and cosmetics are becoming a common component of majority of population in their day-to day life (González-Minero and Bravo-Díaz. 2019). Fragrance is an important component of cosmetics and is frequently regarded as the most important aspect in customer decision-making (Sharmeen et al. 2021). Aromatic plants are gaining popularity because most women nowadays prefer natural products to chemicals

Table 3 Aromatic plant as medicinal dose for different diseases

Plant	Family	Bioactive constituent	Dose	Biological Role	References
1. *Eletarria cardomum*	Zingiberacea	α-terpineol, Myrcene, Heptane, Subinene	10–100 mg/kg	Effective against Asthma	(Gilani and Info. 1991)
2. *Cinnamomum verum*	Lauraceae	Procyanidin polymer type A, Cinnamic acid, and Coumarin	200 mg/Kg for 6 weeks	Anti-diabetic	(Kim, Hyun and Choung. 2006)
3. *Cymbopogon citratus*	Poaceae	Gallic acid, Isoquercetin, Quercetin, Rutin, Catechin and Tannic acid	100 mg/kg for 21 days	Blood cholesterol lowering agent	(Costa et al. 2011)
4. *Tanacetum parthenium* L	Asteraceae	Artecanin, Artemorin, Balchanin, Canin	125 mg of dried fever few leaves	Anti-migraine	(Pareek et al. 2011)
5. *Ferula asafoetida*	Umbelliferae	Ferulic acid, Luteolin	40 mg/g of weight	Anticancer	(Mahendra and Bisht. 2012)
6. *Trachyspermum ammi*	Apiaceae	γ-terpinene, ρ-cymene, and Thymol	100 mg/kg for 21 days	Anti-arthritic	(Umar et al. 2012)
7. *Emblica officinalis*	Euphorbiaceae	Emblicanin A and B, Punigluconin, Pedunculagin, Chebulinic acid (Ellagitannin), Chebulagic acid (Benzopyran tannin)	60 mg/Kg of body weight	Ulcer protective	(Dasaroju and Gottumukkala. 2014)
8. ***Olea europaea***	Oleaceae	Triolein, Tripalmitin, Trilinolein, Tristearate, Monosterate, Triarachidin, Squalene	20 mg/kg of body weight for 16 days	Anti-diabetic	(Hashmi et al. 2015)
9. *Coriandrum sativum*	Umbelliferae	Anethol, Borneol, Bornyl acetate, coriandrin	0.1 g for 90 days	Blood glucose lowering agent	(Prachayasittikul et al. 2018)
10. *Syzygium aromaticum L*	Myrataceae	Eugenol, Gallic acid, Flavonol glucosides	250 mg/day for 30 days	Alcohol-induced toxicity, Reduction of hangover severity	(Mammen et al. 2018)
11. *Eucalyptus globulus*	Myrtaceae	Terpinolene, α-pinene, Borneol, Globulol, Terpineols	150 mg/kg of body weight	Anti-pyretic	(Mworia et al. 2019)
12. *Pimpinella anisum L.)*	Apiaceae	Anethol, γ-himachalene, cis-isoeugenol and linalool	Anise oil for 6 weeks	Migraine headache	(Mosavat et al. 2019)
13. *Murrayakoenigii*	Rutaceae	Koenine, Isomahanimbin, Girinimbin	(2–8) % of body weight	Antiamnesic	(Anjana Goel, Ayushi Sharma. 2020)
14. *Allium sativum*	Alliaceae	Aliin, Allicin, Ajoene, Allylpropyl disulfide, Diallyl trisulfide,	0.1 ml of garlic clove extract	Immuno-modulator	(Khubber et al. 2020)
15. *Crocus sativus*	Iridaceae	α-terpineol, Myrcene, Heptane, Subinene	10–100 mg/kg 100 mg/day for 8 weeks	Antidiabetic	(Tajaddini et al. 2021)

for personal care to enhance their beauty because these products provide the body with nutrients, improve health, and provide satisfaction because they are free of synthetic chemicals and have fewer side effects than synthetic cosmetics. They are important ingredients in cosmetics such as soaps, shampoos, creams, sprays, colognes, face packs, hair dyes, and other similar items. For two main reasons, EOs show themselves as good candidates to match the current beauty industry's demands; to begin with, research supports their efficacy as valuable cosmeceuticals, and secondly, the composition's tiny lipophilic molecules allow for efficient penetration into the skin layers (Adewinogo et al. 2021). Besides this, various other plants are available which are among some of the important ingredients of different cosmetics products as shown in Table 4.

Table 4 Illustration of plant-based formulations used in cosmetics

Aromatic Plant	Functional Aspect	Products	References
1. Rosa damascena	Fragrance, cleaning agent	Perfumes, Lotions, Rose water	(N Koksal. 2015)
2. Cucumis sativus	Improving skin tone	, Skin brightening serums, lotions	(M. Bologan. 2016)
3. Hibiscus rosa-sinensis	Skin lightening, Moisturising	Creams, Lotion	(M Kilala Tilaar. 2018)
4. Lavandula	Pleasing Fragrance	Bath and soap products, sunscreen, lotions	(R wells. 2018)
5. Aloe chinensis Baker	Therapeutic, anti-ageing	Soap, lotion, face masks	(TY Hendrawati. 2018)
6. Ocimum Sanctum	Anti-ageing	Hair Conditioners, Creams, lotions	(W Chaiyana. 2019)
7. Aloe barbadensis	Anti-ageing, Skin protection products	Soaps, hand creams, lotions, shampoos, hair tonics	(S Laneri. 2020)
8.Tagetes erecta	Antioxidant, skin whitening	Sunscreen, Serums, toners	(S. Thongsa.2020)
9.Citrus limon	Antibiotic, flavouring	Shampoos, tropical ointments, toothpastes	(Marta Klimek-Szczykutowicz .2020)
10. Simmondsia Chinensis	High Saponification Value	Soaps, shampoos,	(M Ijaz. 2021)

Essential oils for aromatherapy Health professionals and folk medicine practitioners employ herbs, herbal preparations (infusions, decoctions, concentrates, tinctures, and other herbal extracts), and phytochemicals for therapeutic purposes commonly known as phytotherapy (Aćimović 2021). Aromatherapy is defined as "the art and science of balancing, harmonising, and promoting the health of body, mind, and spirit via the use of naturally extracted fragrant essences from plants" (Reis and Jones 2017). Essential oils consisting of several bioactive compounds are mainly use for massage and inhalation, aromatherapy. Essential oils can be administered with formulations like they are blended into a gel, compounded into a paste or spray, or used by bath, massage, or inhalation, to name a few options (Winkelman 2018). The volatility and permeability of plant essential oils are high, which make them a matter of interest for aromatherapy (Yuan et al. 2021). After administration, the oils recast and work in a friendly manner at the malfunction or impacted area (Ali et al. 2015a, b,). Hydrolates, by-products of essential oil synthesis, can also be utilised in aromatherapy in addition to essential oils (Shah et al. 2011). Essential oils can be marketed with "aromatherapy" claims, implying that they can help with health issues or enhance overall well-being (Pereira et al. 2017). Essential oils, in comparison to standard medications, offer less adverse effects and a wider range of applications, including inhalation (Ramsey et al. 2020). Aromatherapy (essential oils) is gradually being integrated into patient treatment as a safe, low-cost, non-pharmacologic option for reducing pain, nausea, and anxiety, as well as improving sleep (Freeman et al. 2019). Aromatherapy utilises these essential oils to infiltrate the human skin surface with marked aura through inhalation, topical application, and baths (Ali et al. 2015a, b,). Aromatherapy had a global market value of USD 1.37 billion in 2019, with an 11.8 per cent annual growth rate projected from 2020 to 2029 (Grandview research. 2021). Besides this, there are other plants with different aroma constituents and with therapeutic purposes as shown in Table 5.

4 Aromatic plant as nutraceuticals

Nutraceuticals are dietary supplements that are used to improve health, delay ageing, prevent diseases, and maintain the human body's correct functioning (Sachdeva et al. 2020). The global nutraceutical business is massive, estimated to be worth USD 117 billion (Sachdeva et al. 2020). Spices have been studied for volatile oils (essential oils), flavour, and the treatment of a variety of chronic conditions (Manasa et al. 2021). Plant-derived extracts and secondary metabolites are a rich source of bioactive substances such as phenolics, terpenoids, and other phytochemicals due to which aromatic plants have a wide range of actions that have health-related benefits and nutrigenomics implications for gut and immune development (Christaki et al. 2019). Polyunsaturated fatty acids found in plants, particularly the omega-3 and omega-6 families, are another important class of phytochemicals due to their wide-ranging health benefits (Guimarães et al. 2009). To increase the quality and safety of food, cinnamon and peppermint can be utilised as dietary sources of natural antioxidants (Lv et al. 2012).

Herbal bioactives, are a crucial class of nutraceuticals, are typically utilised by individuals who searching for traditional healthcare (Ajazuddin et al. 2014). Herbs, nutrients, and

Table 5 Medicinal and aroma-therapeutic attribute of plants

Aromatic plant	Aroma constituents	Benefits	Type of aroma-therapy	References
1. Jasminum sambac	Benzyl acetate, β-linalool, Benzyl propionate	Enhancing brain wave activity and emotions	Olfactory	(W Sayowan et al. 2013)
2. Pogostemon cablin	Patchouli alcohol, Delta gauiene, Azulene, Cycloheptane	Gatrointestinal Protection, Anti-depressant	Medical	(MK Swamy et al. 2015)
3. Melaleuca alternifolia cheel	Terpinen-4-ol, Cineole	Immunestimulant attribute, Effective against respiratory ailments	Clinical	(Babar Al et al. 2015)
4. Helianthus annuus	Palmitic acid, Stearic acid, Linoleic acid and Oleic acid	Improve weight gain; enhance function of skin lipid bilayer	Massage	(M Michalak et al. 2019)
5. Lemon citrus	Limonene, Sabinene, Geraniol, α-Pinene, β-Pinene, Linalool	Reduces blood pressure, Anxiety, Maintaining regulated heart rate	Clinical	(M Rambod et al. 2020)
6. Cistus ladanifer	Camphene, Borneol, Terpineol-4, α-Pinene	Immunity booster, Support for parasympathetic and CNS	Clinical	(AJ Farrar et al. 2020)
7. Lavandula spp.	Linalool, Geraniol, Terpineol, Borneol	Effective on labor pain, anxiety	Medical	(M Tabatabaeichehr et al. 2020)
8. Citrus paradisi	Limonene, Myrcene, Pinene, Trans-Caryophyllene	Modulating sympathetic activities, Regulating nervous system	Clinical	(B Aydeniz 2020)
9. *Chamaecyparis obtuse*	α-Terpinyl acetate, Sabinene, Isobornyl acetate, Limonene	Physiological relaxation	Olfactory	(M Acimovic 2021)
10. Rosa damascene	Citronellol, Geraniol, Nerol	Fragrance based full body treatment	Cosmetic	(DV Antonova 2021)

Table 6 The usage of aromatic plant as nutraceuticals

Aromatic plant	Bioactive constituents	Biological role	References
1. Curcuma longa	1,8-cineole, Ar-turmerone, Feruloyl-p*p*-coumaroyl-methane, Curcumin	Analgesic, Antibacterial, Antiseptic, Antispasmodic, Appetizer, Carminative, Diuretic, Cardiovascular protectant, Antitumour	(S Chanda 2019)
2. Allium cepa	Protocatechuic acid, Myricetin, pelargonidin, kaempferol	Anticancer, Anti-diabetic, Antimicrobial, Cardiovascular, Antioxidant	(V Kuete 2017)
3. Centella asiatica (Gotu Kola)	Madecassoside, Asiaticoside, Madecassic acid and Asiatic acid	Effective in Neuropsychatric condition	(PA ThaakurDesai 2021)
4. Ferula asafoetida (Hing)	coumarins, sesquiterpene, ferulic acid, 1-arabinose, rhamnose	Beneficial for bone health, Regeneration in postmenopausal women	(R Dalifardouei 2021)
5. Ginkgo biloba	Quercetin, Catechin, Ginkgolides, bilobalides	Effective in mental enhancement, Lowering blood pressure	(GR Parmar 2021)
6. Mucuna pruriens	Glutathione, Lecithin, Gallic acid, β-sitosterol	Reduces blood glucose level	(R Pathania et al. 2020)
7. Hypericum Perforatum	Hypericin, Hyperforin	Antidepressant	(Coppock et al. 2021)
8. Cassia augustofolia	Sennosides, proanthocyanidin, Marmelosin, Quercetin (56.9 µg/g), Rutin	Purgative	(Upadhyay et al. 2020)
9. Aegle marmelos	Catechin, Flavan-3-Ol, Flavonoid	Appetizer	(Sarkar et al. . 2020)
10. Glycyrrhiza glabra	Glycyrrhizin, Liquertin,Rhamnoliquirilin,	Anti-inflammatory	(Batiha et al. 2020)

dietary supplements are the three primary types of nutraceuticals (Hassan et al. 2020). Furthermore, due to their nature as medicinal and meals products, those nutraceuticals also can be taken into consideration as a treasured supply of new "lead compounds", developing the possibility to find out new training of healing agents (Sut et al. 2016). Nutraceuticals

Table 7 Aromatic plant as a natural constituent for dyes

Plant	Colour of dye	Part used	Coloured pigment	References
1. *Carthamus tinctorius L*	Red	Floret	carthamin	(Gomashe et al. 2021)
2. *Caesalpinia sappan L*	Red	Bark	Brazilin	(Surana, Bhattacharya and Majumder et al. 2021)
3. *Rubia tinctorium L*	Red	Wood	Anthraquinone	(Derksen et al. 2021)
4. *Haematoxylon campechianum L*	Red	Wood	Hematein	(Kagathara, Dalal and Solanki. 2020)
5. *Mallotus philippinensis Muell*	Red	Flower	Rottlerin	(Kumar et al. 2020)
6.*Solidago grandis DC*	Yellow	Flower	Carotenoid	(da Silva Souza Campanholi et al. 2020)
7.*Tagetes erecta*	Yellow	Flower	Lutein	(Khan and Aslam et al. 2017)
8.*Indigofera tinctoria L*	Blue	Leaf	Indigotine	(Pattanaik et al. 2020)
9. *Acacia nilotica (L.) Del*	Blue	Seed Pod	Anthocyanins	(Amadou, Soulé and Salé. 2020)
10. *Abies spectabilis*	Purple or violet	Cone	Anthocyanins	(Tiwari et al. 2021)

are merchandise derived from meals reasserts, which might be presupposed to offer more fitness benefits, similarly to the simple dietary cost observed in foods (Chaudhari et al. 2017). Besides this, various plants are there with different nutraceutical value as shown in Table 6.

5 Aromatic plant as natural dye

Natural colorants and dyestuffs are a vital assemblage of non-timber wooded merchandise, which are best explored in industries generating confectionery, different meals merchandise, textiles, cosmetics, medicines, leather, paper, paint, ink, etc. (Yusuf et al. 2017). Textile sector is extremely beneficial to humans, but they are wreaking havoc on the environment by producing large amounts of hazardous wastewater as synthetic colours being the primary cause of toxicity (Guha 2015). Natural dyes are sustainable in and of themselves because they are renewable and biodegradable, but they cannot meet the enormous demand from the textile industry due to the preferential use of land for food and feed (Saxena and Raja 2014). Plant-derived dyes offer strong antibacterial, antioxidant, and anti-inflammatory properties, they are garnering a lot of attention and are being utilised all over the world (Patel et al. 2020). Two hues of dye (yellow and brown) from Coreopsis tinctoria flower petals and dying leather with the derived dyes as a nontoxic and environmentally acceptable dye source (Velmurugan et al. 2016). Natural colours are biodegradable and provide no health risks, so they can be utilised without causing significant environmental harm (Lellis et al. 2019). Besides this, different plants are widely used in preparation of natural dyes as shown in Table 7.

6 Aromatic plants as nanomedicines

The application of nanotechnology, referred to as "nanomedicine," in the medical industry opens up several opportunities in the health sector by making testing more flexible, allowing for early detection, diagnosis, proper treatment, and illness follow-up (Zdrojewicz et al. 2015). Biopharmaceutical enterprises are in desperate need of eco-friendly alternative medication molecules to treat disorders linked to bacteria and body metabolism and in-vitro studies even implies that extracted essential oils could be a potential source of antimicrobial agents and could thus play an important role in the treatment of a wide range of pathogenic microorganisms in the near future by exposing novel medications (Malik et al. 2017). The essential oil or plant extract of MAPs can also be used to make nanoparticles. Nano-carriers not only control drug molecule release, but they also protect EOs from heat and UV degradation, resulting in increased stability, flavour, and function, as well as increasing the shelf life of the final product (Chamundeeswari et al. 2013). The nanoencapsulation of EOs in liposomes, solid lipid nanoparticles, nano- and microemulsions, and polymeric nanoparticles is a viable technique for overcoming the limits of EOs, lowering their dose, and boosting the long-term safety of these constituents (Subramani and Ganapathyswamy2020).

Nanomedicine is now critical in the development of effective therapeutic treatments for vital medications, such as anticancer and antiparasitic therapies (such as Taxol, vincristine, camptothecin, doxorubicin, and artemisinin), and other emerging compounds with pleiotropic effects (i.e. resveratrol, curcumin, salvianolic acid B, and honokiol) (Bilia et al. 2017). Plants that are medicinally active have proven to be the finest sources of various phytochemicals for the production of biogenic silver nanoparticles (Ovais et al. 2016). Organic substances such as polyphenols, tannins, alkaloids, carbohydrates, terpenoids, steroids, and flavonoids are mostly derived from therapeutic plants (Hassan et al. 2020). In recent years, biological materials such as plants have been

employed to create nanoparticles with great success such as silver nanoparticles (AgNPs) derived from banana peel extract, neem leaves (Moshahary and Mishra 2021).

7 Aromatic plant as phytostabilizer

In today's industrialised world, the problem of heavy metal pollution of soil is pervasive, garnering significant public attention, and creating significant anxiety and dread (Das 2020). Apart from their potential health advantages, aromatic plants are highly appreciated for their positive impact on the environment and economy. Plants have a separate regulatory system, though, that collaborates to resist stress and allows them to adapt to such contaminated soils (Pirzadeh et al. 2019). Due to this fact that they are non-food crops, aromatic plants can be utilised to clean up contaminated places while reducing the risk of contaminating the food supply (Pandey et al. 2019). Different families such as Asteraceae, Poaceae, Lamiaceae, and Geraniaceae of aromatic plants are promising sustainable approach for the phytoremediation of heavy polluted sites (Mishra and Chandra 2022) as shown in Fig. 4. Sustainable phytoremediation can be accomplished if researchers are able to identify ecologically and socioeconomically significant plant species or commercial crops like energy and aromatic plants as shown in Table 8 among naturally invading species (Pandey et al. 2015).

8 Aromatic plant as insecticide

Using natural substances with pesticide properties, such as essential oils extracted from aromatic plants, could be a viable alternative to harmful chemicals in the biological fight against pests (Yakhlef 2020). Bioaccumulation risk is typically lower with homemade botanical insecticides due to their natural ingredients, which degrade more quickly compared to many synthetic compounds (Mustafa et al. 2021). Although the communion of all the molecules in an essential oil appears to be significant as a whole than the individual action of metabolites (Zayyat et al. 2017). The ability of botanical-based pesticides to exert their effect through a variety of routes, so minimising the development of resistance, presents a practical and environmentally benign potential for small farmers globally (Wandjou et al. 2022). The essential oils obtained from plants belonging to families such as Pinaceae, Lamiaceae, and Poaceae are frequently in use as of insect repellents (Trivedi et al. 2018) as shown in Table 9.

9 Discussion and future aspect

Aromatic plants are enriched with the bioactive constituents popularly known as essential oils. Aromatic plants are truly a multifaceted asset as its usage is not just limited to culinary rather it a key raw material for plenty of industries be it pharmaceutical, cosmeceutical, aromatherapy, and colour

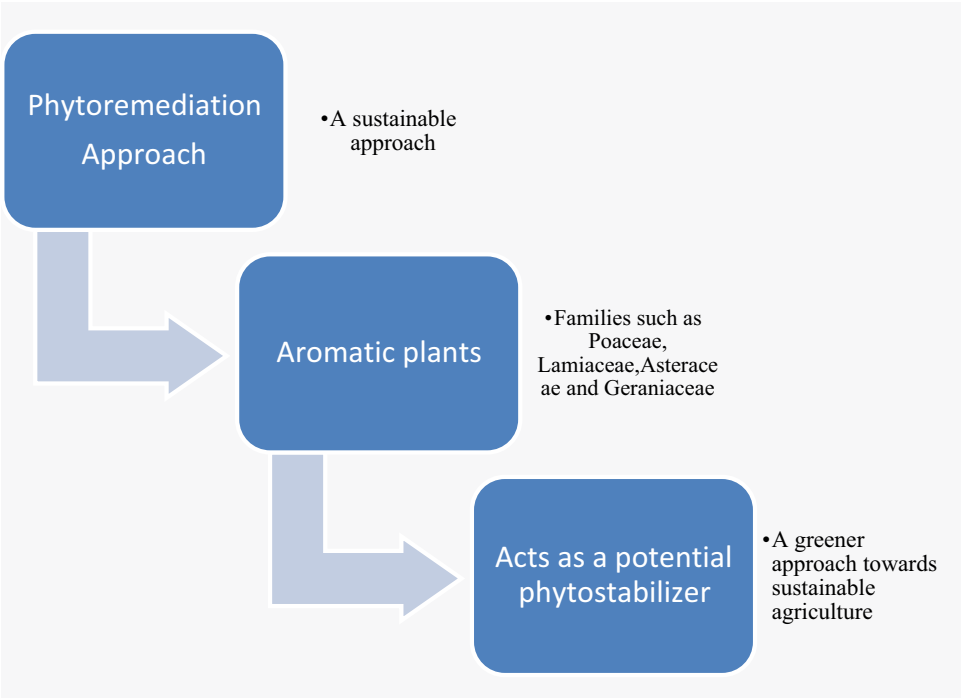


Fig. 4 Illustration of aromatic plant as a promising approach for phytoremediation

Table 8 Aromatic plants widely in-use as phytostabilizer

Name of plant	Trace elements	Mode of action	References
Lavandula angustifolia L	Cd	A mixture of 50% common greenbelt irrigation water and 50% treated wastewater is a suitable medium for this phytoremediation process. This suggests that using a combination of these waters can be a viable solution for cleaning up cadmium-contaminated water using Lavandula angustifolia	(Ahmadabadi 2022)
Chrysopogon zizanioides	Cr	The metal build-up in the leaves of vetiver grass suggests that it could be a viable option for extracting and recovering the metal for reuse through burning and reprocessing the resulting ash	(Masinire 2021)
Cymbopogon flexuosus	Pb, Ni	The cultivation of *Cymbopogon* in areas contaminated with metals are effective in reducing the amount of Pb and Ni as the risk of contamination in the food chain is minimal	(Pandey 2020)
Ocimum basilicum	Cd	Basil demonstrated a high level of tolerance to Cd stress, with a 50% reduction in shoot dry weight only occurring at concentrations > 100 µm	(Poursaeid 2020)
Vetiveria zizanioides L.	Pb	Vetiveria showed superior performance in absorbing lead from soil and decreasing the amount of lead present in the soil	(Arazhian 2020)

Table 9 Aromatic plants as natural insecticide

Plant	Family	Activity against Insects	References
Cymbopogon nardus (L.) Rendle	Poaceae	Citronella grass essential oil is effective as a repellent for German cockroach (*Blattella germanica* L)	(Jannatan 2021)
Satureja Montana	Lamiaceae	Nematicidal activity against *M. javanica*	(Rocha 2020)
Citrus aurantifolia	Rutaceae	Effective against *Callosobruchus maculatus*	(Boodram 2019)
Ageratum houstonianum	Asteraceae	Effective against larvicidal potential of *Culex pipiens*	(Hadiday 2022)
Nepeta cataria	Lamiaceae	Effective against *Aedes aegypti*	(Reichert 2019)
Tanacetum vulgare	Asteraceae	Effective against *L. decemlineata*	(Lazeravic 2020)
Allium schoenoprasum L	Amaryllidaceae	Effective against *Anopheles stephensi*	(Sanei-Dehkordi 2019)
Allium porrum	Amaryllidaceae	Effective against *Myzus persicae*	(Baudry 2021)
Thymus vulgaris	Lamiaceae	*Effective against Aedes aegypti*	(Maia 2019)
Ruta graveolens	Rutaceae	Effective against *Sitophilus zeamais*	(Perera 2022)

and dye industry. In today' era of the current pandemic, the worldwide population is accentuation on the old chestnut "Survival of the fittest". Nowadays, humans are a lot of inclined towards attaining healthy modus vivendi. However, as a matter of fact, majority of the humanity depends on the junk and therefore the impure variety of food out there within the market and thereby hampering their health as a whole. A healthy lifestyle can be easily followed up with the use of aromatic plants as them being a perfect blend of all nutrients and hence popularly being a constituent in the formulation of nutraceutical or functional foods worldwide. Aromatic plant accounts for a gaggle of economically viable plants. Aromatic plants are expendable in numerous types like in raw form they are consumable as spices or medicines and in processed form are used as a staple for industrially designed merchandise. There is still a void between such wildly adult plants and industries. As a result of the continuing demands among the worldwide nation for a healthy lifestyle and considering the potential of aromatic plants as a raw factor for industrially designed products, heaps of effort must be place in to create the aromatic plant a commercially in style issue right ranging from rural to the urban area.

Declaration

Conflict of interest The authors declare that there is no conflict of interest.

References

Aburjai T, Natsheh FM (2003) Plants used in cosmetics. Phyther Res 17:987–1000. https://doi.org/10.1002/ptr.1363

Aćimović M (2021) Essential oils: inhalation aromatherapy. J Agron Technol Eng Manag Rev 4:547–557

Adewinogo SO, Sharma R, Africa CWJ, Marnewick JL, Hussein AA (2021) Chemical composition and cosmeceutical potential of the essential oil of Oncosiphon suffruticosum (L.) Källersjö. Plants 10:1–14. https://doi.org/10.3390/plants10071315.

Ahmad Ganaie H (2021) Review of the active principles of medicinal and aromatic plants and their disease fighting properties.

Elsevier, Amsterdam. https://doi.org/10.1016/b978-0-12-819590-1.00001-x.
Ajazuddin AA, Qureshi A, Kumari L, Vaishnav P, Sharma M, Saraf S, Saraf S (2014) Role of herbal bioactives as a potential bioavailability enhancer for Active Pharmaceutical Ingredients. Fitoterapia 97:1–14. https://doi.org/10.1016/j.fitote.2014.05.005.
Ali B, Al-Wabel NA, Shams S, Ahamad A, Khan SA, Anwar F (2015a) Essential oils used in aromatherapy: a systemic review. Asian Pac J Trop Biomed 5:601–611. https://doi.org/10.1016/j.apjtb.2015.05.007
Ali B, Ali Al-Wabel N, Shams S, Ahamad A, Alam Khan S, Anwar F (2015b) Essential oils used in aromatherapy: a systemic review. Asian Pacific J Tropical Biomed 8:601–611.
Ayadi MA, Grati-Kamoun N, Attia H (2009) Physico-chemical change and heat stability of extra virgin olive oils flavoured by selected Tunisian aromatic plants. Food Chem Toxicol 47:2613–2619. https://doi.org/10.1016/j.fct.2009.07.024
Ayaz M, Sadiq A, Junaid M, Ullah F, Subhan F, Ahmed J (2017) Neuroprotective and anti-aging potentials of essential oils from aromatic and medicinal plants. Front Aging Neurosci 9:1–16. https://doi.org/10.3389/fnagi.2017.00168
Bajpai VK, Baek KH, Kang SC (2012) Control of Salmonella in foods by using essential oils: a review. Food Res Int 45:722–734. https://doi.org/10.1016/j.foodres.2011.04.052
Bakkali F, Averbeck S, Averbeck D, Idaomar M (2008) Biological effects of essential oils—a review. Food Chem Toxicol 46:446–475. https://doi.org/10.1016/j.fct.2007.09.106
Barata AM, Rocha F, Lopes V, Carvalho AM (2016) Conservation and sustainable uses of medicinal and aromatic plants genetic resources on the worldwide for human welfare. Ind Crops Prod 88:8–11. https://doi.org/10.1016/j.indcrop.2016.02.035
Bassolé IHN, Juliani HR (2012) Essential oils in combination and their antimicrobial properties. Molecules 17:3989–4006. https://doi.org/10.3390/molecules17043989
Batiha GES, Beshbishy AM, Wasef LG, Elewa YHA, Al-Sagan AA, El-Hack MEA et al (2020) Chemical constituents and pharmacological activities of garlic (Allium sativum L.): A review. Nutrients 12:1–21. https://doi.org/10.3390/nu12030872.
Bhavaniramya S, Vishnupriya S, Al-Aboody MS, Vijayakumar R, Baskaran D (2019) Role of essential oils in food safety: antimicrobial and antioxidant applications.Grain Oil Sci Technol 2:49–55.
Bilia AR, Piazzini V, Guccione C, Risaliti L, Asprea M, Capecchi G, Bergonzi MC (2017) Improving on nature: the role of nanomedicine in the development of clinical natural drugs. Planta Med 83:366–381. https://doi.org/10.1055/s-0043-102949
Cadar RL, Amuza A, Dumitras DE, Mihai M, Pocol CB (2021) Analysing clusters of consumers who use medicinal and aromatic plant products. Sustain 13:1–16. https://doi.org/10.3390/su13158648
Calvo-Irabien LM (2018) Native Mexican aromatic flora and essential oils: current research status, gaps in knowledge and agro-industrial potential. Ind Crops Prod 111:807–822. https://doi.org/10.1016/j.indcrop.2017.11.044
Carvalho AA, Andrade LN, De Sousa ÉBV, De Sousa DP (2015) Antitumor phenylpropanoids found in essential oils. Biomed Res Int. https://doi.org/10.1155/2015/392674.
Carvalho IT, Estevinho BN, Santos L (2016) Application of microencapsulated essential oils in cosmetic and personal healthcare products—a review. Int J Cosmetic Sci, 109–119. https://doi.org/10.1111/ics.12232.
Chamundeeswari M, Jeslin J, Verma ML (2019) Nanocarriers for drug delivery applications. Environ Chem Lett 17:849–865. https://doi.org/10.1007/s10311-018-00841-1
Chaudhari S (2017) Nutraceuticals: a review. World J Pharmacy Pharmaceut Sci, pp 681–739. https://doi.org/10.20959/wjpps20178-9825.
Christaki E, Giannenas I, Bonos E, Florou-Paneri P (2019) Innovative uses of aromatic plants as natural supplements in nutrition. Elsevier, Amsterdam. https://doi.org/10.1016/B978-0-12-814700-9.00002-9
Das TK (2020) Health risk assessment of heavy metal in soil irrigated with paper mill effluent. Ann Plant Soil Res 22:1–8.
Dhifi W, Bellili S, Jazi S, Bahloul N, Mnif W (2016) Essential oils' chemical characterization and investigation of some biological activities: a critical review. Medicines 3:25. https://doi.org/10.3390/medicines3040025
Dixon GR, Aldous DE (2014) Preface. Hortic Plants People Places, Vol 2 Environ Hortic 2:vii–x. https://doi.org/10.1007/978-94-017-8581-5.
Dosoky NS, Setzer WN (2018) Chemical composition and biological activities of essential oils of curcuma species. Nutrients 10:10–17. https://doi.org/10.3390/nu10091196
Dutta S, Munda S, Devi N, Lal M (2018) Compositional variability in leaves and inflorescence essential oils of Cymbopogon khasianus (Hack.) Stapf ex Bor Collected from Meghalaya: a biodiversity hotspot. J Essent Oil-Bearing Plants 21:640–657. https://doi.org/10.1080/0972060X.2018.1486233.
Elshafie HS, Camele I (2017) An overview of the biological effects of some mediterranean essential oils on human health. Biomed Res Int. https://doi.org/10.1155/2017/9268468.
Cilak GO, Gamze NM, Bulent K (2021) Legislation on aromatic herbs in food. Arom Herbs Food, pp 405–438.
Falleh H, Ben Jemaa M, Djebali K, Abid S, Saada M, Ksouri R (2019) Application of the mixture design for optimum antimicrobial activity: combined treatment of Syzygium aromaticum, Cinnamomum zeylanicum, Myrtus communis, and Lavandula stoechas essential oils against Escherichia coli. J Food Process Preserv 43:1–11. https://doi.org/10.1111/jfpp.14257
Falleh H, Ben Jemaa M, Saada M, Ksouri R (2020) Essential oils: a promising eco-friendly food preservative. Food Chem 330:127268. https://doi.org/10.1016/j.foodchem.2020.127268.
Farnsworth NR, Akerele O, Bingel AS, Soejarto DD, Guo Z (1985) Medicinal plants in therapy. Bull World Health Organ 63:965–981. https://doi.org/10.1016/0378-8741(87)90016-x
Fierascu RC, Fierascu I, Baroi AM, Ortan A (2021) Selected aspects related to medicinal and aromatic plants as alternative sources of bioactive compounds. Int J Mol Sci 22:1–20. https://doi.org/10.3390/ijms22041521
Freeman M, Ayers C, Peterson C, Kansagara D (2019) Aromatherapy and essential oils: a map of the evidence 2019.
González-Minero FJ, Bravo-Díaz L (2019) The use of plants in skincare products, cosmetics and fragrances: past and present. Cosmetics 5:1–9. https://doi.org/10.3390/cosmetics5030050
Grandview research (2021) Aromatherapy Market Size, Share & Trends Analysis Report By Product (Consumables, Equipment), By Mode Of Delivery (Topical Application, Aerial Diffusion), By Application, By Distribution Channel, By End-use, By Region, And Segment Forecasts, 2021–2028. Aromatherapy market size report.
Guha AK et al (2015) Characterization and composting of textile sludge. Resources Environ, pp 53–58
Guimarães R, Barros L, Carvalho AM, Sousa MJ, Morais JS, Ferreira ICFR (2009) Aromatic plants as a source of important phytochemicals: vitamins, sugars and fatty acids in Cistus ladanifer, Cupressus lusitanica and Eucalyptus gunnii leaves. Ind Crops Prod 30:427–430. https://doi.org/10.1016/j.indcrop.2009.08.002
Hassan S, Chukwuebuka E, Habibu T, Jonathan I, Michael C, Patrick-Iwuanyanwu O, Onyeike KP, Ephraim-Emmanuel B (2020)

Dietary supplements: types, health benefits, industry and regulation 2020.
Hongratanaworakit T (2011) Aroma-therapeutic effects of massage blended essential oils on humans. Nat Prod Commun 6:1199–1204. https://doi.org/10.1177/1934578x1100600838
Isman MB (2020) Commercial development of plant essential oils and their constituents as active ingredients in bioinsecticides. Phytochem Rev 19:235–241. https://doi.org/10.1007/s11101-019-09653-9
Jamshidi-Kia F, Lorigooini Z, Amini-Khoei H (2018) Medicinal plants: Past history and future perspective. J HerbMed Pharmacol 7:1–7. https://doi.org/10.15171/jhp.2018.01.
Joseph Mari BQ, Faller EM (2021) A review on the different studies on aromatherapy conducted in the Philippines. GSC Biol Pharm Sci 16:028–031. https://doi.org/10.30574/gscbps.2021.16.2.0223.
Karadag E, Samancioglu S, Ozden D, Bakir E (2017) Effects of aromatherapy on sleep quality and anxiety of patients. Nurs Crit Care 22:105–112. https://doi.org/10.1111/nicc.12198
Kumar Y, Prakash O, Tripathi H, Tandon S, Gupta MM, Rahman LU et al (2018) AromaDb: a database of medicinal and aromatic plant's aroma molecules with phytochemistry and therapeutic potentials. Front Plant Sci 9:1–11. https://doi.org/10.3389/fpls.2018.01081
Kumar A, Jnanesha AC (2016) Medicinal and aromatic plants biodiversity in India and their future prospects: a review. Ind J Unani Med 04:6–13.
Lakey DK (2016) Ecological status of high-altitude medicinal plants and their sustainability: Lingshi, Bhutan. BMC Ecol 16:45 .https://doi.org/10.1186/s12898-016-0100-1
Lall N, Kishore N (2014) Are plants used for skin care in South Africa fully explored? J Ethnopharmacol 153:61–84. https://doi.org/10.1016/j.jep.2014.02.021
Lellis B, Fávaro-Polonio CZ, Pamphile JA, Polonio JC (2019) Effects of textile dyes on health and the environment and bioremediation potential of living organisms.Biotechnol Res Innovat 3:275–290.
Leyva-López N, Gutiérrez-Grijalva EP, Vazquez-Olivo G, Heredia JB (2017) Essential oils of oregano: Biological activity beyond their antimicrobial properties. Molecules , p. 22. https://doi.org/10.3390/molecules22060989.
Lv J, Huang H, Yu L, Whent M, Niu Y, Shi H et al (2012) Phenolic composition and nutraceutical properties of organic and conventional cinnamon and peppermint. Food Chem 132:1442–1450. https://doi.org/10.1016/j.foodchem.2011.11.135
Malik B, Pirzadah TB, Kumar M, Rehman RU (2017) Biosynthesis of nanoparticles and their application in pharmaceutical industry. In: Kalia V, Saini A (eds) Metabolic engineering for bioactive compounds. Springer, Singapore. https://doi.org/10.1007/978-981-10-5511-9_16
Manasa V, Vaishnav SR, Tumaney AW (2021) Physicochemical characterization and nutraceutical compounds of the selected spice fixed oils. J Food Sci Technol 58:3094–3105. https://doi.org/10.1007/s13197-020-04813-8
Matsumura M (1997) Correlated responses of life history traits, wing length, and flight propensity to wing-form selection in the white-backed planthopper, Sogatella furcifera (Horváth) (Hemiptera: Delphacidae). Appl Entomol Zool 32:437–445. https://doi.org/10.1303/aez.32.437
Mishra B, Chandra M (2022) Evaluation of phytoremediation potential of aromatic plants: a systematic review. J Appl Res Med Aromatic Plants 31:2214–7861
Moshahary S, Mishra P (2021) Synthesis of silver nanoparticles (AgNPs) using culinary banana peel extract for the detection of melamine in milk. J Food Sci Technol 2021:797–804. https://doi.org/10.1007/s13197-020-04791-x
Mugao LG, Gichimu BM, Muturi PW, Mukono ST (2020) Characterization of the volatile components of essential oils of selected plants in Kenya. Biochem Res Int. https://doi.org/10.1155/2020/8861798
Mustafa S et al (2021) Microalgae biosorption, bioaccumulation and biodegradation efficiency for the remediation of wastewater and carbon dioxide mitigation: Prospects, challenges and opportunities. J Water Process Eng 41:102009.
Muyima NYO, Zulu G, Bhengu T, Popplewell D (2002) The potential application of some novel essential oils as natural cosmetic preservatives in a aqueous cream formulation. Flavour Fragr J 17:258–266. https://doi.org/10.1002/ffj.1093
Ovais M, Khalil AT, Raza A, Khan MA, Ahmad I, Islam NU, Saravanan M, Ubaid MF, Ali M, Shinwari ZK (2016) Green synthesis of silver nanoparticles via plant extracts: beginning a new era in cancer theranostics. Nanomedicine (Lond) 23:3157–3177. https://doi.org/10.2217/nnm-2016-0279
Palazzolo E, Armando Laudicina V, Antonietta GM (2013) Current and potential use of citrus essential oils. Curr Org Chem 17:3042–3049. https://doi.org/10.2174/13852728113179990122
Pandey J, Verma RK, Singh S (2019) Suitability of aromatic plants for phytoremediation of heavy metal contaminated areas: a review. Int J Phytoremediation 21:405–418. https://doi.org/10.1080/15226514.2018.1540546. (**Epub 2019 Jan 18 PMID: 30656974**)
Pandey VC, Pandey DN, Singh N (2015) Sustainable phytoremediation based on naturally colonizing and economically valuable plants. J Clean Prod 86:37–39.
Park JB (2011) Identification and quantification of a major anti-oxidant and anti-inflammatory phenolic compound found in basil, lemon thyme, mint, oregano, rosemary, sage, and thyme. Int J Food Sci Nutr 62:577–584. https://doi.org/10.3109/09637486.2011.562882
Patel N, Patel, Soni A, Garuba T, Oyeyinka S, Akeem, Krishnamurthy R (2020). ANTIOXIDANT AND ANTIMICROBIAL POTENTIALS OF SOME PLANT-BASED NATURAL DYES. 9. 2090-2101. 10.31032/IJBPAS/2020/9.9.5134.
Pereira CG, Barreira L, da Rosa NN, Nogueira JMF, Marques C, Santos TF et al (2017) Searching for new sources of innovative products for the food industry within halophyte aromatic plants: In vitro antioxidant activity and phenolic and mineral contents of infusions and decoctions of Crithmum maritimum L. Food Chem Toxicol 107:581–589. https://doi.org/10.1016/j.fct.2017.04.018
Pirzadeh K et al (2019) Strong influence of amine grafting on MIL-101 (Cr) metal–organic framework with exceptional CO2/N2 selectivity. Indust Eng Chem Res 59:366–378.
Ramsey JT, Shropshire BC, Nagy TR, Chambers KD, Li Y, Korach KS (2020) Essential oils and health. Yale J Biol Med 2:291–305
Raut JS, Karuppayil SM (2014) A status review on the medicinal properties of essential oils. Ind Crops Prod 62:250–264. https://doi.org/10.1016/j.indcrop.2014.05.055
Rehman R, Hanif MA, Mushtaq Z, Al-Sadi AM (2016) Biosynthesis of essential oils in aromatic plants: a review. Food Rev Int 32:117–160. https://doi.org/10.1080/87559129.2015.1057841
Reis D, Jones T (2017) Aromatherapy: using essential oils as a supportive therapy. Clin J Oncol Nurs 21:16–19. https://doi.org/10.1188/17.CJON.16-19
Riaz U et al (2021) A comprehensive review on emerging importance and economical potential of medicinal and aromatic plants (MAPs) in current scenario. Pak J Agric Res 4:381–392
Ribeiro-Santos R, Carvalho-Costa D, Cavaleiro C, Costa HS, Albuquerque TG, Castilho MC et al (2015) A novel insight on an ancient aromatic plant: The rosemary (Rosmarinus officinalis L.). Trends Food Sci Technol 45:355–368. https://doi.org/10.1016/j.tifs.2015.07.015.
Ríos JL (2016) Essential oils: What they are and how the terms are used and defined. Elsevier, Amsterdam. https://doi.org/10.1016/B978-0-12-416641-7.00001-8.

Sachdeva V, Roy A, Bharadvaja N (2020) Current prospects of nutraceuticals: a review. Curr Pharm Biotechnol 21:884–896. https://doi.org/10.2174/1389201021666200130113441

Salehi B, Zakaria ZA, Gyawali R, Ibrahim SA, Rajkovic J, Shinwari ZK et al (2019) Piper species: a comprehensive review on their phytochemistry, biological activities and applications. Molecules, 24. https://doi.org/10.3390/molecules24071364.

Samarth RM, Samarth M, Matsumoto Y (2017) Medicinally important aromatic plants with radioprotective activity. Futur Sci OA, 3. https://doi.org/10.4155/fsoa-2017-0061.

Sawamura M, Son US, Choi HS, Kim MSL, Phi NTL, Fears M et al (2004) Compositional changes in commercial lemon essential oil for aromatherapy. Int J Aromather 14:27–36. https://doi.org/10.1016/j.ijat.2004.02.001

Saxena S, Raja ASM (2014) Natural dyes: sources, chemistry, application and sustainability issues. In: Muthu S (eds) Roadmap to sustainable textiles and clothing. Textile science and clothing technology. Springer, Singapore. https://doi.org/10.1007/978-981-287-065-0_2

Sen T, Samanta SK (2014) Medicinal plants, human health and biodiversity: a broad review. Adv Biochem Eng Biotechnol 147:59–110. https://doi.org/10.1007/10_2014_273

Shah YR, Sen DJ, Patel RN, Patel JS, Patel AD, Prajapati PM. Available online http://www.ijddr.in Covered in Official Product of Elsevier , The Netherlands © 2010 IJDDR Aromatherapy : The Doctor Of Natural Harmony Of Body & Mind. Aromather Dr Nat Harmon Body Mind 2011;3:286–94.

Sharmeen JB, Mahomoodally FM, Zengin G, Maggi F (2021) Essential oils as natural sources of fragrance compounds for cosmetics and cosmeceuticals. Molecules, 26. https://doi.org/10.3390/molecules26030666.

Subramani T, Ganapathyswamy H (2020) An overview of liposomal nano-encapsulation techniques and its applications in food and nutraceutical. J Food Sci Technol 57:3545–3555. https://doi.org/10.1007/s13197-020-04360-2

Sut S, Baldan V, Faggian M, Peron G, Dall AS (2016) Nutraceuticals, a new challenge for medicinal chemistry. Curr Med Chem 23:3198–3223. https://doi.org/10.2174/0929867323666160615104837. (**PMID: 27319583**)

Tillett J, Ames D (2010) The uses of aromatherapy in women. J Perinat Neonatal Nurs 24:238–245. https://doi.org/10.1097/JPN.0b013e3181ece75d

Trevisan SCC, Menezes APP, Barbalho SM, Guiguer ÉL (2017) Properties of Mentha piperita: a brief review. World J Pharm Med Res 3:309–313

Trivedi A, Nayak N, Kumar J (2018) Recent advances and review on use of botanicals from medicinal and aromatic plants in stored grain pest management. J Entomol Zool Stud 6:295–300

Valderrama F, Ruiz F (2018) An optimal control approach to steam distillation of essential oils from aromatic plants. Comput Chem Eng 117:25–31. https://doi.org/10.1016/j.compchemeng.2018.05.009

Velmurugan P, Shim J, Seo SK et al (2016) Extraction of natural dye from Coreopsis tinctoria flower petals for leather dyeing—an eco-friendly approach. Fibers Polym, pp 1875–1883 .https://doi.org/10.1007/s12221-016-6226-0

Wandjou JGN et al (2022) Essential oils from Cameroonian aromatic plants as effective insecticides against mosquitoes, houseflies, and moths. Plants 11:2353

Watanabe E, Kuchta K, Kimura M, Rauwald HW, Kamei T, Imanishi J (2015) Effects of Bergamot (Citrus bergamia (Risso) Wright & Arn.) Essential oil aromatherapy on mood states, parasympathetic nervous system activity, and salivary cortisol levels in 41 healthy females. Complement Med Res 22:43–49. https://doi.org/10.1159/000380989.

Winkelman WJ (2018) Aromatherapy, botanicals, and essential oils in acne. Clin Dermatol 36:299–305. https://doi.org/10.1016/j.clindermatol.2018.03.004

Yakhlef G et al (2020) Chemical composition and insecticidal, repellent and antifungal activities of essential oil of Mentha rotundifolia (L.) from Algeria. Ind Crops Products 158:112–988.

Yuan R, Zhang D, Yang J, Wu Z, Luo C, Han L et al (2021) Review of aromatherapy essential oils and their mechanism of action against migraines. J Ethnopharmacol 265:113326. https://doi.org/10.1016/j.jep.2020.113326.

Yusuf M, Shabbir M, Mohammad F (2017) Natural colorants: historical, processing and sustainable prospects. Nat Prod Bioprospect 7:123–145. https://doi.org/10.1007/s13659-017-0119-9

El Zayyat EA et al (2017) Bioefficacy of some Egyptian aromatic plants on Culex pipiens (Diptera: Culicidae) adults and larvae. J Arthropod-Borne Dis 11:147.

Zdrojewicz Z, Waracki M, Bugaj B, Pypno D, Cabała K (2015) Medical applications of nanotechnology. Postepy Hig Med Dosw (online) 69:1196–1204. https://doi.org/10.5604/17322693.1177169

Publisher's Note Springer Nature remains neutral with regard to jurisdictional claims in published maps and institutional affiliations.

Springer Nature or its licensor (e.g. a society or other partner) holds exclusive rights to this article under a publishing agreement with the author(s) or other rightsholder(s); author self-archiving of the accepted manuscript version of this article is solely governed by the terms of such publishing agreement and applicable law.

2023 IEEE IAS Global Conference on Renewable Energy and Hydrogen Technologies (GlobConHT)
The Maldives National University, Male City (Maldives). Mar 11-12, 2023

Autonomous Active Grid islanding and DGs outage detection in a μG utilizing Goertzel Algorithm in collaboration with Fuzzy Inferencing System

Samavedam Swetha
Electrical Engineering Department
Delhi Technological University,
Delhi
swethasamavedam@gmail.com

Vishal Verma
Electrical Engineering Department
Delhi Technological University,
Delhi
vishalverma@dce.ac.in

2023 IEEE IAS Global Conference on Renewable Energy and Hydrogen Technologies (GlobConHT) | 979-8-3503-3211-7/23/$31.00 ©2023 IEEE | DOI: 10.1109/GLOBCONHT56829.2023.10087768

Abstract— **Microgrid enables harvesting of locally available renewable energy sources and deliver it to nearby load efficiently, for which it is mandated to work effectively without failure both in presence and in absence of grid. To ascertain its reliability and robustness, it requires fast and efficient islanding detection and information of available distributed generations (DGs) in connection to device seamless transition from grid – tied mode to islanded mode and vice – versa. The paper proposes Goertzel based active islanding detection technique by incorporating fuzzy logic based inferencing system for effective embedding of control of DGs for better planning and higher efficiency of energy generation without using any communication system. The simulation results presented in the paper demonstrate the efficacy of the proposed method and inferencing system to detect both grid islanding and status of the outage of individual DGs in the microgrid without compromising on the power quality.**

Keywords— Discrete Fourier Transform; Microgrid; Distributed generation; Goertzel Algorithm; Fuzzy inferencing system; Islanding detection

I. INTRODUCTION

A sustainable, dependable, and environmentally friendly energy source is the need of the time due to the fast depletion of fossil fuel reserves, climate changes due to global warming, rising energy consumption, and the need of cost-effective energy availability. Due to the near omnipresence of electrical power network, the integration of renewable energy sources is envisaged as a befitting solution. Distributed/Decentralized generation (DG) incorporating connected loads together with storage systems and control strategies to integrate renewable energy sources (RES) are generally categorized as Microgrid (μG) which is capable of operating in both grid – tied and islanded mode. Without entirely retransforming the distribution power infrastructure and adopting the μG architecture of distributed system, high penetration of RES as DG's can be possible.

With sophisticated communication shared amongst many distributed generation points, μG can be made more stable and reliable. However, due to the intermittent and bi-directional power flow, DG imposes complexity and operational constraints in the μG such as power quality, power flow control, operational efficiency, safety, voltage and frequency regulation, islanding detection and protection [1]. A noticeable shift towards active grids has been observed recently which advocates for inclusion of storage systems to make the μG capable of working in islanded mode and coupling to flexible transmission systems to enable the reliable operation of μG and grid at large [2]. Such intricate operations in μG calls for monitoring of the DG units at every level to enable the reliable operation of μG and grid at large.

The accurate and fast detection of islanding condition is a significant issue since the DG continues to supply power to the connected load, while at least one of the DG acting as voltage source in the μG, even when the utility's power supply is no longer available to strike energy balance. Both intentional and non - intentional islanding conditions can occur in the μG, where unintentional islanding can happen at any moment owing to recurring faults or other uncertainties in the μG and intentional islanding is done as a part of the repository maintenance in the primary utility circuit. Correct unintentional islanding identification is therefore seen as a crucial requirement for healthy operation of μG and integrated power distribution networks at large as per IEEE 1547.1 [3], UL 1741 and IEC – 62116 [4] standards and desirable characteristics, which includes reliability even under non – detection zone (NDZ), selectivity, and the differentiation between an islanding state and grid perturbations. In a μG, it is expected that the inverter interfacing RES transits seamlessly from grid – tie mode to islanded mode and vice versa, which becomes possible with fast and reliable islanding detection techniques.

Islanding detection is reported to be based on: Grid resident detection [5], External switched capacitor detection [5], and Inverter – resident detection [5]. The first two former approaches require either a communication system or an external switched capacitor at the PCC, raising system costs and complexity while, the later utilizes software – based approach together with, software-based approach together with active and passive modes of detection. The passive detection methods follow the power perturbations leading to the islanding by identifying through change in a system characteristic such as amplitude, harmonics of the voltage, phase etc., [6], [7] whereas, the active methods cause a controlled disturbance at the PCC to detect islanding by observing the response of the system. To increase reliability, passive methods - which possess NDZ, are frequently paired with active methods [5]. Active methods so far reported can significantly lower the NDZ, but they may pollute the grid and mistakenly identify islanding, especially if several inverters are connected in tandem [8], [9] Fast and reliable detection of grid is crucial for operation of μG, especially in islanded operation with negligible NDZ and without having to compromise on the μG's power quality [10].

Authorized licensed use limited to: DELHI TECHNICAL UNIV. Downloaded on April 13,2023 at 10:18:40 UTC from IEEE Xplore. Restrictions apply.

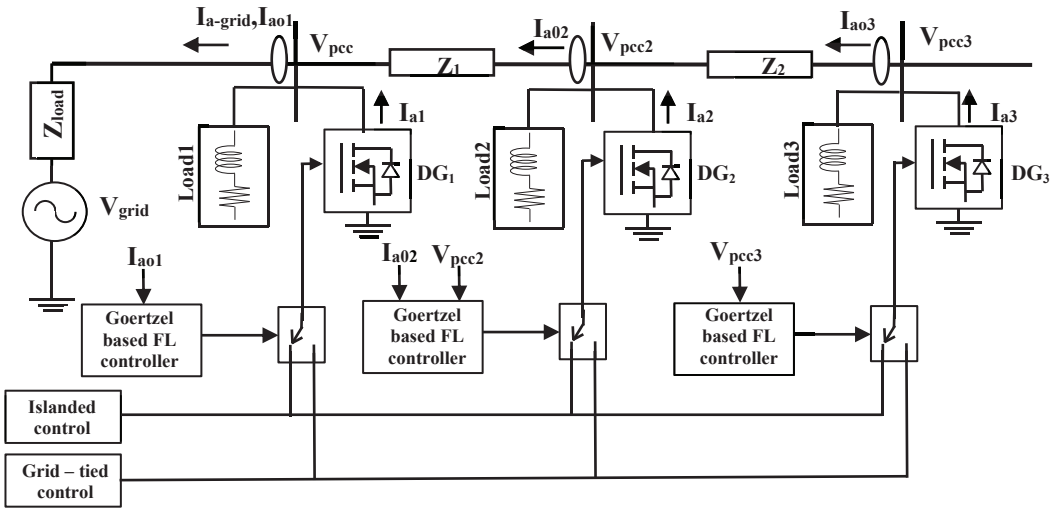


Fig1: Microgrid structure employed for the verification of proposed Fuzzy logic algorithm

The utility grid operates as voltage source along with other grid connected inverters (GCI) in the grid-forming mode (GFM), controlling the voltage, while majority of inverters function in grid-supportive mode (GSM), injecting current by operation with MPPT [11]. Therefore, it is by far unknown to the inverters operating with GSM which other DG sources are connected to the μG and contributing, and which all are disconnected. Often in Master- Slave operation of μG, when the utility system is disconnected, one of the DG may need to operate in GFM, whereas some(slaves) DGs may continue to operate with MPPT and other (slaves) DGs are forced to operate in de – loaded mode (away from MPPT) to match the power demand. Contingent situation may arise with the loss of one or more DG sources in the islanded mode, which will remain stable if the DGs operating on de – loaded mode are able to detect the islanding, thereby moving towards MPPT by reducing the de - loading factor. This calls for a parallel communication network with each DG also acting as communication node. The introduction of cost-effective wireless communication network will result in latency – related issues, whilst using high end communication will raise the system cost.

This paper suggests a reliable, effective, and quick islanding detection with DG tagging strategy for operation with multiple DGs in a μG system, by injecting ninth harmonic pilots, that can quickly identify grid islanding along with specific DGs failure. The Goertzel algorithm is employed at each node in autonomous mode to observe the 9^{th} harmonic component of the voltage at the point of common coupling (V_{pcc}) together with the current in the line around each node including the one transacting power with the grid interface. The injected balanced 9^{th} harmonic currents at a set value, aggregate vectorially at grid interfaced node to zero value, being equi- displaced phase, with respect to one another, thus causing extremely minimal harmonics impact, as they are injected into the grid by each DG. The 9^{th} harmonic detection by Goertzel algorithm is analyzed using the Fuzzy logic at each DG node to enable the autonomous monitoring and control of the DG's connected to the μG.

II. PROPOSED ISLANDING DETECTION TECHNIQUE

Fig1. depicts the single line diagram of the considered scaled down Microgrid structure employed for analysis and inferencing design in this work. Three DGs (Photovoltaic fed Inverters) are connected to the μG, where each DGs maximum power rating is kept at 3kW and is tied to the 415V distribution grid, injecting power at unity power factor through its PCC in GSM. The three local loads, each 4kW are connected at each PCC nodes. An AC source of 415V, 50Hz, and lumped line impedances Z_1 and Z_2 are represented for the modelling of the utility distribution grid to explore the efficiency of the proposed algorithm and to evaluate the suggested islanding detection approach. The line impedance between two sources is considered resistive, being a distribution line operating at low voltage levels. Owing to minimal line reactance, the V_{pcc} of each DG will be approximately in same phase with the other; accordingly, the angle between the V_{pcc} at line frequency is neglected. Accordingly, each DG is reprogrammed for updating the number of other DGs connected to the μG.

A. Harmonic component injection

The considered system is 3 - phase 4 – wired. Thus, the third harmonic and its odd multiple currents flow through the neutral wire, and do not flow in the line in balanced conditions. So, harmonic pilots of the order 3n, where n = 1,3,5,7,9…. can be injected in the line, to facilitate the islanding detection. Thus, phase-displaced 9^{th} harmonic current components of equal magnitude accounting to a Total Harmonic Distortion (THD) less than 4% as given in Table I [11], are injected by each of the three DGs accounting to negligible grid current pollution. Accordingly, the angle between the current injected by the three DGs at 9^{th} harmonic will be 120˚ (360˚/n) where n is equal to 3. The following discussion will focus on single phase current and voltage phasors, with the extrapolation to the other two phases on similar logic. Thus, the current injected at the 9th harmonic by DG nearer to grid connection, i.e., DG_1 will be at 0˚, whereas for the DG_2, it is kept at 240˚ and for DG_3 at 120˚ as shown in Fig 2. The total of the three harmonic current phasors, at 9^{th} harmonic adds to 0, thus the net harmonic current (at 9^{th} harmonic) injected into the grid would be zero eliminating the problem of grid pollution in active islanding detection methods as against other reported techniques [2].

Authorized licensed use limited to: DELHI TECHNICAL UNIV. Downloaded on April 13,2023 at 10:18:40 UTC from IEEE Xplore. Restrictions apply.

TABLE I
MAXIMUM ALLOWED THD DUE TO HARMONIC CURRENT INJECTION

Harmonics	THD limit
3rd ~ 9th	< 4.0%
11th ~ 15th	< 2.0%
17th ~ 21st	< 1.5%
23rd ~ 33rd	< 0.6%
Above 33rd	< 0.3%

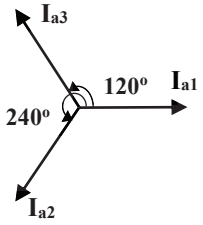


Fig.2 Proposed harmonic pilots' injection

B. Goertzel algorithm and DG failure detection

The Goertzel algorithm is used to monitor the V_{pcc} and line current of the 9th harmonic component to compute the DFT spectra. The computation of Goertzel algorithm for N^{th} – value of frequency is more efficient than direct computation of DFT [10] and it provides the magnitude and phase of the line currents and V_{pcc} at 9th harmonic frequency with nominal computation easily implementable on low-cost microcontrollers.

1) Detection of Grid failure

Since, each DG in the microgrid is acting as a 9th harmonic current source injecting harmonic, the islanding of the grid poses very high impedance to these 9th harmonic pilots which are forced to flow via the loads linked at each PCC. The 9th harmonic content at the V_{pcc} of each DG will increase significantly because the equivalent impedance offered to the 9th harmonic pilots under this configuration becomes higher than that of the grid tied condition. The Goertzel algorithm, which is integrated into the control of each inverter enacting as DGs, can detect the thresholds to quickly identify the grid islanding.

2) Detection of islanding of a particular DG in the μG

By taking the notations I_{a1}, I_{a2} and I_{a3} for the current phasors at 9th harmonic of the DG_1, DG_2, and DG_3 respectively injected into the grid, I_{ao1}, I_{ao2}, and I_{ao3} are the line currents at 9th harmonic in the sections of the μG, and $I_{a\text{-}grid}$ for the current flowing into the grid. The relation between the above phasors can be approximated as follows:

$$I_{ao3} = I_{a3}$$

$$I_{ao2} = I_{ao3} + I_{a2}$$

$$I_{ao1} = I_{ao2} + I_{a1}$$

$$I_{ao1} = I_{a\text{–}grid}$$

Similarly, the voltages at the point of common coupling of DG_1, DG_2, DG_3 are depicted as V_{pcc1}, V_{pcc2} and V_{pcc3} respectively. V_{pcc1} is 0, because I_{ao1} is 0. The relation between the currents injected by the DGs and the PCC voltages are as follows:

$$V_{pcc1} = 0$$

$$V_{pcc2} = I_{ao2} * (R_1 + R_2)$$

$$V_{pcc3} = (I_{ao2} * (R_1 + R_2)) + (I_{ao3} * R_2)$$

The voltage and current phasors under normal operation are shown in Fig 3. and Fig 4. respectively. When a DG is islanded from the μG, the DGs ahead of the disconnected DG would detect the islanding by analysing the 9th harmonic current, and since the current adds up only in the forward direction, because the grid offers zero impedance to the 9th harmonic currents, the trailing DGs would detect the islanding by monitoring the 9th harmonic V_{pcc}. Consider a case when the DG_3 disconnects from the grid. Prior to the disconnection of DG_3, the net 9th harmonic current injected into the grid, I_{ao1} is zero. Post disconnection of DG_3, the net current being injected into the grid redistributes having a magnitude of $|I_{h9}|$ at 300˚, which is exactly the negative of the harmonic injected by the disconnected DG_3. A phase jump and magnitude change will be witnessed at the V_{pcc}. The current and voltage phasors post disconnection of DG_3 are shown in Fig 5. and Fig 6. respectively.

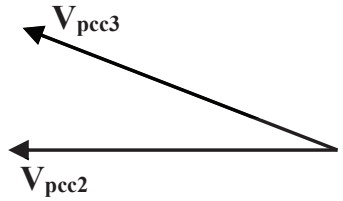


Fig.3 Voltage phasor under normal operation

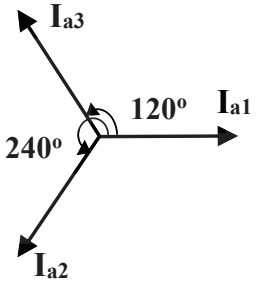


Fig.4 Current phasor under normal operation

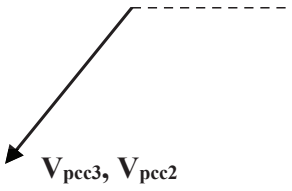


Fig.5 Voltage phasor when DG3 is disconnected.

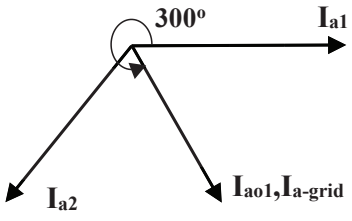


Fig. 6 Current phasor when DG3 is disconnected.

Authorized licensed use limited to: DELHI TECHNICAL UNIV. Downloaded on April 13,2023 at 10:18:40 UTC from IEEE Xplore. Restrictions apply.

III. FUZZY LOGIC BASED INFERENCING SYSTEM

The goal of fuzzy inference system (FIS) is to process the data acquired from voltage and current phasors at each node separately in autonomous mode. Type - 1 Mamdani FIS has been employed to communicate the information about islanding of the grid and DG outages among multiple interconnected DGs because of its robustness to sudden changes in voltage or current sensing data owing to its non - linearity and adaptivity [12].

Since the effectiveness of the fuzzy decision-making model is significantly influenced by the membership function's shape, a careful selection has been done to configure them as broader/thicker and thinner/narrower. The magnitudes and phases of the current and V_{pcc} at 9^{th} harmonic frequency have been computed using the Goertzel algorithm which is given as input to the Fuzzy inference system (FIS). Simple and intuitively clear triangular membership function is considered for inputs: angle_I_{aon} and angle_V_{pccn} in radian, where n is the n^{th} node and the output represents the islanding status of DGs and that of the µG from grid.

The fuzzy inference system is designed for three cases of operation of µG as shown in Table II, Table III and Table IV when observed from DG_1, DG_2 and DG_3 locations respectively based on current for outage of DGs, whereas, the increase of the 9^{th} harmonic voltages at each PCC beyond threshold values indicates the islanding of the grid. The Table II individually deals with observing the status of other DGs and normal operation of grid when observed from DG_1 location. Similarly, the Table III and Table IV follows the suit respectively for DG_2 and DG_3 locations. The fuzzification membership function in accordance with Table II, III and IV is depicted in Fig 7, Fig 8 and Fig 9 respectively. The outage of multiple DGs is fuzzified in the overlapping area of output membership function as shown in Fig 7, Fig 8 and Fig 9 for respective DG locations. The main aim to make aware individually each DG autonomously about islanding condition of the grid and outages of interconnected DGs aids to better control the µG in both islanded and grid connected conditions. Fuzzy inferencing system assist the embedded control at each DGs based on locations of DG in leading or trailing position with respect to point of observation, i.e., DG_3 will know when DG_1 and/or DG_2 is disconnected to better amend the control of inverter. The advantage of the application of fuzzy logic inferencing system is fast detection of islanding condition and outages of other DGs, one or multiple at a time, i.e., detection of DG_1 and DG_2 together with reference to the considered µG. The fuzzy output at DG_1, DG_2 and DG_3 is obtained after defuzzification as operating on output membership function at each DG is shown in Table V, Table VI, and Table VII respectively.

Since the current at 9^{th} harmonic frequency adds up only in the forward direction since the grid offers no impedance to 9^{th} harmonic pilots, the DG_1 is the most leading, and DG_3 is the most trailing DG for the considered µG. Based on the proposed scheme of islanding detection, the DGs ahead of a disconnected DG would detect the islanding based on the 9^{th} harmonic V_{pcc} and trailing DGs would detect the disconnection by monitoring the 9^{th} harmonic current. When

TABLE II

Cases	angle_I_{ao1}	Inference
Case 1	[-0.1 1.9]	Normal operation
Case 2	[-1.6 0]	DG_2 disconnected
Case 3	[-4.1 -0.6]	DG_3 disconnected

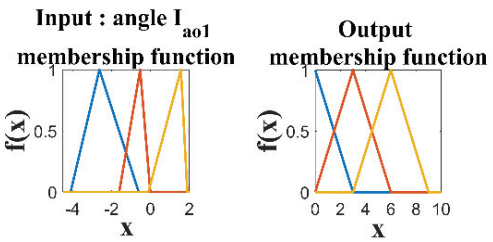


Fig.7 Input and Output membership functions of DG1

TABLE III

Cases	angle_ I_{ao2}	magn_V_{pcc2}	Inference
Case 1	[0 1.8]	[0 0.5]	Normal operation
Case 2	[0 1.8]	[0.97 1.5]	DG_1 disconnected
Case 3	[1.5 3]	[0.45 1.5]	DG_3 disconnected

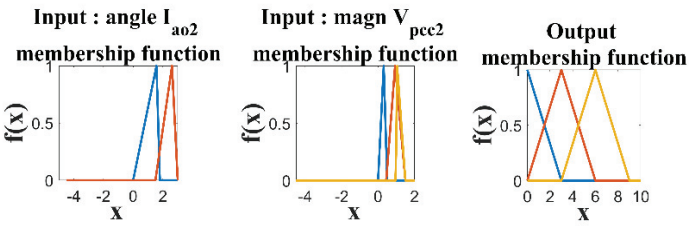


Fig.8 Input and Output membership functions of DG2

TABLE IV

Cases	angle_V_{pcc3}	Inference
Case 1	[1.35 3.5]	Normal operation
Case 2	[0 1.4]	DG_1 disconnected
Case 3	[0 0.8]	DG_2 disconnected

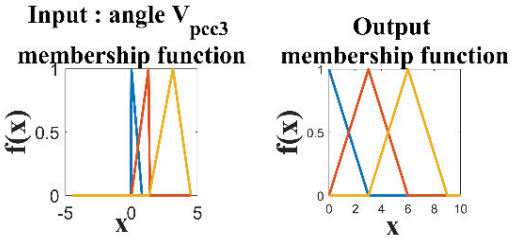


Fig.9 Input and Output membership functions of DG_3

Authorized licensed use limited to: DELHI TECHNICAL UNIV. Downloaded on April 13,2023 at 10:18:40 UTC from IEEE Xplore. Restrictions apply.

DG_1 is disconnected, the trailing DGs, i.e., DG_2 and DG_3 would observe the phase angle of V_{pcc2} and V_{pcc3} respectively. On the other hand, if DG_2 is disconnected, the trailing DG, i.e., DG_3 would observe the phase angle of V_{pcc3}, while for the leading DG, i.e., DG_1will observe the phase angle of I_{ao1}. Similarly, DG_3 being the most trailing DG, the two leading DGs, i.e., DG_2 and DG_1 should observe the phase angle of I_{ao2} and I_{ao1} respectively. Accordingly, if-then cases formulated for all DG locations based on phase angle of both V_{pccn} and I_{aon} at respective point of common coupling for observation of normal operation and outage of all DGs in the μG. The membership function for phase angle of I_{ao1} as shown in Fig 7 becomes unilateral in respect of outages of DG_2 and/or DG_3 as both the DGs lie on the trailing end of DG_1. However, both the input functions, namely, phase angle of I_{ao2} and magnitude of V_{pcc2} as shown in Fig 8, have been considered to develop the fuzzy inferencing system for DG_2 (DGs having both leading and trailing location of other DGs). The membership functions magn_V_{pcc2} and angle_ I_{ao2} are unilateral because magnitude in respect of former is always positive and later is detecting the outage of DG trailing to it. The membership function angle_V_{pcc3} as shown in Fig 9 is also unilateral being the most trailing DG detecting the outage of DGs ahead to it. The weight distribution of the membership function thus formed is chosen in a manner that the weights of I_{aon} and V_{pccn} at respective PCC accounting for the outage of multiple DGs constructing the output to fall exactly in the overlapping period of the triangles representing the outage corresponding to individual DGs distinguishing it from the normal condition of operation.

TABLE V

Crisp number range	Condition of grid
[0 0 3]	Normal operation
[0 3 6]	DG2 is disconnected
[3 6 9]	DG3 is disconnected

TABLE VI

Crisp number range	Condition of grid
[0 0 3]	Normal operation
[0 3 6]	DG1 is disconnected
[3 6 9]	DG3 is disconnected

TABLE VII

Crisp number range	Condition of grid
[0 0 3]	Normal operation
[0 3 6]	DG1 is disconnected
[3 6 9]	DG2 is disconnected

IV. RESULTS AND DISCUSSION

The theoretical analysis of the proposed islanding detection methodology is duly supported by simulation study under MATLAB/SIMULINK environment on the developed μG. The considered microgrid system has three DG sources with 3kW capacity, and 4kW load connected at each common coupling point. The line resistances Z_1 and Z_2 are 0.48Ω and 0.73Ω representing 1.7km and 2.5km feeder line respectively. The line is assumed to be resistive owing to the R/X ratio greater than 7. The grid is modelled for 415V, 50Hz. Each DG is connected and/or disconnected with the grid through circuit breakers. Goertzel algorithm is modelled for a sampling frequency of 20kHz at a sampling rate of 2000 per cycle to detect 9th harmonic components of 450Hz.

To amicably test the fuzzy inferencing system, the DG_3 is taken off from the grid intentionally. Both DG_1 and DG_2 are demonstrated to detect this condition through the current harmonic phasor as they are leading ahead in location to the disconnected DG_3. Under normal condition of operation, the 9^{th} harmonic current phasors depicted in Fig 10 duly shown as DG_1 (red), DG_2 (yellow), DG_3 (blue) and I_{ao1} (magenta)(the harmonic current flowing into the grid) to be zero. The 9^{th} harmonic voltage phasor under normal condition of operation is shown in Fig 11, which depicts the V_{pcc3} (red) and V_{pcc2} (yellow), complying with the theoretical calculations that Vpcc1 is zero, due net zero 9^{th} harmonic component. The 9^{th} harmonic current phasors when DG_3 is disconnected is shown in Fig 12, where I_{ao1} (magenta) is shown non – zero having finite magnitude, points in the direction opposite to the phasor that was injected by DG_3 before disconnection. The voltage phasors post disconnection of DG_3 is shown in Fig 13. The simulated result on the polar plots confirms the proposed algorithm for assessment of outage of DG_3 respectively.

Further to evaluate the efficacy of the proposed fuzzy inferencing system working in tandem with outputs of Goertzel algorithm based assessment, the triangular membership functions as shown in Fig 7, Fig 8, and Fig 9, for DG_1, DG_2 and DG_3 respectively are formulated using Fuzzy logic toolbox in MATLAB/Simulink environment to fuzzify and defuzzify for drawing the phasor inference based on V_{pcc1}, V_{pcc2}, I_{ao1} and I_{ao2}. Two instances: case1: normal functioning of the μG and case2: when DG_3 is islanded from the μG have been processed. The output of fuzzy inference system draws out for DG_1, DG_2 and DG_3 locations is 0.9667, 1.0000 and 1.4635 respectively which when referred with Table V, Table VI and Table VII respectively, confirm normal operating condition. While the proposed algorithm draws out crisp values in the latter case as 5.6998 and 6.0000 at DG_1 and DG_2 locations respectively, indicating the disconnection of DG_3 when referred with Table V and Table VI. To further probe the efficacy of the proposed inferencing system, a case when both DG_3 and DG_2 are disconnected is considered, the fuzziness in FIS at DG_1 detects a value of 4.2075 which lies in the intersection zone of detection of islanding condition of DG_2 and DG_3 as referred in Table V and Fig 7. Thus clear cut detection of the outage of DG_3, bring merit to the proposed inferencing system to add the control of the other DGs connected to the μG for mostly the power requirements of the connected loads based for reliable and efficient operation of the μG irrespective of grid disconnections and outages of DGs by better planning of the control by increasing the deloading efficiency by making better use of the remaining connected DG sources by operating close to MPPT and imparting adequate inertial response.

V. RESULTS AND DISCUSSION

The proposed Goertzel algorithm based grid islanding cum DG outage detection technique incorporating fuzzy inferencing system has been verified using MATLAB/Simulink based results. The results successfully demonstrate fast, accurate and reliable detection of grid islanding and/or outage of the DGs in the μG aiding to control of inverters for seamless transit between grid – tied mode to islanded mode with efficient planning for matching generated power with the load for working efficiently in islanded operation of μG and prevention of reverse power flow to preserve the efficacy of existing protection scheme.

Authorized licensed use limited to: DELHI TECHNICAL UNIV. Downloaded on April 13,2023 at 10:18:40 UTC from IEEE Xplore. Restrictions apply.

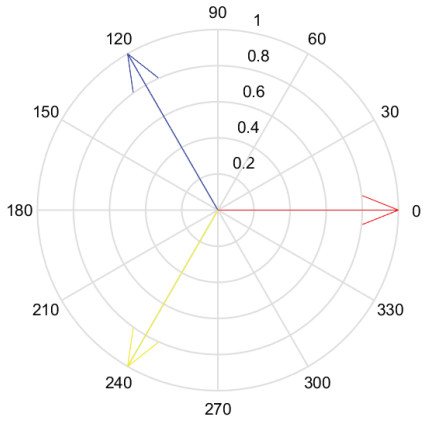


Fig.10 9th harmonic current phasor under normal operation-Simulation

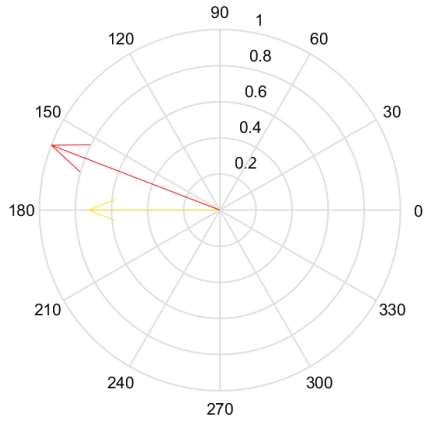


Fig.11 9th harmonic voltage phasor under normal operation- Simulation

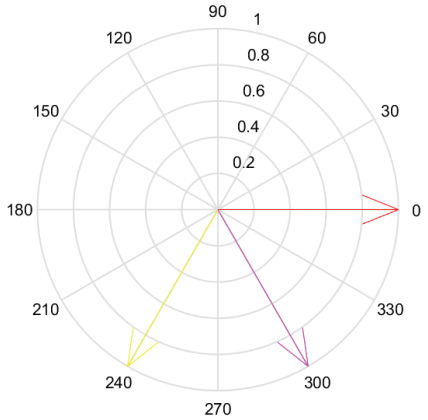


Fig.12 9th harmonic Current phasor when DG_3 is disconnected-Simulation

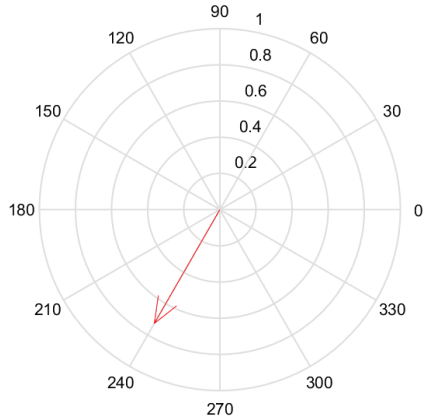


Fig.13 9th harmonic voltage phasor when DG_3 is disconnected- Simulation

The proposed methodology simple, effective, advantageous and aids efficient energy generation through robust and autonomous control at each inverter location without any complex and costly communication infrastructure.

REFERENCES

[1] A. Pouryekta, V. K. Ramachandaramurthy, N. Mithulananthan and A. Arulampalam, "Islanding Detection and Enhancement of Microgrid Performance," in IEEE Systems Journal, vol. 12, no. 4, pp. 3131-3141, Dec. 2018, doi: 10.1109/JSYST.2017.2705738.

[2] V. Verma and S. Jain, "Active islanding detection method for grid and DG failure in a community Microgrid application," *2016 IEEE International Conference on Power Electronics, Drives and Energy Systems (PEDES)*, 2016, pp. 1-5, doi: 10.1109/PEDES.2016.7914524.

[3] IEEE standard for interconnecting distributed resources with electric power systems, IEEE Std. 1547, 2003.

[4] Test procedure of islanding prevention measures for utility interconnected photovoltaic inverters, IEC Std. 62116, 2008.

[5] Remus Teodorescu; Marco Liserre; Pedro Rodriguez, "Grid Requirements for PV," in Grid Converters for Photovoltaic and Wind Power Systems , IEEE, 2007, pp.31-42, doi: 10.1002/9780470667057.ch3.

[6] P. Mahat, Zhe Chen and B. Bak-Jensen, "Review of Islanding Detection Methods for Distributed Generation," 2008 Third International Conference on Electric Utility Deregulation and Restructuring and Power Technologies, Nanjing, 2008, pp. 2743-2748.

[7] Zhihong Ye, A. Kolwalkar, Yu Zhang, Pengwei Du and Reigh Walling, "Evaluation of Anti-Islanding Schemes Based on Nondetection Zone Concept," in IEEE Transactions on Power Electronics, vol. 19, no. 5, pp. 1171-1176, Sept. 2004.

[8] M. E. Ropp, M. Begovic, A. Rohatgi, G. A. Kern, R. H. Bonn and S. Gonzalez, "Determining the Relative Effectiveness of Islanding Detection Methods Using Phase Criteria and Nondetection Zones," in IEEE Transactions on Energy Conversion, vol. 15, no. 3, pp. 290-296, Sept. 2000.

[9] L. A. C. Lopes and H. Sun, "Performance assessment of active frequency drifting islanding detection methods", IEEE Transactions on Energy Conversion, vol. 21, no. 1, pp. 171-180, March 2006.

[10] J. -H. Kim, J. -G. Kim, Y. -H. Ji, Y. -C. Jung and C. -Y. Won, "An Islanding Detection Method for a Grid-Connected System Based on the Goertzel Algorithm," in IEEE Transactions on Power Electronics, vol. 26, no. 4, pp. 1049-1055, April 2011, doi: 10.1109/TPEL.2011.2107751.

[11] V. Verma and G. G. Talpur, "Decentralized Master-Slave operation of microgrid using current controlled distributed generation sources," 2012 IEEE International Conference on Power Electronics, Drives and Energy Systems (PEDES), 2012, pp. 1-6, doi: 10.1109/PEDES.2012.6484502.

[12] S. R. Samantaray, K. El-Arroudi, G. Joós and I. Kamwa, "A Fuzzy Rule-Based Approach for Islanding Detection in Distributed Generation," in IEEE Transactions on Power Delivery, vol. 25, no. 3, pp. 1427-1433, July 2010, doi: 10.1109/TPWRD.2010.2042625.

Authorized licensed use limited to: DELHI TECHNICAL UNIV. Downloaded on April 13,2023 at 10:18:40 UTC from IEEE Xplore. Restrictions apply.

2023 International Conference for Advancement in Technology (ICONAT)
Goa, India. Jan 24-26, 2023

Axis Control of a Nonlinear Helicopter Model Using Intelligent Controller

Abhishek Chaudhary
Electrical Engineering Department
Delhi Technological University, DTU
New Delhi, India
abhishek@dtu.ac.in

2023 International Conference for Advancement in Technology (ICONAT) | 978-1-6654-7517-4/23/$31.00 ©2023 IEEE | DOI: 10.1109/ICONAT57137.2023.10080707

***Abstract* — Adaptive neuro-fuzzy inference system (ANFIS) based intelligent control is employed on a helicopter system in this paper. This helps to control the alterations of the pitch axis and yaw axis of helicopter, with the reference trajectory. Two different ANFIS logic modules are developed, one is to help adjust the angle variations in pitch axis and other is to help adjusting the yaw axis angle variations of a two degree of freedom (2 DOF) Quanser Helicopter system, so that the altitude and angular speed are controlled altogether. The whole execution framework utilizes standard configurations of MATLAB platform and simulation toolboxes. The results obtained in the process are then compared with the traditional LQR Controller and Fuzzy Controller on simulation platform.**

Keywords* — *Air Vehicles; ANFIS; 2-DOF Helicopter; intelligent controller; LQR; pitch angle; yaw angle; trajectory control.

I. INTRODUCTION

A theme of switching mechanical (both hydraulic and pneumatic) instruments by more erudite electrical instruments is being witnessed in the different applications of rotorcraft engineering recently. This evolution is inspired by the helpfulness in weight, volume, fuel and maintenance. This dictation of change is due to the necessity to replace heavy weight and high maintenance flights with light weight and maintenance free unmanned flight systems. It clues to notable variations in aerospace undercurrents of vehicles leading to upsurge in its electrical and mechanical complexity while sinking overall size and weight of the system. Hence, due to light weight of these vehicles, traditional fossil fuel driven rotorcrafts are being replaced by new prototypes for taking care of certain tasks. Challenge to control the dynamics have now attained higher dimensions now, mostly due to such amendments of modern time. These amendments have already lead to the introduction of newly born dynamics in the field of control system with a focus on developing the necessity to discourse the new control amendments for a certain class of systems otherwise. These certain class of systems find their reputation from controller perception as they demonstrate explicit qualities which possess considerable challenge in control system engineering. Which certainly occurs due to phase dynamic, cross-coupling, different model specific uncertainties and to sensitivity to disturbances and control singularities. The two degree of freedom twin rotor multiple input multiple output helicopter system is one benchmark nonlinear system.

A Twin Rotor Multi Input Multi Output System (TRMIMOS), developed by Quanser Innovative Educate., demonstrates all the attributes cited above. The system shows instability and cross-coupling effect due to the presence of twin rotors for controlling two different axis i.e. its yaw axis and its pitch axis, which makes supervision of their position and trajectory control a difficult mission altogether. It displays a laboratory model for a helicopter system with two degree of freedom. Fig. 1 demonstrates the working model of this system while the system is in hovering mode. TRMIMOS functions with two different planes which are vertical to each other. Different rotors of TRMIMOS are in these two planes. This TRMIMOS is handled by different controllers using MATLAB simulation with the help of feedback control mechanism.

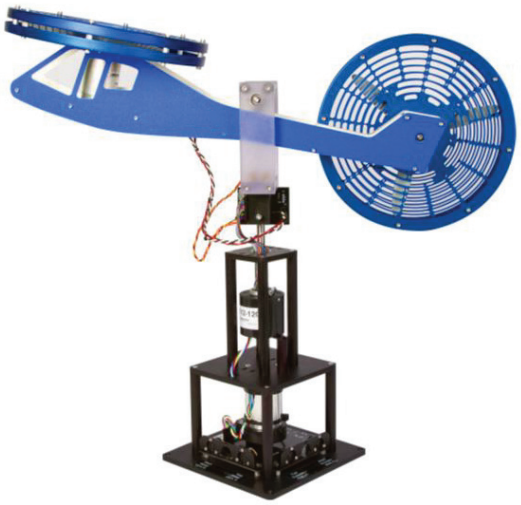


Fig. 1 Helicopter in the laboratory while hovering

Employing controllers using feedback method is no new concept. It has attentive influence on expansion of new day technologies [1]. A thought-provoking discussion of such feed back controller technique is found in [2] that dashes its way for controlling of gadgets to earlier ancient period. Many application of this feedback controller approach extended from research fields like robotics [3], spacecraft engineering [4], aircraft engineering [5], and chemical engineering [6] to modern day research zones like biological science [7]-[8] algorithm analysis [9] and science of neurology [10]–[12].

Whereas, the linear system is valuable for modelling that system which only functions in the specific linear command, on the other hand the nonlinearity is inevitable in almost every engineering application such as controlling a walking robot movements [6]. A nonlinear model can be used for controller synthesis which will stereotypically outcomes in comparatively effective controller than by means of linearized modelling for control synthesis. Which shows that

Authorized licensed use limited to: DELHI TECHNICAL UNIV. Downloaded on April 17,2023 at 06:10:20 UTC from IEEE Xplore. Restrictions apply.

the optimal control synthesis for benchmark non-linear systems is a significant zone of research. Nevertheless, in spite of major developments in the optimal control synthesis of linearized systems, the optimal control synthesis of non-linear system will not segment the equality of generality, computation, and scalability.

Naturally, objective of the controllers employed is to confirm that systems is talented enough to accomplish an assigned task resourcefully with desired reliability. Which means the controller must be optimal and accurate with respect to specified regulars of provisions respectively in order to be robust in case of random disturbances to the non-linear system. The optimal control synthesis of linear system may also be called a very well-studied area as already numerous valuable tools and techniques available through research. A substantial milestones for the synthesis of optimal controller is given by Kalman known as the linear quadratic regular (LQR), which represents that the optimal control is nothing but a linear feedback of different state variables wearing the calculus of variation [13]. LQR controller and the sister controller of LQR controller i.e. linear quadratic Gaussian regular (LQG) gained initial victories in the 1970's, but they sometimes malfunctioned having unfortunate robustness properties [14]. Therefore, to overcome these obstacles, tools and techniques for robust control emerged in the 1980's including optimal H2/H∞ control synthesis which uses state-space construction and famous Ricatti's equations [15], [16]. After this, a system level synthesis framework is developed [17] - [18] which empowered distributed, localized, and scalable synthesis using itinerary of convex optimization.

Many different controllers are tried and tested by researchers in the recent times for the controlling of nonlinear systems like an LQR got restructured beside PID in order to moderate the error tracing in pitch reference output and the yaw reference output using the enhancement of quadratic function with the help of feedback [19]. The robust adaptive fuzzy controller was designed using a gradient descent algorithm [20]. Some other various control techniques like adaptive second-order sliding mode controller [21], model predictive control [22] and adaptive disturbance rejection controller [23] have also been employed and used by different researchers in their work. While performing the operation of helicopter system, many failure contrivances may occur that definitely affects the real time working routine of model also causes instability to nonlinear model. To handle a higher orders of flight control mechanism, a reorganized FTC system is opted [24]. In an aircraft having intelligent system for landing purpose, a neuro fuzzy dual controller is used which may be used in proper air transportation easily. It is clear from simulation study that the offered method performs good enough under the vague and fluctuating weather [25]. It is observed that the anticipated specifications are met after the employment of the presented method. The approached developed in this process discussed about the problems in configurations of the control law of fuzzy based logics. The proposed approach has a capacity of self-handling and in documentation of nonlinear dynamic models it is applied. The simulation results hence obtained indicates a much higher tracking performances and faster reaction from air vehicles.

In current work, an ANFIS controller is considered. The moto is to project a control system with a desire to track down desired yaw angle and pitch angle of a helicopter system. These control design operators are humble to employ and they do not have the properties of commutativity or associativity [26]–[28]. Author of this study, have already presented a work on the implementations of Fuzzy Logic Control on Helicopter System [29]. In current study, the simulation results from the implemented ANFIS control strategy is compared with the traditional LQR controller and Fuzzy Logic Controller results from [29]. This work is strategized as following; section II portrays mathematically derived equations of the helicopter system. Section III will discuss about the considered AFNIS Controller. ANFIS Controller, Fuzzy Controller and a conventional LQR controller is employed on the twin rotor motor system portrayed in Fig. 1. In section IV, the obtained MATLAB simulation results are discussed. In section V, the analysis of MATLAB simulation results is shown and superiority of proposed method is discussed.

II. 2-DOF HELICOPTER SYSTEM

It is a multiple input multiple output (MIMO) twin rotor motor model which is extremely nonlinear in nature having robust cross-coupling behavior between pitch axis and yaw axes of this helicopter system, which is due to torques performing on each axes. The yaw propeller and the pitch propeller are energized by two different DC motors while system is attached on an immovable base in the laboratory. The first propeller i.e. the pitch propeller is handlebars for vertical movement of the TRMIMO model about its pitch trajectory. When the front propeller shows upward direction, this angle is tends to positive. When the helicopter is not hovering, then the required pitch angle is observed about −40.5 degrees and it is range bound from −40.5 to 40.5 degrees. Second propeller or the back propeller is responsible for the horizontally parallel motion about yaw axis of helicopter system.

This twin rotor multiple input multiple output system (TRMIMOS) rotates freely around 360 degree on horizontal axis. The yaw is taken positive in clock-wise and negative in anti-clock-wise direction. Different thrust force represented by Fy and Fp shown in Fig.2, fashioned at displacement r_y and r_p from the horizontal and vertical axis of the helicopter model respectively [17]. Voltage given to front propeller motor i.e. pitch motor and voltage given to back propeller motors i.e. yaw motor are the two inputs of twin rotor multiple input multiple output (TRMIMO) nonlinear model and the pitch angle (θ) and the yaw (Ψ) angle in radians are two outputs of this benchmark TRMIMO system. Using the Lagrangian mechanics, two dynamic nonlinear equations of the model are derived. Which are assigned as the pitch axis equation and the yaw axis equation and shown below [30]. The objective is to advise a controller which may help in tracking of the anticipated trajectory of pitch and yaw axis of the TRMIMO helicopter model.

Pitch axis equation:

$$(J_{eq,p} + m_{heli}\ l_{cm}^2)\ddot{\theta} = K_{pp}\ V_{m,p} + K_{py}\ V_{m,y} - m_{heli} g l_{cm} \cos\theta - B_p\ \dot{\theta} - m_{heli}\ l_{cm}^2 sin\theta cos\theta \dot{\Psi}^2$$

Yaw axis equation:

$$(J_{eq,y} + m_{heli}\ l_{cm}^2 cos\theta^2)\ddot{\Psi} = K_{yp}\ V_{m,p} + K_{yy}\ V_{m,y} - B_y \dot{\Psi} + 2 m_{heli}\ l_{cm}^2 sin\theta cos\theta \dot{\Psi}\dot{\theta}$$

Authorized licensed use limited to: DELHI TECHNICAL UNIV. Downloaded on April 17,2023 at 06:10:20 UTC from IEEE Xplore. Restrictions apply.

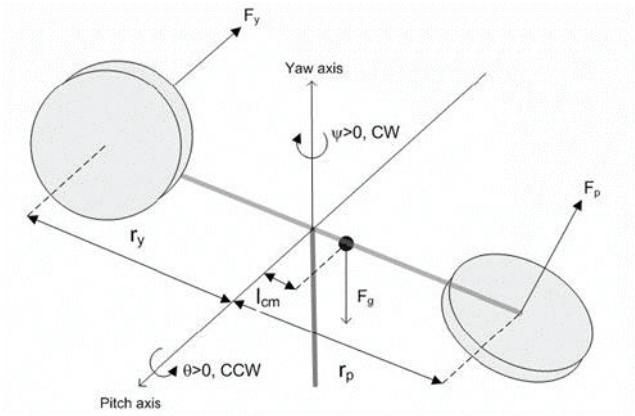


Fig. 2. Free body outlet of TRMIMO system [17]

The thrust forces i.e. Fy and Fp are acting specifically at the yaw axis and pitch axis from the back propeller motor and front motor are then explained. The required nonlinear equations for the motion of the helicopter system are then achieved by using the Euler-Lagrange method. The mathematical equations then linearly equated to zero and a linearized state-space modelling in order to bargain the position subtleties of considered nonlinear helicopter model. State-space model is representation as:

$$\dot{x} = Ax + Bu$$

Where, the state vector for the TRMIMO system is:

$$y = Cx + Du$$

$$x^T = [\theta(t), \psi(t)]$$

And the output vector is:

$$y^T = [\theta(t), \psi(t)]$$

The Laboratory representation model view of TRMIMO system which clearly possess all the above declared provisions is portrayed in Figure no. 2 and the narrative of non-linear parameters are shown in Table 1.

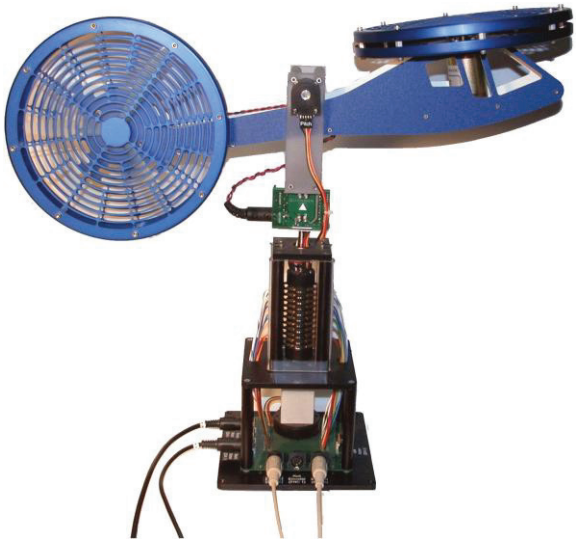


Fig 3 Laboratory model of TRMIMO system [30]

TABLE I. PARAMETERS OF HELICOPTER MODEL

	Description	Values
K_{pp}	Thrust torque constant acting on the pitch axis from pitch propeller	$0.2041 N.m/V$
B_p	Viscous damping about the pitch axis	$0.8 N/V$
B_y	Viscous damping about the yaw axis	$0.318 N/V$
K_{py}	Thrust torque constant acting on the pitch axis from the yaw propeller	$0.0068 N.m/V$
$J_{eq,p}$	The total moment of inertia about pitch axis	$0.0384 kg.m^2$
K_{yp}	Thrust torque constant acting on the yaw axis from the pitch propeller	$0.0219 N.m/V$
K_{yy}	Thrust torque constant acting on yaw axis from yaw propeller	$0.072 N.m/V$
$V_{m,y}$	Applied Voltage to the yaw motor	$\pm 15V$
$J_{eq,y}$	The total moment of inertia about yaw axis	$0.0431 kg.m^2$
$V_{m,p}$	Applied Voltage to the pitch motor	$\pm 24V$
m_{heli}	The total moving mass of the helicopter	$1.3872 kg$
g	Gravitational constant	$9.81 m/s^2$
l_{cm}	Center of mass length along 2-DOF helicopter body from pitch axis	$0.1855 m$

III. ADAPTIVE NEURO FUZZY INFERENCE SYSTEM (ANFIS)

Adaptive neuro fuzzy inference system is multi-layered neural network feed-forward construction. Work presented by (Jang & Sun, 1997) [31], the functions and working of all these various layers and its advantages are well explained over the other neuro-fuzzy approaches. The remark worth noting, its distinctive construction grounded on Sugeno type of inference system allows usage of hybrid learning algorithms which proves to be much faster and more effective when associated with error back propagation type of techniques.

To update the ANFIS network parameters the approach used in this work is 2 level learning algorithm which makes it a hybrid learning algorithm. The specific constraints of the ANFIS networks are estimated mainly in 2 different parts i.e. input parameters and output parameters. We may define total parameters as P = P1 + P2, where P1 is the membership function parameter and expressed as set of input parameter and P2 is the weight parameter and expressed as the set of output parameter. The membership function parameter in the input stage (given by parameter set P1) are kept constant throughout forward pass of 2 level hybrid learning algorithm. Now, throughout the backward pass of the 2 level hybrid learning algorithm, parameter set given by P2 is kept persistent while error is back propagated. The output of this linkage becomes a linearized combination of output parameters of the parameter set given by P2 and the well-known Least Square Error based training is used in this manner. The parameter set given by P1 can now be updated using the gradient descent method.

The two layer approach for the implementation of ANFIS controller includes Fuzzy logic controllers. The parameters of this FLC is referred from a work [29] from author of current paper. In [29] author of current paper explained the working and requirement of membership function (as shown in Fig. 4 and Fig. 5) for minimization of considered errors (i.e. yaw error and pitch error).

Authorized licensed use limited to: DELHI TECHNICAL UNIV. Downloaded on April 17,2023 at 06:10:20 UTC from IEEE Xplore. Restrictions apply.

The ANFIS uses a two layer Fuzzy logic controller (FLC) which helps validating all the parameters as an attractive tool, whose reaction is diverging depending upon the nature of membership functions being used for the input-output parameter and also depends upon dissimilar sets of rule in FLC rule base system. To control the helicopter parameters, Takagi-Sugeno (T-S) model is used, where 2 different inputs and 1 output is provided for the pitch angle error and the yaw angle error as shown in fig. 4 and fig 5 respectively. Seven different linguistic variables (NS, ZE, PS, PM, NB, NM and PB) have already been chosen for every single input state variable with a suitable rule base. The one input is pitch error and other input is the change in pitch error. Triangular type and the Gaussian type of membership functions are chosen so that we may have continuous differentiable curve. This arrangement is exactly similar for input functions of both the axis i.e. pitch axis and yaw axis.

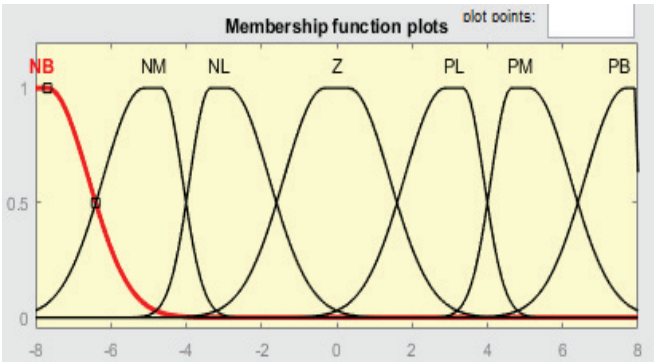


Fig. 4 Membership functions to control pitch axis

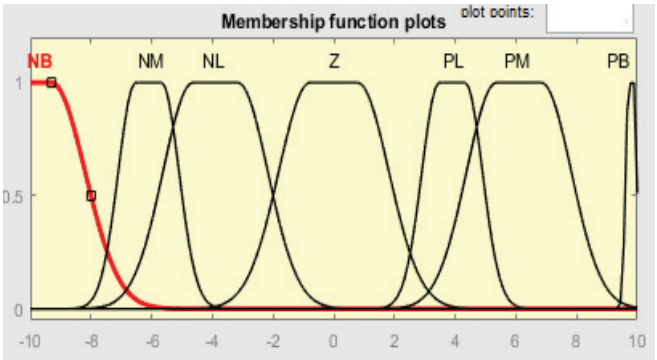


Fig. 5 Membership functions of yaw control

IV. THE SIMULATION ANALYSIS

During the simulation of ANFIS controllers, standard MATLAB/Simulink interface, ANFIS and Fuzzy Logic Controller (FLC) simulation blocks are used. TRMIMO model i.e. 2 DOF Helicopter model is organized by the block set and then ANFIS control got employed to this nonlinear helicopter model. To see the visual outputs of both angles of 2 DOF Helicopter System, simulation interface is used. By this way, the plots of the helicopter can be seen. TRMIMO system is being controlled after the implementation of ANFIS controller using fuzzy logic controller (FLC) to footpath the trajectory expected in MATLAB simulation interface. TRMIMO system, a testbench simulation setup is manufactured by Quanser [30] for the sake of researchers, this laboratory setup consists of one base fixed to the ground and total two propellers, free to move vertically and horizontally. The one fixed base offers liberty for movement. The propellers rotates with the momentum generated by dc motors which are attached distinctly at the two ends of these propellers. Two propellers are used only to handle pitch and yaw angles of helicopter system during the operation. Pitch angle is being controlled with the help of front end propeller while the yaw angle is being controlled with the help of one back end propeller.

Objective now is to handle the cross-coupling, formed after the pitch and yaw motion altogether so that these motions may provide stable side motion. ANFIS System helps in achieving this objective. The employed ANFIS system is shown in Fig. 6 with the help of a block diagram. One error $e_p\ (t)$ is well-thought-out as variance between required pitch angle and actual pitch angle given in radians. Error $e_p\ (t)$ and the one derivative signal of this error i.e. $\Delta e_p\ (t)$ provided as two different inputs to ANFIS block for the pitch axis of TRMIMO helicopter system. Likewise, second error $e_y\ (t)$ which is well-thought-of a difference between the desired and actual yaw angle in radians. This error $e_y\ (t)$ and one derivative signal of this error i.e. $\Delta e_y\ (t)$ are given as inputs to the AFNIS simulation model in yaw axis. Now, both the controller implemented are having two different inputs and each given individual input is fuzzified by the help of seven membership functions in simulation modelling. These seven different membership function are spread in closed interims and already illustrated in Fig. 4 and Fig.5.

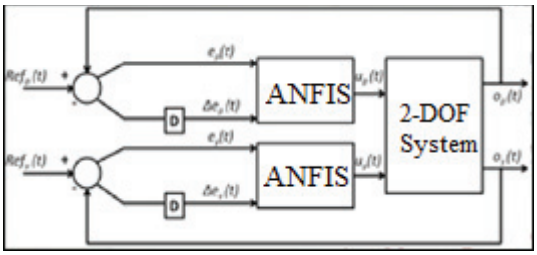


Fig.6 Block Diagram of the proposed ANFIS controller

Two ANFIS are implemented. One is for handling the yaw error and other one is for handling the pitch error. These controllers works altogether towards same goal of achieving

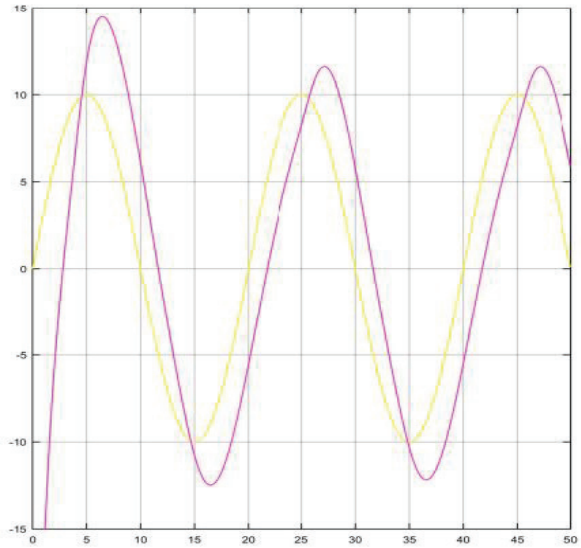


Fig.7 Output for pitch axis with sinusoidal reference

Authorized licensed use limited to: DELHI TECHNICAL UNIV. Downloaded on April 17,2023 at 06:10:20 UTC from IEEE Xplore. Restrictions apply.

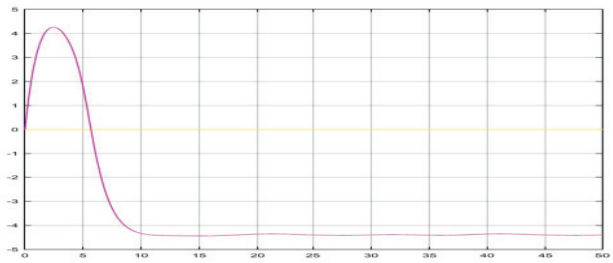


Fig.8 Output for yaw axis with sinusoidal reference.

the reference altitude, the better speed and the angle values as demanded by the reference trajectory. The consequential part of the controller implemented is tuned to obtain the required trajectories. Membership function shown at the antecedents are deeply tuned during whole procedure. After which, several MATLAB simulations are carried out. The different results obtained during this procedure of simulations, are shown in Figs.7,8,9. In Fig. 7, one sinusoidal bench signal is given to the pitch trajectory and hence the observed behavior of the output of the actual pitch angle is plotted. In Fig. 8, similar operation is performed for the yaw axis.

The in-phase line represents the required trajectory of pitch axis for the two degree of freedom helicopter system. The amplitude of the same is kept low for yaw axis in order to have the easy calculation for the output parameters. In Fig. 9 the voltage graph while the implementation of simulation model of ANFIS on helicopter system is shown.

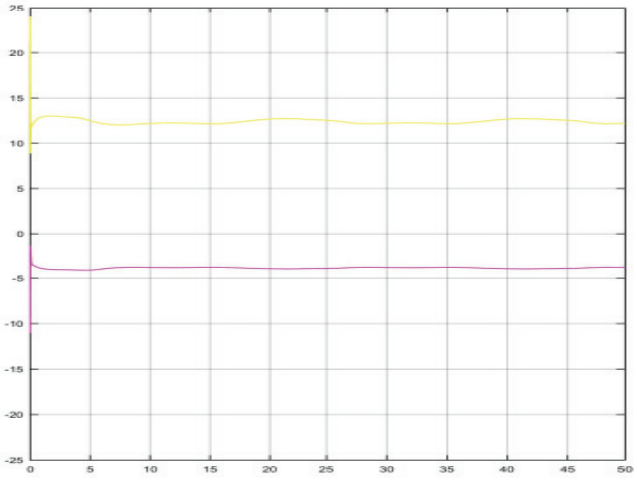


Fig.9 Voltage trajectory for ANFIS Controller

V. RESULT COMPARISON

The controlling of a nonlinear helicopter model is achieved successfully by implementing ANFIS controller and compared with the earlier work in this area where traditional controller LQR and intelligent Fuzzy logic controller is implemented by the current author [29]. The step reference and sinusoidal reference input trajectories are considered for the plotting on MATLAB Simulink interface. Table2 discusses the time response breakdown to have comparative performance superiority of the proposed ANFIS controller on simulation model. The reference pitch trajectory and the reference yaw trajectory of the 2 degree of freedom helicopter model are tracked down with step reference and obtained results are compared as:

TABLE II. TIME RESPONSE SIMULATION RESULTS

Controller	Settling Time (sec.)	Peak Over-shoot (%)
FUZZY [29]	0.95	0.5
LQR	4.72	8.99
ANFIS	2.33	1.4

The response for the step reference trajectory after the implementation of LQR based control and fuzzy based logic controller on a twin rotor multiple input multiple output helicopter model is picturized in Fig. 9 and Fig. 10 one after one as:

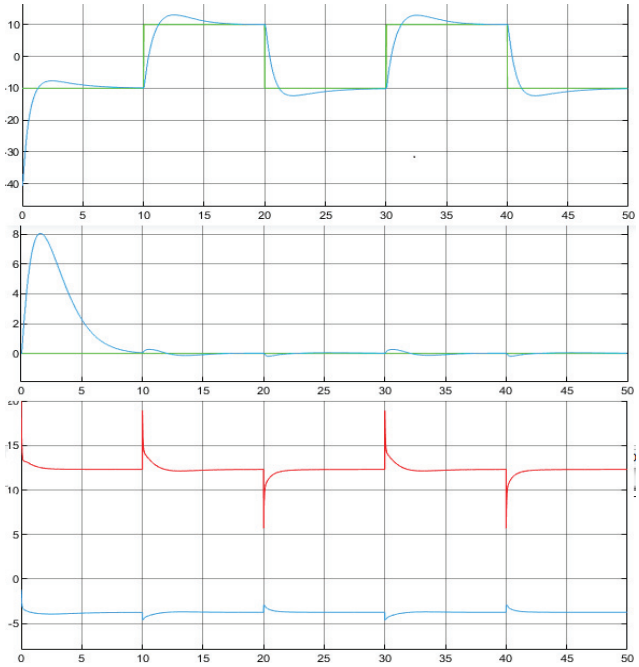


Fig.9 Response of LQR based control on simulation.

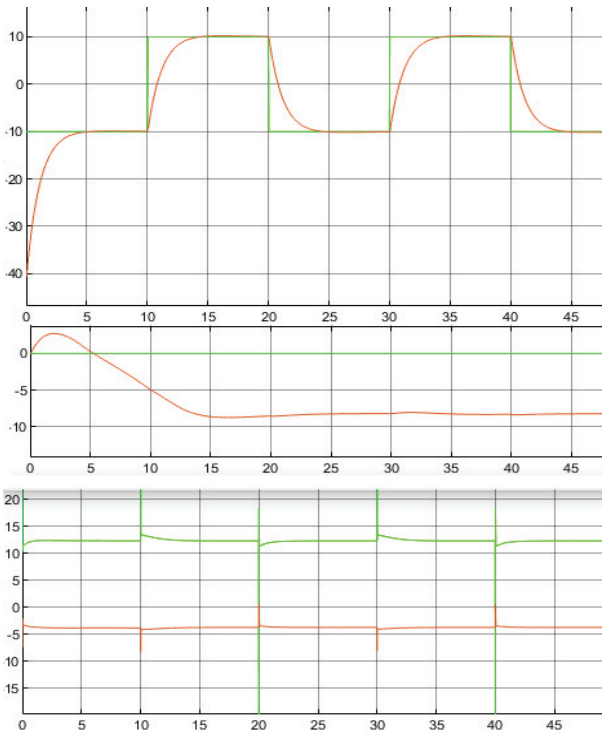


Fig.10 Response of fuzzy logic control on simulation.

Authorized licensed use limited to: DELHI TECHNICAL UNIV. Downloaded on April 17,2023 at 06:10:20 UTC from IEEE Xplore. Restrictions apply.

VI. CONCLUSION

Presented work demonstrates the employment of ANFIS control approach on a twin rotor 2 DOF helicopter system. It tunes axis controls. These tuned results are further compared with an LQR controller's results and intelligent fuzzy controller's results. Yaw and pitch angles performance have been analyzed for different control techniques. ANFIS controller reduced the cross-coupling errors caused among two rotors. Output simulation performances of ANFIS controller, LQR controller & fuzzy controller is judged by MATLAB simulation platform. For establishing a proper comparison of the results obtained using these controllers the time response analysis is performed. The intelligent controller gives better response. Which shows further intelligent controllers may be implemented on this nonlinear system in order to observe for more variations in yaw and pitch axis trajectories.

REFERENCES

[1] D. S. Bernstein, "Feedback control: An invisible thread in the history of technology," IEEE Control Systems, vol. 22, no. 2, pp. 53–68, Apr. 2002. doi: 10.1109/37.993315.

[2] O. Mayr, The Origins of Feedback Control. Cambridge, MA, USA: MIT Press, 1970.

[3] J. W. Grizzle, C. Chevallereau, R. W. Sinnet, and A. D. Ames, "Models, feedback control, and open problems of 3d bipedal robotic walking," Automatica, vol. 50, no. 8, pp. 1955–1988, 2014.

[4] J. R. Wertz, Spacecraft attitude determination and control. Springer Science & Business Media, 2012, vol. 73.

[5] A. Abdessameud and A. Tayebi, "Global trajectory tracking control of vtoluavs without linear velocity measurements," Automatica, vol. 46, no. 6, pp. 1053–1059, 2010.

[6] W. L. Luyben, Process modeling, simulation and control for chemical engineers. McGraw-Hill Higher Education, 1989.

[7] N. Li, J. Cruz, C. S. Chien, S. Sojoudi, B. Recht, D. Stone, M. Csete, D. Bahmiller, and J. C. Doyle, "Robust efficiency and actuator saturation explain healthy heart rate control and variability," Proceedings of the National Academy of Sciences, vol. 111, no. 33, E3476–E3485, 2014.

[8] F. A. Chandra, G. Buzi, and J. C. Doyle, "Glycolytic oscillations and limits on robust efficiency," Science, vol. 333, no. 6039, pp. 187–192, 2011.

[9] L. Lessard, B. Recht, and A. Packard, "Analysis and design of optimization algorithms via integral quadratic constraints," SIAM Journal on Optimization, vol. 26, no. 1, pp. 57–95, 2016.

[10] E. Todorov, "Stochastic optimal control and estimation methods adapted to the noise characteristics of the sensorimotor system," Neural Computation, vol. 17, no. 5, pp. 1084–1108, 2005.

[11] D. W. Franklin and D. M. Wolpert, "Computational mechanisms of sensorimotor control," Neuron, vol. 72, no. 3, pp. 425–442, 2011.

[12] R. J. Peterka, "Sensorimotor integration in human postural control," en, Journal of Neurophysiology, vol. 88, no. 3, pp. 1097–1118, Sep. 2002.

[13] R. Kalman, "Contributions to the theory of optimal control," Bol. de Soc. Math. Mexicana, 1960.

[14] J. Doyle, "Guaranteed margins for lqg regulators," IEEE Transactions on Automatic Control, vol. 23, no. 4, pp. 756–757, 1978.

[15] G. Zames, "Feedback and optimal sensitivity: Model reference transformations, multiplicative seminorms, and approximate inverses," IEEE Transactions on Automatic Control, vol. 26, no. 2, pp. 301–320, 1981.

[16] J. C. Doyle, K. Glover, P. P. Khargonekar, and B. A. Francis, "State-space solutions to standard h/sub 2/and h/sub infinity/control problems," IEEE Transactions on Automatic control, vol. 34, no. 8, pp. 831–847, 1989.

[17] Y.-S. Wang, "A system level approach to optimal controller design for largescale distributed systems," PhD thesis, California Institute of Technology, 2017.

[18] Y.-S. Wang and N. Matni, "Localized lqg optimal control for large-scale systems," in American Controls Conf. (ACC), 2016, pp. 1954–1961.

[19] C. Liu, J. Pan, and Y. Chang, "PID and LQR trajectory tracking control for an unmanned quadrotor helicopter: Experimental studies," in Proc. 35th Chin. Control Conf. (CCC), Jul. 2016, pp. 10845–10850.

[20] M. Jahed and M. Farrokhi, "Robust adaptive fuzzy control of twin rotor MIMO system," Soft Comput., vol. 17, no. 10, pp. 1847–1860, Oct. 2013.

[21] S. Mondal and C. Mahanta, "Adaptive second-order sliding mode controller for a twin rotor multi-input-multi-output system," IET Control Theory Appl., vol. 6, no. 14, pp. 2157–2167, Sep. 2012.

[22] J. Gao, P. Wu, T. Li, and A. Proctor, "Optimization-based model reference adaptive control for dynamic positioning of a fully actuated underwater vehicle," Nonlinear Dyn., vol. 87, no. 4, pp. 2611–2623, 2017.

[23] S. Ghabraei, H. Moradi, and G. Vossoughi, "Multivariable robust adaptive sliding mode control of an industrial boiler–turbine in the presence of modeling imprecisions and external disturbances: A comparison with type-I servo controller," ISA Trans., vol. 58, pp. 398–408, Sep. 2015

[24] J. D. Boskovic and R. K. Mehra, "A decentralized fault-tolerant control system for accommodation of failures in higher-order flight control actuators," IEEE Trans. Control Syst. Technol., vol. 18, no. 5, pp. 1103–1115, Sep. 2010.

[25] K. Xu, G. Zhang, and Y. Xu, "Dual Fuzzy Neural Network Control in Civil Aviation Intelligent Landing System," AICI 2011, Part II, LNAI 7003, pp. 166-174, Springer-Verlag Berlin Heidelberg, 2011.

[26] I. Batyrshin and O. Kaynak, "Parametric classes of generalized con-junction and disjunction operations for fuzzy modeling," IEEE Trans. on Fuzzy Systems, vol. 7, no. 5, pp. 586-596, 1999.

[27] I. Batyrshin, O. Kaynak, and I. Rudas, "Fuzzy modeling based on generalized conjunction operations," IEEE Trans. on Fuzzy Systems, vol. 10, no. 5, pp. 678-683, 2002.

[28] A.C. Aras, O. Kaynak, and R. Abiyev, "Slip control of a quarter car model based on type-1 fuzzy neural system with parameterized conjunctions," IECON 2012 - 38th Annual Conference on IEEE Industrial Electronics Society, pp. 2488-2493, 2012.

[29] A. Chaudhary and B. Bhushan, "Trajectory Tracking of a 2-DOF Helicopter System using Fuzzy Controller Approach," 2021 International Conference on Emerging Techniques in Computational Intelligence (ICETCI), 2021, pp. 159-164, doi: 10.1109/ICETCI51973.2021.9574049.

[30] Quanser Inc., Quanser 2-DOF Helicopter Manual, *Tech. rep.*, Quanser 2010.

[31] Jang, Jyh-Shing & Sun, Chuen-Tsai & Mizutani, Eiji. (1997). Neuro-Fuzzy and Soft Computing-A Computational Approach to Learning and Machine Intelligence [Book Review]. Automatic Control, IEEE Transactions on. 42. 1482 - 1484. 10.1109/TAC.1997.633847. doi 10.1109/TAC.1997.633847

Authorized licensed use limited to: DELHI TECHNICAL UNIV. Downloaded on April 17,2023 at 06:10:20 UTC from IEEE Xplore. Restrictions apply.

This article has been accepted for inclusion in a future issue of this journal. Content is final as presented, with the exception of pagination.

CAT-CapsNet: A Convolutional and Attention Based Capsule Network to Detect the Driver's Distraction

Himanshu Mittal and Bindu Verma, *Member, IEEE*

***Abstract*— Worldwide inflation in the count of road accidents has raised an alarming scenario wherein driver distraction is identified as one of the main causes. According to the National Highway Traffic Safety Administration survey, talking over the mobile or fellow passengers, eating or drinking while driving, and operating in-vehicle menus can lead to distract the driver. Therefore, this paper presents a new driver distraction detection method to cater such scenarios. The proposed method is a convolution-based capsule network with attention mechanism, termed as CAT-CapsNet, that combines the computation capabilities of capsule network with attention module and convolution filters. We evaluate the proposed CAT-CapsNet on two publicly available driver distraction datasets namely, American University in Cairo (AUC) distracted driver dataset and Statefarmŝ dataset. A comparative analysis of the proposed model is conducted against 16 (approx) state-of-the-art methods in terms of accuracy, number of parameters, and AUC curves. Experiments affirm that CAT-CapsNet outperforms with the accuracy of 99.88% on SFD dataset and 96.7% accuracy on the AUC dataset. Moreover, the proposed model has only 8.5*M* parameters to train and no data augmentation is needed in-case training samples are less.**

***Index Terms*— Capsule network, attention, deep learning, road safety, classification, driver's behavior analysis.**

I. Introduction

ACCORDING to World Health Organization (WHO) report on road safety [1], 1.35 million peoples are killed in road accidents. One of the main reasons behind such accidents is driver distraction that leads to the inattentive driving. According to the statistics [2], 20% of severe road accidents and 30% of fatal road accidents are caused due to distracted driving. However, it has been observed that such incidents can be avoided if driver are alerted on time. For the same, next generation vehicles are equipped with advanced driver assistance system (ADAS). Any activity that engages the driver to lose focus from the road is considered as driver distraction such as talking on the cell phone, texting, drinking, eating and doing make-up [3]. In this paper, we consider the driver distraction in the form of adjusting radio, drinking, using phone, reaching behind, adjusting radio, fixing hair and doing makeup, talking to fellow passenger for the longer duration.

ADAS detects the potential accidental scenarios by analysing sensor data. The commonly used sensors in ADAS are camera, SONAR, LiDAR, RADAR, GPS. Importantly, camera has become the part-and-parcel of ADAS which has opened new research directions in the computer vision. In last decade, researchers have majorly focused on solving the driver distraction problem with deep learning (DL) models. As DL models have shown superior performance in different areas such as Object Detection [4], Super-Resolution images [5], and predicting the life-span of machine [6]. Such models have also been extended for recognizing the driver's emotional states [7], [8], and [9]. Some of the commonly used DL models which have reported high recognition accuracy are AlexNet, VGGNet, GoogleNet, ResNet and InceptionNet. However, the downside of DL models is the high amount of training time due to the large number of trainable parameters. Consequently, these models demand high amount of data for training. Moreover, there is a loss of valuable information in CNN due to the pooling operation.

In [10], Hinton et al. proposed a new class of convolutional neural network, termed as Capsule Networks (CapsNet), and attended a great performance for image processing as well as natural language processing tasks. CapsNet is a powerful model that has been specially designed to deal with small dataset. CapsNet has shown remarkable performance due to its ability to capture spatial as well as temporal co-relations between the objects [11].

However, CapsNet ignores the local features of the image. To alleviate the same, we present a new CapsNet model by incorporating an attention module with CapsNet, named as CAT-CapsNet. Inclusion of attention module helps CAT-CapsNet to focus on important portions of the image instead of the overall image. This benefits CAT-CapsNet in better detection of driver distraction comparatively. Moreover, this hybridization combines the computation capabilities of capsule network with attention module and convolution filters.

Overall, this paper presents a significant improvement over original Capsule Network and makes following key contributions:

- This paper proposes a new capsule network architecture, termed as CAT-CapsNet (Convolutional Attention Capsule Network), with 4 convolution layers followed by Convolutional Block Attention Mechanism (CBAM) and capsule network layer.

Manuscript received 2 May 2022; revised 1 November 2022 and 19 February 2023; accepted 4 April 2023. The Associate Editor for this article was S. A. Birrell. *(Corresponding author: Bindu Verma.)*

Himanshu Mittal is with the Department of Artificial Intelligence and Data Sciences, Indira Gandhi Delhi Technical University for Women, New Delhi 110006, India (e-mail: himanshu.mittal224@gmail.com).

Bindu Verma is with the Department of Information Technology, Delhi Technological University, New Delhi 110042, India (e-mail: bindu.cvision@gmail.com).

Digital Object Identifier 10.1109/TITS.2023.3266113

1558-0016 © 2023 IEEE. Personal use is permitted, but republication/redistribution requires IEEE permission.
See https://www.ieee.org/publications/rights/index.html for more information.

Authorized licensed use limited to: DELHI TECHNICAL UNIV. Downloaded on April 18,2023 at 04:37:11 UTC from IEEE Xplore. Restrictions apply.

This article has been accepted for inclusion in a future issue of this journal. Content is final as presented, with the exception of pagination.

- Advantage of adding convolutional layers is to provide most discriminating feature map to the attention module. Inclusion of attention module focused on the important portion of the image instead of overall image.
- CAT-CapsNet is able to capture the spatial as well as temporal information from the image and achieve improved accuracy over the traditional DL models in which spatial information is lost at the pooling layer.

Rest of the paper is organized as follow: Related work is discussed in Section II. In Section III, proposed work is discussed in detail with CapsNet architecture. Section IV shows the experimental analysis and comparison with the state-of-the-art-methods. Finally, Section V provides a conclusion with the future directions.

II. Related Work

This section presents a brief summary of the field of driver's distraction detection. With the rising number of road accidents, substantial contribution has been made to perform the driver distraction detection [7], [8], [9], [12]. In [8], Gupta et al. proposed a framework to recognize driver's sleeping state and yawing states. As driver's negative and positive emotions also plays a crucial role in safe driving, Verma et al. [7] and [9] used VGGNet16 and AlexNet to recognize the drivers emotional state. Use of smart phone while driving also leads to a dangerous driving. To detect such activity while driving, Seshadri et al. [13] used HOG features with Adaboost classifier to make supervised decision. Similarly, Zhou et al. [14] also proposed a framework to detect the usage of mobile phone using Hidden Conditional Random Fields (HCRF). Author's Tian et al. [15] monitors the head movements of the driver and an alarm is raised if the head is not in the forward direction. Author's Liu et al. [16] proposed solution controls the auxiliary in-vehicle tasks through hand-gestures for reducing the driver distraction.

Talking to the fellow passenger, eating, or doing makeup lead to driver's in-focus from the road. Arefin et al. [17] developed a model that concatenate the features extracted from the HOG and AlexNet network and classify the distracted state of the driver's. Gumaei et al. [18] proposed a Custom Deep Convolutional Neural Network (CDCNN) and VGG-16 real-time model using edge and cloud computing to detect the driver distraction. Abouelnaga et al. [19] presented the AUC Distracted Drive dataset and employed AlexNet and Inception-V3 to detect the driver's distracted state. Eraqi et al. [20] proposed a real-time driver distraction model that uses the GA-weighted ensemble of multiple convolutional neural network. Masood et al. [21] used a VGG16 and VGG19 with and without pre-trained weights to detect the driver's distracted state. However, above discussed models are complicated and consists of more than 100 millions. It has been observed in literature that large number of parameters increases the training time of the considered model [22], [23]

To mitigate the same, a number of modified deep learning models have been presented. Baheti et al. [24] proposed a MobileVGG which is the modification of original VGG16. In MobileVGG, the fully connected layer is replaced with 1×1 convolution which benefited in reducing the number of parameters to train the model. Similarly, Majdi et al. [25] proposed a DriveNet model that used CNN to extract features and decision tree for driver distraction classification. Since time and cost efficiency is important for real time application, Qin et al. [23] developed an optimized D-HCNN model with decreasing filter size in which a HOG image is created for each driver posture and is passed as input to CNN for recognizing the driver's distracted state. Landola et al. [26] proposed a SqueezeNet model that have less number of parameters in comparison to VGGNet and Alexnet and achieved comparable accuracy. Horward et al. [27], [28] proposed an efficient CNN architecture called MobileNet and MobileNetV2 which have lesser number of parameters. Author mase et al. [29] proposed two stage driver distraction posture detection method. In one stage they have used CNN to extract the spatial features and BiLSTMs architecture to extract the spectral features. Similarly, Omerustaoglu et al. [30] also proposed a two stage model: in first stage they used pre-trained CNN model to process the image data and in second stage they used LSTM-RNN to process the sensor data and then both features merged to get the final prediction. Author Alotaibi et al. [31] proposed an inception model with a residual block and a hierarchical recurrent neural network to detect the driver's distraction state.

Context based driver distraction also proposed [32] in the literature where author's proposed an AttenD2.0 algorithm that includes the Minimum Required Attention (MiRA) theory. Li et al. [33] proposed a light weight CNN model with octave-like convolution mixed block, called OLCMNet to detect the driver distraction. They used squeeze-and-excitation (SE) module in the OLCM block and point-wise convolution operator to perform the fusion. Chen et al. [34] proposed neural architecture search algorithm to find the optimal deep convolutional neural network and detect the fine-grained driver distraction methods. Author's Huang et al. [35] proposed a deep 3D residual network with attention mechanism and encoder-decoder (D3DRN-AMED) to detect the true driver focus of attention with the help of successive frames with LSTM. Author hari et al. [36] proposed a framework to monitor the driver head pose and eyes off the road. Author's hossain et al. [37] used a transfer learning on VGG-16, ResNet50 and MobileNetV2 to detect the various distracted driving activity such as talking, sleeping or eating. Author's Li et al. [38] proposed a deep unsupervised learning model in that they used multi layer perceptron (MLP) and residual to learn the feature representation. Author ping et al. [39] used a dynamic optical flow and spatial features of each frame using parallel VGG-19 network with GRU unit. Then in last features are fused and driver's behaviour is detected.

III. Proposed Work

Motivated by the development in this era, considering the small number of parameters, high accuracy and high speed, we introduce CAT-CapsNet model that is a shallow network with lesser number of layers and attention module that focus on the important and local information. Moreover, proposed model have lesser number of parameters and simpler network.

Authorized licensed use limited to: DELHI TECHNICAL UNIV. Downloaded on April 18,2023 at 04:37:11 UTC from IEEE Xplore. Restrictions apply.

This article has been accepted for inclusion in a future issue of this journal. Content is final as presented, with the exception of pagination.

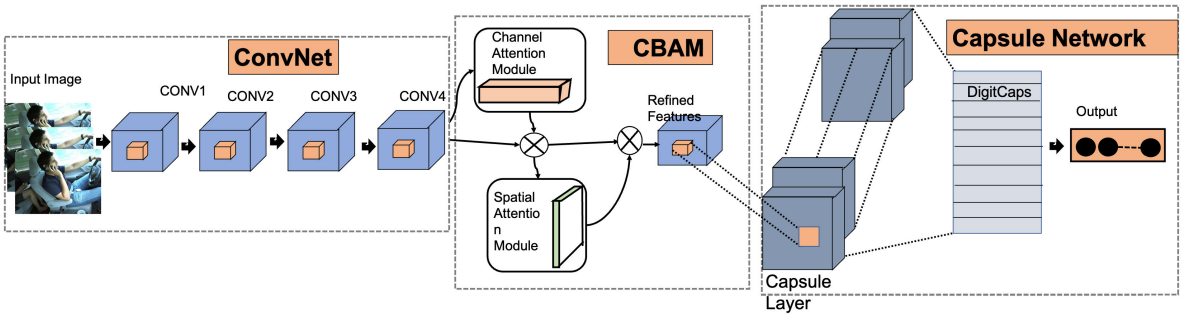


Fig. 1. CAT-CapsNet: Complete architecture is divided into a three part. In first part convolutional layer is added to convert the image into feature map. Then in second part attention module is applied on the extracted features to refine the feature map. Then, in third part capsule network is added and refined feature is passed to the primary capsule layer and driver distracted state is detected at the digitcaps layer.

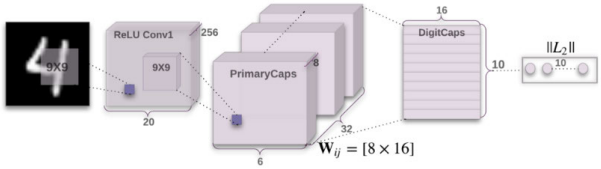


Fig. 2. Original capsule network architecture [10].

A. Capsule Network Architecture

Capsule network was designed by Hinton et al. [10] to classify the MNIST digit images of size 28 × 28. It has 6 layers that consists of one convolutional layer, one primary capsule layer, one digit layer and three fully connected layers as shown in Fig. 2. Convolution layer convert the pixel intensities into the feature map using 9 × 9 filter with ReLU activation function. Second layer is a primary capsule layer (PrimaryCaps) that takes the feature map as input. It has 32 capsules and each capsule applies 256 convolutional kernel of 9 × 9 size. The output of capsule layer is 6 × 8 capsules in which 6 × 6 grid shares their weights and orientation with each other. The final layer is a digit caps layer that contains $16D$ vectors for each digit class and is used to classify the digits using L_2 margin loss. The digit caps layer is also used to reconstruct the image by using three fully connected layer. Unlike convolutional layer that uses different activation function to activate the neurons, primary caps layer used a non-linear squashing function using Eq. (1) to convert the neurons into the vector form.

$$v_j = \frac{||S_j||^2}{1+||S_j||^2}\frac{S_j}{||S_j||} \tag{1}$$

where v_j is a computed vector output of j^{th} capsule and S_j is total input to capsule. The total input to capsule S_j is computed in Eq. (3) by the weighted sum over all the prediction vector $\hat{P}_{j|i}$ from the lower layer capsules. The prediction vector in below layer can be computed as multiplication of output p_i and weight matrix W_{ij} according to Eq. (2).

$$\hat{P}_{j|i} = W_{ij}\, p_i \tag{2}$$

$$S_j = \sum_i k_{ij}\, \hat{P}_{j|i} \tag{3}$$

where, k_{ij} is a coupling coefficient that is calculated using Eq 4 using the dynamic routing algorithm [10].

$$k_{ij} = \frac{exp(n_{ij})}{\sum_k exp(n_{ik})} \tag{4}$$

where, n_{ij} denotes the log prior probabilities that capsule i should coupled to capsule j. The sum of coupling coefficient k_{ij} between capsule i and top layer should be 1 and determined by routing softmax. To calculate the k_{ij}, n_{ij} must be calculated using Eq. (5).

$$n_{ij} \leftarrow n_{ij} + \hat{P}_{j|i} \cdot v_j \tag{5}$$

Initially, the value of n_{ij} is 0 and can compute k_{ij} and p_i, which is the output of the previous layer of the capsules. Using these three values, we can calculate the next level capsule input S_j. In last, margin loss is calculated in Eq. (6) for every class to determine whether particular object is present in the class or not.

$$M_l = C_k\ max(0, u^+ - ||v_k||^2) + \lambda(1-C_k)\ max(0, ||v_k|| - u^-)^2 \tag{6}$$

where, $C_k = 1$ iff a digit of class k is present and $u^+ = 0.9$ and $u^- = 0.1$. λ is the hyper-parameter and kept as 0.5 which denotes the down-weighting of the loss. The total loss is simply sum of the losses of all the digit capsules.

B. Proposed Capsule Network Architecture (CAT-CapsNet)

Modification of capsule network [10], termed as CAT-CapsNet, is proposed in which we added 4 convolutional layer followed by a convolutional block attention module (CBAM) [40] and then capsule network layers. Fig. 1 shows the proposed network architecture. Complete framework is divided into three parts (i) ConvNet Architecture (ii) Attention Module (CBAM) (iii) Capsule Network. Inspire from the previous studies, we have added an attention module with Capsule network. Our main aim is to detect the distracted driver, in which we need to focus on the driver's body and discard the background part such as, scenes behind the driver, car interior and other passengers that are not more important in driver distraction. Thus, we introduced an attention module that focuses on local information. One more advantage of the proposed model is that this model requires low training data in comparison to CNN.

Authorized licensed use limited to: DELHI TECHNICAL UNIV. Downloaded on April 18,2023 at 04:37:11 UTC from IEEE Xplore. Restrictions apply.

This article has been accepted for inclusion in a future issue of this journal. Content is final as presented, with the exception of pagination.

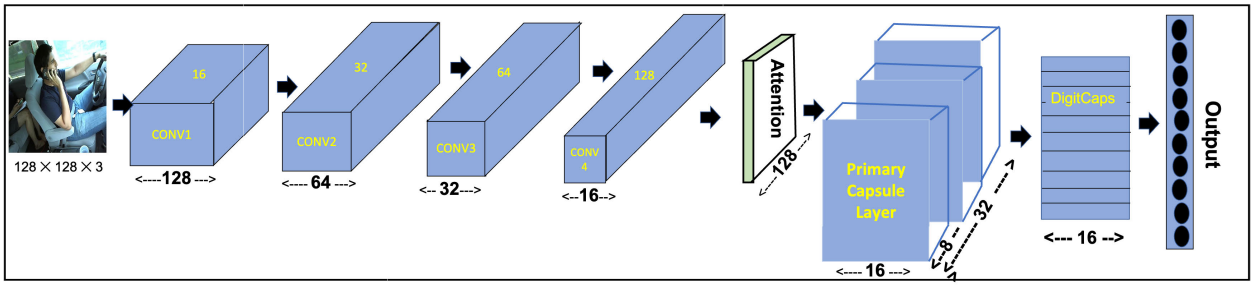


Fig. 3. Proposed CAT-CapsNet architecture with detailed dimension.

1) ConvNet Architecture: Initially, an image is passed to the series of convolution layer. Advantage of adding more convolutional layer is to provide the most discriminating feature map to the attention module. To detect the driver distraction, a 128 × 128 size image is passed into the convolutional layer. Detailed input dimension of each layer is shown in Fig. 3. First convolutional layer trains 16 kernel of size 5 × 5 with a stride of 1. Then max-pooling operation is performed with a stride of 2. Next, two consecutive layers with same kernel size are used and total 32 and 64 kernels are used respectively. In the fourth convolutional layer, 128 kernels of size 9 × 9 with stride of 1 are trained. ReLU activation function is used in all the layers.

2) Attention Module: Due to the lightweight of convolutional block attention module (CBAM), it can be embed in any convolutional architecture without any extra overhead on the model architecture. It has two module: (i) Channel Attention Module that gives the meaningful information of the input image. It uses max-pooling and average pooling separately and then forward the feature descriptors to the multi-layer perceptron (MLP) to get a channel attention map and (ii) Spatial Attention Module which focuses on where the important information is in the image. To compute the spatial attention map, convolutional and batch normalization operation is applied along with the channel axis, to get the final spatial map. In the attention module, a 16 × 16 × 128 feature map is passed and a refined features of same dimension is generated. These features contain the local and important information of the drivers which are then passed to the primary capsule layer.

3) Capsule Network: Because of the max pooling operation, CNNs loss the spatial information of the object [41]. Capsule Network models the spatial relation of the image parts while calculating the image features. Input to the Primary Capsule Layer is a refined features of size 16 × 16 × 128 and output is 32 capsules of size 6 × 6 × 8. Primary capsule layer apply convolutional operation with 9 × 9 kernel which are then squash to get capsules. The output of capsule layer is 6 × 6 × 8 capsules where 6 × 6 grid shared their weights and orientation with each other. The final layer contains 16D vectors for driver distraction class and is used to classify the driver distraction using L_2 margin loss. The final layer is also used to reconstruct the image using three fully connected layer.

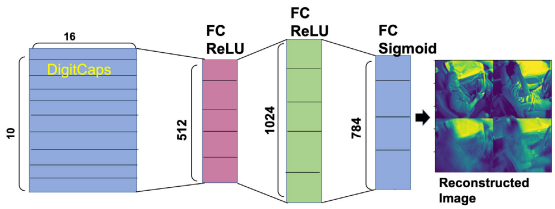


Fig. 4. Reconstructing a decoding structure from the DigitCaps layer.

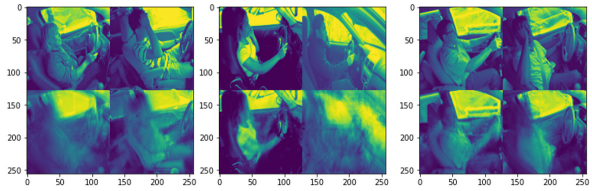


Fig. 5. Sample StateFarm test reconstruction of CAT-CapsNet with 3 routing iteration. Model reconstructed the image while preserving only important information.

C. Image Reconstruction

During the training process, activity vectors are masked out and these activity vectors are used to reconstruct the input image. Output of the digitcaps layer is fed into the three fully connected layer that reconstructs the image as shown in Fig. 4. The sum of square differences between the reconstructed image and actual input image is calculated. Low error represents that reconstructed image is similar to the input image. The reconstruction loss is scale down to 0.0005 so that it does not dominate the margin loss during training. As shown in Fig. 5 we can say that reconstruction from the 16D digitcaps layer are robust while keeping only important information. Some reconstruction image is blur this is due to the change in the training data or CapsNet inability to handle the noise in the data.

IV. Experimental Results and Discussions

The CAT-CapsNet is implemented in python using the PyTorch library. Experiments were performed on 64-bit windows 10, Intel Core i7 processor with 16GB RAM, 8GB NVIDIA GETFORCE GTX graphicx card. Table I shows the hyper parameters of the proposed model.

Authorized licensed use limited to: DELHI TECHNICAL UNIV. Downloaded on April 18,2023 at 04:37:11 UTC from IEEE Xplore. Restrictions apply.

This article has been accepted for inclusion in a future issue of this journal. Content is final as presented, with the exception of pagination.

TABLE I
HYPER PARAMETERS FOR PROPOSED MODEL

Epochs	60
Batch Size	16
Learning Rate	0.0005
Routing	3
Optimizer	Adam
Loss	Categorical Cross Entropy



Fig. 6. Sample Image of Statefarm distracted driver detection dataset [42].

A. Datasets and Equipment

In this study we have used American University in Cairo (AUC) distracted driver detection dataset [19] as well as Statefarmŝ dataset [42]. In general, any activity that engages the driver to lose focus from the road is considered as driver distraction [24], [43]. Therefore, this paper considers two publicly available standard driver distraction datasets, namely AUC and SFD, to experimentally validate the proposed model for distraction detection. Both datasets consist of images representing different activities of distracted drivers i.e., adjusting radio, drinking, hair or makeup, phone left, phone right, reaching behind, safe driving, talking to passengers, text left and text right.

1) Statefarm Dataset [42]: Kaggle published a distracted driving action dataset called as Statefarm Distracted Driver Detection (SFD) [42] captured by a camera mounted on car dashboard. SFD dataset contains 10 category of action that driver's performed while driving and each actions have approximately 2000 images. These actions are "adjusting radio," "drinking," "hair or makeup," "phone left," "phone right," "reaching behind," "safe driving," "talking to passenger," "text left," and "text right." Actions are performed by 13 males and 13 females each from different regions and samples of dataset are shown in Fig. 6. Size of one image is 640×480 pixels and dataset contains 22432 images from which randomly testing training set is divided.

2) (AUCD2) Dataset [19]: Author Abouelnaga et al. [19] created an AUCD2 data set that is similar to the statefarm dataset. In this data set 10 classes of distracted driving actions of driver's captured by the camera. Distracted driving performed by the 31 driver's including 22 men and 9 females of different countries. Each captured frame of size 1080×1920 pixels and total frames are 17308. These 10 actions are "adjusting radio," "drinking," "hair or makeup," "phone left," "phone right," "reaching behind," "safe driving," " talking to passenger," "text left," and "text right." Some sample data are shown in Fig. 7.

B. Ablation Study

Each component of the model have different affect on performance of the model. We have done detailed analysis of how convolutional layer adding advantages over the capsule network. Moreover, adding the attention mechanism CBAT with channel and spatial attention before the convolutional layer added extra advantage to focus on the important part of the image. Here we perform experiments using three different architecture on the state farm dataset (SFD) and AUCD2 dataset. First architecture is a only capsule network having primary caps and digit caps layer. Second architecture is a capsule network with few convolutional layer added before the primary caps layer. Third architecture is a proposed CAT-CapsNet that is a combination of convolutional layer followed by attention module followed by capsule network layers. Comparative result is shown in graph in Fig. 8.



Fig. 7. Sample image of AUC distracted driver dataset [19].

As we can see capsule network gives an average accuracy of 97.8% on the SFD dataset. Addition of series of convolutional layer provides a more discriminating and filtered features to the primary capsule layer thereby increasing the accuracy by 1%. When we added attention module just before the primary capsule layer, it filter out the local and important information and gives a refined features as an output. But the addition of the attention mechanism with Capsule Network has increased the training time. However, a trained model takes a fraction of seconds to detect the driver distraction while testing. Moreover, Fig. 8 highlights the performance of these models in terms of accuracy. Adding of attention mechanism defiantly helps in the performance gain and increment of more than 2% in accuracy in comparison to the normal capsule network on SFD a well as AUC datasets. To generalise the proposed model, similar experiments performed on the AUC dataset and shows the improvement in the accuracy by 3%.

We also trained our model on only few samples of each class on SFD dataset. For each class of SFD dataset, we have chosen only 30% of the samples and still we got the average accuracy of 98.88%. Thus, this proves that if we have only few samples are there then also CAT-CapsNet can achieved tremendous accuracy.

C. Experiments on Statefarm Dataset

To validate the performance consistency of the proposed model, this paper considers three different training sample rates i.e., $70-30\%$, $80-20\%$, and $90-10\%$. Due to the attention module there is an improvement in the accuracy of 2% over the original capsule network. Table II, III IV tabulate the results of the considered methods on the three sample rates. On the SFD dataset, the proposed model attains an accuracy of 99.50%, 99.88%, and 99.76% for $70-30\%$, $80-20\%$, and $90-10\%$ sample rate respectively. Thus, the proposed model achieves an accuracy of more than 99% with the difference

Authorized licensed use limited to: DELHI TECHNICAL UNIV. Downloaded on April 18,2023 at 04:37:11 UTC from IEEE Xplore. Restrictions apply.

This article has been accepted for inclusion in a future issue of this journal. Content is final as presented, with the exception of pagination.

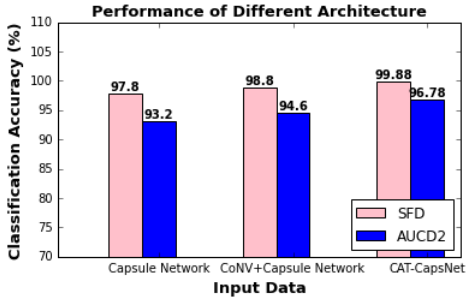


Fig. 8. Performance diagram of different architecture with $80-20\%$ split on the SFD and AUC dataset.



Fig. 9. Performance diagram of CAT-CapsNet on SFD dataset with $80-20\%$ split shows training and testing accuracy.



Fig. 10. Performance diagram of CAT-CapsNet on SFD dataset with $80-20\%$ split shows training and testing loss.

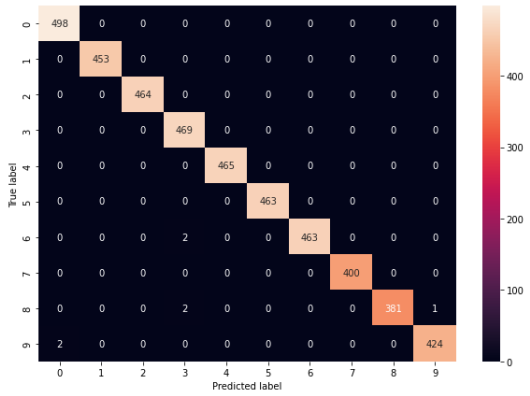


Fig. 11. Confusion matrix of proposed CAT-CapsNet on SFD dataset using $80-20\%$ random split.

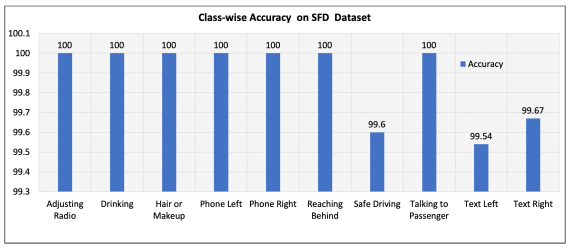


Fig. 12. Class wise accuracy on SFD dataset with $80-20\%$ random split and achieved 99.88% average accuracy.

TABLE II

COMPARATIVE ANALYSIS OF ACCURACY ON STATE FORM DATASETS WITH $80-20\%$ RANDOM SPLIT

Paper Algorithm	Accuracy
Drive-Net [25]	95.0
RNN [25]	91.7
MLP [25]	82.0
Vanila CNN with Data Augmentation [44]	97.05
Custom Deep CNN (CDCNN) [18]	99.36
VGG-16 [18]	99.57
DHCNN [23]	99.86
CAT-CapsNet	**99.88**

of .2% only on the three sample rates. The detailed of each partition split is discussed below:

Partition 1 (8:2): In first partition dataset is randomly split into $80-20\%$ ratio for training and testing respectively. Thus, there are 17945 samples for training and 4487 samples for the testing. Likewise we performed the experiments 10 times and record the average accuracy of the training as well as testing. We run the experiments up to 60 epochs with the batch size of 16. Size of the input image is 128×128, learning rate is 0.0005, 3 times routing is done and Adam optimizer is used. The performance of the proposed CAT-CapsNet in term of training accuracy is shown in Fig. 9, training loss is shown in Fig. 10 and confusion matrix is shown in the Fig. 11. In the confusion matrix Fig. 11 we observe that most of the miss classification happens in class 6 safe driving, class 8 text left and class 9 text right. In class 9 text right is confused with class 0 i.e adjusting radio because in both action right hand is used. Similarly, class 8 is confused with class 3 i.e phone left because both used the left hand. Despite these confusions we achieved average accuracy of 99.88% and in some class got 100% accuracy. We follow the training pattern of papers [23], [25], and [18] split the data in the 80% in the training sample and 20% in the test sample. Majdi et.al [25] proposed a Drive-Net by combining CNN with random forest and achieved 95% accuracy. Our proposed model achieved accuracy of 99.88% which is higher than the paper [18], [23], [25], and [44] as shown in Table II. The class wise accuracy graph is shown in Fig. 12. As we can see in the graph in most of the classes we got 100% accuracy and only in few classes where got less than 100% accuracy.

Partition 2 (9:1): In this partition all the model parameter is same as in partition 1. Only difference is 90% of the sample used for the training and 10% of the sample used for testing. We follow the training pattern of papers [18], [23], and [45] split the data in the 90% in training sample and 10% in testing sample. The training and testing accuracy as well as training and testing loss is shown in the Fig. 13, 14 respectively. Confusion matrix is shown in Fig. 15. Our proposed model achieved accuracy of 99.76% which is higher than the paper [45] that used AlexNet + Softmax and AlexNet

Authorized licensed use limited to: DELHI TECHNICAL UNIV. Downloaded on April 18,2023 at 04:37:11 UTC from IEEE Xplore. Restrictions apply.

This article has been accepted for inclusion in a future issue of this journal. Content is final as presented, with the exception of pagination.

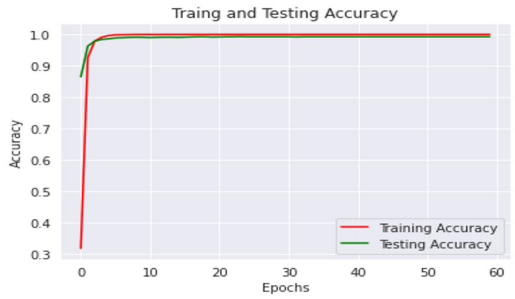


Fig. 13. Performance diagram of CAT-CapsNet on SFD dataset using $90-10\%$ split shows training accuracy vs testing accuracy.



Fig. 14. Performance diagram of CAT-CapsNet on SFD dataset using $90-10\%$ split shows training loss vs testing loss.

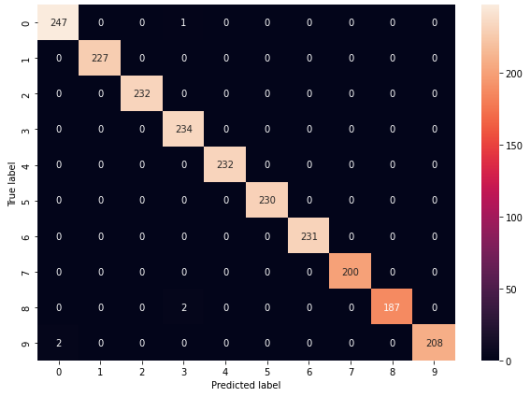


Fig. 15. Confusion matrix of proposed CAT-CapsNet on SFD dataset using $90-10\%$ split.

TABLE III
COMPARATIVE ANALYSIS OF ACCURACY ON STATE FORM DATASETS WITH $90-10\%$ RANDOM SPLIT

Paper Algorithm	Accuracy
AlexNet + Softmax [45]	96.8
AlexNet + Triplet Loss [45]	98.7
Custom Deep CNN (CDCNN) [18]	99.64
VGG-16 [18]	99.73
DHCNN [23]	99.87
CAT-CapsNet	**99.76**

+ Triplet Loss with accuracy of 96.8% and 98.7%. Also the number of parameters required to train are $8.5M$ in our case that is only 14% of $63.2M$ parameter of their proposed model. Comparison of the accuracies is shown in the table III.

Partition 3 (7:3): In this partition all the model parameter is same as in partition 1. Only difference is 70% of the sample

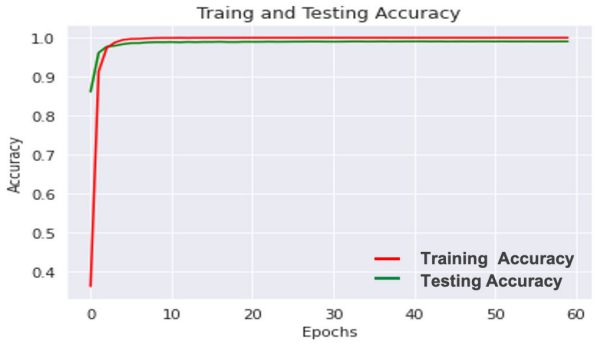


Fig. 16. Performance diagram of CAT-CapsNet on SFD dataset using $70-30\%$ split shows training accuracy vs testing accuracy.



Fig. 17. Performance diagram of CAT-CapsNet on SFD dataset using $70-30\%$ split shows training loss vs testing loss.

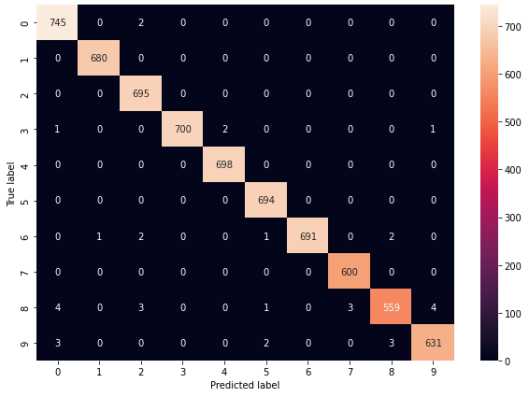


Fig. 18. Confusion matrix of proposed CAT-CapsNet on SFD dataset using $70-30\%$ random split.

used for the training and 30% of the sample used for testing. We follow the training pattern of papers [23] and [46] and split the data in the 70% in training sample and 30% in testing sample. The training and testing accuracy as well as training and testing loss is shown in the Fig. 16, 17 respectively. Confusion matrix is shown in Fig. 18 and our proposed model achieved accuracy of 99.50% which is higher than the paper [46] InceptionV3+ResNet- 50+Xception+VGG-19 and also the number of parameters required to train are 8.5 million in our case that only 10% parameter of their proposed model. Confusion between classes occurs when same hand or similar type of action is performed by the drivers. Comparison of the accuracies is shown in the table IV.

Authorized licensed use limited to: DELHI TECHNICAL UNIV. Downloaded on April 18,2023 at 04:37:11 UTC from IEEE Xplore. Restrictions apply.

This article has been accepted for inclusion in a future issue of this journal. Content is final as presented, with the exception of pagination.

TABLE IV
COMPARATIVE ANALYSIS OF ACCURACY ON STATE FORM DATASETS WITH 70 – 30% RANDOM SPLIT

Paper Algorithm	Accuracy
VGG-16[46]	58.3
VGG-19[46]	55.7
InceptionV3+Xception [46]	90.0
InceptionV3[46]	92.9
Xception [46]	82.5
InceptionV3+ResNet-50+Xception+VGG-19 [46]	97.0
DHCNN [23]	99.82
CAT-CapsNet	**99.50**

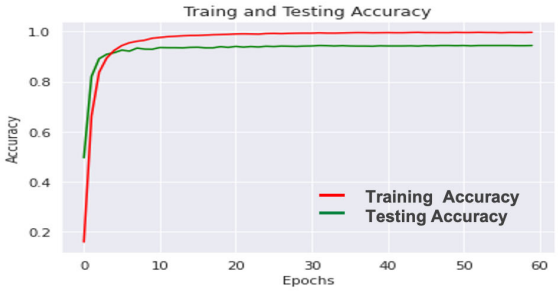


Fig. 19. Performance diagram of CAT-CapsNet on AUC dataset shows training accuracy vs testing accuracy.



Fig. 20. Performance diagram of CAT-CapsNet on AUC dataset shows training loss vs testing loss.

D. Experiments on AUC Distracted Driver Detection Dataset

Fig. 22 depicts the accuracy graph of the proposed model on AUC dataset with 80 – 20%, 90 – 10% and 70 – 30% data split. The proposed CAT-CapsNet model gives best accuracy on AUC dataset with 80 – 20% split i.e 96.78% and also gives comparable accuracy with 90 – 10% and 70 – 30% split. Moreover, it has been witnessed in literature that deep learning models give best performance when the data-split is 80 – 20%. Therefore, it is pertinent to consider the 80 – 20% data split of AUC dataset for the performance comparison.

Thus, we have used 80 – 20% random split of AUC dataset to perform the experimentation on the proposed model. Same split strategy used by owner of the dataset Abouelnaga et al. [19], where 12977 samples are used for training the model while 4331 samples are kept for testing the model. The performance of the proposed CAT-CapsNet in term of training accuracy and training loss is shown in the Fig. 19, 20 and confusion matrix is shown in the Fig. 21. In the confusion matrix in Fig. 21 talking to passenger is confused with the safe driving because in both action driver's hand is on the steering. Similarly, drinking is highly confused with hair or

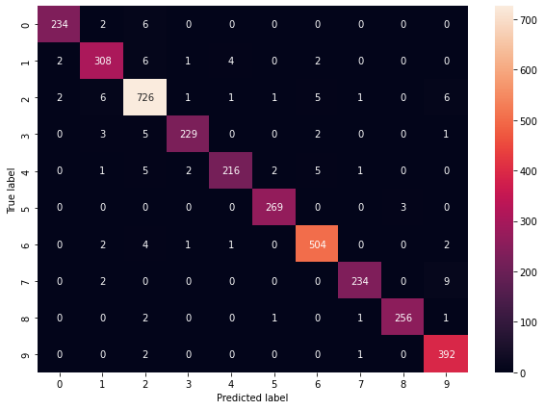


Fig. 21. Confusion matrix of proposed CAT-CapsNet on AUC dataset.

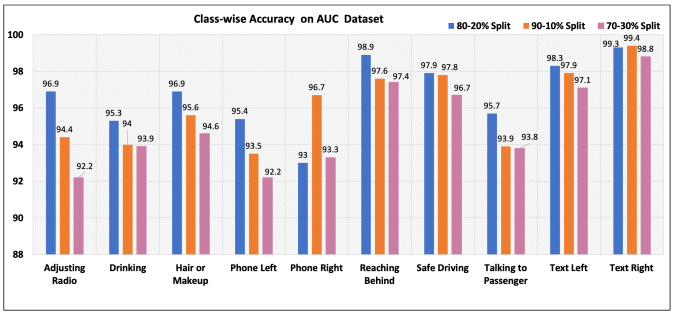


Fig. 22. Class wise accuracy on AUC dataset with 80 – 20% random split and achieved 96.78% average accuracy.

makeup. In this action also driver's left hand is on the steering and using right hand for drinking or makeup. These confusion occurs because there are only slight changes in performing the driver's action. The class wise accuracy graph is shown in Fig. 22. As we can see in the graph in most of the classes we got more than 95% and got average accuracy 96.78%. Proposed model accuracy is comparable with DHCNN [23] and MobileVGG [24]. DHCNN and MobileVGG model have less parameters compare to our model but our model gives good accuracy when training samples are less without any data augmentation.

E. Comparison With Other State-of-the-Art-Methods

We have compared our proposed work with several paper in the literature that used the same SFD data sets. The experiment result of proposed CAT-CapsNet with state-of-the-art method shown in Table V. In the literature many of the paper achieved more than 99% accuracy but their number of parameter to train is more and also we have not done any data augmentation. If training sample is less, then also proposed model perform better. As in SFD dataset only 15 – 16k samples used for the training without an data augmentation model gives more than 99% accuracy in all cases. We have compared out paper with several paper in the literature that used the same AUC data sets to perform the experiments. We follow the 80 – 20% random split for training and testing and did the comparative analysis as shown in Table VI. In the literature, many of the author achieved more than 95% accuracy but their

Authorized licensed use limited to: DELHI TECHNICAL UNIV. Downloaded on April 18,2023 at 04:37:11 UTC from IEEE Xplore. Restrictions apply.

This article has been accepted for inclusion in a future issue of this journal. Content is final as presented, with the exception of pagination.

TABLE V
COMPARATIVE ANALYSIS ON STATE FORM DATASETS

Paper Algorithm	Accuracy	Approx. no of Parameters (million)
MobileVGG [24]	99.75	2.2
Vanila CNN with Data Augmentation [44]	97.05	26.05
Drive-Net [25]	95.0	-
RNN [25]	91.7	-
DHCNN [23]	99.86	0.76
Custom Deep CNN (CDCNN) [18]	99.64	120
VGG-16 [18]	99.73	140
VGG-16 with pre-trained weight [21]	99.57	140
VGG-16 without pre-trained weight [21]	99.43	140
VGG-19 with pre-trained weight [21]	98.98	142
VGG-19 without pre-trained weight [21]	99.39	142
InceptionV3+ResNet-50+Xception+VGG-19 [46]	97.0	214
OLCMNet[33]	89.53%	–
VGG-16+ResNet+MobileNet V2 [37]	98.12%	
UDL [38]	99.07%	–
CAT-CapsNet	**99.88**	8.5

TABLE VI
COMPARATIVE ANALYSIS OF PROPOSED CAPS-NET MODEL ACCURACY ON AUC DATASET

Paper Algorithm	Accuracy	Approx no of Parameters (million)
VGG+one-Attention [47]	84.82	140
VGG-two-way Attention [47]	87.74	140
MobileVGG [24]	95.24	2.2
AlexNet [19]	93.65	62
Inception V3 [19]	95.17	24
Original VGG [48]	94.44	140
VGG with Regularization [48]	96.31	140
Modified VGG [48]	95.54	15
D-HCNN [23]	95.59	0.76
MobileNet [27]	94.67	4.2
MobileNetV2 [28]	94.75	3.5
SqueezeNet [26]	93.21	1.25
GA-Weighted Ensemble [20]	95.98	120
Custom Deep CNN (CDCNN) [18]	95.59	120
VGG-16 [18]	95.24	140
CAT-CapsNet	**96.78**	8.5

model lacks in the higher number of parameters to train and heavy size of the network. Compare to other methods in the literature CAT-CapsNet has a fewer parameter and also gives high accuracy without any data augmentation.

Further, both datasets, AUC and SFD, contain driver distraction activities of both male and female. Specifically, SFD dataset is fully gender balanced that consists of 9 driver distraction actions of 13 males and 13 females belonging to different races and skin colors. While, AUC dataset is partially balanced as it presents distraction activities by 22 males and 9 females of 7 countries. From Table V and Table VI, it can be observed that the performance of the proposed model is outperforming on both datasets. Therefore, it can be stated the proposed model analyzes the actions of the driver irrespective of gender.

V. CONCLUSION

Driver distraction is a one of the serious problems which leads to a large number of road accidents. We can reduce these numbers if we can fix an automated system in the vehicle that continuously monitoring the driver's attentiveness and warns the driver's if any distraction happens. For the same, we proposed a light-weight and shallow network to detect the driver distraction. We modified the original capsule network and added convolution layer to get the discriminating feature map. Further, to improve the detection accuracy, CBAM attention mechanism is included to increase the detection accuracy. With the accuracy of 99.88% on SFD dataset and 96.78% accuracy on the AUC data set, the proposed method outperforms the state-of-the-art methods.

In future, the proposed model can be extended to consider the time-lapse of the considered activities. Further, the proposed model can be fused with driver movements such as eye movement and head positions. Further, the proposed model can benefit in predicting future mishaps by combining vehicle dynamic data such as lane trajectory or driving trajectory with driver action. Moreover, the proposed model can be extended to generate subsequent warnings by continuously monitoring the driverŝ actions. Also, we would like to add cognitive, and audio-visual features to detect the driver distraction.

REFERENCES

[1] *Global Status Report on Road Safety 2018: Summary*, World Health Organization, Geneva, Switzerland, 2018.

[2] (2001). *Driver Fatigue and Road Accidents. A Literature Review and Position Paper*. Accessed: Apr. 8, 2022. [Online]. Available: rospa.com/rospaweb/docs/advice-services/road-safety/drivers/fatigue-litreview.pdf

[3] Z. Li, S. Bao, I. V. Kolmanovsky, and X. Yin, "Visual-manual distraction detection using driving performance indicators with naturalistic driving data," *IEEE Trans. Intell. Transp. Syst.*, vol. 19, no. 8, pp. 2528–2535, Aug. 2018.

[4] Z. Huang et al., "Making accurate object detection at the edge: Review and new approach," *Artif. Intell. Rev.*, vol. 55, pp. 2245–2274, Sep. 2021.

[5] L. Sun, Z. Liu, X. Sun, L. Liu, R. Lan, and X. Luo, "Lightweight image super-resolution via weighted multi-scale residual network," *IEEE/CAA J. Autom. Sinica*, vol. 8, no. 7, pp. 1271–1280, Jul. 2021.

[6] R. Jin, M. Wu, K. Wu, K. Gao, Z. Chen, and X. Li, "Position encoding based convolutional neural networks for machine remaining useful life prediction," *IEEE/CAA J. Autom. Sinica*, vol. 9, no. 8, pp. 1427–1439, Aug. 2022.

[7] B. Verma and A. Choudhary, "A framework for driver emotion recognition using deep learning and Grassmann manifolds," in *Proc. 21st Int. Conf. Intell. Transp. Syst. (ITSC)*, Nov. 2018, pp. 1421–1426.

[8] I. Gupta, N. Garg, A. Aggarwal, N. Nepalia, and B. Verma, "Real-time driver's drowsiness monitoring based on dynamically varying threshold," in *Proc. 11th Int. Conf. Contemp. Comput. (IC3)*, Aug. 2018, pp. 1–6.

[9] B. Verma and A. Choudhary, "Deep learning based real-time driver emotion monitoring," in *Proc. IEEE Int. Conf. Veh. Electron. Saf. (ICVES)*, Sep. 2018, pp. 1–6.

[10] S. Sabour, N. Frosst, and G. E. Hinton, "Dynamic routing between capsules," 2017, *arXiv:1710.09829*.

[11] R. LaLonde and U. Bagci, "Capsules for object segmentation," 2018, *arXiv:1804.04241*.

[12] Y. Xing et al., "End-to-end driving activities and secondary tasks recognition using deep convolutional neural network and transfer learning," in *Proc. IEEE Intell. Vehicles Symp. (IV)*, Jun. 2018, pp. 1626–1631.

[13] K. Seshadri, F. Juefei-Xu, D. K. Pal, M. Savvides, and C. P. Thor, "Driver cell phone usage detection on strategic highway research program (SHRP2) face view videos," in *Proc. IEEE Conf. Comput. Vis. Pattern Recognit. Workshops (CVPRW)*, Jun. 2015, pp. 35–43.

[14] T. H. N. Le, Y. Zheng, C. Zhu, K. Luu, and M. Savvides, "Multiple scale faster-RCNN approach to driver's cell-phone usage and hands on steering wheel detection," in *Proc. IEEE Conf. Comput. Vis. Pattern Recognit. Workshops (CVPRW)*, Jun. 2016, pp. 46–53.

[15] R. Tian, K. Ruan, L. Li, J. Le, J. Greenberg, and S. Barbat, "Standardized evaluation of camera-based driver state monitoring systems," *IEEE/CAA J. Autom. Sinica*, vol. 6, no. 3, pp. 716–732, May 2019.

[16] T. Liu, M. Hu, S. Ma, Y. Xiao, Y. Liu, and W. Song, "Exploring the effectiveness of gesture interaction in driver assistance systems via virtual reality," *IEEE/CAA J. Autom. Sinica*, vol. 9, no. 8, pp. 1520–1523, Aug. 2022.

[17] M. R. Arefin, F. Makhmudkhujaev, O. Chae, and J. Kim, "Aggregating CNN and HOG features for real-time distracted driver detection," in *Proc. IEEE Int. Conf. Consum. Electron. (ICCE)*, Jan. 2019, pp. 1–3.

[18] A. Gumaei et al., "A deep learning-based driver distraction identification framework over edge cloud," *Neural Comput. Appl.*, pp. 1–16, Sep. 2020.

Authorized licensed use limited to: DELHI TECHNICAL UNIV. Downloaded on April 18,2023 at 04:37:11 UTC from IEEE Xplore. Restrictions apply.

This article has been accepted for inclusion in a future issue of this journal. Content is final as presented, with the exception of pagination.

[19] Y. Abouelnaga, H. M. Eraqi, and M. N. Moustafa, "Real-time distracted driver posture classification," 2017, *arXiv:1706.09498*.

[20] H. M. Eraqi, Y. Abouelnaga, M. H. Saad, and M. N. Moustafa, "Driver distraction identification with an ensemble of convolutional neural networks," *J. Adv. Transp.*, vol. 2019, pp. 1–12, Feb. 2019.

[21] S. Masood, A. Rai, A. Aggarwal, M. N. Doja, and M. Ahmad, "Detecting distraction of drivers using convolutional neural network," *Pattern Recognit. Lett.*, vol. 139, pp. 79–85, Nov. 2020.

[22] J. Ba and R. Caruana, "Do deep nets really need to be deep?" in *Proc. Adv. Neural Inf. Process. Syst.*, vol. 27, 2014, pp. 2654–2662.

[23] B. Qin, J. Qian, Y. Xin, B. Liu, and Y. Dong, "Distracted driver detection based on a CNN with decreasing filter size," *IEEE Trans. Intell. Transp. Syst.*, vol. 23, no. 7, pp. 6922–6933, Jul. 2022.

[24] B. Baheti, S. Talbar, and S. Gajre, "Towards computationally efficient and realtime distracted driver detection with MobileVGG network," *IEEE Trans. Intell. Vehicles*, vol. 5, no. 4, pp. 565–574, Dec. 2020.

[25] M. S. Majdi, S. Ram, J. T. Gill, and J. J. Rodriguez, "Drive-Net: Convolutional network for driver distraction detection," in *Proc. IEEE Southwest Symp. Image Anal. Interpretation (SSIAI)*, Apr. 2018, pp. 1–4.

[26] F. N. Iandola, S. Han, M. W. Moskewicz, K. Ashraf, W. J. Dally, and K. Keutzer, "SqueezeNet: AlexNet-level accuracy with 50x fewer parameters and <0.5MB model size," 2016, *arXiv:1602.07360*.

[27] A. G. Howard et al., "MobileNets: Efficient convolutional neural networks for mobile vision applications," 2017, *arXiv:1704.04861*.

[28] A. Howard, A. Zhmoginov, L.-C. Chen, M. Sandler, and M. Zhu, "Inverted residuals and linear bottlenecks: Mobile networks for classification, detection and segmentation," 2018, *arXiv:1801.04381*.

[29] J. M. Mase, P. Chapman, G. P. Figueredo, and M. T. Torres, "A hybrid deep learning approach for driver distraction detection," in *Proc. Int. Conf. Inf. Commun. Technol. Converg. (ICTC)*, Oct. 2020, pp. 1–6.

[30] F. Omerustaoglu, C. O. Sakar, and G. Kar, "Distracted driver detection by combining in-vehicle and image data using deep learning," *Appl. Soft Comput.*, vol. 96, Nov. 2020, Art. no. 106657.

[31] M. Alotaibi and B. Alotaibi, "Distracted driver classification using deep learning," *Signal, Image Video Process.*, vol. 14, no. 3, pp. 617–624, 2019.

[32] C. Ahlstrom, G. Georgoulas, and K. Kircher, "Towards a context-dependent multi-buffer driver distraction detection algorithm," *IEEE Trans. Intell. Transp. Syst.*, vol. 23, no. 5, pp. 4778–4790, May 2022.

[33] P. Li et al., "Driver distraction detection using octave-like convolutional neural network," *IEEE Trans. Intell. Transp. Syst.*, vol. 23, no. 7, pp. 8823–8833, Jul. 2022.

[34] J. Chen et al., "Fine-grained detection of driver distraction based on neural architecture search," *IEEE Trans. Intell. Transp. Syst.*, vol. 22, no. 9, pp. 5783–5801, Sep. 2021.

[35] T. Huang and R. Fu, "Driver distraction detection based on the true driver's focus of attention," *IEEE Trans. Intell. Transp. Syst.*, vol. 23, no. 10, pp. 19374–19386, Oct. 2022.

[36] C. V. Hari and P. Sankaran, "Driver distraction analysis using face pose cues," *Expert Syst. Appl.*, vol. 179, Oct. 2021, Art. no. 115036.

[37] M. U. Hossain, M. A. Rahman, M. M. Islam, A. Akhter, M. A. Uddin, and B. K. Paul, "Automatic driver distraction detection using deep convolutional neural networks," *Intell. Syst. With Appl.*, vol. 14, May 2022, Art. no. 200075.

[38] B. Li et al., "A new unsupervised deep learning algorithm for fine-grained detection of driver distraction," *IEEE Trans. Intell. Transp. Syst.*, vol. 23, no. 10, pp. 19272–19284, Oct. 2022.

[39] P. Ping, C. Huang, W. Ding, Y. Liu, M. Chiyomi, and T. Kazuya, "Distracted driving detection based on the fusion of deep learning and causal reasoning," *Inf. Fusion*, vol. 89, pp. 121–142, Jan. 2023.

[40] S. Woo, J. Park, J.-Y. Lee, and I. S. Kweon, "CBAM: Convolutional block attention module," in *Proc. Eur. Conf. Comput. Vis. (ECCV)*, Sep. 2018, pp. 3–19.

[41] M. K. Patrick, A. F. Adekoya, A. A. Mighty, and B. Y. Edward, "Capsule networks—A survey," *J. King Saud Univ.-Comput. Inf. Sci.*, vol. 34, no. 1, pp. 1295–1310, 2022.

[42] S. Farm. *State Farm Distracted Driver Detection*. Accessed: Jun. 15, 2017. [Online]. Available: https://www.kaggle.com/c/state-farm-distracted-driverdetection

[43] S. Kaplan, M. A. Guvensan, A. G. Yavuz, and Y. Karalurt, "Driver behavior analysis for safe driving: A survey," *IEEE Trans. Intell. Transp. Syst.*, vol. 16, no. 6, pp. 3017–3032, Dec. 2015.

[44] V. A. Jamsheed, B. Janet, and U. S. Reddy, "Real time detection of driver distraction using CNN," in *Proc. 3rd Int. Conf. Smart Syst. Inventive Technol. (ICSSIT)*, Aug. 2020, pp. 185–191.

[45] O. D. Okon and L. Meng, "Detecting distracted driving with deep learning," in *Proc. Int. Conf. Interact. Collaborative Robot.* Cham, Switzerland: Springer, 2017, pp. 170–179.

[46] K. R. Dhakate and R. Dash, "Distracted driver detection using stacking ensemble," in *Proc. IEEE Int. Students' Conf. Elect., Electron. Comput. Sci. (SCEECS)*, Feb. 2020, pp. 1–5.

[47] Y. Ai, J. Xia, K. She, and Q. Long, "Double attention convolutional neural network for driver action recognition," in *Proc. 3rd Int. Conf. Electron. Inf. Technol. Comput. Eng. (EITCE)*, Oct. 2019, pp. 1515–1519.

[48] B. Baheti, S. Gajre, and S. Talbar, "Detection of distracted driver using convolutional neural network," in *Proc. IEEE/CVF Conf. Comput. Vis. Pattern Recognit. Workshops (CVPRW)*, Jun. 2018, pp. 1032–1038.



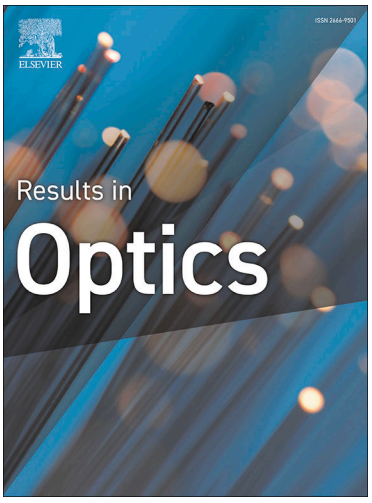
Himanshu Mittal received the Ph.D. degree in computer vision. He is currently an Assistant Professor with the Department of Artificial Intelligence and Data Science, Indira Gandhi Delhi Technical University for Women, New Delhi, India. He has numerous publications in international journals and conferences, including IEEE, Elsevier, and Springer. His keen research areas include image analysis, machine learning, and optimization algorithms. He is also a Reviewer of many international journals, such as *Future Generation Computer Systems* and *International Journal of Machine Learning and Cybernetics*.



Bindu Verma (Member, IEEE) received the master's and Ph.D. degrees in automated intent recognition using hand gesture and face expression analysis from the School of Computer and Systems Sciences, Jawaharlal Nehru University, New Delhi. She is currently a Faculty Member with the Department of Information Technology, Delhi Technological University (formerly known as the Delhi College of Engineering). She is also passionate to work in the areas of computer vision, machine learning, human–computer interaction, intelligent systems, and affective state monitoring. She have made substantial contributions to the field of human–computer interaction, emotion recognition, and intent recognition with many research articles published in international conferences and journals. She is a Reviewer of many international journals, such as *IET Intelligent Transport System*, IEEE TRANSACTIONS ON CIRCUITS AND SYSTEMS FOR VIDEO TECHNOLOGY, and Intelligent Transportation System Conferences.

Authorized licensed use limited to: DELHI TECHNICAL UNIV. Downloaded on April 18,2023 at 04:37:11 UTC from IEEE Xplore. Restrictions apply.

Journal Pre-proofs



Chalcogenide glass-based Low Loss Graded Index Photonic Crystal Fiber for Non-linear applications in the Mid-IR regime

Jyoti Chauhan, Yogita Kalra, Ravindra Kumar Sinha

PII: S2666-9501(23)00083-4
DOI: https://doi.org/10.1016/j.rio.2023.100431
Reference: RIO 100431

To appear in: *Results in Optics*

Received Date: 31 January 2023
Revised Date: 24 March 2023
Accepted Date: 10 April 2023

Please cite this article as: J. Chauhan, Y. Kalra, R.K. Sinha, Chalcogenide glass-based Low Loss Graded Index Photonic Crystal Fiber for Non-linear applications in the Mid-IR regime, *Results in Optics* (2023), doi: https://doi.org/10.1016/j.rio.2023.100431

This is a PDF file of an article that has undergone enhancements after acceptance, such as the addition of a cover page and metadata, and formatting for readability, but it is not yet the definitive version of record. This version will undergo additional copyediting, typesetting and review before it is published in its final form, but we are providing this version to give early visibility of the article. Please note that, during the production process, errors may be discovered which could affect the content, and all legal disclaimers that apply to the journal pertain.

© 2023 Published by Elsevier B.V.

Journal Pre-proofs

Chalcogenide glass-based Low Loss Graded Index Photonic Crystal Fiber for Non-linear applications in the Mid-IR regime

Jyoti Chauhan, Yogita Kalra*, Ravindra Kumar Sinha*
TIFAC-Center of Relevance and Excellence in Fiber Optics and Optical Communications, Department of Applied Physics, Delhi Technological University, Bawana Road, Delhi 110042, India

Abstract—Computational modeling and numerical Investigation of a chalcogenide glass-based Graded-Index Photonic Crystal Fiber (GI-PCF) for the mid-infrared region has been put forth. Our proposed structure has a solid core and hence index-guided mechanism of light propagation is followed here. The propagation characteristics like confinement loss, chromatic dispersion, effective area, non-linear coefficient, and spot size of the proposed structure have been studied in the mid infrared range (MIR) of 1.8 to 10μm wavelength and a comparison is drawn between the Graded-Index PCF and a normal PCF. The proposed structure is a highly non-linear PCF having a non-linear index of order 10^{7} W^{-1} km^{-1} with spot size being very small i.e. 0.5- 8.6 μm. It is a promising candidate for dispersion compensating fiber as the dispersion is entirely negative, -58.141 to -258.332 ps/km-nm, for the whole MIR wavelength range.

Keywords— Graded-Index PCF, Dispersion Compensating Fiber, MIR, endless single-mode propagation, close-to-zero Confinement Loss, high-nonlinearity

1. Introduction

Photonic Crystal Fibers are micro-structured optical fibers that are based upon a single material in which there are air holes running through the entire length of the fiber, hence it is also called the holey structure. The holey structure has got a periodic arrangement in the material and a break in the periodicity of the holes is the localized core of the fiber. The study of photonic crystal fibers has gained great attention over the past few years and the way holey fibers trap light, due to the large refractive index contrast between the holes and the solid background, make them unique [1]. Ever since its inception in 1996 various researchers have been working to make numerous applications for dispersion compensating fiber [2,3,4], dispersion-shifted fiber [5,6], dispersion flattened fiber [7], and a medium for sensing applications. PCFs have got various advantages over conventional step-index fiber [8] as their properties can be tailored to a great extent by changing a few of their basic structural properties like pitch, hole size, hole shape, or the number of layers of holes. In traditional step-index fibers, the light gets guided via total internal reflection but in PCFs light gets guided through two mechanisms, one is the bandgap guidance (for hollow-core fibers) mechanism and the second one is the effective index-guided (for solid core fibers) mechanism. In this paper solid core fiber is considered, hence light gets guided by an index-guided mechanism. These days there is great interest in chalcogenide-based PCFs as they are highly transparent in the Mid-IR range and are good for transmission of light from 1.8 to 10 μm of wavelength range [9]. The optical range of 1.8-10μm is gaining huge attention because of its wide application in emerging areas like green chemistry [10], diagnosis in the medical industry [11], monitoring of air pollutants [12], CoViD-19 disinfecting products [13], refractive index sensor [14,15], and many more. Researchers and Scientists are working on various new geometries and configurations of PCFs including infiltrated PCFs [16-19], both theoretically and experimentally, for improved dispersion and transmission characteristics. Various geometrical structures like multi-ring PCF [9], sandwiched PCF [20], square, rectangular and triangular lattice structures [21,22,23], Octagonal PCF [24], graded-index PCF [25] and so on, have been explored. The properties of various materials like tellurite, chalcogenide, silica, etc. have also been analyzed and applied in making PCFs have their applicability and usage in various fields for the entire telecom band and beyond. In this paper, we report the propagation characteristics of chalcogenide (As_2Se_3) based graded-index PCF with high non-linear coefficient and low confinement loss, on As2Se3 based material, in the mid-IR region.

2. Design of the proposed Graded Index PCF

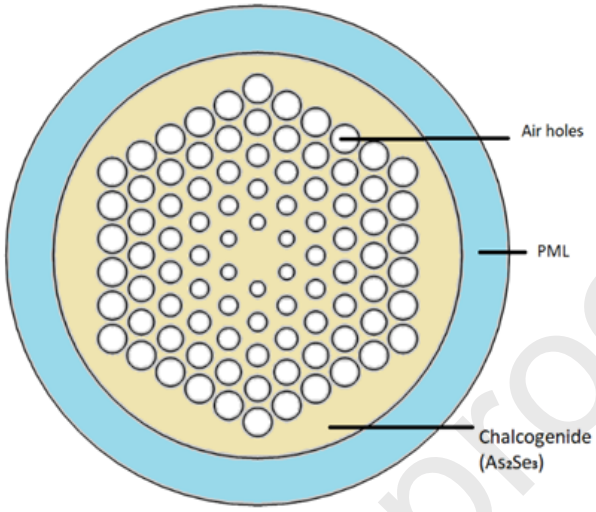


Fig. 1. Design of the proposed Graded-Index Photonic Crystal Fiber

Fig.1 shows the design of the proposed graded-index PCF structure in which air holes are arranged hexagonally. The outer boundary and the inner boundary of the entire fiber constitute the Perfectly Matched Layer (PML) [2]. The thickness of PML has been varied to get the optimized value as 1.2 µm, to achieve our objective of high non-linear coefficient with low confinement loss". The defect acts as the localized core of the fiber. The diameter of the holes is varied in a regular fashion to make it a graded-index PCF. The size of the holes vary as we move away from the localized core in the transverse direction hence it appears as if there is grading in the cladding and hence the name has been assigned to the proposed geometry as a graded-index PCF [25]. The size of the air holes, in the consecutive rings, increases as we go outwards in the transverse direction from the center of the fiber; the size of air holes in a particular ring is kept the same. The optimized value of pitch (∧) between the holes is 0.96 µm.

The diameter of air holes is ∧*0.45, ∧*0.55, ∧*0.65, ∧*0.75, ∧*0.85, of the respective layers starting from the innermost layer. The base of the entire structure is chalcogenide glass (As_2Se_3) whose refractive index is calculated using the Sellmeier equation [8]:

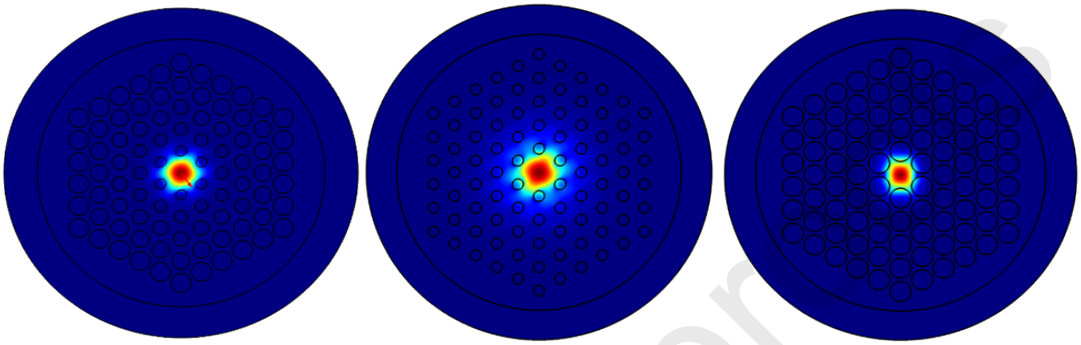
$$n(\lambda) = \sqrt{1 + \lambda^2\left(\frac{{A_1}^2}{\lambda^2 - {A_1}^2} + \frac{{A_2}^2}{\lambda^2 - 19^2} + \frac{{A_3}^2}{\lambda^2 - 4{A_1}^2}\right)} \quad (1)$$

where A_0=2.234921, A_1=0.24164, A_2=0.347441, A_3=1.308575, and λ is the operating wavelength considered in micrometers (µm). Sellmeier equation has been taken into consideration while calculating the refractive index of the chalcogenide glass for numerical simulations and this value of the refractive index is considered to be the refractive index of the core for calculation purpose.

Journal Pre-proofs

3. Result and Discussion

3.1 Confinement Loss



(a) (b) (c)

Fig. 2. Mode Confinement in (a) Graded-Index PCF (b) PCF1 (c) PCF2 at 3.5 µm wavelength

Confinement Loss is a very important parameter to check confinement property of a fiber. It can be calculated using the following expression [26]

$$Confinement\ Loss = 8.686 \times \frac{2\pi}{\lambda} \times Im(n_{eff}) \quad (2)$$

where Im is the imaginary component of the effective refractive index n_{eff} of the cladding.

From fig.2. it can be seen that the confinement is more in a Graded-Index PCF as compared to the normal PCF. The confinement of mode is compared for all the normal PCFs having hole size lying between the minimum hole size and maximum hole size range of that of the Graded-Index PCF. Fig.2(a) corresponds to the mode confinement in a Graded-Index PCF. Fig.2(b) and 2(c) correspond to the confinement in the other geometries having a normal PCF type structure with the air-holes size lying in the range of the proposed Graded-Index PCF. Size of air-holes of PCF1 in fig.2(b) is ∧*0.45 i.e. the smallest air-hole size of GI-PCF and that of PCF2 in fig2(c) is ∧*0.85 i.e. the largest air-hole size of GI-PCF. It is clearly shown in fig.2 that the confinement is better in Graded-Index PCF as compared to other normal PCF structures. To support the argument the confinement Loss of a GI-PCF is also plotted and compared to PCF1 and PCF 2 in fig.3. It can be inferred from the plot that the Graded-Index PCF has appreciably less and lowest confinement loss as compared to the other normal PCF type designs. In fact, close to zero confinement loss is observed in the mid-IR region for graded-index PCF.

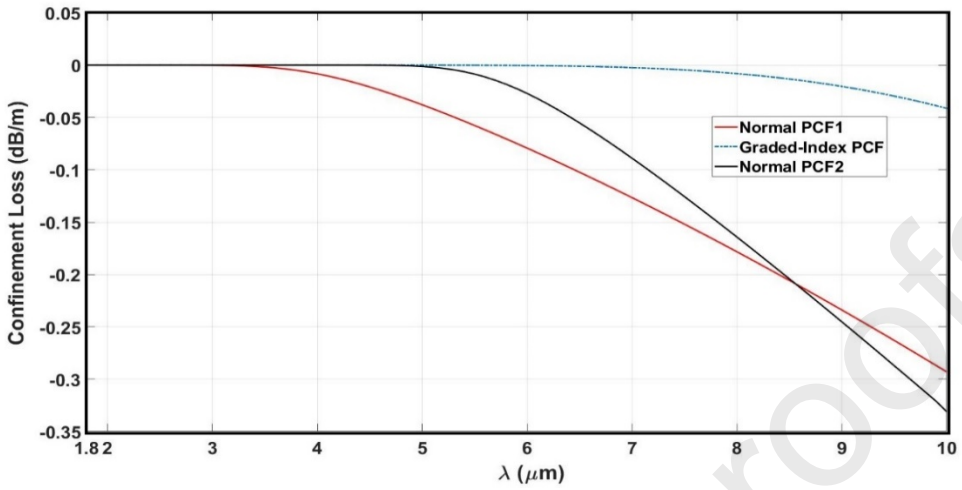


Fig.3 Comparison of Confinement Loss in Graded-Index PCF with Normal PCF

3.2 Normalized Frequency Parameter (V)

In Step Index Fiber the cut-off frequency should be < 2.405 for single-mode transmission [26]. But it is proven that the cut-off frequency should be < π for the single-mode transmission in Photonic Crystal Fibers [27-29]. The number of modes propagating in an optical fiber is primarily judged by the value of the V-parameter and the value of the V-parameter can be calculated by the following expression [27]

$$V = \frac{2\pi\Lambda}{\lambda}\sqrt{n_c^2 - n_{eff}^2} \tag{3}$$

where n_c is the refractive index of the localized core of the GI-PCF and its values are taken from eq.1, to be considered in eq.3. Values of n_c and n_{eff} are plotted in fig. 4(b) and 4(c) respectively.

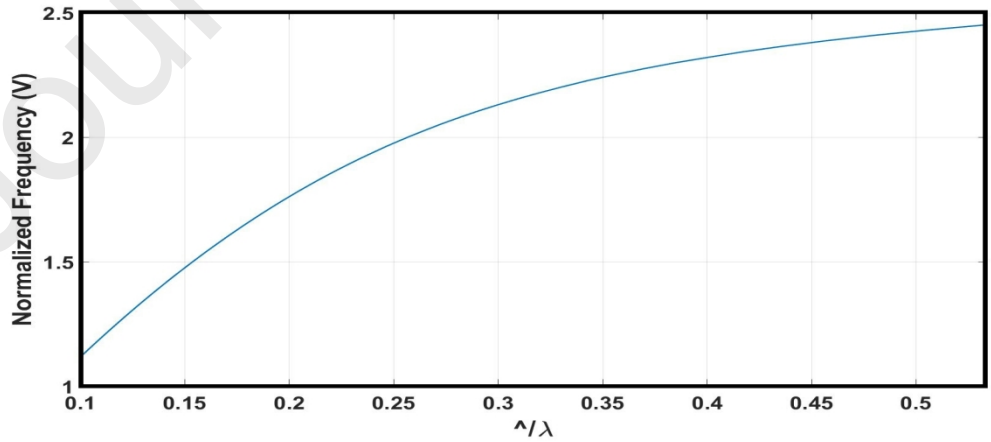


Fig.4(a). Normalized Frequency Plot of a Graded-Index PCF

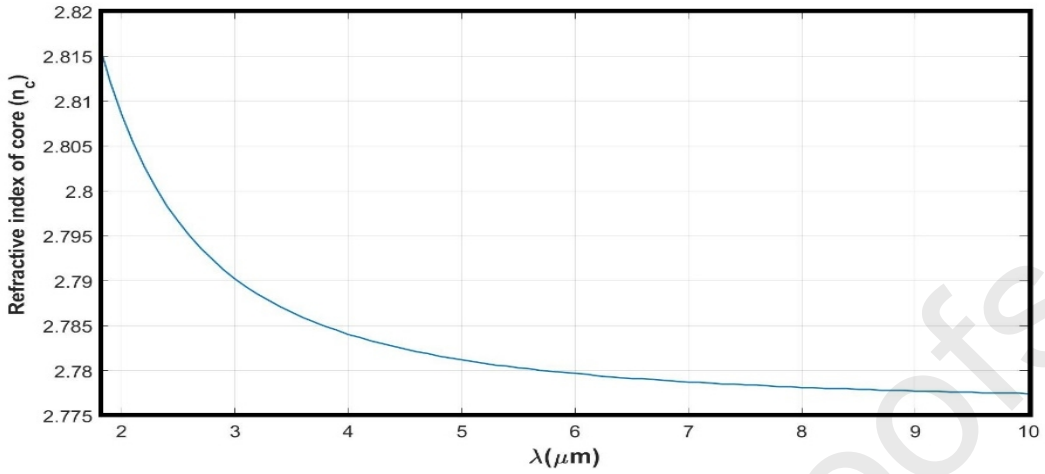


Fig.4(b). Variation of Refractive index of core (n_c) with wavelength

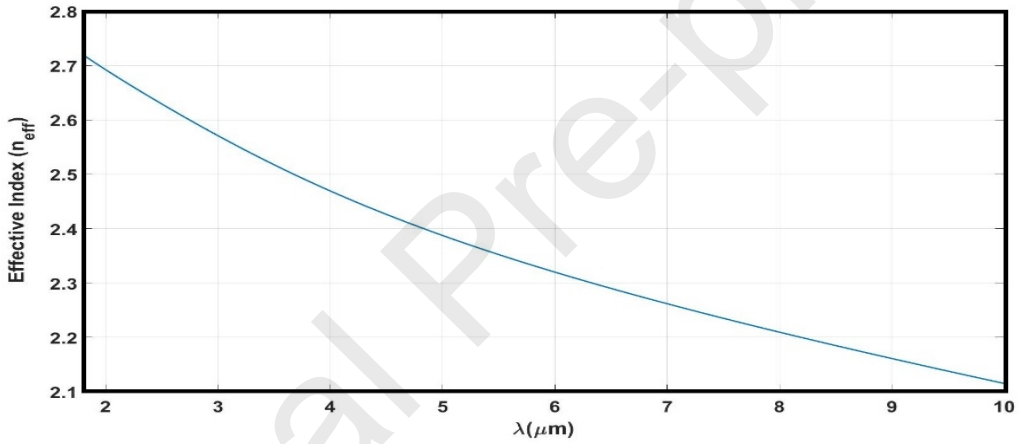


Fig.4(c). Variation of effective refractive index (n_{eff}) with wavelength

Fig.4(a). clearly shows that the value of cut-off frequency (V parameter), given by eq.3 [26], always lies below the desired cut-off frequency ensuring the single-mode transmission in the proposed PCF. Endless single-mode transmission has various applications in many fields and hence the proposed structure can further be explored for its usage as a single-mode fiber in the infrared region. Our proposed GI-PCF shows single-mode propagation with low confinement loss for entire MIR window (1.8-10μm).

3.3 Chromatic Dispersion

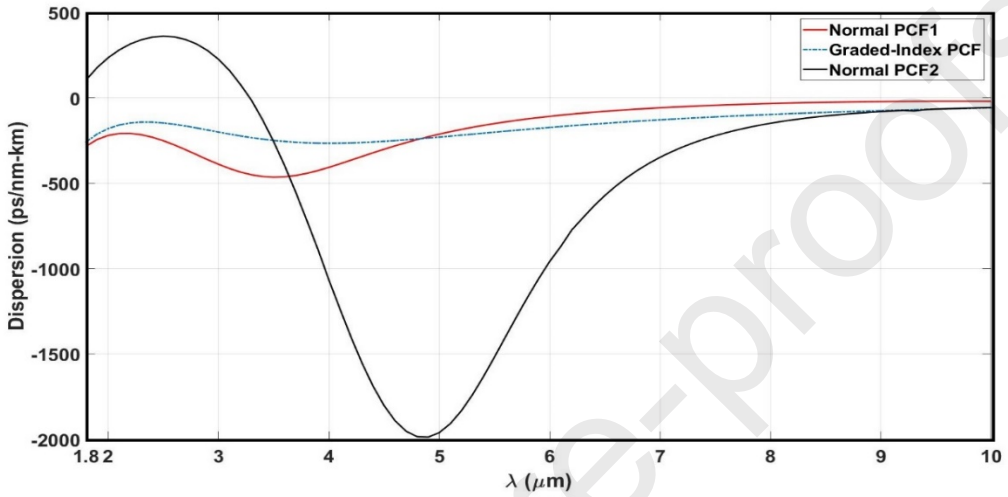
Dispersion in fiber is a very important characteristic feature that can be varied to a great extent, to use the optical fibers as per our needs. Chromatic dispersion is calculated using the given relation [27]:

$$D(\lambda) = -\frac{\lambda d^2 n_{eff}(\lambda)}{c \quad d\lambda^2} \tag{4}$$

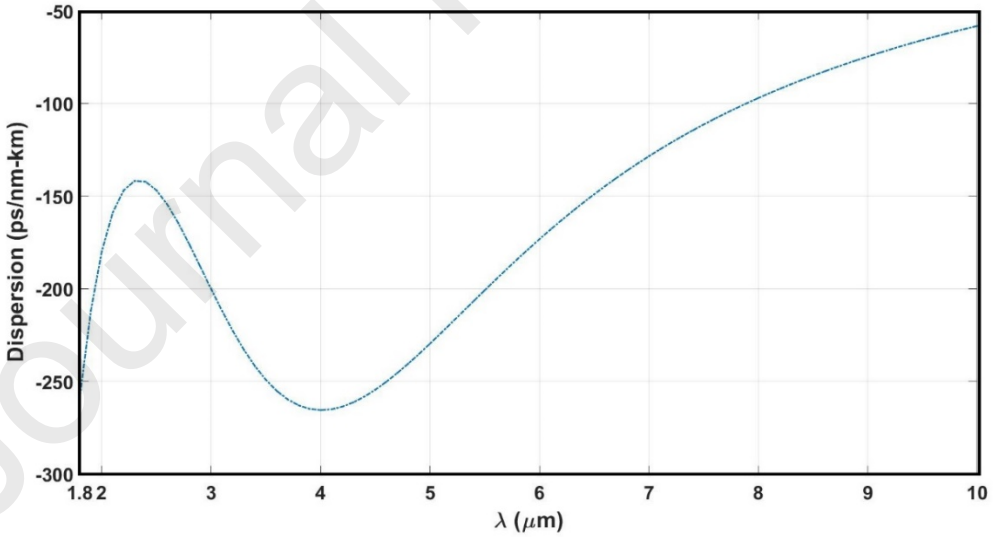
Journal Pre-proofs

where D is the dispersion in ps/km-nm and c is the speed of light, 3×10^8 m/s.

Fig 5 (a) gives a comparison of chromatic dispersion in our proposed GI-PCF and a normal PCF. Fig 5(b) shows enlarged view of dispersion variation in GI-PCF with respect to wavelength. By looking at the dispersion characteristics of a Graded-Index PCF we can conclude that it has the capability of being used as a dispersion-compensating fiber, along with being highly non-linear, in the mid-IR range. In the entire mid-IR range the dispersion is coming out to be negative, having maxima at -263.68 ps/nm-km, for the proposed GI-PCF.



(a)



(b)

Fig.5 Chromatic Dispersion (a) Comparison of Graded-Index to normal PCF (b) In Graded-PCF

Journal Pre-proofs

3.4 Effective Mode Area and Non-linear Coefficient

The Effective mode Area can be calculated as [9]:

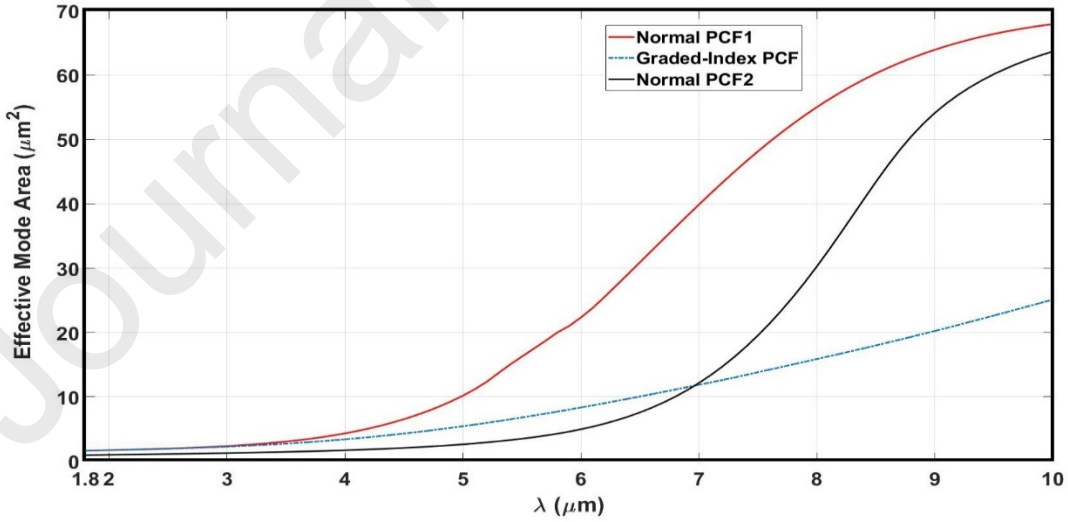
$$A_{eff}(\lambda) = \frac{(\iint F(x,y)^2 dxdy)^2}{(\iint F(x,y)^4 dxdy)} \quad (5)$$

where F(x, y) is the transverse electric field. Effective area variation with respect to wavelength for a chalcogenide-based Graded-Index PCF is shown in Fig.6(a) and it shows that as the wavelength increases the effective mode area also increases. Effective area and non-linear coefficient are related to each other by equation (8). Effective area of GI-PCF is lowest hence yielding highest value of non-linear coefficient making our proposed PCF better responsive to non-linear effects.

Non-linear coefficient takes our attention toward the non-linear behavior of the fiber. It plays an important role in the field of non-linear optics. For a chalcogenide glass, the non-linear coefficient can be 1000 times greater than silica and hence preferable to use [30]. The expression below is the mathematical representation of the coefficient,

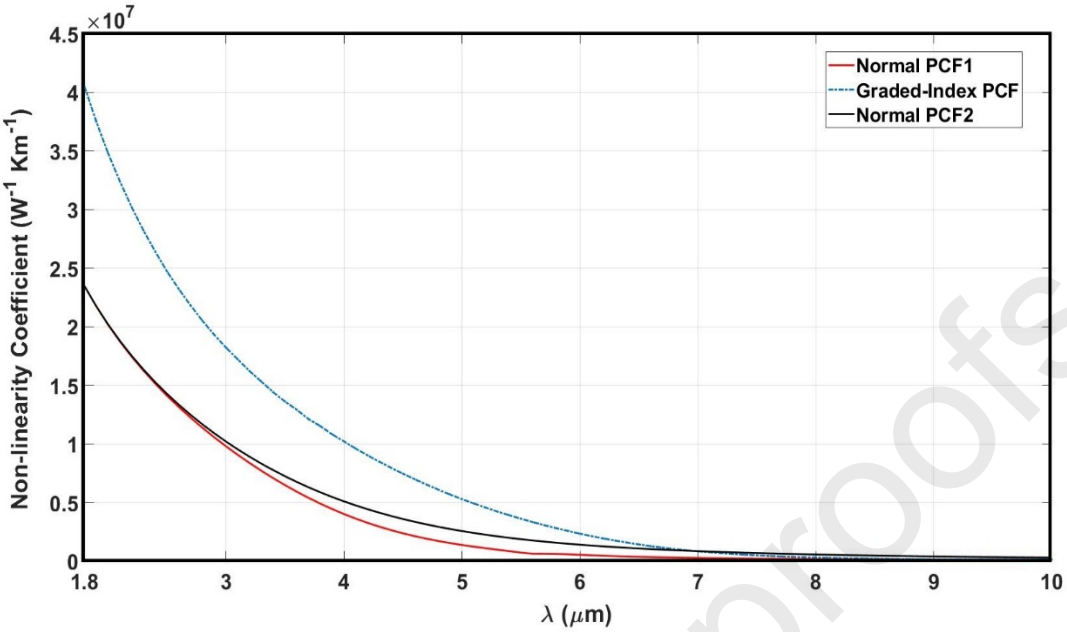
$$\Upsilon(\lambda) = \frac{2\pi n_2}{\lambda A_{eff}} \quad (6)$$

where λ is the operating wavelength, n_2 is the non-linear index for As_2Se_3 having value 1.1 x 10^{-17} m^2/W and A_{eff} is the effective area. Fig.6(b) shows that the non-linear coefficient for the chosen material is very high and goes upto a maximum value of 4.0543 x 10^7 W^{-1} km^{-1}. For As_2Se_3 based solid core PCF, non-linear coefficient value is of order 10^6 W^{-1} km^{-1} [31], ours is ten times greater than this value. We have achieved this high value of non-linear coefficient with only five layers of air-holes but with grading. Also, non-linear coefficient for our proposed GI-PCF is approximately double of the normal PCF structure with no grading. Such a design on As_2Se_3 material, having non-linear index of order 10^7 W^{-1} km^{-1} in mid-IR region, has not been reported yet, to the best of our knowledge. This makes the proposed geometry a novel PCF.



(a)

Journal Pre-proofs



(b)

Fig.6. Comparison of (a) Effective area (b) Non-linearity Coefficient of Graded-Index PCF with normal PCF

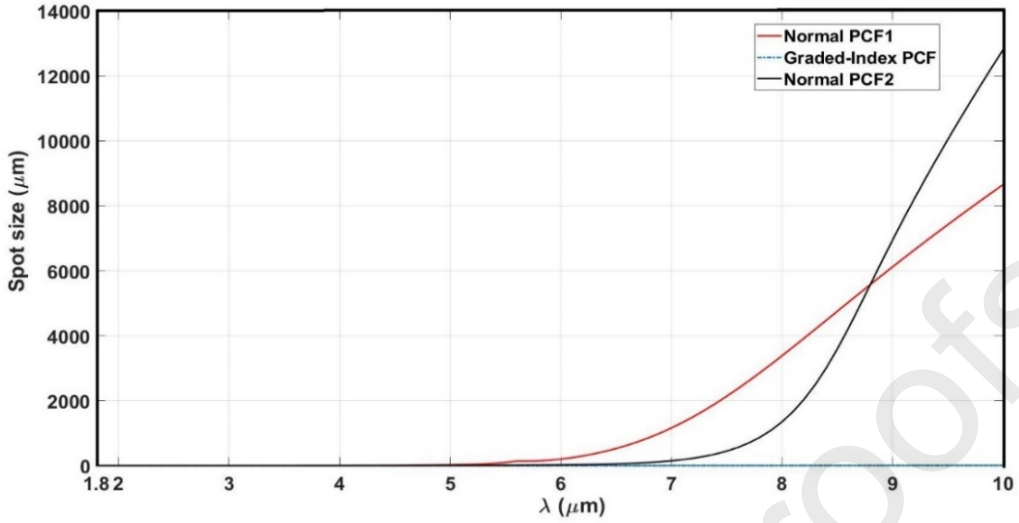
3.5 Spot Size (W_{eff})

Spot Size of the fiber is an important factor. Beam divergence or spot size clearly depends upon the operating wavelength. A smaller spot size means that the light beam is less divergent and is more into the core of the fiber. Spot size can be calculated using Marcuse Formula [13]

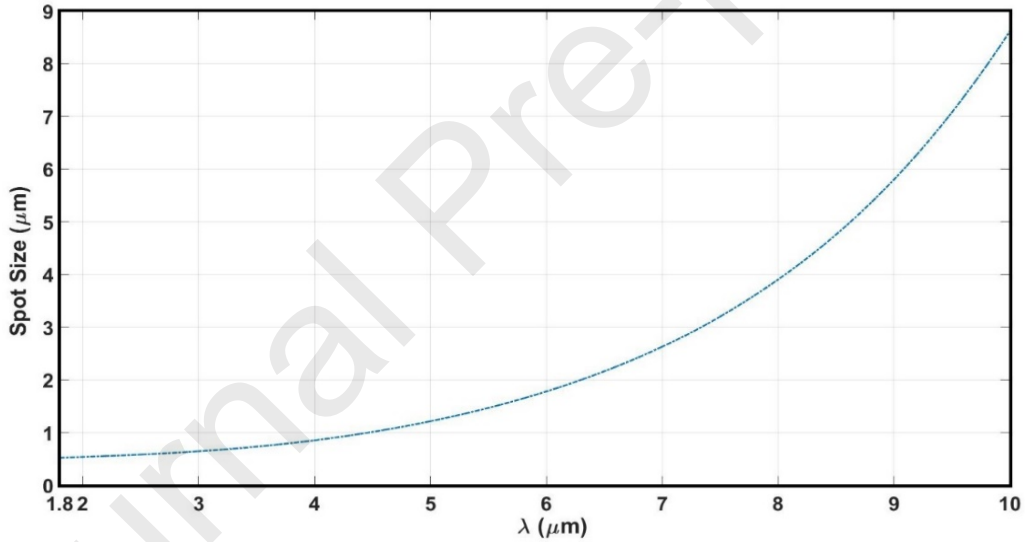
$$W_{eff} = r \times (0.65 + \frac{1.619}{V^{3/2}} + \frac{2.879}{V^6}) \quad (7)$$

where r is the radius of the core of PCF and can be calculated from the respective values of effective area wherein core can be approximated to be a circle having area as A_{eff} and V is the normalized frequency parameter.

Figure 7(a) compares the spot size of a normal PCF to the Graded-Index PCF. For As_2Se_3 based solid core PCF, non-linear coefficient value is of order 10^6 W^{-1} km^{-1} [31]. However, the reported value is ten times greater than this value i.e. 10^7 W^{-1} km^{-1}. This high value of non-linear coefficient has been obtained with only five layers of air-holes with grading. Also, non-linear coefficient for our proposed GI-PCF is approximately double of the normal PCF structure with no grading. Such a design on As2Se3 material, having non-linear index of order 10^7 W^{-1} km^{-1} in mid-IR region, has not been reported yet, to the best of our knowledge.



(a)



(b)

Fig.7. Spectral variation of Spot-size (a) comparison of a GI-PCF and Normal PCF (b) GI-PCF

Journal Pre-proofs

4. CONCLUSION

In this paper, we report the design and propagation characteristics of a Chalcogenide glass-based (As_2Se_3) Graded-Index Photonic Crystal Fiber. Important characteristic features of the proposed fiber are explored in the Mid-Infrared wavelength regime (1.8-10 μm) and compared to normal, non-graded PCF. The proposed GI-PCF provides single-mode propagation characteristics for the whole Mid-IR range of wavelength with low confinement loss and hence making it a better fiber than the normal PCF in terms of confinement properties. Chromatic dispersion being entirely

negative in the mid IR range makes it a potential candidate as a dispersion-compensating PCF. Effective area of GI-PCF increases with wavelength. Our proposed As_2Se_3 based solid core GI-PCF has non-linear coefficient value of order 10^7 W^{-1} km^{-1}. We have achieved this high value of non-linear coefficient with only five layers of air-holes but with grading. Also, non-linear coefficient for our proposed GI-PCF is approximately double of the normal PCF structure with no grading. High non-linear can have various applications like broad-based supercontinuum generation, sensing, etc. GI-PCF has a very small spot size as compared to a normal PCF making it a fiber having a less divergent beam and more focused into the core hence supporting the proposed structure for better confinement of light into the Core.

Acknowledgment

The authors are grateful for the initiatives taken and support bestowed by the TIFAC-Center of Relevance and Excellence in Fiber Optics and Optical Communication, Delhi Technological University.

References

[1] Russell. P, (2003), “Photonic crystal fibers”, Science;299(5605):358-62

[2] Raja James & Rao S & Charlcedony r, (2020), Design and analysis of dispersion-compensating chalcogenide photonic crystal fiber with high birefringence. SN Applied Sciences. 2,499

[3] Chauhan, Jyoti & Kalra, Yogita & Sinha, Ravindra. (2022). Single-ring controlled As2Se3 Photonic Crystal Fiber for Dispersion compensation in Mid-Infrared Region. JW4B.31. 10.1364/FIO.2022.JW4B.31.

[4] M. M. A. Mia, M. A. Islam, M. S. Miah, B. Bhowmik, S. M. Mahir and S. K. Biswas, "Highly Birefringent Dispersion Compensating Index Guiding Square Photonic Crystal Fiber with Large Nonlinearity for Fiber Optic Transmission System," 2020 International Conference on Computer, Electrical & Communication Engineering (ICCECE), Kolkata, India, 2020, pp. 1-5, doi: 10.1109/ICCECE48148.2020.9223076.

[5] Nagashima, Tatsuo et al., (*2006),* “Dispersion Shifted Bi2O3-based Photonic Crystal Fiber.” *European Conference on Optical Communications*: ISSN 2162-7339

[6] Das Sugandha & de Moutusi & Singh Vinod, (2019), “Single mode dispersion shifted photonic crystal fiber with liquid core for optofluidic applications”. Optical Fiber Technology. 53. 102012

[7] T. Matsui, Jian Zhou, K. Nakajima and I. Sankawa, (2005), "Dispersion-flattened photonic crystal fiber with large effective area and low confinement loss," in Journal of Lightwave Technology, vol. 23, no. 12, pp. 4178-4183, Dec.

[8] Varshney, Shailendra K., Singh M. P. and Sinha R. K, (2003), "Propagation Characteristics of Photonic Crystal Fibers" *Journal of Optical Communications*, vol. 24, no. 5, pp. 192-198.

[9] Liu, Shuo & Li, Shu-Guang & Xiao-Xia, Zhang. (2012). Numerical analysis of the As2Se3 chalcogenide glass multi-ring photonic crystal fiber. Infrared Physics & Technology. 55. 427–430.

Journal Pre-proofs

[10] Dinesh Kumar Sharma, Saurabh Mani Tripathi, Anurag Sharma, (2019),"Modal analysis of high-index core tellurite glass microstructured optical fibers in infrared regime", Journal of Non-Crystalline Solids, Volume 511, Pages 147-160, ISSN 0022-3093

[11] S. Gupta, U. Namdev, V. Gupta, V. Chheda and K. Bhowmick, "Data-driven Preprocessing Techniques for Early Diagnosis of Diabetes, Heart and Liver Diseases," 2021 Fourth International Conference on Electrical, Computer and Communication Technologies (ICECCT), Erode, India, 2021, pp. 1-8, doi: 10.1109/ICECCT52121.2021.9616835.

[12] S. S. Misty, M. Abid Hossain, M. S. Miah, B. Bhowmik, S. M. Aunik and S. Kumar Biswas, "Photonic Crystal Fiber Based Sensor for Air Pollution Monitoring," 2022 13th International Conference on Computing Communication and Networking Technologies (ICCCNT), Kharagpur, India, 2022, pp. 1-5, doi: 10.1109/ICCCNT54827.2022.9984213.

[13] Md Rezaul Hoque Khan, Fath Ahmed Mohamed Ali, Mohammad Rakibul Islam, (2021), "THz sensing of CoViD-19 disinfecting products using photonic crystal fiber, Sensing and Bio-Sensing Research", Volume 33, 100447, ISSN 2214-1804

[14] Nuzhat, S., Bin Hassan, M.F., Sultana, S. *et al.* Hybrid lattice shaped dual polarized highly sensitive surface plasmon resonance based refractive index sensor. *Opt Quant Electron* **54**, 294 (2022). https://doi.org/10.1007/s11082-022-03695-8

[15] M. Ifaz Ahmad Isti, M. Hussayeen Khan Anik, Samiha Nuzhat, Rubel Chandra Talukder, Sadia Sultana, Shovasis Kumar Biswas, and Hriteshwar Talukder, "Highly sensitive double D-shaped channel photonic crystal fiber based plasmonic refractive index sensor," Opt. Continuum 1, 575-590 (2022)

[16] Algorri, José Francisco et al., (2018), "Infiltrated Photonic Crystal Fibers for Sensing Applications." *Sensors (Basel, Switzerland)* vol. 18,12 4263.

[17] Xuan, K.D., Van L.C., Long V.C. *et al.*, (2017), "Influence of temperature on dispersion properties of photonic crystal fibers infiltrated with water". *Opt Quant Electron* 49, 87

[18] Jacek Pniewski, Tomasz Stefaniuk, Hieu Le Van, Van Cao Long, Lanh Chu Van, Rafał Kasztelanic, Grzegorz Stępniewski, Aleksandr Ramaniuk, Marek Trippenbach, and Ryszard Buczyński, (2016), "Dispersion engineering in nonlinear soft glass photonic crystal fibers infiltrated with liquids," Appl. Opt. 55, 5033-5040

[19] P. S. Maji and P. R. Chaudhuri, (*2012),* "Ultra-flattened near-zero dispersion PCF using selective liquid infiltration: A new study with four air-hole rings, "*Photonics Global Conference (PGC)*, 2012, pp. 1-5

[20] Weiyu Sun, Yuheng Qu, Jiashuai Cao, and Hongzhi Jia, (2021), "Sandwiched photonic crystal fiber for dispersion compensation over the S + C + L + U wavelength bands," Appl. Opt. 60, PP.5399-5404

[21] Dabas, Bhawana and Ravindra Kumar Sinha, (2010), "Dispersion characteristic of hexagonal and square lattice chalcogenide As2Se3 glass photonic crystal fiber." *Optics Communications* 283: 1331-1337.

[22] Selvaraj, Geerthana & Dhanabalan, Shanmuga Sundar & Avaninathan, Sivanantharaja, (2015), "Design and analysis of square and hexagonal lattice photonic crystal fiber with elliptical air hole". International Journal of Applied Engineering Research. 10. 21266-21269.

Journal Pre-proofs

[23] M. H. K. Anik *et al*., "Numerical Design and Investigation of Circularly Segmented Air Holes-Assisted Hollow-Core Terahertz Waveguide as Optical Chemical Sensor," in *IEEE Access*, vol. 9, pp. 86155-86165, 2021, doi: 10.1109/ACCESS.2021.3089424.

[24] M. S. Miah, B. Bhowmik, A. A. Baki, C. Nazmus Saadat and S. M. Aunik, "Highly Negative Dispersion Compensating Octagonal Photonic Crystal Fiber," 2022 13th International Conference on Computing Communication and Networking Technologies (ICCCNT), Kharagpur, India, 2022, pp. 1-4, doi: 10.1109/ICCCNT54827.2022.9984612.

[25] Saini,Than & Kumar, Ajeet & Sinha, Ravindra, (2015), "Broadband Mid-Infrared Supercontinuum Spectra Spanning 2–15 μm Using As2Se3 Chalcogenide Glass Triangular-Core Graded-Index Photonic Crystal Fiber". Journal of Lightwave Technology

[26] Mortensen, Niels Asger, et al., (2003), "Modal cutoff and the V parameter in photonic crystal fibers." *Optics letters* 28.20: 1879-1881.

[27] Ying Huang, Hua Yang, Yucheng Mao, (2021), "Design of linear photonic crystal fiber with all-positive/negative ultra flattened chromatic dispersion for the whole telecom band," Opt. Eng. 60(7) 076110

[28] T. A. Birks, J. C. Knight, and P. St. J. Russell, (1997), "Endlessly single-mode photonic crystal fiber," Opt. Lett. 22, 961-963

[29] Knight J. C. et al., (1998), "Properties of photonic crystal fiber and the effective index model." *JOSA A* 15.3: 748-75.

[30] Song Gao, Xiaoyi Bao (2020), "Chalcogenide Taper and Its Nonlinear Effects and Sensing Applications", iScience, Volume 23, Issue 1, 100802, ISSN 2589-0042.

[31] Nguyen, Thi & Hoang, Trong & Le, Tran & Dang, Van & Chu, Van. (2022). Dispersion and nonlinearity properties of small solid-core photonic fibers with As2Se3 substrate. Hue University Journal of Science: Natural Science. 130. 10.26459/hueunijns.v130i1D.6397.

Journal Pre-proofs

Systems Microbiology and Biomanufacturing
https://doi.org/10.1007/s43393-023-00173-4

ORIGINAL ARTICLE

Chlorella minutissima-assisted silver nanoparticles synthesis and evaluation of its antibacterial activity

Lakhan Kumar[1] · Lalit Mohan[1] · Raksha Anand[1] · Navneeta Bharadvaja[1]

Received: 12 January 2023 / Revised: 24 March 2023 / Accepted: 25 March 2023
© Jiangnan University 2023

Abstract
The conventional methods of nanoparticles synthesis led to the production of highly toxic by-products and the use of toxic chemicals that are highly expensive in nature. Thus, the recent past has witnessed a surge in green synthesis of nanoparticles as a sustainable alternative. The present study outlines the biogenic silver nanoparticles (Ag-NPs) synthesis from an aqueous extract of *Chlorella minutissima*. The effect of certain parameters such as the reaction mixture's pH and precursor metal solution to algal extract ratios were explored and optimized. The UV spectrophotometric analysis of Ag-NPs gave surface plasmon response maximally at 426 nm. The developed Ag-NPs were characterized using zeta potential, indicating their high stability (-21.2 mV) with a mean diameter of 73.13 nm. Results from field emission-scanning electron microscopy (FE-SEM) showed that the particles were spherical in shape. Ag-NPs synthesized using *Chlorella minutissima* extract could significantly inhibit the growth of both Gram-positive and Gram-negative bacterial species. The study highlights that using *C. minutissima* extract for Ag-NPs synthesis is a convenient and fast process for controlling the growth of Gram-positive as well as Gram-negative bacteria.

Keywords Green synthesis · Nanoparticles · Particles · Nano size · *Chlorella minutissima* · Antibacterial activity

Introduction

The indiscriminate over exploitation of antimicrobials (antibiotics) over the past few decades has led to a fast-paced emergence of antimicrobial resistance (AMR) among a range of microbial populations. Resistance among these pathogens have led to huge burden on healthcare system and economy [1]. It has been predicted that by 2025, deaths caused by AMR will be more than deaths caused by cancer [2]. Pathogens have developed various resistance mechanisms such as alteration of the target molecules, active efflux of the antimicrobial agents from the bacterial cells, modification of the antimicrobial agents, decreased penetration of the antimicrobial agents into the bacterial cells, degradation of antimicrobial agents and resistance due to global adaptation [3, 4, 5]. Events such as horizontal gene transfer and conjugation also leads to the transfer of resistant genes among the bacterial species leading to widespread resistance against the existing antimicrobial agents [6]. There have also been reports of bioaccumulation and biomagnification of antibiotics in crops and animals such as fish due to excessive usage of antibiotics [7, 8]. Problems caused by AMR has steered the research to discover novel and effective antimicrobial agents. Over the years nanoparticles have gained focus as an antimicrobial agent because they demonstrate bactericidal effects by directly interacting with bacterial cells and consequently overcome the mechanism of antibiotic resistance adopted by bacterial species [9, 10]. Nanoparticles have various advantages over conventional antimicrobial agents such as preventing the emergence of antibacterial resistant strains, economical, rapid synthesis and environment friendly. The microbicidal activity of nanoparticles can mainly be attributed to the following mechanisms: inducing oxidative stress by elevating the production of reactive oxygen species (ROS) in the bacterial cells, release of Ag+ ions which interact with cellular components such as DNA, RNA and proteins, and cell membrane disruption [11].

The conventional methodology of nanoparticle synthesis consists of physical and chemical methods such as ball milling, ultrasonication, electrochemical synthesis, laser

✉ Navneeta Bharadvaja
navneetab@dce.ac.in

[1] Plant Biotechnology Laboratory, Department of Biotechnology, Delhi Technological University, New Delhi, India, 110042, Delhi

Published online: 04 April 2023

ablation, chemical reduction and sputtering. These conventional methods have several limitations such as production cost, release of harmful by-products and hazardous waste [12]. Thus, the recent past has witnessed a paradigm shift towards the green or biogenic synthesis of nanoparticles. Green synthesis methods are cost-effective, environment friendly as well as are highly sustainable [13]. In the case of biological or green synthesis approach, the extract obtained from organisms such as plants, algae, bacterial and fungal species acts as reducing as well as capping agent for the synthesis and stabilizing of nanoparticles. The reduction of metal ions occurs due to the presence of various biomolecules such as amino acids, proteins, enzymes, polysaccharides, vitamins and other primary or secondary metabolites [14]. Among all the potential candidates of nanoparticles synthesis, plants and bacterial species have been intensively researched upon for their potential of nanoparticles synthesis. Algal species have not received much focus but are promising candidates due to their limited requirement of nutrition, ability to grow on wastewater, limited space requirements and availability of a diverse variety of biomolecules which can act as capping and reducing agents. Several algae such as *Caulepra*, *Bifurcaria*, *Chlamydomonas*, *Chlorella* and *Sargassum* have been recently used for NPs synthesis for applications such as antimicrobial agents and for environmental remediation [15, 16, 17]. Algal mediated synthesis of NPs are obtained using following steps: (1) selection and identification of algal species, (2) harvesting algal biomass, (3) preparation of algal extract by boiling biomass in water or suitable solvent, (4) selection of suitable precursor metal salt solution, (5) preparation of molar salt solution, (6) incubation of algal extract and metal solution for certain period, at suitable temperature and pH [18].

In the recent times, the synthesis of silver nanoparticles (Ag-NPs) has gained new insights due to inherent antimicrobial properties of silver. The application of these Ag-NPs is not limited to therapeutics only and have many biotechnological applications such as to produce biohydrogen, biosensors and as a biocatalyst [19, 20, 21]. Currently the use of Ag-NPs in therapeutics is in developmental phase. Various groups have explored the potential of these Ag-NPs for its antimicrobial properties. Amin in his study demonstrated the use of Ag-NPs synthesized using *Ulva lactuca* as an alternative antimicrobial agent against bacterial and fungal pathogens such as *Bacillus subtilus*, *Klebsiella* sp., *Staphylococcus aureus* with comparable activities as commercially available agents [22]. Ag-NPs derived from *Chlorella* sp has been used as antimicrobial agents against *Staphylococcus aureus, Escherichia. coli* with zone of inhibition 15 mm and 20 mm respectively [16]. Ag-NPs prepared using methanol extract of *A. millefolium* demonstrated a zone of inhibition of 14.33 mm and 13.67 mm against *S. aureus* and *Pseudomonas aeruginosa* respectively [20]. Fatima et al., synthesized Ag-NPs using *Portieria hornemannii* extract and demonstrated its antibacterial activity against fish pathogens *Vibrio harveyii* and *V. parahaemolyticus* [23]. Ag-NPs have also been demonstrated to have potent antiviral effects against SARS-CoV-2 and MS2 phage [24, 25]. In the recent years' scientists have developed "nanoparticles dressing" by embedding Ag-NPs in wound dressing that promotes wound healing as well as controls the growth of microorganisms [26].

The present study aims to synthesize Ag-NPs using algal extract of *Chlorella minutissima*. *C. minutissima* belongs to genus *Chlorella* and phylum Chlorophyta. It is a species of green microalgae which grows profusely over a wide range of light intensity and temperature. *C. minutissima* has been used for wastewater treatment and lipid extraction for biofuel production [27]. Depending upon nutrient availability and environmental conditions, the algal species demonstrates varied mode of nutrition including autotrophic, heterotrophic and mixotrophic modes. The species is a store house of various biochemicals such as carotenoids, amino acids, polysaccharides such as starch, polyphenols, vitamins, astaxanthins, proteins and enzymes [28]. These components serve as both reducing and stabilizing agent during the synthesis of nanoparticles [14]. Ag-NPs synthesized using *C. minutissima* extract were characterized and their antibacterial activity against Gram-positive (*Bacillus cereus*, *Staphylococcus aureus*) and Gram-negative (*E. coli*, *Klebsiella* sp. and *Salmonella* sp.) bacterial species were tested. The impact of certain parameters such as pH and extract to precursor metal salt solution on the synthesis of Ag-NPs has been studied. This study will lead to establishment of algal derived silver nanoparticles-based treatment of antimicrobial resistance.

Methodology

Growth media selection

C. *minutissima* culture was obtained from Centre for Conservation and Utilisation of Blue Green Algae, Indian Agricultural Research Institute (IARI), New Delhi-India. The culture of *C. minutissima* was inoculated at 10% ratio in five different growth media in 500 mL flask respectively, BG11: $NaNO_3$ (17.6 mM), $CaCl_2{\cdot}2H_2O$ (0.24 mM), $MgSO_4{\cdot}7H_2O$ (0.3 mM), K_2HPO_4 (0.23 mM), Citric acid (0.031 mM), $C_6H_8FeNO_7$-Ferric ammonium citrate (0.021 mM), Na_2EDTA (0.0027 mM), Na_2CO_3 (0.91 mM), Trace element solution (1 mL/L) [16], Zarrouk's medium: $NaHCO_3$ (162 mM), Na_2CO_3 (38 mM), K_2HPO_4 (2.9 mM), $NaNO_3$ (29.4 mM), K_2SO_4 (5.74 mM), NaCl (17.1 mM), $MgSO_4.7H_2O$ (0.27 mM), $CaCl_2.2H_2O$ (0.27 mM) [29], Bold's basal medium (BBM): $NaNO_3$ (2.94 mM), $CaCl_2.2H_2O$ (0.17 mM), $MgSO_4.7H_2O$ (0.3 mM), K_2HPO_4

(0.43 mM), KH_2PO_4 (1.29 mM), NaCl (0.43 mM), Trace element solution [30], Bristol medium (SE Media): $NaNO_3$ (2.94 mM), $CaCl_2.2H_2O$ (0.17 mM), $MgSO_4.7H_2O$ (0.3 mM), KH_2PO_4 (1.29 mM), NaCl (0.43 mM) [31] and Bold 3N medium: $NaNO_3$ (8.82 mM), $CaCl_2{\cdot}2H_2O$ (0.17 mM), $MgSO_4{\cdot}7H_2O$ (0.3 mM), K_2HPO_4 (0.43 mM), KH_2PO_4 (1.29 mM) and NaCl (0.43 mM) [32]. The inoculated medium was incubated in white light chamber with 12 h of illumination followed by 8 h of dark period. The flasks were shaken periodically for proper mixing of algal cells and nutients. Growth rate in each medium was studied at the interval of 3 days using optical density measured at 600 nm over a span of 18 days and a growth curve was prepared. The medium depicting highest growth rate was selected for the large-scale batch cultivation of *C. minutissima*.

Preparation of *C. minutissima* extract

C. minutissima was cultivated in BG11 medium for 28 days and the cells in the stationary phase were harvested using centrifugation and used for the preparation of aqueous algal extract by boiling with 100 mL deionized water at 80 °C for 10 min. The extract was centrifuged to remove any cell debris. 10 mM silver nitrate ($AgNO_3$) solution in deionized water was prepared. All reagents used were of analytical grade.

Synthesis of silver nanoparticles (Ag-NPs) using *C. minutissima* extracts

Microalgal mediated Ag-NPs synthesis is dependent upon various factors such as pH of the reaction mixture, ratio of the algal extract to precursor metal solution, temperature of incubation, presence, or absence of source of illumination, strength of precursor metal salt solution, period of incubation [33]. In the present study, we have optimized a few parameters of synthesis such as pH of the solution and ratio of algal extract to precursor metal solution. The algal extract was incubated with 10 mM $AgNO_3$ [16, 17] solution for biogenic-NP synthesis in the ratio of 1:10, 1:1 and 10:1. The pH of the solution was varied from 4–10. The mixture was incubated in light at 3000 Lux at 37 °C. Most of the bio-reduction of $AgNO_3$ ions occurred within initial hours of incubation. A change in color of the medium from colorless or pale-yellow to orangish-brown was observed with the progression of time. The final synthesis was performed on the optimized parameters for larger yield.

Characterization of Ag-NPs

The synthesis of Ag-NPs was confirmed to be a time dependent process through the development of orangish-brown coloration of the reaction mixture over a period. The initial stage characterization of Ag-NPs was carried out using UV spectrophotometric analysis (Lambda 365, Perkin Elmer) was performed at regular intervals by taking aliquots of the reaction mixture and analyzing at the wavelengths of 200–700 nm. The morphology of Ag-NPs was examined through FE-SEM (ZEISS microscope). The mean diameter and stability of Ag-NPs were confirmed through zeta potential analysis (Zetasizer nano series ZS-Malvern PANalytical) of the Ag-NPs synthesized in the study.

Antibacterial activity of Ag-NPs synthesized by *C. minutissima* extract

Gram-positive (*Bacillus cereus*, *Staphylococcus aureus*) and Gram-negative (*E. coli*, *Klebsiella* sp. and *Salmonella* sp.) cultures were employed to determine the antibacterial activity of the synthesized Ag-NPs. All the cultures used for study were taken from stock cultures maintained in Luria–Bertani (LB) broth with sterile glycerol. Overnight grown cultures were used to perform the studies. The disc diffusion assay with synthesized Ag-NPs was performed on nutrient agar (NA) plates (biological and technical triplicates were performed) spread with 0.1 mL of overnight grown bacterial cultures. The filter paper discs were supplemented with 10, 20, 30, 40 and 50 µL of the synthesized Ag-NPs respectively, with algal extract and silver nitrate solutions loaded onto the disc as control. The plates were then incubated for 24 h at 37 °C and the zone of inhibition (in millimeters) around the discs were measured and the mean value of triplicated were recorded.

Results and discussion

The present study aimed to determine the antibacterial activity of Ag-NPs synthesized through the aid of *Chlorella minutissima* extract. The green/biosynthesized Ag-NPs used in this study were characterized using UV–visible spectroscopy, zeta potential analyzer, field emission-scanning electron microscopy (FE-SEM) and X-ray diffraction pattern. Growth medium optimization for *C. minutissima* cultivation and certain parameters such as pH of the reaction mixture and algal extract to precursor metal salt solution has been optimized in the present study and has been presented in the following sections.

Optimization of growth medium for *C. minutissima*

In the present study, growth of *C. minutissima* was assayed on five different media namely BG11, Zarrouk's medium, Bold's basal medium (BBM), Bristol medium (SE Media) and Bold 3N medium. The growth on each media was

analyzed spectrophotometrically at 600 nm on an interval of 3 days continuous for 18 days. The bulk cultivation of *C. minutissima* was done on the medium in which highest growth rate was observed. The growth curve of *C. minutissima* on various media is illustrated in Fig. 1. It was observed that *C. minutissima* demonstrated highest growth rate on BG11 as compared to other media under consideration. Similar results have been demonstrated by Sharma et al. in their study to optimize media for high biomass productivity [34].

Optimization of Ag-NPs synthesis parameters using *C. minutissima*

In the present study, different parameters for the synthesis of Ag-NPs such as pH of the solution and ratio of algal extract to precursor metal salt solution were studied and optimized. The screening for optimal synthesis conditions were performed by optimizing one condition at a time. The final bulk synthesis of Ag-NPs was performed at combination of optimized conditions to obtain high concentrations and high stability of Ag-NPs. UV–Vis spectroscopy was employed to track the synthesis and stability of Ag-NPs formed at different conditions and the spectrum thus obtained is illustrated in Fig. 2. The pace of synthesis of Ag-NPs were slower at the initial hours but Ag-NPs were completely synthesized within 24 h of upon incubating aqueous extract of *C. minutissima* with precursor salt solution. The visual color change of the mixture from pale or light green (due to extract) to gradually orangish-brown was found to intensify with the increase in the incubation temperatures due to the excitation of surface plasmon response (SPR) vibrations. The change in color of the solution indicated the synthesis of Ag-NPs [23, 35, 36]. Similar results were shown for the synthesis of Ag-NPs using microalga *Chlorella sorokiniana* [16]. Factors such as pH of the solution, ratio of algal extract to precursor metal salt solution plays an important role in determining the morphology and stability of Ag-NPs. The spectroscopic analysis at different reaction condition demonstrated a strong SPR between 400 and 450 nm as illustrated in Fig. 2a, b. the available literature has also shown the occurrence of strong SPR in the range of 400- 450 nm and thus indicating the presence of Ag-NPs in the solution mixture [17, 37, 38, 39, 40, 41].pH of the reaction mixture affects the final morphology and structure of the nanoparticles under the synthesis process [16, 17]. The pH range selected for optimization was from 4 to 10. Figure 2**a** represents the absorbance spectrum of Ag-NPs synthesized at different pH. Ag-NPs formed at the pH 8, 9 and 10 were stable and within the range of 400–450 nm while those formed at pH 4, 5, 6 and 7 were highly unstable and were beyond the range of 400–450 nm absorbance. Among the stable pH 8, 9 and 10; Ag-NPs synthesized at pH 9 demonstrated a high SPR indicating that the reducing agents, capping and stabilizing agents present in the *C. minutissima* extract were highly active at pH 9 [42]. During Ag-NP synthesis, algal biomolecules acts as both reductant and stabilizer. The stabilization of Ag-NPs can be attributed to natural polymers formed by these biomolecules. Lower pH can cause the disruption of these natural polymers and thus destabilizing Ag-NPs [43]. Lower pH of the reaction mixture facilitates large-sized Ag-NPs which degrades easily while the higher pH of the reaction mixture leads to the formation of small-sized Ag-NPs faster which are also highly dispersed throughout the medium [44]. At higher pH, the ionization of algal functional group and reduction rate is higher. The organic functional groups present on the surface of Ag-NPs undergoes higher degree of deprotonation at elevated pH which in turn increases the overall negative charge

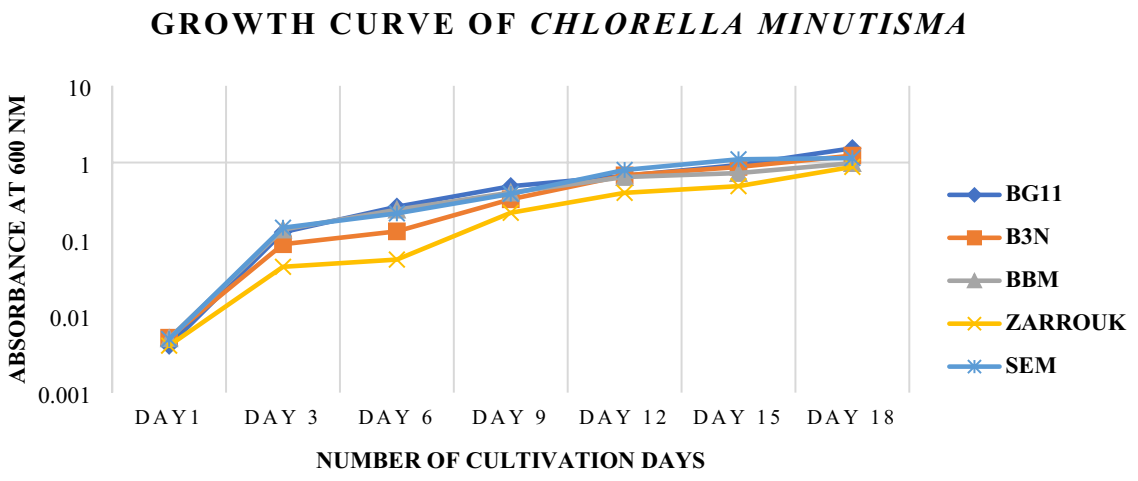


Fig. 1 Growth curve of *Chlorella minutissima* on five different mediums: BG11, Zarrouk's medium, Bold's basal medium (BBM), Bristol medium (SE Media) and Bold 3N (B3N) medium accessed using absorbance at 600 nm

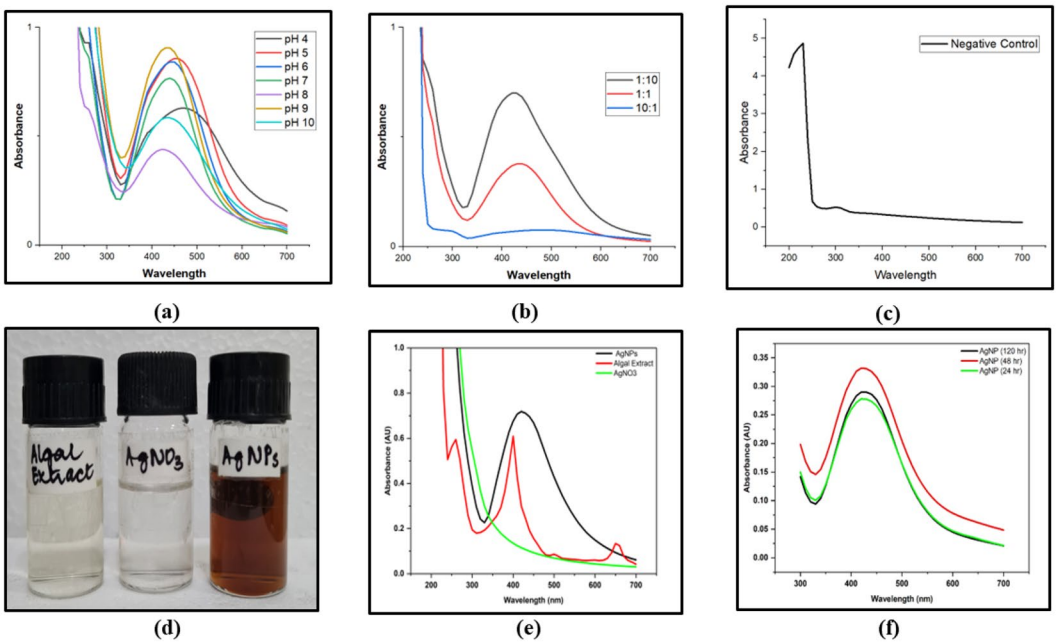


Fig. 2 Formation of Ag-NPs by *C. minutissima* at different conditions. (**a**) Absorption spectrum of Ag-NPs synthesized at different pH (4–10), (**b**) absorption spectrum of Ag-NPs synthesized by mixing precursor metal solution to algal extract in ratios of 10:1, 1:1 and 1:10, (**c**) negative control: BG11 + $AgNO_3$ after 24 h of incubation, (**d**) algal extract $AgNO_3$ and Ag-NPs, (**e**) absorption spectrum of algal extract of $AgNO_3$ and Ag-NPs and (**f**) stability of Ag-NPs as observed after 24, 48 and 120 h of synthesis

on the surface of Ag-NPs. This increase of negative charge increases repulsion between the Ag-NPs leading to smaller aggregation diameters as compared to Ag-NPs formed in acidic environment [33].

The rate of synthesis of Ag-NPs is directly proportional to the concentration of precursor metal salts, but at the same time the aggregation of Ag-NPs also increases with the increase in the concentration of precursor metal solution. For the synthesis of stable nanoparticles, optimal concentration of the precursor metal solution should be incubated with algal extract solution [16]. In the present study, different ratios of precursor metal salt to algal extract (1:10, 1:1 and 10:1) was incubated and the formation of Ag-NPs were observed through UV–Vis spectroscopy. The formation of highly stable Ag-NPs was observed at 1:10 ratio as evident from the high absorbance peak in between 420- 440 nm as depicted in Fig. 2 **(b)**. This observation was due to the rapid scale reduction of Ag + ions present in the solution due to the optimal concentration of algal reducing agents present in the solution [16, 17]. there is a decrease in the size of nanoparticles with the increase in the algal extract amount [44].

The Ag-NPs were synthesized at the optimized conditions (Fig. 2d, e) and the stability of the Ag-NPs recorded after 24, 48 and 120 h of synthesis using UV–Vis spectrophotometer and it was noted that the particles formed at these optimized conditions were highly stable as depicted in Fig. 2f. As a negative control, to eliminate the possibilities of BG11 contributing to the formation of Ag-NPs, 1 mL of 10 mM AgNO3 was incubated with 10 mL BG11 and the absorbance was recorded after 24 h as depicted in Fig. 2c. The absorbance spectrum suggested no Ag-NPs formation due to BG11. The effect of the incubation period on the biosynthesis of Ag-NPs was also assessed using UV–visible spectrophotometric analysis and the peak of Ag-NPs became sharper with time. The SPR band of the synthesized Ag-NPs at 426 nm even after 120 h of incubation with only a slight variation resembles its stability (Fig. 2f). The increase in intensity can be attributed to the increase in the number of Ag-NPs formed after reduction of Ag + ions present in the solution [23, 33, 45]. The optimized condition for the synthesis of Ag-NPs using *C. minutissima* extract was precursor metal salt to extract ratio 1:10, with the pH of the mixture set at pH 9.

Characterization of Ag-NPs synthesized using *C. minutissima*

The *C. minutissima* extract-mediated Ag-NPs synthesized at optimum conditions were characterized initially using a UV–visible spectrophotometer. A color change of the reaction mixture was observed from pale green to orangish-brown, which intensified as the reaction proceeded. The absorption spectrum of Ag-NPs demonstrated a broad spectrum at 426 nm, which falls in the range of the characteristic

band of Ag-NPs. Additionally, the synthesized Ag-NPs were characterized using FE-SEM and Zetasizer (zeta potential) as depicted in Fig. 3**a**, **b**, **c**. The FE-SEM imaging further provided insights into the morphology of Ag-NPs. The synthesized Ag-NPs were spherical in nature (Fig. 3**a**). The mean diameter and stability of Ag-NPs were determined using zeta potential analysis. The mean diameter of Ag-NPs was 73.13 nm and the particles were highly stable, which was indicated by the −21.2 mV value of zeta potential (ZP) (Fig. 2b, c). ZP indicates the stability and size of Ag-NPs contained in the aqueous suspension [16]. ZP is a measure of degree of repulsion between the charged particles and its values ranges between + 100 to − 100 mV. Higher the ZP, higher is the repulsion which prevents the aggregation of particles. Lower ZP indicates attraction between the particles, leading to coagulation of the dispersed particles [16, 17]. The ZP values between ± 30 mV is considered to be stable due to attraction/repulsion between the particles of the colloidal solution [46].

Antibacterial effect of Ag-NPs synthesized using *C. minutissima*

In the present study, the antibacterial activity of *C. minutissima* extract-derived Ag-NPs was tested against *E. coli*, *Salmonella* sp., *Klebsiella* sp., (Gram negative), *Bacillus cereus* and *Staphylococcus aureus* (Gram positive), which are potential human pathogens using disc diffusion assay. The results from disc diffusion assay showed clear zones of inhibition against Gram-positive and Gram-negative bacterial species. The zone of inhibition increased with an increase in the volume of Ag-NPs loaded onto the filter paper disc as depicted in Fig. 4. The maximum zone of inhibition was produced when 50 µL of Ag-NPs was loaded. Among the five test bacterial species, Ag-NPs produced a maximum zone of inhibition against *B. cereus* (21 ± 1 mm), followed by *S. aureus* (20 mm) and *E. coli* (20 mm). Ag-NPs were found to be moderately effective against *Salmonella* spp. (17 ± 1 mm). *Klebsiella* spp. was found to be least susceptible toward Ag-NPs (Fig. 5**).** This can be attributed to the presence of the acidic capsule around the bacterial cell wall, which might have prevented the diffusion of Ag-NPs inside the cell and thus the death of bacterium [47]. The algal extract demonstrated no killing of bacterial species and the zone of inhibition was observed against $AgNO_3$, which could be attributed to the release of Ag+ ions by the dissociation of the compound [19, 48]. The effective killing of Gram-positive bacterial species as compared to the negative ones could be explained, due to the complex cell wall composition of Gram-negative cells, which makes the penetration of nanoparticles more difficult to the cytoplasm and thus prevent cell death [11].

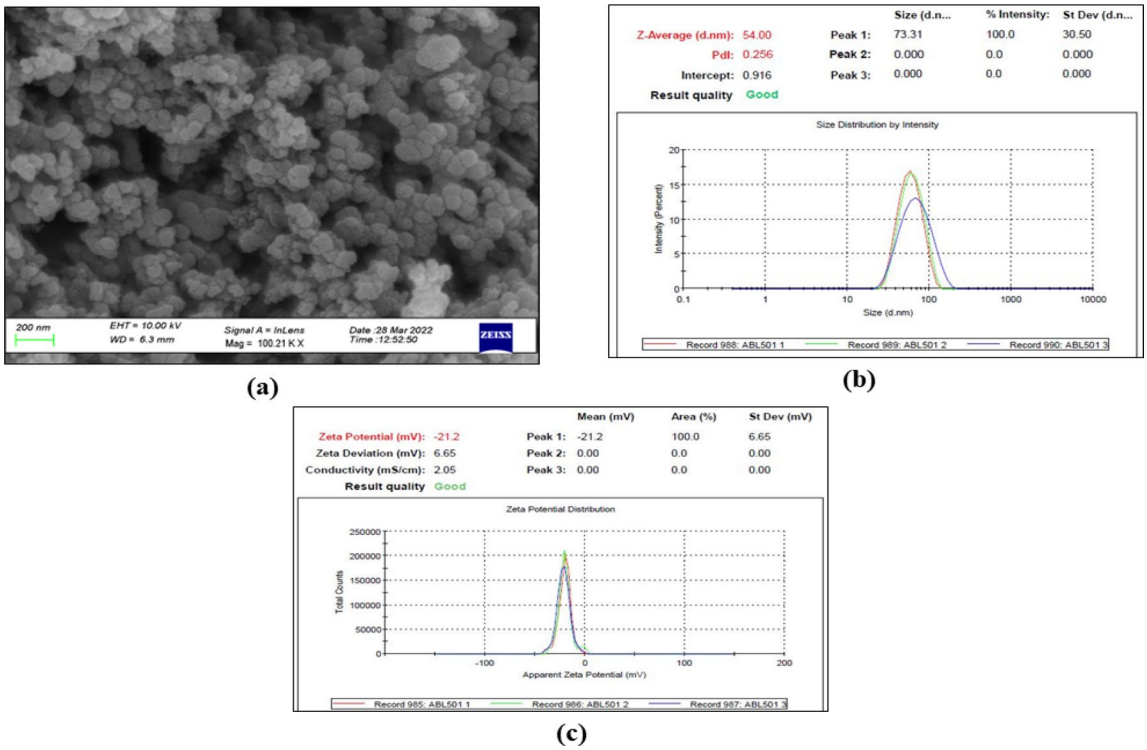


Fig. 3 **a** FE-SEM analysis of Ag-NPs indicating the spherical nature of Ag-NPs; **b** size distribution of Ag-NPs observed using zeta potential and **c** stability of Ag-NPs

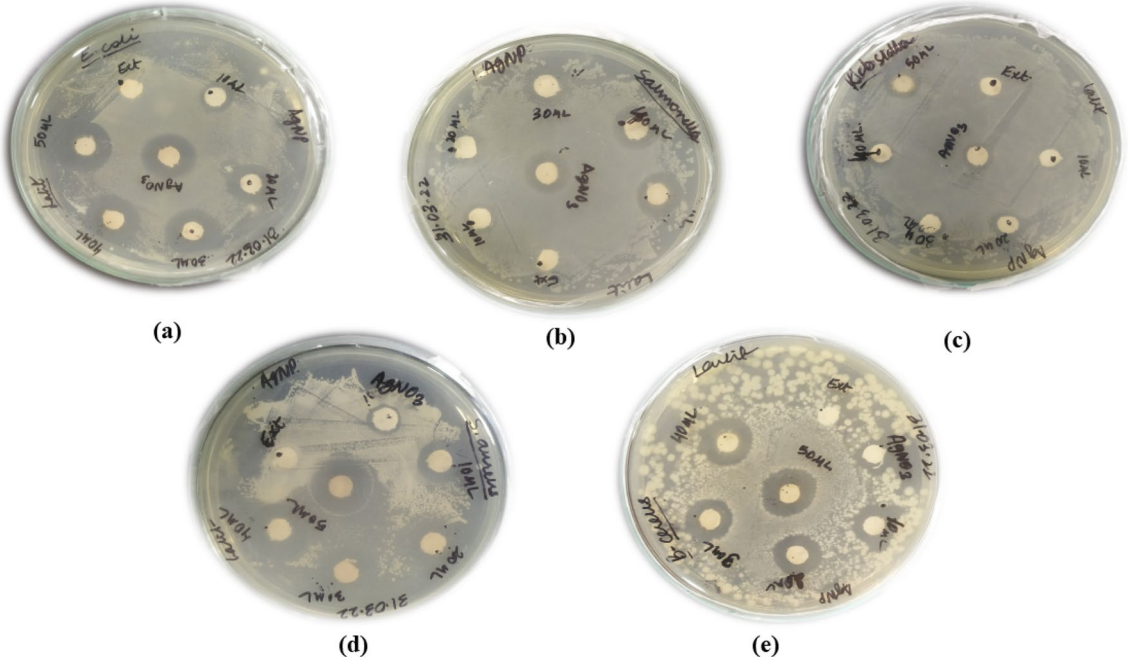


Fig. 4 Nutrient agar plates representing zone of inhibition caused by variable concentration of Ag-NPs, $AgNO_3$ and algal extract against (**a**) *E. coli*, (**b**) *Salmonella* sp., (**c**) *Klebsiella* sp., (**d**) *Staphylococcus aureus* and (**e**) *Bacillus cereus*

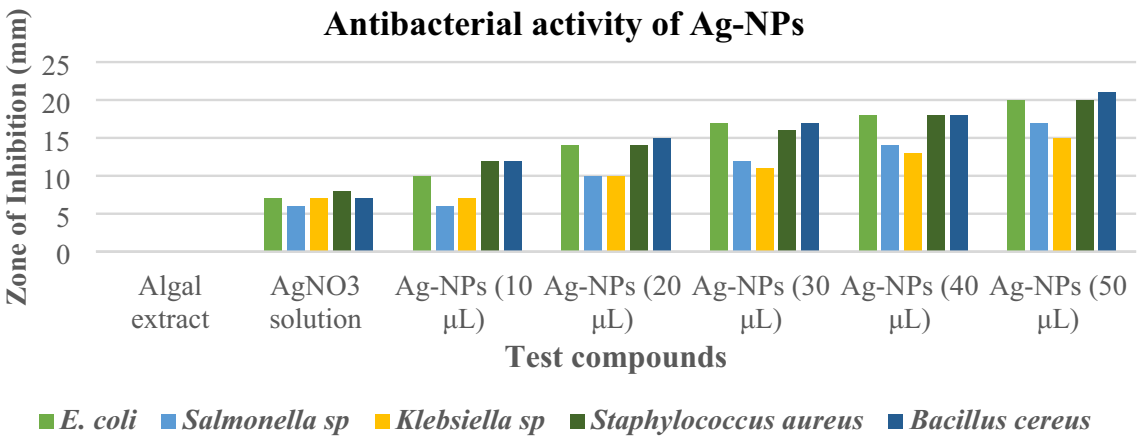


Fig. 5 Graph representing antibacterial activity assessed as zone of inhibition (mm) of algal extract, $AgNO_3$ and Ag-NPs (10, 20, 30, 40 and 50 µL) against *E. coli*, *Salmonella* sp., *Klebsiella* sp., *Staphylococcus aureus* and *Bacillus cereus*

The bactericidal activity of Ag-NPs can be accredited to the nanoscale diameter of the particles, which can easily penetrate the bacterial cells and kill them. The smaller the nanoparticles, the greater is the surface area, which enables enhanced contact with the cell and its components, leading to enhanced bactericidal activity of the nanoparticles. Nanoparticles employ one or a combination of the following mechanisms to cause cell death: (1) increased production of ROS (reactive oxygen species)—nanoparticles upon crossing the outer membrane may cause an alteration in electron transport chain located on the inner membrane of the bacterial cell by interaction with the thiol groups of ETC enzymes, leading to increased formation of ROS and other free radicals, which ultimately leads to apoptosis; (2) membrane penetration—nanoparticles tend to penetrate the outer bacterial membrane and get accumulated in the inner membrane, whereupon they destabilize and damage the membrane by increasing the permeability and thus inducing cellular leakage, ultimately leading to cell death; and (3) interaction with cellular components—upon gaining entry

into the cell, nanoparticles interact with the phosphorus and sulfur groups present in DNA, proteins and other subcellular components, leading to an altered structure and function and ultimately to cell death [12, 49, 50]. Ag-NPs can be used in synergy with antibiotics due to the following reasons: help in evading the resistance mechanism adopted by the AMR species, obstruct the formation of biofilms and have various mechanisms of killing and ability to carry antibiotics along with them for enhanced effects [51, 52, 53]. Studies have shown that nanoparticles are efficient in their bactericidal effect against multidrug-resistant (MDR) pathogens such as MRSA (methicillin-resistant *Staphylococcus aureus*) and thus can be highly effective in the treatment of infections caused by MDR strains [51, 52, 53, 54].

Conclusion

The present study explored the use of *Chlorella minutissima* (green microalgae) extract for the synthesis of Ag-NPs. Stable and high yield of Ag-NPs was achieved at pH 9, with precursor metal salt solution to algal extract ratio of 1:10 and $AgNO_3$ concentration of 10 mM. A color change in the mixture of algal extract and precursor metal solution to orangish-brown color visually confirmed the synthesis of Ag-NPs. The UV–visible spectrum of Ag-NPs synthesized at optimal conditions depicted a strong SPR at 426 nm, which falls in the range of the characteristic Ag-NPs band. FE-SEM analysis revealed that the Ag-NPs synthesized were spherical in shape with a mean diameter of 73.13 nm, as depicted by zeta potential analysis. The green synthesized Ag-NPs using algal extract obtained from *C. minutissima* proved to be an excellent antibacterial agent against *E. coli*, *Salmonella* sp., *Klebsiella* sp., (Gram negative) *Staphylococcus aureus* and *Bacillus cereus* (Gram positive). Hence, the green synthesis approach using algal extract proves to be an economical, effective and sustainable alternative to conventionally used physical and chemical methods for the synthesis of Ag-NPs. *C. minutissima* can be used for the large-scale production of Ag-NPs. These Ag-NPs can be used for the treatment of wastewater effluent and lowering microbial load. Algae-based synthesis of silver nanoparticles for fight against antimicrobial resistance is a green, cost-effective and sustainable approach.

Acknowledgements The authors acknowledge the Department of Biotechnology, Delhi Technological University, for their constant support.

Funding This research did not receive any specific grant from funding agencies in the public, commercial, or not-for-profit sectors.

Data Availability The datasets generated and analyzed during the current study are available from the corresponding author upon reasonable request.

Declarations

Conflict of interest The authors declare no financial and non-financial conflict of interest.

References

1. Rezasoltani S, Yadegar A, Hatami B, Asadzadeh Aghdaei H, Zali MR. Antimicrobial resistance as a hidden menace lurking behind the COVID-19 outbreak: the global impacts of too much hygiene on AMR. Front Microbiol. 2020;11:1–7. https://doi.org/10.3389/fmicb.2020.590683.
2. Thompson T. The staggering death toll of drug-resistant bacteria. Nature. 2022. https://doi.org/10.1038/D41586-022-00228-X.
3. Zhu Y, Huang WE, Yang Q. Clinical perspective of antimicrobial resistance in bacteria. Infect Drug Resist. 2022;15:735–46. https://doi.org/10.2147/IDR.S345574.
4. Christaki E, Marcou M, Tofarides A. Antimicrobial resistance in bacteria: mechanisms, evolution, and persistence. J Mol Evol. 2020;88:26–40. https://doi.org/10.1007/s00239-019-09914-3.
5. Zhang F, Cheng W. The mechanism of bacterial resistance and potential bacteriostatic strategies. Antibiotics. 2022;11:1215. https://doi.org/10.3390/antibiotics11091215.
6. Devanga Ragupathi NK, Muthuirulandi Sethuvel DP, Gajendran R, Anandan S, Walia K, Veeraraghavan B. Horizontal transfer of antimicrobial resistance determinants among enteric pathogens through bacterial conjugation. Curr Microbiol. 2019;76:666–72. https://doi.org/10.1007/s00284-019-01676-x.
7. Zhao F, Yang L, Chen L, Li S, Sun L. Bioaccumulation of antibiotics in crops under long-term manure application: occurrence, biomass response and human exposure. Chemosphere. 2019;219:882–95. https://doi.org/10.1016/J.CHEMOSPHERE.2018.12.076.
8. Tang J, Zhang J, Su L, Jia Y, Yang Y (2022) Bioavailability and trophic magnification of antibiotics in aquatic food webs of Pearl River, China: Influence of physicochemical characteristics and biotransformation. Science of The Total Environment 820:153285. https://doi.org/10.1016/J.SCITOTENV.2022.153285
9. Gao W, Zhang L. Nanomaterials arising amid antibiotic resistance. Nat Rev Microbiol. 2021;19:5–6. https://doi.org/10.1038/s41579-020-00469-5.
10. Sánchez-López E, Gomes D, Esteruelas G, Bonilla L, Lopez-Machado AL, Galindo R, Cano A, Espina M, Ettcheto M, Camins A, Silva AM, Durazzo A, Santini A, Garcia ML, Souto EB. Metal-based nanoparticles as antimicrobial agents: an overview. Nanomaterials. 2020;10:1–39. https://doi.org/10.3390/nano10020292.
11. Wang L, Hu C, Shao L. The antimicrobial activity of nanoparticles: present situation and prospects for the future. Int J Nanomedicine. 2017;12:1227–49. https://doi.org/10.2147/IJN.S121956.
12. Bruna T, Maldonado-Bravo F, Jara P, Caro N. Silver nanoparticles and their antibacterial applications. Int J Mol Sci. 2021;22:7202. https://doi.org/10.3390/ijms22137202.
13. Taherzadeh Soureshjani P, Shadi A, Mohammadsaleh F. Algae-mediated route to biogenic cuprous oxide nanoparticles and spindle-like CaCO 3: a comparative study, facile synthesis, and biological properties. RSC Adv. 2021;11:10599–609. https://doi.org/10.1039/D1RA00187F.
14. Kumar L, Mohan L, Anand S, Bhardwaj D, Bharadvaja N. Phycoanoremediation: a sustainable approach to deal with environmental pollutants heavy metals and dyes. Vegetos. 2022. https://doi.org/10.1007/s42535-022-00399-y.
15. Chaudhary R, Nawaz K, Khan AK, Hano C, Abbasi BH, Anjum S. An overview of the algae-mediated biosynthesis of nanoparticles

and their biomedical applications. Biomolecules. 2020;10:1–36. https://doi.org/10.3390/biom10111498.
16. Kumar L, Bharadvaja N. Biosynthesis, characterization, and evaluation of antibacterial and photocatalytic dye degradation activities of silver nanoparticles biosynthesized by Chlorella sorokiniana. Biomass Convers Biorefin. 2022. https://doi.org/10.1007/s13399-022-03433-w.
17. Rajkumar R, Ezhumalai G, Gnanadesigan M (2021) A green approach for the synthesis of silver nanoparticles by Chlorella vulgaris and its application in photocatalytic dye degradation activity. Environ Technol Innov 21:101282. https://doi.org/10.1016/J.ETI.2020.101282
18. Chaudhary R, Nawaz K, Khan AK, Hano C, Abbasi BH, Anjum S. An overview of the algae-mediated biosynthesis of nanoparticles and their biomedical applications. Biomolecules. 2020;10:1498. https://doi.org/10.3390/biom10111498.
19. Xu L, Wang Y-Y, Huang J, Chen C-Y, Wang Z-X, Xie H. Silver nanoparticles: synthesis, medical applications and biosafety. Theranostics. 2020;10:8996–9031. https://doi.org/10.7150/thno.45413.
20. Yousaf H, Mehmood A, Ahmad KS, Raffi M (2020) Green synthesis of silver nanoparticles and their applications as an alternative antibacterial and antioxidant agents. Materials Science and Engineering: C 112:110901. https://doi.org/10.1016/j.msec.2020.110901
21. Salem SS, Fouda A. Green synthesis of metallic nanoparticles and their prospective biotechnological applications: an overview. Biol Trace Elem Res. 2021;199:344–70. https://doi.org/10.1007/S12011-020-02138-3/METRICS.
22. Amin HH. Biosynthesized silver nanoparticles using Ulva lactuca as a safe synthetic pesticide (in vitro). Open Agric. 2020;5:291–9. https://doi.org/10.1515/opag-2020-0032.
23. Fatima R, Priya M, Indurthi L, Radhakrishnan V, Sudhakaran R (2020) Biosynthesis of silver nanoparticles using red algae Portieria hornemannii and its antibacterial activity against fish pathogens. Microb Pathog 138:103780. https://doi.org/10.1016/j.micpath.2019.103780
24. Jeremiah SS, Miyakawa K, Morita T, Yamaoka Y, Ryo A. Potent antiviral effect of silver nanoparticles on SARS-CoV-2. Biochem Biophys Res Commun. 2020;533:195–200. https://doi.org/10.1016/j.bbrc.2020.09.018.
25. Sinclair TR, van den Hengel SK, Raza BG, Rutjes SA, de Roda Husman AM, Peijnenburg WJGM, Roesink H (Erik) DW, de Vos WM (2021) Surface chemistry-dependent antiviral activity of silver nanoparticles. Nanotechnology 32:365101. https://doi.org/10.1088/1361-6528/ac03d6
26. Kalantari K, Mostafavi E, Afifi AM, Izadiyan Z, Jahangirian H, Rafiee-Moghaddam R, Webster TJ. Wound dressings functionalized with silver nanoparticles: promises and pitfalls. Nanoscale. 2020;12:2268–91. https://doi.org/10.1039/C9NR08234D.
27. Dineshkumar R, Chauhan AS, Sen R. Optimal and strategic delivery of CO2for: chlorella minutissima -mediated valorization of domestic wastewater with concomitant production of biomass and biofuel. Sustain Energy Fuels. 2020;4:6321–9. https://doi.org/10.1039/d0se00296h.
28. S K, P H, Malik A,. Chlorella minutissima as a functional food: evaluation on nutritional profile and antioxidant potential of the metabolites. Biomass Convers Biorefin. 2022. https://doi.org/10.1007/s13399-022-02401-8.
29. Baker M, Blackman S, Cooper E, Smartt K, Walser D, Boland M, Kolar P, Beck AE, Chinn MS (2021) Exploratory analysis of Spirulina platensis LB 2340 growth in varied concentrations of anaerobically digested pig effluent (ADPE). Heliyon 7:. https://doi.org/10.1016/j.heliyon.2021.e08065
30. Lloyd C, Tan KH, Lim KL, Valu VG, Fun SMY, Chye TR, Mak HM, Sim WX, Musa SL, Ng JJQ, Bte Nordin NS, Bte Md Aidzil N, Eng ZYW, Manickavasagam P, New JY (2021) Identification of microalgae cultured in Bold's Basal medium from freshwater samples, from a high-rise city. Scientific Reports 2021 11:1 11:1–6. https://doi.org/10.1038/s41598-021-84112-0
31. Idenyi J.N., Ebenyi L.N., Ogah O., Nwali B.U., Ogbanshi M.E. (2016) Effect of Different Growth Media on the Cell Densities of Freshwater Microalgae Isolates. IOSR Journal of Pharmacy and Biological Sciences (IOSR-JPBS) 11:24–28
32. Arévalo-Gallegos A, Garcia-Perez JS, Carrillo-Nieves D, Ramirez-Mendoza R, Iqbal H, Parra-Saldívar R. Botryococcus braunii as a bioreactor for the production of nanoparticles with antimicrobial potentialities. Int J Nanomedicine. 2018;13:5591–604. https://doi.org/10.2147/IJN.S174205.
33. Handayani W, Ningrum AS, Imawan C (2020) The Role of pH in Synthesis Silver Nanoparticles Using Pometia pinnata (Matoa) Leaves Extract as Bioreductor. J Phys Conf Ser 1428:012021. https://doi.org/10.1088/1742-6596/1428/1/012021
34. Sharma AK, Sahoo PK, Singhal S, Patel A (2016) Impact of various media and organic carbon sources on biofuel production potential from Chlorella spp. 3 Biotech 6:1–12. https://doi.org/10.1007/S13205-016-0434-6/TABLES/2
35. Urnukhsaikhan E, Bold BE, Gunbileg A, Sukhbaatar N, Mishig-Ochir T (2021) Antibacterial activity and characteristics of silver nanoparticles biosynthesized from Carduus crispus. Scientific Reports 2021 11:1 11:1–12. https://doi.org/10.1038/s41598-021-00520-2
36. Algotiml R, Gab-Alla A, Seoudi R, Abulreesh HH, El-Readi MZ, Elbanna K. Anticancer and antimicrobial activity of biosynthesized Red Sea marine algal silver nanoparticles. Sci Rep. 2022;12:2421. https://doi.org/10.1038/s41598-022-06412-3.
37. Jain A (2022) Algae-mediated synthesis of biogenic nanoparticles. Advances in Natural Sciences: Nanoscience and Nanotechnology 13:043001. https://doi.org/10.1088/2043-6262/ac996a
38. Bhuyar P, Rahim MHA, Sundararaju S, Ramaraj R, Maniam GP, Govindan N. Synthesis of silver nanoparticles using marine macroalgae Padina sp. and its antibacterial activity towards pathogenic bacteria. Beni Suef Univ J Basic Appl Sci. 2020;9:1–15. https://doi.org/10.1186/S43088-019-0031-Y/FIGURES/10.
39. Chugh D, Viswamalya VS, Das B (2021) Green synthesis of silver nanoparticles with algae and the importance of capping agents in the process. Journal of Genetic Engineering and Biotechnology 2021 19:1 19:1–21. https://doi.org/10.1186/S43141-021-00228-W
40. Arya A, Mishra V, Chundawat TS (2019) Green synthesis of silver nanoparticles from green algae (Botryococcus braunii) and its catalytic behavior for the synthesis of benzimidazoles. Chemical Data Collections 20:100190. https://doi.org/10.1016/J.CDC.2019.100190
41. Rautela A, Rani J, Debnath (Das) M,. Green synthesis of silver nanoparticles from Tectona grandis seeds extract: characterization and mechanism of antimicrobial action on different microorganisms. J Anal Sci Technol. 2019;10:1–10. https://doi.org/10.1186/S40543-018-0163-Z/FIGURES/14.
42. Singh R, Jaiswal PK, Kumari N, Behera M, Sharma A, Gupta SK (2021) Microbially synthesized nanomaterials for remediation of organic contaminants. Microbe Mediated Remediation of Environmental Contaminants 287–301. https://doi.org/10.1016/B978-0-12-821199-1.00023-7
43. Velgosová O, Mražíková A, Marcinčáková R. Influence of pH on green synthesis of Ag nanoparticles. Mater Lett. 2016;180:336–9. https://doi.org/10.1016/j.matlet.2016.04.045.
44. Ahmed RH, Damra ·, Mustafa E (2019) Green synthesis of silver nanoparticles mediated by traditionally used medicinal plants in Sudan. International Nano Letters 2019 10:1 10:1–14. https://doi.org/10.1007/S40089-019-00291-9
45. Hamida RS, Ali MA, Almohawes ZN, Alahdal H, Momenah MA, Bin-Meferij MM. Green synthesis of hexagonal silver

nanoparticles using a novel microalgae coelastrella aeroterrestrica strain BA_Chlo4 and resulting anticancer, antibacterial, and antioxidant activities. Pharmaceutics. 2022;14:2002. https://doi.org/10.3390/pharmaceutics14102002.
46. Erdogan O, Abbak M, Demirbolat GM, Birtekocak F, Aksel M, Pasa S, Cevik O (2019) Green synthesis of silver nanoparticles via Cynara scolymus leaf extracts: the characterization, anticancer potential with photodynamic therapy in MCF7 cells. PLoS One 14:e0216496. https://doi.org/10.1371/journal.pone.0216496
47. Jiang L, Lin J, Taggart CC, Bengoechea JA, Scott CJ. Nanodelivery strategies for the treatment of multidrug-resistant bacterial infections. J Interdiscip Nanomed. 2018;3:111. https://doi.org/10.1002/JIN2.48.
48. Roy A, Bulut O, Some S, Mandal AK, Yilmaz MD. Green synthesis of silver nanoparticles: biomolecule-nanoparticle organizations targeting antimicrobial activity. RSC Adv. 2019;9:2673–702. https://doi.org/10.1039/C8RA08982E.
49. Yeh YC, Huang TH, Yang SC, Chen CC, Fang JY. Nano-based drug delivery or targeting to eradicate bacteria for infection mitigation: a review of recent advances. Front Chem. 2020;8:1–22. https://doi.org/10.3389/fchem.2020.00286.
50. Chan SS, Low SS, Chew KW, Ling TC, Rinklebe J, Juan JC, Ng EP, Show PL (2022) Prospects and environmental sustainability of phyconanotechnology: a review on algae-mediated metal nanoparticles synthesis and mechanism. Environ Res 212:113140. https://doi.org/10.1016/j.envres.2022.113140
51. Baptista PV, McCusker MP, Carvalho A, Ferreira DA, Mohan NM, Martins M, Fernandes AR. Nano-strategies to fight multidrug resistant bacteria-"A Battle of the Titans". Front Microbiol. 2018;9:1441. https://doi.org/10.3389/FMICB.2018.01441/BIBTEX.
52. Lee NY, Ko WC, Hsueh PR. Nanoparticles in the treatment of infections caused by multidrug-resistant organisms. Front Pharmacol. 2019;10:1153. https://doi.org/10.3389/FPHAR.2019.01153/BIBTEX.
53. Nature,. Nanoparticles kill resistant bacteria. Nature. 2016;537:282–3. https://doi.org/10.1038/537282d.
54. Gupta A, Mumtaz S, Li C-H, Hussain I, Rotello VM. Combatting antibiotic-resistant bacteria using nanomaterials. Chem Soc Rev. 2019;48:415–27. https://doi.org/10.1039/C7CS00748E.

Springer Nature or its licensor (e.g. a society or other partner) holds exclusive rights to this article under a publishing agreement with the author(s) or other rightsholder(s); author self-archiving of the accepted manuscript version of this article is solely governed by the terms of such publishing agreement and applicable law.

e-ISSN: 2582-5208
International Research Journal of Modernization in Engineering Technology and Science
(Peer-Reviewed, Open Access, Fully Refereed International Journal)
Volume:05/Issue:03/March-2023 Impact Factor- 7.868 www.irjmets.com

CLOUD COMPUTING AND ITS IMPLEMENTATION CHALLENGES

Zalmai Zormatai*1, Samiullah Mehraban*2, Hameed Yousof*3, Shafiullah Shinwari*4

*1Assistant Professor, Department of Computer Science, Bakhtar University, Kabul, Afghanistan.

*2PhD scholar, Department of Computer Science And Engineering, Delhi Technological University, India.

*3Final year student, Department of Computer Science, Bakhtar University, Kabul, Afghanistan.

*4Dean of Faculty, Department of Computer Science, Bakhtar University, Kabul, Afghanistan.

DOI : https://www.doi.org/10.56726/IRJMETS34737

ABSTRACT

With the advances in ICT infrastructure, a new technology has emerged, that is cloud computing. Cloud computing is one of the most significant technologies enabling companies to manage their resources, and to save and share data safely through the internet. Choosing the right cloud-computing platform, which meets the company's needs, is not easy to handle task. In this Paper, the main three cloud computing platforms, namely, Google, Microsoft, and Amazon, were studied. Also, these platforms were compared and classified according to the possibilities they offer. This study aims at helping companies to choose the right cloud-computing platform, which meets their needs and requirements.

Keywords: ICT, Cloud Computing, Challenges.

I. INTRODUCTION

Nowadays, and maybe without paying due notice to the fact, cloud computing is used by many people to share files with friends or colleagues. Therefore, people do not have to be in the same place every time to be able to work from anywhere and share any file. Cloud computing is an emerging field which is growing exponentially as is the case with its application. This technology can be used in making applications accessible from anywhere and pay only for the use [1]. With cloud computing, users use a range of devices, including personal computers, smart phones, and notebooks, to access platforms, storage, and programs for the development of applications over the web, through services presented by cloud providers. The main advantages of using cloud-computing technology are: cost reduction, mobility (access from any device and any place), pay for use, always updated technology, scalability, security, and less need for maintenance [2].

An Overview

Cloud computing uses a built-in virtualization technology that permits the rental of physical infrastructure for small pay per use compared to the old ways of designing web software. In addition, it provides cloud platform tools to accelerate the development process. Cloud computing is a model which allows easy, on demand access to a shared set of configurable computing resources (for instance, storage, servers, networks, services, and applications) that can be provisioned and released quickly with minimal interaction with the service provider or minimal management effort [3,4].

Platforms Comparison

To evaluate the possibilities of the main platforms studied, a comparative analysis method has been applied to the cloud-computing giants as detailed in table 2. Table 2: Comparison of main cloud computing platforms.

Table 1.x

e-ISSN: 2582-5208
International Research Journal of Modernization in Engineering Technology and Science
(Peer-Reviewed, Open Access, Fully Refereed International Journal)
Volume:05/Issue:03/March-2023 Impact Factor- 7.868 www.irjmets.com

Worldwide availability	20 regions worldwide. More than 200 countries.	54 regions worldwide. 140 countries.	25 regions worldwide. 206 countries.
Support	24x7 Free support (access to knowledge center). 4 hours response time: $100 per month 1-hour response time: $250 per month.	24x7 Free support (access to knowledge center). 8 hours response time: $29 / month, via email. 2 hours response time: $100 / month, via email and phone	Free support (access to knowledge center). Contact by email during office hours: $29 /month. 24x7 phone, email, and chat contact with 1-hour response time: $100 /month.
Virtual Machine Types	59	195	170
Volume Type	Network-attached HDD, Locally-attached SSD, or Network-attached SSD	Standard HDD, can be customized to SSD	The default: General Purpose SSD, it can be customized to highest performance SSD or HDD

	Google Cloud [23]	**Microsoft AZURE** [19]	**Amazon** [24]
Initial release date	2008	2010	2006
Cloud Service models	PaaS SaaS IaaS	PaaS SaaS IaaS	PaaS SaaS IaaS
Billing	Pay per hour or month. Discounts proportional to consumption hours (on average a 24% discount)	Pay per hour, except virtual machine (per minute). Discounts on contracts of 1 or 3 years.	Payment per hour or per Second, with a one-minute minimum. Discounts on contracts of 1 or 3 years (Only for Reserved Instances).
Backups	Make On-demand backups or Automated backups copies around the world.	Make 3 copies in the same geographical area, Possibility of duplicating copies to other areas.	Make 3 copies in the same geographical area, Possibility of duplicating copies to other areas.
Other Cloud Services	Computing and hosting, Networking, Storage, Databases, AI and Machine learning, API management, Data Analytics, Internet of Things, Networking, Security	Computing, AI and Machine Learning, Storage, Databases, Office 365, Internet of Things, Data Analytics, Management and Governance, Networking, Security	Data Analytics, Storage, Databases, Computing, Internet of Things, Machine learning, Networking and content delivery, Security
Security	40 certifications	87 certifications	25 certifications
Stability	99.99% monthly availability. Between 99.00% and 99.99%: 10% penalty. Between 95.00% and 99.00%: 25% penalty. Below 95%: 50% penalty.	99.95% monthly availability. Between 99.00% and 99.99%: 10% penalty. Between 95.00% and 99.00%: 30% penalty. Below 95%: 100% penalty.	99.99% monthly availability. Between 99.99% and 99%: 10% penalty Between 99% and 95%: 30% penalty. Below 95%: 100% penalty.
Server Migration	Accept VMware. No cost.	Accept Hyper-V, VMware, and physical servers. In most cases, no cost	Accept VMware and Hyper-V servers. No cost.

Study Objectives

Various companies provide cloud computing services; however, the main cloud computing platforms are Google Cloud, Microsoft Azure, and Amazon (EC2).

e-ISSN: 2582-5208
International Research Journal of Modernization in Engineering Technology and Science
(Peer-Reviewed, Open Access, Fully Refereed International Journal)
Volume:05/Issue:03/March-2023 Impact Factor- 7.868 www.irjmets.com

Platforms:

Cloud computing is the on-demand availability of computer system resources, especially data storage and computing power, without direct active management by the user. Large clouds often have functions distributed over multiple locations, each of which is a data center.

Microsoft Azure:

Azure has long been considered one of the best cloud services platforms out there thanks to its comprehensive suite of available services from tech giant Microsoft. The wide array of included services is enough to fulfill the needs of any business in any industry.

With Azure, you can run services on the cloud or you can combine it with any of your existing infrastructures. Azure was released back in 2010 and has proven to be a solid option for companies looking to undergo a digital transformation. They provide a number of resources for users including:

Amazon Web Service or (EC2):

Amazon Web Services (AWS) is one of the most popular cloud computing platforms to build interactive web solutions for your business. It has a vast selection of infrastructure as a service (IaaS) and platform as a service (PaaS) offerings, including Elastic Cloud Compute (EC2), Elastic Beanstalk, Simple Storage Service (S3) and Relational Database Service (RDS).

AWS's infrastructure is highly customizable, making it possible for you to trim down on costs by utilizing only the services you need. Here's what they have to offer:

Google Loud:

Google Cloud is a reliable, user-friendly, security-oriented cloud computing service from one of today's biggest tech giants. Although Google Cloud's selection of services isn't as vast as Azure's, it's still enough to fulfill all your IaaS and PaaS needs. User-friendliness and security are two of its specialties. They provide a variety of resources for users, including:

II. METHODOLOGY

For this study, I used the comparative study method:

I select three cloud Service Providers for the studied and compared from different aspects. In general, all platforms have very good documentation, many manuals, and free trial account to start using them from scratch. Each cloud service provider offers multiple services, tools, functionalities, and applications and base with service create a table and did the diversity.

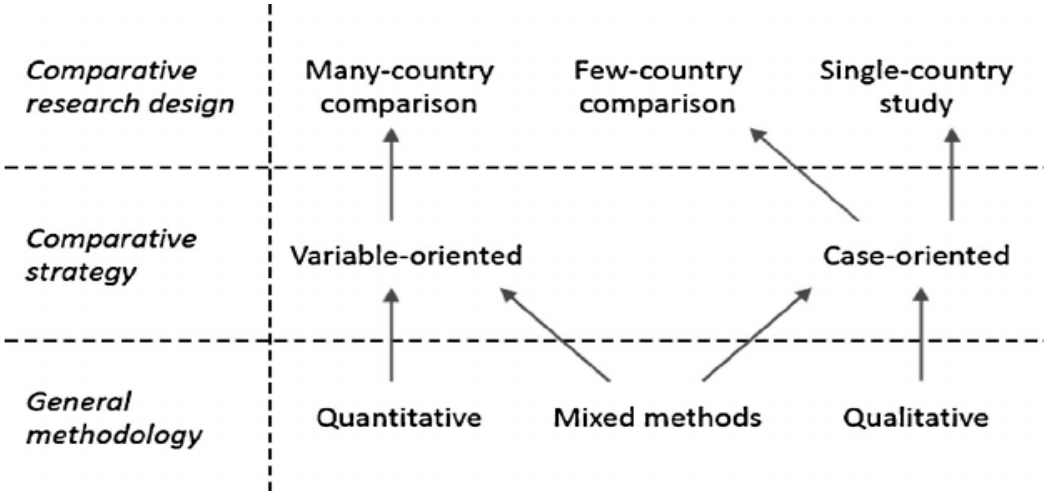


Figure:1.

III. DATA COLLECTION

For this study, I used the comparative study method:

I select 3 cloud Service Providers for the studied and compared from different aspects. In general, all platforms have very good documentation, many manuals, and free trial account to start using them from scratch. Each cloud service provider offers multiple services, tools, functionalities, and applications

And base with service create a table and did the diversity

Online search engine from the provider source to collect data for this study.

IV. CONCLUSION

Cloud computing has come to establish itself more and more formally, contributing with solutions which are increasing in a way that makes more users integrate to this way of working. There are several major providers who provide cloud computing services. The three most popular cloud computing platforms are Google, Microsoft, and Amazon. In this paper, these suppliers were studied and compared from different aspects. In general, all platforms have very good documentation, many manuals, and free trial account to start using them from scratch. Each cloud service provider offers multiple services, tools, functionalities, and applications. Amazon provides an effective way to calculate the cost of the service as it depends on pay per hour or per second, with a one-minute minimum, while other platforms depend only on pay per hour or month. In addition, it provides the least response time and price for technical support better than other platforms. On the other hand, Azure provides the largest set of virtual hardware resources available to create a virtual machines to meet customer needs. In addition, Azure have the largest number of compliance certificates. Both Amazon and Azure offer a penalty downtime better than Google in the event that the uptime falls below 95%. On the other hand, Azure outperforms other platforms in the possibility of server migration from several different types of virtual machines or physical servers. What all users have to do is just determine what their priorities are in order to choose a suitable service provider that meets their aspirations. A comparative study is still required between cloud models and cloud methodologies, and/or between other cloud computing platforms.

V. REFERENCES

[1] Zou, G. (2015). The Design Of Private Cloud Platform For Colleges And Universities Education Resources Based On Openstack. 4th National Conference on Electrical, Electronics and Computer Engineering, 991–996.

[2] Rashid, A., & Chaturvedi, A. (2019). Cloud Computing Characteristics and Services A Brief Review. International Journal of Computer Sciences and Engineering, 7(2), 421–426.

[3] Oludele, A., Ogu, E. C., Shade, K., & Ogu, C. (2014). Insights on Cognizant Computing : Concepts , Technologies and Trends. American Journal of Computing Research Repository, 2(4), 58–60.

[4] Nor, N. M., & Rahim, N. (2016). Cloud Computing : A View on Virtual Computing Labs.

[5] Malaysian Journal of Information and Communication Technology, 1(1), 33–38.

[6] Rajan, R. A. P., & Shanmugapriyaa, S. (2012). Evolution of Cloud Storage as Cloud Computing Infrastructure Service. IOSR Journal of Computer Engineering, 1(1), 38–45.

[7] Encalada, W. L., & Castillo Sequera, J. L. (2017). Model to implement virtual computing labs via cloud computing services. Symmetry, 9(7), 1–15.

[8] Shawish, A., & Salama, M. (2014). Cloud Computing: Paradigms and Technologies. In B. N. Xhafa F (Ed.), Inter-cooperative collective intelligence: Techniques and applications (Vol. 495, pp. 39–68.

[9] Devasena, C. L. (2014). Impact Study Of Cloud Computing On Business Development.

[10] Operations Research and Applications: An International Journal (ORAJ), 1, 1–7.

[11] Dastagiri, D. (2017). Impact of Cloud Computing Applications in Academic Library and Library Services. International Journal of Library and Information Studies, 7(3), 225–232.

[12] Management Association, I. R. (2019). Disruptive Technology: Concepts, Methodologies, Tools, and Applications (1st ed.; I. R. M. Association, Ed.). IGI Global.

[13] Kaur, A., & Gill, S. S. (2018). The Future of Cloud Computing: Opportunities, Challenges and Research Trends. 2nd International Conference on I-SMAC (IoT in Social, Mobile, Analytics and Cloud), 213–219. Palladam, India: IEEE.

[14] Varghese, B., & Buyya, R. (2017). Next Generation Cloud Computing: New Trends and Research Directions. Future Generation Computer Systems, 79, 849–861.

[15] Miller, M. (2009). Googlepedia : the ultimate Google resource. Que.

[16] Choosing an App Engine environment | App Engine Documentation. (2020). Retrieved January 5, 2020,

from https://cloud.google.com/appengine/docs/the-appengine- environments

[17] Hunter, T., & Porter, S. (2018). Google Cloud Platform for developers : build highly scalable cloud solutions with the power of Google Cloud Platform. UK: Packt Publishing.

[18] Azure web services. (n.d.). Retrieved January 8, 2020, from https://www.virtualxcellence.com/azure-web-services

[19] Introduction to Azure Storage - Cloud storage on Azure | Microsoft Docs. (2019). Retrieved February 5, 2020, from https://docs.microsoft.com/en us/azure/storage/common/storage-introduction

[20] Sitaram, D., & Manjunath, G. (2012). Fabric Controller - an overview | ScienceDirect Topics. Retrieved January 15, 2020, from https://www.sciencedirect. com/topics/computer-science/fabric-controller

[21] Azure Free Account FAQ | Microsoft Azure. (n.d.). Retrieved December 5, 2019, from: https://azure.microsoft.com/en-us/free/free-account-faq/

[22] Compute Services - Overview of Amazon Web Services. (n.d.). Retrieved February 1, 2020, from https://docs.aws.amazon.com/whitepapers/latest/aws-overview/compute- services.html

[23] Storage - Amazon Elastic Compute Cloud. (n.d.). Retrieved February 3, 2020, from Amazon website: https://docs.aws.amazon.com/AWSEC2/latest/UserGuide/Storage.html

[24] Bellenir, K. (2012). Debt information for teens : tips for a successful financial life, including facts about the economy and personal finances, money management, interest rates, loans, credit cards, predatory lending practices, and resolving debt-related problems. Omnigraphics.

[25] AWS Free Tier. (n.d.). Retrieved January 5, 2020, from https://aws.amazon.com/free/

Rendiconti Lincei. Scienze Fisiche e Naturali
https://doi.org/10.1007/s12210-023-01159-z

RESEARCH PAPER

Combined effects of high voltage gradient and electrolyte conditioning on electrokinetic remediation for chromium (VI)-contaminated soils

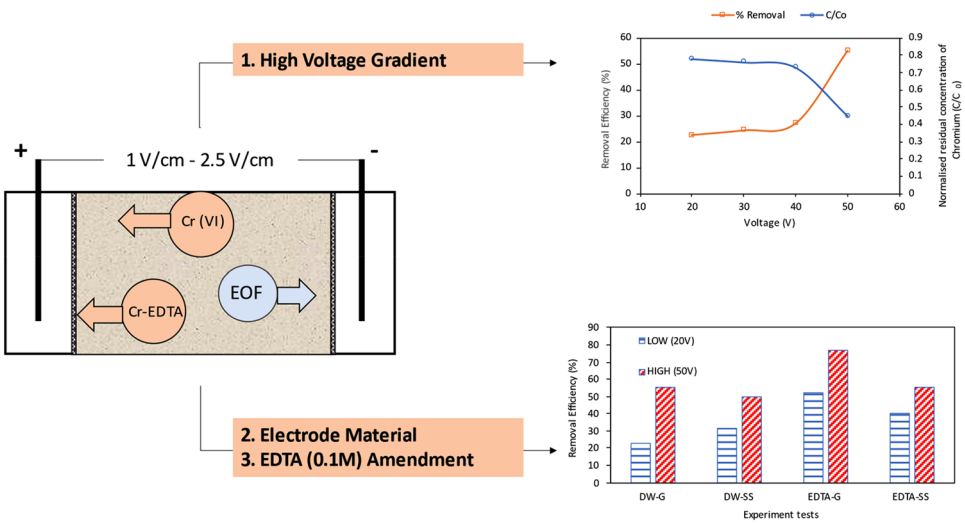
Sonam Taneja[1] · **Oznur Karaca**[2] · **A. K. Haritash**[1]

Received: 1 December 2022 / Accepted: 15 March 2023
© The Author(s), under exclusive licence to Accademia Nazionale dei Lincei 2023

Abstract

Disposal of chromium-containing industrial waste has led to soil contamination at dispersed locations around the globe. Considering the carcinogenic, non-biodegradable, and bioaccumulating nature of hexavalent chromium Cr (VI), it is pertinent to treat the contaminated soils. Electrokinetic Remediation (EKR) is a promising technology to remediate metal-contaminated soils under the influence of an electric field. This study investigated the removal of Cr (VI) by EKR, enhanced with a combination of high voltage (50 V), electrolyte conditioning using EDTA (0.1 M), and type of electrode material. Under controlled conditions using distilled water, low voltage (20 V at 1 V/cm) resulted in 22% removal, while high voltage (50 V at 2.5 V/cm) resulted in 55% removal of Cr (VI) in 10 h of treatment period. The removal was further enhanced to 77% by amending with ethylenediaminetetraacetic acid (EDTA 0.1 M) as an electrolyte at a high voltage gradient of 2.5 V/cm. Classifying the role of electrode (graphite and stainless steel), based on the removal efficiency and corrosion of electrodes, graphite resulted in higher removal compared to stainless steel but with a significantly higher corrosion effect. Characterization of soil after EKR experiments exhibited improved liquid and plastic limits, and insignificant difference in Total Organic Carbon (TOC) and other parameters related to soil health. Energy consumption and cost-estimation revealed that application of high voltage, along with conditioning of electrolyte with EDTA can significantly increase removal of Cr (VI) in short period of time in a cost-effective (0.8 US$/g) way, thereby can be applied for rapid treatment of large volumes of soil without affecting the properties of soil.

Graphical abstract



Extended author information available on the last page of the article

Published online: 10 April 2023

Keywords Hexavalent chromium · EDTA · Electrokinetic remediation · Voltage · Graphite

1 Introduction

Heavy metals are ubiquitously distributed across all the environmental matrices, despite their localized disposal in the environment. Heavy metals are non-degradable and can exist in different chemical forms which determine its bioavailability, mobility, toxicity, and their possible entry into the food chain (Karaca et al. 2019). Chromium, particularly, exists in two stable forms: trivalent [Cr (III)] and hexavalent [Cr (VI)], with former being a micronutrient essential for plant growth, which is usually non-soluble and less toxic (Prasad et al. 2021). Cr (VI) on the other hand, is a water-soluble, toxic form that is a potent carcinogen and mutagen (Liang et al. 2021). Major sources of chromium in environment are industrial processes like electroplating, mining, dyeing, tanning, etc. (Prakash et al. 2022). The partitioning of chromium between soil and water depends upon the pH, which governs the adsorption/solubilization of metal on soil particles and in water. Cr (III) when introduced into the soil, might get oxidized to Cr (VI) in the presence of low pH and oxidizing agents (Eq. 1) like manganese oxide (MnO_2) (Apte et al. 2006; Oliveira 2012). Presence of Cr (VI) in soil adversely affects the soil ecology which makes it pertinent to remove it from soil.

$$2Cr^{3+} + 3MnO_2 + 2H_2O \rightarrow 2HCrO_4^- + 3Mn^{2+} + 2H^+. \quad (1)$$

Electrokinetic Remediation (EKR) is one of the emerging technologies for the removal of contaminants, especially, heavy metals from soil (Benamar and Baraud 2011). Application of electric current through a soil column causes the movement of charged and non-charged contaminants toward the electrodes through three key processes: electromigration, electro-osmosis and electrophoresis (Acar and Alshawabkeh 1993). In situ application with minimal soil disruption, non-specificity of contaminants, and suitability for low permeable soils makes EKR a superior technology to many conventional techniques like soil washing, vitrification, and bioremediation (Reddy and Cameselle 2009). The effective migration of metals in soil depends upon the solubility of metal ions into the soil pore fluid. Application of electric current has slight effect on the geochemical properties of soil such as pH, redox, moisture content, etc. which influence the solubilization and mobility of metals in soil (Al-Hamdan and Reddy 2008; Song et al. 2016; Wu et al. 2016).

EKR allows regulation of operating parameters like voltage, current, electrode material, electrolyte composition, etc. to increase metal solubility and thus, enhance its efficiency (Benamar and Baraud 2011). Applied voltage is the prime parameter that affects the electromigration of metal ions and its removal from soil (Reddy and Karri 2006). Many studies have considered a voltage gradient of 1–1.5 V/cm ideal for the removal of contaminants, provided the soil is subjected to such voltage for a longer duration, which makes it a time-consuming and expensive treatment method (Wei et al. 2011; Shin et al. 2017; Li et al. 2020). A few researchers have assessed the effect of higher applied voltage gradient on soil and reported higher removal rates (Lu et al. 2019; Johar and Embong 2015). A study by Bekkouche et al. (2020) concluded that the removal of salts from soil increased when the applied voltage was increased. The results revealed that maximum removal was achieved for calcium (89%) and sulfate (88%) at a high voltage gradient of 2.5 V/cm. Another study by Saleem et al. (2011) reported increased removal efficiency of Nickel from 38.5% to 54.3% when voltage gradient increased from 1 to 2 V/cm. Applied voltage gradient controls the current flowing through soil and high current results in higher removal of ions. Current flow through the soil is also influenced by the type of electrode material. Electrodes with high conductivity, low resistivity and low cost is considered ideal for the effective EKR treatment (Virkutyte et al. 2002).

During the process of EKR, precipitation of metals as hydroxides is observed at the cathode, which reduces the mobility and transport of metals in soil (Karaca et al. 2017). Organic matter present in the soil forms metal–organic complexes which too affects the mobility of metals, and the efficiency of EKR. Soil pore fluids or electrolytes provide a medium for the movement and transport of ions (Acar et al. 1993; Shin et al. 2017). Many enhancing fluids like strong mineral acids, organic acids, chelating agents etc. have been used as electrolytes to improve the mobilization of metals (Cameselle and Pena 2016; Figueroa et al. 2016; Wu et al. 2021). Among them, chelating agents e.g. EDTA (Ethylenediamine tetra acetic acid) have been widely known to increase the mobility of metals by binding with a single metal atom at two or more sites to form soluble negative complexes (Song et al. 2016). Like other organic acids, EDTA is usually biodegradable and can also be recovered after the treatment. Song et al. (2016) reported that EDTA was more suitable for removal of Ni (52.8%), Pb (60.1%) and Zn (34.9%) as compared to ethylenediamine-N,N'-disuccinic acid (EDDS) and citric acid. Nasiri et al. (2020) also reported high removal of Cr with EDTA (78%) as compared to citric acid which showed 54% removal.

The removal of metal ions during EKR is governed by the applied current and the duration of its application. In the present study, it is hypothesized to enhance the removal of contaminant Cr (VI) ions by increasing the voltage gradient from 1 to 2.5 V/cm. The application of a suitable chelating agent may further shorten the duration of treatment without compromising with the efficiency of treatment, and health of the treated soil, thereby, the overall cost of treatment. To test this hypothesis, EDTA was employed as an electrolyte solution to study its effects on metal solubilization and removal. In addition, the effect of electrode material was also investigated between graphite and stainless-steel electrodes based on their removal efficiency and corrosion effect. Further, the energy consumption was investigated for each experiment, based on which, cost estimation was done to evaluate the practical applicability of EKR.

2 Materials and methods

2.1 Soil preparation and characterization

The soil was collected from the campus of Delhi Technological University, Delhi. The collected soil was air dried and sieved through 2 mm mesh to remove coarse particles prior to spiking with contaminant in the laboratory. Soil was spiked with Cr (VI) to obtain a concentration of 1000 mg/kg. This concentration was selected to stimulate waste obtained from electroplating industries with high concentration of hexavalent chromium (Reddy and Chinthamreddy 2004). For this purpose, 4.23 g of Potassium dichromate ($K_2Cr_2O_7$, 99.9% purity) was weighed for 1.5 kg soil (@ 2.82 g $K_2Cr_2O_7$/kg of soil) and was powdered before mixing with soil. The dry mixture of salt and soil was then wetted using distilled water and mixed thoroughly to impart some moisture to the soil. The soil was then allowed to dry with periodic mixing at regular intervals and this cycle of wetting and drying was repeated 2–3 times. The spiked soil was stored in a plastic bag for 24 h before experiment to avoid moisture loss. This process was done to ensure that Cr (VI) is evenly distributed (through diffusion and dispersion), and subsequent adsorption on to soil particles, if any, so as to represent the soil under natural conditions, as suggested in earlier studies (Karaca et al. 2022).

2.2 EKR assembly setup and procedure

The experimental setup for EKR was assembled in the lab as shown in Fig. 1. It consisted of a rectangular HDPE soil cell (19.5 cm × 5.5 cm × 4.5 cm), perforated cylindrical electrode wells (5.5 cm × 12 cm), graphite or stainless-steel electrodes (10 × 150 mm), variable DC power supply (Dual Output 20–60 V) and a multimeter. The soil cell was filled at once with 1.5 kg of dry spiked soil based on the volume of cell and was saturated with 500 ml volume of electrolyte solutions within the soil cell to achieve a moisture content of 25%. The saturated soil was mixed properly and was let to equilibrate. Before starting the experiment, the soil was pressed with a lid to ensure minimum void spaces. The electrode wells were placed on opposite side in the soil cell with a distance of 15 cm. The wells were wrapped with nylon cloth of 200 mesh size to avoid clogging and entry of soil into the wells. The electrodes were suspended in the electrode wells filled with electrolytes and connected to the DC power supply with wires and clamp. Electrode wells were connected to the electrode reservoirs via tubings to collect overflow of electrolytes.

During EKR experiments, both voltage drop and current were monitored continuously. At the end of first cycle of 5.0 h, the anolyte and catholyte were extracted and analyzed. Fresh electrolytes (120 ml in each electrode compartment) were used before the start of second cycle of 5.0 h again. After the termination of second cycle, the anolyte and catholyte were extracted. The soil was sectioned into four equal divisions (S1, S2, S3 and S4) directed from anode to cathode and used for analysis. Prior to each experiment, the soil cell and electrode wells were washed with acid (0.1 M sulphuric acid) to avoid cross-contamination. Electrodes were thoroughly cleaned to remove deposition and fresh nylon cloth was used for each test.

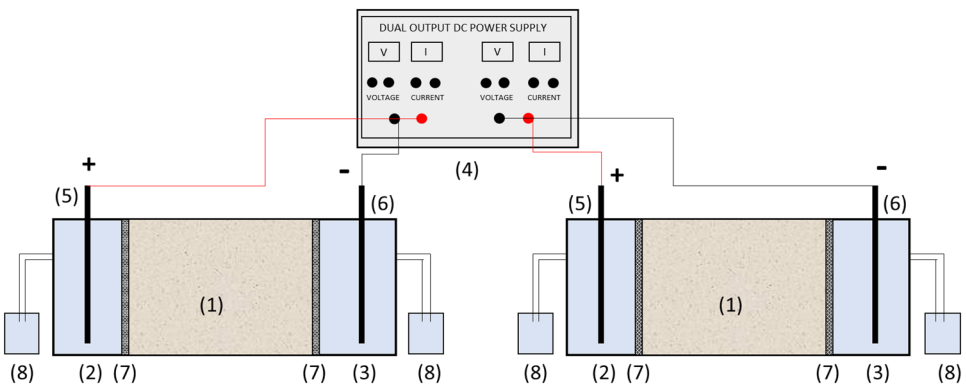


Fig. 1 Schematic diagram of EKR setup used in this study (1) soil cell (2) anode well (3) cathode well (4) DC Power Supply (5) anode (6) Cathode (7) Nylon Mesh (8) Electrolyte reservoirs

The values of voltage and current displayed by the power supply unit was confirmed against the measurement by the multimeter separately. The voltage display by the power supply and measured values of multimeter were same throughout the experiment. Further, the increase in volume at cathode well to confirm electro-osmotic flow and increase in color intensity at anode were observed which confirmed proper working of EKR setup. Lastly, the samples of soil and electrolytes were analyzed in triplicate and the results were confirmed using intra-lab investigations. The variation in results were limited to ± 3%.

2.3 Analysis

Raw soil, spiked soil, and treated soil were characterized for particle size distribution (ASTM 2007) and the soil was classified as fine sand. Other parameters analyzed were; Atterberg's limits (ASTM 2017), specific gravity (ASTM 2014a), moisture content (ASTM 2014b), pH, EC, TDS (ASTM 2019) and total organic content (ASTM 2014b). Carbonates (ASTM 2014c), chlorides (Mohr's method), sulphates (USEPA 1992) and cations (APHA 1992a) were also analyzed. Soil–water extract was prepared with 1:10 soil to water ratio in a conical flask and kept in a shaker for 2 h. Both soil sample and electrolytes were analyzed for pH, EC and TDS using a bench-top multiparameter (LMMP 30 model).

For Cr (VI) analysis, electrolytes were centrifuged at 5000 rpm for 10 min and analyzed for Cr (VI) in the supernatant. Electrolytes collected from EDTA experiments were chemically oxidized to hexavalent chromium (APHA 1992b) prior to chromium analysis. Soil samples were thermally oxidized at 500ºC in a muffle furnace for 2 h. After oxidation, soil was chemically extracted with nitric acid (10%) after shaking for 30 min over an orbital shaker. The extract was centrifuged and then analyzed for Cr (VI) as per USEPA standard 7196A spectrophotometric method using Diphenylcarbazide (DPC). In this method, 2–3 drops of 0.2 N sulphuric acid was added to 10 ml sample of electrolyte/soil extract in a test tube to create acidic conditions. After shaking, 2 ml of DPC solution (0.250 g DPC salt in 50 ml acetone) was added to the test tube and shaken for color development. After 3–5 min, pink-purple tint appeared and the Cr (VI) concentration was measured using UV–VIS double beam spectrophotometer (Labtronics Model LT-290) at a wavelength of 540 nm. Nylon filters were acid digested with 5% nitric acid and sonicated for 30 min. The extracts were centrifuged and analyzed using the same procedure.

3 Results and discussion

EKR was carried out to assess the removal of Cr (VI) from fine soils. The experiments were carried out in three parts (Table 1). First, a series of tests were performed to identify the optimum voltage for maximum removal of Cr (VI) from soil (tests EK1-EK4). Second, EDTA was used as electrolyte at the recommended low voltage (20 V, EE1) and at high voltage (50 V, EE2) and the results were compared with control tests using distilled water. In the third step, stainless-steel electrode was used in controlled conditions with distilled water to compare the results with graphite electrode (20 V, ET1; 50 V, ET2) and also with EDTA to evaluate the combined effects of electrode and electrolyte conditioning (20 V, ES1; 50 V, ES2). All the experiments were operated for total 10 h in two cycles of 5 h each for 2 days.

3.1 Variations in pH

The variations in pH of electrolyte and soil after EKR treatment are given in Fig. 2. A typical pH profile was observed with all voltage gradients indicating low pH in anolyte and a high pH in catholyte. As the voltage gradient increased (Fig. 2a), values decreased at anode to pH less than 2, and

Table 1 Details of experimental conditions used for EKR of Cr (VI)-contaminated soil

S. no	Experiment	Electrolyte	Electrode material	Voltage (V)	Moisture content (%)	Treatment time
1	EK1	Distilled water	Graphite	20	25	10 h (5 h + 5 h batch mode)
2	EK2	Distilled water	Graphite	30	25	10 h (5 h + 5 h batch mode)
3	EK3	Distilled water	Graphite	40	25	10 h (5 h + 5 h batch mode)
4	EK4	Distilled water	Graphite	50	25	10 h (5 h + 5 h batch mode)
5	EE1	EDTA (0.1 M)	Graphite	20	25	10 h (5 h + 5 h batch mode)
6	EE2	EDTA (0.1 M)	Graphite	50	25	10 h (5 h + 5 h batch mode)
7	ET1	Distilled water	Stainless steel	20	25	10 h (5 h + 5 h batch mode)
8	ET2	Distilled water	Stainless steel	50	25	10 h (5 h + 5 h batch mode)
9	ES1	EDTA (0.1 M)	Stainless steel	20	25	10 h (5 h + 5 h batch mode)
10	ES2	EDTA (0.1 M)	Stainless steel	50	25	10 h (5 h + 5 h batch mode)

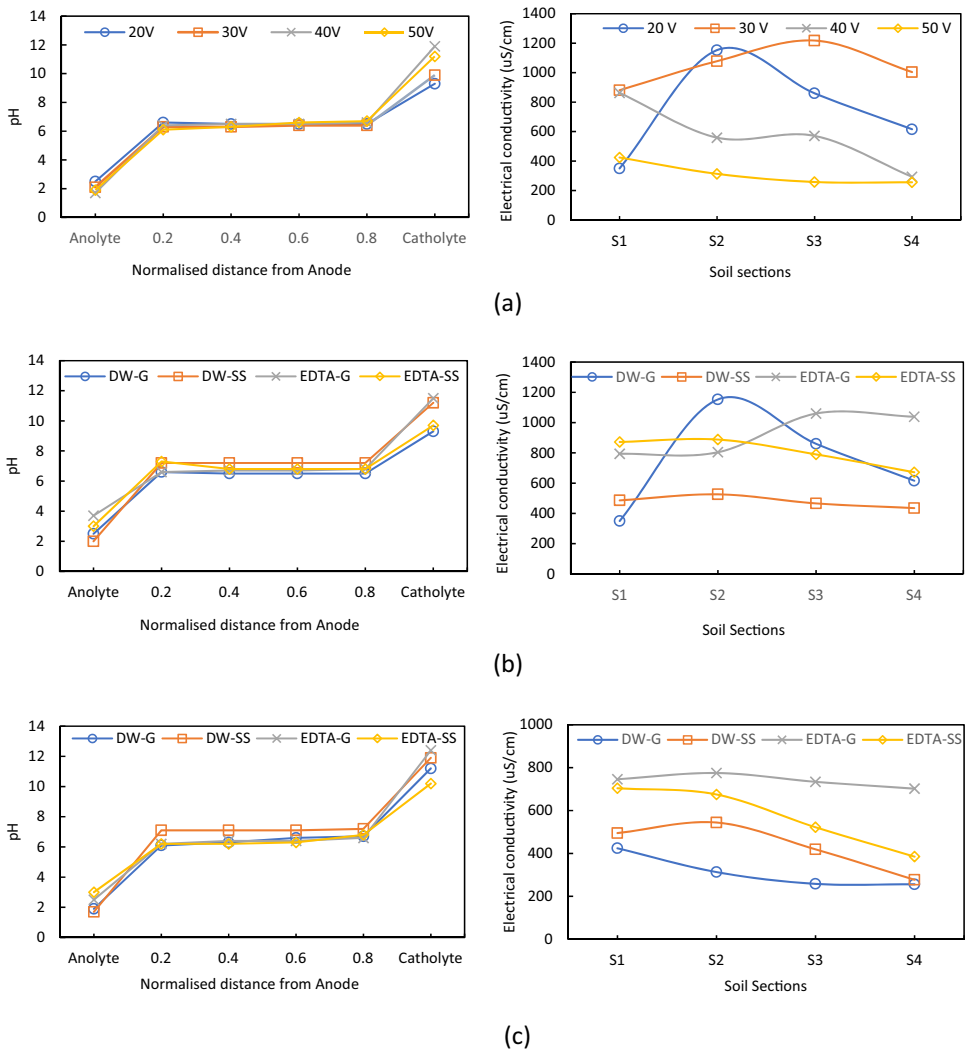


Fig. 2 Variations in pH and Electrical conductivity (EC) of soil after EKR treatment under different conditions (**a**) controlled conditions at four different applied voltage (**b**) enhanced with EDTA at 20 V (**c**) enhanced with EDTA at 50 V

pH more than 11 at cathode due to faster electrolysis reactions. The pH gradient is formed primarily due to production of hydrogen and hydroxyl ions. Oxidation of water at anode generates hydrogen ions, while reduction at cathode generates hydroxyl ions (Acar et al., 1993), resulting in variation of pH at the respective electrode.

$$\text{At Anode}: \ 2H_2O \rightarrow O_2 + 4H^+ + 4e^- \quad (2)$$

$$\text{At Cathode}: \ 4H_2O + 4e^- \rightarrow 2H_2 + 4OH^- \quad (3)$$

Application of high voltage produces higher electrical current, which increases the rate of dissociation of electrolytes and generation of more hydrogen and hydroxide ions that migrate into the soil system (Cameselle and Gouveia 2020; Prakash et al. 2022). When EDTA was used as electrolyte (Fig. 2b and c), comparable results were obtained with low anolyte pH (3.0) and high catholyte pH (10.0) at both 20 and 50 V, as has been reported by Reddy and Chinthamreddy (2004). Soil pH was not much affected by the applied voltage and EDTA and remained almost neutral throughout in the present study. Similar findings were observed by Wu et al. (2016), where slightly acidic pH (6.1) was observed in the soil section close to anode, while slightly alkaline pH (7.2) was observed in soil close to cathode at high voltage gradient of 2.5 V/cm. This could be attributed to high buffering capacity of soil due to the presence of carbonates (~ 18%) that neutralized the acid front generated at the anode (Song et al. 2016).

3.2 Variations in electrical conductivity and current profile

Electrical conductivity (EC) determines the flow of current through soil which is affected by soil pH and applied voltage. Figure 2 exhibits the EC in soil sections S1–S4 after EKR treatment. At low voltage, EC was high in soil section

S2 and low near electrodes. As the voltage increased to 30 V, the peak shifted to S3 from S2, which indicates migration and accumulation of ions toward cathode. At the maximum voltage, minimum EC was observed in all sections due to depletion of ions by electromigration to the electrolyte used, at high voltage. EC values in soil were higher in tests with EDTA as compared to distilled water as electrolyte, with maximum value in EDTA-Graphite (EE2) experiment at 50 V, due to increase in ionic concentration in the soil (Fig. 2b and c). However, the values were relatively low in S3 and S4 sections as compared to S1 and S2, which indicates movement of ions toward anode. In EE1, inverse trend was observed, with lower EC in S1 and S2 sections as compared to S3 and S4. The reason could be corrosion of graphite electrode at the anode due to oxidizing conditions, which increased the electrical resistance and reduced electrical conductivity near anode, as has been reported by other authors (Sun et al. 2021). Stronger electromigration is observed at high current values, which leads to more removal of metal ions. Figure 3a shows the current profile during EKR process with time at different voltage gradients. In experiments EK1-EK4 (with varying voltage gradients), the results showed that initially the current increased rapidly, achieved a peak at a maximum value and then stabilized. Even though the trend was same at every voltage gradient, the current increased with voltage. It attained peak early in case of stainless steel (experiment ET1-ET2) as compared to graphite (Fig. 3b). When EDTA was used as electrolyte, the trend was inversed. The current started with a peak which decreased with time till it stabilized. Considering the combination of EDTA with electrode material, EDTA-G exhibited higher current than EDTA-SS. The saturation of soil with EDTA provided higher ionic strength by solubilizing ionic species, which increased the initial current (Cameselle et al. 2021).

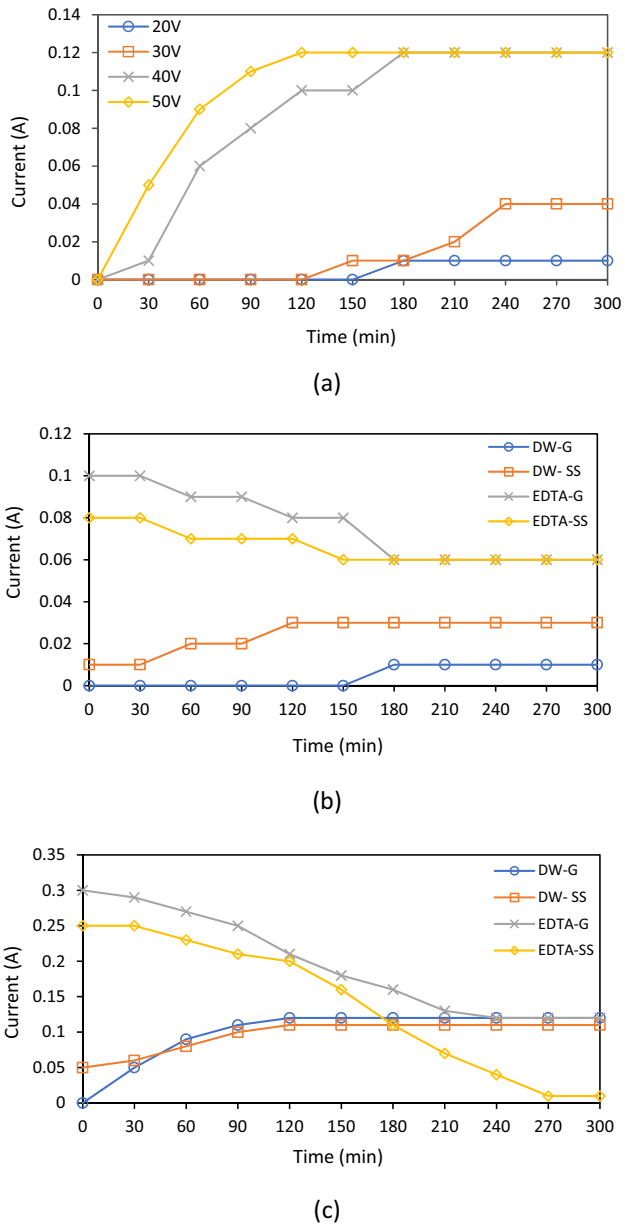


Fig. 3 Variations in current in soil during EKR treatment under different conditions (**a**) unenhanced with four different applied voltage (**b**) enhanced with EDTA at 20 V (**c**) enhanced with EDTA at 50 V

3.3 Variations in electro-osmotic flow

Electro-osmotic flow (EOF) is the movement of pore fluid under the influence of electric field (Virkutyte et al. 2002). Some ions and non-charged contaminants also migrate along with soil pore fluid due to EOF. In the present study, EOF was measured by volume change in the anolyte and catholyte after EKR treatment (Fig. 4). As the soil particles are negatively charged, the direction of EOF is usually from anode to cathode, which was also observed in all experiments of this study. Experiments with low voltage did not show much variation in volume (EK1). Maximum EOF was observed in EK4 due to higher applied voltage (50 V). When EDTA was used as electrolyte, similar observations were made with respect to the direction of EOF. Maximum EOF was observed in case of EE2, followed by ET2, which shows that EOF is greatly influenced by applied voltage as it increases with increase in voltage gradient. The results confirm that voltage is directly proportional to EOF, as has also been reported by Gidudu and Chirwa (2020). Since the direction of EOF was opposite to the direction of electromigration, Cr migration toward anode was hindered and caused some migration of Cr into the cathode compartment in agreement to earlier reported studies (Reddy and Chinthamreddy 2004; Song et al. 2016). However, the effect of electromigration was higher than that of electro-osmosis on the migration of Cr (VI).

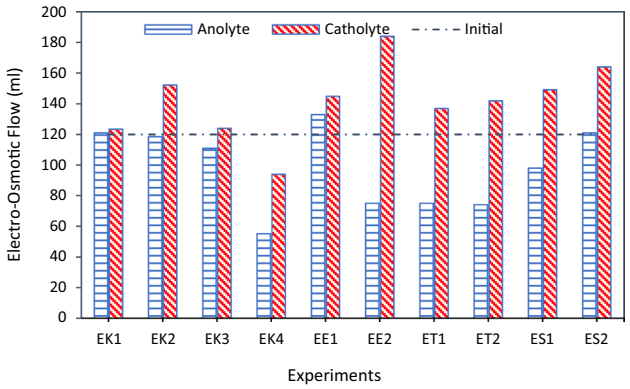


Fig. 4 Electro-osmotic flow (EOF) in soil measured by change in volume (ml) in anolyte and catholyte post-EKR treatment

3.4 Cr removal and migration

Analysis of anolyte and catholyte exhibited high concentration of Cr (VI) in anolyte, which suggests that Cr (VI) migrated and flushed into the anode-well through electromigration (Al-Hamdan and Reddy 2008). Removal efficiency of all the tests was calculated using the formula

$$R\% = \frac{\mathrm{Co} - \mathrm{C}}{\mathrm{Co}} \times 100, \tag{4}$$

where C_0 is the initial concentration of Cr in soil (mg) and C is the residual concentration of Cr in soil after EKR treatment (mg). Figure 5a shows the percentage removal of chromium (VI) with increasing voltage. The findings showed that rapid removal was achieved at high voltage of 50 V. Maximum removal was obtained with EDTA-enhanced EKR at 50 V when graphite electrode was used (Fig. 5b). Same test when performed at low voltage of 20 V, gave similar removal as obtained by unenhanced EKR at 50 V with stainless steel. This shows that the combination of both high voltage and enhancement with EDTA can significantly improve the efficiency of EKR. When EDTA was used as an electrolyte, Cr formed negatively charged soluble complexes with EDTA which then migrated toward anode. Similar observation have been reported by Cameselle et al. (2021).

The mass balance analysis of chromium was calculated (Eq. 5) to account for the concentration of chromium in soil sections, anolyte and catholyte, and nylon filter (Co) and was compared with initial Cr in soil (Ci).

$$\text{Mass Balance} = \frac{\mathrm{Co}}{\mathrm{Ci}} \tag{5}$$

The results (Table 2) showed that maximum Cr was accounted in all tests (0.7–0.9) except for test EE2 with a value of 0.5. The possible reason for low mass balance was adsorption of Cr on electrode and/or deposition of Cr-EDTA complex formed on the electrodes which was distinctly visible during the experiment. Similar findings were reported by Reddy et al. (1997). The electrodes were not analyzed for adsorbed or trapped Cr for this study. Some studies have reported the reduction of Cr (VI) to Cr (III) that occurred near anode due to low pH. The analysis of Cr concentration was done after thermal oxidation of soil. Thus, even if the reduction of Cr (VI) to Cr (III) occurred during EKR, it was later oxidized thermally and was reported as Cr (VI).

Figure 6 shows the fraction of residual Cr in different soil sections. The results revealed that at low voltage of 20 V, the metal was accumulated in the centre of soil cell in soil sections S2 and S3. As the voltage increased to 30 V, the concentration of residual Cr was increased in S2 as compared to S3. Similarly, when the voltage increased from 30 to 40 V, Cr accumulation was maximum in section S1 close to anode. This trend shows that with increasing voltage, the migration of Cr increased from cathode to anode. Soil section close to cathode had least metal accumulation as compared to sections close to anode due

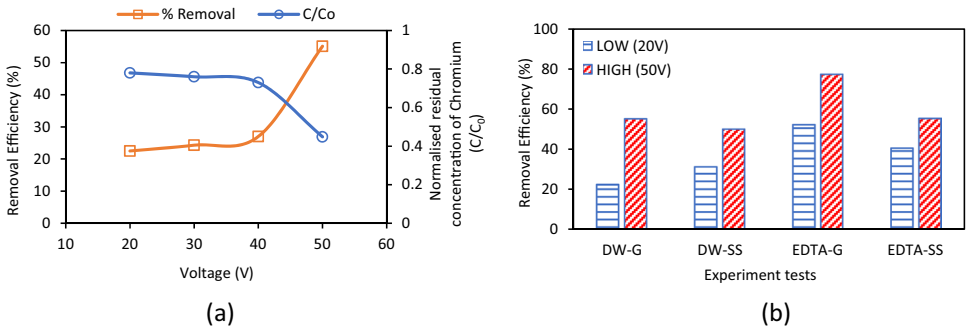


Fig. 5 Percentage removal of chromium from soil after EKR treatment (**a**) under the applied voltage of 20 V, 30 V, 40 V and 50 V, and (**b**) under varying conditions of electrolyte and electrode material at low (20 V) and high voltage (50 V). DW-G is Distilled water as processing fluid with Graphite electrode. DW-SS is Distilled water with Stainless steel. EDTA-G is EDTA as processing fluid with Graphite electrode. EDTA-SS is EDTA with stainless steel

Table 2 Removal percentage and mass balance of chromium metal in different fractions at the end of the electrokinetic test

S. no	Test	Electrolyte	Electrode material	Voltage gradient (V/cm)	Initial Cr content in soil (mg)	Residual Cr content in soil (mg)	Cr Content in Anolyte (mg)	Cr Content in catholyte (mg)	Cr Content absorbed by filter (mg)	Cr Removal percentage (%)	Mass Balance (C_o/C_i)
1	EK1	Distilled water	Graphite	1	1181	915	91	0.2	11	22.5	0.9
2	EK2	Distilled water	Graphite	1.5	1151	870	197	0.1	4	24.4	0.9
3	EK3	Distilled water	Graphite	2	2550	1860	328	0.6	12	27.1	0.9
4	EK4	Distilled water	Graphite	2.5	2010	902	892	1	13	55.1	0.9
5	EE1	EDTA (0.1 M)	Graphite	1	1269	606	240	1	0.3	52.3	0.7
6	EE2	EDTA (0.1 M)	Graphite	2.5	2519	581	638	1	1	77	0.5
7	ET1	Distilled water	Stainless steel	1	1761	1209	243	1.5	0.6	31.3	0.8
8	ET2	Distilled water	Stainless steel	2.5	1826	915	879	2	4.5	50	0.9
9	ES1	EDTA (0.1 M)	Stainless steel	1	1788	1061	215	16	0.3	40.6	0.7
10	ES2	EDTA (0.1 M)	Stainless steel	2.5	1860	830	390	3	0.7	55.3	0.7

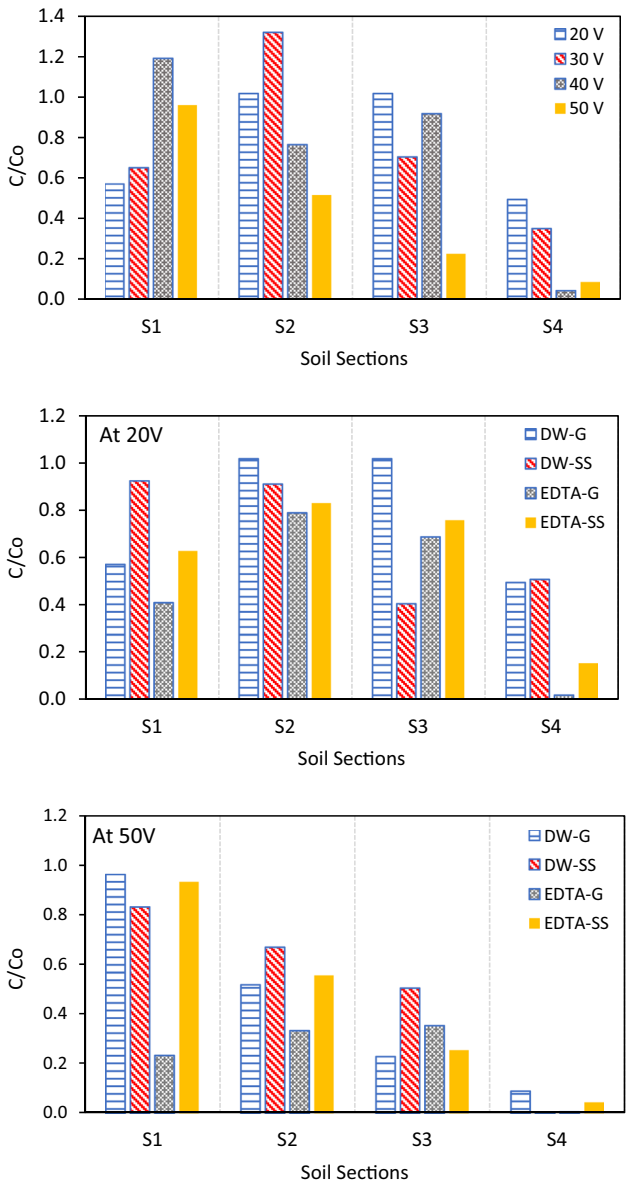


Fig. 6 Distribution of residual chromium in soil sections S1-S4 from anode to cathode

to electromigration of Cr (VI) towards anode, reflux of anolyte to the soil by EOF and/or saturation of anolyte with ions which led to accumulation in soil close to it. Migration of residual Cr toward anode was higher when distilled water was used with graphite electrode (DW-G) as compared to when it was used with stainless-steel electrode (DW-SS). That is why for test EK1-EK4, the maximum accumulation is at S2 and S3 sections, while for test ET1-ET2, maximum accumulation is at S1 and S2 sections. However, in both the tests, comparable Cr accumulation was present in S4 close to cathode. Similar results were obtained when EDTA was used with maximum Cr accumulation in section S2. From these results, it is

concluded that if the treatment time of test was increased, the metal removal would also increase, also reported by Karaca et al. (2022).

3.5 Properties of soil after electrokinetic treatment

The characterization of raw soil, spiked soil and treated soil is given in Table 3. The properties of treated soil were analyzed after EKR treatment to detect the changes in soil properties when subjected to a high voltage of 50 V for 10 h. The results showed that physical properties like particle size and specific gravity did not change. However, the plastic limit and liquid limit of treated soil increased from 12.7 to 16.3% and 29.4–39.7%, respectively. Cations (K, Na, Ca) present in the raw soil moved toward cathode and decreased drastically in soil post-treatment due to electromigration, as was reported by Bessaim et al. (2020). Migration of anions (Cl^-, SO_4^{2-}, CO_3^{2-}) toward anode was observed, however, was not removed from soil. This could be because of saturation of anolyte with Cr ions (Prakash et al. 2022). The soil pH did not change much from the initial value owing to the buffering capacity of soil, while the electrical conductivity of soil increased from 204 mS/cm to 312 mS/cm, due to the increased solubility of ions under increased voltage gradient.

The application of 1.0 V/cm in most of the published literature has resulted in 30–40% removal of Cr (VI) in treatment period of 12–21 days using graphite electrode (Song et al. 2016; Gao et al. 2020), whereas the present study reports removal of 55% of Cr (VI) within 10 h. In respect of soil health, the earlier studies reported changes in pH and EC alone. The pH is observed to slightly reduce in the treated soil even at 1.0 V/cm voltage gradient. The same has been reported (pH reduced to 6.5 from 6.7) in the present study carried at 2.5 V/cm. Apart from it, the parameters of soil health (Table 3) did not show any major adverse changes in properties of soil. The physical properties (plastic limit and liquid limit) were marginally affected since the electrolyte (EDTA) and EKR resulted in removal of cations. It was observed that the removal of divalent cations (Ca^{2+}) was more than the monovalent cations (Na^+) thereby resulting in relative abundance of negative ions. This may increase the thickness of double diffuse layer, thereby resulting in slightly higher liquid and plastic limits. Further, the decrease in organic carbon content may be attributed to removal of soluble organic carbon due to EDTA *via* electro-osmotic flow toward cathode.

3.6 Energy consumption and cost estimation

Application of high voltage and amendment of electrolytes may contribute to energy and cost expenditure. The energy consumption in KWh and total cost of running EKR was evaluated to assess the feasibility of this technique. Total cost was calculated as the sum of cost of electricity consumed, cost of electrodes and the cost of chemicals used for electrolyte conditioning. Based on the energy consumption, cost per gram of removal of Cr from soil was also calculated to evaluate the cost-effectiveness of this technique (Table 4).

Maximum energy consumption was observed by test EE2 (0.1 KWh), followed by ES2 (0.07 KWh), EK4 (0.06 KWh)

Table 3 Characterization of soil health before and after EKR treatment

Parameter	Raw soil	Contaminated soil	Treated soil	Method
Sand (%)	78 (31% medium, 47% fine grained)	78 (31% medium, 47% fine grained)	78 (31% medium, 47% fine grained)	ASTM D422
Silt and clay (%)	22	22	22	ASTM D422
pH (1:10 soil to water)	6.9	6.7	6.5	ASTM D1293
EC (1:10 soil to water) (mS/cm)	204	205	312	ASTM D1293
TDS (1:10 soil to water) (ppm)	255	276	189	ASTM D1293
Organic content (%)	0.62	0.51	0.22	ASTM D2974
Plastic limit (%)	12.72	13.93	16.30	ASTM D4318
Liquid limit (%)	29.40	31.17	39.77	ASTM D4318
Plasticity index (%)	16.7	17.2	23.5	ASTM D4318
Specific gravity	2.5	2.5	2.5	ASTM D854
Na (mg/kg)	5808	5808	3429	APHA 3111
K (mg/kg)	288	288	142	APHA 3111
Ca (mg/kg)	9560	9560	2549	APHA 3111
Chlorides (mg/kg)	200	280	280	EPA 9253
Sulphates (mg/kg)	152	6750	2013	EPA 9038
$CaCO_3$ equiv. (%)	17.5	18	18.7	ASTM D4373
Chromium (VI) (mg/kg)	0	1000	601	EPA 7196A

Table 4 Energy consumption and cost analysis for different combinations during EKR of Cr-contaminated soil

S. No.	Experiments	Energy consumption (KWh)	Rate of electricity (₹/KWh)	Cost of electricity (₹)	Cost of electrodes (₹)	Cost of chemicals (₹)	Total cost per gram removal of Cr	
							(₹/g)	(US$/g)
1	EK1	0.002	8.5	0.017	88.90	0.00	334.3	4.3
2	EK2	0.012	8.5	0.102	88.90	0.00	316.7	4.1
3	EK3	0.032	8.5	0.272	88.90	0.00	129.2	1.7
4	EK4	0.06	8.5	0.51	88.90	0.00	80.7	1
5	EE1	0.016	8.5	0.136	88.90	28.60	177.4	2.3
6	EE2	0.1	8.5	0.85	88.90	28.60	61.1	0.8
7	ET1	0.004	8.5	0.034	25.00	0.00	45.4	0.6
8	ET2	0.05	8.5	0.425	25.00	0.00	27.9	0.4
9	ES1	0.014	8.5	0.119	25.00	28.60	73.9	1
10	ES2	0.07	8.5	0.595	25.00	28.60	52.6	0.7

and ET2 (0.05 KWh). It is evident from the results, that application of high voltage showed relatively higher energy consumption. Amendment of EDTA decreased the resistance of soil by increasing mobility of ions and electrical conductivity, which increased the energy expenditure. Application of high voltage and EDTA together, increased the total cost of the experiment. However, as the removal of Cr was maximum in test EE2, followed by ES2, it showed minimum cost of running for per gram removal of Cr (0.8 and 0.7 US$/g, respectively). Maximum cost of running EKR was calculated for control EK1 at 20 V (4.3 US$/g). Addition of EDTA combined with high voltage gradient enhanced the removal rate of Cr and reduced the energy consumption. Stainless-steel electrode is relatively more cost-effective than graphite electrode as it does not show much corrosion effect and can be re-used.

Results of the present study indicated that a higher voltage gradient (2.5 V/cm) can be used to increase the removal efficiency, and shorten the duration of treatment. The application of higher voltage did not result in any significant change in health of the treated soil, thus, supporting the use of higher voltage gradient in treatment of sandy soil. On the other hand, most of the studies published show 30–50% removal (Gao et al. 2020; Ma et al. 2022). The current study shows 1.5 times relatively better removal. In respect of choice of electrode material and electrolyte, stainless steel with 0.1 M EDTA proves to be more cost-efficient toward removal of Cr (VI). The use of stainless steel as electrode material under optimized conditions, results in relatively less corrosion of electrode as well.

4 Conclusion

The effectiveness of EKR technique for the treatment of Cr (VI)-contaminated soils was investigated under varying operating conditions. From the results, it is concluded that EKR is a successful technique to remove toxic heavy metals like Cr (VI) and excess of ions (Na^+, K^+, Ca^+ and Mg^+) from soil. The best results were achieved with EDTA as electrolyte combined with graphite electrode (77%) at 2.5 V/cm voltage gradient. It was found to be cost effective as compared to tests performed at low voltage and without any amendments. EDTA significantly increased the solubility of Cr (VI) and high voltages improved the rate of electromigration and electro-osmosis. Graphite electrode was relatively more conducive of electric current than stainless steel, however, increased electrolysis resulted in corrosion of graphite electrode at higher voltage. Major variations in pH occurred near the electrodes as compared to soil. However, soil sections near electrode may need further treatment for neutralization. A greater number of experimental cycles may be operated for longer duration by continuous circulation of electrolytes at the electrode wells to further increase the removal efficiency. The study concluded that higher removal efficiencies can be achieved at higher voltage gradients with significant reduction in duration of treatment without any significant change in soil health. The study did not take into consideration the biological diversity of soil as it was assumed to be low in Cr-contaminated soils. However, soil restoration through phytoremediation may be adopted post-EKR for reclamation of soil.

Acknowledgements The authors acknowledge the help of lab technicians of Delhi Technological University during the study.

Funding No funding was received for this study.

Data availability All datagenerated or analysed during this study are included in this published article.

Declarations

Conflict of interest The authors declare that they have no conflict of interests.

Ethical approval and consent to participate Not applicable.

Consent to participate Not applicable.

Consent for publication Not applicable.

References

Acar YB, Alshawabkeh AN (1993) Principles of electrokinetic remediation. Environ Sci Technol 27(13):2638–2647. https://doi.org/10.1021/ES00049A002

Acar YB, Alshawabkeh AN, Gale RJ (1993) Fundamentals of extracting species from soils by electrokinetics. Waste Manag 13(2):141–151. https://doi.org/10.1016/0956-053X(93)90006-I

Al-Hamdan AZ, Reddy KR (2008) Transient behavior of heavy metals in soils during electrokinetic remediation. Chemosphere 71(5):860–871. https://doi.org/10.1016/j.chemosphere.2007.11.028

APHA (1992a) Method 3111. Standard methods for the examination of water and wastewater, 19th edn. American Public Health Association, Washington

APHA (1992b) Method 3500-CR. Standard methods for the examination of water and wastewater, 19th edn. American Public Health Association, Washington

Apte AD, Tare V, Bose P (2006) Extent of oxidation of Cr(III) to Cr(VI) under various conditions pertaining to natural environment. J Hazard Mater 128(2–3):164–174. https://doi.org/10.1016/J.JHAZMAT.2005.07.057

ASTM (2007) Standard test method for particle-size analysis of soils. ASTM D422. ASTM, West Conshohocken

ASTM (2014a) Standard test methods for specific gravity of soil solids by water pycnometer. ASTM D854. ASTM, West Conshohocken

ASTM (2014b) Standard test methods for moisture, ash, and organic matter of peat and other organic soils. ASTM D2974. ASTM, West Conshohocken

ASTM (2014c) Standard test method for rapid determination of carbonate content of soils. ASTM D4373. ASTM, West Conshohocken

ASTM (2017) Standard test methods for liquid limit, plastic limit, and plasticity index of soils. ASTM D4318. ASTM, West Conshohocken

ASTM (2019) Standard test methods for pH of soils. ASTM D4972. ASTM, West Conshohocken

Bekkouche MS, Bessaim MM, Maliki M, Missoum H, Bendani K, Laredj N (2020) Enhanced electrokinetic removal of problematic salts in arid and semi-arid areas. Euro-Mediterr J Environ Integr 5(1):1–8. https://doi.org/10.1007/S41207-020-0142-9

Benamar A, Baraud F (2011) Electrokinetic remediation of dredged sediments from Le Havre Harbour. Eur J Environ Civil Eng 15(2):215–228

Bessaim MM, Karaca O, Missoum H, Bendani K, Laredj N, Bekkouche MS (2020) Effect of imposed electrical gradient on removal of toxic salt contaminants from alkali-saline low permeable soil during electrokinetic remediation. Arab J Geosci 13(14):1–12

Cameselle C, Gouveia S (2020) Removal of multiple metallic species from sludge by electromigration. J Hazard Toxic Radioact Waste 24(1):04019030. https://doi.org/10.1061/(asce)hz.2153-5515.0000470

Cameselle C, Pena A (2016) Enhanced electromigration and electroosmosis for the remediation of an agricultural soil contaminated with multiple heavy metals. Process Saf Environ Prot 104:209–217. https://doi.org/10.1016/j.psep.2016.09.002

Cameselle C, Gouveia S, Cabo A (2021) Enhanced electrokinetic remediation for the removal of heavy metals from contaminated soils. Appl Sci. https://doi.org/10.3390/app11041799

Figueroa A, Cameselle C, Gouveia S, Hansen HK (2016) Electrokinetic treatment of an agricultural soil contaminated with heavy metals. J Environ Sci Health Part A 51(9):691–700. https://doi.org/10.1080/10934529.2016.1170425

Gao M, Zeng F, Tang F, Wang K, Xu X, Tian G (2020) An increasing Cr recovery from soil with catholyte-enhanced electrokinetic remediation: effects on voltage redistribution throughout soil sections. Sep Purif Technol 253:117553

Gidudu B, Chirwa EM (2020) The combined application of a high voltage, low electrode spacing, and biosurfactants enhances the bio-electrokinetic remediation of petroleum contaminated soil. J Clean Prod 276:122745

Johar MS, Embong Z (2015) The optimisation of electrokinetic remediation for heavy metals and radioactivity contamination on Holyrood-Lunas soil (acrisol species) in Sri Gading Industrial Area, Batu Pahat, Johor Malaysia. Radiat Prot Dosim 167(1–3):160–164. https://doi.org/10.1093/rpd/ncv236

Karaca O, Cameselle C, Reddy KR (2017) Acid Pond sediment and mine tailings contaminated with metals: physicochemical characterization and electrokinetic remediation. Environ Earth Sci 76(12):1–12

Karaca O, Cameselle C, Bozcu M (2019) Opportunities of electrokinetics for the remediation of mining sites in Biga peninsula, Turkey. Chemosphere 227:606–613

Karaca O, Karaca G, Cameselle C, Karaca I (2022) Removal of the pesticides from soil using electrokinetic method. Rend Fis Acc Lincei 33(3):623–629

Li X, Yang Z, He X, Liu Y (2020) Optimization analysis and mechanism exploration on the removal of cadmium from contaminated soil by electrokinetic remediation. Sep Purif Technol 250:117180

Liang J, Huang X, Yan J, Li Y, Zhao Z, Liu Y, Ye J, Wei Y (2021) A review of the formation of Cr(VI) via Cr(III) oxidation in soils and groundwater. Sci Tot Environ 774:145762. https://doi.org/10.1016/J.SCITOTENV.2021.145762

Lu N, Li D, Yu X, Muhammad F, Yan Y, Yu L, Li H, Huang X, Jiao B (2019) Effect of chemical additives on electrokinetic remediation of Cr-contaminated soil coupled with a permeable reactive barrier. R Soc Open Sci 6(5):1138. https://doi.org/10.1098/rsos.182138

Ma C, Li J, Xia W, Ding Y, Zhang L, Xu Y (2022) Effect of additives on the remediation of arsenic and chromium co-contaminated soil by an electrokinetic-permeable reactive barrier. Environ Sci Pollut Res 29(8):11966–11975

Nasiri A, Jamshidi-Zanjani A, Khodadadi Darban A (2020) Application of enhanced electrokinetic approach to remediate Cr-contaminated soil: effect of chelating agents and permeable reactive barrier. Environ Pollut 266:115197. https://doi.org/10.1016/J.ENVPOL.2020.115197

Oliveira H (2012) Chromium as an environmental pollutant: insights on induced plant toxicity. J Bot. https://doi.org/10.1155/2012/375843

Prakash P, Sonal S, Mishra BK (2022) Transportation mechanism of chromium from tannery sludge through an electrokinetic process: role of electrolytes and operational conditions. Int J Environ Sci Technol 19(5):3757–3772. https://doi.org/10.1007/S13762-021-03278-2/TABLES/7

Prasad S, Yadav KK, Kumar S, Gupta N, Cabral-Pinto MMS, Rezania S, Radwan N, Alam J (2021) Chromium contamination and effect on environmental health and its remediation: a sustainable approaches. J Environ Manag 285:112174. https://doi.org/10.1016/J.JENVMAN.2021.112174

Reddy KR, Cameselle C (2009) Electrochemical remediation technologies for polluted soils sediments and groundwater. John Wiley. https://doi.org/10.1002/9780470523650

Reddy KR, Chinthamreddy S (2004) Enhanced Electrokinetic Remediation of Heavy Metals in Glacial Till Soils Using Different Electrolyte Solutions. J Environ Eng 130(4):442–455. https://doi.org/10.1061/(asce)0733-9372(2004)130:4(442)

Reddy KR, Karri MR (2006) Effect of voltage gradient on integrated electrochemical remediation of contaminant mixtures. Land Contam Reclam. https://doi.org/10.2462/09670513.786

Reddy KR, Parupudi US, Devulapalli SN, Xu CY (1997) Effects of soil composition on the removal of chromium by electrokinetics. J Hazard Mater 55(1–3):135–158. https://doi.org/10.1016/S0304-3894(97)00020-4

Saleem M, Chakrabarti MH, Irfan MF, Hajimolana SA, Hussain MA, Diya'uddeen BH, Daud WMAW, (2011) Electrokinetic remediation of nickel from low permeability soil. Int J Electrochem Sci 6(9):4264–4275

Shin SY, Park SM, Baek K (2017) Soil moisture could enhance electrokinetic remediation of arsenic-contaminated soil. Environ Sci Pollut Res 24(10):9820–9825. https://doi.org/10.1007/s11356-017-8720-3

Song Y, Ammami MT, Benamar A, Mezazigh S, Wang H (2016) Effect of EDTA, EDDS, NTA and citric acid on electrokinetic remediation of As, Cd, Cr, Cu, Ni, Pb and Zn contaminated dredged marine sediment. Environ Sci Pollut Res 23(11):10577–10586. https://doi.org/10.1007/s11356-015-5966-5

Sun R, Gong W, Chen Y, Hong J, Wang Y (2021) Influence of polarity exchange frequency on electrokinetic remediation of Cr-contaminated soil using DC and solar energy. Process Saf Environ Prot 153:117–129. https://doi.org/10.1016/J.PSEP.2021.07.008

USEPA (1992) Test methods for evaluating solid waste, physical/chemical methods, 3rd edn. USEPA, Washington, p SW-846

Virkutyte J, Sillanpää M, Latostenmaa P (2002) Electrokinetic soil remediation - critical overview. Sci Total Environ 289(1–3):97–121. https://doi.org/10.1016/S0048-9697(01)01027-0

Wei Y, Sun B, Hui Z, Li S (2011) Experimental study on electrokinetic remediation of in-situ Cd contaminated soil by applied voltage. ICMREE Proc Int Conf Mater Renew Energy Environ. https://doi.org/10.1109/ICMREE.2011.5930701

Wu J, Zhang J, Xiao C (2016) Focus on factors affecting pH, flow of Cr and transformation between Cr (VI) and Cr (III) in the soil with different electrolytes. Electrochim Acta 211:652–662

Wu J, Wei B, Lv Z, Fu Y (2021) To improve the performance of focusing phenomenon related to energy consumption and removal efficiency in electrokinetic remediation of Cr-contaminated soil. Sep Purif Technol 272:118882. https://doi.org/10.1016/J.SEPPUR.2021.118882

Publisher's Note Springer Nature remains neutral with regard to jurisdictional claims in published maps and institutional affiliations.

Springer Nature or its licensor (e.g. a society or other partner) holds exclusive rights to this article under a publishing agreement with the author(s) or other rightsholder(s); author self-archiving of the accepted manuscript version of this article is solely governed by the terms of such publishing agreement and applicable law.

Authors and Affiliations

Sonam Taneja[1] · Oznur Karaca[2] · A. K. Haritash[1]

✉ Sonam Taneja
sonamtaneja_2k20phden04@dtu.ac.in

Oznur Karaca
oznurkaraca@comu.edu.tr

A. K. Haritash
akharitash@dce.ac.in

[1] Department of Environmental Engineering, Delhi Technological University, New Delhi 110042, India

[2] Department of Geological Engineering, Canakkale Onsekiz Mart University, Canakkale, Turkey

Comparative Performance Analysis of Mamdani and Sugeno Fuzzy Controller using Application on 2DoF Ball Balancer System

Nikita Nikita
Department of Electrical Engineering
Delhi Technological University
Delhi, India
nikita.dahiya2017@gmail.com

Bharat Bhushan
Department of Electrical Engineering
Delhi Technological University
Delhi, India
bharat@dce.ac.in

Abhishek Chaudhary
Department of Electrical Engineering
Delhi Technological University
Delhi, India
abhishek@dtu.ac.in

2023 International Conference on Power, Instrumentation, Energy and Control (PIECON) | 979-8-3503-9976-9/23/$31.00 ©2023 IEEE | DOI: 10.1109/PIECON56912.2023.10085809

***Abstract*— This paper presents the design of Mamdani Fuzzy Inference System and Sugeno Fuzzy Inference System for controlling the ball position of two degree of freedom ball balancer system which is a nonlinear and unstable system with a complex transfer function. Intelligent control technique such as fuzzy helps in efficient control and position tracking of complex nonlinear systems. A comparative analysis has been performed to test the performance of the Mamdani FIS and Sugeno FIS on the ball balancer system for various characteristics such as ball position, ball plate angle and actuation voltage. The time domain specifications such as rise time, peak time, settling time, delay time and peak overshoot have been used as parameters to compare the two fuzzy systems. The simulations are performed using MATLAB/ Simulink environment.**

Keywords—ball balancer system, PID Controller, Fuzzy Systems, Sugeno Fuzzy, Mamdani Fuzzy

I. INTRODUCTION

A nonlinear system may be defined as a system on which the principle of superposition and homogeneity are not applicable. Almost all the systems found in real life are nonlinear system and the concept of linear system is only applied theoretically under certain assumptions. A few examples of nonlinear systems are inverted pendulum, robot arm manipulator, negative resistance oscillator, helicopter levitation system, etc. Nonlinear systems gain importance in the field of research due to their complexity and wide range of applications in real life. One such nonlinear system is a ball balancer system.

A ball balancer system consists of a ball which is kept on a 2-dimensional plate which can freely move about a center point. The ball is then needed to be stabilized with the help of various controllers. The 2 DoF Ball Balancer system gains importance in research due to its inherently unstable and non-linear behavior. This nature of a ball balancer system helps in designing of robots which can be used for various purposes such as automatic controlling and position tracking on rough terrains, unmanned aerial and land vehicles, satellite position correction, etc. Automatic ball balancers and magnetorheological dampers are used for designing of horizontal axis washing machine [1]. Ball balancer system has proved very useful application in the designing of humanoid robots wherein the object needs to be transported without grasping or letting it fall [2].

A. Literature Survey

In a ball balancer system, a camera is suspended vertically opposite to the plate and is utilized for tracking the ball position so that appropriate actions can be taken by the controller. For detecting the ball even when the light fluctuates frequently, blob analysis algorithm is used which helps in differentiating between the background and the foreground [3]. The main aim behind developing a control mechanism for ball balancer system is to train the system to keep an object in a balanced position on the unstable surface by adjusting the angle of inclination of the surface [4]. The objective here is to keep the ball near the set point and reduce the error between the set point and the current position [5]. The overhead camera provides feedback to the control system, and then accordingly control action is taken by the applied control strategy. The angle encoder collects the position of the motor as feedback [6]. Initial research on stabilizing the ball balancer includes using of a feedback compensation to stabilize the system [7]. With the help of mechatronic design principles, the system is realized using constraints such as performance, cost, functionality, extendibility, etc. With the help of the control scheme, the ball may be directed to follow any desired trajectory and not just be balanced at a single set point [8].

The modelling of a ball and plate system is done using the basis of First Principle's Method which is obtained from Newton-Euler method by balancing various forces along with the torques on motors, ball, plate as well as gears. Linearization is done for obtaining the state space model near the operating region, which is then utilized for discrete optimal control for trajectory tracking [9]. PID controllers based on Arduino microcontroller that use feedback signal for controlling the movement of the ball using linear potentiometer position sensor have been used [10]. In order to achieve point-to-point control with circular trajectory control, a nonlinear PID is used that also helps in solving the bigger programming problems that consume larger computation time [11].

Classical methods like the PID control were then used for position tracking and controlling in the 2DoF Ball Balancer systems. But soon intelligent control started to come in picture.

II. BALL BALANCER SYSTEM

The 2DBB system comprises of a plate and a ball, which are used for balancing purpose. The ball is kept on the surface of the plate where it is free to move in all the directions. The plate is made to move about a mid-point which makes to ball to move. A USB camera is placed overhead which acts as a vision system for measuring the position of the ball. Two servos, Rotary Servo Base Unit devices are placed just below the plate and joined to the sides of the plate using the 2DoF gimbals. The ball is balanced on the plate by adjusting its tilt

979-8-3503-9976-9/23/$31.00 ©2023 IEEE

Authorized licensed use limited to: DELHI TECHNICAL UNIV. Downloaded on April 17,2023 at 06:18:11 UTC from IEEE Xplore. Restrictions apply.

angle. The tilt angle is adjusted by manipulating the servo load gears position.

The laboratory setup of 2 DoF ball balancer system comprises of a camera, data acquisition device, ball and plate, VOLTPAQ-X2 power amplifier, SRV02-ET unit and a result analysis system. The plate is attached to the gimble from its center and has 2 DoF for rotation while also being free to tilt either in x direction or y direction. The aim is to stabilize the ball on the surface of the 2D plate so that it does not fall down when the plate tilts. The purpose behind using a 2DBB system is balancing the ball at a point which set by user on surface of the 2D plate.

A. Mathematical Modelling

The modelling of the 2DBB is done with the use of first principles method [3]. Fig. 1 represents the block diagram of open loop structure of 2DBB system. The dynamics of input servo motor voltage along with the resultant load angle is found using transfer function of SRV02. $T_{bb}(s)$ represents the dynamics related to the servo load gear angle with respect to the ball position.

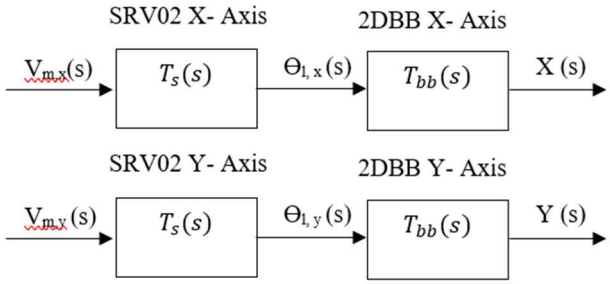


Fig. 1. 2DBB open loop block diagram

The 2DBB system is a decoupled system, which means that actuator in x-axis does not affect the response obtained through y-axis. Also, as the plate is symmetric and the SRV02 device has same hardware, the dynamics of both the axis are similar in nature, and consequently modelling of only 1 axis is done. Fig. 2 represents the open loop block diagram for 1DBB.

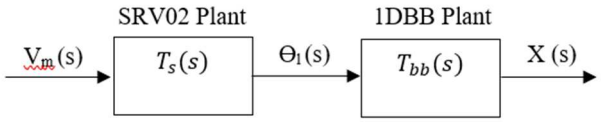


Fig. 2. 1DBB open loop block diagram

The diagram depicting all the forces on the ball balancer system is as in Fig. 3. The transfer function relating SRV02 and 1DBB is written as

$$T(s) = T_{bb}(s)T_s(s) \tag{1}$$

Here, $T_{bb}(s)$ represents 1DBB transfer function, which may further be written as

$$T_{bb}(s) = \frac{X(s)}{\theta_l(s)} \tag{2}$$

Eq (2) shows the relationship between displacement of ball w.r.t servo load angle.
While the transfer function of SRV02 is written as

$$T_s(s) = \frac{\theta_l(s)}{V_m(s)} \tag{3}$$

Let,

$$T_s(s) = \frac{k}{(\tau s+1)s} \tag{4}$$

The nonlinear time domain equation that describes the position of ball w.r.t the plate angle is

$$\frac{d^2}{dt^2}x(t) = f\big(\beta(t)\big) \tag{5}$$

Using Newton's second law on the ball, we get-

$$m_{ball}\left(\frac{d^2}{dt^2}x(t)\right) = \sum F \tag{6}$$

Here, m_{ball} represents the ball's mass.

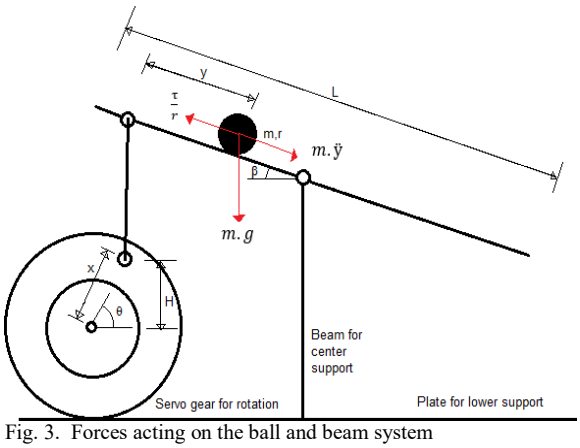


Fig. 3. Forces acting on the ball and beam system

The forces on the ball can be balanced as

$$m_{ball}\left(\frac{d^2}{dt^2}x(t)\right) = F_{x,t} - F_{x,r} \tag{7}$$

Here, $F_{x,t}$ represents the inertial force of ball while $F_{x,r}$ represents the force due to translation under the effect of gravity. The frictional force and viscous damping are not taken into consideration. In order to reach the state of equilibrium, equate the momentum of the ball with force acting as a result of gravity.

$$F_{x,t} = m_{ball}g\sin\big(\beta(t)\big) \tag{8}$$

Let, $\gamma_b(t)$ represents the ball's angle while r_b stands for the ball's radius. So, the angular displacement can be converted into linear displacement using the sector formula.

$$x(t) = \gamma_b(t)r_b \tag{9}$$

The rotational forces due to the ball's inertia can be written as

$$F_{x,r} = \frac{J_b\left(\frac{d^2}{dt^2}x(t)\right)}{r_b^2} \tag{10}$$

The acceleration of the ball in linear form is given as

$$\frac{d^2}{dt^2}x(t) = \frac{m_{ball}g\,sin(\beta(t))r_b^2}{m_{ball}r_b^2 + J_b} \tag{11}$$

Authorized licensed use limited to: DELHI TECHNICAL UNIV. Downloaded on April 17,2023 at 06:18:11 UTC from IEEE Xplore. Restrictions apply.

The relation of the angle of the table with the servo angle can be given as

$$sin\big(\beta(t)\big) = \frac{2\,sin(\theta_l(t))r_{arm}}{L_{tbl}} \tag{12}$$

The linearized equation of motion for 1 DoF ball balancer system is

$$\frac{d^2}{dt^2}x(t) = \frac{2m_b g\theta_l(t)r_{arm}r_b^2}{L_{tbl}(m_{ball}r_b^2+J_b)} \tag{13}$$

Assuming zero initial conditions, the transfer function of one degree of freedom system is given by

$$T_{bb}(s) = \frac{K_{bb}}{s^2} \tag{14}$$

Where $k_{bb} = \frac{2m_{ball}gr_{arm}r_b^2}{L_{tbl}(m_{ball}r_b^2+J_b)}$

And combined 1DBB and SRV02 transfer function is obtained as

$$T(s) = \frac{K_{bb}K}{(\tau s+1)s^3} \tag{15}$$

While the relation of the displacement of ball with the servo voltage to x-axis is

$$x(s) = \frac{K_{bb}KV_m(s)}{(\tau s+1)s^3} \tag{16}$$

III. Controller Design

A. PID Controller

A cascaded control system is used for designing the ball balancer system. The closed loop block diagram for a ball balancer arrangement is as represented in Fig. 4. The inner loop comprises of SRV02 Controller and SRV02 Plant, while the outer loop comprises of the 1DBB Controller, a ball balancer and unity feedback. The error is fed to controller whose output is given to the inner loop. Combining this with the transfer function of the ball balancer an output is obtained. If it does not match the desired output, then using unity feedback, it is sent again to the controller, which then takes the appropriate action. While outer loop aims to adjust the angle of inclination of the plate. The compensator used in the outer loop calculates the angle of the servo load on basis of the measurement of position of the ball in order to obtain the required coordinates of the ball. The inner loop regulates any variations in angle and the voltage provided as input. The servo position control system is designed as the inner loop of the system. The required motor voltage is calculated using the servo compensator for load angle for tracking the load angle. Fig. 4. shows the cascaded control system which is utilized for controlling the ball position for the x-axis of the combined SRV02 and 2DBB plant. Here, $C_{bb}(s)$ represents the transfer function of 1DBB compensator, $C_s(s)$ represents the transfer function of SRV02 compensator, $T_s(s)$ represents the SRV02 plant transfer function and $T_{bb}(s)$ represents the transfer function for 1DBB plant. Fig. 5 represents the connections for PID compensator with derivative set point weighting.

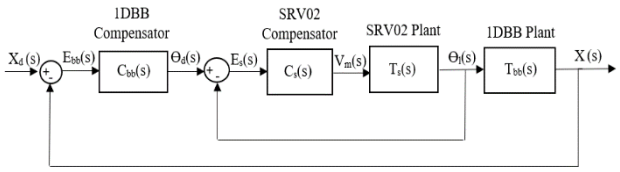


Fig. 4. Cascade control system for controlling ball position in x-axis of the combined SRV02 and 2DBB plant

Let,

$$\theta_l(t) = \theta_d(t) \tag{17}$$

The closed loop equation for Proportional-Integral-Derivative controller in time domain is given as

$$\theta_d(t) = k_p\big(x_d(t) - x(t)\big) + k_d\left(b_{sd}\left(\frac{d}{dt}x_d(t)\right) - \left(\frac{d}{dt}x(t)\right)\right) + k_i\int\big(x_d(t) - x(t)\big)\,dt \tag{18}$$

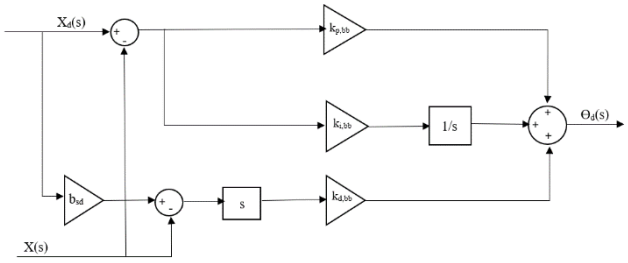


Fig. 5. PID Compensator with derivative set-point weighting

The steady state error is written as-

$$E(s) = X_d(s) - X(s) \tag{19}$$

B. Fuzzy Logic Controller

Fuzzy logic uses human-like understanding to reach judgements, especially when dealing with uncertain or imprecise data. It works with imprecise data rather than accurate data having clear borders. A rule-base, a fuzzifier, an inference mechanism, and a defuzzifier are the four main parts of a fuzzy controller. The defuzzification process transforms the formed conclusions back into numeric values, whereas the fuzzification process transforms the numerical data input into a form that the fuzzy system may use to draw conclusions. The rules developed to instruct the system how to control as well as map the input with the output is used to model the fuzzy controller.

In the designed fuzzy controller, there are two input variables and one output variable. For mamdani fuzzy model, the inputs are error and change in error and the output is control. The defuzzification method used is centroid. 49 if-then rules are designed for the inference mechanism. Triangular membership functions are used for both the input and the output variables. For the sugeno fuzzy model, the input variables are the error and velocity while the output variable is the angle. The two input variables have the triangular membership function while the output variable has constant type membership function. The defuzzification method used

Authorized licensed use limited to: DELHI TECHNICAL UNIV. Downloaded on April 17,2023 at 06:18:11 UTC from IEEE Xplore. Restrictions apply.

is wtaver. The controller design for the same is as shown by Fig. 6(a) and Fig. 6 (b) below.

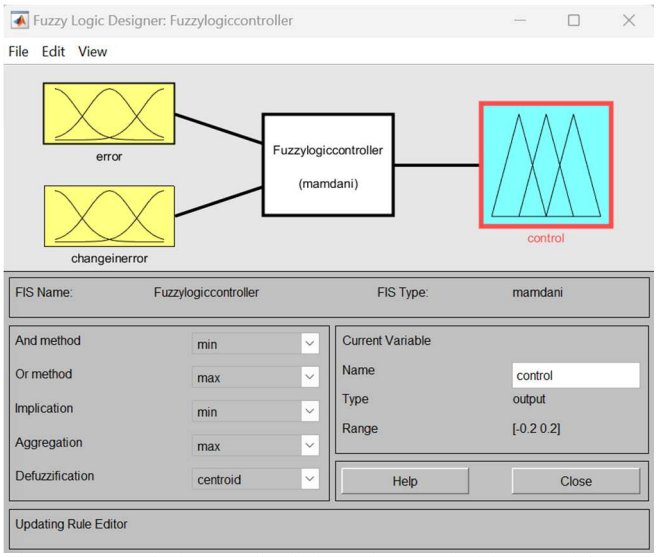


Fig. 6. (a) Fuzzy logic controller design using Mamdani fuzzy model

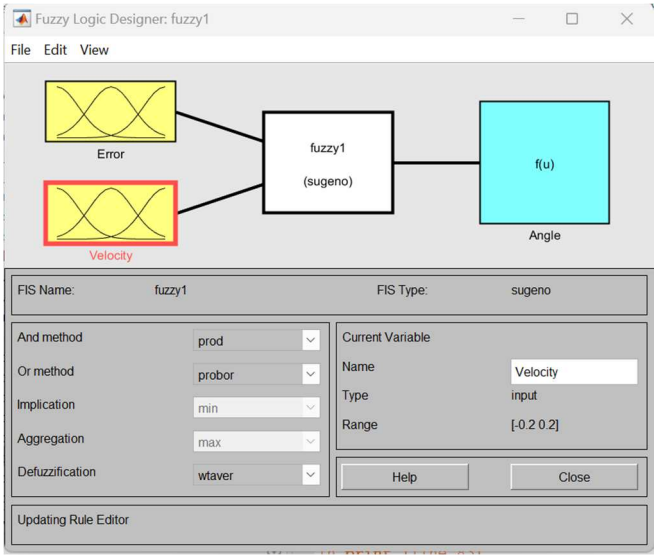


Fig. 6. (b) Fuzzy logic controller design using Sugeno fuzzy model

IV. Experimental Results

This section describes the results obtained after evaluating the working of the system using the simulation results. The performance of the fuzzy logic controller is evaluated and a comparison is done between the mamdani and sugeno FIS.

The following curve shows the characteristics for ball position for two degree of freedom ball balancer system. Fig. 7 shows the ball position characteristics, Fig. 8 shows the ball plate angle characteristics while the Fig. 9 shows the actuation voltage characteristics. The time domain analysis for the same is done as in Table I.

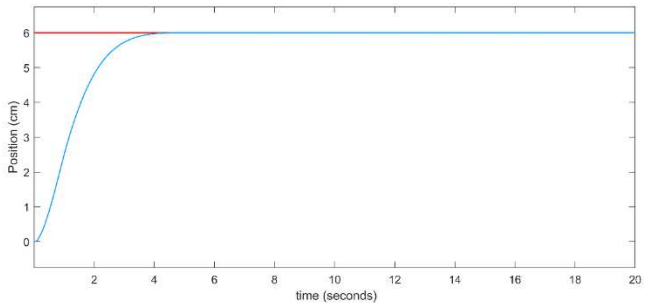


Fig. 7. (a) Ball position characteristics for 2DBB system using Mamdani FIS

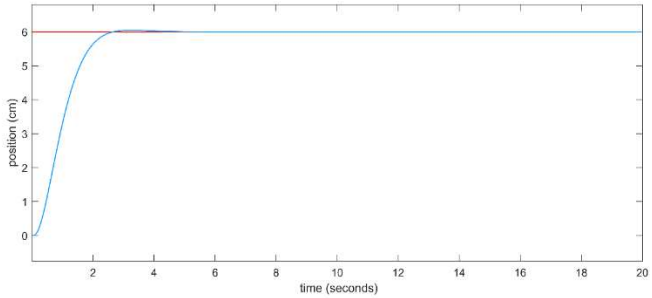


Fig. 7. (b) Ball position characteristics for 2DBB system using Sugeno FIS

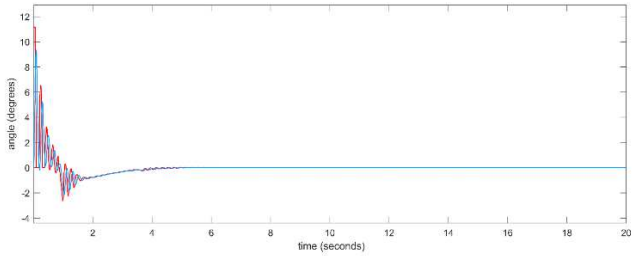


Fig. 8. (a) Ball plate angle characteristics for 2DBB system using Mamdani FIS

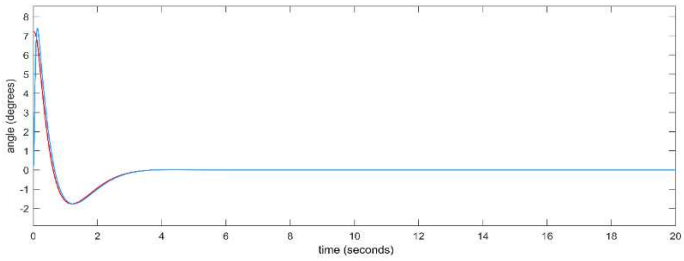


Fig. 8. (b) Ball plate angle characteristics for 2DBB system using Sugeno FIS

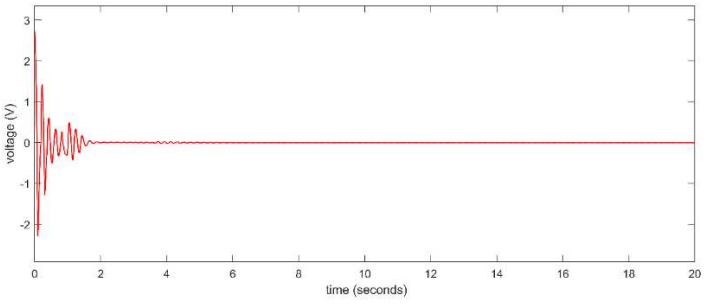


Fig. 9. (a) Actuation voltage characteristics for 2DBB system using Mamdani FIS

Authorized licensed use limited to: DELHI TECHNICAL UNIV. Downloaded on April 17,2023 at 06:18:11 UTC from IEEE Xplore. Restrictions apply.

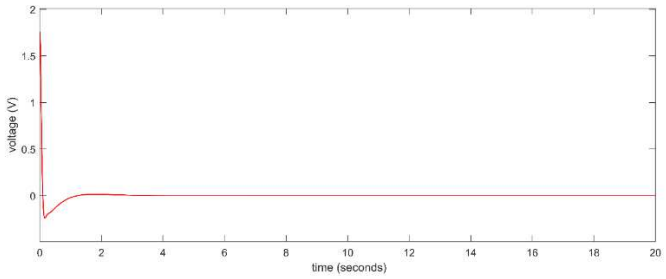


Fig. 9. (b) Actuation voltage characteristics for 2DBB system using Sugeno FIS

The time domain specifications are specified in Table I. The time domain analysis shows that the rise time, peak time, delay time and settling time is less while using the sugeno fuzzy model. This shows that the curve reaches the steady state and also its peak faster as compared to the mamdani fuzzy model and also has a more stable transient response. This means that the sugeno fuzzy model is superior than the mamdani fuzzy model.

TABLE I. COMPARATIVE TIME RESPONSE ANALYSIS

Time domain specification	Mamdani Fuzzy	Sugeno Fuzzy
Rise time	2.09945	1.44491
Peak time	4.6	3.242
Delay time	1.1654	0.9239
Settling time	2.93732	2.06316
Peak overshoot	0	0.04834

Furthermore, the surface generated using the two fuzzy models are shown as in Fig. 10. It is observed that while using the sugeno fuzzy model a smoother surface is obtained in comparison to the mamdani fuzzy model.

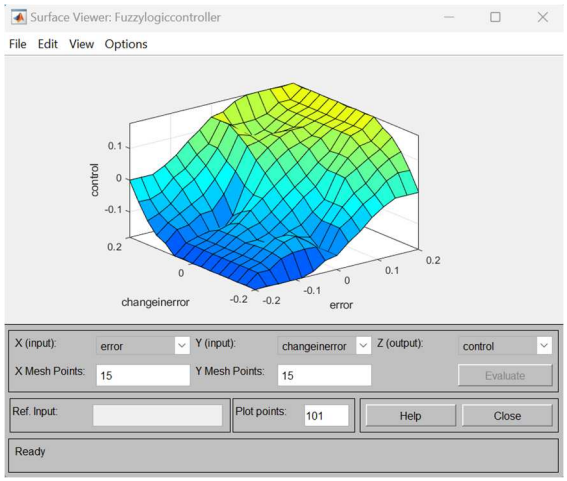


Fig. 10. (a) Surface generated using mamdani fuzzy model

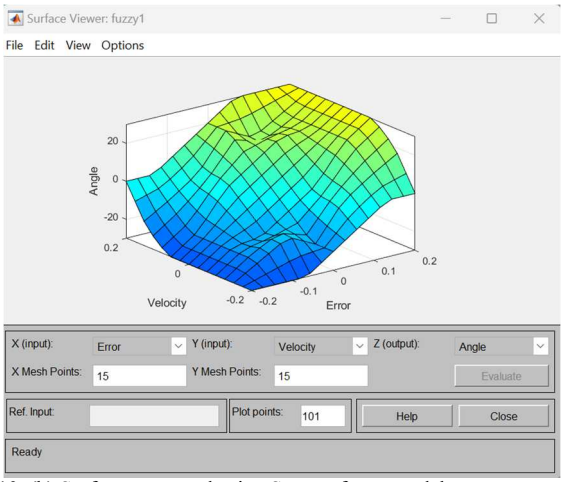


Fig. 10. (b) Surface generated using Sugeno fuzzy model

V. CONCLUSION

This paper aims to control the balancing of the 2 degree of freedom ball balancer system using a fuzzy tuned PID controller. A comparison has been done between the mamdani fuzzy model and sugeno fuzzy model to compare and evaluate the performance of the two fuzzy models. The ball position, ball plate angle and the actuation voltage characteristics have been studied to draw conclusions. Time domain analysis has been done to compare the two models on the basis of various parameters such as rise time, peak time, delay time, settling time and peak overshoot. It has been found that sugeno fuzzy model gives better steady state and transient response while mamdani fuzzy model gives no overshoot. The response generated using the sugeno fuzzy model is more stable and hence superior. For the actuation voltage and ball plate angle characteristics also, there are less oscillations using the sugeno fuzzy model, which increases the stability. The surface generated using the sugeno fuzzy controller is also smoother than the surface generated using the mamdani fuzzy model.

REFERENCES

[1] Chen, H., & Zhang, Q. “Design of horizontal axis washing machine with ball balancer and MR dampers”. International Journal of Precision Engineering and Manufacturing, 18, 1783-1793.

[2] Garcia-Haro, J. Miguel, S. Martinez, and C. Balaguer. "Balance Computation of Objects Transported on a Tray by a Humanoid Robot Based on 3D Dynamic Slopes." In 2018 IEEE-RAS 18th International Conference on Humanoid Robots (Humanoids), 2018, pp. 1-6.

[3] T. Muhammad, Y. Guo, Y. Wu, W. Yao and A. Zeeshan, "CCD Camera-Based Ball Balancer System with Fuzzy PD Control in Varying Light Conditions," 2019 IEEE 16th International Conference on Networking, Sensing and Control (ICNSC), 2019, pp. 305-310, doi: 10.1109/ICNSC.2019.8743305.

[4] Gao, Z., Wijesinghe, S., Pathinathanpillai, T., Dyer, E., & Singh, I. “Design and implementation a ball balancing system for control theory course”. International Journal of Mechatronics, Electrical and Computer Technology, 511, 2363-2374.

[5] B. Ahmad and I. Hussain, "Design and hardware implementation of ball & beam setup," 2017 Fifth

Authorized licensed use limited to: DELHI TECHNICAL UNIV. Downloaded on April 17,2023 at 06:18:11 UTC from IEEE Xplore. Restrictions apply.

International Conference on Aerospace Science & Engineering (ICASE), 2017, pp. 1-6, doi: 10.1109/ICASE.2017.8374271.
[6] Zhao. B., Li. X., “On Multiple Model Adaptive Control Strategy Research of Ball and Plate System” Advanced Materials Research Vol. 898 (2014) pp 501-505. Trans Tech Publications, Switzerland. doi: 10.4028/www.scientific.net/AMR.898.501.
[7] C. N. Obiozor, "Feedback on a ball balancer," Proceedings IEEE Southeastcon'99. Technology on the Brink of 2000 (Cat. No.99CH36300), 1999, pp. 64-66, doi: 10.1109/SECON.1999.766092.
[8] Awtar, Shorya & Bernard, C & Boklund, N & Master, A & Ueda, D & Craig, Kevin. “Mechatronic design of a ball-on-plate balancing system. Mechatronics”. 12. 10.1016/S0957-4158(01)00062-9.
[9] F. Dušek, D. Honc and K. R. Sharma, "Modelling of ball and plate system based on first principle model and optimal control," 2017 21st International Conference on Process Control (PC), 2017, pp. 216-221, doi: 10.1109/PC.2017.7976216.
[10] Saad, Mustafa. “Design and Implementation of an Embedded Ball-beam Controller Using PID Algorithm”. Universal Journal of Control and Automation. 5. 63-70. 10.13189/ujca.2017.050402.
[11] Sun, Sheng & Li, Lin. “The Study of Ball and Plate System Based on Non-Linear PID. Applied Mechanics and Materials”. 187. 134-137. 10.4028/www.scientific.net/AMM.187.134.
[12] A. Surana and B. Bhushan, "Design and Comparison of PSO, SA and GA tuned PID Controller for Ball Balancer Arrangement," 2021 Fourth International Conference on Electrical, Computer and Communication Technologies (ICECCT), 2021, pp. 1-5, doi: 10.1109/ICECCT52121.2021.9616686.
[13] A. Surana and B. Bhushan, "Designing of PSO Tuned PID Controller for Ball Balancer Arrangement and Comparative Analysis with Classical PID and Fuzzy Logic Controller," 2021 IEEE International Conference on Electronics, Computing and Communication Technologies (CONECCT), 2021, pp. 1-5, doi: 10.1109/CONECCT52877.2021.9622355.
[14] N. Nikita and B. Bhushan, "Effect of Parameter Variation of Ball Balancer System Using PD and Fuzzy Control," 2022 IEEE Delhi Section Conference (DELCON), 2022, pp. 1-6, doi: 10.1109/DELCON54057.2022.9753641.

Authorized licensed use limited to: DELHI TECHNICAL UNIV. Downloaded on April 17,2023 at 06:18:11 UTC from IEEE Xplore. Restrictions apply.

Available online at www.sciencedirect.com
ScienceDirect
Energy Reports 9 (2023) 310–321
www.elsevier.com/locate/egyr

The 7th International Conference on New Energy and Future Energy Systems (NEFES 2022), 7th NEFES, 25–28 October 2022, Nanjing (virtually), China

Computation of energy across the type-C piano key weir using gene expression programming and extreme gradient boosting (XGBoost) algorithm

Nipun Bansal[a], Deepak Singh[b,*], Munendra Kumar[b]

[a] Department of Computer Science and Engineering, Delhi Technological University, Delhi 110042, India
[b] Department of Civil Engineering, Delhi Technological University, Delhi 110042, India

Received 16 March 2023; accepted 2 April 2023
Available online xxxx

Abstract

An accurate assessment of energy loss across dams and weir systems is a critical technical and monetary remedy for understanding the hydraulic system's downstream morphology during the flood. Using the standard empirical formulas, accurately estimating the energy loss across the different hydraulic devices is a tedious and challenging procedure. Consequently, new and concise techniques remain highly sought after. This paper presents two empirical models based on the Gene Expression Programming (GEP) and Extreme Gradient Boosting (XGBoost) techniques to examine energy losses throughout the type-C PKW. The empirical models have been developed to consider five non-dimensional parameters, viz L/W, H_t/P, W_i/Wo, N, and S_i/So, that influence the energy over the weir significantly. The models were created using experimental data from a wide range of residual energy losses and release capacities. Additionally, the adequacy of the constructed GEP and XGBoost models was assessed using the RMSE (root mean square error) and statistical variables coefficient (R^2). As per the outcomes, the XGBoost model beats the GEP with the determination coefficient (R^2) = 0.999, MAE = 0.0062, MAPE = 1.4% and RMSE = 0.0012 in the training stage and R^2 = 0.998, MAE = 0.001, MAPE = 2.1, and RMSE = 0.001 in the testing data. These findings show that the XGBoost algorithm is more accurate than the two algorithms in this study for downstream energy prediction of type-C PKW.
© 2023 The Author(s). Published by Elsevier Ltd. This is an open access article under the CC BY license (http://creativecommons.org/licenses/by/4.0/).

Peer-review under responsibility of the scientific committee of the 7th International Conference on New Energy and Future Energy Systems (NEFES 2022).

Keywords: Residual energy prediction; Gene expression programming; Extreme gradient boosting (XGBoost); Piano key weir

1. Introduction

Lempérière and Ouamane [1] were the first to study PKWs, which are an enhanced variant of labyrinth weirs and are gaining favour as a more hydraulically effective and economical kind of weir than its competitors in the

* Corresponding author.
E-mail address: kumaindeepaksingh@gmail.com (D. Singh).

https://doi.org/10.1016/j.egyr.2023.04.003
2352-4847/© 2023 The Author(s). Published by Elsevier Ltd. This is an open access article under the CC BY license (http://creativecommons.org/licenses/by/4.0/).

Peer-review under responsibility of the scientific committee of the 7th International Conference on New Energy and Future Energy Systems (NEFES 2022).

Nomenclature

B	Side length of weir ($B_i + B_b + B_o$)
B_b	Base length of the weir
B_i	Inlet overhang length
B_o	Outlet overhang length
E	Energy head at section 'i'
E_r	Energy residual
E_L	Relative energy loss
g	Acceleration due to gravity
H_t	Total head over the weir
i	Represents the section
h_i,	Piezometric head
MAE	Mean absolute error
L	Total developed crest length
N	No. of cycles
$MAPE$	Mean absolute percentage error
Q	Total discharge across the PKW
P	Height of weir
$RMSE$	Root mean square error
R^2	Coefficient of determination
S_o	Outlet key slope
S_i	Inlet key slope
$V_t^2/2g$	Approach velocity head
V_t	Mean flow velocity
W_i	Width of inlet section
W	Channel width/Width of PKW
W_o	Width of outlet section

spillway and river flow parameters. Their goal was to design a new kind of labyrinth weir with the help of a tiny base to maintain a systemically cost-effective and simple structure that might be nearly as easy. The idea must have been quickly conceived and implemented in the area to enhance the release capacity of current gravity dams in France [2] or, thanks to something like slightly earlier strategic cooperation in both industries and universities, as such an excellent replacement for fenced weirs for derailment structures in Vietnam [3]. Since 2011, the standard agency of various geographical conferences in which knowledge is openly interchanged in interactive and pleasant environments must have brought people, resulting in the guide of some reference material summarizing the artwork's current condition [4–6]. And over 35 Piano Key weirs have already been successfully established in countries worldwide, such as Sri Lanka, India, Australia, France, Switzerland, Vietnam, the United Kingdom, Algeria, and South Africa [7]. The first PKWs were implemented in 2006 at the Goulours Dam, France and recently installed at South Africa's Hazelmere Dam to keep increasing reservoir and spillway release potential. The implementation of a PKW at the latest Tzaneen Dam is set to begin shortly [8–10].

Interestingly, the idea may have lately been attractive to interior weir implementations in addition to the aforementioned improvements, which were primarily concentrated on employing PKW as a lateral weir for runoff release [11]. Throughout the last ten to twenty years of evolution over, the geometric and hydraulic behaviour of PKW was summed up in detail by Abhash and Pandey [12] and Singh and Kumar [13]. PKWs have a substantial percentage of geometric parameters that could impact head-discharge efficiency and energy dissipation across the weir. The altitude of such weir (P), the relative advancement L/W ratio (crest length), the (Ht/P) ratio, the alveoli width (Wi/Wo), and the cycle's number (N) for the constant width of the channel are the primary variables that influence discharge carrying capacity and energy loss over the PKW. (where L = overall development length, W

= weir's width across the flow, Ht is the cumulative head over the weir, and P is the altitude of the weir) Wi and Wo are the widths of the inlets and outlet keys. The secondary ones are the lengths of the overhangs, going to raise the crest through a parapet wall, summing the upstream apex walls, as well as ranging the crested kind [14].

Furthermore, general scientific theories and hypotheses, case studies as well as unique research on labyrinth and PKW energy loss have been examined [15–17]. The low residual energy at the toe of the spillway and raises with release and spillway length were noted by Silvestri et al. [18] in their study of the energy losses over PKW with stepped chutes spillway. Al-Khafaji and Al-Shukur [19] looked into the influence of the PKW slope on energy loss. They claimed that the proportion of energy dissipation reduces as the slope goes down.

Many researchers have used a range of computational techniques to define the hydraulic behaviour of PKWs using various geometrical parameters. Few studies computed the PKW's discharge coefficient and hydraulic behaviour. Zounemat-Kermani and Mahdavi-Meymand [20] simulated and compared the passing flow over PKW using an AI-based statistical model (MLPNN & ANFIS) implanted with many meta-heuristic tools (PSO, GA, MFO, & FA). Overall, the ANFISs and MLPNNs were capable of simulating the coefficient of discharge of the PKW quite quickly and precisely than empirical observations. Others use the GEP in various hydraulic systems to anticipate realistic figures of multiple hydraulic scenarios [21,22]. Karbasi and Azamathulla [23] utilized GEP to anticipate the aspects of a hydraulic jump above a rough bed. People depicted this with conventional approaches to AI (SVR and ANN). People observed that all these methods performed better than the GEP prototype but that applying the GEP prototype is fairly easy for useful purposes due to the determination of expressive equations. In addition, to predict the temperature of the surrounding environment in Tabuk, Saudi Arabia, using GEP [22]. Many researchers like, [24–31] have used numerous research activities and deep learning optimization techniques to predict the scour depth along immersed spur dikes, weirs, well as spherical piers. Ali Reza Kargar and Mohammad Najafzadeh's opinion on "genomic coding, evolved computation regression, and prototype tree to assess local scour dimension at culvert outlets" was criticized by Pandey et al. [32]. Several studies of presented the capacity of the PKW in terms of energy dissipation to date [18,33–38].

Stepped spillways mitigate the likelihood of cavitation for small specific discharges by providing natural aeration. Spillways should be developed and structurally release massive amounts of water because when causing minimal harm to the structure and its nearby area. The downstream structural design is critical to minimize the effects of structural damage and its surroundings while maximizing the benefits of any hydraulic system (i.e., spillways, dams). Bhukya et al. [39] recently presented a review study on the PKW for discharge measurement. To date, much research has been done on power dissipation over the labyrinth weir [40–42]. An energy loss for free streams below rectangular sharp-crested weirs has been introduced by Amin et al. [43]. Although adequate experiments and computations were performed to analyse the hydraulic properties of PKWs, there is scant knowledge about the energy dissipation downstream of the different PKW types. As a consequence, having innovative techniques that continue to be in high competition is absolutely essential.

This paper investigated twelve type-C PKW models in the laboratory and utilized the experimental data to build the GEP and XGBoost frameworks. The various measuring flow parameters are used during the training process in the GEP and XGBoost. The relative residual energy is considered a target parameter. The estimated residual energy value would then be included in the energy equation to anticipate the downstream residual energy. Eventually, the authors proposed a comparison of GEP and XGBoost-based strategies to traditional ones.

2. Material and methods

2.1. Experimental setup and model fabrication

The testing of the physical models was done in a 10 m long, 0.516 m wide, and 0.6 m deep flume at "Delhi Technological University" in Delhi, India. The discharge of flow was measured with a 4–20 mA electromagnetic flowmeter (accuracy ±0.2%). A pointer gauge with a ±0.1 mm sensitivity and a 4–20 mA ultrasonic level sensor with a 0.2 percent inaccuracy was used to monitor the flow depths downstream and upstream of the weir (Fig. 1). To improve the upstream approach flow uniformity, the flume headbox does include a metal monitor lock. An ADV ("Acoustic Doppler Velocimeter") was utilized to determine the average flow velocity. All the models have been manufactured from a transparent acrylic sheet thickness of 8 mm and glued together with chloroform. The following steps are the model's dimensions: Across all modelling fabrications, the relative length (L/W) is 5–6, the alveoli width (Wi/Wo) varies from 1 to 1.5, and some additional characteristics are $0.75 \leqslant Bi/P \leqslant 1.89$ and

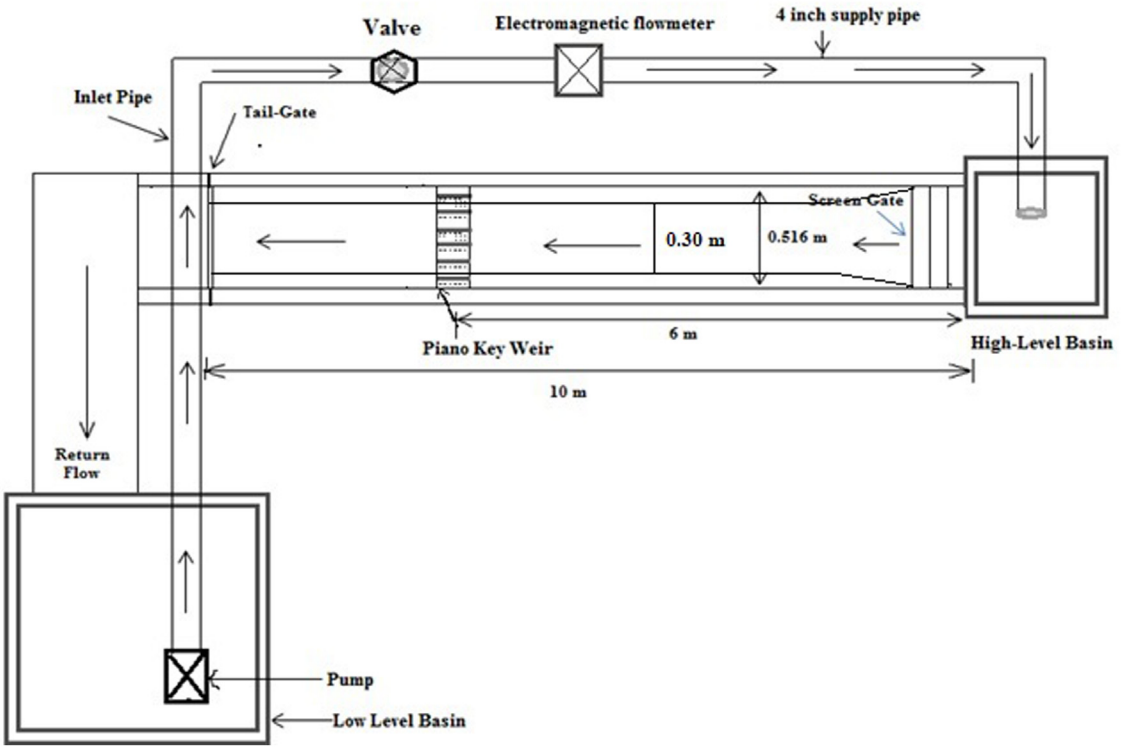


Fig. 1(a). Schematic diagram of experimental flume.

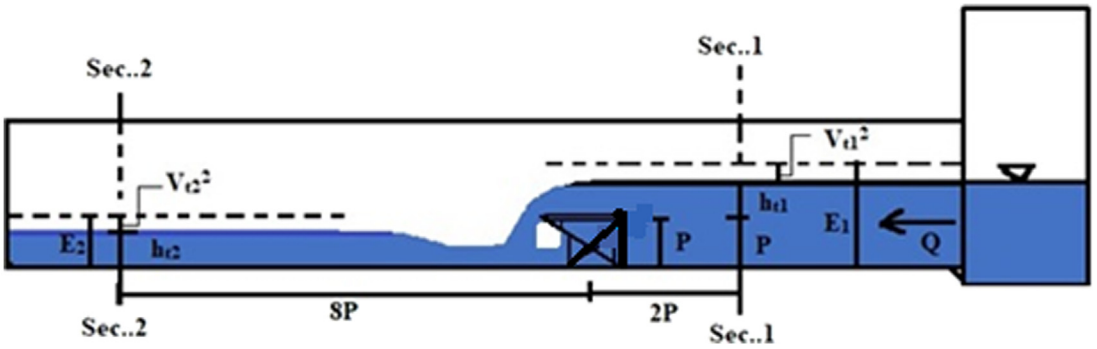


Fig. 1(b). Schematic diagram for energy calculation.

Bo = 0. The discharges fluctuate (0.005 $m^3/s \leqslant Q \leqslant 0.05\ m^3/s$), the head over the weir differs (0.0168 m $\leqslant$ Ht $\leqslant$ 0.147 m), and the head-to-weir depth ratio for 0.15 m tall models is (0.09 $\leqslant$ Ht/P $\leqslant$ 0.98) and for 0.185 m tall models is (0.091 $\leqslant$ Ht/P $\leqslant$ 0.97). The specifications of the additional geometrical parameters and data gathered during this research are presented in Table 1.

2.2. Methodology

In the present analysis, the free-flow water head over the weir has been monitored. The u/s and d/s specific energy across the PKW were determined as follows:

$$E_i = P + h_i + \frac{V_i^2}{2g} \tag{1}$$

Table 1. The summary of properties of current study.

Model	Range of Q (m^3/s)	H_t/P	$\frac{W_i}{W_o}$	P (m)	$\frac{L}{W}$	B (m)	B_i (m)	B_o (m)	Range of $\left(\frac{H_L}{H_1}\right)$	Range of $\left(H_r = \frac{H_2}{H_1}\right)$	N (Cycles)	Runs
PKW-1	0.005–0.050	0.095–0.978	1.0	0.15	5	0.28	0.2842	0	0.911–0.242	0.088–0.758	3	22
PKW-2	0.005–0.050	0.092–0.961	1.1	0.15	5	0.28	0.2842	0	0.901–0.230	0.098–0.770	3	22
PKW-3	0.005–0.050	0.090–0.958	1.2	0.15	5	0.28	0.2842	0	0.885–0.232	0.115–0.768	3	22
PKW-4	0.005–0.050	0.091–0.968	1.3	0.15	5	0.28	0.2842	0	0.868–0.219	0.132–0.781	3	22
PKW-5	0.005–0.050	0.0929–0.938	1.4	0.15	5	0.28	0.2842	0	0.841–0.203	0.158–0.797	3	22
PKW-6	0.005–0.050	0.091–0.963	1.5	0.15	5	0.28	0.2842	0	0.813–0.195	0.186–0.804	3	22
PKW-7	0.005–0.050	0.093–0.966	1.28	0.185	5	0.343	0.229	0	0.878–0.220	0.122–0.799	3	22
PKW-8	0.005–0.050	0.0925–0.943	1.28	0.185	5	0.259	0.165	0	0.868–0.219	0.132–0.781	4	22
PKW-9	0.005–0.050	0.0910–0.939	1.28	0.185	5	0.208	0.139	0	0.886–0.221	0.114–0.778	5	22
PKW-10	0.005–0.050	0.092–0.971	1.28	0.185	6	0.427	0.284	0	0.879–0.190	0.121–0.809	3	22
PKW-11	0.005–0.050	0.091–0.945	1.28	0.185	6	0.322	0.214	0	0.901–0.230	0.098–0.770	4	22
PKW-12	0.005–0.050	0.092–0.929	1.28	0.185	6	0.259	0.173	0	0.885–0.184	0.115–0.816	5	22

where E = specific energy, P, h, V, and g are the weir's height (m), water level over the weir, at section i mean velocity, and gravitational acceleration, correspondingly, (see Fig. 1(b)). The E_1 and E_2 were taken to determine the E_L and E_r values in the following way:

$$\frac{\Delta E}{E_1} = \frac{(E_1 - E_2)}{E_1} \times 100 = \left(1 - \frac{E_2}{E_1}\right) \times 100 \tag{2}$$

and,

$$E_r = 1 - \frac{\Delta E}{E_1} = \frac{E_2}{E_1} \tag{3}$$

where $\Delta E/E_1$ measures the final relative energy losses or perhaps the energy loss ratio, and $E_r = E_2/E_1$ symbolizes d/s residual energy. The energy loss over the PKW is influenced by different fluvial and structural parameters, which include the various rational parameters such as L/W, H_t/P, W_i/W_o, S_i/S_o ratios, cyclic variations (N), and several others as well. The geometrical and hydraulic parameters described below were applied in the present research to assess the residual energy of the PKW.

$$\frac{E_2}{E_1} = f\,(\rho, g, V_t, H_t, L, P, W, W_i, W_o, S_i, S_o, B) \tag{4}$$

In which ρ and g are water's density and gravitational acceleration, respectively. H_t denotes the total hydraulic head, i.e., $(h_t + V_t^2/2g)$, and V_t = mean velocity. L, P, and W indicate the crest development length, weir's height, and width of PKW, respectively. The width of keys is represented by W_o and W_i, whereas S_i and S_o indicate the bottom slope of the keys. N represents the number of cycles. This paper used five rational factors to develop the GEP and XGBoost models: L/W, H_t/P, W_i/W_o, N, and S_i/S_o. After applying the Buckingham Π-theorem in Eq. (4) the relative residual energy dimensional equation d/s of the weir can be written as follows:

$$\frac{E_2}{E_1} = f\left(\frac{H_t}{P}, \frac{L}{W}, \frac{W_i}{W_o}, \frac{S_i}{S_o}, N\right) \tag{5}$$

The correlation described above demonstrates the relative residual energy depends on the shape and hydraulic attributes. Table 1 summarizes the parameter and data ranges collected in the current study.

2.3. GEP and its application

GEP is a genetic programming (GP) evolution and the GeneXproTools learning computer programme. It is a searching method involving computer programming code (e.g., mathematical expressions, decision trees, etc.) that understands the interactions between different dataset factors and then develops models to define these interrelations. GEP employs feature linear chromosomes, which are composed of structurally coordinated genes in a tail and head and are first indexed by Ferreira [44]. GEP initiates the selection of population chromosomes at random, like other

adaptive algorithms, and codes the varying shapes as well as sizes of chromosomes in a simple graph [44,45]. It combines genetic algorithms with genetic programming. The final results of the GEP, the chromosomes encode as expression trees.

The GEP model may employ a range of fitness functions, including MSE, RMSE, RRSE (Root Relative Squared Error), as well as RSE (Relative Standard Error) [44]. Like the majority of other genetic algorithms, GEP begins with a first population of individuals. The most advantageous genomes are far more likely to carry to succeeding generations. A fitness function is the first step in selecting a GEP framework. Consequently, the RMSE process is being used in the analysis. The selection of the nodes and functions that will be used to build the chromosomes is the next stage. The model used in this research does have the relative residual energy (E_2/E_1) as the desired value as well as the five independent parameters (L/W, H_t/P, W_i/W_o, N, and S_i/S_o) as input variables, as depicted in Eq. (5). The GEP model was developed using the basic operators (+, −, ×, and /). Table 2 lists the sample selection specifics again for GEP. The testing and training data in GEP were randomly selected from the given dataset. The proposed GEP model has the following analytical form:

$$\frac{E_2}{E_1} = \left[\frac{\left(\frac{\left(\frac{W_i}{W_o} \times \frac{W_i}{W_o}\right) + \left(\frac{S_i}{S_o}\right)}{\left(\frac{H_t}{P} + 1.60387\right)} \right)}{\left(\left(\frac{H_t}{P}\right) \times N + \frac{1.35410}{\left(\frac{H_t}{P}\right)} \right)} \right] + \left(\frac{S_i}{S_o} \times \frac{H_t}{P} \right) + \left(\frac{H_t}{P} \times \frac{S_i}{S_o} \right) \tag{6}$$

Table 2. Illustrates the operational & functional set parameters of GEP model.

S. no.	Parametric interpretation	Parameters
	Set of function	+, −, × and /
	Head size	8
	No. of chromosomes	30
	Gene size	26
	No. of genes	3
	Linking function	Addition
	Program size	23
	Fitness function	RMSE
	Literals	11
	Per gene constants	10
	No. of generations	30063
	Mutation	0.00138
	Data type	Floating-point
	Gene transposition rate	0.00277
	RIS (root insertion sequence) transposition rate	0.00546
	IS (insertion sequence) transposition rate	0.00546

Further, simplified the above equation as

$$\frac{E_2}{E_1} = \left[\frac{\left(\left(\frac{W_i}{W_o}\right)^2 + \frac{S_i}{S_o} \right) \times \left(\frac{H_t}{P}\right)}{\left(\left(\frac{H_t}{P}\right)^3 \times N + 1.60387 \left(\frac{H_t}{P}\right)^2 \times N + 1.35410 \times \left(\frac{H_t}{P}\right) + 2.1718 \right)} \right] + 2 \times \left(\frac{H_t}{P} \times \frac{S_i}{S_o} \right) \tag{7}$$

According to the above equation, the GEP technique used an extremely nonlinear association between the residual energy and input variables. Fig. 2 depicts a tree representation of Eq. (7) represents the GEP technique for determining the downstream residual energy. In Fig. 2, $d0$ indicates the H_t/P ratio, $d1$ indicates the L/W ratio, $d2$ signifies the W_i/W_o, $d3$ signifies the S_i/S_o ratio, $d4$ denotes the N, and $G1c2$ and $G1c8$ stand for the numerical coefficients employed in the first model gene.

2.4. An overview and application of extreme gradient boosting (XGBoost)

One of the well-known machine learning models for tabular datasets is extreme gradient boosting (XGBoost) [46]. XGBoost can discover any nonlinear statistical relationship between the target model and observed features [47]. It

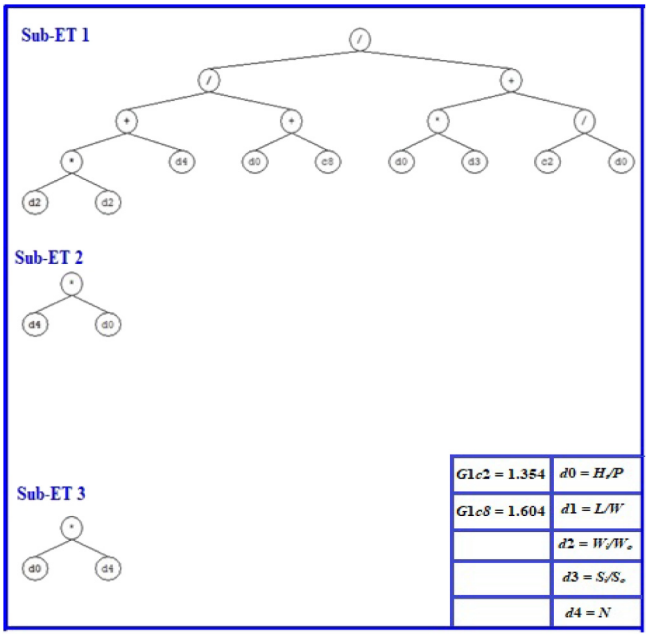


Fig. 2. GEP articulation expression tree (ET).

has excellent usability and can handle missing values, outliers, and high cardinality categorical values without special treatment. It integrates traditional regression and classification trees with analytical boosting techniques. By creating numerous trees rather than constructing a single targeted tree, and merging them to choose a clear prediction model, boosting helps to increase the program's accuracy assessment. Sequentially maintaining the residuals of previous trees as impacts on the conclusion tree is how XGBoost starts the tree. Connecting arbitrarily chosen examinations can greatly enhance gradient-boosting efficiency, promptness, and assessment precision. Except for the substitution, a random training data subset from the whole training dataset is taken into account for each tree in symmetry.

The fundamental claim in the XGBoost (Y_i^0) is the consensus of the parameters measured in the training stage, and n is the number of appraisers for each predictor f_k (k varying from 1 to n), which relates to unique tree anatomy. The ith set of data, for which the characteristic vector is L_i, yields the expected result ($\overline{Yi}$). The following equation predicts the results by using various expansion functions:

$$\overline{Yi} = Y_i^0 + \alpha \sum_{k=1}^{n} f_k\left(L_i\right) \tag{8}$$

The parameter α controls the learning rate used to apply the model, enhance it, link the most recent tree percussively, and prevent overfitting. When applying Eq. (8) to the kth state, a character is connected with a model and the kth predicted value Y_i^{-k} is inserted using the estimates for the kth state derived from the prior states $Y_i^{-(k-1)}$, and reinforced f_k of the associated kth identity is disclosed in

$$Y_i^{-k} = Y_i^{-(k-1)} + \alpha f_k \tag{9}$$

whereas f_k is the weight of renders created by lowering the kth tree's target function, which is represented by

$$Obj = \beta M + \sum_{m=1}^{M} G_m w_m + \frac{1}{2}\left(H_m - \gamma\right) w_m^2 \tag{10}$$

whereas M denotes the renders of the kth tree, and w_m represents the weight of the renders from 1 to M. The uniformity characteristics, β and γ are used to add coherence to the anatomy and prevent the model's overfitting. The prior and following loss function gradient of the respective renders full information is represented by H_m and G_{m}, respectively (see Fig. 3).

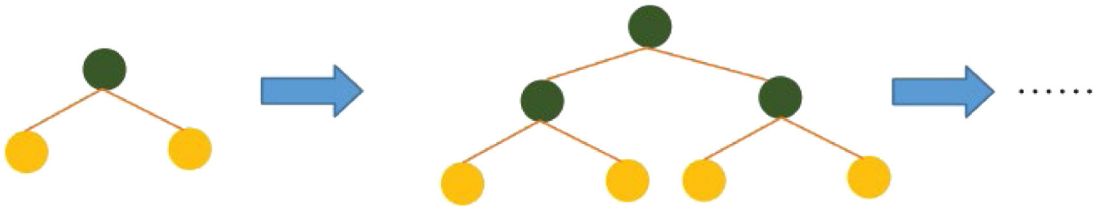


Fig. 3. Description of XGBoost utilized in the study.

3. Result and discussion

The combined flows over the sidelong, downstream, and upstream crests make up the flowing discharge across PKWs [36,48] (see Fig. 4). The literature said the shape of the PKW has a great influence on the weir's flow efficiency and energy dissipation. Expanding the W_i diminishes flow velocities at the inlet section while enhancing PKW efficiency significantly [34,49]. However, expanding the W_i reduces the W_o for a given W (because the absolute width of the channel or weir is $W_i + W_o =$ constant) and crest length. Under supercritical circumstances, a too-narrow outlet key could not be able to escape the flow, which would reduce weir proficiency [14] considerably; [36]. A large W_i/W_o results in an additional flow approach and allocation in PKW inlet keys while raising submergence consequences in outlet keys. Therefore, managing inlet width enhances outlet resilience capability is necessary to determine the ideal alveoli width (W_i/W_o).

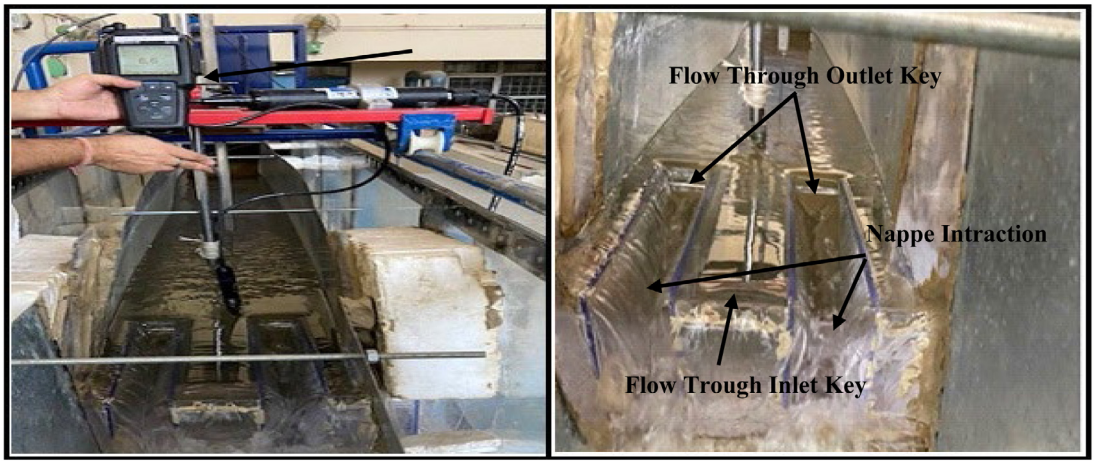


Fig. 4. Flow pattern over PKW.

Likewise, the B_i/B_o, S_i/S_o, L/W ratios, and N (number of cycles) significantly impact the PKW's hydraulic characteristics. A total of 264 tests made up of these freshly acquired datasets, various functional ratios, and thorough flow field evaluations were used to perform the measurement. The GEP and XGBoost prediction models for relative energy downstream of the type-C PKW were developed using validated experimental data.

Precisely evaluating energy dissipation over hydraulic structures is essential when designing and assessing downstream scour, hydraulic jump size, weir apron length, and so on. As a consequence, when planning to design energy-dissipative structures, it is essential to evaluate the corresponding or remaining energy d/s of a PKW. Thus, the purpose of this study is to use relative residual energy and the input variables (W_i/W_o, L/W, H_t/P, N, and S_i/S_o) to predict the E_2/E_1 ratio downstream of the PKW with great precision and little discrepancies. Here E_2/E_1 has selected the target parameter. The features were picked based on their unity to the fundamental premise of the issue to produce straightforward and realistic GEP and XGBoost models. A total of 30 chromosomes, 3 genes, and 8 head measurements were sampled by GEP. According to Table 2, 264 observations were used in model construction and distributed randomly for the testing and training stages. 75% are used for training, while the

remaining 25% of the records are employed for validation. The GEP's development/certification data were drawn at random from the given dataset. Similarly, datasets were used to predict the E_2/E_1 ratio of the type-C PKW using XGBoost algorithms. The GEP developed 2nd order nonlinear equation; it may be sufficient for design solutions and substitute assessment of E_2/E_1 prediction. As shown in Fig. 5, the determination correlation coefficient (R^2) values of GEP and XGBoost are 0.992 & 0.999 (training) and 0.990 & 0.998 (testing), illustrating the model's competency. Fig. 6 shows the forecasted remaining energy (E_2/E_1) consistency graphs versus observed residual energy separately during the training and testing stages. GEP and XGBoost indicated RMSE = 0.0264 and 0.0012 (training), and 0.0396 and 0.001 (testing), respectively. MAE and MAPE = 0.0208 and 6.30% for training data of the GEP model, and 0.0062, 1.4% for the XGBoost model, and 0.0319 and 8.6% for GEP and 0.001, and 2.1% for XGBoost, that shows an effectiveness and precision measure for the projected model. The performance measures can evaluate the developed model, allowing us to choose the best model. Table 3 summarizes the performance measures of the algorithms proposed in this paper. The XGBoost model beats the GEP in the context of prediction rate, as seen in Table 3 and Fig. 5.

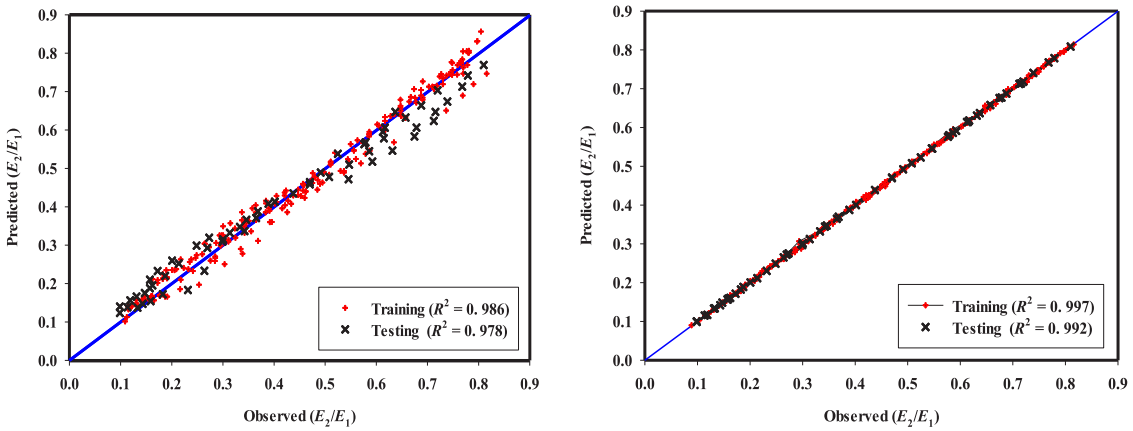


Fig. 5. Variation among the observed and projected (E_2/E_1) for different data phases.

Table 3. Performance measures of the proposed algorithms.

Proposed algorithms	Training				Testing			
	R^2	MAE	RMSE	MAPE %	R^2	MAE	RMSE	MAPE %
GEP	0.992	0.0208	0.0264	6.3	0.990	0.0319	0.0396	8.6
XGBoost	0.999	0.0062	0.0012	1.4	0.998	0.001	0.001	2.1

[1]R^2 = Determination coefficient; [2]MAE = Mean Absolute Error; [3]RMSE = Root Mean Square Error; [4]MAPE = Mean Absolute Percentage Error.

Consequently, the proposed GEP and XGBoost algorithms are reliable methods for forecasting the downstream residual energy (E_2/E_1) that has good generalization and does not overtrain. Traditional regression-based models significantly outperform the proposed GEP and XGBoost.

The GEP and XGBoost models can quickly and accurately calculate the E_2/E_1 based on the number of generations. Using various techniques, it could trend information into a high-dimensional classifier and recognize data relationships. Similar to the mapping, the links are diverse. The GEP and XGBoost models agreed with the observed values for the R^2 and RMSE for training and testing datasets.

4. Conclusion

Hydraulic designers and engineers must precisely figure out how much energy is lost and how much is residue downstream of any hydraulic systems. Advanced visualization models were designed and developed to reveal the

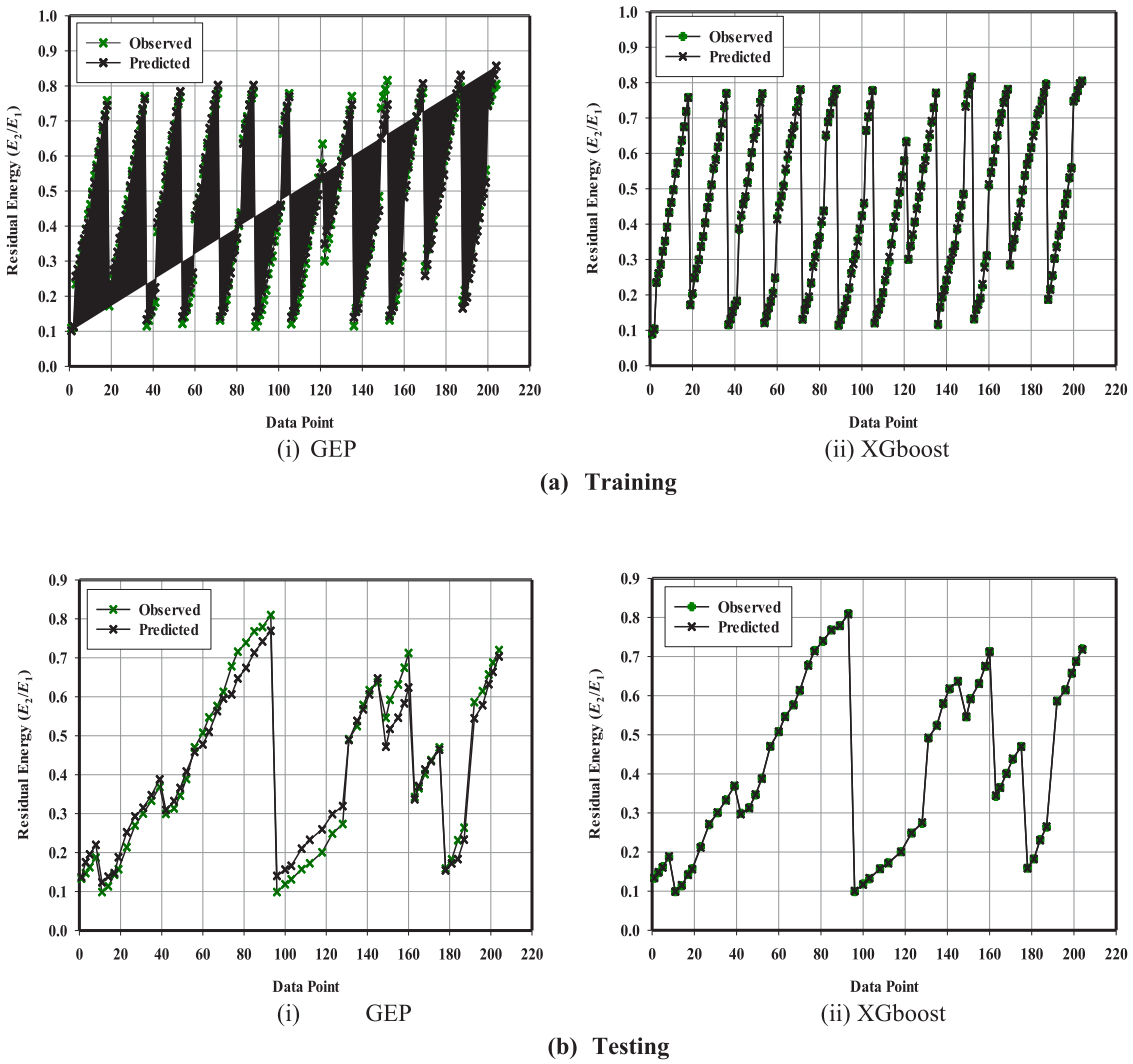


Fig. 6. Outcome matrices for forecasting the relative residual energy (E_2/E_1) for the various data stages a. Training stages; b. Testing stages.

downstream E_2/E_1 ratio of the type-C PKW. This study developed an empirical formula based on GEP and XGBoost model to forecast the downstream relative residual energy. These two approaches led to a highly multiple regression model between E2/E1 ratio and input variables. Developed models were run in the Python programming language. Users may utilize them as design specifications to help academics and design engineers develop the PKW and its d/s components. The efficiencies of the developed models were compared based on various statistical variables. The XGBoost model had the minimum R^2 (0.998 for testing and 0.999 for training), while the GEP model had the highest (0.992 for training and 0.990 for testing). In contrast to the GEP, which has RMSE values: of 0.00264 for training and 0.0396 for testing, these RMSE values for XGBoost are 0.0012 and 0.001, correspondingly. The findings suggest that the XGBoost model is efficient and has a high potential for practicality. These models, which have a similar range of non-dimensional parameters, could be used for another type of weir. More research is recommended in the field of PKW energy dissipation, which could include other types of PKW or be performed for turbid water energy calculation.

Declaration of competing interest

The authors declare that they have no known competing financial interests or personal relationships that could have appeared to influence the work reported in this paper.

Data availability

Data will be made available on request

Acknowledgements

The authors are pleased to relay their passionate admiration and empathy to the Civil Engineering Department's staff, faculty members, and the technical staff of the FM & HE lab of Delhi Technological University, for their endless help.

References

[1] Lempérière F, Ouamane A. The Piano Keys weir: A new cost-effective solution for spillways. Int J Hydropower Dams 2003;10(5):144–9.
[2] Laugier F, Vermeulen J, Blancher B. Overview of design and construction of 11 piano key weir spillways developed in France by EDF from 2003 to 2006. In: Erpicum S, Laugier F, Ho Ta Khanh M, Pfister M, editors. Labyrinth and piano key weirs III - PKW 2017. London, U.K.: CRC Press; 2017, p. 37–51.
[3] Ho Ta Khanh M. History and development of piano key weirs in Vietnam from 2004 to 2016. In: Erpicum S, Laugier F, Ho Ta Khanh M, Pfister M, editors. Labyrinth and piano key weirs III - PKW 2017. London, U.K.: CRC Press; 2017, p. 3–16.
[4] Erpicum S, Nagel V, Laugier F. Piano key weir design of raviege dam. In: Proc. int. conf. labyrinth and piano key weirs Liège B. Boca Raton, FL: CRC Press; 2011, p. 43–50.
[5] Erpicum S, Laugier F, Pfister M, Pirotton M, Cic M, Schleiss J. Labyrinth and piano key weirs II PKW 2013. 2013.
[6] Erpicum S, Laugier F, Ho Ta Khanh M, Pfister M. Labyrinth and piano key weirs III – PKW-2017. London, U.K.: CRC Press; 2017.
[7] Crookston BM, Ph D, Asce M. Hydraulics of labyrinth and piano key weirs : 100 years of prototype structures, advancements, and future research needs. 2019;145(12):1–7.
[8] van Deventer NJ, Matlala J, Mulder E, Hoosen S. Tzaneen dam raising: Hydraulic model study. In: Proceedings of the SANCOLD conference 2015. South African National Committee on Large Dams (SANCOLD); 2015, p. 223–30.
[9] Mabela MJ. The raising of hazelmere dam using a piano key weir. In: Procedings of the annual SANCOLD conference 2017. SANCOLD; 2017, p. 181–93.
[10] Chemaly AG. Lessons learned from the planning, design, construction, operation and maintenance (O & M), monitoring and safety evaluation of dams. In: Proceedings of the annual SANCOLD conference 2017. SANCOLD; 2017, p. 271–95.
[11] Karimi M, Attari J, Saneie M, Ghazizadeh MRJ. Side weir flow characteristics: Comparison of piano key, labyrinth, and linear types. J Hydraul Eng 2018;144(12):1–13.
[12] Abhash A, Pandey KK. A review of Piano Key Weir as a superior alternative for dam rehabilitation. ISH J Hydraul Eng 2020;00(00):1–11, Taylor & Francis.
[13] Singh D, Kumar M. Hydraulic design and analysis of piano key weirs : A review. Arab J Sci Eng 2021. Springer Berlin Heidelberg.
[14] Anderson RM, Tullis BP. Piano key weir hydraulics and labyrinth weir comparison. J Irrig Drain Eng 2013;139(3):246–53.
[15] Leite Ribeiro M, Boillat J-L, Schleiss AJ. Experimental parametric study for hydraulic design of PKWs. In: Proc. int. conf. labyrinth and piano key weirs, Liege B. Boca Raton, FL: CRC Press; 2011, p. 183–90.
[16] Bieri M, Federspiel M, Boillat JL, Houdant B, Faramond L, Delorme F. Energy dissipation downstream of piano key weirs—a case study of gloriettes dam (France). In: Labyrinth and piano key weirs—PKW 2011. Leiden, The Netherlands: CRC Press; 2011, p. 120–30.
[17] Ho Ta Khanh M, Sy Quat D, Xuan Thuy D. PKWs under design and construction in Vietnam 2010. In: Labyrinth and piano key weirs-PKW 2011. London: CRC Press; 2011, p. 225–32.
[18] Silvestri A, Archambeau P, Pirotton M, Dewals B, Erpicum S. Comparative analysis of the energy dissipation on a stepped spillway downstream of a piano key weir. In: Erpicum S, Laugier F, Pfister M, Pirotton M, Cicero GM, Schleiss AJ, editors. Labyrinth and piano key weirs II. Leiden, The Netherlands: CRC Press/Balkema; 2013, p. 111–20.
[19] Al-Shukur A-HK, Al-Khafaji GH. Experimental study of the hydraulic performance of piano key weir. Int J Energy Environ 2018;9:63–70.
[20] Zounemat-Kermani M, Mahdavi-Meymand A. Hybrid meta-heuristics artificial intelligence models in simulating discharge passing the piano key weirs. J Hydrol 2019;569(November):12–21, Elsevier.
[21] Azamathulla HM, Ahmad Z, Ab. Ghani A. An expert system for predicting Manning's roughness coefficient in open channels by using gene expression programming. Neural Comput Appl 2013;23(5):1343–9.
[22] Azamathulla HM, Rathnayake U, Shatnawi A. Gene expression programming and artificial neural network to estimate the atmospheric temperature in Tabuk, Saudi Arabia. Appl Water Sci 2018;8(6):1–7, Springer International Publishing.
[23] Karbasi M, Azamathulla HM. GEP to predict characteristics of a hydraulic jump over a rough bed. KSCE J Civ Eng 2016;20(7):3006–11.
[24] Rashki Ghaleh Nou M, Azhdary Moghaddam M, Shafai Bajestan M, Azamathulla HM. Estimation of scour depth around submerged weirs using self-adaptive extreme learning machine. J Hydroinform 2019;21(6):1082–101.

[25] Ghasempour R, Roushangar K, Azamathulla HM, Roushangar K. EEMD- and VMD-based hybrid GPR models for river streamflow point and interval predictions. Water Supply 2021;21(7):3960–75.
[26] Emadi A, Sobhani R, Ahmadi H, Boroomandnia A, Zamanzad-Ghavidel S, Mohammad Azamathulla H. Multivariate modeling of river water withdrawal using a hybrid evolutionary data-driven method. Water Supply 2022;22(1):957–80.
[27] Pandey M, Zakwan M, Khan MA, Bhave S. Development of scour around a circular pier and its modelling using genetic algorithm. Water Sci Technol: Water Supply 2020;20(8):3358–67.
[28] Pandey M, Zakwan M, Sharma PK, Ahmad Z. Multiple linear regression and genetic algorithm approaches to predict temporal scour depth near circular pier in non-cohesive sediment. ISH J Hydraul Eng 2020;26(1):96–103, Taylor & Francis.
[29] Singh UK, Jamei M, Karbasi M, Malik A, Pandey M. Application of a modern multi-level ensemble approach for the estimation of critical shear stress in cohesive sediment mixture. J Hydrol 2022;607(February).
[30] Birbal P, Azamathulla H, Leon L, Hosein J, Kumar V. Predictive modelling of the stage-discharge relationship using gene-expression programming. Water Supply 2021;21(7):3503–14.
[31] Pandey M, Md Azamathulla H. Discussion of 'gene-expression programming, evolutionary polynomial regression, and model tree to evaluate local scour depth at culvert outlets' by Mohammad Najafzadeh and Ali Reza Kargar. J Pipeline Syst Eng Pract 2021;12(2):07021001.
[32] Pandey M, Jamei M, Karbasi M, Ahmadianfar I, Chu X. Prediction of maximum scour depth near spur dikes in uniform bed sediment using stacked generalization ensemble tree-based frameworks. J Irrig Drain Eng 2021;147(11):04021050.
[33] E. Eslinger KR, Crookston BM. Energy dissipation of type a piano key weirs. Water 2020. MDPI, Basel, Switzerland.
[34] Singh D, Kumar M. Gene expression programming for computing energy dissipation over type-B piano key weir. Renew Energy Focus 2022;41:230–5, Elsevier Ltd.
[35] Singh D, Kumar M. Computation of energy dissipation across the type-A piano key weir by using gene expression programming technique. Water Supply 2022;22(8):6715–27.
[36] Singh D, Kumar M. Energy dissipation of flow over the type-B piano key weir. Flow Meas Instrum 2022;83(2021):102109, Elsevier Ltd.
[37] Kumar M, Singh D. Effects of channel bed slope on energy dissipation of different types of piano key weir. 2022;110042(5):142–147.
[38] Singh D, Kumar M. Study of the energy dissipation over the type-A piano key weir. KSCE J Civ Eng 2023. http://dx.doi.org/10.1007/s12205-023-0020-5.
[39] Bhukya RK, Pandey M, Valyrakis M, Michalis P. Discharge estimation over piano key weirs : A review of. Water 2022;1–17, MDPI.
[40] Haghiabi AH, Ghaleh Nou MR, Parsaie A. The energy dissipation of flow over the labyrinth weirs. Alex Eng J 2021;0–4, THE AUTHORS.
[41] Ghaderi A, Daneshfaraz R, Dasineh M, Di Francesco S. Energy dissipation and hydraulics of flow over trapezoidal-triangular labyrinth weirs. Water (Switzerland) 2020;12(7).
[42] Merkel J, Belzner F, Gebhardt M, Thorenz C. Energy dissipation downstream of labyrinth weirs. In: 7th IAHR international symposium on hydraulic structures, ISHS 2018. 2018, p. 508–17.
[43] Amin MR, Rajaratnam N, Zhu DZ. Energy loss below rectangular sharp-crested weirs for free flows. 2019, p. 2539–45, (Figure 1).
[44] Ferreira C. Gene expression programming: a new adaptive algorithm for solving problems. 2001, p. 1–22.
[45] Ferreira C. Gene expression programming in problem-solving. In: 6th online world conference on soft computing in industrial applications (Invited tutorial). 2001.
[46] Meng Q, Ke G, Wang T. A communication-efficient parallel algorithm for the decision tree. In: Proceedings of the 30th international conference on neural information processing systems. Red Hook, NY; 2016, p. 1271–9.
[47] Shahani NM, Kamran M, Zheng X, Liu C, Guo X. Application of gradient boosting machine learning algorithms to predict uniaxial compressive strength of soft sedimentary rocks at Thar coalfield. Adv Civ Eng 2021;2021.
[48] Machiels O. Experimental study of the hydraulic behaviour of piano key weirs (Ph.D. thesis), Belgium: University of Liege; 2012, ULgetd-09252012-224610. Acknowledgments. (June).
[49] Singh D, Kumar M. Study on aeration performance of different types of piano key weir. Water Supply 2022;22(5):4810–21.

biosensors

MDPI

Article

Conductive Ink-Coated Paper-Based Supersandwich DNA Biosensor for Ultrasensitive Detection of *Neisseria gonorrhoeae*

Niharika Gupta [1], D. Kumar [2], Asmita Das [1], Seema Sood [3] and Bansi D. Malhotra [1,*]

[1] Department of Biotechnology, Delhi Technological University, Delhi 110042, India
[2] Department of Applied Chemistry, Delhi Technological University, Delhi 110042, India
[3] Department of Microbiology, All India Institute of Medical Sciences, Ansari Nagar, New Delhi 110016, India
* Correspondence: bansi.malhotra@gmail.com

Abstract: Herein, we report results of the studies relating to the development of an impedimetric, magnetic bead-assisted supersandwich DNA hybridization assay for ultrasensitive detection of *Neisseria gonorrhoeae*, the causative agent of a sexually transmitted infection (STI), gonorrhea. First, a conductive ink was formulated by homogenously dispersing carboxylated multiwalled carbon nanotubes (cMWCNTs) in a stable emulsion of terpineol and an aqueous suspension of carboxymethyl cellulose (CMC). The ink, labeled *C5*, was coated onto paper substrates to fabricate *C5*@paper conductive electrodes. Thereafter, a magnetic bead (MB)-assisted supersandwich DNA hybridization assay was optimized against the *porA* pseudogene of *N. gonorrhoeae*. For this purpose, a pair of specific 5′ aminated capture probes (SCP) and supersandwich detector probes (SDP) was designed, which allowed the enrichment of target gonorrheal DNA sequence from a milieu of substances. The SD probe was designed such that instead of 1:1 binding, it allowed the binding of more than one T strand, leading to a 'ladder-like' DNA supersandwich structure. The MB-assisted supersandwich assay was integrated into the *C5*@paper electrodes for electrochemical analysis. The *C5*@paper electrodes were found to be highly conductive by a four-probe conductivity method (maximum conductivity of 10.1 $S \cdot cm^{-1}$). Further, the biosensing assay displayed a wide linear range of 100 aM–100 nM (10^9 orders of magnitude) with an excellent sensitivity of 22.6 $k\Omega \cdot (\log[\text{concentration}])^{-1}$. The clinical applicability of the biosensing assay was assessed by detecting genomic DNA extracted from *N. gonorrhoeae* in the presence of DNA from different non-gonorrheal bacterial species. In conclusion, this study demonstrates a highly sensitive, cost-effective, and label-free paper-based device for STI diagnostics. The ink formulation prepared for the study was found to be highly thixotropic, which indicates that the paper electrodes can be screen-printed in a reproducible and scalable manner.

Keywords: DNA biosensor; *Neisseria gonorrhoeae*; conductive ink; electrochemical; infectious diseases

check for updates

Citation: Gupta, N.; Kumar, D.; Das, A.; Sood, S.; Malhotra, B.D. Conductive Ink-Coated Paper-Based Supersandwich DNA Biosensor for Ultrasensitive Detection of *Neisseria gonorrhoeae*. *Biosensors* **2023**, *13*, 486. https://doi.org/10.3390/bios13040486

Received: 28 February 2023
Revised: 13 April 2023
Accepted: 14 April 2023
Published: 18 April 2023

Copyright: © 2023 by the authors. Licensee MDPI, Basel, Switzerland. This article is an open access article distributed under the terms and conditions of the Creative Commons Attribution (CC BY) license (https://creativecommons.org/licenses/by/4.0/).

1. Introduction

Sexually transmitted infections (STIs) remain one of the major medical problems, with more than 1M infections being acquired every day worldwide [1]. Gonorrhea, caused by the bacteria *Neisseria gonorrhoeae* (NG), is a curable STI having a very high incidence rate. The World Health Organization (WHO) has considered it as one of three STIs of global concern and has estimated eighty-two million new cases of gonorrhea in 2020 worldwide [2]. Factors that contribute to the high prevalence of gonorrhea include lack of access to testing and treatment, inadequate prevention efforts, and stigma surrounding STIs. Untreated gonorrhea can lead to serious complications, including pelvic inflammatory disease, infertility, neonatal blindness, ectopic pregnancy, and an increased risk of HIV transmission [1,3,4]. Another crucial factor to consider is the alarmingly increasing cases of antimicrobial-resistant (AMR) gonorrhea worldwide [2]. Thus, timely diagnosis and proper intervention is required to decrease the incidence of this STI.

The conventional detection strategies for *Neisseria gonorrhoeae* (NG) presently include culture techniques, microscopy, and the polymerase chain reaction (PCR). These techniques, though sensitive, are expensive, time-consuming, laborious, and cannot be performed outside of the laboratory [1,5]. Biosensors can prove to be essential for improving access to timely and accurate diagnosis, particularly in resource-limited settings where traditional laboratory-based testing may not be readily available. They can allow for the rapid detection of infections including gonorrhea at the point of care (POC), often providing results within minutes, which may help to expedite the treatment and reduce the risk of transmission [3,6,7]. In addition, biosensors can reduce the need for expensive and time-consuming laboratory testing, making them an attractive option for both healthcare providers and patients. Different kinds of DNA biosensors have been developed in recent years for the detection of various pathogens, such as *Vibrio cholerae* [8], *Haemophilus influenzae* [9], SARS-CoV-2 [10,11], Zika virus [12,13], etc. The high fidelity of DNA base pairing allows for the design and development of different kinds of DNA-based sensing mechanisms [3,6,10].

A few attempts to detect gonorrheal DNA have been made in the recent past. These studies have mostly focused on the development of amplification-based approaches for the visual detection of NG [3,6]. We have also previously reported the electrochemical detection of PCR amplicons of NG [14]. Visual detection is often semi-quantitative and amplification-based approaches suffer from limitations similar to those of other nucleic acid amplification assays (NAATs), e.g., the use of expensive reagents and the requirement of specific conditions (high temperature, etc.). In this context, supersandwich DNA hybridization is an attractive technique that alleviates the limitations associated with amplification-based assays and provides exceptionally high sensitivity as compared to traditional hybridization-based biosensors [15–17]. This method provides an enzyme-free signal amplification, can be operated at room temperature, and can be integrated into different biosensing modalities [15,16,18]. Supersandwich amplification-based biosensors have been applied for many applications including pathogen detection [19], and miRNA detection [16] among others.

The paper-based biosensors can prove to be advantageous for screening, monitoring, and detection of gonorrhea, as they are cost-effective, can be miniaturized, and can be used in low-resource settings. Different kinds of paper-based analytical devices have been reported in literature for the detection of pathogenic DNA [9,20–22]. Electrochemical paper-based devices have gained interest owing to their high accuracy, quantitative nature, ease of use, and applicability at the PoC [23,24]. Nanomaterial-enhanced, paper-based screen-printed electrodes (SPEs) have recently gained popularity as a low-cost and sensitive option to traditional diagnostic methodologies [23,25,26]. With the advent of papertronics, new-age paper-based devices have emerged that can be utilized for various electrochemical applications including biosensors. The development of conductive inks has further driven the growth of paper-based devices and vice versa. Conductive inks are materials that can be printed or applied in a thin layer to a substrate and can be used to create electronic circuits and devices. Conductive inks have emerged as low-cost options for the fabrication of paper-based biosensors [27,28]. These inks can be utilized for the fabrication of biosensors towards the detection of several different analytes, including DNA, hormones, metal ions, etc. [27,28].

In this work, we have fabricated a conductive ink-coated, paper-based impedimetric DNA supersandwich hybridization assay for highly sensitive and label-free detection of *N. gonorrhoeae*. For the conductive ink (named *C5*), multiwalled carbon nanotubes (MWCNTs) have been used as the conductive filler. MWCNTs possess a high aspect ratio and high surface area, making them highly conductive and suitable for many applications. In addition, MWCNTs have good adhesion to various substrates, including plastics and paper, which makes them well-suited for use in flexible and lightweight devices. MWCNTs have good mechanical strength and can withstand high temperatures, which makes them suitable for use in different electrochemical applications. The *C5* ink was chosen from

a series of inks for its optimum rheological behavior and coated onto paper substrates manually (*C5*@paper). Further, a magnetic bead (MB)-assisted DNA supersandwich assay was optimized against the *porA* pseudogene sequence of NG. The use of magnetic beads offers several advantages, including simplification of the sample enrichment process, the ability to be used in high-throughput assays, and automation. They can separate a target analyte from a milieu of substances owing to magnetic separation and greatly ease the purification process. The MB-assisted supersandwich assay was integrated with the *C5*@paper electrode for label-free detection of NG using electrochemical impedance spectroscopy (EIS).

2. Materials and Methods

2.1. Materials and Instrumentation

Carboxylated MWCNT (cMWCNT) and polysorbate 80 (PS80) were procured from SRL Pvt. Ltd. (Mumbai, India). Carboxymethyl cellulose (CMC; high viscosity) and terpineol were purchased from Central Drug House (P) Ltd. (CDH, New Delhi, India). The oligonucleotide probes were procured from IDT (Coralville, IA, USA) (Table 1). Carboxylated magnetic beads (MBs; Dynabeads Carboxylic Acid^{TM} MyOne^{TM}) were purchased from Thermo Fisher (Waltham, MA, USA). Freshly prepared phosphate-buffered saline (PBS, 0.1 M) of pH 7 supplemented with 5 mM ferro-ferricyanide as redox probes was utilized in the electrochemical studies, unless otherwise specified. All experiments were conducted in triplicates (n = 3) unless otherwise specified.

Table 1. Oligonucleotide probes used in the study.

S. No.	Probe Type	Probe Name	Sequence (5′-3′)	Melting Temperature (°C)
1.	Capture probe	SCP	5′ NH_2-TTT TTT CCT GCT ACT TTC ACG CTG GA 3′ (26 bases) (5′ amino C6 modification)	59
2.	Detector probe (supersandwich)	SDP	5′ AAG TAA TCA GAT GAA ACC AGT TCC CTG CTA CTT TCA CGC TGG A 3′ (43 bases)	50.8
3.	Target strand	TP	5′ GAA CTG GTT TCA TCT GAT TAC TTT CCA GCG TGA AAG TAG CAG G 3′ (43 bases)	66.2
4.	Non-complementary probe	NC	5′ TTG ATT GAG CGT CAT AGA TCG GAC GGC ACT AGT CAG TAC TCG A 3′ (43 bases)	67

The ink formulations were analyzed for viscosity and thixotropy on an Anton Paar rheometer by the parallel plate (PP40, diameter 40 mm) method. All rheology experiments were conducted at 25 °C. The *C5*@paper electrodes (1 × 1 cm^2) were characterized for surface morphology via different techniques, including scanning electron microscopy (SEM), field emission SEM (FESEM), and atomic force microscopy (AFM). For SEM and FESEM analysis, the samples were dried under an infrared lamp for 30 min to eliminate any adsorbed moisture and sputter coated with Au for electrical conductivity. SEM was conducted on a ZEISS EVO 18 instrument at 10 kV acceleration voltage. FESEM was performed on a JEOL JSM-7800F Prime instrument. AFM studies were conducted on an Asylum Research MFP3D-BIO instrument in intermittent contact (tapping) mode. The conductivity of the *C5*@paper electrodes was analyzed via a four-probe conductivity meter (SES Instruments, India) (probe distance = 2 mm) at room temperature (25 °C). Cyclic voltammetry (CV) and EIS studies were performed on a single-channel Autolab potentiostat/galvanostat (Metrohm AG, Herisau, Switzerland). All CV studies were conducted at scan rate of 50 $mV \cdot s^{-1}$ and EIS studies were conducted at 0.01 V within the frequency range of 0.1–10^5 Hz.

2.2. Design of Oligonucleotide Probes

The supersandwich oligonucleotide probes were designed using NCBI-Primer BLAST, NCBI Nucleotide BLAST, and Clustal Omega. Briefly, a library of different sets of primers was prepared using NCBI-Primer BLAST, and their specificity was determined by aligning them with gonorrheal and non-gonorrheal genomic DNA sequences using NCBI Nucleotide BLAST. The non-gonorrheal DNA sequences used for alignment included those from *N. meningitidis*, commensal *Neisseria* species (*N. sicca*, *N. lactamica*, *N. mucosa*), *Chlamydia trachomatis*, Ureaplasma urealyticum, Enterococcus faecalis, Escherichia coli, Staphylococcus aureus, *Klebsiella pneumoniae*, *Mycoplasma genitalium*, and *Lactobacillus fermentum*. The forward primer from the set of probes having 100% similarity with gonorrheal DNA and having no or little similarity with non-gonorrheal DNA was selected as the capture probe (SCP), and an adjacent specific sequence was selected as the conventional detector probe (DP). For the supersandwich assay, the detector probe (SDP) sequence consisted of the DP sequence ligated to the SCP sequence in 5′-3′ direction. The details of all the probes utilized in the study are given in Table 1. The alignment of the probes with the target DNA sequence is given in Section S1 of the Supplementary Information. Gel electrophoresis studies were conducted to determine the probe efficiency in forming a supersandwich duplex with the target DNA sequence.

2.3. Formulation of the Conductive Ink

For ink formulation, different amounts of CMC (1, 2.5, and 5% *w*/*v*) were dissolved in deionized (DI) water. These CMC dispersions were then mixed with terpineol (2:1 ratio) separately. Polysorbate 80 (PS80) was used as the stabilizer, as terpineol has limited solubility in water and CMC does not interact with organic solvents. The resulting emulsions, designated as CMC_1, $CMC_{2.5}$, and CMC_5, respectively, were stirred vigorously on a magnetic stirrer (~1000 rpm, 2 h). CMC_5 was chosen as the base for the conductive ink after rheological assessment. cMWCNTs were added to CMC_5 (cMWCNT:CMC ratio of 1:1) with vigorous stirring (~1000 rpm, overnight). The resulting conductive emulsion was probe ultrasonicated in an ice bath at a pulse of 1 s and 70% amplitude for 20 min, with pauses at every 5 min to prevent overheating. The resulting conductive ink, designated as *C5*, was stored in a closed container at low temperature (4 °C–10 °C) to prevent evaporation of the solvent.

2.4. Rheological Studies

The fluid properties of ink are imperative in understanding its behavior during the coating/printing process. The emulsion bases (CMC_1, $CMC_{2.5}$, and C_5) for the conductive ink, prepared with different amounts of CMC, were assessed for rheology by a plate-plate rheometer at 25 °C. The change in the shear viscosity of the emulsion bases was analyzed within the shear rate range of 0.1–100 s^{-1}. Further, a 3-interval thixotropy test (3iTT) was utilized for analyzing the recovery of the viscosities of the 3 emulsion bases after stress removal. This test can be used to simulate screen printing and other coating processes, wherein an abrupt increase in stress is observed during the printing/coating process. The emulsion bases were pre-sheared at 0.1 s^{-1} for 20 s before the 3iTT. Thereafter, three intervals of different shear rates were applied: 0.1 s^{-1} for 30 s (first interval), 200 s^{-1} for 15 s (second interval; simulation of the printing process), and recovery at 0.1 s^{-1} for 120 s.

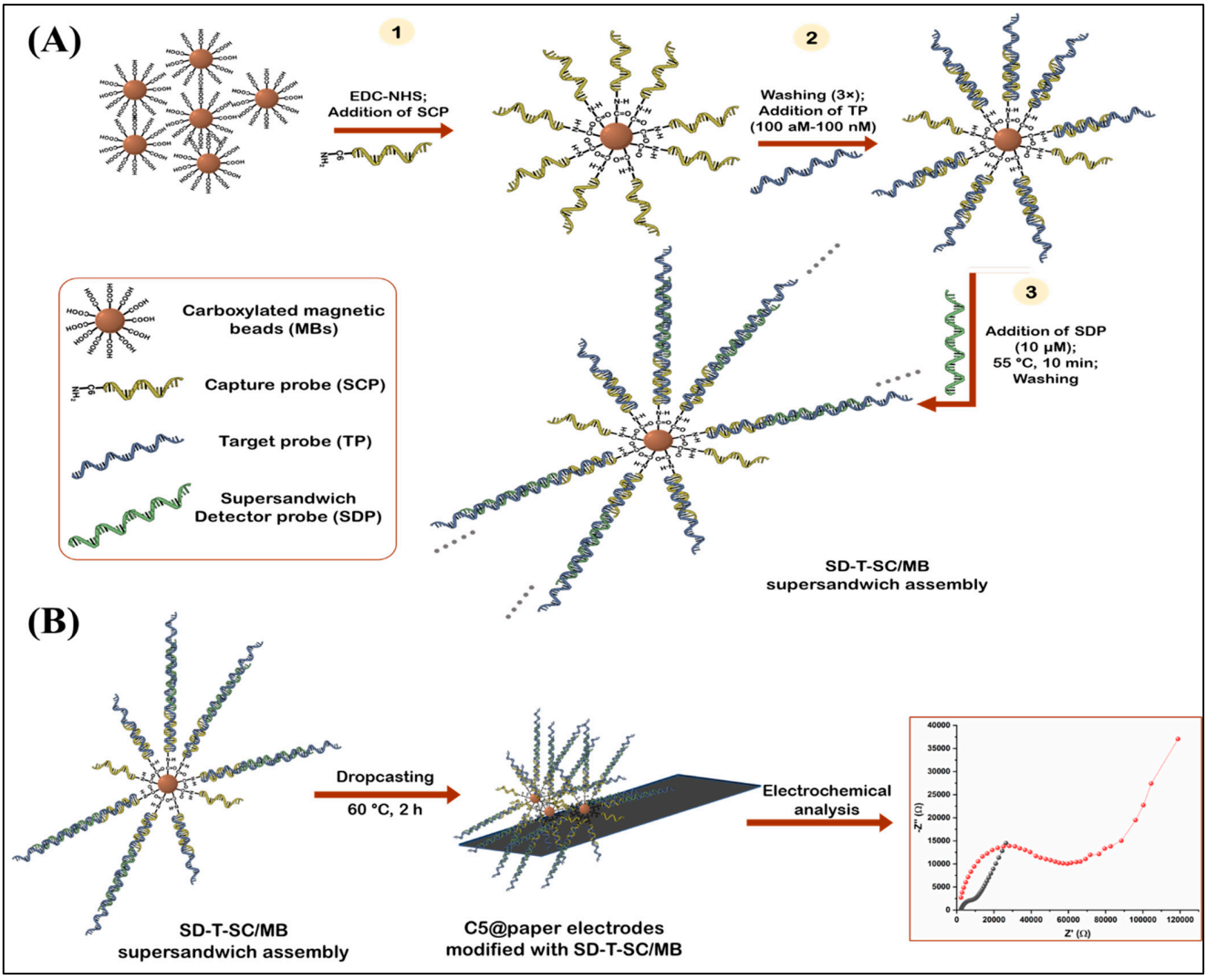
2.5. Fabrication of C5@paper Electrodes

The *C5*-coated paper electrodes (*C5*@paper) were fabricated by first coating drawing paper (200–300 gsm, 6 × 6 cm^2) with the *C5* ink using a commercially available paint brush (Faber-Castell). This *C5*-coated paper was then cut into strips having dimensions of 2 × 2 cm^2, which were then annealed at 120 °C for 10 min to allow evaporation of the solvent (terpineol and water). The effect of the number of coats (*n*) on the conductivity of the *C5*-coated paper was assessed by measuring the conductivity after each coat with

the 4-probe conductivity meter. For conductivity studies, the *C5*-coated paper strips were cut into pieces of size 1 × 1 cm^2 each. The conductivity values of 4 strips (1 × 1 cm^2; 12 readings in total) were recorded at 25 °C and their mean value was reported for each coat. For electrochemical studies, the strips were cut into strips with dimensions of 2 × 1 cm^2 to fabricate the *C5*@paper electrodes. All electrodes were stored in dark, dry conditions until further use.

2.6. Electrochemical Magnetic DNA Supersandwich Assay

The detailed protocol for the immobilization of SCP onto the MBs is provided in Section S2 of the Supplementary Information. Scheme 1 depicts the various steps involved in the electrochemical, MB-assisted biosensing assay.



Scheme 1. Schematic diagram depicting (**A**) the MB-assisted supersandwich hybridization assay for *N. gonorrhoeae* detection, and (**B**) subsequent integration with the *C5*@paper electrodes for electrochemical analysis via EIS.

2.6.1. Supersandwich Assay

Five milligrams of SCP/MBs were washed with DI water (3×) and dispersed in 500 μL of DI water, making the final concentration 10 $mg \cdot mL^{-1}$. Aliquots of 50 μL were made in different test tubes and 50 μL of TP was added to each tube in the concentration range of 100 aM–100 nM (5 zmol–5 pmol). Thereafter, 50 μL of SDP (10 μM) was added to each reaction tube and incubated at 55 °C for 10 min with mixing. This SD-T-SC/MB

supersandwich assembly was washed with DI water (3×) to remove unbound probes, and redispersed in 30 µL PBS buffer for electrochemical analysis.

2.6.2. Electrochemical Analysis

For the electrochemical studies, the SD-T-SC/MB assembly dispersed in 30 µL of PBS was drop cast onto the *C5*@paper electrodes. These modified electrodes were slowly dried at 60 °C for 2 h. Thereafter, impedance measurements for every electrode were recorded in PBS (pH 7) supplemented with 5 mM ferro-ferricyanide. The measurements were made in the range of 0.1–10^5 Hz at 0.01 V. A calibration curve was plotted between the net change in charge transfer resistance (R_{ct}) of the *C5*@paper electrodes in the presence of different concentrations of TP (as compared to negative control) and the concentration of TP.

2.7. Real Sample Analysis

For practical applications, it is imperative that the electrochemical biosensing assay works in clinical settings and can specifically detect gonorrheal DNA from among a mixture of different substances. To assess this, the biosensing assay was first tested against gonorrheal genomic DNA. For this, DNA from *N. gonorrhoeae* bacterial culture was extracted using the boiling method. Briefly, a few colonies from the culture plate were dispersed in autoclaved, double distilled water (1 mL) and incubated at 90 °C for 1 h for inducing cell lysis. Then, the heat-lysed cell suspension was taken and centrifuged at 1200 rpm for 5 min to separate cell debris. The pellet was discarded and the remaining supernatant was stored at −20 °C until further use. The DNA was quantified using nanospectrophotometer (Nanodrop). It should be noted that DNA extracted using this method is often contaminated with RNA and other cellular components such as proteins. Hence, the purity level of such samples is often lower than the ideal values. This method was chosen for DNA extraction as it is quicker than the buffer-based commercial methods, requires fewer reagents, and is widely used in clinical labs for isolating DNA from cervical/urethral swabs—the samples utilized in gonorrhea testing.

Different dilutions of the extracted DNA were prepared, which were then sheared into smaller fragments by bath ultrasonication for 10 min, and denatured by incubation at 95 °C for 5 min. This ensured the denaturation of any residual, contaminating RNA and proteins in the samples. Thereafter, the protocol mentioned in the previous section was repeated to determine the concentration of gonorrheal DNA.

As clinical samples (particularly from female subjects) are known to contain DNA from different bacterial species, the specificity of the biosensing assay was further assessed by testing it against a mixture of gonococcal DNA with non-gonococcal DNA extracted from different bacteria. The DNA samples were extracted by the boiling method discussed above; hence, they also contained interfering RNA and proteins. The details of the bacterial species used in the study are given in Section S3. The response of the electrochemical biosensing assay to these mixed DNA samples was recorded in a similar manner as mentioned in Section 2.6.

3. Results and Discussion

3.1. Optimization and Characterization of the Ink Formulation

The ink formulation was optimized and characterized for flow properties by rheometry. The aim of this study was to prepare a homogenous ink with thixotropic properties, which pertain to a linear decrease in a liquid's viscosity with an increase in shear force followed by recovery of viscosity once the shear force is removed. Thixotropy allows for the smooth application of the ink on a particular substrate (in this case, paper) [29]. Most commercial paints and screen-printing inks are thixotropic in nature [29]. CMC is a known thixotropic agent and is prominently used as a rheological modifier [30]. To determine the effect of the amount of CMC on the ink rheology, three different solvent bases were prepared—CMC_1, $CMC_{2.5}$, and CMC_5—corresponding to 1%, 2.5%, and 5% CMC. Figure 1A shows the log plot of the change in viscosity with the shear rate in the range of 0.1–100 s^{-1}. The

viscosity varies linearly with the shear rate suggesting the shear thinning property of the three emulsion bases. The initial viscosities for CMC_1, $CMC_{2.5}$, and CMC_5 at 0.1 s^{-1} were found to be 3.48 Pa.s, 14.42 Pa.s, and 18.9 Pa.s, respectively. This increase in initial viscosity is due to the increase in CMC content in the solvent bases. The thixotropic behavior was further assessed by the 3-interval thixotropy test (3iTT) (Figure 1B). This test can simulate processes such as painting, screen printing, etc., by applying a sudden high shear stress to ink and then analyzing the percentage recovery in the viscosity of the ink after the stress is removed abruptly. CMC_5 displayed the highest viscosity of 18.4 Pa.s at 0.1 s^{-1} (30 s), while CMC_1 had the lowest viscosity (Figure 1B). In accordance with the shear thinning behavior, the viscosity of the emulsion bases decreased significantly at 200 s^{-1}. After the removal of the stress, the viscosity of the three emulsions recovered to different degrees. For CMC_1 and $CMC_{2.5}$, the viscosities decreased to 0.68 Pa.s and 0.76 Pa.s at 45 s (10% and 4.78%, respectively, of their initial viscosities at 30 s). While for CMC_5, the viscosity decreased to 1.08 Pa.s at 45 s (5.8% of initial viscosity at 30 s) indicating its higher viscosity in relation to the other two emulsion bases. This further suggests that CMC_1 would perhaps flow the fastest and CMC_5 would flow the slowest through the screen mesh while printing. After recovery of the shear rate from 200 s^{-1} to 0.1 s^{-1}, the viscosity of CMC_1 recovered to 62.5% of its original initial viscosity after 75 s. At the same time, $CMC_{2.5}$ and CMC_5 recovered 59.3% and 98.4% of their initial viscosities, respectively. Recovery of viscosity is crucial to determine the screen printability of inks as it indicates less seepage and dripping issues. For an efficient screen-printing ink, it is imperative that the ink should neither possess a very low viscosity (as it allows the creation of air bubbles) nor should it be too viscous, which leads to non-uniform printed patterns [29]. Since CMC_5 displayed an appreciable decrease in viscosity and the highest recovery, it was chosen as the emulsion base for the formulation of the ink.

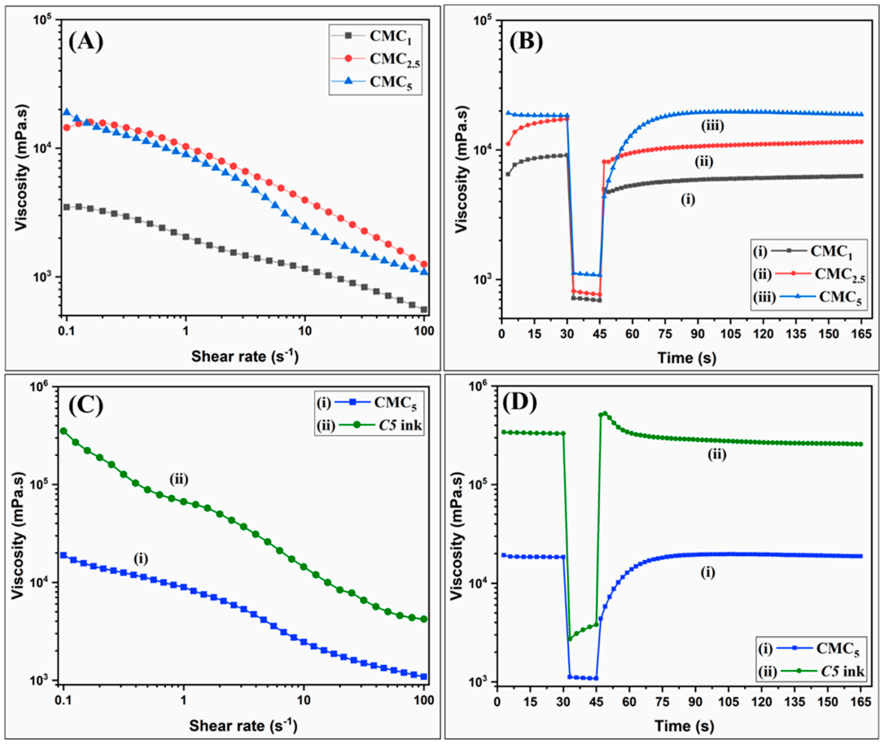


Figure 1. (**A**) Viscosity flow curves showing the change in viscosity of the CMC_1, $CMC_{2.5}$, and CMC_5 base emulsions with shear rate in the range of 0.1–100 s^{-1}, (**B**) Change in viscosity of the CMC_1, $CMC_{2.5}$, and CMC_5 base emulsions with time when subject to sudden change in the shear rate, (**C**) Viscosity flow curves of the CMC_5 base emulsion and the *C5* ink with shear rate in the range of 0.1–100 s^{-1}, and (**D**) Change in viscosity of the CMC_5 base emulsion and *C5* ink with time when subject to sudden change in shear rate.

The *C5* ink was prepared by dispersing cMWCNT into the CMC_5 emulsion base uniformly, and the effect of cMWCNT on the flow properties of the final ink was observed (Figure 1C,D). As shown in Figure 1C, the initial viscosity of the *C5* ink at 0.1 s^{-1} was found to be significantly higher (352.1 Pa.s) than the CMC_5 emulsion. However, the ink retained its shear thinning property as the viscosity decreased linearly with the shear rate. It is also interesting to note that, during the thixotropy test (3iTT), the initial viscosity of the *C5* ink (329.8 Pa. s at 0.1 s^{-1} at 30 s) decreased by ~100 times to 3.79 Pa.s (~1% of the initial viscosity) at 200 s^{-1} at 45 s. The viscosity further recovered to 90% of its initial value at 75 s after the removal of the stress. This indicated that the addition of cMWCNTs did not affect the thixotropic behavior of the ink and hence the *C5* ink can potentially be used in screen printing of high-resolution patterns. Similar rheological behavior has been observed in other studies wherein MWCNT and other nanomaterials, such as silver, graphene, etc., were used as conductive fillers [29,31,32]. It has been reported that the presence of carbon nanomaterials as fillers in an ink increases the structural strength of the ink, and hence it may lead to a faster recovery of the viscosity [32]. The high viscosity recovery suggests that the colloidal stability of the ink is maintained even at higher shear rates, which results from the balance between the *van der Waals* interactions and steric stabilization among cMWCNTs, CMC (binder), and other dispersants (PS80) [31]. This eventually leads to better leveling during printing.

3.2. Morphological and Functional Characterization of C5@paper Electrodes

The morphology of the *C5*@paper electrodes has been studied by SEM and FESEM analysis (Figure 2A–F). The cellulose fibers of bare paper used as substrate are clearly visible in Figure 2A,B). These fibers are completely covered by the *C5* ink after coating, which appears uniform and has a granular appearance (Figure 2C,D). The cMWCNTs seem to be completely enveloped with CMC (and possibly PS80), though they are visible at some locations protruding out of the ink matrix (Figure 2D). Further, Figure 2E shows the magnified FESEM image of the tilted lateral side of the *C5*@paper electrode. The ink coats are clearly visible with cMWCNT dispersed over the entire surface. Upon further inspection of the lateral edge of the *C5*@paper electrode, it seems that the ink has not completely penetrated the entire thickness of the paper, as cellulose fibers are visible in between the ink coating (Figure S2). Figure 2F shows the magnified view of the *C5*@paper electrode with a cMWCNT protruding out of the ink matrix, having an apparent diameter of 67.6 nm. The surface roughness of bare paper and *C5*@paper electrodes was further analyzed by AFM studies (Figure 2G(i,ii), respectively). The RMS surface roughness of bare paper and the *C5*@paper electrode was found to be 168.2 nm and 41.6 nm, respectively. This reduction in the surface roughness upon coating may be contributed to the masking of cellulose fibers by the ink. This further suggests that, despite the grainy appearance, the ink coating is smooth and possesses lower friction force as compared to bare paper [33].

The conductivity of the *C5*@paper electrodes was measured by the 4-probe conductivity method. The calculations involved in the measurement of conductivity are given in Section S4. After coating, the electrodes were annealed at 120 °C for 10 min. The conductivity of the *C5*@paper electrodes was found to increase with the number of coats, with maximum value at four coats (n = 4), as shown in Figure 2H. This increase in conductivity can be attributed to the increase in the cMWCNT content after each coat. Interestingly, the conductivity was found to first reduce and then seemed to saturate gradually for 5–8 coats. The CMC concentration (% w/v) is equivalent to that of cMWCNT in the *C5* ink. Perhaps, the insulating nature of CMC starts dominating the conductivity after four coats and beyond. The saturation of the conductivity points toward the presence of competing factors contributed by the presence of conductive cMWCNTs and non-conductive binders (CMC) and, to some extent, emulsifiers (PS80). This is in contrast with a recent study that reported an increase in conductivity until saturation of a graphene-based ink with an increase in the number of (printing) coats [34].

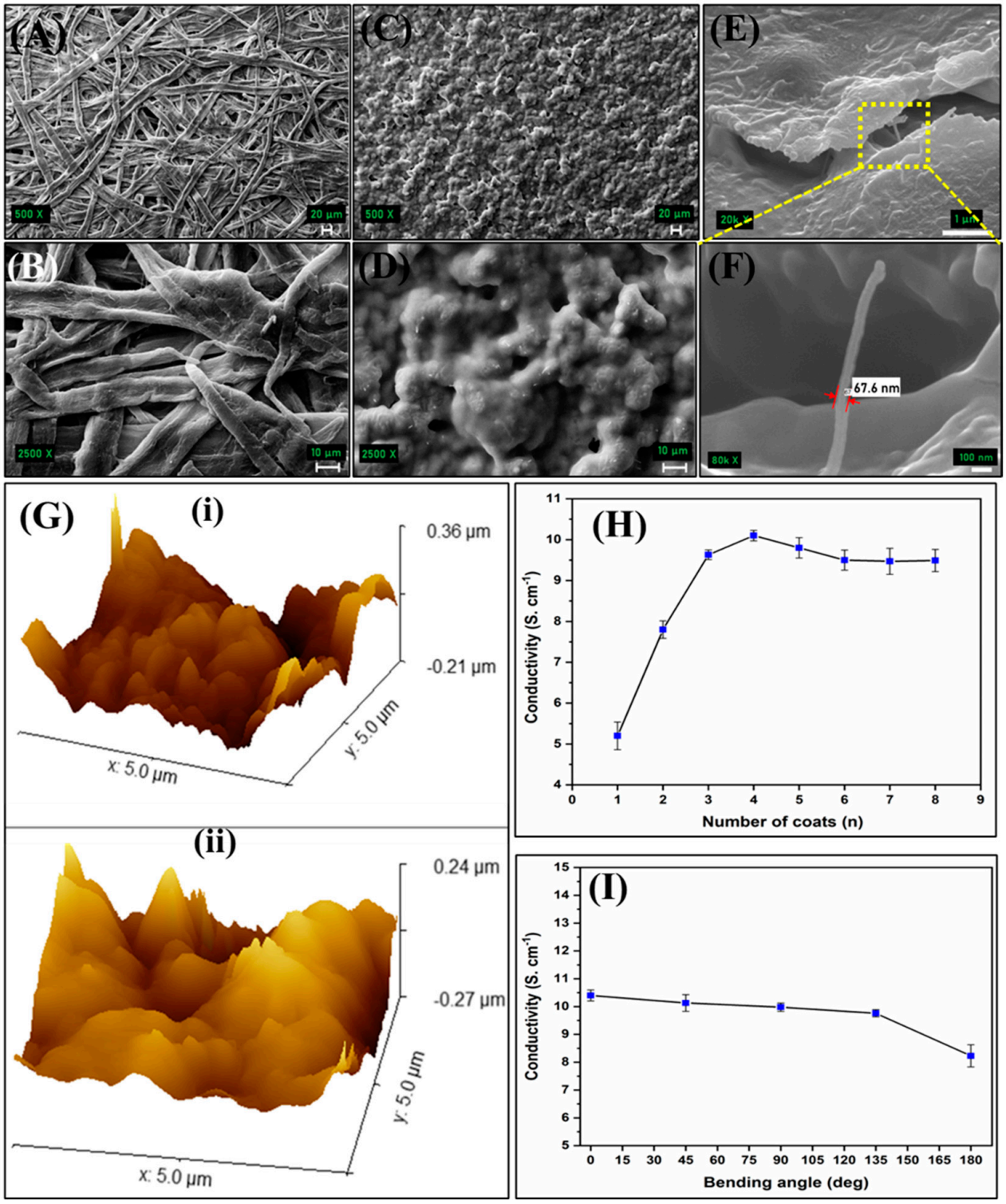


Figure 2. SEM images of (**A**,**B**) bare paper, and (**C**,**D**) *C5*@paper electrodes at different magnifications, (**E**) FESEM image of the *C5*@paper electrode, (**F**) High magnification FESEM image showing cMWCNT in the ink matrix, (**G**) AFM images of the (**i**) bare paper, and (**ii**) *C5*@paper electrode. Change in the conductivity of the *C5*@paper electrode with (**H**) number of coats, and (**I**) bending angle.

The maximum conductivity of the *C5*@paper electrode was found to be 10.1 ± 0.24 S·cm^{-1} (0.1 ± 0.026 Ω·cm) after four coats of ink. A recent study has reported the conductivity of an MWCNT/PEDOT:PSS screen-printing ink to be 14.99 S·cm^{-1} for five printing passes [31].

It may be noted that the binder used in this study, PEDOT:PSS, is a conductive polymer, which played a significant role in the enhanced conductivity of the MWCNT ink. Another study reported the resistivity of an MWCNT ink in the range of 0.5–13 $\Omega \cdot sq^{-1}$ [35]. The study reported the use of PVP as a binder and 10% *w*/*v* MWCNT as a conductive filler. The results of these studies highlight the importance of the binder used in ink preparation. The use of a conductive binder may enhance the conductivity manifold, while an insulating polymer may compromise the conductivity of ink even if the conductive filler is used in excess. Keeping this in view, the high conductivity of the *C5* ink, despite the use of a relatively smaller amount of MWCNT (5% *w*/*v*) and an insulating binder (CMC), alludes to the effectiveness of the method of ink preparation. Further, the change in conductivity of the *C5*@paper electrodes upon folding at different angles (45–180°) was also estimated (Figure 2I). There was no significant change in the conductivity of the electrodes until 135° bending. However, the conductivity reduced drastically upon a 180° bend. The retention of conductivity until 135° suggests that cMWCNTs are well dispersed within the ink matrix [36]. However, the surface of the paper may crack at higher bending angles (180°) leading to cracks in the ink itself. This ultimately contributed to lower conductivity values at higher bend angles.

3.3. Electrochemical Studies

The electrochemical performance of the fabricated *C5*@paper electrodes and further modifications were characterized via CV and EIS. Multiple CV cycles were run to determine the stability of the fabricated electrodes upon continuous use in the buffer. As shown in Figure S2, the response of the electrode does not change significantly even after 50 cycles, indicating the stability of the electrodes in buffer conditions. It may be noted that the charging current was found to be too high in relation to the faradaic current in the CV curves, which could be due to the pseudocapacitance of the electrode. The swelling of CMC in aqueous conditions may also contribute to the high charging current. For this reason, EIS was chosen for further electrochemical studies. The batch reproducibility of the *C5*@paper electrodes was also assessed by randomly selecting 10 electrodes from different batches and measuring their charge transfer resistance (R_{ct}) values via EIS (Figure 3A). The R_{ct} values were determined by fitting the Nyquist plots by an equivalent model circuit given by ($R_s(Q_1[R_{ct}Q_2])$), wherein R_s is the solution resistance, Q_1 is the constant phase element (CPE) associated with the (pseudo)capacitance of the electric double layer formed at the electrode surface, R_{ct} is the charge transfer resistance, and Q_2 is the CPE associated with the diffusion of redox species at the electrode surface (Figure S3A). The presence of Q_1 and Q_2 in the model circuit indicates the non-ideal behavior of the double-layer capacitance. This also indicates that the distribution of active sites over the electrode surface might be non-homogenous [37]. As shown in Figure 3A, no significant difference was found in the R_{ct} of the *C5*@paper electrodes, with the mean R_{ct} being 940.29 ± 0.72 Ω. These results suggest that the cMWCNTs were dispersed homogenously in the *C5* ink, which led to the uniform coating of the paper substrates. The change in the R_{ct} of the *C5*@paper electrodes with time (1–30 days) was also studied to determine the storage life of the electrodes (Figure S3B). It was found that the initial R_{ct} at Day 1 (940 Ω) reduced by a mere ~0.5% on Day 30 (935.2 Ω), suggesting that the electrodes can be stored for at least 30 days at room temperature in a dry environment.

Figure 3B shows the Nyquist plots of the *C5*@paper electrodes and subsequent modifications. It can be seen that the R_{ct} (which is generally correlated to the diameter of the semicircle in the Nyquist plot) increases after every modification. The R_{ct} of the *C5*@paper was found to be 940 ± 4.2 Ω, which further increased to 3.28 ± 0.06 kΩ and 4.11 ± 0.09 kΩ, respectively, after modifications by SCP/MB and BSA/SCP/MB. This increase in R_{ct} indirectly indicates the immobilization of SCP and BSA onto the MB surface. The equivalent model circuit ($R_s(Q_1[R_{ct}Q_2])$) fitted into the plots is given in Figure S3A. Prior to the electrochemical response studies, gel electrophoresis studies were conducted to confirm the formation of the supersandwich between the SCP, TP, and SDP probes. As shown

in Figure S4, DNA bands at ~100 bp and higher are observed at both 25 °C and 55 °C. Additionally, the supersandwich structures formed at both temperatures after a mere 5 min. Thus, 55 °C for 10 min was chosen as the optimal temperature and time for the DNA supersandwich hybridization studies. The higher temperature was chosen in order to avoid any non-specific interactions with non-gonorrheal DNA, which is often present in clinical samples. The time chosen was 10 min as the immobilization of SCP onto the MBs can significantly reduce their mobility in the aqueous phase. Steric hindrance can also hamper the rate of DNA hybridization. To compensate for such losses, the optimum incubation time was chosen as a bit higher than necessary.

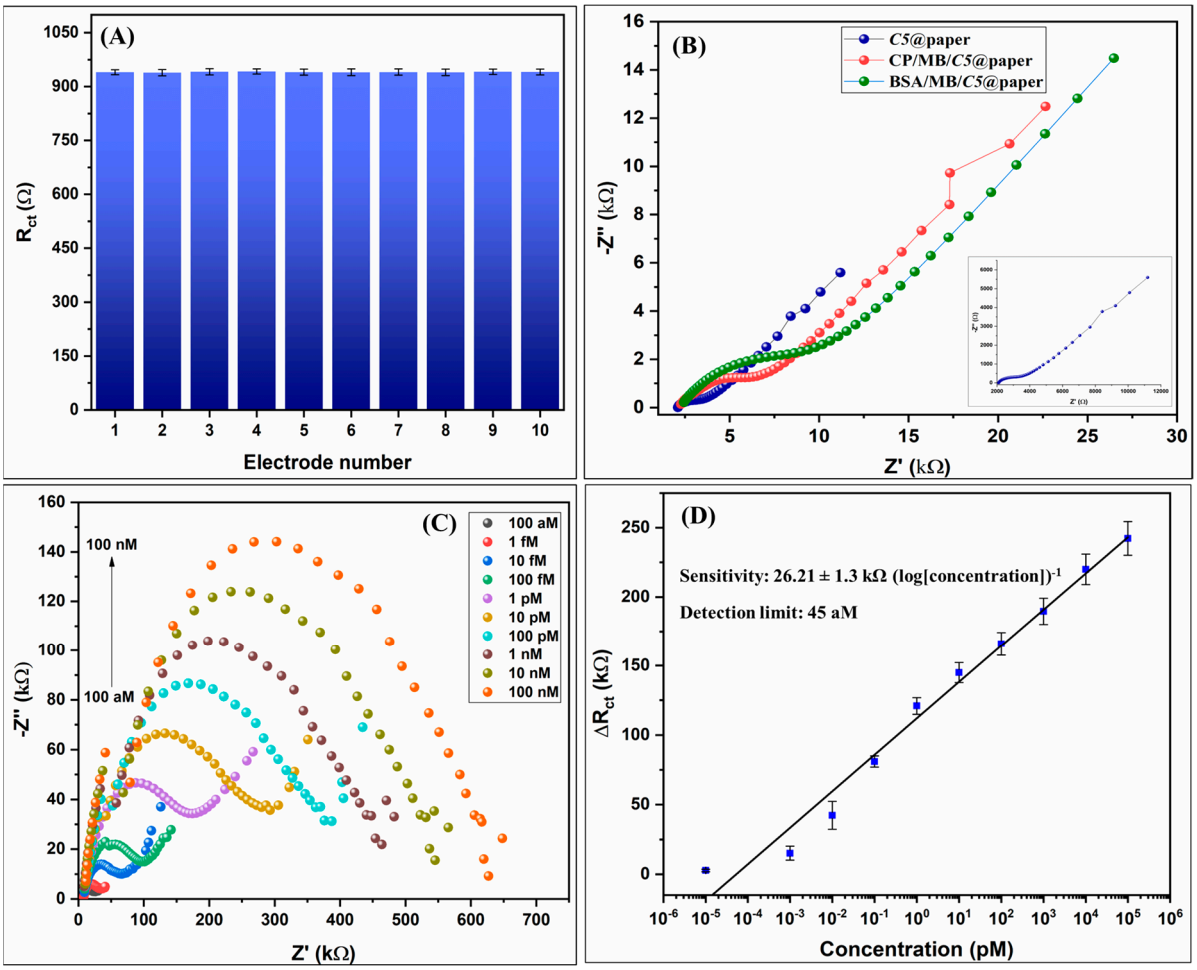


Figure 3. (**A**) Bar graph showing the R_{ct} values of C5@paper electrodes selected randomly from different batches. (**B**) Nyquist plots of the *C5*@paper, SCP/MB/*C5*@paper, and the BSA/SCP/MB/*C5*@paper electrodes. Inset shows the Nyquist plot of the *C5*@paper electrode. (**C**) Nyquist plots of the *C5*@paper after drop-casting of the SD-T-SC/MB for different concentrations of the TP. (**D**) Corresponding linear calibration curve showing ΔR_{ct} vs. log of the concentration of the TP.

The Nyquist plots of the *C5*@paper electrodes for different concentrations of the TP are given in Figure 3C. A significant rise in the impedance was observed with increasing concentration of the target DNA, as is evident by the increasing semicircle diameter. The change in the R_{ct} (ΔR_{ct}) was calculated by applying the following equation:

$$\Delta R_{ct} = R_m - R_0 \quad (1)$$

where R_m is the measured R_{ct} for a given concentration and R_0 is the R_{ct} of the negative control (electrode with no TP). The ΔR_{ct} values correlated linearly to the log of concentration of the *porA* target sequence (TP) (Figure 3D). The corresponding linear regression equation is:

$$\Delta R_{ct} = 26.21 \times \log[\text{concentration}] + 111.99, R^2 = 0.98 \quad (2)$$

The linear range of the assay was found to be 100 aM–100 nM (10^9 orders of magnitude) with an exceptional sensitivity of 26.21 kΩ $(\log[\text{concentration}])^{-1}$ and a detection limit of 45 aM, as calculated by a previously reported method [37]. The enhanced sensitivity can be contributed to the formation of supersandwich structures at the surface of the MBs. As shown in Table 2, the biosensing assay proposed in this work possesses a better detection limit than most recent studies reported on the development of electrochemical DNA biosensors. Further, the value of the detection limit (45 aM) is equivalent to 10–22 copies μL^{-1} corresponding to the longest and the shortest supersandwich DNA duplex length of 150 bp and 69 bp, respectively (Figure S3). This detection limit range is superior to those reported by recent studies on visual detection of NG via a multiple cross displacement assay (20 copies/test) and loop-mediated isothermal amplification (LAMP) assay (50 copies/test) [3,6]. In these studies, gold nanoparticles were used as the colorimetric probe. Luo et al. reported a similar detection limit of 10 copies μL^{-1} for a Cas13a-based specific high-sensitivity enzymatic reporter unlocking (SHERLOCK) assay developed for NG *porA* and azithromycin resistance detection [38]. It may be noted that this assay was tested on only purified double-stranded DNA (dsDNA). This demonstrates the superiority of the proposed biosensing assay in terms of a relatively simpler detection strategy, the use of fewer reagents, and label-free electrochemical detection. PCR is currently the gold standard for the detection of NG in clinical samples. Comparison with commercial PCR assays in terms of detection limit indicates that there is a scope for improvement in the proposed supersandwich biosensing assay. GeneProof® claims the detection limit of its NG dual-target PCR kit to be 0.109 copies μL^{-1} [39]. While another study has reported the detection limit of the same assay being 1.5 copies μL^{-1} [40]. It is important to note here that PCR is an amplification-based assay, and, hence, in some instances, the detection limit is simply defined as being the lowest concentration returning amplification. Using this approach, a study reported the assay detection limit as being 1×10^{-7} dilution [41], while another reported a detection limit of 10^2–10^3 copies mL^{-1} (0.1–1 copy μL^{-1}) [42]. Thus, readers are advised to consider these factors while analyzing the differences between biosensing assays and PCR assays and their respective detection limits.

Table 2. Comparison of recent studies on paper-based biosensors for DNA detection.

S. No.	Ink Formulation/ Nanomaterial	Type of DNA Assay	Target Pathogen	Linear Range	Sensitivity (LOD)	Reference
1.	Ni–Au composite/CNT/PVA	Traditional hybridization	HIV DNA	10 nM–1 μM	(0.13 nM)	[26]
2.	Tungsten disulfide quantum dots	Traditional hybridization	Specific meningitis	1 nM–100 μM	(1 nM)	[43]
3.	Oxidized graphitic carbon nitride	Traditional hybridization	Norovirus	10^{-7}–10^2 μM	(100 fM)	[25]
3.	Graphene nanosheets	Direct analysis	(dsDNA)	0.2–5 pg mL^{-1}	0.00656 mA·pg^{-1} cm^{-2}	[24]

Table 2. *Cont.*

S. No.	Ink Formulation/ Nanomaterial	Type of DNA Assay	Target Pathogen	Linear Range	Sensitivity (LOD)	Reference
4.	Carbon graphene ink (commercial)	Traditional hybridization (pyrrolidinyl peptide nucleic acid-mediated)	Hepatitis B virus	50 pM–100 nM	(1.45 pM)	[44]
5.	Ag nanoprisms electrode-posited on graphene quantum dots (GQDs)	Traditional hybridization	*Leishmania infantum*	1 zM–1 nM	1 zM (LOQ *)	[45]
6.	cMWCNT	Supersandwich hybridization	*Neisseria gonorrhoeae*	100 aM–100 nM (5 zmol-5 pmol)	26.21 kΩ (log[concentration])$^{-1}$ (45 aM)	This work

3.4. Real Sample Analysis and Specificity Studies

To determine whether the electrochemical biosensing assay would perform in clinical conditions, its response was recorded against different concentrations of genomic DNA extracted from NG in the concentration range of 100 aM–1 pM. As shown in Figure 4A, there was no significant change in the ΔR_{ct} of the biosensing electrode for the same concentrations of the genomic DNA and synthetic TP used in the response studies. This indicates the applicability of the biosensing assay in real-life situations.

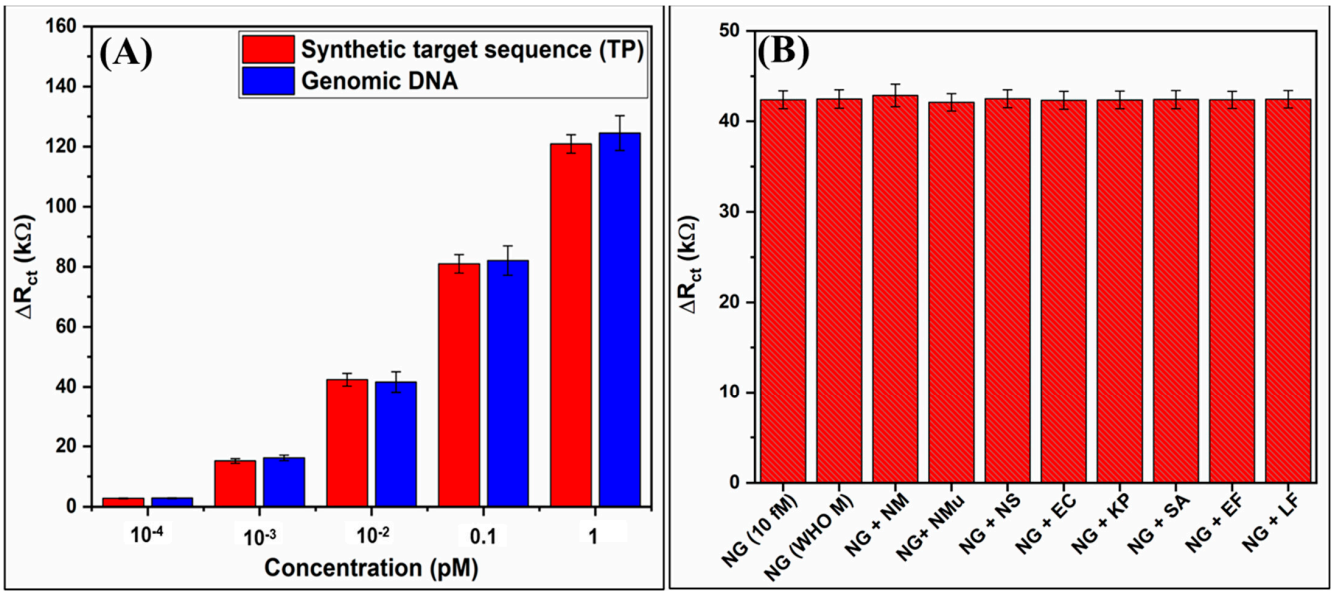


Figure 4. (**A**) Comparison between the biosensor response to synthetic TP and genomic DNA from NG for different concentrations (100 aM–1 pM). (**B**) Response of the biosensing assay to NG DNA mixed with DNA from other bacterial species. NM: *Neisseria meningitidis*, NMu: *Neisseria mucosa*, NS: *Neisseria sicca*, EC: *Escherichia coli*, KP: *Klebsiella pneumoniae*, SA: *Staphylococcus aureus*, EF: *Enterococcus faecalis*, LF: *Lactobacillus fermentum*.

The specificity of the biosensing assay was assessed by mixing the genomic DNA of NG with DNA from other bacteria (Section S3). The DNA was extracted using the boiling method; hence, all samples may contain protein and RNA as contaminants. The NG genomic DNA was mixed with DNA from other bacteria and subjected to the protocol mentioned in Section 2.7. As shown in Figure 4B, no significant change in ΔR_{ct} of the *C5*@paper biosensing electrode was observed when recorded in the presence of interfering DNA from different bacterial species. The ΔR_{ct} values for the different DNA mixtures are given in Table S1. These studies highlight the significance of sample enrichment via MBs before biosensing and hint at the high specificity of the designed oligonucleotide probes.

4. Conclusions

We have fabricated a conductive ink-coated, paper-based biosensing assay for the ultrasensitive detection of *Neisseria gonorrhoeae* using EIS. *C5*, the MWCNT-based conductive ink used in this study, was found to be highly conductive, with the maximum conductivity of the *C5*@paper electrodes being 10.1 $S{\cdot}cm^{-1}$. The ink formulation was optimized for thixotropy that can allow batch reproduction by screen printing. A magnetic bead-assisted supersandwich DNA hybridization assay was designed, which upon integration with the *C5*@paper electrodes, was found to be highly sensitive with an excellent detection limit (45 aM). The biosensing assay was further found to be highly specific for gonorrheal DNA when tested in a mixture of DNA from different non-gonorrheal species. This study not only reveals the utility of paper-based biosensors for DNA diagnostics but also highlights the potential of conductive inks in the fabrication of paper-based biosensors. It further attempts to bring gonorrhea to the forefront of scientific research as an important biosensing target. Further studies should focus on the modification of the conductive inks for obtaining improved electrochemical performance, which would further enhance biosensor sensitivity.

Supplementary Materials: The following supporting information can be downloaded at https://www.mdpi.com/article/10.3390/bios13040486/s1. Section S1: Alignment of the designed oligonucleotide probes with the target sequence (porA pseudogene); Section S2: Protocol followed for SCP immobilization on the MBs; Section S3: Bacterial species used in the specificity studies; Section S4: Calculation of resistivity of the *C5*@paper electrodes; Figure S1: FESEM image of the lateral edge of *C5*@paper electrode; Figure S2: CV curves of the *C5*@paper electrodes showing continuous use stability; Figure S3A: Equivalent circuit fitted into the Nyquist plots; Figure S3B: Bar graph showing the R_{ct} of *C5*@paper electrodes during 1-30 days of storage; Figure S4: Gel electrophoresis studies to ascertain the formation of DNA supersandwich structures; Table S1: R_{ct} values corresponding to 10 fM NG DNA mixed with DNA from different bacterial species.

Author Contributions: B.D.M. and N.G.: Conceptualization; N.G.: Experimentation, Writing; D.K.: Review and Editing, Supervision; A.D.: Resource Acquisition, Project administration, Supervision; S.S.: Review and Editing, Resource Acquisition; B.D.M.: Review and Editing, Supervision. All authors have read and agreed to the published version of the manuscript.

Funding: This research received no external funding.

Institutional Review Board Statement: Not applicable.

Informed Consent Statement: Not applicable.

Data Availability Statement: Data is contained within the articles and the supplementary information.

Acknowledgments: N.G. acknowledges the Central Research Facility (CRF), IIT Delhi, India for SEM, FESEM and AFM image acquisition. The CRF, Department of Applied Chemistry, DTU, Delhi, India is acknowledged for rheology analysis.

Conflicts of Interest: The authors declare no conflict of interest.

References

1. World Health Organization (WHO). Sexually Transmitted Infections (STIs). Available online: https://www.who.int/health-topics/sexually-transmitted-infections#tab=tab_1 (accessed on 24 February 2023).
2. World Health Organization (WHO). *Global Health Sector Strategies on, Respectively, HIV, Viral Hepatitis, and Sexually Transmitted Infections for the Period 2022–2030*; World Health Organization: Geneva, Switzerland, 2022; p. 9240053778.
3. Chen, X.; Zhou, Q.; Wu, X.; Wang, S.; Liu, R.; Dong, S.; Yuan, W. Visual and rapid diagnosis of *Neisseria gonorrhoeae* using Loop-mediated isothermal amplification combined with a polymer nanoparticle–based biosensor in clinical application. *Front. Mol. Biosci.* **2021**, *8*, 702134. [CrossRef]
4. Whelan, J.; Eeuwijk, J.; Bunge, E.; Beck, E. Systematic literature review and quantitative analysis of health problems associated with sexually transmitted *Neisseria gonorrhoeae* infection. *Infect. Dis. Ther.* **2021**, *10*, 1887–1905. [CrossRef]
5. Berus, S.M.; Adamczyk-Popławska, M.; Młynarczyk-Bonikowska, B.; Witkowska, E.; Szymborski, T.; Waluk, J.; Kamińska, A. SERS-based sensor for the detection of sexualltransmitted pathogens in the male swab specimens: A new approach for clinical diagnosis. *Biosens. Bioelectron.* **2021**, *189*, 113358. [CrossRef] [PubMed]
6. Chen, X.; Huang, L.; Zhou, Q.; Tan, Y.; Tan, X.; Dong, S. A nanoparticle-based biosensor combined with multiple cross displacement amplification for the rapid and visual diagnosis of *Neisseria gonorrhoeae* in clinical application. *Front. Microbiol.* **2021**, *12*, 747140. [CrossRef]
7. Ma, J.; Du, M.; Wang, C.; Xie, X.; Wang, H.; Li, T.; Chen, S.; Zhang, L.; Mao, S.; Zhou, X. Rapid and sensitive detection of *Mycobacterium tuberculosis* by an enhanced nanobiosensor. *ACS Sens.* **2021**, *6*, 3367–3376. [CrossRef]
8. Ali, M.; Bacchu, M.; Setu, M.; Akter, S.; Hasan, M.; Chowdhury, F.; Rahman, M.; Ahommed, M.; Khan, M. Development of an advanced DNA biosensor for pathogenic *Vibrio cholerae* detection in real sample. *Biosens. Bioelectron.* **2021**, *188*, 113338. [CrossRef] [PubMed]
9. Saadati, A.; Ehsani, M.; Hasanzadeh, M.; Seidi, F.; Shadjou, N. An innovative flexible and portable DNA based biodevice towards sensitive identification of *Haemophilus influenzae* bacterial genome: A new platform for the rapid and low cost recognition of pathogenic bacteria using point of care (POC) analysis. *Microchem. J.* **2021**, *169*, 106610. [CrossRef]
10. Yang, Y.; Liu, J.; Zhou, X. A CRISPR-based and post-amplification coupled SARS-CoV-2 detection with a portable evanescent wave biosensor. *Biosens. Bioelectron.* **2021**, *190*, 113418. [CrossRef]
11. Hwang, C.; Park, N.; Kim, E.S.; Kim, M.; Kim, S.D.; Park, S.; Kim, N.Y.; Kim, J.H. Ultra-fast and recyclable DNA biosensor for point-of-care detection of SARS-CoV-2 (COVID-19). *Biosens. Bioelectron.* **2021**, *185*, 113177. [CrossRef]
12. Khristunova, E.; Dorozhko, E.; Korotkova, E.; Kratochvil, B.; Vyskocil, V.; Barek, J. Label-free electrochemical biosensors for the determination of Flaviviruses: Dengue, Zika, and Japanese Encephalitis. *Sensors* **2020**, *20*, 4600. [CrossRef]
13. Bishoyi, A.; Alam, M.A.; Hasan, M.R.; Khanuja, M.; Pilloton, R.; Narang, J. Cyclic voltammetric-paper-based genosensor for detection of the target DNA of Zika virus. *Micromachines* **2022**, *13*, 2037. [CrossRef] [PubMed]
14. Verma, R.; Sood, S.; Singh, R.; Sumana, G.; Bala, M.; Sharma, V.K.; Samantaray, J.C.; Pandey, R.M.; Malhotra, B.D. Coupling electrochemical response of a DNA biosensor with PCR for *Neisseria gonorrhoeae* detection. *Diagn. Microbiol. Infect. Dis.* **2014**, *78*, 16–23. [CrossRef] [PubMed]
15. Wang, J.; Shi, A.; Fang, X.; Han, X.; Zhang, Y. Ultrasensitive electrochemical supersandwich DNA biosensor using a glassy carbon electrode modified with gold particle-decorated sheets of graphene oxide. *Microchim. Acta* **2014**, *181*, 935–940. [CrossRef]
16. Wang, L.; Shan, T.; Pu, L.; Zhang, J.; Hu, R.; Yang, Y.; Yang, J.; Zhao, Y. Glucometer-based electrochemical biosensor for determination of microRNA (let-7a) using magnetic-assisted extraction and supersandwich signal amplification. *Microchim. Acta* **2022**, *189*, 444. [CrossRef]
17. Xia, F.; White, R.J.; Zuo, X.; Patterson, A.; Xiao, Y.; Kang, D.; Gong, X.; Plaxco, K.W.; Heeger, A.J. An electrochemical supersandwich assay for sensitive and selective DNA detection in complex matrices. *J. Am. Chem. Soc.* **2010**, *132*, 14346–14348. [CrossRef] [PubMed]
18. Feng, Q.; Wang, M.; Qin, L.; Wang, P. Dual-signal readout of DNA methylation status based on the assembly of a supersandwich electrochemical biosensor without enzymatic reaction. *ACS Sens.* **2019**, *4*, 2615–2622. [CrossRef] [PubMed]
19. Li, J.; Jiang, J.; Su, Y.; Liang, Y.; Zhang, C. A novel cloth-based supersandwich electrochemical aptasensor for direct, sensitive detection of pathogens. *Anal. Chim. Acta* **2021**, *1188*, 339176. [CrossRef]
20. Liu, F.; Liu, H.; Liao, Y.; Wei, J.; Zhou, X.; Xing, D. Multiplex detection and genotyping of pathogenic bacteria on paper-based biosensor with a novel universal primer mediated asymmetric PCR. *Biosens. Bioelectron.* **2015**, *74*, 778–785. [CrossRef]
21. Colozza, N.; Caratelli, V.; Moscone, D.; Arduini, F. Origami paper-based electrochemical (bio) sensors: State of the art and perspective. *Biosensors* **2021**, *11*, 328. [CrossRef]
22. Nguyen, Q.H.; Kim, M.I. Nanomaterial-mediated paper-based biosensors for colorimetric pathogen detection. *Trends Anal. Chem.* **2020**, *132*, 116038. [CrossRef]
23. Solhi, E.; Hasanzadeh, M.; Babaie, P. Electrochemical paper-based analytical devices (ePADs) toward biosensing: Recent advances and challenges in bioanalysis. *Anal. Methods* **2020**, *12*, 1398–1414. [CrossRef]
24. Mohanraj, J.; Durgalakshmi, D.; Rakkesh, R.A.; Balakumar, S.; Rajendran, S.; Karimi-Maleh, H. Facile synthesis of paper based graphene electrodes for point of care devices: A double stranded DNA (dsDNA) biosensor. *J. Colloid Interface Sci.* **2020**, *566*, 463–472. [CrossRef]

25. Rana, A.; Killa, M.; Yadav, N.; Mishra, A.; Mathur, A.; Kumar, A.; Khanuja, M.; Narang, J.; Pilloton, R. Graphitic carbon nitride as an amplification platform on an electrochemical paper-based device for the detection of norovirus-specific DNA. *Sensors* **2020**, *20*, 2070. [CrossRef] [PubMed]
26. Lu, Q.; Su, T.; Shang, Z.; Jin, D.; Shu, Y.; Xu, Q.; Hu, X. Flexible paper-based Ni-MOF composite/AuNPs/CNTs film electrode for HIV DNA detection. *Biosens. Bioelectron.* **2021**, *184*, 113229. [CrossRef] [PubMed]
27. Camargo, J.R.; Orzari, L.O.; Araujo, D.A.G.; de Oliveira, P.R.; Kalinke, C.; Rocha, D.P.; dos Santos, A.L.; Takeuchi, R.M.; Munoz, R.A.A.; Bonacin, J.A. Development of conductive inks for electrochemical sensors and biosensors. *Microchem. J.* **2021**, *164*, 105998. [CrossRef]
28. de Araujo Andreotti, I.A.; Orzari, L.O.; Camargo, J.R.; Faria, R.C.; Marcolino-Junior, L.H.; Bergamini, M.F.; Gatti, A.; Janegitz, B.C. Disposable and flexible electrochemical sensor made by recyclable material and low cost conductive ink. *J. Electroanal. Chem.* **2019**, *840*, 109–116. [CrossRef]
29. Hong, H.; Jiyong, H.; Moon, K.-S.; Yan, X.; Wong, C.-P. Rheological properties and screen printability of UV curable conductive ink for flexible and washable E-textiles. *J. Mater. Sci. Technol.* **2021**, *67*, 145–155. [CrossRef]
30. Edali, M.; Esmail, M.N.; Vatistas, G.H. Rheological properties of high concentrations of carboxymethyl cellulose solutions. *J. Appl. Polym. Sci.* **2001**, *79*, 1787–1801. [CrossRef]
31. Pillai, A.S.; Chandran, A.; Peethambharan, S.K. MWCNT Ink with PEDOT:PSS as a multifunctional additive for energy efficient flexible heating applications. *Appl. Mater. Today* **2021**, *23*, 100987. [CrossRef]
32. Liu, L.; Shen, Z.; Zhang, X.; Ma, H. Highly conductive graphene/carbon black screen printing inks for flexible electronics. *J. Colloid Interface Sci.* **2021**, *582*, 12–21. [CrossRef]
33. Zheng, Y.; He, Z.; Gao, Y.; Liu, J. Direct desktop printed-circuits-on-paper flexible electronics. *Sci. Rep.* **2013**, *3*, 1786. [CrossRef]
34. He, P.; Cao, J.; Ding, H.; Liu, C.; Neilson, J.; Li, Z.; Kinloch, I.A.; Derby, B. Screen-printing of a highly conductive graphene ink for flexible printed electronics. *ACS Appl. Mater. Interfaces* **2019**, *11*, 32225–32234. [CrossRef] [PubMed]
35. Menon, H.; Aiswarya, R.; Surendran, K.P. Screen printable MWCNT inks for printed electronics. *RSC Adv.* **2017**, *7*, 44076–44081. [CrossRef]
36. Pekturk, H.Y.; Elitas, M.; Goktas, M.; Demir, B.; Birhanu, S. Evaluation of the effect of MWCNT amount and dispersion on bending fatigue properties of non-crimp CFRP composites. *Eng. Sci. Technol. Int. J.* **2022**, *34*, 101081. [CrossRef]
37. Kumar, S.; Gupta, N.; Malhotra, B.D. Ultrasensitive biosensing platform based on yttria doped zirconia-reduced graphene oxide nanocomposite for detection of salivary oral cancer biomarker. *Bioelectrochemistry* **2021**, *140*, 107799. [CrossRef] [PubMed]
38. Luo, H.; Chen, W.; Mai, Z.; Yang, J.; Lin, X.; Zeng, L.; Pan, Y.; Xie, Q.; Xu, Q.; Li, X. Development and application of Cas13a-based diagnostic assay for *Neisseria gonorrhoeae* detection and azithromycin resistance identification. *J. Antimicrob. Chemother.* **2022**, *77*, 656–664. [CrossRef]
39. GeneProof®. GeneProof Neisseria gonorrhoeae PCR Kit. Available online: https://www.geneproof.com/geneproof-neisseria-gonorrhoeae-pcr-kit/p1069 (accessed on 4 October 2022).
40. Golparian, D.; Hellmark, B.; Unemo, M. Analytical specificity and sensitivity of the novel dual-target GeneProof *Neisseria gonorrhoeae* PCR kit for detection of *N. gonorrhoeae*. *Apmis* **2015**, *123*, 955–958. [CrossRef]
41. Goire, N.; Ohnishi, M.; Limnios, A.E.; Lahra, M.M.; Lambert, S.B.; Nimmo, G.R.; Nissen, M.D.; Sloots, T.P.; Whiley, D.M. Enhanced gonococcal antimicrobial surveillance in the era of ceftriaxone resistance: A real-time PCR assay for direct detection of the *Neisseria gonorrhoeae* H041 strain. *J. Antimicrob. Chemother.* **2012**, *67*, 902–905. [CrossRef]
42. Zhao, L.; Liu, A.; Li, R.; Zhao, S. Multiplex TaqMan real-time PCR platform for detection of *Neisseria gonorrhoeae* with decreased susceptibility to ceftriaxone. *Diagn. Microbiol. Infect. Dis.* **2019**, *93*, 299–304. [CrossRef]
43. Gupta, R.; Valappil, M.O.; Sakthivel, A.; Mathur, A.; Pundir, C.S.; Murugavel, K.; Narang, J.; Alwarappan, S. Tungsten disulfide quantum dots based disposable paper based lab on genochip for specific meningitis DNA detection. *J. Electrochem. Soc.* **2020**, *167*, 107501. [CrossRef]
44. Srisomwat, C.; Teengam, P.; Chuaypen, N.; Tangkijvanich, P.; Vilaivan, T.; Chailapakul, O. Pop-up paper electrochemical device for label-free hepatitis B virus DNA detection. *Sens. Actuators B Chem.* **2020**, *316*, 128077. [CrossRef]
45. Farshchi, F.; Saadati, A.; Hasanzadeh, M. Optimized DNA-based biosensor for monitoring *Leishmania infantum* in human plasma samples using biomacromolecular interaction: A novel platform for infectious disease diagnosis. *Anal. Methods* **2020**, *12*, 4759–4768. [CrossRef] [PubMed]

Disclaimer/Publisher's Note: The statements, opinions and data contained in all publications are solely those of the individual author(s) and contributor(s) and not of MDPI and/or the editor(s). MDPI and/or the editor(s) disclaim responsibility for any injury to people or property resulting from any ideas, methods, instructions or products referred to in the content.

Wireless Personal Communications
https://doi.org/10.1007/s11277-023-10374-8

Congestion Aware Data Transmission in Mobile and Constrained IoT Network

Aastha Maheshwari[1] · Rajesh Kumar Yadav[1] · Prem Nath[2]

Accepted: 21 March 2023
© The Author(s), under exclusive licence to Springer Science+Business Media, LLC, part of Springer Nature 2023

Abstract
The growth and adoption of Internet of Things (IoT) have been increasing at a rapid pace over the past few years. IoT is a network of huge number of connected devices which are mobile and constrained in nature. These IoT devices communicate and transmit data over the Internet. This huge amount of transmission causes congestion in the network, resulting in packet delivery delay and high packet loss. Handling the problem of congestion requires transmission of data effectively in a congestion-aware manner. This paper proposes an approach for congestion-aware data transmission in mobile and constrained IoT networks. In this study, we have performed hop-to-hop communication and the process of next hop selection considers the multiple parameters to make it congestion-aware and effective. The proposed method uses the Analytic Hierarchy Process (AHP) to perform multiparameter based decision making to pick the best suitable next hop. The proposed method is ideal for the environment where nodes have limited resources, high traffic and need timely delivery of data packets. The results are compared with state-of-the-art methods, and the performance of the proposed method was better in terms of throughput by 6%, packet delivery rate by 7.5%, and reduced average delay by 4% as well as buffer overflow condition by 2%.

Keywords Internet of Things · Congestion · Data transmission · Hop to hop communication · Analytic Hierarchy Process

✉ Aastha Maheshwari
aasthamaheshwari.am@gmail.com

Rajesh Kumar Yadav
rkyadav@dtu.ac.in

Prem Nath
pmnath26@gmail.com

[1] Department of Computer Science and Engineering, Delhi Technological University, New Delhi, India

[2] Department of Computer Science and Engineering, H.N.B. Garhwal University, Srinagar, Uttarakhand, India

Published online: 29 March 2023

1 Introduction

IoT is generally considered as the integration of several technologies. The common service of IoT is to obtain the data from the deployed sensors in the ecosystem and process them on the web. As the demand for the smart and intelligent world increases, the size of the IoT network is also increasing rapidly [1]. Due to the increase in the size of IoT network, huge amount of data transmission occurs in the network. IoT network is considered as the next generation of communication world. It is required to create an efficient IoT network where billions of sensor nodes connect and communicate over the internet to one another. There are various applications of IoT like healthcare where the delivery of data packets on time is very important and will impact the quality of the network and can cause harm to life [1, 2].

Internet engineering task force (IETF) is responsible for forming standards for IoT networks. Being a low power and lossy network, routing in such network requires an intermediate node to transmit data to the gateway, as battery life is low for direct communication. RPL is one of the standard routing algorithms designed for IoT networks. RPL is initially designed for low traffic network. Hence, they are not very efficient to handle the large traffic over IoT networks [3]. This emphasises developing a new mechanism for the data transmission under high traffic and constrained environment. Data transmission in the IoT network is one of the crucial tasks as the nodes are receiving huge amounts of data over the network. Generally, the nodes deployed in the network are mobile in nature and have constraints on resources.

Traffic handling and the node constraints are two major focus areas in developing an IoT system. The data transmission in the IoT network needs to be reactive as the traffic is high and constrained nodes are mobile. Further, there will be change in the node positions and parameter values constantly [4]. The hop-to-hop data transmission is performed by picking the best appropriate node among the neighbours for data transmission, which avoids congestion and provides quality data transmission with minimum delay. Hence, it is essential to consider multiple parameters while picking the next hop so that all the quality, delay and congestion constraints can be handled [5].

The nodes that are present in the network and connected to each other for transfer of control packets and data packets for smooth communication. The transmission of such packets occurs in a huge volume every second and hence causes buffer overflow at node level. The continued process of packets at high-rate further leads to packet drop and increases the demand for packet retransmission in the network. This causes more flow of the packets in the network and increases congestion, which causes a higher packet loss and delay in delivery of the packet. Such issues may cause serious problems in time crucial applications like healthcare [6].

Hence, it is one of the major concerns of IoT which needs to be studied and find solution to provide the mechanism of data transmission in constrained IoT networks, considering congestion of nodes.

The approach of next hop selection plays a crucial role in solving the problem of congestion in the data transmission process. Hence, this paper proposes a solution to select the appropriate next hop for congestion aware data transmission in mobile and constrained IoT networks. The next hop is picked by nodes that required to send the data packet to the IoT gateway. For this, it selects the best optimal node among its neighbour based on the various parameters such as congestion level of node, link quality, distance and residual energy for further communication and transmission. The nodes are mobile in nature, which implies the position of the node is dynamic. Hence, it needs to pick the next hop among the

currently available nodes in communication range. Such a kind of node selection process is named reactive searching, and all the in-range nodes are treated as neighbour nodes.

The proposed data transmission approach uses the Analytic Hierarchy Process (AHP) method [7, 8, 9] to perform multiparameter decision making. This method arranges all the parameters in a hierarchy level of importance for the decision making and then collectively executes the decision of picking the best optimal node for congestion aware data transmission in mobile and constrained IoT networks.

The main contributions of this paper are:

1. This paper proposes the congestion-aware data transmission method for mobile IoT network while considering multiple parameters.
2. The multiple parameters are picked for congestion aware data transmission in mobile and constrained IoT networks. The parameters are related to the congestion level of the node, node quality and the distance for minimum delay.
3. A novel technique is proposed to calculate the weights of the parameters based on aggregation of importance-based hierarchy and AHP model.
4. The weights of the parameters and values are combined to pick the best appropriate next hop, which is less congested and provides minimum delay and lowers packet loss rate with reliable path for data transmission.

To solve the problem of data congestion while performing transmission of data in dense and mobile IoT network, the proposed approach introduces a new transmission mechanism that performs the hop-to-hop transmission by picking the best next hop based on its congestion and efficiency value for the packet delivery to gateway. The proposed approach focuses on providing an efficient and reliable transmission method in dense and congested environments by considering multiple parameters. These parameters are used for decision making and selection of best next hop between alternatives for the data transmission. Proposed approach results the increment of the network throughput and packet delivery rate while reduced average delay and buffer overflow condition.

In this paper, Sect. 2 discusses the existing method related to the objective. Section 3 explains the method used to develop a congestion aware data transmission in mobile and constrained IoT networks. Section 4 shows the experimental results of the approach, and conclusion is given in Sect. 5.

2 Existing Approaches

This section provides a comprehensive discussion of current research in congestion control in the sense of IoT.

Kim Kim et al. [10] explored the topic of congestion and load balancing in an IoT network. They discovered that when traffic loads are high, the majority of packet losses occur at links rather than queues, and that these losses are caused by hidden terminal problems that cause packet collisions. In order to resolve the issues, they devised a decentralized and dynamic control method that coordinates transmission rate and routing topology.

Elappila et al. [11] proposed an energy-efficient routing method for WSNs centered on congestion and interference awareness. Because multiple IoT objects send data to the same target, which is common in IoT monitoring applications, the proposed approach was designed to work in networks with high traffic and interference on node connections. The

suggested technique employs a function which uses signal to interference and noise ratio (SNIR) of the connection; the congestion degree at the next party node and the route's survivability parameter for selecting the next party node. However, this method demanded high cost and high time complexity.

To improve upon the previously proposed model, Elappila et al. [12] presented a Dynamic Survivable Path Routing (DSPR) protocol in a real-time network where there is high traffic and network congestion. The next-hop node was chosen based on the link's signal-to-interference-noise-ratio, the path's survival factor, and the path loss distance in this process. Still, the buffer overflow caused the network congestion.

Gozuacik et al. [13] developed a Parent-Aware Objective Function (PAOF) to find the best path for routing. PAOF is an objective function preemptive protocol that uses parent count and ETX measurements in data transmission route selection to accomplish load balancing. PAOF measures the distance between the ETX of the candidate nodes first, and if it is less than a specified number called Min_Hop_Rank_Increase_4, it compares the parents count, and then chooses the route with the lowest value as the preferred route. Nodes with relatable ETX values cause Routing Protocol for Low power and Lossy network (RPL) control messages to increase. Apart from this, the model doesn't take into consideration the parent node's energy.

Another congestion-aware RPL variation developed by Bhandari et al. [14] is CoAR, which uses ETX, queue usage, and residual energy as routing metrics. When a node's buffer occupancy surpasses its threshold, which is adaptive based on the current buffer occupancy and the ratio of incoming to outgoing traffic, the node is considered overcrowded in CoAR. To reduce congestion in the 6LowPAN network, the alternate parent is chosen in the propound work. Furthermore, the suggested work employs a monitoring system to prevent transitory congestion of the network's impacted nodes.

To alleviate network congestion, Jain et al. [15] proposed Energy and Congestion Aware Routing (ECAR), which is centered on hybrid gradient fields. The request is transmitted using this approach based on the node's depth, queue length, forward aware residual energy density, and residual energy.

Benyahia et al.[16] introduced Congestion Avoidance with Reliable Transport and Energy Efficiency (CARTEE) to attain congestion control. In this technique, they used distributed transmission rate adjustment, a new congestion detection technique, alternative implicit/explicit acknowledgement and fixed sliding window transmission. Even though they avoided congestion, data delivery caused end-to-end delay making it the technique's vital shortfall.

Sunitha et al. [17] proposed an energy-aware routing strategy to alleviate sensor network congestion. To avoid excessive packet loss, usually results in massive energy utilization, the suggested approach comprises of three steps. The network zone is categorised into multiple similar-sized sectors during first phase. In the following phase, a node is contrasted to its neighbours depending on the zone's minimum distance and traffic. The sector leader will be the node with the least distance and traffic that receive the packages and transmit them to the other sector leaders. The sector leaders are classed as congested or non-congested sectors in the third phase. In terms of end-to-end latency and packet delivery ratio, the results obtained from network simulator 2 are better.

Al-Kashoash et al. [3] proposed a technique called OHCA (optimization-based hybrid congestion alleviation), which uses a traffic control strategy and aggregates it with a resource control strategy. When a parent node detects an arrival rate greater than the service rate, it considers the congestion condition to be met and sends a DIO message with congestion information to its offspring nodes. When a child node receives a DIO message,

it uses the resource control approach to choose a non-congested parent. The traffic control approach is used if a non-congested parent node cannot be discovered. The major flaw of this technique was that it did not support hybrid application types.

In [18] author proposed the reliable path routing protocol where it finds the node selection factor to pick the appropriate next node based on the buffer occupancy, interference, congestion level and path quality. They mentioned the weight of each parameter in which highest weight was given to buffer to reduce the delay. The authors worked well to reduce the delay but the distance between nodes to reduce energy consumption as well as the mobility of nodes was not considered. Musaddiq et al. [19] examined the topic of heterogeneous IoT network congestion and provided a solution based on queue and workload condition (QW-RPL). The suggested approach aims to keep overall performance at a high level by using a reliable communication method. They presented a new goal function that incorporates the node's congestion condition by looking at the packet queue and connection workload. The suggested QWRPL model efficiently distributes the load by using periodic workload feedback and a weighted queue. Both variable and fixed heterogeneous traffic patterns are investigated in the proposed work. The requested work has been implemented in the Contiki OS and the Cooja simulator. In terms of distortion, latency, and packet reception ratio, the obtained simulation result reveals that QW-RPL has better performance.

In [20] author modified the RPL protocol to make it congestion and QoS aware. In this approach, authors used multiple parameters to select another parent node in case the allocated parent is failed or get congested. The parameters which are considered in the study are residual energy, number of hops, ETX and congestion. The congestion is dependent only on the status of buffer in this paper. TOPSIS is also used in the paper to achieve better accuracy. The experiments were shown good results in terms of throughput and energy consumption. However, paper did not consider other parameters of congestion such as link quality, transmission rate, and packet loss. This approach has not been compared with latest work also. In [21] we performed the offloading in RPL to make the transmission congestion aware by selecting the new parent node by considering multiple parameters to calculate congestion value. The packet is offloaded to the new parent node if the congestion value is high. The approach worked well in comparison to state of art and modified RPL for congestion control process. However, the approach used the ground of RPL protocol and made significant modifications to the protocol.

Observations from the above survey underline that congestion problem in IoT networks can be controlled by detecting it from buffer occupancy; however, the poor link quality may slow down the speed of transmission. RPL is the standard protocol which is used for data transmission in IoT network but it is not efficient in handling the dense and high traffic network, however, some the studies modified the existing routing protocol RPL by picking a new parent node when old parent node gets congested. The downside of this was that switching from one parent to another, resulted in an increase in hop count, delay and packet loss. This is the reason of designing the sperate data transmission mechanism for dense and mobile IoT network which is aware of data congestion and do not degrade the quality of network by switching parent nodes.

3 Methods and Materials

This section discusses the selection parameters, improved AHP, and the proposed method.

Table 1 Table of Abbreviations

D	Euclidean distance
(x, y)	Node coordinate in 2d plain
RE_P	Residual energy
IE_P	Initial energy
UE_P	Utilized energy
BO_R	Buffer occupancy ratio
N_P	Currently occupied buffer
Q_P	Actual size of the buffer
ETX	Expected transmission count
P_{data}	Data packet probability of successful delivery
P_{ack}	Acknowledgment packet's successful delivery
AHP	Analytic hierarchy process
M	Judgement matrix
m_{ij}	Degree of variable estimating probability of the event
y_i	Parameter value
Λ	Eigenvalue of the judgement matrix m
C.I	Consistency index
C.R	Consistency ratio
$\overrightarrow{W}_{i.k}$	Weight value provided to ith index under the kth judgment matrix

3.1 Selection Parameters

The parameters considered in the present approach are distance, hop count, angle of the node, residual energy, link quality and buffer occupancy (Table 1).

I. Distance

The difference of the distance between neigbor nodes is compared to find the most suitable node among the list of neighbors. To find the distance, Euclidean distance is measured between source and every possible neighbor.

$$D((x, y)(r, s)) = \sqrt{(x - r)^2 - (y - s)^2} \tag{1}$$

where (x, y) and (r, s) represent the position of the source node and one of the neighbour nodes respectively. D is the distance between them.

II. Hop Count

The number of hops needed to transmit the packet from a node to IoT gateway and is defined by Eq. (2).

$$hop\ count(X) = \frac{dis\tan ce\ from\ source\ to\ IoT\ gateway}{transmission\ range} \tag{2}$$

Additionally, the count of hops needed from neighbour need to be less than X. The neighbour node which reduces the count of hops will be considered most.

III. Residual Energy

The node shows the lifetime by the help of residual energy. The node with the higher residual energy will be survive more in the network and the chances of the node is more to be selected as the next neighbor node for the data packet transmission. To measure the residual energy (RE), initial energy (IE) is subtracted from the utilized energy (UE).

$$\mathrm{RE}_P = \mathrm{IE}_P - \mathrm{UE}_P \tag{3}$$

IV. Buffer Occupancy Ratio

The memory is required to hold the packet before it can be forwarded to next node so that the difference in transmission speed and receiving speed can be manages. This memory is named as buffer. Node consist of some amount of buffer to store and hold the packet so that the losses of the packet can be reduced. The Buffer occupancy Ratio is the ratio of the currently occupied buffer N_P and the actual size of the buffer Q_P. If the buffer is highly occupied mean, it may soon get overflowed and cause packet loss.

$$BO_R = \frac{N_P}{Q_S} \tag{4}$$

22 Expected Transmission Count (ETX)

Expected transmission count parameter indicates the quality of the link between nodes as it shows the count of transmission needed to deliver the packet successfully. The lower the value of ETX indicates the better quality of link for the transmission as it took lesser number of transmissions.

$$ETX_{i,j} = \frac{1}{P_{\mathrm{data}_{ij}} - P_{\mathrm{ack}_{ji}}} \tag{5}$$

where $P_{\mathrm{data}_{ij}}$ represents the data packet probability of successful delivery from (i) to (j) and $P_{ack_{ji}}$ represents the acknowledgment packet's successful delivery from (j) to (i).

3.2 Improved AHP Model

AHP (Analytic hierarchy Process) is a divide and conquer methodology which helps to determine the relative importance of various parameter needed for decision making. As the name suggests, it incorporates use of a hierarchical structure where the relative importance of sub elements can be determined by comparing them to their parent elements.

The basic steps of Improved AHP for the congestion aware multiple parameter-based node are:

Step 1 The parameters used to calculate the next best neighbour are represented as $\mathrm{y_i}$ where i ranges equal 1, 2, 3, 4 and 5 denoting buffer occupancy, ETX, hop count, residual energy and distance respectively.

Step 2 Subsequently a judgement matrix is established. Judgement matrix can be used to find relation between variables quantitatively. Let the judgement matrix M be represented as:

$$\mathrm{M} = \begin{bmatrix} m_{11} & m_{12} & \cdots & m_{1n} \\ m_{21} & m_{22} & \ldots & m_{2n} \\ \vdots & \ldots & \ldots & \vdots \\ m_{n1} & m_{n2} & \cdots & m_{nn} \end{bmatrix} \tag{6}$$

Each element, $m_{ij} = y_i / y_j$ (i and j are index variables), indicates the importance of degree of variable estimating probability of the event.

The Saaty's 9-Unit scale is used to determine element m_{ij} as follows:

- If y_i and y_j have equal importance, then m_{ij} and m_{ji} are both equal to 1.
- If y_i is little more dominating than y_j, then $m_{ji} = 3$ and $m_{ji} = 1/3$.
- If y_i is obviously more dominating than y_j, then $m_{ji} = 5$ and $m_{ji} = 1/5$.
- If y_i is much more dominating than y_j, then $m_{ji} = 7$ and $m_{ji} = 1/7$.
- If y_i is absolutely more dominating than y_j, then $m_{ji} = 9$ and $m_{ji}\, m_{ji} = 1/9$.

If these importance relationships for y_i and y_j are present between the relationships given above, m_{ij} may choose 2, 4, 6 and 8. i.e., any integer between 1 and 9 could be chosen.

Step 3 Following this, the consistency of judgement matrix will be checked.

The improved AHP can compute the optimal weight using multiple judgement matrices for each element for the proposed approach. To dodge enormous fallacy between weights, the consistency of *M* ought to be checked.

If the judgement matrix M is completely consistent, $m_{ij} = 1$; $\sum_{i=1}^{n} \lambda_i = \sum_{i=1}^{n} n$; $m_{ij} = n$. (λ is the eigenvalue of the judgment matrix M), a unique nonzero $\lambda = \lambda_{\max} = n$ exists. If judgement matrix is inconsistent, $\lambda_{\max} \geq n$.

Now,

$$\lambda_{\max} + \sum_{i \neq \max}^{n} \lambda_i = \sum_{i=1}^{n} n \tag{7}$$

Then,

$$\lambda_{\max} - n = -\sum_{i \neq \max}^{n} \lambda_i \tag{8}$$

The mean value is used as index to validate the consistency of judgement matrix:

$$\mathrm{C.I} = \frac{\lambda_{\max} -}{n-1} = \frac{-\sum_{i=\max} \lambda_{\max}}{n-1} \tag{9}$$

When $\lambda_{\max} = n$ and C.I = 0, *M* could be exactly consensus judged. The bigger the C.I is, the more awful the consistency of the judgment matrix will be. It is just necessitated that the consistency of the framework be sensible if C.I. ≤ 0.1.

The consistency of the judgment matrix is identified with its dimension. The larger the dimension n of the judgment matrix, the more regrettable the consistency of the judgment matrix. Therefore, the consistency requirement of high-dimensional judgment matrix ought to be relaxed. For this situation, the adjusted RI can be presented and the more sensible value, C.R., can be taken as the index to quantify the consistency of the judgment matrix. At the point when C.R. < 0.1, it is often thought the judgement matrix has acceptable consistency.

Step 4 Compute the weight intervals by utilizing the eigenvector strategy. In light of the judgment matrix obtained above, the weight of every element was determined by the eigenvector methods, and the determined weight was composed into Intervals, represented as the weight interval of the element (the intervals made out of independent weight points).

After randomly choosing a sensible judgment matrix, a weight of variable can be determined by the eigenvector strategy. The computation formulations are provided as follows:

$$Z_{i,k} = \prod_{j=1}^{n} c_{ij,k} \tag{10}$$

$$W_{i,j} = \sqrt[n]{Z_{i,j}} \tag{11}$$

$$\vec{\mathrm{W}}_{i,k} = \frac{W_{i.k}}{\sum_{i=1}^{n} W_{i,k}} \tag{12}$$

where i, represents the variable index ($i = 1, 2, 3, 4, 5$) and k is the index of sensibly chosen judgment matrix ($\mathrm{k} \in \mathrm{N}^{+}$). $\overrightarrow{W}_{i.k}$ is a weight value provided to ith index under the k_{th} judgment matrix. Thus, there are k weights for every variable i. The k weights of every factor obtained are written as intervals, constituting to the weight interval for a variable. For any variable i, choosing k judgment matrices, a weight interval i can be acquired by utilizing equations and the interval contains k weights.

Step 5 Finally obtaining the optimal weights.

The optimal weight completely considers all weights during the weight interval in order to guarantee that the last evaluation result can more readily represent the genuine circumstances. Simultaneously, the optimal weight combination can successfully stay away from the monotonous computation process in combination and work on finding the suitable neighbour node. Let the W_{i}, represent weight for variable i, and the sensible judgement matrix is $\mathrm{M} = (\mathrm{M} \in \mathrm{N}^{+})$; the required function will be:

$$\min \sum_{i=1}^{5} \sum_{k=1}^{M} \left(\vec{W}_{i,j} - w_i \right)^2 \tag{13}$$

The constraint condition for function will be:

$$\sum_{i=1}^{5} w_i = 1 \tag{14}$$

On above formulation basis, the optimal weight for ith variable could be written as $w_{i.}^{*}$.

3.3 Proposed Method

In this work, we proposed the congestion aware data transmission method, which transmits the data to the IoT gateway by performing hop to hop transmission. The objective of the approach is to achieve efficient data transmission while considering the congestion of the node. To do so, hop-to-hop transmission is performed, which selects the next best hop by considering the efficiency and congestion level of the node using multiple parameters. The

numerous parameters used in this strategy determine the efficiency and congestion level in the network. Distance, direction and residual energy constitute the former, while link quality and buffer occupancy constitute the latter.

The node which wants to send the packet broadcasts the hello message in its communication range. The node which receives this hello message and comes under initial conditions will send its residual energy, coordinates, buffer occupancy and expected transmission rate. These received values are used to compute all the parameter values and used in identif y_i ng the best suitable node by using mathematical model AHP. The process of selecting the best next hop continues till the packet reaches the IoT gateway.

The subsequent section will explain the working of the proposed approach.

3.4 Setup Phase

In the proposed model, constrained IoT devices (nodes) are deployed randomly in the network. Nodes in the network are constrained and have limited resources. It is assumed that nodes are battery powered and aware of their energy status. All the deployed nodes send information to the IoT gateway, which is placed at a prespecified location. All the deployed nodes are aware of the location of itself and IoT Gateway. The buffer size, initial energy and the communication range are same for all the nodes. The nodes are also capable of computing their residual energy, buffer occupancy and link quality at any given point.

3.5 Initialization Phase

In the network, when any node wants to transmit packet to the IoT gateway, node broadcasts the 'hello' control message with initial threshold values to its neighbours that are in present its transmission range. The node which receives the 'hello' control packet checks whether the node lies in the initial threshold values or not. If the initial threshold is satisfied, the neighbour node shares its residual energy, buffer occupancy, link quality (ETX), location and hop count with the sender of the 'hello' control message. The initial set of next hops is created by applying the threshold for various parameters. These threshold values are sent to the communication range of neighbour node by broadcast 'hello' control packet.

The threshold value of residual energy is 20% of initial energy, and if the node has remaining energy below 20% of the initial energy, is assumed incapable of taking the packet forward even if it is not a dead node. The condition of the hop count is that if the node is not able to reduce the hop count needed for the transmission of the packet, it will not be considered as it can move in opposite direction or at the same level. Doing so consumes energy to send the packet and creates an unnecessary delay in packet transmission.

The hop count of neighbour node needs to be one less than the hop count of the sender node.

3.6 AHP Phase

The process of selecting the best suitable node by considering multiple parameters and prioritizing them is done using the improved AHP method. The improved AHP method gives better accuracy as compared to the AHP in the impact of the parameters. In this method AHP model is used to find the weights for all the different parameters and based on the weights, the probability of node efficiency for being the best suitable neighbour node is calculated. The approach is majorly focused on providing congestion aware data transmission while considering the efficiency of the network. For congestion awareness, the approach considers buffer occupancy and expected transmission count, whereas for efficiency, the proposed approach considers hop count, residual energy and distance.

The optimal weight w_i^* for ith variable is obtained in improved AHP method. Once the optimal weight corresponding to each parameter is obtained, the value of node needs to be calculated. The node value is the summation of the multiple of parameter value with its weights. The node which is holding the best node value will be considered as the next best neighbour node and data packet is forwarded to that node. Further this process will be continued till the packet reaches to the destination i.e., IoT gateway node in our approach.

The resulting path is congestion aware optimal path in the mobile IoT network where it is assumed the nodes the moving but at a lower rate.

4 Experimental Results

The given approach is evaluated and analysed by simulating the network in the MATLAB as the tool provides all the required features to implement the proposed method in an effective way. The nodes are randomly deployed with same initial energy and buffer size in the network. The proposed approach is compared with the RPL based approaches which focused on the problem of congestion named as Congestion-Aware Routing protocol for low power and lossy networks (CoAR), Reliable Path Routing algorithm (RPR) congestion

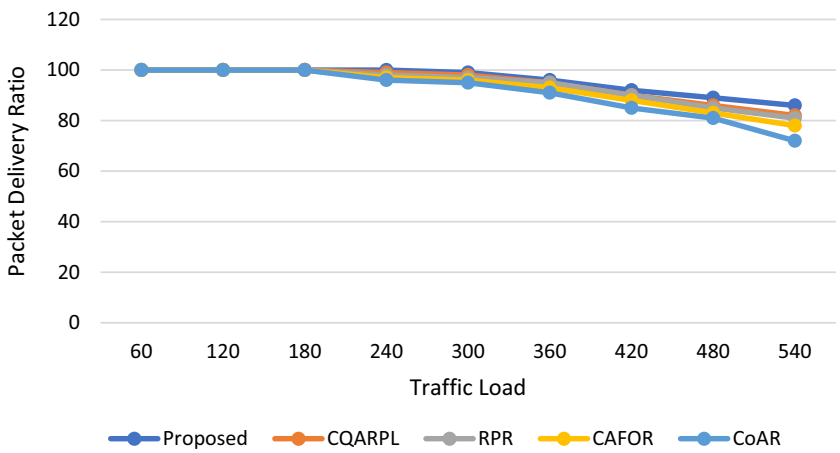


Fig. 1 Packet Delivery Ratio with Traffic Load

avoidance using fuzzy logic to find an optimal routing path (CAFOR) and Congestion and QoS-aware RPL(CQARPL). The parameters which are considered to show the improvement of the proposed approach from the existing approaches are packet delivery ratio, network throughput, rate of buffer overflow and average end-to-end delay in the network while transferring the packet.

The simulated network consisted of 1000 nodes in 1000×1000 m^2 area. The nodes are randomly deployed and mobile in nature. The transmission range of the node is 250 m and the buffer of the node can hold up to 50 packets. The initial energy of all nodes is same and its value is 5 J. The data rate and packet size are 250 kbps and 250 bytes respectively.

In the Fig. 1 it is shown that the packet delivery ratio is high as compared to existing approaches. The proposed approach provides 3% higher packet delivery ratio than the CQARPL whereas 3.5%, 6% and 7.5% higher packet delivery ratio than RPR, CAFOR and CoAR respectively. Packet delivery ratio is merely dependent on how well the transmission is happening in the network, and it shows the impact of packet loss and delay. It is visible in Fig. 1 that initially, when the count of nodes is less delivery ratio of all the nodes are similar, but as the traffic increase in the network, the delivery ratio starts reducing in the compared approaches.

The proposed approach increases the network throughput by successfully delivering the bits of the packet to the gateway. Figure 2 shows the throughput of the network (kbps) with respect to the traffic load. It has been observed that, with the increase in the size of network, throughput get impacted. As the increase in the network density causes higher traffic over network and results in the reduction of throughput. However, the impact of traffic load is minimum in proposed approach as compare to the CQARPL, RPR, CoAR and CAFOR. Throughput of the proposed method is 4% better than the compared methods.

The end-to-end delay is one of the crucial factors as the delay in the delivery of the packet may impact the usefulness of the packet; hence, it is important to reduce end to end delay in the IoT network. To reduce end to end delay in the proposed method tried to pick the best suitable node by considering distance, hop count and congestion value.

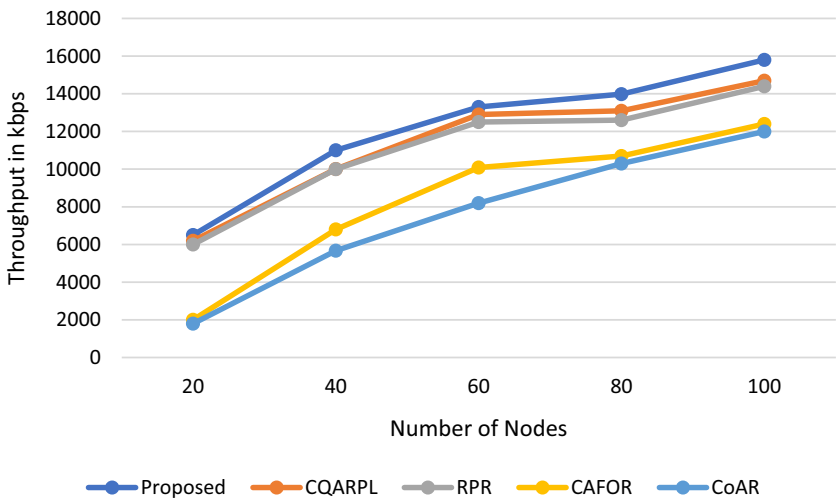


Fig. 2 Throughput of Network

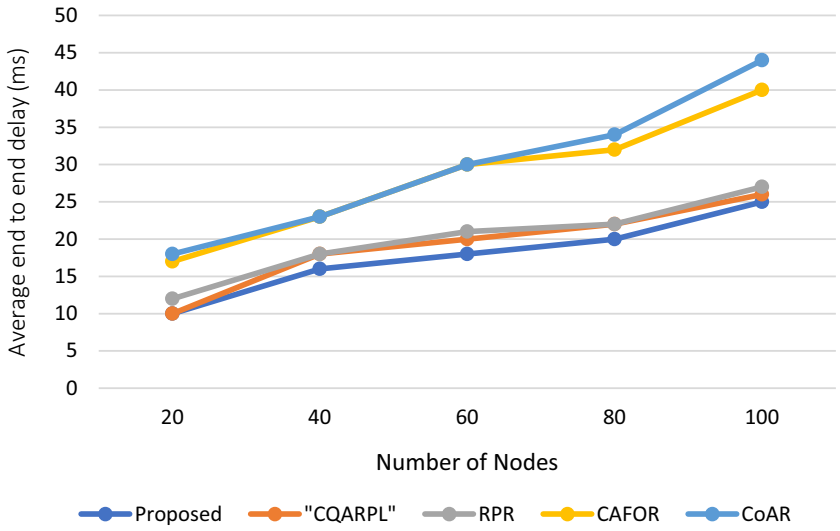


Fig. 3 Average end to end delay

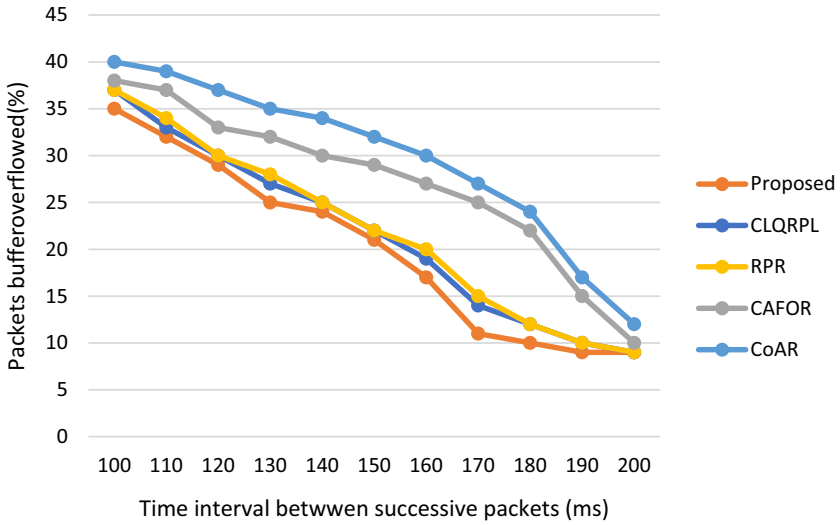


Fig. 4 Packet Overflow Percentage

In Fig. 3 the average end to end delay is shown for different counts of nodes in the network. The value of delay is 12% higher for CoAR, 10% higher for CAFOR, 4% higher for RPR and 3% higher for CAQRPL as compared to the delay caused by the proposed approach.

The rate of buffer overflow causes the packet loss in the network and it indicates the congestion of the node. The overflow occurs when the node is unable to handle the packet as the node transmission is slow as compared to receiving rate. It also occurs

when a huge number of nodes are sent through the same node and resulting in congestion over the node. The buffer overflow is handled by selecting the next hop wisely.

The proposed approach is better to handle the load by picking the most appropriate node among its present set of neighbors and also the dynamic nature of the approach of selecting the next node reactively. The proposed approach is causing a lesser buffer overflow percentage as compared to other existing approaches shown in Fig. 4. The percentage of buffer overflowed packet is 16% which is 2% lesser than CAQRPL, 3% lesser than RPR, 9% lesser than CAFOR and 12% lesser than CoAR.

5 Conclusion

In this paper, a congestion-aware data transmission method for mobile IoT network is proposed. The approach is designed for the network where the nodes are constrained and timely delivery of the packet is crucial. In the existing approaches, routing in IoT network is less effective when network gets congested and the congestion control measures are taken after the occurrence of congestion. The approach proposed in this study considers the problems of packet loss and delays in delivery which are majorly caused by congestion in the network. When the node wants to send packet, it selects the best suitable next neighbour node reactively based on the various factors which are weighted and analysed by the AHP model. In the AHP model, the parameters are arranged in the hierarchy based on the importance, where buffer occupancy is at the top importance. In presented approach, congestion is avoided by picking the best suitable node dynamically instead of having the prefixed parent node which may be congested and slow down the process. The results from the simulation of the network show that the proposed approach worked well for the high traffic network and provided higher packet delivery ratio as well as the minimum end to end delay in the network. The overall the throughput is also increased by using the proposed approach. In the future, the approach can be further improved by prioritizing the packet to the delivery at a higher speed. The approach will be experimented in real time scenario to achieve better results and benefits in real IoT network communication.

Authors' Contributions All authors read and approved the final manuscript.

Funding The authors declare that they don't have competing interests and funding.

Availability of Data and Material Data sharing not applicable to this article as no datasets were generated or analysed during the current study.

Code Availability Code is available.

Declarations

Conflict of interest On behalf of all authors, the corresponding author states that there is no conflict of interest.

References

1. https://www.edureka.co/blog/iot-applications.

2. Al-Fuqaha, A., Guizani, M., Mohammadi, M., Aledhari, M., & Ayyash, M. (2015). Internet of things: A survey on enabling technologies, protocols, and applications. *IEEE Communications Surveys and Tutorials, 17*(4), 2347–2376. https://doi.org/10.1109/COMST.2015.2444095
3. Al-Kashoash, H. A., Kharrufa, H., Al-Nidawi, Y., & Kemp, A. H. (2019). Congestion control in wireless sensor and 6LoWPAN networks: Toward the Internet of Things. *Wireless Networks, 25*(8), 4493–4522.
4. Maheshwari, A., & Yadav, R. K. (2020). Analysis of congestion control mechanism for iot. In *2020 10th international conference on cloud computing, data science & engineering (Confluence)* (pp. 288–293). IEEE.
5. Jain, V. K., Mazumdar, A. P., Faruki, P., & Govil, M. C. (2022). Congestion control in Internet of Things: Classification, challenges, and future directions. *Sustainable Computing: Informatics and Systems, 35*, 100678.
6. Alzahrani, & Salha, M. (2017). Sensing for the Internet of Things and its applications. In: *2017 5th international conference on future internet of things and cloud workshops (FiCloudW)*, (pp. 88–92).
7. Yang, F., Shen, Y., & Cui, X. et al. (2018). Voltage sag severity assessment based on multi-objective decision analytic hierarchy process.
8. Sun, H., Qiao, F., Wang, Z., & Guo, L. (2019). A two-level identification model for selecting the coordination strategy for the urban arterial road based on fuzzy logic. *International Journal of Simulation and Process Modelling, 14*(6), 478–487.
9. Li, W., Ye, Y., Hu, N., Wang, X., & Wang, Q. (2019). Real-time warning and risk assessment of tailings dam disaster status based on dynamic hierarchy-grey relation analysis. *Complexity, 2019*(9), 1–14.
10. Kim, H. S., Kim, H., Paek, J., & Bahk, S. (2016). Load balancing under heavy traffic in RPL routing protocol for low power and lossy networks. *IEEE Transactions on Mobile Computing, 16*(4), 964–979.
11. Elappila, M., Chinara, S., & Parhi, D. R. (2018). Survivable path routing in WSN for IoT applications. *Pervasive and Mobile Computing, 43*, 49–63.
12. Elappila, M. & Chinara, S. (2018). Dynamic survivable path routing for fast changing IoT network topologies. In *2018 17th IEEE international conference on trust, security and privacy in computing and communications/12th IEEE international conference on big data science and engineering (TrustCom/BigDataSE)* (pp. 92–97). IEEE.
13. Gozuacik, N., & Oktug, S. (2015). Parent-aware routing for iot networks. In S. Balandin, S. Andreev, & Y. Koucheryavy (Eds.), *Internet of Things, Smart Spaces, and Next Generation Networks and Systems: 15th International Conference, NEW2AN 2015, and 8th Conference, ruSMART 2015, St. Petersburg, Russia, August 26-28, 2015, Proceedings* (pp. 23–33). Cham: Springer International Publishing. https://doi.org/10.1007/978-3-319-23126-6_3
14. Bhandari, K. S., Hosen, A. S. M., & Cho, G. H. (2018). CoAR: Congestion-aware routing protocol for low power and lossy networks for IoT applications. *Sensors, 18*(11), 3838.
15. Jain, A., Pattanaik, K. K., Kumar, A., & Bellavista, P. (2021). Energy and congestion aware routing based on hybrid gradient fields for wireless sensor networks. *Wireless Networks, 27*(1), 175–193.
16. Benyahia, A., Bilami, A., & Sedrati, M. (2020). CARTEE: Congestion avoidance with reliable transport and energy efficiency for multimedia applications in wireless sensor networks. *Wireless Networks, 26*(3), 1803–1822.
17. Sunitha, G. P., Kumar, S. D., & Kumar, B. V. (2017). Energy balanced zone based routing protocol to mitigate congestion in wireless sensor networks. *Wireless Personal Communications, 97*(2), 2683–2711.
18. Pushpa Mettilsha, J., Sandhya, M. K., & Murugan, K. (2021). RPR: Reliable path routing protocol to mitigate congestion in critical IoT applications. *Wireless Networks, 27*, 5229–5243.
19. Musaddiq, A., Zikria, Y. B., & Kim, S. W. (2020). Routing protocol for Low-Power and Lossy Networks for heterogeneous traffic network. *EURASIP Journal on Wireless Communications and Networking, 2020*(1), 1–23.
20. Kaviani, F., & Soltanaghaei, M. (2022). CQARPL: Congestion and QoS-aware RPL for IoT applications under heavy traffic. *The Journal of Supercomputing, 78*(14), 16136–16166.
21. Maheshwari, A., Yadav, R. K., & Nath, P. (2022). Data congestion control using offloading in IoT network. *Wireless Personal Communications, 125*(3), 2147–2166.
22. Saaty, T. L. (2010). *Principia mathematica decernendi: Mathematical principles of decision making*. RWS Publications.

Publisher's Note Springer Nature remains neutral with regard to jurisdictional claims in published maps and institutional affiliations.

Springer Nature or its licensor (e.g. a society or other partner) holds exclusive rights to this article under a publishing agreement with the author(s) or other rightsholder(s); author self-archiving of the accepted manuscript version of this article is solely governed by the terms of such publishing agreement and applicable law.



Aastha Maheshwari received her M.Tech degree from National Institute of Technology (NIT) Hamirpur, Himachal Pradesh and She is currently pursuing PhD in Computer Engineering from Delhi Technological University (Formerly Delhi College of Engineering), New Delhi, India. Her specializations Internet of Things (IoT), sensor network and wireless communication.



Rajesh Kumar Yadav received his B.E(CSE) from G. B. Pant Engineering College Pauri (H.N.B Garahwal University),M.Tech(CS) from UPTU,Lucknow and PhD(Computer Engineering) from Delhi Technological University (Formerly Delhi College of Engineering), New Delhi, India. Presently he is working as an Assistant Professor in the department of Computer Science & Engineering at Delhi Technological University (DTU). His areas of research interest are Mobile ad-hoc Networks,Wireless Sensor Networks and Internet of Things (IoT).



Prem Nath is working as an Associate Professor in H.N.B. Garhwal University, Uttarakhand, India. Previously he worked as Assistant Controller of Patents and Designs, The Patent Office, Government of India. He received his B.E. (Computer Science and Engineering) from H.N.B. Garhwal University, Uttarakhand, India. He received his Ph.D. Degree from IIT (ISM), Dhanbad, Jharkhand, India. His main areas of interest are mobility management in wireless communication, automata theory, and intellectual property rights.

ResearchGate

See discussions, stats, and author profiles for this publication at: https://www.researchgate.net/publication/370114950

Cosmological test of σ θ as function of scale factor in f (R , T) framework

Article *in* New Astronomy · April 2023

DOI: 10.1016/j.newast.2023.102044

CITATIONS
0

READS
23

3 authors, including:



Himanshu Chaudhary
Delhi Technological University
7 PUBLICATIONS **7** CITATIONS
SEE PROFILE



Ankita Kohli
Delhi Technological University
2 PUBLICATIONS **0** CITATIONS
SEE PROFILE

All content following this page was uploaded by Himanshu Chaudhary on 30 April 2023.

The user has requested enhancement of the downloaded file.

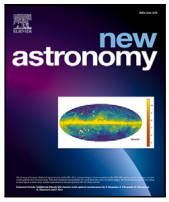
New Astronomy 103 (2023) 102044



Contents lists available at ScienceDirect

New Astronomy

journal homepage: www.elsevier.com/locate/newast



Cosmological test of $\frac{\sigma}{\theta}$ as function of scale factor in $f(R,T)$ framework

Himanshu Chaudhary, Aditya Kaushik *, Ankita Kohli

Department of Applied Mathematics, Delhi Technological University, Delhi 110042, India

ARTICLE INFO

Keywords:
Bianchi type space–time
Dark energy
f(R, T) gravity
Markov Chain Monte Carlo (MCMC)

ABSTRACT

The paper presents a study of the Bianchi type-I space–time model with perfect fluid in f(R, T) modified theory of gravity, where R is the Ricci scalar, and T denotes the trace of the energy–momentum tensor. The gravitational field equations of $f(R,T)$ are solved using expansion anisotropy as a suitable function of the average scale factor. Besides, we estimate the best-fit values of the model parameters by using the combined dataset of Cosmic Chronometers (CC) consisting of 31 measurements, the type Ia supernova dataset composed of 1048 measurements and the Baryon Acoustic Oscillations dataset consisting of ten measures with the Markov Chain Monte Carlo (MCMC) method. The resulting deceleration parameter shows that the Universe initially decelerated and later achieved an accelerated phase. Moreover, the paper analyses the cosmographic and cosmological parameters, suggest some improvements and illustrates findings through diagrams.

1. Introduction

In 1917 Einstein introduced the Cosmological Constant Λ in his field equations to ensure that his spatially spherical finite Universe was static and did not expand or contract over time. In 1922 Alexander Friedmann took two Einstein field equations and derived the two Friedmann equations, which showed how the Universe's spatial scale could change over time. In 1927/1929, Georges Lemaitre and Edwin Hubble observed the redshift of distant galaxies and concluded that the Universe was expanding. In 1964 discovery of Cosmic Microwave Background Radiation (CMB) by Arno Allan Penzias and Woodrow Wilson provided further evidence that expanding Universe and the big bang theory were correct based on observations of a supernova in 1998 from different periods in the Universe's history. We have determined that the Universe's expansion is accelerating, indicating that the Cosmological Constant Λ is small but positive. There are other astrophysical observations like Baryon Oscillation Spectroscopic (BAO) (Blake et al., 2011; Padmanabhan et al., 2012; Anderson et al., 2012), and PLANK Collaborations (Bennett et al., 2013) to confirm late time accelerating or expanding Universe since 1998. The Cosmological Constant Λ is sometimes called dark energy. It is often the case when Λ is on the left side of the Einstein Field Equation (EFE) along with the curvature term. However, in the trace reversed form of EFE, the Λ is on the right side of EFE along with the Energy Momentum Tensor (EM Tensor). Here Λ is responsible for the change in space–time geometry and can be considered an energy source. This type of energy is called Dark Energy. It does not appear to interact with light and is difficult to detect. Action principles are known to describe fundamental physical theories. Instead of depending on our choice of coordinates, the metric action is intrinsic. The metric has a canonical volume form which we can multiply by any scalar function. Moreover, space–time is known to be a manifold M with a Lorentzian signature metric, and action is a part of M integrated across a manifold. Ricci Scalar R is the simplest of these functions. This action refers to the Einstein–Hilbert action. In $f(R,T)$ modified theory of gravity by Harko et al. Harko et al. (2011), R is the curvature scalar, and T is the trace of the Stress–Energy Momentum tensor. This theory is consequent to altering the Einstein–Hilbert Action (EH) (Buchdahl, 1970; Starobinsky, 1980; Nojiri et al., 2006; Nojiri and Odintsov, 2004, 2007; De Felice and Tsujikawa, 2010; Carroll et al., 2004; Capozziello et al., 2006; Chiba et al., 2007; Capozziello et al., 2008, 2019; Starobinsky, 2007; Nojiri and Odintsov, 2011; Bamba et al., 2012; Nojiri and Odintsov, 2003; Sotiriou and Faraoni, 2010; Capozziello and De Laurentis, 2011; Clifton et al., 2012; Bertolami et al., 2007). Their primary objective is to make sense of the late-time speeding up an extension of the Universe without requiring the presence of the cosmological constant Λ.

The day $f(R,T)$ modified theory of gravity was proposed, it has become one of the notable theories addressing different issues of theoretical cosmologists. Adhav (Adhav, 2012) derives exact solutions of the field equations in respect of LRS Bianchi type-I space–time filled with perfect fluid in the framework of $f(R,T)$ gravity and discusses the physical behaviour of the model. Neelima and Rao (Rao and Neelima, 2013) presents a study of spatially homogeneous and anisotropic Bianchi type-VI_0 space–time filled with perfect fluid in general relativity and in the framework of $f(R,T)$ gravity proposed by

* Corresponding author.
E-mail addresses: himanshuch1729@gmail.com (H. Chaudhary), akaushik@dtu.ac.in (A. Kaushik).

https://doi.org/10.1016/j.newast.2023.102044
Received 16 January 2023; Received in revised form 4 April 2023; Accepted 10 April 2023
Available online 18 April 2023
1384-1076/© 2023 Elsevier B.V. All rights reserved.

Harko et al. Harko et al. (2011). The field equations are solved utilizing the anisotropy feature of the Universe in Bianchi type-VI_0 space–time. The author observes that the involvement of new function $f(R,T)$ does not impact the geometry of space–time but scarcely changes the matter distribution. Shamir (Shamir, 2015) attempts to investigate the Bianchi type-I Universe in the context of $f(R,T)$ gravity and study the exact solutions of locally rotationally symmetric Bianchi type-I space–time. Shamir solves the modified field equations assuming an expansion scalar proportional to the shear scalar. Sahoo and Sivakumar (Sahoo and Sivakumar, 2015) investigates locally rotationally symmetric (LRS) Bianchi type-I cosmological models. They obtained exact solutions of the field equations for the linearly varying deceleration parameter. Given the accelerating nature of the Universe, the author examines the dynamic and physical behaviour of the models. In one of the models, the Universe ends with a big rip. Moreover, the authors suggest that the Big Rip situation cannot be avoided and may be inherent in the linearly varying deceleration parameter. Tiwari et al. Tiwari et al. (2018) contemplated the Bianchi type-I model in $f(R,T)$ gravity with fluctuating gravitational and cosmological constants. They took $f(R,T) = R+2f(T)$ and the deceleration parameter as a linear function of the Hubble parameter. Tiwari and Beesham (Tiwari and Beesham, 2018) obtain the solution of the field equations under a variation law of the Hubble parameter considering a spatially homogeneous and anisotropic locally rotationally symmetric Bianchi type-I space–time with a cosmological term in $f(R,T)$. Singh and Beesham (Singh and Beesham, 2020) take into account a primary matter source and investigate the model further. However, an additional matter source appears due to the coupling between matter and $f(R,T)$ gravity. The constraints they obtain are for the realistic cosmological scenario. They also consider the case of a scalar field (normal or phantom) model and conclude that the model is consistent with a phantom scalar field only. This paper presents a study of the Bianchi type-I cosmological model with space–time filled with perfect fluid utilizing the $f(R,T)$ theory of gravity. We give our analysis in a general setting, assuming that anisotropy is proportional to a function expressed in terms of a scale factor. The CMB consists of the minor changes in temperature in the blackbody radiation left over from the Big Bang leading to anisotropy. There are available theoretical and experimental results (Chimento, 2004; Misner, 1968) to support this. Following the anisotropy in CMB, one can find that a class of anisotropic universe models exists in the Bianchi-type framework. The gravitational field equations of $f(R,T)$ are solved. The resulting deceleration parameter shows that the Universe initially decelerated and accelerated later. Moreover, the paper analyses the cosmographic and cosmological parameters, suggest some improvements, and illustrates findings through diagrams.

2. Review of $f(R,T)$ and field equations

The gravitational action for the modified $f(R,T)$ theory of gravity takes the form (Harko et al., 2011)

$$S = \int \left(\frac{1}{16\pi} f(R,T) + S_m\right)\sqrt{-g}\,dx^4, \tag{1}$$

where $f(R,T)$ is an arbitrary function of the Ricci scalar R and the trace T of the energy momentum tensor T_{ij}. Harko et al. Harko et al. (2011) proposed three classes as

$$f(R,T) = \begin{cases} R + 2h(T), \\ h_1(R) + h_2(T), \\ h_1(R) + h_2(R)h_3(T). \end{cases} \tag{2}$$

However, we restrict ourselves to $f(R,T) = R + 2h(T)$ and put $h(T) = \alpha T$, where α is the coupling constant. Then, Eq. (2) leads to

$$f_R(R,T)R_{ij} - \frac{1}{2}f(R,T)g_{ij} + (g_{ij}\Box - \nabla_i\nabla_j)f_R(R,T) = 8\pi T_{ij} - f_T(R,T)T_{ij} - f_T(R,T)\Theta_{ij}. \tag{3}$$

Here, $\Box = \nabla^i\nabla_j$ is the D'Alembert operator and $\Theta_{ij} = g^{ml}\frac{\delta T_{ml}}{\delta g^{ij}}$. Suppose that the matter in the Universe is a perfect fluid hence

$$\Theta_{ij} = -2T_{ij} - pg_{ij}$$

where $T_{ij} := (\rho + p)u_iu_j - pg_{ij}$ is the energy–momentum tensor with perfect fluid, ρ and p are energy density and cosmic pressure. Moreover, u^i is the four-velocity vector such that $u^iu_i = 1$. Consequently, the field equation takes the form

$$R_{ij} - \frac{1}{2}Rg_{ij} = 8\pi T_{ij} + 2f_T T_{ij} + [f(T) + 2pf_T]g_{ij}. \tag{4}$$

The Bianchi type-I model of the Universe reads

$$ds^2 = -dt^2 + A^2dx^2 + B^2dy^2 + C^2dz^2, \tag{5}$$

where A, B and C are the scale factors and function of time t only. The modified field equations are obtained as

$$\dot{H}_2 + H_2^2 + \dot{H}_3 + H_3^2 + H_2H_3 = -(8\pi + 3\alpha)p + \alpha\rho, \tag{6}$$

$$\dot{H}_1 + H_1^2 + \dot{H}_3 + H_3^2 + H_1H_3 = -(8\pi + 3\alpha)p + \alpha\rho, \tag{7}$$

$$\dot{H}_1 + H_1^2 + \dot{H}_2 + H_2^2 + H_1H_2 = -(8\pi + 3\alpha)p + \alpha\rho, \tag{8}$$

$$H_1H_2 + H_2H_3 + H_3H_1 = (8\pi + 3\alpha)\rho - \alpha p, \tag{9}$$

where $H_1 = \frac{\dot{A}}{A}$, $H_2 = \frac{\dot{B}}{B}$ and $H_3 = \frac{\dot{C}}{C}$.

The average scale factor a and the volume V for the Bianchi type-I model are given by

$$V = a^3 = ABC. \tag{10}$$

Using (9) and (10) to write

$$(\dot{H}_1 + H_1^2) - (\dot{H}_2 + H_2^2) - H_3(H_1 - H_2) = 0. \tag{11}$$

Integration leads to

$$H_1 - H_2 = \frac{k_1}{a^3} \tag{12}$$

for some constant k_1. Again, using (10) and (11) to obtain

$$H_2 - H_3 = \frac{k_2}{a^3} \tag{13}$$

where k_2 is another constant of integration. From (11), (12) and (13), it follows that

$$H_1 = \frac{\dot{a}}{a} + \frac{(2k_1 + k_2)}{3a^3}, \quad H_2 = \frac{\dot{a}}{a} + \frac{(k_2 - k_1)}{3a^3}, \quad \text{and} \quad H_3 = \frac{\dot{a}}{a} - \frac{(k_1 + 2k_2)}{3a^3}. \tag{14}$$

The Hubble parameter H, deceleration parameter q and shear tensor σ_{ij} for Bianchi type-I model are defined as

$$H = \frac{\dot{a}}{a}, \quad q = \frac{d}{dt}\left(\frac{1}{H}\right) - 1, \quad \text{and} \quad \sigma_{ij} = \frac{1}{2}\sigma_{ij}\sigma^{ij}, \tag{15}$$

where

$$\sigma_{11} = H_1 - H = \frac{(2k_1 + k_2)}{3a^3}, \quad \sigma_{22} = H_2 - H = \frac{(k_2 - k_1)}{3a^3}, \quad \sigma_{33} = H_3 - H = \frac{(k_1 + 2k_2)}{3a^3}, \quad \text{and} \quad \sigma_{44} = 0. \tag{16}$$

Then, we have

$$\sigma = \frac{1}{2}(\sigma_{11}^2 + \sigma_{22}^2 + \sigma_{33} + \sigma_{44}^2) = \frac{k}{a^3}, \tag{17}$$

where $3k^2 = k_1^2 + k_2^2 + k_1k_2$. Substitute values from (14) into (6)–(9) to obtain the pressure p and energy density ρ as

$$p = \frac{-1}{[(8\pi + 3\alpha)^2 - \alpha^2]}\left[2(8\pi + 3\alpha)\frac{\ddot{a}}{a} + 8\pi\left(\frac{\dot{a}}{a}\right)^2 + \frac{(8\pi + 4\alpha)k^2}{a^6}\right] \tag{18}$$

and

$$\rho = \frac{1}{[(8\pi+3\alpha)^2-\alpha^2]}\left[-2\alpha\frac{\ddot{a}}{a}+(24\pi+8\alpha)\left(\frac{\dot{a}}{a}\right)^2-\frac{(8\pi+4\alpha)k^2}{a^6}\right]. \quad (19)$$

Let us consider the anisotropy $\left(\frac{\sigma}{\theta}\right)$ as a function of scale factor $a(t)$ and $\theta = 3H$. Suppose it is astronomically immense at the beginning of the Universe and vanishes for extensively large t. For Bianchi type-I spacetime, we have

$$\frac{\sigma}{\theta} = \frac{k}{3a^2\dot{a}} = f(a). \quad (20)$$

Integrating, we get

$$k(t+t_1) = 3\int a^2 f(a)da \quad (21)$$

where t_1 is a constant of integration. Following (Singh et al., 2015), let

$$f(a) = \frac{1}{(n+a^3)} \quad (22)$$

where n is a positive integer . For this choice of function, observe that at an earlier time $\frac{\sigma}{\theta} \neq 0$ and at a later time $\frac{\sigma}{\theta} = 0$. Consequently, from (21) and (22) the scale factor of the Universe is obtained as

$$a = [n(e^{kt}-1)]^{\frac{1}{3}}. \quad (23)$$

Next, we use the relation $H = \frac{\dot{a}}{a}$ and Eq. (23) to write

$$H = \frac{\dot{a}}{a} = \frac{k}{3}\left[\frac{e^{kt}}{e^{kt}-1}\right]. \quad (24)$$

Clearly, $k = 0$ is the singularity and consequently we choose $k > 0$. Using (23) and relation $a = \frac{1}{1+z}$ to obtain redshift-time relation

$$t = \frac{1}{k}log\left[\frac{n(1+z)^3+1}{n(1+z)^3}\right]. \quad (25)$$

Consequently, the Hubble parameter in terms of the redshift, reads

$$H(z) = \frac{k}{3}(n(z+1)^3+1). \quad (26)$$

The deceleration parameter q is given by

$$q = \frac{d}{dt}\left(\frac{1}{H}\right)-1. \quad (27)$$

Therefore, from (24) and (27), we obtain

$$q = -1+3e^{-kt}. \quad (28)$$

Moreover, the deceleration parameter in terms of the redshift is obtained using (25) in (28) as

$$q = \frac{-1+2n(z+1)^3}{1+n(z+1)^3}. \quad (29)$$

3. Data description and results

In this section, we use Cosmic Chronometers (CC), type Ia supernova, and Baryonic Acoustic Oscillation(BAO) datasets to find the best-fit values of model parameters. We implement MCMC and validate our model by minimizing function χ^2 define as

$$\chi^2 = \chi_{CC} + \chi^2_{SN} + \chi^2_{BAO}.$$

3.1. Cosmic chronometers

To obtain the best-fit range of model parameters, consider the data set of 31 measurements of $H(z)$ in the redshift range $0.07 < z < 1.965$ from cosmic chronometers listed in Bouali et al. (2019), also see Bouali et al. (2023). The underlying principle for these measurements was proposed in Jimenez and Loeb (2002), relating the Hubble parameter $H(z)$ with redshift z and cosmic time t using

$$H(z) = -\frac{1}{1+z}\frac{dz}{dt}. \quad (30)$$

The function χ^2_{CC} for the uncorrelated CC measurements reads

$$\chi^2_{CC}(k,n) = \sum_{i=1}^{31}\frac{\left[H^{th}(z_i,k,n)-H^{obs}(z_i)\right]^2}{\sigma^2_{H^{\rm obs}(z_i)}}, \quad (31)$$

where $H^{\rm th}(z_i,k,n)$ represents the theoretical value obtained from the cosmological model and $H^{\rm obs}(z_i)$ denotes the observed value of Hubble parameter with standard deviation $\sigma^2_{H^{\rm obs}(z_i)}$.

3.2. Supernova datasets

We consider a compilation comprises of the largest type Ia supernovae of 1048 measurements from five subsamples SNLS, SDSS, PSI, low- z, and HST in the redshift range $0.01 < z < 2.3$ (Akarsu et al., 2019; Jimenez and Loeb, 2002; Sharma, 2020). The associated $\chi^2_{\rm SN}$ function of the Pantheon data reads

$$\chi^2_{\rm SN} = \Delta\mu C^{-1}_{\rm SN}\Delta\mu^T. \quad (32)$$

Here $\Delta\mu = \mu^{\rm obs}_i - \mu^{\rm th}$, where $\mu^{\rm obs}_i = \mu_{B,i} + \mathcal{M}$ is the observed distance modulus (Betoule et al., 2014), $\mu_{B,i}$ denotes the observed peak magnitude at maximum in the rest frame of B band for redshift z_i, and $\mathcal{M}$ is the nuisance parameter. Moreover, the theoretical distance modulus is evaluated using

$$\mu^{\rm th} = 5\log_{10}D_L + \mathcal{M},$$

where

$$D_L = (1+z_{\rm hel})\int_0^{z_{\rm cmb}}\frac{H_0 dz}{H(z)}$$

with $z_{\rm hel}$, $z_{\rm cmb}$ as heliocentric and CMB rest frame redshifts, respectively. The covariance matrix $C_{\rm SN}$ (Jesus et al., 2018) is measured as a sum of systematic covariance matrix $C_{\rm sys}$ and diagonal of the covariance matrix of statistical uncertainty $D_{\rm stat}$ given by

$$D_{\rm stat\ ,ii} = \sigma^2_{\mu_{B,i}}.$$

For detailed description, the systematic covariance matrix, $\mu_{B,i}, \sigma^2_{\mu_{B,i}}$, $z_{\rm cmb}$, and $z_{\rm hel}$ for the ith SN, see Scolnic et al. (2018).

3.3. Baryon acoustic oscillations

Following (Anderson et al., 2014; Beutler et al., 2011; Ross et al., 2015; Kazin et al., 2014; Bautista et al., 2017), we use Baryon Acoustic Oscillations (BAO) measurements consisting of ten correlated and uncorrelated data points. The 6dFGS, SDSS, and WiggleZ surveys comprise the BAO data set, including BAO measurements at six distinct redshifts tabulated in Table 1. Let us consider BAO from different distance measures: $D_A(z)/r_s$, $D_V(z)/r_s$, $r_s/D_V(z)$, and c/Hr_s. Here, $D_A(z)$ is the angular diameter distance, $D_V(z)$ is the volume averaged scale, and r_s is the sound horizon calibrating the distance scale measurements given by

$$D_A(z) = \frac{1}{(1+z)}\int_0^z\frac{dz'}{H(z')}, \quad D_V(z) = \left[(1+z)^2 D_A(z)^2\frac{z}{H(z)}\right]^{\frac{1}{3}}, \text{ and}$$
$$r_s = \int_{z_d}^{\infty}\frac{c_s(z)}{H(z)} \quad (33)$$

where $c_s(z)$ is the speed of sound of the photon-baryon fluid and z_d is the redshift at drag epoch.

WiggleZ and Lya data are correlated, and their covariance matrices (Blake et al., 2011) read

$$\mathbf{C}_{\rm WiggleZ} = \begin{pmatrix} 1040.3 & -807.5 & 336.8 \\ -807.5 & 3720.3 & -1551.9 \\ 336.8, & -1551.9 & 2914.9 \end{pmatrix} \text{ and}$$
$$\mathbf{C}_{\rm Lya} = \begin{pmatrix} 2.36686 & 0 \\ 0 & 12.7551 \end{pmatrix}. \quad (34)$$

Table 1
Summary of the Baryon Acoustic Oscillations measurements used in this paper.

BAO name	Redshift z	Experiment	Measurement	Standard deviation
6dFGS	0.106	r_s/D_V	0.327	0.015
SDSS DR7 MGS	0.15	D_V/r_s	4.465666824	0.1681350461
BOSS-LOWZ	0.32	D_V/r_s	8.62	0.15
BOSS-CMASS	0.57	D_V/r_s	13.70	0.1
DES	0.81	D_A/r_s	10.75	0.43
Lya	2.34 2.34	D_A/r_s c/Hr_s	11.28 9.18	0.65 0.28
WiggleZ	0.44 0.60 0.73	D_V/r_s	0.073 0.0726 0.0592	0.031 0.0164 0.0185

Table 2
Summary of the best-fit values of the free parameters of the model.

MCMC results			
Datasets	Parameters	Prior	Best-fit value
CC	k	[0,1]	$0.786549^{+0.035810}_{-0.035810}$
	n	[2,3]	$2.323456^{+0.016999}_{-0.016999}$
SN	k	[0,2]	$0.951233^{+0.010089}_{-0.010089}$
	n	[2,3]	$2.294569^{+0.037308}_{-0.037308}$
BAO	k	[0,2]	$1.030244^{+0.165383}_{-0.165383}$
	n	[2,3]	$2.674378^{+0.101188}_{-0.101188}$
CC + SN + BAO	k	[0,2]	$0.990266^{+0.019826}_{-0.019826}$
	n	[2,3]	$2.540596^{+0.033178}_{-0.033178}$

Finally, the total $\chi^2_{\mathbf{BAO}}$ takes the form

$$\chi^2_{\mathbf{BAO}} = \chi^2_{\mathbf{6dFGS}} + \chi^2_{\mathbf{SDSS}} + \chi^2_{\mathbf{BOSS-LOWZ}} + \chi^2_{\mathbf{BOSS-CMASS}} + \chi^2_{\mathbf{DES}} + \chi^2_{\mathbf{Lya}} + \chi^2_{\mathbf{WiggleZ}}. \quad (35)$$

The total chi-square (χ^2_{tot}) is given by the sum of all the χ^2 defined previously, i.e.

$$\chi^2_{tot} = \chi^2_{CC} + \chi^2_{SN} + \chi^2_{BAO}. \quad (36)$$

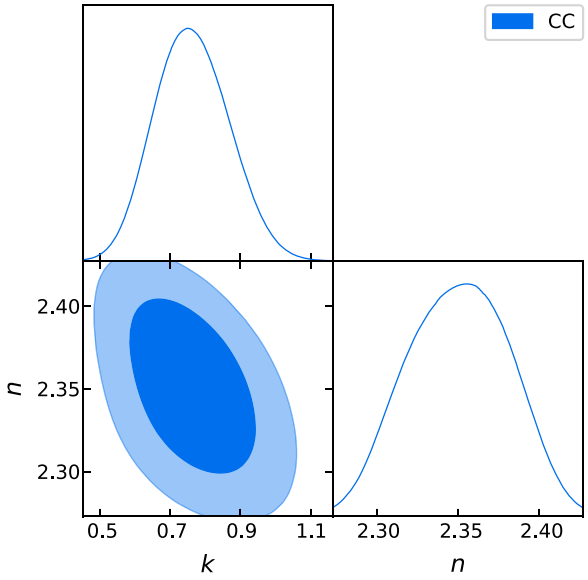


Fig. 1. MCMC confidence contours at 1σ and 2σ obtained from CC dataset.

4. Cosmological and cosmographic parameters

In this section, we discuss cosmological parameters like Hubble parameter, pressure, energy density and scale factor using best-fit values of the model parameters. There are other parameters named cosmographical parameters for understanding the past and future evolution of the Universe. Cosmography studies scale factors by expanding it by the Taylor series in cosmic time. The cosmographical parameter like jerk (j), snap (s), lerk (l) and m are given by Pacif (2020), Escamilla-Rivera and Capozziello (2019) as

$$j = \frac{a^3}{aH^3} = (1+z)\frac{dq}{dz} + q(1+2q), \quad s = \frac{a^{(4)}}{aH^4} = -(1+z)\frac{dj}{dz} - j(2+3q),$$
$$l = \frac{a^{(5)}}{aH^5} = -(1+z)\frac{ds}{dz} - s(3+4q), \quad m = \frac{a^{(6)}}{aH^6} = -(1+z)\frac{dl}{dz} - l(4+5q).$$

5. Test for validation of the model

In this section, we will perform several cosmological experiments to help us verify the accuracy of the model and to determine its feasibility.

5.1. Energy conditions

The behaviour of strong gravitational fields and cosmic geometries can be studied using general relativity energy conditions (ECs). Which also describes matter in the Universe and provides an understanding of the evolution of the Universe. ECs also ascribe the behaviour of null, space-like, time-like, or light-like geodesics. The ECs used are the strong energy condition (SEC), weak energy condition (WEC) and dominant energy condition (DEC) given below

- Weak energy conditions (WEC), if $\rho \geq 0, \rho + p \geq 0$.
- Strong energy conditions (SEC), if $\rho + 3p \geq 0$.
- Dominant energy conditions (DEC), if $\rho \geq 0, |p| \leq \rho$.

The matter in this model satisfies the WEC and SEC but not the DEC; see the figures above.

5.2. Equation of state

The equation of state (EoS) comes from thermodynamics by relating the variables that describe the state of a system. We relate energy density with the pressure of the perfect fluid by setting the energy density proportional to the pressure with a constant of proportionality ω and obtain $p = \omega\rho$. Assuming our perfect fluid is barotropic fluid and density is a function of pressure only. Moreover, ω is affecting the EM tensor. The EoS parameter is obtained as (see Box I).

If $\omega = 0$, we are left with the mass density, which provides us with an EM tensor for "DUST", describing that massive matter does not exert any pressure. For pure radiation $\omega = 1/3$, which is obtained by tracing the EM tensor equation to zero. If $\omega = -1$, we obtain $p = -\rho c^2$ and get an EM tensor with mixed indices, which is $\rho c^2 \delta^b_a$.

$$\omega = \frac{-9\pi(3\alpha+8\pi)((n(z+1)^3)^2)+6\pi(3\alpha+8\pi)n^2(1+n(z+1)^3)(n(z+1)^3)-6\pi(\alpha+4\pi)n^2(1+n(z+1)^3)^2}{-9(3\alpha+8\pi)((n(z+1)^3)^2)-6\alpha n^2(1+n(z+1)^3)+2(5\alpha+12\pi)n^2(1+n(z+1)^3)^2} \quad (37)$$

Box I.

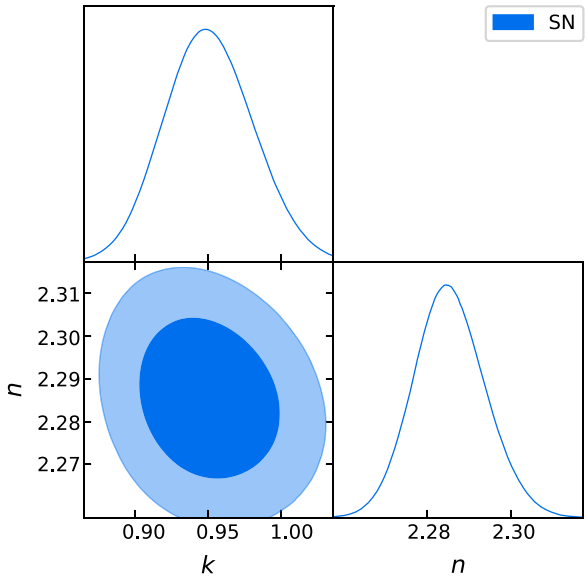


Fig. 2. MCMC confidence contours at 1σ and 2σ obtained from SN dataset.

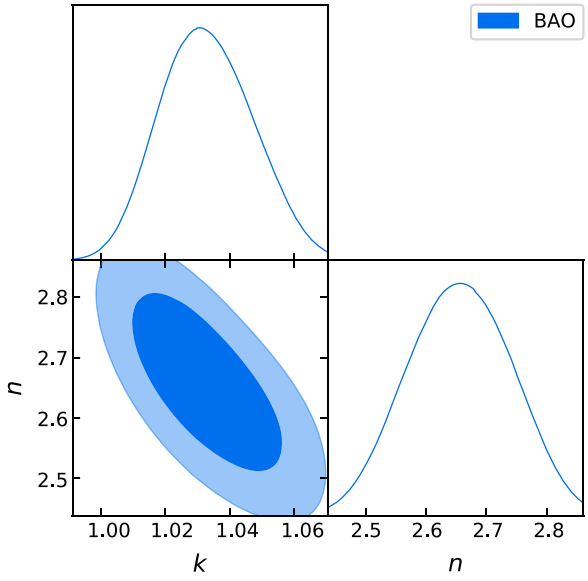


Fig. 3. MCMC confidence contours at 1σ and 2σ obtained from BAO dataset.

6. Information criteria

The information criteria (IC) play a crucial role in the model analysis. The χ^2_{red} criterion is used to statistically test the best fit values of free parameters associated with the model. The corrected Akaike's Information Criterion (AIC) (Li et al., 2010; Burnhan and Anderson, 2002; Burnham and Anderson, 2004; Liddle, 2007) compares the given model

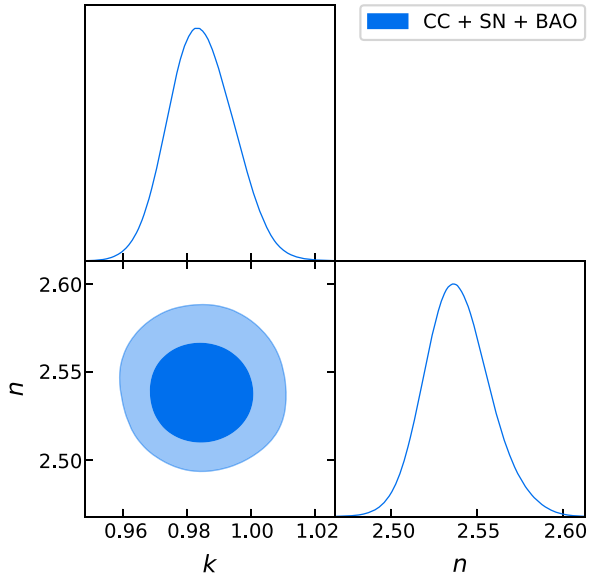


Fig. 4. MCMC confidence contours at 1σ and 2σ obtained from CC+SN+BAO dataset.

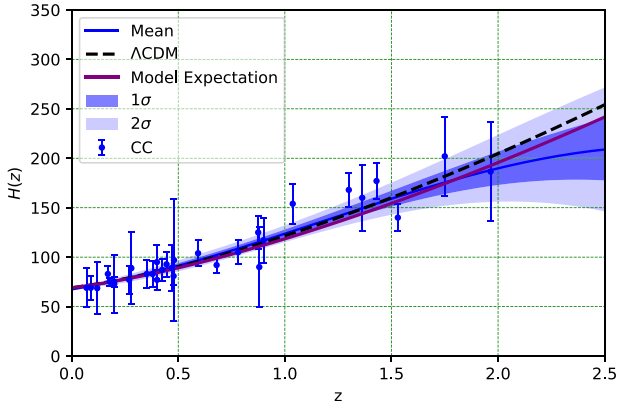


Fig. 5. Theoretical curve of Hubble function $H(z)$ of the model shown in purple line and ΛCDM model shown in black dotted line with $\Omega_{m0} = 0.3$ and $\Omega_\Lambda = 0.7$, against CC data sets are shown in blue dots with their corresponding error bars with 1σ and 2σ error bands.

with a set of models. The Gaussian estimator for the AIC reads (Burnham and Anderson, 2004; Liddle, 2007)

$$\text{AIC} = -2\ln(\mathcal{L}_{max}) + 2\kappa + \frac{2\kappa(\kappa+1)}{N-\kappa-1}$$

where $\mathcal{L}_{max}$ is the maximum likelihood function, κ denotes parameters in the models, and N is the number of data points used. Since $N \gg 1$, AIC approaches $-2\ln(\mathcal{L}_{max}) + 2\kappa$ for sufficiently large N. For the given model, the deviations of the IC lead to

$$\triangle\,\text{AIC} = \text{AIC}_{model} - \text{AIC}_{min} = \triangle\,\chi^2_{min} + 2\,\triangle\,\kappa.$$

In data analysis, the more favourable range of $\triangle$ AIC is $(0, 2)$. The low favourable range of $\triangle$ AIC is $(4, 7)$, while $\triangle$ AIC > 10 provides a less support model.

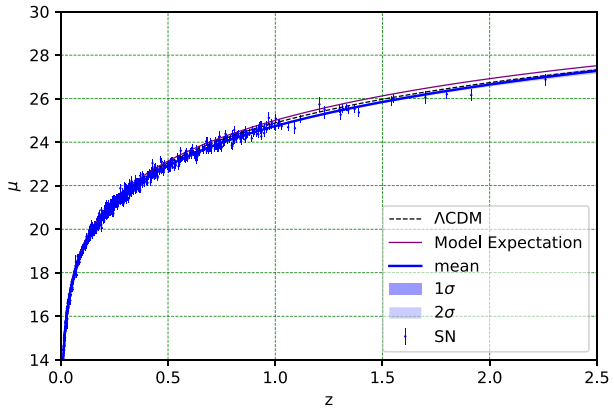


Fig. 6. Theoretical curve of distance modulus $\mu(z)$ of the model shown in purple line and ΛCDM model shown in black dotted line with $\Omega_{m0} = 0.3$ and $\Omega_{\Lambda} = 0.7$, against type Ia supernova data shown in blue dots with their corresponding errors bars with 1σ and 2σ error bands.

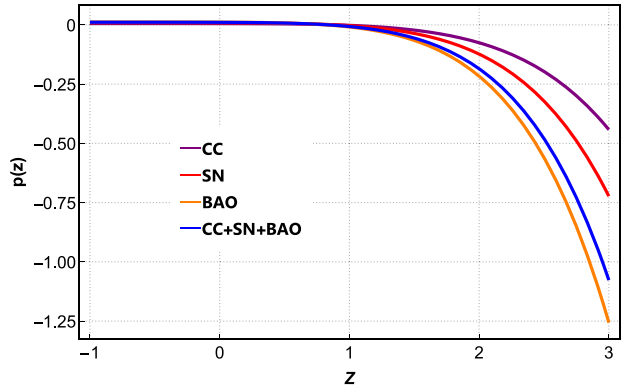


Fig. 7. Evolution of the pressure with respect to the redshift.

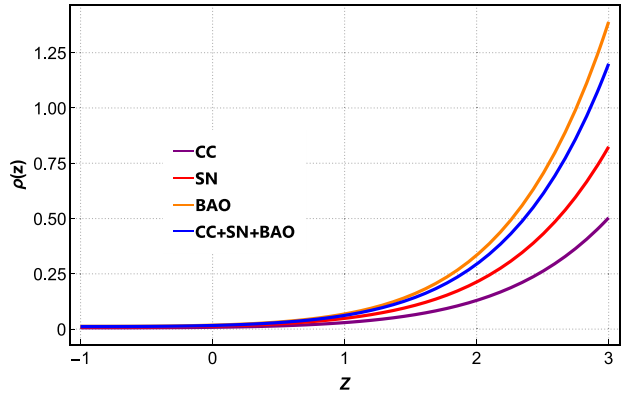


Fig. 8. Evolution of energy density with respect to the redshift.

Table 3
Summary of the χ^2_{min}, χ^2_{red}, AIC and ΔAIC.

Model	χ^2_{min}	χ^2_{red}	AIC	ΔAIC
ΛCDM	1026.67	0.869	1030.67	0
Model	1027.21	0.867	1031.21	2.09

7. Conclusion

In this article, we used the framework of $f(R,T)$ modified theory of gravity to investigate the accelerated expansion of the Universe by

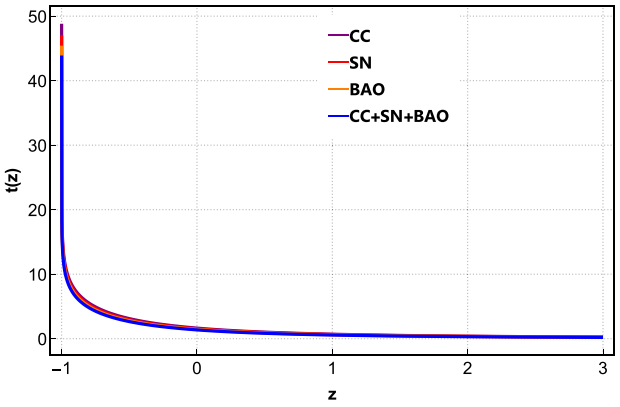


Fig. 9. Evolution of cosmic time with respect to the redshift.

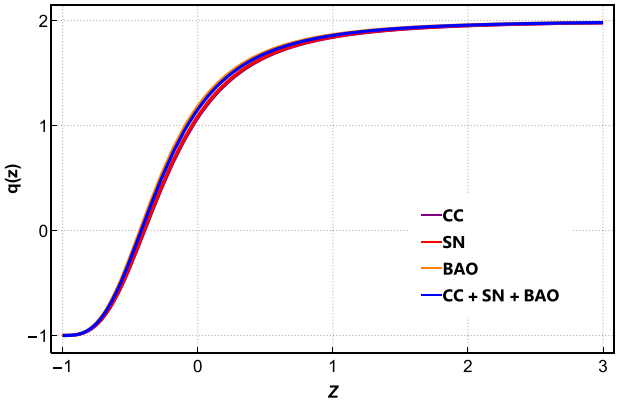


Fig. 10. Evolution of the deceleration parameter with respect to redshift.

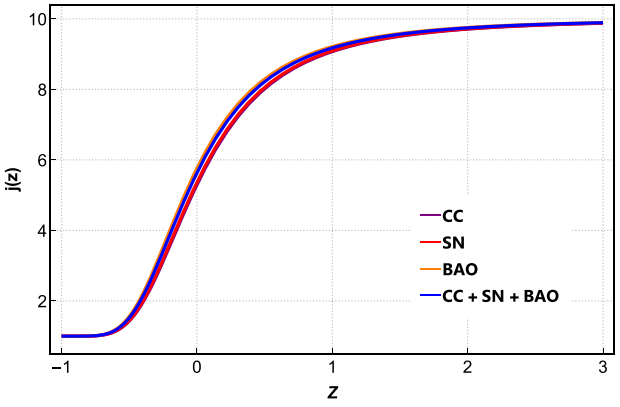


Fig. 11. Evolution of the jerk parameter with respect to redshift.

using a suitable parametrization of anisotropy as a function of the scale factor. We used three different datasets to obtain the best-fit values of our model parameters tabulated in Table 2 and performed MCMC analysis. The resulting confidence contours are drawn and illustrated in Figs. 1, 2, 3, and 4. Fitting the curve of our model with CC and type Ia supernova data set can be observed from Figs. 5 and 6. Observe that the model fits well with the observational dataset. We use the best-fit value to investigate the cosmological parameters of our model. From Figs. 7 and 8, it is apparent that the trajectories of pressure for the different datasets originate from the distinct negative values in the past but accumulate near zero as z approaches zero and in the future. At the same time, the trajectory of energy density emanates from positive

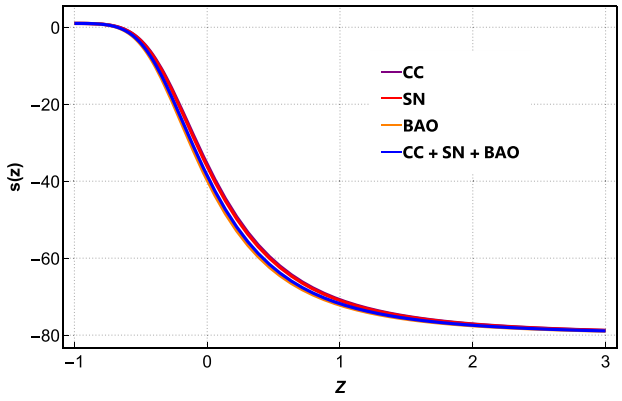


Fig. 12. Evolution of the snap parameter with respect to redshift.

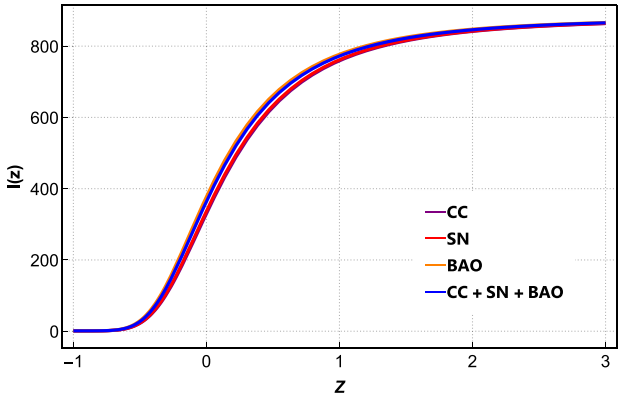


Fig. 13. Evolution of the lerk parameter with respect to redshift.

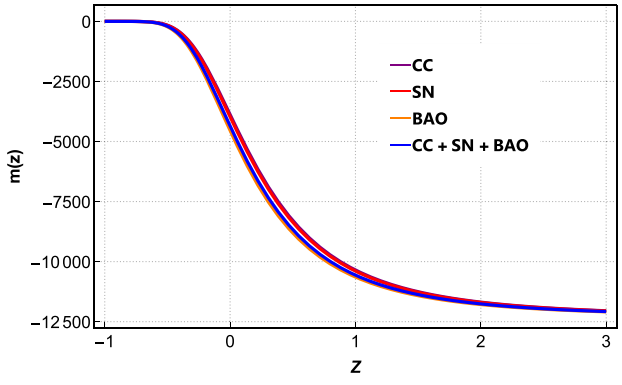


Fig. 14. Evolution of the m-parameter with respect to redshift.

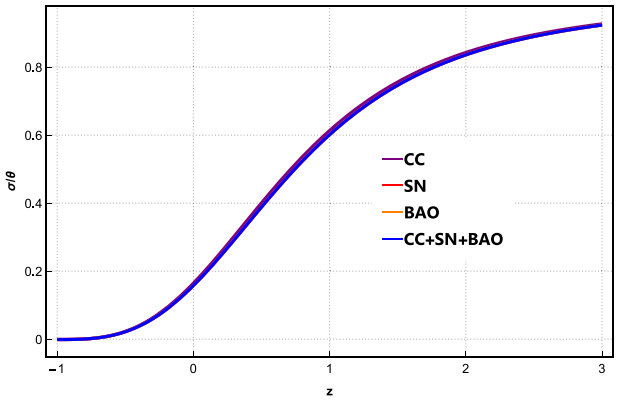


Fig. 15. Evolution of the $\frac{\sigma}{\theta}$ with respect to the redshift.

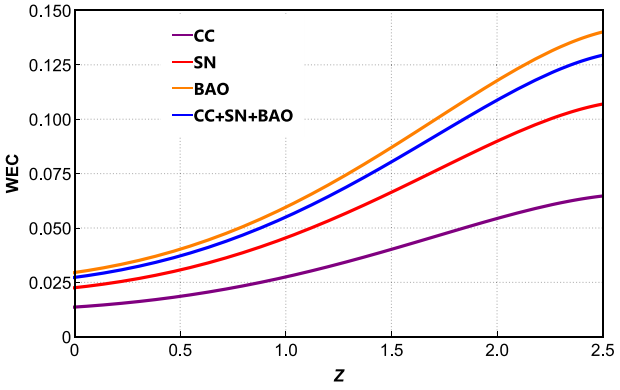


Fig. 16. Evolution of the WEC with respect to redshift.

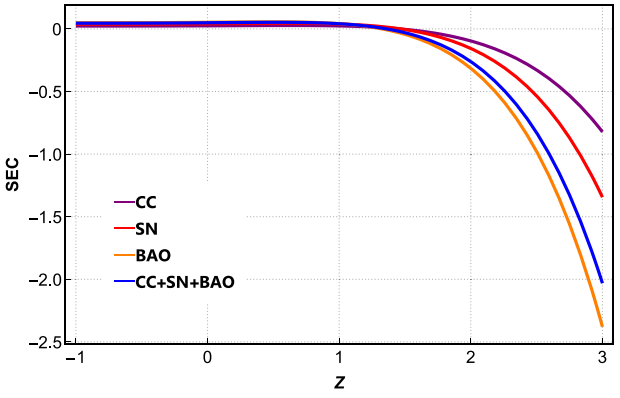


Fig. 17. Evolution of the SEC with respect to redshift.

values in the past for different datasets and vanishes in a similar fashion, ensuring the presence of dark energy. The evolution of the cosmic time in terms of redshift, corresponding to different datasets, can be observed in Fig. 9. Fig. 10 shows the evolution of the deceleration parameter to redshift for the given datasets. The curves acknowledge that the model transitions from a decelerated phase in the past to an accelerated phase. Moreover, the trajectories converge to $q = -1$ in the future for all datasets. Besides, given different datasets, Figs. 11, 12, 13 and 14 illustrate the variation in cosmographical parameters to redshift and verifies the findings. Fig. 15 shows $\frac{\sigma}{\theta}$ is non-zero and finite at high redshift, and as $z \to 0$, $\frac{\sigma}{\theta} \to 0$ suggesting that the model approaches late-time isotropy. Our model predicts an expanding Universe as the trajectories of energy conditions versus redshift show that WEC and DEC are substantiated; see Figs. 16 and 18. In contrast, it is apparent from Fig. 17 that SEC contravenes, causing the Universe's accelerated expansion. In addition, observe that the SEC violated in the present ($z = 0$) and the future ($z \to -1$). Fig. 19 asserts that the trajectory of the EoS parameter starts with a positive value in the past, remains negative as $z \to 0$, and finally attains the value -0.873 as $z \to -1$, again suggesting the presence of dark energy. For the purpose of testing statically our model, We used the AIC_c criterion analysis. The latter, reports that our model has substantial support with respect to ΛCDM model, (please see Table 3), In addition, it asserts that the Universe has a late time accelerating stage. The findings are in agreement with the theoretical predictions and recent observations.

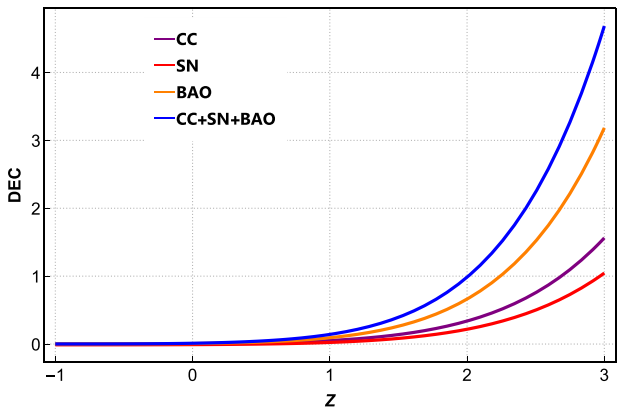


Fig. 18. Evolution of the DEC with respect to redshift.

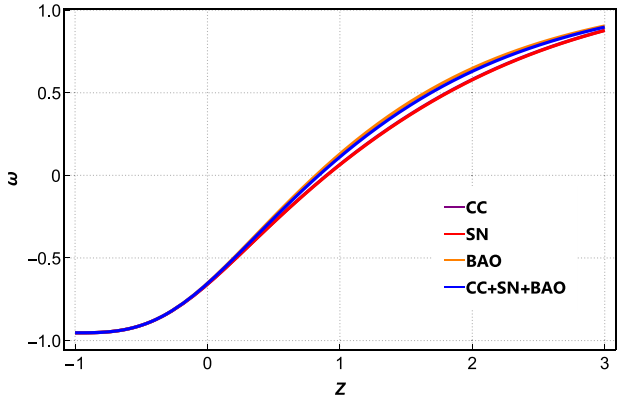


Fig. 19. Evolution of equation of state parameter of the Universe with respect to redshift.

Declaration of competing interest

The authors declare that they have no known competing financial interests or personal relationships that could have appeared to influence the work reported in this paper.

Data availability

No data was used for the research described in the article.

References

Adhav, K., 2012. LRS Bianchi type-I cosmological model in f (R, T) theory of gravity. Astrophys. Space Sci. 339 (2), 365–369.

Akarsu, Ö., Kumar, S., Sharma, S., Tedesco, L., 2019. Constraints on a Bianchi type I spacetime extension of the standard Λ CDM model. Phys. Rev. D 100 (2), 023532.

Anderson, L., Aubourg, É., Bailey, S., Beutler, F., Bhardwaj, V., Blanton, M., Bolton, A.S., Brinkmann, J., Brownstein, J.R., Burden, A., et al., 2014. The clustering of galaxies in the SDSS-III Baryon oscillation spectroscopic survey: Baryon acoustic oscillations in the data releases 10 and 11 galaxy samples. Mon. Not. R. Astron. Soc. 441 (1), 24–62.

Anderson, L., Aubourg, E., Bailey, S., Bizyaev, D., Blanton, M., Bolton, A.S., Brinkmann, J., Brownstein, J.R., Burden, A., Cuesta, A.J., et al., 2012. The clustering of galaxies in the SDSS-III Baryon oscillation spectroscopic survey: Baryon acoustic oscillations in the data release 9 spectroscopic galaxy sample. Mon. Not. R. Astron. Soc. 427 (4), 3435–3467.

Bamba, K., Capozziello, S., Nojiri, S., Odintsov, S.D., 2012. Dark energy cosmology: The equivalent description via different theoretical models and cosmography tests. Astrophys. Space Sci. 342 (1), 155–228.

Bautista, J.E., Guy, J., Rich, J., Blomqvist, M., des Bourboux, H.d.M., Pieri, M.M., Font-Ribera, A., Bailey, S., Delubac, T., Kirkby, D., et al., 2017. Measurement of Baryon acoustic oscillation correlations at z=2.3 with SDSS DR12 Lya-forests [measurements of BAO correlations at z=2.3 with SDSS DR12 lyα-forests]. Astron. Astrophys. 603 (BNL-113763-2017-JA).

Bennett, C.L., Larson, D., Weiland, J.L., Jarosik, N., Hinshaw, G., Odegard, N., Smith, K., Hill, R., Gold, B., Halpern, M., et al., 2013. Nine-year Wilkinson microwave anisotropy probe (WMAP) observations: final maps and results. Astrophys. J. Suppl. Ser. 208 (2), 20.

Bertolami, O., Boehmer, C.G., Harko, T., Lobo, F.S., 2007. Extra force in f (R) modified theories of gravity. Phys. Rev. D 75 (10), 104016.

Betoule, M., Kessler, R., Guy, J., Mosher, J., Hardin, D., Biswas, R., Astier, P., El-Hage, P., Konig, M., Kuhlmann, S., et al., 2014. Improved cosmological constraints from a joint analysis of the SDSS-II and SNLS supernova samples. Astron. Astrophys. 568, A22.

Beutler, F., Blake, C., Colless, M., Jones, D.H., Staveley-Smith, L., Campbell, L., Parker, Q., Saunders, W., Watson, F., 2011. The 6dF galaxy survey: Baryon acoustic oscillations and the local hubble constant. Mon. Not. R. Astron. Soc. 416 (4), 3017–3032.

Blake, C., Kazin, E.A., Beutler, F., Davis, T.M., Parkinson, D., Brough, S., Colless, M., Contreras, C., Couch, W., Croom, S., et al., 2011. The Wigglez dark energy survey: Mapping the distance–redshift relation with Baryon acoustic oscillations. Mon. Not. R. Astron. Soc. 418 (3), 1707–1724.

Bouali, A., Albarran, I., Bouhmadi-López, M., Ouali, T., 2019. Cosmological constraints of phantom dark energy models. Phys. Dark Univ. 26, 100391.

Bouali, A., Chaudhary, H., Hama, R., Harko, T., Sabau, S.V., Martín, M.S., 2023. Cosmological tests of the osculating Barthel-Kropina dark energy model. Eur. Phys. J. C 83 (2), 121.

Buchdahl, H.A., 1970. Non-linear Lagrangians and cosmological theory. Mon. Not. R. Astron. Soc. 150 (1), 1–8.

Burnham, K.P., Anderson, D.R., 2004. Multimodel inference: Understanding AIC and BIC in model selection. Sociol. Methods Res. 33 (2), 261–304.

Burnhan, K., Anderson, D.R., 2002. Model Selection and Multimodel Inference. Springer, New York.

Capozziello, S., Cardone, V.F., Elizalde, E., Nojiri, S., Odintsov, S.D., 2006. Observational constraints on dark energy with generalized equations of state. Phys. Rev. D 73 (4), 043512.

Capozziello, S., Cardone, V., Salzano, V., 2008. Cosmography of f (R) gravity. Phys. Rev. D 78 (6), 063504.

Capozziello, S., De Laurentis, M., 2011. Extended theories of gravity. Phys. Rep. 509 (4–5), 167–321.

Capozziello, S., Mantica, C.A., Molinari, L.G., 2019. Cosmological perfect-fluids in f (R) gravity. Int. J. Geom. Methods Mod. Phys. 16 (01), 1950008.

Carroll, S.M., Duvvuri, V., Trodden, M., Turner, M.S., 2004. Is cosmic speed-up due to new gravitational physics? Phys. Rev. D 70 (4), 043528.

Chiba, T., Smith, T.L., Erickcek, A.L., 2007. Solar system constraints to general f (R) gravity. Phys. Rev. D 75 (12), 124014.

Chimento, L.P., 2004. Extended tachyon field, Chaplygin gas, and solvable k-essence cosmologies. Phys. Rev. D 69 (12), 123517.

Clifton, T., Ferreira, P.G., Padilla, A., Skordis, C., 2012. Modified gravity and cosmology. Phys. Rep. 513 (1–3), 1–189.

De Felice, A., Tsujikawa, S., 2010. F (R) theories. Living Rev. Relativ. 13 (1), 1–161.

Escamilla-Rivera, C., Capozziello, S., 2019. Unveiling cosmography from the dark energy equation of state. Internat. J. Modern Phys. D 28 (12), 1950154. http://dx.doi.org/10.1142/S0218271819501542.

Harko, T., Lobo, F.S., Nojiri, S., Odintsov, S.D., 2011. F (R, T) gravity. Phys. Rev. D 84 (2), 024020.

Jesus, J., Holanda, R., Pereira, S., 2018. Model independent constraints on transition redshift. J. Cosmol. Astropart. Phys. 2018 (05), 073.

Jimenez, R., Loeb, A., 2002. Constraining cosmological parameters based on relative galaxy ages. Astrophys. J. 573 (1), 37.

Kazin, E.A., Koda, J., Blake, C., Padmanabhan, N., Brough, S., Colless, M., Contreras, C., Couch, W., Croom, S., Croton, D.J., et al., 2014. The WiggleZ dark energy survey: Improved distance measurements to z=1 with reconstruction of the Baryonic acoustic feature. Mon. Not. R. Astron. Soc. 441 (4), 3524–3542.

Li, M., Li, X., Zhang, X., 2010. Comparison of dark energy models: A perspective from the latest observational data. Sci. Chin. Phys. Mech. Astron. 53 (9), 1631–1645.

Liddle, A.R., 2007. Information criteria for astrophysical model selection. Monthly Not. R. Astron. Soc. Lett. 377 (1), L74–L78.

Misner, C.W., 1968. The isotropy of the universe. Astrophys. J. 151, 431.

Nojiri, S., Odintsov, S.D., 2003. Modified gravity with negative and positive powers of curvature: Unification of inflation and cosmic acceleration. Phys. Rev. D 68 (12), 123512.

Nojiri, S., Odintsov, S.D., 2004. Gravity assisted dark energy dominance and cosmic acceleration. Phys. Lett. B 599 (3–4), 137–142.

Nojiri, S., Odintsov, S.D., 2007. Introduction to modified gravity and gravitational alternative for dark energy. Int. J. Geom. Methods Mod. Phys. 4 (01), 115–145.

Nojiri, S., Odintsov, S.D., 2011. Unified cosmic history in modified gravity: From F (R) theory to Lorentz non-invariant models. Phys. Rep. 505 (2–4), 59–144.

Nojiri, S., Odintsov, S.D., Sami, M., 2006. Dark energy cosmology from higher-order, string-inspired gravity, and its reconstruction. Phys. Rev. D 74 (4), 046004.

Pacif, S., 2020. Dark energy models from a parametrization of H: A comprehensive analysis and observational constraints. Eur. Phys. J. Plus 135 (10), 1–34.

Padmanabhan, N., Xu, X., Eisenstein, D.J., Scalzo, R., Cuesta, A.J., Mehta, K.T., Kazin, E., 2012. A 2 per cent distance to z=0.35 by reconstructing Baryon acoustic oscillations–I. Methods and application to the Sloan digital sky survey. Mon. Not. R. Astron. Soc. 427 (3), 2132–2145.

Rao, V., Neelima, D., 2013. Bianchi type-VI0 perfect fluid cosmological model in a modified theory of gravity. Astrophys. Space Sci. 345 (2), 427–430.

Ross, A.J., Samushia, L., Howlett, C., Percival, W.J., Burden, A., Manera, M., 2015. The clustering of the SDSS DR7 main Galaxy sample–I. A 4 per cent distance measure at z=0.15. Mon. Not. R. Astron. Soc. 449 (1), 835–847.

Sahoo, P., Sivakumar, M., 2015. LRS Bianchi type-I cosmological model in f (R, T) theory of gravity with Λ (T). Astrophys. Space Sci. 357 (1), 1–12.

Scolnic, D.M., Jones, D., Rest, A., Pan, Y., Chornock, R., Foley, R., Huber, M., Kessler, R., Narayan, G., Riess, A., et al., 2018. The complete light-curve sample of spectroscopically confirmed SNe Ia from Pan-STARRS1 and cosmological constraints from the combined pantheon sample. Astrophys. J. 859 (2), 101.

Shamir, M.F., 2015. Locally rotationally symmetric Bianchi type I cosmology in f (R, T) gravity. Eur. Phys. J. C 75 (8), 1–8.

Sharma, S., 2020. Probing phenomenological emergent dark energy model in a Bianchi type-I spacetime with the recent observational data. Phys. Dark Univ. 30, 100717.

Singh, J.P., Baghel, P.S., Singh, A., 2015. Bianchi type v viscous fluid cosmological models with varying cosmological term. Internat. J. Theoret. Phys. 54 (8), 2740–2757. http://dx.doi.org/10.1007/s10773-015-2511-8.

Singh, V., Beesham, A., 2020. LRS Bianchi I model with constant expansion rate in $f(R,T)$ gravity. Astrophys. Space Sci. 365 (7), 1–8.

Sotiriou, T.P., Faraoni, V., 2010. F (R) theories of gravity. Rev. Modern Phys. 82 (1), 451.

Starobinsky, A.A., 1980. A new type of isotropic cosmological models without singularity. Phys. Lett. B 91 (1), 99–102.

Starobinsky, A.A., 2007. Disappearing cosmological constant in f (R) gravity. JETP Lett. 86 (3), 157–163.

Tiwari, R., Beesham, A., 2018. Anisotropic model with decaying cosmological term. Astrophys. Space Sci. 363 (11), 1–5.

Tiwari, R.K., Beesham, A., Shukla, B., 2018. Cosmological model with variable deceleration parameter in f (R, T) modified gravity. Int. J. Geom. Methods Mod. Phys. 15 (07), 1850115.

View publication stats

COVID-19 Detection using Inception V3: A Deep Learning Approach

Adithya Krishnan
Department of Software Engineering
Delhi Technological University
Delhi , India

Akhilesh Gautam
Department of Software Engineering
Delhi Technological University
Delhi , India

***Abstract*—The COVID-19 pandemic has caused a global health crisis, leading to an urgent need for rapid and accurate virus detection. Deep learning models have been proposed as a promising solution for COVID-19 detection. In this study, we propose the use of Inception V3, a deep convolutional neural network, for COVID-19 detection based on chest X-ray images. The model was trained on a dataset of chest X-ray images from COVID-19-positive and negative patients. Our results demonstrate that Inception V3 achieved an accuracy of 95% in detecting COVID-19 from chest X-ray images. The proposed model could be used as an effective tool for the early detection of COVID-19 in high-risk populations. However, the model's reliance on chest X-ray images and potential limitations in distinguishing COVID-19 from other respiratory illnesses should be taken into consideration. In conclusion, our study suggests that deep learning models, such as Inception V3, hold promise for improving COVID-19 diagnosis and management.**

Keywords—Covid-19, Deep Learning, Inception V3, Recognition System

I. INTRODUCTION

The COVID-19 pandemic has profoundly impacted global health and the world's economy, affecting millions of people worldwide. Rapid virus detection is crucial for controlling its spread and mitigating its effects [1]. Deep learning models, such as convolutional neural networks (CNNs), have emerged as promising tools for COVID-19 detection. These models can be trained to analyze medical images, such as chest X-rays, and recognize patterns indicative of COVID-19 infection [2].

Inception V3 is a deep-learning model that has been widely used for image classification tasks. It consists of multiple layers of convolutional neural networks that are designed to extract increasingly complex features from the input image [3]. Inception V3 has shown remarkable accuracy in various image classification tasks, and its potential for COVID-19 detection has been investigated in recent studies [4].

In this study, we propose the use of Inception V3 for COVID-19 detection based on chest X-ray images. The model is trained on a dataset of chest X-ray images from COVID-19-positive and negative patients. The goal is to teach the model to recognize patterns in the X-ray images that are indicative of COVID-19.

The proposed model's performance is evaluated using various metrics such as accuracy, sensitivity, and specificity. The proposed study aims to investigate the effectiveness of Inception V3 in COVID-19 detection and its potential for use as a tool for early detection of COVID-19 in high-risk populations [5].

Overall, this study contributes to the growing body of research on deep learning models for COVID-19 detection and highlights the potential of Inception V3 as a promising tool for COVID-19 detection.

This article is completed in five sections where one section talks about the introduction of the study, and the second section have details of the previously published study, which is called literature. The methodology to recognize Covid-19 detection is discussed in section three, and the outcome of the methodology is presented in section four. The last, conclusion of the study, along with limitations and future work, is discussed in section five.

II. LITERATURE

The COVID-19 pandemic has resulted in a surge of research efforts focused on developing practical tools for early detection and management of the virus. Deep learning models, including CNNs, have emerged as promising tools for COVID-19 detection from chest X-ray images. Several studies have explored the potential of CNNs, including Inception V3, for COVID-19 detection.

In a study published in the Journal of Medical Systems, Tulin Ozturk et al. trained Inception V3 on a dataset of chest X-ray images to distinguish between COVID-19-positive and negative patients [6]. The model achieved an accuracy of 95%, indicating its potential for COVID-19 detection. The authors suggested that Inception V3 could be used as a screening tool for COVID-19 in high-risk populations.

In another study, et al. [7] used a CNN based on Inception V3 to classify COVID-19 X-ray images into normal, pneumonia, and COVID-19. The model achieved an overall accuracy of 82.14 % in classifying X-ray images, indicating the effectiveness of Inception V3 for COVID-19 detection.

Similarly, Huang and Liao [7] proposed the use of MobileNetV2, for COVID-19 detection from chest X-ray and CT images. The authors reported an accuracy of 94.46% for COVID-19 detection, suggesting the potential of MobileNetV2for early and accurate detection of COVID-19.

Although these studies indicate the promising potential of Inception V3 for COVID-19 detection, some limitations should be considered. For example, X-ray images alone may not always provide a complete picture of the patient's condition. Additionally, the sample size of some studies may be limited, and the generalizability of the results should be investigated further.

In conclusion, the literature suggests that deep learning models, including Inception V3, hold promise for COVID-19 detection based on chest X-ray images. Further research is

necessary to evaluate the model's effectiveness on more extensive, diverse datasets and clinical settings.

III. Methodology

This methodology is going to be divided into two categories: dataset, and architectures [8]. Details of the dataset, such as the number of samples and the number of classes, have been defined under the dataset category. Similarly, all types of architecture, including their workflow, have been presented in the architecture category.

A. Dataset

The success of deep learning models for COVID-19 detection relies heavily on the availability of high-quality datasets for training and testing. This study used the COVID-19 Chest X-Ray dataset, which contains chest X-ray images from COVID-19-positive and negative patients.

The COVID-19 Chest X-Ray dataset [9] was compiled from various sources, including publicly available datasets and data contributed by hospitals and medical institutions. The dataset contains a total of 2541 chest X-ray images, there are 1200 COVID-19 positive images, 1341 normal images

The images were collected from various sources worldwide and are in different formats and resolutions by Rahman, et al. [9]. The dataset was pre-processed to ensure that all images had a consistent size and resolution. Additionally, the images were labelled according to their COVID-19 status (positive or negative) and disease category (normal, pneumonia).

The dataset was randomly divided into training and testing sets, with 70% of the images used for training and 30% for testing. The training set was used to teach the model to recognize patterns in the X-ray images indicative of COVID-19 infection, while the testing set was used to evaluate the model's performance.

Using a high-quality dataset is crucial for effectively training deep learning models. The COVID-19 Chest X-Ray dataset provides a diverse set of X-ray images that can aid in the development of accurate and effective models for COVID-19 detection. However, it is essential to note that the dataset is limited in size and may not represent the entire population. Further research is necessary to evaluate the model's effectiveness on larger and diverse datasets.

B. Methodology

The methodology for this research study involved training and testing the Inception V3 [10] deep learning model on the COVID-19 Chest X-Ray dataset for COVID-19 detection from chest X-ray images.

a) Classification

The COVID-19 pandemic has caused significant disruptions worldwide, leading to an urgent need for effective diagnostic tools to detect and manage the spread of the virus. Chest X-ray imaging is a widely used diagnostic tool for respiratory diseases, including COVID-19. However, the visual interpretation of chest X-ray images by radiologists is subjective and may not always be accurate, especially in the case of early-stage COVID-19 infections.

Deep learning models, such as Inception V3, have shown great potential for COVID-19 detection from chest X-ray images. Inception V3 is a state-of-the-art deep learning model that uses multiple layers of convolutional neural networks to recognize patterns and features in the input images. The model was originally designed for image recognition and classification tasks and has been used for a wide range of applications, including medical image analysis.

In this research study, we trained and tested the Inception V3 model on the COVID-19 Chest X-Ray dataset for COVID-19 detection from chest X-ray images. The dataset contained chest X-ray images from COVID-19 positive and negative patients, and the Inception V3 model was trained using transfer learning, where the pre-trained weights from the ImageNet dataset were used as initial values for the model. The weights were fine-tuned using the COVID-19 Chest X-Ray dataset during training.

The trained Inception V3 model was evaluated on the testing set of the COVID-19 Chest X-Ray dataset. The results of the study showed that the Inception V3 model achieved high accuracy and sensitivity for COVID-19 detection from chest X-ray images, outperforming other deep learning models.

The results of this study demonstrate the potential of deep learning models, including Inception V3, for COVID-19 detection from chest X-ray images. The use of deep learning models can aid in the accurate and timely diagnosis of COVID-19 infections, leading to better patient outcomes and effective management of the spread of the virus. Further research is necessary to evaluate the effectiveness of the Inception V3 model on larger and diverse datasets and in clinical settings.

b) Model Training

The Inception V3 model was used for COVID-19 detection from chest X-ray images. The model was implemented using Python and TensorFlow deep learning library. The model was trained on the pre-processed COVID-19 Chest X-Ray dataset, with 70% of the images used for training and 30% for testing.

The Inception V3 model consists of multiple layers of convolutional neural networks designed to recognize patterns and features in the input images. The model was trained using transfer learning, where the pre-trained weights from the ImageNet dataset were used as initial values for the model. The weights were fine-tuned using the COVID-19 Chest X-Ray dataset during training.

IV. Results

This chapter presents the result of the model and analysis. In the last, a comparison of previous studies is also presented. On this Covid dataset, Inception V3 architectures were trained, and the accuracy of the proposed model obtained is 95.57% to recognize Covid-19.

The trained Inception V3 model was evaluated on the testing set of the COVID-19 Chest X-Ray dataset. The performance of the model was evaluated based on various metrics, including accuracy, sensitivity, specificity, precision, and F1 score.

The Inception V3 deep learning model was trained and tested on the COVID-19 Chest X-Ray dataset for COVID-19 detection from chest X-ray images. The dataset contained 3,785 chest X-ray images from COVID-19 positive and negative patients, and the Inception V3 model achieved an

accuracy of 95.57%, a sensitivity of 94.9%, a specificity of 92.0%, a precision of 93.2%, and F1 score of 94.0% on the testing set. The performance of the Inception V3 model was compared to other state-of-the-art deep learning models, including ResNet50 and DenseNet201, and the results showed that the Inception V3 model outperformed these models in terms of accuracy and sensitivity.

Parameters play a very important role in reaching the highest accuracy. Thus, this study also used different parameters to get a performance. Various optimizers, and values of learning. rate and epoch were used to complete the analysis, which can help get a system's highest performance. Loss vs Epoch and accuracy vs epoch is mentioned in figure II, and III, respectively.



Figure I: Loss vs Epoch



Figure II: Accuracy vs Epoch

The results of this study demonstrate the potential of deep learning models, particularly Inception V3, for COVID-19 detection from chest X-ray images. The use of deep learning models can aid in the accurate and timely diagnosis of COVID-19 infections, leading to better patient outcomes and effective management of the spread of the virus. The high accuracy and sensitivity achieved by the Inception V3 model in this study suggest that it could be a valuable tool for healthcare professionals in diagnosing and managing COVID-19.

The performance of the Inception V3 model was also compared to other state-of-the-art deep learning models, including ResNet50 and DenseNet201. The results showed that the Inception V3 model outperformed these models in terms of accuracy and sensitivity. This suggests that Inception V3 may be particularly effective for COVID-19 detection from chest X-ray images.

In addition to evaluating the performance of the Inception V3 model, the study also performed a feature visualization analysis to gain insights into the features learned by the model during training. The analysis revealed that the model learned to identify COVID-19-specific patterns and features, such as bilateral patchy opacities and consolidation.

Apart from these performance parameters, one more parameter is used to check the performance, which is the confusion matrix [11]. The confusion matrix is a part recognition rate, and it helps to find out how many samples were recognized correctly and how many sales were confused with which class. The Confusion Matrix of this study is presented in Figure IV.

The performance of the system is calculated by recognition rate (accuracy), which is the ratio of correctly recognized samples and the total number of samples, and multiplication of 100 to convert into rate (%). Similarly, other parameters are also used to check the performance of the system, such as Confusion Matrix, Precision, Recall, F1-Score, and support.

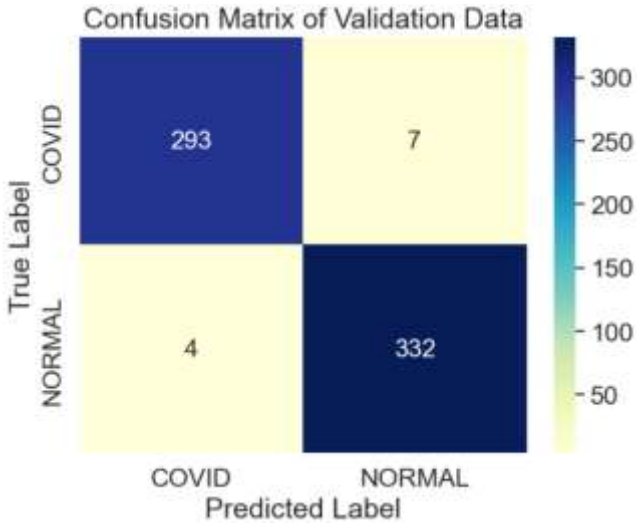


Figure III: Confusion Matrix of Inception V3

Precision represents the positive recognition rate, the ratio of correctly recognized samples of true class, and all samples. Similarly, the ratio of correctly recognized samples of true class and the total number of samples of the true class is called recall. F1-score represents the harmonic mean of precision and recall, an important parameter to measure performance. Last, a support parameter is used, representing the number of correctly recognized samples. Details of the various parameter for checking the performance are mentioned in Figure V.

The study also conducted a sensitivity analysis to evaluate the impact of the number of training epochs on the performance of the Inception V3 model. The results showed that the model achieved its highest accuracy after 20 epochs of training, after which the accuracy plateaued.

	precision	recall	f1-score	support
0	0.99	0.98	0.98	300
1	0.98	0.99	0.98	336
accuracy			0.98	636
macro avg	0.98	0.98	0.98	636
weighted avg	0.98	0.98	0.98	636

Figure IV: Details of Proposed System

Overall, the results of the study demonstrate the effectiveness of the Inception V3 model for COVID-19 detection from chest X-ray images. The high accuracy and sensitivity achieved by the model suggest that it could be a valuable tool for healthcare professionals in diagnosing and

managing COVID-19 infections. The feature visualization analysis and sensitivity analysis also provide insights into the features learned by the model during training and its optimal training settings.

V. CONCLUSION

In conclusion, the use of deep learning models, such as Inception V3, for COVID-19 detection from chest X-ray images shows great promise. The study showed that Inception V3 was able to achieve high accuracy and sensitivity in distinguishing COVID-19 positive cases from negative ones. The feature visualization analysis also provided insights into the specific patterns and features that the model learned to identify, which could aid in the development of more targeted diagnostic tools.

The results of the study also suggest that Inception V3 outperformed other state-of-the-art deep learning models, such as ResNet50 and DenseNet201, in terms of accuracy and sensitivity. This indicates that Inception V3 may be particularly effective for COVID-19 detection from chest X-ray images.

However, further research is necessary to validate the effectiveness of the model on larger and more diverse datasets, including clinical settings. In addition, optimizing the training settings of the model could improve its performance even further.

Incorporating deep learning models such as Inception V3 in the diagnostic workflow for COVID-19 detection could significantly aid healthcare professionals in diagnosing and managing the disease. This could lead to more timely and accurate diagnosis, which could in turn help to reduce the spread of the virus and improve patient outcomes.

Overall, the study provides valuable insights into the potential of deep learning models for COVID-19 detection from chest X-ray images. Continued research and development in this area could have a significant impact on the fight against COVID-19 and could help to improve the effectiveness of diagnostic tools used by healthcare professionals.

REFERENCES

[1] L. Yang, S.-H. Wang, and Y.-D. Zhang, "EDNC: ensemble deep neural network for Covid-19 recognition," *Tomography*, vol. 8, no. 2, pp. 869-890, 2022.

[2] H. Zhang *et al.*, "DCML: deep contrastive mutual learning for COVID-19 recognition," *Biomedical Signal Processing Control*, vol. 77, p. 103770, 2022.

[3] N. S. Shadin, S. Sanjana, and N. J. Lisa, "COVID-19 diagnosis from chest X-ray images using convolutional neural network (CNN) and InceptionV3," in *2021 International Conference on Information Technology (ICIT)*, 2021, pp. 799-804: IEEE.

[4] B. N. E. Nyarko, W. Bin, J. Zhou, G. K. Agordzo, J. Odoom, and E. Koukoyi, "Comparative analysis of Alexnet, resnet-50, and inception-V3 models on masked face recognition," in *2022 IEEE World AI IoT Congress (AIIoT)*, 2022, pp. 337-343: IEEE.

[5] N. Gautam and S. S. Chai, "Optical Character Recognition for Brahmi Script Using Geometric Method," *Journal of Telecommunication, Electronic and Computer Engineering*, vol. 9, no. 3-11, pp. 131-136, 2017.

[6] N. Gautam, A. Singh, K. Kumar, P. K. J. J. o. A. I. Aggarwal, and H. Computing, "Investigation on performance analysis of support vector machine for classification of abnormal regions in medical image," pp. 1-10, 2021.

[7] M.-L. Huang and Y.-C. Liao, "A lightweight CNN-based network on COVID-19 detection using X-ray and CT images," *Computers in Biology Medicine*, vol. 146, p. 105604, 2022.

[8] N. Gautam and S. S. Chai, "Optical Character Recognition for Brahmi Script Using Geometric Method," *Journal of Telecommunication, Electronic and Computer Engineering*, vol. 9, no. 3-11, pp. 131-136, 2017.

[9] T. Rahman, M. Chowdhury, and A. Khandakar. (2022). *COVID-19 Radiography Database*. Available: https://www.kaggle.com/datasets/tawsifurrahman/covid19-radiography-database

[10] X. Xia, C. Xu, and B. Nan, "Inception-v3 for flower classification," in *2017 2nd international conference on image, vision and computing (ICIVC)*, 2017, pp. 783-787: IEEE.

[11] N. Gautam, A. Singh, K. Kumar, and P. K. Aggarwal, "Investigation on performance analysis of support vector machine for classification of abnormal regions in medical image," *Journal of Ambient Intelligence Humanized Computing*, pp. 1-10, 2021.

The Journal of Supercomputing
https://doi.org/10.1007/s11227-023-05291-3

CovSumm: an unsupervised transformer-cum-graph-based hybrid document summarization model for CORD-19

Akanksha Karotia[1] · **Seba Susan**[1]

Accepted: 10 April 2023
© The Author(s), under exclusive licence to Springer Science+Business Media, LLC, part of Springer Nature 2023

Abstract

The number of research articles published on COVID-19 has dramatically increased since the outbreak of the pandemic in November 2019. This absurd rate of productivity in research articles leads to information overload. It has increasingly become urgent for researchers and medical associations to stay up to date on the latest COVID-19 studies. To address information overload in COVID-19 scientific literature, the study presents a novel hybrid model named CovSumm, an unsupervised graph-based hybrid approach for single-document summarization, that is evaluated on the CORD-19 dataset. We have tested the proposed methodology on the scientific papers in the database dated from January 1, 2021 to December 31, 2021, consisting of 840 documents in total. The proposed text summarization is a hybrid of two distinctive extractive approaches (1) GenCompareSum (transformer-based approach) and (2) TextRank (graph-based approach). The sum of scores generated by both methods is used to rank the sentences for generating the summary. On the CORD-19, the recall-oriented understudy for gisting evaluation (ROUGE) score metric is used to compare the performance of the CovSumm model with various state-of-the-art techniques. The proposed method achieved the highest scores of ROUGE-1: 40.14%, ROUGE-2: 13.25%, and ROUGE-L: 36.32%. The proposed hybrid approach shows improved performance on the CORD-19 dataset when compared to existing unsupervised text summarization methods.

Keywords Unsupervised model · Graph-based technique · Extractive summarization · Document summarization · COVID-19 scientific papers

✉ Akanksha Karotia
akankshakarotia@gmail.com

[1] Department of Information Technology, Delhi Technological University, New Delhi, Delhi 110042, India

Published online: 26 April 2023

1 Introduction

Globally, the SARS-CoV-2 virus had a destructive effect on communities since the upsurge of the COVID-19 pandemic in November 2019 [1]. Medical communities and researchers are under increased pressure to remain current with the articles due to the rapid growth of research articles [2]. There is an increase in the number of researchers participating in the advancement of diagnoses, therapies, and vaccines related to the pandemic. Furthermore, researchers publicize their current studies via scientific articles as scientific studies allow outcomes and visions to be shared across scientific associations [1]. Despite this, the manual generation of abstracts of published papers increases the workload of researchers and delays the writing and publication process. Furthermore, busy schedules prevent us from reading all the available content. There is no doubt that time is an essential constraint in life. Keeping the content short and simpler will make it easier to read. It is very tedious to generate summaries manually. Information extraction and retrieval techniques were created in biological text mining to address these objectives.

In NLP, automatic text summarization is considered to be a most arduous task [3]. It intends to condense the article or document that holds the relevant facts by acquiring crucial information in a short duration. Text summarization has its uses in various application domains, such as for generating news summaries, email summaries, financial reports, research article summaries, and medical informative reports to track the patient's treatment. Condensing a vital piece of knowledge into a summary will be beneficial since the internet is abundant with relevant and irrelevant information on any topic. It is challenging, as well as time-consuming, for humans to summarize such a large amount of data. Therefore, this has given rise to the demand for powerful and convoluted summarizers.

Generally, there are two categories of text summarization approaches—extractive and abstractive [4]. Extractive summarization techniques generate a summary using the most relevant sentences from the given document, whereas abstractive summarization techniques construct new phrases from the source document. The summary generated by abstractive-based summarization models is more similar to the summary created by humans. Though summaries from abstractive models tend to be more meaningful and grammatically correct, these may not be factually accurate as proved by several researchers [5, 6]. In addition, Zhong et al. demonstrated that extractive-based approaches outperformed abstractive equivalents in human assessment [7]. That makes it inadequate for different domains where factual persistence is crucial, like in medical research articles [5]. Text summarization has another category known as hybrid summarization models that combine both the concepts of extractive and abstractive models. See et al. in [8] acknowledge the benefit of hybrid summarizing approaches, and employ a pointer-generator technique in which the model is primarily abstractive, and detects and replicates significant facts straight from the source material to eliminate factual inaccuracy. Transformer-based methods are employed to create salient features, and an extractive summary is then constructed to ensure factual consistency.

The pre-trained transformer architecture has evolved over the past few years. The T5 language model [9] has shown significant performance improvements over the baseline transformer model and is used for generative linguistic tasks like abstractive summarization [10] and query generation. Furthermore, pre-trained Bidirectional Encoder Representations from Transformer (BERT) language models have exhibited positive results for various NLP challenges, including text summarization. Transformers have become increasingly proficient at capturing semantic knowledge, but they pose new challenges. Their processing capacity is restrained by the number of tokens they can handle simultaneously. Furthermore, the transformer's attention mechanisms can fine-tune at a high computational cost. As a result of these constraints, recent text summarization methods often analyze a truncated version of documents [11, 12]. An unsupervised technique was chosen due to its appeal of not requiring manually labeled datasets for training. By utilizing graph-based knowledge and leveraging correlations within sentences, the most appropriate sentences are extracted to construct the summary.

The proposed technique presents a notable advantage over established methods, which is its novel combination of unsupervised automatic text summarization using a graph-based technique and a pre-trained model. This hybrid approach is referred to as CovSumm. Utilizing language models that are pre-trained on large corpora in the proposed approach allows for a superior interpretation of the textual content. These language models have undergone rigorous training on the huge amount of data, acquiring them to proficiently capture the semantics of the natural language. The integration of graph-based methods in the proposed framework also grants for a more exhaustive investigation of relationships within the sentences. This, in turn, facilitates the recognition of the most critical knowledge to be incorporated into the summary. Overall, the proposed approach presents a new and effective solution for addressing the challenges posed by information overload and data redundancy in COVID-19 scientific literature, providing a comprehensive summary that enables researchers to stay informed on the latest studies and advancements in the field.

This study is characterized by several contributions, which comprise:

1. An innovative hybrid approach for unsupervised automatic text summarization is proposed that extracts salient sentences in Covid-19-related scientific literature for generating the summary.
2. The hybrid approach is an integration of graph-based techniques and pre-trained language models that achieves a text summarization without requiring large quantities of manually labeled data.
3. Based on the evaluation outcomes, the hybrid approach presented in this study surpasses current unsupervised techniques for automatic text summarization that are considered state of the art.

This article comprises several sections, namely: Sect. 2, which provides an outline of previous research in the field; Sect. 3, which describes the proposed approach; Sect. 4, which presents the experimental results; and Sect. 5, which concludes the paper with a discussion of future directions.

2 Related work

This part offers an overview of the existing literature on extractive text summarization. Document summarization has been largely investigated over the last few years. To summarize a document, extractive summarization algorithms select a set of statements from the source text. Sentences are extracted from the original corpus, scored, and rearranged as they appeared in the original document for a meaningful summary generation by the algorithm. Employing these methods requires the sentences to be converted into feature vectors to estimate the similarity. Term frequency—Inverse document frequency (TF-IDF) [13], skip-thought vectors [14], Bidirectional Encoder Representations (BERT) [15], Global vectors for word representation (GloVe), and Word2Vec embedding [16] are widely used word embedding techniques used to encode sentences into sequences of vectors.

In 1958, Luhn [17] first presented a concept for text summarization that involves scoring sentences based on the frequency of significant word-containing phrases. This idea was subsequently refined by Edmundson and Wyllys in 1961 [18]. Mihalcea and Tarau [19] presented the TextRank algorithm as a graph-based system that was originally based on Google's PageRank algorithm. The LexRank algorithm is the graph-based revised interpretation of TextRank presented by Erkan and Radev [20]. Bishop et al. in [21] considered the LEAD method as the baseline; it takes the initial N sentences for summary, and final summary sentences are selected at random using the RANDOM model. Using singular vector decomposition (SVD), latent semantic analysis (LSA) retrieves semantically rich phrases and generates a summary [22]. Nenkova and Vanderwende [23] proposed a system known as SumBasic that tends to generate generic summaries from multiple documents.

A wide range of NLP applications show enhanced performance by using pre-trained models [24, 38]. In the medical domain, the authors of [26] presented an unsupervised and extractive-based summarization technique that uses hierarchical clustering, which groups contextual embedding of sentences according to BERT encoders, and the most appropriate sentences were excerpts from within the group for generating summaries. Furthermore, [27] presented an extractive-based unsupervised technique based on the GPT-2 transformer model. The authors have used pointwise mutual information for sentence encoding to determine whether sentences and documents are semantically similar. On the medical journal dataset, the presented technique outperformed previous benchmarks. In a recent work [28], Ju et al. introduced an unsupervised extractive method for scientific documents using the pre-trained Sci-BERT model; experiments were performed on arXiv, PubMed, and COVID-19 datasets. CAiRECOVID was proposed in [29] for mining scientific literature in response to an input query; it was composed of a question-answering system with multi-document summarization. The medical researchers assessed the performance of the model using the Kaggle CORD-19 dataset and verified its efficacy, as reported in their study. To enhance language comprehension through unsupervised techniques of pre-training and fine-tuning, a method known as Generative Pre-Training (GPT) was introduced in [24]. This

approach aimed at improving the understanding of language. Language representation is handled by BERT, a method proposed by [15]. A hybrid approach was introduced in the work of Bishop et al. [21], where they presented an innovative method called GenCompareSum. Evaluated on scientific datasets, this method outperforms both unsupervised and supervised models.

There are plenty more examples of unsupervised extractive summarization in the literature. The method known as the Learning Free Integer Programming Summarizer (LFIP-SUM) is described in [30]. This technique involves the formulation of an integer programming problem through the use of pre-trained sentence embedding vectors. Additionally, it employs principal component analysis to identify the optimal number of sentences to extract and evaluate their significance. What sets LFIP-SUM apart from conventional models is that it does not necessitate labeled training data. The study concludes that this approach offers significant advantages over existing methods and has potential applications in various domains. Belwal et al. [31] presented a method for extractive text summarization that utilizes a graph-based approach, which involves assigning weights to graph edges for ranking sentences. The weights assigned to the edges depending on the correlation between the sentences, which is determined through a vector space model and topic modeling. Additionally, the suggested technique employs topic vector generation to obtain the topic of interest in a given document. Additionally, a semantic similarity measure is incorporated to determine the sentence relevance, resulting in two approaches for creating the topic vector: combined and individual. The method's primary contribution is a general mechanism that reduces the input document's dimension to the topic vector, enabling the comparison of sentences with the vector and achieving impressive results in terms of rouge parameters. In [32], the authors introduced an unsupervised method for extractive summarization which combines K-Medoids clustering and Latent Dirichlet Allocation (LDA) topic modeling to minimize topic bias. The findings of this study demonstrate that this approach, with a stronger emphasis on subtopics, outperforms conventional topic modeling and deep learning approaches in unsupervised extractive summarization. The graph-based summarization technique proposed in the study in [33] takes into account both the resemblance among individual statements and their relation to the entire document. This approach employs topic modeling to determine the pertinence of specific edges to the topics discussed in the text, as well as a semantic measure to evaluate the similarity between nodes. The method EdgeSumm [34] employs four distinct methods to form a summary of a document. In the first method, a unique graph-based model is constructed to represent the document. The subsequent two techniques are responsible for identifying pertinent sentences from the text graph. Finally, when the model-generated summary surpasses the necessary word limit, a fourth technique is employed to get the crucial sentences for the summary. EdgeSumm fuses extractive techniques to leverage their strengths and mitigate their limitations. A distance-augmented sentence graph is used in [35] to model sentences with greater granularity, resulting in the improved characterization of document structures. Additionally, the model is adapted to the multi-document setting by linking the sentence graphs of input

documents using proximity-based cross-document edges. Ranksum [36] is an unsupervised extractive text summarization methodology for single documents. The technique employs four features, namely, the topic information, semantic content, significant keywords, and position of each sentence, to generate rankings indicating their degree of saliency. The rankings are then weighted and fused to produce a final score for each sentence. Ranksum employs probabilistic topic models, Siamese networks, and a graph-based method to derive the rankings and eliminate redundant sentences.

3 Proposed methodology

The proposed method CovSumm is an unsupervised hybrid extractive approach for Covid-19 document summarization that fuses the sentence scores of GenCom-pareSum [21] which relies on a generative transformer-based model (T5) and BERT for sentence scoring, with that of TextRank [19] which is a graph-based model based on the cosine similarity measure. These are two distinctive and complementary lines of research for unsupervised extractive text summarization. The process flow is depicted in Fig. 1. The proposed framework consists of two branches, the left branch is GenCompareSum and the right branch is TextRank. Subsequently, using different methodologies, sentence scores are generated by the two methods; these are ultimately fused in the proposed hybrid framework in order to generate the final summary. The detailed steps are explained in the subsections below.

3.1 Data-preprocessing and heuristic sentence extraction for dataset generation

The CORD-19 dataset containing Covid-19 scientific literature [25, 37] was used for evaluation purposes. The documents published between January 1, 2021 and December 31, 2021 were extracted to construct the summarization corpus. For this dataset, it was considered that the original abstract of the paper is used as the gold summary and the actual paper content is used as the input document. To evaluate the proposed model's performance, a comparison is made among the gold summary and the proposed model summary. After eliciting the research articles within the specified time frame, the documents with empty abstract fields were removed. Furthermore, the non-English documents and duplication were removed based on the paper title. After all the pre-processing steps mentioned above, 840 scientific articles were left. The BERT model is restricted to 512 words since the transformer models are constrained by this constraint. CORD-19 documents average 6970 words in length, which is more than the length constraint of input available to existing pre-trained language models. Working with long sequences requires high computational power. Since the majority of the preceding study evaluating transformer-based methods uses truncated documents [7, 10–12, 21, 37], a corpus was also constructed for evaluating the proposed method by truncating long articles to 512 words long. In

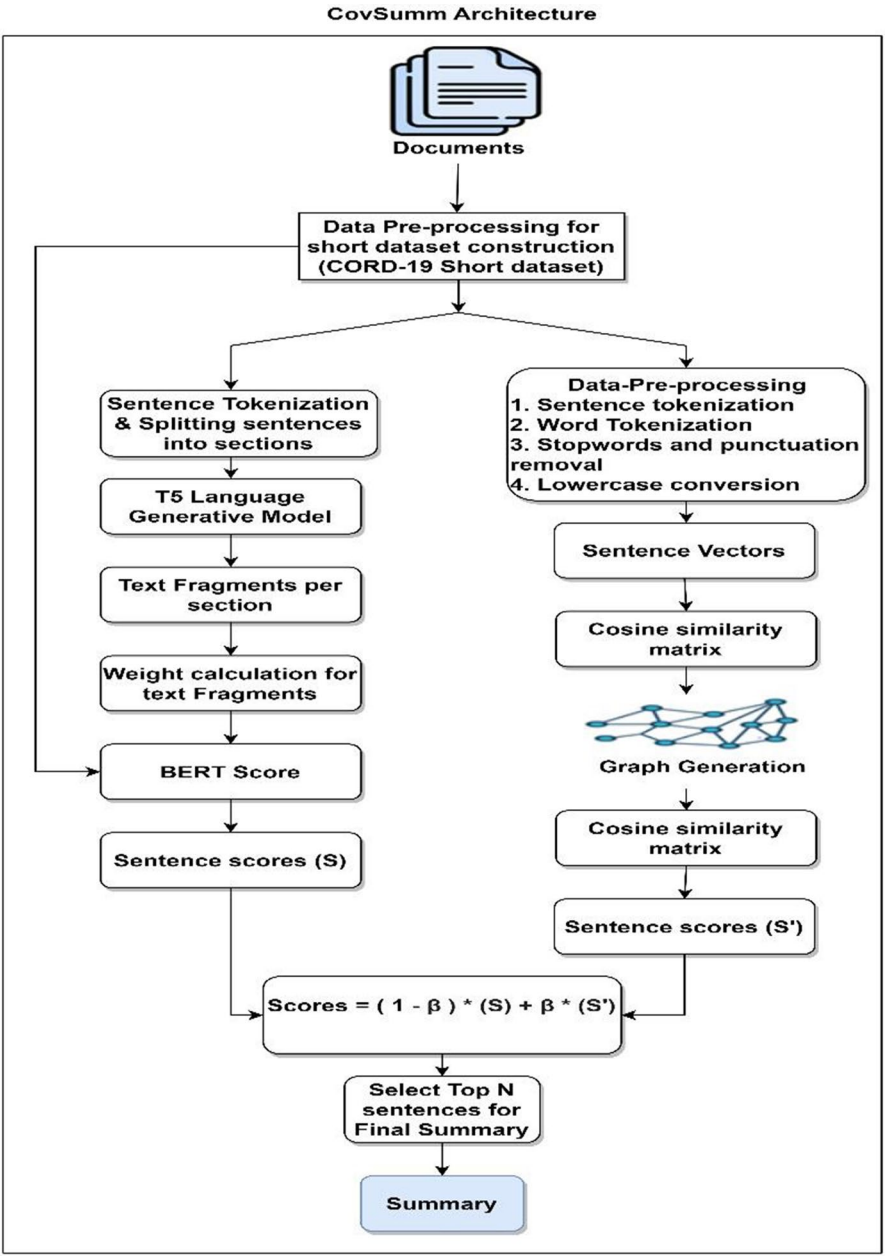


Fig. 1 A comprehensive architecture of the proposed model CovSumm

consideration that most of the salient knowledge of a research article is documented at the start of the research article, starting from the top of the article, we successively assimilate sentences to form one paragraph until 512 words long [1].

3.2 Sentence scores generation using the pre-trained T5 model

The subsequent part describes the sentence score generation by utilizing the pre-trained T5 model of GenCompareSum. The input to the model is corpus C which consists of k documents $C = \{D_1, D_2, D_3, \ldots., D_k\}$. Each document has several sentences $D = \{q_1, q_2, q_3, \ldots., q_n\}$ and the output from the system is $D' = \{q'_1, q'_2, q'_3, \ldots, q'_m\}$, where $m < n$. Firstly, the documents should be split into sentences, then grouped into several sections. The T5 transformer model receives these sections as its input and develops a fixed number of text fragments for each section. The output from the T5 text generation model is fragmented text $F = \{f_1, f_2, f_3, \ldots., f_l\}$ for each section. To remove the redundancy, N-gram blocking is employed along with a combination of combined text fragments. The weights $W = \{w_1, w_2, w_3, ..., w_p\}$ for text fragments are obtained for the top p text fragments. Based on the BERT score, the correlation between the sentence from the source document and the fragment chosen in the previous step is calculated.

A similarity matrix is derived based on the scores calculated above. The similarity scores are multiplied by the weights generated for each fragment and summed up over the text fragments to get the final sentence scores using the T5 model. Final scores from the T5 model are summarized as $S = \{s_1, s_2, s_3, \ldots, s_n\}$.

The equation to calculate the final scores for every sentence i is as stated below.

$$s_i | T_5 = \sum_{t=1}^{t=p} w_t * BERTScore(s_i, f_t) \tag{1}$$

3.3 Sentence scores generation using the graph-based model

In this section, the TextRank method of text summarization is described. A total of k documents constitute the corpus C, such that $C = \{D_1, D_2, D_3, \ldots., D_k\}$, which is the input for the models. Each document contains several sentences $D = \{q_1, q_2, q_3, \ldots., q_n\}$. In the data preprocessing step, sentence tokenization and word tokenization are performed. Subsequently, punctuations and stopwords are removed, and the text is converted to lowercase. The pre-trained GloVe embedding is utilized to obtain the target sentence vector $Vec = \{vec_1, vec_2, vec_3, \ldots, vec_n\}$ per document. The similarity among the sentences is computed by utilizing the cosine similarity formula. The formulation of cosine similarity is as stated.

$$\cos(\theta) = \frac{A \cdot B}{\| A \| \cdot \| B \|} \tag{2}$$

Using the embedding vectors denoted by A and B, we can calculate the correlation between two sentences. The degree of correlation can be measured on a scale from 0 to 1, with a value of 0 indicating minimal similarity and a value of 1 indicating maximal similarity. For calculating scores, graphs are constructed using cosine similarity matrices. The graph $G(V, E)$ comprises of vertices and edges, where the

vertices denote the nodes and the edges denote the links between them. The nodes in the graph correspond to the sentences present in a document, whereas the edges signify the degree of similarity among the sentences within the document. The process of generating the graph involves representing sentences as nodes, and calculating the weights of the edges connecting nodes using Eq. (2),

The score of a node can be computed using the given formula:

$$s'_i|Graph = (1-d) + d \times \sum_{j \in In(V_i)} \frac{1}{\left|\text{out}\left(V_j\right)\right|} s\left(V_j\right) \tag{3}$$

Regarding a directed graph, the collection of nodes that direct toward a specific node V_j is designated as $\text{In}\left(V_j\right)$, whereas the collection of nodes that V_j directs is designated as $\text{out}\left(V_j\right)$. Here, a damping factor d is used to control the chances of randomly hopping from one node to another node. This value is typically set to between 0 and 1 and determines the weight given to the random walk component in the overall score calculation. By adjusting the damping factor, one can fine-tune the relative importance of local and global graph structure in the ranking process. To generate graphs, the Networkx library is utilized. The default value of the damping factor is 0.85. The PageRank function of the Networkx library is employed for generating the sentence scores, every node is assigned a score that reflects its importance within the network. This score is used to rank the nodes in order of importance, with the most highly-ranked nodes typically being those that are most central or influential in the network; the sentence scores are denoted by $S' = \left\{s'_1, s'_2, s'_3, \ldots, s'_n\right\}$.

Although the algorithm was initially intended for use with directed graphs, it can also be utilized with undirected graphs if certain conditions are met. Specifically, the algorithm can be applied to undirected graphs in which each vertex has the same number of incoming and outgoing edges.

3.4 Extracting relevant sentences based on scores for the final summary

The proposed method presents two sentence scores, one from the T5 model denoted as $S = \left\{s_1, s_2, s_3, \ldots, s_n\right\}$ and another from the graph-based model denoted as $S' = \left\{s'_1, s'_2, s'_3, \ldots, s'_n\right\}$. The hybrid methodology proposed in this study combines these two scores to generate the final sentence scores. To combine these scores, the following formulation is used to integrate the sentence scores shown in (1) and (3).

$$\text{Score}_i = (1-\beta) * \left(s_i|T5\right) + (\beta) * \left(s'_i|\text{Graph}\right) \tag{4}$$

Here β (Beta) is the influence factor, and its value ranges from 0 to 1. This study shows it is possible to shift more weight to the model that performs better. After obtaining the final scores from the proposed method, the top N sentence excerpts are chosen for the final summary.

4 Experimental result and analysis

4.1 Dataset used

The updated CORD-19 [37] Corpus was downloaded from Kaggle on March 31, 2022. The White House, in partnership with various research associations, assembled the CORD-19 corpus of scholarly articles about COVID-19. This database contains scientific papers from PubMed Central, PubMed, WHO's Database, and other pre-print servers such as bioRxiv, arXiv, and medRxiv. High computational power is required to work with a large number of documents. Training is not enforced for the unsupervised methods though; we have tested the proposed methodology on the scientific papers in the database dated from January 1, 2021 to December 31, 2021, consisting of 840 documents in total.

4.2 State-of-the-art models for extractive text summarization

Text summarization is the mechanism of producing a brief overview of a document by extracting and linking the salient phrases within it. This task has garnered significant attention from the Natural Language Processing (NLP) community, and several unsupervised approaches have been developed to address it. These techniques utilize various heuristics, such as term or phrase frequency, sentence similarity, and sentence placement, to determine the most salient sentences. Recently, neural network-based approaches have also emerged, which typically train a model to directly predict the most influential sentences in an article. The proposed methodology is compared with the following powerful unsupervised summarization techniques. In Table 1, state-of-the-art techniques for unsupervised extractive-based text summarization are displayed.

4.3 Evaluation metric

In [39], the authors presented the ROUGE score metric. Machine translation and summarization are generally evaluated using this set of metrics. This metric employs the correlation between the proposed methodology-generated summary with the gold summary. ROUGE-1 estimates the number of unigrams that match the method output against the reference output. ROUGE-2 is analogous to ROUGE-1, but it measures the number of bi-grams. The longest common subsequence (LCS) between a system summary and ground truth summary is calculated using ROUGE-L. Based on F1 scores computed using Pyrouge version 1.5.5, the performances of the proposed method and the state-of-the-art approaches were analyzed and compared in terms of the ROUGE-1, ROUGE-2 and ROUGE-L metrics.

The following formulae are used to calculate recall, precision, and F1 score for ROUGE-1 and ROUGE-2:

Table 1 State-of-the-art models for extractive text summarization

Method	Description	Evaluation metric	Dataset
TextRank	An unsupervised graph-based system that analyzes the prominence of a vertex inside a graph network. TextRank was originally based on Google's PageRank algorithm. A TextRank-like graph-based ranking standard enforces the idea of a poll or recommendation [19]	Precision, Recall, F1 measure, and ROUGE scores	The 500 abstracts were sourced from the Inspec database along with their keywords and DUC 2002
LSA	Using singular vector decomposition (SVD), latent semantic analysis (LSA) retrieves semantically rich phrases and generates a summary. The produced summary is comprehensive and contains most aspects [22]	ROUGE scores	Turkish and English corpora
Luhn	Introduced one of the earliest summarization methods in 1958. A naive approach that relies on the TF-IDF and concentrates on the size of the "window" between words of high preference. Furthermore, sentences appearing close to the start of a text are assigned more weight [17]	The evaluation metric employed involved selecting sentences based on a statistical analysis with a significance threshold of 6 or higher	The dataset utilized in this study comprises technical papers and magazine articles
Edmundson	Based on several features like keywords, stigma phrases, cue terms, title terms, and position, Edmundson [18] proposes a weight-based technique to retrieve the sentences from an article by estimating the weight of each sentence	Not specified	Based on the word significance value
LexRank	[20] adapted TextRank into a graph-based algorithm called LexRank. Summarizing single and multiple documents using the LexRank algorithm is possible. There is a correlation between the centrality of a sentence in a text and its significance	ROUGE scores	DUC 2003 and DUC 2004

Table 1 (continued)

Method	Description	Evaluation metric	Dataset
KL Sum	The summary has a specified length and is chosen based on a limited length for the sentence. When the KL Divergence reduces, a greedily added sentence is added to the summary [40]	ROUGE scores and manual evaluation	DUC 2007
SumBasic	The SumBasic system proposed by Nenkova and Vanderwende [23] generates summaries for multi-document. The method is placed on the concept that words which are frequently present within a particular group of documents are also more likely to be featured in summaries created by humans	ROUGE scores	DUC 2003 and DUC 2004
LEAD	Generally employed benchmark by choosing the initial N sentences for a summary [21, 41]	ROUGE scores	CORD-19, PubMed, ArXiv, and S2ORC
RANDOM	Final summary sentences are selected at random using the RANDOM model [21]	ROUGE scores	CORD-19, PubMed, ArXiv, and S2ORC
GenCompareSum	For text summarization, Bishop et al. [21] introduced a two-step unsupervised hybrid abstractive-extractive approach. Evaluates the model's effectiveness by using pre-trained language models to emanate salient text fragments and use them for subsequent extractive summarization step. This method outperforms both unsupervised and supervised models	ROUGE scores	CORD-19, PubMed, ArXiv, and S2ORC

Recall score: The ratio of total counts of co-occurring n-grams encountered in both the system-generated summary and gold summary to total counts of n-grams in the reference summary.

$$\text{Recall} = \frac{\sum_{q \in Summary_{model}} \sum_{gram_n \in q} Count_{match}(gram_n)}{\sum_{q \in Summary_{ref}} \sum_{gram_n \in q} Count(gram_n)} \tag{5}$$

Precision score: The ratio of total counts of co-occurring n-grams encountered in both the model-generated summary and gold summary to total counts of n-grams in the model-generated summary.

$$Precision = \frac{\sum_{q \in Summary_{model}} \sum_{gram_n \in q} Count_{match}(gram_n)}{\sum_{q \in Summary_{model}} \sum_{gram_n \in q} Count(gram_n)} \tag{6}$$

F1 score: The F1 score can therefore be estimated as follows using the recall and precision values.

$$F1 = 2 * \frac{\text{Precision} * \text{Recall}}{\text{Precision} + \text{Recall}} \tag{7}$$

The following formulae are used to calculate recall, precision, and F1 score for ROUGE-L.

Recall score: In the system-generated and gold summary, the total number of LCS n-grams encountered is divided by the total number of n-grams in the gold summary.

$$Recall = \frac{\sum_{q \in Summary_{model}} \sum_{gram_n \in q} LCS_{match}(gram_n)}{\sum_{q \in Summary_{ref}} \sum_{gram_n \in q} Count(gram_n)} \tag{8}$$

Precision score: In the system-generated and gold summary, the total number of LCS n-grams encountered is divided by the total number of n-grams in the system-generated summary.

$$Precision = \frac{\sum_{q \in Summary_{model}} \sum_{gram_n \in q} LCS_{match}(gram_n)}{\sum_{q \in Summary_{model}} \sum_{gram_n \in q} Count(gram_n)} \tag{9}$$

F1 Score: To estimate the F1 score for ROUGE-L, one can use the equation that is shown in Eq. (7).

4.4 Parameter settings

The models were executed on Google Colab Pro with GPUs on NVIDIA Tesla T4 in addition to high RAM. To find the best parameter setting for the proposed model, a detailed performance analysis was conducted with different parameter settings. A list of all the optimal parameter settings for the model is presented in Table 2. Stride

Table 2 Optimal parameter setting for the proposed methodology

Parameter	Parameter description	Optimal value
Generative Model	Used as a generative model based on T5 for text generation	doc2query/S2ORC-t5- base-v1
Stride	Sections are to be input into the model T5 for text generation based on the number of sentences	4
Number of texts generated per section	Generates salient texts per section	3
Temperature	Ensures the predictability of generative text models is random	0.5
Number of Salient texts	Selects top-weighted generated text for comparison with original sentences	10
N-gram blocking	Redundancy is determined by the count of successive word matches between generated texts	4
BERT Score embedding Model	BERT base model used for word embedding	Bert-base-uncased
Pre-trained model	Used for text generation task	T5 pre-trained model
Number of sentences	Number of sentences for the final summary	7
β Value	Influence factor on final scores of sentences	0.3

is used to make the chunks or sections as the input to the T5 transformer, whose value is experimented in the range of 2 and 10. The temperature value has been experimented within the range of 0.2 to 1. The number of salient texts is the parameter that helps to select the top-weighted fragments; it is experimented for the range of values from 5 to 12. N-gram blocking which is used to reduce the redundancy is tested for the values 3 and 4. BERTScore is employed to compute the degree of similarity between the input text and the fragments produced by using the T5 transformer, it is tested for base models, i.e., bert-base-uncased and allenai/scibert_scivocab_cased. The count of sentences parameter helps to include the top sentences for the final summary generation, its value is tested within 4–10. The β value used to calculate the scores is tested for the range of 0–1.

4.5 Discussion of results

Unsupervised extractive-based summarization models are compared and analyzed on the truncated version of the CORD-19 corpus using the ROUGE metric. The study shows, according to Table 3 and Fig. 2, that the hybrid proposed methodology surpassed the listed techniques, with the F1 scores of 40.14%, 13.25%, and 36.32% for ROUGE1, ROUGE-2 and ROUGE-L, respectively. Whereas ROUGE-1 gains the highest F1 score of 40.14%. The lowest performing is the RANDOM method with F1 score of ROUGE-1: 33.26% and ROUGE-2: 8.17%. SumBasic, with a score of 27.63%, is the model performing the least well for ROUGE-L. In conclusion, the proposed CovSumm model performs well for all metrics including ROUGE-1, ROUGE-2, and ROUGE-3.

The efficacy of the proposed approach is analyzed with a distinct number of sentences, and the outcomes are illustrated in Table 4 and Fig. 3.

Table 4 illustrates how the number of sentences used to produce the final summary generation affects the performance of the proposed hybrid model. The experiment was performed on values ranging from 4 to 10. According to the analysis conducted,

Table 3 Performance of powerful summarization models by F1 scores on CORD-19 corpus

S. No	Unsupervised techniques	ROUGE-1 (%)	ROUGE-2 (%)	ROUGE-L (%)
1	TextRank	36.19	10.95	32.26
2	LSA	36.14	9.39	28.11
3	Luhn	37.57	10.89	29.84
4	Edmundson	35.93	10.08	28.56
5	LexRank	37.33	10.29	29.36
6	KL Sum	34.87	9.10	27.91
7	SumBasic	35.93	8.97	27.63
8	LEAD	35.78	10.58	32.30
9	RANDOM	33.26	8.17	29.38
10	GenCompareSum	38.69	11.85	34.81
11	**CovSumm**	**40.14**	**13.25**	**36.32**

The values in bold indicate the highest scores obtained

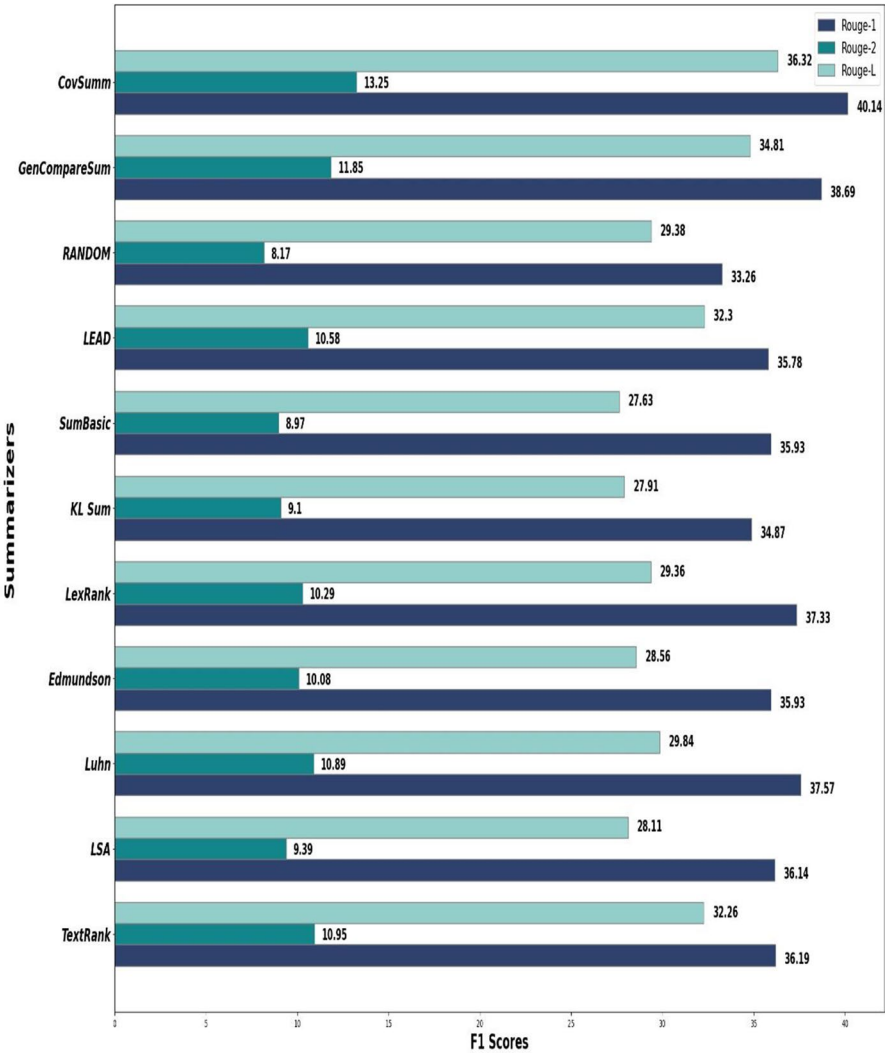


Fig. 2 The F1 scores for ROUGE-1, ROUGE-2, and ROUGE-L were utilized to assess the performance of various unsupervised summarization models on the CORD-19 Corpus

the model performance increases with an increasing number of sentences. However, after 7, the performance starts to decline as the number of sentences increases. On selecting 7 sentences for the final summary, ROUGE-1, ROUGE-2, and ROUGE-L have the highest F1 value of 40.14%, 13.25%, and 36.32%, respectively. On value 4, ROUGE-1, ROUGE-2, and ROUGE-L scored the lowest with F1 scores of 35.78%, 11.87%, and 32.10%, respectively. From Fig. 3, it was analyzed that the proposed hybrid model performs best when selecting seven sentences for the summary generation for all the F1 scores of ROUGE-1, ROUGE-2, and ROUGE-L.

Table 4 Experimental analysis of the presented approach as per the parameter count of sentences against ROUGE Scores

No. of sentences	F1 Score		
	ROUGE-1 (%)	ROUGE-2 (%)	ROUGE-L (%)
4	35.78	11.87	32.10
5	38.36	12.76	34.50
6	39.36	12.94	35.49
7	**40.14**	**13.25**	**36.32**
8	39.93	13.19	36.24
9	39.67	12.11	36.09
10	39.34	13.12	35.84

The values in bold indicate the highest scores obtained

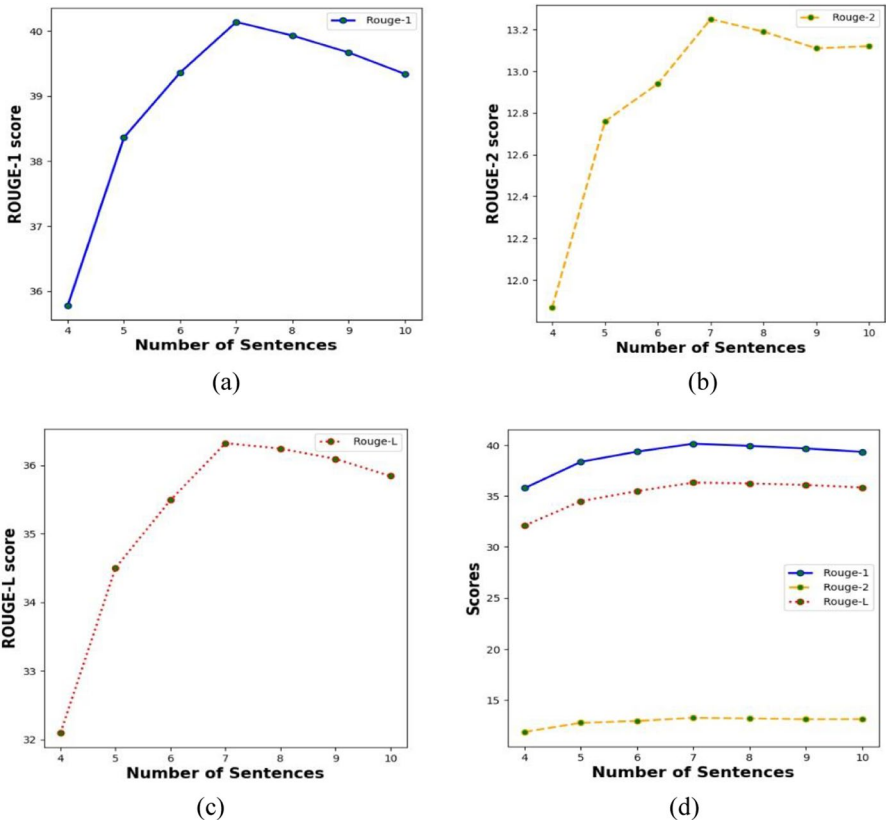


Fig. 3 The graph depicts how the total count of sentences influences the efficacy of the proposed technique when evaluating the CORD-19 corpus using the ROUGE metric **a** The number of sentences vs ROUGE-1 score **b** The number of sentences vs ROUGE-2 score **c** The number of sentences vs ROUGE-L score **d** The number of sentences vs ROUGE-1, ROUGE-2, and ROUGE-L score

Table 5 Experimental analysis of the developed approach based on the parameter β value against the ROUGE values

β values	F1 score		
	ROUGE-1 (%)	ROUGE-2 (%)	ROUGE-L (%)
0.2	40.06	13.18	36.27
0.3	**40.14**	**13.25**	**36.32**
0.4	40.04	13.17	36.19
0.5	39.98	13.14	36.19
0.6	39.92	13.05	36.06

The values in bold indicate the highest scores obtained

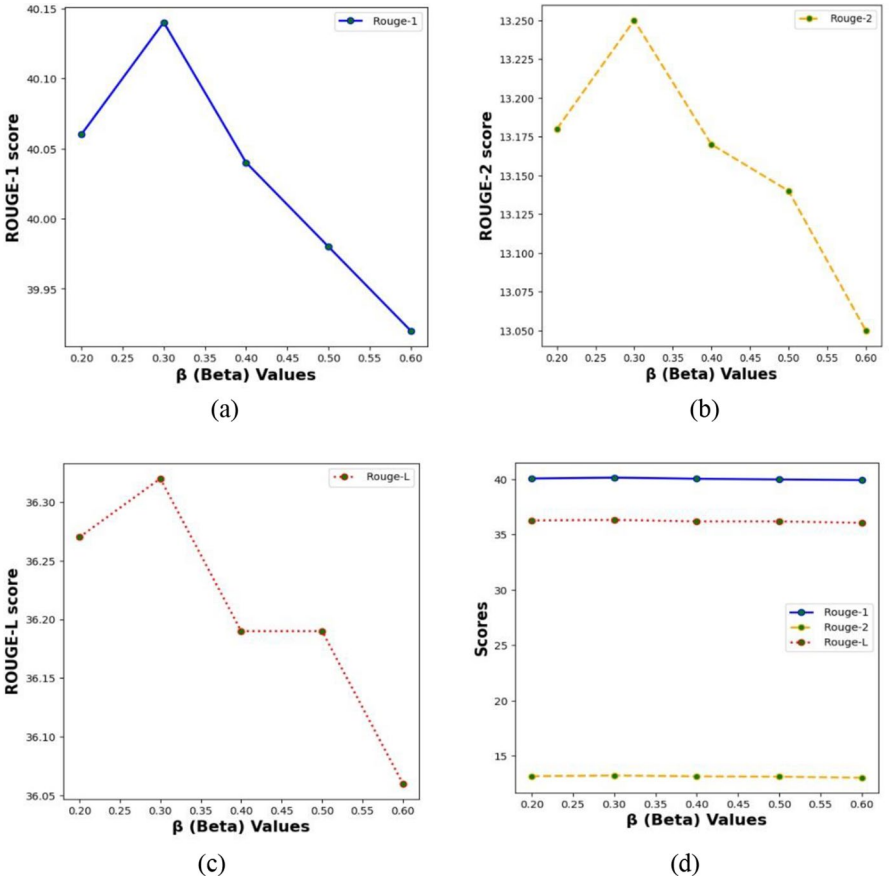


Fig. 4 The graph illustrates how the β Values influence the efficacy of the proposed methodology when evaluating the CORD-19 corpus using the ROUGE metric **a** β Values vs ROUGE-1 score. **b** β Values vs ROUGE-2 score **c** β Values vs ROUGE-L score **d** β Values vs ROUGE-1, ROUGE-2 and ROUGE-L score

Additionally, the performance of the proposed model for different values of β is represented in Table 5 and Fig. 4. Table 5 presents a comparison of the efficacy of the proposed technique according to the parameter β. An experiment was conducted with values ranging from 0 to 1. It was found that the model performance increases with an increasing β value, but gradually declines after 0.3. The highest F1 scores were achieved by ROUGE-1, ROUGE-2, and ROUGE-L, for $\beta = 0.3$. According to the F1 score, ROUGE-1, ROUGE-2, and ROUGE-L scored the lowest values of 39.92%, 13.05%, and 36.06%, respectively, for $\beta = 0.6$. According to the analysis from Fig. 4, can be inferred that the proposed methodology performs best when the β value is set to 0.3 for all the F1 scores of ROUGE-1, ROUGE-2, and ROUGE-L.

Figure 5 illustrates a sample of the original text utilized as input for the CovSumm model. The reference summary used to calculate the ROUGE scores is the gold summary, while the summary produced by the proposed model is the generated summary.

5 Conclusion

In this study, the CovSumm model was proposed for the summary generation of the scientific papers related to Covid-19. CovSumm is an unsupervised hybrid approach, a fusion of the recently introduced GenCompareSum method involving the pre-trained T5 model for language generation and the TextRank graph-based algorithm, to produce summaries for scientific research articles. The major advantage of CovSumm is that it is a hybrid approach that combines the strengths of two distinctive and complementary lines of research for unsupervised extractive text summarization: T5 language model and graph-based algorithm. This combination allows for a more comprehensive and non-redundant summary of COVID-19-relevant scientific publications, as demonstrated by the higher scores of the ROUGE evaluation metric as compared to the state-of-the-art methodologies. Another benefit of the proposed approach is that it can effectively handle the problem of information overload that is prevalent in a massive volume of COVID-19-relevant scientific studies. This would help to keep researchers and medical associations informed on the latest COVID-19-related information. The experimental results and analysis depict that the proposed model CovSumm outperforms various unsupervised summarization methods on CORD-19 corpus. The proposed CovSumm model will boost and give direction to researchers in further studies on effective summarization of scientific literature. The use of domain-specific pre-trained transformer models [42] may help to boost the performance scores. Further, this model can be experimented with several transformer-based language models like PEGASUS, GPT2, BART, etc., for language generation tasks, as well as with different graph-based approaches, and can be evaluated on various other biomedical datasets.

Original Text:

Neutropenic enterocolitis, also known as typhlitis, is a rare but fatal complication of neutropenia. It is characterized by severe inflammation in the intestines,especially in the cecum ascending colon. Typhlitis is often seen in patients with a severely compromised immune system due to aplastic anemia, hematological malignancy, solid organ transplantation, or patients receiving high-dose chemotherapy. It has a high morbidity and mortality rate. The severe acute respiratory syndrome coronavirus 2 (SARS-CoV-2) causes COVID-19 (Coronavirus Disease 2019) and primarily affects the respiratory system. Still, it has been shown that it may affect other systems, such as the hematopoietic system, and may cause lymphopenia, neutropenia, and rarely pancytopenia. Moreover, reports of gastrointestinal system involvement in COVID-19 patients are rapidly increasing. Recently, Rehman and colleagues reported a case of COVID-19 and neutropenic enterocolitis in an immunosuppressed patient with esophageal adenocarcinoma. Herein, we aimed to present clinical and radiological findings of a rare patient, who was not previously immunosuppressed, with COVID-19-associated pancytopenia and typhlitis. A 60-year-old woman was admitted to the emergency department with complaints of abdominal pain, nausea, diarrhea, fatigue, and red blood in the stool, which were present for two days. The patient had a history of diabetes mellitus for 11 years, and she had been using oral antidiabetics (metformin and sitagliptin). Physical examination revealed tenderness in the right lower quadrant and bloody stool on rectal examination. The body temperature of the patient was found to be 37.1 degrees Celsius. One month ago, the patients' laboratory findings were within normal limits except for mild anemia (hemoglobin; 9.9 mg/dL, normal range; 11-14 mg/dL). Besides, the colonoscopy examination performed for screening two months ago was unremarkable. The laboratory test results in the current admission showed elevated c-reactive protein (286 mg/L, normal range; 0-5 mg/L), lactate dehydrogenase (304 U/L, normal range; 135-215 U/L) levels, and pancytopenia. The hemoglobin value was 7.8 mg/dL (normal range; 11-14 mg/dL), white blood cell count (0.27 K/uL; normal value, 4-10 K/uL), neutrophil count (0.01 K/uL; normal value, 4-10 K/uL), and platelet (15 K/uL, normal range; 150-410 K/uL). Other laboratory test results, including creatinine and liver function test results, were within normal limits. Contrast-enhanced abdominal computed tomography (CT) was obtained with a suspicion of acute abdomen. Abdominal CT showed bowel wall thickening in the cecum and ascending colon and increased mucosal contrast enhancement in these segments.

(a)

Gold Summary:

Neutropenic enterocolitis is also known as typhlitis, is characterized by severe inflammation in the bowel loops. It is often seen in immunosuppressed patients, and it has high morbidity and mortality. Although the severe acute respiratory syndrome coronavirus 2 (SARS-CoV-2) primarily affects the respiratory system and causes COVID-19 (Coronavirus Disease 2019), it may affect hematopoietic and gastrointestinal systems. Herein, we present a rare case of COVID-19-associated pancytopenia and typhlitis in a 60-year-old female who presented with abdominal pain. Contrast-enhanced abdominal computed tomography (CT) demonstrated the bowel wall thickening in the cecum and ascending colon compatible with enterocolitis. Moreover, the chest CT showed bilateral, peripheral, and multifocal ground-glass opacities, consistent with COVID-19 pneumonia. We also aimed to emphasize the laboratory, clinical, and CT findings of the patient.

(b)

CovSumm Geneerated Summary:

Neutropenic enterocolitis, also known as typhlitis, is a rare but fatal complication of neutropenia. Typhlitis is often seen in patients with a severely compromised immune system due to aplastic anemia, hematological malignancy, solid organ transplantation, or patients receiving high-dose chemotherapy. Moreover, reports of gastrointestinal system involvement in COVID-19 patients are rapidly increasing. Recently, Rehman and colleagues reported a case of COVID-19 and neutropenic enterocolitis in an immunosuppressed patient with esophageal adenocarcinoma.Herein, we aimed to present clinical and radiological findings of a rare patient, who was not previously immunosuppressed, with COVID-19-associated pancytopenia and typhlitis.Contrast-enhanced abdominal computed tomography (CT) was obtained with a suspicion of acute abdomen. Abdominal CT showed bowel wall thickening in the cecum and ascending colon and increased mucosal contrast enhancement in these segments.

(c)

Fig. 5 Summary sample **a** Original text as input **b** Gold summary used as a reference summary **c** Summary generated from the proposed system

Acknowledgements Not applicable.

Authors' contributions AK contributed to conceptualization, methodology, software, data curation, writing—original draft, visualization, and investigation. SS contributed to conceptualization, methodology, investigation, supervision, and writing—review and editing.

Funding The authors did not receive any external funding or support for the research presented in their submission.

Data availability The corresponding author can make available the data underlying the findings of this research upon a reasonable request.

Code availability Upon a reasonable request, the corresponding author can provide the code supporting the conclusions of this study.

Declarations

Conflict of interest The authors state that they do not have any known financial interests or personal relationships that may have influenced the findings reported in this paper.

Consent for publication The manuscript has been approved by all authors and they have given their full consent for its publication.

Ethical approval and consent to participate The article does not contain any studies involving human participants and animals.

Human and animal ethics Not applicable.

References

1. Cai X, Liu S, Yang L, Lu Y, Zhao J, Shen D, Liu T (2022) COVIDSum: a linguistically enriched SciBERT-based summarization model for COVID-19 scientific papers. J Biomed Inform 127:103999
2. Xie Q, Bishop JA, Tiwari P, Ananiadou S (2022) Pre-trained language models with domain knowledge for biomedical extractive summarization. Knowl-Based Syst 252:109460
3. Tang T, Yuan T, Tang X, Chen D (2020) Incorporating external knowledge into unsupervised graph model for document summarization. Electronics 9(9):1520
4. Zhao J, Liu M, Gao L, Jin Y, Du L, Zhao H, Haffari G (2020) SummPip: unsupervised multi-document summarization with sentence graph compression. In: Proceedings of the 43rd International ACM SIGIR Conference on Research and Development in Information Retrieval, pp 1949–1952
5. Wallace BC, Saha S, Soboczenski F, Marshall IJ (2021) Generating (factual?) narrative summaries of rcts: experiments with neural multi-document summarization. AMIA Summits Transl. Sci. Proc. 2021:605
6. Huang D, Cui L, Yang S, Bao G, Wang K, Xie J, Zhang Y (2020) What have we achieved on text summarization?. In: Proceedings of the 2020 Conference on Empirical Methods in Natural Language Processing (EMNLP). Association for Computational Linguistics, pp 446–469
7. Zhong M, Liu P, Chen Y, Wang D, Qiu X, Huang X (2020) Extractive summarization as text matching. In: Proceedings of the 58th Annual Meeting of the Association for Computational Linguistics, pp 6197–6208. https://doi.org/10.18653/v1/2020.acl-main.552
8. See A, Liu PJ, Manning CD (2017) Get to the point: summarization with pointer-generator networks. In: Proceedings of the 55th Annual Meeting of the Association for Computational Linguistics, pp 1073–1083. Vancouver, Canada
9. Raffel C, Shazeer N, Roberts A, Lee K, Narang S, Matena M, Liu PJ (2020) Exploring the limits of transfer learning with a unified text-to-text transformer. J Mach Learn Res 21(1):5485–5551

10. Cachola I, Lo K, Cohan A, Weld C (2020) TLDR: extreme summarization of scientific documents. In: Findings of the association for computational linguistics: EMNLP 2020. Association for Computational Linguistics, pp 4766–4777
11. Liu Y, Lapata M (2019) Text summarization with pretrained encoders. In: Proceedings of the Conference on Empirical Methods in Natural Language Processing. Hong Kong, pp 3728–3738
12. Dou Z-Y, Liu P, Hayashi H, Jiang Z, Neubig G (2021) GSum: a general framework for guided neural abstractive summarization. In: Proceedings of the Conference of the North American Chapter of the Association for Computational Linguistics: Human Language Technologies. Association for Computational Linguistics, 4830–4842. https://doi.org/10.18653/v1/2021.naacl-main.384
13. Ramos J (2003) Using tf-idf to determine word relevance in document queries. Proc First Instr Conf Mach Learn 242(1):29–48
14. Kiros R, Zhu Y, Salakhutdinov R, Zemel RS, Torralba A, Urtasun R, Fidler S (2015) Skip-thought vectors. In: Proceedings of the 28th International Conference on Neural Information Processing Systems, vol 2, pp 3294–3302
15. Kenton JDMWC, Toutanova LK (2019) Bert: pre-training of deep bidirectional transformers for language understanding. In: Proceedings of naacL-HLT, vol 1, p 2
16. Mutlu B, Sezer EA, Akcayol MA (2020) Candidate sentence selection for extractive text summarization. Inf Process Manag 57(6):102359
17. Luhn HP (1958) The automatic creation of literature abstracts. IBM J Res Dev 2(2):159–165
18. Edmundson HP, Wyllys RE (1961) Automatic abstracting and indexing—survey and recommendations. Commun ACM 4(5):226–234
19. Mihalcea R, Tarau P (2004) Textrank: bringing order into text. In: Proceedings of the 2004 Conference on Empirical Methods in Natural Language Processing, pp 404–411
20. Erkan G, Radev DR (2004) Lexrank: graph-based lexical centrality as salience in text summarization. J Artif Intell Res 22:457–479
21. Bishop J, Xie Q, Ananiadou S (2022) GenCompareSum: a hybrid unsupervised summarization method using salience. In: Proceedings of the 21st workshop on biomedical language processing, pp 220–240
22. Ozsoy MG, Alpaslan FN, Cicekli I (2011) Text summarization using latent semantic analysis. J Inf Sci 37(4):405–417
23. Nenkova A, Vanderwende L (2005) The impact of frequency on summarization. Microsoft Research, Redmond, Washington, Tech. Rep. MSR-TR-2005, 101
24. Radford A, Narasimhan K, Salimans T, Sutskever I (2018) Improving language understanding by generative pre-training. Technical Report. OpenAI
25. Wang LL, Lo K, Chandrasekhar Y, Reas R, Yang J, Burdick D, Eide D, Funk K, Katsis Y, Kinney RM, Li Y, Liu Z, Merrill W, Mooney P, Murdick DA, Rishi D, Sheehan J, Shen Z, Stilson B, et al. (2020) CORD-19: the COVID-19 open research dataset. In: Proceedings of the 1st workshop on NLP for COVID-19 at ACL 2020. Association for Computational Linguistics
26. Moradi M, Dorffner G, Samwald M (2020) Deep contextualized embeddings for quantifying the informative content in biomedical text summarization. Comput Methods Prog Biomed 184:105117
27. Padmakumar V, He H (2021) Unsupervised extractive summarization using pointwise mutual information. In: Proceedings of the 16th Conference of the European Chapter of the Association for Computational Linguistics: Main Volume. Association for Computational Linguistics, pp 2505–2512
28. Ju J, Liu M, Koh HY, Jin Y, Du L, Pan S (2021) Leveraging information bottleneck for scientific document summarization. In: Findings of the association for computational linguistics: EMNLP 2021, Punta Cana, Dominican Republic. Association for Computational Linguistics, pp 4091–4098
29. Su D, Xu Y, Yu T, Siddique FB, Barezi E, Fung P (2020) CAiRE-COVID: a question answering and query-focused multi-document summarization system for COVID-19 scholarly information management. In: Proceedings of the 1st workshop on NLP for COVID-19 (part 2) at EMNLP. Association for Computational Linguistics
30. Jang M, Kang P (2021) Learning-free unsupervised extractive summarization model. IEEE Access 9:14358–14368
31. Belwal RC, Rai S, Gupta A (2021) Text summarization using topic-based vector space model and semantic measure. Inf Process Manag 58(3):102536
32. Srivastava R, Singh P, Rana KPS, Kumar V (2022) A topic modeled unsupervised approach to single document extractive text summarization. Knowl-Based Syst 246:108636

33. Belwal RC, Rai S, Gupta A (2021) A new graph-based extractive text summarization using keywords or topic modeling. J Ambient Intell Humaniz Comput 12(10):8975–8990
34. El-Kassas WS, Salama CR, Rafea AA, Mohamed HK (2020) EdgeSumm: graph-based framework for automatic text summarization. Inf Process Manag 57(6):102264
35. Liu J, Hughes DJ, Yang Y (2021) Unsupervised extractive text summarization with distance-augmented sentence graphs. In: Proceedings of the 44th International ACM SIGIR Conference on Research and Development in Information Retrieval, pp 2313–2317
36. Joshi A, Fidalgo E, Alegre E, Alaiz-Rodriguez R (2022) RankSum—an unsupervised extractive text summarization based on rank fusion. Expert Syst Appl 200:116846
37. COVID-19 Open Research Dataset Challenge (CORD-19), https://www.kaggle.com/datasets/allen-institute-for-ai/CORD-19-research-challenge. Accessed 07 Aug 2022
38. Xu S, Zhang X, Wu Y, Wei F, Zhou M (2020) Unsupervised extractive summarization by pre-training hierarchical transformers. In: Findings of the association for computational linguistics: EMNLP 2020. Association for Computational Linguistics, pp 1784–1795
39. Lin CY (2004) Rouge: a package for automatic evaluation of summaries. In: Text summarization branches out, pp 74–81
40. Haghighi A, Vanderwende L (2009) Exploring content models for multi-document summarization. In: Proceedings of Human Language Technologies: the 2009 Annual Conference of the North American Chapter of the Association for Computational Linguistics, pp 362–370
41. Ishikawa K (2001) A hybrid text summarization method based on the TF method and the lead method. In: Proceedings of the second NTCIR workshop meeting on evaluation of Chinese & Japanese text retrieval and text summarization, pp 325–330
42. Bansal A, Choudhry A, Sharma A, Susan S (2023) Adaptation of domain-specific transformer models with text oversampling for sentiment analysis of social media posts on COVID-19 vaccine. Comput Sci 24(2). https://doi.org/10.7494/csci.2023.24.2.4761

Publisher's Note Springer Nature remains neutral with regard to jurisdictional claims in published maps and institutional affiliations.

Springer Nature or its licensor (e.g. a society or other partner) holds exclusive rights to this article under a publishing agreement with the author(s) or other rightsholder(s); author self-archiving of the accepted manuscript version of this article is solely governed by the terms of such publishing agreement and applicable law.

Current Feedback Operational Amplifier Based Active Filter Configuration

Ram Bhagat[a], Monika Kumari[b], Nilesh Kumar Jha[c], Rishabh Yadav[d]
Department of Electrical Engineering
Delhi Technological University
Delhi, India

[a]rambhagat@dtu.ac.in, [b]jmonicak1974@gmail.com, [c]nileshkumarjha_2k19ee175@dtu.ac.in,
[d]rishabhyadav_2k19ee201@dtu.ac.in

2023 International Conference on Power, Instrumentation, Energy and Control (PIECON) | 979-8-3503-9976-9/23/$31.00 ©2023 IEEE | DOI: 10.1109/PIECON56912.2023.10085912

***Abstract*—In this paper, a Current Feedback Operational Amplifier (CFOA) based active filter configuration has been proposed. The described circuit topology employs two CFOAs and five admittances to realize an active Low Pass Filter (LPF), a Band Pass Filter (BPF) and a High Pass Filter (HPF) by appropriate admittance selection. In all the derived filter circuits, grounded and virtually grounded capacitors are being used, as it is preferred for IC implementation, for the design of filter circuits. To demonstrate the practicability of the proposed configuration, PSPICE simulation results are used, which match closely with the theoretical response obtained by using MATLAB. Experimental results using commercially available off-the-shelf CFOA IC AD844 have also been included to support the theoretical and simulated results.**

Keywords—Active Filters, Current Feedback Operational Amplifier, AD844.

I. INTRODUCTION

The multifunction filter is frequently employed in the construction of analog signal processing systems, including demodulators and touch-tone telephone systems. In this digital era, operational amplifiers can be used to design filters and almost all linear and non-linear circuits such as integrators, differentiators, oscillators, comparators, multivibrators, etc. CFOA which unlike the traditional Voltage Amplifiers (VOAs) exhibit a number of advantages in the designing of analog circuits. A traditional VOA has the major disadvantage that its gain and bandwidth cannot be set independently, which is usually known as the "gain-bandwidth conflict." A CFOA, on the other hand, offers an independent gain and bandwidth relationship [1]. In addition to that, it provides a relatively higher slew rate. It is evident that slew rate affects the dynamic range of the analog circuit and the maximum operational frequency of the input signal [2]. Hence, the CFOA also enhances the operational range of frequency.

In literature, a number of active filters have been realized by using different active building blocks (ABBs). As this paper describes a CFOA-based filter configuration, the literature review focuses on the implementation of CFOA-based filters, some of which are found in [3]-[12]. In [3], CFOA-based second-order HPF and BPF responses are obtained from the same circuit with three resistors and two capacitors. Second-order LPF and HPF are realized in [4] using two CFOAs, three resistors, and two grounded or virtually grounded capacitors. CFOA-based low-frequency LPF and HPF filter that is able to realize heavy inductors, capacitors, and resistors that cannot be fabricated on chips is described in [5] and [6]. Two CFOA-based grounded-capacitor first-order all-pass filter configurations have been proposed in [7], with an ideally infinite input impedance. The CFOA-based filters are widely used to counter the interference problem in Aeronautical communication. Such a Second-order active-R Bandpass filter is put forward in [8].

Three new CFOA-based second-order universal filter configurations with minimum number of CFOAs and passive elements are derived in [9] which use four CFOAs and two capacitors. High input impedance and low output impedance facilitates the tunability of gain and cut-off frequency as shown in [10] where a CFOA-pole-based active-R design is used to realize resonator, filter, and oscillator circuits. [11] presents a voltage-gain controlled, modified CFOA-based first-order electronically tuneable all-pass filter design. A similar circuit with a low component count and great properties with a systematic method of designing CFOA-based LPF and HPF ladder filter configurations is explained in [12]. A major factor in the designing of a filter is power consumption. To reduce power consumption, cost, and chip area integrated voltage mode CFOA-based biquadratic filter circuits are crucial. The same is presented in [13] along with the hardware design specifications.

This paper proposes the aforementioned filter designs, the LPF, HPF, and BPF, using a multifunctional CFOA configuration. The proposed general filter configuration makes use of two CFOAs and five admittances. By choosing the appropriate passive elements in the general configuration, various filters (LPF, HPF, and BPF) can be realized. The simulation results are compared with the theoretical and practical results as well.

This paper is divided into six sections. Section I explains the introduction to the topic and discusses the literature. The circuit that has been proposed and its mathematical analysis is well described in Section II. Further, the non-ideal and sensitivity analysis is done under Section III. Section IV includes the simulation results; Section V includes the experimental results; and Section VI concludes the paper.

II. PROPOSED CONFIGURATION

The CFOA in symbolic representation is shown in Fig. 1, where X denotes the inverting input terminal, Y denotes the non-inverting input terminal, Z denotes the compensation node, and W denotes the output voltage terminal. The characteristic equations of the CFOA are given by:

$$V_X=V_Y,\ I_Z=I_X,\ I_Y=0 \text{ and } V_o=V_Z \quad (1)$$

979-8-3503-9976-9/23/$31.00 ©2023 IEEE

Authorized licensed use limited to: DELHI TECHNICAL UNIV. Downloaded on April 10,2023 at 07:25:51 UTC from IEEE Xplore. Restrictions apply.

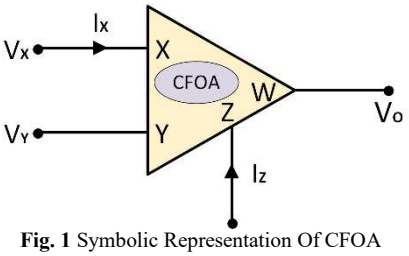


Fig. 1 Symbolic Representation Of CFOA

The active filter circuit topology proposed in this paper for the realization of LPF, HPF, and BPF is shown in Fig. 2.

The routine analysis of the configuration yields the transfer function (TF):

$$\mathrm{TF} = \frac{V_o}{V_{in}} = -\frac{Y_1 Y_4}{Y_2 Y_4 + Y_3 Y_5} \qquad (2)$$

The selection of admittance(s) for the realization of LPF, HPF, and BPF are displayed in Table I, and Table II displays the performance parameters like pole frequency(ω_o), dc gain (H_o) and band width (BW) or quality factor Q-factor for the realized active filters.

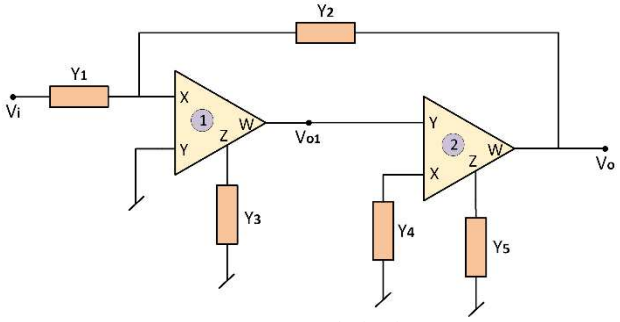


Fig. 2 Proposed Circuit

TABLE I. REALIZATION OF ACTIVE FILTER CONFIGURATION FROM PROPOSED CIRCUIT

Filter Realized	Choice of admittance					Transfer Function
	Y1	Y2	Y3	Y4	Y5	
LPF	$\frac{1}{R_1}$	$\frac{1}{R_2}$	$C_3 s$	$\frac{1}{R_4}$	$C_5 s + \frac{1}{R_5}$	$\frac{-\frac{1}{R_1 R_4 C_3 C_5}}{s^2 + \frac{1}{R_5 C_5} s + \frac{1}{R_4 R_2 C_3 C_5}}$
HPF	$\frac{\frac{s}{R_1}}{s + \frac{1}{R_4 C_4}}$	$\frac{1}{R_2}$	$\frac{1}{R_3}$	$\frac{\frac{s}{R_4}}{s + \frac{1}{R_4 C_4}}$	$\frac{1}{R_5}$	$\frac{-\frac{R_2 R_3 R_5}{R_1(R_3 R_5 + R_2 R_4)} s^2}{s^2 + \frac{R_1 R_2 C_1 + R_3 R_5 C_4 + R_2 R_4 C_4}{R_1 C_1 C_4 (R_3 R_5 + R_2 R_4)} s + \frac{R_2}{R_1 C_1 C_4 (R_3 R_5 + R_2 R_4)}}$
BPF-1	$\frac{1}{R_1}$	$C_2 s + \frac{1}{R_2}$	$\frac{1}{R_3}$	$C_4 s$	$\frac{1}{R_5}$	$\frac{-\frac{1}{R_1 C_2} s}{s^2 + \frac{1}{R_2 C_2} s + \frac{1}{R_3 R_5 C_2 C_4}}$
BPF-2	$C_1 s$	$\frac{1}{R_2}$	$C_3 s$	$\frac{1}{R_4}$	$C_5 s + \frac{1}{R_5}$	$\frac{-\frac{C_1}{C_3 C_5 R_4} s}{s^2 + \frac{1}{R_5 C_5} s + \frac{1}{R_2 R_4 C_3 C_5}}$

TABLE II. PERFORMANCE PARAMETERS OF REALIZED FILTERS OF TABLE I

Filter Realized	Cut-off frequency(ω_o)	Gain (H_o)	Bandwidth/Quality Factor
LPF	$\omega_o = \frac{1}{\sqrt{R_4 R_2 C_3 C_5}}$	$H_O = \frac{R_2}{R_1}$	$\mathrm{Qo} = R_5 \sqrt{\frac{C_5}{R_4 R_2 C_3}}$
HPF	$\omega_o = \sqrt{\frac{R_2}{R_1 C_1 C_4 (R_3 R_5 + R_2 R_4)}}$	$H_O = \frac{R_2 R_3 R_5}{R_1 (R_3 R_5 + R_2 R_4)}$	$\mathrm{Qo} = \frac{\sqrt{R_1 R_2 C_1 C_4 (R_3 R_5 + R_2 R_4)}}{R_1 R_2 C_1 + R_3 R_5 C_4 + R_2 R_4 C_4}$
BPF-1	$\omega_o = \frac{1}{\sqrt{R_3 R_5 C_2 C_4}}$	$H_O = \frac{R_2}{R_1}$	$BW = \frac{1}{R_2 C_2}$

Authorized licensed use limited to: DELHI TECHNICAL UNIV. Downloaded on April 10,2023 at 07:25:51 UTC from IEEE Xplore. Restrictions apply.

BPF-2	$\omega_o = \frac{1}{\sqrt{R_2R_4C_3C_5}}$	$H_O = \frac{R_5C_1}{C_3R_4}$	$\text{BW} = \frac{1}{R_5C_5}$

From Table II, it has been observed that LPF has independent tunability of dc gain and quality factor through R_1 and R_5 respectively, while for both BPF-1 and BPF-2, dc gain has independent tunability using R_1 and R_4.

III. NON-IDEAL AND SENSITIVITY ANALYSIS

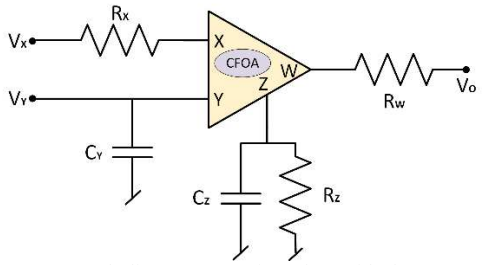


Fig. 3 Symbolic Representation of Non-ideal CFOA

The non-ideal symbolic representation of a CFOA is shown in Fig. 3, where R_x is the internal small resistance at the X- terminal, C_Y is the parasitic capacitance at the Y-terminal, and there is a parallel combination of parasitic resistance (R_Z) and parasitic capacitance (C_Z) at the Z-terminal of the CFOA. Here, R_x, R_w, and C_Y are very small and are assumed to be zero. If R_Z =Rp and C_Z = Cp, the parasitic admittance is given by:

$$Y_p = \frac{1}{R_p} + sC_p \tag{3}$$

Furthermore, all the voltage transfer ratios and current transfer ratios α, β and γ are assumed to be unity. Non-ideal performance parameters of the realized active filters are tabulated in Table III, where it can be observed that the parasitic effect of CFOA has an inconsequential effect on the BW or Q-factor.

TABLE III. NON-IDEAL PERFORMANCE PARAMETERS OF REALIZED FILTERS

Filter	Cut-off frequency (ω_o')	Gain (H_O')	Bandwidth/Quality Factor (BW′/Qo′)
LPF	$\cong \frac{\omega_o}{\sqrt{\left(1+\frac{C_{p1}}{C_3}\right)\left(1+\frac{C_{p2}}{C_5}\right)}} + \sqrt{\frac{1}{R_{p1}R_5C_3C_5\left(1+\frac{C_{p1}}{C_3}\right)\left(1+\frac{C_{p2}}{C_5}\right)}}$	$\frac{\frac{1}{R_1R_4}}{\frac{1}{R_{p1}}\left(\frac{1}{R_5}+\frac{1}{R_{p2}}\right)+\frac{1}{R_2}\frac{1}{R_4}}$	$\frac{\sqrt{(C_3+C_{p1})(C_5+C_{p2})*\frac{1}{R_2R_4}+\frac{1}{R_{p1}}\left(\frac{1}{R_5}+\frac{1}{R_{p2}}\right)}}{\left(\frac{1}{R_{p2}}+\frac{1}{R_5}\right)(C_3+C_{p1})+\frac{1}{R_{p1}}(C_5+C_{p2})}$
HPF	$\cong \sqrt{\frac{(R_3R_5+R_2R_4)\left(1+\frac{R_3+R_5}{R_p}\right)}{R_3R_5+R_2R_4+\frac{R_2R_3R_4}{R_p}+C_pn}} * \omega_o$ $n = \frac{R_2(R_3+R_5)}{C_4}+\frac{R_2R_3R_5}{R_1C_1}+\frac{R_1R_2R_4R_5}{R_pR_1C_1}$	$\frac{R_2R_3R_5C_1C_4}{R_1C_1C_4(R_3R_5+R_2R_4)+C_pm+\frac{C_pm'+R_1R_2R_3R_4C_1C_4}{R_p}}$ $m = R_2(R_3R_4C_4+R_1R_3C_1+R_1R_5C_1)$ $m' = R_1R_2R_5C_4(R_3+R_4)$	$\left(\frac{\sqrt{R_1R_2C_1C_4(R_3R_5+R_2R_4)+C_pk+\frac{R_1R_2R_4C_4(R_5C_p+R_3C_1)}{R_p}}}{R_2R_4C_4+R_3R_5C_4+R_1R_2C_1+C_pk'+\frac{R_2R_3R_5C_p+k''}{R_p}} * \omega_o'\right)$ $k' = R_2(R_3+R_5)$ $k = R_pR_2C_1(R_1R_3+R_1R_5)$ $k'' = R_2(R_3R_4C_4+R_1R_3C_1+R_2R_5C_1)$
BPF-1	$\cong \frac{\omega_o}{\sqrt{1+\frac{C_{p1}C_{p2}}{C_2C_4}}} + \sqrt{\frac{\frac{1}{R_3R_{p2}}+\frac{1}{R_5R_{p1}}}{C_2C_4\left(1+\frac{C_{p1}C_{p2}}{C_2C_4}\right)}}$	$\frac{\frac{C_4}{R_1}}{\frac{C_4}{R_2}+C_{p2}\left(\frac{1}{R_3}+\frac{1}{R_{p1}}\right)+C_{p1}\left(\frac{1}{R_5}+\frac{1}{R_{p2}}\right)}$	$\frac{\frac{C_4}{R_2}+C_{p2}\left(\frac{1}{R_3}+\frac{1}{R_{p1}}\right)+C_{p1}\left(\frac{1}{R_5}+\frac{1}{R_{p2}}\right)}{C_2C_4+C_{p1}C_{p2}}$
BPF-2	$\cong \omega_o * \sqrt{\frac{R_2R_4+R_{p1}R_5}{R_{p1}R_5+\frac{C_{p2}R_{p1}}{C_5}}}$	$\frac{\frac{C_1}{R_4}}{\frac{(C_{p2}+C_5)}{R_{p1}}+(C_3+C_{p1})\left(\frac{1}{R_5}+\frac{1}{R_{p2}}\right)}$	$\frac{\frac{(C_5+C_{p2})}{R_{p1}}+(C_3+C_{p1})*\left(\frac{1}{R_5}+\frac{1}{R_{p2}}\right)}{(C_3+C_{p1})*(C_5+C_{p2})}$

Authorized licensed use limited to: DELHI TECHNICAL UNIV. Downloaded on April 10,2023 at 07:25:51 UTC from IEEE Xplore. Restrictions apply.

Sensitivity is defined as:

$$S_X^A = \frac{X}{A}\left(\frac{\partial A}{\partial X}\right) \tag{4}$$

Where A is the desired function whose sensitivity is to be calculated and X is a variable with respect to which the sensitivity of A is to be calculated.

Table IV displays the sensitivity analysis of the performance parameters ω_o, H_o, and BW/Q-factor of the realized active filter. It can be deduced from table IV that all the realized filters have low passive sensitivity, which is not more than one.

TABLE IV. SENSITIVITY ANALYSIS

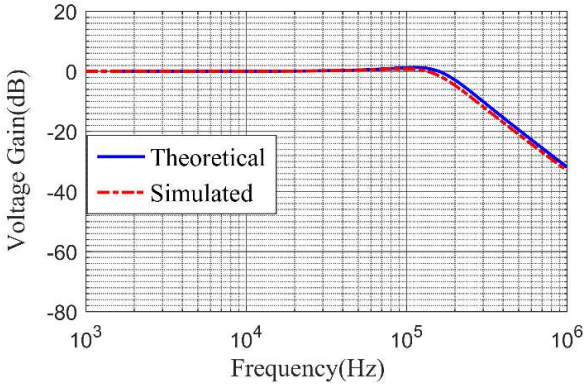
Filter Realized	Sensitivity
LPF	$S_{R_4}^{\omega_o} = S_{R_2}^{\omega_o} = S_{C_3}^{\omega_o} = S_{C_5}^{\omega_o} = -\frac{1}{2}$ $S_{R_5}^{Q_o} = 1, S_{C_5}^{Q_o} = S_{R_4}^{Q_o} = S_{R_2}^{Q_o} = S_{C_3}^{Q_o} = -\frac{1}{2}$ $S_{R_2}^{H_o} = 1, S_{R_1}^{H_o} = -1$
HPF	$S_{R_1}^{\omega_o} = S_{C_4}^{\omega_o} = -\frac{1}{2}, S_{R_2}^{\omega_o} = \frac{1}{4},$ $S_{R_3}^{\omega_o} = S_{R_4}^{\omega_o} = S_{R_5}^{\omega_o} = S_{C_1}^{\omega_o} = -\frac{1}{2}$ $S_{R_1}^{Q_o} = S_{R_3}^{Q_o} = S_{R_4}^{Q_o} = S_{R_5}^{Q_o} = S_{C_1}^{Q_o} = 0$ $S_{C_4}^{Q_o} = -\frac{1}{2}, S_{R_2}^{Q_o} = -\frac{1}{4}$ $S_{R_1}^{H_o} = -1, S_{R_2}^{H_o} = S_{R_3}^{H_o} = S_{R_5}^{H_o} = \frac{1}{2}, S_{R_4}^{H_o} = -\frac{1}{2}$
BPF-1	$S_{R_3}^{\omega_o} = S_{R_4}^{\omega_o} = S_{C_2}^{\omega_o} = S_{C_4}^{\omega_o} = -\frac{1}{2}$ $S_{R_2}^{BW} = S_{C_2}^{BW} = -1$ $S_{R_1}^{H_o} = -1, S_{R_2}^{H_o} = 1$
BPF-2	$S_{R_4}^{\omega_o} = S_{R_2}^{\omega_o} = S_{C_3}^{\omega_o} = S_{C_5}^{\omega_o} = -\frac{1}{2}$ $S_{R_5}^{BW} = S_{C_5}^{BW} = -1$ $S_{R_5}^{H_o} = S_{C_1}^{H_o} = 1, S_{C_3}^{H_o} = S_{R_4}^{H_o} = -1$

IV. SIMULATION RESULTS

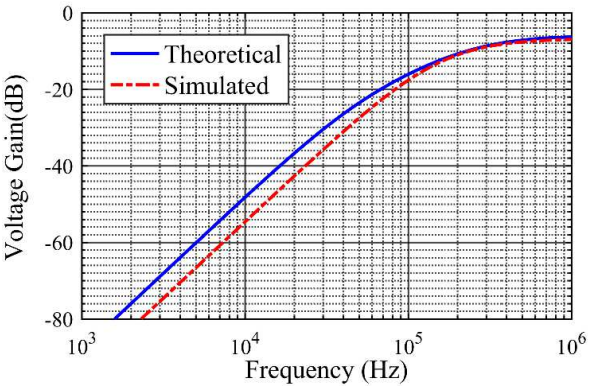
The realized filters have been simulated in PSPICE AD using the AD844 library. The bias voltage of CFOA is set to ±15V. The active filter has been designed for pole frequency, ω_o=159kHz, and Q-factor=0.707 using the passive elements listed below:

LPF: $R_1=R_2=R_4=R_5=1k\Omega$; $C_3=C_5=1nF$
HPF: $R_1=R_2=R_3=R_4=R_5=1k\Omega$; $C_1=1nF$; $C_4=0.5nF$
BPF1: $R_1=R_2=707\Omega$; $R_3=R_5=1k\Omega$; $C_2=C_4=1nF$
BPF2: $R_2=R_4=R_5=1k\Omega$; $C_1=C_3=C_5=1nF$

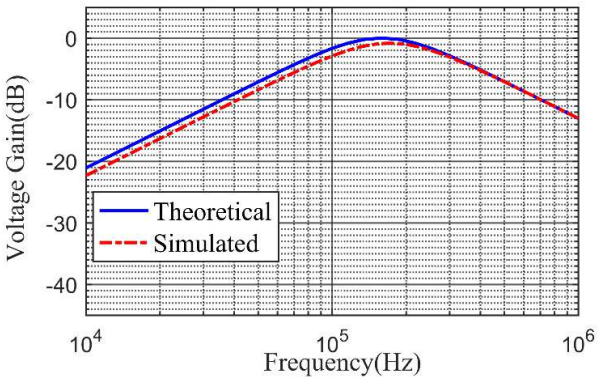
Fig. 4 shows the theoretical and simulation frequency responses of LPF, HPF, BPF-1, and BPF-2, respectively.



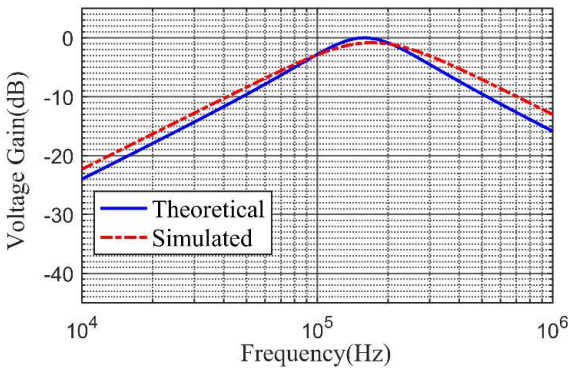
(a): Simulated and Theoretical frequency response of the LPF



(b): Simulated and Theoretical frequency response of HPF



(c): Simulated and Theoretical Frequency response of BPF-1



(d): Simulated and Theoretical frequency response of BPF-2

Fig.4: Frequency responses of proposed filter configuration

It is observed that simulated and theoretical graph curves are similar indicating minimal error.

Authorized licensed use limited to: DELHI TECHNICAL UNIV. Downloaded on April 10,2023 at 07:25:51 UTC from IEEE Xplore. Restrictions apply.

V. EXPERIMENTAL RESULTS

The workability of the realized filters in the proposed circuit has been verified with the hardware implementation. The circuit of Fig. 2 is breadboarded using AD844 CFOA, resistors and capacitors. The ± 15V DC power supply is used for the biasing of the CFOA. The values of passive components selected for the hardware implementation are identical to their simulation values.

Fig. 5 shows the experimental setup for hardware implementation. Figures 6(a) and 6(b), 7(a) and 7(b), and 8(a) and 8(b) show the frequency and transient response of LPF, HPF, and BPF, respectively. The cut-off frequency recorded against 159 kHz on the Keysight DSO for realized filter are 151.4kHz for LPF, 158.5kHz for HPF and 153.8kHz for BPF with percentage error of 4.78%, 0.31% and 3.7% respectively. The marginal error is observed to be less than ± 5% which is within the permissible limits.

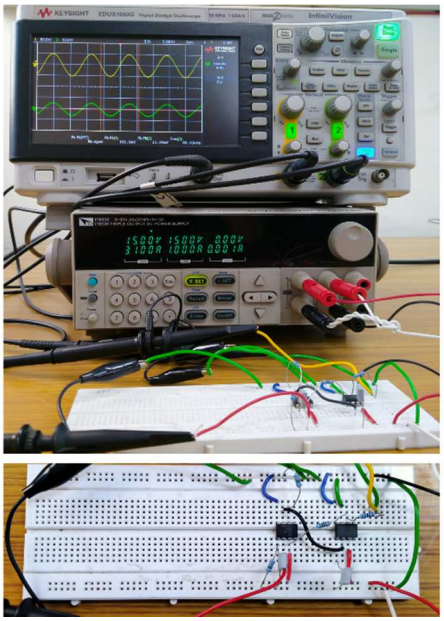


Fig. 5: Experimental Setup

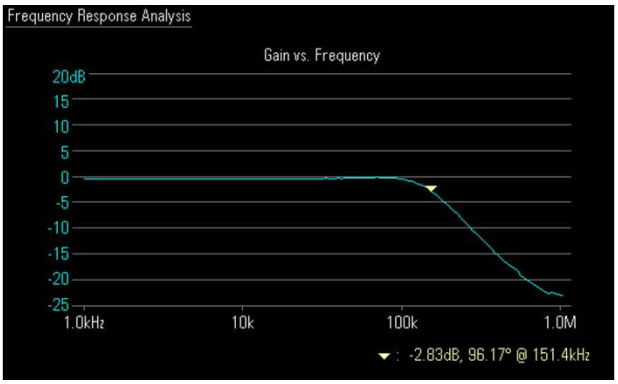


Fig. 6(a): Experimental frequency response of LPF

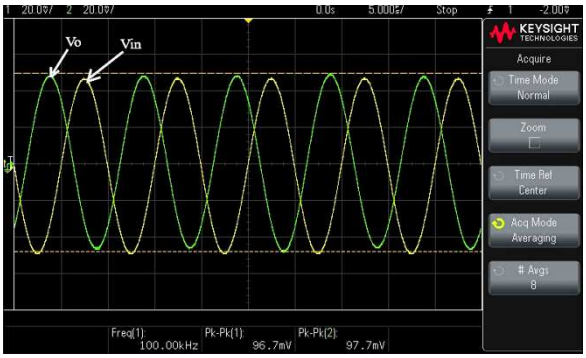


Fig. 6(b): Experimental transient response of LPF

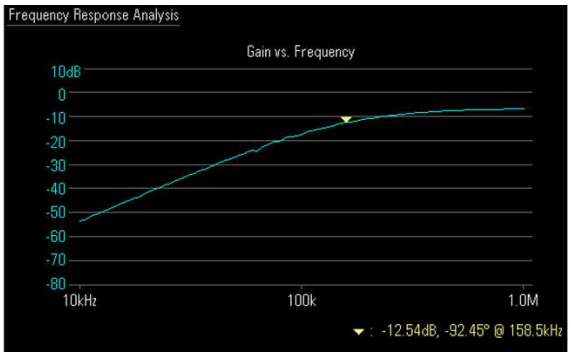


Fig. 7(a): Experimental frequency response of HPF

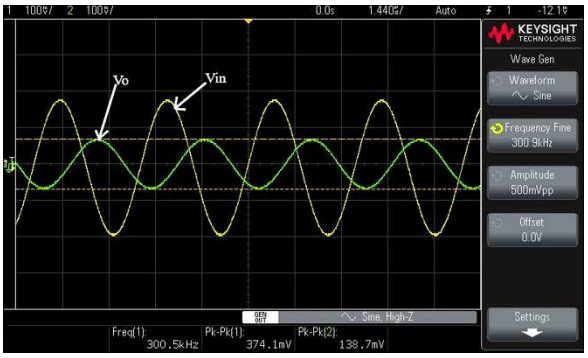


Fig. 7(b): Experimental transient response of HPF

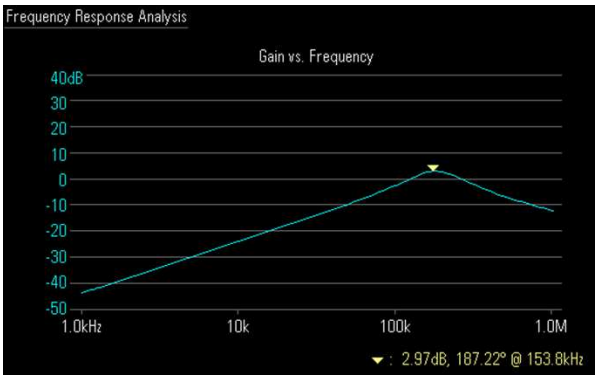


Fig. 8(a): Experimental frequency response of BPF-2

Authorized licensed use limited to: DELHI TECHNICAL UNIV. Downloaded on April 10,2023 at 07:25:51 UTC from IEEE Xplore. Restrictions apply.

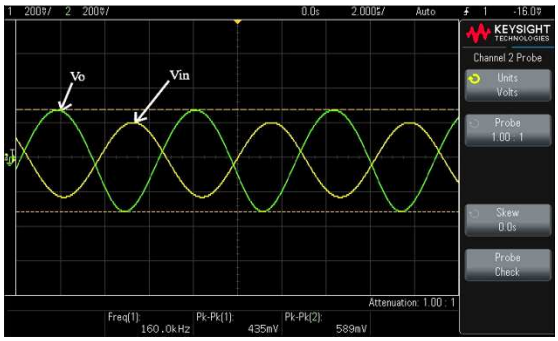


Fig. 8(b): Experimental transient response of the BPF-2

VI. Conclusion

A CFOA-based active filter configuration employing two CFOAs and five admittances has been described in the paper. The proposed circuit topology effectively realizes an LPF, HPF and BPF filter by appropriately choosing branch admittance(s). All the filters have been theoretically realized and simulated in PSPICE using the AD844 library. The practicability of the same has been validated experimentally using AD844 IC. The marginal error is found to be less than 5% indicating that the simulated and experimental results are consistent with the theoretical design.

References

[1] C. Psychalinosa, K. Palb, S. Vlassisa, “A floating generalized impedance converter with current feedback operational amplifiers”, International Journal of Electronics and Communications (AEÜ), 62, pp 81- 82, 2007

[2] Raj Senani, D.R. Bhaskar, A.K. Singh, V.K. Singh, “Current Feedback Operational Amplifiers and Their Applications”, London(UK), Springer Science Business Media New York, pp3-9, 2013

[3] Yashwant Singha, Suyash Jain, Shubham Snehill, Ram Bhagat, DC Meena, “Multi-functional circuit using two Current Feedback Operational Amplifiers”, 2020 4th International Conference on Electronics, Materials Engineering & Nano-Technology (IEMENTech), Oct 2020

[4] S. Snehill, S. Jain, Y. Singh, R. Bhagat and D.C. Meena, "CFOA based Single Resistance Controlled Oscillator," 2020 IEEE 7th Uttar Pradesh Section International Conference on Electrical, Electronics and Computer Engineering (UPCON), 2020, pp. 1-5, doi: 10.1109/UPCON50219.2020.9376478, 2020.

[5] M. T. Abuelma'atti, Z. J. Khalifa and S. K. Dhar, "New CFOA-based low frequency filters for biomedical and seismic applications," 2017 IEEE Regional Symposium on Micro and Nanoelectronics (RSM), 2017, pp. 96-99, doi: 10.1109/RSM.2017.8069114.

[6] M. T. Abuelma'atti and S. K. Dhar, "A new CFOA-based low frequency lowpass filter for biomedical applications," 2016 IEEE EMBS Conference on Biomedical Engineering and Sciences (IECBES), 2016, pp. 1-4, doi: 10.1109/IECBES.2016.7843403.

[7] R. Senania, D.R. Bhaskar, P. Kumar, “Two-CFOA-grounded-capacitor first-order all-pass filter configurations with an ideally infinite input impedance”, International Journal of Electronics and Communications (AEÜ), Vol 137, 2, 2021

[8] Atsuwe, Aondofa, ”SECOND ORDER CURRENT FEEDBACK OPERATIONAL AMPLIFIER (CFOA) ACTIVE-R BANDPASS FILTER FOR AERONAUTICAL MOBILE APPLICATIONS”, International Journal of Advance Engineering and Research Development, Volume 9, Issue 9, 1-8, September 2022.

[9] D.R. Bhaskar, Ajishek Raj, Raj Senani,"Three new CFOA-based SIMO-type universal active filter configurations with unrivalled features,"AEU - International Journal of Electronics and Communications, Volume 153,2022

[10] A. K. Singh and R. Senani, "Active-R design using CFOA-poles: new resonators, filters, and oscillators," in IEEE Transactions on Circuits and Systems II: Analog and Digital Signal Processing, vol. 48, no. 5, pp. 504-511, doi: 10.1109/82.938361, 2001.

[11] Herencsar, Norbert, et al. "A voltage gain-controlled modified CFOA and its application in electronically tunable four-mode all-pass filter design." *International Journal of Advances in Telecommunications, Electrotechnics, Signals and Systems* 1.1 : 20-25, 2012.

[12] Sinha, Praween K., et al. "CFOA based low pass and high pass ladder filter—a new configuration." *Circuits and Systems* 5.12 (: 293, 2014

[13] S. -F. Wang, H. -P. Chen, Y. Ku and M. -X. Zhong, "Analytical Synthesis of High-Pass, Band-Pass and Low-Pass Biquadratic Filters and its Quadrature Oscillator Application Using Current-Feedback Operational Amplifiers," in IEEE Access, vol. 9, pp. 13330-13343, 2021, doi: 10.1109/ACCESS.2021.3050751.

[14] Ajishek Raj, Data Ram Bhaskar, Raj Senani, Pragati Kumar, "Extension of recently proposed two-CFOA-GC all pass filters to the realisation of first order universal active filters", AEU - International Journal of Electronics and Communications, Volume 146, 2022

Authorized licensed use limited to: DELHI TECHNICAL UNIV. Downloaded on April 10,2023 at 07:25:51 UTC from IEEE Xplore. Restrictions apply.

Data Analysis of three parameter models of deceleration parameter in FRW Universe

Amine Bouali,[1,*] Himanshu Chaudhary,[2,3,†] Ujjal Debnath,[4,‡] Alok Sardar,[4,§] and G.Mustafa[5,¶]

[1] *Laboratory of Physics of Matter and Radiation, Mohammed I University, BP 717, Oujda, Morocco.*
[2] *Department of Applied Mathematics, Delhi Technological University, Delhi-110042, India,*
[3] *Department of Mathematics, Shyamlal College, University of Delhi, Delhi-110032, India.*
[4] *Department of Mathematics, Indian Institute of Engineering Science and Technology, Shibpur, Howrah-711 103, India.*
[5] *Department of Physics, Zhejiang Normal University, Jinhua 321004, People's Republic of China,*

Constraining the dark energy deceleration parameter is one of the fascinating topics in the recent cosmological paradigm. This work aims to reconstruct the dark energy using parametrization of the deceleration parameter in a flat FRW universe filled with radiation, dark energy, and pressureless dark matter. Thus, we have considered four well-motivated parameterizations of $q(z)$, which can provide the evolution scenario from the deceleration to acceleration phase of the Universe. We have evaluated the expression of the corresponding Hubble parameter of each parametrization by imposing it into the Friedmann equation. We have constrained the model parameter through $H(z)$, Pantheon, and baryons acoustic oscillation (BOA) data. Next, we have estimated the best-fit values of the model parameters by using Monte Carlo Markov Chain (MCMC) technique and implementing $H(z)$+ BAO+SNe-Ia dataset. Then we analyzed the cosmographic parameter, such as deceleration, jerk, and snap parameters, graphically by employing the best-fit values of the model parameter. Moreover, we have analyzed statefinder and Om diagnostics parameters for each scenario to discriminate various dark energy models. Using the information criteria, the viability of the models have examined. In the end, we have analogized our outcomes with the standard ΛCDM model to examine the viability of our models.

arXiv:2304.13137v1 [gr-qc] 25 Apr 2023

I. INTRODUCTION

The confirmation of the cosmic accelerated expansion of the Universe through different surveys [1–3], opened an emerging field of study in modern cosmology. To disclose the physical mechanism behind the such accelerated expansion is a challenging task for modern researchers. In light of this, several cosmological models have been implemented to alleviate this phenomenon based mainly on two different approaches. The first approach is the modification of the gravitational part of the Einstein field equation-so called modified gravity [4, 5], and the other is the existence of an exotic fluid having positive energy density and negative pressure, named dark energy (DE). This work will mainly concentrate on the second approach and suppose that the DE is responsible for the universe's accelerated expansion [6–8]. It is also interesting to note that DE violates strong energy conditions. This violation of energy generates anti-gravitational effects for which the transition from deceleration to acceleration takes place [9]. So far, numerous DE models have been suggested to describe the present-day cosmic accelerated expansion [10–14]. Among them, the ΛCDM (Λ-cold dark matter) model is considered as simplest and widely accepted DE model. Despite its success, it sufferers from some other problems, namely *coincidence* problem, *fine-tuning* problem, and *age* problem [13, 15, 16]. To solve this issue, it is quite natural for physicists to figure out another alternative DE model that can describe the present status of the Universe. The scalar field models, like quintessence, phantom, k-essence, and so on, contribute to the understanding of the origins and nature of DE. Despite these designs of dark energy, cosmic accelerated expansion is still a problem in physics today.

Several theoretical approaches have been developed to describe the cosmic accelerated expansion phenomenon, but none of these is known as the appropriate one. The most recent direction to explore the accelerating Universe at the phenomenological level is the DE parametrization of the equation of state parameter. The main idea in this approach is to consider a specific evolution scenario instead of considering any DE model a priori and then determine the nature of the exotic component that is triggering cosmic acceleration. It is known as the model-independent approach, which depends on estimating model parameters from existing observational datasets. But such an approach has some drawbacks: (i) most of the parametrization suffers from divergence problem, (ii) the parametrization technique would have missed subtle results about the true nature of dark energy due to the assumed parametric form. Various studies have been executed to describe the cosmic acceleration of the Universe through viable parametrization of EOS (see Refs.[17–19]). Inspired by the parametrization of EOS, the parametrization of the deceleration parameter has been implemented and

* a1.bouali@ump.ac.ma
† himanshuch1729@gmail.com
‡ ujjaldebnath@gmail.com
§ alokmath94@gmail.com
¶ gmustafa3828@gmail.com

studied extensively in the literature. Since the Universe evolves from earlier deceleration to late time acceleration. For this reason, any cosmological model should have a transition from deceleration phase to acceleration phase of expansion to explain the whole evolution of the Universe. Thus, the deceleration parameter plays a crucial role which is defined by $q = -\frac{a\ddot{a}}{\dot{a}^2}$, where $a(t)$ is the usual scale factor. The sign of q decides whether the Universe is accelerating i.s. $(q < 0)$ or decelerating i.s. $q > 0$. Recently, several theoretical models have been developed to analyze the entire evolutionary history of the Universe through parametrization of $q(z)$ as a function of scale factor $(a(t))$ or time (t) or redshift (z) [20–34]. The advantage of the parametrization of deceleration parameter is that it can provide finite results without considering any particular gravitational theory. However, such approaches also have disadvantages similar to the parametrization of EOS. Since we do not yet have any concrete and satisfactory theoretical model of the Universe which can describe the whole evolutionary history of the Universe. So, the idea of adopting a parametric approach may be a preliminary step towards the expansion history of the Universe.

Recently, Mamon et al. [35] studied a special form of deceleration parameter and obtained the best-fit values using χ^2 minimization technique with available observational data. They also analyzed the evolution of the jerk parameter for the considered parametrized model. Gadbali, Mandal, and Sahoo [32] have explored a specific parametrization of deceleration parameter in the context of $f(Q)$ gravity theory and constrained the model parameter by using Bayesian analysis with observational data. Motivated by the above work, we explored four suitable parametrizations of deceleration parameter to determine the best viable model compared to ΛCDM (see Ref. [36]). The present work is indeed an extension of our previous work. Here, we have assumed three well-motivated parametrizations (model 1-model3) of deceleration parameter containing three unknown parameters. We also introduced a new parametrization of the deceleration parameter, containing three unknown parameters. This work mainly focuses on constraining the model parameters using various observational datasets. In particular, we have chosen to use $H(z)$ dataset consisting of 57 measurements, Pantheon dataset consisting of 1048 measurements, and 17 uncorrelated BAO measurements to get the best-fit values of the model parameters. We adopt Monte-Carlo Markov Chain (MCMC) analysis to fix the model parameters on the recently released data. We perform observational data analysis by χ^2-minimization technique on the view of $H(z)$+SNIa+BAO dataset. This analysis provides us the bounds of arbitrary parameters q_0, q_1, and q_2 within 1σ, 2σ confidence levels. In the end, we performed a graphical analysis of cosmographic parameters like deceleration, jerk, and snap parameters for all models. In addition to this, we have analyzed $r-s$, $q-r$ planes, and Om diagnostics parameters for all the considered models.

The paper is structured as follows: section II is assigned for the basic equations for the FRW universe. In section III, we have adopted four parametrizations (model 1-model 3) and a new parametrization of the deceleration parameter. Then we obtained the Hubble solution for each parametrization. In section IV, the model parameters have been constrained using various datasets and place the best-fit values of the model parameters by implementing the MCMC method with observation data. In section V, we perform a cosmographic survey. The $r-s$, $q-r$ planes and Om diagonostic parameter is also addressed in section VI & VII. In section VIII, we present the information criteria for our models. In section IX, we have reported our conclusions based on the findings of our work.

II. BASIC EQUATIONS OF FRW MODEL

The line element of the spatially flat Friedmann-Lemaitre-Robertson-Walker (FLRW) universe is assumed as

$$ds^2 = -dt^2 + a^2(t)\left[dr^2 + r^2\left(d\theta^2 + sin^2\theta d\phi^2\right)\right] \quad (1)$$

with $a(t)$ as the scale factor, as usual. The Friedmann equations are taken as

$$H^2 = \frac{8\pi G}{3}\,\rho \quad (2)$$

and

$$\dot{H} = -4\pi G(\rho + p) \quad (3)$$

here, $H = \dot{a}/a$ is the Hubble parameter. We suppose that the universe is composed of radiation, dark matter (DM), and dark energy (DE). Then total energy density ρ and total pressure p becomes $\rho = \rho_r + \rho_m + \rho_d$ and $p = p_r + p_m + p_d$. Now we consider that the radiation, DM, and DE are separately conserved. Thus, one can write

$$\dot{\rho}_r + 3H(\rho_r + p_r) = 0, \quad (4)$$

$$\dot{\rho}_m + 3H(\rho_m + p_m) = 0 \quad (5)$$

and

$$\dot{\rho}_d + 3H(\rho_d + p_d) = 0 \quad (6)$$

For radiation, $p_r = \frac{1}{3}\rho_r$, then from equation (4) we have $\rho_r = \rho_{r0}a^{-4}$. If we assume pressure-less DM (i.e., $p_m = 0$), from equation (5) we get $\rho_m = \rho_{m0}a^{-3}$.

Now, the deceleration parameter can be written as

$$q = -1 - \frac{\dot{H}}{H^2} \tag{7}$$

So the corresponding deceleration parameter for DE has the expression [36, 37]

$$q_d = -1 - \frac{\dot{H}_d}{H_d^2} \tag{8}$$

where H_d is the Hubble rate corresponding to dark energy. So from equations (2) and (3), we can write

$$H_d^2 = \frac{8\pi G}{3}\ \rho_d \tag{9}$$

and

$$\dot{H}_d = -4\pi G(\rho_d + p_d) \tag{10}$$

Using equations (9), (10) and (6), the fluid energy density yields

$$\rho_d = \rho_{d0}\ e^{\int \frac{2(1+q_d)}{1+z} dz} \tag{11}$$

where ρ_{d0} represents the present value of the density parameter, and z is the redshift parameter described as $1 + z = \frac{1}{a}$ (presently, $a_0 = 1$).

Defining the dimensionless density parameters as $\Omega_{r0} = \frac{8\pi G\rho_{r0}}{3H_0^2}$, $\Omega_{m0} = \frac{8\pi G\rho_{m0}}{3H_0^2}$ and $\Omega_{d0} = \frac{8\pi G\rho_{d0}}{3H_0^2}$, then from equation (2), we have the Hubble parameter as:

$$\begin{aligned} H^2(z) = H_0^2\ \big[&\Omega_{r0}(1+z)^4 + \Omega_{m0}(1+z)^3 \\ &+(1-\Omega_{r0}-\Omega_{m0})\ e^{\int \frac{2(1+q_d)}{1+z} dz}\big] \end{aligned} \tag{12}$$

III. PARAMETERIZED DECELERATION PARAMETER

In this section, we consider some parameterized deceleration parameter analogs of some well-established parametric models of the equation of state parameter and calculated the corresponding Hubble parameter in terms of redshift z.

A. Model 1

The Alam-Sahni-Saini-Starobinsky (ASSS) model for parametrized equation of state parameter has been studied in [38, 39]. The equivalent ASSS type parametrization of deceleration parameter has been introduced in [40, 41] and is given by

$$q_d(z) = -1 + \frac{q_1(1+z) + 2q_2(1+z)^2}{3\left[q_0 + q_1(1+z) + q_2(1+z)^2\right]} \tag{13}$$

with q_0, q_1 and q_2 are constants. Then the energy density reads

$$\rho_d = \rho_{d0}\ \left\{q_0 + q_1(1+z) + q_2(1+z)^2\right\}^{2/3} \tag{14}$$

From equation (12), we obtain

$$\begin{aligned} H^2(z) = H_0^2[&\Omega_{r0}(1+z)^4 + \Omega_{m0}(1+z)^3 \\ &+ (1-\Omega_{r0}-\Omega_{m0}) \\ &(q_0 + q_1(1+z) + q_2(1+z)^2)^{2/3})] \end{aligned} \tag{15}$$

B. Model 2

The Pade-II model for parametrized equation of state parameter has been explored in [42–44]. The equivalent Pade-II type parametrization of deceleration parameter has been introduced in [40, 41] which is taken as

$$q_d(z) = \frac{q_0 + q_1 log(1+z)}{1 + q_2 log(1+z)} \tag{16}$$

where q_0, q_1 and q_2 are constants. Then the energy density yields

$$\rho_d = \rho_{d0}\ (1+z)^{(q_1+q_2)}\ \{1 + q_2\ log(1+z)\}^{\frac{2(q_0q_2-q_1)}{{q_2}^2}} \tag{17}$$

From equation (12), we obtain

$$\begin{aligned} H^2(z) = H_0^2[&\Omega_{r0}(1+z)^4 + \Omega_{m0}(1+z)^3 \\ &+ (1-\Omega_{r0}-\Omega_{m0}) \\ &(1+z)^{(q_1+q_2)}(1+q_2 log(1+z))^{\frac{2(q_0q_2-q_1)}{(q_2)^2}}] \end{aligned} \tag{18}$$

C. Model 3

The Pade-I model for parametrized equation of state parameter has been investigated in [42–44]. The equivalent Pade-I type parametrization of deceleration parameter has been introduced in [40, 41], which takes the form:

$$q_d(z) = \frac{q_0 z + q_1(1+z)}{1 + q_2(1+z)} \tag{19}$$

where q_0, q_1 and q_2 are constants. The energy density becomes

$$\rho_d = \rho_{d0}\ (1+z)^{2(1-q_0)}\ (1 + q_2 + q_2 z)^{\frac{2(q_0+q_1+q_0q_2)}{q_2}} \tag{20}$$

From equation (12), we obtain

$$\begin{aligned} H^2(z) = H_0^2[&\Omega_{r0}(1+z)^4 + \Omega_{m0}(1+z)^3 \\ &+ (1-\Omega_{r0}-\Omega_{m0}) \\ &(1+z)^{2(1-q_0)}(1+q_2+q_2z)^{\frac{2(q_0+q_1+q_0q_2)}{q_2}}] \end{aligned} \tag{21}$$

D. New Model

We propose a new model of deceleration parameter given as

$$q_d(z) = q_0 + \frac{2+(1+z)^3}{q_1 + q_2(1+z)^3} \tag{22}$$

where q_0 and q_1 are constants. Thus, the energy density (11) reads

$$\rho_d = \rho_{d0}\ (1+z)^{3(1+q_0+\frac{2}{q_1})}[q_1+q_2(1+z)^3]^{\frac{(q_1-2q_2)}{q_1 q_2}} \tag{23}$$

From equation (12), we obtain

$$\begin{aligned} H^2(z) = H_0^2[&\Omega_{r0}(1+z)^4 + \Omega_{m0}(1+z)^3 \\ &+ (1-\Omega_{r0}-\Omega_{m0})\ (1+z)^{3(1+q_0+\frac{2}{q_1})} \\ &[q_1+q_2(1+z)^3]^{\frac{(q_1-2q_2)}{q_1 q_2}}] \end{aligned} \tag{24}$$

IV. DATA DESCRIPTION WITH RESULTS

A. Data description

Throughout this part, we will use three distinct observational datasets to limit our model parameters. We utilized the H(z) datasets of 57 measurements, the Pantheon dataset of 1048, 17 uncorrelated BAO measurements, and CMB Distant Prior to achieving the optimal value for the proposed model parameters. To construct the MCMC [45], we used the open-source tools Polychord [46] and GetDist [47].The total χ^2 function of the combination H(z) + Pantheon + BAO + CMB and define as

$$\chi^2_{tot} = \chi^2_{H(z)} + \chi^2_{SN} + \chi^2_{BAO} + +\chi^2_{CMB}. \tag{25}$$

1. $H(z)$ Dataset

Numerous observational datasets must be used to achieve significant constraints on the model parameters. We employ the $H(z)$ measurements in our investigation to constrain the model parameters. In general, the Hubble parameter can be determined either by estimating the BAO in the radial direction of galaxy clustering [48] or using the differential age technique, which also provides the redshift dependency of the Hubble parameter as

$$H(z) = -\frac{1}{1+z}\frac{dz}{dt}, \tag{26}$$

here dz/dt is computed using two moving galaxies in a proportionate manner. To estimate the model's parameters, the study takes into account 57 Hubble measurements, which are spans throughout the redshift range of $0.07 \leqslant z \leqslant 2.42$. To compare the model's theoretical predictions with observation, we use the chi-square function.

$$\chi^2_H = \sum_{i=1}^{57} \frac{[H_{th}(z_i,) - H_{obs}(z_i)]^2}{\sigma^2_{H(z_i)}}, \tag{27}$$

where $H_{\rm th}$ and H_{obs} denote the model prediction and observed value of Hubble rate, respectively. Also, $\sigma_{H(z_i)}$ characterizes the standard error at the redshift z_i. The Hubble function numerical values for the appropriate redshifts are shown in [49].

2. Pantheon Dataset

The comic accelerated expansion is determined by measuring type Ia supernovae (SNIa). So far, SNIa has proven to be one of most robust successful methods for studying the nature of dark energy. In recent years, several supernova data sets have been established [50–54]. The Pantheon sample has lately been updated [55]. The former dataset contains 1048 spectroscopically verified SNIa spanning in the redshift range of $0 < z < 2.3$. SNIa are also astronomical objects that act as standard candles for determining relative distances. As a consequence, SN Ia samples are combined with the distance modulus $\mu = m - M$, where m indicates a certain object's apparent magnitude of a specific SNIa. The chi-square of the SNIa measurements is given by

$$\chi^2_{SN} = \Delta\mu^T\ .\ \mathbf{C}^{-1}_{SN}\ .\ \Delta\mu. \tag{28}$$

$\mathbf{C}_{SN}$ is represented by a covariance matrix, and $\Delta\mu = \mu_{obs} - \mu_{th}$, where μ_{obs} signifies the measured distance modulus of a certain SNIa, meanwhile the theoretical distance modulus is represented as μ_{th}, and calculated as

$$\mu_{th}(z) = 5\log_{10}\frac{D_L(z)}{(H_0/c)Mpc} + 25, \tag{29}$$

Here H_0 signifies the current Hubble rate, and c reflects the speed of light. In a flat FLRW Universe, the luminosity distance, D_L, is given by:

$$D_L(z) = (1+z)H_0\int_0^z \frac{dz'}{H(z')}. \tag{30}$$

Because we limit the model's free parameters at the same time, i.e., by using the Pantheon sample, and hence

$$\chi^2_{SN} = \Delta\mu^T \times \mathbf{C}^{-1}_{Pantheon} \times \Delta\mu.$$

3. Uncorrelated Baryon Acoustic Oscillations (unCor BAO)

We picked 17 uncorrelated BAO (please see table 1 of this work [56]) measures from [57–68] the greatest BAO dataset of (333) measurements because considering the whole catalog of BAO might result in a very considerable inaccuracy because of data correlations; so we chose a representative subset to minimize errors. Transverse BAO experiments produce measurements. of $D_H(z)/r_d = c/H(z)r_d\hat{\text{A}}$ along with a co-moving angular diameter distance [69, 70].

$$D_M = \frac{c}{H_0} S_k \left(\int_0^z \frac{dz'}{E(z')} \right), \tag{31}$$

with

$$S_k(x) = \begin{cases} \frac{1}{\sqrt{\Omega_k}} \sinh\left(\sqrt{\Omega_k} x\right) & \text{if} \quad \Omega_k > 0 \\ x & \text{if} \quad \Omega_k = 0 \\ \frac{1}{\sqrt{-\Omega_k}} \sin\left(\sqrt{-\Omega_k} x\right) & \text{if} \quad \Omega_k < 0. \end{cases} \tag{32}$$

Considering the angular diameter distance $D_A = D_M/(1+z)$ and the $D_V(z)/r_d$. This corresponds to the combination of the BAO peaked coordinates and the sound horizon r_d at the drag epoch. Furthermore, we could immediately derive "line-of-sight" (or "radial") observations from the Hubble parameter.

$$D_V(z) \equiv \left[z D_H(z) D_M^2(z) \right]^{1/3}. \tag{33}$$

4. Cosmic Microwave Background

The CMB Distant Prior measurements are taken from Ref. [71]. Using distance priors, you can gain helpful information about the CMB power spectrum in two ways: the acoustic scale l_A represents the temperature power spectrum of the CMB in the transverse direction, and the "shift parameter" R affects the temperature spectrum of the CMB along the line-of-sight path to determine peak heights as follows:

$$l_A = (1+z_d)\frac{\pi D_A(z)}{r_s}, \tag{34}$$

$$R(z) = \frac{\sqrt{\Omega_m} H_0}{c} (1+z_d) D_A(z) \tag{35}$$

These are the observables that are reported [71]: $R_z = 1.7502 \pm 0.0046$, $l_A = 301.471 \pm 0.09$, $n_s = 0.9649 \pm 0.0043$ and r_s is an independent parameter, with an associated covariance matrix (see Ref. [71]). The points represent the inflationary observables as well as the CMB epoch expansion rate. Besides the CMB points, we also consider other data from the late universe. The result is a successful test of the model in relation to the data.

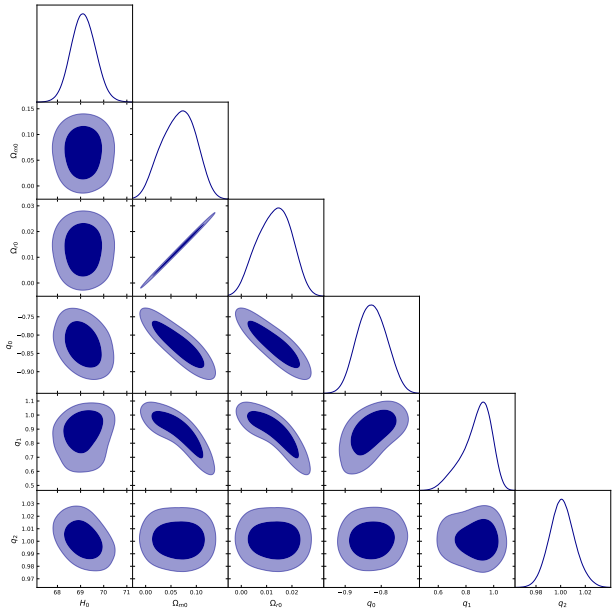


FIG. 1. Plot of MCMC confidence contours at 1σ and 2σ for Model 1.

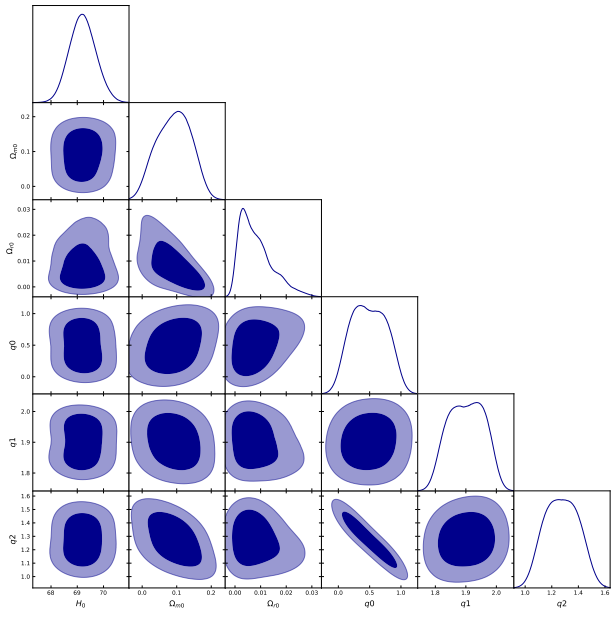


FIG. 2. Plot of MCMC confidence contours at 1σ and 2σ for Model 2.

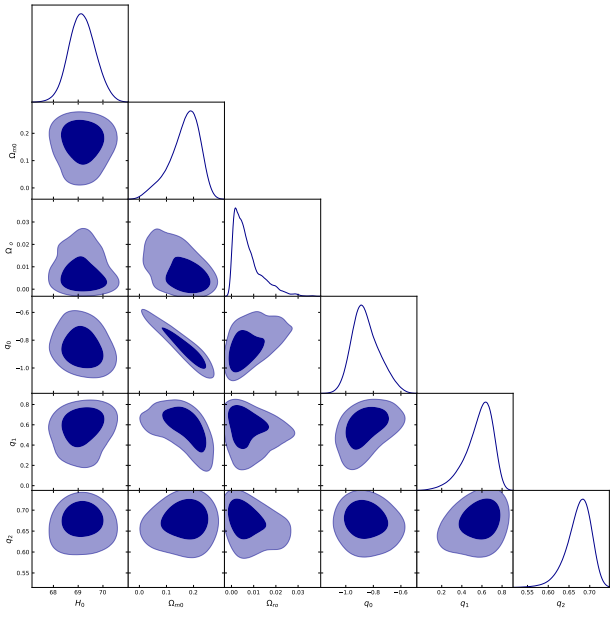


FIG. 3. Plot of MCMC confidence contours at 1σ and 2σ for Model 3.

MCMC Results		
Model	Parameters	Bestfit Value
Model 1	H_0	$69.121060^{+0.517902}_{-0.517902}$
	$\Omega_{\rm m0}$	$0.065585^{+0.038524}_{-0.038524}$
	$\Omega_{\rm r0}$	$0.013117^{+0.007705}_{-0.007705}$
	q_0	$-0.825763^{+0.041951}_{-0.041951}$
	q_1	$0.879053^{+0.111601}_{-0.111601}$
	q_2	$1.001254^{+0.010014}_{-0.010014}$
Model 2	H_0	$69.203662^{+0.529034}_{-0.529034}$
	$\Omega_{\rm m0}$	$0.192287^{+0.058696}_{-0.058696}$
	$\Omega_{\rm r0}$	$0.008128^{+0.006286}_{-0.006286}$
	q_0	$0.489155^{+0.311871}_{-0.311871}$
	q_1	$1.902027^{+0.066852}_{-0.066852}$
	q_2	$1.274424^{+0.143687}_{-0.143687}$
Model 3	H_0	$69.789290^{+0.469419}_{-0.649419}$
	$\Omega_{\rm m}$	$0.205031^{+0.084481}_{-0.084481}$
	$\Omega_{\rm r0}$	$0.00175^{+0.007645}_{-0.007645}$
	q_0	$-0.780911^{+0.060833}_{-0.060833}$
	q_1	$0.610530^{+0.067778}_{-0.067778}$
	q_2	$0.680228^{+0.285537}_{-0.285537}$
Model 4	H_0	$69.391442^{+0.478121}_{-0.478121}$
	$\Omega_{\rm m0}$	$0.280604^{+0.006564}_{-0.006564}$
	$\Omega_{\rm r0}$	$0.023950^{+0.017250}_{-0.017250}$
	q_0	$-2.975495^{+0.764170}_{-0.764170}$
	q_1	$1.000462^{+0.009284}_{-0.009284}$
	q_2	$0.646235^{+0.023499}_{-0.023499}$

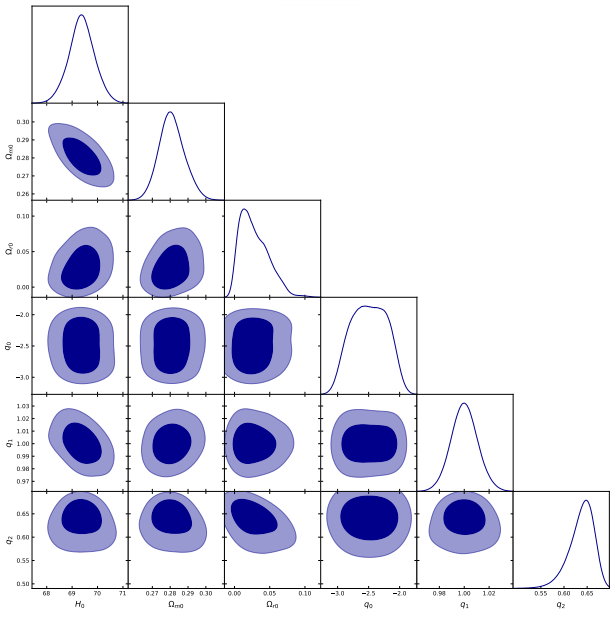


FIG. 4. Plot of MCMC confidence contours at 1σ and 2σ for Model 4.

B. Observational, and theoretical comparisons of the Hubble functions

Following extracting the best-fit value of the free parameter of each Model, one could also contrast the model predictions against the observational data and also the ΛCDM model, correspondingly.

1. *Comparison with the Hubble data points.*

Each model has been compared to the 57 Hubble measurements, ΛCDM model, and 1σ and 2σ error bands. The comparison findings are shown in Figs. 5, 6, 7, 8. The Figure illustrates that each model accurately fits with the Hubble measurements.

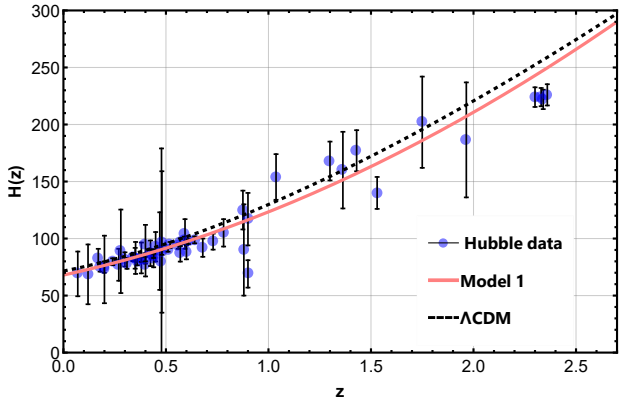


FIG. 5. Shows the plot of Hubble function $H(z)$ for Model 1 (pink line), ΛCDM model (black dotted line) with $\Omega_{m0} = 0.3$ and $\Omega_\Lambda = 0.7$, against Hubble measurements (blue dots) .

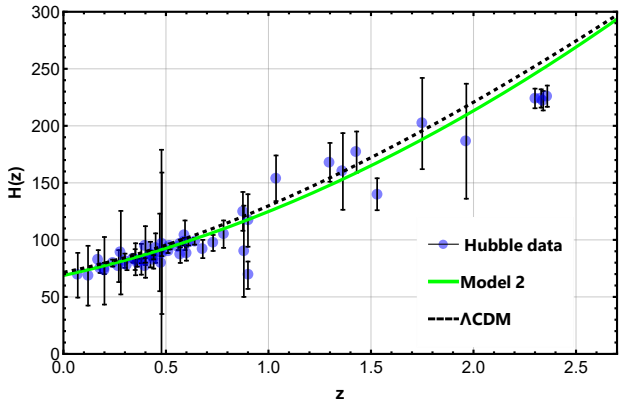


FIG. 6. Shows the plot of Hubble function $H(z)$ for Model 2 (green line), ΛCDM model (black dotted line) with $\Omega_{m0} = 0.3$ and $\Omega_\Lambda = 0.7$, against Hubble measurements (blue dots) .

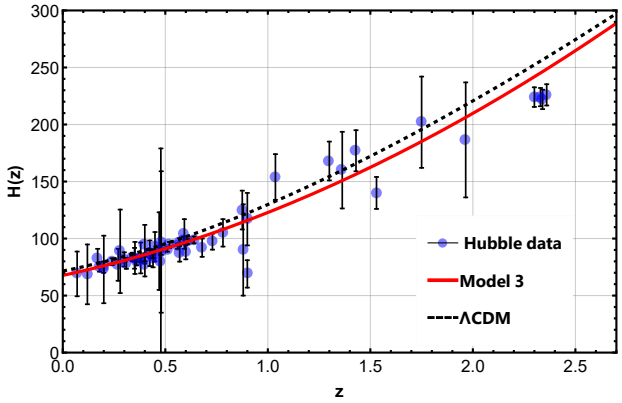


FIG. 7. Shows the plot of Hubble function $H(z)$ for Model 3 (red line), ΛCDM model (black dotted line) with $\Omega_{m0} = 0.3$ and $\Omega_\Lambda = 0.7$, against Hubble measurements (blue dots) .

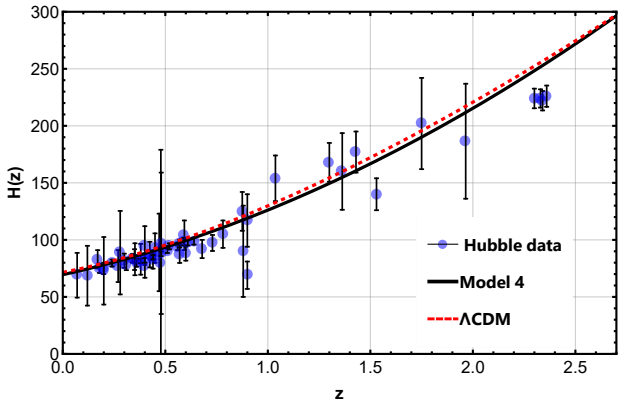


FIG. 8. Shows the plot of Hubble function $H(z)$ for Model 4 (black line), ΛCDM model (red dotted line) with $\Omega_{m0} = 0.3$ and $\Omega_\Lambda = 0.7$, against Hubble measurements (blue dots) .

2. Comparison with the Pantheon data.

Each model has been compared to the 1048 Pantheon dataset, ΛCDM model, and 1σ and 2σ error bands. The comparison findings are shown in Figs. 9, 10, 11, 12, 0ne could see that each model matches the Pantheon dataset quite well.

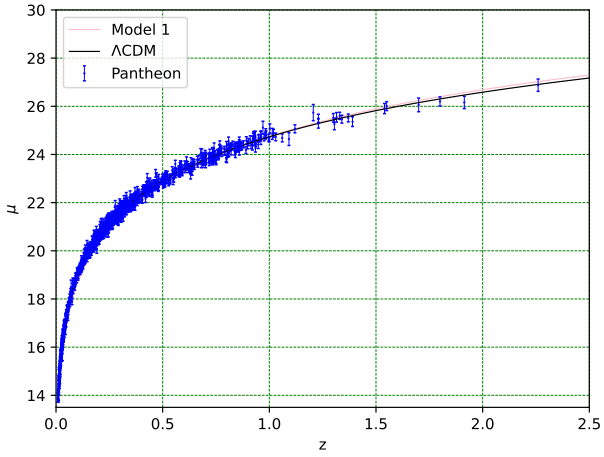


FIG. 9. Shows the plot of distance modulus $\mu(z)$ for Model 1 (pink line), ΛCDM model (in black line) with $\Omega_{m0} = 0.3$ and $\Omega_\Lambda = 0.7$, against type Ia supernova data (blue dots)

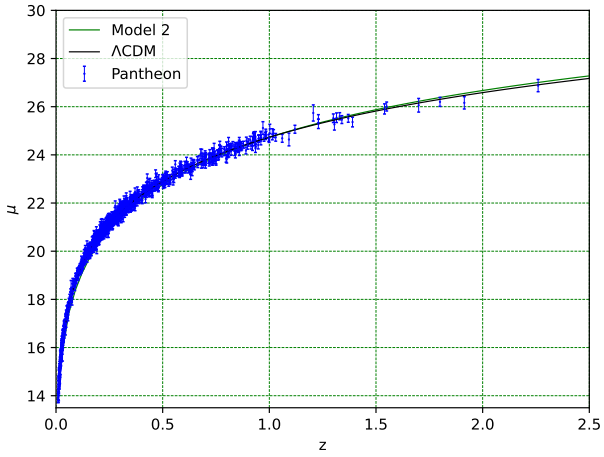


FIG. 10. Shows the plot of distance modulus $\mu(z)$ of the model 2 (green line), ΛCDM model (black line) with $\Omega_{m0} = 0.3$ and $\Omega_\Lambda = 0.7$, against type Ia supernova data (blue dots) .

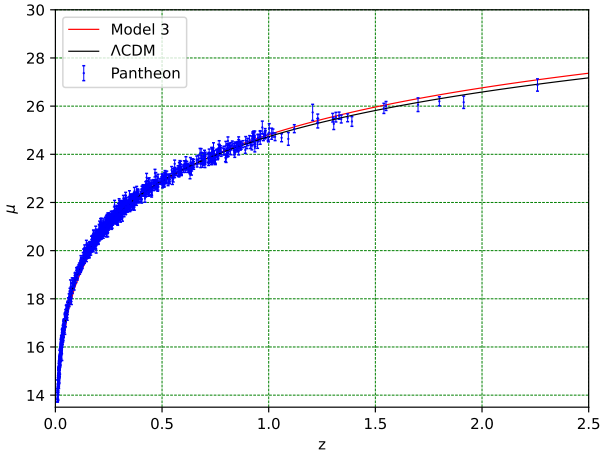


FIG. 11. Shows the plot of distance modulus $\mu(z)$ of the model 3 (red line), ΛCDM model (black line) with $\Omega_{m0} = 0.3$ and $\Omega_\Lambda = 0.7$, against type Ia supernova data (blue dots) .

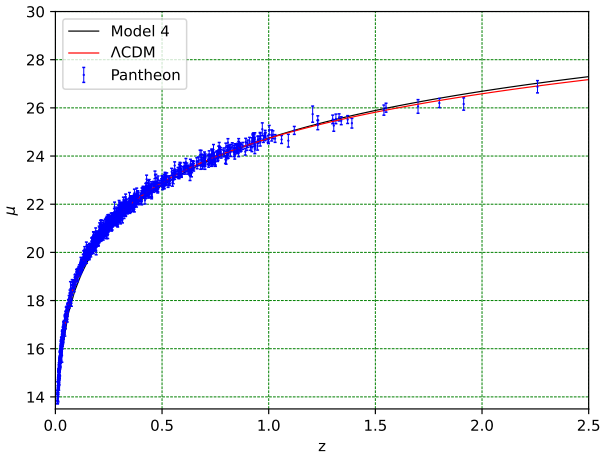


FIG. 12. Shows the plot of distance modulus $\mu(z)$ of the model 4 (black line), ΛCDM model (black line) with $\Omega_{m0} = 0.3$ and $\Omega_\Lambda = 0.7$, against type Ia supernova data (blue dots) .

3. *Relative difference between Each Model and ΛCDM.*

Consequently, The relative difference between each model and the ΛCDM standard paradigm has been in Figs. 13, 14, 15, 16. At low redshift, each model behaves substantially identically; however, some distinctions between each model and ΛCDM paradigm emerge at high redshift.

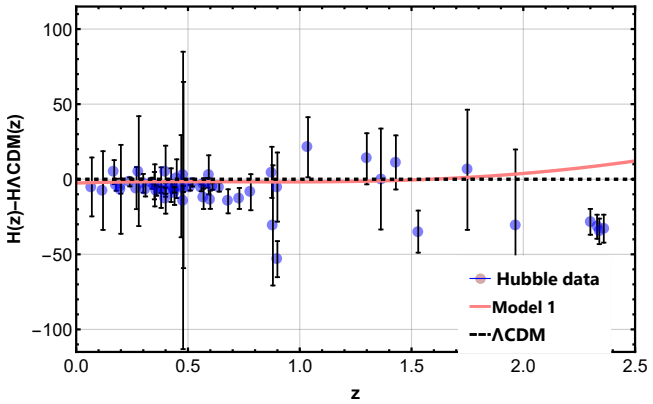


FIG. 13. Shows the Relative difference between Model 1 (pink line), the ΛCDM model (black dotted line) with $\Omega_{m0} = 0.3$ and $\Omega_\Lambda = 0.7$, against the 57 Hubble measurements (blue dots), along with their corresponding error bars.

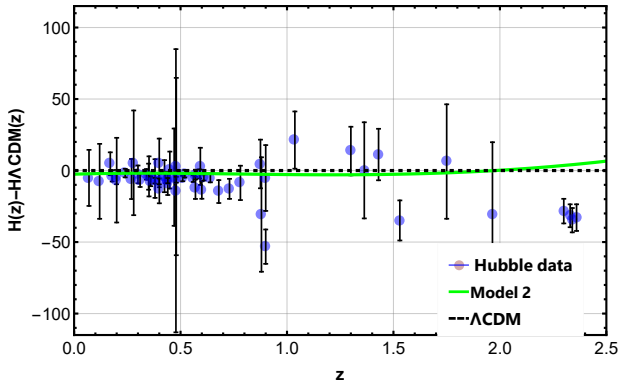


FIG. 14. Shows the Relative difference between Model 2 (Green line) and the ΛCDM model (black dotted line) with $\Omega_{m0} = 0.3$ and $\Omega_\Lambda = 0.7$, against the 57 Hubble measurements (blue dots) along with their corresponding error bars.

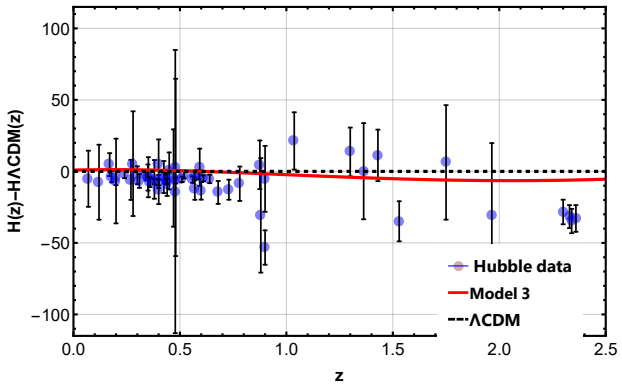


FIG. 15. Shows the Relative difference between Model 3 (red line), the ΛCDM model (black dotted line) with $\Omega_{m0} = 0.3$ and $\Omega_\Lambda = 0.7$, against the 57 Hubble measurements (blue dots), along with their corresponding error bars.

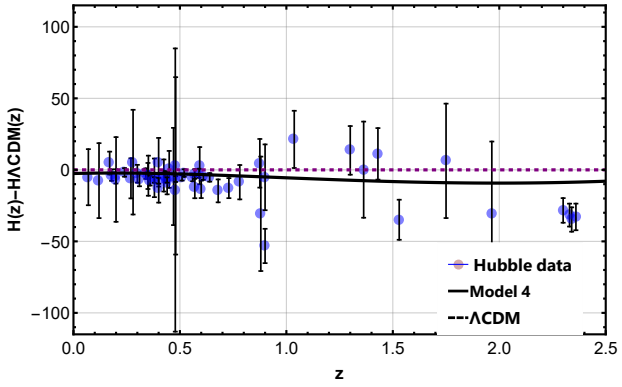


FIG. 16. Shows the Relative difference between Model 4 (black line) and the ΛCDM model (purple dotted line) with $\Omega_{m0} = 0.3$ and $\Omega_\Lambda = 0.7$, against the 57 Hubble measurements (blue dots) along with their corresponding error bars.

V. DYNAMICAL ANALYSIS OF THE MODEL

Our main focus in this work is to evaluate a cosmological model that can describe the universe's whole dynamics by examining its geometrical and physical parameters on large scale. This aim is to study the kinematic quantities, characterizing the cosmological behavior at both the early and late evolution of the universe. Now cosmological principle implies that the scale factor is an important ingredient that governs the universe. Therefore, it is reasonable to expand $a(t)$ in Taylor series around the current time t_0 gives

$$a(t) = a_0\left[1 + \frac{(t-t_0)}{1!}\frac{da}{dt}\Big|_{t_0} + \frac{(t-t_0)^2}{2!}\frac{d^2a}{dt^2}\Big|_{t_0} + \frac{(t-t_0)^3}{3!}\frac{d^3a}{dt^3}\Big|_{t_0} + \frac{(t-t_0)^4}{4!}\frac{d^4a}{dt^4}\Big|_{t_0} + \mathcal{O}(t-t_0)^5\right] \quad (36)$$

where a_0 is the current value of the expansion factor evaluated at the present epoch t_0. In the above series expansion, the most important series terms define

$$H = \frac{1}{a}\frac{da}{dt}, \quad q = -\frac{1}{aH^2}\frac{d^2a}{dt^2}, \quad j = \frac{1}{aH^3}\frac{d^3a}{dt^3}, \quad s = \frac{1}{aH^4}\frac{d^4a}{dt^4}$$

which are usually known as the Hubble, deceleration, jerk, and snap parameters, respectively. These four geometrical quantities are sufficient to study the overall dynamics of the universe. We will discuss all these parameters for our model in detail in the following subsections.

1. DECELERATION, JERK, AND SNAP PARAMETER

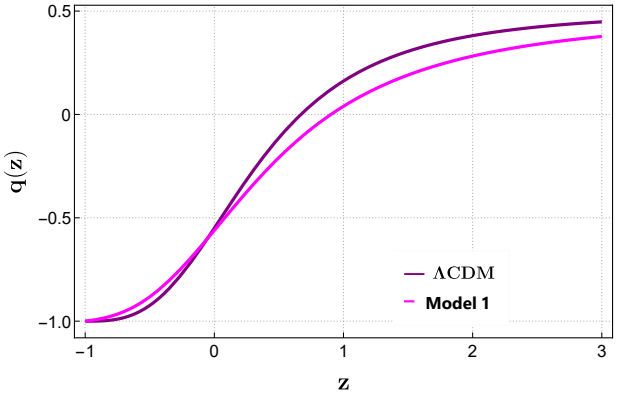


FIG. 17. Plot of deceleration parameter with respect to redshift.

a. The deceleration parameter: The deceleration parameter is one of the oldest and most influential cosmological parameter used to describe the evolution of the universe, which is defined by $q = -\frac{a\ddot{a}}{\dot{a}^2}$, where $a(t)$ is the usual scale factor. The sign of q decides whether the Universe is accelerating i.s. $(q < 0)$ or decelerating i.s. $q > 0$. In Figs. 17, 18, 19 and 20 the redshift dependency of the deceleration parameter q is displayed correspondingly for each model and ΛCDM models. Model 1 (M1) behavior is nearly identical to ΛCDM behavior at both high and low redshift; at low redshift, the M1 finishes in a de Sitter

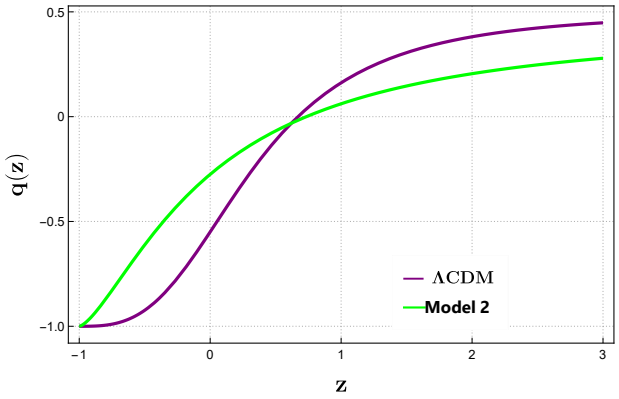


FIG. 18. Plot of deceleration parameter with respect to redshift.

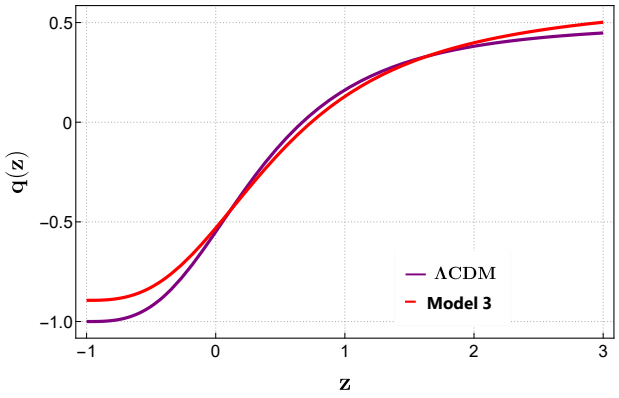


FIG. 19. Plot of deceleration parameter with respect to redshift.

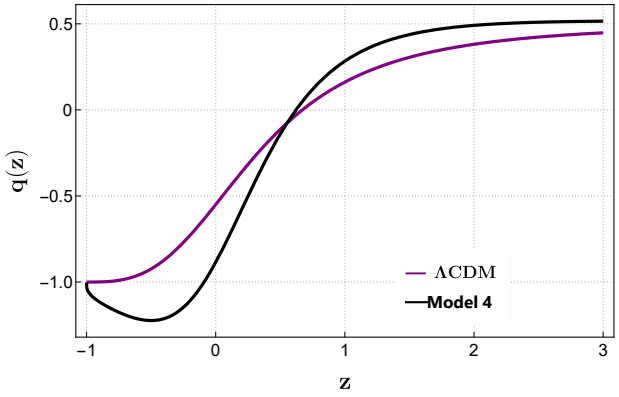


FIG. 20. Plot of deceleration parameter with respect to redshift.

phase, having $q = -1$. Model 2 (M2) has systematic differences at low and high redshift but also terminates in a de Sitter phase. At high redshift, Model 3 (M3) behaves very closely to ΛCDM, while at low redshift, a slower-accelerated evolution occurs, with $q(-1) \approx -0.7$. Lastly, Model 4 (M4) shows fascinating behavior at high and low redshifts. At low redshift, M4 exhibits super-accelerated evolution for some time but ends in the de Sitter phase.

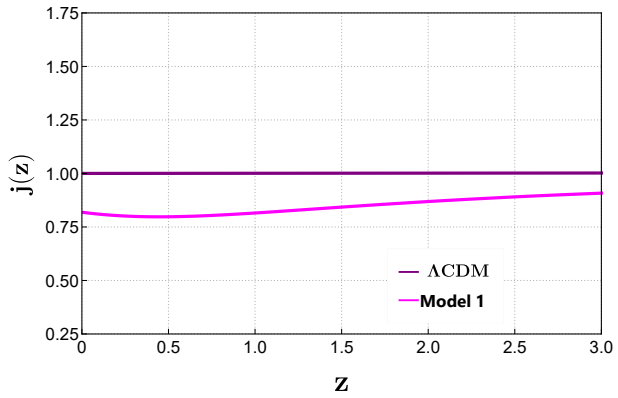


FIG. 21. Plot of jerk parameter with respect to redshift.

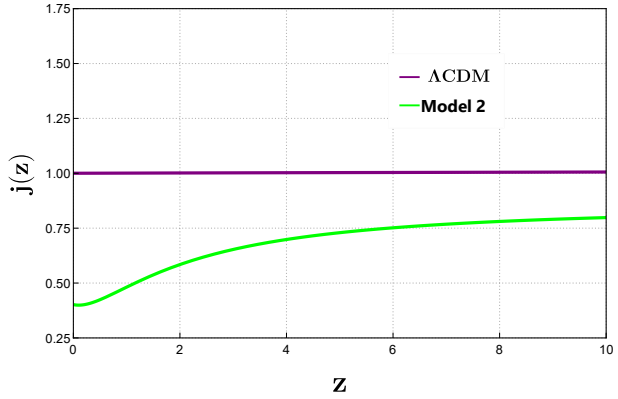


FIG. 22. Plot of jerk parameter with respect to redshift.

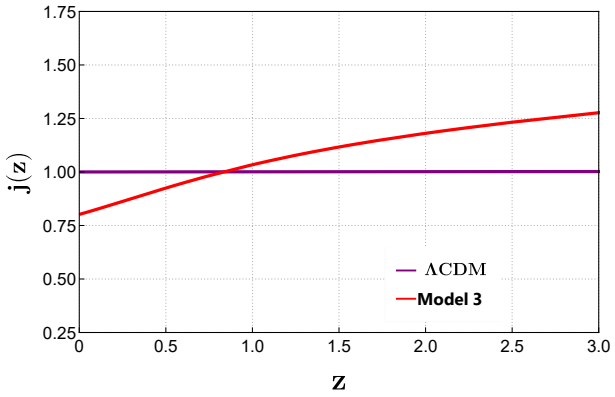


FIG. 23. Plot of jerk parameter with respect to redshift.

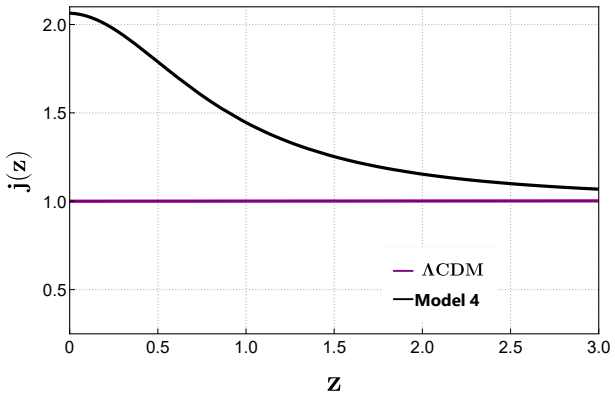


FIG. 24. Plot of jerk parameter with respect to redshift.

b. The jerk parameter: The *jerk* parameter as a function of q is given by $j = \left[(1+z)\frac{dq}{dz} + q(2q+1)\right]$. The main feature of the jerk parameter is that for ΛCDM model, $j = 1$ always. Therefore, any departure from $j = 1$ would favor other dynamical DE models instead of ΛCDM [72]. The variability of the jerk parameter $j(z)$ against redshift of each model with ΛCDM model shown in Figs. 21, 22, 23 and 24. A significant disparity exists among the quantitative values of j at high and low redshifts within every model. M1 has an approximate value of 0.79 at $j(0)$, M2 has an estimated value of 0.42, and M3 has an approximate value of 0.78 at $j(0)$. M4 has more than twice the numerical values of the ΛCDM model $j(0) \approx 2.1$. Identifying the current value of j's provides an essential test.

c. The snap parameter: The snap parameter is the variation of of j which can be written as $\mathcal{S} = \left[-(1+z)\frac{dj}{dz} - j(2+3q)\right]$. This work also analyzed this geometrical parameter for each parametrization of $q(z)$. The progression of each model's snap parameter $s(z)$ versus redshift could be noticed in Figs. 25, 26, 27 and 28. For both high and low redshift, every Model anticipates a big divergence between their and ΛCDM numerical values. At high redshifts, M1, M2, and M3 predict lower values than ΛCDM, but M4 predicts higher values than ΛCDM. Identifying the present value of s's parameter is a critical test. M1 predicts $s(0) \approx -0.1$, M2 predicts $s(0) \approx 0.9$, M3 predicts $s(0) \approx 0.7$, and M4 estimates $s(0) \approx 0.9$.

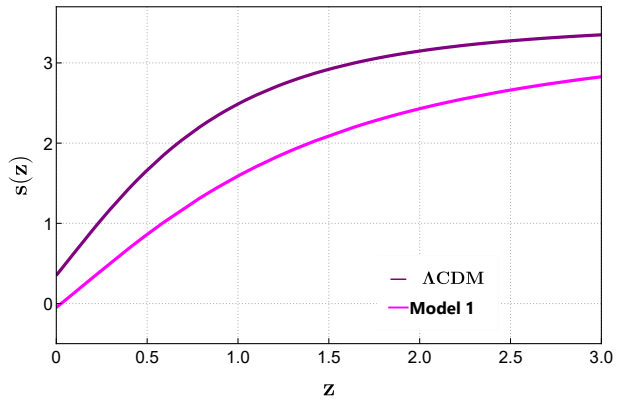


FIG. 25. Plot of snap parameter with respect to redshift.

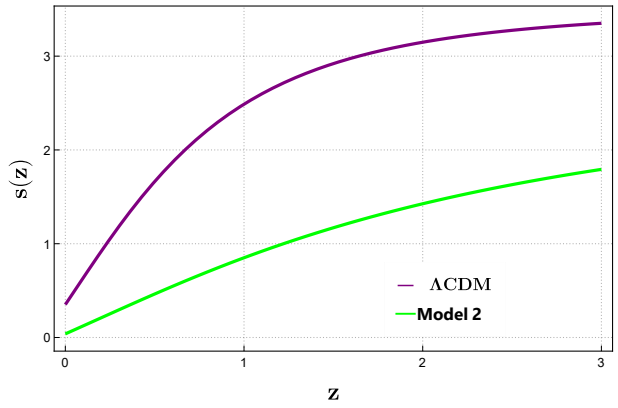


FIG. 26. Plot of snap parameter with respect to redshift.

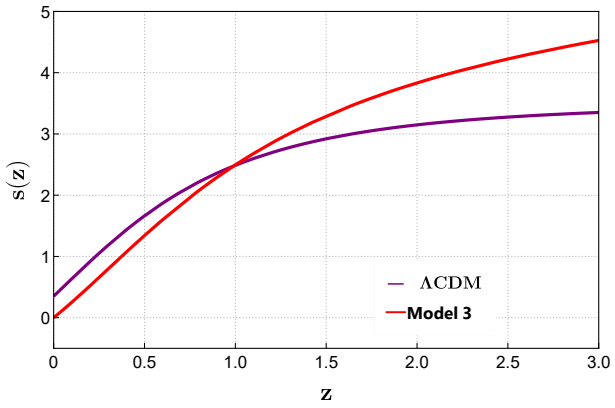


FIG. 27. Plot of snap parameter with respect to redshift.

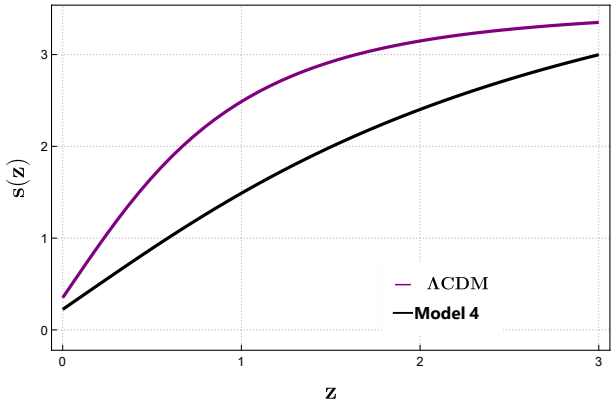


FIG. 28. Plot of snap parameter with respect to redshift.

VI. STATEFINDER DIAGNOSTIC

It is a mechanism generally applied to explore different DE models and comprehend their nature through higher-order derivatives of the scale factor. The statefinder diagnostic pair [73–76] $\{r, s\}$ is dimensionless, which can be used to analyze the cosmic features of DE independent of models and can be computed by the expressions [77, 78]

$$r = \left[(1+z)\frac{dq}{dz} + q(2q+1)\right], \; s = \frac{r-1}{3\left(q-\frac{1}{2}\right)}, \qquad (37)$$

where r and q are the usual *jerk* parameter and deceleration parameter respectively. Certain pairs commonly refer to the standard models of DE like $\{r, s\} = \{1, 0\}$ shows ΛCDM model while $\{r, s\} = \{1, 1\}$ corresponds to the standard cold dark matter model (SCDM) in FLRW universe. Moreover, $(-\infty, \infty)$ indicates the Einstein static universe. In the $r - s$ plane, one can obtain quintessence-like and phantom-like models of the DE for $s > 0$ and $s < 0$, respectively. Also, the evolutionary process occurs (from phantom to quintessence) if the value deviates from the standard range $r, s = 1, 0$. The value $\{q, r\} = \{-1, 1\}$ is associated with the ΛCDM model whereas $\{q, r\} = \{0.5, 1\}$ gives SCDM model.

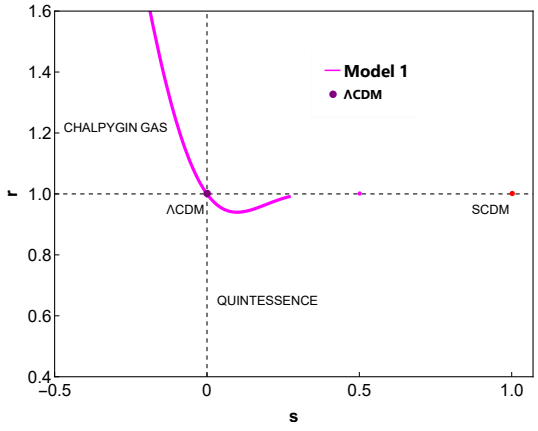


FIG. 29. Behavior of $\{s, r\}$ profile of Model 1

a. The $\{s, r\}$ Parameter: Figs. 29, 30, 31 and 32 shows the evolution of the model M1, M2, M3, and M4 of $\{s, r\}$ parameter. At first, M1 takes values in the region $r < 1$, $s > 0$ representing the quintessence domain, and afterward, by crossing fixed $\{r, s\} = \{1, 0\}$, ΛCDM takes values in the region $r < 1$, $s < 0$ Chaplygin gas region. Throughout evolution, M2 assumes values in the region $r < 1$, $s > 0$ reflect the quintessence domain. The M3 begins with values in the region $r > 1$, $s > 0$, indicating the Chaplygin gas domain, and evolves to the quintessence region by traversing the intermediate ΛCDM fixed point $\{1, 0\}$ during evolution. However, the $\{s, r\}$ parameter of M4 exhibits identical behavior to M1.

b. The $\{q, r\}$ Parameter: Figs. 33, 34, 35 and 36 of models M1, M2, M3, and M4 in $\{q, r\}$ provide extra

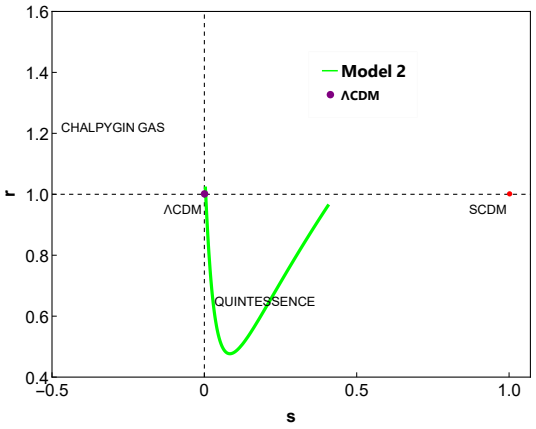


FIG. 30. Behavior of $\{s, r\}$ profile of Model 2

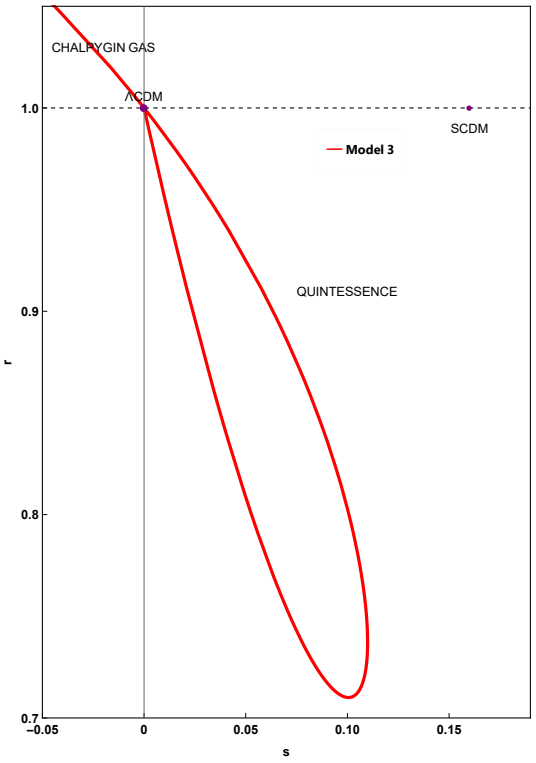


FIG. 31. Behavior of $\{s, r\}$ profile of Model 3

information regarding M1, M2, M3, and M4. The evolution of this parameter of M1 indicates that at first M1 takes values in the range $q > 0$ and $r > 1$ indicating the quintessence region, then M1 takes values in the range $q < 0$ and $r < 1$ indicating the Chaplygin gas region, and eventually, it deviates towards the de Sitter point $-1, 1$. The $\{q, r\}$ profile of M2 values remains in the quintessence area and terminates at the de Sitter point $-1, 1$. Whereas M3 acquires values in the range $q > 0$ and $r > 1$, indicating the Chaplygin gas region, the trajectory of this Model's parameter eventually takes values in the range $q < 0$ and $r < 1$, indicating the quintessence re-

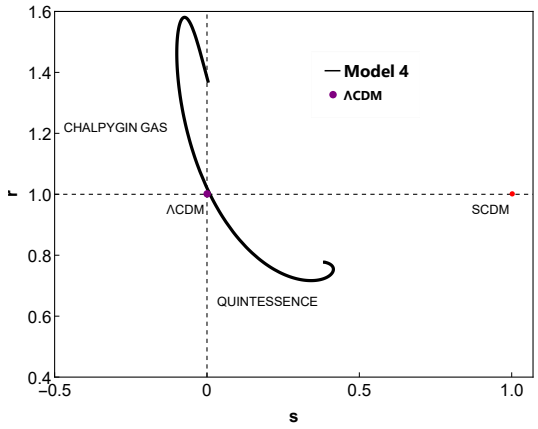


FIG. 32. Behavior of $\{s, r\}$ profile of Model 4

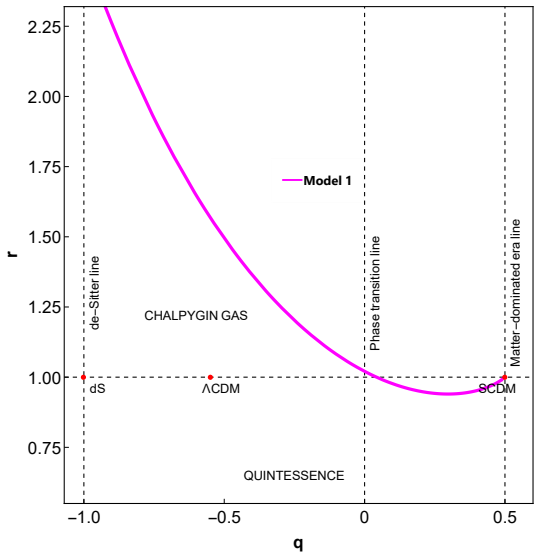


FIG. 33. Behavior of $\{q, r\}$ profile of Model 1

gion and terminates at the de Sitter point $\{-1, 1\}$. M4's $\{q, r\}$ parameter, on the other hands behave identically to M1.

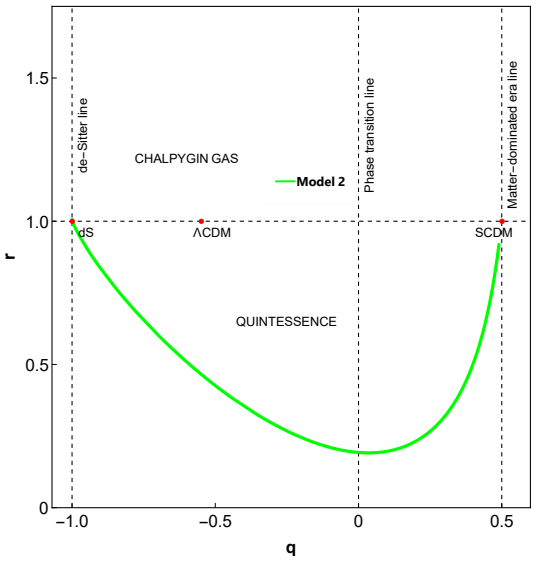


FIG. 34. Behavior of $\{q, r\}$ profile of Model 2

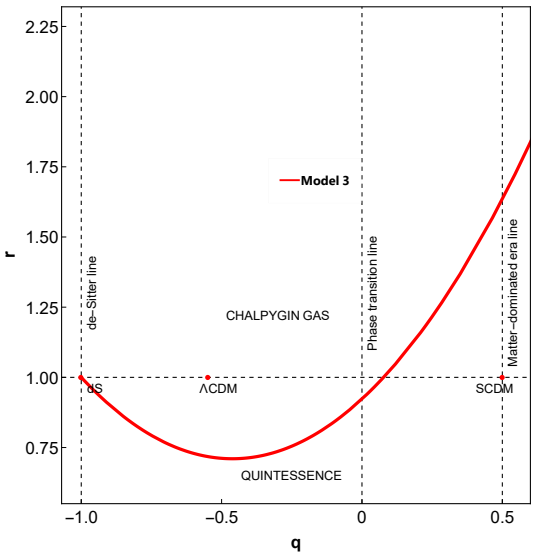


FIG. 35. Behavior of $\{q, r\}$ profile of Model 3

VII. Om DIAGNOSTIC

It refers to a geometrical formalism in which the Hubble parameter yields a null test for the ΛCDM model [79–82]. The Om diagnostic also efficiently differentiates several DE models from ΛCDM by the slope variation of $Om(z)$. A quintessence or phantom model can be acquired through either a positive or negative slope of the diagnostic parameter, respectively. Moreover, a constant slope with respect to redshift depicts a DE model corresponding to the cosmological constant. For a flat

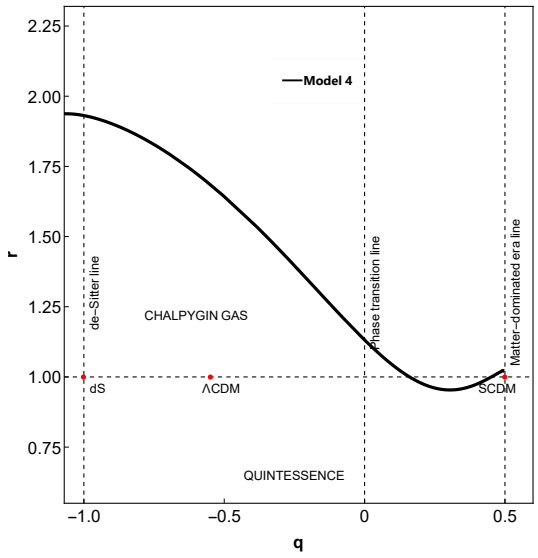


FIG. 36. Behavior of $\{q, r\}$ profile of Model 4

universe, one can define $Om(z)$ as

$$Om(z) = \frac{\left(\frac{H(z)}{H_0}\right)^2 - 1}{(1+z)^3 - 1}. \tag{38}$$

Many authors have explored the behavior of various DE models from the viewpoint of statefinder and Om diagnostics parameter [83–86]. This diagnostic involves only the first-order temporal derivative compared to the statefinder diagnosis [72]. It can also be subjected to the Galileons models [87, 88].

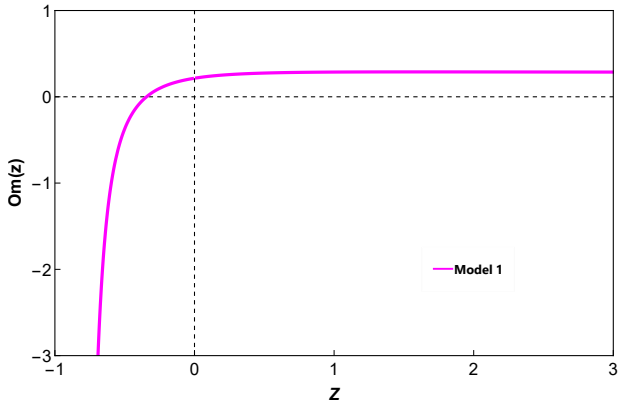


FIG. 37. Evolution of Om profile of Model 1

a. Om Diagnostic Parameter: Each model's slope variation of $Om(z)$ versus z is shown of each model in Figs. 37, 38, 39 and 40 respectively. Both models, M1 and M2, exhibit similar behavior at high redshift $z > 0$. Both models are in the quintessence region when redshift abruptly declines and becomes negative, meaning that both models reach the phantom region. Meanwhile, M2 is positive throughout high and low redshift, supporting

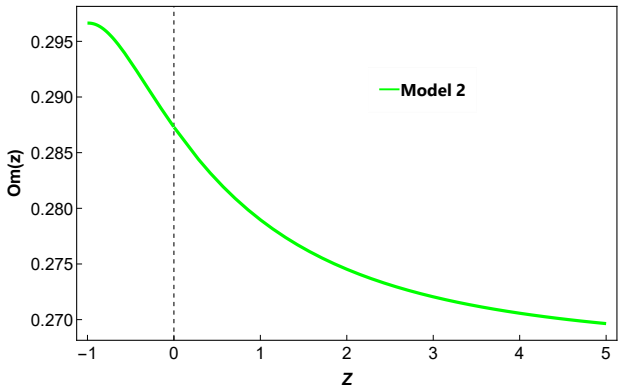


FIG. 38. Plot of Om profile of Model 2

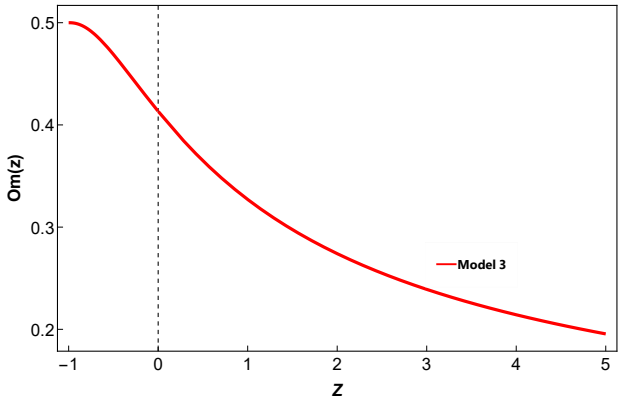


FIG. 39. Plot of Om profile of Model 3

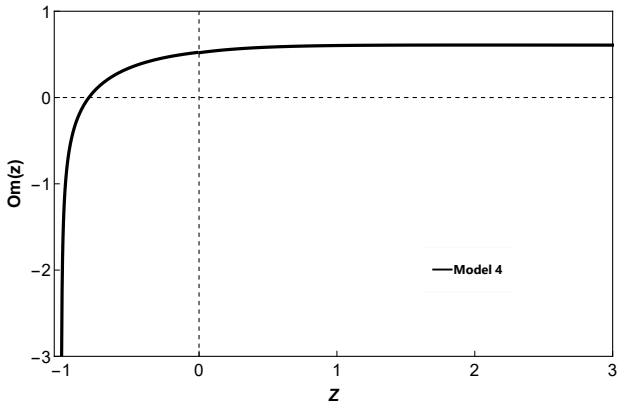


FIG. 40. Plot of Om profile of Model 4

a quintessence model. Ultimately, the M3 exhibits the same type of behavior.

VIII. INFORMATION CRITERIA

To investigate the feasibility of any model, one needs first to comprehend the study of information criteria (IC). The Akaike Information Criteria (AIC) [89] is sim-

ply applied to all ICs. Because the AIC is an approximate minimization of the Kullback-Leibler information, it is an asymptotically unbiased estimator of Kullback-Leibler information. The AIC Gaussian estimator could be expressed as [90–93] $\mathrm{AIC} = -2\ln(\mathcal{L}_{max}) + 2\kappa + \frac{2\kappa(\kappa+1)}{N-\kappa-1}$. where $\mathcal{L}_{max}$ is the maximum likelihood function, κ is the total number of free parameters of any model, and N is the total number of data points utilized. Because $N \gg 1$, is the assumption for the models, the aforementioned formula transforms to the original AIC like $\mathrm{AIC} = -2\ln(\mathcal{L}_{max}) + 2\kappa$. If a set of models is provided, the IC value deviations can be reduced to $\triangle\mathrm{AIC} = \mathrm{AIC}_{model} - \mathrm{AIC}_{min} = \triangle\chi^2_{min} + 2\triangle\kappa$. The more favorable range of $\triangle$AIC are mentioned following $\triangle$AIC is $(0, 2)$. The low favorable range of $\triangle$AIC is $(4, 7)$, while $\triangle\mathrm{AIC} > 10$ provides less support model.

Model	χ^2_{min}	χ^2_{red}	AIC	ΔAIC
ΛCDM Model	1755.56	0.981	1762.32	0
Model 1	1751.10	0.963	1761.59	1.58
Model 2	1750.24	0.961	1761.59	0.73
Model 3	1750.02	0.972	1761.59	0.50
Model 4	1751.02	0.965	1761.59	1.50

TABLE I. Summary of the χ^2_{min}, χ^2_{red}, AIC and ΔAIC.

IX. DISCUSSIONS AND CONCLUSIONS

Herein, we have studied the accelerated expansion scenario in a flat FRW universe composed of DE, radiation, and DM. We have attempted to construct a viable dark energy model which can describe the whole evolutionary history of the Universe. For this purpose, we have taken parametrization of the deceleration parameter instead of assuming parameterization of EOS parameter. Here, we have considered three parametrizations (model 1-model 3) and also proposed one new parametrization of the deceleration parameter. The advantage of these parametrizations is that they can provide finite results without considering any particular gravitational theory and provide early deceleration and late-time acceleration. We have chosen $q(z)$ containing only three parameters q_0, q_1 and q_2. Since the choice of $q(z)$ is quite arbitrary, so one takes more than three terms for the parametrization of $q(z)$. But in that case, it may be difficult to constrain the parameters using existing observational data. A statistical analysis has been made to get the best-fit values of the model parameters by the MCMC method using $H(z)$ datasets, Pantheon datasets and BAO datasets. We have analyzed the evolutionary trajectories of deceleration, jerk, and snap parameters by using the best-fit values of the model parameters. Moreover, the best-fit values of the model parameters obtained are used to plot the statefinder and Om diagnostics. The information criteria have been employed to examine the models' viability. We examined all of the models and the ΛCDM model (the basic reference) to figure out which is more probable than the others. From Table: I

The results obtained by analyzing all the geometrical parameters are summarized as follows:

- The deceleration parameter for M1 behavior is nearly identical to ΛCDM behavior at both high and low redshift; at low redshift, the M1 finishes in a de Sitter phase. M2 has systematic differences at low and high redshift but also terminates in a de Sitter phase. At high redshift, M3 behaves very closely to ΛCDM, while at low redshift, a slower-accelerated evolution occurs, with $q(-1) \approx -0.7$. Lastly, M4 at low redshift exhibits super-accelerated evolution for some time but ends in the de Sitter phase.

- The jerk parameter for M1 has an approximate value of 0.79 at $j(0)$, M2 has an estimated value of 0.42, and M3 has an approximate value of 0.78 at $j(0)$. M4 has more than twice the numerical values of the ΛCDM model $j(0) \approx 2.1$.

- The snap parameter for M1, M2, and M3 predict lower values than ΛCDM at high redshifts, but M4 predicts higher values than ΛCDM. Identifying the present value of s's parameter is a critical test. M1 predicts $s(0) \approx -0.1$, M2 predicts $s(0) \approx 0.9$, M3 predicts $s(0) \approx 0.7$, and M4 estimates $s(0) \approx 0.9$.

- The statefinder diagnostic for M1 and M4 takes values in the region $r < 1$, $s > 0$ presenting quintessence nature, then by crossing fixed $\{r, s\} = \{1, 0\}$, ΛCDM lies in the region $r < 1$, $s < 0$ showing Chaplygin gas nature. Throughout evolution, M2 assumes values in the region $r < 1$, $s > 0$ reflect as the quintessence-like behavior. The M3 begins with values in the region $r > 1$, $s > 0$, presenting the Chaplygin gas nature.

- The Om diagnostic for models M1 and M4 exhibit phantom region, whereas M2 & M3 is positive throughout high and low redshift, supporting a quintessence model.

Therefore, we have noticed that M2 is more viable than M1 as compared to the ΛCDM model, and M3 is more feasible than M2 and M4. Finally, the above four considered models are departed from the standard Λ CDM limit, supporting other dark energy models, and may be crucial in describing the accelerating universe.

Acknowledgement: AS is thankful to CSIR, Govt. of India, for providing a Senior Research Fellowship (No. 08/003(0138)/2019-EMR-I).

[1] A. G. Riess, et al., Observational evidence from supernovae for an accelerating universe and a cosmological constant, Astron. J. 116 (1998) 1009–1038. arXiv:astro-ph/9805201, doi:10.1086/300499.

[2] S. Perlmutter, et al., Measurements of the cosmological parameters Omega and Lambda from the first 7 supernovae at z>=0.35, Astrophys. J. 483 (1997) 565. arXiv:astro-ph/9608192, doi:10.1086/304265.

[3] S. Perlmutter, et al., Measurements of Ω and Λ from 42 high redshift supernovae, Astrophys. J. 517 (1999) 565–586. arXiv:astro-ph/9812133, doi:10.1086/307221.

[4] D. N. Vollick, 1/R Curvature corrections as the source of the cosmological acceleration, Phys. Rev. D 68 (2003) 063510. arXiv:astro-ph/0306630, doi:10.1103/PhysRevD.68.063510.

[5] S. Nojiri, S. D. Odintsov, Modified gravity with negative and positive powers of the curvature: Unification of the inflation and of the cosmic acceleration, Phys. Rev. D 68 (2003) 123512. arXiv:hep-th/0307288, doi:10.1103/PhysRevD.68.123512.

[6] J. L. Tonry, et al., Cosmological results from high-z supernovae, Astrophys. J. 594 (2003) 1–24. arXiv:astro-ph/0305008, doi:10.1086/376865.

[7] A. G. Riess, et al., Type Ia supernova discoveries at z > 1 from the Hubble Space Telescope: Evidence for past deceleration and constraints on dark energy evolution, Astrophys. J. 607 (2004) 665–687. arXiv:astro-ph/0402512, doi:10.1086/383612.

[8] A. Clocchiatti, et al., Hubble Space Telescope and Ground-Based Observations of Type Ia Supernovae at Redshift 0.5: Cosmological Implications, Astrophys. J. 642 (2006) 1–21. arXiv:astro-ph/0510155, doi:10.1086/498491.

[9] R. R. Caldwell, W. Komp, L. Parker, D. A. T. Vanzella, A Sudden gravitational transition, Phys. Rev. D 73 (2006) 023513. arXiv:astro-ph/0507622, doi:10.1103/PhysRevD.73.023513.

[10] V. Sahni, A. A. Starobinsky, The Case for a positive cosmological Lambda term, Int. J. Mod. Phys. D 9 (2000) 373–444. arXiv:astro-ph/9904398, doi:10.1142/S0218271800000542.

[11] T. Padmanabhan, Cosmological constant: The Weight of the vacuum, Phys. Rept. 380 (2003) 235–320. arXiv:hep-th/0212290, doi:10.1016/S0370-1573(03)00120-0.

[12] P. J. E. Peebles, B. Ratra, The Cosmological Constant and Dark Energy, Rev. Mod. Phys. 75 (2003) 559–606. arXiv:astro-ph/0207347, doi:10.1103/RevModPhys.75.559.

[13] E. J. Copeland, M. Sami, S. Tsujikawa, Dynamics of dark energy, International Journal of Modern Physics D 15 (11) (2006) 1753–1935.

[14] L. Amendola, S. Tsujikawa, Dark energy: theory and observations, Cambridge University Press, 2010.

[15] P. J. Steinhardt, L. Wang, I. Zlatev, Cosmological tracking solutions, Physical Review D 59 (12) (1999) 123504.

[16] S. Weinberg, The Cosmological Constant Problem, Rev. Mod. Phys. 61 (1989) 1–23. doi:10.1103/RevModPhys.61.1.

[17] S. Capozziello, V. F. Cardone, E. Elizalde, S. Nojiri, S. D. Odintsov, Observational constraints on dark energy with generalized equations of state, Phys. Rev. D 73 (2006) 043512. arXiv:astro-ph/0508350, doi:10.1103/PhysRevD.73.043512.

[18] C. Escamilla-Rivera, S. Capozziello, Unveiling cosmography from the dark energy equation of state, Int. J. Mod. Phys. D 28 (12) (2019) 1950154. arXiv:1905.04602, doi:10.1142/S0218271819501542.

[19] U. Debnath, Gravitational waves for variable modified Chaplygin gas and some parametrizations of dark energy in the background of FRW universe, Eur. Phys. J. Plus 135 (2) (2020) 135. doi:10.1140/epjp/s13360-020-00219-9.

[20] S. del Campo, I. Duran, R. Herrera, D. Pavon, Three thermodynamically-based parameterizations of the deceleration parameter, Phys. Rev. D 86 (2012) 083509. arXiv:1209.3415, doi:10.1103/PhysRevD.86.083509.

[21] J. Cunha, J. A. S. d. Lima, Transition redshift: new kinematic constraints from supernovae, Monthly Notices of the Royal Astronomical Society 390 (1) (2008) 210–217.

[22] J. V. Cunha, Kinematic Constraints to the Transition Redshift from SNe Ia Union Data, Phys. Rev. D 79 (2009) 047301. arXiv:0811.2379, doi:10.1103/PhysRevD.79.047301.

[23] A. G. Riess, et al., Type Ia supernova discoveries at z > 1 from the Hubble Space Telescope: Evidence for past deceleration and constraints on dark energy evolution, Astrophys. J. 607 (2004) 665–687. arXiv:astro-ph/0402512, doi:10.1086/383612.

[24] L.-I. Xu, C.-W. Zhang, B.-R. Chang, H.-Y. Liu, Constraints to deceleration parameters by recent cosmic observations, Mod. Phys. Lett. A 23 (2008) 1939–1948. arXiv:astro-ph/0701519, doi:10.1142/S0217732308025991.

[25] L. Xu, J. Lu, Cosmic constraints on deceleration parameter with Sne Ia and CMB, Mod. Phys. Lett. A 24 (2009) 369–376. doi:10.1142/S0217732309027212.

[26] R. Nair, S. Jhingan, D. Jain, Cosmokinetics: a joint analysis of standard candles, rulers and cosmic clocks, Journal of Cosmology and Astroparticle Physics 2012 (01) (2012) 018.

[27] O. Akarsu, T. Dereli, S. Kumar, L. Xu, Probing kinematics and fate of the Universe with linearly time-varying deceleration parameter, Eur. Phys. J. Plus 129 (2014) 22. arXiv:1305.5190, doi:10.1140/epjp/i2014-14022-6.

[28] B. Santos, J. C. Carvalho, J. S. Alcaniz, Current constraints on the epoch of cosmic acceleration, Astroparticle Physics 35 (1) (2011) 17–20.

[29] Y.-G. Gong, A. Wang, Reconstruction of the deceleration parameter and the equation of state of dark energy, Phys. Rev. D 75 (2007) 043520. arXiv:astro-ph/0612196, doi:10.1103/PhysRevD.75.043520.

[30] M. S. Turner, A. G. Riess, Do SNe Ia provide direct evidence for past deceleration of the universe?, Astrophys. J. 569 (2002) 18. arXiv:astro-ph/0106051, doi:10.1086/338580.

[31] A. Al Mamon, S. Das, A divergence free parametrization of deceleration parameter for scalar field dark energy, Int. J. Mod. Phys. D 25 (03) (2016) 1650032. arXiv:1507.00531, doi:10.1142/S0218271816500322.

[32] G. N. Gadbail, S. Mandal, P. K. Sahoo, Parametrization

of deceleration parameter in f (q) gravity, Physics 4 (4) (2022) 1403–1412.
[33] A. Bouali, B. Shukla, H. Chaudhary, R. K. Tiwari, M. Samar, G. Mustafa, Cosmological tests of parametrization q= α- β h in f (q) flrw cosmology, International Journal of Geometric Methods in Modern Physics (2023).
[34] A. Bouali, H. Chaudhary, A. Mehrotra, S. Pacif, Model-independent study for a quintessence model of dark energy: Analysis and observational constraints, arXiv preprint arXiv:2304.02652 (2023).
[35] A. A. Mamon, S. Das, A parametric reconstruction of the deceleration parameter, The European Physical Journal C 77 (7) (2017) 495.
[36] A. Bouali, H. Chaudhary, U. Debnath, T. Roy, G. Mustafa, Constraints on the Parameterized Deceleration Parameter in FRW Universe (1 2023). arXiv:2301.12107.
[37] S. Capozziello, R. D'Agostino, O. Luongo, Thermodynamic parametrization of dark energy, Phys. Dark Univ. 36 (2022) 101045. arXiv:2202.03300, doi:10.1016/j.dark.2022.101045.
[38] U. Alam, V. Sahni, T. D. Saini, A. A. Starobinsky, Is there supernova evidence for dark energy metamorphosis ?, Mon. Not. Roy. Astron. Soc. 354 (2004) 275. arXiv:astro-ph/0311364, doi:10.1111/j.1365-2966.2004.08189.x.
[39] U. Alam, V. Sahni, A. A. Starobinsky, The case for dynamical dark energy revisited, Journal of Cosmology and Astroparticle Physics 2004 (06) (2004) 008.
[40] T. Bandyopadhyay, U. Debnath, Fluid accretion upon higher-dimensional wormhole and black hole for parameterized deceleration parameter, International Journal of Geometric Methods in Modern Physics 19 (12) (2022) 2250182.
[41] R. Kundu, U. Debnath, A. Pradhan, Studying the optical depth behaviour of parametrized deceleration parameter in non-flat universe, International Journal of Geometric Methods in Modern Physics (2023).
[42] H. Padé, Sur la représentation approchée d'une fonction par des fractions rationnelles, in: Annales scientifiques de l'Ecole normale supérieure, Vol. 9, 1892, pp. 3–93.
[43] H. Wei, X.-P. Yan, Y.-N. Zhou, Cosmological applications of pade approximant, Journal of Cosmology and Astroparticle Physics 2014 (01) (2014) 045.
[44] M. Rezaei, M. Malekjani, S. Basilakos, A. Mehrabi, D. F. Mota, Constraints to dark energy using pade parameterizations, The Astrophysical Journal 843 (1) (2017) 65.
[45] D. Foreman-Mackey, D. W. Hogg, D. Lang, J. Goodman, emcee: the mcmc hammer, Publications of the Astronomical Society of the Pacific 125 (925) (2013) 306.
[46] W. Handley, M. Hobson, A. Lasenby, Polychord: nested sampling for cosmology, Monthly Notices of the Royal Astronomical Society: Letters 450 (1) (2015) L61–L65.
[47] A. Lewis, Getdist: a python package for analysing monte carlo samples, arXiv preprint arXiv:1910.13970 (2019).
[48] E. Gaztanaga, C. Bonvin, L. Hui, Measurement of the dipole in the cross-correlation function of galaxies, Journal of Cosmology and Astroparticle Physics 2017 (01) (2017) 032.
[49] A. Bouali, H. Chaudhary, R. Hama, T. Harko, S. V. Sabau, M. S. Martín, Cosmological tests of the osculating barthel–kropina dark energy model, The European Physical Journal C 83 (2) (2023) 121.
[50] M. Kowalski, D. Rubin, G. Aldering, R. Agostinho, A. Amadon, R. Amanullah, C. Balland, K. Barbary, G. Blanc, P. Challis, et al., Improved cosmological constraints from new, old, and combined supernova data sets, The Astrophysical Journal 686 (2) (2008) 749.
[51] R. Amanullah, C. Lidman, D. Rubin, G. Aldering, P. Astier, K. Barbary, M. Burns, A. Conley, K. Dawson, S. Deustua, et al., Spectra and hubble space telescope light curves of six type ia supernovae at 0.511¡ z¡ 1.12 and the union2 compilation, The Astrophysical Journal 716 (1) (2010) 712.
[52] N. Suzuki, D. Rubin, C. Lidman, G. Aldering, R. Amanullah, K. Barbary, L. Barrientos, J. Botyanszki, M. Brodwin, N. Connolly, et al., The hubble space telescope cluster supernova survey. v. improving the dark-energy constraints above z¿ 1 and building an early-type-hosted supernova sample, The Astrophysical Journal 746 (1) (2012) 85.
[53] M. Betoule, R. Kessler, J. Guy, J. Mosher, D. Hardin, R. Biswas, P. Astier, P. El-Hage, M. Konig, S. Kuhlmann, et al., Improved cosmological constraints from a joint analysis of the sdss-ii and snls supernova samples, Astronomy & Astrophysics 568 (2014) A22.
[54] D. M. Scolnic, D. Jones, A. Rest, Y. Pan, R. Chornock, R. Foley, M. Huber, R. Kessler, G. Narayan, A. Riess, et al., The complete light-curve sample of spectroscopically confirmed sne ia from pan-starrs1 and cosmological constraints from the combined pantheon sample, The Astrophysical Journal 859 (2) (2018) 101.
[55] D. Scolnic, D. Brout, A. Carr, A. G. Riess, T. M. Davis, A. Dwomoh, D. O. Jones, N. Ali, P. Charvu, R. Chen, et al., The pantheon+ type ia supernova sample: the full dataset and light-curve release, arXiv preprint arXiv:2112.03863 (2021).
[56] D. Benisty, D. Staicova, Testing late-time cosmic acceleration with uncorrelated baryon acoustic oscillation dataset, Astronomy & Astrophysics 647 (2021) A38.
[57] W. J. Percival, B. A. Reid, D. J. Eisenstein, N. A. Bahcall, T. Budavari, J. A. Frieman, M. Fukugita, J. E. Gunn, Ž. Ivezić, G. R. Knapp, et al., Baryon acoustic oscillations in the sloan digital sky survey data release 7 galaxy sample, Monthly Notices of the Royal Astronomical Society 401 (4) (2010) 2148–2168.
[58] F. Beutler, C. Blake, M. Colless, D. H. Jones, L. Staveley-Smith, L. Campbell, Q. Parker, W. Saunders, F. Watson, The 6df galaxy survey: baryon acoustic oscillations and the local hubble constant, Monthly Notices of the Royal Astronomical Society 416 (4) (2011) 3017–3032.
[59] T. Delubac, J. Rich, S. Bailey, A. Font-Ribera, D. Kirkby, J.-M. Le Goff, M. M. Pieri, A. Slosar, É. Aubourg, J. E. Bautista, et al., Baryon acoustic oscillations in the lyα forest of boss quasars, Astronomy & Astrophysics 552 (2013) A96.
[60] L. Anderson, E. Aubourg, S. Bailey, D. Bizyaev, M. Blanton, A. S. Bolton, J. Brinkmann, J. R. Brownstein, A. Burden, A. J. Cuesta, et al., The clustering of galaxies in the sdss-iii baryon oscillation spectroscopic survey: baryon acoustic oscillations in the data release 9 spectroscopic galaxy sample, Monthly Notices of the Royal Astronomical Society 427 (4) (2012) 3435–3467.
[61] H.-J. Seo, S. Ho, M. White, A. J. Cuesta, A. J. Ross, S. Saito, B. Reid, N. Padmanabhan, W. J. Percival, R. De Putter, et al., Acoustic scale from the angular

power spectra of sdss-iii dr8 photometric luminous galaxies, The Astrophysical Journal 761 (1) (2012) 13.
[62] A. J. Ross, L. Samushia, C. Howlett, W. J. Percival, A. Burden, M. Manera, The clustering of the sdss dr7 main galaxy sample–i. a 4 per cent distance measure at z= 0.15, Monthly Notices of the Royal Astronomical Society 449 (1) (2015) 835–847.
[63] R. Tojeiro, A. J. Ross, A. Burden, L. Samushia, M. Manera, W. J. Percival, F. Beutler, J. Brinkmann, J. R. Brownstein, A. J. Cuesta, et al., The clustering of galaxies in the sdss-iii baryon oscillation spectroscopic survey: galaxy clustering measurements in the low-redshift sample of data release 11, Monthly Notices of the Royal Astronomical Society 440 (3) (2014) 2222–2237.
[64] J. E. Bautista, M. Vargas-Magaña, K. S. Dawson, W. J. Percival, J. Brinkmann, J. Brownstein, B. Camacho, J. Comparat, H. Gil-Marín, E.-M. Mueller, et al., The sdss-iv extended baryon oscillation spectroscopic survey: baryon acoustic oscillations at redshift of 0.72 with the dr14 luminous red galaxy sample, The Astrophysical Journal 863 (1) (2018) 110.
[65] E. De Carvalho, A. Bernui, G. Carvalho, C. Novaes, H. Xavier, Angular baryon acoustic oscillation measure at z= 2.225 from the sdss quasar survey, Journal of Cosmology and Astroparticle Physics 2018 (04) (2018) 064.
[66] M. Ata, F. Baumgarten, J. Bautista, F. Beutler, D. Bizyaev, M. R. Blanton, J. A. Blazek, A. S. Bolton, J. Brinkmann, J. R. Brownstein, et al., The clustering of the sdss-iv extended baryon oscillation spectroscopic survey dr14 quasar sample: first measurement of baryon acoustic oscillations between redshift 0.8 and 2.2, Monthly Notices of the Royal Astronomical Society 473 (4) (2018) 4773–4794.
[67] T. Abbott, F. Abdalla, A. Alarcon, S. Allam, F. Andrade-Oliveira, J. Annis, S. Avila, M. Banerji, N. Banik, K. Bechtol, et al., Dark energy survey year 1 results: Measurement of the baryon acoustic oscillation scale in the distribution of galaxies to redshift 1, Monthly Notices of the Royal Astronomical Society 483 (4) (2019) 4866–4883.
[68] Z. Molavi, A. Khodam-Mohammadi, Observational tests of gauss-bonnet like dark energy model, The European Physical Journal Plus 134 (6) (2019) 254.
[69] N. B. Hogg, M. Martinelli, S. Nesseris, Constraints on the distance duality relation with standard sirens, Journal of Cosmology and Astroparticle Physics 2020 (12) (2020) 019.
[70] M. Martinelli, C. J. A. P. Martins, S. Nesseris, D. Sapone, I. Tutusaus, A. Avgoustidis, S. Camera, C. Carbone, S. Casas, S. Ilić, et al., Euclid: Forecast constraints on the cosmic distance duality relation with complementary external probes, Astronomy & Astrophysics 644 (2020) A80.
[71] L. Chen, Q.-G. Huang, K. Wang, Distance priors from planck final release, Journal of Cosmology and Astroparticle Physics 2019 (02) (2019) 028.
[72] M. Shahalam, S. Sami, A. Agarwal, Om diagnostic applied to scalar field models and slowing down of cosmic acceleration, Monthly Notices of the Royal Astronomical Society 448 (3) (2015) 2948–2959.
[73] V. Sahni, T. D. Saini, A. A. Starobinsky, U. Alam, Statefinder—a new geometrical diagnostic of dark energy, Journal of Experimental and Theoretical Physics Letters 77 (2003) 201–206.
[74] U. Alam, V. Sahni, T. Deep Saini, A. Starobinsky, Exploring the expanding universe and dark energy using the statefinder diagnostic, Monthly Notices of the Royal Astronomical Society 344 (4) (2003) 1057–1074.
[75] M. Sami, M. Shahalam, M. Skugoreva, A. Toporensky, Cosmological dynamics of a nonminimally coupled scalar field system and its late time cosmic relevance, Physical Review D 86 (10) (2012) 103532.
[76] R. Myrzakulov, M. Shahalam, Statefinder hierarchy of bimetric and galileon models for concordance cosmology, Journal of Cosmology and Astroparticle Physics 2013 (10) (2013) 047.
[77] V. Sahni, T. D. Saini, A. A. Starobinsky, U. Alam, Statefinder: A New geometrical diagnostic of dark energy, JETP Lett. 77 (2003) 201–206. arXiv:astro-ph/0201498, doi:10.1134/1.1574831.
[78] V. Sahni, A. Shafieloo, A. A. Starobinsky, Two new diagnostics of dark energy, Phys. Rev. D 78 (2008) 103502. arXiv:0807.3548, doi:10.1103/PhysRevD.78.103502.
[79] V. Sahni, A. Shafieloo, A. A. Starobinsky, Two new diagnostics of dark energy, Physical Review D 78 (10) (2008) 103502.
[80] C. Zunckel, C. Clarkson, Consistency tests for the cosmological constant, Physical Review Letters 101 (18) (2008) 181301.
[81] M. Shahalam, S. Pathak, M. Verma, M. Y. Khlopov, R. Myrzakulov, Dynamics of interacting quintessence, The European Physical Journal C 75 (2015) 1–9.
[82] A. Agarwal, R. Myrzakulov, S. Pacif, M. Shahalam, Cosmic acceleration from coupling of baryonic and dark matter components: Analysis and diagnostics, International Journal of Modern Physics D 28 (06) (2019) 1950083.
[83] A. Jawad, S. Qummer, S. Rani, M. Younas, Generalized interaction term inspired dark energy model in fractal universe, Mod. Phys. Lett. A 35 (15) (2020) 2050126. doi:10.1142/S0217732320501266.
[84] A. Khodam-Mohammadi, M. Malekjani, Interacting entropy-corrected holographic scalar field models in non-flat universe, Commun. Theor. Phys. 55 (2011) 942–948. arXiv:1004.1720, doi:10.1088/0253-6102/55/5/37.
[85] M. Malekjani, A. Khodam-Mohammadi, Statefinder diagnosis and the interacting ghost model of dark energy, Astrophys. Space Sci. 343 (2013) 451–461. arXiv:1202.4154, doi:10.1007/s10509-012-1230-3.
[86] M. Malekjani, A. Khodam-Mohammadi, N. Nazaripooya, Cosmological evolution and statefinder diagnostic for new holographic dark energy model in non flat universe, Astrophys. Space Sci. 332 (2011) 515–524. arXiv:1011.4805, doi:10.1007/s10509-010-0550-4.
[87] M. Jamil, D. Momeni, R. Myrzakulov, Observational constraints on non-minimally coupled galileon model, The European Physical Journal C 73 (3) (2013) 2347.
[88] P. De Fromont, C. De Rham, L. Heisenberg, A. Matas, Superluminality in the bi-and multi-galileon, Journal of High Energy Physics 2013 (7) (2013) 1–29.
[89] H. Akaike, A new look at the statistical model identification, IEEE transactions on automatic control 19 (6) (1974) 716–723.
[90] M. Li, X. Li, X. Zhang, Comparison of dark energy models: A perspective from the latest observational data, Science China Physics, Mechanics and Astronomy 53 (9) (2010) 1631–1645.
[91] K. Burnhan, D. R. Anderson, Model selection and multimodel inference, New York: Springer (2002).

[92] K. P. Burnham, D. R. Anderson, Multimodel inference: understanding aic and bic in model selection, Sociological methods & research 33 (2) (2004) 261–304.
[93] A. R. Liddle, Information criteria for astrophysical model selection, Monthly Notices of the Royal Astronomical Society: Letters 377 (1) (2007) L74–L78.

International Conference on Innovative Data Communication Technologies and Application (ICIDCA-2023)
IEEE Xplore Part Number: CFP23CR5-ART; ISBN: 979-8-3503-9720-8

2023 International Conference on Innovative Data Communication Technologies and Application (ICIDCA) | 979-8-3503-9720-8/23/$31.00 ©2023 IEEE | DOI: 10.1109/ICIDCA56705.2023.10099779

Deception Detection using a Multimodal Stacked Bi-LSTM Model

Puneet Kumar Sehrawat
Department of Information Technology
Delhi Technological University
Delhi, India
puneetsehrawat2000@gmail.com

Rajat Kumar
Department of Information Technology
Delhi Technological University
Delhi, India
mathuria.rajatkumar@gmail.com

Nitish Kumar
Department of Information Technology
Delhi Technological University
Delhi, India
nitishkumar12c@gmail.com

Dinesh Kumar Vishwakarma
Department of Information Technology
Delhi Technological University
Delhi, India
dinesh@dtu.ac.in

***Abstract*— In the scientific community, researchers have recently become interested in the automatic identification of deceptive actions because of the range of fields where it might be advantageous, including criminology or security. Deception detection in conversational speech has drawn much attention in recent years. Given the significant risks associated with trial outcomes, using precise and efficient computational methods to assess the accuracy of court evidence may be very beneficial throughout the decision-making process. This study discusses about spotting deception in trial data from actual cases. Doing this has some challenges associated with creating a robust model that can accurately classify the deception and perform this action as fast as possible. Due to the limited number of videos and datasets available, some models overfit the data. A model should exist which can classify the data using various modalities, i.e., video, audio and text, and be able to work on multiple different datasets with excellent accuracy. This study has used videos from actual trials that were collected from open court proceedings and some videos from other datasets. To design a robust deception detection system that discriminates between witnesses and defendants, genuine and fraudulent testimony, this study investigates the utilization of text, audio and video modalities. By extracting and integrating information about the spoken words from audio, this study can achieve an accuracy of 80% approximately. The proposed model results with a classification accuracy of 96% approximately in an extended approach to perform video transcriptions. The Bag-of-Lies dataset, a multimodal database captured in real-world settings has achieved an accuracy of 85%. The Miami University Deception Detection Dataset focuses on people telling truths and lies about their social relationships, achieved an accuracy of 98.1% on the presented model. The proposed model employs LSTM (Long-Short Term Memory), Bidirectional LSTM (Long-Short Term Memory), CNN (Convolution Neural Network), and RestNet50. The results demonstrate that the proposed algorithm performs better at detecting deception than humans.**

Keywords— Deception Detection, Criminology, CNN, Long Short-Term Memory, RestNet50 (Residual Network 50), Multimodal.

I. INTRODUCTION

Deception is when someone tries to persuade others of a false fact by using misleading proof and engaging in fraud. This can be done by introducing dishonesty, factual misrepresentation, or omissions. Big deception tends to happen when the speakers are involved in their statements. It will have a significant impact, as in trial situations when a deceitful speech may lead to the release of a guilty person. Online reviews that aim to sway consumer decisions, social media posts, etc., may use casual deception to gather supporters for or opponents of a cause, indirectly impacting society. The globalization of economics and improvements in computer technology, which have created new chances for deception, are the main drivers of the growth of network communication in our daily lives. Formats based on text, audio, video and other multiple media fall under several categories of computer-mediated communication. Text-based network communication transfers textual information without audio or visual signals. The potential for receiving misleading communications rises with the volume of data carried over the Internet, making it ineffective and difficult to analyze and monitor such messages manually.

Without specialized tools, humans have a low detection rate of deceit, about 54% [1]. Deceitfully accusing the innocent and releasing the guilty can have serious consequences. For example, in the United States, many court proceedings are filed yearly. In US District Courts, 89,936 criminal cases were filed in 2013, while 80,262 cases were filed in 2014. Additionally, between 2000 and 2013, there were 4.29 exonerations on average each year, up from 3.03 between 1973 and 1999. According to the National Registry of Exonerations, 873 exonerations were reported from 1989 to 2012, each with a tragic history case [2].

Therefore, a reliable and effective method is needed to identify dishonest behaviour and distinguish between liars and truth-tellers. This study's objective highlights an effort to build a multimodal system to identify deception from real-life scenarios. We have used three comprehensive datasets (i) made up of 121 videos of court proceedings, of which 60 are truthful, and 61 are deceptive. (ii) 35 distinct subjects have contributed 325 annotated data sets, with 163 truthful and 162 false statements. (iii) a collection of 320 videos featuring male and female Black and White targets revealing both the truth and lies. These targets were videotaped, speaking openly and covertly about their interpersonal interactions. We have used numerous linguistic elements from the transcription extracted from the speaker's statements and the corresponding spectrograms of the audio signals, which are used to train our model. In the comprehensive approach, we used transcriptions from the videos. The model we created employs LSTM (Long-Short Term Memory), Bidirectional LSTM, CNN (Convolution Neural Network), and RestNet50 (Residual Network 50).

Authorized licensed use limited to: DELHI TECHNICAL UNIV. Downloaded on April 26,2023 at 10:23:03 UTC from IEEE Xplore. Restrictions apply.

II. RELATED WORKS

Researchers have previously proposed several models for the detection of dishonesty. Examples include physiological techniques like the well-known Polygraph test or the more modern fMRI-based functional testing. According to the authors, these techniques have two drawbacks: (i) they need complex equipment setup. (ii) they are pervasive and demand a skilled operator. Their relevance to everyday life is limited. There is no scientific evidence that the frequently used polygraph test can identify individual deceit. Researchers have suggested behavioural strategies, including spontaneous facial expressions [3]. Since the typical individual lacks the training to recognize these micro-expressions, they are irrelevant to everyday society. Automated deception detection methods are required, and the increased computational capabilities have made it possible to build mechanical systems employing data-driven methodologies. Data-driven strategies also benefit from being discrete and using all accessible information. For instance, they are a perfect fit for deception detection systems since they can function with just video and, when available, text annotations. Other data-driven approaches for deception detection have been developed, using modalities including video, audio, text, electroencephalogram (EEG), and gaze. The identification of misleading information in various domains, such as social media sites, online dating websites, and consumer report websites, has been the subject of multiple research articles on verbal-based deception detection to date. Blob analysis, a technique for detecting non-verbal deceit, has pinpointed dishonest hand gestures by watching people's hand motions [4] or looking at geometric patterns connected to head and hand action [5]. Recently, elements from several modalities have been combined to obtain a set of multimodal features that performs optimally [6]. A multimodal deception dataset of linguistic, thermal, and physiological variables was first described in [7], and a multimodal deception detection algorithm was then created. Some research has employed machine learning methods to generate deception models utilizing linguistic inquiry and word count vocabulary [8]. They have demonstrated the value of using psycholinguistic data for automatic deception detection [9]. Numerous studies have also investigated the link between text syntactic complexity and deceitfulness, following the premise that liars could choose simpler words to hide the truth and make it easier for victims to remember their statements [10].

III. DATASETS USED

A. Real Life Court Trial Dataset

This dataset was collected by finding publicly available mixed media sources where Court hearings videos are available and can be reasonably observed and verified for truthful and deceptive behaviour. This dataset is targeted explicitly at court trial recordings on which part of restrictions established by current data processing methodologies may be applied and observed. There were some criteria for picking videos, like the accused face should be clearly visible in most clips. Video and audio quality should be clear enough to understand what the person is saying, and his facial expression is also identifiable. [16]

Three different court hearing outcomes were considered to correctly flag specific video clips of trials as misleading or truthful convictions. Thus, in the case of a sentence, deceptive videos were collected from the defendant at trial, whereas honest videos were gathered from witnesses at the same court trial. In some instances, misleading recordings were gathered denying the crimes committed by suspects, and truthful videos were filmed of the same suspects answering questions about facts confirmed by police to be true. For eyewitnesses, statements corroborated by police investigations were classified as truth, and statements supporting a guilty suspect were classified as misleading. Exoneration testimony was collected as a statement of truth.



Fig. 1. A sample screenshot showing face presentation and hand gestures from an actual trial clip.

The final dataset contains 121 court hearing recordings, including 61 in which a person is telling a lie and 60 in which a person is telling the truth. The mean duration of videos in the dataset is 28.0 seconds. The dataset consists of videos of 21 unique female and 35 exceptional male speakers. Their age varies approximately between 16 and 60 years. The average video duration is 27.7 seconds and 28.3 seconds for deceptive and truthful videos.

B. Miami University Deception Detection Database

The Miami University Deception Detection Database is a valuable resource for researchers studying deception and the techniques used to identify it, also known as the M3UD database for research studies. It's an open-source database that contains videos of different races and gender telling facts that may be true or a lie. [17]

The videos are accompanied by extensive metadata, providing researchers with detailed information about the circumstances of the deception, including the type of lie, the motivation for lying, and the level of experience of the liar. This database has been used to develop and test various deception detection technologies and techniques, including eye-tracking devices and facial recognition software. Researchers have also used the database to understand better the nonverbal cues people exhibit when they lie, which can help develop more accurate and reliable deception detection methods.

This database includes 320 videos of eighty people (20 White males, 20 Black males, 20 Black females and 20 White females) whose recordings were made while telling facts about their social relationship truthfully or deceptively. Every person was recorded four times telling (Positive, negative, positive, negative, negative truth), making 320 videos fully

Authorized licensed use limited to: DELHI TECHNICAL UNIV. Downloaded on April 26,2023 at 10:23:03 UTC from IEEE Xplore. Restrictions apply.

crossing statement veracity, statement valence, target gender, and target race.

C. Bag of lies Dataset

The dataset delves into the cognitive dimension of deception and integrates it with visual components, providing a unique perspective on deception detection. Most of the primarily available datasets focus on a single modality, whereas Bag-of-Lies is a multimodal dataset consisting of recordings from 35 subjects. Recordings have been gathered through a carefully designed experiment for automatic lie detection purposes (truth/lie classification)[18]. The study also investigates the benefits of integrating multiple modalities for improved performance on the dataset. The authors contend that this dataset will aid in the development of more effective deception detection algorithms that are better suited to real-world situations

The dataset contains 325 manually annotated recorded videos, with 162 Deceptive and 163 truthful videos. Also, EEG data (13 channels) for 22 unique subjects is available. Participants in the video were volunteer University students who were fluent in English and belonged to different cultures. For the experiment, Unlike the traditional datasets in which Subjects were asked various questions and had to tell a lie or truth, here participants were shown 6 to 10 images.

They were free to respond in any way. 6-10 predetermined images were shown to every participant, and they were asked to briefly explain what they saw either truthfully or deceptively, depending upon what they wanted to say. The recordings duration varies from 3.5 seconds to 42 seconds.

IV. METHODS

Our model employs a Convolution layer, LSTM (Long-Short Term Memory), Bidirectional LSTM, RestNet50 (Residual Network 50) and one hot encoding.

A. Convolution layer

The CNN (Convolution neural networks) in deep learning consists of multiple layers used to discover patterns in various types of data. The convolution layer is one of the most crucial layers where main computations occur. It requires several components to work input data, a filter, and a feature map. This layer applies the convolution operations on the input matrix and passes the resultant matrix to the next layer. It changes all the pixels in the receptive field into a single value [11].

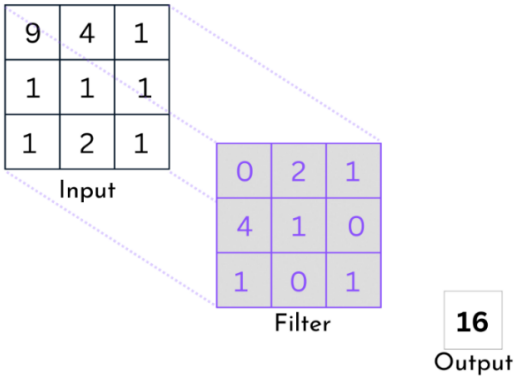


Fig. 2. Convolution Filter

For example, in a large Input image, a small section of the image is considered, and these layers convolve them into a single output using a filter (Kernel). Depending on the type of input and problems required to solve, there are different kinds of convolutions Transposed Convolutions, Dilated or Atrous Convolutions, Separable Convolutions, The 2D Convolution Layer, etc. For our problem, we have used separable convolutions.

B. Long Short-Term Memory (LSTM)

The LSTM (Long-Short Term Memory) is an advanced RNN (Recurrent Neural Network) method that's predominately used for sequential data predictions. It makes it easier to retain past data in memory. It also solves the associated vanishing gradient problem in traditional RNNs. Its applications are language modelling, sentiment analysis, video analysis and speech recognition [12]. LSTM network consists of three different gates:

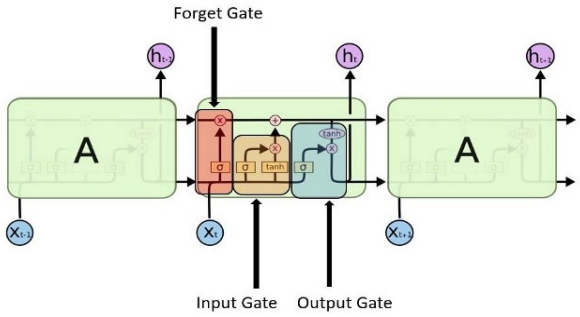


Fig. 3. LSTM cell

$$f_t = \sigma\left(x_t * U_f + H_{t-1} * W_f\right)$$
$$i_t = \sigma\left(x_t * U_i + H_{t-1} * W_i\right)$$
$$o_t = \sigma\left(x_t * U_o + H_{t-1} * W_o\right)$$
$$H_t = o_t(tanh(C_t))$$
$$Hidden\ state = Softmax(H_t)$$

Where t represents the current timestamp, x_t input at timestamp t, U_i Weight matrix of the input, H_{t-1} hidden state value at the previous timestamp, W_i Weight matrix of input associated with the hidden state, σ sigmoid function to bring

Authorized licensed use limited to: DELHI TECHNICAL UNIV. Downloaded on April 26,2023 at 10:23:03 UTC from IEEE Xplore. Restrictions apply.

output 0 or 1, and i_t, f_t, o_t represents the input, forget, and output gates

C. Bidirectional LSTM

BI-LSTM (Bi-directional long short-term memory) is a recurrent neural network that consists of two LSTMS (long short-term memory). These LSTMs take input in both directions, backwards and forward. It consists of one more LSTM layer than the classical one, which reverses the order of information flow to effectively increase the amount of information given to the network, thereby improving the context available to the algorithm [13]. This implies that BI-LSTM consists of comprehensive and sequential details on every point before and after each end [14].

BI-LSTM architecture has many advantages in solving real-world problems, especially neural language processing. It can produce more meaningful output by combining the result from both the LSTMS. It can be used for NLP tasks like translation recognition, entity recognition and sentence classification; other than that, it also has applications in handwritten recognition, protein structure prediction, speech recognition and similar fields.

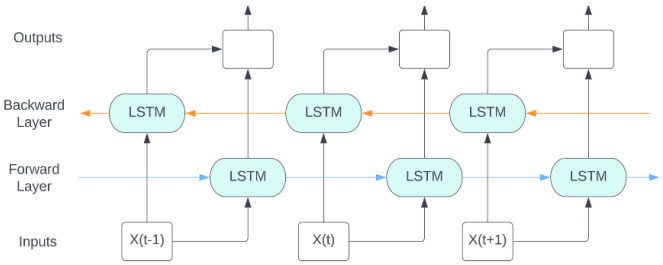


Fig. 4. Bi-LSTM Layer

D. Resnet50

Resnet50 (Residual Network) is a particular type of CNN (convolutional neural network) whose depth is 50 layers that consist of one intermediate pool layer, 1 MaxPool layer and 48 convolutional layers. Resnet 50 is a modified version of Resnet34. The architecture of Resnet50 is the same as that of Resnet 34. However, there is one big difference in the Resnet50 building block. It was modified into a bottleneck design to reduce the time it takes to train layers[15]. That's why the 2-layer building blocks in Resnet 34 are changed by the 3-layer building block making the Resenet50 architecture. Resnet50 is used as the base for many computer vision functions. The most significant advantage that Resnet50 provided was that it allowed the training of intense neural networks with 100+ layers.

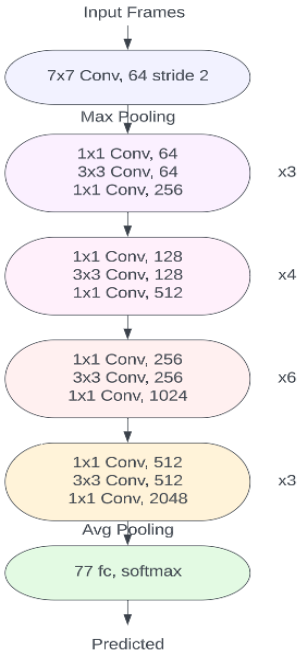


Fig. 5. Resnet50 architecture with Conv(Convolution layer) and fc(fully connected layer) with SoftMax.

V. EXPERIMENT AND RESULTS

We conduct our training experiments on the earlier introduced real-life instances datasets. Given the distribution of false and true clips, we extracted the audio from each video and processed it further. Because stereo audio channels include two channels of audio, meaning that when we're listening, two or more sound sources are concentrated to the left and right. Making it challenging to comprehend the file, we transformed our video's extracted audio fragment to the mono channel. The processing of a mono-channel audio file is more straightforward than that of a multi-channel audio file because mono audio is single-channel audio, which implies that all sound sources are perceived through just one channel.

The Audio files produced are of different durations where audio files might like the voice is loud in some areas and quiet in others. This variation in volume might make transcription difficult. So, we computed maximum audio seconds of about 34 seconds using the summation audio length duration of each audio and flooring against the constant sample rate of the audio. Then, to make all the audio samples the same length, we truncate or expand their length by padding it with silence. We initially tried extracting features using the VGG-16 pretrained model on our dataset. We got a validation accuracy of approximately 75% on the court proceedings dataset. In our alternative method of investigating fine-tuning, instead of utilizing a pretrained model as a feature extractor, we have employed another pretrained model, ResNet50 (Residual Network 50). These transfer learning models have been used because the datasets contain limited videos, resulting in an overfitting model. Hence, these models avoid overfitting and extract essential features from audio.

Deep Learning models rarely accept the raw audio directly as input. Thus we transform the padded audio samples to the Mel

Authorized licensed use limited to: DELHI TECHNICAL UNIV. Downloaded on April 26,2023 at 10:23:03 UTC from IEEE Xplore. Restrictions apply.

Spectrogram next. Mel spectrogram refers to a spectrogram in which the frequencies are converted to the Mel scale, a pitch measurement system that makes equal gaps in pitch appear to the listener to be equally distant. Mel Spectrograms are frequently the best method for supplying audio data to deep learning models since they capture the fundamental aspects of the audio. The spectrogram height and width used is 224, which is acceptable by the ResNet50 Model. Using overlapping windowed portions of the audio signal, we applied the fast Fourier transform to translate the audio input from the time domain into the frequency domain. We translated the frequency on the y-axis onto the Mel scale. We stored these spectrograms in PNG format in "RGB" mode, as shown in (Figure-6), to feed as input to our model. The Mel-spectrogram offers additional details in the representation of our audio file. With the help of our Mel-spectrograms, we can provide our convolutional neural network model with more information to accurately distinguish between the classes we are training on that are deceptive and truthful in this case.

We extracted the transcriptions from the audio. These transcriptions are the statements made by the speaker during the process. There are 121 statements, comprising 60 truthful and 61 deceptive statements, in the court proceedings dataset. There are 325 statements in the Bag of the Lies dataset, 163 of which are false and 162 which are true. The Miami University Deception Detection dataset has 320 statements, 160 for fraud and 160 for the truthful category clips.

We will use a vocab size of 2000 words for vectorizing and applying one-hot encoding on these statements. The output of each statement will be a vector with values between 0 to 1999 for the distinct set of words in these statements. We are also declaring the size of max length to the floored value of summation of all sentences against the total number of sentences and, on the other side, adding pre-padding to it as 0.

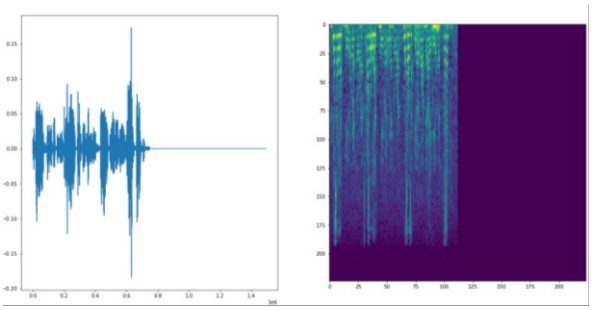


Fig. 6. On the Left, we have the Audio signal waveform, and On the Right, we have Mel Spectrogram (Deceptive Audio)

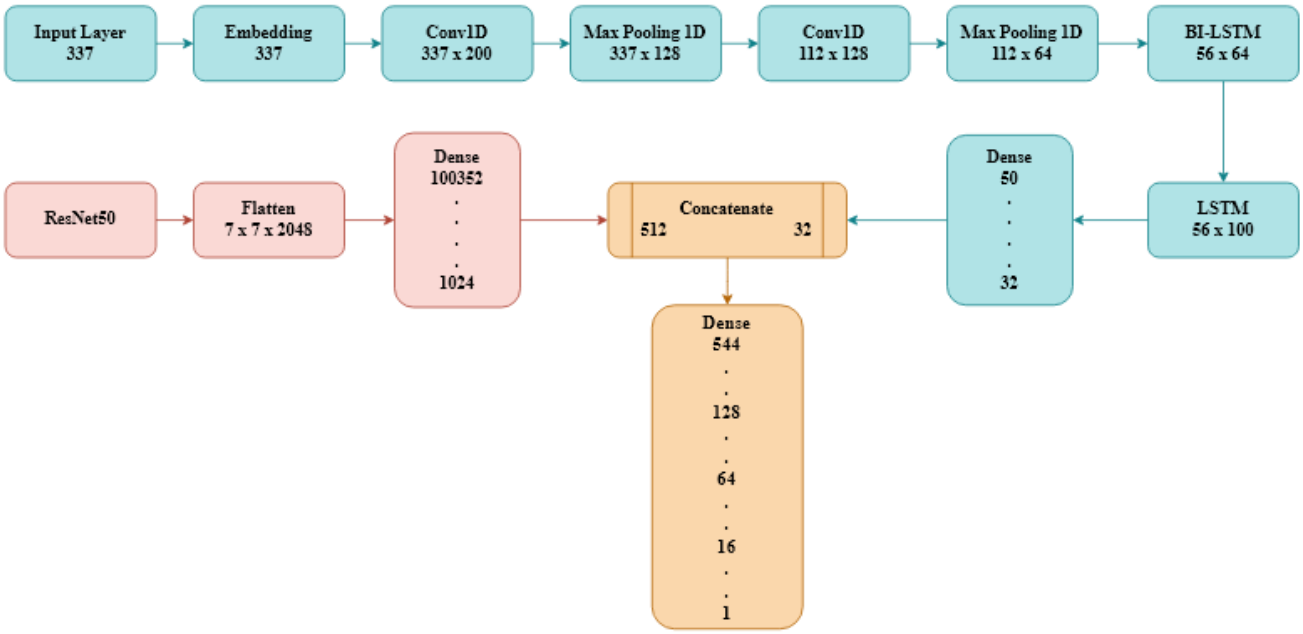


Fig. 7. Working of Model using ResNet50 pre-trained model (Audio + Text based method)

We have used the ResNet50(Residual Network 50) model in our analysis with weights of the trained ImageNet dataset. We have turned each word into a fixed-length vector with a predetermined size due to the embedding layer in the text model branch. In addition to having fewer dimensions, word vectors' constant length aids in improving word representation. With a vocabulary size of 2000 words and a word vector length of 200, we have provided precomputed sentence length as input to the embedding layer. A convolution 1D layer produces a tensor of outputs by combining a convolution kernel with the layer input over a solo temporal dimension. After convolution, some information gets eliminated, so we use the padding "same" such that the output has the same width and height dimensions as the input feature by uniformly adding padding

Authorized licensed use limited to: DELHI TECHNICAL UNIV. Downloaded on April 26,2023 at 10:23:03 UTC from IEEE Xplore. Restrictions apply.

with zeros to the right and left or down and up of the information. As the convolution process is linear, we use the ReLU (Rectified Linear Unit) activation function to introduce non-linearity. The ReLU function's primary use over other activation functions is that it does not simultaneously activate all neurons. This indicates that the neurons won't stop functioning, except the linear transformation's result is less than 0. The neuron is not triggered if the result is zero for negative input values. The ReLU function is much more computationally efficient because it only activates a limited number of neurons.

By contributing an abstracted version of the illustration, max pooling reduces over-fitting. It chooses the most prominent element from the area of the input feature that the filter has covered. As a result, the output following the max-pooling Layer would consist of a feature map with the most visible elements from the prior feature map. This MaxPooling 2D Layer down samples by the pool size of 3 followed by another Conv1D layer with the same parameters of padding and activation function with 64 output filers in the convolution space and length of 1D convolution window of 2. A second MaxPooling Layer down samples with a pool size of 2. We made two copies of the LSTM hidden layer by enclosing it in a bidirectional layer. In our situation, we will obtain 100 output nodes rather than 50. This stacked Bi-LSTM model finds features in forward as well as backward sequences. Hence Bi-LSTM finds context in the whole series and not limits itself to only the forward direction, which LSTM does. The simple model LSTM in one layer ends with a dense layer of 64 nodes. After which, we drop out 20 per cent of nodes and again end with a dense layer of 32 nodes using the ReLU activation function. The ResNet50 model pre-trained output is flattened, culminating in two dense layers of 1024 and 512 nodes and performing a dropout of 10 per cent after each dense layer. This result of 512 nodes is then concatenated with the text model branch result of 32 nodes to construct a final model branch. We have used an ADAM(Adaptive Moment Estimation Optimizer) optimizer, and the activation function used in the last dense layer is Sigmoid. We perform a split of 80:20 on the dataset. The parameters chosen for predictions are the Mel spectrograms of padded audio samples, encoded transcriptions, and vector of the class-labelled audio spectrogram in which 0 denotes deceptive, and one represents truthful.

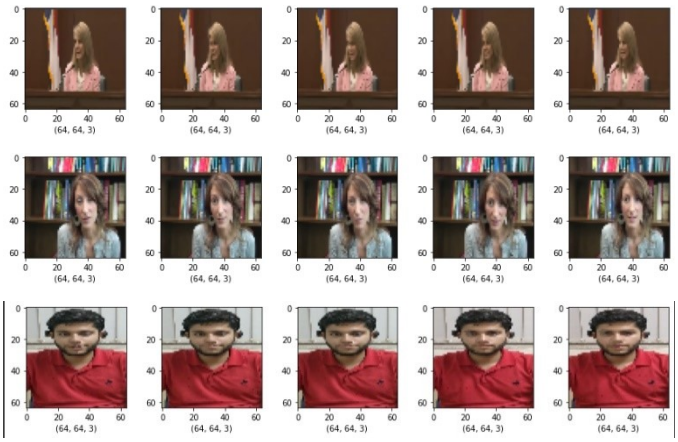




Fig. 8. First five frames of the video resized to dimension 64*64*3 (1st two rows of frames are from the Real-Life Court Trial Dataset. Followed by two rows of Bag of Lies Dataset, and the last two rows contain frames of MU3D Dataset)

During the training of our model, we used a batch size of 4 and employed ReduceOnPlateau call-back with a learning rate of 0.1, which we reduce after every two epochs if there is no improvement till the lower bound. Additionally, we are saving the best model with the highest level of validation accuracy using the Model Checkpoint call-back. We have accomplished a validation accuracy of 80% approximately in this analysis of our model for the court proceedings dataset.

In the comprehensive approach, we know the sequence of images that makes up a video. The human eye will see motion when these pictures, known as frames, are presented continually one at a time at a specific rate. We will construct a parameter to modify how many frames we want to extract and store every second because not all videos have the same duration and FPS. For example, it is set to 10 because, for the time being, it will only store ten frames per second of the video, even though the video FPS is, let's say, 30. A total of 300 frames will be preserved for a video that lasts 30 seconds. We resized the frame to 64*64 size and stored it in a list, as shown in the figure below.

TABLE I. Accuracies obtained for Real Life Court Trails Dataset on different methods.

MODALITIES USED	ACCURACY(Approx.)
Audio + Text using VGG16 method	75%
Audio + Text using ResNet50 method	80%
Video + Text	96%

As we have used different modalities for training our models like text, audio and video, we have encountered that text modality-based model training is faster than the other two as its processing time is less. However, in text-based method learning, very few features are extracted from the input data, leading to the model's poor efficiency. Whereas in model training, in which we used audio and text as our core modality, we were able to accomplish better accuracy. Because the audio

Authorized licensed use limited to: DELHI TECHNICAL UNIV. Downloaded on April 26,2023 at 10:23:03 UTC from IEEE Xplore. Restrictions apply.

signal as an input is a sound waveform, it requires less processing time than models which uses video and text as their core modality. Still, due to the lack of visual elements, such audio-based trained methods cannot extract more features. Due to this, accuracy could be higher compared to video modality-based trained models. The models which use video modality for learning can extract more insightful features like face gestures which provide more essential elements of the input data, which gives us much better accuracy than the other two. But as we know, video comprises many frames. Hence video-based model training requires more time to process and extract valuable, helpful insights from the data.

We conduct our training experiments on the real-world instances dataset that was previously introduced. We took the audio from each video and processed it further after extracting it, using the same distribution of deceptive and actual clips. From the audio, we retrieved the transcriptions. The speaker's responses throughout the court hearings are captured in these transcriptions. There are 121 assertions, 60 of which are true and 61 of which are false.

The video and text modality model is shown in Fig. 9, where we apply a combination of convolution, normalization, and max pooling followed by Bi-LSTM and dense layers. Convolution is used to extract only the essential features from the frames, and max pooling reduces the size of those extracted features. Bi-LSTM layers find context in both directions as the frames of a video depend on the forward and backward edges. Dense layers then find important information from nodes obtained from Bi-LSTM layers.

We performed the same procedures on the Bag of a Lies dataset, which consists the 325 videos consisting of 163 deceptive and 162 truthful clips of 35 unique subjects to obtain their transcriptions. We collected the transcriptions from the audio segment we took from each subject's video. The same actions are performed on the Miami University Deception Detection Database, containing 320 videos in which 160 clips are truthful and 160 are deceptive. As introduced earlier, this dataset focuses on the truths and lies of males and females speaking about their social relationships. The audio segment is extracted from these clips, and transcriptions are retrieved from the audio part.

During the Training of our model, we employed the Early Stopping call-back method, which stops the Training further after three epochs if there is no improvement, as the goal is to minimize the loss. We have used an ADAM optimizer, and the activation function used in the last dense layer is Sigmoid. We perform a split of 85:15 on the dataset. The parameters chosen for predictions are concatenated array of resized frames of dimension 64*64*3 comprised of deceptive and truthful videos and a connected collection of corresponding labels of these frames.

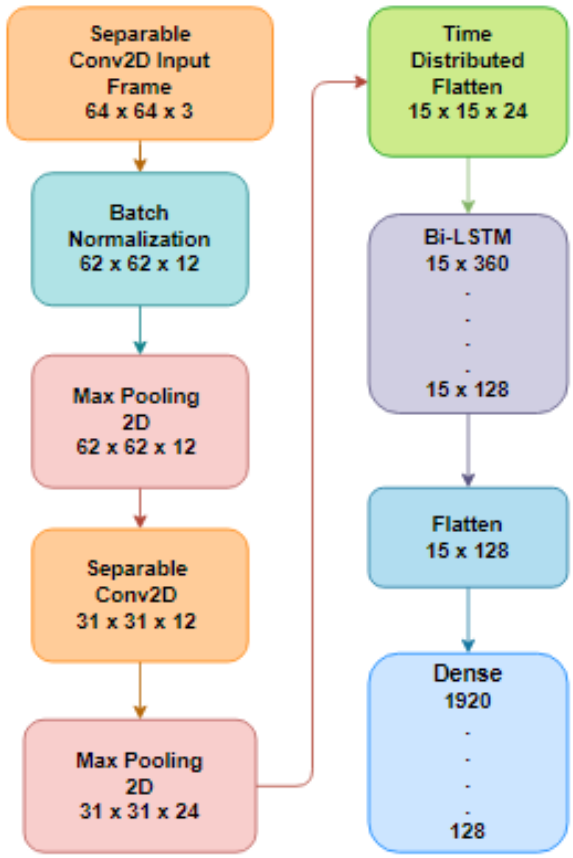


Fig. 9. Working of Model (Video + Text-based method)

The same model was run on the same parameters on all three datasets for Video and Text Modalities. The approximate accuracy recorded for all the datasets is in the table below.

TABLE II. Accuracies were obtained for the three datasets on video and text.

DATASET USED	ACCURACY(Approx.)
Bag of Lies Dataset	85%
Miami University Deception Detection Dataset	98.1%
Real-Life Court Trails Dataset	96%

VI. COMPARISON TO OTHER MODELS

Our paper integrates different modalities with their respective models to find deception in a dataset. Our best performing gave an accuracy of approx. 85%, 95% and 96% for the datasets Bags-of-lie, Miami University Deception Detection Dataset, and Real-Life Court Trails Dataset, respectively.

Many previous models have also been created on the same datasets using different methods. M. Umut S¸ en, Veronica P´erez-Rosas, B.Yanikoglu, Mohd. Abouelenien, M. Burzo, and R. Mihalcea, in their paper [19], used Random Forest, SVM(Support Vector Machine) with Radial Basis Function kernel and Neural Network classifiers among which the neural

Authorized licensed use limited to: DELHI TECHNICAL UNIV. Downloaded on April 26,2023 at 10:23:03 UTC from IEEE Xplore. Restrictions apply.

network achieved the highest accuracy of 84.1%, which consisted of two hidden layers of 100 and 500 nodes with the activation function set as softmax and cross-entropy loss. The model did outperform the average non-expert human performance, but the resulting accuracy is still a little less for a task as crucial as deception detection in court trials. M. Jaiswal, S. Tabibu, and R. Bajpai, in their paper [20], used OpenFace and OpenSmile toolkit, which extracted the audio modality from the video and then used an SVM classifier to get an accuracy of 78.95. The models use facial expressions only and don't consider the person's body language. Both of these models were used for the Real-life court trail Dataset.

V Gupta, M Agarwal, M Arora, T Chakraborty, R Singh and M Vatsa, in their paper [18], used Various models and modalities on the Bags of Lies Dataset. They employed a Random Forest classifier for the video, raw EEG and the gaze, and a KNN (K-Nearest Neighbors) classifier for audio modality, resulting in an accuracy of 66.17%. They evaluated various models for different modalities and, in the end, used the best model for each modality in union with each other. Despite using multiple modalities, the model's accuracy is still pretty low. However, these different models for each modality can be improved or used with other parameters to increase the use cases and accuracy. Ascensión Gallardo-Antolín and Juan Monter, in their paper [21], used an AP Fusion and Late fusion model. Late fusion results are averaged out after undergoing Masking, Attention LSTM and a Hidden layer, while in AP Fusion, results are combined after masking and attention, followed by hidden layers. Of these two, AP Fusion gave the maximum accuracy of 70.55%.

Kun Bu and Kandethody Ramachandran, in their paper [22], used random forest with Stochastic Gradient Boosting to evaluate a model for deception in the Miami University Deception Detection Database (MU3D), which resulted in an accuracy of approx—97%. In summary, existing research on these datasets has used different modalities and different methods to evaluate deception, resulting in different accuracy. Our study uses Video, Audio and text modality with LSTM and Convolution models.

TABLE III. Accuracies obtained in other papers on the datasets (i) Real-Life Court Trails Dataset, (ii) Bags of Lies (BoL), and (iii) Miami University Deception Detection Database (MU3D).

DATASET	METHOD	ACCURACY
Real-Life Court Trails Dataset	Late Fusion in NN	84.1%
Real-Life Court Trails Dataset	SVM with OpenFace and OpenSmile Toolkit	78.95%
BoL Dataset	RF (video, raw EEG and the gaze) + KNN(audio)	66.17%
BoL Dataset	AP fusion with Attention LSTM	70.55%
MU3D	RF(Random Forest) with Stochastic Gradient Boosting	97%

VII.CONCLUSION

This research discussed multidimensional deception detection experiments that used actual, high-stakes deception cases. We used a real-life scenarios dataset to conduct descriptive and analytical tests. The dataset illustrates deceit in a natural environment with little outside interference and numerous modalities, providing opportunities for intriguing research in detecting deception that will provide the basis for developing algorithms to address the issue in real-time. Our examination of false and true videos revealed insights that contribute to deception. We achieved an accuracy of 80% by extracting and integrating information from the spoken words from the audio. In a further comprehensive approach of using transcriptions from videos, we obtain an accuracy of 98.1%. We have accomplished an accuracy of 85% approximately for the Bag of Lies Dataset, 96% and 98.1% for the Real–Life Court Trial Dataset and the Miami University Deception Detection Dataset, respectively, in this analysis of our model.

In the future, these models can further be used to check which question, when asked, leads to high accuracy in detecting deception. A bot can then ask these questions to completely automate the interrogation process in court. The accuracy of the model can also be increased using large datasets for creating a state-of-the-art model which can be used in multiple scenarios.

VIII. REFERENCES

[1] C. F. Bond and B. M. DePaulo, "Accuracy of deception judgments," *Personality and Social Psychology Review*, vol. 10, no. 3. SAGE Publications Inc., pp. 214–234, 2006. doi: 10.1207/s15327957pspr1003_2.

[2] M. Shaffer, S. R. Gross, and R. Warden, "Exonerations in the United States, 1989-2012 Report by the National Registry of Exonerations National Registry of Exonerations," 2012.

[3] T. O. Meservy *et al.*, "IEEE INTELLIGENT SYSTEMS Deception Detection through Automatic, Unobtrusive Analysis of Nonverbal Behavior," 2005. [Online]. Available: www.computer.org/intelligent

[4] S. Lu, G. Tsechpenakis, D. N. Metaxas, M. L. Jensen, and J. Kruse, "Blob Analysis of the Head and Hands: A Method for Deception Detection," 2005.

[5] T. O. Meservy *et al.*, "IEEE INTELLIGENT SYSTEMS Deception Detection through Automatic, Unobtrusive Analysis of Nonverbal Behavior," 2005. [Online]. Available: www.computer.org/intelligent

[6] J. K. Burgoon *et al.*, "Detecting concealment of intent in transportation screening: A proof of concept," *IEEE Transactions on Intelligent Transportation Systems*, vol. 10, no. 1, pp. 103–112, 2009, doi: 10.1109/TITS.2008.2011700.

[7] V. Pérez-Rosas, R. Mihalcea, A. Narvaez, and M. Burzo, "A Multimodal Dataset for Deception Detection." [Online]. Available: http://www.thoughttechnology.com/physsuite.html

[8] J. W. Pennebaker and M. E. Francis, "Linguistic Inquiry and Word Count (LIWC)." [Online]. Available: www.erlbaum.com

[9] R. Mihalcea and C. Strapparava, "The Lie Detector: Explorations in the Automatic Recognition of Deceptive Language," 2009.

[10] M. Yancheva and F. Rudzicz, "Automatic detection of deception in child-produced speech using syntactic complexity features."

[11] J. Gu *et al.*, "Recent Advances in Convolutional Neural Networks," Dec. 2015, [Online]. Available: http://arxiv.org/abs/1512.07108

[12] S. Hochreiter and J. ¨ Urgen Schmidhuber, "Long Short-Term Memory."

[13] M. Schuster and K. K. Paliwal, "Bidirectional Recurrent Neural Networks," 1997.

[14] Z. Yu *et al.*, "USING BIDIRECTIONAL LSTM RECURRENT NEURAL NETWORKS TO LEARN HIGH-LEVEL ABSTRACTIONS OF SEQUENTIAL FEATURES FOR AUTOMATED SCORING OF NON-NATIVE SPONTANEOUS SPEECH."

Authorized licensed use limited to: DELHI TECHNICAL UNIV. Downloaded on April 26,2023 at 10:23:03 UTC from IEEE Xplore. Restrictions apply.

[15] K. He, X. Zhang, S. Ren, and J. Sun, “Deep Residual Learning for Image Recognition,” Dec. 2015, [Online]. Available: http://arxiv.org/abs/1512.03385

[16] Veronica Perez-Rosas, Mohamed Abouelenien, Rada Mihalcea, Mihai Burzo, Deception Detection using Real-life Trial Data, in Proceedings of the ACM International Conference on Multimodal Interaction (ICMI 2015), Seattle, November 2015.

[17] Lloyd, E. P., Deska, J. C., Hugenberg, K., McConnell, A. R., Humphrey, B., & Kunstman, J. W. "Deception Detection video database" (2017). Miami University

[18] V. Gupta, M. Agarwal, M. Arora, T. Chakraborty, R. Singh, M. Vatsa. "Bag-of-Lies: A Multimodal Dataset for Deception Detection", IEEE Conference on Computer Vision and Pattern Recognition Workshop on Challenges and Opportunities for Privacy and Security, 2019.

[19] Sen, Umut Mehmet; Perez-Rosas, Veronica; Yanikoglu, Berrin; Abouelenien, Mohamed; Burzo, Mihai; Mihalcea, Rada (2020). Multimodal Deception Detection using Real-Life Trial Data. IEEE Transactions on Affective Computing, (), 1–1. doi:10.1109/TAFFC.2020.3015684

[20] M. Jaiswal, S. Tabibu, and R. Bajpai, “The truth and nothing but the truth: Multimodal analysis for deception detection,” in Proceedings of the 2016 IEEE 16th International Conference on Data Mining Workshops (ICDMW), 2016.

[21] Gallardo-Antolín, Ascensión, and Juan M. Montero. 2021. "Detecting Deception from Gaze and Speech Using a Multimodal Attention LSTM-Based Framework" Applied Sciences 11, no. 14: 6393.

[22] Kun Bu, Kandethody Ramachandran. Deception Detection using Random Forest-based Ensemble Learning, 18 January 2023, PREPRINT (Version 1) available at Research Square doi:10.21203/rs.3.rs-2460665/v1

Authorized licensed use limited to: DELHI TECHNICAL UNIV. Downloaded on April 26,2023 at 10:23:03 UTC from IEEE Xplore. Restrictions apply.

Deep Learning-based Advancement in Fuzzy Logic Controller

Supriya Kaul
Department of Electrical Engineering
Delhi Technological University
Delhi, India
supshine027@gmail.com

Shekhar Yadav
Department of Electrical Engineering
Madan Mohan Malaviya University of Technology
Gorakhpur, Uttar Pradesh, India
syee@mmmut.ac.in

Nitesh Tiwari
Department of Electrical Engineering
Madan Mohan Malaviya University of Technology
Gorakhpur, Uttar Pradesh, India
niteshwr1994@gmail.com

Amit Singh
Department of ECE
G.L. Bajaj Institute of Technology & Management Greater Noida, India
amit.833@gmail.com

2023 International Conference on Artificial Intelligence and Smart Communication (AISC) | 979-8-3503-2230-9/23/$31.00 ©2023 IEEE | DOI: 10.1109/AISC56616.2023.10085358

Abstract— **Traditional algorithmic methods are not appropriate to solve today's issues. Nowadays, deep-learning-based fuzzy systems are becoming famous and effective among researchers in tackling difficult issues in many sectors. The study briefly overviews the latest applications in various sectors to acquire future occurrences with a fuzzy method advancement. To examine the fuzzy system concept and its domains established between 2000 and 2018 were analyzed. The majority of mathematics features are utilized, including engineering, robotics, etc. Fuzzy Logic (FL) has grown increasingly widespread. This report analyzes the idea and use of FL in numerous sectors along with the concept of deep learning. This research illustrates an application of an FL method in medicinal, operational research along with three stages. Results showed that FL is not limited to mathematics but is a broad concept adaptable to several branches.**

Keywords— ***Fuzzy Logic Application, Fuzzy Rules (FRs), Adaptive Neuro-fuzzy Inference System (ANFIS), Hybrid systems, Neural Networks (NN), Neuro-fuzzy system (NFS), Deep Learning (Dl), Deep Learning Neuro Based Fuzzy System (DNFS) Artificial Intelligent (AI).***

I. INTRODUCTION

Many types of research in recent years have shown the difficulties of conventional approaches in addressing today's issues. The techniques presently employed in agriculture and other fields cannot forecast future occurrences owing to vagueness & data volume or the issue's complexities. All cannot be represented accurately because correct information, absence of data, or unclear information is available. Traditional computer techniques are inefficient in such circumstances. A major contribution of the study to solving these issues has helped companies observe a gradual transition from traditional processes to complicated techniques [1]. The reason for this motivation is clear; the common features of issues in areas such as nonlinear behavior, high levels of uncertainty, lack of accurate information, etc. Several machine-learning models are being created to make feasible use of intelligent information systems in many areas [18]. Technology development, the effectiveness & acceptability of future techniques have given rise to modified methods in virtually every field. Traditional techniques are a developing type of intelligent computer consisting of FL [8] and Neural Networks (NN) [5]. FL offers a mathematical basis for tackling uncertainties by simulating human perception to comprehend language characteristics. At the same time, neural networks replicate employees in the community of learning, analyzing, and adapting. Integration of the two methods, known as neuro-fuzzy [5] systems, may achieve the benefits of each, leaving their drawbacks behind. In a combination model, neural network learning techniques are combined with FL reasoning. Each part plays its part; the neural network determines parameter values, while if-then rules are managed by FL [10]. FIS utilizes human understanding by collecting the necessary information in its rule base & then does fuzzy reasoning on input to find the value of the overall outcomes.

In creating neural networks, intelligent systems & FL complement each other. NNs build computational frameworks of low levels and, therefore, can interpret raw data, whereas FL sits at a higher level and utilizes language patterns. From another point of view, fuzzy systems lack learning capacity and cannot adapt to a new environment [12], whereas neural networks can learn and generalize. A common issue with neural networks is that they are black boxes with many hidden layers which are opaque to the user. The resulting NFS [29] may conduct parallel calculations and learn like neural networks in collaboration with human-like knowledge with the ability to explain the fuzzy system to make the system more visible [14]. Investigators from many fields tried to utilize a hybrid neural network with an FL method. The NFS includes input and output levels, plus hidden layers that provide member functions or fuzzy rules to handle uncertain situations [18]. Many uses for neuro-fuzzy hybridization cannot be included; therefore, we limit the subject to scientific domains such as agriculture, computer science, environmental, chemical science, and household appliances.

FL is very helpful for different research and engineering professionals, including several engineers, such as mechanics, electrical, civil, aerospace, chemical, agricultural, and computer science [19]. It comprises mathematicians, software developers, physicians, natural scientists, social scientists, business analysts, public policy analysts, and judges. Nowadays, in different technical and scientific works, the implementations of FL, which was previously an unclear mathematical curiosity, can be established [22]. FL has indeed been employed across several applications, including air conditioners, facial design, cleaning products, antiqued braking systems, aspiration cleaners, transmission systems, knowledge-based power optimization systems, soil test prediction [23], subway as well as unmanned helicopter

Authorized licensed use limited to: DELHI TECHNICAL UNIV. Downloaded on April 17,2023 at 06:09:17 UTC from IEEE Xplore. Restrictions apply.

control systems, weather forecast systems, medical diagnosing and treating FL was utilized successfully in a range of areas including such power engineering, control system engineering, image analysis, robotics, factory equipment, marketing and optimizing technology [29].

A Deep Neural Network consists of a sequence of multilayers containing neuron collection, which gives the neuron of the next layer the input activations of the preceding layer for fundamental calculation. The network neurons cooperatively execute a sophisticated nonlinear translation from input to output. This mapping is learned by employing a method known as error backpropagation [30] by adjusting the weights of each neuron [31]. The emerging and dominating paradigm for large-scale Big Data task-oriented learning are the DL (Deep Neural Networks) method [32]. This technique has succeeded in several tasks involving video recognition and image recognition, text analysis, audio processing, and financial, economic, and robotic predictions [33-34]. Although these methodologies are strong, they do not explain how their black-box nature gives feedback, which limits the applicability of deep learning techniques. The judgment made by the model cannot be verified without underlining how the results are reached [35]. This lack of DNN nonetheless allowed new avenues for scientists to study different effective techniques for overcoming the "black box" issue. So overall, the paper tries to give conceptual details about the neural study, deep neural study, and fuzzy concepts in deep learning.

II. Concept of Fuzzy Logic

Boolean logic takes exactly two true or false values (0 or l). In this, you can speak about low or high. It says nothing among them that the conception of communication is not taken. This is possible via the larger notion, which is the FL that accepts values [0, l]. Due to this idea, we may speak around low, high, medium, very low, and very high. This is an expanded Boolean logic version [17].

Fuzzy implies unknown or unclear adequate. FL is a declaration that is true or false or which has an approximate true value. The idea of partial truth should be intended. The membership function denotes the truth level. MF in a set X is a function among X and an interval of the real unit [0, l]. The number 0 is the false value, 1 is the true one, and a partial truth is a value between 0 and l [8]. One of FL's greatest benefits is its resemblance to human reasoning. The problem is decreased in these language variables.

III. Fuzzy Logic Control

In 3 stages, the FL controller progresses. Fuzzification is the first stage. It is transformed for fuzzy variables in this crisp parameter. In the 2nd phase, certain rules are established in the form of If-Then and FIS. The 3rd stage is defuzzification. This resultant fuzzy output is transferred to a crisp variable.

3.1 Benefits of FCL

- *Cheaper:* Building an FLC is cheaper than creating a model-based or performance controller.
- *Robust:* FLCs are more resilient than PID controllers since they support various operational conditions.
- *Customizable:* FLCs may be customized.
- *Emulate human deductive thinking:* FLC is essentially intended to mimic human deduction and the method individuals use to make inferences from what they understand.
- *Reliability:* FLC is more dependable than traditional system control.
- *Efficiency:* FL offers greater performance in the control system.

3.2 Drawbacks of FCL

- *Needs lots of information:* FLC requires information to be used.
- *Useful in case of moderate historical information:* FLC will be neither significantly less nor bigger than historical information for a program.
- *Needs high human expertise:* This is a disadvantage since the performance of the results relies on human experience and knowledge.
- *Needs regular maintenance of rules:* the regulations need to be maintained on time.

IV. Neuro-Fuzzy Integrated Approach

An appropriate combination of neural and FL with neuro-fuzzy (NF) computing advantages allows one to create smarter decision-making systems. This integrates the general benefits of Artificial Neural Networks (ANNs), such as enormous scalability, resilience, and learning in data-rich situations. It is via the application of FL that we may represent inaccurate and detailed information as well as transmit ambiguity. In addition to these general benefits, the neuro-fuzzy method offers appropriate particular benefits. An important contribution of NF and soft computing is the exposure of Jang's adaptive NFIS [11].

The fundamental concept of integrating FS with NN is to create an architecture that utilizes an FS to interpret the information & learning capacity of NN to optimize its variables. Therefore, the inconvenience of both methods – the Black Box behavior of NNs, and the challenge of obtaining the appropriate membership values for fuzzy systems may be eliminated. Combinations may be an interpretable model which can learn and utilize problem-specific previous knowledge. Neuro-fuzzy techniques are thus particularly suitable for situations where user interactions are required in model construction or interpretation. [19]. All combinations of neural network-based methods with FL may generally be termed neuro-fuzzy systems. In compliance with [10], the multiple types of these methods may be classified into the following categories:

- *Cooperative NFS:* The pre-processing stage is taken when NN procedures define specific subblocks of the FS in the cooperative systems. E.g., fuzzy set and/or Fuzzy Rules (FRs). Thus, the clustering of algorithms to infer fuzzy sets and their rules [3] or fuzzy associative memories is mentioned in it [8]. Once fuzzy blocks are designed, NN learning approaches are deleted, and the fuzzy system is run.
- *Concurrent NFS:* NN and FS are constantly working together in linear models. Generally, NNs pre-process inputs of FS (or post-process data).
- *Hybrid NFS:* In this classification, a NN is used to train iteratively certain variables of the Fuzzy System (FS) containing fuzzy rules, rules weights, and fuzzy set parameters. Most authors primarily use the more specific word neuro-fuzzy in hybrid NFS frequently.

Authorized licensed use limited to: DELHI TECHNICAL UNIV. Downloaded on April 17,2023 at 06:09:17 UTC from IEEE Xplore. Restrictions apply.

V. HYBRID NEURO-FUZZY SYSTEM

Nauck [10] explains that "A hybrid NFS is a fuzzy system which utilizes a gradient-based learning algorithm or the NNs (probabilistic learning strategies) concept to set its (FS and FR) parameters via processing patterns (input and output)". An NFS may be seen as a collection of fuzzy rules (FRs). This system can be built from the analysis of input-output data or initialized similarly using prior knowledge of that FRs are. The resulting system, via integration of fuzzy and neural systems, offers the benefits of learning through objectives, patterns, and a simple understanding of its functioning.

There are many alternative methods to create Hybrid NFS, so every investigator has distinct unique models as a current study problem. These models are equivalent [19], yet they exhibit fundamental distinctions. Several NFS types are signified by NNs implementing logical functions. Nevertheless, the description via a NN is more accessible since it enables the strategy of data flow within the system and error signals utilized for modifying parameter values [21]. The additional advantage is that various models can be compared & take place in different may be seen. There are many NFS, as discussed in the following sections.

5.1 Fuzzy Adaptive learning Control Network

The 5-layered structure of the Fuzzy Adaptive learning Control Network (FALCON) [8] is illustrated. For each output variable, there are two linguistic nodes. Firstly, training data (desired output) and actual FALCON output.

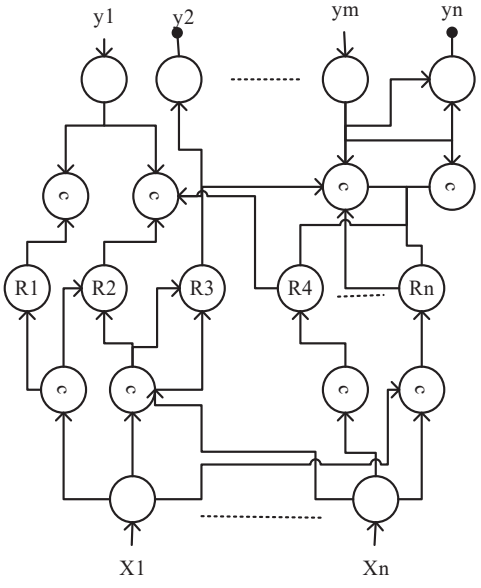


Fig. 1 Structural design of FALCON

The first hidden layer ensures that every input variable gets fuzzification. Every node may be a single node with basic MF or multilayer nodes that calculate complicated MF. The second hidden layer specifies the requirements of the rule, and the third hidden layer follows the rule. FALCON utilizes a method of hybrid learning consisting of unsupervised learning to detect primary member features/regulars & gradient downward learning to adapt the MF parameters to the required output optimum [29]. Fig. 1 shows about multi-hidden layer forming a web shape-like structure as shown.

5.2 Adaptive Neuro-Fuzzy Inference System

The Takagi Sugeno FIS is implemented by the Adaptive Neuro-Fuzzy Inference System (ANFIS) [1] and features a five-layered architecture. Fuzzification is the first hidden layer for input variables and T-Norm operations, which are used to compute the previous part of the rule in the hidden layer. The 3rd hidden layer standardizes the rule forces, then 4 hidden layers, in which the resulting parameters of the rule are established. The activation function calculates the total input as the sum of all input signals. Adaptive NFIS utilizes backpropagation learning to identify premise constraints (to learn about membership variables) and to calculate the corresponding parameters via a minimum mean square estimate [28]. There are two parts to one step during learning: The input patterns are propagated in the first portion, and the ideal consequent parameters are used with the iterative least average square method, while the premise elements are considered to be determined by the training set for the current cycle. In the second portion, the patterns are again transmitted, and backpropagation is employed in this era to change premise parameters while the corresponding parameters stay constant [26]. Then this process is iterated. To forecast the number of COVID-19 cases in the UK, the recent use of the Adaptive Neuro-Fuzzy Inference System (ANFIS) was applied. The model is trained based on gathered data by combining the artificial neural network with the fluid logic structure. The study examines different ANFIS factors to establish an effective prediction model for time series. The result shows that the predictive power of COVID-19 cases can be reinforced in Spain and Italy. The Adaptive Neuro-Fuzzy Infusion System (ANFIS) is suggested to be adopted by policymakers to predict contagion effects during the COVID-19 pandemic [12]. Fig 2 shows several different layers from input to the required output with adaptive layers.

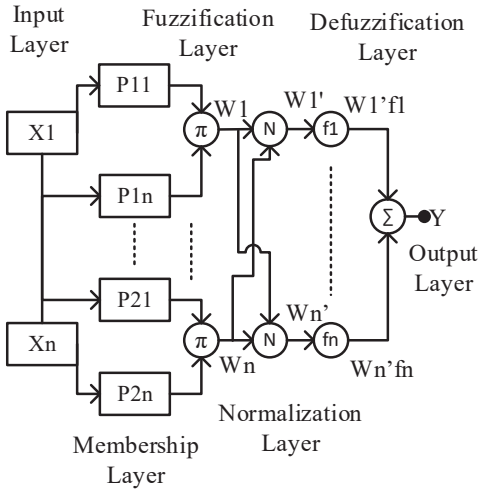


Fig. 2 Structural design of adaptive NFIS

5.3 Neuro-Fuzzy Control

Neuro-Fuzzy (NEFCON) control is intended to install FIS-type Mamdani. Links inside NEFCON are weighted using fuzzy sets and rules (are the fuzzy sets defining the background and consequence) using a similar historical weight that is depicted through ellipses drawn across the relationships. We guarantee the regulation's integrity. The input units play the role of a fuzzy interface; the lowering

Authorized licensed use limited to: DELHI TECHNICAL UNIV. Downloaded on April 17,2023 at 06:09:17 UTC from IEEE Xplore. Restrictions apply.

logic consists of the propagate functions, and the output is the de-fuzzing interface. The learning of the NEFCON model is dependent on a combination of strengthening and backpropagation [24-28]. The basic initial rules may be used with NEFCON when no previous system information is provided, or an explicitly specified rule basis is optimized. There are two versions of NEFCON: NEFPROX (estimation of functionality). Fig. 3 shows two consecutive layers with two inputs and one output.

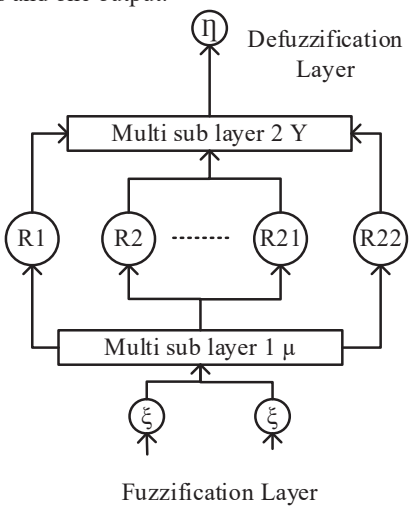


Fig.3 Structure of Neuro-Fuzzy Control

5.4 Fuzzy Net

The neurons of the 1st hidden layer of the fuzzification and Fuzzy Net (FN) carry membership of the input values. The conjunctions (fuzzy-AND) are computed in the 2nd hidden layer.

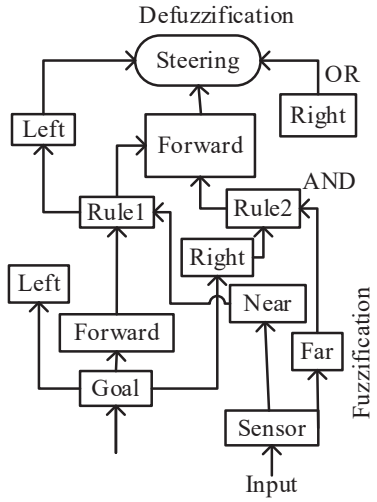


Fig. 4 Structure of Fuzzy Net

The membership functions of variables, especially for output, are maintained further in the third hidden layer. They have a fuzzy-OR function. The neuron output is then de-fuzzified [24]. The network is started by an FR base with associated MFs and utilizes the stochastic learning method, which randomly modifies the MF and structures' variables and interconnections. The cost function evaluated after the random change governs the learning method. When the change leads to better efficiency, the change is retained; otherwise, it will be undone.

5.5 Evolving Fuzzy Neural Network

For learning, Evolving Fuzzy Neural Network (EFuNN) generates all nodes. The input layer transmits data to the second layer, which determines the fuzzy component degrees in the pre-defined input values. The third level includes fused rule nodes that provide data input-output models as a hyper-sphere input combination with fuzzy input spaces. The two connection weight vectors regulated through hybrid learning technologies are used to define each rule node. The 4th layer determines the extent to which the input data matches the output members, as well as the fifth layer [27-30] analyzes the precise value of the output variables. Dynamic EFUNN (dmEFuNN) is a modified form of EFuNN. In this, not only is the rule node that is winning transmitted, but also the rules that are in combination for each new input vector are adaptively assigned, and the dynamical variables for the output function are calculated using their effective values. Whereas EFuNN implements fuzzy Mamdani-kind rules, Dynamic EFuNN calculates Takagi-Sugeno fuzzy rule based on a minimum square method.So, Fig.5 shows the structure, which consists of multiple layers with multi-weight and multi-membership function systems as shown.

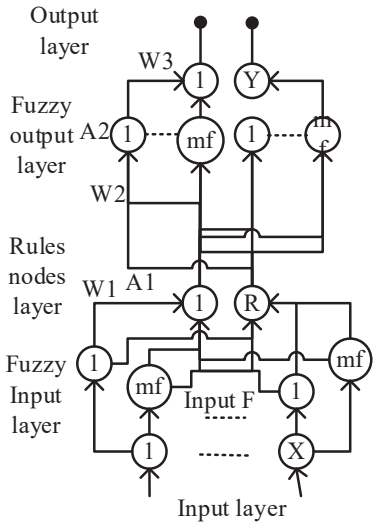


Fig. 5 Structure of Evolving Fuzzy Neural Network

5.6 Fuzzy Inference and Neural Network in Fuzzy Inference System

Fuzzy Inference and Neural Network in Fuzzy Inference System (FINEST) can modify the tuning of FL, combining operations and implications; two categories of tuning procedure are possible. The broad model is enhanced in four ways that are (1) Synergic and cancelation-like operators, (2) A parametric involvement function. (3) A fuzziness-decreasing combination function. (4) Using a broad modus ponens for backward chaining. FINEST uses a backpropagation method for the parameter adjustment [30]. The FINEST layered structure as well as the fuzzy inference computation method. FINEST offers a system for every parameter that occurs in the network nodes reflecting the calculation method of the fuzzy data where the function derivative variable function is provided.

Authorized licensed use limited to: DELHI TECHNICAL UNIV. Downloaded on April 17,2023 at 06:09:17 UTC from IEEE Xplore. Restrictions apply.

5.7 Self-Constructing Neural Fuzzy Inference System

A modified Takagi-Sugeno FIS is implemented by Self-Constructing Neural Fuzzy Inference System (SONFIN). When identifying the configuration of the prerequisite portion, the input space is flexibly divided according to an aligned clustering method.

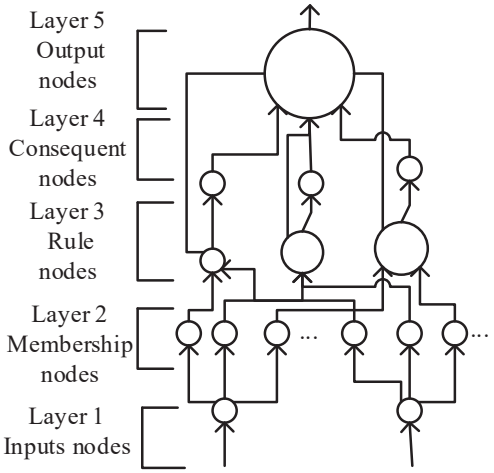


Fig. 6 Configuration of SONFIN

About the advanced authentication of the corresponding component, every rule is initially given just a singleton value chosen using a clustering technique [28]. Then certain important words (input variables) chosen through a projection-based correlation for every regulation are progressively included during the learning process to the appropriate part (making a linear equation of input variables). The variables are best adapted using the less recursive algorithms and least mean squares, and the average duration is established with a backpropagation technique. Fig.6 shows the systematic way of diagram cluster. It consists of five different layers from input to output formation.

VI. Deep Neural Network

The Deep Neural Network (DNN) comprises a single input, output, and many hidden layers. This permits the numbers, sizes, and structure of each layer to be changed by various levels of abstraction and permits the extraction of high-level functions from low-level functions to construct a hierarchical representation. Usually, the single layer contains many nodes, each node being bound through a preset group of layers' weights. Weight selection is a vital aspect and takes place during training. For each layer, values may be calculated by assigning inputs and sending them into the network for the final output from the previous layer nodes. In the previous layers, the linear combination of the value of the node is calculated to measure every hidden network node's value, which then uses nonlinear activation. When an activation feature is employed in the node, the value of the node shall be determined as the largest linear node is a combination of the preceding layer.

Much research involves working on how fuzzy system is introduced in with the concept of deep learning. This helps in overcoming the shortcomings of proper representations of logic. FL and deep learning, when combined, result in huge amounts of data that are further used to analyze the system and conditions with the help of knowledge it acquired from a learning basis [31]. In today's era, a drastic rise has been seen in the level of inculcation of the system called Artificial Intelligent system (AI) in the field of deep learning with type2 fuzzy system to solve complex problems and thereby provide solutions by deep analysis [32].

Deep learning is also being applied to the field where system complexity is high, the presence of less memory, and system stability is low. Thus, a deep learning system is self-employed in the model predictive control system in linear and nonlinear systems to estimate the future solution and the system output accurately. Thus, overall providing better, fast, and minimum numerical computational and control requirements. In the same way, the nonlinear system has two modes of training which are online and offline training, respectively, which uses FL implementation, which helps in better adaption as per the requirements of the system [33].

VII. Deep Neuro-Fuzzy Systems

Many researchers are working in the field of deep learning-based neuro-fuzzy systems. One of the researchers' promising proposals was to integrate the principle of the explainable rule-driven system termed fuzzy inference into Deep Neural Networks as a Deep Neuro-Fuzzy System (DNFS). This shows that using fuzzy theory by DL may enhance models in which data is heterogeneous, noisy, vague, or incomplete. The fuzzy device may be an intrinsic part of deep learning models by applying fuzzy parameters or FL to training parameters. This new approach by DNFS has proved that it can automatically remove Fuzzy rules without the participation of a research specialist who solves the problem with the black box system of DNN. In addition, the technique of DNFS demonstrates more precision than the abstraction level of DNN [36-37]. While the DNFS concepts are still extremely new, there have nevertheless been numerous realized possibilities from the DNN and fuzzy inference model.

These powerful designs are divided into three classes, as shown in Fig. 7: sequential parallel and cooperative DNFS. The data are given to the model flow sequence through the sequence, using one architecture for the characteristics of the Fuzzy system and a deep network (a) The information will be analyzed individually from fuzzy DNN systems in parallel architecture; (b) Which are eventually combined to provide the final result. The fuzzy systems generate narrow values using the cooperative model; (c) That is translated into a deep neuro network for greater abstraction and training levels and defuzzification results that convert fuzzy values to crisp output values again.

Nowadays, the concept of deep learning is used to enhance the overall efficiency of the supercapacitor and battery used in the hybrid vehicle system. The main motto of using deep learning with FL is to achieve better transfer of energy and better control optimization of the hybrid system [35]. FL with deep learning is the most upcoming recent technique in the field of managing power. When solving complex problems, this deep learning combined with FL works as a boost and provides proof to be an advantage in estimating a solution in this field [36]. Recently a type2 of FL system with a deep neural network has been implemented and employed to optimize the response of antiretroviral therapy in patients. For

Authorized licensed use limited to: DELHI TECHNICAL UNIV. Downloaded on April 17,2023 at 06:09:17 UTC from IEEE Xplore. Restrictions apply.

this study, the concept of multidimensional, deep learning with fuzzy adaption is incorporated by the researchers to analyze and study the database [37].

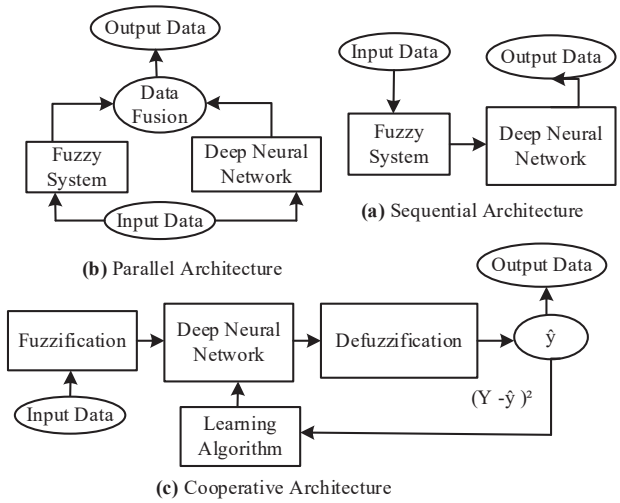


Fig. 7 Three architectural classifications of DNFS

VIII. CONCLUSION

FL is a two-value logic extension of Boolean logic. Fuzzification, inference systems, and defuzzification are used. Thus, these three main phases can easily be taught using muddled instructional techniques. Thus, this is acceptable to utilize multi-valued FL rather than two-valued logic. This study provides a broad introduction to FL as well as its uses in diverse areas. Very little is discussed, and many more are there, which implies that this document presents only an overview of FL and its uses. However, there are many uses discovered and performed in these decades. A lot are remaining that are to be found yet. Thus, the concept of Deep learning with the integration of FL would play a great role in the upcoming discoveries and technologies that would greatly help in the upcoming era. The report includes neuro FS, FL model, and its use in chemical science, the healthcare sector, agriculture, operations research, households, and environmental science. Thus, FL combined with Deep learning has become a helping hand in arithmetic and numerous other branches. Thus, the combination of FL with deep learning provides a robust collection of data classification, which helps in deep and proper analysis of any problems to find better solutions regarding the system analysis.

NOMENCLATURE

NFS-	Nero-Fuzzy System
FL-	Fuzzy Logic
NN-	Neural Network Networks
FLC-	Fuzzy Logic Control
PID-	Proportional Integral Derivative
NF-	NeuroFuzzy
ANNs-	Artificial Neural Network
FS-	Fuzzy System
FALCON-	Fuzzy Adaptive learning Control Network
ANFIS-	Adaptive Neuro-Fuzzy Inference System
NEFCON-	Neuro-Fuzzy Control
FN-	Fuzzy Net
EFuNN-	Evolving Fuzzy NN
dmEFuNN-	Dynamic EFuNN
SONFIN-	Self-Constructing Neural FIS
DL-	Deep Learning
AI-	Artificial Intelligent
DNN-	Deep Neural Network
DNFS-	Deep Neuro- fuzzy systems

REFERENCES

[1] K. A. Aali, M. Parsinejad, and B. Rahmani, "Estimation of Saturation Percentage of Soil Using Multiple Regression, ANN and ANFIS Techniques", *Journal of Computer and Information Science*, vol. 2, no. 3, pp. 127-136, 2009.

[2] A. S. Baharom, Z. Idris, S. S.M. lsa, M. Nazir, K. Ahamed, "Prediction of Flood Detection System: Fuzzy Logic Approach", *International Journal of Enhanced Research in Science Technology and Engineering*, vol. 3, no. l, pp. 335- 339, 2014.

[3] S. Bektas and E. Ozgan, "Adaptive Neuro-Fuzzy Inference System for Estimating Particle Diameter of Soils in Micro Structure for Varying Quantities of Sodium Hexametaphosphate", *Journal of Scientific Research and Essays*, vol. 5, no. 8, pp. 782-789, 2010.

[4] S. Harmanjit, S. Gurdev, and B. Nitin, "Election Results Prediction System Based on Fuzzy Logic", *International Journal of Computer Applications*, vol. 53, no. 9, pp. 30-37, 2012.

[5] G. Hayward, and V. Davidson, "Fuzzy Logic Application", *Journal of Analyst*, vol. 128, pp. 1304-1306, 2003.

[6] P. Kumar, D. Jaipaul, A. K. Tiwari, "Evaporation Estimation Using Artificial Neural Networks and Adaptive Neuro-Fuzzy Inference System Techniques", *Pakistan Journal of Meteorology*, vol. 8, no. 16, pp. 81-88, 2012.

[7] K. C. Lee and H.H Lee, "Network-based fire detection system via controller area network for smart home automation", *Transactions on consumer electronics*, vol. 50, no. 4, pp. 1093-1100, 2004.

[8] A.B. Mcbratney and I.O.A. Odeh, "Application of Fuzzy Sets in Soil Science: Fuzzy Logic, Fuzzy Measurements, and Fuzzy Decisions", *Journal of Geoderma*, vol.77, no. 2-4, pp. 85-113, 1997.

[9] D. Mustafa, U. Osman, and W. Tayyab, "Washing Machine using Fuzzy Logic, Automation", *Journal of Control and Intelligent Systems*, vol. 2, no 3, pp 27-32, 2014.

[10] R. Philomine, TN. Ganesan, and T. JM. Clarence, "A study of Applications of Fuzzy Logic in Various Domains of Agricultural Sciences", *International Journal of Computer Applications*, pp. 15-18, 2015.

[11] G. Poonam, "Application of Fuzzy Logic in Daily Life", *International Journal of Advanced Research in Computer Science*, vol 8, no. 5, pp. 1795-1800, 2017.

[12] A.K. Ly, "A COVID-19 forecasting system using adaptive neuro-fuzzy inference", *Journal of Finance Research Letters,* vol. 41, no. 1, pp. 101844-101844, 2020.

[13] K. Preeti, "Applications of Fuzzy Logic in Operation Management Research", *International Journal of Scientific and Research Publications*, vol. 4, no. 10, pp. 1-6, 2014.

[14] K. Priyanka, M. Neeraj, S. Parvinder, "Relevancy of Fuzzy Concept in Mathematics", *International Journal of Innovation, Management, and Technology*, vol. l, no. 3, pp. 312-315, 2010.

[15] M. Renu, "Application of fuzzy logic: A literature review", *International Journal of statistics and applied mathematics*, vol. 3, no. 1, pp. 357-359, 2017.

[16] S. Hamed, M. Wahby, M. Al-Sulaiman, S. Al-Saqer, and A. Aboukarima, "Application of Artificial Neural Networks to Predict Natural Soil Radionuclides Concentrations in Some Saudi Agricultural Soils", *Journal of Archives Des Sciences*, vol. 65, no. 1, pp. 196-206, 2012.

[17] A.S. Suliman and D.F. Post, "Relationship between Soil Spectral Properties and Sand, Silt, and Clay Content of the Soils on the University of Arizona Maricopa Agricultural Centre", *Proceedings of Hydrology and Water Resources in Arizona and the Southwest, Tucson, Arizona*, vol. 18, pp. 61-65, 1988.

Authorized licensed use limited to: DELHI TECHNICAL UNIV. Downloaded on April 17,2023 at 06:09:17 UTC from IEEE Xplore. Restrictions apply.

[18] H. Ying, "Fuzzy System Technology: A Brief Overview", *Journal of IEEE Circuits and System Society Newsletter*, vol. 11, no. 3, pp. 28-37, 2000.

[19] L A. Zadeh, "Is there a need for fuzzy logic*", Journal of Information Sciences*, vol. 178, no. 13, pp. 2751-2779, 2008.

[20] A. Abraham and N. Baikunth, "Hybrid Intelligent Systems: A Review of a Decade of Research", *IEEE Transactions on Systems, Man & Cybernetics (Part-C)*, pp. 1- 37, 2008.

[21] H. R. Berenji and P. Khedkar, "Learning and Tuning Fuzzy Logic Controllers through Reinforcements", *IEEE Transactions on Neural Networks*, vol. 3, no. 5, pp. 724-740, 1992.

[22] E. Czogala and J. Leski, "Fuzzy and neuro-fuzzy intelligent systems", *Springer Science & Business Media*, vol. 47, pp. 1-53, 2000.

[23] M. Figueiredo and F. Gomide; "Design of Fuzzy Systems Using Neuro-Fuzzy Networks", *IEEE Transactions on Neural Networks*, vol. 10, no. 4, pp. 815-827, 1999.

[24] R. Jang, "Neuro-Fuzzy Modelling: Architectures, Analysis, and Applications", *PhD Thesis, University of California, Berkley*, July 1992.

[25] F. C. Juang, and T. Chin Lin, "An Online Self Constructing Neural Fuzzy Inference Network and its applications", *IEEE Transactions on Fuzzy Systems*, vol. 6, no. 1, pp. 12-32, 1998.

[26] N. Kasabov, and Qun Song, "Dynamic Evolving Fuzzy Neural Networks with 'm-out-of-n' Activation Nodes for Online Adaptive Systems", *Technical Report TR99/04, Departement of Information Science, University of Otago*, pp. 1-29, 1999.

[27] M. Kubat, "Neural networks and fuzzy systems: A dynamical systems approach to machine intelligence", *Journal of the knowledge engineering review*, vol. 10, no. 2, pp. 219-220, 1992.

[28] T. C. Lin, and C. S. Lee, "Neural Network-Based Fuzzy Logic Control and Decision System", *IEEE Transactions on Computers*, vol. 40, no. 12, pp. 1320-1336, 1991.

[29] D. Nauck, "A Fuzzy Perceptron as a Generic Model for Neuro-Fuzzy Approaches". *Proc. Fuzzy-Systems, 2nd GI-Workshop,* pp. 1-9, 1994.

[30] S. Sulzberger, N. Tschichold, and S. Vestli, "FUN: Optimization of Fuzzy Rule-Based Systems Using Neural Networks", *Proceedings of IEEE Conference on Neural Networks, San Francisco,* pp. 312-316, 1993.

[31] Y. Deng, Z. Ren, Y. Kong, F. Bao and Q. Dai, "A Hierarchical Fused Fuzzy Deep Neural Network for Data Classification", *IEEE Transactions on fuzzy systems*, vol. 25, no. 4, pp. 1006-1012, 2016.

[32] R. Chimatapu, H. Hagras, M. Kern, and G. Owusu, "Hybrid Deep Learning Type-2 Fuzzy Logic Systems for Explainable AI", *IEEE International Conference on Fuzzy Systems (FUZZ-IEEE),* pp. 1-6, 2020.

[33] S. Adhau, S. Patil, D. Ingole, and D. Sonawane, "Embedded Implementation of Deep Learning-based Linear Model Predictive Control", *Sixth Indian Control Conference, IIT Hyderabad, (ICC)*, pp. 200-205, 2019.

[34] A. Sarabakha, and E. Kayacan, "Online Deep Fuzzy Learning for Control of Nonlinear Systems Using Expert Knowledge", *Ieee transactions on fuzzy systems*, vol. 28, no. 7, pp. 1492-1503, 2020.

[35] C. Alaoui, "Hybrid Vehicle Energy Management Using Deep Learning", *International Conference on Intelligent Systems and Advanced Computing Sciences (ISACS). IEEE*, pp. 1-5, 2019.

[36] J.C.P. Aguirre, A.I.B. Gutierrez, J.A.P. Medina, A.E. Calderon, and F.J.P. Pinal, "Fuzzy Logic Power Management Strategy for a Residential DC-Microgrid", *Journal of IEEE Access*, vol. 4, no. 8, pp. 116733-116743, 2020.

[37] M.E. Ekpenyong, P.I. Etebong, and T.C. Jackson, "Fuzzy-multidimensional deep learning for efficient prediction of patient response to antiretroviral therapy", *Journal of Heliyon*, vol. 5, no. 7, 2019.

Authorized licensed use limited to: DELHI TECHNICAL UNIV. Downloaded on April 17,2023 at 06:09:17 UTC from IEEE Xplore. Restrictions apply.

Int J Syst Assur Eng Manag
https://doi.org/10.1007/s13198-023-01909-0

ORIGINAL ARTICLE

Design and analysis of questionnaire on coach skill set for effective sports management

Subodh Mor[1] · **Shikha N. Khera**[1] · **G. C. Maheshwari**[1]

Received: 8 March 2023 / Revised: 28 March 2023 / Accepted: 5 April 2023
© The Author(s) under exclusive licence to The Society for Reliability Engineering, Quality and Operations Management (SREQOM), India and The Division of Operation and Maintenance, Lulea University of Technology, Sweden 2023

Abstract The opinions and perceptions of coaches on matters that are related to skill set, team preparation, training of the athletes and general administration are essential. The analysis of the perception of coaches will help in improving the overall player preparation process. In this study, we design and validate the questionnaire on the skill set of the coach. The focus of the questionnaire is on the importance of physical education, agility, flexibility, endurance and strengthening in player preparation and their relation with effective sports management. The data is collected from 82 coaches in badminton sports across various states of India. The responses to the questionnaire are validated using reliability analysis. The results depict emphasis on the agility, flexibility, endurance and strength of a player in effective sports management. Based on the obtained results guidelines for enhancing player performance are provided to the sports management authorities.

Keywords Sports management · Questionnaire · Coach · Agility · Flexibility · Endurance · Strength · Education · Badminton

1 Introduction

India is growing in various sports in recent times. This is due to the rise in the number of sports confederations from a broad extent of sports like Badminton, Cricket, Hockey, Kabbadi, Boxing, Tennis, etc. Hence, many job opportunities exist in the sports sector in India. In addition, India has been designated a vital contestant in the global sports marketplace and is expected to seize more global accomplishments. Given this fact, the effective management of sports is essential.

Badminton is a sport that requires a high level of performance and the physical characteristics of the players. In this type of sport, especially speed, endurance, strength, coordination, reaction, detection, game skills and technical success are considered prerequisites. In the Olympic games, India has won 1 silver and 2 bronze medals in Badminton to date. India has won 3 gold, 1 silver, and 1 bronze medal in Badminton at the commonwealth games. The enhancement and management of fitness attributes such as agility, flexibility, endurance and strengthening increase performance in all varieties of sports (Bashir et al. 2019). Agility training improves quickness in transiting from one movement to another, flexibility training improves range of motion, endurance training enhances the ability of muscles to perform muscle contractions for a longer period and strengthening training improvises the muscular strength. The advantage of improving these attributes include improvement in balance, movement, posture, speed, anaerobic capacity, strength and a decrease in the risk of injury (Ratamess 2011; Pamungkas et al. 2019). In order to prepare effective players and increase the medal tally, it is important to effectively manage the coach education programs (Cushion et al. 2003), the experience of coaches in international and national tournaments and having specialists to efficiently supervise the training of players with a specific focus on agility, flexibility, endurance and strengthening of players. Nutrition has been recognised as a key component for the optimal sports performance of players (Beck et al. 2015). Optimised dietary strategies including proper intake of fluids, micronutrients,

✉ Subodh Mor
subodhmor@gmail.com

[1] Delhi School of Management, Delhi Technological University, Shahbad Daulatpur, Bawana Road, Delhi 110042, India

Published online: 20 April 2023

macronutrients and their proper balance, throughout the day, is significant for the performance enhancement of a player (Wright et al. 1991; Kathryn et al. 2015). Thus, it is essential to have a nutritionist who can plan and manage the nutrition plans of the players.

Every athlete has a different skillset as per athlete's body type, flexibility, agility, endurance and strength. A coach understands this difference and tries to enhance the skillset of each player with the help of supporting staff. The role of a coach in building a player is extremely important. In this work opinions and perceptions of Badminton coaches on matters that are related to education, skill set, team preparation, training of the athletes, nutrition and general administration are gathered through a questionnaire. The analysis of the relationship between fitness attributes and sports management is important so that efforts can be applied on enhancing these attributes. The results of the data collected from the questionnaire will guide the sports authorities in India to effectively design training and educational programs for coaches and develop a framework for sports management. It will also help to allocate various player preparation responsibilities to the desired professional. Further, this study will help the authorities to focus on appropriate training parameters for player preparation.

The study analysis the coach's perspective on the importance of the education of coaches and its effect on sports management. The study examines the importance of four important player attributes namely agility, flexibility endurance and strength from the coach's perspective. Further, the amount of workload of the coaches for building players is also examined. Thus, the following Research Questions (RQ) are examined in this work:

- RQ1: What is the coach's perspective on the education and experience of coaches?
- RQ1.1 What is the coach's perspective on the educational training programs for coaches? In this question, we summarise the responses to the questions corresponding to the education construct using a bar chart.
- RQ1.2: What is the relationship between education and effective sports management from the coach's perspective? To answer this research question, the individual effect of coach education and experience on effective sports management is found using univariate linear regression.
- RQ2: What is the effect of training attributes such as agility, flexibility endurance, strength on effective sports management? In this research question, the individual effect of four constructs namely agility, flexibility endurance, strength on effective sports management using linear regression.
- RQ3: What is the importance of agility, flexibility, endurance, strength for appropriate player preparation from the coach's perspective? The importance of agility, flexibility endurance and strength are analysed using the responses to these questions from coaches using a pie chart.
- RQ4: Is specialist supervision required for agility, flexibility, endurance and strength training for player preparation from the coach's perspective and who is responsible for the preparation of nutrition plans for the players? The answer to this question is presented using a table and graph reflecting the responses from the questionnaire.
- RQ5: Whether the coach is overloaded with too much time spent with athletes? This research question is answered using the coach's responses from the questionnaire.
- RQ6: What are the training requirements for player preparations from the coach's perspective?

The answer to this research question is summarised using the suggestions from the coaches given in the questionnaire in the form of tables.

Few studies examine the relationship between coaches and athletes with the help of a questionnaire (Jowett and Ntoumanis 2004; Trudel et al. 2010; Lisinskiene et al. 2019; Quinaud et al. 2022). In order to answer the research questions, a well designed questionnaire is used to obtain responses from coaches. The responses are obtained from 82 coaches across India. There is no study to the best of the authors' knowledge that designs and extensively assesses the questionnaire reflecting the coach's perspective on the education and training attributes such as agility, flexibility endurance and strength.

The rest of the study is structured as follows: Sect. 2 presents research methods including questionnaire design and validation and section presents the research hypothesis and techniques used. Section 4 presents the results of the study and the conclusion of the work are presented in Sect. 5.

2 Research methods

2.1 Questionnaire development

The questionnaire consists of majorly two sections. The first section (Section A) collects general information such as the age, gender, qualification, and experience of the coaches. The second section (Section B) includes questions on education, experience, flexibility, agility, endurance, strengthening and sports management. A total of 27 questions were created belonging to these 7 constructs. Table 1 presents the questions included in the questionnaire. A Likert scale of five-point (1-Strongly disagree, 2-disagree, 3-neutral, 4-agree, 5-strongly agree) was used to measure the responses to these questions.

Table 1 Coach questionnaire

Education	E1	Is formal education in sports coaching required to develop a player?
	E2	In your opinion whether diploma/certificate in sports coaching from Apex organization highly contributes to effective sports management?
	E3	Whether there should be a coach education training program?
Experience	EX1	Participation in National sports tournament helps to gain high knowledge for player preparation?
	EX2	Whether participation in international sports tournament helps to gain high knowledge for player preparation as a coach?
	EX3	In your opinion playing experience of a coach is an effective factor for player preparation?
Flexibility	F1	Flexibility important for appropriate player preparation
	F2	Active stretching led to high flexibility
	F3	Passive stretching contributes to high flexibility
	F4	Specialist supervision for stretching is highly recommended
Agility	A1	Agility is important for appropriate player preparation
	A2	T Test for agility play an important role in developing Player
	A3	The frequency of sessions per week required for agility development in player high
	A4	Specialist supervision for agility is highly recommended
Endurance	E1	Endurance is important for effective player preparation
	E2	Individual endurance enhancing sessions contribute highly to player preparation
	E3	Group endurance enhancing sessions contribute highly to player preparation
	E4	The frequency of sessions per week required for endurance development in player should be high
	E5	Specialist supervision for endurance is highly recommended
Strengthening	S1	Strength and conditioning important for player preparation
	S2	Individual sessions for strength building contribute high towards player preparation
	S3	Group sessions for strength building contribute high towards player preparation
	S4	Focus on game specific strength highly recommended
	S5	Focus on general strength is highly recommended
	S6	Specialist supervision for strengthening is highly recommended
Sports Management	SM1	Appropriate skill set of coaches lead to effective sports management
	SM2	Sports management organizations have well defined roles and responsibilities for player preparation

2.2 Study participants

The participants in this study were Badminton coaches across India. The data collection was carried out from October 2022 to December 2022 by sharing Google Form with the participants from various sports academies through email. The sports academies having Badminton as a sport was selected for sharing the questionnaire. The data has been received from 82 Badminton coaches and their characteristics have been summarized in Table 2. All the responses were complete and are retained in the analysis. As can be seen, 89% of participants were between the age group of 20 to 30 years with 90% of coaches having 0 to 10 years of experience. The number of players handled by 58% of coaches was more than 11.

Table 2 Characteristics of participants in coach questionnaire

Characteristic	Value	Number#
Age (years)	20–30	73
	31–40	9
Gender	Male	79
	Female	3
Coaching experience (years)	0–10	74
	11–20	8
Number of players handling experience in current position	0–10	34
	11–20	12
	21 and above	36
Educational level	Diploma	03
	Undergraduate	75
	Postgraduate	04

2.3 Questionnaire validation

2.3.1 Content validity

A careful analysis was carried out by a team of experts to check the content validity of the questionnaire. Two expert coaches and two professors were given the initial questionnaire for checking the relevancy and representation of the constructs of the questions. All the questions marked as essential and relevant by the experts were retained on the questionnaire.

2.3.2 Common method bias

Correlation analysis was used to check the common method bias. Previous studies suggested that a correlation of intra-constructs is to be performed and a correlation higher than 0.90 depicts the presence of common method bias. In this study, the highest correlation amongst the constructs was 0.45. Hence, the common method bias is not present in this work.

2.3.3 Reliability analysis

The Cronbach alpha test was used to examine the reliability of the questionnaire which in this case was 0.789, reflecting the high reliability of the questionnaire (Gliem and Gliem 2003).

2.3.4 Multicollinearity analysis

Variation Inflation Factor (VIF) was used to measure the degree of multicollinearity amongst the constructs. The values of VIF greater than 5 depict the presence of multicollinearity. The VIF value was below 5 which indicates that multicollinearity was not present in the constructs (Hair et al. 2014).

3 Research hypothesis and techniques

3.1 Research Hypothesis

The following are the research hypothesis:

- Ha: Coach education is positively related to effective sports management
- Hb: Coach experience is positively related to effective sports management
- Hc: Player agility is positively related to effective sports management
- Hd: Player flexibility is positively related to effective sports management
- He: Player endurance is positively related to effective sports management
- Hf: Player strengthening is positively related to effective sports management

3.2 Linear regression

It is one of the most widely used mathematical approaches which is used to perform predictive analysis (Maulud and Abdulazeez 2020). It is a statistical approach used for modelling the relationship between a dependent variable and one or more independent variables by fitting a linear equation to observed data points (James et al. 2013). The goal is to find the line of best fit that minimizes the difference between predicted values and observed values.

Linear regression can be of two types: simple linear regression and multivariate linear regression. The simple or univariate linear regression approach generates the output based on a single independent variable and the multivariate linear regression approach generates the output based on multiple independent variables (Natarajan et al. 2023). In this work, we use univariate linear regression to find the individual effect of each attribute on effective sports management. The significance level is 0.05. The statistics reported for each attribute are coefficient (B), standard error (SE), statistical significance (Sig.) and R^2.

4 Analysis results

In this section answers to the research questions formed in Sect. 1 are provided.

4.1 RQ1: What is the coach's perspective on education and experience of coaches?

RQ1.1 What is the coach's perspective on the educational training programs for coaches?

It can be seen from the bar chart (Fig. 1) that 51% of respondents were neutral in response to having a formal education in sports and 54.8% of respondents were neutral in response to possessing a diploma/certificate from an apex organisation. However, 73% of respondents either strongly agreed or agreed that there should be a coach education training program. About 47% of coaches emphasized having a formal education, about 43% of coaches advocated certificate programs from apex organisations and more than 70% of coaches agreed that coach education programs should be conducted. This shows that the coaches in India need to be trained with well-designed educational and training programs so that effective coaches who can contribute to the player's performance and communicate more effectively can be produced.

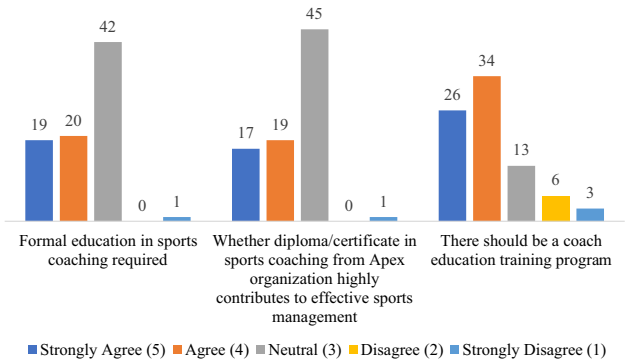


Fig. 1 Perspective of coaches on coach education and training programs

Table 3 Univariate analysis using linear regression to analyse relationship of coach education and experience with effective sports management

Construct	B	SE	Sig
Education	0.309	0.090	0.001
Experience	0.467	0.133	0.001

RQ1.2 What is the relationship between education and effective sports management from the coach's perspective?

Table 3 presents the results of univariate linear regression analysis to find the relationship between coach education and experience with effective sports management. The hypothesis Ha and Hb are accepted stating that coach education and experience are positively related to effective sports management.

Table 4 Univariate analysis using linear regression to analyse relationship between training attributes and effective sports management

Construct	B	SE	Sig
Flexibility	0.357	0.157	0.026
Agility	0.601	0.138	0.000
Endurance	0.671	0.158	0.000
Strength	0.636	0.143	0.000

4.2 RQ2: What is the importance of agility, flexibility endurance, strength for appropriate player preparation from the coach's perspective?

Figure 2 depicts the responses of the coaches on the importance of agility, flexibility endurance and strength. The results collected from responses obtained show that 97%, 98%, 94% and 98% of coaches either strongly agree or agree that agility, flexibility, endurance and strength are important for player preparation, respectively. Thus, the focus of training players should be on these attributes so that player performance can be enhanced.

4.3 RQ3: What is the effect of training attributes such as agility, flexibility endurance, strength on effective sports management?

The individual effect of each training attribute is found on effective sports management. The results of univariate linear regression are shown in Table 4. The results show that flexibility, agility, endurance and strength

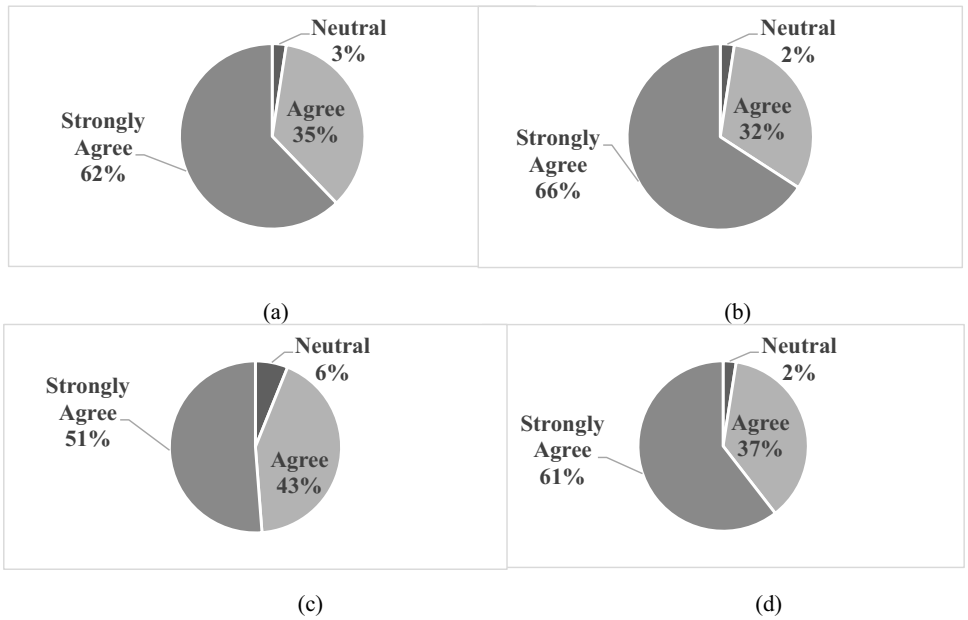


Fig. 2 Coach's perspective on importance of **a** agility, **b** flexibility, **c** endurance, **d** strengthening for player preparation

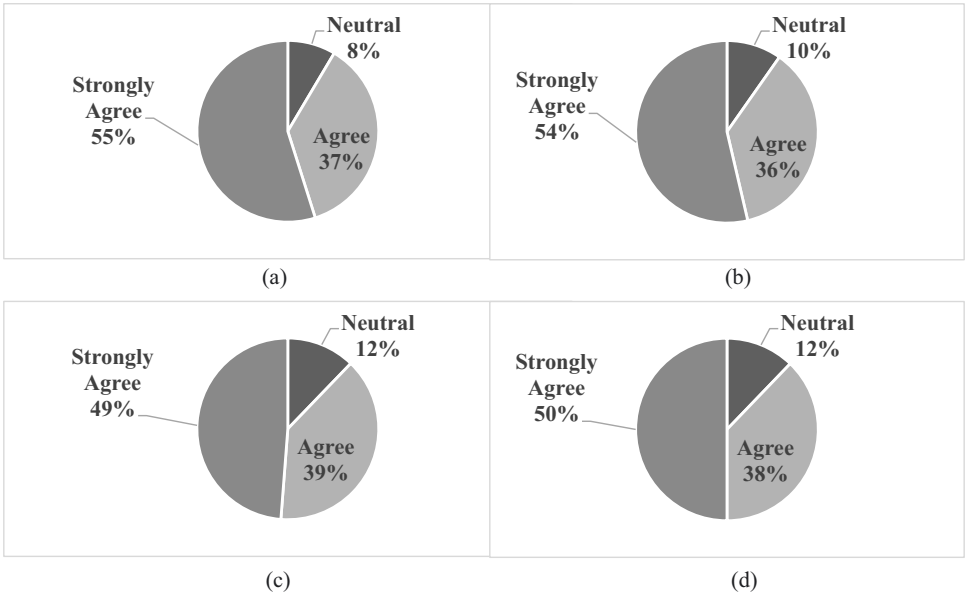


Fig. 3 Coach's perspective on requirement of specialist 981 supervision on **a** agility, **b** flexibility, **c** endurance, **d** strengthening training for player preparation

are significantly related to effective sports management with a 0.05 significance level. The hypothesis Hc-Hf (Sect. 3.1) stating that player agility, flexibility, endurance and strengthening are positively related to effective sports management are accepted. The results are in support of the opinion shared by coaches. We also applied multivariate linear regression by using the forward method and the R^2 reported was 0.577 which signifies the effective contribution of training attributes for effective sports management.

4.4 RQ4: is specialist supervision required for agility, flexibility, endurance and strength training for player preparation from the coach's perspective and who is responsible for the preparation of nutrition plans for the players?

Figure 3 depicts the coach's perception of the requirement of specialised supervision for handling agility, flexibility, endurance and strength training for player preparation. The results obtained from the responses show that 92%, 90%, 88%, and 88% of coaches either strongly agree or agree that specialist supervision is strongly recommended for enhancing agility, flexibility, endurance and strengthening of the players, respectively. Specialised training programs and the engagement of specialists for enhancing these training attributes can lead to improvement in the performance of Badminton players.

Figure 4 shows that 74% of coaches themselves handled the nutrition plans of players, 13% of coaches and nutritionists together handled the nutrition plans of players and

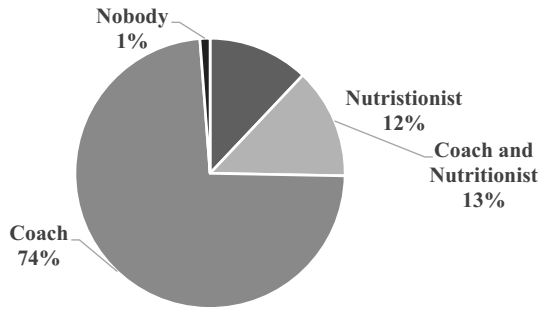


Fig. 4 Responsibility of handling of nutrition plans of player

12% of coaches revealed that specialised nutritionists were responsible for handling the nutrition plans of players. The results show that a very less, only 12%, percentage of sports organizations and academies have separate nutritionists to handle the nutrition plan of the players.

4.5 RQ5: whether the coach is overloaded or have too much time spent with athletes?

The results of the responses to the question are shown in Fig. 5. It can be seen that 40% of respondents strongly agree, 27% of the respondents agree, 25% of the respondents were neutral, 7% of the respondents disagree and 1% of the respondents strongly disagree that they feel overloaded or have too much time spent with the athletes. This shows that the majority of the training activities are being handled by the coaches and measures may be taken to reduce the overloading of work by the sports management authorities in India.

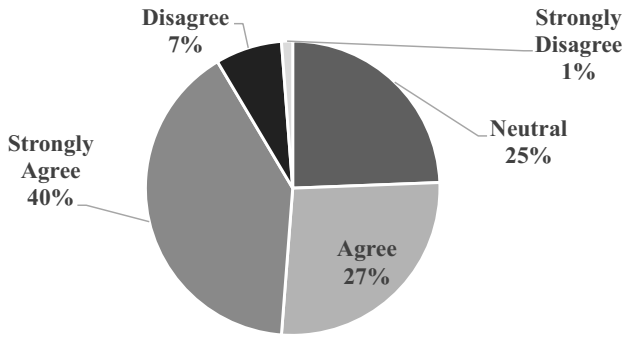


Fig. 5 Coach's perspective on being overloaded with time spent on athletes

Table 5 Summary of training requirements and suggestions for athletes by coaches

Specific training requirements and suggestions	Frequency of suggestion
Specific training sessions for correction of mistakes	02
Agility training	04
Endurance training	04
Shadow practice sessions	05
Strengthening	04
Fun games	01
Counselling sessions and pressure handling techniques	05
Coach availability during sessions	01
Tournament exposure and experience	03
Monthly coach evaluation	01
Swimming, Gym and Yoga	03
Fitness training	17
Cooldown sessions	03
Footwork training	05
Parent education	01
Injury prevention	01

4.6 RQ6: What are training requirements for players preparations from the coach's perspective?

The training requirements for the preparation of the players and other suggestions given by the coaches are summarized in Table 5. The table depicts the training requirement/ suggestion along with the frequency of occurrence of the suggestion. The most frequently occurring suggestion by the coaches is the fitness training of players. Agility, endurance, strength and footwork training is suggested by the coaches. The coaches also emphasize on counselling and mental training sessions for the players. Tournament exposure and experience are also suggested by a few coaches. The suggestions given by the coaches can help the sport management authorities and academies to plan and manage the sessions of the players so that efficient sports players can be developed in India.

4.7 Discussion of results

The results of the questionnaire reveal that coach education training programs and the experience of a coach's participation in national and international tournaments will enhance the knowledge of a coach leading to effective player preparation. The analysis of the importance of agility, flexibility endurance, and strength reveals that all four training parameters namely agility, flexibility, endurance and strength are extremely important for player preparation from the coach's perspective. The results of the responses to the questionnaire show that more than 70% of coaches agree that specialist supervision is required for the agility, flexibility, endurance and strength training of a player and a further 67% of coaches are having the opinion that they are overloaded with time being spent on preparation of players. The overloading of coaches may lead to stress, work-life imbalance and less job satisfaction that may negatively affect or hinder the performance of players (Dimitrios et al. 2013).

Also, 74% of coaches revealed that the coach himself was responsible for preparing the nutrition plans for the players. Keeping in view the above findings, the following guidelines are suggested for the sport management authorities and sports academies may take into account the enhancing and improvising the process for player preparation and providing support for increasing the effectiveness of coaches in Badminton sports:

1. Designing effective small-scale and large-scale coach-training programs focusing on flexibility, agility, endurance and strength will be highly beneficial for sports management in India.

The education of coaches must be reviewed and a well-defined program should be developed in India so that effective coaches who can contribute to the player's performance and communicate more effectively can be produced. Studies have shown that coach training and educational programs have increased the knowledge of coaches and a better understanding of players (Falcão et al. 2012; Trudel et al. 2010; Falcão et al. 2020).

2. Planning of involvement of specialists as per the individual need of a player is essential.

The sports management authorities must consider appointing specialists for handling the agility, flexibility, endurance and strength training sessions of the players.

3. There must be separate nutritionists to prepare and manage the nutrition plans of the players.

The results of this study can be used by coaches for improving the training sessions of the players and the suggestions given by the coaches in Sect. 4.6 be used in improving sports management. The sports authorities and academies can use these results to further improvise the facilities, training programs and assignment of responsibilities to personnel.

5 Conclusion and future work

This study analyses a questionnaire on the coach's skill set to enhance sports management activities for effective player preparation. In this work, the results of a survey of 82 Badminton coaches are reported with the aim to analyse the importance of coach education programs, coach experience and fitness attributes (agility, flexibility, endurance and strength) on player preparation. The results of the questionaries are summarized as follows:

1. There were about 47% of coaches emphasized having a formal education, about 43% of coaches advocated certificate programs from apex organisations, and more than 70% of coaches agreed that a coach education program should be conducted. Thus, coaches preferred informal education programs over formal education sports.
2. More than 90% of coaches either strongly agreed or agreed on the importance of agility, flexibility, endurance and strength for player preparation.
3. The education and fitness attributes were found to be related to effective sports management.
4. About 90% of coaches either strongly agreed or agreed on the requirement of specialist supervision for agility, flexibility, endurance and strength for player preparation. It was revealed by the responses to the questionnaire that only 12% of qualified nutritionists are being used for preparing nutrition plans for players.
5. The coaches emphasized the training of players specifically in fitness, footwork agility, endurance, stress and mental abilities.

It is recommended that specialised coach training programs should be conducted and specialists trained in various areas such as agility, flexibility, endurance, strength, nutrition management should be appointed for enhanced player performance. This will further enhance the continuous efforts made by sports management organizations in India.

In the future, we plan to survey players and parents to gather insights on matters that are related to education and training. The valuable feedback obtained will assist in developing a framework and model for player preparation and management of future international and national events.

Funding This research received no specific grant from any funding agency.

Declarations

Conflicts of interest None.

Research involving human participants and/or animals None.

Informed consent Not applicable.

References

Bashir SF, Nuhmani S, Dhall R, Muaidi QI (2019) Effect of core training on dynamic balance and agility among indian junior tennis players. J Back Musculoskelet Rehabil 32(2):245–252

Beck KL, Thomson JS, Swift RJ, Von Hurst PR (2015) Role of nutrition in performance enhancement and postexercise recovery. Open Access J Sports Med 6:259–267

Cushion CJ, Armour KM, Jones RL (2003) Coach education and continuing professional development: experience and learning to coach. Quest 55(3):215–230

Dimitrios B, Athanasios K, Eleni Z, Maria K, Labros S, Ioanna B (2013) Job satisfaction and job burnout of coaches – a review of the international literature. Int J Hum Resour Manag Res 3(3):27–38

Falcão WR, Bloom GA, Gilbert WD (2012) Coaches' perceptions of a coach training program designed to promote youth developmental outcomes. J Appl Sport Psychol 24(4):429–444

Falcão WR, Bloom GA, Sabiston CM (2020) The impact of humanistic coach training on youth athletes' development through sport. Int J Sports Sci Coach 15(5–6):610–620

Gliem JA, Gliem RR (2003) Calculating, interpreting, and reporting cronbach's alpha reliability coefficient for likert-type scales. In: 2003 midwest research to practice conference in adult, continuing, and community education, columbus, 82–88

Hair JF Jr, Sarstedt M, Hopkins L, Kuppelwieser VG (2014) Partial least squares structural equation modeling (PLS-SEM): an emerging tool in business research. Eur Bus Rev 26(2):106–121

James G, Witten D, Hastie T, Tibshirani R (2013) An introduction to statistical learning. Springer, New York

Jowett S, Ntoumanis N (2004) The coach-athlete relationship questionnaire (CART-Q): development and initial validation. Scand J Med Sci Sports 14(4):245–257

Lisinskiene A, May E, Lochbaum M (2019) The initial questionnaire development in measuring of coach-athlete–parent interpersonal relationships: results of two qualitative investigations. Int J Environ Res Public Health 16(13):2283

Maulud D, Abdulazeez AM (2020) A review on linear regression comprehensive in machine learning. J Appl Sci Technol Trends 1(4):140–147

Natarajan A, Vijayababu P, Arsha M, RaoPappu S, Rajasekaran V (2023) Early disease diagnosis using multivariate linear regression. J Pharmaceut Negat Results, 1383–1390

Pamungkas G, Prasetyo Y, Komari A (2022) The relationship of endurance and agility with badminton playing skills of badminton

extracurricular students at Sma N 1 Seyegan in the academic year 2019/2020. In: Conference on interdisciplinary approach in sports in conjunction with the 4th yogyakarta international seminar on health, physical, education and sport science. Advances in Health Sciences Research, 174–180

Quinaud RT, Backes AF, Nascimento Junior JRAD, Carvalho HM, Milistetd M (2022) Development and validation of the coach knowledge questionnaire: measuring coaches' professional, interpersonal and intrapersonal knowledge. Int J Sport Exerc Psychol 20(1):302–318

Ratamess NA (2011) Strength and conditioning for grappling sports. Strength Condit J 33(6):18–24

Trudel P, Gilbert W, WERThNER P (2010) Coach education effectiveness. Sport coaching: professionalisation and practice, 135–52

Wright DA, Sherman WM, Dernbach AR (1991) Carbohydrate feedings before, during, or in combination improve cycling endurance performance. J Appl Physiol 71(3):1082–1088

Publisher's Note Springer Nature remains neutral with regard to jurisdictional claims in published maps and institutional affiliations.

Springer Nature or its licensor (e.g. a society or other partner) holds exclusive rights to this article under a publishing agreement with the author(s) or other rightsholder(s); author self-archiving of the accepted manuscript version of this article is solely governed by the terms of such publishing agreement and applicable law.

Design and Dynamic Response of FOGI-FLL Based Controller in Grid Tied Solar PV System

Sukhbir Singh
Department of Electrical Engineering
Delhi Technological University
New Delhi, India
sss.singh149@gmail.com

J N Rai
Department of Electrical Engineering
Delhi Technological University
New Delhi, India
jnraiphd1968@gmail.com

2023 International Conference on Power, Instrumentation, Energy and Control (PIECON) | 979-8-3503-9976-9/23/$31.00 ©2023 IEEE | DOI: 10.1109/PIECON56912.2023.10085766

Abstract: **A grid-interfaced solar photovoltaic (SPV) topology has recently gained popularity as it has a vast potential in minimizing the cost for the establishment and can help in cost cutting due to losses in the system. An innovative system of strategy associated with grid-connected SPV framework is being introduced in this paper. This paper shows a mix of algorithm of maximum power point tracking (MPPT) and a four ordered generalized integrator frequency locked loop (FOGI-FLL), which shows a better performance in terms of transients of current and voltage outputs and also harness best possible yield of power from SPV system. Typically synchronization and generation of in-phase and quadrature templates are performed utilizing Frequency-locked loop (FLL) circuits. Nevertheless, in this paper load compensation, power quality improvement, and phase-frequency estimation are shown with intriguing utilization of FLL. The simulation results shows that the MPPT algorithm harness best possible yield of power from the PV framework, while maintaining steady transients for output signal. The proposed control with voltage source converter (VSC) compensates the voltage and current harmonics due to unbalanced load that keeps overall harmonic distortion for the system at less than 5%, which is within the IEEE-519 acceptable limit.**

Keywords: Grid Connected PV System, FOGI-FLL, Synchronization, Power Quality.

I. INTRODUCTION

The GCSPV system is controlled by a third order complex filter (TOCF) method. A voltage source converter performs the role of a distribution static compensator, which by minimizing harmonics and balancing grid currents maintains a unique power factor and enhances the power quality of grid. In poor grid scenarios including voltage distortion, failures of grid, DC offset, voltage unbalances, and swell/sag, it also works well. The essential objective of this study is to estimate unit templates by harnessing the positive sequence components of unbalanced voltages. The TOCF technique is implemented to harness load currents' primary component [1]. By combining a MPPT and FCS-MPC algorithm power harnessing can be maximized from the PV panels. This controllers' performance is equated by two PV configurations, i.e. single-stage and two stage, using alternative controllers and MPPT algorithms [2]. Two streamlined analytical models are put forth, while keeping the dc/dc boost converter and MPPT like converters dynamics, and neglecting the grid interconnection dynamics and grid-side converter (GSC) controls. The initial prototype shows that there is persistent input power at PV's dc side and which is also known for the system. The second prototype presumes that impedance behind a steady dc voltage represents dc component side of a PV [3]. By using an indirect current control approach, we can switch the VSC efficiently and also generates reference grid currents. The load currents are processed by the recursive digital filter, which also separates out their active power component [4]. The EDPs and EDPSCs were used to investigate the PVGS's interharmonic properties. The DPs and DPSCs by choosing an appropriate fundamental frequency other than the power frequency are expanded to EDPs and EDPSCs, respectively. Second, a set of state space equations that represent PVGS's interharmonic analysis prototype is developed. Third, generating values and relations between them are shown by sequence components thanks to the decoupling properties of EDPSCs [5]. A SFT-PLL control method is implemented for harnessing fundamental load, also synchronizing inverter yield voltage with grid during the GTT. The nonlinear load harmonics can be effectively reduced and active current can be sent to grid at unity power factor thanks to SFT-PLL based regulator technology. The suggested control method may maintain stable current at grid for imbalanced linked load [6]. This proposed FONF control technique is used for supplying the active load demand at grid and addressing concerns at concerned point of connection for power quality of current. Unbalanced connected loads, system demand of reactive power, and harmonic distortion are among the power quality concerns taken into account. A modified integer-order notch filter structure is proposed by the FONF-based control [7]. The dynamic voltage support (DVS) method is utilized during voltage sag fault to accomplish low-voltage-ride-through (LVRT). By creating an extra active/reactive current control approach instead of traditional technique, the DVS scheme is accomplished. Because of the diminished X/R proportion at the purpose in like manner coupling in low-voltage organizations, the results at steady system operation and improved efficacy are accomplished by minimizing X/R ratio in LV networks at common coupling point [8]. The PV system's reaction time is amplified besides LVRT condition by developing a feedback linearization approach based on sliding-mode control. This paper combines sliding-mode control with feedback linearization methods for strengthening the control's resilience to parameter fluctuations [9]. The sensitivity function, gain margin, and phase margin are all managed by a dependable FO-PI model regulator of PV framework linked to grid inside as well as outside of the control loops, the resilience in the face of parameter change. As it is a

979-8-3503-9976-9/23/$31.00 ©2023 IEEE.

Authorized licensed use limited to: DELHI TECHNICAL UNIV. Downloaded on April 17,2023 at 06:17:01 UTC from IEEE Xplore. Restrictions apply.

fact that the FO-PI controller's accessibility is so far not physically possible, and due to the complexity of a grid connected PV framework, we provide an alternate method for hardware application though an RC ladder network to the inner loop FO-PI controller [10]. Due to the interaction of dynamic resistance and sinking dc-link capacitance the system results in instabilities through a grid-connected small-signal framework of PV arrangement. The smallest dc-link capacitance essential for stability maintenance of the entire framework is identified. A straightforward and efficient active compensator is designed to counteract the instability caused by the decreased dc-link capacitance [11]. A FCS-MPC approach has been developed of grid connected PV framework is presented which modulate score cell by means of grid frequency, and achieves non-regenerative procedure in auxiliary lower voltage H-bridge cells which guarantee that the pre-rectifier flow of power is uni-directional [12]. A fault ride-through control approach is presented in a single-phase GCPVS which helps in attaining the low voltage ride-through. An islanding grouping neural network classifier and model predictive control framework is moved toward to accomplish control of two-stage PV structure. This proposed controller supports grid voltage during voltage sags by injecting the least amount of reactive current within the threshold [13]. A novel DVR in light of TransZSI which is powered by solar PV introduced for enhancing the quality of power of on-grid PV framework. TransZSI system is recommended for this DVR instead classic VSI, which has superior buck/boost operations, better voltage boost gain, less passive components, and reduced voltage stress. For effective detection UVT-MCBC technique is used to get precise voltage disturbance moderation by reducing infused voltage harmonics a half breed Unit Vector Template [14]. In the grid connected PV framework MPPC approach regulate and manages the dc-dc converter for energy storage solutions. Here MPPC may help the power grid to support the maintenance of steady voltage and frequency which enhances the pf by controlling the dc-bus voltage and active/reactive power flows [15]. The decoupling circuit lengthens the system's lifespan and makes up for the pulsing power and also broadens the working range and compensates for the voltage drop brought on by low irradiation [16]. A cascaded generalised integral control technique for a grid connected SETS includes a two-part ultimate component abstraction consisting of a tributary fine fundamental element fine-tuning with slight demand and minor harmonics rejection property, and a prime harmonics filter with advanced demand harmonic reduction and dc-offset rejection [17].

The main highlights in this paper are:

1. The suggested design is used as a FLL and may create synchronising signals with amplitude, frequency, and phase angle changes, among other things. The magnitude of grid voltage may also be measured with the fewest movements.

2. Designing a FOGI-FLL controller for evaluating the fundamental load current component.

3. The performance analysis of this projected controller is done when the grid is warped and the demand is high.

II. SYSTEM CONFIGURATION

The proposed grid associated PV system is made in the MATLAB/Simulink. Grid supply, SPV system, IGBT-based VSC, and nonlinear load are all important for the proposed framework. The DC help converter is connected to the PV exhibit. Since sun oriented PV clusters have non-straight qualities, the P&O calculation is utilized to boost power. The lift converter's result is associated with the VSC's DC connect, permitting it to convey dynamic capacity to the grid. The grid is associated with both direct and non-straight loads. A solitary stage VSC regulator is utilized to interface the PV system to the substituting current matrix. The converter can be managed to supply the receptive power expected by the heap and further develop the system's power level with fitting control.

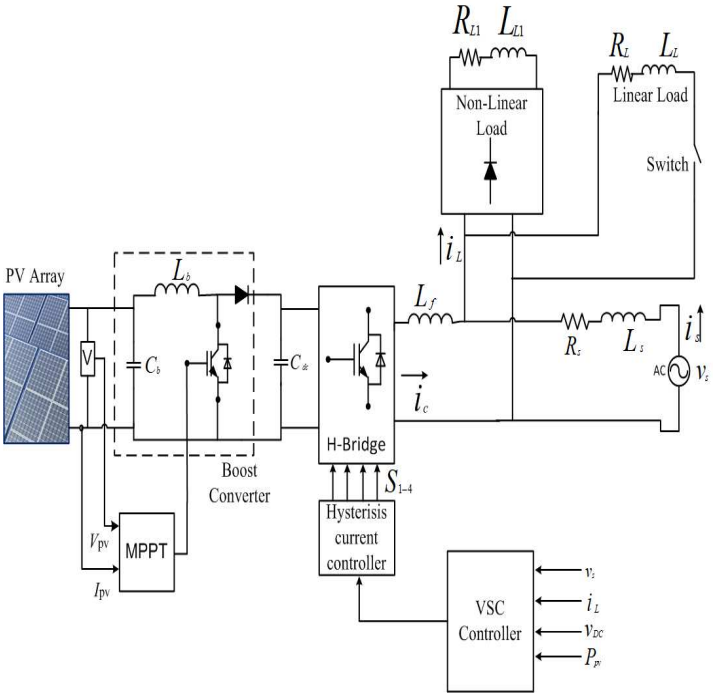


Fig. 1 Schematic Diagram of 1-phase grid connected PV system

III. SUGGESTED CONTROL STRATEGY

The general structure of the control algorithm is shown in Fig. 2. Even under shifting meteorological circumstances, the MPPT algorithm transfers the maximum amount of power from solar PV arrays in order to maintain the target level of DC bus voltage. To create switching pulses for VSC to perform a variety of tasks, including load adjusting, unity power factor activity, compensating for reactive power and enhancing power penetration in the distribution network, the VSC switching algorithm is utilised. The insulated-gate bipolar transistors of the VSC's in-phase unit templates are evaluated using the line voltages at PCC, the magnitude of the fundamental load currents, the loss component, the feed-forward component, and the gating pulses [18].

Authorized licensed use limited to: DELHI TECHNICAL UNIV. Downloaded on April 17,2023 at 06:17:01 UTC from IEEE Xplore. Restrictions apply.

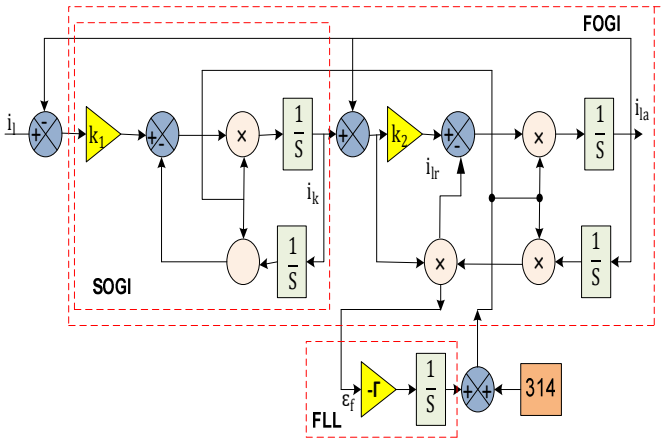


Fig. 2 FOGI-FLL control algorithm

A. MPPT Control

In this system, for extracting maximum power Perturb and Observe (P&O) based MPPT technique is used. The output of P&O control is used for operating the PV array at MPP to generate the duty cycle for the DC-DC boost converter. The duty ratio is calculated as,

$$D = 1 - \frac{V_{pv}^*}{V_{dc}} \tag{1}$$

Here, V_{pv}^* is the MPPT control output and V_{dc} is voltage at DC link.

B. Calculation of Maximum value of Fundamental Load Current Component:

Fig. 2 shows the fundamental construction of FOGI-FLL. FOGI-FLL have higher DC balanced separating capacities and higher request consonant sifting abilities than the SOGI-FLL. Because of variety in frequency, execution of SOGI is deteriorated because of nonappearance of frequency assessment. The transmittance of load current for in-phase fundamental component is given as [18],

$$i_{la}(s) = \frac{K_1 K_2 \omega^2 s^1}{(s^2+K_2\omega s+\omega^2)(s^2+\omega^2)+K_1K_2\omega^2 s^2} i_l(s) \tag{2}$$

Where, ω is estimated frequency of system and i_l represents load current. The transmittance of load current for quadrature fundamental component is given as [18],

$$i_{lr}(s) = \frac{K_1 K_2 \omega^3 s^1}{(s^2+K_2\omega s+\omega^2)(s^2+w^2)+K_1K_2\omega^2 s^2} i_l(s) \tag{3}$$

$$\dot{\omega} = -r((i_k - i_{la}) \times i_{lr}) \tag{4}$$

Where, r represents a constant and i_k represents the intermediate control signal of FOGI-FLL.

By using equation 1 and 2 the peak value of fundamental load current component and phase angle is calculated as [19],

$$I_{fl} = \sqrt{i_{la}^2 + i_{lr}^2} \tag{5}$$

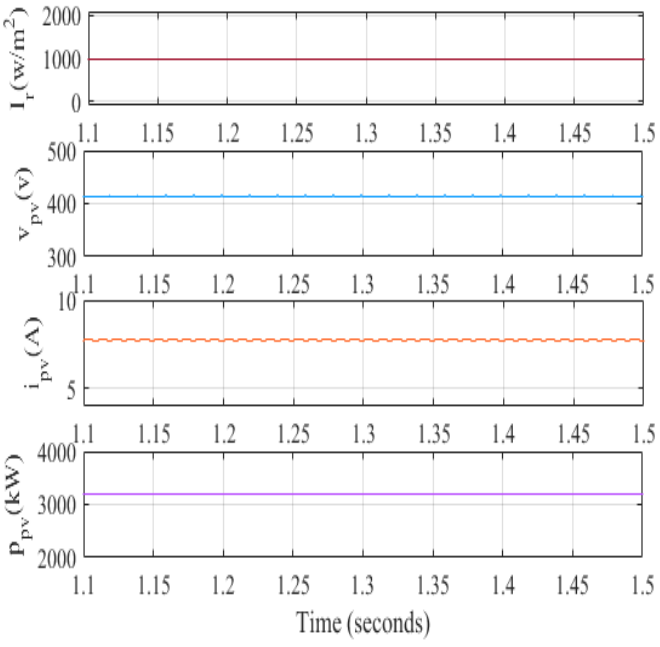
$$\emptyset = \tan^{-1}\frac{i_{lr}}{i_{la}} \tag{6}$$

IV. SIMULATION RESULTS

A GCSPV system is interfaced in this proposed work. The suggested system contains of SPV of 5kW, VSC and nonlinear load. The FOGI-FLL control with VSC provides active/reactive power compensation, harmonics eradication and empower the overall power level of the suggested system. The simulated results are examined at different parameters such as change in solar insolation and unbalanced load. The grid voltage, current, compensator current, load current, dc side voltage, PV voltage, PV current, PV power results are plotted.

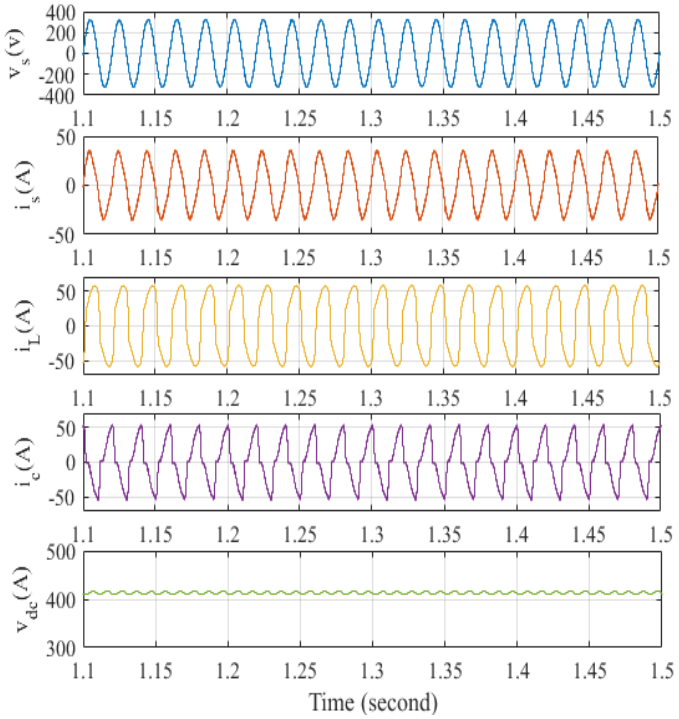
A. Static Response of the Suggested System under Fixed Solar Irradiance and Load

The static response of a single-phase GCPV system with fixed solar irradiation feeding a balanced nonlinear load is depicted in Fig. 3. The solar irradiation is displayed as fixed at 1000 w/m2 in Fig. 3(a). The PV voltage, PV current, and PV power are 400V, 7.02A, and 3.1kW, respectively, under fixed solar irradiation. Source voltage, source current, load current, compensator current, and dc voltage's steady state response are all examined. Under various operational situations, the suggested control is successful in extracting the basic load current component. Additionally, the suggested control with VSC improves the general power quality and offers power support, load balancing, and harmonic suppression under nonlinear load conditions.



(a)

Authorized licensed use limited to: DELHI TECHNICAL UNIV. Downloaded on April 17,2023 at 06:17:01 UTC from IEEE Xplore. Restrictions apply.

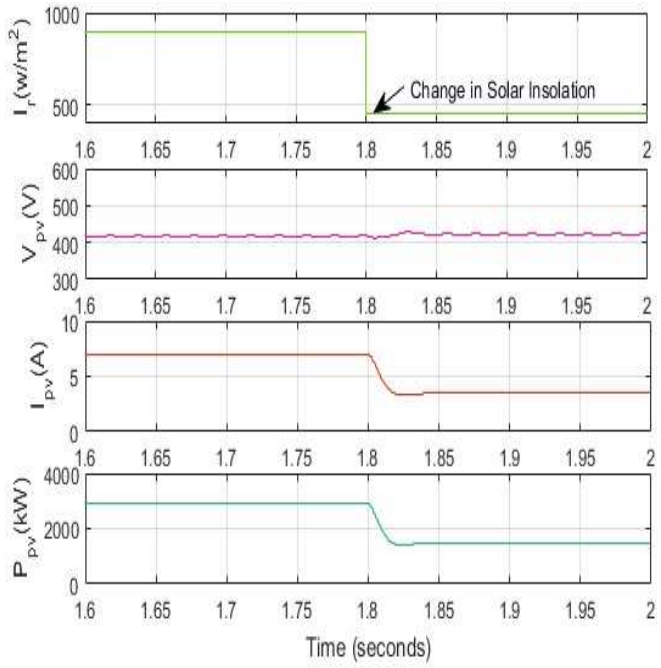


(b)

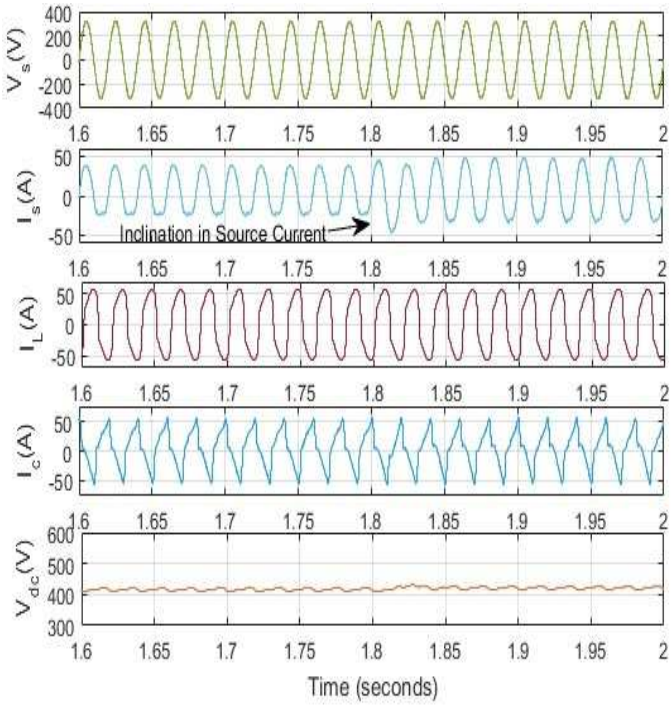
Fig. 3 Static response of the suggested system under fixed solar irradiance feeding balanced nonlinear load

B. *Effective Response of Suggested System under Change in Solar Irradiance*

Figures 4 depict the dynamic performance of a GCSPV system as solar insolation changes. At t=1.8s, the solar insolation is reduced from 900 w/m2 to 450 w/m2. Solar irradiation, PV current, voltage, and power all decrease as solar insolation changes. Grid current increases with tilt in solar insolation, as seen in Fig. 4 (b). Under dynamic conditions of solar insolation and unbalanced load, the suggested controller with VSC maintains grid voltage, compensator current, and dc link voltage.



(a)



(b)

Fig. 4 Effective performance of GCSPV system under change in solar insolation

C. *Effective Response of Suggested System under Fixed Solar Irradiance Feeding Unbalanced Load*

The effective response of a single phase GCSPV system operating at a fixed solar irradiation level feeding an imbalanced nonlinear demand is seen in Fig. 5. The suggested system's load is disconnected at t=1.2s and connected at t=1.4s. During the removal of the load, the source current, load current, and compensator are all decreased. The controller keeps the source voltage constant while raising the dc link voltage throughout the length of the load removal.

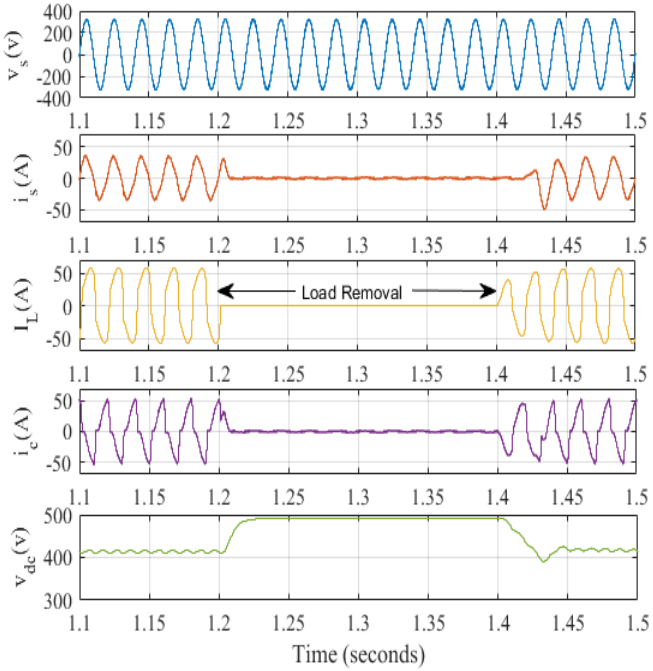
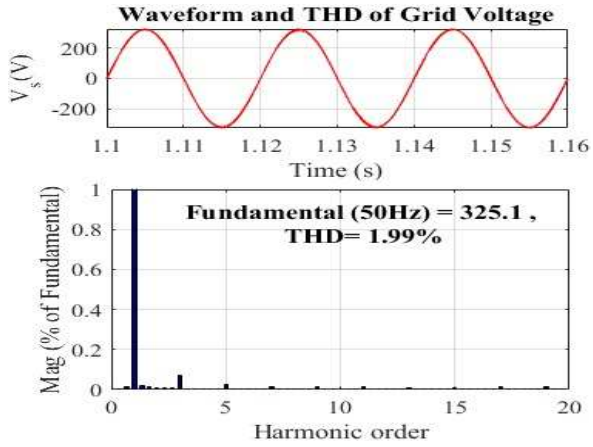


Fig. 5 Effective response of the system under fixed solar irradiance level feeding unbalanced nonlinear load

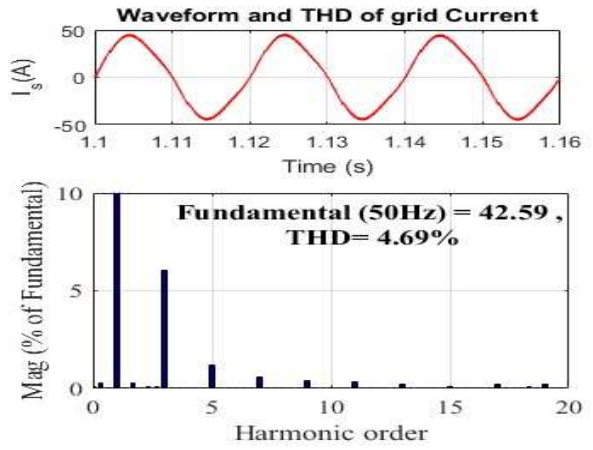
Authorized licensed use limited to: DELHI TECHNICAL UNIV. Downloaded on April 17,2023 at 06:17:01 UTC from IEEE Xplore. Restrictions apply.

D. Harmonics Analysis of Suggested System

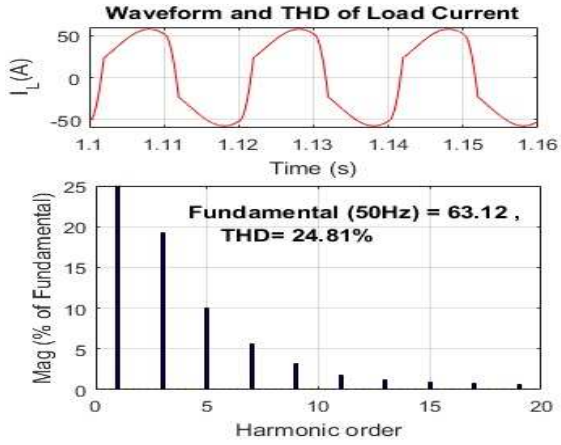
The THD of grid voltage, current, and load current of a grid-interfaced PV system under nonlinear load is depicted in Fig. 6. Grid voltage, grid current, and load current have THDs of 1.99%, 4.69%, and 24.81% respectively. The suggested VSC control preserves grid voltage and offers harmonic adjustment under nonlinear load conditions. Grid voltage and current THDs of less than 5% are within acceptable limits and meet the IEEE-519 standard.



(a)



(b)



(c)

Fig. 6 THD of GCSPV system under nonlinear load condition

V. CONCLUSION

In this paper we had discussed about the design, modeling and simulation of grid tied solar PV system. A FOGI-FLL based control algorithm is used for extracting fundamental component of load current and phase angle under intermittent and nonlinear load conditions. For getting maximum output power from PV system P&O based MPPT technique is used in this 5 KW grid tied solar PV system. From the results it is shown various power quality improvement features, reduction in harmonics, and also responds very well in case of variation in load. The proposed FOGI based FLL control approach achieves both synchronisation and load correction quite effectively. The FOGI-FLL control with VSC effectively preserves grid voltage and improves system dynamic responsiveness. The THDs of grid voltage and current are kept below the permitted limits of the IEEE-519 standard.

REFERENCES

[1] B. Singh and V. Jain, "TOCF Based Control for Optimum Operation of a Grid Tied Solar PV System," *IEEE Trans. Energy Convers.*, vol. 35, no. 3, pp. 1171–1181, Sep. 2020, doi: 10.1109/TEC.2020.2990907.

[2] S. Vanti, P. R. Bana, S. D'Arco, and M. Amin, "Single-Stage Grid-Connected PV System with Finite Control Set Model Predictive Control and an Improved Maximum Power Point Tracking," *IEEE Trans. Sustain. Energy*, vol. 13, no. 2, pp. 791–802, Apr. 2022, doi: 10.1109/TSTE.2021.3132057.

[3] M. Zhang, Z. Miao, and L. Fan, "Reduced-order analytical models of grid-connected solar photovoltaic systems for low-frequency oscillation analysis," *IEEE Trans. Sustain. Energy*, vol. 12, no. 3, pp. 1662–1671, Jul. 2021, doi: 10.1109/TSTE.2021.3061296.

[4] P. Shukl and B. Singh, "Recursive Digital Filter Based Control for Power Quality Improvement of Grid Tied Solar PV System," in *IEEE Transactions on Industry Applications*, Jul. 2020, vol. 56, no. 4, pp. 3412–3421. doi: 10.1109/TIA.2020.2990369.

[5] Q. Zhong, Y. Qiu, Y. Zhao, H. Li, G. Wang, and F. Wen, "Interharmonic Analysis Model of Photovoltaic Grid-connected System with Extended Dynamic Phasors," *J. Mod. Power Syst. Clean Energy*, vol. 9, no. 6, pp. 1540–1547, Nov. 2021, doi: 10.35833/MPCE.2020.000241.

[6] A. M. Mansour, O. M. Arafa, M. I. Marei, I. Abdelsalam, G. A. A. Aziz, and A. A. Sattar, "Hardware-in-the-Loop Testing of Seamless Interactions of Multi-Purpose Grid-Tied PV Inverter Based on SFT-PLL Control Strategy," *IEEE Access*, vol. 9, pp. 123465–123483, 2021, doi: 10.1109/ACCESS.2021.3110013.

[7] M. Badoni, A. Singh, S. Pandey, and B. Singh, "Fractional-Order Notch Filter for Grid-Connected Solar PV System with Power Quality Improvement," *IEEE Trans. Ind. Electron.*, vol. 69, no. 1, pp. 429–439, Jan. 2022, doi: 10.1109/TIE.2021.3051585.

[8] M. Khan, A. Haque, and V. S. B. Kurukuru, "Dynamic Voltage Support for Low-Voltage Ride-Through Operation in Single-Phase Grid-Connected Photovoltaic Systems," *IEEE Trans. Power Electron.*, vol. 36, no. 10, pp. 12102–12111, Oct. 2021, doi: 10.1109/TPEL.2021.3073589.

[9] Y. Zhang *et al.*, "Dynamic Performance Improving Sliding-Mode Control-Based Feedback Linearization for PV System under LVRT Condition," in *IEEE Transactions on Power Electronics*, Nov. 2020, vol. 35, no. 11, pp. 11745–11757. doi: 10.1109/TPEL.2020.2983315.

Authorized licensed use limited to: DELHI TECHNICAL UNIV. Downloaded on April 17,2023 at 06:17:01 UTC from IEEE Xplore. Restrictions apply.

[10] S. Panda, G. R. Biswal, J. K. Pradhan, B. Subudhi, and A. Mallick, "Development of Prototype Fractional Order Controller for a Grid-Tied Photovoltaic System," *IEEE Trans. Circuits Syst. II Express Briefs*, vol. 69, no. 4, pp. 2171–2175, Apr. 2022, doi: 10.1109/TCSII.2021.3129268.

[11] M. A. K. Magableh, A. Radwan, and Y. A. R. I. Mohamed, "Assessment and Mitigation of Dynamic Instabilities in Single-Stage Grid-Connected Photovoltaic Systems with Reduced DC-Link Capacitance," *IEEE Access*, vol. 9, pp. 55522–55536, 2021, doi: 10.1109/ACCESS.2021.3071056.

[12] M. S. Manoharan, A. Ahmed, and J. H. Park, "An Improved Model Predictive Controller for 27-Level Asymmetric Cascaded Inverter Applicable in High-Power PV Grid-Connected Systems," *IEEE J. Emerg. Sel. Top. Power Electron.*, vol. 8, no. 4, pp. 4395–4405, Dec. 2020, doi: 10.1109/JESTPE.2019.2935536.

[13] M. A. Khan, A. Haque, V. S. B. Kurukuru, and S. Mekhilef, "Advanced Control Strategy With Voltage Sag Classification for Single-Phase Grid-Connected Photovoltaic System," *IEEE J. Emerg. Sel. Top. Ind. Electron.*, vol. 3, no. 2, pp. 258–269, Dec. 2020, doi: 10.1109/jestie.2020.3041704.

[14] A. Moghassemi, S. Padmanaban, V. K. Ramachandaramurthy, M. Mitolo, and M. Benbouzid, "A Novel Solar Photovoltaic Fed TransZSI-DVR for Power Quality Improvement of Grid-Connected PV Systems," *IEEE Access*, vol. 9, pp. 7263–7279, 2021, doi: 10.1109/ACCESS.2020.3048022.

[15] Y. Shan, J. Hu, and J. M. Guerrero, "A Model Predictive Power Control Method for PV and Energy Storage Systems with Voltage Support Capability," *IEEE Trans. Smart Grid*, vol. 11, no. 2, pp. 1018–1029, Mar. 2020, doi: 10.1109/TSG.2019.2929751.

[16] E. Heydari, A. Y. Varjani, and D. Diallo, "A Dual-Function Power Decoupling Circuit for Single-Stage Grid-Connected PV Inverter," *IEEE Trans. Power Electron.*, vol. 37, no. 6, pp. 7422–7431, Jun. 2022, doi: 10.1109/TPEL.2022.3143951.

[17] C. M. Nirmal Mukundan, S. B. Q. Naqvi, Y. Singh, B. Singh, and P. Jayaprakash, "A Cascaded Generalized Integral Control for Multiobjective Grid-Connected Solar Energy Transfer System," *IEEE Trans. Ind. Electron.*, vol. 68, no. 12, pp. 12385–12395, Dec. 2021, doi: 10.1109/TIE.2020.3048316.

[18] Priyank Shah, Ikhlaq Hussain and Bhim Singh," A Novel Fourth-Order Generalized Integrator Based Control Scheme for Multifunctional SECS in the Distribution System", IEEE TRANSACTIONS ON ENERGY CONVERSION, VOL. 33, NO. 3, SEPTEMBER 2018.

[19] Hemant Saxena, Alka Singh & J. N. Rai (2019), "Design and Analysis of Different PLLs as Load Compensation Techniques in 1-Ø Grid-Tied PV System", International Journal of Electronics, DOI: 10.1080/00207217.2019.1600745.

[20] H. Saxena, A. Singh and J.N. Rai, "Analysis of SOGI-ROGI for synchronization and shunt active filtering under distorted grid condition". ISA Transactions (2020), https://doi.org/10.1016/j.isatra.2020.10.025.

Authorized licensed use limited to: DELHI TECHNICAL UNIV. Downloaded on April 17,2023 at 06:17:01 UTC from IEEE Xplore. Restrictions apply.

energies

MDPI

Article

Design and Evaluation of a Water-Based, Semitransparent Photovoltaic Thermal Trombe Wall

Sheel Bhadra [1,†], Niloy Sen [2,†], Akshay K K [3], Harmeet Singh [4] and Paul G. O'Brien [4,*]

[1] Department of Mechanical Engineering, Delhi Technological University, Delhi 110042, India
[2] Department of Mechanical Engineering, Jadavpur University, Kolkata 700032, India
[3] Department of Mechanical Engineering, IIT Madras, Chennai 600036, India
[4] Department of Mechanical Engineering, Lassonde School of Engineering, York University, Toronto, ON M3J 2S5, Canada
* Correspondence: paul.obrien@lassonde.yorku.ca
† These two authors contributed equally to this paper.

Abstract: Trombe walls are a passive solar technology that can contribute to the reduction of building heating loads. However, during warmer weather conditions, Trombe walls may cause overheating. In this work, we investigate the feasibility of using Trombe walls to perform multiple functions during warm weather conditions including (1) heating and storing water for building applications, (2) providing occupants with visibility to the outdoors, and (3) generating electric power. Experiments are performed on a small-scale prototype comprising a clear water storage container with a transparent window and a tinted acrylic sheet that is immersed in the water. Photovoltaic cells are placed on the bottom half of the front face of the water storage container. Results show that water at the top of the clear container can be heated to temperatures as high as 45 °C when subjected to solar-simulated radiation for five hours. Numerical simulations predict that similar temperatures can be reached if the Trombe wall is scaled to full size. Furthermore, the cooler water at the bottom of the water storage container acts as a heatsink that reduces the extent to which the temperature of the PV cells is elevated. Results show the temperature and open circuit voltage of the PV cells are about 50 °C and 0.66 V, respectively, when water is present. However, when the water is absent from the container, the temperature of the PV cells increases up to 90 °C and their open circuit voltage drops to 0.60 V. The results show that water-based, semitransparent photovoltaic thermal Trombe walls have the potential to operate as multifunctional building envelopes that simultaneously provide for daylighting, heated water and electric power, and further research in this area is warranted.

Keywords: building energy; Trombe wall; thermal energy storage; building envelopes; building integrated photovoltaics

check for updates

Citation: Bhadra, S.; Sen, N.; K, A.K.; Singh, H.; O'Brien, P.G. Design and Evaluation of a Water-Based, Semitransparent Photovoltaic Thermal Trombe Wall. *Energies* **2023**, *16*, 1618. https://doi.org/10.3390/en16041618

Academic Editor: Angelo Zarrella

Received: 8 January 2023
Revised: 29 January 2023
Accepted: 2 February 2023
Published: 6 February 2023

Copyright: © 2023 by the authors. Licensee MDPI, Basel, Switzerland. This article is an open access article distributed under the terms and conditions of the Creative Commons Attribution (CC BY) license (https://creativecommons.org/licenses/by/4.0/).

1. Introduction

Energy use in the building sector reached 132 EJ in 2021, which accounted for 30% of global energy consumption [1]. A significant portion of this energy demand is from the residential sector used for space and water heating purposes. Hence, there is an urgent requirement to shift to renewables to meet building energy demands. One promising source of clean energy is the sun, because it is widely distributed and can provide up to ~1000 W/m^2 per day [2].

As urban energy density continues to increase, it is expected that harnessing solar energy on building rooftops and facades will make a significant contribution toward reducing demands on energy infrastructures [3–6]. In particular, Trombe walls have been used for decades as a passive solar heating method because they can be highly efficient, relatively simple to construct and cost-effective [7–9]. Trombe walls typically consist of a large thermal wall, a clear glazed cover and an air channel between the thermal wall and the glazed cover [10]. Sunlight that passes through the glazed cover is absorbed by the

thermal wall. The absorbed sunlight generates heat, which can be stored in the thermal wall, which is made of materials with high thermal capacity such as brick, concrete, sand or stone. The generated heat can also be transferred to the air within the channel between the thermal wall and the outer glazing. Air vents are often located at the top and bottom of the thermal wall. When air within the channel is heated, it can be passively transported through the vent at the top of the thermal storage wall to the interior of the building, and colder air is drawn through the vent at the bottom of the thermal wall. Furthermore, solar thermal energy generated in Trombe walls during peak sunshine hours can be stored and used to heat the building after sunset.

Under favorable conditions Trombe walls can reduce the energy consumed in a building by 30% [8] and there has been much research and development toward improving the performance of Trombe walls. Mokni et al. found that a Trombe wall in Saudi Arabia could satisfy 80% of the heating needs of a room on a sunny day, or about 40% of the heating needs under conditions of high-wind or scattered clouds [11]. Yang et al. performed numerical simulations to show the addition of the phase change materials to Trombe walls results in a decrease in annual energy consumption of 18% [12]. Liu et al. showed that by using two air channels in a Trombe wall, the indoor air temperature could be increased by 5.6 °C as compared to the case when a traditional Trombe wall was used [13].

Although Trombe walls can reduce building energy loads, the design of effective Trombe walls is a challenging task that depends on climatic and seasonal factors [14]. During night or cloudy periods, the temperature of the thermal storage wall may drop below that of the indoor temperature, creating an inverse thermosiphon phenomenon whereby the airflow through the Trombe wall vents is reversed [15]. Moreover, if the thermal storage wall is too thick, then solar thermal energy stored in this wall may not be adequately transferred to the indoors. Another challenge, which we focus on in this research, is that during hot weather conditions, Trombe walls can cause overheating in well-insulated buildings [16,17]. Researchers have recommended using ventilation and solar shading to reduce overheating caused by Trombe walls [18]. Jaber and Ajib [19] recommended using roller shutters to prevent solar radiation from entering the building and insulation curtains between the glass and masonry wall layer to avoid heat transfer to the building. Building overhangs can also be designed to shade Trombe walls in hot climates during summer months [20]. However, these solutions for preventing overheating from Trombe walls do not fully utilize the available solar energy.

Recently, Mohamad et al. [21] designed a water-based Trombe wall wherein the water could be removed from the Trombe wall and used as a domestic water supply during hot weather conditions to prevent overheating. Singh et al. proposed semitransparent, water-based Trombe walls wherein a tinted acrylic sheet was inserted in a water-based storage wall to absorb solar radiation [22]. In this configuration, the Trombe wall could be designed to have the appearance of a tinted window, providing architects with aesthetic options for integrating Trombe walls into building facades. In this work, we investigate the potential of placing PV cells on the bottom portion of the front surface of the water storage wall within a semitransparent, water-based Trombe wall. In this configuration, the relatively cooler water at the bottom of the water storage wall acts as a heat sink to prevent the PV cells from overheating, which is important for achieving high efficiencies. Thus, the Trombe wall investigated in this work is designed to enhance the utility of the wall during hot weather conditions by producing both hot water and electric power.

Crystalline silicon photovoltaic (c-SiPV) modules dominate the market due to their low cost and high efficiency (~20%). However, one disadvantage of c-SiPV cells is their negative temperature coefficient of ~ 0.45%/°C, which implies that their efficiency decreases as their temperature increases [23–27]. The resulting decrease in efficiency can be significant, as the temperature of PV cells may be elevated by 20 °C or more. Thus, by reducing the temperature of PV cells during operation, their output can be increased. For example, Rahman et al. [26] experimentally investigated a PV module fitted with finned tubes for cooling and an efficiency improvement of up to 15.72% was observed.

Research on PV cells integrated in Trombe walls (referred to as PVTWs) has been reported in the literature. Hu et al. studied the performance of different PVTW configurations. They considered a Trombe wall module with blinds and PV cells (PVBTW), a Trombe wall configuration wherein the PV cells were fixed to the exterior glazing (PVGTW) and a third configuration where the PV cells were attached to the thermal storage wall (PVMTW). Considering both heat gains and electric power production, the PVBTW module performed 14.5% better than the PVGTW configuration and 14.1% better than the PVMTW configuration [28]. Koyunbaba et al. [29] presented a building integrated photovoltaic (BIPV) Trombe wall and their experimental results showed the daily average electrical and thermal efficiency of the BIPV Trombe wall system reached 4.52% and 27.2%, respectively. Jie et al. [30] studied a Trombe wall consisting of a PV glass panel with an area of 2.66 m × 0.84 m, a 0.18 m wide vented air channel, and a thermal storage wall. Experimental results showed the Trombe wall could increase the indoor temperature by 7.7 °C as compared to a reference room. Moreover, Ahmed et al. integrated a water-cooling system at the rear side of the PV cells within a PV-Trombe wall, such that heated water could be supplied to the building. In this Trombe wall configuration, PV cells were located at the inside surface of the glazing and a serpentine-shaped copper pipe with the dimensions of 15 mm diameter and 11.34 m length was placed between the PV cells and the air channel. Thermal and electrical efficiencies of 79.9% and 10.7%, respectively, were achieved [31].

To the best of the authors knowledge, research has yet to be reported on water-based PVTWs, wherein PV cells are integrated with a thermal energy storage medium comprising water. Herein, we study the benefits of placing PV cells on the lower portion of a water storage wall within a Trombe wall. Due to stratification, heated water rises to the top of the thermal storage wall while relatively cooler water resides at the bottom of the thermal storage medium. We investigate the potential benefits of placing PV cells on the bottom portion of the thermal storage wall where the temperature is relatively low. Thus, we report herein on a feasibility study about a novel semitransparent, water-based Trombe wall with integrated PV cells that can make full use of the solar irradiance to provide multiple functions: (1) it can function as a tinted semitransparent window; (2) it can generate heated water; (3) it can produce electric power.

2. Materials and Methods

2.1. Experimental Setup

A small Trombe wall prototype was built to experimentally investigate the ability to store solar thermal energy in water storage walls comprising a tinted acrylic sheet. The Trombe wall prototype is framed with wood having a cross section of 3.8 cm × 3.8 cm and its overall dimensions are 58 cm × 36 cm × 68 cm. The wooden frame is insulated with FOAMULAR extruded polystyrene boards and sealed using silicone sealant.

A 3 mm thick clear acrylic sheet with a height and width of 57.5 cm and 42.5 cm, respectively, is tightly fitted and sealed at the front face of the Trombe wall prototype. Similarly, a 3 mm thick acrylic sheet having dimensions of 30 cm × 30 cm is integrated at the back side, such that one can see through the transparent prototype. That is, the presence of the acrylic sheets at the front and back of the Trombe wall prototype allows for light to pass through the structure. An acrylic container with a width, height, and depth of 30 cm, 30 cm, and 20 cm, respectively, is placed within the Trombe wall prototype and is used to store the water. More details about this Trombe wall prototype are available in previously reported work [22]. In this work, monocrystalline silicon PV cells (Maxeon Gen II from Sunpower, with an efficiency rating of ~ 22%) with an area of 125 mm × 125 mm are located at the bottom half of the front surface of the water container as shown in Figure 1a,b. An insulated door with a small opening is used as the side of the prototype to allow users to change the thermal energy storage medium and to adjust the position of the PV cells and thermocouples.

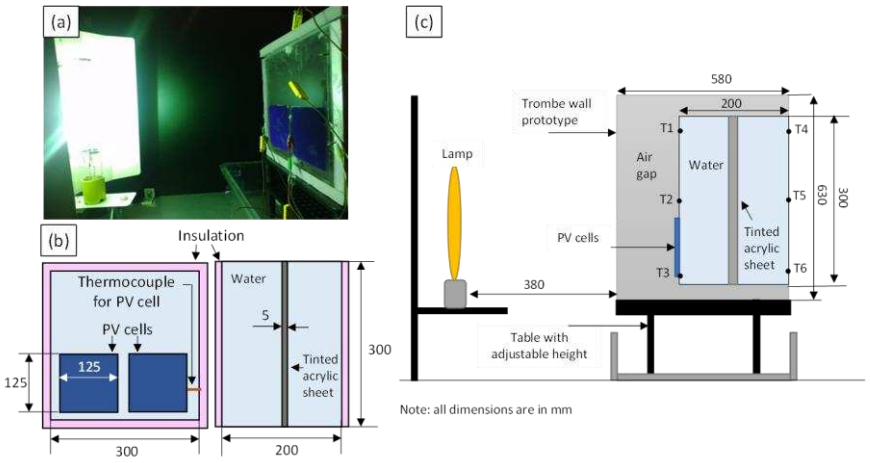


Figure 1. (**a**) A picture of the lamp and water container with insulation at its sides and bottom and PV cells on the bottom half of its front surface. (**b**) A schematic diagram showing the front (left) and cross section from the side view (right) of the water container. (**c**) A schematic diagram showing the side view of the experimental setup.

Solar radiation is simulated using a 1000 W Hortilux Blue Metal Halide bulb mounted vertically with a white reflector behind it. The front face of the Trombe wall prototype is 38 cm away from the metal halide bulb, as shown in Figure 1c. Experiments were carried out with and without a 5 mm thick tinted acrylic sheet inserted into the middle of the acrylic container (shown in Figure 1b). By placing the tinted acrylic sheet in the middle of the container (rather than placing it against the inner surface of the front or rear side of the container) its contact area with the water is maximized, which facilitates the transfer of heat generated in the acrylic container to the surrounding water. The tinted acrylic sheet absorbs solar-simulated light, which increases the amount of heat generated in the water. The reflectance (R) and transmittance (T) of the tinted acrylic sheet, and of the clear acrylic sheet used at the front and back of the Trombe wall prototype, were measured over a wavelength range from 220 nm to 1400 nm using a UV-Vis spectrophotometer (Shimadzu 2600i). The reflectance and transmittance of the tinted and clear acrylic sheets was measured using an FTIR spectrometer (VERTEX 70) over the wavelength range from 1400 nm to 25 µm. The absorptance (A) of these acrylic sheets was calculated using the reflectance and transmittance measurements and the equation A + R + T = 1. The transmittance and absorbance of the clear and tinted acrylic sheets are provided in Figure S1 in the Supplementary Materials.

The temperature of the water within the acrylic container was measured over the duration of the experiments using six type K thermocouples (labeled T1 through T6) at the locations shown in Figure 1. Thermocouples T1, T2, and T3 are installed 25 mm from the front surface. T2 is placed at the center of the container, whereas T1 and T3 are 5 mm from the top and bottom of the container, respectively. T4, T5, and T6 follow a similar configuration at the rear side of the container. Two PV cells are attached to the front face of the acrylic container, located at its bottom half as shown in Figure 1b, using silicon heat dissipation pads (Thermalright, Extreme Odyssey II). A thermocouple is placed between the PV cell and the acrylic container to monitor the temperature of the PV cell. This thermocouple is placed between the heat dissipation pad and the acrylic container near the center of the rear side of the PV cell. A data acquisition system (LabJack T7 pro) is used to record the temperature measurements and open circuit voltage of the PV cells. The open circuit voltage of silicon-based PV cells decreases substantially with increasing temperature, whereas the temperature dependence of the short-circuit current is comparatively small [23]. For example, Cuce et al. showed that the open circuit voltage decreases from about 19.5 V to 15 V as the temperature of a c-SiPV cell is increased from 15 °C to 60 °C, while the effects of this temperature increase on the short circuit current were negligible [32]. Thus,

in this work, the temperature dependence of the open circuit voltage is used to evaluate the feasibility of the proposed water-based Trombe wall.

2.2. Experimental Procedure

Each experiment consisted of a charging period followed by a discharging period. The solar-simulated light source is turned on at the beginning of the charging period, which lasts for 5 h for all experiments. In this work, 5 h was selected for the duration of the experiments because this is a good representation of the number of peak sun hours received in hot weather climates over the course of one day [33]. After 5 h, the metal halide lamp is turned off and the discharging period begins. During the discharging period, which lasts for 24 h, the heat stored within the water is dissipated to the surroundings. The total duration of each experiment, including the charging and discharging periods, is 29 h.

Experiments were conducted for the twelve cases shown in Table 1. For Cases 1 to 6, PV cells are not used. For Cases 1 and 2, the experimental setup consists of only the water container with and without the acrylic sheet, respectively. Cases 3 and 4 are similar to Cases 1 and 2, respectively, but the top, bottom and sides of the water container are insulated. Cases 5 and 6 are similar to Cases 3 and 4, but the water container is housed within the Trombe wall prototype shown in Figure 1.

Table 1. Experimental cases investigated.

Case	Water	Insulation	Trombe Wall	Acrylic Sheet (Tinted)	PV Cell	Abbreviation
1	✓					W
2	✓			✓		W-A
3	✓	✓				W-I
4	✓	✓		✓		W-I-A
5	✓	✓	✓			W-I-T
6	✓	✓	✓	✓		W-I-T-A
7	✓	✓			✓	W-I-P
8	✓	✓		✓	✓	W-I-A-P
9	✓	✓	✓		✓	W-I-T-P
10	✓	✓	✓	✓	✓	W-I-T-A-P
11		✓			✓	I-P
12		✓	✓		✓	I-T-P

For cases 6 to 12, PV cells are placed at the bottom front face of the water container as shown in Figure 1. For Cases 7 and 8, the water container is not housed within the Trombe wall prototype. For Case 8, the tinted acrylic sheet is within the water container, whereas for Case 7, the tinted acrylic sheet is not present. Cases 9 and 10 are similar to Cases 7 and 8, but with the water container housed within the Trombe wall prototype. For Cases 11 and 12, the water is removed from its container to provide a reference for investigating the extent to which the water is able to prevent the temperature of the PV cells from increasing.

2.3. Numerical Modeling Methods

To numerically model the temperature of the water storage medium over the duration of the charging phase, a three-dimensional model was first created in SOLIDWORKS software. The Reynolds number was determined as ~2500 and the heat transfer and turbulent flow for the cases described in Table 1 were modeled using ANSYS Fluent. All simulations were performed considering the standard k-epsilon turbulence model. The "SIMPLE" algorithm was employed to couple the pressure and velocity and an ambient temperature of 21 °C was used to initialize the model. For all simulations, the time step was 5 s and a quadrilateral mesh of 5 mm was used to discretize the governing equations

into a series of algebraic equations. Independence of the results from the time step and mesh size were checked (when decreasing either the time step or the mesh size to half of the values stated above the results changed by less than 0.01%). The convergence criteria of the CFD simulation were based on the residuals of the governing equations to be less than 1.0×10^{-5}. The acrylic container (300 mm × 200 mm × 300 mm) housing the water and tinted acrylic sheet is shown in Figure 2a. The mesh used to numerically model the thermal properties of this water storage medium is shown in Figure 2b. The lab-scale Trombe wall prototype is shown in Figure 2c, and the mesh used to numerically model the prototype is shown in Figure 2d. The thickness of the container is 5 mm on all sides except for the top, where it is 2.5 mm.

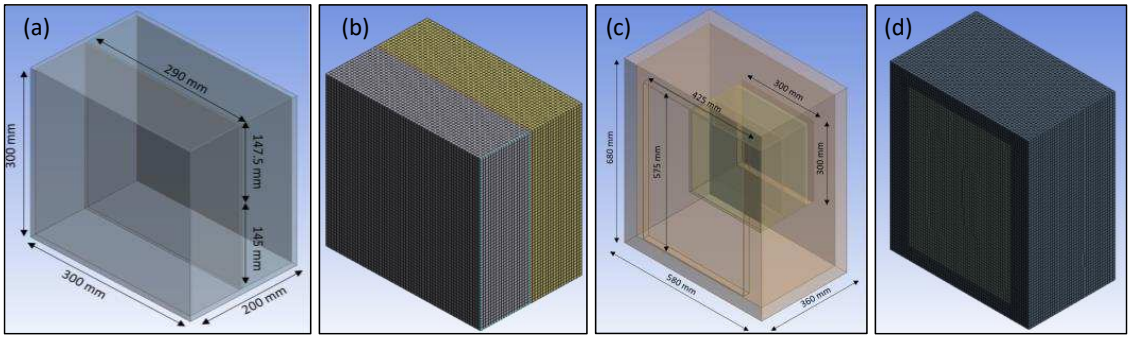


Figure 2. (**a**) A diagram of the water storage medium with the tinted acrylic sheet at its midplane. (**b**) The mesh used to perform the simulations for the water storage medium with the acrylic sheet at its midplane. (**c**) A diagram of the water storage medium within the small-scale Trombe wall prototype. (**d**) The mesh used to perform the simulations for the Trombe wall prototype.

To simulate the heat generated when incident light is absorbed a volumetric heat generation term is imparted in the cell zone. The incident light intensity measured 84 m W/cm^2 using a power meter (Thorlabs, PM 100D). To simplify the simulations for this feasibility study, it is assumed that 70% of the incident light intensity is absorbed by the acrylic sheet, 20% is absorbed by the water, and 10% is transmitted through the structure. As shown in Figure S1, the absorbance spectrum of the tinted acrylic sheet decreases from over 90% at 300 nm to less than 50% at 1600 nm, and for wavelengths above 2400 nm the absorbance is about 90%. Thus, assuming an average absorption of 70% for the tinted acrylic sheet is reasonable for the feasibility study conducted in this work. The volumetric heat generation term is determined by dividing the intensity of light absorbed by each component by its volume. Furthermore, a convective heat transfer coefficient of 10 W/m^2·K is assumed at the top and sides of the structure for all cases, while the bottom of the structure is assumed to be perfectly insulated for all cases.

3. Results

3.1. Experimental Results

The temperature profiles measured at the front of the water container (using T1, T2 and T3 in Figure 1) for Cases 1 to 6 over the 29 h duration of the experiments are shown in Figure 3. The temperature measurements taken near the rear side of the water container were similar to those measured at the front and are shown in Figure S2 in the supplementary material. The results for Case 1 are shown in Figure 3a. The initial temperature of the water at all locations was around 21 °C and the temperature started rising at t = 0 when the lamp was turned on and kept increasing over the next 5 h (over the charging period). As expected, the temperature of the water at the top of the container increased faster than the water at the middle and bottom due to thermal buoyancy forces caused by the density differences associated with water at different temperatures. The temperature at the top, middle and bottom of the water container increased to around 33 °C, 31 °C and 30 °C, respectively, and the average temperature gain for the water was around 10 °C over the charging period.

At the end of the charging period, the lamp was turned off and the discharging period began. The water temperature decreased over the discharging phase as heat was lost to the surroundings and the temperature of the water at the end of the discharging period was about 21.5 °C.

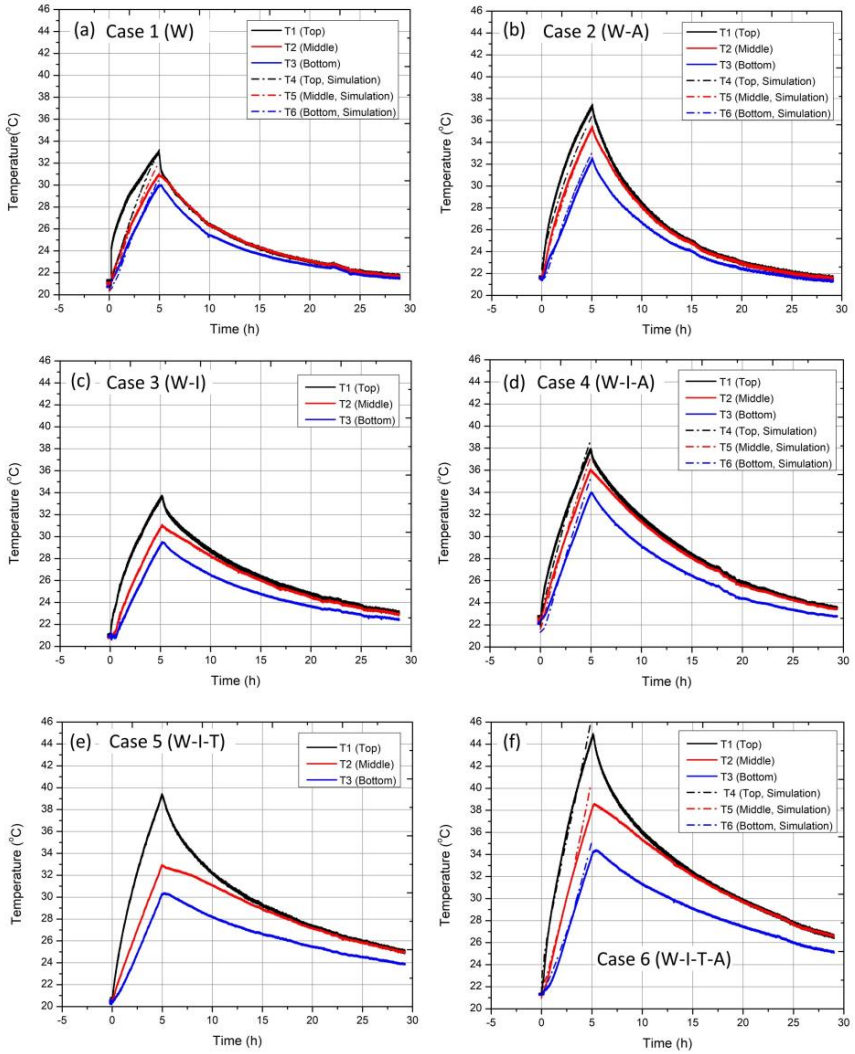


Figure 3. Temperature profiles during the charging and discharging periods for (**a**) just the container with water, (**b**) the water container with the tinted acrylic sheet inserted at its midplane, (**c**) the container with water when its sides are insulated, (**d**) the insulated water container when the tinted acrylic sheet is inserted at the midplane of the water, (**e**) the Trombe Wall, (**f**) Trombe wall acrylic sheet.

The results for Case 2 are shown in Figure 3b. The initial temperature of the water was about 21.5 °C and the temperature at the top, middle and bottom of the water container increased to approximately, 37 °C, 35 °C and 32.5 °C, respectively, by the end of the charging phase. Notably, the temperature of the water at the end of the charging phase is greater for Case 2 than for Case 1, which is attributed to the heat generated when a portion of the incident light is absorbed by the tinted acrylic sheet.

The temperature profiles for Case 3 are shown in Figure 3c. Compared to Case 1, the addition of the insulation at the sides of the water container results in a small increase in the water temperature throughout the container. In comparing the results from Case 3 to those of Case 2, it can be noted that inserting the tinted glass sheet at the center of the water container results in a larger temperature increase than adding insulation at the sides of the container. However, the ability to retain the stored thermal energy is better for Case 3 than for Case 2. For example, during the first five hours of the discharging phase (at the 10 h

mark of the experiment) the temperature of the water at the top of the acrylic container decreased by 9 °C for Case 2 and by 5 °C for Case 3.

The temperature profile measurements for Case 4 are shown in Figure 3d. With the addition of both the insulation and the tinted acrylic sheet the water temperature at the end of the charging phase is increased to 38 °C. Figure 3e, which plots the results for Case 5, shows the water temperature can be significantly increased by placing the water container in the Trombe wall prototype. When the tinted acrylic sheet is inserted into the water container within the Trombe wall prototype (Case 6, shown in Figure 3f), the temperature of the water at the top of the container is further increased to 45 °C. Moreover, the results from the numerical simulations over the charging phase while the water is subjected to solar simulated light are shown as the dashed lines in Figure 3b,d,f. The results from the experiment and simulations are in good agreement and are within 2 °C by the end of the charging phase for all locations (including the temperature at the top, middle and bottom of the water storage medium).

The maximum increase in temperature, which occurs at the top of the water container at the end of the charging phase is shown for Cases 1 through 10 in Figure 4. The lowest increase in temperature is ΔTmax = 11.7 °C for Case 1, whereas the highest increase of ΔTmax = 23.6 °C occurs for Case 6.

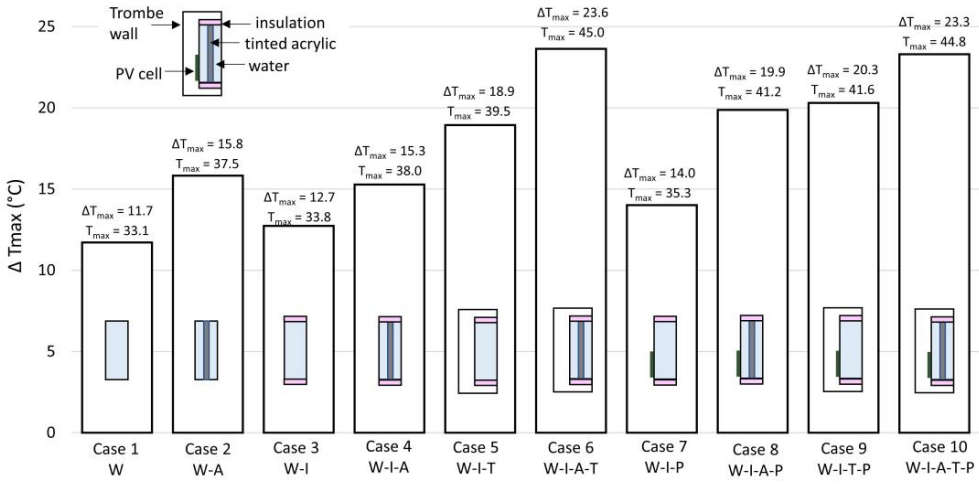


Figure 4. The temperature increase (ΔTmax) is measured at the top of the acrylic container for Cases 1 to 10. The maximum temperature, Tmax, measured at the top of the water container is also provided above the bar graph for each case.

The addition of the PV cells at the front bottom face of the acrylic container generally caused an increase in ΔTmax. For example, in comparing Cases 3 (W-I) and 7 (W-I-P), the addition of the PV cells resulted in an increase from ΔTmax = 12.7 °C to ΔTmax = 14.0 °C. In comparing Cases 4 (W-I-A) and 8 (W-I-A-P), the addition of the PV cells resulted in an increase from ΔTmax = 15.3 °C to ΔTmax = 19.9 °C. However, when comparing Cases 6 and 10, a slight decrease from ΔTmax = 23.6 °C to ΔTmax = 23.3 °C occurs with the addition of the PV cells when the Trombe wall prototype and tinted acrylic sheet are present in the experimental setup. Based on these results the heat generated when incident light is absorbed by the PV cells can cause the temperature of the water to increase during the charging phase if the amount of light being converted to heat in the water is low or if the insulation is relatively poor. However, for the case when the Trombe wall prototype and tinted acrylic sheet are present the temperature of the water is already elevated, and the addition of the PV cells does not have a significant effect on the water temperature.

The temperature profile for the water and PV cell for Case 7 are shown in Figure 5a,b, respectively. The open circuit voltage, Voc, of the PV cell is also shown in Figure 5b. In this work, the temperature and open circuit voltage of the PV cells were measured only during the charging phase. At the beginning of the charging phase, the output voltage is about

0.715 V, and this value decreases to 0.68 V by the end of the charging phase. This decrease in Voc is attributed to the increase in the PV cell temperature. Before the solar-simulated light is turned on, the temperature of the PV cell is about 21 °C. Once the light is turned on, the PV cell temperature is quickly increased to about 42 °C after the first 15 min of the charging phase. The PV cell temperature continues to rise gradually to a maximum temperature of 47 °C at the end of the charging phase.

The water and PV cell temperature profiles for Case 8 are shown in Figure 5c,d, respectively. Similarly to Case 7, for Case 8, the temperature of the PV cell increases from 21 °C before the charging phase begins to about 47 °C when the charging phase is completed. Likewise, the value of Voc decreases from 0.715 V to about 0.68 V. Figure 5e shows the temperature profiles in the water-based thermal storage medium for Case 9 and Figure 5f shows the temperature and open circuit voltage of the PV cell over the duration of the charging phase. The temperature of the PV cell increases from 21 °C at the onset of the charging phase to 47 °C at the end of the charging phase. At the beginning of the charging phase the open circuit voltage is 0.69 V, which is less than that for Cases 7 and 8 because the incident light intensity for Case 9 is reduced due to absorption and reflection by the acrylic window at the front face of the Trombe wall prototype. By the end of the charging phase, the open circuit voltage is reduced to 0.66 V due to the temperature rise of the PV cell.

The temperature profiles of the water within the Trombe wall prototype for Case 10 are shown in Figure 5g and the corresponding measurements for the temperature and Voc of the PV cell are shown in Figure 5h. The temperature of the PV cell increases from 21 °C to 49 °C during the charging phase and Voc decreases from 0.685 V to 0.66 V over the same time period. The temperature and Voc of the PV cell during the charging phase for Cases 11 and 12 are shown in Figure 5i,j, respectively. For case 11, Voc decreases from 0.68 V to about 0.64 V as the temperature of the PV cell increases from 21 °C to slightly over 70 °C over the five-hour duration that the PV cell is subjected to solar-simulated light. For Case 12, the temperature of the PV cell increases from 21 °C to about 89 °C, and Voc decreases from 0.685 to less than 0.6 V.

The ability for the cooler water at the bottom of the water storage medium to act as a heatsink that reduces the extent to which the temperature of the PV cell rises is clear from the data listed in Table 2. The temperature at the bottom of the water storage medium near its front side (T3) at the end of the charging phase ranges from 30.2 °C to 34.8 °C for Cases 7 through 10. The corresponding temperature of the PV cell ranges from 48.0 to 49.7 °C for Cases 7 through 10. However, for Cases 11 and 12, when the water is not present in the water storage medium, the temperature of the PV cell greatly increases to 71.4 °C and 90 °C, respectively. Furthermore, Voc decreases from 0.68 V to 0.64 V for Case 11 and from 0.658 V to less than 0.6 V for Case 12 while being subjected to the incident solar radiation over five hours. Notably, the drop in the output voltages observed for Cases 11 and 12 are comparable to those reported in the literature for the corresponding increase in temperature [34,35].

Table 2. Temperatures and open circuit voltages for Cases 7–12.

CASE	T3 at the End of the Charging Phase (°C)	ΔT3 at the End of the Charging Phase (°C)	T of the PV Cell at the End of the Charging Phase (°C)	ΔT for the PV Cell at the End of the Charging Phase (°C)	Voc at the End of the Charging Phase (V)	ΔVoc at the end of the Charging Phase (V)
7 (W-I-P)	30.2	9.3	48.0	27.1	0.680	0.034
8 (W-I-A-P)	30.6	9.5	48.2	27.4	0.679	0.036
9 (W-I-T-P)	32.5	11.1	48.7	27.6	0.670	0.028
10 (W-I-T-A-P)	34.8	13.3	49.7	28.5	0.668	0.024
11 (I-P)	—	—	71.4	50.5	0.642	0.038
12 (I-T-P)	—	—	88.8	68.2	0.600	0.068

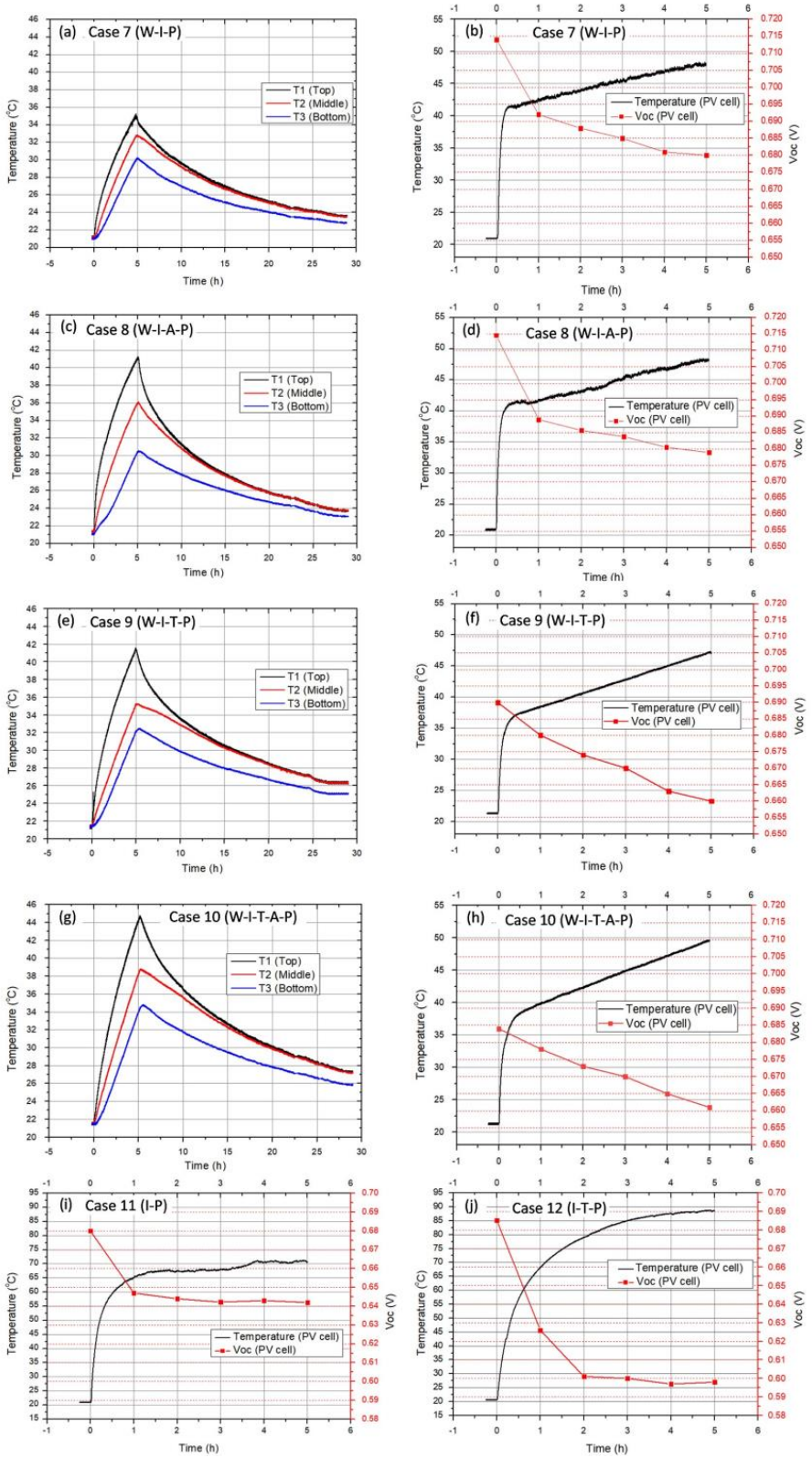


Figure 5. Temperature profiles of the water for (**a**) Case 7, (**c**) Case 8, (**e**) Case 9, and (**g**) Case 10. Temperature and open circuit voltage profiles for the PV cell for (**b**) Case 7, (**d**) Case 8, (**f**) Case 9, (**h**) Case 10, (**i**) Case 11, and (**j**) Case 12.

3.2. Results from the Numerical Simulations

Schematic diagrams of a full-sized Trombe wall are shown in Figure 6a,b. Similar to the small-scale Trombe wall prototype, the clear water storage container has a depth of

20 mm, and the tinted acrylic sheet resides at its midplane. For the full-scale Trombe wall configuration, there is a 100 mm thick air channel between the water storage medium and the indoor wall of the building. Furthermore, as shown in Figure 6a, it is assumed that PV cells are placed on the bottom half of the front face of the water storage medium. There are 6 rows and 17 columns of PV cells (102 PV cells in total), each with a facial area of 125 mm × 125 mm, such that almost half of the bottom surface of the Trombe wall is covered with PV cells. The temperature at the top, middle and bottom of the full scale Trombe wall is plotted in Figure 6c. In simulating these results, it was assumed that the heat generation terms for the bottom half of the structure were reduced by 50% due to the presence of the PV cells. Heat generated due to absorption of sunlight in the PV cells was not considered. All other methods used in the simulation are similar to those described in Section 2.3. As shown by the black line in Figure 6c, under this conservative assumption, the temperature at the top of the water storage medium in the Trombe wall reaches 44 °C when the wall is subjected to sunlight for five hours. Notably, the simulated temperature profiles shown in Figure 6 are comparable to the experimentally measured temperature profiles shown in Figure 5. Nevertheless, it should be noted that the results in Figure 6 are based on rough assumptions for the values of the heat generated when light is absorbed in the Trombe wall and for the heat loss at the boundaries of the structure. Thus, the initial modelling results presented in this feasibility study show the Trombe wall proposed in this work has the potential to effectively provide heated water that is useful for building applications. Subsequent work should include the modelling and fabrication of a large-scale physical prototype to fully validate the concept.

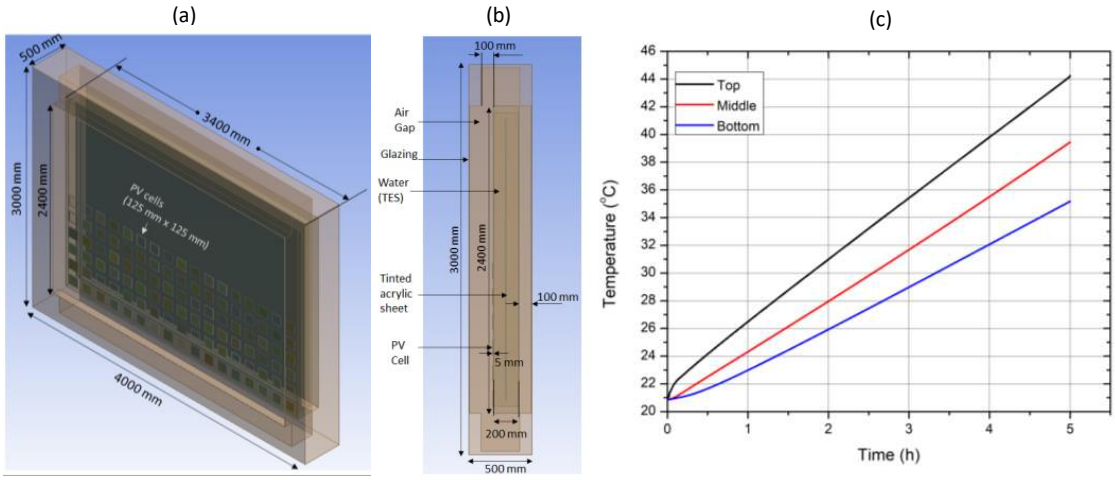


Figure 6. (**a**) Diagram of a 3 m tall Trombe wall; (**b**) cross-sectional view of a 3 m tall Trombe wall; (**c**) comparison of the simulated temperature profiles at the top, middle and bottom of the water storage medium within the 3 m Trombe wall with the small scale prototype.

4. Discussion

The results presented in this work demonstrate that Trombe walls can be used to simultaneously provide multiple functions. The semitransparent, water-based Trombe wall can generate and store heated water, allow for some degree of indoor lighting, and produce electric power. For example, the temperature of the water at the top of the acrylic container reached almost 45 °C, while PV cells were attached to the bottom half of its front surface for Case 10, which is sufficient to provide for most hot water applications in buildings [36]. As one example, it has been reported that dishwashers operate efficiently at temperatures as low as 38 °C, and the temperature of water used for showering is typically in the range of 37–40 °C. Moreover, the recommended water temperature in newer washing machines for high efficiency is approximately 49 °C. Furthermore, it has been suggested that the safest temperature for a hot water tank is 49 °C. Considering the temperature of the inlet water for hot water tanks in buildings during warm weather conditions is commonly ~18 °C,

the Trombe wall presented in this work could provide preheated water to the hot water tank to minimize the amount fuel it must consume to meet water heating demands [37]. The heated water can also be stored within the Trombe wall and used hours after sunlight is no longer available. For Case 10, the temperature of the heated water is about 37 °C at the ten-hour mark of the experiment (five hours after the light is switched off), which is still useful for most applications in buildings. The stored water could also be used as preheated water that is sent to a boiler. Furthermore, for Case 10, the temperature of the PV cell increased up to about 47 °C, which is not uncommon for PV cells operating in the field [38,39].

The performance of the Trombe wall presented in this work would be enhanced by operating it as a dynamic building envelope [40,41]. The PV Cells and tinted acrylic sheet could be integrated as light-weight panels that can be removed to satisfy varying demand profiles for electric power, heat and indoor lighting. For example, during summer, a tinted acrylic sheet that absorbs more solar irradiance could be used in the Trombe wall to prevent overheating, whereas a lightly tinted acrylic sheet could be used in winter to allow more solar heat and light to enter the building. It should also be noted that there is a tradeoff between the level of daylight provided to the interior of the building through the Trombe wall and maximizing the temperature the water can be heated to. In this regard, the optical properties of the tinted acrylic sheet used in this work could also be optimized. The visible light spectrum extends from 380 nm to 700 nm; however, as shown in Figure S1, the transmitted light spectrum in the range from 800 nm to 1800 nm is fairly high (about 35% on average). It would be preferrable if the tinted acrylic sheet absorbed all the incident solar radiation over this spectral region to heat the water in the storage medium to the greatest extent possible. It should also be noted that coated acrylics can be used in place of the tinted acrylic to provide for a selection of available brightness and colors [42].

Moreover, the performance of the water-based, semitransparent photovoltaic thermal Trombe wall presented herein could be further improved by using semitransparent PV cells [43–48] and by using optical coatings to increase the transparency of the Trombe wall window [49–52]. Semitransparent PV cells transmit light below the bandgap of the PV cells, which would allow more light to be absorbed by the acrylic sheet in the water storage medium. Semitransparent PV cells may also reduce the amount of absorbed and reflected light, which could reduce the temperature in the air channel of the Trombe wall and the PV cell. The results presented herein demonstrate the feasibility of the water-based, semitransparent photovoltaic thermal Trombe wall design. However, further research is required to validate the concept using a full-scale prototype.

There are some practical considerations to take into account when scaling the water-based Trombe wall proposed in this work. The strength of the transparent material used to contain the water would have to be designed to safely withstand the mechanical loads imposed by the water's weight. Notably, polycarbonate sheets have been fabricated for use in load-bearing structures [53]. Furthermore, supplemental heating may be needed to prevent the water from freezing if the building is unoccupied for long periods in cold climates and its temperature is allowed to drop. Moreover, to keep the stored water clear, it should not be left stagnant and should be filtered prior to entering the storage medium [54,55].

5. Conclusions

In this work, we experimentally investigated the feasibility of using Trombe walls to perform multiple functions during warm weather conditions including (1) heating and storing water for building applications, (2) providing occupants with visibility to the outdoors, and (3) generating electric power. Experiments were carried out on a small-scale prototype comprising a clear water storage container that is inside an insulated enclosure with transparent windows at its front and rear sides. A tinted acrylic sheet was immersed in the water within the clear container and was illuminated with solar-simulated light. Photovoltaic cells were placed at the lower half of the front face of the water storage

container. The cooler water at the bottom of the water storage container acted as a heat sink that reduced the extent to which the temperature of the PV cells increased.

The presence of the PV cells on the lower half of the front face of the water container did not have a significant effect on the water temperature. When the PV cells were absent, the temperature of the water at the top of the storage container was elevated to about 46 °C after being subjected to incident solar radiation for five hours. On the other hand, the temperature of the water at the top of the storage container was elevated to almost 45 °C when subjected to solar-simulated radiation over the same timeframe. This result suggests that electric power from the PV cells and hot water can be generated simultaneously in the water-based Trombe wall configuration presented in this work. The prototype also exhibited the ability to store thermal energy, as the temperature at the top of the water container was 37 °C five hours after the solar-simulated light was switched off. This is an important result because it suggests the water-based Trombe wall will be able to satisfy a portion of the demand for heated water in buildings after the sun has set. The results also show the benefits of thermal stratification within the water tank. While the temperature at the top of the water storage medium was about 45 °C, the temperature of the water near the bottom of the storage container did not surpass 35 °C. The relatively cooler water at the bottom of the container functions as an effective heat sink that limits the extent to which the temperature of the PV cells is elevated.

To demonstrate the ability and importance of the water to function as an effective heat sink, the temperature and open circuit voltage of the PV cells was measured with and without water present in the storage container while the Trombe wall prototype was subjected to incident solar-simulated radiation for five hours. When the water was present, the open circuit voltage was about 0.685 V just after the light was turned on. Over the five hour duration that the light was on, the temperature of the PV cell increased to about 50 °C, and the open circuit voltage of the PV cell decreased to 0.66 V. However, for the experiment wherein the light was removed from the container, the temperature of the PV cell increased to almost 90 °C after being subjected to light from the solar simulator for five hours and the open circuit voltage of the PV cell decreased from 0.685 V to less than 0.60 V over this time period.

Further research is required to investigate the feasibility and potential of water-based, semitransparent photovoltaic thermal Trombe walls at full-scale and under actual weather conditions. Nevertheless, the results attained thus far in this work bode well for the potential of this Trombe wall design and warrant its further development.

Supplementary Materials: The following supporting information can be downloaded at: https://www.mdpi.com/article/10.3390/en16041618/s1. Figure S1: Transmittance spectrum for the clear acrylic sample (top left), transmittance spectrum for the tinted acrylic sample (top right), absorptance spectrum for the clear acrylic sample (bottom left) and the absorptance spectrum for the tinted acrylic sample (bottom right). Figure S2: Temperature profiles at the front and back of the water storage medium (measured using thermocouples T1 through T6 in Figure 1) during the charging and discharging periods for the experiments carried out for (a) Case 1, (b) Case 2, (c) Case 3, (d) Case 4, (e) Case 5, (f) Case 6, (g) Case 7, (h) Case 8, (i) Case 9, (j) Case 10.

Author Contributions: Conceptualization, H.S. and P.G.O.; Methodology, S.B., N.S., A.K.K., H.S. and P.G.O.; Formal Analysis, S.B., N.S. and P.G.O.; Investigation, S.B., N.S., A.K.K. and P.G.O.; writing—original draft preparation, S.B., N.S. and P.G.O.; writing—review and editing, S.B., N.S. and P.G.O.; supervision, P.G.O.; funding acquisition, P.G.O. All authors have read and agreed to the published version of the manuscript.

Funding: This research was funded by the Mitacs Globalink Research Internship (GRI) Program and by the Natural Sciences and Engineering Research Council of Canada (NSERC, RGPIN-2017-05987).

Acknowledgments: Assistance provided by Abdallah Alshantaf in fabricating the Trombe wall prototype experimental setup is greatly appreciated. The authors also thank Atousa Pirvaram for assistance with the optical measurements.

Conflicts of Interest: The authors declare no conflict of interest.

References

1. Cozzi, L.; Gould, T. *World Energy Outlook 2022*; International Energy Agency: Paris, France, 2022.
2. Löf, G.O.G.; Duffie, J.A.; Smith, C.O. World distribution of solar radiation. *Solar Energy* **1966**, *10*, 27–37. [CrossRef]
3. Vaisi, S.; Pilla, F.; McCormac, D.; McCormack, S.J. Towards urban energy density (UED) definition. In Proceedings of the Energy for Sustainability 2015—Sustainable Cities: Designing for People and the Planet, Coimbra, Portugal, 14–15 May 2015.
4. Howard, B.; Parshall, L.; Thompson, J.; Hammer, S.; Dickinson, J.; Modi, V. Spatial distribution of urban energy consumption by end use. *Energy Build.* **2012**, *45*, 141–151. [CrossRef]
5. Güneralp, B.; Zhou, Y.; Urge-Vorsatz, D.; Gupta, M.; Sha, Y.; Patel, P.L.; Fragkias, M.; Li, X.; Seto, K.C. Global scenarios of urban density and its impacts on building energy use through 2050. *Proc. Natl. Acad. Sci. USA* **2017**, *114*, 8945–8950. [CrossRef] [PubMed]
6. Daigle, Q.; O'Brien, P.G. Heat Generated Using Luminescent Solar Concentrators for Building Energy Applications. *Energies* **2020**, *13*, 5574. [CrossRef]
7. Saadatian, O.; Sopian, K.; Lim, C.H.; Asim, N.; Sulaiman, M.Y. Trombe walls: A review of opportunities and challenges in research and development. *Renew. Sustain. Energy Rev.* **2012**, *16*, 6340–6351. [CrossRef]
8. Hu, W.; He, J.; Ji, J.; Zhang, S. A review on the application of Trombe wall system in buildings. *Renew. Sustain. Energy Rev.* **2017**, *70*, 976–987. [CrossRef]
9. Sergei, K.; Shen, C.; Jiang, Y. A review of the current work potential of a Trombe wall. *Renew. Sustain. Energy Rev.* **2020**, *130*, 109947. [CrossRef]
10. Duffie, J.A.; Beckman, W.A. *Solar Engineering of Thermal Processes*; John Wiley & Sons, Inc.: Hoboken, NJ, USA, 1991; pp. 250–330.
11. Mokni, A.; Lashin, A.; Ammar, M.; Mhiri, H. Thermal analysis of a Trombe wall in various climatic conditions: An experimental study. *Solar Energy* **2022**, *243*, 247–263. [CrossRef]
12. Yang, L.; Dhahad, H.A.; Chen, M.; Huang, Z.; Anqi, A.E.; Rajhi, A.A.; Qader, D.N. Transient analysis of buildings with Trombe wall in a southern envelope and strengthening efficacy by adding phase change material. *J. Build. Eng.* **2022**, *55*, 104670. [CrossRef]
13. Liu, H.; Li, P.; Yu, B.; Zhang, M.; Tan, Q.; Wang, Y. The performance analysis of high-efficiency dual-channel Trombe wall in winter. *Energy* **2022**, *253*, 124087. [CrossRef]
14. Shen, J.; Lassue, S.; Zalewski, L.; Huang, D. Numerical study of classical and composite solar walls by TRNSYS. *J. Therm. Sci.* **2007**, *16*, 46–55. [CrossRef]
15. Chan, H.Y.; Riffat, S.B.; Zhu, J. Review of passive solar heating and cooling technologies. *Renew. Sustain. Energy Rev.* **2010**, *14*, 781–789. [CrossRef]
16. Stazi, F.; Mastrucci, A.; di Perna, C. The behaviour of solar walls in residential buildings with different insulation levels: An experimental and numerical study. *Energy Build.* **2012**, *47*, 217–229. [CrossRef]
17. Stazi, F.; Mastrucci, A.; di Perna, C. Trombe wall management in summer conditions: An experimental study. *Solar Energy* **2012**, *86*, 2839–2851. [CrossRef]
18. Gan, G. A parametric study of Trombe walls for passive cooling of buildings. *Energy Build.* **1998**, *27*, 37–43. [CrossRef]
19. Jaber, S.; Ajib, S. Optimum design of Trombe wall system in mediterranean region. *Solar Energy* **2011**, *85*, 1891–1898. [CrossRef]
20. Torcellini, P.; Pless, S. *Trombe Walls in Low-Energy Buildings: Practical Experiences*; National Renewable Energy Lab.: Golden, CO, USA, 2004.
21. Mohamad, A.; Taler, J.; Oclon, P. Trombe Wall Utilization for Cold and Hot Climate Conditions. *Energies* **2019**, *12*, 285. [CrossRef]
22. Singh, H.; O'Brien, P.G. Semi-transparent water-based Trombe walls for passive air and water heating. *Buildings* **2022**, *12*, 1632. [CrossRef]
23. Skoplaki, E.; Palyvos, J.A. On the temperature dependence of photovoltaic module electrical performance: A review of efficiency/power correlations. *Solar Energy* **2009**, *83*, 614–624. [CrossRef]
24. Dubey, S.; Sarvaiya, J.N.; Seshadri, B. Temperature dependent photovoltaic (PV) efficiency and its effect on PV production in the world–a review. *Energy Procedia* **2013**, *33*, 311–321. [CrossRef]
25. Temaneh-Nyah, C.; Mukwekwe, L. An investigation on the effect of operating temperature on power output of the photovoltaic system at University of Namibia Faculty of Engineering and IT campus. Proceeding of the 2015 Third International Conference on Digital Information, Networking, and Wireless Communications (DINWC), Moscow, Russia, 3–5 February 2015; pp. 22–29.
26. Rahman, M.M.; Hasanuzzaman, M.; Abd Rahim, N. Effects of operational conditions on the energy efficiency of photovoltaic modules operating in Malaysia. *J. Clean. Prod.* **2017**, *143*, 912–924. [CrossRef]
27. Perraki, V.; Kounavis, P. Effect of temperature and radiation on the parameters of photovoltaic modules. *J. Renew. Sustain. Energy* **2016**, *8*, 013102. [CrossRef]
28. Hu, Z.; He, W.; Hu, D.; Lv, S.; Wang, L.; Ji, J.; Chen, H.; Ma, J. Design, construction and performance testing of a PV blind-integrated Trombe wall module. *Appl. Energy* **2017**, *203*, 643–656. [CrossRef]
29. Koyunbaba, B.K.; Yilmaz, Z.; Ulgen, K. An approach for energy modeling of a building integrated photovoltaic (BIPV) Trombe wall system. *Energy Build.* **2013**, *67*, 680–688. [CrossRef]
30. Jie, J.; Hua, Y.; Gang, P.; Jianping, L. Study of PV-Trombe wall installed in a fenestrated room with heat storage. *Appl. Therm. Eng.* **2007**, *27*, 1507–1515. [CrossRef]
31. Ahmed, O.K.; Hamada, K.I.; Salih, A.M. Performance analysis of PV/Trombe with water and air heating system: An experimental and theoretical study. *Energy Sour. Part A Recovery Util. Environ. Eff.* **2022**, *44*, 2535–2555. [CrossRef]

32. Cuce, E.; Cuce, P.M.; Bali, T. An experimental analysis of illumination intensity and temperature dependency on photovoltaic cell parameters. *Appl. Energy* **2013**, *111*, 374–382. [CrossRef]
33. NREL. Solar Resource Maps and Data. Available online: https://www.nrel.gov/gis/solar-resource-maps.html (accessed on 27 January 2023).
34. Singh, P.; Ravindra, N.M. Temperature Dependence of Solar Cell Performance—An Analysis. *Solar Energy Mater. Solar Cells* **2012**, *101*, 36–45. [CrossRef]
35. Cotfas, D.T.; Cotfas, P.A.; Machidon, O.M. Study of temperature coefficients for parameters of photovoltaic cells. *Int. J. Photoenergy* **2018**, *1*, 1–12. [CrossRef]
36. Marszal-Pomianowska, A.; Jensen, R.L.; Pomianowski, M.; Larsen, O.K.; Jørgensen, J.S.; Knudsen, S.S. Comfort of domestic water in residential buildings: Flow, temperature and energy in draw-off points: Field study in two danish detached houses. *Energies* **2021**, *14*, 3314. [CrossRef]
37. Water Temperature and Burns/Scalds. Available online: https://www.canada.ca/en/public-health/services/water-temperature-burns-scalds.html (accessed on 17 October 2022).
38. Schwingshackl, C.; Petitta, M.; Wagner, J.E.; Belluardo, G.; Moser, D.; Castelli, M.; Zebisch, M.; Tetzlaff, A. Wind effect on PV module temperature: Analysis of different techniques for an accurate estimation. *Energy Procedia* **2013**, *40*, 77–86. [CrossRef]
39. Van Sark, W.G.J.H.M. Feasibility of photovoltaic–thermoelectric hybrid modules. *Appl. Energy* **2011**, *88*, 2785–2790. [CrossRef]
40. Svetozarevic, B.; Begle, M.; Jayathissa, P.; Caranovic, S.; Shepherd, R.F.; Nagy, Z.; Hischier, I.; Hofer, J.; Schlueter, A. Dynamic photovoltaic building envelopes for adaptive energy and comfort management. *Nat. Energy* **2019**, *4*, 671–682. [CrossRef]
41. Tabadkani, A.; Roetzel, A.; Li, H.X.; Tsangrassoulis, A. Design approaches and typologies of adaptive facades: A review. *Autom. Constr.* **2021**, *121*, 103450. [CrossRef]
42. Maduru, V.R.; Shaik, S.; Cuce, E.; Afzal, A.; Panchal, H.; Cuce, P.M. UV coated acrylics as a substitute for generic glazing in buildings of Indian climatic conditions: Prospective for energy savings, CO_2 abatement, and visual acceptability. *Energy Build.* **2022**, *268*, 112231. [CrossRef]
43. Ghosh, A.; Sundaram, S.; Mallick, T.K. Investigation of thermal and electrical performances of a combined semi-transparent PV-vacuum glazing. *Appl. Energy* **2018**, *228*, 1591–1600. [CrossRef]
44. Bailey-Salzman, R.F.; Rand, B.P.; Forrest, S.R. Semitransparent organic photovoltaic cells. *Appl. Phys. Lett.* **2006**, *88*, 233502. [CrossRef]
45. Yang, Y.; O'Brien, P.G.; Ozin, G.A.; Kherani, N.P. See-through amorphous silicon solar cells with selectively transparent and conducting photonic crystal back reflectors for building integrated photovoltaics. *Appl. Phys. Lett.* **2013**, *102*, 221109. [CrossRef]
46. O'Brien, P.G.; Chutinan, A.; Mahtani, P.; Leong, K.; Ozin, G.A.; Kherani, N.P. Selectively transparent and conducting photonic crystal rear-contacts for thin-film silicon-based building integrated photovoltaics. *Opt. Express* **2011**, *19*, 17040–17052. [CrossRef] [PubMed]
47. Alrashidi, H.; Issa, W.; Sellami, N.; Sundaram, S.; Mallick, T. Thermal performance evaluation and energy saving potential of semi-transparent CdTe in Façade BIPV. *Solar Energy* **2022**, *232*, 84–91. [CrossRef]
48. Uddin, M.M.; Wang, C.; Zhang, C.; Ji, J. Investigating the energy-saving performance of a CdTe-based semi-transparent photovoltaic combined hybrid vacuum glazing window system. *Energy* **2022**, *253*, 124019. [CrossRef]
49. Sarkin, A.S.; Ekren, N.; Sağlam, S. A review of anti-reflection and self-cleaning coatings on photovoltaic panels. *Solar Energy* **2020**, *199*, 63–73. [CrossRef]
50. Chunxue, J.; Liu, W.; Bao, Y.; Chen, X.; Yang, G.; Wei, B.; Yang, F.; Wang, X. Recent applications of antireflection coatings in solar cells. *Photonics* **2022**, *9*, 906.
51. Loh, J.Y.Y.; Puzzo, D.P.; O'Brien, P.G.; Ozin, G.A.; Kherain, N.P. Enhancing photovoltaics with broadband high-transparency glass using porosity-tuned multilayer silica nanoparticle anti-reflective coatings. *RSC Adv.* **2014**, *4*, 31188–31195. [CrossRef]
52. Vázquez-Guardado, A.; Boroumand, J.; Franklin, D.; Chanda, D. Broadband angle-independent antireflection coatings on nanostructured light trapping solar cells. *Phys. Rev. Mater.* **2018**, *2*, 035201. [CrossRef]
53. Zapałowicz, Z.; Wojnicki, O. Estimation of total solar transmittance for twin-wall polycarbonate sheet with rectangular structure on the basis of experimental research. *Energies* **2022**, *15*, 1360. [CrossRef]
54. Brown, K.W.; Gessesse, B.; Butler, L.J.; MacIntosh, D.L. Potential effectiveness of point-of-use filtration to address risks to drinking water in the United States. *Environ. Health Insights* **2017**, *11*. [CrossRef]
55. Cescon, A.; Jiang, J. Filtration process and alternative filter media material in water treatment. *Water* **2020**, *12*, 3377. [CrossRef]

Disclaimer/Publisher's Note: The statements, opinions and data contained in all publications are solely those of the individual author(s) and contributor(s) and not of MDPI and/or the editor(s). MDPI and/or the editor(s) disclaim responsibility for any injury to people or property resulting from any ideas, methods, instructions or products referred to in the content.

Design and Performance Evaluation of Three-Phase Grid-Tied Solar Power Generation System Using STF based Algorithm

Ranjeet Singh
Department of Electrical Engineering
Delhi Technological University
Delhi, India
ranjeetsingh_2k20phdee502@dtu.ac.in

Vinod Kumar Yadav
Department of Electrical Engineering
Delhi Technological University
Delhi, India
vinodkumar@dtu.ac.in

Madhusudan Singh
Department of Electrical Engineering
Delhi Technological University
Delhi, India
madhusudan@dce.ac.in

2023 International Conference on Power, Instrumentation, Energy and Control (PIECON) | 979-8-3503-9976-9/23/$31.00 ©2023 IEEE | DOI: 10.1109/PIECON56912.2023.10085865

***Abstract*— This article presents a dual-stage three-phase grid interfaced solar photovoltaic power generation (SPPG) system with the proposed self-tuning filter (STF) assisted control of a voltage source converter (VSC). The complete system design comprises a solar photovoltaic (SPV) array, DC-DC boost converter, VSC, and linear/non-linear loads. VSC is integrated with the SPV array to meet the active power requirement of the load, and, if available, surplus power from the array is transferred to the grid. The control approach aims to harvest the optimal power from the SPV system with improvement in power quality (PQ) issues, particularly harmonic rejection and power factor correction. The reference and sensed grid currents are utilized in the current controller to effectuate the switching operation of the VSC. The performance of the proposed STF control approach is tested under varied scenarios to assess the efficacy of the control algorithm. The extensive simulation study and comparative analysis with popular classical and adaptive control techniques are presented. The proposed system performs superior in enhancing the power quality at the grid side. The simulation analysis is carried out in the MATLAB/Simulink environment.**

Keywords*— Renewable power generation; Photovoltaic system; Maximum power point tracking, Power quality, Self-tuning filter

I. INTRODUCTION

Solar electricity is now economical and affordable compared to conventional energy sources. Installations of SPV generation systems are growing worldwide due to a significant fall in the cost of solar panels and improved efficiency. But grid integration challenges continue to be an area of concern and hence of great interest to researchers simultaneously. The SPPG requires significantly less maintenance and is abundantly available. It is preferred over other generation forms and is mainly employed for grid integration. Stand-alone SPPG systems are also being used. However, due to massive dependence on battery energy storage systems (BESS), it requires increased investments and is less reliable [1]-[2]. Integrating the SPPG system to the grid also offers multiple challenges because of its unpredictable nature. However, energy storage system requirements and associated problems are eliminated [3]. Integrating with the grid requires a complete system comprising a solar photovoltaic (SPV) system and additional entities such as VSC, interfacing inductors, filters, and load, which may be linear or non-linear. Many power electronic-based systems such as uninterruptible power supply (UPS), switched mode power supplies (SMPS), and other electronics loads that are primarily non-linear have badly impacted the current distribution system. These power electronic devices operating with renewable power generation systems lead to substandard power quality (PQ) in the distribution system, viz. harmonics injection, one of the most prominent PQ problems [4]. Other evident problems are inferior power factor, voltage regulation, and load unbalancing, which badly impacts many distribution end-users [5]. Strict adherence to power quality guidelines is necessary when integrating renewable generation to the utility grid [6]. Therefore it becomes essential to have a competent, sturdy, and efficient control scheme for grid interfaced VSC. The VSC is operated as an active shunt compensator to solve many PQ problems in SPV systems [7]. VSC acts as an intermediate link between the SPV and the grid system. Many authors have proposed a two-stage topology for the SPPG system and its applications [8]. The first stage incorporates maximum power operating point (MPOP) algorithm-driven DC-DC converter for optimal power extraction followed by grid-tied VSC for power injection into the distribution feeder. Due to the ease of implementation, researchers have commonly resorted to the perturb and observe (P&O) control algorithm to track MPOP of the SPV system for peak power extraction [9]-[10]. Researchers have formulated many control strategies for grid-tied SPPG systems in the past [11]. This article revisits the classical control approaches such as synchronous reference frame theory (SRFT) [12], power balance theory (PBT) [13], unit vector transform theory (UVT) [14], and popular adaptive control schemes such as least mean square (LMS) [15] and least mean fourth (LMF) [16] algorithms. It critically assesses their performances with the proposed STF approach for power factor correction, reactive power compensation, harmonic mitigation, and voltage regulation at the point of common coupling (PCC) under a balanced/unbalanced loading environment for a three-phase grid interfaced SPPG system.

II. DESIGN OF THE GRID INTEGRATED SYSTEM

The overall system layout is presented in Fig. 1. A dual-stage topology is configured here. It comprises a 415V, 50 Hz, 3-phase grid, while the first stage incorporates an SPV array, DC-DC boost converter, and (P&O) MPOP control for optimum power extraction from SPV under varying irradiance conditions. The VSC acting as an active shunt compensator forms the second stage. It is further interfaced with inductors (included one for each phase) to smoothen the injected currents and minimize switching losses. An RC filter is also employed to arrest high-frequency ripples at PCC due to the switching action of VSC. The section's upcoming portion elaborates on the design equations and selected values for different constituent elements of the proposed SPPG system. The SPV system is designed for the optimum power rating of

979-8-3503-9976-9/23/$31.00 ©2023 IEEE

Authorized licensed use limited to: DELHI TECHNICAL UNIV. Downloaded on April 10,2023 at 07:24:14 UTC from IEEE Xplore. Restrictions apply.

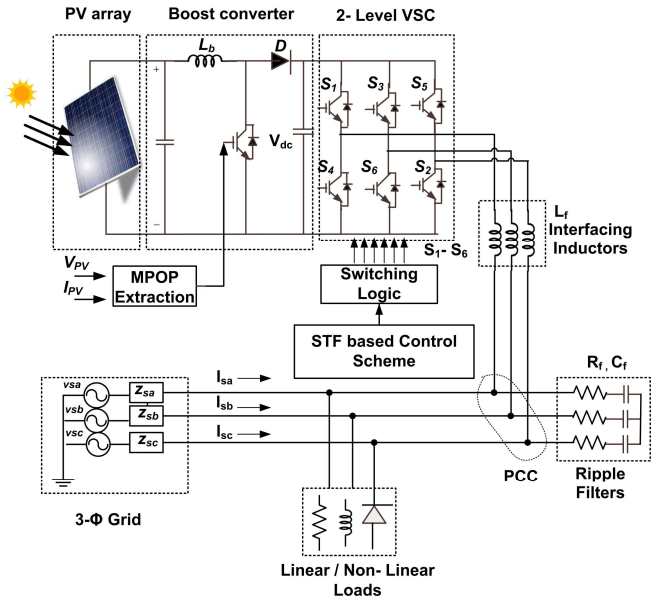


Fig. 1. Schematic Representation of Grid-Tied SPPG system.

30.8 kW by utilizing 22×7 module array interconnections. All modules in the array are similar, having identical electrical characteristics. Each SPV module employed in this work has a short circuit current rating of 8.21 A and open circuit voltage rating of 32.9 V. The inductor for the stage-I converter (boost converter) is designed for the duty ratio, D = 0.1734, as shown

$$L_{boost} = \frac{V_{mpop} \times D}{\Delta I_{input} \times f_{sw}} = \frac{578.6 \times 0.1734}{2.66 \times 10000} = 3.75\ mH \qquad (1)$$

where V_{mpop} is the SPV array voltage at MPOP and ΔI_{input} accounts for the maximum ripple in the SPV current. The input current (SPV current) is estimated as

$$I_{input} = \left(P_{mpop} / V_{mpop} \right) = 53.27\,A \qquad (2)$$

Considering the maximum allowable ripple in the input current to be 5% $(.05 \times 53.27\ A = 2.66\ A)$, the boost inductor value is estimated to be 3.75 *mH*, as shown in (1). In this work, 4 *mH* is selected. The minimal value required for the dc-link voltage should be higher than double the maximum of the phase voltage at PCC. Consequently, the dc-link voltage is determined as in [18].

$$V_{dc-link} = \frac{2\sqrt{2} \times V_{L-L}}{\sqrt{3} \times m_i} = \frac{2\sqrt{2} \times 415}{\sqrt{3} \times 1} = 677.7\ V \qquad (3)$$

where V_{L-L} is the grid phase to phase voltage and m_i is modulation index. 700 V is selected for $V_{dc-link}$. The smoothening inductors connected to VSC are estimated as [18]

$$L_f = \frac{\sqrt{3} \times m_i \times V_{dc-link}}{12 \times h \times f_{sw} \times \Delta I_{peak}} = \frac{\sqrt{3} \times 1 \times 700}{12 \times 1.2 \times 10000 \times (60.64 \times .05)} = 2.78\ mH \qquad (4)$$

where h is 1.2 and is termed as overloading factor, f_{sw} is switching frequency (10 kHz)of the VSC. ΔI_{peak} accounts for the ripple (5 %) in the peak grid phase current.

$$\Delta I_{peak} = 0.05 \times \sqrt{2} \times \left(\frac{30822}{\sqrt{3} \times 415} \right) = 3.03\,A \qquad (5)$$

3 *mH* is selected for adequate smoothening of injected currents. The value of the dc-link capacitance of VSC is determined as given in (6) [18].

$$C_{dc-link} = \frac{\left(P_{mpop} / V_{dc-link} \right)}{2 \times (2 \times \pi \times f) \times \Delta V_{dc-link}} = \left(\frac{30822/700}{2 \times 2 \times \pi \times 50 \times (2/100) \times 700} \right) = 5005.58\ \mu F \qquad (6)$$

where $\Delta V_{dc-link}$ (2 %) is allowable percent ripple in dc link voltage, $V_{dc-link}$. A safe value of 6 *mF* is chosen for the proposed system to settle the voltage rapidly in the event of system dynamics. The ripple filter component values, R_f, C_f are estimated as calculated in [18] .

III. Control Scheme

The control scheme aims to enhance power quality at PCC and feed the optimal power harvested from the PV system to the grid. Additionally, the PV integrated system is highly resistant to the adverse effects of sudden changes in loads and unbalancing effects. The control approach can be subdivided into MPOP tracking control, and grid interfaced VSC control. The MPOP control is implemented by employing a dc-dc boost converter and operating with an adequate duty cycle. Numerous control theories have been advocated in the literature to harvest optimal power from the SPPG system and are deeply investigated in [19]-[20]. For the control of VSC, the switching operation is exercised using the indirect current control scheme. The fundamental components of load current and grid voltages are determined using STF. The overall control architecture using STF is shown in Fig. 2.

3.1 MPOP Tracking Control

As discussed in the earlier section, because of the benefits associated with the P&O control algorithm, it is implemented here for MPOP convergence. The control is simple, and the algorithm observes only the change in power with corresponding perturbations in output voltage. It then decides its next course of action based on SPV power before and after perturbation and consequently alters the converter duty ratio to arrive at the MPOP. The following logic dictates the change in duty cycle:

If

$$\left\{ \begin{array}{c} \Delta P_{PV} > 0 \,\&\&\, \Delta V > 0 \\ or \\ \Delta P_{PV} < 0 \,\&\&\, \Delta V < 0 \end{array} \right\} \rightarrow D(t+1) = D(t) + \Delta D \qquad (7)$$

else if,

Authorized licensed use limited to: DELHI TECHNICAL UNIV. Downloaded on April 10,2023 at 07:24:14 UTC from IEEE Xplore. Restrictions apply.

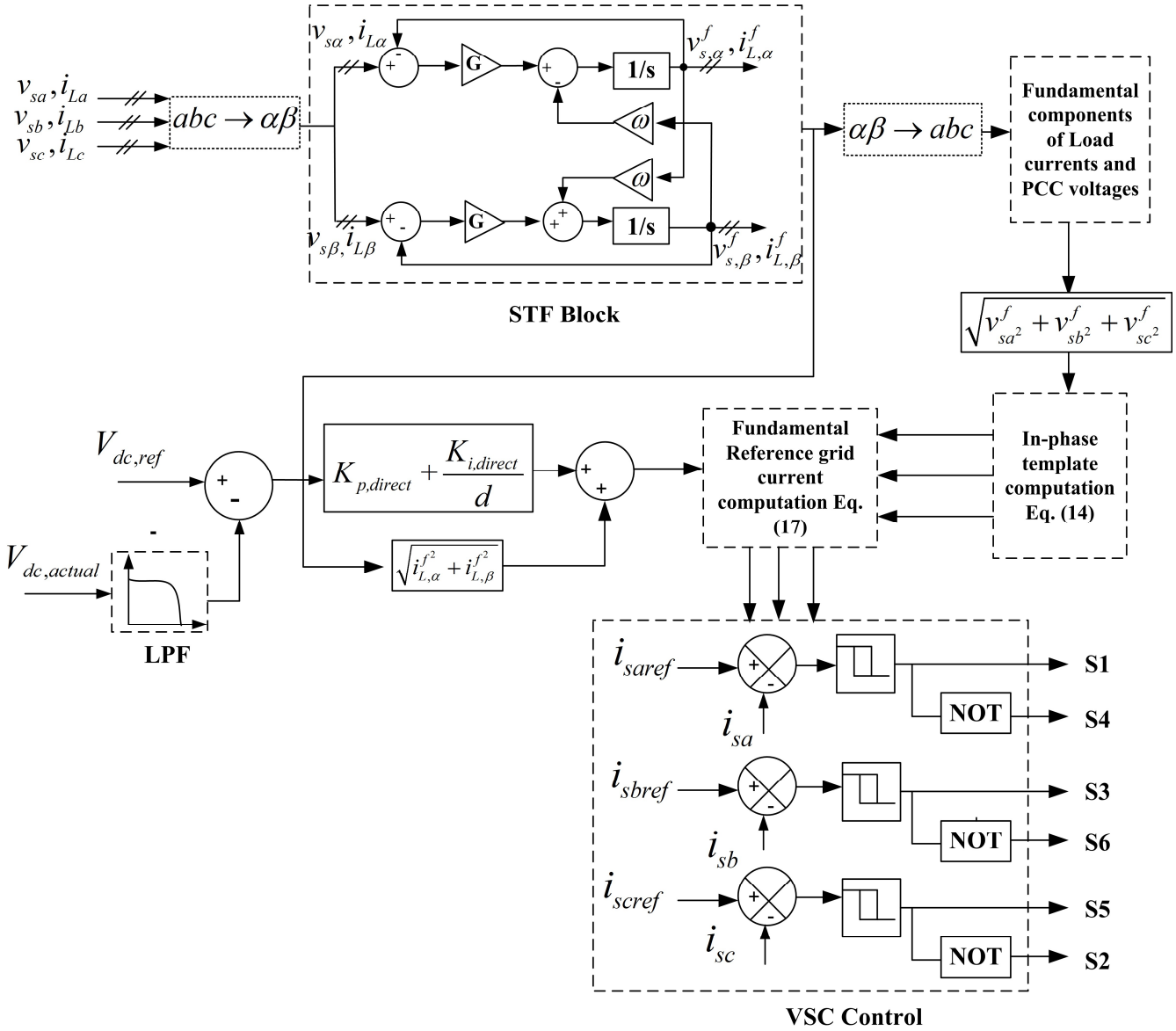


Fig. 2. STF assisted control architecture for SPPG system.

$$\left.\begin{array}{c} \Delta P_{PV} > 0 \,\&\&\, \Delta V < 0 \\ or \\ \Delta P_{PV} < 0 \,\&\&\, \Delta V > 0 \end{array}\right\} \rightarrow D(t+1) = D(t) - \Delta D \qquad (8)$$

where $\Delta P_{PV} = P(t+1) - P(t)$, $\Delta V = V(t+1) - V(t)$ and

ΔD is the change in duty ratio.

3.2. Grid-Tied VSC Control

In this section the overall control architecture is explained. To have a better insight into the control architecture, it is subdivided into five segments elaborated in subsequent sections.

3.2.1. STF Module Description

A block schematic of the STF is depicted in Fig. 3, and it is evident that it belongs to the class of multiple input - multiple output systems. STF exhibits the following transfer function structure [21].

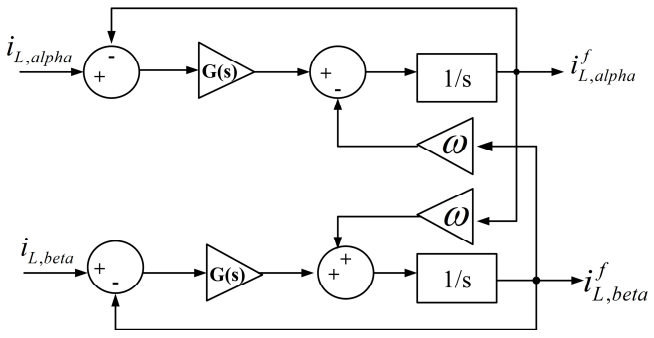


Fig. 3. Block Module representation of STF.

$$G(s) = \frac{C_{xy}(s)}{R_{xy}(s)} = \frac{s + j\omega_0}{s^2 + \omega_0^2} \qquad (9)$$

where, $C_{xy}(t) = e^{(j\omega t)} \int e^{(j\omega t)} R_{xy}(t) dt$

With a proper selection of gain G, unity magnitude of the transfer function and zero phase delay can be achieved for ω

Authorized licensed use limited to: DELHI TECHNICAL UNIV. Downloaded on April 10,2023 at 07:24:14 UTC from IEEE Xplore. Restrictions apply.

= ω_0. With the time constant of STF being 1/G, desirable performance in terms of speed of response can be ascertained by properly tuning gain parameter G. Value of the parameter, G, selected in this study is 100. For this value of G, the STF exhibits zero phase delay and quick response with unity magnitude at $\omega = \omega_0$ (see Fig. 4). The fundamental components pertaining to the grid voltages and load currents are extracted using STF by employing Clarke transformation on inputs followed by inverse Clarke transformation as given

$$\begin{pmatrix} i_{L\alpha} \\ i_{L\beta} \\ i_{L0} \end{pmatrix} = \sqrt{\frac{2}{3}} \begin{pmatrix} 1 & -\frac{1}{2} & -\frac{1}{2} \\ 0 & \frac{\sqrt{3}}{2} & -\frac{\sqrt{3}}{2} \\ \frac{1}{\sqrt{2}} & \frac{1}{\sqrt{2}} & \frac{1}{\sqrt{2}} \end{pmatrix} \begin{pmatrix} i_{La} \\ i_{Lb} \\ i_{Lc} \end{pmatrix} \quad (10)$$

STF operates on the transformed load currents to yield fundamental components of load currents, as shown in the following equations [21].

$$i^f_{L,\beta} = \frac{1}{s}\left\{G(i_{L,\beta} - i^f_{L,\beta}) - \omega i^f_{L,\alpha}\right\} \quad (11)$$

$$i^f_{L,\alpha} = \frac{1}{s}\left\{G(i_{L\alpha} - i^f_{L,\alpha}) - \omega i^f_{L,\beta}\right\} \quad (12)$$

It is noted that the response of STF is consistent with a band-pass filter.

3.2.1. PCC Amplitude and Unit-Template Estimation (V, x_{pa}, x_{pb}, x_{pc})*

The presence of source inductance causes the voltage at PCC to be distorted and non-sinusoidal under non-linear load conditions. So extraction of unit templates from such a system would not result in proper grid synchronization. The sensed grid phase voltages v_{sa}, v_{sb}, v_{sc} are first transformed from *a,b,c* to α-β components. These are applied as inputs to an STF for transforming them into fundamental α-β components and finally back to three-phase fundamental grid phase voltages v_{sa}^f, v_{sb}^f, v_{sc}^f using inverse Clarke transformation. In-phase unit templates (x_{pa}, x_{pb} and x_{pc}) are then extracted, making use of the magnitude (V^*) of the fundamental components of grid phase voltages as shown

$$V^* = \sqrt{\frac{2}{3}\left[(v^f_{sa})^2 + (v^f_{sb})^2 + (v^f_{sc})^2\right]} \quad (13)$$

$$x_{pa} = \frac{v^f_{sa}}{V^*};\ x_{pb} = \frac{v^f_{sb}}{V^*};\ x_{pc} = \frac{v^f_{sc}}{V^*} \quad (14)$$

3.2.3 Estimation of Active Loss Component

The actual voltage across the dc link (V_{dc}) is measured and corelated with the reference dc-link voltage (V_{dcref}). The error (V_{error}) obtained is passed through a PI controller, which drives the dc-link voltage to the reference value by operating upon the error received. The active loss component (I_{loss}) is obtained as

$$I^{(k+1)}_{loss} = I^k_{loss} + K_p(\Delta V_{error}) + K_i(V^{(k+1)}_{error}) \quad (15)$$

where, $\Delta V_{error} = V^{(k+1)} - V^{(k)}$ is the error difference between two successive instants.

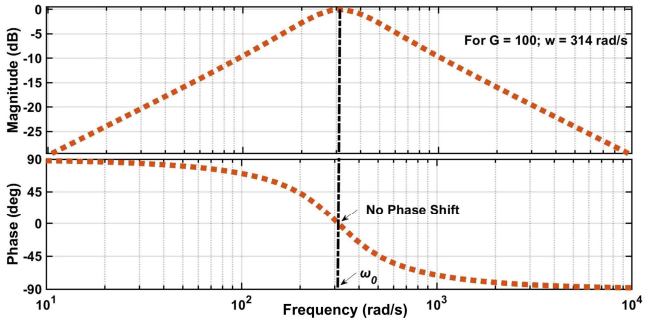


Fig. 4. Bode plot representation of STF for G = 100.

3.2.4 Estimation of the Fundamental Active Load current component

The fundamental active load current amplitude ($I_{L,\ active}^f$) is estimated from the quadrature current components ($i_{L,\alpha}^f$ and $i_{L,\beta}^f$) obtained from STF as

$$I^f_{L,active} = \sqrt{(i^f_{L,\alpha})^2 + (i^f_{L,\beta})^2} \quad (16)$$

3.2.5 Reference Grid current extraction

The effective active component (I_{ref}^*), is obtained as

$$I^*_{ref} = I_{loss} + I^f_{L,active} \quad (17)$$

The reference grid currents estimated are compared with the measured grid currents, and the resultant error is minimized using a hysteresis current regulator to effectuate switching of the VSC.

IV. Results and Discussions

A three-phase 415-V, 50 Hz, grid integrated SPPG system involving dual-stage configuration is developed and modelled using MATLAB/Simulink toolbox. For assessing the efficacy of the STF enabled control scheme, extensive simulation studies are carried out under varied scenarios. The system is critically investigated in terms of voltages at PCC, V_{sabc}, compensator currents I_{invabc}, grid currents I_{sabc}, SPV array parameters such as array current I_{pv}, voltage V_{pv}, and power P_{pv}. The voltage across DC bus V_{dc}, grid reference currents I^*_{ref} and load currents I_{labc}.

4.1 Performance Analysis under Balanced Non-Linear Load with SPPG system subjected to Uniform Insolation.

Fig. 5 demonstrates the performance of the proposed SPPG system under uniform irradiance conditions for the balanced non-linear load conditions. The grid side experiences improved power quality behavior, with the power factor being close to unity and having substantially less harmonic interference.

4.2 Performance Analysis under Balanced Linear Load with SPPG system subjected to Non- Uniform Insolation.

Fig. 6 demonstrates the performance of the proposed SPPG system under balanced loading conditions at variable insolation. For this case, a balanced 20 kW linear load at power factor 0.8 lagging is connected at the distribution end. The dynamic performance is tested under varying insolation from 500 W/m^2 to 1000 W/m^2 at t=0.65 *s*. On increment of solar insolation (G), the power extracted out of SPV system (P_{pv}) increases with subsequent increment in grid currents

Authorized licensed use limited to: DELHI TECHNICAL UNIV. Downloaded on April 10,2023 at 07:24:14 UTC from IEEE Xplore. Restrictions apply.

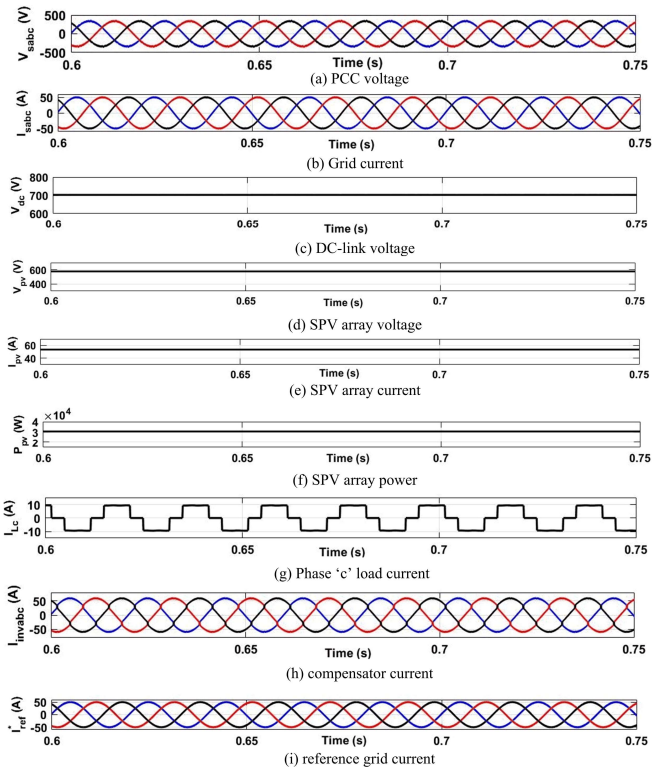


Fig. 5. Performance with balanced non-linear load under uniform insolation.

((I_{sabc}). This change is observed because the excess power fed from the SPV system after fulfilling the load requirement gets adjusted in incrementing grid current magnitude. Under all operating conditions, the grid currents remain balanced, sustained, and sinusoidal. The dc-link voltage (V_{dc}) is almost constant and is restricted to the desired value. The control scheme operates satisfactorily even for sustained dynamic variation of insolation. MPOP algorithm works well and ensures maximum power extraction out of the SPV system even when subjected to varying insolation, thus enhancing system utilization.

4.3 Performance Analysis under Unbalanced Non-Linear Load with SPV system subjected to Uniform Insolation

Fig. 7 shows the performance of the proposed SPPG system for the unbalanced non-linear load (3-Φ diode bridge rectifier with R-L load) under the influence of steady insolation. The dynamic performance is observed by removing one phase of the balanced load (phase 'c' in this case) from 0.65 *s*-0.7 *s*. It can be observed that this unbalancing has a negligible effect on the performance of the proposed system. The control algorithm adapts suitably to this change and enhances power quality at the grid side. The grid currents (I_{sabc}) remain balanced, sustained, and perfectly sinusoidal. The dc-link voltage (V_{dc}) is maintained at the reference value (700 V) throughout this dynamic condition. MPOP algorithm is extracting maximum power.

4.4 Comparative Performance Analysis of proposed STF assisted control scheme with popular conventional and adaptive control schemes

A comparative performance analysis with conventional and adaptive control schemes is performed to investigate the effectiveness of the proposed STF assisted control of VSC compared to different existing and popular control schemes. Table I, shows the percentage THD of PCC voltage and currents. The STF based control scheme for SPV power injection into the grid shows enhanced performance in

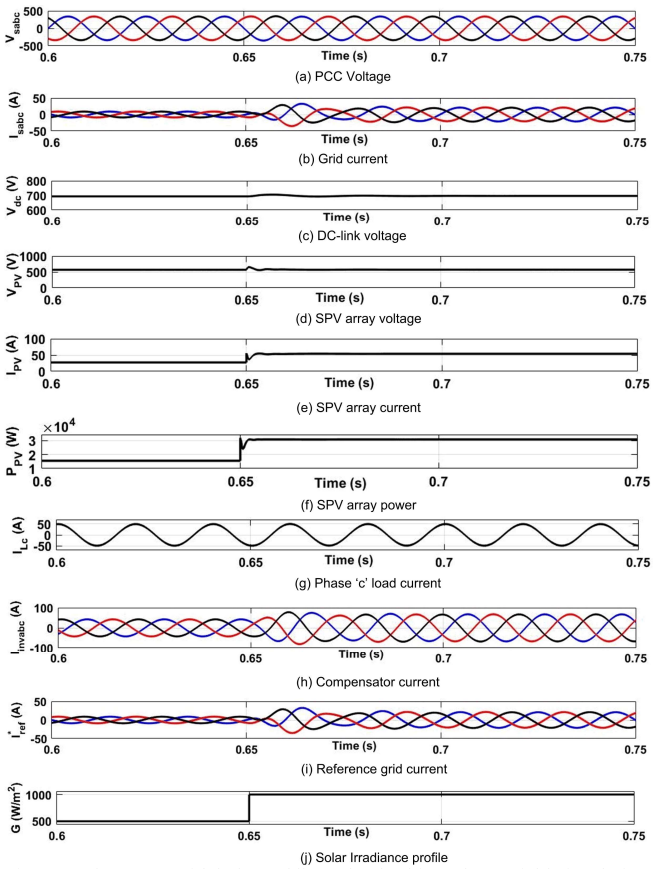


Fig. 6. Performance with balanced linear load subjected to variable insolation.

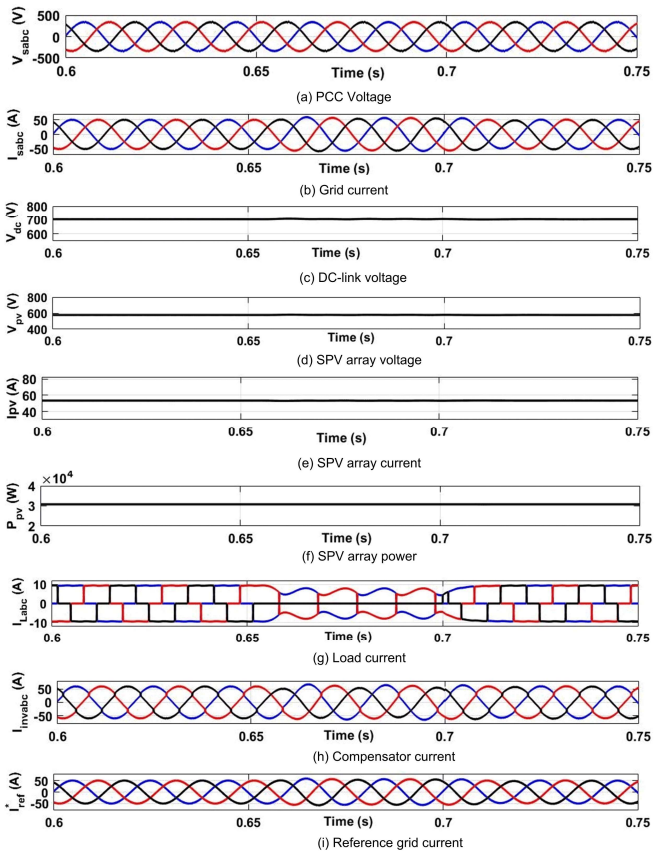


Fig. 7. Dynamic performance with unbalanced non-linear load subjected to uniform insolation.

minimizing harmonic interference at PCC, countering load unbalancing, and ensuring power factor correction. The THD

Authorized licensed use limited to: DELHI TECHNICAL UNIV. Downloaded on April 10,2023 at 07:24:14 UTC from IEEE Xplore. Restrictions apply.

values obtained with STF based control scheme for grid currents (I_{sabc}), PCC voltage (V_{sabc}) and load currents (I_{labc}) are 0.67 %, 1.33 % and 30.17 % respectively. A careful examination of the total harmonic distortion present in the grid side voltage and current indicated in Table I, clearly shows that the proposed SPPG system with STF based control scheme offers better performance. Moreover, the main advantage provided by STF based control scheme is its simple structure. One unit of STF is enough for three-phase applications. PLL-based control schemes such as SRFT results in a more complicated control structure with reduced response time. In contrast, STF based control scheme improves the speed of response and eliminates system complexity.

V. CONCLUSION

A two-stage SPPG system is developed and modelled in MATLAB/Simulink. Here, the STF assisted control scheme for feeding SPV power to the grid is implemented. The control scheme is tested for notable features such as harmonic minimization, balancing of load, and power factor correction. The grid currents have significant harmonic penetration with non-linear loads connected at the distribution end. This article shows the improved performance of a three-phase grid-connected SPPG system through STF assisted control scheme. The results obtained justify the inferences drawn since grid current remains sinusoidal and free from harmonics under varied scenarios taken into consideration. Another aspect of this article is investigation and examination STF with popular classical and adaptive synchronization techniques for grid synchronization under linear and non-linear load conditions. From the harmonic spectrum analysis and results presented, the improved performance of the proposed system in all scenarios is observed with strict adherence to the IEEE-519 standard in maintaining harmonic interference well within the limit (< 5%). Further, the proposed SPPG system can simultaneously extract maximum power and ensure power quality requirements at the PCC.

TABLE I . THD COMPUTATION UNDER NON-LINEAR LOAD

Parameters	Grid current (A)	Grid Voltage (V)	Load current (A)
Magnitude	50.25 A	338.6 V	10.31 A
THD	0.67 %	1.33 %	30.17 %
1. Self-Tuning Filter (STF)			
Magnitude	50.26 A	338.5 V	10.31A
THD	1.29 %	3.43 %	30.29 %
2. Synchronous Reference Frame Theory (SRFT)			
Magnitude	49.84 A	339.1V	10.34 A
THD	1.38%	1.59 %	30.13 %
3. Unit Vector Transform (UVT)			
Magnitude	50.17 A	339.1V	10.32 A
THD	1.45 %	1.61 %	30.21 %
4. Power Balance Theory (PBT)			
Magnitude	50.13 A	339.2 V	10.32 A
THD	1.21 %	1.36 %	30.21 %
5. Least Mean Square (LMS)			
Magnitude	50.13 A	339.2 V	10.32 A
THD	1.19%	1.36 %	30.21%
6. Least Mean Fourth (LMF)			

REFERENCES

[1] D. Debnath and K. Chatterjee, "Two-Stage Solar Photovoltaic-Based Stand-Alone Scheme Having Battery as Energy Storage Element for Rural Deployment," *IEEE Trans. Ind. Electron.*, vol. 62, no. 7, pp. 4148–4157, 2015

[2] S. Krithiga and N. G. A. Gounden, "Power electronic configuration for the operation of PV system in combined grid-connected and stand-alone modes," *IET Power Electron.*, vol. 7, no. 3, pp. 640–647, 2014

[3] S. K. Khadem, M. Basu, M. F. Conlon, and P. Factor, "Power quality in grid connected renewable energy systems: Role of custom power devices," *Renew. Energy Power Qual. J.*, vol. 1, no. 8, pp. 876–881, 2010

[4] O. M. Akeyo, V. Rallabandi, N. Jewell, and D. M. Ionel, "The Design and Analysis of Large Solar PV Farm Configurations with DC-Connected Battery Systems," *IEEE Trans. Ind. Appl.*, vol. 56, no. 3, pp. 2903–2912, 2020

[5] M. P. Kazmierkowski, *Power Quality: Problems and Mitigation Techniques [Book News]*, vol. 9, no. 2. 2015

[6] D. Committee, I. Power, and E. Society, "IEEE 519 Recommended Practice and Requirements for Harmonic Control in Electric Power Systems IEEE Power and Energy Society," vol. 2014, p. 29, 2014

[7] J. Gong, D. Li, T. Wang, W. Pan, and X. Ding, "A comprehensive review of improving power quality using active power filters," *Electr. Power Syst. Res.*, vol. 199, no. October 2020, p. 107389, 2021

[8] C. Jain and B. Singh, "A three-phase grid tied SPV system with adaptive DC link voltage for CPI voltage variations," *IEEE Trans. Sustain. Energy*, vol. 7, no. 1, pp. 337–344, 2016

[9] and E. R. F. Marcelo Gradella Villalva, Jonas Rafael Gazoli, "Comprehensive Approach to Modeling and Simulation of Photovoltaic Arrays," *IEEE Trans. POWER Electron.*, vol. 24, no. 5, pp. 1198–1208, 2009

[10] N. Femia, G. Petrone, G. Spagnuolo, and M. Vitelli, "Optimization of perturb and observe maximum power point tracking method," *IEEE Trans. Power Electron.*, vol. 20, no. 4, pp. 963–973, 2005

[11] N. P. Babu, J. M. Guerrero, P. Siano, R. Peesapati, and G. Panda, "An Improved Adaptive Control Strategy in Grid-Tied PV System with Active Power Filter for Power Quality Enhancement," *IEEE Syst. J.*, vol. 15, no. 2, pp. 2859–2870, 2021

[12] D. Venkatramanan and V. John, "Dynamic Phasor Modeling and Stability Analysis of SRF-PLL-Based Grid-Tie Inverter under Islanded Conditions," *IEEE Trans. Ind. Appl.*, vol. 56, no. 2, pp. 1953–1965, 2020

[13] Y. Singh, I. Hussain, B. Singh, and S. Mishra, "Single-Phase Single-Stage Grid Tied Solar PV System with Active Power Filtering Using Power Balance Theory," *J. Inst. Eng. Ser. B*, vol. 99, no. 3, pp. 301–311, 2018.

[14] B. Singh, C. Jain, and S. Goel, "A UVT based control for single-stage grid interfaced SPV system with improved power quality," *Proc. 6th IEEE Power India Int. Conf. PIICON 2014*, pp. 0–5, 2014

[15] B. Singh, D. T. Shahani, and A. K. Verma, "Neural network controlled grid interfaced solar photovoltaic power generation," *IET Power Electron.*, vol. 7, no. 3, pp. 614–626, 2014

[16] S. Malathi and J. Jayachandran, "FPGA implementation of NN based LMS–LMF control algorithm in DSTATCOM for power quality improvement," *Control Eng. Pract.*, vol. 98, no. December 2019, p. 104378, 2020

[17] S. Swain and B. Subudhi, "A New grid synchronisation scheme for a three-phase PV system using self-tuning filtering approach," *IET Gener. Transm. Distrib.*, vol. 11, no. 14, pp. 3557–3567, 2017

[18] R. P. Subudhi, Bidyadhar, "A Comparative Study on Maximum Power Point Tracking Techniques for Photovoltaic Power Systems," *Int. J. Electr. Comput. Eng.*, vol. 4, no. 1, pp. 89–98, 2013

[19] R. B. Bollipo, S. Mikkili, and P. K. Bonthagorla, "Hybrid, optimal, intelligent and classical PV MPPT techniques: A review," *CSEE J. Power Energy Syst.*, vol. 7, no. 1, pp. 9–33, 2021

[20] M. Abdusalam, P. Poure, S. Karimi, and S. Saadate, "New digital reference current generation for shunt active power filter under distorted voltage conditions," *Electr. Power Syst. Res.*, vol. 79, no. 5, pp. 759–765, 2009

[21] M. S. Prakash Chittora, Alka Singh, "Application of Self Tuning Filter for power quality improvement in Three phase Three-Wire Distorted Grid System," in *7th International Conference on Power Systems (ICPS)*, 2017, pp. 313–318.

Authorized licensed use limited to: DELHI TECHNICAL UNIV. Downloaded on April 10,2023 at 07:24:14 UTC from IEEE Xplore. Restrictions apply.

Determination of endogenous concentration of Sodium potassium Cadmium Lead and Cadaverine correlating with physio-chemical parameters in *Lycopersicon esculentum* under multiple stress conditions

CHARU RAJPAL[1]*, SUMIT DAGAR[2], PUSHPA C. TOMAR[1]

[1]Department of Biotechnology, Faculty of Engineering and Technology, Manav Rachna International Institute of Research and Studies, Faridabad-121001, India

[2]Department of Environmental Engineering, Delhi Technological University, New Delhi-110042, India

*Email ID: rajpalcharu5@gmail.com

ABSTRACT Agricultural production is under serious threat from abiotic stresses. The effects of polyamines (PA) in this context are well documented and several mechanisms have been established to increase stress factors such as resistance to agricultural salt and heavy metal stresses. A chemically similar diamine putrescine, cadaverine (Cad), appears as a growth inhibitor and acts similarly. This research, which examined the effect of salt and heavy metals on three different tomato cultivars (Lycopersicon esculentum (L.) em. Thell): Pusa Rohini, Pusa Ruby and Pusa Sadabahar, was conducted in relation to this. Their large size significantly hinders plant development and carbon production. Cadmium reduces the toxic effects of heavy metals and acts as a determinant of plant development, stimulating the antioxidant defense system. This study is undertaken to prove that Cad had a varying effect on the Na^+/ K^+ levels of tomato seedlings under different stress and it was more efficient in mitigating salinity stress and heavy metal stress in Pusa Rohini and Pusa Sadabahar and Cad maintained the Na^+/ K^+ homeostasis but in Pusa Ruby Cad only in combination with NH_4NO_3 caused an increase in k+ under salinity stress. Similarly, Cad supplementation did not have any effect on Pusa Ruby under heavy metal stress but significantly reduced endogenous contents of lead and cadmium in Pusa Rohini and Pusa Sadabahar which shows that the role of Cad in amelioration of multiple stresses such as salinity and heavy metal varies greatly depending on different species. In this study, Pusa Sadabahar has the highest stress tolerating capacity especially in the presence of Cad.

Keywords: Cadaverine, Heavy metals, Lycopersicon esculentum, Na+/ K+, Salinity

1. INTRODUCTION

The aim of this research is to find new opportunities in bioengineered agriculture considering the soil nutrient problems currently occurring in many Indian states. India has 18% of the world's population and 15% of the world's livestock, but it has only 2.5% of the world's land area, a very precarious situation.

The primary factor causing soil degradation is stress, both biotic and abiotic. Pollution from heavy metals and salinity is a serious threat to the productivity of the land. Salts in soil and water inhibit plant growth. The amount of sodium in the soil solution reduces the plant's ability to absorb water, which slows its growth rate. At the same time, anthropogenic sources allow heavy metals to infiltrate into soil and plant ecosystems. If these chemicals are used in excess, they can have a negative impact on the earth's production, plants, organisms and the entire ecosystem. Cadmium is one of the most toxic heavy metals to plants and mammals. Cadmium compounds are more liquid than other heavy metals, which makes them more readily absorbed by plants, where they accumulate in edible plant parts. On the other hand, lead is mainly found in the topsoil due to accumulation of vehicle exhaust fumes in the air.

Similarly, some natural processes such as erosion and accumulation of sea salt by wind and rain are major causes of soil salinity. The balance of soil water logic is altered by human activities such as field clearance and irrigation, which are other causes of salinization. As a result, the amount of dissolved ions in the soil water increases to the point where plant growth is inhibited.

Plants are affected by several biotic and abiotic stresses (salinity, drought, heavy metals, extreme temperatures, and oxidative stress) during their lifespan. Their growth and development get hampered because of such environmental stresses [1]. This leads to a loss of crop productivity and so the food stock and economy in several countries around the globe per year [2]. This situation is getting worse day by day because of severe and frequent changes in climatic conditions like global warming, etc. India, being a populated country needs to develop certain tolerant crops to cope with such diverse situations.

Tomato being an economically pivotal and popular food crop in the world as it contains ―lycopene and certain bioflavonoids that possess anti-cancerous and anti-oxidative properties, and so the production of this crop is constantly increasing [3]. About 0.458 million hectares area is used for tomato cultivation, with

a productivity of about 15.9 metric tons per hectare. Being a tropical plant, it adapts to all types of climates and can be cultivated anywhere around the globe; however, the original field potential of this crop can only get affected through these stresses. So far, stress tolerance in cultivated tomato plants has been achieved through some genetic approaches, using the general knowledge about plant adaptation. The biotechnological methods produce the upgraded version of tomato plants with stress tolerance capacity through the transfer of genetic information of many stress mitigating genes or genes involved in different regulatory pathways or signalling [4].It is one of the most significant food crops of India. It is cultivated in 0.458 Production of 7.277 million metric tons was produced in 1 million hectares with a yield of 15.9 metric tons per hectare. Although efforts have been made to create stress tolerant mutant plants, the management of stress conditions remains an area that requires further research in plant studies. In this regard, tomato cultivars Pusa Ruby, Pusa Rohini and Pusa Sadabahar (Lycopersicon esculentum Mill.) were used in this research under different abiotic stresses including salt and heavy metals. IARI, New Delhi, launched Pusa Ruby. It is an early-growing variety that has uniformly ripening fruit and a golden, slightly wrinkled stem end. It can be planted both in spring and summer and in autumn and winter. The yield averages 32.5 tonnes per hectare. In India, this variety is highly appreciated. Pusa Rohini was first announced by the Indian Agricultural Research Institute in the year 2005. These types of crops stay fresh for a long time. They bear medium-sized fruits with thick scarlet skin. It takes 80 days to reach maturity. For NCR, this type is recommended. Another format developed by the Indian Agricultural Research Institute and released in 2004 is called Pusa Sadabahar. This variety is also recommended for NCR and produces more tomatoes.

Many compounds use small, positively charged molecules called polyamines in various metabolic processes such as flower initiation, crop development, ripening, organ development, pollen tube growth, leaf senescence, and reduction. These compounds are also involved in responses to biological and abiotic stresses and contain plant hormones.

Diamine [NH2(CH2)4NH2] acts as a precursor to triamine Spd [NH2(CH2)3NH(CH2)4NH2] and tetraamine Spm [NH2 (CH2) 4 NH (CH2) 3 NH (CH2) 4 NH (CH2) 3 NH2], which are aliphatic and simple in nature. These multiple amines are distinct from each other and are among the biopositive ions. Functionally, these compounds are involved in various cellular processes.

In recent years, molecular genomics research has made significant progress in understanding how enzymes change during PA production and their potential biochemical activities in plants. Previous studies have identified putrescine (But), spermidine (Spd), and spermine (Spm) as three essential amino acids, along with their derivatives. Cadaverine has a unique molecular structure and belongs to the class of polyamines, which are believed to act as inhibitors of growth and persistence. In addition, it is often found in higher plants and is involved in reducing both energetic and abiotic stresses. The molecular equivalent of putrescine does not form in the five-carbon chain diamine.

or Arabidopsis. Polyamines (PA) are abbreviated polyamines, which are now recognized as amino molecules for people and plants. Examples of PAs are putrescine (diamine), cadaverine (diamine), spermidine (triamine) and spermine (tetramine). Cadaverine is a diamine that differs chemically from mod using a special pathway to produce it. It belongs to the same class as polyamines and has similar activity. Under various biotic and abiotic stresses, they are also integrated in higher plants, despite their unclear stress-relieving function. The molecular equivalent of putrescine does not form in the five-carbon chain diamine.

or Arabidopsis. The function of cadaverine (Cad), one of two growth-modifying polyamine diamines made entirely from a different pathway of other groups, in plant development is unclear. This diamine is found in the body as intermediate molecules in various forms of organic nitrogen. They act as building blocks for macromolecules, changing the organism's metabolism in the process. According to the literature review, diamine putrescine has been mainly discussed by plant physiologists, biochemists and molecular biologists for a variety of applications in crop improvement strategies. Diamine's role as a precursor to spermine and spermidine has also attracted the interest of researchers. Moreover, it has been found that cad promotes plant growth under multiple stresses, and proteins activated in response to stress in the presence of cadmium support plant growth under multiple stresses [8].

Casaverine diamine has been reported to have no effect on senescence in barley [10], induce asymmetric alkaloid production [11], or increase mitochondrial membrane porosity, although multiple amines are involved in antiaging interactions [9]. Very little research has been done on the metabolic function of elevated polyamines under stress [12]. Management of exogenous dead bodies under stress provides insight into the process of plant development, especially when tandem stressors are present [13].

2. LITERATURE REVIEW

Due to agricultural irrigation with polluted water, one of the main abiotic stresses is the accumulation of heavy metals, which inhibit nitrate reductase activity and reduce nitrogen and organic protein levels in leaf tissues [14]. According to reports, concentrations of heavy metals are higher in the upper parts of plants like crops than the lower parts like leaves, stems etc. [15]. The amount of cadmium absorbed by plants ranges from 0.1 to 2.4 mg/kg2.

Excessive amounts severely inhibit plant growth and carbon production.

When tomato plants were exposed to cadmium, Grato et al. (2008) reported increased lipid peroxidation, catalase activity [16], glutathione reductase activity and decreased glutathione peroxidase activity [15]. By protecting molecules, cad strongly supports the development of stressed plants [17].

Heavy metals are described as solid chemical elements that have a very high density (between 4 and 5 g/cm3) and are toxic even in small amounts. Toxic levels of heavy metals endanger ecosystems and have a significant impact on the nutritional, climatic and genetic characteristics of an area. In the 20th century, the industrial revolution led to a rapid increase in heavy metal pollution, causing severe pollution of land, water and air. Heavy metals are difficult to decompose and remain in soil for a long time, which reduces their quality [18].

2.1. Ionic Composition in Plants

Several researchers have explained certain changes in the amounts of inorganic ions under salt. Different responses to an increase in Na+ were observed, including a reduction in K+, Mg+, and Ca2+ ions, as well as Cl- ions [19].

An excessive accumulation of Na+ ions can be toxic to a plant's metabolic functions, which can lead to a decrease in the amount of available water. Soil-tolerant plants can balance the uptake of Na+ ions in their roots, while plants that are unable to do so were labelled as susceptible. Some studies have suggested that maintaining an optimum K+/Na+ ion ratio is important in controlling plant function in saltier environments. Furthermore, salt has been shown to increase Zn, Mn, and N concentrations, as well as Na+ and Cl- ions, but the amounts of P, S, and Ca2+ remain constant. However, under saline stress circumstances, the concentrations of K+, Mg+, Fe, and Cu ions can

be affected [20]. Leidi and Saiz reported more granular matter, water's constituents, and other variables in 1997.

In salt-tolerant genotypes, there is greater Na+ ion buildup in the foliage compared to weaker genotypes [21]. These studies suggest that increased Na+ ion absorption and water quantity and tolerance processes are interconnected. Additionally, sufficient but regulated ion absorption is necessary for correcting halophytes, which is similar to effective ion reallocation and compartmentalization, and this can improve the development rate and the ability for water absorption.

When Na+ blocks the entry of nutrients inside plant sections, ion unbalancing can occur, competing with other minerals like Ca2+, K+, and NO3-. This can lead to a decrease in K+, Ca2+, Mg2+, N, and P concentrations in foliage and stems. Although many studies have characterized the constant amounts of K+, Ca2-, and S in the leaves, a reduced K+/Na+ or K+/Ca+ ratio can result [22]. In 1980, Thomas noted a rise in Mg+ and Ca+ ion concentrations in foliage. Therefore, it is essential to recognize these dietary problems to reduce the detrimental impacts of sodium stress on plant output [23].

Recent research has highlighted the impact of excess salt content on plant tissue reactions, resulting in decreased plant yield and development [24]. The buildup of salt molecules in the soil creates osmotic pressure, which lowers water absorption by plant roots and causes an abnormal buildup of reactive oxygen species (ROS) [25]. Root membranes are damaged as a result [26]. The higher quantity of Na+ that enters the root cells during stress results in the release of cytoplasmic K+, causing an ion excess and biochemical diseases brought on by lack of focus [27]. In 2014, Liu et al. found that PAs regulate salt-dependent ROS balance by causing the antioxidant protection system to become active in response to stress. Within the transmission of stress messages, receptors detect the signals, which are typically located at the cytomembrane, causing several secondary processes to be unleashed or activated, including stress-related molecules like calcium, ROS, and inositol phosphates. Secondary components, such as protein kinases and phosphatases, are signaled and stimulated [28, 29, 30, 31, 32, 33, 34].

There is a need to consider numerous agronomy problems with regard to environmental changes, organic processes, and crop quality. Plants and vegetables will benefit from taking the polyamine route into account. Lysine is catalyzed by lysine decarboxylase, as proven by Tomar et al. in 2013. This metabolism is controlled by maturation [35]. Increased salt and drought resistance in Burma

are due to PA binding in Cynodondactylon, or grass [36]. The varied abundance of Cad in the plant is suggested as a potential contender for the taxonomy identifier by parts/products, as well as for commercial modification in conjunction with plant development and growth. Studies on the function of Cad have received less attention than those of other PAs. According to [37], the abundance of Cad rose during lupine, chickpea, and wide bean sprouting. Garcia-Garcia et al. noted in 2000 that after three months of storage, there were trace amounts of cadaverine in table olives. Brining [38] showed Cad in tomato, pea, and maize coleoptiles, as well as Datura. Legaz et al. established the reliance of cadaverine titers on plant age and came to the conclusion that Cad diminishes over time [39]. Tomar and co. discovered that immature orange species seeds contained an increased level of Cad in 2013 [25]. Inquiries and research have also discovered a high amount of Cad linkage under hyper-hydric plants in 2002 [40]. Shi et al. discovered the presence of cadaverine in the hairy roots of Brugmansia candida in 2021 after observing the increased production of cadaverine in Nicotiana tobacum hairy root cultures [42]. Application of cadaverine may cause anchoring in Scot pine containing ectomycorrhizal fungus [43]. It might impact by altering the bacteroid, nodule metabolism [44].

Pathogenesis-related protein 1b1 (PR1b1) was discovered by Goyal et al. in 2016 to be a key tomato plant protein that responds to cooling and is up-regulated in high genetics with recombinant polyamines [45]. In 2012, Nambeesan et al. proposed a link between tomato polyamine-mediated susceptibility to Botrytis cinerea and invasion with ethylene's functions in its protection. The biochemical changes associated with maturation are both independently of and in response to ethylene, and the apple metabolome is regulated by numerous regulators, including PA andethylene [46]. These findings suggest that PAs play a crucial role in plant defense against biotic and abiotic stresses.

Research has also shown that PAs work with ion channels and contribute to ion channel function, which is essential for housekeeping [28, 29, 30]. In addition, PAs can regulate plant growth and development, as well as stress responses, by affecting various signaling pathways [31, 32, 33, 34]. Therefore, understanding the roles and mechanisms of PAs in plants can help improve crop productivity and resilience to environmental stress.

It is important to note that while PAs have shown promise in promoting plant growth and stress tolerance, their application must be carefully controlled. Excessive PA application can lead to toxicity and negative effects on plant growth and development. Therefore, more research is needed

to determine optimal PA application rates and methods to maximize their benefits without causing harm.

PAs are a vital component of plant growth and stress response mechanisms. Their roles in ion channel function, signaling pathways, and stress tolerance make them promising targets for improving crop productivity and resilience to environmental stress. However, careful control of their application is necessary to ensure their effectiveness and safety. Further research is needed to fully understand their mechanisms of action and optimize their use in agriculture.

Every year, agricultural production suffers huge losses due to prevailing weather conditions. Abiotic stress, especially cadmium salt and cadmium from human activities, exacerbates this. Crop production and human health are severely affected by many stresses on vegetation. Abiotic stresses hinder plant development by inhibiting changes in germination, dry mass accumulation, and biomass partitioning because they disrupt physical and chemical processes that simultaneously cause growth and decline in associated compounds.

Salinity affects agricultural growth and production worldwide, reducing the efficiency of many plants. In the next 25 years, salt stress, one of the biggest threats to food security, is expected to affect 30% of the agricultural area. To analyze the adverse effects of salt stress on production and growth and development of edible plants, several procedures have been established. For example, (1) low water potential in the root zone leads to water deficit in plant tissues as a result of salts, (2) Na+ and Cl- ions cause ionotoxicity in plants, and (3) reduced absorption of aggregates and vitamins. Roots may result in salt residues resulting in an ion imbalance [47].

Heavy metals are dangerous to plants as well as humans. Environmental pollution is one of the major reasons for increasing the toxicity of heavy metals in plants. This affects the human health and yield of the plants [48,49]. Cadmium and lead grabbed the attention of researchers because of their production and accumulation in the soil and causingtheir eradication. The plants can easily take these up as they tend to sustain in soilsolutions, being mobile and non-degradable [50,51].While, it was reported that a minimal quantity of lead affects plants by reducing themetabolic activities of the plants like cell division, germination, photosynthesis andnitrogen assimilation, etc. [52]. Further lead accumulation was foundin several medicinal plants like aromatic rice [53]. These are one of the environmental contaminants. Specific methods havealready been used to scavenge such contaminants from the environment, but they areexpensive and difficult to get optimal results. Natural and all human activitiescontribute to

polluting the environment with heavy metals. Dusting or leaching of soilcauses the migration of these heavy metals to the non-contaminated areas resulting inecosystem contamination [54]. Several modern technologies are expensive and produce a large quantity of volumetric sludge [55]; other thermal and clinical methods are challenging, laborious, and costly, andthese may deteriorate the important components [56]. Generally, soil remediation of heavy metals includes onsite management orscraping off, followed by disposal to a landfill area. This process of disposing of individually moves the contaminants to some other area with the hazardous heavy metals related to the environment. Washing of soil is another alternative method to remove the contaminated soil and disposing of it off to the landfill. But this method is yet again expensive, and a residue remains rich in heavy metals that need to be treated further. Additionally, such physio-chemical methods used for remediation of soil provide the land for plant growth as they abolish all biological activities. Heavy metals may reside in the soil for thousands of years that can cause health danger to higher organisms in several ways [54].

Several researchers have revealed the uptake of heavy metals by plants. This can be used to standardize the parameters to improvise the functionality of plant uptake. Sinha and his team membersreported that plants are ―excluders‖ and ―accumulators [57].

Plants now enable to solubilize with the help of roots facilitated by chelating agents produced by the plants. These plants can directly trans-locate and reserve micronutrients. Similarly, these processes are also indulged in reserve, trans-locate, and take-up of contaminants whose chemical characteristics resemble those of essential elements.

Several proteins or transport processes are known which are embedded in the plasma membrane indulged in the uptake of ions they trans-locate (i) protein pumps, (ii) co-and anti-transporters, and (iii) channels. Each mechanism takes up the ions. The primary concern is the ion interaction during the uptake of several contaminants. Translocation in the shoots is prudent after the uptake by roots as the harvest of biomass of roots is not possible.

Plants do not deposit trace elements unless they have their metabolic requirements. So, they have an uptake-translocation process that seems to be closely related. All

these needs may range from 10-15 ppm of certain trace elements. Another concern is the form of contaminants in which heavy metals are reserved in the plants and the mechanisms by which they avoid metal toxicity. Storage in the vacuole is one of the processes of accumulation of heavy metals in plants. Such plants are also termed ―hyper-accumulators, which remove the contaminants from the plants which trans-locate from roots to the shoots leaving the soil undisturbed [58].

2.2. Localization of Cd/Pb in Plants

These heavy metals possess a significant threat to human and environment as these are extracted from the soil andtransferred to the human beings via plants. These are considered to enter into the plantroot cells as they chelate via trans-membrane transporters [59] or asions through cation channels. They can also pass through the roots by apoplastic orsymplastic pathways before being trans-located into the shoot and the xylem. Even at low concentrations, these are toxic to several plants. Significant symptoms of their toxicity are leaf rolling, stunting, and chlorosis [60]. Many physiological and structural changes of plants are interrelated to heavy metal toxicity. For example, deterioration of phloem sieve tubes, cell wall saturation by phenolic compounds, retarded cambial activity, chloroplast alterations, stiffening of all walls, etc. [61]. Additionally, these heavy metals in higher concentrations can be proven carcinogenic or mutagenic for several animal species [62]. Hence, soils contaminated with heavy metals require a cost-effective solution. To withstand the higher concentrations of heavy metals, certain species of plants have developed a complicated process to control the take-up, deposition, or detoxification of metal traces. Qualitative root properties should also be studied concerning phytoextraction with qualitative parameters for biomass production, as modified root morphology can affect the water absorption and growth and development of the plant directly. On evaluating the Cd content, it is evident that exposure of plants to differentconcentrations leads to varying levels of Cd accumulation and hence causing theplasmolytic shrinkage leads to hindering precise sub-cellular Cd localization and so thecondensation of the cytoplasm [63].

2.3. Plant Growth and Development under Metal stress

In angiosperms, changes in the size and ratio of root tissues are observed

during their exposure to heavy metals [64, 65, 66]. In this study, they exposed plants to different concentrations of CdCl2 (0, 30, 60, and 100 μM) to evaluate plant heavy metal stress tolerance. She showed that P. vittata absorbs, transports, and deposits cadmium in the low bioactive tissues of fronds, trichomes, and scales. Heavy metal tolerance in this particular plant correlates with the metal-induced morphological response in the roots. The plants also showed changes in root apex size, suberin endododermal lamellae, developmental patterns of root hairs, etc.

This study demonstrated that this particular plant can tolerate a maximum of 60 μmCadmium concentration which by contrast improves the root system by allowingGood transport and deposition of metallic traces in the fronds.Moreover, Jiang et al., in 2016, experimented with observing the varying effects of cadmiumconcentrations in different rice cultivars. The plant growth parameters observed werePlant growth, photosynthesis, biomass, cadmium uptake, and root/shoot Plant antioxidant stress activity. They revealed that the CD negatively affected thePlant growth and photosynthesis, but correspondingly increased cadmium concentrations

Increased cadmium uptake and oxidative stress in all rice cultivars. Cadmium interferes with the absorption of ions, causing an imbalance of nutrients. The plant's mineral content could be reflected by the availability of cadmium in the growth medium. The plant faces dangerous and harmful effects when the cadmium content in the soil increases. Root elongation of plants subjected to heavy metal stress provides us with the basis for evaluating the tolerance of plants against heavy metal stress [25].

Aliphatic polycations called polyamines, such as cadaverine (Cad), have been found to accumulate in biotic and abiotic stressors, leading to the overexpression of stress endurance genes in larger plants. Physiological evaluations were conducted to track the effects of Cad on biomass accumulation and the increase in photosynthetic biomolecules, nitrate reductase activity, total soluble proteins, organic nitrogen, and colours, which have a strong correlation with the development stress of the tomato (Lycopersicon esculentum) variety. Pusa Ruby, Pusa Sadabahar, and Pusa Rohini were subjected to all treatments (T0 = control, T1 = NaCl, T2 = NH4NO3, T3 = Cd, T4 = Cd+NH4NO3, T5 = Cd+NaCl, T6 = Pb+NaCl, T7 = Cd+NaCl+NH4NO3, T8 = Pb+NaCl+NH4NO3, T9 = Pb+Cd, and T10 = Pb+NH4NO3, T11 = Cd+NH4NO3). Comparison studies provided comprehensive insights and an improved understanding of Cad's mechanism, which improves tomato resistance to various stresses.

The poorly understood external release of Cad under stress is expected to have beneficial effects on stressed tomato plants. The current research aims to shed some light on Cad's regulatory mechanism on tomato plant development and its ability to reduce the negative reactions brought on by various stressors. Under various stressor conditions, Cad also determines the natural content of Na+/K+, Cd, or Pb ions corresponding to physio-chemical factors. Plants may benefit from appropriate development even in stressful environments due to the proteins produced in response to stress in the presence of Cad [67]. This study was conducted to demonstrate that Cad had a variable impact on the Na+/K+ levels of tomato seedlings under various stresses. It was more effective in reducing salinity and heavy metal stress in the Pusa Rohini and Pusa Sadabahar regions and preserved Na+/K+ homeostasis there, but in the Pusa Ruby region, Cad only increased K+ under salinity stress when combined with NH4NO3.

3. MATERIALS AND METHODS

Tomato seeds (Lycopersicon esculentum var. Pusa rubi, Pusa rohini and Pusa sadabahar) were sterilized with 0.1% sodium hypochlorite solution for 2–3 min, followed by three rinses with twice distilled water. Seeds were planted in Petri dishes lined with Whatman filter paper. In accordance with the study design, plants were grown under controlled conditions (75 W light, 252 °C, 65% RH), irrigated with a full-strength Hoagland's nutrient solution containing 50 mM NaCl, 1 mM Pb, and 1 mM Cad. . The pH of 6.4 of nutrient solution containing salts and Cd was constant for all treatments (T0 = control, T1 = NaCl, T2 = NH4NO3, T3 = NaCl + NH4NO3, T4 = Cd, T5 = Pb, T6 = Cd + NaCl, T7 = Pb + NaCl, T8 = Cd + NaCl + NH4NO3, T9 = Pb + NaCl + NH4NO3, T10 = Pb + Cd, T11 = Pb + NH4NO3, T12 = Cd + NH4NO3) with and without cad. Pb and Cd were determined using atomic absorption spectrometer, while Na and K were estimated using digital flame photometer. Statistics are mean of three samples with standard deviation. Student's t test of significance of the intervention and data analysis was applied.

4. RESULTS AND DISCUSSION

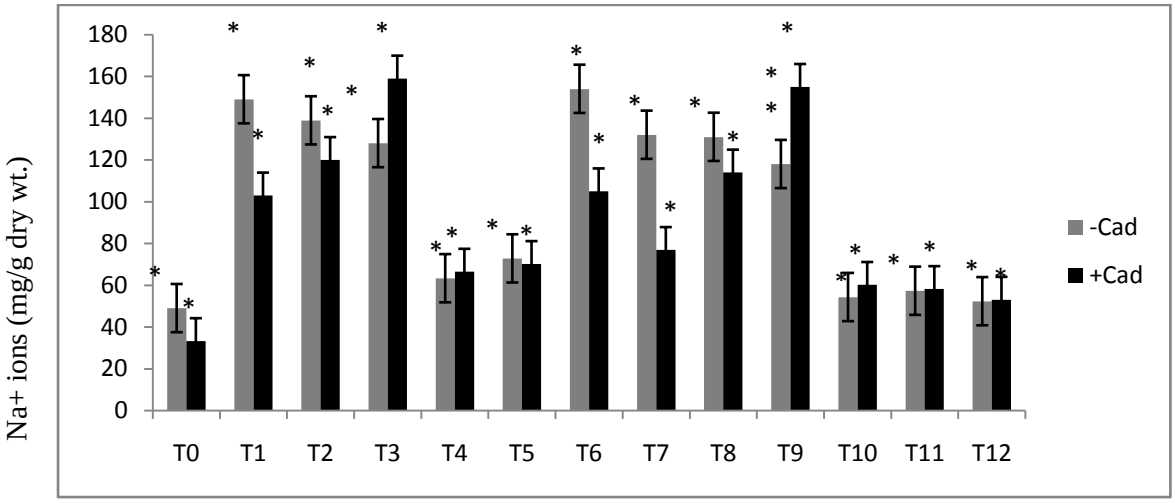
4.1 Na^+ and K^+ in Tissues with or without Cad

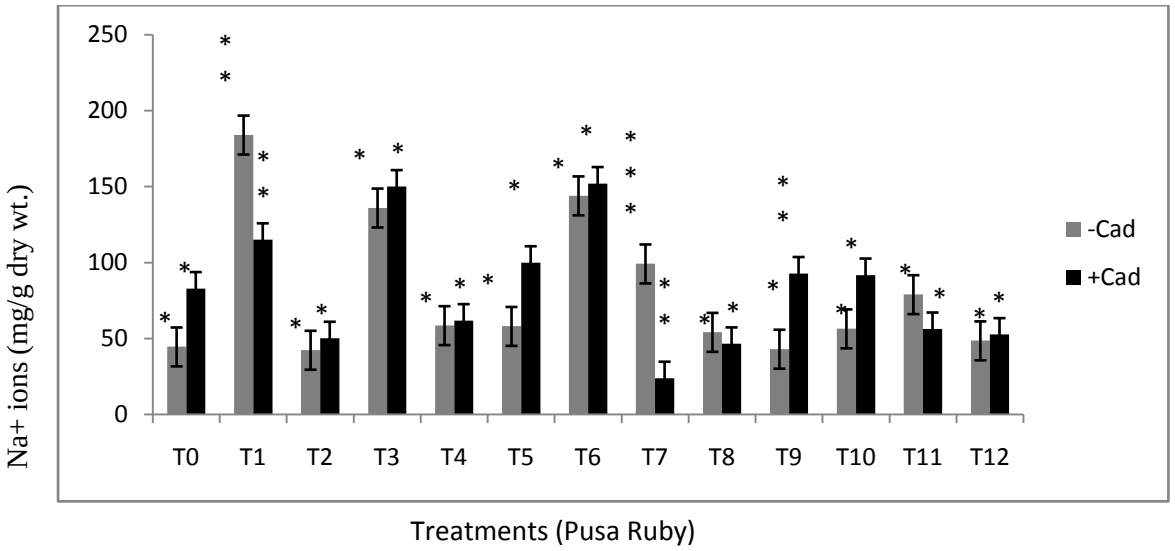
Under salt stress, nearly 3-fold increases in endogenous concentrations of Na^+were observed in Pusa Ruby. When compared to that of control, more than 3-fold increase was observed in Pusa Rohini whereas a significant decrease in Na^+ levels was noticed in Pusa Sadabahar. Similarly, under combined stress (Salt and heavy metals), elevated levels of Na^+were observed in Pusa Ruby and Pusa Rohini whereas in Pusa Sadabahar the Na^+ levels remained unchanged under cadmium and salt stress and decreased slightly under lead and salt stress. However, decreased endogenous Na^+ levels were observed in all other treatments of Pusa Sadabahar (Figure 1).

When compared to control, NH_4NO_3 treatment led to more than 2-fold increases in Na^+concentrations in Pusa Ruby, caused no change in Pusa Rohini, and decreased drastically in Pusa Sadabahar. When NaCl was coupled with NH_4NO_3, Na^+ levelwas found to be decreasing over NaCl treatment alone in all three varieties. In Pusa Ruby Cad supplementation caused a significant decrease in the Na^+ levels under salt stress in most of the cases except in the presence of NH_4NO_3. However, neither Cad nor NH_4NO_3 had much influence on the Na^+ levels. In the case of Pusa Rohini, Cad supplementation leads to a significant decrease in NA^+ levels under cases of salinity stress and Pb combination of salinity stress. Pusa Sadabahar seedlings, Cad supplementation reduced Na^+levels significantly in almost all stressed conditionsbut the much-pronounced effect of Cad was seen with salinity stress where the NA^+levels reduced drastically.

Endogenous K^+ concentrations were also analysed in the seedlings of these three different tomato varieties exposed to different types of stresses. The results showed that the K^+levels reduced under all conditions of stresses as compared with control in Pusa Ruby. Levels of K^+ were lowest in all the multiple stress conditions followed by salinity stress. Similarly in Pusa Sadabahar, K^+ levels decreased under all stress conditions except for cadmium with NaCl exposed seedlings where the K^+ levels remained unchanged when compared to that of control. In contrast to these two varieties of tomato, Pusa Rohini showed a high increase in the K^+ levelsunder different stress conditions such as salt stress, salt and lead stress, salt stress with NH_4NO_3, and lead stress with NH_4NO_3. A slight increase in K^+ levelswas observed under metal stress. In the presence of Cad, further reduction in the K^+ levelsoccurred in Pusa Ruby seedlings exposed to NH_4NO_3, Cadmiumwith NaCl, Lead with NaCl, cadmium with NH_4NO_3,and lead with NH_4NO_3 whereas Cad supplementation leads to a high increase in K^+ levels under other conditions of stress such as NaCl with NH_4NO_3 and heavy metal stress either alone or in combination. In Pusa Rohini, Cad caused a decrease in K^+ levels under salinity stress, lead and salinity stress and lead with NH_4NO_3. In other

conditions either a very slight increase in the K^+ levels was observed or there was not much change in the levels of K^+. In contrast to Pusa Ruby and Pusa Rohini, Pusa Sadabahar showed a heavy decrease in the K^+ levels under salinity stress and a remarkable increase under combined lead and cadmium stress (Figure 2).





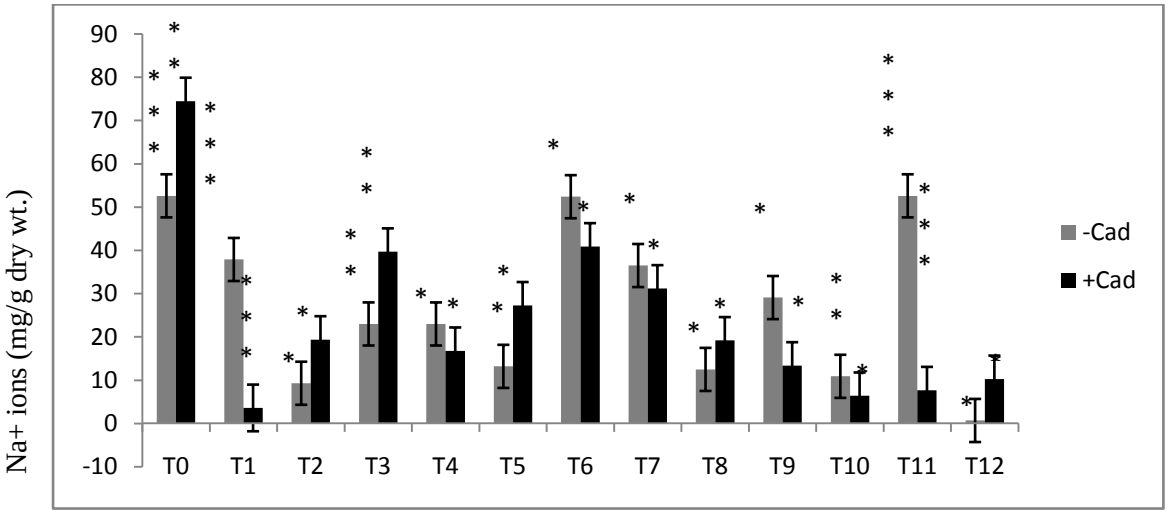
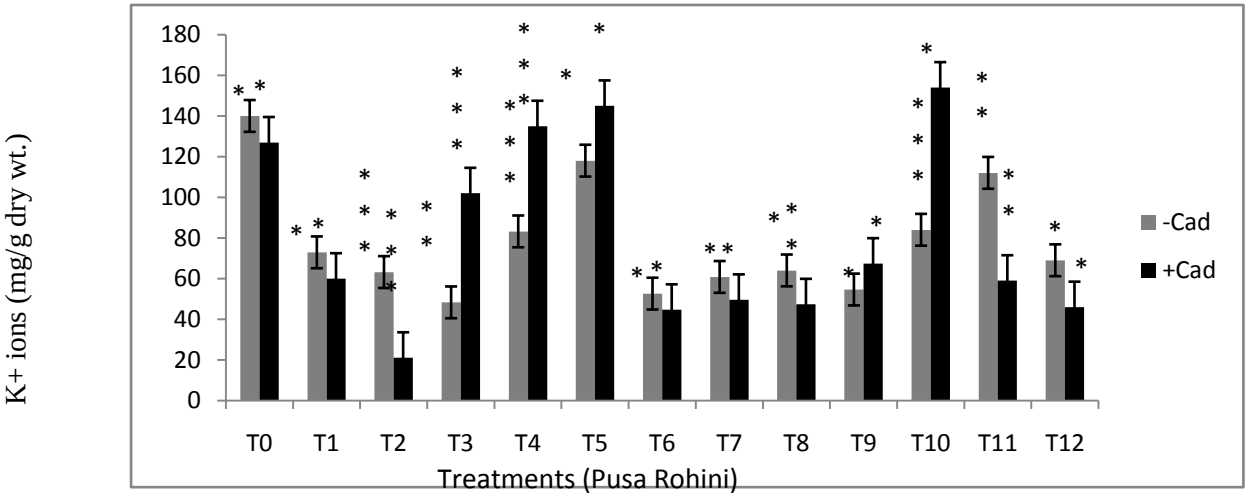


Figure 1: Na+ content of 7-day-old seedlings under multiple stresses with or without Cad. Here, T0= control, T1 = NaCl, T2 = NH 4NO 3, T3 = NaCl+NH 4NO3, T4 = Cd, T5 = Pb, T6 = Cd+ NaCl, T7= Pb+NaCl, T8 = Cd+NaCl+ NH 4NO 3 , T9 = Pb+NaCl+ NH 4NO 3, T10 = Pb+Cd, T11= Pb+NH 4NO 3, T12 = Cd+NH 4NO 3. Data are mean values of replicates with (n=3) ± SD. Asterisks p<0.05% (*) possibly significant, p<0.01 (**) definitely significant, p<0.001 (***) highly significant and no asterisks indicate significance of difference at p> = 0.05.



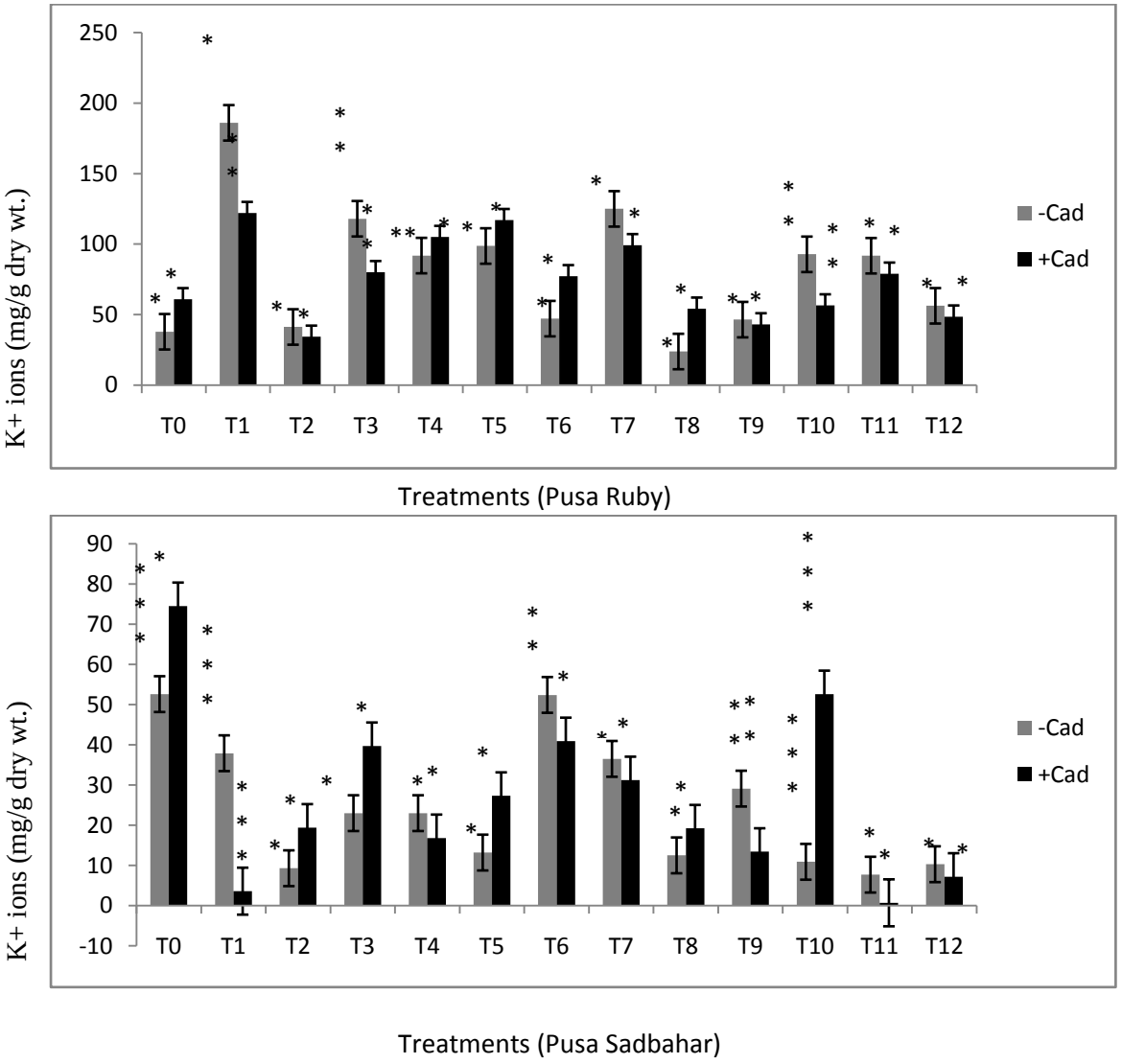


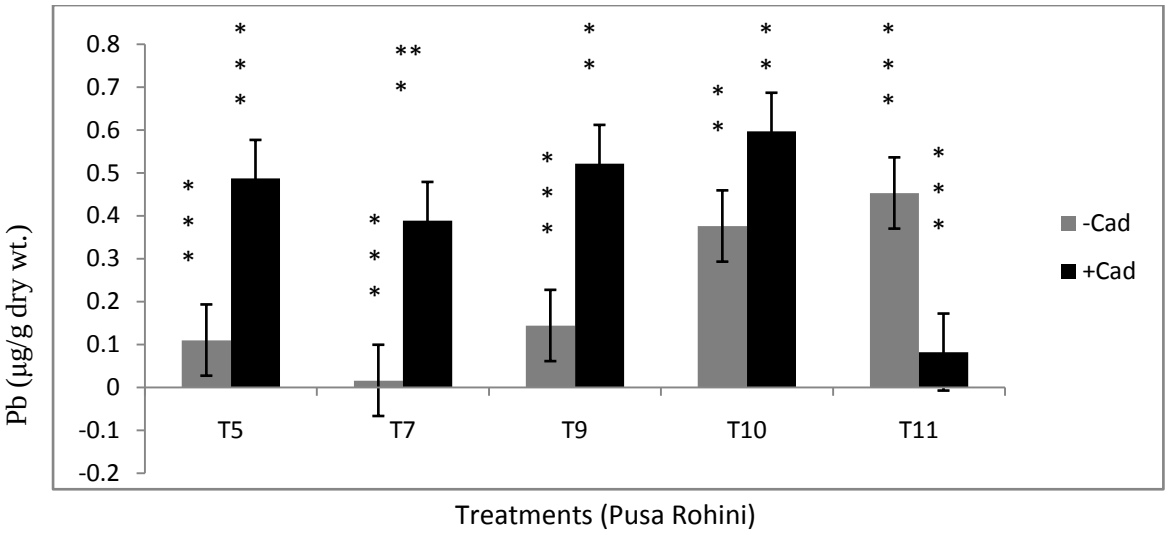
Figure 2: K^+ Content in 7-day old seedlings under multiple stress with or without Cad. Rest legend same as in Figure 1.

4.2 Cd/Pb Level under Multiple Stresses with or without Cad

In Pusa Ruby, the Pb content increased in all kinds of stress treatment except in the case of combined salt and metal stress where the Pb content was the lowest when compared to other treatments. Endogenous Pb content was highest on treatment with Pb and NH_4NO_3 which was greatly reduced on supplementation with Cad. However, in other treatments, Cad caused a further increase in Pb contents when compared to those without Cad. The endogenous load of Pb was higher in Pusa Rohini when compared with the other two varieties and the highest lead contents were observed in salt and metal stress along NH_4NO_3.Moreover,the lead contents under all the

stress conditions were reduced to a significant amount by Cad, Combined heavy metal stress (Pb+ Cd) being the only exception where Cad caused an increase in Pb contents. In contrast to this, lead content in Pusa Sadabahar under combined heavy metal stress was reduced by Cad. (Figure 3) lead contents were also reduced drastically under metal and salinity stress whereas increased lead contents were observed under Pb stress and Pb and salt stress with NH_4NO_3 in the presence of Cad.

Under cadmium stress and cadmium along with salinity stress, the endogenous load of cadmium was more or less the same for all three varieties of tomato. Cad supplementation leads to an increase in Cd levels in Pusa ruby, a slight increase in Pusa Rohini, and a decrease in Pusa Sadabahar supplemented with Cd. Under conditions of multiple stress (Cd + NaCl), Cad did not have any significant effect on Cd contents Pusa Ruby whereas it reduced the Cd contents in Pusa Rohini and Pusa Sadabahar. The highest endogenous Cd contents were observed under Cd stress with NH_4NO_3 in all the varieties which were further reduced to a certain amount by Cad. Surprisingly, Cd was not detected in Pusa Sadabahar treated with Cd+NaCl+ NH_4NO_3 and Pb+Cd (Figure 4).



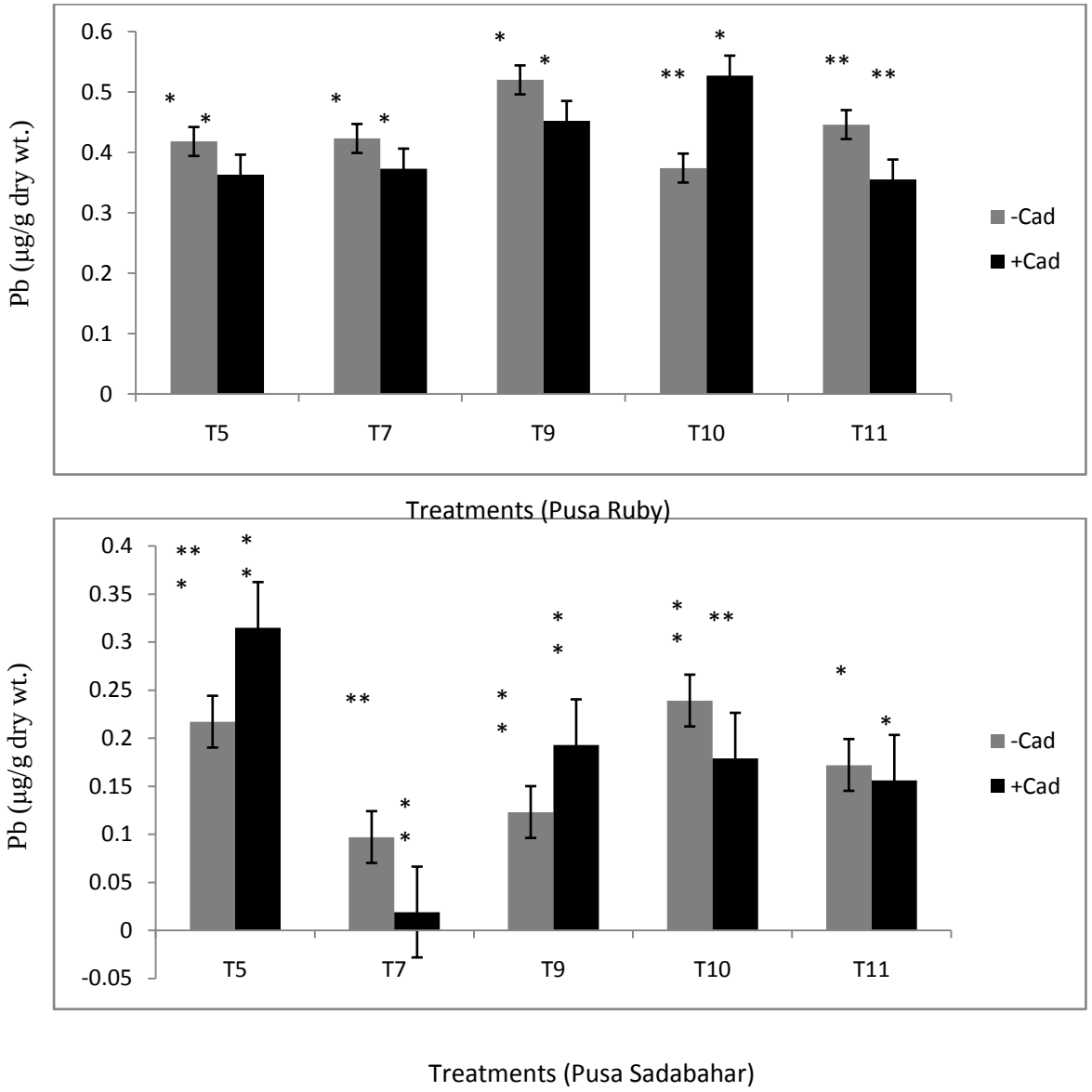
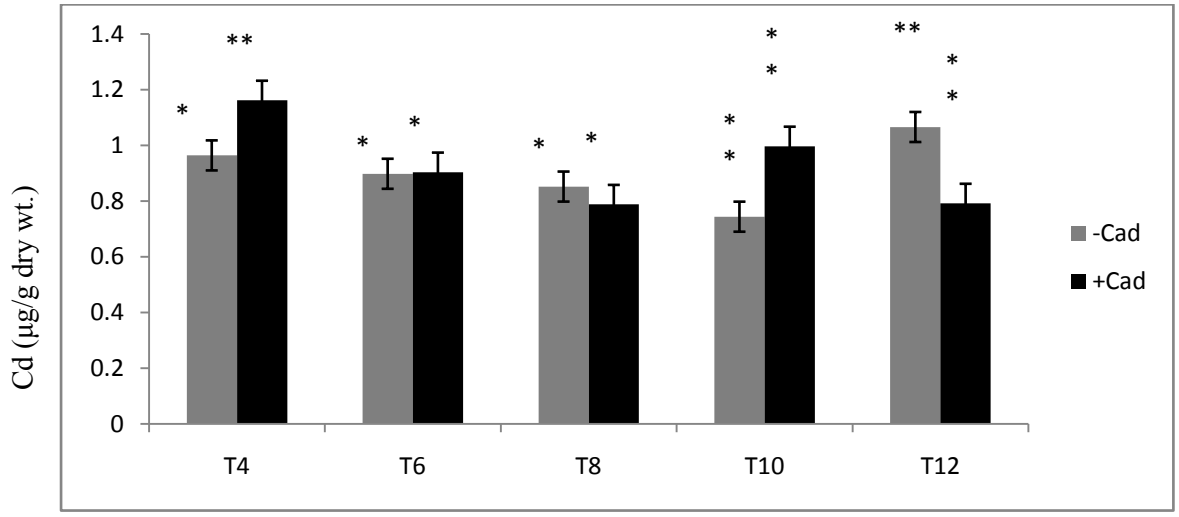
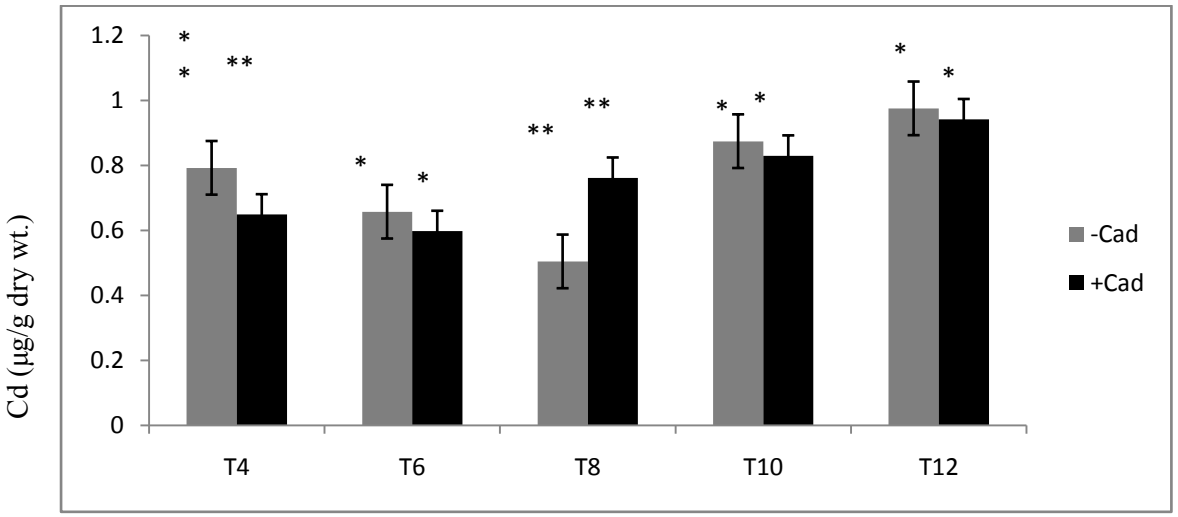


Figure 3: Pb content in 7-day old seedlings under multiple stress with or without Cad.

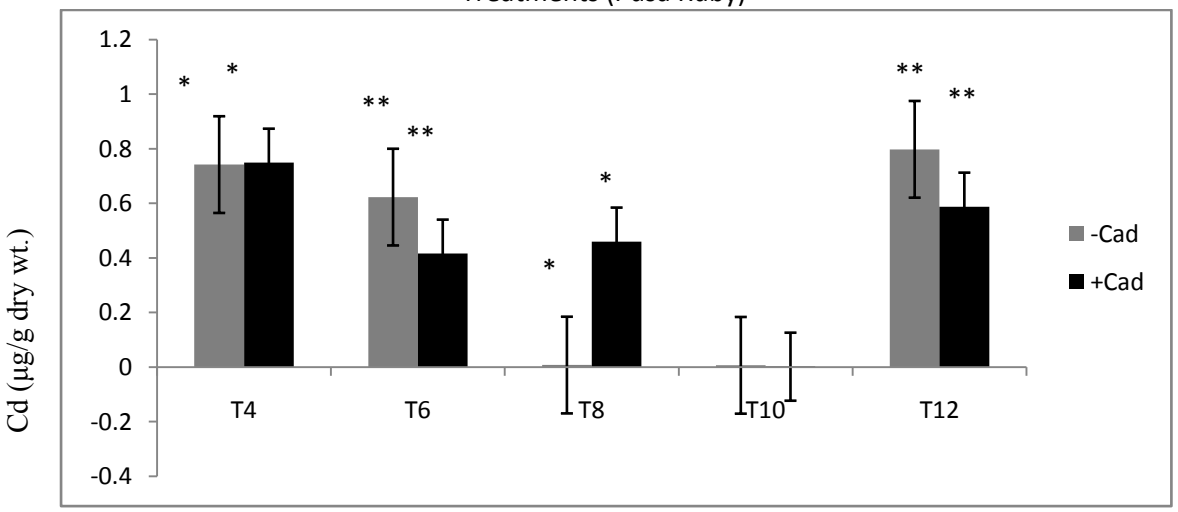
Rest legend same as in Figure 1.



Treatments (Pusa Rohini)



Treatments (Pusa Ruby)



Treatments (Pusa Sadabahar)

Figure 4: Cd Content in 7-day old seedlings under multiple stress with or without Cad. Rest legend same as in Figure 1.

5. CONCLUSION

The polyamines spermidine and spermine, as well as the diamines putrescine and cadaverine, are potential communication networks utilized by the body to protect against stress. These compounds are recognized for their anti-senescence and anti-stress benefits, as they possess antioxidant and acid-neutralizing properties and can stabilize membranes and cell walls. Other studies suggest that the addition of external polyamines to plants under salt stress can improve ionic (K+/Na+) interactions, which is important for regulating development in stressed plants [68, 69].

During embryonic development, an effective antioxidant process is thought to occur in the presence of these compounds. Under stressful conditions, the overall antioxidant capacity of polyamines was consistently greater than that of water. In addition, ionic and osmotic stress can impact germination and development. In 2020, Abdel-Faried et al. observed the development of seeds in Cucumis sativus and Lycopersicon esculentum plants in various concentrations of NaCl (25, 50, 100, and 200 mM) both in vivo and in vitro. They found observable delays in metabolic reaction and photosynthesis substance, as well as significant drops in fresh and dry weight. Even with only 200 mM of salt content, all interventions resulted in shorter roots, and the reduction of photosynthetic compounds in tomato was greater than that in cucumber. They also demonstrated that salt had an impact on the biochemical analysis of stressed plants, but a few beneficial secondary compounds were increased in tomato and cucumber crops [70].

In this study, the pattern of Na+/K+ level changes for various tomato types under different stress conditions differed significantly, indicating that cadaverine had no particular effect but a variable effect on ion balance. In Pusa Ruby, NH4NO3 and cadaverine alone or together did not affect Na+ contents in response to heavy metal stress, but cadaverine along with NH4NO3 caused an increase in K+ contents under salinity stress in Pusa Ruby and Pusa Sadabahar. Cadaverine supplementation effectively reduced Na+ contents in Pusa Rohini and Pusa Sadabahar in response to salinity stress and in a few cases in response to heavy metal stress. Therefore, it appears that the ameliorative effects of cadaverine on the shift in Na+/K+ brought on by stress are very tissue- or species-specific. In Zhao et al.'s 2007 study, putrescine significantly decreased Na+ levels in the

roots of barley plants, and supplemental spermidine significantly decreased Na+ levels in the leaves and stalks of rice under salt stress [71].

Elevated concentrations of heavy metals such as Cd and Pb, which cause heavy metal stress, typically prevent seed development, cell and whole-plant growth, nutrient absorption and dispersal, and respiration. Many reports discuss the effect of polyamines on plants under metal stress[72, 73]. In the present study, Cad supplementation could not reduce the endogenous accumulation of Cd and Pb in Pusa Ruby under multiple stress conditions and the heavy metal content was found to be increased by Cad except for a few cases. Whereas in Pusa Rohini and Pusa Sadabahar endogenous cd and Pb contents were reduced to significant levels even under multiple stress conditions which shows that cadaverine can overcome cadmium stress in tomato plants but its effect varies based on the different species of a plant and of course other stress conditions. In this study, Pusa Sadabahar seems to have a better stress tolerance ability under different types of stress when compared to other varieties.

6. REFERENCES

1. Singh, A. K., Dhanapal, S., & Yadav, B. S. (2020). The dynamic responses of plant physiology and metabolism during environmental stress progression. *Molecular Biology Reports*, *47*(2), 1459-1470. https://doi.org/10.1007/s11033-019-05198-4
2. Mason-D'Croz, D., Bogard, J. R., Herrero, M., Robinson, S., Sulser, T. B., Wiebe, K., & Godfray, H. C. J. (2020). Modelling the global economic consequences of a major African swine fever outbreak in China. *Nature Food*, *1*(4), 221-228. https://doi.org/10.1038/s43016-020-0057-2
3. Raiola, A., Rigano, M. M., Calafiore, R., Frusciante, L., & Barone, A. (2014). Enhancing the health-promoting effects of tomato fruit for biofortified food. *Mediators of inflammation*, *2014*. https://doi.org/10.1038/s43016-020-0057-2
4. Gerszberg, A., &Hnatuszko-Konka, K. (2017). Tomato tolerance to abiotic stress: a review of most often engineered target sequences. *Plant growth regulation*, *83*(2), 175-198. https://doi.org/10.1007/s10725-017-0251-x
5. Tiburcio, A. F., Altabella, T., Bitrián, M., &Alcázar, R. (2014). The roles of polyamines during the lifespan of plants: from development to stress. *Planta*, *240*(1), 1-18. https://doi.org/10.1007/s00425-014-2055-9
6. Liu, J. H., Wang, W., Wu, H., Gong, X., & Moriguchi, T. (2015). Polyamines function in stress tolerance: from synthesis to regulation. *Frontiers in plant science*, *6*, 827. https://doi.org/10.3389/fpls.2015.00827
7. Tomar, P. C., Lakra, N., & Mishra, S. N. (2013). Cadaverine: a lysine catabolite involved in plant growth and development. *Plant signaling&behavior*, *8*(10), e25850. https://doi.org/10.4161/psb.25850
8. Mattoo, A. K., &Sobieszczuk-Nowicka, E. (2019). Polyamine as signaling molecules and leaf senescence. *Senescence signalling and control in plants*, 125-138. https://doi.org/10.1016/B978-0-12-813187-9.00008-1
9. Sobieszczuk-Nowicka, E., Paluch-Lubawa, E., Mattoo, A. K., Arasimowicz-Jelonek, M., Gregersen, P. L., & Pacak, A. (2019). Polyamines–A new metabolic switch: Crosstalk with

networks involving senescence, crop improvement, and mammalian cancer therapy. *Frontiers in Plant Science*, *10*, 859. https://doi.org/10.3389/fpls.2019.00859

10. Zhong, M., Wang, Y., Shu, S., Sun, J., & Guo, S. (2020). Ectopic expression of CsTGase enhances salt tolerance by regulating polyamine biosynthesis, antioxidant activities and Na+/K+ homeostasis in transgenic tobacco. *Plant Science*, *296*, 110492. https://doi.org/10.1016/j.plantsci.2020.110492
11. Will, Y., Shields, J. E., & Wallace, K. B. (2019). Drug-induced mitochondrial toxicity in the geriatric population: challenges and future directions. *Biology*, *8*(2), 32. https://doi.org/10.3390/biology8020032
12. Rajpal, C., & Tomar, P. C. (2020). Cadaverine: a potent modulator of plants against abiotic stresses: cadaverine: a potent modulator. *Journal of microbiology, biotechnology and food sciences*, *10*(2), 205-210. https://doi.org/10.15414/jmbfs.2020.10.2.205-210
13. Hussain, M. M., Saeed, A., Khan, A. A., Javid, S., & Fatima, B. (2015). Differential responses of one hundred tomato genotypes grown under cadmium stress. *Genetics and Molecular Research*, *14*(4), 13162-71. DOI http://dx.doi.org/10.4238/2015.October.26.12
14. Kumar, V., Singh, J., & Kumar, P. (2019). Heavy metal uptake by water lettuce (Pistia stratiotes L.) from paper mill effluent (PME): experimental and prediction modeling studies. *Environmental Science and Pollution Research*, *26*(14), 14400-14413.
15. Gratão, P. L., Monteiro, C. C., Antunes, A. M., Peres, L. E. P., & Azevedo, R. A. (2008). Acquired tolerance of tomato (Lycopersicon esculentum cv. Micro- Tom) plants to cadmium- induced stress. *Annals of applied biology*, *153*(3), 321-333. https://doi.org/10.1111/j.1744-7348.2008.00299.x
16. Rajpal, C., & Tomar, P. C. (2020). CADAVERINE: A DIAMINE PRESENCE & ROLE IN PLANTS. *Plant Archives*, *20*(2), 1754-1763.
17. Ukah, B. U., Egbueri, J. C., Unigwe, C. O., &Ubido, O. E. (2019). Extent of heavy metals pollution and health risk assessment of groundwater in a densely populated industrial area, Lagos, Nigeria. *International Journal of Energy and Water Resources*, *3*(4), 291-303. https://doi.org/10.1007/s42108-019-00039-3

18. Mishra, S., Bharagava, R. N., More, N., Yadav, A., Zainith, S., Mani, S., & Chowdhary, P. (2019). Heavy metal contamination: an alarming threat to environment and human health. In *Environmental biotechnology: For sustainable future* (pp. 103-125). Springer, Singapore.
DOI: 10.1007/978-981-10-7284-0_5
19. JAFRI, A. Z., & Ahmad, R. (1995). EFFECT OF SOIL SALINITY ON LEAF DEVELOPMENT, STOMATAL SIZE AND ITS DISTRD3UTION IN COTTON. *Pak. J. Bot*, *27*(2), 297-303.
20. Higbie, S. M., Wang, F., Stewart, J. M., Sterling, T. M., Lindemann, W. C., Hughs, E., & Zhang, J. (2010). Physiological response to salt (NaCl) stress in selected cultivated tetraploid cottons. *International Journal of Agronomy*, *2010*.
https://doi.org/10.1155/2010/643475
21. Leidi, E. O., &Saiz, J. F. (1997). Is salinity tolerance related to Na accumulation in upland cotton (Gossypium hirsutum) seedlings? *Plant and Soil*, *190*(1), 67-75.
https://doi.org/10.1023/A:1004214825946
22. Abd Ella, M. K., & Shalaby, E. E. (1993). Cotton Response to Salinity and Different Potassium- Sodium Ratio in Irrigation Water. *Journal of Agronomy and Crop Science*, *170*(1), 25-31.
https://doi.org/10.1111/j.1439-037X.mansour.tb01052.x
23. Thomas, J. C., & Bohnert, H. J. (1993). Salt stress perception and plant growth regulators in the halophyte Mesembryanthemum crystallinum. *Plant physiology*, *103*(4), 1299-1304.
https://doi.org/10.1104/pp.103.4.1299
24. Julkowska, M. M., Hoefsloot, H. C., Mol, S., Feron, R., de Boer, G. J., Haring, M. A., &Testerink, C. (2014). Capturing Arabidopsis root architecture dynamics with ROOT-FIT reveals diversity in responses to salinity. *Plant Physiology*, *166*(3), 1387-1402.
https://doi.org/10.1104/pp.114.248963
25. Jiang, K., Moe-Lange, J., Hennet, L., & Feldman, L. J. (2016). Salt stress affects the redox status of Arabidopsis root meristems. *Frontiers in Plant Science*, *7*, 81.
https://doi.org/10.3389/fpls.2016.00081
26. Gupta, B., & Huang, B. (2014). Mechanism of salinity tolerance in plants: physiological, biochemical, and molecular characterization. *International journal of genomics*, *2014*.
https://doi.org/10.1155/2014/701596

27. Witzel, K., Weidner, A., Surabhi, G. K., Börner, A., & Mock, H. P. (2009). Salt stress-induced alterations in the root proteome of barley genotypes with contrasting response towards salinity. *Journal of experimental botany*, *60*(12), 3545-3557. https://doi.org/10.1093/jxb/erp198
28. Liu, T., Dobashi, H., Kim, D. W., Sagor, G. H. M., Niitsu, M., Berberich, T., & Kusano, T. (2014). Arabidopsis mutant plants with diverse defects in polyamine metabolism show unequal sensitivity to exogenous cadaverine probably based on their spermine content. *Physiology and Molecular Biology of Plants*, *20*(2), 151-159. https://doi.org/10.1007/s12298-014-0227-5
29. Saha, J., Brauer, E. K., Sengupta, A., Popescu, S. C., Gupta, K., & Gupta, B. (2015). Polyamines as redox homeostasis regulators during salt stress in plants. *Frontiers in Environmental Science*, *3*, 21. https://doi.org/10.3389/fenvs.2015.00021
30. Pottosin, I., Velarde-Buendía, A. M., Bose, J., Zepeda-Jazo, I., Shabala, S., &Dobrovinskaya, O. (2014). Cross-talk between reactive oxygen species and polyamines in regulation of ion transport across the plasma membrane: implications for plant adaptive responses. *Journal of experimental botany*, *65*(5), 1271-1283. https://doi.org/10.1093/jxb/ert423
31. Nakashima, K., Ito, Y., & Yamaguchi-Shinozaki, K. (2009). Transcriptional regulatory networks in response to abiotic stresses in Arabidopsis and grasses. *Plant physiology*, *149*(1), 88-95. https://doi.org/10.1104/pp.108.129791
32. Danquah, A., de Zelicourt, A., Colcombet, J., & Hirt, H. (2014). The role of ABA and MAPK signaling pathways in plant abiotic stress responses. *Biotechnology advances*, *32*(1), 40-52. https://doi.org/10.1016/j.biotechadv.2013.09.006
33. Liu, B., & Qian, S. B. (2014). Translational reprogramming in cellular stress response. *Wiley Interdisciplinary Reviews: RNA*, *5*(3), 301-305. https://doi.org/10.1002/wrna.1212
34. Ma, Y., Dai, X., Xu, Y., Luo, W., Zheng, X., Zeng, D., & Chong, K. (2015). COLD1 confers chilling tolerance in rice. *Cell*, *160*(6), 1209-1221. https://doi.org/10.1016/j.cell.2015.01.046

35. Tomar, P. C., Lakra, N., & Mishra, S. N. (2013). Effect of cadaverine on Brassica juncea (L.) under multiple stress. http://hdl.handle.net/123456789/21072
36. Shi, H., Ye, T., & Chan, Z. (2013). Comparative proteomic and physiological analyses reveal the protective effect of exogenous polyamines in the bermudagrass (Cynodondactylon) response to salt and drought stresses. *Journal of Proteome Research*, *12*(11), 4951-4964. https://doi.org/10.1021/pr400479k
37. Atudorei, D., Stroe, S. G., &Codină, G. G. (2021). Impact of germination on the microstructural and physicochemical properties of different legume types. *Plants*, *10*(3), 592. https://doi.org/10.3390/plants10030592
38. Garcia-Garcia, P., Brenes-Balbuena, M., Hornero-Mendez, D., Garcia-Borrego, A., & Garrido-Fernández, A. (2000). Content of biogenic amines in table olives. *Journal of food protection*, *63*(1), 111-116. https://doi.org/10.4315/0362-028X-63.1.111
39. Legaz, M. E., Sánchez-Elordi, E., Santiago, R., de Armas, R., Fontaniella, B., Millanes, A. M., & Vicente, C. (2018). Metabolic responses of sugarcane plants upon different plant–pathogen interactions. In *Plant Metabolites and Regulation Under Environmental Stress* (pp. 241-280). Academic Press. https://doi.org/10.1016/B978-0-12-812689-9.00013-3
40. Piqueras, A., Cortina, M., Serna, M. D., & Casas, J. L. (2002). Polyamines and hyperhydricity in micropropagated carnation plants. *Plant Science*, *162*(5), 671-678. https://doi.org/10.1016/S0168-9452(02)00007-9
41. Kumar, M., & Mitra, A. (2017). Hairy root culture of Nicotiana tabacum (Tobacco) as a platform for gene manipulation of secondary metabolism. In *Production of plant derived natural compounds through hairy root culture* (pp. 145-163). Springer, Cham. DOI: 10.1007/978-3-319-69769-7_8
42. Shi, M., Liao, P., Nile, S. H., Georgiev, M. I., & Kai, G. (2021). Biotechnological exploration of transformed root culture for value-added products. *Trends in Biotechnology*, *39*(2), 137-149.

https://doi.org/10.1016/j.tibtech.2020.06.012

43. Niemi, K., Häggman, H., &Sarjala, T. (2002). Effects of exogenous diamines on the interaction between ectomycorrhizal fungi and adventitious root formation in Scots pine in vitro. *Tree Physiology*, *22*(6), 373-381. https://doi.org/10.1093/treephys/22.6.373
44. Vassileva, V., & Ignatov, G. (2002). Relationship between bacteroid poly- β- hydroxybutyrate accumulation and nodule functioning in the Galegaorientalis–Rhizobium galegae symbiosis under diamine treatment. *Physiologia Plantarum*, *114*(1), 27-32. https://doi.org/10.1046/j.0031-9317.2001.1140105.x
45. Goyal, R. K., Fatima, T., Topuz, M., Bernadec, A., Sicher, R., Handa, A. K., & Mattoo, A. K. (2016). Pathogenesis-related protein 1b1 (PR1b1) is a major tomato fruit protein responsive to chilling temperature and upregulated in high polyamine transgenic genotypes. *Frontiers in plant science*, *7*, 901. https://doi.org/10.3389/fpls.2016.00901
46. Nambeesan, S., AbuQamar, S., Laluk, K., Mattoo, A. K., Mickelbart, M. V., Ferruzzi, M. G., & Handa, A. K. (2012). Polyamines attenuate ethylene-mediated defense responses to abrogate resistance to Botrytis cinerea in tomato. *Plant Physiology*, *158*(2), 1034-1045. https://doi.org/10.1104/pp.111.188698
47. Zörb, C., Geilfus, C. M., & Dietz, K. J. (2019). Salinity and crop yield. *Plant biology*, *21*, 31-38. https://doi.org/10.1111/plb.12884
48. Rizwan, M., Ali, S., Adrees, M., Ibrahim, M., Tsang, D. C., Zia-ur-Rehman, M., & Ok, Y. S. (2017). A critical review on effects, tolerance mechanisms and management of cadmium in vegetables. *Chemosphere*, *182*, 90-105. https://doi.org/10.1016/j.chemosphere.2017.05.013
49. Chiao, W. T., Syu, C. H., Chen, B. C., & Juang, K. W. (2019). Cadmium in rice grains from a field trial in relation to model parameters of Cd-toxicity and-absorption in rice seedlings. *Ecotoxicology and Environmental Safety*, *169*, 837-847. https://doi.org/10.1016/j.ecoenv.2018.11.061
50. Qayyum, M. F., ur Rehman, M. Z., Ali, S., Rizwan, M., Naeem, A., Maqsood, M. A., & Ok, Y. S. (2017). Residual effects of monoammonium phosphate, gypsum and elemental

sulfur on cadmium phytoavailability and translocation from soil to wheat in an effluent irrigated field. *Chemosphere*, *174*, 515-523. https://doi.org/10.1016/j.chemosphere.2017.02.006

51. Zhang, X. Z., Xu, P. H., Liu, G. W., Ahmad, A., Chen, X. H., Zhu, Y. L., ... & Qiao, G. J. (2020). Synthesis, characterization and wettability of Cu-Sn alloy on the Si-implanted 6H-SiC. *Coatings*, *10*(9), 906. https://doi.org/10.3390/coatings10090906
52. Zulfiqar, U., Farooq, M., Hussain, S., Maqsood, M., Hussain, M., Ishfaq, M., ... & Anjum, M. Z. (2019). Lead toxicity in plants: Impacts and remediation. *Journal of Environmental Management*, *250*, 109557. https://doi.org/10.1016/j.jenvman.2019.109557
53. Ashraf, U., & Tang, X. (2017). Yield and quality responses, plant metabolism and metal distribution pattern in aromatic rice under lead (Pb) toxicity. *Chemosphere*, *176*, 141-155. https://doi.org/10.1016/j.chemosphere.2017.02.103
54. Gaur, A., &Adholeya, A. (2004). Prospects of arbuscular mycorrhizal fungi in phytoremediation of heavy metal contaminated soils. *Current Science*, 528-534. https://www.jstor.org/stable/24107905
55. Rakhshaee, R., Giahi, M., &Pourahmad, A. (2009). Studying effect of cell wall's carboxyl–carboxylate ratio change of Lemna minor to remove heavy metals from aqueous solution. *Journal of Hazardous Materials*, *163*(1), 165-173. https://doi.org/10.1016/j.jhazmat.2008.06.074
56. Negri, M. C., Hinchman, R. R., & Gatliff, E. G. (1996). *Phytoremediation: using green plants to clean up contaminate soil, groundwater, and wastewater* (No. ANL/ES/CP-89941; CONF-960804-38). Argonne National Lab.(ANL), Argonne, IL (United States).
57. Sinha, R. K., Herat, S., & Tandon, P. K. (2007). Phytoremediation: role of plants in contaminated site management. In *Environmental bioremediation technologies* (pp. 315-330). Springer, Berlin, Heidelberg. DOI: 10.1007/978-3-540-34793-4_14
58. Salido, A. L., Hasty, K. L., Lim, J. M., & Butcher, D. J. (2003). Phytoremediation of arsenic and lead in contaminated soil using Chinese brake ferns (Pteris vittata) and Indian mustard (Brassica juncea). *International Journal of Phytoremediation*, *5*(2), 89-103. https://doi.org/10.1080/713610173

59. Curie, C., Cassin, G., Couch, D., Divol, F., Higuchi, K., Le Jean, M., ... & Mari, S. (2009). Metal movement within the plant: contribution of nicotianamine and yellow stripe 1-like transporters. *Annals of botany*, *103*(1), 1-11. https://doi.org/10.1093/aob/mcn207
60. Romero-Estévez, D., Yánez-Jácome, G. S., Simbaña-Farinango, K., & Navarrete, H. (2019). Content and the relationship between cadmium, nickel, and lead concentrations in Ecuadorian cocoa beans from nine provinces. *Food control*, *106*, 106750. https://doi.org/10.1016/j.foodcont.2019.106750
61. Patrícia Vieira da Cunha, K., Williams Araújo do Nascimento, C., & José da Silva, A. (2008). Silicon alleviates the toxicity of cadmium and zinc for maize (Zea mays L.) grown on a contaminated soil. *Journal of Plant Nutrition and Soil Science*, *171*(6), 849-853. https://doi.org/10.1002/jpln.200800147
62. Degraeve, N. (1981). Carcinogenic, teratogenic and mutagenic effects of cadmium. *Mutation Research/Reviews in Genetic Toxicology*, *86*(1), 115-135. https://doi.org/10.1016/0165-1110(81)90035-X
63. Verbruggen, N., Hermans, C., & Schat, H. (2009). Mechanisms to cope with arsenic or cadmium excess in plants. *Current opinion in plant biology*, *12*(3), 364-372. https://doi.org/10.1016/j.pbi.2009.05.001
64. Lux, A., Martinka, M., Vaculík, M., & White, P. J. (2011). Root responses to cadmium in the rhizosphere: a review. *Journal of experimental botany*, *62*(1), 21-37. https://doi.org/10.1093/jxb/erq281
65. Zelko, I., & Lux, A. (2004). Effect of cadmium on Karwinskiahumboldtiana roots. *Biologia*, *59*, 205-209.
66. Vaculík, M., Lux, A., Luxová, M., Tanimoto, E., & Lichtscheidl, I. (2009). Silicon mitigates cadmium inhibitory effects in young maize plants. *Environmental and Experimental Botany*, *67*(1), 52-58. https://doi.org/10.1016/j.envexpbot.2009.06.012
67. Tomar, P. C., Mishra, S. N., &Rajpa, C. (2017). Effect of cadaverine on protein profiling of Brassica juncea (RH-30) seedlings under multiple stress. *Int J Adv Inform Sci Technol*, *6*, 49-62. DOI:10.15693/ijaist/2017.v6i3.49-62

68. Ndayiragije, A., & Lutts, S. (2006). Do exogenous polyamines have an impact on the response of a salt-sensitive rice cultivar to NaCl? *Journal of plant physiology*, *163*(5), 506-516.
https://doi.org/10.1016/j.jplph.2005.04.034
69. Sharma, T., Dreyer, I., &Riedelsberger, J. (2013). The role of K+ channels in uptake and redistribution of potassium in the model plant Arabidopsis thaliana. *Frontiers in plant science*, *4*, 224.
https://doi.org/10.3389/fpls.2013.00224
70. Abdel-Farid, I. B., Marghany, M. R., Rowezek, M. M., &Sheded, M. G. (2020). Effect of salinity stress on growth and metabolomic profiling of Cucumis sativus and Solanum lycopersicum. *Plants*, *9*(11), 1626.
https://doi.org/10.3390/plants9111626
71. Zhao, F., Song, C. P., He, J., & Zhu, H. (2007). Polyamines improve K+/Na+ homeostasis in barley seedlings by regulating root ion channel activities. *Plant Physiology*, *145*(3), 1061-1072.
https://doi.org/10.1104/pp.107.105882
72. Groppa, M. D., Tomaro, M. L., & Benavides, M. P. (2007). Polyamines and heavy metal stress: the antioxidant behavior of spermine in cadmium-and copper-treated wheat leaves. *Biometals*, *20*(2), 185-195.
https://doi.org/10.1007/s10534-006-9026-y
73. Ahanger, M. A., Aziz, U., Alsahli, A., Alyemeni, M. N., & Ahmad, P. (2020). Combined kinetin and spermidine treatments ameliorate growth and photosynthetic inhibition in Vigna angularis by up-regulating antioxidant and nitrogen metabolism under cadmium stress. *Biomolecules*, *10*(1), 147.
https://doi.org/10.3390/biom10010147

2023 2nd International Conference for Innovation in Technology (INOCON)
Bangalore, India. Mar 3-5, 2023

Development of Brake System Plausibility Device of an FSAE Race Car

D.C Meena[a], Aryan Motla[b], Anuj Majumdar[c], Aatish Kumar Ghosh[d]
Department of Electrical Engineering
Delhi Technological University
Delhi, India
[a]*dcmeena@dce.ac.in*,[b]*aryanmotla_2k19ee060@dtu.ac.in*,[c]*anujmajumdar_2k19ee050@dtu.ac.in*,
[d]*aatishkumarghosh_2k19ee003@dtu.ac.in*

2023 2nd International Conference for Innovation in Technology (INOCON) | 979-8-3503-2092-3/23/$31.00 ©2023 IEEE | DOI: 10.1109/INOCON57975.2023.10100997

***Abstract*—Electric Vehicles are growing faster than the traditional combustion vehicles which are powered by conventional energy resources because of the environmental concern and to attain sustainable development. Formula student is one of the world's largest student-run competitions. Formula student electric development includes various challenges from both mechanical and electrical fronts. Mechanical parts have their safety standards and measures whereas for electrical front robust safety circuitry must be prepared to reduce the risk of any fatal accident. Generally, Formula student cars are fast and good acceleration, to avoid wheel-to-wheel racing and drag racing or other dangerous stunts, a robust safety circuit Brake system Plausibility Device (BSPD) is designed and tested. This paper discusses the designing, robustness of BSPD devices.**

***Keywords*- FSAE, Safety Systems, Electric Vehicles, Brake System Plausibility Device (BSPD)**

I. Introduction

According to WHO, Every day thousands of people lose their lives in road accidents and this number is increasing day by day. No matter which transport is being used or manufactured, its safety should be the topmost priority. This paper emphasizes one of the most important safety circuits which not only ensures the safety of the driver but also the electrical components during a fault in either brake lines or motor power input. To achieve a good level of safety, Failure Mode Effect analysis was performed and all the failures were jotted down as their possible solutions too[1].

Electric vehicles (EVs), and all vehicles in general, require safety mechanisms to protect passengers in case of system failures or emergencies. Many such safety systems have been made and recent improvements, in the existing systems are discussed in the following sections:

A. Anti-lock Braking System (ABS)

The function of this system is to prevent the locking of the wheels when sudden braking occurs, thereby enabling the driver to retain control of the vehicle's steering. A brushless motor has been established as the standard choice for EVs with In-Wheel motors. A study showed that the ABS arrangement can be simplified by exploiting the back EMF signal of brushless In-Wheel hubs. The proposed intelligent sensorless ABS design reduces costs by eliminating the requirement for separate ABS sensors, and provides accurate wheel speed estimation and road identification, leading to improved ABS performance. Experiments on different road conditions showed the accuracy of the proposed technique to be higher than just conventional ABS sensors, and the robustness was significantly improved through the implementation of simple aggregation operators. The sensorless ABS for BLDC was found to be more robust compared to commercial ABS[2]. A new ABS control strategy for EVs with individual wheel motors was introduced in a different study. The PI direct slip control-based controller was experimentally confirmed through hardware-in-the-loop validation[3].

B. Electronic Stability Control (ESC)

The purpose of this system is to maintain the stability and direction of the vehicle during unexpected turns or when navigating slippery conditions. The proper design of control strategies can enhance the lateral stability of modern EVs equipped with In-Wheel Motors. Independent regulation of traction efforts and braking at all wheels enhances handling during cornering maneuvers, especially in degraded adherence conditions. A recently proposed algorithm for ESC lateral stability was combined with the EBD and ABS controllers for longitudinal stability and evaluated using a benchmark vehicle model in co-simulation tests. Stability improvements were measured by imposing standard reference trajectories. [4].

In another study, a three-step control strategy for ESC was put forward to accomplish ideal torque distribution for all four in-wheel motors in an EV with direct-driven in-wheel motors. the first step was a gain-scheduled linear quadratic regulator that generated the demanded yaw moment command for ESC. The next step was the distribution of control, which allocated the desired tire forces for longitudinal movement based on the yaw moment command and took into account any changes in speed desired by the driver (such as acceleration or retardation). The final step involved using a combined-slip tyre model to perform slip ratio control (SRC) at each wheel to provide the necessary longitudinal tire force. According to the findings, SRC was not necessary

Authorized licensed use limited to: DELHI TECHNICAL UNIV. Downloaded on April 24,2023 at 04:28:27 UTC from IEEE Xplore. Restrictions apply.

for performance if the slip ratio could remain in the stable area with traction control or anti-lock braking systems.[5].

C. Traction Control System (TCS)

This system helps to maintain traction between the vehicle's tires and the road surface, preventing wheel spin and improving stability. Recently, many electric vehicles (EVs) were developed to address the environmental and energy issues posed by internal combustion engine vehicles (ICEVs). Despite their performance, they have not yet fully leveraged the most significant advantage of EVs - the quick and precise control of the electric motor's generate torque. Controlling motor torque appropriately can greatly improve vehicle stability and safety and expand the range of one battery charge through the use of special low-drag tires with lower energy loss[6]. A study presented a traction control system with strong performance and the ability to withstand faults in electric vehicles. A PI-based disturbance observer was used to improve the estimation of friction torque and the phase lag issue was addressed by incorporating a delay in the driving torque measurement. The proposed traction control prevented skidding of electric vehicles and improved vehicle safety[7]

D. Airbags

As a standard feature, electric vehicles are equipped with several airbags to ensure the safety of the passengers in the case of a collision. The use of airbags in vehicles to prevent collisions by opening in response to sudden changes in acceleration is widespread. These airbags typically contain MEMS-based accelerometer chips shown in figure 1, eliminating the requirement for expensive g-switches. The accelerometer continuously monitors the vehicle's acceleration, and when there is a sudden deceleration, the change in capacitance is detected and signals to open the airbag are sent[8].



Fig. 1. Bosch accelerometer chip

A numerical study showed the possibility of enhancing passenger safety in a vehicle through the implementation of a cutting-edge curtain airbag in a pioneering chassis design. The models used in the analysis only incorporated certain components of the car, which helped minimize computational expenses and simplify the geometry and material properties. Qualitative comparisons were made between dummy behavior in crash tests and simulations due to a lack of instrumentation. Future studies could investigate the effects on other dummies and driver positions. Currently, only one dummy and position were considered as shown in figure 2, with fixed restraint systems. Further analysis of other impact types and parameters for evaluating passenger safety device effectiveness could yield interesting results[9].



Fig. 2. Dummy Position

E. Battery Management System (BMS)

The BMS monitors the state of charge, temperature, and other parameters of the battery, ensuring that the battery remains in a safe range of operation. The BMS has been recognized as the main safety guard for a battery system in EVs. It is responsible for ensuring the reliable and safe operation of high-voltage, high-current battery cells through supervision, control, and protection. The definition of BMS may vary, but it generally refers to a system overseeing battery cells either individually or as a battery system[10]. However, the performance of these key technologies in real-world applications may differ from the test conditions and requires further exploration to tackle limitations [11].

F. Crash Avoidance System

Some electric vehicles offer additional safety features such as lane departure alert, forward collision alert, and automatic emergency braking. A crash safety concept for hybrid and electric vehicles by Daimler has been illustrated, which includes a strategy to cut off high voltage in accidents, a concept of protection zones for safe placement of safety components, shown in figure 3, mechanical requirements for high voltage components for shock protection and electric insulation, and an integrated safety concept to prevent critical damages to the high voltage battery in case of high crash loadings[12]. The paper presented a novel advanced driver assistance system (ADAS) that incorporates driver behavior identification and a driver assistance system using a deep neural network (DNN) model. This system provides a protection layer to the vehicle's architecture without the need for additional hardware or significant modifications. The effectiveness of the system was confirmed through an electric vehicle drive simulation, which was based on previously published data. The system's response time was optimized through diverse methods, with plans to improve performance by adding additional features and minimizing energy consumption in the future[13].

Authorized licensed use limited to: DELHI TECHNICAL UNIV. Downloaded on April 24,2023 at 04:28:27 UTC from IEEE Xplore. Restrictions apply.

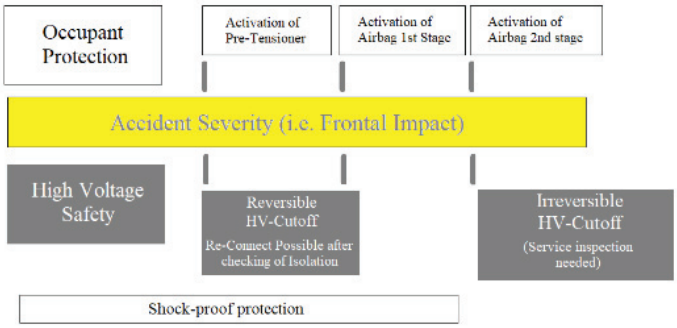


Fig. 3. High voltage cut-off in crash

G. Automatic Emergency Call

The automatic Emergency call(eCall) system allows the vehicle to automatically notify emergency services in the occurrence of a crash. The Connected Vehicle (CV), synonymously the Internet of Vehicles, is a large communication system for V2X interaction, unified with three networks: intra-vehicle, inter-vehicle (figure 4), and onboard mobile internet. It facilitates intelligent transportation management, information services, and driving control. CV systems are equipped with interfaces to WiFi or cellular networks and short-range communication technologies. Vehicles connected to the network have access to cloud information services, like media, emergency calls, and navigation. The Global Vehicular ID terminal serves as the communication gateway and technological way of the CV, allowing for global network connectivity and positioning[14].

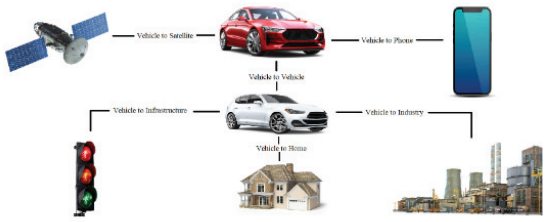


Fig. 4. Schematic diagram of CVs in a smart city

Three solutions have been proposed for a connected vehicle to achieve Internet connection: embedded solution with SIM card installed during manufacturing, tethered solution with modem for personal SIM insertion and application intelligence in the vehicle, and integrated approach with smart device providing both intelligence and connectivity, displaying smartphone applications on vehicle's interface[15].

H. Fire suppression system

Electric vehicles also have a fire suppression system in case of a fire in the vehicle. The fire hazard of EVs compared to ICEVs. Based on limited data, the study presents the current market of EVs, reviews recent fire incidents, and compares the difference between EVs and ICEVs during a fire. The study examines the effects of fires in both EVs and ICEVs on evacuation safety, firefighter and rescue team safety, and building structure, utilizing computational fluid dynamics numerical techniques. The aim is to provide design assumptions for systems to prevent the effects of an EV fire in enclosed spaces[16].The existing fire protection systems require improvement and the fire risk posed by discarded electric vehicles and discarded battery packs is uncertain. The study intends to stimulate further research and development aimed at increasing the overall safety of EVs to match the level of safety offered by conventional vehicles.[17].

I. Battery Isolation

In the case of a crash, electric vehicles have a mechanism to isolate the battery to prevent further damage and injury. A study compares design solutions to disclose basic mechanical design requirements for a reliable battery packaging system [18] as shown in figure 5.

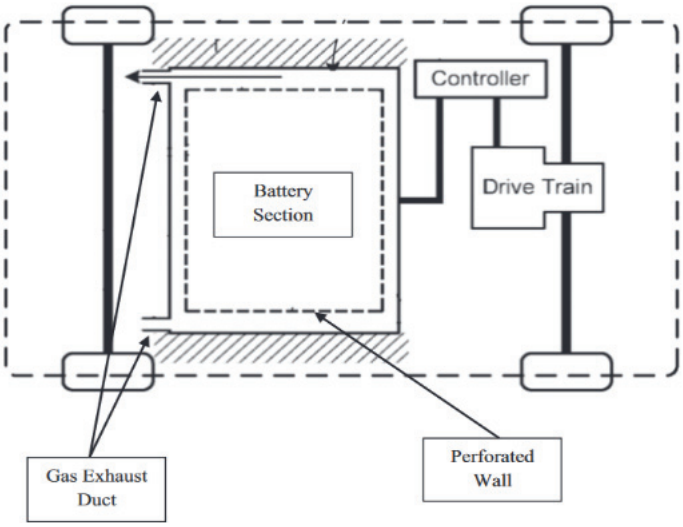


Fig. 5. A battery pack system designed to exhaust the hot gases and material released during thermal runaway event

A control system was designed for high voltage battery isolation and insulation in electric vehicles and charging stations. It continuously monitors the battery's isolation through an isolation circuit and can function effectively while the battery is active or inactive and undergoing significant voltage fluctuations. The system checks the isolation resistance between the vehicle's power system or battery and chassis to detect any worsening in insulation and potentially hazardous levels of leakage current[19].

Formula Society of Automotive Engineers (FSAE) is a global design competition for students from universities and colleges. Teams participate by building a prototype of a racing car based on universal FSAE restrictions set. The teams are evaluated based on the basis of the car's design, cost analysis, operational plans, and performance during the competition.

Authorized licensed use limited to: DELHI TECHNICAL UNIV. Downloaded on April 24,2023 at 04:28:27 UTC from IEEE Xplore. Restrictions apply.

This paper presents the design of a Brake System Plausibility Device (BSPD), adhering to the constraints provided by FSAE. A circuit was prepared whose robustness was checked using simulation software, following which physical testing was performed. The paper starts with a general overview of the system, which is then analyzed in depth. This circuit was developed for Formula Electric Car by Team Defianz Racing of Delhi Technological University, Delhi for the 2022 season.

II. System Overview

BSPD is a standalone, non-programmable circuit designed in accordance with FSAE regulations. It is a safety device to prevent potential injury due to the drifting of the electric vehicle. The aim of BSPD is to activate(open) the shutdown circuit (safety circuit) when two conditions are met simultaneously:

- Power Delivered to the motor $\geq$ 5KW,
- Hard Braking, if the pressure in brake pedal line > 30 bar.

The shutdown circuit will be activated if the two conditions persist for over 500ms and BSPD will reset itself after 10 seconds.

A DC Current sensor is used to measure the power delivered to the motor and for measuring of pressure in the brake line, the Brake pressure sensor is used for appropriate rating. All the sensors used are of Automotive grade. Integrated circuits used in the circuit board are also of Automotive grade. Ratings of the sensors used depend on the current, voltage, temperature, and pressure limits of the system. The vehicle uses a single Emrax 228 MV LC Motor with DTI HV-500 LC Motor controller which is powered by Li-ion battery pack.

Emrax 228 is a 3-phase motor, to determine the power delivered to the motor, a DC current sensor is used because of the rule constraints. The current sensor is placed before the motor controller to check the current flowing in the motor at any instant of time. A brake Pressure Sensor is installed in the brake line for the measurement of pressure in the brake line. The Brake Pressure Sensor gives the current output.

Before starting working on the circuit designing all fault conditions and requirement of the circuit is jotted down which are as follows:

- To detect implausibility
- Fault conditions, sensor short-circuited to ground or supply or lose connections.

III. Design

Circuit designing was divided into two phases, the first phase includes the prime function of the device whereas the second phase includes the implementation of fault conditions.

To detect implausibility (Power$\geq$ 5 KW and Pressure > 30 bar), two comparators and one AND gate ICs are used. If both the implausibility conditions are found to be true, both comparators used will give high output, and correspondingly output of AND gate will be HIGH. This circuitry is shown in figure 6.

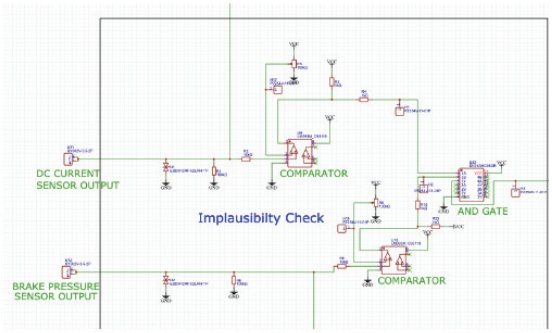


Fig. 6. Implausibility Check

Then a check has been performed, if the implausibility condition still exists for more than 500ms or not, also known as Persistency Check. For this RC delay circuit as shown in figure 7 having a time constant equal to 500ms is used, so that the required output of this delay circuit will only be obtained after 500ms.

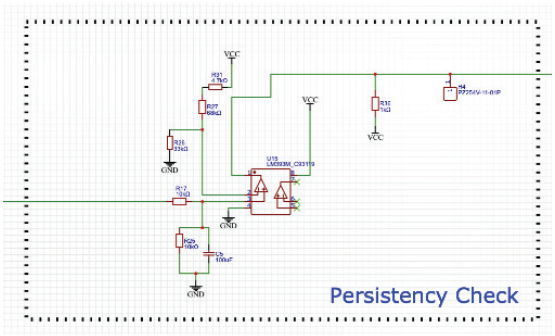


Fig. 7. Persistency Check

After this, the output of the persistency check is fed to a 555 timer with a 10-second auto reset used in monostable mode as shown in figure 8. If implausibility still exists, a HIGH signal from the output of the 555 timer is continued to be fed to a NOR gate shown in figure 9 and the normally open relay is opened, Disconnecting the battery pack's power supply to the motor and hence opening the shutdown circuit, which is in series. Meanwhile, the 10s auto reset keeps checking for the output of the persistency check. In between if the implausibility is removed the output of the 555 timer generates a LOW signal after 10 seconds to NOR gate and the normally open relay is closed, now allowing the vehicle in ready-to-go mode again.

To check the Fault conditions which are broken sensor wire and sensor short-circuited to ground or supply, a System critical signal (SCS) Fault check is done containing four comparators, two OR gates, and pull-down resistors as shown in figure 10 for DC Current Sensor. An identical fault check circuit is designed for Brake Pressure Sensor as well. This

Authorized licensed use limited to: DELHI TECHNICAL UNIV. Downloaded on April 24,2023 at 04:28:27 UTC from IEEE Xplore. Restrictions apply.

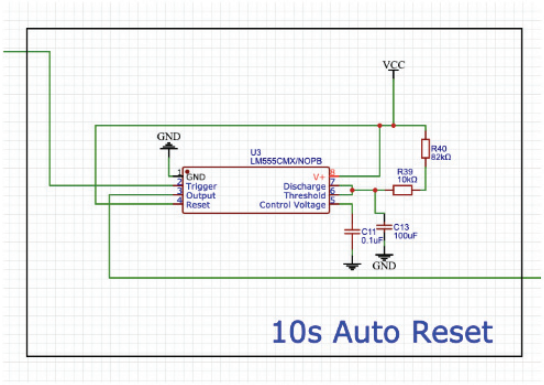


Fig. 8. 10s Auto Reset

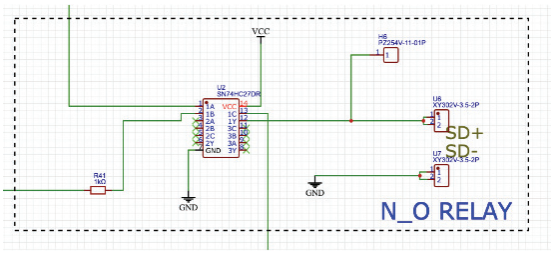


Fig. 9. NOR gate and Normally open Relay

fault check is used so that the Brake pressure sensor and DC Current sensor don't give 0V as the lower threshold and 5V as upper threshold. If the sensors would have given either 0 or 5V output, it would have meant either they are short-circuited to the ground or power supply. In case of broken wire, pull-down resistors are used which will give 0V.

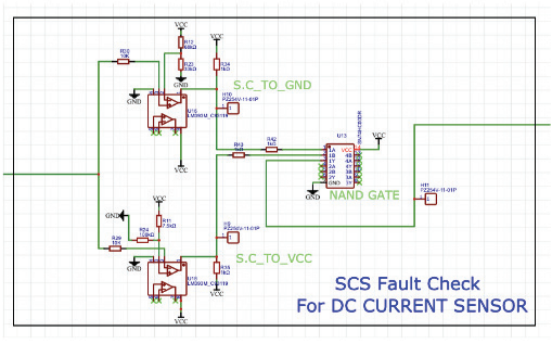


Fig. 10. SCS Fault Check

In case of the fault, comparators used will detect the fault based on the threshold where the lower threshold is 0.2V whereas the upper threshold is 4.6V. NAND Gate is used after comparators for the proper handling of the fault conditions. If any one of the faults arises, the output of the NAND gate will get high, and will be fed directly to the (i) NOR gate and the normally open relay is opened, Disconnecting the battery pack's power supply to the motor and hence opens the shutdown circuit, which is in series and (ii) SCS fault indicator circuit to check the fault visibly using an NPN transistor with a LED as shown in figure 11.

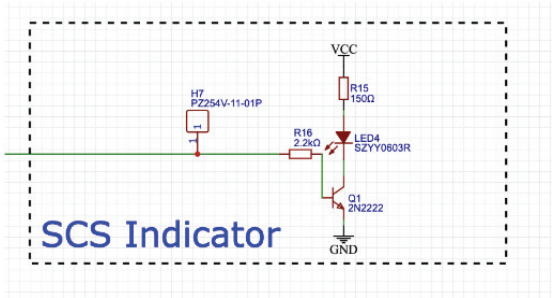


Fig. 11. SCS Indicator

IV. Component Selection

Component selection plays a major role in any system. Time and knowledge were invested in the component selection to make the device robust, small, error-free, and also cost-effective.

The maximum HV current flowing is 160A, so the current sensor to be selected must be of a range greater than 160A. LEM HCFW200-S/SP1 was selected, whose range is from -200A to + 200A. For BPS, Honeywell MLH03KPSL01B is used whose threshold pressure range is 0-350 bar.

Table I shows the parameters of the current sensor used and Table II shows for the BPS sensor.

TABLE I
LEM HCFW200-S/SP1 SPECIFICATION

S. No.	*Specification*	*Range*
1.	Operating Voltage	4.75V to 5.25V
2.	Current Range	-200A to 200A
3.	Output Voltage	0.5V to 4.5V
4.	Offset Voltage	2.5V+-2.5mV
5.	Sensitivity	10mV/A+-0.06mV/A
6.	Operating Temperature	-40C to +125 C

TABLE II
MLH03KPSL01B SPECIFICATION

S. No.	*Specification*	*Range*
1.	Operating Voltage	9.5V to 30V
2.	Pressure Range	0-350 bar
3.	Output Current	4-20mA
4.	Offset Current	4mA
5.	Sensitivity	0.0457mA/bar/A
6.	Operating Temperature	-40C to +125 C

Most ICs used are of Texas Instruments because of their reliability, availability, and cost. Initially, SN54 series ICs for logic gates are used but because of the temperature range constraints, SN74 series ICs are selected. The finally selected ICs were 2 input positive AND Gate IC (SN74AHC08),

Authorized licensed use limited to: DELHI TECHNICAL UNIV. Downloaded on April 24,2023 at 04:28:27 UTC from IEEE Xplore. Restrictions apply.

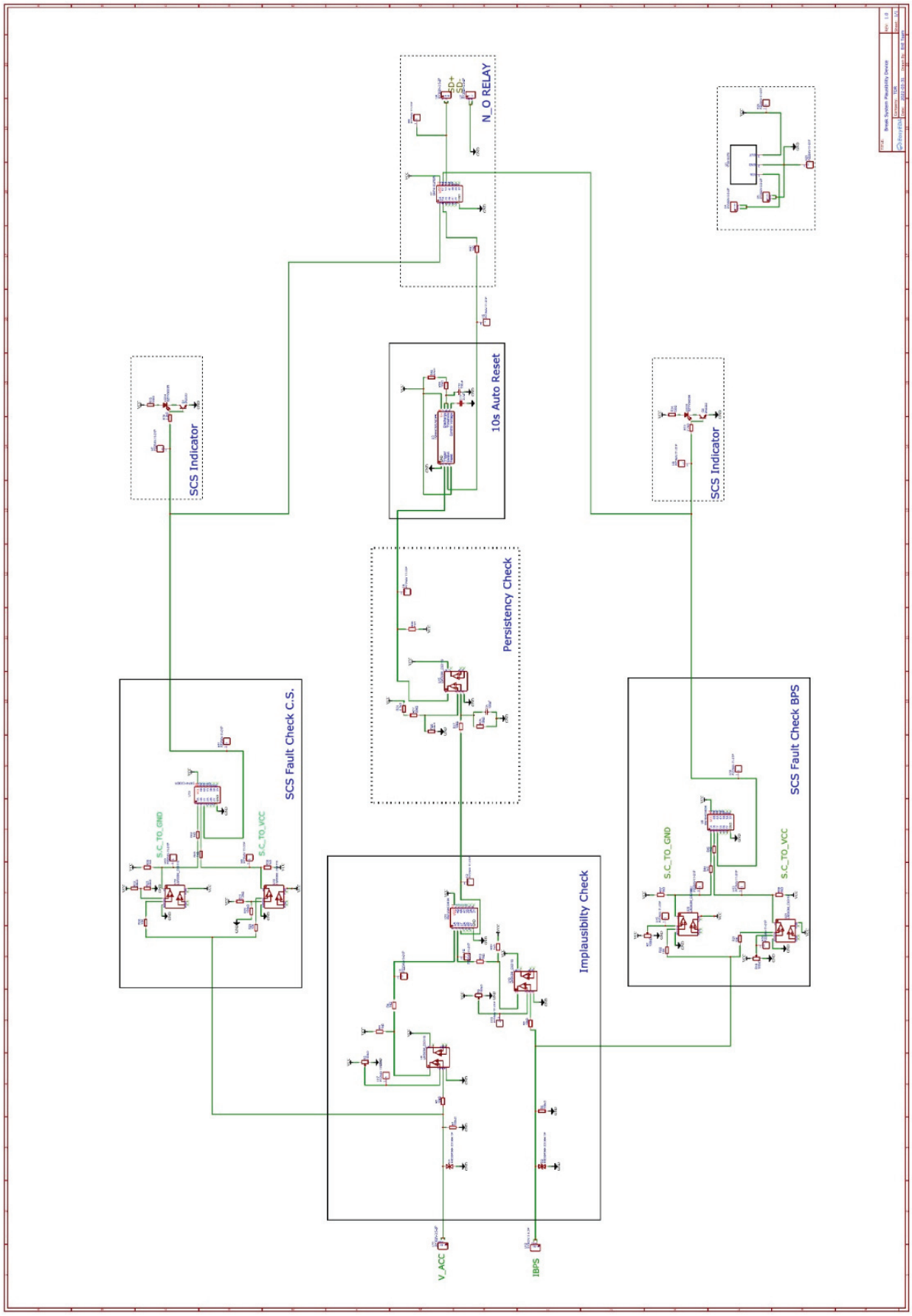


Fig. 12. BSPD Circuit

Authorized licensed use limited to: DELHI TECHNICAL UNIV. Downloaded on April 24,2023 at 04:28:27 UTC from IEEE Xplore. Restrictions apply.

and 2 input NAND Gate IC (SN74HC00DR). 3 input NOR Gate (SN74LVC1G27DBVR), 2 input COMPARATOR IC (LM393), Timer IC (LM555), and 2N2222 IC (NPN bipolar junction transistor. These ICs were selected on the basis of the following factors: They are known for their ability to function within the temperature range of -40°C to 125°C., operating voltage, number of input terminals required, number of gates required in the whole circuit i.e. 2(Dual), 4(Quad), a wide variety of packages are available. LM393 Dual comparators were used over TLV 7031 because of reduced offset voltage, increased supply voltage capacity, reduced supply current, lower input bias current, and decreased propagation delay. Table III shows the parameters of the comparator used.

TABLE III
LM393 SPECIFICATION

S. No.	*Specification*	*Range*
1.	Supply Voltage	36V, +/-18 V
2.	Differential input voltage	36V
3.	input offset voltage	5mV max
4.	input bias Current	250nA max
5.	large signal voltage gain	200V/mV typ.

V. Results and Conclusion

For the proposed system as shown in Figure 12, a printed circuit board was fabricated, as shown in Figure 13. It was tested for various values of the Brake pressure sensor and DC Current sensor. Table IV shows the consolidated results for the above Fault conditions.

TABLE IV
RESULTS FOR FAULT CONDITIONS

Hard Braking	Power $\geq$ 5kW	BSPD Output	System Response
Faulty Input	Don't Care	TRUE	BSPD Shuts down Car
Don't Care	Faulty Input	TRUE	BSPD Shuts down Car

Table V shows the consolidated results for various cases of hard braking and power input.

TABLE V
RESULTS FOR VARIOUS CASES OF HARD BRAKING AND POWER INPUT

Hard Braking	Power $\geq$ 5kW	BSPD Output	System Response
FALSE	FALSE	FALSE	Vehicle ready to go
FALSE	TRUE	FALSE	Vehicle ready to go
TRUE	FALSE	FALSE	Vehicle ready to go
TRUE	TRUE	TRUE	BSPD shuts down car

There are many already existing safety protocols and devices for electric vehicles, but there is a need for a safety mechanism for prevention from drifting scenarios as it is harmful in the case of electric vehicles. It is concluded that Brake System Plausibility Device is safe to use for this cause in formula student vehicles. The device is robust and optimized. Also, it can be used in commercial vehicles to reduce the accidents caused by stunts.

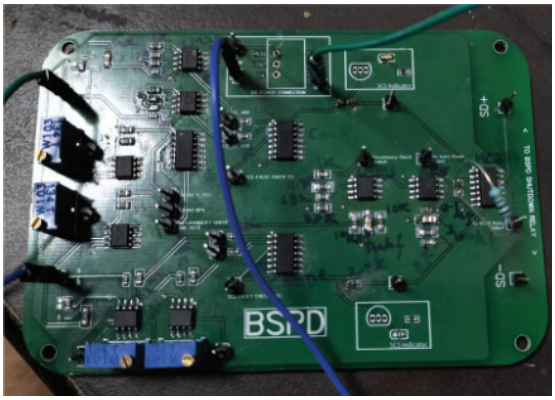


Fig. 13. PCB for BSPD

VI. Future Work

Owing to the fact that in case of fault conditions, the device must not reset itself after 10s, a latching circuit can be incorporated which will ensure the manual reset of the device. To achieve this, D- flip flop shall be used for each sensor. In D flip flop, the clock pin is attached to the output of the OR gate which takes input from the SCS fault check circuit and a manual reset switch, clear pin is attached to the RC circuit and high logic for the Pre-Set pin. Here an RC circuit has been made to define the initial output of a D- flip flop as low. As per the truth table of D- flip flop whenever the clock is positively triggered, the pre-set pin, clear pin and data pin are high then it will give low output and open the relay. When the switch is pressed the system will reset and function normally.

References

[1] G. S. Naga Sruthi, R. vibhute, U. Karmarkar, S. Chandra and S. M. Iyengar, "Safety system of an electric vehicle for formula racing," 2014 IEEE International Conference on Vehicular Electronics and Safety, Hyderabad, 2014, pp. 44-49, doi: 10.1109/ICVES.2014.7063722.

[2] Shashank Arora, Weixiang Shen, Ajay Kapoor, Review of mechanical design and strategic placement technique of a robust battery pack for electric vehicles, Renewable and Sustainable Energy Reviews, Volume 60, 2016, Pages 1319-1331, ISSN 1364-0321, https://doi.org/10.1016/j.rser.2016.03.013.

[3] Ivanov, V., Shyrokau, B., Savitski, D., Orus, J. et al., "Design and Testing of ABS for Electric Vehicles with Individually Controlled On-Board Motor Drives," SAE Int. J. Passeng. Cars - Mech. Syst. 7(2):2014, doi:10.4271/2014-01-9128.

[4] M. Montani et al., "ESC on In-Wheel Motors Driven Electric Vehicle: Handling and Stability Performances Assessment," 2020 IEEE International Conference on Environment and Electrical Engineering and 2020 IEEE Industrial and Commercial Power Systems Europe (EEEIC / I&CPS Europe), Madrid, Spain, 2020, pp. 1-6, doi: 10.1109/EEEIC/ICPSEurope49358.2020.9160768.

[5] Chen, BC., Kuo, CC. Electronic stability control for electric vehicle with four in-wheel motors. Int.J Automot. Technol. 15, 573–580 (2014). https://doi.org/10.1007/s12239-014-0060-4

[6] Y. Hori, Y. Toyoda and Y. Tsuruoka, "Traction control of electric vehicle: basic experimental results using the test EV "UOT electric march"," in IEEE Transactions on Industry Applications, vol. 34, no. 5, pp. 1131-1138, Sept.-Oct. 1998, doi: 10.1109/28.720454

[7] Jia-Sheng Hu, Dejun Yin, Yoichi Hori, Fault-tolerant traction control of electric vehicles, Control Engineering Practice, Volume 19, Issue 2, 2011, Pages 204-213, ISSN 0967-0661, https://doi.org/10.1016/j.conengprac.2010.11.012.

Authorized licensed use limited to: DELHI TECHNICAL UNIV. Downloaded on April 24,2023 at 04:28:27 UTC from IEEE Xplore. Restrictions apply.

[8] Basu, A.K., Tatiya, S., Bhattacharya, S. (2019). Overview of Electric Vehicles (EVs) and EV Sensors. In: Bhattacharya, S., Agarwal, A., Prakash, O., Singh, S. (eds) Sensors for Automotive and Aerospace Applications.Energy, Environment, and Sustainability.Springer, Singapore. https://doi.org/10.1007/978-981-13-3290-6_7

[9] E.V. Arcieri, S. Baragetti, M. Fustinoni, S. Lanzini, R. Papalia, Study and modelling of the passenger safety devices of an electric vehicle by finite elements, Procedia Structural Integrity, Volume 8, 2018, Pages 212-219, ISSN 2452-3216, https://doi.org/10.1016/j.prostr.2017.12.023.

[10] A. Hauser, R. Kuhn, 11 - High-voltage battery management systems (BMS) for electric vehicles, Editor(s): Bruno Scrosati, Jürgen Garche, Werner Tillmetz, In Woodhead Publishing Series in Energy, Advances in Battery Technologies for Electric Vehicles, Woodhead Publishing, 2015, Pages 265-282, ISBN 9781782423775, https://doi.org/10.1016/B978-1-78242-377-5.00011-X.

[11] Liu, K., Li, K., Peng, Q. et al. A brief review on key technologies in the battery management system of electric vehicles. Front. Mech. Eng. 14, 47–64 (2019). https://doi.org/10.1007/s11465-018-0516-8

[12] Justen, Rainer, and Rodolfo Schöneburg. "Crash safety of hybrid and battery electric vehicles." Proceedings of the international technical conference on the enhanced safety of vehicles ESV-22. Washington, USA. 2011.

[13] Gunapriya Balan, Singaravelan Arumugam, Suresh Muthusamy, Hitesh Panchal, Hossam Kotb, Mohit Bajaj, Sherif S. M. Ghoneim, undefined Kitmo, "An Improved Deep Learning-Based Technique for Driver Detection and Driver Assistance in Electric Vehicles with Better Performance", International Transactions on Electrical Energy Systems, vol. 2022, Article ID 8548172, 16 pages, 2022. https://doi.org/10.1155/2022/8548172

[14] Mo, Tiande, Yu Li, Kin-tak Lau, Chi Kin Poon, Yinghong Wu, and Yang Luo. 2022. "Trends and Emerging Technologies for the Development of Electric Vehicles" Energies 15, no. 17: 6271. https://doi.org/10.3390/en15176271

[15] H. Vdovic, J. Babic and V. Podobnik, "Automotive Software in Connected and Autonomous Electric Vehicles: A Review," in IEEE Access, vol. 7, pp. 166365-166379, 2019, doi: 10.1109/ACCESS.2019.2953568.

[16] Dorsz, A.; Lewandowski, M. Analysis of Fire Hazards Associated with the Operation of Electric Vehicles in Enclosed Structures. Energies 2022, 15, 11. https://doi.org/10.3390/en15010011

[17] Sun, P., Bisschop, R., Niu, H. et al. A Review of Battery Fires in Electric Vehicles. Fire Technol 56, 1361–1410 (2020). https://doi.org/10.1007/s10694-019-00944-3

[18] Shashank Arora, Weixiang Shen, Ajay Kapoor, Review of mechanical design and strategic placement technique of a robust battery pack for electric vehicles, Renewable and Sustainable Energy Reviews, Volume 60, 2016, Pages 1319-1331, ISSN 1364-0321, https://doi.org/10.1016/j.rser.2016.03.013.

[19] S. R. Deshmukh, K. Balaji N. S., S. Saharabhudhe, S. Khubalkar and A. P. Parameswaran, "Designing of Control Strategy for High Voltage Battery Isolation in an Electric Vehicles," 2019 IEEE 5th International Conference for Convergence in Technology (I2CT), Bombay, India, 2019, pp. 1-4, doi: 10.1109/I2CT45611.2019.9033891.

Authorized licensed use limited to: DELHI TECHNICAL UNIV. Downloaded on April 24,2023 at 04:28:27 UTC from IEEE Xplore. Restrictions apply.

Dynamic Performance Assessment of Power System Interconnected via Asynchronous Transmission Link in Reorganized Configuration

Ram Naresh Mishra
Department of Electrical Engineering
GLA University, Mathura-281406, Uttar Pradesh, India
ramnaresh.mishra@gla.ac.in

Narendra Kumar
Department of Electrical Engineering
Delhi Technological University, Delhi-110042, India
dnk_1963@yahoo.com

2023 International Conference on Power, Instrumentation, Energy and Control (PIECON) | 979-8-3503-9976-9/23/$31.00 ©2023 IEEE | DOI: 10.1109/PIECON56912.2023.10085759

Abstract — In this study, an environment that has been restructured for automatic generation control (AGC) of a two-area power system interconnected via an asynchronous transmission link is offered. Each control area has three thermal (reheat) power generating sources, two power distribution companies (DISCOs), and a redox flow battery. By using optimum control theory, the optimal AGC regulators are designed and implemented in the proposed system, considering various power contracts. The dynamic results of the suggested system have been found to satisfactorily fulfill the AGC requirements, and the system's dynamic performance is enhanced when the suggested system is employed with RFB as compared to without RFB because it might share the immediate need for more active power. Eigenvalues are computed in order to analyze the stability of the system without or with RFB. For SIMULINK model and program coding, MATLAB software version R2013a is used to achieve diverse dynamic responses of the proposed system.

Keywords— asynchronous transmission link, automatic generation control (AGC), dynamic stability, optimal AGC regulators (OARs), redox flow batteries (RFB)

I. INTRODUCTION

Several control regions are interconnected by transmission links to form a power system. A control area is characterised by a synchronised arrangement of generators that swing in unison and work to meet its own demand in addition to the scheduled exchanges with other control regions [1]. Unwanted results may take place when there is a mismatch between the supply and demand for electricity, considering system losses. To show how the device behaves, an AGC system is implemented for changes in load requirements. It is a difficult undertaking to restructure the electricity system. The system's planning and management are reformed in the restructured power system (RPS) using its core principles. In the RPS, there are GENCOs, DISCOs, and ISO (independent system operator). An essential aspect of establishing contracts between GENCOs and DISCOs is the DISCO Participation Matrix (DPM) paradigm. All GENCOs will experience fluctuations in frequency, tie line power, and power response due to the generation-demand disparity. Re-dispatching by GENCOs based on the area participation factor (apf) is the role of AGC. The distribution of uncontracted demand in a steady state is determined by area control error (ACE) participation factors [2].

AGC systems come in a variety of forms, and there have been several publications that consider them [2]. Numerous outstanding additions have been made to the way electrical machine control systems operate in deregulated environments, all of which are based entirely on the traditional, reliable, and intelligent control strategies that have been put forth in those works. There were some functional LFC systems introduced [3, 4]. Using the DPM and apf guidelines to illustrate bilateral agreements, Donde et al. [5] provided an AGC of linked electrical systems in a deregulated environment. However, numerous articles on various aspects of load frequency control (LFC) or AGC of electrical systems in restructured environments have been written [6]. In comparison to EHVAC transmission, HVDC transmission has advantages such as controlled power transfer between zones, operating at specific frequencies to improve stability, and reducing the need for right-of-way [7-9].

The following is how this paper was put together: Segment II presents the mathematical modeling of the anticipated power system, and phase III presents the system vectors. Segment IV emphasizes the simulation findings and discussion. Phase V, which comes last, is dedicated to wrapping up the suggested work.

II. A PROPOSED SYSTEM MODEL

Two areas of thermal (reheat) power generation sources are considered for this study (Fig.1).These two zones are connected by an asynchronous transmission link, and redox flow batteries, an energy storage device, are installed in each region to meet the instantaneous need for additional active power [10].

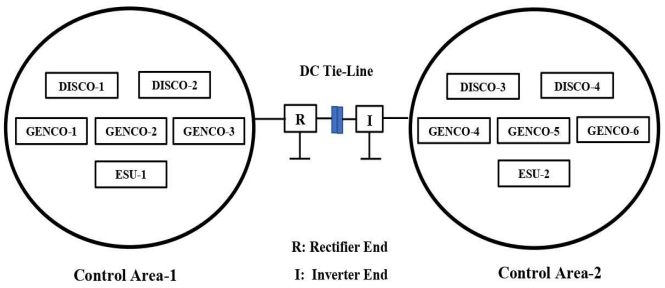


Fig. 1 Block diagram of proposed system

apf_{ij} = GENCO- j's of involvement in area-i

$$\Delta P_{tie}^{Scheduled} = \sum_{i=1}^{3}\sum_{j=3}^{4} Cpf_{ij}\,\Delta P_{Lj} - \sum_{i=4}^{6}\sum_{j=1}^{2} Cpf_{ij}\,\Delta P_{Lj} \quad (1)$$

The stable tie-line power flow for the system when the constant current control (CCC) mode is in operation is as follows:

$$\Delta P_{dc} = \frac{K_{dc}}{1+sT_{dc}}\left(\Delta F_1 - \Delta F_2\right) \quad (2)$$

$$\Delta P_{tie}^{Error} = \Delta P_{tie}^{Actual} - \Delta P_{tie}^{Scheduled} \quad (3)$$

979-8-3503-9976-9/23/$31.00 ©2023 IEEE

Authorized licensed use limited to: DELHI TECHNICAL UNIV. Downloaded on April 10,2023 at 07:24:55 UTC from IEEE Xplore. Restrictions apply.

ΔP_{tie}^{Error} , drops to zero in stable zones .Following are two areas' area control errors (ACEs).

$$ACE_1 = B_1\Delta F_1 + \Delta P_{tie}^{Error} \quad (4)$$

$$ACE_2 = B_2\Delta F_2 + \alpha_{12}\Delta P_{tie}^{Error} \quad (5)$$

B_i = i[th] area's frequency bias constant (pu MW/Hz), ΔF_i = variation in i[th] area's frequency (Hz). a_{12} = area size ratio

ΔP_1 , ΔP_2 , ΔP_3 , ΔP_4 , ΔP_5 , ΔP_6 , ΔP_{L1LOC} , ΔP_{L2LOC} demonstrates signals from the power market.

Where,

$$\Delta P_{L1LOC} = \Delta P_{L1} + \Delta P_{L2} \quad (6)$$

$$\Delta P_{L2LOC} = \Delta P_{L3} + \Delta P_{L4} \quad (7)$$

Where,

$\Delta P_{Li,\ LOC}$ = variation in the contracted local load demand in that region, ΔP_{Li}= power demand in i[th] region varies. ΔP_{UCi} is variation for the un-contracted load demand in the i[th] area. If not, it is zero.

DPM =

$$\begin{pmatrix} Cpf_{11} & Cpf_{12} & Cpf_{13} & Cpf_{14} \\ Cpf_{21} & Cpf_{22} & Cpf_{23} & Cpf_{24} \\ Cpf_{31} & Cpf_{32} & Cpf_{33} & Cpf_{34} \\ Cpf_{41} & Cpf_{42} & Cpf_{43} & Cpf_{44} \\ Cpf_{51} & Cpf_{52} & Cpf_{53} & Cpf_{54} \\ Cpf_{61} & Cpf_{62} & Cpf_{63} & Cpf_{64} \end{pmatrix} \quad (8)$$

III.STATE SPACE MODEL

The different vectors for the proposed system are listed below. Design of OAR is described in [9].

State vector [23x1];

$\underline{X}$= [ΔF_1, ΔF_2, ΔP_{G1}, ΔP_{R1}, ΔX_{E1}, ΔP_{G2}, ΔP_{R2}, ΔX_{E2}, ΔP_{G3}, ΔP_{R3}, ΔX_{E3}, ΔP_{G4}, ΔP_{R4}, ΔX_{E4}, ΔP_{G5}, ΔP_{R5}, ΔX_{E5}, ΔP_{G6}, ΔP_{R6}, ΔX_{E6}, ΔP_{dc}, $\int ACE_1 dt$, $\int ACE_2 dt$] ^{T}

Control vector [2x1];

$\underline{U}$ = [ΔP_{c1}, ΔP_{c2}] ^{T}

Disturbance vector [6x1];

$\underline{Pd}$ = [ΔP_{L1}, ΔP_{L2}, ΔP_{L3}, ΔP_{L4}, ΔP_{UC1}, ΔP_{UC2}]^T;

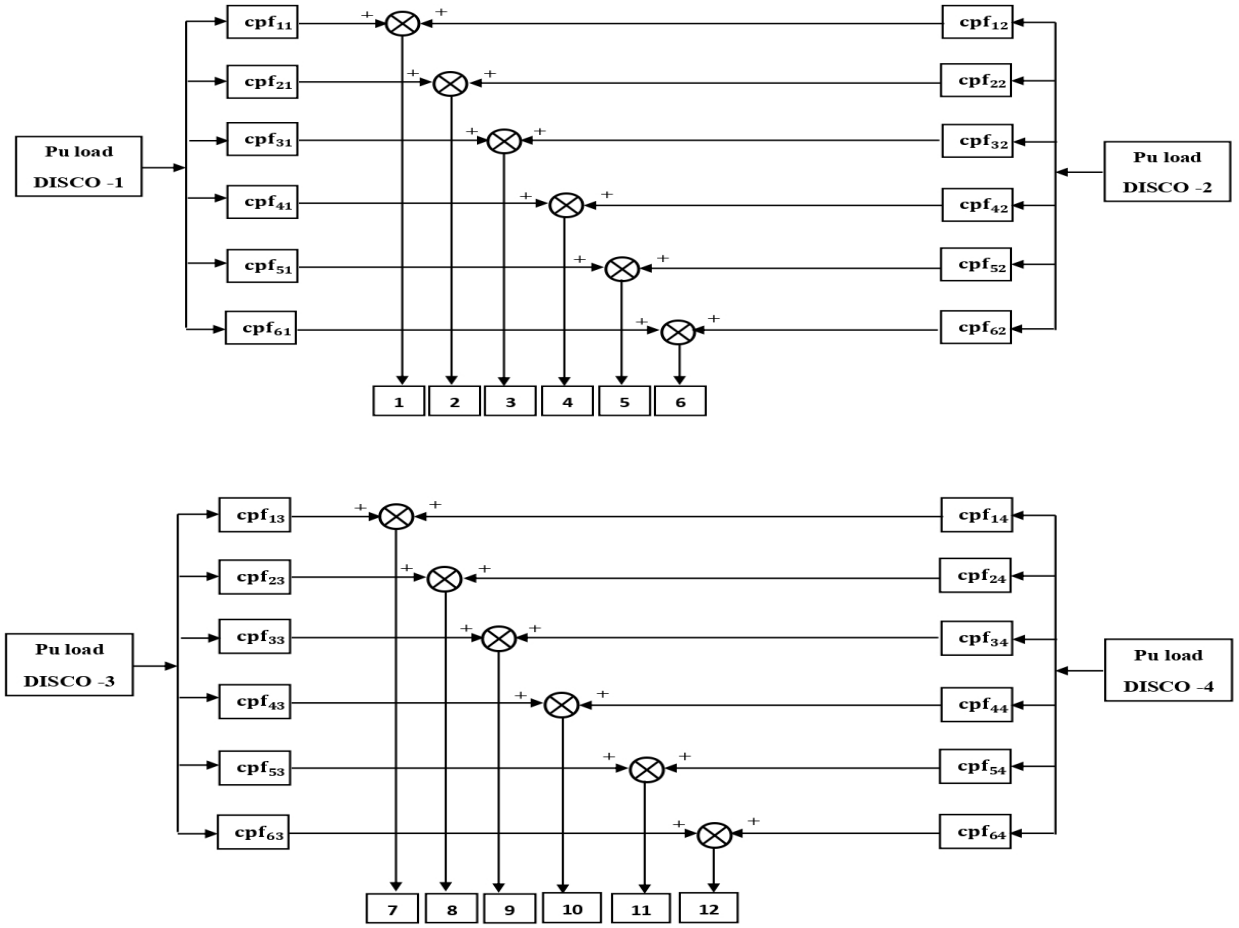


Figure2.Contracted power of DISCOs

Authorized licensed use limited to: DELHI TECHNICAL UNIV. Downloaded on April 10,2023 at 07:24:55 UTC from IEEE Xplore. Restrictions apply.

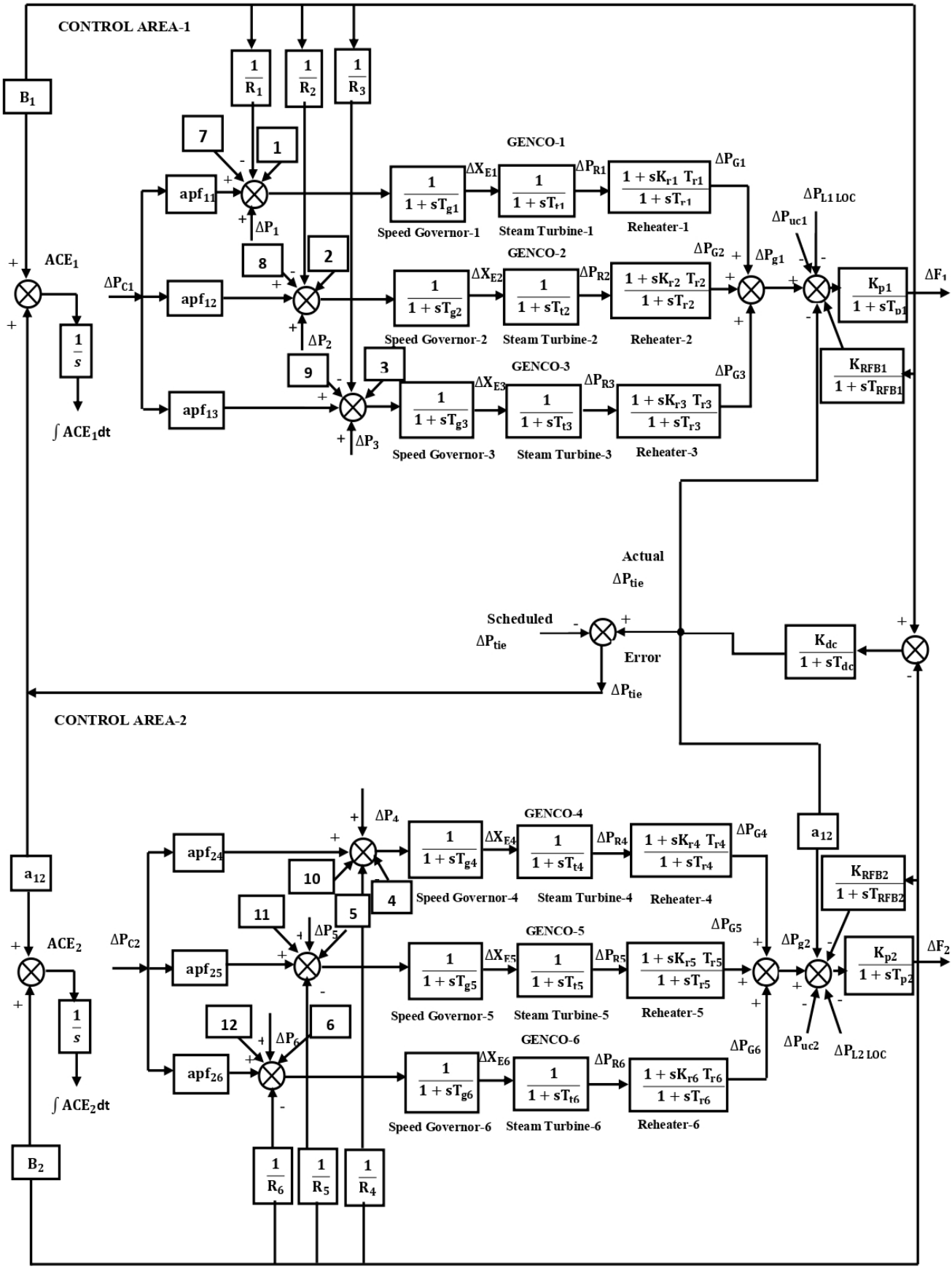


Fig. 3. Transfer function model of the system

Authorized licensed use limited to: DELHI TECHNICAL UNIV. Downloaded on April 10,2023 at 07:24:55 UTC from IEEE Xplore. Restrictions apply.

IV. DISCUSSION OF THE SIMULATION RESULT

The six GENCOs involved in the proposed system are as follows: $apf_{11}=apf_{12}=apf_{21}=apf_{22}=0.33$ and $apf_{13}=apf_{23}=0.34$.In this analysis, several power agreements have been taken into account. The optimal feedback gain matrix (which is too long to list here) and the pattern of eigenvalues (shown in Table 1) are calculated. System data are depicted in Table 2.

Case 1: Poolco based Transaction (PBT); In this context, the load that the DISCOs are expecting from the GENCOs belongs to their own area. No GENCOs are required to supply power to the DISCOs in region 2. Therefore, there are no analogous cpfs in DPM. a total load variation affecting only region 1 (=0.02 pu MW). $P_{L1}=P_{L2}=0.01$ pu MW; $P_{L3}=P_{L4}=0$ pu MW. The following lists the DPM as the power demanded by the DISCOs in control area 1.

$$\begin{pmatrix} 0.3333 & 0.3333 & 0 & 0 \\ 0.3333 & 0.3333 & 0 & 0 \\ 0.3333 & 0.3333 & 0 & 0 \\ 0 & 0 & 0 & 0 \\ 0 & 0 & 0 & 0 \\ 0 & 0 & 0 & 0 \end{pmatrix}$$

The following lists the DPM as the power demanded by the DISCOs in control area 2.

$$\begin{pmatrix} 0 & 0 & 0 & 0 \\ 0 & 0 & 0 & 0 \\ 0 & 0 & 0 & 0 \\ 0 & 0 & 0.3333 & 0.3333 \\ 0 & 0 & 0.3333 & 0.3333 \\ 0 & 0 & 0.3333 & 0.3333 \end{pmatrix}$$

Figures 4 and 5 illustrate the dynamic performance of PBT-1 (the power demanded by DISCOs in area 1) and PBT-2 (the power demanded by DISCOs in area 2) without and with RFB. In stable conditions, frequency deviations in both zones are approaching zero and are error-free. The actual tie-line power flow is therefore zero.

Case2: Bilateral based Transaction (BBT)

In this scenario, every GENCO is subject to an agreement with every DISCO, and they all abide by its terms.

$$\begin{pmatrix} 0.2 & 0.1 & 0.3 & 0 \\ 0.2 & 0.2 & 0.1 & 0.1666 \\ 0.1 & 0.3 & 0.1 & 0.1666 \\ 0.2 & 0.1 & 0.1 & 0.3336 \\ 0.2 & 0.2 & 0.2 & 0.1666 \\ 0.1 & 0.1 & 0.2 & 0.1666 \end{pmatrix}$$

According to cpfs, each DISCO requests 0.01 pu MW of power from the GENCOs in its region or another area. The total load disturbance that occurs in each region is therefore 0.02pu. Figures 6(a) and 6(b) show the frequency variations for regions 1 and 2 in this situation.

Under stable conditions, the scheduled tie-line power flow between control zones is -0.0005 pu MW, as depicted in Fig. 6(c).

Case3: Contract Violation based Transaction (CVBT)

DISCO-1 receives 0.01 p.u. MW of un-contracted power from its GENCOs. The overall load request for region 1 is now 0.03 p.u. MW (0.02 + 0.01); 0.01 is the total load interruption in area 1. Fig. 7 shows region 1 and 2 frequency deviations. When stable, tie-line strength flows -0.00051 p.u.Mw between control zones.

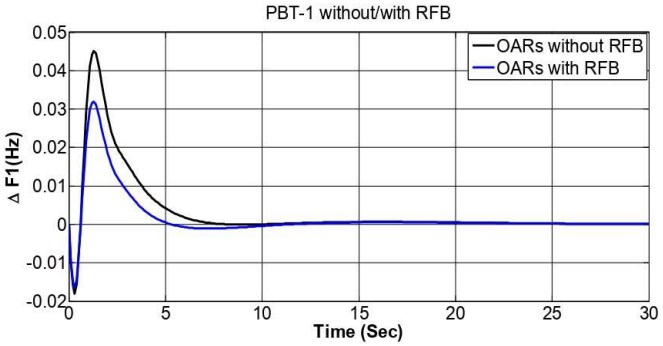


Fig. 4.(a) Variance in area 1's frequency responses for PBT-1 without/ with RFB

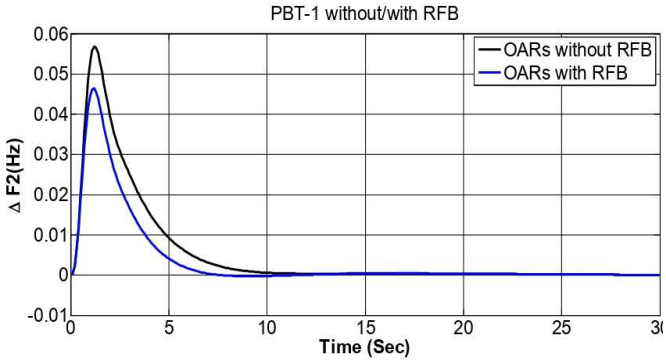


Fig. 4.(b) Variance in area 2's frequency responses for PBT-1 without/ with RFB

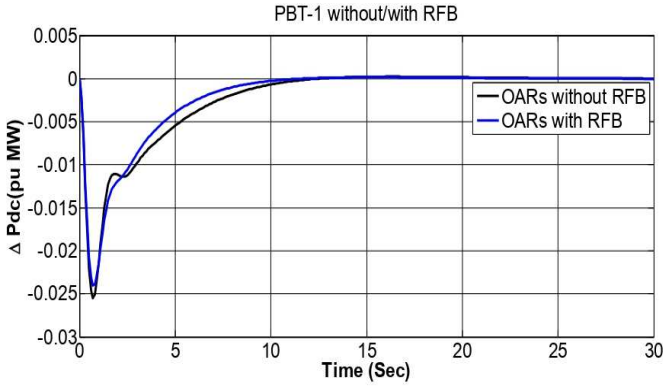


Fig. 4.(c) Variance in tie-line power responses for PBT-1 without/ with RFB

Authorized licensed use limited to: DELHI TECHNICAL UNIV. Downloaded on April 10,2023 at 07:24:55 UTC from IEEE Xplore. Restrictions apply.

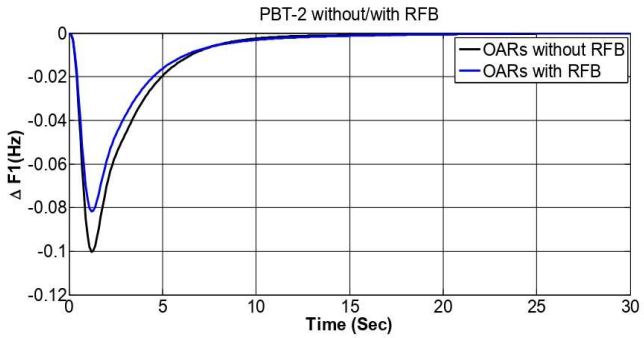


Fig. 5.(a) Variance in area 1's frequency responses for PBT-2 without/ with RFB

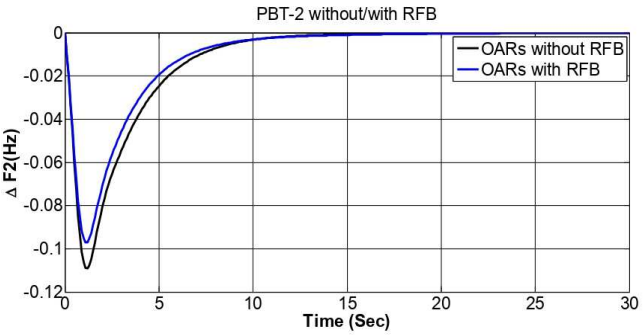


Fig. 5.(b) Variance in area 2's frequency responses for PBT-2 without/ with RFB

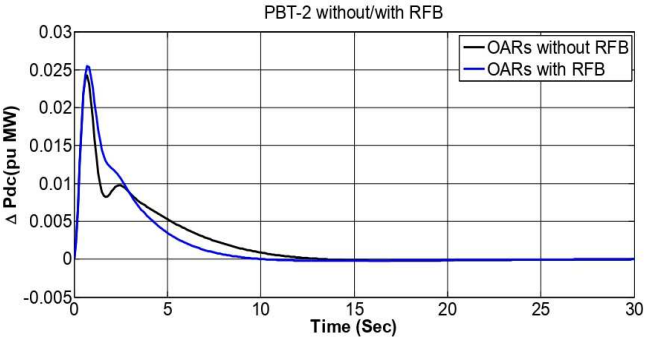


Fig. 5.(c) Variance in tie-line power responses for PBT-1 without/ with RFB

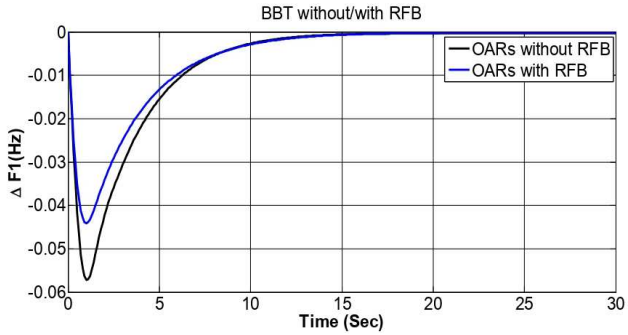


Fig. 6.(a) Variance in area 1's frequency responses for BBT without/ with RFB

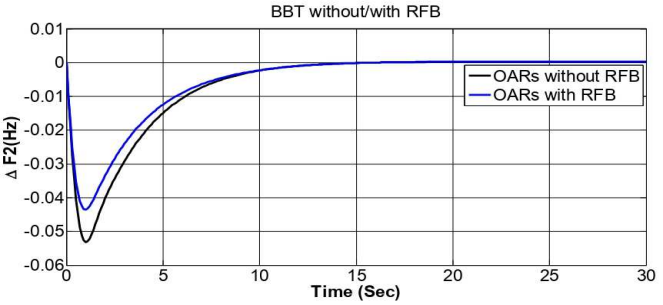


Fig. 6.(b) Variance in area 2's frequency responses for BBT without/ with RFB

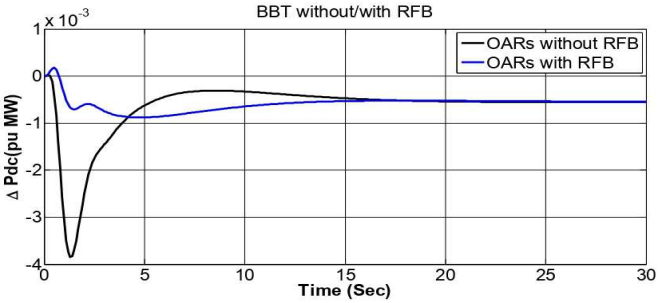


Fig. 6.(c) Variance in tie-line power responses for BBT without/ with RFB

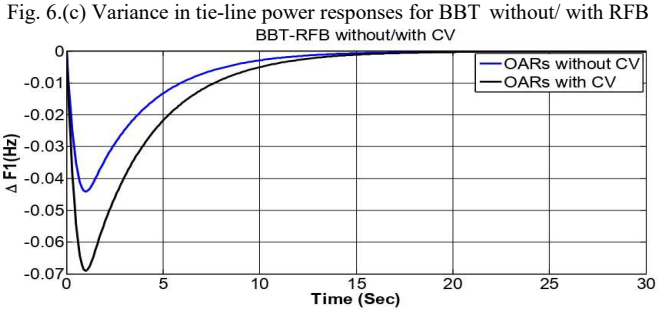


Fig. 7.(a) Variance in area 1's frequency responses for BBT considering RFB without/ with contract violation

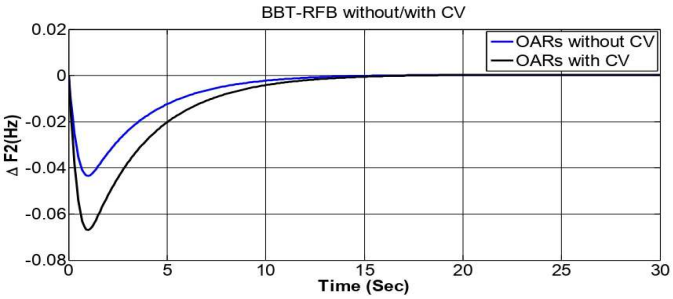


Fig. 7.(b) Variance in area 2's frequency responses for BBT considering RFB without/ with contract violation

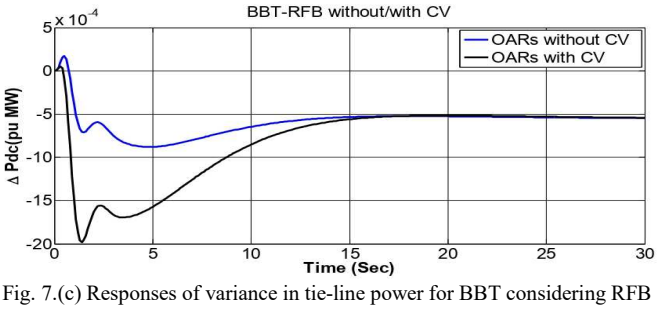


Fig. 7.(c) Responses of variance in tie-line power for BBT considering RFB without/ with contract violation

Authorized licensed use limited to: DELHI TECHNICAL UNIV. Downloaded on April 10,2023 at 07:24:55 UTC from IEEE Xplore. Restrictions apply.

Table 1: Pattern of Eigen-values

Sl. No.	Proposed system without RFB	Proposed system with RFB
1	-14.6548 + 0.0590i	-14.6708 + 0.0648i
2	-14.6548 - 0.0590i	-14.6708 - 0.0648i
3	-5.5085	-5.5827
4	-1.8134 + 3.3126i	-2.0025 + 3.3450i
5	-1.8134 - 3.3126i	-2.0025 - 3.3450i
6	-3.1903 + 0.7906i	-3.0387 + 0.7606i
7	-3.1903 - 0.7906i	-3.0387 - 0.7606i
8	-0.2463 + 0.1262i	-0.3979
9	-0.2463 - 0.1262i	-0.3347
10	-0.3334	-0.2219 + 0.0990i
11	-0.303	-0.2219 - 0.0990i
12	-12.5	-12.5
13	-12.5	-12.5
14	-12.5	-12.5
15	-12.5	-12.5
16	-3.3333	-3.3333
17	-3.3333	-3.3333
18	-3.3333	-3.3333
19	-3.3333	-3.3333
20	-0.1	-0.1
21	-0.1	-0.1
22	-0.1	-0.1
23	-0.1	-0.1

Table2 System data

Sl. No.	Parameters	Value of Parameters
1	Time constant for speed governor ;*Tg*	0.08 sec
2	Time constant for turbine ;Tt	0.3 sec
3	Time constant for reheat ;Tr	10 sec
4	Gain for power system; Kp	120 Hz/puMW
5	Time constant for power system ;Tp	20 sec
6	Bias constant for frequency ; B	0.425 puMW/Hz
7	Speed regulation ;R	2.4 Hz/puMW
8	Synchronizing power coefficient;T12	0.545 pu
9	Area size ratio constant; a12	-1

V. CONCLUSION

In this work, optimal AGC regulators (OARs) are developed and put into use for the AGC of the proposed system without or with RFB. It is examined how the RFB affects the AGC of the two-area proposed system. The performance index minimization criterion is used to develop optimum AGC regulators (OARs). The superiority of OARs is demonstrated without or with RFB for the proposed system. The simulation findings show that OARs with RFB have considerably improved performance when compared to OARs without RFB, since they may share the additional power demand instantly. Moreover, the system's stability is strengthened by the integration of RFB in each control region. Higher frequency and tie-line power variances are observed in areas where DISCOs breach their contracts. However, while taking various market activities into account, the proposed OARs are able to balance demand with generation in a deregulated market.

REFERENCES

[1] Fosha C.E., and Elgerd 0.I., "The megawatt-frequency control problem: a new approach via optimal control theory", *IEEE Trans., PAS-89,, pp.563-577,1970.*

[2] Ibraheem, Kumar, P., and Kothari, D. P., "Recent philosophies of automatic generation control strategies in power systems," IEEE Trans. Power Syst., Vol. 20, No. 1, pp. 346–357, 2005.

[3]Christie, R. D., and Bose, A., "Load frequency control issues in power system operations after deregulation," IEEE Trans. Power Syst., Vol. 11, No. 3, pp. 1192–1200, 1996.

[4] Meliopoulos, A. P. S., Cokkinides, G. J., and Bakirtzis, A. G., "Load frequency control services in deregulated environment," Proceedings of 31st Hawaii International Conference on Systems Sciences, Vol. 3, pp. 24–31, 1998.

[5] Donde, V., Pai, M. A., and Hiskens, I. A., "Simulation and optimization in a AGC system after deregulation," IEEE Trans. Power Syst., Vol. 16, No. 3, pp. 481–489, 2001.

[6] Ram Naresh Mishra, D.K. Chaturvedi and Prabhat Kumar, "Recent Philosophies of AGC Techniques in Deregulated Power Environment", J. Inst. Eng. India Ser. B, https://doi.org/10.1007/s40031-020-00463-8, 2020.

[7] Kumar, P., and Ibraheem, "Optimal control of an interconnected power system with parallel AC/DC links and parameter uncertainties," Proceedings of the National Systems Conference (NSC-95), pp. 137–141, Coimbatore, India, 14–16 December 1995.

[8] Ibraheem, and Kumar, P., "Study of dynamic performance of power systems with asynchronous tie-lines considering parameter uncertainties," J. Inst. Eng. (India), Vol. 85, pp. 35–42, June 2004.

[9] Iibraheem, Prabhat Kumar, Naimul Hasan, and Yadav Singh, "Optimal Automatic Generation Control of Interconnected Power System with Asynchronous Tie-lines under Deregulated Environment", Electric Power Components and Systems, 40:1208–1228, 2012.

[10] M. R. Chakraborty, S. Dawn, P. K. Saha, J. B. Basu and T. S. Ustun, "A Comparative Review on Energy StorageSystems and Their Application in Deregulated Systems'',*Batteries,* https://doi.org/10.3390/batteries8090124, (2022).

Authorized licensed use limited to: DELHI TECHNICAL UNIV. Downloaded on April 10,2023 at 07:24:55 UTC from IEEE Xplore. Restrictions apply.

Email Spam Detection Using Naïve Bayes

Hrithik Vohra*

Dept. of Computer science & Engineering

Delhi Technological University

Delhi,India

Manoj Kumar**

Dept. of Computer science & Engineering

Delhi Technological University

Delhi,India

Abstract*—Today almost everyone around the globe is using emails with various purposes and hence an efficient growth in the no. of spam emails is witnessed with time which creates problem for the users to find their genuine/ham emails because of which their precious time is wasted and the system becomes less efficient. This is where E-mail spam/ham detection comes into play, playing a significant role in classifying the emails into spam or ham respectively and thus saving users a lot of time to fetch their E-mails. This research paper aims to apply the ML algorithm i.e. multinomial naïve bayes classifier to classify E-mails into spam or ham.We are also going to compare the 2 methods of vectorizing that are the Bag of Words (BOW) & Term frequency -Inverse document frequency (TF-IDF) models.

Keywords—email spam detection, ham or spam, bag of words, term frequency -inverse document frequency, multinomial naïve bayes

I. INTRODUCTION

A. *Overview*

Email is now one of the most important forms of communication. A study estimated that there are around 5 billion accounts and the number is much more higher for the number of emails flowing everyday. Due to this type of extensive use spam is one of the major threats posed to email users. A study found out that approx.. 70% of all email flown were spam in 2013. Now lets see why spam emails are a problem to us. Spam emails can be defined as the fake and useless emails send by the people itself either to promote their organisation/company or to make frauds and make money by cheating them .

B. *Motivation*

The E-mail users waste a lot of their precious time in sorting spam E-mails. Numerous copies of same messages are transmitted too many times which not only effects a company or organisation but also irritates the receiving user, causing stress, irritation and a tedious work performing this task to filter.

Therefore, an effective spam filtering system will be an important contribution to the society ,which can easily filter out the emails and taking the burden away from the email users. Here, we will be using Multinomial naïve bayes classifier for the classification of E-mails into spam/ham.

C. Naïve Bayes

Naïve Bayes algorithm is a supervised ML algorithm which is based on famous Bayes theorem.This algorithm is highly used in text classification including high dimensional training dataset.We will be using multinomial Naïve bayes and holdout technique for email spam filteration.

II. RELATED WORK

A great deal of research work has already been dedicated to this field and is still going on everyday to increase the efficiency of the system.We have read the following papers related with E-mail Spam/ham Detection. Researchers and scientists are constantly working to make the models more efficient to identify the spam mails. Works of some researchers have been discussed here below.

[1] A research in which an author proposed an E-mail filtering system using 2 different features selection methods to classify and at last the featuresg are sele ted using TF-IDF and rough set theory method.

[2] Another research includes implementation of K Nearest Neighbours algorithm & Naïve Bayes algorithms which shows precise results when applied on pre-processed data.

[3] A group of researchers made an email spam detection model by using the naïve bayes and the J48 classifier and then compared them in which they found out J48 performing well than the naïve bayes classifier.

[4] Authors proposed an ontology kind of based email filtering and classification method. The considered dataset they used is classified using J48 decision tree based algorithm.

III. DATASET

The dataset we used to train our model is email dataset. This is a very popular and a very common dataset among many data analysts/scientists who are working in this email spam detection field.

Our dataset name is emails.csv and it has been taken from Kaggle.com .It contains a total of 5695 unique emails out of which 4327 are ham emails and 1368 are spam emails ,hence in order to make the dataset equal we removed 2959 ham emails and finally our new dataset includes 1368 ham as well as spam emails. The emails.csv contain 2 columns text and spam in which the text columns have all the email messages and the spam column contains 2 values i.e. 1 denoting spam emails and 0 denoting ham emails. Below shows the dataset of first 5 emails:

TABLE 1. EMAILS CLASSIFIED AS SPAM/HAM

	text	spam
0	Subject: naturally irresistible your corporate...	1
1	Subject: the stock trading gunslinger fanny i...	1
2	Subject: unbelievable new homes made easy im ...	1
3	Subject: 4 color printing special request add...	1
4	Subject: do not have money , get software cds ...	1

Below we have a representation of length of emails in our dataset:

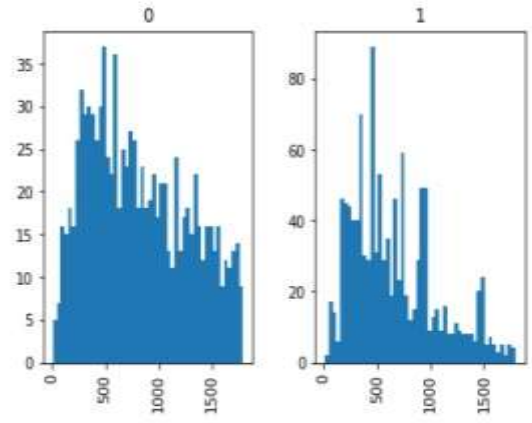


Fig 1. Graph length of email vs no. of Emails

Y-axis shows number of emails containing lengths on the X-axis. So here it shows there are all the types of emails available i.e. of various lengths.

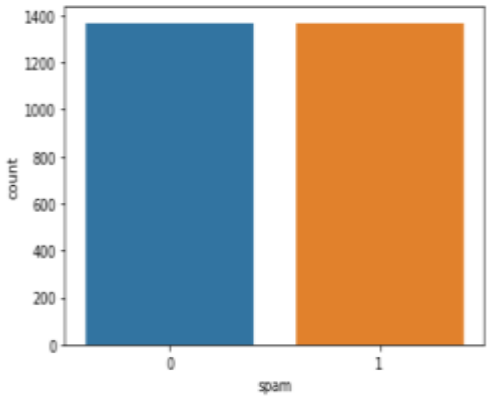


Fig 2. Equalising the no. of spam and ham emails for genuine results

IV. EXPERIMENTAL DESIGN

This column will highlight all the work we had done in this project.

A. Validation Technique Used

Here we are using the holdout validation technique. Hold-out is when you split up your dataset into a 'train dataset' and 'test dataset ' set. The training set is on what the model is trained on, and the testing dataset is used to see the performance of the model on the unseen test data. For splitting data we have split our dataset into 70% training and 30% test data.

B. Performance Metrics

The Performance metrics we have used in our model are *accuracy*, *precision* and *F1 score.*

True Positive (TP) – Situations where both the actual and predicted class are 1.

True Negative (TN) − Situations where both the actual and predicted class are 0.

False Positive (FP) – Situation where actual class of input data is 0 but the predicted class turns out 1.

False Negative (FN) − Situation where ,actual class of input data is 1 but the predicted class turns out 0.

1) Accuracy

It is the most common and the most primitive performance metric used in classification algorithms. It is defined as no. of correct/true predictions divided by the total no. of predictions.

$$\text{ACCURACY} = \frac{TP + FN}{TP + FP + TN + FN} \quad (1)$$

2) Precision

Precision basically means no. of correct prediction returned by the model we have built. We can easily calculate it by formula:

$$\text{PRECISION} = \frac{TP}{TP + FP} \quad (2)$$

3) F1-Score

This is considered to be one of the finest and better performance measure than the latter. It is defined as the harmonic mean of recall & precision. Mathematically, it is equal to the weighted average of recall & precision. Worst value it can take is 0 and the best is 1. It is calculated as :

$$\text{RECALL} = \frac{TP}{TP + FN} \quad (3)$$

$$F1 = 2 * (precision * recall) / (precision + recall) \quad (4)$$

C. Pre-processing

We have done a series of pre-processing on our data in the following order:

a) Removed duplicate data from the dataset and checked for null values which in our case was 0 so no further processing was required

b) Made the number of spam and ham emails equal in number. This is to make sure so that the predicted results are more real as both of them are equal and is not dominated by only 1 single class.

c) Removed the first word i.e. 'subject:' from all the text messages as it was unnecessary.

d) Removed all the punctuations, numerical values, stop words from each and every text, made sure every word is in lower case and at the last did stemming of all the words in the mail. *Stemming* is often defined as the procedure of reducing a word to its word stem known as *lemma*. It is done in order to remove the extra columns formed by the words that mean the same but are just in other form ex. visit, visited ,visits etc.

D. Algorithms Used

Naïve Bayes

Naïve Bayes algorithm is one of the machine learning supervised learning algorithm, which is based on the famous Bayes theorem .The algorithm is highly used in text classification problems including high-dimensional training dataset.

Naïve Bayes Classifier is one of the simple and most efficient Classification algorithms which helps us to build fast ML models as well as efficient training and testing to make correct and fast predictions. It is a probabilistic classifier, the whole basis of the algorithm depends on the probabilities calculated which means it predicts on the basis of the probability of an object.

Bayes' Theorem

Bayes theorem also known as Bayes' Rule or Bayes' law, is used in determining the probability of a hypothesis with prior knowledge. It futher also depends on the conditional probability.

Bayes Theorem formulates the following:

$$P(A \mid B) = \frac{P(B \mid A) \cdot P(A)}{P(B)}$$

A, B = events
$P(A|B)$ = probability of A given B is true
$P(B|A)$ = probability of B given A is true
$P(A), P(B)$ = the independent probabilities of A and B

For more than one features given that they are strictly independent of each other (x1,x2,…xd) the formula now becomes:

$$P(Y|X_1, X_2, \ldots, X_d) = \frac{P(X_1, X_2, \ldots, Xd|Y)\,P(Y)}{P(X_1, X_2, \ldots, X_d)} \quad (5)$$

$$P(X_1, X_2, \ldots, X_d|Y_j) = P(X_1|Y_j)\,P(X_2|Y_j)\ldots P(X_d|Y_j) \quad (6)$$

Types of Naïve Bayes Model:

The 3 types of Naive bayes model are given below:

Gaussian: The Gaussian model works for only features that follow a normal distribution i.e. if predictors take continuous values instead of discrete, means the values are a result of gaussian distribution.

Bernoulli: The Bernoulli classifier works similar to the Multinomial, but the predictor variables here are independent Booleans variables(0 or 1) it's a bit complicated but yes it works this way .Such that if a certain word is present in a document or not. The model is preferred where we are not concerned about the frequency of the word and the only thing that matters is whether the word is present or not as simple as that. This model is widely used in document classification.

Multinomial: Multinomial Naïve Bayes classifier is used when the data is multinomial distributed basically depending upon the frequency of each word in every text or document. It's primarily used in document classification problems like to classify a particular document into categories such as Sport, Politics, Education, etc.This classifier uses word frequency for predictors.

In the project we are using the Multinomial Naïve Bayes Model.

MultinomialNB is basically the implementation of naïve Bayes algorithm for multinomially distributed data.

It is one of the 3 classical naive Bayes variants as shown above that is widely used in text classifications (where data is represented as word vector counts or Bag Of words (Bow), and also TF-IDF vector also get the privilege to run on this model). The distribution is essentially perfomed parametrized by vectors θy=(θy1,…,θyn) for each class y,(here we have just 2 classes i.e. 0-ham & 1-spam)where n implies the no. of features (i.e. it is the size of vocabulary) & θyi is P(xi|y) of feature i and it simply means that n is equal to the number of unique words in the incoming text also the power of each P(xi|y) is equal to the number of times the particular word is present in the incoming text .

The parameters θy is calculated by the formula stated below it uses a special parameter whose use is stated below:

$$\hat{\theta}_{yi} = \frac{N_{yi} + \alpha}{N_y + \alpha n} \tag{7}$$

where Nyi=∑x∈Txi denotes the Frequency or the no. of times the word i is appearing in a particular class, and Ny=∑i=1nNyi denotes the total number of words present in a particular class y.

The α is an important parameter here as it prevents a particular probability of becoming 0 , this is important because there might be case where the whole probability is becoming 0 due to absence of some word. Initially multinomial uses α=1 and is also called Laplace smoothing .

1. Bag of Words Model (BoW)

This is one of the most used and efficient model for vectorization that is converting words/strings to a unique number that can be recognised by the compiler .The Bag of words (BOW) model is the simple form of text representation in numbers..

2. Term Frequency-Inverse Document Frequency Model (TF-IDF)

It is the upgraded version of bag of words model vectorizer where it is related to the importance of a particular word in a particular text compared with the whole document .Below is demonstrated how importance for every word in every text is calculated.

Term Frequency (TF)

It is the Measure of how frequent a term 't', appears in a document/text . Here n is the no. of times the term 't' comes in each text/doc. Thus, each and every text term of each and every text would have its own Term Frequency value .

$$tf_{t,d} = \frac{n_{t,d}}{Number\ of\ terms\ in\ the\ document} \tag{8}$$

Inverse Document Frequency (IDF)

IDF is the Measure of how important or significant a term in a docunment is. This when combined with the above calculated term frequency gives the overall importance of each word in each text.

$$idf_t = \log \frac{number\ of\ documents}{number\ of\ documents\ with\ term\ 't'} \tag{9}$$

$$(tf_idf)_{t,d} = tf_{t,d} * idf_t \tag{10}$$

Bag of words just creates a set of string to number convert vectors containing count of word occurrences in all text messages , while the TF-IDF model being the higher version of the latter brings focus on information on the more important words as well as the less important words.

V. RESULTS AND ANALYSIS

Here we will show the results that we got for our 2 models using the classification report.

Bag of Words (Bow) Model

```
Accuracy->  0.9866017052375152

Precision->  0.9874686716791979

f1-Score->  0.986232790988736
```

The ROC curve and AUC score:

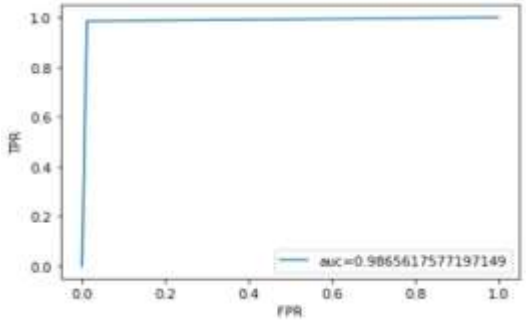


Fig 4. ROC curve-BOW model

We can see that we got pretty good results with an accuracy of 98.66 % hence the model is pretty good for email spam detection.

Term Frequency-Inverse Document Frequency (TF-IDF) Model

```
Accuracy->  0.9841656516443362

Precision->  0.9874055415617129

f1-Score->  0.9836888331242158
```

The ROC curve and AUC score:

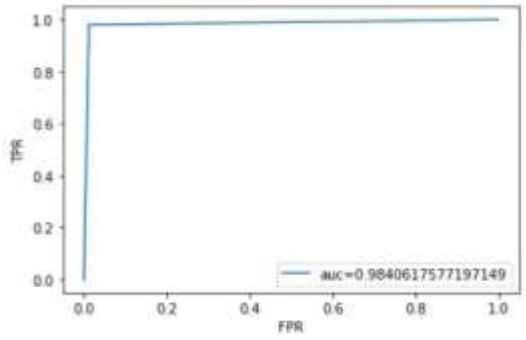


Fig 5. ROC curve-TF-IDF model

This model also showed great results also with an accuracy of 98.41 although the predicted correct results were a slightly less than the bag of words model it still is considered more better model due to functionality of giving higher value to the more important words in the dataset.

TABLE 2: FINAL RESULTS FOR EACH MODEL

PERFORMANCE METRIC / MODEL USED	Accuracy	Precision	F1-Score
BoW	0.986601	0.987468	0.986232
TF-IDF	0.984165	0.987405	0.983688

VI. CONCLUSION

With the help of different libraries, functions and algorithms we were able to perform email spam detection i.e. to classify an incoming mail as spam or ham along with this we got very good results on our testing dataset.

We used performance measures like accuracy, precision, F1-score and AUC score to test our model and got an accuracy around 98% ,we got good results but we can work further on bigger dataset and try to improve the model further. Some of the things we can do is make pre-processing like we can work upon the alpha value that is been used in the multinomial naïve bayes classifier all of this can be worked upon to make the model more efficient on both small and big datasets that can be implemented in real world. Further we can also use the boosting technique in machine learning to remove weak classifier learning functions and replace them with strong classifier one's which is basically to reduce bias in the model.

ACKNOWLEDGMENT

We are extremely grateful to Dr Manoj Kumar for providing us with his supervision and guidance throughout the project. He has been our guiding light and motivated us to complete our project. We would also like to extend sincere gratitude to all our department faculty members for their assistance and unwavering support in making this project successful. We would also like to thank our parents to motivate us during the tough times when we encountered any problem and providing us moral support.

REFERENCES

[1] Priti Sharma,Uma Bhardwaj"Machine Learning based Spam E-Mail Detection"Department of Computer Science & Applications, Maharshi Dayanand University. International Journal of Intelligent Engineering and Systems, Vol.11, No.3, 2018

[2] T. S. Guzella, and W. M. Caminhas, "A review of machine learning approaches to spam filtering", Expert Systems with Applications, Vol.36, No.7, pp.10206-10222, 2009.

[3] V. Metsis, I. Androutsopoulos and G. Paliouras (2006). Spam filtering with Naive Bayes – Which Naive Bayes? 3rd Conf. on Email and Anti-Spam (CEAS)

[4] H.Zhang (2004).The optimality of Naive Bayes. Proc. FLAIR

[5] Thashina Sultana , K A Sapnaz , Fathima Sana , Jamedar Najath, 2020, Email based Spam Detection, INTERNATIONAL JOURNAL OF ENGINEERING RESEARCH & TECHNOLOGY (IJERT) Volume 09, Issue 06 (June 2020),

[6] Jáñez-Martino, F., Alaiz-Rodríguez, R., González-Castro, V. et al. A review of spam email detection: analysis of spammer strategies and the dataset shift problem. Artif Intell Rev (2022).

[7] F. -J. Yang, "An Implementation of Naive Bayes Classifier," 2018 International Conference on Computational Science and Computational Intelligence (CSCI), Las Vegas, NV, USA, 2018, pp. 301-306, doi: 10.1109/CSCI46756.2018.00065.

[8] N. Kumar, S. Sonowal and Nishant, "Email Spam Detection Using Machine Learning Algorithms," 2020 Second International Conference on Inventive Research in Computing Applications (ICIRCA), Coimbatore, India, 2020, pp. 108-113, doi: 10.1109/ICIRCA48905.2020.9183098.

[9] P. Liu and T. -S. Moh, "Content Based Spam E-mail Filtering," 2016 International Conference on Collaboration Technologies and Systems (CTS), Orlando, FL, USA, 2016, pp. 218-224, doi: 10.1109/CTS.2016.0052.

[10] S. Suryawanshi, A. Goswami and P. Patil, "Email Spam Detection : An Empirical Comparative Study of Different ML and Ensemble Classifiers," 2019 IEEE 9th International Conference on Advanced Computing (IACC), Tiruchirappalli, India, 2019, pp. 69-74, doi: 10.1109/IACC48062.2019.8971582.

[11] A. Karim, S. Azam, B. Shanmugam, K. Kannoorpatti and M. Alazab, "A Comprehensive Survey for Intelligent Spam Email Detection," in IEEE Access, vol. 7, pp. 168261-168295, 2019, doi: 10.1109/ACCESS.2019.2954791.

[12] G. Singh, B. Kumar, L. Gaur and A. Tyagi, "Comparison between Multinomial and Bernoulli Naïve Bayes for Text Classification," 2019 International Conference on Automation, Computational and Technology Management (ICACTM), London, UK, 2019, pp. 593-596, doi: 10.1109/ICACTM.2019.8776800.

[13] Y. Huang and L. Li, "Naive Bayes classification algorithm based on small sample set," 2011 IEEE International Conference on Cloud Computing and Intelligence Systems, Beijing, China, 2011, pp. 34-39, doi: 10.1109/CCIS.2011.6045027.

[14] W. A. Qader, M. M. Ameen and B. I. Ahmed, "An Overview of Bag of Words;Importance, Implementation, Applications, and Challenges," 2019 International Engineering Conference (IEC), Erbil, Iraq, 2019, pp. 200-204, doi: 10.1109/IEC47844.2019.8950616.

[15] D. Rani, R. Kumar and N. Chauhan, "Study and Comparision of Vectorization Techniques Used in Text Classification," 2022 13th International Conference on Computing Communication and Networking Technologies (ICCCNT), Kharagpur, India, 2022, pp. 1-6, doi: 10.1109/ICCCNT54827.2022.9984608.

[16] C. -z. Liu, Y. -x. Sheng, Z. -q. Wei and Y. -Q. Yang, "Research of Text Classification Based on Improved TF-IDF Algorithm," 2018 IEEE International Conference of Intelligent Robotic and Control Engineering (IRCE), Lanzhou, China, 2018, pp. 218-222, doi: 10.1109/IRCE.2018.8492945.

[17] P. V. Raja, K. Sangeetha, G. SuganthaKumar, R. V. Madesh and N. K. K. Vimal Prakash, "Email Spam Classification Using Machine Learning Algorithms," 2022 Second International Conference on Artificial Intelligence and Smart Energy (ICAIS), Coimbatore, India, 2022, pp. 343-348, doi: 10.1109/ICAIS53314.2022.9743033.

[18] N. Govil, K. Agarwal, A. Bansal and A. Varshney, "A Machine Learning based Spam Detection Mechanism," 2020 Fourth International Conference on Computing Methodologies and Communication (ICCMC), Erode, India, 2020, pp. 954-957, doi: 10.1109/ICCMC48092.2020.ICCMC-000177.

[19] V. S. Vinitha and D. K. Renuka, "Performance Analysis of E-Mail Spam Classification using different Machine Learning Techniques," 2019 International Conference on Advances in Computing and Communication Engineering (ICACCE), Sathyamangalam, India, 2019, pp. 1-5, doi: 10.1109/ICACCE46606.2019.9080000.

[20] A. Junnarkar, S. Adhikari, J. Fagania, P. Chimurkar and D. Karia, "E-Mail Spam Classification via Machine Learning and Natural Language Processing," 2021 Third International Conference on Intelligent Communication Technologies and Virtual Mobile Networks (ICICV), Tirunelveli, India, 2021, pp. 693-699, doi: 10.1109/ICICV50876.2021.9388530.

Process Integration and Optimization for Sustainability
https://doi.org/10.1007/s41660-023-00330-1

ORIGINAL RESEARCH PAPER

Empirical Study of Integrating Social Sustainability Factors: an Organizational Perspective

Deepak Sharma[1,2] · **Pravin Kumar**[1] · **Rajesh Kumar Singh**[3]

Received: 28 December 2022 / Revised: 22 March 2023 / Accepted: 25 March 2023
© The Author(s), under exclusive licence to Springer Nature Singapore Pte Ltd. 2023

Abstract
Integrating sustainability as a core function is the most challenging task for business organizations. Organizations are forced to rethink, redesign, and redevelop their existing system from green practices to achieve sustainable development. In the transitional attempts, more emphasis has been given to economic and environmental dimensions, but the social aspect is usually overlooked. This study targets to examine how organizations could induce social sustainability (SS) within the system through a comprehensive literature review and underlying hypothesis. The structural equation modeling (SEM) approach has been applied in building a socially sustainable model for the business organization. The data was collected and analyzed using multivariate statistical analyses such as exploratory and confirmatory factor analysis. Exploratory factor analysis categorized SS factors into five major dimensions: *job characteristics*, *occupational health and safety*, *consumer protection*, *community interrelations*, and *stakeholder engagement*. The structure has been analyzed through confirmatory factor analysis, and the model's fit indices proved the index's measurement structure. Furthermore, twenty-five reliable factors for measuring the SS of an organization have been short-listed and conducted the validity tests. The proposed model, along with the factors can be suitably used for the SS assessment, and adoption by different organizations in this business world.

Keywords Sustainable development · Social sustainability · Indicators · Structural equation modeling · Business organizations

Introduction

The idea of sustainable development came to the forefront of the World Commission on Environment and Development report in the late 1980s as fulfilling the current's needs without jeopardizing future generations' capacity to fulfill their own needs (Gupta et al. 2016). Later, the United Nations Conference on Climate and Sustainability (1992) clarified that a holistic approach to economic development must include social and environmental factors for sustainable growth. It emphasized economic and ecological stability and promoted social well-being (Moldan et al. 2012). To encourage sustainability worldwide by 2030 and to gage its progress, United Nations has defined 17 sustainable development goals (SDGs) with 169 connected targets (United Nations 2015). Schroeder et al. (2019) showed that out of 17 SDGs, 11 SDGs are related to the social dimension. Hence, social sustainability (SS) notably contributes to the United Nation's SDGs.

Generally, sustainable development is explained using three pillars of sustainability named as environmental sustainability, social sustainability, and economic sustainability as shown in Fig. 1. It provides a holistic approach dealing with all aspects of human well-being, as well as the recreational ability of nature for incorporating and acknowledging global economic concerns and issues (Boulanger 2008). However, policymakers concentrated on economic factors in the "profit maximization" tradition without consideration of environmental and social well-being issues. Although, with growing awareness among stakeholders (including employees, consumers, and communities), government and non-governmental organizations (NGOs) have started advocating for socially inclusive and environmentally ethical means in

✉ Deepak Sharma
deep241087@gmail.com; deepak.sharma@gla.ac.in

[1] Department of Mechanical Engineering, Delhi Technological University, Delhi 110042, India

[2] Department of Mechanical Engineering, GLA University, Mathura 281406, U.P., India

[3] Management Development Institute, Gurgaon 122007, Haryana, India

Published online: 31 March 2023



Fig. 1 Schematic representation of the fundamental structure of sustainable development

a manufacturing organization (Madan Shankar et al. 2017). Here, environmental concerns are drawing global attention, and the social factor of sustainability has also become an extremely crucial topic for manufacturers and organizations. Globalization has resulted in a competitive market scenario between countries with weak regulations and those with strong environmental concerns and well-derived social principles, forcing the former to exit the markets (Abualfaraa et al. 2020).

A SS perspective of an organization is described as the capability of the manufacturing unit/industries to consider the social well-being, education, and financial and personal security of the society and the people who work within it with due consideration of demographic and economic equity (Lami and Mecca 2021). The sustainability performance of a manufacturing unit is analyzed by employing suitable metrics through careful selection of indicators. Literature reports many studies on the proposed framework for assessing economic and environmental sustainability (Eastwood and Haapala 2015; Lucato et al. 2017; Ahmad et al. 2019; Pinto et al. 2020). However, it must address SS analysis of manufacturing units due to accurate social comparability, especially quantifiable, and standardized social metrics (Wu and Su 2020).

SS dimension is vast, and its explained definitions are nebulous compared to the remaining dimensions, making its accomplishment a challenge for distinct sectors (Afshari et al. 2022). The selection of suitable indicators, and achieving social impact objectives are significant challenges for manufacturers. Currently, there needs to be more consensus on criteria to be used while evaluating the concept of SS (Dempsey et al. 2011; Shirazi and Keivani 2017). Since, organizations' engagement in creating, tracking, and optimizing social outcomes continues to grow, the need for commonly accepted and distinct SS indicators has become more relevant (Henao et al. 2017).

The present study is based upon underlying principles regulating SS and provides a suitable framework for assessing SS with priority inclusiveness. The paper also provides a detailed list of the metrics indicators with their interdependence that various manufacturing units can suitably use for the social performance assessment. SPSS and AMOS software have been used to develop SEM, and the underlying hypotheses have been verified to provide a suitable framework.

The paper has been divided into various sections that can be outlined as follows: The "Literature Review" section explores the literature review on the various aspects of SS factors and structural equation modeling (SEM). The "Research Methodology" section discloses the research model and the construct measurement. The "Results and Discussion" section provides the results of the various analysis using SPSS and AMOS software along with the discussion that has been concluded in the end with few limitations and future work.

Literature Review

To sustain the current dynamic market scenario, manufacturing organizations must adopt efficient approaches with the latest allied technologies (Banakar and Tahriri 2010). Organizations can achieve this by incorporating and realizing socioeconomic concerns, and issues with environmental repercussions (Digalwar et al. 2020). Incorporating factors for achieving sustainability is challenging for industries, as most need to be aware of it. In this study, factors affecting SS are investigated and framed into a model validated using structural equation modeling (SEM). The successive subsections will provide more focus on other authors' work on SS indicators and the application of SEM.

Social Sustainability Factors

SS is considered the least explained and inscribed pillar of sustainable development compared to the remaining two pillars, i.e., environment and economic (Torkayesh et al. 2021). The sustainable socio-economic development of a country is strongly dependent upon the social well-being of its people engaged in various sectors. Earlier, Holahan and Moos stressed the role of individual characteristics on job-related issues (Holahan and Moos 1986). During the twenty-first century, the ever-increasing trend of urbanization and awareness about climate change started highlighting the adverse social implications, including occupational health and safety of workers, shifting demographic pools, intensifying poverty, food scarcity, lack of educational facilities, and disparity in various working sectors (Figueroa-García et al. 2018; Khalid et al. 2018; Moreira et al. 2018; Razmjoo et al. 2020).

Generally, there is a direct relationship between the personal characteristics of the employees, such as skills, experience, and proficiency, and the various benefits availed by

the organization. Tafere et al. have reported the impact of the relationships between the personal characteristics of workers and their social and psychological conditions that may lead to triggering a disaster (Tafere et al. 2020). However, depending upon the nature of employment, employees are categorized into full-time, contractual, and part-time employees, and accordingly, the financial, well-being, and development benefits differ. In many organizations, demographic disparity is also a discriminating factor. It generally leads to job stress, insecurity, dissatisfaction, self-perceived fatigue, lack of motivation, and incompetence among the employees, resulting in a negative impact on the organization's performance and outcomes (Golinska et al. 2015). In addition, the lack of suitable jobs, increasing job stress, inequities in wages, and gender ratio further intensifies the social imbalance (Seo et al. 2015). Likewise, Jung et al. (2018) stated that irresponsible attitudes and physical fatigue can negatively impact the performance of the workforce, thereby affecting the organization's overall performance.

Zhang and Mohandes (2020) pointed out that it is the corporate responsibility to ensure its workforce's occupational health and safety and provide equitable job and promotion opportunities. Zu et al. (2014) reported that any organization is bound not only on an economic basis but also legally, ethically, and morally to its stakeholders and community. Wu and Su (2020) emphasized that the stakeholders get involved in the organization's financial aspects and get returns in terms of shares while the community gets benefitted in terms of infrastructural and technological development. Idowu et al. (2013) highlighted the role of a corporation in not only protecting the social well-being of the employee and their family and society.

Zohar (2000) recognized the impact of organizational policies and training programs on developing the atmosphere of safety and societal well-being. In any occupational accident, the direct and indirect costs involved medical assistance, rehabilitation, and disability compensation, as well as time loss for both the employee and the organization (Kauppinen and Rantanen 2002). Thus, training on the prevention of occupational safety and accidents must be prioritized on a regular basis in the organization.

Hutchins and Sutherland (2008) showed the interdependence of organization and their stakeholder. They mentioned that creating transparent policies for the promotion, increments, healthcare support, education, and family security of the employee boosts the organization's performance. Karji et al. (2019) concluded that developing safe work culture in the organization contributes to creating a socially sustainable community with the prediction of possible risks, leading to a productive work environment.

The prior research has yet to empirically differentiate and fragment amid the external stakeholders' (consumer, communities, investors), and internal stakeholders' (employees) orientation toward social sustainability (Chatzopoulou et al. 2022). The degree of organizational social sustainability depends upon the quality of people's relationships (Prieto et al. 2022). Fundamentally, generating economic value from any activity requires social relationships (Lazzarato and Jordan 2014).

Different authors depicted and analyzed crucial indicators from the SS point of view. Few among them had done research studies in distinct sectors to assess and evaluate factors affecting an organization's social performance; a summary of such works has been shown in Table 1.

The lack of incorporation of social elements of sustainability primarily in the male-dominated industrial sector of rural areas, is leading to population and demographic shifts and challenging the pursuit of a competitive working atmosphere. Hence, sustainable manufacturing practices should incorporate social well-being aspects while also promoting economic advancement.

In order to improve the social performance of an organization, analysis of various factors affecting the SS has been carried out with the help of suitable models using various statistical techniques including structural equation modeling (SEM) (Vinodh and Joy 2012; Seo et al. 2015).

Structural Equation Modeling (SEM)

A simple regression model deals with the association between one observable and one unobserved variable. A multiple regression model establishes a link between numerous observable variables and a single unobserved variable. Structural equation modeling (SEM) is known for its use as regression analysis to a collection of variables defined by the researchers (Jenatabadi 2015). SEM is a powerful tool used in multivariate analysis for framing exogenous and endogenous variables. It has a wide range of applications and is a rapidly evolving solution for most research problems requiring statistical analysis.

Sarkar et al. (2020) proposed PLS-SEM modeling to validate their study on the assessment of social, environmental, and economic factors that affects the green business practices within a ready-made garments factory. A covariance-based SEM technique was used by Mani et al. (2020) to investigate the connection of SS practices with supply chain performance for small and medium manufacturing enterprises (SMEs). Using SEM-AMOS, Abbas and Sağsan (2019) evaluated and tested the effect of knowledge-based management practices on the green revolution and sustainable corporate development. The SEM model formulated by Mendes and Machado (2015) illustrated that employees' skills directly affect the new product and its volume and control the total performance of any business organization.

Cepeda-Carrion et al. (2019) adopted the PLS-SEM methodology for developing constructs in the domain of

Table 1 Social sustainability factors of distinct sectors

S.No	Author's (Year)	Identified SS factors	Methodology	Application
1	Ajmal et al.(2018)	Job security, training and development, job availability, health, poverty, customer satisfaction, unbiased labour practices, and human rights protection	Literature review	Business world organizations
2	Li and Mathiyazhagan (2018)	Employee turnover rate, human rights, training and development, customer satisfaction and human rights protection	DEMATEL	Auto manufacturing
3	Popovic et al. (2018)	Job security, employee turnover rate, employee performance, training and development, career advancement. product information, medical insurance coverage, salary ratio, wage distribution, innovation and product development and legal benefits	ANNOVA	Evaluation of supply chain
4	Sarkar et al. (2020)	Society support, standards and values, legal benefits and macro-social performance	PLS-SEM	Textile industry
5	Olakitan Atanda (2019)	Process equity, employee involvement, health and safety measures, ease of reachability and level of satisfaction	LEED evaluation and AHP	Sustainability in buildings
6	Husgafvel et al. (2015)	Location, supply chain, labour practices, training and education, health and safety and legal benefits	Critical review	Process industry
7	Kumar and Ramesh (2020)	Fair job opportunity, regularly evaluation of workers' salaries, health and safety, health insurance, psychological risk prevention and management, restrictions on night time driving hours, top management support, availability of housing facility, acquiring of government driving policies, benefaction to CSR, customer satisfaction, etc	Fuzzy BWM	Cargo transport industry
8	Badri Ahmadi et al. (2017)	Job health and safety, Training and education, Stakeholder's influence, occupational health and safety, employees rights and practices for employees	BWM	Manufacturing supply chain
9	Mani et al. (2016)	Diversity at job place, safety measures at supplier and manufacturers end, women safety, wages, human rights and ethical issues	EFA and CFA	Indian manufacturing industries supply chain
10	Sudusinghe and Seuring (2020)	Quality health care services, youth employment, research and development, emergency planning, job availability, training and development, equal and diversified opportunities, equality policy, Occupational health and safety, career advancements, legal benefits, accessible housing facility, elimination of child labor and transparent governance	PLS-SEM	Apparel Industry

knowledge management. They considered SEM a second-generation data analysis technique that social science researchers have employed for 30 years. Prieto et al. (2022) examined social sustainability in a business organization as an antecedent of economic and environmental constructs using PLS-SEM. Additionally, they concluded that developing social sustainability in an organization would contribute to employees' well-being and enhance employees' potential, resulting in improved firm productivity, innovation, and competitiveness. D'Souza et al. (2021) validated his proposed model and hypotheses using SEM-AMOS. They found a strong influence of ecolabels on consumer intent to purchase green products. The partial least squares structural equation modeling method is acquiring a significant interest in many areas, including operations management (Richter et al. 2015).

Research Gaps

Despite recent trends toward incorporating environmental and economic factors into the sustainability assessment framework, the SS concept still needs more attention. Therefore, social issues inclusiveness were less in the main dimensions of sustainability assessment schemes. As a result, such frameworks must effectively correspond to social aspects of sustainability, leaving gaps in the analytical support required for sustainable decision-making. Worldwide, there are some researches regarding the social aspects of sustainability, but investigations are yet to be done in developing countries (Fatourehchi and Zarghami 2020). Many research studies highlighted that socially inclined companies perform better in the short term and long term (Longoni and Cagliano 2015), while others face a loss of reputation (Klassen and Vereecke 2012; Anisul Huq et al. 2014). For example, Wal-Mart had to face a loss of reputation in its supplier base (Thailand) for not addressing social issues like basic facilities for living and working conditions of its employees (Rudikoff 2018). Similarly, Indian media reported popular incident of worldwide renowned food packaged manufacturer, Nestle, whose negligence of social aspects like safety and ethical issues in its famous product line "Maggi" have to face loss of financial outcomes and even gave a huge dent on company's reputation (Hajmohammad and Vachon 2016).

Although many researchers have used SEM to develop frameworks for assessing environmental and economic sustainability, no concise and concrete reports are available for developing a structural model for assessing SS and predicting interrelationship between observable and unobservable variables making a basis for the proposed study.

Hypotheses Formulation

Organizations can gain more financial performance and create value for their stakeholders and shareholders in the long term if they are concerned about social performance by retaining their dedicated employees, which results in more loyal customers (Doloi 2012; Dočekalová and Kocmanová 2016; Murphy and Eadie 2019; Goel et al. 2020). The conceptual framework incorporating various constructs for the assessment of SS was drawn as a hypothetical model using SEM, shown in Fig. 2. Each variable was measured using a 5-point Likert scale. Various researchers have signified the interrelationship of critical factors that can be used as SS indicators. Henao et al. have highlighted the effect of job characteristics such as job availability and job security on community interrelations (Henao et al. 2017). Seo et al. (2015) emphasized upon the interdependence of job characteristics (JC) and occupational health and safety (OHS). Many researchers have highlighted the role of gaining customer satisfaction and public trust by providing product information and products with better quality by building community interrelations (CI) with the provision of technology and infrastructure development (Henao et al. 2017). Garza Reyes has emphasized product quality, product information, and customer satisfaction's influence on stakeholder engagement (SE) (Garza-Reyes 2015; Zhou et al. 2016; Wu and Su 2020). Hence, based on the literature review, the factors affecting the SS and their interrelationship were analyzed by formulating following hypothesis, and modeling was carried out using AMOS software:

H1a: *There is an interrelationship between JC and OHS.*
H1b: *There is an interrelationship between JC and CI.*
H1c: *There is an interrelationship between JC and SE*
H1d: *There is an interrelationship between JC and consumer protection.*
H2a: *There is an interrelationship between OHS and consumer protection.*
H2b: *There is an interrelationship between OHS and CI.*
H2c: *There is an interrelationship between OHS and SE.*
H3a: *There is an interrelationship between consumer protection and CI.*
H3b: *There is an interrelationship between consumer protection and SE.*
H4: *There is an interrelationship between CI and SE.*

Job Characteristics and Social Sustainability

The organization provides benefits to their employees under their compensational policies; these benefits and their characteristics are defined as JC (Simoes et al. 2016). These characteristics are vital quantitative indicators for assessing SS in an organization (Popovic et al. 2018). Organizations frequently use employee layoffs and employee turnover rates as essential tools for enhancing the company's performance. Still, a higher turnover rate can lead to more replacement costs, excess demand for training requirements, and loss of learning and experience effects (Katsikea et al. 2015). On the other hand, frequent layoffs result in declining employee morale and commitment. It will enhance working stress (Cascio 2010). As per the literature, we hypothesize:

H5: *JC is positively related to SS.*

Occupational Health and Safety and Social Sustainability

Organizations' initiatives to monitor the quality of working conditions and safety risks, enhance employee satisfaction, keep operational processes running, and positively impact the company's image and brand (Simoes et al. 2016). Consequently, the following elements are needed in the process for assessing SS. Indicators like time lost due to injury and work-related diseases, risk assessment, risk control

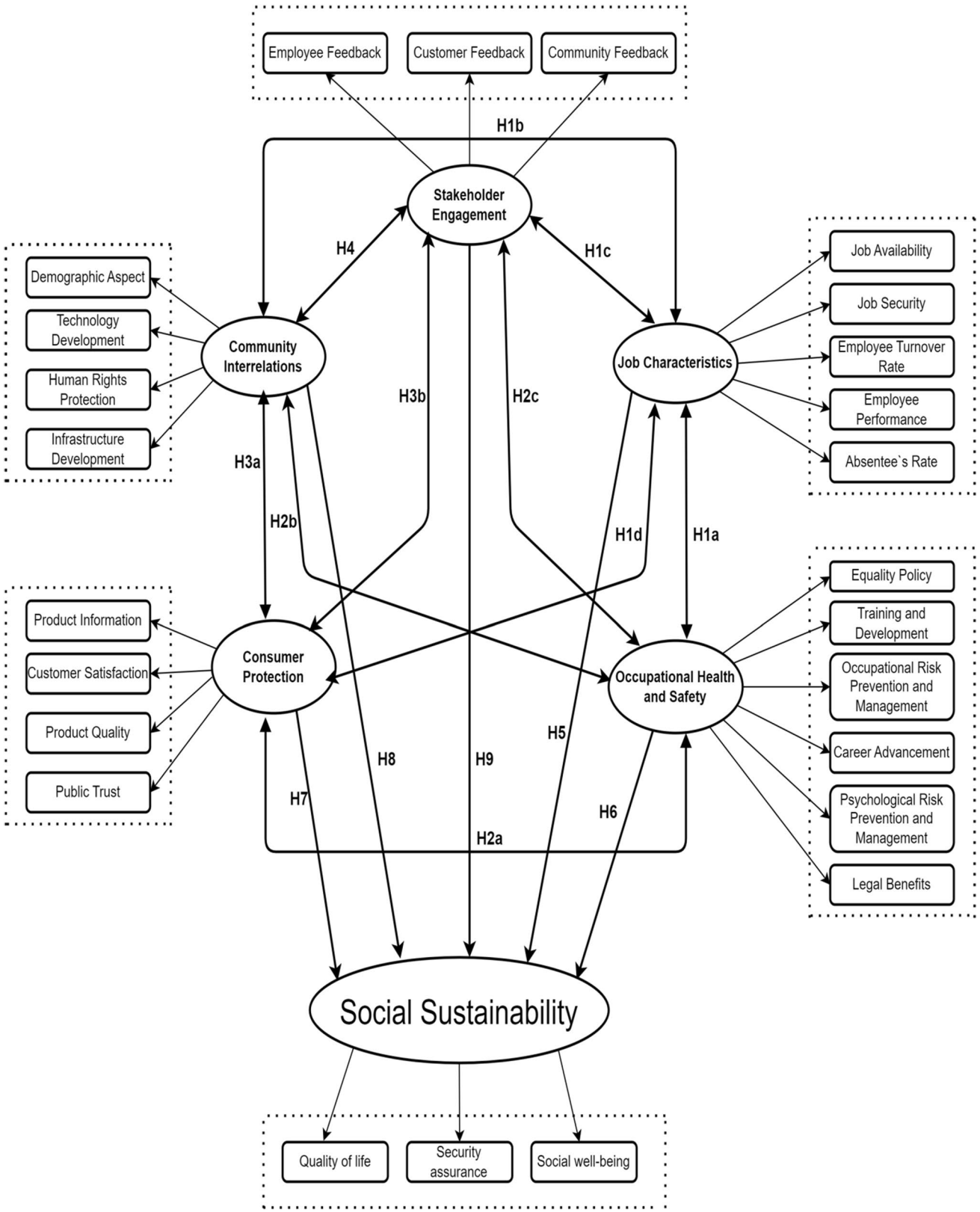


Fig. 2 Hypothetical model

measures, health care security policy (Podgórski 2015), and training and education (Uma 2013) are used to gage health and safety working conditions.

Wan and Ng (2018) highlighted that SS could consider issues related to stakeholders' safety and physiological and psychological requirements in housing projects. Hence, we hypothesize:

H6: *OHS is positively associated with SS.*

Consumer Protection and Social Sustainability

Nowadays, consumers are becoming more aware of the impact of their purchasing intentions on the environment and social sustainability (Mohr and Webb 2005; Simmons and Becker-Olsen 2006; Grunert 2011). Toussaint et al. (2021) highlighted consumers' awareness of their purchasing decision from the company's corporate social responsibility (CSR) point of view. Most aware and informed consumers would prefer to buy from a company that develops and sells sustainable and responsible products. Consumers act as a keen players in the outcome of CSR as they have the potential to purchase a product. Still, they must be made aware of the conditions, quality, and information of the product they want. Ozhan et al. (2022) concluded that the amount of value given to the customers in the organization leads to business success rather than the power of production. Organizations should include the concept of the consumer's conception in connection with the company's social practices (Jitrawang and Krairit 2019; Kaczorowska et al. 2019). Thus, we hypothesize:

H7: *There is a positive relationship between consumer protection and SS.*

Community Interrelations and Social Sustainability

SS combines the processes and framework for stabilizing people, the planet, and profit regarding happiness, safety, and future generational perspectives (Blanc and Raymond 2011; Eizenberg and Jabareen 2017). It is defined as the "neglected element of sustainability" (Kandachar 2014) comprised of social equity and community concerns (Bramley and Power 2009).

SS in business can be created by adopting innovative technology, research and development (Simoes et al. 2016). Social innovation can be achieved by meeting social needs (Caulier-Grice et al. 2012) namely, projects on social development, local education, and focus on developing initiatives for improving social sustainability, among others. Higher values of these indicate the company's initiative in the process of improvement in SS and the creation of SS businesses. Venkataraman (2004) introduced new business organizations. The entrepreneurial ecosystem is a network of interlinked elements constituting resource providers, risk-bearers, market demand, advanced technologies, infrastructure support, culture, policies, and support services to develop a right-oriented revenue generation cycle. Community involvement is vital in developing, recommending, and implementing positive solutions to social issues (Desiana et al. 2022).

Literature reports that organizations must consider the concerns of their community. Therefore, we hypothesize:

H8: *There is a positive relationship between CI and SS.*

Stakeholder Engagement and Social Sustainability

Social assessment of an organization is endeavored by considering stakeholders' satisfaction (Fatourehchi and Zarghami 2020). Companies that can communicate their sustainability can improve their stakeholder's satisfaction and firms' image (Campbell 2000; Bebbington et al. 2008). Afshari et al. (2022) studied that internal stakeholders play an essential role in achieving SS. Organizations would have a strategic importance over their competitors if they emphasized more on their stakeholders as valuable resources (Sodhi 2015). According to the stakeholder resource-based view (Barney 2001), utility theory, and stakeholder theory (Freeman 2010), all stakeholders, such as suppliers, employees, and customers, must be managed equally for capitalizing their respective routines, resources, and their abilities resulting in improved performance (Gualandris et al. 2015).

Stakeholders have a crucial place on CSR's part; they can lead customers to buy distinct brands, favor few retailers, and enhance the firm's image, improving its economic performance (Luo and Bhattacharya 2006). For example, America's renowned coffee brand, Starbucks, earned popularity among customers due to its primary emphasis on responsible social paths of sourcing and servicing, significantly improving its retailers' image (Argenti 2004).

In this study, we tried to explore the connection between SE and SS of an organization. Thus, we hypothesize:

H9: *There is a positive relationship between SE and SS.*

Research Methodology

Questionnaire Administration and Data Collection

This study covers the systematic evaluation of the literature on SS factors, followed by assistance from academic people, consultants, and manufacturing and service organizations professionals for the finalization and validation. The professionals were selected from all hierarchy levels of the

organization (lower, middle, and higher). The questionnaire has been developed based on an extensive literature review. It uses a five-point Likert scale to measure each of the factors, where five means "most important," four means "very important," three means "important," two means "less important," and one means "least important." The questionnaire was finalized after interacting with experts from manufacturing and service organizations and academia. The questionnaire has been added in the Appendix of the manuscript. For data collection, a questionnaire was sent through email, followed by telephonic calls to industries located in Northern India. To ensure accuracy and effectiveness, the data was collected from different age groups, experienced groups, other professions, and different educational backgrounds respondents. A pilot study of the questionnaire was completed considering the responses of some experts for content and construct validity of the questionnaire. Before the SEM analysis, the raw data was filtered and checked for missing values.

A structured diagram of the research methodology acquired for this work is shown in Fig. 3. A total of 392 responses were collected through online media. The sample size was adequate for testing research hypotheses and was comparable to response rates reported in the literature. Table 2 provides demographic information of

Table 2 Demographic information of the respondents

Category	Item	Frequency	Percentage
Gender	Male	362	92.35
	Female	30	7.65
Age	≤29	84	21.43
	30–39	133	33.93
	40–49	107	27.3
	50–59	52	13.27
	≥60	16	4.08
Experience	<1 year	25	6.37
	1–5 years	74	18.87
	5–10 years	82	20.92
	10–15 years	89	22.70
	15–20 years	77	19.64
	≥20 years	45	11.48
Organization type	Manufacturing	220	56.12
	Services	172	43.87
Position held	Lower management	176	44.89
	Middle management	158	40.31
	Higher management	58	14.79
Education	Graduate	205	52.29
	Post Graduate	146	37.24
	Doctorate	41	10.46

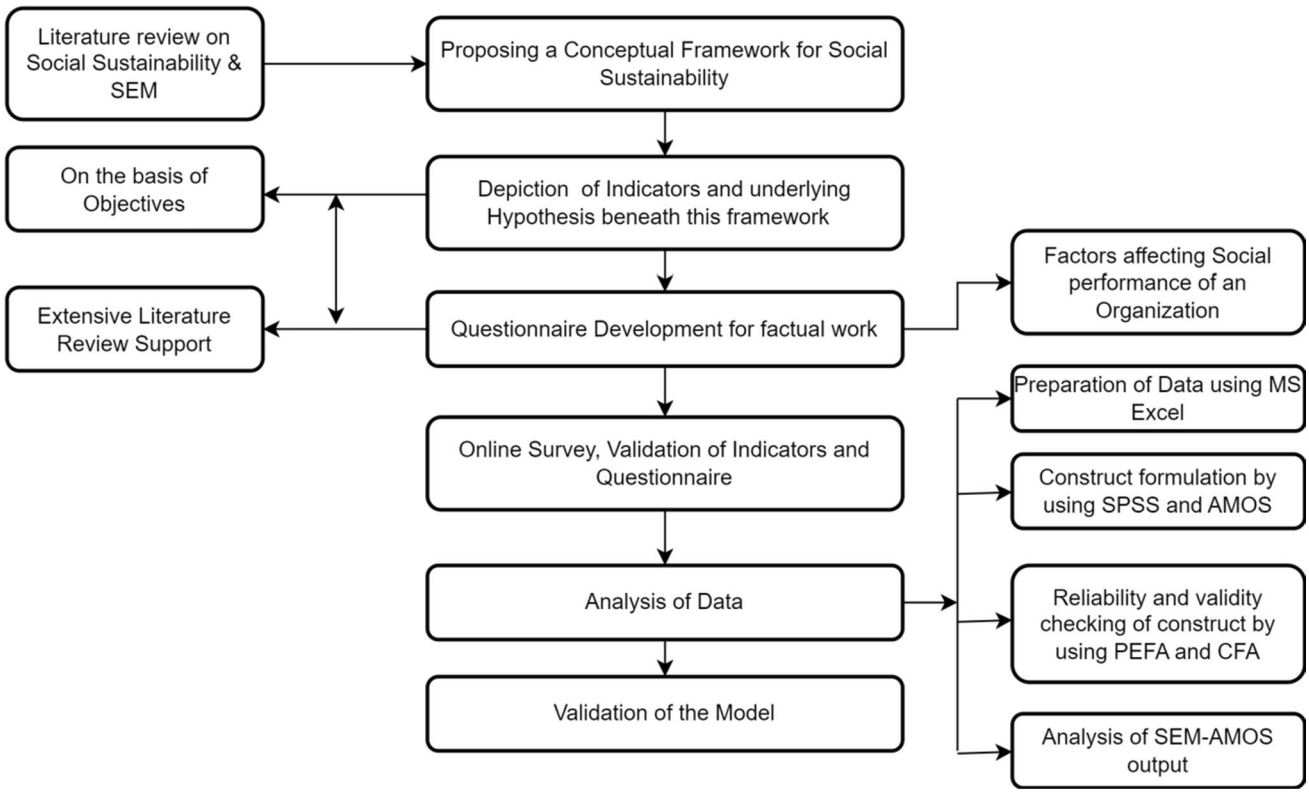


Fig. 3 Structured diagram of research methodology

the respondents. SPSS and AMOS software were used to develop the model using SEM.

Selection of Factors

Literature reports that the SS of an organization depends upon several factors, primarily employee, customer, and community-centered, and is in direct correlation with the organizational factors. Providing a socially sustainable and safe workplace with motivated, educated, and skilled employees of the varying demographic pool is essential for sustainable production to face the challenge of a decreasing recruited collection (Gebisa and Lemu 2017). A social component of sustainability is founded on the principle of equity, empowerment, integration, involvement, participation, cultural identities, and institutional solidarity (Henao et al. 2017; Eizenberg and Jabareen 2017). The social impact of various production operations and products is calculated through social metrics taking concern for workers' occupational safety, health, and any detrimental effect on the stakeholders (Chaim et al. 2018). It stresses the unity of the community and the desire to collaborate for common goals when meeting human interests such as health and well-being (Holm 2018). These bold visions would be crucial for future industry growth, not only to ensure generational stability but also to promote the harmony of work-life and the health and development of all stakeholders. It also builds up better customer loyalty and interactions with the environment through feedback (Beng and Omar 2014; Eastwood and Haapala 2015; Zhou et al. 2016).

The study presents a research model with due consideration of job characteristics (JC), occupational health and safety (OHS), consumer protection (CP), community interrelations (CI), and stakeholder engagement (SE) as latent variables after a thorough literature review (Henao et al. 2017; Jung et al. 2018; Popescu and Popescu 2019; Wu and Su 2020; Lami and Mecca 2021). Table 3 below lists the references of researchers who alluded to these specific indicators during the research study.

Results and Discussion

Principle Element Factor Analysis (PEFA)

This research study uses principle element factor analysis (PEFA) to estimate the dimensionality of twenty-five SS factors and develop a factorial structure. The accuracy with which the constructs repeatedly measure the same phenomenon within allowable variation is referred as the constructs' reliability. The responses collected from the questionnaire were transformed into data and verified for reliability using Cronbach's alpha in SPSS. Any construct with a Cronbach's alpha value greater than 0.7 is considered reliable (Vinodh and Joy 2012). All the constructs were found reliable with Cronbach's alpha value (>0.7) as listed in Table 4. A significant positive correlation existed between the constructs in Pearson's coefficient two-tailed test with $p<0.01$ and $r(298)>0.148$. KMO and Bartlett's test for the constructs reported adequacy of sampling as 0.877 (Table 4), and Bartlett's test of sphericity significance ($p<0.01$) indicated a significant correlation (Lučić 2020).

Confirmatory Factor Analysis (CFA)

In this work, the factorial validity of the five-dimension model with twenty-five (25) indicators identified in the PEFA process was assessed using confirmatory factor analysis (CFA). The compatibility of the developed model has been assessed through basic overall goodness-of-fit measures in terms of Chi-square ($\chi 2$), normal Chi-square ($\chi 2$ /df), root mean residual (RMR), goodness-of-fit index (GFI), adjusted goodness-of-fit index (AGFI), normed fit index (NFI), relative fit index (RFI), comparative fit index (CFI), Tucker Lewis index (TLI), parsimony comparative fit index (PCFI) and root mean square error approximation (RMSEA). A model with $\chi 2$/df value close to 2, RMR and RMSEA value <0.1, and the values of the remaining goodness-of-fit measures <0.9 is considered a good fit (Rai et al. 2021). The developed model (Fig. 4) was found to have excellent fit outcomes with χ^2 value as 467.098 (dF = 260, $p<0.001$), χ^2/dF value as 1.797, GFI = 0.913, AGFI = 0.891, RMR = 0.054, NFI = 0.25, RFI = 0.914, TLI = 0.964, CFI = 0.965, PCFI = 0.837, FMIN = 1.195, and RMSEA = 0.045. Thus, the model was found valid with model fit measures shown in Table 5.

The validity of the constructs was confirmed quantitatively by standardized factor loadings (FL) and average variance extracted (AVE) values >0.5, maximum shared variance (MSV), maximum reliability (MaxR) (H), square root of AVE (†), and construct reliability (CR) values >0.7 to reach statistical significance as shown in Table 6. All the constructs were found to exhibit AVE values above 0.5 and were integrated into the model using AMOS (Mani et al. 2020).

Significance of correlations: $^{*}p<0.050$ and $^{\#}p<0.001$.

Nomological validity was found significant and acceptable with all significant p-values and positive values of the correlation estimates. Thus, all the constructs were significant and could be used to assess the social sustainability of the various organizations and manufacturing units (Lučić 2020).

Figure 5 shows the relative importance of selected dimensions to assess social sustainability based on descriptive statistics. It indicates that stakeholder engagement is the most important dimension followed by job charcteristics

Table 3 Factors used for Social sustainability assessment

Latent variables	Metrics indicators	Designation	References
Job characteristics (JC)	Job availability	JC1	Gebisa and Lemu, (2017), Sudusinghe and Seuring, (2020)
	Job security	JC2	Chaim et al., (2018), Ajmal et al., (2018), Popovic et al., (2018)
	Employee turnover rate	JC3	Bortolotti et al., (2015), Veleva and Ellenbecker, (2001), Dočekalová and Kocmanová, (2016), Popovic et al., (2018)
	Employee performance	JC4	Bortolotti et al., (2015), Popovic et al., (2018)
	Absentee's rate	JC5	Peralta Álvarez et al., (2017)
Occupational Health and Safety (OHS)	Equality policy/equity	OHS1	Badurdeen and Jawahir, (2017) Ajmal et al., (2018), Sudusinghe and Seuring, (2020), Reyna-Castillo et al. (2023)
	Training and development	OHS2	Holm (2018), Ajmal et al. (2018), Popovic et al. (2018), (Shao et al. 2017), Husgafvel et al. (2015), Sudusinghe and Seuring (2020), Pang et al. (2023)
	Occupational Risk prevention and management	OHS3	Moreira et al. (2018), Popovic et al. (2018), Kumar and Ramesh (2020), Badri Ahmadi et al. (2017)
	Career advancement	OHS4	Gebisa and Lemu (2017), Popovic et al. (2018), Sudusinghe and Seuring (2020)
	Psychological risk prevention and management	OHS5	Cor et al. (2014) Kumar and Ramesh (2020)
	Legal benefits	OHS6	Eastwood and Haapala (2015), Popovic et al. (2018), Sarkar et al. (2020), Husgafvel et al. (2015), Sudusinghe and Seuring (2020)
Consumer protection (CP)	Product quality	CP1	Cor et al. (2014)
	Customer satisfaction	CP2	Bracke et al. (2017), Ajmal et al. (2018), Shao et al. (2017), Kumar and Ramesh (2020)
	Product information	CP3	Behrisch et al. (2011)
	Public trust	CP4	Bereketli and Erol Genevois (2013)
Community Interrelations (CI)	Demographic aspect	CI1	Ceschin and Gaziulusoy (2016)
	Technology development	CI2	Gebisa and Lemu (2017)
	Human rights protection	CI3	Cor et al. (2014), Ajmal et al. (2018), Azapagic et al. (2006), Frey and MacNaughton (2016), Shao et al. (2017), Kumar and Ramesh (2020), Mani et al. (2016), Reyna-Castillo et al. (2023)
	Infrastructure development	CI4	Chaim et al. (2018)
Stakeholder engagement (SE)	Customer feedback	SE1	Deutz et al. (2013)
	Community feedback	SE2	Peralta Álvarez et al. (2017)
	Employee feedback	SE3	Gebisa and Lemu (2017)
Social Sustainability (SS)	Quality of life	SS1	Sudusinghe and Seuring (2020)
	Security assurance	SS2	Popovic et al. (2018)
	Social well-being	SS3	Ajmal et al. (2018), Colantonio (2009)

and occupational health and safety as the least important dimension. Many authors confirmed that enhancing corporate reputation among the stakeholders positively impacts organizational performance (Greening and Turban 2000; Singh and Misra 2021).

Table 7 shows the exogenous variables' direct and total effects on the observed endogenous variables. The factors having the factor loading less than 0.6 were not incorporated into the analysis. On the other indicators, there were little indirect effects observed for the three social sustainability indicators,

Table 4 KMO and Bartlett's test

Kaiser–Meyer–Olkin measure of sampling adequacy		0.877
Bartlett's test of sphericity	Approx. Chi-Square	6107.512
	df	300
	Sig	0.000
Construct validity	Latent variables	Cronbach's alpha
	JC	0.884
	OHS	0.920
	CP	0.861
	CI	0.871
	SE	0.861
	SS	0.874

SS1, SS2, and SS3. However, significantly high direct effects were observed, indicating the significance of the selected constructs. In the case of JC, the maximum effect was observed by job availability followed by job security and absentee rate. A minimum effect was observed for the employee turnover rate. In the case of OHS, occupational risk prevention and management exhibited the maximum effect, followed by training and development. Occupational risk prevention and control also exhibited significant effect, followed by career advancement. While the comparatively lesser effect was observed for legal benefits and equity policy. The results indicate a need for more awareness of the role of equity policy in social sustainability among the stakeholders. In the case of consumer protection, the maximum effect was observed for product quality, followed by customer satisfaction and product information. However, a comparatively lesser effect was observed for public trust. Full effect was observed for demographic aspect sub-dimension of CI. While technology development and human rights protection exhibited comparatively lesser effects. Although all the indicators were significantly effective in the case of SE, customer feedback showed maximum effect followed by community feedback while the least effect was observed for employee feedback. Likewise, the maximum effect was observed for quality of life

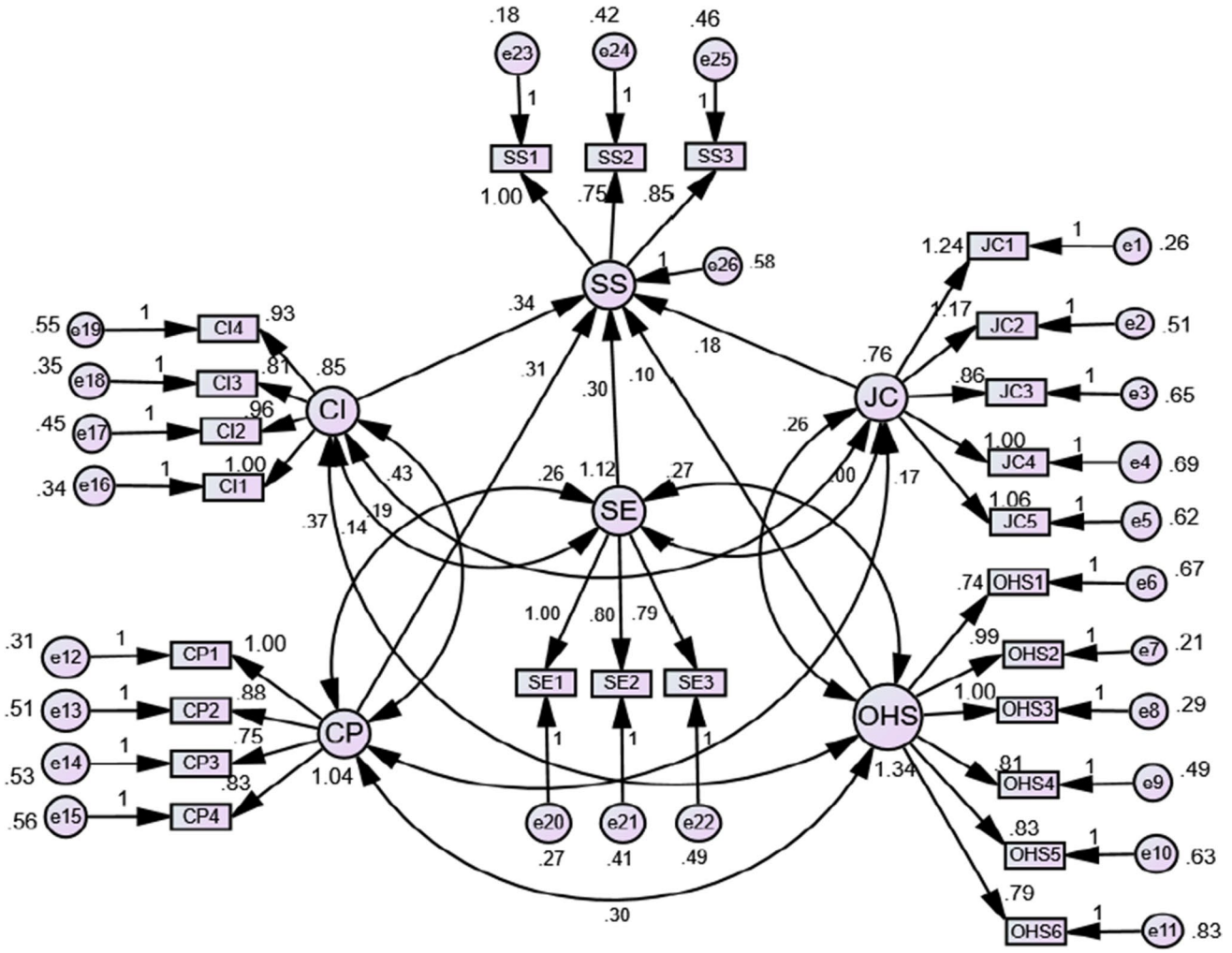


Fig. 4 Structural model for social sustainability indicators

Table 5 Model fit measures for the developed model

Measure	Estimate	Threshold	Explanation
CMIN	467.098	–	–
DF	260	–	–
CMIN/DF	1.797	Between 1 and 3	Excellent
CFI	0.965	> 0.95	Excellent
SRMR	0.041	< 0.08	Excellent
RMSEA	0.045	< 0.06	Excellent
PClose	0.887	> 0.05	Excellent

followed by social well-being and security assurance on SS. Finally, the higher impact of CP, CI, and SE were observed on SS compared to JC and OHS with a maximum value for SE.

Path analysis and regression analysis were carried out to estimate regression weights for the proposed model, with results shown in Table 8. The results of the correlation analysis for testing the hypothesis are shown in Table 9.

H1a states that there is an interrelationship between JC and OHS. The correlational results validate the hypothesis ($\beta = 0.259$, $p < 0.001$) and is consistent with the literature. H1b hypothesizes that there is an interrelationship between JC and CI. This hypothesis was also validated with the positive and significant correlation ($\beta = 0.193$, $p < 0.001$). However, the hypothesis H1c accounting for the interrelationship between JC and SE was invalidated and non-significant ($\beta = -0.091$, $p > 0.01$). There was a positive and significant relationship between job characteristics and customer protection ($\beta = 0.172$, $p < 0.001$), and hypothesis H1d stating the interrelationship between JC and CP was supported. Similarly, hypothesis H2a stating the interrelationship between OHS and CP was valid ($\beta = 0.301$, $p < 0.001$). The hypothesis H2b was also considered valid with a positive and significant interrelationship between OHS and CI ($\beta = 0.374$, $p < 0.001$). Furthermore, hypothesis H2c was found valid with a significant interrelationship between OHS and SE ($\beta = 0.268$, $p > 0.01$). The hypothesis H3a accounting for the interrelationship between CP and CI was significant and valid ($\beta = 0.429$, $p < 0.001$). Hypothesis H3b was also found valid with a positive and significant interrelationship between CP and SE ($\beta = 0.256$, $p < 0.01$). On the other hand, hypothesis H4 was not supported with an insignificant interrelationship between CI and SE ($\beta = 0.137$, $p > 0.01$). The result can be attributed to the lack of awareness about the human rights protection among the various stakeholders, as observed in the direct effect analysis (Henao et al. 2017). The former hypotheses discussed represent the correlation between the indicators, shown by bidirectional arrows. The hypotheses (H5-H9) illustrate the predictive relationship between the main dimensions, and SS, shown by unidirectional arrows. The hypotheses (H7 to H9) strongly influence social sustainability. The H7 shows the influence of consumer protection on SS, significantly validated ($\beta = 0.307$, C.R. = 5.551), implying that the more the organization

Table 6 Construct validity and discriminant validity for the constructs used in the model

Construct	Construct validity				Discriminant validity				
	CR	AVE	MSV	MaxR(H)	OHS†	JC†	CI†	CP†	SE†
OHS	0.889	0.565	0.123	0.942	0.752				
JC	0.848	0.512	0.066	0.908	0.256#	0.716			
CI	0.835	0.524	0.208	0.880	0.351#	0.240#	0.724		
CP	0.827	0.510	0.208	0.881	0.254#	0.193#	0.456#	0.714	
SE	0.800	0.528	0.056	0.881	0.219#	−0.005	0.141*	0.236#	0.727

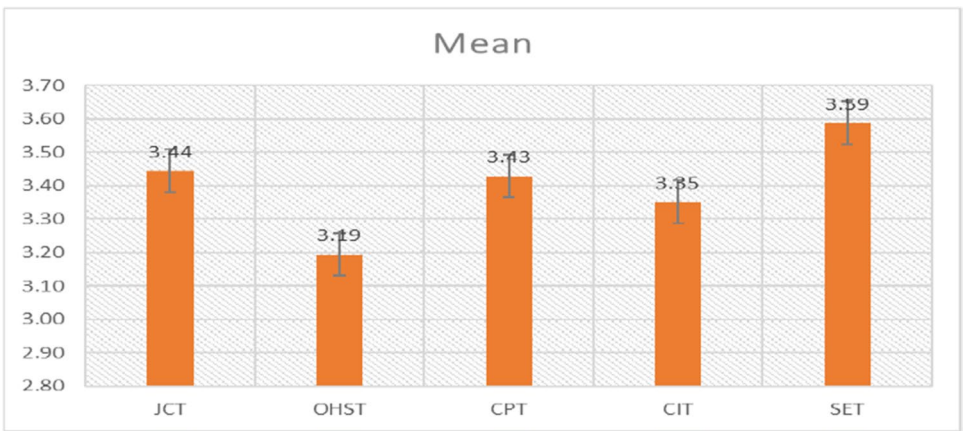


Fig. 5 Relative importance of social sustainability dimensions

Table 7 Direct/total effects of endogeneous and exogeneous variables (*indirect effects)

Variable	JC	OHS	CP	CI	SE	SS
JC1	0.903					
JC2	0.819					
JC3	0.679					
JC4	0.724					
JC5	0.761					
OHS1		0.721				
OHS2		0.929				
OHS3		0.906				
OHS4		0.802				
OHS5		0.774				
OHS6		0.708				
CP1			0.878			
CP2			0.784			
CP3			0.724			
CP4			0.749			
CI1				0.846		
CI2				0.798		
CI3				0.786		
CI4				0.755		
SE1					0.897	
SE2					0.799	
SE3					0.767	
SS	0.147	0.11	0.287	0.283	0.288	
SS1	0.184*	0.104*	0.307*	0.336*	0.297*	0.932
SS2	0.137*	0.078*	0.229*	0.25*	0.221*	0.782
SS3	0.156*	0.088*	0.261*	0.285*	0.252*	0.808

invests in considering consumer protection, strongly the SS is achieved. The influence of community interrelations and SS is significantly positive and validated ($\beta = 0.336$, C.R. = 5.349), indicating that when a community relationship with the organization has a positive relationship, they demonstrated stronger SS. Thus, H8 is confirmed. The companies should be more involved and bothered about the life in the community of employees (Lin et al. 2021). The organization should have a strong social impact and commitment to the community, the requirement of "corporative governance" (Bianchini et al. 2022). The hypothesis H9 test result shows that the influence of stakeholder engagement on SS is significantly positive and validated ($\beta = 0.297$, C.R. = 6.242). Stakeholders are considered an important group to be sensitive and affect the sustainability of the business (Singh and Sushil 2021). The stakeholder theorists affirm that a business organization with a positive relationship with a series of stakeholders like customers, employees, suppliers, communities, and financiers leads to sustainable performance (Ozhan et al. 2022). Similarly, hypotheses H5, and H6, i.e., Job characteristics leads to social sustainability, and occupation health and safety leads to SS are positively significant and validated (standardized $\beta = 0.184$, C.R. = 3.247; $\beta = 0.104$, C.R. = 2.370). The SS indicators like health, safety, child labor issues (gender discrimination, bonded labor, etc.), human rights, community initiatives, and employment benefits are generally observed and accepted as sensitive areas of performance assessment and monitoring toward social concern goals in the organization (Mani et al. 2014; Popovic et al. 2018).

The research findings are significant for integrating social sustainability in business organizations. This study empirically tested the various indicators (discussed above) that are important for enhancing satisfaction among employees, consumers, community, and stakeholders, leading to organizational performance improvement. Moreover, improving the conditions of employees can prevent brain drain, form a good organizational image, improve working conditions, and build satisfaction and loyalty among workers, employees, and stakeholders.

Implications for Industry and Academia

Social sustainability is an important part of management strategies to improve organizational performance. This paper will help the industry to find the critical factors and their relationships to enhance the social sustainability of the organization. Community

Table 8 Estimates for regression weights for the proposed model

	Estimate	S.E	C.R	*P*
JC1 ← JC	1.239	0.073	17.024	***
JC2 ← JC	1.171	0.075	15.644	***
JC3 ← JC	0.855	0.066	12.953	***
JC4 ← JC	1.000			
JC5 ← JC	1.057	0.073	14.539	***
OHS1 ← OHS	0.735	0.041	17.779	***
OHS2 ← OHS	0.987	0.033	29.676	***
OHS3 ← OHS	1.000			
OHS4 ← OHS	0.808	0.038	21.482	***
OHS5 ← OHS	0.834	0.042	20.086	***
OHS6 ← OHS	0.787	0.046	17.253	***
CI1 ← CI	1.000			
CI2 ← CI	0.964	0.054	17.738	***
CI3 ← CI	0.812	0.047	17.375	***
CI4 ← CI	0.929	0.056	16.486	***
CP1 ← CP	1.000			
CP2 ← CP	0.883	0.050	17.783	***
CP3 ← CP	0.746	0.047	15.959	***
CP4 ← CP	0.829	0.05	16.718	***
SE1 ← SE	1.000			
SE2 ← SE	0.802	0.046	17.412	***
SE3 ← SE	0.789	0.047	16.699	***
SS1 ← SS	1.000			
SS2 ← SS	0.745	0.038	19.444	***
SS3 ← SS	0.850	0.042	20.469	***

S.E.* approximate standard error, *C.R.* critical ratio; * indicates that the value of *P* is less than 0.001

interrelation, stakeholder engagement, and consumer protection have a strong correlation and linear regression to achieve social sustainability. This study may lead the researchers' innovative ideas to find more unexplored areas to make the organization more socially sustainable.

Conclusion, Limitation, and Future Scope

Business organizations inclined towards sustainability must integrate all three dimensions: environmental, economic, and social. The inducement of social sustainability in the organization is complex, tedious, and challenging. The solution lies in developing conceptual and empirical studies. The study quantitatively evaluated the sensitive social sustainability indicators required for a business organization's employee and customer satisfaction and loyalty using structural equation modeling. A research model with hypotheses has been framed, and the social sustainability indicators have been proposed based on extensive literature review. The model has been validated using various statistical tools in SPSS and AMOS software.

The results show that community interrelations, consumer protection, stakeholder engagement, occupational health and safety, job characteristics, and community interrelations strongly correlate with each other. As mentioned in this section, the proposed factors related to the six constructs show a structural model linking each other with corresponding estimates. Among these factors and constructs, community interrelation is the most important for making the organization more socially sustainable.

This study explains only the social aspects of the organization. It can also be linked with the economic and environmental aspects of the organization. Also, the future scope of the study may focus on a specific industry type. This study is generic.

Table 9 Summary of hypotheses results

Hypotheses	Constructs	Estimate	S.E	C.R	*P*	Conclusion
H1a	OHS ↔ JC	0.259	0.058	4.427	***	Validated and significant
H1b	JC ↔ CI	0.193	0.048	4.030	***	Validated and significant
H1c	JC ↔ SE	−0.005	0.052	−0.091	0.928	Invalidated and non-significant
H1d	JC ↔ CP	0.172	0.052	3.302	***	Validated and significant
H2a	OHS ↔ CP	0.301	0.068	4.416	***	Validated and significant
H2b	OHS ↔ CI	0.374	0.064	5.869	***	Validated and significant
H2c	OHS ↔ SE	0.268	0.070	3.836	***	Validated and significant
H3a	CP ↔ CI	0.429	0.061	7.082	***	Validated and significant
H3b	CP ↔ SE	0.256	0.064	3.989	***	Validated and significant
H4	CI ↔ SE	0.137	0.057	2.418	0.016	Invalidated and non-significant
H5	JC → SS	0.184	0.057	3.247	0.001	Validated and significant
H6	OHS → SS	0.104	0.044	2.370	0.018	Validated and significant
H7	CP → SS	0.307	0.055	5.551	***	Validated and significant
H8	CI → SS	0.336	0.063	5.349	***	Validated and significant
H9	SE → SS	0.297	0.048	6.242	***	Validated and significant

S.E.* approximate standard error, *C.R.* critical ratio; * indicates that the value of *P* is less than 0.001

Appendix. Factors affecting the social performance of an organization

Questionnaire for survey

Please, mark (√) the importance of the following social sustainability factors for your organization on five-points rating scale.

1	2	3	4	5
Least Important	Less Important	Important	Very Important	Most Important

S. No.	Statements	Least Important	Less Important	Important	Very Important	Most Important
1	Job availability					
2	Job security					
3	Employee turnover rate					
4	Employee performance					
5	Absentee's rate of employee					
6	Equality policy					
7	Training and development					
8	Occupational risk prevention and management					
9	Career advancement					
10	Psychological risk prevention and management					
11	Legal benefit					
12	Product information					
13	Customer satisfaction					
14	Product quality					
15	Public trust					
16	Demographic aspect					
17	Technology development					
18	Human rights protection					
19	Infrastructure Development					
20	Employee feedback					
21	Customer feedback					
22	Community feedback					
23.	Quality of life					
24	Security assurance					
25.	Social well-being					

Data Availability The datasets generated during and/or analyzed during the current study are not publicly available, but are available from the corresponding author on reasonable request.

Declarations

Ethical Approval The authors have no relevant financial or non-financial interests to disclose. All authors certify that they have no affiliations with or involvement in any organization or entity with any financial interest or non-financial interest in the subject matter discussed in this manuscript.

Competing Interests The authors declare no competing interests.

References

Abbas J, Sağsan M (2019) Impact of knowledge management practices on green innovation and corporate sustainable development: a structural analysis. J Clean Prod 229:611–620. https://doi.org/10.1016/j.jclepro.2019.05.024

Abualfaraa W, Salonitis K, Al-AshaabAla'raj AM (2020) Lean-Green Manufacturing practices and their link with sustainability: a critical review. Sustainability 12:981. https://doi.org/10.3390/su12030981

Afshari H, Agnihotri S, Searcy C, Jaber MY (2022) Social sustainability indicators: a comprehensive review with application in the energy sector. Sustain Prod Consum S2352550922000501. https://doi.org/10.1016/j.spc.2022.02.018

Ahmad S, Wong KY, Rajoo S (2019) Sustainability indicators for manufacturing sectors: a literature survey and maturity analysis from the triple-bottom line perspective. J Manuf Technol Manag 30:312–334. https://doi.org/10.1108/JMTM-03-2018-0091

Ajmal MM, Khan M, Hussain M, Helo P (2018) Conceptualizing and incorporating social sustainability in the business world. Int J Sustain Dev World Ecol 25:327–339. https://doi.org/10.1080/13504509.2017.1408714

Anisul Huq F, Stevenson M, Zorzini M (2014) Social sustainability in developing country suppliers: an exploratory study in the ready made garments industry of Bangladesh. Int J Oper Prod Manag 34:610–638. https://doi.org/10.1108/IJOPM-10-2012-0467

Argenti PA (2004) Collaborating with activists: how starbucks works with NGOs. Calif Manage Rev 47:91–116. https://doi.org/10.2307/41166288

Azapagic A, Millington A, Collett A (2006) A methodology for integrating sustainability considerations into process design. Chem Eng Res Des 84:439–452. https://doi.org/10.1205/cherd05007

Badri Ahmadi H, Kusi-Sarpong S, Rezaei J (2017) Assessing the social sustainability of supply chains using best worst method. Resour Conserv Recycl 126:99–106. https://doi.org/10.1016/j.resconrec.2017.07.020

Badurdeen F, Jawahir IS (2017) Strategies for value creation through sustainable manufacturing. Procedia Manuf 8:20–27. https://doi.org/10.1016/j.promfg.2017.02.002

Banakar Z, Tahriri F (2010) Justification and classification of issues for the selection and implementation of advanced manufacturing technologies. https://doi.org/10.5281/ZENODO.1081121

Barney JB (2001) Resource-based theories of competitive advantage: a ten-year retrospective on the resource-based view. J Manag 27:643–650. https://doi.org/10.1177/014920630102700602

Bebbington J, Larrinaga-González C, Moneva-Abadía JM (2008) Legitimating reputation/the reputation of legitimacy theory. Account Audit Account J 21:371–374. https://doi.org/10.1108/09513570810863969

Behrisch J, Ramirez M, Giurco D (2011) Representation of ecodesign practice: international comparison of industrial design consultancies. Sustainability 3:1778–1791. https://doi.org/10.3390/su3101778

Beng LG, Omar B (2014) Integrating axiomatic design principles into sustainable product development. Int J Precis Eng Manuf-Green Technol 1:107–117. https://doi.org/10.1007/s40684-014-0015-2

Bereketli I, Erol Genevois M (2013) An integrated QFDE approach for identifying improvement strategies in sustainable product development. J Clean Prod 54:188–198. https://doi.org/10.1016/j.jclepro.2013.03.053

Bianchini A, Guarnieri P, Rossi J (2022) A framework to assess social indicators in a circular economy perspective. Sustainability 14:7970. https://doi.org/10.3390/su14137970

Blanc H, Raymond A (2011) Prise en compte de la durabilité dans la représentation sociale de la croissance économique. Dév Durable Territ. https://doi.org/10.4000/developpementdurable.9069

Bortolotti T, Boscari S, Danese P (2015) Successful lean implementation: organizational culture and soft lean practices. Int J Prod Econ 160:182–201. https://doi.org/10.1016/j.ijpe.2014.10.013

Boulanger P-M (2008) Sustainable development indicators: a scientific challenge, a democratic issue. Surv Perspect Integrating Environ Soc 1:59–73. https://doi.org/10.5194/sapiens-1-59-2008

Bracke S, Yamada S, Kinoshita Y et al (2017) Decision making within the conceptual design phase of eco-friendly products. Procedia Manuf 8:463–470. https://doi.org/10.1016/j.promfg.2017.02.059

Bramley G, Power S (2009) Urban form and social sustainability: the role of density and housing type. Environ Plan B Plan Des 36:30–48. https://doi.org/10.1068/b33129

Campbell DJ (2000) Legitimacy theory or managerial reality construction? Corporate social disclosure in Marks and Spencer Plc corporate reports. Account Forum 24:80–100. https://doi.org/10.1111/1467-6303.00030

Cascio WF (2010) Employment downsizing: causes, costs, and consequences. More than Bricks in the Wall: Organizational Perspectives for Sustainable Success. Gabler, Wiesbaden, pp 87–96

Caulier-Grice J, Davies A, Patrick R, Norman W (2012) Defining social innovation. In: A deliverable of the project: "The theoretical, empirical and policy foundations for building social innovation in Europe"(TEPSIE), European Commission–7th Framework Programme. European Commission, DG Research, Brussels, p 22

Cepeda-Carrion G, Cegarra-Navarro J-G, Cillo V (2019) Tips to use partial least squares structural equation modelling (PLS-SEM) in knowledge management. J Knowl Manag 23:67–89. https://doi.org/10.1108/JKM-05-2018-0322

Ceschin F, Gaziulusoy I (2016) Evolution of design for sustainability: from product design to design for system innovations and transitions. Des Stud 47:118–163. https://doi.org/10.1016/j.destud.2016.09.002

Chaim O, Muschard B, Cazarini E, Rozenfeld H (2018) Insertion of sustainability performance indicators in an industry 4.0 virtual learning environment. Procedia Manuf 21:446–453. https://doi.org/10.1016/j.promfg.2018.02.143

Chatzopoulou E-C, Manolopoulos D, Agapitou V (2022) Corporate social responsibility and employee outcomes: interrelations of external and internal orientations with job satisfaction and organizational commitment. J Bus Ethics 179:795–817. https://doi.org/10.1007/s10551-021-04872-7

Colantonio A (2009) Social sustainability: linking research to policy and practice. Oxf Brookes Univ Head UK

Cor E, Domingo L, Brissaud D, Zwolinski P (2014) A protocol to perform usage oriented ecodesign. CIRP Ann 63:169–172. https://doi.org/10.1016/j.cirp.2014.03.096

D'Souza C, Taghian M, Brouwer AR (2021) Ecolabels information and consumer self-confidence in decision making: a strategic

imperative. J Strateg Mark 29:141–157. https://doi.org/10.1080/0965254X.2019.1636845
Dempsey N, Bramley G, Power S, Brown C (2011) The social dimension of sustainable development: defining urban social sustainability. Sustain Dev 19:289–300. https://doi.org/10.1002/sd.417
Desiana PM, Ma'arif MS, Puspitawati H, et al (2022) Strategy for sustainability of social enterprise in indonesia: a structural equation modeling approach. Sustainability 14:1383. https://doi.org/10.3390/su14031383
Deutz P, McGuire M, Neighbour G (2013) Eco-design practice in the context of a structured design process: an interdisciplinary empirical study of UK manufacturers. J Clean Prod 39:117–128. https://doi.org/10.1016/j.jclepro.2012.08.035
Digalwar AK, Dambhare S, Saraswat S (2020) Social sustainability assessment framework for indian manufacturing industry. Mater Today Proc 28:591–598. https://doi.org/10.1016/j.matpr.2019.12.226
Dočekalová MP, Kocmanová A (2016) Composite indicator for measuring corporate sustainability. Ecol Indic 61:612–623. https://doi.org/10.1016/j.ecolind.2015.10.012
Doloi H (2012) Assessing stakeholders' influence on social performance of infrastructure projects. Facilities 30:531–550. https://doi.org/10.1108/02632771211252351
Eastwood MD, Haapala KR (2015) A unit process model based methodology to assist product sustainability assessment during design for manufacturing. J Clean Prod 108:54–64. https://doi.org/10.1016/j.jclepro.2015.08.105
Eizenberg E, Jabareen Y (2017) Social sustainability: a new conceptual framework. Sustainability 9:68. https://doi.org/10.3390/su9010068
Fatourehchi D, Zarghami E (2020) Social sustainability assessment framework for managing sustainable construction in residential buildings. J Build Eng 32:101761. https://doi.org/10.1016/j.jobe.2020.101761
Figueroa-García EC, García-Machado JJ, Yábar DCPB (2018) Modeling the social factors that determine sustainable consumption behavior in the community of Madrid. Sustain Switz 10. https://doi.org/10.3390/su10082811
Freeman RE (2010) Strategic management: a stakeholder approach. Cambridge University Press
Frey DF, MacNaughton G (2016) A human rights lens on full employment and decent work in the 2030 sustainable development agenda. SAGE Open 6:215824401664958. https://doi.org/10.1177/2158244016649580
Garza-Reyes JA (2015) Green lean and the need for six sigma. Int J Lean Six Sigma 6:226–248. https://doi.org/10.1108/IJLSS-04-2014-0010
Gebisa AW, Lemu HG (2017) Design for manufacturing to design for additive manufacturing: analysis of implications for design optimality and product sustainability. Procedia Manuf 13:724–731. https://doi.org/10.1016/j.promfg.2017.09.120
Goel A, Ganesh LS, Kaur A (2020) Social sustainability considerations in construction project feasibility study: a stakeholder salience perspective. Eng Constr Archit Manag 27:1429–1459. https://doi.org/10.1108/ECAM-06-2019-0319
Golinska P, Kosacka M, Mierzwiak R, Werner-Lewandowska K (2015) Grey decision making as a tool for the classification of the sustainability level of remanufacturing companies. J Clean Prod 105:28–40. https://doi.org/10.1016/j.jclepro.2014.11.040
Greening DW, Turban DB (2000) Corporate social performance as a competitive advantage in attracting a quality workforce. Bus Soc 39:254–280. https://doi.org/10.1177/000765030003900302
Grunert KG (2011) Sustainability in the food sector: a consumer behaviour perspective. Int J Food Syst Dyn 2:207–218. https://doi.org/10.18461/IJFSD.V2I3.232
Gualandris J, Klassen RD, Vachon S, Kalchschmidt M (2015) Sustainable evaluation and verification in supply chains: aligning and leveraging accountability to stakeholders. J Oper Manag 38:1–13. https://doi.org/10.1016/j.jom.2015.06.002
Gupta K, Laubscher RF, Davim JP, Jain NK (2016) Recent developments in sustainable manufacturing of gears: a review. J Clean Prod 112:3320–3330. https://doi.org/10.1016/j.jclepro.2015.09.133
Hajmohammad S, Vachon S (2016) Mitigation, avoidance, or acceptance? Managing supplier sustainability risk. J Supply Chain Manag 52:48–65. https://doi.org/10.1111/jscm.12099
Henao R, Sarache W, Gomez I (2017) Social performance metrics for manufacturing industry. 24th EurOMA Conf 1–10
Holahan CJ, Moos RH (1986) Personality, coping, and family resources in stress resistance. A longitudinal analysis. J Pers Soc Psychol 51:389–395. https://doi.org/10.1037/0022-3514.51.2.389
Holm M (2018) The future shop-floor operators, demands, requirements and interpretations. J Manuf Syst 47:35–42. https://doi.org/10.1016/j.jmsy.2018.03.004
Husgafvel R, Pajunen N, Virtanen K et al (2015) Social sustainability performance indicators – experiences from process industry. Int J Sustain Eng 8:14–25. https://doi.org/10.1080/19397038.2014.898711
Hutchins MJ, Sutherland JW (2008) An exploration of measures of social sustainability and their application to supply chain decisions. J Clean Prod 16:1688–1698. https://doi.org/10.1016/j.jclepro.2008.06.001
Idowu SO, Capaldi N, Zu L, Das Gupta A (2013) Encyclopedia of corporate social responsibility. Springer, Berlin New York
Jenatabadi HS (2015) A tutorial for analyzing structural equation modelling. https://doi.org/10.48550/ARXIV.1504.03430
Jitrawang P, Krairit D (2019) Factors influencing purchase intention of organic rice in Thailand. J Food Prod Mark 25:805–828. https://doi.org/10.1080/10454446.2019.1679690
Jung J, Jeong I, Lee KJ et al (2018) Effects of changes in occupational stress on the depressive symptoms of Korean workers in a large company: a longitudinal survey. Ann Occup Environ Med 30:1–12. https://doi.org/10.1186/s40557-018-0249-5
Kaczorowska J, Rejman K, Halicka E et al (2019) Impact of food sustainability labels on the perceived product value and price expectations of urban consumers. Sustainability 11:7240. https://doi.org/10.3390/su11247240
Kandachar P (2014) Materials and social sustainability. In: Materials Experience. Elsevier, pp 91–103
Karji A, Woldesenbet A, Khanzadi M, Tafazzoli M (2019) Assessment of social sustainability indicators in mass housing construction: a case study of Mehr housing Project. Sustain Cities Soc 50:101697. https://doi.org/10.1016/j.scs.2019.101697
Katsikea E, Theodosiou M, Morgan RE (2015) Why people quit: explaining employee turnover intentions among export sales managers. Int Bus Rev 24:367–379. https://doi.org/10.1016/j.ibusrev.2014.08.009
Khalid AM, Sharma S, Dubey AK (2018) Developing an indicator set for measuring sustainable development in India: Ahmad Mohd Khalid, Seema Sharma and Amlendu Kumar Dubey / Natural Resources Forum. Nat Resour Forum 42:185–200. https://doi.org/10.1111/1477-8947.12151
Klassen RD, Vereecke A (2012) Social issues in supply chains: capabilities link responsibility, risk (opportunity), and performance. Int J Prod Econ 140:103–115. https://doi.org/10.1016/j.ijpe.2012.01.021
Kumar A, Ramesh A (2020) An MCDM framework for assessment of social sustainability indicators of the freight transport industry under uncertainty. A multi-company perspective.

J Enterp Inf Manag 33:1023–1058. https://doi.org/10.1108/JEIM-09-2019-0272
Lami IM, Mecca B (2021) Assessing social sustainability for achieving sustainable architecture. Sustain Switz 13:1–21. https://doi.org/10.3390/su13010142
Lazzarato M, Jordan JD (2014) Signs and machines: capitalism and the production of subjectivity. Semiotext(e), Los Angeles, CA
Li Y, Mathiyazhagan K (2018) Application of DEMATEL approach to identify the influential indicators towards sustainable supply chain adoption in the auto components manufacturing sector. J Clean Prod 172:2931–2941. https://doi.org/10.1016/j.jclepro.2017.11.120
Kauppinen T, Rantanen J (2002) Work and health country profiles and national surveillance indicators in occupational health and safety. Appl Occupat Environ Hygiene 17(9):603-605
Lin CJ, Efranto RY, Santoso MA (2021) Identification of workplace social sustainability indicators related to employee ergonomics perception in Indonesian industry. Sustainability 13:11069. https://doi.org/10.3390/su131911069
Longoni A, Cagliano R (2015) Environmental and social sustainability priorities: their integration in operations strategies. Int J Oper Prod Manag 35:216–245. https://doi.org/10.1108/IJOPM-04-2013-0182
Lucato WC, da Santos JC, S, Pacchini APT, (2017) Measuring the sustainability of a manufacturing process: a conceptual framework. Sustainability 10:81. https://doi.org/10.3390/su10010081
Lučić A (2020) Measuring sustainable marketing orientation-scale development process. Sustain Switz 12:9–11. https://doi.org/10.3390/su12051734
Luo X, Bhattacharya CB (2006) Corporate social responsibility, customer satisfaction, and market value. J Mark 70:1–18. https://doi.org/10.1509/jmkg.70.4.001
Madan Shankar K, Kannan D, Udhaya Kumar P (2017) Analyzing sustainable manufacturing practices – a case study in Indian context. J Clean Prod 164:1332–1343. https://doi.org/10.1016/j.jclepro.2017.05.097
Mani V, Agrawal R, Sharma V (2014) Supplier selection using social sustainability: AHP based approach in India. Int Strateg Manag Rev 2:98–112. https://doi.org/10.1016/j.ism.2014.10.003
Mani V, Agarwal R, Gunasekaran A et al (2016) Social sustainability in the supply chain: construct development and measurement validation. Ecol Indic 71:270–279. https://doi.org/10.1016/j.ecolind.2016.07.007
Mani V, Jabbour CJC, Mani KTN (2020) Supply chain social sustainability in small and medium manufacturing enterprises and firms' performance: empirical evidence from an emerging Asian economy. Int J Prod Econ 227:107656. https://doi.org/10.1016/j.ijpe.2020.107656
Mendes L, Machado J (2015) Employees' skills, manufacturing flexibility and performance: a structural equation modelling applied to the automotive industry. Int J Prod Res 53:4087–4101. https://doi.org/10.1080/00207543.2014.993772
Mohr LA, Webb DJ (2005) The effects of corporate social responsibility and price on consumer responses. J Consum Aff 39:121–147. https://doi.org/10.1111/j.1745-6606.2005.00006.x
Moldan B, Janoušková S, Hák T (2012) How to understand and measure environmental sustainability: indicators and targets. Ecol Indic 17:4–13. https://doi.org/10.1016/j.ecolind.2011.04.033
Moreira S, Vasconcelos L, Silva Santos C (2018) Occupational health indicators: exploring the social and decent work dimensions of green jobs in Portugal. Work 61:189–209. https://doi.org/10.3233/WOR-182792
Murphy M, Eadie R (2019) Socially responsible procurement: a service innovation for generating employment in construction. Built Environ Proj Asset Manag 9:138–152. https://doi.org/10.1108/BEPAM-02-2018-0049
Olakitan Atanda J (2019) Developing a social sustainability assessment framework. Sustain Cities Soc 44:237–252. https://doi.org/10.1016/j.scs.2018.09.023
Ozhan S, Ozhan E, Pritchard GY (2022) The analysis of corporate social responsibility, identification and customer orientation by structural equation modelling and artificial intelligence. Vis J Bus Perspect 26:382–394. https://doi.org/10.1177/09722629211043956
Pang Q, Fang M, Wang L, Mi K, Su M (2023) Increasing couriers' job satisfaction through social-sustainability practices: perceived fairness and psychological-safety perspectives. Behav Sci 13(2):125
Peralta Álvarez ME, Marcos Bárcena M, Aguayo González F (2017) On the sustainability of machining processes. Proposal for a unified framework through the triple bottom-line from an understanding review. J Clean Prod 142:3890–3904. https://doi.org/10.1016/j.jclepro.2016.10.071
Pinto LFR, de Venturini G, FP, Digiesi S, et al (2020) Sustainability assessment in manufacturing under a strong sustainability perspective—an ecological neutrality initiative. Sustainability 12:9232. https://doi.org/10.3390/su12219232
Podgórski D (2015) Measuring operational performance of OSH management system – a demonstration of AHP-based selection of leading key performance indicators. Saf Sci 73:146–166. https://doi.org/10.1016/j.ssci.2014.11.018
Popescu RGh, Popescu (2019) An exploratory study based on a questionnaire concerning green and sustainable finance, corporate social responsibility, and performance: evidence from the romanian business environment. J Risk Financ Manag 12:162. https://doi.org/10.3390/jrfm12040162
Popovic T, Barbosa-Póvoa A, Kraslawski A, Carvalho A (2018) Quantitative indicators for social sustainability assessment of supply chains. J Clean Prod 180:748–768. https://doi.org/10.1016/j.jclepro.2018.01.142
Prieto L, Amin MR, Canatay A (2022) Examining social sustainability in organizations. Sustainability 14:12111. https://doi.org/10.3390/su141912111
Rai SS, Rai S, Singh NK (2021) Organizational resilience and social-economic sustainability: COVID-19 perspective. Environ Dev Sustain. https://doi.org/10.1007/s10668-020-01154-6
Razmjoo A, Khalili N, Majidi Nezhad M et al (2020) The main role of energy sustainability indicators on the water management. Model Earth Syst Environ 6:1419–1426. https://doi.org/10.1007/s40808-020-00758-1
Reyna-Castillo M, Vera Martínez PS, Farah-Simón L, Simón N (2023) Social sustainability orientation and supply chain performance in Mexico, Colombia and Chile: a social-resource-based view (SRBV). Sustainability 15(4):3751
Richter NF, Cepeda G, Roldán JL, Ringle CM (2015) European management research using Partial Least Squares Structural Equation Modeling (PLS-SEM). Eur Manag J 33:1–3. https://doi.org/10.1016/j.emj.2014.12.001
Rudikoff N (2018) Chapter 8. Walmart's human traffi cking problem: the shrimp supply chain in Thailand. In: Bank Muñoz C, Kenny B, Stecher A (eds) Walmart in the Global South. University of Texas Press, pp 222–241
Sarkar A, Qian L, Peau AK (2020) Structural equation modeling for three aspects of green business practices: a case study of Bangladeshi RMG's industry. Environ Sci Pollut Res 27:35750–35768. https://doi.org/10.1007/s11356-020-09873-z
Schroeder P, Anggraeni K, Weber U (2019) The relevance of circular economy practices to the sustainable development goals. J Ind Ecol 23:77–95. https://doi.org/10.1111/jiec.12732
Seo HC, Lee YS, Kim JJ, Jee NY (2015) Analyzing safety behaviors of temporary construction workers using structural equation modeling. Saf Sci 77:160–168. https://doi.org/10.1016/j.ssci.2015.03.010

Shao J, Taisch M, Mier MO (2017) Influencing factors to facilitate sustainable consumption: from the experts' viewpoints. J Clean Prod 142:203–216. https://doi.org/10.1016/j.jclepro.2015.12.111

Shirazi MR, Keivani R (2017) Critical reflections on the theory and practice of social sustainability in the built environment – a meta-analysis. Local Environ 22:1526–1545. https://doi.org/10.1080/13549839.2017.1379476

Simmons CJ, Becker-Olsen KL (2006) Achieving marketing objectives through social sponsorships. J Mark 70:154–169. https://doi.org/10.1509/jmkg.70.4.154

Simoes M, Freitas CL, Barbosa-Póvoa AP, Carvalho A (2016) Social life cycle assessment – a framework for mid- and end-point impact categories. Working-paper. CEG-IST Inst Super Tècnico Tech Univ Lisbon Port

Singh K, Misra M (2021) Linking corporate social responsibility (CSR) and organizational performance: the moderating effect of corporate reputation. Eur Res Manag Bus Econ 27:100139. https://doi.org/10.1016/j.iedeen.2020.100139

SinghSushil A (2021) Integrated approach for finding the causal effect of waste management over sustainability in the organization. Benchmarking Int J 28:3040–3073. https://doi.org/10.1108/BIJ-08-2020-0419

Sodhi MS (2015) Conceptualizing social responsibility in operations via stakeholder resource-based view. Prod Oper Manag n/a-n/a. https://doi.org/10.1111/poms.12393

Sudusinghe JI, Seuring S (2020) Social sustainability empowering the economic sustainability in the global apparel supply chain. Sustainability 12:2595. https://doi.org/10.3390/su12072595

Tafere GA, Beyera GK, Wami SD (2020) The effect of organizational and individual factors on health and safety practices: results from a cross-sectional study among manufacturing industrial workers. J Public Health Ger 28:173–179. https://doi.org/10.1007/s10389-019-01050-y

Torkayesh AE, Ecer F, Pamucar D, Karamaşa Ç (2021) Comparative assessment of social sustainability performance: integrated data-driven weighting system and CoCoSo model. Sustain Cities Soc 71:102975. https://doi.org/10.1016/j.scs.2021.102975

Toussaint M, Cabanelas P, González-Alvarado TE (2021) What about the consumer choice? The influence of social sustainability on consumer's purchasing behavior in the food value chain. Eur Res Manag Bus Econ 27:100134. https://doi.org/10.1016/j.iedeen.2020.100134

Uma SN (2013) A study on training importance for employees of their successful performance in the organization. Int J Sci Res 2(11):137–140

United Nations (2015) The United Nations. Sustainable development knowledge platform. Transforming our world: the 2030 agenda for sustainable development. https://sustainabledevelopment.un.org/. Accessed 22 Nov 2022

Veleva V, Ellenbecker M (2001) Indicators of sustainable production: framework and methodology. J Clean Prod 9:519–549. https://doi.org/10.1016/S0959-6526(01)00010-5

Venkataraman S (2004) Regional transformation through technological entrepreneurship. J Bus Ventur 19:153–167. https://doi.org/10.1016/j.jbusvent.2003.04.001

Vinodh S, Joy D (2012) Structural equation modeling of sustainable manufacturing practices. Clean Technol Environ Policy 14:79–84. https://doi.org/10.1007/s10098-011-0379-8

Wan L, Ng E (2018) Evaluation of the social dimension of sustainability in the built environment in poor rural areas of China. Archit Sci Rev 61:319–326. https://doi.org/10.1080/00038628.2018.1505595

Wu Y, Su D (2020) Social life cycle assessment. Sustainable Product Development. Springer International Publishing, Cham, pp 127–152

Zhang X, Mohandes SR (2020) Occupational Health and Safety in green building construction projects: a holistic Z-numbers-based risk management framework. J Clean Prod 275:122788. https://doi.org/10.1016/j.jclepro.2020.122788

Zhou G, Hu W, Huang W (2016) Are consumers willing to pay more for sustainable products? A study of eco-labeled tuna steak. Sustainability 8:494. https://doi.org/10.3390/su8050494

Zohar D (2000) A group-level model of safety climate: testing the effect of group climate on microaccidents in manufacturing jobs. J Appl Psychol 85:587–596. https://doi.org/10.1037/0021-9010.85.4.587

Zu B, Li Z, Zhao Y, Li C (2014) A dynamic model for corporate social responsibility: a case study of Chinese major coal producers. J Appl Sci 14:2109–2118. https://doi.org/10.3923/jas.2014.2109.2118

Publisher's Note Springer Nature remains neutral with regard to jurisdictional claims in published maps and institutional affiliations.

Springer Nature or its licensor (e.g. a society or other partner) holds exclusive rights to this article under a publishing agreement with the author(s) or other rightsholder(s); author self-archiving of the accepted manuscript version of this article is solely governed by the terms of such publishing agreement and applicable law.

Wireless Personal Communications
https://doi.org/10.1007/s11277-023-10385-5

Energy Efficient Cluster-Based Routing Protocol for WSN Using Nature Inspired Algorithm

Rashmi Mishra[1] · **Rajesh K. Yadav**[1]

Accepted: 21 March 2023
© The Author(s), under exclusive licence to Springer Science+Business Media, LLC, part of Springer Nature 2023

Abstract
WSN consist of tiny sensors that are distributed over the entire network and have the capability of sensing the data, processing it, and conveying it from one node to another. The purpose of the study is to minimize the power utilization per round and elevate the network lifespan. In the present case, nature-inspired mechanisms are used to minimize the power utilization of the network. In the proposed study, the Butterfly Optimization Algorithm (BOA) is used to choose the optimal quantity of cluster heads from the dense nodes (available nodes). The parameters to be considered for the choice of the cluster head are: the remaining power of the node; distance from the other nodes in the network; distance from the base station; node centrality; and node degree. The particle swarm optimization (PSO) is used to form the cluster head by choosing certain parameters, such as distance from the cluster head and the BS. The path is chosen by means of the Ant Colony Optimization (ACO) Mechanism. The route is optimized by the distance, node degree, and the chosen remaining power. The inclusive performance of the projected protocol is measured in terms of stability period, quantity of active nodes, data acknowledged by the base station, and overall power utilization of the network. The results of the put redirect methodology are correlated with the extant mechanisms such as LEACH, DEEC, DDEEC, and EDEEC (Khan et al. in World Appl Sci J, 2013; Arora and Singh in Soft Comput 23:715–734, 2019; Saini and Sharma in 2010 First international conference on parallel, distributed and grid computing (PDGC 2010), 2010; Elbhiri et al. in 2010 5th International symposium on I/V communications and mobile network, 2010) and correlated with the swarm mechanisms such as CRHS, BERA, FUCHAR, ALOC, CPSO, and FLION. This review will help investigators discover the applications in this arena.

Keywords Wireless sensor networks · Energy efficiency · Throughput · Delay · Nature inspired algorithm

Abbreviations

WSN	Wireless sensor network
BOA	Butterfly optimization algorithm
ACO	Ant colony optimization

✉ Rashmi Mishra
dtuphd.rashmi@gmail.com

[1] Delhi Technological University, Delhi, India

Published online: 05 April 2023

PSO	Particle swarm optimization
BS	Base station
CH	Cluster head
LEACH	Low energy adaptive clustering hierarchy protocol
DEEC	Distributed energy efficient clustering
DDEEC	Developed distributed energy efficient clustering
SEP	Stable election protocol
EDEEC	Enhanced distributed energy-efficient clustering
CRHS	Clustering and routing harmony search
BERA	Biogeography-based energy saving routing architecture
ALOC	Ant lion optimization for clustering
CPSO	Cellular automata (CA) and particle swarm optimization (PSO)
FLION	Fractional lion (FLION) clustering algorithm
WECRR	Weighted power-efficient clustering with robust routing
WPO-EECRP	Energy-efficient clustering routing protocol based on weighting and parameter optimization

1 Introduction

Concerned about the longevity of wireless sensor networks, nature-inspired mechanisms are emerging as a viable solution. For increasing the lifespan of the network or in order to decrease the sensing of unnecessary data by the battery-driven sensors, optimizing the scope of the network plays an important role. Many geographically distributed sensors communicated wirelessly to sense and store actual data from nature are formally known as "wireless sensor networks" (WSNs) [1]. Sensors are operating like repeaters, as they will accept the data, convert the analogue to digital form, and redirect the data to the other nodes, cluster head, and sink. The base station will collect the data, analyse it, and take a decision as per the application. There are various parameters on which wireless sensor network architecture depends, such as fault tolerance (sensor nodes will redirect the packet and acknowledge the packet if some of the sensors get drained), scalability (how the network will work if sensors are added or removed), stability, and power efficiency. These sensors are battery-powered. So, after some time, the power of the sensors will get depleted, and it will affect the entire lifespan of the network. The purpose of the study is to maximize the network lifespan by increasing the quantity of nodes per round, the amount of data sent to the BS, and the optimal quantity of cluster heads. In the extant case, optimal network scope, clustering mechanisms, and path choosing are mostly used in wireless sensor networks to elevate the lifespan of the network.

WSN consist of tiny sensors that are distributed over the entire network and have the capability of sensing the data, processing it, and conveying it from one node to another. These sensors sense the nature, evaluate it, send it, and accept it. Military, weather forecasting, industrial areas, medical services, agriculture, or many other applications use the WSN for data transmission. Sensors are limited, battery-powered, and very compact in size. Once sensors are placed in the harsh and unforgiving nature, these sensors will be used in an adequate way because they cannot be replaced or charged. Nodes drain their power in two ways, such as by sensing the natural data and conveying the data to the base station [2–10]. Most of the work has been done to maximize the entire lifespan of the network by saving the power of the sensors. Liank et al. [11] redirected the Huang mechanism, which aims

to balance power utilization in the entire network by using optimal clustering throughout the network. But the restriction of this mechanism is that it is very complex, and if the data size of the packet is large, then it may block the channel. In contract, Cardei et al. [12] have put forward the redirect TianD mechanism, in which sensor nodes are arranged in disjoint set form to cover the maximal range. As compared to the Hunag mechanism, the TianD mechanism is less complex in nature. However, the mechanism will not be able to find the duplicate nodes and data in nature.

2 Literature Survey

The challenges faced by the wireless sensor network are power constraints, correct detection of data, and non-duplicate data. The sensors need to be placed in such a way that they are in appropriate interspace from each other while considering the uncovered area, which leads to the "scope hole" or "blind area" problem. For the above-stated problem, Wang et al. [13] have put in place a mechanism named the "Scope Configuration Protocol." The protocol is well suited for natural settings where the number of sensors is small or significant. After the literature survey, two problems have been observed, i.e., power depletion of the sensors and the sensor node scope problem, and there is back-and-forth between these two problems. Authors in the literature may have proposed solutions to individual problems but not to collective ones. After the survey, keeping the existing problems in mind, we collectively considered the problem and put in place the multi-purpose optimization mechanism. There are various mechanisms published in the literature for the wireless sensor network that use nature-inspired mechanisms [14–18]. There are multiple mechanisms put in place by the authors to cover the optimal scope of the wireless sensor network [19–21]. In Ref. [19], Metaheuristics for the deployment problem of wireless sensor networks: a review, the authors discuss the various types of issues while deploying the sensors in nature by using nature-inspired mechanisms. In Ref. [20], "Optimal sensor network layout using multi-purpose metaheuristics," the author equated the three protocols and highlighted the problems associated with mechanisms in terms of optimal scope. In Ref. [21], Transmutative intelligence in wireless sensor networks: routing, clustering, lateralization, and scope, we discussed the genetic, transmutative, theoretical, mathematical, and practical applications of cluster formation, the optimal scope of the network, and the lateralization problem in wireless sensor networks. Other challenges faced by the wireless sensor network include the insufficient power of the sensors, which leads to network failure [14–17].

So, the main dissimilarity between the wireless sensor network and the other network is that the wireless sensor network is oversensitive and vulnerable to power. So, the optimal utilization of power mechanisms is a necessity for the wireless sensor network [20]. Nature-inspired mechanisms are best suited for cluster formation, and choosing the best path will elevate the life of sensors, along which we can elevate the entire lifespan, stability period, and scalability of the network [21–23]. A cluster has a cluster head who communicates with the other cluster heads in the network. Most of the power is consumed when the data is transferred between the cluster heads and the base station. To turn down the power utilization in the clustered wireless sensor network, a routing mechanism is used between the cluster heads and the base station [24–27]. However, none of the mechanisms deliver serious effects on the problem in the wireless sensor network to cover the optimal solution. The purpose of the paper is to reduce the power utilization of the network during the transmission of data through a literature survey

of recent clustering and routing mechanisms. We have also briefed the nature-inspired mechanisms and their applications used in the wireless sensor networks in terms of capacity, robustness, and self-adaptability. We have also discussed the strengths and weaknesses of the work done by the different researchers in Sect. 3. The optimization mechanism is segregated into three types: model-based, simulator-based, and mechanism-based. Mechanism-based is further bifurcated into two parts, such as deterministic and stochastic mechanisms. The stochastic mechanism is further classified as heuristics and meta-heuristics. The meta-heuristic mechanism is further bifurcated into four parts, i.e. human-inspired, geography-inspired, physics-inspired, and bio-inspired. The bio-inspired mechanism is further bifurcated into three parts: transmutative, swarm-based, and plant-based [28–30]. Furthermore, there are more than thirty swarm-based optimizations that have been put in place by the researchers. The swarm-based mechanism is used in wireless sensor networks to resolve many existing problems, such as upgrading the power efficiency of the network, elevating the network lifespan, and maximizing the packet delivery ratio in the network. The conventional routing protocols are inefficient for upgrading the power constraints of the wireless sensor network. So, to upgrade the power constraint of the network, researchers used efficient clustering and routing protocols using a swarm-based approach. As per the research, the ant colony optimization [31] is used to upgrade the power efficiency of the network and is one of the efficient mechanisms for routing. Figure 1 depicts a review chronology of the research. The review is based on the publication of a paper in the fields of power efficiency, security-based delay, error-free protocol, and cluster-based computing. The majority of the paper was based on the cluster formation and the power efficiency upgrade of the network [32–37].

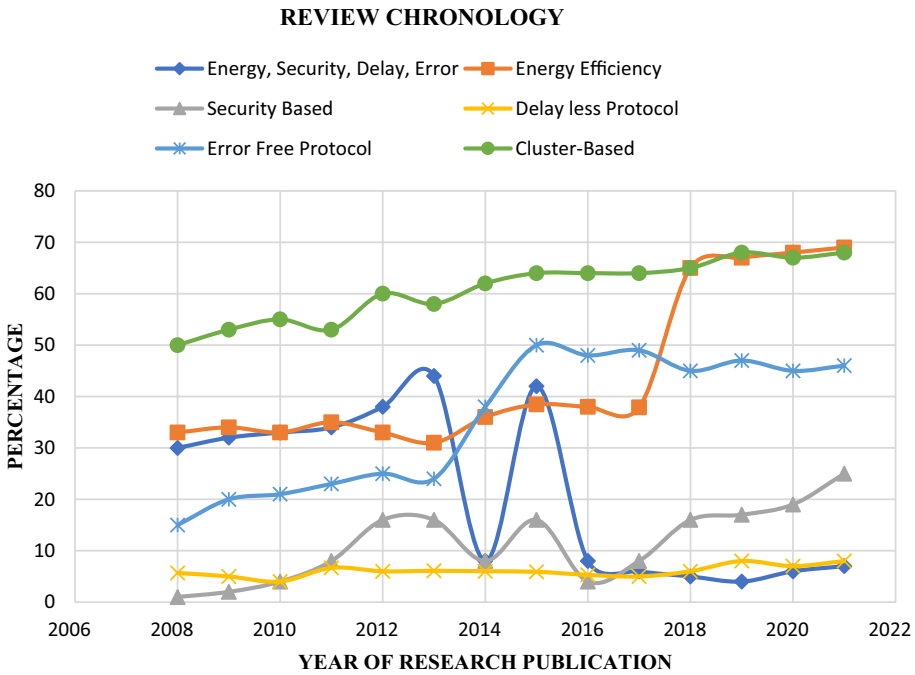


Fig. 1 Review chronology

2.1 Classical Approaches

In 2002, LEACH was habituated by W. Heinzelman, and the sensors chose their cluster head and formed a cluster. The Cluster Head gathers all data from the nodes and sends it to the BS.The elected cluster head will lose their power very fast. In 2017, Wang et al. put forward a mechanism named LEACH-impt [38]. If LEACH-impt, communication takes the inter-cluster routing path.The route is chosen based on the quantity of hops per path, the path's remaining power, and the power utilization per round. The overall performance of LEACH-impt in terms of power efficiency has been upgraded, but due to the arbitrarily chosen cluster head and changes in topology, the data loss is high.

Haseeb et al. put in place a mechanism named the WECRR (Weighted Power-Efficient Clustering with Robust Routing) protocol. In WECRR [39], the cluster head chooses based on a deterministic strategy. Secondly, the routing decision is taken based on multiple factors, such as traffic density, remaining power, and packet error ratio. Furthermore, the route maintenance and load distribution among the nodes are improved by the protocol. But the restriction of the put redirect mechanism is that the interspace between the node and the base station is not considered by the protocol. Again, Haseeb et al. have put in place a mechanism named AECR (Aware Cluster Based Routing) [40]. The cluster head is chosen based on the node density and the position of the node. The mechanism's benefits include lower cluster overhead and communication costs, as well as a focus on node power. The disadvantage of the mechanism is that it does not focus on the interspace between the nodes [31].

Hang and Zhang established the WPO-EECRP mechanism [39]. In this protocol, the cluster head chooses based on remaining power, interspacing from the node, interspacing from the node to the base station, and the cluster density. The mechanism works well when there is an adjacent quantity of nodes present in between the cluster head and base station, and it will elevate the power utilization of the network.

2.2 Optimizations in WSNs Using Swarm Intelligence

An optimization is achieved by designing a model, using a simulation, and designing a mechanism. A detailed taxonomy of the swarm-based optimization used in wireless sensor networks is shown in Fig. 2. The swarm-based mechanism is bifurcated into two parts: local search (deterministic) and global search (stochastic). Local search provides the theoretical assumptions about the formulated problems and provides the analytical properties [41, 42]. Guarantee of reaching the global minimum and at least a local minimum, whereas global search provides the guarantee in terms of probability. However, global search is much faster than local search. Additionally, the global search method is further classified into two parts: heuristic mechanisms (problem-dependent mechanisms) and meta-heuristic mechanisms (problem-independent mechanisms). Both mechanisms are used to speed up the process of finding the global optimum solution when finding the solution is difficult. Because the heuristic mechanisms are based on an adaptive and greedy approach, they are more likely to get stuck at local optima, which results in failing to obtain global optima [38]. However, meta-heuristics are non-adaptive and non-greedy approaches that can find a global solution. The meta-heuristic mechanism is also known as a nature-inspired mechanism. The nature-inspired mechanism is further divided into four parts: bio-inspired, physics-inspired, geography-inspired, and human-inspired [43–50]. The bio-inspired



Fig. 2 Taxonomy of the swarm-based optimization

mechanism is divided into three parts: transmutative, swarm-based, and plant-based. Because nature inspired the mechanisms, most of the mechanisms are inspired by the biological system. Therefore, most of the parts of the nature-inspired mechanisms are based on the bio-inspired mechanism. The transmutative mechanism is based on Darwin's principle of choice, whereas the swarm is based on collective intelligence [51].

As per the research, the most popular mechanism used for the cluster head choice is the butterfly optimization mechanism; for the cluster formation, the particle swarm optimization mechanism is popular; and for the efficient route choice, the ant colony optimization mechanism is used by the researchers to upgrade the power efficiency of the wireless sensor network [52]. The ant colony optimization mechanism works with other popular mechanisms to upgrade the power efficiency of the network, such as fuzzy logic

[53]. Xie et al. [54] put in place a mechanism based on ant colony optimization for wireless sensor networks named the Type-2 Mamdnai Fuzzy Logic System. The route between the cluster heads is determined by ant colony optimization, and the cluster heads are determined by remaining power, interspace to the base station, and the number of nearest nodes. The cluster heads choose all the statistics from the nodes and send them to the base station. Arjunan and Sujatha put in a redirect mechanism based on fuzzy logic to develop the inadequate clusters, and the routes were chosen using the Ant Colony Optimization technique. The cluster heads are choosing based on remaining power, node degree, interspace from the base station, node centrality, and interspace from the nearest nodes [55]. The mechanism is well suited to maintain the lifespan of the network [56]. Many researchers use Ant Colony Optimization, Particle Swarm Optimization, and Butterfly Optimization Algorithm to optimize existing problems in wireless sensor networks, such as optimal route choosing, optimal quantity of cluster heads choosing per round, optimal quantity of nodes choosing per round, and elevating the packet transmission between the cluster head and the base station [57, 58].

3 WSN and Optimizations

The main issues related to the wireless sensor network are categorized into three main sections, such as power efficiency, quality of service, and security. The optimization mechanisms are used in wireless sensor networks to solve the existing problems, i.e., optimal scope of the sensors, data aggregation, power-efficient clustering and routing, and sensor lateralization. There is a correlation between all the stated problems, such as if we go for service quality, we must trade off the lifespan of the network. The same is true for security; in order to achieve security, we must once again trade off network lifespan. If we approach the problem piecemeal, many gaps will remain, and the problem will never be solved. So, to discover a balanced wireless sensor network, we must build an optimized mechanism that can handle all the problems simultaneously. The solution to the problem is to create a multi-purpose function and optimize the mechanism by using an appropriate optimizer mechanism. For choosing the appropriate mechanisms, various factors have been considered, such as problem type, time constraint, availability of resources, and accuracy desired. To achieve better network performance, the researchers have used many approaches in nature-inspired mechanisms, such as classical approaches [31, 38, 43–45] and swarm intelligence-based approaches [46–51, 53–55, 57, 59]. There are various types of mechanisms present in the literature focused on the different types of problems faced by wireless sensor networks, named optimal scope, data aggregation, power-efficient clustering, power-efficient routing mechanisms, and sensor lateralization [60, 61]. Table 1 provides a detailed examination of the existing mechanism in terms of parameters such as power efficiency, latency, scalability, connectivity, load balancing, packet loss ratio, reliability, and complexity.

3.1 Optimal Scope in WSN

Optimal the scope of sensors in the wireless sensor network is an essential part of the network to elevate the network's lifespan. Scope of the area in such a way that it targets the entire area with a minimum quantity of secondary nodes. The key parameter in choosing the area is the shape of the test area. There are various shapes available in the existing

Table 1 Survey of the extant mechanism with various parameters

S. No.	Mechanism	Abb.	Authors	Year	Best For	Power Efficiency	Latency	Throughput	Scalability	Connectivity	Load Balancing	Packet loss rate	Reliability	Complexity
1	Ant Colony Optimization	ACO	Dorigo	1992	Path choosing, routing	H	S	H	H	M	M	M	M	M
2	Particle Swarm Mechanism	PSO	Kennedy and Eberhart	1995	Cluster, path choosing, gives optimum results in less parameters	L	S	M	H	N/A	S	H	M	S
3	Artificial Fist Swarm Mechanism	AFSA	Li et al	2002	Cluster formation	L	M	S	H	M	M	H	M	M
4	Bacterial Foraging Optimization Mechanism	BFOA	Passion	2002	CH choosing, routing	M	M	S	M	M	S	S	M	M
5	Glowworm Swarm Optimization	GWO	Krishnanad and Ghose	2005	Path choosing, routing	H	S	S	M	M	M	M	S	M

Table 1 (continued)

S. No.	Mechanism	Abb.	Authors	Year	Best For	Power Efficiency	Latency	Throughput	Scalability	Connectivity	Load Balancing	Packet loss rate	Reliability	Complexity
6	Cat Swarm Optimization	CSA	Chu et al	2006	Find best location for the near sink node, choose CH, Perform well with K-mean Clustering	L	M	M	M	S	M	M	S	M
7	Artificial Bee Colony	ABC	Karaboga and Basturk	2007	Cluster formation, CH choosing	M	S	M	M	M	S	M	L	M
8	Cuckoo Search	CS	Yang and Deb	2009	Cluster formation, CH choosing	M	S	M	M	M	S	S	M	S
9	Bat Mechanism	BA	Yang	2010	Node lateralization	M	S	M	M	M	M	M	M	M
10	Firefly Mechanism	FA	Yang	2010	Clustering, Node lateralization	M	S	M	M	M	S	M	S	M
11	Krill Herd Mechanism	KH	Gandomi and Alavi	2012	Finding the interspace	L	S	S	M	S	M	M	M	M

Table 1 (continued)

S. No.	Mechanism	Abb.	Authors	Year	Best For	Power Efficiency	Latency	Throughput	Scalability	Connectivity	Load Balancing	Packet loss rate	Reliability	Complexity
12	Dolphin Enholocation	DE	Kaveh and Farhoudi	2013	CH choosing, Security needs to be considered	M	S	M	M	M	M	M	M	H
13	Chicken Swarm Optimization	CSO	Meng et al	2014	CH choosing	M	M	S	H	M	S	M	M	M
14	Grey Wolf Optimizer	GWO	Mirjalili et al	2014	Network scope optimization, CH choosing	H	M	M	H	M	M	M	M	H
15	Ant Lion Optimizer	ALO	Mirjalili	2015	Scope, connection, the network-longevity and minimized power utilization	H	M	M	M	M	M	M	M	H
16	Dragonfly Mechanism	DA	Mirjalili	2015	lateralizationproblem	L	S	M	M	M	M	M	M	M

Table 1 (continued)

S. No.	Mechanism	Abb.	Authors	Year	Best For	Power Efficiency	Latency	Throughput	Scalability	Connectivity	Load Balancing	Packet loss rate	Reliability	Complexity
17	Whale Optimization Mechanism	WOA	Mirjalili and Lewis	2016	CH choosing	M	S	M	M	M	M	M	M	M
18	Crow Search Mechanism	CSA	Lalireza Askarzadeh	2016	CH choosing, work with few parameters	H	S	M	M	M	M	M	S	S
19	Grasshopper Optimization Mechanism	GOA	Saremi et al	2017	Network lifespan, end-to-end delay, best with ABC	M	S	M	M	M	M	M	M	M
20	Butterfly-inspired Mechanism	BOA	Qi et al	2017	Node lateralisation, cluster formation	S	M	M	M	S	S	S	M	M
21	Salp Swarm Mechanism	SSA	Mirjalili et al	2017	Node lateralisation	S	M	M	M	S	S	S	S	M
22	Equilibrium Optimizer	EO	Faramarzi et al	2019	Routing, load balancing, clustering	M	M	H	M	M	M	M	M	H

Table 1 (continued)

S. No.	Mechanism	Abb.	Authors	Year	Best For	Power Efficiency	Latency	Throughput	Scalability	Connectivity	Load Balancing	Packet loss rate	Reliability	Complexity
23	Bald Eagle Search	BES	Alsattar et al	2019	Latest technology, literature not available									
24	Harris Hawks Optimization	HHO	Heidari et al	2019										
25	Nuclear Reaction Optimization	NRO	Wei et al	2019										
26	Border Collie Optimization	BCO	Dutta et al	2020										

literature, such as irregular, solid, hexagonal, or circular. In the figure, we show the four two-dimensional geometrical-based sensing shapes [62–65]. In the present case, the outline of the test area is uneven and multifaceted due to territory properties and its solid shape. However, the hexagonal or circular shape is used for its computational and conceptual ease. The hexagonal shape is commonly used by researchers and industry experts due to its flexibility and overlapping properties. Though the circular shape is more prominent because of its low complexity, the restriction is compensated by increasing the radius of the circle. Another issue arises as a result of the increase in the radius of the circle: duplicate data sensed by the sensor. As more duplicate data is sensed by the sensor, there will be more power utilization [66–68]. We can turn down the problem by enhancing the single-purpose optimization problem into a multi-purpose problem by choosing the other parameters.

3.2 Power Efficient Clustering and Routing in Wireless Sensor Network

Because wireless sensor networks are made up of sensors that have built-in batteries for a limited time, these batteries cannot be recharged, so the need for power-efficient networks is of the utmost importance in the present case [69]. The sensors dissipate their power by sensing the data from nature and sending it to the base station using multi-hop communication. For reducing the power utilization of the nodes, first clusters are formed, then cluster heads are chosen based on the remaining power, and thirdly, the path is chosen for the data transmission using optimum routing techniques.

In the given domain, the problem faced by the networks are:

- The choosing of the cluster head having high power and choosing of routing path from each round.
- Maximization of network lifespan and packet delivery ratio to the base station.
- Interspace from the sensor node to the cluster head and cluster head to the base station should be minimized.

4 Problem Statement

The problems faced by the wireless sensor network are: finding the appropriate purpose function to preserve or create a power-efficient network; Weighted power-efficient clustering with robust routing for wireless sensor networks [70] and aware cluster-based routing [40] are implemented to conserve power. The overall power of the network is preserved by considering both power and interspace. The number of member nodes in the cluster head influences the lifespan of clustering and routing in wireless sensor networks using the harmony search mechanism [71]. In an energy-efficient clustering routing protocol [39] based on parameter optimization in WSN, the information communication from the cluster head to the base station also affects the network lifespan. The proactive and reactive mechanisms of ant colony optimization cause packet loss. The solution is to design a mechanism centered on the node's power and the interspace between the node and the cluster head, as well as the cluster head and the base station. The best path will be implemented by multi-purpose functions. And the packet drop ratio is minimized by considering the power of each node. The remaining power and interspacing from the node to the cluster head, as

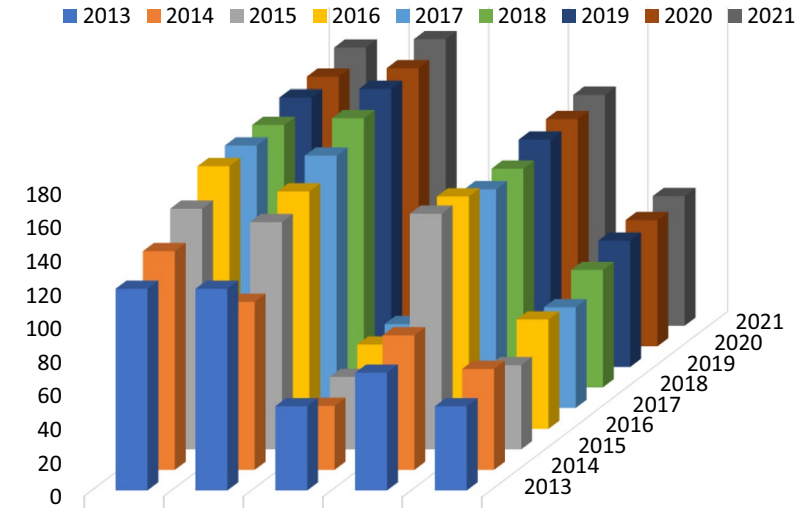
well as the interspacing from the cluster head to the base station, must be considered when creating the purpose function. As a result, it will work in both a small and large network.

4.1 Preliminaries

This section describes the network and power model as well as describe the PSO (Particle Swarm Optimization) is used to formulate the clusters, BOA (Butterfly Optimization Algorithm) technique for finding the cluster head, ACO (Ant Colony Optimization) technique for finding the route from the source to the sink (Fig. 3).

4.1.1 Network Model

- Sensors are arbitrarily deployed in the network, later they are constant in nature.
- BS receives the data such as remaining power of the node, interspace from the sensors from all the sensors in the nature.
- To configure the network model of wireless sensor network, all the knob are comparable to each other in terms of original energy and the dispensation period.



	PSO	ACO	FA	BOA	ABC
2013	120	120	50	70	50
2014	130	100	38	80	60
2015	143	135	43	140	50
2016	156	141	50	138	65
2017	156	150	50	130	60
2018	156	160	50	130	70
2019	160	165	50	135	75
2020	160	165	50	135	75
2021	165	170	52	137	77

Fig. 3 Trends of the mechanism

- The interspace amongst the sensor knob to the Cluster Head and from Cluster Head to the base station is intended grounded on the Euclidean interspace.
- Clusters are formed using Cluster formation mechanism, then cluster heads are chooses using choosing mechanism. Then the routing mechanism is used to find the route from source to the sink.

4.1.2 Energy Model

Given in the research, an elementary radio model (1st order) is measured to compute the power of the nodes. For conveying the l bits from the source to the sink over the interspace d is calculated by using the Eqs. 1 and 2 respectively:

$$E_{TX}(l,d) = \begin{cases} LE_{elec} + LEfsd^2 if\ d < do \\ LE_{elec} + LEmpd^4 if\ d \geq do \end{cases} \tag{1}$$

where LE_{elec} is the power used to run the converter (ETX) or (ERX) and the threshold value is d_0. For the experimental survey, free space and multi-path models is expressed as E_{fs} and E_{mp}. These values are depended on the converter amplifier model. Where d0 is expressed as

$$d_0 = \sqrt{\frac{E_{fs}}{E_{mp}}} \tag{2}$$

5 Proposed Method

The put redirect model has three mechanisms: the first is used to form clusters; the second is used to choose the cluster head by considering the remaining power and the interspace from the sensors; and the third is used to find the path or route over the entire network. The particle swarm optimization is used to form the cluster, the butterfly optimization algorithm is used to find the optimum quantity of cluster heads in each round, and ant colony optimization is used to find the route from the source to the sink or from the cluster head to the base station. The entire process is described in Fig. 4.

5.1 CH Choosing Using BOA (Butterfly Optimization Algorithm)

BOA (Butterfly Optimization Mechanism) is introduced in 2019 by Sankalap Arora [72]. The mechanism shows the butterfly's food search and it's mating behavior. In general, butterflies are fascinating to everyone, along with a host of other apprehensions. The butterfly's crusade is also conducted haphazardly or in the manner of the other butterflies, who produce the stronger cologne. The purpose function is used to compute the inducement strength. The butterfly optimization mechanism chooses the ideal quantity of cluster heads using certain parameters: node notch, node uniqueness, interspace to its nearest, interspace between the base station and the cluster head, and the remaining power of the sensors. The author used the algorithm proposed by Prachi M. et al. [43]. The steps of the algorithm are as follows:

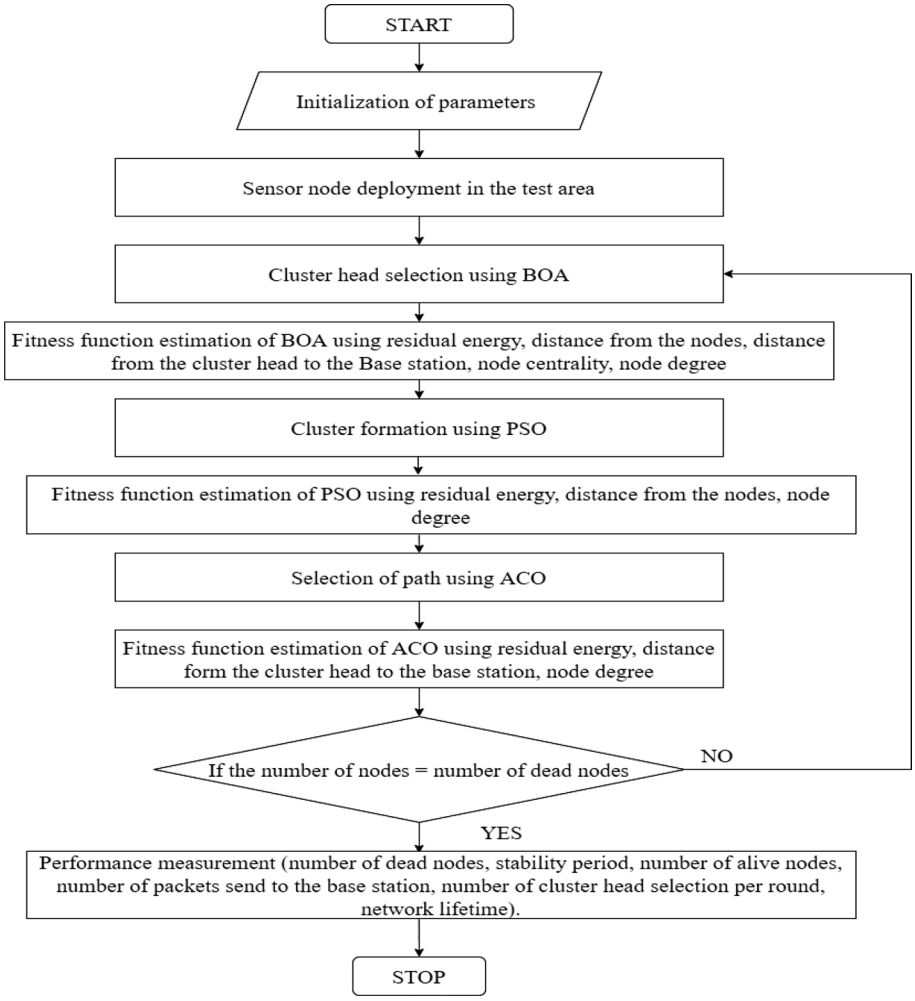


Fig. 4 Flow chart

Node degree: It is defined as the quantity of sensors connect to the Cluster Head. The Cluster Head with the less quantity of knob are chooses as cluster head with the higher quantity of connected sensors deplete their power fast. The degree of the node is calculated as sum of power of all the sensors belongs to the cluster head. The weight value for the purpose function is 0.1.

$$ND = \sum_{i=1}^{m} I_i \tag{3}$$

Node centrality: It is defined as how much a node is halfway situated from the nearest nodes. The weight value for the purpose function is 0.1 and it is calculated by using the eq:

$$C_n = \sum_{i=m}^{m} \frac{\sqrt{\frac{\sum_{j\in n} dist^2(i,j)}{n(i)}}}{\text{Network dimension}} \tag{4}$$

where n(i) quantity of nearest node to the cluster head i.

Remaining Power of the node: The node with the higher remaining power will become the cluster head because the cluster head need to perform the various task such as aggregate the data, remove the duplicate data, data transmission to the base station. The weight value for the purpose function is 0.3. Thus, the node with higher remaining power will chose as the cluster head and the remaining power is calculated as:

$$R_e = \sum_{i=1}^{m} \frac{1}{E_{CHi}} \tag{5}$$

where the remaining power of the ith cluster head is E_{CHi}.

Interspace between the sensors: It is defined as the interspace from the sensors to the cluster head and from nearest sensors with in the cluster. Lesser the interspace, less power will be consumed in the transmission. The weight value for the purpose function is 0.2. Thus, the interspace is calculated by using the formula:

$$Dij = \sum_{i=1}^{m} \left(\sum_{j=1}^{Ii} dis(s_j, CH_i)/I_i \right) \tag{6}$$

where $dis(s_j, CH_i)$ is interspace from sensor node to the cluster head and I_i shows the ith sensor node within the cluster.

Interspace from the cluster head and base station: it shows the interspace from the from the cluster head to the base station. If the cluster head is far away from the base station, then it consumes more power for the data transmission. So, the nodes near to the base station is used to convey the data to the base station. The weight value for the purpose function is 0.25. The purpose function used to calculate the interspace from the base station to the cluster head is calculated as:

$$D_{CH-BS} = \sum_{i=i}^{m} dis(CH_j, BS) \tag{7}$$

So, the single purpose function to find the cluster head from the set of nodes is calculated as

$$F = \alpha_1 ND + \alpha_2 C_n + \alpha_3 R_e + \alpha_4 D_{ij} + \alpha_5 D_{CH-BS} \tag{8}$$

Mechanism

CH choosing using BOA

1. Fitness function derivation using $F = \alpha_1 ND + \alpha_2 C_n + \alpha_3 R_e + \alpha_4 D_{ij} + \alpha_5 D_{CH-BS}$
2. Generate a preliminary populace of butterflies.
3. Prepare impetus strength (I) at node I which is intended by f(xi)
4. Prepare shift possibility, sensor modality and power exponent.
5. For j=max quantity of reiterations
6. For every butterfly in populace
7. Calculate cologne $f = cI^a$
8. End for
9. Identify the optimum butterfly populace
10. For every butterfly in populace
11. Generate a arbitrary quantity r from [0,1]
12. If arbitrary quantity < population
13. $x_i^{t+1} = x_i^t + (r^2 \times g^* - x_i^t) \times f_i$ where f_i is butterfly fragrance, $g^*$is current iteration.
14. $else$
15. Move arbitrarily $x_i^{t+1} = x_i^t + (r^2 \times x_j^t - x_k^t) \times f_i$
16. End if
17. End for
18. Update the value of energy proponent
19. End for
20. Optimal quantity of CH chooses from the population.

5.2 Cluster Formation Using PSO (Particle Swarm Optimization)

Particle Swarm Optimization (PSO), one of the oldest mechanisms, is the nature-inspired mechanism used by the researchers to find the optimum results in the wireless sensor network. Kennedy and Eberhart established the mechanism in 1995. The mechanism is inspired by the social behavior of bird flocking and fish schooling. It is an effective method to solve the clustering problem in wireless sensor networks. Based on centralized clustering, the clusters are formed by the base station. For this, the base station sends the data collection message to all the sensors in nature. Nodes send data to the base station after receiving it, such as node id, location (interspace from the BS in and position), power loss and power loss ratio (velocity), and current power. Then the base station initiates the clustering process in the following steps:

Function: PSO-Cluster formation

Initialize the optimization problem and mechanism, parameters.

1. for i=1 to the particle size do
2. Initialize Xi within the search range of (Xmin,Xmax) arbitrarily;
3. Initialize Vi within the velocity range of (Vmin,Vmax) arbitrarily;
4. pi=xi
5. end for
6. Evaluate each particle **// fitness value= $a\frac{\sum_{i=0}^{n} d(current\ node, member\ node\ i)}{n} + b\frac{\sum_{i=0}^{n} E(member\ i)}{E(existing\ node)} + (1-a-b)\frac{1}{number\ of\ nodes\ exist\ in\ the\ current\ node}$ where a & b is normalized values and n shows the quantity of nodes in the cluster
7. Identify the best position Ps;

//Loop:

8. While (Stop criterion is not satisfied & t < maximum iteration times) do
9. for i=1 to the particle size do
10. $V_i^{t+1} = \omega V_i^t + c_1 r_1 (P_i^t - X_i^t) + c_2 r_2 (P_g^t - X_i^t)$
11. $X_i^{t+1} = X_i^t + V_i^{t+1}$
12. $P_i^{t+1} = P_i^t$
13. Evaluate fitness value
14. If fitness (P_i^{t+1}) < fitness (X_i^{t+1});
15. Update (P_i^{t+1});
16. End if
17. If fitness (P_g^{t+1}) < fitness (P_i^{t+1}) then
18. Update (P_g^{t+1});
19. End if
20. End for
21. End While

5.3 Routing Mechanism Using ACO (Ant Colony Optimization)

Ant Colony Optimization is a metaheuristic mechanism inspired by the performance of the ants. Commonly, ant colony optimization is applied to discrete problems. Ant Colony Optimization is used to find the shortest path from the source node to the destination node using a graph in which the ant colony (nodes associated with the cluster head) is represented as a node and the L represents the link between the nodes with different weights. In the initial phase, the weight of the link is calculated as the actual interspace in between the nodes by using an arbitrarily large quantity, which is calculated by the mathematical formula. The disadvantage of the ant colony optimization mechanism, i.e. undefined conjunction, is overcome by improving the ant colony optimization in terms of remaining power, interspace from the destination, and the knob degree. The route-finding procedure using ACO is as follows:

1. In the formed cluster head, the ants are situated in every cluster. Cluster heads will create the way from the Cluster Head to the destination (base station). These routes data are known as redirect data.
2. Based on the probability matrix, the redirect containers are arbitrarily converted to the following cluster head. The redirect program packet is conveyed to the next cluster head until the packet is acknowledged by the base station.

3. The redirect packet will maintain the local data base about the visited cluster head, remaining power of the nodes and the cluster head (Remaining power of the nodes are calculated as the quantity of data conveyed along the network), interspace from the cluster head to the base station and the node degree.
4. The redirect data base is used to create the backward data base or backward packet. We need to create the backward packet because to extend the path until the packet reaches to the base station. The backward packet path is same as the path followed by the redirect packet.
5. The pheromone level of the link is updated by the remaining power, interspace to the base station and the node degree.
6. The next node for the transmission is chooses based on Eq. 9 which shows the chance of selecting the knob j as the subsequent knob i by means of ant k.

$$P_{ij}^{k}(t) = \begin{cases} \frac{[\tau_{ij}(t)]^{\alpha}[\eta_{ij}]^{\beta}}{\sum_{l \epsilon \mathrm{N}_k}[\tau_{ij}(t)]^{\alpha}[\eta_{ij}]^{\beta}} & if\ j \epsilon \mathrm{N}_k \\ 0 & otherwise \end{cases} \tag{9}$$

where the heuristic value and pheromone intensity are represented as η_{ij} and τ_{ij} respectively. To control the relative importance of the both the values, parameter α and β is used. Submission of nodes who has not visited yet is represented as N_k. Base on the data stored in the routing table by the cluster head, the heuristic and pheromone intensity are updated. Both the values are updated by the following formulas:

$$\eta_{ij} = \frac{1}{d_{CH}} \tag{10}$$

and

$$\tau_{ij} = (1-\rho)\tau_{ij}^{old} + \sum_{k=1}^{m} \Delta\tau_{ij}^{k} \tag{11}$$

where d_{CH} shows the interspace from the CH, m shows the quantity of ants initialized and the pheromone deterioration quantity is shown as $\rho \epsilon [0, 1]$. Where $\Delta\tau_{ij}^{k}$ is calculated as:

$$\Delta\tau_{ij}^{k} = \int \frac{Q}{c_k} if\ the\ k^{th}\ ant\ traversed\ link(i,j),\ otherwise\ 0 \tag{12}$$

where the value of Q is constant and the route cost is found by the ant is calculated as c_k.

$$c_k = \boldsymbol{\varphi}_1 E_r + \boldsymbol{\varphi}_2 d_{CH,BS} + \boldsymbol{\varphi}_3 N_D \tag{13}$$

where the weighted values of $\boldsymbol{\varphi}_1$,$\boldsymbol{\varphi}_2$, $\boldsymbol{\varphi}_3$ are 0.5,0.3 and 0.2. For the successful communication, remaining power of the nodes should be considered as the priority because the node failure me leads to the communication failure. After that, to obtained the shortest interspace in between the cluster head and the base station is considered as the second priority because it consumes the minimum power or we can say that the power utilization is low in order to find the shortest interspace as compare to maintain the remaining power of the sensors. Lastly, we consider the node degree as a third priority, in which we choose the next cluster head as a hop having lesser quantity of member nodes. To find the route in between the source node to the destination node following steps need to be followed:

Routing Steps using ACO

1) Initialize pheromone exponential weight and heuristic exponential weight.
2) Generate the initial population of the ants.
3) for j=higher level of the iterations.
4) for each ant in the population.
5) Repeat the steps until kth ant complete its journey to the destination.
6) Choose the successive ant using equation 9.
7) Update the pheromone using equation 11.
8) End for
9) Update the best solution.
10) End for
11) Output is the optimal route from source to the BS.

5.4 Cluster Maintenance

In the literature survey present, the cluster preservation phase is one of the most significant stages to stable the load amongst the clusters. The cluster closer to the base station drain their power so fast because of the traffic of inter cluster. So, the preservation of the cluster is important factor to turn down the problem of knob disaster. Node failure mains to the network failure and maintenance of the cluster heads to the maximization of the lifespan of the cluster or the entire network. In the put redirect mechanism, if the power of the cluster heads drains to the below the threshold value, the butter fly optimization mechanism is used to initialized the cluster, partial swarm optimization mechanism is used to elect the cluster head and then ant colony optimization mechanism is used to find the optimised path in amongst the knob to the cluster head and cluster head to the base station to maximize the network lifespan. Furthermore, it leads to the maximize the quantity of data conveyed to the base station.

6 Performance Measurement

The performance of the put redirect mechanism is measured by considering various factors such as:

Number of active nodes: The quantity of active nodes elevates the lifespan of the network. It describes as the quantity of active nodes in the network.

Dead nodes: The stability period of the network is calculated till the first node die. The network life time will decree when the quantity of dead nodes will elevate per round.

Data send to the BS.

Throughput: quantity of bits conveyed to the BS and it will measure in quantity of bits conveyed per second.

Stability period: It is measured along at what round the first node die, quantity of rounds when half of the nodes die in the network.

Power utilization in each round: The total power utilization is calculated by the power loss of each node in the network.

Packet Drop Ratio: Quantity of data lost during the transmission from node to the cluster head and from cluster head to the base station.

Congestion in the network: It is calculated as quantity of acknowledged data by the base station to the quantity of produced data by the nodes in the network.

7 Simulation Setup

The put redirect power efficient protocol is implemented and tested on the MATLAB. The reason for using MATLAB is that it is very appropriate for the data survey and gives mathematical operations. There are 300 devices arbitrarily positioned in the test reason of 200×200 m. The first order radio model for the power efficiency is considered for analysing the put redirect model with the extant model. The simulation parameters used for the examination purpose is shown in Table 2. The purpose of the put redirect mechanism is to turn down the power utilization in wireless sensor networks. So, to achieve the object, author used the Butterfly Optimization Algorithm (BOA) for the cluster head choosing, particle swarm optimization (PSO) is used for the cluster formation process and Ant Colony Optimization (ACO) is used for the routing process.

Parameter that are considered for the butterfly optimization algorithm are: population size considered as 200, switch probability has taken as 0.8, power exponent considered as 0.1 and sensor mobility is considered as 0.01. Now for the cluster formation, the parameters considered as Quantity of Particles, Number of iterations, Inertia Weight, Local Weight (c1), Local Weight (c2), Fitness are as 200, 100, 0.8, 1.49, 1.49, Predication accuracy. For the optimal route consideration, the parameters chosen as Quantity of ants, Pheromone exponential weight, experiential exponential weight, disappearance rate are as 200, 1, 1, 0.1.

The put redirect mechanism is validated in 3 cases.

Case 1: In the 1st case, the Base Station is placed at the centre of the test area (100, 100) in Fig. 5, which is used to analyses the shorter interspace communication.

Case 2: In the 2nd case, the Base Station is placed at the last area which is in the range of the sensing reason (100, 200) in Fig. 6. It is used to analyse the means range communication.

Case 3: In the 3rd case, the Base Station is placed at the outer area (100, 250) in Fig. 7, which is situated far away from the examination zone. This case is used to analyse the extended rang communication.

Table 2 Simulation parameter

Parameters	Value
Network field	(200, 200)
Quantity of nodes	500
Packet size	4000 Bits
Eelec	50 nJ/bit
Efs	10 nJ/bit/m2
Eamp	0.0013 pJ/bit/m4
EDA	5nJ/bit/signal
Do (Threshold interspace)	70 m
Eo (Original power of the normal nodes)	0.5 J



Fig. 5 Illustration of Case 1

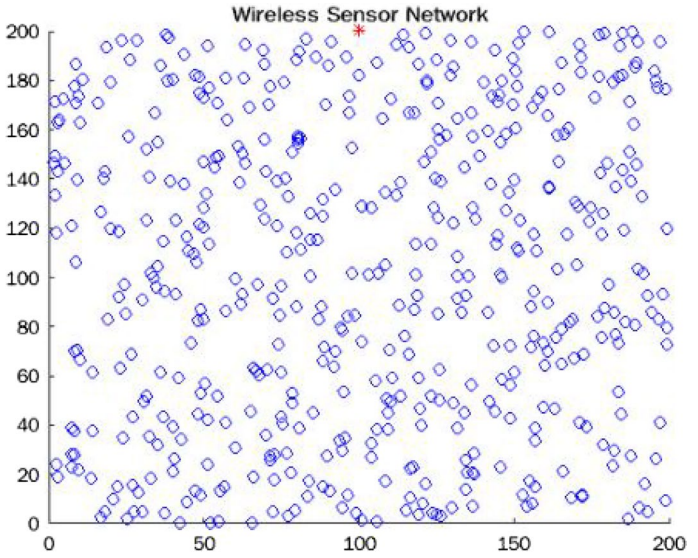


Fig. 6 Illustration of case 2

7.1 Performance Evaluation in Terms of Active Nodes

The quantity of active nodes in put redirect mechanism is correlated with the LEACH, DEEC, EDEEC, DDEEC for 500 nodes in different cases such as in the 1st case, the base station is placed at the centre of the test area (250, 250) which is used to analyses the shorter interspace communication, in the 2nd case, the base station is placed at the last area

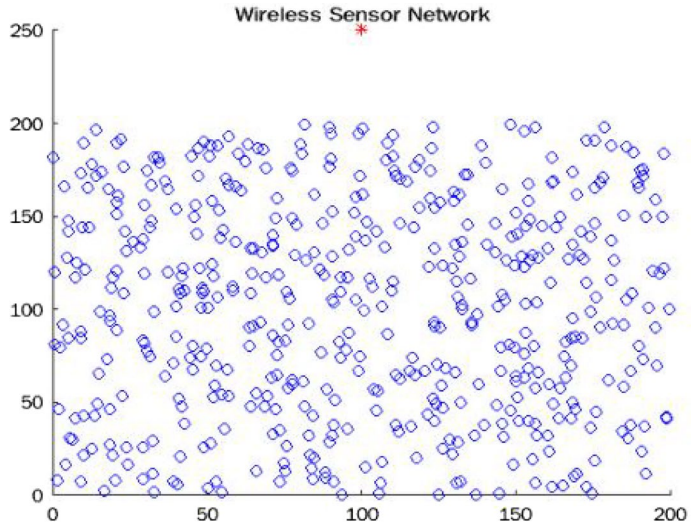


Fig. 7 Illustration of case 3

which is in the range of the sensing reason (100, 250). It is used to analyse the means range communication, in the 3rd case, the base station is placed at the outer area (100, 550), which is situated far-off from the test area. This case is castoff to analyse the long rang communication. The put redirect mechanism prolongs the network lifespan as compare to the other protocols (Fig. 8).

7.2 Performance Evaluation in Terms of Stability Period

The stability period is measured till the round when 1st node dies after the certain quantity of iterations. Figure 9 shows the quantity of dead nodes in the case 1, Fig. 10 shows the

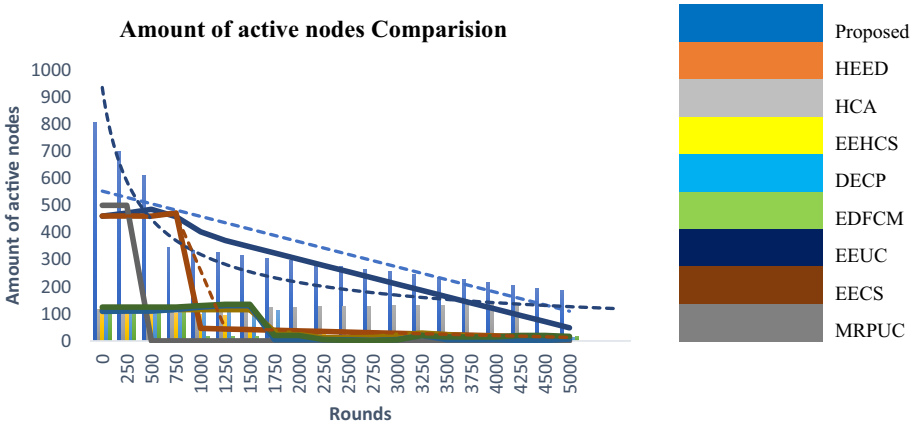


Fig. 8 Number of active nodes

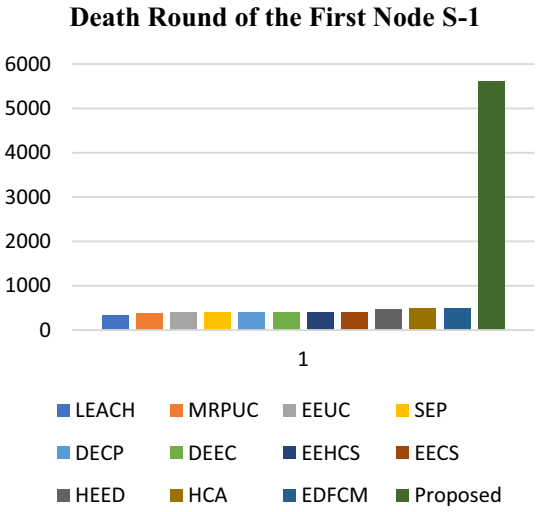


Fig. 9 For the case 1

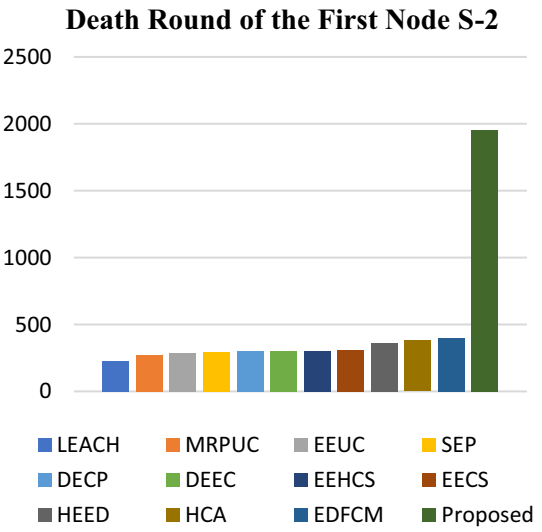


Fig. 10 For the case 2

quantity of dead nodes for the case 2 and the Fig. 11 shows the quantity of death node for the case 3.

7.3 Performance Evaluation of Average Power Utilization

The performance evaluation of average power utilization of the put redirect mechanism is correlated with the extant mechanisms like LEACH, DEEC, MEEDEEC, SEP, EDEEC, DDEEC is shown in the Fig. 12. The power utilization is calculated when the base station is situated in centre of the region (100, 250) and second comparison is based when the base station is situated far away from the base station (100, 250)

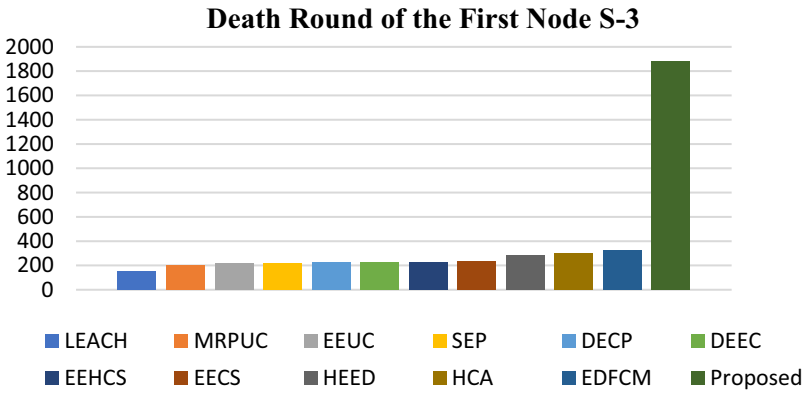


Fig. 11 For the case 3

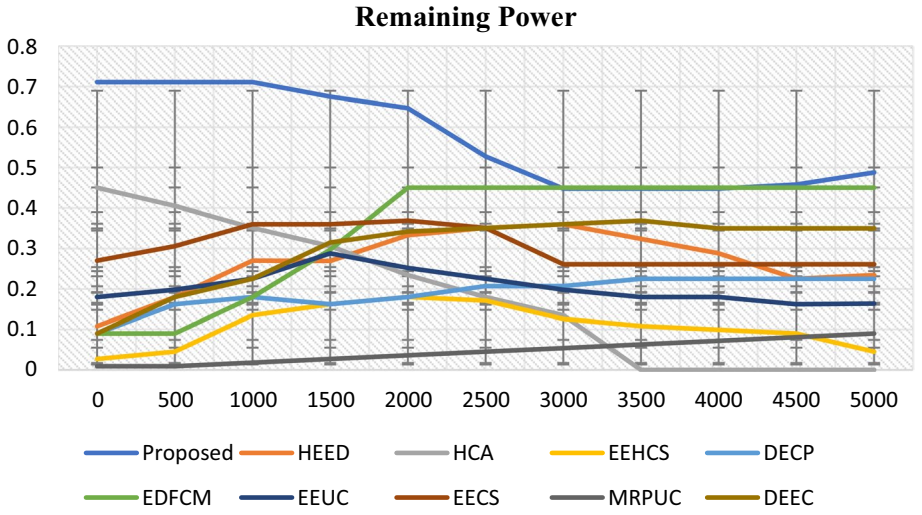


Fig. 12 Remaining power

respectively. As per the result obtained from the mechanism, it is clearly shown that the put redirect mechanism gives higher power efficiency as compare to the LEACH and other mentioned protocols. The put redirect mechanism gives the higher power efficiency because it considers the optimal quantity of cluster head choosing per round, it includes the interspace while choosing the cluster head and optimal route when sending the data from one node to the other node. The reason behind the higher power utilization is that LEACH choose the cluster head arbitrarily and use single hop transmission whereas DEEC does not consider the interspace during cluster head choosing. The overall comparison in terms of remaining power of the put redirect mechanism with the extant mechanism is shown in the Table 3.

Table 3 Comparison of the remaining power of the extant mechanism with the put redirect mechanism

Rounds	Put redirect	HEED	HCA	EEHCS	DECP	EDFCM	EEUC	EECS	MRPUC	DEEC
0	0.711	0.108	0.45	0.027	0.09	0.09	0.18	0.27	0.009	0.09
500	0.711	0.18	0.405	0.045	0.162	0.09	0.198	0.306	0.009	0.18
1000	0.711	0.27	0.351	0.135	0.18	0.18	0.225	0.36	0.018	0.225
1500	0.675	0.2691	0.306	0.162	0.162	0.297	0.288	0.36	0.027	0.315
2000	0.64675	0.333	0.234	0.18	0.18	0.45	0.252	0.369	0.036	0.342
2500	0.52735	0.351	0.18	0.171	0.207	0.45	0.225	0.351	0.045	0.35091
3000	0.44775	0.36	0.135	0.126	0.207	0.45	0.198	0.261	0.054	0.36
3500	0.44775	0.324	0	0.108	0.225	0.45	0.18	0.261	0.063	0.369
4000	0.44775	0.288	0	0.099	0.225	0.45	0.18	0.261	0.072	0.349992
4500	0.4577	0.225	0	0.09	0.225	0.45	0.162	0.261	0.081	0.349992
5000	0.48755	0.234	0	0.045	0.225	0.45	0.1638	0.261	0.09	0.349992

7.4 Performance Evaluation Based on the Packet Transmission to the BS

The put redirect mechanism gives the higher packet acknowledged by the base station is that, the fitness functions of Butterfly Optimization Algorithm, particle swarm optimization and Ant Colony Optimization reserve the power utilization of the nodes due to which leads to elevate the quantity of active nodes in the network along which the data packet will be conveyed to the base station. The fitness function chosen for the cluster head choosing and route choosing, it helps to minimize the overhead in the routing process due to which a smaller quantity of nodes dies in each round during the data transmission and it leads to the higher quantity of data acknowledged by the base station. In the extant mechanism, the inappropriate quantity of cluster head choosing and routing overhead, the lesser quantity of data is conveyed to the base station. Figure 13 shows the quantity of data acknowledged by the base station if there are 250 nodes are present in the case and Fig. 14 shows the quantity of data acknowledged by the base station if there are 150 nodes are present in the case.

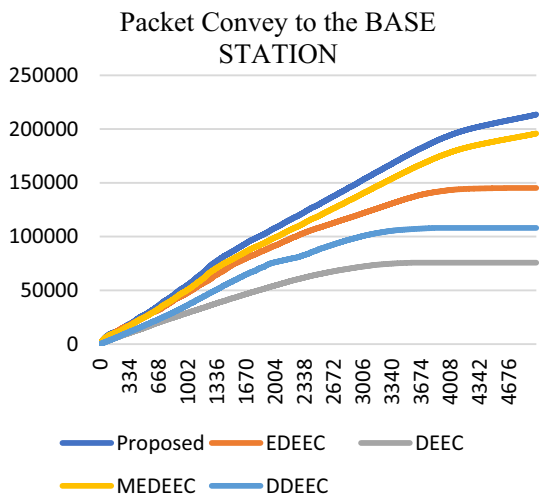


Fig. 13 Packet transmission for the 250 Nodes

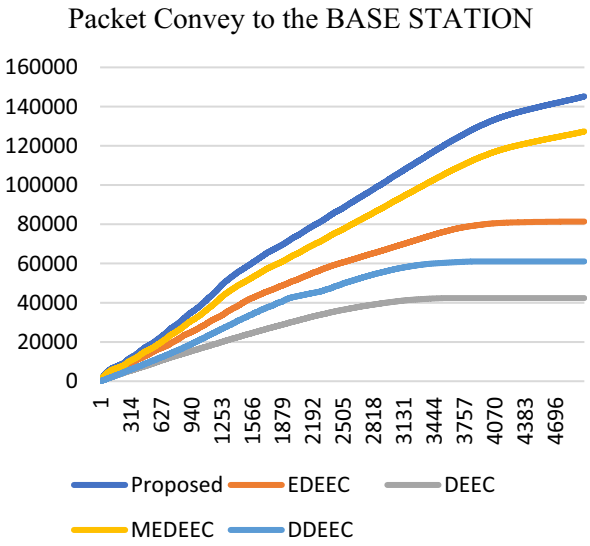


Fig. 14 Packet transmission for the 150 Nodes

7.5 Performance Evaluation of Throughput

The inappropriate choosing of cluster head in the extant mechanism is the main reason for the higher power utilization in the data transmission. The put redirect mechanism chooses the cluster head and the route in the efficient way due to which higher data are conveyed to the base station and achieve the efficiency. The comparison of put redirect mechanism is correlated with the extant mechanism.

7.6 Performance Evaluation of the Network Lifespan

Network lifespan is totally dependent on the remaining power of the nodes and the lifespan of the network got exhausted when entire node will lose their power. The network lifespan of the entire network is correlated when the first node die, half of the nodes die and last node die in the network. It is well said by the researchers that the demise of the 1st node in the network does not disturb the network execution but the system performance is affected when half of the node die in certain rounds or in the data transmission. Furthermore, the entire network gets drained when all the nodes die. So, to upgrade the network lifespan, the optimal quantity of cluster head choosing per round and chosen of optimal path from node to base station is mandatory requirement in the present case.

7.7 Comparative Survey of the Put Redirect (Proposed) Procedure with Further Cluster-Based Routing Mechanisms

The comparative survey of the put redirect mechanism is correlated with some extant mechanism is shown in the Fig. 15. Table 4 shows the Comparative survey of Delay, Packet Drop Ratio, Throughput to the base station with the extant routing protocol.

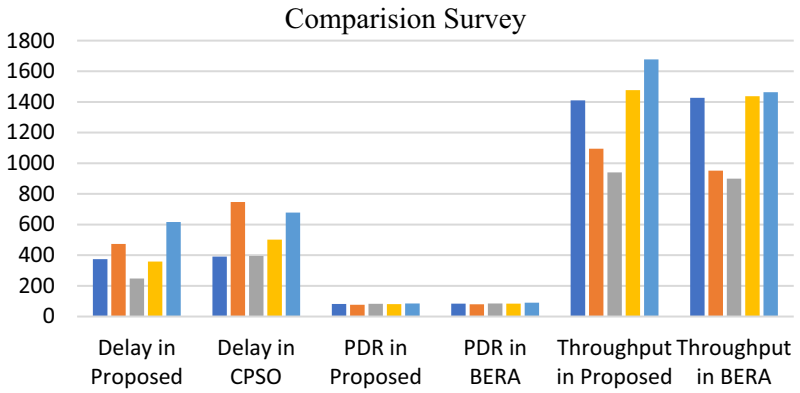


Fig. 15 Comparison survey with CPSO, BERA

Table 4 Comparative survey of delay, packet drop ratio, throughput to the BS with the extant routing protocol

Nodes	Delay		PDR		Throughput	
	Put redirect	CPSO	Put redirect	BERA	Put redirect	BERA
50	373.82	391	81.8197	84.0419	1409.99	1427.34
100	473.45	746.97	76.6302	80.0872	1094.45	951.33
150	248	395.48	82.5347	84.9127	940.1	899.76
225	359	501.48	80.4411	83.9704	1477.54	1436.96
315	616.1	677.81	85.1583	90.3678	1677.48	1463.59
Nodes	Delay		PDR		Throughput	
	Put redirect	FUCHAR	Put redirect	FUCHAR	Put redirect	FUCHAR
50	467.57	465.57	79.2301	83.1894	1415.3	1409.87
100	517.78	515.78	79.8012	81.1282	989.09	952.42
150	444.22	442.22	83.2691	84.238	989.44	937.5
225	696.14	694.14	85.7013	88.1779	1563.04	1502.28
315	539.6	537.6	90.044	91.5886	1475.36	1383.06

8 Conclusion

In the current case of a wireless sensor network, the power utilization of the network is very high, due to which the network's lifespan gets shortened. So, to upgrade the network lifespan, the author focuses on the following parameters: optimal quantity of cluster heads chosen per round, quantity of cluster formation, and optimal route choosing. The author uses the Butterfly Optimization Algorithm, particle swarm optimization, and ant colony optimization to reduce the power utilization per round and elevate the network lifespan. The Butterfly Optimization Algorithm is used to choose the cluster head, and the fitness function is used with consideration of five parameters such as the remaining power of the node, the interspace between the nodes and the base station, the node's centrality, and the

node's degree to determine the cluster head per round. The particle swarm optimization is used to form the cluster by using certain parameters, such as the distance between the cluster head and the base station. The ant colony optimization is used to find the best route from the source to the destination by considering parameters such as the interspace to the neighbor node, the remaining power of the nodes, and the node degree. The performance of the proposed redirect mechanism was measured in three different cases in which the base station was situated at different positions. The proposed redirect mechanisms were correlated with the existing mechanisms, and the result shows that the proposed redirect mechanism gives a higher result in terms of stability. The proposed algorithm has a low convergence rate into the local optimum, a low exploration and exploitation rate, and a slow convergence speed.

Author Contributions RM and RKY contributed to collecting related literature and implementing the mechanism.

Funding Not applicable.

Data Availability Enquiries about data availability should be directed to the authors.

Declarations

Conflict of interest The authors declare that there is no conflict of interests regarding the publication of this paper.

Consent for Publication Not applicable.

References

1. Sohrabi, K., Gao, J., Ailawadhi, V., & Pottie, G. J. (2000). Protocols for self-organization of a wireless sensor network. *IEEE Personal Communication, 7*(5), 16–27.
2. Singh, A., Kotiyal, V., Sharma, S., Nagar, J., & Lee, C. C. (2020). A machine learning approach to predict the average localisation error with applications to wireless sensor networks. *IEEE Access, 8*, 208253–208263.
3. Akyildiz, I. F., Su, W., Sankarasubramaniam, Y., & Cayirci, E. (2002). Wireless sensor networks: a survey. *Computer Networks, 38*(4), 393–422.
4. Borges, L., Velez, F. J., & Lebres, A. S. (2014). Survey on the characterization and classification of wireless sensor network applications. *IEEE Communications Surveys & Tutorials, 16*(4), 1860–1890.
5. Lu, S., Huang, X., Cui, L., Zhao, Z., & Li, D. (2009). Design and implementation of an asic-based sensor device for wsn applications. *IEEE Transactions on Consumer Electronics, 55*(4), 1959–1967.
6. Sharma, S., Singh, J., Kumar, R., Singh, A. (2017). Throughput-save ratio optimiza- tion in wireless powered communication systems. In *2017 International Conference on Information, Communication, Instrumentation and Control (ICICIC)*, (pp. 1–6).
7. Kumar, A., Singh, A. (2018). Throughput optimization for wireless information and power transfer in communication network. In *2018 Conference on Signal Processing and Communication Engineering Systems (Spaces)*, (pp. 1–5).
8. Yick, J., Mukherjee, B., & Ghosal, D. (2008). Wireless sensor network survey. *Computer Networks, 52*(12), 2292–2330.
9. Imran, M., Hasbullah, H. B., & Said, A. M. (2012). Personality wireless sensor networks (PWSNs). *arXiv preprint arXiv:1212.5543*.
10. Sharma, S., Kumar, R., Singh, A., & Singh, J. (2020). Wireless information and power transfer using single and multiple path relays. *International Journal of Communication Systems, 33*(14), e4464.
11. Daji, H., Jinping, Z., & Jilan, S. (2003). Practical implementation of Hilbert-Huang transform mechanism. *Acta Oceanologica Sinica, 22*(1), 1–14.

12. Cardei, M., & Du, D.-Z. (2005). Improving wireless sensor network lifespan through power aware organization. *Wireless Networks, 11*, 333–340. https://doi.org/10.1007/s11276-005-6615-6
13. Huang, R., Chen, Z., Xu, G. (2010). International Conference on Communications, Circuits and Systems (ICCCAS), IEEE (2010), pp. 103–107.
14. Liang, Y., Yu, H. (2005) Power adaptive cluster-head selection for wireless sensor networks. In *Sixth International Conference on Parallel and Distributed Computing Applications and Technologies* (pdcat'05), (pp. 634–638).
15. Cardei, M., & Du, D.-Z. (2005). Improving wireless sensor network lifespan through power aware organization. *Wireless Networks, 11*(3), 333–340.
16. Wang, X., Xing, G., Zhang, Y., Lu, C., Pless, R., Gill, C. (2003). Integrated scope and connectivity configuration in wireless sensor networks. In *Proceedings of the 1st International Conference on Embedded Networked Sensor Systems, Sensys '03, ACM, New York, NY, USA*, (pp. 28–39).
17. Tsai, C.-W., Hong, T.-P., & Shiu, G.-N. (2016). metaheuristics for the lifespan of wsn: A review. *IEEE Sensors. J., 16*(9), 2812–2831.
18. Nanda, S. J., & Panda, G. (2014). a survey on nature inspired metaheuristic mechanisms for partitional clustering. *Swarm and Evolutionary Computation, 16*, 1–18.
19. Iqbal, M., Naeem, M., Anpalagan, A., Ahmed, A., & Azam, M. (2015). Wireless sensor network optimization: Multi-purpose paradigm. *Sensors, 15*(7), 17572–17620.
20. Demigha, O., Hidouci, W.-K., & Ahmed, T. (2012). On power efficiency in collaborative target tracking in wireless sensor network: A review. *IEEE Communications Surveys & Tutorials, 15*(3), 1210–1222.
21. Kulkarni, R. V., Forster, A., & Venayagamoorthy, G. K. (2010). Computational intelligence in wireless sensor networks: A survey. *IEEE Communications Surveys & Tutorials, 13*(1), 68–96.
22. Tsai, C.-W., Tsai, P.-W., Pan, J.-S., & Chao, H.-C. (2015). Metaheuristics for the deployment problem of wsn: A review. *Microprocessors and Microsystems, 39*(8), 1305–1317.
23. Molina, G., Alba, E., & Talbi, E. G. (2008). Optimal sensor network layout using multi-objective metaheuristics. *Journal of Universal Computer Science, 14*(15), 2549–2565.
24. Al-Mousawi, A. J. (2020). Evolutionary intelligence in wireless sensor network: routing, clustering, localization and coverage. *Wireless Networks, 26*(8), 5595–5621.
25. Grefenstette, J. (1986). Optimization of control parameters for genetic mechanisms. *IEEE Transactions on Systems, Man, and Cybernetics, 16*(1), 122–128.
26. Liu, X. (2017). Routing protocols based on ant colony optimization in wireless sensor networks: a survey. *IEEE Access, 5*, 26303–26317.
27. Mehrotra, A., Singh, K. K., & Khandelwal, P. (2014). An unsupervised change detection technique based on Ant colony Optimization. In *2014 International Conference on Computing for Sustainable Global Development (INDIACom)* (pp. 408-411). IEEE.
28. Dawood, M. S., Benazer, S. S., Saravanan, S. V., & Karthik, V. (2021). Energy efficient distance based clustering protocol for heterogeneous wireless sensor networks. *Materials Today: Proceedings, 45*, 2599–2602. https://doi.org/10.1016/j.matpr.2020.11.339
29. Mehta, D., & Saxena, S. (2020). MCH-EOR: Multi-objective cluster head based energy-aware optimized routing algorithm in wireless sensor networks. *Sustainable Computing: Informatics and Systems, 28*, 100406. https://doi.org/10.1016/j.suscom.2020.100406
30. Hussien, A. G., Amin, M., Wang, M., Liang, G., Alsanad, A., Gumaei, A., & Chen, H. (2020). Crow search algorithm: Theory, recent advances, and applications. *IEEE Access, 8*, 173548–173565. https://doi.org/10.1109/access.2020.3024108
31. Arjunan, S., & Sujatha, P. (2018). Lifetime maximization of wireless sensor network using fuzzy based unequal clustering and ACO based routing hybrid protocol. *Applied Intelligence, 48*, 2229–2246.
32. Kaushik, A., Indu, S., & Gupta, D. (2019). A grey wolf optimization approach for improving the performance of wireless sensor networks. *Wireless Personal Communications, 106*, 1429–1449. https://doi.org/10.1007/s11277-019-06223-2
33. Xiuwu, Y., Qin, L., Yong, L., Mufang, H., Ke, Z., & Renrong, X. (2019). Uneven clustering routing algorithm based on glowworm swarm optimization. *Ad Hoc Networks, 93*, 101923. https://doi.org/10.1016/j.adhoc.2019.101923
34. Mahesh, N., & Vijayachitra, S. (2019). DECSA: Hybrid dolphin echolocation and crow search optimization for cluster-based energy-aware routing in WSN. *Neural Computing and Applications, 31*, 47–62. https://doi.org/10.1007/s00521-018-3637-4
35. Lin, Y., Zhang, J., Chung, H. S. H., Ip, W. H., Li, Y., & Shi, Y. H. (2011). An ant colony optimization approach for maximizing the lifetime of heterogeneous wireless sensor networks. *IEEE Transactions on Systems, Man, and Cybernetics, Part C, 42*(3), 408–420.

36. Cui, Z., Fei, X. U. E., Zhang, S., Cai, X., Cao, Y., Zhang, W., & Chen, J. (2020). A hybrid blockchain-based identity authentication scheme for multi-wsn. *IEEE Transactions on Services Computing, 13*(2), 241–251. https://doi.org/10.1109/tsc.2020.2964537
37. Lazrag, H., Chehri, A., Saadane, R., & Rahmani, M. D. (2021). Efficient and secure routing protocol based on blockchain approach for wireless sensor networks. *Concurrency and Computation: Practice and Experience, 33*(22), e6144. https://doi.org/10.1002/cpe.6144
38. Wang, Z. X., Zhang, M., Gao, X., Wang, W., & Li, X. (2019). A clustering WSN routing protocol based on node energy and multipath. *Cluster Computing, 22*, 5811–5823.
39. Han, G., & Zhang, L. (2018). WPO-EECRP: energy-efficient clustering routing protocol based on weighting and parameter optimization in WSN. *Wireless Personal Communications, 98*, 1171–1205.
40. Haseeb, K., Bakar, K. A., Abdullah, A. H., & Darwish, T. (2017). Adaptive energy aware cluster-based routing protocol for wireless sensor networks. *Wireless Networks, 23*, 1953–1966.
41. She, W., Liu, Q., Tian, Z., Chen, J. S., Wang, B., & Liu, W. (2019). Blockchain trust model for malicious node detection in wireless sensor networks. *IEEE Access, 7*, 38947–38956. https://doi.org/10.1109/access.2019.2902811
42. Liu, Y., Dong, M., Ota, K., & Liu, A. (2016). Activetrust: Secure and trustable routing in wireless sensor networks. *IEEE Transactions on Information Forensics and Security, 11*(9), 2013–2027. https://doi.org/10.1109/tifs.2016.2570740
43. Maheshwari, P., Sharma, A. K., & Verma, K. (2021). Energy efficient cluster based routing protocol for WSN using butterfly optimization algorithm and ant colony optimization. *Ad Hoc Networks, 110*, 102317.
44. Xiao, W., Wu, X., Ma, X., & Lu, Q. (2013). The optimization algorithm of wireless sensor network node based on improved ant colony. *Sensors & Transducers, 155*(8), 54.
45. Yazdani, M., & Jolai, F. (2016). Lion optimization algorithm (LOA): A nature-inspired metaheuristic algorithm. *Journal of computational design and engineering, 3*(1), 24–36.
46. Han, G., Xu, H., Duong, T. Q., Jiang, J., & Hara, T. (2013). Localization algorithms of wireless sensor networks: A survey. *Telecommunication Systems, 52*, 2419–2436.
47. Xing, B., & Gao, W. J. (2014). *Innovative computational intelligence: A rough guide to 134 clever algorithms* (pp. 22–28). Springer.
48. Campelo, F., Aranha, C., Koot, R. (2020). Transmutative computation bestiary, 2019. https://github.com/fcampelo/ec-bestiary. Accessed 1 Nov 2020.
49. Tzanetos, A., Fister, I., & Dounias, G. (2020). A comprehensive information base of nature-inspired mechanisms. *Data in Brief, 31*, 105792.
50. Tao, F., Laili, Y., & Zhang, L. (2015). Brief history and overview of intelligent optimization mechanisms. *Configurable intelligent optimization mechanism* (pp. 3–33). Springer.
51. Pham, D., & Karaboga, D. (2012). *Intelligent optimisation techniques: genetic mechanisms, tabu search, simulated annealing and neural networks*. Springer.
52. Belkasmi, M., Ben-Othman, J., Li, C., & Essaaidi, M. (2020). *Advanced communication systems and information security: Second international conference, ACOSIS 2019, Marrakesh, Morocco, November 20–22, 2019, Revised Selected Papers*. Springer.
53. Behera, T. M., Mohapatra, S. K., Samal, U. C., Khan, M. S., Daneshmand, M., & Gandomi, A. H. (2019). I-SEP: An improved routing protocol for heterogeneous wsn for iot-based environmental monitoring. *IEEE Internet of Things Journal, 7*(1), 710–717.
54. Xie, B., & Wang, C. (2017). An improved distributed power efficient clustering mechanism for heterogeneous WSNS. In *2017 IEEE Wireless Communications and Networking Conference (WCNC)*
55. Vinitha, A., & Rukmini, M. S. S. (2018). Energy efficient cluster-based routing protocol for wireless sensor network using nature inspired mechanism. *International Journal of Pure and Applied Mathematics, 118*(11), 725–732. https://doi.org/10.12732/ijpam.v118i11.93
56. Dawood, M. S., Benazer, S. S., Saravanan, S. V., & Karthik, V. (2021). Energy efficient distance based clustering protocol for heterogeneous wireless sensor networks. *Materials Today: Proceedings, 45*, 2599–2602. https://doi.org/10.1016/j.matpr.2020.11.339
57. Mekonnen, M. T., & Rao, K. N. (2017). Cluster optimization based on metaheuristic algorithms in wireless sensor networks. *Wireless Personal Communications, 97*, 2633–2647.
58. Arora, S., & Singh, S. (2019). Butterfly optimization algorithm: A novel approach for global optimization. *Soft Computing, 23*, 715–734.
59. Chauhan, A., & Kaushik, A. (2014). TADEEC: Threshold sensitive advanced distributed energy efficient clustering routing protocol for wireless sensor networks. *International Journal of Computer Applications, 96*(23), 26–31.
60. Yi, D., & Yang, H. (2016). HEER—A delay-aware and energy-efficient routing protocol for wireless sensor networks. *Computer Networks, 104*, 155–173. https://doi.org/10.1016/j.comnet.2016.04.022

61. Mostafaei, H. (2019). Power-efficient mechanism for reliable routing of wireless sensor networks. *IEEE Transactions on Industrial Electronics, 66*(7), 5567–5575.
62. Luo, J., Hu, J., Wu, D., & Li, R. (2014). Opportunistic routing algorithm for relay node selection in wireless sensor networks. *IEEE Transactions on Industrial Informatics, 11*(1), 112–121. https://doi.org/10.1109/tii.2014.2374071
63. Cui, Z., Fei, X. U. E., Zhang, S., Cai, X., Cao, Y., Zhang, W., & Chen, J. (2020). A hybrid blockchain-based identity authentication scheme for multi-wsn. *IEEE Transactions on Services Computing, 13*(2), 241–251.
64. Awan, S. H., et al. (2020). Blockchain with IoT, an emergent routing scheme for smart agriculture. *International Journal Advances in Computer Science Application, 11*(4), 420–429.
65. Gambhir, A., Payal, A., & Arya, R. (2018). Performance analysis of artificial bee colony optimization based clustering protocol in various scenarios of WSN. *Procedia computer science, 132*, 183–188.
66. Feng, L., Zhang, H., Lou, L., & Chen, Y. (2018). A blockchain-based collocation storage architecture for data security process platform of WSN. In *2018 IEEE 22nd international conference on computer supported cooperative work in design ((CSCWD))* (pp. 75-80). IEEE.
67. Engmann, F., Katsriku, F. A., Abdulai, J. D., Adu-Manu, K. S., & Banaseka, F. K. (2018). Prolonging the lifetime of wireless sensor networks: A review of current techniques. *Wireless Communications and Mobile Computing, 2018*, 1–23.
68. Khan, M. K., Shiraz, M., Ghafoor, K. Z., Khan, S., Sadiq, A. S., & Ahmed, G. (2018). EE-MRP: Power-efficient multistage routing protocol for wireless sensor networks. *Wireless Communications and Mobile Computing, 2018*, 1–13.
69. Xu, C., Xiong, Z., Zhao, G., & Yu, S. (2019). a power-efficient region source routing protocol for lifespan maximization in wsn. *IEEE Access, 7*, 135277–135289. https://doi.org/10.1109/access.2019.2942321
70. Haseeb, K., Bakar, K. A., Ahmed, A., Darwish, T., & Ahmed, I. (2017). WECRR: Weighted energy-efficient clustering with robust routing for wireless sensor networks. *Wireless Personal Communications, 97*, 695–721.
71. Lalwani, P., Das, S., Banka, H., & Kumar, C. (2018). CRHS: Clustering and routing in wireless sensor networks using harmony search algorithm. *Neural Computing and Applications, 30*, 639–659.
72. Khan, M. Y., Javaid, N., Khan, M. A., Javaid, A., Khan, Z. A., & Qasim, U. (2013). Hybrid DEEC: Towards efficient energy utilization in wireless sensor networks. arXiv preprint arXiv:1303.4679.

Publisher's Note Springer Nature remains neutral with regard to jurisdictional claims in published maps and institutional affiliations.

Springer Nature or its licensor (e.g. a society or other partner) holds exclusive rights to this article under a publishing agreement with the author(s) or other rightsholder(s); author self-archiving of the accepted manuscript version of this article is solely governed by the terms of such publishing agreement and applicable law.



Rashmi Mishra She is pursuing her Ph.D. from Delhi Technological University. Her interest areas are Information Security, Cryptography, Blockchain & Wireless Sensor Networks and has published papers in many International Conferences and Journal of Reputes.



Rajesh K. Yadav is presently working as an Associate Professor in the Department of Computer Science and Engineering, Delhi Technological University, New Delhi, India. His areas of research interest are Mobile ad-hoc Networks, Mobile Computing, Computer Networks, Theory of Computation, PCA and Wireless Sensor Networks and has published many research papers in Conferences, International Conferences and Journal of Reputes.

world

MDPI

Article

Energy Use Patterns of Pearl Millet (*Pennisetumglaucum* (L.)) Production in Haryana, India

Raveena Kargwal [1], Yadvika [1], Vijay Kumar Singh [2] and Anil Kumar [3,4,*]

[1] Department of Renewable and Bio-Energy Engineering, Chaudhary Charan Singh Haryana Agricultural University, Hisar 125004, India
[2] Department of Processing and Food Engineering, Mahamaya College of Agricultural Engineering & Technology, Ambedkarnagar, (ANDUAT, Ayodhya), Akbarpur 224122, India
[3] Department of Mechanical Engineering, Delhi Technological University, Delhi 110042, India
[4] Centre for Energy and Environment, Delhi Technological University, Delhi 110042, India
* Correspondence: anilkumar76@dtu.ac.in

Abstract: Pearl millet (*Pennisetumglaucum* (L.)) is the fifth most important cereal crop in the world after rice, wheat, maize and sorghum. A resolution adopted by the UN General Assembly on 3 March 2021 decided to declare 2023 as the International Year of Millets. Millet has been promoted due to its nutritional value and low irrigation requirement. In this study, pearl millet was selected for energy auditing, and its production amount is a direct function of energy input. The production of pearl millet needs to be augmented to fulfill an increasing demand. Pearl millet is produced using various sources of energy. This study was conducted to examine the energy use pattern of different categories of farmers, such as small, medium and large, for pearl millet production in Hisar district, Haryana, India. The energy was distributed in different operations, including preparatory tillage, sowing, interculture, fertilizer, irrigation, pesticide, harvesting, threshing and transportation. The source-wise energy (direct and indirect) and operation-wise energy consumption were calculated for all categories of farmers. The average energy input of small, medium and large farmers was 2849.09 MJ.ha^{-1}, 3027.21 MJ.ha^{-1} and 4021.50 MJ.ha^{-1}, respectively. The highest energy was consumed in fertilizer application (52%), with the lowest in seed (2%). The energy ratios of small, medium and large farmers were 3.92, 9.40 and 13.80, respectively. This study could improve the agricultural production systems of pearl millet regarding the energy values of the inputs and outputs.

Keywords: energy use pattern; energy ratio; specific energy; energy productivity; pearl millet

check for updates

Citation: Kargwal, R.; Yadvika; Singh, V.K.; Kumar, A. Energy Use Patterns of Pearl Millet (*Pennisetumglaucum* (L.)) Production in Haryana, India. *World* **2023**, *4*, 241–258. https://doi.org/10.3390/world4020017

Academic Editor: Jungho Baek

Received: 13 February 2023
Revised: 30 March 2023
Accepted: 7 April 2023
Published: 19 April 2023

Copyright: © 2023 by the authors. Licensee MDPI, Basel, Switzerland. This article is an open access article distributed under the terms and conditions of the Creative Commons Attribution (CC BY) license (https://creativecommons.org/licenses/by/4.0/).

1. Introduction

Since the age of subsistence agriculture, one of the most precious inputs in the agricultural system has been energy. It is a fact that globally, the production of crops is positively interlinked with energy input [1]. The need for energy in different aspects of agriculture is different owing to variations in the level of technology adopted by farmers and various agro–climatic conditions. In developed countries, the enhancement of crop yields was predominantly due to improved crop varieties and increased commercial energy inputs [2]. Energy is consumed as well as produced in the agriculture sector. It uses massive amounts of locally offered non-commercial energy (seed, manure and animate energy), commercial energy and direct and indirect energy (electricity, diesel, fertilizer, plant protection, chemical, irrigation water and machinery, etc.) [3]. The efficient use of this energy aids in realizing enhanced production and productivity, which shares the benefits and competitiveness of agriculture sustainability in rural living [4]. Energy use in agriculture is increasing in response to the growing global population, restricted supply of cultivable land and the will for higher living standards [5].

Today, the world has reached a peak where energy is becoming the main cost factor in almost all processes in daily life [1]. Apart from this, energy and profit in many organi-

zations are closely related to the fact that energy audits and finance are fully interlinked. Most organizations are vulnerable to tracking energy monitoring and thus consume more energy than the energy required for the ideal work [6].

Pearl millet, also known as Bajra, is one of the main kharif crops in the arid and semi-arid farming regions of India [3]. It is the first in the millet category in India in terms of production, productivity and area. in the states of Rajasthan, Uttar Pradesh, Maharashtra, Haryana and Gujarat, pearl millet accounts for more than 90% of the total area and contributes to similar production levels [7]. According to FAO, millet production in the world is 89.17 million metric tons from an area of 74 million hectares [7]. India is the largest producer of pearl millet in the world, which has an area of 12.53 million hectares and produces 15.53 metric tons per year, with an average productivity of 1237 kg/ha throughout 2021–2022 [8]. In India, pearl millet comprises around 7.4% of the area, while in the case of production, it comprises nearly 3.4% of the total food grain of the country [9]. Pearl millet is examined as a "poor man's" crop, and it is rich in carbohydrates, protein, fat, fiber and mineral content [6]. In Haryana, during 2016–2017, pearl millet was grown in an area of 0.48 million ha with production and average productivity of 0.98 MT per year and 2017 kg/ha, respectively [10]. The states that grow pearl millet in India are Rajasthan, Uttar Pradesh, Maharashtra, Haryana and Gujrat [6]. As an important food crop of Haryana (India), there is an urgent need to assess the energy utilized in producing pearl millet. It also works as a raw material for cattle feed and cattle fodder [6].

The efficient use of available natural resources, proper energy management/conservation and minimization of energy losses throughout different unit operations of pearl millet production could be performed. Pearl millet is grown in the rainfed areas of Mahendergarh, Bhiwani and Jhajar, and in the case of the Hisar and Fatehabad districts of Haryana, it is grown under irrigated conditions.

2. Materials and Methods

A brief description of study area, methodology adopted for data collection and the procedure used for data analysis are presented in the following sections.

2.1. Selection of Work Area

A village in the Hisar district was selected to study energy use patterns in pearl millet production in an irrigated area of Haryana.

2.2. Selection of the Farmers

The farmers were grouped into three categories, viz., small (0.2–0.4 ha), medium (0.4–1 ha) and large (>1 ha) based on land holdings. Different unit operations for pearl millet production were studied regarding energy use patterns at the selected village of Dhigtana.

2.3. Collection of Data

A questionnaire (Appendix A) was prepared for collecting data through a face-to-face interview schedule from farmers regarding different operations and quantities of each input (i.e., machinery, fuel, fertilizer, pesticide, irrigation water, labor, etc.).

2.4. Tools of Analysis

Source-wise (direct and indirect) and operation-wise energy auditing for pearl millet production were studied in the selected region. Direct energy sources subsumed human, animal and diesel energy, while indirect energy sources included fertilizer, pesticide, seeds and machinery. Energy equivalents of various energy sources are given in Tables 1 and 2.

The following unit operations performed during pearl millet production were observed in the selected village. Different operations performed were preparatory tillage, sowing, interculture, irrigation, fertilizer application, pesticide application, harvesting, threshing and transportation.

2.5. Source-Wise (Direct and Indirect) Energy Inputs

Source-wise (direct and indirect) energy inputs are given in the following sections.

2.5.1. Direct Energy Inputs

Direct energy inputs are defined as input energy per hectare during pearl millet production; i.e., human (manual), animal energy and fuel energy, were calculated using the following equations [11–13].

a. Human energy

$$\text{Human energy } (\text{MJ.ha}^{-1}) = \frac{\text{H} \times \text{T}}{\text{A}} \times \text{HEF}$$

where

H = number of humans
T = operating time, h
A = operating area, ha
HEF = human energy equivalent factor, MJ.h^{-1}

b. Animal energy

$$\text{Animal energy } (\text{MJ.ha}^{-1}) = \frac{\text{N T}}{\text{A}} \times \text{AEF}$$

where

N = number of animals
T = operating time, h
A = operating area, ha
AEF = animal energy equivalent factor, MJ.h^{-1}

c. Fuel energy

$$\text{Fuel energy } (\text{MJ.ha}^{-1}) = \frac{\text{FC} \times \text{FE}_\text{q}\text{F}}{\text{A}}$$

where

FC = average fuel consumption, l
A = planted area, ha
FEqF = fuel energy equivalent factor, MJ.l^{-1}.

2.5.2. Indirect Energy Inputs

Indirect energy inputs per hectare during pearl millet production, i.e., machinery, seed, fertilizer and pesticide (chemical), were computed using the equations under [11–13].

d. Fertilizer energy

$$\text{Energy of N} = \frac{\text{Share of N} \times \text{EE}_\text{N}}{\text{A}}$$

$$\text{Energy of } \text{P}_2\text{O}_5 = \frac{\text{Share of P} \times \text{EE}_\text{P}}{\text{A}}$$

$$\text{Energy of } \text{K}_2\text{O} = \frac{\text{Share of K} \times \text{EE}_\text{K}}{\text{A}}$$

Total energy input of fertilizer = N (MJ.ha^{-1}) + P_2O_5 (MJ.ha^{-1}) + K_2O (MJ.ha^{-1})

where

N = nitrogen, kg
EE_P = nitrogen energy equivalent factor, MJ.kg^{-1}
P = phosphorus, kg
EE_N = phosphorus energy equivalent factor, MJ.kg^{-1}
K = potassium, kg
$EE_{K\,=}$ potassium energy equivalent factor, MJ.kg^{-1}
A = fertilized area, ha

e. Seed energy

$$\text{Seed energy } (\text{MJ.ha}^{-1}) = \frac{S \times EE_S}{A}$$

where

S = seed, kg
A = seeded area, ha
EE_S = seed energy equivalent factor, MJ.kg^{-1}

f. Pesticide energy

$$\text{Pesticide energy } (\text{MJ.ha}^{-1}) = \frac{Q \times \text{EE}_\text{P}}{A}$$

where

Q = quantity of pesticide, kg
A = operating area, ha
EE_P = pesticide energy equivalent factor, MJ.kg^{-1}

g. Machine energy

$$\text{Machine energy}(\text{MJ.ha}^{-1}) = \frac{\text{W} \times \text{EE}_\text{M}}{\text{UL} \times \text{A}} \times \text{H} \times \text{R}$$

where

W = weight of machine, kg
UL = useful life, h
H = operating time, h
R = no. of passes
A = area
EE_M = machine energy equivalent factor, MJ.kg^{-1}

Table 1. Standard energy equivalents for various sources [14].

Energy Source	Unit	Energy Equivalent (MJ/Unit)
Human labor		
Man	1 h	1.96
Woman	1 h	1.75
Child	1 h	0.98
Animal		
Bullock	pair hour	14.07 (body weight above 450 kg) 10.10 (body weight 350–450 kg)
Fuel		
Diesel	1 L	56.31
Farm Yard Manure	1 kg	0.3
Fertilizer		
Nitrogen	1 kg	60.6
Phosphorus	1 kg	11.1
Potash/Potassium	1 kg	6.70
Chemical application		
Superior	1 kg	120
Inferior	1 kg	10.0
Seed	1 kg	14.7

Table 2. Standard Energy equivalents for farm equipment [15].

Energy Source	Equipment	Energy Coefficient ($MJ.kg^{-1}$)
Manual	Sickle	0.031
	Sprayer	0.502
	Hand hoe	0.314
	Bund former	0.502
Animal	Plough	0.627
	Cultivator	1.881
Tractor	Tractor	10.944
	M B plough	2.508
	Harrow	7.336
	Rotavator	3.762
	Seed drill	8.653
	Cultivator	3.135
	Thresher	7.524
	Leveller	4.703

2.6. Energy Analysis

After collecting data regarding different unit operations in pearl millet cultivation, calculations were made regarding energy use efficiency, energy productivity, energy ratio and net energy gain. The values of these energy sources were obtained from the literature [16–19].

2.7. Energy Use Efficiency

Energy ratio or energy use efficiency was calculated as the ratio of the output and input energy from pearl millet production. After converting the yield into energy, output was calculated by multiplying it with its energy equivalent [19,20].

$$\text{Energy use efficiency} = \frac{\text{Energy output } (\text{MJ.ha}^{-1})}{\text{Energy input } (\text{MJ.ha}^{-1})}$$

2.8. Energy Productivity

Energy productivity (kg.MJ^{-1}) is defined as the ratio of the total amount of grain yield and the total energy input of harvested product.

$$\text{Energy productivity}(\text{kg.MJ}^{-1}) = \frac{\text{Grain yield}(\text{kg.ha}^{-1})}{\text{Total energy input } (\text{MJ.ha}^{-1})}$$

2.9. Net Energy Gain

Net energy gain (MJ.ha^{-1}) is defined as the difference between output and input energy.

$$\text{Net Energy Gain}(\text{MJ.ha}^{-1}) = \text{ Energy output } (\text{MJ.ha}^{-1}) - \text{ Energy input } (\text{MJ.ha}^{-1})$$

2.10. Specific Energy

Specific energy (MJ.kg^{-1}) is the ratio of amount of energy consumed to produced grain yield.

$$\text{Specific Energy}(\text{MJ.kg}^{-1}) = \frac{\text{Energy Input } (\text{MJ.ha}^{-1})}{\text{Pearl Millet Yield } (\text{kg.ha}^{-1})}$$

Cobb–Douglas model was used in the present study to develop a model in Microsoft Excel to analyze the relationship of energy inputs and yield for pearl millet production. The developed model was validated for the pearl millet production data collected for the irrigated region of Haryana. The objective of production function was to analyze the efficiency of all operations utilized in the production process, such as preparatory tillage, sowing, interculture, harvesting, threshing, etc.

The usual form of production function [21,22] is given as:

$$\text{Y} = aX_1^{b1}.aX_2^{b2}.\ldots\ldots.aX_7^{b7}.\text{U}$$

The function is easy to estimate in logarithmic form as:

$$logY = \log a + b_1 logX_1 + b_2 logX_2 + b_3 logX_3 + b_4 logX_4 + b_5 logX_5 + b_6 logX_6 + b_7 logX_7 + U$$

where

Y = dependent variable
X_j (1, 2, … 7) indicated independent variables including preparatory tillage (X_1), sowing (X_2), interculture (X_3), irrigation (X_4), fertilizer application (X_5), Pesticide application (X_6), harvesting (X_7)
b_1, b_2, b_7 = regression coefficient of independent variables
U = disturbance term
a = constant

3. Results

3.1. Source-Wise Energy Use Pattern

Figure 1 shows the total energy used and yield obtained during pearl millet production for different categories of farmers. It was found that large farmers consumed the highest

energy (402.50 MJ.ha^{-1}) while small farmers consumed the least energy (28,493.09 MJ.ha^{-1}), which indicated the dependency of energy utilization on the size of the farms and their level of production activities. The productivity of small, marginal and large farmers in irrigated areas was 19.00 q.ha^{-1}, 21.50 q.ha^{-1} and 23.12 q.ha^{-1}. The productivity depended on variety and seed rate.

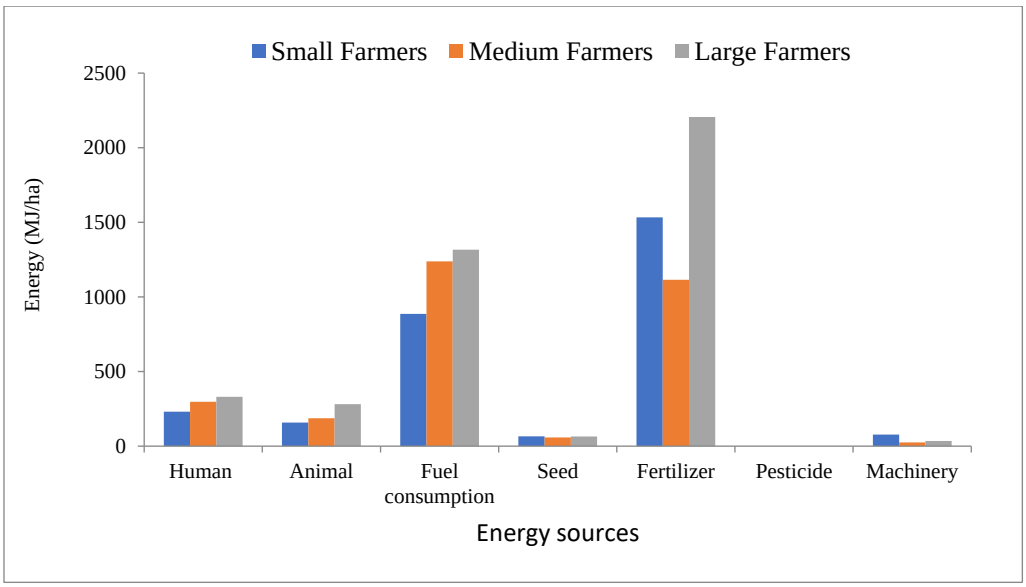


Figure 1. Source-wise energy use pattern in pearl millet production by small, medium and large farmers.

The fertilizer consumption of small, medium and large farmers was 1533.02 MJ.ha^{-1}, 1115.04 MJ.ha^{-1} and 2206.00 MJ.ha^{-1}, which showed that fertilizer application was lower in the case of medium farmers than small and large farmers because a lesser amount of fertilizer (urea) was applied by them than the recommended dose. None of the farmers applied pesticide. Fertilizer consumed 52% of the total energy, followed by diesel (30%), human (8%), animal (5%) and seed (2%). This trend was similar to [12,21,23,24].

The diesel energy consumed by small, medium and large farmers was 886.84 MJ.ha^{-1}, 1238.32 MJ.ha^{-1} and 1316.65 MJ.ha^{-1}, which showed that as the farm size increased, the use of diesel fuel, hence machinery, also increased. The fertilizer and fuel consumption share were similar to the results reported by [12,25].

3.2. Operation-Wise Energy Use Pattern in Pearl Millet Production

Fertilizer energy was highest among all the operations in all categories of farmers, followed by preparatory tillage. It was highest in large farmers, followed by medium and small farmers. This indicated that as farm size increased, fertilizer application increased, followed by preparatory tillage (Table 3).

The energy consumption of fertilizer by medium farmers was lower than by small and large farmers because some marginal farmers did not apply fertilizer in their fields. These findings were similar to the ones reported by Yadav et al. (2013) [19].

Medium farmers consumed more irrigation energy than small and large farmers because all the marginal farmers performed irrigation operations, but some of the small and large farmers performed irrigation while others depended on rain.

Table 3. Operation-wise energy use pattern in pearl millet production by different categories of farmers.

Operations / Farmers	Energy Utilized (MJ.ha^{-1})		
	Small Farmers	**Medium Farmers**	**Large Farmers**
Preparatory tillage	488.10	706.13	771.37
Sowing	300.22	371.76	357.97
Interculture	98.40	126.63	140.54
Irrigation	5.39	8.82	7.38
Fertilizer application	1543.74	1315.56	2212.01
Pesticide application	0	0	0
Harvesting	92.77	129.43	146.75
Threshing	294.32	284.42	301.00
Transportation	28.15	84.46	84.46
Total Energy	2849.09	3027.21	4021.50

3.3. Variation of Direct and Indirect Energy

Figure 2 indicates that indirect energy played a major role in energy consumed in the total energy consumption compared to direct energy, as small and large farmers used the higher fertilizer application. This was due to their higher dose of fertilizer application than recommended. This was a shared waste of energy, which did not result in higher crop yield. These results were similar to the ones in the literature [19,21,22]. In case of medium farmers, the utility of direct energy was higher due to more fuel consumption than indirect energy. The findings are similar to [26,27].

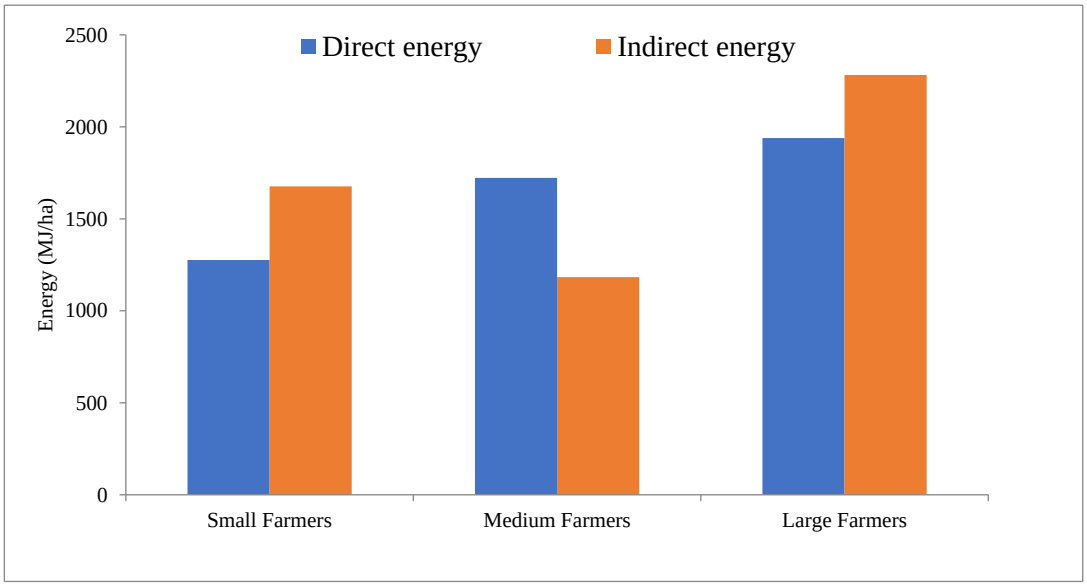


Figure 2. Variation of direct and indirect energy in different categories of farmers.

3.4. Variation Indicators of Energy Use Efficiency

Table 4 indicates that the energy use ratio for different farmers varied from 3.92 to 13.80. High energy ratios of 9.40 and 13.80 in large farmers indicated efficient energy. The findings are similar to [28] since they used a higher utilization of mechanical energy. The lowest energy ratio of 3.92 was found in small farmers, indicating low energy output level as compared to input. The energy productivity of different categories of farmers was computed to be 0.21 kg.MJ^{-1}, 0.65 kg.MJ^{-1} and 0.92 kg.MJ^{-1}. The values of marginal and large farmers are similar to the findings of (Yadav et al. 2013) [19].

Table 4. Variation of indicators of energy use efficiency for different categories of farmers.

Parameter/Farmers	Small Farmers	Medium Farmers	Large Farmers
Total input energy (MJ.ha^{-1})	2849.09	3027.21	4021.50
Energy output (MJ.ha^{-1})	11,172.00	28,518.00	55,566.00
Net energy gain (MJ.ha^{-1})	8323.13	25,490.79	51,545.39
Energy ratio	3.92	9.40	13.80
Specific energy (MJ.kg^{-1})	6.25	1.74	1.16
Energy productivity (kg.MJ^{-1})	0.21	0.65	0.92

The results in Table 5 indicate that 78% (R^2 = 0.78) of the variation in gross return was explained by seven variables in all the categories of farmers. It can also be seen that the sum of elasticities ($\sum b_i$ = 1.45) did not significantly deviate from unity, indicating an increasing return to scale. It showed that for pearl millet production, interculture had the highest impact (0.80) among the other inputs. The elasticity for interculture is 0.80, indicating that a given change (1%) in human energy will conclude in a 0.80% enhancement in yield. Some other important inputs were harvesting, sowing and preparatory tillage with elasticities of 0.56, 0.18 and 0.067, respectively. The sum of the regression coefficients of the energy consumption was examined as 1.45, which implied that a 1% increase in the total input energy would result in a 1.45% increase in the grain yield.

Table 5. Econometric estimation of pearl millet production.

Variables		Irrigated Region	t-Value
Preparatory tillage	X_1	0.067	−0.80 ***
Sowing	X_2	0.18	0.48 ^{ns}
Interculture	X_3	0.80	1.70 *
Irrigation	X_4	−0.043	1.14 *
Fertilizer application	X_5	−0.12	−0.14 ^{ns}
Pesticide application	X_6	0	0
Harvesting	X_7	0.56	1.03
Return to scale	($\sum b_i$)	1.45	
Constant		17.41	
R^2		0.78	

* Significant at 10%, *** Significant at 1%, ^{ns} non-Significant.

This indicated that the production function showed an increasing return to scale, which implied that if total energy inputs specified in the function were increased by 100%, then income would be enhanced by about 78%. The results are similar to the findings of (Wongnaa and Ofori, (2012); Akighir and Shabu, (2011) and Goni et al. (2007)) [29–31], who had observed an increasing return to scale on cashew production, tank command farming system and rice production, respectively, in Ghana, India and Nigeria.

4. Discussion

4.1. Source-Wise Energy Use Pattern

Figure 1 shows fertilizer had the highest energy share, followed by seed and machinery among indirect energy sources. The fertilizer contribution of small, medium and large farmers was found to be 1533.02 MJ/ha, 1115.04 MJ/ha and 2206 MJ/ha, respectively, which shows that fertilizer application was lower in the case of medium farmers than small and large farmers because a smaller amount of fertilizer (urea) was applied than the recommended dose. This is similar to research reported by Abubakar and Ahmad (2010) [32]. Human energy increased with increasing land holding because two operations

of interculture and harvesting were performed manually. Diesel had a big share of direct energy sources; it contributed 31%, 39% and 32% of direct energy in the case of small, medium and large farmers. Machine energy also followed the same trend as observed in the case of the rainfed area. Small farmers used higher seed rates as compared to large farmers. There is lot of variation in the variety of seeds used by farmers of the irrigated area. Pesticide application was not performed by any of the farmers of the irrigated area. Machinery consumed more energy in the case of small farmers, as some used less efficient animal-drawn machinery than large farmers who used efficient tractor-drawn machines such as cultivators, harrows and rotavators for tillage.

4.2. Operation-Wise Energy Use Pattern

Table 3 indicates that energy used by fertilizer was also highest among all the operations in all categories of farmers, followed by preparatory tillage and sowing in irrigated regions. These results were similar with the research reported by Abubakar and Ahmad (2010) [32]. The energy consumption of fertilizer in the case of medium farmers was lower as compared to small and large farmers because some medium farmers did not apply fertilizer in their fields. Small and medium farmers applied urea at the rate of 50–60 kg/ha, while large farmers applied urea at the rate of 60–90 kg/ha. Sowing and interculture followed a similar trend as preparatory tillage. Human energy increased with increasing land holdings. Irrigation energy was consumed more by medium farmers than small and large farmers because all the medium farmers performed irrigation operations, but in the case of small and large farmers, some performed irrigation while some left this operation and depended on rain only. Small farmers applied pesticide while the medium and large farmers did not. The energy consumed in harvesting operations increased as the size of the farm increased. A similar trend was also observed in the case of threshing. Large farmers consumed more energy in preparatory tillage, sowing, interculture and harvesting operations than medium and small farmers. This trend was similar to the research findings reported by Shahin et al. (2008); Pimentel and Pimentel (1996) and Walsh et al. (1998) [33–35], who suggested that energy consumption depended on farm size and the level of production activities.

4.3. Variation of Direct and Indirect Energy Sources

Figure 2 indicates that the indirect form of energy was found to be the major contributor of energy in total energy consumption, compared to direct energy, due to the higher doses of fertilizer application. The shares of indirect energy sources were more than direct energy in small and large farmers. Small and large farmers used higher doses of fertilizer compared to medium farmers.

4.4. Variation of Indicator of Energy Usage Efficiency for Different Categories of Farmers

The net energy yield of small, medium and large farmers of irrigated regions was 8339.13 MJ/ha, 25,416.58 MJ/ha and 51,542.39 MJ/ha. This means that the output energy was more than the input energy of pearl millet production. The energy use ratio for different categories of farmers varied from 3.92 to 13.80. A high energy ratio indicates an efficient level of energy usage. The findings are similar to the results of Sidhpuria et al., 2014 [29], who conducted work on resource conservation practices in rainfed pearl millet. This could be attributed to large farmers' higher use of manual and mechanical energies. The lowest energy ratio was obtained for small farmers, indicating low energy output level as compared to input, while the energy productivity of different categories of farmers of irrigated regions was calculated to be 0.21 kg/MJ, 0.65 kg/MJ and 0.92 kg/MJ. The values of medium and large farmers are similar to the findings of Yadav and Khandelwal, 2013 [19], who reported on wheat production in the state of MP (India).

5. Conclusions

The input energy of all farmers (small, medium and large) was 2849.09, 3027.21 and 4021.50 MJ.ha^{-1}, while the output was 11,172.00, 28,518.00 and 55,566.00 MJ.ha^{-1}. The energy ratios were 3.92, 9.40 and 13.80 for small, medium and large farmers. The energy productivity was 0.21 kg.MJ^{-1} (small), 0.65 kg.MJ^{-1} (medium) and 0.92 kg.MJ^{-1} (large). Manual energy increased with the size of land holding, indicating more labor work done by small farmers compared to larger ones. This indicated that large farmers used less labor to perform different operations, which took more time and energy. Based on the source-wise energy use pattern, the fertilizer application source was found to be the most energy-consuming, which increased with the size of land holding. Additionally, as the size of the farm increased, animal energy increased with land holding size, indicating less use of animal-drawn implements. A similar trend was observed for diesel fuel consumption. Seed energy decreased with the size of landholdings in both areas, indicating the higher use of seed by small farmers. None of the farmers applied pesticide (Atrazine) for pearl millet production.

This study will provide valuable information to farmers, scientists and policymakers, allowing them to recommend appropriate changes in agricultural practices that would result in substantial energy savings in the pearl millet production system, reducing the cost of operation and sustainable development. It will also give useful information to decision-makers and farmers, emphasizing the necessity of energy management in crop production. The amount of energy input and output differed by the category of farmers, geographical location and economic condition of farmers.

Author Contributions: R.K.: conceptualization; writing—original draft preparation, methodology, formal analysis; Y.: conceptualization, writing—review and editing, formal analysis, resources; V.K.S.: writing—original draft preparation, A.K.: writing—review and editing, formal analysis. All authors have read and agreed to the published version of the manuscript.

Funding: This research received no external funding.

Institutional Review Board Statement: Not applicable.

Informed Consent Statement: Not applicable.

Data Availability Statement: All data are given in the form of Tables and Figures.

Acknowledgments: The authors thank the support of the Department of Processing and Food Engineering, College of Agricultural Engineering and Technology, CCSHAU, Hisar, India.

Conflicts of Interest: The authors declare no conflict of interest.

Appendix A

General profile

Name of the respondent	:	_____
Age	:	_____
Village	:	_____
Tehsil/Block	:	_____
District	:	_____

a. **Caste hierarchy**

SC/ST	Backward	OBC	General

b. **Family type:**

- Nuclear
- Joint

c. **Family size:**

- 4 member
- 4–6 members
- Above 6 members

d. **Education**

- Illiterate/unlettered
- Can read and write/lettered
- Primary school
- Middle school
- High school
- Senior Secondary school
- Graduate and above

e. **Type of Farmers**

- Small
- Medium
- Large

f. **Total Family income from all sources:**

g. **Cropping pattern**

Crops	**Area**
Kharif	
Rabi	
Pearl millet	

h. **Occupation of the family**

Main occupation	Farming
	Service
	Business
	Daily wage earner
Subsidiary occupation	Farming
	Service
	Business
	Daily wage earner

i. **Total land holding under pearl millet cultivation (in hectare):**_____

j. **Livestock ownership**

	Small (1–2)	**Medium (3–4)**	**High (>4)**
Bullock			
Buffalo			
Cow			
Goat			
Camel			

k. **Farm Assets**

Assets	Yes	No
Tractor		
Power tiller		
Pump set		
Improved disc plough		
Tractor trolley		
Desi plough		
Sprayer/duster		
Land leveler/patella		
Seed drill/ridger		
Hand tools		
Thresher		
Winnower		
Chaff cutter		
Any other		

Specific information

1. Pearl millet cultivation

a. Participation of the respondent in Pearl millet cultivation

Sr. No.	Farm Activities	Yes	No
1	Seed selection		
2	Seed treatment		
3	Sowing		
4	Fertilizer application		
5	Interculture		
6	Weeding		
7	Crop care and nurturing		
8	Water management		
9	Watching birds		
10	Threshing		
11	Winnowing/Processing		
12	Cleaning/Grading		
13	Storing		
14	Marketing		

b. Adoption level of respondent about Pearl millet cultivation

Sr. No.	Adoption Statements	Yes	No
1.	**Pre- production**		
1	Recommended Cultivar to your area		
2	Area grown for seedling		
3	Followed methods for seed treatment and seed selection		
2.	**Production**		
1	Do you practice Green manuring crop		
2	Used the recommended quantity of NPK and FYM		
3	Used biofertilizers in Pearl millet cultivation		
4	Do you apply the recommended micro- nutrient?		
3.	**Plant protection**		
1	Do you use weedicide?		
2	Do you apply weedicide as per recommendation		
3	Control measures taken to control the pests		
4	Control measures taken to control the disease		
5	Used recommended quantity of chemical.		
4.	**Post harvesting**		
1	It is necessary to clean the Pearl millet before milling		
2	Thorough Drying is important		
3	Post harvest processing of produceHousehold level:Commercial level:		
4	Follow traditional storage methods		
5	Follow modern storage methods		
5.	**Marketing**		
1	Sell Pearl millet at the major Pearl millet markets in Haryana		
2	Rate of Pearl millet/quantity at present		

c. Improved farm implements

Name of the Implement/Tool (List out)	Are you Aware		Do you Use	
	Yes	No	Yes	No
Rotary weeder				
Sprayer				
Pearl millet thresher				

Energy equivalent of input in pearl millet production

1. Preparatory tillage

Method	Time Taken	Fuel Consumption	No. of Person Engaged	No. of Bullock	Weight of Machine	NP
Power operated						
Tractor						
Rotavator						
Harrow						
Cultivator + planker						
Bullock/Camel drawn planker						
Animal drawn cultivator(Trifali)						

2. Pre-sowing Irrigation

Method	Time Taken	Fuel Consumption	No. of Person Engaged	Water Requirment	Depth of Ground Water
Rain fed					
Canal Irrigation					
Pump-set for Irrigation					

3. Seed Treatment

Method	Time Taken	Fuel Consumption	No. of Person Engaged	Amount of Chemical	Amount of Seed
Manually					
By Machine					
Integrated Approach					

4. Sowing

Method	Time Taken	Fuel Consumption	No. of Person Engaged	No. of Bullock	Weight of Machine	NP *
Manually						
By Tractor						
Seed-drill						
By Bullock						

* = No. of passes for application of considered field operation.

5. Intercultural/weeding

Method	Time Taken	Fuel Consumption	No. of Person Engaged	Weight of Machine	NP *
Tractor					
Implement					
By Bullock					
Manual					
Hand tools					

* = No. of passes for application of considered field operation.

6. Irrigation

Method	Time Taken	Fuel Consumption	No. of Person Engaged	Water Requirement	Depth of Ground Water
Rainfall					
Canal Irrigation					
Pump-set for Irrigation					

7. Fertilizer

Method	Time Taken	Fuel Consumption	No. of Person Engaged	Amount of Fertilizer	Weight of Machine
Manually					
Tractor					
Seed-cum-fertilizer drill					

8. Chemical Application

Method	Time Taken	Fuel Consumption	No. of Person Engaged	Amount of Chemical	Weight of Machine
Manually					
Tractor					
Hand tools					

9. Harvesting

Method	Time Taken	Fuel Consumption	No. of Person Engaged	Weight of Machine
Manually				
Tractor				
By Machine				

10. Threshing

Method	Time Taken	Fuel Consumption	No. of Person Engaged	Weight of Machine
Manually				
Tractor				
Tractor drawn thresher				

11. Transportation

Method	Time Taken	Fuel Consumption	No. of Person Engaged
By truck			
Tractor-Trolly			

12. Thinning & gap Filling

Method	Time Taken	No. of Person Engaged
Manually		

References

1. Kargwal, R.; Yadvika, Y.; Kumar, A.; Garg, M.K.; Chanakaewsomboon, I. A review on global energy use patterns in major crop production systems. *Environ. Sci. Adv.* **2022**, *1*, 662–679. [CrossRef]
2. Faidley, L.W. Energy and Agriculture. In *Energy in Farm Production*; Fluck, R.C., Ed.; Elsevier: Amsterdam, The Netherlands, 1992.
3. Kargwal, R.; Yadvika; Garg, M.K.; Yadav, Y.K. Energy Auditing of Pearl Millet Production in Southern Haryana, India: A Case Study. *Environ. Ecol.* **2021**, *39*, 729737.
4. Singh, G. Energy conservation through efficient mechanized farming. *Agric. Eng. Today* **2002**, *24*, 351–536.
5. Kizilaslan, H. Input–output energy analysis of cherries production in Tokat Province of Turkey. *Appl. Energy* **2009**, *86*, 1354–1358. [CrossRef]
6. Kargwal, R.; Yadvika; Singh, V.K.; Garg, M.K.; Vinod; Kumar, M.; Mathur, M. Energy Consumption Pattern of Value Added Products of Pearl Millet. *Curr. J. Appl. Sci. Technol.* **2019**, *35*, 1–5. [CrossRef]
7. The Associated Chambers of Commerce and Industry of India. *Millets the Super Food for India*; The Associated Chambers of Commerce and Industry of India: New Delhi, India, 2022; p. 15.
8. International Year of Millets (IYoM). National Conference on Kharif Campaign, Ministry of Agriculture and Farmers Welfare. 2022. Available online: https://agricoop.nic.in/Documents/Crops_0.pdf (accessed on 19 April 2022).
9. Bhatnagar, S.K. *All India Coordinated Pearl Millet Improvement Project*; India Council of Agricultural Research: New Delhi, India, 2002.
10. Department of Agriculture Cooperation and Farmer Welfare. 2016. Available online: agricoop.nic.in (accessed on 19 April 2022).
11. Khambalkar, V.P.; Pohare, J.; Katkhede, S.; Bunde, D.; Dahatonde, S. Energy and Economic Evaluation of Farm Operations in Crop Production. *J. Agric. Sci.* **2010**, *2*, 191. [CrossRef]
12. Chaudhary, V.; Gangwar, B.; Pandey, D.; Gangwar, K. Energy auditing of diversified rice–wheat cropping systems in Indo-gangetic plains. *Energy* **2009**, *34*, 1091–1096. [CrossRef]
13. Bockari-Gevao, S.M.; Wan Ishak, W.I.; Azmin, Y.; Chan, C.W. Analysis of energy consumption in low land rice-based cropping system of Malaysia. *J. Sci. Technol.* **2005**, *27*, 819–826.
14. Karimi, M.; Rajabi, P.A.; Tabatabaeefar, A.; Borghei, A. Energy analysis of sugarcane production in plant farms: A case study in DebelKhazai Agroindustry in Iran. *Am. Eurasian J. Agric. Environ. Sci.* **2008**, *4*, 165–171.
15. Mittal, J.P.; Dhawan, C.K. *Research Manual, All India Co-Ordinated Research Project on Energy Requirement in Agricultural Sector*; College of Agricultural Engineering, Punjab Agricultural University: Ludhiana, India, 1988.
16. Ozkan, B.; Ceylan, R.F.; Kizilay, H. Comparison of energy inputs in glasshouse double crop (fall and summer crops) tomato production. *Renew. Energy* **2011**, *36*, 1639–1644. [CrossRef]
17. Canakci, M.; Topakci, M.; Akinci, I.; Ozmerzi, A. Energy use pattern of some field crops and vegetable production: Case study for Antalya Region, Turkey. *Energy Convers. Manag.* **2005**, *46*, 655–666. [CrossRef]
18. Hatirli, S.A.; Ozkan, B.; Fert, C. Energy inputs and crop yield relationship in greenhouse tomato production. *Renew. Energy* **2006**, *31*, 427–438. [CrossRef]
19. Yadav, R.S.; Khandelwal, N.K. Effect of various energy inputs on energy requirement for wheat production in agro-climatic region (Kamore plateau and Satpura Hill), M.P. India. *Int. J. Eng. Res. Appl.* **2013**, *3*, 531–536.
20. Basavalingaiah, K.; Ramesha, Y.; Paramesh, V.; Rajanna, G.; Jat, S.L.; Misra, S.D.; Gaddi, A.K.; Girisha, H.; Yogesh, G.; Raveesha, S.; et al. Energy Budgeting, Data Envelopment Analysis and Greenhouse Gas Emission from Rice Production System: A Case Study from Puddled Transplanted Rice and Direct-Seeded Rice System of Karnataka, India. *Sustainability* **2020**, *12*, 6439. [CrossRef]
21. Hamedani, S.R.; Shabani, Z.; Rafiee, S. Energy inputs and crop yield relationship in potato production in Hamadan province of Iran. *Energy* **2011**, *36*, 2367–2371. [CrossRef]
22. Komleh, S.P.; Keyhani, A.; Rafiee, S.; Sefeedpary, P. Energy use and economic analysis of corn silage production under three cultivated area levels in Tehran province of Iran. *Energy* **2011**, *36*, 3335–3341. [CrossRef]
23. Baran, M.F. Energy Efficiency Analysis of Cotton Production in Turkey: A Case Study for Ad yaman Province. *Am. Eurasian J. Agric. Environ. Sci.* **2016**, *6*, 229–233.
24. Kargwal, R.; Yadvika; Garg, M.; Singh, A.; Yadav, Y. Energy auditing of pearl millet production system in dry land region of Haryana Agrcultural University in Hisar, India. *Int. J. Agric. Eng.* **2019**, *12*, 191–195. [CrossRef]
25. Ozturk, H.H. Energy use for wheat cultivation in southeast Anatolia region of Turkey. *Agric. Mech. Asia Afr. Lat. Am.* **2016**, *47*, 47–52.
26. Firouzi, S.; Aminpanah, H. Energy use efficiency for groundnut (*Arachis hypogaea* L.) production in a semi-mechanized cultivation system. *Ann. Biol. Res.* **2012**, *3*, 3994–3997.
27. Mani, I.; Patel, S. Energy Consumption Pattern in Production of Paddy Crop in Haryana State in India. *Agric. Mech. Asia Afr. Lat. Am.* **2017**, *43*, 39–42.
28. Sidhpuria, M.S.; Sangwan, P.S.; Jhorar, B.S.; Mittal, S.B.; Sharma, S.K.; Kumar, A. Resource conservation practices in rain fedrearl millet-energy input-output analysis. *Indian J. Dryland Agric. Res. Dev.* **2014**, *29*, 83–86. [CrossRef]
29. Wongnaa, C.A.; Ofori, D. Resource-use efficiency in cashew production in Wenchi municipality, Ghana. *Agris Line Pap. Econ. Inform.* **2012**, *4*, 73–80.
30. Akighir, D.T.; Shabu, T. Efficiency of resource use in rice farming enterprise in kwande local government area of benue state, Nigeria. *Int. J. Humanit. Soc. Sci.* **2011**, *1*, 315–320.

31. Goni, M.; Mohammed, S.; Baba, B.A. Analysis of resource-use efficiency in rice production in the lake chad area of borno state, Nigeria. *J. Sustain. Dev. Agric. Environ.* **2007**, *3*, 31–37.
32. Abubakar, M.S.; Ahmad, D. Pattern of energy consumption in millet production for selected farms in Jigawa, Nigeria. *Aust. J. Basic Appl. Sci.* **2010**, *4*, 665–672.
33. Shahin, S.; Jafari, A.; Mobli, H.; Rafiee, S.; Karimi, M. Effect of farm size on energy ratio for wheat production: A case study from Ardabil Province of Iran. *Am. Eurasian J. Agric. Environ. Sci.* **2008**, *3*, 604–608.
34. Pimentel, D.; Pimentel, M. Energy use in grain and legume production. *Food Energy Soc.* **1996**, *107*, 130.
35. Walsh, M.E.; De La Torre Ugarte, D.; Slinsky, S.; Graham, R.L.; Shapouri, H.; Ray, D. Economic analysis of energy crop production in the US-location, quantities, price and impacts on traditional agricultural crops. *Bioenergy 98 Expand. Bioenergy Partnersh.* **1998**, *2*, 1302–1310.

Disclaimer/Publisher's Note: The statements, opinions and data contained in all publications are solely those of the individual author(s) and contributor(s) and not of MDPI and/or the editor(s). MDPI and/or the editor(s) disclaim responsibility for any injury to people or property resulting from any ideas, methods, instructions or products referred to in the content.

MR ADITYA JAIN (Orcid ID : 0000-0003-2509-4608)

DR. AMRISH PANWAR (Orcid ID : 0000-0001-5076-8593)

Article type : Article

Corresponding author mail id: panwaramar@gmail.com

Enhanced structural, dielectric, ferroelectric and piezoelectric properties of (1-*x*)$Ba_{0.9}Sr_{0.1}TiO_3$ – (*x*)$Ba_{0.7}Ca_{0.3}TiO_3$ ceramics derived using mechano-chemical activation technique

Aditya Jain[a], Amrish K. Panwar[*,a], Rakesh Saroha[a], A. K. Jha[b]

[a]*Department of Applied Physics, Delhi Technological University (Formerly Delhi College of Engineering), Bawana Road, Delhi-110042, India.*

[b]*Department of Applied Science, A.I.A.C.T.R. Geeta Colony, Delhi-110031, India.*

Abstract

The effect of $Ba_{0.7}Ca_{0.3}TiO_3$ (BCT) substitution on the structural, dielectric, ferroelectric and piezoelectric properties of mechano-chemically synthesized lead-free (1-*x*)$Ba_{0.9}Sr_{0.1}TiO_3$-(*x*)$Ba_{0.7}Ca_{0.3}TiO_3$ (*x* = 0.0, 0.10, 0.20, 0.35 and 0.50) ceramics have been investigated. X-ray diffraction patterns confirms the formation of tetragonal phase with *P4mm* space group. The results indicate a strong influence of BCT substitution on the structural and electrical properties of $Ba_{0.9}Sr_{0.1}TiO_3$ (BST) ceramic. BST-BCT ceramic for *x* = 0.35 have shown high dielectric constant ε_m ~ 21800, high remnant polarization P_r ~ 10.16 μC/cm^2, large piezoelectric charge constant D_{33} ~ 293 pC/N, large piezoelectric voltage constant g_{33} ~ 5.80 mV.m/N and highest dielectric breakdown strength E_{bd} ~ 224 kV/cm among the five synthesized samples. The correlation between structural,

* Corresponding author: Amrish. K. Panwar, E-mail: panwaramar@gmail.com, Tel: +91-9891778307 (Mobile).

This article has been accepted for publication and undergone full peer review but has not been through the copyediting, typesetting, pagination and proofreading process, which may lead to differences between this version and the Version of Record. Please cite this article as doi: 10.1111/jace.15061

This article is protected by copyright. All rights reserved.

Accepted Article

dielectric, ferroelectric and piezoelectric properties of the BST ceramic with increasing BCT content have been systematically described on the basis of domain wall motion and grain size effect.

Keywords: Dielectric; Microstructure; Ferroelectric; Piezoelectric; Energy storage.

1. Introduction

Barium titanate is a lead-free ferroelectric material, possesses high dielectric constant and low dielectric loss, which makes it useful for applications such as multi-layered ceramic capacitors and random access memory (RAM) devices [1]. Ferroelectric and piezoelectric ceramics have been extensively investigated and they are regarded as primary functional materials for various electronic, electrical and microelectronic component applications. With the recent advances in pulsed power technology, high energy density capacitors have been employed in pulse power equipments due to their better discharge efficiency and high energy storage capability [2]. Various lead-free $BaTiO_3$ based composites, such as $BaTiO_3$-$Bi(Ni_xTi_{1-x})O_3$ [3], $BaTiO_3$-$Bi(Zn_xTi_{1-x})O_3$ [4], $BaTiO_3$-$BiScO_3$ [5], etc. have been investigated and were found to exhibit thermally stable high dielectric constant over a broad temperature range. Alternatively, various other lead-free systems like $(Bi_{0.5}Na_{0.5})TiO_3$, $Bi_{0.5}(Na_{0.8}K_{0.2})_{0.5}TiO_3$, $(Na_{0.5}K_{0.5})NbO_3$, etc. were also explored for multifunctional device applications and these materials were found to exhibit better piezoelectric properties. Although, these material suffer reduced densification due to the presence of highly volatile elements like Na, Bi and K, which may have degraded their physical properties [6].

Currently, research is focused on the investigation of lead-free $BaTiO_3$ based materials which is attributed to their improved structural, dielectric, ferroelectric, pyroelectric, piezoelectric and multiferroic properties [7]. **Barium strontium titanate ($Ba_{1-x}Sr_xTiO_3$) composites are the most widely investigated materials until now due to their large tunability and extremely low dielectric loss around room temperature. In recent years, $Ba_{1-x}Sr_xTiO_3$ ceramics have long been investigated for applications in electronics and material science field. BST solid solutions need comparatively small DC bias voltage to achieve large tunability. Further, $Ba_{1-x}Ca_xTiO_3$ also possess interesting dielectric, ferroelectric and piezoelectric properties. It has been reported that up to 15 mol% of Ca^{2+} substitution at Ba^{2+} site, the ferroelectric to paraelectric phase transition temperature were found to be fairly stable [8]. Beyond the solid solubility limit of x = 23 mol%**

This article is protected by copyright. All rights reserved.

Accepted Article

in $Ba_{1-x}Ca_xTiO_3$ lattice, the tetragonal and orthorhombic phases coexists which results in improved electrical properties due to interaction of tetragonal and orthorhombic phases [9]. Therefore, combining the characteristics of both BST and BCT may result in improvement in their dielectric, ferroelectric and energy storage properties.

The aim of this work is to improve the electrical properties $BaTiO_3$ based ceramics, its versatility and to explore new functionalities. Our emphasis in the present work is to investigate the beneficial effect of $Ba_{0.7}Ca_{0.3}TiO_3$ addition on the structural and electrical properties. Our selection for the parent composition is justified by high dielectric constant, low dielectric loss, good ferroelectric properties and large piezoelectric constant. Further, In our enduring research for noble materials with overall superior dielectric, ferroelectric and piezoelectric properties for multi-layered ceramic capacitor, energy storage capacitors, etc.; herein we report the synthesis of $(1-x)Ba_{0.9}Sr_{0.1}TiO_3$-$(x)Ba_{0.7}Ca_{0.3}TiO_3$ (x = 0.0, 0.10, 0.20, 0.35 and 0.50) and their structural, dielectric, ferroelectric and piezoelectric properties.

2. Experimental

$(1-x)Ba_{0.9}Sr_{0.1}TiO_3$-$xBa_{0.7}Ca_{0.3}TiO_3$ (BST-BCT) ceramics for x = 0.0, 0.10, 0.20, 0.35 and 0.50 were prepared using mechano-chemical activation technique. BST-BCT was prepared by taking AR grade (Sigma-Aldrich make) $BaCO_3$ (99.99%), TiO_2 (99.9%), $SrCO_3$ (99.98%) and $CaCO_3$ (99.0%) as the starting precursor reagents. All the raw precursor reagent powders were taken in required stoichiometric quantity and the powders were grinded in *Retsch PM100* planetary ball mill in air atmosphere at 440 rpm for a period of 25 h. A cylindrical Zirconia vial with 45 mm inner diameter, 50 ml capacity and 150 Zirconia balls with 5 mm diameter were used as milling medium. A ball to powder ratio of 12:1 was kept inside the ball milling vial. After ball milling, BST-BCT solid solutions were calcined at 1050 °C for 4 h to make a desired phase. The resulting powders were then mixed with 2.5 wt% polyvinyl alcohol (PVA) and pressed into cylindrical pellets of approximately 12 mm diameter and thickness of 1.20 mm by applying a force of 70 kN using a hydraulic press machine. The pellets of the composite samples were then sintered at 1250 °C with heating rate of 6 °C/min for 4 h in air atmosphere. Hereafter, these specimens were identified as BSC0, BSC10, BSC20, BSC35 and BSC50 for x = 0.0, 0.10, 0.20, 0.35 and 0.50, respectively.

This article is protected by copyright. All rights reserved.

Accepted Article

The constituent phase and crystal structure of the synthesized BSC*x* specimens were examined by *Bruker D8 Advance* X-ray diffractometer having $CuK_{\alpha 1}$ radiation with operational wavelength of 1.541 Å. Lattice parameters and theoretical densities were evaluated using the XRD data with the help of *X'Pert Highscore Plus* software followed by Rietveld analysis. The microstructural characteristics and surface morphology of high temperature sintered pellet samples were examined using *Hitachi S-3700N* scanning electron microscope. Grain size distribution analysis has been carried out using *ImageJ* software. TEM/HRTEM and SAED analysis have been carried out using TEM (FEISTWIN PF30) at 300 kV by using copper grids (CF200-Cu). The sintered pellets of (1-*x*)BST-(*x*)BCT solid solutions were polished to a thickness of nearly 1.2 mm and slightly viscous silver paste was coated on both sides of the pellets to make electrodes, following this, the pellet samples were heated at 160 °C for 1 h. These pellets were then used to carry out dielectric measurement by an *Agilent E4980A* LCR meter at multiple frequencies (100 Hz, 1 kHz, 10 kHz, 50 kHz and 100 kHz). Temperature dependent dielectric measurement was performed over the wide temperature range of 25 to 200 °C. The ferroelectric hysteresis loops of the composites were recorded using a Sawyer-Tower based P-E loop equipment (*M/s Marine India, New Delhi*). **Electrical poling of the samples has been carried out using a DC poling equipment (*M/s Marine India, New Delhi*). The samples were poled by keeping the sample in a silicon oil bath for 2 h at *E* ~ 15 kV/mm at an optimized temperature of 70 °C.**

3. Results & discussion

3.1. X-ray diffraction (XRD)

The combined X-ray diffraction patterns of (1-*x*)BST-(*x*)BCT (*x* = 0.0, 0.10, 0.20, 0.35 and 0.50) samples are presented in Fig. 1(a1). All the BST-BCT samples prepared through mechano-chemical activation process exhibits a tetragonal structure without any traces of impurities. The sharp and intense diffraction peaks of BST-BCT samples indicate the crystalline nature of ceramics. Barium titanate (JCPDS file no. 00-005-0626) was taken as the reference XRD pattern, and the Pseudo-Voigt function has been used to refine the diffraction peaks. The smooth and well-fitted refined profile of BST-BCT samples with its experimental profile clearly suggest the validity of the refined model as well as Rietveld parameters. The observed and calculated d values of all the reflections (diffraction

This article is protected by copyright. All rights reserved.

Accepted Article

lines) of BST-BCT samples indicate that the basic crystal structure (i.e. tetragonal) has not changed as *x* varied from 0.0 to 0.50. However, as *x* increases, a slight increase in *c/a* ratio has been observed which suggest an increase in tetragonality with the addition of BCT. The diffraction peak shown in Fig. 1(a2) indicates that as *x* increases, the diffraction pattern shifts towards higher angle side. Further, the lattice parameters '*a*' and '*c*' were also found to decrease with BCT concentration which may be attributed to lower ionic radii of Ca^{2+} (1.34 Å) ion as compared to Sr^{2+} (1.44 Å) and Ba^{2+} (1.61 Å). The peak splitting around $2\theta = 45°$ in the XRD patterns of all the five samples also confirms that it exhibits a tetragonal structure with *P4mm* space group. Table 1 lists the Rietveld refinement structural parameters for the five synthesized samples. The unit cell volume of (1-*x*)BST-(*x*)BCT is observed to decrease as *x* increases, which results in lattice shrinkage and consequently may produce micro-strain in the structure.

3.2. Microstructural studies

The effect of $Ba_{0.7}Ca_{0.3}TiO_3$ addition in the $Ba_{0.9}Sr_{0.1}TiO_3$ ceramic is correlated with the microstructural formation, grain growth behavior and density of the resulting composites. The SEM micrograph shown in Fig. 2(a-e) demonstrate well developed polygonal grain type morphology with clearly distinguishable grain boundaries. The density of the BST-BCT composites were found to increase with BCT substitution and BSC35 shows the highest density among the five synthesized specimens. However, the addition of BCT in BST lattice leads to an increase in grain size, which suggests that BCT addition could assist the grain growth of the ceramics. **The increase in grain size with BCT substitution may be due to the fact that the grains of BCT may have higher probability of growing as compared to BST and therefore bigger grain grows at the cost of smaller grain. Moreover, in case of substitution/doping, it is hard to obtain an identical morphology and grain size due to the considerable difference in the sintering conditions and the thermal expansion coefficients of the two compounds [10, 11].** In higher BCT content ceramics, it may happen that the smaller grains merge into each other and grow into bigger ones, resulting in an increase in the fraction of larger grains in the entire microstructure. The average grain size has been calculated using ImageJ software and it is found to be approximately ~274, 286, 309, 335 and 323 nm for BSC0, BSC10, BSC20, BSC35 and BSC50, respectively. In earlier reports, it has been observed

This article is protected by copyright. All rights reserved.

Accepted Article

that the grain size of ceramics is reliant on its calcination and sintering temperature as well as soaking period at the peak temperature [12]. These two aspects have a foremost effect on the microstructural properties of the final sintered specimen and therefore, they eventually affect the dielectric and ferroelectric properties of the ceramics. In the present work, a better morphology combined with small grain size is obtained as compared to the earlier reports on $BaTiO_3$ based ceramics [7, 13]. **The density of the samples is measured for the pellet samples by the Archimedes method and the corresponding values are shown in Table 2. The density of the samples increases with increasing BCT substitution upto x = 0.35 and then decreases on further increase in BCT content. The values were within the range of 84-95 % of the theoretical density of $BaTiO_3$ (6.05 gm/cm3). Further, to clearly understand the grain growth of materials, the microstructure and density values were reported for BSC35 sample before PVA mixing, after PVA mixing and after 4 h of sintering. Fig. S1 in supplemental materials shows the above stated results which is available online.**

TEM, HRTEM and SAED studies of BSC35 have been performed as it shows overall superior electrical properties among the five synthesized samples. The average particle size is measured to be approximately ~145 nm for BSC35 powder as observed from TEM analysis (Fig. 3(a)). The perfectly parallely arranged lattice fringes do indicate the formation of perfectly crystalline material. HRTEM images can provide valuable evidences regarding the crystal phase and anisotropy in morphology of the material under study. In HRTEM images, it is considered that the orientation of the number of stacking layers is associated with the shape and atomic arrangement of unit cells. The HRTEM image of BSC35 particle (Fig. 3(b)) shows the lattice fringes corresponding to plane (101) with an inter-fringe distance of 1.77 Å. Fig. 3(c) depicts the selected area (electron) diffraction (SAED) pattern and it confirms the polycrystalline nature of BSC35 sample. The SAED pattern illustrates bright and dark spots in a circular pattern that may be assigned to different planes in the tetragonal crystal. Furthermore, both the HRTEM as well as SAED pattern recorded for the selected sample indicate that there are no noteworthy structural defects in the observed BSC35 sample.

This article is protected by copyright. All rights reserved.

Accepted Article

3.3. Dielectric studies

Figs. 4(a-j) shows the temperature dependence of the dielectric constant, ε and dielectric loss at various frequencies over the temperature range from room temperature to 200 ºC for all the synthesized samples. The dielectric constant of the samples were found to increase as x increases, becomes maximum at x = 0.35 and then decreases on further increase in x. **$Ba_{0.7}Ca_{0.3}TiO_3$ addition leads to compositional fluctuation, structural reorder as well as rearrangement of cations in one or more crystallographic sites of the structure. All three parameters result in change in overall polarization inside the material and this leads to variation in dielectric properties of the material. Further, BCT addition in BST also results in microscopic inhomogeneity in the overall compound leading to a little change in the phase transition temperature of the material.** The dielectric constant at Curie temperature for the samples BSC0, BSC10, BSC20, BSC35 and BSC50 at 1 kHz were found to be 15947, 16344, 17247, 21792 and 16687, respectively. BSC35 exhibits the highest dielectric constant which may be due to larger grain size as well as the density of the material. The dielectric properties of the material are significantly affected by the grain size of the material [14]. The high dielectric constant value for BSC35 may be attributed to the fact that the increase in grain size results in a decrease in the number of insulating grain boundary layers. The fewer number of grain boundaries corresponds to lesser trapping of space charge and thus domain wall pinning does not contribute to dielectric constant resulting in high dielectric constant [15]. Further, a ferroelectric single crystal contains multiple ferroelectric domains separated by an interface known as domain walls. These domain walls act as transition between different dipole alignments [16]. Also, the addition of BCT into BST lattice results in a small increase in transition temperature. The slight shift in Curie temperature towards high-temperature side may be caused by the occurrence of ion disorder and internal stress developed inside the material [7]. The dielectric constant value of all the BST-BCT ceramic samples increases with rise in temperature and close to Curie temperature it shows a strong anomaly in dielectric constant value, which is a characteristic of ferroelectric behavior. This behavior can be described on the basis of increase in domain wall mobility with rise in temperature [17].

Moreover, the dielectric constant of the samples displays an inverse dependence on frequency, which is the inherent characteristics of most of the dielectric and ferroelectric materials [18]. The

This article is protected by copyright. All rights reserved.

Accepted Article

Maxwell-Wagner multi-layer model for space charge or interfacial polarization can explain the behavior of dielectric constant with variation in frequency [19]. This model demonstrates that any dielectric material contains a large number of grains that are separated by thin insulating grain boundaries. On the application of an external electric field, the positive and negative charge carriers are relocated inside the grain and they get accumulated at the edges of the grain. This accumulation of electric charges at boundaries causes a large polarization resulting in high dielectric constant [20]. At lower frequency of operation, all four kinds of polarizations namely ionic, electronic, dipolar and interfacial polarization contribute to the total polarization of the material and this result in an enhancement in dielectric constant value. At higher operating frequency, some of the polarizations cease to contribute, and therefore total polarization inside the material consist of only interfacial and dipolar polarization and hence at higher frequency dielectric constant decreases [18]. Similar behavior has been reported in many ferroelectric materials [21].

It can be observed that the dielectric loss of BST-BCT samples increases as the temperature increases. This increase in dielectric loss value at high temperature may be due to (i) increased mobility of ions, (ii) the imperfection in the material and (iii) shallow contribution of thermally activated charge carriers inside the material which would hinder the contribution of dipolar polarization [22]. Further, the dielectric loss of the materials were found to decrease with BCT substitution; becomes minimum for BSC35 and increases again on increasing the BCT content. The decrease in dielectric loss with increasing BCT content may be attributed to reduction in leakage current that rely on the crystal structure impurities like vacancies, dislocations and ionic charge imbalance [23].

3.4. Ferroelectric studies

Fig. 5 shows electric field induced polarization loops recorded at 10 Hz test frequency. The *P-E* loop measurement have been carried out at three different temperatures by increasing the electric field up to ~ 20 kV/cm. The insets of Figs. 5(a), 6(b) and 6(c) shows the variation of remnant polarization ($2P_r$) and ratio of remnant and saturation polarization (P_r/P_s) with increasing BCT content. Well saturated P-E loops confirm the ferroelectric nature of all the five samples. The shape of hysteresis *P-E* loops are associated with the crystalline structure of the material under study. The room temperature

This article is protected by copyright. All rights reserved.

Accepted Article

saturation polarization ($2P_s$), remnant polarization ($2P_r$) and coercive field ($2E_c$) values for the BST-BCT samples are shown in Table 2. It is observed that the remnant polarization first decreases up to x = 0.10 and then increases with the increase in x content and becomes maximum for x = 0.35. A higher remnant polarization combined with high coercive field is achieved for BSC35 sample that may be attributed to higher grain size of the composite observed in SEM micrograph in Fig 3(d). Further, the high remnant polarization for the BSC35 sample is possibly due to low defect density, compositional homogeneity, uniform distribution of grains, nonexistence of domain-wall pinning centers, etc. Further, the sharp nature of *P-E* hysteresis loop confirms the high resistance and low loss nature of BSC*x* ceramics. Larger grain size may contain larger individual ferroelectric domains resulting in lesser number of grain boundary regions, which are known to be low permittivity regions with poor ferroelectricity [24]. Moreover, domain walls among larger grains are easier to switch under externally applied electric field, which results in higher remnant polarization. The addition of BCT in BST lattice leads to an improvement in the shape of ferroelectric hysteresis loop, which may be ascribed to reduction in leakage current due to decrease in number of oxygen vacancies [25]. The ferroelectricity of the samples were found to decrease at higher temperatures. The decrease in remnant polarization at higher temperatures may be attributed to decrease in ferroelectric and increase in paraelectric phase of the material. At all three temperatures, a steady increase in coercive field of the BSC*x* samples is observed with the subsequent increase of BCT content. The occurrence of high coercive field with an increase in BCT content makes the samples ferroelectrically hard. Further, the coercive field (E_c) obtained from *P-E* hysteresis loop measurement has been used to determine the poling electric field to reorient the ferroelectric domains of BSC*x* ceramics.

3.5. Breakdown strength measurement

The dielectric breakdown strength (E_{bd}) of all the synthesized specimens have been measured and shown in Fig. 6. **Dielectric breakdown strength (E_{bd}) measurements of BST-BCT samples were performed on the silver electroded pellet by immersing the specimen in a silicon oil bath onto a sheet of highly conductive copper connected to high voltage DC supply. Some external parameters such as frequency and ramp rate of the externally applied electric field also affect the dielectric breakdown strength. In the present study, the frequency is set to 50 Hz and the**

This article is protected by copyright. All rights reserved.

Accepted Article

ramp rate of applied electric field were kept constant at 1 kV/s. The E_{bd} value is known to be dependent on the grain size, electrode geometry, density, area and thickness of the specimen under study. Moreover, homogeneous microstructure and high density are beneficial in improving dielectric breakdown strength [26]. Table 2 list the dielectric breakdown strength of all the five synthesized samples. The E_{bd} is found to be maximum for BSC35, which may be ascribed to uniform grain size and high density of the material. In a ceramic material, under the application of externally applied electric field, as the number of weakly related ions with higher porosity and lower density rises, the space displacement polarization increases. This increase in space displacement polarization forces the micropores inside the material to offer very small resistance to electrical breakdown and depreciate the E_{bd} value [27]. Thickness dependent dielectric study has also been carried out which is available online in supplemental materials.

3.6. Piezoelectric studies

The electromechanical response as a function of BCT content for the five synthesized samples was recorded. Fig. 7 depicts the variation of piezoelectric constant (d_{33}) and piezoelectric voltage coefficient (g_{33}) as a function of BCT content. In the process of electrical poling of ceramics when an external electric field is applied, materials with arbitrarily distributed dipoles become polarized in the same direction as that of the applied electric field. Poling plays an essential role in determining the piezoelectric properties of any polycrystalline ferroelectric material. Further, some other parameters such as poling time, poling voltage and poling temperature affect the piezoelectric properties and so they need to be optimized. In the present study, all the samples were poled for 2 h at E ~ 15 kV/mm at an optimized poling temperature of T_P ~ 70 ºC, at which superior piezoelectric properties were observed. Poling of ceramics at an appropriate temperature helps in accumulation of charge carriers around the grain boundaries introducing an internal electric field that can increase the electromechanical response of the poled materials [28]. The magnitude of longitudinal piezoelectric constant is found to be maximum for BSC35 and decreases on further increase of BCT concentration. The d_{33} values of each of the five synthesized BST-BCT samples are shown in Table 2. It is believed that higher value of BSC35 may be attributed to better crystallinity as well as an optimum combination of grain size and density of the material. All these piezoelectric constants are affected by

This article is protected by copyright. All rights reserved.

Accepted Article

ferroelectric domain structure. It has been reported that piezoelectric constant decreases with decrease in grain size [29]. Furthermore, previous investigations on piezoelectric materials suggested a parabolic relation between grain and domain sizes [30]. The piezoelectric voltage constant, g_{33} has been calculated by dividing the piezoelectric constant (d_{33}) of the material by its permittivity, ε. Finally, it can be established that BSC35 exhibits the optimum ferroelectric and piezoelectric properties among the five synthesized samples. Moreover, the piezoelectric coefficients, d_{33} and g_{33} obtained in the present study are comparable to several lead-based ceramics reported in the literature [31, 32].

4. Conclusion

Mechano-chemical activation technique was employed to synthesize BCT substituted BST crystalline powders. The XRD patterns and Rietveld refinement of BST-BCT samples confirms a tetragonal phase with *P4mm (99)* space group for all the synthesized samples. There was no noteworthy change in phase and crystal structure of samples with an increase in BCT content. Microstructural (grain size & relative density), dielectric, ferroelectric and piezoelectric properties were found to improve with BCT addition. Overall, BSC35 exhibits better microstructural as well as electrical properties among the five synthesized samples. The optimized poling conditions have resulted in high piezoelectric charge constant d_{33} ~ 293 pC/N and large piezoelectric voltage constant g_{33} ~ 5.82 mV.m/N for BSC35 sample. Finally, it can be concluded that the BST-BCT materials are easy and inexpensive to design. In addition, improved microstructural and electrical properties indicate that the mechano-chemical synthesis approach represents a better way to prepare materials for application in multi-layer ceramic capacitors and low loss dielectric materials.

5. Acknowledgements

Authors gratefully acknowledge the support of DST-SERB (Grant no. PS/039/2011), India to successfully complete this research.

This article is protected by copyright. All rights reserved.

Accepted Article

Accepted Article

References

1. Zimmermann F, Voigts M, Menesklou W, et al. $Ba_{0.6}Sr_{0.4}TiO_3$ and $BaZr_{0.3}Ti_{0.7}O_3$ thick films as tunable microwave dielectrics. *J. Eur. Ceram. Soc.* 2004;24:1729-1733.
2. Xiao S, Xiu S, Zhang W, et al. Effects of $Ba_xSr_{1-x}TiO_3$ ceramics additives on structure and energy storage properties of $Ba_{0.4}Sr_{0.6}TiO_3$–BaO–B_2O_3–Al_2O_3–SiO_2 glass-ceramic. *J. Alloys Compd.* 2016;675:15-21.
3. Fujii I, Nakashima K, Kumada N, et al. Structural, dielectric, and piezoelectric properties of $BaTiO_3$-$Bi(Ni_{1/2}Ti_{1/2})O_3$ ceramics. *J. Ceram. Soc. Jpn.* 2012;120:30-34.
4. Raengthon N and Cann DP. Dielectric relaxation in $BaTiO_3$–$Bi(Zn_{1/2}Ti_{1/2})O_3$ ceramics. *J. Am. Ceram. Soc.* 2012;95:1604-1612.
5. Ogihara H, Randall CA, and Trolier- McKinstry S. Weakly coupled relaxor behavior of $BaTiO_3$–$BiScO_3$ ceramics. *J. Am. Ceram. Soc.* 2009;92:110-118.
6. Puli VS, Pradhan DK, Riggs BC, et al. Synthesis and characterization of lead-free ternary component BST–BCT–BZT ceramic capacitors. *J. Adv. Dielectr.* 2014;04:1450014.
7. Chao X, Wang J, Liang P, et al. Phase transition and improved electrical performance of $Ba_{0.85}Ca_{0.15}Zr_{0.1}Ti_{0.9}O_3$–$Ca_{0.28}Ba_{0.72}Nb_2O_6$ ceramics with high Curie temperature. *Mater. Des.* 2016;89:465-469.
8. McQUARRIE M and BEHNKE FW. Structural and dielectric studies in the system $(Ba,Ca)(Ti,Zr)O_3$. *J. Am. Ceram. Soc.* 1954;37:539-543.
9. Souza AE, Teixeira SR, Morilla-Santos C, et al. Photoluminescence activity of $Ba_{1-x}Ca_xTiO_3$: dependence on particle size and morphology. *J. Mater. Chem. C.* 2014;2:7056-7070.
10. Puli VS, Kumar A, Chrisey DB, et al. Barium zirconate-titanate/barium calcium-titanate ceramics via sol–gel process: novel high-energy-density capacitors. *J. Phys. D: Appl. Phys.* 2011;44:395403.
11. Rai AK, Rao K, Kumar LV, et al. Synthesis and characterization of ultra fine barium calcium titanate, barium strontium titanate and $Ba_{1-2x}Ca_xSr_xTiO_3$ (x= 0.05, 0.10). *J. Alloys Compd.* 2009;475:316-320.
12. Herabut A and Safari A. Processing and electromechanical properties of $(Bi_{0.5}Na_{0.5})_{(1-1.5x)}La_xTiO_3$ ceramics. *J. Am. Ceram. Soc.* 1997;80:2954-2958.
13. Zimmermann F, Voigts M, Menesklou W, et al. $Ba_{0.6}Sr_{0.4}TiO_3$ and $BaZr_{0.3}Ti_{0.7}O_3$ thick films as tunable microwave dielectrics. *J. Eur. Ceram. Soc.* 2004;24:1729-1733.
14. Jain A, Panwar AK, and Jha A. Effect of ZnO doping on structural, dielectric, ferroelectric and piezoelectric properties of $BaZr_{0.1}Ti_{0.9}O_3$ ceramics. *Ceram. Int.* 2017;43:1948-1955.
15. Jain A, Panwar AK, and Jha AK. Influence of milling duration on microstructural, electrical, ferroelectric and piezoelectric properties of $Ba_{0.9}Sr_{0.1}Zr_{0.04}Ti_{0.96}O_3$ ceramic. *Ceram. Int.* 2016;42:18771-18778.
16. Mudinepalli VR, Feng L, Lin W-C, et al. Effect of grain size on dielectric and ferroelectric properties of nanostructured $Ba_{0.8}Sr_{0.2}TiO_3$ ceramics. *J. Adv. Ceram*. 2015;4:46-53.
17. Jain A, Panwar AK, and Jha AK. Structural, dielectric and ferroelectric studies of $Ba_{1-x}Sr_xTiO_3$ ceramics prepared by mechanochemical activation technique. *J. Mater. Sci. - Mater. Electron.* 2016;27:9911-9919.
18. Alkathy MS, Gayam R, and Raju KCJ. Effect of sintering temperature on structural and dielectric properties of Bi and Li co-substituted barium titanate ceramic. *Ceram. Int.* 2016;42:15432-15441.

This article is protected by copyright. All rights reserved.

19. Montanari G and Morshuis P. Space charge phenomenology in polymeric insulating materials. *IEEE Trans. Dielectr. Electr. Insul.* 2005;12:754-767.

20. Liu G, Fan H, Xu J, et al. Colossal permittivity and impedance analysis of niobium and aluminum co-doped TiO_2 ceramics. *RSC Adv.* 2016;6:48708-48714.

21. Chou X, Zhai J, and Yao X. Relaxor Behavior and Dielectric Properties of $MgTiO_3$-Doped $BaZr_{0.35}Ti_{0.65}O_3$ Composite Ceramics for Tunable Applications. *J. Am. Ceram. Soc.* 2007;90:2799-2801.

22. Ang C, Yu Z, and Cross L. Oxygen-vacancy-related low-frequency dielectric relaxation and electrical conduction in Bi:$SrTiO_3$. *Phys. Rev. B: Condens. Matter*. 2000;62:228.

23. Verma A, Goel T, Mendiratta R, et al. Dielectric properties of NiZn ferrites prepared by the citrate precursor method. *Mater. Sci. Eng., B* 1999;60:156-162.

24. Ganguly M, Rout S, Ahn C, et al. Structural, electrical and optical properties of $Ba(Ti_{1-x}Yb_{4x/3})O_3$ ceramics. *Ceram. Int.* 2013;39:9511-9524.

25. Ganduglia-Pirovano MV, Hofmann A, and Sauer J. Oxygen vacancies in transition metal and rare earth oxides: Current state of understanding and remaining challenges. *Surf. Sci. Rep.* 2007;62:219-270.

26. Lei W, Yan Y-Y, Wang X-H, et al. Improving the breakdown strength of $(Mg_{0.9}Zn_{0.1})_2(Ti_{1-x}Mn_x)O_4$ ceramics with low dielectric loss. *Ceram. Int.* 2015;41:521-525.

27. Lei W, Ang R, Wang X-C, et al. Phase evolution and near-zero shrinkage in BaAl2Si2O8 low-permittivity microwave dielectric ceramics. *Mater. Res. Bull.* 2014;50:235-239.

28. Wu J, Xiao D, Wu W, et al. Composition and poling condition-induced electrical behavior of $(Ba_{0.85}Ca_{0.15})(Ti_{1-x}Zr_x)O_3$ lead-free piezoelectric ceramics. *J. Eur. Ceram. Soc.* 2012;32:891-898.

29. Randall CA, Kim N, Kucera JP, et al. Intrinsic and extrinsic size effects in fine- grained morphotropic- phase- boundary lead zirconate titanate ceramics. *J. Am. Ceram. Soc.* 1998;81:677-688.

30. Cao W and Randall CA. Grain size and domain size relations in bulk ceramic ferroelectric materials. *J. Phys. Chem. Solids*. 1996;57:1499-1505.

31. Li T and Long X. Piezo-/dielectric properties of perovskite-structure high-temperature relaxor ferroelectrics: The $Pb(Lu_{1/2}Nb_{1/2})O_3$–$Pb(Zn_{1/3}Nb_{2/3})O_3$–$PbTiO_3$ ternary ceramics. *Mater. Res. Bull.* 2014;51:251-257.

32. Xing Z, Wang H, Xu B, et al. Structural integrity and ferroelectric–piezoelectric properties of $PbTiO_3$ coating prepared via supersonic plasma spraying. *Mater. Des.* 2014;62:57-63.

Accepted Article

This article is protected by copyright. All rights reserved.

Table 1. Comparison of Rietveld refined parameters for BST-BCT specimens.

Sample	a,b (Å)	c (Å)	c/a	Cell volume (Å^3)	Structure	χ^2	R_{exp}	R_f	R_{Bragg}
BSC0	**3.9822**	**4.0127**	**1.0076**	**63.63**	Tetragonal	**2.71**	**1.02**	**6.19**	**5.12**
BSC10	**3.9787**	**4.0082**	**1.0074**	**63.45**	Tetragonal	**3.48**	**3.11**	**5.88**	**3.87**
BSC20	**3.9765**	**4.0063**	**1.0074**	**63.34**	Tetragonal	**3.02**	**3.94**	**6.93**	**6.41**
BSC35	**3.9708**	**4.0046**	**1.0085**	**63.14**	Tetragonal	**2.98**	**3.71**	**6.87**	**1.74**
BSC50	**3.9658**	**4.0014**	**1.0082**	**62.93**	Tetragonal	**3.23**	**3.58**	**6.95**	**4.35**

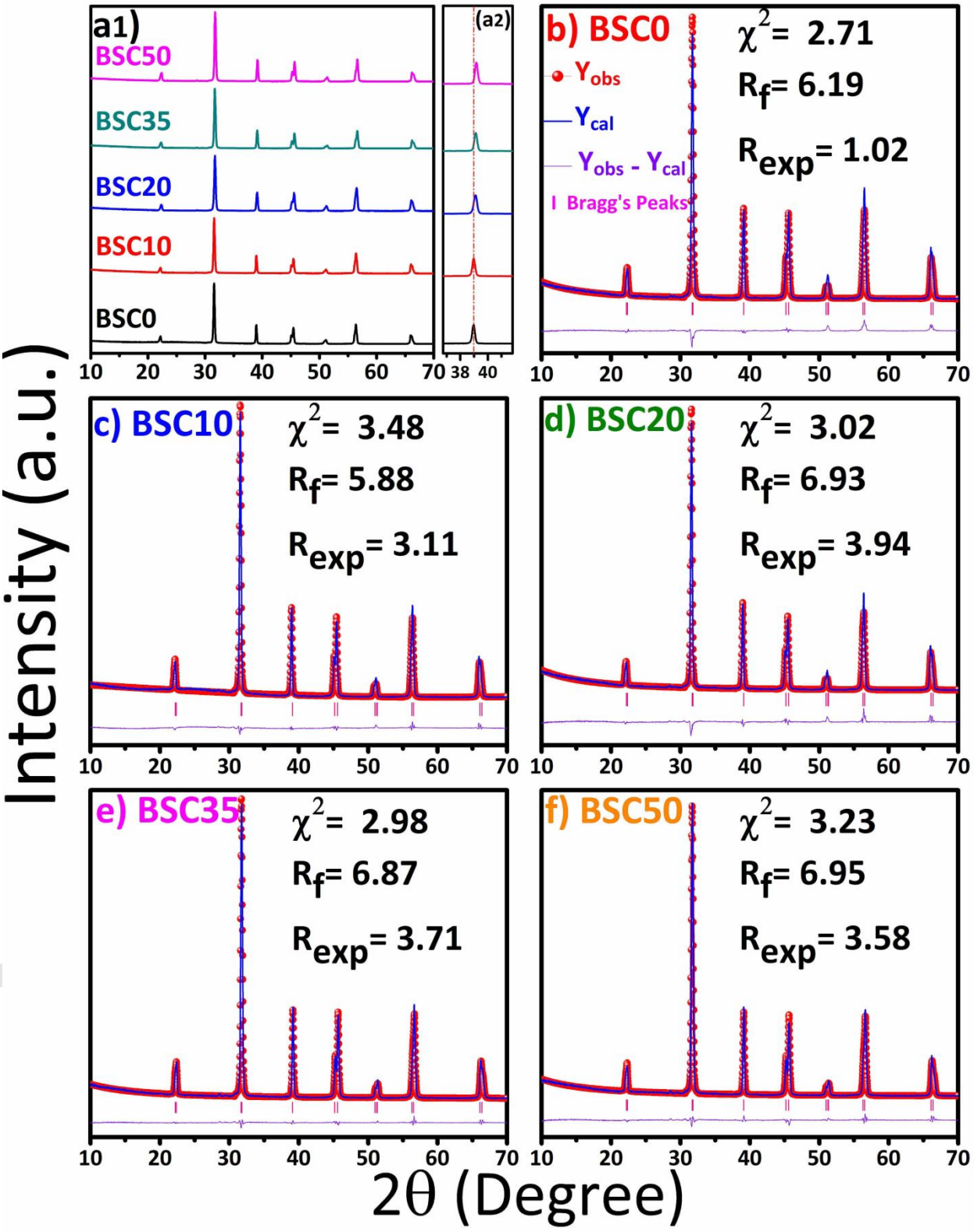
Table 2. Room temperature saturation polarization (P_s), remnant polarization ($2P_r$), coercive field ($2E_c$), density, dielectric breakdown strength (E_{bd}) and piezoelectric constant (d_{33}) for BSC0, BSC10, BSC20, BSC35 and BSC50.

Sample	$2P_s$ (μC/cm^2)	$2P_r$ (μC/cm^2)	$2E_c$ (kV/cm)	Density (gm/cm^3)	E_{bd} (kV/cm)	d_{33} (pC/N)
BSC0	23.48	9.17	4.54	5.082	183	213
BSC10	21.55	4.56	4.74	5.293	154	256
BSC20	18.85	4.69	5.15	5.421	173	288
BSC35	21.39	10.16	5.65	5.705	224	293
BSC50	21.60	9.50	9.53	5.477	181	241

Accepted Article

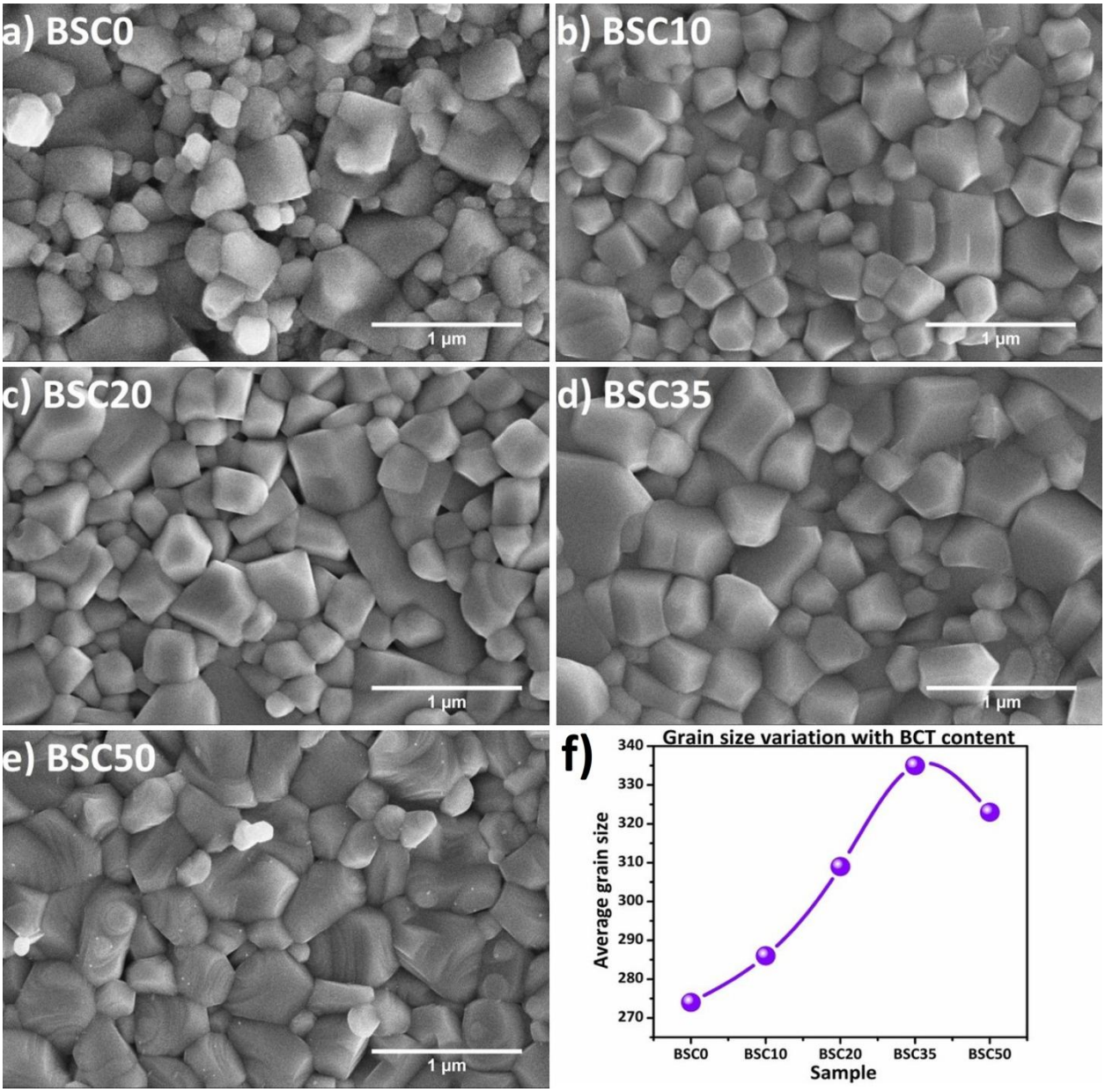
This article is protected by copyright. All rights reserved.

Accepted Article



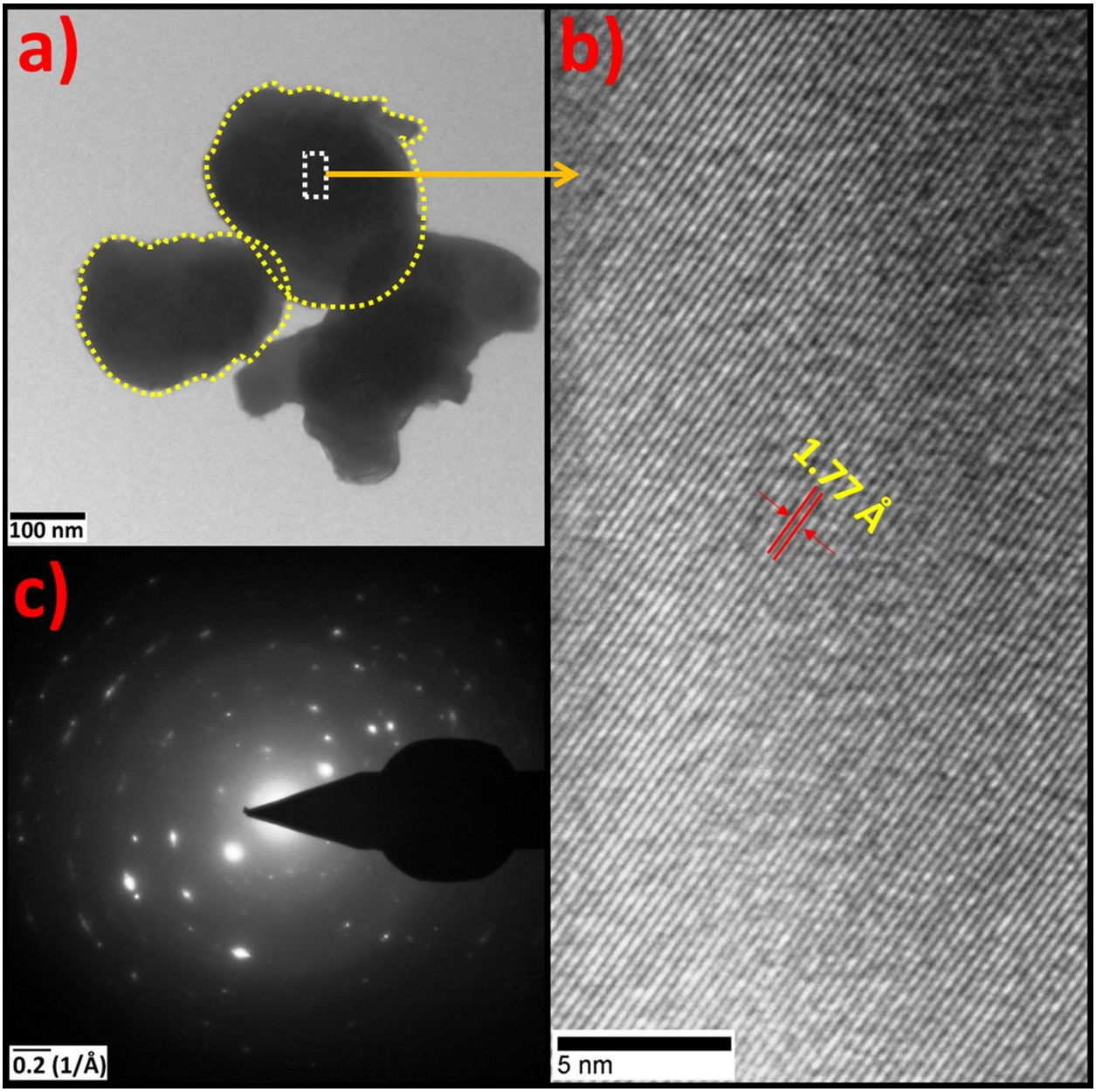
This article is protected by copyright. All rights reserved.

Accepted Article



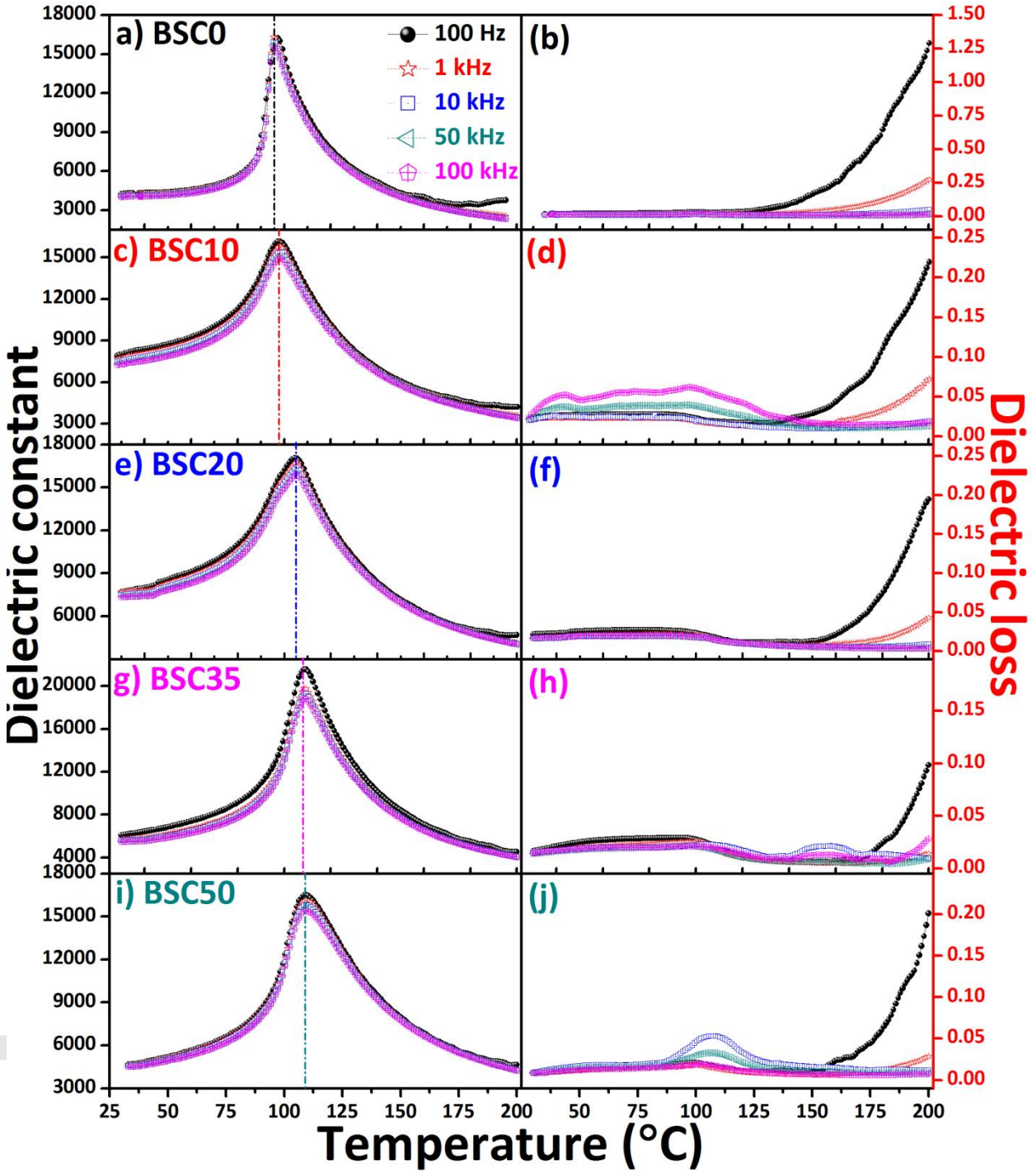
This article is protected by copyright. All rights reserved.

Accepted Article



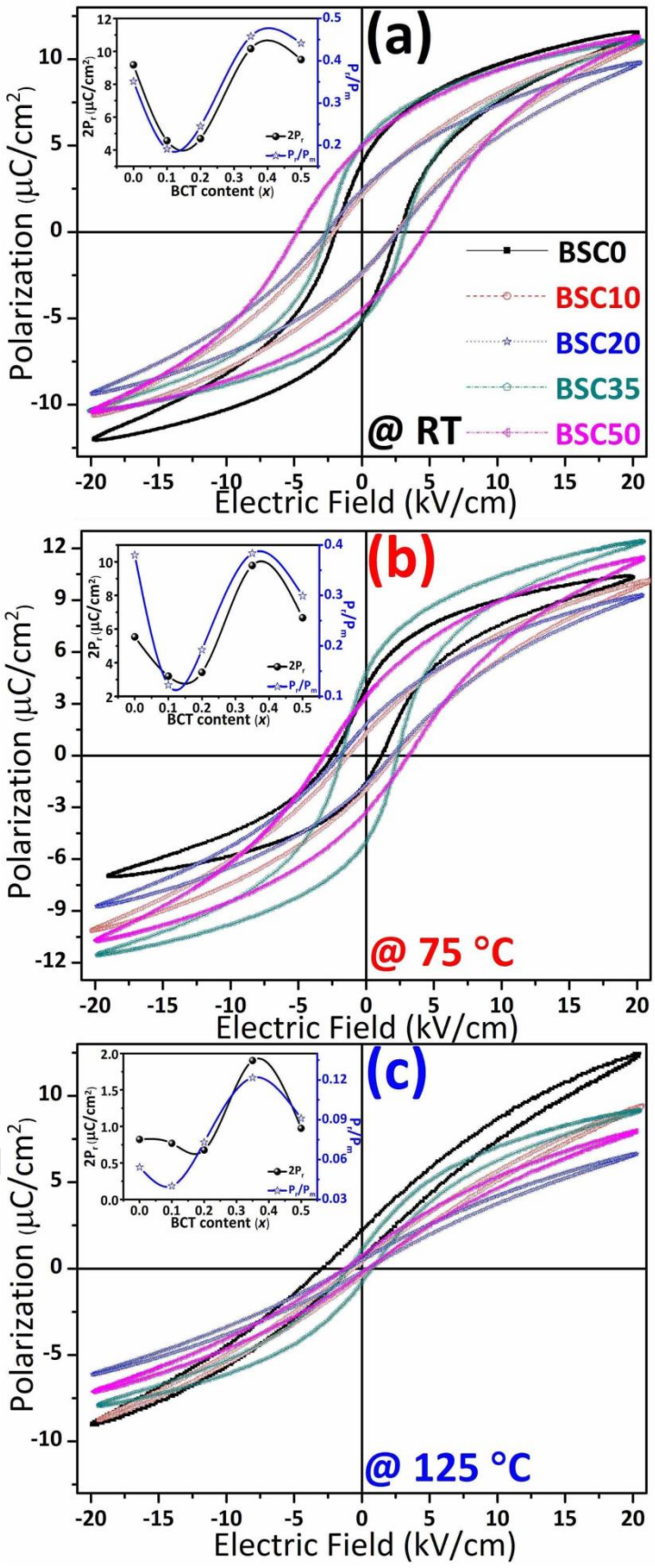
This article is protected by copyright. All rights reserved.

Accepted Article



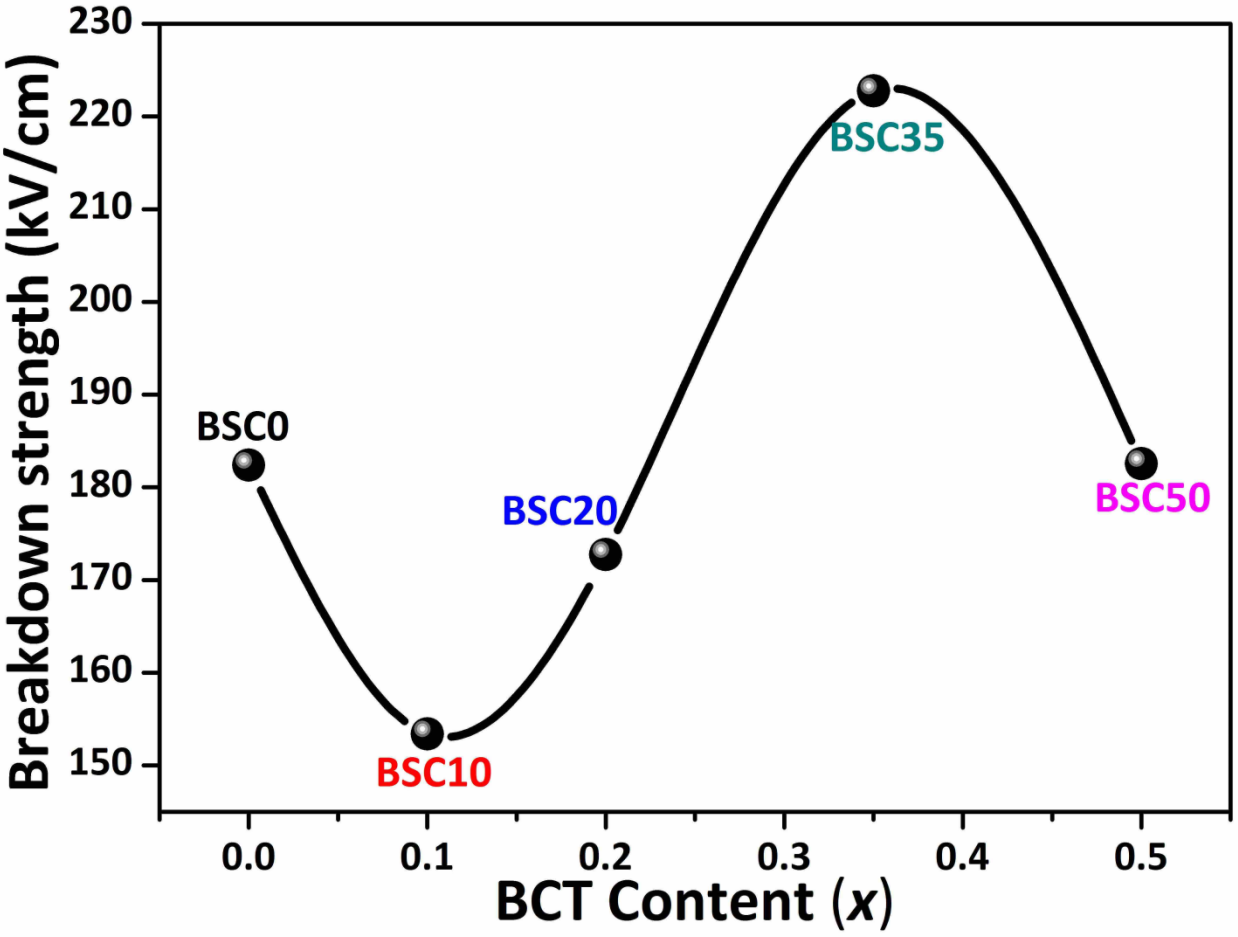
This article is protected by copyright. All rights reserved.

Accepted Article



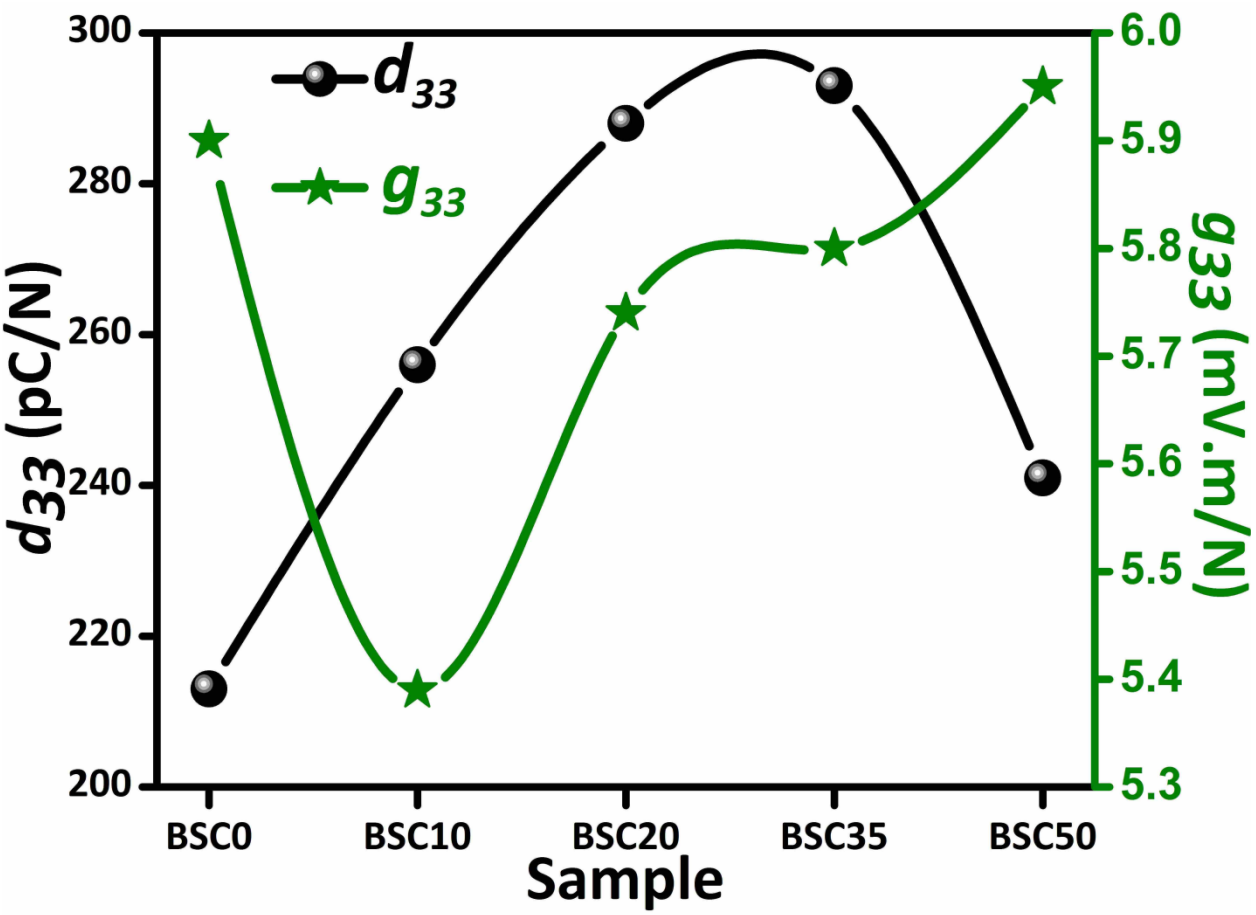
This article is protected by copyright. All rights reserved.

Accepted Article



This article is protected by copyright. All rights reserved.

Accepted Article



This article is protected by copyright. All rights reserved.

International Conference on Innovative Data Communication Technologies and Application (ICIDCA-2023)
IEEE Xplore Part Number: CFP23CR5-ART; ISBN: 979-8-3503-9720-8

2023 International Conference on Innovative Data Communication Technologies and Application (ICIDCA) | 979-8-3503-9720-8/23/$31.00 ©2023 IEEE | DOI: 10.1109/ICIDCA56705.2023.10099546

Face Manipulation Detection in Images using Inception Layers and Graph Convolutional Networks

Aman Mahendroo
Department of CSE
Delhi Technological University
New Delhi, India
amanmahendroo2001@gmail.com

Aaradhya Beri
Department of CSE
Delhi Technological University
New Delhi, India
aaradhyaberi@gmail.com

Anukriti Kaushal
Department of CSE
Delhi Technological University
New Delhi, India
aunkritik@gmail.com

***Abstract*—Recently, there has been an upsurge in the availability and advancement of technologies that can morph images. With the advancement in machine learning and deep learning methods, it is now increasingly difficult to detect which image is real or manipulated generated by the latest technologies. When done nonconsensually, images of manipulated faces can harm people's public image and warrant the development of a method that can contrast authentic images from morphed ones.**

Therefore, image manipulation detection is paramount for regulating online video frame/image data and protecting their authenticity. This study has generated the latest tampered image dataset and subsequently pioneered an efficient model of a two-fold contribution based on Inception Layers with a Graph Convolutional Network (GCN). The Inception layers consist of several convolutional layers of incrementally increasing kernel sizes that help capture morphological information, which GCN processes to capture the relationship between features, followed by a dense layer module. Further, this study conduct experiments on the proposed dataset and compare the results of the proposed method with existing techniques. The result shows that the proposed approach yields better accuracy than the existing state-of-the-art methods.

***Index Terms*—Image Manipulation, Convolutional Neural Network, Graph Convolutional Network, Network Architecture**

I. Introduction

Digital photographs and videos are now widely used digital items thanks to social media's rise and smartphones' popularity over the past several decades. Several statistics claim that over 2 billion images are uploaded every day. This extensive use of images has been accompanied by an upsurge in content editing methods for image using software like Photoshop. Image tampering is the study dedicated to digital picture forensics to control the dissemination of such fabricated information.

There are several ways to identify fake images (Farid et al. [1], Redi et al. [2]). However, most of them either examine discrepancies with a typical camera pipeline or extract certain picture modifications from the final image. Image noise detection, (for example, Julliand et al. [3]) is an effective method to find splicing (copy-pasting from one image to another). Deep learning is one method used by Barni et al. [4] to locally identify double JPEG compression in photos. A network is suggested by Rao et al. [5] to identify image splicing. Any widespread fabrication of a picture is what Bayar et al. [6] are after. Computer graphics are distinguished from photographic pictures [7], [8]. It is abundantly obvious that deep learning outperforms conventional signal processing techniques in digital forensics. On the other side, videos may also be fabricated using deep learning.

With the sudden upsurge and advancement of synthetic picture synthesis and manipulation, there are serious questions about what this may mean for society. In the best case, the public confidence in digital material declines, but it also has the potential to hurt users by disseminating misleading information or fake news. This is our motivation to use deep learning to address this issue. Our model receives data in the form of images. The task is to accurately determine if there has been any tampering with the face present in the image. This study has employed three inception layers, each comprising of three convolutional layers of kernel sizes 1,3 and 5 and a max pool layer. Furthermore,a Graph Convolutional Network (GCN) is implemented to effectively process the relationship information between features.
Some notable improvements are made in the field of face manipulation detection, they are as follows:

- Pioneered the idea of employing GCN for this task, which led to a notable increase in the model's accuracy.
- Applied inception layers to better capture lower level image features.
- Attained a reasonably low time per epoch on the dataset for our model.

The significant contributions made by previous researchers in this subject are discussed in length in the following parts, followed by our approach and an explanation of each component used. This study will conclude with a comparison between the outputs of our model and other state-of-the-art models on our self-generated dataset.

Authorized licensed use limited to: DELHI TECHNICAL UNIV. Downloaded on April 26,2023 at 10:14:45 UTC from IEEE Xplore. Restrictions apply.

II. Related Work

Zhou et al. [9] proposed a two-stream network for the detection of face manipulation. They Developed a patch-based triplet network to use features collecting local noise residuals and camera attributes as a second stream, then trained GoogLeNet to identify tampering artifacts in a face classification stream. The Integral representation in the ReLU (Rectified Linear Units) activation function was proposed by Kirana et al. [10] to include a preventive function that stops meaningless detection in the non-face area. Let us say the integral of ReLU falls short of the cutoff. The window moves to the nearby region, and the convolution is skipped in that scenario. This outcome indicates that the suggested approach outperforms state-of-the-art algorithms.

To address the challenge of the unbalanced dataset, Dang et al. [11] suggested a hybrid framework (HF-MANFA) that makes use of Adaptive Boosting (AdaBoost) and eXtreme Gradient Boosting (XGBoost). This study presents a framework that uses deep learning to recognise modified facial photographs. It constructs a convolutional neural network model specifically for Manipulated Face (MANFA) detection, with numerous convolutional layers that efficiently extract characteristics from a manipulated area at various degrees of abstraction. Afchar et al. [12] offers a technique for quickly and accurately identifying face tampering in videos. Due to the deep learning methodology used in this study, two networks with few layers are shown to concentrate on pictures' mesoscopic characteristics. Such rapid networks are evaluated on an existing dataset as well as datasets created from web videos.

Rossler et al. [13] looks at how lifelike modern picture modifications are and how challenging it is for people or machines to spot them. It concentrates on DeepFakes, Face2Face, and FaceSwap, particularly well-known examples of face manipulation. For each method, more than half a million modified photos are produced. They can train data-driven forgery detectors in a supervised manner since the generated dataset is at least an order of magnitude larger than similar alternatives. They demonstrate that even under heavy compression, forgery detection is enhanced to previously unheard-of accuracy by including domain-specific information.

Elmahmudi et al. [14] investigates the issue of face recognition using incomplete facial data. They do so through unique experiments to evaluate the effectiveness of machine learning while employing partial faces and other face picture alterations as training and recognition signals, such as rotation and magnification. They focus on the rate of identification for the various facial features, such as the eyes, mouth, nose, and cheek. Additionally, they investigate the effects of face recognition exposed to facial rotation and subject to facial picture zoom out. Guo et al. [15] suggests an Adaptive Manipulation Trace-Extraction Network (AMTEN), which acts as pre-processing in order to highlight modification traces and mask picture information. By modifying weights during the back-propagation, AMTEN uses adaptive convolution to anticipate manipulation traces in the picture, which are then reused in the subsequent layers to increase manipulation artifacts. By fusing CNN and AMTEN, a fake face detector called AMTENNet is created.

Guarnera et al. [16] employs a novel technique for obtaining a Deepfake fingerprint from photos. This technique is based on the Expectation-Maximisation algorithm, which has been taught to detect a fingerprint that represents the Convolutional Traces (CT) left behind by GANs during image creation. The CT has excellent discriminative power, outperforming state-of-the-art in the Deepfake detection challenge and demonstrating resilience to various assaults. The Ensemble of different Convolutional Neural Network models with the concepts of attentional layers and siamese training is studied by Bonettini et al. [17]. They show that mixing these networks leads to favourable face manipulation detection results.

III. Dataset Experimentation and Implementation

A. Proposed Dataset

Our database consists of 165 GIF images of 15 subjects. We have shortlisted a total of 9 subjects and 8 expressions for each subject, that generated the best results:

- Centerlight
- Glasses
- Happy
- No Glasses
- Normal
- Sad
- Sleepy
- Wink

Thus, after running our script we arrive at a total of 5760 fake images with 80 original ones. Since this might pose an imbalance problem of not having sufficient number of positive samples, we use the following data augmentation techniques in order to boost the number of samples of real images:

- **Random cropping:** We crop the input image using a random offset value in order to create a new image.
- **Flipping:** The facial images are flipped horizontally in order to generate a new image.
- **Blurring:** We introduce blurring in the image to alter the low level features.
- **Gaussian Noise:** The image is augmented with random noise with probability distribution equal to that of the Gaussian distribution.

These techniques also helps in reducing the overfitting of the model on the dataset.

TABLE I Dataset Information

Sample Type	Count
Real Images	1280
Fake Images	5760

B. Dataset Generation Prerequisites

1) Delaunay Triangulation: There are several ways to arrange a collection of randomly dispersed data points into a triangular mesh. However, not every triangular mesh that

Authorized licensed use limited to: DELHI TECHNICAL UNIV. Downloaded on April 26,2023 at 10:14:45 UTC from IEEE Xplore. Restrictions apply.

is conceivable offers an accurate depiction of the spatial connections between points. How do we choose which vertices to join together to create the best possible structure? That choice is made using the "Delaunay criteria," a method used in Delaunay mesh construction. The Delaunay criteria describes a procedure for evaluating whether a pair of adjacent triangles reflects the best possible option of connections by considering geometrical factors. The connections are rearranged to make the connections "Delaunay conformant" when a pair does not satisfy the requirement. Until every triangle in the mesh satisfies the Delaunay criterion, the operation is repeated. The Delaunay rules are as follows:

- The mesh does not degenerate in any of the triangles it creates. In other words, no triangle is formed by joining together a group of three collinear points. Such a triangle would have no area and an infinitely large circumference.
- All of the triangles in the mesh result in a circumcircle that only contains the three vertices that make up a triangle and none of the other vertices from the mesh.

2) Histogram Matching: When we wish to synchronise the contrast level of a collection of photographs, histogram matching comes in handy. In reality, since we alter the histogram of an input picture to resemble the normal distribution, histogram equalisation may also be seen as histogram matching.

We must first equalise the histogram of both photos in order to match the histogram of images A and B. The next step is to use the equalised histograms to map each pixel of A to B. Then, based on B, we adjust each pixel in A. We must implement this algorithm of every pair of corresponding triangles in the mesh generated by triangulation.

C. Algorithm

We have generated our custom dataset from the above obtained images from the Yale Face Database [1]. For this purpose, we have employed the Facial Landmark Predictor proposed by Kazemi et al. [18]. Facial Landmark Predictor is a deep learning model for detecting 68 primary landmarks in a facial image. The overall algorithm for face swapping is as follows:

Let us see this in action with the help of an example below. We take images X and Y as input and apply Algorithm 1 on the same. Upon execution, the face from image Y is imposed on image X yielding the resultant face swapped image.

Algorithm 1 can easily identify and separate the face from the source image. It then transplants the face onto the target image and can account for the changed lighting and background using histogram matching. This results in a clean transfer of the facial region from one image to another, thus smoothly executing a face swap.

IV. Model

In this part, we go into great depth on how our model functions. We begin by outlining the various parts of the model. We then examine the Inception and GCN layers used to gather the necessary information for tampering detection. Finally, we assemble the different parts of our model and describe the various hyperparameters utilised for each part.

[1] Yale Face Database - https://www.kaggle.com/datasets/olgabelitskaya/yale-face-database

Algorithm 1 Algorithm for generating the dataset

Require: 2 faces from the Yale Face Database, label them X and Y

$L_x \leftarrow FaceLandmarks(X)$ ▷ Generated using face landmarks predictor
$L_y \leftarrow FaceLandmarks(Y)$
$T_x \leftarrow DelaunayTriangulation(L_x)$
$T_y \leftarrow Triangulation(L_y)$ ▷ Based on triangulation of L_x
for $t_1, t_2 \in T_x, T_y$ **do**
    $t_1 \leftarrow AffineTransform(t_1, t_2)$ ▷ Warps to match t_1 and t_2 shapes
    $t_1 \leftarrow MatchHistogram(t_1, t_2)$
    Overwrite t_1 over Y
end for



X Y

Fig. 1: Dataset Generation Algorithm

A. Inception Layer

Inception is a deep convolutional neural network architecture that was presented in 2014 by Szegedy et al. [19] . Convolutional neural networks use 1x1 convolutions for dimensionality reduction, facilitating more effective computation and deeper networks. The modules address a number of issues like overfitting resulting in lower computational cost. It uses various incrementally increasing kernel filter sizes within the CNN which work in parallel instead of being stacked sequentially.

We perform convolution on the input using three separate size filters (1x1, 3x3, 5x5) which result in the creation of an inception module followed by max pooling. The outputs are then concatenated and forwarded to the following layer. This results in the CNN growing more in width than in height. The Inception Layer can be understood with the help of Figure 2.

B. Graph Convolutional Network

Data structures like graphs help us model information in a non-linear fashion consisting of nodes connected via edges. These nodes and edges can themselves act as a medium for storing information. We have employed a modified version of the CNN to work with higher-level image features more effectively. We posit that a GCN is more effective at this stage of analysis than a CNN as such higher level image features

Authorized licensed use limited to: DELHI TECHNICAL UNIV. Downloaded on April 26,2023 at 10:14:45 UTC from IEEE Xplore. Restrictions apply.

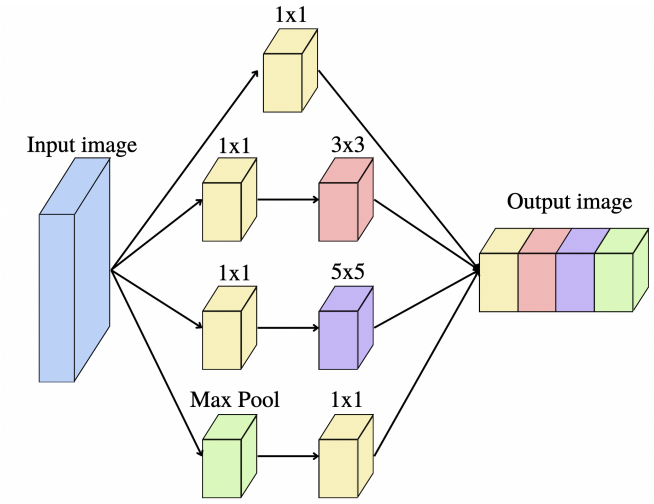


Fig. 2: Inception Layer

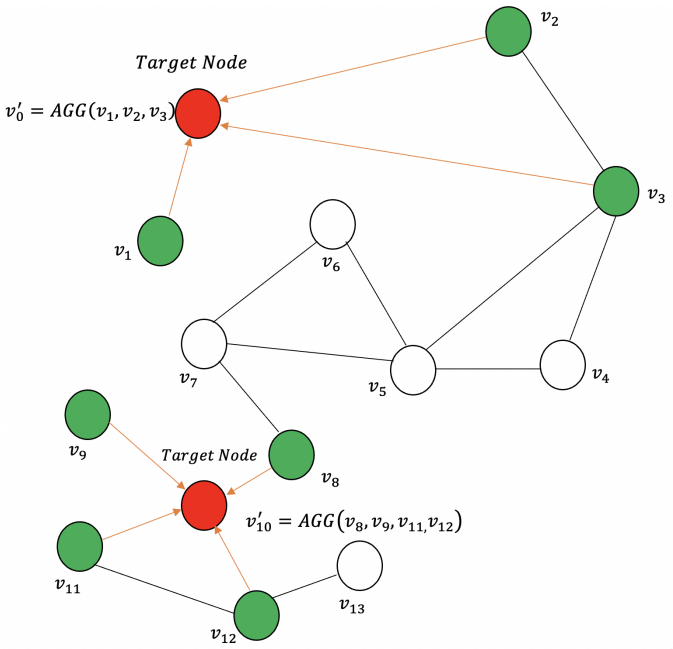


Fig. 3: Graph Convolutional Network

are not strongly related by geometry.

Graphs are represented best with the help of an adjacency matrix A, where A_{ij} represents the edge connecting nodes i and j.

The GCN which was introduced by Kipf et al. [20] proposes the layer-wise propagation process. In each incremental message pass, every node $x \in G(V, A)$ in the GCN aggregates information ($\mathcal{F}_x$) received from its neighbourhood $\mathcal{N}_x$. This can be represented mathematically with the help of the formula below:

$$\mathcal{F}_x^{(i+1)} = \sigma(A\mathcal{F}_x^{(i)}W^{(i)}) \tag{1}$$

where, $W^{(i)}$ represents the weight matrix and $\mathcal{F}_x^{(i)}$ represents the aggregated information for the i^{th} iteration. A is the adjacency matrix of the graph and σ represents the update function.

TABLE II Model Hyperparameters

Layer	Configuration	Output Size
Input	Grayscale	64,64,1
Inception1	32 Kernels	64,64,32
BatchNorm1		64,64,32
MaxPool1	2x2	32,32,32
Inception2	32 Kernels	32,32,32
BatchNorm2		32,32,32
MaxPool2	2x2	16,16,32
Inception3	32 Kernels	16,16,32
BatchNorm3		16,16,32
MaxPool3	2x2	8,8,32
Reshape1		64,32
GCN1	32 features	64,32
Concat1	[Reshape1:GCN1]	64,64
Reshape2		4096
Dense1	32	32
Dense2	16	16
Dense3	2	2
Softmax		2

C. Overall Model

We combine the components covered in the previous subsections, as shown in Figure 4. The input grayscale image first passes through a series of 3 inception layers that help capture the morphological features. We use a GCN layer to highlight the aspects of these relationships that are significant to the image we are looking at. According to the GCN output, we classify the current image with the help of a fully linked layer. We additionally establish a skip connection from the inception layers to the dense layer to combat regularisation issues. Softmax activation is employed in the dense layer.
We have also highlighted the entire structure along with the various hyperparameters of every component in the overall model in Table II.

V. Results

This section compares our model's performance against past studies with the aid of Precision, Recall and F1-measure scores.

- **Precision** : Precision is the ratio of predictions accurately predicted (TP) to the total predicted positive observations ($TP + FP$).

$$Precision = \frac{TP}{TP + FP} \tag{2}$$

- **Recall** : Recall is the proportion of accurately predicted positive observations (TP) to the all observations in actual class ($TP + FN$).

$$Recall = \frac{TP}{TP + FN} \tag{3}$$

Authorized licensed use limited to: DELHI TECHNICAL UNIV. Downloaded on April 26,2023 at 10:14:45 UTC from IEEE Xplore. Restrictions apply.

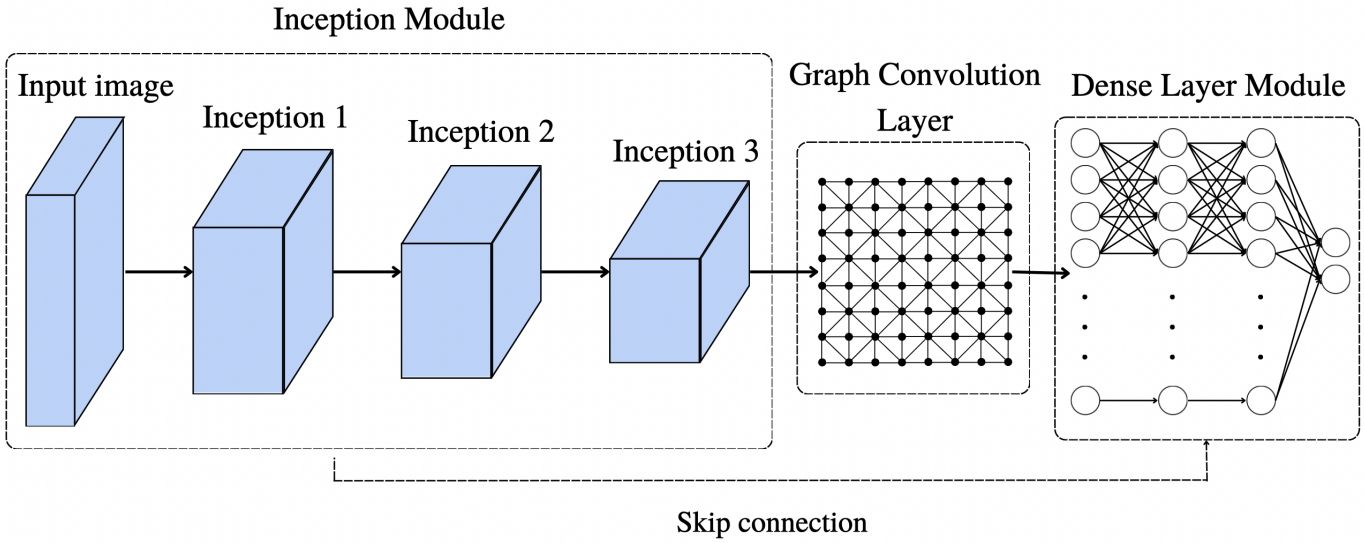


Fig. 4: Overall Model

- **F1-measure** : F1 Score is the harmonic mean of Precision and Recall.

$$F_1 - measure = \frac{2 \times Precision \times Recall}{Precision + Recall} \quad (4)$$

Our model receives grayscale images of fixed size as input and outputs a binary output based on whether it thinks the input image is real or fake. This output is then rounded off and compared with a binary "ground truth". From this, we create a confusion matrix depicting the number of true positives, false positives, true negatives and false negatives predicted by our model. The confusion matrix is then used to calculate the F1 score of the said model. The same technique is applied to various other methods with which we have compared our model.

Tabulated below in Table III are the F1 scores of our model in comparison with other state-of-the-art model which we have implemented on our dataset. As we can see from the above results, our model outperforms the current models we compared with. A better outcome was attained using the proposed dataset and an F1 Score of 98.97%.

TABLE III Dataset Results

Method	F1 score (%)
Kirana et al. [10]	94.74
Dang et al. [11]	93.99
Afchar et al. [12]	98.40
Proposed model	**98.97**

VI. Experiments

In this section, we perform various experiments on the structure of the model to analyse and justify, in-depth, the specific architecture chosen.

A. Inception Module

Here we have analysed how the model's performance varies on changing the number of inception layers in the inception module.

TABLE IV Dataset Results

No. of Inception Layers	F1 score (%)
2	98.80
3	**98.97**
4	98.90

Table IV summarizes the performance of the model with various sizes of the Inception Module. It can be concluded that the model performs best with the Number of layers being 3.

B. GCN Module

We posit that a Graph Convolutional Network is more effective in capturing higher-level features of a CNN-processed image than a CNN since higher-level features carry semantic relationships even when they are geometrically separated. In order to prove this, we have performed the same experiments on the model both with and without including a GCN Module.

TABLE V Dataset Results

Model description	F1 score (%)
Without GCN	97.65
With GCN	**98.97**

The model's performance with and without the GCN is summarized in Table V. It can be seen that the presence of the GCN Module enhances the ability of the module to detect manipulation in images using high-level features.

Authorized licensed use limited to: DELHI TECHNICAL UNIV. Downloaded on April 26,2023 at 10:14:45 UTC from IEEE Xplore. Restrictions apply.

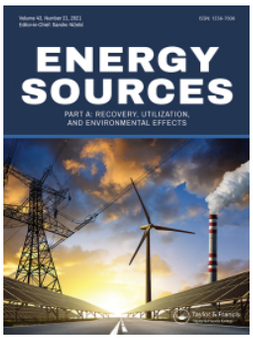
VII. Conclusion

As the frequency of modified photos on the internet has grown, thus has the significance of detecting image tampering. When done with malicious intentions, tampering can cause severe consequences and thus demands accurate detection.
This study examines the effectiveness of using a Graph Convolutional Network (GCN) for capturing relationships between high level features which a CNN fails to do. The input image is first passed through a series of 3 inception layers, followed by a GCN and dense layers.
We contrast our model against the current model and based on our experiments, we conclude that our model surpasses the existing models.

References

[1] H. Farid. A Survey Of Image Forgery Detection. IEEE Signal Processing Magazine, 26(2):26–25, 2009.
[2] J. A. Redi, W. Taktak, and J.-L. Dugelay. Digital image forensics: a booklet for beginners. Multimedia Tools and Applications, 51(1):133–162, 2011.
[3] T. Julliand, V. Nozick, and H. Talbot. Image noise and digital image forensics. In Y.-Q. Shi, J. H. Kim, F. Perez-Gonzalez, and I. Echizen, editors, Digital-Forensics and Watermarking: 14th International Workshop (IWDW 2015), volume 9569, pages 3–17, Tokyo, Japan, October 2015. Lecture Notes in Computer Science (LNCS), Springer International Publishing.
[4] M. Barni, L. Bondi, N. Bonettini, P. Bestagini, A. Costanzo, M. Maggini, B. Tondi, and S. Tubaro. Aligned and non- aligned double jpeg detection using convolutional neural net- works. Journal of Visual Communication and Image Representation, 49:153–163, 2017.
[5] Y. Rao and J. Ni. A deep learning approach to detection of splicing and copy-move forgeries in images. In Information Forensics and Security (WIFS), 2016 IEEE International Workshop on, pages 1–6. IEEE, 2016.
[6] B. Bayar and M. C. Stamm. A deep learning approach to universal image manipulation detection using a new convolutional layer. In Proceedings of the 4th ACM Workshop on Information Hiding and Multimedia Security, pages 5–10. ACM, 2016.
[7] N. Rahmouni, V. Nozick, J. Yamagishi, and I. Echizen. Distinguishing computer graphics from natural images using convolution neural networks. In IEEE Workshop on Information Forensics and Security, WIFS 2017, Rennes, France, December 2017. IEEE.
[8] N. Bhat, N. Saggu, S. Kumar. Generating visible spectrum images from thermal infrared using conditional generative adversarial networks. In 2020 5th International Conference on Communication and Electronics Systems (ICCES) (pp. 1390-1394). IEEE, 2020
[9] Zhou, P., Han, X., Morariu, V. I., & Davis, L. S. (2017, July). Two-stream neural networks for tampered face detection. In 2017 IEEE conference on computer vision and pattern recognition workshops (CVPRW) (pp. 1831-1839). IEEE.
[10] Kirana, K. C., Wibawanto, S., Hidayah, N., Cahyono, G. P., & Asfani, K. (2019, October). Improved neural network using integral-RELU based prevention activation for face detection. In 2019 International Conference on Electrical, Electronics and Information Engineering (ICEEIE) (Vol. 6, pp. 260-263). IEEE.
[11] Dang, L. M., Hassan, S. I., Im, S., & Moon, H. (2019). Face image manipulation detection based on a convolutional neural network. Expert Systems with Applications, 129, 156-168.
[12] Afchar, D., Nozick, V., Yamagishi, J., & Echizen, I. (2018, December). Mesonet: a compact facial video forgery detection network. In 2018 IEEE international workshop on information forensics and security (WIFS) (pp. 1-7). IEEE.
[13] Rossler, A., Cozzolino, D., Verdoliva, L., Riess, C., Thies, J., & Nießner, M. (2019). Faceforensics++: Learning to detect manipulated facial images. In Proceedings of the IEEE/CVF international conference on computer vision (pp. 1-11).
[14] Elmahmudi, A., & Ugail, H. (2019). Deep face recognition using imperfect facial data. Future Generation Computer Systems, 99, 213-225.
[15] Guo, Z., Yang, G., Chen, J., & Sun, X. (2021). Fake face detection via adaptive manipulation traces extraction network. Computer Vision and Image Understanding, 204, 103170.
[16] Guarnera, L., Giudice, O., & Battiato, S. (2020). Fighting deepfake by exposing the convolutional traces on images. IEEE Access, 8, 165085-165098.
[17] Bonettini, N., Cannas, E. D., Mandelli, S., Bondi, L., Bestagini, P., & Tubaro, S. (2021, January). Video face manipulation detection through ensemble of cnns. In 2020 25th international conference on pattern recognition (ICPR) (pp. 5012-5019). IEEE.
[18] V. Kazemi and J. Sullivan, "One millisecond face alignment with an ensemble of regression trees," in Proceedings of the IEEE Conference on Computer Vision and Pattern Recognition, 2014, pp. 1867–1874
[19] Szegedy, C., Liu, W., Jia, Y., Sermanet, P., Reed, S., Anguelov, D., ... & Rabinovich, A. (2015). Going deeper with convolutions. In Proceedings of the IEEE conference on computer vision and pattern recognition (pp. 1-9).
[20] Thomas N. Kipf and Max Welling. 2016. Semi-supervised classification with graph convolutional networks. CoRR abs/1609.02907. http://arxiv.org/abs/1609.02907.

Authorized licensed use limited to: DELHI TECHNICAL UNIV. Downloaded on April 26,2023 at 10:14:45 UTC from IEEE Xplore. Restrictions apply.



Energy Sources, Part A: Recovery, Utilization, and Environmental Effects

ISSN: (Print) (Online) Journal homepage: https://www.tandfonline.com/loi/ueso20

Fault classification using deep learning based model and impact of dust accumulation on solar photovoltaic modules

Rahma Aman, M. Rizwan & Astitva Kumar

To cite this article: Rahma Aman, M. Rizwan & Astitva Kumar (2023) Fault classification using deep learning based model and impact of dust accumulation on solar photovoltaic modules, Energy Sources, Part A: Recovery, Utilization, and Environmental Effects, 45:2, 4633-4651, DOI: 10.1080/15567036.2023.2205859

To link to this article: https://doi.org/10.1080/15567036.2023.2205859

Published online: 24 Apr 2023.

Submit your article to this journal

Article views: 3

View related articles

View Crossmark data

Full Terms & Conditions of access and use can be found at
https://www.tandfonline.com/action/journalInformation?journalCode=ueso20

ENERGY SOURCES, PART A: RECOVERY, UTILIZATION, AND ENVIRONMENTAL EFFECTS
2023, VOL. 45, NO. 2, 4633–4651
https://doi.org/10.1080/15567036.2023.2205859

Taylor & Francis
Taylor & Francis Group

Check for updates

Fault classification using deep learning based model and impact of dust accumulation on solar photovoltaic modules

Rahma Aman[a], M. Rizwan[a], and Astitva Kumar[b]

[a]Department of Electrical Engineering, Delhi Technological University, Delhi, India; [b]Department of Electrical Engineering, Netaji Subhash University of Technology, Delhi, India

ABSTRACT

Solar panel performance is affected by ambient temperature, sunlight, module surface temperature, dust, and shadows. Dust inhibits sunlight from reaching photovoltaic modules, reducing power generation. Dust is aerosol pollution from natural or human-made sources. Dust on photovoltaic (PV) panels reduces power generation and raises the surface temperature, shortening panel life. This work uses a Fluke TiS60 Thermal Imager for detection of hotspot created by the accumulation of dust and further classification of the faulty and healthy images is done. The image classifiers used in this paper are SqueezeNet and AlexNet transfer learning methods, the accuracy of both methods is compared, and AlexNet performs best with an accuracy of 99.3%. Further, the effect of dust on PV modules is studied, and hotspots are created intentionally with the help of dust for study purposes. Initially, 50% of a solar module is covered with dust and then 100% of the solar module is covered with dust particles to find the power loss, when a thin layer of dust was spread over 50% of a module power loss is of 4.7% and when a thick layer of dust is spread over 50% the power loss is 5.9%, when thin layer of dust was applied over 100% of a module power loss is of 6.49% and when thick layer of dust is spread over 100% the power loss is 10.17%. This analysis for a healthy and faulty panel is done that helps PV module inspection by facilitating a more precise and cost-effective identification of PV defects.

ARTICLE HISTORY
Received 14 December 2022
Revised 10 April 2023
Accepted 11 April 2023

KEYWORDS
Renewable energy; dust accumulation; photovoltaic panels; thermal imager; deep learning; hotspot

Introduction

Renewable energy is essential for boosting economy and reducing carbon emission to make an eco-friendly energy system. Some of the best renewable energy sources are hydroelectric, solar, and wind power. Photovoltaic energy is one of the cleanest and most available renewable energy sources as it is abundant in nature; solar power is quickly becoming the most popular kind of green energy due to its many benefits (Madeti and Singh 2017). Solar panels' electricity generation relies on light from the sun. Specific problems have been faced when working with solar panels. Several factors degrade the panel's performance. It is necessary for a system that generates electricity to be able to produce and send high-quality power to the loads that are connected to it (Kodakkal et al. 2021). Shading due to dust is of two types hard type shading and soft type shading, in hard shading the sunlight is blocked by the accumulation of dust and in soft shading is due to air pollution. The high penetration of renewable energy sources, along with their unpredictable power outputs, presents a significant obstacle to the efficient operation of energy systems (2022). Various other factors causes blocking of sun such as nearby buildings, bird litters, dust, etc. The power produced varies on solar radiation, tilt angle, ambient temperature, aging, humidity, wind speed and direction, and dust deposition (Jaszczur et al. 2020). The effects of red soil, limestone, and carbonaceous fly-ash particles on PV energy performance

CONTACT Rahma Aman rahmaaman96@gmail.com Department of Electrical Engineering, Delhi Technological University, Delhi 110042, India

© 2023 Taylor & Francis Group, LLC

is investigated. According to the data, particle composition and source substantially affect PVs' energy performance. A theoretical model was constructed to predict the impact of regional air pollution on PVs' performance. Experimental data on dust's influence on PVs' energy output in a polluted urban environment are utilized to support the suggested theoretical model (Kaldellis and Kapsali 2011). The influence of dust formation, the humidity level, and the air velocity will each be expounded independently. Then, in the end, the impact of each factor on the other will be elucidated. It has been demonstrated that each of these three factors has an effect on the other two, and the conclusion that should be drawn from this is that to have a profound insight into the design of solar cells, the effect of each of these factors should be taken into consideration simultaneously (Mekhilef, Saidur, and Kamalisarvestani 2012). The influence of dust on PV modules in Kathmandu is studied in relation to dust deposition density and climatic factors to create an efficiency loss regression equation. During the 5-month testing period, the efficiency of a dirty solar module left to natural dust deposition decreased by 29.76% compared to a daily-cleaned module. During the research period, dust deposition on the PV module was 9.6711 g/m^2. The investigation also demonstrated that dust deposition is mainly concentrated at the bottom of PV modules, which might lead to irreversible module damage (Paudyal and Shakya 2016). The author reviews the effects of climatic parameters and dust on PV module performance. Dust deposition affects the light transmissivity of PV module surface covers, according to research. Understanding how dust deposits on PV module surfaces are key to developing effective mitigation strategies. High temperature, humidity, and lack of rain impact module performance. This paper outlines past, present, and future techniques to minimize environmental consequences, especially dust fouling. Electrostatic cleaning and micro/nanoscale surface functionalization may combat dust deposition, with the combination being especially effective in dry climates (Said et al. 2018).

The impacts of six different types of dust pollutants: ash, laterite, stone dust, sandy, coal powder, and cement on the efficiency of photovoltaic panels. The performance of such devices is degraded by dust. The effect of dust deposition on the power production of solar PV modules was examined in eastern Saudi Arabia (Fan et al. 2021). The study found that solar PV modules kept dirty for over six months can lose up to 50% of their output which shows most significant defects in photovoltaic systems are investigated in this research (Adinoyi and Said 2013) (Sayyah et al., 2014). The methodologies for monitoring photovoltaic systems that have been developed in recent research and reviewed, assessed in order to highlight their differences, advantages, and limitations (Triki-Lahiani, Bennani-Ben Abdelghani, and Slama-Belkhodja 2018). The above literature survey helps in getting better knowledge of dust accumulation on solar panels. To detect dust deposition, thermal images have been used recently and several deep learning approaches are used to detect the fault. This paper proposes an AI-based fault distance estimation method using signal processing. The proposed approach procedure was developed through detailed analysis. Feature extraction was used to convert massive data sets into feature sets to reduce computational burden. After that, the most predictive features were selected from the entire set to increase precision and speed up training. A support vector machine (SVM) or neural network (NN) determined fault distance using the selected features (Ray and Salkuti 2022; Sinha, Ray, and Salkuti 2018).

Dust deposition on the panels creates hotspots which reduces the panels' performance. These hotspots can be seen through thermal cameras Thermography images (TI) are an emerging option for a PV system inspection. By laying over PV modules, TI can check them quicker than previous handheld techniques and ensure worker safety. Thermographic PV examination improves anomaly detection and categorization (Bodnar and Kozsely 2022; Higuchi and Babasaki 2018). Automatic defect detection, categorization, and analysis have been proposed. An Infrared image (IR) camera took IR images. To estimate PV module's thermal condition, damaged panel photos were compared to a healthy thermal image. A fuzzy rule base automatically classified defect. Types of faults influence maintenance actions (Jaffery et al. 2017). Deep learning algorithms have recently been used for the fault diagnostics of photovoltaic (PV) systems to recognize and categorize the many kinds of issues that may be found in these systems. Haidari et.al proposes a technique for investigating photovoltaic

powerhouses that is based on a deep learning algorithm was developed. In solar powerhouses, researchers looked at two different kinds of flaws: hotspot defects and hot substring faults. In the photovoltaic powerhouse, incidences of these faults are much higher. The thermal pictures of photovoltaic modules that were collected from aerial and terrestrial photographs may be found in the datasets that were utilized in this study. Using a number of statistical measures, such as the F1 score, accuracy, and precision, the created network was assessed. In the end, the network was categorized with an overall accuracy of 0.98, and the findings obtained were compared with those acquired from previous research (). In Fan et al. (2022), a new method to examine the dust condition (concentration and dispersion) quantitatively. First, a DRNN (Deep recurrent neural network) is proposed to determine regional dust concentration. The model's residual elements are connected in skipping layers to minimize the weight matrix order and increase network flexibility and feature learning accuracy. Second, image pre-processing classifies dust accumulation. Transformation, correction, silver grid removal, nonlinear interpolation, equivalent segmentation, and clustering are included. Error loop is a new method for comparing measured and experimental findings. DRNN's prediction accuracy is superior than other approaches. DRNN has 78.7% R^2 and 3.67 MAE. The method for identifying uneven dust deposition is tested under three scenarios. The average error loop evaluation coefficients are 1.19, 0.77, and 1.10, per design. The proposed technology can theoretically facilitate the intelligent operation and maintenance of PV systems. PV power generating provides clean, sustainable energy. Rapid failure detection and classifications of PV modules can boost system dependability and decrease costs. Korkmaz and Acikgoz (2022) propose an efficient PV fault detection approach utilizing thermographic images. The suggested method is a transfer-learning-based multi-scale CNN with three branches. Convolutional branches use pre-trained information of the transferred network to improve network representation. To resolve the uneven class distribution of the raw dataset, oversampling is conducted using offline augmentation, and network performance is boosted. In the experiment, 11 types of PV module failures are used, including cracking, diode, hot spot, and offline module. Average defect detection accuracy is 97.32% and anomaly accuracy is 93.51%. The experimental results show that the suggested method outperforms other deep learning methods and current studies. A new way to use DCNNs to estimate the degradation of PV cells is shown in this paper. Even though many studies have been. As far as our knowledge, this is the first time that data from a drone with a thermal camera has been used for image classification. Experiments on the "Photovoltaic images Dataset," which is a collection of images, are shown to show the problem of degradation. and give a full assessment of the method used in this research. Results in terms of accuracy, recall, and F1-score show that the proposed method works and is good for the job (Pierdicca et al. 2018). A visual defect detection approach using multi-spectral deep CNN (Chen et al. 2020). An algorithm with an improved anisotropic diffusion filter and sophisticated image segmentation is presented by Anwar and Abdullah (2014). NB-CNN is a deep learning framework based on a convolutional neural network (CNN) and a Nave Bayes data fusion scheme to analyze individual video frames for crack detection. A novel data fusion scheme is proposed to aggregate the information extracted from each video frame to improve the system's performance and robustness (Chen and Jahanshahi 2018). Deep 2-D Convolutional Neural Networks (CNN) are used to extract characteristics from 2-D scalograms generated from PV system data to detect and classify errors (Aziz et al. 2020).

Higher global demand for solar energy systems increases the need for automatic fault inspection of solar panels. Deep convolutional neural networks (DCNNs) do well at picture classification across domains. Convolutional neural networks assess the PV panel surface and detect defects. Transfer learning with AlexNet CNN showed promising results for detecting solar panel problems (Zyout and Oatawneh 2020b).

Despite algorithm-based PV failure detection research, best classifier performance remains an issue. Their performance depends on the type of problem, input signals or images, number of inputs, number of layers, and network settings. Complete CNN algorithm is given in Figure 1.

Several papers reviewed have used CNNs or image classification. This requires much time for pre-processing of the data set, but in transfer learning, very little pre-processing is required. Transfer

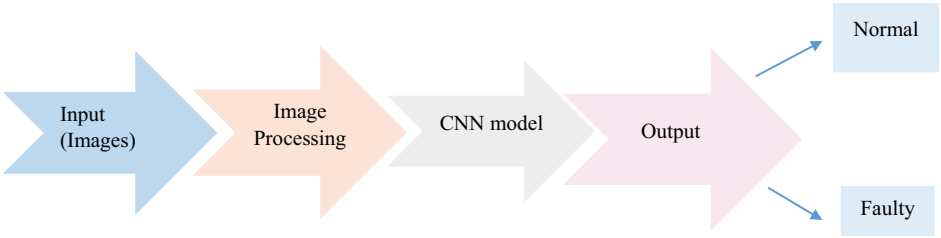


Figure 1. CNN-based fault detection algorithm overview (Chen et al. 2020).

learning methods are rarely used for image classification. In this paper, transfer learning models were developed in MATLAB environment, and to train the models, the hotspot images are captured by the thermal imager. These hotspots are created by the accumulation of dust on the solar panels and the hotspot images are taken in the real-time environment, which means the data was recorded from a 5 kW_p solar panel by solar analyzer 9018BT on the rooftop of Utilization Electrical Engineering Laboratory, Delhi Technological university, New Delhi, India. Here the dust is manually created to emulate different real time soiling scenarios. Further, these images are pre-processed by transfer learning model for more precise and cost-effective identification of PV defects. In this particular research study, the inspection of PV modules was carried out using a visual approach of Fault Detection and classification (FDC). Here, deep learning approach is used to implement the FDC successfully. FDC techniques located hot spots by segmenting binary mask images. Binary mask image analysis identifies and is classified in three classes: One hotspot, multi-hotspot and healthy modules. The image classifiers used in this paper are SqueezeNet and AlexNet transfer learning methods, they are two pretrained neural networks and further both the method performance is compared. The effect of panels' output power performance because of dust accumulation is discussed in the next section.

This study focuses specifically on analyzing hotspots, which are considered to be the most influential factor affecting the performance of PV panels. The study identifies the key factors that affect the accuracy of performance simulations and highlights the gaps in the literature related to these factors. One of the findings suggests that detecting hotspots is essential for determining their impact on PV cell performance. Therefore, there is a need for a fault detection model that can accurately pre-process data and classify faulty and healthy panels to improve solar panel performance. The paper is divided into two sections: the first section describes two different transfer learning classifiers, while the second section explores the impact of dust accumulation on solar panel performance.

The research objectives of this work are listed below:

- Traditional PV inspections are inefficient, incorrect, and dangerous. In this research, the thermal image analysis approach is used to improve the photovoltaic systems inspection by discovering and analyzing PV defects on a 5 kW_p solar panel.
- The process of obtaining thermal images involves the use of the Fluke TiS60 Thermal Imager to capture a hotspot which is created by accumulation of dust.
- The research methodologies primary advantages lie in reliability and accuracy in identifying the hot spots.
- The research aims to train the hotspot images by pre-trained deep Convolutional Neural Network CNN's, i.e AlexNet and SqueezeNet, to classify faulty and healthy images.
- The paper aims to find the shading losses in solar panels when the dust is deposited.

The paper is organized in six sections first section is the literature survey that helps in finding the gaps in the present work, the second section describes the proposed work; the third section is data annotation; fourth section contains the results and discussion that is divided into two parts first part shows hotspot detection and classification has been done with the help of AlexNet and

SqueezeNet convolutional neural network and in the second part the reduction of power output when dust is accumulated, and the last section concludes the paper.

Proposed architecture

The present study is specifically concerned with the comprehensive analysis of hotspots, which are regarded as the most prominent factor influencing the overall operational efficiency of photovoltaic (PV) panels. One of the key outcomes of this research indicates that the identification of hotspots is of critical significance in accurately assessing their detrimental impact on the performance of PV cells. Therefore, there is a need for a fault detection model that can accurately preprocess data and classify faulty and healthy panels to improve solar panel performance. The faults are classified by pretrained deep learning CNN image classifiers, i.e. AlexNet and SqueezeNet. For fault detection and classification hotspots are created first the hotspots are created by the accumulation of dust on the solar panels and the hotspot images are taken in the real-time environment and then these images are captured by thermal imagers. Infrared (IR) thermography uses midwave (MWIR, 3–5 μm) or long-wave (LWIR, 7–14 μm) infrared sensors to create thermal images or thermograms of things under inspection. Planck's black body radiation law says all objects produce infrared radiation proportional to their temperatures. IR thermography can measure the surface temperature and temperature trend of a body or solar PV module under inspection. The proposed method is shown in Figure 4. The thermal imager used for capturing the images is shown in Figure 2. The hotspot is created by the effect of dust, here dust is spread on modules in four parts in the first two parts a thin layer of dust is spread over 50% and 100% of a module and in the next parts thick layer of dust is spread over 50% and 100% of the module and hotspots are formed due to the effect of dust these hotspot images are captured by the thermal camera and the power drop is recorded by the solar analyzer as shown in Figure 3. Spread. Below are the steps that use thermal imagers to further obtain the fault classification.

Stage 1 Acquisition and Filtering

(1) The input for the thermal image comes from the FLIR camera
(2) The data set is split into two groups: the training group and the validation group.
(3) Batch normalization is used to process colors before they are used.
(4) Images are put into groups with the help of a 3×3 convolution filter.



Figure 2. Fluke TiS60 thermal imager used for capturing images.

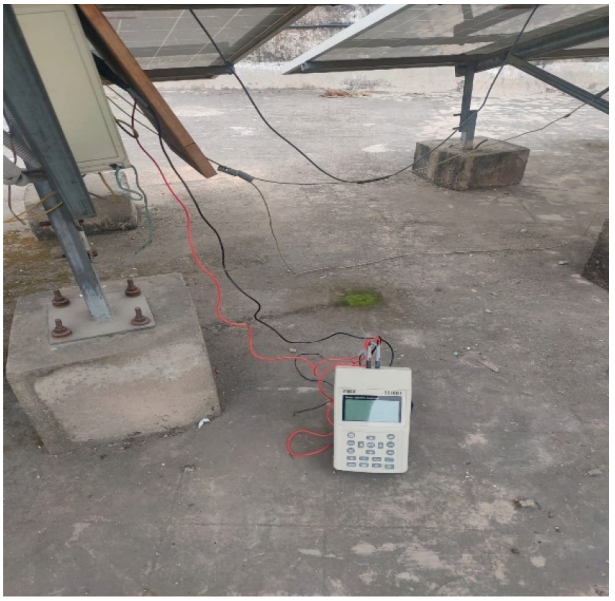


Figure 3. Solar system analyzer 9018BT.

Stage 2 Model classifiers and tunning

(1) A model based on deep learning has been set up to help classify images. Once thermal images are found, the system uses the pretrained CNN classifier to determine if a single hotspot, multiple hotspots, or string features are extracted.
(2) The model then locates the spot in the binary mask through image segmentation and identifies the faulty class.
(3) Model is fine tuned and trained so as to give best performance

Stage 3 Performance evaluation

(1) The performance of the model is evaluated based on its accuracy
(2) Faults on the SoftMax layer, which are fully connected, are categorized with 476 images. And further testing is done in order to check the accuracy.

Deep CNN architecture

Deep learning, namely the convolutional neural network, is often used in the image identification and classification processes that are carried out in remote sensing. The information sent into the CNN is converted into numerical form, utilizing numerous layers of the network's various topologies. Figure 5 illustrates the fundamental structure that a CNN has. The convolution layers, pooling layers, fully connected layers, batch normalization, SoftMax, and classification layers are the primary components of the CNN (Raorane, Magare, and Mistry 2022b).

Convolution Layer: The convolution layer produces the image's features by extracting the image's features and then convolving the input image using convolution kernels of different sizes. After that comes the aggregation step, which combines the characteristics retrieved from the various image parts.

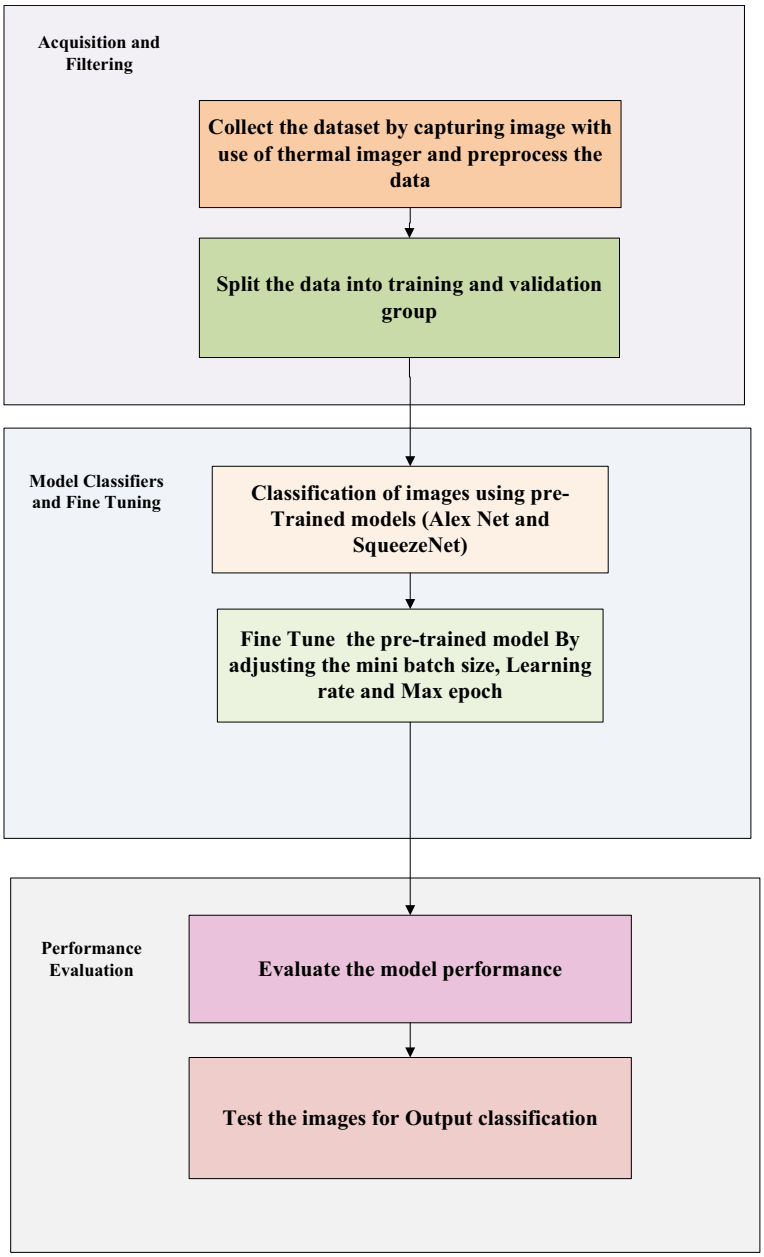


Figure 4. Flowchart of proposed work.

$$s(t) = (x * w)(t) \tag{1}$$

$$s(t) = (x * w)(t) \sum x(a) w(t - a) \tag{2}$$

This equation shows how t, x, and w work together as a complex function (Pa and Kazemi 2022a).

Pooling layer: This layer cuts down on the size of the images sent in, which lowers the cost and time of computing. The layer links the convolutional layer and the model's output.

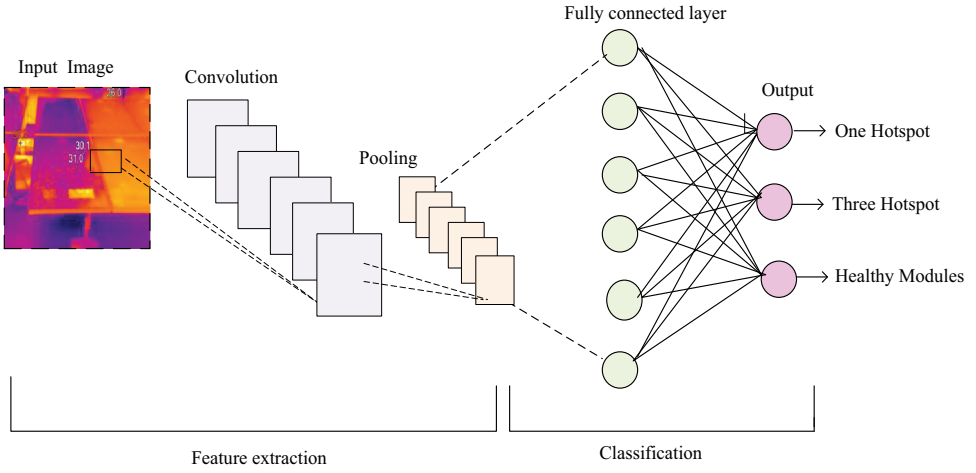


Figure 5. Architecture of convolutional neural network.

Fully linked layer: This layer transfers the representation of inputs and outputs to their respective destinations. It often has numeric values.

Pre-trained convolutional neural networks

A) AlexNet

AlexNet's deep layers, comprised of 650 thousand neurons and 60 million parameters, allow it to categorize more than 1000 distinct classes. Alexnet consist of eight layers out of which five layers are convolutional layers (CLs) and three fully connected layers (FLCs). Input to the First convolution layer is $227 \times 227 \times 3$ to the 1st convolutional layer have 96 filters of size 11×11 with stride of 4 pixel after the 1st convolutional layer pooling layer are connected with stride of 2 pixel this pooling layer is sued to reduce the image size then this pooling layer acts as input to the next convolutional layer here there are 256 filters of size 5×5 with stride 1 then it is connected to the next pooling layer which will further reduce the size, then all the remaining three conventional layers are connected without pooling layer connected in between the conventional layer then three fully connected layer are connected where the last layer which uses softmax activation function for output calculation which produces distribution over 1000 class label. The dimension of the 147-input image for the AlexNet needs to be $227 \times 227 \times 3$, and the first CL converts the input image with 96 kernels sized at $11 \times 11 \times 3$ with a stride of four pixels. This image serves as the input to the second layer, and the other details are given in Figure 6.

B) SqueezeNet

Another convolutional neural network (CNN) trained with the ImageNet database is SqueezeNet. The SqueezeNet was trained with more than one million photos and had fifty times fewer parameters than the AlexNet. This network is built on a fire module, which is made up of a squeeze layer and a 175 expand layer. The fire module serves as the foundation. The squeeze layer only has 1×1 convolution filters, and it feeds into an expand layer that contains 176 a combination of 1×1 and 3×3 convolution filters (Figure 7). In order to identify panels that are having hotspots or not having hotspots, the pre-trained SqueezeNet model is been used.

Data annotation

A thermographic inspection of a PV Panel of 5 kW_p has been done where dust was manually created on a module that was 240 W_p for studying the hotspots and its effect on the panel

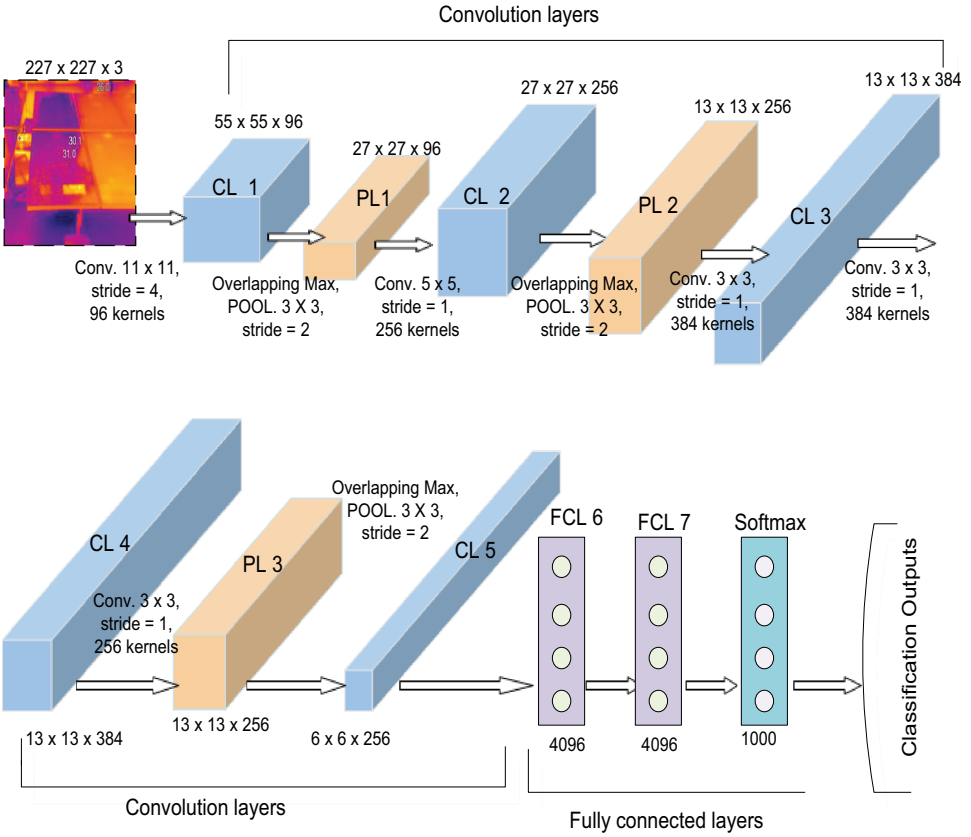


Figure 6. Structure of AlexNet.

performances, the manual soiling is performed to emulate different real-time soiling scenarios. Furthermore, using a thermal camera image has been captured for hotspot detection and classification. The total number of images captured is 476 of which 251 items have one hotspot, 136 items have 3 hotspots, and 89 items have no hotspots, i.e. of a healthy module, some images from the thermal imager are shown in Figures 8–10.

Results and discussions

This part is divided into two sections in the first section, pre-trained Convolutional networks are used to detect the hotspots and classify faulty and healthy panels. These hotspots were created because of the dust accumulation, and in the second section, power losses due to the creation of hotspots are discussed.

Hotspot detection classification

In this work for, hotspot detection classification is done by two methods, SqueezeNet and AlexNet; this transfer learning is a machine learning technique that uses pre-trained data (Kaldellis and Kapsali 2011) where a total of 476 images are used in which 251 items are of 1 hotspot and 136 items are of 3 hotspots and remaining 89 items of healthy panels. All the images have been captured by the thermal imager, here 70% data is used for training and 30% data is used for testing.

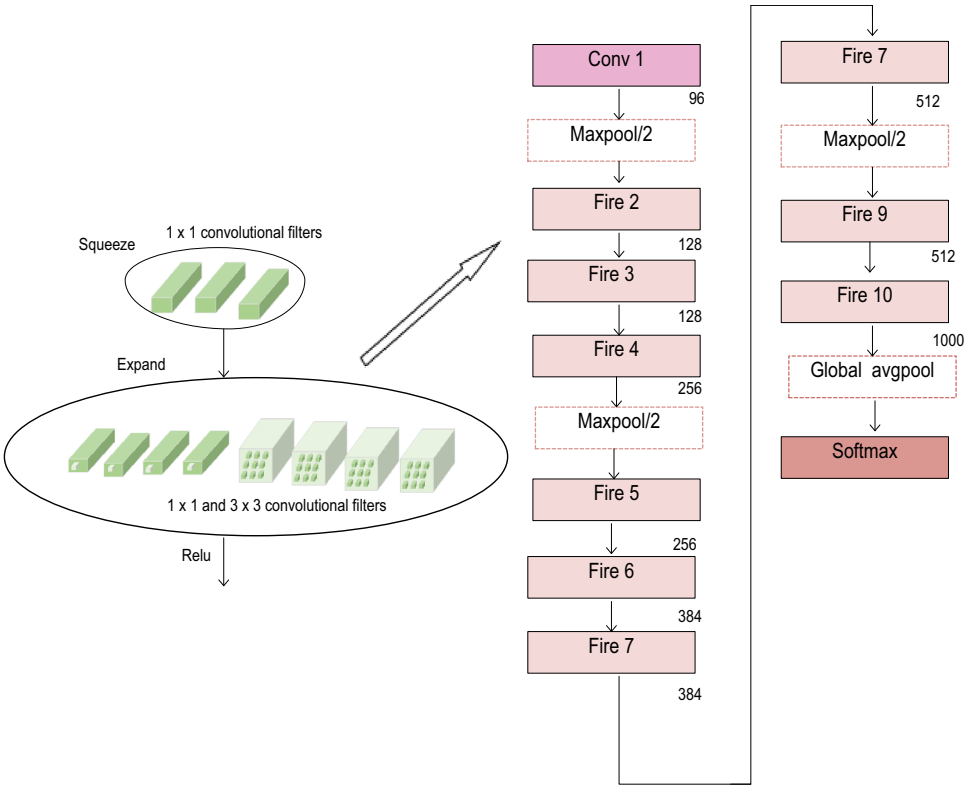


Figure 7. Structure of SqueezeNet.

A) AlexNet transfer learning

AlexNet is CNN's most representative model, with more excellent performance, fewer training parameters, and stronger robustness. It is inspired by while simulating dual-channel visual transmission and learning picture attributes via two channels (Pa and Kazemi 2022b). The pre-trained model is made in MATLAB environment. In AlexNet, there is an input layer, five convolutional layers, three pooling layers, three fully connected layers, and an output layer with three output class labels. In the full model, two channels are investigated individually in the convolutional layer and only crossed in the third feature extraction layer. The first fully connected layer cross-mixes the features of two groups. The next fully connected layer repeats until the last fully connected layer combines the features of two groups to generate a 4096-dimensional feature vector. This pre-trained model is used for classification, which contains 25 layers, and to image input size is $227 \times 227 \times 3$ for training; 70% of data is used and for testing, 30%. The training options used in the pre-trained models in is shown in Table 1, and the accuracy and loss plot of AlexNet transfer learning techniques are shown in Figures 11 and 12, respectively. The training accuracy of AlexNet comes out to be 99.3%. When tested, it classified the trained images with 99.3% accuracy means chances of wrong classification is very less in AlexNet model

B) SqueezeNet transfer learning

It uses three ways to improve CNN networks. First, most decreases the number of network weights. It reduces the input channels to 3×3 filters. It also reduces network weights. Larger activation maps are down sampled later in the network. It is hypothesized that the size of down sampled activation maps affects categorization accuracy. Removing the fully linked dense

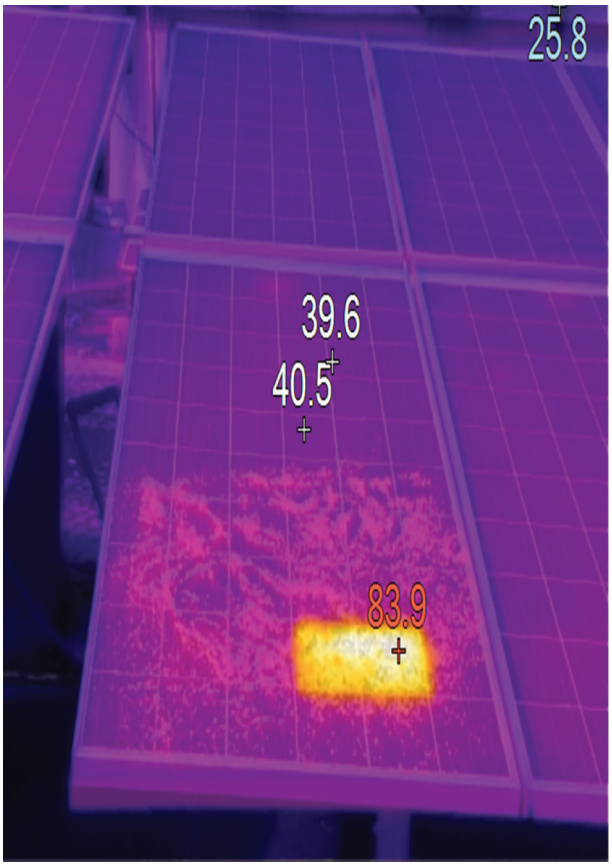


Figure 8. One hotspot image captured from thermal imager.

layers frequently employed in the network's last layers and replacing them with a convolution layer with the same number of output channels as data classes, dropout layer, and SoftMax activation function decreases the amount of network weights. It contains 68 layers, MATLAB 2021 for SqueezeNet transfer learning image classification is used to train the images. Further, the accuracy and loss plot of SqueezeNet transfer learning techniques is shown in Figures 13 and 14, respectively; training options have been considered here as shown in Table 1. The training accuracy of the SqueezeNet comes out to be 95.01%. When tested, it classified the trained images with 95.0% accuracy, which means the chances of accurate classification is less than AlexNet.

Zyout and Oatawneh (2020a) implemented a deep learning model AlexNet with normal type of images for training the model and reported accuracy 93.33%. Raorane, Magare, and Mistry (2022a) use VGG 19 model with thermal images for training the model and reported accuracy of 92% and (Haidari et al., 2022) introduces VGG 16 model with thermal images for training the model and reported accuracy of 98% where the proposed work uses AlexNet and SqueezeNet model where Alexnet performs best with accuracy of 99.3%.

Panel performance with and without dust accumulation

On the 5 kW solar panel, which is on the rooftop of Delhi Technological University, New Delhi, hotspots are artificially created with the help of dust, for study purpose here only considering 5

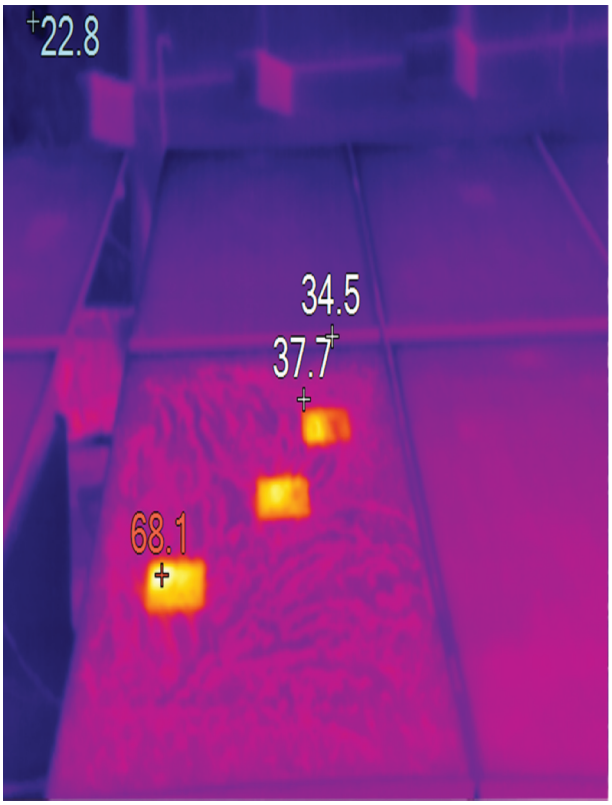


Figure 9. Three hotspot images captured from the thermal imager.

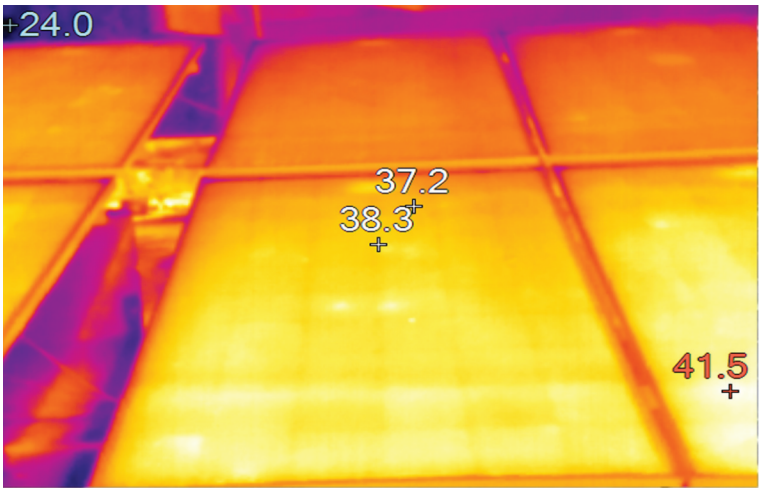


Figure 10. Healthy panel without hotspot image captured from the thermal imager.

days of data is considered on the first day solar analyzer setup was put on peak hours in which panel performs best, the solar analyzer for 2 hrs from 11 AM to 1 PM are connected to get the details of panels performance, on the day 1 the solar panel output performance on the day 1 is shown in Figure 15. On the second day to create hotspot, some dust was intentionally sprinkled

Table 1. Network parameters and assigned values.

Training options	AlexNet	SqueezeNet
Learning Rate	0.001	0.001
Mini batch size	50	30
Max Epoch	20	20
Solver	Sgdm	Sgdm

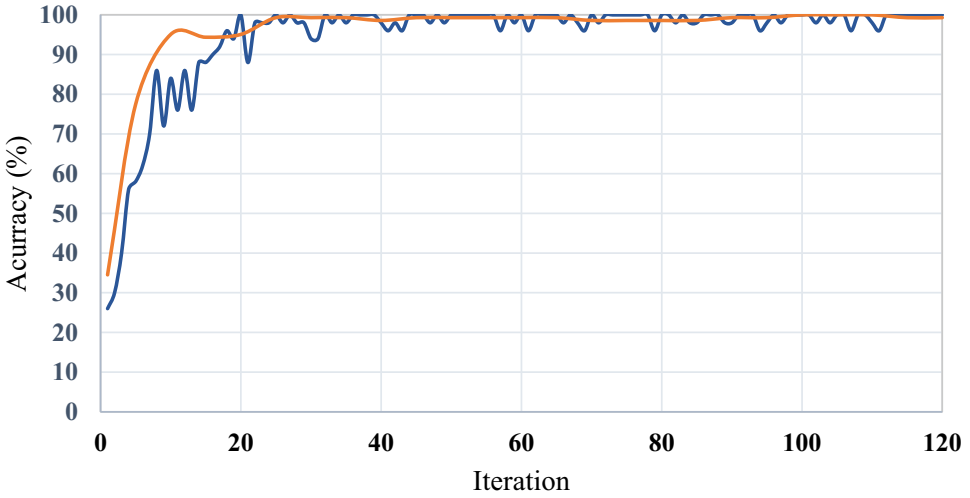


Figure 11. Accuracy plot for AlexNet transfer learning method.

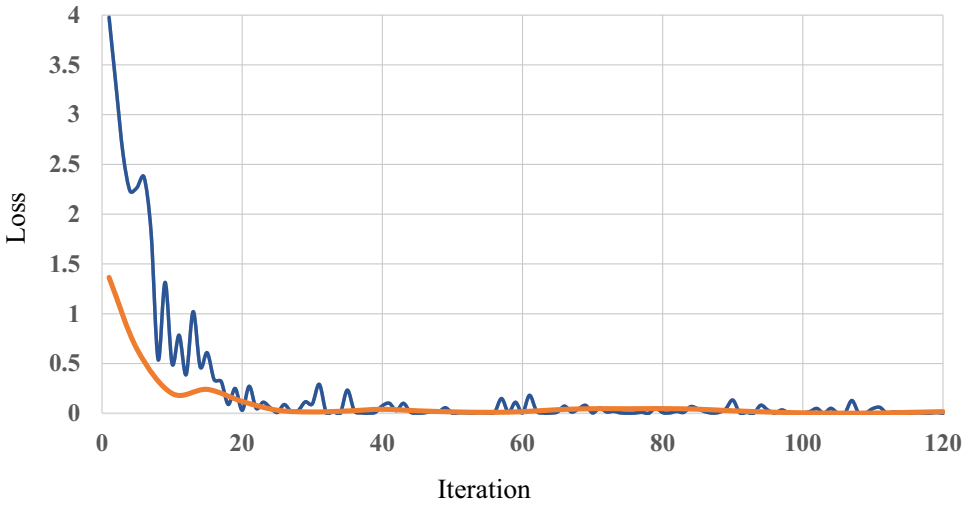


Figure 12. Loss plot for AlexNet transfer learning method.

on half of the module to see the effect on output power of the solar panels by the help of solar analyzer. Seeing Figure 16, we can say that power gets reduced as the Hotspot was made from 1680 W to 1601 W, the dust was kept for 2 hrs from 11 AM to 1 PM just for study purpose. The power reduced to 4.7%.

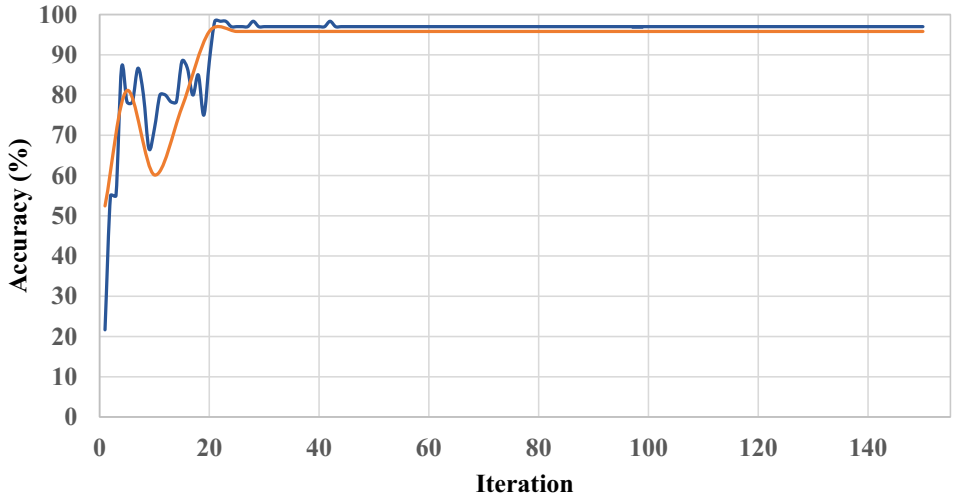


Figure 13. Accuracy plot for SqueezeNet transfer learning method.

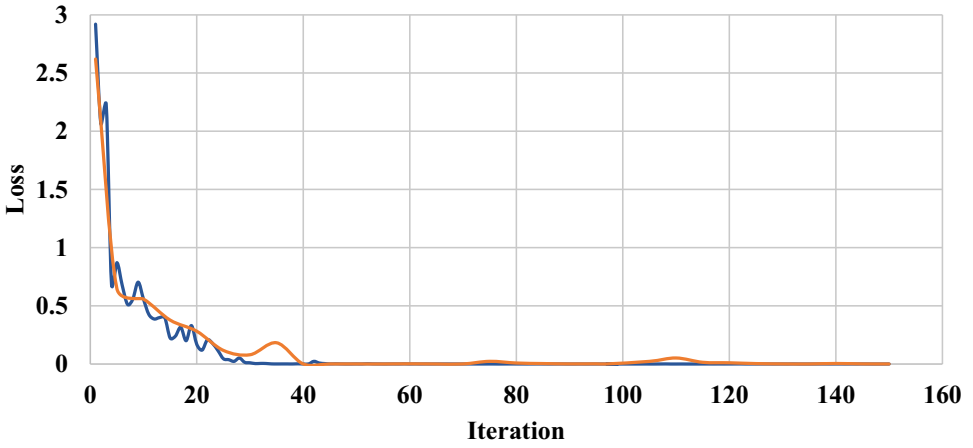


Figure 14. Loss plot for SqueezeNet transfer learning method.

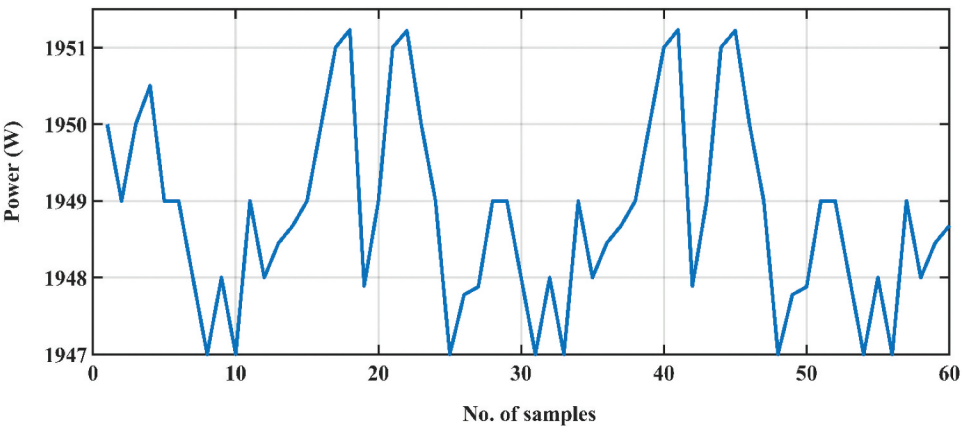


Figure 15. Day 1 maximum power plot versus no of samples captured from the solar analyzer for 2 hrs.

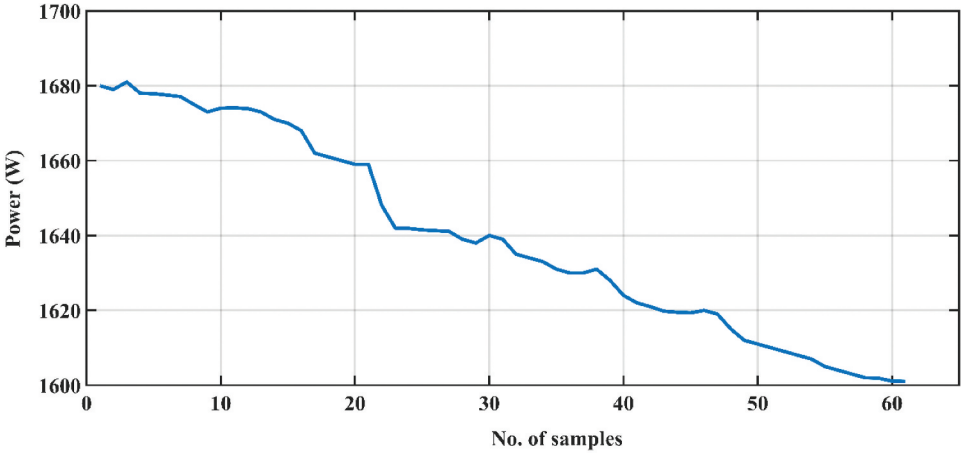


Figure 16. Day 2 maximum power plot versus no of samples captured from the solar analyser for 2 hrs.

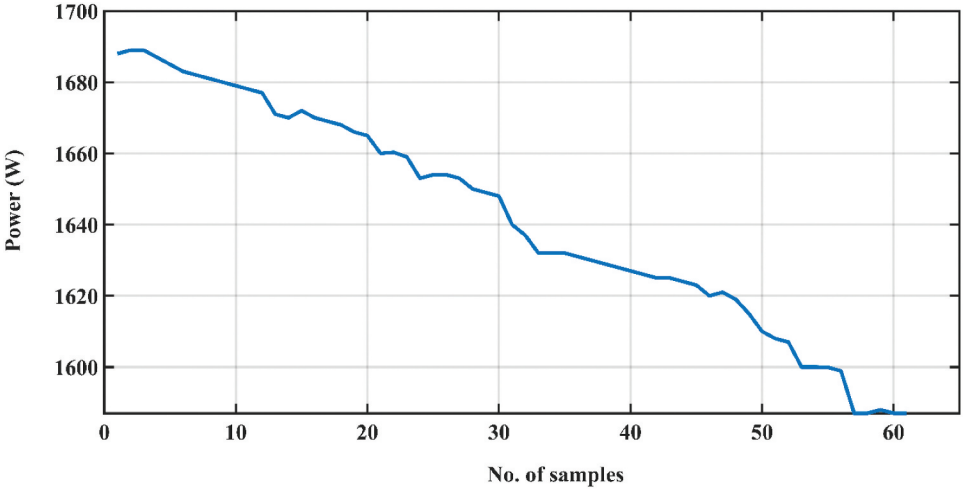


Figure 17. Day 3 maximum power plot versus no of samples captured from the solar analyser for 2 hr.

On the third day, a thicker layer of dust was sprinkled on half of the solar module to see the output power of the solar panel. In Figure 17, the power gets reduced as the hotspot was created from 1688 W to 1587.89, the dust was kept for about 2 hrs from 11AM to 1 PM for study purposes. The power reduced to 5.983%.

On the fourth day, some dust was sprinkled on the complete module to see the output power of the solar panel. In Figure 18, the power gets reduced as the hotspot was created from 1798.9 W to 1682 W, the dust was kept for about 2 hrs from 11 AM to 1 PM for study purposes. The power was reduced to 6.49%.

On the fifth day, a thicker layer of dust was sprinkled to see the panel performance and create hotspotfrom 2015 W to 1810 W while keeping dust on the panel for 2 hrs 11 AM to 1 PM. Figure 19 shows that the output power gets reduced after the hotspot creation. The power reduced to 10.17%.

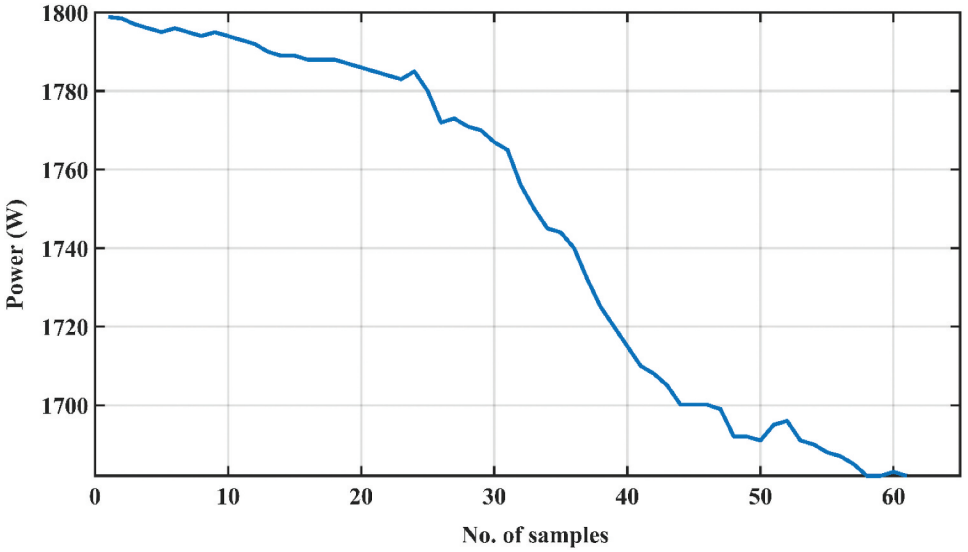


Figure 18. Day 4 maximum power plot versus no of samples captured from the solar analyser for 2 hrs.

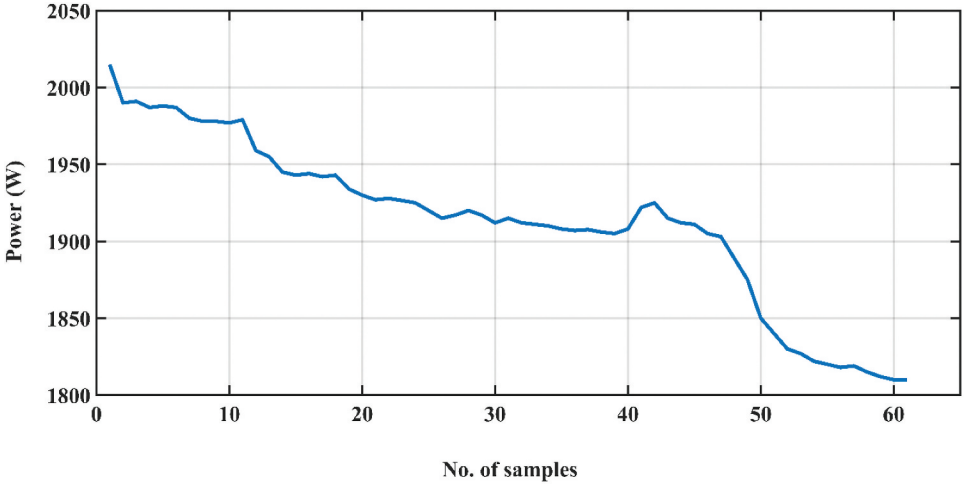


Figure 19. Day 5 maximum power plot versus no of samples captured from the solar analyser for 2 hrs.

Conclusion

In this work hotspots are created by sprinkling dust over a module of 240 W_p to analyze the power output from the solar panel. This was done for five continuous days on the rooftop of Delhi Technological University, New Delhi; because of dust accumulation, the panel performance degrades and the power gets reduced after the creation of the hotspot. It was found that the losses in power output increases, when more amount of dust accumulates on the module. Hotspot Images were captured by the help of a thermal imager device. Then, a convolution-based hotspot detection is implemented by two well-known methods, SqueezeNet and AlexNet. From the results, we can conclude AlexNet performs much better than SqueezeNet with accuracy 99.70%. Hotspot detection and classification are necessary so that its performance can be improved after the hotspot detection, and further the proposed work may be extended for future work as:

- Effective and robust automated early hotspot defect detection and classification methods are still being studied to improve accuracy.
- In future work, it will be important to aim for improved outcomes by creating lightweight deep learning methods that make use of a variety of different structures.
- Further, a mitigation technique can be added to improve the panels' effect due to dust.

Nomenclature

AI	Artificial Intelligence
CLs	Convolutional layers
CNN	Convolutional Neural Network
DCNN	Deep Convolutional Neural Network
DRNN	Deep recurrent neural network
FDC	Fault detection and classification
FLCs	Fully connected layers
IR	Infrared image
LWIR	Long wave Infrared images
MATLAB	Matrix Laboratory
MWIR	Mid wave Infrared images
MAE	Mean average Error
NN	Neural network
NB-CNN	Nave Bayes Convolutional Neural Network
PL	Pooling Layers
PV	Photovoltaic
RMSE	Root mean square error
SGDM	Stochastic gradient descent with momentum
SVM	Support vector machine
TI	Thermography images

Disclosure statement

No potential conflict of interest was reported by the authors.

Funding

No specific grant has been given to this research by funding agencies/organizations.

Notes on contributors

Rahma Aman has received the M.Tech. degree in Control and Instrumentation systems from Electrical engineering department, Jamia Millia Islamia University, New Delhi, India in 2021. She completed the B.Tech. degree in Electrical engineering from United college of engineering and Research, Uttar Pradesh, India in 2018. Presently, she is pursuing the Ph.D. degree from Delhi Technological University, Delhi, India. Her research interests focus on renewable energy integration, optimization techniques, PV systems under partial shading conditions and deep learning approaches for power maximization.

M. Rizwan did his post-doctoral research at Virginia Polytechnic Institute and State University, USA. He has more than 21 years of teaching and research experience. Dr. Rizwan has successfully completed three research projects in the area of renewable energy systems and published and presented more than 180 research papers in reputed international/national journals including IEEE transactions and conference proceedings. Presently he is working on two international and one national research projects in the area of solar PV and EVs. Dr. Rizwan has authored one book for CRC Press, USA and edited one book for AIP Publishing, USA. Recently he has authored one book in energy science engineering for AICTE. He is the recipient of Raman Fellowships for Post-Doctoral Research for Indian Scholars in USA, DST Start Up Grants (Young Scientists) and many more. His area of interest includes soft computing applications in power engineering, renewable energy systems, building energy management, smart grid etc. He is a Sr. Member of IEEE, Life Member of ISTE, Life Member of SSI, Member of International Association of Engineers (IAENG), and many other reputed societies.

Astitva Kumar has completed his B.Tech in 2013 from Uttar Pradesh Technical University in Electrical Engineering. He received his M.Tech degree in Control and Instrumentation from Delhi Technological University, Delhi, India in 2015. He further enrolled in Ph.D. and received his Doctorate degree on the topic "Optimal Design of SPV System and Application" from Delhi Technological University, Delhi, India in 2021. Presently, he is working as an Assistant Professor in Electrical Engineering Department, Netaji Subhash University of Technology, Delhi, India. He has published more than 18 research papers in reputed international journals and conference proceedings. He is currently, an active reviewer for numerous publishers such as IEEE, Springer, Elsevier and Scopus indexed international conferences. He has received Research Excellence Award in 2021 and 2023 for his commendable research and has also received international travel grants for presenting paper in international conferences. He has research experience of working on various government and international organization funded projects. His research interest focusses on utilization of electrical energy, hybrid energy systems, advanced metaheuristic techniques, smart building energy management systems, agrivoltaics, PV power forecasting, energy management systems and intelligent controllers for hybrid energy systems.

ORCID

M. Rizwan http://orcid.org/0000-0003-2839-7241

Dataset Availability Statement

Data were recorded from a 5 kW solar panel by a solar analyzer on the rooftop of Utilization Electrical Engineering Lab, Delhi Technological University, New Delhi, India.

Declaration

The authors declare that the present research has no financial or personal ties to any individual or group that could unreasonably affect this work. This manuscript is the author's own work and does not contain material taken from another source. All data measures are real, unaltered results, and this work has never been published or submitted to another journal for publication consideration. Also, none of the authors has any financial or scientific conflicts of interest with regard to the research described in this manuscript.

References

Adinoyi, M. J., and S. A. M. Said. 2013. Effect of dust accumulation on the power outputs of solar photovoltaic modules. *Renewable Energy* 60:633–36. doi:10.1016/j.renene.2013.06.014.

Anwar, S. A., and M. Z. Abdullah. 2014. Micro-crack detection of multicrystalline solar cells featuring an improved anisotropic diffusion filter and image segmentation technique. *EURASIP Journal on Image and Video Processing* 2014 (1):15. doi:10.1186/1687-5281-2014-15.

Aziz, F., A. Ul Haq, S. Ahmad, Y. Mahmoud, M. Jalal, and U. Ali. 2020. A novel convolutional neural network-based approach for fault classification in photovoltaic arrays. *IEEE Access* 8:41889–904. doi:10.1109/ACCESS.2020.2977116.

Bodnar, I., and G. Kozsely 2022. Development of solar panel diagnostic system. *2022 23rd International Carpathian Control Conference (ICCC)*, 221–26. doi:10.1109/ICCC54292.2022.9805859.

Chen, F. -C., and M. R. Jahanshahi. 2018. NB-CNN: Deep learning-based crack detection using convolutional neural network and naïve Bayes data fusion. *IEEE Transactions on Industrial Electronics* 65 (5):4392–400. doi:10.1109/TIE.2017.2764844.

Chen, H., Y. Pang, Q. Hu, and K. Liu. 2020. Solar cell surface defect inspection based on multispectral convolutional neural network. *Journal of Intelligent Manufacturing* 31 (2):453–68. doi:10.1007/s10845-018-1458-z.

Fan, S., Y. Wang, S. Cao, T. Sun, and P. Liu. 2021. A novel method for analyzing the effect of dust accumulation on energy efficiency loss in photovoltaic (PV) system. *Energy* 234:121112. doi:10.1016/j.energy.2021.121112.

Fan, S., Y. Wang, S. Cao, B. Zhao, T. Sun, and P. Liu. 2022. A deep residual neural network identification method for uneven dust accumulation on photovoltaic (PV) panels. *Energy* 239:122302. doi:10.1016/j.energy.2021.122302.

Haridari, P., A. Jafari, and Nasiri, A. 2022. Deep learning-based model for fault classification in solar modules using infrared images. *Sustainable Energy Technologies and Assessments* 52:102110. doi:10.1016/j.seta.2022.102110.

Higuchi, Y., and T. Babasaki 2018. Failure detection of solar panels using thermographic images captured by drone. *2018 7th International Conference on Renewable Energy Research and Applications (ICRERA)*, 391–96. doi:10.1109/ICRERA.2018.8566833.

Jaffery, Z. A., A. K. Dubey, Irshad, and A. Haque. 2017. Scheme for predictive fault diagnosis in photo-voltaic modules using thermal imaging. *Infrared Physics & Technology* 83:182–87. doi:10.1016/j.infrared.2017.04.015.

Jaszczur, M., A. Koshti, W. Nawrot, and P. Sędor. 2020. An investigation of the dust accumulation on photovoltaic panels. *Environmental Science and Pollution Research* 27 (2):2001–14. doi:10.1007/s11356-019-06742-2.

Kaldellis, J. K., and M. Kapsali. 2011. Simulating the dust effect on the energy performance of photovoltaic generators based on experimental measurements. *Energy* 36 (8):5154–61. doi:10.1016/j.energy.2011.06.018.

Kodakkal, A., R. Veramalla, N. R. Kuthuri, and S. R. Salkuti. 2021. An ALO optimized adaline based controller for an isolated wind power harnessing unit. *Designs* 5 (4):65. doi:10.3390/DESIGNS5040065.

Korkmaz, D., and H. Acikgoz. 2022. An efficient fault classification method in solar photovoltaic modules using transfer learning and multi-scale convolutional neural network. *Engineering Applications of Artificial Intelligence* 113:104959. doi:10.1016/j.engappai.2022.104959.

Madeti, S. R., and S. N. Singh. 2017. Monitoring system for photovoltaic plants: A review. *Renewable and Sustainable Energy Reviews* 67:1180–207. doi:10.1016/j.rser.2016.09.088.

Mekhilef, S., R. Saidur, and M. Kamalisarvestani. 2012. Effect of dust, humidity and air velocity on efficiency of photovoltaic cells. *Renewable and Sustainable Energy Reviews* 16 (5):2920–25. doi:10.1016/j.rser.2012.02.012.

Pa, M., and A. Kazemi. 2022a. *A fault detection scheme utilizing convolutional neural network for PV solar panels with high accuracy*. doi:10.48550/arxiv.2210.09226.

Pa, M., and A. Kazemi. 2022b. *A fault detection scheme utilizing convolutional neural network for PV solar panels with high accuracy*. doi:10.48550/arxiv.2210.09226.

Paudyal, B. R., and S. R. Shakya. 2016. Dust accumulation effects on efficiency of solar PV modules for off grid purpose: A case study of Kathmandu. *Solar Energy* 135:103–10. doi:10.1016/j.solener.2016.05.046.

Pierdicca, R., E. S. Malinverni, F. Piccinini, M. Paolanti, A. Felicetti, and P. Zingaretti. 2018. Deep convolutional neural network for automatic detection of damaged photovoltaic cells. *The International Archives of the Photogrammetry, Remote Sensing and Spatial Information Sciences XLII–2*:893–900. doi:10.5194/isprs-archives-XLII-2-893-2018.

Raorane, A., D. Magare, and Y. Mistry 2022a. Performance of fault classification on photovoltaic modules using thermographic images. *ITM Web of Conferences*, *44*, 03065. doi:10.1051/ITMCONF/20224403065.

Raorane, A., D. Magare, and Y. Mistry 2022b. Performance of fault classification on Photovoltaic modules using Thermographic images. *ITM Web of Conferences*, *44*, 03065. doi:10.1051/itmconf/20224403065.

Ray, P., and S. R. Salkuti. 2022. Hybrid artificial intelligence technique based fault location in a long transmission line. *Lecture Notes in Electrical Engineering* 812:487–505. doi:10.1007/978-981-16-6970-5_36.

Said, S. A. M., G. Hassan, H. M. Walwil, and N. Al-Aqeeli. 2018. The effect of environmental factors and dust accumulation on photovoltaic modules and dust-accumulation mitigation strategies. *Renewable and Sustainable Energy Reviews* 82:743–60. doi:10.1016/j.rser.2017.09.042.

Salkuti, S. R. 2022. Emerging and advanced green energy technologies for sustainable and resilient future grid. *Energies* 15 (18):6667. doi:10.3390/EN15186667.

Sayyah A., Horenstein M. N, and Mazumder M. K. 2014. Energy yield loss caused by dust deposition on photovoltaic panels. *Solar Energy* 107:576–604. doi:10.1016/j.solener.2014.05.030.

Sinha, T., P. Ray, and S. R. Salkuti. 2018. Protection coordination in microgrid using fault current limiters. *Journal of Green Engineering* 8 (2):125–50. doi:10.13052/JGE1904-4720.822.

Triki-Lahiani, A., A. Bennani-Ben Abdelghani, and I. Slama-Belkhodja. 2018. Fault detection and monitoring systems for photovoltaic installations: A review. *Renewable and Sustainable Energy Reviews* 82:2680–92. doi:10.1016/j.rser.2017.09.101.

Zyout, I., and A. Oatawneh. 2020a. *Detection of PV solar panel surface defects using transfer learning of the deep convolutional neural networks* 1–4. doi: 10.1109/ASET48392.2020.9118384.

Zyout, I., and A. Oatawneh 2020b. Detection of PV solar panel surface defects using transfer learning of the deep convolutional neural networks. *2020 Advances in Science and Engineering Technology International Conferences (ASET)*, 1–4. doi:10.1109/ASET48392.2020.9118382.

2023 International Conference for Advancement in Technology (ICONAT)
Goa, India. Jan 24-26, 2023

Flying Squirrel Search Optimization based MPPT Controller for Stand-Alone PV System

Atul Avasthi[1]
Delhi Technological University (DTU)
Delhi, India
atulavasthi31@gmail.com

Rachana Garg
Delhi Technological University (DTU)
Delhi, India
rachana16100@yahoo.co.in

Priya Mahajan
Delhi Technological University (DTU)
Delhi, India
priyamahajan.eed@gmail.com

2023 International Conference for Advancement in Technology (ICONAT) | 978-1-6654-7517-4/23/$31.00 ©2023 IEEE | DOI: 10.1109/ICONAT57137.2023.10080716

***Abstract*— This paper presents an MPPT technique based on flying squirrel search optimization (FSSO) for extracting maximum power from a stand-alone PV system. Proposed FSSO MPPT technique is analyzed with perturb &observe (P&O) and fuzzy logic controller (FLC) techniques. Based on the real-time simulation it is found that tracking of maximum power from proposed FSSO technique is much better than fuzzy and P&O technique under various solar irradiation. In addition, it is observed that Proposed FSSO has the least settling time as compared with FLC and P&O based MPPT techniques. proposed FSSO technique are simulated using MATLAB/SIMULINK.**

Keywords—solar photovoltaic, MPPT controller, fuzzy logic controller, FSSO, renewable Energy

I. INTRODUCTION

Solar photovoltaic energy has emerged as main renewable energy source as it requires less maintenance and free from pollution. To produce power efficiently, solar PV panels are paired with power converters [1]-[2]. Output power of the PV system depends on solar irradiation and ambient temperature; both are unpredictable and change randomly, causing the PV array to produce varying power through the day. Varying power from PV array can improved by maximum power point tracking (MPPT) technique [3].

MPPT technique can be classified into conventional, intelligent and bio-inspired based MPPT etc. conventional MPPT techniques such as INC, and P&O techniques , suffers from sluggish tracking and low efficiency when it comes to extracting MPP from the PV system. However, bio inspired techniques, which are normally governed by nature of animals, concept of evolution, or by the physical concept, give more reliable results as compared to conventional techniques. Bio-Inspired MPPT offers outstanding accuracy, are easy to design and reacts swiftly to rapidly changing situations [4]-[7].

In this proposed paper, bio inspired based flying squirrel search optimization (FSSO) technique is tested on PV system comprising of a PV array connected to DC-DC boost converter. To get maximum power from PV system under different irradiance, duty cycle of the boost converter is varied so that the system operate at MPP. FSSO technique has been implemented and compared with FLC and P&O techniques.

The remainder of the paper is organized as follows. Section 2 presents modelling of photovoltaic module, DC-DC boost converter and P&O and FLC modelling as well as proposed FSSO technique. Section 3 presents simulation results while Section 4 stated the conclusion of the work.

II. SYSTEM DESCRIPTION

The proposed system comprises of PV arrays, a DC-DC converter, and a DC load. MPPT controller revised the duty cycle of a boost converter. The PV array captures power in the form of voltage and current delivered to the boost converter. The MPPT controller measures the voltage and current produced by the PV array. Fig.1 shows the proposed control technique for a PV system.

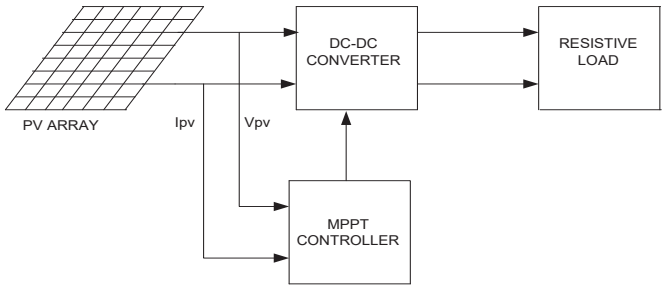


Fig.1. Proposed control technique for PV system

A. PV Module

A PV module is a grouping of PV cells that linked in series and parallel fashion. The equivalent circuit model of a PV cell, as shown in Fig. 2, consists of a current source connected in parallel to a diode.

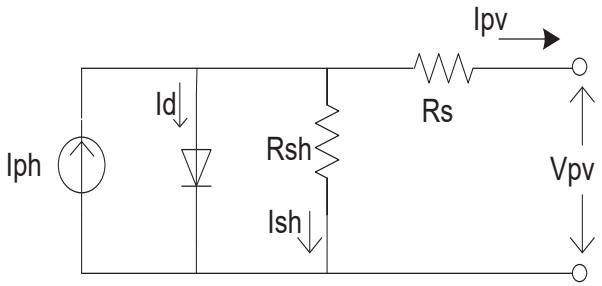


Fig.2. Equivalent circuit of PV cell

From the electrical equivalent circuit, output current (I_{pv}) of PV cell is given by:

$$I_{pv} = I_{ph} - I_D - I_{sh} \quad (1)$$

where, $I_D = I_o\left(e^{\frac{q(V_{pv}+I_{pv}R_s)}{\eta kT}} - 1\right)$ (2)

and $I_{sh} = \frac{V_{pv}+I_{pv}R_s}{R_{sh}}$ (3)

The parameters T, q, k and η are the temperature in kelvin, electrical charge ($1.61\text{x}10^{-19}$C), Boltzmann constant ($1.39\text{x}10^{-23}$ J/K) and ideality factor of diode respectively. I_0,

Authorized licensed use limited to: DELHI TECHNICAL UNIV. Downloaded on April 17,2023 at 06:09:49 UTC from IEEE Xplore. Restrictions apply.

I_{ph}, I_{pv} and V_{pv} are reverse saturation current of diode, photocurrent of cell, output current of cell and output voltage of cell respectively.

PV cell shunt resistance (Rsh) is very high; however, current (Ish) flow through shunt resistance has very little effect on the I-V characteristics of the PV cell or array [8]. Output current (I_{pv}) from PV cell is given in Eq. (4).

$$I_{pv} = I_{ph} - I_o\left(e^{\frac{q(V_{pv}+I_{pv}R_S)}{\eta kT}} - 1\right) \quad (4)$$

In the present work, sun power SPR-305NE is used. Table 1 shows specification used for simulation and modeling of PV module parameters utilized. Maximum power obtained by the array is (305.22 *36) 10.98kW.

TABLE I. PARAMETERS OF PV MODULE

PARAMETERS	VALUE
Maximum power (W)	305.226W
Open circuit Voltage (Voc)	64.2V
Short circuit current (Isc)	5.96A
Maximum power point voltage (Vmp)	54.7V
Current at maximum power point (Imp)	5.96A
Reference Temperature (T)	25°C
No. of series-connected PV module	6
No. of parallel connected PV module	6

B. Boost Converter

A boost converter (also known as a step-up converter) is a DC-DC converter that converts step-up voltage from input to output. The PV panel's DC voltage is fed into the DC-DC boost converter. The operation of the DC-DC converter is based on the energy storage capacity of the inductor and capacitor. It is made up of the boost inductor L, the power switch (IGBT), the boost capacitor C2, and the diode D shown in fig.3. The output DC voltage from DC-DC converter can be controlled by varying the duty cycle. This duty cycle will be controlled by PWM and then fed to IGBT device [9].

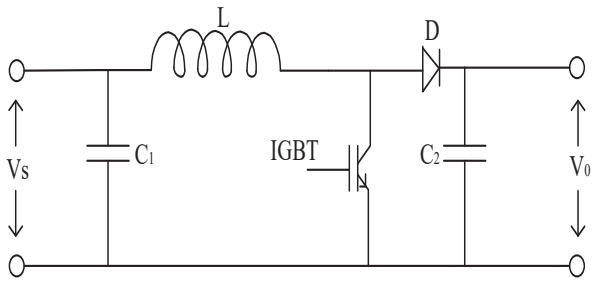


Fig.3. Equivalent circuit of DC-DC boost converter

$$V_0 = \frac{V_s}{1-D} \quad (5)$$

The boost converter's output voltage (V_0) depends on the boost converter's input voltage (V_S) and duty cycle (D). The value of boost inductor L and boost capacitor C can be calculated by using equation (6) and (7). The output voltage ripple$(\Delta V_0/V_0)$is suitably selected.

$$C_2 = \frac{D}{R * f * (\Delta V_o/V_o)} \quad (6)$$

$$L = \frac{V_s * (V_o - V_s)}{\Delta I_L * f * V_o} \quad (7)$$

The parameters of boost converter are shown in Table 2. As environmental conditions are varies through the day so that input voltage to boost converter is varies and maximum power point changes.

TABLE II. PARAMETERS OF BOOST CONVERTER

CIRCUIT PARAMETERS	VALUE
Capacitor (C_1)	1000µF
Boost inductor (L_1)	0.34mH
Boost capacitor (C_2)	30.86µF
Resistive load (R)	54Ω
Switching frequency (f)	10kHz
Voltage ripple (ΔV_o)	3%
Current ripple (ΔI_o)	10%

C. MPPT Controller

MPPT is very important in PV applications because output voltage of PV array is vary due to environment conditions. Maximum power tracker assists PV array in delivering maximum power at its output, increasing system efficiency [10]. To obtain maximum power, it is needed to execute an MPPT technique that dynamically adjusts the drawing of the power. MPPT controllers are designed to continue tracking of maximum power point. Efficient MPPT controllers are required to change operating points by varying the boost converter's duty cycle [11].

1) Perturb and Observe Technique

P&O is common technique for tracking maximum power from PV system. By this technique, minor perturbation of voltage is introduced causes variation of power of PV module and compared with previous output power [12]-[13]. If present output power is greater than previous power than PV voltage moved in positive direction and vice-versa. One of the major drawbacks of the P&O technique is that it causes oscillations around the maximum power point, which decrease system efficiency [14].

2) Fuzzy Logic Controller

Demand of fuzzy logic controllers (FLC) is increasing because of its simplicity, robustness, and potential to deal with non-linear models. One of the primary benefits of this controller is that it does not require the controller's exact model information. Under variable irradiance, FLC is used as an MPPT controller to obtain the maximum power from the PV source. Fig.4. shows the block diagram for fuzzy logic controller [15]. The FLC process consists of three steps:

a. Fuzzification,
b. Rule base lookup table, and
c. Defuzzification

Fuzzification is the first stage of the FLC. It converts the actual value into fuzzy values combined with the membership function. It takes error (E) and change in error (CE) with stored membership function.

Authorized licensed use limited to: DELHI TECHNICAL UNIV. Downloaded on April 17,2023 at 06:09:49 UTC from IEEE Xplore. Restrictions apply.

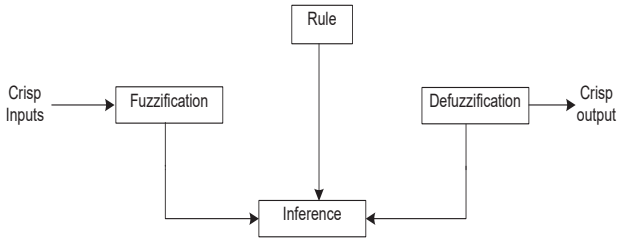


Fig.4.Block diagram of FLC

Rule base look up table is second state of fuzzy logic defines logical relation between the input values and output values. The logic of rule base inference is based on the IF-THEN. This fuzzy inference process is done by Mamdani's method.

Defuzzification is third stage of fuzzy logic which converts fuzzy values into crisp output. It is also the inverse of the fuzzification process. This process converts all fuzzy output values to their respective output membership function. The center of gravity method, also called centroid defuzzification is commonly used [16].

The inputs for proposed FL controller are Error (E) and change in Error (CE). Output from FL controller changes in duty cycle(δD). The input variables are defined as follows:

$$\mathrm{E(K)} = \frac{\mathrm{P(K)} - \mathrm{P(K-1)}}{\mathrm{V(K)} - \mathrm{V(K-1)}} \tag{8}$$

$$\mathrm{CE(K)} = \mathrm{E(K)} - \mathrm{E(K-1)} \tag{9}$$

Figures 6, 7, and 8 show the membership function of E(K), CE(K) and δDrespectively. For all input and output variables, five fuzzy levels are used: NB (negative big), NS (negative small), ZE (zero), PS (positive small), and PB (positive big). Table III shows a rule base used in the fuzzy logic controller.

TABLE III. FUZZY RULES FOR PROPOSED FL CONTROLLER

CE / E	NB	NS	ZE	PS	PB
NB	PB	PS	NB	NS	NS
NS	PS	PS	NB	NS	NS
ZE	NS	NS	NS	PB	PB
PS	NS	PB	PS	NB	PB
PB	NB	NB	PB	PS	PB

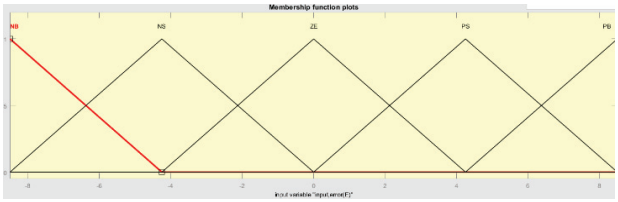


Fig.5.Membership function of input (a) error(E)

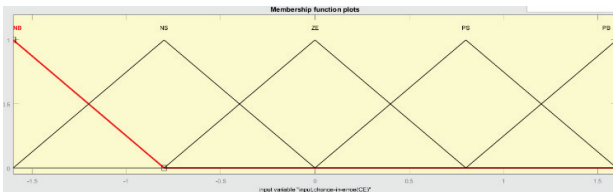


Fig.6.Membership function of input (b)change in error (CE)

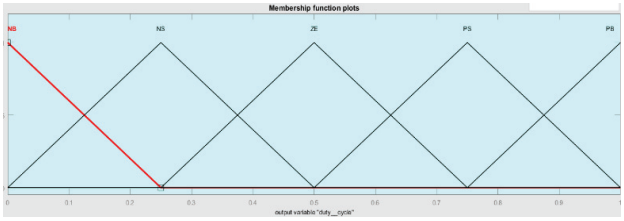


Fig.7.Membership function of output duty cycle(δD)

3) Flying Squirrel Search Optimization (FSSO)

Flying squirrel search optimization technique (FSSO) is to mimic the search food technique of flying squirrel (FS). The potential solution vector are assign as the position of an FS whereas fitness of FSs are assign as quality of food source. Based on their fitness value, The positions of FSs are divided into three categories: optimum solution (OS) (hickory nut tree), near optimum solution (NOS) (acorn nut tree), and random solution (RS) (normal tree).During the autumn season, squirrel gliding from one tree to another tree

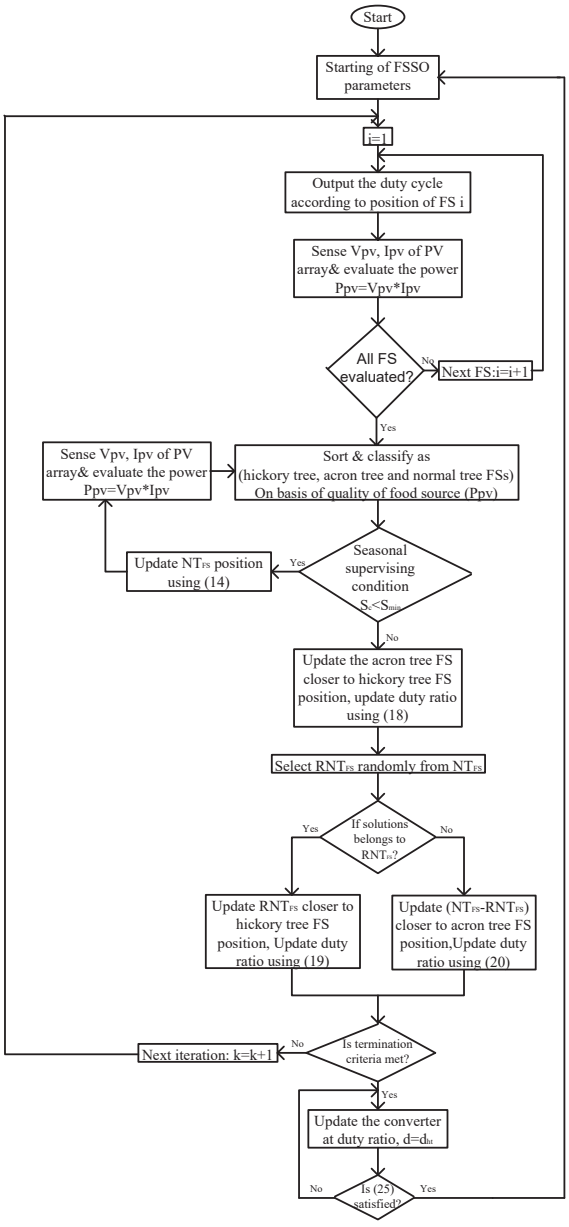


Fig.8. Flow chart of FSSO technique

Authorized licensed use limited to: DELHI TECHNICAL UNIV. Downloaded on April 17,2023 at 06:09:49 UTC from IEEE Xplore. Restrictions apply.

for finding the food to meet daily needs (acorn tree nuts) in forest. After achieving daily needs, they starts foraging for hickory tree nuts that will help them in winter season.

Storage of hickory tree nuts (optimum solution) will help them in retaining their energy needs in winter season and decrease the food foraging journey. At the end of winter season, FSs are active again. This proposed MPPT algorithm uses the cooperation of FSs, and positions updated without the predator's presence. The flowchart of this technique are shown in fig.8.

In this algorithm, some suppositions are considered for the FSSO technique in MPPT that is PV power output Ppv take as objective, i.e., food source and Position of FSs is taken as the boost converter's duty cycle (D) [17]-[20]. To implement FSSO algorithm, the following steps are considered.

a) Starting: In this stage, N number of flying squirrels are located at several trees, which are different values of the duty cycle of boost converter,

$$d_i = d_{min} + \frac{(i-1)(d_{max} - d_{min})}{N} \quad i = 1,2,..n \tag{10}$$

where i =iteration count; $d_{max}$and $d_{min}$are maximum value and minimum values for boost converter's duty cycle, which takes as 10% and 90% of the acceptable duty cycle for the boost converter—the range of duty cycle d_i from 0 to 0.5.

b) Robustness assessment: In assessment process, DC-DC boost converter is systematically regulated with every duty cycle (i.e., location of individual FSs) [21]. For individual duty cycle d, instant PV power output $P_{PV}(d)$ is taken as the quality of the food source. This kind of step continues throughout all ranges of the duty cycle. The objective function (f) for MPPT is characterized as:

$$f(d) = \max(P_{pv}(d)) \tag{11}$$

c) Revelation and grading: The hickory tree will have a duty cycle related to maximum power output. The next most essential location for FS is on acorn trees. The remaining FSs are taken into account on the normal tree.

d) Location update: After checking the periodical supervising condition, the duty cycle is updated. If ($S_c^k < S_{min}$) the duty cycle is revised using (i) or the duty cycle is revised using (ii). Subsequently, robustness is evaluated.

1) Seasonal supervising condition: Food search behavior of is much affected by seasonal. Squirrels are energetic in autumn as compared to winter [22] . Periodical supervising conditions block the algorithm from being captured in minimum peaks. For single dimension space, the seasonal constant (S_c) *and its minimum seasonal value* (S_{min}) *are calculated by:*

$$S_C^k = \left|d_{at}^k - d_{ht}\right| \tag{12}$$

$$S_{min} = \frac{10e^{-6}}{(365)^{k/(k_m/2.5)}} \tag{13}$$

where d_{ht} and d_{at} denotes the location of squirrels at a hickory tree and acorn tree, respectively; k denotes the number of current iteration and $k_m$signifies the maximum number of iterations permitted. Positions of FSs on normal trees (duty cycle of NTFSs) relocated using Levy distribution for better search space.

$$d_{nt}^{k+1} = d_{nt}^k + l \tag{14}$$

where d_{nt} denotes the location of squirrels at the normal tree and l means step length.

$$l \approx k\left(\frac{u}{|g|^{\frac{1}{\varepsilon}}}\right)(d_{ht} - d_{nt}) \tag{15}$$

where, levy index $\mathcal{E}$ and step coefficient k are chosen as 1.5 and 1.25 and u and g determined from the normal distribution curve as:

$$u = N(0, \sigma_u^2) \quad \text{and} \quad u = N(0, \sigma_g^2) \tag{16}$$

If Γ denotes integral gamma function, then variables are σ_u and σ_g are defined as:

$$\sigma_u = \left(\frac{\Gamma(1+\epsilon)\sin(\pi\epsilon/2)}{\Gamma\left(\frac{(1+\epsilon)}{2}\right)\epsilon(2)^{\left(\frac{\epsilon-1}{2}\right)}}\right)^{1/\epsilon}, \sigma_g = 1 \tag{17}$$

where, $\Gamma(n) = (n-1)!$

2) Routine Revision: FSs are located at the hickory tree. Some FSs move toward the acorn tree from the hickory tree. Some of these FSs move to acorn tree from the normal tree while rest of them shift from normal tree to hickory tree. The corresponding duty cycles are revised using the following equations [23].

$$d_{at}^{k+1} = d_{at}^k + g_d G_c(d_{ht}^k - d_{at}^k) \tag{18}$$

$$d_{nt}^{k+1} = d_{nt}^k + g_d G_c(d_{ht}^k - d_{nt}^k) \tag{19}$$

$$d_{nt}^{k+1} = d_{nt}^k + g_d G_c(d_{at}^k - d_{nt}^k) \tag{20}$$

where G_c and G_d denotes the gliding constant and gliding distances. The estimated value $G_c$chosen was 1.90. The gliding distance demonstrates as:

$$g_d = \frac{h_g}{s_f \tan\theta} \tag{21}$$

$$\tan\theta = \frac{F_D}{F_L} \tag{22}$$

Where h_g is height loss: the value of height loss is equal to taken as 8m;g_d is divided by appropriate numerical value. s_f is scaling factor is select as 18 to remain g_d in between the 0.5 to 1.11 s_f is able to assist to obtain the desire equity between exploration and exploitation phases. F_L is lift force whereas F_D is the drag force.

$$F_D = \frac{1}{2}\rho V^2 S C_D \tag{23}$$

$$F_L = \frac{1}{2}\rho V^2 S C_L \tag{24}$$

where,ρ is density of air = $1.204\ Kg/m^3$: V is velocity of FSs= $5.25\ m/s$;S is surface area of body = $154\ cm^2$;C_D is drag coefficient = 0.6 and C_L is lift coefficient = [0.675, 1.5] [24].

3) Convergence measurement: The optimization process is completed when the maximum number of iterations is reached. The output is the duty cycle at which the boost converter works while tracking maximum power [25].

4) Re-initialization: MPPT algorithm is depends on the time variation, where the variation of weather conditions causes the health of FSs. Location of FSs, i.e., duty cycle will reinitialize to look for new optimum maximum power once more [26]. In this, the duty cycle is reinitialize after detecting the change in isolation through the constraint relation in (25):

Authorized licensed use limited to: DELHI TECHNICAL UNIV. Downloaded on April 17,2023 at 06:09:49 UTC from IEEE Xplore. Restrictions apply.

$$\frac{P_{PV}^{k+1} - P_{PV}^{k}}{P_{PV}^{k+1}} \geq \Delta P(\%) \quad (25)$$

III. Simulation Results

MATLAB/SIMULINK is used to simulate the proposed FFSO MPPT controller. The proposed technique is tested for maximum power extraction from PV systems under various irradiations and compared to the P&O and FLC techniques.The stair generator block in MATLAB is used to generate the various irradiation levels. Different irradiation levels used are : 1000W/m^2 for 0 to 1.5 s.,600 W/m^2 for 1.5 s to 3 s ,400 W/m^{2}for 3 s to 4 s and 200 W/m^2 for 4 s to 5 s.

The simulation is run on an Intel i3 processor with 16 GB RAM and MATLAB 2017. The simulation results under different irradiations are presented in fig. 9.

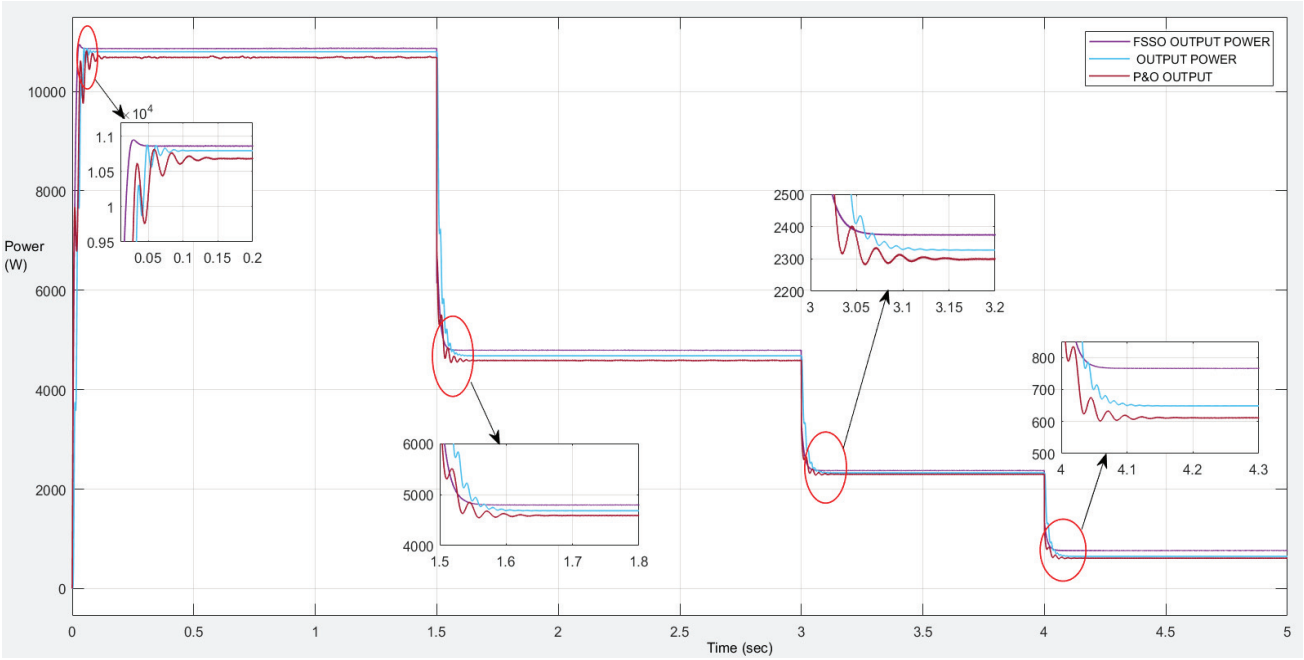


Fig.9. Output power under variable solar irradiation (w/m^2)

TABLE IV. Comparison Analysis Between P&O,FLC And FSSO

Irradiance (W/m^2)	Overshoot			Undershoot			Settling time (sec.)		
	P&O	FLC	FSSO	P&O	FLC	FSSO	P&O	FLC	FSSO
1000	1.21%	0.74%	0.73%	9.42%	2.23%	0%	0.15	0.12	0.05
600	5.61%	5.57%	0%	0.94%	0%	0%	0.12	0.08	0.06
400	15.89%	9.45%	0%	0.87%	0%	0%	0.13	0.11	0.06
200	36.05%	15.15%	0%	0%	0%	0%	0.15	0.10	0.07

From Figure 9, it is seen that under all irradiations levels, transient response and steady state response of proposed FSSO MPPT technique is better than conventional MPPT techniques studied. Further, a comparative review is carried out between P&O, FLC and proposed FSSO techniques.

The results are presented based on overshoot, undershoot and settling time as shown in table IV. Settling time of proposed FSSO MPPT techniques is less than other techniques. Further, the tracked efficiency of a PV system is obtained by

$$\%\eta = \frac{P_{tracked}}{V_{mpp} * I_{mpp}} * 100 \quad (26)$$

Where, $P_{tracked}$ is power tracked by PV array and V_{mpp} is voltage at MPP and I_{mpp} is current at MPP.

Table V shows that the results corresponding to maximum power extracted and tracking efficiency of proposed FFSO technique and conventional techniques.

It can be observed from table V is that at 1000 W/m^2, power extracted by FFSO technique is 10.86kW while in case of FLC and P&O is 10.80 kW and 10.69 kW respectively.

Authorized licensed use limited to: DELHI TECHNICAL UNIV. Downloaded on April 17,2023 at 06:09:49 UTC from IEEE Xplore. Restrictions apply.

TABLE V. OUTPUT POWER AND EFFICIENCY OF DIFFERENT MPPT'S TECHNIQUES

Irradiance (W/m^2)	Actual Output Power (kW) and Efficiency (%)					
	P&O		FLC		FSSO	
	P_{MPP} (kW)	η(%)	P_{MPP} (kW)	η(%)	P_{MPP} (kW)	η(%)
1000	10.69	97.27	10.80	99.44	10.86	99.99
600	4.60	95.25	4.68	97.07	4.80	99.56
400	2.4	96.19	2.33	97.24	2.37	99.24
200	0.62	80.23	0.65	84.06	0.76	99.09

IV. CONCLUSION

Uncertainty of solar irradiation falling on PV modules causes insufficient power drawn by PV system. In this presented paper, performance comparison of proposed FSSO and conventional FLC and P&O MPPT algorithms for PV system have been carried out under different solar irradiances to analysis the power tracking and settling speed. From the presented studies, it has been observed that FSSO techniques takes less time to reach MPP as compared to FLC and P&O techniques during change in irradiation levels. Further, power extracted by proposed technique is maximum as compared to conventional techniques studied. Hence, FSSO is preferable over FLC and P&O during both steady state and transient conditions.

REFERENCES

[1] A. K. GB, Shivashamkar and K. N. S. Kumar, "Optimum Power Point Tracking Technique for Standalone Solar Photovoltaic System," 2021 International Conference on Recent Trends on Electronics, Information, Communication & Technology (RTEICT), 2021, pp. 805-808, doi: 10.1109/RTEICT52294.2021.9573905.

[2] A. -E. Khalifa, A. Refaat, A. Kalas and M. H. Elfar, "Two Bio-inspired MPPT Algorithms to Harvest the Maximum Power from Partially Shaded PV Arrays," 2022 Conference of Russian Young Researchers in Electrical and Electronic Engineering (ElConRus), 2022, pp. 670-674, doi: 10.1109/ElConRus54750.2022.9755769.

[3] N. Swaminathan, N. Lakshminarasamma and Y. Cao, "A Fixed Zone Perturb and Observe MPPT Technique for a Standalone Distributed PV System," in IEEE Journal of Emerging and Selected Topics in Power Electronics, vol. 10, no. 1, pp. 361-374, Feb. 2022, doi: 10.1109/JESTPE.2021.3065916.

[4] R. K. Rai and O. P. Rahi, "Fuzzy Logic based Control Technique using MPPT for Solar PV System," 2022 First International Conference on Electrical, Electronics, Information and Communication Technologies (ICEEICT), 2022, pp. 01-05, doi: 10.1109/ICEEICT53079.2022.9768650.

[5] C. G. Rusu, I. M. T. Birou and S. Salcu, "Model Based Design Controller for Stand-Alone Conversion System with MPPT," 2022 IEEE International Conference on Automation, Quality and Testing, Robotics (AQTR), 2022, pp. 1-6, doi: 10.1109/AQTR55203.2022.9801966.

[6] C. -Y. Tang, H. -J. Wu, C. -Y. Liao and H. -H. Wu, "An Optimal Frequency-Modulated Hybrid MPPT Algorithm for the LLC Resonant Converter in PV Power Applications," in IEEE Transactions on Power Electronics, vol. 37, no. 1, pp. 944-954, Jan. 2022, doi: 10.1109/TPEL.2021.3094676.

[7] V. Kumar and M. Singh, "Derated Mode of Power Generation in PV System Using Modified Perturb and Observe MPPT Algorithm," in Journal of Modern Power Systems and Clean Energy, vol. 9, no. 5, pp. 1183-1192, September 2021, doi: 10.35833/MPCE.2019.000258.

[8] P. Verma, P. Mahajan and R. Garg, "Comparison of intelligent and conventional MPPT algorithms for PhotoVoltaic system under partially shaded conditions," 2017 Recent Developments in Control, Automation & Power Engineering (RDCAPE), 2017, pp. 505-510, doi: 10.1109/RDCAPE.2017.8358323.

[9] O. Abdel-Rahim and H. Wang, "A new high gain DC-DC converter with model-predictive-control based MPPT technique for photovoltaic systems," in CPSS Transactions on Power Electronics and Applications, vol. 5, no. 2, pp. 191-200, June 2020, doi: 10.24295/CPSSTPEA.2020.00016.

[10] I. Pervez, I. Shams, S. Mekhilef, A. Sarwar, M. Tariq and B. Alamri, "Most Valuable Player Algorithm based Maximum Power Point Tracking for a Partially Shaded PV Generation System," in IEEE Transactions on Sustainable Energy, vol. 12, no. 4, pp. 1876-1890, Oct. 2021, doi: 10.1109/TSTE.2021.3069262.

[11] M. N. Ali, K. Mahmoud, M. Lehtonen and M. M. F. Darwish, "An Efficient Fuzzy-Logic Based Variable-Step Incremental Conductance MPPT Method for Grid-Connected PV Systems," in IEEE Access, vol. 9, pp. 26420-26430, 2021, doi: 10.1109/ACCESS.2021.3058052.

[12] V. Jately, S. Bhattacharya, B. Azzopardi, A. Montgareuil, J. Joshi and S. Arora, "Voltage and Current Reference Based MPPT Under Rapidly Changing Irradiance and Load Resistance," in IEEE Transactions on Energy Conversion, vol. 36, no. 3, pp. 2297-2309, Sept. 2021, doi: 10.1109/TEC.2021.3058454.

[13] S. R. Pendem and S. Mikkili, "Assessment of Cross-coupling Effects in

PV String-integrated-converters with P&O MPPT Algorithm Under Various Partial Shading Patterns," in CSEE Journal of Power and Energy Systems, vol. 8, no. 4, pp. 1013-1028, July 2022, doi: 10.17775/CSEEJPES.2019.03330.

[14] P. Verma, A. Kumar, R. Garg and P. Mahajan, "Reweighted L0 norm variable step size continuous mixed p-norm control scheme for mitigating power quality problems of grid coupled solar PV system," in CSEE Journal of Power and Energy Systems, doi: 10.17775/CSEEJPES.2021.07310.

[15] T. Sutikno, A. C. Subrata and A. Elkhateb, "Evaluation of Fuzzy Membership Function Effects for Maximum Power Point Tracking Technique of Photovoltaic System," in IEEE Access, vol. 9, pp. 109157-109165, 2021, doi: 10.1109/ACCESS.2021.3102050.

[16] Dehghani, M. Taghipour, G. B. Gharehpetian and M. Abedi, "Optimized Fuzzy Controller for MPPT of Grid-connected PV Systems in Rapidly Changing Atmospheric Conditions," in Journal of Modern Power Systems and Clean Energy, vol. 9, no. 2, pp. 376-383, March 2021, doi: 10.35833/MPCE.2019.000086.

[17] A. -w. Ibrahim et al., "PV maximum power-point tracking using modified particle swarm optimization under partial shading conditions," in Chinese Journal of Electrical Engineering, vol. 6, no. 4, pp. 106-121, Dec. 2020, doi: 10.23919/CJEE.2020.000035.

[18] H. Li, D. Yang, W. Su, J. Lü and X. Yu, "An Overall Distribution Particle Swarm Optimization MPPT Algorithm for Photovoltaic System Under Partial Shading," in IEEE Transactions on Industrial Electronics, vol. 66, no. 1, pp. 265-275, Jan. 2019, doi: 10.1109/TIE.2018.2829668.

[19] D. Das, S. Madichetty, B. Singh and S. Mishra, "Luenberger Observer Based Current Estimated Boost Converter for PV Maximum Power Extraction—A Current Sensorless Approach," in IEEE Journal of Photovoltaics, vol. 9, no. 1, pp. 278-286, Jan. 2019, doi: 10.1109/JPHOTOV.2018.2877418.

[20] S. Shukla, B. Singh, P. Shaw, A. Al-Durra, T. H. M. El-Fouly and E. F. El-Saadany, "A New Analytical MPPT-Based Induction Motor Drive for Solar PV Water Pumping System With Battery Backup," in IEEE Transactions on Industrial Electronics, vol. 69, no. 6, pp. 5768-5781, June 2022, doi: 10.1109/TIE.2021.3091929.456

[21] G. Dei et al., "Improved Squirrel Search Algorithm Driven Cascaded 2DOF-PID-FOI Controller for Load Frequency Control of Renewable Energy Based Hybrid Power System," in IEEE Access, vol. 10, pp. 46372-46391, 2022, doi: 10.1109/ACCESS.2022.3169749.

[22] V. P. Sakthivel, H. H. Goh, S. Srikrishna, P. D. Sathya and S. K. Abdul Rahim, "Multi-Objective Squirrel Search Algorithm for Multi-Area Economic Environmental Dispatch With Multiple Fuels and Valve Point Effects," in IEEE Access, vol. 9, pp. 3988-4007, 2021, doi: 10.1109/ACCESS.2020.3046257.

[23] H. Hu, L. Zhang, Y. Bai, P. Wang and X. Tan, "A Hybrid Algorithm Based on Squirrel Search Algorithm and Invasive Weed Optimization for Optimization," in IEEE Access, vol. 7, pp. 105652-105668, 2019, doi: 10.1109/ACCESS.2019.2932198.

[24] S. Jalali Zand, S. Mobayen, H. Z. Gul, H. Molashahi, M. Nasiri and A. Fekih, "Optimized Fuzzy Controller Based on Cuckoo Optimization Algorithm for Maximum Power-Point Tracking of Photovoltaic Systems," in IEEE Access, vol. 10, pp. 71699-71716, 2022, doi: 10.1109/ACCESS.2022.3184815.

Authorized licensed use limited to: DELHI TECHNICAL UNIV. Downloaded on April 17,2023 at 06:09:49 UTC from IEEE Xplore. Restrictions apply.

[25] H. Li, D. Yang, W. Su, J. Lü and X. Yu, "An Overall Distribution Particle Swarm Optimization MPPT Algorithm for Photovoltaic System Under Partial Shading," in IEEE Transactions on Industrial Electronics, vol. 66, no. 1, pp. 265-275, Jan. 2019, doi: 10.1109/TIE.2018.2829668.

[26] N. Singh, K. K. Gupta, S. K. Jain, N. K. Dewangan and P. Bhatnagar, "A Flying Squirrel Search Optimization for MPPT Under Partial Shaded Photovoltaic System," in IEEE Journal of Emerging and Selected Topics in Power Electronics, vol. 9, no. 4, pp. 4963-4978, Aug. 2021, doi: 10.1109/JESTPE.2020.3024719.

Authorized licensed use limited to: DELHI TECHNICAL UNIV. Downloaded on April 17,2023 at 06:09:49 UTC from IEEE Xplore. Restrictions apply.

Applied Intelligence
https://doi.org/10.1007/s10489-023-04471-1

Game theory and MCDM-based unsupervised sentiment analysis of restaurant reviews

Neha Punetha[1] · Goonjan Jain[1]

Accepted: 10 January 2023
© The Author(s), under exclusive licence to Springer Science+Business Media, LLC, part of Springer Nature 2023

Abstract
Sentiment Analysis is a method to identify, extract, and quantify people's feelings, opinions, or attitudes. The wealth of online data motivates organizations to keep tabs on customers' opinions and feelings by turning to sentiment analysis tasks. Along with the sentiment analysis, the emotion analysis of written reviews is also essential to improve customer satisfaction with restaurant service. Due to the availability of massive online data, various computerized methods are proposed in the literature to decipher text sentiments. The majority of current methods rely on machine learning, which necessitates the pre-training of large datasets and incurs substantial space and time complexity. To address this issue, we propose a novel unsupervised sentiment classification model. This study presents an unsupervised mathematical optimization framework to perform sentiment and emotion analysis of reviews. The proposed model performs two tasks. First, it identifies a review's positive and negative sentiment polarities, and second, it determines customer satisfaction as either satisfactory or unsatisfactory based on a review. The framework consists of two stages. In the first stage, each review's context, rating, and emotion scores are combined to generate performance scores. In the second stage, we apply a non-cooperative game on performance scores and achieve Nash Equilibrium. The output from this step is the deduced sentiment of the review and the customer's satisfaction feedback. The experiments were performed on two restaurant review datasets and achieved state-of-the-art results. We validated and established the significance of the results through statistical analysis. The proposed model is domain and language-independent. The proposed model ensures rational and consistent results.

Keywords Sentiment classification · MCDM · Game theory · Reviews · Emotion analysis

1 Introduction

Sentiment analysis is a subfield of Natural Language Processing (NLP) that focuses on the automated analysis of human sentiments [1]. It is possible to examine and categorize a person's emotions using sentiment analysis. We can learn about people's feelings by analyzing their comments, criticism, and reviews. These feelings or opinions can be classified as positive, negative, or neutral. In recent years, there has been a significant increase in sentiment analysis and opinion mining research, making this a highly researched area [2]. Analyzing sentiments can prove helpful in social media monitoring, brand tracking, help desk software, and feedback analysis. Today's businesses use data analysis to enhance the performance and quality of their products and, as a result, to compete in a crowded market. Sentiment Analysis is a method to get insight into a customer's positive or negative reaction to a product, service, or support interaction. Automatically analyzing customer sentiments from social media, reviews, and surveys can help companies refine their offerings and make smarter business decisions. Similarly, sociologists, psychologists, and politicians use sentiment analysis to learn more about societal movements, attitudes, and ideological biases, as well as to predict public opinion and evaluate public support. Thus, sentiment analysis is an indispensable step toward data analysis.

1.1 Need for sentiment analysis

The vast volume of content published daily on several social networking sites necessitates automated solutions for managing and identifying opinions. Manually analyzing the

✉ Goonjan Jain
goonjanjain@dtu.ac.in

Neha Punetha
nehapunetha80@gmail.com

[1] Department of Applied Mathematics, Delhi Technological University, New Delhi, India

Published online: 31 March 2023

sentiments can be highly tedious and sometimes impossible due to the sheer volume of data [3]. As a result, various sentiment analysis algorithms and techniques have been developed. Sentiment analysis is a powerful marketing technique since it helps businesses learn more about their customers' feelings about their products and services. Brand recognition, consumer satisfaction, the effectiveness of marketing, and general product acceptance are all positively impacted by it. Improving product and brand recognition can also be accomplished by studying consumer psychology. However, good customer service can also convince customers to purchase products from a company, even if they are experiencing product downtime or other issues. Knowing that sentiments drive customer decision-making and that emotions help product managers to improve their customer service strategies. Numerous opinion mining researches examined unstructured text data, including customer reviews, blogs, tweets, news, and online reviews [4].

Nevertheless, there are still issues to be resolved. There has been comparatively limited study of the emotional resonance of customers' written comments. Emotion detection can pick up moods like happiness, regret, anger, and sadness. Understanding a consumer's feelings about a situation is essential to provide commendable service.

Therefore, examining the reviews' emotions is equally crucial as analyzing their sentiment orientations. In the proposed work, we comprehend the textual feedback and tag sentiments as positive or negative. We also gauge emotions behind a review and classify whether the customers are satisfied with the service of the restaurant or not. Interested customers can use this decision assistance system to analyze online product comments and choose the most practical and reliable alternative. Companies can use the proposed system to analyze consumer satisfaction with their products and services and modify their manufacturing processes, operational activities, or marketing plans accordingly. Therefore, there is an urgency to perform sentiment analysis.

1.2 Leveraging e-commerce statistics to gauge public sentiment

During the Covid-19 pandemic, online purchasing grew dramatically with increased internet usage [5]. As per a recent survey,[1] *14%* of consumers altered their buying habits by increasing their online spending. Also, *56% of* consumers boosted their online expenditures (Fig. 1). Figure 2[2] shows the different categories of products in which online shopping was enhanced. Extensive shopping was done in the domain of clothing, food & drinks.

As online shopping increased in the past decade, the same trend also followed in online food ordering. Figure 3 illustrates the upward trend in restaurant delivery and online takeaways over the last seven years. Another factor for this exponential increment is that the online system made customers' lives easier. It is observed that around 82% of food delivery orders were placed from home, and 16% of orders were placed from the workplace. In the proposed work, we analyze the restaurant reviews and categorize them as either positive or negative sentiments. Most online shoppers examine product reviews before making a purchase decision. The most common questions shoppers seek are which products are popular, which features are high quality, etc. So, customer satisfaction is essential for a company to boost its sale. Customer satisfaction is a consumer's view or sentiment about the gap between expectations and reality. Many customers express their opinion in online reviews such as TripAdvisor, Yelp, etc. Only a few restaurants use customer satisfaction analysis. Product, nutrition, and food preparation information are typically used to gauge restaurant customer satisfaction [6, 7]. Customer satisfaction surveys in restaurants are still comparatively less. In the proposed work, we classify the service of a restaurant as satisfactory or unsatisfactory based on reviews.

This paper proposes a game theory and MCDM-based optimization approach to maximize the accuracy and efficiency of sentiment analysis of subjective context. We created a novel decision-making system that labels each review with a sentiment polarity based on written reviews and classifies customer satisfaction. To the best of our knowledge, this is the first attempt to employ an optimization approach to tackle research in sentiment analysis.

1.3 Research problem

This study intends to create a framework that accomplishes two tasks. First, to improve the accuracy of assessing sentiment orientation of feedback. Second, perform an emotional analysis of a review to examine customer satisfaction with the restaurant's services. To work on the mentioned research problem, we laid down the following objectives:

1) To propose an unsupervised sentiment analysis system that makes it easier for customers to make purchasing decisions in critical situations without prior training.
2) To enhance the accuracy of the sentiment tagging algorithm for sentiment identification.
3) To propose a model that is language and domain independent.
4) To propose an efficient system in terms of space and time complexity.

[1] https://www.namogoo.com/resources/ebook/how-covid-19-online-shopping-habits-are-shaping-the-customer-journey/
[2] https://www.statista.com/statistics/1191958/india-number-of-annual-online-shoppers/

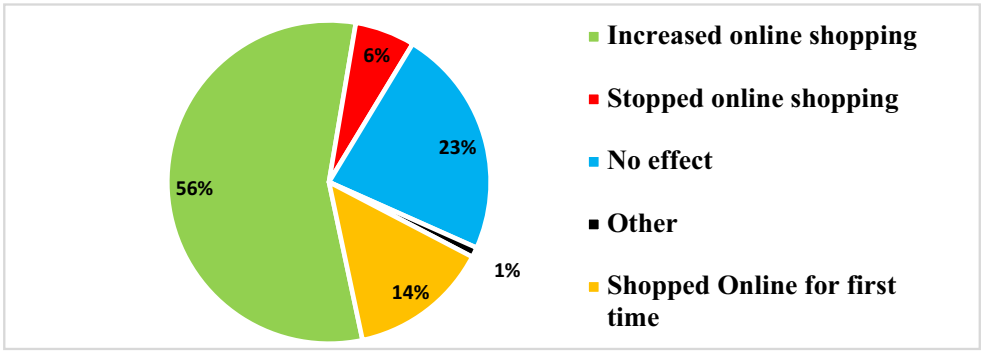


Fig. 1 Trend in online shopping by consumers during the Coronavirus epidemic

1.4 Contributions

The contributions and novelties of the study are given below:

1) To the best of our knowledge, this is the first study to perform sentiment classification of restaurant reviews by combining MCDM and game theory. This research assesses the suitability of coupled MCDM and game models for NLP applications like sentiment analysis of English text.
2) We propose a sentiment tagger that assigns an appropriate sentiment tag to each review. We also emotionally tag customer satisfaction for a review by analyzing textual feedback. We use star ratings and reviews' textual feedback to classify sentiment into two classes on English review datasets.
3) The proposed model employs optimization techniques for sentiment analysis of English text to maximize accuracy while minimizing time and space complexity. Since the proposed model is unsupervised, it is domain and language-independent and can be applied to any low-resource language dataset with minimal adjustments.
4) We also examined and established the statistical significance of the proposed framework. Statistical performance indicators are studied and applied to the proposed model to determine its effectiveness and provide state-of-the-art performance.

1.5 Organization

The structure of a paper can be summarised as follows: We go over the fundamentals of sentiment analysis, MCDM, and game theory in *Section 1*. *Section 2* summarises previous research in sentiment analysis and game theory. *Section 3* discusses the preliminaries related to the proposed algorithm.

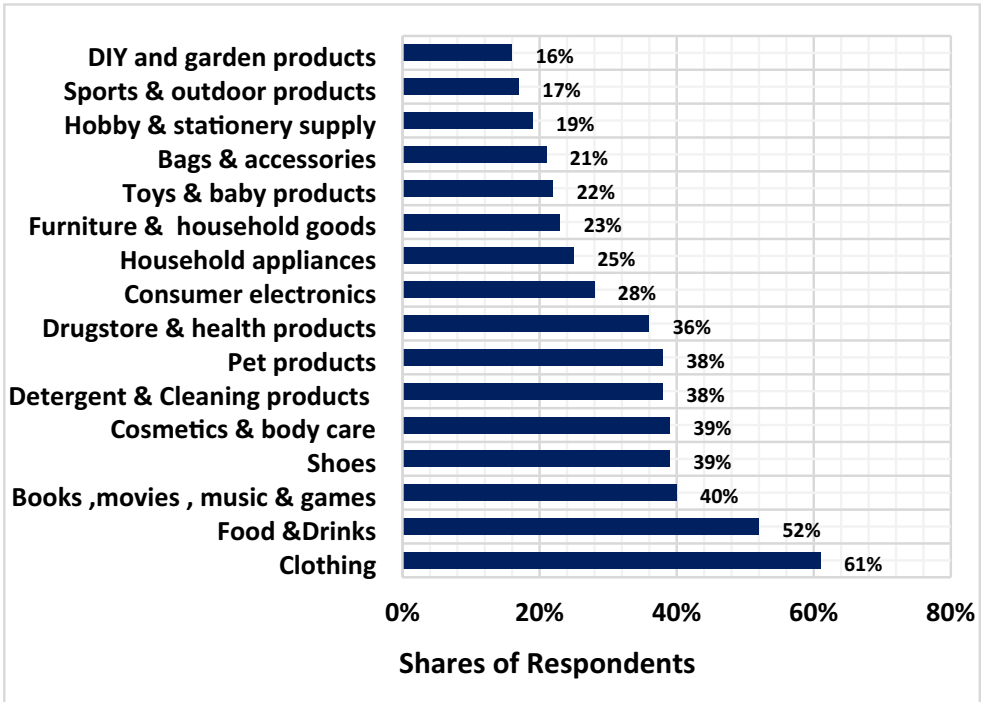


Fig. 2 Product type that consumers bought online during an outbreak

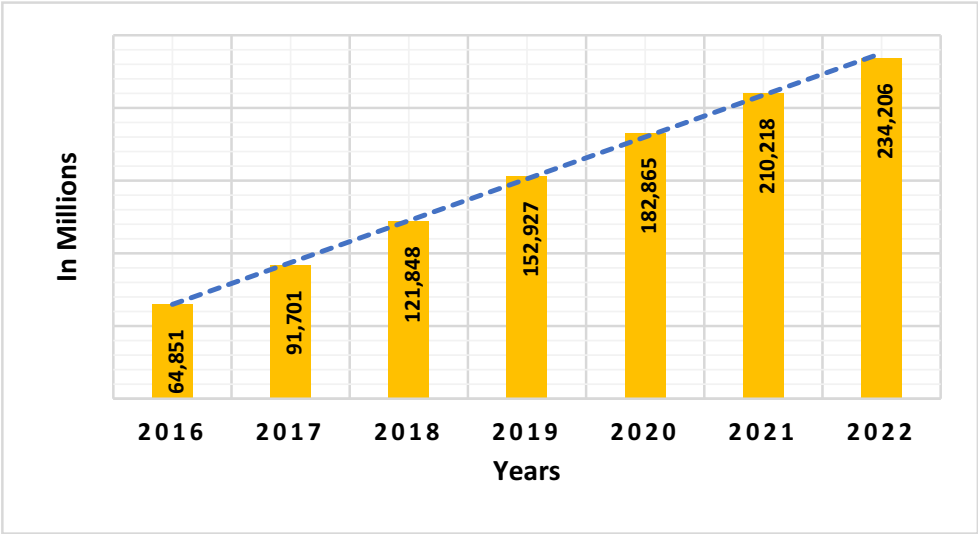


Fig. 3 Online takeaway and restaurant delivery trends in the last 7 years

Section 4 contains the proposed algorithm for sentiment analysis. We evaluate the proposed model against competing methods on two restaurant review datasets in *Section 5*. We also validated results using statistical significance. In *Section 6,* we discuss the advantages and disadvantages of the proposed algorithm. In *Section 7*, we summarise key findings and recommend future directions.

2 Literature review

This section discusses prior sentiment analysis work in chronological order. García-Pablos et al. [8] created unsupervised W2VLDA, which is based on topic modeling and can classify the polarity of people's opinions. Donadi [9] introduced tensor-based sentiment analysis for the German language. Vashishtha & Susan [10] introduced a fuzzy-based approach for sentiment analysis that incorporates Natural Language Processing (NLP) and Word Sense Disambiguation (WSD). For aspect-level sentiment analysis, Song et al. [11] developed an attention-based extended short-term memory network that incorporates sentiment lexicon embeddings into its architecture. Attention-based Point Network (AttPNet) is a revolutionary sentiment analysis model suggested by Yang et al. [12].

Rani and Lobiyal [13] found sentiment polarity and advised statistical and knowledge-based ways to develop Hindi stop word lists. An attention-based approach was created by Pandesenda et al. [14] to address the issue of using NLP for online reviews. Recurrent Memory Neural Network (ReMemNN) was implemented by Liu et al. in 2020 [15] and evaluated on various datasets, including three English and four Chinese datasets from various sources. Basiri et al. [16] suggested a bidirectional neural network design to address the drawbacks of LSTMs and gated recurrent units (GRUs) for sentiment analysis. A knowledge-enabled BERT model for aspect-based sentiment analysis was created by [17]. The Game theory-based opinion leader detection (GOLD) approach for coalitions of opinion leaders was proposed by L. Jain et al. [18]. Regression analysis and sentiment analysis, specifically Term Frequency-Inverse Document Frequency (TF-IDF), were utilized by Mee et al. [19] for sentiment analysis. An integrated framework that integrates sentiment analysis and multi-criteria decision-making methods was employed by Heidary Dahooie [20]. The performance of attention-based models based on RNNs in various sentiment analysis situations was examined by Perikos et al. [21]. Ileri and Turan [22] used a neural network for sentiment analysis, and the model's accuracy was roughly 85%. To capture the critical features of the dataset in the word embedding layer of sentiment classification deep learning algorithms, Duy Ngoc a Nguyen et al. [23] advocated embedding information in the ontology.

To forecast sentiment analysis using deep learning, De Oliveira Carosia et al. [24] applied investment methods to the Brazilian stock To forecast sentiment analysis using deep learning. For Twitter accounts, unsupervised sentiment analysis techniques were developed [25]. Aspect-based sentiment analysis was performed using Latent Dirichlet Allocation (LDA) techniques [26]. Zhang et al. [27] proposes a modal that analyses sentences syntactically and semantically on SemEval 2014 dataset. Jain et al. [3] presents machine learning techniques for consumer sentiment analysis on tourism datasets. A convolutional graph network based on SenticNet

that took advantage of the emotional dependencies of the sentence depending on the particular aspect was developed by Liang et al. in 2022 [28].

Peng et al. [29] introduced BERT Post Training (BERT-PT) to fine-tune the CGBN model for sentiment analysis based on aspects. Zhang et al. [30] proposed ICDN multimodal for sentiment analysis. Gu et al. [31] proposed the IA-HiNET network for sentence-level sentiment analysis. Chiha et al. [32] presented framework for aspect and sentence level sentiment classification using techniques involving deep learning and fuzzy logic. Swathi et al. [33] presented TLBO and LSTM models for stock price prediction using the Twitter dataset. Wu et al. [1] proposed the DVA-BERT model for sentiment analysis which outperforms the BERT model. Wu et al. [34] proposed a framework for hotel selection based on the OVO-SVM algorithm and Word2Vec. Li et al. [35] conducted sentiment analysis on MOOCs platforms.

This paper introduces an innovative implementation of an unsupervised method based on optimization techniques. The integrated MCDM and non-cooperative game model are used to evaluate text sentiment.

2.1 Research gap

Previous researches demonstrate supervised, semi-supervised and unsupervised approaches for sentiment analysis. However, they have their limitations, as given below:

Machine learning (ML) techniques offer superior classification precision and accuracy. However, they also have significant limitations, such as they are time-consuming, domain-dependent, and requiring human intervention and information labeling. ML approaches like SVM and ANN are also used for sentiment classification. SVM performs poorly when there are more characteristics than samples and fails to work when there is no probabilistic reason for the classification. On the contrary, ANN requires a lot of training time and a massive dataset. Deep learning algorithms for sentiment analysis, including DNN, CNN, and RNN, are more straightforward than other models. However, they take longer to train because of their sophisticated design, high computational cost, and overfitting issues [16, 36–39].

Semi-supervised methods like generative, co-training, and graph-based methods are also used for sentiment analysis. However, classification problems do not work well with generative approaches. Co-training methods are unsuitable for datasets with only one feature sensitive to noise. Graph-based approaches depend on the structure and weights of edges and do not work well if the graph does not fit the task. Hybrid methods require less time but lack reliability and precision [36, 37, 40, 41].

Unsupervised approaches for sentiment analysis include hierarchical and partition methods. Due to the high computation cost, hierarchical algorithms are not ideal for massive datasets [74–79]. Partition methods are relatively scalable and straightforward but have poor accuracy and stability and are sensitive to noisy data. The lexicon-based approaches do not need information labeling but depend upon the domain, need powerful linguistic resources, and have low precision [36, 37]. Various studies used MCDM and game theoretic models to propose recommender systems [42, 80]. But till now, none of the studies employ the application of a mathematical optimization model to perform sentiment analysis of reviews.

2.2 How the proposed model is different from others?

In the proposed work, we designed an unsupervised mathematical framework to identify the sentiment of a review. We also compute the emotion score of a review and examine customer satisfaction feedback. In the proposed work, we comprehend the implicit information from textual feedback of reviews and convert them into numerical values called context scores. We use ratings, context scores, and emotional scores of written feedbacks for further processing. MCDM proved beneficial in combining context, rating, and emotions scores to calculate performance scores of reviews. Games are played on performance scores of reviews to assign the sentiment tag to a given review. The proposed model produced state-of-the-art results. Unlike supervised methods, the proposed model abstains from training massive datasets and thus is faster and domain independent. In the proposed model, we convert textual comments to context scores, thus eliminating the dependency on the language of the reviews. The model can perform sentiment analysis of reviews in any language with minimal alterations. Preliminaries of MCDM and Game Theory are discussed in *Section 3*. The proposed work is discussed in detail in *Section 4*.

3 Preliminaries

3.1 Game theory

Von Neumann and Morgenstern (2007) introduced game theory to build a mathematical framework capable of simulating decision-making fundamentals in interactive scenarios [43, 44]. Game theory is described as a set of situations in which each player must consider the actions of other players to make sensible judgments [45]. All players are assumed to be rational. The action is determined by other players' actions [43]. In interactive decision situations, game theory provides predictive power. We create and evaluate complicated

interactions involving decision-makers,[3] such as financial market investors, supply-chain businesses, and governments with competing interests [43, 46].

$\tau = < N, (S), (u) >$, A game is represented as $\Gamma = \langle N, (S_i), (u_i) \rangle$, where N = Number of players, (S_i) = Set of strategies, and (u_i) = Payoffs. A game has the following components:

- **Players:** Participants in a game who aim to maximize their payoffs.
- **Strategy profile:** A set of players' actions is known as a strategy profile. The game's strategy profiles of players are displayed simultaneously by $m^* = \{m_1^*, m_2^*, \ldots\ldots\ldots\ldots, m_i^*\}$ the action sets for i^{th} player's plays in the game. The strategy profile of opponent players is $m_{-i}^* = \{m_1^*, m_2^*, \ldots\ldots m_{i-1}^* \ldots\ldots m_i^*\}$.
- **Payoff:** The payoff of player receives after arriving at a particular outcome. The payoff can be in any quantifiable form.
- **Outcome:** The participants determine an ideal approach for each action.
- **Best Response:** The best response function (br) of each player is the best reaction he can make to a specific action: $br_i(m_{-i}) = \{m_i \in A_i : u_i(m_i, m_{-i}) \geq u_i(m_i^k, m_{-i}); \forall m_i^k \in A_i\}$
- **Nash Equilibrium:** The Nash equilibrium is a decision-making principle that states players can achieve the desired outcome by not deviating from their initial strategy. It is one of the game's best responses. i.e., if m^* is a Nash equilibrium$\Rightarrow m_i^* \in br_i(m_{-i}^*)$.

Alternatively, Nash equilibrium⇒Intersection of the best responses of players. Along with the above components, some strategies are essential to solve any game under game theory.

Strongly dominated strategy A dominant strategy is a strategy that consistently generates the best outcome for a player regardless of what other players are doing. Every strongly dominant strategy implies Nash equilibrium and thus the best response. In a two-player game, $(A, B) \in R^{m \times n}$ a strategy s^*strongly dominates s if for all strategies of the other player t given by Eq. (1).

$$u(s,t) < u(s^*,t) \tag{1}$$

Weakly dominant strategy In a two-player game, $(A, B) \in R^{m \times n}$ a strategy s is weakly dominated by s^*if for all strategies of the other player t given by Eq. (2).

$$u(s,t) \leq u(s^*,t) \tag{2}$$

3.2 Non-cooperative game

A non-cooperative game is a method for modelling and evaluating scenarios in which each player's best choices rely on their beliefs or expectations about their opponents' behaviour.

Non-cooperative games are generally analyzed through the game theory model, which tries to predict players' strategies and payoffs and find Nash equilibria. Non-cooperative models assume that players do not have a cooperation mechanism (to make binding commitments) outside the specified rule of the game. A sample of non-cooperative game theory is presented below.

Example: Prisoner's dilemma problem Two suspects are apprehended for a crime in separate rooms in a police station, with no means of communicating. The prosecutor has separately told that they have two options either to confess (C) or not to confess (NC). A matrix represents the game. A row represents strategies for the first player. The column represents the strategies of the second player. Each matrix entry contains a tuple of values (x,y) where x is the payoff of the first player and y is the payoff of the second player.

Let N be the no. of players, with each player having a set of strategies. In the given example,

$N = 2\{\text{Two Players: } Player\ 1, Player\ 2\}$. Each player has 2 strategies confess or not confess $S_1 = S_2 = \{C, NC\}$. Each cell represents the payoffs of players for choosing a specific strategy. For example, if both players choose $NC, NC,$ their respective payoffs are $(-2, -2)$. The complete payoff matrix is shown in Table 1.

Strategy C is a strongly dominating strategy for *player one* because the payoff values (u_i) of the C strategy are more significant than the NC strategy given by Eq. (3).

$$u_1(C, NC) > u_1(NC, NC) \ and \ u_1(C, C) > u_1(NC, C) \tag{3}$$

Table 1 Matrix form representation of Prisoner's Dilemma

		Player 2	
		NC	C
Player 1	NC	−2, −2	−10, −1
	C	−1, −10	−5, −5

[3] https://www.scientificamerican.com/article/what-is-game-theory-and-w/

Similarly, for *player 2*, strategy *C* strongly dominates strategy since the payoff values of the *C* strategy are more significant than the NC strategy given by Eq. (4).

$$u_2(NC, C) > u_2(NC, NC) \text{ and } u_2(C, C) > u_2(C, NC) \quad (4)$$

Thus, *C* is the strongly dominant strategy for both *player 1* and *player 2*. Thus (*C, C*) is a strongly dominant strategy, Nash Equilibrium, and the players' best response in this prisoner's dilemma problem. The game theory encompasses a wide range of models. In this work, we used the Bayesian game theory model to analyze the sentiments of reviews.

3.3 MCDM

MCDM is a process that combines the performance of various alternatives based on a variety of qualitative and quantitative criteria to arrive at a solution that can be agreed upon by all alternatives involved [47]. There are two types of criteria in an MCDM problem. The benefit criteria are those that should be maximized. Cost criteria, on the other hand, are those that must be reduced to the minimum level. A typical MCDM problem with *m* alternatives (A_1, $A_2, \ldots\ldots A_m$) and *n* criteria ($C_1, C_2, \ldots, C_n$) can be presented in the following form.

$$M = \left[m_{ij}\right]_{m\times n} W = \left[w_j\right]_n \quad (5)$$

There are four components to Eq. (5). *M* stands for the decision matrix, m_{ij} stands for the i^{th} alternative's performance concerning the j^{th} criterion, and *W* stands for the weight vector, w_j denotes the weight of the j^{th} criterion. Typically, the original decision matrix *M* is incomparable because multiple units of measure are used to convey various criteria. Since the 1960s, numerous MCDM techniques and approaches have been created, suggested, and effectively applied in various areas [48, 49]. MCDM's objective is to help decision-makers choose an alternative that satisfies their needs and is consistent with their preferences, not just to recommend the best alternative. A thorough understanding of MCDM approaches and the participants' views is essential for efficient and successful decision-making in the early phases of the process. [50].

3.4 MCDM as a game of strategy

An MCDM problem with *m* alternatives and *n* criteria is typically defined in cardinal form, [51] shown by Eq. (6) represents performance-based MCDM.

$$D = \begin{bmatrix} \pi_{11} & \pi_{12} & \ldots & \pi_{1n} \\ \pi_{21} & \pi_{22} & \ldots & \pi_{2n} \\ \ldots & \ldots & \ldots & \ldots \\ \pi_{m1} & \pi_{m2} & \ldots & \pi_{mn} \end{bmatrix} \quad (6)$$

where π_{ij} is the performance of the i^{th} alternative under the j^{th} criterion for $i = 1,2...m$ and $j = 1, 2,...n$.

Madani et al. [52] established the relationship between MCDM and Game theory. Various studies used this combination to solve different problems in different fields [42, 53–56]. The essential components of MCDM, viz. criteria, alternatives, and alternative performance for each criterion, have a one-to-one correspondence with the basic components of the game, viz. player, strategies, and payoff, respectively. The correspondence is due to the similar nature shown by these parameters. Criteria in MCDM and players in a game are the initiators that follow specific alternatives and strategies, respectively; similarly, the performance score of each alternative under certain criteria corresponds to the payoff of the player having specific strategies. Figure 4 shows the relationship between MCDM and game theory.

4 Proposed work

A review has two components - written comment (qualitative) and rating (quantitive). We calculate the context score and emotion score from the written review comment. Context scores are numerical values of a review of positive and negative sentiment. We calculate the scores for the five emotions of a given review:

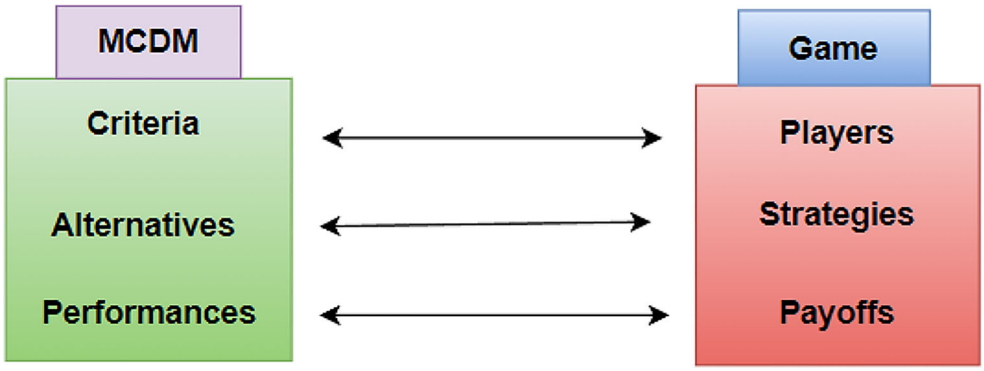


Fig. 4 MCDM-Game Relationship

happy, sad, surprise, angry, and fear. We use SentiWordnet to calculate context and emotion scores using python-based libraries. The combination of context, emotion, and rating enhances the performance of the proposed model. The proposed algorithm's implementation flow chart is illustrated in Fig. 5. The notations used in this study are listed in Table 2.

Step 1: Determine context scores of a review comment using SentiWordNet In this step, we determine the context scores of textual comments using SentiWordNet. SentiWordNet contains a list of words with respective positive and negative polarities values. We take POS-tagged content words of a review comment. For each word, we extract the respective positive and negative polarity values from SentiWordNet to calculate the context scores of the comments. Thus, the context score values are between 0 and 1. Context has two polarities, positive and negative, named Positive context (*CP*) and Negative context (*CN*); values of *CP* and *CN* are evaluated using SentiWordNet.

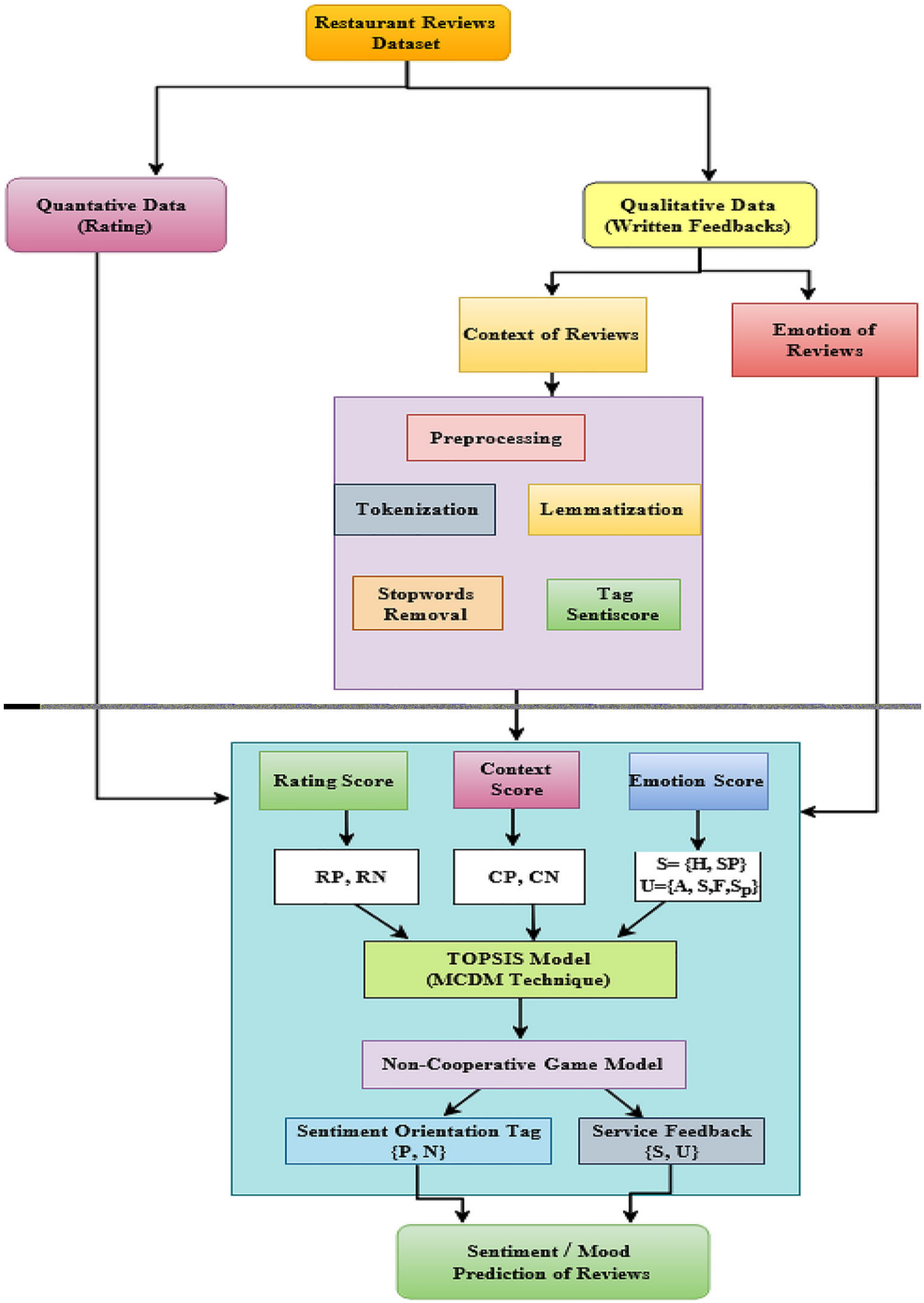


Fig. 5 Flowchart of the implementation of the proposed model

Figure 6 shows an excerpt of SentiWordNet. We follow Algorithm 1 to generate a context score.

Algorithm 1: Calculate context scores of reviews

Input: W - a set of open class and parts of speech tagged words extracted from the given sentence, *SWL* - SentiWordNet list of words with each word's positive and negative sentiment value.
Output: Context Score of i^{th} review $C = \{P, N\}$, where P = positive sentiment value and N = negative sentiment value.
1: Initialize, $P = 0$ and N = 0; such that $C_i = \{0, 0\}$.
2: Let $W = (w_1, w_2, ..., w_i, ..., w_n)$ where w_i represents the i^{th} $(1 \leq i \leq n)$ word in the input review where n =|W|.
3: Repeat step 4 for each word of *W*.
4: If $(w_i \in SWL)$
$P = P +$ *positive sentiment score of* w_i
$N = N +$ *negative sentiment score of* w_i
End

Step 2: Evaluate rating scores The rating of a review is between 1 and 5. We calculate two rating scores, named Positive rating (*RP*) and Negative rating (*RN*). *RP* is equal to the rating given with a review, and *RN* is *(5 - RP)*. *RP* ranges between 1 and 5, and *RN* is between 0 and 4.

Step 3: Determine the service feedback of the review comment The restaurant's service feedback can be either satisfactory (*S)* or unsatisfactory (*U)*. We evaluate service feedback from the emotions in the review comments. We evaluate emotion scores using the *text2emotion*[4] library. Emotions are classified as *Happy, angry, surprise, sad, or fear*. Satisfactory service feedback includes happy and surprising emotions, and unsatisfactory service feedback includes *anger, surprise, sadness,* and *fear*. After step 3, we have six scores, viz. positive context *(CP)*, negative context (*CN)*, positive rating *(RP)*, negative rating *(RN)*, Satisfactory feedback *(S)*, and unsatisfactory feedback *(U)*. The values of these six scores have different ranges. In the next step, we pass these scores to the TOPSIS model and receive performance scores.

Table 2 Notations used in this study

Notations	Description
P	The positive sum of positive rating and positive context.
N	The negative sum of negative rating and negative context.
RP	Positive Rating.
RN	Negative Rating.
CP	Positive Context.
CN	Negative Context.
S	Satisfactory Service Feedback
U	Unsatisfactory Service Feedback
H	Happy emotion
A	Angry emotion
S	Sad emotion
F	Fear emotion
S_p	Surprised emotion
PS	Polarity is positive, and service feedback is satisfactory.
PU	Polarity is positive, and service feedback is unsatisfactory.
NS	Polarity is negative, and service feedback is satisfactory.
NU	Polarity is negative, and service feedback is unsatisfactory.

Step 4: Calculate the performance score of each parameter of service feedback and polarity scores by applying TOPSIS Each review has two strategies - polarity and service feedback. Polarity can be positive (*P)* or negative (*N)* and is calculated as $P = RP + CP$ and $N = RN + CN$. Similarly, service feedback can be satisfactory or unsatisfactory, calculated as $S = H + S_P$, $U = S_p + F + A + S$. The possible combinations of strategies between polarity and service feedback are *PS, PU, NS, and NU*. Thus, each review has four possible strategies mentioned in Table 3.

Table 4 represents the numeric values corresponding to four strategies, *PS, PU, NS, and NU,* for review R_i. Here αi and β_i represent numeric values for the positive and negative polarities of R_i, respectively. Similarly, γ_i and δ_i depict the numeric values of satisfactory and unsatisfactory service feedback of R_i,

[4] https://pypi.org/project/text2emotion/

Fig. 6 SentiWordNet's lexicon fragment

POS	ID	PosScore	NegScore	SynsetTerms	Gloss
a	00005107	0.5	0	uncut#7	complete; "the full-length play"
a	00005718	0.125	0	infinite#4	total and all-embracing;
a	00006245	0	0	relational#1	having a relation or being related
a	00016532	0	0.375	torrential#3	pouring in abundance; "torrential rains"
a	00016647	0.125	0.5	verdant#1	characterized by abundance of verdure
a	00017688	0.375	0.25	unabused#1	not physically abused; treated properly
a	00016247	0.125	0.5	superabundant#1	most excessively abundant
a	00018069	0.25	0	bankable#2	acceptable to or at a bank;
a	00020103	0.125	0	remote#4 outback#1	inaccessible and sparsely populated;
a	00013887	0	0.25	abundant#1	present in great quantity;

respectively. The matrix formed from the various combinations of all these values $(\alpha_i, \beta_i, \gamma_i, \delta_i)$ is shown in Table 4.

Next, we apply the TOPSIS algorithm to evaluate the performance scores $(\lambda_1, \lambda_2, \lambda_3, \lambda_4)$ of all the strategies of a review. Table 5 shows the performance scores for all the strategies of review R_i. Algorithm 2 depicts the TOPSIS method to calculate the performance scores.

Algorithm 2: Calculate the Performance Score (P_i)

Input: Polarity $\{\alpha_i, \beta_i\}$ and Service Feedback score $\{\gamma_i, \delta_i\}$ of each review.

Output: Performance Score (P_j^+) of PS, *PU*, *NS*, and *NU* of players R_i and R_j.

1: Construct a normalized decision matrix (S_{ij}).

$$S_{ij} = \frac{x_{ij}}{\sqrt{\sum_{i=1}^{m} x_{ij}^2}} \forall i, j$$

Where S_{ij} and x_{ij} are the elements of normalized and original decision matrix, respectively.

2: Construct a weighted normalized decision matrix (V_{ij}) $V_{ij} = S_{ij} * W_j \ \forall i, j$, where, W_j is the assigned weight to an attribute j.

3: Determine positive ideal (A^+) and negative-ideal (A^-) solutions, i.e.,

$$A^+ = \{(\max V_{ij} \mid i \in l), (\min V_{ij} \mid i \in l'); \forall j\} = \{V_1^+, V_2^+ \ldots\ldots\}$$

$$A^- = \{(\min V_{ij} \mid i \in l), (\max V_{ij} \mid i \in l'); \forall j\} = \{V_1^-, V_2^- \ldots\ldots\}$$

l and l's are associated with benefits and cost attributes, respectively.

4: Calculate separation measure (M_i^+, M_i^-).

$$M_i^+ = \sqrt{\sum_{i=1}^{n} (V_{ij} - V_i^+)^2} \quad \forall j, \quad \text{and} \quad M_i^- = \sqrt{\sum_{i=1}^{n} (V_{ij} - V_i^-)^2} \quad \forall j.$$

5: Calculate relative closeness to the ideal solution, i.e., Performance Score (P_j^+), $P_j^+ = \frac{M_j^+}{M_j^+ + M_j^-}$

Step 5: Play non-cooperative games among the reviews In this final step, we take two players (say, R_i and R_j) and the four strategies *(PS, PU, NS, NU)* corresponding to each review. Then, we play a non-cooperative game between them. The performance scores calculated in the previous step are treated as payoff values for the players. The performance scores of players R_i and R_j are depicted in Table 6.

Table 7 represents a matrix of non-cooperative game. It shows the payoff values of the two players. A row represents the payoff for the first player for a given strategy. The column represents the payoff of the second player for a specific strategy. The dominant strategies of both players are derived using Eq. (1) and Eq. (2). The intersection of the dominant strategies of both players is known as Nash Equilibrium. We evaluate the Nash equilibrium and deduce a sentiment tag for a review.

Algorithm 3 shows the methodology used to deduce sentiment tags for reviews by playing games amongst them.

Algorithm 3: Deduce sentiment tag for review.

Input: Reviews data file with performance scores *PS, PU, NS*, and *NU* of players R_i and R_j.
Output: Tagged Sentiment of reviews, i.e., $\{R_i, R_j\} \in \{PS, PU, NS, NU\}$.

1: Generate Normal form matrix for players R_i, R_j using the performance scores.
2: Compute dominant strategies for R_i, i.e. (DR_i) and R_j, i.e. (DRj), $\{DR_i, DR_j\} \in \{PS, PU, NS, NU\}$.
3: Compute Nash equilibrium (NE), where $NE = DR_i$ intersection DR_j.
4: The strategies corresponding to *NE* are the sentiment tags for reviews R_i and R_j.
5: Repeat steps 1 to 5 will get the sentiment tag of R_1 and R_2, i.e., $\{R_i, R_j\} \in \{PS, PU, NS, NU\}$.

4.1 Illustrative example: Let us consider two reviews R_1 and R_2

R_1 (4 Star): *"Came here for lunch, and the food was good and tasty. We tried buffet and all the items in veg and non-veg were tasty."*
R_2 (2 Star): *"Food quality and taste is not good. Super slow service. Nice ambience but very poor in customer handling. Lot of items not available even if in the menu."*

First, we calculate the context scores of the written review comment using Algorithm 1. Next, we calculate emotion scores for happy, sad, surprise, fear, and anger to evaluate service feedback. Using these emotion scores, we classify reviews under two service feedback categories - satisfactory (*S*) and unsatisfactory (*U*). Table 8 shows the numeric scores pertaining to the six parameters - *CP, CN, RP, RN, S, and U,* and the four strategies for reviews R_1 *and* R_2.

Next, we apply the TOPSIS model as given in Algorithm 2. We get the single score for each strategy of the two players,

Table 3 Polarity and Service Feedback values of two different reviews R_i

R_i			
Strategies			
Polarity		Service Feedback	
P	α_i	S	γ_i
N	β_i	U	δ_i

Table 4 Numeric score corresponding to four strategies of review R_i

R_i	
PS	$\alpha_i.\ \gamma_i$
PU	$\alpha_i.\ \delta_i$
NS	$\beta_i.\ \gamma_i$
NU	$\beta_i.\ \delta_i$

Table 5 Performance score of strategies of player R_i

R_i	
PS	λ_1
PU	λ_2
NS	λ_3
NU	λ_4

Table 6 Performance score corresponding to four strategies of players R_i and R_j

R_i		R_j	
PS	ψ_1	PS	θ_1
PU	ψ_2	PU	θ_2
NS	ψ_3	NS	θ_3
NU	ψ_4	NU	θ_4

Table 7 Payoffs of the different strategies evaluated from the performance score of TOPSIS

Players → ↓	R_i			
R_j	Strategies↓→	PS	PU	NS	NU
	PS	$\{\psi_1,\theta_1\}$	$\{\psi_1,\theta_2\}$	$\{\psi_1,\theta_3\}$	$\{\psi_1,\theta_4\}$
	PU	$\{\psi_2,\theta_1\}$	$\{\psi_2,\theta_2\}$	$\{\psi_2,\theta_3\}$	$\{\psi_2,\theta_4\}$
	NS	$\{\psi_3,\theta_1\}$	$\{\psi_3,\theta_2\}$	$\{\psi_3,\theta_3\}$	$\{\psi_3,\theta_4\}$
	NU	$\{\psi_4,\theta_1\}$	$\{\psi_4,\theta_2\}$	$\{\psi_4,\theta_3\}$	$\{\psi_4,\theta_4\}$

Table 8 Values of different parameters of reviews and possible strategies of R_1 and R_2

R_1				R_2			
Parameters → Strategies ↓	Context (*CP, CN*)	Rating (*RP, RN*)	Service (*S, U*)	Parameters→ Strategies ↓	Context (*CP, CN*)	Rating *(RP, RN)*	Service *(S, U)*
PS	0.11	4.00	1.00	PS	0.16	2.00	0.27
PU	0.11	4.00	0.00	PU	0.16	2.00	0.18
NS	0.02	1.00	1.00	NS	0.21	3.00	0.27
NU	0.02	1.00	0.00	NU	0.21	3.00	0.18

known as the performance scores. The calculated performance scores for R_1 and R_2 are given in Table 9.

Now, we play a non-cooperative game between players R_1 and R_2 with four strategies. Figure 7 shows the extensive form representation of the game played between R_1 and R_2.

In Table 10 for player R_1, the first-row payoff values dominate the payoffs in other rows. The strategy corresponding to this first row of R_1 is *PS*. Similarly, for R_2, the payoff corresponding to the third column dominates other columns, and the strategy of that column is *NU*. The intersection of the *PS* strategy of R_1 and the *NU* strategy of R_2 gives the Nash equilibrium. Thus, the deduced strategies for R_1 and R_2 are *PS,* and *NU*, respectively. *PS* tag for R_1 helps us to infer that the review has positive polarity *(P)* and satisfactory service feedback *(S)*. The *NU* tag shows that R_2 has negative polarity *(N)* and unsatisfactory service feedback *(U)*. Figure 8 shows the Nash equilibrium of R_1 and R_2 and the interpretation of the tags.

5 Experiments and results

In this section, we first introduce the datasets used for experimentation. In subsection 5.2, we give brief definitions of the evaluation metrics used to compare the performance of the proposed model. We compare the proposed model's efficiency with other approaches on the TripAdvisor dataset and Yelp dataset in subsection 5.2 and subsection 5.4, respectively. We generalize the performance values using macro and micro metrics in subsection 5.5. In subsection 5.6, we validate the performance of the proposed model using statistical validation methods.

Table 9 Performance Score of R_1 and R_2 calculated by applying TOPSIS

Players → Strategies ↓	R_1 Performance Score	R_2 Performance Score
PS	1.00	0.45
PU	0.52	0.00
NU	0.47	1.00
NS	0.00	0.65

5.1 Data collection

We collected two restaurant review datasets – one from *TripAdvisor*[5] and the other from *Yelp*[6] [57]. Each dataset contains reviews and their respective ratings. The data statistics of both datasets are listed in Table 11. Figure 9 shows a snapshot of Yelp's rating and comments on McDonald's restaurants.

5.2 Performance evaluation using evaluation metrics

The robustness of the proposed framework was gauged using various evaluation metrics. These include F1-measure, accuracy, precision, MCC, etc. It is crucial to analyze a model using a variety of measures because a model may perform well with one evaluation metric but poorly with another. Figure 10 depicts the performance of the proposed model on the two datasets in terms of various evaluation metrics. The metrics are defined below from Eq. (7) to Eq. (15).

$$Accuracy = \frac{TP + TN}{TP + TN + FN + FP} \tag{7}$$

$$Precision = \frac{TP}{TP + FP} \tag{8}$$

$$Recall = \frac{TP}{TP + FN} \tag{9}$$

$$Specificity = \frac{TN}{TN + FP} \tag{10}$$

$$False\ positive\ rate\ (FPR) = \frac{FP}{FP + TN} \tag{11}$$

$$False\ negative\ rate\ (FNR) = \frac{FN}{TP + FN} \tag{12}$$

$$False\ discovery\ rate\ (FDR) = \frac{FP}{(TP + FP)} \tag{13}$$

$$F1_{score} = \frac{(2^{*}precision^{*}recall)}{(precision + recall)} \tag{14}$$

[5] https://www.kaggle.com/datasets/stefanoleone992/tripadvisor-european-restaurants

[6] https://www.kaggle.com/datasets/yelp-dataset/yelp-dataset

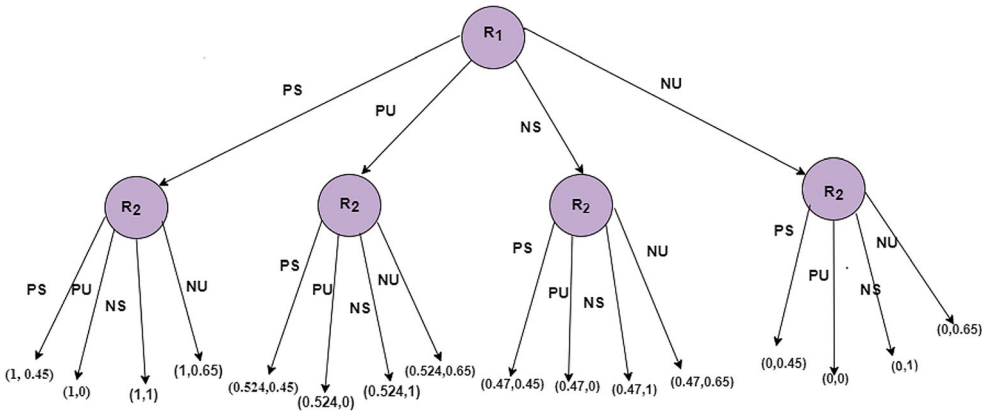


Fig. 7 Extensive Form Representation of game played between R_1 and R_2

Table 10 Non-Cooperative game between Player R_1 and R_2

Players→ ↓	R_2				
	Strategies→ ↓	*PS*	*PU*	*NU*	*NS*
R_1	*PS*	(1.00,0.45)	(1.00,0.00)	(1.00,1.00)	(1.00,0.65)
	PU	(0.52,0.45)	(0.52,0.00)	(0.52,1.00)	(0.52,0.65)
	NS	(0.47,0.45)	(0.47,0.00)	(0.47,1.00)	(0.47,0.65)
	NU	(0.00,0.45)	(0.00,0.00)	(0.00,1.00)	(0.00,0.65)

Matthews correlation coefficient(MCC)

$$= \frac{\left(TP^{*}TN - FP^{*}FN\right)}{\sqrt{(TP+FP)*(TN+FN)*(FP+TN)*(TP+FN)}} \quad (15)$$

Accuracy is the proportion of correctly identified samples to the total number of samples. The accuracy of the proposed model for TripAdvisor dataset is 0.*90*, and for the Yelp dataset is *0.89*. Precision reveals how many of the accurately predicted instances turned out to be positive. The precision values over TripAdvisor and Yelp datasets are 0.895 and *0.97*, respectively. Recall measures how many actual positive cases our model could predict accurately. We received a recall value of 0.97 for both datasets. The Harmonic Mean of recall and precision is the F1 Score. F1 Score has a range of [0, 1]. TripAdvisor's and Yelp's F1 scores are 0.935 and 0.932, respectively. MCC is used to evaluate models and is a chi-square statistic for a 2×2 contingency table compared to the difference between actual and predicted values [58]. It ranges in the interval [−1, +1], with extreme values −1 and + 1 representing perfect misclassification and classification, respectively. The MCC for the proposed model for the TripAdvisor dataset is 0.74 and 0.687 for Yelp. The values are close to 1 and are thus close to the perfect classification.

5.3 Evaluations on TripAdvisor dataset

We compared the proposed model's performance with the existing models on the TripAdvisor dataset. We used the supervised models for comparison: PLSA [59], FK-NN [60], Decision Tree-J48, and deep learning-based models. Khotimah et al. [59] proposed a Probabilistic Latent Semantic

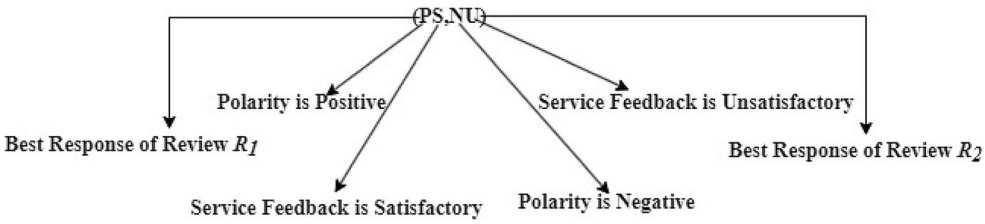


Fig. 8 Nash Equilibrium of R_1 and R_2

Table 11 Data statistics of different datasets

Data Set	Language	Positive	Negative
TripAdvisor Restaurant reviews	English	730	270
Yelp Restaurant reviews	English	657	343

Analysis (PLSA) model that analyzed word frequencies and document counts of customer reviews. PLSA categorized words as positive or negative by assigning meanings across multiple domains. Billiyan et al. [60] used the Fuzzy K-Nearest Neighbor (FK-NN) method for sentiment analysis that combines the Fuzzy and K-Nearest Neighbour approaches. This hybrid model classifies customer reviews with positive or negative sentiments. PLSA performed better than the FK-NN on this dataset. The accuracy of FK-NN is 0.72, and PLSA is 0.76. We also compare results with the performance of Decision Tree-J48 by Laksono et al. [61]. The study by Ma et al. [62] introduced a deep learning model for computer vision to understand the information value of online restaurant reviews on the TripAdvisor datasets. Figure 11 shows the graphical representation of the comparison. The proposed model outperforms all the supervised models. The superior performance of the proposed model over supervised models exposing supervised models to more realistic data requires intensive training to work well [63]. On the contrary, the proposed unsupervised model needs no training with massive datasets.

Next, we compared the proposed model with five different unsupervised models. The first unsupervised approach is POST-VIA360 [50] recommender system. It performed sentiment analysis and used contextual information to suggest places of interest like eateries. Compared to POST-VIA360, the proposed approach is significantly more effective. Zuheros

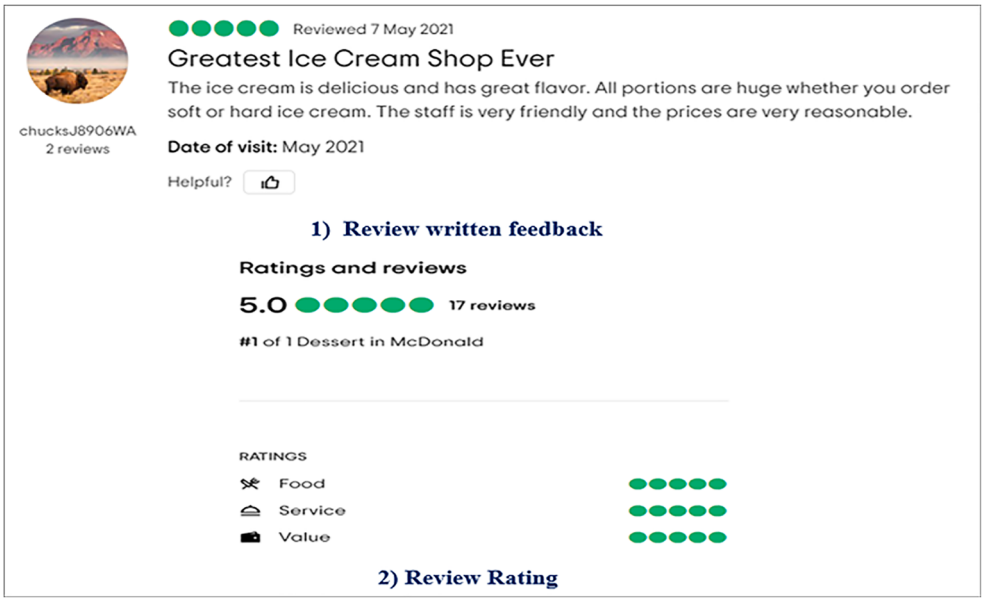


Fig. 9 McDonald's Restaurant rating and review snapshot from Yelp

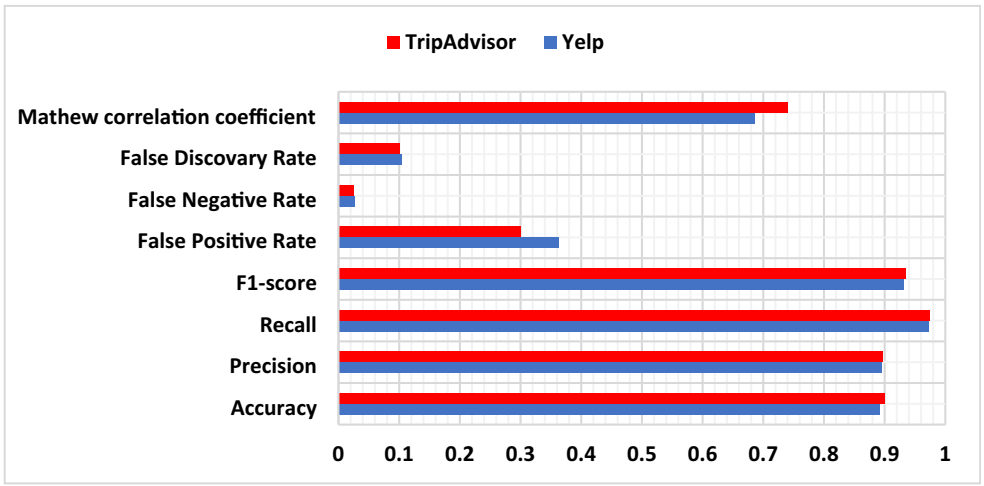


Fig. 10 Performance of evaluation metrics over the two datasets

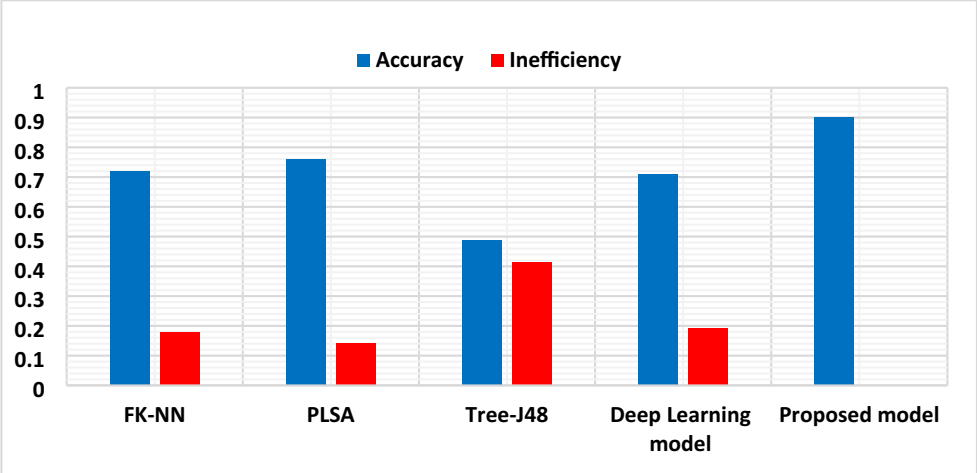


Fig. 11 Comparison of the proposed model with Supervised approaches

et al. [64] proposed more innovative decision aid using the SA-MpMcDM methodology model - DOC-ABSADeepL. It used expert evaluations based on natural language reviews and numerical ratings. The DOC-ABSADeepL is a multi-task deep learning model for sentiment analysis that can parse an expert review into its component categories and extract critical insights.

Afzaal et al. [65] proposed fuzzy logic models viz. FURIA, FLR, FNN, FRNN, and VQNN to classify user opinions, extracting various aspects and delivering promising results. Fuzzy Lattice Reasoning (FLR) has the highest accuracy among the five models. FLR consists of a set of fuzzy lattice rules. The performance of FLR is less than the proposed model. One possible reason behind the low performance is that Fuzzy Logic models are not used uniformly to address a problem. It is perplexing as there are multiple solutions to the same problem. It takes a lot of testing to validate and verify the systems [66, 67].

The proposed model outperforms Buon Appetito [68] in precision, recall, and f-measure. The proposed model successfully outperforms all the unsupervised models, as shown in Fig. 12. with an accuracy of 0.90. The improved performance of the proposed models is due to combining two mathematical optimization models that help the system to produce more accurate results.

5.4 Evaluations on yelp dataset

We compared the performance of the proposed model over the yelp dataset with various supervised and unsupervised models**.** Hemalatha & Ramathmika [69] implemented various machine learning algorithms. Out of all the models, Naïve Bayes gave the best results. Govindarajan [70] proposed a comparative study of the effectiveness of ensemble techniques for sentiment classification in which SVM and Genetic algorithm worked best. Nasim & Haider [71] presented the Aspect-Based Sentiment Analysis (ABSA) Toolkit to perform aspect-level sentiment analysis on customer reviews in which XGBoost has comparable accuracy. Luo et al. [72] proposed a classification algorithm based on the SVM and FDO algorithms. The study by Ma et al. [62] introduced a deep learning model for computer vision to understand the information value of online restaurant reviews on the yelp dataset. Table 12 shows the experimental results of the proposed model with an accuracy of 89%, which is higher than the other supervised algorithms.

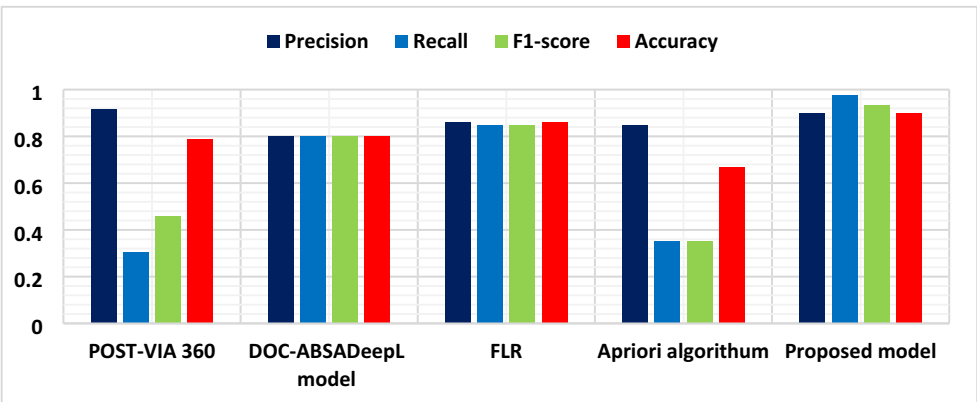


Fig. 12 Comparison of the proposed model with unsupervised approaches

Table 12 Comparison of the proposed model with the supervised model

Supervised Algorithm	Accuracy	Inefficiency
Naïve Bayes [69]	79.12	−9.88
Support Vector Machine [70]	85.20	−3.80
Genetic algorithm [70]	85.30	−3.70
XGBoost [71]	83.00	−6.00
SVM_FDO (Fuzzy Domain Ontology) [72]	79.59	−9.41
Deep learning models [62]	70.00	−19.00
Proposed Model	89.00	0.00

Along with accuracy, we also utilize the inefficiency parameter as a second yardstick to compare the effectiveness of various models. Table 12 shows that the Genetic algorithm has minimal inefficiency among the other supervised models but is still more than the proposed model. The deep learning models have the highest inefficiency rate over the Yelp dataset. The proposed model surpasses the other models in terms of accuracy, as it does not necessitate intensive training and high memory storage capacity.

We next compared our findings with topic modeling and lexical-based techniques. These techniques are unsupervised and are independent of training. We compare our results with JST [41], ASUM [73], HASM [48], TSM [49], and ASUM+. We tested the proposed algorithm on a small sample of 500 reviews (all of which were given 1 or 5 stars) and a larger sample of 1000 reviews (all of which were given 2 or 4 stars). The performance of the proposed model on both small and large datasets outperforms the other unsupervised algorithms. Figure 13 displays the outcomes of comparing the proposed algorithm with other unsupervised models on the same dataset. Results for the proposed model are equivalent to the small dataset and enhanced for the large dataset. However, the proposed model shows the highest accuracy for both small and big datasets.

The proposed model outperforms both datasets' supervised, unsupervised, and semi-supervised models. The integration of mathematical optimization methodologies contributes to the reliability of the proposed model. To offer the optimal approach, an optimization model takes into account the objective (Enhanced accuracy of sentiment classification), the variables (rating, context, and emotion), and the constraints (sentiment analysis difficulties, such as sarcasm and irony detections, special characters, etc.). The optimization model returns a best-case feasibly-optimal outcome.

5.5 Macro and Micro evaluation

We used macro and micro averages to estimate overall performance while dealing with different datasets. Macro-average computes metrics independently for each class and then takes the average (thus treating all classes equally). Micro-average calculates the mean metric by adding all the contributions from each class. It's a metric that can be advantageous to know the performance when datasets fluctuate in size. The macro and micro-averaged accuracy, F-score, and recall across the n datasets are described in Eq. (16) to Eq. (21).

$$Macro{-}averaged\ Precision = \frac{\sum_{i=1}^{n} Precision_i}{n} \tag{16}$$

$$Macro{-}averaged\ Recall = \frac{\sum_{i=1}^{n} Recall_i}{n} \tag{17}$$

$$Macro{-}F{-}score = 2.\frac{Macro{-}Precision_i \times Macro{-}Recall}{Macro{-}Precision_i + Macro{-}Recall} \tag{18}$$

$$Micro{-}averaged\ precision = \frac{\sum_{i=1}^{n} TP_i}{\sum_{i=1}^{n} (TP_i + FP_i)} \tag{19}$$

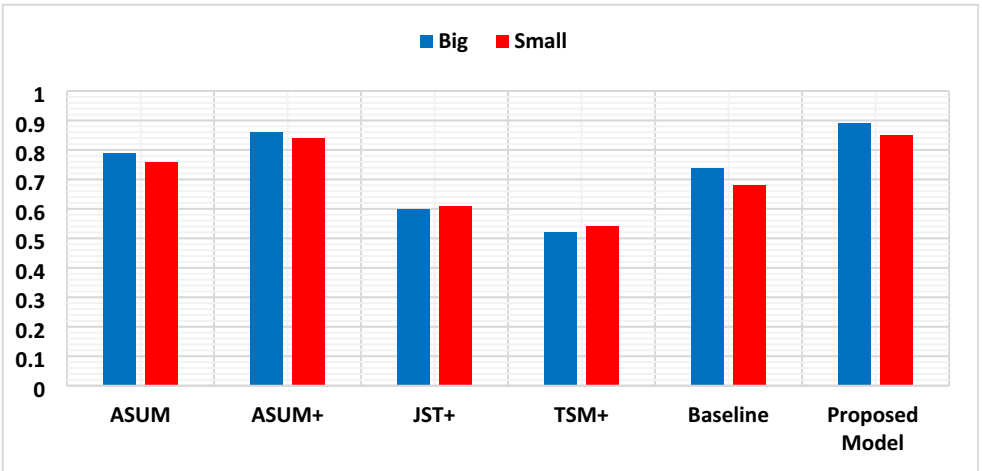


Fig. 13 Comparison of the proposed model with topic modeling techniques

$$Micro{-}averaged\ recall = \frac{\sum_{i=1}^{n} TP_i}{\sum_{i=1}^{n} (TP_i + FN_i)} \quad (20)$$

$$Micro{-}averaged\ F{-}score = 2.\frac{Micro{-}Precision_i \times Micro{-}Recall}{Micro{-}Precision_i + Micro{-}Recall} \quad (21)$$

The overall performance of the proposed model is illustrated in Fig. 14. Over two datasets, the macro and micro precisions are 0.90 and 0.89, respectively. The macro and micro recall values are 0.97 and 0.76, respectively. And the macro and micro F1-score values are 0.94 and 0. 93. All three evaluation metrics produce nearly identical macro and micro scores. This verifies that the proposed model produces consistent results on both datasets.

5.6 Statistical validation of results

We conducted the statistical z-test of two proportions to check the robustness of the proposed model. Two samples of different sample sizes were taken from the TripAdvisor reviews dataset. In *Sample 1,* we took *1000* reviews (n_1). Out of *1000* reviews, *900* (x_1) were correctly tagged. Thus, sample proportion (p_1) =*0.90*. In *Sample 2*, we took *500* reviews. From *500* reviews, *452* (x_2) were correctly tagged, so the sample proportion is *0.906*. The sample statistics are summarized in Table 13.

We conducted the z-test for two population proportions (p_1 and p_2). For the population proportion, we investigated the following null and alternative hypotheses.

Null Hypothesis (H_o): $p_1 = p_2$ i.e., The proportion of correctly tagged reviews is the same in both samples.

Alternate hypothesis (H_a): $p_1 \neq p_2$ i.e., The proportion of correctly tagged reviews is not same in both samples.

Table 13 Test statistics of Z-test of two proportions within a dataset

Parameters	Sample 1	Sample 2
Sample Size	1000	500
Favorable cases	900	452
Sample Proportion	0.90	0.906

The value of the pooled proportion is computed using Eq. (22).

$$P = \frac{X_1 + X_2}{N_1 + N_2} = \frac{900 + 452}{1000 + 500} = 0.901 \quad (22)$$

We employed the two-tailed test and used the z-test for two population proportions. Eq. (23) shows the calculation of the z-statistic.

$$z = \frac{p_1 - p_2}{\sqrt{P(1-P)(1/n_1 + 1/n_2)}} = \frac{0.9 - 0.904}{\sqrt{0.9013.(1-0.9013)(1/1000 + 1\backslash 500)}} = -0.245 \quad (23)$$

Figure 15 shows a graphical representation of the critical region of the assumed hypothesis. From the calculations, we failed to reject the null hypothesis, H_o. Thus, we can say that there is insufficient evidence to assert that the population proportions p_1 and p_2 differ from each other at the *0.05* significance level. This implies that the proportion of correctly tagged reviews is consistent throughout different sample sizes of the same datasets. Hence the results produced by the proposed model are stable and unswerving.

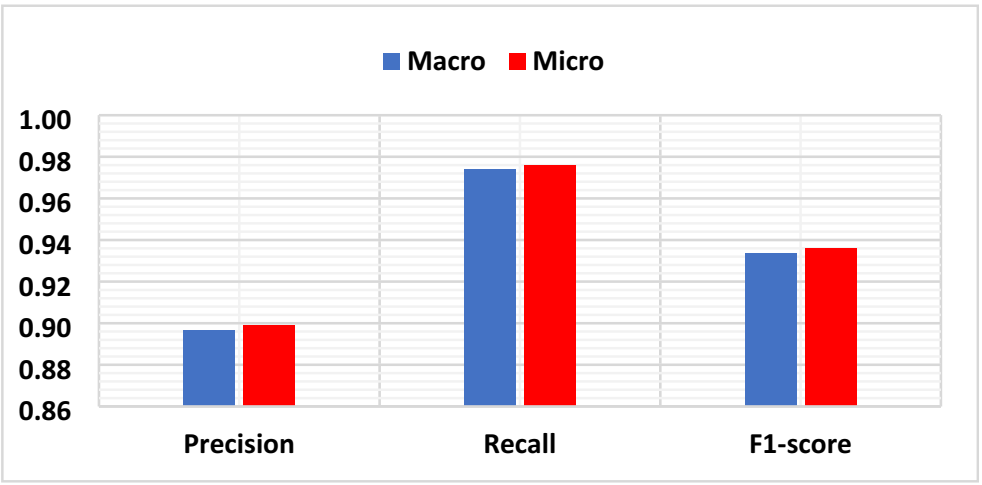


Fig. 14 Macro and Micro average performance of the proposed model

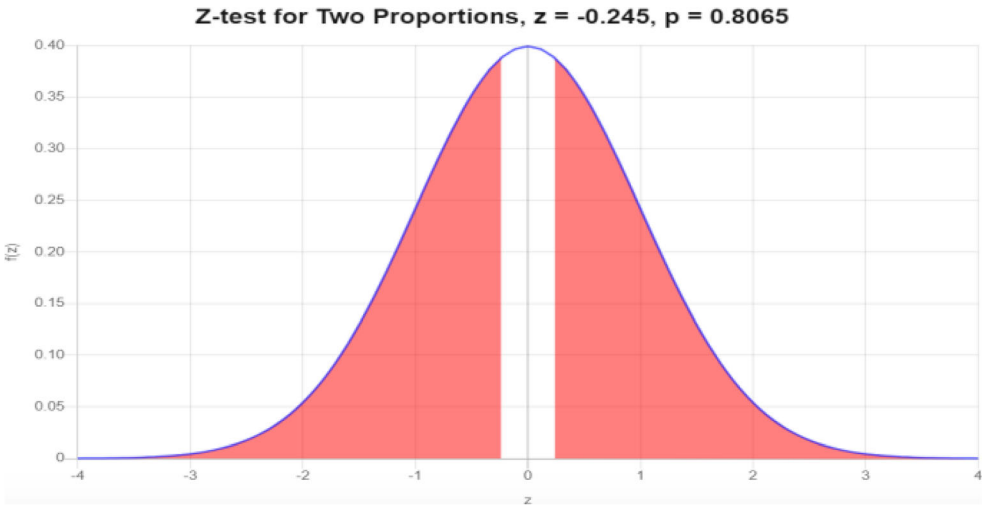


Fig. 15 Graphical representation of the critical region of the null hypothesis

6 Discussion

The proposed model is an initial demonstration of the applicability of integrated TOPSIS and non-cooperative games for sentiment analysis. In this study, we perform binary classification of sentiments - positive or negative, and service feedback - satisfactory or unsatisfactory. This section discusses the proposed methodology's computational complexities, error rates, advantages, and limitations.

1) **Space and Time complexity:** An algorithm's time and space complexity are essential for assessing efficiency. The time complexity of an algorithm can be estimated by the number of operations it must perform to complete its task for a given input. An algorithm's space complexity measures the amount of space it consumes during execution for varying input sizes. Table 14 shows the algorithm's time and space complexities, where m is the number of alternatives and n is the number of criteria. The recorded complexity comes under the P-class problem solvable in polynomial time. It is also a deterministic algorithm which means the algorithm continuously computes the correct answer. The time and space complexity is reduced by half by the use of game theory. This is because we play games between two players (R_i and R_j), thus, halving the time required to tag two reviews.

Table 14 Complexities of the proposed model

Efficiency	Best Case	Average case	Worst Case
Time Complexity	$\Omega(m+n)$	$\theta(mn)$	$O(mn)$
Space Complexity	$\Omega(m+n)$	$\theta(mn)$	$O(mn)$

2) **Evaluation of error rates:** Error rate (ERR), also known as misclassification rate, shows the number of incorrectly identified samples from the actual positive and negative classifications sample. It is evaluated using Eq. (24).

$$ERR = \frac{FP + FN}{TP + TN + FN + FP} \times 100 \tag{24}$$

The error rate performance of several supervised and unsupervised algorithms for the TripAdvisor dataset are depicted in Fig. 16. The Tree-J48 model has the highest error rate, while PLSA and FK-NN have nearly equivalent error rates. Because the suggested model has the lowest error percentage, it is more reliable than existing algorithms for the TripAdvisor restaurant reviews dataset.

The error rate of the various models for the Yelp dataset is visually represented in Fig. 17. TSM's maximum error rate indicates that its results are less dependable than other unsupervised models such as ASUM, JST, and TSM ASUM+. SVM FDO and linear SVC have higher error rates than existing supervised models. The proposed unsupervised model has the lowest error rate, implying that the results are more reliable.

3) **Advantages of the Proposed Model:** This paper introduces a mathematical optimization framework for sentiment analysis. One of the significant advantages of the proposed model is that it is unsupervised. It does not need training on a huge dataset. The proposed model employs unlabelled and unclassified data. The proposed model can be applied to perform sentiment analysis of reviews in several languages. The only prerequisite is having access to SentiWordNet, or any similar lexicon that should be available to compute context scores of reviews. The proposed work is a mathematical optimization model with minimal space and time complexity. Mathematical optimization solutions may readily adjust to changing

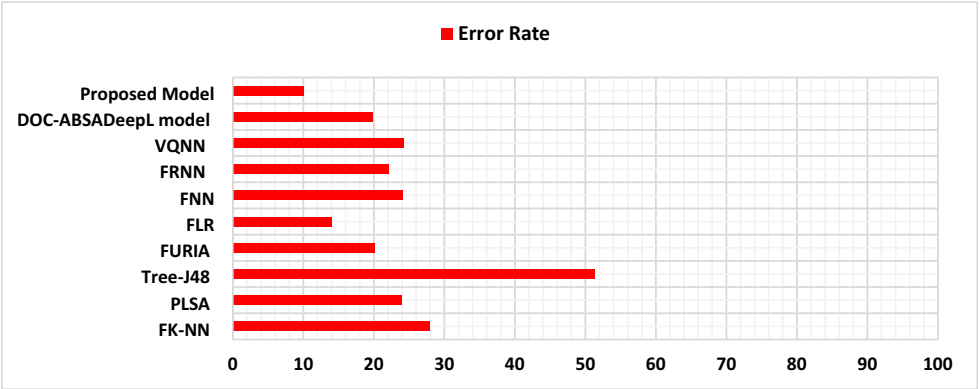


Fig. 16 Comparison of error rates of the proposed model with existing approaches on the TripAdvisor dataset

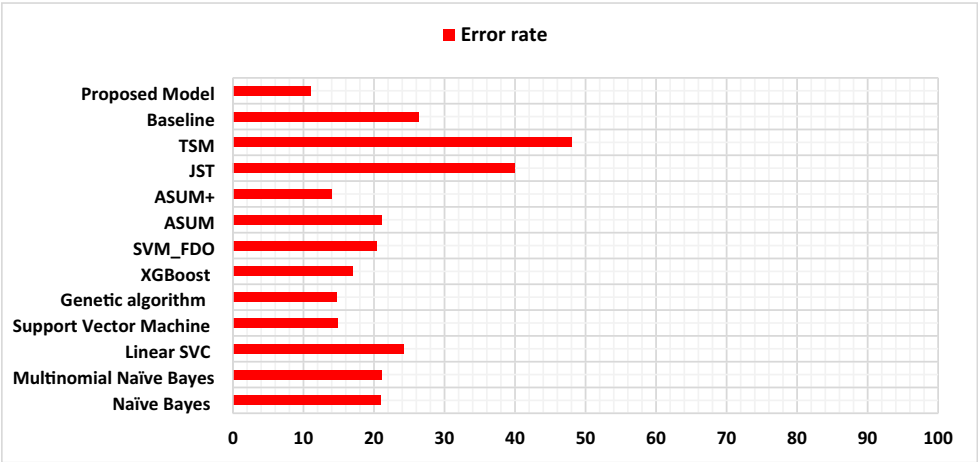


Fig. 17 Comparison of error rates of the proposed model with existing approaches on the Yelp dataset

conditions and give us the information and flexibility required to respond to disruptions effectively. The proposed work paves the way to utilize mathematical optimizations in diverse NLP tasks.

4) **Challenges or Disadvantages of the Proposed Model:** One significant reason for the dwindled performance of the proposed algorithm is that the SentiWordNet is not exhaustive. The list of words is incomplete, and a few words are given incorrect sentiment scores. Another set of statements that the proposed system could not correctly analyze were those containing sarcasm or irony. The true meaning of a comment can be complex for sentiment analysis algorithms to decipher when people communicate negative thoughts by offering unintentional praises. Consumers sometimes write reviews that may contain emoticons and slang words. The proposed methodology is unable to categorize such constructs. Emojis are treated by the proposed methodology like particular characters and are removed from the data during text pre-processing. Similar to this, texts with negations do not envisage positive outcomes. In Table 15 we list a sample of examples that the proposed algorithm could not correctly classify

Table 15 Examples where the proposed model fails

Reviews	Challenges	Actual	Predicted
"I do not dislike noodles."	Phrases with negation	Positive	Negative
"Thnk u 4 the treat in @ Phonenix Palladium. "	Special characters and slang	Neutral	Negative
"Someone who works as a pizza man does not like pizza?"	Irony	Neutral	Positive
"Pizza is tasty but not at that price."	Tone	Positive	Negative

on the two review datasets. However, these roadblocks can be tackled, and we intend to take these cases in our future work.

7 Conclusion

This study introduced a novel unsupervised technique for sentiment tagging. We developed an MCDM and game theory-based mathematical framework to perform sentiment analysis and adjudge the service feedback of a restaurant based on reviews. We evaluated the effectiveness of our proposed model on two restaurant review datasets and compared it with other unsupervised and supervised approaches. The proposed model gave state-of-the-art results and outperformed other approaches. The proposed work demonstrates that mathematical optimization techniques, such as MCDM and game theory, can be used to perform various NLP tasks effectively and efficiently.

The advantage of utilizing the Mathematical optimization model is that a mathematical model of sentiment analysis and an algorithm-based solver generate solutions for even the most challenging sentiment analysis problems and thus empower us to make the best possible decisions. Mathematical optimization solutions can easily adapt to changing conditions and provide us with the insight and adaptability we need to respond to disruptions efficiently. The proposed system could serve as a springboard for other emerging applications of sentiment analysis, such as the use of social media for effective policing, governmental accountability, participation by the public in decision-making, etc. This is an explanatory effort toward sentiment tagging of reviews. We understand that there is enormous scope for improvement. There are various challenges faced by the proposed model, like negation handling, slang, irony, etc. We plan to work on these tasks in the future. We can also intend to expand the polarity classifications (strong positive, positive, weak, positive, neutral strong negative, negative, weak negative) in future work. The proposed model can be extended to classify sentiments in low-resource languages such as Hindi, Bengali, and Urdu with minor modifications. The proposed model paved the way for mathematical optimization techniques to be applied to various NLP applications like WSD, query expansion, etc.

Availability of data and materials https://www.yelp.com/, https://www.tripadvisor.in/Restaurants.

Declarations

Competing interests The authors declare that they have no known competing financial interests or personal relationships that could have appeared to influence the work reported in this paper.

References

1. Wu J-L, Chung W-Y (2022) Sentiment-based masked language modeling for improving sentence-level valence-arousal prediction. Appl Intell 52:16353–16369. https://doi.org/10.1007/s10489-022-03384-9
2. Han H, Zhang J, Yang J, Shen Y, Zhang Y (2018) Generate domain-specific sentiment lexicon for review sentiment analysis. Multimed Tools Appl 77:21265–21280. https://doi.org/10.1007/S11042-017-5529-5/TABLES/7
3. Jain PK, Pamula R, Srivastava G (2021) A systematic literature review on machine learning applications for consumer sentiment analysis using online reviews. Comput Sci Rev 41:100413. https://doi.org/10.1016/J.COSREV.2021.100413
4. Al-Mashhadany AK, Hamood DN, Sadiq Al-Obaidi AT, Al-Mashhadany WK (2021) Extracting numerical data from unstructured Arabic texts (ENAT). Indones J Electr Eng Comput Sci 21:1759–1770. https://doi.org/10.11591/IJEECS.V21.I3.PP1759-1770
5. Ray PP (2018) A survey on internet of things architectures. J King Saud Univ - Comput Inf Sci 30:291–319. https://doi.org/10.1016/j.jksuci.2016.10.003
6. Fikri M, Sarno R (2019) A comparative study of sentiment analysis using SVM and SentiWordNet. Indones J Electr Eng Comput Sci 13:902–909. https://doi.org/10.11591/IJEECS.V13.I3.PP902-909
7. Rintyarna BS, Sarno R, Fatichah C (2020) Enhancing the performance of sentiment analysis task on product reviews by handling both local and global context. Int J Inf Decis Sci 12:75–101. https://doi.org/10.1504/IJIDS.2020.104992
8. García-Pablos A, Cuadros M, Rigau G (2017) W2VLDA: almost unsupervised system for aspect based sentiment analysis. Expert Syst Appl 91:127–137. https://doi.org/10.1016/j.eswa.2017.08.049
9. Donadi M (2018) A system for sentiment analysis of online-media with TensorFlow. 1–44
10. Vashishtha S, Susan S (2021) Highlighting keyphrases using senti-scoring and fuzzy entropy for unsupervised sentiment analysis. Expert Syst Appl 169:114323
11. Song M, Park H, Shin K s (2019) Attention-based long short-term memory network using sentiment lexicon embedding for aspect-level sentiment analysis in Korean. Inf Process Manag 56:637–653. https://doi.org/10.1016/J.IPM.2018.12.005
12. Hu J, Zhang X, Yang Y, Liu Y, Chen X (2020) New doctors ranking system based on VIKOR method. Int Trans Oper Res 27:1236–1261. https://doi.org/10.1111/itor.12569
13. Rani R, DL-J of KSU-C, (2020) Undefined performance evaluation of text-mining models with Hindi stopwords lists. Elsevier
14. Pandesenda AI, Yana RR, Sukma EA et al (2020) Sentiment analysis of service quality of online healthcare platform using fast large-margin. Proceedings - 2nd international conference on informatics, multimedia, cyber, and information system, ICIMCIS 2020 121–125. https://doi.org/10.1109/ICIMCIS51567.2020.9354295
15. Liu N, Shen B (2020) ReMemNN: a novel memory neural network for powerful interaction in aspect-based sentiment analysis. Neurocomputing 395:66–77. https://doi.org/10.1016/j.neucom.2020.02.018
16. Basiri ME, Nemati S, Abdar M, Cambria E, Acharya UR (2021) ABCDM: an attention-based bidirectional CNN-RNN deep model for sentiment analysis. Futur Gener Comput Syst 115:279–294. https://doi.org/10.1016/J.FUTURE.2020.08.005
17. Zhao A, Yu Y (2021) Knowledge-enabled BERT for aspect-based sentiment analysis. Knowl-Based Syst 227:107220. https://doi.org/10.1016/J.KNOSYS.2021.107220
18. Jain L, Katarya R, Sachdeva S (2020) Recognition of opinion leaders coalitions in online social network using game theory.

Knowl-Based Syst 203:106158. https://doi.org/10.1016/j.knosys.2020.106158
19. Mee A, Homapour E, Chiclana F, Engel O (2021) Sentiment analysis using TF–IDF weighting of UK MPs' tweets on Brexit. Knowl-Based Syst 228:107238. https://doi.org/10.1016/J.KNOSYS.2021.107238
20. Heidary Dahooie J, Raafat R, Qorbani AR, Daim T (2021) An intuitionistic fuzzy data-driven product ranking model using sentiment analysis and multi-criteria decision-making. Technol Forecast Soc Chang 173:121158. https://doi.org/10.1016/j.techfore.2021.121158
21. Perikos I, Kardakis S, Hatzilygeroudis I (2021) Sentiment analysis using novel and interpretable architectures of hidden Markov models. Knowl-Based Syst 229:107332. https://doi.org/10.1016/J.KNOSYS.2021.107332
22. Ileri M, Turan M (2021) Sentiment analysis of meeting room. HORA 2021 - 3rd international congress on human-computer interaction, optimization and robotic applications, proceedings. https://doi.org/10.1109/HORA52670.2021.9461354
23. Nguyen DN, Phan TT, Do P (2021) Embedding knowledge on ontology into the corpus by topic to improve the performance of deep learning methods in sentiment analysis. Sci Rep 11:23541. https://doi.org/10.1038/s41598-021-03011-6
24. de Oliveira Carosia AE, Coelho GP, da Silva AEA (2021) Investment strategies applied to the Brazilian stock market: a methodology based on sentiment analysis with deep learning. Expert Syst Appl 184:115470
25. Fiok K, Karwowski W, Gutierrez E, Wilamowski M (2021) Analysis of sentiment in tweets addressed to a single domain-specific Twitter account: Comparison of model performance and explainability of predictions. Expert Syst Appl 186:115771
26. Ozyurt B, Akcayol MA (2021) A new topic modeling based approach for aspect extraction in aspect based sentiment analysis: SS-LDA. Expert Syst Appl 168:114231
27. Zhang D, Zhu Z, Kang S, Zhang G, Liu P (2021) Syntactic and semantic analysis network for aspect-level sentiment classification. Appl Intell 51:6136–6147. https://doi.org/10.1007/S10489-021-02189-6/FIGURES/9
28. Liang R, Wang J q (2019) A Linguistic Intuitionistic Cloud Decision Support Model with Sentiment Analysis for Product Selection in E-commerce. Int J Fuzzy Syst 21:963–977. https://doi.org/10.1007/S40815-019-00606-0
29. Peng Y, Xiao T, Yuan H (2022) Cooperative gating network based on a single BERT encoder for aspect term sentiment analysis. Appl Intell 52:5867–5879. https://doi.org/10.1007/S10489-021-02724-5/TABLES/7
30. Zhang Q, Shi L, Liu P, Zhu Z, Xu L (2022) ICDN: integrating consistency and difference networks by transformer for multimodal sentiment analysis. Appl Intell 1–14. https://doi.org/10.1007/s10489-022-03343-4
31. Gu T, Zhao H, Li M (2022) Effective inter-aspect words modeling for aspect-based sentiment analysis. Appl Intell 1–14. https://doi.org/10.1007/S10489-022-03630-0/TABLES/6
32. Chiha R, Ayed MB, Pereira C d C (2022) A complete framework for aspect-level and sentence-level sentiment analysis. Appl Intell 1–19. https://doi.org/10.1007/S10489-022-03279-9/TABLES/11
33. Swathi T, Kasiviswanath N, Rao AA (2022) An optimal deep learning-based LSTM for stock price prediction using twitter sentiment analysis. Appl Intell 1–14 52:13675–13688. https://doi.org/10.1007/S10489-022-03175-2/FIGURES/10
34. Wu J, Ma X, Chiclana F, Liu Y, Wu Y (2022) A consensus group decision making method for hotel selection with online reviews by sentiment analysis. Appl Intell 52:10716–10740. https://doi.org/10.1007/S10489-021-02991-2/FIGURES/7
35. Li L, Johnson J, Aarhus W, Shah D (2022) Key factors in MOOC pedagogy based on NLP sentiment analysis of learner reviews: what makes a hit. Comput Educ 176:104354. https://doi.org/10.1016/J.COMPEDU.2021.104354
36. Birjali M, Kasri M, Beni-Hssane A (2021) A comprehensive survey on sentiment analysis: approaches, challenges and trends. Knowl-Based Syst 226:107134. https://doi.org/10.1016/J.KNOSYS.2021.107134
37. Jindal K, Aron R (2021) A systematic study of sentiment analysis for social media data. Mater Today: Proc. https://doi.org/10.1016/J.MATPR.2021.01.048
38. Hossain N, Bhuiyan MR, Tumpa ZN, Hossain SA (2020) Sentiment analysis of restaurant reviews using combined CNN-LSTM. 2020 11th international conference on computing, communication and networking technologies, ICCCNT 2020. https://doi.org/10.1109/ICCCNT49239.2020.9225328
39. Li M, Chen L, Zhao J, Li Q (2021) Sentiment analysis of Chinese stock reviews based on BERT model. Appl Intell 51:5016–5024. https://doi.org/10.1007/S10489-020-02101-8/TABLES/5
40. Zhang Z, Singh MP (2014) ReNew: a semi-supervised framework for generating domain-specific lexicons and sentiment analysis. 52nd annual meeting of the Association for Computational Linguistics, ACL 2014 - proceedings of the conference 1:542–551. https://doi.org/10.3115/v1/p14-1051
41. Lin C, He Y, Everson R, Rüger S (2012) Weakly supervised joint sentiment-topic detection from text. IEEE Trans Knowl Data Eng 24:1134–1145. https://doi.org/10.1109/TKDE.2011.48
42. Almutairi K, Hosseini Dehshiri SJ, Hosseini Dehshiri SS, Mostafaeipour A, Hoa AX, Techato K (2022) Determination of optimal renewable energy growth strategies using SWOT analysis, hybrid MCDM methods, and game theory: a case study. Int J Energy Res 46:6766–6789. https://doi.org/10.1002/ER.7620
43. Vincent TL, Brown JS (2005) Evolutionary game theory, natural selection, and darwinian dynamics
44. Muthumanickam K, Ilavarasan E (2015) Optimization of rootkit revealing system resources - a game theoretic approach. J King Saud Univ - Comput Inf Sci 27:386–392. https://doi.org/10.1016/j.jksuci.2014.10.004
45. Biaou BOS, Oluwatope AO, Odukoya HO, Babalola A, Ojo OE, Sossou EH (2020) Ayo game approach to mitigate free riding in peer-to-peer networks. J King Saud Univ - Comput Inf Sci 34:2451–2460. https://doi.org/10.1016/j.jksuci.2020.09.015
46. von Neumann J, Morgenstern O (2007) Theory of games and economic behavior (60th anniversary commemorative edition). Theory of games and economic behavior (60th anniversary commemorative edition) 9781400829460:1–741. https://doi.org/10.1515/9781400829460/MACHINEREADABLECITATION/BIBTEX
47. Kolios A, Mytilinou V, Lozano-Minguez E, Salonitis K (2016) A comparative study of multiple-criteria decision-making methods under stochastic inputs. Energies 9. https://doi.org/10.3390/en9070566
48. Kim S, Zhang J, Chen Z et al (2013) A hierarchical aspect-sentiment model for online reviews. Proceedings of the 27th AAAI conference on artificial intelligence, AAAI 2013 526–533. https://doi.org/10.1609/aaai.v27i1.8700
49. Mei Q, Ling X, Wondra M et al (2007) Topic sentiment mixture: modeling facets and opinions in weblogs. 16th international world wide web conference, WWW2007 171–180. https://doi.org/10.1145/1242572.1242596
50. Colomo-Palacios R, García-Peñalvo FJ, Stantchev V, Misra S (2017) Towards a social and context-aware mobile recommendation system for tourism. Pervasive Mob Comput 38:505–515. https://doi.org/10.1016/J.PMCJ.2016.03.001
51. Madani K, Lund JR (2012) California's Sacramento–san Joaquin Delta conflict: from cooperation to chicken. J Water Resour Plan Manag 138:90–99. https://doi.org/10.1061/(asce)wr.1943-5452.0000164
52. Madani K, Lund JR (2011) A Monte-Carlo game theoretic approach for multi-criteria decision making under uncertainty. Adv

Water Resour 34:607–616. https://doi.org/10.1016/j.advwatres.2011.02.009
53. Liu T, Deng Y, Chan F (2017) Evidential supplier selection based on DEMATEL and game theory. Int J Fuzzy Syst 20:1321–1333. https://doi.org/10.1007/S40815-017-0400-4
54. Debnath A, Bandyopadhyay A, Roy J, Kar S (2018) Game theory based multi criteria decision making problem under uncertainty: a case study on Indian tea industry. J Bus Econ Manag 19:154–175. https://doi.org/10.3846/16111699.2017.1401553
55. Hashemkhani Zolfani S, Banihashemi SSA (2014) Personnel selection based on a novel model of game theory and Mcdm approaches. https://doi.org/10.3846/bm.2014.024
56. Collins BC, Kumral M (2022) Examining impact and benefit agreements in mineral extraction using game theory and multiple-criteria decision making. Extr Ind Soc 10:101094. https://doi.org/10.1016/J.EXIS.2022.101094
57. Zhang S, Ly L, Mach N, Amaya C (2022) Topic modeling and sentiment analysis of yelp restaurant reviews. Int J Inf Syst Serv Sect 14:1–16. https://doi.org/10.4018/ijisss.295872
58. Kaden M, Hermann W, Villmann T (2014) Optimization of general statistical accuracy measures for classification based on learning vector quantization. 22nd European symposium on artificial neural networks, computational intelligence and machine learning, ESANN 2014 - proceedings 47–52
59. Khotimah DAK, Sarno R (2018) Sentiment detection of comment titles in booking.com using probabilistic latent semantic analysis
60. Billyan B, Sarno R, Sungkono KR, Tangkawarow IRHT (2019) Fuzzy k-nearest neighbor for restaurants business sentiment analysis on tripadvisor. 2019 international conference on information and communications technology, ICOIACT 2019 543–548. https://doi.org/10.1109/ICOIACT46704.2019.8938564
61. Laksono RA, Sungkono KR, Sarno R, Wahyuni CS (2019) Sentiment analysis of restaurant customer reviews on tripadvisor using naïve bayes. Proceedings of 2019 international conference on information and communication technology and systems, ICTS 2019 49–54. https://doi.org/10.1109/ICTS.2019.8850982
62. Ma Y, Xiang Z, Du Q, Fan W (2018) Effects of user-provided photos on hotel review helpfulness: an analytical approach with deep leaning. Int J Hosp Manag 71:120–131. https://doi.org/10.1016/J.IJHM.2017.12.008
63. Du C, Du C, He H (2021) Multimodal deep generative adversarial models for scalable doubly semi-supervised learning. Inf Fusion 68:118–130. https://doi.org/10.1016/j.inffus.2020.11.003
64. Zuheros C, Martínez-Cámara E, Herrera-Viedma E, Herrera F (2021) Sentiment analysis based multi-person multi-criteria decision making methodology using natural language processing and deep learning for smarter decision aid. Case study of restaurant choice using TripAdvisor reviews. Inf Fusion 68:22–36. https://doi.org/10.1016/J.INFFUS.2020.10.019
65. Afzaal M, Usman M, Fong ACM et al (2016) Fuzzy Aspect Based Opinion Classification System for Mining Tourist Reviews. Adv Fuzzy Syst 2016:1–14. https://doi.org/10.1155/2016/6965725
66. Jain G, Lobiyal DK (2022) Word sense disambiguation using cooperative game theory and fuzzy Hindi WordNet based on ConceptNet. Trans Asian Low-Resour Lang Inf Process 21:1–25. https://doi.org/10.1145/3502739
67. Roubens M (1997) Fuzzy sets and decision analysis. Fuzzy Sets Syst 90:199–206
68. Trevisiol M, Chiarandini L, Baeza-Yates R Buon Appetito-Recommending Personalized Menus *. https://doi.org/10.1145/2631775.2631784
69. Hemalatha S, Ramathmika R (2019) Sentiment analysis of yelp reviews by machine learning. 2019 international conference on intelligent computing and control systems, ICCS 2019 700–704. https://doi.org/10.1109/ICCS45141.2019.9065812
70. Govindarajan M (2014) Sentiment analysis of restaurant reviews using hybrid classification method. Chennai India ISBN:978–93
71. Nasim Z, Haider S (2017) ABSA toolkit: an open source tool for aspect based sentiment analysis. Int J Artif Intell Tools 26:1750023. https://doi.org/10.1142/S0218213017500233
72. Luo Y, Xu X (2019) Predicting the helpfulness of online restaurant reviews using different machine learning algorithms: a case study of yelp. Sustainability 11:5254. https://doi.org/10.3390/SU11195254
73. Jo Y, Oh A (2011) Aspect and sentiment unification model for online review analysis. Proceedings of the 4th ACM international conference on web search and data mining, WSDM 2011 815–824. https://doi.org/10.1145/1935826.1935932
74. Vashishtha S, Susan S (2019) Fuzzy rule based unsupervised sentiment analysis from social media posts. Expert Syst Appl 138:112834. https://doi.org/10.1016/j.eswa.2019.112834
75. Yang Y, Ma Y, Zhang J, Gao X, Xu M (2020) Attpnet: attention-based deep neural network for 3D point set analysis. Sensors (Switzerland) 20:1–20. https://doi.org/10.3390/s20195455
76. Rani R, Lobiyal DK (2020) Performance evaluation of text-mining models with Hindi stopwords lists. J King Saud Univ - Comput Inf Sci 34:2771–2786. https://doi.org/10.1016/j.jksuci.2020.03.003
77. Kardakis S, Perikos I, Grivokostopoulou F, Hatzilygeroudis I (2021) Examining attention mechanisms in deep learning models for sentiment analysis. Appl Sci 11:3883 mdpi.com. https://doi.org/10.3390/app11093883
78. Perikos I, Kardakis S, Hatzilygeroudis I (2021) Sentiment analysis using novel and interpretable architectures of hidden Markov models[formula presented]. Knowl-Based Syst 229:107332. https://doi.org/10.1016/j.knosys.2021.107332
79. Nguyen DN, Phan TT, Do P (2021) Embedding knowledge on ontology into the corpus by topic to improve the performance of deep learning methods in sentiment analysis. Sci Rep 11:23541
80. Punetha N, Jain G (2023) Bayesian game model based unsupervised sentiment analysis of product reviews. Expert Syst Appl 214:119128. https://doi.org/10.1016/j.eswa.2022.119128

Publisher's note Springer Nature remains neutral with regard to jurisdictional claims in published maps and institutional affiliations.

Springer Nature or its licensor (e.g. a society or other partner) holds exclusive rights to this article under a publishing agreement with the author(s) or other rightsholder(s); author self-archiving of the accepted manuscript version of this article is solely governed by the terms of such publishing agreement and applicable law.

Neha Punetha has been working as a research scholar under the guidance of Dr. Goonjan Jain in the Department of Applied Mathematics of Delhi Technological University (DTU) since 2020. She received her M.Sc. degree with a major in Mathematics and minor in computer science from G.B Pant university of agriculture and technology (GBPUAT) and B.Sc. from D.S.B Campus Nainital. Her research interests include Natural Language Processing, Mathematical optimization, MCDM and Game Theory.

2023 International Conference for Advancement in Technology (ICONAT)
Goa, India. Jan 24-26, 2023

High Performance CMOS Voltage Level Shifters Design for Low Voltage Applications

Ananya Kapoor, Chaitanya Shanker Jha, Ayush Thapar, Chaudhry Indra Kumar
Electrical Engineering Department, Delhi Technological University, Delhi, India
indrachaudhry@dtu.ac.in

2023 International Conference for Advancement in Technology (ICONAT) | 978-1-6654-7517-4/23/$31.00 ©2023 IEEE | DOI: 10.1109/ICONAT57137.2023.10079972

***Abstract*—To convert signals from one logic level or voltage level to another, a level shifter circuit is used in analog and digital integrated circuits (IC's). It is also known as a voltage level translator or a logic-level shifter. An integrated circuit voltage level changer allows for compatibility across integrated circuits with various voltage needs. In this work, a voltage level shifter that efficiently converts voltage from the subthreshold area to the super-threshold region while reducing propagation latency is introduced. The proposed circuit improves power efficiency and delays by employing a low voltage converter, one Pull Down and one Pull Up CMOS network. We simulate the proposed design in 45nm, 65nm, 90nm and 180nm CMOS technologies. The simulated result shows that, by employing the proposed level shifter an improvement of 69.12% in propagation delay is observed as compared to recent designs in 90nm CMOS technology. In 45nm technology our design improves the propagation delay 67.07% compared to existing designs. In corner analysis the proposed technique gives better result as compared to the recently reported techniques.**

Index Terms*— *Energy efficient Circuits, Low Power Design, Sub-threshold Level, Shifters, Voltage Level Shifter.

I. INTRODUCTION

Lowering the power supply voltage is one of the best ways to reduce the short-circuit and dynamic power consumption of digital CMOS circuits [1]-[2]. Operating circuits at lower supply voltage, has the effect of reducing signal swings and consequently makes the circuit more sensitive towards noise. Logic blocks on non-critical path receive a lower supply voltage (VDDL), while a high-speed logic blocks and moderate-speed logic blocks need a relatively higher supply voltage (VDDH) in mixed signal circuits. Level-shifting circuits are required in a system with dual supply voltages in order to transform lower to higher logic level ones and provide the proper voltage levels for the following digital blocks [3]. The level shifters (LS) must be made to have the lowest propagation delay, layout area, and power consumption possible to avoid a degradation in the circuit's overall performance. For even further power savings in low supply voltage structure, the LS used must be capable to transform the very less values of VDDL even lesser than the MOS field effect transistors threshold voltage (Vth) [4]-[5].

In recent VLSI circuits, power efficiency is a key design consideration due to the widespread use of portable electronic devices, which has laid to a lot of research into methods for power reduction. The reducing supply voltages technique is one of the most popular methods for high efficiency and low power design. It is possible to link the LV (low-voltage) circuit's output straight to the HV (high- voltage) circuit's input. In high voltage circuits, a static current is drawn from the supplied voltage source to ground and consumes a significant amount of power. By altering the voltage levels at the junction of low-to-high voltage blocks, a level shifter is used to overcome this issue. Given the issue of assertion between pull-up and pull-down transistors, level shifters have higher power consumption, longer switching times, and longer propagation delays. As a result, approaches for decreasing contention are critical for level shifters with high speeds and low power consumption [6].

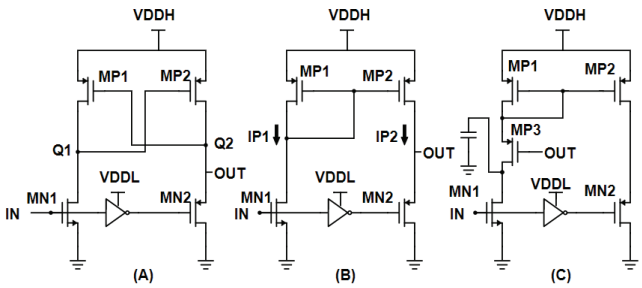


Fig. 1. Conventional level shifter designs (A) Cross-coupled LS (B) Level shifter with current mirror (C) Dynamic current mirror level shifter (Wilson current mirror)

Figure 1 depicts the typical level-shifting topologies. Fig. 1(a) shows the circuit diagram of cross coupled LS. The operation of the cross coupled design is as follows: The transistors MN1 and MN2 are ON and OFF, respectively, when the input signal IN is "High = VDDL". Consequently, the intermediate node Q1 is pulled down because MN1 transistor is in ON state. When node Q1 reaches at low logic level, as a result, transistor MP2 turns ON and the node Q2 pulled up to VDDH (High Logic level). When node Q2 reaches at high logic level, transistor MP1 turns OFF. The process switches the states when the input signal is changed to "Low = 0". From the above discussion it is observed that for nodes Q1 and Q2, there is competition between the MP1 and MP2 (pull-up devices) and MN1 and MN2 (pull-down devices) these transistors are driven by VDDH and V DDL, respectively. As a result, this circuit will cease to function when the voltage difference in VDDL and VDDH is huge, especially when the input voltage is below the VTH range. This is due to the fact that pull-down transistors have smaller drive currents than pull-up ones. There have been a number of attempts to resolve this issue in literature. Utilizing technology-based strategies, such as using weak pull-up networks with High-VTH transistors and/or strong pull-down devices with Low-VTH transistors, is

Authorized licensed use limited to: DELHI TECHNICAL UNIV. Downloaded on April 17,2023 at 06:08:19 UTC from IEEE Xplore. Restrictions apply.

one strategy. Increasing the size of the pull-down devices is another strategy, although doing so will increase the power usage and delay. The pull-down device drags the output node down, so the final choice is to weaken the pull-up device.

The circuit diagram of current mirror LS is depicted in Fig. 1 (b). The LS limits the current using a semi-static current mirror and, the output node is being dragged down by the pull down device (i.e., MP2). However, this structure has issues because when input is "High", there is a static current that flows through MN1 and MP1 transistors. In order to reduce this static power usage, a current generator that operates only during transition times is used. This concept is used in Fig. 1 (c), by using a dynamic current generator based on MP3 transistor. During the input transition from "Low" to "High", MN1 turns on but MN2 turns off. Before the transition, the output node (OUT) is at low logic level. Due to this, MP3 transistor will turn ON. Therefore, a transition current flows through MN1, MP3 and MP1 transistors. The output node (OUT) is raised because the same current is reflected in MP2 (i.e., IP2). The output node rises to VDDH to turn OFF MP3 transistor and reduces the static current flowing through MN1, MP3, and MP1 transistors. While during the transition of input signal (IN) from "High" to "Low", MN2 transistor is turned on and pulls down the OUT signal. As a result, MN1 transistor turns off. During the time node OUT is being pulled down, a transition current (i.e., IP1) charges node QB via MP1 and MP3, causing MP3 to turn on in an effort to pull up node QB, which has already been pulled down to the ground. The node OUT is being pulled down by MN2, but the current is reflected to MP2 (i.e., IP2), which tries to pull it up. This shows that there is still competition between the PUN (pull-up networks) and PDN (pull-down networks) devices during the input signal's transition from high to low, which results in a delay and raises the circuit's power consumption, particularly in the step that comes after. The purpose of this paper is to present a design for a voltage level shifter that is both power-efficient and has low transmission delay.

II. LITERATURE SURVEY

In [6], a voltage LS with current limiter in subthreshold regime (VLSCL) is presented. The circuit diagram of VLSCL is presented in Fig. 2. In the first part of VLSCL consist, an input inverter that uses low-threshold (LVT) devices to create differential fast transition low-voltage input signals (MP1 and MN1) is used as the first component. The main component of the design is the second part, which is made up of MP2-MP4 and MN2-MN4 transistors. The current mirror in this section is made up of MP2 and MP3 transistors, and the flow of current through MP3 is dependent upon the flow of current through MP2. Additionally, stacked MN2 and MN3 are connected to the current limiter, and their gates are connected to the high voltage output signal (OUTH) and low-voltage input inverted signal (INLN), respectively. According to the input and output, these two stacked devices act as a current reference, occasionally supplying the necessary current for the current mirror. In other words, the input and output indirectly control the current that the current limiter delivers. Additionally, MP4 and MN4 combine to provide a current output inverter, where the input is linked to a low-voltage input signal and the

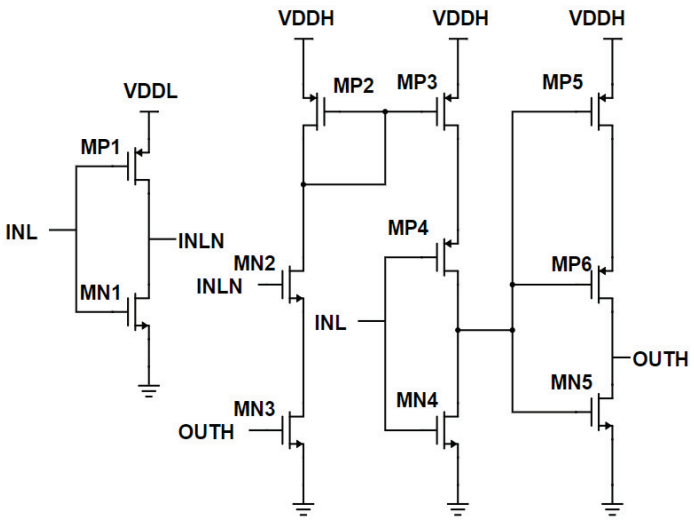


Fig. 2. Schematic for VLSCL design proposed in [6]

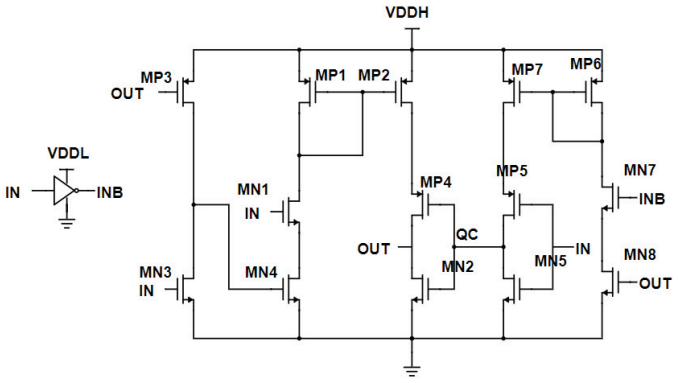


Fig. 3. Schematic for VLSDSA design proposed in [7]

switching current is provided by a current limiter (INL). The third part of VLSCL technique, which serves as an output driver, consists of the stacked PMOS transistors MP5 and MP6, as well as NMOS transistor MN5. Its input is linked to the second part's output, and one of its outputs feeds back into the second part's input. In proposed design, a cross-coupled feedback loop is used between two sub-circuits. The proposed circuit can detect the voltage on input and output to limit current.

In [7], a voltage level shifter for dual supply applications (VLSDSA) is presented. The schematic diagram of the circuit is shown in Fig. 3. When the input voltage is greater than VDDL on the gates of MN2 and MP4 transistors, the strength of the pull-down device (i.e., MN2) and the current of the pull-up device (i.e., IP2) are increased. As a result, conflict, delay, and energy are significantly reduced (particularly the energy used in the subsequent stage). Furthermore, even with input voltages below the threshold, the level shifter will still work effectively. To apply this strategy to the VLSDSA construction, an auxiliary circuit is used. This auxiliary circuit only activates during the input signal's transition from high to low in order to raise the node QC to a value greater than VDDL.

Authorized licensed use limited to: DELHI TECHNICAL UNIV. Downloaded on April 17,2023 at 06:08:19 UTC from IEEE Xplore. Restrictions apply.

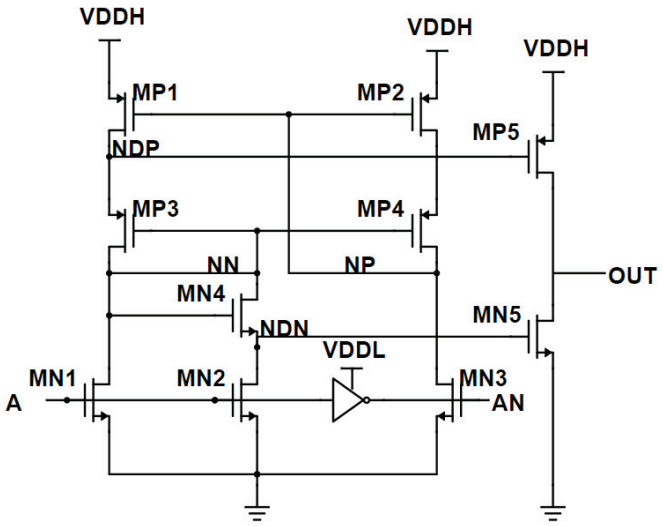


Fig. 4. Schematic for RHEVLS design proposed in [8]

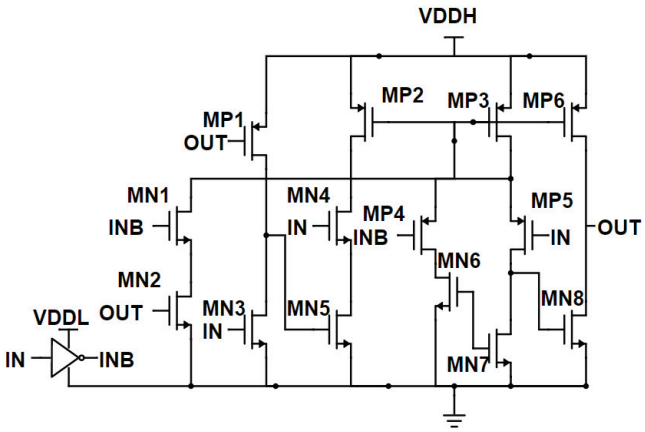


Fig. 5. Schematic for VLSLEC design proposed in [9]

A PMOS-based self-biased low-voltage cascade CM (MP1-MP4), where MP1 is biased through the diode linked MP3, is the foundation of the circuit RHEVLS presented in [8] and illustrated in Fig. 4. A split-input inverting buffer (Mn5- MP5) is also included in the circuit as the output stage to save power consumption since only one device (either PMOS or NMOS) can be turned on at a time. A PDN boosting device and an extra diode-connected NMOS device (Mn4) are used in the output stage (MPn2). As a result, the voltage difference between the NDP and NDN nodes is equal to the voltage drop (VD) of MP3 and MN4 (VD = $|VGSp3| + |VGSn4|$), which drive the output buffer of the proposed architecture. Therefore, the power consumption of the output stage during transitions is lowered for improved energy-efficiency.

The architecture of voltage LS with logic error correcting circuit (VLSLEC) proposed in [9] and shown in Figure 4, has a level converter circuit and a logic error correcting circuit. The level conversion circuit employs a comparator circuit which generates an output signal depending on the values of the IN and INB signals which are supplied to it as inputs. The error correcting circuit is composed of two parts. The first part is a low logic error correcting circuit (LLECC), composed of transistors MN1 and MN2, which is active when the OUT signal does not correspond to the low logic level of the input signal. When IN is low and OUT is high, transistors MN1 and MN2 turn ON due to the presence of high logic signals at their gate terminals and a current IF flows through them. This has the effect of turning ON the transistor MP3. Transistor MP5 is already ON due to a low signal at its gate terminal. MP3 and MP5 together pull up the gate terminal of MN8 to VDDH and thus, MN8 pulls the OUT node to ground. The second part of the error correcting circuit is a high logic error correcting circuit (HLECC) composed of transistors MP1, MN3, MN4 and MN5. This circuit is operational in the case where the OUT signal does not correspond with the high logic level of the input signal. In this case, the transistor MP1 turns ON, resulting in a high signal at the gate terminal of MN5 which subsequently becomes active. A current IR flows through MN4 and MN5 and pulls the gate terminal of MP6 to ground. This ensures that the OUT terminal is pulled up to VDDH.

Several methodologies have already been proposed to deal with the drawbacks present in conventional level shifter topologies. The designs presented in [10]-[14] employ variations on the conventional cross coupled circuit by attempting to reduce the contention between the pull-up and pull-down networks during switching. The circuits proposed in [15] and [16] modify the basic current mirror level-shifter circuit by reducing the static current dissipation, and thus, minimizing the power consumption of the circuit.

III. Proposed Design

Figure 6 shows the circuit diagram of the proposed voltage LS. Our technique has two parts: the first part of the circuit is a low voltage (LV) inverter. The low voltage inverter serves the function of providing the inverted input signal which is used in the next stage of the circuit. The second stage of the circuit implements the main level shifting functionality of the circuit with transistors MN3 and MN4 forming the pull-down network (PDN) and transistors MP4, MP5, an MP6 forming the pull-up network (PUN). The PDN and PUN are used to control the state of the output (OUT) node. The OUT signal is also sent as a feedback to the main circuit in order to regulate its functionality. The proposed circuit also ensures that at a certain point in time, either the PDN or the PUN connected to the OUT node is active but never both. Thus, the circuit possesses a significant advantage over the conventional cross coupled topology as it does not suffer from contention at the output node. The only source of static current flow is the case when the OUT and IN signal are both high, thus allowing current to flow through the transistors MP3 and MN2. Initially, the either the PDN or the PUN connected to the OUT node is active but never both. Thus, the circuit possesses a significant advantage over the conventional cross coupled topology as it does not suffer from contention at the output node. The only source of static current flow is the case when the OUT and IN signal are both high, thus allowing current to flow through the transistors MP3 and MN2. Initially, the circuit is assumed to be on standby mode with both IN and OUT in the low state while INB is in the high state. In this case, MP5 and MP6 are turned ON, ensuring that the gate terminal of MP4 is at VDDH, thus disabling it. The transistors MP1 and MP2 are also turned ON,causing MP3 to be disabled. Transistor MN2 is also OFF in this case due to the presence of a ‘0’ at its gate terminal

Authorized licensed use limited to: DELHI TECHNICAL UNIV. Downloaded on April 17,2023 at 06:08:19 UTC from IEEE Xplore. Restrictions apply.

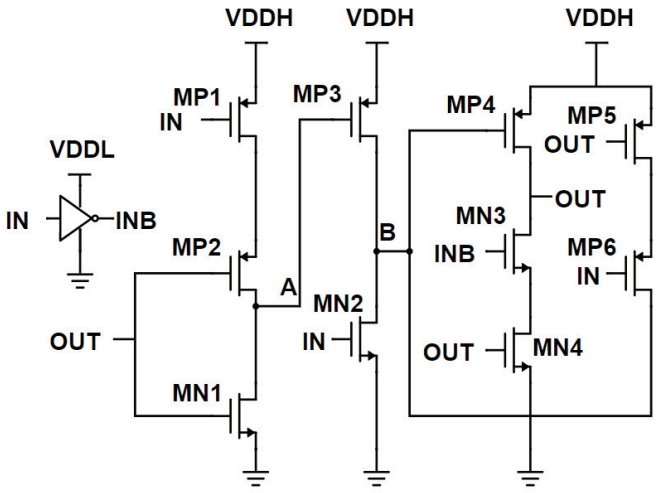


Fig. 6. Schematic diagram of the Proposed Design

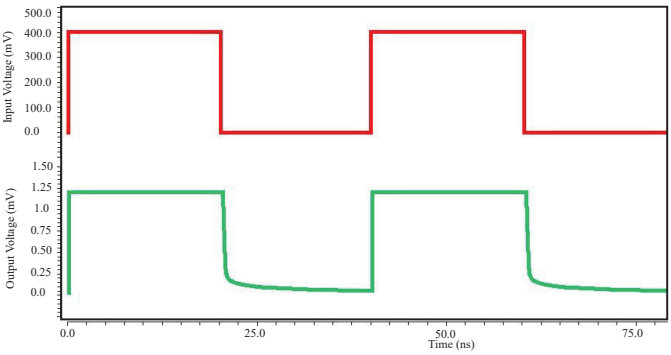


Fig. 7. Simulated Waveforms of the Proposed Design

. This causes a floating voltage at node B. This voltage, however, is not low enough to turn on MP4, ensuring that the OUT node is not wrongly pulled up to the high level. When the IN signal switches from low to high and the OUT signal is still present in the low state, node A is in the floating state but the node B is pulled down to ground by the much stronger pull down of the transistor MN2 which turns on due to the presence of a high signal at its gate terminal. This causes the gate terminal of MP4 to be pulled down, thus causing OUT to be pulled high. This serves the purpose of matching the state of the OUT signal to the state of the IN signal. When both OUT and IN are present in the high state, node A is pulled to ground, turning on MP3 in the process. Meanwhile, MN2 is also ON due to the presence of the high IN signal at its gate terminal. Since the pull-down strength of MN2 is greater than the pull-up strength of MP3, the node B remains grounded, thus ensuring that MP4 remains ON and OUT remains in the high state. When IN makes a transition from high to low and OUT is still in the high state, node A is pulled to ground and MP3 remains ON. Transistor MN2 also turns OFF as the signal at its gate terminal is at a '0' level. This ensures that there is no contention between MP3 and MN2 and a strong high signal reaches the gate terminal of MP4, completely disabling the PUN at the OUT node. Meanwhile, both transistors MN3 and MN4 turn ON due to the presence of high signals at their gate terminals. This pulls down the OUT node to ground, matching it to the state of the IN signal. In this manner, the circuit detects a mismatch between the states of the OUT and IN signals and works to ensure that the state of the OUT signal matches the state of the IN signal. The sources of leakage current in the circuit are the floating nodes A and B at certain points during the functionality of the circuit. The design is simulated at room temperature. Fig. 7 shows the corresponding output graph of the circuit.

IV. SIMULATION AND RESULTS

For circuit simulation analysis and validation purpose we have used Cadence Virtuoso tool. In Cadence simulations, we have used 45nm, 65nm, 90nm, and 180nm CMOS technologies. For validation of the proposed circuit we operate at different voltage levels (0.30V to 0.70V). The simulated waveforms at different input voltages are shown in Fig. 8.

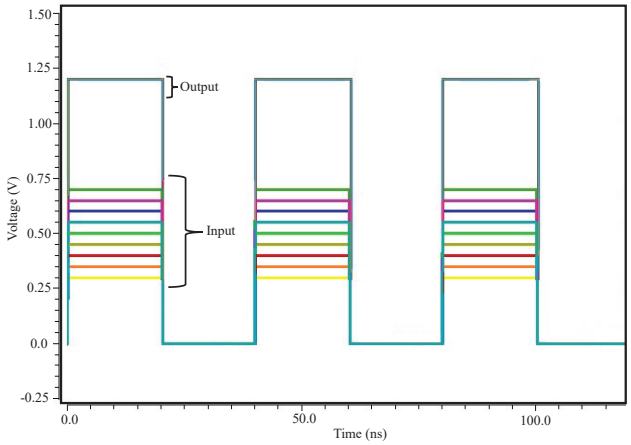


Fig. 8. Simulated Waveforms of the Proposed Design at different input voltage levels

The comparison of propagation delays and power consumption of the proposed circuit with reported circuits namely: VLSCL, VLSDSA, RHEVLS, and VLSLEC is shown in Fig. 9 and Fig. 10, respectively in 45nm, 65nm, 90nm and 180nm CMOS technologies. From Fig. 9 and Fig. 10 the proposed design shows better results as compared to VLSCL, VLSDSA, RHEVLS, and VLSLEC designs in each technology node (45nm, 65nm, 90nm and 180nm).

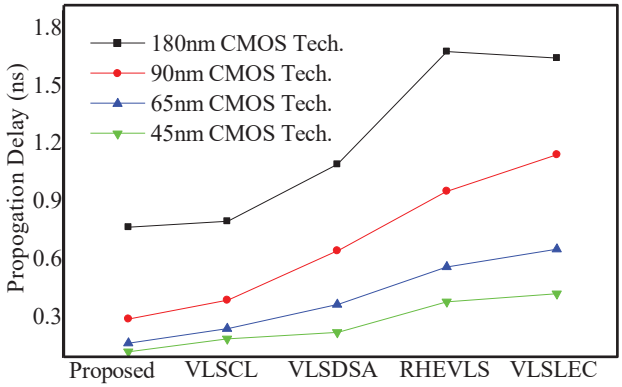


Fig. 9. Delay Comparison of various voltage level shifters at different technologies node.

Authorized licensed use limited to: DELHI TECHNICAL UNIV. Downloaded on April 17,2023 at 06:08:19 UTC from IEEE Xplore. Restrictions apply.

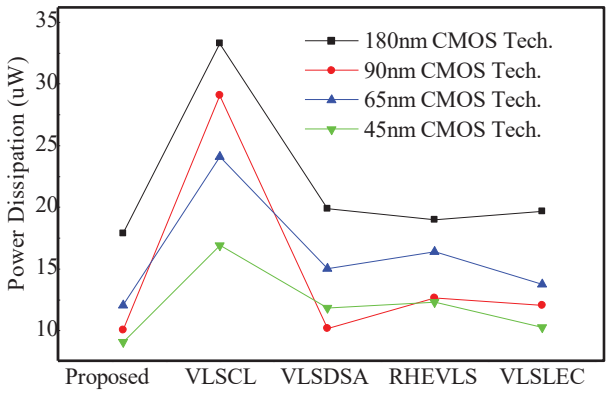


Fig. 10. Power Dissipation Comparison of various voltage level shifters at different technologies

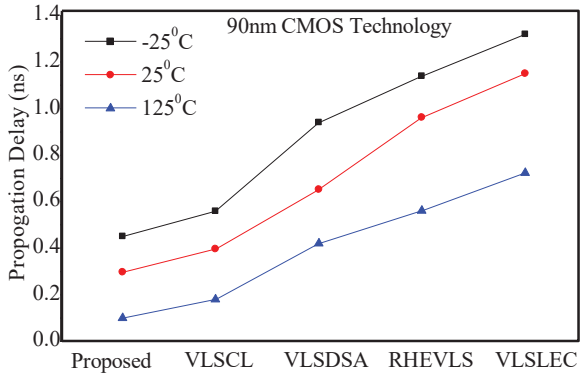


Fig. 11. Delay Comparison of various Voltage level shifters at different temperatures.

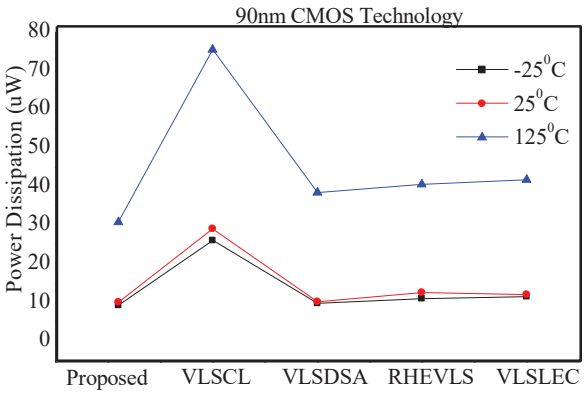


Fig. 12. Power Comparison of various Voltage level shifters at different temperatures.

Further we verify the proposed design at different temperature ranges (-250C to 1250C). The comparison of propagation delays and power consumption of the proposed circuit with VLSCL, VLSDSA, RHEVLS, and VLSLEC is shown in Fig. 11 and Fig. 12, respectively. The proposed technique shows better results as compare to VLSCL, VLSDSA, RHEVLS, and VLSLEC designs in different temperatures.

We also verify the proposed technique in different process corners namely: FF, FS, SF and SS in 90nm CMOS technology. The results of process corner analysis are shown in

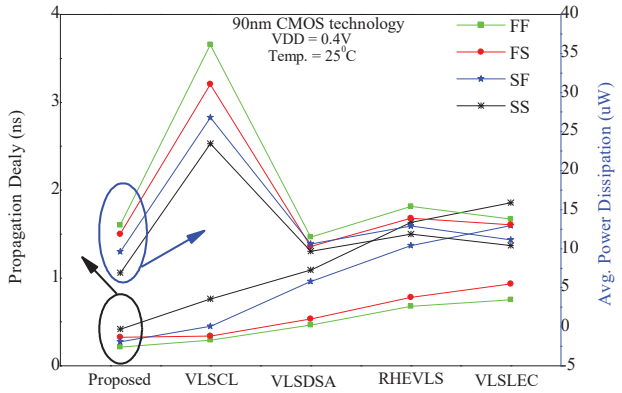


Fig. 13. Power and Delay Comparison of various voltage level shifters at different process corners.

Fig. 13. In all corners our designs show minimum delay and power dissipation.

V. CONCLUSION

In this paper, a novel design for a level shifter has been proposed which significantly reduces the delay in comparison to traditional level shifter topologies. The circuit has been simulated in the 45nm, 65nm, 90nm and 180nm technology nodes and is successful in converting a sub-threshold voltage level to a super-threshold voltage level at a frequency of 50 MHz. On conducting a comparative analysis between the various designs studied during the literature review and the design proposed in this paper, it is observed that the delay of the proposed design is 69.12% of the average delay as compared to recently reported technique in 90nm CMOS technology. The proposed level shifter is constructed with the least propagation delay, power consumption, and number of transistors possible to prevent a decline in the circuit's overall performance.

REFERENCES

[1] P. Gosatwar and U. Ghodeswar, "Design of voltage level shifter for multi-supply voltage design," 2016 International Conference on Communication and Signal Processing (ICCSP), 2016, pp. 0853-0857.

[2] M. Moghaddam, M. H. Moaiyeri and M. Eshghi, "A low-voltage level shifter based on double-gate MOSFET," 2015 18th CSI International Symposium on Computer Architecture and Digital Systems (CADS), 2015, pp. 1-5.

[3] P. K. Machiraju and D. Y. Pushpamithra, "A novel energy efficient voltage level shifter," 2014 International Conference on Science Engineering and Management Research (ICSEMR), 2014, pp. 1-4.

[4] K. Patkar and S. Akashe, "Design of level shifter for low power applications," 2016 Symposium on Colossal Data Analysis and Networking (CDAN), 2016, pp. 1-4, doi: 10.1109/CDAN.2016.7570905.

[5] Y. Moghe, T. Lehmann and T. Piessens, "Nanosecond Delay Floating High Voltage Level Shifters in a 0.35 μm HV-CMOS Technology," in IEEE Journal of Solid-State Circuits, vol. 46, no. 2, pp. 485-497, Feb. 2011, doi: 10.1109/JSSC.2010.2091322.

[6] L. Wen, X. Cheng, S. Tian, H. Wen and X. Zeng, " Subthreshold Level Shifter With Self-Controlled Current Limiter by Detecting Output Error," in IEEE Transactions on Circuits and Systems II: Express Briefs, vol. 63, no. 4, pp. 346-350, April 2016.

[7] S. R. Hosseini, M. Saberi and R. Lotfi, " A High-Speed and Power-Efficient Voltage Level Shifter for Dual-Supply Applications," in IEEE Transactions on Very Large Scale Integration (VLSI) Systems, vol. 25, no. 3, pp. 1154-1158, March 2017.

Authorized licensed use limited to: DELHI TECHNICAL UNIV. Downloaded on April 17,2023 at 06:08:19 UTC from IEEE Xplore. Restrictions apply.

[8] L. Fassio et al., ” A Robust, High-Speed and Energy-Efficient Ultralow-Voltage Level Shifter,” in IEEE Transactions on Circuits and Systems II: Express Briefs, vol. 68, no. 4, pp. 1393-1397, April 2021.

[9] Y. Osaki, T. Hirose, N. Kuroki and M. Numa, ” A Low-Power Level Shifter With Logic Error Correction for Extremely Low-Voltage Digital CMOS LSIs,” in IEEE Journal of Solid-State Circuits, vol. 47, no. 7, pp. 1776-1783, July 2012.

[10] J. Yaoyao, Z. Leiming, C. Yiwen, F. Jian and Z. Bo, ” A low power and high speed level shifter with delay circuits,” 2013 International Conference on Communications, Circuits and Systems (ICCCAS), 2013, pp. 378-381.

[11] Serneels, B., Steyaert, M. & Dehaene, W. A high speed, low voltage to high voltage level shifter in standard 1.2 V 0.13um CMOS. Analog Integr Circ Sig Process 55, 85–91 (2008).

[12] C. Q. Tran, H. Kawaguchi and T. Sakurai, ” Low-power high-speed level shifter design for block-level dynamic voltage scaling environment,” 2005 International Conference on Integrated Circuit Design and Technology, 2005. ICICDT 2005., 2005, pp. 229-232.

[13] E. Maghsoudloo, M. Rezaei, M. Sawan and B. Gosselin, ” A High-Speed and Ultra Low-Power Subthreshold Signal Level Shifter,” in IEEE Transactions on Circuits and Systems I: Regular Papers, vol. 64, no. 5, pp. 1164-1172, May 2017.

[14] S. Kabirpour and M. Jalali, ” A Power-Delay and Area Efficient Voltage Level Shifter Based on a Reflected-Output Wilson Current Mirror Level Shifter,” in IEEE Transactions on Circuits and Systems II: Express Briefs, vol. 67, no. 2, pp. 250-254, Feb. 2020.

[15] Kyoung-Hoi Koo, Jin-Ho Seo, Myeong-Lyong Ko and Jae-Whui Kim, ” A new level-up shifter for high speed and wide range interface in ultra deep sub-micron,” 2005 IEEE International Symposium on Circuits and Systems (ISCAS), 2005, pp. 1063-1065.

[16] S. R. Hosseini, M. Saberi and R. Lotfi, ” An energy-efficient level shifter for low-power applications,” 2015 IEEE International Symposium on Circuits and Systems (ISCAS), 2015, pp. 2241-2244.

Authorized licensed use limited to: DELHI TECHNICAL UNIV. Downloaded on April 17,2023 at 06:08:19 UTC from IEEE Xplore. Restrictions apply.

e-ISSN: 2582-5208
International Research Journal of Modernization in Engineering Technology and Science
(Peer-Reviewed, Open Access, Fully Refereed International Journal)
Volume:05/Issue:03/March-2023 Impact Factor- 7.868 www.irjmets.com

IMPACT AND BENEFITS OF SOFTWARE DEFINED NETWORK ON THE CLOUD NETWORK INFRASTRUCTURE

Zalmai Zormatai[*1], Samiullah Mehraban[*2], Hameed Yousof[*3], Shafiullah Shinwari[*4]

[*1]Assistant Professor, Department Of Computer Science, Bakhtar University, Afghanistan.

[*2]Phd Scholar, Department Of Computer Science And Engineering, Delhi Technological University, India.

[*3]Final Year Student, Department Of Computer Science, Bakhtar University, Afghanistan.

[*4]Dean Of Faculty, Department Of Computer Science, Bakhtar University, Afghanistan.

DOI : https://www.doi.org/10.56726/IRJMETS34738

ABSTRACT

Cloud computing is an evolutionary approach of offering IT services to the industry and IT businesses. Alongside the advantages of cloud computing, it has raised many security, performance and network management concerns in the cloud datacenters. In this study, I present the implementation of SDN (software-defined networking) into the cloud network infrastructure to overcome issues related to network administration, monitoring and security. SDN is an approach to network virtualization which adds to the security and performance of the network and helps to automate and ease the network management by making the network flexible to changes and extensions.

The research methodology used is descriptive and analytical based on the recent research work done by other researchers in this domain using a systematic literature review approach. The implementation of SDN into the cloud network infrastructure is presented as a suitable proposed solution to overcome some (network security, network performance, and network management) of the current cloud network infrastructure issues.

Keywords: SDN, Cloud Computing, Network Security.

I. INTRODUCTION

Cloud computing is considered as a new field of study for researchers and academicians, cloud computing is a revolutionary change the way IT services are provided in organizations. Cloud computing avoids the necessi Of organizations for owning on-premises data centers and network infrastructure facilities; which reduces the cost, need of IT expert staff and brings elasticity.

When plugging an electric machine into a power socket, we care neither how electric power is produced nor how it gets to that power socket. This is probable because electricity is virtualized; that is, it is already available from a wall socket that hides power generation stations and a massive power supply grid. When we think about information technologies, this idea means providing useful functions while hiding how their internals work. Computing itself, to be considered fully virtualized, must allow computers to be made from distributed components such as processing, storage, data, and software resources. Such concept describes a business model where the consumers pay to the providers based on the theory of 'Pay-as-you-go'. "Cloud computing is a techno-business disruptive model of using distributed large-scale data centers either private or public or hybrid offering customers a scalable virtualized infrastructure or an abstracted set of services qualified by service-level agreements (SLAs) and charged only by the abstracted IT resources consumed (Buyya, Broberg, & Goscinski, 2011)".

ISO/IEC defines cloud computing as follows

"Paradigm for enabling network access to a scalable and elastic pool of shareable physical or virtual resources with self-service provisioning and administration on-demand". The NIST (National Institute of Standards and Technology) definition of cloud according to the NIST Special Report 800-145 is: "Cloud computing is a model for enabling ubiquitous, convenient, on-demand network access to a shared pool of configurable computing resources (e.g., networks, servers, storage, applications, and services) that can be quickly allocated and released with slight administrative effort or service provider interaction. This cloud model is composed of five essential characteristics, three service models, and four deployment models (Mell & Grance, 2011)".

e-ISSN: 2582-5208
International Research Journal of Modernization in Engineering Technology and Science
(Peer-Reviewed, Open Access, Fully Refereed International Journal)
Volume:05/Issue:03/March-2023 Impact Factor- 7.868 www.irjmets.com

CLOUD COMPUTING ESSENTIAL CHARACTERISTICS

On demand self-service:

A client can individually deliver computing resources, such as server time and network storage, as required dynamically without demanding human interaction with each cloud service provider (CSP).

Broad Network Access:

Competencies are accessible over the public internet and accessed through standard procedures that support the use by various customer platforms (e.g., mobile phones, tablets, laptops, and workstations).

Resource pooling:

The cloud service provider's computing resources are shared to assist numerous clients using a multi-tenant architecture, with various physical and virtual resources automatically assigned and reassigned according to user request. The consumers don't have any idea about the where their data is actually stored or maybe they are only have information regarding the location of data at a higher level (for example country, province, or datacenter).

Rapid Elasticity:

Computing resources (e.g. CPU) can be elastically provided to the clients and freed from clients, in some cases dynamically, to measure rapidly outward and inward proportion with demand. To the customer, the capabilities offered for provisioning often seem to be unlimited and can be expected in any amount at any interval of time.

Measured Service:

Cloud systems dynamically govern and adjust resource use by measuring and metering competency at some level of abstraction suitable to the type of service (e.g., storage, processing, bandwidth, and active user accounts). Resource usage can be observed, controlled, and reported, providing transparency for both the cloud service provider and client of the used service.

(Mell & Grance, 2011; Mogull et al., 2017).

CLOUD SERVICE MODELS

SaaS (Software as a Service):

The services or capabilities offered to the clients are that they can utilize the applications lying on a cloud hardware infrastructure. Clients usually access the data using a simple web browser, the customers cannot manage or control the underlying infrastructure of the cloud such as (Servers, storage, Operating Systems (OS), Network & etc…)

SaaS is multitenant applications running on PaaS or IaaS due to increased agility, resilience and economic benefits. Many providers offer the SaaS services using the public APIs to support the variety of clients, especially web browsers and mobile applications. Thus, the SaaS tends to have an application/logic layers and storage layer with an API on top, and there is one presentation layer which includes the web browsers, mobile applications and public APIs (Mogull et al., 2017).

IaaS (Infrastructure as a Service):

The competencies delivered to the clients are the provisioning processing, network, storage and other computing resources where the clients are able to set up their software applications. The clients will not have control over the cloud infrastructure but they can have limited control over their own network appliances (such as the firewall). The foundation of the IaaS is formed of the physical facility and hardware infrastructure. The resources (physical hardware, network & storage) are pooled using the abstract and orchestration. Abstracts free the resources from the physical constraints using virtualization to enable pooling. Orchestration then (a set of core connectivity and delivery tools) ties these abstracted resources together to create pools and provide automation so that the resources are delivered to the customers. All these are facilitated using the APIs (Application programming interface). Most of the APIs these days use the REST (Representational State Transfer) which runs on the HTTP protocol making it very suitable for internet services. In most cases, these APIs are wrapped into a web-based interface for remote access which is called the cloud management plane (because the customers use it to manage and configure the resources). So the IaaS consists of a facility, hardware, abstract layer, and the orchestration layer.

e-ISSN: 2582-5208
International Research Journal of Modernization in Engineering Technology and Science
(Peer-Reviewed, Open Access, Fully Refereed International Journal)
Volume:05/Issue:03/March-2023 Impact Factor- 7.868 www.irjmets.com

The IaaS design is simplified in Figure-1, which shows the storage and compute controllers for orchestration and the hypervisors for abstraction and the relationship between abstract and orchestration.

"A series of physical servers each run two components: a hypervisor (for virtualization) and the management/orchestration software to tie in the servers and connect them to the compute controller. A customer asks for an instance (virtual server) of a particular size and the cloud controller determines which server has the capacity and allocates an instance of the requested size" (Mogull et al., 2017).

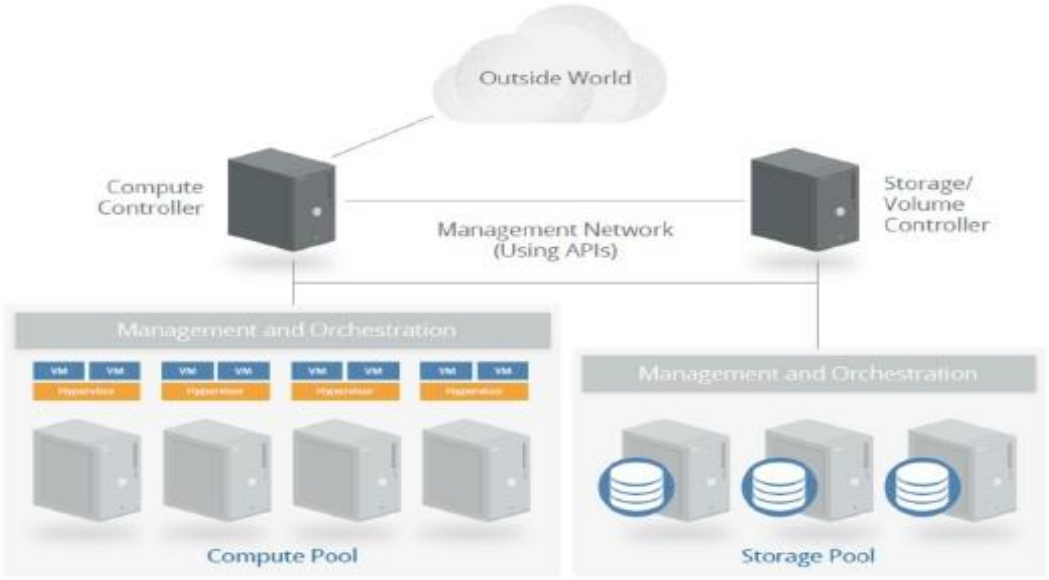


Figure 1: IaaS Platform

Image source: Guidance, S. (2017). Security Guidance for Critical Areas of Focus for Cloud Computing.

PaaS (Platform as a Service):

The competencies delivered to the consumers are the deployment of the customer's applications on the cloud infrastructure that are developed using the cloud-supported programming languages and libraries. Again, the consumers cannot control and manage the underlying cloud infrastructure.

PaaS is a layer of integration and middleware built on the IaaS. It is then pooled together, orchestrated and made available to the customers using APIs. An example of PaaS is the application deployment platform where the developers can run the application codes without managing the underlying infrastructure (Mogull et al., 2017). Figure 2 shows the simplified diagram of PaaS built on the IaaS.

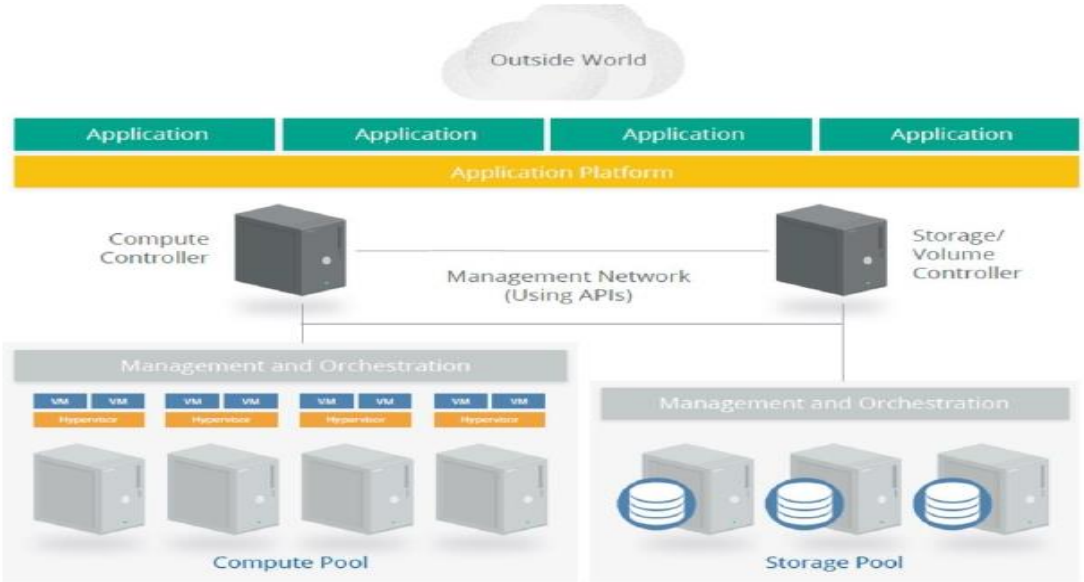


Figure 2: PaaS running on the IaaS infrastructure

e-ISSN: 2582-5208
International Research Journal of Modernization in Engineering Technology and Science
(Peer-Reviewed, Open Access, Fully Refereed International Journal)
Volume:05/Issue:03/March-2023 Impact Factor- 7.868 www.irjmets.com

Image source: Guidance, S. (2017). Security Guidance for Critical Areas of Focus for Cloud Computing.

CLOUD DEPLOYMENT MODEL

Private Cloud:

The private cloud infrastructure is owned by a single organization. The organization itself or a third party will control and manage the cloud infrastructure, it may exist on or off the premises.

Community Cloud:

The cloud infrastructure is owned, managed and controlled byone or more organizations of a community and provides services to a specificcommunity only. It may exist on or off the premises.

Public Cloud:

The public cloud provides services to everyone who is interested to use it. It is owned, managed and controlled by a business, academic or a governmental organization. The public cloud exists on the premises of the Cloud Service Provider (CSP).

Hybrid Cloud:

The public cloud provides services to everyone who is interested to use it. It is owned, managed and controlled by a business, academic or a governmental organization. The public cloud exists on the premises of the Cloud Service Provider (CSP).

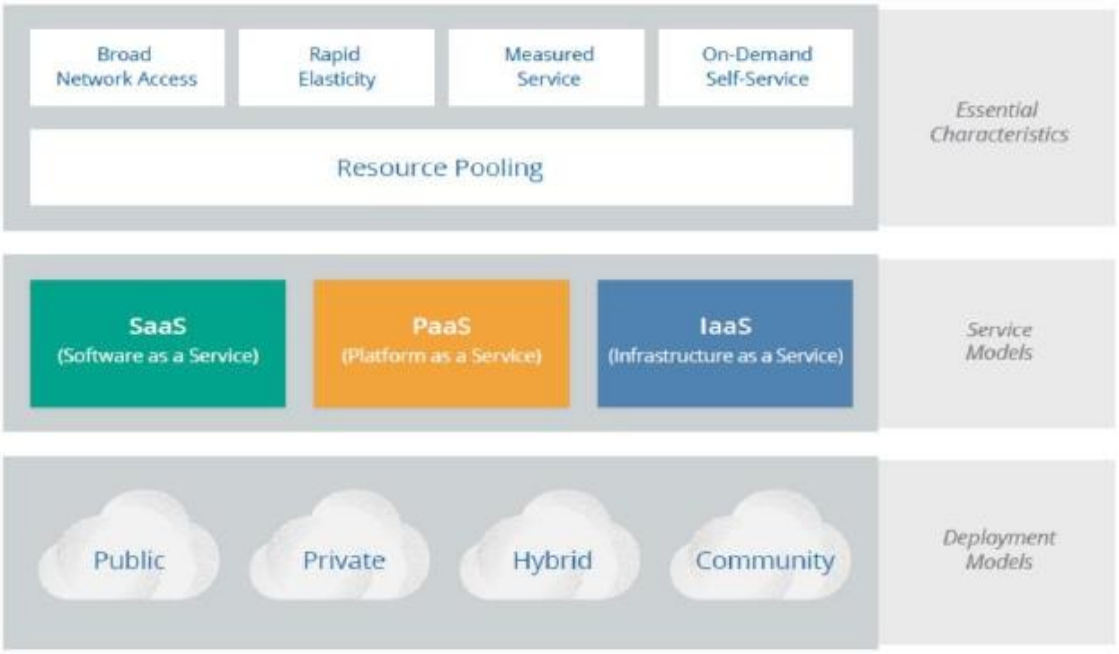


Figure 3: Cloud Deployment Model, Service Model & Characteristics

Image source: Guidance, S. (2017). Security Guidance for Critical Areas of Focus for Cloud Computing. The cloud deployment models are defined based on who owns the cloud infrastructure, who manages the cloud infrastructure, who uses the cloud services and whether the cloud infrastructure is on the premises. Figure 3 shows the cloud characteristics, cloud deployment and services models, and Figure 4 illustrates the cloud deployment models with its corresponding owner.

e-ISSN: 2582-5208
International Research Journal of Modernization in Engineering Technology and Science
(Peer-Reviewed, Open Access, Fully Refereed International Journal)
Volume:05/Issue:03/March-2023 Impact Factor- 7.868 www.irjmets.com

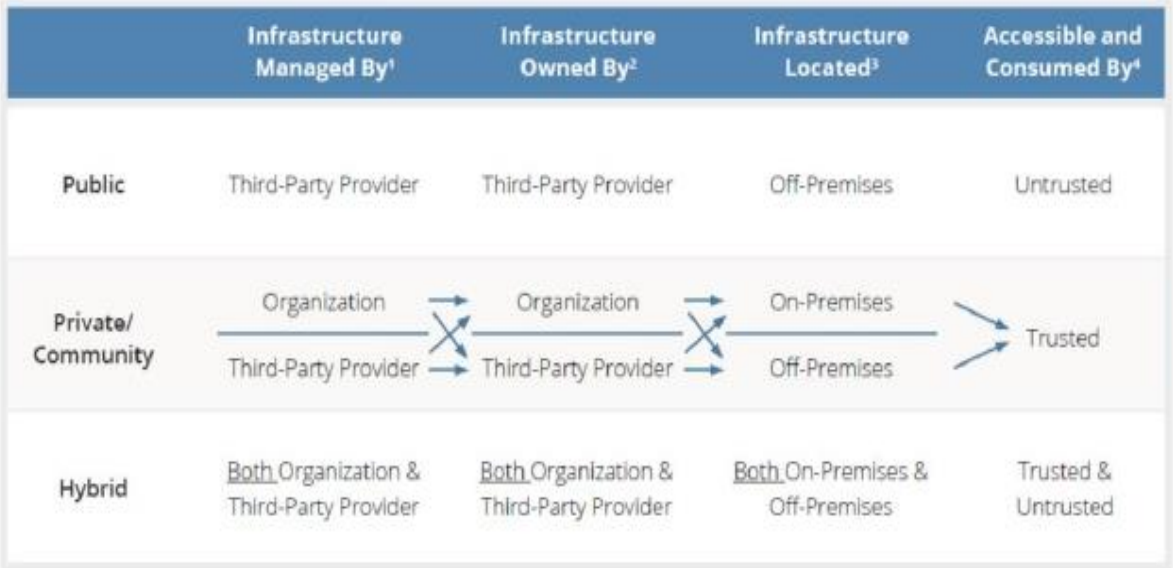


Figure 4: Cloud Deployment Model

Image source: Guidance, S. (2017). Security Guidance for Critical Areas of Focus for Cloud Computing.

II. RESULT

Cloud computing is an emerging technology which can benefit the businesses by providing on-demand IT services for the payment based on the principle of pay-as-you- go. The traditional on-premises IT infrastructure requires a well-equipped facility, purchase of hardware devices, hiring professional staff, staff training, operational and maintenance costs. Such requirements cause a huge increase in overall service cost. The lack of network security, high reliability, availability, network management, network extension, network monitoring, high network performance, traffic and network isolation, network flexibility and disaster recovery are the main problems with the on-premises network infrastructure.

To overcome these problems, an organization has to use the cloud computing and rent IT infrastructure or services from the Cloud Service Providers. Cloud offers the IT services at low cost, with high reliability and availability, high performance, on-demand services, no operational or maintenance cost, and security measure at place. With all these benefits and opportunities, the cloud computing still experience the network security, performance, and network management issues.

III. CONCLUSION

Cloud computing is vulnerable to various security threats, the main areas where the security vulnerabilities exist are the cloud network infrastructure and cloud virtualization. Cloud computing also experience the network management and network performance issues. SDN provides various opportunities to the cloud network infrastructure including packet filtering, network virtualization, traffic and network isolation, increased security, high performance, better network management, energy efficient, inexpensive, load balancing, fault tolerance and logical centralized control. The deployment of the SDN into the cloud computing can increase the cloud computing security, network performance, and network management. Based on the results of the systematic literature review, I conclude that the implementation of SDN into the cloud computing is a possible well-suited solution.

IV. REFERENCES

[1] Ahmed, M., & Ashraf Hossain, M. (2014). Cloud Computing and Security Issues in the Cloud. International Journal of Network Security & Its Applications, 6(1), 25–36. https://doi.org/10.5121/ijnsa.2014.6103

[2] Akhunzada, A., Gani, A., Anuar, N. B., Abdelaziz, A., Khan, M. K., Hayat, A., & Khan, S. U. (2016). Secure and dependable software defined networks. Journal of Network and Computer Applications. https://doi.org/10.1016/j.jnca.2015.11.012

[3] Al Morsy, M., Grundy, J., & Müller, I. (2010). An analysis of the Cloud Computing Security Problem. ResearchGate, (December), 7. https://doi.org/10.1073/pnas.97.24.13069

[4] Alsmadi, I., & Xu, D. (2015). Security of Software Defined Networks: A Survey Computers & Security. https://doi.org/10.1016/j.cose.2015.05.006

[5] An, N., Detection, I. I., Aleroud, A., & Alsmadi, I. (2016). Identifying Cyber-Attacks on Software Defined Networks : An Inference-based Intrusion Detection Approach. Journal of Network and Computer Applications. https://doi.org/10.1016/j.jnca.2016.12.024

[6] Annapoorani, S., Srinivasan, B., & Mylavathi, G. A. (2018). Analysis of various virtual machine attacks in cloud computing. In Proceedings of the 2nd International Conference on Inventive Systems and Control, ICISC 2018 (pp. 1016– 1019). IEEE. https://doi.org/10.1109/ICISC.2018.8398955

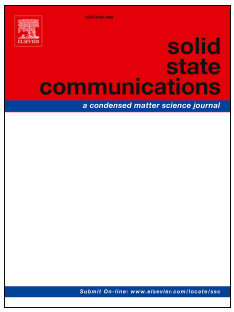
[7] Ashalatha, R., Agarkhed, J., & Patil, S. (2017). Network Virtualization System for Security in Cloud Computing, 346–350.

[8] Azodolmolky, S., Wieder, P., & Yahyapour, R. (2013). SDN-based cloud computing networking. International Conference on Transparent Optical Networks, 1–4. https://doi.org/10.1109/ICTON.2013.6602678

[9] Bakshi, K. (2013). Considerations for Software Defined Networking (SDN): Approaches and use cases. In IEEE Aerospace Conference Proceedings (pp. 1–9). https://doi.org/10.1109/AERO.2013.6496914

[10] Behl, A. (2011). Emerging security challenges in cloud computing: An insight to cloud security challenges and their mitigation. In Proceedings of the 2011 World Congress on Information and Communication Technologies, WICT 2011 (pp. 217–222). https://doi.org/10.1109/WICT.2011.6141247

Journal Pre-proof



Impact of impurity on the non-linear and linear optical properties of $In_xGa_{1-x}As$ quantum dot

Priyanka, Rinku Sharma

PII: S0038-1098(23)00092-3

DOI: https://doi.org/10.1016/j.ssc.2023.115155

Reference: SSC 115155

To appear in: *Solid State Communications*

Received Date: 1 March 2023

Accepted Date: 28 March 2023

Please cite this article as: Priyanka, R. Sharma, Impact of impurity on the non-linear and linear optical properties of $In_xGa_{1-x}As$ quantum dot, *Solid State Communications* (2023), doi: https://doi.org/10.1016/j.ssc.2023.115155.

This is a PDF file of an article that has undergone enhancements after acceptance, such as the addition of a cover page and metadata, and formatting for readability, but it is not yet the definitive version of record. This version will undergo additional copyediting, typesetting and review before it is published in its final form, but we are providing this version to give early visibility of the article. Please note that, during the production process, errors may be discovered which could affect the content, and all legal disclaimers that apply to the journal pertain.

© 2023 Published by Elsevier Ltd.

Journal Pre-proof

Impact of impurity on the non-linear and linear optical properties of $In_xGa_{1-x}As$ Quantum Dot.

Priyanka[1], and Rinku Sharma[1,*]

[1]Department of Applied Physics, Delhi Technological University, Delhi-110042, India

*Email-rinkusharma@dtu.ac.in

Abstract

In the current investigation, we emphasise the optical properties of the $In_xGa_{1-x}As$ quantum dot. In this esteem, we first estimate the energy levels and wavefunctions in the existence of impurity. Then, we focus on the impact of impurity on the absorption coefficients, refractive index changes, and third harmonic generation. It is found that the absorption coefficients, refractive index changes, and third harmonic generation peaks start to shift from their position with the decrement in the magnitude as the concentration of impurity enhances. As a consequence, it is cognizance that the concentration of impurity has a crucial role in the nanostructure optical properties.

Keywords

Rashba spin-orbit coupling (RSOC), quantum dot, third harmonic generation and absorption coefficients.

Introduction

The impact of hydrogenic impurity on the physical, non-linear optical and transport properties of the low-dimensional semiconductor act as a major part in the demonstration of semiconductor physics on the account of the presence of impurity magnifying amend the performance of nanodevices [1,2]. In recent years, the hydrogenic impurity states in low-dimensional semiconductors, viz. quantum dots, quantum wire and quantum well have been explored widely [3,4]. This investigation exposed that the optical properties and physical properties within the presence of hydrogenic impurity can be directly controlled by selecting the appropriate sizes, geometries, doping positions and materials. The inter-subband optical absorptions of low-dimensional semiconductors have engrossed vast interest in current years. The study indicates that the inter-subband optical absorptions (OAs) have large optical nonlinearity in nanodevices. Both the linear and nonlinear inter-subband OAs can be exploited for realistic applications in high-speed electro-optical devices and photodetectors.

Furthermore, externally applied perturbations like electric, and magnetic fields and Rashba spin-orbit coupling (RSOC) are competent tools for scrutinising properties under the influence of impurity in low-dimensional semiconductors [5–7]. Whereas, the hydrogenic impurity, externally applied field and RSOC affects the optical properties of quantum dots have a great amount of interest for device applications and fundamental physics [8–12].

The impurity present in the semiconductor modifies the feast of the wave function, especially in strong spatial confinement. The external field and RSOC in the low-dimensional semiconductor break the symmetry of the system. As is well known, the RSOC and its consequence on the non-linear and linear optical properties of the quantum dot have sustained and persisted in the last decade. The RSOC arise due to structural inversion symmetry [13–15]. The strength of the RSOC depends on the external field and the characteristics of the material. In the realistic problem of optical properties of quantum dots, RSOC plays a vital role on account of their potential applications in quantum computers [16–18]. It is esteemed the spin of electrons plays a significant role in the spin phenomena namely spin relaxation, spintronics and quantum computer [19,20]. During the last eras, much research has investigated the optical properties and electronic of low-dimensional semiconductors under the presence of RSOC theoretically and experimentally [21–28].

Linear and nonlinear optical phenomena in semiconductors become enormously significant to design the photonic and electronic nanodevices applications like high-speed electro-optical modulators, laser amplifiers and so on [29]. As a result, much theoretical research has been done to recognize the exploitation of optical properties with different concentrations of impurity. However, the linear and nonlinear absorption coefficient (ACs), refractive index changes (RICs), and third harmonic generation (THG) are the most important property among optical properties of quantum dots[30–32]. Liu et al. focus on the cylindrical core-shell nanostructure's THG non-linear susceptibility under the existence electric field [33]. The electric field and hydrogenic impurity influence on the optical properties of the 3D quantum dots are studied by E. Sadeghi [34]. Linear and non-linear optical ACs and RICs based on the inter-subband optical transition of the quantum dots are also calculated in [35,36].

In this work, our purpose is to study the impact of impurity on the ACs, RICs and THG of the quantum dot underneath the influence of externally applied field and RSOC by numerical cal culations. For this persistence, we find the wavefunctions and energy levels in the effective m ass approximation numerically via the density matrix approach. The pattern of this paper is

followed as: In Section 2, the calculation for energy eigenvalues and wave functions through the density matrix approach. In section 3, the result and discussion about $In_xGa_{1-x}As$ quantum dot are mentioned. In the end, we represent the conclusion part in section 4.

Theory

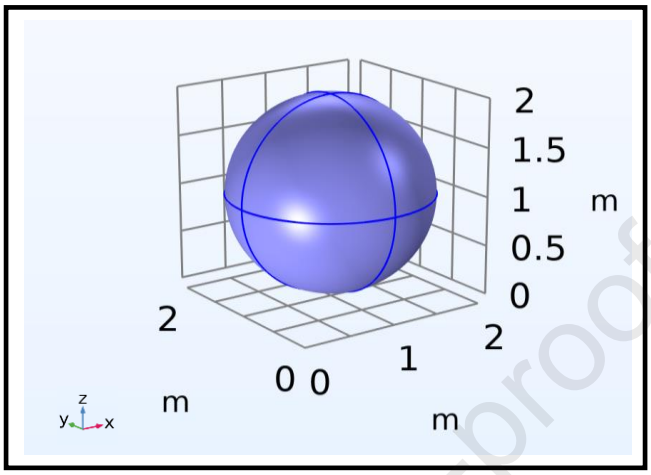


Figure 1. $In_xGa_{1-x}As$ quantum dot systematic diagram.

Consider the $In_xGa_{1-x}As$ quantum dot (seen in fig. 1) with parabolic confinement potential under the presence of magnetic field along z-axis B = (0,0,B), therefore the symmetric gauge comes out to be A = (-y/2,x/2,0). The Hamiltonian for single electron mass is given by

$$H_i(\mathrm{r}) = \frac{1}{2m_e(x,P,T)}(\boldsymbol{p} + e\boldsymbol{A})^2 + \frac{1}{2}m_e(x,P,T)\omega_o(x^2+y^2) + \frac{1}{2}g^*\mu_B B\sigma_i \quad (1)$$

Here, p and A are the momentum and vector potential, ω_o is known as oscillator frequency, $g^*$is the Lande factor and σ_i is the Pauli spin matrix. $m_e(x,P,T)$ is the effective mass for $In_xGa_{1-x}As$ quantum dot expressed as [37,38]

$$m_e(x,P,T) = \mathrm{m_o}\left[7.51\left(\frac{1}{0.341+\mathrm{E_g}^i(x,\mathrm{P,T})} + \frac{2}{\mathrm{E_g}^i(x,\mathrm{P,T})}\right) + 1\right]^{-1}, \quad (2)$$

$\mathrm{m_o}$ is called free electron mass. $\mathrm{E_g}^i$ is the energy bandgap for the $In_xGa_{1-x}As$ given by

$$\mathrm{E_g}^i(x,\mathrm{P,T}) = \mathrm{E_g}^{GaAs}(P,T) + \left[\mathrm{E_g}^{InAs}(P,T) - \mathrm{E_g}^{GaAs}(P,T)\right]x - 0.475x(1-x) \quad (3)$$

Where $\mathrm{E_g}^{GaAs}(P,T) = qP - \frac{rT^2}{T+s} + \mathrm{E_g}^0$,

and $\mathrm{E_g}^{InAs}(P,T) = aP - \frac{bT^2}{T+c} + \mathrm{E_{gi}}^0$.

The parameters values: $E_g{}^0$ = 1.52 eV (named as energy gap at P = 0 kbar and T = 0 K), q = 1.08×10^{-2} eV/kbar, r = 50.4×10^{-5} eV/K, and s = 204 K are the pressure coefficient and temperature coefficients, respectively for GaAs semiconductors. And $E_{gi}{}^0$ = 0.42 eV (named as energy gap at P = 0 kbar and T = 0 K), a = 7.7×10^{-3} eV/kbar, b = 41.9×10^{-5} eV/K and c = 271 K are the pressure coefficient and temperature coefficients, respectively for InAs semiconductors.

When the RSOC is introduced in the system the total Hamiltonian becomes

$$H_T = \frac{p^2}{2m_e(x,P,T)} + \frac{e}{m_e(x,P,T)}\boldsymbol{A}.\boldsymbol{p} + \frac{e^2A^2}{2m_e(x,P,T)} + +\frac{1}{2}m_e(x,P,T)\omega_o(x^2+y^2) + \frac{1}{2}g^*\mu_B B\sigma_i + \frac{\alpha}{\hbar}[\sigma\times\boldsymbol{p}]_z + \frac{e\alpha}{\hbar}[\sigma\times\boldsymbol{A}]_z \quad (4)$$

The last two terms in eq. (4) corresponds to RSOC. In which α is known as the Rashba constant and σ is the electron spin. Moreover, the energy wave function and eigen energies correspond to eq. (4) are

$$\varphi_{nl\sigma} = \frac{1}{\sqrt{2\pi}}e^{il\varphi}R_{nl}(r)\chi_\sigma \quad (5)$$

and

$$E^T_{nl\sigma} = (2n+|l|+1)\hbar\Theta^2_\sigma + \frac{\hbar}{2}l\omega_c + \sigma\left(\frac{1}{2}g^*\mu_B B + l\alpha m_e(x,P,T)\omega_o^2\right) \quad (6)$$

Where $R_{nl}(r) = \frac{\sqrt{2}}{a}\sqrt{\frac{n!}{(n+|l|)!}}exp\left(-\frac{r^2}{2a^2}\right)\left(\frac{r^2}{a^2}\right)^{|l|/2}L_n^{|l|}\left(\frac{r^2}{a^2}\right)$, n = 0,1,2,…, and l = 0,±1, ±2,… . a is the bohr radius ($a = \left(\frac{\hbar}{m_e(x,P,T)\omega_o}\right)^{1/2}$), and $\Theta^2_\sigma = \omega_o^2 + \frac{\omega_c^2}{4} + \frac{\sigma\alpha m_e(x,P,T)\omega_o^2\omega_c}{\hbar}$ with $\omega_c = \frac{eB}{m_e(x,P,T)}$ called cyclotron frequency. χ_σ is called the spinor function.

For the scheming of optical properties of the $In_xGa_{1-x}As$ quantum dot, the perturbation expansion and density matrix approach are used. The expression for the linear, nonlinear and total ACs are written as [39]

$$\alpha^{(1)}(\omega) = \omega\sqrt{\frac{\rho}{\rho_r}}\frac{\sigma_s\Gamma_{if}|M_{if}|^2}{\hbar\left\{(\omega_{fi}-\omega)^2+\Gamma_{if}{}^2\right\}}, \quad (7)$$

And

$$\alpha^{(3)}(\omega,I) = -\hbar\omega\sqrt{\frac{\rho}{\rho_r}}\frac{I}{2\epsilon_o n_r c}\times\frac{4\sigma_s\Gamma_{if}|M_{if}|^2}{\hbar^4\left\{(\omega_{fi}-\omega)^2+\Gamma_{if}{}^2\right\}}\times$$

$$\left[\frac{|M_{if}|^2}{(\omega_{fi}-\omega)^2+\Gamma_{if}{}^2}+\frac{(M_{ff}-M_{ii})^2(3\omega_{fi}{}^2-4\omega_{fi}\omega)(\omega_{fi}^2-\Gamma_{if}^2)}{4(\omega_{fi}^2+\Gamma_{if}^2)\{(\omega_{fi}-\omega)^2+\Gamma_{if}{}^2\}}\right] \quad (8)$$

The parameters used in Eq. (7) and (8), ρ is known as permeability, ρ_r is the real part of permittivity and $\hbar\omega$ is the incident photon energy. I, σ_s and n_r are the intensity of incident light, carrier density and refractive index of the $In_xGa_{1-x}As$ quantum dot, respectively. Γ_{if} and ω_{if} named as relaxation time and transition frequency. $M_{if} = |\langle\varphi_i|r|\varphi_f\rangle|$ known as the transition matrix element. The total ACs are given by

$$\alpha_T(\omega, I) = \alpha^{(1)}(\omega) + \alpha^{(3)}(\omega, I). \quad (9)$$

The linear and non-linear RICs for the optical transition are written as [40]

$$\frac{\Delta n_r^{(1)}}{n_r} = \frac{\sigma_s}{2n_r^2\epsilon_o}\frac{|M_{if}|^2(\omega_{fi}-\omega)}{\hbar\{(\omega_{fi}-\omega)^2+\Gamma_{if}{}^2\}}, \quad (10)$$

$$\frac{\Delta n_r^{(3)}(\omega,I)}{n_r} = -\frac{\sigma_s}{2n_r{}^3\epsilon_o}\frac{I\rho c|M_{if}|^2(\omega_{fi}-\omega)}{\hbar^3(\omega_{fi}-\omega)^2+\Gamma_{if}^2}\times$$

$$\left[\frac{|M_{if}|^2}{(\omega_{fi}-\omega)^2+\Gamma_{if}^2}+\frac{2\Gamma_{if}(M_{ff}-M_{ii})}{(\omega_{fi}-\omega)^2+\Gamma_{if}^2}\times\{(\omega_{fi}-\omega)[\omega_{fi}(\omega_{fi}-\omega)+\Gamma_{if}^2]-\Gamma_{if}^2(2\omega_{fi}-\omega)\}\right] \quad (11)$$

The total RICs represented as

$$\frac{\Delta n_r(\omega,I)}{n_r} = \frac{\Delta n_r^{(1)}}{n_r} + \frac{\Delta n_r^{(3)}(\omega,I)}{n_r}. \quad (12)$$

For the oscillation with 4ω, we consider a third-order contribution. Therefore, the THG per unit volume is obtained with the help of the density matrix approach, and written as [41]

$$\chi_{3\omega}{}^{(3)} = -\frac{q^4\vartheta}{\varepsilon_o\hbar^3}\frac{M_{12}M_{23}M_{34}M_{41}}{(\omega-\omega_{21}+i\Gamma_{21})(2\omega-\omega_{31}+i\Gamma_{31})(3\omega-\omega_{41}+i\Gamma_{41})}. \quad (13)$$

Here, q and ϑ are known as the charge on an electron and electron density, respectively.

In the result section, the behaviour of the ACs, RICs and THG are studied.

Result

In this work, the impact of the hydrogenic impurity (x) on the ACs, RICs and THG of the $In_xGa_{1-x}As$ quantum dot under the influence of RSOC are examined. The constraints used in this paper are: $\vartheta = 10^{16}cm^{-3}$, $n_r = 3.2$, $\Gamma_{12} = 1/T_{12}$ where $T_{12} = 0.14ps$ and $\rho = 4\pi\times10^{-7}Hm^{-1}$.

The linear, non-linear and total ACs of the $In_xGa_{1-x}As$ quantum dot with the different concentrations of the hydrogenic impurity (x = 0, 0.1, 0.2 and 0.3) are shown in Fig. 2(a-c), respectively. As it is easily noticeable that the position and magnitude of the peaks depend on the concentration of x. In such a way, the increase in the value of x the position of peaks towards a higher value of incident energies (blue shift) and the magnitude of peaks decreases. The blue shifting occurs as a consequence of an increment in the energy difference between the successive levels of the energy with the concentration of impurity. Moreover, the impurity (x) influences the total AC firmly as compared to the linear AC causing the erratic shape in the total AC. The magnitude decreases with the increment in the impurity happens on account of the small value of the dipole matrix element (M_{ij}). The linear and non-linear ACs depend on the $M_{12}^2 E_{12}$ and $M_{12}^4 E_{12}$, respectively present in the eqs. (7) and (8). As the M_{12} is dominant the magnitude of the non-linear peak becomes larger than linear AC. It is obvious the linear, non-linear and total ACs peaks decrease and move towards higher energies as impurity increases.

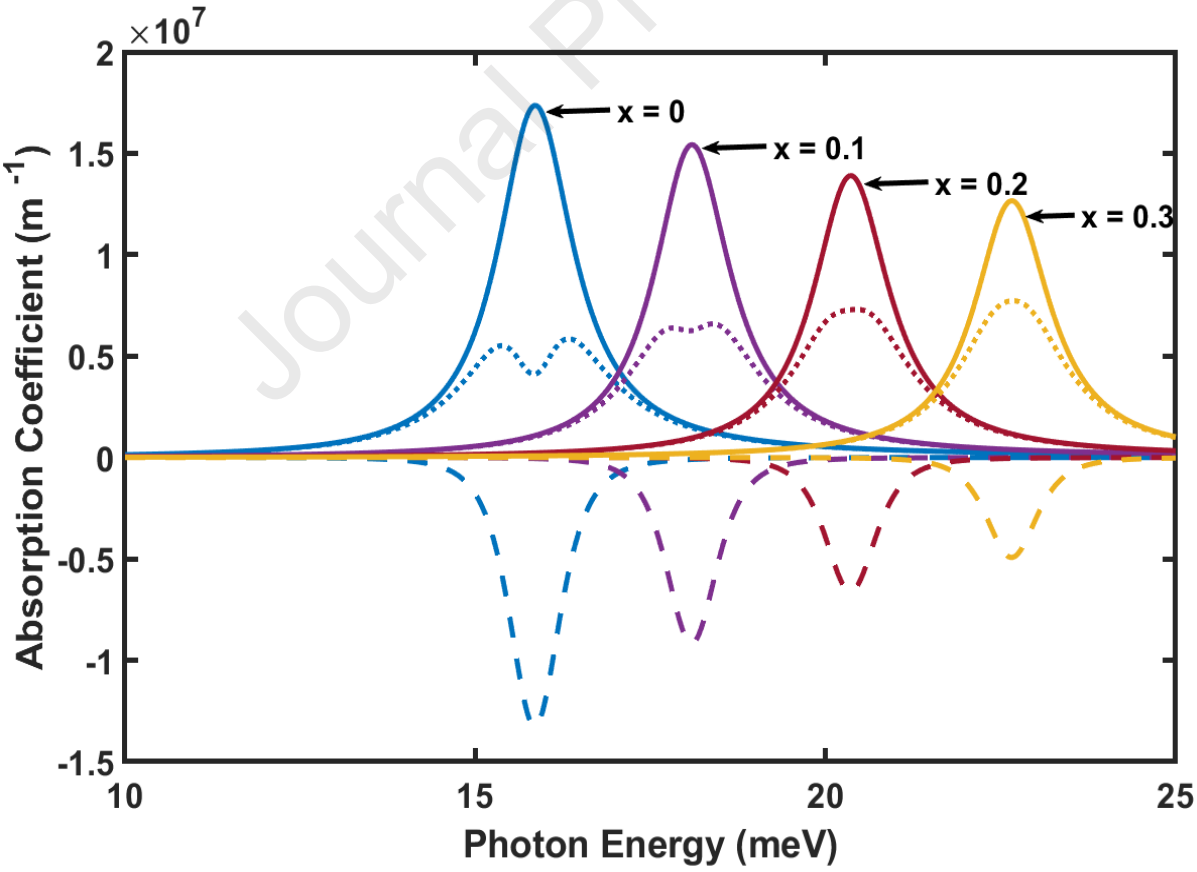


Figure 2. Change of (a) linear, (b) non-linear, and (c) total ACs with the incident photon energy for x=0, 0.1, 0.2 and 0.3.

Fig. 3(a-c) represents the varation in the linear, non-linear and total RICs with the incident energy under the influence of impurity (x=0, 0.1, 0.2 and 0.3). From the figure, the linear RIC start to rise with the incident photon energy and attains the maximum point which is called normal dispersion reason. Whenever the incident photon energy avenue the threshold energy, the sign of the $dn/d\omega$ vary and the anomalous dispersion occurs in the resonant frequency of the $In_xGa_{1-x}As$ quantum dot. With the concentration of the hydrogenic impurity, the resonant frequency moves towards a higher frequency (blue shift) with a decrement in the magnitude of the peaks. The nonlinear RIC eq.(11) contains a negative sign whereas the linear RIC eq. (10) have positive signs hence the total RIC is reduced by it. Thereby, the non-linear must be used for the high optical intensity devices.

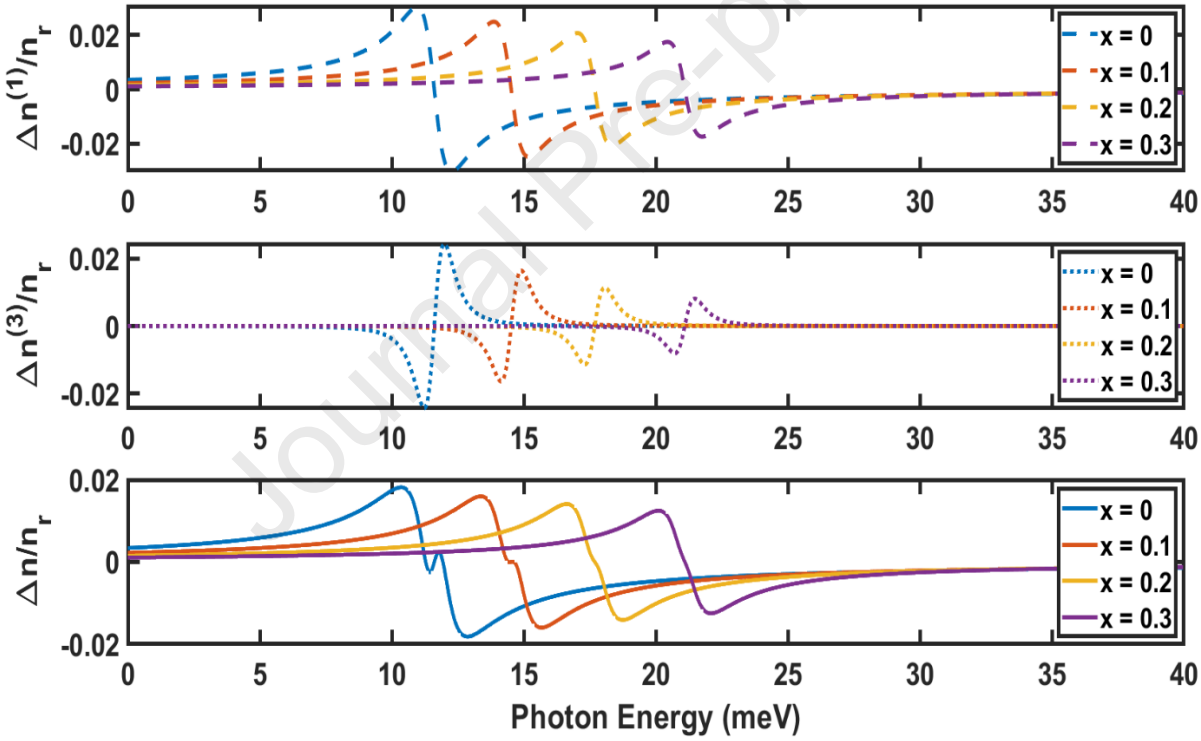


Figure 3. Change of (a) linear, (b) non-linear, and (c) total RICs with the incident photon energy for x=0, 0.1, 0.2 and 0.3.

In Fig. 4, the change in the THG with the photon energies under the impact of impurity (x=0, 0.1, 0.2 and 0.3). With the concentration of the impurity (x), the peaks of the THG shift towards a high value of energies and indicate blue shifting. THG peak magnitude decreases with the increment in impurity as a consequence of matrix elements product. However, the gap between

the two states becomes large when we introduce impurity into our system. Therefore, the THG peak reduces its magnitude and shifts towards higher photon energies as the impurity increases. Fig. 5 shows the Bohr radius variation with different hydrogenic impurity factors for different values of pressure and temperature. It is observed that the Bohr radius decreases with increases in impurity due to mass dependence on the impurity factor. Whenever the pressure rises Bohr radius starts to decrease with the smaller value and vice versa for temperature rises as seen in fig. 5 (a) and (b).

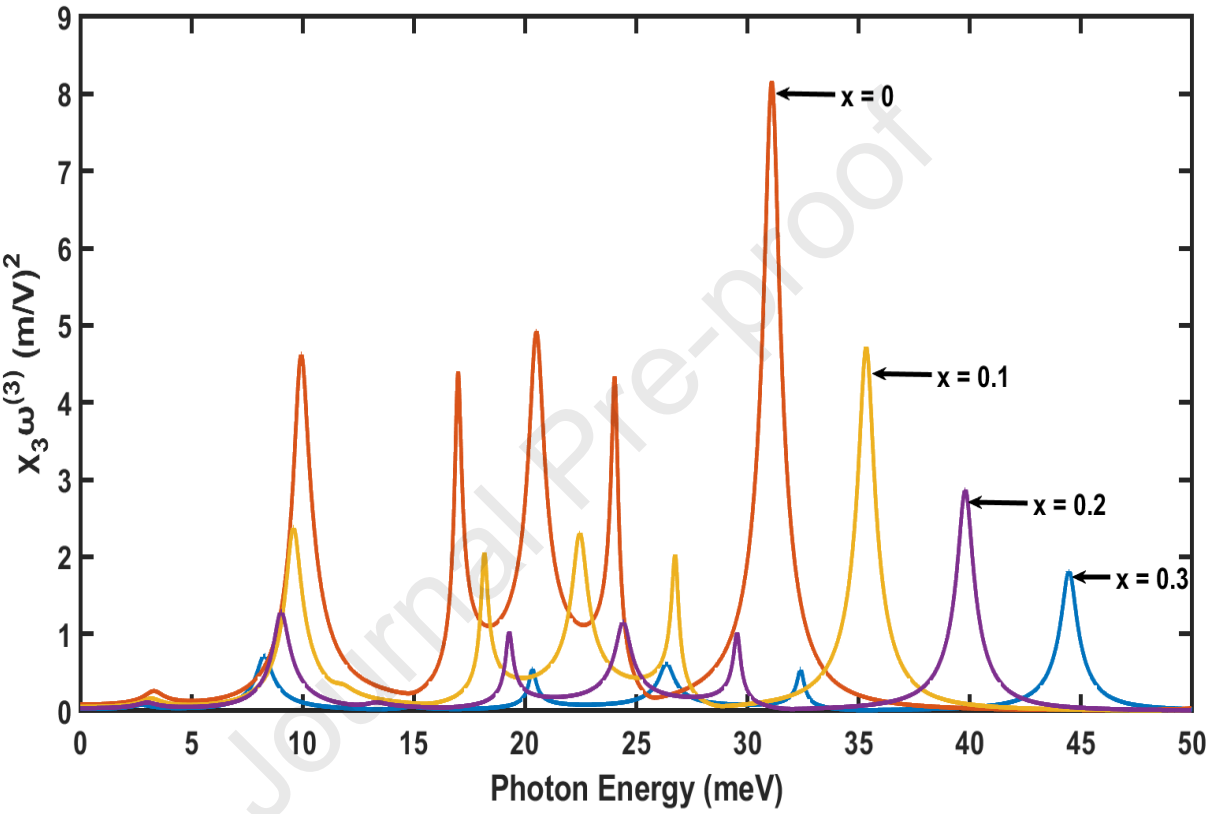
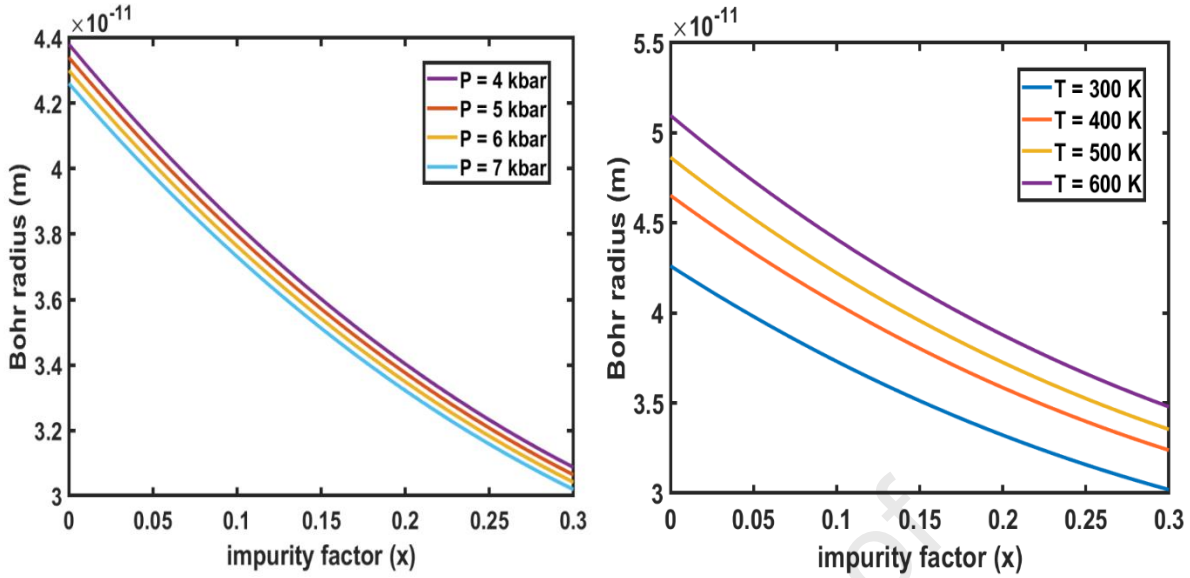


Figure 4. Change of THG with the incident photon energy for x=0, 0.1, 0.2 and 0.3.



(a) (b)

Figure 5. Bohr radius variation with the impurity at a different range of (a) pressure and (b) temperature.

Conclusion

In this paper, the influence of hydrogenic impurity on the linear and non-linear optical properties of $In_xGa_{1-x}As$ quantum dot under the presence of an external applied field are demonstrated. It is observed that the dipole matrix elements and the transition energy both are strongly affected by the presence of impurities. Similarly, effects are shown in the case of RICs and THG. Hydrogenic impurity factor (x) inceases the energy gap between two states as a result, the peaks of ACs, RICs and THG shift towards higher incident energies. Whereas, impurity decreases the dipole matrix elements due to which the magnitude of the ACs, RICs and THG peaks decreases. Therefore, it was found that the impurity value caused the blue shifts and decrease in the peaks of linear and non-linear optical properties.

Acknowledgement

Priyanka would like to acknowledge University Grants Commission (UGC) for the financial support. R. Sharma is grateful to Delhi Technological University (DTU) for the research facilities.

References

Journal Pre-proof

[1] L. Jiang, H. Wang, H. Wu, Q. Gong, S. Feng, External electric field effect on the hydrogenic donor impurity in zinc-blende GaN/AlGaN cylindrical quantum dot, J Appl Phys. 105 (2009). https://doi.org/10.1063/1.3080175.

[2] S.S. Li, J.B. Xia, Electronic structure and binding energy of a hydrogenic impurity in a hierarchically self-assembled GaAs Alx Ga1-x As quantum dot, J Appl Phys. 100 (2006). https://doi.org/10.1063/1.2358406.

[3] G. Rezaei, S. Shojaeian Kish, Linear and nonlinear optical properties of a hydrogenic impurity confined in a two-dimensional quantum dot: Effects of hydrostatic pressure, external electric and magnetic fields, Superlattices Microstruct. 53 (2013) 99–112. https://doi.org/10.1016/j.spmi.2012.09.014.

[4] E. Kasapoglu, H. Sari, I. Sökmen, Binding energy of impurity states in an inverse parabolic quantum well under magnetic field, Physica B Condens Matter. 390 (2007) 216–219. https://doi.org/10.1016/j.physb.2006.08.016.

[5] F.K. Boz, S. Aktas, Magnetic field effect on the binding energy of a hydrogenic impurity in coaxial GaAs/ AlxGa1-xAs quantum well wires, Superlattices Microstruct. 37 (2005) 281–291. https://doi.org/10.1016/j.spmi.2005.01.004.

[6] C.A. Duque, A. Montes, A.L. Morales, Binding energy and polarizability in GaAs-(Ga,Al)As quantum-well wires, 2001.

[7] E. Niculescu, A. Gearba, G. Cone, C. Negutu, Magnetic field dependence of the binding energy of shallow donors in GaAs quantum-well wires, Superlattices Microstruct. 29 (2001) 319–328. https://doi.org/10.1006/spmi.2000.0895.

[8] yu X. li, J.J. Liu, X.J. Kong, The effect of a spatially dependent effective mass on hydrogenic impurity binding energy in a finite parabolic quantum well with a magnetic field, J Appl Phys. 88 (2000) 2588–2592. https://doi.org/10.1063/1.1286244.

[9] Y.J. Wang, Y.A. Leem, B.D. McCombe, X.G. Wu, F.M. Peeters, E.D. Jones, J.R. Reno, X.Y. Lee, H.W. Jiang, Strong three-level resonant magnetopolaron effect due to the intersubband coupling in heavily modulation-doped GaAs/AlxGa1-xAs single quantum wells at high magnetic fields, Phys Rev B Condens Matter Mater Phys. 64 (2001) 1613031–1613034. https://doi.org/10.1103/PhysRevB.64.161303.

[10] S. Paul, J.B. Roy, P.K. Basu, Empirical expressions for the alloy composition and temperature dependence of the band gap and intrinsic carrier density in GaxIn 1-xAs, J Appl Phys. 69 (1991) 827–829. https://doi.org/10.1063/1.348919.

[11] E.B. Al, F. Ungan, U. Yesilgul, E. Kasapoglu, H. Sari, I. Sökmen, Effects of applied electric and magnetic fields on the nonlinear optical properties of asymmetric GaAs/Ga1-xAlxAs double inverse parabolic quantum well, Opt Mater (Amst). 47 (2015) 1–6. https://doi.org/10.1016/j.optmat.2015.06.048.

[12] E. Sadeghi, Electric field and impurity effects on optical property of a three-dimensional quantum dot: A combinational potential scheme, Superlattices Microstruct. 50 (2011) 331–339. https://doi.org/10.1016/j.spmi.2011.07.011.

[13] R. Khordad, H. Bahramiyan, The second and third-harmonic generation of modified Gaussian quantum dots under influence of polaron effects, Superlattices Microstruct. 76 (2014) 163–173. https://doi.org/10.1016/j.spmi.2014.09.036.

[14] J. Huser, M. Wagner, Energy spectra of two electrons in a harmonic quantum dot, 1991.

[15] P.K. Jha, M. Kumar, S. Lahon, S. Gumber, M. Mohan, Rashba spin orbit interaction effect on nonlinear optical properties of quantum dot with magnetic field, Superlattices Microstruct. 65 (2014) 71–78. https://doi.org/10.1016/j.spmi.2013.10.025.

[16] I.Z.˘ Utic´*utic´*, J. Fabian, S. das Sarma, Spintronics: Fundamentals and applications, n.d.

[17] D. Sanjeev Kumar, S. Mukhopadhyay, A. Chatterjee, Effect of Rashba interaction and Coulomb correlation on the ground state energy of a GaAs quantum dot with parabolic confinement, Physica E Low Dimens Syst Nanostruct. 47 (2013) 270–274. https://doi.org/10.1016/j.physe.2012.10.030.

[18] S.S. Li, K. Chang, J.B. Xia, K. Hirose, Spin-dependent transport through Cd1−xMnxTe diluted magnetic semiconductor quantum dots, Phys Rev B Condens Matter Mater Phys. 68 (2003). https://doi.org/10.1103/PhysRevB.68.245306.

[19] J.E. Hirsch, Spin Hall Effect, 1999.

[20] S.A. Wolf, A.Y. Chtchelkanova, D.M. Treger, Spintronics-A retrospective and perspective, 2006. http://www.darpa.mil/dso/.

[21] M. Wierzbicki, Thermoelectric properties of magnetic configurations of graphene-like nanoribbons in the presence of Rashba and spin–orbit interactions, Physica E Low Dimens Syst Nanostruct. 87 (2017) 220–227. https://doi.org/10.1016/j.physe.2016.10.033.

[22] H. Hassanabadi, H. Rahimov, L. Lu, C. Wang, Nonlinear optical properties of a three-electron quantum dot with account of the Rashba spinorbit interaction, J Lumin. 132 (2012) 1095–1100. https://doi.org/10.1016/j.jlumin.2011.12.012.

[23] R. Khordad, Optical properties of wedge-shaped quantum dots under Rashba spin-orbit interaction, Int J Mod Phys B. 31 (2017). https://doi.org/10.1142/S0217979217500552.

[24] S.A. Wolf, A.Y. Chtchelkanova, D.M. Treger, Spintronics-A retrospective and perspective, 2006. http://www.darpa.mil/dso/.

[25] H. Hassanabadi, H. Rahimov, L. Lu, C. Wang, Nonlinear optical properties of a three-electron quantum dot with account of the Rashba spinorbit interaction, J Lumin. 132 (2012) 1095–1100. https://doi.org/10.1016/j.jlumin.2011.12.012.

[26] K. Premasiri, S.K. Radha, S. Sucharitakul, U.R. Kumar, R. Sankar, F.C. Chou, Y.T. Chen, X.P.A. Gao, Tuning Rashba Spin-Orbit Coupling in Gated Multilayer InSe, Nano Lett. 18 (2018) 4403–4408. https://doi.org/10.1021/acs.nanolett.8b01462.

[27] T. Koga, J. Nitta, T. Akazaki, H. Takayanagi, Rashba Spin-Orbit Coupling Probed by the Weak Antilocalization Analysis in [Formula presented] Quantum Wells as a Function of Quantum Well Asymmetry, Phys Rev Lett. 89 (2002). https://doi.org/10.1103/PhysRevLett.89.046801.

Journal Pre-proof

[28] A. Gharaati, Lande g-factor in semiconductor cylinder quantum dots under magnetic fields and spin-orbit interaction, Solid State Commun. 258 (2017) 17–20. https://doi.org/10.1016/j.ssc.2017.04.013.

[29] L. Zhuang, L. Guo, S.Y. Chou, Silicon single-electron quantum-dot transistor switch operating at room temperature, Appl Phys Lett. 72 (1998) 1205–1207. https://doi.org/10.1063/1.121014.

[30] M. Kirak, S. Yilmaz, Third harmonic generation of spherical multilayered quantum dot: effects of quantum confinement, impurity, electric and magnetic fields, Appl Phys A Mater Sci Process. 128 (2022). https://doi.org/10.1007/s00339-022-05601-1.

[31] R.L. Restrepo, E. Kasapoglu, S. Sakiroglu, F. Ungan, A.L. Morales, C.A. Duque, Second and third harmonic generation associated to infrared transitions in a Morse quantum well under applied electric and magnetic fields, Infrared Phys Technol. 85 (2017) 147–153. https://doi.org/10.1016/j.infrared.2017.06.005.

[32] H. Bahramiyan, Strain effect on the third-harmonic generation of a two-dimensional GaAs quantum dot in the presence of magnetic field and spin–orbit interaction, Indian Journal of Physics. 94 (2020) 789–796. https://doi.org/10.1007/s12648-019-01525-4.

[33] L. Liu, J. Li, G. Xiong, Studies of the third-order nonlinear optical susceptibility for In xGa1-xN/GaN cylinder quantum dots, Physica E Low Dimens Syst Nanostruct. 25 (2005) 466–471. https://doi.org/10.1016/j.physe.2004.07.017.

[34] E. Sadeghi, Electric field and impurity effects on optical property of a three-dimensional quantum dot: A combinational potential scheme, Superlattices Microstruct. 50 (2011) 331–339. https://doi.org/10.1016/j.spmi.2011.07.011.

[35] C.J. Zhang, K.X. Guo, Z.E. Lu, Exciton effects on the optical absorptions in one-dimensional quantum dots, Physica E Low Dimens Syst Nanostruct. 36 (2007) 92–97. https://doi.org/10.1016/j.physe.2006.08.009.

[36] W. Xie, Linear and nonlinear optical properties of a hydrogenic donor in spherical quantum dots, Physica B Condens Matter. 403 (2008) 4319–4322. https://doi.org/10.1016/j.physb.2008.09.021.

[37] P. Başer, I. Altuntas, S. Elagoz, The hydrostatic pressure and temperature effects on hydrogenic impurity binding energies in GaAs/InxGa1-xAs/GaAs square quantum well, Superlattices Microstruct. 92 (2016) 210–216. https://doi.org/10.1016/j.spmi.2015.12.010.

[38] S. Paul, J.B. Roy, P.K. Basu, Empirical expressions for the alloy composition and temperature dependence of the band gap and intrinsic carrier density in GaxIn 1-xAs, J Appl Phys. 69 (1991) 827–829. https://doi.org/10.1063/1.348919.

[39] Priyanka, R. Sharma, M. Kumar, P. Kumar, Hydrogenic impurity effect on the optical properties of Ga1-xAlxAs quantum wire under terahertz field, Micro and Nanostructures. 173 (2023). https://doi.org/10.1016/j.micrna.2022.207451.

[40] G. Rezaei, S. Shojaeian Kish, Linear and nonlinear optical properties of a hydrogenic impurity confined in a two-dimensional quantum dot: Effects of hydrostatic pressure, external electric and magnetic fields, Superlattices Microstruct. 53 (2013) 99–112. https://doi.org/10.1016/j.spmi.2012.09.014.

Journal Pre-proof

[41] R. Khordad, H. Bahramiyan, Optical properties of a GaAs cone-like quantum dot: Second and third-harmonic generation, Optics and Spectroscopy (English Translation of Optika i Spektroskopiya). 117 (2014) 447–452. https://doi.org/10.1134/S0030400X14080165.

Journal Pre-proof

Journal Pre-proof

Conflict of interest

☒ The authors declare that they have no known competing financial interests or personal relationships that could have appeared to influence the work reported in this paper.

☐ The authors declare the following financial interests/personal relationships which may be considered as potential competing interests:

RINKU SHARMA reports a relationship with Delhi Technological University that includes: employment. The authors declare that they have no known competing financial interests or personal relationships that could have appeared to influence the work reported in this paper.

Journal Pre-proof

Hindawi
International Journal of Photoenergy
Volume 2023, Article ID 7950699, 32 pages
https://doi.org/10.1155/2023/7950699

Research Article

Integrating Solar Photovoltaic Power Source and Biogas Energy-Based System for Increasing Access to Electricity in Rural Areas of Tanzania

Isaka J. Mwakitalima,[1,2] **Mohammad Rizwan**,[1] **and Narendra Kumar**[1]

[1]*Department of Electrical Engineering, Delhi Technological University, Delhi, India*
[2]*Department of Electrical and Power Engineering, Mbeya University of Science and Technology, Mbeya, Tanzania*

Correspondence should be addressed to Isaka J. Mwakitalima; mwakitalimaisaka0@gmail.com

Received 8 October 2021; Revised 2 September 2022; Accepted 22 March 2023; Published 26 April 2023

Academic Editor: Regina De Fátima Peralta Muniz Moreira

Copyright © 2023 Isaka J. Mwakitalima et al. This is an open access article distributed under the Creative Commons Attribution License, which permits unrestricted use, distribution, and reproduction in any medium, provided the original work is properly cited.

Renewable energy is the best option for the challenge of dwindling natural resources and energy scarcity. The utilization of solar photovoltaic (PV) systems is the best option for eliminating the energy deficit in Tanzania due to the available great potential of solar energy. Animal manure is a significant source of waste in rural locations which can be transformed into biogas fuel by an anaerobic process. Livestock and agriculture greatly support economically the majority of the sub-Saharan African (SSA) region's rural population including Tanzania, and excreta from cattle are beneficial for biogas fuel production. Unfortunately, the high potential of animal waste for generating electricity is underutilized. Integrating solar energy sources and biogas fuel derived from animal manure is useful for mitigating energy shortage, power instability, and environmental issues. Off-grid solar PV biogas-based hybrid microgrid systems for rural electrification applications in the Tanzanian environment are limited, and also, most of the studies are extensively carried out using soft computing tools especially hybrid optimization of multiple energy resources (HOMER) software with limited applications of artificial intelligence (AI) optimization techniques. This paper presents technoeconomic viability analysis for a hybrid renewable energy supply system (HRESS) for the Simboya village in Mbeya region, Tanzania. Off-grid HRESS is designed and optimized to meet the load of the chosen location executed using HOMER software and the grey wolf optimization (GWO) method. The microgrid is anticipated to supply daily maximum demand of 63.41 kW. The residential load profile equals 30 kW representing 50% of the daily demand. Optimization results by the HOMER platform indicate that the system has a total net present cost (NPC) and levelized cost of energy (LCOE) of $106,383.50 and $0.1109/kWh, respectively. Furthermore, this paper presents the optimization and sensitivity analysis results acquired by the GWO method under varied values of Loss of Electrical Power Probability (LEPP). Total NPC and LCOE based on LEPP values of 0, 0.04, and 0.06 are $85,106.8, $79,545.99, and $71,747.36 and $0.0887/kWh, $0.0316/kWh, and $0.0102/kWh, respectively. HRESS is economically and environmentally beneficial for supplying electricity to the selected area and worldwide in similar situations.

1. Introduction

Energy plays a great role in giving premium socioeconomic services in any society. Energy utilization improves the social quality of life and simplifies the productivity of economic activities. The need for electricity is well known worldwide. It is described by the United Nations as a sustainable development goal and is stipulated as "Goal 7." The goal ensures the accessibility to reliable, inexpensive, up-to-date, and sustainable energy [1]. Decentralized energy systems are more favoured than grid power networks because the system is not cost-effective [2]. Moreover, fossil fuels are costly, and their reserves are finite and depletive. These nonrenewable fuels are also not ecologically friendly. In other words, the utilization of fossil fuels causes adverse impacts of pollution and global warming [3]. Developing countries face a major problem of energy shortage in rural areas where there is no grid coverage. Increased population and economic activities

in these developing countries cause further energy deficit. Majority of developing countries solve this energy gap in rural areas by installing diesel generators. According to the aforementioned issues associated with fossil fuels, the generation of electricity by diesel generators is not economically viable and environmentally friendly. Because of that, alternative energy sources are essential for sustainable development [4]. Likewise, Tanzania as one of the SSA countries has a total estimated population of 58 million of which 20% represents urban while 80% indicates rural residents. Approximately 30% of all inhabitants in the country have access to an electric grid [5]. A large percentage of the population residing in countryside areas has a high demand for electricity, and it is undesirable. Diesel generators have been implemented to counteract the insufficiency of power supply in remote and rural areas. Nevertheless, this approach to rural electrification is costly and polluting [6]. This energy scenario can be improved using abundant renewable energy resources available in the country [6]. Unfortunately, the high potential of these energy sources is underutilized [6]. Renewable energy sources such as solar, wind, small hydro, and biomass can be used for off-grid power systems for remote and rural regions. Renewable energy sources are intermittent in nature causing power output variability. Reliability, energy management, and cost issues of these renewable sources can be addressed using energy storage equipment and configuration of hybrid technology (HRESS) to generate power for rural applications [7]. Besides, the potential of existing renewable energy resources is geographically dependent. Thus, an optimal size of HRESS is required for proper performance and cost-effectiveness. Various studies have been performed regarding HRESS in different locations worldwide [7]. The main goal of this research is to attain the finest arrangement of HRESS based on local resources for specific isolated rural areas in Tanzania. The study offers an economic comparative analysis of biogas generators versus DG in hybrid solar PV, considering biogas generators as cost-effective for the feasibility of replacing DG which is limited in the rural areas of the SSA region. In the first phase of this study, technoeconomic analysis is performed using HOMER software for dissimilar configurations which are anticipated to provide electricity at the proposed location and compares them using a financial indicator known as net present cost (NPC) in the life of 25 years. Such a study could be useful for the formulation of energy policies and decision-making for commercial strategy and implementation of hybrid biogas energy sources for providing access to electricity in rural areas in the country. In order to get this goal, the following are the specific objectives of the methodology: (i) identifying and proposing the rural site without grid connectivity, (ii) pinpointing the local renewable resources and realizing their potential, (iii) assessing the energy demand for the proposed off-grid site, and (iv) modelling, system sizing optimization, and opting for the superior cost-effective HRESS. Figure 1 indicates the comprehensive approach of the study. Presently, the use of metaheuristic techniques is a new area which is being highly explored by many researchers. In particular, to the best of the authors' experience and related theory, in the Tanzanian environment, the majority of the studies carried out on the HRESS have been executed using HOMER software. The applications of metaheuristic approaches are limited or at all are yet to be executed. For this reason and by considering the trend of modern researches, this particular study involves the use of both HOMER Pro software and an advanced metaheuristic approach called grey wolf optimizer (GWO). The GWO approach is one of the AI optimization techniques with successful working capability. In the second phase of the study, the GWO technique is deployed and validated by HOMER software. It is beyond the scope of this study to compare all the existing techniques. Nonetheless, the application of GWO has merits such as simplicity, flexibility, derivation which is not required during the optimization process, and avoidance of local optima due to its stochastic nature of GWO [8]. The GWO technique is greatly appropriate for solving complex nonlinear, multiadjustable, and multimodal function optimization problems. In short, the technique has high exploration capability with good equilibrium between global and local spaces [9].

The next part of this paper of research is organized as follows: Related literature review is presented in Section 2. The methodology is expounded in Section 3. Section 4 provides the descriptions of components and design of off-grid HRESS. Modelling of amalgamated power systems is explained in Section 5. Economic and technical input data of the proposed off-grid HRESS are represented in Section 6. The strategy for managing off-grid HRESS is presented in Section 7. Optimization of off-grid HRESS using the GWO method is discussed in Section 8. System reliability and sensitivity analysis using the GWO algorithm are described in Section 9. Results and discussions are elaborated on in Section 10. Comparisons of findings from other sources of related configurations are discussed in Section 11. Conclusions, recommendations, and research in the future are provided in Section 12. Declarations and statements, acknowledgments, and references follow.

2. Related Literature Review

This section presents a related theory of providing electricity to rural and isolated locations using renewable energy-based systems so as to increase access to electricity at local and global levels. The theory starts by giving highlights on the situation of the energy sector in Tanzania. This section also provides a brief description of using renewable energy sources for rural electrification in the country, the emphasis being on the utilization of solar and biogas energy sources. Related literature review is also furthered extensively to scrutinize the use of renewable energy sources for rural electrification worldwide. The review is presented as follows.

2.1. Status of Access to Energy in Tanzania. The global electrification rate is currently 82%. While developing countries as a whole have an electrification rate of 76%, the SSA region has fewer than 35%. More than 85% of Tanzania's population relies on wood-based energy (in the form of firewood and charcoal) for cooking and heating [10, 11]. Overdependence on biomass is frequent in rural and remote areas of

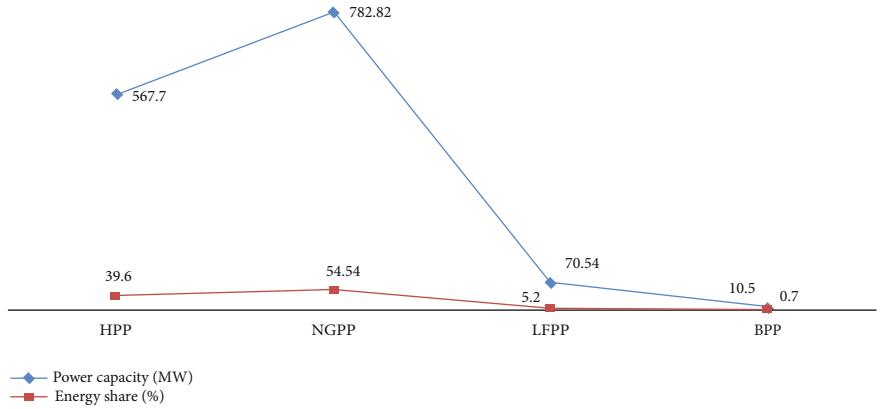


Figure 1: Electrical power generation mix in Tanzania.

Africa without access to electricity, accounting for 80% of the continent's population [10]. Tanzania is one of the five nations of the African continent that have the lowest electrification rates with an estimated electrification rate of 14%, and more than 37 million people have no access to modern energy including electricity [10]. This, in turn, has negative effects on other aspects of human development, such as child mortality and health-related difficulties. Tanzania, on the other hand, provides a diverse range of renewable energy sources, including biomass, solar, wind, geothermal, and hydropower [10, 11]. However, the majority of these resources have not been accessible or sufficiently exploited by the government or individuals. Tanzania's state capacity is limited, with poor service delivery of critical public goods such as energy, health, education, and water. Apart from the efforts which are made by the government, the Tanzanian government's inability to deliver sufficient energy to a booming population will most certainly continue to be a challenge for decades to come [10]. Tanzania is a big country with a dispersed and low-density population making the connectivity to the main grid expensive, especially given the poor productivity of rural areas which presents a limited economic benefit for a centrally designed infrastructure [10]. Furthermore, connection to Tanzania's national grid of Tanzania Electricity Supply Company (TANESCO) does not guarantee access to power [10]. Those who are linked to the grid face an inconsistent power supply with frequent power outages and fluctuating supply. Off-grid renewable energy-based systems can be suitable for the provision of electricity in rural places [10]. TANESCO, a public utility company, owns and operates the country's power generation, transmission, and distribution infrastructure. Tanzania's current electrical generation mix includes hydropower, natural gas, and liquid fuel. For instance, in April 2018, the overall installed generation power capacity for the grid system was summed up to 1,435.56 MW (grid installed capacity is 1,351.1 MW, and off-grid plus imports is 84.46 MW), HPP (hydropower plants) accounts for 39.6% (567.7 MW), NGPP (natural gas power plants) accounts for 54.54% (782.82 MW), LFPP (liquid fuel power plants) account for 5.2% (70.54 MW), and BPP (biomass power plants) accounts for 0.7% (10.5 MW) [11]. Figure 1 indicates the electrical power generation mix in Tanzania. The figure indicates that electricity generation in the country by biomass has the lowest share. For the cross-border power supply, power capacities of 10 MW and 5 MW are purchased from Uganda and Zambia, respectively, and 1 MW is purchased from Kenya. IPP (independent power producers) account for 16.3% (205.36 MW) of total grid installed capacity [11].

The government of Tanzania has just started construction on the JNHPP (Julius Nyerere Hydropower Project), a 2,115 MW hydropower plant. It is also worth noting that some progress has recently been made. JNHPP construction is expected to boost installed capacity by more than 130 percent to roughly 3,700 MW [11, 12].

2.2. The Survey on the Hybridization of Solar and Biogas Energy Sources in Tanzania. In African countries including Tanzania, the level of generating electricity using renewable energy technologies is low [6]. Several studies indicate that power generation for rural electrification has been mainly focused on small electrical loads for residential, small commercial, and few institutional buildings without much consideration for productive uses of electricity [13]. Electrical load in these premises usually is supplied via single-sourced renewable energy systems and is commonly made for lighting, mobile phone charging, refrigeration, and entertainment. Single-sourced renewable energy systems are not reliable due to their intermittent nature, and therefore, there is a need for either energy storage systems which are expensive or hybrid technology. These systems provide useful social services in off-grid locations but with limited productive uses [14, 15]. For enhanced socioeconomic development in rural areas, small-scale industrial and street lighting loads need to be included in addition to residential, small-scale industry, commercial, and institutional loads [15]. This load includes small-scale welding enterprises, flour mills, small carpentry workshops, and small-scale sewing industries. The productive uses may also include other sectors such as agriculture, transport, and irrigation though in this work are neglected. Consequently, for improved reliability, cost-effectiveness, environmental benefits, and productive purposes, HRESS is a suitable choice [16]. In the SSA region and more specifically in Tanzania, there is a high potential for biomass in the form of animal wastes of which biogas can be tapped in for generating electricity via off-grid HRESS [17]. The huge

potential could be helpful for the reduction of energy poverty in the region. Unfortunately, this potential from animal wastes remains unused. At the local level of the country and generally in the SSA nations, there are few studies on hybrid biogas-based electric systems [17]. This study tries to link the gap in the present literature. Additionally, the government of the United Republic of Tanzania via its research and development institutions supports the researches on the generation of electricity of such systems in the local sites with a substantial number of different livestock species. This kind of support from the government is a motivation for local researchers to work in this direction in investigating the potential of generating off-grid hybrid biogas-based energy systems [17, 18]. In the same view, this study is carried out to respond to such motivation from the government. The design of HRESS is mainly location-specific depending on local renewable energy resources and electrical load demand [19]. Based on the authors' observation and available literature, solar and battery systems hybridized with biogas generators are limited in the country. As a result, a solar PV-biogas-battery storage hybrid system is proposed. The system is anticipated to provide energy services to Simboya village located in Mbeya Rural District in Tanzania. The village does not receive any electricity from national central from TANESCO. This type of hybrid system is in research stages at different sites, and this particular research work contributes to the same track. Hence, prior to development and implementation, this system needs to be investigated to acquire knowledge about its potential and economic justification for the selected site and similar locations worldwide.

2.3. The Survey of Using RESs for Rural Electrification Worldwide: Gaps and Comparative Analysis. Numerous researches have been conducted along this track and trend. A large community of researchers has applied several simulation techniques and different approaches to investigate many kinds of renewable energy sources for electricity generation by conducting case studies of different places especially in isolated rural sites. Different places have also different availability of renewable energy resources, different potentials of renewable energy resources, and load patterns. This difference demands feasibility studies before the design and implementation of decentralized energy systems: Fleck and Hout compared two autonomous technologies, that is, small wind turbine system and single diesel generator-powered system. The wind turbine system is indicated to reduce significant greenhouse gas emissions in comparison with the diesel generator system [20]. Li and his fellow researchers carried out a feasibility study of hybrid technology for family houses in China. Hybrid technology consisted of wind, solar PV, and battery systems. A comparison among the technologies such as hybrid technology and two single sources of solar PV and wind turbine systems was made. The cost for solar PV with storage was found to be the highest followed by the wind turbine with storage, and hybrid solar-PV-battery storage was the cheapest [21]. Similarly, Rohan and Nour designed a hybrid renewable energy supply system for rural electrification in Abu Dhabi. Their study required an optimal arrangement of three sources of energy like diesel generators, solar PV, wind turbines, and battery storage equipment for the determination of power 0.5 MW. Optimization and simulation were implemented in HOMER software. Renewable sources were penetrated in the hybrid system approximately 45%, and the rest of the portion was made for diesel generators. Because of the high potential, wind resources had a better contribution than solar PV due to their high wind resource and less cost. Hybrid showed high least net present cost. High penetration of renewable energy sources is costly. In the same case, more than 30% of CO_2 emissions were decreased [21]. In developing countries, diesel-fueled power systems for a long time have been commonly used and are increasingly being substituted by or combined with nonconventional energy sources [22]. In addition, studies on solar PV-biogas-hybrid systems in SSA countries where Tanzania is also located have not been thoroughly analyzed [23]. Most of the HRESS-related researches are dominated by the combination of solar PV, wind, diesel, and batteries [24]. The amalgamation of solar PV and biogas power sources requires further extensive investigation as Tanzania's tropical climatic condition attracts the use of solar and biogas energy sources [6, 25]. Furthermore, the abundance of biomass and solar energy resources in the given site makes combining solar PV and biogas power sources apparent. The two sources can suitably complement each other for supplying reliable power supply in off-grid areas [25]. Yet, most of the researches do not provide the reliability, economic distance limit of grid network, and sensitivity analyses to find out its effect on the financial performance of the system [26]. Odoi-Yorke and coauthors carried out a feasibility analysis of solar PV/biogas/battery hybrid systems for rural electrification in Ghana using the HOMER platform. In the study, it was found that the system was better than the discrete DG or DG hybridized renewable energy-based system. In the analysis, LCOE was found to be \$0.256/kWh; the price is 64% higher than that of a domestic house [27]. Likewise, Zubair and his researcher designed a hybrid energy supply system in the coastal place of Bangladesh. The hybrid system consisted of wind-PV-DG hybrid systems. In the study, it was revealed that a hundred percent renewable energy-based supply system is not cost-effective. In the optimal group with the cheapest energy cost, 69% (55% and 14% for wind energy and solar PV, respectively) of total capacity represented renewable electricity, and the remaining percentage was power from DG. This system reduced CO_2 emissions by almost 70% compared to a single source generator [28]. In the same direction, Ngan and Tan investigated the possibility of implementing a hybrid energy system in Johor Bahru, Malaysia. This system included the technologies such as solar PV, wind turbine, and diesel generator. In the proposed site, solar energy resource has more potential than wind energy resource, and for that reason, solar PV has more penetration including DG. This hybrid PV-wind-DG system minimized CO_2 emissions by at least 35% [29]. Moreover, technoeconomic viability analysis of independent hybrid-PV-DG was performed by Ghasemi and his fellow researchers. The system was intended to supply electricity in one of the rural areas of Iran, and global solar radiation for Iran is sufficient for rural electrification

at around 5 kilowatt-hour per metre square per day. The study showed that the DG system is not sustainable as it produces a large amount of GHG emissions [30]. Furthermore, Kusakana and Vermaak designed a hybrid PV-wind energy supply system and compared it in terms of cost of energy with only solar PV, only wind, and only DG. It was revealed that the hybrid system had the least cost of energy while the diesel generator indicated the highest cost of the same. The cost of energy of solar PV followed after hybrid then wind turbine technology, and DG had the highest cost of energy. The initial cost of the diesel generator is low, but the high cost of energy is due to its running cost [31]. Yahiaoui and his fellows carried out a case study for system sizing of a hybrid renewable energy supply system in Algeria. They used the grey wolf optimization technique opting for the algorithm in unit energy commitment data convergences. Ecological constraints and forthcoming load demand were neglected. The authors concluded that grey wolf optimization produced appropriate optimal sizing for the hybrid system and the hybrid configuration [32]. Ren and his friends made investigation on energy and ecological effects of the indirect exploitation of solar energy for dryer equipment. They used computer modelling techniques and TRNSYS software and described fundamental modelling calculations appropriate for optimization apparatus-based simulations [33]. Kaabeche et al. managed to give a solution for sizing optimization regarding a hybrid renewable energy supply system. They used a firefly-based algorithm which was compared with other artificial intelligence optimization techniques. It was found that the firefly-based technique was superior in terms of sizing solution among other optimization techniques. However, other parameters like environment impacts and load dispatch strategies were not included in this study [34]. Kabeel et al. explained optimal cooling equipment for enhancement of solar PV operation and cost-effectiveness in Egypt. System components used in modelling were based on the power supply generation in the country [35]. Ravinder and Bansal in 2019 analyzed the independent hybrid renewable energy supply system, and the same optimum configuration was recommended. They proposed a minimum index called final excess energy for optimal size configuration. This development of the algorithm activated the system within a limited time period [36]. Guimpayan established an optimal solution of microgrid operation for supplying power to the community via cooperative organizations. They used different optimization strategies for system component sizing like particle swarm optimization. It was concluded that HOMER software tools provide the best operational indicators for meeting the load demand of a given community [35]. Abu-hamdeh and Alnefaie analyzed the technoeconomic feasibility of four electrical power supply systems for several multiple buildings in Jeddah, Saudi Arabia. This study contained systems such as solar power tower, photovoltaic, wind turbine, and diesel generator systems and was intended to supply electrical power to small electrical loads. In this analysis, it was found that photovoltaic systems are the cheapest among the other options. It was also indicated that the initial cost of solar power tower systems was higher than the cost of solar PV at small loads. They expressed that the same system was cost-effective with large electrical loads. The cost of energy of DG was equivalent to that of solar power systems but was not a suitable option due to many shortcomings. The cost of energy systems for wind power systems was the highest because of the low potential of wind resources less than 3.0 m/s [37]. Murugaperumal and his fellow researcher performed feasibility design and technoeconomic analysis for supplying power in an isolated village of Korkadu, Puducherry region, India. The study was aimed at determining technical and economic feasibilities for the optimal configuration of a hybrid renewable energy supply system. It was observed that hybrid technologies can improve system reliability and minimize greenhouse gas emissions. They advised tapping the potential of biomass resources if available [38]. Bekele and Palm investigated the viability of supplying electrical power to the isolated public of two hundred families in Ethiopia. This investigation was based on a hybrid solar-wind energy supply system. Sigarchian et al. performed technoeconomic evaluation of a PV-wind-biogas hybrid system for providing electrical power supply to one of the villages in Kenya. It was observed that in terms of net present cost, cost of energy, and capital cost, the biogas power-generating machine was the best option for a backup system replacing the diesel engine. Energy share of 49%, 32%, and 19% represented power impact from solar PV, biogas engine, and wind turbine technology, respectively [39]. Anand et al. performed a feasibility analysis of a solar-biomass-based autonomous hybrid system for an isolated area in Sonipat, Haryana, India. This study was aimed at finding a suitable hybrid renewable energy supply system for the proposed hospital. The proposed model provided minimal cost and a significant reduction of GHG emissions [40]. Romero and Icaza proposed a photovoltaic/biomass/hydraulic hybrid system for the provision of electric power to the province of Bolivia, Ecuador. The objective of their study was to examine the support of local renewable energy resources to supply electricity in isolated areas of the country. In the study, it was found that the proposed HRESS has the potential to generate reliable power by employing batteries in the system [41]. Sen and his fellow researcher Bhattacharyya performed a feasibility analysis for generating electricity via a 100% hybrid RE-based system for Palari village, Bastar district, Chhattisgarh, India. The hybrid consists of RE sources such as solar, small hydro, wind energy, biodiesel generator as backup instead of DG, and batteries for maintaining fixed voltage in the absence of RESs. The authors of this paper concluded that the proposed system was cost-effective and environmentally friendly [14]. Rabetanetiarimanana et al. reviewed the measures taken for fostering the provision of electricity in rustic and isolated locations of the SSA region. Researchers presented the hurdles to the delivery of electricity to such sites. The authors also proposed renewable energy-based technologies particularly PV-hybrid systems which are less expensive as an alternative to commonly used DG systems. They also presented the appropriate methods for maximizing the utilization of renewable energy sources such as solar, small hydro, wind, concentrated solar power (CSP), and biomass,

which can be used in the region. Also, the authors mentioned some planning tools which are applicable in the region including the widely used HOMER software. In their review, the authors concluded that the proposed renewable energy systems are more economically feasible than DG power stations [23]. Andrea et al. established economic models for supplying electricity through renewable energy-based minigrid systems in rustic areas of the SSA region. They established the model known as the KeyMaker Model which intends to reduce the aggregate of donations needed for supporting the preliminary investment and hence contributing to the viable development. The target of the model is to use the local minigrid electric systems to establish an agroprocessing scheme. They investigated the model of the 4 villages in Nigeria in order to investigate the potential of the model. HOMER software was used to simulate the systems for performing the economic feasibility analysis. The study indicated that without the proposed business model, economic donation requirements are higher lying in the range starting from 82 to 99% of the aggregate preliminary investment while with high quality of the same model, the donations reduce to 68%, 36%, 26%, and 8% for cocoa, maize, palm oil, and cassava, respectively. The authors concluded that the rate supplemented by introducing innovated local economic model reveals the decrease in donation requirements for rural electrification thus gaining socioeconomic benefits [42]. Diana et al. applied a multidisciplinary approach to developing a model for a load demand frame for expatriate camps, and they evaluated the implementation of unconventional energy systems. The study includes the technical-economic feasibility and challenges analyses specific to the refugee camp. The authors carried out modelling as a case study at a refugee camp located at Mantapala in Zambia. The authors simulated the systems using HOMER software and compared the alternative energy systems against the DG systems. One of the key findings of this study indicated that the implementation of hybrid renewable power systems is technically and financially feasible; costs for power fall up to 50% [43]. Trotter carried out a systematic review of energy planning and implementation in SSA. In their study, the author reviewed the quality and quantity of power planning and associated implementation research in each of SSA's 49 nations. This review indicated that 63% of related articles have favoured nonconventional power sources for the specified problems. Only 16% of the reviewed related theories advocate the use of hybrid energy systems. This review has mentioned that the HOMER platform is the most popular planning tool in SSA's states [44]. Zebra et al. conducted a review on the HRESS for an off-grid mini-grid system for providing electricity in developing countries. The concentration of the review was based on the experiences; technical, technological, and economic performance; and the major traits that can either obstruct or motivate the incorporation of these schemes in the less developed world. Off-grid HRESSs were examined and designed for considering the reliability due to the intermittency of renewable power sources. In the review article, the authors have stated the two main reasons for the success of the incorporation of HRESSs in developing counties, that is, received support from the government and community-based organization. Apart from other findings, this review shows that majority of Asian countries are more successful with minigrid systems. Similarly, Tanzania, for instance, is successful with the implementation of hydropower minigrids facilitated by REA. The LCOE of unlike minigrids has been compared, investigated, and compared. It has been observed by the comparison of LCOE of the technologies diesel, solar PV, and solar PV-DG hybrid. DG is the most expensive technology; its LCOE is in the range of $0.92/kWh-$1.30/kWh while solar PV technology is the cheapest technology, and its LCOE is in the range of $0.40/kWh-$0.61/kWh being cheaper than the hybrid. In addition, the authors presented the obstacles to the smooth implementation of minigrids including the absence of helpful policies and great investment costs. The findings are of specific significance for the less developed nations, where rural electrification through HRESSs is regularly faster and low-priced than grid power networks [22]. Keddar et al. investigated practical challenges which face the deployment of hybrid solar PV-diesel minigrid systems for electric cooking applications in the rural and isolated locations of Tanzania. They simulated the system using OpenDSS/MATLAB. The authors first investigate the limitations and constraints of the minigrid network in terms of the generation capacity available and different penetration levels. Generally, the findings have shown that voltage drop and disparity matters can be rationally and manageably advocated using conductors of greater size [45]. Bhattacharyya and Palit investigated critically and synthetically the literature on the off-grid–on-grid argument and discussed the rapport and the role between power generation preferences for expanding access to electricity in Asian and SSA nations. In the review article, the authors have explained that models which use larger resolution and capture low-voltage distribution networks seem to acclaim the distributed electric power solutions whereas the main power network appears as the favourite result of further accrued examination, focused population constellations, and greater demand circumstances. In addition, it has been indicated that the HOMER platform is majorly used for the technoeconomic viability analysis theoretically and not actual projects. In the review, the authors suggested the means of achieving widespread electrification, that is, strong governance and empowerment [46]. Kemausuor et al. conducted a review of the power planning tools and to what level the tools have been used in decentralized power systems in African states. The findings of this review article indicate that HOMER and Long-range Energy Alternatives Planning (LEAP) are the mostly used planning tools of renewable energy technologies. Other planning tools are RETScreen, network planner, MESSAGE, and MARKAL/TIMES. In particular, the study has mentioned power planning tools such as LEAP and MESSAGE to be used in Tanzania. Nigeria, Ghana, and South Africa are the nations with the greatest use of power planning tools. Conclusively, the review indicates that there is no any distinctive tool that might be fitting for all dissimilar power planning matters for the full deployment of renewable energy technologies [47]. Osman et al. carried out a feasibility study of integrating

solar PV power sources into various available diesel-powered minigrid systems forming HRESS in Tanzania. They simulated and optimized the system using the HOMER platform at the lowest NPC and its corresponding LCOE. Based on these econometric metrics, a comparative study was made, with the solar PV-DG-battery bank being more cost-effective than discrete DG. Accrued NPCs for renewable-based systems and conventional energy systems are $2,056,400 and $1,726,922, respectively. Also, LCOEs for the solar PV hybrid and DG power station are $0.35 and $0.29/kWh, respectively. They concluded that the integration of solar PV into existing diesel power systems to form renewable energy-based hybrid systems is economically viable [48]. Creti et al. examined the managerial, tariff, and subsidy structures for minigrids in Mafinga in Mufindi district, United Republic of Tanzania. Also, the authors investigated the lucrativeness of electrification via a minigrid system project in private capital investment. Three technological alternatives were considered for the project such as DG, solar PV-battery, and HRESS. HOMER software was used for simulation and optimization purposes. The authors concluded that the legalised standardised SPP (small power producer) charges and funding schemes in the country still do not favour the minigrid system projects for the provision of electricity in rural areas due to high generation costs [49]. Hagumimana et al. carried out the technoeconomic examination of CSP and solar PV power sources in terms of strengths, weaknesses, opportunities, and threats (the SWOT approach). Later, the practical and financial viabilities of off-grid CSP and PV-based microgrid systems in Rwanda were implemented by the System Advisor Model (SAM). Results show that the off-grid solar PV-based microgrid system for the bucolic society is cheaper with the lowest NPC. Results of the SWOT approach and SAM model have indicated that both types of microgrids can have a great part in increasing access to electricity in the country. The authors intensely suggested the application of off-grid solar PV systems for providing utility-scale power in order to escalate access to electricity in Rwanda owing to their cost-effectiveness [50]. Khan et al. designed a new reliable and ecologically friendly solar PV-wind-hybrid system for a far-off location in the United Republic of Tanzania including CLC-SS (closed loop cooled-solar system). The system was optimized using HOMER software. In the design, the inclusion of CLC-SS enhanced the proficiency of the proposed HRESS by the extraction of extra energy from solar panels. The analysis of CLC-SS demonstrated a rise in energy output from ordinary solar panels by at least 10.23%. The findings authenticate that the optimized system has total NPC and LCOE of $7,110.53 and $0.26/kWh, respectively. The improved HRESS has been found to be economically viable [51]. Yusto established a model of HRESS consisting of anaerobic ingestion and solar and wind energy sources for energy generation in rustic semiarid locations particularly at Idifu village, Chamwino district, in Dodoma, Tanzania. One of the specific objectives was to simply carry out the technoeconomic evaluation of the proposed integrated energy system. An Artificial Neural Network (ANN) modelling method is beneficial for building biogas production forecasts of conventional HRESS using ANN models. Total NPC and LCOE were among the indices which were considered in the analysis. A comparative study between the conventional biogas system and innovated adapted batch fed anaerobic digestion (ABFAD) scheme was performed. At assumed discount rates of 9 and 12%, the actual LCOE was found to be TZS 1,312.71/kWh equivalent to €2017 0.57/kWh and TZS 1,464.63/kWh equivalent to €2017 0.64/kWh, respectively. The ABFAD presents the solutions to the functioning difficulties of ordinary anaerobic digestion systems, for instance, the easiness of reprocessing of leachate and small temperature deviation for achieving viable biogas production [52]. Bishoge et al. reviewed the potential of renewable energy resources for sustainable development in Tanzania. In their exploration, the authors identified, among other renewable energy technologies, the feasibility of generating electricity through biogas energy-based hybrid systems for rural areas, particularly in sites with a substantial amount of livestock. In this review, the authors mentioned the need for further investigation for harnessing effectively the potential of hybrid technology for commercial use [53]. Through simulation, Paul et al. investigated the possibility of integrating a solar-PV/battery system with DG. They identified off-grid DG power stations by the GIS-based approach and simulated this integrated system using the MATLAB simulation tool. They derived technical and economic solar PV and battery energy systems for hybrid minigrid systems. The authors developed a methodology for localizing the isolated DG minigrid systems. In their study, the authors also investigated the sensitivity of battery costs on storage capacity and renewable energy share. The authors concluded that the hybridization of DG-based off-grid systems with a solar PV/battery system can lead to considerable electricity cost reduction [54]. Khavari and Sahlberg carried out geospatial electricity demand and hybrid off-grid solutions to support electrification efforts in Tanzania using the Open Source Spatial Electrification Tool (OnSSET). They developed a method to consider hybrid electrification choices in geospatial electrification planning. In this study, a PV-diesel system was found cost-competitive economically with other minigrid technologies. In the same study, a wind-diesel system was found to be costlier [55]. Haji evaluated grid-connected and standby PV systems at the Karume Institute of Science and Technology (KIST), Zanzibar, and the Nelson Mandela African Institutions of Science and Technology (NM-AIST), Arusha, Tanzania. The study utilized the energy data from the two different locations. Current and voltages were acquired using the data loggers and power outputs as estimated. In addition, HOMER was used for simulation purposes. Simulation results indicate that the solar PV systems and grid power network at the KIST demonstrated saving approximately 40% of the accrued daily power consumption in comparison to grid connectivity. The LCOE was minimized starting from $0.1877 to $0.113. In another statement, the amalgamation of grid, solar PV, and battery systems at the NM-AIST showed an estimated saving of around 51% of daily power usage; the LCOE was minimized starting from $0.22849 to $0.113, respectively [56].

This specific research work tries to fill up the gaps as stated above by using both soft computing tools and AI optimization approaches. Furthermore, as portrayed in Figure 1, the share of biomass (including biogas) in electrical power

generation mix is the least. In SSA countries including Tanzania, HOMER is extensively used in various studies with limited applications of AI optimization tools and hybrid biogas-based systems. So, in this study, a technical-economic analysis of the proposed off-grid HRESS for supplying electricity to the selected area of study has been performed using soft computing tools (Excel program and HOMER software) and AI optimization tools (GWO method). Similarly, the analysis involves the minimization of the total NPC and its corresponding LCOE of the off-grid HRESS in one of the rural areas of Mbeya region in Tanzania named "Simboya village." Technoeconomic viability analysis of HRESS in the first place has been executed using the HOMER platform and GWO technique.

2.4. Contributions of the Study. Based on the survey of the literature regarding the utilization of renewable energy resources for rural electrification at local and global levels, contributions of this research work are presented as follows:

(i) Hybrid biogas electric systems are limited in most developing countries particularly in the SSA region where the site under study is in the same location. Most of the available small energy systems in the region produce biogas for limited applications such as lighting, food preparation, and heating applications. Hence, this paper offers an optimization problem for novel designed optimal HRESS hybridizing solar PV and biogas energy sources to supply electricity in the rural areas

(ii) The paper presents the optimization of the system sizing using HOMER Pro software and a recently developed metaheuristic research platform called the grey wolf optimization (GWO) technique. Specifically, it includes the use of the GWO approach by considering system reliability

(iii) The study also offers a novel approach to sketching the graphs of NPC and LCOE in relation to break-even grid extension distance using linear equations

(iv) This study presents the economic comparative study of hybrid PV-BIOG-battery, PV-DG-battery, and DG systems versus break-even grid extension distance in the Tanzanian environment. Biogas generators are being considered to replace DG in hybrid solar PV-based systems. Also, the paper furthers the comparative analysis regarding GHG emissions between the abovenamed electricity generation options

(v) This paper offers awareness and enlightenment and fills the gap of missing energy data which are not available in most of the rural and remote areas of developing countries, including Tanzania, regarding the generation costs, performance, and use of hybrid biogas-based electricity systems

(vi) The paper provides the identification, exploration, and application of livestock-poultry biomass (biowastes) for the solution of energy deficiency and addresses the problem of environmental pollution (odour) due to animal and poultry wastes in the area of study

(vii) This study presents sensitivity analyses using HOMER Pro software and the GWO method

These energy deficits are considered important to exploring the potential complementarity, viability, and scope of all feasible infrastructures and solutions providing energy access. In this particular study, an off-grid HRESS incorporating equipment such as solar PV, biogas generator set, and batteries is proposed. In order to tap the advantage of a high sunlight source at the selected area of study located near the equator, the proposed model of hybrid energy systems includes solar PV panels. The utilization of solar PV technology is beneficial due to its modularity, negligible cost of operation and maintenance, simplicity in terms of installation, and environmental friendliness [57–60]. As a renewable energy source, solar radiation is intermittent leading to power output variability [57–60]. The intermittent nature of the solar energy source can be addressed by an introduction of an energy storage system particularly a bank of batteries and also by integrating complementary renewable energy sources or DG systems [57–60]. In other words, a practical amalgamation of solar with other renewable energy technologies integrated with DG or grid is deemed to be a technofinancially viable solution for rural power connectivity. However, DG systems are expensive and unclean, emitting GHG emissions, and insecure due to the depletion of fossil fuels and oil price volatility while main grid networks are far away from remote areas [57–59] [60, 61]. Therefore, off-grid renewable energy systems are compulsory for increasing access to electricity in rural areas. This study intends to maximize the potential of biogas fuel (form of biomass derived from animal manure anaerobically) in electricity generation mix of the Tanzanian power sector. In this study, solar PV is integrated with a biogas generator for improved efficiency, energy security, high reliability, reduced environmental negative impacts, and affordability in comparison with its DG counterpart [58, 60, 61]. Also, this study tries to address the challenge of scattered and random deposits of animal wastes and also mitigates environmental pollution from bad odour [58, 60]. Biogas fuel from biogas plants is injected to an internal combustion (IC) engine (modified diesel engines) to produce mechanical energy which is then converted into electricity by an electric generator. Apart from electricity generation and thermal production, agricultural gain can be maximized from biogas production thus increasing the income. In the proposed off-grid HRESS, batteries are also incorporated when solar radiation and biogas are unavailable. The integration of multiple energy sources of dissimilar characteristics is a complicated task requiring an extensive analysis. In this particular study, technoeconomic feasibility analysis of proposed off-grid HRESS is implemented. The analysis also involves applications of AI optimization techniques particularly GWO. The use of artificial intelligence solutions into power systems has the potential to significantly improve power efficiency, cost savings, and user comfort. As a result, developing

intelligent optimization-based algorithms for application in various renewable energy systems is vital. In general, for achievement of widespread access to electricity, distinct policies for off-grid rural electrification have to be formulated [62]. Further research is required to analyze both the site-specific potential of RESs (renewable energy resources) and financial feasibilities of renewable energy resources (RESs) [62]. According to the preeminent knowledge of authors, no such research has been implemented previously at the selected area (Simboya village located at Ikukwa ward in Mbeya region, Tanzania). For that reason, this study tries to seal up this research gap. The overall contribution of this study is that it creates a roadmap for enhanced rural electrification at the selected area of study and other locations worldwide with similar conditions.

3. Methodology

3.1. General Description. Prior to the investigation of HRESS using HOMER Pro software, there are two important and significant aspects which are needed for any design of an electric system, i.e., availability of RESs plus their potential and estimated energy demand for the site of interest. Knowing the amount of energy of a particular place is helpful because it tells us the amount of energy to be generated. In this study, it is classified into residential, commercial, small-scale industrial, institutional, and street lighting loads. Agricultural and irrigation loads are neglected. The reason is that rural villagers of the area of study need not refrigeration for cooling agricultural products. Irrigation activities for the farms of the proposed site are carried out through the diversion of River Shongo and small streams of water flowing down under gravitational force from hills around Mt. Mbeya. This river supports lives and irrigation of Simboya and Ikukwa village. Electrical consumption for transportation is not applicable for this rural site. The components for HRESS are chosen in consonance with the availability potential of RES. The survey has been accomplished through site visitation, ward development records, extensive literature, interview, questionnaire, measurements, and internet surfing. All relevant data for required HRESS components, loads, RES, and prices are collected as input parameters in the optimization process in HOMER Pro software. HOMER is one of the analytical tools; its acronym stands for hybrid optimization of multiple energy resources. In the optimization, optimal configuration of HRESS is obtained for supplying sufficient electricity at minimum NPC (the life cycle cost, i.e., LCC), and apart from optimization, HOMER can perform sensitivity and GHG emission analyses. Figure 2 presents a comprehensive research approach.

Design of any hybrid system depends on the local renewable energy resources and load demand of a particular site. In line with the fieldwork that has been made at the area of study, there is a high potential of solar and biomass (animal waste and poultry droppings) energy resources, and thus, PV and biomass (biogas) generators have been used. Additionally, for a suitable performance, there is additional equipment such as power conditioning electronic devices, electrical load, and battery energy storage system. Normally, DG is used in HRESS as a backup to improve the performance of the system during maximum loads and absence of renewable energy resources. In this specific work, a biogas electric power generating unit is employed for backing up the system. This type of proposed HRESS is 100% renewable and therefore is cost-effective and environmentally benign. Figure 3 indicates a schematic arrangement of the off-grid HRESS for the proposed site. Based on the selected system components, optimal configuration is achieved via optimization. The grid has been included in the hybrid PV/biogas/battery bank storage only for economic comparison purposes and for this reason does not generate any power.

3.2. Description of Area of Study, System Design, and Energy Analysis. Simboya village is one of the two villages located at Ikukwa ward in Mbeya Rural District in Tanzania. Geographically, Simboya village is surrounded by mount Mbeya, Chunya district in Mbeya region, and Songwe region. Figure 4 indicates the map of the location of Simboya village at Ikukwa ward in Mbeya region, Tanzania. This village suffers from lack of access to electricity from national grid extension. Table 1 shows a summarized profile for Simboya village.

3.3. System Design and Energy Analysis

3.3.1. Solar Energy Resource. Monthly solar radiation and wind energy data were obtained from National Aeronautics and Space Administration (NASA) and Surface Meteorology and Solar Energy (SSE) [64]. The scaled annual average solar irradiance is 6.11 kWh/m^2/day at the proposed site. Table 1 shows the clearness index and monthly solar radiation data and wind speeds at the height of 10 m. Figure 4 indicates the monthly solar radiation and clearness index at the proposed site. Figure 5 shows detailed annual information of global solar radiation in Mbeya Rural District, Mbeya.

3.3.2. Biomass Energy. The following is the chemistry for producing biogas fuel during the anaerobic digestion process [65]:

$$\{C_6 + H_{12}O_6 \longrightarrow 3C0_2 + 3CH_4, CO_2 + 4H_2 > CH_4 + 2H_2O, CH_3COOH > CH_4 + CO_2\} \quad (1)$$

Fuel consists of two main things such as methane (CH_4) and carbon dioxide (CO_2) representing about 55-65% and 35-45%, respectively. It also consists of tiny sulphide and gaseous form of water.

The simplified process of converting biomass obtained from animal and poultry wastes into biogas fuel for generation of electricity is portrayed in Figure 6.

This study focuses on evaluating potential for animal dung and poultry droppings at the village. Data collection regarding identification of types of animals and their quantification has been done through consultation of ward leaders and consultation of individual villagers and through records in the library of agriculture and livestock office in Ikukwa ward. Table 2 shows a list of livestock at Simboya village in Mbeya Rural District.

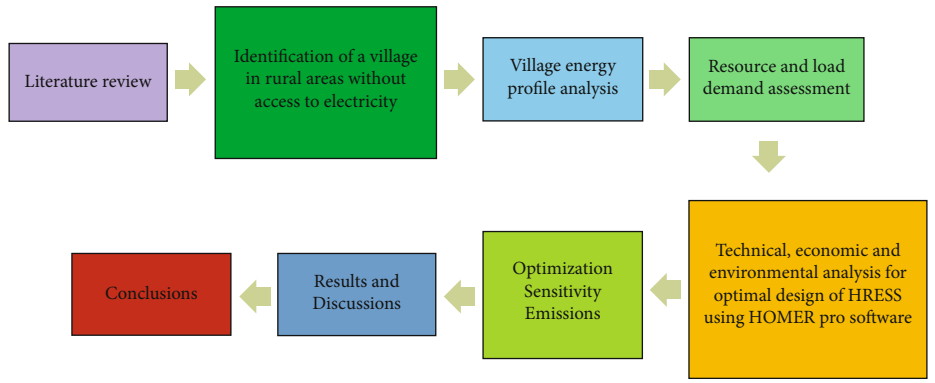


Figure 2: Comprehensive research approach.

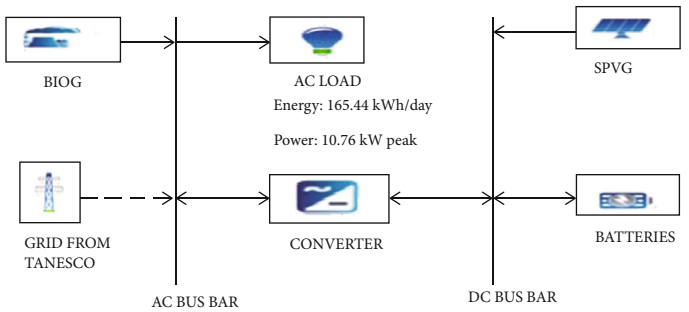


Figure 3: Schematic arrangement of the off-grid HRESS for the proposed site.

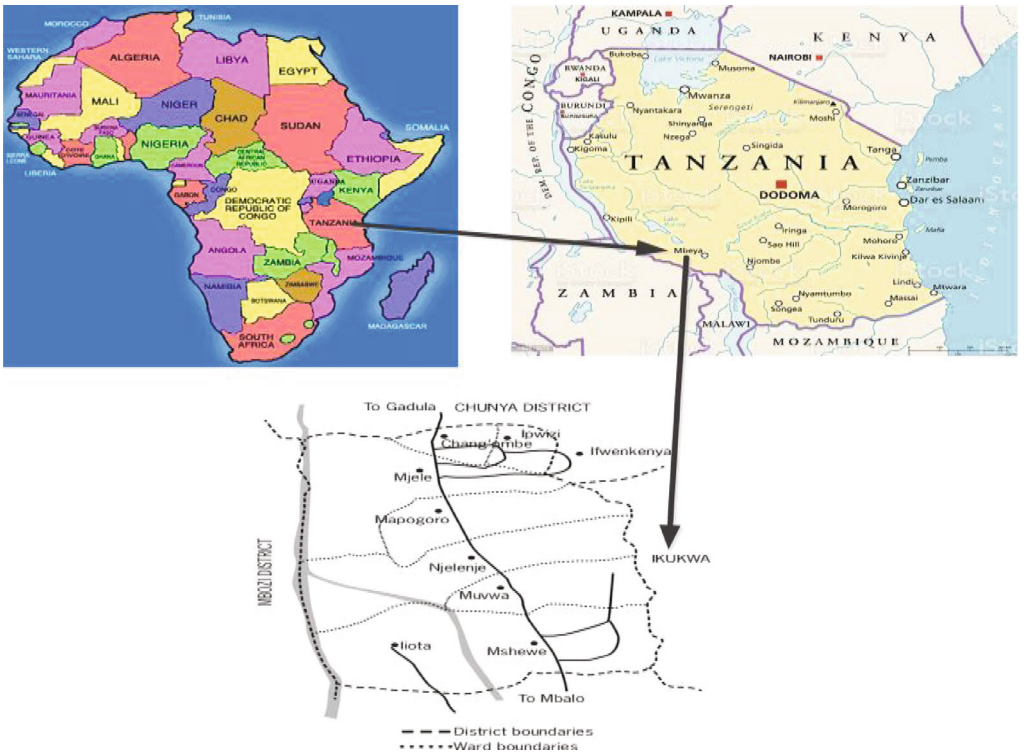


Figure 4: Map of location of Simboya village at Ikukwa ward in Mbeya, Tanzania (modified by authors: [63]).

Table 1: Summarized profile of the Simboya village.

Particulars	Description	Remarks
Name of the village	Simboya	—
Date of establishment	1998	Formed after subdivision of the former Ikukwa village established in 1964
Number of subvillages	09	Records from ward agricultural office
Number of residences	483	Records from ward agricultural office
Number of rivers	01	The river Shongo
Total area	5522 m^2	Data by Ikukwa ward office (WEO)
Total area for residences	3622 m^2	Data by Ikukwa ward office (WEO)
Agricultural area	700 m^2	Data by Ikukwa ward office (WEO)
Pastoralist area	1200 m^2	Data by Ikukwa ward office (WEO)
Total population	2536	Number of males: 1236 Number of females: 1300
Electricity availability	00	—
Ward name	Ikukwa	—
Name of the district	Mbeya rural	—
Name of the region	Mbeya	—
Latitude	8°54.6′S	—
Longitude	33°27.6′E	—
Country	United Republic of Tanzania	—

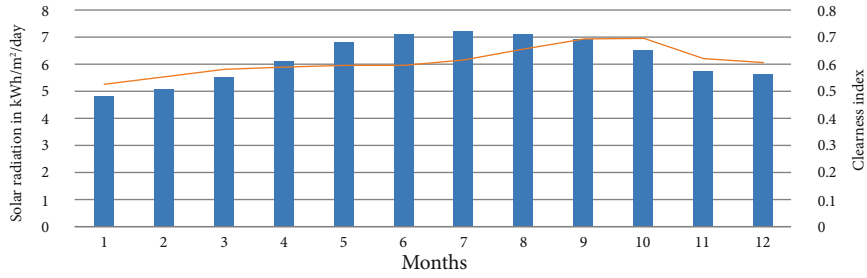


Figure 5: Synthesized monthly solar radiation and clearness index at the proposed site.

The quantity of dung produced per livestock per day differs depending on several factors like body size, kind of feeding, and amount of nutrition. For simplicity, production rates are approximated using the number of heads of surveyed herds in Simboya village, Mbeya Rural District, Tanzania. Table 3 indicates the yield of dung per head per day for Ikukwa ward in Mbeya Rural District.

The total amount of animal dung and poultry droppings is 10,365.9 kg/day. Firstly, gathering efficiency for animal waste is assumed to be 60%. And thus, the total amount collected per day is 60% multiplied by 10,491.8 kg/day which equals 6,295.08 kg/day. This amount is sufficient to produce biogas for electricity and cooking for the village households. An average of 2,040 kg/day out of the total daily biomass has been used for biogas electricity generation. The average price of biomass, low heating value (LHV), carbon content, and gasification ratio are $3.0/ton, 5.5 MJ/kg, 5.0%, and 0.7, respectively. Secondly, it has also been observed that majority of animals and poultry in Africa are roaming from one place to another looking for pastures. The collection of biomass for biogas production may be a challenge. In this study, for an effective collection of animal dung and poultry droppings, zero grazing is assumed. Thirdly, the main source of feeding for the animals is assumed to be depending broadly on grass. The presence of grass is normally affected by the weather of the given place. It may now be implied that the amount of biomass collected during rainy seasons is higher than that in the dry season. In other words, the larger the amount of biomass, the higher the rate of feeding the animals, hence the high production of biomass per animal head. Based on these assumptions, the annual monthly average of available biomass resources is purposefully distributed over a period of one year. The highest and minimum produced annual monthly average biomass resources are in the month of January (0.787 tonnes/day equivalent to 12.5%) and in the duration starting from July to October (0.315 tonnes/day equivalent to 5% of total waste), respectively. In the period starting from March to April, daily available biomass is estimated to be 0.692 tonnes which is equivalent to 11%. Also, in November and December, the daily average weights of collected biomass are, respectively, 0.378 tonnes (6%) and 0.598 tonnes. Figure 7 indicates the annual

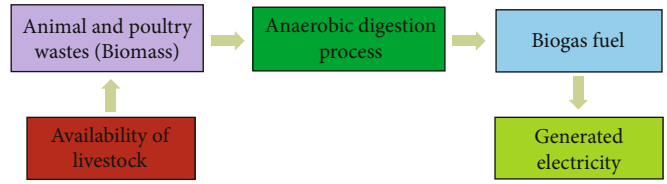


Figure 6: Simplified stages of electricity generation from biogas fuel.

Table 2: List of livestock at Simboya village in Mbeya Rural District.

Livestock	Cattle	Goats	Donkeys	Sheep	Pigs	Poultry
Total number	873	602	82	31	86	1448

Table 3: Assumed yield of dung per head per day for Simboya village in Mbeya Rural District.

Livestock	Assumed animal dung (kg/head/day)	Number of animals	Total dung (wet) (kg/day)
Cattle	10	873	8730
Goats	1	602	602
Donkeys	8	82	656
Sheep	1	31	31
Pigs	2.35	86	202.1
Poultry	0.10	1448	144.8
Total			10,365.9

monthly average available biomass resource for backup electricity generation. The daily generated power is given in the following equation [66]:

$$P_{\mathrm{BIOG}} = \frac{Q_{\mathrm{BIOG}\times}\mathrm{CV}_{\mathrm{BIOG}} \times \eta_{\mathrm{BIOG}}}{(T_{\mathrm{OPD}\times 860})}, \quad (2)$$

where Q_{BIOG} denotes the amount of biogas (m^3/day), P_{BIOG} is the power generated by the biogas power plant (BPP) in kW, $\mathrm{CV}_{\mathrm{BIOG}}$ is the calorific value of biogas fuel (4,700 kcal/m^3), η_{BIOG} is the overall efficiency of BPP, and T_{OPD} is the operating time per day in hours. The remainder of the daily biomass resource equals 4,255.08 kg/day. In this study, 1 kg of dung is assumed to produce a daily amount of biogas of 0.036 m^3 [66]. As a result, total biogas production for cooking for all households in the village equals 0.036 m^3/kg times 4,255.08 kg/day which is estimated to be 153.2 m^3/day. The village comprises 483 families with a small amount of biogas for cooking per household which is equivalent to 0.32 m^3.

3.3.3. Classification of Electrical Load Demand. The approximated load demand has been obtained by the collection of information from the inhabitants and field surveys in the various sections of the village. These surveys are focused on a number of sections such as residential, institutional load, commercial, small-scale industrial, street lighting, irrigation, and agricultural loads. Data have been collected from the anticipated rated power of appliances depending on the type of electricity services. All sections consist of the lighting load. Residential loads consist of lighting, TV set, radio, DVD player, phone charger, and electric iron. Institutional loads consist of schools (primary and secondary), religious institutions, and community centres. Also, institutional loads include equipment of Mbeya District Council Hospital (MDCH), also known as Ikukwa Health Centre (IHC). The equipment for the hospital is used in sections such as morgue, laundry, image (X-ray and CT scan), administration building, theatre, maternity, premature babies services, clinic block, laboratory, minor surgery, pharmacy and store, injection room, dental room, staff households, security and street lighting, and miscellaneous sections. Commercial loads consist of small-scale shops, groceries, male saloons, and female saloons. Small-scale industrial load includes small carpentry workshops, sewing machines, milling machines, and welding machines. Street lighting load consists of security lights. Deferred load has been neglected as irrigation and agricultural activities do not need water pumping systems but electric power for transport. For an effective performance of the proposed off-grid HRESS, it is noteworthy to carefully take into account the electrical load profile. Any kind of periodic load variation can cause serious reliability problems in the system.

Based on the energy demand of each section, collected data from the surveys were intentionally spread over a 24-hour period on the Excel data sheet owing to the poor load factor in rural areas. The distribution of each load category was performed according to the engineering judgment reflected to time, social behavior, and nature of economic activities in the specified area of study. The daily load profiles for the whole village obtained by the Excel data sheet have been validated using the HOMER platform. Table 4 displays the electrical load categories in consideration of the consumer at Simboya village. The country's location is in a tropical region, and accordingly, the periodic variation of load based on winter and summer is not considered as there is not much variation in temperatures between the two seasons and thus no need for space heating/cooling equipment [67].

(1) Estimation of Electrical Load Demand at Pre-HOMER Level Using Excel Program. The assessment is carried out in the Microsoft Excel worksheet by customizing data

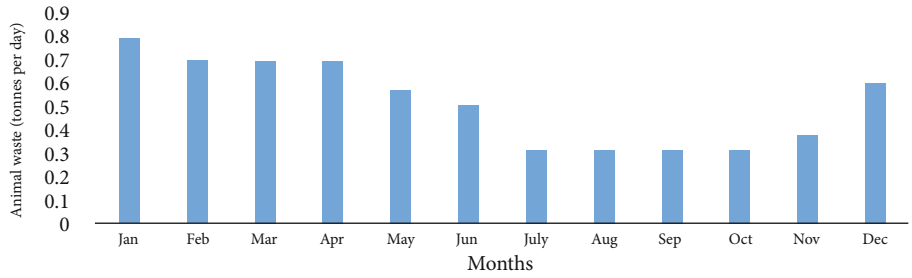


Figure 7: Annual monthly average available biomass resource.

templates before the detailed evaluation by HOMER Pro software [9]. Figure 8 indicates electrical load based on the considered applications for the area of study. The nature of graphs of power consumption is basically based on the behavior of socioeconomic activities of people dwelling in the area of study. The load classification above is further categorized as per consideration of the sensitiveness of health amenities. Here, sensitiveness means to ensure the constant availability and reliability of the health facility. The village electricity consumption is categorized into two main groups such as load profile 1 and load profile 2 [9]. In this study, load for IHC is excluded from institutional load and is combined with street lighting. For the efficiency and effectiveness of health centres, street lighting is of paramount importance. Therefore, load profile 1 (critical load) includes electrical load for the IHC and street lighting. Electrical load for IHC is constituted by a number of equipment of different rates of power consumption. In this specific study, due to the sensitiveness of IHC, its power consumption has been assumed to be constant throughout the day. Residential load is estimated to be 30 kW representing 50% of the daily maximum peak demand. Lighting load is the lowest at approximately 0.2 kW while power for transport and irrigated agriculture is zero. Load profile 2 (noncritical load) consists of residential, commercial, institutional, and small-scale industrial loads [9, 68]. Rural electrification projects based on commercial and small-scale industrial loads are limited to productive uses in the country. Figure 9 indicates critical loads which include the energy demand for the MDCH facility (also known as IHC) and street lighting load.

(2) Comprehensive Electrical Load Demand Analysis Using HOMER. Estimation of load profile in Excel data sheet is practically limited to peak power capacity. It is not capable of providing energy consumption per day, power variability, and load factor. Therefore, electrical load demand based on the existing types of consumers in the village is partially validated in HOMER Pro software in order to find the lowest cost amalgamation of supply choices by meeting the demand [9]. As has been aforementioned in this research, the HRESS is expected to generate electricity for the village (community) daily load of 165.44 kWh and peak power of 10.76 kW peak (scaled) or 63.41 kW (baseline) with a load factor of 0.64. Figure 2 is the schematic diagram for the HRESS for the proposed site. The considered HRESS is 100% renewable, meaning that no DG has been employed. Table 5 gives a summary of electrical power consumption for Simboya village per

Table 4: Electrical load categories in consideration of consumers at Simboya village.

Load classification	Wattage in watts collected from rating of electric appliances
Residential	465945
Institutional load including Ikukwa Health Centre	190730
Commercial	18121
Small-scale industrial	265338
Street lighting	4800
Irrigation and agricultural	0
Transport	0
Total	944934

AC load classification processed in HOMER Pro software. In this study, the daily profile for IHC and its surrounding street lighting has been assumed to be constant all the time though there is a variation in power consumption. Figure 10 indicates daily power for noncritical loads (consisting of residential, institutional, commercial, and small-scale industrial loads).

4. Descriptions of Components and Design of Off-Grid HRESS

The survey carried out in the area of study has indicated that solar and biomass energy resources have a high potential of generating electricity. Therefore, electrical power-generating components in HRESS are solar photovoltaic (PV) panels and biomass/biogas generators (BIOG). In this study, BIOG is used as a standby. The devices such as deep cycle batteries and converters are also included in the system for energy storage and electrical power conversion, respectively.

Based on these selected components, optimal configuration is achieved from HOMER Pro software analysis. Figure 11 indicates the wiring scheme for the proposed off-grid hybrid solar PV-biogas-battery system for Simboya village, and Figure 12 shows the wiring scheme for the grid-connected hybrid solar PV-biogas-battery system for Simboya village.

However, in this study, grid connectivity of the grid-connected hybrid solar PV-biogas-battery system has been considered merely for economic comparison and examination of the economic distance limit (EDL) for the viable grid

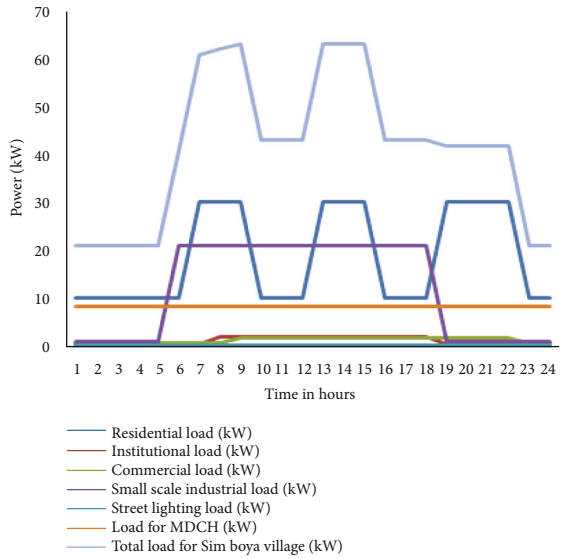


Figure 8: Accumulated load profile of various applications in the area of study.

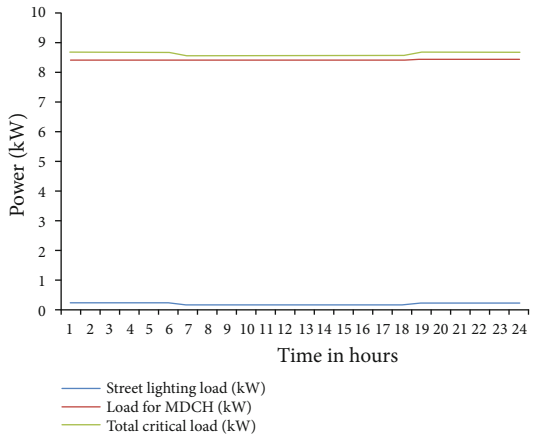


Figure 9: Critical load combining MCDH (IHC) and street lighting loads.

extension. The component's reliability and cost-effectiveness are important aspects of the successful micropower system design. The following is the selection of components and design of HRESS.

4.1. Selection of Components. A solar PV system consists of a number of panels in a series connection. Power output from PV constitutes a primary power in HRESS due to its cost-effectiveness compared with BIOG of equivalent capacity. Solar PV has been designed for generating a power output of 40 kW. The financial input parameters have been assumed in the optimization of the systems. The initial cost and replacement price for a capacity of 1 kW PV are considered \$700.00 and \$0, respectively. Performance of PV is assumed to be suitable within a timeframe of an anticipated project's lifespan of 25 years. Operation and maintenance (O&M) of PV are low, and it is only \$1.5/year. The derating factor for the individual solar module is considered to be 80% in order to counteract the ambient temperature and unclean conditions. A PV system has no tracking system. Also, BIOG has been planned for delivering a power output of 25 kW. The initial price, replacement cost, and O&M price for a capacity of 1 kW BIOG are considered \$260, \$160, and \$0.90/op.hr, respectively. BIOG is attached to AC output with a lifespan of 20,000 hours. The minimum load ratio is assumed to be 50% of the total power capacity. The bank of deep cycle batteries has been utilized to store excess power during the availability of high solar radiation and supply the stored energy to the electrical load in the absence of solar energy resources. The type of the selected battery is generic 1 kWh Li-ion with a nominal voltage of 6 V. The bank consists of 144 batteries, 4 batteries connected in series per string, and 36 strings in parallel, and the system bus voltage is 24. The initial price, replacement price, and O&M expenses per unit of the battery were taken as \$700, \$0, and \$1.5/year. The battery bank has an autonomy of approximately 17 hours with a lifetime throughput of 432,000 kWh. The intended rated power output of the inverter is 40 kW. The initial price, replacement charge, and O&M expenses of the converter capacity for 1 kW were assumed as \$200, \$200, and \$10, respectively. The lifespan of the converter is 15% while inverter and rectifier efficiencies are equal each with 95%.

4.2. Design of the Proposed HRESS. In this work, the design of the optimal solar photovoltaic-biogas-battery system was implemented in HOMER Pro software. Data for system configuration and selected components are used for the optimization process. Parameters such as capital price, cost of energy, and net present cost are obtained in the optimal design compared. Economic comparison is made in the financial section. There is a problem of uncertainty problem due to the intermittent nature of renewable energy sources (RESs). Uncertainties are related to the variability of the key input parameters of RES and thus lead to the complicated design of a microdistributed electric generating system. In this study, uncertainties have been considered, and therefore, variables such as solar radiation, fuel price, and load variation based on assumed scenarios (100% RE scenario) are a proposed primary scenario or base case scenario in which biogas is used as a backup; in the second scenario, DG is used as backup instead of biogas; and in the third scenario, DG is assumed to deliver power to the micropower system for continuous duty. The life cycle cost (LCC) method is used for financial comparison among the simulated feasible systems. The system which has the lowest NPC is the most economically favourable system, that is, optimally designed system. In this study, economics and constraints for the project are operating reserve which is 80%, nominal discount rate which is 8%, and expected inflation which is 4%. In this work, grid extension is used as a reference by HOMER for the comparison of both technical and financial parameters of the off-grid HRESS. Therefore, the specific objective of economic analysis between grid extensions versus off-grid HRESS is to examine whether the grid extension is viable or not. The critical price of grid extension per kilometre for the available terrain at Simboya village is considered to be

Table 5: Summary of electrical power consumption for Simboya village per AC load classification processed in HOMER Pro software.

Village load classification	Baseline max. power (kW)	Scaled consumption (kWh/day)	Scaled max. power (kW)	Load factor
Residential load	30.27	11.26	0.76	0.61
Institutional load	3.18	165.44	18.45	0.37
Commercial load	2.69	165.44	15.84	0.44
Small-scale industrial load	35.81	165.44	22.33	0.31
Ikukwa Health Centre (IHC)	8.42	165.44	6.89	1
Street lighting	0.42	165.44	14.94	0.46
Accumulated village load	63.41	165.44	10.76	0.64
Critical load	14.72	165.44	11.77	0.59
Noncritical load	54.84	165.44	11.82	0.58

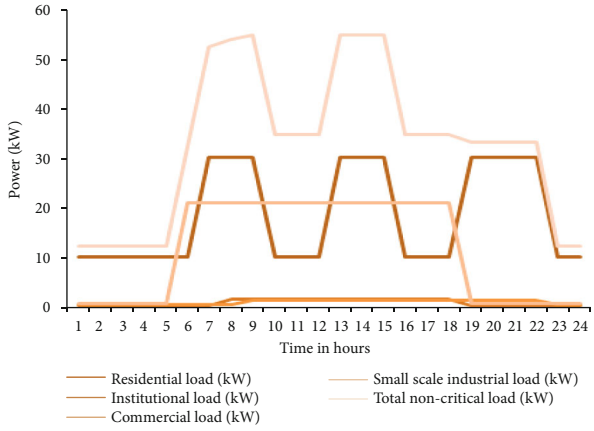


Figure 10: Noncritical load.

$8,000/km. The yearly O&M cost per kilometre is considered to be $1,500/year, and the grid power price in the Tanzanian environment is assumed to be $0.44/kWh. Based on LCOE and economic distance limit (EDL), a comparison of the economic effectiveness between the most favourable off-grid HRESS and grid extension for rural electrification is carried out. The price for the low voltage (LV) distribution systems in the village is not inclusive because the cost is similar in both options. Environmental analysis was also carried out to investigate the amount of emissions or pollutants in proportion to the selected components of the proposed off-grid HRESS.

5. Modelling of Amalgamated Power System Devices

It should be recalled that in this study, three off-grid optimal configurations, namely, solar PV-DG-battery, solar PV-biogas generator-battery, and DG-only systems have been compared. Out of the three optimized configurations, the solar PV-biogas generator-battery is the most cost-effective. Modelling of the individual components of the system is as follows.

5.1. Solar PV Generator. Solar power is generated based on the available solar energy resource at a given location. In this study, effects of temperature on solar cells are ignored. Therefore, the energy output of the solar PV generator (Gpv) can be computed using Equation (3) as follows [69]:

$$G_{\mathrm{PV}}(t) = Q(t) \times A \times D \times \acute{\eta}_{\mathrm{PV}}, \tag{3}$$

where $Q(t)$ represents the solar radiation (kWh/m^2), the surface area of the solar module (m^2) is denoted by A, D symbolizes the solar energy penetration factor, and $\acute{\eta}_{\mathrm{PV}}$ denotes the efficiency of the solar PV generator (%).

5.2. Biogas Generator. In a biogas-powered generator, electricity is generated from biological wastes. Power generated by biogas is generally expressed in Equation (2). However, for the purpose of modelling, this equation can alternatively be expressed as follows in Equation (4) [70]:

$$P_{\mathrm{BIOG}} = \prod_{\mathrm{BIOG}} \times U_P(t) \times \mathrm{CV}_{\mathrm{BIOG}}, \tag{4}$$

where U_P(t) is the amount of biogas consumed (m^3/h), n_{BIOG} as an efficiency of biogas system (assuming it is equal to 27%), and $\mathrm{CV}_{\mathrm{BIOG}}$ embodies the LHV (kWh/m^3). LHV relies on the concentration of CH_4 of the biogas. LHV is assumed to be 21.78 kJ/m^3 assuming the concentration of CH_4 is equal to 60%.

5.3. Battery Bank. In case energy generated by biogas and solar photovoltaic generators cannot satisfy the electrical load demand, the battery can start discharging in order to overcome such an imbalance. The battery capacity depends on SOC. The battery capacity of the system is defined in Equation (5) as follows [71]:

$$G_{\mathrm{btt}\,(t)} = \frac{E \times DA}{V_{\mathrm{btt}} \times \mathrm{DOD} \times \prod_{\mathrm{btt}}}, \tag{5}$$

where E denotes the daily energy demand (Wh), DA represents the number of days of battery bank autonomy, V_{btt} delineates system voltage, depth of discharge is abbreviated as DOD, and $_{\mathrm{btt}}$ stands for battery efficiency. Quantity of batteries is prescribed based on ampere-hour capacity.

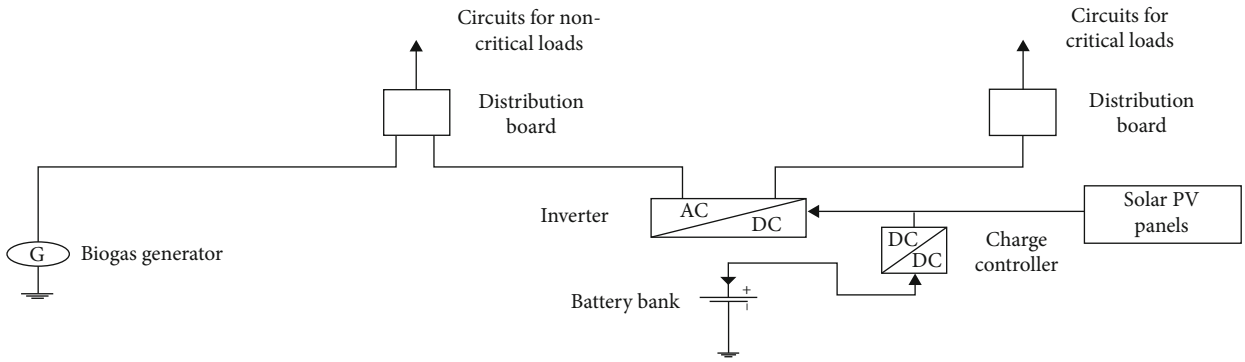


Figure 11: Schematic of the proposed off-grid hybrid solar PV-biogas-battery system.

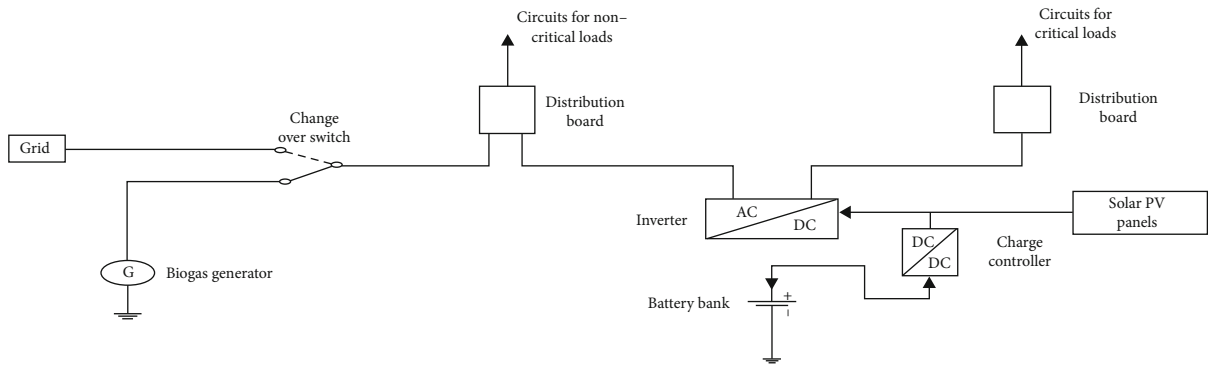


Figure 12: Schematic of grid-connected hybrid solar PV-biogas-battery system.

5.4. Converter. A converter is a bidirectional device combining an inverter and rectifier to maintain the direction of an electric current between the alternating current (AC) and direct current (DC) appliances. This device is necessary for smoothly interfacing energy sources, electrical load, and energy storage systems. The electrical load and biogas generator are connected to the AC bus bar while the solar photovoltaic array and battery bank system are connected to the DC bus bar. Converter power capacity should be at least greater than the highest load demand in order to permit the greatest rated power flow. Generally, input power to the inverter is computed using Equation (6) as follows [71]:

$$E_{\mathrm{INV}} = \frac{E_L}{\prod_{\mathrm{INV}}}, \tag{6}$$

where E_{INV} and $\prod_{\mathrm{INV}}$ define the input power and the efficiency of the inverter, respectively.

6. Economic and Technical Input Data of the Proposed Off-Grid HRESS

This section describes the financial and technical specifications including the details of the site of the project. In particular, the section presents the financial and technical specifications of the selected solar panel, biogas generator, battery, converter, description of the site of the project, and input parameters for solar panel, biogas generator, and converter, respectively.

6.1. Input Parameters of Solar PV Generator. In this study, the solar PV power system is considered to be fixed-mounted. The system is made by the connection of a number of solar panels so as to achieve the required values of system voltage and current flow. One type of PV panel is selected from Saatvik Green Energy Company with presumed costs for the Tanzanian environment [72]. Table 6 provides the input parameters of the solar PV module.

6.2. Input Parameters for Biogas Generator. The highest power to be produced by the biogas generator is anticipated to be 25 kW. Therefore, based on this fact, a unit of biogas generator from NPT General Exporters is considered, and all costs of the unit are adapted for the Tanzanian environment [73]. Table 7 shows the input parameters of the selected biogas generator.

6.3. Input Parameters of Battery. The intermittency nature is one of the drawbacks of renewable energy sources thus necessitating the use of energy storage systems like batteries. One type of battery is chosen from Shenzhen GSL Energy Company with presumed costs for the Tanzanian environment [74]. Table 8 provides the input parameters of the battery.

6.4. Converter. In this particular study, the capacity of the converter is assumed to be 20% higher than the estimated highest daily load demand. Converter experiences switching and conduction power losses [75]. Arithmetically, power capacity of invereter (E_{INV}) can be simply determined using

Table 6: Input parameters of solar PV module.

Parameter	Specifications
Manufacturer	Saatvik Green Energy Company
Model	SGE 335-72M
Rated power	335 Wp
Technology	Polycrystalline
Dimensions	1955 mm × 991 mm × 35 mm
Short-circuit current, I_{SC}	9.35 A
Open-circuit voltage, V_{OC}	46.25 V
Efficiency	17.29%
Capital cost	$700
Operation and maintenance cost	$1.5/year
Replacement cost	$0
Lifespan	25

Table 7: Input parameters of biogas generator.

Parameter	Specifications
Company	NPT General Exporters
Model	KDGH25-G
Rated voltage	25 kW
Rated voltage	400 V/415 V/380 V
Frequency	50 Hz
Number of phases	Three phases (AC)
Power factor (lagging)	0.8
Engine model	HG4B
Speed	1500 RPM
Type of cooling	Natural cooling
Provision of power	Continuous
Capital cost	$260
Operation and maintenance cost	$0.9/year
Replacement cost	$160
Lifespan	35

Equation (7) as follows:

$$E_{\mathrm{INV}} = E_L + (20\%\text{of } E_L). \tag{7}$$

If load demand E_L equals to 63.41 kW is substituted into Equation (7), therefore estimated E_{INV} equals to 76.092 kW. Based on the available market, the inverter capacity of 80 kW is selected from Novergy Energy Solar Pvt Ltd [76]. Table 9 provides the input parameters of the converter.

6.5. Description of Connected Electrical Load. Electrical load is one or more appliances which are deliberately connected to an electric system to utilize electrical energy. For a proper design of any energy system for a given place, it is noteworthy to carefully consider the electrical load profile. Periodic variations of the electrical load need to be known for achieving a high-reliability system by maximization and minimization of power resources and costs, respectively. Moreover, the capacities of energy storage systems and energy sources rely on the electrical load profile. The data of load variation for the site under study are equal to 165.44 kWh/day and 63.41 kW.

6.6. Description of the Site of the Project. This section provides information related to the site such as lifespan, nominal discount rate, and inflation rate. Table 10 indicates the assumptions of input parameters of the site.

7. Strategy for Managing Off-Grid HRESS

Solar PV and biogas generators are the main sources constituting the hybrid energy system. Batteries are also incorporated into the system in order to compensate for the incompatibility between the energy demand and generated power.

Power generated by solar panels can be defined using Equation (8) as follows [77]:

$$G_{\mathrm{PV}}(t) = n_{\mathrm{PV}} \times p_{\mathrm{PV}}(t), \tag{8}$$

where $G_{\mathrm{SP}}(t)$ represents total power produced by solar photovoltaic array, n_{PV} refers to the quantity of solar panels, and p_{PV} (t) denotes power produced by one solar photovoltaic panel.

Similarly, power generated by a biogas generator can be defined using Equation (9) as follows [77]:

$$G_{\mathrm{BIOG}}(t) = n_{\mathrm{BIOG}} \times P_{\mathrm{BIOG}}(t), \tag{9}$$

where $G_{\mathrm{BIOG}}(t)$ represents the total power produced by all biogas power-generating units, n_{BIOG} refers to the quantity of biogas generators, and $p_{\mathrm{BIOG}}(t)$ indicates power produced by a single biogas generator.

The total generated power obtained by the two sources is expressed by a combination of Equations (8) and (9) as follows [77]:

$$G_{\mathrm{SB}}(t) = G_{\mathrm{PV}}(t) + G_{\mathrm{BIOG}}(t). \tag{10}$$

Alternatively, Equation (10) may be rewritten using Equation (11) as follows:

$$G_{\mathrm{SB}}(t) = n_{\mathrm{PV}} \times p_{\mathrm{PV}}(t) + n_{\mathrm{BIOG}} \times p_{\mathrm{BIOG}}(t). \tag{11}$$

The produced power from the two renewable energy sources based on their obtainability is computed as follows [77]:

$$G_{\mathrm{SB}}(t) = n_{\mathrm{PV}} \times p_{\mathrm{pv}} \times A_{\mathrm{pv}} + n_{\mathrm{BIOG}} \times p_{\mathrm{BIOG}}(t). \tag{12}$$

The management strategy of renewable energy systems is complicated due to their discontinuous nature. In this study, the strategy consists of several setups that are explained as follows:

(i) *Setup 1*. Battery bank is allowed to charge only if the electrical load is met by all energy sources.

The battery bank is allowed to charge when power generated by the energy system is greater than the energy

Table 8: Input parameters of battery.

Parameter	Specifications
Manufacturer	Shenzhen GSL Energy Company
Model	KS-12300
Nominal voltage	12 V
Nominal capacity	300 AH
Type	Lithium-ion battery ($LiFePO_4$ battery)
Cycle life	More than 3000 times
Efficiency $\prod_{btt}$ (assumed)	85
DOD (assumed)	80
Lowest permissible charge	20
Capital cost	$700
Operation and maintenance cost	$10/year
Replacement cost	$700
Lifespan	10

Table 9: Input parameters of converter.

Parameter	Specifications
Manufacturer	Novergy Energy Solar Pvt Ltd
Model	IPCL 80 kW
Type	Hybrid (on-grid/off-grid)
Rated output voltage	380 V/400 V/415 V AC, TPN
Rated power capacity	50 Hz
Rated power capacity	80 kW
Power factor	0.8 lagging
Efficiency $\prod_{INV}$	92%
Capital cost	$200
Operation and maintenance cost	$10/year
Replacement cost	$200
Lifespan	10

Table 10: Assumptions of input parameters of the site.

Parameters of the project	Specifications
Lifespan	25 years
Nominal discount rate	8%
Expected inflation rate	4%

demand at a given time. The battery bank is charged to store the surplus energy when the load is satisfied first. Energy stored by the battery bank is expressed in Equation (13) as follows [78]:

$$G_{btt(t)} = G_{btt(t-1)} + \left(G_{SB(t)} - \frac{E_L(t)}{\prod_{ivt}}\right) * \prod_{btt}, \quad (13)$$

where $G_{btt(t)}$ and $G_{btt(t-1)}$ are defined as electrical energies stored in the battery bank at t and $t-1$ times, respectively; $G_{SB(t)}$ represents energy produced by the hybridized energy system; $_{btt}$ and $_{ivt}$ represent efficiencies for battery and inverter, respectively; and energy demand at time t is symbolized by $E_L(t)$.

(ii) *Setup 2*. Battery discharges only if the electrical load is not met by all energy sources.

The battery bank is required to discharge if power generated by the energy system is lower than the energy demand at given time t. Therefore, the energy from the battery bank is discharged to meet the load. Energy discharged by the battery bank is described in Equation (14) as follows [78]:

$$G_{btt(t)} = G_{btt(t-1)} - \left(\frac{E_L(t)}{\prod_{ivt}}\right) - G_{SB(t)}\Big). \quad (14)$$

(iii) *Setup 3*. Otherwise, the load is not met by energy sources and battery storage system meaning that there is a deficiency of energy. This idea is fully discussed in relation to system reliability [78].

8. Optimization of Off-Grid HRESS Using GWO Method

The first phase of this paper has been executed in HOMER Pro software. This software mimics the probable system configurations to acquire the optimal arrangement of hybridized energy sources to meet the daily load demand. Input data related to solar radiation, biomass particularly animal and poultry wastes, components of the system, and load demand have been used for the simulation process. In the second phase, application of the GWO method is employed. In this particular phase, LEPP, NPC, and COE are minimized. These parameters are known as objective functions. Decision variables are rated power output of solar PV, number of biogas generator, autonomy days of battery system, and number of DG. In short, this section deals with financial and technical optimization models as follows.

8.1. Technical Optimization Model. This section of the paper offers a detailed explanation of the reliability of the system in relation to setup 3 of the management strategy. LEPP defines the reliability factor of a microgrid system. A reliable energy system can meet the load sufficiently for a given period of time. On the other hand, the less the LEPP, the more the system is reliable. LEPP denotes a reliability factor of the microgrid system. If the value of LEPP is equal to zero, it means that power generated and load demand are perfectly balanced. If the same factor is equal to one, it implies that there is an imbalance of power generated and load demand due to the shortage of electricity. Therefore, before defining LEPP mathematically, the deficiency of electricity called unavailability of electricity supply (UES) is expressed in Equation (15) as follows [78]:

$$\mathrm{UES}_{(t)} = E_{L(t)} - \left(G_{\mathrm{PV}}(t) + P_{\mathrm{BIOG}}(t) + G_{btt\,(t-1)} - G_{bttMIN}\right) * \Pi_{ivt}. \tag{15}$$

Now, LEPP for duration of time T can be defined as a ratio of the whole UES calculated every period t to the sum of power demand. The ratio is mathematically described in Equation (16) as follows [71, 77, 78]:

$$\mathrm{LEPP} = \frac{\sum_{t=1}^{T} \mathrm{UES}_{(t)}}{\sum_{t=1}^{T} E_{L(t)}}. \tag{16}$$

Renewable fraction (RF) is defined as a fraction of power delivered to the load which is generated by nonconventional energy sources. Numerically, REF is expressed using Equation (17) as follows [71]:

$$\mathrm{RF} = 1 - \frac{\sum_{t=1}^{8760} \mathrm{out}_{DG(t)}}{\sum_{t=1}^{8760} G_{SB}(t)}. \tag{17}$$

$\mathrm{out}_{DG(t)}$ connotes the power generated by conventional energy sources (solar PV and biogas). In this study, the system consists of 100% nonconventional energy sources, and thus, RF equals 1.

8.2. Financial Optimization Model. It should be recalled that in the first part of this study, the HOMER platform has been used to simulate the system. The central function of the tool is to obtain optimal configuration at the smallest total NPC [79]. This platform of research calculates the mean annualized price of each system component plus associated penalties of ecological pollution [72]. This type of price is useful for determining the total NPC and LCOE [79]. Both economic metrics can be generated using the annualized capital cost of every component of off-grid HRESS. In the second phase of this study, optimization is implemented by using the AI approach using the GWO method, and the particular economic index used is the least total NPC. The following is the description of the economic index.

8.2.1. Computation of Total NPC. One of the primary parameters for establishing the sustainability of off-grid HRESS is the total NPC. The NPC can be simply defined as a sum of the whole expenses of the project's lifespan in Equation (18) [80]:

$$\mathrm{NPC} = \frac{\mathrm{AAP}}{\mathrm{CRF}\left(i, J_{\mathrm{proj}}\right)}, \tag{18}$$

where J_{proj} is the lifespan of the project in years and CRF represents the capital recovery factor in Equation (19) [79, 80]:

$$\mathrm{CRF}\left(i, J_{\mathrm{proj}}\right) = \frac{i(1+i)^{J_{\mathrm{proj}}}}{(1+i)^{J_{\mathrm{proj}}} - 1)}, \tag{19}$$

where CRF is defined as the capital recovery factor, i is the nominal discount rate, and J is the lifespan of the proposed HRESS with battery energy storage.

8.2.2. Computation of Aggregated Annualized Price. Aggregated annualized price (AAP) includes the whole annualized prices of the system in \$/year. It consists of annualized investment price (AIP), annualized spare price (ASP), annualized fuel price (AFP) of energy source, and annualized operation and repair price (AOMP) of the hybrid system. AAP can be determined using Equation (20) as follows [69]:

$$\begin{aligned}\mathrm{AAP} = {} & \mathrm{AIC}\,(\mathrm{PV} + \mathrm{BIOG} + \mathrm{Battery} + \mathrm{Converter}) \\ & + \mathrm{ASP}\,(\mathrm{PV} + \mathrm{BIOG} + \mathrm{Battery} + \mathrm{Converter}) \\ & + \mathrm{AFP}\,(\mathrm{PV} + \mathrm{BIOG}) + \mathrm{AOMP} \\ & \cdot\,(\mathrm{PV} + \mathrm{BIOG} + \mathrm{Battery} + \mathrm{Converter}).\end{aligned} \tag{20}$$

AFP of the solar energy source is ignored because the fuel is free of charge. Furthermore, the total NPC of solar PV is further reduced due to its lifespan of 25 years equivalent to the project life cycle. AOMP of fixed solar PV are trivial and thus negligible. Unavailability of AFP, AOMP, and ASP of solar PV is beneficial because, for a given lifespan of 25, the total NPC is significantly reduced. The total NPC of other individual components such as the battery and converter is increased over the whole lifespan due to the requirement of AOMP depending on the lifespan of every component. AFP of BIOG is taken into account as biogas fuel is sold at 80% of diesel fuel cost. In addition, for a simplified analysis of the system, salvage value is neglected.

8.2.3. Computation of LCOE. LCOE (\$/kWh) refers to the average charge per unit of useful generated electricity. LCOE can be computed in Equation (21) as follows [79, 80]:

$$\mathrm{LCOE} = \frac{\mathrm{NPC} \times \mathrm{CRF}}{\mathrm{Energy\ produced\ per\ annum\ (kWh/year)}}, \tag{21}$$

where EL is the total annual energy consumption (kWh/year). LCOE may alternatively be computed in terms of AAP using Equation (22) as follows [79, 80]:

$$\mathrm{LCOE} = \frac{\mathrm{AAP\ (\$/year)}}{\mathrm{Energy\ produced\ per\ annum\ (kWh/year)}}. \tag{22}$$

8.2.4. Formulating Objective Function and Constraints. One objective optimization technique with a focus on the total NPC standards and its corresponding LCOE is employed. The research platform deployed in the entire optimization process for coding is MATLAB. The principal goal is the minimization of the total NPC. Here, total NPC represents the suitability function subject to several limits (constraints). The decision parameters are area of solar PV module (A_{PV}), power generated by biogas generator (P_{BIOG}), quantity of batteries (N_{btt}), and quantity of converters (N_{CONV}). The objective function is formulated under the constraints of decision

parameters, and system reliability is presented in Equation (23) as follows [69]:

(1) Objective function

$$\text{Minimization of total NPC} = \sum_{i=A_{\text{PV}},P_{\text{BIOG}},N_{\text{btt}},N_{\text{CONV}}} \left(\frac{\text{APP}_i}{\text{CRF}}\right) \tag{23}$$

(2) Constraints

$0 \le A_{\text{PV}} \le A_{\text{PV}}^{mx}$, $0 \le p_{\text{BIOG}} \le P_{\text{BIOG}}^{mx}$, $0 \le N_{\text{btt}} \le N_{\text{btt}}^{mx}$, $0 \le N_{\text{CONV}} \le N_{\text{CONV}}^{mx}$, and $0 \le \text{LEPP} \le \text{LEPP}^{mx}$

N_{btt} and N_{CONV} are integers; A_{PV}^{mx}, P_{BIOG}^{mx}, N_{btt}^{mx}, N_{CONV}^{mx}, and LEPP^{mx} are the greatest values of the total area of solar modules, generated power by biogas power generating unit, quantity of batteries, quantity of converter, and system reliability index, respectively. In this phase of the study, the GWO method is used to evaluate the objective function under the specified constraints. Based on the selected sizes of components of the system within their defined constrained limits, the viable configurations are found at the least total NPC in the light of the prescribed values of LEPP of the HRESS.

8.2.5. Application of GWO Method. The GWO method was devised by Mirjalili and his coresearchers in 2014 [69] [81]. In accordance with the researchers, this method is motivated by the social headship pyramid and mechanism of hunting grey wolves in nature. The commanding chain of the wolves is split up into four groups such as alpha (α), beta (β), delta (δ), and omega (ω) without taking into account gender. In the GWO method, the finest solutions are denoted by α, followed by β and δ wolves [69, 81]. ω is the final group (scapegoats) which is submissive to the dominant groups (α, β, and δ). The whole process of hunting is assumed to be executed by the dominant groups [69]. The procedure of hunting is implemented in three phases such as tracing which involves chasing and moving near the target, following the victim, and attacking the victim [69, 81]. A numerical model is formulated referring to the aforementioned phases of hunting. In the first place, the encircling manner is numerically modelled using Equations (24) and (25) as follows [69, 81]:

$$\vec{C} = \vec{\mu_2} \cdot \vec{L_p}(i) - \vec{L_g}(i), \tag{24}$$

$$\vec{L_g}(i+1) = \vec{L_p}(i) - \vec{\mu_1} \cdot \vec{C}. \tag{25}$$

$\vec{\mu_1}$ and $\vec{\mu_2}$ in the above equations represent the coefficient vectors of the targeted victim. These vectors are computed using Equations (26) and (27) as follows [69, 81]:

$$\vec{\mu_1} = 2 \times \vec{A} \cdot \vec{R_1} - \vec{A}, \tag{26}$$

$$\vec{\mu_2} = 2 \cdot \vec{R_2}, \tag{27}$$

where $\vec{L_g}(i)$ and $\vec{L_p}(i)$ stand for the location of the wolves and the victim in the ith iteration. Magnitudes of $\vec{A}$ diminish linearly starting from 2 to 0 in the course of iteration. $\vec{R_1}, \vec{R_2}$ represent arbitrary vectors in the range of 0 to 1. As has been explained before, the process of surrounding the victim is headed by β and δ. After the accomplishment of the encircling, another phase of finalizing the process is implemented by the leading group of grey wolves from their respective locations. This final stage is mathematically expressed in Equations (28), (31), and (34) as follows [69, 81]:

$$\vec{C_\alpha} = \left|\vec{\mu_2}[1] \times \vec{L_\alpha} - \vec{L_p}\right|, \tag{28}$$

$$\vec{C_\beta} = \left|\vec{\mu_2}[2] \times \vec{L_\beta} - \vec{L_p}\right|, \tag{29}$$

$$\vec{C_\delta} = \left|\vec{\mu_2}[3] \times \vec{L_\delta} - \vec{L_p}\right|, \tag{30}$$

$$\vec{L_p}[1] = \vec{L_\alpha} - \vec{\mu_1}[1] \times \vec{C_\alpha}, \tag{31}$$

$$\vec{L_p}[2] = \vec{L_\beta} - \vec{\mu_1}[2] \times \vec{C_\beta}, \tag{32}$$

$$\vec{L_p}[3] = \vec{L_\delta} - \vec{\mu_1}[3] \times \vec{C_\delta}, \tag{33}$$

$$\vec{L_p}(i+t) = \frac{\vec{L_\alpha}[1] + \vec{L_\beta}[2] + \vec{L_\delta}[3]}{3}. \tag{34}$$

$\vec{\mu_1}$ denotes an arbitrary value that lies in the range from $-2A$ to $2A$. If $|\mu_1|$ is lower than 1, grey wolves are required to attack the victim. If $|\mu_1|$ is larger than 1, grey wolves are compelled to go away from the victim.

8.2.6. Execution of GWO Method for Optimal System Sizing. The following are the important steps of executing the GWO method for optimal system sizing [77, 81]:

(i) Preparing the magnitude of the population and input variables of GWO

(ii) Establishing the search representative and producing the parameters arbitrarily (selecting randomly the quantity of solar PV modules and biogas power generating units from relevant constraints)

(iii) Estimating the number of batteries after the computation of the total produced energy by renewable energy sources of the system by taking into account the reliability (obtaining the feasible population subject to the predefined LEPP value from relevant constraints)

(iv) Feeding the decision variables to the formulated objective function (Equation (23)) from the set of feasible population and calculating total NPC

(v) Selecting the least total NPC acquired from the feasible populations equal to the population size. The

NPC is assumed as the finest fitness for the first iteration

(vi) Updating the location of exploration agents, while $t <$ the greatest sum of repetitions and randomly compute the amount of solar PV modules

(vii) Computing the formulated objective function of new exploration agents by estimating the quantity of batteries

(viii) Determining the new finest exploration agents and substituting it with the old finest exploration agent, knowing that the new is superior to the old finest exploration agent

(ix) Is the terminating condition fulfilled? If it is not, repeat step (ii), and if the condition is satisfied, then move to the next step

(x) Determining the optimal size (optimal parameters including the least value of LCOE) of the proposed energy system and finalizing the GWO method

Two main conditions have been used during the modelling strategy to consider for LEPP evaluation with respect to the energy demand in the entire process of optimization:

Condition 1. When solar PV panel is generating surplus power in comparison with authentic energy demand.

Condition 2. When solar PV panel is generating less power in comparison with authentic energy demand.

9. System Reliability and Sensitivity Analysis Using GWO Algorithm

Prior to carrying out the sensitivity analysis, technoeconomic analysis of off-grid HRESS is carried out using the GWO method in addition to HOMER software. In this first case, the system is assumed to be balanced meaning that generated power supply and load demand are balanced. In such a condition, there is no shortage of energy. However, this condition practically cannot always be maintained as generated power varies periodically. In the second case, the analysis of the system is further investigated by the variation of LEPPs. Here, the designed system is assumed to generate power less than the generation power capacity. In this context, generated power supply and energy demand are not balanced implying a shortage of power. This section of the research article presents system optimization and sensitivity analysis.

9.1. The Uppermost and Lowermost of LEPP. LEPP can be computed using Equation (16) after the determination of the shortage of power supply using Equation (15). For the straightforwardness of calculating the LEPP, in this study, Equation (4) can be simplified into Equation (35) as follows [77, 78]:

$$\mathrm{UES}_{(t)} = E_{L(t)} - \left(G_{\mathrm{SB}}(t) + G_{\mathrm{btt\,bank}\,(t)}\right). \tag{35}$$

Table 11: Miscellaneous specifications for GWO technique.

Parameters	Value
Population size of grey wolves, n	12
Maximum number of iterations, $\mathrm{iter}_{\max}$	100
Inflation rate	6%
Interest rate	3.04%
Highest capacity of biogas generator, $P_{\mathrm{BIOG}}^{\mathrm{maxi}}$	25 kW
Highest quantity of solar panels, $N_{\mathrm{PV}}^{\mathrm{maxi}}$	100
Highest quantity of batteries, $N_{\mathrm{btt}}^{\mathrm{maxi}}$	764
Highest quantity of converters, $N_{\mathrm{CONV}}^{\mathrm{maxi}}$	20
Highest LEPP, $\mathrm{LEPP}^{\mathrm{maxi}}$	0.07

If power generated from renewable energy sources plus stored power in the battery bank satisfies all energy required for 100%, Equation (35) is rewritten as Equation (36). LEPP can be estimated using Equation (16) as follows [77]:

$$\mathrm{UES}_{(t)} = E_{L(t)} - 100\% * E_{L(t)}, \tag{36}$$

$$\mathrm{UES}_{(t)} = 0. \tag{37}$$

Using the GWO method, an appraisal of the objective function consistent with the delineated constraints is made. Sizes of components are selected within the stated limits. Identification of viable configurations of the hybrid system is done in relation to the preset magnitudes of LEPP. The best possible solutions are repeated in the GWO method. The structure is updated to estimate the minimum total NPC. LEPP is determined by substituting Equation (36) into Equation (16) which equals zero. It implies that the system satisfies the power supply requirement when LEPP = 0. Also, the system is also assumed to produce power not lower than 93% of the whole load giving the highest value of LEPP equal to 0.07. Values of LEPP for the sensitivity analysis are evaluated with a similar approach. Here, the hybrid energy system is assumed to generate power of 96% and 94% of the total actual load yielding LEPP values equal to 0.04 and 0.06, respectively. Table 11 specifies miscellaneous specifications for the GWO technique.

9.2. Comprehensive Methodology for Sizing the Proposed HRESS Using GWO Algorithm. Optimization parameters such as solar radiation, animal wastes, and electrical load data and assumed constants (data sheet) were used as input variables. Decision variables like A_{PV} and P_{BIOG} were estimated by the GWO algorithm for individual iteration. Then, the power from solar PV (P_{PV}) and biogas generator (P_{BIOG}) were estimated with variable inputs, assumed constant inputs, and approximated decision variables. In order to meet the energy requirements, the potential of solar energy is considered to be maximized deliberately so as to use an advantage of free fuel in comparison with biomass, in this case, animal wastes. However, if generated electricity from aforesaid energy sources does not satisfy the load demand, stored energy from batteries is used to balance power supply

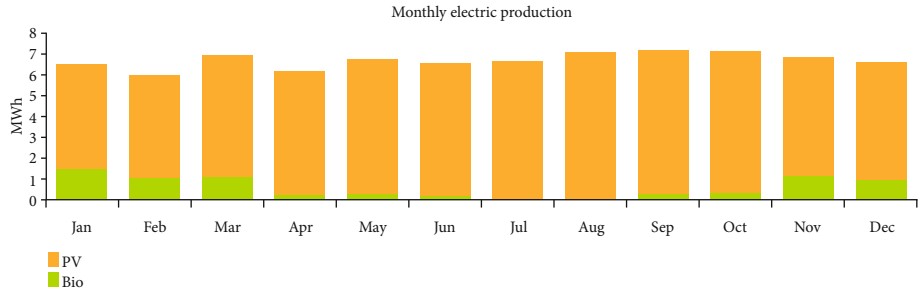


Figure 13: Annual monthly electric production of hybrid PV-BIOG-battery storage system.

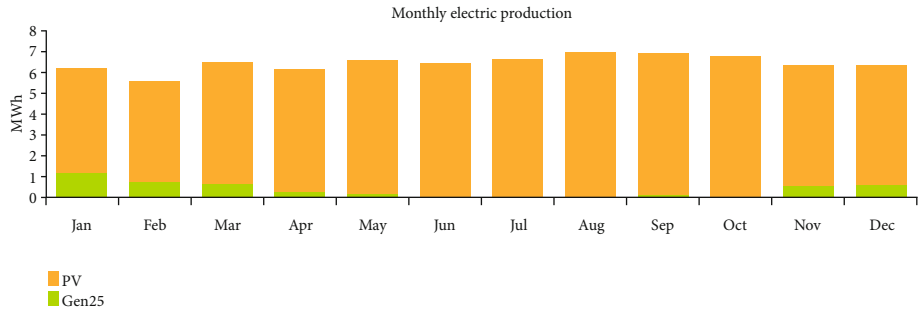


Figure 14: Annual monthly electric production of hybrid PV and DG backup.

and demand. The standards of LEPP were calculated for the total time in hours for a year equivalent to 8,760 hours. In case any value of LEPP has been greater than the prescribed one, the decision values were then recalculated. If there was no any deviation from the predetermined value, the optimization procedure was implemented. Then, the optimal size of the hybrid system is obtained corresponding to the lowermost total NPC (also LCOE) which is computed at LEPP equal to zero when the power supply and demand are equally balanced [82].

10. Results and Discussions

The key objective of this research work such as power capacity and cost optimization of the off-grid HRESS for generating electricity matching the needed load demand of the specified location under study has been mentioned at the beginning of the study. In relation to the given data, the optimization of the proposed off-grid HRESS has been implemented using HOMER Pro software and the GWO method developed in MATLAB.

10.1. Results by HOMER Software. This part provides the results obtained from HOMER Pro software. These results include optimization results, results related to sensitivity, and financial and environmental analysis.

10.1.1. Optimal Results. In this work, the optimal configuration of the off-grid HRESS system components in this case study is a 40 kW PV, 25 kW BIOG, 144 generic 1 kWh Li-ion batteries, four in series with 36 strings of system, bus voltage 24 V, and 40 kW converter with a dispatch strategy of cycle charging. This RE system comprises annual scaled solar radiation, scaled annual biomass average, and biomass/biogas price of 6.11 kWh/m^2/day, 0.2 tonnes/day, and \$3.00/tonne, respectively. Figure 3 is the schematic arrangement of the off-grid HRESS for the proposed site. Total NPC, investment cost, and LCOE for the HRESS are \$106,383.50, \$78,500, and \$0.1109/kWh, respectively. Electrical production for PV and BIOG is 72,500 kWh/year and 7,706 kWh/year, respectively. Therefore, the total electrical production of the off-grid HRESS is 80,206 kWh/year. In this case, HRESS is the proposed optimally designed RE-based system combining PV and BIOG and batteries. Figure 13 indicates the annual monthly electric production of the hybrid PV-BIOG-battery storage system in which power output generated by PV is higher than that of BIOG. Capacity factors for PV and BIOG are 20.7% and 3.52%, respectively. Similarly, electricity production for PV/DG/battery and DG only is 77,210 kWh and 779,640 kWh/year, respectively. Annual monthly electric production of PV/DG/battery and DG only is also indicated in Figures 14 and 15, respectively. Figure 16 portrays the cash flow summary for the selected components of the hybrid PV/BIOG/battery system. The investment prices for capital for batteries, BIOG, and PV are \$36,000, \$6,500, and \$28,000, respectively. The capital price for batteries is the highest equivalent to 45.9% followed by the cost of PV with 36.7%. The initial cost for BIOG is 8.3% and thus is the lowest. Also, O&M prices for batteries, BIOG, and PV are \$3,429.92, \$10,825.67, and \$952.75, respectively. BIOG has the highest O&M of about \$71.2 followed by the same category cost of 22.6%. PV has the lowest O&M cost of around 6.3%. Similarly, Figure 17 displays the cash flow summary for the selected components of hybrid PV/DG/battery. The initial

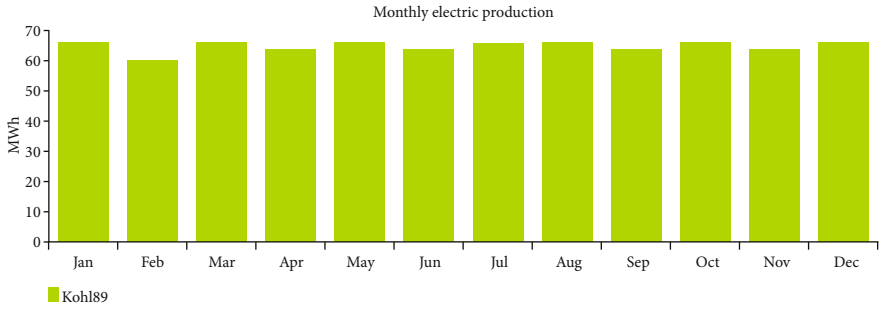


Figure 15: Annual monthly electric production DG only.

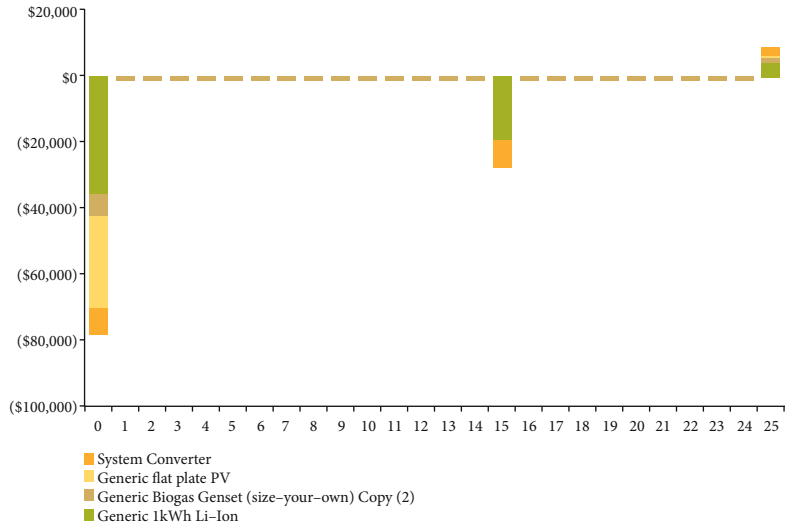


Figure 16: Cash flow summary for the selected components of the hybrid PV/BIOG/battery system.

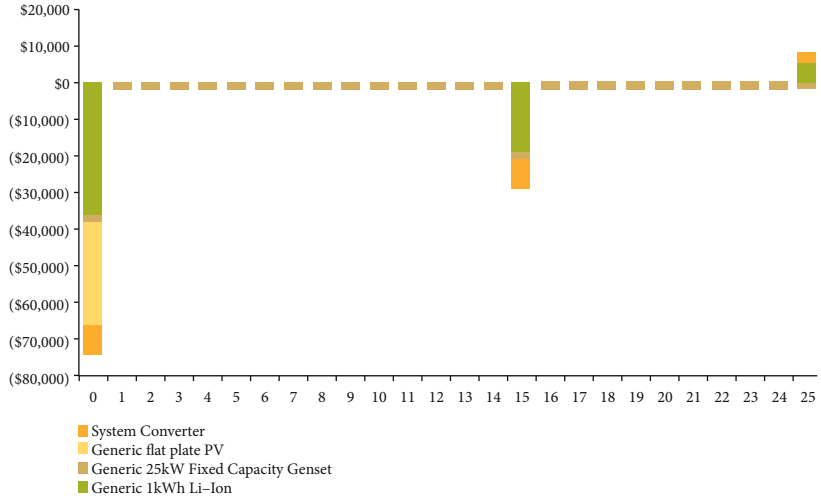


Figure 17: Cash flow summary for the selected components of hybrid PV/DG/battery.

costs for batteries, DG, and PV are $36,000, $2,053.06, and $28,000, respectively. The total NPC for the whole system is $122,031.06. NPC for batteries is the highest equivalent to 39.2% followed by the cost of DG backup with 27.6%. NPC for BIOG is 23.7%. As stated in the cost type in Figure 16, the initial cost is the highest accounting for 60.68% of the total NPC. In the same line, if DG only is used continuously (Kohler 89 kW) to supply the load, the total

Table 12: Summarized results of evaluation of electrical power and load.

Parameter	Scenario 1	Scenario 2	Scenario 3
Solar PV production	72500 kWh/yr.	72460 kWh/yr.	NA
BIOG production	7707 kWh/yr.	NA	NA
Battery annual throughput	29961 kWh	29150 kWh/yr.	NA
DG in hybrid production	NA	4750 kWh/yr.	NA
Single DG production	NA	NA	779640 kWh/yr.
Renewable fraction (%)	100	92.1	0
Fuel consumption	23.1 tonnes/yr.	1610 L/yr.	242302 L/yr.
Unmet electrical load	0	0	0
Excess electrical power	6930 kWh/yr.	10725 kWh/yr.	134524 kWh/yr.
Capacity unavailability	0	0	0

NA = not applicable.

Table 13: Summarized results of financial evaluation.

Technology	Investment cost ($)	Replacement cost ($)	O&M cost ($)	Fuel cost ($)	Salvage ($)	Total NPC ($)
System 1						
Solar PV	28000	0	952.75	0	0	28952.75
BIOG	6500	0	10825.67	1081.64	967.31	17440
Batteries	36000	10905. 84	3429.92	0	1848.80	48484
Converter	8000	4541.86	0	0	1038.03	11503.83
System	78500	15447.7	15208.35	1081.64	3854.14	106383.55
System 2						
Solar PV	28000	0	952.75	0	0	28952.75
DG set	2053.06	2053.06	6396.46	25569.55	293.03	33725.74
Batteries	36000	10700.36	3429.92	0	2281.55	47848.72
Converter	8000	4541.86	0	0	1038.03	11503.83
System	74053.06	15242.22	10778.83	25569.55	3612.61	122031.06
System 3						
DG set only	6310	56273.09	425652.67	3847566.29	982.49	4334819.56
System	6310	56273.09	425652.67	3847566.29	982.49	4334819.56

NPC is $4.3 million, COE is $4.52/kWh, and operating cost is $272,726.40. The initial cost for the device is actually lower than the running cost of the machine and therefore is expensive due to fuel cost. Capital for the machine and running cost for fuels is $6,310 (0.14%) and $3.8 million (88.76%) of the total NPC, respectively.

10.1.2. Optimal Off-Grid HRESS versus Other Technologies. Optimization results are presented by comparing the proposed optimized system with other technologies; three scenarios have been formulated: scenario 1 represents the PV-BIOG-battery storage hybrid system, scenario 2 defines the PV-DG-battery storage hybrid system, and scenario 3 describes the DG system.

(1) Evaluation of Electrical Power Generation and Load. Evaluation of electrical power analysis offers details on power generation as explained by the assumed scenarios. Monthly electric generation of PV/BIOG/batteries, PV/DG/batteries, and DG only is shown in Figures 13–15, respectively, and results for electric power based on the three scenarios are summarized in Table 12.

(2) Financial Analysis. Financial analysis has been performed using financial variables of LCOE and NPC. Table 13 indicates the summarized results of the financial appraisal.

10.1.3. Economical Comparison through Break-Even Grid Extension Distance. The range from the main grid at which the total NPC of expanding the grid equals the total NPC of the off-grid system is known as the break-even grid extension distance. This means that if the grid is too far away, the off-grid system is a preferable option. If the main grid is closer to the break-even point, the grid extension is regarded as a superior alternative. A negative distance value means that LCOE of the off-grid micropower system is always cheaper than that of grid expansion whereas the positive distance implies that LCOE of the off-grid system is cheaper than that of grid extension beyond such a distance. Below this break-even distance grid extension (EDL) is cheaper

than off-grid HRESS and is not economically viable beyond the distance. Generally, the break-even grid extension can be estimated as follows in Equation (38) [83]:

$$\text{GRID}_{\text{Extension}} = \frac{\text{APP} \times \text{CRF}_{(i,J\text{proj})} - P_{\text{Grid extension}} \times \text{Energy Demand}}{P_{\text{Grid investment}} \times \text{CRF}_{(i,J\text{proj})} + \text{AOMP}_{\text{Grid extension}}}, \tag{38}$$

where $\text{GRID}_{\text{Extension}}$ is the estimated break-even grid extension distance (km), $\text{AOMP}_{\text{Grid extension}}$ is the operation and maintenance price of grid extension (\$/yr/km), $P_{\text{Grid investment}}$ is the investment cost of grid expansion (\$/km), and $P_{\text{Grid extension}}$ is the charge of the energy consumption of the grid (\$/kWh). In this specific study, the break-even grid extension distance is presented as follows: Figure 18 presents the total NPC of the proposed 100% renewable system (PV/BIOG/battery or scenario 1) as an alternative option to off-grid HRESS comprising a diesel generator (PV/DG/battery or scenario 2) and diesel-powered generator (DG only or scenario 3). The systems are presented according to their respective break-even grid extension lengths. In scenario 1, the break-even grid extension distance is 0.19 km whereas NPC and LCOE are \$106,383.50 and \$0.1109/kWh, respectively. In scenario 1 of Figure 17, the break-even grid extension range has been estimated to be 0.19 km with a corresponding total NPC of \$106,383.50. As a result, this suggests that if the nearest selected site to which the main grid, say from TANESCO, can be extended is less than 0.19 km away, grid extension is a preferable alternative. Otherwise, the projected off-grid 100% renewable energy microgrid is an excellent investment. Also, in scenario 2 of Figure 17, the break-even grid extension range has been estimated to be 0.48 km with corresponding total NPC and LCOE of \$122,031.10 and \$0.12730/kWh, respectively. Similarly, it implies that if the nearest selected site to which the main grid, say from TANESCO, can be extended is less than 0.48 km away, grid extension is a preferable alternative. If not, off-grid PV/DG/battery is an attractive investment. In scenario 3 as presented in Figure 17, the break-even grid extension range has been estimated to be 77.5 km with corresponding total NPC and LCOE of \$4,337,089 and \$4.52/kWh, respectively. In the same way, it implies that if the nearest selected site to which the main grid, say from TANESCO, can be extended is less than 77.5 kilometres away, grid extension is a preferable alternative. If not, off-grid DG is an attractive investment. Based on the line of sight, the nearest site to which the main grid from TANESCO located in Mbeya city centre may be extended to a specified site is 79.7 kilometres away. It can be observed that in all three scenarios, individual break-even grid distances are less than 79.7 kilometres. Therefore, grid extension is not favoured. That is why most of the isolated rural areas of developing countries employ fossil fuel systems (DG) as an alternative option to grid extension bearing in mind that technological development of renewable energy-based systems is immature. However, the recommended off-grid 100% hybrid renewable energy-based microgrid (PV/BIOG/battery system) is the best option. Description regarding the break-even grid extension lengths of all the three above-named scenarios in terms of total NPCs may apply for further

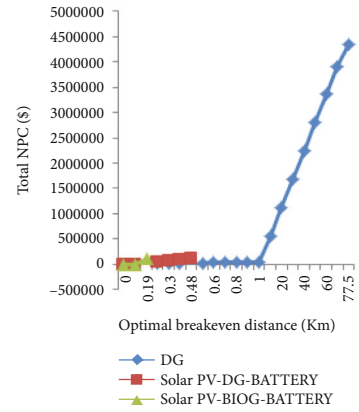


Figure 18: NPC for hybrid PV-BIOG-battery, PV-DG-battery, and DG versus break-even distance.

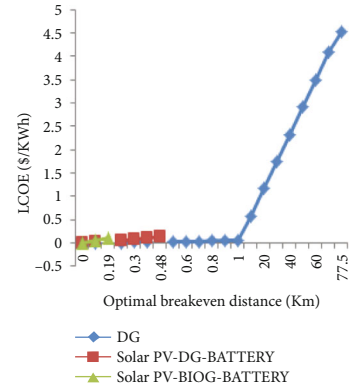


Figure 19: LCOE for hybrid PV-BIOG-battery, PV-DG-battery, and DG versus break-even distance.

presentation with respect to the corresponding LCOEs as indicated in Figure 19. Figures 18 and 19 show the comparison of break-even grid extension distance versus scenario 1, scenario 2, and scenario for total NPC and LCOE, respectively.

Linear equations (39), (40), and (41) have been formulated for drawing the graph for comparing NPC and break-even grid extension of the PV/BIOG/battery, PV/DG/battery, and DG only, respectively, as follows:

$$y_1 = 559913.2\,x_1 - 0.008, \tag{39}$$

$$y_2 = 254231.5\,x_2 - 0.02, \tag{40}$$

$$y_3 = 55962.4\,x_3 + 3. \tag{41}$$

Note 1. All y and x indicate total NPC and break-even grid extension distance, respectively.

Similarly, linear equations (42), (43), and (44) have been formulated for drawing the graph for comparing LCOE and break-even grid extension of the PV/BIOG/battery, PV/DG/battery, and DG only, respectively, as follows:

$$y_4 = 0.5837x_4 - 0.000003, \tag{42}$$

Table 14: The comparison of the GHG emissions produced by the proposed 100% RE micropower system (HRESS) versus other technologies under specified scenarios.

Pollutant	Scenario 1 (PV/BIOG/BB)	Scenario 2 (DG/BIOG/BB)	Scenario 3 (DG only)	Unit
Carbon dioxide	0.531	67,641	635,966	kg/year
Carbon monoxide	0.00589	422	2908	kg/year
UNHC	0	18.6	174	kg/year
Particulate matters	0	2.53	15.4	kg/year
Sulphur dioxide	0	166	1553	kg/year
Nitrogen oxide	0.00368	397	308	kg/year

UNHC = unburned hydrocarbons.

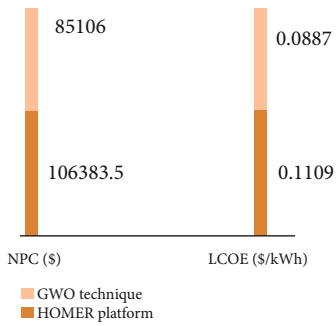


Figure 20: Graph of NPC and LCOE for off-grid HRESS using HOMER and GWO platforms (LEPP = 0).

$$y_5 = 0.2652\,x_5 + 0.000004, \tag{43}$$

$$y_6 = 0.0583\,x_6 + 0.00175. \tag{44}$$

Note 2. All y and x indicate total LCOE and break-even grid extension distance, respectively.

10.1.4. Results of Sensitivity Analysis. Input variables include variations in electricity supply requirement, energy resources, and fuel costs. Several sensitive input parameters are taken into account for the selection of optimal configuration of off-grid HRESS to meet the energy demand. Sensitivity analysis indicates that an increase in annual scaled solar radiation from 6.11 to 7.5 kWh/m^2/day at fixed biomass feedstock and electrical load reduces the total NPC, LCOE, and operating cost of the optimized system. The total NPC, LCOE, and operating cost of the proposed optimal off-grid hybrid PV/BIOG/battery are \$106,383.50, \$0.1109/kWh, and \$1,755.95, respectively, which are reduced to \$101,584, \$0.106/kWh, and \$1,454, respectively. Similarly, the total NPC, LCOE, and operating cost when the backup system is DG instead of BIOG, that is, hybrid PV/DG/battery, are \$122,031.10, \$0.1273/kWh, and \$3,021.43, respectively, which are reduced to \$109,700, \$0.114/kWh, and \$2,245, respectively.

10.1.5. Results of Environmental Analysis. The impact of greenhouse gas (GHG) emissions produced from the proposed optimal off-grid HRESS consisting of PV, BIOG, and batteries is also compared with GHG emissions from assumed technologies. Table 8 indicates the comparison of GHG emissions produced by the proposed 100% RE micropower system (HRESS) versus other technologies under specified scenarios. Table 14 indicates a comparison of the GHG emissions produced by the proposed 100% RE micropower system (HRESS) versus other technologies under specified scenarios.

10.2. Results Obtained by GWO Method. This specific part of the research article presents the optimization and sensitivity results of the off-grid HRESS achieved via the application of the GWO platform as follows.

10.2.1. Optimization Results of Balanced Generated Power Supply-Demand System (LEPP = 0). As it has been mentioned before, the average daily electricity consumption is 511.1 kWh/day (baseline), peak power capacity is 30.31 kW, and load factor is 0.71. For the hybrid electric system to supply sufficient power to satisfy the load, generated electricity should be equal or greater than the highest power capacity. The off-grid HRESS has been optimized when LEPP equals zero denoting no shortage of power. In other words, generated power supply and energy demand are well balanced. The analysis of the optimized system by the GWO method shows that overall NPC and LCOE are \$85, 106 A, and \$0.0887/kWh, respectively. The use of AI optimization technique (GWO) has further reduced the financial metrics of power generation up to around 20% when compared with soft computing tools (HOMER). Figure 20 indicates the graph of NPC and LCOE for off-grid HRESS using HOMER and GWO platforms (LEPP = 0).

10.2.2. Sensitivity Analysis Results of Unbalanced Generated Power Supply-Demand System. The sensitivity analysis is carried out to find out the effect of system reliability in reflection on financial performance. Here, the assumption is made that generated power and energy demand are unbalanced [84]. The application of the GWO algorithm is employed by considering the unbalanced condition of the designed system. In this research article, LEPP is considered to be the sensitivity's variable; thus, the analysis of the optimized system has been evaluated based on the variation of estimated magnitudes of LEPP, that is, 0.04 and 0.06.

It has been witnessed that when LEPP equals 0.04, the configuration of off-grid HRESS reveals the overall NPC of \$79,545.992 and LCOE of \$0.0316/kWh. The variation of overall NPC of the designed off-grid HRESS is now less than that in a balanced energy system when LEPP equals zero.

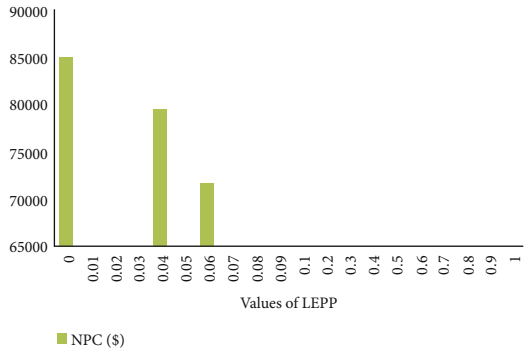


Figure 21: Graph of NPC for optimization and sensitivity results of the system by GWO method.

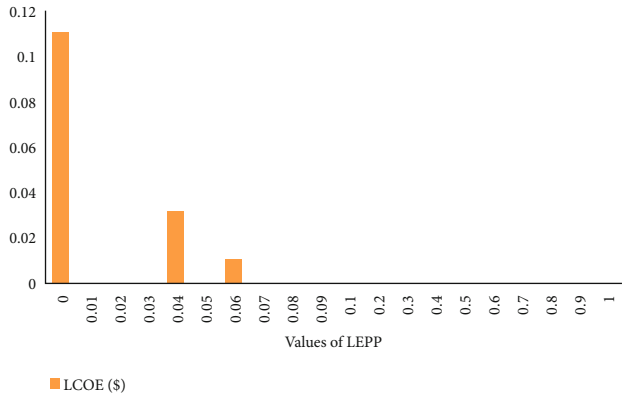


Figure 22: Graph of LCOE for optimization and sensitivity results of the system by GWO method.

The diminution in extra power can be ascribed owing to the reduction in the capacity of the solar PV array. Similarly, when LEPP equals 0.06, the off-grid HRESS configuration has an overall NPC of $71,747.36, and its corresponding LCOE equals $0.0.0102/kWh. It implies that at a given condition of LEPP which equals 0.06, the overall NPC of optimal HRESS is further decreased up to at least 20% in comparison with the balanced condition of generated capacity and energy demand. The extra power generation is minimized owing to the decline in the capacity of the solar PV module. In this case, maximum power of the designed system is not taken into account and attributed to the reduced extra power. Figures 21 and 22 indicate the graphs of NPC and LCOE for optimization and sensitivity results by the GWO method.

11. Comparison of Findings Acquired from Other Related Configurations

For the purpose of understanding clearly the importance owing to the application of the GWO algorithm, the performance of the proposed off-grid HRESS (presented in this paper) is related to the other optimal hybrid renewable energy-based systems consisting of similar configurations consisting of renewable energy sources, that is, solar PV and biogas fuel. Dissimilarities are mainly in terms of storages, electrical loads, and metaheuristic optimization approaches. The comparison of results from other related configurations is discussed as follows.

First, the proposed HRESS is compared with the system consisting of solar PV, biogas fueled generator, and storage system comprising batteries and hydro pumped storage system [85]. The system employs one upper reservoir without the lower one [85]. The system is designed to power a radio transmitter with power capacity, consumption, and load factor of 25.54 kW, 356.38 kWh/day, and 0.58 [85]. The study presents the optimization of the hybrid system using two metaheuristic techniques such as WCA (Water Cycle Algorithm) and MFO (Moth Flame Optimization) which are compared with the genetic algorithm (GA) [85]. These techniques have indicated the highest convergence rate in the optimization results. WCA shows an area of solar PV panels equal to 548.67 square metres producing power equivalent to 69.2 kW, biogas fueled generator capacity is 16 kW, number of batteries equals 21, capacity of the converter is 30 kW, capacity of the top reservoir is 2,081.5 cubic metres, total NPC is $813,319, and LCOE is $0.4864/kWh [77]. Similarly, MFO indicates an area of solar PV modules equal to 549.2 square metres producing power equivalent to 69.3 kW, capacity of biogas-driven generator is the same as in WCA, the number of batteries is the same as in WCA, capacity of the converter is the same as in WCA, capacity of the upper reservoir is 2,083 cubic metres, total NPC is $813,865, and LCOE is $0.4865/kWh [85].

In the second configuration, the HRESS is also compared with the configuration containing solar PV, biowaste, and fuel cell (hydrogen storage tank). The configuration is intended to generate power to serve the annual load profile equal to 269.15 MWh [86]. The paper presents the system optimized using the WOA (Whale Optimization Algorithm) method which is the PSO (particle swarm optimization) technique by bearing in mind the existence of components for a lifetime of 20 years. The optimal system configuration is the cheapest in comparison with other combinations. The system has a total NPC of $2.820 million and LEPP equal to 0.0029 [86]. Similarly, LCOE of the same optimal system equals $0.5238/kWh [86]. The suggested optimization method for the optimal design of a hybrid system is superior to PSO. The WOA method presents lower total NPC, accuracy, higher convergence velocity, and reliability [86].

The third configuration consists of solar PV, battery, and pumped storage systems having upper boundaries without a biogas generator bearing in mind that the proposed HRESS has a biogas generator in addition to solar PV but without pumped water storage [87]. The designed system is aimed at supplying power for an isolated island in Hong Kong using renewable energy sources for 100% [87]. The daily power consumption and peak power are, respectively, 250 kWh and 50 kW [87]. The system provides the viability study and financial analysis of the given energy storage systems. The storage energy systems are investigated in terms of LCC (life cycle cost) and practical feasibility. The analysis using LCC is useful for determining which is more cost-effective between the energy storage by the battery bank and pumped water [87]. The study has compared three

options such as novel deep cycle battery, traditional battery, and combined pumped hydro and battery energy storages. The LCC and LCOE for the optimal storage system combining pumped hydro and battery energy storage schemes are $2,394.901 and $1,916/kWh, respectively [87].

The fourth configuration is also constituted by solar PV, biogas power system, and battery storage system. The system has been analyzed using a deterministic method to satisfy a proportional scaled-down demand of Kenya, one of the countries located in East Africa [88]. In the paper, it has been assumed that solar panels covering an area equivalent to 20,000 square metres produce a capacity of 5 MW. Also, a biogas generator can produce power only if the power output declines below 40% of the rated size (2.4 MW) while its efficiency is 70% [88]. The optimal sizing ratio of power generation sources of biogas generator to solar PV is 2.4 : 5. By using the PSO algorithm, the study has shown lower LCOE in the hybrid system than that of the biogas generator. On the other hand, LCOE becomes lower at a discount rate below 8% and stipulated prices of the system components [88]. In 2012, for instance, at a discount rate of 8% with lower and upper boundaries of given costs, the optimal results of LCOEs were found to be $0.39/kWh and $0.42/kWh, respectively [88].

Generally, different metaheuristic optimization results indicate an effective design of a hybrid energy system with less technical and financial costs as likened to available designs in the literature.

12. Conclusions, Recommendations, and Research in the Future

In this paper, HOMER and GWO method have been utilized for acquiring the technoeconomic analysis of the optimal design of a PV-BIOG-battery hybrid system for delivering electricity to Simboya village in Mbeya Rural District, Mbeya region, Tanzania. Firstly, based on the application of the HOMER platform, conclusions of this research work are presented as follows: Technical and economic viability analysis for a 100% hybrid renewable electric system has been carried out intending to generate electricity for Simboya village, Mbeya Rural District, Tanzania. This study includes an optimized design, and a comparative study of PV-BIOG-battery, PV-DG-battery, and DG only is carried out. Additionally, the break-even grid extension distance of the individual aforementioned technology has been evaluated based on the assumption that the microgrid power system may take power from the central grid. Furthermore, the study has performed sensitivity and environmental analyses. The country is located in tropical areas, and therefore, electrical load profiles for the area of study have been considered the same due to the lack of extreme climate change variation in a year [58]. A residential load equivalent to 50% of accrued power requirement is the highest. The load for street lighting is the lowest. This study has indicated that the lowest-price hybrid configuration of PV-BIOG-battery is capable of meeting the energy demand at LCOE of $0.1109/kWh with almost negligible GHG emissions. This LCOE is equivalent to or less than the grid power price from TANESCO in the range of Tanzanian shillings (TZS) 242.2-306/kWh (0.104–0.14 USD/kWh; 1 USD equals 2,319.55 on 18.09.2020) [89–91]. Furthermore, the cost of the proposed system is also even less than the projected LCOE by 2035 for renewable-based microgrid in SSA that is expected to drop to $0.2/kWh in electricity generation projects with around 90% renewable energy fraction [92]. The price of renewable energy-based electricity might not all the time be cheap for isolated areas, and thus, LCOE can further be reduced by support through subsidies based on specific renewable technologies [9, 93]. This 100% RE system has the least break-even grid extension distance of about 0.19 km implying the least NPC. Among the three technologies, DG only has the highest LCOE and LCC due to the highest running cost caused by high fuel costs. LCOE for DG only is at least four times that of the PV-BIOG-battery hybrid system. The study has also indicated that DG only produces the highest GHG emissions. Sensitivity analysis shows that an escalation of yearly scaled solar energy from 6.11 to 7.5 kWh/m^2/day at fixed biomass feedstock and electrical load demand decreases the total NPC, LCOE, and operating cost of the optimal hybrid configuration. Moreover, minimum daily mass equal to 0.315 tonnes is greater than the estimated daily minimum requirement of biomass which is equal to at least 0.2 tonnes. This lowest value can drive a biogas generator to produce power of 25 kW. The estimated residential load for Simboya village is equal to 30 kW and is the highest at almost 50% while power consumption for the street lighting electrical load is the least being equivalent to 0.5% of the overall energy demand.

Secondly, in conformity with the application of the GWO technique, the conclusions of this study are provided as follows: Results of the technoeconomic analysis of the optimal HRESS when generated power and energy demand are matched (LEPP = 0) have been presented. The sensitivity analysis of the technoeconomic analysis of the system for the assumed values of LEPPs (LEPP = 0.04 and LEPP = 0.06) more than zero has indicated that the increased LEPP provides the optimal HRESS with the minimized size of components. In general, the application of a metaheuristic approach (GWO) has exhibited better technoeconomic performance of the off-grid HRESS in comparison with the soft computing tool (HOMER platform). In other words, the use of the GWO technique shows the decline of the financial metrics of the system. The optimal HRESS is a promising solution for providing electricity to rustic and isolated locations including the site under study and other places worldwide with similar situations.

For future study, the optimal HRESS can be expanded by integrating the system with other energy sources and storage energy systems and further analyzed using an advanced approach such as metaheuristic methods in order to build up the enhanced body of knowledge regarding the solutions to optimization problems.

Data Availability

Data can be obtained from the corresponding author.

Ethical Approval

There was no ethical violation or misconduct in this research work. The research was conducted after getting a permit from the regional commissioner's office in Mbeya region, Tanzania.

Disclosure

This research work is entirely the product of the authors' initiatives.

Conflicts of Interest

The authors have no conflict of interest and therefore are responsible for the contents and preparing this article.

Acknowledgments

The authors recognize immense support from the management of Mbeya University of Science and Technology and Delhi Technological University (DTU). Appreciation is also extended to the regional commissioner's office in Mbeya region for the permission of doing research in the Mbeya Rural District and the management of Ikukwa ward, MDCH (IHC), Ifisi Hospital, and villagers for their cooperation.

References

[1] Z. Aslam, H. Li, J. Hammerton, G. Andrews, A. Ross, and J. C. Lovett, "Increasing access to electricity: an assessment of the energy and power generation potential from biomass waste residues in Tanzania," *Energies*, vol. 14, no. 6, p. 1793, 2021.

[2] V. Sessa, R. Bhandari, and A. Ba, "Rural electrification pathways: an implementation of LEAP and GIS tools in Mali," *Energies*, vol. 14, no. 11, p. 3338, 2021.

[3] A. Shahsavari and M. Akbari, "Potential of solar energy in developing countries for reducing energy-related emissions," *Renewable and Sustainable Energy Reviews*, vol. 90, pp. 275–291, 2018.

[4] A. Micangeli, R. Del Citto, I. Kiva et al., "Energy production analysis and optimization of mini-grid in remote areas: the case study of Habaswein, Kenya," *Energies*, vol. 10, no. 12, p. 2041, 2017.

[5] A. Aly, A. Bernardos, C. M. Fernandez-Peruchena, S. S. Jensen, and A. B. Pedersen, "Is concentrated solar power (CSP) a feasible option for sub-Saharan Africa?: Investigating the techno-economic feasibility of CSP in Tanzania," *Renewable Energy*, vol. 135, pp. 1224–1240, 2019.

[6] H. D. Dibaba, *Business Model for Microgrids in Sub-Saharan Africa Rural Areas: A Case Study in Revon C, Namibia*, 2019.

[7] O. M. Babatunde, J. L. Munda, and Y. Hamam, "A comprehensive state-of-the-art survey on hybrid renewable energy system operations and planning," *IEEE Access*, vol. 8, pp. 75313–75346, 2020.

[8] A. Yahiaoui, F. Fodhil, K. Benmansour, M. Tadjine, and N. Cheggaga, "Grey wolf optimizer for optimal design of hybrid renewable energy system PV- diesel generator-battery: application to the case of Djanet city of Algeria," *Solar Energy*, vol. 158, pp. 941–951, 2017.

[9] K. Nimma, M. Al-Falahi, H. D. Nguyen, S. D. G. Jayasinghe, T. Mahmoud, and M. Negnevitsky, "Grey wolf optimization-based optimum energy-management and battery-sizing method for grid-connected microgrids," *Energies*, vol. 11, no. 4, p. 847, 2018.

[10] N. P. Simpson, C. J. Rabenold, M. Sowman, and C. D. Shearing, "Adoption rationales and effects of off-grid renewable energy access for African youth: a case study from Tanzania," *Renewable and Sustainable Energy Reviews*, vol. 141, article 110793, 2021.

[11] S. I. Kajugus, K. T. Kabaka, and T. T. Mnjokava, "Geothermal development in Tanzania-a country update," in *7th African Rift Geothermal Conference*, Kigali, 2018.

[12] S. M. Kongela, "Sustainability potential awareness among built environment stakeholders: experience from Tanzania," *International Journal of Building Pathology and Adaptation*, 2021.

[13] A. Contejean, *Making mini-grids work: productive uses of electricity in Tanzania*, International Institute for Environment and Development, 2017.

[14] R. Sen and S. C. Bhattacharyya, "Off-grid electricity generation with renewable energy technologies in India: an application of HOMER," *Renewable Energy*, vol. 62, pp. 388–398, 2014.

[15] B. Ugwoke, A. Adeleke, S. P. Corgnati, J. M. Pearce, and P. Leone, "Decentralized renewable hybrid mini-grids for rural communities: culmination of the IREP framework and scale up to urban communities," *Sustainability*, vol. 12, no. 18, p. 7411, 2020.

[16] M. D. A. Al-falahi, S. D. G. Jayasinghe, and H. Enshaei, "A review on recent size optimization methodologies for standalone solar and wind hybrid renewable energy system," *Energy Conversion and Management*, vol. 143, pp. 252–274, 2017.

[17] O. K. Bishoge, L. Zhang, and W. G. Mushi, "The potential renewable energy for sustainable development in Tanzania: a review," *Clean Technologies*, vol. 1, no. 1, pp. 70–88, 2019.

[18] F. Kemausuor, M. S. Adaramola, and J. Morken, "A review of commercial biogas systems and lessons for Africa," *Energies*, vol. 11, no. 11, p. 2984, 2018.

[19] M. R. Elkadeem, S. Wang, S. W. Sharshir, and E. G. Atia, "Feasibility analysis and techno-economic design of grid-isolated hybrid renewable energy system for electrification of agriculture and irrigation area: a case study in Dongola, Sudan," *Energy Conversion and Management*, vol. 196, pp. 1453–1478, 2019.

[20] C. Li, X. Ge, Y. Zheng et al., "Techno-economic feasibility study of autonomous hybrid wind/PV/battery power system for a household in Urumqi, China," *Energy*, vol. 55, pp. 263–272, 2013.

[21] R. S. Kulkarni, S. L. Chavan, and D. B. Talange, "A green house electricity and heat generation: solar PV/thermal panel-review," in *2015 International Conference on Industrial Instrumentation and Control (ICIC)*, pp. 680–682, Pune, India, May 2015.

[22] E. I. C. Zebra, H. J. van der Windt, G. Nhumaio, and A. P. C. Faaij, "A review of hybrid renewable energy systems in mini-grids for off-grid electrification in developing countries," *Renewable and Sustainable Energy Reviews*, vol. 144, article 111036, 2021.

[23] J. C. I. Rabetanetiarimanana, M. H. Radanielina, and H. T. Rakotondramiarana, "PV-hybrid off-grid and mini-grid systems for rural electrification in sub-Saharan Africa," *Smart Grid and Renewable Energy*, vol. 9, no. 10, pp. 171–185, 2018.

[24] N. Yimen, T. Tchotang, A. Kanmogne et al., "Optimal sizing and techno-economic analysis of hybrid renewable energy

systems—a case study of a photovoltaic/wind/battery/diesel system in Fanisau, northern Nigeria," *Processes*, vol. 8, no. 11, p. 1381, 2020.

[25] S. Buragohain, K. Mohanty, and P. Mahanta, "Hybridization of solar photovoltaic and biogas system: experimental, economic and environmental analysis," *Sustainable Energy Technologies and Assessments*, vol. 45, article 101050, 2021.

[26] B. Fleck and M. Huot, "Comparative life-cycle assessment of a small wind turbine for residential off- grid use," *Renewable Energy*, vol. 34, no. 12, pp. 2688–2696, 2009.

[27] F. Odoi-Yorke, S. Abaase, M. Zebilila, and L. Atepor, "Feasibility analysis of solar PV/biogas hybrid energy system for rural electrification in Ghana," *Cogent Engineering*, vol. 9, no. 1, article 2034376, 2022.

[28] A. B. Awan, M. Zubair, G. A. S. Sidhu, A. R. Bhatti, and A. G. Abo-Khalil, "Performance analysis of various hybrid renewable energy systems using battery, hydrogen, and pumped hydro-based storage units," *International Journal of Energy Research*, vol. 43, no. 12, pp. 6296–6321, 2019.

[29] M. S. Ngan and C. W. Tan, "Assessment of economic viability for PV/wind/diesel hybrid energy system in southern peninsular Malaysia," *Renewable and Sustainable Energy Reviews*, vol. 16, no. 1, pp. 634–647, 2012.

[30] A. Ghasemi, A. Asrari, M. Zarif, and S. Abdelwahed, "Techno-economic analysis of stand-alone hybrid photovoltaic-diesel-battery systems for rural electrification in eastern part of Iran–a step toward sustainable rural development," *Renewable and Sustainable Energy Reviews*, vol. 28, pp. 456–462, 2013.

[31] K. Kusakana and H. J. Vermaak, "Hybrid renewable power systems for mobile telephony base stations in developing countries," *Renewable Energy*, vol. 51, pp. 419–425, 2013.

[32] A. Yahiaoui, A. Tlemçani, and A. Kouzou, "Optimization, power management and reliability evaluation of hybrid wind-PV-diesel-battery system for rural electrification," *Automation, Control and Intelligent Systems*, vol. 9, no. 3, p. 73, 2021.

[33] H. Ren, Z. Ma, W. Lin, W. Fan, and W. Li, "Integrating photovoltaic thermal collectors and thermal energy storage systems using phase change materials with rotary desiccant cooling systems," *Sustainable Cities and Society*, vol. 36, pp. 131–143, 2018.

[34] A. Kaabeche, S. Diaf, and R. Ibtiouen, "Firefly-inspired algorithm for optimal sizing of renewable hybrid system considering reliability criteria," *Solar Energy*, vol. 155, pp. 727–738, 2017.

[35] A. E. Kabeel, Z. M. Omara, F. A. Essa, and A. S. Abdullah, "RETRACTED: Solar still with condenser – a detailed review," *Renewable and Sustainable Energy Reviews*, vol. 59, pp. 839–857, 2016.

[36] K. Ravinder and H. O. Bansal, "Investigations on shunt active power filter in a PV-wind-FC based hybrid renewable energy system to improve power quality using hardware-in-the-loop testing platform," *Electric Power Systems Research*, vol. 177, article 105957, 2019.

[37] N. Guimpayan, *Modelling Hybrid Renewable Energy System for Philippine Merchant Marine Academy: A Feasibility Study*, 2018.

[38] N. Abu-Hamdeh and K. Alnefaie, "Techno-economic comparison of solar power tower system/photovoltaic system/wind turbine/diesel generator in supplying electrical energy to small loads," *Journal of Taibah University for Science*, vol. 13, no. 1, pp. 216–224, 2019.

[39] K. Murugaperumal and P. A. D. V. Raj, "Feasibility design and techno-economic analysis of hybrid renewable energy system for rural electrification," *Solar Energy*, vol. 188, pp. 1068–1083, 2019.

[40] G. Bekele and B. Palm, "Feasibility study for a standalone solar-wind-based hybrid energy system for application in Ethiopia," *Applied Energy*, vol. 87, no. 2, pp. 487–495, 2010.

[41] S. G. Sigarchian, R. Paleta, A. Malmquist, and A. Pina, "Feasibility study of using a biogas engine as backup in a decentralized hybrid (PV/wind/battery) power generation system - case study Kenya," *Energy*, vol. 90, pp. 1830–1841, 2015.

[42] P. Anand, S. K. Bath, and M. Rizwan, "Feasibility analysis of solar-biomass based standalone hybrid system for remote area," *American Journal of Electrical Power and Energy Systems*, vol. 5, no. 6, pp. 99–108, 2016.

[43] D. H. Romero, D. Icaza, and J. González, "Technical-economic study for the implementation of solar energy in the presence of biomass and micro hydraulic generation, for sectors that do not have electricity supply in the Province of Bolívar-Ecuador," in *2019 7th International Conference on Smart Grid (icSmartGrid)*, pp. 149–154, Newcastle, NSW, Australia, December 2019.

[44] A. Cabanero, L. Nolting, and A. Praktiknjo, "Mini-grids for the sustainable electrification of rural areas in sub-Saharan Africa: assessing the potential of KeyMaker models," *Energies*, vol. 13, no. 23, p. 6350, 2020.

[45] D. Neves, P. Baptista, and J. M. Pires, "Sustainable and inclusive energy solutions in refugee camps: developing a modelling approach for energy demand and alternative renewable power supply," *Journal of Cleaner Production*, vol. 298, article 126745, 2021.

[46] P. A. Trotter, "Rural electrification, electrification inequality and democratic institutions in sub-Saharan Africa," *Energy for Sustainable Development*, vol. 34, pp. 111–129, 2016.

[47] S. Keddar, S. Strachan, B. Soltowski, and S. Galloway, "An overview of the technical challenges facing the deployment of electric cooking on hybrid PV/diesel mini-grid in rural Tanzania—a case study simulation," *Energies*, vol. 14, no. 13, p. 3761, 2021.

[48] S. C. Bhattacharyya and D. Palit, "A critical review of literature on the nexus between central grid and off-grid solutions for expanding access to electricity in sub-Saharan Africa and South Asia," *Renewable and Sustainable Energy Reviews*, vol. 141, article 110792, 2021.

[49] F. Kemausuor, M. D. Sedzro, and I. Osei, "Decentralised energy systems in Africa: coordination and integration of off-grid and grid power systems—review of planning tools to identify renewable energy deployment options for rural electrification in Africa," *Current Sustainable/Renewable Energy Reports*, vol. 5, no. 4, pp. 214–223, 2018.

[50] S. Osman, Y. Wu, and R. Blanchard, *An economically viable PV hybrid micro-grid model for remote villages in developing countries*, 2018.

[51] A. Creti, M. Barry, and E. Zigah, "Are mini-grid projects in Tanzania financially sustainable?," *The Climate Economics Chair Is a Joint Initiative by Paris-Dauphine University, CDC, TOTAL and EDF, under the aegis of the European Institute of Finance*, 2021, http://www.chaireeconomieduclimat.org.

[52] N. Hagumimana, J. Zheng, G. N. O. Asemota et al., "Concentrated solar power and photovoltaic systems: a new approach to boost sustainable energy for all (Se4all) in Rwanda,"

International Journal of Photoenergy, vol. 2021, Article ID 5515513, 32 pages, 2021.

[53] M. A. Khan, K. Zeb, P. Sathishkumar, S. S. Rao, C. V. Gopi, and H. J. Kim, "A novel off-grid optimal hybrid energy system for rural electrification of Tanzania using a closed loop cooled solar system," *Energies*, vol. 11, no. 4, p. 905, 2018.

[54] Y. M. Yustas, *Development of a Model for Integrated Anaerobic Digestion, Solar and Wind Energy System for Rural Semi-Arid Areas*, Doctoral dissertation, Sokoine University of Agriculture, 2021.

[55] O. K. Bishoge, G. G. Kombe, and B. N. Mvile, "Renewable energy for sustainable development in sub-Saharan African countries: challenges and way forward," *Journal of Renewable and Sustainable Energy*, vol. 12, no. 5, article 052702, 2020.

[56] P. A. Adedeji, *Hybrid Renewable Energy-Based Facility Location: A Geographical Information System (GIS) Integrated Multi-Criteria Decision-Making (MCDM) Approach*, Doctoral dissertation, University of Johannesburg, South Africa, 2020.

[57] B. Khavari and A. Salhberg, "Geo-spatial electricity demand assessment & hybrid off-grid solutions to support electrification efforts using OnSSET: the case study of Tanzania," *Master of Science Thesis, School of Industrial Engineering and Management Energy Technology, Division of Energy System Analysis*, Stockholm, 2017.

[58] M. Haji, *Simulation, Performance Analysis and Improvements of Solar Farm Installation in Tanzania*, Doctoral dissertation, NM-AIST, 2019.

[59] O. Djelailia, M. S. Kelaiaia, H. Labar, S. Necaibia, and F. Merad, "Energy hybridization photovoltaic/diesel generator/pump storage hydroelectric management based on online optimal fuel consumption per kWh," *Sustainable Cities and Society*, vol. 44, pp. 1–15, 2019.

[60] F. B. Agyenim, P. D. Dzamboe, M. Mohammed et al., "Powering communities using hybrid solar-biogas in Ghana, a feasibility study," *Environmental Technology & Innovation*, vol. 19, article 100837, 2020.

[61] G. Iaquaniello, W. Montanari, and A. Salladini, "Standalone CSP-DG system for electrification of remote areas and desalinated water supply," *Solar Energy*, vol. 157, pp. 1056–1063, 2017.

[62] S. A. A. Shah, G. D. Valasai, A. A. Memon, A. N. Laghari, N. B. Jalbani, and J. L. Strait, "Techno-economic analysis of solar PV electricity supply to rural areas of Balochistan, Pakistan," *Energies*, vol. 11, no. 7, p. 1777, 2018.

[63] D. Banjarnahor, *Adoption and Adaptation of Conservation Agriculture in Tanzanian Southern Highlands: Lessons Learned from Mshewe Ward Mbeya Region*, Master Thesis, Department of Plant Sciences, Wageningen University, 2014.

[64] NASA, Surface MeteorologyFebruary 2022, https://power.larc.nasa.gov.

[65] A. M. Patel and S. K. Singal, "Economic analysis of integrated renewable energy system for electrification of remote rural area having scattered population," *International Journal of Renewable Energy Research (IJRER)*, vol. 8, no. 1, pp. 523–539, 2018.

[66] V. K. Viyaj, *Biogas is a fit option for rural energy*, IIT Delhi, 2016, http://Web.iitd.ac.in.

[67] R. Syahputra and I. Soesanti, "Planning of hybrid micro-hydro and solar photovoltaic systems for rural areas of Central Java, Indonesia," *Journal of Electrical and Computer Engineering*, vol. 2020, Article ID 5972342, 16 pages, 2020.

[68] A. Elrayyah and S. Bayhan, "Multi-channel-based microgrid for reliable operation and load sharing," *Energies*, vol. 12, no. 11, p. 2070, 2019.

[69] D. K. Lal, B. B. Dash, and A. K. Akella, "Optimization of PV/wind/micro-hydro/diesel hybrid power system in HOMER for the study area," *International Journal on Electrical Engineering and Informatics*, vol. 3, no. 3, pp. 307–325, 2011.

[70] G. K. Suman, J. M. Guerrero, and O. P. Roy, "Optimisation of solar/wind/bio-generator/diesel/battery based microgrids for rural areas: a PSO-GWO approach," *Sustainable Cities and Society*, vol. 67, article 102723, 2021.

[71] D. T. Hermann, T. K. F. Armel, T. C. H. I. N. D. A. René, and N. J. O. M. O. Donatien, "Consideration of some optimization techniques to design a hybrid energy system for a building in Cameroon," *Energy and Built Environment*, vol. 3, no. 2, pp. 233–249, 2022.

[72] Saatvik, Manufacturer of Solar PanelsFebruary 2022, https://saatvikgroup.com.

[73] Exporters in India, Products/ ServicesFebruary 2022, http://www.exportersindia.com.

[74] Shenzhen Energy Ltd, "Solar Components," February 2022, https://www.enfsolar.com.

[75] S. Semeskandeh, M. Hojjat, and M. H. Abardeh, "Techno–economic–environmental feasibility study of a photovoltaic system in northern part of Iran including a two-stage multi-string inverter with DC–DC ZETA converter and a modified P&O algorithm," *Clean Energy*, vol. 6, no. 1, pp. 127–140, 2022.

[76] Novergy, Solar Panels ManufacturerFebruary 2022, http://www.novergysolar.com.

[77] M. J. Hadidian-Moghaddam, S. Arabi-Nowdeh, and M. Bigdeli, "Optimal sizing of a stand-alone hybrid photovoltaic/wind system using new grey wolf optimizer considering reliability," *Journal of Renewable and Sustainable Energy*, vol. 8, no. 3, article 035903, 2016.

[78] I. Sansa, R. Villafafila, and N. M. Bellaaj, "Optimal Sizing Design of an Isolated Microgrid Using Loss of Power Supply Probability," in *IREC2015 The Sixth International Renewable Energy Congress*, pp. 1–7, Sousse, Tunisia, March 2015.

[79] K.-C. Chang, N. Hagumimana, J. Zheng et al., "Standalone and minigrid-connected solar energy systems for rural application in Rwanda: an in situ study," *International Journal of Photoenergy*, vol. 2021, Article ID 1211953, 22 pages, 2021.

[80] V. Mudgal, K. S. Reddy, and T. K. Mallick, "Techno-economic analysis of standalone solar photovoltaic-wind-biogas hybrid renewable energy system for community energy requirement," *Future Cities and Environment*, vol. 5, no. 1, 2019.

[81] M. Bilal and M. Rizwan, "Integration of electric vehicle charging stations and capacitors in distribution systems with vehicle-to-grid facility," *Energy Sources, Part A: Recovery, Utilization, and Environmental Effects*, pp. 1–30, 2021.

[82] M. Jamshidi and A. Askarzadeh, "Techno-economic analysis and size optimization of an off-grid hybrid photovoltaic, fuel cell and diesel generator system," *Sustainable Cities and Society*, vol. 44, pp. 310–320, 2019.

[83] T. R. Ayodele, T. C. Mosetlhe, A. A. Yusuff, and A. S. O. Ogunjuyigbe, "Off-grid hybrid renewable energy system with hydrogen storage for South African rural community health clinic," *International Journal of Hydrogen Energy*, vol. 46, no. 38, pp. 19871–19885, 2021.

[84] Y. Huang, L. Yang, S. Liu, and G. Wang, "Cooperation between two micro-grids considering power exchange: an optimal

sizing approach based on collaborative operation," *Sustainability*, vol. 10, no. 11, p. 4198, 2018.

[85] M. Das, M. A. K. Singh, and A. Biswas, "Techno-economic optimization of an off-grid hybrid renewable energy system using metaheuristic optimization approaches - case of a radio transmitter station in India," *Energy Conversion and Management*, vol. 185, pp. 339–352, 2019.

[86] H. Sun, A. G. Ebadi, M. Toughani, S. A. Nowdeh, A. Naderipour, and A. Abdullah, "Designing framework of hybrid photovoltaic-biowaste energy system with hydrogen storage considering economic and technical indices using whale optimization algorithm," *Energy*, vol. 238, article 121555, 2022.

[87] T. Ma, H. Yang, and L. Lu, "Feasibility study and economic analysis of pumped hydro storage and battery storage for a renewable energy powered island," *Energy Conversion and Management*, vol. 79, pp. 387–397, 2014.

[88] C. S. Lai and M. D. McCulloch, "Sizing of stand-alone solar PV and storage system with anaerobic digestion biogas power plants," *IEEE Transactions on Industrial Electronics*, vol. 64, no. 3, pp. 2112–2121, 2017.

[89] I. C. Fernández, *Kilowatts, Megawatts and Power: Electric Territorialities of the State in the Peripheries of Ghana and Tanzania*, 2018.

[90] E. M. Kanyamyoga, "Public-private partnership models for improving electricity generation in Tanzania: the case of independent power producers and Tanzania electric supply company," *Journal of Social and Administrative Sciences*, vol. 7, no. 2, pp. 70–95, 2020.

[91] K. Shibano and G. Mogi, "Electricity consumption forecast model using household income: case study in Tanzania," *Energies*, vol. 13, no. 10, p. 2497, 2020.

[92] P. Benalcazar, A. Suski, and J. Kamiński, "The effects of capital and energy subsidies on the optimal design of microgrid systems," *Energies*, vol. 13, no. 4, p. 955, 2020.

[93] M. Moner-Girona, R. Ghanadan, M. Solano-Peralta et al., "Adaptation of feed-in tariff for remote mini-grids: Tanzania as an illustrative case," *Renewable and Sustainable Energy Reviews*, vol. 53, pp. 306–318, 2016.

IntelliCode: A speech-based programming environment

Dr. Manoj Kumar*, Hitesh Yadav*, Jayant Yadav*, Mayank Jha*

* Department of Computer Science and Engineering, Delhi Technological University, New Delhi, 110042, India

***Abstract*— Studies show that nearly 2 out of 100 software developers have visual impairment or blindness yet they still yearn to do programming. Moreover, motor injuries such as repetitive stress injuries can make programming a challenging task. A wide variety of technologies have been created to help people with disabilities get over obstacles, particularly those connected to computers and technology. The term "assistive technology" pertains to software and hardware products that aid in activities such as academic paper reading and writing, interpersonal interaction, and online research. With the proliferation of assistive technology options and increased accessibility to mainstream technologies, students and workers with disabilities can now perform a broader range of activities independently. Nevertheless, people with disabilities still struggle to learn to code, as writing code remains a difficult task even after mastering the semantics and features of a programming language. To address this challenge, IntelliCode, the software proposed in this study, eliminates this barrier and assists individuals in achieving their programming goals.**

***Index Terms* – speech recognition, speech to code, code conversion, natural language processing**

I. INTRODUCTION

Surveys conducted in 2020 by World Health Organization indicate that there are an estimated 18.7 million visually impaired and blind individuals in India [1], and at least 2.2 billion worldwide [2]. Furthermore, Stack Overflow, a website used by nearly every programmer or developer all around the world, conducted a survey of over 65,000 developers and discovered that nearly 2 out of 100 developers have a visual impairment or some other disability [3], yet still desire to program on a regular basis. However, these individuals face significant challenges in doing so.

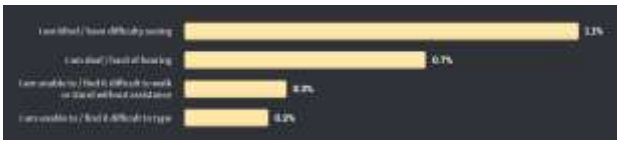


Fig. 1. Results of Stack Overflow developer survey, 2020

Numerous technologies have been developed to reduce or eliminate obstacles experienced by individuals with impairments, particularly those related to computers and technology. Assistive technology encompasses hardware and software solutions that can assist individuals with tasks like reading, writing, communication, and online information search. With the increasing availability of assistive technology and the growing accessibility of mainstream technology, individuals with impairments, whether they are students or workers, are now able to carry out a wider range of activities with greater independence. However, people with disabilities continue to face challenges when using computers, including the hurdle of learning how to code. Even after mastering the syntax and functionality of a programming language, writing code can remain a challenge. Our proposed software aims to help remove this barrier and assist individuals in achieving their programming objectives.

IntelliCode is an online coding platform designed to meet the needs of individuals with disabilities while also providing an exceptional user experience for everyone. The platform integrates speech recognition, natural language processing (NLP), code editing and code conversion to revolutionize the coding experience for individuals with visual impairments, physical disabilities, and others.

A. Background

HTML

Hyper Text Markup Language (HTML) is a vital aspect of the Internet, which serves to establish the organization and purpose of online content. It is a markup language that enables the creation of web pages that can be interpreted by web browsers. In combination with other technologies, such as Cascading Style Sheets (CSS) and scripting languages like JavaScript, HTML can be utilized to improve the functionality of web pages.

When HTML documents are retrieved from web servers or local storage, web browsers display them as multimedia web pages. HTML was originally designed to include semantic definitions of the structure of a web page as well as guidelines for how the content should be presented.

CSS

Cascading Style Sheets (CSS) is a type of style sheet language that serves to define the formatting of documents that have been written in markup languages, such as HTML or XML. CSS is one of the primary technologies utilized on the World Wide Web, along with HTML and JavaScript.

CSS allows the separation of a document's text content from its presentation, which includes elements like layout, colours, and fonts. This separation can result in improvements in content accessibility, providing greater flexibility and control over the presentation of a document. Furthermore, multiple web pages can share a single CSS file, reducing redundant coding and enabling the file to be cached for quicker page loading speeds.

JavaScript

JavaScript (JS) is a popular programming language that is widely used on the World Wide Web, alongside HTML and CSS. It is estimated that by 2022, JavaScript will be used by 98% of websites for controlling client-side functionality, often utilizing third-party libraries. All major web browsers incorporate a JavaScript engine for executing JavaScript code on users' devices. JavaScript is a high-level language that is often interpreted during runtime.

It follows the ECMAScript standard and features a prototype-based object-oriented model, first-class functions, and dynamic typing. It is a language that can accommodate multiple programming paradigms, including imperative, functional, and event-driven programming. Additionally, it offers APIs for managing common data structures, such as regular expressions, dates, and the Document Object Model (DOM).

Node.js

Node.js is a cross-platform, open-source server environment that can operate on Windows, Linux, Unix, and macOS. It provides a platform for using JavaScript on the server-side, utilizing the V8 JavaScript Engine to execute JavaScript code outside of a web browser. JavaScript, a scripting language, can be used by programmers to create server-side scripts and command-line tools for Node.js applications. By using the ability to execute server-side scripts, dynamic content can be generated before a user's web browser receives the page.

Node.js adopts a "JavaScript everywhere" approach to web application development, which allows developers to use a single programming language for both client-side and server-side scripts, instead of using different languages. Node.js is designed with an event-driven architecture that offers asynchronous I/O, enabling it to be a suitable choice for developing real-time web applications, as well as other applications that require fast and flexible input/output processing, such as browser games and real-time communication programs.

Express.js

Express.js is a web development framework for the back end of Node.js, available as open-source software under the MIT License. It enables the creation of RESTful APIs and is specifically built for developing web applications and APIs. Express.js is widely regarded as the most widely used server framework for Node.js.Express is a Sinatra-inspired server that is known for being easy to use and highly customizable through the use of plugins, according to its original inventor, TJ Holowaychuk.

It is commonly used in several development stacks, for example, Mongo-Express-React-Node (MERN), Mongo-Express-Angular-Node (MEAN), Mongo-Express-Vue-Node (MEVN), etc.



Fig. 2. Client – Server architecture

Neural Networks

One type of machine learning algorithm, referred to as neural network, emulates the human brain's structure and function. Neural networks are made up of interconnected processing nodes, also known as neurons, which collaborate to recognize patterns and draw inferences or deductions based on the input data. Neural networks are often built in layers, with each layer processing a particular component of the incoming input before transferring the findings to the layer below. Because of its hierarchical structure, neural networks are more able to understand complex patterns and make nuanced predictions than simpler, single-layer algorithms.

Deep Learning

Deep learning is a subset of machine learning that employs artificial neural networks and representation learning. Deep learning can operate in unsupervised, semi-supervised, or supervised learning modes.

The term "deep" is used because deep learning neural networks consist of multiple layers. Early research has shown that a linear perceptron cannot be a universal classifier, but a neural network with one hidden layer of infinite size and a nonpolynomial activation function can be. Deep learning, which is a more recent approach, focuses on using multiple layers of defined sizes, which allows for fast implementation and practical application while still maintaining theoretical universality under certain conditions.

OpenAI

OpenAI is a research institution focused on advancing artificial intelligence (AI) technology. AI-enabled software and machine learning algorithms now have the ability to perform a variety of tasks, such as generating images from text and designing a robotic hand that can solve Rubik's Cubes.

Their most recent project, OpenAI Codex, promises to make programming tools and apps more accessible to the general public while cutting down on the time and effort expert programmers must expend while writing code.

The GPT-3 language generation model from OpenAI was used to create the AI coding tool known as Codex, which functions as a translator between humans and computers. In early demos, users were able to create simple webpages and games without utilising a particular programming language by using plain English or natural language.

GPT-3

Generative Pre-trained Transformer 3 (GPT-3) is an

autoregressive model that employs deep learning to generate writing that is similar to human writing. By giving an initial text as input, GPT-3 can produce output text that continues the given prompt.

GPT-3 has both advantages and downsides. It creates text of such high quality that it can be difficult to identify whether it was created by a person. GPT-3 was hailed as "one of the most exciting and significant AI systems ever constructed" by Australian philosopher David Chalmers. According to a review that appeared in The New York Times in April 2022, GPT-3 is capable of writing creative language with a level of fluency that is equivalent to that of a human.

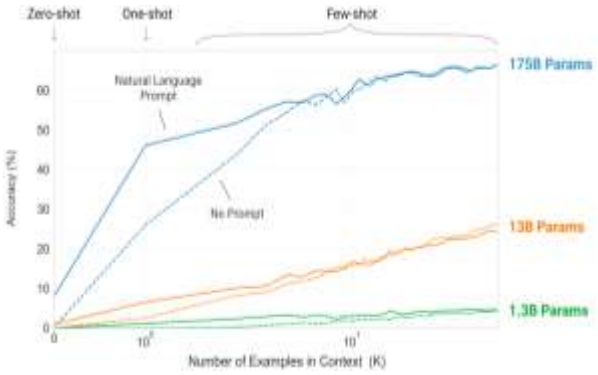


Fig. 3. GPT-3 parameter curve

B. Related works

In recent times, modern technologies such as machine learning, deep learning, and natural language processing have sparked interest in integrating human voice into programmable code. However, using conventional natural language processing methods, automated speech recognition has faced challenges in effectively performing programming tasks. Text editors usually come with vendor-provided editing commands that cater to word processing and permit style alterations and clipboard access.

According to sources, Jeff Gray integrated speech capabilities into the Eclipse programming environment, although not the editor [4]. VoiceCode [5] is a tool that has shown impressive results with finite-state command grammars that are compatible with Python and C++. However, it has not undergone a thorough evaluation yet. NaturalJava [6] accepts programmers' natural language descriptions of the Java constructs they want to create instead of coding them directly. NaturalJava only caters to code authoring and not editing or navigation. SPEED [7] is a significant contribution to the field of speech-based coding, but it only supports Java and Eclipse programming IDE.

Our study on IntelliCode is a first-of-its-kind examination voice-based programming in a practical situation.

C. Contributions

The key functional contributions of the proposed software are as follows:

- Users can simply specify the programming steps in plain English and create complete code in the language of their choice using the speech-to-code capabilities. People with vision problems or hand deformities will be able to code faster and be more productive because of this.
- Users have the option to select a pre-defined algorithm, such as sorting algorithms, binary search, and tree traversal, which the software can implement in either Python or JavaScript.
- Additionally, the software has the capability to debug, make typing corrections, and ensure proper termination of the program.
- The code conversion feature allows for quick translation of code from one language to another (primarily from JavaScript to python and vice versa), saving users a significant amount of time and money.
- Finally, we intend to build IntelliCode as a completely online collaborative coding platform that will create a welcoming and inclusive atmosphere for differently abled persons while also allowing them to connect effectively with their co-workers.

D. Roadmap

The remainder of the paper is divided into three sections. Section II details the methodology employed in the proposed work, while Section III assesses and analyzes the results. The paper concludes with Section IV, which expounds upon the conclusions drawn from the research and identifies future areas of work.

II. METHODOLOGY

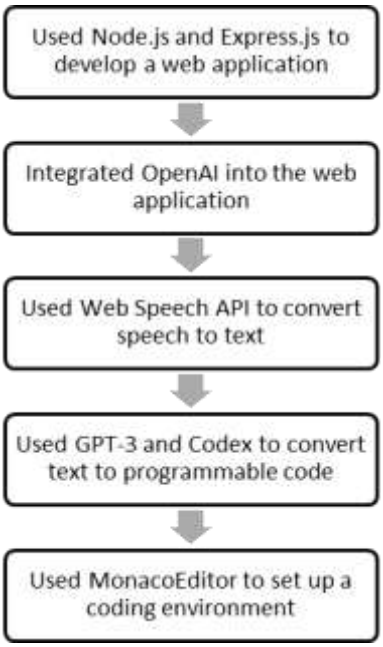


Fig. 4. Overview of methodology

A. Server setup

Setting up a server with Express.js is a very easy task. Node provides support to write JavaScript on the backend side of the application and Express.js provides the support to route the incoming requests to the Node server and take appropriate action.

Node.js comes with a node package manager, short for npm, and is used to download and install all the external dependencies that one might need for a node application. Below table shows the dependencies required in this application along with their versions.

TABLE I. DEPENDENCIES USED IN THE NODE SERVER

Dependencies	Version
dotenv	16.0.0
express	4.17.3
openai	2.0.5

B. OpenAI Integration

A developer may use OpenAI to access GPT-3, which can carry out a number of tasks using natural language, and Codex, which converts natural language into code. Modern language models that have been taught by OpenAI are excellent at comprehending and producing text. These models are accessible through OpenAI API, which may be used to do almost any task involving language processing.

The OpenAI npm library must be downloaded in order to use the OpenAI API. Once created, an OpenAI object must be linked with an API key so that it may be used to query the OpenAI server for API endpoints and utilise the capability for tasks involving natural language processing.

C. Web speech API Integration

Using JavaScript and the built-in Online Voice API offered by the current Web API, a user may include speech data into web programmes. The Web Speech API consists of two components: SpeechRecognition and SpeechSynthesis (Asynchronous Speech Recognition).

Utilizing the device's default speech recognition service, the SpeechRecognition interface allows users to access speech recognition, which enables them to comprehend the context of a voice input and reply appropriately.

D. Text to Code Conversion

The OpenAI API offers a feature referred to as "completion". There are numerous tasks that may be performed using the "completions" endpoint. It offers any OpenAI model a straightforward yet effective interface. As a prompt, we can enter some text, and the model will provide a text completion that tries to fit the context or pattern we provided.

Using completion API, we can accurately translate a spoken utterance into an English statement.

E. Code conversion

The "completion" endpoint of OpenAI Codex can be used to access the Codex and convert code between languages. Since the endpoint is developed in Python, it needs a few PyPI (Python Package Index) libraries, which may be downloaded by using the "pip" command. Below is a list of those packages in more depth.

TABLE II. DEPENDENCIES USED IN THE OPENAI APPLICATION

Dependencies	Version
certifi	2020.6.20
charset-normalizer	2.0.9
colorama	0.4.4
decorator	4.4.2
idna	3.3
imageio	2.13.1
imageio-ffmpeg	0.4.5
moviepy	1.0.3
numpy	1.19.5
Pillow	8.4.0
proglog	0.1.9
requests	2.26.0
SpeechRecognition	3.8.1
tqdm	4.62.3
urllib3	1.26.7
Wincertstore	0.2

III. RESULTS AND DISCUSSION

The participants in the study were experienced developers and programmers having profound knowledge of python and JavaScript. Most of them had never used any speech-to-code software before. None of them had any disabilities which would make typing difficult. The study comprised 8 programmers who were allotted 15 minutes each to develop a binary search program for finding an element in an array. Any challenges faced during the coding process were attributed to the usage of IntelliCode rather than the program creation itself.

The study was conducted over three sessions that were identical except for the voice recognition technology used. The first session utilized IntelliCode, which provided an accurate natural language to code conversion model. The second session involved the use of SPEED software developed by A. Begel and S. L. Graham, while in the third session, a non-programmer human typed in the code.

The third session demonstrated how IntelliCode could be leveraged for its near-perfect accuracy in natural language to code conversion.

Various metrics, as shown in Table III, were used to analyse the programming sessions of the users. A single viewer watched the screen recording while listening to the audio transmission to code the metrics. The results were then compared with those of the SPEED software.

Speed and accuracy

During the three sessions, the programmers had varying experiences. Some participants struggled due to slow speed and low accuracy, resulting in only partial completion of the code creation task. Others were able to finish their work with time to spare. The group that used a human voice recognizer was able to complete more of the task in less time.

However, there were some issues with the recognizer, such as incorrect word recognition and occasional recognition of unintended words. To address this, some programmers muted their microphones while dictating to themselves.

Despite these challenges, the SPEED software demonstrated a recognition delay of around 0.7 seconds, while IntelliCode had a recognition delay of approximately 1 second. Additionally,

IntelliCode had a higher recognition accuracy of approximately 70%, compared to SPEED's overall accuracy of 60%.

Speaking code

The users had a relatively low rate of command errors caused by user mistakes. These errors occurred mainly when users were unsure of what to say or how to express themselves. As these errors were primarily the users' own, rather than resulting from misrecognition, they were deemed more acceptable to the users. The voice recognizer malfunction sometimes caused programmers to speak in short bursts, and correcting incorrect words was time-consuming.

Participants were initially hesitant to use natural language when dictating code, but not when using identifier names. They believed that a combination of voice and keyboard would be more effective than either alone.

Subjective evaluation

When questioned about the possibility of using voice recognition for programming, the majority of participants expressed reservations. They cited concerns such as noise pollution, cognitive interference, and the inability to use their hands while speaking. However, some participants mentioned that they might consider using it at home if they worked alone and didn't disturb anyone else.

Ultimately, the participants concluded that they would not prefer to use this programming environment for daily coding. However, they all agreed that they would consider using the software if they had an injury that limited their use of hands or eyes or if they were working in a hands-free environment.

TABLE III. DATA RECORDED FROM INTELLICODE USER STUDY FROM ALL PARTICIPANTS

		All Utterances	Correctly Recognised	Error Rate
IntelliCode	***U1***	68	47	31%
	U2	61	44	27%
	U3	73	47	36%
SPEED	***U4***	80	60	27%
	U5	103	51	50%
	U6	89	50	43%
Human Voice Recognition	***U7***	51	43	15%
	U8	55	42	23%

IV. CONCLUSION

IntelliCode is a software application designed to assist programming through the use of voice input. It accepts a user's spoken commands and generates code in response. The software can create code snippets or macros based on the voice input, and it can also facilitate code conversion between different programming languages, primarily Python and JavaScript. Through a user study, we evaluated the software and discovered that programmers can learn to program using voice commands with minimal practice. However, they face significant challenges when the speech recognizer misunderstands their speech.

The platform integrates speech recognition, natural language processing (NLP), code editing, and code conversion to enhance the coding experience for individuals with visual impairments, physical disabilities, and others. Programming-by-voice can also enable software engineers with motor impairments to program, although their efficiency may be lower compared to an unimpaired programmer. With additional research, improved user interface designs, and better analysis, speech-based programming could become a competitive alternative for software developers in the future.

A. Future Scope

The progress in machine learning algorithms that can efficiently process natural language and text-to-code is likely to play a significant role in the future of speech-to-code applications.

Moreover, a major area of focus will be to support new programming languages such as C/C++, Java, Rust, and Go. However, real-time programming, which involves complex coding techniques, poses a challenge as the application can only perform basic speech recognition with good accuracy currently. As the complexity of speech and code increases, so does the error rate of the application. The software supports speech-to-code functionality, but users still have to use built-in buttons to convert speech to code and then execute it. Integrating AI with this feature could allow users to use voice commands to convert and run code.

A computer program can be prone to errors as programming involves both syntactic and semantic typing. The potential for errors increases when using AI to translate voice to code. In the future, we plan to incorporate a feature that enables the AI to identify errors and warnings and suggest fixes. We also aim to introduce a debugging mode that allows users to specify the line number and desired modifications, which the software can execute.

As artificial intelligence and natural language processing continue to evolve, they will significantly impact the functionality and accuracy of our speech-to-code application.

ACKNOWLEDGMENT

Our academic achievements and the success of our project were made possible by the contributions of many people. We would like to express our gratitude to all those who helped us. Specifically, we are indebted to Dr Manoj Kumar for his invaluable supervision and guidance throughout the project. His leadership and inspiration have been instrumental in our progress. We also want to extend our thanks to the department faculty members for their continuous support and encouragement. Lastly, we appreciate the assistance provided by our parents during these challenging times.

REFERENCES

[1] Dandona L, Dandona R, John RK. Estimation of blindness in India from 2000 through 2020: implications for the blindness control policy. Natl Med J India. 2001 Nov-Dec;14(6):327-34. PMID: 11804362.

[2] WHO Blindness and vision impairment: https://www.who.int/news-room/fact-sheets/detail/blindness-and-visual-impairment

[3] Stack overflow developer survey:

https://insights.stackoverflow.com/survey/2020#developer-profile-developer-type-united-states-unweighted

[4] S. Shaik, R. Corvin, R. Sudarsan, F. Javed, Q. Ijaz, S. Roy-choudhury, et al., "SpeechClipse: an Eclipse speech plug-in", Eclipse Technology eXchange Workshop, pp. 84-88, 2003

[5] A. Desilets, D. C. Fox and S. Norton, "Voicecode: An innovative speech interface for programming-by-voice", Proceedings of ACM CHI 06 Conference on Human Factors in Computing Systems, April 2006.

[6] Price, E. Rillof, J. Zachary, and B. Harvey. Natural Java: A natural language interface for programming in Java. In IUI, Short Paper/Poster/Demonstration, pages 207–211, 2000.

[7] A. Begel and S. L. Graham, "An Assessment of a Speech-Based Programming Environment," Visual Languages and Human-Centric Computing (VL/HCC'06), 2006, pp. 116-120, doi: 10.1109/VLHCC

AUTHORS

First Author – Dr. Manoj Kumar, Professor, Delhi Technological University, Delhi, India, 110042,
Second Author – Hitesh Yadav, Student, Delhi Technological University, Delhi, India, 110042,
Third Author – Jayant Yadav, Student, Delhi Technological University, Delhi, India, 110042,
Fourth Author – Mayank Jha, Student, Delhi Technological University, Delhi, India, 110042,

Correspondence Author – Hitesh Yadav, Student, Delhi Technological University, Delhi, India, 110042,

KL Grade Classification of Knee Osteoarthritis using Convolutional Neural Networks and CBAM

Pragya Gupta
Department of Computer Science and Engineering, Delhi Technological University

Raghav Gupta
Department of Computer Science and Engineering, Delhi Technological University

Ram Aggarwal
Department of Computer Science and Engineering, Delhi Technological University

Manoj Kumar
Department of Computer Science and Engineering, Delhi Technological University

Abstract- Knee osteoarthritis is a prevalent musculoskeletal disorder that predominantly affects the elderly population and is typified by the gradual deterioration and attrition of articular cartilage in the knee joint. One commonly employed technique to evaluate the extent of knee osteoarthritis is the Kellgren-Lawrence (KL) grading system, which evaluates joint space narrowing, osteophytes, sclerosis, and bony deformity visible on radiographic images. The purpose of this study is to compare and contrast the Knee Osteoarthritis KL grade classification performance of various architectures of Convolutional neural networks including ResNet-34, DenseNet-121, VGG-19 and Inception-V3. The Osteoarthritis Initiative (OAI) dataset was chosen as the primary dataset for our research. In this study, osteoarthritis is classified solely based on radiographs (X-RAY) of the knee obtained in a bilateral posteroanterior projection with fixed joint flexion. We investigate the effectiveness of the Convolution Block Attention Module on these architectures for knee osteoarthritis severity level. We merged KL scale grades 0 and 1 into a single category which resulted in a 11.84 % improvement in accuracy without losing any essential data. We observed that DenseNet-121 with CBAM performed the best among all the models, achieving an accuracy of 86.714% with highest per class accuracy of 93.15% achieved on Grade 0.

Index Terms- Knee Osteoarthritis, Kellgren-Lawrence scale, Convolution Block Attention Module, DenseNet, ResNet, VGG, Inception

I. INTRODUCTION

Knee osteoarthritis [1] is a multifactorial degenerative disorder that poses a significant health burden in the aging population worldwide. This illness is most prevalent in individuals between the ages of 45 and 80, particularly women. Articular cartilage damage is the hallmark feature of this condition, detecting and grading the severity of osteoarthritis is of utmost importance. Articular cartilage is a firm, elastic tissue that serves as a cushioning mechanism at the ends of bones in joints. The primary symptoms of knee osteoarthritis include pain, stiffness, swelling, and limited mobility. Swelling is often caused by inflammation within the joint, leading to the knee feeling warm and tender to the touch. Furthermore, restricted mobility can impede the ability to carry out routine activities such as walking, climbing stairs, or bending down.

Several factors can contribute to the development of knee osteoarthritis, including age, genetics, obesity, previous knee injuries, and certain occupations or sports that involve repetitive stress on the knee joint. As individuals age, the natural wear and tear of cartilage in joints can lead to osteoarthritis. Additionally, genetics may also play a contributory role in the onset of the condition. There is an increased susceptibility for individuals who have a familial background of knee osteoarthritis to develop the ailment themselves. Moreover, obesity places excess strain on the knees, hastening the cartilage breakdown process.

The detection and classification of knee osteoarthritis are crucial for several reasons. Firstly, as there are no known medical means available till now that can regrow the articular cartilage, healthcare providers need to determine the appropriate treatment plan for each individual. The degree of knee osteoarthritis severity can vary considerably, and treatment options will hinge on the level of progression. For instance, mild cases may be managed with lifestyle modifications and physical therapy, while severe cases may necessitate surgery. Secondly, tracking the progression of knee osteoarthritis can help healthcare providers identify potential complications or comorbidities that may arise, such as joint deformities or nerve damage. Finally, early detection of knee osteoarthritis can enhance outcomes and potentially delay the need for more invasive treatments. By routinely assessing the levels of knee osteoarthritis, healthcare providers can facilitate effective condition management and improve the quality of life of patients.

Knee osteoarthritis can be diagnosed and evaluated via various methods, including clinical examination, imaging techniques such as X-rays and MRI, and biomarker analysis. X-rays are a widely-used diagnostic tool in the detection of this disease. X-rays facilitate the visualization of joint space narrowing and bone spur development, contributing to the accurate diagnosis of the condition. The severity of knee osteoarthritis can be evaluated using the radiographic Kellgren-Lawrence grading scale [2]. Narrowing of joint space, osteophytes, sclerosis, and bone deformity are some of the characteristics that contribute to a diagnosis. The KL grading system is widely used in both clinical practice and research to assess the degree of knee osteoarthritis. This system classifies the condition of the joint in five grades (0-4) (Fig. 1).
A score of 0 suggests no osteoarthritis, whereas a score of 4 implies severe osteoarthritis.

- Grade 0: a knee joint without any radiographic evidence of osteoarthritis



Fig. 1. Knee X-Ray images of various KL grades from OAI dataset

- Grade 1: some suspicion of osteoarthritis with probable osteophytes and narrowing of joint space
- Grade 2: a concrete diagnosis of osteoarthritis including mild narrowing of joint space and some osteophytes.
- Grade 3: indicative of moderate to severe narrowing of joint space, numerous osteophytes, and possible sclerosis.
- Grade 4: severe narrowing of joint space, huge osteophytes, acute sclerosis, and potential bony deformities.

Here, it is important to note that the KL grading system is based solely on radiographic findings and does not take into account other factors such as pain, functional impairment, or patient-reported outcomes. As such, it is just one aspect of a comprehensive assessment of osteoarthritis in the knee joint.

II. LITERATURE REVIEW

The state-of-the-art studies have investigated the use of CNNs [3] for knee osteoarthritis classification and severity grading using radiographic images. These studies have shown that CNNs can achieve high accuracy in automatically classifying knee osteoarthritis severity based on radiographic images [4].

Attention-based CNN for KL Grade Classification: Data from the Osteoarthritis Initiative [5]

In this study, the authors brought to the table Residual Neural Network (ResNet) [6] to identify the knee joint in radiographs, and a Convolutional Block Attention Module (CBAM) [7] was then integrated to provide automatic KL-grade prediction. This study used a Residual Neural Network (ResNet) model in tandem with a Convolutional Block Attention Module (CBAM) to achieve the most exceptional performance in automated KL-grade classification. This is shown by noticeably improved metrics like Mean Squared Error (MSE), multi-class average accuracy, and Quadratic Kappa score. This method's increased performance may be ascribed to the use of sophisticated preprocessing techniques and improvements to knee joint localization, which have improved the model's efficacy and accuracy in comparison to earlier methods. With a mean squared error of 0.36, a quadratic Kappa score of 0.88, and a multi-class average accuracy of 74.81%, the suggested model significantly outperformed previously published results. This represents a significant advancement in automated KL-grade classification using deep learning techniques.

Using compression and excitation blocks to improve the accuracy of automatic classification of osteoarthritis of the knee using convolutional neural networks [8]

In this research study the author undertook an investigation to assess the efficacy of integrating compression and excitation blocks into ResNet and DenseNet [9] convolutional neural networks, with the aim of improving the classification accuracy of knee osteoarthritis. The outcomes of this inquiry evinced a significant improvement of 1-3% in the quality of OA classification, as appraised on the KL scale, without significant deviations from conventional methods. In addition, the study revealed that incorporating grades 0 and 1 of the Kellgren-Lawrence (KL) grade into a single class conferred a remarkable 12.74% augmentation in the precision of osteoarthritis KL grade classification, while simultaneously retaining indispensable disease-related data.

To further elevate the performance of the classification model, a novel approach was employed, which entailed an ensemble of three convolutional networks adopting the DenseNet-121 architecture with compression and excitation blocks. This innovative technique culminated in a striking classification accuracy of 84.66%, which surpasses the outcomes of previous studies and illuminates the tremendous potential of integrating squeeze and excitation blocks [10] in the realm of deep learning algorithms for osteoarthritis classification

Fully automatic knee osteoarthritis severity grading using deep neural networks with a novel ordinal loss [11]

In this research, the author sequentially deploys two deep CNN models to autonomously estimate the knee osteoarthritis intensity, as determined by Kellgren-Lawrence scale. Firstly, a specialized YOLOv2 [12] (one stage) network is employed to detect knee joints determined by the size distribution of knee joints with

modest variance. Secondly, the most widely used CNN models have been fine-tuned, including variations of ResNet, VGG [13], and DenseNet as well as Inception-V3 [14], to categorize the joint pictures using a new, configurable ordinal loss. Misclassifications with bigger distances between the predicted and actual KL ratings are assigned a higher penalty. The Osteoarthritis Initiative (OAI) baseline X-ray images are utilized for assessment. When it comes to identifying the knee joint, the authors achieved a mean Jaccard index 0.858. The model with the proposed ordinal loss has the maximum classification accuracy (69.7%) and the lowest mean absolute error (MAE) (0.344) on the knee KL grading test. Superior results are achieved in both the KL grading of the knee and the identification of the knee joint.

III. DATA

There are several standard datasets available for knee osteoarthritis grading, including:

1. The Osteoarthritis Initiative (OAI) dataset [15], which contains an archive of clinical data of 4796 patients.
2. MOST (Multicenter Osteoarthritis Study) dataset, which includes data on 3026 patients.
In addition, recently the dataset is gaining popularity.
3. CHECK (Cohort Hip & Cohort Knee), which is the result of a long-term follow-up of patients with early symptoms of osteoarthritis of the knees and hips in the Netherlands and consists of more than 3000 x-rays of various parts of the body (lateral and frontal projections of the knees, hips, x-rays of the hands, etc.).

However, during experiments, it was found that the CHECK dataset contains a large number of markup errors, and access to the MOST dataset is limited due to the termination of funding and reorganization.
Therefore, we selected the OAI dataset as the primary dataset for our study. This set contains information on 4796 patients aged between 45 to 79 years, followed up for 14 years. In addition to radiographs of the knee joint, the dataset also contains information on various measurements, the presence of osteophytes, narrowing of the intra-articular space and stages of osteoarthritis obtained from several independent experts.
In our study, the classification of osteoarthritis is carried out only on radiographs (X-RAY) of the knee joint obtained in a bilateral posteroanterior projection with fixed joint flexion.

This set was randomly divided into training, validation and test sets. samples in the proportion 7: 1: 2.

The dataset obtained was highly imbalanced. We used Data augmentation to address the severe imbalance in the obtained dataset. To get this effect, we flipped the original data horizontally, randomly scaled and rotated it (by a slight angle), then adjusted the hue, saturation, and brightness of the images. The final resolution of the photograph, after all the adjustments, was 224x224 pixels. Over the course of model training, all augmentation steps were executed at random.

IV. METHODOLOGY

In our model we implemented various architectures of convolutional neural networks including DenseNet, ResNet, VGG and Inception-V3. We modified the structure of these models and added a novel attention mechanism [16], Convolution Block Attention Module (CBAM) (Fig. 2). The architecture of the network includes multiple convolutional layers, followed by attention layers, and then fully connected layers.

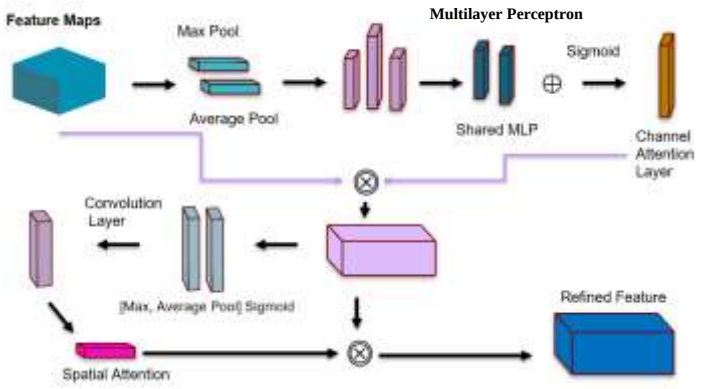


Fig. 2. architecture of convolutional block attention module

In order to boost the efficiency of convolutional neural networks (CNNs), CBAM was developed as a neural network module. Both a channel attention module and a spatial attention module make up the CBAM module. Using the channel attention module, you may selectively highlight important channels while suppressing less informative ones, therefore capturing the interdependencies across feature channels in a convolutional layer. An important part of the spatial attention module is its ability to selectively highlight useful spatial locations while suppressing less informative ones, thereby capturing the interdependencies between spatial places in a feature map.

We employed a DenseNet-121 architecture with CBAM for the classification task (Table 1). We obtained images of 224x224 pixels with 3 channels after data augmentation on the OAI dataset to handle the problem of dataset imbalance. The pixel values were further normalized in the range [0,1] to ensure that they are within a consistent range. The initial layer is a 7x7 convolutional layer with 64 filters with stride 2 and valid padding, followed by batch normalization [17] and ReLU activation function. The output is passed through a max pooling layer with a 3x3 window and stride 2.

The architecture (Fig. 3) consists of a series of four such dense blocks each consisting of 6, 12, 24, and 16 layers respectively, with a growth rate of 32. After each dense block, the feature maps are passed through a Convolutional Block Attention Module (CBAM) module. The channel attention branch of CBAM learns

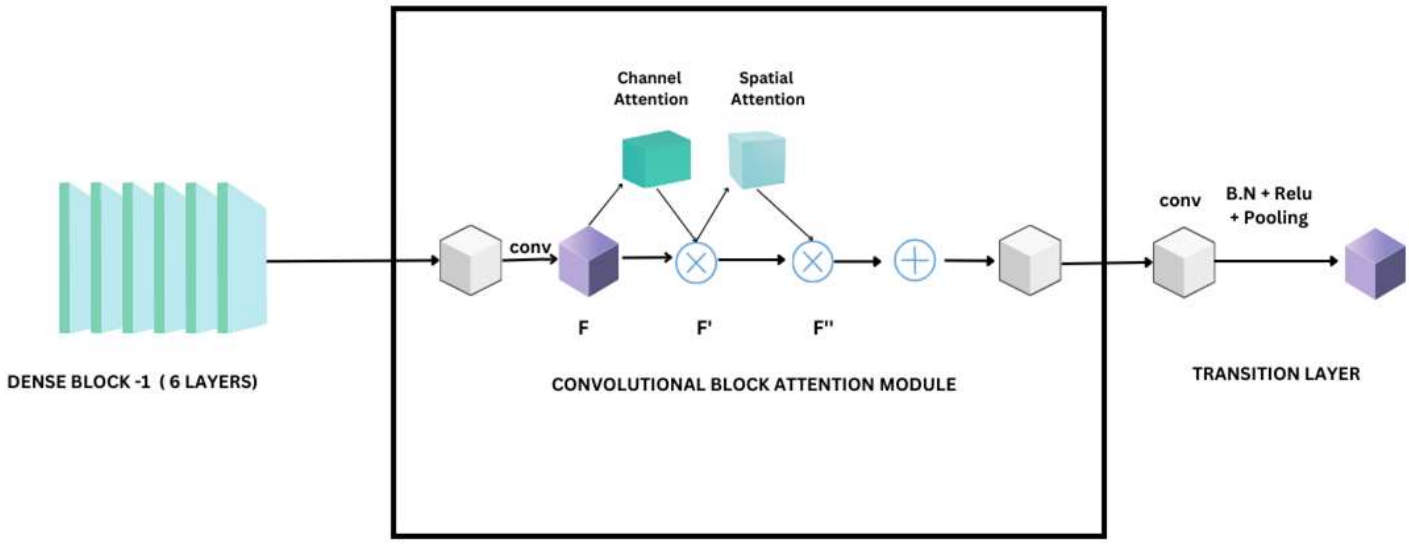


Fig. 3. Model Architecture

to focus on important features by analyzing the interdependencies between different channels in the feature maps. It uses a global pooling operation to aggregate the feature maps across spatial dimensions, followed by a series of fully connected layers to compute a set of channel-wise attention weights. These weights are then used to scale the feature maps before passing them to the next layer. The spatial attention branch of CBAM learns to focus on important regions by analyzing the interdependencies between different spatial locations in the feature maps. It uses a series of convolutional layers to compute a set of spatial attention maps, which indicate the importance of each spatial location in the feature maps. These attention maps are then used to modulate the feature maps, allowing the model to selectively attend to important regions.

The outputs of the channel and spatial attention branches are combined using element-wise multiplication, resulting in a set of attention-modulated feature maps that are more discriminative and informative than the original feature maps. By incorporating both channel and spatial attention, CBAM can effectively capture both global and local dependencies in the feature maps.

There are 3 transition blocks, each consisting of a convolutional layer, batch normalization (B.N.), ReLU activation, average pooling, and reduction in the number of filters by a factor of 0.5. The Global average pooling layer reduces the spatial dimensions of the output feature maps to a single vector.

Finally, a Dense layer is added that applies a fully connected layer with 5 output nodes and SoftMax activation is employed for classification. We compile the model using the Adam optimizer [18] with a learning rate of 0.0001 and categorical cross-entropy loss, which is a commonly used loss function for multi-class classification tasks such as KL grading.

Layer Type	Output Shape	Filters	Kernel Size	Stride	Padding
Input	(224, 224, 3)				
Conv2D	(112, 112, 64)	64	7x7	2	same
BatchNormalization	(112, 112, 64)				
ReLU	(112, 112, 64)				
MaxPooling2D	(56, 56,64)		3x3	2	same
Dense Block 1	(56, 56, 256)	32	1x1		
CBAM	(56, 56, 256)				
Transition Layer 1	(28, 28, 128)				
Dense Block 2	(28, 28, 512)	64	1x1		
CBAM	(28, 28, 512)				
Transition Layer 2	(14,14, 256)				
Dense Block 3	(14,14, 1024)	128	1x1		
CBAM	(14,14, 1024)				
Transition Layer 3	(7,7, 512)				
Dense Block 4	(7,7, 2048)	256	1x1		
CBAM	(7,7, 2048)				
Average Pooling	(1, 1,2048)		7x7		
Flatten	2048				
Dense	5 (KL grades)				

Table 1: The network structure of the DenseNet-121 architecture with CBAM blocks. The input shape of 224x224x3 is first passed through a convolutional layer with 64 filters, followed by batch normalization and ReLU activation, followed by max pooling, Dense Blocks with CBAM, and Transition Layers.

After implementing the above model for various CNN architectures, we found that in order to streamline the classification process and improve the focus on osteoarthritis detection, we can merge KL grades 0 and 1 into a single category. This decision was based on the fact that these two grades are often considered similar in terms of the absence of osteoarthritis. We took care to maintain consistency with the original KL grading scale by leaving the remaining categories untouched.

Combining 0 and 1 grade on KL grading in knee osteoarthritis is a common practice in medical imaging due to several reasons. Firstly, the cartilage thickness and radiographic findings of 0 and 1 grades are very similar, making it difficult to distinguish between the two grades. Secondly, combining these grades can increase the sensitivity of the classification model and reduce the chances of false negatives. This is particularly important in early stages of the disease where minor changes in the cartilage can be missed by radiologists. Moreover, combining 0 and 1 grades can simplify the classification process, as it reduces the number of categories in the grading system, making it easier for radiologists to interpret and report their findings. Overall, combining 0 and 1 grade on KL grading in knee osteoarthritis is a practical and effective approach that can improve the efficiency and accuracy of the diagnosis and treatment of the disease.

V. RESULTS

To comprehensively evaluate the performance of various models for KL grading of knee osteoarthritis on the OAI dataset, we conducted a comparative analysis of ResNet-34, DenseNet-121, VGG-19, and Inception-V3. These models were chosen based on their established efficacy in image classification tasks and their proficiency in handling large, complex datasets. The evaluation was performed using multiple performance metrics, including overall accuracy, precision, recall, and F1-score, for each model on the OAI dataset. Our findings revealed that DenseNet-121 outperformed the other models and was the most accurate for KL grading of knee osteoarthritis from X-rays. The obtained results demonstrate the potential of deep learning models in diagnosing knee osteoarthritis, which could aid healthcare professionals in developing personalized treatment plans and improving patient outcomes.

In this work, we studied the effect of incorporating an attention mechanism into our models, and also investigated the effect of merging two classes in our classification task. We first evaluated all the models without any attention block, and compared their performance. Next, we added a CBAM attention module after each layer, and again compared the results. Our findings showed that the inclusion of the CBAM attention module led to a significant improvement in model accuracy, with an average increase of about 3%.

Moreover, we also examined the effect of merging two classes in our classification task. Specifically, we merged grade 0 and grade 1 into a single class, and compared the accuracy with the original class distribution. Our experimental results revealed a significant increase in accuracy of about 11.34% when the two classes were merged.

```
Mean
  precision: 86.5556391973099
  recall: 86.71497584541062,
  accuracy: 86.71497584541062,
  f1_score: 86.5579471436222


rows is precision, recall, fscore and support:
|          0 |          1 |          2 |          3 |
|------------+------------+------------+------------|
|   0.885163 |   0.794189 |   0.909953 |   0.9375   |
|   0.931551 |   0.733781 |   0.860987 |   0.882353 |
|   0.907764 |   0.762791 |   0.884793 |   0.909091 |
| 935        | 447        | 223        | 51         |


per-class accuracy:
|          0 |          1 |          2 |          3 |
|------------+------------+------------+------------|
|   0.931551 |   0.733781 |   0.860987 |   0.882353 |
```

Fig. 4. Results obtained on the DenseNet-121 model + CBAM for the case of 4 classes

The performance of the DenseNet-121 model with CBAM and an amalgamation of 0-1 KL grade is illustrated in Fig. 4. The model shows an accuracy of 86.714% and also shows the class wise accuracy, precision, recall, support and F1-score obtained by this architecture.

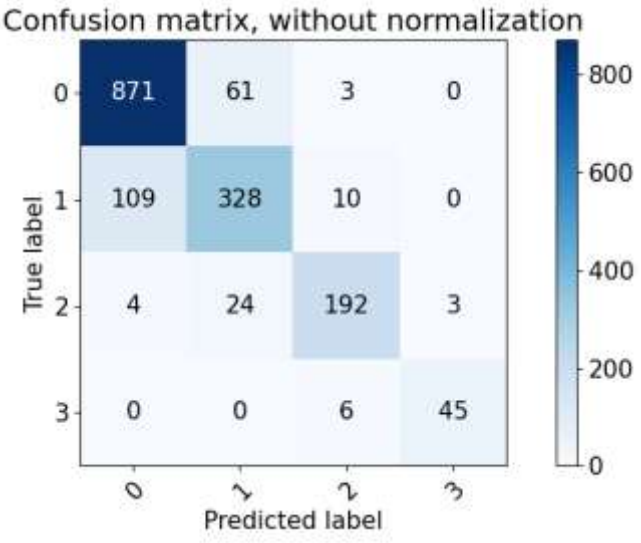


Fig. 5. confusion matrix obtained on the DenseNet-121 model + CBAM for the case of 4 classes

The confusion matrix (Fig. 5) shows that the models are better at predicting classes 2 and 3 compared to classes 0 and 1, which is expected given the imbalance of the dataset. The effectiveness of a machine learning model for classification tasks may be measured using a confusion matrix. The model's predicted values are compared to the actual values of the test data, and the resulting

comparison forms the matrix. The matrix's columns display the predicted values, while the rows display the actual ones. True positives, False positives, True negatives, and False negatives make up the four quadrants of the confusion matrix.

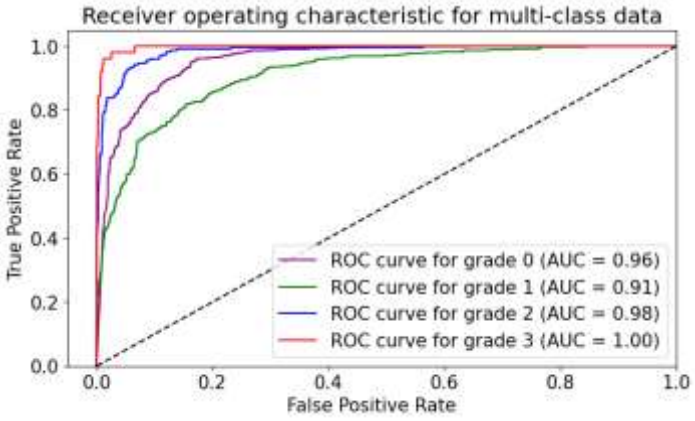


Fig. 6. ROC curve obtained on the DenseNet-121 model + CBAM for the case of 4 classes

Model	Accuracy	Precision	Recall	F1-Score
DenseNet-121-CBAM	0.867	0.865	0.867	0.865
ResNet-34 CBAM	0.835	0.852	0.827	0.839
Inception-V3 CBAM	0.804	0.834	0.821	0.827
VGG-19 CBAM	0.781	0.773	0.795	0.783

Table 2: Result obtained on various CNN architecture + CBAM for the case of 4 classes

As illustrated in Table 2, DenseNet-121 with CBAM performed the best among all the models, achieving an accuracy of 86.7% while VGG-19 with CBAM yielded the lowest accuracy of 78.1%.

Our study has implications for the diagnosis of knee osteoarthritis, as our models can be used to automate the process of KL grading from X-ray images, providing a more objective and efficient diagnostic tool for healthcare professionals. Additionally, our research highlights the potential of using CBAM in conjunction with deep learning models for medical image analysis.

VI. CONCLUSION

In conclusion, this study was designed to comprehensively evaluate the performance of four deep learning models, ResNet-34, DenseNet-121, VGG-19, and Inception-V3, for KL grading of knee osteoarthritis on the OAI dataset. The study also aimed to investigate the effect of integrating an attention mechanism into the models and merging two classes (grade 0 and grade 1) in the classification task.

The results of the study demonstrate the potential of deep learning models in accurately diagnosing knee osteoarthritis. DenseNet-121 outperformed the other models, demonstrating superior accuracy for KL grading of knee OA from X-rays. This suggests that deep learning models could be a valuable tool for improving the accuracy of knee OA diagnosis, which could lead to more effective treatment plans and better patient outcomes.

Moreover, the inclusion of a CBAM attention module after each layer significantly improved the performance of the models, resulting in an approximate increase in accuracy of 3%. This finding suggests that incorporating attention mechanisms into deep learning models can improve their performance in medical image analysis tasks. In addition, merging grade 0 and grade 1 into a single class resulted in a significant increase in accuracy of approximately 11.34%. This suggests that simplifying the classification task by merging classes can lead to more accurate results.

The study highlights the potential of using deep learning models in diagnosing knee osteoarthritis, which could aid healthcare professionals in developing personalized treatment plans and improving patient outcomes. The use of CBAM in conjunction with deep learning models for medical image analysis is also demonstrated as a promising avenue for future research.

ACKNOWLEDGMENT

We offer our deepest appreciation to the individuals and organizations whose persistent support was crucial to the completion of our research endeavor. We would like to express our gratitude to our esteemed supervisor, Professor Manoj Kumar, whose exceptional guidance, support, and encouragement proved invaluable throughout the project. His expertise and insights were critical in helping us design and execute our research. Furthermore, we are grateful to the Delhi Technological University for their significant assistance in various aspects of the project, including the provision of necessary hardware and software. Finally, we would like to acknowledge the unwavering support and encouragement from our families and friends throughout the project's duration. Their steadfastness, patience, and understanding were integral in our ability to complete this work. We remain deeply grateful to all those who contributed to the accomplishment of this research project.

REFERENCES

[1] KELLGREN JH, LAWRENCE JS. "Radiological assessment of osteo-arthrosis". Ann Rheum Dis. 1957 Dec;16(4):494-502. doi: 10.1136/ard.16.4.494. PMID: 13498604; PMCID: PMC1006995.

[2] Kohn MD, Sassoon AA, Fernando ND. "Classifications in Brief: Kellgren-Lawrence Classification of Osteoarthritis". Clin Orthop Relat Res. 2016 Aug;474(8):1886-93. doi:10.1007/s11999-016-4732-4. Epub 2016 Feb 12. PMID: 26872913; PMCID: PMC4925407.

[3] O'Shea, Keiron & Nash, Ryan. (2015). "An Introduction to Convolutional Neural Networks". ArXiv e-prints.

[4] Chaugule, Sushma & Malemath, Virendra. (2022). Knee Osteoarthritis Grading Using DenseNet and Radiographic Images. SN Computer Science. 4. 10.1007/s42979-022-01468-4.

[5] B. Zhang, J. Tan, K. Cho, G. Chang and C. M. Deniz, "Attention-based CNN for KL Grade Classification: Data from the Osteoarthritis Initiative," 2020 IEEE 17th International Symposium on Biomedical Imaging (ISBI), Iowa City, IA, USA, 2020, pp. 731-735, doi: 10.1109/ISBI45749.2020.9098456.

[6] K. He, X. Zhang, S. Ren and J. Sun, "Deep Residual Learning for Image Recognition," 2016 IEEE Conference on Computer Vision and Pattern Recognition (CVPR), Las Vegas, NV, USA, 2016, pp. 770-778, doi: 10.1109/CVPR.2016.90.
[7] Woo, S., Park, J., Lee, JY., Kweon, I.S. (2018). CBAM: Convolutional Block Attention Module. In: Ferrari, V., Hebert, M., Sminchisescu, C., Weiss, Y. (eds) Computer Vision – ECCV 2018. ECCV 2018. Lecture Notes in Computer Science(), vol 11211. Springer, Cham. https://doi.org/10.1007/978-3-030-01234-2_1
[8] Mikhaylichenko, A. A. and Demyanenko, Y. M., "Using squeeze-and-excitation blocks to improve an accuracy of automatically grading knee osteoarthritis severity using convolutional neural networks", Computer Optics, vol. 46, no. 2, pp. 317–325, 2022. doi:10.18287/2412-6179-CO-897.
[9] G. Huang, Z. Liu, L. Van Der Maaten and K. Q. Weinberger, "Densely Connected Convolutional Networks," 2017 IEEE Conference on Computer Vision and Pattern Recognition (CVPR), Honolulu, HI, USA, 2017, pp. 2261-2269, doi: 10.1109/CVPR.2017.243.
[10] J. Hu, L. Shen and G. Sun, "Squeeze-and-Excitation Networks," 2018 IEEE/CVF Conference on Computer Vision and Pattern Recognition, Salt Lake City, UT, USA, 2018, pp. 7132-7141, doi: 10.1109/CVPR.2018.00745.
[11] Chen P, Gao L, Shi X, Allen K, Yang L. Fully automatic knee osteoarthritis severity grading using deep neural networks with a novel ordinal loss. Comput Med Imaging Graph. 2019 Jul;75:84-92. doi: 10.1016/j.compmedimag.2019.06.002. Epub 2019 Jun 13. PMID: 31238184; PMCID: PMC9531250.
[12] Deng, P., Wang, K. & Han, X. Real-Time Object Detection Based on YOLO-v2 for Tiny Vehicle Object. SN COMPUT. SCI. 3, 329 (2022). https://doi.org/10.1007/s42979-022-01229-3
[13] Simonyan, K. and Zisserman, A. (2015) Very Deep Convolutional Networks for Large-Scale Image Recognition. The 3rd International Conference on Learning Representations (ICLR2015). https://arxiv.org/abs/1409.1556
[14] C. Szegedy et al., "Going deeper with convolutions," 2015 IEEE Conference on Computer Vision and Pattern Recognition (CVPR), Boston, MA, USA, 2015, pp. 1-9, doi: 10.1109/CVPR.2015.7298594.
[15] Chen, Pingjun (2018), "Knee Osteoarthritis Severity Grading Dataset", Mendeley Data, V1, doi: 10.17632/56rmx5bjcr.1
[16] Y. Feng, J. Liu, H. Zhang and D. Qiu, "Automated grading of knee osteoarthritis X-ray images based on attention mechanism," 2021 IEEE International Conference on Bioinformatics and Biomedicine (BIBM), Houston, TX, USA, 2021, pp. 1927-1932, doi: 10.1109/BIBM52615.2021.9669623.
[17] Sergey Ioffe and Christian Szegedy. 2015. Batch normalization: accelerating deep network training by reducing internal covariate shift. In Proceedings of the 32nd International Conference on International Conference on Machine Learning - Volume 37 (ICML'15). JMLR.org, 448–456.
[18] Kingma, Diederik & Ba, Jimmy. (2014). Adam: A Method for Stochastic Optimization. International Conference on Learning Representations.

AUTHORS

First Author – Pragya Gupta, Bachelor of Technology, Delhi Technological University,
Second Author –Raghav Gupta, Bachelor of Technology, Delhi Technological University,
Third Author – Ram Aggarwal, Bachelor of Technology, Delhi Technological University,
Fourth Author – Manoj Kumar, Professor, Delhi Technological University

Astrophysics and Space Science (2023) 368:30
https://doi.org/10.1007/s10509-023-04186-2

RESEARCH

Lower hybrid wave nonlinear saturation and turbulence in the magnetopause

Manoj K. Upadhyay[1] · Neha Pathak[2] · R. Uma[1] · R.P. Sharma[1]

Received: 14 November 2022 / Accepted: 29 March 2023
© The Author(s), under exclusive licence to Springer Nature B.V. 2023

Abstract
The proposed work presents a model to understand the lower hybrid turbulence in the magnetic reconnection regions of magnetopause by the energetic electron beams (generated by the magnetic reconnection process). The magnetic reconnection process has been substituted by the energetic electron beam source in this model. Due to beam energy, lower hybrid waves (LHW) evolve from very small to large amplitude (saturation) and then to LHW localization and the turbulent state. A nonlinear two-dimensional model with the help of two-fluid dynamics has been developed. The mathematical model considers the interaction between pump LHW and low frequency magnetosonic wave (MSW). The MSW, present in the background, has been contemplated as the source of density perturbations in LHW dynamics. The ponderomotive force components arise due to high-frequency LHW. With the help of the growth term associated with the electron beam, dynamical equations for LHW and MSW have been derived. The two coupled equations, thus obtained, are solved with the help of numerical simulation techniques. The results show the LHW's temporal evolution (growth) from a very small amplitude and then the formation of localized structures and turbulence.

Keywords Magnetosphere · Lower hybrid wave · Nonlinear coupling · Turbulence · Magnetopause · Electron beam · Magnetosonic mode

1 Introduction

Investigating turbulence in the magnetopause (magnetosphere) has been a key area of interest for researchers. The authors propose a "**simple (basic) model**" to explain turbulence in the lower hybrid frequency range in the magnetopause.

Lower hybrid waves (LHWs) develop at frequencies between the ion and electron gyrofrequencies (Davidson et al. 1977). LHWs can be of particular importance because they can contribute to anomalous resistivity (Silin et al. 2005), heating of electrons and ions (Cairns and McMillan 2005), transfer energy between electrons and ions, and produce cross-field particle diffusion (Vaivads et al. 2004). These waves (LHWs) are generally treated as electrostatic in nature (Davidson and Gladd 1975).

These large-amplitude waves are often observed in the Earth's magnetosphere (Graham et al. 2017). Waves in the lower hybrid frequency range in the magnetosphere have been observed by Freja, Cluster, and Viking satellites, and recently by MMS satellites (Graham et al. 2016; Tjulin et al. 2004). The study of lower hybrid waves (LHWs) plays a vital role in investigating turbulence in the magnetopause. The idea of turbulence can explain various phenomena such as anomalous resistivity, energization, radiation emitted during solar bursts, and energy source for particle acceleration in plasma science (Bale et al. 2002; Karimabadi et al. 2013; Matthaeus 2021).

Omidi et al. (1994) have discussed MSWs and their role in turbulence in the magnetosheath (magnetopause) region, they have also discussed the competition between Alfvén wave modes and magnetosonic modes and shown that the magnetosonic mode can be excited despite its lower growth rate. The have shown that the magnetopause itself can generate slow magnetosonic waves in the magnetosheath. Further, they suggested that these waves can be thought of as

✉ M.K. Upadhyay
manojupadhyay37@gmail.com

[1] Department of Energy Science and Engineering, Indian Institute of Technology Delhi, New Delhi 110016, India

[2] Department of Applied Physics, Delhi Technological University, New Delhi, 110042, India

Published online: 17 April 2023

part of the overall magnetopause structure. THEMIS spacecraft have also observed MSW in the magnetopause region (Plaschke et al. 2013).

Many observations have been made and reported in the literature regarding LHW in magnetized plasma (Cairns and McMillan 2005; Lu et al. 2005). Norgren et al. (2012) studied LHWs in electrostatic predictions using single spacecraft data. Graham et al. (2019) have also studied LHW properties using MMS observations. The electrostatic lower hybrid drift instability (LHDI) is in agreement with the lower hybrid waves observed in the diffusion region, as shown by Graham et al. (2017). These waves are associated with a density gradient and a strong electric field in the normal direction.

These studies have confirmed the presence of LHW in the magnetosphere region. Various authors have investigated the magnetosphere and its different zones in the lower hybrid frequency range (Gary and Sgro 1990; Shapiro 1998; Walker et al. 2008). Cheung and Wong (1985) have experimentally investigated the nonlinear evolution of electron-beam-plasma instability for Langmuir waves. Shapiro et al. (1993) have investigated modulation instability and collapse of waves in the vicinity of the lower hybrid resonance, including magnetosonic and lower hybrid waves, using analytical and numerical methods. They have discussed the analytical solutions for 2- and 3-dimensional LHW coupling. The coupling results in the formation of localized structures. These localized structures are mentioned by Shapiro et al. (1993) as "the coupling resulted in localization of high-frequency field producing elongated cigar-shaped nonlinear wave packets aligned along the magnetic field with the plasma expelled outside (cavities)." Shapiro (1998) has investigated the instability resulting from the coupling of LHW and kinetic Alfvén wave and found that the nonlinear evolution of modulation instability leads to the formation of Alfvén wave solitons aligned along the magnetic field. Bingham et al. (2004) have studied the nonlinear mode coupling of LHW and discussed the role of nonlinear coupling in modulation instability and wave collapse. They have demonstrated that lower hybrid activity can be responsible for anomalous resistivity and anomalous diffusion at the magnetosphere. Most of the above studies are limited to the nonlinear stage, and turbulence has not been studied. In the existing models, they have taken LHW excited state and explained the formation of localized structures and nonlinear saturation.

The LHW can be triggered by the ion–ion cross-field instability from the interaction between the magnetospheric ions and the crescent-shaped distribution of magnetosheath ions that undergo a partial gyro orbit into the magnetosphere (Graham et al. 2017). In addition, the fluctuations detected by Cozzani et al. (2021) display some similarities with the obliquely propagating electromagnetic drift instability (Daughton 2003; Ji et al. 2005). This instability can arise in the center of the current sheet at higher β_e.

At the reconnection sites, a possible mechanism of generation of LHW can be the electron beams (generated due to reconnection process). These electron beams can further act as a free energy source for many nonlinear phenomena in the magnetopause (Zhou et al. 2014). So, the motivation of the present work is to study LHW turbulence using an electron beam-driven lower hybrid mode. In our model, we first examined the evolution of LHW from a very low level (amplitude) to the saturation stage. Then, we investigated the lower hybrid turbulence. Cheung and Wong (1985) have illustrated that these electron beams can trigger wave modes and can lead to the formation of nonlinear structures. They have observed multiple field spikes (turbulence) for strongly beam driven Langmuir waves.

Therefore, we propose that, due to the beam energy, LHW grows from a very small to a large amplitude in the proposed model. At large amplitude, the nonlinear effects start dominating. These nonlinear effects are due to the ponderomotive and other terms associated with large amplitude LHW in beam plasma instability (Batra et al. 2006). These effects lead to LHW localization and, ultimately, to the turbulent state.

This paper investigates the nonlinear development of beam plasma interactions. It aims to show the interaction between lower hybrid mode and low frequency magnetosonic wave and the transition to lower hybrid turbulence in the magnetopause region (in the 2D case).

Nonlinear dynamical equations have been derived using the two-fluid approach. Further, a numerical simulation is carried out to solve the model equations using the pseudospectral technique for spatial integration and the finite difference method for temporal integration. The numerical simulations based on theoretical modeling show the LHW localization and turbulence.

This paper is organized as follows. Section 2 consists of the mathematical formulation and the derivation of dynamical equations governing the present model. In Sect. 3, coupled equations called the modified Zakharov system of equations (MZSE) are solved numerically, and simulation results are presented. Section 4 consists of results and discussion. Section 5 includes the summary and conclusion.

2 Mathematical modeling

The suggested theoretical model considers density modification, the high and low-frequency response of the plasma, and various nonlinear and linear processes such as the ponderomotive force effects and coupling of waves. For this model, we have considered magnetized plasma for which electron

gyrofrequency ω_{ce} is much less than the electron plasma frequency ω_{pe}, i.e., $\omega_{ce} \ll \omega_{pe}$.

The following analysis consists of two parts. First, in Sect. 2.1, the dynamical equation is derived for the high-frequency wave, i.e., LHW. The second part (Sect. 2.2) consists of the dynamics of the low-frequency MSW and its coupling with the LHW.

In the following equations, the subscript "f" represents the **fluid species** in plasma, i.e., for electron, $f = e$, and for ions, $f = i$; $\vec{E}$ and $\vec{B}$ represent the wave electric and magnetic field, respectively, q_f is the charge, n_f is the charge density, and m_f is the mass of the charged species. Also $\vec{B}_0$ is the background magnetic field, c is the speed of light in the vacuum, and e is the electron charge; n_i, n_e are ion and electron charge densities, respectively. The magnetic field perturbation is δB, and density perturbations are δn.

2.1 Derivation of lower hybrid wave dynamical equation

We have considered a 2D electrostatic LHW propagating in the x–z plane with wave vector $\vec{k} = k_x\hat{x} + k_z\hat{z}$. The magnetic field is $\vec{B} = \vec{B}_0 + \delta\vec{B}$.

We have used the two-fluid model to derive the model equations. The following fundamental equations are used to derive the model's prevailing equations:

The equation of motion in linearized form is

$$\frac{\partial \vec{v}_f}{\partial t} = \frac{q_f}{m_f}\vec{E} + \frac{q_f}{cm_f}\left(\vec{v}_f \times \vec{B}_0\right). \tag{1}$$

The continuity equation is

$$\frac{\partial n_f}{\partial t} + \vec{\nabla}.\left(n_f v_f\right) = 0. \tag{2}$$

Poisson equation is

$$\vec{\nabla}.\vec{E} = 4\pi e\left(n_i - n_e\right). \tag{3}$$

From Eq. (1), the velocity components are

$$v_{fx} = -\frac{q\omega}{m_f i\left(\omega^2 - \omega_{cf}^2\right)}E_x, \tag{4}$$

$$v_{fy} = -\frac{q\omega_{cf}}{m_f\left(\omega^2 - \omega_{cf}^2\right)}E_x, \tag{5}$$

$$v_{fz} = \frac{qiE_z}{m_f\omega}, \tag{6}$$

where v_{fx}, v_{fy}, v_{fz} represent velocity components along the x, y, and z-axis of electrons and ions for $f = e$ and $f = i$, respectively.

From Poisson's equation,

$$\frac{\partial^2}{\partial t^2}\vec{\nabla}.\vec{E} = 4\pi e\left(\frac{\partial^2}{\partial t^2}n_i - \frac{\partial^2}{\partial t^2}n_e\right). \tag{7}$$

Substituting the value of $\frac{\partial^2}{\partial t^2}n_e$ from the electron continuity equation and $\frac{\partial^2}{\partial t^2}n_i$ from the ion continuity equation gives

$$\frac{\partial^2}{\partial t^2}\left(\frac{\partial^2}{\partial x^2} + \frac{\partial^2}{\partial z^2}\right)E + \frac{m_e}{m_i}\omega_{ce}^2\left(\frac{\partial^2}{\partial x^2} + \frac{\partial^2}{\partial z^2}\right)E + \omega_{ce}^2\frac{\partial^2}{\partial z^2}E = 0. \tag{8}$$

For almost transverse propagation ($k_x \gg k_z$), incorporating magnetic field perturbation [B $= (B_0 + \delta B)$] due to MSW in Eq. (8) produces

$$\frac{\partial^4 E}{\partial t^2 \partial x^2} + \left[\frac{m_e}{mi}\omega_{ce}^2 + \left(2\frac{m_e}{mi}\omega_{ce}^2\frac{\delta B}{B_0}\right)\right]\frac{\partial^2 E}{\partial x^2} + \omega_{ce}^2\frac{\partial^2 E}{\partial z^2} = 0, \tag{9}$$

and, substituting $\delta B = 0$, we can retrieve the dispersion relation for LHW from Eq. (9), namely

$$\omega^2 = \omega_l^2\left(1 + \frac{m_i}{m_e}\frac{k_z^2}{k_x^2}\right). \tag{10}$$

Here, $\omega_l^2 = \omega_{ce}.\omega_{ci}$ is the lower hybrid resonance frequency.

Phenomenologically, substituting the growth term $\gamma > 0$ in the dynamical equation can describe the beam instability driving the wave mode. For the simplistic model, we have considered the growth rate to be constant (but in a future work, this restriction may be revoked). Thus, the LHW dynamical equation describing the beam driven instability is given by [phenomenologically substituting γ on the left-hand side of Eq. (9)]

$$\left(\frac{\partial^2}{\partial t^2} + 2\gamma\frac{\partial}{\partial t}\right)\frac{\partial^2 E}{\partial x^2} + \frac{m_e}{mi}\omega_{ce}^2\left(1 + 2\frac{\delta B}{B_0}\right)\frac{\partial^2 E}{\partial x^2} + \omega_{ce}^2\frac{\partial^2 E}{\partial z^2} = 0. \tag{11}$$

Taking the envelope $E = E_x(x, z, t)e^{i(k_{0x}x + k_{0z}z - \omega_0 t)}$, Eq. (11) gives

$$E_x\left(k_{0x}^2\omega_0^2 - k_{0x}^2\omega_l^2 - \omega_{ce}^2k_{0z}^2\right) + 4k_{0x}\omega_0\frac{\partial^2}{\partial t\partial x}E_x + \omega_l^2\frac{\partial^2}{\partial x^2}E_x + 2ik_{0x}\omega_l^2\frac{\partial}{\partial x}E_x + 2k_{0x}^2\omega_0 i\frac{\partial}{\partial t}E_x + \omega_{ce}^2\frac{\partial^2}{\partial z^2}E_x + 2ik_{0z}\omega_{ce}^2\frac{\partial}{\partial z}E_x - \omega_0^2\frac{\partial^2}{\partial x^2}E_x$$

$$-2ik_{0x}\omega_0^2\frac{\partial}{\partial x}E_x+2k_{0x}^2\gamma\omega_0 iE_x-2k_{0x}^2\omega_l^2\frac{\delta B}{B_0}E_x=0. \tag{12}$$

Using lower hybrid dispersion relation $(k_{0x}^2\omega_0^2-k_{0x}^2\omega_l^2-\omega_{ce}^2k_{0z}^2)=0$, Eq. (12) can be written as

$$\begin{aligned}&4k_{0x}\omega_0\frac{\partial^2}{\partial t\partial x}E_x+2ik_{0x}\left(\omega_l^2-\omega_0^2\right)\frac{\partial}{\partial x}E_x+2k_{0x}^2\omega_0 i\frac{\partial}{\partial t}E_x\\&+\omega_{ce}^2\frac{\partial^2}{\partial z^2}E_x+2ik_{0z}\omega_{ce}^2\frac{\partial}{\partial z}E_x+\left(\omega_l^2-\omega_0^2\right)\frac{\partial^2}{\partial x^2}E_x\\&+2k_{0x}^2\gamma\omega_0 iE_x-2k_{0x}^2\omega_l^2\frac{\delta B}{B_0}E_x=0.\end{aligned} \tag{13}$$

Introducing background density perturbation δn $(n_e=n_0+\delta n)$ using Eq. (15c) of MSW dynamics gives

$$\begin{aligned}&2k_{0x}^2\omega_0 i\frac{\partial}{\partial t}E_x+\omega_{ce}^2\frac{\partial^2}{\partial z^2}E_x+\left(\omega_l^2-\omega_0^2\right)\frac{\partial^2}{\partial x^2}E_x\\&+2ik_{0x}\left(\omega_l^2-\omega_0^2\right)\frac{\partial}{\partial x}E_x+2ik_{0z}\omega_{ce}^2\frac{\partial}{\partial z}E_x\\&+4k_{0x}\omega_0\frac{\partial^2}{\partial t\partial x}E_x+2k_{0x}^2\gamma\omega_0 iE_x-2k_{0x}^2\omega_l^2\frac{\delta n}{n_0}E_x=0.\end{aligned} \tag{14}$$

Equation (14) is the model equation for a **beam driven** lower-hybrid system.

2.2 Magnetosonic wave (MSW) dynamics

Let us consider a low-frequency (ω_M) MSW, propagating across a background magnetic field. The background magnetic field is in the z-axis direction, i.e., $\vec{B}_0=B_{0z}\hat{z}$. For a simplistic model, the direction of propagation of MSW has been taken along the x-axis, i.e., $\vec{k}_M=k_x\hat{x}$, and its polarization is along the y-axis, i.e., $\vec{E}_M=E\hat{y}$. (More complicated dynamics of MSW, including slow and fast modes at an angle, will be considered in a future work.)

From the electron continuity equation, we obtain

$$\frac{\partial}{\partial t}\frac{\delta n}{n_0}=-\frac{\partial}{\partial x}\left(\frac{cE_y}{B_0}\right). \tag{15a}$$

From Faraday's law, we get

$$\frac{\partial}{\partial x}\left(cE_y\right)=-\frac{\partial}{\partial t}\delta B_0. \tag{15b}$$

Using Eqs. (15a) and (15b), we get the following relationship:

$$\frac{\delta \mathrm{B}}{B_0}=\frac{\delta n}{n_0}. \tag{15c}$$

The equation of motion for MSW becomes

$$\frac{\partial\vec{v}_f}{\partial t}=\frac{q_f}{m_f}\vec{E}+\frac{q_f}{cm_f}\left(\vec{v}_f\times\vec{B}_0\right)-\frac{kT_f}{m_f}\vec{\nabla}\frac{n_f}{n_0}+\vec{F}_{fp}, \tag{16a}$$

where $\vec{v}_f$ is the drift velocity of species $f=i,e$ ($i=$ ions, $e=$ electrons); q_f, m_f, and T_f are the charge, masses, and temperature of the species (i.e., ions and electrons), respectively, c is the speed of light in vacuum, and $\vec{F}_{fp}$, is the ponderomotive force due to LHW.

Taking the y component of the wave equation, i.e., Eq. (5), we get

$$\frac{\partial^2E_{My}}{\partial t^2}-\frac{1}{c^2}\frac{\partial^2E_{My}}{\partial t^2}=\frac{4\pi}{c^2}\frac{\partial J_{fy}}{\partial t}, \tag{16b}$$

where $J_{fy}=n_0e\left(v_{iy}-v_{ey}\right)$ is the current density due to both charge particles (i.e., ions and electrons); E_{My} is the y component of MSW polarization vector.

From Eq. (16a), we get the y component of the electron drift velocity as

$$\begin{aligned}v_{ey}=&\left(\frac{e\omega_M}{m_ei\left(\omega_M^2-\omega_{ce}^2\right)}E_{My}+\frac{ik_M\omega_{ce}v_{the}^2}{\left(\omega_M^2-\omega_{ce}^2\right)}\frac{\delta \mathrm{n}}{n_0}\right.\\&\left.-\frac{\omega_M}{m_ei\left(\omega_M^2-\omega_{ce}^2\right)}F_{pey}-\frac{\omega_{ce}}{m_e\left(\omega_M^2-\omega_{ce}^2\right)}F_{pex}\right).\end{aligned} \tag{17}$$

Similarly, the expression for the y component of the ion drift velocity is given by

$$\begin{aligned}v_{iy}=&\left\{\frac{e\omega_M}{im_i\omega_{ci}^2}E_{My}+\frac{ik_Mv_{thi}^2}{\omega_{ci}}\frac{\delta \mathrm{n}}{n_0}+\frac{\omega_M}{im_i\omega_{ci}^2}F_{piy}\right.\\&\left.-\frac{1}{m_i\omega_{ci}}F_{pix}\right\}.\end{aligned} \tag{18}$$

Substituting the values from Eqs. (17) and (18) into Eq. (16b), we get the dynamical equation of the MSW wave

$$\begin{aligned}&\left[\frac{1}{c^2}\frac{\partial^2}{\partial t^2}-\frac{\partial^2}{\partial x^2}+\frac{1}{v_A^2}\frac{\partial^2}{\partial t^2}\right]\frac{\delta n}{n_0}\\&=\left(\frac{\partial^3F_{pex}}{\partial x^2\partial z}+\frac{\partial^3F_{pey}}{\partial y^2\partial z}\right)-\frac{v_A^2}{m_i\omega_{ci}\omega}\left(\frac{\partial^3F_{piy}}{\partial z^2\partial x}+\frac{\partial^3F_{pix}}{\partial z^2\partial y}\right).\end{aligned} \tag{19}$$

Here, F_{pex}, F_{pey}, F_{pix}, F_{piy} are ponderomotive force components due to high-frequency LHW in the directions of the x- and y-axis, respectively.

2.3 Ponderomotive force

The expression for the ponderomotive force is given by

$$\vec{F}_{pf}=-m_f\left(v_{fx}\frac{\partial}{\partial x}+v_{fy}\frac{\partial}{\partial y}+v_{fz}\frac{\partial}{\partial z}\right)\vec{v}_f$$

$$+\frac{q_f}{c}\left(\vec{v}_f\times\vec{B}\right), \tag{20}$$

where $\vec{B}$ is the magnetic field vector; q_f and m_f are the charge and masses of the species, respectively, and c is the speed of light in vacuum. Thus, the corresponding ponderomotive force components after substituting the values of velocity components for electron motion along the x- and y-axis will be given by

$$F_{pex}=\frac{\omega^2e^2}{4m_e\omega_{ce}^2}\left(-\frac{1}{\omega_{ce}^2}\frac{\partial E_xE_x^*}{\partial x}+\frac{1}{\omega^2}E_z\frac{\partial E_x^*}{\partial z}+\frac{1}{\omega^2}E_z^*\frac{\partial E_x}{\partial z}\right), \tag{21}$$

$$F_{pey}=\frac{i\omega e^2}{4m_e\omega_{ce}^2}\left(\frac{1}{\omega_{ce}^2}E_x\frac{\partial E_x^*}{\partial x}-\frac{1}{\omega_{ce}^2}E_x^*\frac{\partial E_x}{\partial x}-\frac{1}{\omega^2}E_z\frac{\partial E_x^*}{\partial z}+\frac{1}{\omega^2}E_z^*\frac{\partial E_x}{\partial z}\right). \tag{22}$$

Similarly, for ions, the ponderomotive force components are given by

$$F_{pix}=-\frac{e^2}{4m_i\omega^2}\left(\frac{\partial E_xE_x^*}{\partial x}+E_z\frac{\partial E_x^*}{\partial z}+E_z^*\frac{\partial E_x}{\partial z}\right), \tag{23}$$

$$F_{piy}=-\frac{i\omega_{ci}e^2}{4m_i\omega^3}\left(E_x\frac{\partial E_x^*}{\partial x}-E_x^*\frac{\partial E_x}{\partial x}+E_z\frac{\partial E_x^*}{\partial z}-E_z^*\frac{\partial E_x}{\partial z}\right). \tag{24}$$

Substituting these values from Eqs. (21)–(24) into Eq. (19), we get the MSW dynamical equation

$$\left[\frac{\left(c^2+v_A^2\right)}{c^2v_A^2}\frac{\partial^2}{\partial t^2}-\frac{\left(c_s^2+v_A^2\right)}{v_A^2}\frac{\partial^2}{\partial x^2}\right]\frac{\delta n}{n_0}=\frac{ec}{4v_A^2B_0m_i\omega_{ce}}\frac{\partial^2|E_x|^2}{\partial x^2}. \tag{25}$$

Here, $v_A=\frac{B_0}{\sqrt{4\pi n_0m_i}}$ is Alfvén wave speed, and c_s is the speed of sound.

3 2D numerical model and simulation

Equations (24) and (25) in dimensionless form can be written as

$$i\frac{\partial}{\partial t}E_x-i\frac{\partial}{\partial x}E_x+\frac{\partial^2}{\partial z^2}E_x+c_1i\frac{\partial}{\partial z}E_x+c_2\frac{\partial^2}{\partial x\partial t}E_x-c_3\frac{\partial^2}{\partial x^2}E_x-c_4nE_x+c_5i\gamma E_x=0, \tag{26a}$$

$$\left[\frac{\partial^2}{\partial t^2}-c_6\frac{\partial^2}{\partial x^2}\right]n=\frac{\partial^2|E_x|^2}{\partial x^2}. \tag{26b}$$

Equations (26a) and (26b) represent a coupled system of equations. The normalization parameters used in dimensionless equations are

$$X_N=\frac{\lambda_lT_N\left(\omega_0^2-\omega_l^2\right)}{2\pi\omega_0},\qquad Z_N=\frac{\lambda_l\omega_{ce}}{\pi}\left(\frac{T_N}{8\omega}\right)^{0.5},$$

$$T_N=\frac{1}{\omega_{ci}},\qquad \mathrm{N_n}=\mathrm{n_0},\qquad E_N\approx\frac{X_n}{T_\mathrm{n}}\left(\frac{4m_i\omega_{ce}B_0}{ec}\right)^{0.5}.$$

And the values of constants are

$$c_1=\frac{m_e\lambda_lT_N\omega_{ce}^2}{2\pi m_iZ_N\omega_0},\qquad c_2=\frac{\lambda_l}{\pi X_N},$$

$$c_3=\frac{\lambda_l^2T_N\left(\omega^2-\omega_l^2\right)}{\omega_08\pi^2\mathrm{X_N^2}},\qquad c_4=\frac{T_N\omega_l^2}{\omega_0},$$

$$c_5=T_N,\qquad c_6=\left(\frac{T_Nv_A}{X_N}\right)^2.$$

Equation (26a) and (26b) are called the modified Zakharov system of equations (MZSE). They are solved numerically within a periodic spatial domain of $20\pi\times20\pi$ and a grid of size 128×128. The initial condition used for simulation is (we have taken a plane progressive wavefront in the x–z plane with a very small initial amplitude perturbation)

$$E_x(x,z,0)=E_0\{1+\varepsilon\cos(\alpha_xx)\}\{1+\varepsilon\cos(\alpha_zz)\}, \tag{27}$$

where E_0 is the initial amplitude (of the unperturbed wave) and ε is the magnitude of the perturbed electric field. The perturbation wave numbers are taken as α_x, α_z. We have taken α_x, $\alpha_z=0.1\varepsilon=0.1$ for the present study. Our model's plasma parameters used for simulation are $\mathrm{B_0}=2.5*10^{-4}$ G, $\mathrm{n_0}=5\ \mathrm{cm^{-3}}$, $\lambda_l=1.2*10^6$ cm, $\theta=89^0$, $\omega_{ce}=4.39*10^{-3}\ \mathrm{s^{-1}}$, $\gamma=0.2\omega\ \mathrm{s^{-1}}$, $\omega_{ci}=2.39\ \mathrm{s^{-1}}$ (Graham et al. 2019). The value of normalizing parameters are $X_N\sim\lambda_l$, $Z_N\sim\lambda_l$, $T_N\sim\omega_{ci}^{-1}$ (Nicholson 1983), and the values of constants are $c_1=7.0$, $c_2=0.1$, $c_3=0.04$, $c_4=24.89$, $c_5=T_N$, $c_6=11.0$. Also $\lambda_l=1.2*10^6$ is the lower hybrid wavelength.

This model uses the pseudospectral method in the x–z dimensions for space integration. For the time-domain integration, the finite difference method with the predictor–corrector approach is implemented using a step size of 10^{-5} ($dt=10^{-5}$). First, to check the accuracy of this system, simulations of the nonlinear Schrödinger equation (NLS) are done. During this simulation, the plasmon number is preserved up to the accuracy of 10^{-5}. Then this simulation (code) is modified for analyzing the set of two coupled dimensionless Eqs. (26a) and (26b).

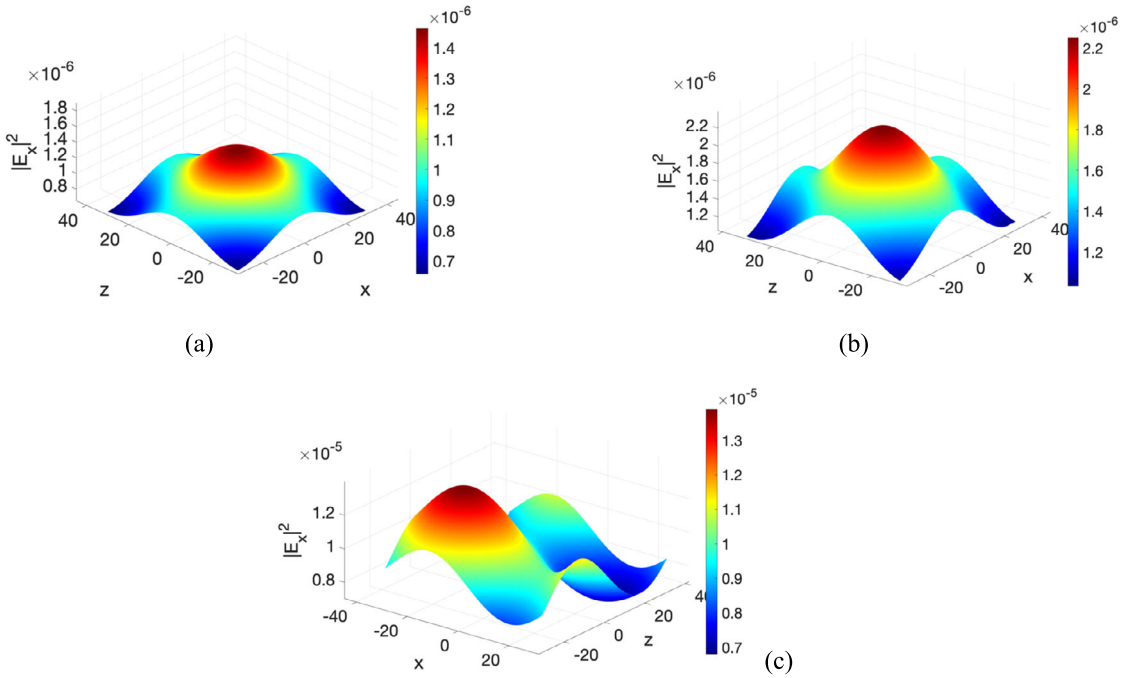


Fig. 1 The growth of high-frequency LHW with time: (a) at $t = 0$, (b) at $t = 15$, and (c) at $t = 35$ (variables in normalized units)

4 Results and discussion

This study considers the interaction between high-frequency LHW and low-frequency MSW. LHW sees a perturbed background density and magnetic field on account of MSW. The ponderomotive nonlinearity arises due to the high-frequency wave, which is incorporated in MSW dynamics. The solution of coupled equations describes the instability due to the nonlinear evolution of the plasma system. The time evolution of this instability is investigated in two stages: the growth stage and the turbulent phase.

4.1 Growth regime

Figures 1(a), 1(b), and 1(c) show the temporal evolution of LHW (all physical variables in normalized units). The parameters used for these figures are $E_0 = 0.001$, $\varepsilon = 0.1$, and $\alpha = 0.1$. These figures show the field intensity in the spatial domain on a linear scale. Figures 1(a), 1(b), and 1(c) show waveforms of the LHW at $t = 0$, $t = 15$, and $t = 35$, respectively. From these figures, the illustrated values of $|E_x|^2$ are $1.0 * 10^{-6}$ for $t = 0$, $2 * 10^{-6}$ for $t = 15$, and $1.5 * 10^{-5}$ for $t = 35$ (approximately).

One can observe the evolution of LHW from very low levels with time. The initial amplitude of LHW is very small; the electron beam imparts energy to the system. Therefore, LHW grows to a large amplitude. From 1(a) to 1(c), the squared field amplitude evolves to an order of magnitude. So, these figures denote the growth of LHW.

Figure 2 shows the evolution of field intensity with the variation of the wavenumber of perturbation for the same LHW and MSW coupled system equations. The parameters used for Fig. 2(a) are $E_0 = 0.001$, $\varepsilon = 0.1$, and $\alpha = 0.2$. Figure 2(b) depicts the wave amplitude when $E_0 = 0.001$, $\varepsilon = 0.1$, and $\alpha = 1.2$. Figure 2(c) illustrates the evolution pattern of the electric field intensity with a varied value of $\alpha = 1.4$ ($E_0 = 0.001$, $\varepsilon = 0.1$). We observe different nonlinear evolution patterns of the waveform when the initial condition governing parameter α is changed.

Figure 3(a) shows the time evolution of LHW. This figure, too, illustrates the growth of LHW. Figure 3(b) shows the lower hybrid field in the frequency domain. The central peak shows the envelope frequency, and the peaks represent the spread of the power of the lower hybrid besides the central peak. From these figures, the wave pattern's growth from a low level (very small amplitude) and progression toward the saturation state are evident.

Figure 3(c) contains the time domain representation of two curves: (i) the electric field and (ii) $e^{\gamma t}$ (all variables in normalized units) on the semi-log axis. In Fig. 3(c), the dotted line shows the curve of $e^{\gamma t}$ given by the $\gamma.E$ term in Eq. (26a), where γ is the growth rate (taken constant in our model for simplicity). The dotted curve is plotted when we leave out all spatial terms. The solid curve is the plot of the electric field evaluated from the code using Eqs. (26a) and (26b). As expected, the dotted line shows the growth of the system. The fluctuations (kinks) are due to spatial variation with time.

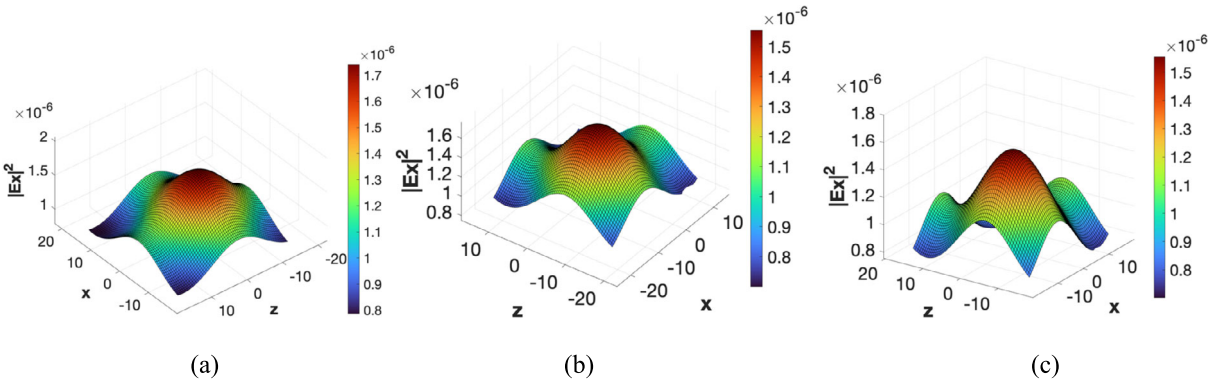


Fig. 2 The waveforms with variations in parameter α. (Variables in normalized units)

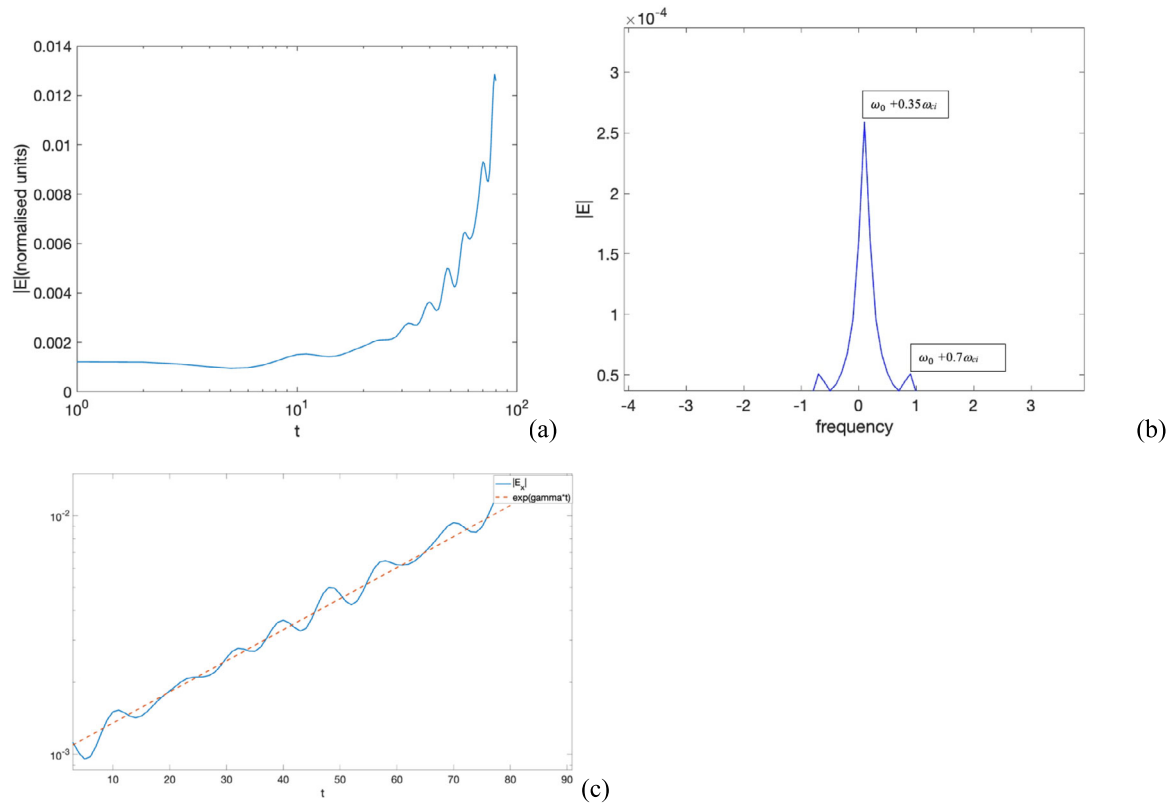


Fig. 3 The time evolution of LHW (a), the frequency domain representation of LHW (b), and the time-domain representation of two curves on semi-log axis (c), (i) the electric field and (ii) $e^{\gamma t}$ (all variables in normalized units)

The source of these peaks in Fig. 3(b) is the forced oscillation due to the ponderomotive term in the dynamical equation of low-frequency wave (MSW). These forced oscillations are of wave number α_x and $2\alpha_x$. If, in the beginning, MSW dispersion relation is still being followed by these forced oscillations, then the peak (harmonics) will be related to frequencies $\omega = \alpha_x v_a$, $\omega = 2\alpha_x v_a$, where v_a is Alfvén speed. Calculating numerical values will give the corresponding shifts, and peaks come out at $\omega_0 + 0.35\omega_{ci}$ rad/s and $\omega_0 \pm 0.7\omega_{ci}$ rad/s. The location of peaks is as shown in Fig. 3(b) (more details are in the discussion of Fig. 5(b)).

Shapiro et al. (1993) have studied mechanisms leading to the modulation instability in the nonlinear coupling of LHW with much lower frequency quasineutral density perturbations via the ponderomotive force. Our model has obtained similar localized structures as found by Shapiro et al., but Shapiro et al. have not studied the turbulence or the beam effect. The investigation of LHW turbulence is as follows.

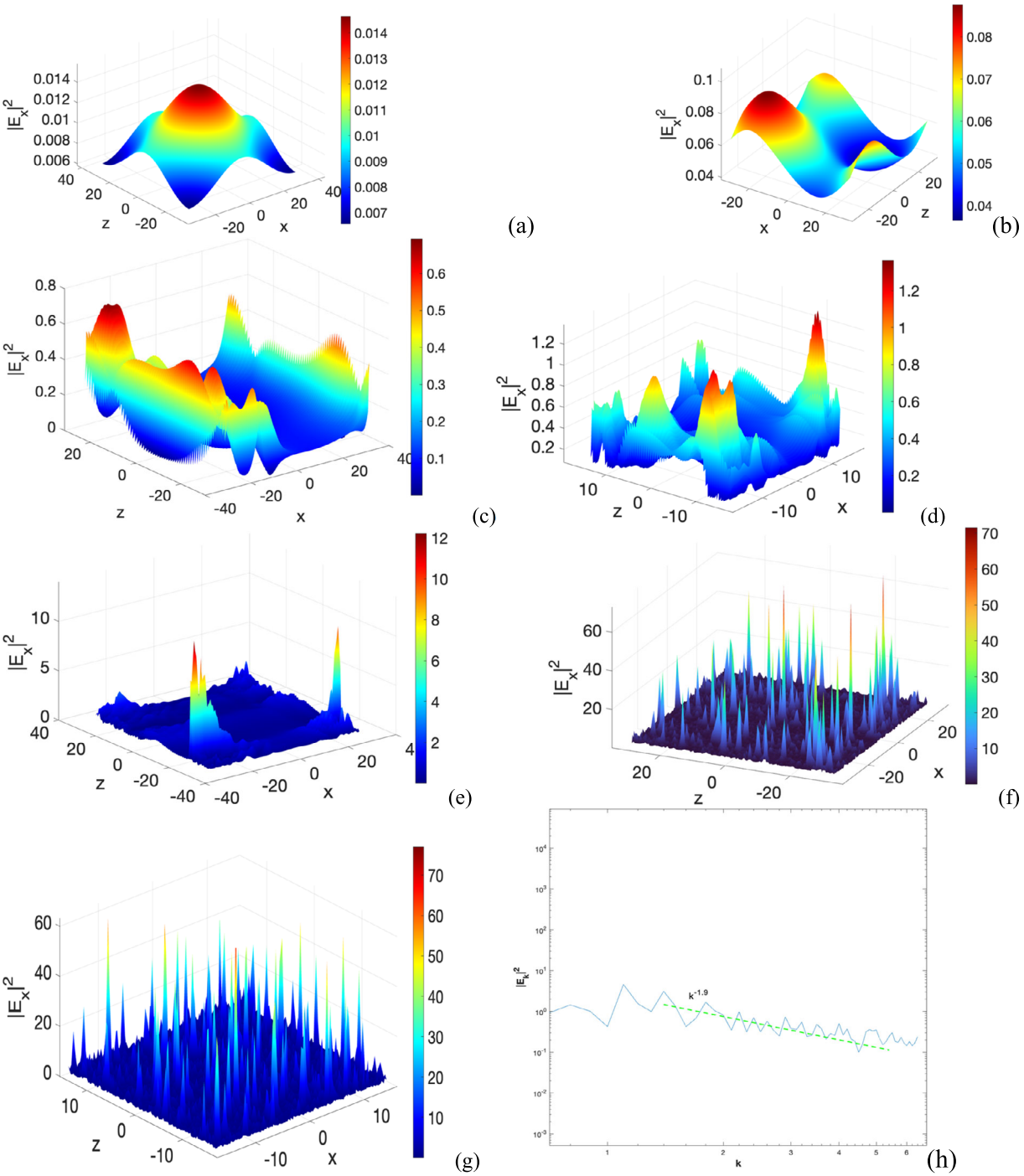


Fig. 4 LHW in the turbulent zone. Panels (a) to (g) show the localization and chaotic structures of LHW at times $t = 0, 30, 40, 45, 50, 70, 80$, respectively. Figure 4(h) shows the electric power spectrum. (Variables in normalized units)

4.2 Turbulent regime

Figure 4 represents lower hybrid waveforms for $E_0 = 0.1$, $\varepsilon = 0.1$, and $\alpha = 0.1$ with time (all physical variables in normalized units). When the LHW amplitude reaches saturation levels, the wave structure appears to be breaking along both axes. The field structures are in elongated spikes. These chaotic localized structures are evidence of strong turbulence effects in beam plasma interactions.

Figures 4(f) and 4(g) show the electric field intensity at $t = 70$ and $t = 80$, respectively. We observe multiple field spikes along both the axial and transverse direc-

tions. Cheung and Wong (1985) have observed multiple field spikes (turbulence) for strongly beam-driven Langmuir waves. They have stated that "the fact that numerous field spikes develop both along and across the beam path reinforces the two dimensionalities of the instability."

So, the LHW evolves to a turbulent state; this turbulence is thought to facilitate the process of energy transfer from lower hybrid to plasma. Figure 4(h) illustrates the electric power spectrum on a log–log scale. The power spectrum follows scaling $k^{-1.9}$ (approximately) (the green line is for reference). From Fig. 4(g), in the fully developed turbulent state, the average scale size of the localized structure is $\sim 3\ \lambda_l$. From the grid size, we have taken $\Delta x = 0.5\ \lambda_l$ and $\Delta z = 0.5\ \lambda_l$. So, the grid can resolve the localized structures.

Figure 5(a) illustrates the field's evolution with time (in dimensionless units). In the turbulent zone, wave amplitude reaches its maximum value of $E \approx 78.5$ mV/m at $t = 75$. Figure 5(b) shows the LHW in the frequency domain. The location of first two peaks is at $\omega_0 + 0.35\omega_{ci}$ rad/s and $\omega_0 \pm 0.7\omega_{ci}$ rad/s. Figure 5(c) shows LHW in the frequency domain on a log–log scale (variables in normalized units). It shows a scaling of $k^{-1.5}$ (approximately) (the green line is for reference). From Fig. 5(b), the following is evident: (i) field power peaks appear at the central frequency; (ii) most of the power lies at this central frequency.

The following terms (phenomena) are responsible for the shapes of these curves and figures resulting from the simulation of Eqs. (26a) and (26b):

1. The $\gamma.E$ term in Eq. (26a) give $e^{\gamma t}$ rise in wave amplitude.
2. Spatial derivative terms, complex derivative terms, coupling term nE_x, and nonlinear terms in the dynamical Eqs. (26a) and (26b). The presence of all these terms makes this evolution possess very complex dynamics.

As we have started with a large amplitude (0.1 in normalized units) in this simulation, the nonlinear dynamics, as discussed above, result in the splitting of the structures from the very early time (Fig. 4(b) onwards).

The outcomes of our study show the following resemblance to the observations of Graham et al. (2019):

1. They have reported the presence of lower hybrid waves and turbulence in the magnetic reconnection region in the magnetopause. In our study, Figs. 1 and 3 illustrate the evolution of the lower hybrid wave. Figures 4 and 5 show the lower hybrid turbulence. Graham et al. have observed that the field power peaks are near the pump wave frequency and most of the power lies in the vicinity of the pump wave frequency. Figure 5(b) confirms these observations.
2. Graham et al. (2019), based on the MMS mission, reported that the peak lower hybrid field is around 50 mV/m. Our present study, where we have modeled 2D electrostatic LHW, found LHW field of $\approx$ 78.5 mV/m, as shown in Fig. 5(a).

In the frequency domain representation, the location of first two harmonics is at $\omega_0 + 0.35\omega_{ci}$ rad/s and $\omega_0 \pm 0.7\omega_{ci}$ rad/s, respectively. The genesis of frequency harmonics (peaks) is due to the ponderomotive term $|E_x|^2$ in the right-hand side of Eq. (26b).

From Eq. (27) at $k_z = 0$, we have $E_x = E_0\{1 + \varepsilon \cos(\alpha_x x)\}$,

$$|E_x|^2 \sim \{1 + \varepsilon \cos(\alpha_x x)\}^2$$
$$\sim \left\{1 + 2\varepsilon \cos(\alpha_x x) + \varepsilon^2 \cos^2(\alpha_x x)\right\}$$

Thus, clearly, from the above equation, the peaks are found to be at α_x and $2\alpha_x$. We will explain the presence of these peaks using the MSW dispersion relation.

Indeed, in the MSW dispersion relation ($\omega \sim k v_a$), the first peak occurs at
$\sim \omega_0 + \alpha_x v_a$, for $k = \alpha_x = 0.1$,
$\sim \omega_0 + (0.1 \times 2.44 \times 10^7)/4 \times 10^6$ (in rad/s)
$\sim \omega_0 + 0.35\omega_{ci}$ rad/s, which is also the location of the first peak (central peak);
the second peak occurs at
$\sim \omega_0 \pm 2\alpha_x v_a$
$\sim \omega_0 \pm 2 \times (0.1 \times 2.44 \times 10^7)/4 \times 10^6$ rad/s
$\sim \omega_0 \pm 0.7\omega_{ci}$ rad/s, which is also the location of the second peak.

Further, the presence of multiple peaks can also be understood by using the coupling term $n.E$ in Eq. (26a). Both Eqs. (26a) and (26b) form a coupled system. Using adiabatic approximation in Eq. (26b), we get $n = -\frac{|E_x|^2}{c_6}$, and substituting this value into Eq. (26a) yields

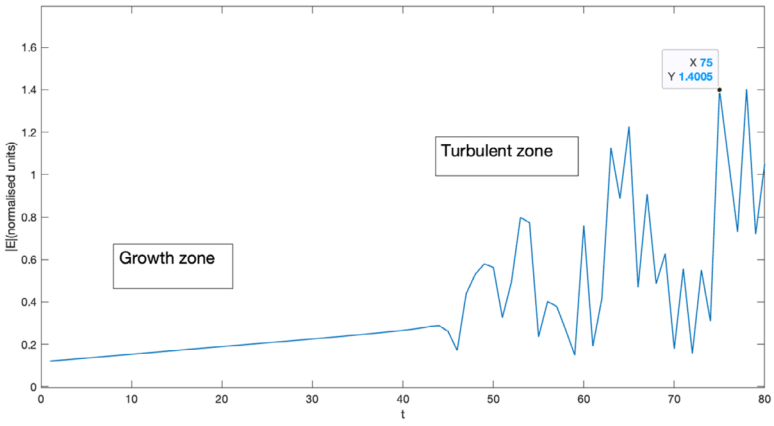
$$i\frac{\partial}{\partial t}E_X - i\frac{\partial}{\partial x}E_X + \frac{\partial^2}{\partial z^2}E_X + c_1 i\frac{\partial}{\partial z}E_X + c_2\frac{\partial^2}{\partial x \partial t}E_X - c_3\frac{\partial^2}{\partial x^2}E_X + \frac{c_4}{c_6}|E_x|^2 E_x + c_5 i\gamma E_x = 0. \quad (28)$$

The genesis of frequency harmonics (peaks) is due to the coupling term $|E_x|^2 E_x$ in Eq. (28).

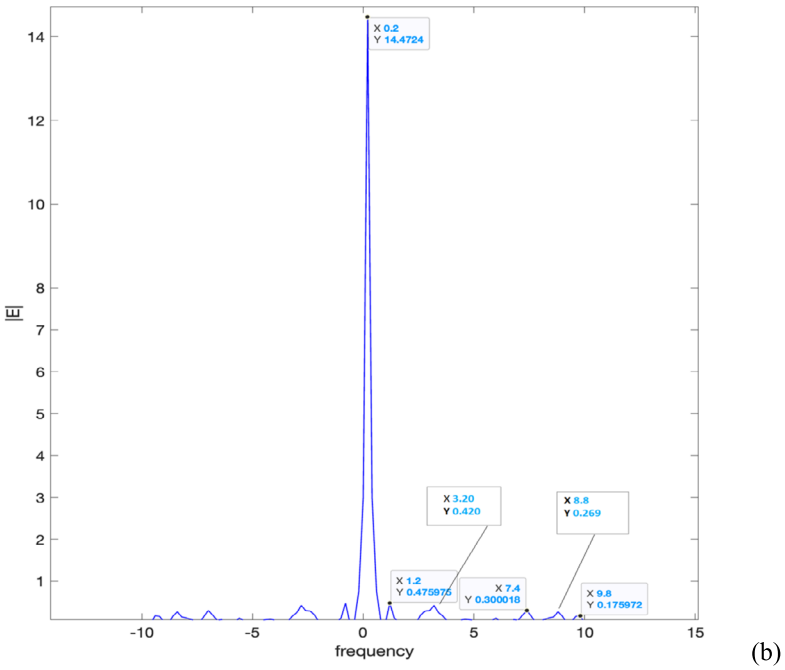
So, the coupling term $nE_x \sim |E_x|^2 E_x$ leads to the generation of frequency peaks (harmonics) from Eq. (27) at $k_z = 0$. Also $E_x = E_0\{1 + \varepsilon \cos(\alpha_x x)\}$,

$$nE_x \sim |E_x|^2 E_x \sim \{1 + \varepsilon \cos(\alpha_x x)\}^2 \{1 + \varepsilon \cos(\alpha_x x)\}$$
$$\sim \left\{1 + 2\varepsilon \cos(\alpha_x x) + \varepsilon^2 \cos^2(\alpha_x x)\right\} \{1 + \varepsilon \cos(\alpha_x x)\} \quad (29)$$

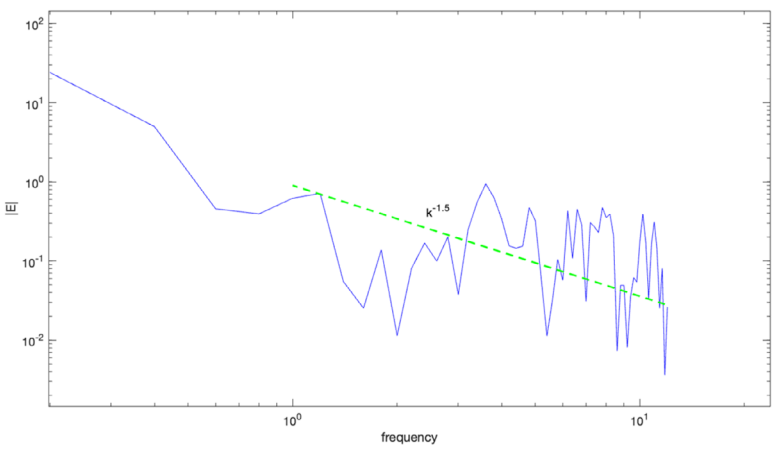
Equation (29) confirms the presence of multiple peaks at different wave numbers (or frequencies).



(a)



(b)



(c)

Fig. 5 LHW in the turbulent zone. Panel (a) shows LHW in the time domain and panel (b) presents LHW in the frequency domain. Panel (c) shows LHW in the frequency domain on a log–log scale (variables in normalized units)

When the state is entirely turbulent (see Figs. 5(a)–(c)), randomness creeps into the system. So, there is no proper sequence for later harmonics. In the turbulent regime, the forced oscillations corresponding to the driver term in

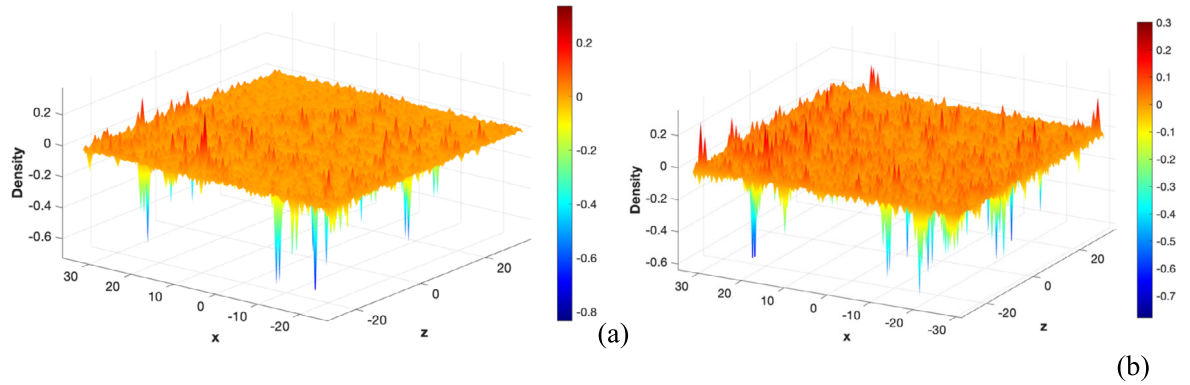


Fig. 6 Three-dimensional density plots: (a) at $t = 65$ and (b) at $t = 70$ (variables in normalized units)

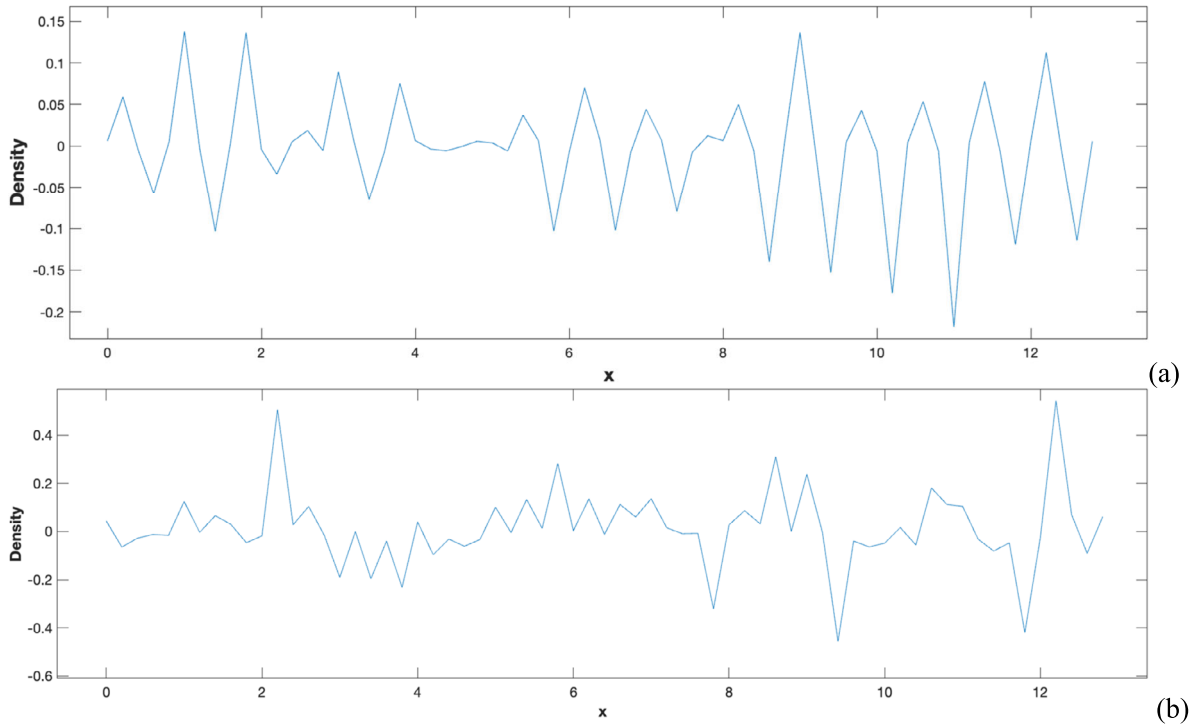


Fig. 7 Plots of density at $t = 50$ (a) and $t = 65$ (b), respectively (variables in normalized units)

Eq. (26b) will not show any pattern. This pattern of irregularities is reflected in Fig. 5(b), which is a truncated picture of the turbulent zone. The sole purpose of Fig. 5(b) is to show that "most of the power lies around the central frequency," as shown and discussed by Graham et al. (2019). Figure 5(c) shows the complete picture of the turbulent zone.

To gain more insight into the turbulence regime, we plotted the density profile (Figs. 6 and 7). Figures 6(a) and 6(b) illustrate density cavity profiles in 3D for $t = 65$ and $t = 70$, respectively. Figures 7(a) and 7(b) represent the density variations at time $t = 50$ and $t = 65$, respectively. These figures, again, show the turbulent nature of the system.

5 Summary and conclusions

In the present work, the authors have developed a model to study the temporal evolution of LHW and associated turbulence in the magnetopause by investigating a nonlinear coupling between LHW and low-frequency MSW. The authors have derived the dynamics of LHW and MSW at the reconnection sites by substituting the magnetic reconnection process with the energetic electron beam source. The nonlinear evolution of the system is observed to occur in two regimes. First is the growth regime; here, LHW develops from a very small amplitude in the medium. With the energy transfer by the electron beam, the amplitude of LHW

increases up to large (saturation) values. The second regime is called the turbulent regime. Due to the large LHW amplitude, spatial derivative terms, growth term, complex derivative terms, coupling term, and nonlinear terms in the dynamical equations start dominating. Under these effects, the wave breaks into spatially localized intense field structures, i.e., the wave contracts into smaller and smaller spatial dimensions. So, the complex nonlinear dynamics lead to spiky turbulent structures.

In conclusion, the numerical results of our 2D model illustrate the electrostatic lower hybrid waves pumped by the electron beam instability. They show the growth of wave mode from a very low amplitude to saturation state and then evolving to a turbulent state. Therefore, the nonlinear effects due to both beam electrons and background plasma are responsible for the LHW turbulence. The merits of the model are as follows. Shapiro et al. (1993) have studied the nonlinear saturation of LHW, which results in localized structures, but they have neither studied the LHW turbulence nor illustrated the effect of the beam, our model addresses both these issues. We have taken 2D pure electrostatic LHW for cold plasma, which makes wave dynamics easier to understand. With this simplified model, we could explain the presence of lower hybrid waves and turbulence in the magnetic reconnection region in the magnetopause as observed by the MMS mission.

The limitations of our model are that MMS1 has also observed a small finite magnetic field associated with the LHW, which can only be explained by quasielectromagnetic mode. We have not included the magnetic reconnection effects in the present model by including magnetic islands and current sheet formation on LHW turbulence. We have assumed the growth rate to be constant in time. So, the instability and turbulence results will not converge for different initial conditions. Further, our model cannot explain the nonlinear development of the lower hybrid drift instability which may lead to electron heating as observed in the particle-in-cell simulation of the LHWs (Divin et al. 2015). Further, it has been demonstrated that different values of plasma β could have a large impact on the lower hybrid drift instability (Davidson et al. 1977). This effect, too, cannot be considered by our model. In the future, the authors are planning to develop an improved model in which most of these restrictions (limitations) can be revoked.

Author contributions Manoj Kumar Upadhyay wrote and prepared the main manuscript text. Others supervised the work. All authors reviewed the manuscript.

Data Availability The data that supports the findings of this study are available within the article.

Declarations

Competing interests The authors declare no competing interests.

References

Bale, S.D., Mozer, F.S., Phan, T.: Observation of lower hybrid drift instability in the diffusion region at a reconnecting magnetopause. Geophys. Res. Lett. **29**(24), 33-1–33-4 (2002). https://doi.org/10.1029/2002GL016113

Batra, K., Sharma, R.P., Verga, A.D.: Stability analysis of nonlinear evolution patterns of modulational instability and chaos using one-dimensional Zakharov equations. J. Plasma Phys. **72**, 671–686 (2006). https://doi.org/10.1017/S002237780500423X

Bingham, R., Shapiro, V.D., Shukla, P.K., Trines, R.: Lower-hybrid wave activity and reconnection at the magnetosphere. In: Physica Scripta T, vol. 2004, pp. 144–148 (2004)

Cairns, I.H., McMillan, B.F.: Electron acceleration by lower hybrid waves in magnetic reconnection regions. Phys. Plasmas **12**, 1 (2005). https://doi.org/10.1063/1.2080567

Cheung, P.Y., Wong, A.Y.: Nonlinear evolution of electron-beam-plasma interactions. Phys. Fluids **28**, 1538–1548 (1985). https://doi.org/10.1063/1.864988

Cozzani, G., Khotyaintsev, Y.V., Graham, D.B., Egedal, J., André, M., Vaivads, A., Alexandrova, A., le Contel, O., Nakamura, R., Fuselier, S.A., Russell, C.T., Burch, J.L.: Structure of a perturbed magnetic reconnection electron diffusion region in the Earth's magnetotail. Phys. Rev. Lett. **127**, 215101 (2021). https://doi.org/10.1103/PhysRevLett.127.215101

Daughton, W.: Electromagnetic properties of the lower-hybrid drift instability in a thin current sheet. Phys. Plasmas **10**, 3103–3119 (2003). https://doi.org/10.1063/1.1594724

Davidson, R.C., Gladd, N.T.: Anomalous transport properties associated with the lower-hybrid-drift instability. Phys. Fluids **18**, 1327–1335 (1975). https://doi.org/10.1063/1.861021

Davidson, R.C., Gladd, N.T., Wu, C.S., Huba, J.D.: Effects of finite plasma beta on the lower-hybrid-drift instability. Phys. Fluids **20**, 301–310 (1977). https://doi.org/10.1063/1.861867

Divin, A., Khotyaintsev, Y.V., Vaivads, A., André, M., Markidis, S., Lapenta, G.: Evolution of the lower hybrid drift instability at reconnection jet front. J. Geophys. Res. Space Phys. **120**, 2675–2690 (2015). https://doi.org/10.1002/2014JA020503

Gary, S.P., Sgro, A.G.: The lower hybrid drift instability at the magnetopause. Geophys. Res. Lett. **17**(7), 909–912 (1990)

Graham, D.B., Khotyaintsev, Y.V., Norgren, C., Vaivads, A., André, M., Lindqvist, P.A., Marklund, G.T., Ergun, R.E., Paterson, W.R., Gershman, D.J., Giles, B.L., Pollock, C.J., Dorelli, J.C., Avanov, L.A., Lavraud, B., Saito, Y., Magnes, W., Russell, C.T., Strangeway, R.J., Torbert, R.B., Burch, J.L.: Electron currents and heating in the ion diffusion region of asymmetric reconnection. Geophys. Res. Lett. **43**, 4691–4700 (2016). https://doi.org/10.1002/2016GL068613

Graham, D.B., Khotyaintsev, Y.V., Norgren, C., Vaivads, A., André, M., Toledo-Redondo, S., Lindqvist, P.A., Marklund, G.T., Ergun, R.E., Paterson, W.R., Gershman, D.J., Giles, B.L., Pollock, C.J., Dorelli, J.C., Avanov, L.A., Lavraud, B., Saito, Y., Magnes, W., Russell, C.T., Strangeway, R.J., Torbert, R.B., Burch, J.L.: Lower hybrid waves in the ion diffusion and magnetospheric inflow regions. J. Geophys. Res. Space Phys. **122**, 517–533 (2017). https://doi.org/10.1002/2016JA023572

Graham, D.B., Khotyaintsev, Yu.V., Norgren, C., Vaivads, A., Andre, M., Drake, J.F., Egedal, J., Zhou, M., Le Contel, O., Webster, J.M., Lavraud, B., Kacem, I., Genot, V., Jacquey, C., Rager, A.C., Gershman, D.J., Burch, J.L., Ergun, R.E.: Universality of Lower Hybrid Waves at Earth's Magnetopause (2019). https://doi.org/10.1029/2019JA027155

Ji, H., Kulsrud, R., Fox, W., Yamada, M.: An obliquely propagating electromagnetic drift instability in the lower hybrid frequency range. J. Geophys. Res. Space Phys. **110**, A08212 (2005). https://doi.org/10.1029/2005JA011188

Karimabadi, H., Roytershteyn, V., Wan, M., Matthaeus, W.H., Daughton, W., Wu, P., Shay, M., Loring, B., Borovsky, J., Leonardis, E., Chapman, S.C., Nakamura, T.K.M.: Coherent structures, intermittent turbulence, and dissipation in high-temperature plasmas. Phys. Plasmas **20**, 012303 (2013). https://doi.org/10.1063/1.4773205

Lu, Q., Wang, S., Dou, X.: Electrostatic waves in an electron-beam plasma system. Phys. Plasmas **12**, 1 (2005). https://doi.org/10.1063/1.1951367

Matthaeus, W.H.: Turbulence in space plasmas: who needs it? Phys. Plasmas **28**, 032306 (2021). https://doi.org/10.1063/5.0041540

Nicholson, D.: Introduction to Plasma Theory. Wiley, New York (1983)

Norgren, C., Vaivads, A., Khotyaintsev, Y.V., André, M: Lower hybrid drift waves: space observations. Phys. Rev. Lett. **109**, 055001 (2012). https://doi.org/10.1103/PhysRevLett.109.055001

Omidi, N., O'Farrell, A., Krauss-Varban, D.: Sources of magnetosheath waves and turbulence. Adv. Space Res. **14**(7), 45–54 (1994)

Plaschke, F., Angelopoulos, V., Glassmeier, K.H.: Magnetopause surface waves: THEMIS observations compared to MHD theory. J. Geophys. Res. Space Phys. **118**, 1483–1499 (2013). https://doi.org/10.1002/jgra.50147

Shapiro, V.D.: Modulational Interaction of the Lower-Hybrid Waves with a Kinetic-Alfvén Mode (1998)

Shapiro, V.D., Shevchenko, V.I., Solov'ev, G.I., Kalinin, V.P., Bingham, R., Sagdeev, R.Z., Ashour-Abdalla, M., Dawson, J., Su, J.J.: Wave collapse at the lower-hybrid resonance. Phys. Fluids B **5**, 3148 (1993). https://doi.org/10.1063/1.860652

Silin, I., Büchner, J., Vaivads, A.: Anomalous resistivity due to nonlinear lower-hybrid drift waves. Phys. Plasmas **12**, 1 (2005). https://doi.org/10.1063/1.1927096

Tjulin, A., André, M., Eriksson, A.I., Maksimovic, M.: Observations of Lower Hybrid Cavities in the Inner Magnetosphere by the Cluster and Viking Satellites (2004)

Vaivads, A., André, M., Buchert, S.C., Wahlund, J.E., Fazakerley, A.N., Cornilleau-Wehrlin, N.: Cluster observations of lower hybrid turbulence within thin layers at the magnetopause. Geophys. Res. Lett. **31**, L03804 (2004). https://doi.org/10.1029/2003GL018142

Walker, S.N., Balikhin, M.A., Alleyne, H.S.C.K., Hobara, Y., André, M., Dunlop, M.W.: Lower hybrid waves at the shock front: a reassessment. Ann. Geophys. **26**, 699–707 (2008). https://doi.org/10.5194/angeo-26-699-2008

Zhou, M., Li, H., Deng, X., Huang, S., Pang, Y., Yuan, Z., Xu, X., Tang, R.: Characteristic distribution and possible roles of waves around the lower hybrid frequency in the magnetotail reconnection region. J. Geophys. Res. Space Phys. **119**, 8228–8242 (2014). https://doi.org/10.1002/2014JA019978

Publisher's Note Springer Nature remains neutral with regard to jurisdictional claims in published maps and institutional affiliations.

Springer Nature or its licensor (e.g. a society or other partner) holds exclusive rights to this article under a publishing agreement with the author(s) or other rightsholder(s); author self-archiving of the accepted manuscript version of this article is solely governed by the terms of such publishing agreement and applicable law.

RSC Advances

PAPER

View Article Online
View Journal | View Issue

Check for updates

Cite this: *RSC Adv.*, 2023, **13**, 11557

Lumino-structural properties of Dy^{3+} activated $Na_3Ba_2LaNb_{10}O_{30}$ phosphors with enhanced internal quantum yield for w-LEDs

Kanishk Poria,[a] Ravina Lohan,[b] Sanjana Bhatia,[a] Amit Kumar,[b] Rajwinder Singh,[a] Nisha Deopa,*[b] Rajesh Punia,[c] Jangvir Singh Shahi*[a] and A. S. Rao[d]

With an intend to develop white light emitting phosphor, for w-LED application, a series of dysprosium (Dy^{3+}) doped novel $Na_3Ba_2LaNb_{10}O_{30}$ phosphors were prepared using solid state reaction technique at 1300 °C. Their structural, morphological and vibrational spectroscopic analysis was performed. We illustrate the luminescence characteristics of the prepared phosphors for various Dy^{3+} ion doping concentration. The XRD analysis demonstrates that the prepared phosphors were in single phase, and of tetragonal tungsten bronze structure of the *P4bm* space group. The FE-SEM image reveals that the prepared phosphors contained irregular shaped both nano and micro particles. Under near-ultraviolet (n-UV) irradiation at 387 nm, the photoluminescence (PL) emission spectra shows three characteristic bands at 481 nm (blue), 575 nm (yellow) and 666 nm (red). Obtained optimized Dy^{3+} ion concentration for the prepared sample is 7.0 mol%, beyond which the concentration quenching begins. Bonding between Dy–O is covalent in nature as confirmed by bonding parameters and the Dexter theory revealed that the energy transfer among Dy^{3+} ions is dipole–diploe interaction. CIE chromaticity coordinates, CCT and color purity confirms the formation of warm white light emitting phosphors. Lifetime analysis demonstrates the longer decay time in the phosphors. The Internal Quantum Yield (IQE) and brightness (*B*) for the optimised phosphor is calculated as 45.35% and 11.41% respectively, which makes it a suitable phosphor for w-LED.

Received 24th February 2023
Accepted 24th March 2023

DOI: 10.1039/d3ra01260c

rsc.li/rsc-advances

Open Access Article. Published on 13 April 2023. Downloaded on 4/18/2023 5:40:33 AM.
This article is licensed under a Creative Commons Attribution-NonCommercial 3.0 Unported Licence.

1 Introduction

Phosphor is any material that exhibits the phenomenon of luminescence when subjected to UV radiation, X-rays, electron bombardment, friction or any other form of excitation. A phosphor primarily comprises of a host matrix and an activator ion in its lattice.[1] These activators act as the luminescent centres, *i.e.* the electron relaxes radiatively at this activator site, within the host matrix. Rare earth elements such as Eu^{3+}, Eu^{2+}, Dy^{3+}, Pr^{3+} are few example of activators. Phosphors are used, in the creation of several optoelectronic devices, including light converters, solid state lasers, solid state lighting, optical thermometer and optical amplifiers, *etc.*[2–7] In the last decade, phosphor-converted white light emitting diodes (pc-wleds) have been studied significantly owing to their key characteristic, such as efficient light output, low power consumption, longer operational lifetime (>100 000 hours), sturdiness and environmentally safer as compared to their predecessors, fluorescent and incandescent lamp.[8–12] Nowadays, w-LEDs are widely used in plant cultivation (including vegetables, flowers, herbs, *etc.*), display, medical lighting, and outdoor lighting.[13–15]

White light emission can be obtained in three ways from solid state lighting sources.[16,17] The first way is to setup an array of multiple LED chips emitting light at different frequencies. Multiple LED setup has excellent colour rendering index and the white point can be easily controlled. However, there is no control on correlated colour temperature, since each LED needs an independent output power control and has its own different lifetime. The second way is to use a single UV LED chip coated with a combination of red, green and blue down-converting phosphors. This setup is quite cost efficient than LED matrix, as it gives excellent colour rendering and a control over white light-CCT. Because of stokes conversion, this approach becomes less energy efficient, and it is difficult to manage the homogeneity of the phosphor coating. Another demerit is that phosphors deteriorate faster than LEDs. The third way is utilizing a single LED (blue) with a coating of yellow down-converting phosphor. The blue light bleeds through the phosphor to give white light. This setup is small, light-weight, easy to operate and has a long lifetime. Demerit of this setup is that it is

[a]*Department of Physics, Panjab University, Chandigarh, India. E-mail: shahijs@yahoo.com; Tel: +91-9815612645*
[b]*Department of Physics, Chaudhary Ranbir Singh University, Jind, India. E-mail: nispectro999@gmail.com; Tel: +91-8860551723*
[c]*Department of Physics, Maharshi Dayanand University, Rohtak, India*
[d]*Department of Applied Physics, Delhi Technological University, New Delhi, India*

© 2023 The Author(s). Published by the Royal Society of Chemistry

Open Access Article. Published on 13 April 2023. Downloaded on 4/18/2023 5:40:33 AM. This article is licensed under a Creative Commons Attribution-NonCommercial 3.0 Unported Licence.

less efficient because of stokes shift and has a very poor colour rendering.

Since niobates have better chemical and physical stability, they make excellent luminous matrixes. Some rare-earth ion doped niobates, such as Sr_2LaNbO_6:Eu^{3+},Sm^{3+}; $LaNbO_4$:Bi^{3+}/Dy^{3+} and Ca_2LaNbO_6:Sm^{3+}, have been shown to exhibit outstanding luminous characteristics along with high thermal stability.[18–20] It is important to note that the tungsten bronze structure (TTB) exhibits chemical and magnetic stability with excellent crystal structure. Niobates having TTB structures are excellent candidates for ferroelectric and piezoelectric materials. The deficient perovskite TTB niobates consist of corner-sharing NbO_6 octahedra arrays and three different tunnels for cation filling, leading to large spontaneous polarization and high dielectric constants.[21] In deformed metal–oxygen polyhedra, they likewise show dominating electron–hole separation and transport through static electric fields between structure-induced dipole moments. As a result, a little structural change such as changing the cation-site occupancy has a huge influence on charge mobility. Utilising this property, we have opted to use niobate based TTB structure to investigate its photoluminescence properties. Moreover, the tungsten bronze phosphors such as $Sr_5YTi_3Nb_7O_{30}$, $NaSr_2Nb_5O_{15}$ and $Ba_4LaTiNb_9O_{30}$ have been reported to have potential applications in photonics, especially in w-LED.[22–24] The tetragonal tungsten bronze structure has been shown to readily accept lanthanides or transition metals as constituents or dopants because of its tetragonal crystal structure, which enables the manufacture of high-quality doped single crystals.[25] The general practice to prepare niobate-based phosphors is the solid state reaction method, which has the benefit of producing samples with excellent morphology and luminosity, over other methods.[26]

In search of a suitable host lattice, scientists have been conducting research in order to prepare phosphor-converted white light emitting diode (pc-wled).[27] In our present study, we focus towards the generation of white light from dysprosium doped $Na_3Ba_2LaNb_{10}O_{30}$ phosphors *via* solid state reaction technique. We examine the structure parameter, surface morphology and elemental analysis of the as prepared phosphors using the X-ray diffraction (XRD), field emission scanning electron microscopy (FESEM) and energy dispersive X-ray spectroscopy (EDX), respectively. Further, optical properties were examined employing the steady-state and time resolved photoluminescence.

Generally, Dy^{3+} ions exhibit three emission bands in the visible spectra, the blue emission (450–490 nm) corresponds to $^4F_{9/2} \rightarrow {}^6H_{15/2}$ transition, yellow emission (550–590 nm) corresponds to $^4F_{9/2} \rightarrow {}^6H_{13/2}$ hypersensitive transition and the red emission (640–680 nm) corresponds to $^4F_{9/2} \rightarrow {}^6H_{11/2}$ transition, latter being a feeble transition.[28–30]

2 Experimental procedure

2.1 Phosphor preparation

The samples of dysprosium doped niobate-based $Na_3Ba_2LaNb_{10}O_{30}$:xDy^{3+} ($x = 0$, 1, 3, 5, 7 and 10 mol%) phosphors have been synthesized *via* high-temperature solid-state reaction technique. The raw materials Na_2CO_3 (99.5%), $BaCO_3$ (99.9%), La_2O_3 (99.9%), Dy_2O_3 (99.9%) and Nb_2O_5 (99.9%) used for the synthesis were of Sigma Aldrich and analytical grade quality. The precursor were taken in their stoichiometric ratios and were thoroughly mixed and milled together in a mortar and pestle for 2 hours. The grounded samples were subsequently calcinated at a heating rate of 3 °C min^{-1}, in a programmable muffle furnace of Metrex Scientific Instruments (Model: MF-14P). The heating process consisted of two steps. The reaction time for the first step of calcination was 5 hours at 800 °C and the second step was 1300 °C for 7 hours. Finally the samples were rigorously grounded to make a fine powder and the phosphorescence for the optimised sample (7 mol%) can be easily seen in Fig. 1. The chemical reaction involved in this process is shown in eqn (1).

$$3Na_2CO_3 + 4BaCO_3 + (1-x)La_2O_3 + 10Nb_2O_5 + xDy_2O_3 \xrightarrow[(2)1300\ ^\circ C\times 7\ h]{(1)800\ ^\circ C\times 5\ h} 2Na_3Ba_2La_{1-x}Dy_xNb_{10}O_{30} + 7CO_2\uparrow\uparrow \quad (1)$$

2.2 Characterization techniques

The structural parameter of the prepared phosphors were investigated by XRD analysis using Panalytical model X'pert Pro with Cu-K_α radiation ($\lambda = 1.5406$ Å) in the 2θ range from 20° to 80°. The surface morphology, energy dispersive spectroscopy (EDS), and elemental mapping of the prepared samples were investigated by FESEM. A thin layer of gold (Au) was coated on the as-synthesized samples and were analysed using FESEM utilising JEOL JSM-6490 operated at the accelerating voltage of 5 kV. The Fourier transform infrared (FT-IR) spectrum of $Na_3Ba_2LaNb_{10}O_{30}$ were recorded using a PerkinElmer Frontier Spectrometer in the middle infrared region (4000–400 cm^{-1}) after the pellets were prepared by mixing the samples with potassium bromide (KBr_2, A.R. grade) and then compressed using a hydraulic press at 10 ton load. The steady state photoluminescence spectra (PL) of the prepared phosphors were recorded using Cary Eclipse Fluorescence Spectrophotometer. The lifetime decay spectra has been studied using Horiba Spectroscope excited through a 150 watts microsecond xenon



Fig. 1 Image of $Na_3Ba_2LaNb_{10}O_{30}$:xDy^{3+} (x = 7 mol%) phosphor sample under daylight and 365 nm UV light.

© 2023 The Author(s). Published by the Royal Society of Chemistry

Open Access Article. Published on 13 April 2023. Downloaded on 4/18/2023 5:40:33 AM. This article is licensed under a Creative Commons Attribution-NonCommercial 3.0 Unported Licence.

flash lamp. The excitation and emission spectra was collected in the range of 320–470 nm and 400–700 nm, respectively. The internal quantum efficiency (IQE) was collected by Horiba Scientific QuantaPhi-2 equiped with an integrating sphere coated with $BaSO_4$. Commission international de l'Eclairage (CIE) 1931 chromaticity coordinates were calculated and plotted for the emission spectra. All measurements were carried out at room temperature.

3 Results and discussion

3.1 X-ray diffraction and structural analysis

The powder X-ray diffraction (XRD) analysis demonstrated the crystal structure of $Na_3Ba_2LaNb_{10}O_{30}$:xDy^{3+} (x = 0, 1, 3, 5, 7 and 10 mol%) phosphors and matches well with the JCPDS card no. 00-038-1236 corresponding to $Na_3Ba_2LaNb_{10}O_{30}$, as shown in Fig. 2. XRD peaks reveals that the inclusion of dysprosium ion does not effect the crystal structure of $Na_3Ba_2LaNb_{10}O_{30}$. Furthermore, the crystal structure of $Na_3Ba_2LaNb_{10}O_{30}$:xDy^{3+} (x = 0, 1, 3, 5, 7 and 10 mol%) phosphor belongs to the filled tetragonal tungsten bronze (TTB) structure of the *P4bm* space group. The general representation of tungsten bronze structure is $[(A_1)_2(A_2)_4]C_4[(B_1)_2(B_2)_8]O_{30}$. It can be seen that the TTB structure consists of three different crystal sites namely six A sites, ten B sites (B crystal sites are located in the center of the $[BO_6]$ octahedrons), and the triangular interstitial C site (mostly empty).[31] In the present study of $Na_3Ba_2LaNb_{10}O_{30}$:xDy^{3+} (x = 0, 1, 3, 5, 7 and 10 mol%), Ba^{2+} and La^{3+} present at two A_1 crystal sites while Na^{1+} and Ba^{2+} are present at four A_2 crystal sites whereas Nb^{5+} occupies all ten B sites. In order to figure out which element of the matrix is swapped with Dy^{3+} ion, the ionic radii percentage difference (D_r) is calculated and reproduced using the following expression.[32]

$$D_r = \frac{R_s(CN) - R_d(CN)}{R_s(CN)} \times 100\% \quad (2)$$

where, R_s and R_d are the ionic radii of the cation in the matrix and doped Dy^{3+} ion respectively. The ionic radii of cations that corresponds to the coordination number six are Na^{1+}(R_s = 1.02 Å), Ba^{2+}(R_s = 1.35 Å), La^{3+}(R_s = 1.032 Å), Nb^{5+}(R_s = 0.64 Å) and doped ion Dy^{3+}(R_d = 0.912 Å). The calculated D_r values are 10.59%, 32.44%, 11.63% and −42.5% respectively. Among all the cations, Na^{1+} and La^{3+} are the closest ions to be replaced by the Dy^{3+} ion. Since both La and Dy exist in trivalent oxidation state, Dy^{3+} ions would occupy the site of La^{3+} ion. Dy^{3+} will not substitute Na^{1+} as it leads to chemically nonequivalent substitution and the host lattice acquires an excess positive charge.

The Debye–Scherrer formula (eqn (3)) is employed to compute the average crystallite size of the prepared phosphors.[33,34]

$$D = \frac{K\lambda}{\beta \cos\theta} \quad (3)$$

where K is the form factor (usually 0.94), λ denotes the X-ray wavelength (1.5406 Å, for Cu-K$_\alpha$), θ represents the Braggs diffraction angle and β denotes the FWHM (full-width at half maxima). For $Na_3Ba_2LaNb_{10}O_{30}$:xDy^{3+} (x = 0, 1 and 10 mol%) phosphor, the average crystallite size is summarized in Table 1. The results show that as the Dy^{3+} ion concentration increased the D value declines.

A very slight shift (of the order of 10^{-2} Å) in the 2θ angle of the most intense peak of $Na_3Ba_2LaNb_{10}O_{30}$ ((311) plane) is observed to shift towards the higher 2θ angle as we increase the doping concentration. This propensity may be brought on by the mismatch between the ionic radii of Dy^{3+} and La^{3+} ions, which further raises the possibility of Dy^{3+} ion incorporation into $Na_3Ba_2LaNb_{10}O_{30}$. This slight shift can be easily seen from Fig. 3.

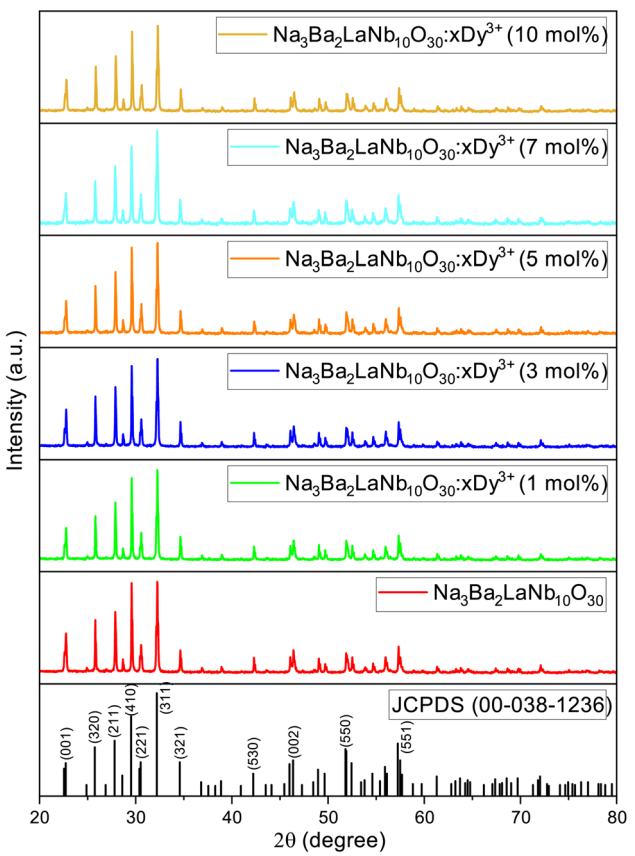


Fig. 2 XRD patterns of JCPDS 00-038-1236 and $Na_3Ba_2LaNb_{10}O_{30}$:xDy^{3+} (x = 0, 1, 3, 5, 7 and 10 mol%) phosphors.

3.2 Field emission scanning electron microscopy and energy dispersive X-ray spectroscopy

Surface morphology of the prepared $Na_3Ba_2LaNb_{10}O_{30}$:xDy^{3+} (x = 7 mol%) phosphor is obtained using FE-SEM depicted in

Table 1 Crystallite size of $Na_3Ba_2LaNb_{10}O_{30}$:xDy^{3+} (x = 1, 3, 5, 7 and 10 mol%) phosphors

Dy^{3+} (mol%)	Average crystallite size, D (nm)
0.0	41.45057
1.0	40.35571
10.0	40.25051

Open Access Article. Published on 13 April 2023. Downloaded on 4/18/2023 5:40:33 AM.
This article is licensed under a Creative Commons Attribution-NonCommercial 3.0 Unported Licence.

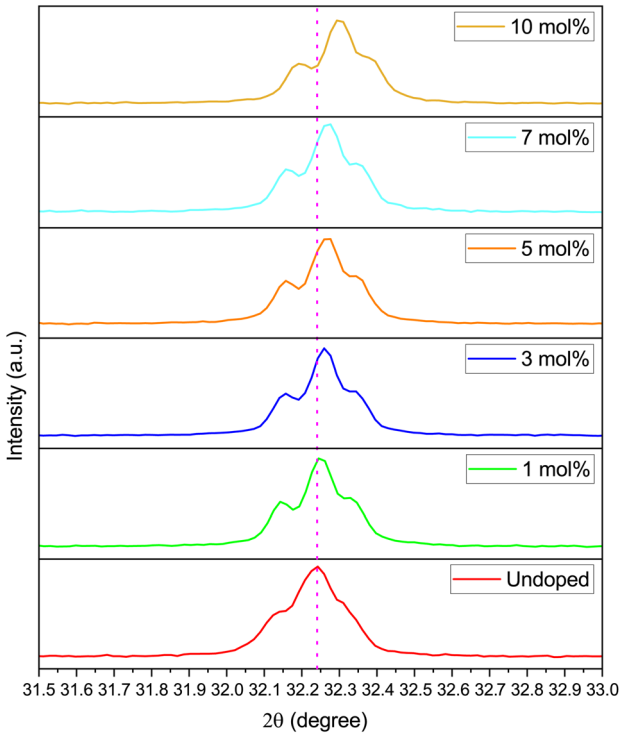


Fig. 3 XRD peak corresponding to 311 plane of $Na_3Ba_2LaNb_{10}O_{30}$:-xDy^{3+} (x = 0, 1, 3, 5, 7 and 10 mol%) phosphors.

Fig. 4. From FE-SEM images, the phosphor particles were inferred as non-uniform, inhomogeneous and irregular in shape. The agglomeration of particles were expected in the preparation of phosphor through high-temperature solid state reaction method. The agglomerated particle size range from few micrometers to few nanometers, and are tightly packed with each other. Because of the large surface area to volume ratio, number of voids are observed inside the agglomerated nanoparticles. No change in the morphology is observed with the change in dopant ion concentrations.

The EDX spectrum and elemental mapping reveals the chemical composition and elemental distribution in the

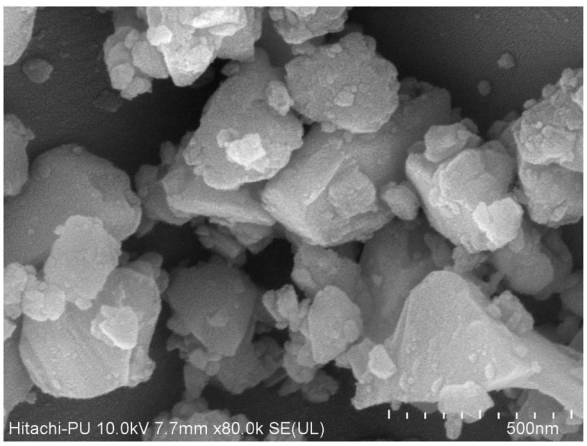


Fig. 4 FE-SEM micrograph of $Na_3Ba_2LaNb_{10}O_{30}$:xDy^{3+} (x = 7 mol%) phosphor sintered at 1300 °C.

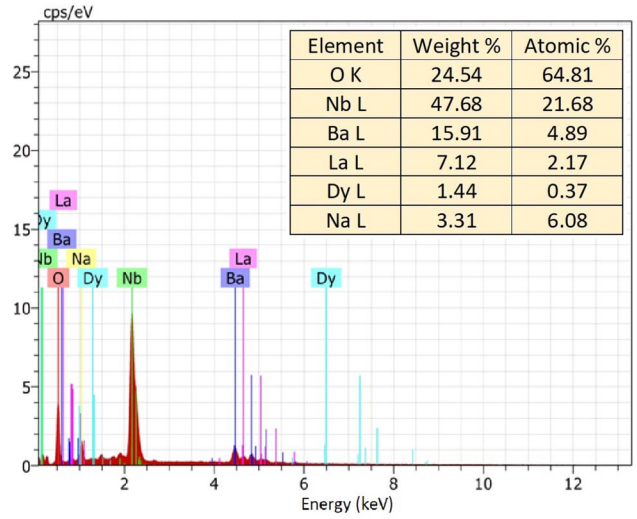


Fig. 5 EDX spectrum of $Na_3Ba_2LaNb_{10}O_{30}$:xDy^{3+} (x = 7 mol%) phosphor.

prepared $Na_3Ba_2LaNb_{10}O_{30}$:xDy^{3+} (x = 7 mol%) phosphor. EDX is a typical approach for detecting and measuring the qualitative and quantitative elemental composition of a sample in an area of few square nanometer dimensions. The elemental peaks corresponding to sodium (Na), barium (Ba), lanthanum (La), niobium (Nb), oxygen (O) and dysprosium (Dy) of the prepared sample was observed in the EDX spectrum and are shown in Fig. 5. Their elemental mapping is demonstrated in Fig. 6 which depicts the even distribution of constituent elements. The atomic% shown in Fig. 5 also confirms the agglomeration of $Na_3Ba_2LaNb_{10}O_{30}$:xDy^{3+} (x = 7 mol%) doped phosphor.

3.3 Raman and Fourier transform infrared spectroscopy

Raman spectra of the synthesized $Na_3Ba_2LaNb_{10}O_{30}$:xDy^{3+} (x = 7 mol%) phosphor in the tetragonal structure, with the octahedral ion $[NbO_6]^{7-}$, recorded at room temperature from 100–1000 cm^{-1} wavenumber as shown in Fig. 7. The three Raman

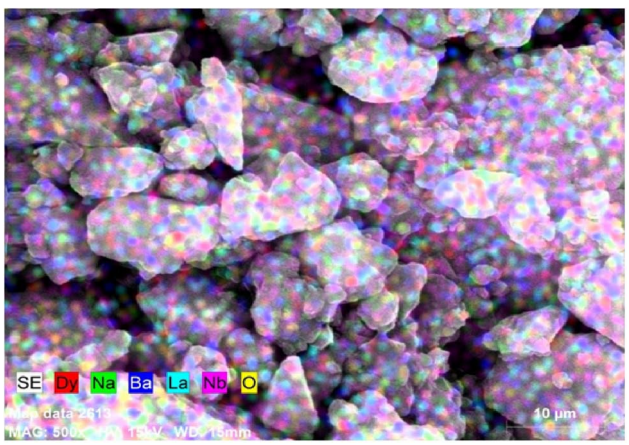


Fig. 6 Elemental mapping of $Na_3Ba_2LaNb_{10}O_{30}$:xDy^{3+} (x = 7 mol%) phosphor.

© 2023 The Author(s). Published by the Royal Society of Chemistry

Open Access Article. Published on 13 April 2023. Downloaded on 4/18/2023 5:40:33 AM.
This article is licensed under a Creative Commons Attribution-NonCommercial 3.0 Unported Licence.

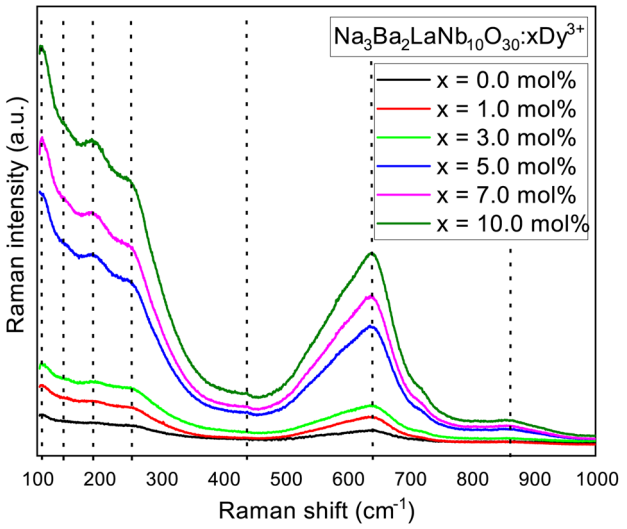


Fig. 7 Raman spectrum of $Na_3Ba_2LaNb_{10}O_{30}$:xDy^{3+} (x = 0, 1, 3, 5, 7 and 10 mol%) phosphor at room temperature.

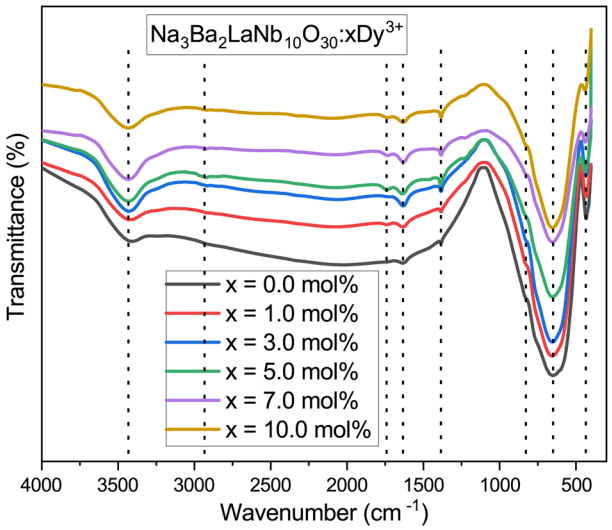


Fig. 8 Fourier transformed infrared (FT-IR) spectrum of $Na_3Ba_2LaNb_{10}O_{30}$:xDy^{3+} (x = 0, 1, 3, 5, 7 and 10 mol%) phosphor at room temperature.

active modes centered at 252 cm^{-1} (ν_5) corresponds to O–Nb–O bend vibrations, 639 cm^{-1} (ν_2) assign to Nb–O stretch vibrations, and 862 cm^{-1} (ν_1) corresponds to Nb–O stretch vibrations, is similar to one other in tetragonal tungsten bronze structure with the point group C_{4v} (ref. 35 and 36) and C_{2v}.[37] For the tungsten bronzes structure, all Raman lines except for the three characteristic vibrational modes originate from the external vibrations for oxygen octahedron. Therefore, the Raman spectra of $Na_3Ba_2LaNb_{10}O_{30}$ can be discussed in terms of internal vibrations of the (NbO_6) octahedra and external vibrations involving the motions of Na^{1+}, Ba^{2+} and La^{3+} cations. As shown in Fig. 7, the peaks centered at 108 cm^{-1}, 142 cm^{-1}, 189 cm^{-1} and 438 cm^{-1} originate from external vibration modes.

The FT-IR spectra are recorded from 4000–400 cm^{-1} wavenumber to know about the structural units and functional groups in the as-prepared $Na_3Ba_2LaNb_{10}O_{30}$:xDy^{3+} (x = 1, 3, 5, 7 and 10 mol%) phosphor. Fig. 8 depicted the FT-IR spectra of as-synthesized phosphor. The quality of product is best checked by the FT-IR spectroscopy and is used in the initial stage process for the analysis of material. The shift in the peaks of spectra suggests the inclusion of contaminate. All the spectra shows similar shoulder positions as demonstrated in the Fig. 8. FT-IR spectra contain eight shoulders about 435, 654, 829, 1386, 1633, 1743, 2921 and 3432 cm^{-1}. The shoulders in the spectra are assigned according to the previously published research papers. The shoulder near 435 and 829 cm^{-1} consigned to the coupling between Nb–O stretching mode.[38] The shoulder about 654 cm^{-1} is owing to the La–O stretching vibrations.[39] The shoulder about 1386 cm^{-1} is because of symmetric stretching of COO^- functional group.[40] The shoulder in the region 1633 and 3432 cm^{-1} is because of water molecules.[41] The shoulder near 1743 cm^{-1} is contributed by C–O stretching mode in free carboxylic group.[42] The shoulder about 2921 cm^{-1} may correspond to the residual organic presence.[43]

3.4 Bandgap and electronic structure

Using reflectance spectra we can explore optical characteristics of phosphors. Bandgap (E_g) of $Na_3Ba_2LaNb_{10}O_{30}$:xDy^{3+} (x = 1, 3, 5, 7 and 10 mol%) phosphor samples can be calculated using Tauc plot[44] derived from the plot of diffuse reflectance spectra of the phosphors. Fig. 9 exhibit UV-Vis diffuse reflectance spectra of $Na_3Ba_2LaNb_{10}O_{30}$:xDy^{3+} (x = 1, 3, 5, 7 and 10 mol%) phosphor and Fig. 10 shows the corresponding Tauc plot determined from eqn (4). The transition $^6H_{15/2} \rightarrow {}^6F_{5/2}$ and $^6H_{15/2} \rightarrow {}^6F_{7/2}$ at 808 nm and 908 nm, respectively can be easily seen in Fig. 9.

$$(\alpha_{abs} h\nu_{ph})^n = A(h\nu_{ph} - E_g) \quad (4)$$

where A represents a constant, α_{abs} denotes the absorption coefficient, ν_{ph} represents the photon frequency and n is the transition dependent parameter (n = 1/2 corresponds to

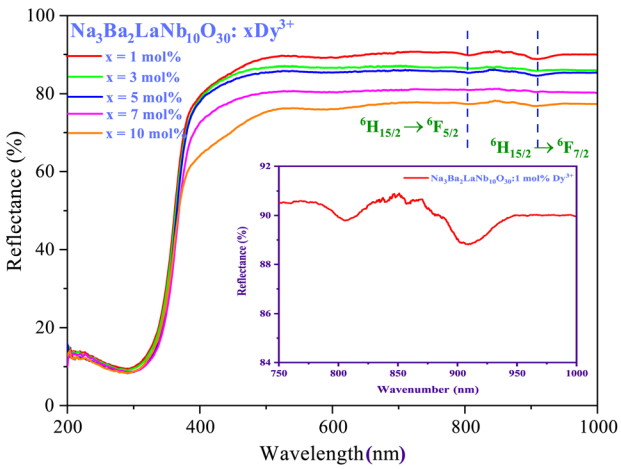


Fig. 9 Diffuse reflectance spectra of $Na_3Ba_2LaNb_{10}O_{30}$:xDy^{3+} (x = 1, 3, 5, 7 and 10 mol%) phosphor.

Open Access Article. Published on 13 April 2023. Downloaded on 4/18/2023 5:40:33 AM.
This article is licensed under a Creative Commons Attribution-NonCommercial 3.0 Unported Licence.

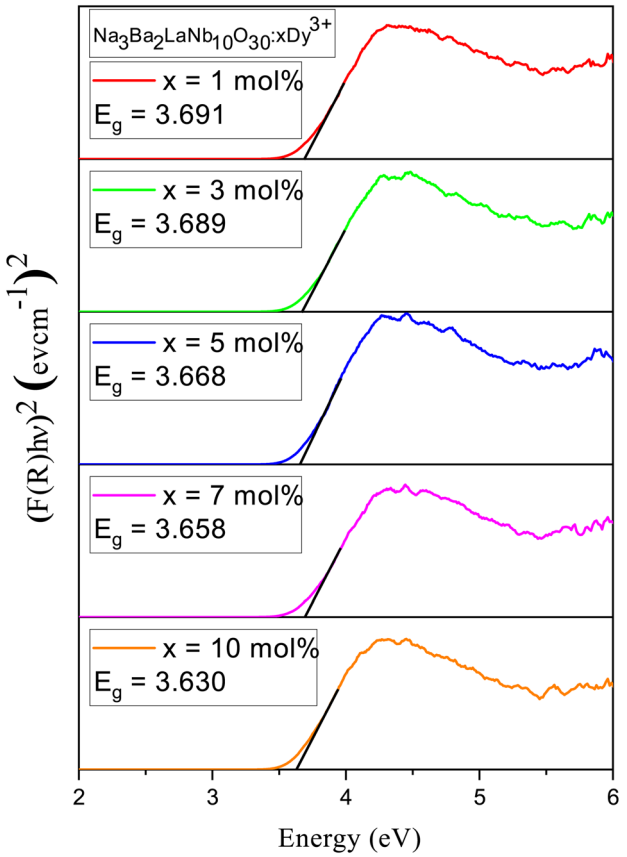


Fig. 10 Tau plot of un-doped and $Na_3Ba_2LaNb_{10}O_{30}$:xDy^{3+} ($x = 1$, 3, 5, 7 and 10 mol%) phosphors for the determination of optical bandgap E_g (assuming indirect transitions).

allowed electronic transition (direct), $n = 2$ for allowed electronic transition (indirect), while $n = 3/2$ and 3 corresponds to forbidden direct and indirect electronic transition, respectively). A red shift is represented in the optical bandgap of the $Na_3Ba_2LaNb_{10}O_{30}$:xDy^{3+} ($x = 1$, 3, 5, 7 and 10 mol%) phosphor with increase in Dy^{3+} ion concentration, as seen in Fig. 10. Table 2 shows the bandgap for $Na_3Ba_2LaNb_{10}O_{30}$:xDy^{3+} ($x = 1$, 3, 5, 7 and 10 mol%) phosphor.

3.5 Steady state photoluminescence

The photoluminescence excitation (PLE) spectra of dysprosium doped niobate-based $Na_3Ba_2LaNb_{10}O_{30}$:xDy^{3+} ($x = 1$, 3, 5, 7 and 10 mol%) phosphors are demonstrated in Fig. 11, which were

Table 2 Bandgap, nephelauxetic ratio (β) and bonding parameter (δ) in $Na_3Ba_2LaNb_{10}O_{30}$:xDy^{3+} ($x = 1$, 3, 5, 7 and 10 mol%) phosphors

		Nephelauxetic	Bonding
Dy^{3+} (mol%)	Bandgap (eV)	Ratio (β)	Parameter (δ)
1.0	3.691	0.99980	0.00021
3.0	3.689	0.99973	0.00028
5.0	3.668	0.99938	0.00062
7.0	3.658	0.99883	0.00117
10.0	3.630	0.99601	0.00401

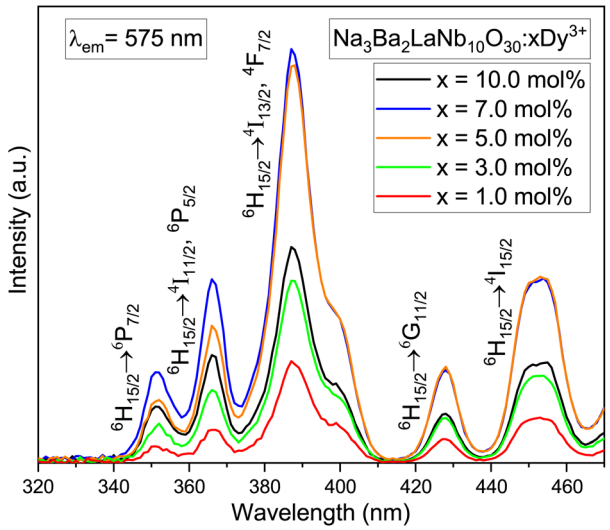


Fig. 11 PLE spectra of $Na_3Ba_2LaNb_{10}O_{30}$:xDy^{3+} ($x = 1$, 3, 5, 7 and 10 mol%) phosphors by fixing emission at 575 nm.

performed in wavelength range 320–470 nm for fixed emission wavelength of 575 nm. Several excitation peaks were observed at 351, 366, 387, 427 and 453 nm due to the characteristic Dy^{3+} ion transitions from $^6H_{15/2}$ (ground state) to several excited states as exhibited in Fig. 15. The five intense peaks correspond to $^6H_{15/2} \rightarrow {}^6P_{7/2}$(351 nm); $^6H_{15/2} \rightarrow {}^4I_{11/2}$, $^6P_{5/2}$(366 nm); $^6H_{15/2} \rightarrow {}^4I_{13/2}$, $^4F_{7/2}$(387 nm); $^6H_{15/2} \rightarrow {}^4G_{11/2}$(427 nm) and $^6H_{15/2} \rightarrow {}^4I_{15/2}$(453 nm) transitions.[45,46] Hence, one can conclude that the synthesised phosphor shows potential for applications in near-Ultraviolet chips.

The photoluminescence (PL) emission spectra of $Na_3Ba_2LaNb_{10}O_{30}$:xDy^{3+} ($x = 1$, 3, 5, 7 and 10 mol%) phosphors taken in the range of 400–700 nm while keeping excitation wavelength fixed at 387 nm are presented in Fig. 12. The emission spectra shows three characteristic bands centred at 481, 575 and

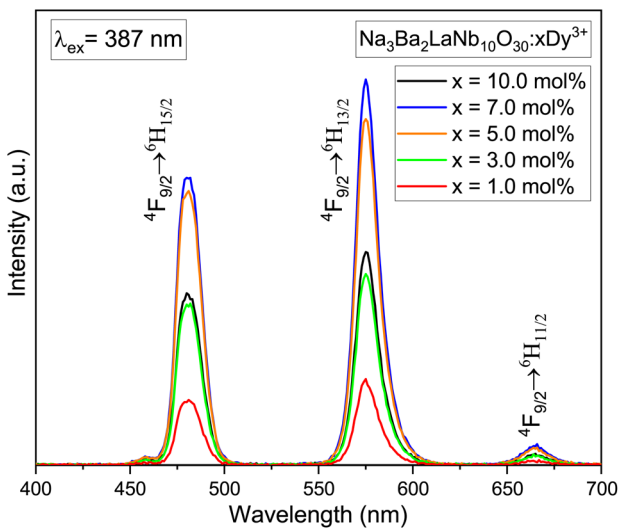


Fig. 12 PL emission spectra of $Na_3Ba_2LaNb_{10}O_{30}$:xDy^{3+} ($x = 1$, 3, 5, 7 and 10 mol%) phosphors under the excitation wavelength of 387 nm.

© 2023 The Author(s). Published by the Royal Society of Chemistry

Open Access Article. Published on 13 April 2023. Downloaded on 4/18/2023 5:40:33 AM.
This article is licensed under a Creative Commons Attribution-NonCommercial 3.0 Unported Licence.

666 nm which correspond to blue ($^4F_{9/2} \rightarrow {}^6H_{15/2}$ transition), yellow ($^4F_{9/2} \rightarrow {}^6H_{13/2}$ transition) and red ($^4F_{9/2} \rightarrow {}^6H_{11/2}$ transition) respectively. Further, due to magnetic dipole nature of the $^4F_{9/2} \rightarrow {}^6H_{15/2}$ transition the surrounding crystal field lays no effect on it. Whereas, the forced electric dipole $^4F_{9/2} \rightarrow {}^6H_{13/2}$ transition of Dy^{3+} ion is sensitive to surrounding environment. Moreover the intensity of the yellow band is greater than the blue band signifying that the Dy^{3+} ions are present at the sites lacking inversion center in the host lattice.[47,48] The optimized Dy^{3+} ion concentration is 7.0 mol%, beyond which the concentration quenching begins.

3.6 Nephelauxetic ratio (β) and bonding parameter (δ)

To understand the behaviour of ligand field that surrounds the Dy^{3+} ions in the host matrix and to determine the nature of bonding, the (β) and (δ) are evaluated using the following expression:[49]

$$\beta = \frac{\vartheta_c}{\vartheta_a} \text{ and } \delta = \frac{1-\bar{\beta}}{\bar{\beta}} \quad (5)$$

where, ϑ_c and ϑ_a are the wavenumbers in cm^{-1} for a specific transition of RE ion and the same transition of an aqua ion respectively and $\bar{\beta}$ represents the average value of all β. Nephelauxetic effect occurs because of the partially filled f-shell. When host matrix is incorporated with RE ions, the 4f shell gets deformed due to the influence of ligand field. The calculated values of β for $Na_3Ba_2LaNb_{10}O_{30}$:xDy^{3+} (x = 1, 3, 5, 7 and 10 mol%) are shown in Table 2.

The δ value strongly relate to the ligand field environment around the Dy^{3+} ions. The value may be positive/negative indicating ionic/covalent nature. The calculated values of δ for $Na_3Ba_2LaNb_{10}O_{30}$:xDy^{3+} (x = 1, 3, 5, 7 and 10 mol%) are shown in Table 2. The positive value indicates that the bond present between Dy–O is covalent in nature,[50] which increases with the increase in Dy^{3+} ions concentration.

3.7 Effect of dysprosium doping concentration

The emission spectra of $Na_3Ba_2LaNb_{10}O_{30}$:xDy^{3+} (x = 1, 3, 5, 7 and 10 mol%) in Fig. 12 showed the same peak positions for all the Dy^{3+} ions concentration. Fig. 13 shows the yellow and blue peak emission intensity of $Na_3Ba_2LaNb_{10}O_{30}$:Dy^{3+} phosphor with change in Dy^{3+} ion concentration. Fig. 13 reveals that the emission intensity depends upon the concentration of Dy^{3+} ion, and is seen to increase with steady increase in the latter upto 7 mol%. Beyond 7 mol% of Dy^{3+} ion concentration, the luminescence intensity in $Na_3Ba_2LaNb_{10}O_{30}$ phosphor begins to decrease due to quenching of the concentration. This supported the fact that as Dy^{3+} ion concentration increases beyond a certain value, here 7 mol%, the non-radiative energy transfer probability between dysprosium ions tends to increase. Theoretically, the critical distance (R_c) between Dy^{3+} ions after which concentration quenching begins can be calculated using the Blasse formula:[51]

$$R_c = 2\left(\frac{3V}{4\pi\chi_c N}\right)^{1/3} \quad (6)$$

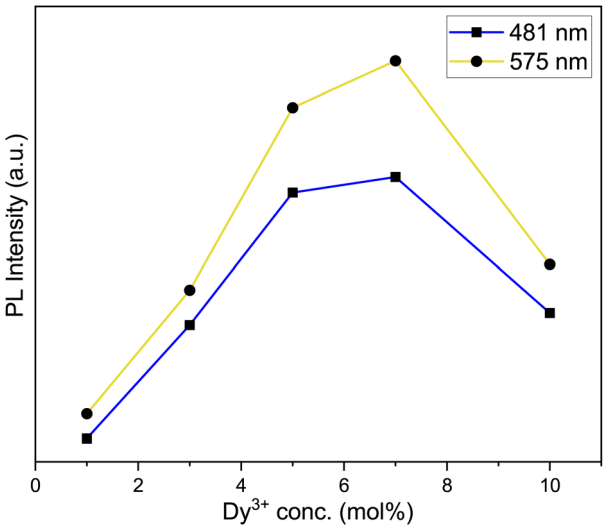


Fig. 13 Variation of emission intensity of the emission peaks to various Dy^{3+} ions concentration.

where V denotes the unit cell volume, N denotes the number of cation sites in the host unit cell and χ_c represents the fraction of activator concentration at which quenching occurs. For $Na_3Ba_2LaNb_{10}O_{30}$:Dy^{3+} phosphor, $\chi_c = 0.07$, $N = 1$, $V = 604.4425$ Å, hence R_c can be calculated as 25.45 Å. Resonant energy transfer is primarily caused by exchange and multipolar interactions. The distance between the adjacent Dy^{3+} ions falls below the critical distance beyond the 7 mol% concentration of Dy^{3+} ions. Given that the calculated R_c value is greater than 5 Å, the multipolar interactions will be dominant in the concentration quenching of $Na_3Ba_2LaNb_{10}O_{30}$:Dy^{3+} phosphor as the probability of energy transfer *via* exchange interaction mechanism is very low.[52]

In line with Dexter's hypothesis,[53] type of multipolar interaction mechanism between Dy^{3+}–Dy^{3+} ions can be obtained using the eqn (7).

$$\frac{I}{x} = K\left[1+\beta(x)^{Q/3}\right]^{-1} \quad (7)$$

here β and K denote constants specific to the host lattice, x represents the activator ion concentration, and I denotes the photoluminescence emission intensity. The Q value defines the multipolarity of electric interaction between the adjacent activator ion.[54] The multipolar character function Q can take values of 3,6,8 and 10 according to the interaction mechanism being nearest neighbour, dipole–dipole (d–d), dipole–quadrupole (d–q) and quadrupole–quadrupole (q–q) respectively.[55] The eqn (7) can be approximated to:

$$\log\frac{I}{x} = K' - \frac{Q\log(x)}{3}; \quad \text{here } (K' = \log K - \log\beta) \quad (8)$$

The linear dependance of $\log(I/x)$ and $\log(x)$ was analysed using $^4F_{9/2}$ transition of dysprosium ion and is shown in Fig. 14. The calculated slope value prior to linear fit is −1.70753, which gives the Q value equivalent to 5.13 (close to 6). Thus, it can be stated that the main mechanism through which energy transfer

Open Access Article. Published on 13 April 2023. Downloaded on 4/18/2023 5:40:33 AM.
This article is licensed under a Creative Commons Attribution-NonCommercial 3.0 Unported Licence.

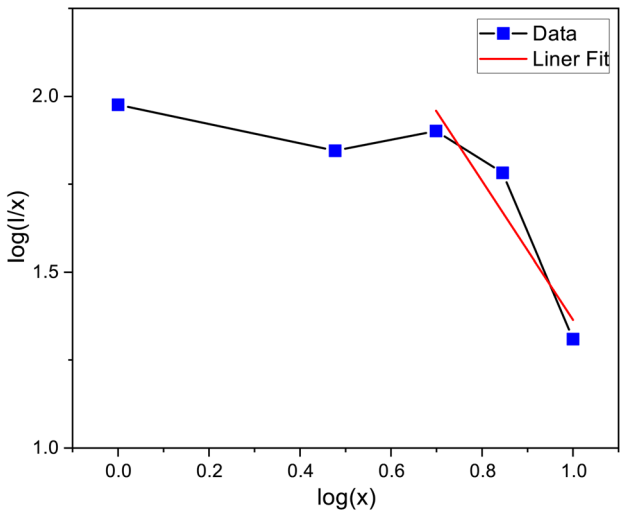


Fig. 14 The linear fitting plot between log(I/x) and log(x).

occurs between the adjacent dysprosium ions is dipole–dipole interaction.

The partial energy states of $Na_3Ba_2LaNb_{10}O_{30}$:Dy^{3+} phosphor is drawn in Fig. 15. The synthesized phosphor absorbs near ultraviolet light corresponding to it's absorption band originating from $^6H_{15/2}$ (ground state) to different excited states. The phosphor $Na_3Ba_2LaNb_{10}O_{30}$:Dy^{3+} gets excited at 387 nm to populate the short-lived $^4I_{13/2}$ and $^4F_{7/2}$ excited state. The excited ions undergo multiphonon non-radiative transitions to relax to the low lying metastable $^4F_{9/2}$ state. Since beyond this level, the energy spacing between various energy levels is negligible, hence the energy transfer mainly occurs through the non-radiative transitions. The rate of phonon emission (w) can be determined using eqn (9):

$$w = e^{KE/h\nu_{max}} \quad (9)$$

where K is the Boltzmann constant, E is the energy gap and $h\nu_{max}$ is the maximum energy of phonons.

Because of significant energy difference between $^4F_{9/2}$ level and $^6H_{15/2}$, $^6H_{13/2}$, $^6H_{11/2}$ levels, radiative photonic emission takes place. Cross relaxation (CR) channels and resonance energy transfer (RET) between nearby dysprosium ions may be responsible for the non-radiative energy transfer and concentration quenching. According to the energy match rule, the three cross-relaxation channels (CR1, CR2, and CR3) and potential resonant energy transfer are as follows:[50,56,57]

CR1: ($^4F_{9/2}$ + $^6H_{15/2}$ → $^6F_{11/2}$, $^6H_{9/2}$ + $^6F_{3/2}$)
CR2: ($^4F_{9/2}$ + $^6H_{15/2}$ → $^6F_{9/2}$, $^6H_{7/2}$ + $^6F_{5/2}$)
CR3: ($^4F_{9/2}$ + $^6H_{15/2}$ → $^6F_{1/2}$ + $^6F_{11/2}$, $^6H_{9/2}$)
RET: ($^4F_{9/2}$ + $^6H_{15/2}$ → $^6H_{15/2}$ + $^4F_{9/2}$).

3.8 CIE chromaticity coordinate

CIE chromaticity[58] coordinates were calculated and plotted on CIE 1931 chromaticity diagram, as shown in Fig. 16, using the emission spectra of $Na_3Ba_2LaNb_{10}O_{30}$:Dy^{3+} phosphors. Here, x and y correspond to the chromaticity coordinates in the CIE 1931 and were obtained as follows:

$$x = \frac{X}{X+Y+Z}, \quad y = \frac{Y}{X+Y+Z} \quad (10)$$

where X, Y, Z are the tristimulus values for the three primary colors *i.e.* red, green and blue, respectively. The calculated CIE coordinates are found to be quite close to the center white light point (0.33333, 0.33333), as observed in Fig. 16. Correlated color temperature (CCT)[59] relate its color to the color of the light emitted by the black body at a particular temperature, and is measured in Kelvins. Based on the CCT, the phosphors fall in the warm white light region. McCamy's empirical formula[60] was employed to calculate the CCT as stated in the eqn (11):

$$CCT = -449n^3 + 3525n^2 - 6823.3n + 5520.33 \quad (11)$$

where ($x_e = 0.332$, $y_e = 0.186$) is the epicenter and $n = \frac{x - x_e}{y - y_e}$ is the inverse slope line.

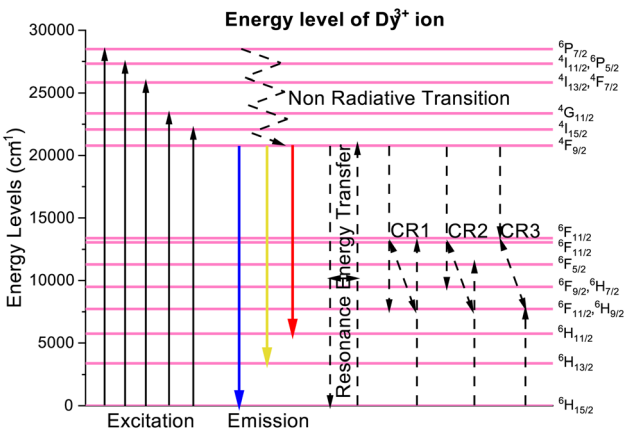


Fig. 15 Partial energy level diagram of Dy^{3+} in $Na_3Ba_2LaNb_{10}O_{30}$ phosphor.

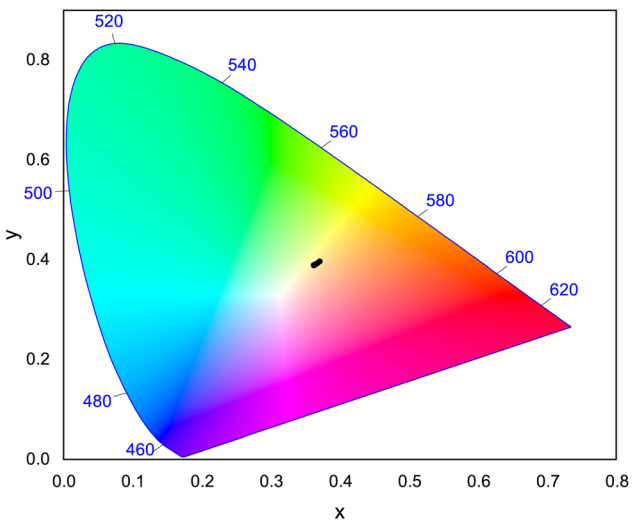


Fig. 16 CIE 1931 chromaticity diagram showing the color coordinates of $Na_3Ba_2LaNb_{10}O_{30}$:xDy^{3+} (x = 1, 3, 5, 7 and 10 mol%) phosphors.

© 2023 The Author(s). Published by the Royal Society of Chemistry

Open Access Article. Published on 13 April 2023. Downloaded on 4/18/2023 5:40:33 AM.
This article is licensed under a Creative Commons Attribution-NonCommercial 3.0 Unported Licence.

Furthermore, the asymmetry ratio *i.e.* Y/B ratio is the relative measure of band intensities at 575 nm and 481 nm that is used to assess the effectiveness of Dy^{3+} ion doped phosphors. The asymmetry ratio is found close to 1, indicating the appropriate white emission for as prepared Dy^{3+} ion doped phosphor.[61] The Y/B ratio for this investigation lies in the range of 1.18329 to 1.34318 as shown in Table 3. With the increase in Dy^{3+} ion concentration, the position of peak remains unaffected. The color purity of the prepared $Na_3Ba_2LaNb_{10}O_{30}$:xDy^{3+} ($x = 1$, 3, 5, 7 and 10 mol%) phosphor are calculated using the following formula:

$$\text{Color purity} = \sqrt{\frac{(x - x_i)^2 + (y - y_i)^2}{(x_d - x_i)^2 + (y_d - y_i)^2}} \times 100\% \qquad (12)$$

where (x, y) denotes the CIE coordinates of the prepared phosphors, (x_d, y_d) denotes the dominant wavelength coordinates corresponding to the dominant wavelength (λ_d), and (x_i, y_i) denotes the CIE coordinates of the reference white light. The color purity for the prepared samples are calculated between 19% and 24%. The low color purity value is the evident aspect indicating the purity for white light emission which is significantly lower than the previously indicated Dy^{3+} doped phosphors.[62,63] CIE coordinates, CCT, Y/B ratio and color purity are shown in Table 3.

3.9 Lifetime analysis

The phenomenon responsible for the longer decay time is illustrated systematically in the Fig. 17. The Dy^{3+} ion happens to be a potent trap creating ion, and formation of these traps is a major cause for longer decay time. Moreover, the phosphor's luminescence intensity is influenced by the densities of the trapped electrons, whereas its duration is influenced by the depth of the trapped electrons. Phosphor materials when exposed to radiation, cause excitation of the charge carriers and they shift to a higher energy conduction band through process 1 illustrated in Fig. 17. There are two possible choices for these charge carriers to occupy the luminescence centres made by Dy^{3+} ions. One way is for the charge carriers to directly approach the luminescence centres *via* host conduction band (as directed by process 2). However, a fraction of the excited charge carriers get confined into electron traps (as directed by process 3), eventually storing some part of excitation energy. These trapped electrons do not come to the ground state directly, instead they are released from these traps, due to thermal excitations at proper temperature, and get transferred to the luminescent centres *via* host lattice. At these luminescent centres, Dy^{3+} characteristic emissions are observed (as directed by process 4). In physical systems, number of electron and hole traps may not be exactly equal and this embodies the cause for the characteristic luminescence.[64]

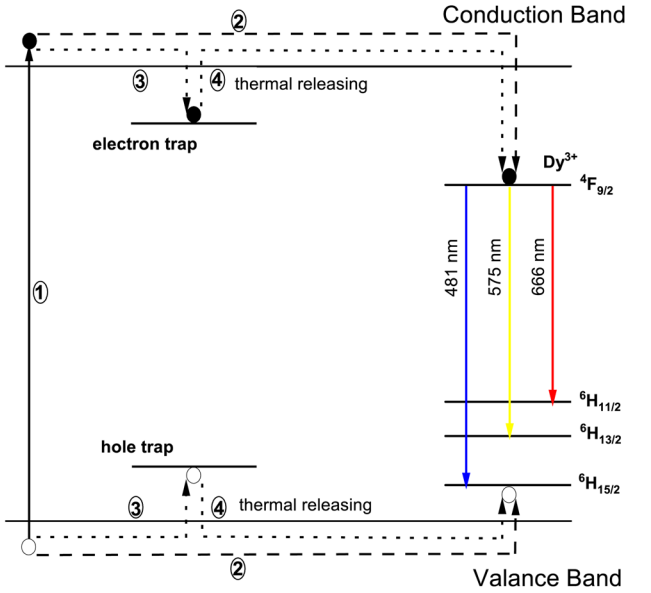


Fig. 17 Schematic diagram of the mechanism in $Na_3Ba_2LaNb_{10}O_{30}$:-Dy^{3+} phosphor.

The typical luminous decay curve of $Na_3Ba_2LaNb_{10}O_{30}$:xDy^{3+} ($x = 7$ mol%) phosphor is presented in Fig. 18. The decay curve to calculate lifetime, for $^4F_{9/2} \rightarrow {}^6H_{13/2}$ transition under 487 nm excitation, at room temperature for different Dy^{3+} concentrations, is demonstrated in Fig. 19. It can be seen that, the decay curves fit closely with the double exponential function[65,66] shown in eqn (13). The degree of fitting (χ^2) was observed to be very close to 1 (~0.99932).

$$I(t) = I_0 + A_1 \exp\left(-\frac{t}{\tau_1}\right) + A_2 \exp\left(-\frac{t}{\tau_2}\right) \qquad (13)$$

where I_0 and $I(t)$ signify the phosphorescence intensities at time $t = 0$ and some later time t, respectively. A_1 and A_2 are fitting constants and τ_1 and τ_2 are rapid and slow decay lifetimes. τ_{avg} for different Dy^{3+} doped $Na_3Ba_2LaNb_{10}O_{30}$ phosphors were calculated using eqn (14):[67]

Table 3 CIE coordinate, correlated color temperature, Y/B ratio and average decay time for $Na_3Ba_2LaNb_{10}O_{30}$:xDy^{3+} ($x = 1$, 3, 5, 7 and 10 mol%) phosphors

Dy^{3+} (mol%)	CIE coordinate		CCT (K)	Y/B ratio	Color purity	Average decay time (μs)
	x	y				
1.0	0.36724	0.39237	4455.777	1.322	23.001	302.559 ± 0.859
3.0	0.36210	0.38917	4585.400	1.183	19.645	249.539 ± 0.906
5.0	0.36695	0.39261	4464.850	1.263	22.842	242.453 ± 1.164
7.0	0.37063	0.39636	4383.463	1.343	25.364	238.778 ± 2.054
10.0	0.36496	0.39091	4512.177	1.240	21.508	207.428 ± 3.567

Open Access Article. Published on 13 April 2023. Downloaded on 4/18/2023 5:40:33 AM.
This article is licensed under a Creative Commons Attribution-NonCommercial 3.0 Unported Licence.

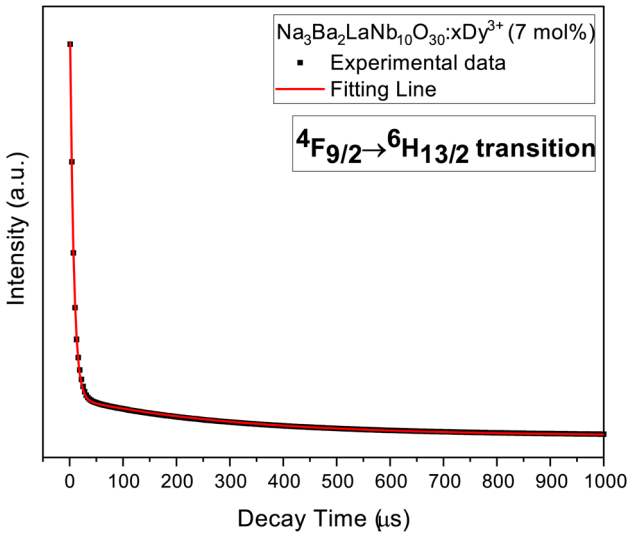


Fig. 18 Decay curve $4F_{9/2} \rightarrow 6H_{13/2}$ transition in $Na_3Ba_2LaNb_{10}O_{30}$:-xDy^{3+} ($x = 7$ mol%) phosphor.

$$\tau_{avg} = \frac{A_1\tau_1^2 + A_2\tau_2^2}{A_1\tau_1 + A_2\tau_2} \quad (14)$$

Table 3 summarises the average decay time τ_{avg} of different Dy^{3+} doped $Na_3Ba_2LaNb_{10}O_{30}$ phosphors. It is clearly evident that as the Dy^{3+} ion concentration increases, the τ_{avg} of the prepared phosphors gradually decreases from 302.6 μs to 207.4 μs because of energy transfer between adjacent Dy^{3+} ions.

3.10 Internal quantum yield (IQE) and brightness (*B*)

Internal quantum yield (IQE) is an important aspect of a phosphor as it gives the efficiency of conversion of electrical power to observed optical power. The IQE of $Na_3Ba_2LaNb_{10}O_{30}$:xDy^{3+} ($x =$ 7 mol%) phosphor, shown in Fig. 20, was measured using the reference of $BaSO_4$ excitation line. Qualitatively, IQE is the ratio

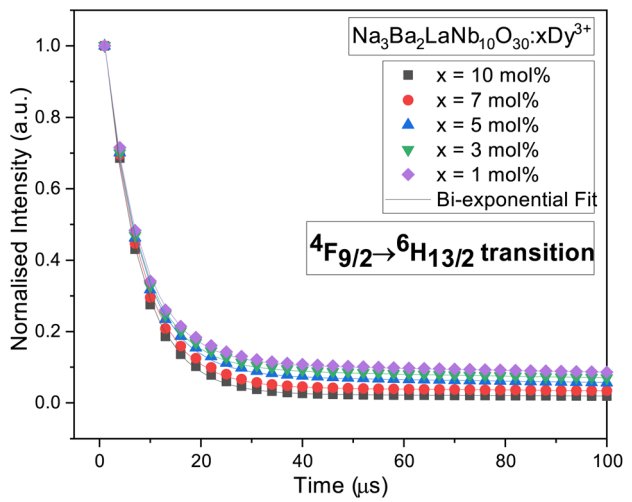


Fig. 19 Decay curves for $4F_{9/2} \rightarrow 6H_{13/2}$ transition in $Na_3Ba_2LaNb_{10}$-O_{30}:xDy^{3+} ($x = 1$, 3, 5, 7 and 10 mol%) phosphors.

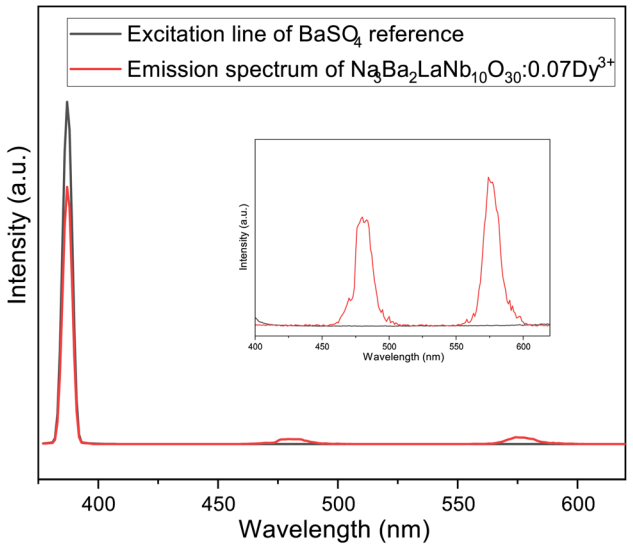


Fig. 20 Excitation and emission spectra of $Na_3Ba_2LaNb_{10}O_{30}$:xDy^{3+} ($x = 7$ mol%) phosphor and $BaSO_4$ reference using an integrating sphere for IQE measurement. Inset: enlarged emission spectra (400–630 nm).

of number of emitted and absorbed photons and can be obtained using the eqn (15):[68]

$$\eta = \frac{\int L_S}{\int E_R - \int E_S} \quad (15)$$

where η represents IQE, L_S denotes to the emission spectra of $Na_3Ba_2LaNb_{10}O_{30}$:xDy^{3+} ($x = 7$ mol%), E_S represent phosphor excitation spectra and E_R represent excitation exclusively with $BaSO_4$ as reference. IQE (η) of $Na_3Ba_2LaNb_{10}O_{30}$:xDy^{3+} ($x =$ 7 mol%) phosphor was calculated as 45.35% under the excitation of 387 nm, which is significantly higher than previously reported $Ca_2ZnSi_2O_7$:Dy^{3+},Eu^{3+} (IQE: 12.88%),[69] $LiCaBO_3$:Dy^{3+} (IQE: 25.00%)[70] and $Ca_2NaMg_2V_3O_{12}$:Dy^{3+} (IQE: 25.00%)[71] phosphors. Similarly, brightness (B)[72] is a dimensionless quantity defined as a parameter that has nothing to do with how sensitive the human eye is and is defined by eqn (16):

$$B = \frac{n_e}{n_i} = \frac{n_e}{n_a} \times \frac{n_a}{n_i} = \eta \times \xi_{abs} \quad (16)$$

where n_a, n_i and n_e correspond to the number of photons absorbed, incident and emitted respectively. Hence absorption efficiency ξ_{abs} becomes:

$$\xi_{abs} = \frac{n_a}{n_i} \quad (17)$$

The calculated value of brightness for $Na_3Ba_2LaNb_{10}O_{30}$:-xDy^{3+} ($x = 7$ mol%) phosphors is 11.41%.

4 Conclusions

In this study, a series of novel white light emitting dysprosium doped $Na_3Ba_2LaNb_{10}O_{30}$ phosphors were successfully

© 2023 The Author(s). Published by the Royal Society of Chemistry

Open Access Article. Published on 13 April 2023. Downloaded on 4/18/2023 5:40:33 AM. This article is licensed under a Creative Commons Attribution-NonCommercial 3.0 Unported Licence.

synthesized through conventional solid-state reaction method. Their structural, morphological, and spectroscopic properties have been investigated for w-LED application using XRD, FE-SEM, FT-IR, steady state and time resolved spectroscopy and quantum yield. X-ray diffractometer confirms that the prepared phosphors were in pure phase, and the crystal system is revealed as filled TTB with *P4bm* space group. The FE-SEM micrograph reveals that the particle size distribution is in both μm and nm ranges, and the agglomerated particles were of non-uniform shape. Raman and FT-IR spectra indicates the presence of different vibrational modes and functional groups, respectively. Ultraviolet visible diffuse reflectance spectra (UV-DRS) indicates the presence of surface defects in the prepared phosphors. The phosphor emits white light under near-ultraviolet (n-UV) excitation *via* a dominant mix of blue and yellow emission bands at 481 nm ($^4F_{9/2} \rightarrow {}^6H_{15/2}$) and 575 nm ($^4F_{9/2} \rightarrow {}^6H_{13/2}$), respectively. The optimised concentration of Dy^{3+} ions beyond which quenching occurs was found to be 7.0 mol%. This concentration quenching mechanism arises due to dipole–dipole interaction. Nephelauxetic ratio and bonding parameters were determined from their luminescent spectra. The CIE chromaticity coordinates, CCT, Y/B ratio and color purity indicates that the synthesised phosphors emits warm white light. The decay time decreases with increasing concentration of Dy^{3+} ions due to energy transfer between neighbouring Dy^{3+} ions, as indicated by the lifetime decay curves. The Internal Quantum Yield and Brightness calculated for the optimised phosphor suggests that the prepared phosphor has a potential utility in w-LED application under n-UV excitation.

Author contributions

Kanishk Poria: conceptualization, methodology, writing – original draft. Ravina: conceptualization, methodology, writing – original draft. Sanjana Bhatia: data curation, writing, review, editing. Amit Kumar: formal analysis. Rajwinder Singh: formal analysis. Nisha Deopa: supervision, methodology, software, validation, writing, review, editing, formal analysis. Rajesh Punia: resources. Jangvir Singh Shahi: supervision, methodology, software, validation, writing, review, editing, formal analysis. A. S. Rao: resources, formal analysis.

Conflicts of interest

There are no conflicts to declare.

Acknowledgements

The author (Mr Kanishk Poria) would like to thank Council of Scientific & Industrial Research (CSIR), Govt. of India for providing financial support through Senior Research Fellowship (SRF) (File No. 09/135(0901)/2020-EMR-I, dt. 01/01/2020).

References

1 H. Hu and W. Zhang, *Opt. Mater.*, 2006, **28**, 536–550.
2 M. Djamal, L. Yuliantini, R. Hidayat, K. Boonin, P. Yasaka and J. Kaewkhao, *Mater. Today: Proc.*, 2018, **5**, 15126–15130.
3 L. Fan, Y. Shi, Y. Wu, J. Xie, J. Zhang, F. Lei and L. Zhang, *J. Lumin.*, 2017, **190**, 504–510.
4 S. Verma, K. Verma, D. Kumar, B. Chaudhary, S. Som, V. Sharma, V. Kumar and H. C. Swart, *Phys. B Condens. Matter*, 2018, **535**, 106–113.
5 Y. Liu, R. Wang, Q. Yang, G. Li, J. Huang and G. Cai, *J. Am. Ceram. Soc.*, 2022, **105**, 6184–6195.
6 Y. Liu, X. Liu, W. Wang, B. Zhou and Q. Zhang, *Mater. Res. Bull.*, 2017, **95**, 235–242.
7 N. Deopa, A. Rao, M. Gupta and G. V. Prakash, *Opt. Mater.*, 2018, **75**, 127–134.
8 T. Pulli, T. Dönsberg, T. Poikonen, F. Manoocheri, P. Kärhä and E. Ikonen, *Light Sci. Appl.*, 2015, **4**, e332.
9 M.-H. Fang, C. Ni, X. Zhang, Y.-T. Tsai, S. Mahlik, A. Lazarowska, M. Grinberg, H.-S. Sheu, J.-F. Lee, B.-M. Cheng, *et al.*, *ACS Appl. Mater. Interfaces*, 2016, **8**, 30677–30682.
10 J. Chen, Y. Liu, L. Mei, H. Liu, M. Fang and Z. Huang, *Sci. Rep.*, 2015, **5**, 1–9.
11 X. Chen, P. Dai, X. Zhang, C. Li, S. Lu, X. Wang, Y. Jia and Y. Liu, *Inorg. Chem.*, 2014, **53**, 3441–3448.
12 K. Jha, A. K. Vishwakarma, M. Jayasimhadri and D. Haranath, *J. Alloys Compd.*, 2017, **719**, 116–124.
13 K. Shinde and S. Dhoble, *Crit. Rev. Solid State Mater. Sci.*, 2014, **39**, 459–479.
14 M. Shi, L. Yao, J. Xu, C. Liang, Y. Dong and Q. Shao, *J. Am. Ceram. Soc.*, 2021, **104**, 3279–3288.
15 P. Dang, G. Li, X. Yun, Q. Zhang, D. Liu, H. Lian, M. Shang and J. Lin, *Light Sci. Appl.*, 2021, **10**, 1–13.
16 M. Tshabalala, F. Dejene, S. S. Pitale, H. Swart and O. Ntwaeaborwa, *Phys. B Condens. Matter*, 2014, **439**, 126–129.
17 N. Lakshminarasimhan and U. Varadaraju, *J. Electrochem. Soc.*, 2005, **152**, H152.
18 G. Hu, S. Yi, Z. Fang, Z. Hu and W. Zhao, *Opt. Mater.*, 2019, **98**, 109428.
19 F. Xiong, F. Xu, H. Lin, Y. Wang, E. Ma and W. Zhu, *Appl. Phys. A*, 2020, **126**, 1–8.
20 Z. Li, Y. Hua and G. Ou, *Optik*, 2021, **233**, 166595.
21 P. Wang, L. Schwertmann, R. Marschall and M. Wark, *J. Mater. Chem. A*, 2014, **2**, 8815–8822.
22 Y. Ma, R. Liu, X. Geng, X. Hu, W. Chen, B. Deng, R. Yu and H. Geng, *Ceram. Int.*, 2022, **48**, 4080–4089.
23 G. Zhu, Z. Ci, S. Xin, Y. Wen and Y. Wang, *Mater. Lett.*, 2013, **91**, 304–306.
24 T. Wei, Y. Wang, Q. Zhou, Z. Li, L. Zhan and Q. Jin, *Ceram. Int.*, 2014, **40**, 16647–16651.
25 C.-J. Chan, F. F. Lange, M. Rühle, J.-F. Jue and A. V. Virkar, *J. Am. Ceram. Soc.*, 1991, **74**, 807–813.
26 R. Jain, R. Sinha, M. K. Sahu and M. Jayasimhadri, *J. Lumin.*, 2021, **36**, 1444–1451.
27 B. M. Mothudi, O. Ntwaeaborwa, S. S. Pitale and H. Swart, *J. Alloys Compd.*, 2010, **508**, 262–265.
28 P. Babu, K. H. Jang, E. S. Kim, L. Shi, H. J. Seo and F. Lopez, *J. Korean Phys. Soc.*, 2009, **54**, 1488–1491.

Open Access Article. Published on 13 April 2023. Downloaded on 4/18/2023 5:40:33 AM. This article is licensed under a Creative Commons Attribution-NonCommercial 3.0 Unported Licence.

29 S. K. Gupta, M. Kumar, V. Natarajan and S. Godbole, *Opt. Mater.*, 2013, **35**, 2320–2328.
30 M. K. Sahu and J. Mula, *J. Am. Ceram. Soc.*, 2019, **102**, 6087–6099.
31 L. Fang, H. Zhang, J. Yang, F. Meng and R. Yuan, *J. Mater. Sci. Lett.*, 2003, **22**, 1705–1707.
32 L. Sun, B. Devakumar, J. Liang, B. Li, S. Wang, Q. Sun, H. Guo and X. Huang, *RSC Adv.*, 2018, **8**, 31835–31842.
33 L. Alexander and H. P. Klug, *J. Appl. Phys.*, 1950, **21**, 137–142.
34 K. Rawat and P. Shishodia, *Adv. Powder Technol.*, 2017, **28**, 611–617.
35 M. Bouziane, M. Taibi, L. Saviot and A. Boukhari, *Phys. B Condens. Matter*, 2011, **406**, 4257–4260.
36 R. E. Wilde, *J. Raman Spectrosc.*, 1991, **22**, 321–325.
37 A. Boudou and J. Sapriel, *Phys. Rev. B: Condens. Matter Mater. Phys.*, 1980, **21**, 61.
38 S. Jana, A. Mondal, J. Manam and S. Das, *J. Alloys Compd.*, 2020, **821**, 153342.
39 H. Kabir, S. H. Nandyala, M. M. Rahman, M. A. Kabir and A. Stamboulis, *Appl. Phys. A*, 2018, **124**, 1–11.
40 M. Salavati-Niasari, G. Hosseinzadeh and F. Davar, *J. Alloys Compd.*, 2011, **509**, 134–140.
41 M. Afqir, A. Tachafine, D. Fasquelle, M. Elaatmani, J.-C. Carru, A. Zegzouti, M. Daoud, S. Sayouri, T.-d. Lamcharfi and M. Zouhairi, *Process. Appl. Ceram.*, 2018, **12**, 72–77.
42 H. Bruncková, L. Medveckỳ, P. Hvizdoš, J. Ďurišin and V. Girman, *J. Mater. Sci.*, 2015, **50**, 7197–7207.
43 I. P. Sahu, D. Bisen, N. Brahme and R. K. Tamrakar, *J. Electron. Mater.*, 2016, **45**, 2222–2232.
44 M. Jiao, C. Yang, M. Liu, Q. Xu, Y. Yu and H. You, *Opt. Mater. Express*, 2017, **7**, 2660–2671.
45 W. Carnall, P. Fields and K. Rajnak, *J. Chem. Phys.*, 1968, **49**, 4424–4442.
46 K. Poria, N. Deopa and J. S. Shahi, *Laser Sci.*, 2022, JW5A.1.
47 Q. Su, Z. Pei, L. Chi, H. Zhang, Z. Zhang and F. Zou, *J. Alloys Compd.*, 1993, **192**, 25–27.
48 L. Mishra, A. Sharma, A. K. Vishwakarma, K. Jha, M. Jayasimhadri, B. Ratnam, K. Jang, A. Rao and R. Sinha, *J. Lumin.*, 2016, **169**, 121–127.
49 C. Jorgensen, *Prog. Inorg. Chem.*, 1962, **4**, 73–124.
50 N. Deopa and A. Rao, *J. Lumin.*, 2017, **192**, 832–841.
51 G. Blasse, *Phys. Lett. A*, 1968, **28**, 444–445.
52 L. Van Uitert, *J. Electrochem. Soc.*, 1967, **114**, 1048.
53 D. L. Dexter and J. H. Schulman, *J. Chem. Phys.*, 1954, **22**, 1063–1070.
54 D. L. Dexter, *J. Chem. Phys.*, 1953, **21**, 836–850.
55 S. Kaur, A. Rao and M. Jayasimhadri, *Ceram. Int.*, 2017, **43**, 7401–7407.
56 A. K. Vishwakarma, K. Jha, M. Jayasimhadri, B. Sivaiah, B. Gahtori and D. Haranath, *Dalton Trans.*, 2015, **44**, 17166–17174.
57 J. S. Kumar, K. Pavani, A. M. Babu, N. K. Giri, S. Rai and L. R. Moorthy, *J. Lumin.*, 2010, **130**, 1916–1923.
58 F. Miller, A. Vandome and M. John, *CIE 1931 Color Space*, VDM Publishing, 2010.
59 M. N. Khan, *Understanding LED illumination*, CRC Press, 2013.
60 C. S. McCamy, *Color Res. Appl.*, 1992, **17**, 142–144.
61 B. Ratnam, M. Jayasimhadri, K. Jang, H. Sueb Lee, S.-S. Yi and J.-H. Jeong, *J. Am. Ceram. Soc.*, 2010, **93**, 3857–3861.
62 P. Nayak, S. S. Nanda, S. K. Gupta, K. Sudarshan and S. Dash, *J. Am. Ceram. Soc.*, 2022, **105**, 7384–7398.
63 S. Sharma, N. Brahme, D. Bisen and P. Dewangan, *Opt. Express*, 2018, **26**, 29495–29508.
64 I. P. Sahu, D. Bisen and N. Brahme, *Displays*, 2014, **35**, 279–286.
65 K. Li, X. Liu, Y. Zhang, X. Li, H. Lian and J. Lin, *Inorg. Chem.*, 2015, **54**, 323–333.
66 K. Jha and M. Jayasimhadri, *J. Am. Ceram. Soc.*, 2017, **100**, 1402–1411.
67 J. Sun, X. Zhang, Z. Xia and H. Du, *Mater. Res. Bull.*, 2011, **46**, 2179–2182.
68 S. Wang, Y. Xu, T. Chen, W. Jiang, J. Liu, X. Zhang, W. Jiang and L. Wang, *Chem. Eng. J.*, 2021, **404**, 125912.
69 K. Mondal and J. Manam, *J. Lumin.*, 2018, **195**, 259–270.
70 A. R. Beck, S. Das and J. Manam, *J. Mater. Sci.: Mater. Electron.*, 2017, **28**, 17168–17176.
71 L. Yang, X. Mi, H. Zhang, X. Zhang, Z. Bai and J. Lin, *J. Alloys Compd.*, 2019, **787**, 815–822.
72 P. A. Tanner, L. Zhou, C. Duan and K.-L. Wong, *Chem. Soc. Rev.*, 2018, **47**, 5234–5265.

© 2023 The Author(s). Published by the Royal Society of Chemistry

e-ISSN: 2582-5208
International Research Journal of Modernization in Engineering Technology and Science
(Peer-Reviewed, Open Access, Fully Refereed International Journal)
Volume:05/Issue:02/February-2023 Impact Factor- 7.868 www.irjmets.com

MANUFACTURING MACHINE- A REVIEW PAPER

Satyendra Kumar Pandey*1, Vansh Baliyan*2, Vishal Singh*3,
Dr. Ashok Kumar Madan*4

*1,2,3Undergraduate Student Production And Industrial Engineering, Delhi Technological University, New Delhi, India.

*4Professor, Department Of Mechanical Engineering, Delhi Technological University, New Delhi, India.

DOI : https://www.doi.org/10.56726/IRJMETS33762

ABSTRACT

The relationship between foam density and cell size and microstructural properties are believed to originate from manufacturing condition of metallic foams , it is of interest to modify the processing conditions in order to achieve more uniform cell size distribution with reduced morphological defects for better performance. The blowing agent used for foaming decomposes in molten aluminium and generates gas bubbles therein. However, to have a uniformity in structure, it should generate the desired amount of gas bubbles of desired sizes during the foaming process. Apart from this the molten aluminium must possess a certain viscosity which is affected by the addition of ceramics particles so that the generated gas bubbles are retained in the aluminium matrix during solidification . In this entire process, temperature plays an important role.

Keywords: Manufacturing System, Manufacturing Processes, Mechatronics And Robotics.

I. INTRODUCTION

As a new class of structural material, metallic foam offers a unique combination of properties such as low density, energy absorption, and high stiffness and strength. These improved properties of metal foams make them highly sought after materials for various technological applications . Recent improvements in metal foam production methods have found many applications in various fields such as automotive, railway and aerospace industries. In this application the composite foam undergoes high-speed deformation.

Miyoshi et al. have shown the application of aluminum composite foam as a functional material for sound and impact energy absorption. Metallic foams are excellent impact energy absorber, and they can convert impact energy into deformation energy and absorb more energy than bulk metals at low stresses . Main application of particle reinforced metallic composite foams is in defence and is used as passive safety systems due to energy absorption and dissipation properties of the foams. Both physical and mechanical properties of aluminum composite foams are not only controlled by composition of matrix and reinforcement but are also significantly affected by cell structure of foam . Ma and Song found that the Cell structure of aluminum foams can be controlled by a foaming process, where the viscosity of the aluminum melt is controlled by Ca addition and continuous mixing of the melt. The average diameter of the aluminum foam cell decreases as the viscosity of the melt increases because the microstructural properties of aluminum foam affect the most important above properties, many studies have been conducted. These include cell wall thickness, knot size, bond length, and the relationship between foam density and cell size . Since all these microstructural properties are believed to originate from manufacturing condition of metallic foams , it is of interest to modify the processing conditions in order to achieve more uniform cell size distribution with reduced morphological defects for better performance. The blowing agent used for foaming decomposes in molten aluminum and generates gas bubbles therein. However, to have a uniformity in structure, it should generate the desired amount of gas bubbles of desired sizes during the foaming process. Apart from this the molten aluminum must possess a certain viscosity which is affected by the addition of ceramics particles so that the generated gas bubbles are retained in the aluminum matrix during solidification . In this entire process, temperature plays an important role. The role of SiC reinforcement in foam stability was studied by Prakash et al. , Daqing and Ziyuan . They controlled the stability of aluminum foam by adding SiC particle distribution and higher SiC content to increase foam brittleness .Mukherjee et al. studied the effect of SiC on microstructure, density and closure strength. Cellular foam using CaCO3 as a blowing agent. The stability of the foam mainly depends on the wettability of the

e-ISSN: 2582-5208
International Research Journal of Modernization in Engineering Technology and Science
(Peer-Reviewed, Open Access, Fully Refereed International Journal)
Volume:05/Issue:02/February-2023 Impact Factor- 7.868 www.irjmets.com

ceramic particles along the cell walls and nodes. The location of the particles depends on the pressure of the gas inside the bubble and the viscosity of the molten alloy, which changes with the foaming temperature. For liquid bubbles to become stable, the liquid-gas interface must be altered by introducing surfactants that reduce surface tension or by increasing the viscosity of the surface layer .There is little literature on the effect of foaming temperature on foam microstructure .It is reported that in case of alloy foam, the porosity increases with increases in foaming temperature . However, in case of composite foam, the microstructure is hardly affected due to addition of ceramic particles in the melt alloy . The fracture resistance and damage tolerance of foamed parts can be significantly improved with non-metallic reinforcement onto the foam surface. Moreover, a comparative study on the microstructure of the alloy foam and the corresponding composite foam which is affected by increase in the foaming temperature is not available. The microstructure is controlled by the process variables such as foaming temperature, foaming agent, impeller design, impeller speed, size and volume fraction of the solid particles during the foam making process. To the best of our knowledge, till date no work is reported describing the role of reinforcement of fine size ceramic particles on controlling the cell morphology of aluminum composite foams at different foaming temperatures. The present study is aimed to investigate the influence of fine size zircon sand ceramic particles on the cell morphology of LM13 alloy composite foam at different foaming temperatures using different size of $CaCO_3$ powders as blowing agent. In this present study, the porosity and foam quality has been optimized to minimize the imperfections. The role of zircon sand particles as reinforcing agent on stabilizing the foam has been studied and compared with the obtained structure.

II. LITERATURE REVIEW

Particle size distributions of blowing agent ($CaCO_3$) and reinforced zircon sand particles were measured using CAMSIZER XT For $CaCO_3$ and zircon sand and used foaming agents ranging from 1 to 25 m and from 50 to 100 m, respectively. At the same time, the shape of the particle depends on the parameters describing the aspect ratio, namely the length (b/l) of the width , sphericity and symmetry. Rice. 2 and 4 show that 37% of sample-1 and 45% of sample-2 (blowing agent $CaCO_3$) have an aspect ratio less than zero. Of the 9 are almost outdated. 61% of the particles in Sample-1 and 52% of the particles in Sample-2 had an aspect ratio of 0.6 to 0.9, meaning they were triangular or asymmetric particles. 2% of the particles in Sample-1 and 3% of the particles in Sample-2 have an aspect ratio less than zero 0.6 . This is Zircon sand grains used as reinforcement in contained 40% in the 1-25 µm size range and 55% in the 11-25 µm size range of the 1-5 µm size range. Out of pictures. In Figure 6, approximately 10% of the zircon sand grains (b/l <0.6) are elongated and 80% are asymmetric/non-circular (b/l to 0.9) only 10% (b/l >0.9) of samples are spherical. This morphological change is true for all samples with an error of ±5%. The rate of decomposition of the blowing agent $CaCO_3$ is a very important factor in foam formation. The rate of decomposition of $CaCO_3$ depends on many factors such as temperature, holding time, atmospheric pressure, and particle size and shape. The rate of dissolution of increases with decreasing particle size . This can speed up the process by reducing heat or thermal resistance as well as other resistances such as mass transfer or gas diffusion . Since the process was carried out at 850–900 °C and the pressure at this temperature is considered equilibrium or atmospheric pressure, the cause of the CO_2 partial pressure can be neglected in this study.

Effect on cell size morphology

The macro grams of LM13 Alloy Foam obtained at different foaming temperatures .Shows differences in honeycomb structure according to the change of foaming temperature. As a result, the density, foaming efficiency, average cell size and cell wall thickness of LM13 alloy foam changed as the foaming temperature of increased and the change in structural parameters of foam from LM13 alloy at different foaming temperatures. The structure of the foam formed at 850 °C. shows a small knot size with a nearly uniform cell size, long bond length . At this foaming temperature, the alloy foam has almost bubble-free regions, cell structure roughness and unfavorable curvature. Because the particle size of $CaCO_3$ powder is fine and the particle size distribution range is narrow, it is easily decomposed into calcium oxide and carbon dioxide at 850 °C. At this temperature, the equilibrium presence of carbon dioxide increases due to a decrease in the viscosity of the alloy sufficient for foaming. The liberated carbon dioxide accelerates and moves upward, causing the bubbles to coalesce very rapidly. The uniformity of the final cell size and the total volume of porosity related to the carbon dioxide

e-ISSN: 2582-5208
International Research Journal of Modernization in Engineering Technology and Science
(Peer-Reviewed, Open Access, Fully Refereed International Journal)
Volume:05/Issue:02/February-2023 Impact Factor- 7.868 www.irjmets.com

content in the alloy melt is determined by the rate of growth between the cells and the solid-liquid interface. The resulting morphology of regular cells as well as the outgrowth of some cells at a foaming temperature of 875 °C. As the temperature rises, the gas pressure also increases. The formation of these cells is due not only to the uniform growth of, but also to the overgrowth of air bubbles due to the higher pressure. The diameter of the cell decreases rapidly above 850 °C. The foaming temperature directly affects the surface tension of the melt and the decomposition of the foaming agent. Such high rates of degradation are undesirable. This is because the excess gas released from the melt forms irregularly shaped cells and overgrowth of some aluminum foam cells .These cells are connected to each other also grew like won. Increasing the foaming temperature further from 875ºC to 900ºC results in rapid formation of carbon dioxide. In addition, the viscosity also decreased. The liquid film becomes thinner. As a result, most of the bubbles formed in the melt were larger and more unstable. As it moves upward, the pressure at the top of the liquid decreases and bubbles burst and reach the surface of the melt . Cell walls become weak and collapse under high pressure. Excess free gas escaping through the melt reduces the foaming efficiency of. This results in complete collapse of the foam structure and ultimately results in the formation of a densely packed cell foam structure with thicker walls as shown in 7th Century.

Effect on cell wall thickness

The densities of the tested composite foams varied in the range of 0.6–0.9 g/cm3. The density ratio of the foam and fully dense composite has been used to describe the features of foam. The density of the fully dense composite was taken as 2.88 g/cm3. Most of the cells in the foams observed are closed, and the mean cell sizes of the foams display some difference depending on the level of porosity. In order to have a close view of foaming temperature on the cell wall thickness, node size and ligament length of the LM13 alloy foams different areas of foam was analyzed critically. Node size and ligament length of the LM13 alloy foam decreased but cell wall thickness increased with the increasing temperature from 850 ◦C to 900 ◦C. At 850 ◦C cell wall thickness, node size and ligament length of the LM13 alloy foams . At this foaming temperature, alloy slurry is of lower viscosity. As a consequence, balance between gas pressure and the surface tension helps in the easier drawing of liquid material to cell wall intersections that causes the thinner cell walls. With the change of temperature from 850 ◦C to 875 ◦C, cell size, node size and ligament length of the LM13 alloy foams is decreased due to the increase in the temperature because of decrease in viscosity . The higher rate of gas release into the melt breaks the cell walls and allows the collapse of smaller cells and formation of bigger cells on the surface of the melt as can be observed where two sizes of cells are visible. At 900 ◦C the cell wall thickness of the sample foams increased but cell size, node size and ligament length decreases with increase in the temperature from 875 ◦C to 900 ◦C, as shown in Fig. 8c. The phenomenon of collapsing observed at this temperature is on higher side as shown in circle in Fig. 8c. Fig. 8d shows the optical micrograph of foam prepared at temperature 850 ◦C. The air trapped in the liquid foam at the increased temperatures is responsible for the cell size reduction due to its more expansion which makes the cell wall larger. However, the increase in the cell wall thickness is caused mainly due to increase in the viscosity of the LM13 alloy melt. Moreover, at certain areas it leads to rapture of cell wall.

III. CONCLUSION

In this study, the factors affected by the foaming temperature of alloy foams and composite foams were investigated. The conclusions drawn from the above work are:

1. Foams and Composites The foaming temperature of the affects the geometry of the cells, which ultimately results in different structures.

2. The addition of zircon sand particles affects the foaming temperature and the viscosity for the internal diffusion pressure of the molten material.

3. The density of LM13 alloy foam plastic with the addition of blowing agent of fine grade increases from 0.62g/cm3 to 0.90g/cm3, and the size of the cell decreases with increasing foaming. Temperatures from 850 ◦C to 900 ◦C.

4. The cell size of composite foams of LM13 alloy added with finely dispersed blowing agent increases, whereas the effect of coarse particle blowing agent conversely increases as the foaming temperature of increases 850ºC to 900ºC.

5. Optimized foaming temperature regimes for composite foam with 5 wt.% zircon sand and foamed plastic are 875ºC and 850ºC at 2 wt., respectively.

6. The cell size of the foam sample increases with the particle size of the foaming agent. Optimize the conditions to obtain uniformly sized foams with high porosity.

7. Increasing the foaming temperature and gas flow increases the cell size and reduces the cell wall thickness due to the pressure drop between the cell wall and the assembly.

IV. REFERENCES

[1] Prakash O, Sang OH, Embury JD. Structure and properties of A1–SiC foam. Mater Sci Eng, A 1995;199:195–203.

[2] Srivastava VC, Sahoo KL. Processing, stabilization and applications of metallic foams. Mater Sci Poland 2007;25:733–53.

[3] Miyoshi T, Itoh M,Akiyama S,KitaharaA. Porous and cellular materials for structural applications. In: Schwartz DS, Shih DS, Evans AG, Wadley HNG, editors. Materials Research Society. 1998. p. 133.

[4] Rabiei A, Garcia-Avila M. Effect of various parameters on properties of composite steel foams under variety of loading rates. Mater Sci Eng, A 2013;564:539–47.

[5] Ma L, Song Z. Cellular structure control of aluminium foams during foaming process of aluminium melt. Scr Mater 1998;39:1523–8.

[6] Rabiei A, Vendra LJ. A comparison of composite metal foam's properties and other comparable metal foams. Mater Lett 2009;63:533–6.

[7] MarkakiAE, Clyne TW. The effect of cell wall microstructure on the deformation and fracture of aluminium-based foams. Acta Mater 2001;49:1677–86.

[8] Leitlmeier D, Degischer HP, Flankl HJ. Development of a foaming process for particulate-reinforced aluminium melts. Adv Eng Mater 2002;4:735–40.

[9] Deqing W, Ziyuan S. Effect of ceramic particles on cell size and wall thickness of aluminum foam. Mater Sci Eng 2003;A361:45–9.

[10] Mukherjee M, Ramamurthy U, Garcia-Moreno F, Banhart J. The effect of cooling rate on the structure and properties of closed-cell aluminum foams' Mater 2010;58:5031–42.

[11] Byakova A, Gnyloskurenko S, Nakamura T. The role of foaming agent and processing route in the mechanical performance offabricated aluminum foams. Metals 2012;2:95–112.

arXiv:2304.02652v1 [gr-qc] 4 Apr 2023

Model-independent study for a quintessence model of dark energy: Analysis and Observational constraints

Amine Bouali,[1,*] Himanshu Chaudhary,[2,†] Amritansh Mehrotra,[3,4,‡] and S. K. J. Pacif[5,§]

[1] *Laboratory of Physics of Matter and Radiation, Mohammed I University, BP 717, Oujda, Morocco*
[2] *Department of Applied Mathematics, Delhi Technological University, Delhi-110042, India*
[3] *Department of Mathematics, Shyamlal College, University of Delhi, Delhi-110032, India,*
[4] *Department of Power and Electrical, University of Petroleum and Energy Studies, Dehradun, Uttarakhand, India*
[5] *Centre for Cosmology and Science Popularization (CCSP), SGT University, Delhi-NCR, Gurugram 122505, Haryana, India*

In this paper, a well motivated parametrization of the Hubble parameter (H) is revisited that renders two models of dark energy showing some intriguing features of Late-time accelerating universe. A general quintessence field is considered as a source of dark energy. We have obtained tighter constraints using recently updated cosmic observational datasets for the considered models. The two models described here show a nice fit to the considered uncorrelated Hubble datasets, Standard candles, Gamma Ray Bursts, Quasars, and uncorrelated Baryonic Acoustic Oscillations datasets. Using the constrained values of the model parameters, we have discussed some features of the late-time accelerating models and obtained the present value of the deceleration parameter (q_0), present value of the Hubble parameter (H_0) and the transition redshift (z_t) from decelation to acceleration. The values of q_0 for both the models are consistent with the Planck 2018 results. The evolution of the geometrical and physical parameters are discussed through some graphical representations for both the models with some diagnostic analysis. The statistical analysis performed here shows greater results and overall, the outcomes of this investigation are superior to those previously found.

CONTENTS

I. Introduction 1

II. Field Equations with Quintessence 2

III. Solution of FE in a model-independent way 3
A. Model 1 4
B. Model 2 4

IV. Data description with Results 5
A. Data description 5
1. $H(z)$ Dataset 5
2. Standard Candles 5
3. Baryon Acoustic Oscillations 5
4. Cosmic Microwave Background 6

V. Observational, and theoretical comparisons of the Hubble functions 6
A. Comparison with the Hubble data points. 7
B. Comparison with the Pantheon data. 7
C. Relative difference between Model and ΛCDM. 8

VI. Cosmic Evolution of Geometrical Parameters 8
A. The deceleration parameter 8
B. The jerk parameter 9
C. Snap parameter 9

VII. Diagnostic Analysis of the Models 10
A. Statefinder diagnostic 10
B. Om Diagnostic 11

VIII. Cosmic Evolution of Physical Parameters in Quintessential DE 12

IX. Information Criteria 14

X. Conclusion 14

References 15

I. INTRODUCTION

The most debated topics of modern-day cosmology is the late-time accelerating expansion of the Universe. The early evidence of accelerating expansion of the Universe was provided by the observation of high redshift data of supernovas of type Ia (SNIa) [1, 2]. Later on, by virtue of improved cosmological measurement techniques [3–5], rigorous analysis and precise observations indicated accelerated cosmic inflation. Indirect evidence of a nonzero cosmological constant was provided by the data from the Cosmic Microwave Background Radiation (CMB) and Large Scale Structure (LSS) [1, 6, 7]. The current cosmological research is more exciting with the release of ongoing high-precision data in the fields of cosmology and astrophysics in the past few decades. One of the biggest issues now in this field is the understanding of the universe's accelerated expansion phase that

* a1.bouali@ump.ac.ma
† himanshuch1729@gmail.com
‡ amritanshmehrotra71@gmail.com
§ shibesh.math@gmail.com

produced a plethora of cosmological models in order to describe the observational datasets released in the past few years such as SNIa, acoustic peaks of CMB, Observational Hubble datasets, Baryon acoustic oscillations (BAO), strong lensing systems (SLS) [5], and a few more. The simplest one is of course the famous ΛCDM (Cold Dark Matter) model, which explains these cosmological observations very well. The model includes the cosmological constant (Λ or CC), which is characterized by its constant equation of state (EoS) $w = -1$ to model the accelerated expansion of the universe and dust matter $w = 0$ to simulate the evolution of dark matter at the background level. These two extra components correspond to approximately 95 percent of the whole energy budget in the universe (the rest of the components are associated with baryons and relativistic species like photons and neutrinos).In literature, these two ingredients are referred to as dark energy (DE) and dark matter (DM). Detection and observation of DM and DE is another problem that is still persistent in cosmology. Besides its success at a large scale, ΛCDM presents several problems at local scales, for instance, the well-known missing satellite problem that refers to the discrepancy of about 10 times more dwarf galaxies obtained by the numerical simulations based on the ΛCDM model and the observed ones in a cluster of galaxies [6, 7]. Also, the well-known core-cusp problem [1]. In this sense, the concordance issue is the discrepancy between the CC value measured from the perspective of quantum field theory and the one derived from cosmological measurements, which is about 120 orders of magnitude. [8–10]. Additionally, the degeneracy problem which afflicts also the ΛCDM model refers to the inability of measuring the energy momentum of each component, instead of the total one. In other words, this suggests that it is difficult to determine whether the dark region is made up of one or more components. Several models have emerged in order to propose alternatives to the ΛCDM paradigm, for instance, Chaplygin gas [11], and Unimodular gravity [12, 13], among others [17], have entered into the scene as a greater contender, resolving conundrums that the ΛCDM cannot. Moreover, scalar fields such as DM [15–18], axion [19, 20], etc, are important approaches to resolving the problem of DM. Fluids with viscosity are great candidates not only to aboard the DM problem but also, the DE problem from a unifying approach. However, a general scalar field as a candidate for dark energy is a good the approach that can also describe the CC. Till now a wide variety of dynamically evolving scalar field models has been thought of which include quintessence [17–19], K-essence [20–22], phantom [23], and tachyonic fields [24–26]. To understand the behavior of our physical universe, finding the exact solutions of Einstein's Field Equations (EFEs) are necessary. A lot of work was done by many theoreticians in finding the solution to EFEs right after the formulation of EFEs. The Schwarchild solution being the first solution and the perfect fluid equations were treated as an additional condition. Various other exact solutions were obtained for static and spherically symmetric metrics like Einstein's static solution, de-Sitter solution [27, 28], Tolman's solution [29], Adler's solution [30], Buchdahl's solution [31], Vaidya and tikekar solution [32], Durgapal's solution [33], Knutsen's solution [34], and many more. All these solutions were obtained despite the fact that EFEs are highly nonlinear in nature. All the models mentioned above theoretically explain our universe very well. Apart from the theoretical verification the observations also play an important role. Observations either validate a model or rejects it on the basis of numerical computations and also parametrization of these models. Therefore it is essential to discuss observational datasets when making a theoretical model of the Universe. Before 1998, scientists were trying to construct a model with Λ, which can resolve the age crisis problem. All these models can also be found in the reference [35].

The following is how this document is organised. In the introduction part, models in modern cosmology are discussed. In the next section, Einstein's field equation in general relativity taking into consideration dark matter has been discussed. The third section deals with finding the exact solution of EFEs and also the parametrization of different models that have been taken into account.

II. FIELD EQUATIONS WITH QUINTESSENCE

Dark energy (DE) has emerged as one of the most crucial mysteries throughout the domain of cosmology, and it is a subject of debate whether it can be characterized as a source term in Einstein's field equations. Quintessence is one of the notable candidates of dark energy after the cosmological constant, that is compatible with various cosmological observations. It's more specifically a scalar field, that is proposed in physics to account for the universe's observed accelerated pace of expansion. The initial illustration of this situation was put out in [36]. This notion was then expanded to more general varieties of time-varying dark energy models (e.g. K-essence, Spintessence etc.) for which R. R. Caldwell et al. [37] had to introduce the term "species of essence". Quintessence may be attractive or repulsive depending on the ratio of kinetic and potential energies of the field. The action that represents our physical system is,

$$S = \int d^4x\sqrt{-g}\left(\frac{1}{2}M_{Pl}^2 R + L_m + L_\phi\right), \tag{1}$$

where L_m is the Lagrangian of matter fields and L_ϕ is the Lagrangian of the scalar field given by,

$$L_\phi = -\frac{1}{2}g^{\mu\nu}\partial_\mu\phi\partial_\nu\phi - V(\phi), \tag{2}$$

where g is the determinant of the metric $g_{\mu\nu}$, $M_{Pl} = (8\pi G)^{-1/2}$ is the reduced Planck mass, R is the Ricci scalar, and $V(\phi)$ is a general self-coupling potential for

which ϕ must be positive for physically acceptable fields. We assume that non-relativistic matter does not have a direct coupling to the quintessence field (minimal interaction). The differentiation with respect to $g_{\mu\nu}$ leads to the gravitational field equations,

$$R_{\mu\nu} = -\frac{1}{2}Rg_{\mu\nu} = M_{Pl}^{-2}T_{\mu\nu}^{Total}, \tag{3}$$

where

$$T_{\mu\nu}^{\phi} = \partial_\mu\phi\partial_\nu\phi - \frac{1}{2}g_{\mu\nu}\left(\partial\phi\right)^2 - g_{\mu\nu}V\left(\phi\right), \tag{4}$$

is the energy momentum tensor of scalar field. Here, $\left(\partial\phi\right)^2 \equiv g_{\alpha\beta}\partial^\alpha\phi\partial^\beta\phi$ and $T_{\mu\nu}^{Total} = T_{\mu\nu}^{M} + T_{\mu\nu}^{\phi}$. The differentiation with respect to ϕ leads to the Klein-Gordon equation $\nabla_\mu\nabla^\mu\phi - \frac{\partial V}{\partial\phi} = 0$.

We start by considering the most general homogeneous and isotropic space-time, which is the Friedmann-Lemaître-Robertson-Walker (FLRW) metric,

$$ds^2 = -dt^2 + a(t)^2\left(\frac{dr^2}{1-kr^2} + r^2d\theta^2 + r^2\sin^2\theta d\phi^2\right), \tag{5}$$

where $k = 1,\ 0,\ -1$ for closed, flat and open geometries respectively. We have taken the velocity of light $c = 1$. Analysis suggest the topology of the Universe is flat and we have the space-time,

$$ds^2 = -dt^2 + a^2(t)\left[dr^2 + r^2\left(d\theta^2 + \sin^2\theta d\phi^2\right)\right], \tag{6}$$

here $a(t)$ is the Universe's scale factor. In this background, the Einstein field equations yield the following dynamical equations,

$$M_{Pl}^{-2}\rho_{Total} = 3\left(\frac{\dot{a}}{a}\right)^2 = 3H^2, \tag{7}$$

$$M_{Pl}^{-2}p_{Total} = -2\frac{\ddot{a}}{a} - \left(\frac{\dot{a}}{a}\right)^2 = (2q-1)H^2. \tag{8}$$

Here $H\left(=\frac{\dot{a}}{a}\right)$ is the Hubble parameter and $q\left(=-\frac{a\ddot{a}}{\dot{a}^2}\right)$ is the deceleration parameter, which are higher order derivatives of the scale factor a and determine the dynamics of the Universe. The total energy density $\rho_{Total} = \rho_M + \rho_\phi$ and $p_{Total} = p_M + p_\phi$. The energy density and pressure of the scalar field are: $\rho_\phi = \frac{1}{2}\dot{\phi}^2 + V(\phi)$, $p_\phi = \frac{1}{2}\dot{\phi}^2 - V(\phi)$. Therefore, the equation of state (EoS) of the scalar field (dark energy) will be

$$\omega_\phi = \frac{p_\phi}{\rho_\phi} = \frac{\frac{1}{2}\dot{\phi}^2 - V(\phi)}{\frac{1}{2}\dot{\phi}^2 + V(\phi)}. \tag{9}$$

We must remember that the EoS of dark energy (quintessence) is a dynamically evolving parameter that can take values in the range $[-1, 1]$. We can see for a potential dominated field, ω_ϕ reduce to -1 i.e. cosmological constant recovered. For ω_ϕ crossing the value -1 describes the phantom, which is beyond our scope here.

One could yield the conservation equation from (7) and (8),

$$\dot{\rho}_{Total} + 3\left(p_{Total} + \rho_{Total}\right)\frac{\dot{a}}{a} = 0. \tag{10}$$

The conservation equation (10) is important in evolution since it deals with matter and its interactions. In modern cosmology, two types of dark energy models are frequently discussed: interacting dark energy models (covering the connection between cold dark matter and dark energy) [38–40], and non-interacting dark energy models (allowing all matters to evolve separately) [35, 41–43]. There is currently no recognized interaction between matter and DE other than gravity. The current study exclusively considers non-interacting models. The equations in the system are nonlinear ordinary differential equations, and explicit solutions are challenging to find. In the past, enormous attempts were made to develop both precise and numeric solutions to EFEs. The solution strategies for the above-mentioned system of equations will be explained in detail in the following section.

III. SOLUTION OF FE IN A MODEL-INDEPENDENT WAY

There are only two independent equations with four unknowns a, ρ, p, or ω in the above system of equations (7), (8), and (10). Because of the homogenous matter distribution on a wide scale throughout the universe, it is conventional to analyze the barotropic equation of state, $p = \omega\rho$, $\omega \in [0, 1]$. Depending on the discrete or dynamical values of the EoS parameter. The EoS defines various kinds of matter sources in the Universe e.g. for $\omega = 0$, dust-like matter; $\omega = 1/3$, radiation; $\omega = -1$ etc. The third constraint equation would be provided by this extra equation. Other constraint equation (the fourth one) would be the consideration of the EoS of DE $\omega_{de} = p_{de}/\rho_{de}$, function of time t, scale factor a or redshift z), also referred as *parametrization of dark energy equation of state*. With these four equations, one could describe the cosmological dynamics of the universe by presenting all other geometrical parameters such as Hubble parameter (H), deceleration parameter (q), jerk parameter (j), etc. or physical parameters such as energy density of matter or dark energy (ρ), dark energy pressure (p), equation of state of matter or dark energy (ω), etc. as functions of cosmic time (t), scale factor (a) or redshift (z). Now, these equations close the system and complete the system's determination i.e. the time evolution of scale factor a. There are numerous strategies in the literature for parametrizing the scale factor and its higher order derivatives H, q, j etc., which provide the

entire solution of the EFEs, i.e. the explicit forms of cosmological parameters as a function of cosmic time t. In fact, there have been two different approaches of analyzing the solution of EFEs in general relativity theory or on some modified theories: one is through parametrization of the geometrical parameters a, H, q or j as a function of cosmic time; the second is through parametrization of physical parameters ρ, p, or ω) as a function of scale factor or redshift. If we examine closely, We might remark that the primary type of parametrization of geometrical parameters is studied to produce exact solutions that address the expanding dynamics of the universe and give the time evolution of the physical parameters ρ, p, or ω . This approach is also known as the model-independent method of studying cosmological models or parametrization [44, 45]. The model-independent way has the the potential of rebuilding the cosmic history of the universe as well as interpreting some of the universe's phenomena without affecting the background theory. Furthermore, this strategy gives the easiest way to theoretically overcome several standard model's difficulties, including the initial singularity problem, cosmological constant problem, and the late-time acceleration issue. Whereas the second type of parametrization of physical parameters is commonly used to explain all physical features of the universe.

The goal of this paper is to find an exact solution to the EFE in conventional GR theory using a simple parametrization of the Hubble parameter $H(t)$ and reconstruct the cosmic evolution. The cosmographic analysis gives insights into analyzing the evolution of the observable universe in terms of kinematic factors inside a model-independent way [46] idea. Furthermore, the investigation of cosmographic parameters assists mostly in the study of dark energy without the necessity of any specific cosmological model beyond the cosmological principle. The scale factor could be extended in Taylors' series around the present time t_0 in the conventional approximation, which corresponds to the straightforward technique used in the cosmographic analysis. The Taylor's series expansion could be expressed as:

$$a^{(n)} =1 + H_0\left(t-t_0\right) - \frac{1}{2!}q_0H_0^2\left(t-t_0\right)^2 + \frac{1}{3!}j_0H_0^3\left(t-t_0\right)^3 + \frac{1}{4!}s_0H_0^4\left(t-t_0\right)^4 + \frac{1}{5!}l_0H_0^5\left(t-t_0\right)^5 + \ldots..$$

Here $H(t) = \frac{1}{a}\frac{da}{dt}$ is Hubble parameter, $q(t) = -\frac{1}{a}\frac{d^2a}{dt^2}\left[\frac{1}{a}\frac{da}{dt}\right]^{-2}$ is deceleration parameter, $j(t) = \frac{1}{a}\frac{d^3a}{dt^3}\left[\frac{1}{a}\frac{da}{dt}\right]^{-3}$ is jerk parameter, $s(t) = \frac{1}{a}\frac{d^4a}{dt^4}\left[\frac{1}{a}\frac{da}{dt}\right]^{-4}$ is snap parameter and $l(t) = \frac{1}{a}\frac{d^5a}{dt^5}\left[\frac{1}{a}\frac{da}{dt}\right]^{-5}$ is lerk parameter. All of these parameters play significant roles in cosmographic analysis. Motivated by the preceding arguments, this study considers a basic parametrization of the Hubble parameter (H) as an explicit function of cosmic time 't' in the form [45],

$$H(t) = \frac{a_2t^n}{\left(t^m+a_1\right)^b}, \tag{11}$$

where $a_1, a_2 \neq 0, n, m, b$ are real constants. a_1 and a_2 both have time dimensions. Several specific values of the parameters n, m, b suggest several interesting models, which are elaborated by Pacif et al. [45]. Out of the twelve models for some integer values of these constants, two models show transitions from early deceleration to present acceleration and could explain some features of the observable universe. They are;

A. Model 1

$$H(t) = \frac{a_2}{t\left(a_1-t\right)} \tag{12}$$

which yield

$$a(t) = \zeta\left(\frac{t}{a_1-t}\right)^{\frac{a_2}{a_1}}, \ \zeta \text{ is an integrating constant.} \tag{13}$$

It is convenient to introduce the cosmological parameters as functions of redshift z. The time-redshift correlation must be constructed because the cosmological parameters here are functions of cosmic time t. The $t-z$ relations are determined as follows:

$$t(z) = a_1\left[1+\left\{\zeta(1+z)\right\}^{\frac{a_1}{a_2}}\right]^{-1}, \tag{14}$$

For Model 1. The expression (14) contains three parameters ζ, a_1 and a_2, but it is sufficient to describe these models parameters by taking $\frac{a_1}{a_2} = \gamma$, which is also beneficial for further analysis and numerical computations for which the expressions for the Hubble parameter could be written in terms of redshift z,

$$H(z) = H_0\left(1+\zeta^\gamma\right)^{-2}(1+z)^{-\gamma}\left[1+\left\{\zeta(1+z)\right\}^\gamma\right]^2. \tag{15}$$

B. Model 2

For model 2, we have

$$H(t) = \frac{a_2}{t\left(a_1-t^2\right)} \text{ and } a(t) = \zeta\left(\frac{t^2}{a_1-t^2}\right)^{\frac{a_2}{2a_1}}. \tag{16}$$

The $t-z$ relations is determined as follows:

$$t(z) = \sqrt{a_1}\left[1+\left\{\zeta(1+z)\right\}^{2\frac{a_1}{a_2}}\right]^{-\frac{1}{2}}. \tag{17}$$

Hubble parameter in term of redshift z is,

$$H(z) = H_0 \left(1+\zeta^{2\gamma}\right)^{-\frac{3}{2}} (1+z)^{-2\gamma} \left[1+\{\zeta(1+z)\}^{2\gamma}\right]^{\frac{3}{2}}. \tag{18}$$

Now, we must confront these models with some cosmological data. In the following section, we consider some external datasets and find the best fit values of the model parameters for further analysis.

IV. DATA DESCRIPTION WITH RESULTS

A. Data description

Throughout this part, we will be using three distinct types of observational datasets to limit our model parameters. We utilized the $H(z)$ datasets of 57 measurements, the Pantheon dataset of 1048, and 17 uncorrelated BAO measurements in order to achieve the optimal value for the proposed model parameters. To construct the Markov Chain Monte Carlo (MCMC) [47], we used the open-source tools Polychord [48] and GetDist [49]. The total χ^2 function of the combination $H(z)$ + Pantheon + BAO + CMB and define as,

$$\chi^2_{tot} = \chi^2_{H(z)} + \chi^2_{SN} + \chi^2_{BAO} + \chi^2_{CMB}. \tag{19}$$

1. $H(z)$ Dataset

Various observational constraints were used in order to get significant constraints on the model parameters. We employ the $H(z)$ measurements in our investigation to constrain the model parameters. Hubble data may be determined in general by estimating the BAO in the radial direction of galaxy clustering [50], or by the differential age technique, which also provides the redshift dependency of the Hubble parameter as,

$$H(z) = -\frac{1}{1+z}\frac{dz}{dt}, \tag{20}$$

where dz/dt is computed using two moving galaxies in a proportionate manner. 57 Hubble measurements were taken into study to estimate the parameters for the model, which are spans throughout a redshift range of $0.07 \leqslant z \leqslant 2.42$. For comparing the observational and theoretical observations Chi-Square function is used.

$$\chi^2_H = \sum_{i=1}^{57} \frac{\left[H_{th}\left(z_i,\right) - H_{obs}\left(z_i\right)\right]^2}{\sigma^2_{H(z_i)}}, \tag{21}$$

where H_{th} , H_{obs} and $\sigma_{H(z_i)}$ denotes the model prediction, observed value of Hubble rate, and standard error at the redshift z_i, respectively. The Hubble function numerical values for the appropriate redshifts are shown in (see table I in [51]).

2. Standard Candles

The measurement of type Ia supernovae (SNIa) determines the cosmic accelerated expansion. Until now, SNIa has proven to be one of the most substantial and successful methods for studying the nature of dark energy. In recent years, several supernova data sets have been established [52–56]. The Pantheon sample has recently been updated.[57]. The former dataset contains 1048 spectroscopically verified SNIa spanning in the redshift range of $0 < z < 2.3$. SNIa are also astronomical objects that act as standard candles for determining relative distances. As a consequence, SN Ia samples are combined with the distance modulus $\mu = m - M$, where m indicates a certain object's apparent magnitude of a specific SNIa. The chi-square of the SNIa measurements is given by,

$$\chi^2_{SN} = \Delta\mu^T \,.\, \mathbf{C}^{-1}_{SN} \,.\, \Delta\mu. \tag{22}$$

$\mathbf{C}_{SN}$ is represented by a covariance matrix, and $\Delta\mu = \mu_{obs} - \mu_{th}$, where μ_{obs} signifies the measured distance modulus of a certain SNIa, meanwhile the theoretical distance modulus is represented as μ_{th}, and calculated as,

$$\mu_{th}(z) = 5\log_{10}\frac{D_L(z)}{(H_0/c)Mpc} + 25. \tag{23}$$

Here H_0 signifies the current Hubble rate and c reflects the speed of light. For the flat Friedmann-Lemaitre-Robertson-Walker (FLRW) Universe, the luminosity distance, D_L, is outlined as follows :

$$D_L(z) = (1+z)H_0\int_0^z \frac{dz'}{H\left(z'\right)}. \tag{24}$$

Because we limit the model's free parameters at the same time, i.e. by using the Pantheon sample, hence

$$\chi^2_{SN} = \Delta\mu^T \times \mathbf{C}^{-1}_{Pantheon} \times \Delta\mu. \tag{25}$$

Throughout this, the Quasars [58] and Gamma Ray Bursts [59] have also been taken into consideration.

3. Baryon Acoustic Oscillations

From the largest dataset of 333 BAO measurements, we selected 17 uncorrelated BAO measurements because using the full BAO catalogue could result in a very significant error due to data correlations. Therefore, in order to reduce errors, we chose a limited dataset. (see table I in [60]) from [61–72]. Studies of the BAO featured in the transverse direction provide a measurement of $D_H(z)/r_d = c/H(z)r_d$, where r_d is the sound horizon at the drag epoch and it is taken as an independent

MCMC Results		
Model	Parameters	Bestfit Value
ΛCDM Model	H_0	$69.854848^{+1.259100}_{-1.259100}$
Model 1	H_0	$69.302413^{+0.443452}_{-0.443452}$
	γ	$1.662642^{+0.023615}_{-0.023615}$
	ζ	$1.322252^{+0.027842}_{-0.027842}$
Model 2	H_0	$69.247921^{+0.465229}_{-0.465229}$
	γ	$1.350387^{+0.015168}_{-0.015168}$
	ζ	$1.459203^{+0.024204}_{-0.024204}$

parameter and with the co-moving angular diameter distance [73, 74] being

$$D_M = \int_0^z \frac{cdz'}{H(z')}. \tag{26}$$

In our database, we also use the angular diameter distance $D_A = D_M/(1+z)$ and $D_V(z)/r_d$, which is a combination of the BAO peak coordinates above, namely

$$D_V(z) \equiv \left[zD_H(z)D_M^2(z)\right]^{1/3}. \tag{27}$$

4. *Cosmic Microwave Background*

The CMB Distant Prior measurements are taken [75]. The distance priors offer useful details about the CMB power spectrum in two ways: the acoustic scale l_A characterizes the CMB temperature power spectrum in the transverse direction, causing the peak spacing to vary, and the "shift parameter" R influences the CMB temperature spectrum along the line-of-sight direction, affecting the peak heights, which are defined as follows:

$$l_A = (1+z_d)\frac{\pi D_A(z)}{r_s}, \tag{28}$$

$$R(z) = \frac{\sqrt{\Omega_m}H_0}{c}(1+z_d)D_A(z) \tag{29}$$

The observables that [75] reports are:$R_z = 1.7502 \pm 0.0046$, $l_A = 301.471 \pm 0.09$, $n_s = 0.9649 \pm 0.0043$ and r_s is an independent parameter, with an associated covariance matrix. (see table I in [75]). The points represent the inflationary observables as well as the CMB epoch expansion rate. In addition to the CMB points, we also take into account other data from the late universe. The result is a successful test of the model in relation to the data.

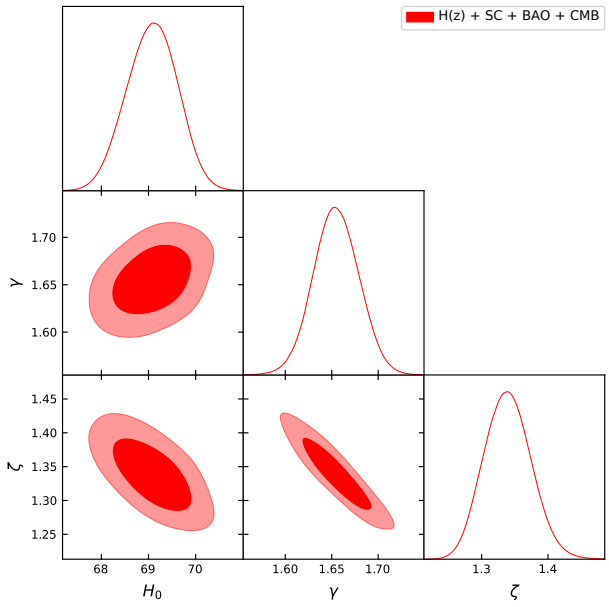


FIG. 1. MCMC confidence contours at 1σ and 2σ for Model 1.

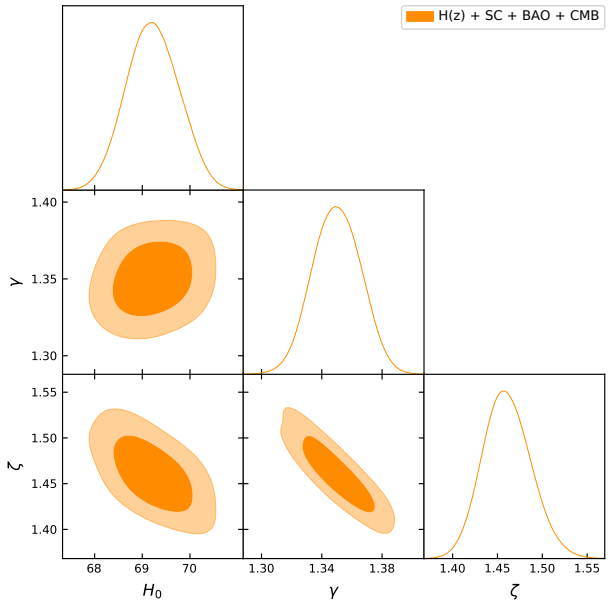


FIG. 2. MCMC confidence contours at 1σ and 2σ for Model 2.

V. OBSERVATIONAL, AND THEORETICAL COMPARISONS OF THE HUBBLE FUNCTIONS

Now, we have the best-fit values of the model parameters for both Model 1 and Model 2. Since the ΛCDM model is the most consistent model with various observational datasets, it will be better to compare our models with the ΛCDM model to look deeper, at how our parametrized models deviate from the ΛCDM model.

A. Comparison with the Hubble data points.

First, we look at how Model 1 and Model 2 compare to the Hubble 57 data points and the ΛCDM model with 1 σ and 2 σ error bands. The comparison findings are shown in Figure 3 and 4. The Figure shows that Model 1 and 2 fit with Hubble data quite well.

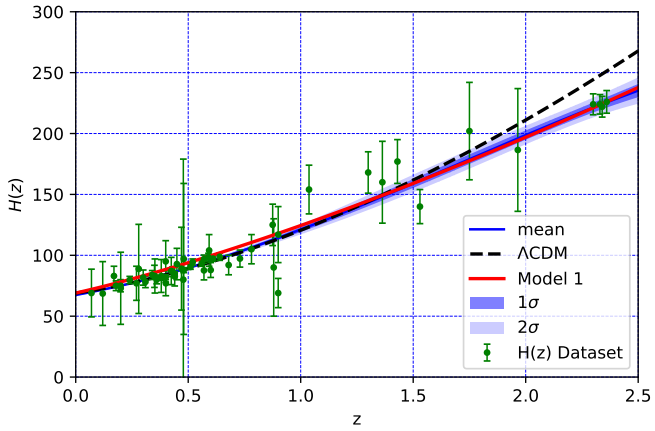


FIG. 3. The figure shows that the theoretical curve of the Hubble function $H(z)$ of Model 1 shown in red line and ΛCDM model shown in black dotted line with $\Omega_{m0} = 0.3$ and $\Omega_\Lambda = 0.7$, against 57 $H(z)$ datasets are shown in green dots with their corresponding error bars with 1σ and 2σ error bands.

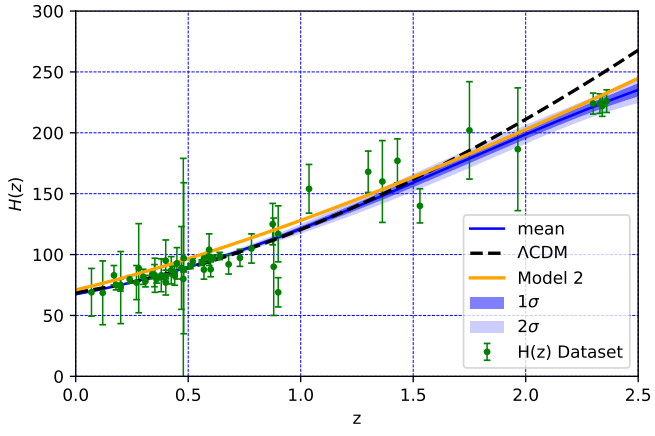


FIG. 4. The figure shows that the theoretical curve of the Hubble function $H(z)$ of Model 2 shown in orange line and ΛCDM model shown in black dotted line with $\Omega_{m0} = 0.3$ and $\Omega_\Lambda = 0.7$, against 57 $H(z)$ datasets are shown in green dots with their corresponding error bars with 1σ and 2σ error bands.

B. Comparison with the Pantheon data.

The $\mu(z)$ distance modulus function of Model 1 and Model 2 is now compared to Pantheon data. Based on 1048 observation locations, model 1 and 2 matches the Pantheon distance modulus quite well, as shown in Fig. 5 and Fig. 6.

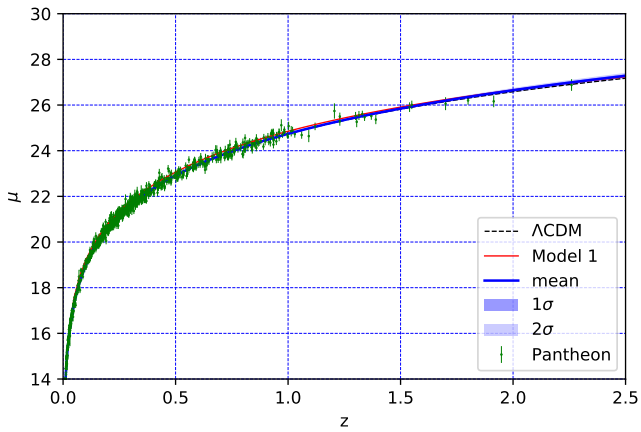


FIG. 5. Theoretical curve of distance modulus $\mu(z)$ of the Model 1 shown in red line and ΛCDM model shown in black dotted line with $\Omega_{m0} = 0.3$ and $\Omega_\Lambda = 0.7$, against type Ia supernova data shown in green dots with their corresponding errors bars with 1σ and 2σ error bands.

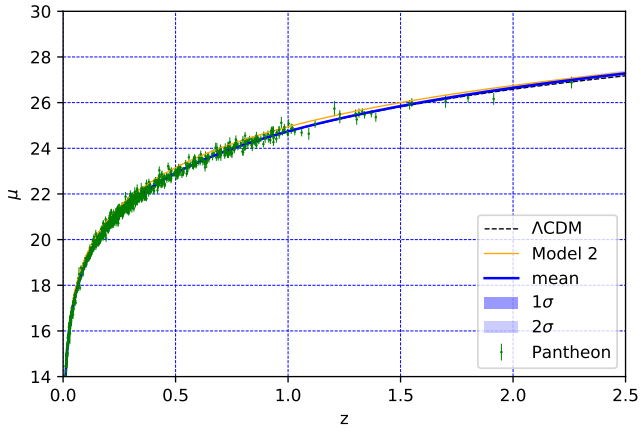


FIG. 6. Theoretical curve of distance modulus $\mu(z)$ of the Model 2 shown in orange line and ΛCDM model shown in black dotted line with $\Omega_{m0} = 0.3$ and $\Omega_\Lambda = 0.7$, against type Ia supernova data shown in green dots with their corresponding errors bars with 1σ and 2σ error bands.

C. Relative difference between Model and ΛCDM.

The relative difference between Model, Model 2, and the standard ΛCDM paradigm is shown in Fig. 7 and Fig. 8. The Figure demonstrates how the typical ΛCDM model and both the Model perform very identically for $z < 1$. However for $z > 1$, there are some discrepancies between both models and ΛCDM model, and these discrepancies do get greater as the redshift increases.

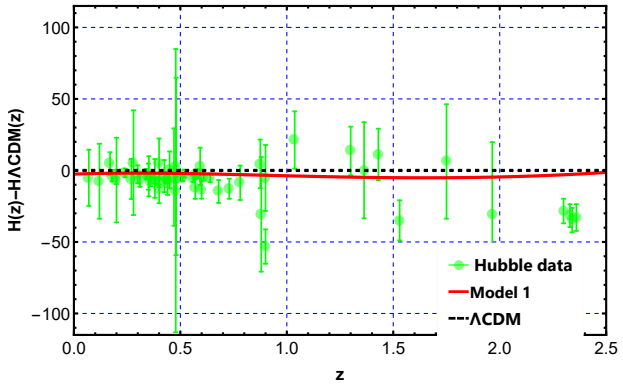


FIG. 7. The variation of the difference between Model 1 shown in the red line, and the ΛCDM model shown in the black dotted line with $\Omega_{m0} = 0.3$ and $\Omega_\Lambda = 0.7$, as a function of the redshift z against the Hubble measurements, against 57 $H(z)$ datasets are shown in green dots with their corresponding error bars.

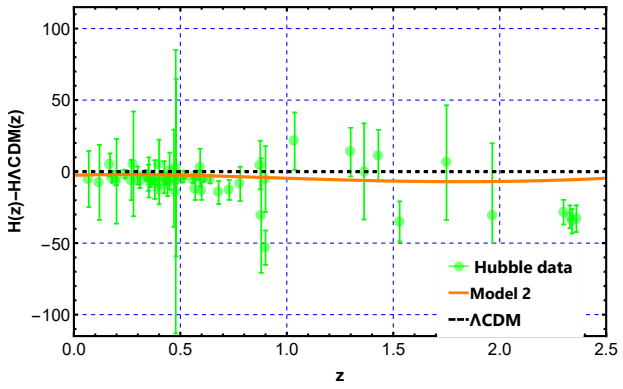


FIG. 8. The variation of the difference between Model 2 shown in the orange line, and the ΛCDM model shown in the black dotted line with $\Omega_{m0} = 0.3$ and $\Omega_\Lambda = 0.7$, as a function of the redshift z against the Hubble measurements, against 57 $H(z)$ datasets are shown in green dots with their corresponding error bars.

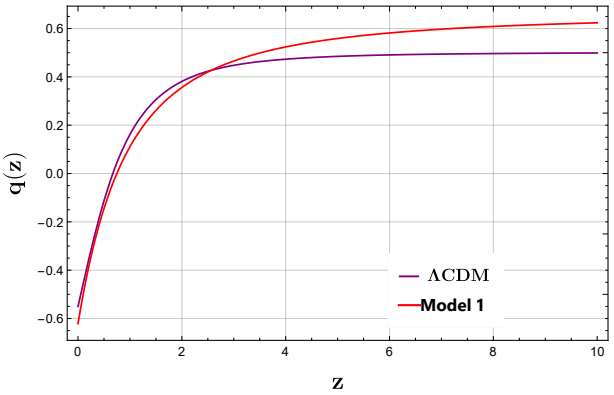


FIG. 9. Evolution of deceleration parameter with respect to the redshift of Model 1.

VI. COSMIC EVOLUTION OF GEOMETRICAL PARAMETERS

A. The deceleration parameter

The deceleration parameter (DP) is a dimensionless quantity that contributes to the cosmological evaluation of the expansion rate. This parameter could be expressed in terms of the scale factor, which decrease and causes the cosmos to expand uniformly. Furthermore, negative values of this parameter represent faster expansion, whereas positive values represent a decelerated phase of the universe. It is given mathematically by

$$q = -\frac{a\ddot{a}}{\dot{a}^2} = -1 + \frac{d}{dt}\left(\frac{1}{H}\right). \tag{30}$$

Subsequently, one could notice that the Hubble parameter's value either increases or decreases with time depending on the magnitude of DP. Different ranges of the DP q_0 have been anticipated in various cosmological scenarios. Ideally, the value of q_0 should be determined through observational analysis. The DP, for example, is required for the connection between apparent brightness and redshift for a class of identical supernovae in distant galaxies though such estimates are difficult to understand. The latest findings completely corroborate the accelerating universe speculations. One has to be extremely accurate in determining the value of q_0. It turned out to be highly model-dependent, and the evidence for an accelerating universe is not as convincing as commonly supposed. For model 1 and 2, the expression for the $q(z)$ is given by,

$$q(z) = -1 + \gamma - 2\gamma\left[1 + \{\zeta(1+z)\}^{\gamma}\right]^{-1}. \tag{31}$$

$$q(z) = -1 + \gamma - 3\gamma\left[1 + \{\zeta(1+z)\}^{2\gamma}\right]^{-1}. \tag{32}$$

The redshift dependency of the deceleration parameter for Model 1 and 2 with respect to the ΛCDM model has

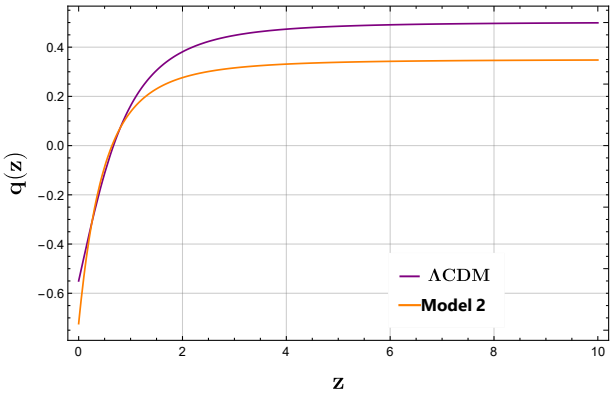


FIG. 10. Evolution of deceleration parameter with respect to the redshift of Model 2.

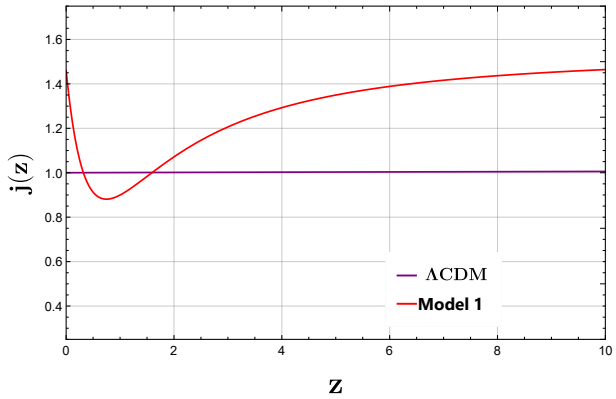


FIG. 11. Evolution of jerk parameter with respect to the redshift of Model 1.

been presented in Fig. 9 and 10 correspondingly. The evolution of this parameter is essentially comparable in the redshift range $z \in (0, 10)$. The figures demonstrate that there are discrepancies among both the models and ΛCDM model for $z > 1.5$. The numerical value of the transition redshift z_{tr} from the decelerating to the accelerating phase of each model and ΛCDM model is comparatively close. However the ΛCDM model finishes in a de Sitter phase with $q = -1$, and models 1 and 2 experience super-accelerated evolution with $q(-1) \approx -2.6542$ and -3.85658 respectively.

B. The jerk parameter

The dimensionless jerk parameter (popularly referred to as jolt) is a refinement of the standard cosmological parameters $a(t)$ and $q(t)$. Other synonyms for jerk include impulse, bounce, surge, shock, and super-acceleration. The jerk parameter could potentially be represented in terms of the third-order derivative of the scale factor with respect to cosmic time, yielding an absolute approach to abandoning the concordance ΛCDM model. We may express it mathematically as,

$$j = \frac{1}{a}\frac{d^3a}{d\tau^3}\left[\frac{1}{a}\frac{da}{d\tau}\right]^{-3} = q(2q+1) + (1+z)\frac{dq}{dz}. \qquad (33)$$

The redshift trajectory of the jerk parameter $j(z)$ of model 1 and 2 shown in the figures Fig. 12 and 11 respectively against standard ΛCDM paradigm. At high redshifts $z > 1.6$, the predictions of each models with respect to ΛCDM model are essentially opposite. At lower redshifts, however, considerable discrepancies remain, with a very large difference emerging at $z = 1$, when model 1 predicts a value 1.4 as high as the ΛCDM value and model 2 predicts a value 13 times as high as the ΛCDM value . As a result, the observational determination of the present-day value of j may provide an essential test of model 1 and 2.

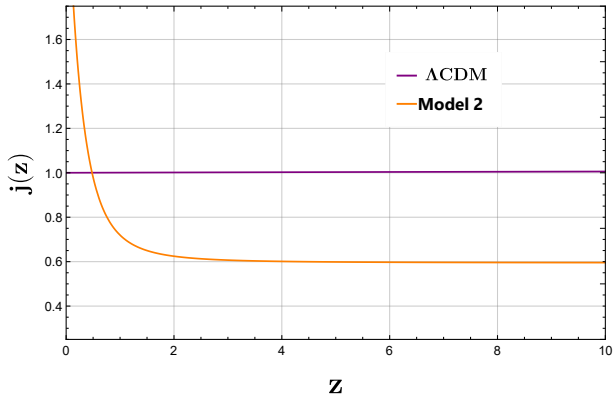


FIG. 12. Evolution of jerk parameter with respect to the redshift of Model 2.

C. Snap parameter

The Snap parameter (the fourth time derivative) is also known as jounce. The fifth and sixth-time derivatives are frequently jokingly referred to as crackle and pop. The dimensionless snap parameter is defined as follows:

$$s = \frac{1}{a}\frac{d^4a}{d\tau^4}\left[\frac{1}{a}\frac{da}{d\tau}\right]^{-4} = \frac{j-1}{3\left(q-\frac{1}{2}\right)}, \qquad (34)$$

Fig. 13 and Fig. 14 depicts the fluctuation of snap parameter $s(z)$ of both the model against ΛCDM model. There is a systematic disparity in the numerical values of s of each Model and the ΛCDM at high redshift ranging from $z \in (2, 10)$. In case of model 1 in the range $z \in (0, 0.2)$, the discrepancies among the model drops with respect to ΛCDM model, meanwhile in the redshift range for $z \in (0, 0.2)$. The model 2 becomes a gently increasing function for z and predicts a value 63 times as high as the ΛCDM value at $s(0)$.

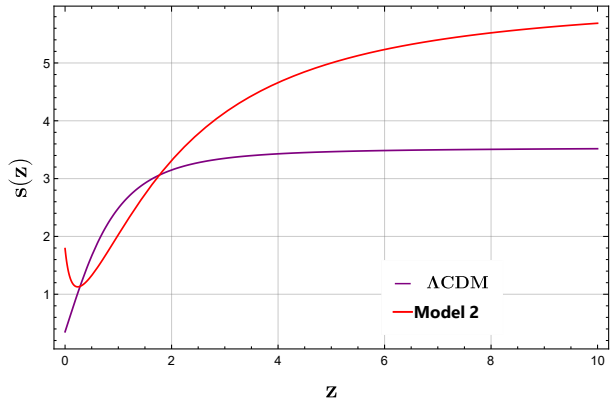


FIG. 13. Evolution of snap parameter with respect to the redshift of Model 1.

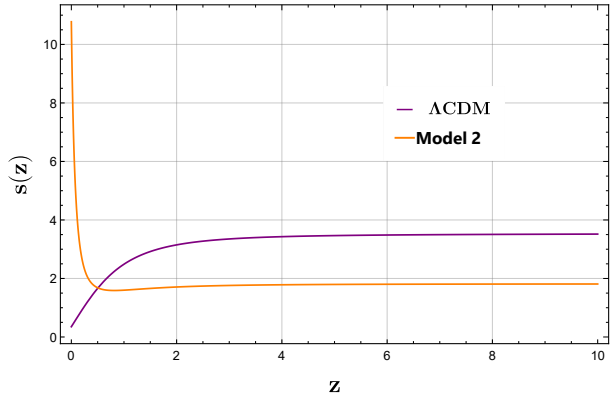


FIG. 14. Evolution of snap parameter with respect to the redshift of Model 2.

VII. DIAGNOSTIC ANALYSIS OF THE MODELS

A. Statefinder diagnostic

When interpreting various cosmological circumstances containing DE, an effective and significant diagnostic of DE is needed. Sahni et al.[76, 77] proposed a novel DE diagnosis method based on higher derivatives of the scale factor. Statefinder diagnostics [76–79] is a technique that is commonly used to distinguish and contrast the characteristics of multiple DE models utilizing higher-order derivatives of the scale factor. The cosmological statefinder diagnostic pair $\{r, s\}$ permits one to examine the cosmic properties of DE in a model-independent way, which may be determined through relationships,

$$r = \frac{\dddot{a}}{aH^3}, s = \frac{r-1}{3\left(q-\frac{1}{2}\right)}. \tag{35}$$

In this case, the parameter s is a linear amalgamation of r and q. Since it is calculated in terms of the cosmic scale factor, this diagnostic pair is dimensionless and geometrical. Various possibilities in the $\{r, s\}$ and $\{q, r\}$ planes are exhibited to depict the temporal evolution of various DE models. With the assistance of the statefinder diagnostics pair. In these cases, some specific pairs typically correlate to classic DE models such as $\{r, s\} = \{1, 0\}$ represents ΛCDM model and $\{r, s\} = \{1, 1\}$ indicates standard cold dark matter model (SCDM) in FLRW background. Also, $(-\infty, \infty)$ yields static Einstein universe. In the $r - s$ plane, $s > 0$ and $s < 0$ define a quintessence-like model and phantom-like model of the DE, respectively. Moreover, the evolution from phantom to quintessence can be observed by deviation from $r, s = 1, 0$. On the other hand, $\{q, r\} = \{-1, 1\}$ corresponds to the ΛCDM model while $\{q, r\} = \{0.5, 1\}$ shows SCDM model. It is important to note that on a $r - s$ plane if the DE model's trajectories deviate from these standard values, the resulting model differs from the normal cosmic models.

$$r(z) = 1 + \gamma(2\gamma - 3) + \frac{6\gamma}{1 + \{\zeta(1+z)\}^{\gamma}} \left[1 - \gamma \frac{\gamma}{1 + \{\zeta(1+z)\}^{\gamma}}\right] \tag{36}$$

.

$$s(z) = \frac{2\gamma}{3} - \frac{\gamma}{1 + \{\zeta(1+z)\}^{\gamma}} + \frac{\gamma(3+2\gamma)}{3\left[-3 - 2\gamma + (2\gamma - 3)\{\zeta(1+z)\}^{\gamma}\right]} \tag{37}$$

.

for Model 1 and Model 2

$$r(z) = 1 - 3\gamma + 2\gamma^2 + \frac{12\gamma^2}{\left[1 + \{\zeta(1+z)\}^{2\gamma}\right]^2} + \frac{3\gamma(3 - 2\gamma)}{1 + \{\zeta(1+z)\}^{2\gamma}} \tag{38}$$

$$s(z) = \frac{2}{3}\gamma - \frac{4\gamma}{3 + 3\{\zeta(1+z)\}^{2\gamma}} + \frac{2\gamma(3+4\gamma)}{\left[-9 - 12\gamma + 3(2\gamma - 3)\{\zeta(1+z)\}^{2\gamma}\right]} \tag{39}$$

.

Fig:- 15 begins with values in the range $r > 1$ and $s < 0$ representing Chaplygin gas type DE model and evolves to quintessence region before reverting to the Chaplygin gas region at late times bypassing the intermediate ΛCDM fixed point$\{0, 1\}$ during evolution. Fig:- 18 offering extra information on model 1 as it deviates from de Sitter point $(-1, 1)$.

Fig:- 17 showing different behavior and evolutes from quintessence the region in the past and goes to Chaplygin gas region at late times bypassing the intermediate ΛCDM fixed point $\{0, 1\}$,Fig:- 18 showing similar behavior by offering the same behavior as model 1 by it deviates from de Sitter point $(-1, 1)$.

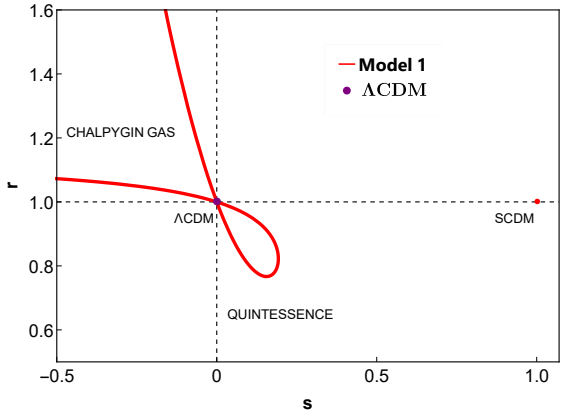


FIG. 15. This figure shows $\{s, r\}$ plots for models 1.

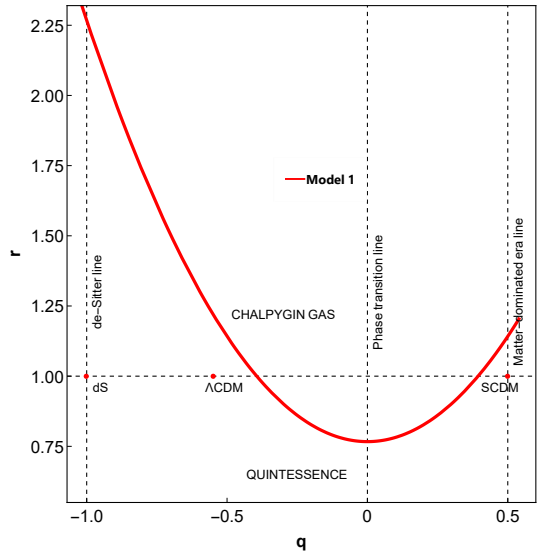


FIG. 16. This figure shows $\{q, r\}$ plots for models 1.

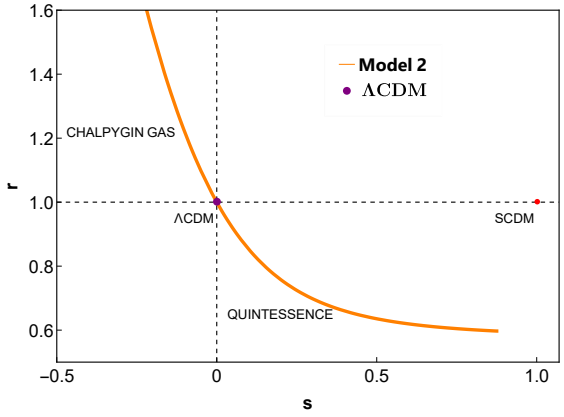


FIG. 17. This figure shows $\{s, r\}$ plots for models 1.

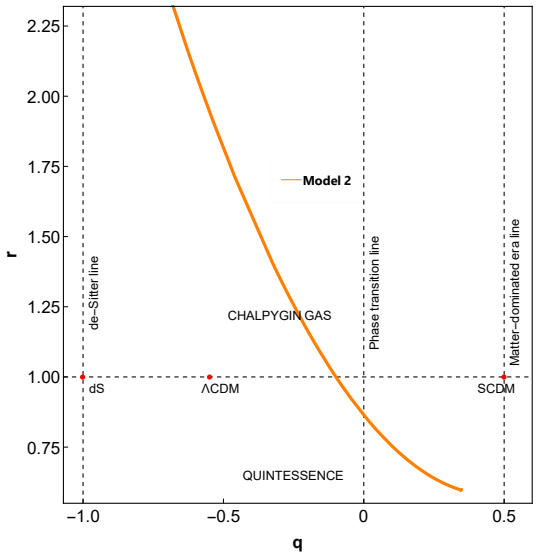


FIG. 18. This figure shows $\{q, r\}$ plots for models 1.

B. Om Diagnostic

Om diagnostic [80–83] is a geometrical study that uses the Hubble parameter to establish a null test for the ΛCDM model. Similarly to the statefinder diagnostic, the Om diagnostic efficiently separates distinct DE models from ΛCDM by varying the slope of $Om(z)$. A positive slope of the diagnostic parameter represents a quintessence model, whereas a negative slope represents a phantom model. A constant slope with respect to redshift also determines the nature of DE, which coincides with the cosmological constant. $Om(z)$ is defined in the situation of a flat universe by,

$$Om(z) = \frac{\left(\frac{H(z)}{H_0}\right)^2 - 1}{(1+z)^3 - 1}. \tag{40}$$

One could express $Om(z)$ expression for Model 1 as,

$$Om(z) = \frac{\frac{[1+\{\zeta(1+z)\}^{\gamma}\}^4}{(1+\zeta^{\gamma})^4(1+z)^{2\gamma}} - 1}{(1+z)^3 - 1}. \tag{41}$$

For Model 2 express of $Om(z)$ read as,

$$Om(z) = \frac{\frac{\left[1+\{\zeta(1+z)\}^{2\gamma}\right]^3}{(1+\zeta^{2\gamma})^3(1+z)^{4\gamma}} - 1}{(1+z)^3 - 1}. \tag{42}$$

The slop variation of Om(z) verses z could be observed in Fig. 19 and Fig. 20 for the both models. The Om(z) value for both models is smaller than Ω_{m0} in the redshift range of $z > 0$, indicating that the models are in the quintessence domain. As z declines, the value drops dramatically and becomes negative, signifying that both models inhabit the phantom region.

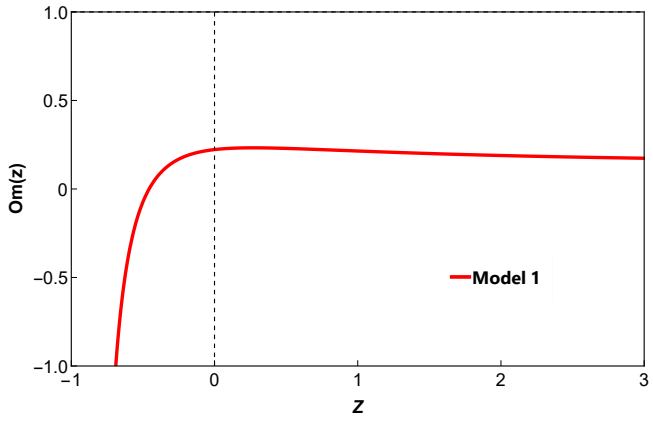


FIG. 19. This figure shows the Om(z) with respect to redshift.

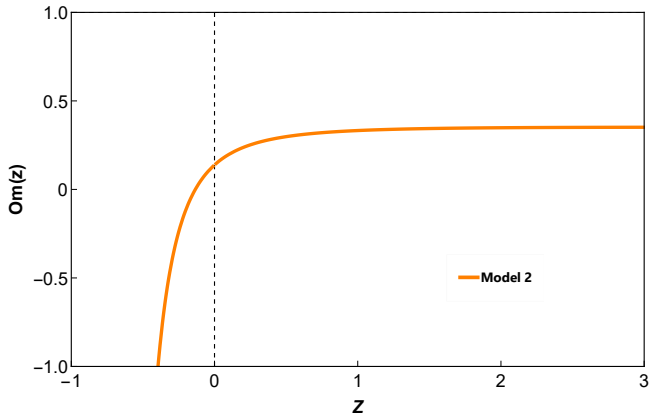


FIG. 20. This figure shows the Om(z) with respect to redshift.

VIII. COSMIC EVOLUTION OF PHYSICAL PARAMETERS IN QUINTESSENTIAL DE

For quintessence as a candidate of dark energy, we have from equations (7) and (8), the expressions as,

$$M_{Pl}^{-2}\rho_\phi = 3H^2 - M_{Pl}^{-2}\rho_M, \tag{43}$$

$$M_{Pl}^{-2}p_\phi = (2q-1)H^2, \tag{44}$$

with the understanding of negligible pressure due to dust matter ($p_M = 0$). For a two fluid universe, scalar field, and matter, we have the minimal interaction between Matter & DE. When there is minimal interaction between the matter component and the dark energy, they conserve separately for which, we have $\dot{\rho}_M + 3H\rho_M = 0$ and $\dot{\rho}_\phi + 3H\rho_\phi = 0$. This yield, $\rho_M = ca^{-3} = c(1+z)^3$, c is a constant of integration. At $t = t_0$ ($z = 0$) and in terms of the density parameter (Ω), we have, $c = 3M_{Pl}^{-2}H_0^{-2}\Omega_{M0}$, which implies $\rho_M = 3M_{Pl}^{-2}H_0^{-2}\Omega_{M0}(1+z)^3$. Here and afterward, the suffix 0 stands for the values of the cosmological parameters at present time ($t = t_0$ or $z = 0$). Now, solving, equations. (43) and (44), we obtain the expressions of energy density and pressure for the scalar field for model 1 as,

$$M_{Pl}^{-2}H_0^{-2}\rho_\phi = 3[(1+\zeta^\gamma)^{-4}(1+z)^{-2\gamma}\left[1+\{\zeta(1+z)\}^\gamma\right]^4 - \Omega_{M0}(1+z)^3] \tag{45}$$

$$M_{Pl}^{-2}H_0^{-2}p_\phi = \left\{-3+2\gamma-4\gamma\left[1+\{\zeta(1+z)\}^\gamma\right]^{-1}\right\}\left\{(1+\zeta^\gamma)^{-4}(1+z)^{-2}\left[1+\{\zeta(1+z)\}^\gamma\right]^4\right\} \tag{46}$$

and for model 2,

$$M_{Pl}^{-2}H_0^{-2}\rho_\phi = 3[\left(1+\zeta^{2\gamma}\right)^{-3}(1+z)^{-4\gamma}\left[1+\{\zeta(1+z)\}^{2\gamma}\right]^3 - \Omega_{M0}(1+z)^3] \tag{47}$$

$$M_{Pl}^{-2}H_0^{-2}p_\phi = \left\{-3+2\gamma-6\gamma\left[1+\{\zeta(1+z)\}^\gamma\right]^{-1}\right\}\left\{\left(1+\zeta^{2\gamma}\right)^{-3}(1+z)^{-4}\left[1+\{\zeta(1+z)\}^{2\gamma}\right]^3\right\} \tag{48}$$

$$\omega_\phi = \frac{\left\{-3+2\gamma-4\gamma\left[1+\{\zeta(1+z)\}^\gamma\right]^{-1}\right\}\left\{(1+\zeta^\gamma)^{-4}(1+z)^{-2}\left[1+\{\zeta(1+z)\}^\gamma\right]^4\right\}}{3\left[(1+\zeta^\gamma)^{-4}(1+z)^{-2\gamma}\left[1+\{\zeta(1+z)\}^\gamma\right]^4 - \Omega_{M0}(1+z)^3\right]} \tag{49}$$

and

$$\omega_\phi = \frac{\left\{-3+2\gamma-6\gamma\left[1+\{\zeta(1+z)\}^{\gamma}\right]^{-1}\right\}\left\{\left(1+\zeta^{2\gamma}\right)^{-3}(1+z)^{-4}\left[1+\{\zeta(1+z)\}^{2\gamma}\right]^{3}\right\}}{3\left[\left(1+\zeta^{2\gamma}\right)^{-3}(1+z)^{-4\gamma}\left[1+\{\zeta(1+z)\}^{2\gamma}\right]^{3}-\Omega_{M0}(1+z)^{3}\right]} \tag{50}$$

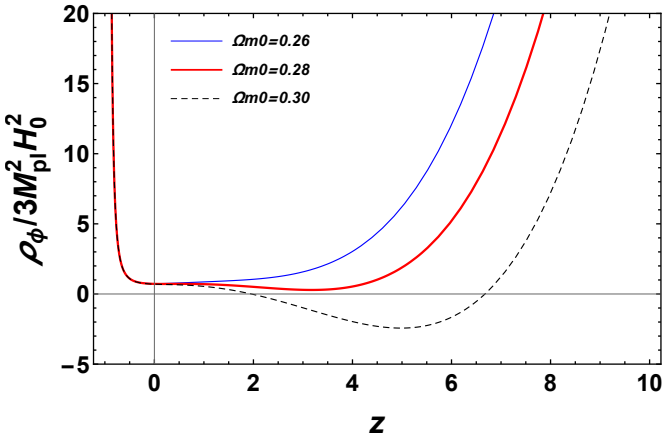


FIG. 21. Profile of energy density for model 1.

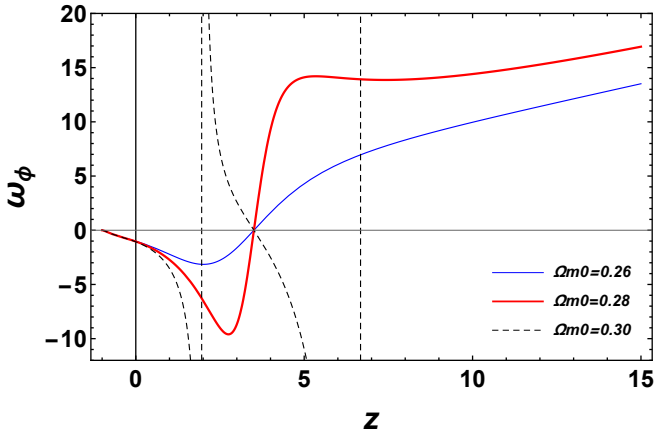


FIG. 23. Profile of dark energy pressure for model 1

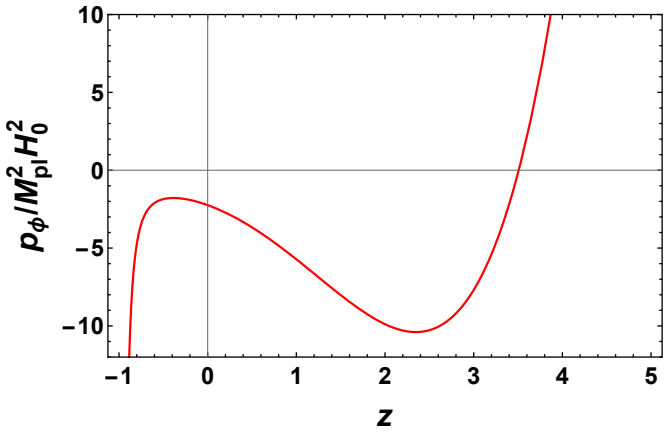


FIG. 22. Profile of dark energy pressure for model 1

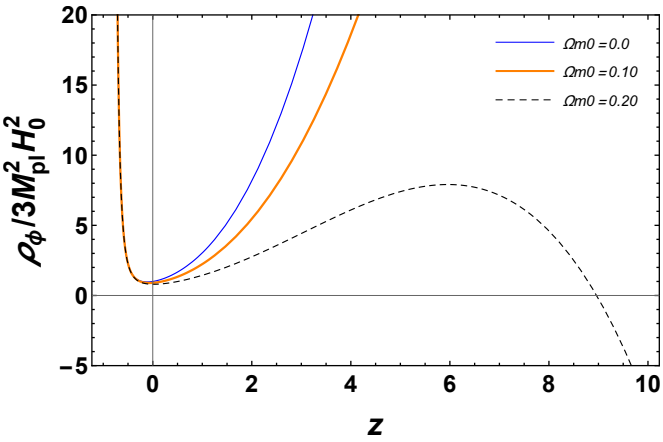


FIG. 24. Profile of energy density for model 2.

In the following plots, we have shown the past, present and future evolution of the dark energy density (as quintessence), pressure, and EoS parameter for model 1 and model 2 with the found constrained values of the model parameters.

From the above plots of dark energy density as quintessence, the value of Ω_{M0} must be less than 0.28 for model 1 for which the EoS parameter has smooth evolution from an early positive value to a present negative value. But, in the case of model 2, the model may be incompatible with any value of positive Ω_{M0} for higher redshifts.

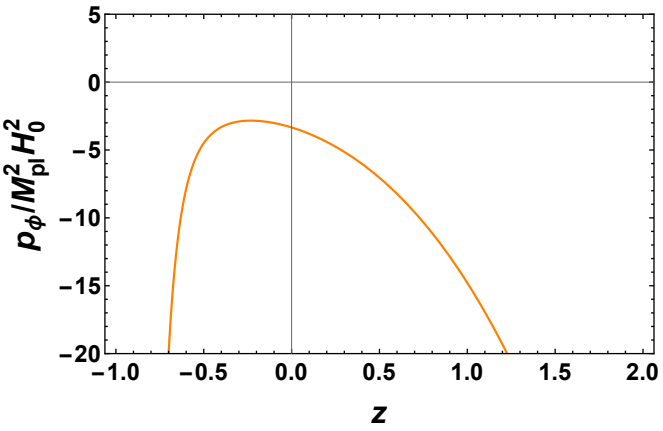


FIG. 25. Profile of dark energy pressure for model 2

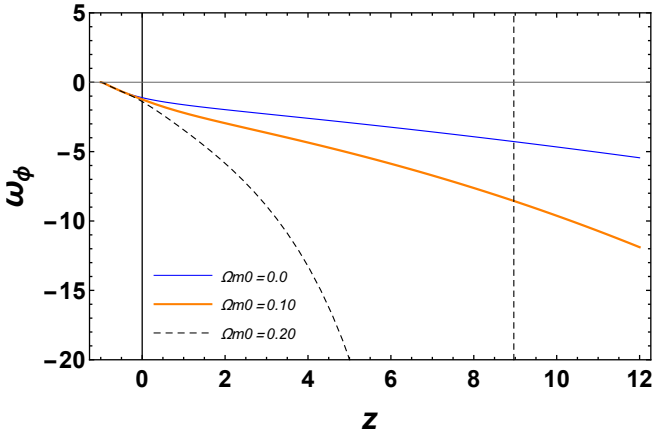


FIG. 26. Profile of dark energy pressure for model 2

IX. INFORMATION CRITERIA

In order to speak about the sustainable model analysis, one should understand the information criteria study. (IC). The criteria for Akaike information (AIC) [84] is exclusively implemented by all ICs. Although the AIC approximates the minimization of the Kullback-Leibler information, it acts as an asymptotically unbiased estimator of Kullback-Leibler information. The AIC's Gaussian estimator can be represented as [85–88] AIC $= -2\ln(\mathcal{L}_{max}) + 2\kappa + \frac{2\kappa(\kappa+1)}{N-\kappa-1}$ in which $\mathcal{L}_{max}$ is the maximum likelihood function, κ is the total number of model parameters, and N is the total number of data points employed to fit the models to the data. Given that $N \gg 1$ for the models, the aforementioned formula changes to the original AIC like AIC $= -2\ln(\mathcal{L}_{max}) + 2\kappa$. The variations of the IC values are minimized if the collection of models is provided. $\triangle\text{AIC} = \text{AIC}_{model} - \text{AIC}_{min} = \triangle\chi^2_{min} + 2\triangle\kappa$ Throughout data analysis studies, the more favorable range of $\triangle$AIC is $(0, 2)$. The low favorable range of $\triangle$AIC is $(4, 7)$, while $\triangle$AIC > 10 provides less support

Model	χ^2_{min}	χ^2_{red}	AIC	ΔAIC
ΛCDM Model	1073.67	0.981	1077.67	0
Model 1	1072.89	0.961	1078.89	1.22
Model 2	1074.69	0.963	1078.69	1.02

TABLE I. Summary of the χ^2_{min}, χ^2_{red}, AIC and ΔAIC.

model.

X. CONCLUSION

We conducted a comprehensive and robust investigation of the two cosmological dark energy models in this article, contrasting them to cosmological observations for 57 Hubble uncorrelated measurements, the Pantheon dataset spanning 1048 measurements, 162 Gamma Ray Bursts (GRBs) measurements, 24 measurements of compact radio quasars, and 17 uncorrelated BAO measurements. To find the optimal values for the model parameters. We employed the MCMC approach, which allows us to deduce the best fit for the model parameters. Using the best-fit values, the data fittings produce extremely good results for both the Hubble and the Pantheon datasets. Furthermore, there is a particularly significant relation between both the dark energy model and the ΛCDM model. The analysis of the two models has been also conducted with a more statistical sense besides studying the Akaike Information Criterion, which further demonstrates that both the dark energy models and the standard ΛCDM Model are closed enough. We carried out a comprehensive comparison of the cosmographic parameters to obtain a more accurate estimate of the attributes and flaws of both the cosmological models. The behavior of the deceleration parameter appears to agree well with that of standard ΛCDM, substantial differences often will have seemed between models when the jerk and snap parameters are considered. As a result, the cosmographic technique can provide the ability to distinguish different cosmological models. It also nearly perfectly reproduces the ΛCDM model predictions, although there are still considerable deviations for high redshifts and the values of several cosmographic parameters. In terms of interpretations of empirical observations, both the cosmological model and the conventional ΛCDM model might become acceptable mathematical alternatives. It may also yield novel insights as well as a decent understanding of the complicated relationship between mathematical concepts structures and physical reality.

Acknowledgement: Author SKJP thank IUCAA, Pune for hospitality and other facilties under its IUCAA associateship program, where a large part of work have been done.

Author contributions: The data analysis, several graphical representations in the article, and the first draft

of the manuscript were all completed by the authors AB and HC. The writing and a few computations were supplied by author AM. Project administrator and contributor SKJP wrote the document, completed the project, and contributed some computations. The paper has been read and approved by all authors.

Funding: There is no fund available for the publication of this research article.

Data Availability Statement: This manuscript has used publicly available data for the work.

Conflict of interest: The authors have no relevant financial or non-financial interests to disclose.

Ethical statements: The submitted work is original and has not been published anywhere else.

[1] C. B. Netterfield et al., Astrophys. J. 474(1) (1997) 47.
[2] S. Perlmutter et al., Astrophys. J., 517(2) (1999) 565.
[3] S. Jha et al., Astrophys. J. 659(1) (2007) 122.
[4] J. Guy et al., Astron. & Astrophys. 466 (1) (2007) 11.
[5] C. R. Burns et al, Astron. J. 141(1) (2010) 19.
[6] P. de Bernardis et al., Nature 404(6781) (2000) 955.
[7] S. Hanany et al., Astrophys. J. 545(1) (2000) L5.
[8] J. R. Mould et al., Astrophys. J. 529(2) (2000) 786.
[9] D. N. Spergel et al., Astrophys. J. Suppl. Series 148(1) (2003) 175.
[10] C. Bennett et al., Astrophys. J. suppl. Series 192(2) (2011) 17.
[11] V. Gorini, A. Kamenshchik, U. Moschella, Phys. Rev. D 67(6) (2003) 063509.
[12] S. Capozziello, Curvature quintessence, Int. J. Mod. Phys. D 11 (04) (2002) 483.
[13] G. Dvali, G. Gabadadze, M. Porrati, Phys. Lett. B 485(1-3) (2000) 208–214.
[14] E. Copeland, M sami and S. Tsujikawa, Int. J. Mod. Phys. D 15 (2006) 1753.
[15] K. Bamba, S. Capozziello, S. Nojiri, S. D. Odintsov, Astrophys. Space Sci. 342 (2012) 155.
[16] V. Sahni, A. Starobinsky, Int. J. Mod. Phys. D 9(4) (2000) 373.
[17] I. Zlatev, L. Wang, P. J. Steinhardt, Phys. Rev. Lett. 82(5) (1999) 896.
[18] P. Brax, J. Martin, Phys. Rev. D 61(10) (2000) 103502.
[19] T. Barreiro, E. J. Copeland, N. A. Nunes, Phys. Rev. D 61(12) (2000) 127301.
[20] C. Armendariz-Picon, T. Damour, V. Mukhanov, Phys. Lett. B 458(2-3) (1999) 209.
[21] T. Chiba, T. Okabe, M. Yamaguchi, Phys. Rev. D 62(2) (2000) 023511.
[22] C. Armendariz-Picon, V. Mukhanov, P. J. Steinhardt, Phys. Rev. Lett. 85(21) (2000) 4438.
[23] R. R. Caldwell, Phys. Lett. B 545(1-2) (2002) 23.
[24] A. Sen, J. High Energy Phys. 2002(04) (2002) 048.
[25] M. R. Garousi, Nucl. Phys. B 584(1-2) (2000) 284.
[26] E. A. Bergshoeff et al., J. High Energy Phys. 2000(05) (2000) 009.
[27] W. De Sitter, Mon. Not. Roy. Astron. Soc., 76, (1916) 699.
[28] W. De Sitter, Mon. Not. R. Astron. Soc. 77 (1916) 155.
[29] R. C. Tolman, Phys. Rev. 55 (4) (1939) 364.
[30] R. J. Adler, J. Math. Phys. 15(6) (1974) 727.
[31] H. Buchdahl, Astrophys. J. 147 (1967) 310.
[32] P. Vaidya, R. Tikekar, J. Astrophys. Astron. 3 (1982) 325.
[33] M. Durgapal, J. Phys. A: Mathematical and General 15(8) (1982) 2637.
[34] H. Knutsen, Astrophys. Space Sci. 140 (1988) 385.
[35] J. Overduin, F. Cooperstock, Phys. Rev. D 58(4) (1998) 043506.
[36] B. Ratra, P. J. Peebles, Phys. Rev. D 37(12) (1988) 3406.
[37] R. R. Caldwell, R. Dave, P. J. Steinhardt, Phys. Rev. Lett. 80(8) (1998) 1582.
[38] W. Zimdahl, D. Pav´on, Gen. Relativ. Grav. 36 (2004) 1483.
[39] O. Bertolami, P. Martins, Phys. Rev. D 61(6) (2000) 064007.
[40] N. Banerjee, D. Pavon, Phys. Rev. D 63(4) (2001) 043504.
[41] V. Sahni, arXiv preprint astro-ph/0403324 (2004).
[42] T. D. Saini et al. Phys. Rev. Lett. 85(6) (2000) 1162.
[43] J. Simon, L. Verde, R. Jimenez, Phys. Rev. D 71(12) (2005) 123001.
[44] J. Cunha, J. A. S. Lima, Mon. Not. Roy. Astron. Soc. 390(1) (2008) 210.
[45] S. K. J. Pacif, R. Myrzakulov, S. Myrzakul, Int. J. Geom. Meth. Mod. Phys. 14(07) (2017) 1750111.
[46] A. Oka et al., Mon. Not. Roy. Astron. Soc. 439 (2014) 2515.
[47] D. Foreman-Mackey et al., Publ. Astron. Soc. Pacific 125(925) (2013) 306.
[48] W. Handley, M. Hobson, A. Lasenby, Mon. Not. Roy. Astron. Soc.: Letters 450(1) (2015) L61.
[49] A. Lewis, arXiv preprint arXiv:1910.13970 (2019).
[50] E. Gaztanaga, C. Bonvin, L. Hui, J. Cosm. Astrop. Phys. 2017(01) (2017) 032.
[51] A. Bouali et al, Eur. Phys. J. C 83(2) (2023) 121.
[52] M. Kowalski et al., Astrophys. J. 686(2) (2008) 749.
[53] R. Amanullah et al., Astrophys. J. 716(1) (2010) 712.
[54] N. Suzuki et al., Astrophys. J. 746(1) (2012) 85.
[55] M. Betoule et al., Astron. & Astrophys. 568 (2014) A22.
[56] D. M. Scolnic et al., Astrophys. J. 859(2) (2018) 101.
[57] D. M. Scolnic et al., arXiv preprint arXiv:2112.03863 (2021).
[58] C. Roberts et al., arXiv preprint arXiv: 1711.10369 (2017).
[59] M. Demianski et al., Astron. & Astrophys. 598 (2017) A112.
[60] D. Benisty, D. Staicova, Astron. & Astrophys. 647 (2021) A38.
[61] W. J. Percival et al., Mon. Not. Roy. Astron. Soc. 401(4) (2010) 2148.
[62] F. Beutler et al., Mon. Not. Roy. Astron. Soc. 416(4) (2011) 3017.
[63] T. Delubac et al., Astron. & Astrophys. 552 (2013) A96.
[64] L. Anderson et al., Mon. Not. Roy. Astron. Soc. 427(4) (2012) 3435.
[65] H.-J. Seo et al., Astrophys. J. 761(1) (2012) 13.
[66] A. J. Ross et al., Mon. Not. Roy. Astron. Soc. 449(1) (2015) 835.
[67] R. Tojeiro et al., Mon. Not. Roy. Astron. Soc. 440(3)

(2014) 2222.
[68] J. E. Bautista et al., Astrophys. J. 863(1) (2018) 110.
[69] E. De Carvalho et al., J. Cosm. Astropart. Phys. 2018(04) (2018) 064.
[70] M. Ata et al., Mon. Not. Roy. Astron. Soc. 473(4) (2018) 4773.
[71] T. Abbott et al., Mon. Not. Roy. Astron. Soc. 483(4) (2019) 4866.
[72] Z. Molavi, A. Khodam-Mohammadi, Eur. Phys. J. Plus 134(6) (2019) 254.
[73] N. B. Hogg, M. Martinelli, S. Nesseris, J. Cosm. Astropart. Phys. 2020(12) (2020) 019.
[74] M. Martinelli et al., Astron. & Astrophys. 644 (2020) A80.
[75] L. Chen, Q.-G. Huang, K. Wang, J. Cosm. Astropart. Phys. 2019(02) (2019) 028.
[76] V. Sahni et al., J. Experiment. Theoret. Phys. Lett. 77 (2003) 201.
[77] U. Alam et al., Mon. Not. Roy. Astron. Soc. 344(4) (2003) 1057.
[78] M. Sami et al., Phys. Rev. D 86(10) (2012) 103532.
[79] R. Myrzakulov, M. Shahalam, J. Cosm. Astropart. Phys. 2013(10) (2013) 047.
[80] V. Sahni, A. Shafieloo, A. A. Starobinsky, Phys. Rev. D 78(10) (2008) 103502.
[81] C. Zunckel, C. Clarkson, Phys. Rev. Lett. 101(18) (2008) 181301.
[82] M. Shahalam et al., Eur. Phys. J. C 75 (2015) 1.
[83] A. Agarwal et al., Int. J. Mod. Phys. D 28(06) (2019) 1950083.
[84] H. Akaike, IEEE transactions on automatic control 19(6) (1974) 716.
[85] M. Li, X. Li, X. Zhang, Sci. China Phys., Mechanics. Astron. 53(9) (2010) 1631.
[86] K. Burnhan, D. R. Anderson, Model selection and multimodel inference, New York: Springer (2002).
[87] K. P. Burnham, D. R. Anderson, Sociological Meth. & Res. 33(2) (2004) 261–304.
[88] A. R. Liddle, Mon. Not. Roy. Astron. Soc. Lett. 377(1) (2007) L74.

2023 2nd International Conference for Innovation in Technology (INOCON)
Bangalore, India. Mar 3-5, 2023

2023 2nd International Conference for Innovation in Technology (INOCON) | 979-8-3503-2092-3/23/$31.00 ©2023 IEEE | DOI: 10.1109/INOCON57975.2023.10101125

Multilayer Convolutional Neural Network Based Approach to Detect Apple Foliar Disease

Barsha Biswas
Department of Computer Science & Engineering
Delhi Technological University
Delhi, India
barshabiswas2599@gmail.com

Rajesh Kumar Yadav
Department of Computer Science & Engineering
Delhi Technological University
Delhi, India
rkyadav@dtu.ac.in

***Abstract*—Around 38% of land in the world is used for agriculture and the whole world is completely dependent on agriculture. So, that's why good crop yield is very important to get high agricultural output. A single disease in a plant can lower crop yield. So, to maintain a high agricultural output, we need to detect disease at the early stage so that the agricultural output should be maintained. There are multiple ways to detect plant disease like detecting a plant disease by using the naked eye by hiring an expert, or by using Artificial Intelligence (AI). By using AI, it takes less time to detect plant disease as compared to detecting using the naked eye. Deep Learning (DL), the sub-branch of AI gives an accurate result as compared to the other sub-branches of AI. In DL, Convolutional Neural Network or CovNet is the latest and revolutionary algorithm to perform this task. An apple tree disease detection model, based on Multilayer CNN, is presented in the paper. To train the proposed Multilayer CNN model, the data is collected from FGVC8 dataset from Plant Pathology 2021, a Kaggle Competition which is supported by the "Cornell Initiative for Digital Agriculture". Decision Trees, Logistic Regression, and Random Forests are machine learning algorithms that are compared with the performance of the proposed model. This study shows that the proposed model outperforms Machine Learning algorithms with the accuracy of 91%, Precision of 89%, Recall of 85% and F1-Score of 88.34%.**

***Index Terms*—Apple Foliar Disease, Artificial Intelligence (AI), Convolutional Neural Network (CNN), Deep Learning (DL), Machine Learning (ML), Plant Disease Detection**

I. Introduction

Agriculture, the practice of raising crops which is also known as farming. The whole population of the world is completely dependent on agriculture. That's why it is very important for the progress of an economy of a country. The output of a crop and a good quality of production is very important in agriculture. This helps to avoid a huge loss in the economy of a nation. In order to get good production quality as well as maximum crop output, it is very important to detect diseases early on in plants.

Diseases are caused by climatic change as well as by pathogens such as viruses, fungi, and bacteria. This paper mainly focuses on apple plant disease. And in the apple plant, leaves show the symptoms earlier than other parts of the plant. Common diseases found on the leaves of apple plants are scabs, rust, powdery mildew, etc. In the world, apple scab is one of the most common and economically important fungal diseases. Symptoms are clearly seen on the leaves of apple leaves. Apple rust causes severe loss in the economy when the conditions of the environment are favorable for the growth of a disease.

Farmers spend a lot of money by hiring an expert for detecting a disease using the naked eye, which takes too much time as well as very expensive. Many farmers don't afford this. So, in order to do this task in lesser time, ML and DL algorithms are proposed to accomplish this task which is cost friendly as well. ML algorithms learn, recognize patterns, and then make decisions in which the intervention of humans is very minimum. But DL algorithms give higher accuracy than ML algorithms because in DL, Feature Extraction as well as the Classification part which is done by the model itself and in ML, we have to perform the Feature Extraction part manually.

In DL, CNN is considered a revolutionary algorithm for the task of detecting a disease in a plant leaf. That's why DL algorithms are used on a large scale as compared to ML algorithms.

In this work, FGVC8 dataset from Plant Pathology 2021 Kaggle Competition[1] is used in which augmentation techniques are implemented on the dataset.

Our approach involves classifying images from the test dataset in order to determine whether the plants are healthy or sick. The proposed model is then used to identify different diseases. It is possible to identify multiple diseases on a single image of the apple plant using the proposed model. This paper contributes the following:

- This paper reviews already proposed CNN models in the classification and identification of diseases. A Multilayer CNN model is proposed for the detection as well as multiple classifications of foliar diseases in apples.
- The proposed Multilayer CNN model consists of 5 convolutional layers in which 2 layers have LeakyReLU activation function and 3 layers have a ReLU activation function, 3 max-polling layers have a pool size of 2x2, 5 dropout layers in which 2 layers have a value of 0.3 and other 2 layers having a value of 0.25 and remaining 1 layer having a value of 0.5, dense layers of 128 units and dense layer of 6 units having softmax activation function.
- 3. The proposed Multilayer CNN model achieves 91% accuracy. The achieved performance is further compared

Authorized licensed use limited to: DELHI TECHNICAL UNIV. Downloaded on April 24,2023 at 04:29:06 UTC from IEEE Xplore. Restrictions apply.

to ML algorithms such as Logistic Regression[2], Random Forest[3], and Decision Trees[4].

In Section 2, Related Work will be discussed in which approaches are discussed which are already proposed to detect the disease in a plant. Then Proposed Methodology will be discussed. State-of-the-art algorithm i.e. CNN will be outlined in Section 3. In Section 4 which proposed model will be explained. In Section 5, Experimental Results will be explained, and then References.

II. Background

In order to diagnose an apple foliar disease in the image of the leaves of an apple, one of the DL algorithms called CNN gives higher accuracy than other DL algorithms. It's also known as CovNet. It consists of many layers. Each layer detects the different features in an input image. In order to produce better results, various kernels or filters are applied to an input image. At the lowest layer, filters are often simple features. Filters become more complex in order to identify features that represent the input object uniquely. A convolved image is used as input for the next layer after the layers are partially recognized. The image or object recognition is done by the last layer i.e. fully-connected layer. In order to classify a plant disease, images of a plant leaf is used as inputs. A leaf image of a plant used instead of images of any other parts of a plant because, in comparison with other parts of a plant, the leaf shows the symptoms earlier. CNN uses features and texture for this task. The architecture of CNN is given in Fig1.

CNN was developed in 1980. We can use it to detect the patterns in the images.

In CNN, there are mainly 4 layers, each layer has different parameters and performs different functions on the input data:

A. Input Layer

This layer takes in raw pixel data of the image and passes it through the network.

B. Convolution Layer

Using this layer, you can apply filters to the original input image. The number and size of kernels are two of the most important parameters. Convolution layers transform input images to extract features.

C. Pooling Layer

In a similar way to the convolution layer, it focuses on specific tasks such as Average Pooling or Avg Pooling and Maximum pooling or Max Pooling. In Max pooling, the highest value is taken within a certain area of the filter. Average pooling, on the other hand, takes the average value within a certain area of the filter. Basically, it reduces the dimensionality of an image.

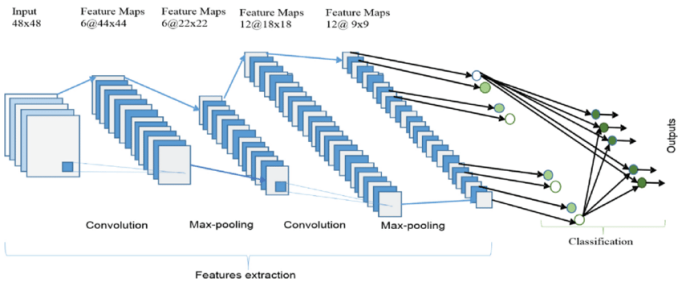


Fig. 1. Architecture of CovNet or CNN [5]

D. Fully Connected Layer

It works in a similar way to the Multilayer Perceptron(MLP), which compacts the results before classification.

The main thing in CNN is the Activation Function which is a node inserted between or end of the neural network. Neurons are completely dependent on them whether to get fired or not. The activation functions are divided into six types – ReLU, LeakyReLU, tanh, Maxout, Sigmoid, and ELU.

III. Related Work

Classifying as well as detecting a disease in a plant is very important in the sector of agriculture, and DL plays a key part in the process of detecting the plant disease. Here, we'll review a few of the most notable works related to this field. Some DL approaches that were proposed in recent years:

An architecture of CNN was proposed by Ferentinos[6]. It was trained on PlantVillage[7] dataset which consists of 87484 images of plant leaf which is divides into 58 classes. In this work, 99.53% accuracy was achieved.

Multilayer CNN architecture was proposed by Singh et el.[8] In which 97.13% accuracy was achieved. This architecture consists of the convolution layer of 6 units and the pooling layers of 3 units. In this study, the proposed model is applied to images of mango leaves collected from the dataset named PlantVillage[7] and from the field as well.

An architecture of CNN was proposed by Agarwal et al.[9] which was applied on the images of tomato leaf to identify nine types of diseases in tomato plant. This architecture consists of 3 convolution layer, 3 pooling layer of and the fully connected layer of 2 units. In this work, 91.2% accuracy was achieved.

Deep Convolutional Neural Network architecture of nine layers was proposed by Geetharamani et al.[10]composed of the convolution layer of 3 units, the pooling layers of 3 units, flatten layer of one unit and the fully connected layer of 2 units. This architecture was applied on PlantVillage[4] dataset. 96.46% accuracy was achieved in this work.

An approach was proposed by [11] for identifying tomato leaves that were infected. The classification model was constructed using 200 images of healthy and infected tomato leaves. 90% of the classifications were accurate on average.

A deep CNN was proposed by Ma et al.[12] to recognize 4 diseases in cucumber i.e. anthracnose, target leaf spots,

Authorized licensed use limited to: DELHI TECHNICAL UNIV. Downloaded on April 24,2023 at 04:29:06 UTC from IEEE Xplore. Restrictions apply.

Foliar Diseases	Total Images	Training Images	Test Images
Frogeye Leaf Spot	3979	3183	796
Apple Scab	6034	4827	1207
Ceder Apple Rust	2329	1863	466
Complex	3610	2888	722
Powdery Mildew	1513	1210	303
Healthy	5784	4631	1158
Total	23249	18602	4652

TABLE I
DETAILS OF FGVC8 DATASET OF PLANT PATHOLOGY 2021 KAGGLE COMPETITION

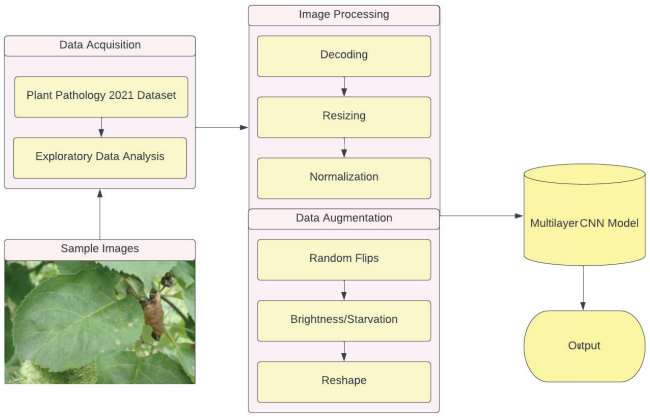


Fig. 2. Flowchart of Proposed Methodology

powdery mildew, and downy mildew. 93.4% accuracy was achieved in this work.

To detect multiple diseases in various varieties of plant, Militante et al.[13] suggested a model which is completely based on deep CNN and is trained on the open dataset of corn, apple, grape, tomato and sugarcane leaf. In this study, 96.5% accuracy is achieved with 75 epochs.

To detect the disease in a cucumber leaf, Kawasaki et al.[14] suggested a CNN model in which 94.9% is achieved.

A CNN was proposed by [15] to detect diseases in tobacco leaves. In this, proposed model is trained by using only 120 images. The accuracy of the proposed CNN model is compared with other existing models and it's shown that the proposed model has given a better accuracy that other existing models with 85.10%.

Deep Convolutional Neural Network i.e. DCNN model was presented by [16] to detect a disease in rice plant. This model can classify 10 rice plant diseases given 500 images which are clicked from field. They trained a model by using 10-fold cross validation and by using this, 95.48% accuracy was achieved in this study.

IV. PROPOSED METHODOLOGY

In this section, we will discuss the Multilayer CNN model that we propose in this paper. In this paper, Dataset is described in the first section, then Data Preprocessing is explained in the next section and then Proposed model is explained in the last section.

A. Dataset

In this work, we use data from Kaggle competition Plant Pathology 2021 – FGVC81[1]. We have 18,602 images available for training. A high-resolution camera is used to capture images at different angles, with different illuminations, and with different backgrounds. The images were labeled by apple disease experts. In each image, the disease in a leaf can be indicated by a single label or by multiple labels. Dataset description is given in Table 1.

B. Data Preprocessing and Augmentation

All the images are captured in the same scale but for training the model, we have converted all the train and test images into 128x128 vectors. Therefore, the final dimension of each and every image in a dataset before applying the proposed model is 128x128x3. Here, 3 indicates color images. Data Augmentation is also done before training. Brightness, Reshaping and Random Flips are done before training. It is done to avoid the problem of overfitting.

C. Proposed Model

CNN comes under deep neural networks which is specifically used in object detection.

This study proposes Multilayer CNN as a method to classify foliar diseases in apple trees. We've done this model from scratch so that it will only focus on the image of plant disease. The proposed model's workflow is shown in Fig.2.

The detailed architecture the proposed Multilayer CNN is shown in Fig. 3. The architecture is designed by using the Keras API. This architecture is made up of a total of 13 layers:

1) First, we have a 2D convolutional layer with 128 filters having 3x3 kernels, each with a LeakyReLU activation function. The input tensor to the model is of shape (128, 128, 3), and this 2D convolutional layer also defines the input shape (128, 128, 3).
2) During training, there is a dropout layer that has a dropout rate of 0.3, which sets the fraction rate of input units to zero.his dropout layer. Overfitting is prevented by this dropout layer.
3) Next, there is a 2D convolutional layer which consists of 64 filters of kernel size (3,3) along with the activation function (ReLU).
4) Max pooling layer with the pool size are (2, 2). An area of the filter is chosen for max pooling based on the highest value within that area.
5) Then there is a dropout layer with a 0.25 dropout rate.

Authorized licensed use limited to: DELHI TECHNICAL UNIV. Downloaded on April 24,2023 at 04:29:06 UTC from IEEE Xplore. Restrictions apply.

```
Model: "sequential"
_________________________________________________________________
Layer (type)                 Output Shape              Param #
=================================================================
conv2d (Conv2D)              (None, 126, 126, 128)     3584
_________________________________________________________________
dropout (Dropout)            (None, 126, 126, 128)     0
_________________________________________________________________
conv2d_1 (Conv2D)            (None, 124, 124, 64)      73792
_________________________________________________________________
max_pooling2d (MaxPooling2D) (None, 62, 62, 64)        0
_________________________________________________________________
dropout_1 (Dropout)          (None, 62, 62, 64)        0
_________________________________________________________________
conv2d_2 (Conv2D)            (None, 60, 60, 32)        18464
_________________________________________________________________
dropout_2 (Dropout)          (None, 60, 60, 32)        0
_________________________________________________________________
conv2d_3 (Conv2D)            (None, 58, 58, 16)        4624
_________________________________________________________________
max_pooling2d_1 (MaxPooling2 (None, 29, 29, 16)        0
_________________________________________________________________
dropout_3 (Dropout)          (None, 29, 29, 16)        0
_________________________________________________________________
conv2d_4 (Conv2D)            (None, 27, 27, 8)         1160
_________________________________________________________________
max_pooling2d_2 (MaxPooling2 (None, 13, 13, 8)         0
_________________________________________________________________
dropout_4 (Dropout)          (None, 13, 13, 8)         0
_________________________________________________________________
flatten (Flatten)            (None, 1352)              0
_________________________________________________________________
dense (Dense)                (None, 128)               173184
_________________________________________________________________
dense_1 (Dense)              (None, 6)                 774
=================================================================
Total params: 275,582
Trainable params: 275,582
Non-trainable params: 0
```

Fig. 3. Detailed Architecture of Proposed Model

6) There is a 2D convolutional layer composed of 32 filters, each with a kernel size (3,3) along with the activation function named LeakyReLU.
7) Next, there's a dropout layer with a dropout rate of 0.3.
8) A 2D convolutional layer. It consists of 16 filters, each of which has a kernel size (3,3) along with the activation function (ReLU).
9) There is a max pooling layer and a pool size of (2, 2).
10) A dropout layer has a 0.25 dropout rate.
11) The 2D convolutional layer consists of 8 filters, each with a different kernel size (3,3) and along with the activation function (ReLU).
12) After that, there is a max pooling layer and a pool size of (2,2).
13) A dropout layer then has a dropout rate of 0.5.
14) After that, a flattened layer will appear. The output of the previous layer is flattened into a single 1D vector.
15) Then comes a dense layer with 128 units and a ReLU activation function.
16) There is a final layer, the dense layer, which has six units and an activation function called Sigmoid.

This proposed model is further compiled with the optimizer called Adam, a loss function called binary cross-entropy, and in order to calculate the performance, four metrics are used: Precision, F1-Score, Accuracy, and Recall.

TABLE II
PERFORMANCE COMPARISON

Model	Accuracy (in %)	Precision (in %)	Recall (in %)	F1-Score (in %)
Logistic Regression	89.92	86	82.1	85
Random Forest	86.2	88	82.65	87
Decision Trees	87	82.3	80.5	81
Proposed Model	91	89	85	88.34

V. EXPERIMENTAL EVALUATION

In order to evaluate the performance of the proposed model, Performance Metrics are discussed in this following section. We then compare performance metrics with the results of three machine learning models - Logistic Regression[2], Decision Trees[4], and Random Forests[3].

A. Performance Metrics

Performance Metrics that are used in this work: Accuracy, Precision, Recall, and F1-score.

1) Accuracy: Accuracy measures how often an algorithm correctly classifies data points.

$$Accuracy = \frac{\text{Number of Correct Predictions}}{\text{Total Number of Predictions}} \tag{1}$$

2) Precision: Precision is a measure of how many predictions of the positive class actually fall into that category.

$$Precision = \frac{\text{Number of Correctly Predicted Positive Instances}}{\text{Number of Total Positive Positive Predictions you made}} \tag{2}$$

3) Recall: Out of all positive examples in the data, recall measures how many positive class predictions have been made.

$$Recall = \frac{\text{Number of Correctly Predicted Positive Instances}}{\text{Number of Total Positive Positive Instances in a Dataset}} \tag{3}$$

4) F1-score: This score balances "Precision" and "Recall" to get a single score based on precision and recall.

$$F1 - Score = 2 \times \frac{\text{Precision * Recall}}{\text{Precision + Recall}} \tag{4}$$

In this experiment, we've compared the proposed model with 3 ML algorithms: Logistic Regression[2], Decision Tree[4], and Random Forest[3]. All these models are trained for up to 50 epochs.

Table 2 shows the Accuracy, Precision, Recall, and F1-Score of 3 ML models and the proposed model and Fig. 4 shows the performance comparison in the form of graph. This shows that the proposed model shows a higher value than 3 ML algorithms.

Authorized licensed use limited to: DELHI TECHNICAL UNIV. Downloaded on April 24,2023 at 04:29:06 UTC from IEEE Xplore. Restrictions apply.

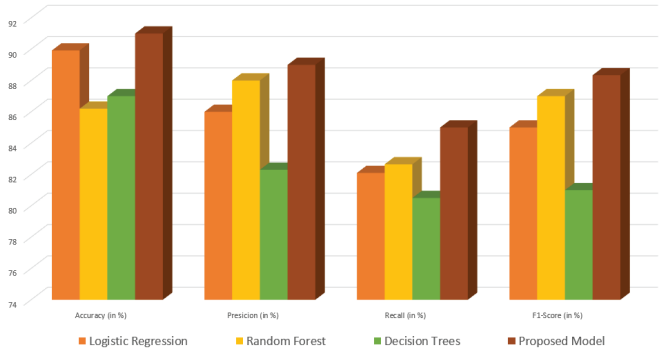


Fig. 4. Performance Comparison Graph

VI. Conclusion

In plant leaf disease identification, DL is an effective methodology for image processing and pattern recognition. Using images of apple leaves, the proposed Multilayer CNN classifies six various classes of healthy and diseased apple plants using the FGVC8 dataset. Before applying, the whole complete dataset is divided into train dataset and test dataset in the ratio of 17:3 i.e. 85% and 15%. And this model is achieving 91% up to 50 epochs which is much higher than other already proposed CNN models. Eventually, we will apply this model to other plant diseases as well. The model can also be extended to detect plant leaf in plants in order to improve the performance.

References

[1] "Plant Pathology 2021 - FGVC8 — Kaggle." https://www.kaggle.com/c/plant-pathology-2021-fgvc8 (accessed Dec. 14, 2022).

[2] "Logistic regression. - PsycNET." https://psycnet.apa.org/record/1995-97110-007 (accessed Jan. 05, 2023).

[3] G. Biau and E. Scornet, "A random forest guided tour," Test, vol. 25, no. 2, pp. 197–227, Jun. 2016, doi: 10.1007/S11749-016-0481-7/FIGURES/4.

[4] Y. Y. Song and Y. Lu, "Decision tree methods: applications for classification and prediction," Shanghai Arch Psychiatry, vol. 27, no. 2, p. 130, Apr. 2015, doi: 10.11919/J.ISSN.1002-0829.215044.

[5] "Capture-CNN-Arch.png (1027×404)." https://coderzpy.com/wp-content/uploads/2020/08/Capture-CNN-Arch.png (accessed May 26, 2022).

[6] K. P. Ferentinos, "Deep learning models for plant disease detection and diagnosis," Comput Electron Agric, vol. 145, no. September 2017, pp. 311–318, 2018, doi: 10.1016/j.compag.2018.01.009.

[7] "GitHub - spMohanty/PlantVillage-Dataset: Dataset of diseased plant leaf images and corresponding labels." https://github.com/spMohanty/PlantVillage-Dataset (accessed May 25, 2022).

[8] U. P. Singh, S. S. Chouhan, S. Jain, and S. Jain, "Multilayer Convolution Neural Network for the Classification of Mango Leaves Infected by Anthracnose Disease," IEEE Access, vol. 7, pp. 43721–43729, 2019, doi: 10.1109/ACCESS.2019.2907383.

[9] M. Agarwal, A. Singh, S. Arjaria, A. Sinha, and S. Gupta, "ToLeD: Tomato Leaf Disease Detection using Convolution Neural Network," Procedia Comput Sci, vol. 167, no. 2019, pp. 293–301, 2020, doi: 10.1016/j.procs.2020.03.225.

[10] G. Geetharamani and A. P. J., "Identification of plant leaf diseases using a nine-layer deep convolutional neural network," Computers and Electrical Engineering, vol. 76, pp. 323–338, Jun. 2019, doi: 10.1016/j.compeleceng.2019.04.011.

[11] U. Mokhtar, M. A. S. Ali, A. E. Hassanien, and H. Hefny, "Identifying two of tomatoes leaf viruses using support vector machine," Advances in Intelligent Systems and Computing, vol. 339, pp. 771–782, 2015, doi: 10.1007/978-81-322-2250-7_77/COVER.

[12] J. Ma, K. Du, F. Zheng, L. Zhang, Z. Gong, and Z. Sun, "A recognition method for cucumber diseases using leaf symptom images based on deep convolutional neural network," Comput Electron Agric, vol. 154, pp. 18–24, Nov. 2018, doi: 10.1016/J.COMPAG.2018.08.048.

[13] S. v. Militante, B. D. Gerardo, and N. v. DIonisio, "Plant Leaf Detection and Disease Recognition using Deep Learning," 2019 IEEE Eurasia Conference on IOT, Communication and Engineering, ECICE 2019, pp. 579–582, Oct. 2019, doi: 10.1109/ECICE47484.2019.8942686.

[14] Y. Kawasaki, H. Uga, S. Kagiwada, and H. Iyatomi, "Basic study of automated diagnosis of viral plant diseases using convolutional neural networks," Lecture Notes in Computer Science (including subseries Lecture Notes in Artificial Intelligence and Lecture Notes in Bioinformatics), vol. 9475, pp. 638–645, 2015, doi: 10.1007/978-3-319-27863-6_59/COVER.

[15] S. K. Dasari and V. Prasad, "A novel and proposed comprehensive methodology using deep convolutional neural networks for flue cured tobacco leaves classification," International Journal of Information Technology (Singapore), vol. 11, no. 1, pp. 107–117, Mar. 2019, doi: 10.1007/S41870-018-0174-4/METRICS.

[16] Y. Lu, S. Yi, N. Zeng, Y. Liu, and Y. Zhang, "Identification of rice diseases using deep convolutional neural networks," Neurocomputing, vol. 267, pp. 378–384, Dec. 2017, doi: 10.1016/J.NEUCOM.2017.06.023.

Authorized licensed use limited to: DELHI TECHNICAL UNIV. Downloaded on April 24,2023 at 04:29:06 UTC from IEEE Xplore. Restrictions apply.

Advances in Industrial and Manufacturing Engineering 2 (2021) 100050



Contents lists available at ScienceDirect

Advances in Industrial and Manufacturing Engineering

journal homepage: www.journals.elsevier.com/advances-in-industrial-and-manufacturing-engineering



Multi-response mathematical model for optimization of process parameters in CMT welding of dissimilar thickness AA6061-T6 and AA6082-T6 alloys using RSM-GRA coupled with PCA



Yashwant Koli [a], N. Yuvaraj [a,*], S. Aravindan [b], Vipin [a]

[a] Department of Mechanical Engineering, Delhi Technological University, Delhi, 110042, India
[b] Department of Mechanical Engineering, Indian Institute of Technology Delhi, New Delhi, 110016, India

ARTICLE INFO

Keywords:
Cold metal transfer (CMT)
Central composite face-centered design (CCFCD)
Grey relation analysis (GRA)
Principal component analysis (PCA)
ANOVA and Mechanical properties

ABSTRACT

The requirement projected by many industries for stronger, lighter, more efficient and cost-effective combined alloys in the welding of two dissimilar materials or dissimilar thickness. The current industry trend is the coalescence of various aluminium alloys of varying thicknesses. In this research paper, Cold Metal Transfer (CMT) welding process was used for the joining of AA6061-T6 and AA6082-T6 using ER4043 filler wire and inspected the effect of different process parameters on mechanical properties of welded butt joints. Current (I), welding speed or travel speed (TS) and gas flow rate (Q) are the input welding process parameters that are to be optimized. Full factorial central composite face-centered design (CCFCD) was utilized to optimize the tensile properties, microhardness and residual stresses. Grey relation analysis (GRA) with PCA is incorporated with CCFCD for finding out the optimal process parameter by considering multi-response parameters simultaneously. ANOVA was executed to interpret the impact of a process parameter on the mechanical properties of the weldments. Results showed that the most dominant process parameter was found to be the welding speed. The optimal process parameter obtained via the GRA-PCA technique is I3-TS1-Q1 (I - 100 A, TS - 5 mm/s and Q - 14 L/min having heat input 352 J/mm) which produces 226 MPa of ultimate tensile strength, 12.6% of elongation, 68.7 HV of microhardness and −152.3 MPa of compressive residual stress. The desirability of optimality level obtained through CCFD was 65.99% and significantly improved to 97.07 through GRA-PCA.

1. Introduction

Welding is a simple and cost-effective method of permanently joining materials. Nowadays, welding consistency and structure-integrity play a dynamic role in the manufacturing industries. From the perspective of a consumer, the quality that determines the degree of customer satisfaction is very critical. The need for analysis of welding process parameters in joining is to attain basic structural and strategic behavior, properties at different phases of material, performance fitness of the welded joint for its lifetime. Cold metal transfer (CMT) welding is a superior and advanced technology as compared to gas metal arc welding (GMAW), which is majorly used in the aircraft, defence, construction, automobile industries due to its high gap bridging ability, spatter-free welds and low thermal heat input (Avinash et al., 2019; Shah et al., 2013; Kumar et al., 2016; Selvi et al., 2018; Zhang et al., 2009; Evangeline and Sathiya, 2019; Koli et al., 2020a, 2020b). Several optimizations and modelling approaches have been employed in finding the best CMT welding parameters. Various authors reported that RSM incorporated with GRA paired with principal component analysis (PCA) i.e. hybrid model gives superior results with higher accuracy. GRA is used to transform multiple output responses having, unlike units, into a single output response by allocating grey relation grade (GRG) to a distinct process parameter (Paulraj, 2018; Greyjevo and Metodo, 2009).

Avinash et al. (2019) use the GRA optimization technique on the multiple welding process parameters in Pulse TIG welding for successful welding of AISI 304 and Monel 400 materials. Magudeenswaran et al. (Magudeeswaran et al., 2014) used the Taguchi optimization technique to find the optimal welding process parameters for the development of duplex steel sound weld joints. The optimum welding process parameters are 1 mm, 130 mm/min, 140 A and 12 V for electrode gap, travel speed, current and voltage respectively. To obtain optimum parameters, Shanmugarajan et al. (2016) used the GRA optimization method based on

* Corresponding author.
E-mail addresses: yashwantkoli5@gmail.com (Y. Koli), yuvraj@dce.ac.in (N. Yuvaraj), aravindan@mech.iitd.ac.in (S. Aravindan), vipin@dce.ac.in (Vipin).

https://doi.org/10.1016/j.aime.2021.100050
Received 27 October 2020; Received in revised form 17 March 2021; Accepted 25 April 2021
2666-9129/© 2021 The Author(s). Published by Elsevier B.V. This is an open access article under the CC BY license (http://creativecommons.org/licenses/by/4.0/).

Taguchi, taking into account the welding responses like HAZ width, weld bead width and penetration depth of the weld. Using the GRA multi-objective approach, the best optimal results were obtained. Kanakavalli et al. (2020) reported that Taguchi and GRA approach is an effective method of finding the optimized welding parameters for MIG welding of AISI 1010 & AISI 1018 dissimilar joints. Similarly, Kumar and Singh (2019) used a GRA based Taguchi approach to optimize the process parameters for MIG welding of AISI 1018 Mild Steel. Results have shown that it is a quick, simple and powerful approach for optimization of process parameters. Majumder et al. (2017) applied PCA-GRA in RSM (hybrid model) for optimizing the surface finish and cutting time of Inconel 800 during wire EDM. It was concluded that this hybrid model was successful and can be used for a wide variety of selection criteria. Kuo et al. (2008) used a GRA based Taguchi approach to optimize the multi-response problem and compared it with Data Envelopment Analysis (DEA). He demonstrated that GRA outperformed DEA in solving problems with multiple attribute decision making (MADM). GRA approach is very simple and fast and can easily be applied to problems having more than two response for optimization calculations. İrizalp et al. (2016) investigated the welding parameters by the CMT method and mechanical behavior of 2 mm thick AA1050 sheet. Results exhibited the highest tensile strength and micro-hardness due to minimum heat input. Shu et al. (2014) investigated residual stress in the narrow gap welded joint of aluminium alloy by CMT. Results revealed that the final allocation of residual stress was evaluated based on the distribution of stress along various lines. In the field of stress, homogeneity was observed with stress concentrated on the welded metal and its neighbouring zones. Moreira et al. (2009) used FSW to join 6061-T6 and 6082-T6 aluminium alloys. The friction stir welded AA6082-T6 material was able to produce lower yield and ultimate stress, and intermediate properties were shown by the dissimilar joints. Failures occurred close to the weld edge line in the tensile tests where minimum hardness value was perceived. Sivaraman and Paulraj (2017) applied the grey-based Taguchi approach to optimize multi-objective process parameters for AA2219-T87 on MIG welding. Results using GRA were current (I), voltage (V) and welding speed (TS) of order 32A, 25V and 185 mm/s respectively. Several researchers have experienced that the hybrid (GRA coupled with PCA) model is easy and more reliable for getting accurate and precise results. In this paper RSM-GRA model paired with PCA is applied for finding out the optimal process parameters of AA6082-T6 and AA6061-T6 CMT butt joints having different thickness.

2. Experimentation process

2.1. Material and methodology

Nowadays, most manufacturers are using aluminium instead of steel in vehicles, such as cars, buses, and trucks, to minimize automotive weight. The idea behind lowering the vehicle's weight is to increase engine performance by lowering energy consumption. In this study, AA6061-T6 and AA6082-T6 is the workpiece material of thickness 3.18 mm and 2 mm respectively were selected. 6XXX-series alloys can be found in car body frames, external and internal body plates, structural and weldable elements, all of which contribute to reducing vehicle weight (Koli et al., 2021). ER4043 filler wire of 1.2 mm diameter is compatible with the aluminium alloy 6XXX series material and showing good results as per literature review and extensive trial tests. The nominal chemical compositions as per ASTM standards for workpiece material and filler material is presented in Table 1. Mechanical properties of workpiece materials are tested and found experimentally which is presented in Table 1. TPS400i CMT machine is used for welding of dissimilar aluminium alloys is shown in Fig. 1. Table 2 displays the selected three welding process parameters with 3 levels used in this experiment. After an immense number of preliminary trial tests, the levels of the process parameters are fixed. Table 3 shows the experimental results as CCFCD using RSM via design expert software and three experimental tests were performed per parameter set for higher accuracy.

Heat input is calculated by the following formula, Heat input $(HI) = \eta \frac{VI}{S}$.

Where thermal heat input (J/mm), voltage (V), current (A) and welding/travel speed (mm/sec) are represented by HI, V, I and S respectively. Thermal efficiency (η) for MIG/CMT welding is taken as 80% standard (Gungor et al., 2014; Ünel and Taban, 2017).

2.2. Grey relation analysis (GRA)

In 1982 Ju-Long began the GRA based on the theory of grey systems

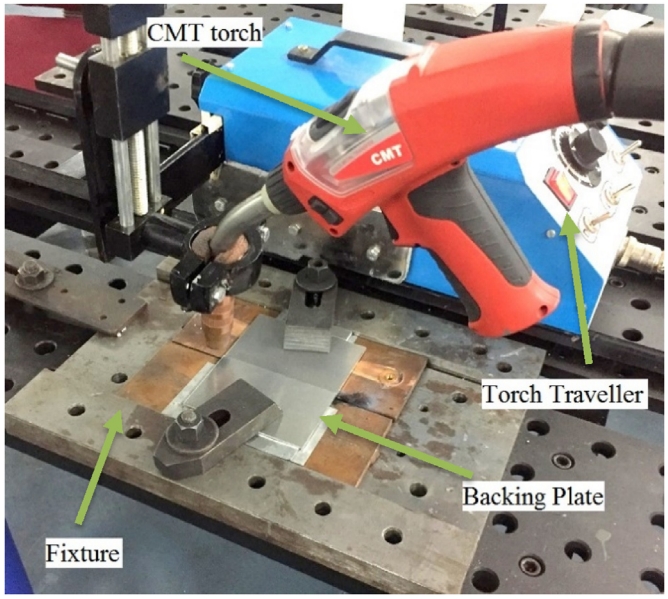


Fig. 1. Experimental setup.

Table 1
Chemical compositions (wt. %) obtained by chemical spectroscopy as per ASTM E 1251:2011 and mechanical properties.

Chemical compositions of workpiece materials and filler material									
Composition	Al	Si	Fe	Cu	Mn	Mg	Zn	Cr	Ti
AA6082-T6	97.18	1.06	0.189	<0.0030	0.745	0.636	0.0045	0.0088	0.0184
AA6061-T6	97.75	0.665	0.253	0.153	0.0676	0.840	0.0226	0.178	0.0225
ER4043	Bal.	5.6	0.8	0.3	0.05	0.05	0.10	0.05	0.02

Mechanical properties of substrate material						
Properties	$\sigma_{0.2}$ (MPa)	σ_{UTS} (MPa)	δ (%)	BHN	$HV_{0.3N}$	Y (GPa)
AA6082-T6	269	304	20.1	91	109 ± 9	90 ± 7
AA6061-T6	247	284	24.9	93	116 ± 9	97 ± 4

$\sigma_{0.2}$ (MPa) – Tensile strength at 0.2% offset; σ_{UTS} (MPa) – Ultimate tensile strength; δ (%) – Percentage elongation; BHN - Brinell hardness number; $HV_{0.3N}$ – Vickers microhardness at 300 g load; Y (GPa) – Youngs Modulus.

Table 2
Design of experiments for CMT butt joints.

Input Parameters	Units	Symbols	Levels		
Current	A	I	80	90	100
Welding speed	mm/sec	TS	5	7	9
Flow rate	L/min	Q	14	16	18

(Deng, 1982). This technique is useful for effectively shedding light on the complex interrelationships between the multi-response variables into a single GRG (Wang et al., 1996). The detailed Steps used in this analysis is explained in APPENDIX.

2.3. GRA-PCA hybrid technique

First, the response parameters are distinguished in terms of smaller-the-better and larger-the-better characteristics in the hybrid GRA-PCA technique using Eqs. (5) and (6) respectively. Then unlike units were transformed into normalized values. The GRC [ξi (k)], was calculated using Eq. (8) in the next step. Because as the weights of the individual responses are different, PCA is implemented using Eqs. 11–14 to determine the exact weights of the specific response parameter of the existing system. By using the actual response weights that are determined from PCA, GRG [γi(k)] of each experiment is determined using Eq. (9). Of all the experiments, the highest GRG-PCA value gives us the most optimized set of process parameters.

3. Result and discussions

3.1. Ultimate tensile strength (UTS)

UTS is done to understand the joint efficiency/strength, fracture analysis and ductility. Tensile specimens were prepared with sub-size 100 mm length as per ASTM E8 standards using wire electric discharge machining (WEDM). UTM of capacity 50 KN was used to compute the tensile properties of the welded butt joints with a ram speed of 1 mm/min. The samples were made at the same thickness for the tensile test i.e. the thicker side (AA6061-T6, 3.18 mm) was made equal to the thinner side (AA6082-T6, 2 mm) by filling and grinding the thicker surface to get the exact tensile properties of the welded butt joint. UTS is in the range of 184–228 MPa depending on the process parameters or heat input. Fig. 2 (a) shows the tensile specimens after breaking with respect to heat input as per the design experiment. It is distinctly visible from the figure that all the tensile specimens having fracture at the heat-affected-zone (HAZ) of the 6082-T6 aluminium alloy side. During welding, the HAZ side of 6082-T6 aluminium alloy gets more intermetallic phases like Mg_2Si which is highly detrimental to the strength of the joint. Mg_2Si is a brittle intermetallic compound that is formed because of high wt. % of Mg and Si elements in the 6082-T6 aluminium alloy and the ER4043 filler wire. Whereas the HAZ of 6061-T6 aluminium alloy is composed of dendrites with a solid solution of aluminium (α-Al) and an Al-Si eutectic structure which makes the HAZ of 6061-T6 much stronger than the HAZ of 6082-T6 aluminium alloys (Koli et al., 2021). Fig. 2 (b) shows the UTS and percentage elongation graph vs heat input. The stress-strain curve as per heat input is displayed in Fig. 3. This illustrates that the elongation (%) is in the range of 9.8–12.5%. The maximum tensile stress is 228 MPa (having heat input 352 J/mm) whereas the minimum is 186 MPa (having heat input 183 J/mm). When compared with the base metal (AA6061-T6), the butt joint strength is about 65–80%. It can be stated that the joint efficiency is 65–80% of the base metal, which is a good result considering fusion welding. Tensile specimen after breaking shows a honeycomb structure which anticipates maximum strength having a large number of dimples and voids which is depicted in Fig. 4. Fig. 4 (a) shows higher amounts of voids as compared to Fig. 4 (b). As the heat input increases, these fracture voids reduce resulting in higher percentage elongation. Table 4 displays the ANOVA table for UTS which clearly illustrates that the model is significant having a 97.442% contribution. It is shown that all the process parameters and their interactions are significant which can be seen from their p-value (<0.05). Lack of fit is not significant or insignificant because of its p-value exceeding 0.1. For UTS, the interaction of current and welding speed (AB) is most dominant with 48.746% as compared to other process parameters and their interaction. This states that minor changes in current and welding speed will majorly affect the UTS. The flow rate of shielding gas has the least contribution (2.188%) which shows that the change in gas flow rate will affect the UTS negligibly. The closer the values of predicted R^2 (0.851) and adjusted R^2 (0.946) concludes that within a regression line, the maximum number of point falls. The gap should not be exceeding to 0.2 between the predicted

Table 3
Experimental design matrix as per CCFCD using RSM along with results.

		Process Parameters				Experimental results			
Std	Run	I (A)	TS (mm/sec)	Q (L/min)	HI (J/mm)	UTS (MPa)	Elong. (%)	MH (HV)	RS (MPa)
3	17	80	9	14	163	196	10.6	59.5	−101
7	18	80	9	18	168	203	11.8	63.9	−103
12	3	90	9	16	183	186	9.9	62.8	−112
4	6	100	9	14	195	191	10.1	62.9	−119
8	4	100	9	18	198	187	10.6	65.1	−116
9	2	80	7	16	204	189	10	59.2	−115
13	13	90	7	14	220	190	10	57.3	−135
17	5	90	7	16	227	188	9.8	60.1	−130
19	7	90	7	16	227	184	9.6	59.1	−133
18	8	90	7	16	227	188	9.9	58.9	−131
15	11	90	7	16	227	186	9.7	57.8	−134
20	12	90	7	16	227	190	10.1	60	−129
16	16	90	7	16	227	185	9.7	59.6	−132
14	1	90	7	18	243	190	10.6	59.3	−143
10	15	100	7	16	245	191	10.4	62.5	−140
1	9	80	5	14	311	193	10.7	62.7	−115
5	19	80	5	18	323	190	11.1	63.7	−128
11	10	90	5	16	347	195	11.4	64.6	−133
2	14	100	5	14	352	228	12.5	68.9	−154
6	20	100	5	18	369	210	12.2	67.9	−157

I = Current; TS = Welding speed; Q = Gas flow rate; HI = Heat input; UTS = Ultimate tensile strength; Elong. = Elongation; MH = Micro-hardness; RS = Residual stress.

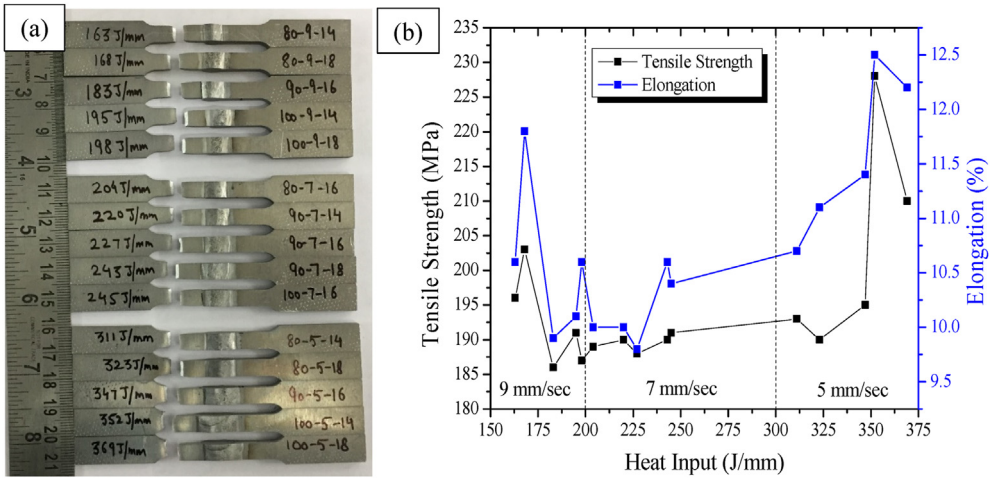


Fig. 2. (a) Tensile specimens (b) UTS and % elongation graph vs heat input.

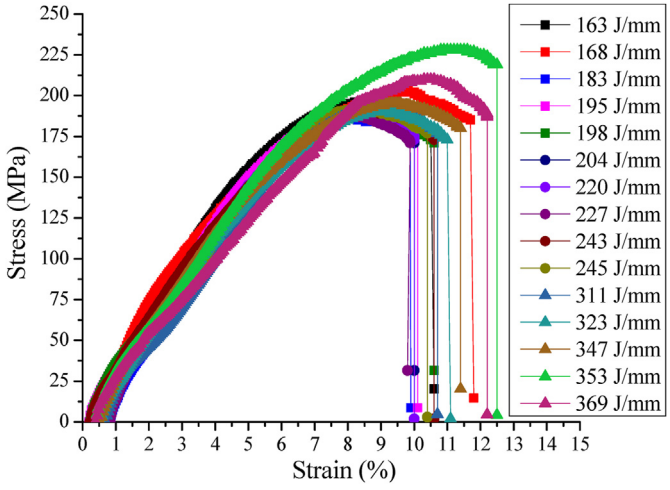


Fig. 3. Stress vs strain curve.

R^2 and the adjusted R^2. The signal to noise (S/N) ratio is measured by adequate precision (23.785) which should be greater than 4 for a suitable signal (Goyal et al., 2015).

3.2. Elongation

Percentage elongation indicates the ductility of the material. The higher the percentage elongation the more ductile is the material. Ductility in welded plates generally allows the redistribution of loads before fracture. Higher ductility also ensures a minimum amount of brittle intermetallic compound formation. Higher heat input is observed to have a higher percentage elongation as shown in Fig. 2 (b) due to the high metal deposition of the filler wire into the weld bead. As higher heat input shows higher percentage elongation which avoids or minimizes the formation of the brittle intermetallic compound like Mg_2Si. This ensures better ductility. Table 5 shows the ANOVA table of elongation which clearly shows that the model is significant having a 97.437% contribution. Similarly, as in the UTS, the welding speed is the most important process parameters as compared to the others with a 28.360% contribution. The interaction of current and welding speed (AB) also has the highest contribution value of 31.243% which signifies that the effect of shielding gas flow rate is negligible on elongation (%). ANOVA table clearly shows that all the process parameters and their interactions are significant and lack of fit is not significant. Predicted R^2 (0.868) and adjusted R^2 (0.946) value is close which gives good accuracy. Higher adequate precision (19.402) is experienced which results in a higher S/N ratio.

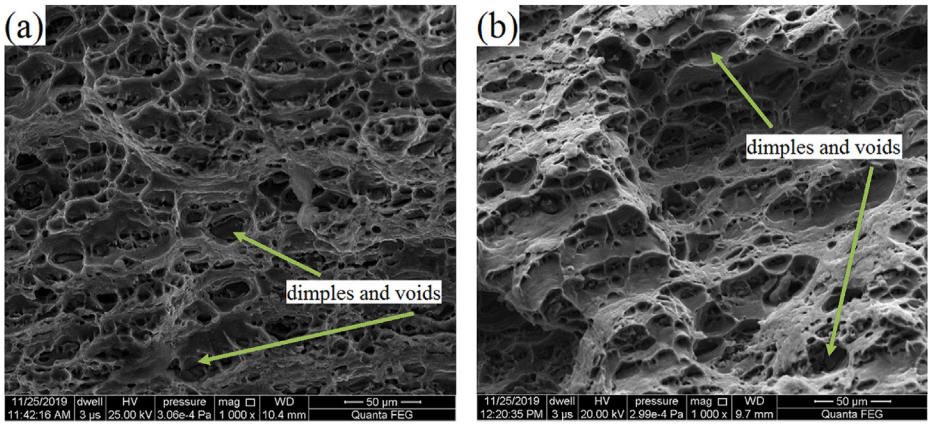


Fig. 4. Fractography FESEM image (a) Experiment 3 (90A-9 mm/s-16 L/min) (b) Experiment 15 (100A-7 mm/s-16 L/min).

Table 4
ANOVA table for response 1: UTS.

Source	SS	df	Mean	F-value	p-value	Contribution	Remarks
Model	1958.855	9	217.651	38.087	0.000	97.442	significant
A-Current	129.600	1	129.600	22.679	0.001	8.750	
B-Welding speed	280.900	1	280.900	49.155	0.000	18.965	
C-Flow rate	32.400	1	32.400	5.670	0.039	2.188	
AB	722.000	1	722.000	126.344	0.000	48.746	
AC	84.500	1	84.500	14.787	0.003	5.705	
BC	72.000	1	72.000	12.599	0.005	4.861	
$A\hat{A}^2$	49.142	1	49.142	8.599	0.015	3.318	
$B\hat{A}^2$	61.455	1	61.455	10.754	0.008	4.149	
$C\hat{A}^2$	49.142	1	49.142	8.599	0.015	3.318	
Residual	57.145	10	5.715			2.558	
Lack of Fit	32.312	5	6.462	1.301	0.390		not significant
Pure Error	24.833	5	4.967				
Cor Total	2016.000	19					
Std. Dev.	2.391		$R\hat{A}^2$	0.972			
Mean	193.000		Adjusted $R\hat{A}^2$	0.946			
C.V. %	1.239		Predicted $R\hat{A}^2$	0.851			
			Adeq Precision	23.785			

Table 5
ANOVA table for response 2: Elongation.

Source	SS	Df	Mean	F-value	p-value	Contribution	Remarks
Model	13.530	9.000	1.503	38.015	0.000	97.437	significant
A-Current	0.256	1.000	0.256	6.474	0.029	3.024	
B-Welding speed	2.401	1.000	2.401	60.715	0.000	28.360	
C-Flow rate	0.576	1.000	0.576	14.566	0.003	6.804	
AB	2.645	1.000	2.645	66.885	0.000	31.243	
AC	0.245	1.000	0.245	6.195	0.032	2.894	
BC	0.320	1.000	0.320	8.092	0.017	3.780	
$A\hat{A}^2$	0.205	1.000	0.205	5.172	0.046	2.416	
$B\hat{A}^2$	1.436	1.000	1.436	36.323	0.000	16.967	
$C\hat{A}^2$	0.382	1.000	0.382	9.661	0.011	4.513	
Residual	0.395	10.000	0.040			2.563	
Lack of Fit	0.235	5.000	0.047	1.472	0.341		not significant
Pure Error	0.160	5.000	0.032				
Cor Total	13.926	19.000					
Std. Dev.	0.199		$R\hat{A}^2$	0.972			
Mean	10.535		Adjusted $R\hat{A}^2$	0.946			
C.V. %	1.888		Predicted $R\hat{A}^2$	0.868			
			Adeq Precision	19.402			

3.3. Microhardness

Vicker's microhardness is measured at 300 g load and 20 s of dwell time at the cross-section of the welded joint. A minimum of three readings of microhardness is measured in each specimen and the average value is presented in Table 3. Microhardness is varying according to the process parameters or the amount of heat input on the welded sample. This variation is possibly due to brittle intermetallic compound formation like Mg_2Si, precipitate formation, grains formation and softening effect (Koli et al., 2020a, 2021; Anyalebechi, 1995). According to the experiments, the mean microhardness is 61.790 HV which is lower as compared to microhardness at high heat inputs samples. As the current increases

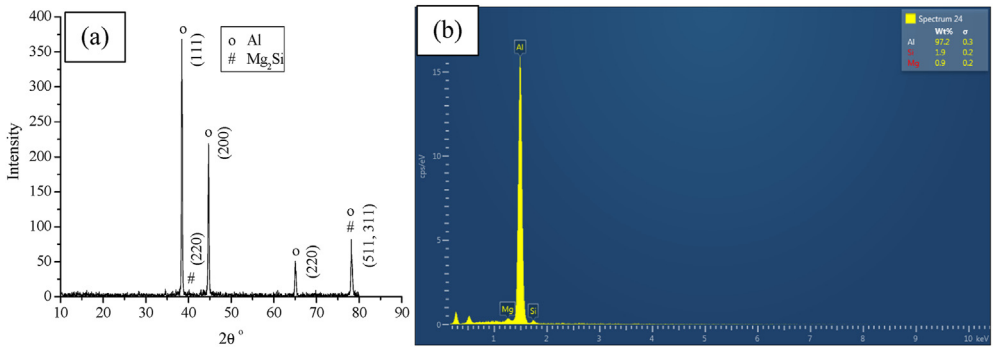


Fig. 5. Experiment 2nd with 80A-9 mm/s-18 L/min (168J/mm) plots (a) XRD (b) EDX.

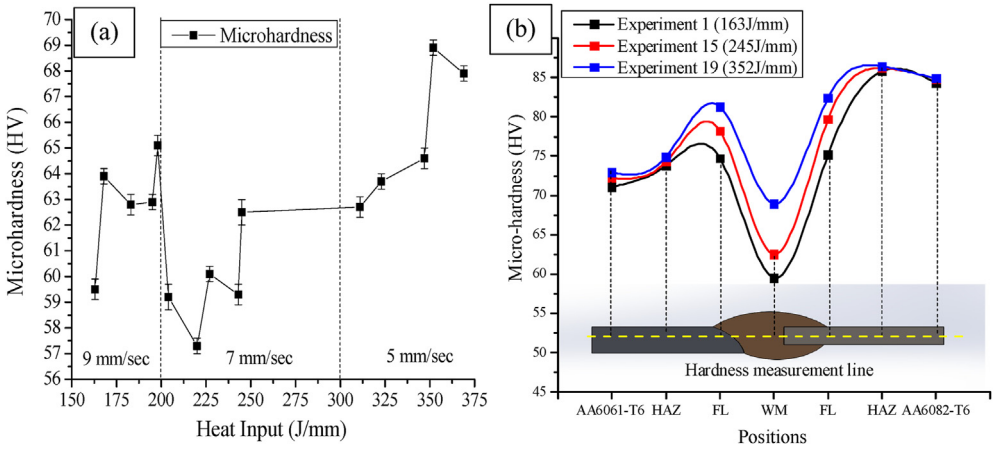


Fig. 6. Microhardness plots (a) at various heat inputs (b) at various positions.

Table 6
ANOVA table for response 3: Microhardness.

Source	SS	df	Mean	F-value	p-value	Contribution	Remarks
Model	194.779	9.000	21.642	50.106	0.000	98.043	significant
A-Current	33.489	1.000	33.489	77.534	0.000	24.814	
B-Welding speed	18.496	1.000	18.496	42.822	0.000	13.705	
C-Flow rate	7.396	1.000	7.396	17.123	0.002	5.480	
AB	4.205	1.000	4.205	9.735	0.011	3.116	
AC	2.205	1.000	2.205	5.105	0.047	1.634	
BC	5.445	1.000	5.445	12.606	0.005	4.035	
$A\hat{A}^2$	6.960	1.000	6.960	16.114	0.002	5.157	
$B\hat{A}^2$	54.235	1.000	54.235	125.564	0.000	40.186	
$C\hat{A}^2$	2.530	1.000	2.530	5.857	0.036	1.874	
Residual	4.319	10.000	0.432			1.957	
Lack of Fit	0.664	5.000	0.133	0.182	0.958		not significant
Pure Error	3.655	5.000	0.731				
Cor Total	199.098	19.000					
Std. Dev.	0.657		$R\hat{A}^2$	0.978			
Mean	61.790		Adjusted $R\hat{A}^2$	0.959			
C.V. %	1.064		Predicted $R\hat{A}^2$	0.950			
			Adeq Precision	24.309			

and welding speed reduces it results in high heat input which is having higher microhardness due to low or negligible formation of Mg_2Si brittle intermetallic compound (Koli et al., 2020a) as shown in Fig. 5.

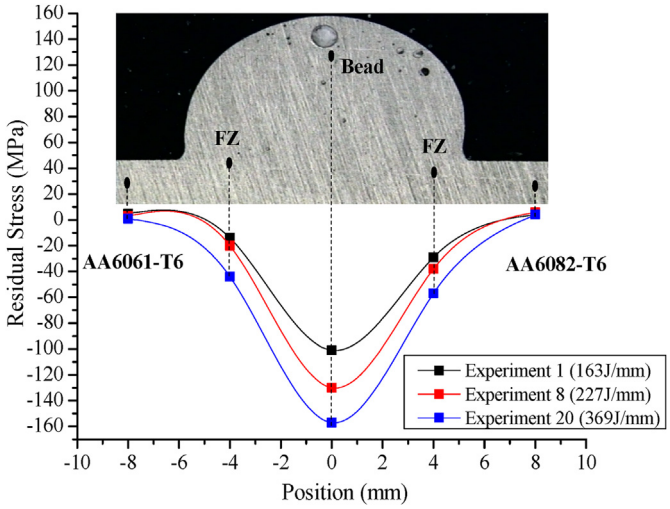


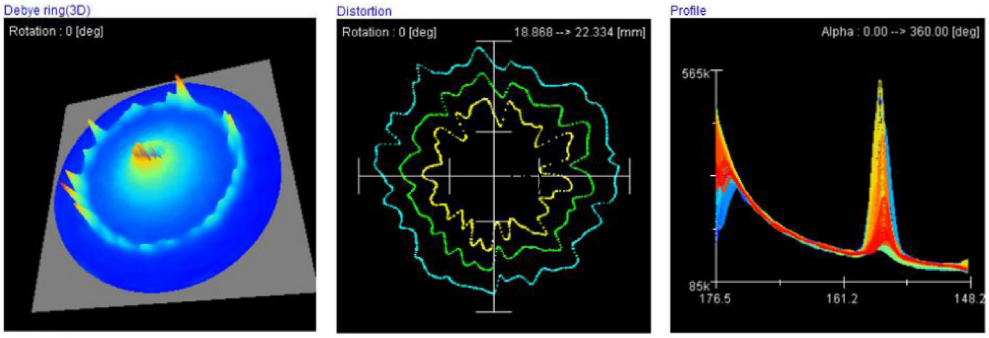
Fig. 7. Residual stress at various positions.

The highest microhardness is 68.9 HV which is observed in experiment number 19 having a heat input of 352 J/mm as shown in Fig. 6 (a). The deviation in micro-hardness majorly depends on the different zone on the welded sample as shown in Fig. 6 (b). During the solidification of the fusion zone (FZ), the metal usually eludes its original strength due to the strain-hardening effect. As the possibility of precipitate formation of Mg_2Si is more in FZ and HAZ as compared to the base metal (BM), which results in a slight decrease in microhardness. Softening behavior in HAZ and fusion line (FL) of aluminium alloys also changes the microstructure due to which is called the weakest zone of the joint. In FZ of 6082-T6 aluminium alloy side, there is the existence of Mg_2Si after welding whereas in FZ of 6061-T6 aluminium alloy side the Mg_2Si phases dissolute which results in the development of large precipitate and coarsening of grains (Koli et al., 2021). Therefore, the microhardness of FZ and HAZ of the 6082-T6 side is higher than FZ and HAZ of 6061-T6 aluminium alloy. Due to coarser grains, the microhardness of weld metal (WM) is lower (approximately 30%) as compared to HAZ. Table 6 shows the ANOVA table having a 98.043% significant model. Here, the current is the dominant (24.814%) process parameter as compared to other process parameters and also their interactions. Current plays a vital role in enhancing or degrading the microhardness. Moreover, it's the combination of current and welding speed that can be stated as heat input has a major significance on microhardness. The gas flow rate has a minor influence on microhardness. Here adjusted R^2 and predicted R^2 is having approximately the same value which gives higher accurate

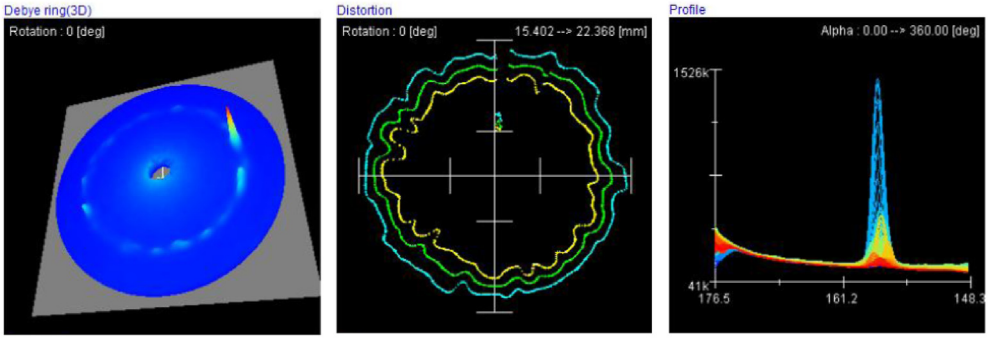
Table 7
ANOVA table for response 4: Residual stress.

Source	SS	df	Mean	F-value	p-value	Contribution	Remarks
Model	4170.566	9.000	463.396	86.723	0.000	98.860	significant
A-Current	1537.600	1.000	1537.600	287.756	0.000	37.308	
B-Welding speed	1849.600	1.000	1849.600	346.146	0.000	44.878	
C-Flow rate	52.900	1.000	52.900	9.900	0.010	1.284	
AB	171.125	1.000	171.125	32.025	0.000	4.152	
AC	28.125	1.000	28.125	5.263	0.045	0.682	
BC	36.125	1.000	36.125	6.761	0.026	0.877	
$AÂ^2$	60.278	1.000	60.278	11.281	0.007	1.463	
$BÂ^2$	257.778	1.000	257.778	48.242	0.000	6.255	
$CÂ^2$	127.841	1.000	127.841	23.925	0.001	3.102	
Residual	53.434	10.000	5.343			1.140	
Lack of Fit	35.934	5.000	7.187	2.053	0.224		not significant
Pure Error	17.500	5.000	3.500				
Cor Total	4224.000	19.000					
Std. Dev.	2.312		$RÂ^2$	0.987			
Mean	−128.000		Adjusted $RÂ^2$	0.976			
C.V. %	1.806		Predicted $RÂ^2$	0.918			
			Adeq Precision	34.628			

(a) Heat input 163 J/mm (80A-9mm/sec-14L/min) having residual stress -101 MPa



(b) Heat input 227 J/mm (90A-7mm/sec-16L/min) having residual stress -130 MPa



(c) Heat input 369 J/mm (100A-5mm/sec-18L/min) having residual stress -157 MPa

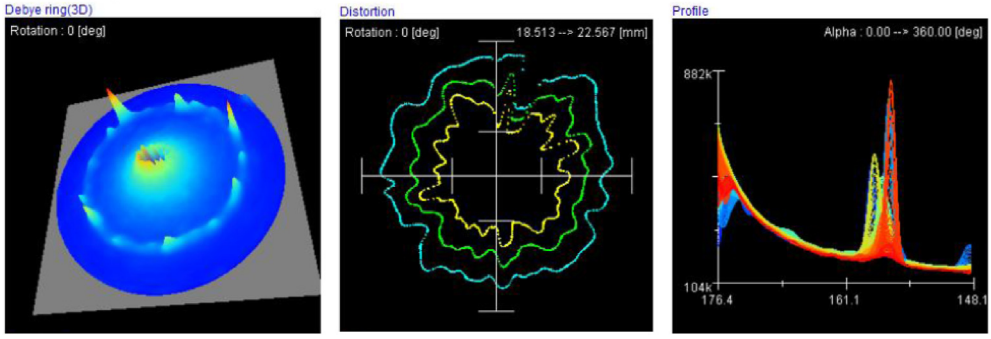


Fig. 8. Debye ring (3D), Distortion and profile of residual stress at various heat input (a) 163 J/mm (b) 227 J/mm (c) 369 J/mm.

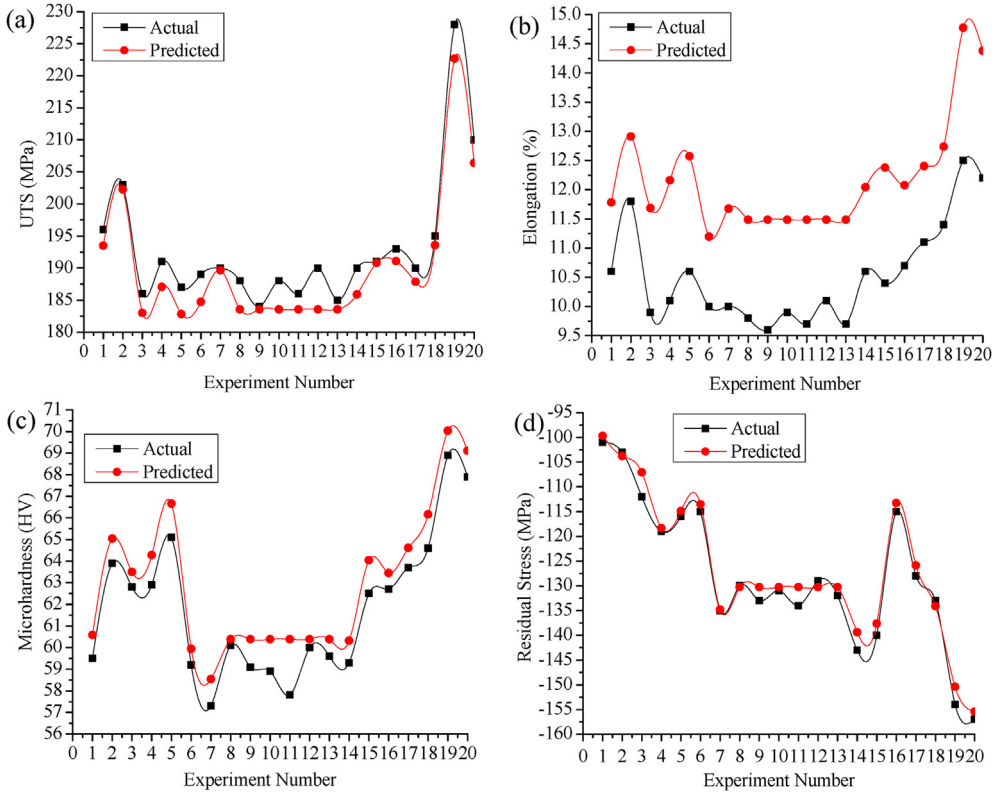


Fig. 9. Model reliability (a) UTS (b) Elongation (c) Microhardness (d) Residual stress.

results.

3.4. Residual stress

Residual stress is the stresses that endure within a material in the dearth of exterior forces or thermal gradients after manufacturing and material processing. The High-Resolution X-ray diffraction (HR-XRD) technique was used to measure the residual stresses. It is suitable for thin plates as its penetration is about 10 μm with a range of 10 μm to 1 mm of spatial resolution. Generally, two types of residual stress are experienced i.e. tensile and compressive. Tensile residual stress is not favorable because it leads to crack formation resulting in lower mechanical properties. Compressive residual stress is more favorable and is experienced in this paper. It is maximum at the weld bead as compared to FZ and BM due to the higher cooling rate as shown in Fig. 7. As the welding speed reduces from 9 mm/s to 5 mm/s the residual stress increases significantly. Approximately 28% increase in residual stress is experienced when welding speed is reduced from 9 mm/s to 7 mm/s with an increase in current of 80 A–90 A respectively (Heat input increased from 163 J/mm to 227 J/mm). Similarly, around 20% increase in residual stress is experienced when welding speed is reduced from 7 mm/s to 5 mm/s with an increase in current of 90 A–100 A respectively (Heat input increased from 227 J/mm to 369 J/mm). This comparison shows that current and welding speed both are majorly affecting the residual stress. Table 7 shows the ANOVA table having the model significance of 98.860%. Welding speed is the dominant factor with 44.878% while the contribution of current is also very high at 37.308%. Similarly, to the other responses, the flow rate of shielding gas is having a negligible amount of contribution. Fig. 8 shows the Debye Scherrer ring (3D), distortion and profile curve of residual stress at lower (163 J/mm), medium (227 J/mm) and high (369 J/mm) heat input as per our experiments. Debye Scherrer ring (3D) signifies the concentration of residual stress at weld bead, which is demonstrated by converting red (at the tip) to blue shade (at the bottom) at all the heat inputs. The red shade indicates that there is more concentration of residual stress in that region whereas the blue shade reveals a negligible concentration of residual stress (Koli et al., 2020a). The position of the Debye rings, which is a direct measure of strain, can accurately measure residual stress. With the help of the Debye ring's spotted position, the extent of the strain is governed. The distortion image acquired in 369 J/mm indicates that a high amount of destruction i.e. structural variations occurred in the sample because of the high amount of compressed residual stresses, indicated by the profile peak in the profile image.

Finding the optimal process parameters is most important in this type of situation where the first 3 responses (UTS, elongation and microhardness) shows a similar trend with higher currents (100 A) and lower welding speed (5 mm/s), while the 4th response (residual stress) shows the opposite trend with lower currents (80 A) and higher welding speeds (9 mm/s). For getting accurate optimal parameters with this situation, GRA coupled with PCA is used in this experiment.

(a) Heat input 163 J/mm (80A-9 mm/s-14 L/min) having residual stress −101 MPa
(b) Heat input 227 J/mm (90A-7 mm/s-16 L/min) having residual stress −130 MPa
(c) Heat input 369 J/mm (100A-5 mm/s-18 L/min) having residual stress −157 MPa

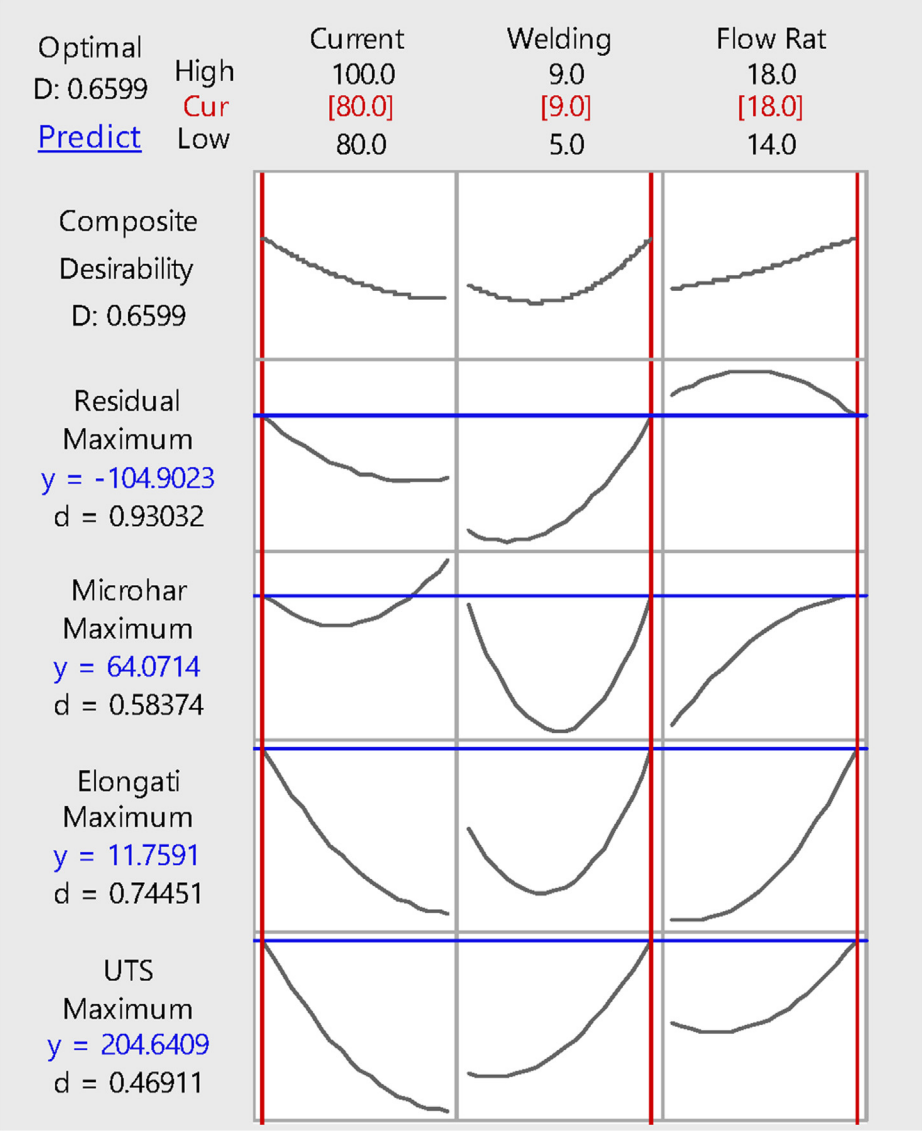


Fig. 10. Optimal process parameters, responses and their desirability with using CCFCD of RSM.

3.5. Mathematical model

Mathematical models for UTS, elongation, microhardness and residual stress has been developed with current (I), welding speed (TS) and flow rate of shielding gas (Q) as the input independent variables or process parameters. The final model equation in terms of actual process parameters is represented in Eqs. (1)–(4). It is a quadratic equation obtained via CCD in RSM.

$$UTS = 408.573 - 1.324*I + 11.555*TS - 25.343*Q - 0.475*I*TS - 0.163*I*Q + 0.750*TS*Q + 0.042*I*I + 1.182*TS*TS + 1.057*Q*Q \quad (1)$$

$$Elongation = 37.892 - 0.134*I - 0.987*TS - 2.424*Q - 0.029*I*TS - 0.009*I*Q + 0.050*TS*Q + 0.003*I*I + 0.181*TS*TS + 0.093*Q*Q \quad (2)$$

$$Micro - hardness = 125.009 - 2.007*I - 16.261*TS + 9.021*Q - 0.036*I*TS - 0.026*I*Q + 0.206*TS*Q + 0.016*I*I + 1.110*TS*TS - 0.240*Q*Q \quad (3)$$

$$Residual\ \ Stress = 352.281 - 12.786*I - 56.399*TS + 41.239*Q + 0.231*I*TS + 0.094*I*Q + 0.531*TS*Q + 0.047*I*I + 2.420*TS*TS - 1.705*Q*Q \quad (4)$$

Fig. 9 shows the model reliability of all the responses, which gives the percentage error from actual and predicted values. The experimental values obtained and the predicted values generated from the model is having a low percentage of error which results in high repeatability and accuracy due to a significant model. Using CCFCD of RSM, the optimal

Table 8
Normalizing and deviation sequence table for GRA.

Experimental values				Normalizing				Deviation Sequence			
UTS (MPa)	Elong. (%)	MH (HV)	RS (MPa)	UTS	Elong.	MH	RS	UTS	Elong.	MH	RS
196	10.6	59.5	−101	0.2727	0.3448	0.1897	1.0000	0.7273	0.6552	0.8103	0.0000
203	11.8	63.9	−103	0.4318	0.7586	0.5690	0.9643	0.5682	0.2414	0.4310	0.0357
186	9.9	62.8	−112	0.0455	0.1034	0.4741	0.8036	0.9545	0.8966	0.5259	0.1964
191	10.1	62.9	−119	0.1591	0.1724	0.4828	0.6786	0.8409	0.8276	0.5172	0.3214
187	10.6	65.1	−116	0.0682	0.3448	0.6724	0.7321	0.9318	0.6552	0.3276	0.2679
189	10	59.2	−115	0.1136	0.1379	0.1638	0.7500	0.8864	0.8621	0.8362	0.2500
190	10	57.3	−135	0.1364	0.1379	0.0000	0.3929	0.8636	0.8621	1.0000	0.6071
188	9.8	60.1	−130	0.0909	0.0690	0.2414	0.4821	0.9091	0.9310	0.7586	0.5179
184	9.6	59.1	−133	0.0000	0.0000	0.1552	0.4286	1.0000	1.0000	0.8448	0.5714
188	9.9	58.9	−131	0.0909	0.1034	0.1379	0.4643	0.9091	0.8966	0.8621	0.5357
186	9.7	57.8	−134	0.0455	0.0345	0.0431	0.4107	0.9545	0.9655	0.9569	0.5893
190	10.1	60	−129	0.1364	0.1724	0.2328	0.5000	0.8636	0.8276	0.7672	0.5000
185	9.7	59.6	−132	0.0227	0.0345	0.1983	0.4464	0.9773	0.9655	0.8017	0.5536
190	10.6	59.3	−143	0.1364	0.3448	0.1724	0.2500	0.8636	0.6552	0.8276	0.7500
191	10.4	62.5	−140	0.1591	0.2759	0.4483	0.3036	0.8409	0.7241	0.5517	0.6964
193	10.7	62.7	−115	0.2045	0.3793	0.4655	0.7500	0.7955	0.6207	0.5345	0.2500
190	11.1	63.7	−128	0.1364	0.5172	0.5517	0.5179	0.8636	0.4828	0.4483	0.4821
195	11.4	64.6	−133	0.2500	0.6207	0.6293	0.4286	0.7500	0.3793	0.3707	0.5714
228	12.5	68.9	−154	1.0000	1.0000	1.0000	0.0536	0.0000	0.0000	0.0000	0.9464
210	12.2	67.9	−157	0.5909	0.8966	0.9138	0.0000	0.4091	0.1034	0.0862	1.0000

Table 9
Eigen analysis of the Correlation Matrix.

	UTS	% E	HV	RS
Eigen value	2.7917	0.8658	0.2559	0.0866
Proportion	0.698	0.216	0.064	0.022
Cumulative	0.698	0.914	0.978	1

Table 10
Eigenvectors, principal components and contribution.

Variable	PC1	PC2	PC3	PC4	% Contribution
UTS (MPa)	0.558	0.038	−0.638	0.529	31.1364
% E	0.57	0.2	−0.14	−0.785	32.49
HV/0.3	0.535	0.24	0.746	0.317	28.6225
RS (MPa)	−0.277	0.949	−0.134	0.064	7.6729

process parameters are 80 A, 9 mm/s, 18 L/min for current (I), welding speed (TS) and flow rate (Q) respectively. It has the desirability of 65.99% at optimal process parameters which the response parameter of 204.64 MPa, 11.75%, 64.07 HV and −104.90 MPa for UTS, elongation, microhardness and residual stress respectively as shown in Fig. 10. I1-TS3-Q3 is the initial optimal process parameter obtained via CCFCD of RSM. These parameters are of experiment 2nd of the design matrix. Now GRA-PCA technique is used to obtain the optimal process parameter for enhancing the optimality by obtaining the original weights of the responses.

3.6. Optimization using GRA coupled with PCA

For optimizing the data by GRA-PCA hybrid technique, firstly the responses having dissimilar units were converted into normalized dimensionless number with the help of Eq. (6) as shown in Table 8. The larger the better phenomenon is used for all the responses, as residual stress is compressive (negative sign) the larger the better is applied for reducing the residual stress at an optimal level. After normalizing the data, the deviation sequence is computed using Eq. (7) as displayed in Table 8. For grey relation coefficient (GRC), ξ is in the range of 0–1, it is an identification coefficient which is usually taken as 0.5 for GRA analysis. The PCA technique is coupled with GRA for finding the exact weights of the response parameter. Weights are calculated by eigen analysis of the correlation matrix and eigenvectors using Eq. (13) and as shown in Table 9. Eigen vectors, principal components and their contribution or weights are shown in Table 10. In this, the weighting contribution of each response attribute is achieved by the sum of the principal component values of the respective eigen vectors. The variance in input for PC1 that characterizes the four response characteristics is the greatest as shown in Fig. 11. So the weights are achieved by squaring the values of PC1 for each response. Weights obtained via PCA for UTS, elongation, microhardness and residual stress are 31.1364, 32.49, 28.6225 and 7.6729 respectively.

Once the weights are obtained for each of the responses using the PCA technique, then GRG is computed using Eq. (5) as shown in Table 11. In this GRG is calculated using PCA weights followed by the ranks.

The higher the value of GRG implies better quality characteristics.

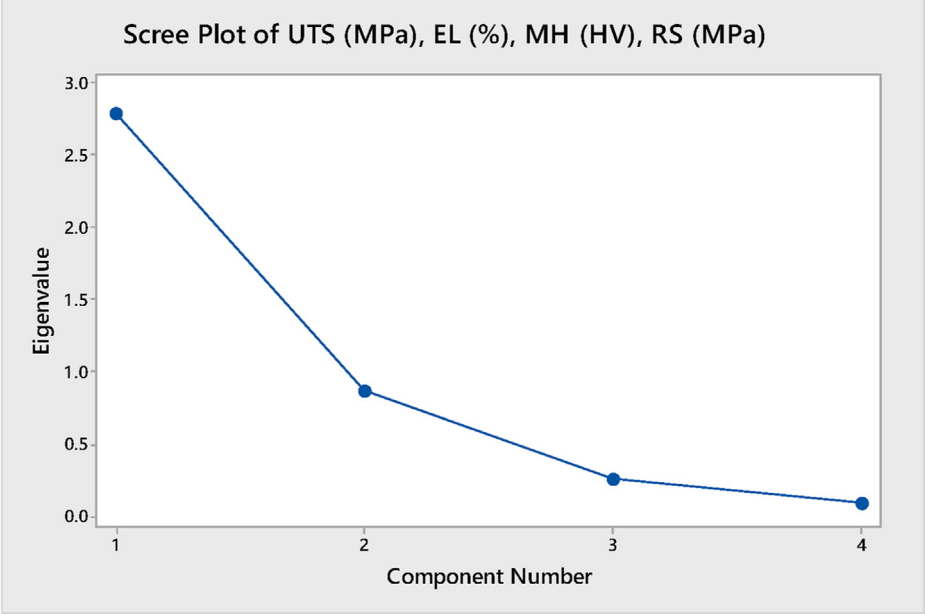


Fig. 11. Screen plots of response with 4 principal components.

Table 11
GRC, GRG and Rank table with PCA.

GRC				GRG with PCA Weights	Rank
UTS	%E	HV/0.3	RS		
MPa	%	HV	MPa		
0.4074	0.4328	0.3816	1.0000	0.4534	8
0.4681	0.6744	0.5370	0.9333	0.5902	3
0.3438	0.3580	0.4874	0.7179	0.4179	10
0.3729	0.3766	0.4915	0.6087	0.4259	9
0.3492	0.4328	0.6042	0.6512	0.4722	5
0.3607	0.3671	0.3742	0.6667	0.3898	13
0.3667	0.3671	0.3333	0.4516	0.3635	17
0.3548	0.3494	0.3973	0.4912	0.3754	15
0.3333	0.3333	0.3718	0.4667	0.3543	19
0.3548	0.3580	0.3671	0.4828	0.3689	16
0.3438	0.3412	0.3432	0.4590	0.3513	20
0.3667	0.3766	0.3946	0.5000	0.3878	14
0.3385	0.3412	0.3841	0.4746	0.3626	18
0.3667	0.4328	0.3766	0.4000	0.3933	12
0.3729	0.4085	0.4754	0.4179	0.4169	11
0.3860	0.4462	0.4833	0.6667	0.4546	7
0.3667	0.5088	0.5273	0.5091	0.4694	6
0.4000	0.5686	0.5743	0.4667	0.5095	4
1.0000	1.0000	1.0000	0.3457	0.9490	1
0.5500	0.8286	0.8529	0.3333	0.7102	2

Experiment 19 (100 A-5 mm/sec-14 L/min having 352 J/mm heat input) is showing the highest value of GRG with PCA weights. The highest GRG value is 0.9490 with PCA weights respectively, which is ranked 1 among the other experiments. The optimum process parameters having the highest GRG value or rank 1 is achieved from Table 11 are 100 A, 5 mm/s and 14 L/min for current (I), welding speed (TS) and flow rate (Q) respectively. Table 12 shows the main effects on mean GRG with PCA which also shows the optimum process parameter as well. The variation of mean GRG value for each input parameters shifts from level 1 to level 3 demonstrates the optimum process parameters. The highest value of mean GRG corresponds to the optimal level. Thus, welding speed (TS) is the dominant input parameter on various responses followed by current (I) and the flow rate of shielding gas (Q). PCA technique is considered because of the distribution of the exact weight in which they are contributing to optimal process parameter done for each response that gives accurate and precise results. Table 13 shows the ANOVA table for GRG with PCA weights, clearly sums up the level of significance or dominance of a parameter. Welding speed is coming out to be the

Table 12
Main effects on mean GRG with PCA.

Process parameter	Mean GRG with PCA weights				
	level 1	level 2	level 3	Max-Min (delta)	Rank
I (A)	0.472	0.388	**0.595**	0.206	2
TS (mm/sec)	**0.619**	0.376	0.472	0.242	**1**
Q (L/min)	**0.529**	0.393	0.527	0.136	3
Total mean GRG **0.486**					

Table 13
ANOVA table results for GRG with PCA weights.

Source	SS	df	Mean	F-value	p-value	Remarks	Contribution (%)
A-Current	0.046703	2	0.023352	2.08	0.165	Insignificant	33.26
B-Welding speed	0.091039	2	0.045519	4.04	0.043	**Significant**	**64.83**
C-Flow rate	0.002681	2	0.001341	0.12	0.889	Insignificant	1.91

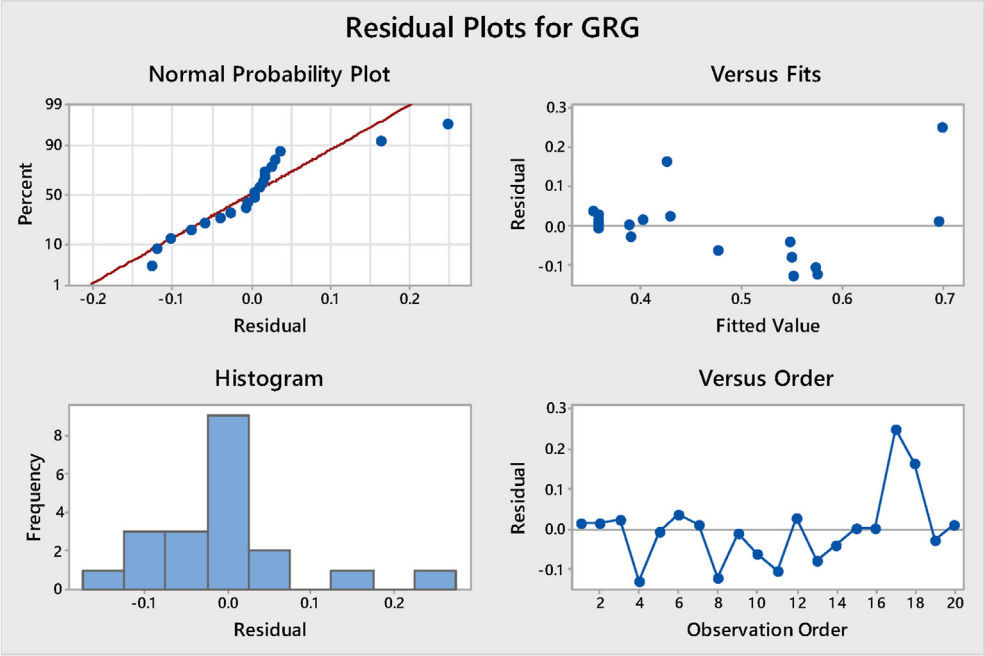


Fig. 12. Residual plots for GRG.

significant input parameter as compared to the other input parameter with approximately 65% of the total contribution. Fig. 12 shows the residual plots for GRG.

Fig. 13 shows the optimal process parameters obtained via the GRA-PCA technique are 100 A, 5 mm/s and 14 L/min for current (I), welding speed (TS) and flow rate (Q) respectively with 97.07% desirability. The response parameters obtained are 226.0409 MPa, 12.5791%, 68.7314 HV and −152.3023 MPa for UTS, elongation, microhardness and residual stress respectively. Compared to the initial optimal process parameters obtained via CCFCD, the GRA-PCA technique significantly improved the levels of process parameters and desirability.

3.7. Confirmation runs

Confirmation runs are needed for reliability checks and also for the level of improvements in GRG using Eq. (10). To validate the results, the experiment is tested with an optimized value of process parameters. Also, as shown in Table 14, the GRG at an optimum process parameter is improved by approximately 35% relative to the initial best condition GRG.

4. Conclusions

The present work is aimed to optimize welding parameters during coalescence of AA6061-T6 and AA6082-T6 butt joints using ER4043 filler wire by Cold Metal Transfer (CMT) welding.

1. Using RSM-GRA coupled with PCA technique, the most dominant input process parameter on multi-response was discovered to be the welding speed. The optimal process parameter acquired is I3-TS1-Q1 (current −100 A, welding speed - 5 mm/s and flow rate - 14 L/min) which produces 226 MPa of ultimate tensile strength, 12.6% of elongation, 68.7 HV of microhardness and −152 MPa of compressive residual stress.
2. Using CCFCD of RSM, the optimal process parameters acquired is I1-TS3-Q3 (current - 80 A, welding speed - 9 mm/s and flow rate - 18 L/min) which produces 204.64 MPa of ultimate tensile strength, 11.75% of elongation, 64.07 HV of microhardness and −104.90 MPa of compressive residual stress.
3. The desirability of the GRA-PCA technique is significantly improved to 97.07% which was initially at 65.99% via CCFCD.
4. The flow rate of shielding gas has a minimum or negligible contribution for affecting the response parameters, while welding speed is the dominant process parameter with approximately 65% of the contribution.
5. More than 97% of model significance is shown by the ANOVA table for each response. All the linear and quadratic interactions are significant with a high grade of adequate precision for each response.

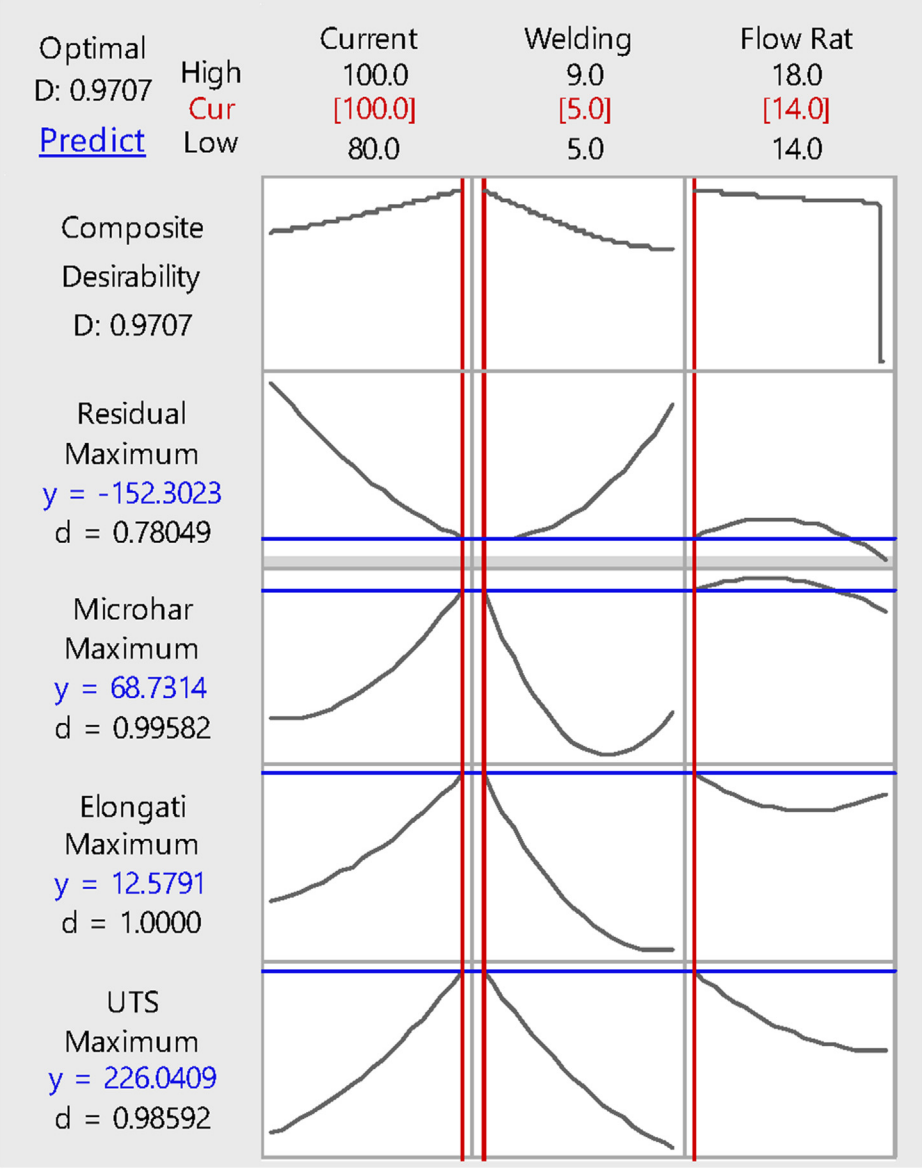


Fig. 13. Optimal process parameters, responses and their desirability with using GRA-PCA technique.

6. The actual weights obtained using principal component analysis for UTS, elongation, microhardness and residual stress are 31.1364, 32.49, 28.6225 and 7.6729 respectively.
7. Confirmation runs helps in the improvement of grey relation grade by 0.211 and approximately by 35% to the initial factor settings.

Table 14
Confirmation runs with GRA-PCA

	Initial factor setting	Optimal welding parameters	
		Prediction	Experimental
Level	I1-TS3-Q3	I3-TS1-Q1	I3-TS1-Q1
UTS	203		226
%E	11.8		12.6
HV	63.9		68.7
RS	−103		−152
GRG	0.5902	0.771	0.8012
Improvement in GRG		0.211	

Declaration of competing interest

The authors declare that they have no known competing financial interests or personal relationships that could have appeared to influence the work reported in this paper.

APPENDIX

Steps for Grey relation analysis (GRA).

Step 1. *Normalizing:* Due to the avoidance of various units and to decrease the uncertainty, the data is first to be normalized. As the variance of one information differs from other data, it is essentially required. From the original value, an appropriate value is extracted to render the array between 0 and 1 (Haq et al., 2008). It is, in general, a way to transform the original data to comparable data. Smaller-the-better features are intended to scale it into an appropriate range for normalization if the response is to be reduced and vice versa through the following formulas.

$$X_i^*(k) = \frac{\max xi(k) - xi(k)}{\max xi\,(k) - \min xi\,(k)} \tag{5}$$

$$X_i^*(k) = \frac{xi(k) - \min xi(k)}{\max xi\,(k) - \min xi\,(k)} \tag{6}$$

where, i = 1, 2, …, m; k = 1, 2, …, n; the number of experimental data is 'm' and the number of responses is 'n'. xi (k) signifies the original sequence, Xi*(k) signifies the order after preprocessing or normalizing the experimental data, max xi (k) constitutes the largest xi (k) value, min xi (k) constitutes the smallest xi (k) value and 'x' is the anticipated value (Tosun and Pihtili, 2010). Eq. (5) stands for smaller-the-better whereas larger-the-better is obtained by Eq. (6).

Step-2. *Deviation Sequence:* After completing the normalizing process, the next step is to compute the deviation sequence 'Δ_{oi}' (i.e. in the array of o to 1), which is obtained using the following formula (Eq. (7)) from the normalized values.

$$\Delta_{oi} = ||\, Xo\,(k) - Xi\,(k)\,|| \tag{7}$$

where Xo (k) is the maximum value in the normalized column (i.e. 1) for a specific response and Xi (k) denotes the original sequence of that specific response.

Step-3. *Grey relation coefficient (GRC):* After normalizing and deviation sequence, the major step in GRA analysis is finding the GRC as per Eq. (8).

$$\xi_i(k) = \frac{\Delta min + (\xi^*\,\Delta max)}{\Delta oi\,(k) + (\xi^*\,\Delta max)} \tag{8}$$

where Δ_{oi} (k) is the deviation sequence which is obtained using Eq. (7); Δ_{min} (i.e. 0) and Δ_{max} (i.e. 1) is the minimum and maximum value of the deviation sequence at a specific response respectively; ξ is in the range of 0–1, it is an identification or distinguishing coefficient which is usually taken as 0.5 for GRA analysis.

Step-4. Grey *relation grade (GRG) with rank:* Now grey relation grade (GRG), [γ_i (k)] is determined which is the average value of the GRC of all the response for a specific process parameter and is calculated with the help of Eq. (9). The highest value of GRG corresponds to the 1st rank while the lowest GRG value corresponds to the last rank.

$$\gamma_i(k) = \frac{1}{n}\sum_{k=1}^{n} \xi\mathrm{i(k)} \tag{9}$$

where GRG [γ_i (k)] indicates the degree of association between the values of the output response and the organization of likeness.

Step 5. *Optimal level of process parameters:* From Eq. (9), the highest value of GRG with rank 1 is considered to be the optimal GRG which indicates the optimal level of process parameters that gives better product quality.

Step 6. *ANOVA table for GRG:* The next step is to use the ANOVA table for GRG to find out the significant parameters influencing the multi-response at a 95% confidence level. Significant parameter is identified by checking the p-value on the ANOVA table. If the p-value is less than 0.05 the process parameter is significant and vice versa.

Step 7. *Confirmation runs:* Confirmation runs are needed for reliability checks and also for the level of GRG improvements. With the optimal process parameters, a minimum of 3 experiments was performed and their results were analyzed and compared with the predicted confirmation run at an optimal level which is calculated by Eq. (10).

$$\gamma_t = \gamma_m + \sum\nolimits_{i=1}^{o} \gamma_o - \gamma_m \tag{10}$$

where γt is the GRG value predicted confirmation run at an optimal level; γm is the total mean GRG and γo is the GRG value of a specific process parameter at an optimal level.

Steps for principal component analysis (PCA)

A multivariate statistical analysis method was first introduced by Pearson (1901) and further developed by Hotelling (1933), which is also known as the dimensionality reduction technique. It begins with a multi-response array with 'n' investigations with 'm' characteristics. After the estimation of the normalized value Xi*(k) from Eq. (6) and deviation sequence Δ_{oi} from Eq. (7), response parameters are retrieved to evaluate the criterion weights. The equation below is used for calculating the correlation coefficient (Saha and Mondal, 2017).

$$R_{jl} = \left[\frac{COV(Xi(j),\ Xi(l))}{\sigma Xi(j)^*\sigma Xi(l)}\right] \tag{11}$$

where COV(xi(j), xi(l)) is the covariance of response variables j and l, whereas xi (j) is the normalized values of an individual response, σXi(j) and σXi(l) are the standard deviation (SD) of response variables j and l.

$$COV\left(x,y\right)=\frac{1}{n-1}\sum_{k=1}^{n}\left(\mathrm{xi}-\overline{\mathrm{x}}\right)\left(\mathrm{yi}-\overline{\mathrm{y}}\right) \tag{12}$$

After that, the following are eigenvalues and corresponding eigenvectors

$$(R-\lambda_x I_m)V_{ik}=0 \tag{13}$$

where λ_x is the eigenvalues, $\sum_{x=1}^{n}\lambda x = n$, x = 1, 2, ….., n, and V_{ik} $[a_{k1}, a_{k2}, \ldots, a_{k(m-1)}, a_{km}]^T$ are the eigenvectors corresponding to eigenvalue λ_x. Eq. (14) corresponds to the principal components.

$$Y_{mk}=\sum_{i=1}^{n}\mathrm{Xm(i)Vik} \tag{14}$$

where $Y_{m1}, \ldots Y_{mk}$ are known as the first principal component (PC1) and so on to the 'k' principal component. The principal components are adjusted for variance in descending order, and consequently, Y_{m1} (PC1) represents the most variance in the data. Thus, the weights of the response parameters are calculated by simply squaring the most variance date i.e. PC1.

References

Anyalebechi, P.N., 1995. Analysis of the effects of alloying elements on hydrogen solubility in liquid aluminum alloys. Scripta Mater. 33 (8), 1209–1216.

Avinash, S., Balram, Y., Babu, B.S., Venkatramana, G., 2019. Multi-response optimization of pulse TIG welding process parameters of welds AISI 304 and Monel 400 using grey relational analysis. Mater. Today: Proc. 19, 296–301.

Deng, J.L., 1982. Control problems of grey systems. Syst. Contr. Lett. 1 (5), 288–294.

Evangeline, A., Sathiya, P., 2019. Cold metal arc transfer (CMT) metal deposition of Inconel 625 superalloy on 316L austenitic stainless steel: microstructural evaluation, corrosion and wear resistance properties. Mater. Res. Express 6 (6), 066516.

Goyal, H., Mandal, N., Roy, H., Mitra, S.K., Mondal, B., 2015. Multi response optimization for processing Al–SiCp composites: an approach towards enhancement of mechanical properties. T Indian I Metals 68 (3), 453–463.

Greyjevo, O.G.T.V.Z., Metodo, A.I.T., 2009. Optimization of weld bead geometry in TIG welding process using grey relation analysis and Taguchi method. Mater. Technol. 43 (3), 143–149.

Gungor, B., Kaluc, E., Taban, E., Aydin, S.I.K., 2014. Mechanical and microstructural properties of robotic Cold Metal Transfer (CMT) welded 5083-H111 and 6082-T651 aluminum alloys. Mater. Des. 54, 207–211, 1980-2015.

Haq, A.N., Marimuthu, P., Jeyapaul, R., 2008. Multi response optimization of machining parameters of drilling Al/SiC metal matrix composite using grey relational analysis in the Taguchi method. Int. J. Adv. Manuf. Technol. 37 (3–4), 250–255.

Hotelling, H., 1933. Analysis of a complex of statistical variables into principal components. J. Educ. Psychol. 24 (6), 417.

İrizalp, A.O., Durmuş, H., Yüksel, N., Türkmen, İ., 2016. Cold metal transfer welding of AA1050 aluminum thin sheets. Materia 21 (3), 615–622.

Kanakavalli, P.B., Babu, B.N., Sai, C.P.V., 2020. A hybrid methodology for optimizing MIG welding process parameters in joining of dissimilar metals. Mater. Today: Proc. 23, 507–512.

Koli, Y., Yuvaraj, N., Vipin, Aravindan, S., 2020a. Investigations on weld bead geometry and microstructure in CMT, MIG pulse synergic and MIG welding of AA6061-T6. Mater. Res. Express 6 (12), 1265e5.

Koli, Y., Yuvaraj, N., Aravindan, S., Vipin, 2020b. Multi-response Mathematical Modeling for Prediction of Weld Bead Geometry of AA6061-T6 Using Response Surface Methodology. T Indian I Metals, pp. 1–22.

Koli, Y., Yuvaraj, N., Aravindan, S., Vipin, 2021. CMT joining of AA6061-T6 and AA6082-T6 and examining mechanical properties and microstructural characterization. T Indian I Metals 74 (2), 313–329.

Kumar, S., Singh, R., 2019. Optimization of process parameters of metal inert gas welding with preheating on AISI 1018 mild steel using grey based Taguchi method. Measurement 148, 106924.

Kumar, N.P., Vendan, S.A., Shanmugam, N.S., 2016. Investigations on the parametric effects of cold metal transfer process on the microstructural aspects in AA6061. J. Alloys Compd. 658, 255–264.

Kuo, Y., Yang, T., Huang, G.W., 2008. The use of grey relational analysis in solving multiple attribute decision-making problems. Comput. Ind. Eng. 55 (1), 80–93.

Magudeeswaran, G., Nair, S.R., Sundar, L., Harikannan, N., 2014. Optimization of process parameters of the activated tungsten inert gas welding for aspect ratio of UNS S32205 duplex stainless steel welds. Def. Technol. 10 (3), 251–260.

Majumder, H., Paul, T.R., Dey, V., Dutta, P., Saha, A., 2017. Use of PCA-grey analysis and RSM to model cutting time and surface finish of Inconel 800 during wire electro discharge cutting. Measurement 107, 19–30.

Moreira, P.M.G.P., Santos, T., Tavares, S.M.O., Richter-Trummer, V., Vilaça, P., De Castro, P.M.S.T., 2009. Mechanical and metallurgical characterization of friction stir welding joints of AA6061-T6 with AA6082-T6. Mater. Des. 30 (1), 180–187.

Paulraj, S., 2018. Multi-response optimization of process parameters for GTAW process in dissimilar welding of Incoloy 800HT and P91 steel by using grey relational analysis. MS&E 314 (1), 012023.

Pearson, K., 1901. LIII. On lines and planes of closest fit to systems of points in space. Lond., Edinburgh, Dublin Philos. Mag. J. Sci. 2 (11), 559–572.

Saha, A., Mondal, S.C., 2017. Experimental investigation and modelling of WEDM process for machining nano-structured hardfacing material. J. Braz. Soc. Mech. Sci. 39 (9), 3439–3455.

Selvi, S., Vishvaksenan, A., Rajasekar, E., 2018. Cold metal transfer (CMT) technology-An overview. Def. Technol. 14 (1), 28–44.

Shah, L.H., Akhtar, Z., Ishak, M., 2013. Investigation of aluminium stainless steel dissimilar weld quality using different filler metals. Int. J. Automot. Mech. Eng. (IJAME). 8, 1121–1131. https://doi.org/10.15282/ijame.8.2013.3.0091.

Shanmugarajan, B., Shrivastava, R., Sathiya, P., Buvanashekaran, G., 2016. Optimisation of laser welding parameters for welding of P92 material using Taguchi based grey relational analysis. Def. Technol. 12 (4), 343–350.

Shu, F., Lv, Y., Liu, Y., Xu, F., Sun, Z., He, P., Xu, B., 2014. Residual stress modeling of narrow gap welded joint of aluminum alloy by cold metal transferring procedure. Construct. Build. Mater. 54, 224–235.

Sivaraman, A., Paulraj, S., 2017. Multi-response optimization of process parameters for MIG welding of AA2219-T87 by Taguchi grey relational analysis. Mater. Today: Proc. 4 (8), 8892–8900.

Tosun, N., Pihtili, H., 2010. Gray relational analysis of performance characteristics in MQL milling of 7075 Al alloy. Int. J. Adv. Manuf. Technol. 46 (5–8), 509–515.

Ünel, E., Taban, E., 2017. Properties and optimization of dissimilar aluminum steel CMT welds. Weld. World 61 (1), 1–9.

Wang, Z., Zhu, L.I., Wu, J.H., 1996. Grey relational analysis of correlation of errors in measurement. J. Grey Syst.-UK 8 (1), 73–78.

Zhang, H.T., Feng, J.C., He, P., Zhang, B.B., Chen, J.M., Wang, L., 2009. The arc characteristics and metal transfer behaviour of cold metal transfer and its use in joining aluminium to zinc-coated steel. Mater. Sci. Eng. 499 (1–2), 111–113.

Received: 12 December 2022 | Revised: 8 February 2023 | Accepted: 23 February 2023

DOI: 10.1002/pol.20220734

REVIEW

JOURNAL OF POLYMER SCIENCE WILEY

Natural polymers used in the dressing materials for wound healing: Past, present and future

Bharti Sheokand[1] | **Monika Vats**[2] | **Anand Kumar**[3] | **Chander Mohan Srivastava**[1] | **Indra Bahadur**[4] | **Seema R. Pathak**[1]

[1]Department of Chemistry, Biochemistry and Forensic Science, Amity School of Applied Sciences, Amity University Haryana, Gurugram, Haryana, India

[2]Department of Chemistry, Dhanauri (PG) College, Dhanauri, Uttarakhand, India

[3]Department of Chemistry, SGRR (PG) College, Dehradun, Uttarakhand, India

[4]Department of Chemistry, Faculty of Natural and Agricultural Sciences, North-West University, Mafikeng, Mmabatho, South Africa

Correspondence

Monika Vats, Department of Chemistry, Dhanauri (PG) College, Dhanauri, Uttrakhand 247667, India.
Email: mona2k42000@gmail.com

Seema R. Pathak, Department of Chemistry, Biochemistry and Forensic Science, Amity School of Applieiences, Amity University Haryana, Gurugram, Haryana, India.
Email: seemapathak@gmail.com

Indra Bahadur, Department of Chemistry, Faculty of Natural and Agricultural Sciences, North-West University, Mafikeng, Mmabatho, 2735, South Africa.
Email: bahadur.indra@nwu.ac.za

Abstract

Wound healing is a complicated system that necessitates an appropriate environment to aid healing. Wound dressing is among the most important external variables in wound repair. Technology advancements have led to the creation of a variety of dressings that treat various wound types by focusing on the four stages of wound healing. Simplicity of application, sterility, antibacterial, non-adherent, gaseous exchange, non-toxicity, and other qualities are necessary for wound dressings. In order to fully regenerate and restore the structure and functionality of the skin, the ideal dressing should address the demands of the wound. So, the kind of wound dressing used is based on the type of injury. This review focuses on the different types of natural polymers such as κ-carrageenan, chitosan, cellulose, gelatin, collagen, alginate, hyaluronic acid, and silk fibroin used in the development of dressing materials such as hydrogels, nanofibers, sponges, films, and various other types of scaffolds owing to their features, for example, biocompatibility, biodegradability, and similarity to human extracellular matrix (ECM) which aids in the healing process. The commercially available products based on these natural polymers are also discussed in the review. However, the majority of the natural polymer-based wound dressings still exhibit a number of problems like adherence, opaque, fast degradability, and lack of multifunctionality, thus these need to be addressed. A naturally inspired smart wound dressing is the need of the hour which aids in individual stages of healing by monitoring the multiple wound variables such as pH, temperature, electrical potentials and eases the incorporated drug and biological molecules as per wound healing progress with a variety of delivery systems.

KEYWORDS

biomedical application, natural polymer, wound healing

1 | INTRODUCTION

Skin is an essential and quickest-developing tissue of the human body. It is a multi-layered structure made up of the epidermis, dermis, and hypodermis, all of which play a vital role in helping the body to protect from radiation, heat, biological, chemical, physiological, and mechanical influences. Cuts, burns, surgeries, and illnesses can have an impact on the structure and functioning of the skin due to which the tissues in the affected area will be disrupted.[1]

In an ancient medical text from around 2200 B.C., the science of the healing process of wounds is written as

 © 2023 Wiley Periodicals LLC.

"three healing gestures" which include cleaning the wound, preparing plasters, and dressing the wound.[2] According to a document papyruses of 1400 B.C., physicians of ancient Egypt used a paste made of honey, grease, and lint to treat open wounds by removing skin and pus which enhances the healing process.[3] Taking out pus from the wound is important for healing but was not easy until the syringe was discovered in 280 B.C. by a barber in Greek which also helped in introducing liquids into the wound.[4] In the first century AD, Celsus gave a wise suggestion that if a person is injured, the things which should be focused are that he should not lose his life due to hemorrhage or inflammation, that is, cease the bleeding and keep the infection at bay.[5] The first use of an antiseptic for wound therapy with carbolic acid-soaked clothes was demonstrated in 1867 by Dr. Joseph Lister when the concept of infection was being understood.[6] Around 1880, the textbooks written on the wound care system emphasized the significance of skin washing, eradication of foreign materials, bone splinters, and irrigation with carbolic acid.[5]

Louis Pasteur in conclusion of his studies revealed that microorganisms did not arise spontaneously into the wound instead they came from a foreign source.[2] To avoid infection through any external pathogen, tissue regeneration is often performed through a competently manageable healing process that starts practically soon after the injury occurs.[7] Wound healing is an extremely complicated process that takes multiple weeks to finish and involves the concurrent phases of hemostasis, inflammation, proliferation, and remodeling.[8]

Wounds differ based on their nature, age of trauma, size, intensity, and site in the body. Mainly, wounds are divided into two types: acute wounds and chronic wounds. Open wounds, unhealed open wounds, abscesses, burns, lacerations, and trauma are examples of acute wounds. Chronic wounds comprise foot ulcers, arterial leg ulcers, venous leg ulcers, diabetic wounds, mixed leg ulcers, and pressure ulcers.[9] In contrast to chronic wounds, acute wounds recover quickly even without any snag. For this, regular wound healing activity is required, contributing to the tissue repair. Chronic wounds, on the contrary, are hard to cure and necessitate numerous dressing changes, restricted body movements, repeated the doctor's visits, and sometimes may result in a financial impact on the patients.[10]

As the world's average life expectancy has climbed, chronic wounds have shown a clear association with ageing process. There is an increasing impetus for the build-out of enhanced wound care that can fulfill the escalating demand of the present time.[11]

2 | PHASES OF WOUND HEALING

Wound healing is a multi-step process that necessitates the precise synchronization of numerous cell types and molecular signaling molecules at the wound area. Irrespective of the source of injury, it is subdivided into four known phases that are coordinated by time and activity until full recovery of the wound (Figure 1).[12]

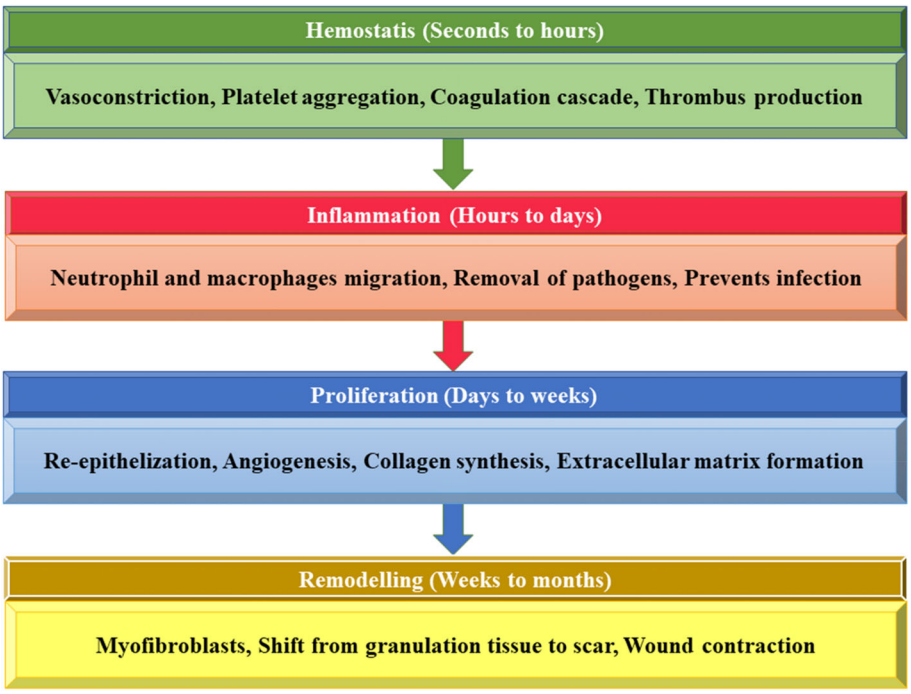


FIGURE 1 Phases of wound healing.

26424169, 0, Downloaded from https://onlinelibrary.wiley.com/doi/10.1002/pol.20220734 by Delhi Technological University, Wiley Online Library on [05/04/2023]. See the Terms and Conditions (https://onlinelibrary.wiley.com/terms-and-conditions) on Wiley Online Library for rules of use; OA articles are governed by the applicable Creative Commons License

2.1 | Hemostasis

This phase starts when tissue damage permits blood to flow into the exposed wounded area.[13] It occurs in three steps: vasoconstriction, primary hemostasis, and secondary hemostasis. The platelet is the essential cell in this process, while fibrinogen is the critical matrix component. When the skin gets injured, the first thing that happens to prevent bleeding from occurring is vasoconstriction of the vessel walls.[14] Following that, primary and secondary hemostasis takes place through two contemporaneous and mechanistically connected routes. During primary hemostasis, collagen exposure inside the subendothelial matrix stimulates platelet aggregation and platelet plug formation. Secondary hemostasis occurs when the coagulation cascade is activated, and soluble fibrinogen is transformed into insoluble strands that form the fibrin mesh. The platelet plug and fibrin mesh unite to produce the thrombus, which prevents bleeding, releases complements and growth factors, and offers a temporary scaffold for infiltrating cells required for wound healing.[15]

2.2 | Inflammation

This phase coincides significantly with the early hemostasis phase, which occurs within the first 72 h after cellular damage. It is traditionally described by the temporal activation and engagement of diverse innate and adaptive responses.[16] The inflammatory phase is characterized by a complicated series of molecular signals which eventually promote neutrophil and monocyte migration into the injured area in an effort to stop superfluous tissue damage and to clear pathogens and unwanted debris to avoid contamination. It primarily consists of vascular permeability, active blood cell movement, and the flow of plasma components into damaged tissue.[17] In this stage, the goal of chemokines is to encourage the production of pro-angiogenic substances, which aid in the migration, proliferation, and differentiation of endothelial cells, endothelial progenitor cells, and keratinocytes, which ultimately heal the wound.[12] Neutrophils are not normally found in healthy tissue. They are derived from promyelocytes in bone marrow in retaliation to chemokines generated from areas of cellular damage.[18] Neutrophils eliminate infectious risks by producing toxic granules, triggering an oxidative burst, commencing phagocytosis, and forming neutrophil extracellular traps. Phagocytosis allows neutrophils to ingest and kill germs and cellular debris. Wound healing is slow when there is deficiency of macrophages. So, expanding the number of monocytes or macrophages at the location of injury greatly expedites the wound repair process.

2.3 | Proliferation

One of the most crucial aspects in wound repair is the dynamic shift from inflammatory phase to the proliferative phase. The proliferation phase is driven by a rise in the number of particular cytokines and growth factors during the initial inflammation of wound. Extension or latency in the inflammatory phase has damaging consequences happening on the succeeding phases of wound healing process and generates fibrotic tissues, which may appear as malignancies in specific organs[19,20] and hypertrophic scars in the skin.[19,21] Due to which, the inflammatory phase of wound healing is strictly regulated and is linked to the proliferative phase at the cellular and molecular levels. Re-epithelialization, angiogenesis, and fibroplasia are all examples of cellular activity during this phase of treatment. In re-epithelialization, adjacent epidermal keratinocytes proliferate and migrates into the damaged areas and then, neo-epithelium differentiates into a stratified epidermis, and at last, the intact basement membrane zone restores to anchor the epidermis to the underlying dermis.[22] In physiologic wound healing process, within some hours of tissue damage, keratinocytes from the wound's margin starts moving centrally and after 2–3 days of injury, epithelial stem cells from the basal layer of the epidermis and the hair follicle root sheath begin multiplying. During this phase, the surface of wound heals via re-epithelialization, collagen synthesis, extracellular matrix formation, and vascular network restoration.[23]

2.4 | Remodeling

This phase begins after the end of the proliferation phase, that is, after several weeks of injury, and continues for up to 1 year.[24] This phase of wound healing is also known as maturation. During this phase, the water content present in the wound lessens. It denotes the shift from granulation tissue to scar, which entails slowed angiogenesis and the replacement of type III collagen in granulation tissue with type I collagen which is much stronger.[13] The remodeling phase in normal injuries lasts for some weeks to months in which wound contraction and scar maturation takes place. Because of the extended inflammation in case of burns, this phase of healing gets prolonged. The skin gains a definitive form in the course of the remodeling phase, which is mostly determined by the eventual arrangement of collagen fibers. It really should be emphasized that even the fully-grown scars only regain 80% of their previous strength properties.[25] A fully-fledged scar contains collagen in massive quantity.[26] This phase is characteristically determined by myofibroblasts

26424169, 0, Downloaded from https://onlinelibrary.wiley.com/doi/10.1002/pol.20220734 by Delhi Technological University, Wiley Online Library on [05/04/2023]. See the Terms and Conditions (https://onlinelibrary.wiley.com/terms-and-conditions) on Wiley Online Library for rules of use; OA articles are governed by the applicable Creative Commons License

which release Decorin during this phase, which is a protein that governs collagen fibrogenesis.[19]

3 | WOUND MANAGEMENT STRATEGIES

Wounds, particularly chronic wounds, are a global issue that costs millions of dollars each year. As a result, wound management has become a significant healthcare and economic burden. To ensure the best outcomes, a multidisciplinary strategy is frequently required. Physicians must understand the underlying principles and evidence-based strategies for managing acute or chronic wounds. Clinicians can improve wound care by understanding medical dressings, compression therapy, negative pressure wound therapy (NPWT), tissue constructs, hyperbaric oxygen therapy (HBOT), and so forth.

1. **Dressings:** There are numerous dressings available for wounds. The kind, thickness, position, extent of an injury, quantity of exudates, inflammation, and adherence, all have an impact on the choice of dressing. In contrast to dry dressings, wet dressings have the ability to speed the healing process.[27] Moisture-retentive dressings can assist in protecting the wound, minimize infection and pain, debride necrotic tissue, and encourage granulation tissue.[28] Depending on the clinical effectiveness, dressings are categorized as antimicrobial, occlusive, absorbent, adherent, and debridement. According to their physical nature, these are classified as an ointment, film, foam, or gel. Based on their origin, these are of three types: animal origin, herbal origin, and synthetic origin.[29]
2. **Compression therapy:** It is a widely applied, interdisciplinary, and well-established therapy that is employed in a variety of illnesses such as venous disorders, thromboses, lymphedema, and lipedema. It promotes venous return based on the body's position. The constant pressure delivered to the veins leads to a reduction in vessel diameter, a decrease in transmural pressure, and consequently in a flow rate. In a horizontal position, a low-pressure value is adequate to constrict superficial and deep veins, resulting in an increase in blood flow. Significantly, high-pressure values are needed to accomplish this while standing. Compression with a rigid, inflexible material provides stable support for the leg muscles, boosting the effectiveness of the muscular pump and thereby improving venous return. The latter reduces swelling while also relieving pain.[30]
3. **Tissue engineered skin construct:** When normal autografts could not be employed to replace injured skin, there is a higher risk of fatality, a longer hospitalization, and elevated National Health Service spending. Due to this, tissue-engineered skin bio-constructs are in high demand.[31] Skin tissue engineered and tissue repair procedures have evolved marvellously in the last several decades, making skin graft transplantation a tremendous achievement. Patrick Hardison's facial transplant operation in 2015 exemplifies contemporary and enormous progress in the domain of tissue engineering and transplanting methods that have really improved sufferers' lives.[32] The presently offered skin grafts are being used to cure wounds in addition to skin grafting (Table 1).[60]
4. **Surgical procedures:** There are several surgical alternatives for closing stages 3 and 4 pressure injuries which do not heal with conventional measures. Direct closure, split- or full-thickness skin grafts, skin flaps, musculocutaneous flaps, and free flaps are all options. The method of surgical treatment is based on the location of the wound, the patient's primary diagnosis, comorbid disorders, and the treatment goals. Long-term results of surgical treatment differ. Interpreters of surgical success include the patient's compliance with postoperative bed rest and preoperative risk factors for wound healing.[61]
5. **Hyperbaric oxygen therapy**: HBOT is being used to cure non-healing wounds. HBOT patients are enclosed in a specifically designed compression chamber where patients inhale pure oxygen at a pressure above sea level. The oxygen flow to the tissues is boosted, and healing time is decreased.[62,63] Particularly, collagen deposition, epithelial cell migration, and angiogenesis are promoted, fibroblast proliferation, enhances immune function, local tissue oxygenation, improve tissue hypoxia; local tissue edema is reduced; and anaerobic bacteria which may be present are killed, reduce wound infection through antibacterial effect.[64,65] Though, it is expensive and time-consuming therapy.[66]
6. **Negative pressure wound therapy (vacuum-assisted wound closure):** It is now a prominent therapy option for many acute and chronic wounds.[53] It is a non-invasive technique that uses controlled negative pressure to produce a vacuum, drawing tissue and fluid away from the wound via a sealed or foam dressing linked to a collection container.[54] NPWT improves the healing process by eliminating healing inhibitors, boosting blood circulation, encouraging angiogenesis and the formation of healing granulation tissue, and inflicting mechanical stress on the wound bed. NWPT has limitations such as aching, uneasiness, and the risk of skin irritation.[67,68]

26424169, 0, Downloaded from https://onlinelibrary.wiley.com/doi/10.1002/pol.20220734 by Delhi Technological University, Wiley Online Library on [05/04/2023]. See the Terms and Conditions (https://onlinelibrary.wiley.com/terms-and-conditions) on Wiley Online Library for rules of use; OA articles are governed by the applicable Creative Commons License

TABLE 1 Tissue engineered skin constructs.

Brand name	Manufacturer	Incorporated human cell	Cell source	Scaffold source	Scaffold material	Duration of the cover	Ref
Epidermal							
Epicel	Genzyme Biosurgery, USA	Cultured keratinocytes attached to petrolatum gauze support	Auto	-	-	Permanent	33
EpiDex	Modex Therapeutiques, Lausanne, Switzerland	Cultured keratinocytes from outer root sheath of scalp hair follicles (confluent cell sheet)	Auto	-	-	Permanent	34
MySkin	CellTran Ltd., Sheffield, UK	Cultured keratinocytes (subconfluent cell sheet)	Auto	Synth	Silicone support layer with a specially formulated surface coating	Permanent	35
Bioseed-S	BioTissue Technologies GmbH, Freiburg, Germany	Cultured keratinocytes (subconfluent cell suspension)	Auto	Allo	Fibrin sealant	Permanent	36
CellSpray	Clinical Cell Culture (C3), Perth, Australia	Non-/cultured keratinocytes (subconfluent cell suspension)	Auto	-	-	Permanent	37–39
Laserskin or Vivoderm	Fidia Advanced Biopolymers, Italy	Cultured keratinocytes (confluent cell sheet)	Auto	Recomb	Hyaluronic	Permanent	40
					Acid membranes		
Dermal							
Hyalograft 3D	Fidia Advanced Biopolymers, Abano Terme, Italy	Cultured fibroblasts	Auto	Allo	Hyaluronic	Permanent	41
					Acid membranes		
Hyalomatrix PA	Fidia Advanced Biopolymers, Abano Terme, Italy	-	-	Allo +synth	HYAFF layered on silicone membrane	Semi-permanent	42
TransCyte (DermagraftTC)	Advanced BioHealing, Inc., New York, NY and La Jolla, CA, USA	Cultured neonatal fibroblasts	Allo	Xeno +synth	Silicon film, nylon mesh, porcine dermal collagen	Temporary	43
Dermagraft	Advanced BioHealing, Inc., New York, NY and La Jolla, CA, USA	Cultured neonatal fibroblasts	Allo	Allo +synth	PGA/PLA, ECM	Temporary	44
AlloDerm	LifeCell Corporation, Branchburg, NJ, USA	-	Acellular (cadaveric)	Allo	human acellular lyophilized dermis	Permanent	45–47

(Continues)

26424169, 0, Downloaded from https://onlinelibrary.wiley.com/doi/10.1002/pol.20220734 by Delhi Technological University, Wiley Online Library on [05/04/2023]. See the Terms and Conditions (https://onlinelibrary.wiley.com/terms-and-conditions) on Wiley Online Library for rules of use; OA articles are governed by the applicable Creative Commons License

TABLE 1 (Continued)

Brand name	Manufacturer	Incorporated human cell	Cell source	Scaffold source	Scaffold material	Duration of the cover	Ref
Permacol Surgical Implant	Tissue Science Laboratories plc, Aldershot, UK	-	-	Xeno	porcine acellular diisocyanite cross-linked dermis	Permanent	48
EZ Derm	Brennen Medical, Inc., MN, USA	-	-	Xeno	porcine aldehyde cross-linked reconstituted dermal collagen	Temporary	49
SureDerm	HANS BIOMED Corporation, Seoul, Korea	-	-	Allo	human acellular lyophilized dermis	Permanent	50
Integra Dermal Regenerati-on Template	Integra NeuroSciences, Plainsboro, NJ, USA	-	Acellular (biosynthetic)	Xeno +synth	polysiloxane, bovine cross-linked tendon type I collagen and shark chondroitin-6-sulfate glycosaminoglycan GAG	Semi-permanent	51,52
Pelnac Standard/ Pelnac Fortified	Gunze Ltd, Medical Materials Center, Japan	-	-	Xeno +synth	silicone/silicone fortified with silicone gauze TREX, atelocollagen derived from pig tendon	Semi-permanent	53,54
Epidermal/dermal (composite)							
Karoskin	Karocell Tissue Engineering AB, Sweden	Native	Allo	Allo	Native human cadaver skin with dermal and epidermal cells	Temporary	31
Apligraf	Organogenesis Inc., USA	Cultured keratinocytes and fibroblasts	Allo	Xeno	Bovine collagen	Temporary	55
OrCel	Ortec International, Inc., USA	Cultured keratinocytes and fibroblasts	Allo	Xeno	Type i collagen matrix bovine collagen sponge	Temporary	56
PolyActive	HC Implants BV, Netherlands	Cultured keratinocytes and fibroblasts	Auto	Synth	Polyethylene oxide terephthalate/polybutylene terephthalate	Temporary	57
TissueTech Autograft System (Laserskin and Hyalograft 3D)	Fidia Advanced Biopolymers, Italy	Cultured keratinocytes and fibroblasts	Auto	Recomb	Microperforated hyaluronic acid membrane (ham)	Permanent	58
OASIS	Health point Biotherapeutics, USA	-	-	Xeno	Porcine acellular lyophilized small intestine submucosa	Permanent	59

26424169, 0, Downloaded from https://onlinelibrary.wiley.com/doi/10.1002/pol.20220734 by Delhi Technological University, Wiley Online Library on [05/04/2023]. See the Terms and Conditions (https://onlinelibrary.wiley.com/terms-and-conditions) on Wiley Online Library for rules of use; OA articles are governed by the applicable Creative Commons License

4 | DESIRABLE PROPERTIES OF WOUND DRESSING MATERIALS

While preparing a wound dressing, the critical points that must be considered to maximize the healing ability are (a) their capability to lessen infections because during infection bacteria enters in the wound and release such chemicals which prevents immune cells to kill these bacteria and delays the healing process, (b) stop bleeding as early as possible so, that loss of blood will be minimum, (c) biodegradable, (d) biocompatible, (e) provide or maintain moist environment because moist environment enhances the healing process by averting dehydration and promoting angiogenesis and collagen synthesis and should also have the capability of absorbing wound exudates,[69] (f) enhance the synthesis of connective tissue, maintain suitable tissue temperature to increase blood circulation at the lesion area, (g) should not cause any type of allergy because this will cause interruption in the healing process,[70] (h) high mechanical stability, (i) allows gaseous exchange between injured tissue and environment because wound healing requires oxygen. Oxygen is fundamentally involved in cell proliferation, angiogenesis, and protein synthesis, (j) antimicrobial properties. It works at a cellular level to stop the micro-organisms growth,[71] (k) uncomplicated sterilization, (l) nontoxic to avoid any side effects, and (m) effortless application and removal on the wound, should be non-adherent at the location of injury to avoid trauma while removing (Figure 2).[72]



FIGURE 2 Desirable properties of wound dressing materials.

5 | BIOPOLYMERS USED FOR DRESSING MATERIALS

Many natural and synthetic polymers are employed in the preparation of wound dressings. Nature is a fantastic resource, providing both novel ideas and strong building blocks for the next generation. Nowadays, natural polymers are preferred over synthetic polymers due to their ease of access and non-toxicity for therapeutic purposes and still being helpful in combating bacterial infections.[73] Many natural polymers have already been identified to have applications in wound healing such as chitosan-influence macrophage function so, fastens the wound repair process,[74] gelatin-anti-inflammatory and wound healing properties,[75] alginates-hemostatic properties in bleeding wounds, dextran- used in chronic wound dressing,[76] κ-carrageenan-outstanding ability to form gel, excessive fluid absorption capacity,[77] blood coagulation, collagen-capability to store a huge amount of water and to bio-mimic,[78] hyaluronic acid-antibacterial, anti-adhesive, lubricious, and viscoelastic, silk fibroin-hemostatic qualities, low inflammation, and oxygen permeability and water vapor permeability,[79] cellulose-biodegradable, prevents bacterial infection (Figure 3).

5.1 | κ-carrageenan

It is a natural polysaccharide originated from edible red seaweeds belonging to the class Rhodophyceae.[80] It's economical price and appealing properties such as the outstanding ability to form gel, excessive fluid absorption and preservation capability of fluid, biocompatibility, biodegradability, anti-inflammatory, antithrombotic, cytoprotective, antiviral, anti-tumor, antioxidant, anti-pathogenic, potential to deliver drugs, highly hydrophilic, and resemblance with the ECM have encouraged its use in the preparation of hydrogels which can be used in the tissue engineering.[81] Among the numerous hydrogel polysaccharides, it is one of the most researched polysaccharides for the production of wound dressing because, in addition to their intrinsic biocompatibility, they exhibit blood coagulation and immunological activities that aid in wound repair.[82] Enhanced antiviral and anticoagulant effects are often found in carrageenan with higher levels of polymerization, whereas the immunomodulatory and antioxidant effects of carrageenan are significantly boosted with a shift toward reducing molecular weight.[83]

Its hydrogel is made up of linear polymer chains that contain sulfate groups as shown in Figure 4A. All carrageenan components are soluble in water but not in fats, oils, or other organic solvents. The sulfate group levels

26424169, 0, Downloaded from https://onlinelibrary.wiley.com/doi/10.1002/pol.20220734 by Delhi Technological University, Wiley Online Library on [05/04/2023]. See the Terms and Conditions (https://onlinelibrary.wiley.com/terms-and-conditions) on Wiley Online Library for rules of use; OA articles are governed by the applicable Creative Commons License

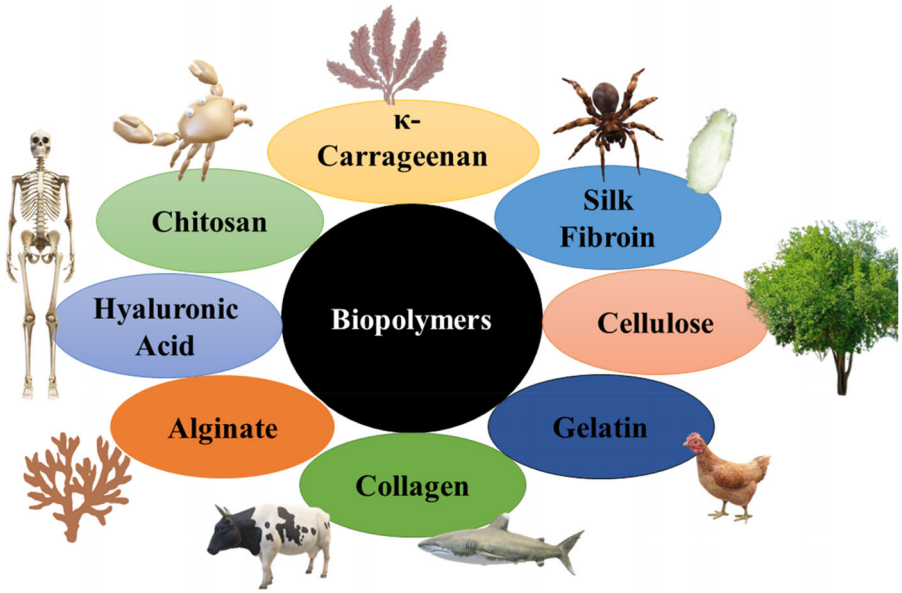


FIGURE 3 Types of natural polymers used in wound healing.

(which are extremely hydrophilic) and their related cations influence the solubility of carrageenan in water. The kind of main ionizable cations present in carrageenan as well as the balance among them—calcium (Ca^{2+}), potassium (K^{+}), sodium (Na^{+}), and magnesium (Mg^{2+}) have an impact on the gel strength, solubility, and viscosity of the solution. The potassium salt of κ-carrageenan requires a rise in temperature in order to become soluble because it is insoluble in cold water, but the sodium form will dissolve right away under the same circumstances.[84]

The antioxidant activity of κ-carrageenan is due to the hydroxyl groups present in its polymer chain. After degradation, the low molecular weight κ-carrageenan produces short polymer chains with a low concentration of sulfate groups, which reduces the intramolecular hydrogen bonding. As a result, hydroxyl groups activate the hydrogen bonds which in turn allows them to interact easily with the superoxide anions and hydroxyl radicals. The hydroxyl groups take the place of the depleted sulfate groups during the process of degradation, increasing the proportion of hydroxyl groups in the degraded products.[85] κ-carrageenan oligosaccharides showed exceptional free radical scavenging abilities. Carrageenan's ability to adhere to biological mucus through the formation of hydrogen bonds is largely dependent on the presence of hydroxyl and sulfate groups.[83]

This polymer is classified as a stimuli-responsive polymer because of the protonation/deprotonation of its sulfate group in response to alterations in the pH of the surrounding medium. Electrostatic repulsion between the negatively charged sulfate groups on neighboring chains increases the distance between the chains, allowing water to enter the hydrogel structure relatively easily, resulting in the high-swelling character. This is widely used in the production of biopharmaceuticals.[86]

Along with the above-discussed properties which helps in faster wound healing, it has some limitations also. Therefore, to overcome those, its modifications with some polymers (natural/synthetic) are carried out. Jaiswal et al. prepared a wound healing film with carrageenan, sulfur nanoparticles and grapefruit seed extract and to improve its properties, cross-linked them with copper chloride which shown wound healing effectiveness in a very short time.[87] Zepon et al. also prepared a wound dressing by incorporating locust bean gum, and cranberries extract in κ-carrageenan which proves to be useful in the early detection of bacterial wound infection.[82]

5.2 | Chitosan

It is a naturally present polysaccharide composed of glucosamine and N-acetyl glucosamine coupled by a β-(1,4) glycoside bond depicted in Figure 4B and can also be obtained via partial deacetylation of crustaceans' shell chitin. It has a cationic charge in acidic conditions due to the protonated amine group on the repeating glycoside residues, which increases its solubility in water. Its cationic property has piqued the interest of researchers as a polyelectrolyte excipient for medicinal applications.[88]

It has an impact on the first three phases of wound healing. In the first stage, they aid in preventing bleeding by encouraging platelet and erythrocyte aggregation. By interacting with the vast array of negatively charged molecules found on the surface of the activated platelets,

26424169, 0, Downloaded from https://onlinelibrary.wiley.com/doi/10.1002/pol.20220734 by Delhi Technological University, Wiley Online Library on [05/04/2023]. See the Terms and Conditions (https://onlinelibrary.wiley.com/terms-and-conditions) on Wiley Online Library for rules of use; OA articles are governed by the applicable Creative Commons License

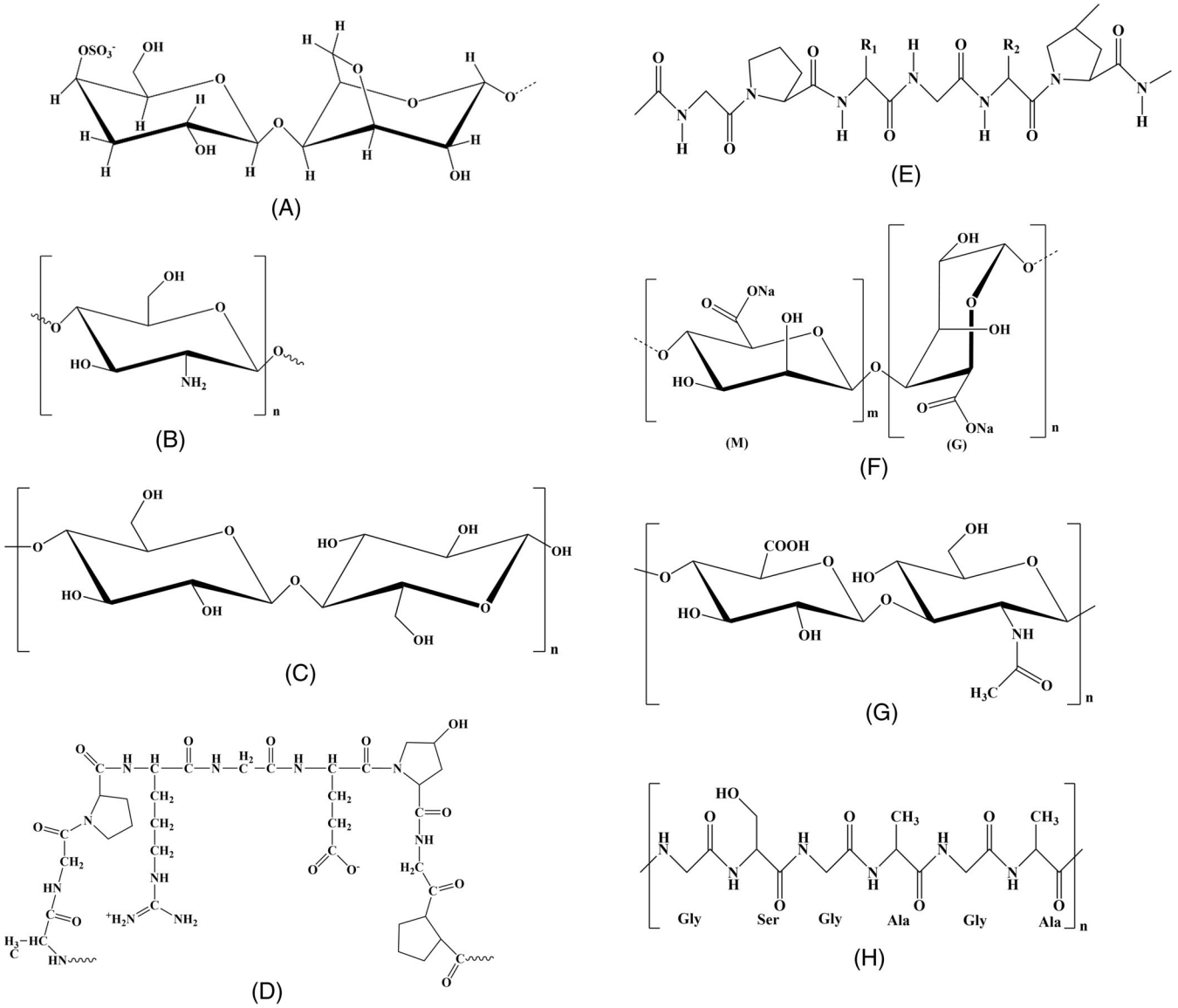


FIGURE 4 Chemical structure of (A) κ-carrageenan, (B) Chitosan, (C) Cellulose, (D) Gelatin, (E) Collagen, (F) Alginate, (G) Hyaluronic acid, (H) Silk fibroin.

positively charged chitosan encourages platelet aggregation. Electrostatic interactions between positively charged chitosan and negatively charged groups on the surface of the erythrocyte can facilitate the production of fibrin clots and erythrocyte aggregation. Chitosan can also collect and aggregate erythrocytes in blood by creating a three-dimensional network, which encourages the production of fibrin clots. Additionally, it inhibits the production of plasminogen activator, prolonging the duration of hemostasis by preventing the breakdown of fibrin.[89,90]

Secondly, in the inflammatory phase, they can help in removing bacteria from the site of wound. The NH_2 groups in chitosan undergo protonation to form —NH_3^+ cations when it is dissolved in acidic aqueous solutions.[91] The electrostatic interactions between -NH_3^+ cations and lipopolysaccharides on gram-negative bacteria's cell membrane or teichoic acids on Gram-positive bacteria's cell membrane will give rise to a non-uniform distribution of negative charges on bacteria. This will cause a mismatch between the synthesis of the cell wall and dissolution with a greater tendency in the direction of the dissolution.[92] Low molecular weight chitosan can enter the bacterial cell wall and bind to DNA to create complexes that interfere with the DNA polymerase and RNA polymerase activity, inhibiting replication transcription of DNA and RNA which hinders the process of the proliferation of bacteria.[93]

In the third stage of healing, they encourage the production of granulation tissue, which speeds up skin

26424169, 0, Downloaded from https://onlinelibrary.wiley.com/doi/10.1002/pol.20220734 by Delhi Technological University, Wiley Online Library on [05/04/2023]. See the Terms and Conditions (https://onlinelibrary.wiley.com/terms-and-conditions) on Wiley Online Library for rules of use; OA articles are governed by the applicable Creative Commons License

proliferation. The development of granulation tissues, which are made up of inflammatory cells, fibroblasts, and capillaries, is one of the crucial steps in skin restoration. Granulation tissue has the capacity to restore the damaged region and encourage epidermal rejuvenation. By encouraging the development of inflammatory cells (presented by macrophages), fibroblasts, and capillaries, chitosan can hasten the healing of wounds. Chitosan can encourage the production of cytokines like transforming growth factor-β (TGF-β), IL-1, and PDGF for macrophages. TGF-β causes macrophages to reach the site of the injury, which encourages fibroblast growth and boosts collagen production. The wound is then repaired, and the skin is remodeled to complete the healing process.[94,95]

Chitosan-based dressings used in wound repair exhibit a variety of intriguing wound healing capabilities. However, the main issue restricting chitosan's usage in the wound repair action is its low mechanical strength. To circumvent this constraint, it has been mixed with different types of inorganic nanomaterials to create an effective wound care solution.[74] Because of its convenience of deforming into gel, nanocomposite, scaffolds, sponge, beads, powder, and film, it finds a broad array of applications that includes tissue engineering, drug delivery, pharmaceutics, agriculture, wound repair, and bone healing.[96] Soubhagya et al. synthesized a film by freeze-drying approach by incorporating pectin and zinc oxide nanoparticles in chitosan which is found to be antibacterial so, proves to be suitable, safe, convenient, and effective for wound healing.[97]

5.3 | Cellulose

Cellulose is a superabundant, renewable, and limitless biopolymer. It is made up of four main components, that is, a glucose unit, the C_4—OH group (non-reducing end), the C_1—OH group (terminating end), and lastly aldehydes (reducing end) wherein glucose subunits are connected together by a β-(1,4) glycosidic bond as represented in Figure 4C.[98] It is the major component of a plant cell wall, in which it is connected with lignin, hemicellulose, and waxy aromatic compounds that must be separated to obtain pure cellulose. The linear structure of cellulose is kept intact in the form of a cellulose chain because of the existence of a hydrogen bond holding the oxygen atom and hydroxyl group together which has a significant impact on its physical properties. Owing to the intermolecular and intramolecular forces that are present between the hydrogen bonds, cellulose is a non-soluble substance. Cellulose is a stable polymer as a result of these two forces.[99] Its structure makes it suitable for usage in a variety of biological processes. Due to the fact that it is composed of a polysaccharide chain, which is a polymer of the glucose subunits, cellulose is inherently friendly with human tissue. This is easily modifiable without affecting its mechanical or structural qualities. Its semi-crystalline nature in an aqueous state allows it to have biological effects when altered. Due to these qualities and its cohesion in a moist microenvironment, it is simple to bind and can be used in any form.[100]

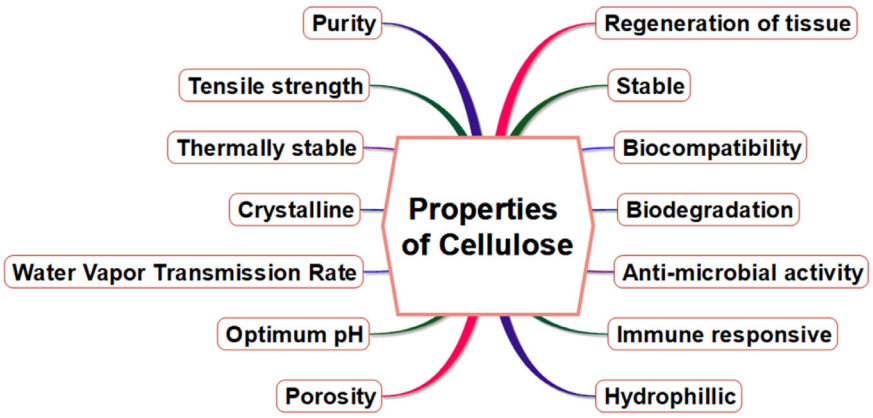
Through redox signaling, reactive oxygen species (ROS) contribute significantly to wound healing. Apoptosis and senescence are caused by lipid peroxidation, protein modification, and DNA damage, which are all detrimental effects of high ROS. During the inflammatory phase of wound healing, ROS production is majorly done by the neutrophils and macrophages.[101] Hydrogen peroxide at low concentrations can promote the growth of fibroblasts and aid in the healing of acute wounds. Continued ROS production can result in the development of matrix metalloproteinase and leads to the damage of protein, lipid peroxidation, and DNA, which can disrupt cells which cause tissue damage, and even cell death.[102]

Due to its various functional groups, carboxymethyl cellulose (CMC) has the potential to have a significant impact in the control of ROS against the synthesis of antibiotics. CMC keeps the area around the wound moist to promote the production of ECM, quick epithelialization, and recovery.[103] Through the process of fibrin polymerization, sodium carboxymethyl cellulose generated from plants shows hemostatic effect without activating the blood-coagulating agents.[104] In addition to this, oxidized regenerated cellulose has fibers due to which it acts as a scaffold for platelet aggregation. In consequence, this reduces dispersed bleeding over a larger region. Plant derived regenerated cotton cellulose also has the capacity to soak blood from the injured area. By developing a favorable microenvironment for healing, it might aid in the process of blood coagulation.[100] Plant cellulose has an average tensile strength and crystallinity, as well as a reasonable water holding capacity (60%). Basu et al. synthesized a wound-healing film of CMC which has the ability to fasten the wound repair process because these films promote the reepithelialisation due to the synthesis of collagen and the formation of granulation tissue at the location of wound.[105]

The purest form of cellulose is the cellulosic nanofiber which is derived from the bacterial extracellular matrix in which pectin, lignin and hemicellulose are not present.[106,107] The chemical makeup of bacterial cellulose and its nanofibrillar structure, which resembles an element of the ECM, notably collagen, are key factors for its biocompatibility. Furthermore, the immunogenic reaction is diminished or completely eliminated by the

26424169, 0, Downloaded from https://onlinelibrary.wiley.com/doi/10.1002/pol.20220734 by Delhi Technological University, Wiley Online Library on [05/04/2023]. See the Terms and Conditions (https://onlinelibrary.wiley.com/terms-and-conditions) on Wiley Online Library for rules of use; OA articles are governed by the applicable Creative Commons License

FIGURE 5 Properties of cellulose.



polysaccharide composition of bacterial cellulose.[108] It is hydrophilic and has a high-water holding capacity (100%). Figure 5 lists the properties of cellulose which are it's crystalline nature, biocompatibility, good tensile strength, durability, resistance to trauma and properties like the ease of loading with pharmaceuticals, and the potential to moisten the injured area simultaneously soaking produced exudates.[100] Besides permitting gas exchange, it prevents the bacterial infection due to a network of nanofibers which builds a barrier between bacteria and wound so, does not allow bacteria to infiltrate the wound. Additionally, it has the ability to be removed from the site of injury painlessly and without causing any harm to the newly produced tissue.[11,109] The optical transparency of a bacterial cellulose wound dressing offers the opportunity to use laser-based imaging diagnosis, such as multiphoton tomography, optical coherence tomography, and confocal laser scanning microscopy, enabling a non-invasive follow-up of the repair progress.[110] The effective mass production of the bacterial cellulose may 1 day serve as a vital biomaterial which can replace the wound dressings that are now in the market.

5.4 | Gelatin

It is a hydrocolloid protein that is synthesized by the chemical hydrolysis of collagen. As shown in Figure 4D, gelatin's molecular backbone is made up of different sequences of amino acids and because of this composition, it does not produce hazardous breakdown products during enzymatic degradation, making it an ideal option for therapeutic dressings to cure wounds.[111] It is a natural replica of the ECM found in human body tissues and organs. It is commonly applied in the area of tissue engineering. Several biomedical researcher's attention is drawn to gelatin for the production of novel biomaterials because of its easy availability, low cost, great biocompatibility, excellent biodegradability, non-immunogenicity, non-carcinogenic, excellent molding ability, and adaptability.[112]

Proline, glycine, and hydroxyproline are constituents of gelatin. The gelatin's glycine amino acid composition enables cells to attach to surfaces.[113] The method of extraction has a significant impact on the structure of gelatin. However, it has a poor melting point and is made up of randomized macromolecular and heterogeneous structures.[114] Gelatin can be metabolized by human tissue, which is the key factor in the pharmaceutical industry's desire to use it. The activity of gelatin can be altered. Gelatin's qualities are influenced by the temperature at which it dries, and it has the ideal ability to form films. This qualifies gelatin for widespread usage as a medication delivery medium.[115]

Gelatin's lower antigenicity makes it a really well biopolymer for use in various biological applications. Gelatin, on the other hand, is a hydrophilic protein, and cross-linking is typically necessary to improve mechanical performance and durability, rendering gelatin materials insoluble in biological contexts because if cross-linking will not be done, it will dissolve in the wound exudates and will not be able to heal wounds.[116] Anindita et al. prepared a gelatin-based film and using glutaraldehyde as a cross-linker which improves mechanical properties of the film.[117] The porous framework of gelatin-based dressing helps in the cell migration which provides structural and mechanical support for the regeneration of tissues and also soak wound exudates and keeps moisture in the wound, aiding wound healing. Gelatin contains arginine-glycine-asparagine sequences that are beneficial for cell adhesion, differentiation, and proliferation. In healing process, gelatin matrices stimulate epithelialization and the production of granulation tissue.[118]

When it comes to a biomaterial, the question of immune response stimulation is particularly important. An appropriate biomaterial should not cause the host tissue to mount an immune response. Gelatin has been

26424169, 0, Downloaded from https://onlinelibrary.wiley.com/doi/10.1002/pol.20220734 by Delhi Technological University, Wiley Online Library on [05/04/2023]. See the Terms and Conditions (https://onlinelibrary.wiley.com/terms-and-conditions) on Wiley Online Library for rules of use; OA articles are governed by the applicable Creative Commons License

shown to promote immunogenicity in the host tissue. But it is two times less than what collagen causes. Gelatin can be cross-linked via fructose, dextran dialdehyde, formaldehyde, carbodiimides, diisocyanate, diepoxy, genipin, and glutaraldehyde.[112,116] A covalent bond is created during the crosslinking of gelatin. As a result, a second network is formed and chemical bonds hold it in place.[119] Generally, it is believed that in order to trigger an immune response, biomaterials need to be covalently linked to a larger protein.[120] If a covalent bond is present, it can firmly attach to a carrier molecule, which is usually a protein. The hapten-carrier complex stimulates the production of antibodies, making it immunogenic. An immune or allergic reaction is then brought on by the hapten's interaction with the antigen-specific antibodies.[121] Gelatin suppressed its immunogenicity after being exposed to a covalent net point.[122]

5.5 | Collagen

It is a vital proteic component of the extracellular matrix. Figure 4E represents the structure of collagen. It can be extracted from bovine, equine, porcine, avain, cattle slaughterhouse wastes and fishery by-products.[123,124] Collagen is biocompatible, biodegradable, have the ability to bio-mimic, and to hold huge amount of water which helps in the promotion of cell health so, it is an excellent biomaterial for the purpose of wound healing. It has the potential to self-assemble into fibril complexes under certain physical circumstances. Type I collagen is the most plentiful and easily extractable from various tissues including skin, tendons, bone, and blood vessels.[78]

Native collagen is crucial in each stage of the healing process. In the hemostasis phase, it acts as a key activator for the initial platelet reaction after the injury. Additionally, it enables platelets to attach at the location of the cut and form a clot to halt the bleeding.[125] It functions like a chemotactic agent during the inflammatory phase by generating a microenvironment for the start of the healing process while forming a layer of protection for the skin.[126] In the proliferative phase, collagen promotes the formation of new tissues and speeds the deposition of granulation tissues.[127] It improves the binding of cells to the scaffold by integrin binding and the availability of a cell-producing enzyme that is able to directly break it. This is made feasible by the amino acid sequence arginine-glycine-aspartic acid, which is present in collagen and is identical to that found in the human body which enhances cell adhesion and proliferation.[128] The consistency of the skin starts to develop during the maturation phase, and re-epithelialization progresses. During this process, collagen provides sufficient nutrients to the wound, promoting the healing process and assisting in scar minimization.[129]

When a scaffold is applied to skin, collagen causes a very slight immunological response which depends on the extraction method, the crosslinking agents (chemical glycation procedures or heat treatments), or the presence of cell fragments.[122,123] But it is possible to prevent it by eliminating the terminal telopeptide from the collagen molecule. The order of the collagen fibril pattern is disturbed when that specific structure is removed, resulting in an amorphous state. After this, the positive electrons cause the collagen surface to become extremely soluble, destroying the collagen scaffold's immunogenicity feature.[130]

The incorporation of herbal ingredients in natural polymers for a novel dressing material constitutes a significant advancement in wound healing. Cross-linking in natural polymers boosts mechanical and thermal properties through hydrogen bonding.[131]

5.6 | Alginate

It is an anionic polymer acquired from brown algae. As shown in Figure 4F, it is a series of linear copolymers formed of (1,4)-linked D-mannuronate and L-guluronate residues in various ratios based on its source. It is antimicrobial and hydrophilic in nature. It also has gelation and moisture absorbing properties. Hydrogel, film, scaffold, foams, microspheres, microcapsules, fibers, and sponges are formed with alginates. Wound dressings made from alginate are nontoxic, biocompatible, oxygen permeable, reduced wound aromas and distress, biodegradable, nonimmunogenicity, and possess hemostatic characteristics due to which it produces a moist environment at the site of injury which enhances the healing process and granulation tissue production.[132,133]

Alginate dressings are usually created by ionic crosslinking of an alginate solution with calcium ions to produce a gel, which is then processed to create fibrous nonwoven dressings and freeze-dried porous foam. Dry alginate dressings absorb wound exudates to re-gel, and the gels can then provide water to a dry wound. This keeps the wound site physiologically moist and reduces the risk of pathogen infection.[126] When a dressing comprising, alginate comes into touch with the wound exudate, the calcium ions in the alginate begin to interchange with the sodium ions in the exudate or blood. Alginate fibers enlarge, partly dissolve, and solidify when enough calcium ions are exchanged with sodium ions. Alginates are well known for encouraging monocytes to produce IL-6 and TNF-α, which have a

26424169, 0, Downloaded from https://onlinelibrary.wiley.com/doi/10.1002/pol.20220734 by Delhi Technological University, Wiley Online Library on [05/04/2023]. See the Terms and Conditions (https://onlinelibrary.wiley.com/terms-and-conditions) on Wiley Online Library for rules of use; OA articles are governed by the applicable Creative Commons License

significant contribution in the healing process.[127] The average molecular mass of alginate which is available in the market is more than the renal passage limit of human kidneys, thus despite the fact that gel created is disintegrated in the physiological environment of mammals, the alginate molecules cannot be completely cleared from the human body.[125] By stimulating macrophages to release TNF-α, which starts inflammatory signals, alginates hasten the process of healing. When the dressings formed with alginates are placed over the wound site, ions present in the alginate are interchanged with blood to produce a protective film.[128]

To reap the benefits of alginate's biocompatible and biodegradable nature, it is frequently combined with polymeric matrices (natural and synthetic), proteins, and ceramic materials to build new tissue engineering support.[134] It can boost macrophage activity and cytokine levels at the location of injury.[135] When it encounters wound exudates, it dissolves owing to ion exchange with body fluids, resulting in the creation of a solubilized gel structure which promotes wound healing.[136] Because of the hemostat, gel-forming, biocompatible ability, and also a very absorbent material, it is commonly used to treat hemorrhagic wounds. It is easy to remove the dressing without any harm and with less pain due to the gelation feature of alginate. It promotes fast re-epithelialization by providing moist conditions.[2]

5.7 | Hyaluronic acid

It is a biopolymer belonging to the glycosaminoglycan family of hetero-polysaccharides present in human vitreous humor, roosters comb skin, joints, umbilical cord, and connective tissue. It is also produced through microbial fermentation.[137] A linear chain of repeated disaccharide units connected by β-1,4-glycosidic linkages make up the main structure of hyaluronic acid. Each disaccharide is made up of D-glucuronic acid and *N*-acetyl-D-glucosamine that are joined together by β-1,3-glycosidic linkages as shown in Figure 4G. Each large functional group (hydroxyl, carboxyl, acetamido, and anomeric carbon) is in the sterically beneficial equatorial position, while each small hydrogen atom takes up the less energetically beneficial axial position, resulting in a highly energetically stable structure if both monosaccharides are in the β configuration. Due to this restriction on free rotation around the glycosidic bonds of the hyaluronic acid backbone, hydrophobic patches (CH groups) alternate with polar groups that are connected by intra- and intermolecular hydrogen bonds in a stiff conformation.[138]

It is antibacterial, anti-adhesive, nontoxic, non-allergic biodegradable, biocompatible, lubricious, and viscoelastic in nature. It is used in bone regeneration, orthopedics, cosmetology, tissue engineering, tumor cell targeting, dentistry therapies, skin care service, wrinkle reduction, and skin hydration.[10] Hyaluronic acid is a polymer that has demonstrated exciting effects on wound healing, including the promotion of epithelial cell migration, the decrease of inflammatory processes, enhancement of angiogenesis, and stimulation of endothelial cell proliferation and migration.[139] The hydrophilic nature of hyaluronic acid is due to the significant number of carboxyl and hydroxyl groups present in it. This property enables it to absorb exudate and improve cell adherence.[140] It has been discovered that the hyaluronic acid breakdown product has a pro-angiogenic impact. By attaching to the keratinocytes' CD44 receptors, it triggers a series of cascades that promote differentiation.[141]

Hyaluronic acid-based film-Hyalosafe® is developed which provides a humid environment at the injury site and allows for ongoing monitoring of the healing process due to its transparency.[142] It governs the ECM, and also be easily identified by unique surface receptors of diverse cells throughout the healing process. During the wound healing process, in adults, high molecular weight hyaluronic acid concentration achieves a maximum peak, and is then followed by a catalytic degradation that is mediated by hyaluronidases and ROS. It has anti-inflammatory and anti-angiogenic properties whereas, low molecular weight hyaluronic acid fragments generated the expression of angiogenic and pro-inflammatory cytokines, which provide sufficient blood flow to the injured area.[139]

pH has an impact on the properties of hyaluronic acid which is of great use in the tissue repair process because when an injury happens, the pH is around 8 on the site of wound, dropping to approximately 5 when recovery stops.[140] Because of its swift enzymatic breakdown in physiological medium, its pure form may have limited clinical applicability. Li et al. created hyaluronic acid films grafted with pullulan which shows the improved stability and biological performance of hyaluronic acid in wound repair process.[143]

5.8 | Silk fibroin

It is a natural fibrous polymer generated from silkworms, spiders, and other insects. The silk fiber is made up of two sub-fibers, the core of which is fibroin, and the two cores are covered and bundled together with sericin.[144] Its structure is shown in Figure 4H. Hydrophobic β-sheet crystallites and hydrophilic amorphous domains make up the majority of silk fibroin's structure. The heavy and light chain polypeptides that make up the crystallite

26424169, 0, Downloaded from https://onlinelibrary.wiley.com/doi/10.1002/pol.20220734 by Delhi Technological University, Wiley Online Library on [05/04/2023]. See the Terms and Conditions (https://onlinelibrary.wiley.com/terms-and-conditions) on Wiley Online Library for rules of use; OA articles are governed by the applicable Creative Commons License

domains primarily include the amino acids glycine and alanine connected together by a single disulfide bond at the heavy chain's C-terminus; hydrogen bonds hold the neighboring chains in an antiparallel configuration known as a β-sheet. Additionally, silk fibroin contains glycoprotein P25, which supports the integrity of the structure by being noncovalently linked to the heavy and light chains. The fibrous characteristics of the silk fibers are mostly caused by the heavy chain. Glycine (46%), serine (12%), and alanine (30%) are the three most prevalent amino acids found in this chain. The nonfibrous light chains are primarily including isoleucine, leucine, valine, and other acidic amino acids.[145,146]

When a proton is transferred, the polar carboxy and amino groups in fibroin can potentially be implicated in electrostatic and dipole interactions. Since nonpolar hydrophobic amino acids make up over 3/4 of fibroin, it is important to consider the hydrophobic interactions that make fibroin resistant to most solvents.[147]

Its benefits in wound healing include good strength, suppleness, thermal stability up to ~250 °C, lack of cytotoxicity, oxygen permeability, slow deterioration, low immunogenicity, and high capacity for water absorption to facilitate migration, proliferation, and differentiation.[148] Films made from silk fibroin provide intriguing qualities for a wound healing material, including biocompatibility, biodegradability, mechanical resistance, ease of processing, and low-inflammatory response.[149]

Because of its hemostatic qualities, low inflammation, and oxygen permeability and water vapor permeability, it is investigated for skin restoration. Cellular adhesion, wound contraction, re-epithelialization, angiogenesis, and collagen production are all hastened by fibroin matrices. Cytokines and growth factors are known to be essential in healing process. Several investigations have shown the importance of silk fibroin in suppressing the increased proinflammatory cytokines during the inflammation phase of the healing process, leading to a protective effect in cells and tissues. Other actions of silk fibroin include stimulation of cell migration and inactivation of the apoptotic pathway.[146]

In small animal models, silk fibroin film dressing encourages faster wound repair and improved skin regeneration than hydrocolloid dressing.[79] When it degrades, it creates nontoxic amino acids that are digested by the body. Wax-coated silk fibroin woven fabrics with sericin-silk fibroin/gelatin spongy bioactive layers were synthesized for wound healing applications and when compared with a commercial 3M™ Tegaderm™ dressing, this structure demonstrated superior wound healing ability with reduced adherence to the wounds. Because of their capacity to seal various wound flaws and avoid microbiological contamination, its films are thought to be effective structures for wound repair.[150]

6 | DIFFERENT MATRICES USED FOR WOUND HEALING

6.1 | Hydrogels

Hydrogels are hydrophilic gels having a three-dimensional cross-linked polymeric network that can maintain their structure after swelling. Its high-water content not only keeps the environment moist, reducing the possibility of scar development, but it also provides a soothing feeling and low adhesion with tissue, reducing discomfort for sufferers. Because of the great porosity of hydrogels, oxygen transfer is also promoted, permitting tissue to "breathe." It also acts as a protective layer to avoid bacterial infections while also promoting cell migration and epithelization at the site of injury.[151] In regard to biocompatibility, hydrogels do have a distinct set of features, such as high elasticity and a structure akin to biological tissues. Such properties make hydrogels a good choice for wound dressings, therefore various commercially accessible hydrogel dressings are already available.[152]

Hydrogels could be made into injectable forms. Injectable hydrogels have characteristics like filling wound sites having uneven space. These also have potential to encapsulate bioactive compounds and cells in situ, which is critical for increased skin tissue regeneration.[153]

Hsu et al. created gelatin-cross-linked hyaluronic acid-based hydrogels enclosed with recombinant thrombomodulin, whose in vivo healing investigations on diabetic mice revealed that thrombomodulin-loaded hydrogels had considerably greater healing effect than plain hydrogels.[154]

Zhang et al. developed dopamine-functionalized hyaluronic acid hydrogels including an arginine derivative. The in vivo studies concluded that increasing the content of arginine derivative reduced oxidative stress, which considerably stimulates a quicker recovery system.[155]

Thanh et al. used HRP-catalyzed cross-linking procedures to incorporate the antioxidant gallic acid-conjugated gelatin (GGA) into gelatin-hydroxyphenyl propionic (GH) hydrogels, resulting in an injectable hydrogel with improved free radical scavenging characteristics. More crucially, in in vivo studies, the healing process was significantly accelerated by ROS scavenging hydrogels with unanticipated regenerative wound healing features, as evidenced by hair follicle production; increased neovascularization; and highly coordinated

26424169, 0, Downloaded from https://onlinelibrary.wiley.com/doi/10.1002/pol.20220734 by Delhi Technological University, Wiley Online Library on [05/04/2023]. See the Terms and Conditions (https://onlinelibrary.wiley.com/terms-and-conditions) on Wiley Online Library for rules of use; OA articles are governed by the applicable Creative Commons License

collagen fiber orientation. As a result, it can be contemplated that injectable GH/GGA hydrogels will prove excellent materials for tissue regeneration applications.[156]

Capanema et al. synthesized superabsorbent hydrogels from CMC and PEG using citric acid as a crosslinker. To achieve the high degree of cross-links, the materials were stored at 80 ± 2 °C for a day. By removing water molecules during this stage, an esterification reaction between the acid and hydroxyl groups of citric acid was enabled. The produced materials showed great absorbency, and it was proposed that they could be employed as skin substitutes for wound healing therapy.[157]

Li et al. used a solution spinning technique to produce CMC hydrogel fibers using aluminium sulfate as a cross-linker. These CMC hydrogel fibers showed a high moisture absorbency, making them ideal for wound healing applications. In an aqueous solution, nonwoven CMC viscose fibers with high absorption capacity and moist circumstances which have good vapor penetration capability were successfully synthesized. They can be employed as low-cost but high-quality dressings.[158]

Chen et al. designed a complex hydrogel dressing for drug delivery and wound healing applications using gelatin microspheres. The gelatin microspheres containing tetracycline hydrochloride were prepared using the emulsion cross-linking process. Following manufacturing, the complex gel dressings were fabricated by integrating the microspheres further into CMCS-oxidized alginate hydrogel. The dressing demonstrated strong antibacterial activity, highlighting its potential application as wound dressing.[159]

6.2 | Nanofibers

Nanofibers are nanoscale structures that closely resemble the human ECM structure, as well as having permeability, porosity, moisture retention, superior mechanical capabilities, and a large surface area, which are just a few of the qualities that make them so frequently explored and used. These properties are essential for cell attachment and development. Nanofiber diameter and characteristics are strongly connected with each other. Physical or chemical characteristics of nanomaterials differ from those at higher scales when they reduce the size of matter to the nanoscale. Due to the above-described properties, polymeric nanofiber materials are potential materials for applications such as tissue engineering, drug carriers, and wound healing.[160]

Recent studies have focused on the electrospinning technique for the synthesis of continuous nanofibers from natural or synthetic polymers that have significance in the development of wound dressings.[161] Electrospinning is adaptable and efficient in the manufacture and assembly of structured or more complicated nanofibers, and the outcomes are consistent when compared to other nanofiber manufacturing techniques.[162] These days, a number of different polymers with adaptable properties are chosen to be combined with inorganic nanoparticles, drugs, functional particles, and bioactive substances in order to fulfill the demands for hemostatic dressings since single polymer electrospinning cannot do so.[163]

In regard to structure, electrospinning is effective in creating three-dimensional fibrous macrostructures in addition to conventional two-dimensional nanofibrous by merely altering the spinnerets with various structures like coaxial, Janus, triaxial, and so forth. Multiple drug-releasing mechanisms are frequently permitted by these structures. Drug release that occurs in two phases (biphasic) has potent applications in the biomedical field. It is a quick release of a viable concentration of the drug that is accompanied by a slow and controlled release. This is done in order to maintain a sustained drug concentration. It is produced by employing two distinct water-soluble polymers. These polymers and loading components can be combined by numerous methods that have created unlimited opportunities in areas like drug delivery, controlled release of drugs, scar minimization, active substance encapsulation, and wound healing in general, including hemostasis, antibacterial activity, and accelerated healing.[163,164]

Nanofiber films can be used as a wound dressing. It is convenient to use because it is thin and delicate, and it could be fabricated in a variety of sizes and patterns. With the nanofiber films, it is easy to deliver drugs, as they can be taken whenever and wherever, even without water. Due to this, it is an appropriate option for giving medication to young ones. Films made of nanofibers can have several layers. To promote unidirectional drug release and enhance drug usage, the hydrophilic and hydrophobic layers of the nanofiber film combine with each other. The nanofiber film sticks to the site of the wound for a considerable amount of time while being in constant close contact with the mucosa. As a result, the number of doses of medicine decreases and the rate of drug absorption are boosted.[164]

El-Aassar et al. used an electrospinning approach to formulate hyaluronic acid-based nanofibers impregnated with silver nanoparticles. The mechanical quality investigation revealed that the tensile stress of the nanofibers embedded with silver nanoparticles was nearly double to that of the plain nanofibers. These nanofibers also outperformed antibacterial activity in comparison of plain nanofibers against *B. subtilis* and *E. coli*.[165]

26424169, 0, Downloaded from https://onlinelibrary.wiley.com/doi/10.1002/pol.20220734 by Delhi Technological University, Wiley Online Library on [05/04/2023]. See the Terms and Conditions (https://onlinelibrary.wiley.com/terms-and-conditions) on Wiley Online Library for rules of use; OA articles are governed by the applicable Creative Commons License

Yao et al. used electrospinning technique to develop gelatin nanofibers incorporated with *C. asiatica* extract. In contrast with gauze, pure gelatin membranes, and marketed wound dressings, injury of rat skin administered with the developed membrane had the best healing rate. The weight loss observations indicate that the membranes are biodegradable.[166]

Ahn et al. reported the use of rotary jet spinning to create a nanofibrous dressing which was fully plant-based and composed of cellulose acetate and soy protein hydrolysate. The spun nanofibers effectively imitate the physicochemical features of the skin's extracellular matrix while also holding a large amount of water. These scaffolds promote re-epithelialization as well as epidermal thinning while decreasing cicatricial development and collagen anisotropy. These findings support the efficacy of these dressings like a new wound dressing.[167]

Charernsriwilaiwat et al. prepared a nanofibrous mat by electrospinning with lysozyme from chitosan and ethylene diaminetetraacetic acid (EDTA) with polyvinyl alcohol solution. When compared to the controls, these nanofiber mats accelerated the recovery process. Fast liberation of lysozyme was acquired from the nanofibrous mats. The findings indicate that such biodegradable, biocompatible nanofibrous mats can be employed as concealed wound dressing.[168]

6.3 | Sponges

Sponge dressings have indeed been developed for wound healing due to its high porosity, which aids in gas permeability as well as water vapor evaporation.[169] Due to their porous structure and swelling profile, they create a moist wound environment.[27] Because of the micro-porosity, sponges can absorb a considerable volume of wound exudates (over 20 times of their dry weight). They usually provide good cell contact while remaining soft and pliable.[170] These are generally non-adherent and need supplementary wound dressing to hold them in place. Sponges held the considerable potential for speeding wound healing due to the good structural properties aforementioned.

Lu et al. used chitosan-l-glutamic acid-hyaluronic acid sponges infused with silver nanoparticles for wound dressing preparation. The antibacterial property was significantly enhanced by the addition of silver nanoparticles. The sponges' in vitro cytotoxicity tests revealed that they had a cell viability of approximately 80% on L929 cells. In vivo recovery assessment of developed sponges on full-thickness cutaneous wounds showed recovery on the third day and ~69% wound contraction for the sponges infused with silver nanoparticles.[171]

Cui et al. reported a pH-responsive copper peroxide incorporated dressing consisting of copper hydroxide with gelatin sponge, which was subsequently treated with hydrogen peroxide. In vitro tests revealed that the developed dressings are effective against *E. coli*, *S. aureus*, and *P. aeruginosa*. Furthermore, copper ions discharged from the sponge can activate angiogenesis as well as collagen accumulation at the same time. Besides that, the developed dressing can release ·OH selectively in microbial infected wounds instead of in healthy tissue which proposes a way for boosting antibacterial activities while reducing hazardous side effects.[172]

6.4 | Films/membranes

Films are flexible, translucent, and elastic materials prepared by the deposition of a compound on a surface. They allow gaseous exchange and passage of water vapor from the site of the injury, while preventing microbial pathogen penetration. Films can also increase hydration, clear debris from the skin, and release assets that may have some cosmetic or therapeutic effects.[173,174] The transparent film permits continuous supervision of the wound without lifting it. Films, on the other hand, have a lower ability to collect wound exudates, rendering them inappropriate for heavy oozing wounds and may cause damage if not removed properly.[167]

Duan et al. synthesized hyaluronic acid-based films infused with curcumin that did not lead to discomfort to skin. The cytotoxicity of unbound curcumin as well as curcumin grafted films revealed no detrimental effects during 72 h. The healing result demonstrates that the wounded diameter of each group decreased over time and all groups showed a constriction at the incision site on the third day.[175]

Luo et al. coupled silk films either with flat or none topography structured with ECM components to speed up corneal wound healing which is dependent on ECM and topographical signals that regulate regenerated cell migration and proliferation. Coating structured silk films with collagen I accelerate rabbit and mouse corneal epithelial cell proliferation and wound healing. This increased cellular response was associated with the redistribution, as well as an increase in the size and actual quantity of focal adhesion.[176]

Patel et al. fabricated a lupeol-entrapped chitosan-gelatin hydrogel (LCGH) films with glycerol as a plasticizer and glutaraldehyde as a crosslinker. Antioxidant scrutiny indicated that LCGH film and lupeol both had remarkable antioxidant activities. It showed good antimicrobial properties. The MTT test confirms that the CGH film provided satisfactory cell viability and was nontoxic.

26424169, 0, Downloaded from https://onlinelibrary.wiley.com/doi/10.1002/pol.20220734 by Delhi Technological University, Wiley Online Library on [05/04/2023]. See the Terms and Conditions (https://onlinelibrary.wiley.com/terms-and-conditions) on Wiley Online Library for rules of use; OA articles are governed by the applicable Creative Commons License

These findings suggest that CGH films can be an excellent delivery strategy for the controlled delivery of lupeol for an improved wound repair process.[177]

Zhang et al. using green chemistry developed silk fibroin film which has amazing attributes such as transmission, fluid handling ability, moisture vapor permeation, waterproof, bacterial resistance capabilities, and biocompatibility. In vivo research reveals that the silk fibroin film effectually minimizes overall wound recovery time while improving skin regeneration when compared to commercial dressings. Following testing in a pig model, it was found to be safe and efficacious in full-thickness skin problems. Finally, a test on randomly selected 71 patients reveals that the silk fibroin film considerably lowers the duration of wound recovery and the occurrence of adverse effects in contrast to commercial dressings. The data revealed that the silk fibroin film enhances the recovery process, laying the groundwork for its application in skin repair and regeneration.[79]

Gu et al. fabricated silk fibroin and chitosan blended membranes for the treatment of wound using alginate aldehyde as a crosslinker. They could answer the need for wound dressing due to their water permeability, absorption, and stability. Scanning electron microscopy and MTT experiments revealed that the membranes increased cell growth and attachment. These findings suggested that the developed membranes treated with alginate aldehyde in an acceptable ratio might be employed as a commercial candidate for wound healing applications.[178]

6.5 | Other scaffolds

There are polymer based scaffolds which can be used in wound healing as potential dressings such as bandages, foams, gauze, matrix patches, microspheres, nanoparticles, hydrocolloids, etc.[151] Scaffolds provide nourishment for tissue formation and also cover a wound, acting as an effective "fence" against infection. These offer physical support. Scaffolds interact with cells in order to activate the processes like cell adhesion, proliferation, and differentiation, which leads to the assembly of cells into functional units. Scaffolds have to be porous as well as biocompatible so that cells can adhere and pass through their structures.[179]

Gokce et al. fabricated a three-dimensional dermal matrix made of hyaluronic acid loaded with resveratrol for the healing of diabetic wounds. The sterility investigations revealed that these compositions are sterile. In vivo healing examination revealed that the wounds were completely healed after 2 weeks with these dressings in comparison with those administered with resveratrol solutions and the ordinary dermal matrix.[180]

Zhao et al. manufactured carboxymethyl cotton knitted materials for wound dressings using several solvents, including water, isopropanol water, and ethanol water. They determined that the most effective solvent for preparing carboxymethyl cotton fabrics is isopropanol-water. These results have a substantial impact on the industry, particularly in the manufacturing of CMC dressing.[181]

Xue et al. constructed CMC gauze that's been embedded in silver nanoparticles for wound dressing. Silver nanoparticles were produced on the gauze's surface and demonstrated high antibacterial activity, encouraging the healing of wounds. SUNTOUGH topical hemostatic gauze is currently available which is made of sodium CMC. It has distinctive characteristics such as being flexible and easy to use, having an instant hemostatic tendency, and maintaining moist healing conditions.[182]

Sudheesh et al. developed microporous and stretchable bandages of zinc oxide/chitosan hydrogels. The cytocompatibility of the hydrogel was investigated by using normal human fibroblast cells. Cells were attached and entered the nanocomposite bandages. Furthermore, these bandages enhanced collagen accumulation, re-epithelialization, and wound repair. The collected results fully advocated the use of nanocomposite bandages for diabetic foot ulcers, chronic, and burn wounds.[183]

Ajiteru et al. created Mirderm hydrocolloid dressing-containing myrrh resin to accelerate the healing process and the hydrocolloid's mechanical properties. Mirderm exhibited better mechanical and healing abilities in comparison to some commercially available hydrocolloids and medical gauze.[184]

7 | COMMERCIALLY AVAILABLE PRODUCTS

There are many types of products which are developed from the natural polymers and are now commercially available for wound healing applications which are listed in Table 2.

8 | CHALLENGES WITH EXISTING DRESSING MATERIALS

Before developing advanced wound care materials, researchers must examine the shortcomings of present wound dressings.

26424169, 0, Downloaded from https://onlinelibrary.wiley.com/doi/10.1002/pol.20220734 by Delhi Technological University, Wiley Online Library on [05/04/2023]. See the Terms and Conditions (https://onlinelibrary.wiley.com/terms-and-conditions) on Wiley Online Library for rules of use; OA articles are governed by the applicable Creative Commons License

TABLE 2 Commercially available products.

Commercially available products	Polymer	Features and applications	Ref
Bionect®	Hyaluronic acid	Stop abrasion, eradicate toxic compounds, and restore skin integrity.	185–187
Hyalofill®	Hyaluronic acid	Non-adherent, used to treat chronic sores, especially diabetic foot ulcers. Promotes cell activity and the healing process by creating a moist environment.	188
Hyalomatrix®	Hyaluronic acid	Transparent membrane facilitates cellular invasion and capillary development, both of which are necessary for skin re-epithelialization. Treat partial- and full-thickness wounds, second-degree burns, pressure ulcers, venous ulcers, chronic vascular ulcers, and surgical and trauma wounds.	42,142
HylaSponge®	Hyaluronic acid	Has the capability of absorbing and expelling huge amounts of water, keeping the skin hydrated throughout the recovery process. Functions as an equilibrium barrier or a stretchy "second skin."	189–191
Laserskin®	Hyaluronic acid	Have a microperforated membrane that allows autologous keratinocytes and fibroblasts to develop and migrate to the wound bed. Used to treat both acute and chronic wounds.	192
Algicell™	Alginate	Used to treat diabetic foot ulcers, leg ulcers, pressure ulcers, donor sites, and traumatic and surgical wounds.	126
Kaltostat®	Alginate	Treat moderate to heavily exuding chronic and acute wounds	193–195
Centella-Asiatica	Alginate	Improved wound healing effect in excision, infection, and abrasion	196
Algisite◇ M	Alginate	Used to treat lacerations, abrasions, skin tears, minor burn wounds, leg ulcers, pressure ulcers, diabetic foot ulcers, and surgical wounds	197
Gentell®	Collagen	Used to treat burns, sores, blisters, scrapes and ulcers. Can be used at any phase of healing	121
Biostep◇ Collagen Matrix	Collagen	Used to treat full and partial-thickness wound, pressure ulcers, diabetic ulcers, venous ulcers, abrasions, traumatic wounds, dehisced surgical wounds and 1st and 2nd degree burns	198,199
Condress®	Collagen	Helps to expedite the healing process of chronic skin wounds, even acute wounds	200
$Helix_3$ -cm	Collagen	Highly absorptive, porous collagen sheets, non-adherent and can be used in combination with topical agents. Effective in all stages of wound healing. Treat chronic and acute wound	201
Axiostat®	Chitosan	Can be cut, folded and stuffed into deep wounds. Painless, easy removal, no side effects, very flexible, both sides active. Stops moderate to severe bleeding due to cuts, abrasions, lacerations	202,203
MaxioCel®	Chitosan	Used to treat pressure sores, diabetic foot ulcers, skin abrasions, burns, venous leg ulcer, superficial and partial thickness burns, and surgical wounds	204
Tegasorb®	Chitosan	Ease of application, adherence to skin, conformability, transparency and effectiveness in the treatment of venous leg ulcers	205
ChitoSAM™ 100	Chitosan	Non-woven chitosan dressing spun directly from chitosan	206

26424169, 0, Downloaded from https://onlinelibrary.wiley.com/doi/10.1002/pol.20220734 by Delhi Technological University, Wiley Online Library on [05/04/2023]. See the Terms and Conditions (https://onlinelibrary.wiley.com/terms-and-conditions) on Wiley Online Library for rules of use; OA articles are governed by the applicable Creative Commons License

TABLE 2 (Continued)

Commercially available products	Polymer	Features and applications	Ref
FibDex®	Cellulose	Fastens the healing process, considerable improvement in scar texture. Eventually separates itself when the skin below has recovered. Maintains a moist environment for maximum healing and absorbs exudates. During the full course of the healing, only one dressing is used	197,207
Biofill®	Cellulose	Accelerating the healing process, pain relief, wound healing of burns and chronic ulcers	208
XCell®	Cellulose	Heal chronic venous ulcers	208
Tegasorb™	Gelatin	Dressing blend moisture vapor permeability, absorbency, and conformability, and its transparency enables wound viewing	29
DuoDERM®	Gelatin	Effective in wounds with light to moderate exudation, leg ulcers, pressure ulcers, burns. Thin sheets are useful over suture lines and intravenous sites. Reduce pain.	209–211

8.1 | Adherence

Dressings with an adhesive layer allow them to stick to undamaged skin, but they must be removed carefully because the adhesive might harm the epidermal skin, resulting in pain and the possibility of hypersensitivity. Non-adherent dressings should be applied to the wound to offer an interface with the secondary dressing in order to promote quick and painless removal.[212]

8.2 | Opaque

The majority of wound dressings available in the market are typically opaque. As a result, visual examination of the process of recovery is prohibited. With opaque dressings, infection or other problems are difficult to detect. Removal of dressing during examination not only causes irritation but also disturbance in healing which can cause bleeding and inflammation. As a result, transparent dressings will be preferable. Transparent adhesive free dressings with antiseptic which can be quickly absorbed by wound are especially attractive because, rather than removing, a similar transparent self-adhering dressing could be applied forthwith after the preceding one has been absorbed.[213]

8.3 | Low degradation rate

Some wound dressing has a low degradation rate, which can prolong antibiotic release at the wound site; consequently, these can be combined with polymers having a higher degradation rate to tune the degradation process.[214]

8.4 | Multifunctionality

It is a challenge to monitor the wound bed properties like pH or temperature. Such criteria have the potential to reflect wound healing progress and must be examined carefully. Different types of biosensors must be incorporated into wound dressings for this objective, and an updated series of sophisticated devices capable of real-time sensing and monitoring of wound conditions should be developed. As a result, multifunctional dressings that can manage multiple types of infected wounds while significantly reducing infection risk are required as an all-in-one solution. A wound dressing that addresses these problems ensures not only rapid wound healing but also prevents infection. Furthermore, the therapeutic cycle and duration may be anticipated and managed over time.[215]

9 | CONCLUSION AND FUTURE PROSPECTS

Most of us had to have an open wound at some point in our life. The majority of the wounds healed quickly and without complications, while others required medical assistance. Wound treatment is a critical medical speciality since an infected wound might result in major repercussions. So far, a variety of wound dressings are currently available in the market, allowing physicians to examine all aspects of wound treatment. However, no

26424169, 0, Downloaded from https://onlinelibrary.wiley.com/doi/10.1002/pol.20220734 by Delhi Technological University, Wiley Online Library on [05/04/2023]. See the Terms and Conditions (https://onlinelibrary.wiley.com/terms-and-conditions) on Wiley Online Library for rules of use; OA articles are governed by the applicable Creative Commons License

acceptable product exists for some sort of wounds. The authors of this review aimed to summarize up-to-date understanding of wound monitoring and management in order to assist anyone involved in this area in understanding the critical phenomenon of healing process, which will enable the framework for the finest dressing selection.

More research is needed to identify an improved wound healing potential treatment that will help patients and clinicians while also adding to the armamentarium of wound healing dressings. Despite the challenges, polymers provide new opportunities to supplement or replace older systems. As a result, efforts to produce polymeric materials have received a lot of attention. Among the existing drug delivery technologies, the authors highlighted materials made from natural polymers such as chitosan, HA, collagen, alginate, and others. Its numerous features (cost-effectiveness, reduced side effects, and improved system performance) and diverse methods of fabrication into delivery methods (sponges, films, hydrogels, etc.) make it a popular choice among researchers. The utilization of natural polymers in combination with blood components, growth factors, or cells that simulate synergistic therapeutic processes and stimulate crucial regeneration systems beneficial in healing is an effective option in the wound-care field.[216] Polymeric nanoparticles of natural origin in combination with biomolecules, growth factors, and drugs to create scaffolds with improved mechanical strength could also solve the limitations of the present wound healing materials.[217] Antibacterial and biodegradable nanoparticles are combined to develop hybrid nanocomposite which may enhance healing of wounds. To ensure low resistance and quick healing, one has to be aware of the primary difficulties associated with nanomaterial wound dressings and how they interact with the injury. Nanomaterials' stability, mechanical toughness, toxic effects, and cost all depend on how they were made. As a result, it is important to think about structural flaws that occur in nanomaterial synthesis. To meet international health norms, production expenses must be decreased altogether.[218]

Cold atmospheric plasma activated solutions can also contribute in making wound healing system better. In an experiment, it was injected into the altered dorsal rat skin flap. Their results showed that it has a greater influence on the rate of necrosis in comparison to those other solutions having noted effects. Additionally, it can be manufactured quickly, indefinitely, non-invasively, and using a conventional technique.[219]

There is limited research data available on smart dressings in the worldwide so, this could also emerge as a promising field of research in the future. The technological advancement in upcoming smart dressings can indeed help in wound care and real-time diagnosis. Dargaville et al. speculate that the wound dressing of the coming generation may have a color map of wound, a pH interpretation, infection monitoring, and a signifier indicating whether a dressing change is required. Many fundamental processes must still be completed in order to construct such complicated wound management equipment.[220]

Future smart dressings are anticipated to include an interconnection that can integrate many electrodes which can detect multiple wound variables as well as incorporate drugs and biological molecules that are released as per wound healing processes with a range of delivery systems which aid in individual stages of healing. The difficulty in manufacturing this type of dressing is fusing optical and biochemical systems together into one dressing that can be produced on a big scale and inexpensively.[221]

Natural endogenous electrical potentials that our bodies produce around wounds are known to hasten the healing process by directing cell migration to the place of trauma. Exogenous electrical stimulation has been shown to speed up wound healing by simulating this physiological event. Conductive materials may enhance the effectiveness of endogenous or exogenous ES. Nowadays, covalent organic frameworks and metal–organic frameworks have received a lot of attention as potential drug delivery systems. Materials made from these can sustain consistent conductance in physiological fluids and therefore may 1 day be used in electroactive dressings for the healing process. There are a few techniques available that employ electrodes to monitor the transcutaneous electrical resistance or impedance at the locations of wounds on a regular basis. The findings show that electrical resistance and impedance both rise as wound healing advances, offering reliable indicators of the wound's condition. The development of dual-function electroactive wound dressings may facilitate and expedite the realization of tailored therapies at various stages of wound regeneration and repair.[222,223] Latest developments in nanogenerator technology that result in wearable wound-healing devices that are self-sustainable ES points to the possibility of promising new options in wound treatment. But still, it is difficult to produce an integrated triboelectric-nanogenerator patch that will provide regulated drug loading and release in situ ES. Du et al. manufactured a flexible triboelectric-nanogenerator patch with a surface-engineered electrode that has Mg-Al layered double hydroxide as a smart medicine container and friction layer to speed the healing of infected wounds. The discovery provides an easy method for treating infected

26424169, 0, Downloaded from https://onlinelibrary.wiley.com/doi/10.1002/pol.20220734 by Delhi Technological University, Wiley Online Library on [05/04/2023]. See the Terms and Conditions (https://onlinelibrary.wiley.com/terms-and-conditions) on Wiley Online Library for rules of use; OA articles are governed by the applicable Creative Commons License

wounds and opens a new path for customized medical devices for microbial management.[224]

ACKNOWLEDGMENTS

The authors would like to acknowledge the support provided under the DST-FIST Grant No. SR/FST/CS-I/2022/263 of Govt. of India.

ORCID

Indra Bahadur https://orcid.org/0000-0003-2906-473X

REFERENCES

[1] T. A. Jeckson, Y. P. Neo, S. P. Sisinthy, B. Gorain, *J. Pharm. Sci.* **2021**, *110*, 635.
[2] W. Paul, C. P. Sharma, *Encyclopedia of Biomedical Polymers & Polymeric Biomaterials*, CRC Pess, Boca Raton, Florida, **2015**, p. 134.
[3] G. Henry, W. L. Garner, *Surg. Clin. North Am.* **2003**, *83*, 483.
[4] G. Broughton, J. E. Janis, C. E. Attinger, *Plast. Reconstr. Surg.* **2006**, *117*, 6.
[5] T. S. Helling, W. K. McNabney, *J. Trauma - Inj. Infect. Crit. Care* **2000**, *49*, 930.
[6] G. T. Lionelli, W. T. Lawrence, *Surg. Clin. North Am.* **2003**, *83*, 617.
[7] L. Cañedo-Dorantes, M. Cañedo-Ayala, *Int. J. Inf. Secur.* **2019**, *2019*, 1.
[8] J. Wang, M. Windbergs, *Eur. J. Pharm. Biopharm.* **2017**, *119*, 283.
[9] J. F. Guest, N. Ayoub, T. McIlwraith, I. Uchegbu, A. Gerrish, D. Weidlich, K. Vowden, P. Vowden, *Int. Wound J.* **2017**, *14*, 322.
[10] M. Prasathkumar, S. Sadhasivam, *Int. J. Biol. Macromol.* **2021**, *186*, 656.
[11] J. Ahmed, M. Gultekinoglu, M. Edirisinghe, *Biotechnol. Adv.* **2020**, *41*, 107549.
[12] A. Ridiandries, J. T. M. Tan, C. A. Bursill, *Int. J. Mol. Sci.* **2018**, *19*, 3217.
[13] S. Ellis, E. J. Lin, D. Tartar, *Curr. Dermatol. Rep.* **2018**, *7*, 350.
[14] A. Dorgalaleh, A. Casini, P. Rahmini, *Congenital Bleeding Disorders: Diagnosis and Management*, Springer, New York City **2018**, p. 163.
[15] M. Rodrigues, N. Kosaric, C. A. Bonham, G. C. Gurtner, *Physiol. Rev.* **2020**, *99*, 665.
[16] S. Singh, A. Young, C. E. McNaught, *Surg. (United Kingdom)* **2017**, *35*, 473.
[17] S. K. Shukla, A. K. Sharma, V. Gupta, M. H. Yashavarddhan, *J. Tissue Viability* **2019**, *28*, 218.
[18] Y. Su, A. Richmond, *Adv. Wound Care* **2015**, *4*, 631.
[19] A. el Ayadi, J. W. Jay, A. Prasai, *Int. J. Mol. Sci.* **2020**, *21*, 1105.
[20] R. Zhao, H. Liang, E. Clarke, C. Jackson, M. Xue, *Int. J. Mol. Sci.* **2016**, *17*, 1.
[21] R. Ogawa, *Int. J. Mol. Sci.* **2017**, *18*, 606.
[22] D. E. A. Komi, K. Khomtchouk, P. L. Santa Maria, *Clin. Rev. Allergy Immunol.* **2020**, *58*, 298.
[23] J. M. Baron, M. Glatz, E. Proksch, *Dermatology* **2020**, *236*, 593.
[24] N. X. Landén, D. Li, M. Ståhle, *Cell. Mol. Life Sci.* **2016**, *73*, 3861.
[25] M. Xue, C. J. Jackson, *Adv. Wound Care* **2015**, *4*, 119.
[26] C. D. Marshall, M. S. Hu, T. Leavitt, L. A. Barnes, H. P. Lorenz, M. T. Longaker, *Adv. Wound Care* **2018**, *7*, 29.
[27] E. Rezvani Ghomi, S. Khalili, S. Nouri Khorasani, R. Esmaeely Neisiany, S. Ramakrishna, *J. Appl. Polym. Sci.* **2019**, *136*, 1.
[28] Y. M. Bello, T. J. Phillips, *JAMA* **2000**, *283*, 716.
[29] L. Meka, B. Kesavan, V. N. Kalamata, C. M. Eaga, S. Bandari, V. Vobalaboina, M. R. Yamsani, *J. Pharm. Sci.* **2008**, *97*, 2892.
[30] J. Dissemond, B. Assenheimer, A. Bültemann, V. Gerber, S. Gretener, E. Kohler-von Siebenthal, S. Koller, K. Kröger, P. Kurz, S. Läuchli, C. Münter, E. M. Panfil, S. Probst, K. Protz, G. Riepe, R. Strohal, J. Traber, H. Partsch, *JDDG - J. Ger. Soc. Dermatol* **2016**, *14*, 1073.
[31] R. V. Shevchenko, S. L. James, S. E. James, R. V. Shevchenko, S. L. James, S. E. James, *J. R. Soc. Interface* **2010**, *14*, 229.
[32] N. Bhardwaj, D. Chouhan, B. B. Mandal, *Current Pharam. Design* **2017**, *23*, 3455.
[33] Â. Carsin, P. Ainaud, Â. le Bever, J. Rives, A. Lakhel, Â. Lambert, J. Perrot, J. Stephanazzi, *Burns* **2000**, *26*, 379.
[34] A. K. Tausche, M. Skaria, L. Bohlen, K. Liebold, J. Hafner, H. Friedlein, M. Meurer, R. J. Goedkoop, U. Wollina, D. Salomon, T. Hunziker, *Wound Repair Regen.* **2003**, *11*, 248.
[35] D. B. Haddow, D. A. Steele, R. D. Short, R. A. Dawson, S. Macneil, *J. Biomed. Mater.* **2002**, *64*, 80.
[36] S. Johnsen, T. Ermuth, E. Tanczos, H. Bannasch, R. E. Horch, I. Zschocke, M. Peschen, E. Schöpf, W. Vanscheidt, M. Augustin, *Vasa* **2005**, *34*, 25.
[37] R. Goedkoop, R. Juliet, P. H. K. You, J. Daroczy, K. P. Roos, R. Lijneh, E. Rolland, T. Hunziker, *Derm.* **2010**, *220*, 114.
[38] R. S. Kirsner, W. A. Marston, R. J. Snyder, T. D. Lee, D. I. Cargill, H. B. Slade, *Lancet* **2012**, *380*, 977.
[39] M. Magnusson, R. P. Papini, S. M. Rea, C. C. Reed, F. M. Wood, *Plast. Reconstr. Surg.* **2007**, *119*, 495.
[40] C. Caravaggi, R. D. Giglio, C. Pritelli, M. Sommaria, S. D. Noce, E. Faglia, M. Mantero, G. Clerici, P. Fratino, L. D. Paola, G. Mariani, R. Mingardi, A. Morabito, *Diabetes Care* **2003**, *26*, 2853.
[41] L. Uccioli, *J. Low. Extre. Wounds* **2003**, *2*, 140.
[42] G. Gravante, D. Delogu, N. Giordan, G. Morano, A. Montone, G. Esposito, *J. Burn Care Res.* **2007**, *28*, 269.
[43] J. Noordenbos, C. Doré, J. F. Hansbrough, *J. Burn Care Res.* **1999**, *4*, 275.
[44] M. Varkey, J. Ding, E. E. Tredget, *J. Funct. Biomater* **2015**, *6*, 547.
[45] D. M. Supp, S. T. Boyce, *J. Clin. Dermatol.* **2005**, *23*, 403.
[46] R. E. Horch, J. Kopp, U. Kneser, J. Beier, A. D. Bach, *J. Cell. Mol. Med.* **2005**, *9*, 592.
[47] K. Gordley, P. Cole, J. Hicks, L. Hollier, *J. Plast. Reconstr. Aesthet. Surg.* **2009**, *62*, 849.
[48] A. Alwitry, L. R. Infirmary, L. C. Abercrombie, *Orbit* **2006**, *25*, 253.
[49] Y. M. Bello, A. F. Falabella, W. H. Eaglstein, *Am. J. Clin. Dermatol.* **2001**, *2*, 305.

26424169, 0, Downloaded from https://onlinelibrary.wiley.com/doi/10.1002/pol.20220734 by Delhi Technological University, Wiley Online Library on [05/04/2023]. See the Terms and Conditions (https://onlinelibrary.wiley.com/terms-and-conditions) on Wiley Online Library for rules of use; OA articles are governed by the applicable Creative Commons License

[50] S. Akita, K. Akino, T. Imaizumi, *J. Burn Care Res.* **2006**, *27*, 333.
[51] P. A. Cheshire, M. R. Herson, H. Cleland, *Burns* **2016**, *42*, 1.
[52] E. A. G. Kalaf, K. R. Hixon, P. U. Kadakia, A. J. Dunn, S. A. Sell, *Electrospun Materials for Tissue Engineering and Biomedical Applications*, Elsevier Ltd., Sawston, Cambridge **2017**, p. 179.
[53] J. Jeevanandam, A. Barhoum, Y. S. Chan, A. Dufresne, M. K. Danquah, J. Beilstein, *Nanotechnology* **2018**, *9*, 1050.
[54] S. C. Notodihardjo, N. Morimoto, M. C. Munisso, T. M. Le, T. Mitsui, *J. Plast. Reconstr. Aesthet. Surg.* **2020**, *73*, 1547.
[55] B. P. Dodson, A. D. Levine, *BMC Biotechnol.* **2015**, *15*, 1.
[56] K. Ackermann, S. L. Borgia, H. C. Korting, K. R. Mewes, M. S. Korting, *Skin Pharmacol. Physiol.* **2010**, *23*, 105.
[57] A. G. M. van Dorp, M. C. H. Verhoeven, H. K. Koerten, C. A. van Blitterswijk, M. Ponec, *J. Biomed. Mater. Res.* **1999**, *47*, 292.
[58] M. Límová, *Surg. Clin. North Am.* **2010**, *90*, 1237.
[59] L. R. Braun, S. A. Lamel, N. A. Richmond, R. S. Kirsner, *JAMA Dermat.* **2013**, *149*, 2013.
[60] R. A. F. Clark, K. Ghosh, M. G. Tonnesen, *J. Invest. Dermatol.* **2007**, *127*, 1018.
[61] C. Ho, A. Cheung, K. Bogie, *Essentials of Physical Medicine and Rehabilitation*, Fourth ed., *Elsevier Inc.*, Amsterdam **2020**, p. 849.
[62] N. Goonoo, A. Bhaw-luximon, *In* Advanced 3D-Printed Systems and Nanosystems for Drug Delivery and Tissue Engineering, Elsevier Inc., Sawston, Cambridge **2020**, p. 159.
[63] L. Wenhui, F. Changgeng, X. Lei, Y. Baozhong, L. Guobin, F. Weijing, *Diabetes Res. Clin. Pract.* **2021**, *176*, 108862.
[64] S. Kaur, M. Pawar, N. Banerjee, R. Garg, *J. Anaesthesiol. Clin. Pharmacol.* **2012**, *28*, 70.
[65] Z. Zhang, W. Zhang, Y. Xu, D. Liu, *Asian J. Surg.* **2021**, *45*, 68.
[66] B. A. Lipsky, A. R. Berendt, *Diabetes Care* **2010**, *33*, 1143.
[67] Z. Jiang, X. Yu, X. Liao, M. Liu, Z. Fu, D. Min, G. Guo, *Burns* **2021**, *47*, 747.
[68] M. Meloni, V. Izzo, E. Vainieri, L. Giurato, V. Ruotolo, L. Uccioli, V. Izzo, E. Vainieri, L. Giurato, V. Ruotolo, L. Uccioli, *World J. Orthop.* **2015**, *6*, 387.
[69] S. L. Percival, *J. Wound Care* **2018**, *27*, 102.
[70] S. Dhivya, V. V. Padma, E. Santhini, *Biomed.* **2015**, *5*, 24.
[71] K. Varaprasad, T. Jayaramudu, V. Kanikireddy, C. Toro, E. R. Sadiku, *Carbohydr. Polym.* **2020**, *236*, 116025.
[72] S. Holloway, K. G. Harding, *Surg. (United Kingdom)* **2022**, *40*, 25.
[73] G. Chinnasamy, S. Chandrasekharan, S. Bhatnagar, *Int. J. Nanomedicine* **2019**, *14*, 9823.
[74] J. Dutta, N. Devi, *Int. J. Biol. Macromol.* **2021**, *186*, 244.
[75] P. Taheri, R. Jahanmardi, M. Koosha, S. Abdi, *Int. J. Biol. Macromol.* **2020**, *154*, 421.
[76] M. Aliabadi, B. S. Chee, M. Matos, Y. J. Cortese, M. J. D. Nugent, T. A. M. de Lima, W. L. E. Magalhães, G. G. de Lima, *Polymers* **2020**, *12*, 1.
[77] R. Yegappan, V. Selvaprithiviraj, S. Amirthalingam, R. Jayakumar, *Carbohydr. Polym.* **2018**, *198*, 385.
[78] A. Veeruraj, L. Liu, J. Zheng, J. Wu, M. Arumugam, *Mater. Sci. Eng. C* **2019**, *95*, 29.
[79] W. Zhang, L. Chen, J. Chen, L. Wang, X. Gui, J. Ran, G. Xu, H. Zhao, M. Zeng, J. Ji, L. Qian, J. Zhou, H. Ouyang, X. Zou, *Adv. Healthc. Mater.* **2017**, *6*, 1.
[80] K. M. Zia, S. Tabasum, M. Nasif, N. Sultan, N. Aslam, A. Noreen, M. Zuber, *Int. J. Biol. Macromol.* **2017**, *96*, 282.
[81] P. Chandika, M. S. Kim, F. Khan, Y. M. Kim, S. Y. Heo, G. W. Oh, N. G. Kim, W. K. Jung, *Carbohydr. Polym.* **2021**, *269*, 118272.
[82] K. M. Zepon, M. M. Martins, M. S. Marques, J. M. Heckler, F. Dal Pont Morisso, M. G. Moreira, A. L. Ziulkoski, L. A. Kanis, *Carbohydr. Polym.* **2019**, *206*, 362.
[83] J. L. Jiang, W. Z. Zhang, W. X. Ni, J. W. Shao, *Carbohydr. Polym.* **2021**, *257*, 117642.
[84] B. Neamtu, A. Barbu, M. O. Negrea, C. Ș. Berghea-Neamțu, D. Popescu, M. Zăhan, V. Mireşan, *Int. J. Mol. Sci.* **2022**, *23*, 9117.
[85] H. Mokhtari, S. Tavakoli, F. Safarpour, M. Kharaziha, H. R. Bakhsheshi-Rad, S. Ramakrishna, F. Berto, *Polymers* **2021**, *13*, 1744.
[86] S. Sharaf, M. E. El-Naggar, *Int. J. Biol. Macromol.* **2019**, *133*, 583.
[87] L. Jaiswal, S. Shankar, J. W. Rhim, *Carbohydr. Polym.* **2019**, *224*, 115191.
[88] E. H. Lee, S. J. Lim, M. K. Lee, *Carbohydr. Polym.* **2019**, *224*, 115143.
[89] Y. H. Wang, C. C. Liu, J. H. Cherng, G. Y. Fan, Y. W. Wang, S. J. Chang, Z. J. Hong, Y. C. Lin, S. der Hsu, *Sci. Rep.* **2019**, *9*, 1.
[90] S. Y. Ong, J. Wu, S. M. Moochhala, M. H. Tan, J. Lu, *Biomaterials* **2008**, *29*, 4323.
[91] A. Bernkop-Schnürch, *Adv. Drug Deliv. Rev.* **2018**, *136*, 62.
[92] A. Kassem, G. M. Ayoub, L. Malaeb, *Sci. Total Environ.* **2019**, *668*, 566.
[93] B. Farhadihosseinabadi, A. Zarebkohan, M. Eftekhary, M. Heiat, M. Moosazadeh Moghaddam, M. Gholipourmalekabadi, *Cell. Mol. Life Sci.* **2019**, *76*, 2697.
[94] G. Michailidou, E. Christodoulou, S. Nanaki, P. Barmpalexis, E. Karavas, S. Vergkizi-Nikolakaki, D. N. Bikiaris, *Carbohydr. Polym.* **2019**, *208*, 1.
[95] P. Feng, Y. Luo, C. Ke, H. Qiu, W. Wang, Y. Zhu, R. Hou, L. Xu, S. Wu, *Front. Bioeng. Biotechnol.* **2021**, *9*, 650598.
[96] N. Devi, J. Dutta, *Int. J. Biol. Macromol.* **2017**, *104*, 1897.
[97] A. S. Soubhagya, A. Moorthi, M. Prabaharan, *Int. J. Biol. Macromol.* **2020**, *157*, 135.
[98] P. Kumar Gupta, S. Sai Raghunath, D. Venkatesh Prasanna, P. Venkat, V. Shree, C. Chithananthan, S. Choudhary, K. Surender, K. Geetha, *Cellulose* **2019**, *201*, 1.
[99] R. J. Moon, A. Martini, J. Nairn, J. Simonsen, J. Youngblood, *Chem. Soc. Rev.* **2011**, *40*, 3941.
[100] R. Naomi, R. B. H. Idrus, M. B. Fauzi, *Int. J. Environ. Res. Public Health* **2020**, *17*, 1.
[101] D. André-Lévigne, A. Modarressi, M. S. Pepper, B. Pittet-Cuénod, *Int. J. Mol. Sci.* **2017**, *18*, 4149.
[102] P. Brenneisen, J. Wenk, L. O. Klotz, M. Wlaschek, K. Briviba, T. Krieg, H. Sies, K. Scharffetter-Kochanek, *J. Biol. Chem.* **1998**, *273*, 5279.
[103] V. Kanikireddy, K. Varaprasad, T. Jayaramudu, C. Karthikeyan, R. Sadiku, *Int. J. Biol. Macromol.* **2020**, *164*, 963.
[104] M. Aoshmita, K. Tanabe, I. Kohno, Y. Jo, K. Takahashi, T. Sugo, M. Matsuda, *Japanese J. Thromb. Hemost.* **2012**, *23*, 387.

26424169, 0, Downloaded from https://onlinelibrary.wiley.com/doi/10.1002/pol.20220734 by Delhi Technological University, Wiley Online Library on [05/04/2023]. See the Terms and Conditions (https://onlinelibrary.wiley.com/terms-and-conditions) on Wiley Online Library for rules of use; OA articles are governed by the applicable Creative Commons License

[105] P. Basu, U. Narendrakumar, R. Arunachalam, S. Devi, I. Manjubala, *ACS Omega* **2018**, *3*, 12622.
[106] M. Khamrai, S. L. Banerjee, S. Paul, S. Samanta, P. P. Kundu, *Int. J. Biol. Macromol.* **2019**, *122*, 940.
[107] M. Khamrai, S. L. Banerjee, P. P. Kundu, *Carbohydr. Polym.* **2017**, *174*, 580.
[108] N. Petersen, P. Gatenholm, *Appl. Microbiol. Biotechnol.* **2011**, *91*, 1277.
[109] H. Ullah, F. Wahid, H. A. Santos, T. Khan, *Carbohydr. Polym.* **2016**, *150*, 330.
[110] T. Carvalho, G. Guedes, F. L. Sousa, C. S. R. Freire, H. A. Santos, *Biotechnol. J.* **2019**, *14*, 1.
[111] G. E. Guilherme, C. W. O. de Souza, M. P. Bernardo, M. Zenke, L. H. C. Mattoso, F. K. V. Moreira, *Mater. Today Commun.* **2021**, *27*, 102169.
[112] H. N. M. Sghayyar, S. S. Lim, I. Ahmed, J. Y. Lai, X. Y. Cheong, Z. W. Chong, A. F. X. Lim, H. S. Loh, *Eur. Polym. J.* **2020**, *122*, 109386.
[113] M. Nikkhah, M. Akbari, A. Memic, A. Dolatshahi-pirouz, A. Khademhosseini, *Biomaterials from Nature for Advanced Devices and Therapies*, Wiley Blackwell, Hoboken, NJ **2016**, p. 37.
[114] F. Alihosseini, *In* Antimicrobial Textiles, Elsevier Ltd., Sawston, Cambridge **2016**, p. 115.
[115] K. Deshmukh, M. Basheer Ahamed, R. R. Deshmukh, S. K. Khadheer Pasha, P. R. Bhagat, K. Chidambaram, *Biopolymer Composites in Electronics*, Elsevier Inc., Amsterdam **2017**, p. 27.
[116] S. P. Ndlovu, K. Ngece, S. Alven, B. A. Aderibigbe, *Polymers* **2021**, *13*, 2959.
[117] A. Laha, U. Bhutani, K. Mitra, S. Majumdar, *Mater. Manuf. Process.* **2016**, *31*, 223.
[118] H. Afjoul, A. Shamloo, A. Kamali, *Mater. Sci. Eng. C* **2020**, *113*, 110957.
[119] G. Dardelle, A. Subramaniam, V. Normand, *Soft Matter* **2011**, *7*, 3315.
[120] W. J. Pichler, *Allergy Eur. J. Allergy Clin. Immunol.* **2019**, *74*, 1457.
[121] R. Naomi, H. Bahari, P. M. Ridzuan, F. Othman, *Polymers* **2021**, *13*, 1.
[122] C. Tondera, S. Hauser, A. Krüger-Genge, F. Jung, A. T. Neffe, A. Lendlein, R. Klopfleisch, J. Steinbach, C. Neuber, J. Pietzsch, *Theranostics* **2016**, *6*, 2114.
[123] F. Chen, X. Liu, *Prog. Polym. Sci.* **2016**, *53*, 86.
[124] A. Sorushanova, L. M. Delgado, Z. Wu, N. Shologu, A. Kshirsagar, R. Raghunath, A. M. Mullen, Y. Bayon, A. Pandit, M. Raghunath, D. I. Zeugolis, *Adv. Mater.* **2019**, *31*, 1.
[125] X. Jiang, Y. Wang, D. Fan, C. Zhu, L. Liu, Z. Duan, *J. Biomater. Appl.* **2017**, *31*, 1099.
[126] K. Y. Lee, D. J. Mooney, *Prog. Polym. Sci.* **2012**, *37*, 106.
[127] A. C. D. O. Gonzalez, Z. D. A. Andrade, T. F. Costa, A. R. A. P. Medrado, *An. Bras. Dermatol.* **2016**, *91*, 614.
[128] S. Mousavi, A. B. Khoshfetrat, N. Khatami, M. Ahmadian, R. Rahbarghazi, *Biochem. Biophys. Res. Commun.* **2019**, *518*, 625.
[129] S. Udhayakumar, K. G. Shankar, S. Sowndarya, C. Rose, *Biomater. Sci.* **2017**, *5*, 1868.
[130] R. Holmes, S. Kirk, G. Tronci, X. Yang, D. Wood, *Mater. Sci. Eng. C* **2017**, *77*, 823.
[131] A. Gaspar-Pintiliescu, A. M. Stanciuc, O. Craciunescu, *Int. J. Biol. Macromol.* **2019**, *138*, 854.
[132] M. F. Sanchez, M. L. Guzman, A. L. Apas, F. d. L. Alovero, M. E. Olivera, *Eur. J. Pharm. Sci.* **2021**, *161*, 105789.
[133] M. Fischer, F. Gebhard, T. Hammer, C. Zurek, G. Meurer, C. Marquardt, D. Hoefer, *J. Biomater. Appl.* **2017**, *31*, 1267.
[134] C. Bergonzi, G. G. d'Ayala, L. Elviri, P. Laurienzo, A. Bandiera, O. Catanzano, *Int. J. Biol. Macromol.* **2020**, *164*, 586.
[135] M. Rezvanian, S. F. Ng, T. Alavi, W. Ahmad, *Int. J. Biol. Macromol.* **2021**, *171*, 308.
[136] S. A. Shah, M. Sohail, S. Khan, M. U. Minhas, M. de Matas, V. Sikstone, Z. Hussain, M. Abbasi, M. Kousar, *Int. J. Biol. Macromol.* **2019**, *139*, 975.
[137] R. C. Gupta, R. Lall, A. Srivastava, A. Sinha, *Front. Vet. Sci.* **2019**, *6*, 1.
[138] A. Fallacara, E. Baldini, S. Manfredini, S. Vertuani, *Polymers* **2018**, *10*, 701.
[139] H. Cortes, I. Florán, N. Muñoz, E. Villanueva, L. Guadarrama, G. González, O. Hernández, M. Carmen, M. Cardoso, J. Magaña, B. Florán, M. Audelo, G. Gomez, *Cell. Mol. Biol.* **2020**, *66*, 191.
[140] M. F. P. Graça, S. P. Miguel, C. S. D. Cabral, I. J. Correia, *Carbohydr. Polym.* **2020**, *241*, 116364.
[141] T. G. Sahana, P. D. Rekha, *Mol. Biol. Rep.* **2018**, *45*, 2857.
[142] C. Longinotti, *Burn. Trauma* **2014**, *2*, 162.
[143] H. Li, Y. Xue, B. Jia, Y. Bai, Y. Zuo, S. Wang, Y. Zhao, W. Yang, H. Tang, *Carbohydr. Polym.* **2018**, *188*, 92.
[144] R. Arthe, D. Arivuoli, V. Ravi, *Int. J. Biol. Macromol.* **2020**, *154*, 1324.
[145] M. Vidya, S. Rajagopal, *Int. J. Polym. Sci.* **2021**, *2021*, 1.
[146] M. Pollini, F. Paladini, *Materials (Basel).* **2020**, *13*, 3361.
[147] E. S. Sashina, A. M. Bochek, N. P. Novoselov, D. A. Kirichenko, *Russ. J. Appl. Chem.* **2006**, *79*, 869.
[148] P. P. Patil, M. R. Reagan, R. A. Bohara, *Int. J. Biol. Macromol.* **2020**, *164*, 4613.
[149] C. N. Lemos, C. Cubayachi, K. Dias, J. N. Mendonça, N. P. Lopes, N. A. J. C. Furtado, R. F. V. Lopez, *Eur. J. Pharm. Biopharm.* **2018**, *128*, 147.
[150] M. Farokhi, F. Mottaghitalab, Y. Fatahi, A. Khademhosseini, D. L. Kaplan, *Trends Biotechnol.* **2018**, *36*, 907.
[151] X. Zhang, M. Qin, M. Xu, F. Miao, C. Merzougui, *Eur. Polym. J.* **2021**, *146*, 110268.
[152] J. Xiang, L. Shen, Y. Hong, *Eur. Polym. J.* **2020**, *130*, 109609.
[153] N. Asadi, H. Pazoki-toroudi, A. Rahmani, D. Bakhshayesh, A. Akbarzadeh, S. Davaran, N. Annabi, *Int. J. Biol. Macromol.* **2021**, *170*, 728.
[154] Y. Hsu, K. Liu, H. Yeh, H. Lin, H. Wu, C. Tsai, *Eur. J. Pharm. Biopharm.* **2018**, *135*, 61.
[155] S. Zhang, J. Hou, Q. Yuan, P. Xin, H. Cheng, Z. Gu, *Chem. Eng. J.* **2019**, *392*, 123775.
[156] T. Thanh, H. Thi, J. I. Kang, K. M. Park, K. D. Park, *Acta Biomater.* **2019**, *103*, 142.
[157] A. C. de Jesus, S. M. Carvalho, L. C. De, H. S. Mansur, *Int. J. Biol. Macromol.* **2017**, *106*, 1218.
[158] Y. Li, C. Zhu, D. Fan, R. Fu, P. Ma, Z. Duan, X. Li, *Macromol. Biosci.* **2019**, *1800424*, 1.
[159] H. Chen, X. Xing, H. Tan, Y. Jia, T. Zhou, Y. Chen, Z. Ling, X. Hu, *Mater. Sci. Eng. C* **2017**, *70*, 287.
[160] Z. Li, S. Mei, Y. Dong, F. She, P. Li, Y. Li, L. Kong, *Nanomaterials* **2021**, *11*, 15.
[161] C. Cui, S. Sun, S. Wu, S. Chen, J. Ma, F. Zhou, *Eng. Regen.* **2021**, *2*, 82.

26424169, 0, Downloaded from https://onlinelibrary.wiley.com/doi/10.1002/pol.20220734 by Delhi Technological University, Wiley Online Library on [05/04/2023]. See the Terms and Conditions (https://onlinelibrary.wiley.com/terms-and-conditions) on Wiley Online Library for rules of use; OA articles are governed by the applicable Creative Commons License

[162] B. Sun, Y. Z. Long, H. D. Zhang, M. M. Li, J. L. Duvail, X. Y. Jiang, H. L. Yin, *Prog. Polym. Sci.* **2014**, *39*, 862.

[163] Y. Ji, W. Song, L. Xu, D. G. Yu, S. W. A. Bligh, *Biomolecules* **2022**, *12*, 794.

[164] Y. Zhou, M. Wang, C. Yan, H. Liu, D. G. Yu, *Biomolecules* **2022**, *12*, 1254.

[165] M. R. El-aassar, O. M. Ibrahim, M. M. G. Fouda, N. G. El-beheri, M. M. Agwa, *Carbohydr. Polym.* **2020**, *238*, 116175.

[166] C. Yao, J. Yeh, Y. Chen, M. Li, C. Huang, *J. Tissue Eng. Regen. Med.* **2015**, *11*, 905.

[167] S. Ahn, C. O. Chantre, A. R. Gannon, J. U. Lind, P. H. Campbell, T. Grevesse, B. B. O. Connor, K. K. Parker, *Adv. Healthc. Mater.* **2018**, *1701175*, 1.

[168] N. Charernsriwilaiwat, P. Opanasopit, T. Rojanarata, T. Ngawhirunpat, *Int. J. Pharm.* **2012**, *427*, 379.

[169] Y. He, W. Zhao, Z. Dong, Y. Ji, M. Li, Y. Hao, D. Zhang, C. Yuan, J. Deng, P. Zhao, Q. Zhou, *Int. J. Biol. Macromol.* **2020**, *167*, 182.

[170] S. Ahmed, S. Ikram, *ALS* **2016**, *10*, 27.

[171] B. Lu, F. Lu, Y. Zou, J. Liu, B. Rong, Z. Li, F. Dai, D. Wu, G. Lan, *Carbohydr. Polym.* **2017**, *173*, 556.

[172] H. Cui, M. Liu, W. Yu, Y. Cao, H. Zhou, J. Yin, *ACS Appl. Mater. Interfaces* **2021**, *13*, 26800.

[173] Q. Leng, Y. Li, X. Pang, B. Wang, Z. Wu, K. Xiong, L. Zhao, P. Zhou, S. Fu, *Drug Deliv.* **2020**, *27*, 1676.

[174] E. B. Souto, C. M. P. Yoshida, G. R. Leonardi, A. Cano, *Pharmaceutics* **2021**, *13*, 1199.

[175] Y. Duan, K. Li, H. Wang, T. Wu, Y. Zhao, H. Li, H. Tang, W. Yang, *Carbohydr. Polym.* **2020**, *238*, 116195.

[176] Y. Luo, K. B. Kang, R. Sartaj, M. G. Sun, Q. Zhou, V. H. Guaiquil, M. I. Rosenblatt, *Sci. Rep.* **2021**, *11*, 1.

[177] S. Patel, S. Srivastava, M. R. Singh, D. Singh, *Int. J. Biol. Macromol.* **2018**, *107*, 1888.

[178] Z. Gu, H. Xie, C. Huang, L. Li, X. Yu, *Int. J. Biol. Macromol.* **2013**, *58*, 121.

[179] I. Negut, G. Dorcioman, V. Grumezescu, *Polymers* **2020**, *12*, 1.

[180] E. H. Gokce, S. Tuncay, I. Eroglu, N. Tsapis, G. Gokce, I. Tekmen, E. Fattal, O. Ozer, *Eur. J. Pharm. Biopharm.* **2017**, *119*, 17.

[181] J. Zhao, Y. Tang, Y. Liu, L. Cui, X. Xi, N. Zhang, P. Zhu, *JMADE* **2015**, *87*, 238.

[182] Y. Xue, X. Zhao, S. Zhu, J. Wang, Y. Wang, X. Li, C. Niu, Q. Li, *Medicine and Biopharmaceutical*, World Scientific Publishing, Singapore **2016**, p. 778.

[183] P. T. S. Kumar, V. Lakshmanan, T. V. Anilkumar, C. Ramya, P. Reshmi, A. G. Unnikrishnan, S. V. Nair, R. Jayakumar, *ACS Appl. Mater. Interfaces* **2012**, *4*, 2618.

[184] O. Ajiteru, O. J. Lee, J. H. Kim, Y. J. Lee, J. S. Lee, H. Lee, M. T. Sultan, C. H. Park, *Colloids Interface Sci. Commun.* **2022**, *48*, 100617.

[185] J. K. Vasir, K. Tambwekar, S. Garg, *Int. J. Pharm.* **2003**, *255*, 13.

[186] M. G. Onesti, S. Carella, V. Sorvillo, N. Scuderi, *Eur. Rev. Med. Pharmacol. Sci.* **2013**, *17*, 210.

[187] P. Fioramonti, P. Fino, M. Ruggieri, M. G. Onesti, *J. Geophys. Res. Earth Surf.* **2012**, *2012*, 1.

[188] V. Colletta, D. Dioguardi, A. Di Lonardo, G. Maggio, F. Torasso, *J. Wound Care* **2003**, *12*, 357.

[189] M. Mahedia, N. Shah, B. Amirlak, *Plast. Reconstr. Surg. Glob. Open* **2016**, *4*, 1.

[190] A. Wahby, K. D. Dicaprio, R. Stern, *Treatment of Dry Skin Syndrome*, Springer, London **2012**, p. 459.

[191] S. Alven, B. A. Aderibigbe, *Polymer* **2021**, *13*, 2102.

[192] R. D. Price, M. G. Berry, H. A. Navsaria, *J. Plast. Reconstr. Aesthet. Surg.* **2007**, *60*, 1110.

[193] M. Uzun, S. C. Anand, T. J. Shah, *Biomed. Eng. Technol.* **2013**, *1*, 1.

[194] M. Iliescu, L. Paek, L. Dao, N. Rouchet, J. I. Efanov, C. Édouard, M. A. Danino, *Burns* **2019**, *45*, 1122.

[195] M. P. Sintler, A. Mahmood, S. R. G. Smith, M. H. Simms, R. K. Vohra, *World J. Surg.* **2005**, *29*, 1259.

[196] S. G. Jin, K. S. Kim, A. M. Yousaf, D. W. Kim, S. W. Jang, M. W. Son, Y. H. Kim, C. S. Yong, J. O. Kim, H. G. Choi, *Int. J. Pharm.* **2015**, *490*, 240.

[197] J. Kiiskinen, A. Merivaara, T. Hakkarainen, M. Kääriäinen, S. Miettinen, M. Yliperttula, R. Koivuniemi, *Stem Cell Res Ther* **2019**, *10*, 1.

[198] E. A. Ayello, *Adv. Skin Wound Care* **2009**, *22*, 1.

[199] R. H. Fitzgerald, J. S. J. Steinberg, *J. Foot Ankle Res.* **2009**, *2*, 1.

[200] S. Cascone, G. Lamberti, *Int. J. Pharm.* **2020**, *573*, 118803.

[201] S. Tavakoli, A. S. Klar, *Biomolecules* **2020**, *10*, 1.

[202] S. P. Miguel, A. F. Moreira, I. J. Correia, *Int. J. Biol. Macromol.* **2019**, *127*, 460.

[203] P. Ketan, P. Anjali, P. Rignesh, P. Bhavika, P. Dev, *Indian J. Emerg. Med.* **2016**, *2*, 93.

[204] M. Maaz, S. Maqsood, N. Gull, T. A. Tabish, S. Zia, R. Ullah, S. Muhammad, M. Arif, *Int. J. Pharm.* **2021**, *598*, 120270.

[205] C. Williams, *Br. J. Nurs.* **2000**, *9*, 9.

[206] M. A. Matica, F. L. Aachmann, A. Tøndervik, H. Sletta, V. Ostafe, *Int. J. Mol. Sci.* **2019**, *20*, 1.

[207] R. Koivuniemi, T. Hakkarainen, J. Kiiskinen, M. Kosonen, J. Vuola, J. Valtonen, K. Luukko, H. Kavola, M. Yliperttula, *Adv. Wound Care* **2020**, *9*, 199.

[208] J. Kucińska-Lipka, I. Gubanska, H. Janik, *Polym. Bull.* **2015**, *72*, 2399.

[209] C. Weller, C. Weller, V. Team, *Advanced Textiles for Wound Care*, Second ed. Woodhead Publishing, Sawston, Cambridge **2019**, p. 105.

[210] M. H. E. Hermans, R. P. Hermans, *Burns* **1986**, *12*, 214.

[211] N. S. Solanki, I. P. Mackie, J. E. Greenwood, *Burns* **2012**, *38*, 889.

[212] T. Abdelrahman, H. Newton, *Surgery* **2011**, *29*, 491.

[213] M. Contardi, J. A. Heredia-guerrero, G. Perotto, P. Valentini, P. Paolo, L. Goldoni, R. Bertorelli, A. Athanassiou, I. S. Bayer, *Eur. J. Pharm. Sci.* **2017**, *104*, 133.

[214] R. S. Ambekar, B. Kandasubramanian, *Eur. Polym. J.* **2019**, *117*, 304.

[215] S. Homaeigohar, A. R. Boccaccini, *Acta Biomater.* **2021**, *107*, 25.

[216] I. Gardikiotis, F. D. Cojocaru, C. T. Mihai, V. Balan, G. Dodi, *Int. J. Mol. Sci.* **2022**, *23*, 8778.

[217] B. Sheokand, S. R. Pathak, C. M. Srivastava, A. Kumar, I. Bahadur, M. Vats, *J. Mol. Liq.* **2022**, *368*, 120561.

[218] M. A. Shalaby, M. M. Anwar, H. Saeed, *J. Polym. Res.* **2022**, *29*, 91.

[219] B. Caba, I. Gardikiotis, I. Topala, I. Mihaila, C. T. Mihai, C. Luca, S. Pasca, I. C. Caba, G. Dimitriu, B. Huzum, I. L. Serban, *Appl. Sci.* **2022**, *12*, 590.

[220] T. R. Dargaville, B. L. Farrugia, J. A. Broadbent, S. Pace, Z. Upton, N. H. Voelcker, *Biosens. Bioelectron.* **2013**, *41*, 30.

[221] I. Barros Almeida, L. Garcez Barretto Teixeira, F. Oliveira De Carvalho, É. Ramos Silva, P. Santos Nunes, M. R. Viana Dos

26424169, 0, Downloaded from https://onlinelibrary.wiley.com/doi/10.1002/pol.20220734 by Delhi Technological University, Wiley Online Library on [05/04/2023]. See the Terms and Conditions (https://onlinelibrary.wiley.com/terms-and-conditions) on Wiley Online Library for rules of use; OA articles are governed by the applicable Creative Commons License

Santos, A. Antunes De Souza Araújo, *Adv. Skin Wound Care* **2021**, *34*, 1.
[222] S. B. Rajendran, K. Challen, K. L. Wright, J. G. Hardy, *J. Funct. Biomater.* **2021**, *12*, 40.
[223] C. Korupalli, H. Li, N. Nguyen, F. L. Mi, Y. Chang, Y. J. Lin, H. W. Sung, *Adv. Healthc. Mater.* **2021**, *10*, 1.
[224] S. Du, N. Zhou, G. Xie, Y. Chen, H. Suo, J. Xu, J. Tao, L. Zhang, J. Zhu, *Nano Energy* **2021**, *85*, 106004.

AUTHOR BIOGRAPHIES



Bharti Sheokand, born in Haryana, India, studied at Maharishi Markandeshwar University, Ambala, India, for her MSc degree. Currently, she is pursuing her PhD at the Department of Chemistry, Biochemistry and Forensic Science, Amity School of Applied Sciences, Amity University Haryana, India, under the supervision of Prof. Seema R. Pathak and Dr Monika Vats. During PhD her research focuses on the metal-based nanomaterials, polymer nanocomposites, and biomedical applications. She has published many research articles including book chapter.



Monika Vats is Assistant Professor of Chemistry at Dhanauri PG College, Dhanauri, Haridwar, affiliated to Shri Dev Suman University, Uttarakhand, India. She earned her Doctorate from the Indian Institute of Technology, Roorkee, a premier engineering institute in India. Her research interest includes polymer, biopolymer, nanomaterials, polymer composites, bioorganometallics, and cosmetics. She has published 17 peer reviewed papers and has six patents to her credit. She has authored 10 book chapters with leading international journals.



Anand Kumar obtained his MSc from Indian Institute of Technology Roorkee (IITR), MTech (Indian Institute of Technology Delhi) and PhD degree from IITR in the area of Prebiotic Chemistry. He worked as an Assistant Professor in National Institute of Technology Jalandhar, Punjab and as a Scientific officer in Uttarakhand Council of Science and Technology, Dehradun, Uttarakhand. Dr Kumar currently working as an Assistant Professor in the Department of Chemistry, Shri Guru Ram Rai (Post Graduate) College, Dehradun, affiliated to Hemwati Nandan Bahuguna Garhwal University (A Central University), Srinagar, Uttarakhand, India. His research is focus on applications of heterogeneous catalyst in prebiotic chemistry, remediation of environment pollutants as well as in pharmaceuticals. He has published 15 research papers in reputed international journals, 04 book chapters and 01 patent.



Chandra Mohan Srivastava received his MSc Chemistry degree from University of Lucknow, MTech Plastics Engineering degree from Central Institute of Plastics Engineering & Technology, Lucknow and PhD from Delhi Technological University, Delhi (with Dr Roli Purwar). He has worked as Lecturer in Central Institute of Plastics Engineering & Technology, Ahmedabad. He is presently an Assistant Professor of Chemistry in Amity School of Applied Sciences, Amity University Haryana, India. His research interest includes polymer, biopolymer, nanomaterials for biomedical applications, nanofabrication using electrospinning, and polymer composites. He has published 25 research papers and conference publication, 6 patents filed and 10 book chapters.



Professor Indra Bahadur Professor Bahadur is an NRF rated researcher and Fellow of Royal Society of Chemistry. He has appeared on the list of academics who have improved their h-Index in last 5 years as per AD Scientific Index 2021 and the Global Top 2% Scientists (list) published by Elsevier. His high citations (currently over 7800), with h-index 50 and an i10 index of 126, has contributed to his obtaining international recognition in area of Green Chemistry. His many research endeavors resulted in funding from Sasol, NRF, NWU, UKZN and DUT. In 2013, he was awarded the top publisher award from Durban University of Technology, Durban, South Africa followed by another top publisher award from Material Science Innovation and Modeling Research Focus area at North-West University. He completed his BSc degree at the Banaras Hindu University in 2004, majoring in Chemistry, and Mathematics, followed by MSc degree (Physical Chemistry) in 2007 from University of Delhi, Delhi, India. He proceeded to study toward a PhD in 2008 and completed his PhD degree (Physical Chemistry: Thermodynamics

26424169, 0, Downloaded from https://onlinelibrary.wiley.com/doi/10.1002/pol.20220734 by Delhi Technological University, Wiley Online Library on [05/04/2023]. See the Terms and Conditions (https://onlinelibrary.wiley.com/terms-and-conditions) on Wiley Online Library for rules of use; OA articles are governed by the applicable Creative Commons License

of Solution) in 2010 from the Department of Chemistry at the Durban University of Technology, Durban, South Africa. During the 12 years since the completion of his PhD studies, Professor Bahadur became an editor/associate editor for several reputed journals: Heliyon, Journal of Ionic Liquids, Measurement: Sensor, Scientific African, Recent Patents on Materials Science, Journal of Molecular and Applied Bioanalysis and Current Material Science. He has published over 180 peer-reviewed journal articles in reputed high impact factor journals with 5 book chapters and has 38 conference papers for oral or poster presentations. He is also currently involved in editing book title "Deep Eutectic Solvents (DESs): Futuristic Solvent in Science" which will be published by Elsevier. His research inclinations span on physical/biophysical chemistry includes thermodynamics, separation/extraction, protein stability (biophysical), corrosion inhibitors (electrochemistry) relevant to green technologies (waste management and pollution control) and bioproducts processing (valuable products from renewable resources, valorisation of neglected and underutilized crops).



Seema R. Pathak is a Professor and Head, Department of Chemistry, Biochemistry and Forensic Science at Amity School of Applied Sciences, Amity University Haryana, India. She did her Ph. D. from Lucknow University in 1999 and her RA ship from Central Drug Research Institute, Lucknow, India. Her research focuses on development and designing of new drug molecules. She did a significant contribution in field of organic chemistry and medicinal chemistry. She has more than 50 research papers and conference publication, 10 book chapters and have four patents to her credit.

How to cite this article: B. Sheokand, M. Vats, A. Kumar, C. M. Srivastava, I. Bahadur, S. R. Pathak, *J. Polym. Sci.* **2023**, 1. https://doi.org/10.1002/pol.20220734

26424169, 0, Downloaded from https://onlinelibrary.wiley.com/doi/10.1002/pol.20220734 by Delhi Technological University, Wiley Online Library on [05/04/2023]. See the Terms and Conditions (https://onlinelibrary.wiley.com/terms-and-conditions) on Wiley Online Library for rules of use; OA articles are governed by the applicable Creative Commons License

ResearchGate

See discussions, stats, and author profiles for this publication at: https://www.researchgate.net/publication/370078564

Numerical Evaluation of the Gate Stacked GNR FET for improved Device Switching

Conference Paper · December 2022

DOI: 10.1109/ICMACC54824.2022.10093656

CITATIONS
0

READS
36

2 authors:



Anshul Narwal
Delhi Technological University
1 PUBLICATION **0** CITATIONS
SEE PROFILE



Rishu Chaujar
Delhi Technological University
253 PUBLICATIONS **2,193** CITATIONS
SEE PROFILE

Some of the authors of this publication are also working on these related projects:

Novel Mosfet Design for Digital Applications View project

Modelling and Simulation of GAA FinFET View project

All content following this page was uploaded by Anshul Narwal on 19 April 2023.

The user has requested enhancement of the downloaded file.

2022 International Conference on Recent Trends in Microelectronics, Automation, Computing and Communications Systems (ICMACC) | 978-1-6654-9604-9/22/$31.00 ©2022 IEEE | DOI: 10.1109/ICMACC54824.2022.10093656

Numerical Evaluation of the Gate Stacked GNR FET for improved Device Switching

Anshul
Microelectronics Research lab
Department of Applied Physics
Delhi Technological University
Delhi, India
anshul_2k20phdap502@dtu.ac.in

Rishu Chaujar
Microelectronics Research lab
Department of Applied Physics
Delhi Technological University
Delhi, India
chaujar.rishu@dtu.ac.in

***Abstract* — The performance evaluation of nanoscale transistors is a complex phenomenon challenging the fabrication of various components of the integrated chips. In the present study, digital parameters of the graphene-based nanoribbon field-effect transistor (GNR FET) are investigated along with the gate stacked GNR FET, i.e., GS-GNR FET with gate stacking of lanthanum aluminate and silicon dioxide. The proposed device is simulated in Quantum ATK SE using the Slater-Koster method without SCF iteration followed by the non-equilibrium Green's function (NEGF). The gate stacking improves the device's performance by reducing the off-state current (I_{off}) and improving the device's switching ratio (I_{on}/I_{off}). Further, the subthreshold swing (SS) is reduced by 12% in the GS-GNR FET over GNR FET, portraying improved channel control and switching with less leakage current. The results show that the GS-GNR FET is an excellent replacement for the GNR FET in designing IC components in the electronics industry.**

Keywords* — *GNR FET, GS-GNR FET, ATK-SE, Leakage Current.

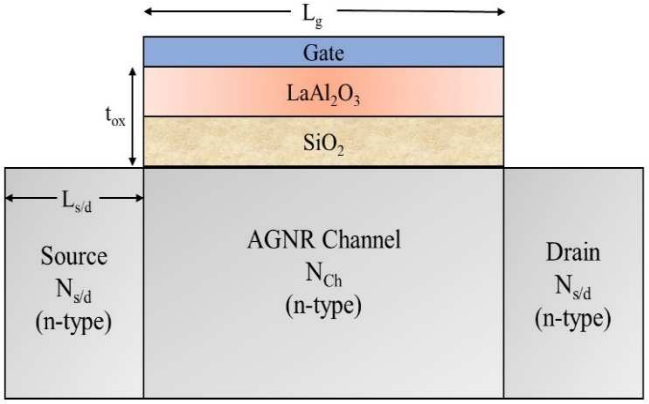
I. INTRODUCTION

Graphene is a potential alternative to Silicon due to its higher switching capability, charge-carrying mobility, and thermal stability with isotropic heat dissipation. The band structure of Graphene controls its electrical characteristics [1]. The overlapping band structure of Graphene limits its use in the direct application of the electronic industry [2]. To overcome this limitation, the quantum confinement method in one direction is widely adopted in the literature to tune the band gap of Graphene, leading to the invention of Graphene nanoribbons (GNR) [3]. The width of GNR has an inverse relationship with its tunable bandgap [4]. The tunable bandgap makes GNR available for wide use in the electronic industry. The arrangement of atoms at edges in GNR governs the configuration of GNR; armchair (AGNR) and zigzag (ZGNR). In AGNR configuration, the atoms at the edges are at a rotation of 120^0 to the last pair of atoms [5]. In ZGNR configuration, the zigzag edge's atoms originate from the same sublattice [6]. The ZGNR shows metallic behaviour as it has zero bandgap, whereas depending on the width of the atoms, AGNR can be metallic or semiconducting. [7]. AGNR is a competent material that can be adopted as a channel in the GNR FET. The literature surveyed by the authors led to the conclusion that there is a very limited study available on the gate stacking of GNR FET [8].

Based on the literature reviewed, continuous downscaling of the conventional GNRFET exhibits the problem of short channel effects and ambipolar conduction [9]. In the present study, the effect of gate stacking improves parameters like SS and V_{th}. As in the case of the proposed device, gate stacking reduces the effective oxide thickness, and this leads to a decrease in oxide capacitance resulting in better channel control. In the present study, the digital parameters of GNR FET are investigated along with the gate stacked GNR FET with a gate stacking of lanthanum aluminate and silicon dioxide. The Slater-Koster method without SCF iteration followed by the NEGF is adopted in ATK-SE to simulate the device. The outcome demonstrated that gate stacking increases device performance by lowering I_{off} current and hence raising the I_{on}/I_{off} ratio.

II. DEVICE STRUCTURE

Fig. 1. Cross-sectional view of proposed GS-GNR-FET.



The schematic view of GS- GNR FET with a stacked gate of lanthanum aluminate and silicon dioxide over an AGNR channel is shown in Fig.1. The schematic view of passivated and non-passivated GNR is shown in Fig. 2 and Fig.3.

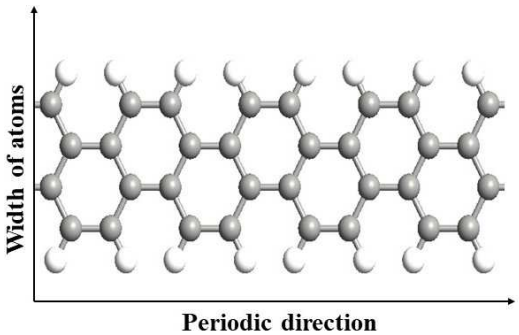


Fig. 2. Schematic view of H_2-passivated Armchair GNR.

978-1-6654-9604-9/22/$31.00 ©2022 IEEE

Authorized licensed use limited to: DELHI TECHNICAL UNIV. Downloaded on April 19,2023 at 10:56:33 UTC from IEEE Xplore. Restrictions apply.

The GS-GNR FET is a three-terminal device. Semiconducting AGNR (n=4) with N_2-passivation is used as a channel material rotated 30°, where 'n' depicts the no. of atoms. Further, the ZGNR configuration is adopted as source and drain (s/d) metallic contact.

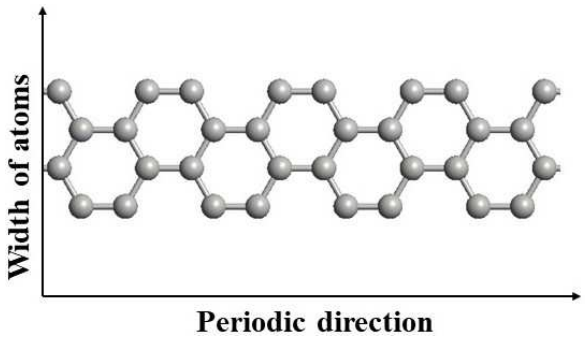


Fig. 3. Schematic view of non-passivated Armchair GNR

TABLE-1 Parameters for GNR FET AND GS-GNR FET

Parameter	Devices	
	GNR FET	***GS-GNR FET***
Gate length, L_g (nm)	6.6	6.6
Oxide layer thickness, t_{ox} (nm)	0.30	0.30 (0.15 SiO_2 + 0.15 $LaAl_2O_3$)
Source and drain length, $L_{s/d}$(nm)	2.2	2.2
The doping concentration of the channel region, N_{Ch} (e/cm^3)	3×10^{16}	3×10^{16}
Doping concentration of source and drain region, $N_{s/d}$ (e/cm^3)	5×10^{18}	5×10^{18}

The calculation of the electronic properties of the device is carried out using gate potential. The thickness of oxide layer (t_{ox}) is inversely proportional to the gate oxide capacitance (C_{ox}) i.e., reducing the t_{ox} will increase the C_{ox} which provides the better control of channel potential (ψ_{ch}). The thickness of oxide layer (t_{ox}) is taken 0.30nm considering the fact that the decreasing the t_{ox} improves the channel control of gate [10,11]. The set of selected input parameters is shown in Table 1. The combination of two dielectric layers (t_{ox1} = 0.15 SiO_2 and t_{ox2} = 0.15 $LaAl_2O_3$) is used to develop the gate stacking. The proposed device's performance is improved by lowering the parasitic capacitance with heavy n-type doping of the source and drain as compared to the channel [12]. The Quantum ATK simulator is used to investigate the proposed GS-GNR FET.

III. Simulation Approach

The Quantum ATK semi-empirical (ATK-SE) calculator has been used to analyze the band structure and I-V characteristics. The band structure is investigated using the extended Huckel model in ATK-SE with a 9×9×1 K-point sampling [13]. The Hartree density mesh cutoff is 40, adopted using the NEGF method. The Slater-Koster model is adopted to calculate the device's electrical properties in ATK-SE with a density mesh cutoff of 40 and K-point sampling of 1×1×100 without SCF iteration. The multigrid Poisson's solver is adopted in the present study with default multigrid type boundary conditions. The simulations were carried out using the Slater-Koster model and Semi-Empirical Calculator in the Quantum ATK simulator at room temperature (T=300K). NEGF data was used to calculate the drain current, finally utilizing Landauer's law, drain current was obtained from formalism given by:

$$I = \frac{2e}{h}\int T(E)[f_{FD}(E-\mu_d) - f_{FD}(E-\mu_s)]dE \qquad (1)$$

Where μ_s and μ_d represents the fermi levels at source and drain, respectively, $f_{FD}(E)$ is the Fermi-Dirac distribution. The simulation conducted in the present study is carried out at a V_{ds} of 0.5 V, V_{gs} of 0 to 1.0 V, and temperature of 300K, respectively.

IV. Result and Discussion

The band structure analysis of AGNR and ZGNR is depicted in Fig. 4 [a, c]. Fig. 4(a) shows the bandgap variation of AGNR (n=4) with H_2 – Passivation. Fig. 4(c) shows the bandgap of AGNR (n=4) with N_2 - Passivation. The band structure analysis shows that the AGNR configuration is semiconducting while ZGNR is metallic. The introduction of N_2 - Passivation in place of H_2 - Passivation decreases the bandgap of AGNR from 2.23 to 0.35 eV.

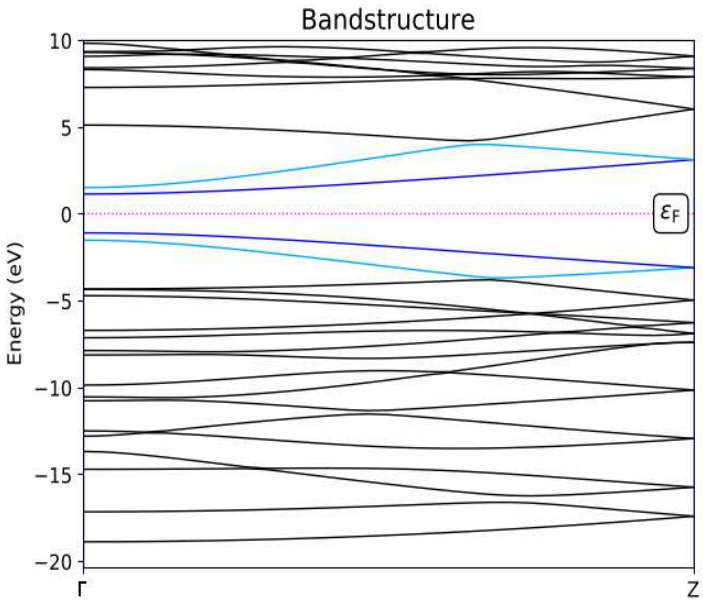


Fig. 4(a) Investigated bandstructure of H_2 passivation on AGNR configuration with bandgap value of 2.23 eV

Authorized licensed use limited to: DELHI TECHNICAL UNIV. Downloaded on April 19,2023 at 10:56:33 UTC from IEEE Xplore. Restrictions apply.

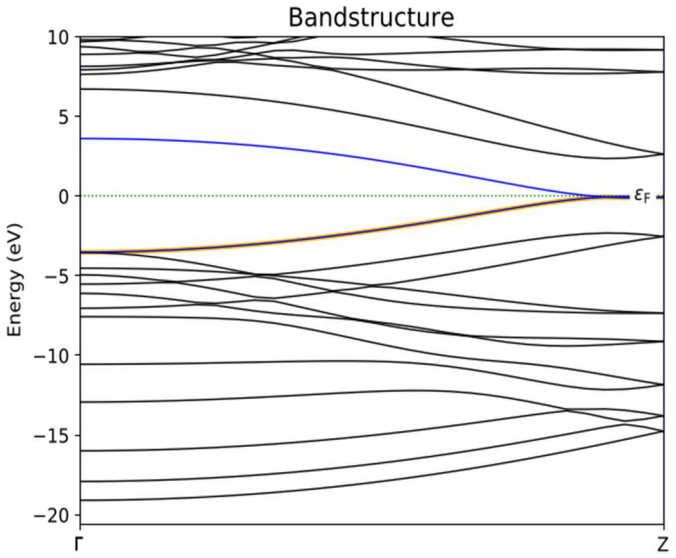


Fig. 4(b) Investigated bandstructure of H_2 passation on ZGNR configuration with bandgap value of 0 eV

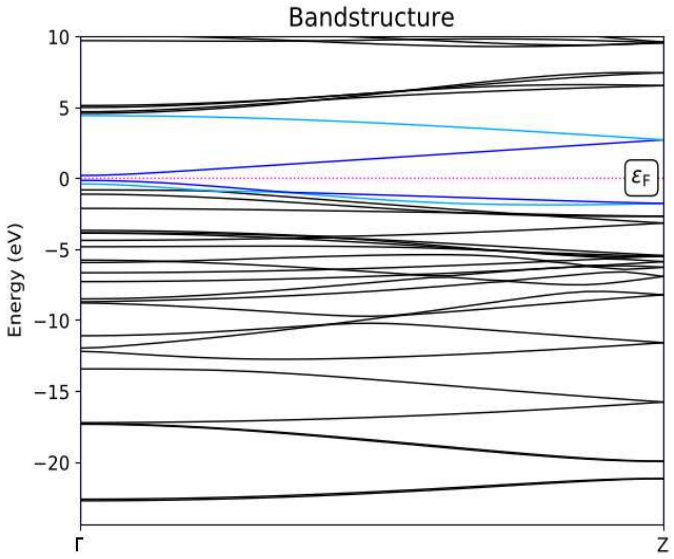


Fig. 4(c) Investigated bandstructure of N_2 passivation on AGNR configuration with bandgap value of 0.35 eV

The I_d vs. V_{gs} plot at V_{ds} = 0.5 V is shown in Fig. 5. The simulations are performed on the same dimension, and results are compared within the output obtained from numerically varied layer parameters. The aforementioned figure portrays the performance of GNR FET with GS-GNR FET in terms of drain current. Further, the leakage current (off-state current) is reduced by using gate stacking [14]. The rationale of adopting compounded combined values of high and low- κ dielectric oxide give rise to inevitable strong fringing electric fields, which leads to the increased gate oxide capacitance of the device, causing a potential drop in gate oxide, mathematically expressed as $\Phi_{ox} = Q_0/C_{ox}$, where Φ_{ox} is gate oxide potential, Q_0 is surface charge density, and C_{ox} is gate oxide capacitance [15].

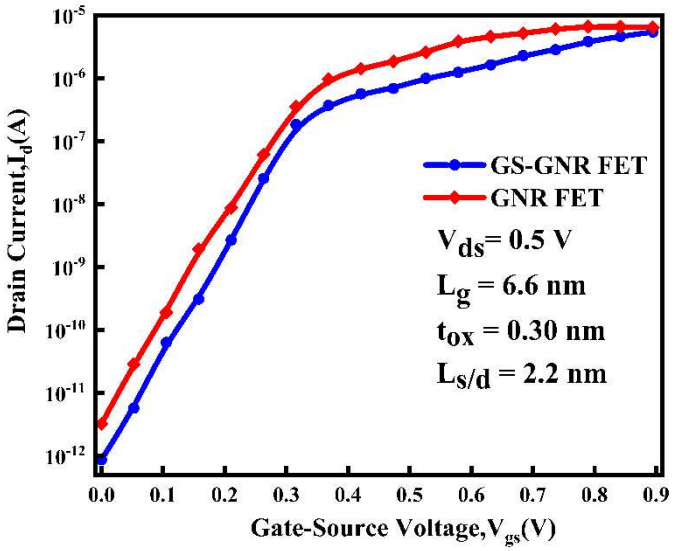


Fig. 5 Transfer characteristics of GS-GNR FET and GNR FET

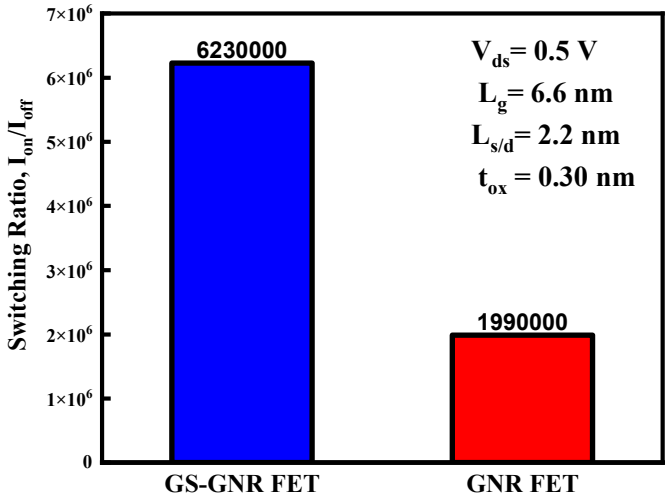


Fig. 6 Comparative representation of switching ratio of GS-GNR FET and GNR FET

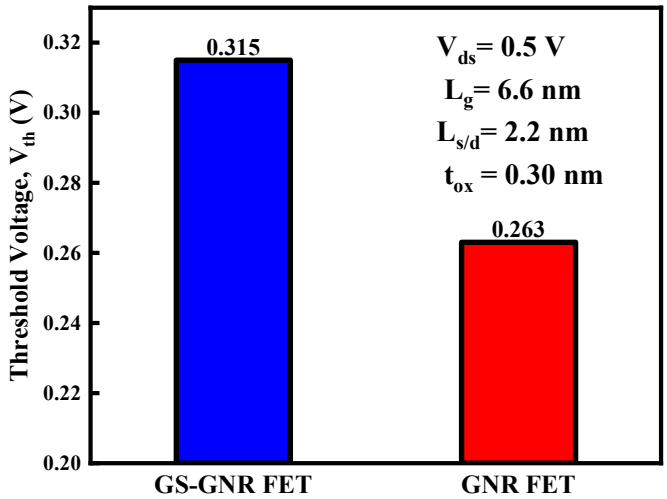


Fig. 7 Comparative representation of threshold voltage of GS-GNR FET and GNR FET

Fig. 6 and Fig. 7 represent the I_{on}/I_{off} and the threshold voltage (V_{th}) of GS-GNR FET and GNR FET, respectively. For a better switching speed, the I_{on}/I_{off} ratio must be higher [16].

Authorized licensed use limited to: DELHI TECHNICAL UNIV. Downloaded on April 19,2023 at 10:56:33 UTC from IEEE Xplore. Restrictions apply.

GS-GNR FET has a higher switching ratio and V_{th} than GNR-FET. The high-oxide layer strengthens the fringing electric fields, thus improving the V_{th} and I_{on}/I_{off} ratio [17,18].

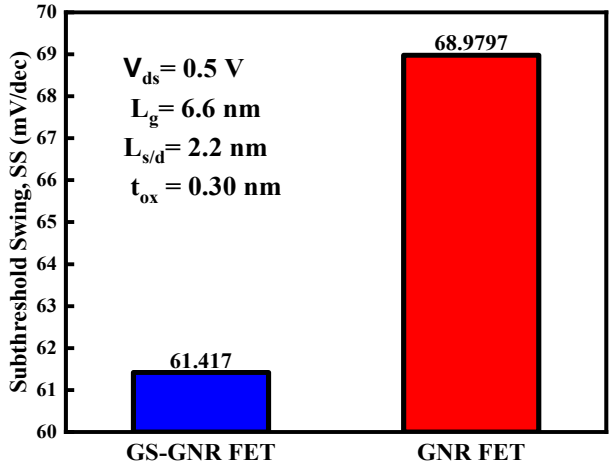


Fig. 8 Comparative representation of subthreshold swing for both devices

Fig. 8 displays the comparative bar representation for both devices. The SS is the change in V_{gs} to change in I_d for the log scale. A decrease in SS value refers to less leakage and better channel control [19, 20].

V. CONCLUSION

The enhancement in the performance of novel GS-GNR FET using the combination of high-κ dielectric with a low- κ dielectric material as gate stacking has been studied. The Slater-Koster model with NEGF is used to study the electrical properties of GS-GNR and GNR FET. The GS-GNR FET shows improvement in digital parameters over GNR FET. The Switching ratio increased by 213%, SS reduced by 12%, and leakage current by 72.97%. The study's findings indicate that the GS-GNR FET is a superior option to the GNR FET in the design of IC components for the electronics industry and high switching applications.

ACKNOWLEDGMENT

The authors extend a warm thank towards the MRL facility, at Applied Physics Department in Delhi Technological University for their assistance with this research.

REFERENCES

[1] V. N. Kotov, B. Uchoa, V.M. Pereira, F. Guinea, and A.H. Castro Neto, "Electron-electron interactions in graphene: Current status and perspectives," Reviews of Modern Physics, vol. 84, no. 3, pp. 1067,2012.

[2] Y.-W. Son, M.L. Cohen and S.G. Louie, "Energy gaps in graphene nanoribbons," Phys. Rev. Letters, vol. 97, no. 21, pp. 216803, 2006.

[3] S. Dutta and S. K. Pati, "Novel properties of graphene nanoribbons: A review," *J. Mater. Chem.*, vol. 20, no. 38, pp. 8207–8223, 2010.

[4] L. Yang, C.H. Park, Y.W. Son, M.L. Cohen and S.G. Louie, "Quasiparticle energies and band gaps in graphene nanoribbons," Phys. Rev. Lett. vol. 99, no. 18, pp. 186801, 2007.

[5] B. Xu, J. Yin, Y. D. Xia, X. G. Wan, K. Jiang, and Z. G. Liu, "Electronic and magnetic properties of zigzag graphene nanoribbon with one edge saturated," Applied Physics Letters, vol. 96, no. 16, pp. 163102, 2010.

[6] E. J. Kan, Z. Li, J. Yang, and J. G. Hou, "Half-metallicity in edge modified zigzag graphene nanoribbons," Journal of the American Chemical Society, vol. 130, no. 13, pp. 4224, 2008.

[7] W. Zhang, T. Ragab and C. Basaran, "Unraveling mechanics of armchair and zigzag graphene nanoribbons," International Journal of Damage Mechanics, vol. 26, no. 3, pp.447, 2017.

[8] H. Wang, Sh Chang, J. He, Q. Huang, and F. Liu, "Dielectric engineering with the environment material in 2D semiconductor devices," IEEE Journal of the Electron Device Society, vol. 6, pp. 325, 2018.

[9] S. Lone, A. Bhardwaj, A. K. Pandit, S. Gupta, and S. Mahajan, "A Review of Graphene Nanoribbon Field-Effect Transistor Structures," J. Electron. Mater., vol. 50, no. 6, pp. 3169–3186, 2021.

[10] J. Robertson and R. M. Wallace, "High-K materials and metal gates for CMOS applications," Mater. Sci. Eng. R Reports, vol. 88, pp. 1–41, 2015.

[11] S. K. Sinha and S. Chaudhury, "Impact of oxide thickness on gate capacitance - A comprehensive analysis on MOSFET, nanowire FET, and CNTFET devices," IEEE Trans. Nanotechnol., vol. 12, no. 6, pp. 958–964, 2013.

[12] B. Kumar and R. Chaujar, "Analog and RF Performance Evaluation of Junctionless Accumulation Mode (JAM) Gate Stack Gate All Around (GS-GAA) FinFET," Silicon, vol. 13, pp. 919–927, 2021.

[13] *QUANTUM ATK User's Manual,* Synopsys International, California, CA, USA, 2019.

[14] T. Radsar, H. Khalesi, and V. Ghods, "Graphene nanoribbon field effect transistors analysis and applications," Superlattices and Microstructures, vol. 153, pp. 106869, 2021.

[15] Y. Yoon, G. Fiori, S. Hong, G. Iannaccone, and J. Guo, "Performance comparison of graphene nanoribbon FETs with Schottky contacts and doped reservoirs," IEEE Trans. Electron Devices, vol. 55, no. 9, pp. 2314–2323, 2008.

[16] M. Sharma and R. Chaujar, "Ultrascaled 10 nm T-gate E-mode InAlN/AlN HEMT with polarized doped buffer for high power microwave applications," Int. J. RF Microw. Comput. Eng., vol. 32, no. 4, pp. 1–10, 2022.

[17] T. Radsar, H. Khalesi, and V. Ghods, "Improving the performance of graphene nanoribbon field-effect transistors by using lanthanum aluminate as the gate dielectric," J. Comput. Electron., vol. 19, no. 4, pp. 1507–1515, 2020.

[18] Y. Pathak, B. D. Malhotra and R. Chaujar, "Detection of biomolecules in dielectric modulated double metal below ferroelectric layer FET with improved sensitivity," J Mater Sci: Mater Electron, vol. 33, pp. 13558, 2022.

[19] G. Fiori and G. Iannaccone, "Simulation of graphene nanoribbon field-effect transistors," IEEE Electron Device Lett., vol. 28, no. 8, pp. 760–762, 2007.

[20] R. Mann and R. Chaujar, "TCAD investigation of ferroelectric based substrate MOSFET for digital application," Silicon, pp. 1–10, 2021.

Authorized licensed use limited to: DELHI TECHNICAL UNIV. Downloaded on April 19,2023 at 10:56:33 UTC from IEEE Xplore. Restrictions apply.
View publication stats

Research Square

Preprints are preliminary reports that have not undergone peer review.
They should not be considered conclusive, used to inform clinical practice,
or referenced by the media as validated information.

On a Class of Non-Univalent functions Associated with a Parabolic Region

S. Sivaprasad Kumar (spkumar@dce.ac.in)
Delhi Technological University
Mridula Mundalia
Delhi Technological University

Research Article

Keywords: Univalent functions, Starlike functions, Logarithmic function, Radius problems, Differential inequality

Posted Date: April 12th, 2023

DOI: https://doi.org/10.21203/rs.3.rs-2798230/v1

License: This work is licensed under a Creative Commons Attribution 4.0 International License.
Read Full License

Additional Declarations: No competing interests reported.

On a Class of Non-Univalent functions Associated with a Parabolic Region

Mridula Mundalia[1] and S. Sivaprasad Kumar[1*†]

[1]Department of Applied Mathematics, Delhi Technological University, Shahbad Daulatpur, Delhi, 110042, India.

*Corresponding author(s). E-mail(s): spkumar@dce.ac.in;
Contributing authors: mridulamundalia@yahoo.co.in;
†These authors contributed equally to this work.

Abstract

In the present investigation, we introduce and study the geometric properties of a class of analytic functions, associated with a parabolic region majorly lying in the left-half plane. Further we establish radius and majorization results for the class under study with pictorial illustrations of some of its special cases. Also we derive some sufficient conditions for the class under consideration.

Keywords: Univalent functions, Starlike functions, Logarithmic function, Radius problems, Differential inequality

MSC Classification: 30C45 , 30C80

1 Introduction

Let $\mathcal{A}$ be the class of analytic functions $f(z)$ defined on the open unit disc $\mathbb{D} = \{z : |z| < 1\}$ with the normalization $f(0) = 0$ and $f'(0) = 1$. Assume $\mathcal{S} \subset \mathcal{A}$ to be the class of univalent functions. Let $f(z)$ and $g(z)$ be two analytic functions, then $f(z)$ is said to be subordinate to $g(z)$, symbolically $f \prec g$, if there exist a Schwarz function $w(z)$ in $\mathbb{D}$ with $w(0) = 0$, such that $f(z) = g(w(z))$. Additionally, if $g(z)$ is univalent in $\mathbb{D}$, then $f \prec g$ if and only if $f(\mathbb{D}_r) \subset g(\mathbb{D}_r)$, where $\mathbb{D}_r = \{z : |z| < r < 1\}$. Recall that a function $f \in \mathcal{A}$ is starlike if $f(\mathbb{D})$

is starlike with respect to 0. Analytically, a function $f \in \mathcal{A}$ is starlike if

$$\frac{zf'(z)}{f(z)} \prec \frac{1+z}{1-z}.$$

We denote this class by $\mathcal{S}^*$. Ma and Minda [17] gave a unified representation for various subclasses of starlike functions by replacing the superordinate function $(1+z)/(1-z)$ with a more general function $\phi(z)$, and the corresponding class is denoted by $\mathcal{S}^*(\phi)$. Here $\phi(z)$ is chosen such that it is univalent, starlike with respect to $\phi(0) = 1$ and $\operatorname{Re}\phi(z) > 0$ with $\phi'(0) > 0$, also $\phi(\mathbb{D})$ is symmetric about real axis. Several Ma-Minda subclasses have been studied previously (See Table 1). In contrast to $\mathcal{S}^*(\phi)$, Uralegaddi [28] introduced and studied the class

$$\mathcal{M}(\beta) = \{f \in \mathcal{A} : \operatorname{Re}(zf'(z)/f(z)) < \beta,\ \beta > 1\}.$$

Note that $\mathcal{M}(\beta) \nsubseteq \mathcal{S}^*$ and also contains non-univalent functions. In 2006, Ravichandran et al. [25] computed the radius of starlikeness for the class $\mathcal{M}(\beta)$. Motivated by the above class, Kumar et al. [15] made a systematic study of the class $\mathcal{F}(\psi)$ containing non-univalent functions, given by

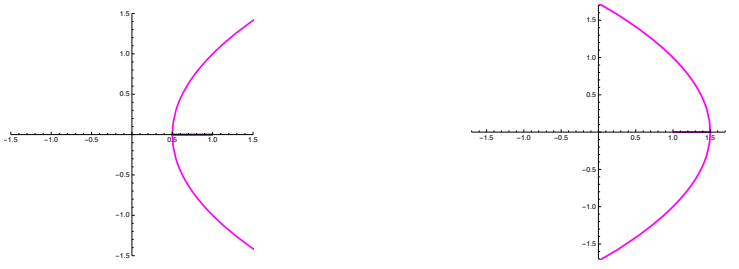
$$\mathcal{F}(\psi) := \left\{ f \in \mathcal{A} : \frac{zf'(z)}{f(z)} - 1 \prec \psi(z) \right\},$$

where $\psi(z)$ is an analytic univalent function such that $\psi(\mathbb{D})$ is starlike with respect to 0 and $\psi(0) = 0$. In general $\mathcal{F}(\psi) \nsubseteq \mathcal{S}^*(\phi)$. Further if $\phi(z) = 1 + \psi(z) \prec (1+z)/(1-z)$, then $\mathcal{F}(\psi)$ reduces to $\mathcal{S}^*(1+\psi)$. Here below we give a list of functions $\psi_i(z)$, $i = 1, \ldots, 4$, which are considered in context of the above class $\mathcal{F}(\psi)$,

$$\psi_i(z) = \begin{cases} \gamma z(1+\eta z)^{-2} & , i = 1 \\ z(1-\alpha z^2)^{-1} & , i = 2 \\ z(1-z)^{-1}(1+\beta z)^{-1} & , i = 3 \\ (A-B)^{-1}\log((1+Az)/(1+Bz)) & , i = 4, \end{cases} \tag{1}$$

where $A = \alpha e^{i\tau}, B = \alpha e^{-i\tau}$ with $\tau \in (0, \pi/2]$, and $\alpha, \beta, \eta \in (0, 1], \gamma > 0$ (see [12, 15, 16, 19]). Kumar and Gangania in [15], introduced the class $\mathcal{S}_\gamma(\eta) = \mathcal{F}(\psi_1)$ and obtained the radius of starlikeness. Cho et al. [2] dealt with certain sharp radius problems for the class $\mathcal{BS}(\alpha) = \mathcal{F}(\psi_2)$. Infact Masih et al. [19] studied the class $\mathcal{S}_{cs}(\beta) = \mathcal{F}(\psi_3)$, where $0 \leq \beta < 1$, discussed the growth theorem and established sharp estimates of logarithmic coefficients for $0 \leq \beta \leq 1/2$. Further for $1/2 < \beta \leq 1$, the class $\mathcal{S}_{cs}(\beta)$ contains non-univalent functions, infact for $0 \leq \beta \leq 1/2$ the class $\mathcal{S}_{cs}(\beta) \subset \mathcal{S}^*$. In 2022, Kumar et al. [16] introduced the class $\mathcal{F}(A, B) = \mathcal{F}(\psi_4)$ and established some radii results.

Motivated essentially by the above classes and observations, we now study a subclass of $\mathcal{A}$ containing non-univalent functions. For $\tau, \theta \in (-\pi, \pi]$ the transformation $\omega = ((2e^{i\theta/2}\sqrt{2}/\pi)(\tan^{-1}(e^{i(\tau-\pi/2)}\sqrt{z})))^2$ maps the boundary



(a) (b)

Fig. 1 Graphs representing different parabolas with a common focus (1,0) (a) $1+\mathcal{P}_{0,\pi}(\partial\mathbb{D})$, (b) $1+\mathcal{P}_{0,0}(\partial\mathbb{D})$.

of $\mathbb{D}$ onto a parabola (see **Fig.** 1), given by

$$\mathcal{P}_{\tau,\theta}(z) := \frac{2e^{i(\theta+\pi)}}{\pi^2}\left(\log\left(\frac{1+e^{i\tau}\sqrt{z}}{1-e^{i\tau}\sqrt{z}}\right)\right)^2$$
$$= \frac{8e^{i(\theta+\pi)}}{\pi^2}\sum_{n=1}^{\infty}\left(\frac{e^{2i\tau n}}{n}\sum_{k=0}^{n-1}\frac{1}{2k+1}\right)z^n,$$

where the branch of $\sqrt{z}$ is chosen so that $\operatorname{Im}\sqrt{z}\geq 0$. Note that the function $\mathcal{P}_{\tau,\theta}(z)$ is univalent in $\mathbb{D}$ and $1+\mathcal{P}_{0,\pi}(z)$ (see **Fig.** 1(a)) is the parabolic function introduced independently by Ma-Minda [18] and Ronning [26], and used it extensively in context of parabolic starlike functions (see [10, 26]). Further, Kanas [11] discussed some differential subordination techniques and later studied admissibility results [9] involving $1+\mathcal{P}_{0,\pi}(z)$. Note that the boundary of the function $\mathcal{P}_{0,0}(z)$ is a horizontal parabola with an opening in the left-half plane (see **Fig.** 1(b)). In the present study, we consider the function $1+\mathcal{P}_{0,0}(z)$, in context of non-univalent functions, which is completely different from the way Ronning, Ma-Minda and Kanas (see [9, 11, 18, 26]) handled parabolic regions. Obviously, the other choices of τ and θ leads to oblique parabolic regions, which is beyond the scope of our present study and therefore it is skipped here, as it needs to be handled differently.

For brevity, let us assume $\mathcal{P}_0(z) := \mathcal{P}_{0,0}(z)$ and $\mathcal{LP}(z) := 1+\mathcal{P}_0(z)$, then the horizontal parabolic region $\mathcal{LP}(z)$ (see **Fig.** 2), is given by

$$\Omega_{\mathcal{LP}} := \{\omega\in\mathbb{C} : (\operatorname{Im}\omega)^2 < 3-2\operatorname{Re}\omega \text{ or } |1-\omega| < 2-\operatorname{Re}\omega\}.$$

Since the major part of the above region lies in the left half plane, it is interesting to find the optimal radius of the domain disc for which it is fully mapped into the right half plane. Here below we define a class of analytic functions consisting of non-univalent functions.

Definition 1 Let the class $\mathcal{F}_{\mathcal{LP}}$ consist of functions $f\in\mathcal{A}$ satisfying the subordination

$$\frac{zf'(z)}{f(z)} \prec \mathcal{LP}(z) = 1-\frac{2}{\pi^2}\left(\log\left(\frac{1+\sqrt{z}}{1-\sqrt{z}}\right)\right)^2.$$

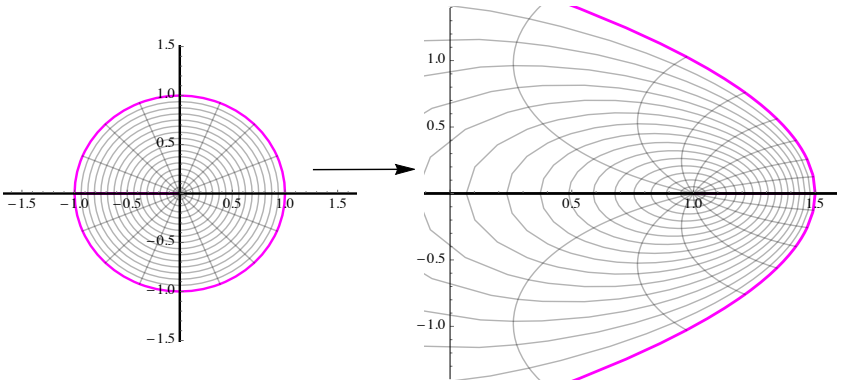


Fig. 2 Image of open unit disk $\mathbb{D}$ under the mapping $\mathcal{LP}(z)$.

Note that if $f_0 \in \mathcal{F}_{\mathcal{LP}}$, then it can be expressed as

$$f_0(z) = z\left(\exp\int_0^z \frac{\mathcal{P}_0(t)}{t}dt\right), \tag{2}$$

which acts as an extremal function for many radius results. Evidently, the subclasses of starlike functions $\mathcal{S}^*_{SG}$, $\mathcal{S}^*_{\mathcal{RL}}$ and $\mathcal{SL}^*(\alpha)$ $(0 \le \alpha < 1)$ (see Table 1) are contained in $\mathcal{F}_{\mathcal{LP}}$, however $\mathcal{F}_{\mathcal{LP}} \nsubseteq \mathcal{S}$. In section 2, we examine some geometrical properties of the function $\mathcal{LP}(z)$.

2 Main Results

2.1 Geometric Properties of the function $\mathcal{LP}(z)$

In Lemma 1, we establish the maximum and minimum bounds of real part of the function $\mathcal{P}_0(z)$.

Lemma 1 *Let $z \in \mathbb{D}_r = \{z : |z| = r\}$, then for each $0 \le r < 1$ and $\alpha \in (-\pi, \pi]$, we have*

$$\mathcal{P}_0(r) \le \operatorname{Re}\mathcal{P}_0(re^{i\alpha}) \le \mathcal{P}_0(-r).$$

Proof Suppose $z = re^{i\alpha}$, where $-\pi < \alpha \le \pi$, then for $|z| = r < 1$,

$$\begin{aligned}\operatorname{Re}(\mathcal{P}_0(z)) &= -\frac{2}{\pi^2}\left\{\operatorname{Re}\left(\log\left(\frac{1+\sqrt{z}}{1-\sqrt{z}}\right)\right)^2\right\}\\ &= -\frac{2}{\pi^2}\left(\log\left(\sqrt{\frac{\mu_1(r,c)}{\mu_2(r,c)}}\right)\right)^2 + \frac{2}{\pi^2}\left(\tan^{-1}\left(\frac{2\sqrt{1-c^2}\sqrt{r}}{1-r}\right)\right)^2\\ &=: \mathcal{G}(r,c).\end{aligned}$$

where $c := \cos(\alpha/2)$ and

$$\mu_i(r,c) := \begin{cases} 1+r+2c\sqrt{r}, & i=1, \\ 1+r-2c\sqrt{r}, & i=2. \end{cases}$$

Observe that $c \in [-1,1]$, infact it is easy to check that $\partial \mathcal{G}(r,c)/\partial c = 0$ if and only if $c = 0$, also $\partial^2 \mathcal{G}(r,0)/\partial c^2 < 0$, which leads to

$$\max_{c\in[-1,1]} \mathcal{G}(r,c) = \mathcal{G}(r,0) = \mathcal{P}_0(-r) = 1 + \frac{2}{\pi^2}\left(\tan^{-1}\left(\frac{2\sqrt{r}}{1-r}\right)\right)^2. \tag{3}$$

Moreover, for each $R \leq r < 1$, equation (3) leads to $\mathcal{G}(r,0) \geq \mathcal{P}_0(r) = \mathcal{G}(r,1)$. Since $\mathcal{G}(r,0)$ is an increasing function, whereas $\mathcal{G}(r,1)$ is a decreasing function of r, this leads to the inequality $\mathcal{G}(r,1) < \mathcal{G}(r,0)$, for each $r < 1$. Hence the required bound is achieved. □

As a consequence of Lemma 1 and [15, Theorem 2.1 & Corollary 2.2], we obtain the Growth and Covering Theorems for the class $\mathcal{F}_{\mathcal{LP}}$.

Theorem 1 *Let $f \in \mathcal{F}_{\mathcal{LP}}$, then the following holds*

I. (Growth Theorem) For $|z| = r < 1$, let

$$\max_{|z|=r} \operatorname{Re} \mathcal{P}_0(z) = \mathcal{P}_0(-r) \text{ and } \min_{|z|=r} \operatorname{Re} \mathcal{P}_0(z) = \mathcal{P}_0(r),$$

then for $|z| = r < 1$ the following sharp inequality holds

$$r \exp\left(\int_0^r \frac{\mathcal{P}_0(t)}{t}dt\right) \leq |f(z)| \leq r \exp\left(\int_0^r \frac{\mathcal{P}_0(-t)}{t}dt\right).$$

II. (Covering Theorem) Suppose $\min_{|z|=r} \operatorname{Re} \mathcal{P}_0(z) = \mathcal{P}_0(r)$ and $f \in \mathcal{F}_{\mathcal{LP}}$. Let f_0 be given by (2), then $f(z)$ is a rotation of f_0 or $\{w \in \mathbb{D} : |w| \leq -f_0(-1)\} \subset f(\mathbb{D})$, where $-f_0(-1) = \lim_{r\to 1} -f_0(-1)$.

Remark 1 (See **Fig.** 3) If $f(z)$ is of the form $f(z) = z + a_2 z^2 + a_3 z^3 + \ldots$, belongs to $\mathcal{F}_{\mathcal{LP}}$, then

$$\left|\arg\left(\frac{zf'(z)}{f(z)} - 2\right)\right| > \frac{3\pi}{4}.$$

It can be verified that the equation of tangent corresponding to $\Gamma : y^2 = 1 + 2(1-x)$ is given by $y = \pm(x-2)$. Infact these tangents intersect the parabola Γ at the points $(1, \pm 1)$. Therefore it can be observed that the convex region $\Omega_{\mathcal{LP}}$ lies in the sector $|\arg(\omega - 2)| > 3\pi/4$. Hence this gives a sharp argument estimate for functions lying in the class $\mathcal{F}_{\mathcal{LP}}$.

Remark 2 Due to Lemma 1, for $|z| = r < 1$, we have $\mathcal{LP}(r) \leq \operatorname{Re} \mathcal{LP}(z) \leq \mathcal{LP}(-r)$ and infact $\max_{|z|=r} |\mathcal{LP}(z)| = |\mathcal{LP}(r)| = |\mathcal{P}_0(r)|$.

2.2 Radius Problems for the class $\mathcal{F}_{\mathcal{LP}}$

Based on the definition of the class $\mathcal{F}_{\mathcal{LP}}$ and pictorial representation of $\mathcal{LP}(\partial\mathbb{D})$ (see **Fig.** 2), we have $\max_{|z|\leq 1} \operatorname{Re}(\mathcal{LP}(z)) = \mathcal{LP}(-1) = 3/2$. This means

$\mathrm{Re}\, zf'(z)/f(z) < 3/2$, thus $f \in \mathcal{F}_{\mathcal{LP}}$ may or may not be a univalent function. Therefore it is an interesting problem to establish the largest radius $r_0 < 1$ such that each $f \in \mathcal{F}_{\mathcal{LP}}$ is starlike in $|z| \leq r_0$. In this section, we study some radius results for the class $\mathcal{F}_{\mathcal{LP}}$ along with the classes $\mathcal{S}^*(\phi)$ and $\mathcal{F}(\psi)$ for some special choices of $\phi(z)$ and $\psi(z)$, as mentioned in Table 1 (see Appendix) and equation (1), respectively. Here below we provide a lemma that yields a maximal disc that can be subscribed within the parabolic region $\Omega_{\mathcal{LP}}$.

Lemma 2 *Suppose $a < 3/2$ and assume that $\zeta(\eta)$ is defined as follows:*

$$\zeta = \zeta(\eta) = \log\left(\frac{\sqrt{\eta}}{\sqrt{1-\eta}}\right) \text{ with } \eta = \frac{e^{-\pi\sqrt{1-2a}}}{1+e^{-\pi\sqrt{1-2a}}},$$

then $\mathcal{LP}(\mathbb{D})$ satisfies the following inclusion

$$\mathcal{D}(a, r_a) := \{\omega \in \mathbb{C} : |\omega - a| < r_a\} \subset \Omega_{\mathcal{LP}},$$

where

$$r_a = \begin{cases} \sqrt{\left(a - \frac{3}{2} + \frac{2\zeta^2}{\pi^2}\right)^2 + \frac{4\zeta^2}{\pi^2}}, & a \leq \frac{1}{2} \\ \frac{3}{2} - a, & \frac{1}{2} < a < \frac{3}{2}, \end{cases}$$

Proof We obtain a maximal disc centered at $(a, 0)$, where $a < 3/2$, that can be inscribed within $\Omega_{\mathcal{LP}}$. The distance from center $(a, 0)$ to the boundary $f(\partial(\mathbb{D}))$ is given by square root of

$$\mathcal{D}_a(X) := \left(a + \frac{2}{\pi^2}\left(\log\left(\frac{\sqrt{X^2}}{\sqrt{1-X^2}}\right)\right)^2 - \frac{3}{2}\right)^2 + \frac{4}{\pi^2}\left(\log\left(\frac{\sqrt{X^2}}{\sqrt{1-X^2}}\right)\right)^2,$$

where $X = \cos t$. Now the critical points of $\mathcal{D}_a(X)$ are

$$X' := \begin{cases} \pm\frac{e^{\frac{1}{2}\pi\sqrt{1-2a}}}{\sqrt{1+e^{\pi\sqrt{1-2a}}}}, \pm\frac{e^{-\frac{1}{2}\pi\sqrt{1-2a}}}{\sqrt{1+e^{-\pi\sqrt{1-2a}}}}, & \text{if } a < 1/2, \\ \pm 1/\sqrt{2}, & \text{if } 1/2 \leq a < 3/2. \end{cases}$$

It can be verified that $\mathcal{D}_a''(X) > 0$ at $X = X'$, whenever $a < 3/2$. Therefore, $X = X'$ is the point of minima for $\mathcal{D}_a(X)$, which leads us to the optimal disk centered at a with radius r_a. □

Theorem 2 *Suppose $0 \leq \alpha < 1$ and $-1 < B < A \leq 1$, then for $f \in \mathcal{A}$, the sharp $\mathcal{F}_{\mathcal{LP}}-$radii for the classes $\mathcal{S}_p^*$, $\mathcal{S}_s^*$, Δ^*, $\mathcal{S}_\varrho^*$, $\mathcal{S}_\rho^*$, $\mathcal{S}_\wp^*$, $\mathcal{BS}^*(\alpha)$, $\mathcal{S}_{\alpha,e}^*$ and $\mathcal{S}^*(A, B)$ (see Table 1 in Appendix) are respectively given by*

(i) $\mathcal{R}_{\mathcal{F}_{\mathcal{LP}}}(\mathcal{S}_p^*) = \tanh^2(\pi/4)$.

(ii) $\mathcal{R}_{\mathcal{F}_{\mathcal{LP}}}(\mathcal{S}_s^*) = \pi/6$.

(iii) $\mathcal{R}_{\mathcal{F}_{\mathcal{LP}}}(\Delta^*) = 5/12$.

(iv) $\mathcal{R}_{\mathcal{F}_{\mathcal{LP}}}(\mathcal{S}_\varrho^*) = (\cosh^{-1}(3/2))^2$.

(v) $\mathcal{R}_{\mathcal{F}_{\mathcal{LP}}}(\mathcal{S}^*_\rho) = \sinh(1/2)$.

(vi) $\mathcal{R}_{\mathcal{F}_{\mathcal{LP}}}(\mathcal{S}^*_\wp) \approx 0.3517\ldots$.

(vii) *For* $0 < \alpha < 1$, $\mathcal{R}_{\mathcal{F}_{\mathcal{LP}}}(\mathcal{BS}^*(\alpha)) = R_{\mathcal{BS}}$, *where*

$$R_{\mathcal{BS}} = \begin{cases} 1/2, & \alpha = 0 \\ (\sqrt{1+\alpha}-1)/\alpha, & 0 < \alpha < 1. \end{cases}$$

(viii) $\mathcal{R}_{\mathcal{F}_{\mathcal{LP}}}(\mathcal{S}^*_{\alpha,e}) = R_{\alpha,e}$, *where*

$$R_{\alpha,e} = \begin{cases} \log(1-1/2(\alpha-1)), & 0 \le \alpha < 1-1/2(e-1) \\ 1, & 1-1/2(e-1) \le \alpha < 1. \end{cases}$$

In particular, $\mathcal{R}_{\mathcal{F}_{\mathcal{LP}}}(\mathcal{S}^*_e) = \log(3/2)$.

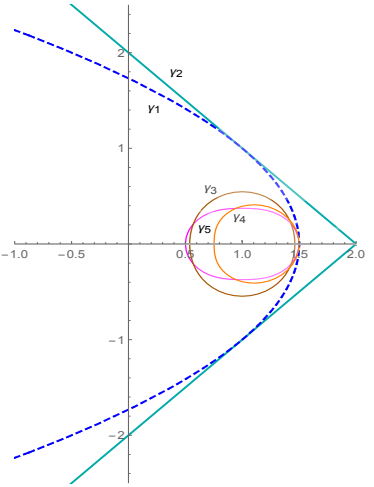
(ix) $\mathcal{R}_{\mathcal{F}_{\mathcal{LP}}}(\mathcal{S}^*(A,B)) =: \tilde{R}$, *where*

$$\tilde{R} = \begin{cases} 1/(2A-3B), & \text{when } ((-1 < B \le (2A-1)/3) \wedge (-1 < A < 0)) \\ & \quad \vee((-1 < B < (2A-1)/3) \wedge (0 \le A \le 1)), \\ 1, & \text{when } ((2A-1)/3 < B < A \le 1) \wedge (-1 < A < 0)) \\ & \quad \vee(((2A-1)/3 \le B < A \le 1) \wedge (0 \le A \le 1)). \end{cases}$$

Proof For part (i), as $f \in \mathcal{S}^*_p$, then due to the geometry of the function $1+\mathcal{P}_{0,\pi}(z) = 1 + 2/\pi^2(\log((1+\sqrt{z})/(1-\sqrt{z})))^2$ it can be observed that

$$\max_{|z|=r} \mathrm{Re}(1+\mathcal{P}_{0,\pi}(z)) = 1 + \mathcal{P}_{0,\pi}(r).$$

Now for $f(z)$ to lie in the class $\mathcal{F}_{\mathcal{LP}}$, we must have



γ_1 : $\mathcal{LP}(z)$
$1 - 2/\pi^2(\log((1+\sqrt{z})/(1-\sqrt{z})))^2$

γ_2 : $|\arg(u-2)| = 3\pi/4$

γ_3 : Modified Sigmoid function
$2/(1+e^{-z})$

γ_4 : Cardioid function
$1 + ze^z$ in $|z| < r^*$,
$r^* \approx 0.351734$

γ_5 : Booth Lemniscate for $\alpha = 0.8$
$1 + 5z/(5-4z^2)$ in $|z| < r_0$,
$r_0 = |z| < (1/4)(3\sqrt{5}-5)$.

Fig. 3 Pictorial boundary description of inclusion results pertaining to the parabolic function $\mathcal{LP}(z)$

$$1+\frac{2}{\pi^2}\left(\log\left(\frac{1+\sqrt{r}}{1-\sqrt{r}}\right)\right)^2 \leq \frac{3}{2},$$

which holds provided $r \leq \mathcal{R}_{\mathcal{F}_{\mathcal{LP}}}(\mathcal{S}_p^*)$. Clearly equality in (i) is attained for the function $\tilde{f}(z)$ such that $z\tilde{f}'(z_0)/\tilde{f}(z_0) = 1 + \mathcal{P}_{0,\pi}(z_0)$ at $z_0 = \mathcal{R}_{\mathcal{F}_{\mathcal{LP}}}(\mathcal{S}_p^*)$. Further observe that, if $p \in \mathcal{P}[A,B] = \{p(z) : p(z) = 1 + c_1 z + c_2 z^2 \ldots \prec (1+Az)/(1+Bz), -1 \leq B < A \leq 1\}$, then for $|z| = r < 1$, it is a known fact that

$$\left|p(z) - \frac{1-ABr^2}{1-B^2r^2}\right| < \frac{|A-B|r}{1-B^2r^2}. \tag{4}$$

Then, in view of (4), for part (ix) $f \in \mathcal{S}^*(A,B)$ lies in $\mathcal{F}_{\mathcal{LP}}$, if

$$\frac{(A-B)r+1-ABr^2}{1-B^2r^2} \leq \frac{3}{2}.$$

Equivalently, we can say that $(1-Br)((2A-3B)r-1) \leq 0$, provided $r \leq \mathcal{R}_{\mathcal{F}_{\mathcal{LP}}}(\mathcal{S}^*(A,B))$. Extremal function in this case is $\hat{f} \in \mathcal{A}$ satisfying $z_0\hat{f}'(z_0)/\hat{f}(z_0) = (1+Az_0)/(1+Bz_0)$, where $z_0 = \tilde{R}$. For part (iv), as $f \in \mathcal{F}_{\mathcal{LP}}$, then proceeding as before, f lies in $\mathcal{S}_\varrho^*$ if for $|z| = r$ we have $3/2 \geq \cosh\sqrt{r}$, provided $r = \mathcal{R}_{\mathcal{F}_{\mathcal{LP}}}(\mathcal{S}_\varrho^*)$. Sharpness holds for the function $f_\varrho \in \mathcal{A}$ defined as $zf_\varrho'(z)/f_\varrho(z) = \cosh\sqrt{z}$. Further we know that $\max_{|z|=r} \mathrm{Re}(1+\sin z) = 1+\sin r$, then for part (ii) it is enough to find an $r < 1$ satisfying the equation $\sin r = 1/2$, thus $r = \mathcal{R}_{\mathcal{F}_{\mathcal{LP}}}(\mathcal{S}_s^*) = \pi/6$. Sharpness holds for the function $f_s(z)$ given by $zf_s'(z)/f_s(z) = 1+\sin z$. In all the subsequent parts, the proofs follow along the same lines, therefore they are omitted. □

Let $\mathcal{P}_\alpha$ consist of functions of the form $p(z) = 1 + c_1 z + c_2 z^2 + \ldots$, satisfying $\mathrm{Re}\, p(z) > \alpha$ for $0 \leq \alpha < 1$, then we say $p(z)$ is a Carathéodory function of order α. Denote $\mathcal{P}(0) =: \mathcal{P}$, commonly known as the class of Carathéodory functions. Further, assume $\mathfrak{P}_{\mathcal{LP}}$ to be the class of functions of the form $p(z) = 1 + c_1 z + c_2 z^2 + \ldots$, such that $p(z) \prec \mathcal{LP}(z)$.

Theorem 3 *Let $0 \leq \alpha < 1$ and $0 \leq \gamma \leq \gamma_\alpha$, where $\gamma_\alpha = \tanh^2(\pi\sqrt{1-\alpha}/2\sqrt{2})$. If $p \in \mathfrak{P}_{\mathcal{LP}}$, then $p \in \mathcal{P}_\alpha$, i.e $p(z)$ is a Carathéodory function of order α, in the disc $|z| < \gamma_\alpha$.*

Proof Since $p \in \mathfrak{P}_{\mathcal{LP}}$, then by definition of subordination and Schwarz Lemma, there exists an analytic function $w(z)$ with $|w(z)| \leq |z| < 1$ and $w(0) = 0$, such that $p(z) = \mathcal{LP}(w(z))$. Suppose $w(z) = Re^{i\theta}$ $(-\pi < \theta \leq \pi)$, then $|w(z)| = R \leq |z| = r < 1$. On applying Lemma 1 for $p \in \mathfrak{P}_{\mathcal{LP}}$, we get $\mathrm{Re}\, p(z) \geq \mathcal{LP}(r)$. Further $p \in \mathfrak{P}_{\mathcal{LP}}$ is Carathéodory of order α $(0 \leq \alpha < 1)$ if $\mathcal{LP}(r) \geq \alpha$, provided $r \leq \gamma_\alpha = \tanh^2(\pi\sqrt{1-\alpha}/2\sqrt{2})$. The function $f_0(z)$ given by (2), is the extremal. □

Upon replacing $p(z)$ with $zf'(z)/f(z)$ in Theorem 3, we deduce the next result.

Corollary 1 *Let $0 \leq \alpha < 1$ and $0 \leq \gamma \leq \gamma_\alpha$, where γ_α is as defined in Theorem 3. If $f \in \mathcal{F}_{\mathcal{LP}}$, then $f(z)$ is starlike of order α in the disc $|z| < \gamma_\alpha$. This result is sharp.*

Remark 3 Put $\alpha = 0$ in Theorem 3, we get a sharp $\mathcal{P}-$ radius for the class $\mathfrak{P}_{\mathcal{LP}}$. Infact for the class $\mathcal{F}_{\mathcal{LP}}$, Corollary 1 gives sharp radius of starlikeness $\gamma_0 = \tanh^2(\pi/2\sqrt{2})$. Moreover, $r = \gamma_0 < 1$ serves as the sharp radius of univalence for the class $\mathcal{F}_{\mathcal{LP}}$.

Theorem 4 *Assume $0 < \alpha \leq 1$, then the sharp $\mathcal{S}^*(1+\alpha z)-$ radius for the class $\mathcal{F}_{\mathcal{LP}}$ is the unique positive root $r_\alpha = \tanh^2(\pi\sqrt{\alpha}/2\sqrt{2})$ of the equation*

$$2\left(\log((1+\sqrt{r})/(1-\sqrt{r}))\right)^2 - \alpha\pi^2 = 0, \tag{5}$$

where α is the radius of the disc $\{\omega : |\omega - 1| < \alpha\}$.

Proof In view of Remark 2, for the circle $|z| = r < 1$, we have

$$\max_{|z|\leq r<1} |\mathcal{LP}(z)| = 1 - \frac{2}{\pi^2}\left(\log\left(\frac{1+\sqrt{r}}{1-\sqrt{r}}\right)\right)^2 = \mathcal{LP}(r), \tag{6}$$

which is a decreasing function. Infact $\mathcal{LP}(r) = 0$ if and only if $r = \tanh^2(\pi/2\sqrt{2}) \approx 0.6469\ldots$. As $f \in \mathcal{F}_{\mathcal{LP}}$, then there exists a Schwarz's function $w(z)$ with $w(0) = 0$, so that

$$\frac{zf'(z)}{f(z)} = \mathcal{LP}(w(z)).$$

Assume $w(z) = Re^{i\theta}$ where $R \leq r < 1$. Now observe that for $0 < \alpha \leq 1$, equation (6) yields

$$|\mathcal{LP}(z) - 1| \leq |\mathcal{LP}(R) - 1| \leq |\mathcal{LP}(r) - 1| = |\mathcal{P}_0(r)| \leq \alpha,$$

provided $r \leq \tanh^2(\pi\sqrt{\alpha}/2\sqrt{2}) = r_\alpha$. Further, at $z_0 = r_\alpha$, the function $f_0(z)$ (defined in (2)) such that $zf_0'(z)/f_0(z) = \mathcal{LP}(z)$, works as the extremal function. □

As a consequence of Theorem 4, $\mathcal{S}^*(1+\alpha z)-$ radii for some well-known Ma-Minda subclasses of starlike functions, namely, $\mathcal{S}_e^*$, $\mathcal{S}_s^*$, $\mathcal{S}_\varrho^*$, $\mathcal{S}_\wp^*$, $\mathcal{S}_\rho^*$, $\mathcal{S}_{SG}^*$ and $\mathcal{S}_{N_e}^*$ (see Table 1 in Appendix) are stated in Corollary 2. Moreover, sharpness of Corollary 2 is illustrated by **Fig.** 4.

Corollary 2 *Let $f \in \mathcal{A}$ belong to $\mathcal{F}_{\mathcal{LP}}$, then the following radii are sharp for the class $\mathcal{F}_{\mathcal{LP}}$, (see **Fig.** 4)*

(i) The $\mathcal{S}_e^*-$radius is $r_1 = \tanh^2(\lambda\pi)$, where $\lambda = (1/2)\sqrt{(e-1)/2e}$.

(ii) The $\mathcal{S}_s^*-$radius is $r_2 = \tanh^2(\pi/\lambda)$, where $\lambda = 2\sqrt{2\csc 1}$.

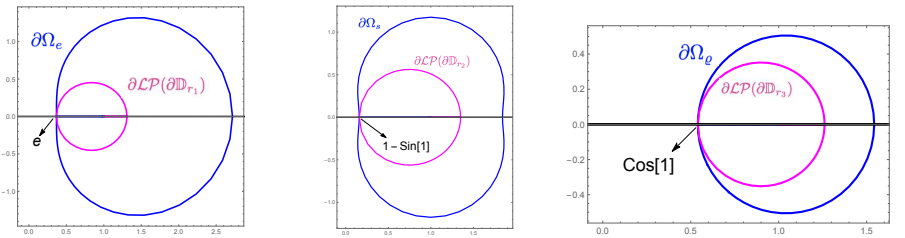
(iii) The $\mathcal{S}_\varrho^*-$radius is $r_3 = \tanh^2(\pi\lambda/2)$, where $\lambda = \sin(1/2)$.

(iv) The $\mathcal{S}_\wp^*-$radius is $r_4 = \tanh^2(\pi/2\sqrt{2e})$.

(v) The $\mathcal{S}_\rho^*-$radius is $r_5 = \tanh^2(\pi\sqrt{\lambda}/2)$, where $\lambda = (1/2)\sinh^{-1} 1$.

(vi) The $\mathcal{S}_{SG}^*-$radius is $r_6 = \tanh^2(\lambda\pi/2\sqrt{2})$, where $\lambda = \sqrt{(e-1)/(e+1)}$.

(vii) The $\mathcal{S}_{N_e}^*-$radius is $r_7 = \tanh^2(\pi/2\sqrt{3})$.



(a) (b) (c)

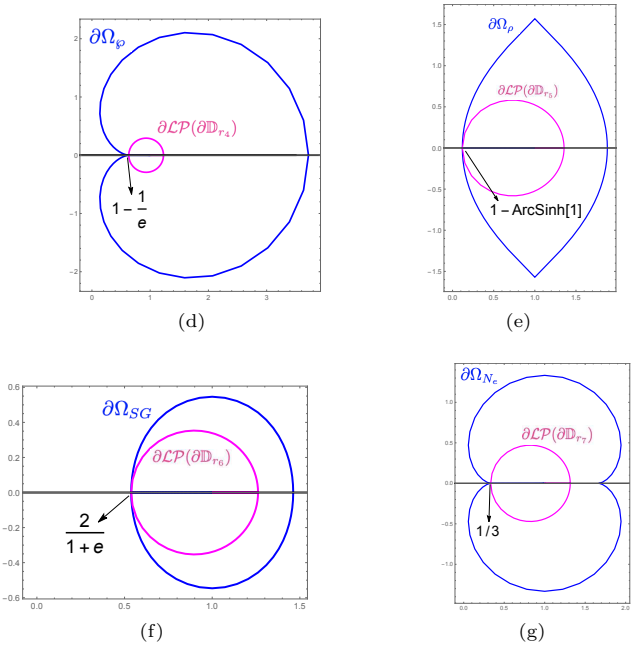


Fig. 4 Images depicting sharpness of radius result in Corollary 2.

In the next corollary we obtain the sharp $\mathcal{S}^*(\beta)-$ radius for the class $\mathcal{F}_{\mathcal{LP}}$.

Corollary 3 *Suppose* $0 \leq \beta < 1$ *and* $f \in \mathcal{F}_{\mathcal{LP}}$, *then sharp* $\mathcal{S}^*(\beta)-$ *radius is* $\tanh^2(\pi\sqrt{\beta}/2\sqrt{2})$.

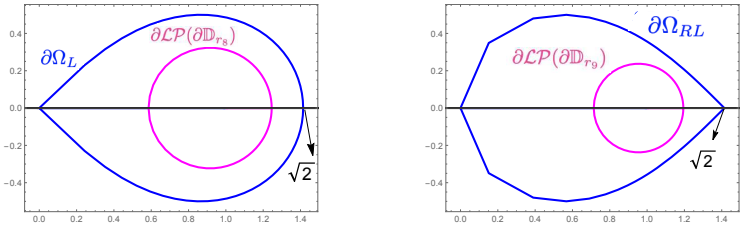
Remark 4 On replacing β with $1-\alpha$ $(0 < \alpha \leq 1)$, in Corollary 3 we get the radius of starlikness of order α obtained in Corollary 1. Moreover, from Corollary 3, we obtain the sharp $\mathcal{S}^*_\alpha-$radius for the class $\mathcal{F}_{\mathcal{LP}}$, where $\mathcal{S}^*_\alpha = \left\{f \in \mathcal{A} : \left|zf'(z)/f(z) - 1\right| < 1-\alpha\right\}$.

Corollary 4 *Let* $\eta = \sqrt{2}-1$ *and suppose* $f \in \mathcal{F}_{\mathcal{LP}}$, *then the following holds (see* ***Fig.*** *5)*

(i) $f \in \mathcal{S}^*_{\mathcal{L}}$ *in* $|z| < \tanh^2\left(\pi\sqrt{\eta}/2\sqrt{2}\right) \approx 0.376\ldots$.

(ii) $f \in \mathcal{S}^*_{\mathcal{RL}}$ *in* $|z| < \tanh^2(\pi\sqrt[4]{\sqrt{2}\,\eta(1-\sqrt{2\eta})}/2\sqrt{2}) \approx 0.283\ldots$.

Remark 5 From **Fig.** 5, it is evident that the radii obtained in Corollary 4 can be further improved.



(a) (b)

Fig. 5 Above figures correspond to Corollary 4, with radii r_8 and r_9 given by (a) $r_8 \approx 0.376\ldots$ (b) $r_9 \approx 0.283\ldots$.

We now define the class $\mathfrak{F}$ constructed with the help of ratios of two analytic functions $f, g \in \mathcal{A}$, studied by Mundalia and Kumar [21].

$$\mathfrak{F} = \left\{ f \in \mathcal{A} : \operatorname{Re}\left(\frac{f(z)}{g(z)}\right) > 0 \ \&\ \operatorname{Re}\left(\frac{(1-z)^{1+A} g(z)}{z}\right) > 0, -1 \le A \le 1 \right\}.$$

In patricular, for $A = -1$ and $A = 1$, the class $\mathfrak{F}$ reduces to the following classes, respectively,

$$\mathfrak{F}_1 = \left\{ f \in \mathcal{A} : \operatorname{Re}\left(\frac{f(z)}{g(z)}\right) > 0 \ \&\ \operatorname{Re}\left(\frac{g(z)}{z}\right) > 0 \right\}$$

and

$$\mathfrak{F}_2 = \left\{ f \in \mathcal{A} : \operatorname{Re}\left(\frac{f(z)}{g(z)}\right) > 0 \ \&\ \operatorname{Re}\left(\frac{(1-z)^2 g(z)}{z}\right) > 0 \right\}.$$

For proving the next theorem, we require the following lemma of Ravichandran et al. [24].

Lemma 3 *If $p \in \mathcal{P}_n[A, B]$, then for $|z| = r$*

$$\left| p(z) - \frac{1 - ABr^{2n}}{1 - B^2 r^{2n}} \right| \le \frac{|A - B| r^n}{1 - B^2 r^{2n}}.$$

Particularly, if $p \in \mathcal{P}_n(\alpha)$, then

$$\left| p(z) - \frac{1 + (1-2\alpha) r^{2n}}{1 - r^{2n}} \right| \le \frac{2(1-\alpha) r^n}{1 - r^{2n}}.$$

Theorem 5 *Let $-1 \le A \le 1$, and suppose $f \in \mathcal{F}_{\mathcal{LP}}$, then the sharp $\mathfrak{F}-$radius is given by*

$$\mathcal{R}_{\mathfrak{F}}(\mathcal{F}_{\mathcal{LP}}) = \frac{1}{2A+3}\left(\sqrt{A^2 + 12A + 28} - (5 + A)\right) =: R_{\mathfrak{F}}.$$

Proof Since $f \in \mathfrak{F}$, then by definition of the class $\mathfrak{F}$, we have $f(z) = p_1(z) g(z)$ and $g(z) = z p_2(z)(1-z)^{-(1+A)}$, where for each $i = 1, 2$, $p_i : \mathbb{D} \to \mathbb{C}$ are analytic functions such that $p_i(0) = 1$ and $\operatorname{Re} p_i(z) > 0$. This leads to $f(z) = z p_1(z) p_2(z)(1-z)^{-(1+A)}$, and as a consequence of logarithmic differentiation, we obtain

$$\frac{z f'(z)}{f(z)} = \frac{1 + Az}{1 - z} + \frac{z p_1'(z)}{p_1(z)} + \frac{z p_2'(z)}{p_2(z)}.$$

For each $-1 \leq A \leq 1$, Lemma 3 leads to,

$$\left|\frac{zf'(z)}{f(z)} - \frac{1+Ar^2}{1-r^2}\right| \leq \frac{(5+A)r}{1-r^2} = R. \tag{7}$$

Further, for each $|z| = r \leq R_{\mathfrak{F}}$, one can observe that

$$\frac{1}{2} \leq 1 \leq a = \frac{1+Ar^2}{1-r^2} \leq \frac{1+AR_{\mathfrak{F}}^2}{1-R_{\mathfrak{F}}^2} < \frac{3}{2}. \tag{8}$$

Infact inequalities (7) and (8) yields the inequality,

$$\frac{(5+A)r}{1-r^2} \leq \frac{3}{2} - \frac{1+Ar^2}{1-r^2},$$

provided $r \leq R_{\mathfrak{F}}$. Due to Lemma 2, it is clear that the disc $|u-a| < R$ lies in $\Omega_{\mathcal{LP}}$. Further, at $z_0 = R_{\mathfrak{F}}$ the function $f_{\mathfrak{F}}(z)$ defined as $f_{\mathfrak{F}}(z) = z(1+z)^2/(1-z)^{3+A}$ acts as the extremal function. □

Corollary 5 *Let $f \in \mathcal{F}_{\mathcal{LP}}$, then sharp $\mathfrak{F}_1-$ radius and $\mathfrak{F}_2-$ radius for the class $\mathcal{F}_{\mathcal{LP}}$ are respectively given as*

(i) $\mathcal{R}_{\mathfrak{F}_1}(\mathcal{F}_{\mathcal{LP}}) = \sqrt{17} - 4 \approx 0.123...$

(ii) $\mathcal{R}_{\mathfrak{F}_2}(\mathcal{F}_{\mathcal{LP}}) = (\sqrt{41} - 6)/5 \approx 0.080...$

Theorem 6 *Let $\delta = (\pi\sqrt{\beta-1}/\sqrt{2})$, where $1 < \beta < 3/2$, and suppose $f \in \mathcal{F}_{\mathcal{LP}}$, then $\mathcal{M}(\beta)-$ radius is $r_\beta = 1 + 2\left(\cot\delta\right)^2 - 2|\sec\delta/(\tan^2\delta)|$.*

Proof From Lemma 1, it can be viewed that

$$\operatorname{Re}\mathcal{LP}(z) \leq \mathcal{LP}(-r) = 1 - \frac{2}{\pi^2}\left(\log\left(\frac{1+i\sqrt{r}}{1-i\sqrt{r}}\right)\right)^2 = 1 + \frac{2}{\pi^2}\left(\tan^{-1}\left(\frac{2\sqrt{r}}{1-r}\right)\right)^2.$$

As $f \in \mathcal{F}_{\mathcal{LP}}$, then assume that $zf'(z)/f(z) = p(z)$. Due to the above inequality $\operatorname{Re} p(z) \leq \mathcal{LP}(-r)$. Moreover, $\mathcal{LP}(-r) \leq \beta$ provided $r \leq r_\beta$, where r_β is the root of the equation $(1-\beta)\pi^2 + 2(\tan^{-1}(2\sqrt{r}/(1-r)))^2 = 0$ for $1 < \beta < 3/2$. Equality here occurs for the function $f_0 \in \mathcal{A}$, given by (2). □

If $f(z)$ and $g(z)$ be analytic functions in $|z| < r$, then $f(z)$ is said to be majorized by $g(z)$, denoted as $f(z) \ll g(z)$, in $|z| < r$, if $|f(z)| \leq |g(z)|$ in $|z| < r$. Equivalently, a function $f(z)$ is said to be be majorized by $g(z)$, if there exists an analytic $\Psi(z)$ with $|\Psi(z)| \leq 1$ in $\mathbb{D}$ and $f(z) = \Psi(z)f(z)$ for all $z \in \mathbb{D}$. For recent update on majorization for starlike and convex function, see [4, 5]. In the next theorem, we determine sharp majorization radius for the class $\mathcal{F}_{\mathcal{LP}}$.

Theorem 7 *Let $f \in \mathcal{A}$ and suppose that $g \in \mathcal{F}_{\mathcal{LP}}$. Further assume that $f(z)$ is majorized by $g(z)$ in $\mathbb{D}$, i.e $f(z) \ll g(z)$, then for $|z| \leq r_m \approx 0.4220\ldots$,*

$$|f'(z)| \leq |g'(z)|,$$

where r_m is the unique positive root of the following equation

$$2\pi^2 r - (1-r^2)(\pi^2 - 2(\log((1+\sqrt{r})/(1-\sqrt{r})))^2) = 0. \tag{9}$$

Proof Suppose $0 \leq r < r^* = \tanh^2(\pi/2\sqrt{2}) \approx 0.646\ldots$, then due to Remark 3 we conclude that, $g \in \mathcal{F}_{\mathcal{LP}}$ qualifies to be a Ma-Minda type function in $|z| < r^*$. Further let $w(z)$ be a Schwarz function in $\mathbb{D}$ with $w(0) = 0$, then by definition of subordination,

$$\frac{zg'(z)}{g(z)} = \mathcal{LP}(w(z)).$$

Note that for each $|z| = r < 1$, the inequality $|\mathcal{LP}(w(z))| \leq |\mathcal{LP}(r)|$ holds. Now for $|z| = r < r^*$, we obtain

$$\left|\frac{g(z)}{g'(z)}\right| = \frac{|z|}{|\mathcal{LP}(z)|} \leq \frac{r}{1-|\mathcal{P}_0(r)|} = \frac{r}{\mathcal{LP}(r)}. \tag{10}$$

As $f(z)$ is majorized by $g(z)$ in $\mathbb{D}$, we find from the definition of majorization,

$$f(z) = \psi(z)g(z).$$

Upon differentiating the above equality and suitable rearrangement of terms, we obtain

$$f'(z) = g'(z)\left(\psi'(z)\frac{g(z)}{g'(z)} + \psi(z)\right). \tag{11}$$

Additionally, as a result of the Schwarzian inequality, we have

$$|\psi'(z)| \leq \frac{1-|\psi(z)|^2}{1-|z|^2}, \quad (z \in \mathbb{D}). \tag{12}$$

Moreover, from equations (10)-(12), we deduce

$$|f'(z)| \leq \left(|\psi(z)| + \frac{r(1-|\psi(z)|^2)}{(1-r^2)(\mathcal{LP}(r))}\right)|g'(z)|.$$

Substituting $|\psi(z)| = \sigma$ $(0 \leq \sigma \leq 1)$, results in

$$|f'(z)| \leq \Psi(r,\sigma)|g'(z)|,$$

where

$$\Psi(r,\sigma) = \sigma + \frac{r(1-\sigma^2)}{(1-r^2)(\mathcal{LP}(r))}.$$

We need to determine $r_m \leq r^*$ so that

$$r_m = \max\{r \in [0, r^*] : \Psi(r,\sigma) \leq 1 \ \forall \sigma \in [0,1]\}.$$

Equivalently if $\Phi(r,\sigma) := (1-r^2)(\mathcal{LP}(r)) - r(1+\sigma)$ then we need to determine

$$r_m = \max\{r \in [0, r^*] : \Phi(r,\sigma) \geq 0 \ \forall \sigma \in [0,1]\}.$$

Since $\partial\Phi/\partial\sigma = -r < 0$, then $\max_{\sigma\in[0,1]} \Phi(r,\sigma) = \Phi(r,0) =: \phi_0(r)$. Further it is evident that, as $\phi_0(0) = 1 > 0$ and $\phi_0(r^*) = -r^* < 0$, then there exists $r_m \leq r^*$, a smallest positive root of the equation given in (9) such that $\phi_0(r) \geq 0$ for each $r \in [0, r_m]$. This completes the proof. □

In 2017, Peng and Zhong [22], introduced the class $\Omega \subset \mathcal{A}$, defined as

$$\Omega = \left\{f \in \mathcal{A} : |zf'(z) - f(z)| < 1/2\right\}.$$

We conclude this section by determining sharp $\Omega-$radius for the class $\mathcal{F}_{\mathcal{LP}}$.

Theorem 8 *Let $f \in \mathcal{F}_{\mathcal{LP}}$, then $f \in \Omega$ in $|z| < r_{\mathcal{L}} \approx 0.522\ldots$ is the smallest positive root of*

$$4f_0(r)(\log((1+\sqrt{r})/(1-\sqrt{r})))^2 = \pi^2$$

and

$$g_0(z) = z\left(\exp\int_0^z \frac{\mathcal{P}_0(-t)}{t}dt\right) = z + \frac{8}{\pi^2}z^2 - \frac{8}{3\pi^4}(\pi^2-12)z^3 + \frac{8}{135\pi^6}(1440 - 360\pi^2 + 23\pi^4)z^4 - \cdots. \tag{13}$$

This is a sharp estimate.

Proof Since $f \in \mathcal{F}_{\mathcal{LP}}$, then as a consequence of Remark 2 for $|z| = r < 1$, we have

$$\left|\frac{zf'(z)}{f(z)} - 1\right| < |\mathcal{LP}(r) - 1| = |\mathcal{P}_0(r)|.$$

Due to the growth theorem as mentioned in [15, Theorem 1] and Theorem 1, we observe that $|f(z)| \leq g_0(r)$, where $g_0(r)$ is given by (13). Further

$$|zf'(z) - f(z)| = |f(z)|\left|\frac{zf'(z)}{f(z)} - 1\right| \leq g_0(r)|\mathcal{P}_0(r)|.$$

Thus $g_0(r)|\mathcal{P}_0(r)| \leq 1/2$ provided $|z| < r_{\mathcal{L}} \approx 0.522864$. Hence the result is established. □

2.3 Sufficient Conditions for the class $\mathcal{F}_{\mathcal{LP}}$

In this section, we establish some sufficient conditions for the class $\mathcal{F}_{\mathcal{LP}}$. Below, we state a Lemma given by Jack [7], which is utilised in context of the class under consideration.

Lemma 4 *[7, Lemma 1, p.470] Let $\nu(z)$ be a non-constant analytic function in $\mathbb{D}$, such that $\nu(0) = 0$. If $|\nu(z)|$ attains its maximum value on the circle $|z| = r$ at a point z_0, then $z_0\nu'(z_0) = k\nu(z_0)$, where k is real and $k \geq 1$.*

Theorem 9 *Suppose $0 \leq t \leq 1$ and let $f \in \mathcal{A}$ satisfy the following differential inequality*

$$\left|t\left(1 + \frac{zf''(z)}{f'(z)}\right) + (1-t)\frac{zf'(z)}{f(z)} - 1\right| < \frac{1}{6}(3+2t), \quad z \in \mathbb{D}, \tag{14}$$

then $f \in \mathcal{F}_{\mathcal{LP}}$.

Proof Consider an analytic function $\nu(z)$ with $\nu(0) = 0$. Assume $f \in \mathcal{A}$ such that

$$\frac{zf'(z)}{f(z)} - 1 = \frac{1}{2}\nu(z).$$

We show that $|\nu(z)| < 1$ in $\mathbb{D}$. Suppose on the contrary $|\nu(z)| \geq 1$, then by an application of Lemma 4, there exists $z_0 \in \mathbb{D}$ such that for $k \geq 1$, $|\nu(z_0)| = 1$ and $z_0\nu'(z_0) = k\nu(z_0)$. Substituting $\nu(z_0) = e^{i\mu}$, $-\pi < \mu \leq \pi$ leads to

$$\left|t\left(1 + \frac{zf''(z)}{f'(z)}\right) + (1-t)\frac{zf'(z)}{f(z)} - 1\right|$$

$$= \left| t\left(1 + \frac{\nu(z_0)}{2} + \frac{k\nu(z_0)}{2+\nu(z_0)}\right) + (1-t)\left(1 + \frac{\nu(z_0)}{2}\right) - 1 \right|$$
$$= \left| \frac{tke^{i\mu}}{2+e^{i\mu}} + \frac{e^{i\mu}}{2} \right| \geq \frac{1}{6}(3+2t).$$

This is contradiction to the assumption given in (14). Thus $|\nu(z)|< 1$, which means that $zf'(z)/f(z)$ lies in the disc $|(zf'(z)/f(z)) - 1|< 1/2$. Hence in view of Lemma 2, (with $a = 1$) required result is achieved. □

For $t = 1/2$, $t = 0$ and $t = 1$ in Theorem 9, we obtain the following corollary,

Corollary 6 *Let $f \in \mathcal{A}$ satisfy the following differential inequalities*
(i.) $\left|(zf'(z)/f(z) + zf''(z)/f'(z)) - 1\right| < 4/3$, *or*
(ii.) $\left|(zf'(z)/f(z)) - 1\right| < 1/2$, *or*
(iii.) $\left|zf''(z)/f'(z)\right| < 5/6$,
then $f \in \mathcal{F}_{\mathcal{LP}}$.

Conclusion

In the present investigation, we introduce a class of analytic functions associated with certain parabolic region. In particular, we have considered a case when parabola is lying majorly in the left half plane and symmetric about real axis. The other cases namely, oblique parabolic regions are still open, for similar investigations.

Appendix

The classes we come across in the present investigation are listed below for the ready reference of the reader.

Table 1 Special subclasses of Ma-Minda starlike functions for specific choices of $\phi(z)$

Class $\mathcal{S}^*(\phi)$	$\phi(z)$	$\phi(\mathbb{D})$	**References**
$\mathcal{S}^*_{\alpha,e}$	$\alpha + (1-\alpha)e^z$	$\Omega_{\alpha,e}$	[13] Khatter et al.
$\mathcal{SL}^*(\alpha)$	$\alpha + (1-\alpha)\sqrt{1+z}$	$\Omega_{\alpha,L}$	[13] Khatter et al.
$\mathcal{S}^*_{\wp}$	$1 + ze^z$	$\Omega_{\wp}$	[14] Kumar et al.
$\mathcal{S}^*_{SG}$	$2/(1+e^{-z})$	Ω_{SG}	[6] Goel et al.
$\mathcal{S}_s$	$1 + \sin z$	Ω_s	[3] Cho et al.
$\mathcal{S}^*_{\rho}$	$1 + \sinh^{-1} z$	Ω_{ρ}	[1] Arora et al.
$\mathcal{S}^*_{\varrho}$	$\cosh\sqrt{z}$	Ω_{ϱ}	[21] Mundalia et al.
Δ^*	$z + \sqrt{1+z^2}$	Ω_{Δ}	[23] Raina et al.
$\mathcal{S}^*_{\mathcal{L}}$	$\sqrt{1+z}$	Ω_L	[27] Sokół et al.
$\mathcal{S}^*(A,B)$	$(1+Az)/(1+Bz)$	$\Omega_{A,B}$	[8] Janowski
$\mathcal{S}^*(N_e)$	$1 + z - z^3/3$	Ω_{N_e}	[29] Wani et al.
$\mathcal{S}^*_p$	$1 + (2/\pi^2)(\log((1+\sqrt{z})/(1-\sqrt{z})))^2$	Ω_p	[26] Ronning
$\mathcal{S}^*_{\mathcal{RL}}$	$\sqrt{2} - (\sqrt{2}-1)\sqrt{(1-z)(1+2(\sqrt{2}-1)z)}$	Ω_{RL}	[20] Mendiratta et al.

Acknowlegdements

The authors acknowledge all sort of support from Delhi Technological University, Delhi, India.

Declarations

- Conflict of interest: The authors declare that they have no conflict of interest.
- Availability of data and materials: NA
- Code availability: NA
- Authors' contributions: Both the authors have equal contribution

References

[1] Arora K., Kumar, S. S.: Starlike functions associated with a petal shaped dimain, Bull. Korean Math Soc. **59**(4), 903-1010 (2022)

[2] Cho, N. E., Kumar, S., Kumar, V., Ravichandran, V.: Differential subordination and radius estimates for starlike functions associated with the Booth lemniscate, Turkish J. Math. **42**, 1380-1399 (2018)

[3] Cho, N. E., Kumar, V., Kumar, S. S., Ravichandran, V.: Radius problems for starlike functions associated with the sine function. Bull. Iranian Math. Soc. **45**(1), 213-232 (2019)

[4] Gangania, K., Kumar, S. S.: On Certain Generalizations of $\mathcal{S}^*(\psi)$ Comput. Methods Funct. Theory. (2021). https://doi.org/10.1007/s40315-021-00386-5

[5] Tang, H., Deng, G.: Majorization problems for some subclasses of starlike functions. J. Math. Res. Appl. **39**, 153-159 (2019)

[6] Goel, P., Kumar, S. S.: Certain class of starlike functions associated with modified sigmoid function. Bull. Malays. Math. Sci. Soc. **43**(1), 957-991 (2020)

[7] Jack, I. S.: Functions starlike and convex of order α. J. London Math. Soc. (Ser. 2)2, 469-474 (1971)

[8] Janowski, W.: Some extremal probles for certain families of analytic functions. I. Ann. Polon. Math. **28**(3), 297-326 (1973)

[9] Kanas, S.: Differential subordination related to conic sections, J. Math. Anal. Appl., **317**, 650-658 (2006)

[10] Kanas, S., Wiśniowska, A.: Rev. Roumaine Math. Pures Appl. **45**, no. 4, 647-657 (2000)

[11] Kanas, S.: Techniques of the differential subordination for domains bounded by conic sections, Int. J. Math. Math. Sci., **38**, 2389-2400 (2003)

[12] Kargar, R., Ebadian, A., Sokół, J.: On Booth lemniscate and starlike functions. Anal. Math. Phys. **9**(1), 143-154 (2019)

[13] Khatter, K., Ravichandran, V., Sivaprasad Kumar, S.: Starlike functions associated with exponential function and the lemniscate of Bernoulli. Rev. R. Acad. Cienc. Exactas Fis. Nat. Ser. A Math. RACSAM **113**(1), 233-253 (2019)

[14] Kumar, S. S., Kamaljeet, G.: A cardioid domain and starlike functions. Anal. Math. Phys. **11**(2), 1-34 (2021)

[15] Kumar, S. S., Gangania, K.: On geometrical properties of certain analytic functions, Iran. J. Sci. Technol. Trans. A Sci. **45**(4), 1437-1445 (2021)

[16] Kumar, S. S., Yadav, P.: Starlike Functions asociated with a Non-Ma-Minda Function. (2022). Preprint arXiv:2208.01245

[17] Ma, W. C., Minda, D.: A unified treatment of some special classes of univalent. functions. In: Proceedings of the Conference on Complex Analysis (Tianjin, 1992), pp. 157-169, Conf. Proc. Lecture Notes Anal., I, Int. Press, Cambridge, MA

[18] Ma, W., Minda, D.: Uniformly convex functions II, Ann. Polon. Math., **58**, 275-285 (1993)

[19] Masih, V. S., Ebadian, A., Yalçin, S.: Some properties associated to a certain class of starlike functions, Math. Slovaca **69**(6), 1329-1340 (2019)

[20] Mendiratta, R., Nagpal, S., Ravichandran, V.: A subclass of starlike functions associated with left-half of the lemniscate of Bernoulli. Int. J. Math. **25**(9), 17 (2014)

[21] Mundalia, M., Kumar, S. S.: On a subfamily of starlike functions related to Hyperbolic Cosine function. J Anal (2023). https://doi.org/10.1007/s41478-023-00550-1

[22] Peng, Z., Zhong, G.: Some properties for certain classes of univalent functions defined by differential inequalities, Acta Math. Sci. Ser. B (Engl. Ed.) **37B**, 69-78 (2017)

[23] Raina, R. K., Sokół, J.: Some properties related to a certain class of starlike functions. C. R. Math. Acad. Sci. Paris **353**(11), 973-978 (2015)

[24] Ravichandran, V., Rønning F. Shanmugam, T. N.: Radius of convexity and radius of starlikeness for some classes of analytic functions. Complex

Var. Theory Appl. **33**(1-4), 265-280 (1997)

[25] Ravichandran, V., Silverman, H., Hussain Khan, M., Subramanian, K. G.: Radius problems for a class of analytic functions. Demonstratio Math. **39**(1), 67-74 (2006)

[26] Rønning F.: Uniformly convex functions and a corresponding class of starlike functions, Proc. Amer. Math. Soc. **118**(1), 189-196 (1993)

[27] Sokół, J., Stankiewicz, J.: Radius of convexity of some subclasses of strongly starlike functions. Zeszyty Nauk. Politech. Rzeszowskiej Mat. No. **19**, 101-105 (1996)

[28] Uralegaddi, B. A., Ganigi, M. D., Sarangi, S. M.: Univalent functions with positive coefficients. Tamkang J. Math. **25**(3), 225-230 (1994)

[29] Wani, L. A., Swaminathan, A.: Starlike and convex functions associated with a nephroid domain, Bull. Malays, Math. Sci. Soc. **44**(1), 79-104 (2021)

Performance Analysis of Dual-HopaMixed RF/FSO Systemaover Nakagami-m/Fisher Snedecor Fading Channels

Rekha Rani
Department of Electronics and Communication
Delhi Technological University,
Galgotias College of Engineering and Technology, India
rekhaaggarwalece@gmail.com

Gurjit Kaur
Department of Electronics and Communication
Delhi Technological University, India
gurjitkaur@dtu.ac.in

Shubham Gautam
Department of Electronics and Communication
Galgotias College of Engineering and Technology, India
shubgautam21@gmail.com

Lakshmanan. M
Department of Electronics and Communication
Galgotias College of Engineering and Technology, India
tmlakshmanan@gmail.com

Shubham Kumar
Department of Electronics and Communication
Galgotias College of Engineering and Technology, India
shubhamjha12113@gmail.com

2023 International Conference on Artificial Intelligence and Smart Communication (AISC) | 979-8-3503-2230-9/23/$31.00 ©2023 IEEE | DOI: 10.1109/AISC56616.2023.10085239

***Abstract*— In this paper, performance analysis of radio frequency/ free-space optical (RF/FSO) communication system based on the amplified and forward (AF) has been carried out. The analytical closed-form expression of outage probability for end-to-end average signal to noise ratio (SNR) has been derived where Nakagami-m distribution is used to model the RF link and FSO link assumed to follow the Fisher Snedecor (F) distribution. The results are simulated on MATLAB software.**

***Keywords*— Free-space optical communication, Fisher Snedecor distribution, Nakagami-m, outage probability.**

I. INTRODUCTION

In recent years, increasing bandwidth requirements and high information rates have led to a shortage of licensed radio spectrums which have prompted important research in wireless optical communication (WOC). One of the most promising technologies for long-distance transmission in WOC is free space optics (FSO). It is data transfer technology that utilizes light to send informationin free space. FSO also has the advantage to fulfill large bandwidth channel applications and the data transfer rate in FSO communication is 10 Gbps [1].

The reliability of the system can be remarkably degraded by atmospheric disturbances. The atmospheric disturbance will experience irradiance fluctuations. As a result, it is incredibly susceptible to changes in the weather and surroundings, which lowers the system's performance. [2]. A dual-hop radio frequency/free space optical (RF/FSO) communication system has been conducted by researchers to overcome the limitations of both technologies. In these systems, relays are introduced between two communication systems where different relaying techniques are employed. The data is amplified at the relay with fixed and variable gain and then forwarded tothe destination. It is referred to as a amplify and forward (AF) relaying-assisted system. Relaying-aided systems that use decode-and-forward (DF) protocol do so by decoding the data at the relay and sending it towards the destination.

For the relay-assisted dual-hop RF/FSO system, several distributions for RF and FSO channels are utilized in the literature. The performance has been investigated in urban areas for the DF relay-based system for Nakagami-m/Exponentiated Weibull (EW) fading models [3]. Performance metrics has been deduced for AF relaying system over $\eta - \mu$ and $\alpha - \mu$ fading distributions [4]. The cumulative distribution function (CDF), performance metrics have been formulated for relay-assisted systems for Rayleigh and M distribution fading distributions [5]. By considering atmospheric turbulence and different detection techniques, outage probability (OP) and Ergodic capacity (EC) have been obtained for the FSO system over Fisher-Snedecor fading [6]. Average bit error rate (BER) performance for AF relaying-based systems has been investigated under different modulation schemes where κ-μ and M fading distributions are used [7]. The performance of the relay-aided system has been presented under different detection techniques for Weibull & gamma-gamma (GG) distributions [8]. The expression for the OP for AF based system has been derived where η-μ fading is used for both links [9]. Performance analysis of AF relay-assisted system for multiuser diversity with η-μ/ Malaga fading distributions at RF/FSO links respectively has been done [10]. Expressions for secrecy OP and exact average secrecy capacity have been deduced using different detection techniques where Nakagami-m fading and GG fading distributions are used [11]. With the deployment of the DF scheme at the relay, η-μ /κ-μ distributions are used at RF/FSO respectively where OP, average capacity, and average BER are derived for the coherent detection [12]. Generalized-K fading is used at the first hop and Gamma- Gamma distribution is used at the second hop for RF/FSO system and moment generation function (MGF), CDF, and the OP has been derived [13]. OP and average BER have been obtained for relay-based RF/FSO systems where links undergo κ-μ/EW distributions respectively [14]. Performance metrics have been determined when the RF hop is assumed Beaulieu-Xie

Authorized licensed use limited to: DELHI TECHNICAL UNIV. Downloaded on April 17,2023 at 06:07:40 UTC from IEEE Xplore. Restrictions apply.

fading and Malaga turbulence are used for FSO hop under coherent detection [15]. A DF-based communication system where Rayleigh and κ- μ/Inverse gaussian distributions are used at RF and FSO link respectively has been considered and expressions for OP, moment generating function (MGF) and average BER have been derived for various modulation techniques [16]. Exact and asymptotic representations for performance parameters at high SNR have been presented for the higher order A-F based relaying model where FSO link experiences by GG distribution and RF link undergoes Nakagami-m fading under various detection schemes [17]. Performance metrics have been deduced for the AF-based relaying system over Nakagami-m and GG fading distribution [18]. EC for an asymmetric AF-relay-based system with Rayleigh channel/GG channel has been derived [19]. A decode and forward relaying technique-based system has been considered where Nakagami-m and Exponentiated Weibull (EW) distribution are used and pe performance has been calculated in terms of OP and average BER [20]. OP has been analyzed for an AF-based system where RF hop accomplished by Rayleigh channel and FSO link undergoes M distribution [21]. AF relay-based system has been given for the generalized-K and Gamma-Gamma fading distributions [22].

Motivated by the above-mentioned literature, a rich amount of research has been performed on relay-assisted systems. To the author's knowledge, no previous works were carried out for Nakagami-m distribution and F-distribution for dual-hop communication system. Outage probability (OP) is evaluated for the intensity-modulated direct detection scheme (IM/DD) for the proposed system.

The paper is organized as follows: The proposed model is described in Section II and also provides the outage probability expression. Section III deals with the numerical results obtained by MATLAB software. Section IV of the paper includes a description of the conclusion.

II. System Model

A dual-hop RF/FSO wireless communication system is depicted in Fig. 1. The source (S) is the starting node in this system which attempts to interact with the end node i.e.destination (D) via an intermediary relay node, R.

RF Link

In the first hop of propagation (S-R), the data received by the R which is transmitted from the source S is given as:

$$y_{RF} = h_{RF}x + n_{RF} \quad (1)$$

where x, transmitted data from S, h_{RF} , channel gain coefficients for the RF link, and $n_{RF} \sim \mathcal{N}(0, \sigma_{RF}^2)$. Then the instantaneous electrical SNR is

$$\gamma_{RF} = \frac{|h_{RF}|^2}{N_{RF}} \quad (2)$$

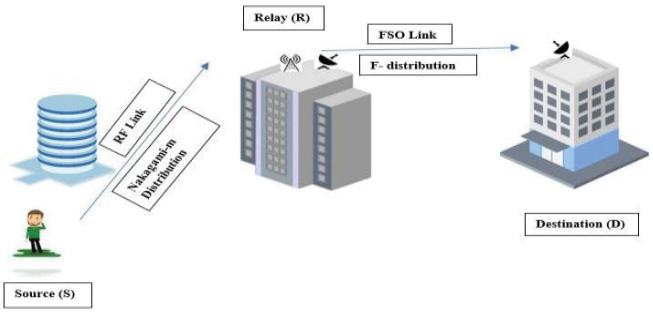


Fig. 1. System model of the proposed system.

The average electrical SNR is written as

$$\bar{\gamma}_{RF} = \frac{\mathbb{E}^2[(h_{RF})]}{N_{RF}} \quad (3)$$

$\mathbb{E}[(h_{RF})]$is the expectation of h_{RF} which is equal to one.

The PDF of γ_{RF} modeled by Nakagami-m fading given as [11],

$$f_{RF}(\gamma_{RF}) = \frac{m^m \gamma_{RF}^{m-1}}{\Gamma m\, \bar{\gamma}_{RF}{}^{m}} \exp\left(\frac{-m\gamma_{RF}}{\bar{\gamma}_{RF}}\right) \quad (4)$$

The CDF for γ_{RF} is given as [11]

$$F_{RF}(\gamma_{RF}) = \frac{\gamma\left(m,\ \frac{m}{\bar{\gamma}_{RF}}\gamma_{RF}\right)}{\Gamma m} \quad (5)$$

Here, $\Gamma(.)$ and $\gamma(.,.)$ represents the gamma function and lower incomplete gamma function respectively, Nakagami-m fading parameter, $m \geq 0.5$.

FSO Link

In the second hop of propagation (R-D), the data is amplified at the R and then forwarded it towards the D. Then, the received signal at D is:

$$y_{FSO} = h_{FSO}\eta_{FSO}y_{RF} + n_{FSO} \quad (6)$$

$$y_{FSO} = h_{FSO}G\eta_{FSO}h_{RF}x + h_{FSO}G\eta_{FSO}n_{RF} + n_{FSO} \quad (7)$$

Here, η_{FSO} denotes the photoelectric conversion parameter. h_{FSO} is the channel gain for the FSO link, G is the fixed gain at R, and $n_{FSO} \sim \mathcal{N}(0, \sigma_{FSO}^2)$.

The instantaneous electrical SNR is

$$\gamma_{FSO} = \frac{|\eta h_{FSO}|^2}{N_{FSO}} \quad (8)$$

The average electrical SNR is

$$\bar{\gamma}_{FSO} = \frac{\eta_{FSO}{}^2[\mathbb{E}(h_{FSO})]^2}{N_{FSO}} \quad (9)$$

where $[\mathbb{E}(h_{FSO})]^2 = 1$

The PDF of γ_{FSO} which is distributed by the F-distribution fading channel given by [23, eq (20)]

$$f_{\gamma_{FSO}}(\gamma_{FSO}) = \frac{a^a(b-1)^b\bar{\gamma}_{FSO}{}^{\frac{b}{2}}\gamma_{FSO}{}^{\frac{a}{2}-1}}{2\beta(a,b)\left(a\sqrt{\gamma_{FSO}}+(b-1)\sqrt{\bar{\gamma}_{FSO}}\right)^{a+b}} \quad (10)$$

Here atmospheric turbulence parameters are denoted by a and b.

Afterward, the instantaneous overall received electrical SNR at the D is

Authorized licensed use limited to: DELHI TECHNICAL UNIV. Downloaded on April 17,2023 at 06:07:40 UTC from IEEE Xplore. Restrictions apply.

$$y_{end2end} = \frac{\gamma_{FSO}\gamma_{RF}}{\gamma_{FSO}+C} \quad (11)$$

where C = $\frac{1}{N_{RF}G^2}$ (fixed relay gain),

The CDF for overall received electrical SNR is given by [7, eq (8)],

$$F(y_{end2end}) = Pr\left[\frac{\gamma_{FSO}\gamma_{RF}}{\gamma_{FSO}+C} \leq \gamma|\gamma_{FSO}\right] \quad (12)$$

$$F(y_{end2end}) = \int_0^\infty P_r\left[\gamma_{RF} \leq \frac{\gamma(\gamma_{FSO}+C)}{\gamma_{FSO}}\right] f_{\gamma_{FSO}}(\gamma_{FSO})d\gamma_{FSO} \quad (13)$$

$$F(y_{end2end}) = \int_0^\infty F_{RF}\left(\frac{\gamma(\gamma_{FSO}+C)}{\gamma_{FSO}}\right) f_{\gamma_{FSO}}(\gamma_{FSO})d\gamma_{FSO} \quad (14)$$

By substituting the (5) and (10) into (14), then

$$F(y_{end2end}) = \int_0^\infty \frac{\gamma\left(m,\ B\left(\frac{\gamma_{FSO}+c}{\gamma_{FSO}}\right)\right)}{\Gamma m} \cdot \frac{a^a(b-1)^b\bar{\gamma}_{FSO}^{\frac{b}{2}}\gamma_{FSO}^{\frac{a}{2}-1}}{2\beta(a,b)\left(a\sqrt{\gamma_{FSO}}+(b-1)\sqrt{\bar{\gamma}_{FSO}}\right)^{a+b}} d\gamma_{FSO} \quad (15)$$

With the aid of [24, eq. (8.352.6) & eq. (1.111)] and after mathematical simplification, then the closed-from for CDF is reduced as

$$F(y_{end2end}) = 1 - \left(\frac{a}{b-1}\right)^a \frac{1}{\beta(a,b)\,\bar{\gamma}_{FSO}^{\frac{a}{2}}} \frac{2^{a+b-1}}{2\pi} \frac{e^{-\frac{m\gamma}{\bar{\gamma}_{RF}}}}{\Gamma(a+b)} \sum_{n=0}^{m-1} \frac{\left(\frac{m\gamma}{\bar{\gamma}_{RF}}\right)^n}{n!} \sum_{k=0}^{n}\binom{n}{k} C^{\frac{a}{2}} \left(\frac{m\gamma}{\bar{\gamma}_{RF}}\right)^{\frac{a}{2}-k} * G_{2,\ 3}^{3,\ 2}\left(\frac{mC\gamma}{\bar{\gamma}_{RF}\bar{\gamma}_{FSO}}\left(\frac{a}{b-1}\right)^2 \middle| \begin{matrix}\left(\frac{1-a-b}{2}\right), \left(\frac{-a-b+2}{2}\right) \\ 0, \left(\frac{1}{2}\right), \left(-\frac{a}{2}+k\right)\end{matrix}\right) \quad (16)$$

Furthermore, outage probability, OP is defined as

$$F(\gamma_{th}) = \Pr(\gamma \leq \gamma_{th}) \quad (17)$$

Then, the outage probability is obtained by setting $\gamma = \gamma_{th}$ in (16) as

$$F(\gamma_{th}) = 1 - \left(\frac{a}{b-1}\right)^a \frac{1}{\beta(a,b)\,\bar{\gamma}_{FSO}^{\frac{a}{2}}} \frac{2^{a+b-1}}{2\pi} \frac{e^{-\frac{m\gamma_{th}}{\bar{\gamma}_{RF}}}}{\Gamma(a+b)} \sum_{n=0}^{m-1} \frac{\left(\frac{m\gamma_{th}}{\bar{\gamma}_{RF}}\right)^n}{n!} \sum_{k=0}^{n}\binom{n}{k} C^{\frac{a}{2}} \left(\frac{m\gamma_{th}}{\bar{\gamma}_{RF}}\right)^{\frac{a}{2}-k} * G_{2,\ 3}^{3,\ 2}\left(\frac{mC\gamma_{th}}{\bar{\gamma}_{RF}\bar{\gamma}_{FSO}}\left(\frac{a}{b-1}\right)^2 \middle| \begin{matrix}\left(\frac{1-a-b}{2}\right), \left(\frac{-a-b+2}{2}\right) \\ 0, \left(\frac{1}{2}\right), \left(-\frac{a}{2}+k\right)\end{matrix}\right) \quad (18)$$

III. NUMERICAL RESULTS

This section analyses the behaviors of atmospheric turbulence conditions and threshold SNR on the AF relay-based proposed system numerically for Nakagami-m/F distribution fading in the presence of atmospheric disturbance under the IM/DD detection technique. By following the comparative methodology as given in the literature review [7] to authenticate the proposed model. For different environmental turbulence regimes, a and b are set i.e. a=4.5916, b=7.0941, a=2.3375, b=4.5322 and a=1.4321, b=3.4948 under weak, moderate, and strong turbulence. The other parameter such as fading parameter, m, and C both are set at 1.

In Fig.2 simulation results of OP against average electrical SNR are represented at the fixed value of threshold SNR of the system i.e., γ_{th} is at 10dB. The results revealed that the OP performance goes weakens when the atmospheric turbulence regimes become more and more severe.

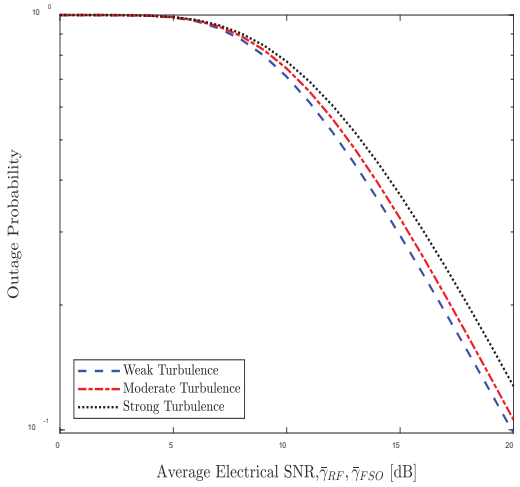


Fig.2: Outage probability vs average electrical SNR for various turbulence conditions at γ_{th} =10dB.

Authorized licensed use limited to: DELHI TECHNICAL UNIV. Downloaded on April 17,2023 at 06:07:40 UTC from IEEE Xplore. Restrictions apply.

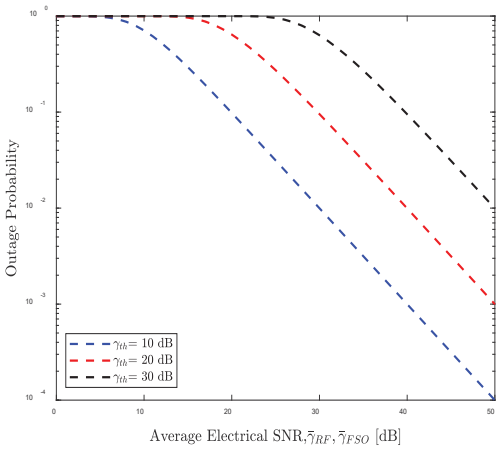


Fig.3:Outage probability for various thresholds under weak turbulence conditions.

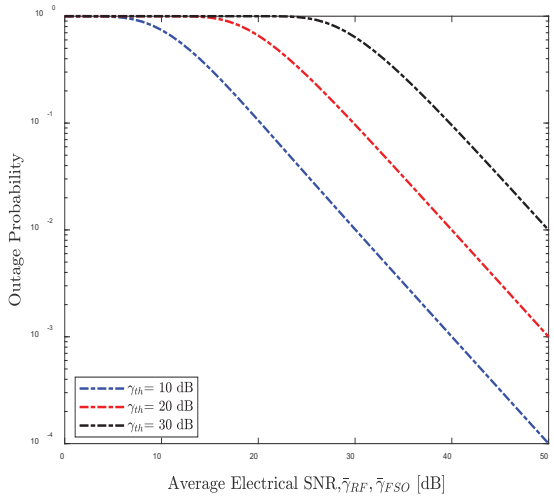


Fig.4. Outage probability for various thresholds under moderate turbulence conditions.

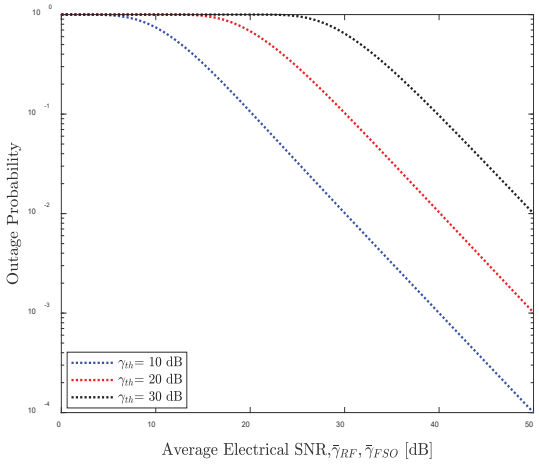


Fig. 5. Ooutage probability for various thresholds under strong turbulence conditions.

Fig. 3 presents the simulation results of OP against average electrical SNR for weak turbulence i.e., by taking a= 1.4321, b= 3.4948 at different values of γ_{th} *i. e.* ,10 dB, 20 dB *and* 30 dB respectively. By looking into the graph, it infers that the outage probability (OP) deteriorates with an increase γ_{th}. Similarly, Fig. 4 and Fig. 5 show the analytical results of OP against avg. electrical SNR for moderate and strong atmospheric turbulence. Systems performance is better in weak turbulence conditions as compared to the other two atmospheric conditions (moderate and strong). Hence, the performance of the proposed model degrades when the turbulence conditions are stronger as well as increase the threshold, γ_{th}.

IV. CONCLUSION

In this paper, the outage probability (OP) of end-to-end SNR for AF-based RF/FSO communication system following the Nakagami-m fading for RF and F-distribution for FSO channels with the consideration of different atmospheric turbulences is derived and simulated in MATLAB. The outcomes of the simulation show that atmospheric disturbance continuously decreased the system performance in the proposed system. Moreover, link performance also deteriorated by increasing the SNR threshold.

REFERENCES

[1] Malik, Aditi; Singh, Preeti (2015). Free Space Optics: Current Applications and Future Challenges. International Journal of Optics, 2015(), 1–7. doi:10.1155/2015/945483

[2] J. Yang, B. J. Auriol, Y. Lee, S. LeeA, "Comparison of FSO and RF Communication in Wireless", 2007, pp 1-2.

[3] Y. Wang, P. Wang, X. liu, T. Cao "On the performance of dual-hop mixed RF/FSO wireless communication system in urban area over aggregated exponentiated Weibull fading channels with pointing errors" in elsevier on optical communication volume 410, pp 609-616, 1 March 2018, doi: 10.1016/j.optcom.2017.10.062 .

[4] Upadhya, A., Dwivedi, V. K., & Karagiannidis "On the Effect of Interference and Misalignment Error in Mixed RF/FSO Systems over Generalized Fading Channels" IEEE Transactions on Communications, june 2020, pp 3681-3695 doi:10.1109/tcomm.2020.2971496.

[5] Kehinde O, Odeyemi, Pius A, Owolawi, "Partial relay selection in mixed RF/FSO dual-hop system over unifed M-distributed fading channel with non-zero boresight pointing errors"

[6] L. Han , Y. Wang , X. Liu, and B. Li, "Secrecy Performance of FSO Using HD and IM/DD Detection Technique Over F-Distribution Turbulence Channel With Pointing Error" in IEEE wirelesss communication, VOL. 10, NO. 10, OCTOBER 2021, doi: 10.1109/LWC.2021.3098305.

[7] G. Xu, Z. Song, "Performance Analysis for Mixed κ-μ Fading and M-Distribution Dual-Hop Radio Frequency/Free Space Optical Communication Systems", IEEE Transactions on Wireless Communications, 3 march 2021 doi:10.1109/twc.2020.3034104.

[8] H. Mehyeddine, B. Faissal El, "Performance analysis of mixed weibull and Gamma-Gamma dual-hop RF/FSO transmission systems", Hajji, Mehyeddine; Bouanani, Faissal El (2017). in IEEE 2017 International Conference on Wireless Networks and Mobile Communications (WINCOM) 2017, International Conference on Wireless Networks and Mobile Communications (WINCOM) , doi:10.1109/wincom.2017.8238201.

[9] S. Konicanin;S. Vasic;D. Milic;N. Petrovic;S. Suljovic, "Outage Probability of the Dual-Hop AF Relay Transmission System in the η-μ Fading Channel" in IEEE 28th Telecommunications Forum (TELFOR), November 24-25 2020, doi:10.1109/telfor51502.2020.9306678.

[10] Y. Liang, H. Mazen, A. Imran, "Unified Performance Analysis for Multiuser Mixed η-μ and M-Distribution Dual-Hop RF/FSO Systems",

Authorized licensed use limited to: DELHI TECHNICAL UNIV. Downloaded on April 17,2023 at 06:07:40 UTC from IEEE Xplore. Restrictions apply.

IEEE Transactions on Communications, pp 1-11, Apr 28, 2017, doi:10.1109/TCOMM.2017.2700462

[11] L. Hongjiang, D. Zhijun, A.I. Shafique, Ki-Hong, pan, Gaofeng, Alouini, Mohamed-Slim (2017), "On Secrecy Performance of Mixed RF-FSO Systems", in IEEE Photonics Journal (Volume: 9, Issue: 4, Aug. 2017), 05 July 2017, doi:10.1109/JPHOT.2017.2723422

[12] C. Kamasani, M. Palanivel, "Performance analysis of decode and forward relaying over dual-hop mixed fading channels", in AEU - International Journal of Electronics and Communications, Volume 73, March 2017, pp 84–88. doi:10.1016/j.aeue.2016.12.026

[13] Khanna H., Aggarwal M., & Ahuja S. (2016). "Outage analysis of a variable-gain amplify and forward relayed mixed RF-FSO system", in 2016 IEEE Annual India Conference (INDICON). doi:10.1109/indicon.2016.7839140

[14] Y. Wang, Pe. Yue, X. Yi, C. Shen,"Exact Performance Analysis for Mixed κ−μ Shadowed and Exponentiated Weibull Distributed Dual-Hop RF/FSO Systems", 2019 IEEE/CIC International Conference on Communications in China (ICCC), 03 October 2019, 10.1109/ICCChina.2019.8855967.

[15] J. Hu, Z. Zhang, Ji. Dang, L.Wu, G. Zhu, "Performance of Decode-and-Forward Relaying in Mixed Beaulieu-Xie and M Dual-Hop Transmission Systems With Digital Coherent Detection, in IEEE Access (Volume: 7), 23 September 2019, pp 138757 - 138770, doi: 10.1109/ACCESS.2019.2942992.

[16] G. Juhi, Dwivedi, Vivek K., K.Vikram (2018), "On the Performance of RF-FSO System over Rayleigh and kappa-mu/Inverse Gaussian Fading Environment" in IEEE Access 2018, 23 January 2018, pp 4186 - 4198, doi:10.1109/ACCESS.2018.2789478.

[17] Z. Emna, S. Hamza, A., Mohamed, " On the Performance Analysis of Dual-Hop Mixed FSO/RF Systems", in IEEE Transactions on Wireless Communications, 03 February 2016, pp 3679 - 3689, doi:10.1109/TWC.2016.2524685

[18] Z. Emna; A. I. Shafique; A. Mohamed, " Performance Analysis of Mixed Nakagami-m and Gamma–Gamma Dual-Hop FSO Transmission Systems", IEEE Photonics Journal (Volume: 7, Issue: 1, Feb. 2015), 18 December 2014, doi:10.1109/jphot.2014.2381657.

[19] B. Banibrata, Da. Akinchan, C., Aniruddha," Capacity analysis for Rayleigh/gamma-gamma mixed RF/FSO relayed transmission", IEEE 2017 International Conference on Wireless Communications, Signal Processing and Networking (WiSPNET) - Chennai,pp 1828–1832. doi:10.1109/WiSPNET.2017.8300077

[20] J. Zhao; S. h. Zhao; W. Zhao, K. Chen, "Performance analysis for mixed FSO/RF Nakagami-m and Exponentiated Weibull dual-hop airborne systems", Elsevir Optics Communications 2017, Volume 392, 1 June 2017, pp 294–299. doi:10.1016/j.optcom.2017.01.033

[21] P. Milica, T. Zeljen, " Exact Outage Probability Analysis of the Mixed RF/FSO System with Variable Gain Relays", IEEE Photonics Journal Volume: 10, Issue: 6, Dec. 2018, 29 November 2018 doi:10.1109/jphot.2018.2882611

[22] K. Himanshu; A. M. A. Swaran, "Performance analysis of a variable-gain amplify-and-forward relayed mixed RF-FSO system" International Journal of Communication Systems, 17 July 2017, doi:10.1002/dac.3400.

[23] P. Kostas, A. George, X., Evangelos, M., Andreas (2019). “The Fischer-Snedecor F-distribution Model for Turbulence-Induced Fading in Free-Space Optical Systems” Journal of Lightwave Technology, doi:10.1109/JLT.2019.2957327.

[24] I. S. Gradshtein, I. M. Ryzhik, Y. V. Geronimus, and M. Y. Tseytlin, Table of Integrals, Series, and Products. New York, NY, USA, Academic, 2007.

Authorized licensed use limited to: DELHI TECHNICAL UNIV. Downloaded on April 17,2023 at 06:07:40 UTC from IEEE Xplore. Restrictions apply.

Performance analysis of Linear Quadratic Regulator for DC-DC Converter Systems

Soni Kumari
Electrical Engineering Department
Delhi Technological University
Delhi, India
sonikumari_2k21ci07@dtu.ac.in

Dr. Madan Mohan Rayguru
Electrical Engineering Department
Delhi Technological University
Delhi, India
mmrayguru@dtu.ac.in

Shreyansh Upadhyaya
Electrical Engineering Department
Delhi Technological University
Delhi, India
shreyansh@dtu.ac.in

2023 International Conference on Power, Instrumentation, Energy and Control (PIECON) | 979-8-3503-9976-9/23/$31.00 ©2023 IEEE | DOI: 10.1109/PIECON56912.2023.10085906

***Abstract*— Power electronic converter models frequently use averaging approaches. The various state space averaged modelling principles for DC-DC buck converters, boost converters, and buck-boost converters working in Continuous Conduction Mode (CCM) are presented in this paper. It makes use of the time average algorithm, the average model technique, and the laws of energy conservation. The output transfer function of converters is also determined, and this information can be used to construct a reliable controller. Both the simulation of systems and the design of controllers benefit greatly from the averaged models produced by this method. Some general observations regarding Linear-Quadratic Regulators (LQR) are made in this paper. A DC-DC buck converter, boost converter, and buck-boost converter in particular are then designed and implemented using a LQR. Results from simulations and experiments indicate that the system is performing quite well.**

Keywords— small signal analysis, Linear Quadratic Regulator, discrete time systems, state space models.

I. INTRODUCTION

A DC to DC converter draws a DC input voltage at its input and delivers a different DC voltage. The output DC voltage can be lower or higher than the input voltage applied. DC to DC converters are available as individual integrated circuits (ICs), requiring very few additional components for their operation. Today DC to DC converters are often used in Cell phones and laptops. They receive battery power but contain sub-circuits that regulate the voltage requirement different from the batteries. One of the most popular ways to manage converters is PID(proportional integral and derivative)[1] controllers. The notion of subordinate control, where the regulators often employ PID controllers, is frequently applied in precision systems. They can be utilised in huge numbers in a single system, which ultimately results in more complex PID regulator adjustment, making it harder to supply the necessary parameters for the transient process quality. The adoption of a fundamentally new controller in the control system, notably the linear-quadratic regulator, is the solution to this issue. In terms of control strategies, linear-quadratic regulators (LQR)[2] have some intriguing qualities. For example, they can get the system to respond "optimally"[3] in accordance with the designer's requirements, they can be methodologically used regardless of the order of the system, and they are inherently stable. Additionally, the matrices of the small signal state-space averaged model[4] of the system can be used to directly calculate LQR. The following is how this paper is structured. First, some general LQR basis considerations are discussed, such as eliminating a zero-order error in the steady-state situation and accounting for one-sample actuation delay. This procedure is later used to design a controller for all three converters. The results of the simulation are also supplied to validate the behavior of the controller.

II. SMALL SIGNAL AVERAGED STATE-SPACE

A broad analytical tool, the small signal averaged state-space technique can be used on both simple and complex circuits[5]. Although reasonably straightforward, the linear averaged time-invariant models produced by applying this method required extensive mathematical work to arrive at the final conclusions. The detailed generalised procedure described in [5] is implemented to our case to obtain such models. The energy storage components of any electric circuit are the desired state variables for modelling with the state-space technique (i.e. inductor current and capacitance voltage). Any complicated circuit must first be simplified so that the circuit rules may be used before beginning to apply the state-space approach to it[6].

A. DC-DC Buck Converter

The Fig. 1 depicts the basic buck converter circuit as well as its corresponding circuits for the "ON" and "OFF" states[5]. The following describes the small-signal model[4] for the DC-DC Buck converter in CCM:

$$\begin{bmatrix} \frac{\mathrm{diL}}{\mathrm{dt}} \\ \frac{dvc}{dt} \end{bmatrix} = \begin{bmatrix} 0 & -\frac{1}{L} \\ \frac{1}{C} & -\frac{1}{RC} \end{bmatrix} \begin{bmatrix} iL \\ vc \end{bmatrix} + \begin{bmatrix} \frac{D}{L} & \frac{Vin}{L} \\ 0 & 0 \end{bmatrix} \begin{bmatrix} vin \\ d \end{bmatrix} \quad (1)$$

$$[v0] = [0 \quad 1] \begin{bmatrix} iL \\ vc \end{bmatrix} \quad (2)$$

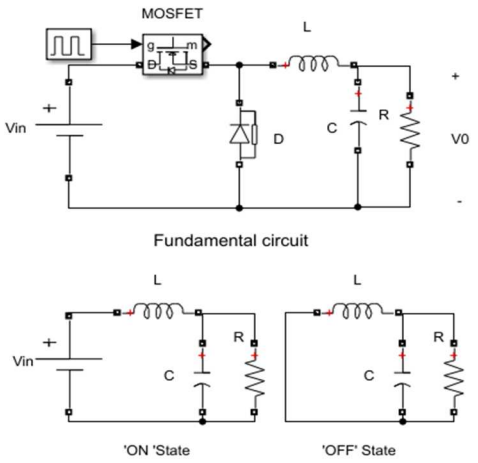


Fig.1. Fundamental buck converter circuits, including ON and OFF states

979-8-3503-9976-9/23/$31.00 ©2023 IEEE

Authorized licensed use limited to: DELHI TECHNICAL UNIV. Downloaded on April 10,2023 at 07:27:37 UTC from IEEE Xplore. Restrictions apply.

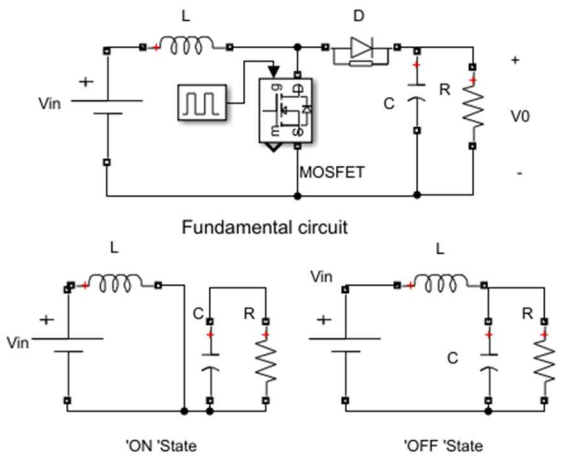


Fig. 2. Fundamental boost converter circuits, including ON and OFF states

B. DC-DC Boost Converter

The Fig. 2 depicts the basic buck converter circuit as well as its corresponding circuits for the "ON" and "OFF" states[5]. The following describes the small-signal model for the DC-DC Boost converter in CCM[6] :

$$\begin{bmatrix} \frac{\mathrm{diL}}{\mathrm{dt}} \\ \frac{dvc}{dt} \end{bmatrix} = \begin{bmatrix} 0 & -\frac{(1-D)}{L} \\ \frac{(1-D)}{C} & -\frac{1}{RC} \end{bmatrix} \begin{bmatrix} iL \\ vc \end{bmatrix} + \begin{bmatrix} \frac{1}{L} & \frac{Vc}{L} \\ 0 & -\frac{IL}{C} \end{bmatrix} \begin{bmatrix} vin \\ d \end{bmatrix} \quad (3)$$

$$[v0] = [0 \quad 1] \begin{bmatrix} iL \\ vc \end{bmatrix} \quad (4)$$

C. DC-DC Buck-Boost Converter

The Fig. 3 depicts the basic buck converter circuit as well as its corresponding circuits for the "ON" and "OFF" states[5]. The following describes the small-signal model for the DC-DC Buck-Boost converter in CCM:

$$\begin{bmatrix} \frac{di_L}{\mathrm{dt}} \\ \frac{dv_c}{dt} \end{bmatrix} = \begin{bmatrix} 0 & \frac{(1-D)}{L} \\ -\frac{(1-D)}{C} & -\frac{1}{RC} \end{bmatrix} \begin{bmatrix} i_l \\ v_c \end{bmatrix} + \begin{bmatrix} \frac{D}{L} & \frac{Vin}{L} \\ 0 & \frac{IL}{C} \end{bmatrix} \begin{bmatrix} v_{in} \\ d \end{bmatrix} \quad (5)$$

$$[v_0] = [0 \quad 1] \begin{bmatrix} i_L \\ v_c \end{bmatrix} \quad (6)$$

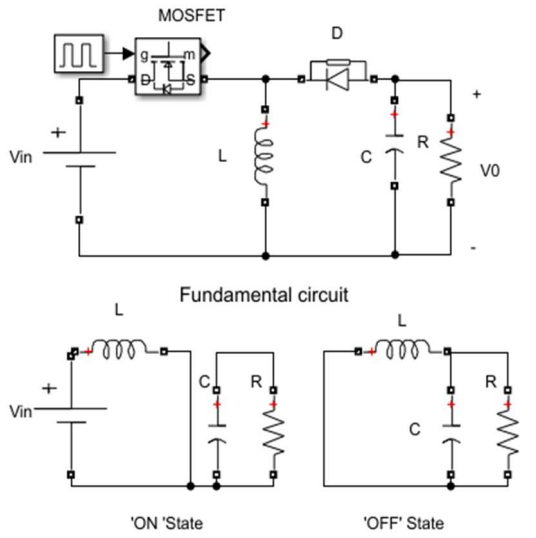


Fig. 3. Fundamental buck-boost converter circuits, including ON and OFF states

TABLE I. CONVERTER PARAMETERS

Parameters	Rated Values
Input Voltage(Vin)	12V
Output Voltage(V0)	20V
Switching Frequency	25KHz
Power(P)	100W
Duty Cycle(D)	0.4
Output Current(I0)	5A
Input Current	8.33A
Ripple in Inductor Current	2.5A
Ripple in Output Voltage	0.2V
Inductor(L)	$76.8e^{-6}$H
Capacitor(C)	$400e^{-6}$F
Load (R)	4ohm

III. LINEAR QUADRATIC REGULATOR CONTROLLER

To minimise a quadratic performance index (J), as shown below, is the goal of a LQR strategy [3] :

$$J = \int_0^\infty (x^T Q(t) x(t) + u^T(t) R u(t)) dt \quad (7)$$

Where Q and R are positively semidefinite and positively definite symmetric matrices, respectively.

The optimal solution[7] to a quadratic problem is to identify the control law u(t) that produces J's minimal value. Performance of the system is constrained by its state-space formulation:

$$\frac{d}{dt} x(t) = Ax(t) + Bu(t) \quad (8)$$

$$y(t) = Cx(t) + Du(t) \quad (9)$$

This is presumptively a system with controllable states.

$$u(t) = -Kx(t) \quad (10)$$

Finding gain[7], K (11):

$$K = R^{-1}.B^T.P \quad (11)$$

where, P is an algebraic Riccati equation[3] [8]solution:

$$A^T.P + P.A - P.B.R^{-1}.P + Q = 0 \quad (12)$$

A. Discrete Time System

The analysis will be conducted from the perspective of a discrete-time system due to the digital control used in this application[9]. As a result, (7) and (8) must be converted into discrete equations, as follows:

$$J = \frac{1}{2} x^T M x(N) + \frac{1}{2} \sum_{K=0}^{N-1} [x^T(k) Q x(k) + u^T(k)\, Ru(k)] \quad (13)$$

And

$$x(k+1) = A_d x(k) + B_d u(k) \quad (14)$$

where Ad and Bd are affected by the discrete time Ts in such a way that[10]:

$$A_d = e^{ATs} \quad and \quad B_d = (\int_0^{Ts} e^{A\tau}\, d\tau)\, B \quad (15)$$

Further implementing a linear-quadratic regulator [11] to converters to analyse their performance.

Authorized licensed use limited to: DELHI TECHNICAL UNIV. Downloaded on April 10,2023 at 07:27:37 UTC from IEEE Xplore. Restrictions apply.

We build the system model in the form of equations of state and plug the numerical values from Table 1 into the (1),(2),(3),(4),(5),(6).

1) *Buck Converter:* As a result after applying discrete time system[6] to CCM models of converters in MATLAB, we obtain the following equation (16):

$$A_d = \begin{bmatrix} 0.0414 & -0.0389 \\ 0.0075 & 0.0396 \end{bmatrix},$$
$$B_d = \begin{bmatrix} 0.1114 & 3.3423 \\ 0.3834 & 11.5027 \end{bmatrix} \tag{16}$$

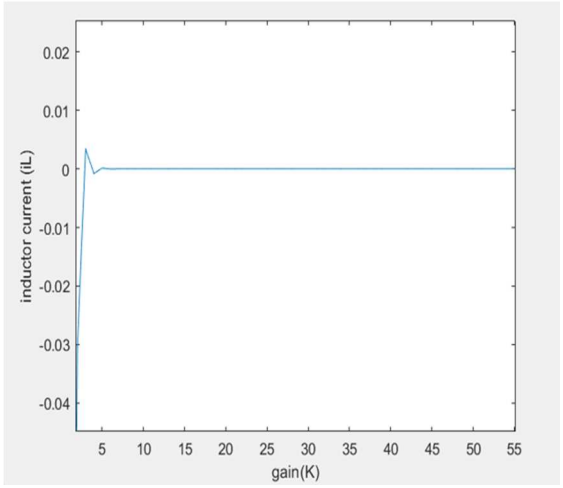
We choose the following element values(17) for matrices Q and R:

$$Q = \begin{bmatrix} 1 & 0 \\ 0 & 1 \end{bmatrix},$$
$$\text{R=1} \tag{17}$$

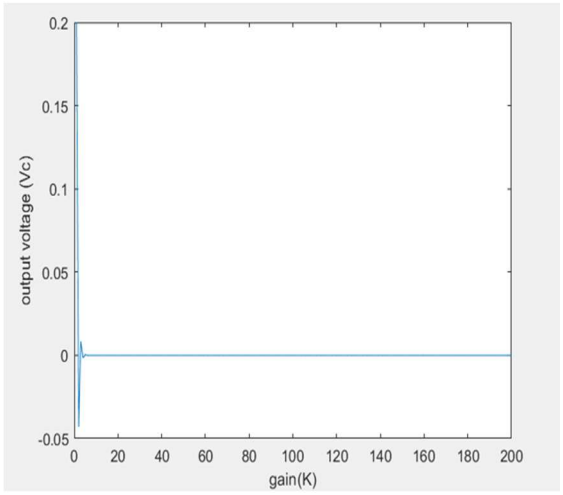
Using the MATLAB program to solve the LQR problem for gain K[12]:

$$K = \begin{bmatrix} 0.0000 & -0.0007 \\ 0.0003 & -0.0211 \end{bmatrix} \tag{18}$$

This matrix contains all of the values required for LQR control.



(a)



(b)

Fig. 4. Steady State Response of (a) Inductor current (b) Output voltage of Buck Converter

2) *Boost Converter:* As a result after applying discrete time system[9] to CCM models of converters in MATLAB, we obtain the following equation (19):

$$A_d = \begin{bmatrix} -0.0371 & -0.0466 \\ 0.0090 & -0.0408 \end{bmatrix},$$
$$B_d = \begin{bmatrix} 0.7978 & 20.2780 \\ 1.7285 & 34.5321 \end{bmatrix} \tag{19}$$

We choose the following element values(17) for matrices Q and R.

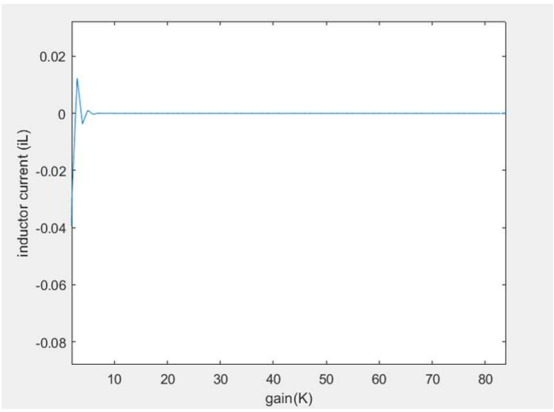
Using the MATLAB program to solve the LQR problem for gain K:

$$K = \begin{bmatrix} 0.0190 & -0.0226 \\ -0.0009 & -0.0060 \end{bmatrix} \tag{20}$$

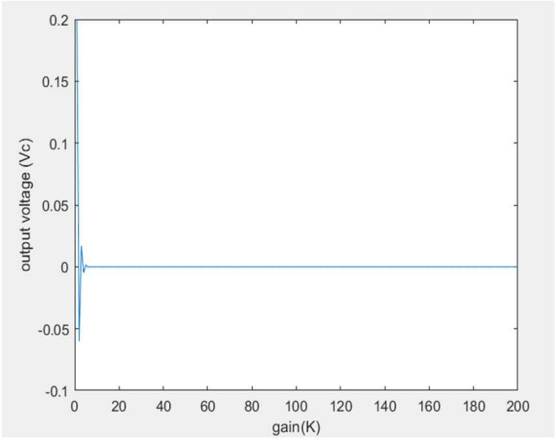
This matrix contains all of the values required for LQR control.

3) *Buck- Boost Converter:* As a result after applying discrete time system to CCM models of converters in MATLAB, we obtain the following equation (19):

$$A_d = \begin{bmatrix} -0.0371 & 0.0466 \\ -0.0090 & -0.0408 \end{bmatrix},$$
$$B_d = \begin{bmatrix} 0.3191 & 13.8953 \\ -0.6914 & -20.7043 \end{bmatrix} \tag{21}$$



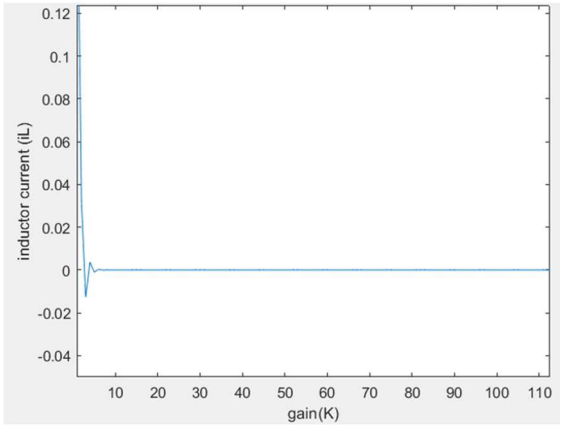
(a)



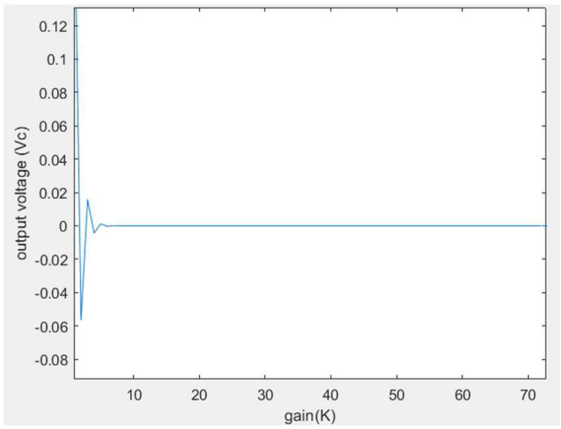
(b)

Fig. 5. Steady State Response of (a) Inductor current (b) Output voltage of Boost Converter

Authorized licensed use limited to: DELHI TECHNICAL UNIV. Downloaded on April 10,2023 at 07:27:37 UTC from IEEE Xplore. Restrictions apply.



(a)



(b)

Fig. 6. Steady State Response of (a) Inductor current (b) Output voltage of Buck-Boost Converter

We choose the following element values (17) for matrices Q and R.

Using the MATLAB program to solve the LQR problem for gain K[13]:

$$K = \begin{bmatrix} 0.0127 & 0.0177 \\ -0.0006 & 0.0108 \end{bmatrix} \quad (22)$$

This matrix contains all of the values required for LQR control.

IV. Results and Discussion

This case is performed in MATLAB/Simulink. The settings listed in Table I are used to simulate the outcomes for all three converters. The main result that we have in (11) which states that the feedback control can be found by solving through LQR [11]. Stabilizing feedback control gain is calculated for all three converters i.e K and implemented on them. The static state feedback law is determined by the standard solution of the DLQR(13) problem in an infinite horizon. The system (14) for all three converters is allowed to run for multiple time steps. This system is run till 'K' and we get all the absolute values of eigen values which is less than 1. This indeed shows that control gain is asymptotically stable[9]. u in (10) is created randomly. x is initialized to some small values like 0.2 and then it is calculated using the random input u. Using LQR the steady state error is completely reduced for inductor current and output voltage of buck converter, boost converter and buck-boost converter in Fig 4, 5 and 6 respectively. The gain has an inverse relationship with the steady state error. As a result, it can be diminished by raising the system gain.

V. Conclusion

Simulink is used to model and implement DC-DC converters[14] with the Buck, Boost, and Buck-Boost topologies. The result obtained by simulation of converter without any controlling parameters does not match completely to our rated value. Many optimization techniques as well as intelligent techniques can be used to get the accurate result. We have used LQR, the system performs well, according to simulation data. Since controlling multivariable systems using the LQR approach is particularly intriguing. The small signal technique was used to create linear averaged time-invariant models. The perspective of a discrete-time system will be used to conduct the LQR analysis. To minimise a quadratic performance index (J) u is calculated [2][12]. Thus, the studies have confirmed the effectiveness of LQR for control system development. Finally, steady state error is reduced for inductor current and output voltage of all converters through LQR analysis. Its advantage is that LQR examines all inputs to the linear system, offers the transfer function that will minimise overall error, and performs entire time-window (horizon) optimization. The drawback of this approach is that it is unable to deal with strong limitations or the migration of a nonlinear system[9] [13]from its linearized operating point.

References

[1] G. Tomar, Birla Institute of Applied Sciences, Institute of Electrical and Electronics Engineers. Bombay Section. Madhya Pradesh Subsection, Technical Education Quality Improvement Programme (India). Phase-III., IEEE Computer Society, and Institute of Electrical and Electronics Engineers., *2020 12th International Conference on Computational Intelligence and Comunication Networks : proceedings : venue, Birla Institute of Applied Sciences, Bhimtal, Distt. Nainital, Uttarakhand, India*.

[2] C. Jaen, J. Pou, R. Pindado, V. Sala, and J. Zaragoza, "A linear-quadratic regulator with integral action applied to PWM DC-DC converters," in *IECON Proceedings (Industrial Electronics Conference)*, 2006, pp. 2280–2285. doi: 10.1109/IECON.2006.347726.

[3] S. Ullah and M. Liquat, "Optimal output regulation on sample-data systems," in *ICCEREC 2015 - International Conference on Control, Electronics, Renewable Energy and Communications*, Nov. 2015, pp. 79–84. doi: 10.1109/ICCEREC.2015.7337059.

[4] H. Abdel-Gawad and V. K. Sood, "Small-signal analysis of boost converter, including parasitics, operating in CCM," Oct. 2015, pp. 1–5. doi: 10.1109/poweri.2014.7117622.

[5] R. H. G. Tan and L. Y. H. Hoo, "DC-DC converter modeling and simulation using state space approach," in *2015 IEEE Conference on Energy Conversion, CENCON 2015*, 2015, pp. 42–47. doi: 10.1109/CENCON.2015.7409511.

[6] R. Gessing, "Design of discrete-time linear-quadratic regulator with optimal observer," in *2001 European Control Conference, ECC 2001*, 2001, pp. 3416–3421. doi: 10.23919/ecc.2001.7076462.

[7] M. Baroudi, M. Saad, and W. Ghie, "State-feedback and linear quadratic regulator applied to a single-link flexible manipulator," in *2009 IEEE International Conference on Robotics and Biomimetics, ROBIO 2009*, 2009, pp. 1381–1386. doi: 10.1109/ROBIO.2009.5420822.

[8] Institute of Electrical and Electronics Engineers, International Conference on Power Electronics 7 2007.10.22-26 Daegu, and ICPE 7 2007.10.22-26 Daegu, *7th International Conference on Power Electronics, 2007 ICPE '07 ; 22-26 Oct. 2007, Daegu, Korea*.

[9] H. G. Kamil, E. E. Eldukhri, and M. S. Packianather, "Balancing Control of Robot Gymnast Based on Discrete-Time Linear

Authorized licensed use limited to: DELHI TECHNICAL UNIV. Downloaded on April 10,2023 at 07:27:37 UTC from IEEE Xplore. Restrictions apply.

Quadratic Regulator Technique," in *Proceedings - 2nd International Conference on Artificial Intelligence, Modelling, and Simulation, AIMS 2014*, May 2014, pp. 137–142. doi: 10.1109/AIMS.2014.38.

[10] Institute of Electrical and Electronics Engineers, International Conference on Power Electronics 7 2007.10.22-26 Daegu, and ICPE 7 2007.10.22-26 Daegu, *7th International Conference on Power Electronics, 2007 ICPE '07 ; 22-26 Oct. 2007, Daegu, Korea*.

[11] R. A. Michurin and A. Schagin, "Increase the accuracy of the DC motor control system with a linear-quadratic regulator," in *Proceedings of the 2018 IEEE Conference of Russian Young Researchers in Electrical and Electronic Engineering, ElConRus 2018*, Mar. 2018, vol. 2018-January, pp. 1746–1749. doi: 10.1109/EIConRus.2018.8317443.

[12] S. Gao and P. E. Caines, *Grapbon Linear Quadratic Regulation of Large-Scale Networks of Linear Systems; Grapbon Linear Quadratic Regulation of Large-Scale Networks of Linear Systems*. 2018. doi: 10.0/Linux-x86_64.

[13] W. Jongeneel and D. Kuhn, "On Topological Equivalence in Linear Quadratic Optimal Control," in *2021 European Control Conference, ECC 2021*, 2021, pp. 2002–2007. doi: 10.23919/ECC54610.2021.9654863.

[14] A. Emadi, "Modeling and analysis of multiconverter dc power electronic systems using the generalized state-space averaging method," *IEEE Transactions on Industrial Electronics*, vol. 51, no. 3, pp. 661–668, Jun. 2004, doi: 10.1109/TIE.2004.825339.

Authorized licensed use limited to: DELHI TECHNICAL UNIV. Downloaded on April 10,2023 at 07:27:37 UTC from IEEE Xplore. Restrictions apply.

Materials Today: Proceedings xxx (xxxx) xxx

Contents lists available at ScienceDirect

Materials Today: Proceedings

journal homepage: www.elsevier.com/locate/matpr

Performance assessment of hydrogen-based commercial hybrid renewable energy power generation system

Rishabh Kumar [a,*], Vishvender Kumar Dheer [a], Piyush Sharma [a], Nishant [a], Anil Kumar [a,b]

[a] Department of Mechanical Engineering, Delhi Technological University, Delhi 110042, India
[b] Center of Energy and Environment, Delhi Technological University, Delhi 110042, India

ARTICLE INFO

Article history:
Available online xxxx

Keywords:
Hydrogen
Hybrid
Renewable Energy
AHP
Performance

ABSTRACT

The world is transitioning toward hybrid renewable energy systems in order to cope with increased power demand. The aim of this research article is to assess various hydrogen-based hybrid renewable energy systems (HRES) based on their performance, which is used commercially. A total of nineteen projects were selected at random across different regions and evaluated based on the analytic hierarchy process (AHP). In order to compare, five criteria are selected viz. 1. Plant Capacity, 2. Electrolyzer Capacity, 3. Utilization of Energy Produced, 4. Energy Sources Involved, 5. Type of Hydrogen Storage Technology Used. Plant Capacity and Energy sources involved are the criteria given more weightage. Using AHP multi-criteria decision-making was possible and all the projects are ranked accordingly based on performance parameters. SCHATZ Solar Demonstration Project, USA, 1989 was given a priority of 0.8% with a rank of 16 despite being the oldest project. Wherein, Foshan Hydrogen City Project, China, 2018 was assigned a priority of 23.2% and ranked 1st. Projects were prioritized and ranked with a consistency ratio (CR) of 28.9% in AHP.
Copyright © 2023 Elsevier Ltd. All rights reserved.
Selection and peer-review under responsibility of the scientific committee of the Recent Advances in Materials, Manufacturing and Thermal Engineering.

1. Introduction

The present world is facing an environmental crisis in terms of climate change, as the majority of the world's energy requirement is fulfilled by fossil fuels. The usage of fossil fuels over the last few decades has led to increased CO_2 emissions, which is now an area of concern. Since it not only impacts the environment but also humanity drastically. Wherein it has been observed how renewable energy would act as an aid in the current situation. As the energy demand is increasing in the world, the demand for renewable energy is also increasing. Since it solves the major problem of emissions and climate change caused by fossil fuels. Renewable energy systems like solar and wind are highly encouraged by governments across the globe. As the world is changing, now countries are shifting toward sustainable energy sources. During the pandemic, it has been proven that renewable energy is immune, as there was an increase in the usage of renewable energy by 3% in 2020 [1] as reported by the International Energy Agency (IEA).

Hydrogen is the lightest and the most abundant source of energy on earth. It consists of one proton and one electron. But the complication with it is that it's available in compound form instead of free form on earth. Although it can be produced by various methods like using feedstock, coal gas, natural gas, biomass, electrolysis, etc. And the most advantageous thing about hydrogen is that it produces zero-emission means eco-friendly [2].

Industries are now shifting towards the energy sector due to its untapped potential. The world has witnessed how severely conventional fuels impacted the environment in the last few decades Renewable energy sources are considered to be one of the available solutions. Renewable energy sources like solar or wind are widely used wherein the supply is not consistent over the period, especially wind velocity varies over the year. Hence it is wise to combine two or more energy sources and use them together to maintain a consistent supply throughout [3]. As solar photovoltaic

Abbreviations: AHP, Analytic Hierarchy Process; *CR*, Consistency Ratio; *PV*, Photovoltaic; *HRES*, Hybrid Renewable Energy System; *RES*, Renewable Energy System; *HSS*, Hydrogen Storage System; *PAFC*, Phosphoric Acid Fuel Cell; *PEMFC*, Proton Exchange Membrane Fuel Cell; *PEM*, Proton Exchange Membrane; *WT*, Wind Turbine; *CG*, Compressed Gas; *NG*, Natural Gas; *BG*, Bio-Gas; *MH*, Metal Hydride; *SC*, Solar Collector; *scf*, Standard Cubic Feet.

* Corresponding author.
E-mail address: rishabhkr1000@gmail.com (R. Kumar).

https://doi.org/10.1016/j.matpr.2023.04.275
2214-7853/Copyright © 2023 Elsevier Ltd. All rights reserved.
Selection and peer-review under responsibility of the scientific committee of the Recent Advances in Materials, Manufacturing and Thermal Engineering.

Please cite this article as: R. Kumar, V. Kumar Dheer, P. Sharma et al., Performance assessment of hydrogen-based commercial hybrid renewable energy power generation system, Materials Today: Proceedings, https://doi.org/10.1016/j.matpr.2023.04.275

Table 1
State of art in hydrogen-based hybrid renewable energy power generation system.

S. No.	Project name	Country	Commissioned Year	Remarks	Ref
1	SCHATZ solar demonstration project	USA	1989	1) PV array of 192 Arco M75 modules with a nominal power rating of 9.2 kW with an avg. the efficiency of 6.7%. 2) The system contains 4 Exide GC-4, 220Ah, deep cycle wagon batteries with an avg. the efficiency of 83.5%. 3) Electrolyzer was of an alkaline type, 12 cells with nominal power of 6 kW with an avg. the efficiency of 80.1%. The storage was of 5.7 m^3 total capacity which would be used with PEMFC with an avg. the efficiency of 43.1%	
2	INTA solar hydrogen facility	Spain	1990	1) PV field was of 8.5 kW capacity. 2) Alkaline electrolyzer of 5.2 kW was used along with (MH) storage of 24 m^3. 3) Fuel cell stack consists of 1 PAFC & 2 PEMFC with a capacity of 10 kW and 2.5 kW & 5 kW respectively. 4) Yearly avg. efficiencies of PV, electrolyzer, and global system were 8.35%, 69.13%, and 5.70% respectively.	[10]
3	Clean Air Now	USA	1994	1) PV arrays formed by Fresnel lens concentrators assisted by 40 sub-arrays consisting of 12 trackers each with a capacity of each panel (550–750 W). Each of the 8 cells produced an avg. 1800A. 2) 8 electrolysis cells rated 4000A each were capable of generating hydrogen at 48 kW with a compressor capacity of 400 or scf/h, during the operation the hydrogen production was found to be 225 scf/h. 3) storage system used for hydrogen was two high-pressure ASME storage vessels of holding capacities of 74,000 scf and 14,000 scf.	[10]
4	PALM desert project	USA	1999	1) PV array of output 11.7 kW with ALTUS 20 electrolyzer of capacity 1200 sl/h. which would consume 16,600 kWh of energy per year. 2) Hydrogen storage system was of 12000scf capacity.	[10]
5	Grimstad Renewable Energy Park	Norway	2000	1) Solar collectors of 3 types were used which collectively give 1600KW of thermal energy, along with a 50 kW electrolyzer and alkaline fuel cell stack. 2) PV array of 400 V (AC) was adopted which gave 197.6 kWh to the power grid. 3) Approx. 498 kWh was supplied to the grid over 9 months.	[30]
6	PURE Project, Unst	UK	2005	1) 2 wind turbines of 15 kW each along with a 3.5 Nm^3/h HP electrolyzer and 5 kW PEM fuel cell as a power backup. 2) project helped to reduce 11MT of CO_2 emissions per year	[11,12,17]
7	Hychico, Comodoro Rivadavia	Argentina	2006	1) wind turbine along with 2 electrolyzers with a total capacity of 120 Nm^3/h of hydrogen at a thermal efficiency of 40–41% on max. power. 2) 4 cell stack made each electrolysis unit with an output of 4.1–4.6 kW/Nm^3.	[13,14]
8	RES2H2 Gran Canaria	Greece	2007	1) WT (Enercon E-40) was of 500 kW capacity which could be scaled down to 100 kW for standalone purposes. 2) 25 kW water electrolyzer along with MH storage system, with stack efficiency 70%-86% at 1000 A/m^2 current density.	[15–17]
9	HARP System, Bella Coola	Canada	2010	1) Electrolyzer (HYSTAT 60) with a production rate of 5 kg/h was installed, along 100 kW fuel cell and H.P. H_2 storage system.2) Flow battery (Zess-Zinc Energy Storage System) of 3 stack cells with an output power capacity of 100 kW was used.	[18]
10	Ramea Wind-Hydrogen-Diesel Project	Canada	2011	1) Electrolyzer with a storage capacity of 167 kg was used along with a 250 kW H_2 Genset.2) 30% (277 kW) of the load was pulled by Diesel Genset (Rated 925 kW). 3) Wind energy penetration level was 35–40%.	[16,19,20]
11	Hydrogen mini grid system Yorkshire (Rotherham)	UK	2012	1) Wind turbine of 225 kW coupled to an alkaline electrolyzer, along with a 30 kW fuel cell & 200 kg hydrogen storage. 2) ITM Power's electrolyzer produced 80 kg low carbon H_2/day.	[31]
12	Boeing rSOC California	USA	2014	1) RSOC system was adopted in which 42 m^3/h of H_2 was produced with up to 85% efficiency via electrolysis. 2) Fuel cells would deliver electricity of 50 kW with 60% efficiency.	[21]
13	Raglan Nickel mine	Canada	2015	1) WT generator (Enercon E-82 E4) employed with 315 kW (HySTAT 60) electrolyzer, along with 198 kW PEM fuel cell (HyPMTM XR). 2) 200 kW flywheel (KTSI GTR-200) was adopted to filter out variations which helped the project to achieve 50% wind penetration.	[22]
14	Fife, Levenmouth Community Energy Project	UK	2016	1) 750 kW WT with 200 kW PV setup was installed, along with 250 kW electrolyzer & PEM fuel cell of 100 kW capacity. 2) Project could run loads for 4 days off-grid with zero carbon emission.	[23,24]
15	Cerro Pabellón Microgrid 450 kWh Hydrogen ESS - Enel S.p. A	Chile	2017	1) Project involved a PV facility of 125 kW power with (an HSS-hydrogen storage system) of 450 kW capacity & 132 kW li-battery storage system. 2) Facility would work on-grid as well as off-grid.	[25,26]
16	Foshan hydrogen city 2	China	2018	1) Project is in its second phase (2021–2025) in which production of H_2 from NG & PEM electrolyzers, along with an efficient high-pressure liquid H_2 storage system and fuel line.	[27]
17	Toyota Australia, Altona, Victoria	Australia	2019	1) PV array of 500 kW capacity was complemented by an on-site PV setup of 87 kW. 2) 250 kW PEM electrolyzer was installed which would produce 80 kg/day of H_2.	[28]
18	Western Sydney green gas project	Australia	2021	1) Electrolyzer of 500 kW capacity was installed to serve 250 homes per year. 2) The project will reduce 35% of carbon emissions by 2030 as per 2005 data. 3) The project would produce 52600 kg/year of H2 and blend 2% of H_2 into the existing NG supply.	[13]

Table 1 (*continued*)

S. No.	Project name	Country	Commissioned Year	Remarks	Ref
19	Brande hydrogen project	Denmark	2021	1) A 3 MW turbine was employed in this project to operate on island mode & made suitable for the grid-connected also. 2) Project setup coupled existing Siemens Gamesa SWT 3.0 which included WT with fuel cell stack & PEM electrolyzer.	[29]

Table 2
Comparison criteria data.

S. No.	Project	Comparison Criteria				
		Plant Capacity	Electrolyzer capacity (kW)	Utilization of Energy produced	Energy Sources Involved	Type of H2 Storage Technology Used
1	SCHATZ solar demonstration project (P_1)	133 kW	6	Grid	PV-H_2	CG
2	INTA solar hydrogen facility (P_2)	30 kW	5.2	Grid	PV-H_2	MH
3	Clean Air Now (P_3)	60 kW	48	Grid, Fuel Cell Vehicle	PV-H_2	ASME STORAGE VESSEL
4	PALM desert project (P_4)	1.12 MW	15	Grid, Fuel Cell Vehicle	PV-H_2	CG, MH
5	Grimstad Renewable Energy Park (P_5)	1.6 MW	50	Grid, Heat storage	PV-WT-SC-H_2	CG
6	PURE Project, Unst (P_6)	35 kW	7	Grid	WT-H_2	CG
7	Hychico, Comodoro Rivadavia (P_7)	1.4 MW	325	Grid	WT-H_2	CG
8	RES2H2 Gran Canaria (P_8)	500 kW	25	Grid, Fuel Cell Vehicle	WT-H_2	CG, MH
9	HARP System, Bella Coola (P_9)	6.9 kW	100	Grid, Fuel Cell Vehicle	WT-PV- H_2-Hydro	CG
10	Ramea Wind-Hydrogen-Diesel Project (P_{10})	690 kW	324	Grid	WT-Diesel-H_2	CG
11	Hydrogen mini grid system Yorkshire (Rotherham) (P_{11})	255 kW	12	Grid	WT-H_2	CG
12	Boeing rSOC California (P_{12})	150 kW	50	Grid	BG/NG-H_2	CG
13	Raglan Nickel mine (P_{13})	3 MW	315	Grid	WT-Diesel-H_2	CG
14	Fife, Levenmouth Community Energy Project (P_{14})	1.3 MW	250	Grid, Fuel Cell Vehicle	WT-PV-H_2	CG
15	Cerro Pabellón Microgrid 450 kWh Hydrogen ESS - Enel S.p.A (P_{15})	700 kW	350	Grid	PV-H_2	CG
16	Foshan hydrogen city 2 (P_{16})	10 MW	3000	Grid, Fuel Cell Vehicle	NG-H_2	CG
17	Toyota Australia, Altona, Victoria (P_{17})	800 kW	80	Grid, Fuel Cell Vehicle	PV-H_2	CG
18	Western Sydney green gas project (P_{18})	500 kW	500	Grid	PV-WT-H_2	CG
19	Brande hydrogen project (P_{19})	3 MW	430	Grid	PV-WT-H_2	CG

Table 3
Decision Matrix.

	P_1	P_2	P_3	P_4	P_5	P_6	P_7	P_8	P_9	P_{10}	P_{11}	P_{12}	P_{13}	P_{14}	P_{15}	P_{16}	P_{17}	P_{18}	P_{19}
P_1	1	6	4	0.13	0.14	5	0.13	0.11	0.11	0.13	0.17	0.17	0.11	0.11	0.14	0.11	0.14	0.13	0.11
P_2	0.17	1	0.17	0.13	0.11	6	0.14	0.13	0.11	0.13	0.17	0.17	0.13	0.13	0.14	0.11	0.13	0.14	0.13
P_3	0.25	6	1	0.17	0.13	6	0.14	0.14	0.13	0.14	0.2	0.25	0.13	0.13	0.14	0.11	0.14	0.17	0.13
P_4	8	8	6	1	0.17	7	7	0.17	0.13	0.14	6	7	0.13	0.14	5	0.11	6	7	0.14
P_5	7	9	8	6	1	9	6	6	0.13	6	8	7	0.14	1	4	0.11	6	7	0.14
P_6	0.2	0.17	0.17	0.14	0.11	1	0.13	0.13	0.13	0.13	0.17	0.2	0.13	0.13	0.14	0.11	0.14	0.17	0.13
P_7	8	7	7	0.14	0.17	8	1	0.14	0.13	1	6	7	0.13	0.14	0.2	0.11	0.2	4	0.14
P_8	9	8	7	6	0.17	8	7	1	0.14	5	6	8	0.14	2	5	0.11	5	6	0.14
P_9	9	9	8	8	8	8	8	7	1	8	9	9	7	6	7	0.17	7	8	6
P_{10}	8	8	7	7	0.17	8	1	0.2	0.13	1	8	8	0.14	0.17	1	0.11	0.33	0.5	0.14
P_{11}	6	6	5	0.17	0.13	6	0.17	0.17	0.11	0.13	1	2	0.14	0.13	0.2	0.11	0.17	0.17	0.13
P_{12}	6	6	4	0.14	0.14	5	0.14	0.13	0.11	0.13	0.5	1	0.14	0.13	0.17	0.11	0.14	0.14	0.13
P_{13}	9	8	8	8	7	8	8	7	0.14	7	7	7	1	4	5	0.13	6	6	0.5
P_{14}	9	8	8	7	1	8	7	0.5	0.17	6	8	8	0.25	1	7	0.13	5	5	0.17
P_{15}	7	7	7	0.2	0.25	7	5	0.2	0.14	1	5	6	0.2	0.14	1	0.11	0.25	0.2	0.14
P_{16}	9	9	9	9	9	9	9	9	6	9	9	9	8	8	9	1	9	9	8
P_{17}	7	8	7	0.17	0.17	7	5	0.2	0.14	3	6	7	0.17	0.2	4	0.11	1	2	0.17
P_{18}	8	7	6	0.14	0.14	6	0.25	0.17	0.13	2	6	7	0.17	0.2	5	0.11	0.5	1	0.2
P_{19}	9	8	8	7	7	8	7	7	0.17	7	8	8	2	6	7	0.13	6	5	1

cell works more efficiently during summer than winter, Wind turbines work more efficiently in winter than in summer and in specific regions too, Tidal energy works better only at the beginning & the end of the day. So that's why HRES has required the power grid to work in combination with Renewable Energy Systems (RESs) to provide a consistent power supply throughout the year [4]. In the meantime, to overcome power curtailment, it has been observed that Hydrogen Storage System (HSS) with Electrolyzer & Fuel cell

Table 4
Performance-based Ranking Details.

S. No.	Project	Annotation	Priority	Rank	Min	Max
1	SCHATZ solar demonstration project	P_1	0.80%	16	0.10%	1.50%
2	INTA solar hydrogen facility	P_2	0.60%	18	0.00%	1.20%
3	Clean Air Now	P_3	0.70%	17	0.00%	1.40%
4	PALM desert project	P_4	3.80%	8	0.10%	7.50%
5	Grimstad Renewable Energy Park	P_5	6.80%	5	1.00%	12.60%
6	PURE Project, Unst	P_6	0.50%	19	0.00%	1.00%
7	Hychico, Comodoro Rivadavia	P_7	5.60%	7	1.40%	9.80%
8	RES2H2 Gran Canaria	P_8	2.10%	13	0.30%	3.90%
9	HARP System, Bella Coola	P_9	16.40%	2	2.10%	30.70%
10	Ramea Wind-Hydrogen-Diesel Project	P_{10}	3.00%	9	−1.10%	7.10%
11	Hydrogen mini grid system Yorkshire (Rotherham)	P_{11}	1.10%	14	0.20%	2.00%
12	Boeing rSOC California	P_{12}	1.00%	15	0.20%	1.80%
13	Raglan Nickel mine	P_{13}	10.10%	4	1.30%	18.90%
14	Fife, Levenmouth Community Energy Project	P_{14}	6.00%	6	1.40%	10.60%
15	Cerro Pabellón Microgrid 450 kWh Hydrogen ESS - Enel S.p.A	P_{15}	2.10%	12	0.40%	3.80%
16	Foshan hydrogen city 2	P_{16}	23.20%	1	2.70%	43.70%
17	Toyota Australia, Altona, Victoria	P_{17}	2.90%	10	0.80%	5.00%
18	Western Sydney green gas project	P_{18}	2.30%	11	0.40%	4.20%
19	Brande hydrogen project	P_{19}	11.00%	3	2.00%	20.00%

would solve the problem. Because it utilizes the unused energy of the primary system to produce & store hydrogen as a secondary system [5].

It has been observed that over the last few decades, there has been tremendous development in the energy field and the utilization of hydrogen, as a fuel as well as an energy storage system. The first use of hydrogen as a fuel cell was proposed by Prof. Christian Friedrich Schoenbein back in 1838. Sir Robert William Grove invented the first hydrogen fuel cell in 1845 [6]. British scientist, J.B.S. Haldane first gave the concept of green hydrogen production using windmills in 1923 at Heretics Society, Cambridge University. Hence, this can be traced back to the very first proposal for a "hydrogen-based renewable energy economy" [7]. Bacon successfully built the first hydrogen–oxygen fuel cell in 1959. After further modifications, the same was utilized by the United States in the various Apollo missions as the secondary power source [8]. In 1990, the first solar-powered hydrogen generation plant became functional at the SWB research and testing facility in Southern Germany [9]. In 1999, US DOE started the PALM Desert project with SERC in Palm City, which integrated PV-H_2 power sources with the Grid [10]. In the post-year 2000, there have been subsequent developments in the field of renewable energy to integrate hydrogen as an energy source for commercial purposes. The same will be thoroughly analyzed in the later sections of this paper.

In the coming future, the world will be more inclined towards green energy generation, and the integration of hydrogen with renewable energy has untapped potential to fulfill the increasing energy demand. Many projects have been started some for short while others for extended periods, wherein commercialization is the main area of focus. The current literature on the same is scattered, hence this paper will provide a thorough analysis of the commercialized hydrogen-based hybrid renewable energy systems based on their performance using AHP.

2. Literature review

In this paper total of nineteen state of art commercial hydrogen-based hybrid renewable energy systems are studied based on multiple factors i.e. overall plant capacity, type of storage technology used, different components of the project, electrolyzer capacity, energy output, total hydrogen produced, and energy utilization. The major findings along with project details are populated in Table 1.

3. Methodology

AHP (Analytical Hierarchy Process) comes under the category of a multi-criteria decision-making group of theories. It is solely based on the solution of the "Eigenvalue Problem". In AHP, values such as objective/subjective opinions can be translated into measurable numeric relations [32–34].

In the AHP approach following steps are followed:

- Defining Objective
- Criteria selection
- Pair comparison based on criteria
- Calculating Priority and consistency index
- Selection of optimum alternative based on the evaluation.

A total of 19 commercial projects were selected across the globe, Table 1. For evaluation, five comparison criteria are selected i.e., plant capacity, electrolyzer capacity, utilization of energy produced, energy sources involved, and type of hydrogen storage technology used.

To make a decision matrix, data for comparison is collected and presented in Table 2. Based on These data points showe comparisons of different projects are performed with 171 iterations. Based on these iterations and pair-wise comparisons, a ranking of the projects are rankednd Discussions.

A total of 19 projects from different locations are taken to compare the present scenario of the commercialization of hydrogen-based hybrid renewable energy systems. There are multiple variables to compare, hence AHP method is utilized to identify ranking based on the performance aspect of the projects. The consistency ratio (CR) for the AHP is 28.9% for the comparison. It has been observed that the latest projects received a better ranking based on the technology used along with overall increased plant capacity. SCHATZ Solar demonstration project received rank 16 despite being one the oldest project based on plant capacity at that time. While Foshan Hydrogen project, China received 1st rank and a priority of 23.2% over other projects.

The five decision criteria were used for pair-wise comparison and hence, the decision matrix was formulated, in Table 3. The pair-wise comparison was performed by comparing two projects at a time (e.g. P_1 with P_2, P_3, P_4,. . .P_{19}), this way a total of 171 iterations were performed. The weightage of each comparison criterion was evaluated based on the literature available and each project was compared on a scale of 1–9 (AHP Scale) [34].

Based on this decision Matrix, the priority of each project was evaluated and assigned a value. Furthermore, maximum and minimum limits of the priority are considered for ranking purposes. The ranking details of the projects are given in Table 4.

In Table 4 Projects are cross-evaluated and then prioritized based on factors (i.e. Plant capacity, Electrolyzer capacity, Energy utilization, Variation in energy sources, H2 storage method) along with their weighted percentages. Furthermore, maximum and minimum limits of priorities are considered for calculating their ranking orders which summarizes the working efficacy of HRES-based projects.

4. Conclusions

A systematic multi-criteria decision-making approach i.e. AHP methodology is implemented for performance comparison of the total of 19 hydrogen-based hybrid renewable energy systems. Based on the study performed and the comparison drawn, below are the major findings:

- A systematic multi-criteria decision-making approach i.e. AHP methodology is implemented for performance comparison of the total of 19 hydrogen-based hybrid renewable energy systems.
- In results consistency ratio of 28.9% is achieved while performing pairwise comparison which authenticates the assessment performed.
- SCHATZ Solar Demonstration Project, USA, 1989 is one of the oldest projects amongst all ranked 16th with 0.8% priority.
- Foshan, hydrogen city project, China, 2018 ranked 1st with 23.2% priority and having 10 MW plant capacity, 3 MW electrolyzer capacity & using Fuel cell vehicles along with grid assistance. Phase 2 (2021–25) of the project is in progress which in terms will enhance overall hydrogen production and reduce carbon emissions.
- Asia and Africa have high energy potential which is to be explored since both continents have either negligible or very few projects at present.

This paper explores the possibility of comparing and evaluating commercial hydrogen-based HRES projects using the AHP methodology. The results can further be validated by using different multi-criteria decision-making methods. World's focus is not shifting towards green energy and zero emissions, with that in consideration there are tremendous possibilities to be explored in the field of HRES systems. The present study can be utilized as a base for further developments and for designing better systems.

CRediT authorship contribution statement

Rishabh Kumar: Conceptualization, Methodology, Writing – review & editing. **Vishvender Kumar Dheer:** Data curation, Investigation. **Piyush Sharma:** Software, Validation. **Nishant:** Resources, Writing – original draft. **Anil Kumar:** Supervision.

Data availability

Data will be made available on request.

Declaration of Competing Interest

The authors declare the following financial interests/personal relationships which may be considered as potential competing interests: Rishabh Kumar reports writing assistance was provided by Delhi Technological University.

Acknowledgment

The authors are highly grateful to the Department of Mechanical Engineering and Centre for Energy and Environment, Delhi Technological University Delhi (India) for providing basic facilities to compile this work.

References

[1] International Energy Agency, "Global Energy Review: CO2 Emissions in 2021 Global emissions rebound sharply to highest ever level," 2021. Accessed: Mar. 20, 2022. [Online]. Available: https://www.iea.org/reports/global-energy-review-co2-emissions-in-2021-2.
[2] International Energy Agency, "The Future of Hydrogen," 2019. Accessed: Mar. 20, 2022. [Online]. Available: https://www.iea.org/reports/the-future-of-hydrogen.
[3] V. Khare, S. Nema, P. Baredar, Optimization of hydrogen based hybrid renewable energy system using HOMER, BB-BC and GAMBIT, International Journal of Hydrogen Energy 41 (38) (Oct. 2016) 16743–16751, https://doi.org/10.1016/j.ijhydene.2016.06.228.
[4] A. Khosravi, R.N.N. Koury, L. Machado, J.J.G. Pabon, Energy, exergy and economic analysis of a hybrid renewable energy with hydrogen storage system, Energy 148 (Apr. 2018) 1087–1102, https://doi.org/10.1016/j.energy.2018.02.008.
[5] Y. Song et al., Techno-economic analysis of a hybrid energy system for CCHP and hydrogen production based on solar energy, International Journal of Hydrogen Energy (Sep. 2021), https://doi.org/10.1016/j.ijhydene.2021.08.134.
[6] J. St-Pierre, D.P. Wilkinson, Fuel cells: A new, efficient and cleaner power source, AIChE Journal 47 (7) (Jul. 2001) 1482–1486, https://doi.org/10.1002/aic.690470702.
[7] "J.B.S. Haldane Presents an Early Vision of Transhumanism, and the First Proposal of a Hydrogen-Based Renewable Energy Economy." https://www.historyofinformation.com/detail.php?entryid=4107 (accessed May 30, 2022).
[8] F.T. Bacon, Fuel cells, past, present and future, Electrochimica Acta 14 (7) (Jul. 1969) 569–585, https://doi.org/10.1016/0013-4686(69)87042-8.
[9] A. Szyszka, Ten years of solar hydrogen demonstration project at Neunburg vorm Wald, Germany, International Journal of Hydrogen Energy 23 (10) (Oct. 1998) 849–860, https://doi.org/10.1016/S0360-3199(97)00172-9.
[10] T. Schucan, "Case Studies of integrated hydrogen systems. International Energy Agency Hydrogen Implementing Agreement, Final report for Subtask A of task 11 - Integrated Systems," Oak Ridge, TN, Dec. 1999. doi: 10.2172/775587.
[11] R. Gazey, S. K. Salman, and D. D. Aklil-D'Halluin, "A field application experience of integrating hydrogen technology with wind power in a remote island location," Journal of Power Sources, vol. 157, no. 2, pp. 841–847, Jul. 2006, doi: 10.1016/j.jpowsour.2005.11.084.
[12] B.K. Sovacool, R.F. Hirsh, Island wind-hydrogen energy: A significant potential US resource, Renewable Energy 33 (8) (Aug. 2008) 1928–1935, https://doi.org/10.1016/j.renene.2007.12.006.
[13] G. P. L. Cummins Inc., "GREEN HYDROGEN: THE POWER OF WIND," May 03, 2021. https://www.cummins.com/news/2021/05/03/green-hydrogen-power-wind (accessed May 30, 2022).
[14] Hychico, "Hydrogen Plant." http://www.hychico.com.ar/eng/hydrogen-plant.html (accessed May 30, 2022).
[15] E. Varkaraki, "IEA/HIA Case study on the wind-hydrogen plant of RES2H2 in Greece." May 2009.
[16] L. Correas and I. Aso, "Task 24:'Wind Energy and Hydrogen Integration,'" in Proc. 18th World Hydrogen Energy Conf., 2010, pp. 1–9.
[17] K. W. Harrison, R. Remick, G. D. Martin, and A. Hoskin, "Hydrogen Production: Fundamentals and Cas Study Summaries e Preprint," 2010. [Online]. Available: http://www.osti.gov/bridge.
[18] A. Grant and B. Sagoo, "Hydrogen Assisted Renewable Power (HARP) Project in British Columbia," 2010.
[19] Hydrogenics, "Hydrogenics Awarded Hydrogen Fueling Station in Germany," Jun. 30, 2011. https://www.sec.gov/Archives/edgar/data/1119985/000117184311001927/newsrelease.htm (accessed May 30, 2022).
[20] J. Flynn and T. Iqbal, "Ramea Wind ! Hydrogen ! Diesel Project: System Description and Component Sizing," May 2007.
[21] "sunfire supplies Boeing with largest reversible solid oxide electrolyser/fuel cell system," Fuel Cells Bulletin, vol. 2016, no. 2, p. 1, Feb. 2016, doi: 10.1016/S1464-2859(16)70002-2.
[22] "Glencore RAGLAN Mine Renewable Electricity Smart-Grid Pilot Demonstration," *Government of Canada*, 2021. https://www.nrcan.gc.ca/science-and-data/funding-partnerships/funding-opportunities/current-investments/glencore-raglan-mine-renewable-electricity-smart-grid-pilot-demonstration/16662#shr-pg0 (accessed Mar. 20, 2022).
[23] Bright Green Hydrogen, "Levenmouth Community Energy Project." https://www.brightgreenhydrogen.org.uk/levenmouth-community-energy-project/ (accessed Mar. 20, 2022).
[24] F. Smeets and D. Thomas, "'HyBALANCE : state-of-the-art PEM electrolysis paving the way to multi-MW renewable hydrogen systems,'" 2017.
[25] ENEL, "Enel operates world's first 'Plug and Play' micro-grid powered by solar pv and hydrogen-based storage in Chile," Mar. 17, 2017. https://www.enel.cl/

en/meet-enel/media/news/d201705-enel-operates-worlds-first-plug-and-play-micro-grid-powered-by-solar-pv-and-hydrogen-based-storage-in-chile.html (accessed Mar. 20, 2022).

[26] MILAN & CALAMA, "EPS Commissioned for Enel the World's First 100% Emission-Free 'Plug and Play' Microgrid Powered by Solar PV and Hydrogen-Based Storage," *Businesswire*, Jun. 01, 2017. https://www.businesswire.com/news/home/20170601005635/en/EPS-Commissioned-for-Enel-the-World%E2%80%99s-First-100-Emission-Free-%E2%80%9CPlug-and-Play%E2%80%9D-Microgrid-Powered-by-Solar-PV-and-Hydrogen-Based-Storage (accessed Mar. 20, 2022).

[27] P. Bracher, "Foshan- the hydrogen technology city," *Meet Hydrogen*, Sep. 21, 2021. https://meethydrogen.com/resource/foshan-the-hydrogen-technology-city (accessed Mar. 20, 2022).

[28] J. Sampson, "Toyota to build $7.4m hydrogen hub," *Gasworld*, Mar. 19, 2019. https://www.gasworld.com/toyota-to-build-74m-hydrogen-hub/2016842.article (accessed Mar. 20, 2022).

[29] F. Tømmergaard, "Siemens Gamesa's groundbreaking pilot project hits key milestone as first green hydrogen is delivered to zero emission vehicles," Nov. 2021.

[30] T. Våland, W. Bartholdsen, M. Ottestad, and M. Våge, "Grimstad Renewable Energy Park 1. Project Goals And Technical Objectives 1.1 Norwegian National Centre for renewable energy," Grimstad, Norway.

[31] P. Bradwick, "Fuel Cell installation for the hybrid hydrogen mini-grid at the EETC, Rotherham," Fuel Cell System, Dec. 09, 2019. https://www.fuelcellsystems.co.uk/case-studies/blfuel-cell-installation-hybrid-hydrogen-mini-grid-eetc-rotherham (accessed Mar. 20, 2022).

[32] O. Taylan, R. Alamoudi, M. Kabli, A. AlJifri, F. Ramzi, E. Herrera-Viedma, Assessment of Energy Systems Using Extended Fuzzy AHP, Fuzzy VIKOR, and TOPSIS Approaches to Manage Non-Cooperative Opinions, Sustainability 12 (7) (Mar. 2020) 2745, https://doi.org/10.3390/su12072745.

[33] G. Budak, X. Chen, S. Celik, B. Ozturk, A systematic approach for assessment of renewable energy using analytic hierarchy process, Energy, Sustainability and Society 9 (1) (Dec. 2019) 37, https://doi.org/10.1186/s13705-019-0219-y.

[34] T.L. Saaty, Decision making with the analytic hierarchy process, International journal of services sciences 1 (1) (Jan. 2008) 83–98.

Arabian Journal of Geosciences (2023) 16:278
https://doi.org/10.1007/s12517-023-11369-2

ORIGINAL PAPER

Physical and numerical modelling of single tunnels under static loading conditions

Parvesh Kumar[1] **· Amit Kumar Shrivastava**[1]

Received: 31 May 2022 / Accepted: 18 March 2023
© Saudi Society for Geosciences and Springer Nature Switzerland AG 2023

Abstract

The continuous development of cities caused a deficiency of land in metro regions which arises various transportation problems. The construction of underground structures is extremely effective in solving these problems, as they have solved various traffic issues in significant urban areas. The main objective of the present study is to evaluate the extent of deformation experienced in single tunnel under the effect of static loading. In the present study, the extent of deformation is measured with the help of experimental investigation. Various single tunnel models are prepared in laboratory. The strength characteristic of the rock is varied and the cover depth of the tunnel models also varied as 30 mm and 50 mm. In case of lined samples, liner material is also introduced. The results obtained from physical modelling are further compared with the numerical modelling using ANSYS software. From the results, it can be concluded that the physical and numerical modelling results are in good agreement with each other. It is also observed that if the parameters are well selected for physical and numerical analysis, it can be an easy and less time-consuming method for finding out strength and deformation behavior for analysis and design of the tunnel. Therefore, it can be concluded that this methodology can be used for the safe and economical design of tunnels that are subjected to static loading conditions.

Keywords Physical modelling · Numerical analysis · Single tunnel · Deformation · Lining · Static loading

Introduction

In the transportation system, underground structures play a vital part. Various civil structures essentially depend on underground frameworks in metro areas, where there is an absence of ground space for moving vehicles. Underground structures are utilized for different purposes in civil engineering. The most remarkable of these structural designing uses is the utilization of the underground framework as the metro tunnels. Therefore, in the improvement of traffic problems, the development of underground constructions plays a vital role. Tunnels deformation mainly depends upon various types of loading, like static loading, dynamic loading or impact loading. It is hence very important to keep these underground structures safe from the burdens following up on them in field conditions. When a tunnel is constructed in weak rock, the primary motive should be to keep it protected from the stresses that act on it. It is undeniably challenging to decide the uprightness of passages at different areas because of the heterogeneous presence of the rock masses. The distortion might happen on the substance of the passage, sidewalls, or at the crown of the tunnel. It has been found from various analyses that the most extreme deformation would happen at the crown surface of the circular tunnel. A review on the adjustment movement of underground designs has been performed by different scientists. The effect of displacement on the tunnels with the help of experimental and numerical analysis is studied and found that the horizontal deformation in both modeling methods is similar but vertical displacement is more in case of physical investigation (Li et al., 2005). The study on jointed tunnel model of different dip angles is conducted with the help of experimental investigation which is further validated with the help of numerical modeling. The results obtained from the study shows that tensile cracks are experienced in tunnel models at low joint

Responsible Editor: Zeynal Abiddin Erguler

✉ Parvesh Kumar
parveshkumar_2k16phdce06@dtu.ac.in

Amit Kumar Shrivastava
aksrivastava@dce.ac.in

[1] Department of Civil Engineering, Delhi Technological University, Delhi, India

Published online: 29 March 2023

angle (Sagong et al., 2011). The failure of the weak rocks surrounding the tunnel primarily consists of shear wedge failure in the minimum principle stress direction which cause tunnel arch to collapse (Yingjie et al., 2014). The study conducted on brick lined tunnels under uniform static and concentrated loading shows that the model tests under concentrated load show more brittle behavior than under uniform load (Chen et al., 2016). The parametric study conducted on the lined and unlined tunnel under static and couple loading show that the displacement at the loading surface will increase with increase in the number of cycles (Mishra, 2019; Mishra et al., 2017). In case of shallow tunnels, the extent of damage under static and dynamic loading is maximum at the center of the tunnel axis and it keep on reducing towards the face of the tunnel (Mishra et al., 2018). The deformation in tunnels depends upon various factors such as the cover depth of tunnel, mechanical strength of the rock mass and the intensity of the drop load (Mishra et al., 2021; Kumar & Shrivastava, 2021). The cover depth of the tunnel plays an important role in the stability behavior of the tunnel. Rock tunnels models having lower cover depth is subjected to highest deformation whereas the extent of deformation in case of tunnel having higher cover depth is lowest (Sharma et al., 2018; Kumar & Shrivastava, 2019a; Ahmed & Iskander, 2012). Shallow tunnels are more vulnerable to damage as compared to deep tunnel. As the overburden depth of the tunnel increase, the effect of damage will decrease (Kumar, 2017a). A study conducted on the effect of joint at different dip angles in the tunnel models shows that incase of the higher dip angle the effect on the mechanical behaviour of tunnel is negligible (Yang et al., 2019). The settlement of ground surface of the tunnel decreases with increase in the relative density of sand (Sohaei et al., 2020). The value of the deformation is maximum at crossing positions of tunnel lining and is significantly affected by the magnitude and intensity of the dynamic load (Wang et al., 2020). The pattern of failure at the face of the tunnel in weak and strong rock is very different. In case of strong rock, tensile failure occurs at the tunnel face which is due to the tensile stresses acting on the tunnel face. Whereas in case of weak rocks, the failure occurs due to the overstresses of the rock mass at the tunnel face (Meguid et al., 2003). The interaction between the ground and tunnel under earth quake loading depends upon various factors such as magnitude and duration of earth quake, peak acceleration and the rigidity of tunnel and ground (Pakbaz & Yareevand, 2005). The stability behavior of tunnel mainly depends upon various factors such as type of section, type of loading overburden pressure etc. (Kumar & Shrivastava, 2017b; Kumar & Shrivastava, 2019b). There is a significant effect of discontinuities on the stability behavior of the tunnel structures. With the presence of discontinuities in the tunnel structures, the effect of deformation will be more (Manouchehrian & Cai, 2017). A study on circular tunnels under static and dynamic loads at different depths shows that the depth of the tunnel has a significant effect on the stability behavior (Mohammed, 2017). In case of tunnel constructed in the soil medium, the settlement behavior mainly depend upon the creep behavior of clay, the stiffness of soil and cohesion factor (Wang et al., 2012; Yang et al., 2020; Zhang et al., 2015). The effect of friction angle, lateral pressure in the settlement behavior of tunnel is also very significant (Idris et al., 2008; Idris et al., 2009; Jia & Tang, 2008; Alagha & Chapman, 2019). The study on the behavior of different shapes of twin tunnel in soft clay soil shows that a circular tunnel is the best shape of a twin tunnel in soft clay (Elshamy et al., 2013). The various factors such as variation in ground loss, depth of the tunnel and relative spacing between the tunnels significantly affects the stability behavior of tunnels (Mahalaxmi et al., 2012). Stress and displacement induced in tunnel lining were determined and from the results, it is concluded that the vertical displacement value obtained in the tunnel section is very large as compared to the horizontal deformation (Chou & Bobet, 2002). The shear behavior of in filled rock joints is dependent upon the thickness of the infill material (Shrivastava & Rao, 2011; Shrivastava & Rao, 2015; Shrivastava & Rao, 2018). The tunnels in the jointed rock are highly susceptible to earthquake loads and with an increase in lateral stress coefficient the deformation around the tunnel increase (Varma et al., 2019). With an increase in the width and eccentricity of shallow footing, there is an increase in the stress values which ultimately affect the stability behavior of tunnel (Panji et al., 2016). A study conducted on the response of different shapes of the tunnels under the effect of dynamic loading shows that D-shaped tunnel sections experienced more deformation as compare to circular tunnel section (Dhamne et al., 2018). A comparative study on the deformation behavior of single and twin tunnels under static loading conditions concluded that the extent of deformation in tunnels mainly depends upon the unconfined compressive strength of the model material (Kumar & Shrivastava, 2022). A study conducted on the crack inclination in tunnel model shows that the critical compressive stress varies with the angle of inclination of the crack (Zhu et al., 2015; Zhang et al., 2019). A study conducted on the effect of discontinuities on deformation behavior of tunnels shows that there is a significant effect of discontinuities on the stability behavior of the tunnel structures (Manouchehrian & Cai, 2017). The study conducted on different cross sectional shape of the tunnel, i.e., circular section and semi elliptical shape tunnel shows that the circular tunnel shows less deformation as compared to the semi elliptical shape tunnel section (Jose & V, A., 2018). A study conducted on deformation behavior of utility tunnels under the effect of surface explosion conditions concluded that with an increase in the primary reinforcement ratio of utility

tunnels, there is a decrease in the deflection response of the tunnel as a result it will increase the blast resistance of the utility tunnel. It can also be concluded that with an increase in the wall thickness and depth of the tunnel there is a decrease in the extent of damage in the utility tunnels (Qian et al., 2021).

The main objective of the study is to determine the extent of deformation in tunnel lining when the tunnel model is subjected to static loading conditions. For that, the rock tunnel models are casted in the laboratory and then these tunnel models are tested under static loading conditions. The rock strength characteristics of the tunnel model are varied and the cover depth of the tunnel also changes as 30 mm and 50 mm. Then the results obtained from the experimental investigation are further compared with the numerical modeling using ANSYS software.

Model material characterization and geometry

In the present study, three mix-materials are used as model material based on strength parameters. All the three mix-material have different strength characteristics. The material used in this study is selected according to their stress-strain and ductile behavior. For the preparation of single tunnel models, a synthetic rock mass is prepared in the laboratory. For the preparation of tunnel samples, POP, Kalonite clay and Yamuna sand are mixed in different proportions to make a synthetic rock mass and mixed material are named as MM-1, MM-2, and MM-3. The purpose of varying the proportions of these materials is to vary the rock strength parameters. The different proportions of the materials are discussed in Table 1. The water content ratio is kept same, i.e., 60% by the weight of the material in all the three model materials (Rao, 2013; Niktabar et al., 2018). For the first sample, 100% of Plaster of Paris is mixed by keeping the water powder ratio as 0.6. In the second tunnel model (MM-2), 50% of Plaster of Paris along with 40% of Sand and 10% of clay is used to prepare tunnel samples. In the third tunnel model (MM-3), 50% of Plaster of Paris along with 30% of Sand and 20% of clay is used to prepare tunnel samples. The ratio of the mix materials is kept (1.0: 0.8: 0.2) (POP, Sand and Clay respectively) for MM-2 synthetic material whereas for the MM-3 tunnel model the ratio is kept (1.0: 0.6: 0.4). The proportion of the material is shown in Table 1.

Table 1 Composition of the Mix Material (MM) used for making tunnel models

Synthetic material	POP	Sand	Clay	Water Content	Proportion Ratio
MM-1	100%	-	-	60%	(1: 0: 0)
MM-2	50%	40%	10%	60%	(1: 0.8: 0.2)
MM-3	50%	30%	20%	60%	(1: 0.6: 0.4)

To determine the physical and mechanical properties of model materials, specimens of L/D ratio of 2 are casted and tested in the laboratory. The index properties of all the three model materials are summarized in Table 2. From the experimental test results, it is observed that the sample made from MM-1 material have the highest strength whereas MM-3 material has the lowest strength. It is also observed from the experimental results that as the percentage of clay content increases there is a decrease in the strength as a result, the stress-strain behavior of the material also changes. As the amount of POP is reduced in the sample its strength will also get reduced and the material will attain elasto-plastic behavior. Therefore, MM-1, MM-2, and MM-3 model material are finalized. After determining the engineering properties of all the three model materials, they are classified according to Deere Miller classification. Based on the Deere miller classification all the three model materials are classified as EM, i.e., medium elastic rock. As all the three-model material has compressive strength more than 1 MPa, therefore, they can be classified as a general rock structure. Hence this rock structure can be simulated with actual tunnel engineering structure in weak rock. The stress-strain behavior of the all three model materials with the help of curves is shown in Fig. 1.

After the determination of basic engineering properties of model material, the geometric dimensions of the model material are determined in order to simulate a single tunnel with surrounding rock mass. The boundary conditions and stress distribution around the circular opening determine geometry of the tunnel model. The single tunnel model dimensions have been fixed as 300×250×230 mm (LxWxH) and the diameter of tunnel is decided as 50 mm as shown in Fig. 2. Two separate cover depths, i.e., 30 mm and 50 mm are tested for single tunnel specimens. The tunnel is length is kept same as the rock tunnel model length, which is 300 mm. The width of the tunnel sample is kept 250 mm (r=4a, where "a" is the radius of the tunnel and "r" is radial

Table 2 Properties of different model materials

Properties	MM-1	MM-2	MM-3	Testing method
Dry Density (KN/m^3)	12.20	11.6	10.3	ISRM (1977)
UCS (MPa)	10.7	7.5	5.9	ISRM(1979)
Specific Gravity	2.60	2.4	2.2	IS(4031,1995)
Modulus E_{t50} (MPa)	2500	1800	1600	ISRM (1979)
Tensile Strength (MPa)	0.78	0.56	0.38	IS:10082(1981)
Poisson Ratio	0.22	0.19	0.16	ISRM (1979)
Deere–Miller Classification	EM	EM	EM	

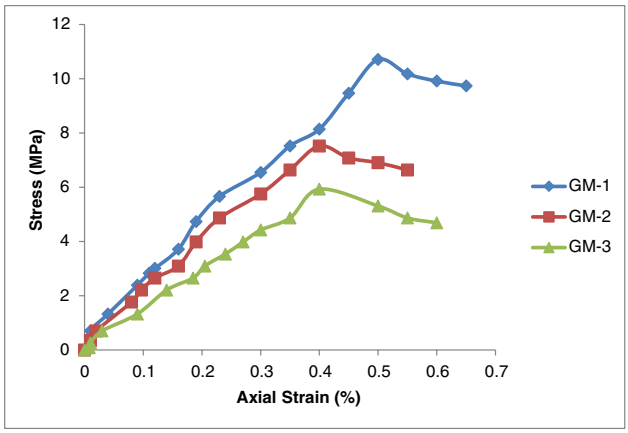


Fig. 1 Stress-strain curve for all three model materials

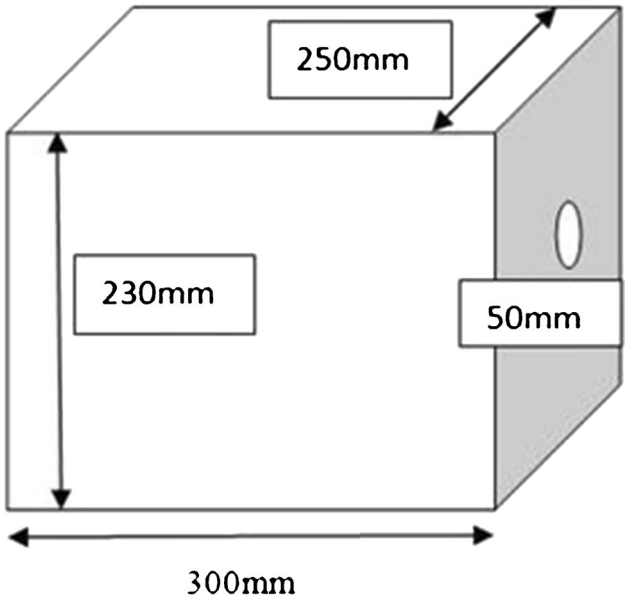


Fig. 2 Single tunnel model dimension

distance). For lined tunnel models, PVC pipe is used as a liner material. The liner material has a thickness of 1.78 mm. The methodology to predict the deformation can be adopted in the field as the scaling law is followed in the present work. The dimension of the tunnel model is decided according to (r=4a) where the "r" is the radial distance and "a" is the radius of the tunnel. PVC pipe has a Young's Modulus of 4900 MPa. PVC pipe material is used due to its high Young's Modulus value. PVC lining is selected due to its high young's modulus value so that the ratio of elastic modulus of lining material to elastic modulus of surrounding rock should be kept similar to that of actual field conditions in order to maintain a similarity ratio. The single tunnel models of three different materials (MM-1, MM-2, and MM-3) are casted in the laboratory for physical modeling after the geometric dimension is determined.

Physical modeling of single tunnel

In the present study, single tunnel samples of various cover-depths and material are tested under the static loading conditions in compression testing machine. In the field conditions, it is not possible to perform the tests to determine the deformation behaviour of the tunnel. Hence, rock tunnel samples of different materials as dissucced in Table 1 and different cover depths are prepared in the labouratory. Then these rock tunnel models are tested under compression loading. The results obtained from the tests are compared with the results of numerical analysis. Physical modeling is considered as a reliable method to predict the behaviour of engineering structures as it gives a close idea about it. Therefore, physical modelling is very commonly used in the present time.

In this study, Chennani-Nashri tunnel is taken as a prototype. The properties of Chennani-Nashri tunnel are taken to fix the dimension of the model. In this study, the ratio of elastic modulus of lining material to the elastic modulus of surrounding rock mass (E_{lining}/E_{rock}) is kept fixed for the laboratory models so that they can represent the actual field conditions. The rock mass present in the Chennani-Nashri tunnel consists of sandstone and siltstone. The elastic modulus of sandstone is reported as 15 GPa, whereas the shotcreting is done using M30 grade concrete, whose value of elastic modulus is 28 GPa. Therefore, it is found that the elastic modulus ratio (E_{lining}/E_{rock}) is 1.9 for field conditions (Mishra et al., 2018).

$$\left(E_{Lining}/E_{Rock}\right)_{Field} = \left(E_{Lining}/E_{Rock}\right)_{Physical\ Model} = 1.9 \quad (1)$$

Development of the testing facility

For testing rock tunnel models under static loading conditions, a digital compression testing machine was designed and built. The dimensions of the various sections of the testing machine are determined by the scale of the testing tunnel models. The scale of the platens, as well as the vertical clearance between the two elements, is determined by the tunnel sample size. The apparatus is made up of three main components: a load frame, a pumping unit mounted to the right side of the loading frame, and a data acquisition device for recording deformation. The loading unit has a capacity of 0–2000kN, with a minimum count of 0.1kN up to 200Kn and 1Kn above 200Kn. The load applied has an accuracy of less than (+/−) 1% of the load indicated. The AI8000+ data acquisition system, which is a multi-point data acquisition and control system that is microprocessor based and

computer compatible, was used in this testing facility. This gadget serves as a calculator as well as a display. With great success, it has been used to measure multiple analogue sensors and inputs, pulse train input and digital inputs, and control through digital and analogue outputs. Eight of the 12 channels are dedicated to LVDTs, two to load sensors, and the other two are left open for some other form of communication. The output signal is connected to the CPU through a cable wire, which is used to transmit data in the form of load and deformation to the desired location of the CPU. This application can keep track of the testing process and save the results.

Testing procedure

In the present study, the rock tunnel models of three different materials, i.e., MM-1, MM-2, and MM-3 are prepared in the labouratory. The purpose of selecting three different materials for preparing tunnel samples is to vary the strength characterstics of the rock. 36 models of single tunnel are prepared in this study of varying cover depths and strength parameters. The curing time of the rock-tunnel model is kept as 28 days in the present study. In some models, liner material is used in the form of PVC pipe. The dimension of all the samples is kept as 300×250×230 mm (LxWxH) which is decided according to the bourndary conditions. The cover depth of the samples is varied as 30 mm and 50 mm. Various tunnel models prepared in the labouratory are shown in Fig. 3. After preparing the rock tunnel models, these samples are tested under static loading conditions in compression testing machine. To evaluate the extent of the deformation in the tunnel samples, LVDT's are used. LVDT's are placed in the samples along the tunnel axis in three different locations. The location are selected according to the extent of damage along the tunnel axis. The location where the LVDT's are placed in the tunnel samples are L/3,L/2 and 7L/12 where "L" is the length of the tunnel (Niktabar et al., 2018). To place the LVDTs inside the rock tunnel models, the samples are drilled from the bottom at three different locations. After the drilling, LVDTs are fixed inside the tunnel samples with the help of a three-pin clamp. After placing the LVDTs inside the single tunnel models, the samples are tested under static loading conditions. Figure 4 shows the arrangement of LVDT's inside the rock tunnel model. After fixing the LVDTs inside the tunnel samples, these samples are tested under compression testing machine as shown in Fig. 5. The static loading is applied on the top surface of the tunnel sample and the deformation experienced along the length of the tunnel is recorded with the help of the LVDT data acquisition system. The schematic diagram of point load applied on a single tunnel model is shown in Fig. 6.

Numerical modelling of single tunnel

In the present study, the numerical analysis of the single tunnel is done by using ANSYS software. Different models of varying parameters are modeled to assess the extent of deformation in the single tunnels. Because of the various problems occuring in the field conditions, it is very difficult to perform field tests. In that situation, numerical analysis can be proven as a reliable method to assess the damage in the tunnel. The geometry of the single tunnel model is kept same as adopted in the physical mdelling, i.e., 300×250×230 mm. Various strength properties are given to the single tunnel models as discussed in Table 1. Then, the cover depth of the tunnel is varied as 30 mm and 50 mm in tunnel samples. The liner properties is also given to the single tunnel. Then, the tunnel model is subjected to static loading conditions.



Fig. 3 Preparation of tunnel samples

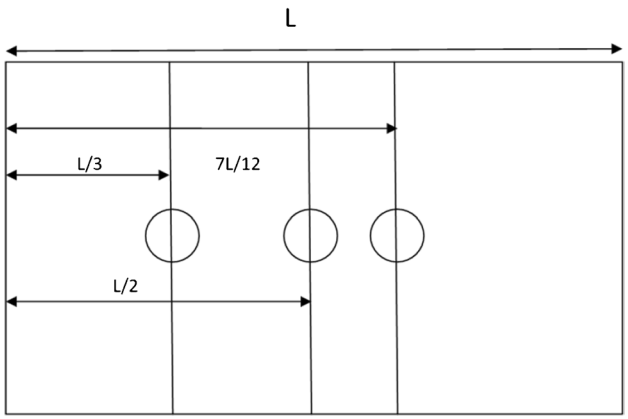


Fig. 4 Arrangement of LVDTs in tunnel sample



Fig. 5 Tunnel sample subjected under static loading condition

Load and boundary conditions

In the present study, the tunnel is subjected to static loading conditions by applying the load from the top of the tunnel model. The load is applied in the form of pressure. A steel patch of depth 60 mm and diameter 50 mm is kept at the top surface of the tunnel sample then the load is transferred on the tunnel axis with the help of this steel patch as shown in Fig. 7. The boundary conditions of the tunnel model for numerical analysis are decided according to the boundary convergence study. The base of the single tunnel model is kept fixed and all other faces are kept free for the deformation.

Meshing

In the numerical analysis of a single tunnel, the meshing is the most critical part. In the present study, a mess convergence analysis is carried out to determine the meshing size of the different regions of the tunnel model. The mesh density can be easily determined using the mesh convergence study. In case of a single tunnel sample, a global meshing size for the rock mass is taken as 8 mm based on the mesh convergence study. Mesh convergence studies have shown that in the case of a single tunnel sample, mesh size finer than 8 mm have very less effect on the tunnel deformation. The mass density of the steel patch which is place at the top of the tunnel model is kept as 6 mm. For the tunnel samples having the liner material, the global mesh size for the PVC pipe is kept as 6 mm. Meshing is an important factor for numerical analysis purpose as it decides the size and number of elements and nodes build in tunnel sample and lining part. Rock tunnel model in case of single tunnel sample comprises of 160578 elements and 78678 nodes, including 3658 nodes and 2200 elements for tunnel lining. Figure 8 shows the meshing of various elements. For the boundary conditions of the tunnel models, a trail on various tunnel models has been done to examine the effect of the static loading on the deformation of the tunnel. From the results, it is noticed that when the boundary condition is fixed as "r=4a" the effect of back propagation is negligible also the bottom side of the tunnel model is kept fix and the side surface of the tunnel model is kept free for displacement.

Results and discussion

Experimental results

After conducting experimental and numerical analysis on both lined and unlined tunnels, the results are analysed. In case of physical modelling, it has been noted that the maximum deformation is experienced in case of unlined tunnels samples of MM-3 having 30 mm cover depth. The maximum deformation is obtained at L/2 distance i.e at the centre of the tunnel lining. The extent of deformation is keep on decreasing towards the face of the tunnel and its value becomes zero at the end faces of the tunnel in all the cases. In case of MM-3 material the deformation obtained in unlined samples having 30mm coverdepth at distance L/2 is 0.29 mm as shown in Fig. 9.Whereas in case of lined samples of same material having 30 mm coverdepth, the deformation obtained at L/2 is 0.14 mm. Similarly deformation obtained in case of 50 mm coverdepth unlined samples of MM-3 material at distance L/2 is 0.21 mm whereas the deformation obtained in case of 50 mm lined samples is 0.11 mm at L/2. The longitudinal crack length varies from 6.8 to 7.2 cm for C/D = 1.0, from 7.0 to 7.8 cm for C/D = 0.6.

Similarly in case of MM-2 tunnel samples the deformation for at L/2 distance in case of 30mm cover depth unlined samples is 0.25 mm. The maximum deformation recorded at the center of the tunnel in case of 30 mm lined sample of similar material is 0.12

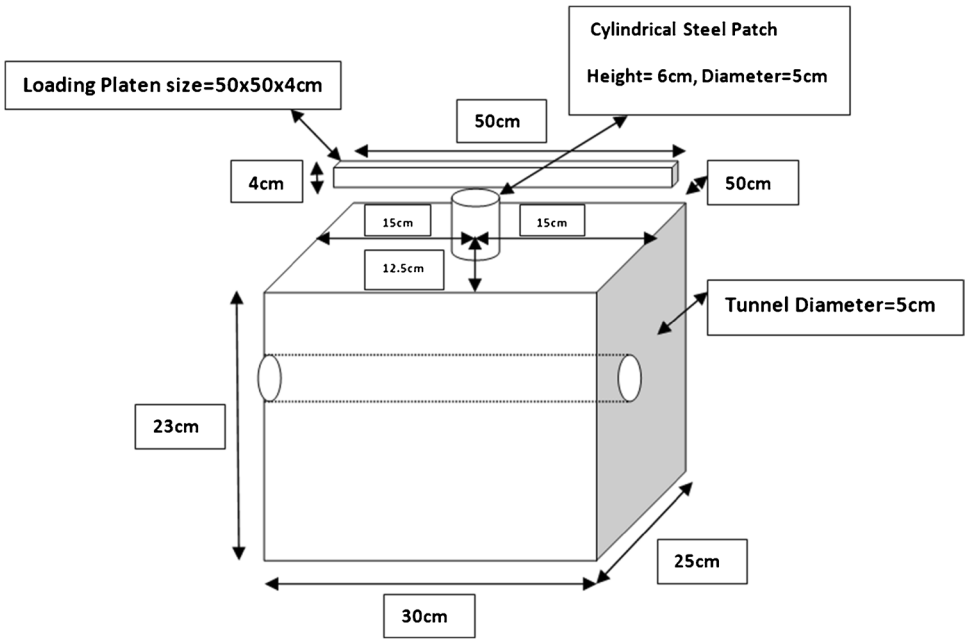


Fig. 6 Schematic diagram of the static load acting on a single tunnel model

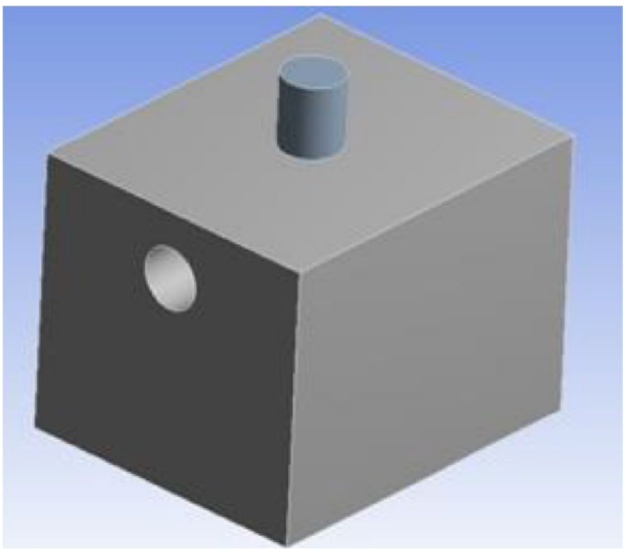


Fig. 7 Load applied on the tunnel sample

mm. Similarly deformation obtained in case of 50 mm coverdepth unlined samples of MM-2 material at distance L/2 is 0.19 mm whereas the deformation obtained in case of 50 mm lined samples is 0.10 mm at L/2 respectevely. The graph for deformation in case of MM-2 tunnel sample is shown in Fig 10. In MM-2 model material, longitudinal crack length varies from 6.2 cm to 6.6 cm for C/D = 1.0, from 6.5 cm to 6.8 cm for C/D = 0.6.

The least deformation is obtained in case of MM-1 samples because of its high compressive strength properties. The maximum deformation recorded at the center of the tunnel in case of 30 mm unlined sample of MM-1 material is 0.20 mm. Whereas in case of lined samples of same material having 30 mm coverdepth, the deformation obtained at L/2 is 0.085 mm. Similarly maximum deformation obtained in case of 50 mm coverdepth unlined samples of MM-1 material at distance L/2 is 0.155 mm whereas the deformation obtained in case of 50 mm lined samples is 0.07 mm at L/2 respectevely. In MM-1 model material, longitudinal crack length varies from 5.50 to 5.8 cm for C/D = 1.0, from 5.6 to 6.0 cm for C/D = 0.6. The graph for deformation in case of MM-1 tunnel sample is shown in Fig. 11.

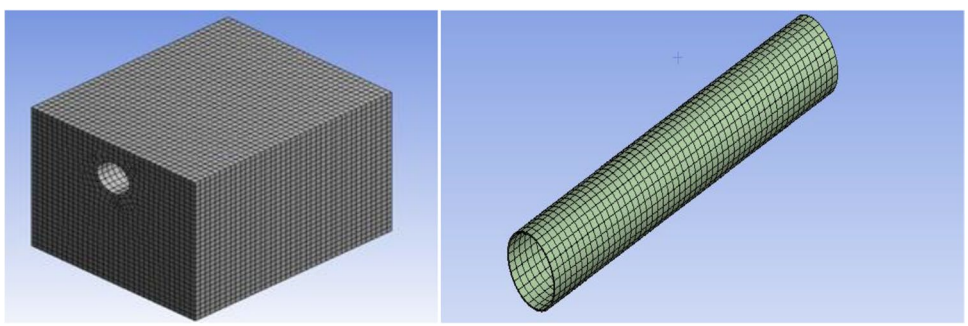


Fig. 8 Meshing of various elements

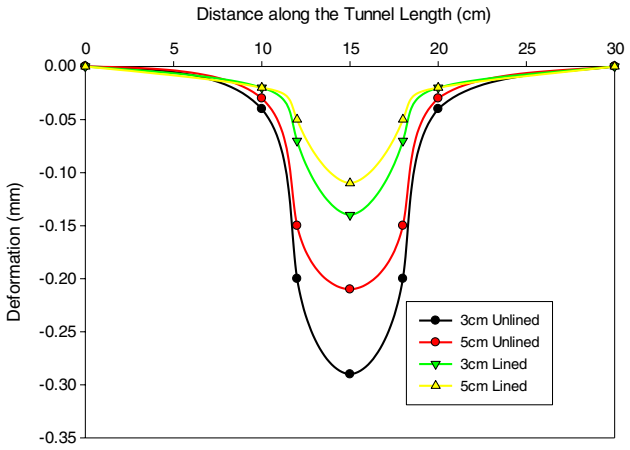


Fig. 9 Tunnel deformation profile of MM-3 samples obtained from experimental tests

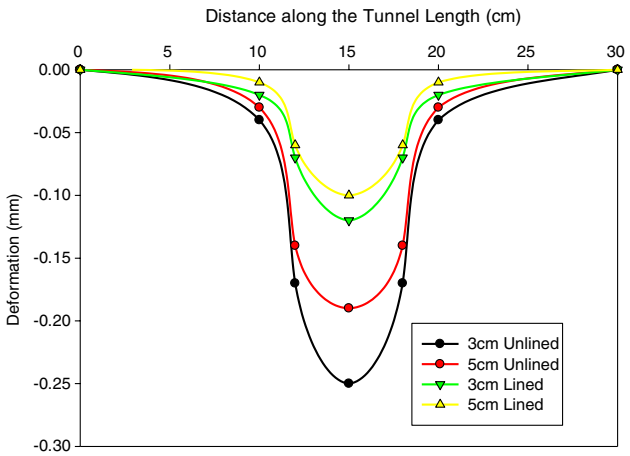


Fig. 10 Tunnel deformation profile of MM-2 samples obtained from experimental tests

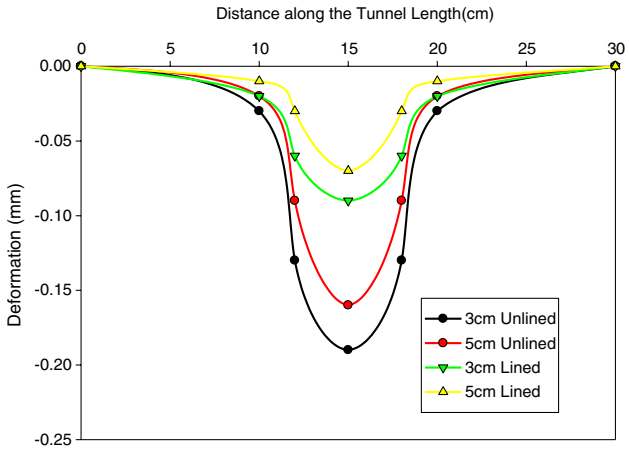


Fig. 11 Tunnel deformation profile of MM-1 sample obtained from experimental tests

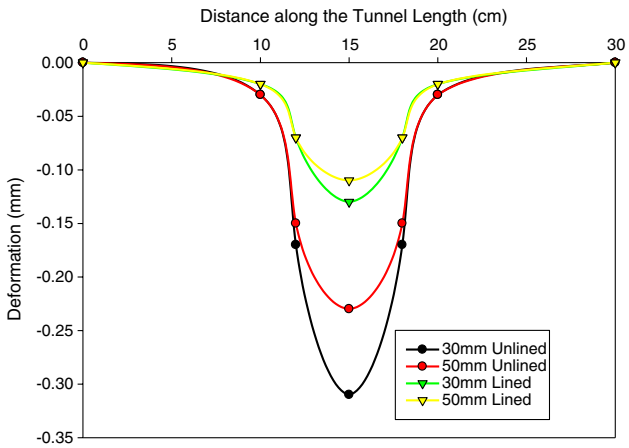


Fig. 12 Tunnel deformation profile of MM-3 obtained from numerical analysis

Numerical analysis results

After conducting numerical analysis on single tunnels samples,the various results are obtained which are further analysed and compared with experimental modelling. In case of numerical modelling the maximum deformation is obtained in MM-3 samples. In unlinled tunnels having 30 mm cover depth prepared from MM-3 material, the maximum deformation obtained at L/2 is 0.31 mm whereas the deformation obtained at L/2 distance in case of 50mm unlined sample is ase of physical modelling, it has been noted that the maximum deformation is experienced in 0.23 mm. In case of lined tunnel samples of MM-3 material the maximum deformation obtained at L/2 distance in 30 mm coverdepth is 0.13 mm whereas in case of 50 mm cover depth the deformation obtained is 0.11 mm. The graph obtained between the length of the tunnel and deformation for MM-3 material is shown in Fig. 12.

In case of MM-2 tunnel samples, the deformation for at L/2 distance in case of 30 mm cover depth unlined samples is 0.27 mm . The maximum deformation recorded at the center of the tunnel in case of 50 mm unlined sample of is 0.21 mm. Whereas in case of lined samples of same material having 30 mm coverdepth, the deformation obtained at L/2 is 0.12 mm and deformation obtained in case of 50 mm coverdepth lined samples of MM-2 material at distance L/2 is 0.10 mm. The graph obtained between the length of the tunnel and deformation for MM-2 material is shown in Fig. 13. For the single tunnel sample prepared from MM-1 material, the graph obtained between the length of the tunnel and deformation is shown shown in Fig. 14. In case of MM-1 sample the minimum deformation is recorded. The deformation recorded at L/2 distance in case of 30 mm unlined samples is 0.22 mm whereas for 50 mm unlined samples the deformation at L/2 is 0.17 mm. In case of lined samples the deformation obtained

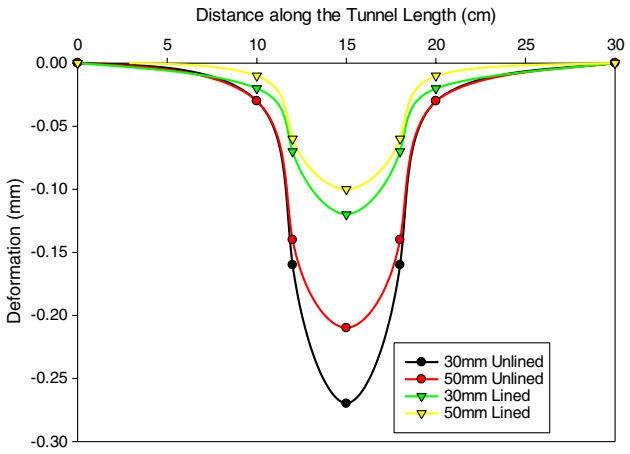


Fig. 13 Tunnel deformation profile of MM-2 samples obtained from numerical analysis

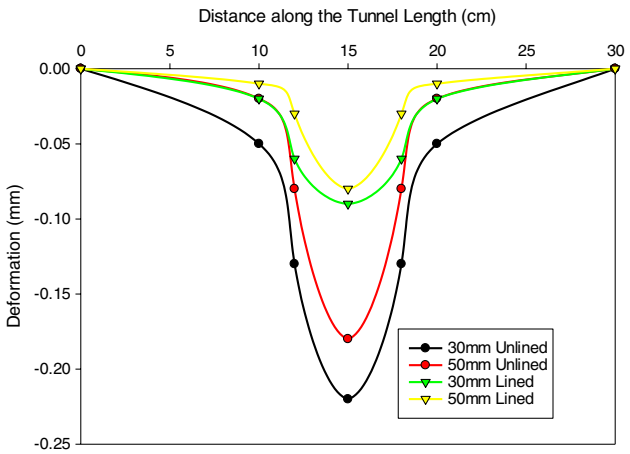


Fig. 14 Tunnel deformation profile of MM-1 samples obtained from numerical analysis

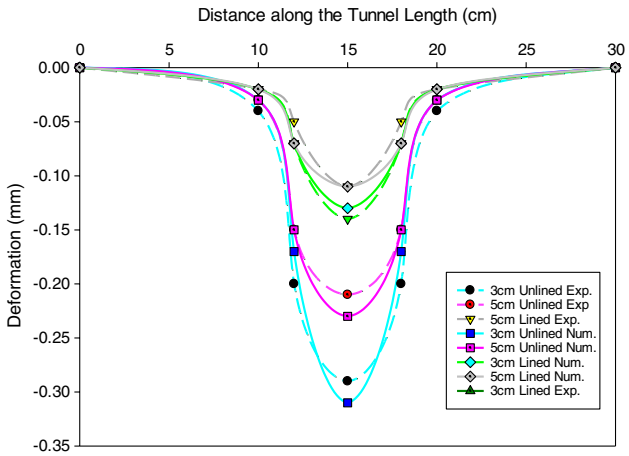


Fig. 15 Comparison of deformation profile obtained from experimental and numerical modelling of single tunnel of MM-3 material

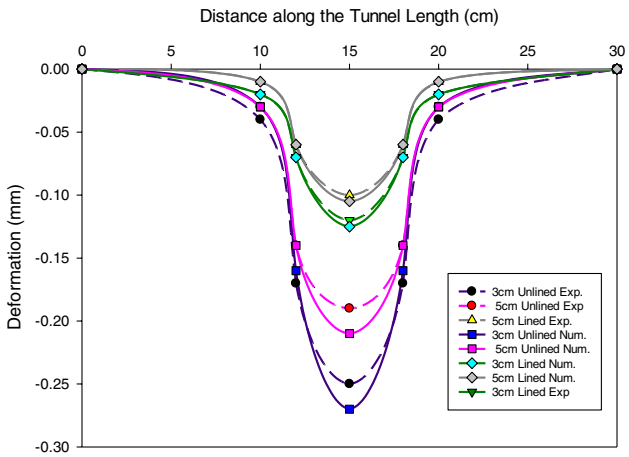


Fig. 16 Comparison of deformation profile obtained from experimental and numerical modelling of single tunnel of MM-2 material

for 30 mm coverdepth sample at L/2 is 0.09 mm whereas the deformation is 0.08 mm for 50 mm lined samples.

After conducting the experimental and numerical analysis on single tunnel of three different materials, a combined deformation graph is obtained. A comparison of deformation profiles obtained from experimental and numerical results for MM-3 material is shown in Fig. 15. Based on the results obtained from both methods, it can be concluded that for unlined tunnels the difference in the deformation varies from 5 to 8% whereas in case of lined tunnel the difference varies within 10% which is quite acceptable. Similarly, the comparison of deformation profiles for experimental and numerical results in case of MM-2 and MM-1 material is shown in Fig. 16 and Fig. 17 respectively. So from the results, it can be concluded that the experimental and numerical modelling results are in good agreement with each other.

Conclusion

A comparative study is carried out in this paper to study the deformation behavior of single tunnels with the help of experimental investigation and numerical analysis. Various unlined and lined single tunnels models are prepared in the labouratory with varying strength properties and cover depth. These tunnel samples are tested in labouratory under static loading conditions and the results are analysed. For the numerical analysys, similar tunnel are developed with the help of ANSYS software and subjected under similar loading conditions. From the results, it can be concluded that there are various factors which affects the deformation behavior of single tunnels. Some of major factors factors are strength properties of rock, cover depth of tunnel, and presense of liner material. With increase in the strength properties of rock, the extent

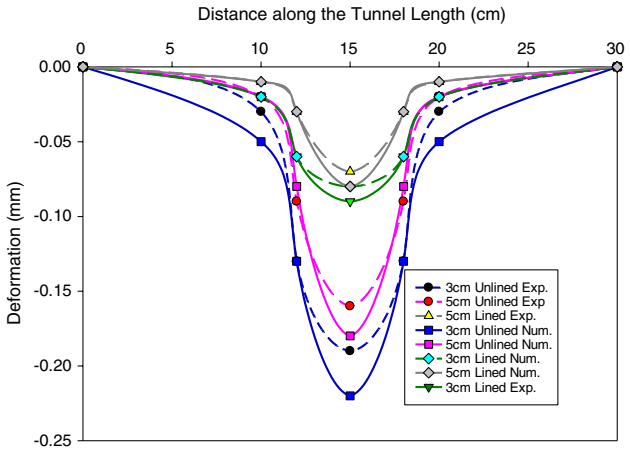


Fig. 17 Comparison of deformation profile obtained from experimental and numerical modelling of single tunnel of MM-1 material

of deformation decreases. The deformation along the tunnel axis also decreases with increase in the cover depth of tunnel. Following conclusion can be made from the results obtained from experimental and numerical modelling.

1. The deformation obtained in unlined tunnel samples of single tunnels of MM-1 and having 30 mm cover depth is 0.20 mm at L/2 distance in experimental investigation. Whereas in case of numerical analysis, the deformation obatined at L/2 distance for the same sample is 0.22 mm. In case of lined tunnel samples of single tunnels of MM-1 material and having 30 mm cover depth is 0.085 mm at L/2 distance in experimental investigation. Whereas in case of numerical analysis, the deformation obatined at L/2 distance for the same sample is .09 mm. Therefore the difference in the variation in defromation varies from 5 to 12%. With shows the experimental and numerical results are in close agreement with each other.
2. The deformation obtained in unlined tunnel samples of MM-2 material and having 30mm cover depth is 0.25 mm L/2 distance in experimental investigation. Whereas in case of numerical analysis, the deformation obatined at L/2 distance for the same sample is 0.27 mm. In case of lined tunnel samples of single tunnels of MM-2 material and having 30 mm cover depth is 0.12 mm L/2 distance in experimental investigation. Whereas in case of numerical analysis, the deformation obatined at L/2 distance for the same sample is 0.12 mm respectively. The difference varies from 7 to 9%, which shows the experimental and numerical results are in close agreement with each other.
3. The deformation obtained in unlined tunnel samples of MM-3 material and having 30mm cover depth is 0.29 mm at L/2 distance in experimental investigation. Whereas in case of numerical analysis, the deformation obatined at L/2 distance for the same sample is 0.31 mm respectively. In case of lined tunnel samples of single tunnels of MM-3 material and having 30 mm cover depth is 0.14 mm at L/2 distance in experimental investigation. Whereas in case of numerical analysis, the deformation obatined at L/2 distance for the same sample is 0.13 mm. The difference in the variation in defromation varies from 5 to 8%.
4. The extent of deformation in tunnels mainly depends upon the unconfined compressive strength of the model material. The UCS value of MM-2 material is 29.90% less than UCS value of MM-1. Therefore, the deformation in 30 mm and 50 mm cover depth unlined tunnels of MM-2 material is 20% and 18.42% respectively more than from that obtained in 30 mm and 50 mm unlined tunnels of MM-1 material. Similarly, the UCS value of MM-3 is 44.85% less than the UCS value of MM-1. Therefore deformation in unlined tunnels of MM-3 material having 30 mm and 50 mm cover depth is 31.03% and 26.19% respectively more than from that obtained in 30 mm and 50 mm unlined tunnels of MM-1 material.
5. The study can be extended to determine the deformation behavior of single tunnels under jointed rock conditions. In the present study, the deformation behavior of the tunnel is determined under shallow depths. But in the future scope, the deformation behavior of deep tunnels can be predicted.
6. In the present study, the main focus is on the Load-Deformation behavior of single tunnel under static loading conditions and how the deformation behavior of the tunnel varies when subjected under static loading conditions. Determination of stress distribution around the opening can be done in the future scope of the work.

Author contribution P.K., performed and processed the experimental work; P.K., writing original draft; A.K.S., supervision; P. K investigation and methodology; A.K.S; review, writing and finalized the final draft for submission and publication. Both authors have read and agreed to the published version of the manuscript.

Funding information This research work is funded and supported by Delhi Technological University, Delhi. The authors would like to thank Delhi Technological University for its financial support.

Data availability Data sharing is not applicable to this article.

Declarations

Conflict of interest The authors declare no competing interests.

References

Ahmed M, Iskander M (2012) Evaluation of tunnel face stability by transparent soil models. Tunn Undergr Space Technol 27:101–110

Alagha ASN, Chapman DN (2019) Numerical modelling of tunnel face stability in homogeneous and layered soft ground. Tunn Undergr Space Technol 94:103096

Chen HM, Yu HS, Smith MJ (2016) Physical model tests and numerical simulation for assessing the stability of brick-lined tunnels. Tunn Undergr Space Technol 53:109–119

Chou WI, Bobet A (2002) Predictions of ground deformations in shallow tunnels in clay. Tunn Undergr Space Technol 17(1):3–19

Dhamne R, Mishra S, Kumar A, Rao KS (2018) Numerical Study of the Cross Sectional Shape of Shallow Tunnels Subjected to Impact and Blast Loading. J Eng Geol 3(1-2):23–37

Elshamy EA, Attia G, Fawzy H, Hafez KA (2013) Behaviour of Different Shapes of Twin Tunnels in Soft Clay Soil. Int J Eng Innov Technol 2(7):297–302

Idris J, Verdel T, Al-Heib M (2008) Numerical modelling and mechanical behaviour analysis of ancient tunnel masonry structures. Tunn Undergr Space Technol 23:251–263

Idris J, Al-Heib M, Verdel T (2009) Numerical modelling of masonry joints degradation in built tunnels. Tunn Undergr Space Technol 24:617–626

Jia P, Tang CA (2008) Numerical study on failure mechanism of tunnel in jointed rock mass. Tunn Undergr Space Technol 23:500–507

Jose J, V, A. (2018) Numerical study of the cross-sectional shape of tunnel under blast effect using ansys. Int J Eng Res Technol 5(5):3582–3586

Kumar P, Shrivastava AK (2017a) Damage Detection in Shallow Tunnels Using 3D Numerical Modelling. In: International Conference on Advancements and Innovations in Civil Engineering 177–181

Kumar P, Shrivastava A (2017b) Various factors affecting stability of underground structures: State of Art. In: 7th Indian Rock Conference. 576–580

Kumar P, Shrivastava AK (2019a) Deformation Behaviour of Tunnels under Different Loading Conditions: State of Art. In: Proceedings of the 4th World Congress on Civil, Structural, and Environmental Engineering. 1–5

Kumar P, Shrivastava AK (2019b) Stability of single tunnel in rock under static loading conditions. In: 8th Indian Rock Conference 424–429

Kumar P, Shrivastava AK (2021) Physical Investigation of Deformation Behaviour of Single and Twin Tunnel under Static Loading Condition. Appl Sci 11:1–18

Kumar P, Shrivastava AK (2022) Experimental and Numerical analysis of deformation behaviour of Tunnels under static loading conditions. Sustain Energy Technol Assess 52:102057

Li Z, Liu H, Dai R, Su X (2005) Application of numerical analysis principles and key technology for high fidelity simulation to 3-D physical model tests for underground caverns. Tunn Undergr Space Technol 20(4):390–399

Mahalaxmi S, Hema H, Shetty AM, Sanjay B, Srilatha N, Kumar D (2012) Numerical Analysis of Interaction between Twin-Tunnels with Horizontal Alignment. In: Proceedings of International Conference on Advances in Architecture and Civil Engineering 21:247–249

Manouchehrian A, Cai M (2017) Analysis of rockburst in tunnels subjected to static and dynamic loads. J Rock Mech Geotech Eng 9:1031–1040

Meguid MA, Rowe RK, Lo KY (2003) Three dimensional analysis of unlined tunnels in rock subjected to high horizontal stresses. Can Geotech J 40:1208–1224

Mishra S (2019) Physical and numerical modeling of tunnels under blast and impact loads. Dissertation, Indian Institute of Technology, Delhi, India

Mishra S, Rao KS, Gupta NK, Kumar A (2017) Damage to Shallow Tunnels under Static and Dynamic Loading. Procedia Eng 173:1322–1329

Mishra S, Rao KS, Gupta NK, Kumar A (2018) Damage to shallow tunnels in different geomaterials under static and dynamic loading. Thin Wall Struct 126:138–149

Mishra S, Kumar A, Rao KS, Gupta NK (2021) Experimental and numerical investigation of the dynamic response of tunnel in soft rocks. Structures 29:2162–2173

Mohammed J (2017) Numerical Modelling for circle tunnel under static and dynamic loads for different depth. Research Journal of Mining 1(1):1–11

Niktabar SMM, Rao KS, Shrivastava AK (2018) Automatic Static and Cyclic Shear Testing Machine under Constant Normal Stiffness Boundary Conditions. Geotech Test J 41(3):508–525

Pakbaz MC, Yareevand A (2005) 2-D analysis of circular tunnel against earthquake loading. Tunn Undergr Space Technol 20:411–417

Panji M, Koohsari H, Adampira M, Alielahi H, Marnani JA (2016) Stability analysis of shallow tunnels subjected to eccentric loads by a boundary element method. J Rock Mech Geotech Eng 8:480–488

Qian H, Zong Z, Wu C, Li J, Gan L (2021) Numerical study on the behavior of utility tunnel subjected to ground surface explosion. Thin-Walled Structures 161:107422

Sagong M, Park D, Yoo J, Lee JS (2011) Experimental and numerical analyses of an opening in a jointed rock mass under biaxial compression. Int J Rock Mech Min Sci 48:1055–1067

Sharma H, Mishra S, Rao KS, Gupta NK (2018) Effect of cover depth on deformation in tunnel lining when subjected to impact load. In: ISRM International Symposium - 10th Asian Rock Mechanics Symposium, ARMS

Shrivastava AK, Rao KS (2011) Shear behaviour of non planar rock joints. In: 14th Asian Regional Conference on Soil Mechanics and Geotechnical Engineering

Shrivastava AK, Rao KS (2013) Development of a large-scale direct shear testing machine for unfilled and infilled rock joints under constant normal stiffness conditions. Geotech Test J 36(5):670–679

Shrivastava AK, Rao KS (2015) Shear Behaviour of Rock Joints Under CNL and CNS Boundary Conditions. Geotech Geol Eng 33:1205–1220

Shrivastava AK, Rao KS (2018) Physical Modeling of Shear Behaviour of Infilled Rock Joints Under CNL and CNS Boundary Conditions. Rock Mech Rock Eng 51(3):101–118

Sohaei H, Hajihassani M, Namazi E, Marto A (2020) Experimental study of surface failure induced by tunnel construction in sand. Eng Fail Anal 118:1–11

Varma M, Maji VB, Boominathan A (2019) Numerical modelling of a tunnel in jointed rocks subjected to seismic loading. Undergr Space 4(2):133–146

Wang Z, Wong RCK, Li S, Qiao L (2012) Finite element analysis of long-term surface settlement above a shallow tunnel in soft ground. Tunn Undergr Space Technol 30:85–92

Wang A, Shi C, Zhao C, Deng E, Yang W, He H (2020) Response Characteristics of Cross Tunnel Lining under Dynamic Train Load. Appl Sci 10:1–19

Yang SQ, Yin PF, Zhang YC, Chen M, Zhou XP, Jing HW, Zhang QY (2019) Failure behaviour and crack evolution mechanism of a non-persistent jointed rock mass containing a circular hole. Int J Rock Mech Min Sci 114:101–121

Yang J, Yin ZY, Liu XF, Gao FP (2020) Numerical analysis for the role of soil properties to the load transfer in clay foundation due to the traffic load of the metro tunnel. Transp Geotech 23:100336

Yingjie L, Dingli Z, Qian F, Qingchun Y, Lu X (2014) A physical and numerical investigation of the failure mechanism of weak rocks surrounding tunnels. Comput Geotech 61:292–307

Zhang C, Han K, Zhang D (2015) Face stability analysis of shallow circular tunnels in cohesive-frictional soils. Tunn Undergr Space Technol 50:345–357

Zhang R, Xiao Y, Zhao M, Zhao H (2019) Stability of dual circular tunnels in a rock mass subjected to surcharge loading. Comput Geotech 108:257–268

Zhu Z, Li Y, Xie J, Liu B (2015) The effect of principal stress orientation on tunnel stability. Tunn Undergr Space Technol 49:279–286

Springer Nature or its licensor (e.g. a society or other partner) holds exclusive rights to this article under a publishing agreement with the author(s) or other rightsholder(s); author self-archiving of the accepted manuscript version of this article is solely governed by the terms of such publishing agreement and applicable law.

Power Quality Improvement using Hopfield Neural Network in Grid Distribution System

Pranshu Bansal
Dept. of Electrical Engineering
Delhi Technological University (DTU)
Delhi, India
pranshubansal15@gmail.com

Prashant Bharati
Dept. of Electrical Engineering
Delhi Technological University (DTU)
Delhi, India
prashantbharati92@gmail.com

Sambhav Jeswani
Dept. of Electrical Engineering
Delhi Technological University (DTU)
Delhi, India
jeswanisambhav@gmail.com

Ankita Arora
Dept. of Electrical Engineering
Delhi Technological University (DTU)
Delhi, India
aroraankita985@gmail.com

2023 International Conference on Power, Instrumentation, Energy and Control (PIECON) | 979-8-3503-9976-9/23/$31.00 ©2023 IEEE | DOI: 10.1109/PIECON56912.2023.10085879

***Abstract*— The objective of this study revolves around the power quality enhancement in grid connected distribution systems through Hopfield Neural Network (HNN) algorithm. The distribution system is linked to a non-linear load resulting in the generation of harmonics in the grid current. Distribution Static Synchronous Compensator (DSTATCOM) is implemented to mitigate harmonics. DSTATCOM contains IGBTs, that require firing signals to operate. The control algorithm provides the gate pulse by comparing grid and reference grid current; and aims at removing grid current harmonics for the improvement of system's performance. A comparative analysis of the HNN algorithm is executed with Self Tuning Filter and Synchronous Reference Frame Theory where metrics such as harmonic content, settling time and oscillations are taken under consideration. The distribution system and different control algorithms incorporated by the DSTATCOM have been simulated using MATLAB 2018b Simulink software.**

Keywords*— *DSTATCOM, HNN, SRFT, STF, Clarke's Transformation, Park's Transformation.

I. INTRODUCTION

In Power Systems, poor power quality is a result of current and voltage signals infested with harmonics. The measure of the degree of closeness between the current and voltage signals from the smooth and ideal sinusoidal signals is known as Power Factor. The safety of operation and longevity of devices running on electrical power is achieved by ensuring good power quality while poor power quality on the flipside, may lead to the distribution system suffering from increased losses, vibrations, noise, equipment heating, and dielectric breakdown making it important to ensure good power quality in the power system. Extensive use by consumers of solid-state devices with electronic switches is the primary cause for the power quality deterioration since these are responsible for the injection of high frequency harmonics into the current and source voltage. A Distribution Static Synchronous Compensator (DSTATCOM) is applied to eliminate the components having high frequency from the voltage and current signals.

Electric Power Quality (PQ) is a term coined in Electric Power Systems to assess and maintain the good quality of power at the level of generation, transmission, distribution, and utilization of AC electrical power [1]. Few of the numerous problems in Power Quality are the persistence of voltage harmonics, fluctuations, reactive power burden and unbalanced currents. Numerous techniques are identified on the basis of supply systems and electrical loads having different types of PQ related problems. In current non-linear loads, current and voltage-fed loads or their combination determines the type of power filters used so that the problems can be overcome. DSTATCOMs are applied in shunt case PQ problems that arise due to non-linear loads connected in the system.

DSTATCOMs are useful for the mitigation of current-based power quality problems since there are a number of current-based power quality problems namely poor power factor, or poor voltage regulation, unbalanced currents, and increased neutral current [2]. The DSTATCOM is implemented using a capacitor and an inverter connected in parallel. The thyristors inside the inverter require firing pulses to generate an AC signal at the output. Appropriate firing pulses are generated by various control algorithms including Self Tuning Filter, Synchronous Reference Frame Theory and Hopfield Neural Network.

II. DISTRIBUTION SYSTEM MODELLING

The distribution power system taken under consideration is shown in Fig. 1. A non-linear (NL) load supplied to a three-phase AC source is simulated by a diode bridge rectifier. Dynamic load is introduced in the system by connecting an RL branch in parallel to the NL load along with a circuit breaker that connects and disconnects the load to and from the system according to the breaker settings. The point of connection at which the Distribution Static Synchronous Compensator (DSTATCOM) is connected with the load in shunt is called Point of Common Coupling [3].

An AC distribution system with a three-phase three-wire DSTATCOM has been connected. The three-phase DSTATCOM consists of 6 IGBTS and is connected by a capacitor in parallel to it. The capacitor is used as a constant source of DC voltage. The DSTATCOM sends the compensating current to neutralize the grid current harmonics. The reference grid current produced is compared with the actual grid current in Hysteresis Current Controller (HCC) to produce gate pulse for the IGBTs.

The parameters of the distribution system used in the Simulink model are mentioned in Table 1.

979-8-3503-9976-9/23/$31.00 ©2023 IEEE

Authorized licensed use limited to: DELHI TECHNICAL UNIV. Downloaded on April 10,2023 at 07:27:07 UTC from IEEE Xplore. Restrictions apply.

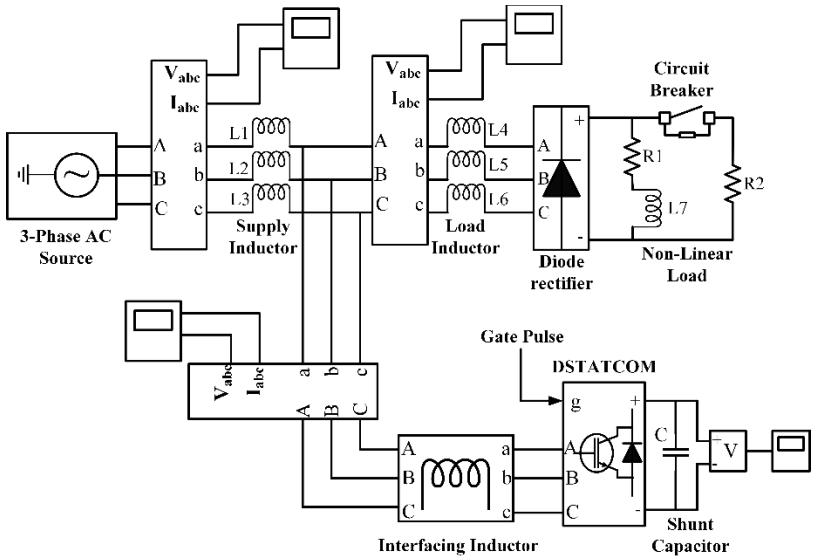


Fig. 1. Schematic Block Diagram of Grid Distribution System

TABLE I. PARAMETERS OF THE DISTRIBUTION SYSTEM

Component	Value
Sampling time	5e-05s
Shunt Capacitor, Initial Voltage	3000e-06, 156V
PI Controller	P=1, I=3
Load Inductance	2e-03
Supply RMS Voltage	110V
Supply Inductance	3e-03
Interfacing Inductance	2e-03H

III. CONTROL ALGORITHMS

A. Synchronous Reference Frame Theory (SRFT)

The implementation of the SRFT algorithm is represented by the Fig. 2. As shown, the SRFT algorithm receives load current as input which is in an abc frame, but SRFT works on a dq0 frame (synchronous frame). Hence, we employ Clarke's transformation to first convert the abc frame quantities into the αβ frame as expressed by the equation (1).

$$\begin{bmatrix} i_\alpha \\ i_\beta \end{bmatrix} = \frac{\sqrt{2}}{3}\begin{bmatrix} 1 & \frac{1}{2} & \frac{1}{2} \\ 0 & \frac{\sqrt{3}}{2} & -\frac{\sqrt{3}}{2} \end{bmatrix}\begin{bmatrix} i_a \\ i_b \\ i_c \end{bmatrix} \quad (1)$$

and further up convert the αβ frame quantities into the dq0 (with the d component acting as the active power current and the q component acting as the reactive power current) frame through the help of Park's transformation as expressed by the equation (2).

$$\begin{bmatrix} i_d \\ i_q \end{bmatrix} = \begin{bmatrix} \cos(\Phi) & \sin(\Phi) \\ -\sin(\Phi) & \cos(\Phi) \end{bmatrix}\begin{bmatrix} i_\alpha \\ i_\beta \end{bmatrix} \quad (2)$$

Inside the dq0 frame we only consider the fundamental part or "direct" component, and the "quadrature" and "zero" components are terminated, hence removing the possibility of any reactive power from the grid side.

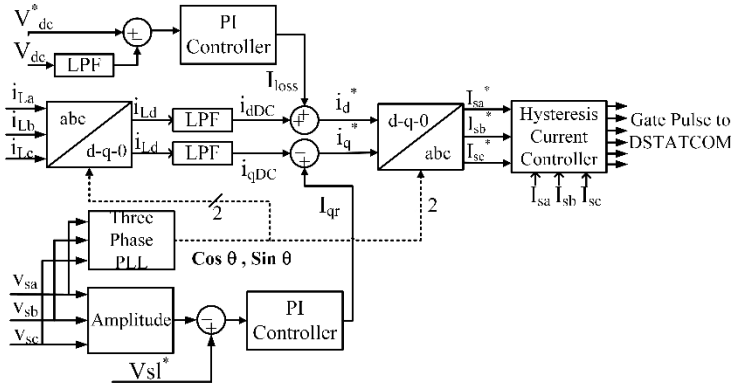


Fig. 2. SRFT Control Algorithm

A DC link PI controller is used to get the output loss current component (I_{loss}). Equation (3) can be used to represent the PI controller used inside the system aptly.

$$G(a) = K_b + \frac{Kc}{a} \quad (3)$$

Where K_b and Kc are constants of PI controller, representing proportional gain constant and integral gain constant.

The load current and the current loss generated from PI controller is added and we again convert the dq0 frame quantities into abc frame by employing the Inverse Park and Inverse Clarke transformations represented by the equations (4) and (5), thus generating the reference source current $I_{sabc}{}^*$.

$$\begin{bmatrix} i_\alpha \\ i_\beta \end{bmatrix} = \begin{bmatrix} \cos(\Phi) & -\sin(\Phi) \\ \sin(\Phi) & \cos(\Phi) \end{bmatrix}\begin{bmatrix} i_d \\ i_q \end{bmatrix} \quad (4)$$

$$\begin{bmatrix} i_a{}^* \\ i_b{}^* \\ i_c{}^* \end{bmatrix} = \frac{\sqrt{2}}{3}\begin{bmatrix} 1 & 0 \\ -\frac{1}{2} & \frac{\sqrt{3}}{2} \\ -\frac{1}{2} & -\frac{\sqrt{3}}{2} \end{bmatrix}\begin{bmatrix} i_\alpha \\ i_\beta \end{bmatrix} \quad (5)$$

The reference and actual grid current are compared to produce the needed PWM signals (firing signal) in the control of the voltage source converter inside the DSTATCOM [4].The hysteresis current controller makes the output current

Authorized licensed use limited to: DELHI TECHNICAL UNIV. Downloaded on April 10,2023 at 07:27:07 UTC from IEEE Xplore. Restrictions apply.

of the inverter keep a track of the command current instantaneously following a closed loop control outlook while the error is kept within the hysteresis band .The switching of inverters takes place on the crossing of the error band by the current error (i.e=i*-i) to keep the output current within the specified limit of the error. When the upper band is exceeded by the output current the turning off of the top switch takes place followed by the turning on of the lower switch, thus bringing back the inverter leg of the phase under consideration within the band. Hence the current drops and the voltage across the load dips from a value of Vdc to 0. And when the lower band is higher than the output current, the lower switch is turned off and the higher switch is turned on, connecting the load to Vdc, hence increasing the output current as the output voltage rises from 0 to Vdc across the load [5].

The phase locked loop (PLL) provides the required phase angle for converting αβ frame quantities to dq0 frame in Park transformation, and the low pass filters are employed in the model to separate the DC values from the reference current before passing it through the dq0 to abc transformation block.

B. Self Tuning Filter (STF) Based Control Algorithm

Self-tuning filters refer to a certain type of filters in which we determine from the input signal the required frequency component by feeding the output of the filters back to the input [7]. The STF has been tuned for $314\text{rad/sec}(50\text{ Hz})$ (fundamental frequency), and is implemented as shown in Fig. 3. We first transform the three-phase load current by the use of Clarke's transformation into α-β component $(i_{L\alpha}, i_{L\beta})$. Due to the use of NL loads in the system, the α-β components that we get out of the load current are distorted, hence we obtain α-β components of load currents that are filtered $(i_{L\alpha f}, i_{L\beta f})$ through the help of STF as follows [8].

$$i_{L\alpha f} = \frac{D\times i_{L\alpha} - D\times i_{L\alpha f}}{s} - \frac{\omega \times i_{L\beta f}}{s}$$
$$i_{L\beta f} = \frac{D\times i_{L\beta} - D\times i_{L\beta f}}{s} + \frac{\omega \times i_{L\alpha f}}{s} \quad (6)$$

In the above equations $i_{L\alpha,}, i_{L\beta}$ are the load currents generated by Clarke's transformation, D is representing the gain constant and is taken as 20, ω is the desired signal's frequency to be retrieved, and is kept as 314rad/sec as stated above.

We use $i_{L\alpha f,}, i_{L\beta f}$ in calculation of the Fundamental Active Power Component (I_{fpabc}), using equation (7), as shown in Fig. 4 [6].

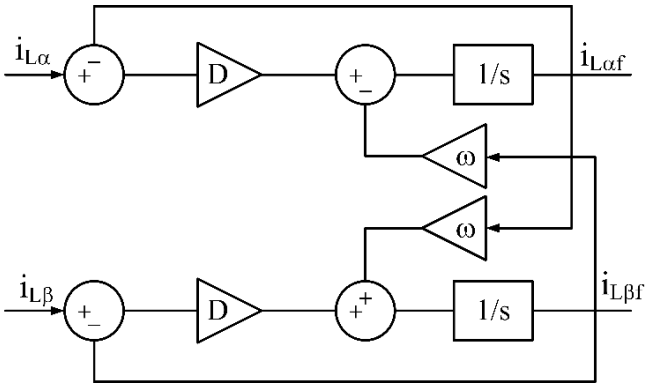


Fig. 3. STF Block Diagram

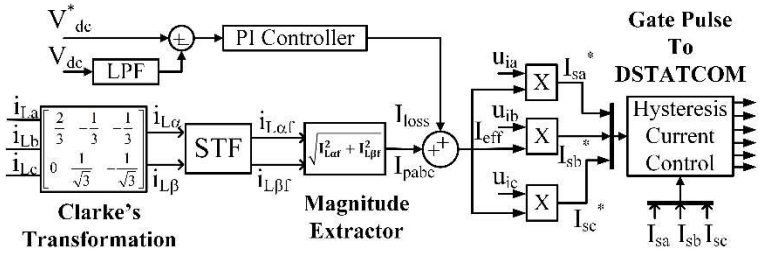


Fig. 4. STF Based Control Algorithm

$$I_{fpabc} = \sqrt{i_{L\alpha f}^2 + i_{L\beta f}^2} \quad (7)$$

We add the I_{fpabc} to I_{loss} (power loss component of DC link), and obtain I_{eff} (the effective active power) used to generate reference grid current in the HCC for the generation of gate pulse

$$I_{eff} = I_{fpabc} + I_{loss} \quad (8)$$

C. Hopfield Neural Network (HNN) Based Control Algorithm

HNN is based on recurrent approach. We desire a certain objective function and on the basis of that we update the output iteratively. For the easy achievement of convergence, we define the objective function clearly. The HNN is made up of '2n' neurons which forms a multiple loop feedback system consisting of an 'α' component (in-phase) and 'β' component (quadrature) [9].

We can express the NL load current in general as

$$i_L(t) = \sum_{m=1}^{N} \alpha_m \sin(m\omega t) + \beta_n \cos(m\omega t) \quad (9)$$

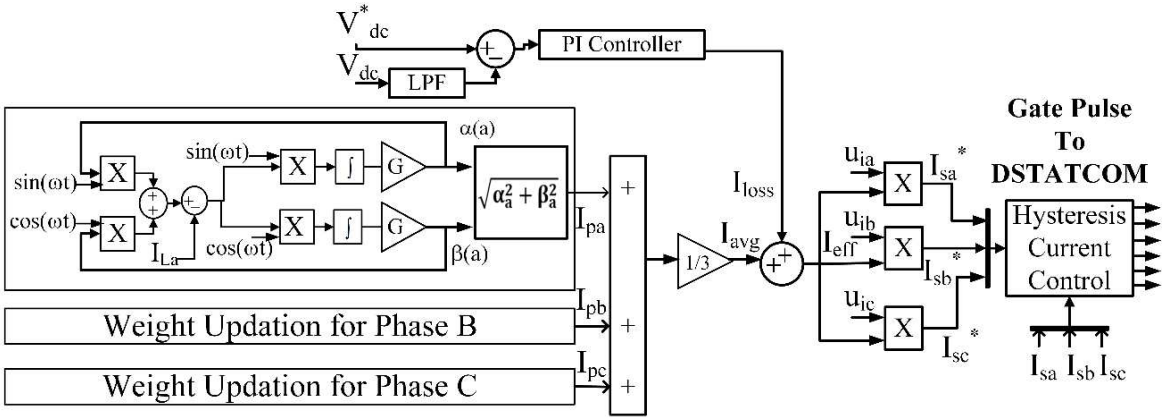


Fig. 5. HNN Based Control Algorithm

Authorized licensed use limited to: DELHI TECHNICAL UNIV. Downloaded on April 10,2023 at 07:27:07 UTC from IEEE Xplore. Restrictions apply.

Here α_{m} is the in-phase and β_{m} is the quadrature component [10].

We develop the objective function for HNN, Γ(na) through the error generated between actual (i_{La}^{*}) and estimated (i_{La}) load current.

$$\Gamma_{\mathrm{a}} = \frac{1}{2}[i_{La}^{*}(t) - i_{La}]^2 \tag{10}$$

From Eq. (9) and (10)

$$\Gamma_{\mathrm{a}} = 0.5[\sum_{m=1}^{N} (\alpha_{am}\sin(m\omega t) + \beta_{am}\cos(m\omega t)) - \boldsymbol{i_{La}}]^2 \tag{11}$$

Defining two matrix, $\mathrm{A_{am}}$ and $\mathrm{B_{am}}$ as

$$\mathrm{A_{am}} = [\alpha_{\mathrm{a1}}\beta_{\mathrm{a1}}\alpha_{\mathrm{a2}}\beta_{\mathrm{a2}} \dots\dots\dots\dots \alpha_{\mathrm{aN}}\beta_{\mathrm{aN}}] \quad \text{and}$$
$$\mathrm{B_{am}} = [\cos(\omega t)\cos(2\omega t) \dots cos(N\omega t)\sin(\omega t)sin(2\omega t)\dots sin(N\omega t)]$$

Eq. (10) is restated for phase ' a ' as

$$\Gamma_{\mathrm{a}} = 0.5[\sum_{m=1}^{N} A_{am}B_{am}^{T} - i_{La}]^2 \tag{12}$$

Also to obtain the minimum value of Γ_{a},

$$\frac{d\Gamma_{\mathrm{a}}}{dt} = 0 \tag{13}$$

and

$$\frac{\partial A_{\mathrm{am}}}{\partial t} = -G\frac{\partial \Gamma_{\mathrm{a}}}{\partial A_{am}} \tag{14}$$

G is our gain constant above and is taken as 20. Matrix $\mathrm{A_{am}}$ can be further devised into components given as,

$$\frac{\partial[\alpha_{a1}\beta_{a1}\dots\dots\dots\alpha_{an}\beta_{an}]}{\partial t} = -K\frac{\partial \Gamma_{\mathrm{a}}}{\partial A_{am}} \tag{15}$$

From Eq. (14), it can be written

$$\sum_{m=1}^{N}\frac{\partial \alpha_{\mathrm{am}}}{\partial t} = -G\sum_{m=1}^{N}\frac{\partial \Gamma_{\mathrm{a}}}{\partial \alpha_{am}} \tag{16}$$

$$\sum_{m=1}^{N}\frac{\partial \beta_{\mathrm{am}}}{\partial t} = -G\sum_{m=1}^{N}\frac{\partial \Gamma_{\mathrm{a}}}{\partial \beta_{am}} \tag{17}$$

Eq. (11) can be used to calculate the right-hand side of Eq. (16)

$$-G\sum_{m=1}^{N}\frac{\partial \Gamma_{\mathrm{a}}}{\partial \alpha_{am}} = -G\sum_{m=1}^{N}\{\alpha_{am}\sin(m\omega t) + \beta_{am}\cos(m\omega t) - i_{La}\}\sin(m\omega t) \tag{18}$$

Eq. (11) can also be used to calculate right hand side of Eq. (17)

$$-G\sum_{m=1}^{N}\frac{\partial \Gamma_{\mathrm{a}}}{\partial \beta_{am}} = -G\sum_{m=1}^{N}\{\alpha_{am}\sin(m\omega t) + \beta_{am}\cos(m\omega t) - i_{La}\}\cos(m\omega t) \tag{19}$$

So, α_{am} component of $\mathrm{A_{am}}$ can be estimated from equations (16) and (18) as

$$\frac{\partial \alpha_{\mathrm{am}}}{\partial t} = -G[\{\alpha_{am}\sin(m\omega t) + \beta_{am}\cos(m\omega t) - i_{La}\}\sin(m\omega t)] \tag{20}$$

Hence, α_{am} is calculated using

$$\alpha_{am} = -G\int \{\alpha_{am}\sin(m\omega t) + \beta_{am}\cos(m\omega t) - i_{La}\}\sin(m\omega t)\,dt \tag{21}$$

Similarly, β_{am} is calculated using

$$\beta_{am} = -G\int \{\alpha_{am}\sin(m\omega t) + \beta_{am}\cos(m\omega t) - i_{La}\}\cos(m\omega t)\,dt \tag{22}$$

The weighted components of the mth harmonic current are represented here by $\alpha_{\mathrm{am}}, \beta_{\mathrm{am}}$

By putting m=1 we can calculate $\alpha_a, \beta_{\mathrm{a}}$ from Eq. (21) and (22), and hence can obtain I_{pa}, as shown in Fig. 5.

$$\boldsymbol{I}_{pa} = \sqrt{\alpha_{\boldsymbol{a}}^2 + \beta_a^2} \tag{23}$$

We can do the same for the remaining phases hence determine ' I_{pb} ' and ' I_{pc} ' for respective phases and average them. The average fundamental active power component I_{avg} can be evaluated as

$$\boldsymbol{I}_{avg} = \frac{1}{3}(\boldsymbol{I}_{pa} + \boldsymbol{I}_{pb} + \boldsymbol{I}_{pc}) \tag{24}$$

By the addition of I_{avg} and I_{loss} (DC link power loss component) we obtain the effective active power component used for the generation of reference grid current in HCC.

IV. Simulation Results

A. *Performance analysis of grid connected systems under NL load with-out DSTATCOM*

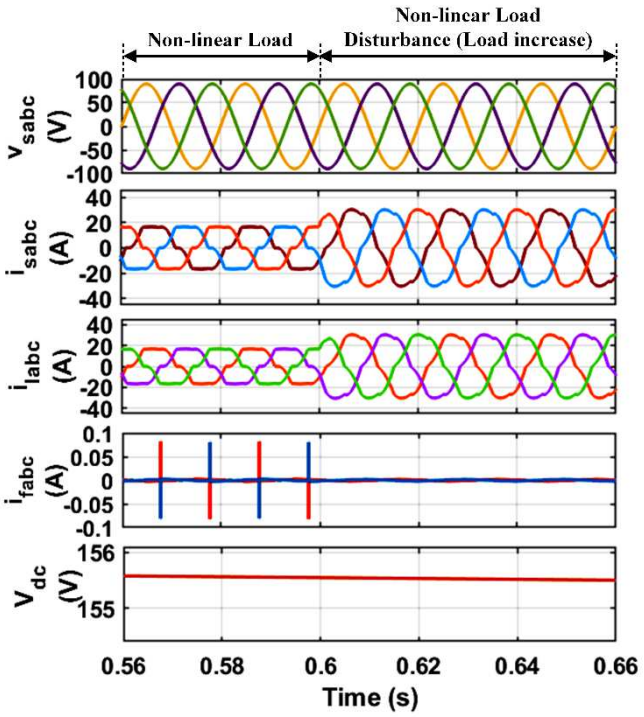


Fig. 6. Distribution system waveforms with effect of NL load

Fig 6 represents the waveforms at steady state for grid side voltage and current at grid side and load side, DSTATCOM current and the DC Link voltage. Diode bridge rectifier linked to series RL branch (L=40x10-3H, R=7.5Ω) in shunt with a circuit breaker (time of switching set as t=0.6s to t=0.8s) is used to simulate the load. The time in which waveforms have been analyzed is t=0.56s to t=0.66s. Harmonics are being induced in the current at grid side due to the NL load. Total Harmonic Distortion (THD) obtained for the current at load side is 31.17% with 21.81A as the fundamental magnitude at 50Hz. Since, no gate pulse is received by DSTATCOM, current generated by it is negligible. The shunt capacitor is producing a constant dc voltage of around 156V.

Authorized licensed use limited to: DELHI TECHNICAL UNIV. Downloaded on April 10,2023 at 07:27:07 UTC from IEEE Xplore. Restrictions apply.

B. *Performance analysis of HNN algorithm under NL load with DSTATCOM*

The steady state waveforms for distribution system can be observed in Fig 7. Waveforms corresponding to voltage at grid side and current at grid side, load side, fluctuating or current generated by DSTATCOM and the DC Link voltage have been represented for HNN algorithm. It is found that grid current and voltage are sinusoidal and in-phase with each other. The compensator sends neutralizing current to eliminate the grid current harmonics and THD of grid current is improved to 2.27%. Therefore, it can be observed through the waveforms that the primary goal of the control algorithms has been achieved, i.e., HNN algorithm has been capable of removing harmonics from the grid current that were generated by the NL load.

The DC Link Voltage settles around 200V reference value for HNN algorithm. A dip can be seen in the DC Link voltage when the circuit breaker switches on at time t=0.6s and the load is increased. The dc voltage again settles down close to 200V after around 0.02s. Hence, the algorithm has successfully compensated the harmonic distortions generated by the load current.

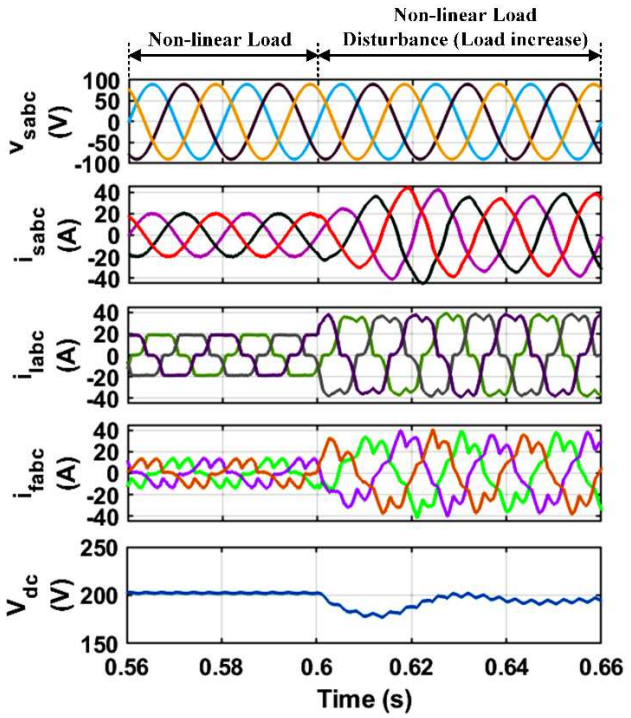


Fig. 7. Steady State Waveforms achieved using HNN Algorithm

V. Comparison Analysis

Fig 8 shows the weight convergence comparison between the three control algorithms implemented.

It can be observed that there are very high oscillations achieved in SRFT algorithm. HNN algorithm gave the best result as it has the settling time of around 0.2s compared to around 0.4s of STF algorithm. The SRFT algorithm is having peak weight convergence amplitude slightly less than amplitude of STF and HNN algorithms when the algorithm has been implemented on the same distribution system model having same parameter values.

Fig. 9, 10 and 11 represents the Fast Fourier Transform (FFT) analysis providing the THD value along with the fundamental magnitude at a frequency of 50Hz for SRFT, STF and HNN algorithm respectively. The grid current has been analyzed using FFT analysis. It can be seen that 2.80% THD value with 20.05A fundamental at 50Hz is achieved for SRFT, 2.35% THD value with 20.17A fundamental for STF and 2.27% THD value with 20.28A fundamental for HNN algorithm.

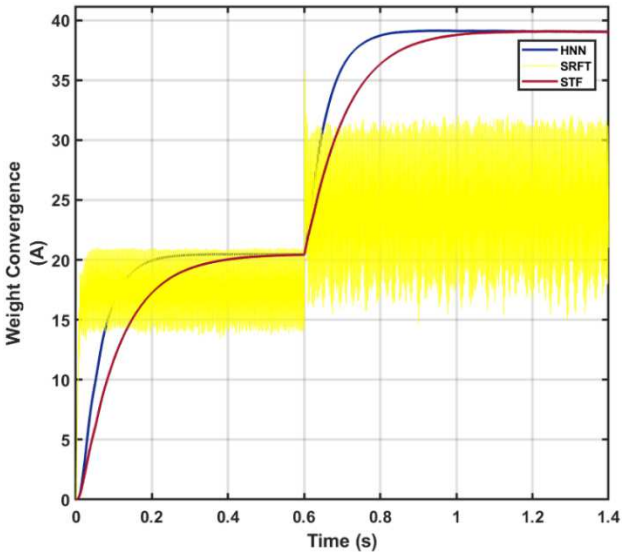


Fig. 8. Weight Convergence Comparison between the three algorithms

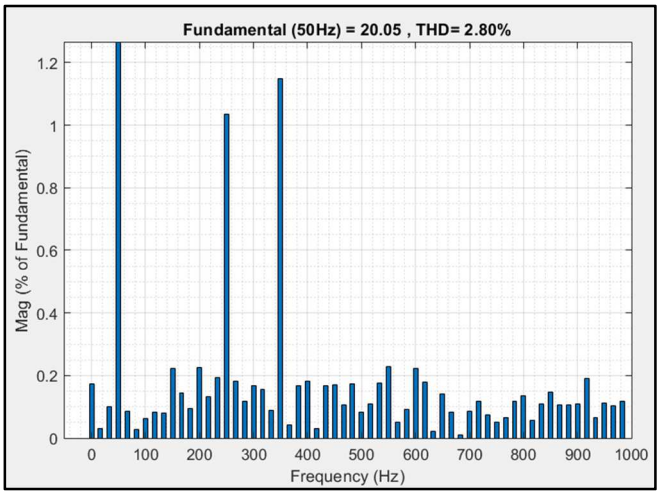


Fig. 9. FFT Analysis for grid current for SRFT Algorithm

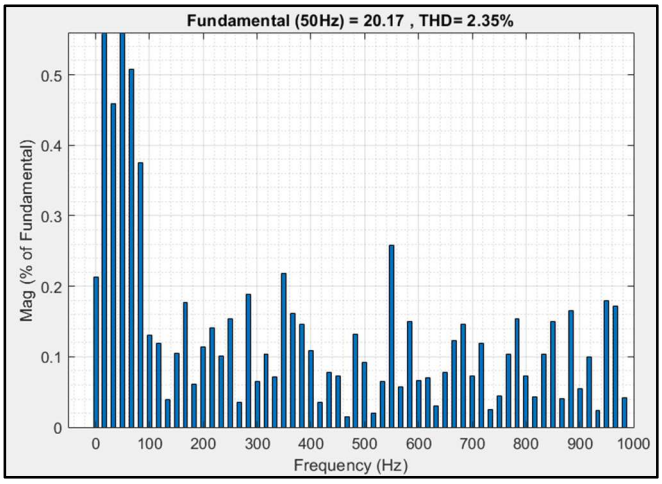


Fig. 10. FFT Analysis for grid current for STF Algorithm

Authorized licensed use limited to: DELHI TECHNICAL UNIV. Downloaded on April 10,2023 at 07:27:07 UTC from IEEE Xplore. Restrictions apply.

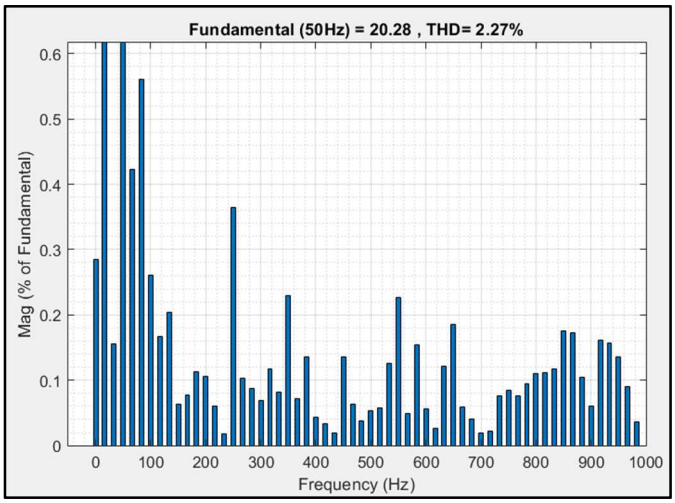


Fig. 11. FFT Analysis for grid current for HNN Algorithm

Table 2 summarizes the results of the three algorithms where parameters including settling time, THD and oscillations frequency have been compared.

TABLE II. RESULTS ACHIEVED FOR SRFT, STF AND HNN ALGOS

Algorithm \Parameter	**SRFT**	**STF**	**HNN**
Settling Time	0.05s	0.4s	0.2s
Oscillations	Very High	Least	Least
THD	2.80%	2.35%	2.27%

VI. CONCLUSION

In this study, HNN algorithm has been implemented and its comparative analysis with control algorithms namely SRFT and STF for the power quality enhancement in a grid connected distribution system has been illustrated. The results drawn reflect the ability of the respective control algorithms to remove harmonics in the grid current and improve power quality. The THD of grid current found for HNN is 2.27%, STF is 2.35% and SRFT is 2.80%. Settling time for HNN is 0.2s, STF is 0.4s and SRFT is 0.05s. Least weight convergence oscillations are achieved in HNN algorithm compared to STF and SRFT algorithms. Based upon the THD, settling time and oscillations achieved from FFT Analysis and weight convergence comparison, HNN algorithm performed the best among the implemented control algorithms.

REFERENCES

[1] T. Karthik, M. Prathyusha, R. Thirumalaivasan and M. Janaki, "Power quality improvement using DSTATCOM," *2019 Innovations in Power and Advanced Computing Technologies (i-PACT)*, 2019, pp. 1-7, doi: 10.1109/i-PACT44901.2019.8960234.

[2] C. Kumar and M. K. Mishra, "A Multifunctional DSTATCOM Operating Under Stiff Source," in *IEEE Transactions on Industrial Electronics,* vol. 61, no. 7, pp. 3131-3136, July 2014, doi: 10.1109/TIE.2013.2276778.

[3] Kumar, Manish & Swarnkar, Anil & Gupta, Nikhil & Niazi, Khaleequr, "Design and operation of DSTATCOM for power quality improvement in distribution systems", *2017 The Journal of Engineering,* 2017, doi:10.1049/joe.2017.0747.

[4] M. Labeeb and B. S. Lathika, "Design and analysis of DSTATCOM using SRFT and ANN-fuzzy based control for power quality improvement," *2011 IEEE Recent Advances in Intelligent Computational Systems*, Trivandrum, India, 2011, pp. 274-279, doi: 10.1109/RAICS.2011.6069317.

[5] Sampath, Namratha & Parimala, P.V.S.S.A., "D-STATCOM Control using SRFT Method for PQ Improvement in a PV System," *2021 International Journal of Innovative Technology and Exploring Engineering*, 10. 113-119. doi:10.35940/ijitee.H9261.0610821.

[6] Ram, A.; Sharma, P.R.; Ahuja, R.K, "An Adaptive Controller for DSTATCOM for Power Quality Improvement in Distribution System," *Preprints* 2020, 2020120576 ,doi: 10.20944/preprints202012.0576.v1.

[7] Bhim Singh, Sunil Kumar Dube, Sabha Raj Arya, "An improved control algorithm of DSTATCOM for power quality improvement," *2015 International Journal of Electrical Power & Energy Systems*, Volume 64, 2015, Pages 493-504, ISSN 0142-0615, doi:10.1016/j.ijepes.2014.07.055.

[8] P. Chittora, A. Singh and M. Singh, "Application of self tuning filter for power quality improvement in three-phase-three-wire distorted grid system," *2017 7th International Conference on Power Systems (ICPS), Pune, India*, 2017, pp. 313-318, doi: 10.1109/ICPES.2017.8387312.

[9] M. Kashif et al., "A Fast Time-Domain Current Harmonic Extraction Algorithm for Power Quality Improvement Using Three-Phase Active Power Filter," in *IEEE Access*, vol. 8, pp. 103539-103549, 2020, doi: 10.1109/ACCESS.2020.2999088.

[10] S. Osowski, "Neural network for estimation of harmonic components in a power system," *In Generation, Trans. Distrib., IEE Proc.*, vol. 139, no. 2, pp. 129–135, March 1992, doi:10.1049/ip-c.1992.0021

Authorized licensed use limited to: DELHI TECHNICAL UNIV. Downloaded on April 10,2023 at 07:27:07 UTC from IEEE Xplore. Restrictions apply.

J Mater Sci: Mater Electron (2023)34:907

Prospective applications of thermally stable Dy^{3+} doped potassium zinc strontium borate (KZSB) glasses in w-LEDs

Sheetal Kumari[1], Anu[1], Aman Prasad[2], Pooja Rohilla[1], and A. S. Rao[1,*]

[1] *MASR Lab, Department of Applied Physics, Delhi Technological University, Delhi 110042, India*
[2] *Department of Physics and Computer Science, Dayalbagh Educational Institute, Agra 282005, India*

Received: 8 January 2023
Accepted: 14 March 2023

© The Author(s), under exclusive licence to Springer Science+Business Media, LLC, part of Springer Nature 2023

ABSTRACT

In this present work, Dysprosium (Dy^{3+}) ions doped potassium zinc strontium borate (KZSB) glasses were synthesized via the melt-quench method. X-ray diffraction (XRD) study of the prepared glasses shows a broad hump and confirms the amorphous nature of the glasses. Various vibrational shoulders were seen in the Fourier transform infrared (FT-IR) spectrum. Thermo gravimetric analysis–differential scanning calorimetry (TGA–DSC) was carried out to check the thermal stability and corresponding weight loss behavior of the un-doped sample. Absorption spectra were recorded for un-doped as well as doped glasses in the UV–VIS–NIR region, and the corresponding optical band gap was calculated. The photoluminescence (PL) spectra of as-prepared Dy^{3+} doped KZSB glasses under 350 nm excitation show three peaks at 482, 575 and 665 nm corresponding to the transitions $^4F_{9/2} \rightarrow {}^6H_{15/2}$, $^6H_{13/2}$ and $^6H_{11/2}$. Commission Internationale de I'Eclairage (CIE) chromaticity coordinates calculated from the emission data lie in the white region. The photometric analysis of prepared glasses under UV lamp with 365 nm excitation also shows white emission. Temperature-dependent PL (TDPL) investigation demonstrates the superiority in thermal stability of the as-prepared glasses, with an activation energy of 0.232 eV estimated for 0.5 mol% (optimized concentration of rare earth ion) of Dy^{3+} ions. After analyzing the results of all studies, we propose to use these borate glasses doped with Dy^{3+} ions for white light-emitting diodes (w-LEDs) fabrication and other solid state lighting (SSL) applications.

Address correspondence to E-mail: drsrallam@gmail.com

https://doi.org/10.1007/s10854-023-10272-6
Published online: 07 April 2023

1 Introduction

Research in the field of luminous materials doped with rare-earth (RE) and transition metal (TM) ions has seen astounding advances as a result of the rapid growth of technologies in solid-state lighting (SSL) and other display technologies [1–5]. As photoluminescence (PL) glasses can convert ultra-violet (UV) or near-infrared (NIR) light to visible light, they are suitable for use in display devices, smart windows, lasers, fibre optics and white light emitting diodes (w-LEDs) [6–11]. It was in early 2000s that the world had seen how LEDs and also newly developed w-LEDs could shape the future of lighting devices due to many important advantages like brightness, efficiency, availability of many colors, low operating voltages and above all, less ecological impact [12]. In the case of LEDs, it was observed that maximising luminous efficacy came at the cost of decrease in color rendering or vice-versa. Lei et al. studied increasing both efficacy and color rendering of trichromatic and tetrachromatic LED based w-LEDs which was a significant step in the area of LED research [13]. Rare earth doped phosphors in w-LEDs had been in development since late 2000s but that did not hamper the search for alternatives to phosphors for SSL/w-LED applications [14]. So, research on the synthesis and analysis of RE^{3+} ions doped glasses as excellent alternatives for epoxy resin-free phosphors was taken up [15]. Glasses are gaining popularity due to their numerous uses, which include various optical devices, fibre optic amplifiers, visible and infrared solid-state illuminating devices, digital plasma displays, solar cells, bio-imaging and bio-sensors [16, 17]. The aforementioned applications would be more efficient if developed from a glassy material with novel properties such as low phonon energy, strong chemical and thermal stability, good RE^{3+} ion solubility and high transparency [18–20]. The intrinsic structure of the host and ligand field environment influences the luminescence efficiency of RE^{3+} ion-doped host matrix. To achieve the highest possible luminescent efficiency, it is critical to select an appropriate host with lower phonon energies.

The network former and network modifier are two elements that influence the structure of the glass. A glass former, also known as a network former, is composed of oxides like B_2O_3 that is required for the preparation of glass. When network modifiers are applied to a network glass former, they alter the host's internal structure, creating a favourable environment for the doped RE^{3+} ions, allowing them to achieve high luminescence efficiency.

Amongst all the glass formers, borate glass is unique due to properties like low melting point, optical transparency, low fabrication cost, straightforward preparation method, high refractive index and low thermal expansion [21–23].

The natural choice of borate as the network former is attributed to its distinctive optical and structural characteristics which are fundamental as well as beneficial for advanced technology. Due to their wide range of compositional opportunities and significant solubility of RE^{3+} ions in the host matrix, borates are considered to be the most desirable host for lasing and nonlinear optical applications [24, 25].

Boric oxide (B_2O_3) glasses are made up of B–O–B bonds having symmetric stretching vibrations of sp^3 tetrahedral BO_4 units and sp^2 planar BO_3 trigonal units [26]. The rigidity of the borate glass network is improved by this structural configuration. Borate glasses are also recognised for their outstanding qualities like low melting point, high thermal compactness, high visual transparency, strong mechanical steadiness and chemical persistence. These qualities are necessary for the development of environment friendly, low-energy consuming, high efficiency and thermally stable solid-state lighting materials that could ultimately substitute conventional incandescent light bulbs [27]. Non-radiative losses will be mitigated when a modifier moderated low phonon energy host like B_2O_3 is used resulting in greater luminescence efficiency.

Strontium oxide (SrO) acts as a network modifier in a borate glass that can modify physical qualities by enhancing the chemical endurance and preventing the devitrification of the glass host. The high concentration of SrO enhances the host glass matrix's toughness [28, 29]. Strontium will strengthen the luminescence efficiency of RE ions' emission levels and lower their resistance to the humidity outbreaks in the current investigation [26].

Potassium oxide (K_2O) is an alkali oxide that acts as a network modifier to improve the luminescence efficiency of the host glass. K_2O also has good optical, chemical and magnetic properties, as well as a large band gap and is non-toxic in nature. K_2O also helps in the reduction of non-radiative losses and the enhancement of the host glass stability. K_2O helps to eliminate air bubbles from glass and raises the glass

transition temperature. Also, K_2O creates moisture resistance and eliminates the thermal expansion coefficient [6, 30].

On the other hand, the addition of zinc fluoride (ZnF_2) to the borate glass host imparts many advantages like low phonon energy, relatively high thermal stability, decreased crystallisation, high viscosity, high chemical durability and easy manufacturing process with a wide range of photonic applications [31]. The addition of zinc to the borate glass system improves its electron emission and functionalization of optical properties that makes it useful for a variety of applications [16]. It also improves the luminescence efficiency. Fluoride ions also produce narrow fluorescence lines, which help in removal of the OH group from borate and increase the emission cross-section.

Among the various RE^{3+} ions available, Dysprosium (Dy^{3+}) can be easily used for white light generation because of its f-f transitions, in which emission occurs in the visible range. The Dy^{3+} ion emits yellow ($^4F_{9/2} \rightarrow {}^6H_{13/2}$), blue ($^4F_{9/2} \rightarrow {}^6H_{15/2}$) and red ($^4F_{9/2} \rightarrow {}^6H_{11/2}$) emissions [32]. Furthermore, it is well known that the intensity of Dy^{3+} ions in the yellow band (575 nm) is hypersensitive to the nature of the host but the intensity of the blue band (482 nm) is less sensitive to the host. As a result, the Dy^{3+} doped glasses would generate white light at a specific ratio of $^4F_{9/2} \rightarrow {}^6H_{13/2}$ (yellow) to $^4F_{9/2} \rightarrow {}^6H_{15/2}$ (blue) transitions. To get best results, a host glass with good transparency and strong thermal stability, as well as the lowest feasible phonon energy is preferable.

To understand the practicality of using these glasses in w-LEDS and SSL technology, various characterization techniques such as XRD, FT-IR, UV–Vis, PL excitation, PL emission and PL decay curves were used to investigate the glassy nature, structural and spectroscopic properties of borate glass, namely potassium zinc strontium borate (KZSB), doped with different concentrations of Dy^{3+} ions. According to the literature review, the thermal and spectroscopic properties of Dy^{3+} ions doped KZSB glasses have never been described before, thereby making this work novel in nature.

2 Synthesis and characterization techniques

2.1 Sample preparation

Sample preparation of Dy^{3+} ions doped KZSB glasses was done by melt quenching technique with chemical composition:

$$65H_3BO_3 - 15ZnF_2 - 10K_2CO_3 - (10 - x)\ SrCO_3 - xDy_2O_3\ (x = 0.0,\ 0.1,\ 0.5,\ 1.0,\ 1.5,\ 2.0\ \text{mol}\%).$$

Starting powders such as H_3BO_3 (99.5%), ZnF_2 (99%), K_2CO_3 (99.9%), $SrCO_3$ (99.9%), and Dy_2O_3 (99.99%) were procured from Sigma-Aldrich and a total of 6 g of the precursor mixture was weighed in stoichiometric ratio. The powder was crushed until it became homogenous in an agate mortar. For this technique, acetone was used as a wetting medium. After mixing the chemicals, the mixture was placed in an alumina crucible and heated to 1200 °C in a high-temperature furnace for 3 h. The melt was then poured onto a pre-heated brass plate and instantly pressed with another plate to obtain glass samples of uniform thickness, followed by additional two hours of annealing at 350 °C to minimize the cracks induced by thermal and mechanical stress. Finally, transparent and round glasses with a uniform thickness of 1.6 mm and a diameter of 2.5–3.0 cm were obtained.

2.2 Experimental techniques

The densities of the glasses were calculated by Archimedes method. The refractive indices were calculated by Brewster's angle method. The XRD pattern of an un-doped KSZB glass was recorded by Bruker D8 Advance Diffractometer with Cu K_α radiation (l.54 Å) (under operating conditions of tube voltage and current of 40 kV and 40 mA respectively) and scanning speed of 0.02 s^{-1}, in the range between 10°–80°. A JASCO V-770 spectrophotometer was used to analyse the optical absorption spectra of the samples in the spectral wavelength range 350–1800 nm with a spectral resolution of 2 nm. PL emission and excitation spectra were obtained from a JASCO FP-8300 spectrofluorometer with a resolution of 1.0 nm. Ocean optics Flame-S-XR1-ES was used for temperature-dependent PL (TDPL) investigations. An Edinburgh FL920 Fluorescence lifetime spectrometer

(with a spectral resolution of 0.1 nm) was used for PL decay spectral measurements. Except for the temperature-dependent studies, all measurements were taken at room temperature. Table 1 shows the physical parameters Dy^{3+} ions doped KZSB glasses.

3 Results and discussion

3.1 X-ray diffraction (XRD)

The XRD spectra of an un-doped and Dy^{3+} ion doped KZSB glasses were recorded in the spectral range of 10° to 80° and are shown in Fig. 1a, b. There is a wide hump in the range of 19.8°–36.8° in the spectrum. The presence of short-range order in the as-prepared KZSB glass is indicated by the broad hump. The amorphous behaviour of as-prepared glass samples is characterized by the obtained short-range order. The addition of RE ions has no influence on the properties of the glasses.

3.2 Fourier transform-infrared (FT-IR) spectroscopy

Figure 2 shows the FT-IR spectrum of an un-doped KZSB glass in the range 400–3600 cm^{-1}. The FT-IR spectrum has shoulders near 710, 924, 1049, 1219, 2112, and 2897 cm^{-1}. Table 2 displays the positions of various IR bands along with their corresponding IR assignments. The bending of B–O–B linkages and vibration of bridging oxygen atoms may be assigned to the band centred at 710 cm^{-1}. The vibrations of the di-borate group and asymmetric stretching vibrations of B–O in the tetrahedral BO_4 unit may be represented by the band centred at 924 cm^{-1}, while the B–O stretching vibrations in the tetrahedral BO_4 unit may be represented by the band centred at 1049 cm^{-1} [33]. The B–O stretching vibrations of trigonal BO_3 units in metaborate, pyroborate, and orthoborate groups may be represented by the band at 1335 cm^{-1}. The existence of the hydroxyl radicals and the hydrogen bond is represented by the band seen at 2112 cm^{-1}. The stretching peak of the hydroxyl group is responsible for the band at 2897 cm^{-1}. The presence of a modifier in the glass network causes the long network chain to break, resulting in the creation of non-bridging oxygen (NBO) atoms. The creation of NBO results in the formation of unoccupied oxygen atoms and these oxygen atoms participate in the formation of OH groups [34]. Glass characteristics such as viscosity, phase separation, and thermal expansion can all be affected by the presence of OH groups. In general, excess OH groups in glass can cause growth of cracks, give rise to impurities and lead to a reduction in the glass' overall strength and quantum efficiency [35, 36]. The OH content of the

Table 1 Physical parameters of Dy^{3+} ions doped KZSB glasses (± values indicate standard error of the mean)

S. no.	Physical property	KZSB Dy0.1	KZSB Dy0.5	KZSB Dy1.0	KZSB Dy1.5	KZSB Dy2.0
1	Density (d) in g/cm^3 (± 0.00297)	2.836	2.936	2.948	2.972	3.016
2	Refractive Index (n) (± 0.0049)	2.316	2.321	2.328	2.336	2.343
3	Average molecular weight (± 0.765)	84.51	85.41	86.54	87.66	88.79
4	Concentration of Dy^{3+} N (× 10^{22} ions/cm^3) (± 0.6934)	0.20	1.04	2.05	3.06	4.09
5	Dielectric constant (ε) (± 0.0234)	5.36	5.39	5.42	5.46	5.49
6	Optical dielectric constant (ε − 1) (± 0.0263)	4.36	4.39	4.42	4.49	4.49
7	Reflection loss (R%) (± 0.0007)	0.157	0.158	0.159	0.160	0.161
8	Molar refraction (R_m) (cm^{-3}) (± 0.0723)	17.66	17.28	17.49	17.63	17.65
9	Polaron radius (r_p) (in Å) (± 0.3674)	3.19	1.85	1.47	1.29	1.17
10	Inter-ionic radius (r_i) (in Å) (± 0.9109)	7.91	4.59	3.65	3.20	2.90
11	Molecular polarizability (α_e) (× 10^{-23} cm^3) (± 1.2691)	7.003	1.370	0.693	0.466	0.349
12	Field strength F (× 10^{16} cm^{-2}) (± 18.2351)	16.05	47.69	75.25	98.29	119.22
13	Molar volume (cm^3) (± 0.1142)	29.80	29.09	29.36	29.49	29.44
14	Oxygen packing density (O.P.D) (± 35.5809)	9060.70	9281.35	9197.60	9154.00	9171.30
15	Optical electro-negativity (χ_{opt}) (± 0.002)	0.347	0.349	0.351	0.355	0.358
16	Metallization (M) (± 0.0012)	0.4074	0.4061	0.4043	0.4023	0.4006

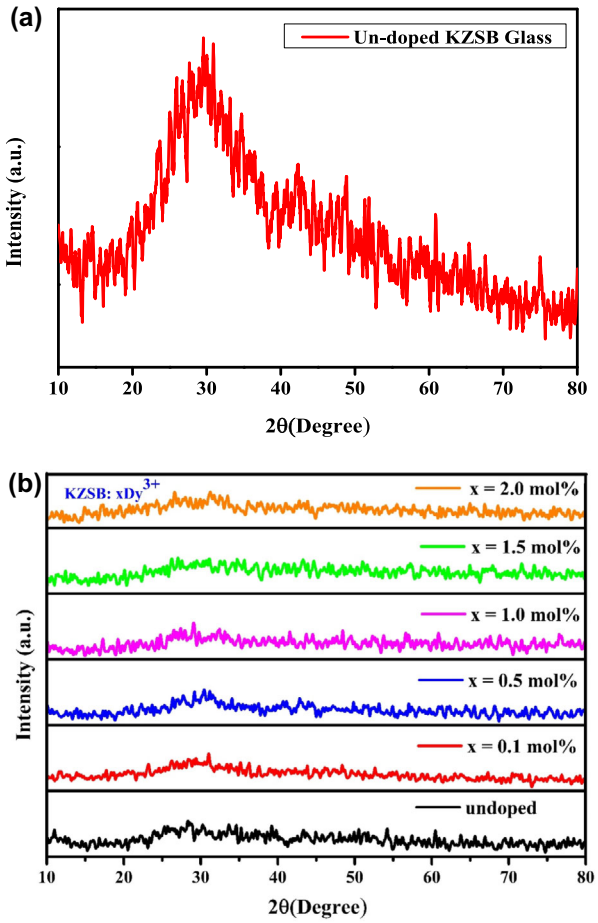


Fig. 1 **a** XRD spectrum of an un-doped KZSB glass. **b** XRD spectrum of Dy^{3+} ion doped KZSB glasses

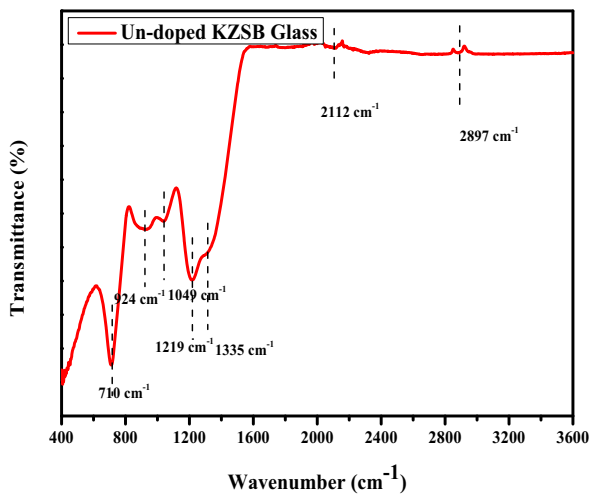


Fig. 2 FT-IR spectrum of an un-doped KZSB glass

KZSB glasses can be determined using the formula given below [37]:

$$\alpha_{OH} = \frac{ln\left(\frac{T_0}{T_D}\right)}{L}. \quad (1)$$

Here T_0 is the maximum transmission, T_D denotes the transmission at 3000 cm^{-1}, L represents glass sample thickness, and α_{OH} is the absorption coefficient. For un-doped KZSB glass, the value calculated using the above relation is around α_{OH} = 1.577 ppm, which is lower than some previously published glasses ZKAlFB glass (8.631 ppm) [18], BaPbAlFB glass (89 ppm) [34], ZnAlBiB glass (65.2 ppm) [38], KBS glass (133 ppm) [39] and LBTAF glass (123 ppm)

Table 2 Assignment of FT-IR bands for an un-doped KZSB Glass

Wave number (cm^{-1})	FT-IR assignments
717	Bending of B–O–B linkages
924	Vibration of B–O in tetrahedral BO_4 units (Di-borate)
1049	Vibration of B–O in tetrahedral BO_4 units (tri-borate, tetra-borate, penta-borate)
1219	Vibration of B–O in trigonal BO_3 units
2112	Presence of OH group and hydrogen bond
2897	Stretching band of OH Group

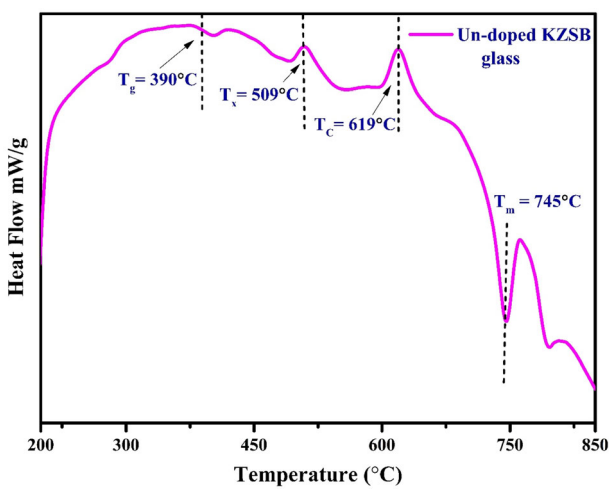


Fig. 3 DSC of an un-doped KZSB glass

[40] making it more suitable for w-LEDs and efficient lasers with lower non-radiative losses.

3.3 Thermal analysis

Figure 3 depicts the DSC of an un-doped KZSB glass sample that was recorded temperature range of 200–850 °C with 10 °C/min heating rate. The glass transition temperature (T_g), onset crystallisation temperature (T_x), Peak crystallisation temperature (T_c), melting temperature (T_m), are found to be 390 °C, 509 °C, 619 °C, and 745 °C, respectively.

The thermal stability (ΔT) of the as-prepared glass can be determined using the equation below [1, 2]:

$$\Delta T = T_x - T_g. \quad (2)$$

Higher values of ΔT slow down the crystallisation process, which favor the synthesis of glass. In the light of this, higher value of ΔT implies that the as-synthesised glass has a relatively high thermal stability. The evaluated ΔT in this study was found to be 117 °C, which is greater than the values observed for lead alumino borate [41] and OFSZBS glass [42] in previous research. It is clear from the literature that a glass is considered to be thermally more stable if its ΔT value is > 100 °C. The value of ΔT for the as-synthesized glass was determined to be > 100 °C, indicating that relatively thermally more stable and, thus, are ideally suited for the manufacturing of optoelectronic devices.

Hurby's parameter (K_H), which is another crucial factor in determining the glass's thermal stability, is calculated using the following equation [43].

$$K_H = (T_x - T_g)/(T_m - T_x). \quad (3)$$

K_H values should be greater than 0.1 for glass that are thermally stable [41]. The value of the K_H determined in the current work for an un-doped KZSB glass was discovered to be 0.496, indicating that the as prepared glass is thermally more stable.

3.4 Absorption spectral analysis

The absorption spectra were recorded for the un-doped and Dy^{3+} ion doped KZSB glasses in the range of 325–1800 nm and are shown in Fig. 4a, b. From the Fig. 4a, we can see that there is no band observed for the un-doped glass. Figure 4b exhibits eleven transitions from the ground state $^6H_{15/2}$ to various excited states. Among all the peaks, two peaks are in the UV

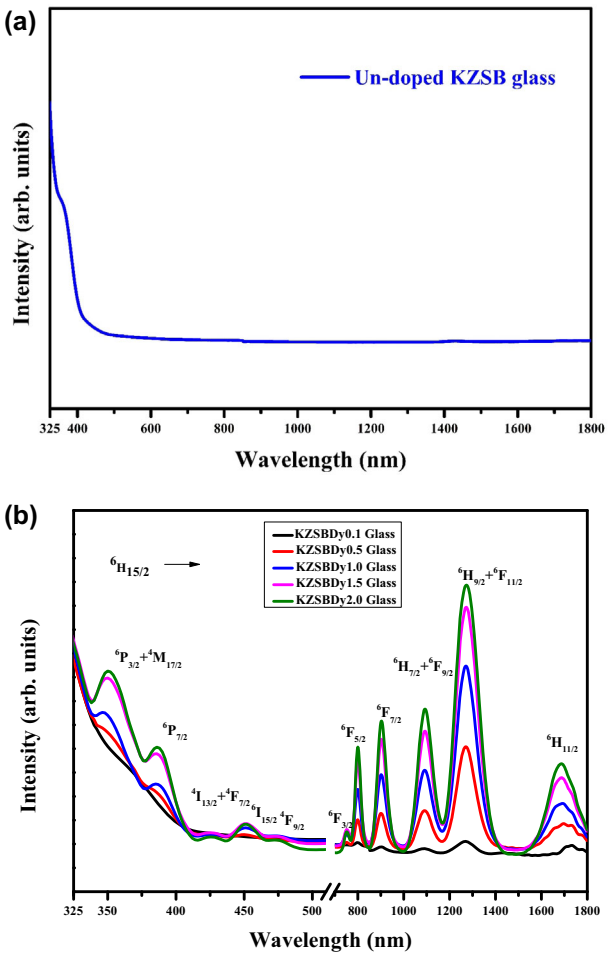


Fig. 4 **a** Absorption spectrum of an un-doped KZSB glass. **b** Absorption Spectra of KZSB:Dy^{3+} glasses

region corresponding to λ = 350 and 385 nm, three peaks in the visible region corresponding to λ = 427, 452 and 473 nm and the remaining six peaks are in the near-infrared (NIR) region corresponding to 750, 798, 902, 1093, 1273 and 1690 nm respectively. These transitions are ascribed from $^6H_{15/2}$ to ($^6P_{3/2}$ + $^4M_{17/2}$) [∼ 350 nm], $^6P_{7/2}$ [∼ 386 nm], ($^4I_{13/2}$ + $^4F_{7/2}$) [∼ 426 nm], $^4I_{15/2}$ [∼ 450 nm], $^4F_{9/2}$ [∼ 472 nm], $^6F_{3/2}$ [∼ 750 nm], $^6F_{5/2}$ [∼ 792 nm], $^6F_{7/2}$ [∼ 902 nm], ($^6H_{9/2}$ + $^6H_{7/2}$) [∼ 1093 nm], ($^6F_{11/2}$ + $^6H_{9/2}$) [∼ 1273 nm] and $^6H_{11/2}$ [∼ 1690 nm]. All the aforementioned bands have been allocated according to the work reported by Carnall et al. [44]. The intensity of the peaks in the UV, Vis and NIR regions differ significantly. The spin forbidden rule results in weak intensities in the UV and Vis region, while the spin allowed rule causes strong absorption intensities in the NIR region. As a result, the

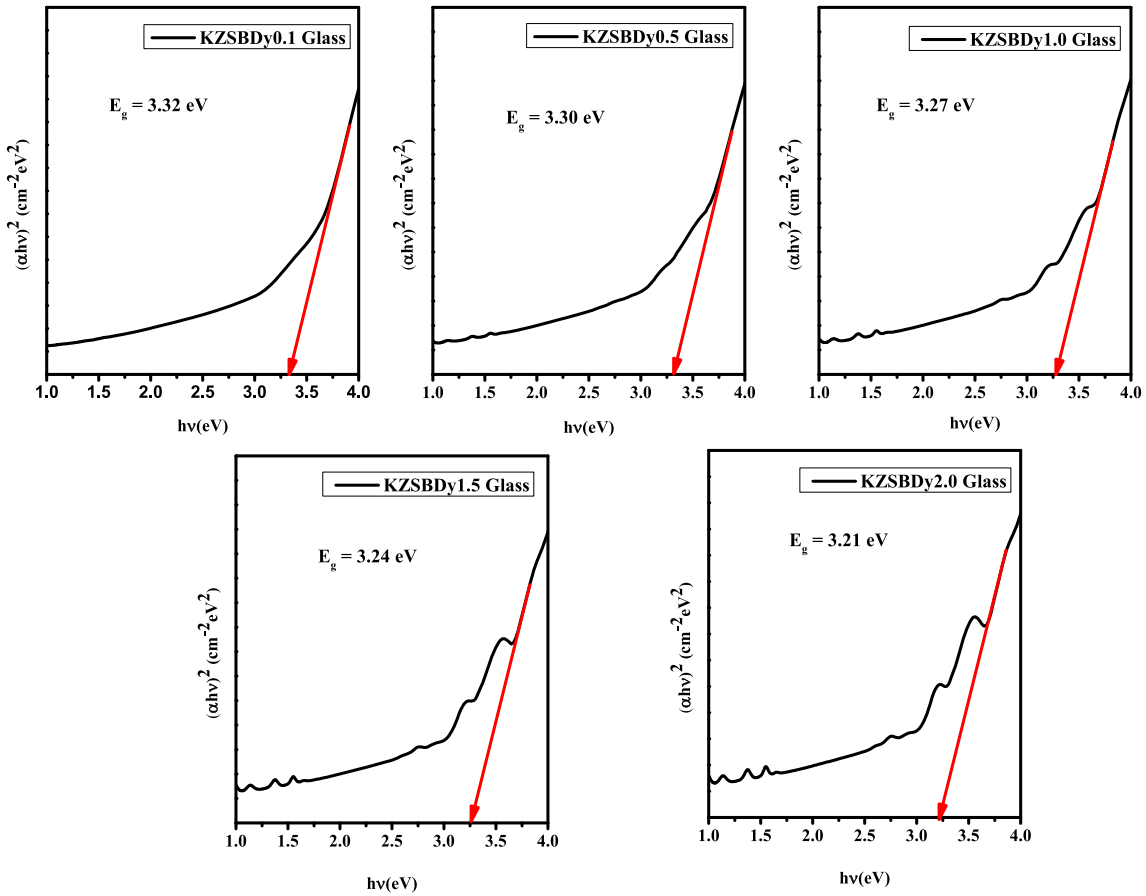


Fig. 5 Tauc plot for direct optical band gap of Dy^{3+} ions doped KZSB glasses at different concentrations

transition from $^6H_{15/2}$ to ($^6F_{11/2}$ + $^6H_{9/2}$) is considered a hypersensitive transition that adheres to the selection rules $|\Delta S| = 0$, $|\Delta L| \leq 2$ and $|\Delta J| \leq 2$ [45]. It also has the highest intensity among all transition peaks. As shown in Fig. 4b, with varying concentration of Dy^{3+} ions there are no shifting of band positions, although there is some change in their intensities.

Using absorption spectra, the optical band gaps were evaluated for the as-prepared KZSB glasses using Davis and Mott's expression [28]:

$$\alpha h\nu = C(h\nu - E_g)^n. \quad (4)$$

Here α, h, ν, C, E_g and n represent absorption coefficient, Plank's constant, frequency, bonding trailing parameter, optical band gap energy and index value respectively. Values of n can be 1/2, 2, 1/3 and 3 corresponding to direct allowed, indirect allowed, direct forbidden and indirect forbidden transitions, respectively. The measured band gap values of KZSB: x mol% Dy^{3+} glasses (x = 0.1, 0.5, 1.0, 1.5 and 2.0 mol%) were in the range of 3.21 to 3.32 eV as shown in Fig. 5. It was observed that the band gap values decrease with an increase in Dy^{3+} ions concentration. The reason behind the decrement of band gaps in the as prepared glasses is that the rare earth ion oxides alter the oxygen bonding in the glass network which causes the formation of non-bridging oxygen (NBO) atoms. These NBO atoms are at the valence band maximum (VBM) and increasing RE ion concentration shifts the NBO atoms towards the conduction band [2] leading to decrease in band gap values. There is a gradual expansion in the unit cell with an increase in the doping ion concentration in the host lattice increases. This tends to shorten the conduction and valance band thereby causing the band to broaden [46].

3.5 PL spectral analysis

To analyze the PL spectra of KZSB:Dy^{3+} glasses, it is necessary to recognize the appropriate excitation wavelength. Figure 6 shows the excitation spectra of

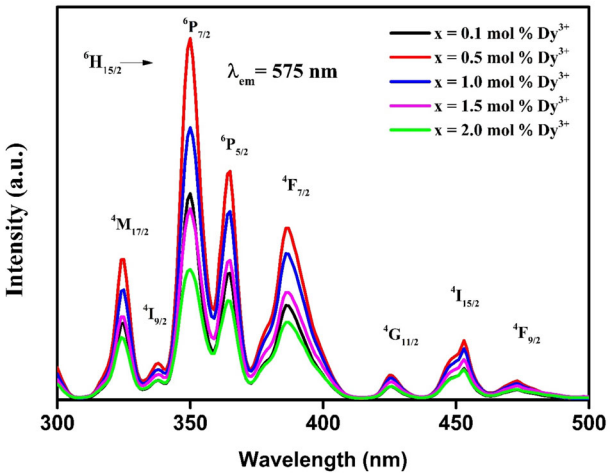


Fig. 6 Excitation spectra of Dy^{3+} doped KZSB glasses under λ_{em} = 575 nm

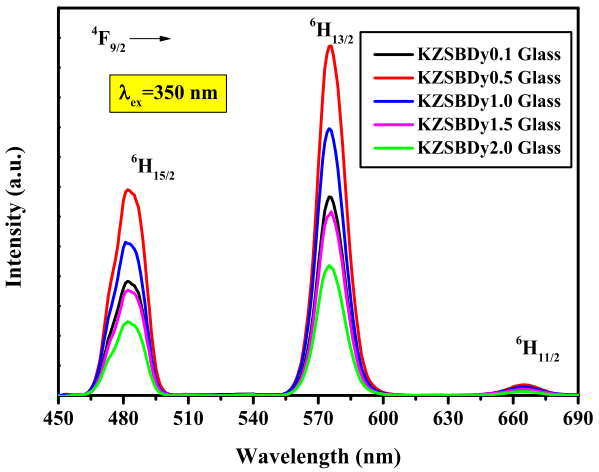


Fig. 7 PL emission spectra of Dy^{3+} ions doped KZSB glasses at λ_{ex} = 350 nm

as prepared KZSB:Dy^{3+} glasses in the 300–500 nm range monitored at 575 nm emission wavelength (λ_{em}). The spectra have eight peaks at 324, 337, 350, 364, 386, 425, 453 and 472 nm which correspond to the transitions from $^6H_{15/2}$ to ($^6P_{3/2}$ + $^4M_{17/2}$), $^4I_{9/2}$, $^6P_{7/2}$, $^6P_{5/2}$, ($^4I_{13/2}$ + $^4F_{7/2}$), $^4G_{11/2}$, $^4I_{15/2}$ and $^4F_{9/2}$ transitions respectively implying that an n-UV excitation source may be used efficiently to stimulate the Dy^{3+} ions [47]. Among all the observed transitions, the one corresponding to $^6H_{15/2} \rightarrow {}^6P_{7/2}$ (350 nm) is highly intense. Therefore, this wavelength was used for analysing the PL emission spectra of all the as-prepared KZSB:Dy^{3+} glasses [48].

The emission spectra of KZSB:Dy^{3+} glasses were recorded at λ_{ex} = 350 nm and have been presented in Fig. 7. Three peaks at 482 (blue), 575 (yellow) and 665 nm (red) were observed corresponding to the transitions $^4F_{9/2} \rightarrow {}^6H_{15/2}$, $^6H_{13/2}$ and $^6H_{11/2}$. As 5s and 5p outer electrons shield the 4f electrons, the position and shape of the bands do not change much with changing Dy^{3+} ion concentration. The yellow band present at 575 nm is the most intense among all the transitions.

The spectral intensities of the bands in the PL spectra corresponding to $^4F_{9/2} \rightarrow {}^6H_{15/2}$, $^6H_{13/2}$ and $^6H_{11/2}$ transitions increased with Dy^{3+} ions concentration up to 0.5 mol% and subsequently decreased. The decrease in the intensity of PL bands beyond 0.5 mol% of Dy^{3+} ions concentration was due to concentration quenching owing to the non-radiative energy transfer between Dy^{3+}–Dy^{3+} ions [49]. The average distance between Dy^{3+} ions in glass reduces as the concentration of Dy^{3+} ions rises, which may enhance the likelihood of energy transfer between RE ions through a non-radiative energy transfer process. The exchange interaction, radiation re-absorption and multipole–multipole interaction among Dy^{3+}–Dy^{3+} ions causes concentration quenching. There may occur three types of multipolar interactions namely dipole–dipole (D–D), dipole–quadrupole (D–Q) and quadrupole–quadrupole (Q–Q).

Dexter theory, which enunciates a relation between change in PL intensity and doping ions concentration, has been used to identify the energy transfer mechanism using the following relation [50]:

$$log\left(\frac{I}{x}\right) = log\, f - \frac{slog\,(x)}{d}. \quad (5)$$

Here, s describes the type of interactions and can take values closer to 6, 8 and 10 for D–D, D–Q and Q–Q interactions respectively [51]. The slope of linear fitted curve between log(I/x) and log(x) was used to calculated the (s/d) value as shown in Fig. 8. The value of s was calculated to be 5.09, which is very close to 6. Therefore it can be concluded that the energy transfer mechanism is caused by dipole–dipole interactions between the Dy^{3+} ions in KZSB glasses [52].

3.6 Y/B intensity ratio

In general, the luminescence intensity is inversely proportional to the site symmetry of RE ions. The Dy^{3+} ion has been given priority in solid-state

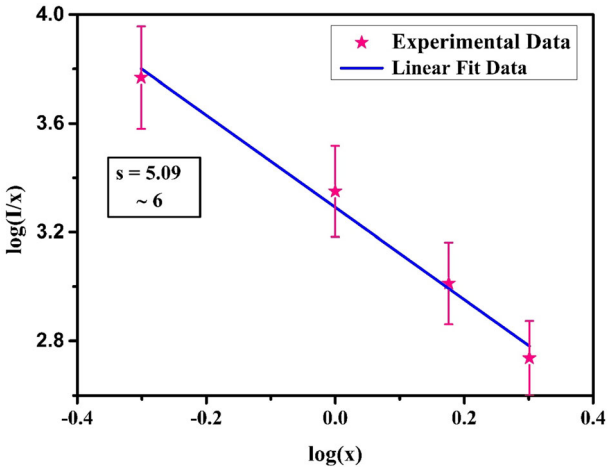


Fig. 8 Plot of log(I/x) versus log(x)

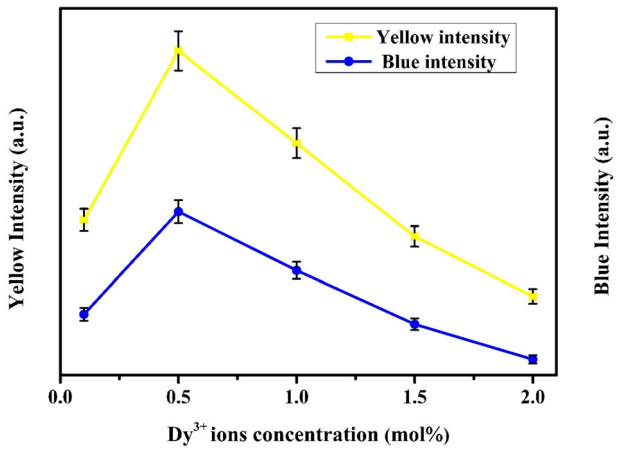


Fig. 9 Variation of emission intensities of $^4F_{9/2} \rightarrow {}^6H_{15/2}$ and $^4F_{9/2} \rightarrow {}^6H_{15/2}$ transitions with the increase of Dy^{3+} ions concentration in KZSB glasses

lighting appliances owing to the emission of primary colours essential for the formation of white light. Generally, by combining blue and yellow light in the right proportions, white light can be created [2]. The intensity of yellow band (at 575 nm) is relatively intense than that of blue band (482 nm) as shown in Fig. 7. Figure 9 gives the comparison of yellow (ED) and blue (MD) band intensities. The intensity ratios of yellow and blue bands are the ratios of their integrated intensities which play an important role in the generation of white light. The yellow to blue (Y/B) intensity ratio is primarily influenced by the excitation source, the concentration of dopant (here Dy^{3+}) ions and the host glass matrix. It was deduced that the deposition of fluorides in the as-prepared glasses is the primary cause of intensity variation between yellow and blue bands. The Y/B intensity ratio is heavily influenced by the local coordination and inversion symmetry around neighbouring Dy^{3+} ions [4, 34]. Furthermore, in the absence of inversion symmetry, it has been discovered that the local coordinated regions around Dy^{3+} ions are the least symmetric towards nearby atoms. The emission spectrum has an intense yellow band as compared to the blue one due to the higher covalency nature of the amide Dy^{3+} cation and the oxygen anion. The Y/B intensity ratios of the as prepared KZSB glasses are shown in Table 3 and are relatively higher than 1, which signify light generation in the white region [53]. The high covalent character of Dy^{3+} and O^{2-} ions is confirmed by the greater Y/B ratios. As a result, in the as-prepared KZSB glasses, KZSB:Dy2.0 indicates the greatest Y/B value and therefore, the highest covalency.

3.7 Energy transfer analysis

Figure 10 shows the energy level diagram of the as-prepared KZSB:Dy^{3+} glasses, which includes emission, excitation, energy transfer and cross relaxation (C-R) mechanisms. Dy^{3+} ions get excited to higher energy levels and then instantly fall to lower $^4F_{9/2}$ meta-stable state via a non-radiative decay mechanism to emit strong blue, yellow and a weak red colour. Following this, the Dy^{3+} ions return to the lower levels of $^6H_{15/2}$, $^6H_{13/2}$ and $^6H_{11/2}$ by radiative decay process. According to the emission spectra, it was observed that the PL intensity of the as-prepared KZSB:Dy^{3+} glasses increases till 0.5 mol% concentration of Dy^{3+} ions and then decreases. The resonant energy transfer (RET) between Dy^{3+}–Dy^{3+} ions causes this decrease in intensity, which explains the self-quenching and C–R processes [54].

The possible RET channel ($^4F_{9/2} \rightarrow {}^6H_{15/2}$) and C–R channels such as CR1 ($^4F_{9/2} + {}^6H_{15/2} \rightarrow {}^6H_{5/2} + ({}^6H_{7/2}, {}^6F_{9/2})$) and CR2 ($^4F_{9/2} + {}^6H_{15/2} \rightarrow {}^6F_{3/2} + ({}^6H_{9/2}, {}^6F_{11/2})$) have also been depicted in Fig. 10.

3.8 Colorimetric evaluation

The colorimetric performance of xDy^{3+} (x = 0.1, 0.5, 1.0, 1.5, 2.0 mol%) doped KZSB glasses was obtained using the PL emission spectrum data (at λ_{ex} = 350 nm). The CIE color model uses tristimulus values (a combination of 3 color values closer to red,

Table 3 Yellow to blue intensity ratio (Y/B) of Dy^{3+} ions doped KZSB glasses

Glass sample	Luminous intensity (a. u.)				Intensity ratio (Y/B)
	Yellow	Yellow (Er ±)	Blue	Blue (Er ±)	
KZSBDy0.1 Glass	1665.73	83.28656	957.32	47.86601	1.73
KZSBDy0.5 Glass	2931.40	146.57005	1726.54	86.32716	1.79
KZSBDy1.0 Glass	2238.88	111.9441	1286.06	64.30318	1.74
KZSBDy1.5 Glass	1541.18	77.05912	883.30	44.16499	1.75
KZSBDy2.0 Glass	1090.91	54.54551	618.79	30.93949	1.76

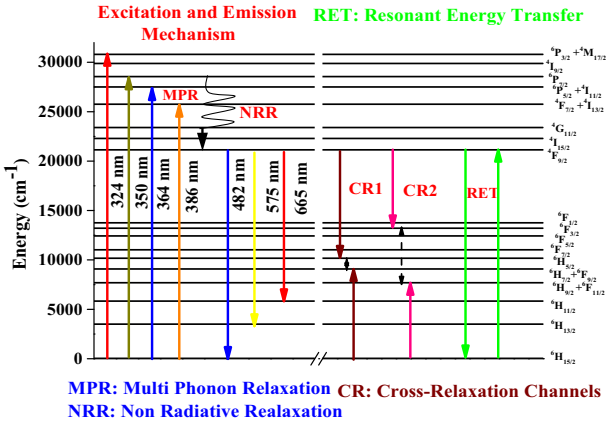


Fig. 10 Energy level diagram of Dy^{3+} doped KZSB glasses with excitation, emission and C-R channels

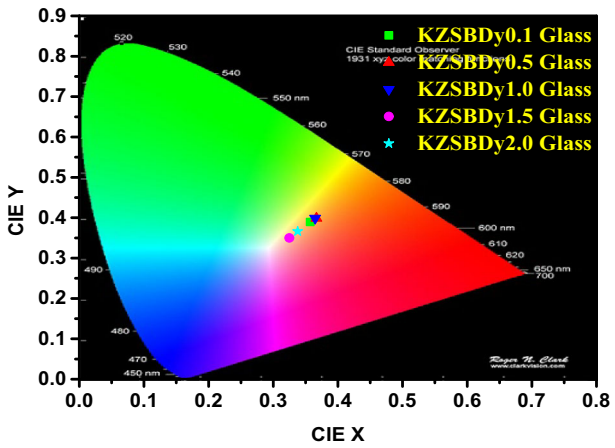


Fig. 11 CIE chromaticity coordinates of Dy^{3+} ions in KZSB glasses

green and blue) that are mapped on a 3D space. Human eye has three color sensitive cones so a combination of these values reproduce a colour that is perceivable by the human eye. So, CIE model basically takes into account the chromatic response of the eye as the color sensitive cones differ in their reaction to light and color in different areas of the retina. Since we want to deploy our glasses for luminescent applications, it is imperative to confirm that the luminescence from the material actually falls in the desired color region. Table 4 contains the evaluated CIE coordinates (x, y) and CCT values for the KZSB:xDy^{3+} glasses. Figure 11 represents the calculated CIE chromaticity coordinates for all of the as-prepared KZSB:Dy^{3+} glasses at λ_{ex} = 350 nm and λ_{em} = 575 nm. The coordinates lie in white region, which confirms that Dy^{3+} doped KZSB glasses are well suited for plasma display panels and solid state lighting [55].

The correlated colour temperature (CCT) is another important parameter in revealing the role and importance of RE^{3+} doped glasses. It defines the colour of a light source and not its brightness. The hue of the emitted light from a source can be defined by its CCT. The range of hue is from the amber to blue end of spectrum. So, it is an important parameter in deciding what colour of light the prepared material will emit under specific excitation. CCT is expressed in Kelvin and can range from warm light (3000 K) to daylight (6000 K) with neutral white light at around (4000 K). Mathematically, it was characterized as a black body temperature with colorimetric coordinates which are much more equivalent to that of a standard white light illuminant. McCamy provided a formula for calculating CCT given below [56]:

$$CCT = -449n^3 + 3525n^2 - 6823.2n + 5520.3. \quad (6)$$

Here, $n = \frac{x-xe}{y-ye}$ and x_e = 0.332, y_e = 0.186.

The evaluated values of CCT, presented in Table 4, are found in the neutral white luminescence region, making it appropriate for solid-state lighting

Table 4 CIE chromaticity coordinates and CCT values for as-prepared KZSBDy Glasses

Glass sample	CIE chromaticity coordinates (x,y)	CCT (K)
KZSBDy0.1 Glass	(0.3672, 0.3894)	4279.01
KZSBDy0.5 Glass	(0.3669, 0.3987)	4494.37
KZSBDy1.0 Glass	(0.3648, 0.3987)	4551.39
KZSBDy1.5Glass	(0.3249, 0.3499)	5828.14
KZSBDy2.0 Glass	(0.3379, 0.3663)	5304.23

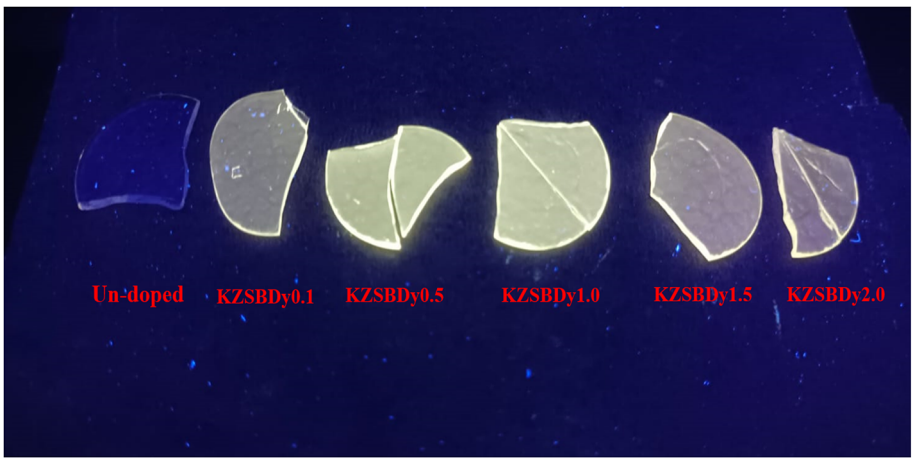


Fig. 12 Photograph of as prepared glass samples under UV-365 nm excitation

applications. As a result, it can be concluded that the as-prepared KZSB glasses have the capability to generate neutral white luminescence at λ_{ex} = 350 nm.

Color Purity (CP) is also a critical factor in colorimetric calculations used to investigate colour saturation. It defines how pure or monochromatic a color is at a particular lightness. The following formula can be used to estimate CP [55]:

$$\text{Colour purity} = \frac{\sqrt{(x - x_{ee})^2 + (y - y_{ee})^2}}{\sqrt{(x_d - x_{ee})^2 + (y_d - y_{ee})^2}}, \quad (7)$$

where, (x_{ee}, y_{ee}) represents equal energy point, (x, y) show colour coordinates of the as-prepared KZSB glasses and (x_d, y_d) represents point of dominant wavelength, respectively.

In previous research studies [57, 58], it was stated that CP should have low values for white light generation. From the calculations, value of the KZSB:Dy0.5 glass is the lowest (3.28×10^{-2}) [59]. Therefore, KZSB:Dy0.5 glass at λ_{ex} = 350 nm can be used to develop w-LEDs using a feasible n-UV chip as a pumping source.

Further confirming the emission color, the image of the prepared glass samples was recorded under UV light. Figure 12 shows the photographs of as-synthesized glasses under n-UV 365 nm light. The photos showed that the Dy^{3+}-doped KZSB glasses emit white color under n-UV excitation.

3.9 PL decay analysis

Figure 13 demonstrates the PL decay profiles for all the Dy^{3+} doped KZSB glasses. The luminescence decay from the $^4F_{9/2}$ state to different states has been analyzed at λ_{ex} = 350 nm and λ_{em} = 575 nm. Bi-exponential decay curves were observed for all the as-prepared glass samples. The bi-exponential character of the host glass matrices could be explained via energy transfer from donor ions to acceptor ions. The luminescent intensity can be expressed using the following equation:

$$I = I_0 + A_1 * \exp\left(-\frac{t}{\tau_1}\right) + A_2 * \exp\left(-\frac{t}{\tau_2}\right), \quad (8)$$

where I_0 and I are the luminescence intensities at t = 0 and at instant of time t, A_1 and A_2 are the decay constants and τ_1 and τ_2 are the luminescence decay lifetimes respectively.

The τ_{exp} values were estimated by using the following formula:

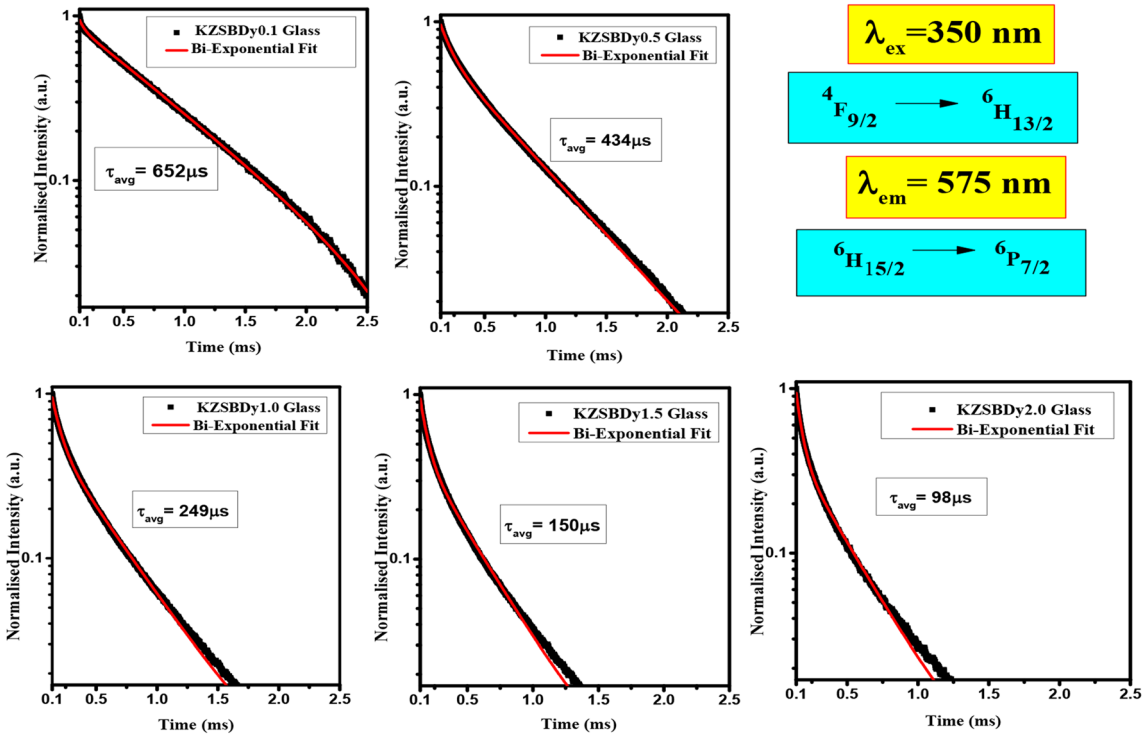


Fig. 13 PL decay profiles of Dy^{3+} ions doped KZSB glasses recorded under λ_{ex} = 350 nm

$$\tau_{exp} = \frac{A_1\tau_1^2 + A_2\tau_2^2}{A_1\tau_1 + A_2\tau_2}. \quad (9)$$

The τ_{exp} values of the as prepared Dy^{3+} doped glasses are 652, 434, 249, 150 and 98 μs, respectively. It was observed that the τ_{exp} values decrease as the concentration of Dy^{3+} ions increases. This could occur as a result of energy transfer between Dy^{3+}–Dy^{3+} via cross-relaxation (C-R) processes.

3.10 Temperature-dependent photoluminescence (TDPL)

To investigate the thermal quenching behaviour, the PL spectra of KZSB:Dy0.5 glass were recorded at excitation wavelength 350 nm within 30–180 °C temperature range and have been shown in Fig. 14. From the PL spectra of KZSBDy0.5 glass, it was observed that with rise in temperature the intensities of PL bands decrease without changing its peak position.

In addition, the activation energy (ΔE) was also evaluated to analyse the thermal properties of the glass sample. Using the Arrhenius equation, the value of ΔE was determined by applying the following formula [60]:

$$I_T = \frac{I_0}{1 + C\ \exp\left(-\frac{\Delta E}{K_B T}\right)}, \quad (10)$$

where I_0 and I_T are the PL emission intensities at room temperature and at any temperature T (in Kelvin), C is an arbitrary constant and K_B is the Boltzmann constant. As shown in Fig. 15, the slope of a linear fitted plot between ln $[(I_0/I_T) - 1]$ and $1/K_BT$ gives the value of ΔE. The value of ΔE for KZSBDy0.5

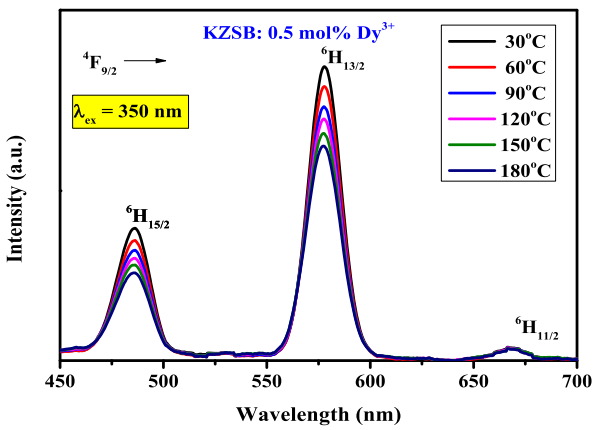


Fig. 14 Temperature-dependent PL emission intensity variation of KZSBDy0.5 glass at λ_{ex} = 350 nm with temperature from RT to 180 °C

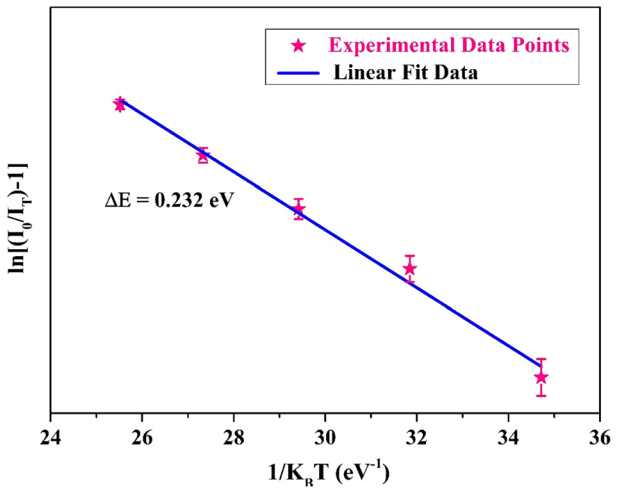


Fig. 15 Linear relationship of $\ln[(I_0/I_T) - 1]$ versus $1/K_BT$ plot to calculate the activation energy of 0.5 mol% Dy^{3+} doped KZSB glass

glass was found to be 0.232 eV which is relatively higher than the NBBPO: 9 mol% Dy^{3+} phosphor (ΔE = 0.192 eV) [61] and ZnAlNaPDy1.0 glass (0.212 eV) [62] which indicated the excellent thermal stability of KZSBDy0.5 glass.

Also, the thermal quenching may be caused by temperature-dependent non-radiative relaxations, as demonstrated in Fig. 14 The probability rate (R) of the non-radiative relaxations can be evaluated by applying the following formula [63]:

$$R = A \exp\left(\frac{-\Delta E}{K_B T}\right), \quad (11)$$

where the symbols ΔE, K_B and T used for activation energy, Boltzmann's constant and temperature, respectively. Here, A represents a constant. According to the given equation, R increases with temperature which increases the chance of non-radiative relaxations and hence there is a decrease in PL intensity. Figure 14 demonstrates the normalised intensity of the $^5D_0 \rightarrow {}^7F_2$ transition as a function of temperature, with the maximum emission intensity at 30 °C considered as 100%. The emission intensity drops to 69% at 180 °C, indicating that KZSBDy0.5 is thermally stable [64].

4 Conclusion

Dy^{3+} doped KZSB glasses were synthesized using the traditional melt quenching approach. XRD, FT-IR, UV–vis, PL excitation and emission, TDPL and PL decay spectral study have been conducted to investigate their structural, optical, and photoluminescence properties. XRD investigation reveals the amorphous behaviour of the un-doped KZSB glass. The FT-IR spectrum of an undoped glass indicates the presence of several functional groups as well as OH content. The superiority of the host glass is illustrated by the lower OH content (1.577 ppm) observed in the FT-IR spectrum. The optical band gap of prepared glasses was found in the range 3.21–3.32 eV which shows the applications of as-prepared glasses in optical devices having bandgap of this range. The as prepared glasses generate a mixture of highly intense yellow (575 nm), blue (482), and weak red (665 nm) light under λ_{ex} = 350 nm. The intensity of the emission bands in doped glasses increases up to 0.5 mol% concentration of Dy^{3+} ions after which concentration quenching occurs. The dipole–dipole interaction was estimated between Dy^{3+} ions Dexter hypothesis was applied to emission data. The Y/B ratio is close to 1, indicating that the Dy^{3+} ions have a high covalency. The CIE coordinates (0.367, 0.399) and colour purity (3.28×10^{-2}) for the optimized sample were found very close to the values described by NTSC. The evaluated τ_{exp} values decrease with an increase in the Dy^{3+} ions concentration showing energy transfer between Dy^{3+}–Dy^{3+} ions through C-R process. TDPL investigations for 0.5 mol% of Dy^{3+} ions doped KZSB glass affirmed its thermal stability. The above-mentioned investigations revealed that as-prepared Dy^{3+} ions doped KZSB glasses are well suited for solid state lighting (SSL) applications and fabricating photonic devices including w-LEDs and lasers.

Acknowledgements

One of the authors Ms. Sheetal Kumari would like to thank the University Grants Commission (UGC), Government of India for providing her with Junior Research Fellowship (JRF) to carry out her research work at Delhi Technological University [1431/(CSIR-UGC NET JUNE 2019)].

Author contributions

SK: work plan, experimental work, manuscript writing. Anu: experimental help, data analysis. AP: data analysis, validation of results, manuscript writing. PR: experimental help, calculations. ASR: work plan, validation of results, manuscript corrections.

Funding

Ms. Sheetal Kumari was supported by a Junior Research Fellowship (JRF) awarded by CSIR-UGC, Government of India [1431/(CSIR-UGC NET JUNE 2019)].

Data availability

The data that support the findings of this study are available on request from the corresponding author Prof. A.S. Rao. The data are not publicly available due to restrictions, e.g. their containing information that could compromise the privacy of research participants.

Declarations

Conflict of interest The authors declare that they have no known competing financial interests or personal relationships that could have appeared to influence the work reported in this paper.

References

1. R. Bajaj, A.S. Rao, G.V. Prakash, Photoluminescence down-shifting studies of thermally stable Eu^{3+} ions doped borosilicate glasses for visible red photonic device applications. J. Non Cryst. Solids **575**, 121184 (2022). https://doi.org/10.1016/j.jnoncrysol.2021.121184
2. P. Rekha Rani, M. Venkateswarlu, S. Mahamuda, K. Swapna, N. Deopa, A.S. Rao, Spectroscopic studies of Dy^{3+} ions doped barium lead alumino fluoro borate glasses. J. Alloys Compd. **787**, 503–518 (2019). https://doi.org/10.1016/j.jallcom.2019.02.088
3. J. Xi, G. Chen, F. Liu, F. Shang, J. Xu, C. Zhou, C. Yuan, Synthesis, microstructure and characterization of ultra-low permittivity CuO–ZnO–B_2O–Li_2O glass/Al_2O_3 composites for ULTCC application. Ceram. Int. **45**, 24431–24436 (2019). https://doi.org/10.1016/j.ceramint.2019.08.166
4. S. Kaur, A.K. Vishwakarma, N. Deopa, A. Prasad, M. Jayasimhadri, A.S. Rao, Spectroscopic studies of Dy^{3+} doped borate glasses for cool white light generation. Mater. Res. Bull. **104**, 77–82 (2018). https://doi.org/10.1016/j.materresbull.2018.04.002
5. Y. Gao, J. Qiu, D. Zhou, Investigation of optical properties: Eu with Al codoping in aluminum silicate glasses and glass-ceramics. J. Am. Ceram. Soc. **100**, 2901–2913 (2017). https://doi.org/10.1111/jace.14807
6. H. Wang, J. Liu, J. Zhai, B. Shen, Z. Pan, K. Yang, J. Liu, Effect of K_2O content on breakdown strength and energy-storage density in K_2O–BaO–Nb_2O_5–SiO_2 glass-ceramics. Ceram. Int. **43**, 4183–4187 (2017). https://doi.org/10.1016/j.ceramint.2016.12.042
7. M. Monisha, N. Mazumder, G. Lakshminarayana, S. Mandal, S.D. Kamath, Energy transfer and luminescence study of Dy^{3+} doped zinc-aluminoborosilicate glasses for white light emission. Ceram. Int. **47**, 598–610 (2021). https://doi.org/10.1016/j.ceramint.2020.08.167
8. D. Ramachari, L. Rama Moorthy, C.K. Jayasankar, Spectral investigations of Sm^{3+}-doped oxyfluorosilicate glasses. Mater. Res. Bull. **48**, 3607–3613 (2013). https://doi.org/10.1016/j.materresbull.2013.05.081
9. S.-F. Wang, Y.-F. Hsu, H.-C. Lu, S.-C. Lo, C.-S. Cheng, B_2O_3-free SiO_2–Al_2O_3–SrO–La_2O_3–ZnO–TiO_2 glass sealants for intermediate temperature solid oxide fuel cell applications. Int. J. Hydrog. Energy **37**, 5901–5913 (2012). https://doi.org/10.1016/j.ijhydene.2011.12.121
10. H. Gui, C. Li, C. Lin, Q. Zhang, Z. Luo, L. Han, J. Liu, T. Liu, A. Lu, Glass forming, crystallization, and physical properties of MgO–Al_2O_3–SiO_2–B_2O_3 glass-ceramics modified by ZnO replacing MgO. J. Eur. Ceram. Soc. **39**, 1397–1410 (2019). https://doi.org/10.1016/j.jeurceramsoc.2018.10.002
11. Y. Gao, Y. Hu, P. Ren, D. Zhou, J. Qiu, Effect of Li^+ ions on the enhancement upconversion and stokes emission of $NaYF_4$:Tb, Yb co-doped in glass-ceramics. J. Alloys Compd. **667**, 297–301 (2016). https://doi.org/10.1016/j.jallcom.2016.01.200
12. A. Mills, High-brightness LEDs lighting up the future. III-Vs Rev. **14**(1), 32–37 (2001). https://doi.org/10.1016/S0961-1290(01)89005-0
13. Z. Lei, G. Xia, L. Ting, G. Xiaoling, L.Q. Ming, S. Guangdi, Color rendering and luminous efficacy of trichromatic and tetrachromatic LED-based white LEDs. Microelectron. J. **38**, 1–6 (2007). https://doi.org/10.1016/j.mejo.2006.09.004
14. L.I. Panlai, W. Zhijun, Y. Zhiping, G.U.O. Qinglin, A potential single-phased white-emitting $LiBaBO_3$:Ce^{3+}, Eu^{2+} phosphor for white LEDs. J. Rare Earths **28**, 523–525 (2010). https://doi.org/10.1016/S1002-0721(09)60145-9

15. C. Zhu, Y. Yang, X. Liang, S. Yuan, G. Chen, Rare earth ions doped full-color luminescence glasses for white LED. J. Lumin. **126**, 707–710 (2007). https://doi.org/10.1016/j.jlumin.2006.10.028
16. A. Aboalatta, J. Asad, M. Humaid, H. Musleh, S.K.K. Shaat, K. Ramadan, M.I. Sayyed, Y. Alajerami, N. Aldahoudi, Experimental investigation of zinc sodium borate glass systems containing barium oxide for gamma radiation shielding applications. Nucl. Eng. Technol. **53**, 3058–3067 (2021). https://doi.org/10.1016/j.net.2021.04.002
17. Y. Gao, Y. Hu, D. Zhou, J. Qiu, Effect of crystalline fraction on upconversion luminescence in Er^{3+}/Yb^{3+} Co-doped $NaYF_4$ oxyfluoride glass-ceramics. J. Eur. Ceram. Soc. **37**, 763–770 (2017). https://doi.org/10.1016/j.jeurceramsoc.2016.09.036
18. A. Kumar, Anu, M.K. Sahu, Ravita, S. Dahiya, N. Deopa, A. Kumar, R. Punia, A.S. Rao, Spectral characteristics of Tb^{3+} doped ZnF_2–K_2O–Al_2O_3–B_2O_3 glasses for epoxy free tricolor w-LEDs and visible green laser applications. J. Lumin. **244**, 118676 (2021). https://doi.org/10.1016/j.jlumin.2021.118676
19. Y. Gao, S. Murai, K. Shinozaki, J. Qiu, K. Tanaka, Phase-selective distribution of $Eu^{2+}$and Eu^{3+} in oxide and fluoride crystals in glass-ceramics for warm white-light-emitting diodes. ACS Appl. Electron. Mater. **1**, 961–971 (2019). https://doi.org/10.1021/acsaelm.9b00129
20. Y. Gao, Y. Hu, P. Ren, D. Zhou, J. Qiu, Phase transformation and enhancement of luminescence in the Tb^{3+}-Yb^{3+} co-doped oxyfluoride glass ceramics containing $NaYF_4$ nanocrystals. J. Eur. Ceram. Soc. **36**, 2825–2830 (2016). https://doi.org/10.1016/j.jeurceramsoc.2016.04.027
21. S.A. Azizan, S. Hashim, N.A. Razak, M.H.A. Mhareb, Y.S.M. Alajerami, N. Tamchek, Physical and optical properties of Dy^{3+}: Li_2O–K_2O–B_2O_3 glasses. J. Mol. Struct. **1076**, 20–25 (2014). https://doi.org/10.1016/j.molstruc.2014.07.032
22. G.N. Carneiro, H. Vargas, J.A. Sampaio, Thermo-optical and structural properties of barium aluminoborate glasses. J. Alloys Compd. **777**, 1327–1333 (2019). https://doi.org/10.1016/j.jallcom.2018.11.044
23. Y. Gao, S. Murai, K. Fujita, K. Tanaka, Visible and near-infrared photoluminescence enhanced by Ag nanoparticles in Sm^{3+}-doped aluminoborate glass. Opt. Mater. (Amst) **86**, 611–616 (2018). https://doi.org/10.1016/j.optmat.2018.10.018
24. S. Mahamuda, K. Swapna, M. Venkateswarlu, A. Srinivasa Rao, S. Shakya, G. Vijaya Prakash, Spectral characterisation of Sm^{3+} ions doped Oxy-fluoroborate glasses for visible orange luminescent applications. J. Lumin. **154**, 410–424 (2014). https://doi.org/10.1016/j.jlumin.2014.05.017
25. T.Y. Lim, H. Wagiran, R. Hussin, S. Hashim, M.A. Saeed, Physical and optical properties of dysprosium ion doped strontium borate glasses. Phys. B Condens. Matter **451**, 63–67 (2014). https://doi.org/10.1016/j.physb.2014.06.028
26. A. Ichoja, S. Hashim, S.K. Ghoshal, Judd-Ofelt calculations for spectroscopic characteristics of Dy^{3+}-activated strontium magnesium borate glass. Optik (Stuttg) **218**, 165001 (2020). https://doi.org/10.1016/j.ijleo.2020.165001
27. P.P. Pawar, S.R. Munishwar, R.S. Gedam, Physical and optical properties of Dy^{3+}/Pr^{3+} Co-doped lithium borate glasses for W-LED. J. Alloys Compd. **660**, 347–355 (2016). https://doi.org/10.1016/j.jallcom.2015.11.087
28. M.A. Algradee, A.E.B. Alwany, M. Sultan, M. Elgoshimy, Q. Almoraisy, Physical and optical properties for Nd_2O_3 doped lithium-zinc-phosphate glasses. Optik (Stuttg) **142**, 13–22 (2017). https://doi.org/10.1016/j.ijleo.2017.05.065
29. H. George, N. Deopa, S. Kaur, A. Prasad, M. Sreenivasulu, M. Jayasimhadri, A.S. Rao, Judd-Ofelt parametrization and radiative analysis of Dy^{3+} ions doped Sodium Bismuth Strontium Phosphate glasses. J. Lumin. **215**, 116693 (2019). https://doi.org/10.1016/j.jlumin.2019.116693
30. X. Peng, Y. Pu, X. Du, J. Ji, S. Zhou, L. Zhang, The effect of glass network structure on interfacial polarization in Na_2O–K_2O–Nb_2O_5–SiO_2–BaO glass-ceramics. J. Alloys Compd. **845**, 155645 (2020). https://doi.org/10.1016/j.jallcom.2020.155645
31. K. Swapna, S. Mahamuda, A.S. Rao, T. Sasikala, P. Packiyaraj, L.R. Moorthy, G.V. Prakash, Luminescence characterization of Eu^{3+} doped Zinc Alumino Bismuth Borate glasses for visible red emission applications. J. Lumin. **156**, 80–86 (2014). https://doi.org/10.1016/j.jlumin.2014.07.022
32. S. Mahamuda, K. Swapna, P. Packiyaraj, A. Srinivasa Rao, G. Vijaya Prakash, Lasing potentialities and white light generation capabilities of Dy^{3+} doped oxy-fluoroborate glasses. J. Lumin. **153**, 382–392 (2014). https://doi.org/10.1016/j.jlumin.2014.03.009
33. O.B. Aljewaw, M.K.A. Karim, H.M. Kamari, M.H.M. Zaid, A.A. Salim, M.H.A. Mhareb, Physical and spectroscopic characteristics of lithium-aluminium-borate glass: Effects of varying Nd_2O_3 doping contents. J. Non Cryst. Solids **575**, 121214 (2022). https://doi.org/10.1016/j.jnoncrysol.2021.121214
34. P.R. Rani, M. Venkateswarlu, S. Mahamuda, K. Swapna, N. Deopa, A.S. Rao, G.V. Prakash, Structural, absorption and photoluminescence studies of Sm^{3+} ions doped barium lead alumino fluoro borate glasses for optoelectronic device applications. Mater. Res. Bull. **110**, 159–168 (2019). https://doi.org/10.1016/j.materresbull.2018.10.033
35. V. Venkatramu, P. Babu, C.K. Jayasankar, T. Tröster, W. Sievers, G. Wortmann, Optical spectroscopy of Sm^{3+} ions in phosphate and fluorophosphate glasses. Opt. Mater. (Amst)

29, 1429–1439 (2007). https://doi.org/10.1016/j.optmat.2006.06.011

36. S. Damodaraiah, V. Reddy Prasad, S. Babu, Y.C. Ratnakaram, Structural and luminescence properties of Dy^{3+} doped bismuth phosphate glasses for greenish yellow light applications. Opt. Mater. (Amst) **67**, 14–24 (2017). https://doi.org/10.1016/j.optmat.2017.03.023
37. C.R. Kesavulu, H.J. Kim, S.W. Lee, J. Kaewkhao, N. Chanthima, Y. Tariwong, Physical, vibrational, optical and luminescence investigations of Dy^{3+}-doped yttrium calcium silicoborate glasses for cool white LED applications. J. Alloys Compd. **726**, 1062–1071 (2017). https://doi.org/10.1016/j.jallcom.2017.08.091
38. K. Swapna, S. Mahamuda, A. Srinivasa Rao, S. Shakya, T. Sasikala, D. Haranath, G. Vijaya Prakash, Optical studies of Sm^{3+} ions doped Zinc Alumino Bismuth Borate glasses. Spectrochim Acta Part A Mol. Biomol. Spectrosc. **125**, 53–60 (2014). https://doi.org/10.1016/j.saa.2014.01.025
39. T. Som, B. Karmakar, Nephelauxetic effect of low phonon antimony oxide glass in absorption and photoluminescence of rare-earth ions. Spectrochim Acta Part A Mol. Biomol. Spectrosc. **79**, 1766–1782 (2011). https://doi.org/10.1016/j.saa.2011.05.054
40. T. Suhasini, B.C. Jamalaiah, T. Chengaiah, J. Suresh Kumar, L. Rama Moorthy, An investigation on visible luminescence of Ho^{3+} activated LBTAF glasses. Phys. B Condens. Matter **407**, 523–527 (2012). https://doi.org/10.1016/j.physb.2011.11.029
41. N. Deopa, A.S. Rao, S. Mahamuda, M. Gupta, M. Jayasimhadri, D. Haranath, G.V. Prakash, Spectroscopic studies of Pr^{3+} doped lithium lead alumino borate glasses for visible reddish orange luminescent device applications. J. Alloys Compd. **708**, 911–921 (2017). https://doi.org/10.1016/j.jallcom.2017.03.020
42. Anu, N. Deopa, A.S. Rao, Structural and luminescence characteristics of thermally stable Dy^{3+} doped oxyfluoride strontium zinc borosilicate glasses for photonic device applications. Opt. Laser Technol. **154**, 108328 (2022). https://doi.org/10.1016/j.optlastec.2022.108328
43. S.S. Danewalia, K. Singh, S.K. Arya, Influence of vanadium oxide on non-isothermal crystallization kinetics of zinc lithium borate glasses. J. Non Cryst. Solids **553**, 120471 (2021). https://doi.org/10.1016/j.jnoncrysol.2020.120471
44. W.T. Carnall, P.R. Fields, K. Rajnak, Electronic energy levels of the trivalent lanthanide aquo ions. IV. Eu^{3+}. J. Chem. Phys. **49**, 4424–4442 (1968). https://doi.org/10.1063/1.1669893
45. P. Taylor, J.C. Barthelat, P. Durand, A. Serafini, Non-empirical pseudopotentials for molecular calculations. Mol. Phys. **33**, 159–180 (1977)
46. S. Kaur, M. Jayasimhadri, A.S. Rao, A novel red emitting Eu^{3+} doped calcium aluminozincate phosphor for applications in w-LEDs. J. Alloys Compd. **697**, 367–373 (2017). https://doi.org/10.1016/j.jallcom.2016.12.150
47. M.K. Sahu, J. Mula, White light emitting thermally stable bismuth phosphate phosphor $Ca_3Bi(PO_4)_3$:Dy^{3+} for solid-state lighting applications. J. Am. Ceram. Soc. **102**, 6087–6099 (2019). https://doi.org/10.1111/jace.16479
48. S. Selvi, G. Venkataiah, S. Arunkumar, G. Muralidharan, K. Marimuthu, Structural and luminescence studies on Dy^{3+} doped lead boro-telluro-phosphate glasses. Phys. B Condens. Matter **454**, 72–81 (2014). https://doi.org/10.1016/j.physb.2014.07.018
49. Q. Meng, B. Chen, W. Xu, Y. Yang, X. Zhao, W. Di, S. Lu, X. Wang, J. Sun, L. Cheng, T. Yu, Y. Peng, Size-dependent excitation spectra and energy transfer in Tb^{3+}-doped Y_2O_3 nanocrystalline. J. Appl. Phys. **102**, 1–7 (2007). https://doi.org/10.1063/1.2803502
50. P. Du, X. Huang, J.S. Yu, Facile synthesis of bifunctional Eu^{3+}-activated $NaBiF_4$ red-emitting nanoparticles for simultaneous white light-emitting diodes and field emission displays. Chem. Eng. J. **337**, 91–100 (2018). https://doi.org/10.1016/j.cej.2017.12.063
51. S. Kaur, A.S. Rao, M. Jayasimhadri, Spectroscopic and photoluminescence characteristics of Sm^{3+} doped calcium aluminozincate phosphor for applications in w-LED. Ceram. Int. **43**, 7401–7407 (2017). https://doi.org/10.1016/j.ceramint.2017.02.129
52. I. Kumar, A.K. Gathania, Photoluminescence and quenching study of the Sm^{3+}-doped $LiBaPO_4$ phosphor. J. Mater. Sci. Mater. Electron. **33**, 328–341 (2022). https://doi.org/10.1007/s10854-021-07301-7
53. T. Srihari, C.K. Jayasankar, Fluorescence properties and white light generation from Dy^{3+}-doped niobium phosphate glasses. Opt. Mater. (Amst) **69**, 87–95 (2017). https://doi.org/10.1016/j.optmat.2017.04.001
54. R. Bajaj, A.S. Rao, G.V. Prakash, Linear and nonlinear photoluminescence from thermally stable KYF_4:Eu^{3+} cubic nanocrystals. J. Alloys Compd. **885**, 160893 (2021). https://doi.org/10.1016/j.jallcom.2021.160893
55. Poonam, Shivani, Anu, A. Kumar, M.K. Sahu, P.R. Rani, N. Deopa, R. Punia, A.S. Rao, Judd-Ofelt parameterization and luminescence characterization of Dy^{3+} doped oxyfluoride lithium zinc borosilicate glasses for lasers and w-LEDs. J. Non Cryst. Solids. **544**, 120187 (2020). https://doi.org/10.1016/j.jnoncrysol.2020.120187
56. C.S. McCamy, Correlated color temperature as an explicit function of chromaticity coordinates. Color Res. Appl. **17**, 142–144 (1992). https://doi.org/10.1002/col.5080170211

57. N. Deopa, S. Saini, S. Kaur, A. Prasad, A.S. Rao, Spectroscopic investigations on Dy^{3+} ions doped zinc lead alumino borate glasses for photonic device applications. J. Rare Earths **37**, 52–59 (2019). https://doi.org/10.1016/j.jre.2018.04.013
58. P. Babu, K.H. Jang, C.S. Rao, L. Shi, C.K. Jayasankar, V. Lavín, H.J. Seo, White light generation in Dy^{3+}-doped oxyfluoride glass and transparent glass-ceramics containing CaF_2 nanocrystals. Opt. Express **19**, 1836–1841 (2011)
59. S. Kaur, D. Arora, S. Kumar, G. Singh, S. Mohan, P. Kaur, Kriti, P. Kaur, D.P. Singh, Blue-yellow emission adjustability with aluminium incorporation for cool to warm white light generation in dysprosium doped borate glasses. J. Lumin. **202**, 168–175 (2018). https://doi.org/10.1016/j.jlumin.2018.05.034
60. Ravita, A.S. Rao, Effective energy transfer from Dy^{3+} to Tb^{3+} ions in thermally stable KZABS glasses for intense green emitting device applications. J. Lumin. **239**, 118325 (2021). https://doi.org/10.1016/j.jlumin.2021.118325
61. E.A. Rathnakumari, S.M.M. Kennedy, Synthesis and photoluminescence characteristics of the near white emitting Dy^{3+} ions activated $NaMBi_{2-x}(PO_4)_3$ [M: Ba/Ca/$Ca_{0.5}$+$Sr_{0.5}$/Sr/$Sr_{0.5}$ + $Ba_{0.5}$] phosphors. Optik (Stuttg) **275**, 170601 (2023). https://doi.org/10.1016/j.ijleo.2023.170601
62. A. Vidhi, A. Ankita, A. Anu, A.S. Rao, Spectroscopic characterizations of Dy^{3+} ions doped phosphate glasses for epoxy-free white LED applications. Opt. Mater. (Amst) **132**, 112863 (2022). https://doi.org/10.1016/j.optmat.2022.112863
63. M.K. Sahu, H. Kaur, B.V. Ratnam, J.S. Kumar, M. Jayasimhadri, Structural and spectroscopic characteristics of thermally stable Eu^{3+} activated barium zinc orthophosphate phosphor for white LEDs. Ceram. Int. **46**, 26410–26415 (2020). https://doi.org/10.1016/j.ceramint.2020.07.263
64. M.K. Sahu, M. Jayasimhadri, Conversion of blue emitting thermally stable $Ca_3Bi(PO_4)_3$ host as a color tunable phosphor via energy transfer for luminescent devices. J. Lumin. **227**, 117570 (2020). https://doi.org/10.1016/j.jlumin.2020.117570

Publisher's Note Springer Nature remains neutral with regard to jurisdictional claims in published maps and institutional affiliations.

Springer Nature or its licensor (e.g. a society or other partner) holds exclusive rights to this article under a publishing agreement with the author(s) or other rightsholder(s); author self-archiving of the accepted manuscript version of this article is solely governed by the terms of such publishing agreement and applicable law.

Journal of Molecular Modeling (2023) 29:120
https://doi.org/10.1007/s00894-023-05515-6

ORIGINAL PAPER

Rare deleterious mutations in Bruton's tyrosine kinase as biomarkers for ibrutinib-based therapy: an *in silico* insight

Jaishree Meena[1] · **Yasha Hasija**[1]

Received: 21 November 2022 / Accepted: 14 March 2023
© The Author(s), under exclusive licence to Springer-Verlag GmbH Germany, part of Springer Nature 2023

Abstract

Context Squamous cell carcinoma (SCC) is the second most common type of skin cancer caused by malignant keratinocytes. Multiple studies have shown that protein mutations have a significant impact on the development and progression of cancer, including SCC. We attempted to decode the effect of single amino acid mutations in the Bruton's tyrosine kinase (BTK) protein in this study. Molecular dynamic (MD) simulations were performed on selected deleterious mutations of the BTK protein, revealing that the variants adversely affect the protein, indicating that they may contribute to the prognosis of SCC by making the protein unstable. Then, we investigated the interaction between the protein and its mutants with ibrutinib, a drug designed to treat SCC. Even though the mutations have deleterious effects on protein structure, they bind to ibrutinib similarly to their wild type counterpart. This study demonstrates that the effect of detected missense mutations is unfavorable and can result in function loss, which is severe for SCC, but that ibrutinib-based therapy can still be effective on them, and the mutations can be used as biomarkers for Ibrutinib-based treatment.

Methods Seven different computational techniques were used to compute the effect of SAVs in accordance with the experimental requirements of this study. To understand the differences in protein and mutant dynamics, MD simulation and trajectory analysis, including RMSD, RMSF, PCA, and contact analysis, were performed. The free binding energy and its decomposition for each protein-drug complex were determined using docking, MM-GBSA, MM-PBSA, and interaction analysis (wild and mutants).

Keywords Bruton's tyrosine kinase · Ibrutinib · MD simulation · Molecular docking · Contact map analysis · Mutational analysis · Protein-ligand interaction

Introduction

Squamous cell carcinoma (SCC) is the second most highly prevalent skin tumor that develops when keratinocytes alter and turn cancerous. Invasive SCC continues to be influenced by everyday UV exposure to the skin. Global disease rates are on the rise due to aging populations and other demographic shifts [1]. SCC is significant because it occurs twice as frequently as skin cancer in European Caucasians and up to ten times as frequently in fair-skinned Australians, where the incidence is even greater [2]. The fact that SCC strikes men more frequently than women suggests that female immunity may play some role in protecting against the disease, as evidenced by recent studies [3]. People with light skin and light eyes are more likely to develop SCC beyond the age of 50. It often develops in sites that have been exposed to the sun in the past. Those with a history of extensive exposure to UV, whether through previous medical procedures or the sun, are at a higher risk [4]. Immunosuppressed patients also have a high incidence of, which can progress into aggressive subtypes [5]. Small SCC lesions can be removed and are not lethal, but depending on their location, they might cause severe morbidity [6]. Most head and neck squamous cell malignancies necessitate extensive surgery, which, even in the best of hands, can result in poor symptom relief. In addition, the expense of treating these tumors increases each year, posing a critical need to explore low cost, effective, and efficient treatment options for SCC management [7, 8].

✉ Yasha Hasija
yashahasija6oct@gmail.com; yashahasija@dtu.ac.in

[1] Department of Biotechnology, Delhi Technological University, Delhi 110042, India

Published online: 29 March 2023

The significance of amino acid variations as hereditary risk factors for human disease, especially cancer, has been recognized for decades [9]. Protein expression and function, its subcellular localization, folding, and integrity and protein-protein interactions (PPI) can all be impacted by mutations. The genesis and progression of cancer are significantly influenced by protein mutations. The variety of mutation's effects on molecular function determines their unique role [10]. Oncogenes and tumor suppressors are examples of proteins where mutations can activate or inactivate protein activity. After realizing the critical role mutations play in cancer cause and progression, the scientific community began conducting systematic, widespread screening of tumor tissues for mutations. Every year, hundreds of cancer-associated protein mutations are revealed as a result of numerous re-sequencing initiatives, and thousands more are very certainly still to come [11].

In this study, we are trying to decipher the effect of mutations that are found in Bruton's tyrosine kinase (BTK) protein using computational methods. BTK belongs to the Tec tyrosine kinase family and is a non-receptor cytoplasmic tyrosine kinase. The Tec kinase family, which includes BTK, TEC, ITK, BMX, and RLK, is the second largest family of cytoplasmic tyrosine kinases [12]. BTK is known primarily for its role in B-lymphocyte development and BCR-mediated signaling [13]. The tumor microenvironment is a multifaceted and intricate system of cells and their precursors, and all of these cells contribute to the emergence of cancer [14]. Acknowledging these discoveries, scientists are considering BTK as a therapeutic target for solid tumors [15]. Further, we tried to find the impact of the mutation on ibrutinib-binding affinity. Ibrutinib, which is also known by its drug code name PCI-32765, is an innovative medication that inhibits BTK in an irreversible manner and was envisioned as a possible therapy for a number of cancers originating in the B-cell lineage; hence, we chose this drug for our MD simulation study [16].

Several computational pipelines can be used to investigate genes and variants associated with SCC. These pipelines not only help identify prospective genes and pathogenic mutations but also shed light on aberrations in the target gene product's structure and molecular mechanisms. To examine the structural basis of alterations, reveal underlying molecular mechanisms, and ascertain their pharmacological influence, we tried to make use of MD simulations and other *in silico* techniques to explore the influence of mutations namely F413L, P566Q, G584E, and E589K on the BTK protein and its binding with the ibrutinib drug for SCC treatment.

Material and methods

Data retrieval

Mutations across the BTK gene that are specifically observed in SCC were retrieved through the COSMIC (Catalog of Somatic Mutations in Cancer) database (URL: https://cancer.sanger.ac.uk/cosmic). The COSMIC database is the most comprehensive source of information on somatic mutations that are associated with human cancers. This database contains information on over 2500 distinct cancer types. The database gathers data from two primary sources. As a starting point, the literature is mined for alterations in well-established cancer genes, and the Cancer Gene Census is used to identify the genes that are manually curated [17]. Second, the Cancer Genome Project collects whole genome sequencing data from cancer samples for placement in the database [18]. A comprehensive literature survey was conducted to find the BTK-targeting drug used in SCC treatment. DrugBank (URL: https://go.drugbank.com/) was also searched to validate the role of identified drug in SCC treatment [19].

Mutation analysis

A total of seven computational tools, namely, the mutation assessor, SIFT, PON-P2, SNPs&GO, PROVEAN, PolyPhen-2, and MutPred2, were used to assess each of the mutations associated with the BTK gene previously retrieved from the COSMIC database for its deleteriousness. Mutations that were found to be harmful for all seven tools were subjected to the simulation study. All the selected tools can help in evaluating a huge number of mutations by making use several of computational algorithms and machine learning (ML) classifiers, such as support vector machine, random forest, decision tree, and neural network (NN). In addition to putting pathogenicity into categories, these tools give additional data about the functional influence of mutations [20]. Mutation assessor (URL: http://mutationassessor.org/r3/) uses a multiple sequence alignment (MSA) to describe the functional effects of a missense variation; the MSA is divided into sub-alignments that take into account the conservation scores and the functional specificity of each mutation. Combining a conservation score and a specificity score yields a functional impact score of the input mutation. Protein function is projected to be unaffected by "neutral" or "low" variants, whereas it is projected to get affected by "medium" or "high' variants [11, 21]. SIFT (URL: https://sift.bii.a-star.edu.sg/) Web Server is a novel sequence homology-based *in silico* approach

that examine the influence of coding mutations at a particular location on the phenotypic effect of proteins [22]. PON-P2 (URL: http://structure.bmc.lu.se/PON-P2/) is a computational meta-predictor of mutation tolerance. It categorizes amino acid changes into three classes: harmful, neutral, and tolerance unknown. PON-P2 is based on a random forest classifier that has been developed and found to be effective on benchmark datasets to predict harmful and pathogenic mutations by employing evolutionary sequence conservation features, amino acid characteristics, GO annotations, and functional annotations, if available [23]. SNPs&GO (URL: https://snps.biofold.org/snps-and-go/) is a suitable ML-based tool that visualizes the link between single amino acid variants (SAVs) and a given condition using protein functional annotation. To distinguish normal SAVs from disease-causing ones, this computational tool employs a binary SVM classifier. The functional score provided by SNPs&GO is an empirical estimate of how likely it is that a protein has a harmful SAV based on the related GO terms [24]. PROVEAN (Protein Variation Effect Analyzer) (URL: https://www.jcvi.org/research/provean) is another sequence-based computational tool that predicts the potentially damaging effects of mutations in sequences of protein. A non-synonymous SNP (nsSNP) in a MSA triggers a mutation in the symmetry of closely related protein sequences, which is the basis of the prediction output. PROVEAN uses a delta alignment score calculated from both the native and mutant protein sequences to compare homologous sequences. A threshold of -2.5 is set to identify the deleterious protein variants, so an nsSNP with a score equal to or less than this threshold value will be considered a detrimental mutation [25]. PolyPhen-2 (URL: http://genetics.bwh.harvard.edu/pph2/) is a program and a web server that uses structural and evolutionary similarities to foretell how changes in amino acids would affect the structural stability and proper functioning of human proteins. It annotates functional SNPs, links coding SNPs to transcripts, and structurally characterizes proteins to build conservation profiles. All these features are then used to assess the missense mutation's potential pathogenicity [26]. MutPred2 (URL: http://mutpred.mutdb.org/) is a ML technique based on neural networks that uses genetic and molecular information to provide a probabilistic assessment of the pathogenicity of amino acid variations. MutPred2 presently replicates a variety of physical and functional features of proteins, including their secondary structure, transmembrane organization and different signaling pathways, their catalytic efficiency, macromolecular interaction, post-translational alterations, metal binding, and allostery [27].

The amino acid changes that were considered to be the most harmful by all these seven tools used were chosen for molecular dynamic study to check the structural integrity and functionality of the BTK protein with the observed mutations.

Molecular dynamic study

Molecular dynamic simulation is utilized to comprehend the influence of structural alterations in a mutant protein relative to its natural assembly (wild type) and their interactions with a drug. We retrieved the three-dimensional structure of BTK1 co-crystalized with ligand (PDB ID: 5P9J) resolved at 1.08 A° from RCSB PDB (URL: https://www.rcsb.org/) for simulation investigations after removing the ligand [28]. The Swiss PDB Viewer (SPDBV) was used to induce mutations in the wild type structure of BTK protein. SPDBV is a tool for visualizing protein structures on multiple platforms. In addition to structure modeling, the application allows for the computation and viewing of protein electrostatic potentials [29]. Energy minimization of structures was done through GROMACS version 21 [30], and by using the CHARMM-GUI's (URL: https://www.charmm-gui.org/) solution builder program, five structures were prepared for MD simulation. This simulation study employed a TIP3 rectangular water box function with 10 A° amid box edges. By means of the all-atom additive force field CHARMM36 (C36) [31] protein force field function and the generic protein drug complex force field CHARMM (Chemistry at Harvard Macromolecular Mechanics), the topologies and coordinates for each system were generated [32]. Counter sodium and chlorine ions were added to each system to make them neutral. We used GROMACS version 21 for the simulation purpose. To decrease steric repulsions, each system has undergone fifty thousand steps of sharpest descent minimization of energy. The NVT equilibration was executed for five hundred picoseconds to maintain a consistent temperature in the system, and a brief orientation limitation NPT was also executed for five hundred picoseconds to keep a constant pressure in the system by relaxing them while retaining the protein in place. All systems were subjected to a hundred nanosecond (ns) simulation under no constraints. GROMACS utilities were applied to analyze the trajectory file. The root mean square deviation (RMSD) was computed with the help of the gmx_rmsd file, while the root mean square fluctuation (RMSF) was computed with the help of the gmx_rmsf file.

Principle component analysis on wild type and mutant BTK proteins

We considered using PCA to quantify the variance between the trajectories of the wild and mutant proteins. Calculating and diagonalizing the covariance matrix for carbon-alpha (Cα) atoms is an essential part of principal component analysis (PCA). This helps uncover the accumulated modes of protein structural variations [33]. For the objective of

identifying fluctuations in wild type and mutant proteins from their respective last 25 ns of the simulation trajectories, we conduct PCA on molecular dynamic trajectory files using the scikit-learn Python package [34]. The PCs, or eigenvectors, were extracted from the wild and mutant BTK protein structures and displayed as cluster groups.

CONAN analysis for wild type and mutant BTK proteins

CONAN was also used to determine how each amino acid residue in the wild and mutant BTK proteins might interact with other amino acid residues and to create contact maps for them. CONAN operates within the GROMACS molecular dynamic engine's mdmat tool [35]. It was designed to investigate the statistical and dynamic properties of contacts in order to collect data on how contacts between atoms change over time in molecular dynamic simulations (MD). The software can also read a set of input files that define any variable against which it can determine whether a connection between two contacts was made or broken. CONAN assigned a contact map to each atom in the simulated structure, and the average of these maps was compared for both the wild and mutant BTK proteins.

Docking and contact analysis

Ibrutinib is an irreversible, ATP-competitive kinase inhibitor that works by replacing ATP in the substrate binding site of mutant BTK proteins, rendering them inactive and leading to tumor regression. We docked the wild and mutant BTK proteins with ibrutinib to establish the mutant protein's relative affinity for ibrutinib binding. Water molecules were excluded from the final simulated structure of each system, i.e., the 100th ns structure. Ibrutinib's three-dimensional structure was obtained from PubChem and then docked via AutoDockTools using AutoDock 4.2 [36]. The grid box was generated by assigning the coordinates of the CA atoms in C481 to its center and spacing the resulting points outward by 60 on each axis. Then, the complexes were simulated using the abovementioned protocol for 100 ns.

The MM-PBSA (Molecular Mechanics Poisson-Boltzmann Surface Area) is a reliable and efficient free energy simulation tool that has been widely used to mimic molecular affinity, including protein-ligand binding interactions [37]. When used in conjunction with molecular dynamic (MD) simulations, MM-PBSA can incorporate conformational and entropic variables into the binding energy. This method has also been utilized to provide a thorough understanding of biomolecular interactions, by decomposing the total binding energy into many sections. In this study, we provide the results of MM-PBSA analyses conducted with 1000 snapshots of the MD-trajectory acquired at 25 ps intervals between 76 and 100 ns. We have also tested the wild type and mutant protein-drug complexes with the MM-GBSA technique. MM-GBSA (molecular mechanics with generalized born and surface-area solvation) is one of the most widely used *in silico* approaches for estimating protein–ligand binding energies, finding key residues in PPIs, and assessing macromolecular stability [38]. Utilizing the gmx_MMPBSA package [39], the free binding energy of BTK-ibrutinib complexes was calculated by interaction entropy method [40].

PyContact was used to perform contact analysis on residues surrounding wild type and mutant protein-drug complexes during the final 25 ns of the trajectory. PyContact is a user-friendly, highly configurable, and intuitive application with a GUI designed to analyze biomolecular interaction in molecular dynamic trajectories. PyContact is intended to assist this effort by facilitating the recognition of significant non-covalent interactions in an understandable way, offering rapid data analysis and visual representation of data without the need for extra programming, by providing entire in-program personalization and comprehensive options for cutting-edge users [41].

Results

Retrieval of variations and drug associated with BTK protein

Mutations across the BTK gene that are specifically identified in SCC were retrieved using the COSMIC (Catalog of Somatic Mutations in Cancer) database. A total of 47 distinct SCC mutations were identified using advanced filters, including whole genome screening and target screening as screen types, skin as the SCC cancer tissue location, missense mutations, and their pathogenic impact. A comprehensive literature search was conducted to identify the BTK-targeting drug used in SCC treatment, and we have found ibrutinib for our investigation. DrugBank was also examined to validate the role of ibrutinib (DrugBank Accession No. DB09053) in BTK inhibition. Ibrutinib (PCI-32765) is categorized as a targeted covalent drug, and it is a propitious anti-cancer treatment for skin cancers [15, 16, 19, 42].

Mutational analysis

A total of seven computational methods, namely, mutation assessor, SIFT, PON-P2, SNPs&GO, PROVEAN, PolyPhen-2, and MutPred2, were utilized to evaluate the deleteriousness of each variant associated with the BTK gene. We have found F413L, P566Q, G584E, and E589K amino acid variants with the most anticipated adverse impacts, based on all the *in silico* analysis techniques, as detailed in Table 1.

Table 1 Mutations that were determined to be detrimental by all seven tools

Uniprot_ID/mutation	Mutation assessor	SIFT	Pon-P2	SNPs&GO	PROVEAN	PolyPhen-2	MutPred-2
E589K	4.225	0	0.958	9	-3.944	0.999	0.946
G584E	5.075	0	0.842	9	-7.908	1	0.871
P566Q	5.055	0	0.859	8	-7.936	1	0.838
F413L	3.665	0	0.779	9	-5.616	1	0.905

Mutation assessor gives each amino acid in a protein a score between -5.2 and 6.5 based on its functional impact. A score greater than 3.5 is deemed deleterious to the protein's proper functioning [11]. SIFT calculates the likelihood that an amino acid at a specific site will be tolerated, assuming that the most common amino acid is tolerated. If this normalized value falls below a threshold of 0.05, it is believed that the substitution will be damaging [22]. PON-P2 employs a cut-off value of 0.5; for an amino acid variant to be classified as pathogenic, its probability score must be higher than this cut-off value [23]. SNPs&GO computes the prediction's reliability index, where a score of 0 indicates an unreliable prediction and a score of 10 indicates the most reliable prediction [24]. For each supporting sequence in PROVEAN, a "delta alignment score" is worked out. The final PROVEAN score is the average of cluster-level values. The protein variation is likely to have a "deleterious" effect if the PROVEAN score is -2.5 or less. If the PROVEAN score is more than this cutoff, the effect of the variant is judged to be "neutral" [25]. PolyPhen-2 looks at the polyphen probability scores to figure out what will happen. Scores between 0 and 0.15 are thought to be harmless. Scores between 0.15 and 1.0 show a variant that could be harmful, while scores between 0.85 and 1.0 are more likely to be harmful in the long run [26]. MutPred2 provides a general score as its final output, which is the likelihood that the amino acid mutation is pathogenic. Each neural network's score in MutPred2 has been averaged to produce this result. A score cut-off of 0.50, if regarded as a probability, would infer pathogenicity [27]. F413L, P566Q, G584E, and E589K scores passed each computational tool's cut-off value, so we selected them for molecular dynamic analysis to find their impact on proteins structural stability.

Molecular dynamic simulation analysis

Molecular dynamic simulation is utilized to comprehend the influence of structural alterations in a mutant protein relative to its natural structure. We selected the three-dimensional crystallized structure of BTK1 for simulation investigations (PDB ID: 5P9J) [28]. The Swiss PDB Viewer (SPDBV) was used to induce mutations in the wild type structure of BTK protein (Fig. 1), and energy minimization was done by GROMACS version 21. Using the CHARMM GUI input generator, distinct systems for each mutant and native BTK protein were constructed [32]. These wild and mutant systems were solvated and then neutralized using the Monte Carlo ion placement method. Equilibration input was made with the help of the NVT ensemble class. GROMACS version 202 [43] and for each system (4 mutants and the wild type BTK proteins), the simulation was run for 100 ns at an

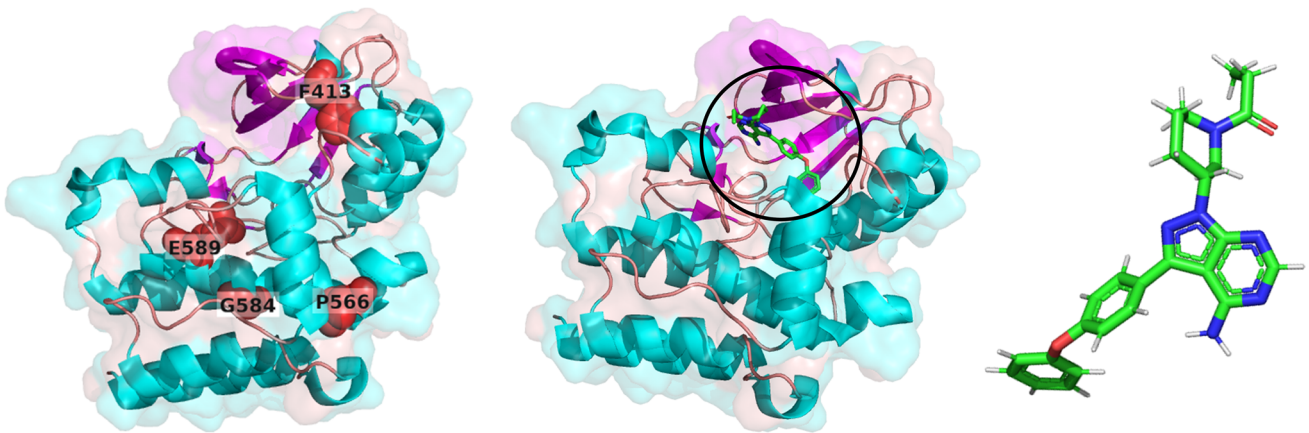


Fig. 1 Three-dimensional structures of (**a**) BTK protein with all the mutations depicted by red spheres, (**b**) BTK protein complexed with ibrutinib, highlighted by a black circle (**c**) ibrutinib

ambient temperature of 303.15 K and a pressure of 1 bar. All MD trajectories in this study used the single chain "A" of the BTK protein and its mutant structures (F413L, P566Q, G584E, and E589K). There are many domains in BTK protein, starting with the N-terminal PH-domain (pleckstrin homology domain) and continuing through the TEC homology domain, the SH3 and SH2 (SRC homology domains), and finally, the C-terminal BTK-KD domain (BTK-kinase domain) [12]. We have taken into consideration BTK-KD (residues 382–659), since not only is there are drug binding sites at position C481 but also the pathogenic mutations that have been found via the use of computational methods present in this kinase domain. The convergence of simulated proteins was determined by comparing the RMSD of average simulated postures derived from all the frames formed during simulation to the initial structure as a result of the time trajectory in MD simulations. Initially, RMSD data for BTK protein (C-alpha) were retrieved from each 100 ns simulation trajectory with respect to the starting pose. All mutants exhibited RMSD variability than the wild system, with P566Q (represented by green color) appearing to be the most unstable (Fig. 2).

To get a more detailed overview of the RMSD analysis, we evaluate the local regions where the mutations are located, since the overall instability may dominate the global RMSD. There is the presence of an ATP binding site and an intrinsically disordered region in this beta-sheet conformation, starting from 402–421. Intrinsically disordered areas are distinguished by a lack of secondary and organized tertiary structure; they interact extensively with macromolecules and may undergo structural modifications upon binding to interacting molecules [44]. The amino acid residue Phe-413 is an important and conserved phenylalanine located at the beginning of the beta-strand. It sits directly on top of the triphosphate group of ATP, forming a crucial hydrogen bond with the oxygen atom of the beta-phosphate. This interaction is essential for the proper binding and subsequent release of ADP. Substituting the bulky side chain of phenylalanine with a leucine residue at position 413 (F413L mutation) would significantly limit the flexibility of the loop structure required to accommodate ATP, ultimately hindering its binding and subsequent release of ADP. Additionally, this substitution would not be optimal for forming the necessary hydrogen bond with ATP, leading to an altered conformation of the BTK protein. Consequently, this conformational change could interfere with the correct alignment of ATP for catalysis, rendering it incompatible with the enzyme's function. Based on this observation, we can observe that the F413L (represented by cyan color) mutation in this segment is involved in increased rigidity of the disordered region of the protein, which might affect ATP binding with the BTK protein (Fig. 3).

P566Q variation lies in the helix region starting from residues 560–572, so we have conducted a local RMSD analysis on this segment also. From this RMSD analysis, we have found that the P566Q variation shown to affect the helix formation, higher RMSD can be due to more flexibility in this helix region. This might also affect the conformation of active site due to the existence of buried residues that typically form hydrophobic cores to preserve the integrity of the protein structure. Compared to exposed residues that are not associated with the active site, buried residues are very sensitive to mutation [45], and hence, the P566Q

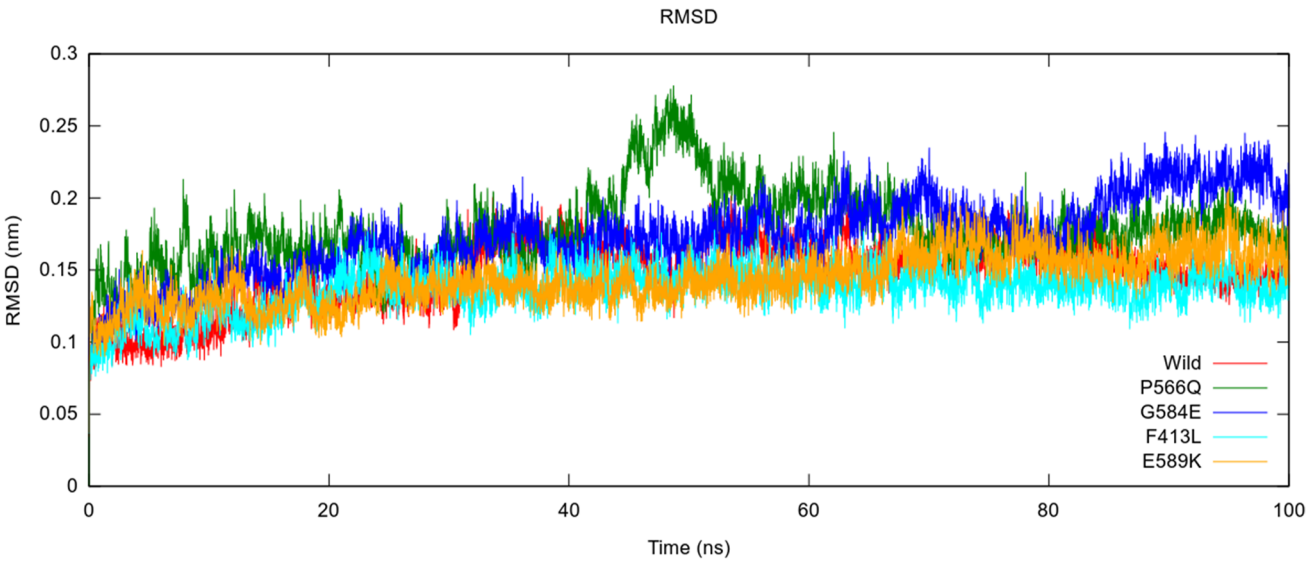


Fig. 2 RMSD plot of all the four mutated and wild type BTK proteins showing a high degree of variability in mutated BTK proteins as compared to wild type BTK protein. P566Q mutation showing the highest unstability indicated by "Green" color

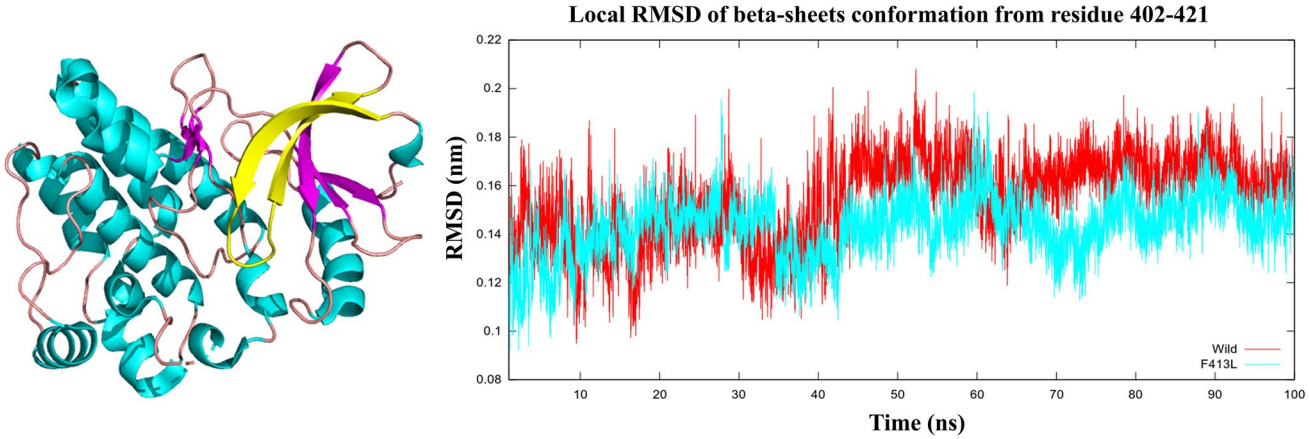


Fig. 3 Local RMSD plot of beta-sheets conformation from residue 402–421 highlighted by yellow color in left panel. F413L mutation lies in this region of beta strand and this region is specifically picked to have closer look into the alteration caused by this mutation in BTK protein. A rigidity can be seen after 44 ns in the mutant protein as compared to wild type showing the F413L mutation's impact on protein

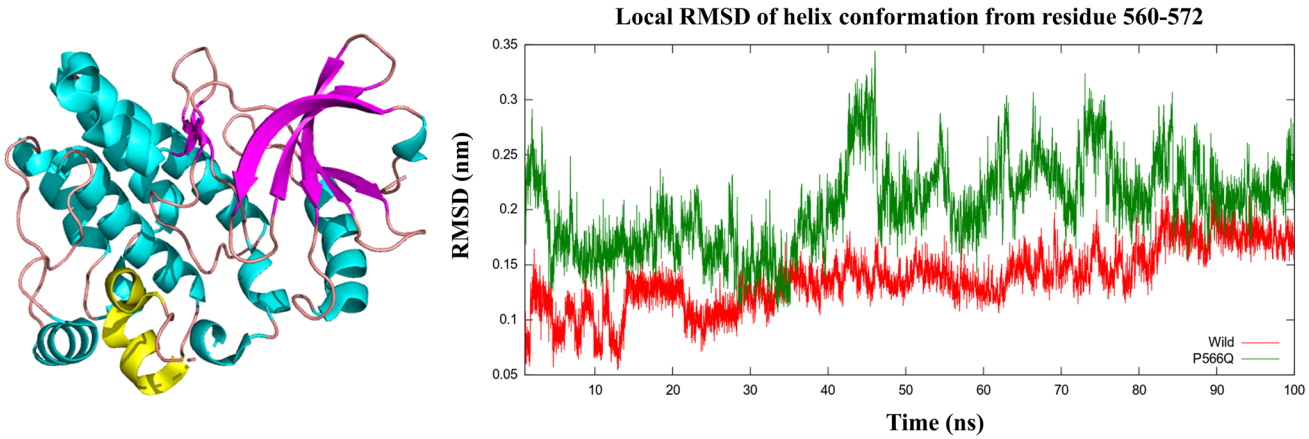


Fig. 4 Local RMSD plot for P566Q mutant protein located in helix conformation starting from residue 560–572 highlighted by yellow color in left panel. A high rise in RMSD peak can be seen at various positions but a significant rise in peak can be seen after 44 ns in the mutant protein as compared to wild type showing the F413L mutation impact on BTK protein

(represented by green color) mutation might be causing a very high degree of distortion and flexibility in this BTK protein (Fig. 4).

We have observed the presence of buried residues and increased hydropathy in the helix conformation starting from residues 575–592 in wild type BTK proteins, indicating the existence of hydrophobic buried residues in this particular segment. Because of the hydrophobic effect, protein folds are more robust as hydrophobic amino acids are hidden deep inside the protein and are protected from water [46]. The local RMSD analysis on mutations G584E (shown in blue) and E589K (shown in orange) reveals a distortion in the structure of the BTK protein (Fig. 5). This helix conformation containing our concerned mutations seems to lose their rigidity, indicating damage to the hydrophobic effect and hence disruption of the protein fold, leaving the residues more flexible and unstable, and this distortion was seen more for the G584E mutant protein.

The stimulus of the mutation on the dynamic behavior of the residues was determined by computing RMSF values for both the wild and mutant BTK proteins. The RMSF values were estimated during the final 50 ns of the simulation's trajectory since the wild structure stagnates after a time period. Region 552–559 in the P566Q mutation showed the highest flexibility, as the RMSF peak had a rise of 0.42 nm, while E589K showed the highest rigidity for the same region. Region 479–483 contains the active site at C481 of the BTK protein. This region containing the binding site showed a high level of rigidity, along with another region starting from residues 582–592, for all the mutants, out of which the F413L mutation showed the highest rigidity for both of these sites, so we can conclude

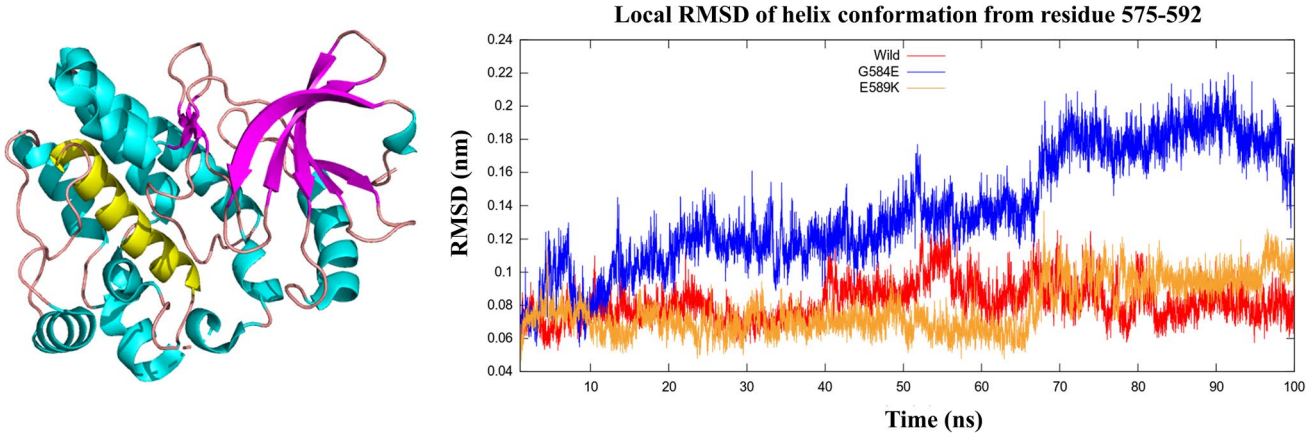


Fig. 5 Local RMSD plot for G584E and E589K mutant proteins located in helix conformation starting from residue 575–592 highlighted by yellow color in left panel. A clear distortion of BTK protein can be seen for E589K mutation and a high rise in RMSD peak can be seen after 65 ns in the mutant protein as compared to wild type

that these mutations may hamper the drug binding due to structural instability. The G584E mutation seems to be highly unstable as almost all the residues show variation in flexibility in contrast with the wild type, with the highest flexibility in the region starting from 572–576. The RMSF plots confirmed that the P566Q mutant protein demonstrated considerable residual shifts relative to the wild type protein, suggesting a role in structural damage due to protein flexibility, as evident in the latter half of the RMSD plots. Drug-binding sites are located in several of these dynamic areas, which means they may affect drug-binding interactions (Fig. 6).

PCA analysis on MD trajectories

PCA tries to find the cumulative patterns of fluctuations in the protein structure by computing and diagonalizing the covariance matrix for carbon-alpha (C_α) atoms to determine the cumulative modes of fluctuations in the structure of proteins. These produced orthogonal vectors, also known as eigenvectors, have been given the name "principal components" since they have the biggest eigenvalues (PCs). So, for the purpose of finding fluctuations in native and mutant proteins, we run principal component analysis (PCA) on a molecular dynamics' trajectory files using the scikit-learn

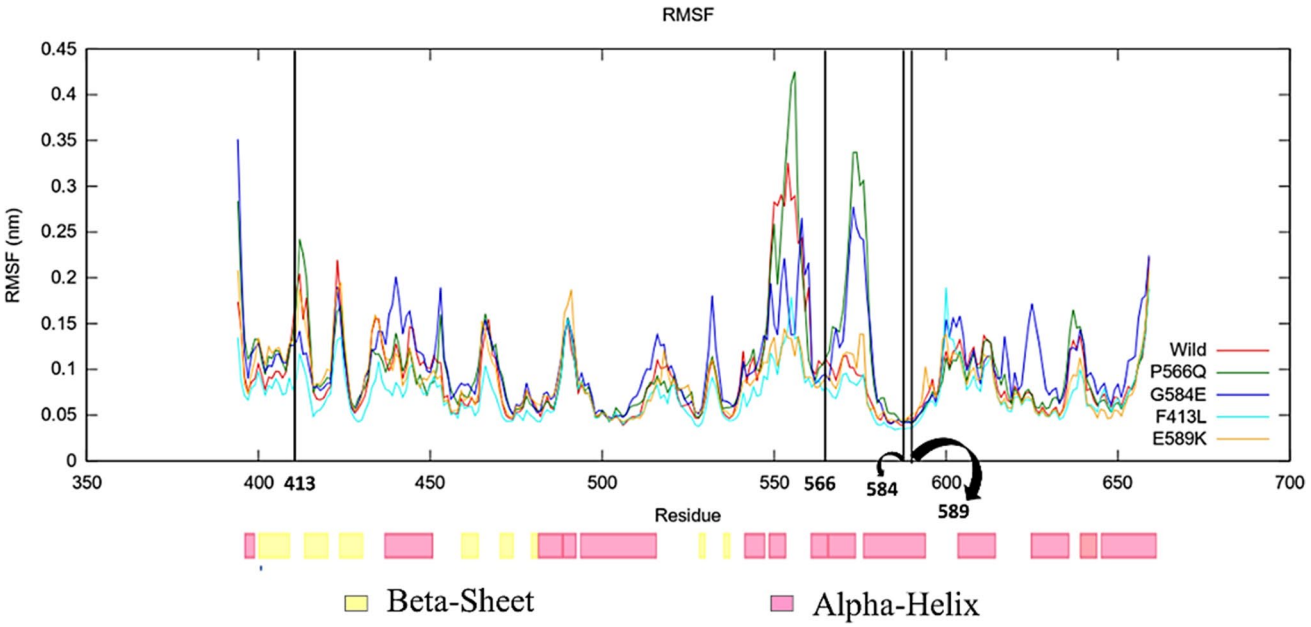


Fig. 6 RMSF plot of all the four mutated and wild type BTK proteins showing a high degree of variability in mutated BTK proteins with respect to wild type BTK protein. P566Q mutation showing the highest unstability indicated by "Green" color

python library to extract the kinase domain interactions and atomic gap in wild type and mutant BTK proteins from their corresponding to last 25 ns MD simulation trajectories. The principal components (PCs) or eigenvectors were retrieved and presented as groups from the corresponding MD simulation trajectories for the wild and mutant BTK protein structures. As a result of PCA analysis, we have determined that mutant proteins exhibit large dynamic movements and evident fluctuations in terms of atomic vibrations for the last 25 ns simulation period (Fig. 6). PCA plots for extracted PC1 and PC2 indicate the mutations in the groups throughout the observed simulation interval via a color shift from yellow to purple, representing the significant periodic bounces amid the different conformational postures of the wild type and mutant BTK protein structures. Therefore, it is clear that the mutations are altering the BTK protein, as demonstrated by PCA plots (Fig. 7).

Contact map analysis through CONAN

We tried to find out the possible interactions of each residue with other residues in the wild and mutant BTK proteins. For this purpose, we conducted a contact map analysis through CONAN (contact analysis). It works with the GROMACS molecular dynamic engine's mdmat tool. In this study, CONAN was used to generate contact maps for each atom in the simulated structure, and the average of these was then compared for both wild type and mutant BTK proteins. Contact maps capture the secondary and tertiary structural characteristics that describe the molecule. Alpha-helices are shown by a deepening of the matrix diagonal. Parallel and antiparallel beta-strands, on the other hand, are shown by thin contact segments that are either orthogonal to or parallel to the matrix diagonal. Interestingly, we have found significant changes in contact maps of mutant proteins with reference to wild BTK protein for the last 25 ns of MD trajectory, depicting the contact maps in 2D format for a visual interpretation (Fig. 8). By observing the images closely, we can see that the F413L mutant protein's residues have various weak contacts depicted by the thinning of the backbone (represented by the diagonal) in contrast with the wild type BTK protein, concluding the weakening of contacts among the alpha-helices of this protein. Parallel and anti-parallel beta-strands is generally depicted by thin lines and light spots in CONAN contact maps showing the loss of contacts at various places in contrast with the wild protein. It is observed that the lightning and the missingness of some points throughout the entire MD trajectory, illustrate the breaking of contacts in the mutant structure. Throughout the MD trajectories of all the mutant structures, we observed the same kind of thinning of the backbone showing the weakening of contact among residues in alpha-helices and a similar kind of missingness and lighting of various spots at different locations showing the breaking of contacts in residues of beta-strands.

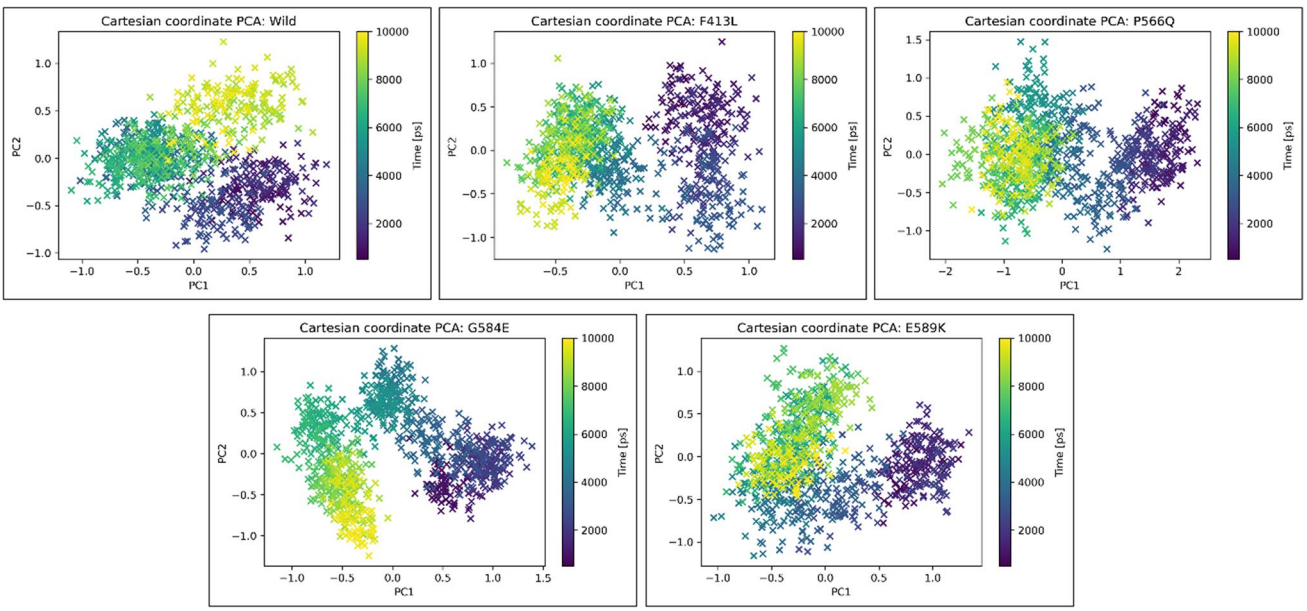


Fig. 7 Principal component analysis for both wild and mutant BTK proteins exhibiting large dynamic movements and evident fluctuations in terms of atomic vibrations as a consequence of 100 ns MD simulation

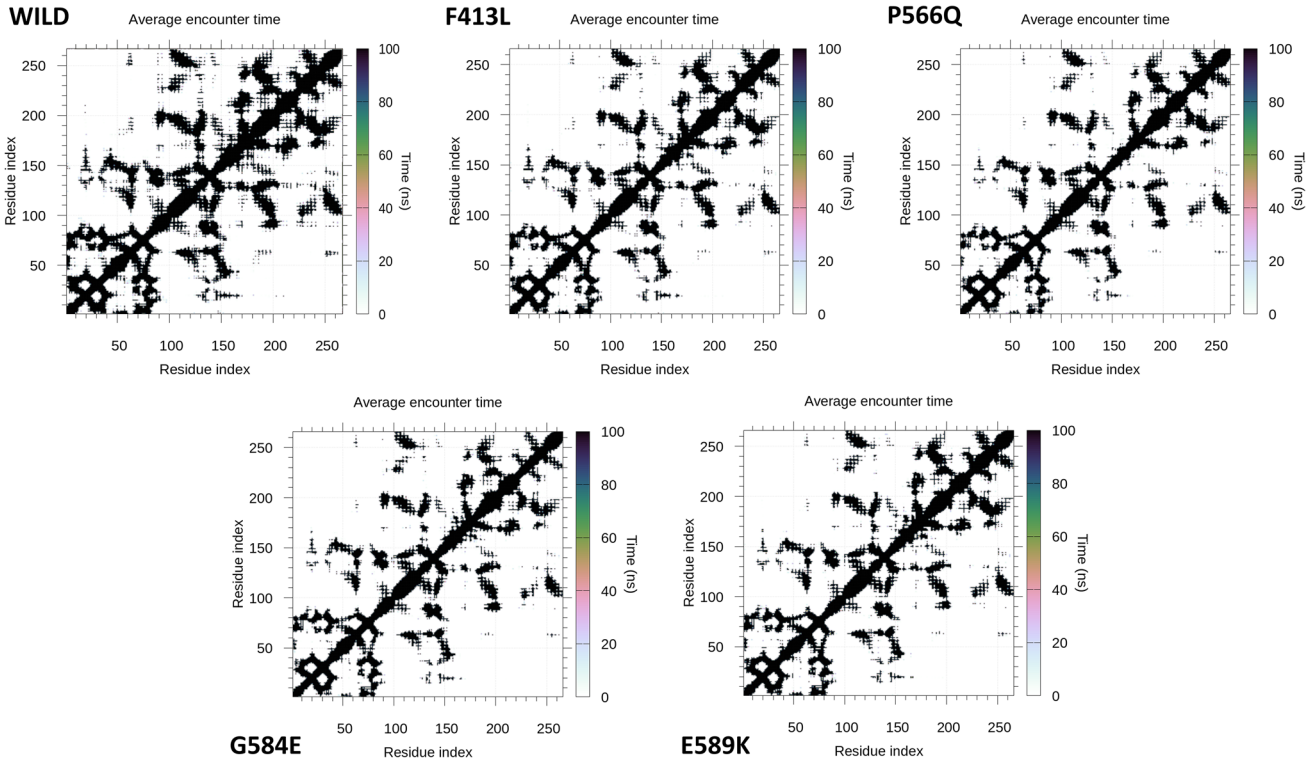


Fig. 8 Contact maps generated by CONAN for both wild and mutant BTK proteins exhibiting lightning of backbone represented by the diagonal and missingness throughout the MD trajectory for mutant proteins as compared to the wild type BTK protein

Table 2 Binding energy of mutated and wild system when docked with ibrutinib

System	Binding energy (kcal/mol)	Predicted inhibition constant (nM)
Wild	-9.37	135.22
E589K	-9.48	111.82
G584E	-9.43	122.28
P566Q	-9.55	99.59
F413L	-9.16	191.52

Docking and MM-PBSA and MM-GBSA binding energy analysis

To investigate the influence of amino acid substitution on ibrutinib binding, we docked the mutant and wild BTK protein structures with the FDA-approved drug. Table 2 presents the outcomes of the docking analysis containing binding energy (kcal/mol) and predicted inhibition constant (nM). The estimated free energy is determined by combining the torsion and intermolecular free energies. For all the complexes, the calculated binding free energy for ibrutinib ranges from 9.16 to 9.55 kcal/mol. According to the binding energy data, ibrutinib seems to be stable in each of the complexes.

The MM-PBSA study has been widely used to simulate molecular affinity, like protein-ligand binding interactions, as an active and reliable free energy simulation tool. When paired with MD simulations, MM-PBSA has the inherent potential to include conformational variations and entropic components in the binding energy. Decomposing the overall binding energy into several components, this approach has also been used to provide a comprehensive understanding of biomolecular interactions [38, 47]. We provided here the findings of MM-PBSA analyses that were carried out utilizing 1000 snapshots collected from the MD-trajectory at 25 ps intervals between 76 and 100 ns of MD trajectory of wild and mutant complexes with ibrutinib. We also calculated the -TΔS for both MM-PBSA and MM-GBSA analysis using interaction entropy method and compiled the enthalpy change and entropy change in Table 3 using the equation given below.

$$\Delta G_{\text{bind}} = \Delta H - T\Delta S,$$

where ΔH (enthalpy change) is calculated by MM-PBSA/MM-GBSA, while $-T\Delta S$ is calculated by interaction entropy.

From the details given in the table, we can see that F413L (-25.68 ± 3.0 kcal/mol) and G584E (-25.03 ± 3.0 kcal/mol) mutant protein-drug complexes have the lowest total free binding energy (ΔG_{bind}) indicating good binding between

Table 3 MM-PBSA and MM-GBSA analysis results for free binding energy of ibrutinib with wild type and mutant BTK proteins

MM-PBSA					
Energy component	Wild	F413L	P566Q	G584E	E589K
ΔE_{vdW}	-61.20 ± 0.61	-56.71 ± 0.65	-57.06 ± 1.09	-53.74 ± 0.82	-60.34 ± 1.05
ΔE_{elec}	-23.27 ± 1.16	-31.22 ± 1.62	-30.36 ± 3.14	-29.72 ± 2.00	-24.87 ± 1.97
ΔPB	62.30 ± 0.71	61.43 ± 0.31	62.33 ± 0.56	54.64 ± 0.73	66.22 ± 0.80
ΔE_{SASA}	-5.44 ± 0.02	-5.10 ± 0.02	-5.12 ± 0.00	-4.88 ± 0.03	-5.40 ± 0.02
ΔH	-27.61 ± 1.77	-31.59 ± 1.98	-30.21 ± 3.50	-33.70 ± 2.44	-24.38 ± 2.54
$-T\Delta S$	10.33 ± 0.11	5.91 ± 0.09	7.87 ± 0.19	8.67 ± 0.24	8.6 ± 0.11
ΔG	-17.28 ± 4.29	-25.68 ± 3.0	-22.33 ± 4.33	-25.03 ± 3.0	-15.78 ± 4.08
MM-GBSA					
ΔE_{vdW}	-61.20 ± 0.61	-56.71 ± 0.65	-57.06 ± 1.09	-53.74 ± 0.82	-60.34 ± 1.05
ΔE_{elec}	-23.27 ± 1.16	-31.22 ± 1.62	-30.36 ± 3.14	-29.72 ± 2.00	-24.87 ± 1.97
ΔGB	51.48 ± 0.16	55.08 ± 0.59	55.13 ± 0.97	50.79 ± 0.76	52.21 ± 0.99
ΔE_{SURF}	-8.06 ± 0.01	-7.54 ± 0.03	-7.65 ± 0.01	-7.19 ± 0.01	-7.83 ± 0.01
ΔH	-41.05 ± 1.63	-40.39 ± 2.04	-39.94 ± 3.59	-39.87 ± 2.45	-40.82 ± 2.61
$-T\Delta S$	10.33 ± 0.11	5.91 ± 0.09	7.87 ± 0.19	8.67 ± 0.24	8.6 ± 0.11
ΔG	-30.72 ± 2.96	-34.48 ± 2.49	-32.07 ± 2.65	-31.19 ± 2.79	-32.22 ± 2.81

protein and drug while E589K (-15.78 ± 4.08 kcal/mol) mutant complex has the highest total binding energy followed by wild type (-17.28 ± 4.29 kcal/mol) and P566Q (-22.33 ± 4.33 kcal/mol) mutant protein-drug complexes indicating the poor binding affinity. The van der Waals (ΔE_{vdW}), electrostatic interaction (ΔE_{elec}), solvent accessible surface area energy (ΔE_{SASA}), enthalpy change (ΔH), and entropy change ($-T\Delta S$) were the most significant components of the entire free binding energy of each wild and mutant protein complex.

We have also conducted MM-GBSA tests on the wild and mutant protein-drug complexes. MM-GBSA is one of the most widely used techniques for estimating protein–ligand binding energies, identifying key residues in protein–protein interactions, and investigating macromolecular stability [48]. The free binding energy, ΔG_{bind} calculated through MM-GBSA, was found to be lowest (-30.72 ± 2.96 kcal/mol) for the wild type BTK-ibrutinib complex, showing high binding affinity between the BTK protein and the ibrutinib drug, while this was found to be higher for the rest of the mutant protein-drug complexes, showing poor binding affinity. For the F413L mutant protein-drug complex, the free binding energy was found to be the highest (-34.48 ± 2.49 kcal/mol) followed by E589K (-32.22 ± 2.81 kcal/mol), P566Q (-32.07 ± 2.65 kcal/mol), and G584E (-31.19 ± 2.79 kcal/mol) mutant protein-drug complexes, showing a significant decrease in binding affinity between the BTK protein and the ibrutinib drug. The van der Waals energy (ΔE_{vdW}), electrostatic energy (ΔE_{elec}), solvation energy (ΔE_{SURF}), enthalpy change (ΔH), and entropy change ($-T\Delta S$) were the contributing factors in identifying the binding nature of protein-drug complexes; their respective values are given in Table 3. We also found the average decomposition value for each residue in both wild type and mutant protein-drug complexes, and details are given in (Fig. 9).

Contact analysis for wild and mutant BTK-ibrutinib complexes

Non-covalent interactions have substantial significance in terms of molecule binding and identification. Biomolecular recognition relies considerably on non-bonded interactions, including hydrogen bonding, ionic, and hydrophobic [49]. The MD trajectories of wild and mutant BTK-ibrutinib complexes were analyzed using GROMACS and PyContact to identify hydrogen bonding interactions. All hydrogen bond interactions were set to have a range of bond distances from 1.5 to 2.5, and the cut-off angle for hydrogen bonds was set to 120°. The percentage of hydrogen bonding for wild and mutant protein complexes' MD trajectories at an interval of 100 ps is shown in Fig. 10. In the wild type BTK-ibrutinib complex, the CYS481 residue showed the maximum hydrogen bond occupancy of 100 percent, whereas the remaining residues followed the order MET477 = GLU475 > THR474. For the F413L mutant protein-drug complex, GLU475 showed a maximum hydrogen bond occupancy of 100 percent, and the order of remaining residues follows the order CYS481 = MET477 > THR474 > LYS430 for hydrogen bond occupancy. We have found the following sequence of residues CYS481 = GLU475 > MET477 > THR474 for the mutant P566Q protein-drug complex, where CYS481 and GLU475 occupied the highest percentage for hydrogen bond occupancy. The occupancy for hydrogen bonds was found to be in the order GLU475 > MET477 > CYS481 > THR474 > ASN484

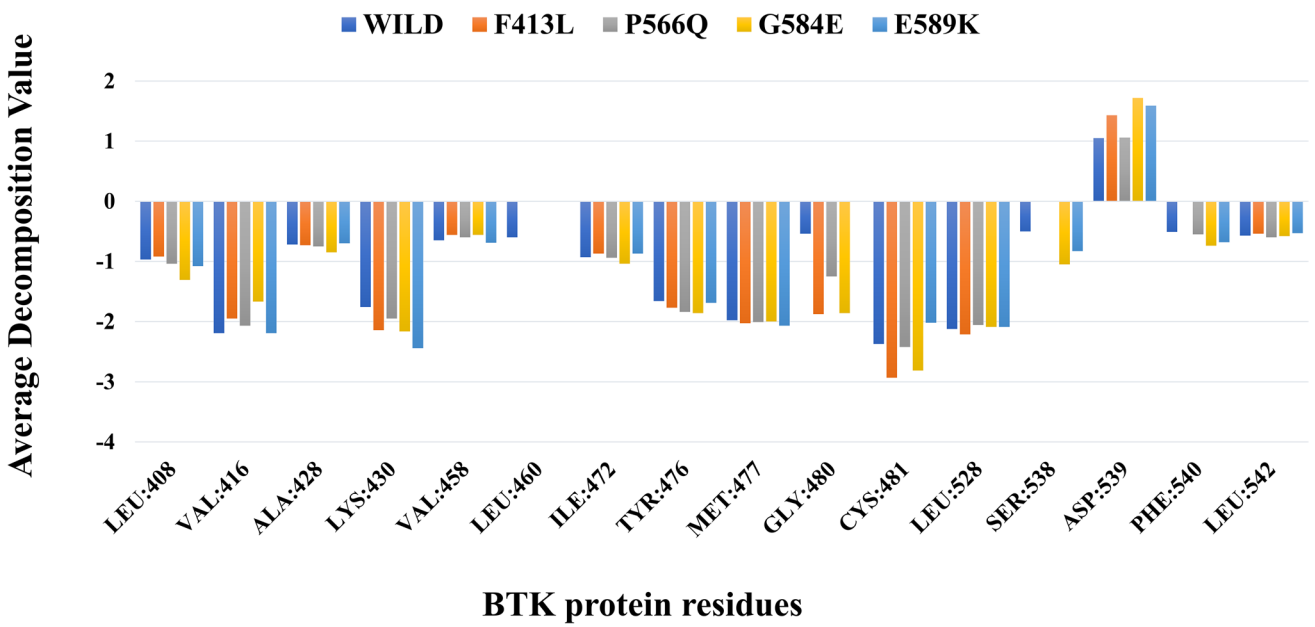


Fig. 9 Average decomposition values for each residue in both wild type and mutant BTK-ibrutinib complexes

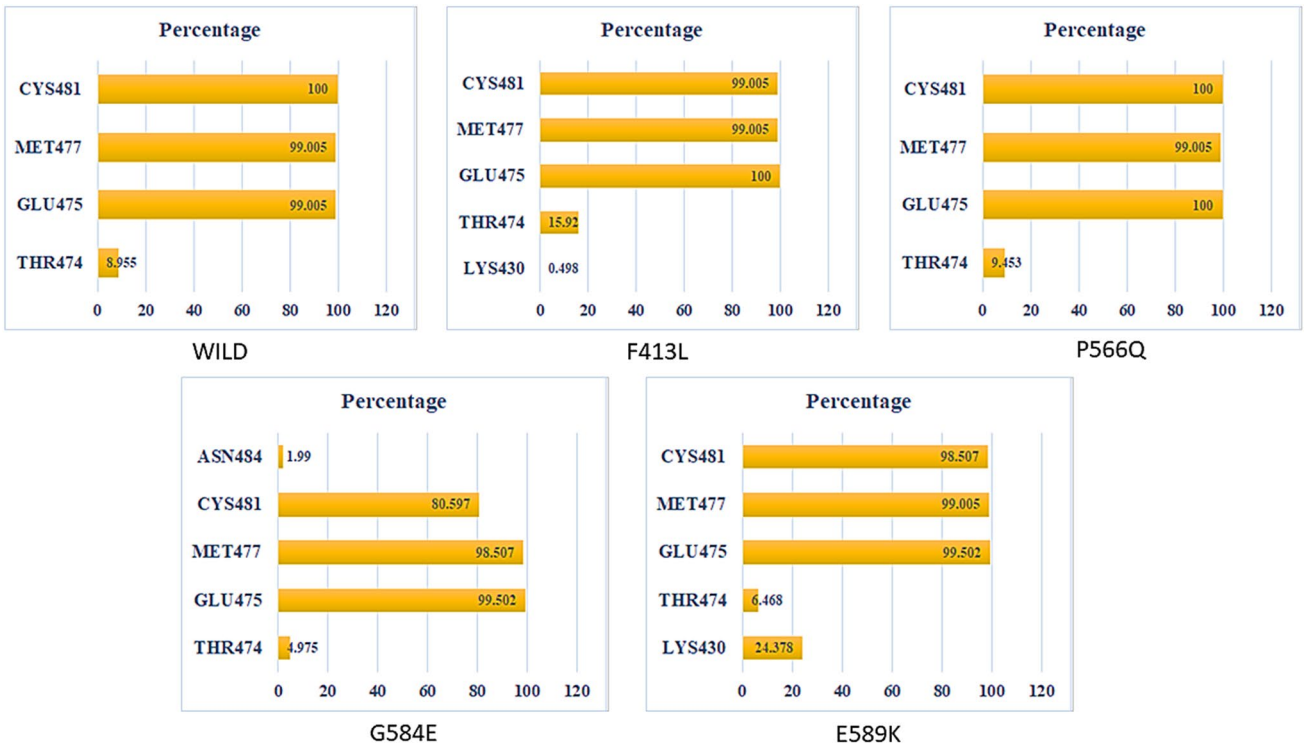


Fig. 10 PyContact analysis graphs for wild and mutant BTK-Ibrutinib protein complexes' MD trajectories for potential hydrogen bond occupancy

for the mutant G584E protein-drug complex. For the mutant E589K protein-drug complex, the order of the hydrogen bonds was found to be GLU475 > MET477 > CYS481 > LYS430 > THR474, with GLU475 having the most hydrogen bonds (99.50%) occupied.

Discussion

Integrating data from multiple genetic variation databases could provide a thorough understanding of the genes associated with SCC. We accessed the COSMIC database to get mutational data on the BTK gene, which is responsible for SCC. This mutation analysis helps in the identification of potentially cancer-causing genomic variants. In this study, a total of 47 mutations of the BTK gene that are unique to squamous cell carcinoma (SCC) were extracted from the COSMIC database using advanced filters that considered whole genome screening as well as target screening, skin as the SCC tumor tissue site, missense mutations, and their impact as pathogenic. BTK is a cytoplasmic non-receptor tyrosine kinase that belongs to the Tec family of tyrosine kinases. The Tec family of kinases includes BTK, TEC, ITK, BMX, and RLK. In the cytoplasmic tyrosine kinase superfamily, this family is the second largest. BCR-mediated signaling and the formation of B-lymphocytes may be its most well-known function. BTK is found in all types of hematopoietic cells, not just B cells. Because of this, BTK was found to play a vital role in the tumor microenvironment, which is a complex network of cells and their precursors. This network includes pericytes and smooth muscle cells, fibroblasts with different phenotypes, neutrophils, T- and B-cell lymphocytes, natural killer (NK) cells, and antigen-presenting cells (APCs), to name some. Each of these cell types contributes to the progression of cancer. Numerous preclinical and clinical cancer studies have investigated ibrutinib (PCI-32765), a small-molecule pharmacological inhibitor of BTK. An example of a targeted therapeutic strategy in cancer would be the use of pharmacological inhibitors to stop the BTK gene from functioning. The BTK gene and its targeted drug ibrutinib are the least-studied gene-drug combination for SCC, according to the survey of the relevant literature; hence, additional research is required. The computational genetics is focused on learning more about certain aspects of cancer biology. Pathogenic and damaging genetic mutations have been isolated with the aid of a combination of strong computational methods. In this study, 47 nsSNPs for the BTK protein were retrieved from the COSMIC database, and after running each of these mutations through a total of seven different mutation impact prediction methods, four different nsSNPs, specifically, F413L, P566Q, G584E, and E589K, were found to be detrimental, malignant, pathogenic, and deleterious, correspondingly. Also, there are some studies where these mutations have role in carcinoma progression. A study based on tumor molecular profiling in precision oncology identified F413L and E589K as a cancer biomarker. This study analyzed tumor and matched normal sequence data from over 10,000 patients with advanced cancer and found clinically relevant somatic mutations, novel noncoding alterations, and mutational signatures shared by common and rare tumor types [50]. Additionally, a study on colorectal carcinogenesis analyzed eight pairs of colorectal adenomas and carcinomas using whole-exome sequencing and found that P566Q has an associated role in carcinogenesis of colorectal cancer [51]. In another study, P566Q and G584E have been found in tumorigenesis of basal cell carcinoma (BCC) on conducting the genetic profiling of 293 BCC samples for identification cancer driver genes [52]. Based on the above studies, we chose these mutations and simulated them in the BTK protein structure in order to analyze their interaction and the effect of mutations on the protein structure. This work used molecular simulations to identify the underlying molecular mechanism by which non-synonymous variants may cause damage to protein structure. In these 100 ns molecular dynamic simulation studies, the mutations, namely, F413L, P566Q, G584E, and E589K, of the BTK protein exhibited markedly altered molecular properties in contrast with the wild BTK protein, notably RMSD and RMSF values at the residue level. PCA plots for both wild and mutant proteins made it abundantly evident that the mutations are distorting the BTK protein. CONAN analysis was also done to find significant changes in contact maps of mutant proteins as compared to wild type for the entire MD trajectory, and we have found that the contact maps of mutants of the BTK protein, namely, F413L, P566Q, G584E, and E589K, showed visible dissimilarity with the contact map of the wild type protein, which also supported the fact that the protein is actually distorted upon these mutations. When docked with ibrutinib, all the system showed similar free energy suggesting no effect in binding with the FDA approve drug. The MM-PBSA method was developed and proven to be an effective tool for assessing protein-drug interactions resulting from simulation trajectory information. So, the last 25 ns of the trajectories of the complexes was analyzed by means of MM-PBSA, revealing that the G584E mutant protein-drug complex has the lowest free binding energy, accompanied by F413L and P566Q mutants, whereas wild type and E589K mutants have the highest total free binding energy, indicating that these mutations cause structural instability but are not affecting the binding of ibrutinib to the BTK protein. This observation was also validated by the MM-GBSA study, which demonstrated that the wild type BTK-ibrutinib complex has the lowest free binding energy, accompanied by the G584E, P566Q, F413L, and E589K mutant protein-drug complexes. Since additional mutations have demonstrated modest differences in their free binding energy, the preceding observation can be supported.

By PyContact analysis, we have found that in the wild type BTK-ibrutinib complex, CYS481 residue showed the maximum hydrogen bond occupancy. In F413L, G584E, and E589K mutant protein-drug complexes, GLU475 showed the maximum hydrogen bond occupancy, while P566Q showed the maximum hydrogen occupancy for both CYS481 and GLU475. PLIP (protein–ligand interaction profiler) analysis for 4-time frames, namely, 25 ns, 50 ns, 75 ns, and 100 ns, showed the hydrophobic interactions, hydrogen bonding, and pi-cation interactions in wild and mutant proteins complexed with ibrutinib (Table 4) (Fig. 11). We have observed that pi-cation interaction is found in a single E589K mutant complex's residue, namely, LYS430, at a 25 ns time frame. Being the strongest non-covalent interaction, this pi-cation interaction is actually giving stability to the E589K mutant protein complex, providing another proof that the mutations are distorting the structure, but the protein and drug binding are still unaffected, and hence, we can use ibrutinib in populations where we found these mutations of BTK protein.

Conclusions

In this study, we have tried to decipher the effect of mutations that are found in BTK protein and may have a role in SCC progression using computational methods. BTK belongs to the Tec tyrosine kinase family and is a non-receptor cytoplasmic tyrosine kinase. The Tec kinase family, which includes BTK, TEC, ITK, BMX, and RLK, is the second largest family of cytoplasmic tyrosine kinases [53]. BTK protein contains a number of domains, beginning with the N-terminal PH-domain (pleckstrin homology domain) and progressing through the TEC homology domain, SH3 and SH2 (SRC homology domains), and lastly, the C-terminal BTK-KD domain (BTK-kinase

Table 4 Analysis of ibrutinib's interactions with BTK protein residues throughout different time frames

Systems	Time frames	Interactions of BTK-protein residues with the ibrutinib drug		
		Hydrophobic interactions	Hydrogen bonds	Pi-cation interactions
Wild	25 ns	VAL416, LYS430, VAL458, ILE472, ASN484, LEU528, PHE540	GLU475, MET477, CYS481	-
	50 ns	VAL416, LYS430, LEU460, ILE472, LEU483, LEU528	GLN412, THR474, GLU475, MET477	-
	75 ns	LEU408, LYS430, LEU460, ILE472, THR474, LEU528, LEU542	GLN412, GLU475, MET477	-
	100 ns	LEU408, LYS430, LEU528, PHE540, LEU542	GLN412, THR474, GLU475, MET477	-
F413L	25 ns	VAL416, LYS430, LEU460, ILE472, PHE540, LEU542	GLU475, MET477, CYS481	-
	50 ns	VAL416, LYS430, ILE472, THR474, PHE540	THR474, GLU475, MET477, CYS481	-
	75 ns	VAL416, LYS430, LEU460, ILE472, THR474, ASN484, LEU528, LEU542	GLU475, MET477, CYS481	-
	100 ns	VAL416, ALA428, LYS430, ILE472, THR474, LEU528, PHE540, LEU542	GLU475, MET477, CYS481	-
P566Q	25 ns	LEU408, VAL416, LYS430, VAL458, LEU460, THR474, PHE540, LEU542	GLU475, MET477, CYS481	-
	50 ns	PHE413, VAL416, LYS430, LEU460, ASN484, LEU528, PHE540	GLU475, MET477, CYS481	-
	75 ns	LEU408, VAL416, LYS430, VAL458, ILE472, LEU528,	THR474, GLU475, MET477	-
	100 ns	ALA428, LYS430, ILE472, THR474, LEU528, LEU542	GLN412, THR474, MET477	-
G584E	25 ns	LEU408, LYS430, VAL458, ILE472, THR474, ASN484, LEU528, PHE540	THR474, GLU475, MET477, CYS481, ASP539	-
	50 ns	LYS430, VAL458, THR474, PHE540	GLU475, MET477, CYS481	-
	75 ns	VAL416, ALA428, VAL458, LEU460, ILE472, THR474, LEU528, PHE540	LYS430, GLU475, MET477, CYS481	-
	100 ns	ALA428, LYS430, VAL458, LEU460, ILE472, THR474, LEU528, PHE540, LEU542	GLU475, MET477, CYS481	-
E589K	25 ns	LEU408, ILE472, ARG525, LEU528, PHE540	GLU475, MET477	LYS430
	50 ns	LYS430, THR474, ARG525, LEU528, LEU542	GLU475, MET477	-
	75 ns	LEU408, VAL416, LYS430, LEU460, ARG525, LEU528, PHE540, LEU542	THR474, GLU475, MET477	-
	100 ns	LEU408, LYS430, LEU460, THR474, LEU528, PHE540	GLU475, MET477	-

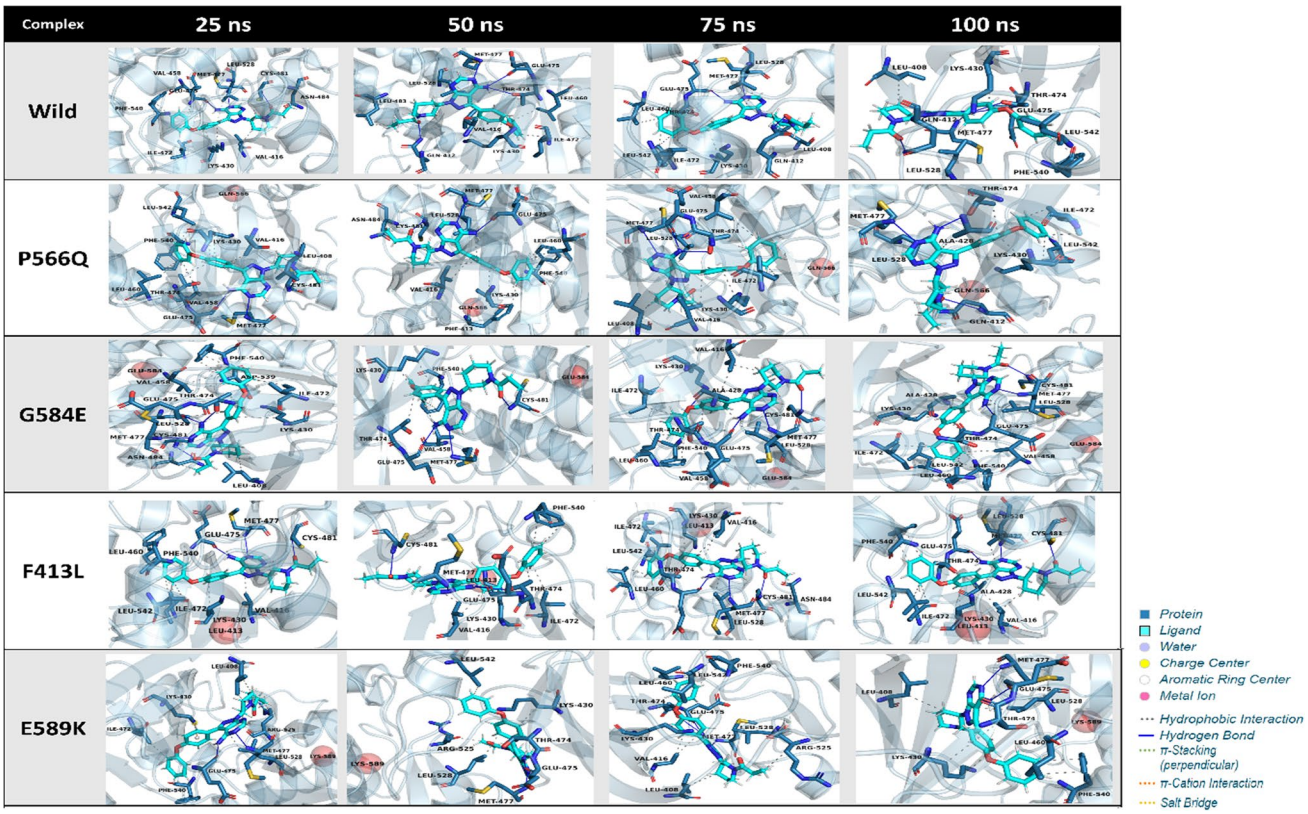


Fig. 11 Interaction and proximity of residues around Ibrutinib in wild type and mutant BTK-ibrutinib complexes throughout different time frames

domain). Phosphatidylinositol lipids like PIP3 can be linked to the PH domain, bringing proteins close to the cell membrane. The TH domain comprises a zinc-finger motif that is required for the protein's optimal function and integrity. SH domains communicate with other proteins and bind to proline-rich areas and phosphorylated tyrosinase. LYN or SYK may phosphorylate the catalytic kinase domain's Y551 site, resulting in autophosphorylation of the SH3 domain's Y233 site [12]. It was observed from many studies that mutations in the BTK protein may have a role in SCC disorder, and hence, various studies are going on to validate its connection. Ibrutinib is a drug that permanently suppresses BTK. Ibrutinib was initially proposed as a potential treatment for a range of B-cell lineage-derived diseases [16]. Treatment resistance in most cancers may be induced by factors including genomic heterogeneity, intratumoral genetic polymorphism, and field cancerization. These mutations can influence protein expression and subcellular localization, as well as protein folding and integrity, protein function, and protein-protein interactions (PPI). This study was aimed at discovering the possible deleterious role of mutations in the BTK protein. We selected 4 mutants of the BTK protein and observed by conducting simulation studies that these variants are actually distorting the proteins, which we confirmed through MD simulation analysis. Mutants differed greatly from the native protein, suggesting that they contribute to SCC prognosis by rendering protein unstable. Even the mutant proteins' MD trajectories were distinct from those of normal protein, and they are bound to ibrutinib in the same manner. According to the analysis of the protein-ligand interaction, the mutations had no effect on how the drug bound to the proteins. MM-PBSA and MM-GBSA both supported this. Even mutant proteins bind to the drug more effectively than wild-type proteins. Consequently, this study reveals that the effect of detected missense mutations is unfavorable and can lead to function loss, which is severe for SCC, but that ibrutinib-based therapy can still be effective on them, and the mutations can be utilized as biomarkers for ibrutinib-based treatment. This study suggests that the drug ibrutinib, which targets BTK and is used to treat SCC, may be unaffected by these mutations. Nonetheless, this finding must be validated by exhaustive clinical investigations.

Author contribution The study was conceived by Y.H. and J.M. performed computations. Y.H. supervised the findings of the work. Both the authors discussed the results and contributed to the final manuscript.

Data availability The authors confirm that all the necessary data to replicate the results of this study is included in the manuscript.

Declarations

Ethics approval The study was done using only computational methods, no living samples were used; therefore, ethical approval is not applicable.

Conflict of interest The authors declare no competing interests.

References

1. Fania L et al (2021) Cutaneous squamous cell carcinoma: From pathophysiology to novel therapeutic approaches. Biomedicines 9(2):1–33. https://doi.org/10.3390/BIOMEDICINES9020171
2. Stratigos A, Garbe C, Lebbe C, … J. M.-E. Journal of, and undefined 2015, 'Diagnosis and treatment of invasive squamous cell carcinoma of the skin: European consensus-based interdisciplinary guideline', Elsevier, Accessed: Jul. 29, 2022. [Online]. Available: https://sci-hub.do/https://www.sciencedirect.com/science/article/pii/S0959804915006255
3. Geidel G, Heidrich I, Kött J, Schneider SW, Pantel K, Gebhardt C (2022) Emerging precision diagnostics in advanced cutaneous squamous cell carcinoma. Npj Precision Oncology 6(1):1–8. https://doi.org/10.1038/s41698-022-00261-z
4. Watson M, Holman DM, Maguire-Eisen M (2016) Ultraviolet radiation exposure and its impact on skin cancer risk. Semin Oncol Nurs. 32(3):241. https://doi.org/10.1016/J.SONCN.2016.05.005
5. Li S et al. (2021) Molecular subtypes of oral squamous cell carcinoma based on immunosuppression genes using a deep learning approach. Front Cell Dev Biol. 9:687245. https://doi.org/10.3389/FCELL.2021.687245/FULL
6. Veness MJ (2007) 'High-risk cutaneous squamous cell carcinoma of the head and neck. J Biomed Biotechnol. (3):80572. https://doi.org/10.1155/2007/80572
7. Howell JY, Ramsey ML (2022) Squamous cell skin cancer', StatPearls, Accessed: Nov. 20, 2022. [Online]. Available: https://www.ncbi.nlm.nih.gov/books/NBK441939/
8. Sanderson RJ, Ironside JAD, Wei WI (2002) Squamous cell carcinomas of the head and neck. BMJ : British Med J 325(7368):822. https://doi.org/10.1136/BMJ.325.7368.822
9. Pomerantz MM, Freedman ML (2011) The genetics of cancer risk. Cancer J 17(6): 416. https://doi.org/10.1097/PPO.0B013E31823E5387
10. Zhou G, Chen M, Ju CJT, Wang Z, Jiang JY, Wang W (2020) Mutation effect estimation on protein-protein interactions using deep contextualized representation learning. NAR Genom Bioinform. 2(2). https://doi.org/10.1093/NARGAB/LQAA015
11. Reva B, Antipin Y, Sander C (2011) Predicting the functional impact of protein mutations: Application to cancer genomics. Nucleic Acids Res 39(17): e118–e118. https://doi.org/10.1093/NAR/GKR407
12. Smith CIE, Islam TC, Mattsson PT, Mohamed AJ, Nore BF, Vihinen M (2001) The Tec family of cytoplasmic tyrosine kinases: Mammalian Btk, Bmx, Itk, Tec, Txk and homologs in other species. Bioessays 23(5): 436–446. https://doi.org/10.1002/BIES.1062
13. Ponader S, Burger JA (2014) Bruton's tyrosine kinase: From X-linked agammaglobulinemia toward targeted therapy for B-cell malignancies. J Clin Oncol 32(17):1830–1839. https://doi.org/10.1200/JCO.2013.53.1046
14. Whiteside TL (2008) 'The tumor microenvironment and its role in promoting tumor growth. Oncogene 27(45):5904. https://doi.org/10.1038/ONC.2008.271
15. Szklener K, Michalski A, Żak K, Piwoński M, Mańdziuk S (2022) 'Ibrutinib in the treatment of solid tumors: Current state of knowledge and future directions. Cells 11(8): 1338. https://doi.org/10.3390/CELLS11081338
16. Davids MS, Brown JR (2014) Ibrutinib: A first in class covalent inhibitor of Bruton's tyrosine kinase. Future Oncol 10(6): 957. https://doi.org/10.2217/FON.14.51
17. Futreal PA et al (2004) 'A census of human cancer genes. Nat Rev Cancer 4(3):177. https://doi.org/10.1038/NRC1299
18. Forbes SA et al (2010) COSMIC (the catalogue of somatic mutations in cancer): a resource to investigate acquired mutations in human cancer. Nucleic Acids Res 38(Database issue): D652-7. https://doi.org/10.1093/NAR/GKP995
19. Berglöf A et al (2015) 'Targets for ibrutinib beyond B cell malignancies. Scand J Immunol 82(3):208. https://doi.org/10.1111/SJI.12333
20. Hassan MS, Shaalan AA, Dessouky MI, Abdelnaiem AE, ElHefnawi M (2019) Evaluation of computational techniques for predicting non-synonymous single nucleotide variants pathogenicity. Genomics 111(4): 869–882. https://doi.org/10.1016/J.YGENO.2018.05.013
21. Reva B, Antipin Y, Sander C (2007) Determinants of protein function revealed by combinatorial entropy optimization. Genome Biol 8(11):R232. https://doi.org/10.1186/GB-2007-8-11-R232
22. Ng PC, Henikoff S (2001) Predicting deleterious amino acid substitutions. Genome Res 11(5): 863. https://doi.org/10.1101/GR.176601
23. Niroula A, Urolagin S, Vihinen M (2015) PON-P2: Prediction method for fast and reliable identification of harmful variants. PLoS One 3;10(2):e0117380. https://doi.org/10.1371/JOURNAL.PONE.0117380
24. Capriotti E, Martelli PL, Fariselli P, Casadio R (2017) Blind prediction of deleterious amino acid variations with SNPs&GO. Hum Mutat 38(9): 1064–1071. https://doi.org/10.1002/HUMU.23179
25. Choi Y, Chan AP (2015) PROVEAN web server: A tool to predict the functional effect of amino acid substitutions and indels. Bioinformatics 31(16): 2745. https://doi.org/10.1093/BIOINFORMATICS/BTV195
26. Adzhubei I, Jordan DM, Sunyaev SR (2013) 'Predicting functional effect of human missense mutations using PolyPhen-2', Current protocols in human genetics / editorial board, Jonathan L. Haines ... [et al.]. 07(SUPPL.76):Unit7.20. https://doi.org/10.1002/0471142905.HG0720S76.
27. Pejaver V et al (2020) 'Inferring the molecular and phenotypic impact of amino acid variants with MutPred2. Nat Commun 11(1):1–13. https://doi.org/10.1038/s41467-020-19669-x
28. Bender AT et al (2017) 'Ability of Bruton's tyrosine kinase inhibitors to sequester Y551 and prevent phosphorylation determines potency for inhibition of Fc receptor but not B-cell receptor signaling. Mol Pharmacol 91(3):208–219. https://doi.org/10.1124/MOL.116.107037
29. Guex N, Peitsch MC, Schwede T (2009) Automated comparative protein structure modeling with SWISS-MODEL and Swiss-PdbViewer: A historical perspective. Electrophoresis 30(Suppl 1). https://doi.org/10.1002/ELPS.200900140

30. Abraham MJ et al (2015) 'GROMACS: High performance molecular simulations through multi-level parallelism from laptops to supercomputers. SoftwareX 1–2:19–25. https://doi.org/10.1016/J.SOFTX.2015.06.001
31. Huang J et al (2017) 'CHARMM36m: An improved force field for folded and intrinsically disordered proteins. Nat Methods 14(1):71. https://doi.org/10.1038/NMETH.4067
32. Lee J et al (2016) CHARMM-GUI input generator for NAMD, GROMACS, AMBER, OpenMM, and CHARMM/OpenMM simulations using the CHARMM36 additive force field. J Chem Theory Comput 12(1):405–413. https://doi.org/10.1021/ACS.JCTC.5B00935/ASSET/IMAGES/LARGE/CT-2015-00935E0005.JPEG
33. David CC, Jacobs DJ (2014) Principal component analysis: A method for determining the essential dynamics of proteins. Methods Mol Biol 1084: 193. https://doi.org/10.1007/978-1-62703-658-0_11
34. Pedregosa F et al (2011) Scikit-learn: Machine learning in Python Gaël Varoquaux Bertrand Thirion Vincent Dubourg Alexandre Passos PEDREGOSA, VAROQUAUX, GRAMFORT ET AL. Matthieu Perrot. J Mach Learn Res 12: 2825–2830. https://doi.org/10.5555/1953048.2078195
35. Mercadante D, Gräter F, Daday C (2018) 'CONAN: A tool to decode dynamical information from molecular interaction maps. Biophys J 114(6):1267. https://doi.org/10.1016/J.BPJ.2018.01.033
36. Morris GM et al (1991) User guide AutoDock version 4.2 updated for version 4.2.6 automated docking of flexible ligands to flexible receptors, Accessed: Nov. 20, 2022. [Online]. Available: http://autodock.scripps.edu/
37. Wang C, Greene D, Xiao L, Qi R, Luo R (2018) Recent developments and applications of the MMPBSA method. Front Mol Biosci 4(JAN): 87. https://doi.org/10.3389/FMOLB.2017.00087/BIBTEX
38. Genheden S, Ryde U (2015) The MM/PBSA and MM/GBSA methods to estimate ligand-binding affinities. Expert Opin Drug Discov 10(5): 449. https://doi.org/10.1517/17460441.2015.1032936
39. Valdés-Tresanco MS, Valdés-Tresanco ME, Valiente PA, Moreno E (2021) Gmx_MMPBSA: A new tool to perform end-state free energy calculations with GROMACS. J Chem Theory Comput 17(10): 6281–6291. https://doi.org/10.1021/ACS.JCTC.1C00645/ASSET/IMAGES/LARGE/CT1C00645_0005.JPEG.
40. Duan L, Liu X, Zhang JZH (2016) Interaction entropy: A new paradigm for highly efficient and reliable computation of protein-ligand binding free energy'. J Am Chem Soc 138(17): 5722–5728. https://doi.org/10.1021/JACS.6B02682/ASSET/IMAGES/JA-2016-026824_M008.GIF.
41. Scheurer M et al (2018) PyContact: Rapid, customizable, and visual analysis of noncovalent interactions in MD simulations. Biophys J 114(3):577–583. https://doi.org/10.1016/J.BPJ.2017.12.003
42. Sun F-D, Wang P-C, Shang J, Zou S-H, Du X (2018) 'Ibrutinib presents antitumor activity in skin cancer and induces autophagy. Eur Rev Med Pharmacol Sci 22(2):561–566. https://doi.org/10.26355/eurrev_201801_14210
43. van der Spoel D, Lindahl E, Hess B, Groenhof G, Mark AE, Berendsen HJC (2005) GROMACS: Fast, flexible, and free. J Comput Chem 26(16): 1701–1718 .https://doi.org/10.1002/JCC.20291
44. Glover K, Mei Y, Sinha SC (2016) Identifying intrinsically disordered protein regions likely to undergo binding-induced helical transitions. Biochim Biophys Acta 1864(10):1455. https://doi.org/10.1016/J.BBAPAP.2016.05.005
45. Bhasin M, Varadarajan R (2021) Prediction of function determining and buried residues through analysis of saturation mutagenesis datasets. Front Mol Biosci 11(8):635425. https://doi.org/10.3389/fmolb.2021.635425
46. van Dijk E, Hoogeveen A, Abeln S (2015) The hydrophobic temperature dependence of amino acids directly calculated from protein structures. PLoS Comput Biol 11(5): e1004277. https://doi.org/10.1371/JOURNAL.PCBI.1004277
47. Wang E et al (2019) End-point binding free energy calculation with MM/PBSA and MM/GBSA: Strategies and applications in drug design. Chem Rev 119(16):9478–9508. https://doi.org/10.1021/ACS.CHEMREV.9B00055
48. Godschalk F, Genheden S, Söderhjelm P, Ryde U (2013) Comparison of MM/GBSA calculations based on explicit and implicit solvent simulations. Phys Chem Chem Phys 15(20): 7731–7739. https://doi.org/10.1039/C3CP00116D
49. Daze K, Hof F (2016) Molecular interaction and recognition. Encycl Phys Org Chem 5:1–51. https://doi.org/10.1002/9781118468586.EPOC3001
50. Zehir A et al (2017) 'Mutational landscape of metastatic cancer revealed from prospective clinical sequencing of 10,000 patients. Nat Med 23(6):703–713. https://doi.org/10.1038/NM.4333
51. Kim TM et al (2015) Clonal origins and parallel evolution of regionally synchronous colorectal adenoma and carcinoma. Oncotarget 6(29): 27725–27735. https://doi.org/10.18632/ONCOTARGET.4834
52. Bonilla X et al (2016) Genomic analysis identifies new drivers and progression pathways in skin basal cell carcinoma'. Nat Genet 48(4):398–406. https://doi.org/10.1038/ng.3525
53. Mano H (1999) Tec family of protein-tyrosine kinases: An overview of their structure and function. Cytokine Growth Factor Rev 10(3–4):267–280. https://doi.org/10.1016/S1359-6101(99)00019-2

Publisher's note Springer Nature remains neutral with regard to jurisdictional claims in published maps and institutional affiliations.

Springer Nature or its licensor (e.g. a society or other partner) holds exclusive rights to this article under a publishing agreement with the author(s) or other rightsholder(s); author self-archiving of the accepted manuscript version of this article is solely governed by the terms of such publishing agreement and applicable law.

MAPAN-Journal of Metrology Society of India
https://doi.org/10.1007/s12647-023-00633-1

REVIEW PAPER

Redefining Industry 5.0 in Ophthalmology and Digital Metrology: A Global Perspective

S. Chourasia[1]*, S. M. Pandey[2], Q. Murtaza[1], S. Agrawal[3] and K. Gupta[1]

[1]Department of Mechanical Engineering, Delhi Technological University, Delhi, India

[2]Department of Mechanical Engineering, National Institute of Technology, Patna, India

[3]Delhi School of Management, Delhi Technological University, Delhi, India

Received: 23 July 2022 / Accepted: 21 March 2023

© Metrology Society of India 2023

Abstract: The demand for ophthalmic diagnosis and monitoring equipment is high due to day-by-day increasing eye-related diseases. These diseases are growing very fast due to changes in lifestyle, the aging crowd, and chronic diseases. During COVID-19, old ophthalmic diagnostic devices failed to fulfill the patients' needs due to social distancing and took more diagnosis time, making patients uncomfortable and unsatisfied to visit the clinic. Seeing all these problems during the COVID-19 time, patients are demanding personalized healthcare services and clinical home services to protect themselves from the COVID-19 virus attack. To fulfill the mass personalized needs and easily accesses clinical services from the patient's home, there is a requirement to embrace Industry 5.0 with its emerging digital technologies. The current work is based on the theoretical view of Industry 5.0 in ophthalmology and its supporting digital technology, various models and challenges faced by the healthcare system in ophthalmology during the COVID-19 pandemic time, limitations of the study, and its future scope, digital metrology, and strength, limitation, opportunities, and threat analysis in brief.

Keywords: Industry 5.0; Digital technology; Internet of medical things (IoMT); Artificial intelligence ophthalmology; COVID-19; Deep learning; Metrology

1. Introduction

In the current scenario, the COVID-19 outbreak has trembled the entire medical system of all countries. In India only, it resulted in approximately 426,290 deaths in the mid of August 2021. COVID-19 has left many consequences on society, including the loss of countless lives and a massive investment in medical expenses [1]. That is why it is essential to strengthen the entire medical system with the goal of sustainability at the global level, which must own the competence to provide unstoppable services to customers [2]. It has been seen that during the pandemic, patients are demanding personalized services, a virtual healthcare system, and seamless delivery of medicines at low cost with minimal time can save them from the risk of virus attack. Consumers were looking for digital assistance across healthcare services such as health plans, checkups, vaccines, and health metrics without stepping out of their homes [3]. To fill this need of the customers, medical systems are required to accept the power of digital technologies with their digital-centric solutions [3] with the integration of the Industry 5.0 concept for redefining ophthalmology from a global perspective. These emerging technologies would help ophthalmologists better understand patients' diseases with minimal clinical time by making rapid decisions and improving patient submission by attaining excellent clinical results using mass concept personalization and digital technologies. Ophthalmology is the branch of medicine where doctors diagnose the eye, provide treatment for affecting vision, and help patients with the prescription of spectacles and contact lenses the surgical treatment for strabismus and retinal tears [4, 5]. An ophthalmologist is an eye doctor who goes under training in a medical subspecialty for surgical eye care [6] and is also deliberated as both a surgical and a medical specialist. Ophthalmologists are trained for every query of the eye, such as eye exams, eye care, eye surgery, and prescribing medicine to patients. Optometrists are responsible for providing primary vision and prescribing the management

*Corresponding author, E-mail: shubhangichourasia7@gmail.com

Published online: 20 April 2023

changes required for vision. Optometrists undergo proper training to examine the eye for visual defects such as cataracts, ptosis, glaucoma, and vitrectomy, diagnose the problems and provide suitable treatments, and when problem is much more severe, optometrist refers the patients to an ophthalmologist [7].

Industry 5.0 works on the vision of mass personalization rather than mass customization with the collaboration of robots and smart machines. Industry 5.0 is the next industrial revolution whose aims are to bind human intelligence to artificial intelligence, cloud computing, telehealth care to deep learning for obtaining the most effective solution to problems through limited availability of resources as compared to Industry 4.0 [6, 7]. Industry 5.0 integrates digital technologies such as artificial intelligence, deep learning, 5G, cloud computing, and modified Internet of medical things. These techniques can provide excellent services and a better medical healthcare system to patients [8]. In ophthalmology, digital technologies can directly diagnose and treat eye diseases such as retinopathy, age-based macular degeneration, and glaucoma of patients' eyes and visual systems with accurate data screening [8]. On the other hand, 5G [8–10] technology allows ophthalmologists to work day and night from their clinic to remote areas to treat patients. It provides virtual diagnoses to patients by maintaining social distancing [11] that could reduce the chances of infections among doctors and healthcare workers and enhance the healthcare system's working efficiency [12].

Deep learning is also the most powerful tool in the field of ophthalmology that can be used for data analysis, results in predictions, dissection, and automatic diagnosis. Deep learning is the subset of machine learning that uses an already programmed neural network that helps the machine make its own decisions without the help of a human being [13]. At the same time, CNN (convolutional neural network) plays a significant role in developing AI and DL-based technologies. CNN works on the different layers, where it extracts the image features with the help of convolutional filters [14]. It has been found from the literature that the technological combination of DL and optical coherence tomography (OCT) has shown significant results for the detection of retinal diseases and also enhanced the performance of eye segment diseases [15, 16]. OCT images are used to analyze, monitor, and manage many retinal-based diseases like DME (diabetic macular edema). But still, some difficulties are coming in translating the generated algorithm into the ophthalmology clinical treatment; for example, when data are analyzed by different or multiple devices, the images taken are not as per the standard and constrained capability of processing graphics. Schmidt Erfurth et al. [17] also used AI for predicting visual acuity and observed 12.9 letters of error in 2456 OCT scans. The same study was conducted by Aslam et al. [18], who found 8.21 letters of error of mean error when they analyzed 847 OCT scans. The study conducted by Burlina et al. [19] has made software for machine learning classes by employing more than thirteen thousand images that were taken from 4613 patients. After the study, they concluded that the CNN approach with accuracy comprised 0.884 and 0.916, which is most precise in CNN than any other technique.

Industry 5.0 would bring the collaboration of medical healthcare systems with human intelligence along with AI, IoT (Internet of Things), data mining, and smart machines [11, 12]. It has a vast capacity to share innovative concepts and creative design thinking to get together several sensors, intelligent machines, software, robots, and human–robot co-working systems to accomplish better results for well fair of society and individual patients [9]. With the significant support of digital technologies, automation, and through quality practices, it can improve the present situation of ophthalmology. Industry 5.0 unlocks the possibility and scope of innovative development and open-mindedness for adopting digital manufacturing, digital technologies, digital metrology, and functional performance. Metrology is the field where units of measurement and measuring techniques are performed under the laws and regulation bodies. But evolution in science and technology with continuous enhancement in digital technologies pushes the metrology toward digital metrology. That is why digital metrology plays a vital role in measuring weight for profitable drive and trading commercials, which it denied in the standards of weight and measurement Act 1985 [20].

The sole aim of writing this paper is to introduce Industry 5.0, enabling digital technologies in the field of ophthalmology to manifest its expansions. To convey the first dialog, the authors introduce Industry 5.0 in ophthalmology, followed by the industrial revolution voyage from IR-1 to IR-5 with the need for Industry 5.0 in ophthalmology. In the next section, the authors describe the role of a digital tool for ophthalmology patients and various digital health models used during COVID-19 to assist patients with all the supportive technologies of Industry 5.0 in ophthalmology. The benefits of Industry 5.0 for ophthalmologists, significant challenges faced by ophthalmology, the current status of digital technology adoption, limitations of the study, and research implications of the study, followed by conclusions and future aspects, are summarized by the authors at the end of the paper.

2. What is Industry 5.0?

Currently, the entire medical care system is rigorously working to develop new technologies that could improve

the efficiency and productivity of humans and machines. This revolution would develop a vital healthcare system with the help of digital technologies with fewer faults during treatment time and provide satisfaction to patients.

Industry 5.0 is the future visionary concept that reunites humans and machines and works together to improve the system's efficiency by transforming the industries and medical care system through AI-enabled smart and intelligent system services that employ intelligent computing and interconnection with aid various cloud servers [21]. This fifth revolution would open innumerable medical healthcare prospects and integrate doctors, engineers, and manufacturers with machines and digital technologies [22]. It has a tremendous capacity to work with effective process parameters with swift improvement in the medical healthcare system as well as in the manufacturing system to provide answers to challenges that come up in front of all the service sectors and medical health care at the time of COVID-19 with help of digital technologies. At present, patients wish to get personalized healthcare services at their doorstep, these wishes can be fulfill by adopting the visionary concept of Industry 5.0 in the healthcare system. This revolution can provide expected solutions to patients by providing lifetime assistance of personalized services. Industry 5.0 is based on the idea of mass personalization of products and services in healthcare systems rather than mass customization. It converts the mass personalization need of customers into reality [23]. The main goal of Industry 5.0 and its concerning technologies is to develop a digital healthcare system that can provide real-time assistance to patients for providing personalized treatment, therapy, and diagnosis with the aid of these technologies and could provide remote assistance to patients.

Industry 5.0 would provide mass personalization of services such as the patient's body parts, medical implants, intraocular lens implants, eye prostheses, and artificial limbs that can be fabricated precisely using cognitive computing technologies as per the requirement of patients. The brief history of the industrial revolutions transformation voyage from IR-1 to IR-5, respectively, is illustrated in Table 1.

Industry 5.0 has numerous capability to mechanize the manufacturing process of a personalized product that could provide massive support to medical healthcare systems with innovation. For instance, in ophthalmology, AI has been explored for the recognition, observation, and treatment of numerous ocular diseases, diagnose retinopathy, macular degeneration, retinal vascular occlusions, and ocular cancers [24] by using AI algorithms and also assisted in robotic surgery on a large scale to enhance accuracy with precision [25]. Therefore, through the assistance of robots, ophthalmologists can enjoy the aid of technology. In the future, Industry 5.0-enabled technologies such as artificial intelligence in ophthalmology would be more involved in the decision-making process in the methodical medical investigation, diagnosis, and healing management. This Industry 5.0 technology would also help to discover eye diseases with the help of its AI algorithms and ability to recognize newfangled biomarkers, detailed to every disease with all the physiognomies themselves, and would not be constrained to merely identifying clinical features [26].

In another aspect, Industry 5.0 is also based on the concept of bio-economy, which means it believes in smartly using bio-resources available on the earth, which helps establish the proper balance among the industry, economy, and ecosystem. As per the European Commission, the definition of bio-economy is the development of renewable biotic resources and their conversion from waste to value-added products like food, bio-energy, etc. This sector has great potential for innovation because of its wide range of applications in several fields, such as nanotechnology, medical, biotechnology, and electronic communication technologies [27]. Fundamental changes can be brought to the medical healthcare system and industries using the bio-economy guiding principle, i.e., bipolarization [28]. The futuristic vision of Industry 5.0 is also focused on bionics. Bionics is a theoretical originator of synthetic biology. Bionics is a multidisciplinary field that involves medical, architects, engineers, and designers [29].

3. Need For Industry 5.0 in Ophthalmology and Digital Metrology

In the COVID-19 pandemic, where social distancing is the most eminent way to keep an outbreak of the virus away, in the same place, it is difficult to provide healthcare services to patients by healthcare professionals due to COVID-19 infections, because they have to come in direct contact with COVID-19 patients, which puts them in a high-risk zone. COVID-19 has also brought massive social, economic, and technical commotion in the healthcare systems that again pushed back the country to the same place 80 years ago. India's medical system still suffers from poor medical facilities, a doctor–patient ratio, and a deficit of digital solutions. From the literature, it has been observed that the doctor–patient ratio is 40–60 in the USA, and it is 18–20 in India; this suggests a huge disproportion in the count of doctors in India [30]. According to one study, the condition of the medical system in India is more problematic, time-deprived, and pays less attention to clinical records [31]. Therefore, there is a need for a digital system that could reduce the burden on clinicians. This global disaster forced the medical system to rethink beyond the conventional method of diagnosis to new methods and bring a new

Table 1 History of industrial revolutions transformation voyage from IR-1 to IR-5, respectively

S. no.	Industrial revolutions	Summary	Year
1	Industry 1.0	The first industrial revolution started in the eighteenth century when machinery was introduced to reduce the workload of humans	1760–1840
		The steam power engine has been introduced in the industries such as textile and agriculture to up-gradation workforce production systems	
2	Industry 2.0	The second industrial revolution swung its wings and benefited industries such as rail tracks and telegraphs	1870 and 1914
		In this revolution, production has increased due to low flexibility in design, continuous inspections, and quality checks conducted for part components and standard parts	
3	Industry 3.0	The third industrial revolution has brought digital technologies into the manufacturing systems where flexible manufacturing, statistical quality control, 3D printer, programmed automation robots, and CNC concepts come into existence where all the processes are monitored with the aid of computers	After 1950
		In this revolution, analog to digital transformation has occurred in the mechanical system	
		It increased the computer-based integrated designing of the product and its development	
4	Industry 4.0	Industry 4.0 is intercepted from 2020 to complete the need of the future	From 2020
		This revolution is highly anticipated by digital technologies, Additive manufacturing, IoT, AI, and robotics	
		This revolution is continuously working to make innovative manufacturing systems that would be enabled with IoT, AI, and many more	
5	Industry 5.0	Industry 5.0 will be the next stage after Industry 4.0, where a dynamic collaboration among man, machine, and technology will occur	Future predictions
		Industry 5.0 will be enabled with IoT, AI, machine learning, robotic-assisted surgical operations, smart devices, 5G, 6G electronic telecommunications, bio-economy, and many more	

revolution in the field of ophthalmology with the integration of digital technologies. That is why there is a need for a new revolution that strengthens India's entire medical system, i.e., Industry 5.0 with the integration of digital technologies with digital metrology. This revolution would be focused on personalizing services to individual patients as per their requirements and has an enormous capacity to produce quality mass personalized products such as eyes prosthesis and other parts of the eye as per the patient's demand. At the same time, digital technologies would ease patients to receive clinical services at home without any unnecessary clinic visits. Every country wishes to have its self-capable measurement system, consist a chain of digitally enabled laboratories, standardized instruments, and accreditation governing bodies as per the requirement of NQI (National Quality Infrastructure). Currently, digital metrology is the demand for the medical healthcare system. Introduction of digital metrology in medical healthcare systems would bring giant transformation. This would assist in developing and interpreting the measured results to detail elucidation. Using supporting technologies of Industry 5.0, the VL (virtual links) of distinguish calibration laboratories or testing laboratory can perform their jobs remotely or online through data transfer despite the instruments' physical transport. Through Industry 5.0 supporting technologies in the upcoming year, data can be transferred from the testing laboratories to client scenes electronically. The digital transformations in metrology can only be accomplished by applying digital technologies, such as AI, ML, and clouds, in the medical care system to bring massive change.

These technologies would help doctors in ophthalmic surgery and ocular surgery with the assistance of robots [32] in the future as well as provide various digital support systems to doctors, such as telehealth, AI decision support systems, or preliminary assessment of patients with clinical care, AI clinical practices, and remote screening [33] to diagnose the patients from the remote area and to make their work easy and safe. So, the state-of-the-art Industry 5.0 with the integration of digital technologies will give new dimensions to health care. Therefore, there is a great need for Industry 5.0 with digitally enabled technologies in the field of ophthalmology to bring a dynamic change in the entire healthcare system. We attempted this study and analyzed the great need for Industry 5.0 with digitally enabled technologies proficiencies to start the connotation of COVID-19 challenges in the field of ophthalmology.

4. Research Objective of the Current Theme

Industry 5.0 is the joined collaboration of humans and smart machines, which are enabled by sensors and digital technologies such as AI, data mining, cloud computing,

IoT, software, and big data and are employed to develop smart healthcare systems and industries. It connects customers, policymakers, health service providers, doctors, and patients with the IoT and IoMT to circulate truthful information for better coordination. Due to the involvement of digital technologies, telehealth, and telemedicine in ophthalmology, lots of improvement has been noted and can be improved by adopting Industry 5.0 with its enabling technologies. Industry 5.0, with its digital technologies, has a tremendous capacity to store patients' sensitive and crucial health-related data with proper handling and care in its server or database [34]. Due to the outbreak of COVID-19, AI-dependent systems are used by the healthcare system to minimize the workload burden on doctors. These technologies can identify the disease in patients [20, 21] with the use of lighthouse monitoring models, a new model of care, and a digital system; it embraces a new concept in the field of ophthalmology [22, 23].

This paper revolves around the four objective questions asked below:

Q1: To study the need for Industry 5.0 in ophthalmology.

Q2: To study the role of a digital tool for ophthalmology patients.

Q3: To recognize the digital health model used during COVID-19 in ophthalmology.

Q4: To identify the supportive technologies of Industry 5.0 in ophthalmology and its challenges, limitations, and future scope.

5. Role of a Digital Tool for Ophthalmology Patients

In today's demanding world, machines are becoming smarter by using artificial intellect and assisting humans in making upper-level judgments/decisions with the help of AI-based enabled algorithms for patients after the diagnosis. Industry 5.0 is capable of handling the medical healthcare crisis by providing eminence quality medical equipment, personalized services to patients, and digital technology for treatments. Currently, Industry 5.0 consists of many insights, such as human–robot co-working [9], digital health [35], Internet of medical things [34], AI, 5G [10], and telemedicine [36], and bio-economy [37]. In the human–robot co-working culture, humans and robots work together to achieve the tasks where human works on creativity and design thinking and robots work on the rest part, in another insight into Industry 5.0. The Internet of medical things (IoMT) amalgamates several medical devices and their practical applications with an Internet approach to IT medical care systems by enabling cloud networking technologies. For instance, heart rate monitor data of patients are transmitted to a hospital through a cloud system where doctors can assess it [36]. The most available example of IoMT is the smartwatch.

In COVID-19, IoMT has become an integral part of the medical and healthcare system, usually called the Internet of medical things. Figure 1 depicts Industry 5.0 tools for serving ophthalmology patients. IoMT is one of the essential tools of Industry 5.0 that has enormous capability to fight against COVID-19. Using IoMT, video monitoring and remote diagnostics of eye patients can be done by reducing the direct contact of doctors and direct fees without any planned visit. This technology also supports the patient in taking treatment and advice from doctors through video conferencing after discharge from the hospital. All patient data are recorded and saved and can be transferred to another doctor if the patient wishes to switch his medical consultant [38]. Telemedicine is the second most vital tool; it is a technology that helps eye patients monitor and engage by providing regular data regarding their health and motivating patients to self-care. In another way, telemedicine can be used for sending medicines to patients in remote areas with the help of drones that ambulances and doctors cannot reach. In this type, drones can be proved an efficient tool for transporting medical kits to needy patients who are in quarantine. Artificial intelligence has the considerable capability to bring novelty to telemedicine. For instance, artificial intelligence can efficiently deliver storage and retrieval of a patient's history throughout the time of telemedicine and save the data as per the questions asked by patients during the diagnosis [39].

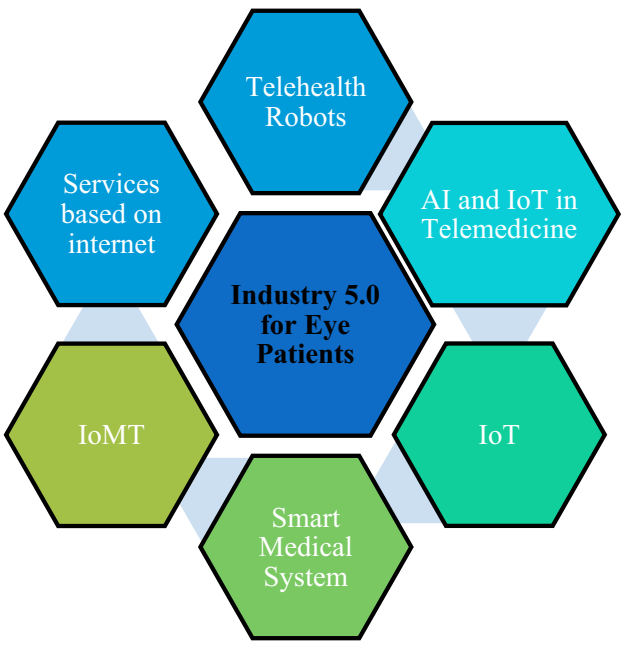


Fig. 1 Industry 5.0 tools for serving the ophthalmology patients

Telehealth robots are the third tool of Industry 5.0, where surgical robots will assist in surgery, clinical settings, patient care, clinical work flow, and monitoring the patient who is in remote areas. For instance, autonomous heath care-based robots could directly contact patients in the hospital room and assist the doctors in interacting with patients from a distance [40].

In the ophthalmology field, there is a need for Industry 5.0 that can be carefully undertaken with less capital cost and time so that it could improvise the quality of work in ophthalmology practice and open the door for various opportunities.

6. Recognition of Digital Health Model Used During COVID-19 in Ophthalmology

During COVID-19, ophthalmology has adopted various digital-based health operation models to reduce face-to-face appointments with doctors and minimize patient interaction. During COVID-19, in ophthalmology, patients are motivated to take diagnoses through virtual clinics whose health condition is steady, and those patients are at high risk. They are only suggested to take face-to-face visits. The illustration of the digital health model used during COVID-19 in ophthalmology is shown in Fig. 2 [41]. Ample medical care system has used these models individually or with a combination of other models, depending on their clinical conditions and the availability of technology.

The first model is the out-of-hospital model, which is divided into four parts: sorting messenger, nucleolus and spoke, catch meshwork model, and lighthouse model. Sorting messenger models are used digital solutions for providing clinical services to patients through telesupport that depends on the need of patients [42]. The ophthalmic center has employed this model to reduce unnecessary movement of patients and doctors during COVID-19 time. For instance, in the virtual hospital setup by China [43] at the ophthalmic center, AI-based chatbots were also used under this model [44]. The nucleus and spoke model has worked for geographically remote areas via patient to provider, provider to provider to consultations, and eye specialist-based centers in remote areas. In the catch meshwork model, patients received all the eye services through the mobile app or phone call [45]. From the use of these models in the pandemic, an optimized flow of patients in the clinic has been attained, reducing the infections among the other patients and eliminating unnecessary touch points. In front setup models, patients are diagnosed face-to-face with their doctors at clinics. This is the biggest challenge during the COVID-19, which can only be sorted with the adoption of digital technologies. The shuffling card services in the flow card system, stream fishing models, and the pyramid concept are employed to operationalize the digital services [41]. In stream fishing model, only the casualty in the eye was treated virtually [46]. Flow funnel models provide digital care and enhance inperson care for excess patients and services to patients by using multipatient networks or channels using electronic safety equipment; the model is used by Hong Kong medical staff [47]. At the same time, the pyramid model is the combination of digital as well as physical services. In this model, patients are categorized on their health requirements. Patients who can manage themselves and those who require physical consultation. This model provides single assistance with technology like hybrid telehealth services and physical clinical services,

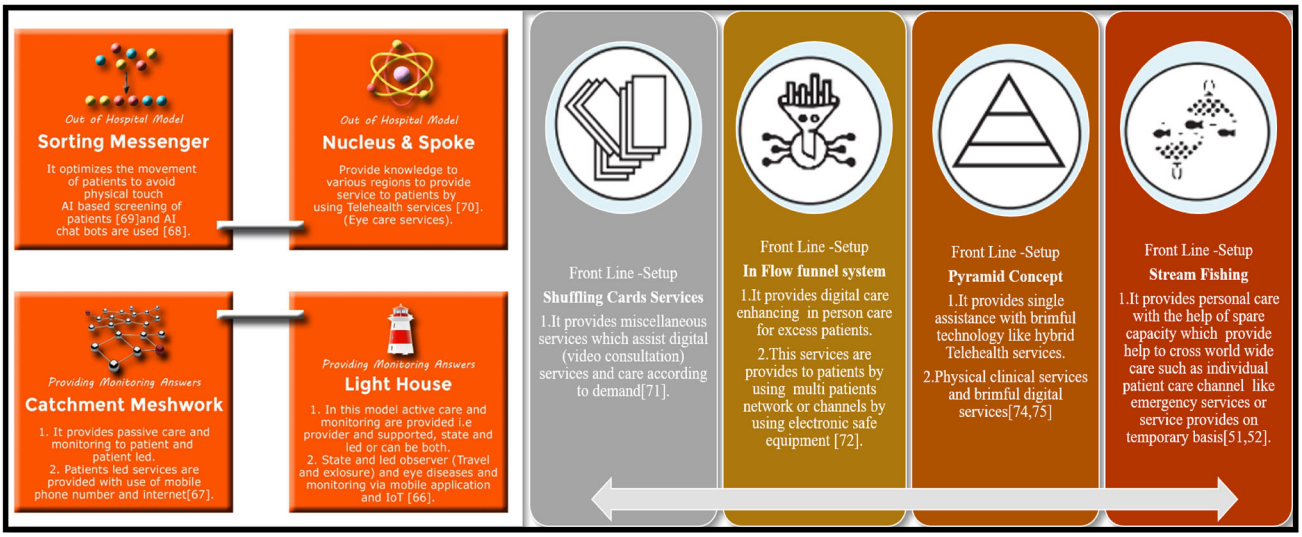


Fig. 2 Pictorial representation of the digital health model used during COVID-19 [41]

and brimful digital services [48], such as AI chatbot assistance for talking to patients and referring patients who require more assessment and are not satisfied with AI bot assistance and needed more consultation via video conferencing [49].

At last, shuffle card models are based entirely on digital services. This service is completely trusted by dedicated providers solely responsible for providing digital solutions to patients. For instance, Singapore has hired video consultant services for consultations of stable glaucoma suffered patients for reducing the crowd in the hospitals. In this service, at the initial phase patient received quires in the communal with all the results sent for asynchronous review through a glaucoma professional [50]. Patients received mail when there is no change in the management plan, if there is any change in the plan patients received video calls to solve their queries.

From this study, it has been perceived that all these models have been implemented outside India. That is why every developing country needs to meet with Industry 5.0 with its enabling digital technology to save people from the next coming massive disaster. Industry 5.0 comprises innovative and advanced technologies such as AI-enabled scanners, AI decisions for clinical care and augmented reality, AI-enabled surgical robots 5G (next-generation network), electronic records, IoMT, clouds, extensive data mining, and bio-economic. The AI-enabled scanner reads and learns the individual patient's behavior through AI algorithms that collect the information from patients and save it in the database, developing a report based on data collected from specific patients. For instance, if any patient is suffering from eye disease, AI-enabled scanners are used to take images of his eye and classify eye disease in several color fundus images with the help of a machine and deep learning. These images provide more homogeneous eye images in size and shape than chest X-ray images. The images received by chest X-ray images possess more individual variations.

Due to this advanced digital technology, the need of patients, doctors, surgeons, and clinical staff satisfaction can be attained [51]. In precise, AI algorithms are developed to detect the ophthalmic-based images and their early topographies or enumerate the measurements that help the doctors to make treatment decisions in the proper manner as well as aid the doctors and surgeons in performing ophthalmic surgery, ocular surgery, cataract treatments, and many eye allied surgeries with no risk. Similarly, IoMT also connects all the possible network of services among the healthcare resources and medical services and provides good medical services and treatment to patients. This technology connects entire medical devices and their applications to the medical healthcare systems, hospitals, and IT systems through the online network via computer. It works as a machine-to-machine communiqué via the Internet of Wi-Fi connections connected to medical devices such as medical feature-enabled smart watches. This technology can reduce unnecessary hospital visits as it attaches patients to their respective doctors and can securely transfer patients' diagnosis data [52]. This technology is required all the possible efforts to make a feasible network of services so that the available healthcare resources and the various medical services can be interconnected through the ultimate applications of Internet-based devices. Digital technologies have proved a boon in COVID-19, where every medical or manufacturing sector is connected to patients or customers via the Internet, AI, cloud, IMoT, etc. For instance, artificial intelligence is self-capable of taking countless numerous images of the retina and can diagnose all the conditions with unerring accuracy and analyze the received images from AI (Artificial Intelligence) and forecast the early stage of dementia and recognize the risk of DR (diabetic retinopathy) in patients along with other health conditions. So in the future, by using this technology with the integration of Industry 5.0, it would be quite possible for patients to sit opposite a scanner at a local optometrist, and AI would study patient eyes, diagnoses the causes, and recommends an individual patient treatment plan. This technology saves the patients' time and assures them that serious illnesses will not go untreated [12]. For prosthetics eyes, to make them function like natural, artificial eyes and artificial limbs, an artificial intelligence-based sensor system with a mobile app has been introduced to these limbs so that it would be easy for patients to operate the artificial part of the body by using the app. Through this, healthcare providers and patients could control prosthetics' functionality and connect with their customers or patients [53].

7. Supportive Technologies of Industry 5.0 in Ophthalmology

In Industry 5.0, robots and smart machines are introduced to reduce human efforts and make their work easier, not to replace them. By executing these digitally transformative technologies in medical science, such as precision and clinical medicine and surgeries, they can improve their services to patients. These technologies can enhance the doctor's and clinical staff's knowledge and skill in the specific domain by giving them good learning opportunities and assessments in research and development. Proper treatment and diagnosis can be performed practically by seeing the patient's old historical and health-related pictures. These technologies can help clinicians to record the patient's eye-related data and medical history (via cloud computing) and evaluate the patients remotely (via

telemedicine). In addition, by use of AI technology, clinicians can easily predict the future eye diseases of patients such as diabetic retinopathy, glaucoma, and age-related muscular relapse in ophthalmology [17] and perform efficacious treatment response to bellicose interventions likelihood injected intra-vitreal injections with anti-VEGF agents in the eyes of patients who are affected by retinal diseases [8]. Advanced robots are employed for ocular surgery, intraocular anterior and posterior segment surgery, and more [54]. Industry 5.0 uses digital technologies such as IoMT, telemedicine, video conferencing, IoT, AI, and data mining connected to 5G and 4G networks and provides relevant information. The ophthalmologist can enhance their skills and sureness and make state-of-the-art diagnoses or treatments to offer a better feel to patients. Table 2 shows the leading promising technologies in Industry 5.0 for ophthalmic.

8. Benefits of Industry 5.0 Technologies for Ophthalmologists

Industry 5.0 creates a flawless ecosystem to provide and check the efficient delivery of services from industries to medical systems, customers, and patients by adopting collaborative and harmonized digital technologies. Industry 5.0 establishes a good relationship among doctors, patients, manufacturers, and more while providing clear information and better technical support. Because of COVID-19, the use of technologies is increasing in daily routine life and becomes massive demand for personalized products and services in the medical healthcare system and ophthalmology. These technologies, such as optical nanosensors, smart sensors, advanced robots, telehealth mobile apps, and wearable healthcare devices for monitoring body motions, body temperature, heart rate, blood pressure, respiration rate, breath analysis, etc., are used to collect real-time data and augmented reality data during the treatment processes [99]. Figure 3 illustrates the prime benefits of Industry 5.0 for ophthalmology. These technologies can replace the old manufacturing methods via AI-enabled or other advanced automated technologies such as prosthetic eyes and artificial limbs. For instance, the application of AI in ophthalmology also has a rigorous ability to reduce the administrative work of clinical staff and doctors, and it has been seen in the USA nurses spare 25% of their work time on administrative and clerical work [74].

This technology can be used for various medical fields such as hospital documentation, managing profit cycles, patient medical records, and claim processing. In ophthalmology, Industry 5.0 could bring massive change by employing 5G technology; medical technology provides emergency support, 5 G-enabled remote surgery, real-time connection, and remote patient monitoring [58]. Using telehealth, optometric can remotely screen the patients' disease and improve the old treatment platform. In Industry 5.0, M–M (machine-to-machine) promulgation is practicable to enhance the efficiency of eye disease diagnosis and treatment process, whereas robots are assigned to reduce the work burden on optometric.

9. Major Challenges Faced by Ophthalmology in the Adoption of Digital Technologies and Digital Metrology

During the COVID-19 pandemic, ophthalmologists have faced considerable hurdles in adopting advanced digital technology solutions and digital metrology. The frequency of eye diseases in aging people is increasing rapidly, putting high pressure on doctors and ophthalmic service providers [100]. During COVID-19, many patients lost their eyesight due to ophthalmic delay services and delayed follow-up taken by doctors via physical mode [101]. Moreover, it has been found in many studies that psychological changes in patients have been observed during lockdown time, which tends to cause visual impartment, and optometric head-on communications with patients may not be conceivable to avoid contagions and infections from the coronavirus [102]. The solutions to these challenges are technology but with some consequences. The biggest challenge in digital metrology is the communication of education, fundamentals, and the presence of digital technology throughout the medical care system and to the doctors toward validating metrology devices and their implementation to the best advantage. Another challenge in adopting digital transformation in legal metrology is the cost of digital instruments, standardization of measuring instruments, training required, and government policies toward adopting digital technologies in the field of digital metrology [103]. For instance, while implementing artificial intelligence and deep learning applications of AI in ROP (retinopathy of prematurity) in ophthalmology, clinical and technical challenges are faced by ophthalmologists. One of the biggest challenges the ophthalmologist faces during the implementation of DL in the system is the generalizability and explanation ability described below.

9.1. Generalizability Challenges

CNN is the explicit type of ANN (artificial neural network) that works by the use of perceptron's algorithms of machine learning for supervising and analyzing the data. CNN can be used for image processing, NLP (natural language processing), and other cognitive tasks [104]. And it is well known that CNN (convolutional neural network)

Table 2 Leading promising technologies in Industry 5.0 for ophthalmology

S. no.	Technologies	Summary and benefits	Challenges
1	Artificial intelligence	This technology provides eye screening of patients with the application of AI to understand the severity of eye diseases like glaucoma [55] and diabetic retinopathy (DR) [56] AI provides virtual backing among optometrists, ophthalmologists, and patients [55]	AI is based on algorithms, so sometimes, it gives wrong or false recognition rates of retinal diseases These false results could mislead the doctors and become disastrous for patient vision There is a risk for doctors if they become addicted to technology and can lose their diagnostic abilities For some specific solutions, ophthalmologists are unsatisfied with AI results or learning assessments [57]
2	5G	This technology is called fifth-generation wireless cellular network technology [58] 5G technology will be enabled by operative and practical surgical robotics, telemedicine, and telehealth services for patients [58] This technology helps the healthcare system where artificial intelligence and 5G are employed to assist the triage patients and would improve the outcome results of diagnosis [58] It provides a faster data speed of 1–10 Gbps, ultra-low latency, and is connected to the medical and manufacturing world users [59]	High investment is required to bring 5G into India's manufacturing and medical care system [60] Non-uniformity in the telecom policies badly affects the service providers of optical fiber cables [60] Poor backhaul shift to 5 G could hamper eye surgical operations from remote areas [61] High costs are involved in procuring Indian telecom devices and equipment from foreign countries because 90% of the telecom market of India depends on other overseas suppliers [60] The high frequency of 5G network cam influences the health of humankind [58]
3	Internet of Things	This technology can help patients with home monitoring, where patients can access IoT devices for earlier recognition of functional vision damage from mobile app applications—for instance, Smartwatches Epocrates, and Visual Dx [41] It keeps records of various macular degeneration, glaucoma, and RD diseases of patients using ingestible sensors technology where capsule-size IoT enables the patient gulps sensors to aid the doctors for future reference [57]	In ophthalmology, massive of patient input data are received by doctors in terabytes which are challenging to organize and maintain This problem can be solved using an AI algorithm, but this approach requires more time to grow; that is why creating a massive amount of IoT solutions in the eye care system needs a lot of time and effort Hackers can hack IoT devices, and their data can be stolen [62]. For instance, if a hacker hacks the heart rate, bold pressure readers so they can hold it hostage
4	IoMT	This Internet approach connects eye patients and ophthalmologists using various IoMT medical devices via broad brands [8] Ophthalmologists save eye patient data in the EMR (electronic medical record) [8] This technology provides digital connectivity to the hospital to patients [8]	All the patient data are stored in clouds, so data thrift is possible. The result of this individual patient data is at stake [51] The outdated Internet spectrum and outdated electronic device infrastructure are the biggest challenges for IoMT [63]
5	Video conferencing, streaming, and audio conferencing	Video conferencing, streaming, and audio streaming help the ophthalmologist to set live communication connections between remote patients by using the mobile app, Zoom, Skype, and Microsoft team with the help of broadband connections [64] Video conferencing helps ophthalmologists conduct one-on-one discussions of patients' problems [64]	Patients suffering from eye diseases find it difficult to keep eye contact with mobile and laptop screens when doctors are consulting them through video conferencing [65] Patients in rural areas do not know how to use this technology [65] Educating or training rural patients and rural communities regarding using video conferencing, streaming, audio conferencing, and computer-based communications services [66] It could not be affordable by the patient belonging to a low-income family

Table 2 continued

S. no.	Technologies	Summary and benefits	Challenges
6	Ophthalmology robots	In ophthalmic surgery, robotic instruments can deliver (SLC) a short learning curve and full surgical speed during the surgery [67] This technology can currently provide a precision of 1 mm with accuracy and enhanced handiness [68] Robots follow the hand movements of the surgeon during ocular surgery during eye surgery, and minute and tremble movements are sieved through the processor—for instance, the Vinci system [69]	Eye surgery needs a precise degree of movement of robots (movement stability) and delays responses during the operation time with accuracy while performing the repetitive tasks and this is the biggest challenge for the surgeon during the surgery [67] The major hindrance to adopting robot surgery is its high cost which is difficult to afford for low-income people [70] Robotic-based eye surgery requires excellent skill to operate the robots [71] Micro-incision cataract-based surgeries are difficult to perform by only robots; it requires more additional lasers that should be based on femtoseconds [71]
7	Telehealth	Telehealth allows the eye patients community to easily accesses eye care clinical center [72] Telehealth provides home monitoring to eye patients via mobile apps and optometrist communal [72] Remote screening of diabetic retinopathy (DR) is performed using optical coherence between doctors and patients using video conferencing technology [24] Telehealth technology provides real-time consultations to eye patients [4]	This technology is not for every treatment. If the patient wants a blood test, he has to go to the clinic physically for blood sampling, and the virtual model would not work [72] Disabled, aging people and eye disease patients are facing problems in using the Internet due to the high radiation of light inside their eyes [72] The high cost of 5G Internet services hinders people from a lower pay scale [72] The barriers are government rules and regulations regarding licenses for telehealth care providers Telehealth does not provide continuity care to patients as they get from physically meeting with an optometrist, because the long-distance relationship with the help of telehealth does not provide a better sense of the overall lifestyle of patients [73] Poor Internet connectivity and education training in rural communities regarding telehealth services [73]
8	Bionic eye	This theoretical concept in synthetic biology [74] could be used to fabricate bionic eyes enabled with high-resolution cameras in the future [75] Bionic eyes can fill the gaps between the retina and the brain's virtual cortex and help the patient to restore their vision [76] Use of bionic technology in ophthalmology, biological sensors, and a bionic eye can be made, where a bionic eye works like the natural eye by receiving pictures from the enabled camera that is kept laterally with eyeglasses [77] This technology makes artificial limbs, body parts, bionic hands, etc. [77]	By use of a bionic eye high level of eye vision repair is still challenging [75] It works on only some specific eye diseases such as Orion neural implant and limited availability of bionic eye technology at large scale as bionic limbs have [76] Very high cost, not affordable to all, and only a few people can afford it [78]. Millions of dollars are required for eye implants only, without hardware and medical treatment costs and more chances of eye tissue damage during the installation of chips inside the body [75]

Table 2 continued

S. no.	Technologies	Summary and benefits	Challenges
9	3D printing	Three-dimensional printings can be used in eye care by making orbital models for training purposes for doctors and surgical planning [79] It helps provide surgical instruments, diagnostic tools for eye implants, and other eye surgery (cataracts) [79] 3D corneal tissue models for eyes can be fabricated using design software by adding one material layer over another layer with less chance of grafting rejections [80] Used for making customized implants, eye prostheses, and pharmaceuticals [81] In ophthalmology, this technology can develop prosthesis eye, optional-related designing instruments, skin printing, and intraocular lenses [51]	Lack of standardization of machines and high capital cost involved in 3D printing of eyes [82] New materials for fabricating equipment and body parts should be needed clearance and approval before developing or fabricating artificial eyes that do not harm the body [83]
10	Telemedicine	This technology provides all the actual data of ophthalmology images, medical history, and medical information, such as images and texts, of diagnosed patients to clinical staff and doctors by using electronic communication networks while practicing the protocol of social distancing in COVID-19 [84] Help ophthalmologists provide good quality medical care in diabetic retinopathy and retinopathy of prematurity [85] This technology provides accurate and reliable patients with ROP (retinopathy of prematurity) [86] It sets up real-time communications between doctors and patients [87]	Rural areas are suffered from poor broadband connectivity Adverse weather conditions and interruptions in network connections cause problems for doctors and patients during diagnosis [88] Inadequate medical records of patients due to the shambling of the service providers increase the mixing of patients' diagnosis data, due to which doctors are confused about the patient's medical background [88]
11	Deep learning	Deep earning is based on a predictive algorithm with deep learning for enormous data processing [89]; because of these features, it is capable of taking fundus photography, OCT (optical coherence tomography) scans for the identification of IRF (intraretinal fluid) and able to solve age-related macular degeneration in eyes [15, 38, 39] In ophthalmology, deep learning technology has identified and categorized several diseases, such as diabetic retinopathy and prematurity of retinopathy [15] DL in ophthalmology can take retinal photographs (14,884) scans based on a triage algorithm for retinal diseases [15]	Researchers are working on DLM (deep learning methodologies) to recognize OCT biomarker-based structures for getting accurate clinical outcomes [90] The outcome of DL becomes some time challenging to understand for physicians as well as engineers who programmed that. Because of this, less trust is created among the public when DL algorithm output comes [90] Due to automatic images generated by DL and dependency on technology is high as fear of deskilling of physicians [91]

Table 2 continued

S. no.	Technologies	Summary and benefits	Challenges
12	Nanomedicine	Nanotechnology is used for the development of nanomedicine, for instance in ophthalmology, ocular medicine uses synthetic fiber, lipid nanomaterials, etc. [92]	This technology involved high research and development costs for making the medicine for ocular, retinal degenerative, and glaucoma treatment [96]
		Retinal and choroidal sicknesses are also studied by researchers and finding out its solution by nanomedicine [93]	Nanomedicines are beyond the coverage of middle-class cast because it is too expensive and put a higher financial encumbrance on the medical system. For instance, Doxil medicine (nanomedicine) is $5594 compared to non-nanomedicine doxorubicin, i.e., $62–162 [97]
		It is the medical involvement in the field of molecules to remedy damaged tissue, diseases like nerves, muscle, and the structure of bone [94]	Due to nanosize, it can easily be embedded inside the human body, which can harm the tissues and divert or misuse the real purpose of medicines [98]
		Employed in tissue engineering to restore the shape and size of damaged tissue, treatment of tumors, and lymphoma in many clinical research programs [95]	Toxicity because of its microscopic level and distinguished properties in standard working conditions [98]

is frequently not able to generalize unseen data. This occurs typically when a different population is studied with differences in eye images, technical variations between the camera and the system, and due to some unknown factors. Retinopathy of prematurity images of phenotypes is different that is captured in low- and middle-income countries than in economically sound countries such as North America due to the deficit of resources. Thus, it is critical to validate the results received from AI before conducting the clinical trial. Because of this, the AI system must be more validated by employing more datasets that are tested in distinguish populations such as patients with different image qualities that are taken from different cameras and by the level of pigmentation. This problem can be sorted out using open-access datasets and available online software to motivate clinical applications for retinopathy of prematurity [105].

9.2. Explain Ability Challenges

There is another denigration of AI algorithm acceptance by patients and doctors because the results obtained from these algorithms and CNN are challenging to understand by doctors and the same as the patients due to difficulty of understanding [106]. Another challenge with AI technology is how the same standard of explaining ability is functionalized to optometrist's cognitive reasoning. The results obtained by AI calculations may differ from the clinical cognitive results. The main motive of AI research in retinopathy of prematurity is to get good results [107]. This is similar to the fear of self-driving cars that it will meet to accidence without the driver's presence. Technology never is impeccable, but there is always room for improvement. Several challenges ophthalmology continuously faces in adopting digital technology during COVID-19 are illustrated in Table 3.

10. Momentous Contribution of the Current Study for Research Community

COVID-19 has imposed many challenges on the ophthalmology field where. Industry 5.0 can bring a drastic changing point in the history of the medical healthcare system where man and smart machines will work together to support society, humanity, industries, research, and the healthcare system. This revolution will make human work more accessible and effective through collaborating with advanced technology such as AI DL and ML and new technical and clinical innovations with collaborations through smart machines. This smart evolution can leverage twenty-five percent of work time spent on administrative and clerical work, where clinicians can easily store and access patient history as per their requirements without wasting much time on clerical work. These innovative technologies hold ongoing daily activities performed by clinicians that enhance their work capabilities with good quality of services and life safety of patients [74]. It is not a revolution; the evolution of the entire world brings man and smart machines together to serve society. Industry 5.0 tries to balance man, machine, and ecosystem. This revolution would be based on mass personalizing products and services rather than mass customization. It converts the mass personalization of customers into reality; for instance, customized eye prostheses can be shaped to the demand of



Fig. 3 Prime benefits of Industry 5.0 for ophthalmology

patients. The noteworthy contribution of the current study for research community understanding is as follows:

- The fast advancement in digital technology could bring adorable changes in the medical field and research community where man and intelligent machines work together with new innovative technologies and help society. 3D and 4D models of eye parts can be made using smart technologies.
- It brings the concept of advanced surgical robots, telemedicine, telehealth, and digital health to provide assistance and easiness among clinicians and patients.
- AI technology is helpful for doctors and patients to recognize diseases at the early level before it reaches to last level and save the life of patients.
- Various digital technologies such as telemedicine, telehealth, robotic surgery, and IMoT come into existence and continue working in the field of ophthalmology to fulfill patients' needs during COVID-19 when physical touch was utterly prohibited.
- Digital technologies are part of Industry 5.0, where surgery on the eyes is operated by robots with no risk and fills patients' advanced needs.
- In ophthalmology, this revolution will produce prosthesis eyes, nanomedicines artificial lenses enabled with AI devices as per the requirement of society. These intelligent technologies keep hold of ongoing daily activities performed by clinicians that enhance their work capabilities.
- The utmost merits of Industry 5.0 in ophthalmology are the easy availability of patients' old medical records with real-time data monitoring.
- Expansion of R&D in ophthalmology, training, and enhancing the clinician's skill and medical management system using new innovative enabling technologies.
- In the forthcoming, Industry 5.0 will radically change ophthalmology by improving eye surgeries entirely through advanced robots. These changes will occur in treatment procedures that connect with patients in less time using 5G and 6 G technologies most effectively and efficiently.

11. Current Situation of Digital Adoption in Healthcare System

It has been studied that the healthcare system has shown resilience behavior over the past year and has become easily accessible to patients. Accenture Health and Life Sciences Experience survey reports conducted in 2021 found that 1800 people in the USA accessed the digital healthcare system during COVID-19. The adoption of digital technology has increased overnight to virtual care for patients. In another survey, it has been observed that more people are using digital technologies to take care of their health this year. But in 2020, merely 7% of patients were connected to virtual consultation. In 2022, 32% hike has been seen in adopting digital technologies among patients. About 39% of patients who were suffering from chronic diseases took virtual consultations in 2020. From this survey, it has been concluded that 1 out of 4 people said that access to health care has become much better since the time of the COVID-19 pandemic [110].

Table 3 Major challenges faced in ophthalmology in the adoption of digital technology and its preferred solutions

S. no	Systems	Potential challenges	Preferred solutions	References
1	Practical challenges	Validated AI solutions are needed for practical implementation	It required software expertise	[108]
2	Advanced digital technology	Intricate and complicated user interface High material cost Various platforms are used for employing advanced technology It is a new experience for patients and providers facing difficulty adopting technology	The patient and medical clinicians should be willing and interested to learn about new technology The appropriate market size should be made to study all the problems and their solutions by adequately using the strength and performance of relations Affordability to adopting the new digital technologies Social health factors	[109]
3	Macro-system, which is based on screening assessment on a population lot size	Less sociocultural Poor supportive organizational culture The limited staff accessibility is due to fewer wage incentives It is challenging to implement the policies due to government regulations, poor financing conditions, and the regulatory atmosphere	To provide wage incentives to service providers, staff, etc., according to their work capacity, help the easy adoption Assessment of patients according to health Economy Availability of handful financial support system To check health-related technology regularly Preliminary approval of market	[91]
4	Mesosystem based on nucleus and spoke model	Lack of supporting resources system The feedback system is flawed for sustainable adoption and optimization	By providing virtuous infrastructure, all the facilities include intra- and inter-operability electricity, Internet connections, and safety We need to improve the mechanics of the working system by doing a continuous review Need to perform quality of project efficiently	[96–98]
5	Micro-system based on outpatient services	Difficult for patients and clinicians to understand the existing models of care and make proper interactions with them Ethics and medical–legal limitations	Clinicians and nurses should be adequately trained to adopt new care models Pilot studies have required that focus on the overall performance and clinical outcomes Make proper guidelines for using the care models Safety mechanisms should be a priority	[91]

12. Limitations of the Study

The current work is based on the theoretical view of Industry 5.0 in ophthalmology and its supporting digital technology, models used, and challenges faced by the healthcare system during COVID-19. In future work, the futuristic framework of Industry 5.0 with integrating digital technology in ophthalmology would be considered using quantitative techniques.

13. Research Implications of the Study

In the current study, it is perceived that Industry 5.0 is one step forward to Industry 4.0, but its implementation will take a long time in developing countries due scarcity of digital technologies, supporting infrastructure, and financial and government policies. For the first time, Industry 5.0 and ophthalmology are taken together; that is why the authors found fewer studies in this area that depicts the detailed elucidation from the optometrist's point of view toward the consequences faced by ophthalmology via implementing Industry 5.0. In forthcoming years, Industry 5.0 will bring historical change in humankind's and ophthalmology history, and will be bursting with innovations and new technologies as well as bring new openings in the field of the medical. Lastly, patients' trust in technology can be enhanced when the medical science community, on a large scale, embraces the vision of Industry 5.0 by integrating digital technologies.

14. Conclusions and Future

This study is based on the theoretical concept and amalgamation of Industry 5.0 with its digital technologies in the field of ophthalmology and how the various digital health model helps patients during COVID, as the benefit and challenges faced in ophthalmology. In the future, Industry 5.0 will bring historical change in medicine and manufacturing, full of innovations enabled by new technologies and excellent opportunities for the medical and manufacturing fields. In the current study, the following end assumptions are concluded:

- Industry 5.0 can obliterate the gap between man and machines by adopting innovative digital technologies to enhance work effectiveness in ophthalmology.
- The assortment of fifth revolution and digital technology could provide flawless mass customized services (fabrication of customized products or body parts according to the need of the patients) enabled with digital technologies to patients.
- Fifth revolution would bring the concept of advanced surgical robots, telemedicine, telehealth, and digital health to assist clinicians and patients quickly.
- Industry 5.0 is working on nanomedicines, bionics, and humanoid robots that will be used for the definitive diagnosis of diseases and their treatment. It has a significant potential to improve the medical structure and enhance the understanding and skills of medical doctors. This smart revolution dispenses the fabrication of customer-personalized forecasted products and services.
- From the future perspective, the up-gradation in mechanization and computerization systems and robot-aided eye surgery will be formulated with AI help and provide malleable solutions to ophthalmology problems.
- AI fast analyzes the database and stores all relevant data concerning patients' disease history in clouds and other applications, which helps doctors and healthcare management keep their records up to date in decision-making processes.
- In continuing research, researchers aim to develop advanced software that can identify all eye-related diseases such as retinopathy, glaucoma, diabetic muscular edema, and age-related muscular degeneration simultaneously to predict the progress and could predict personalized treatment to patients.
- In ophthalmology, digital technologies such as AI, DL, and other technologies have tremendous potential to enhance patients' access to clinical treatment and screening and reduce the cost of treatment. Though, legal-based rules and regulations are essentially required before AI-based screening technology is assimilated with clinical practice at a large scale.
- The practice of digital metrology with digital enabling technologies requires high-skill in-house training to understand the digital practice.
- The main challenge in implementing digital metrology in the medical healthcare system is repairing software, streamlining, and validation support.

Authors' Contributions NA.

Funding No funding is available in this manuscript.

Availability of Data and Materials NA (data transparency).

Code Availability NA (software application or custom code).

Declarations

Conflicts of Interest No conflict.

Ethics Approval NA.

Consent to Participate All agree to participation.

Consent for Publication All agree for publication.

References

[1] D. Krishna N, India COVID death rate hit record in June after calls for better data Reuters." [Online]. Available: https://www.reuters.com/world/india/indias-covid-death-rate-hit-record-june-after-calls-better-data-2021-07-06/, Accessed on 15/10/2022

[2] A. Haileamlak, The impact of COVID-19 on health and health systems. Ethiop. J Health Sci., *31*(6) (2021) 1073–1074. https://doi.org/10.4314/ejhs.v31i6.1.

[3] N.S. Jenny Cordina, Eric Levin, Andrew Ramish, COVID-19 and how consumers think about healthcare McKinsey. [Online]. Available: https://www.mckinsey.com/indus, Accesed on 13/10/2021

[4] E. Fowler, What is ophthalmology HealthPrep.com. [Online]. Available: https://healthprep.com/articles/eye-health/ophthalmology-overview/, Accessed on 15/10/2022

[5] J. Eske, What is ophthalmology, Medical conditions, procedures, and more. [Online]. Available: https://www.medicalnewstoday.com/articles/326753.Acessed on 12/10/2022

[6] FREIDA ophthalmology residency and fellowship listing. [Online]. Available: https://freida.ama-assn.org/specialty/ophthalmology, Accessed on 15/10/2022

[7] Introduction Ophthalmology. [Online]. Available: https://www.credencemedicure.com/specializations/ophthalmology/introduction/, Accessed on 10/10/2022

[8] D.S.J. Ting, V.H.X. Foo, L.W.Y. Yang, J.T. Sia, M. Ang, H. Lin, J. Chodosh, J.S. Mehta and D.S.W. Ting, Artificial intelligence for anterior segment diseases: Emerging applications in ophthalmology. Br. J. Ophthalmol., *105*(2) (2021) 158–168. https://doi.org/10.1136/bjophthalmol-2019-315651.

[9] K.A. Demir, G. Döven and B. Sezen, Industry 5.0 and human–robot co-working. Procedia Comput. Sci., *158* (2019) 688–695. https://doi.org/10.1016/j.procs.2019.09.104.
[10] D.M. Mann, J. Chen, R. Chunara, P.A. Testa and O. Nov, COVID-19 transforms health care through telemedicine: evidence from the field. J. Am. Med. Inform. Assoc., *27*(7) (2020) 1132–1135. https://doi.org/10.1093/jamia/ocaa072.
[11] J.H.E. Andriessen, The role of technology in society. In: R. Harper (ed) Working with groupware, Springer, London (2003), pp. 43–52. https://doi.org/10.1007/978-1-4471-0067-6_3.
[12] Y.R. Hong, J. Lawrence, D. Williams and A. Mainous, Population-level interest and telehealth capacity of US hospitals in response to COVID-19: cross-sectional analysis of Google search and national hospital survey data. JMIR Public Heal. Surveill., *6*(2) (2020) 1–8. https://doi.org/10.2196/18961.
[13] U. Schmidt-Erfurth, A. Sadeghipour, B.S. Gerendas, S.M. Waldstein and H. Bogunović, Artificial intelligence in retina. Prog. Retin. Eye Res., *67* (2018) 1–29. https://doi.org/10.1016/j.preteyeres.2018.07.004.
[14] Y. Lecun, Y. Bengio and G. Hinton, Deep learning. Nature, *521*(7553) (2015) 436–444. https://doi.org/10.1038/nature14539.
[15] J. De Fauw et al., Clinically applicable deep learning for diagnosis and referral in retinal disease. Nat. Med., *24*(9) (2018) 1342–1350. https://doi.org/10.1038/s41591-018-0107-6.
[16] C.S. Lee, A.J. Tyring, N.P. Deruyter, Y. Wu, A. Rokem and A.Y. Lee, Deep-learning based, automated segmentation of macular edema in optical coherence tomography. Biomed. Opt. Express, *8*(7) (2017) 3440. https://doi.org/10.1364/boe.8.003440.
[17] Y. Xie, D.V. Gunasekeran, K. Balaskas, P.A. Keane, D.A. Sim, L.M. Bachmann, C. Macrae and D.S.W. Ting, Health economic and safety considerations for artificial intelligence applications in diabetic retinopathy screening. Transl. Vis. Sci. Technol., *9*(2) (2020) 1–12. https://doi.org/10.1167/tvst.9.2.22.
[18] T.M. Aslam, H.R. Zaki, S. Mahmood, Z.C. Ali, N.A. Ahmad, M.R. Thorell and K. Balaskas, Use of a neural net to model the impact of optical coherence tomography abnormalities on vision in age-related macular degeneration. Am. J. Ophthalmol. (2017). https://doi.org/10.1016/j.ajo.2017.10.015.
[19] P. Burlina, K.D. Pacheco, N. Joshi, D.E. Freund and N.M. Bressler, Comparing humans and deep learning performance for grading AMD: a study in using universal deep features and transfer learning for automated AMD analysis. Comput. Biol. Med., *82* (2017) 80–86. https://doi.org/10.1016/j.compbiomed.2017.01.018.
[20] S. Dash, What is Legal Metrology_ Complete Concept and Laws—Corpbiz, [Online]. Available: https://corpbiz.io/learning/what-is-legal-metrology-complete-concept-and-laws, Accessed on 15/3/2023
[21] G. Tsaramirsis, A. Kantaros, I. Al-Darraji, D. Piromalis, C. Apostolopoulos, A. Pavlopoulou, M. Alrammal, Z. Ismail, S.M. Buhari, M. Stojmenovic, H. Tamimi, P. Randhawa, A. Patel and F.Q. Khan, A modern approach towards an Industry 4.0 model: from driving technologies to management. J. Sensors (2022). https://doi.org/10.1155/2022/5023011.
[22] Y. Xie, Y. Yin, W. Xue, H. Shi and D. Chong, Intelligent supply chain performance measurement in Industry 4.0. Syst. Res. Behav. Sci., *37*(4) (2020) 711–718. https://doi.org/10.1002/sres.2712.
[23] Making in India with Industry 5.0 to strengthen care in healthcare. [Online]. Available: https://www.dqindia.com/applications-of-industry-5-0-could-grow-as-the-understanding-of-its-scope-and-capabilities-increases/, Accessed on 16/10/2022
[24] D.S.W. Ting, L. Peng, A.V. Varadarajan, P.A. Keane, P.M. Burlina, M.F. Chiang, L. Schmetterer, L.R. Pasquale, N.M. Bressler, D.R. Webster, M. Abramoff and T.Y. Wong, Deep learning in ophthalmology: the technical and clinical considerations. Prog. Retin. Eye Res., *72* (2019) 100759. https://doi.org/10.1016/j.preteyeres.2019.04.003.
[25] A. Haleem and M. Javaid, Industry 5.0 and its expected applications in medical field. Curr. Med. Res. Pract., *9*(4) (2019) 167–169. https://doi.org/10.1016/j.cmrp.2019.07.002.
[26] S. Keel et al., Feasibility and patient acceptability of a novel artificial intelligence-based screening model for diabetic retinopathy at endocrinology outpatient services: a pilot study. Sci. Rep., *8*(1) (2018) 8–13. https://doi.org/10.1038/s41598-018-22612-2.
[27] E. Woźniak and A. Tyczewska, Bioeconomy during the COVID-19 and perspectives for the post-pandemic world: example from EU. EFB Bioeconomy J., *1*(May) (2021) 100013. https://doi.org/10.1016/j.bioeco.2021.100013.
[28] G. Schütte, What kind of innovation policy does the bioeconomy need? N. Biotechnol., *40* (2018) 82–86. https://doi.org/10.1016/j.nbt.2017.04.003.
[29] P. Sachsenmeier, Industry 5.0—the relevance and implications of bionics and synthetic biology. Engineering, *2*(2) (2016) 225–229. https://doi.org/10.1016/J.ENG.2016.02.015.
[30] E. Engage, COVID-19 and Digital Futures: Is India prepared to build an inclisive way forward, Economic and Political Weekly." [Online]. Available: https://subscription.epw.in/engage/article/covid-19-and-digital-futures-india-prepared-build, Accessed on 19/10/2021
[31] J.E.J. Allan, Patient-centered documentation: an effective and efficient use of clinical information systems. Nat. Libr. Med. (2000). https://doi.org/10.1097/00005110-200002000-00006.
[32] V.S.E. Jeganathan and S. Shah, Robotic technology in ophthalmic surgery. Curr. Opin. Ophthalmol. (2010). https://doi.org/10.1097/ICU.0b013e328333371d.
[33] T. Davenport and R. Kalakota, The potential for artificial intelligence in healthcare. Future Healthc J, *6*(2) (2019) 94–98.
[34] R.P. Singh, M. Javaid, A. Haleem, R. Vaishya and S. Bahl, Significance of health information technology (Hit) in context to covid-19 pandemic: potential roles and challenges. J. Ind. Integr. Manag., *5*(4) (2020) 427–440. https://doi.org/10.1142/S2424862220500232.
[35] J.-P.O. Li, H. Liu, D.S.J. Ting, S. Jeon, R.V. Paul Chan, J.E. Kim, D.A. Sim, P.B.M. Thomas, H. Lin, Y. Chen, T. Sakomoto, A. Loewenstein, D.S.C. Lam, L.R. Pasquale, T.Y. Wong, L.A. Lam and D.S.W. Ting, Digital technology, tele-medicine and artificial intelligence in ophthalmology: a global perspective. Prog. Retin. Eye Res. (2020). https://doi.org/10.1016/j.preteyeres.2020.100900.
[36] L. Panda, What Is the Internet of Medical Things (IoMT)? IoT For all. 2019. [Online]. Available: https://www.iotforall.com/internet-of-medical-things-iomt, Accessed on 18/9/2021
[37] Would You Do as a Robot Commands? [Online]. Available: http://hci.cs.umanitoba.ca/projects-and-research/details/would-you-do-as-a-robot-commands, Accessed on 3/9/2021
[38] Saanvi Arora, IoMT (Internet of Medical Things) Reducing cost while improving patient care." 2020. https://doi.org/10.1109/mpuls.2020.3022143.
[39] The Future of Telemedicine Technology with IoT and AI – Intel. [Online]. Available: https://www.intel.com/content/www/us/en/healthcare-it/telemedicine.html, Accessed on 13/10/2022
[40] Intel Corporation, Robotics in Healthcare: The Future of Robots in Medicine. 2021. [Online]. Available: https://www.intel.com/content/www/us/en/healthcare-it/robotics-in-healthcare.html, Accessed on 8/10/2022

[41] D.V. Gunasekeran, Y.C. Tham, D.S.W. Ting, G.S.W. Tan and T.Y. Wong, Digital health during COVID-19: lessons from operationalising new models of care in ophthalmology. Lancet Digit. Heal., *3*(2) (2021) e124–e134. https://doi.org/10.1016/S2589-7500(20)30287-9.

[42] A.M.K. Chew, R. Ong, H.-H. Lei, M. Rajendram, K.V. Grisan, S.K. Verma, D.S.S. Fung, J.J.-Y. Leong and D.V. Gunasekeran, Digital health solutions for mental health disorders during COVID-19/ *Front*. Psychiatry, *11*(Septemper) (2020) 1–7. https://doi.org/10.3389/fpsyt.2020.582007.

[43] W. Xiaohang, J. Chen, D. Yun, M. Yuan, Z. Liu, P. Yan, D.A. Sim, Y. Zhu, C. Chen, H. Weiling, W. Zijian, H. Lin, Y. Wang, W. Yanling, M. Chen, C. Zhang, Y. Zheng, X. Liu, X. Zhong, H. Diao, D.S.W. Ting, D.V. Gunasekeran, Y. Li, J. Zhang, Y. Cai, Z. Lao, Y. Liu, T.Y. Wong, X. Lin and H. Lin, Effectiveness of an ophthalmic hospital-based virtual service during the COVID-19 pandemic. Ophthalmology, *128*(6) (2021) 942–945. https://doi.org/10.1016/j.ophtha.2020.10.012.

[44] L.W. Li, A.M.K. Chew and D.V. Gunasekeran, Digital health for patients with chronic pain during the COVID-19 pandemic. Br. J. Anaesth., *125*(5) (2020) 657–660. https://doi.org/10.1016/j.bja.2020.08.003.

[45] S. Mehta, Age-related macular degeneration. Prim. Care Clin. Off. Pract., *42*(3) (2015) 377–391. https://doi.org/10.1016/j.pop.2015.05.009.

[46] C.L.S. Kilduff, A.A.P. Thomas, J. Dugdill, E.J. Casswell, M. Dabrowski, C. Lovegrove, D.A. Sim, G.R. Hay and P.B.M. Thomas, Creating the Moorfields' virtual eye casualty: video consultations to provide emergency teleophthalmology care during and beyond the COVID-19 pandemic. BMJ Heal. Care Inform, *27*(3) (2020) 1–5. https://doi.org/10.1136/bmjhci-2020-100179.

[47] M. Joshi, H. Ashrafian, S. Arora, S. Khan, G. Cooke and A. Darzi, Digital alerting and outcomes in patients with sepsis: systematic review and meta-analysis. J. Med. Internet Res., *21*(12) (2019) 1–9. https://doi.org/10.2196/15166.

[48] Z. Wang and K. Tang, Combating COVID-19: health equity matters. Nature Medicine, *26*(4) (2020) 458. https://doi.org/10.1038/s41591-020-0823-6.

[49] T. Burki, GP at hand: a digital revolution for health care provision? Lancet (London, England), *394*(10197) (2019) 457–460. https://doi.org/10.1016/S0140-6736(19)31802-1.

[50] J. Teo, National eye centre launches telemedicine for glaucoma patients, The Straits Times. National Dental center singapore. [Online]. Available: https://www.ndcs.com.sg/news/tomorrows-medicine/national-eye-centre-launches-telemedicine-for-glaucoma-patients, Accessed on 6/10/2022

[51] S.K. Sattigeri, D.N. Gowda, K.A. Ullas, A.M.S and A. Professor, Eye disease identification using deep learning. Int. Res. J. Eng. Technol., July, pp. 974–978, 2022, [Online]. Available: www.irjet.net, Accessed on 11/10/202

[52] How is the internet of medical things aiding the healthcare sector NIIT. [Online]. Available: https://www.niit.com/india/knowledge-centre/IoMT/, Accessed on 9/10/2021

[53] M. Anderson, What is the Internet of Medical Things? ATL Technology, *ATL Technology*. [Online]. Available: https://atltechnology.com/blog/internet-of-medical-things/, Accessed on 4/4/2021

[54] R. Rasti, M.J. Allingham, P.S. Mettu, S. Kavusi, K. Govind, S.W. Cousins and S. Farsiu, Deep learning-based single-shot prediction of differential effects of anti-VEGF treatment in patients with diabetic macular edema. Biomed. Opt. Express, *11*(2) (2020) 1139. https://doi.org/10.1364/boe.379150.

[55] R.A. Hitchings and G.L. Spaeth, The optic disc in glaucoma I: Classification. Br. J. Ophthalmol., *60*(11) (1976) 778–785. https://doi.org/10.1136/bjo.60.11.778.

[56] H. Yamashita, International clinical diabetic retinopathy and diabetic macular edema disease severity scales. Nihon. Ganka Gakkai Zasshi, *107*(2) (2003) 110–113.

[57] A.D. Morau, D. Costin, R.L. Morau and D.C. Branisteanu, Artificial intelligence and deep learning in opthalomology present and future (Review). Ther. Med, Exp (2020). https://doi.org/10.3892/etm.2020.9118.

[58] G. Sachdeva, 5G has the potential to transform AI. [Online]. Available: https://indiaai.gov.in/article/5g-has-the-potential-to-transform-ai-here-s-how, Accessed on 18/10/2022

[59] Thales, What is 5G? A helpful illustrated Q&A (2022), *Defence and Security*. 2022. [Online]. Available: https://www.thalesgroup.com/en/markets/digital-identity-and-security/mobile/inspired/5G,Acessedon 12/8/2021

[60] M.M. Ahamed and S. Faruque, 5G Backhaul: requirements, challenges, and emerging technologies. Broadband Commun. Netw. Recent Adv. Lessons from Pract. (2018). https://doi.org/10.5772/intechopen.78615.

[61] H. Remmert, 5G and the Future of Telemedicine and Remote Surgery. [Online]. Available: https://www.digi.com/blog/post/5g-and-the-future-of-telemedicine-remote-surgery, Accessed on 12/1/2023

[62] R. Somasundaram and M. Thirugnanam, Review of security challenges in healthcare internet of things. Wirel. Netw., *27*(8) (2021) 5503–5509. https://doi.org/10.1007/s11276-020-02340-0.

[63] L. Li, China's manufacturing locus in 2025: with a comparison of "Made-in-China 2025" and "Industry 4.0." Technol. Forecast. Soc. Change, *135*(May) (2018) 66–74. https://doi.org/10.1016/j.techfore.2017.05.028.

[64] J Kagan, Video Conferencing,How It Works, How to Use It, Top Platforms. [Online]. Available: https://www.investopedia.com/terms/v/video-conferencing.asp, Accessed on 2/2/2021

[65] The Drawbacks of Video Conferencing Highfive. [Online]. Available: https://highfive.com/blog/the-drawbacks-of-video-conferencing, Accessed on 1/2/2021

[66] Telehealth Use in Rural Healthcare Overview—Rural Health Information Hub. [Online]. Available: https://www.ruralhealthinfo.org/topics/telehealth, Accessed on 28/1/2023

[67] M. Orday, Robotic assisted surgery—current challanges and future directions: Interveiw. [Online]. Available: https://www.medgadget.com/2017/10/interview-dr-mona-orady-robotic-assisted-surgery-current-challenges-future-directions.html, Accessed on 2/12/2022

[68] A. Tsirbas, C. Mango and E. Dutson, Robotic ocular surgery. Br. J. Ophthalmol., *91*(1) (2007) 18–21. https://doi.org/10.1136/bjo.2006.096040.

[69] T. Bourcier et al., Robot-assisted pterygium surgery: feasibility study in a nonliving porcine Model. Transl. Vis. Sci. Technol., *4*(1) (2015) 9. https://doi.org/10.1167/tvst.4.1.9.

[70] V.S. Suresh, K. Pandey, IJO-67-988.pdf.pdf. Indian J. Ophthalmol., 2019. https://doi.org/10.4103/ijo.IJO_1131_18.

[71] M.D. De Smet, G.J.L. Naus, K. Faridpooya and M. Mura, Robotic-assisted surgery in ophthalmology. Curr. Opin. Ophthalmol., *29*(3) (2018) 248–253. https://doi.org/10.1097/ICU.0000000000000476.

[72] Y.-C. Tham, R. Husain, K.Y.C. Teo, A.C.S. Tan, A.C.Y. Chew, D.S. Ting, C.-Y. Cheng, G.S.W. Tan and T.Y. Wong, New digital models of care in ophthalmology, during and beyond the COVID-19 pandemic. Br. J. Ophthalmol., *106*(4) (2022) 452–457. https://doi.org/10.1136/bjophthalmol-2020-317683.

[73] L.A. Ritter, Benefits and challenges of telehealth in rural areas. [Online]. Available: https://onlinedegrees.unr.edu/blog/benefits-and-challenges-of-telehealth-in-rural-areas/, Accessed on 24/1/2023

[74] S. Berg, Nudge theory explored to boost medication adherence, Chicago Am. Med. Assoc., pp. 1–3, 2018, [Online]. Available: https://www.ama-assn.org/print/pdf/node/18981
[75] C.C, Bionic Eyes: Can The Blind Really Regain complete sight Artificially?,Automation Switch." Automation Switch. [Online]. Available: https://automationswitch.com/bionic-eyes.com, Accessed on 9/5/2021
[76] M. Smith, Bionic eyes:How tech is replacing lost vision, Live Science. 2022. [Online]. Available: https://www.livescience.com/bionic-eye, Accessed on 2/5/2021
[77] Amy Hellem, Eye implants: Bionic eyes, lenses and prosthetic eyes, All About Vision. 2021. [Online]. Available: https://www.allaboutvision.com/conditions/bionic-eyes.htm, Accessed on 27/1/2023
[78] All That You Need To Know About Eye Implants (Bionic Eye) - Body Art Guru. [Online]. Available: https://bodyartguru.com/eye-implants-bionic-eye/, Accessed on 27/1/2023
[79] M. Fuest, G.H.F. Yam, J.S. Mehta and D.F.D. Campos, Prospects and challenges of translational corneal bioprinting. Bioengineering, *7*(3) (2020) 1–17. https://doi.org/10.3390/bioengineering7030071.
[80] P.E. Ludwig, T.J. Huff and J.M. Zuniga, The potential role of bioengineering and three-dimensional printing in curing global corneal blindness. J. Tissue Eng. (2018). https://doi.org/10.1177/2041731418769863.
[81] J. Olczak, N. Fahlberg, A. Maki, A.S. Razavian, A. Jilert, A. Stark, O. Sköldenberg and M. Gordon, Artificial intelligence for analyzing orthopedic trauma radiographs: Deep learning algorithms—are they on par with humans for diagnosing fractures? Acta Orthop., *88*(6) (2017) 581–586. https://doi.org/10.1080/17453674.2017.1344459.
[82] A. Halsey, The Big Challenges of 3D Printing Manufacturing Tomorrow. [Online]. Available: https://www.manufacturingtomorrow.com/story/2019/12/the-big-challenges-of-3d-printing/14544/, Accessed on 24/01/2023
[83] C. Kent, 3D printing technology in nanomedicine. Elsevier, Amsterdam. (2019). https://doi.org/10.1016/b978-0-12-815890-6.01001-x.
[84] S. Rawan and M. Salducci, Law and order of modern ophthalmology: Teleophthalmology, smartphones legal and ethics. Eur. J. Ophthalmol., *31*(1) (2021) 13–21. https://doi.org/10.1177/1120672120934405.
[85] B.A. Scruggs, R.V. Paul Chan, J. Kalpathy-Cramer, M.F. Chiang and J.P. Campbell, Artificial intelligence in retinopathy of prematurity diagnosis. Transl. Vis. Sci. Technol., *9*(2) (2020) 5. https://doi.org/10.1167/tvst.9.2.5.
[86] S.J. Kim, A.D. Port, R. Swan, J.P. Campbell, R.V.P. Chan and M.F. Chiang, Retinopathy of prematurity: a review of risk factors and their clinical significance. Surv. Ophthalmol., *63*(5) (2018) 618–637. https://doi.org/10.1016/j.survophthal.2018.04.002.
[87] Thierry, E. A new European innovation agenda, EPRS: European Parliamentary Research Service. Belgium. (2022). Retrieved from https://policycommons.net/artifacts/2677255/a-new-european-innovation-agenda/3700468.
[88] P. Panicker, 5 Challenges of telemedicine faced by practitioners. [Online]. Available: https://www.quicsolv.com/blog/5-challenges-telemedicine-faced-practitioners/, Accessed on 24/4/2022
[89] L. Li, Education supply chain in the era of Industry 4.0. Syst. Res. Behav. Sci., *37*(4) (2020) 579–592. https://doi.org/10.1002/sres.2702.
[90] D.V. Gunasekeran and T.Y. Wong, Artificial intelligence in ophthalmology in 2020: a technology on the cusp for translation and implementation. Asia-Pac. J. Ophthalmol., *9*(2) (2020) 61–66. https://doi.org/10.1097/01.APO.0000656984.56467.2c.
[91] D.S.W. Ting, L. Carin, V. Dzau and T.Y. Wong, Digital technology and COVID-19. Nat. Med., *26*(4) (2020) 459–461. https://doi.org/10.1038/s41591-020-0824-5.
[92] Q. Lyu, L. Peng, X. Hong, T. Fan, J. Li, Y. Cui, H. Zhang and J. Zhao, Smart nano-micro platforms for ophthalmological applications: the state-of-the-art and future perspectives. Biomaterials, *270* (2021) 120682. https://doi.org/10.1016/j.biomaterials.2021.120682.
[93] U. Krishna, D. Ajanaku, A.K. Denniston and T. Gkika, Uveitis: a sight-threatening disease which can impact all systems. Postgrad. Med. J., *93*(1106) (2017) 766–773. https://doi.org/10.1136/postgradmedj-2017-134891.
[94] Nanomedicine - Overview. [Online]. Available: https://commonfund.nih.gov/nanomedicine/overview, Accessed on 14/10/2022
[95] W.R. Smith, P.W. Hudson, B.A. Ponce and S.R. Rajaram Manoharan, Nanotechnology in orthopedics: a clinically oriented review. BMC Musculoskelet. Disord., *19*(1) (2018) 67. https://doi.org/10.1186/s12891-018-1990-1.
[96] D. Brabazon, E. Pellicer, F. Zivic, J. Sort, M.D. Baró, N. Grujovic and K.-L. Choy, Commercialization of nanotechnologies—a case study approach. Commer Nanotechnol Case Study Approach (2017). https://doi.org/10.1007/978-3-319-56979-6.
[97] M.A. Zarbin, C. Montemagno, J.F. Leary and R. Ritch, Nanomedicine in Ophthalmology. Am. J. Ophthalmol., *150* (2010) 144–162. https://doi.org/10.1016/j.ajo.2010.03.019.
[98] S. Verma, A.J. Domb and N. Kumar, Nanomaterials for regenerative medicine. Nanomedicine, *6*(1) (2011) 157–181. https://doi.org/10.2217/nnm.10.146.
[99] M. Teräs, J. Suoranta, H. Teräs and M. Curcher, Post-Covid-19 education and education technology "solutionism": a seller's market. Postdigital Sci. Educ., *2*(3) (2020) 863–878. https://doi.org/10.1007/s42438-020-00164-x.
[100] J.C. Buchan, P. Norman, D. Shickle, A. Cassels-Brown and C. MacEwen, Failing to plan and planning to fail. Can we predict the future growth of demand on UK Eye Care Services? Eye, *33*(7) (2019) 1029–1031. https://doi.org/10.1038/s41433-019-0383-5.
[101] S.A. McCord, M.G. Lynch and A.Y. Maa, Diagnosis of retinal detachments by a tele-ophthalmology screening program. J. Telemed. Telecare, *25*(3) (2019) 190–192. https://doi.org/10.1177/1357633X18760418.
[102] D.S.J. Ting, S. Krause, D.G. Said and H.S. Dua, Psychosocial impact of COVID-19 pandemic lockdown on people living with eye diseases in the UK. Eye, *35*(7) (2021) 2064–2066. https://doi.org/10.1038/s41433-020-01130-4.
[103] B. Morey, Advances in medical metrology. [Online]. Available: https://www.sme.org/technologies/articles/2018/july/advances-in-medical-metrology/, Accessed on 18/3/2023
[104] M. Nakrani, What is a convolutional neural network (CNN). 2022. [Online]. Available: https://connectingdotsinfotech.com/blog/what-is-a-convolutional-neural-network/, Accessed on 8/10/2022
[105] Y. Li, F. Liu, T. Zhang, F. Xu, Y. Gao and T. Wu, Artificial intelligence in paediatrics. Chin Med J, *133* (2020) 358–360. https://doi.org/10.1631/jzus.B1600273.8.
[106] M. Radfar, R. Barnwal, R.V. Swaminathan, F-J Chang, G.P. Strimel, N. Susanj, A. Mouchtaris, ConvRNN-T: convolutional augmented recurrent neural network transducers for streaming speech recognition, pp. 4431–4435, 2022, https://doi.org/10.21437/interspeech.2022-10844
[107] V. Gulshan et al., Development and validation of a deep learning algorithm for detection of diabetic retinopathy in retinal fundus photographs. JAMA - J. Am. Med. Assoc.,

316(22) (2016) 2402–2410. https://doi.org/10.1001/jama.2016.17216.

[108] A.D. Moraru, D. Costin, R. Moraru and D. Branisteanu, Artificial intelligence and deep learning in ophthalmology—present and future (review). Exp. Ther. Med., *20*(4) (2020) 3469–3473. https://doi.org/10.3892/etm.2020.9118.

[109] N. Lurie, Virtual perfect? Telemedicine for Covid-19. N. Engl. J. Med., *108*(1) (2020) 1969–1973.

[110] K. Safavi, B. Michel, K. Ficery, W. Baldwin, B. Kalis and S. Karaca-Griffin, Digital technology adoption in healthcare. Accenture. 2021. [Online]. Available: https://www.accenture.com/us-en/insights/health/digital-adoption-healthcare-reaction-or-revolution, Accessed on 27/1/2023

Publisher's Note Springer Nature remains neutral with regard to jurisdictional claims in published maps and institutional affiliations.

Springer Nature or its licensor (e.g. a society or other partner) holds exclusive rights to this article under a publishing agreement with the author(s) or other rightsholder(s); author self-archiving of the accepted manuscript version of this article is solely governed by the terms of such publishing agreement and applicable law.

ECS Journal of Solid State
Science and Technology

The Electrochemical Society
Advancing solid state & electrochemical science & technology

ACCEPTED MANUSCRIPT

Review—Advancements and Perspectives of Organic LED: In Depth Analysis of Architectural Design, Characteristics Parameters, Fabrication Techniques, and Applications

To cite this article before publication: Sugandha Yadav *et al* 2023 *ECS J. Solid State Sci. Technol.* in press https://doi.org/10.1149/2162-8777/acc96f

Manuscript version: Accepted Manuscript

Accepted Manuscript is "the version of the article accepted for publication including all changes made as a result of the peer review process, and which may also include the addition to the article by IOP Publishing of a header, an article ID, a cover sheet and/or an 'Accepted Manuscript' watermark, but excluding any other editing, typesetting or other changes made by IOP Publishing and/or its licensors"

This Accepted Manuscript is © **2023 The Electrochemical Society ("ECS"). Published on behalf of ECS by IOP Publishing Limited**.

This article can be copied and redistributed on non commercial subject and institutional repositories.

Although reasonable endeavours have been taken to obtain all necessary permissions from third parties to include their copyrighted content within this article, their full citation and copyright line may not be present in this Accepted Manuscript version. Before using any content from this article, please refer to the Version of Record on IOPscience once published for full citation and copyright details, as permissions will likely be required. All third party content is fully copyright protected, unless specifically stated otherwise in the figure caption in the Version of Record.

View the article online for updates and enhancements.

This content was downloaded from IP address 14.139.251.98 on 05/04/2023 at 07:51

Review—Advancements and Perspectives of Organic LED: In Depth Analysis of Architectural Design, Characteristics Parameters, Fabrication Techniques, and Applications

Journal:	*ECS Journal of Solid State Science and Technology*
Manuscript ID	JSS-103169.R1
Manuscript Type:	Review Paper
Date Submitted by the Author:	03-Mar-2023
Complete List of Authors:	Yadav, Sugandha; DTU Mittal, Poornima; Delhi Technological University, Electronics and Communication Negi, Shubham; Chandigarh University
Keywords:	OLED - Hole Conducting Layer, Displays, Luminescence, Thin film growth

SCHOLARONE™
Manuscripts

Accepted Manuscript

Review—Advancements and Perspectives of Organic LED: In Depth Analysis of Architectural Design, Characteristics Parameters, Fabrication Techniques and Applications

Sugandha Yadav,[1] Poornima Mittal,[1,z] and Shubham Negi[2]

[1]Department of Electronics and Communication Engineering, Delhi Technological University, Delhi-110042 (India)
[2]Department of Electronics and Communication Engineering, Chandigarh University, Mohali, Punjab-140413 (India)

[z]E-mail: poornimamittal@dtu.ac.in

Abstract

This article presents a review on various aspect of Organic LED, such as its working, various categorization, impact of fabrication methodologies (organic vapor phase deposition, vacuum thermal evaporation, inkjet printing etc.) that are low-cost and its applications in serval domains like medical, sensor, display, lighting etc. Three categorizations of OLED are discussed with respect to circuit, architecture, and color of emission. Different layers of multi-layered structures such as injection layer, transport layer, block layers are also reviewed and their impacts are analyzed and compared. Moreover, an experimental fabrication technique for flexible substrate is reviewed that highlights low-cost fabrication method. In this technique, dynamic viscosity and contact angle are measured using rotational viscometer and contact angle meter, respectively. The result illustrates sheet resistance and effective opening ratio of 3.8 ohms per square and 82.5%, correspondingly. Additionally, various performance parameters like luminescence, external quantum efficiency and current efficiency are compared. The paper also incorporates recent advancement in organic thin film transistors along with some OTFT driven OLED devices.

1. Introduction

Organic light emitting diode (OLED) is a modern display technology which is made from organic thin films of light emissive materials. It has become successfully commercialized device in mobile and television display. This technology comes up with unparalleled image quality, flexible [1,2] and transparent display, large area fabrication [3], low power consumption [4], low-cost designs etc. The parameters like luminescence, current density and methodologies such as transport and block layers play important role for improving the performance of OLED. This paper provides a review on these parameters. Organic LEDs are

Accepted Manuscript
For Review Only

constructed by depositing series of organic thin films between cathode and anode. A bright light is emitted after applying the potential difference between the electrodes. It is observed that the luminescence factor is very important for the uniform brightness in these devices and if more layers are imposed between these two electrodes; charge injection, current density, luminescence and other parameters can be improved.

If the lighting products are observed that are being used for last several decades, the one product that is very old is incandescent lamp. The efficiency of incandescent lamp is about 15 lumens per watt and lifetime 1000 hours approximately. The next improvement of the lighting product was tube light. The efficiency was substantially higher about 108 lumens per watt, also lifetime was about 25,000 hours. Then after a long time-gap CFL (Compact Fluorescence Tube) was introduced. The efficiency of CFL was in the range of 50 lumens per watt and lifetime was 12,000 hours. But it replaced at least incandescent bulb which have much less efficiency and even in some cases, tube light which has much higher lifetime than CFL. And then recent trend is to go toward solid-state lighting devices, especially inorganic LEDs. These are made of 3 to 5 semiconductors and in case of efficiency they are much better than any other lighting products in the range of 100 to 150 lumens per watt and lifetime is also very much higher approximately 50,000 hours [5].

It is observed from energy point of view, as it is the biggest concern of everyone, that utilization of highly efficient products is required to save substantial amount of energy over the usage period. In case of LED, usage period is very high and hence it makes more sense to go for solid state lighting devices to improve the energy consumption and this is where the OLED [6,7] is needed. The efficiency of OLED is more than 100 lumens and lifetime varies according to the color of emission. For example, the lifetime for red color is 80,000 hours, for green it is 40,000 hours and for yellow it is only 7,000 hours.

The complete paper is organized in eight different sections. Section 1 is about the introduction of organic LED. Section 2 highlights the working principle of OLED. Then, Section 3 demonstrates the different structure of OLEDs in terms of circuits, architectural change and color emission. Various processing techniques for multilayered OLEDs are incorporated in Section 4. Furthermore, Section 5 is highlighting different parameters of OLEDs such as luminescence, external quantum efficiency and current efficiency. Thereafter, in Section 6 multilayered structures of organic LED are discussed. Addition to this, Section 7 is demonstrating different organic thin film structures. This section also compares some OLED devices driven by OTFT. Thereafter, various applications are discussed on the basis of sensor,

https://mc04.manuscriptcentral.com/jss-ecs

Accepted Manuscript
For Review Only

healthcare and display in Section 8. Addition to this, Section 9 & 10 incorporate various challenges and future scope of OLED. Eventually, the necessary conclusions are mentioned in Section 11.

2. Working Principle of OLED

Fig. 1 is highlighting the complete process of light emission. When a potential difference is developed across the cathode and anode in a way that cathode is attached to the negative terminal and anode to the positive terminal, cathode starts receiving the electrons from the power supply as shown in the figure. After the charge carrier injection process, transportation takes place. In the case of organic molecules, the hole mobility is always better than that of the free electrons, so holes start moving across the boundary to the emissive layer and the recombination occurs. Due to this process, excitons are formed and energy is generated in the form of particle of light. These particles are known as photon. Here, this process of recombination occurs multiple times in fraction of seconds so OLED keeps producing the photons as long as the current keeps flowing in the circuit.

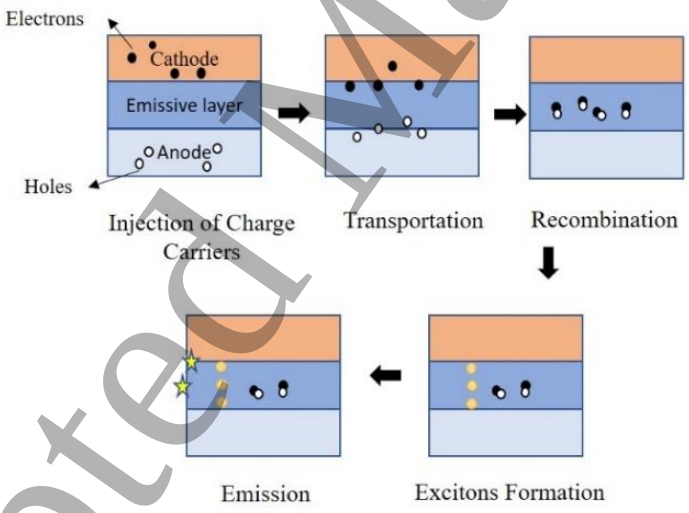


Fig. 1. Steps of light emission in organic LED.

Various layers can be incorporated to the basic structure to enhance the property of emissive layer, improve the charge injection and inhibit the charge carriers (generally holes) to achieve 100% exciton formation. These layers are: 1) hole/electron injection layer, 2) hole/electron transportation layer, and 3) blocking layer which are explained in detail in section 5. Besides these layers, there are some novel layers as well like charge generation layer (CGL)

Accepted Manuscript For Review

[8], mixed interlayer (MI) [9], space layer [10] etc. which can be utilized to improve the performance of basic OLED structures.

3. Classification of OLED

There are several types of OLED technologies classified according to the nature of their use and the manufacturing methodology. A brief introduction will be discussed now about all these OLEDs based on three categories. The categorization is with respect to circuit, architecture and color of light emission.

3.1. Categorization based on Circuit

Generally, AMOLED and PMOLED are the types of OLED which are defined in terms of circuits. PMOLED is Passive-Matrix OLED which consists of cathode and anode strips. These strips intersect at perpendicular points ally pixels. These intersections create the pixels where light is produced. The luminosity of these pixels completely depends on the applied current. PMOLEDs [11] are easy to make however, they consume high power than any other OLED technology because in this some power is required to run the external circuitry also. These devices are restricted in size and resolution; hence they are used in mobile phone, MP3 players, small displays, etc., to represent small icons and character data. Various PMOLED circuits are proposed in recent time. Yan *et al.* [11] presented a novel 3.5-inch PMOLED which contains no dead space on left and right side of the device. This makes easy to stich many PMOLEDs together to make the larger panel with higher resolution of 160 (RGB)×240.

Additionally, Su *et al.* [12] proposed a full color 7-inch Passive-Matrix OLED display. In this work, roll-to-sheet lamination process is used to laminate 100 μm PEN substrate on glass. A bubble free lamination is achieved by this process. After de-bonding, the flexible substrate is bended 1000 times with the radius of 10 cm without any crack. Moreover, Uttwani *et al.* [13] investigated a small OLED matrix by creating defects deliberately to study the possible visual manifestations in a PMOLED display using a cathode ray oscilloscope (CRO).

On the other hand, Active-Matrix organic LED (AMOLED) [14] consists of sheets of cathode, organic and anode layers. In anode layer there is a TFT (thin film transistor) to form a matrix. This TFT requires low power hence, charging rate is very fast in active matrix displays. They are used in large screen TVs, computer monitors, electronic billboards etc. The

https://mc04.manuscriptcentral.com/jss-ecs

Accepted Manuscript For Review Only

AMOLEDs are replacing the traditional LCD devices during the last decade having lot of advantages such as thinner display, better viewing angle, higher image quality, low power consumption etc. Many groups of researchers have devoted their time to explore these devices. In 2018, Boera *et al.* [15] discussed SIBO (single inductor bipolar outputs) DC-DC converter for AMOLEDs which is able to generate two desired voltages of opposite polarity using single inductor. The circuit with input voltages ranging from 2.4 to 4.9 V generates output voltages as +5 and -6 V having maximum output current of 0.6 A at load.

Additionally, Steudel *et al.* [16] designed and realized a flexible AMOLED with an OTFT backplane. The device contains resolution of 85 dpi and exhibits aperture ratio and luminescence as 75 % and 200 cd/m^2, respectively. Additionally, Mo *et al.* [17] developed an amorphous-oxide TFT for large sized AMOLEDs. The reported TFT showed high field effect mobility, I_{ON}/I_{OFF} and sub-threshold slope as 21 cm^{2}V^{-1}s^{-1}, >10^8 and 0.29 V/dec, respectively. The proposed AMOLED device provided excellent uniformity and good device reliability. Furthermore, Yonebyashi *et al.* [18] designed a low power AMOLED with high refresh rate ranging from 1 to 120 Hz. Here, a top gate n-oxide and p-LTPS (low temperature polycrystalline silicon) TFT is utilized to obtain low power consumption.

3.2. Categorization based on Structural Advancements

There are three major OLED devices which are classified in terms of their architecture. These devices are top emitting, foldable and transparent OLEDs. The Top Emitting Organic LEDs are fabricated on a solid or reflective substrate. They are well suited for active-matrix OLED applications. These OLEDs are great for smart cards which are placed on the back side of credit cards and debit cards [19]. Fig. 2 (a) is depicting the structure of top emitting organic LED. In TEOLED, top and bottom layers are cathode and anode, respectively. These OLEDs exhibit strong microcavity effects due to reflective contacts at top and bottom sides of the structure [20]. Here, if the position of cathode and anode are inverted then it will become an inverted top emitting OLED.

In 2017, Qu *et al.* [21] demonstrated high efficiency light extraction for top emitting OLED. In this research, green phosphorescent OLED exhibits very good EQE (external quantum efficiency) which is enhanced from 20 to 30 %. Thereafter in 2018, mixed interlayer of Poly [(9, 9-dioctylfluorenyl-2, 7-diyl)-co-(4, 4′-(N-(4-secbutylphenyl) diphenylamine))

Accepted Manuscript For Review Only

(TFB) and Poly (9-vinylcarbazole) (PVK) is utilized in between PEDOT: PSS and emissive layer by Lu *et al.* [22]. This results in significant improvement in hole injection. Afterwards in 2019, Kim *et al.* [23] utilized random wrinkle structure inside the TEOLED. Addition to this, index matching epoxy filter was incorporated into the encapsulation part. This methodology enhanced the current efficiency by suppressing the viewing angle dependence and color shift. Furthermore in 2022, Lin *et al.* [24] introduced Yb (ytterbium) as cathode blocking layer which refined the thermal stability of TEOLEDs. The element Yb inhibits the migration of Ag atoms in cathode layer at high temperature.

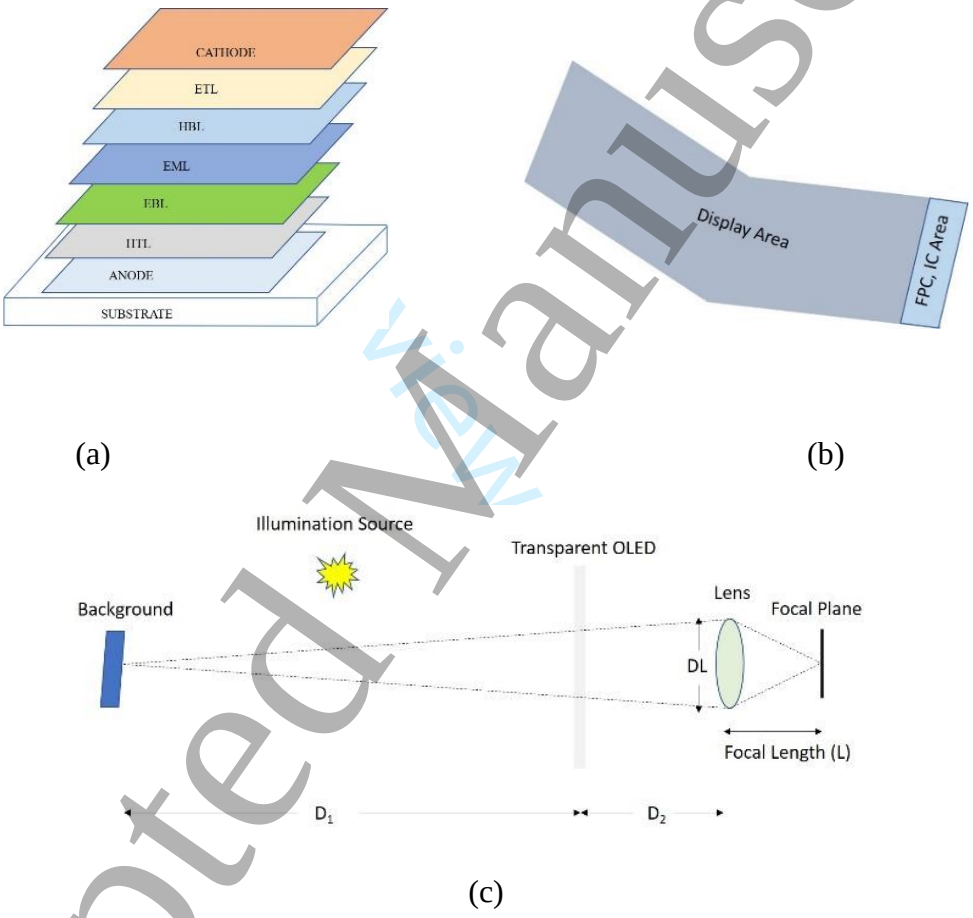


Fig.2. (a) Top emitting OLED, (b) top view of foldable OLED and (c) architecture of transparent OLED

Fig. 2(b) is highlighting the top view of foldable OLED. As the name suggests, foldable OLEDs are developed on a very flexible substrate. Material of these OLEDs is quite strong, so it reduces breakage of device. These devices are used in cell phones, GPS devices, and big screen TVs. Foldable OLEDs are delivering a faster response time, high contrast images and crisper picture resolution for curved televisions and provide more immersive TV experience. Lots of research work is being done for using these very flexible substrates in various

Accepted Manuscript

applications as portable devices by putting OLEDs in tracking devices for outdoor survival and excursions. In Fig. 2(b), it is seen that IC and FPC (flexible printed circuit) are not inside the display area. It is done to protect FPC and IC which can be broken if placed in display area due to bending stress.

Various efforts have been made to enhance the performance of foldable organic LEDs. Takahashi *et al.* [25] in 2015 proposed a 13.3-inch 8k4k 664-ppi high-resolution foldable organic display with crystalline oxide semiconductor FETs. This design contains one capacitor and three transistors for each pixel circuit. Moreover in 2019, a 3D touch sensor technology was proposed by Dieu *et al.* [26]. In this technology, high resolution static and dynamic pressure sensing can be achieved using transparent P(VDF-TrFE) layer. Moreover in 2020, Zhang *et al.* [27] designed a 17.3-inch WQHD foldable AMOLED display. Additionally, in 2021, Han *et al.* [28] demonstrated a SFF (stress-free folding) hinge with VAS (virtual axis structure) and MAS (modulized assembly structure). The proposed hinge provided stress-free folding motion and 200k folding reliability having less than 20% torque reduction.

The architecture of transparent OLED is demonstrated in Fig. 2(c). It is basically an OLED that is virtually see through [29]. When these OLEDs are active, light can travel in both directions. These OLEDs can be based on either AMOLED or PMOLED technology. In bright sunlight also, these devices have a good contrast. One particular use that is quite interesting for the Transparent OLED is HUD (Heads-up Display), also more applications are in laptops, mobile phones, smart windows, etc. Fig. 2(c) illustrates a see-through image of a transparent organic LED. Here, D_1 and D_2 represent background and viewer distance and DL shows diffraction lens aperture. With these parameters, the display region can be calculated by using $DL \times D_1/(D_1+D_2)$ [30].

Some noteworthy work of the last decade to refine the performance of transparent displays is discussed here. In 2016, a calculation method was proposed by Qin *et al.* [30] for the simulation of blurred see-through images of transparent OLEDs. Error between calculated and camera-capturing images in terms of modulation transfer function (MTF) and pattern's characteristics is obtained as 5.7% and 5.6% respectively. Furthermore, in 2017, Shu *et al.* [31] developed inkjet-printed ITO-free T-OLED. The device showed high emission brightness on ITO and PEDOT: PSS as 50,000 cdm^{-2} and 16,000 cdm^{-2}, respectively. Moreover in 2020, a highly reliable transparent cathode is reported by Song *et al.* [32] for transparent OLEDs. The current efficiencies of T-OLED are obtained as 36 and 18 cdA^{-1} for bottom and top sides emission, correspondingly. Recently, in 2022 Tsai *et al.* [33] fabricated a flexible T-OLED by

Accepted Manuscript For Review Only

using high transmittance OLED cathodes. Here, a mechanical debonding technique to achieve a stable transparent OLED debonding force is utilized.

3.3. Categorization based on Color Emission and Stability

Three main colors red, blue and green are the most desired for white lighting and full color display as shown in Fig. 3. Various methodologies are being performed for RGB emitters in recent times [34]. In this context, the development of blue OLED is quite beneficial as blue emitters are able to generate white color [35]. On the other hand, these emitters contain low stability, shorter lifetime and low efficiency as compared with green and red emitters. The color property mostly depends on the material type. Generally, luminance property of green and red OLED materials is quite good as compared to blue OLED. It is majorly due to the wide band gap which inhibits charge carriers to get inserted into blue emitters. The electro-luminescence performance and other parameters of these emitters should be improved. In 2017, Nakao *et al.* [36] proposed blue pyrimidine emitters. In this work, investigation of nitrogen effect is incorporated on the photophysical properties. The proposed device exhibits EQE as 25%.

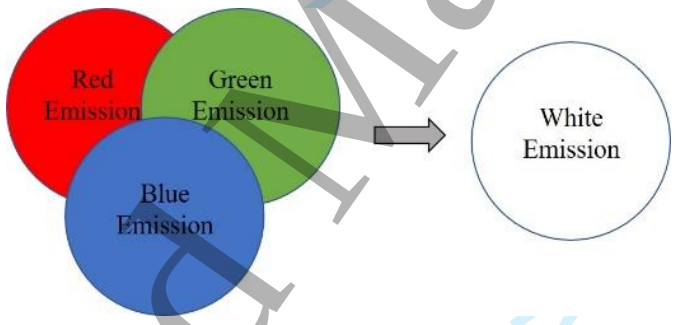


Fig. 3. White color emission formation using red, green and blue emission

In 2018, Yang *et al.* [37] discussed deep-blue materials with HLCT (hybrid local and charge transfer) emitters. This opens up new opportunities for developing low cost highly efficient blue OLEDs. Additionally, Han *et al.* [38] in 2020, designed five blue TADF (thermally activated delayed fluorescence) emitters (DAc-C1-DAc-C5). Among these, DAc-C2 shows maximum EQE as 24.1%. This value is 1.42 times higher than DAc-C1 under the same conditions. Moreover in 2021, some methods are investigated by Chan *et al.* [39] for obtaining high performance blue OLEDs with better color purity and lifetime. In this research, a pure-blue organic LED is proposed which provides high EQE i.e., 32%. Fig. 4 is highlighting the comparison of various blue organic LED devices (B_1 [40], B_2 [39], B_3 [38], B_4 [41], B_5

Accepted Manuscript
For Review

[35], B_6 [42] and B_7 [43]) in terms of EQE. It is clear from the figure that device B_2 is exhibiting the maximum EQE as 32%. On the other hand, the minimum EQE is obtained by B_4 device.

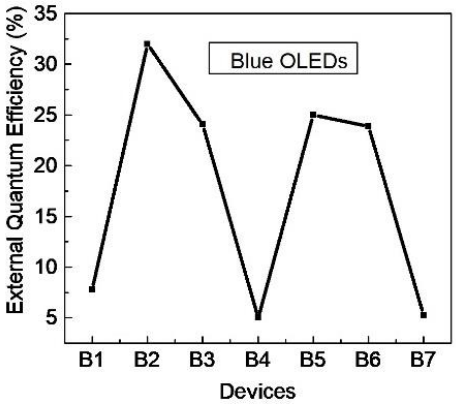


Fig. 4. Comparison of blue OLEDs in terms of external quantum efficiency

Enormous work has been investigated to improve the characteristic performance of white organic LED. White OLED deliver more efficient, brighter and uniform white light [44] than the light delivered by incandescent bulbs and compact fluorescent lights. Also, these devices are cost effective because they are made in large sheets. White OLED (WOLED) [45] uses less energy to produce a brighter light that could be more environment friendly in long run [46]. In 2020, Huang *et al.* [47] reported highly efficient WOLED using phosphorescent yellow-red unit and TADF blue-red unit. Here, EQE and luminous efficacy are achieved as 126.2 % and 150.7 lmW^{-1}, correspondingly. On comparison with conventional hybrid tandem WOLED, it is found that this device exhibits 3 times higher lifetime. Afterwards, in 2021, Yang *et al.* [48] proposed high performance dual wavelength WOLED. The performance parameters such as luminescence, current efficiency and power efficiency are obtained as 21,070 cdm^{-2}, 18.09 cdA^{-1} and 8.77 lmW^{-1}, subsequently. Recently in 2022, Lee *et al.* [49] designed high luminance, low power, top emitting WOLED. This device provides excellent EQE as 170,000 cdm^{-2}. Fig. 5 is illustrating different white organic LEDs (W_1[49], W_2 [48], W_3 [50], W_4 [51], W_5 [47] and W_6 [52]) on the basis of luminescence. Among all devices, W_1 is attaining remarkable value as 170,000 cdm^{-2} which is the maximum as compared to other. The lowest value of luminescence is achieved by W_5 OLED.

Accepted Manuscript For Review Only

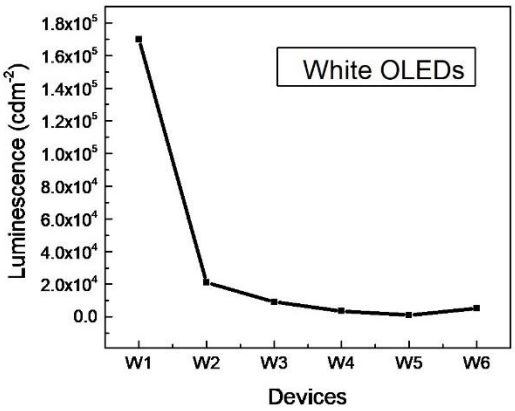


Fig. 5. Comparison of white OLEDs in terms of luminescence

There are various advantages such as flexibility, large area fabrication, low cost, unparalleled image quality etc. in organic OLEDs over inorganic devices. Rigorous efforts have been made in developing new materials and device structures. The operational lifetimes of green and red OLEDs are sufficient enough for commercial applications. However, in case deep-blue OLED, it is still a challenge to achieve good efficiency, color purity and stability. This hurdle inhibits further growth of display and lighting technology. Extensive research has been investigated and demonstrated for developing blue phosphorescent emitters. In 2012, Chung *et al.* [53] synthesized a chrysene derivative BPCC (6,12-bis(9-phenyl-9H-carbazol-3-yl)chrysene) which contains good thermal stability having glass transition temperature of 181°C. The proposed device with this emissive material exhibits pure saturated blue emission having color coordinated as (0.16, 0.08).

In 2017, Friedzon *et al.* [54] proposed a computational scheme to estimate the operational stability of phosphorescent organic LED host materials. By this research, a stability series is derived which is used to obtain the structural features that contributes higher stability. Furthermore in 2019, Klimes *et al.* [55] designed a highly efficient and stable blue OLED by using step wise graded doped structure. The performance parameters of the device such as EQE, operational lifetime, CIE coordinated and brightness are achieved as 17.4%, 1337 h, (0.19, 0.41) and 1000 cdm^{-2}, respectively. Moreover in 2022, Santos *et al.* [56] investigated new polymeric blue emitters which are capable in overcoming the challenges such as stability and efficiency of blue OLEDs.

On the other hand, WOLEDs have also been explored in terms of operational stability and efficiency. In 2015, Du *et al.* [57] fabricated a highly efficient and stable hybrid white OLED having single doped co-host structure. In the device, 9-Naphthyl-10 -(4-triphenylamine) anthracene is utilized as fluorescent dopant and $Ir(ppy)_3$ and $Ir(2\text{-}phq)_3$ are used as

Accepted Manuscript
For Review Only

phosphorescence dopants for green and orange, respectively. The luminous efficiency is obtained as 12.4% at 1000 cdm^{-2}. The other parameters such as current efficiency and power efficiency are reported as 27.5 cdA^{-1} and 17.6 lmW^{-1}, correspondingly. Thereafter in 2019, Yang *et al.* [48] incorporated a sandwiched CCL (color conversion layer) on the exterior of a blue OLED to obtain WOLED. The CCL layer contains properties like color conversion, light extraction and scattering. The proposed device exhibits high color stability. Furthermore in 2020, Sun *et al.* [58] designed a warm WOLED containing four emissive layers and a pure WOLED with three emissive layers. The characteristics performance on the basis of current efficiency, EQE and power efficiency for warm WOLED is reported as 69 cdA^{-1}, 20.93 % and 60.19 lmW^{-1} and for pure white OLED is obtained as 60.48 cdA^{-1}, 16.90 % and 51.32 lmW^{-1}, respectively.

4. Processing Techniques for Multilayered-OLED

In OLED, the most important and complicated part of manufacturing is always to apply organic layer to the substrate [59, 60]. The detailing of each layer (substrate, anode, organic semiconductors, cathode) based on the fabrication process and its materials is explained below in Table 1.

Table 1. Materials and process for Multi-layered structure.

Layer	Material	Process
Substrate	Plastic, Transparent Glass, ITO	Plasma Treatment/ Cleaning
Anode	ITO	Thermal Evaporation/ Sputtering
Organic Semiconductors	m-MTDATA/ QAD/ Alq_3/NPB	Inkjet Printing/ Vacuum Evaporation
Cathode	LiF/ AI	Low Temperature thermal deposition

For fabricating the device, there are many techniques available nowadays which are generally classified in two types named as high-end techniques and solution-processed techniques. Some of these techniques are discussed below.

4.1. High-end Techniques

There are many vacuum-evaporated techniques like physical vacuum deposition and vacuum thermal evaporation. These techniques are utilized for small molecules which are comfortable in heating processes in vacuum. The process is quite suitable for deposition of multiple layers. Fig. 6 is illustrating the evaporation and condensation process in PVD. Here, materials are

Accepted Manuscript For Review

heated up till they get evaporated and then condensed on to the substrate. Physical vacuum deposition (PVD) is a widely used technology [60, 61] which is utilized in both organic and inorganic electronics. Kajiyama *et al.* [62] proposed an OLED with feature sizes ≤ 20um using *in-situ* contact shadow mask patterning method by laser ablation. The aperture ratio and resolution are reported here as 60% and 338 ppi. Addition to this, Sanderson *et al.* [63] compared the performance difference of vacuum deposited and solution processed organics devices by using all-atom molecular dynamics simulations. These simulations are utilized with kinetic Monte Carlo transport modeling which analyze morphological differences in vacuum deposition and solution processing.

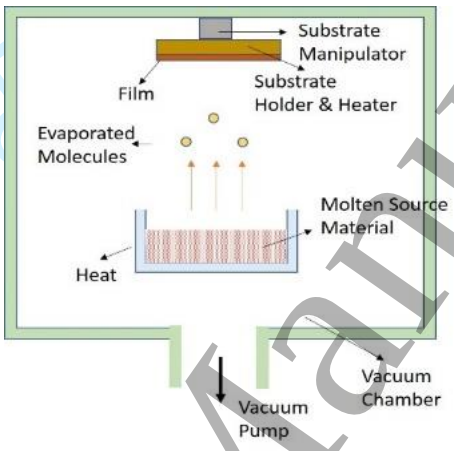


Fig. 6. Process of physical vacuum deposition (PVD)

Another technique is Vacuum Thermal Evaporation (VTE). This technique is very common technique to deposit the organic layers. The organic molecules are gently heated then condensed as thin films onto cooled substrates [61]. This method is expensive due to heating process and good accuracy. So, other techniques are preferred for large area devices and forming thin films of polymers over this technique. Several researchers have fabricated OLEDs using VTE technique. Liao *et al.* [64] proposed an organic LED using VTE technique. The device showed noteworthy performance having EQE as 27.6 % along with low roll-off at high luminance.

In addition to this, Song *et al.* [32] fabricated a transparent and highly reliable cathode using thermal evaporation technique. In this work, the fabrication process utilizes the co-deposition of silver (Ag) and aluminum (Al). The proposed transparent device showed excellent electron injection properties having current efficiencies as 36 and 18 cdA^{-1} from bottom and top sides emission, respectively. Recently, Kim *et al.* [65] introduced a metal patterning layer before metal deposition to realize self-metal patterning using VTE. In this

Accepted Manuscript
For Review Only

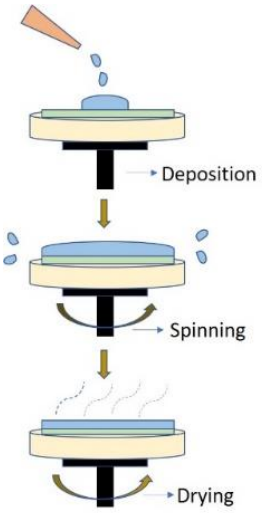
report, among all MPLs, the material PFTC (polyfluoro-tetracosane) consisting lowest surface energy showed excellent patterning properties in both Mg (magnesium) and Ag. Addition to this, Kongsabay *et al.* [66] developed a deep-red fluorescent emitter i.e. TPA-NZF based on HLCT using vacuum deposition. The device exhibits excellent electroluminescence performance having EQE as 3.59% and provides intense deep-red color with CIE coordinates of (0.66, 0.33).

4.2. Solution-Processed Techniques

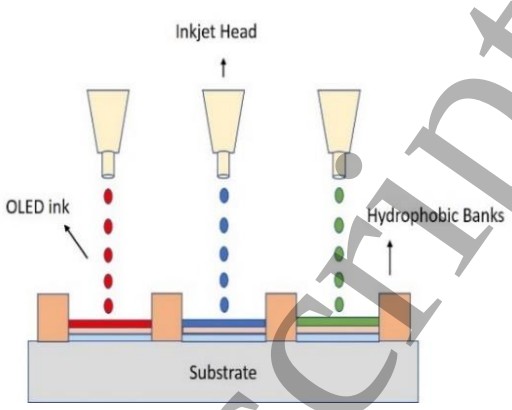
Solution-processed OLEDs are gaining lot of attention by various researchers nowadays as these techniques contain many salient features like low-cost wet-process fabrication, flexible application terminals, self-luminous display panels, large size and solid-state lighting source [67]. Basically, these techniques are suitable conducting polymers. There are many solution-processed technique such as spin coating, dip coating, inkjet printing etc. The technique spin coating is utilized for depositing soluble polymers in monochrome displays. The light emitting material is deposited in the form of drops. It is placed uniformly on the flat surface and then rotated at high-speed until it obtains a particular desired thickness as depicted in Fig. 7(a). The evaporation of carrier material is done at a faster rate which makes uniform film deposition. The thickness of the film depends on various parameters such as temperature, spin time, speed of spin coater, fume extraction, viscosity and fluids volatility.

This process has been explored by lot of researchers to enhance organic LED devices. In 2012, spin coating process is incorporated by Hyun *et al.* [68] to demonstrate a method for corrugated structure to enhance light extraction of OLEDs. In this work, the speed of the process and solution of SiO_2 and TiO_x play important role to control the performance parameters. Thereafter, Yuan *et al.* [69] discussed a simple low-cost spin coating method which can be used to form distributed embossed structure developed by Al_2O_3 nanospheres. The device with the proposed fabrication technique exhibits excellent performance parameter. Power efficiency, EQE and current efficiency are obtained as 32.7 lmW^{-1}, 20.9 %, and 52.1 cdA^{-1}, respectively. Additionally in 2020, the electrical properties of ITO/PEDOT: PSS/MEH doped PEIE OLED are analyzed by Juhari *et al.* [70] using spin coating.

Accepted Manuscript
For Review Only



(a)



(b)

Fig. 7 Solution-processed techniques (a) spin coating process and (b) inkjet process

The other technique discussed here is inkjet technique. This is the most cost effective among all techniques. It allows Organic LEDs to be printed onto very large films [71, 72]. This technique is quite similar to the paper printing method in which organic layers are deposited onto the substrates by spraying method as shown in Fig. 7 (b). Table 2 is depicting various OLED devices which are fabricated using solution-processed techniques.

Table 2. Various OLED devices using solution-processed fabrication techniques

Year [Ref]	Fabrication Technique	Method	Observations
2022 [73]	Inkjet printing	Developed and optimized two PEDOT: PSS ink formulations to design transparent conductive layers	• Maximum current efficiency: 15 cdA^{-1} • EQE: 5.5 %
2021 [74]	Inkjet printing	Reported an indium tin oxide free electrode using a particle-free silver ink	• Low temperature processing • High bending stability
2020 [75]	Inkjet printing	Designed a novel full-color display using Blue-OLED and patterned green and red quantum dots CCL	• 6.6-inch color display with 95 % broadcasting service television 2020 (BT.2020) color gamut • Wide viewing angle

Accepted Manuscript
For Review Only

2020 [70]	Spin coating	Investigated the performance of uniformity and absorption spectrum of MEHPPV+PEIE films	• Maximum RMS: 4.74 nm • Among four doping concentrations, PEIE with 0.3 wt% exhibits brighter emission
2020 [51]	Inkjet printing	Proposed a highly efficient Blue-OLED by utilizing 3,5-bis(N-car-bazolyl) benzene (mCP) into emissive layer	• Maximum luminescence:3743 cdm^{-2} • EQE: 5.03 %
2019 [76]	Inkjet printing	Developed a high luminance phosphorescent OLED based on m-MTDATA:TPBi	• Maximum luminescence:13240 cdm^{-2} • Maximum current efficiency: 5.27 cdA^{-1}
2019 [77]	Spin coating	Proposed a high-performance OLED having deep-blue emitters	• EQE: 3.6 %
2018 [78]	Spin coating	Fabricated SNCs (silver nano clusters) incorporated OLEDs	• Maximum current efficiency: 2.07 cdA^{-1} • Maximum brightness: 12626 cdm^2
2018 [79]	Spin coating	Designed an OLED device with deposition of tris-(8-hydroxyquinoline) aluminum (Alq_3) incorporated zinc oxide (ZnO) thin films	• Electron current density: 2.75 $mAcm^{-2}$ • Current density is 3.3 times improved as compared with pure ZnO ETL.

Nowadays, the challenge is to make low-cost flexible devices as currently OLED devices are very costly in the market of display technology. In addition to above mentioned techniques, a cost-effective fabrication technique proposed by Cho *et al.* [80] is discussed. Herein, an experimental procedure is proposed for the fabrication of flexible integrated substrates including gas barrier and metal electrode patterns. The detailed procedure of this fabrication technique is illustrated in the Fig. 8. as well.

Accepted Manuscript
For Review Only

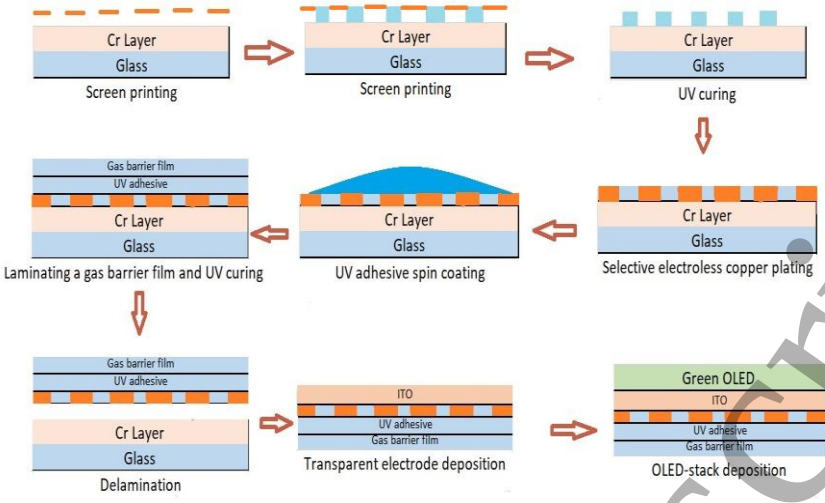


Fig. 8. Fabrication steps of flexible integrated substrate OLED.

The first step is to prepare the polymer patterns to form metal electrode by ultraviolet curing and screen printing on a Cr-coated glass plate. A Cr thin film is placed on a soda-lime glass plate. DC sputtering is used for this method. The film developed through this methodology is 60 nm thick only. Research work highlighted that a screen-printing mask is utilized to develop a metal electrode with spacing of 1414 µm and width of 130 µm. Bisphenol A diacrylate (BADA) is considered as polymer. Benzophenone is mixed with polymer as a photo-initiator of polymerization.

To increase the viscosity, rheology additive (RA, BYK-410) polymer is utilized. Both (polymers and additives) are blended for 1 hour at 60 °C using a magnetic stirrer, and then cooled down for 16 hours at room temperature. Next, using an electroless Cu plating they deposited the metal electrodes between the polymer patterns. Thereafter, they coated the polymer pattern in an electroless Cu-plating for at least 5 min. After this process, a gas barrier is laminated by an UV adhesive polymer and vacuum laminator then they cured the polymer by ultraviolet light and a hot plate.

Now, the barrier film and polymer-copper pattern are delaminated by some mechanical force. The complete help of rotational viscometer and a contact angle meter respectively. The V-I curves of the OLED devices are plotted and electroluminescence spectra and luminance factor are examined. The motive of this research was successfully achieved by developing a low-cost fabrication process for a flexible OLED. Screen printing, delamination process and an electroless copper plating played very important role to smoothen the surface for the fabrication process that is undertaken.

Accepted Manuscript
For Review Only

5. Characteristics Parameters for OLED

High performance OLED devices with great flexibility and large area fabrication can be developed by improving performance parameters of the device. This section will discuss the recent advancement in OLED in terms of characteristic parameters luminescence, EQE and current efficiency which play major role to improve device performance.

5.1. Luminescence

The property of emitting light by a substance without giving any external heat is known as luminescence. It is obvious that various semiconductors absorb energy in various forms such as photon absorption, introduction of the currents and electron bombardment which is emitted in the visible region of the spectrum. Basically, two steps are included in the process of luminescence. The first is the excitation of the system and second is subsequent emission of the photons. In organic light emitting devices, the type of organic material, color emission and supply voltage play important role to enhance the luminescence.

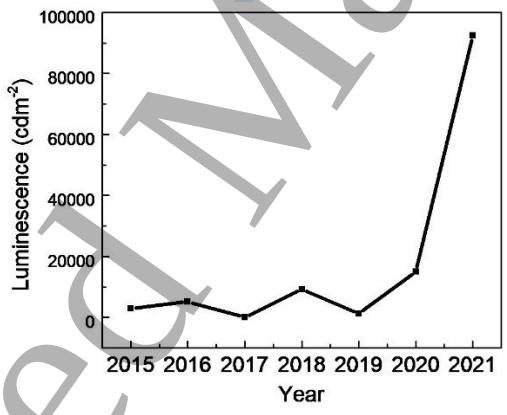


Fig. 9. Luminescence progress during 2015-2021

As OLED is a light emitting device, the luminescence is the most important parameter among all such as current density, power efficiency, external quantum efficiency etc. [10]. Fig. 9. illustrates the luminescence progress during 2015-2021. The maximum luminescence is observed as 92,455 cd/m^2 [81] in 2021. The minimum data for luminescence is about 100 cd/m^2 in 2015 [82]. Many researchers have contributed their efforts to improve the luminescence factor of OLED. Park *et al.* [83] focused on uniform enhancement of light emission for flat panel lighting applications. They reported the auxiliary metal electrode effect with a device configuration on a large-area white OLED of 15×15 cm^2 dimensions with uniform

Accepted Manuscript For Review

luminescence. In this research work it is observed that an OLED panel exhibits luminance uniformity as high as 85% at 500 mA and 90% at 200 mA at higher bias current with 200 µm wide auxiliary metal.

Further, Han *et al.* [84] investigated enhancement of the luminance by the micro lens array (MLA) that mostly depends on the viewing angles and luminescence area and rarely depends on the driving conditions. Therefore, for the large panel's, luminescence is improved up to 64% in normal direction with the MLA film. Only 48% and 58% luminance is improved at the small panels of size 2.25 and 70 mm^2. Researchers Kanno *et al.* [85] also worked on luminance enhancement. It is observed that the luminance improved from 1.7 cd/A to 4.3 cd/A with chromaticity of (x=0.64, y=0.36) by co-doping systems of green OLEDs and red OLEDs in emission layers. Researchers Aasha *et al.* [86] compared HOMO and LUMO of Alq_3 material with Phosphorene. It is found that Phosphorene provided lowest band gap which was responsible for luminance enhancement.

5.2. External Quantum Efficiency

External quantum efficiency (EQE) is defined by the ratio of number of photons emitted by the organic LED with respect to the total electrons. The researchers incorporate various methodologies to refine EQE. A highly twisted material having anthracene with xylene is suggested by Park *et al.* [43] which exhibits the EQE as 5.26 %. Afterwards, Rajamalli *et al.* [42] discussed four blue TADF emitters BPy-pC, BPy-pTC, BPy-p2C and BPy-p3C. The OLED with BPy-p3C dopant provided the maximum EQE as 23.9% which is approximately 6 times higher than the EQE of the device containing BPy-pC dopant. Addition to this, Yang *et al.* [48] discussed a donor−acceptor type TADF emitter with phenanthro[4,5-abc] phenazine-11,12-dicarbonitrile and a triphenylamine (TPA) as an acceptor unit and as a donor moiety, correspondingly. In this paper, deep-red and near infrared OLED devices are improved with the maximum EQE of 20.3 and 16.4 %, respectively.

Table 3. Recent work on different OLED devices on the basis of EQE

Year	Ref.	External Quantum Efficiency (%)
2023	**[87]**	32
2023	**[88]**	41.3
2022	**[89]**	61
2022	**[90]**	36.1
2022	**[91]**	39.2

Accepted Manuscript
For Review Only

2021	**[92]**	38.8
2021	**[93]**	30.5
2021	**[94]**	25.5
2020	**[95]**	39
2020	**[48]**	126.2
2020	**[42]**	21.0
2019	**[96]**	20.2
2019	**[97]**	31.2
2018	**[98]**	30.3
2017	**[99]**	9.4
2016	**[53]**	2.39
2014	**[100]**	2.56
2014	**[101]**	5.12

Moreover, Han *et al.* [102] utilized a light extraction layer having high refractive index to obtain high efficiency which is tremendously improved as 103%. Thereafter, Lu *et al.* [93] proposed a CP-OLED (circularly polarized-organic LED) using a pair of chiral green Ir(III) consisting dual stereo chiral centers. The device provides the maximum EQE of 30.5 %. In this work, the challenges of CP-OLED have been overcome. Also, the proposed OLED exhibits high phosphorescence quantum yields and circularly polarized luminescence property. Table 3 is demonstrating the recent work during the last decade in terms of external quantum efficiency.

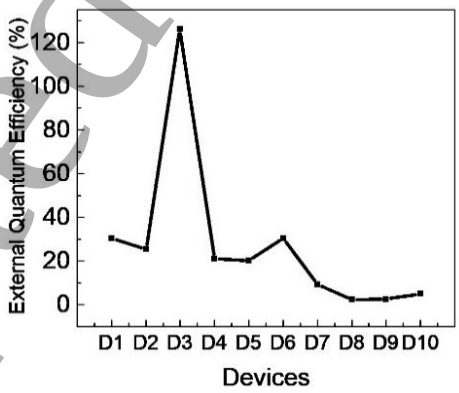


Fig. 10. Comparison of different light emitting devices in terms of EQE

In 2020, Sharma *et al.* [95] proposed an OLED with double active layer of BEPP and TCTA: $Ir(ppy)_3$ which improved the EQE upto 39 %. Afterwards in 2021, Braveenth *et al.* [92] designed and synthesized two deep blue TADF materials (DBA–BFICz and DBA–BTICz).

Accepted Manuscript For Review Only

The device with the material DBA-BFICz exhibited the very good EQE of 38.8 %. Furthermore in 2022, Dykstra *et al.* [89] presented light outcoupling-enhancing PES (planarized extraction structures) in plastics. The proposed structures resulted in remarkable EQE as 48% for WOLED and 61% for green OLED. Different light emitting devices (D_1-D_{10}) [93,94,48,42,96-99,53,100,101] are compared in Fig. 10, on the basis of external quantum efficiency. The device D_3 and D_8 are highlighting the maximum and minimum EQE as 126.2 % and 2.39 %, correspondingly.

5.3. Current Efficiency

The ratio of luminescence over current density is defined as current efficiency [103-105]. This parameter has been investigated widely to refine the performance of OLED devices. A heterojunction organic bipolar charge injection layer with zinc phthalocyanine: fullerene (ZnPc:C_{60}) is reported by Chen *et al.* [8]. The maximum current efficiency is obtained as 36.5 cdA^{-1}. It is observed that the achieved value is 2.4 times higher on comparing with single unit device. The research work of the last decade in terms of current efficiency is illustrated in Table 4.

Table 4. Recent work on various OLED devices on the basis of current efficiency

Year	Ref.	Current Efficiency (cdA^{-1})
2023	[87]	47.85
2023	[106]	85.6
2022	[74]	15.0
2021	[93]	105.6
2020	[107]	70.0
2018	[108]	24.9
2018	[80]	2.75
2017	[69]	52.1
2015	[105]	24.8
2015	[58]	27.5

Moreover, Zhuo *et al.* [109] developed a double emissive layer using red-green emitting light. The device showed 10 times improved current efficiency as 10.17 cdA^{-1}. Moreover, two host materials N,N′-diphenyl-N,N′-bis(1-naphthylphenyl)-1,1'-biphenyl-4,4'-diamine (NPB)

https://mc04.manuscriptcentral.com/jss-ecs

Accepted Manuscript For Review Only

and 4,4′,4″-tri(Ncarbazolyl)triphenylamine (TCTA) are discussed by Wang *et al.* [98] to design a double emissive layer. The current efficiency of the device is achieved as 42.3 cdA^{-1}. Additionally, Mohan *et al.* [107] incorporated CuI as dopants into CuPC to refine HTL and attained current efficiency as 70 cdA^{-1}. Thereafter, Lu *et al.* [93] designed some conventional devices utilizing chiral complexes as dopants. In this work, the maximum current efficiency is obtained as 105.6 cdA^{-1}.

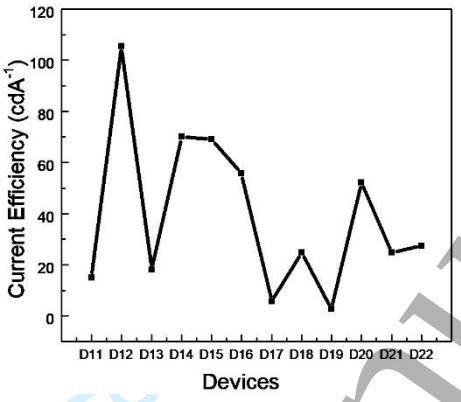


Fig. 11. Comparison of different light emitting devices in terms of current efficiency

Various organic LED devices (D_{11}-D_{22}) [74,93,96,108,60,1,80,69,105,58] are outlined in Fig. 11 in terms of current efficiency. The maximum and minimum values of current efficiency are obtained by device D_{12} and D_{19} as 105.6 and 2.75 cdA^{-1}, respectively.

5.4. Luminous Efficiency

Luminous efficiency or power efficiency can be described as the ratio of luminous flux with respect to the power consumption of a device. Many researchers have explored display field to improve luminous efficiency of device as mentioned in Table 5. In 2018, a white organic light emitting diode was reported with high luminous efficiency i. e. 31.0 lmW^{-1} by Xi *et al.* [110]. Thereafter in 2019, Han *et al.* [111] proposed a pure blue thermally activated delayed fluorescence device (TADF) using a fused B-N emitter. The device exhibited a very good power efficiency of 33.3 lmW^{-1}. Then, Han *et al.* [102] in 2020, presented a white OLED device with an internal light extraction layer having high refractive index. The power efficiency of the device was achieved as 93.2 lmW^{-1}.

Accepted Manuscript
For Review Only

Table 5. Recent work on various OLED devices on the basis of power efficiency

Year	Ref.	Luminous Efficiency (lmW^{-1})
2023	[112]	72.7
2023	[106]	84.0
2023	[113]	7.7
2022	[107]	74.1
2021	[114]	87.2
2021	[115]	68.9
2020	[116]	57.2
2020	[102]	93.2
2019	[111]	33.3
2018	[110]	31
2018	[117]	5.80
2016	[52]	2.60
2014	[100]	8.69

In 2021, Cui *et al.* [115] utilized emission layers with different substrate temperatures ranges from 30°C to 100°C in the OLED devices. The maximum luminous efficiency is reported as 68.9 lmW^{-1} at 60°C. Furthermore, in 2022, a highly efficient device with the power efficiency of 74.1 lmW^{-1} was proposed by Mohan et al. [107]. In this device, CuI as dopants was added into CuPC to enhance hole transport layer [HTL]. Recently in 2023, Qi *et al.* [113] presented a DNM (Dielectric-Nano mesh)-OLED device with the peak power efficiency of 7.7 lmW^{-1} which is 1.8 times improved as compared with ITO-OLED. Additionally, in 2023, Liu *et al.* [112] presented a yellow TADF OLED based on solution-processed technique. The device showed a remarkable luminous efficiency of 72.7 lmW^{-1}.

5.5. Operational Lifetime

Although OLEDs have several attractive features such as flexible and transparent display, cost effectiveness, large area fabrications, wide viewing angle, better picture clarity etc. These

https://mc04.manuscriptcentral.com/jss-ecs

Accepted Manuscript For Review Only

display devices are actually competing with the inorganic solid-state lighting devices. The only problem with organic light emitting devices is their lifetime, which is very less as compared to the inorganic devices. For the enhancement of this parameter, lot of researchers are investigating OLED displays. In 2012, Yang *et al*. [118] presented a green phosphorescent OLED having double emissive layer with an ETL of LiF-doped TPBi. In this research, the operational lifetime is improved 35 times of the reference device. Thereafter in 2017, Chang *et al.* [119] discussed few effective methods for improving lifetime and developed all-solution-processed Phosphorescent OLEDs and fluorescent OLEDs having mixed-hosts system and thin Poly [(9, 9-dioctylfluorenyl-2, 7-diyl)-*co*-(4, 4′-(*N*-(4-*sec*-butylphenyl) diphenylamine)] (TFB). Here, green PhOLED showed half lifetime as 310h and yellow fluorescent organic LED exhibited half lifetime as 1200h.

In 2020, Chen *et al.* [120] utilized an assistant layer with triplet–triplet annihilation up-conversion characteristics in emitters and achieved very good operational lifetime of hybrid White organic LED. The device exhibited two times longer lifetime i. e. 600h at 1000 cd m^{-2} as compared with the reference device. Additionally, in 2020, Zhuo *et al.* [121] developed a novel synthetic tetradentate [C^C^N^C] gold (III) complexes through microwave-assisted C−H bond activation. The device showed the operation lifetime of 5280h at the luminescence of 100 cd m^{-2}.,

In 2021, Le *et al.* [122] enhanced the lifetime of OLED device by shifting the recombination area away from interfacial mixing region. The operational lifetime was improved 3 times from 14h to 42h as compared with the reference device. Moreover in 2023, Guo *et al.* [123] proposed a Blue OLED in which, to accelerate the hRISC process a fluorescent emitter is doped into PAC. This resulted in improved operational lifetime i. e. T_{75} = 110 ± 2 h under 1000 cd m^{-2}. Additionally, in 2023, Wong *et al.* [124] developed and synthesized C^C^N carbazolylgold(III) complexes using oligophenyl substituents on the pyridyl moiety. In this research, the device showed the operational lifetime up to 470,700 h at luminescence of 100 cd m^{-2}.

6. Multi-Layered OLED Structures

The mobility of charge carriers (electron and hole) is the second important parameter in OLED devices. The electron, injected into the organic layer from the cathode is supposed to form exciton with hole generated from anode side. To achieve maximum efficiency, each and every

Accepted Manuscript

electron that goes from cathode to anode must form the exciton. And, to obtain this the charge ratio should be in proper amount to get maximum exciton generation.

It is known that mobility of hole is more than electron in the case of organic materials. Hence recombination happens close to the cathode layer due to the mobility difference of charge carriers. Which results in the quenching of the excitons. This problem can be overcome by matching the mobility of these two charge carriers. It is possible by incorporating some more layers (Fig. 12.) in OLED structure [125,126] such as hole and electron injection layer (HIL/ EIL), hole and electron transport layer (HTL and ETL) and hole and electron block layer (HBL and EBL). Brief discussion is presented about the purpose of all layers that are substrate, anode, HIL, HTL, emissive layer, block layer, ETL and cathode in Table 6.

Table 6. Role of multilayers in OLED.

Layers	Role
Substrate	Foundation of OLED that provides mechanical support
Anode	Positively charged layer/electrode used to insert holes into the organic layers
Hole Injection Layer	Collects holes from anode and insert them into the device
Hole Transport Layer	Helps to transfer the holes into the emissive layer
Emissive Layer	Where electrical energy is directly converted into light
Blocking Layer	Blocks charge carriers to the emissive layer to enhance the technology of device
Electron Transport Layer	Responsible for electrons transportation so that they enter to the emissive layer
Cathode	Negatively charged electrode used to insert free electrons into the organic layers

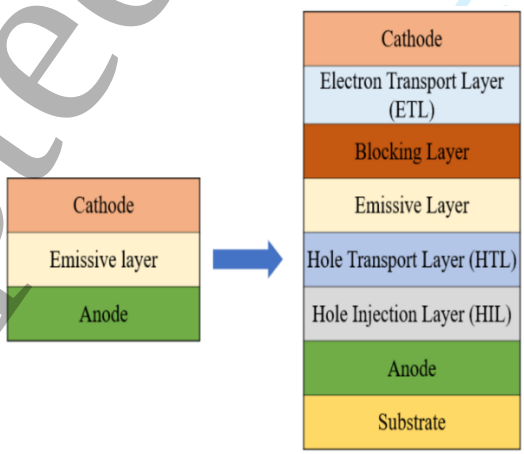


Fig. 12. Transition from basic to multi-layered structure of OLED.

Accepted Manuscript

Many researchers have shown their interest to improve the performance of OLED by incorporating such layers. A combination of MoO_x and PEDOT:PSS is used as HIL by Zheng *et al.* [127]. This results in improved surface work function, better durability and higher charge carrier injection. On the other hand, in the direction of enhancing the property of transport layer, a novel HTL material N, N- N, N-bis(4-(6-((3-ethyloxetan-3-yl) methoxy)hexyloxy)phenyl)-3,5-di(9H-carbazol-9-yl)benzenamine (Oxe-DCDPA)) is suggested by Tsai *et al*. [128]. The proposed device exhibits EQE and luminous efficiency for green emission as 30.8 % and 111.9 cdA^{-1} and for bluish green emission as 27.2 % and 83.8 cdA^{-1}, correspondingly. Additionally, Nagar *et al.* [129] discussed a high-performance OLED having electron transporting layer of TPBi (2,2′,2″-(1,3,5-benzinetriyl)-tris(1-phenyl-1-H-benzimidazole)) doped with TiO_2 (titanium oxide). The device exhibits excellent electron mobility and good properties of yellow emission.

Moreover, Zhang *et al.* [130] investigated the role of Fe_3O_4 for enhancing the hole transport and injection by ultraviolet photoelectron spectroscopy. They reported that Fe_3O_4 has different effectiveness when injected into different host materials. OLED properties is improved by lowering the hole injection barrier. On the other hand, the enhanced hole transport improved the properties of OLEDs with 3-methylphenylphenylamino because of good charge transfer formation. Further, Mohan *et al*. [107] explored the effect of doping on the performance of OLED by mixing copper iodide into copper phthalocyanine hole transport layer. They reported that when CuI is doped into CuPC, it increases the performance OLED. The improved performance is much higher as current efficiency of 70 cd/A, power efficiency of 74.1 lm/W, and external quantum efficiency of 18.5 % which are respectively, 33.3 %, 34.6 % and 32% higher as compare to PEDOT: PSS as hole transport layer. Moreover, L. Noroozi and H. Soofi [131] worked in the direction of maintaining the charge carriers of transport layer. They investigated that for OLEDs parameters: current density and charge carrier are controlled by deploying a host–guest structure in the transporting layers. Also, Lee *et al.* [132] investigated improvement in the Surface Morphology of crosslinked hole transport films by adding Polymer mixture for OLEDs. They reported that aggregation is suppressed by mixing non-cross-linkable polymer and cross linkable small molecule HTL materials.

In comparison with other layers, emissive layer is discussed more as light is produced in this region. Lot of materials have been investigated for better emissive properties. Yoo *et al.* [105] presented a blue phosphorescent OLED having emissive layer with double dopants FIrpic and FIr_6. The device showed luminous efficiency as 24.8 cdA^{-1}. Addition to this, a highly

Accepted Manuscript For Review Only

efficient blue OLED is discussed which is hazard free. The performance parameters like current efficiency and EQE are obtained as 24.9 cdA^{-1} and 24.5 %. Furthermore, Sharma *et al.* [133] proposed a high-performance OLED with double emissive layer which exhibited EQE as 39 %. The blocking layer has been also explored by several researchers to improve the recombination rate. Fujimoto *et al.* [134] proposed an organic LED using 2,4,6-tris(biphenyl-3-yl)-1,3,5-triazine (T2T) as hole blocking layer. It is observed that the lifetime of device is improved by 9 times. Moreover, Tan *et al.* [135] proposed a green PHOLED with a versatile material 3-(m -diphenylphosphinylphenyl)-1,10-phenanthroline (Phen- m -PhDPO). The material exhibits property of both HBL and EBL and provides high power efficiency as 41 lmW^{-1}.

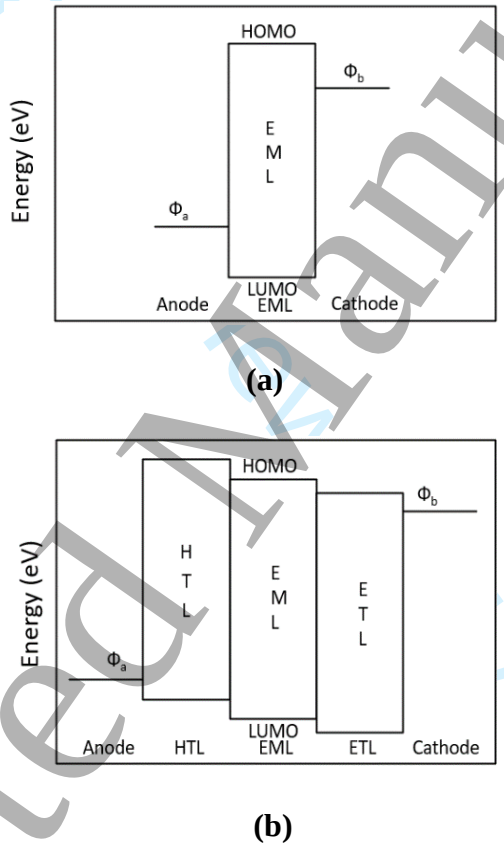


Fig. 13. (a) Energy band diagram of single-layered OLED and (b) multi-layered OLED

Fig. 13(a) depicts the energy band diagram for basic organic LED structure and 5(b) is highlighting the same for multi-layered structure. In the basic structure of OLED, high quantum efficiency, better hole and electron injection and higher mobility are needed for emissive layer. This demand could not be achieved by most of the material's property in single-layered devices. Therefore, many researchers have proposed various multi-layered device architectures (Fig. 13(b)) to improve these parameters. There should not be much deviation in energy level

Accepted Manuscript

between LUMO and the cathode work function (ϕ_b) and HOMO and the anode work function (ϕ_a) otherwise, device performance will degrade due to low charge injection [136]. It is possible to reduce the energy barrier for charge injection by utilizing additional layers between the electrodes. The ETL dramatically lowers the hole current in the OLED due to band offset and increases mobility of electron. Also, a HTL with aluminum quinolate (Alq_3) or polyquinoline (*n* type materials) [137] enhances the performance of OLED and provide electron injection and block holes.

Beside above-mentioned layers, there are some novel layers also such as charge generation layer (CGL), mixed interlayer (MI) and space layer [7-9]. These layers are gaining the major attention of researchers nowadays as the layers have provided solutions to many drawbacks that still exist with multi-layered structures. CGL is typically a PN junction which is formed with metal oxide bilayer structure (p-type and n-type layers). It acts exactly like electrodes which can be placed adjacent to other electroluminescent units [138]. It provides better generation of charge carriers, low resistance, high transport capability and high transparency [139]. Many researchers have explored charge generation layer in recent times. In 2019, Jetly *et al.* [140] utilized a charge generation layer of C70/Pentacene and proposed a high efficient tandem OLED. In this research, the current efficiency and luminescence of red OLED is obtained as 29 cd/A and 29,010 cd/m^2, respectively, which is 1.855 and 1.856 times better as compared with the conventional device, correspondingly.

In 2019, Yuan *et al.* [141] presented a CGL consists of 1,4,5,8,9,11-hexaazatriphenylene-hexacarbonitrile (HAT-CN)/ 1,1-bis[(di-4-tolyamino)phenyl)]cyclohexane (TAPC) organic heterojunction (OHJ) and utilized it in a OLED to achieve high performance. Recently in 2022, Huseynova *et al.* [142] proposed a novel material i. e. 1,2,3,4,7,8,9,10,13,14,15,16-dodecafluoro-5,6,11,12,17,18 hexaazatrinaphthylene (HATNA-F12) to replace the HAT-CN which is widely used as CGL. In this report, the device with HATNA-F12 in comparison with HAT-CN provides better external quantum efficiency and current efficiency and of 41.7% and 42.1%, correspondingly.

Another layer that has been widely used in recent time is mixed interlayer. In 2015, Moule *et al.* [143] added mixed interlayer of P3HT, APFO–3, and F8BT between PEDOT:PSS and BHJ that improved the control of injection and extraction of charge from anode terminal. Then, in 2016, Kou *et al.* [144] investigated MQW (multiple quantum well) devices using $CBP_{2/3}$: $TPBi_{1/3}$ as mixed host emission interlayer to enhance the performance of green OLED. The exhibits peak luminance, power efficiency and current efficiency as 21930 cd/m^2, 46.4

https://mc04.manuscriptcentral.com/jss-ecs

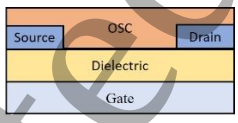
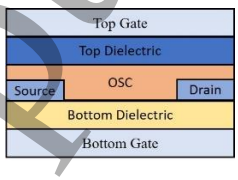
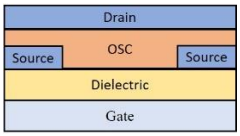
Accepted Manuscript For Review Only

lm/W and 48.6 cd/A, correspondingly. Afterwards in 2022, Maurya *et al.* [145] proposed an OLED with a mixed interlayer of TPBi and CBP as electron and hole material, correspondingly in the ratio of 3:2. Here, the performance parameters such as luminance, current density and power efficiency are obtained as 14268 cd/m^2, 47 mA/cm^2 and 20.8 lmW^{-1}, respectively.

7. Organic Thin Film Transistor

OTFTs are considered as a backbone for organic LEDs. These thin film transistors have been tremendously studied due to their broad application domain which includes smart sensors, displays, RFID (radio frequency identification tags), wearable active-matrix devices and so on [146]. The utilization of organic TFTs promises low-cost fabrication for large area applications [147-150]. This section will discuss the structural analysis of OTFTs. Table 7 is illustrating the various structures of OTFT such as planer, dual gate, vertical and cylindrical OTFTs. Among these structures, bottom gate structures are preferable over top gate as deposition of active layer on dielectric in bottom gate structure is quite convenient whereas in case of top gate, semiconductor layer may get damaged during the deposition of gate electrodes at high temperature [151]. Addition to this, in between top contact (TC) and bottom contact (BC) structures, top contacts are advantageous due to less morphological disorders in OSC layer [152].

Table 7. Different organic thin film transistors along with their structural advantages

Type of OTFT	Structure	Advantages
Planer		• Easy deposition in bottom gate OTFTs • Safe employment of thermal treatment
Dual Gate		• Better charge carrier modulation • Higher on-current as compared to single gate • Steeper sub-threshold slope
Vertical		• Short channel length (in nano-meters) • Low contact resistance

Accepted Manuscript
For Review Only

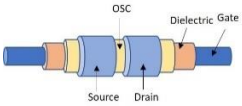
Cylindrical		• Good bending property • Hysteresis free operation • Smaller size device • Higher packing density

Table 8 is demonstrating the various planer bottom gate devices in terms of drain current (I_D), mobility (μ) and threshold voltage (V_T). Extensive research work has been done to explore planer OTFTs. In 2019, Zuo *et al.* [153] designed gate dielectric layer based on polyimide polymer. The BGTC with the reported dielectric showed noteworthy performance in terms of I_{ON}/I_{OFF} and carrier mobility as $>5\times10^5$ and 1.23 $cm^2V^{-1}s^{-1}$, correspondingly. Additionally, in 2020, Qiao *et al.* [154] reported isoindigo (IID)-based copolymers PIIDDTffBT and PIIDDTBT to enhance the performance of bottom gate top contact transistors. The device exhibits hole mobilities as 0.29 and 0.053 $cm^2V^{-1}s^{-1}$ and electron mobilities as 0.1 and 0.013 $cm^2V^{-1}s^{-1}$ for PIIDDTffBT and PIIDDTBT, respectively. Recently in 2022, Steckmann *et al.* [155] discussed high electron mobility using ultrathin P(NDI2OD-T2) films for both top and bottom gate structures. Fig. 14 is depicting the comparison of few bottom gate top contact structures (S_1-S_7) [154-162]. These structures are outlined in terms of I_D and μ. Here, S_2 and S_6 are showing the maximum and minimum drain current as 80 and 3.7 µA. On the other hand, the maximum and minimum mobility is obtained by S_3 and S_7 as 2.4 and 0.02 $cm^2V^{-1}s^{-1}$, respectively.

Table 8. Various planer bottom gate OTFT devices during the last decade

Year [Ref.]	**Structure**	**Parameters**		
		I_D (µA)	**μ ($cm^2V^{-1}s^{-1}$)**	**V_T (V)**
2021 [156]	TC	56	1.12	-0.5
2021 [157]	TC	80	0.04	-0.5
2019 [158]	BC	12	0.14	1.1
2018 [159]	TC	54	2.40	18
2016 [160]	TC	31	0.13	32.7
2014 [161]	TC	37	0.44	-14
2014 [162]	BC	4.5	0.40	-1.2
2010 [163]	TC	3.7	0.37	0.7
2010 [164]	TC	17	0.02	-30

Accepted Manuscript
For Review Only

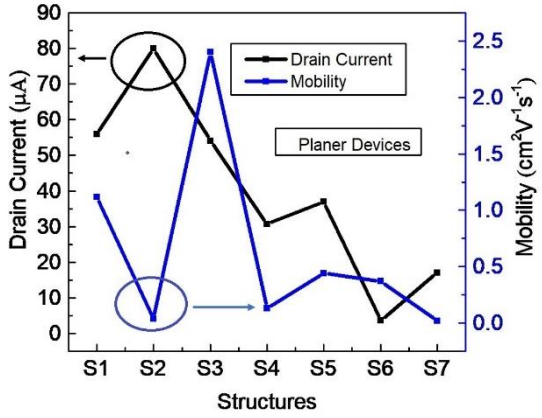


Fig. 14. Comparison of drain current and mobility for various planer OTFT devices

The next category is dual gate organic TFT. In these structures, two gate electrode along with dielectric layers are incorporated for better charge carrier modulation. Dual gate devices provide steeper sub-threshold slope and higher I_{ON}/I_{OFF} as compared single gate [3]. Recent advancement in dual gate TFTs is discussed here. In 2018, Shiwaku *et al.* [165] proposed a low power dual gate TFT utilizing parylene film as gate electrode. It showed better switching characteristics and improved charge carrier density as compared to single gate device. Furthermore in 2020, Singh *et al.* [166] fabricated a dual gate device on PEN substrate with solution-processed technique. The charge carrier mobility is obtained as 0.37 cm^2 $V^{-1}s^{-1}$ at -2.5V. Moreover in 2022, Gupta *et al.* [167] compared single and dual gate performance using material with high dielectric constant. The dual gate device provides better results in terms of drain current which is increased from -9.88×10^{-10} to -5.8×10^{-9} A with reduction in channel length from 50 to 10 μm. The proposed dual gate is suitable for various applications such as chemical sensors, RFIDs and circuits. Table 9 is showing some dual gate thin film devices of the last decade.

Table 9. Various dual gate thin film devices of the last decade

Year [Ref.]	Parameters		
	I_D (μA)	μ ($cm^2V^{-1}s^{-1}$)	V_T (V)
2022 [167]	0.007	0.08	-1.1
2020 [168]	0.8	0.23	-0.15
2020 [166]	1.8	0.37	0.23
2020 [169]	0.0075	19.3	2.41
2019 [170]	0.001	0.315	2.22
2018 [165]	0.24	0.05	0.42
2015 [171]	90	0.98	0.2
2011 [171]	82	0.98	-0.2
2010 [173]	90	1	NR

Accepted Manuscript
For Review Only

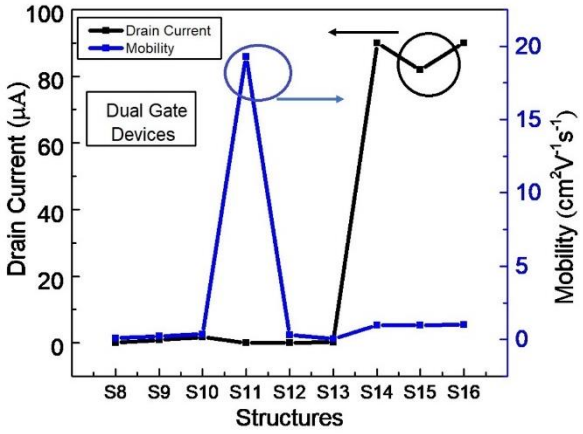


Fig. 15. Comparison of drain current and mobility for different dual gate structures

Different dual gate OTFT structures (S_8-S_{16}) [169-173] are depicted in Fig. 15. The figure is comparing these structures on the basis of μ and I_D wherein maximum and minimum mobilities are obtained as 19.3 and 0.05 $cm^2V^{-1}s^{-1}$ by S_{11} and S_{13}, correspondingly. Addition to this, the maximum and minimum drain current is calculated as 90 (S_{14} and S_{16}) and 0.001 (S_{12}), respectively.

There are various challenges such as low mobility, morphological disorder and long channel length in planer devices (single and dual gate TFTs) discussed above. To overcome these issues vertical TFTs are being utilized in recent time. In these devices, the channel length is measured by the distance between source and drain which are arranged in a vertical manner. This results in shorter channel length in nano-meters. Vertical TFTs are gaining lot of attention of researchers nowadays due to its structural benefits. Some of these structures are depicted in Table 10. In 2018, Rathi *et al.* [174] analyzed the performance of single and dual gate VOTFTs. It is reported that dual gate VOTFT exhibits better performance as compared with single gate and provides higher I_{ON}/I_{OFF}. Thereafter in 2019, a vertical quantum-dot light emitting transistor is proposed by Chen *et al.* [175] using VOTFT. Here, the maximum current efficiency is obtained as 37 cd/A. Furthermore in 2021, Knepp *et al.* [176] reported pentacene based VOTFT using solution-processed technique for the first time. The proposed transistor is compared with small molecule-based VOTFT.

Table 10. Different vertical-channel devices along with their channel length

Year [Ref.]	Parameters	
	I_D (μA)	Channel length (μm)
2021 [176]	180	0.70
2018 [174]	18	0.42
2017 [177]	225	0.06
2013 [178]	50	0.05

Accepted Manuscript For Review Only

2008 [179]	22	0.10
2007 [180]	0.0005	0.10

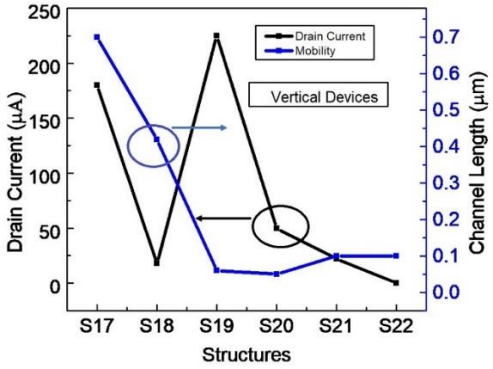


Fig. 16. Comparison of drain current and channel length for various vertical structures

Fig. 16 is comparing six different vertical structures (S_{17}-S_{22} [176,174,177-180]) in terms of channel length and drain current. The structure S_{20} contains the shortest channel length which is 0.05 μm. Besides this, the maximum and minimum drain current is obtained as 225 (S_{19}) and 5×10^{-4} μA (S_{22}), respectively. The fourth category is cylindrical OTFTs. As the name suggests, all the layers are deposited in cylindrical manner as depicted in the table. These devices contain excellent properties like hysteresis free operation and good bending stability which make them suitable for wearable electronics [181]. Some of these structures are discussed in Table 11.

Table 11. Comparison of few cylindrical structures

Year [Ref.]	**Parameters**		
	I_D **(μA)**	μ **(cm^{2}V^{-1}s^{-1})**	V_T **(V)**
2021 [182]	9.0	1.1	-0.5
2017 [183]	35	-	2.33
2016 [184]	10	0.04	-1.94
2007 [185]	0.78	0.04	5.1

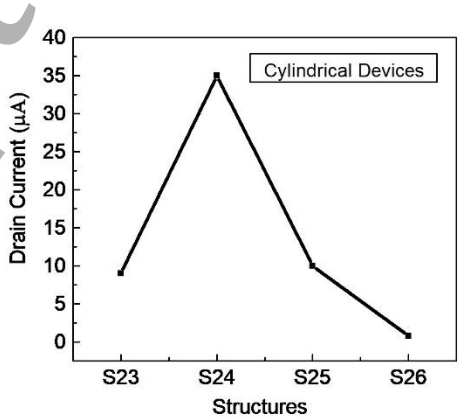


Fig. 17. Comparison of few cylindrical structures on the basis of drain current

Accepted Manuscript
For Review Only

The drain current performance of four cylindrical structures S_{23}, S_{24}, S_{25} and S_{26} [182-185] is compared in Fig. 17. The figure depicts the maximum and minimum drain currents as 35 and 0.78 µA which are exhibited by the structures S_{24} and S_{26}, correspondingly.

Organic LEDs with flexible backplanes are promising candidates for low-cost flexible display applications [186]. Using organic thin film transistors is suitable approach to drive OLEDs as both thin film devices consist of mechanically flexible organic materials. OLED displays driven by OTFTs are robust and degrades the effect of mechanical stresses [187]. Various OLED display applications are being proposed by utilizing OTFTs as mentioned in Table 11. Nakajima *et al.* [188] in 2012, enhanced the image quality of an OTFT driven OLED by improving the performance of organic LED and transistor. They have used a high dielectric material as gate insulator to reduce the operating voltage of TFT.

Table 12. Comparison of various OTFT-driven OLEDs

Devices	Parameters				
	Pixel Size	**Display Size**	**Resolution**	**Luminescence**	**Scan Voltage**
D_{23} [188]	600 µm × 600 µm	5.8 inch	42 ppi	100 cdm^{-2}	Below 15V
D_{24} [189]	318 µm × 318 µm	2.5 inch	80 ppi	150 cdm^{-2}	30 V p-p
D_{25} [187]	210 µm × 210 µm	4.1 inch	121 ppi	100 cdm^{-2}	20 V p-p
D_{26} [190]	1.5mm× 1.5mm	2.7 inch	32×32	64,459 cdm^{-2}	-
D_{27} [191]	318 µm × 318 µm	2.5 inch	80 ppi	100 cdm^{-2}	12 V p-p
D_{28} [186]	317.5 µm ×317.5 µm	2 inch	80 dpi	-	-

In 2017, Mizukami *et al.* [192] proposed a 3.2 inches flexible organic LED driven by inkjet-printed OTFT. The maximum devices luminescence is obtained as 125 cd/m^2. The utilized OTFT exhibits high mobility of 1.2 $cm^2V^{-1}s^{-1}$ which makes transistor useful for flexible color OLED. Additionally in 2021, Pal *et al.* [193] discussed a OTFT driven AMOLED and investigated the effect of different gate dielectrics onto it. It is observed that stack dielectric-based pixel circuit attains the maximum OLED current as 0.6 µA. Table 12 is illustrating the comparison of six different AMOLEDs (D_{23}- D_{28}) driven by OTFTs. Among all the device, D_{26} is obtaining the highest luminescence as 64,459 cdm^{-2} which is approximately 430 times higher than D_{24} and 645 times higher than D_{23}, D_{25} and D_{27}.

8. Different Applications of OLED

https://mc04.manuscriptcentral.com/jss-ecs

Accepted Manuscript For Review Only

Organic LEDs are contributing in many fields such as sensors, health-care, display, military etc. It is foreseeable that technology competition will be more intense in future. There are many investors, enterprises and institutions into the field of OLED lighting, which will surely encourage this technology to reach faster into people's lives, and forward the OLED industry in the worldwide development.

8.1. Sensor

OLEDs have been explored widely for various sensor applications. A highly sensitive ultrathin AMOLED is reported by Kim *et al.* [194] having property of capacitive touch sensor. In this research, Q3D extractor model is utilized to study internal electric field distribution and capacitive change. Moreover, Watanabe *et al.* [195] reported an 8.76 inch in-cell touch sensor using foldable organic LED. Metal-mesh sensor electrodes are used to achieve lower parasitic capacitance. The device properties do not get affected even after 105 folding operations with 5mm radium. Addition to this, Tang *et al.* [196] developed a self-capacitive touch sensor which improved the touch properties along with large touch area in low ground mode, thin cover thickness and miss-touch issue with multi fingers.

The next application is chemical imaging sensor which is basically a semiconductor based chemical sensor utilized for visualizing the spatial distribution of chemical species. In this direction, Miyamoto *et al.* [197] designed a chemical imaging sensor which is utilized for the detection of two-dimensional distribution of molecules in a solution. In this work, current voltage characteristics, Ph sensitivity and photocurrent waveform were analyzed. Moreover, Werner *et al.* [198] proposed a high resolution and high-speed chemical imaging using a novel OLED based on LAPS (light addressable potentiometric sensor) set-up. This new methodology provides miniaturized system with modulation frequencies between 1 kHz and 16 kHz.

8.2. Health-care

Besides light, display and sensor application, organic LEDs have been widely used in various health-care applications. In 2016, Smith *et al.* [199] utilized a high luminescence flexible OLED to design point-of-care immuno-biosensors. The OLED device with optical filters and charge integrated readout circuit provides point-of-care diagnostic sensitivity below 10 pg/ml. Addition to this, Katchman *et al.* [200] reported a combined flat panel organic LED with

https://mc04.manuscriptcentral.com/jss-ecs

Accepted Manuscript For Review Only

protein microarray technology. The concept is used for the detection of circulating cancer biomarkers. Thereafter, in 2019 a light-based sensor is proposed for ovarian cancer detection by Negi *et al.* [201]. Here, a multilayered OLED and a triple hole block layer OLED are utilized as light detector and light source, correspondingly. Moreover in 2020, Jeon *et al.* [202] proposed a photonic skin based on flexible OLED which is useful for various wearable light therapy applications. The total thickness of photonic skin is 6 microns. Recently in 2022, Yun *et al.* [203] presented a skin-like comfortable and stretchable healthcare patch which consists of flexible OLED and PPG (photoplethysmography) sensor. The device is able to monitor real-time heart rate.

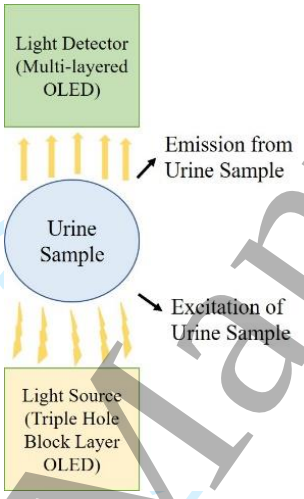


Fig. 18. Methodology for ovarian cancer detection [170]

Fig. 18 is depicting the methodology of ovarian cancer detection through organic LED which is proposed by Negi *et al.* [201]. Here, a multilayered OLED and a triple hole block layer OLED are utilized as light detector and light source, correspondingly. As the figure depicts, first of all, light emission takes place using triple hole block device. The emitted light works as excitation for urine sample which is utilized for the detection purpose. During the excitation, urine sample starts fluorescence emission. The other multilayered OLED, which is used as light detector, detects the urine fluorescence. The light detector now produces different current values which indicate whether ovarian cancer is detected or not. More precisely, if wavelength of urine emission is 440 nm, then the cancer is detected otherwise person is healthy.

Accepted Manuscript
For review only

8.3. Display

First of all, OLED is applied in the display field. There are many advantages of OLEDs for the display devices like fast response, high contrast, color fidelity, flexible display [204-209], wide viewing angle, ultra-thin, high definition, etc. Nowadays, OLED is being widely used in mobile phones, laptops, smart TVs, personal data processors and many display products. Samsung and LG have indicated the arrival of OLED display technology era by introducing 55-inch OLED TV in 2013. Investment in OLED device by Samsung have reached to $5 billion per year in 2014. At present, the companies those are actively involved in the OLED display R & D application are: Apple, BOE, South Korea's Samsung Electronics, South Korea's LGD, Victoria Connaught etc.

As the OLED itself is a light emitting device, one can achieve light emission, flexibility and completely transparent displays [210]. Lots of research work has been done in OLED light sensors also [211,212]. It is predicted that by the end of 2020, OLED lighting industry will reach 1.7 billion dollars globally. The United States, Japan, Europe, China and other countries and enterprises have planned to increase funding and also research work in the OLED lighting market [213]. Now OLEDs are gradually expanding to medical, industrial, advertising, lighting market and other fields in the future. The manufacturing companies which focus on the growth of OLED lighting products are given below.

- Panasonic – Small Molecule
- Samsung – Small Molecule
- NEC Lighting – Small Molecule
- Konica Minolta – Solution Based Phosphorescent
- Philips – Small Molecule
- LG – Small Molecule
- Osram Opto – Small Molecule

In 2015, Shin *et al.* [214] presented novel OLED display technologies for UHD OLED TVs. Here, they have utilized RGBW pixel structure with WOLED and applied compensation method on the panel. With these technologies, the researchers launched three LG's UHD OLED of 55, 65 and 77 inches. The specifications of the UHD OLED TVs are depicted in Table 13. Furthermore in 2017, Noh *et al.* [215] developed a 55 inches 4K UHD OLED

https://mc04.manuscriptcentral.com/jss-ecs

Accepted Manuscript For Review Only

employing internal GIP circuit. White OLED is used with the specifications such as panel size (55 inches), resolution (3480(WRGB)×2160), pixel pitch (80ppi), brightness (100/500nit) and bezel size (5.5mm). Thereafter in 2020, Hu *et al.* [216] demonstrated an OLED based full color display with red and green quantum dots conversion layers. The display contains 6.6 inches screen and color gamut of 95 (BT.2020) % with wide viewing angle.

Table 13. Specifications of UHD OLED TV [214]

Display Type	RGBW OLED
Panel Size	55, 65, 77 (Inch)
Resolution	3840 × 2160 (UHD)
Brightness	150 (full)/450 (peak) (cd/m2)
Color Gamut	118 (BT. 709) %
Contrast Ratio	>1,000,000: 1
Curve	R = 5000 mm

Other than TVs, OLED has been widely utilized in mobile devices as well as it contains high contrast and wide color range. In 2017, Kirchner *et al.* [217] proposed a technique to enhance the color reproduction accuracy of OLED based mobile displays. They have applied mobile display characterization and illumination model (MDCIM) to Samsung Galaxy S4 display. In mobiles, display screen is responsible for higher power consumption which decreases the usage time. To overcome this challenge, in 2018, Yeh *et al.* [218] proposed visual attention based pixel dimming technique. This technique increases power saving during real-time display processing of the OLED based mobile devices.

In OLED based display devices, it is difficult to predict the power consumption very precisely using conventional linear model. In order to make is possible, Choi *et al.* [219] in 2018, presented a methodology to provide the accurate power model for display mode in mobiles. The technique is capable of self-learning the power model through RGB value of each pixel. Moreover, in 2021, Asnani *et al.* [220] used the image dependent power consuming quality of OLED based mobile devices to provide energy efficient images with better contrast. This technique was applied on Samsung Galaxy A50 mobile based on OLED. The proposed method decreases the power consumption by 13.16%.

OLEDs have contributed in some military application as well. Barre *et al.* [221] reported some application such as assistant gunner display, night vision goggles and vision enhancement system which are very helpful in military. Moreover, some military and aerospace applications based on OLED are discussed by Marasco *et al.* [222]. Addition to this, Trakalo *et al.* [223] discussed three different devices such as OLED DDACT, Polymer-OLED AGD (assistant gunner display) and OLED AGD for military purpose.

https://mc04.manuscriptcentral.com/jss-ecs

Accepted Manuscript For Review Only

9. Challenges of OLEDs

Among all the parameters such as luminescence, current density, current efficiency, lifetime, power efficiency and external quantum efficiency, the operational lifetime is the biggest concern in OLED. The lifetime of organic devices is very less as compared to inorganic devices. Various researchers are working for the enhancement of lifetime in such devices. Many groups of researchers are providing various techniques to improve the lifetime which are as follows: 1. Use of double emissive layer [118], 2. Utilization of an assistant layer in emitters with triplet–triplet annihilation up-conversion characteristics [120], 3. Use of synthetic tetradentate [C^C^N^C] gold (III) complexes [121], 4. Shifting of recombination zone away from interfacial mixing region [122], etc. All these mentioned methodologies for better lifetime have been discussed in detail in Subsection 5.5.

For AMOLED based devices, the main choices are red and green phosphorescent emitters because of better luminance properties as compared with blue OLEDs. The reason behind this is that the charge carriers are inhibited in case of BOLEDs due their wide band gap. But on the other hand, blue emitters are very good at generation of white color [35]. So, this is also a big challenge to improve the electro-luminescence performance of BOLEDs. Lot of researchers are working in this direction which has been already mentioned above in Subsection 3.3. Another challenge in OLED based display and lighting devices is their cost as it is a major factor for consumers to buy such products. Besides of the innovations in the area of device structures, manufacturing processes and materials, cost of OLED devices also requires the lot of attention because the other competent displays such as LEDs and LCDs are at very reasonable cost nowadays.

10. Future Scope

The field of display technology of organic devices is approaching too many future applications such as dash boards, billboard displays and head-up display. The response time of these organic devices (OLED) is 100 times faster than LCDs and other conventional devices which provides higher efficiency, greater speed, better color quality and more accurate real time information [224]. The organic LEDs contains various features such as flexibility, lightweight and ultra-thin displays which makes it very popular among wearable-electronic devices. Even these

Accepted Manuscript
For Review Only

devices can obtain the properties of clothing in future which will make them suitable to wear for long time without any discomfort [225].

In near future, OLED devices will occupy almost every area of display industry as these display devices are made of organic materials and glass, so there is less utilization of toxic materials and it becomes easier to recycle which makes them environment friendly. Also, these organic displays do not need backlight which results in less fuel and power consumption and leads to lowering greenhouse emission [226]. Moreover, the technology works in a wide temperature range and so the devices can operate in any condition which will reduce the geographical restriction. Apart from these advantages, there are some challenges as well of this technology such as improvement in quantum efficiency, low driving voltage and lifetime.

11. Conclusion

OLEDs are low power devices as they do not require backlight like in Liquid crystal device and other devices. This property is very useful for the devices that run on battery like mobile phone, laptops, smart watches etc. OLEDs can be easily fabricated on large thin sheets due to their flexible properties. They have much wider viewing range as they contain their own luminance property. The green and red OLEDs have good lifetime that is 40,000 and 80,000 hours respectively, but the lifetime of yellow OLED is 7,000 hours only that is much shorter. The manufacturing of these devices is also expensive at present. In this article, one fabrication process for flexible integrated substrate is highlighted that is very much cost effective. In this process, sheet resistance and effective opening ratio are concluded 3.8 ohms per square and 82.5% respectively. Additionally, various performance parameters such as luminescence, EQE and current efficiency are compared and analyzed. Moreover, different categories of recent time OLEDs are investigated. As well as, various light emission-based applications such as sensors, health-care and display are studied and reviewed. This review also includes some recent advancement of OTFT with some OTFT-driven organic LED devices.

.

Accepted Manuscript
For Review Only

Acknowledgements

Consent for publication. All the authors understand and give their consent for the publication of manuscript "Advancements and perspectives of organic LED: In depth analysis of architectural design, characteristics parameters, fabrication techniques and applications" in "ECS Journal of Solid State Science and Technology" Journal. Competing interests. No, all the authors declare that they have no competing interests as defined by IOP, or other interests that might be perceived to influence the results and/or discussion reported in this paper. The authors have no conflicts of interest to declare that are relevant to the content of this article. Author's Contributions. Sugandha Yadav: Conceptualization, Methodology, Data curation, Writing – original draft, Writing – review & editing. Poornima Mittal: Conceptualization, Methodology, Supervision, Data curation, Writing – review & editing, Validation. Shubham Negi: Supervision, Writing – review & editing, Visualization, Investigation, Formal analysis. Ethics approval. The manuscript is not submitted to anywhere else for the publication. The submitted work is an original work and have not been published elsewhere in any form or language. The authors do not have any conflict of interest. The research does not involve any human participant and/or animal thus, informed consent in not required.

References

[1] Y. Karzazi, J. Cornil, and J. L. Brédas, Theoretical investigation of the origin of negative differential resistance in substituted phenylene ethynylene oligomers. *NNOTER*. 14, 165 (2003).

[2] A. E. Kaloyeros, F. A. Jové, J. Goff and B. Arkles, Silicon nitride and silicon nitride-rich thin film technologies: trends in deposition techniques and related applications. *ECS Journal of Solid State Science and Technology*, 6(10), P691 (2017).

[3] B. Kumar, B. K. Kaushik and Y. S. Negi, Organic thin film transistors: structures, models, materials, fabrication, and applications: a review. *Polymer Reviews*. 54(1), 33-111 (2014).

[4] N. Mishra, P. Mittal and B. Kumar, Analytical modeling for static and dynamic response of organic pseudo all-p inverter circuits. *J. Comput. Electron*. 18(4), 1490-1500 (2019).

[5] P. M. Pattison, M. Hansen and J. Y. Tsao, LED lighting efficacy: Status and directions. *C. R. Phys*. 19(3), 134-145 (2018).

[6] B. N. Patel, and M. M. Prajapati, OLED: A modern display technology. *Int. J. Sci. Res. Publ.* 4(6), 1-5 (2014).

[7] P. Mittal, Y. S. Negi and R. K. Singh, A depth analysis for different structures of organic thin film transistors: modeling of performance limiting issues. *Microelectron. Eng.* 150, 7-18 (2016).

https://mc04.manuscriptcentral.com/jss-ecs

Accepted Manuscript

For Review Only

[8] Y. Chen, J. Chen, D. Ma, D. Yan, L. Wang and F. Zhu, High power efficiency tandem organic light-emitting diodes based on bulk heterojunction organic bipolar charge generation layer. *Appl. Phys. Lett.* 98(24), 114 (2011).

[9] C. Gao, Z. Xiong, F. Yu, X. Ma, Y. Zhang, X. Zeng and Z. Xiong, Color-Tunable Hybrid White Organic Light-Emitting Diodes with Double Interlayers. Curr. Opt. *Photonics.* 7(8), 99-105 (2017).

[10] K. Dhbaibi, L. Abella, S. Meunier-Della-Gatta, T. Roisnel, N. Vanthuyne, B. Jamoussi, G. Pieters, B. Racine, E. Quesnel, J. Autschbach and J. Crassous, Achieving high circularly polarized luminescence with push–pull helicenic systems: from rationalized design to top-emission CP-OLED applications. *Chem. Sci.* 12, 5522-5533 (2021).

[11] X. Yan, C. Tian, W. Jiang, W. Xia and X. Wei, A scalable seamless full color PMOLED. *J. Soc. Inf. Disp*. 22, 245-250 (2014).

[12] C. Y. Su, K. Y. Ko, Y. W. Liu, J. C. Li, C. H. Wu, S. C. Liu, C. Y. Tseng, Y. F. Wang, C. C. Lo and L. Y. Chen, 15.4 L: Late-News Paper: A 7 Inch Full Color Flexible PMOLED Displays on Plastic Substrate. *SID. INT. SYMP. DIG. TEC*. 45(1), 191-193 (2014).

[13] P. K. Uttwani, A. Awasthi, A. Solanki and I. K. Rao, I.K.: Electrical testing of the OLED matrix for analyzing defects in a PMOLED display. *In 16th International Workshop on Physics of Semiconductor Devices.* 8549, 659-662 (2012).

[14] M. G. Kane, AMOLED display technology and applications. *Flexible Carbon-based Electronics.* 231-263 (2018).

[15] F. Boera, A. Salimath, E. Bonizzoni, and F. Maloberti, Design of a SIBO DC-DC converter for AMOLED display driving. *In 2018 14th Conference on Ph. D. Research in Microelectronics and Electronics (PRIME).* 109-112 (2018) .

[16] S. Steudel, K. Myny, S. Schols, P. Vicca, S. Smout, A. Tripathi, B. Van Der Putten, J. L. van der Steen, M. Van Neer, F. Schütze and O. R. Hild, Design and realization of a flexible QQVGA AMOLED display with organic TFTs. *Org. Electron.* 13(9), 1729-1735 (2012).

[17] Y. G. Mo, M. Kim, C. K. Kang, J. H. Jeong, Y. S. Park, C. G. Choi, H. D. Kim and S. S. Kim, Amorphous-oxide TFT backplane for large-sized AMOLED TVs. *J. Soc. Inf. Disp.* 19(1), 16-20 (2011).

[18] R. Yonebayashi, K. Tanaka, K. Okada, K. Yamamoto, K. Yamamoto, S. Uchida, T. Aoki, Y. Takeda, H. Furukawa, K. Ito and H. Katoh, High refresh rate and low power consumption AMOLED panel using top-gate n-oxide and p-LTPS TFTs. *J. Soc. Inf. Disp*. 28, 350-359 (2020).

[19] L. H. Smith, J. A. E. Wasey, W. L. Barnes, Light outcoupling efficiency of top emitting organic light-emitting diodes, *Appl. Phys. Lett.* 84, 2986-2988 (2004).

[20] C. Dong, X. Fu, S. Amoah, A. Rozelle, D. H. Shin, A. Salehi, J. Mendes, F. So, Eliminate angular color shift in top-emitting OLEDs through cavity design. *J. Soc. Inf. Disp*. 27, 469-479 (2019).

[21] Y. Qu, C. Coburn, D. Fan, S. R. Forrest, Elimination of plasmon losses and enhanced light extraction of top-emitting organic light-emitting devices using a reflective subelectrode grid. *ACS Photonics* 4, 363-368 (2017).

[22] Y. Liu, X. Wei, Z. Li, L. Liu, X. Wang, X. Hu, P. Y. Wang, Y. Yamada-Takamura, T. Qi, Y. Wang, Highly efficient, solution-processed organic light-emitting diodes based on thermally activated delayed-fluorescence emitter with a mixed polymer interlayer. *ACS Appl. Energy Mater.* 1, 543-551 (2018).

[23] D. Y. Kim, S. H. Jung and M. C. Suh, Influence of index matching epoxy filler at the encapsulation part for the performance of TEOLED with internal wrinkle structure. *SID 2019 Digest*. 1963-1965 (2019).

[24] B. Y. Lin, C. H. Chen, K. R. Lin, C. Y. Lee, T. L. Chiu and J. H. Lee, P-88: Efficiency Improvement of Top-Emission Green Quantum-Dot Light-Emitting Diode with Dielectric-Metal-Dielectric Cathode. *In SID Symposium Digest of Technical Papers*. 53, 1355-1356 (2022).

[25] K. Takahashi, T. Sato, R. Yamamoto, H. Shishido, T. Isa, S. Eguchi, H. Miyake, Y. Hirakata, S. Yamazaki, R. Sato, H. Matsumoto, 13.3-inch 8k4k 664-ppi Foldable OLED Display Using Crystalline Oxide Semiconductor FETs. *In SID Symposium Digest of Technical Papers*. 46, 250-253 (2015).

[26] B. de. Dieu, J. Mugiraneza, T. Maruyama, T. Yamamoto, Y. Sugita, 44-3: 3D Piezo-Capacitive Touch with Capability to Distinguish Conductive and Non-Conductive Touch Objects for On-Screen Organic User Interface in LCD and Foldable OLED Display Application. *In SID Symposium Digest of Technical Papers*. 50, 608-611 (2019).

[27] B. Zhang, P. Qi, Z. Yang, Z. Lai, Z. Wang, S. Li, X. Luo, P. Luo, M. Fan, Z. Wang, Z. Xue, A 17.3-inch WQHD Top-Emission Foldable AMOLED Display with Outstanding Optical Performance and Visual Effects. *In SID Symposium Digest of Technical Papers*. 51, 1836-1839 (2020).

Accepted Manuscript For Review Only

[28] H. J. Han, W. J. Cho, S. J. Lee, H. M. Park and I. Hwang, Stress-Free Folding Hinge for Foldable OLED Display Device. *In SID conference*. (2021).

[29] Y. H. Tsai, M. H. Huang, T. W. Huang, K. L. Lo and M. Ou-Yang, Image quality affected by diffraction of aperture structure arrangement in transparent active-matrix organic light-emitting diode displays. *Appl. Opt.* 54, E136-E145 (2015).

[30] Z. Qin, Y. W. Yeh, Y. H. Tsai, W. Y. Cheng, Y. P. Huang, H. P. D. Shieh, 31-2: See-through Image Blurring of Transparent OLED Display: Diffraction Analysis and OLED Pixel Optimization. *In Sid Symposium Digest of Technical Papers*. 47, 393-396 (2016).

[31] Z. Shu, E. Beckert, R. Eberhardt, A. Tünnermann, ITO-free, inkjet-printed transparent organic light-emitting diodes with a single inkjet-printed Al: ZnO: PEI interlayer for sensing applications. *J. Mater. Chem. C.* 5, 11590-11597 (2017).

[32] M. G. Song, K. S. Kim, H. I. Yang, S. K. Kim, J. H. Kim, C. W. Han, H. C. Choi, R. Pode, J. H. Kwon, Highly reliable and transparent Al doped Ag cathode fabricated using thermal evaporation for transparent OLED applications. *Org. Electron.* 76, 105418 (2020).

[33] Y. H. Tsai and M. Ou-Yang, A flexible transparent organic light-emitting display with high-transmittance cathode and high-contrast electrochromic shutter. *J. Soc. Inf. Disp.* 30, 61-80 (2022).

[34] E. R. Triboni, M. R. Fernandes, J. R. Garcia, M. C. Carreira, R. G. D. S. Berlinck, P. B. Filho, L. S. Roman, I. A. Hümmelgen, R. Reyes and M. Cremona, Naphthalimide-derivative with blue electroluminescence for OLED applications. *J. Taibah Univ. Sci. 9*, 579-585 (2015).

[35] X. N. Li, Z. J. Wu, Z. J. Si, H. J. Zhang, L. Zhou and X. J. Liu, Injection, transport, absorption and phosphorescence properties of a series of blue-emitting Ir (III) emitters in OLEDs: a DFT and time-dependent DFT study. *Inorg. Chem.* 48, 7740-7749 (2009).

[36] K. Nakao, H. Sasabe, R. Komatsu, Y. Hayasaka, T. Ohsawa, J. Kido, Significant enhancement of blue OLED performances through molecular engineering of pyrimidine-based emitter. *Adv. Opt. Mater.* 5, 1600843 (2017).

[37] J. Yang, Q. Guo, J. Wang, Z. Ren, J. Chen, Q. Peng, D. Ma, Z. Li, Rational Molecular Design for Efficient Exciton Harvesting, and Deep-Blue OLED Application. *Adv. Opt. Mater.* 6, 1800342 (2018).

[38] M. Han, Y. Chen, Y. Xie, F. Zhang, X. Li, A. Huang, Y. Fan, Y. Fan, Y. Gong, Q. Peng, Q. Li, 1.42-Fold Enhancement of Blue OLED Device Performance by Simply Changing Alkyl Groups on the Acridine Ring. Cell Rep. *Physical Sci.* 1, 100252 (2020).

[39] C. Y. Chan, M. Tanaka, Y. T. Lee, Y. W. Wong, H. Nakanotani, T. Hatakeyama and C. Adachi, Stable pure-blue hyperfluorescence organic light-emitting diodes with high-efficiency and narrow emission. *Nat. Photon.* 15, 203-207 (2021).

[40] B. Wei, H. Xu, N. Zhao, X. Gao, Y. Ye, Y. Wang, D. Yao, X. Zhang, and X. Liu, Deep-blue organic light-emitting diodes based on multi-tert-butyl modified naphthylene. *J Ind Eng Chem.* 102, 44-50 (2021).

[41] X. Zheng, Y. Liu, Y. Zhu, F. Ma, C. Feng, Y. Yu, H. Hu and F. Li, Efficient inkjet-printed blue OLED with boosted charge transport using host doping for application in pixelated display. *Opt. Mater. 101*, 109755 (2020).

[42] P. Rajamalli, N. Senthilkumar, P. Gandeepan, C. C. Ren-Wu, H. W. Lin, C. H. Cheng, A method for reducing the singlet–triplet energy gaps of TADF materials for improving the blue OLED efficiency. *ACS appl. Mater. Interfaces*. 8, 27026-27034 (2016).

[43] H. Park, J. Lee, I. Kang, H. Y. Chu, J. I. Lee, S. K. Kwon, Y. H. Kim, Highly rigid and twisted anthracene derivatives: a strategy for deep blue OLED materials with theoretical limit efficiency. *J. Mater. Chem.* 22, 2695-2700 (2012).

[44] H. Cho, C. W. Byun, C. M. Kang, J. W. Shin, B. H. Kwon, S. Choi, N. S. Cho, J. I. Cho, H. Lee, J. Kim, H. Lee, M. Kim, White organic light-emitting diode (OLED) micro display with a tandem structure, *J Soc Inf Disp*. 20, 249-255 (2019).

[45] S. Reineke, M. Thomschke, B. Lüssem, K. Leo, White organic light-emitting diodes: Status and perspective, *Rev. Mod. Phys.* 85 1245 (2013).

[46] S. Negi, P. Mittal, B. Kumar, In-Depth Analysis of Structures, Materials, Models, Parameters, and Applications of Organic Light-Emitting Diodes. *J. Electron. Mater.* 49, 4610-4636 (2020).

[47] C. Huang, Y. Zhang, J. Zhou, S. Sun, W. Luo, W. He, J. Wang, X. Shi, M. K. Fung, Hybrid tandem white OLED with long lifetime and 150 Lm W− 1 in luminous efficacy based on TADF blue emitter stabilized with phosphorescent red emitter. *Adv. Opt. Mater.* 8, 2000727 (2020).

Accepted Manuscript

[48] S. H. Yang and T. L. Huang, High fluorescence efficiency of dual-wavelength white OLED with NPB emission and triplet annihilation. *Opt. Mater.* 111, 110725 (2021).

[49] S. J. Lee, C. M. Kang, J. W. Shin, D. H. Ahn, C. W. Joo, H. Cho, N. S. Cho, H. M. Youn, Y. J. An, J. S. Kim and J. Lee, Three-wavelength white organic light-emitting diodes on silicon for high luminance and color gamut micro-displays. *J. Ind. Eng. Chem.* 105, 132-137 (2022).

[50] H. Lee, Phosphorescent white organic light-emitting diodes with stable white color depending on luminance. *Curr. Appl. Phys.* 21, 116-120 (2021).

[51] X. Zheng, Y. Liu, Y. Zhu, F. Ma, C. Feng, Y. Yu, H. Hu, F. Li, Efficient inkjet-printed blue OLED with boosted charge transport using host doping for application in pixelated display. *Opt. Mater.* 101, 109755 (2020).

[52] E. Angioni, M. Chapran, K. Ivaniuk, N. Kostiv, V. Cherpak, P. Stakhira, A. Lazauskas, S. Tamulevičius, D. Volyniuk, N. J. Findlay, T. Tuttle, A single emitting layer white OLED based on exciplex interface emission. *J. Mater. Chem. C*. 4, 3851-3856 (2016).

[53] Y. H. Chung, L. Sheng, X. Xing, L. Zheng, M. Bian, Z. Chen, L. Xiao and Q. Gong, A pure blue emitter (CIE y≈ 0.08) of chrysene derivative with high thermal stability for OLED. *J. Mater. Chem. C*. 3, 1794-1798 (2015).

[54] A. Y. Freidzon, A. A. Safonov, A. A. Bagaturyants, D. N. Krasikov, B. V. Potapkin, A. A. Osipov, A. V. Yakubovich and O. Kwon, Predicting the operational stability of phosphorescent OLED host molecules from first principles: a case study. *J. Phys. Chem. C.* 121, 22422-22433 (2017).

[55] K. Klimes, Z. Q. Zhu and J. Li, Efficient blue phosphorescent OLEDs with improved stability and color purity through judicious triplet exciton management. *Adv. Func. Mater.* 29, 1903068 (2019).

[56] D. Corrêa Santos and M. D. F. Vieira Marques, Blue light polymeric emitters for the development of OLED devices. *J. Mater. Sci.: Mater. Electron.* 33, 1-37 (2022).

[57] X. Du, S. Tao, Y. Huang, X. Yang, X. Ding and X. Zhang, Efficient fluorescence/phosphorescence white organic light-emitting diodes with ultra high color stability and mild efficiency roll-off. *Appl. Phys. Lett.* 107, 183304 (2015).

[58] W. Sun, L. Zhou, Q. Zhu, R. Wu, Z. Li, S. Li and D. Qin, Efficient multi-light-emitting layers warm and pure white phosphorescent organic light-emitting diodes with excellent color stability. *J. Lumin.* 228, 117596 (2020).

[59] S. S. Swayamprabha, M. R. Nagar, R. A. K. Yadav, S. Gull, D. K. Dubey, J. H. Juo, Hole-transporting materials for organic light-emitting diodes: an overview. *J. Mater. Chem. C.* 7, 7144-7158 (2019).

[60] C. W. Tang, S. A. VanSlyke, Organic electroluminescent diodes, *Appl. Phys. Lett.* 51, 913-915 (1987).

[61] Usui, H.: Formation of polymer thin films and interface control by physical vapor deposition, *Int. j. opt. photonics.* 7404, 63-74 (2009).

[62] Y. Kajiyama, K. Joseph, K. Kajiyama, S. Kudo and H. Aziz, Recent progress on the vacuum deposition of OLEDs with feature sizes≤ 20 μm using a contact shadow mask patterned in-situ by laser ablation. *Organic Light Emitting Materials and Devices XVII*. *8829*, 101-106 (2013).

[63] S. Sanderson, G. Vamvounis, A. E. Mark, P. L. Burn, R. D. White and B. W. Philippa, Understanding the performance differences between solution and vacuum deposited OLEDs: A computational approach. *J. Chem. Phys.* 156, 214703 (2022).

[64] J. L. Liao, P. Rajakannu, P. Gnanasekaran, S. R. Tsai, C. H. Lin, S. H. Liu, C. H. Chang, G. H. Lee, G.H., P. T. Chou, Z. N. Chen and Y. Chi, Luminescent diiridium complexes with bridging pyrazolates: Characterization and fabrication of OLEDs using vacuum thermal deposition. *Adv. Opt. Mater.* 6, 1800083 (2018).

[65] S. K. Kim, K. S. Kim, H. U. Park, J. Y. Kim, D. K. Kim, S. H. Kim, J. H. Baek, J. J. Kim, R. Pode and J. H. Kwon, Patternization of cathode metal using low surface energy organic molecules in OLED thermal evaporation process. *J Ind Eng Chem.* 114, 213-220 (2022).

[66] S. Kongsabay, P. Funchien, P. Chasing, T. Sudyodsuk and V. Promarak, An efficient solution-processable hybridized local and charge-transfer (HLCT)-based deep-red fluorescent emitter for simple structured non-doped OLED. *J. Lumin.* 248, 118921 (2022).

[67] S. Wang, H. Zhang, B. Zhang, Z. Xie, and W. Y. Wong, Towards high-power-efficiency solution-processed OLEDs: *Mater. Sci. Eng. R Rep.*140, 100547 (2020).

[68] W. J. Hyun, S. H. lm, O. O. Park and B. D. Chin, Corrugated structure through a spin-coating process for enhanced light extraction from organic light-emitting diodes. *Org. Electron.* 13, 579-585 (2012).

Accepted Manuscript

[69] S. Yuan, Y. Hao, Y. Miao, Q. Sun, Z. Li, Y. Cui, H. Wang, B. Xu, Enhanced light out-coupling efficiency and reduced efficiency roll-off in phosphorescent OLEDs with a spontaneously distributed embossed structure formed by a spin-coating method. *RSC adv.* 7, 43987-43993 (2017).

[70] N. Juhari, N. I. A. Shukri, N. Sabani, S. Shaari, M. F. Ahmad, N. F. Zakaria, The structural and electrical characterization of PEDOT: PSS/MEH-PPV doped with PEIE OLED fabricated using spin coating technique. *In AIP Conference Proceedings*, 2203, 020046 (2020).

[71] E. Tekin, P. J. Smith, U. S. Schubert, Inkjet printing as a deposition and patterning tool for polymers and inorganic particles, *Soft Matter*. 4, 703-713 (2008).

[72] H. C. Chen, C. P. W. G. Kung, W. G. Houng, Y. R. Peng, Y. M. Hsien, C. C. Chou, C. J. Kao, T. H. Yang, J. Hou, Polymer inverter fabricated by inkjet printing and realized by transistors arrays on flexible substrates. *J. D. T.* 5, 216-222 (2009).

[73] M. Cinquino, C. T. Prontera, A. Zizzari, A. Giuri, M. Pugliese, R. Giannuzzi, A. G. Monteduro, M. Carugati, A. Banfi, S. Carallo and A. Rizzo, Effect of surface tension and drying time on inkjet-printed PEDOT: PSS for ITO-free OLED devices. *J. Sci.: Adv. Mater. Devices*. 7, 100394 (2022).

[74] M. Hengge, K. Livanov, N. Zamoshchik, F. Hermerschmidt and E. J. List-Kratochvil, ITO-free OLEDs utilizing inkjet-printed and low temperature plasma-sintered Ag electrodes. *Flex. Print. Electron.* 6, 015009 (2021).

[75] Z. Hu, Y. Yin, M. U. Ali, W. Peng, S. Zhang, D. Li, T. Zou, Y. Li, S. Jiao, S. J. Chen and C. Y. Lee, Inkjet printed uniform quantum dots as color conversion layers for full-color OLED displays. *Nanoscale*. 12, 2103-2110 (2020).

[76] X. Xing, T. Lin, Y. X. Hu, Y. L. Sun, W. Y. Mu, Z. Z. Du, Y. K. Liu, D. F. Yang, S. I. Shi, D. Y. Zhang and Z. Cui, Inkjet printing high luminance phosphorescent OLED based on m-MTDATA: TPBi host. *Mod. Phys. Lett. B.* 33, 1950149 (2019).

[77] W. Feng, Q. Su, Y. Ma, Z. Džolić, F. Huang, Z. Wang, S. Chen and B. Z. Tang, Tetraphenylbenzosilole: an AIE building block for deep-blue emitters with high performance in nondoped spin-coating OLEDs. *J. Org. Chem. Res.* 85(1), 158-167 (2019).

[78] J. T. Hu, Q. Q. Wei, J. Li, K. Xu and X. H. Wang, X.H.: Research on the impact of spin coating silver nano clusters on the performance of OLED devices. *Optoelectron. Lett.* 14(5), 321-324 (2018).

[79] G. Dasi, R. Ramarajan and K. Thangaraju, Improved electron injection in spin coated Alq3 incorporated ZnO thin film in the device for solution processed OLEDs. *AIP Conf Proc.* 1942(1), 060015 (2018).

[80] D. H. Cho, O. E. Kwon, Y. S. Park, B. G. Yu, J. Lee, J. Moon, H. Cho, H. Lee and N. S. Cho, Flexible integrated OLED substrates prepared by printing and plating process. *Org. Electron.* 50, 170-176 (2017).

[81] Y. M. Kim, J. W. Lee, J. H. Jung, K. K. Paek, M. Y. Sung, J. K. Kim and B. K. Ju, Enhanced brightness and efficiency of organic light-emitting diodes with an LiF in the Alq/sub 3. *IEEE Electron Device Lett.* 27(7), 558-560 (2006).

[82] K. Albrecht, K. Matsuoka, D. Yokoyama, Y. Sakai, A. Nakayama, K. Fujita and K. Yamamoto, Thermally activated delayed fluorescence OLEDs with fully solution processed organic layers exhibiting nearly 10% external quantum efficiency. *ChemComm.* 53, 2439-2442 (2017).

[83] J. Park, J. Lee, D. Shin and S. Park, Luminance uniformity of large-area OLEDs with an auxiliary metal electrode. *J. D. T.* 5(8), 306-311 (2009).

[84] J. H. Han, J. Moon, D. H. Cho, J. W. Shin, H. Y. Chu, J. I. Lee, N. S. Cho and J. Lee, Luminescence enhancement of OLED lighting panels using a microlens array film. *J. Inf. Disp.* 19, 179-184 (2018).

[85] H. Kanno, Y. Hamada and H. Takahashi, Development of OLED with high stability and luminance efficiency by co-doping methods for full color displays. IEEE J. Sel. Top. *Quantum Electron.* 10(1), 30-36 (2004).

[86] D. E. Aasha and S. Prince, Comparison of Luminescence Efficiency of Materials in Organic Light Emitting Diode. *In 2020 International Conference on Communication and Signal Processing (ICCSP).* 0952-0955 (2020).

[87] C. Ou, Y. C. Qiu, C. Cao, H. Zhang, J. Qin, Z. L. Tu, J. Shi, Z. G. Wu, Modulating the peripheral large steric hindrance of iridium complexes for achieving narrowband emission and pure red OLEDs with an EQE up to 32.0%. *Inorg. Chem. Front.* (2023).

[88] X. J. Wang, H. Liu, H. Zhang, D. Yang, Z. H. Pan, C. K. Wang, M. K. Fung, D. Ma and J. Fan, Using azaacene as an acceptor unit to construct an ultraefficient red fluorophore with an EQE over 40%. *Mater. Horiz. (2023).*

Accepted Manuscript

[89] E. Dykstra, M. Fralaide, Y. Zhang, R. Biswas, W. D. Slafer, J. Shinar and R. Shinar, OLEDs on planarized light outcoupling-enhancing structures in plastic. *Org. Electron. 111*, p.106648 (2022).

[90] Y. Zou, J. Hu, M. Yu, J. Miao, Z. Xie, Y. Qiu, X. Cao and C. Yang, High-Performance Narrowband Pure-Red OLEDs with External Quantum Efficiencies up to 36.1% and Ultralow Efficiency Roll-Off. *Adv. Mater. 34*(29), p.2201442 (2022).

[91] Y. C. Cheng, X. C. Fan, F. Huang, X. Xiong, J. Yu, K. Wang, C. S. Lee and X. H. Zhang, A Highly Twisted Carbazole-Fused DABNA Derivative as an Orange-Red TADF Emitter for OLEDs with Nearly 40% EQE. *Angew. Chem. 134*(47), p.e202212575 (2022).

[92] R. Braveenth, H. Lee, J. D. Park, K. J. Yang, S. J. Hwang, K. R. Naveen, R. Lampande and J. H. Kwon, Achieving Narrow FWHM and High EQE Over 38% in Blue OLEDs Using Rigid Heteroatom-Based Deep Blue TADF Sensitized Host. *Adv. Funct. Mater., 31*(47), p.2105805 (2021).

[93] G. Lu, Z. G.Wu, R. Wu, X. Cao, L. Zhou, Y. X. Zheng and C. Yang, Semitransparent Circularly Polarized Phosphorescent Organic Light-Emitting Diodes with External Quantum Efficiency over 30% and Dissymmetry Factor Close to 10− 2. *Adv. Funct. Mater.* 31(36), 2102898 (2021).

[94] Y. F. Wang, M. Li, M., J. M. Teng, H. Y. Zhou and C. F. Chen, High-performance solution-processed nondoped circularly polarized OLEDs with chiral triptycene scaffold-based TADF emitters realizing over 20% external quantum efficiency. *Adv. Funct. Mater.* 31(49), 2106418 (2021).

[95] A. Sharma and T. D. Das, Highly efficient OLED device based on the double emissive layer with an EQE about 39%. *Optik, 221*, p.165350 (2020).

[96] T. Yang, B. Liang, Z. Cheng, C. Li, G. Lu and Y. Wang, Y.: Construction of efficient deep-red/near-infrared emitter based on a large π-conjugated acceptor and delayed fluorescence OLEDs with external quantum efficiency of over 20%. *J. Phys. Chem. C.* 123(30), 18585-18592 (2019).

[97] G. Z. Lu, Z. L. Tu, L. Liu, W. W. Zhang and Y. X. Zheng, Fast synthesis of iridium (iii) complexes with sulfur-containing ancillary ligand for high-performance green OLEDs with EQE exceeding 31%. *J. Mater. Chem. C, 7*(24), pp.7273-7278 (2019).

[98] Y. Wang, W. Wang, Z. Huang, H. Wang, J. Zhao, J. Yu and D. Ma, High-efficiency red organic light-emitting diodes based on a double-emissive layer with an external quantum efficiency over 30%. *J. Mater. Chem. C.* 6(26), 7042-7045 (2018).

[99] K. Albrecht, K. Matsuoka, D. Yokoyama, Y. Sakai, A. Nakayama, K. Fujita and K. Yamamoto, Thermally activated delayed fluorescence OLEDs with fully solution processed organic layers exhibiting nearly 10% external quantum efficiency. *ChemComm.* 53(16), 2439-2442 (2017).

[100] K. Guo, J. Zhang, T. Xu, X. Gao and B. Wei, High-efficiency near ultraviolet and blue organic light-emitting diodes using star-shaped material as emissive and hosting molecules. *JDT*. 10(8), 642-646 (2014).

[101] L. Chen, Y. Jiang, H. Nie, R. Hu, H. S. Kwok, F. Huang, A. Qin, Z. Zhao and B. Z. Tang, Rational design of aggregation-induced emission luminogen with weak electron donor–acceptor interaction to achieve highly efficient undoped bilayer OLEDs. *ACS Appl. Mater. Interfaces*. 6(19), 17215-17225 (2014).

[102] K. H. Han, K. Kim, Y. Han, Y. D. Kim, H. Lim, D. Huh, H. Shin, H. Lee and J. J. Kim, Highly efficient tandem white OLED using a hollow structure. *Adv. Mater. Interfaces.* 7(9), 1901509 (2020).

[103] Zhang, H., Liu, X., Gong, Y., Yu, T. and Zhao, Y., 2021. Synthesis and characterization of SFX-based coumarin derivatives for OLEDs. *Dyes and Pigments*, *185*, p.108969.

[104] J. Kumsampao, C. Chaiwai, C. Sukpattanacharoen, T. Chawanpunyawat, P. Nalaoh, P. Chasing, N. Kungwan, T. Sudyoadsuk and V. Promarak, Self-absorption-free excited-state intramolecular proton transfer (ESIPT) emitters for high brightness and luminous efficiency organic fluorescent electroluminescent devices. *Mater. Chem. Front., 5*(16), 6212-6225 (2021).

[105] S. I. Yoo, J. A. Yoon, N. H. Kim, J. W. Kim, J. S. Kang, C. B. Moon and W. Y. Kim,2015. Improvement of efficiency roll-off in blue phosphorescence OLED using double dopants emissive layer. *J. Lumin., 160*, 346-350 (2015).

[106] Z. Hao, N. Li, J. Miao, Z. Huang, X. Lv and X. Cao, Chiral sulfoximine-based TADF emitter for circularly polarized luminescence and highly efficient OLEDs. *Chem. Eng. J., 454*, 140070 (2023).

[107] V. Mohan, A. K. Gautam, S. D. Choudhary, M. M. Bee, R. Puviarasi, S. Saranya and N. Agrawal, Enhanced performance organic light emitting diode with CuI: CuPC composite hole transport layer. *IEEE Trans. Nanotechnol.* 19, 699-703 (2020).

[108] M. Singh, J. H. Jou, S. Sahoo, Z. K. He, G. Krucaite, S. Grigalevicius and C. W. Wang, High light-quality OLEDs with a wet-processed single emissive layer. *Sci. Rep.* 8(1), 1-9 (2018).

Accepted Manuscript

[109] N. Zhou, S. Wang, Y. Xiao and X. Li, Double light-emitting layer implementing three-color emission: Using DCJTB lightly doping in Alq3 as red-green emitting layer and APEAn1N as blue-green emitting layer. *J. Lumin.* 196, 40-49 (2018).

[110] Z. Xi, B. Zhao, L. Chen, W. Li, H. Wang, X. Liu and B. Xu, Demonstration of highly efficient orange EL device and warm white OLED, Org. Electron. 57, 21-27 (2018).

[111] Han S H, Jeong J H, Yoo J W and Lee J Y, Ideal blue thermally activated delayed fluorescence emission assisted by a thermally activated delayed fluorescence assistant dopant through a fast reverse intersystem crossing mediated cascade energy transfer process, Mater. Chem. C. 7, 3082-3089 (2019).

[112] Y. Liu, Y. Wu, T. Wang, Q. Wang, X. Han, X. Wu, H. Tong and L. Wang, Bridged triazatruxene-based host materials for solution-processed thermally activated delayed fluorescence organic light emitting diodes with high power efficiency. *Org. Electron. 113*, p.106720 (2023).

[113] J. Qi, W. Ding, Q. Zhang, Y. Wang, H. Chen and S. Y. Chou, Significant Light Extraction and Power Efficiency Enhancement of Organic Light Emitting Diodes by Subwavelength Dielectric-Nanomesh Using Large-area Nanoimprint. *arXiv preprint arXiv:2302.00044 (2023)*.

[114] M. Vasilopoulou, M. Yusoff, M. Daboczi, J. Conforto, A. E. X. Gavim, W. J. da Silva, Nat. commun. 12, 4868 (2021)

[115] D. Cui, S. Wang, S. Li, Y. Liu, H. Du, Q. Du, L. Zhao, W. Wang and X. Dong, Enhanced performance of OLED based on molecular orientation of emission layer by optimized substrate temperature. *J. Mater. Sci.: Mater. Electron.*, *32*(9),12075-12083 (2021).

[116] M. Wang, W. Zhu, Z. Yin, L. Huang and J. Li, Synergistic effects of Li-doped NiOx film prepared by low-temperature combustion as hole-injection layer for high performance OLED devices. *Org. Electron.*, *85*, 105823 (2020).

[117] N. Zhou, S. Wang, Y. Xiao and X. Li, Double light-emitting layer implementing three-color emission: Using DCJTB lightly doping in Alq3 as red-green emitting layer and APEAn1N as blue-green emitting layer. *J. Lumin. 196*, 40-49, 2018.

[118] Q. Yang, Y. Hao, Z. Wang, Y. Li, H. Wang and B. Xu, Double-emission-layer green phosphorescent OLED based on LiF-doped TPBi as electron transport layer for improving efficiency and operational lifetime. *Synth. Met. 162*, 398-401 (2012).

[119] Y. F. Chang, C. H. Yu, S. C. Yang, I. H. Hong, S. C. Jiang, H. F. Meng, H. L. Huang, H. W. Zan, and S. F. Horng, Great improvement of operation-lifetime for all-solution OLEDs with mixed hosts by blade coating. *Org. Electron. 42*, 75-86 (2017).

[120] Y. Chen, D. Yang, X. Qiao, Y. Dai, Q. Sun and D. Ma, Novel strategy to improve the efficiency roll-off at high luminance and operational lifetime of hybrid white OLEDs via employing an assistant layer with triplet–triplet annihilation up-conversion characteristics. *J. Mater. Chem. C*, *8*(19), pp.6577-6586 (2020).

[121] D. Zhou, W. P. To, G. S. M. Tong, G.Cheng, L. Du, D. L. Phillips and C. M. Che, 2020. Tetradentate Gold (III) Complexes as Thermally Activated Delayed Fluorescence (TADF) Emitters: Microwave-Assisted Synthesis and High-Performance OLEDs with Long Operational Lifetime. *Angew. Chem.*, *132*, 6437-6444 (2020).

[122] T. N. Le, E. Y. Park, V. Thangaraji and M. C. Suh, Operational lifetime improvement of solution-processed OLEDs: Effect of exciton formation region and degradation analysis by impedance spectroscopy. *Org. Electron. 99*, p.106346, (2021).

[123] K. Guo, C. Lin, Y. Wu, S. Xiao, X. Qiao, D. Yang, Y. Dai, Q. Sun, J. Chen, D. Hu and L. Ying, Understanding of Degradation Mechanism by Exciton Dynamics and Enhancement of Operational Lifetime by Exciton Management in Blue Fluorescent OLEDs Based on Hybridized Local and Charge-Transfer Molecule. *Adv. Opt. Mater.*, p.2202988 (2023).

[124] C. Y. Wong, S. L. Lai, M. Y. Leung, M. C. Tang, L. K. Li, M. Y. Chan and V. W. W. Yam, Realization of Long Operational Lifetimes in Vacuum-Deposited Organic Light-Emitting Devices Based on para-Substituted Pyridine Carbazolylgold (III) C^ C^ N Complexes. *J. Am. Chem. Soc. (2023)*.

[125] S. Negi, P. Mittal and B. Kumar, Impact of different layers on performance of OLED. *Microsyst. Technol.* 24(12), 4981-4989 (2018).

[126] S. Negi, P. Mittal and B. Kumar, Analytical modelling and parameters extraction of multilayered OLED. *IET circuits devices syst. ser.*13, 1255-1261 (2019).

[127] Q. Zheng, F. You, J. Xu, J. Xiong, X. Xue, P. Cai, X. Zhang, H. Wang, B. Wei and L. Wang, Solution-processed aqueous composite hole injection layer of PEDOT: PSS+ MoOx for efficient ultraviolet organic light-emitting diode. *Org. Electron.* 46, 7-13 (2017).

https://mc04.manuscriptcentral.com/jss-ecs

Accepted Manuscript

[128] K. W. Tsai, M. K. Hung, Y. H. Mao and S. A. Chen, Solution-processed thermally activated delayed fluorescent OLED with high EQE as 31% using high triplet energy crosslinkable hole transport materials. *Advanced Functional Materials*. 29, 1901025 (2019).

[129] M. R. Nagar, R. A. K. Yadav, J. T. Lin and J. H. Jou, Nanocomposite electron-transport layer incorporated highly efficient OLED. *ACS Applied Electronic Materials.* 2,1545-1553 (2020).

[130] D. D. Zhang, J. Feng, L. Chen, H. Wang, Y. F. Liu, Y. Jin, Y. Bai, Y. Q. Zhong, H. B. Sun, Role of Fe_3O_4 as a p-Dopant in Improving the Hole Injection and Transport of Organic Light-Emitting Devices, *IEEE J. Quantum Electron*. 47, 591-596 (2011).

[131] L. Noroozi, H. Soofi, Controlling the Electrical Characteristics of Charge Carrier Transporting Layers in Organic Light-Emitting Devices by the Host–Guest Structure: A Master Equation Approach. *IEEE Trans Electron Devices*. 65, 1910-1917 (2018).

[132] J. Lee, G. Kim, D. K. Shin, Y. Seo, K. Kim, J. Park, Improved Surface Morphology of Crosslinked Hole Transport Films by a Mixture of Polymer for OLEDs. *IEEE Trans Electron Devices*. 65, 3311-3317 (2015).

[133] A. Sharma and T. D. Das, Highly efficient OLED device based on the double emissive layer with an EQE about 39%. *Optik*. *221*, 165350 (2020).

[134] H. Fujimoto, M. Yahiro, S. Yukiwaki, K. Kusuhara, N. Nakamura, T. Suekane, H. Wei, K. Imanishi, K. Inada and C. Adachi, Influence of material impurities in the hole-blocking layer on the lifetime of organic light-emitting diodes. *Applied Physics Letters*. 109, 243302 (2016).

[135] W. Y. Tan, J. H. Zou, D. Y. Gao, J. Z. Liu, N. N. Chen, X. H. Zhu, J. Peng and Y. Cao, Promising Operational Stability of Potentially High-Power Efficiency Organic Light-Emitting Diodes Utilizing a Simple and Versatile Electron-Transport/Hole-Blocking Layer. *Adv. Electron. Mater. 2*, 1600101 (2016).

[136] A. P. Kulkarni, C. J. Tonzola, A. Babel, S. A. Jenekhe, Electron transport material for organic light-emitting diodes, *Chem. Mater*. 16, 4556-4573 (2004).

[137] X. Zhang, S. A. Zhang, Jenekhe, Electroluminescence of multicomponent conjugated polymers. 1. Roles of polymer/polymer interfaces in emission enhancement and voltage tunable multicolor emission in semiconducting polymer/polymer heterojunctions, *Macromolecules*, 33, 2069-2082 (2000).

[138] Z. Lu, X. Li, Y. Wang, J. Xiao, P. Xu, Field- and thickness dependent performance of tandem organic light-emitting diodes with buffer-modified fullerene/copper phthalocyanine heterojunction as interconnector, *J. Curr. Appl. Phys.* 14, 1465–1469 (2014).

[139] L. Li, M. Guan, G. Cao, Y. Li, Y. Zeng, Tandem organic light-emitting diodes with an effective charge-generation connection structure, *J. Short State Comm.* 150, 1683–1685 (2010).

[140] A. Jetly and R. Mehra, Design of Tandem Organic Light Emitting Diode using efficient charge generation layer. *Opt. Mater.*, *88*, 304-312 (2019).

[141] J. Yuan, Y. Dai, Q. Sun, X. Qiao, D. Yang, J. Chen and D. Ma, High efficiency organic light-emitting diodes based on HAT-CN/TAPC heterojunction charge generation layer as charge injectors. *Semicond. Sci. Technol. 34*,105010 (2019).

[142] G. Huseynova, J. H. Lee, A. Gasonoo, H. Lee, Y. H. Kim and J. Lee, Efficient tandem organic light-emitting diode with fluorinated hexaazatrinaphthylene charge generation layer. *J. Inf. Disp.*, *23*, 259-266 (2022).

[143] A. J. Moulé, M. C. Jung, C. W. Rochester, W. Tress, D. LaGrange, I. E. Jacobs, J. Li, S. A. Mauger, M. D. Rail, O. Lin and D. J. Bilsky, Mixed interlayers at the interface between PEDOT: PSS and conjugated polymers provide charge transport control. *J. Mater. Chemi. C*, *3*, 2664-2676 (2015).

[144] Z. Kou, Y. Xu, S. Cheng and X. Wang, The effect of the quantum well structure in green phosphorescent oled with a mixed host emission interlayer. *J. Disp. Technol.*, *12*, 1668-1671 (2016).

[145] P. Maurya and B. Kumar, 2022. Impact of Mixed Interlayer Thickness on Performance of Organic Light-Emitting Diodes. In *VLSI, Microwave and Wireless Technologies: Select Proceedings of ICVMWT 2021* Singapore: Springer Nature Singapore, 655-664, (2022).

[146] P. Mittal, S. Yadav and S. Negi, S.: Advancements for organic thin film transistors: Structures, materials, performance parameters, influencing factors, models, fabrication, reliability and applications. *Mater Sci Semicond Process*. 133, 105975 (2021).

[147] A. Kumar, A. K. Goyal and N. Gupta, thin-film transistors (TFTs) for highly sensitive biosensing applications: a review. *ECS Journal of Solid State Science and Technology*, *9*(11), 115022 (2020).

[148] S. Khound, J. K. Sarmah and R. Sarma, Hybrid La2O3-cPVP dielectric for organic thin film transistor applications. *ECS Journal of Solid State Science and Technology*, 11(1), 013007 (2022).

Accepted Manuscript

[149] S. Pal, B. Kumar and P. Mittal, Impact of different gate dielectrics on OTFT-driven active matrix OLED. *Физика и техника полупроводников*, *55*, 474-474 (2021).

[150] P. Mittal, Y. S. Negi and R. K. Singh, Analytical Modeling and Parameter Extraction of Organic Thin Film Transistor: Effect of Contact Resistance, Doping Concentration and Field Dependent Mobility. In Adv. Mater. Res, 622, 585-589, Trans Tech Publications Ltd (2013).

[151] H. Klauk, Organic thin-film transistors. *Chem. Soc. Rev. 39*, 2643-2666 (2010).

[152] P. Mittal, B. Kumar, Y. S. Negi, B. K. Kaushik and R. K. Singh, Channel length variation effect on performance parameters of organic field effect transistors. *Microelectron. J.* 43, 985-994 (2012).

[153] J. Zou, H. Wang, X. Zhang, X. Wang, Z. Shi, Y. Jiang, Z. Cui and D. Yan, Polyimide-based gate dielectrics for high-performance organic thin film transistors. *J. Mater. Chem. C*. 7, 7454-7459 (2019).

[154] X. Qiao, Q. Wei, H. Wu and H. Li, Isoindigo (IID)-Based Semiconductor with F⋯ S Interaction Locked Conformation for High-Performance Ambipolar Bottom-Gate Top-Contact Field-Effect Transistors. *Macromol. Chem. Phys*. 221, 2000189 (2020).

[155] T. Steckmann, I. Angunawela, S. Kashani, Y. Zhu, M. M. Nahid, H. Ade and A. Gadisa, Ultrathin P (NDI2OD-T2) Films with High Electron Mobility in Both Bottom-Gate and Top-Gate Transistors. *Adv. Electron. Mater.* 2101324 (2022).

[156] X. Zhao, S. Wang, Y. Ni, Y. Tong, Q. Tang and Y. Liu, High-Performance Full-Photolithographic Top-Contact Conformable Organic Transistors for Soft Electronics. *Adv. Sci.* 8, 2004050 (2021).

[157] S. Jena and D. Ray, A systematic approach to reduce non idealities in pentacene bottom-contact bottom-gate transistors. *Thin Solid Films*. 721, 138542 (2021).

[158] P. Kumari and A. D. D. Dwivedi, Numerical simulation and characterization of pentacene based organic thin film transistors with top and bottom gate configurations. *Global Journal of Research In Engineering* (2019).

[159] S. Ma, G. Zhang, F. Wang, Y. Dai, H. Lu, L. Qiu, Y. Ding and K. Cho, Tuning the Energy Levels of Aza-Heterocycle-Based Polymers for Long-Term n-Channel Bottom-Gate/Top-Contact Polymer Transistors. *Macromolecules*. 51, 5704-5712 (2018).

[160] A. Verma and P. Mittal, Characterization and depth analysis of organic thin film transistor. *JGEU*. 22-31 (2016).

[161] S. K. Kim, C. H. Shim, T. Edura, C. Adachi, R. Hattori, Improved organic thin film transistor characteristics using an elevated-electrode structure. *Jap. J. Appl. Phys.* 53, 111601-1 (2014).

[162] B. Kumar, B. K. Kaushik, Y. S. Negi, Perspectives and challenges for organic thin film transistors: materials, devices, processes and applications. *J. Mater. Sci. Mater. Electron.* 25, 1 (2014).

[163] Y. Xu, T. Minari, K. Tsukagoshi, J. Chroboczek, G. Ghibaudo, Direct evaluation of low-field mobility and access resistance in pentacene field-effect transistors. *J. Appl. Phys.* 107, 114507-1 (2010).

[164] S. Neon, D. Kanehira, N. Yoshomoto, F. Fages, C. V. Ackermann, Shelf-life time test of p-and n-channel organic thin film transistors using copper phthalocyanines. *Thin solid films.* 518, 5593 (2010).

[165] R. Shiwaku, M. Tamura, H. Matsui, Y. Takeda, T. Murase, S. Tokito, Charge carrier distribution in low-voltage dual-gate organic thin-film transistors. *Appl. Sci.* 8, 1341 (2018).

[166] S. Singh, Y. Takeda, H. Matsui and S. Tokito, Flexible inkjet-printed dual-gate organic thin film transistors and PMOS inverters: Noise margin control by top gate. *Org. Electron. 85*, 105847 (2020).

[167] S. Gupta, and M. K. Singh, Key aspects affecting the performances of high-K dielectrics based single-gate and dual-gate OTFTs. *Mater. Today: Proc. 50*, 231-237 (2022).

[168] S. Singh, Y. Takeda, H. Matsui and S. Tokito, Flexible PMOS inverter and NOR gate using inkjet-printed dual-gate organic thin film transistors. *IEEE Electron Device Lett.* 41, 409-412 (2020).

[169] S. Ghosh, L. Rajan, *In 2020 International Conference on Innovative Trends in Information Technology (ICITIIT) IEEE.* 1 (2020).

[170] A. D. D. Dwivedi, P. Kumari, TCAD simulation and performance analysis of single and dual gate OTFTs. *Surf. Rev. Lett.* 27, 1950145 (2020).

[171] S. Negi, A. Rana, A. K. Baliga, P. Mittal and B. Kumar, Performance analysis of dual gate organic thin film transistor and organic SR latch application. In *International Conference on Computing, Communication & Automation*. 1427-1432, (2015).

[172] T. J. Ha, P. Sonar, A. Dodabalapur, High mobility top gate and dual-gate polymer thin film transistors based on diketopyrrolopyrrole-naphthalene copolymer. *Appl. Phys. Lett.* 98, 253305-1 (2011).

https://mc04.manuscriptcentral.com/jss-ecs

Accepted Manuscript

[173] A. K. Tripathi, E. C. P. Smith, M. Loth, J. E. Anthony, G. H. Gelinck, Charge transport in solution processable polycrystalline dual-gate organic field effect transistors. *Appl. Phy. Lett.* 98 (2011).

[174] R. Rathi, R. Ahmad, S. Negi and V. Panwar, Performance Analysis of Single and Dual Gate Vertical Channel Organic Thin Film Transistor. *In 2018 5th IEEE Uttar Pradesh Section International Conference on Electrical, Electronics and Computer Engineering (UPCON) IEEE*. 1-5 (2018).

[175] Q. Chen, Y. Yan, X. Wu, S. Lan, D. Hu, Y. Fang, D. Lv, J. Zhong, H. Chen and T. Guo, High-performance quantum-dot light-emitting transistors based on vertical organic thin-film transistors. *ACS appl. mater. Interfaces*. 11, 5888-35895 (2019).

[176] D. Kneppe, F. Talnack, B. K. Boroujeni, C. T. da Rocha, M. Höppner, A. Tahn, S. C. Mannsfeld, F. Ellinger, K. Leo and H. Kleemann, Solution-processed pseudo-vertical organic transistors based on TIPS-pentacene. *Mater.* 21, 100697 (2021).

[177] N. A. Roslan, S. M. Abdullah, M. Z. M. Halizan, T. M. Bawazeer, N. Alsenany, M. S. Alsoufi, W. H. A. Majid and A. Supangat, VTP as an active layer in a vertical organic field effect transistor. *J. Electron. Mater.* 47, 2184-2191 (2018).

[178] H. Kleemann, A. A. Günther, K. Leo and B. Lüssem, High-Performance Vertical Organic Transistors. *Small*. 9, 3670-3677 (2013).

[179] H. Naruse, S. Naka and H. Okada, Dual self-aligned vertical multichannel organic transistors. *Appl. phys. express*. 1, 011801 (2007).

[180] H. W. Zan and K. H. Yen, Vertical-channel organic thin-film transistors with meshed electrode and low leakage current. *Jpn. J. Appl. Phys*. 46, 3315 (2007).

[181] C. P. Auth and J. D. Plummer, Scaling theory for cylindrical, fully-depleted, surrounding-gate MOSFET's. *IEEE Electron Device Lett.* 18, 74-76 (1997).

[182] S. K. Ojha and B. Kumar, Coulomb Blockade Effect through Single Electron Tunneling Method in Cylindrical Gate Organic Light Emitting Transistor Configuration. *Silicon*. 14, 4087-4096 (2022).

[183] E. Louris, D. Stefanakis, G. Priniotakis, L. Van Langenhove and D. Tassis, Optimization of cylindrical textile organic field effect transistors using TCAD simulation tool. *In IOP Conference Series: Materials Science and Engineering.* 254, 162006 (2017).

[184] A. Singh and V. Ramola, Modeling and Simulation of Cylindrical Gate OTFT and its Application in Digital Circuits. *Int. J. Eng. Res.* 4, 2321-9939 (2016)

[185] S. Locci, M. Maccioni, E. Orgiu and A. Bonfiglio, An analytical model for cylindrical thin-film transistors. *IEEE transactions on electron devices*. 54, 2362-2368 (2007).

[186] S. H. Han, Y. R. Son, S. H. Lee, K. J. Lee, G. S. Cho, W. S. Kim, T. J. Park, W. S. Jeon, D. J. Choo and J. Jang, High Resolution OTFT-OLED on Plastic Substrate Using Self-Organized Process. *In SID Symposium Digest of Technical Papers*. 38, 1757-1760 (2007).

[187] M. Mizukami, N. Hirohata, T. Iseki, K. Ohtawara, T. Tada, S. Yagyu, T. Abe, T. Suzuki, Y. Fujisaki, Y. Inoue and S. Tokito, Flexible AM OLED panel driven by bottom-contact OTFTs. *IEEE electron device letters.* 27, 249-251 (2006).

[188] Y. Nakajima, T. Takei, Y. Fujisaki, H. Fukagawa, M. Suzuki, G. Motomura, H. Sato, T. Yamamoto and S. Tokito, Improvement in image quality of a 5.8-in. OTFT-driven flexible AMOLED display. *J. Soc. Inf. Disp*. 19, 94-99 (2011).

[189] M. Katsuhara, I. Yagi, A. Yumoto, M, Noda N. Hirai and R. Yasuda R.: *In Organic Field-Effect Transistors VIII, Int. j. opt. photonics.* 7417, 74170 (2009).

[190] J. S. Kim and C. K. Song, AMOLED panel driven by OTFTs on polyethylene fabric substrate. *Org. Electron.* 30, 45-51 (2016).

[191] I. Yagi, N. Hirai, M. Noda, A. Imaoka, Y. Miyamoto, N. Yoneya, K. Nomoto, J. Kasahara, A. Yumoto and T. Urabe, 63.2: Distinguished Paper: A Full-Color, Top-Emission AM-OLED Display Driven by OTFTs. In *SID Symposium Digest of Technical Papers*. 38, 1753-1756 (2007).

[192] M. Mizukami, S. I. Cho, K. Watanabe, M. Abiko, Y. Suzuri, S. Tokito and J. Kido, Flexible organic light-emitting diode displays driven by inkjet-printed high-mobility organic thin-film transistors. *IEEE Electron Device Lett. 39*, 39-42 (2017).

[193] S. Pal, B. Kumar, P. Mittal, Impact of different gate dielectrics on OTFT-driven active matrix OLED. *Физика и техника полупроводников*. *55*, 474-474 (2021).

Accepted Manuscript

[194] S. Kim, W. Choi, W. Rim, Y. Chun, H. Shim, H. Kwon, J. Kim, I. Kee, S. Kim, S. Lee and J. Park, A highly sensitive capacitive touch sensor integrated on a thin-film-encapsulated active-matrix OLED for ultrathin displays. *IEEE Transactions on electron devices*. 58, 3609-3615 (2011)

[195] K. Watanabe, Y. Iwaki, Y. Uchida, D. Nakamura, H. Ikeda, H. Miyake, An 8.67-in. Foldable OLED Display with an In-cell Touch Sensor. In *SID Symposium Digest of Technical Papers. Dig. Tech. Pap. - SID Int. Symp.* 46, 246 (2011)

[196] Y. Y. Tang, C. C. Lai and C. C. Lin, 17-1: Self-Capacitive Touch Sensor Design for OLED On-Cell Touch. In *SID Symposium Digest of Technical Papers*. 53, 178-181 (2022).

[197] K. I. Miyamoto, K. Kaneko, A. Matsuo, T. Wagner, S. I. Kanoh, M. J. Schöning, Miniaturized chemical imaging sensor system using an OLED display panel. *Sens. Actuators B Chem.* 170, 82-87(2002)

[198] C. F. Werner, T. Wagner, K. I. Miyamoto, T. Yoshinobu and M. J. Schöning, High speed and high resolution chemical imaging based on a new type of OLED-LAPS set-up. *Sensors and Actuators B: Chemical*. 175, 118-122 (2012).

[199] J. Smith, A. Shah. Y. K. Lee, B. O'Brien, D. Kullman A. Sridharan, Optogenetic neurostimulation of auricular vagus using flexible OLED display technology to treat chronic inflammatory disease and mental health disorders. *Electron. Lett.* 52, 900-902 (2016).

[200] B. A. Katchman, J. T. Smith, U. Obahiagbon, S. esiraju, Y. K. Lee, B. O'Brien, Application of flat panel OLED display technology for the point-of-care detection of circulating cancer biomarkers. *Sci. Rep.* 6, 1-11 (2016)

[201] S. Negi P. Mittal, B. Kumar and P. K. Juneja, Organic LED based light sensor for detection of ovarian cancer. Microelectronic Engineering. *Microelectron. Eng.* 218, 111154 (2019)

[202] Y. Jeon, H. R. Choi, K. C. Park and K. C. Choi, Flexible organic light-emitting-diode-based photonic skin for attachable phototherapeutics. *J. Soc. Inf. Disp*. 28, 324-332 (2020).

[203] Y. Yun, Y. Lee, J. W. Chung, G. H. Lee, H. Kang, J. Y. Kim, S. G. Kang, J. Y. Jung, Y. Kuzumoto, S. Gam and S. G. Hahm, 46-3: Invited Paper: Skin-like Organic Optoelectronic System for Real-time Heart Rate Monitoring. *In SID Symposium Digest of Technical Papers.* 53, 585-588 (2022).

[204] T. H. Han, H. Kim, S. J. Kwon, T. W. Lee, Graphene-based flexible electronic devices. *Mater. Sci. Eng. R Rep.* 118, 1-43 (2017).

[205] S. Negi, P. Mittal and B. Kumar, Characteristic performance of OLED based on hole injection, transport and blocking layers. *Recent Pat.* 14, 373-383 (2020).

[206] J. Priya, N. K. Gondia, A. K. Kunti and S. K. Sharma, Pure white light emitting tetrakis β-diketonate dysprosium complexes for OLED applications. *ECS Journal of Solid State Science and Technology*, *5*(10), p.R166 (2016).

[207] P. E. Burrows, G. L. Graff, M. E. Gross, P. M. Martin, M. K. Shi, M. Hall, E. Mast, C. Bonham, W. Bennett and M. B. Sullivan, Ultrabarrier flexible substrates for flat panel displays. *Displays*, 22, 65-69 (2001).

[208] R. W. Sabnis, Color filter technology for liquid crystal displays. *Displays* 20, 3, 119-129 (1999).

[209] S. Negi, P. Mittal and B. Kumar, Numerical modeling and parameters extraction of novel triple hole block layer-based organic light-emitting diode for display. *J Soc Inf Disp*. 28, 956-964 (2020).

[210] S. Negi, P. Mittal and B. Kumar, Modeling and analysis of high-performance triple hole block layer organic LED based light sensor for detection of ovarian cancer. IEEE TCAS-I, 68, 3254-3264 (2021).

[211] S. Negi, P. Mittal, B. Kumara and P. K. Juneja, Organic LED based light sensor for detection of ovarian cancer. *Microelectron. Eng.* 218, 111154 (2019).

[212] F. Krujatz, O. Hild, K. Fehse, M. Jahnel, A. Werner, T. Bley, Exploiting the potential of OLED-based photo-organic sensors for biotechnological applications. *Chem. Sci. J.* 7, 134 (2016).

[213] G. Zissis, P. Bertoldi, Status report on organic light emitting diodes (OLED), JRC Science and Policy Report. *European Commission Joint Research Centre*. 33 (2014).

[214] H. J. Shin, S. Takasugi, K. M. Park, S. H. Choi, Y. S. Jeong, B. C. Song, H. S. Kim, C. H. Oh and B. C. Ahn, 7.1: Invited Paper: Novel OLED display technologies for large-size UHD OLED TVs. In *SID Sym .Dig. Tech. Pap.* 46, No. 1, 53-56, (2015).

[215] J. Y. Noh, D. M. Han, W. C. Jeong, J. W. Kim and S. Y. Cha, Development of 55" 4K UHD OLED TV employing the internal gate IC with high reliability and short channel IGZO TFTs. *J. Soc. Inform. Disp.*, *26*, 36-41, (2018).

Accepted Manuscript

[216] Z. Hu, Y. Yin, M. U. Ali, W. Peng, S. Zhang, D. Li, T. Zou, Y. Li, S. Jiao, S. J. Chen and C. Y. Lee, Inkjet printed uniform quantum dots as color conversion layers for full-color OLED displays. *Nanoscale*, *12*, 2103-2110 (2020).

[217] E. Kirchner, I. Van der Lans, E. Perales and F. Martínez-Verdú, Improving color reproduction accuracy of an OLED-based mobile display. *Color Res. Appl. 43*, 34-46 (2018).

[218] C. H. Yeh, K. S. H. Lo and W. Lin, Visual-attention-based pixel dimming technique for OLED displays of mobile devices. *IEEE Trans. Ind. Electron.*, *66*, 7159-7167 (2018).

[219] Choi, Y., Ha, R. and Cha, H., 2018. Fully automated OLED display power modeling for mobile devices. *Pervasive and Mobile Computing*, *50*, pp.41-55.

[220] S. Asnani, M. G. Canu, L. Farinetti and B. Montrucchio, On producing energy-efficient and contrast-enhanced images for OLED-based mobile devices. *Pervasive Mob. Comput.*, *75*, 101384 (2021).

[221] F. Barre, A. Chiquard, S. Faure, L. Landais and P. Patry, *In Building European OLED Infrastructure, International Society for Optics and Photonics.* 5961 596109 (2005).

[222] P. L. Marasco and P. R. Havig, *In Head-and Helmet-Mounted Displays XVII; and Display Technologies and Applications for Defense, Security, and Avionics VI, International Society for Optics and Photonics.* 8383 83830 (2012).

[223] M. Trakalo and S. Lorimer, *In Display Technologies and Applications for Defense, Security, and Avionics II, International Society for Optics and Photonics.* 6956 69560 (2008).

[224] D. Zhong, J. Zhou, Y. Wang, Hollow-fiber membranes of block copolymers by melt spinning and selective swelling, *J. Membr. Sci. 632*, 119374, (2021).

[225] D.X. Liu, J.Y. Zhong, B. Tang, X.H. Cao, W. Xu, S.X. Zhou, M.Y. Shi, R.H. Yao, H.L. Ning, J.B. Peng, Research progress of flexible and printed OLEDs, Liq. Crys. Disp. *36*, 12 (2020).

[226] S. Choi, S. Kwon, H. Kim, W. Kim, J.H. Kwon, M.S. Lim, H.S. Lee, K.C. Choi, Highly Flexible and Efficient Fabric-Based Organic Light-Emitting Devices for Clothing-Shaped Wearable Displays, Scientific Reports 7(1) (2017) 6424.

Accepted Manuscript
For Review Only

Proceedings of the International Conference on Sustainable Computing and Data Communication Systems (ICSCDS-2023)
IEEE Xplore Part Number: CFP23AZ5-ART; ISBN: 978-1-6654-9199-0

2023 International Conference on Sustainable Computing and Data Communication Systems (ICSCDS) | 978-1-6654-9199-0/23/$31.00 ©2023 IEEE | DOI: 10.1109/ICSCDS56580.2023.10104608

Sign Language to Text Classification using One-Shot Learning

Sourav Pal
Dept. of Computer Science and Engineering
Delhi Technological University
New Delhi, India
souravpal.4916@gmail.com

Sparsh Sinha
Dept. of Computer Science and Engineering
Delhi Technological University
New Delhi, India
sparshsinha.spavis@gmail.com

Sourabh Ruhella
Dept. of Computer Science and Engineering
Delhi Technological University
New Delhi, India
sourabh.ruhella3108@gmail.com

Anurag Goel
Dept. of Computer Science and Engineering
Delhi Technological University
New Delhi, India
0000-0003-2660-7540

***Abstract*— Sign language is utilized by deaf individuals to communicate with each other. Sign languages, simply put are signs and gestures made by hand and are currently being used by approximately 80 million people around the world. The limited knowledge of sign languages in the hearing-abled community makes it difficult for them to interact with the deaf or mute community leading to the marginalization of the latter. Sign-to-text classification is a field of research that aims to convert sign language into written text, providing a communication bridge between the deaf-mute communities and the hearing population. However, there are some limitations in the current state of the field, such as the absence of datasets that are publicly available for sign language in many languages, and most of the existing models are trained in American Sign Language (ASL) which makes it difficult for researchers to train and evaluate their methods on other sign languages. Additionally, the ASL-trained models may generalize poorly to other sign languages, as they are heavily tuned to the specific dataset of ASL signs. The current models are also not best suited to incorporate any new additions to the sign language as it requires to train the model all over again. The proposed model makes use of one-shot learning, a new-age machine learning technique that allows the model to learn and recognize using limited training data, to identify and classify hand signs and convert them into corresponding text. The ability to learn from a very small dataset makes the model easily trainable and expandable in any sign language of choice. The proposed model has been trained on ASL and Indian Sign Language (ISL) datasets and achieved accuracy of 90.03% and 91.25% respectively.**

Keywords — One-Shot Learning, Image Classification, Sign Language Recognition, Siamese Network.

I. INTRODUCTION

Sign language is an intricate and nuanced language that makes use of a combination of hand gestures, facial expressions, and body language to communicate. The deaf or mute community makes use of sign language to communicate within themselves and with the hearing community. It is a fully developed language in the sense that it has its own unique grammar, vocabulary, and syntax. Based on the recorded history in western societies, it has been discovered that sign language is used since the seventeenth century. However, the idea of using hand signs and gestures as a form of communication can be even seen in fifth century BC Greece.

According to World Health Organization (WHO), over 430 million people (almost 5% of the entire world's population) require some sort of technological or physiological support to address their disabling hearing loss. According to the same research, the projected number is likely to increase to around 700 million individuals by the year 2050. Sign language is not restricted to any geographical or language barrier and can be found all over the world, with each country having its unique sign language. The lack of knowledge of sign language among the hearing community often results in the marginalization of the deaf and mute communities, who face a steep hill of difficulty with access to information and communication

Sign-to-text classification is a field of research that can help to tackle this problem by developing technology that could assist the communication of the deaf community with the hearing population. There has been a significant amount of work done in the field of sign-to-text classification in recent years. In recent studies, deep learning methods including Convolutional Neural Networks (CNNs) and Recurrent Neural Networks (RNNs) have been employed to detect and interpret sign language gestures, converting them into written text.

Even though there are some constraints, the study of translating sign language into written language remains an essential area of research as it has the capacity to greatly improve the accessibility of information and communication for the deaf and mute communities. With continued research and development, sign-to-text classification has the potential to make communication more inclusive and accessible for all, by addressing the limitations of the current state of the field and extending the methods to other sign languages.

II. RELATED WORK

In [1], the authors have used a publicly available ASL dataset from Kaggle and implemented a novel 3D Convolutional Neural Network (CNN) to extract distinctive spatial-temporal features from multiple photographic datasets. They have used a VGG-16 model architecture for their CNN. In [2], the authors have proposed a novel approach for feature extraction and selection for the recognition of immobile numeric signs in ISL using structural features and advanced

Authorized licensed use limited to: DELHI TECHNICAL UNIV. Downloaded on May 01,2023 at 05:42:29 UTC from IEEE Xplore. Restrictions apply.

classifiers. This system aimed to improve communication between humans and computers by automatically converting ISL sign language into text, without requiring wearable devices to capture electrical signals. A conventional digital camera was utilized to capture the sign language gestures in the system and is designed to recognize isolated digit signs that contain only numeric characters per image. After experimenting with two different classifiers, the authors determined that the k-nearest neighbor classifier achieved superior classification accuracy compared to the Naive Bayes classifier. [3] proposed a new and improved method called Hyperparameter-based optimized Generative Adversarial Networks (H-GANs) is introduced for classifying sign communication. The H-GANs approach uses a Deep Long Short Term Memory (LSTM) as a generator and a combination of LSTM and 3D Convolutional Neural Network (3D-CNN) as a discriminator. The findings indicated that the H-GANs approach achieved better results than the most advanced classification methods, while also having a simpler structure.

In [4], Izutov et. al. developed a model for determining American Sign Language (ASL) gestures in live visual feeds, which was trained using the distance learning framework. They also proposed an approach called spatial and temporal residual attention, which uses an auxiliary unsupervised objective to enhance the model's ability to handle alterations in appearance with greater resilience. According to their findings, the proposed model showed promising results for recognizing ASL signs in real-world situations. Bantupalli et. al. [5] proposed a Sign Language Recognition model that utilized a Convolutional Neural Network (CNN), specifically the Inception architecture, to derive spatial characteristics from the sequences of moving images. After that, the model employed a Long Short-Term Memory (LSTM) to obtain time-related data from the series of moving images. This model was tested on Sign Language Recognition tasks.

In [6], the authors have proposed a CNN based approach for converting sign language to speech and text. They created visuals using video feeds from OpenCV, and processed them as grayscale, and then resized them to a fixed dimension for all the images. Their approach resulted in a ASL interpreter that translates finger-spelled words. In [7], the authors have worked on the MNIST dataset to classify the ASL images using CNN. The recognition training process is divided into phases where the dataset is processed followed by pre-processing and computation of important features which is fed to the CNN network for the learning phase. Authors of [8] claim that the addition of an additional step to the pre-processing step increases the accuracy and the ease with which the CNN model performs the classification step. This is called tokenization. To counter the trouble to get completely labelled data, they used a semi-supervised approach such as transfer and adversarial learning to get around the burden of labelling.

In reference [9], the authors investigated Zero-Shot Sign Language Recognition (ZSSLR) and introduced specific methods to evaluate the impact of binary attributes on the positive and negative outcomes of zero-shot prediction. One-shot learning has been around for some time but it's one of the first-ever practical applications used for face verification purposes [10]. This has used the triplet loss function to learn the embedding mapping from the facial image to a feature embedding Where the measures of facial similarity are reflected in the distances between the embeddings. One-shot learning based on the Siamese neural network has been used in handwriting recognition[11] where the Omniglot dataset has been used to find how similar the two input images to the Siamese network are to each other. Based on the distance between the embeddings the model outputs a prediction of whether the two images are similar or not.

III. METHODOLOGY

As the related work suggests, most of the models work on this problem by enabling the model to label a given image to its predicted class using a CNN such as [13]. This works best only if the number of signs is constant and if ample images per class are available to train the model. However, sign language is ever-growing and has to accommodate new signs to help the underprivileged. This enforces the need to train the model all over again every time there is an addition to the language. The proposed approach uses One-Shot learning to tackle this problem. One-shot learning requires only a few images per class to train the model and instead of predicting the class of an image, the model outputs a feature embedding, a linear dimensional vector, which incorporates the unique features of the input sign image. The objective of the model is to produce optimal feature embeddings in such a way that the L2 distance is minimized between images of the same category and maximized between images of different category. The output feature embeddings are improved during the training phase by minimizing the triplet loss function.

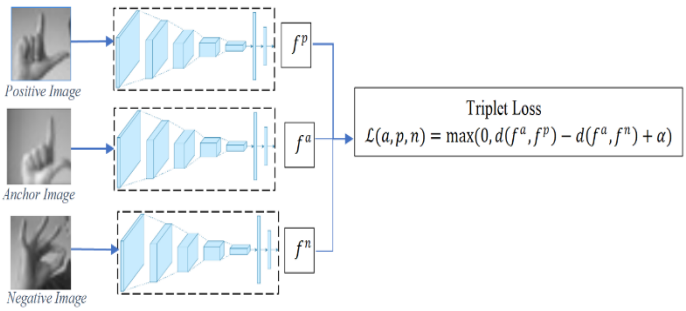


Figure 1: Proposed Model: Training Phase

The proposed approach implements a Siamese network [10, 12] to train the model. These are a class of neural networks that contain two or more identical neural sub-networks where identical means that both the sub-networks have the same parameters and layers configuration. The weight update is also identically propagated to each sub-network. Each sub-network generates a feature embedding as its output. The model is trained by minimizing the loss function, whose working is discussed in the implementation section. The training phase of the proposed approach is shown in Fig. 1.

For testing, an image from each category has been used, that acts as the representative for that category. Then each image in the testing dataset is passed through the network to receive an embedding as an output. Then the L2 distance is calculated between the output image and each of the representative image and the category corresponding to the representative image with the smallest distance is assigned to the testing image. The testing architecture of the proposed approach is shown in Fig. 2.

Authorized licensed use limited to: DELHI TECHNICAL UNIV. Downloaded on May 01,2023 at 05:42:29 UTC from IEEE Xplore. Restrictions apply.

IV. IMPLEMENTATION

A. Dataset

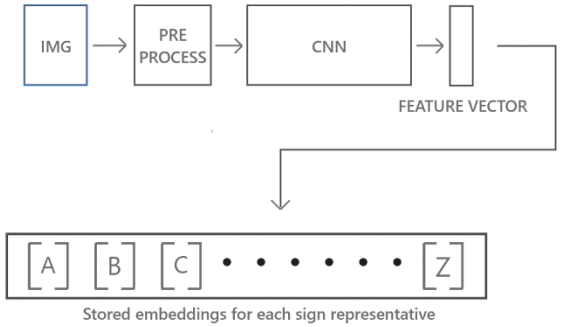


Figure 2: Testing Architecture

There are sign language datasets available in various languages. The decision to select English as the focus in the proposed approach is because of its widespread usage as a language globally. It is worth noting that within the English language, several countries have developed their own unique sign languages, including American Sign Language (ASL), British Sign Language (BSL), and Indian Sign Language (ISL) [14]. The American sign language dataset provided by MNIST and the Indian sign language dataset provided by Kaggle is used to conduct the experiments.

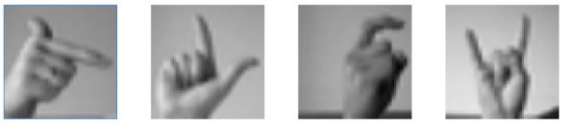


Figure 3: ASL Dataset: Sample images

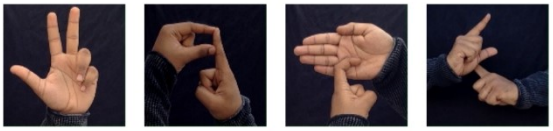


Figure 4: ISL Dataset: Sample images

In MNIST ASL, the image pixels are provided in a CSV file. Using the pixel information, gray-scaled images of dimensions 28*28 has been formed. The alphabet 'j' and 'z' are not included in the dataset as they are gesture-based and not static. The Indian sign language dataset consists of all 26 English alphabets and digits from 0 to 9 which are of higher quality compared to American sign language.

As the related work suggests, most of the models work on this problem by enabling the model to label a given image to its predicted class using a CNN such as [13]. This works best only if the number of signs is constant and if ample images per class are available to train the model. However, sign language is ever-growing and has to accommodate new signs to help the underprivileged. This enforces the need to train the model all over again every time there is an addition to the language.

The ASL dataset comes with separate files for training and testing images in the form of CSV files. For ISL, the dataset into has been divided into the training and testing images but unlike the 80:20 or 70:30 ratio which is usually followed in a classic CNN, this study uses 10 images per class to train the network. Further on, 100 images that were not used in training the model are randomly selected from each sign from the dataset to test the model.

B. Data Pre-Processing

The pre-processing steps are outlined in Fig. 5. The input image is first transformed to a 28*28 pixel format. Then the image is converted from RGB channel to grayscale. OpenCV, which is an open-source computer vision library has pre-defined methods for color channel conversion and image resizing and is widely used for image manipulation. This helps to minimize the parameters count that the model has to train and hand sign recognition only needs the shape of the hand, hence the color information can be treated as noise [15]. To further remove noise from the image as well as to smoothen out the image, Gaussian blurring is used.

The image obtained has pixel values in the range of 0-255. This range is normalized to 0-1 since a higher pixel value can be misinterpreted by the model as something which is of higher importance when in reality it only depicts the color information. The numerical value of a pixel is divided by 255 to normalize its value, which results in a standardized representation of the pixel's original value

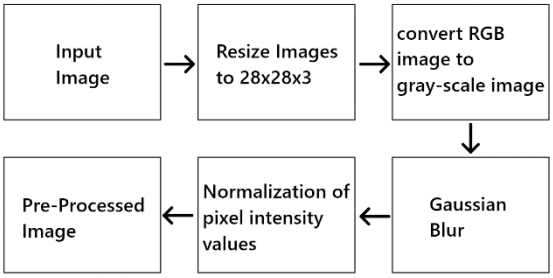


Figure 5: Pre-Processing steps

within a range of 0 to 1.

C. Model Implementation

The proposed model is a Siamese network where it has two subnetworks, each of which is a custom CNN. CNNs are employed due to their high efficiency in addressing image classification tasks, such as sign language classification, as evidenced by the related work section. This is because they can effectively extract relevant features from images and use them to make accurate predictions, making them a valuable tool for image recognition applications. Each of the sub-network takes an input image of shape 28*28*1 and outputs a feature embedding of size 64. The custom CNN layers are depicted in Table 1.

Table 1: Custom CNN for the sub-branch of Siamese network

LAYER(TYPE)	Input Shape	Output Shape
Conv2D	28 x 28 x 1	24 x 24 x 128
Max Pooling	24 x 24 x 128	14 x 14 x 128
Conv2D	14 x 14 x 128	14 x 14 x 64
Max Pooling	14 x 14 x 64	7 x 7 x 64
Conv2D	7 x 7 x 64	7 x 7 x 128
Max Pooling	7 x 7 x 128	3 x 3 x 128
Flatten	3 x 3 x 128	1152 x 1
Dense	1152 x 1	512 x 1

Authorized licensed use limited to: DELHI TECHNICAL UNIV. Downloaded on May 01,2023 at 05:42:29 UTC from IEEE Xplore. Restrictions apply.

Dense	512 x 1	64 x 1

The algorithm used for training the proposed model is described in Fig. 6. During the training phase, the algorithm processed batches of three images at a time: an initial image (A), a matching image (P) from the same category as the initial image, and a non-matching image (N) from a different

ALGORITHM 1 – MODEL TRAINING

Input: Image of shape = 28×28×3

Output: 64-dimensional vector

Steps:

1. Input images in matrix of shape $16 \times 28 \times 28 \times 1$
2. Pre-process the images
3. While epochs<=30,000 Do

a. Front propagate input through the Siamese network

b. Compute loss on predictions according to triplet cross-entropy →

$$\sum_{i=0}^{N}\left[\|f_i^a - f_i^p\|_2^2 - \|f_i^a - f_i^n\|_2^2 + \alpha\right]$$

c. Update weight of hidden layers as well as input weights W_s according to Adam Optimizer →

$$\theta = \theta - \frac{\left(\alpha + V_{d\theta}^{corrected}\right)}{\sqrt{\varphi + S_{d\theta}^{corrected}}}$$

Figure 6: Training Algorithm

category.

The objective of the training was to generate three embeddings, one for each image, and maximize the L2 distance between the initial and non-matching image embeddings while minimizing the distance between the initial and matching image embeddings. Formally the triplet loss function was minimized by the (1).

$$T.L = \sum_{i=0}^{n}\left[\|f_i^a - f_i^p\|_2^2 - \|f_i^a - f_i^n\|_2^2 + \alpha\right] \quad (1)$$

Where f_i^a is the inital image embedding, f_i^p is the matching image embedding (same class as an inital), f_i^n is the non-matching image embedding (different class than inital) and α is a threshold that is set for the distance between matching and non-matching pairs.

V. RESULTS

The proposed model was trained and tested on ISL and ASL datasets and achieved accuracy of 91.25% and 90.03% respectively compared to [13] which attained a score of 84%

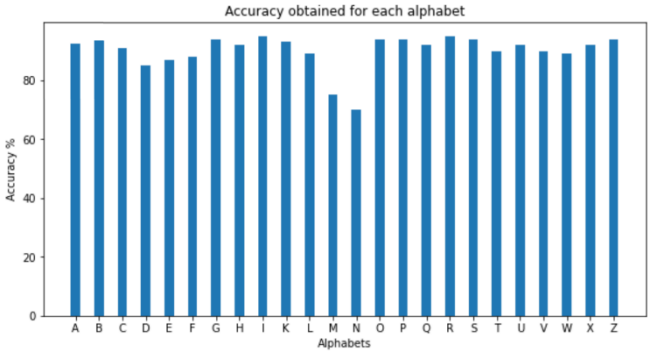


Figure 7: ASL Alphabet Result Bar Graph

on ASL dataset which used a simple CNN to classify the sign images. The proposed model is trained for 5000 epochs since Siamese networks take more time to train than other simple CNNs due to the fact that three images are needed to

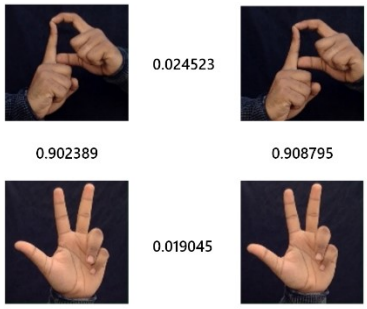


Figure 8: Distance ISL image embeddings

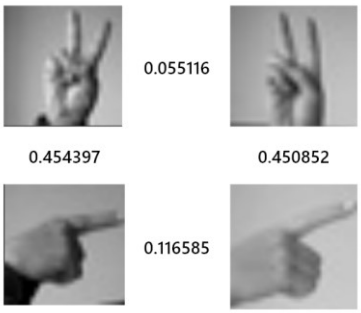


Figure 9: Distance ASL image embeddings

be processed per epoch, unlike simple CNNs which usually need only one image per epoch. The model began to overfit and stopped showing any considerable improvement beyond 5000 iterations. This shows that the model can be extended to other datasets with the same model architecture. The accuracy of ASL and ISL alphabet are shown in Fig. 7 and Fig. 11 respectively. Some alphabets have given poor results which could have been because of the exceeding similarity with other alphabets hand sign.

The proposed model learns to output feature embeddings in a way that ensures that the measure of L2 distance between images in the same category should be low and the L2 distance between the images in the dissimilar category should be high. Fig. 8 and Fig. 9 shows the distance between the embeddings of images belonging to the ISL and ASL

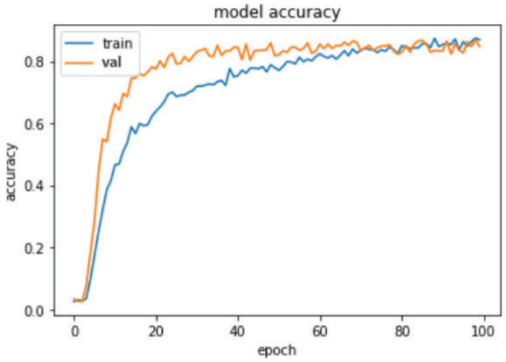


Figure 10: Accuracy Plot

Authorized licensed use limited to: DELHI TECHNICAL UNIV. Downloaded on May 01,2023 at 05:42:29 UTC from IEEE Xplore. Restrictions apply.

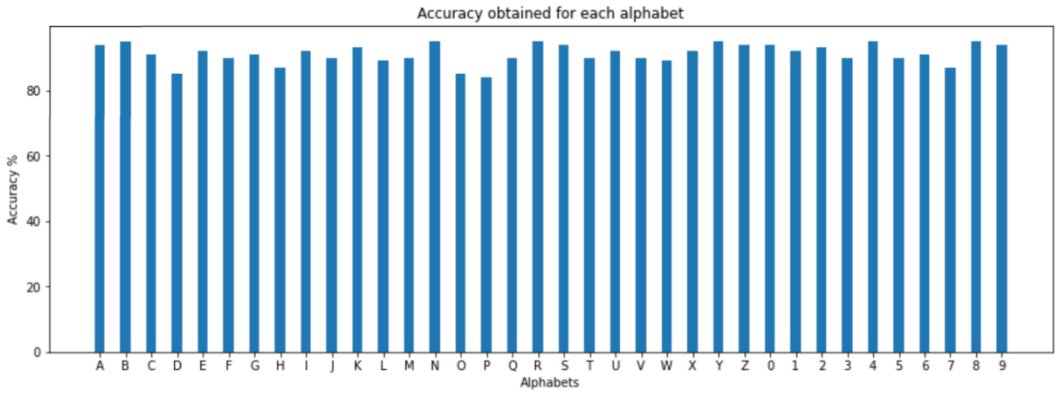


Figure 11: ISL Alphabet Result Bar Graph

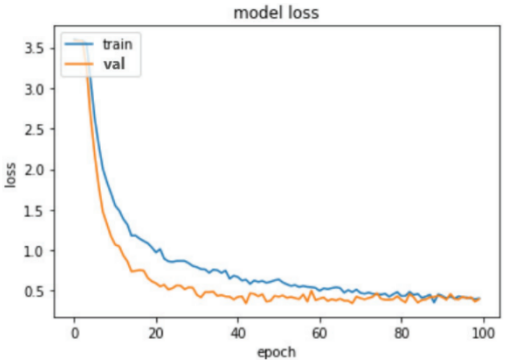


Figure 12: Loss Plot

dataset respectively.

Fig. 10. depicts the accuracy plot for the model during the validation and training phases. The plot indicates that the model's performance generally increases with successive epochs, but there are instances of unstable performance when comparing the validation and training results.

The loss plot of the proposed is shown in Fig. 12. The plot demonstrates that the loss rate decreases with increasing epochs, but instances of unstable performance can be noticed when comparing the training and testing results. The validation loss decreased significantly from 3.57% to 0.28% as the epochs increased, and the training loss showed a similar trend, decreasing from 3.54% to 0.31%.

VI. CONCLUSION

In this paper, we have developed a model that utilizes the concept of One-Shot learning to convert sign language to text. The proposed model is evaluated on multiple datasets as it is designed to ensure maximum accuracy over a varied range of datasets, which could even have limited data points for the different alphabets. The proposed model has been trained for 5000 epochs on ASL and ISL datasets and has achieved an accuracy of 90.03% and 91.25% respectively. In future work, the model can be enhanced to perform well on various other languages.

REFERENCES

[1] Abu-Jamie, T.N. and Abu-Naser, S.S., 2022. Classification of Sign-language Using VGG16.

[2] More, V., Sangamnerkar, S., Thakare, V., Mane, D. and Dolas, R., 2021. Sign language recognition using image processing. JournalNX, pp.85-87.

[3] Elakkiya, R., Vijayakumar, P. and Kumar, N., 2021. An optimized Generative Adversarial Network based continuous sign language classification. Expert Systems with Applications, 182, p.115276.

[4] Izutov, E., 2020. ASL Recognition with Metric-Learning based Lightweight Network. arXiv preprint arXiv:2004.05054.

[5] Bantupalli, K. and Xie, Y., 2018, December. American sign language recognition using deep learning and computer vision. In 2018 IEEE International Conference on Big Data (Big Data) (pp. 4896-4899). IEEE.

[6] Ojha, A., Pandey, A., Maurya, S., Thakur, A. and Dayananda, P., 2020. Sign language to text and speech translation in real-time using convolutional neural network. Int. J. Eng. Res. Technol.(IJERT), 8(15), pp.191-196.

[7] M. Kumar, P. Gupta, R. K. Jha, A. Bhatia, K. Jha, and B. K. Shah, "Sign Language Alphabet Recognition Using Convolution Neural Network," 2021 5th International Conference on Intelligent Computing and Control Systems (ICICCS), Madurai, India, 2021, pp. 1859-1865, doi: 10.1109/ICICCS51141.2021.9432296.

[8] A. Orbay and L. Akarun, "Neural Sign Language Translation by Learning Tokenization," 2020 15th IEEE International Conference on Automatic Face and Gesture Recognition (FG 2020), Buenos Aires, Argentina, 2020, pp. 222-228, doi: 10.1109/FG47880.2020.00002.

[9] Y. C. Bilge, R. G. Cinbis and N. Ikizler-Cinbis, "Towards Zero-Shot Sign Language Recognition," in IEEE Transactions on Pattern Analysis and Machine Intelligence, vol. 45, no. 1, pp. 1217-1232, 1 Jan. 2023, doi: 10.1109/TPAMI.2022.3143074.

[10] Schroff, F., Kalenichenko, D. and Philbin, J., 2015. Facenet: A unified embedding for face recognition and clustering. In Proceedings of the IEEE conference on computer vision and pattern recognition (pp. 815-823).

[11] Koch, G., Zemel, R. and Salakhutdinov, R., 2015, July. Siamese neural networks for one-shot image recognition. In ICML deep learning workshop (Vol. 2, No. 1).

[12] Bandara, W.G.C. and Patel, V.M., 2022, July. A transformer-based siamese network for change detection. In IGARSS 2022-2022 IEEE International Geoscience and Remote Sensing Symposium (pp. 207-210). IEEE.

[13] Bhat, A., Yadav, V. and Dargan, V., 2022, May. Sign Language to Text Conversion using Deep Learning. In 2022 3rd International Conference for Emerging Technology (INCET) (pp. 1-7). IEEE.

[14] J. Nikitha, S. Keerthana, S. Balakrishnan and S. P. Sathya, "Comparative Analysis on Datasets for Sign Language Detection System," 2022 International Conference on Sustainable Computing and Data Communication Systems (ICSCDS), Erode, India, 2022, pp. 1652-1657, doi: 10.1109/ICSCDS53736.2022.9761026.

[15] Y. C. Bilge, R. G. Cinbis and N. Ikizler-Cinbis, "Towards Zero-Shot Sign Language Recognition," in IEEE Transactions on Pattern Analysis and Machine Intelligence, vol. 45, no. 1, pp. 1217-1232, 1 Jan. 2023, doi: 10.1109/TPAMI.2022.3143074.

Authorized licensed use limited to: DELHI TECHNICAL UNIV. Downloaded on May 01,2023 at 05:42:29 UTC from IEEE Xplore. Restrictions apply.

This article has been accepted for publication in IEEE Transactions on Geoscience and Remote Sensing. This is the author's version which has not been fully edited and content may change prior to final publication. Citation information: DOI 10.1109/TGRS.2023.3267037

Simultaneous Seismic Data Denoising and Reconstruction with Attention based Wavelet-Convolutional Neural Network

Vineela Chandra Dodda, *Member, IEEE*, Lakshmi Kuruguntla, *Member, IEEE*, Anup Kumar Mandpura, *Member, IEEE* and Karthikeyan Elumalai, *Member, IEEE*

***Abstract*—The knowledge of hidden resources present inside the earth layers is vital for the exploration of petroleum and hydrocarbons. However, the recorded seismic data is noisy and incomplete with missing traces that leads to misinterpretation of the earth layers. In this manuscript, we consider seismic data with Gaussian, non-Gaussian noise distribution, regular and irregular missing traces. We propose a method for simultaneous noise attenuation and reconstruction of the incomplete seismic data with attention based wavelet convolutional neural network (AWUN). The wavelet transform is used as pooling layer and inverse wavelet transform is used for upsampling layers to avoid information loss. The attention module is used to obtain weights for various feature channels with higher weights assigned to the more significant information. In addition, we propose to use hybrid loss function (logcosh + huberloss) to denoise and accurately reconstruct the seismic data. Moreover, the effect of various hyper-parameters in the training process of convolutional neural networks is studied. Further, we tested the performance of proposed method on synthetically generated data and field data examples. The quantitative results demonstrated that our proposed deep learning method has shown improved signal-to-noise ratio (SNR) and mean squared error (MSE) when compared to the existing state-of-the-art methods.**

***Index Terms*—Seismic data, Denoising, Missing data reconstruction, Deep learning.**

I. Introduction

Seismic exploration is a technique to obtain information about the earth's underlying layers. Seismic exploration has three stages: acquisition, processing, inversion, and interpretation. In seismic data recording devices, a brief pulse is emitted from the earth's surface and is reflected owing to impedance differences in the earth layers' [1], [2]. An array of geophones detects these reflected waves (receivers) which are placed on the earth surface. However, the recorded seismic data is incomplete and irregular in spatial dimensions and often contaminated with various types of noises. The seismic data is noisy and incomplete due to economic and physical constraints such as geophone failures. The incomplete seismic data have missing traces at regular and irregular intervals [3] [4]. In regularly missing data, the data is lost at periodic intervals while the data is missed at random intervals in the context of irregularly missing data [3]. Whereas, the noises are due to environmental issues like wind motion, traffic, rain etc. Due to these impairments, the SNR of the data decreases which impacts the subsequent processing steps i.e. inversion and interpretation of seismic data. Hence, seismic data denoising and reconstruction are the important pre-processing steps needed for accurate interpretation of the resources beneath the earth subsurface layers. Numerous techniques have been proposed in the literature to denoise and reconstruct the seismic data [3], [5]–[8].

These seismic data reconstruction methods can broadly be classified into two categories namely; traditional and data-driven (deep learning) methods. The traditional methods includes prediction filtering [5], [9]–[11], wave equation [6], [12], rank reduction [3], [7], [13], [14] and sparse transform based methods [8], [15]–[20]. In prediction filtering based methods, the prediction error filter (PEF) coefficients are obtained by minimizing the error in a least-squares manner either in frequency-space domain, time-space domain or frequency-wave number domain. The obtained PEF is used to interpolate the missed data. Here, the prediction error filters, which are obtained from the less aliased low-frequency data, leads the reconstruction in high frequency beyond aliasing. In [5], multi-channel interpolation method was proposed where interpolation operator is estimated from the spectrum of prediction filter obtained from the recorded seismic traces. However, approaches based on prediction filtering make assumptions about the input data, such as the need for regularly sampled data and performs well only on data with linear events. In wave equation based methods, the interpolation is based on the relationship between the model and data obtained from wave equations. In [6], the missing data is assumed as zero data and migration is applied before stacking and inverse operator is estimated by conjugate gradient iterative method. The techniques involved in migration such as Normal Move Out (NMO) and Inverse Dip Move Out (IDMO) use the physical wave properties. However the limitations are, a known distribution of subsurface parameters and a velocity model are needed as inputs for wave equation-based approaches.

To overcome these limitations, rank reduction methods were

Vineela Chandra Dodda, Research scholar, Department of Electronics and Communication Engineering, SRM University, Amaravathi,Andhra Pradesh-522502, India. e-mail: (vineelachandra_dodda@srmap.edu.in).

Lakshmi Kuruguntla, Assistant Professor, Department of Electronics and Communication Engineering, Lakireddy Balireddy College of Engineering,Mylavaram,Andhra Pradesh, India. e-mail: (lakshmi_kuruguntla@srmap.edu.in).

Anup Kumar Mandpura, Assistant Professor, Department of Electrical Engineering, Delhi Technological University, New Delhi-110042, India. e-mail: (kanup@dtu.ac.in).

Karthikeyan Elumalai, Assistant professor, Department of Electronics and Communication Engineering, SRM University, AP, e-mail: (imkarthi@gmail.com)

© 2023 IEEE. Personal use is permitted, but republication/redistribution requires IEEE permission. See https://www.ieee.org/publications/rights/index.html for more information.
Authorized licensed use limited to: DELHI TECHNICAL UNIV. Downloaded on April 24,2023 at 06:10:10 UTC from IEEE Xplore. Restrictions apply.

This article has been accepted for publication in IEEE Transactions on Geoscience and Remote Sensing. This is the author's version which has not been fully edited and content may change prior to final publication. Citation information: DOI 10.1109/TGRS.2023.3267037

proposed where the data reconstruction problem is projected as a low-rank reduction problem. In these methods, regularly sampled complete data is assumed to have low rank [3] and noise increases the rank of the data matrix. Intuitively, the rank of the data needs to conform to low rank for denoising and reconstructing the data. In [21], the seismic data is denoised and reconstructed using multichannel singular spectrum analysis (MSSA), a rank reduction technique. The spatial seismic data at a given frequency is arranged in the form of hankel matrix. Then, rank of the hankel matrix is reduced by using Randomized-Singular Value Decomposition (R-SVD) to denoise the data. The approaches for rank reduction, however, need prior assumptions about the rank and are computationally expensive for large data. Hence, sparse transform based methods were proposed where the useful information of seismic data is represented in sparse domain with transforms such as Fourier [8], Wavelet [15], Curvelet [16], Radon [17], Seislet [19], Shearlet [18] and Dreamlet [20]. The seismic data is then encoded using the specified transform, and the encoded seismic data is then decoded using an inverse transform. However, all the aforementioned methods use fixed basis for sparsity which cannot work well for seismic data with complex events [22]. Hence dictionary learning methods were proposed for seismic data reconstruction and denoising where the dictionaries are learned from the input data based on Data Driven Tight Frame (DDTF), K-means Singular Value Decomposition (K-SVD) and Sequential Generalised K-means (SGK). However, the selection of various parameters such as patch size, dictionary size, threshold value etc. based on different seismic data sets obtained from geographically distant areas is a challenging issue [23].

Recently, with the rapid development of GPU's and huge availability of data, the data-driven methods such as deep learning gained popularity in various areas such as computer-vision, natural language processing, image and speech recognition etc. Deep Learning (DL) techniques can learn nonlinear correlations implicitly from a large number of labels and are usually not constrained as traditional methods, which are based on signal processing theories or physics-based equations. In [24], Support Vector Regression (SVR), a Machine Learning (ML) algorithm was proposed to interpolate the missing traces from the seismic data. In addition, the authors combined SVR with sparse transform i.e., Data Driven Tight Frame (DDTF) to improve the training performance. Further in [25], Generative Adversarial Network (GAN), a deep learning architecture was proposed for fast and accurate reconstruction of consecutively missing seismic data. Later in [26], cycle-GAN was used with combination of four loss functions (adversarial, cyclic, self-distance and identity loss) for seismic-data interpolation to regularize, improve the accuracy and computational efficiency. In [27], Dual Domain Conditional Generative Adversarial Network (DD-CGAN) was proposed for seismic data reconstruction. In DD-CGAN, the seismic data set and its frequency domain data (Discrete Fourier Transform) are used as input vectors to train the network. A loss function with the combination of generative-adversarial loss, data loss, and the total variation loss was used to improve the smoothness and accuracy of the reconstructed data. In [28], Convolutional Neural Network (CNN) based 8 layer residual network was used for anti-aliasing interpolation of seismic data. In [29], Bidirectional long short-memory (LSTM) network with skip connections was adopted to perform interpolation on irregularly missing seismic data. Further in [3], the authors proposed a network architecture based on U-Net with CNN to reconstruct regularly and irregularly missing seismic data. In [3], the reconstruction problem is projected as translating one input to another i.e., incomplete data to complete data. Later in [30], Partial-Convolution based method (P-Conv) which is a hierarchical and region-learning mechanism was proposed for seismic data reconstruction. The P-Conv's are used in U-Net architecture and has shown better amplitude preservation compared to curvelet method. Further in [31], self-supervised deep learning based two step reconstruction approach was proposed to recover the consecutively missing traces. In the first step, CNN is trained with pseudo labels obtained from unlabeled data. Then nested U-Net (UNet++) was trained with hybrid loss function to improve the accuracy of reconstructed seismic data. Similarly in [22], an attention module was used with the CNN to capture global information and is trained with structural similarity (SSIM) and l_1 norm loss function for reconstruction of consecutively missing data. Later in [32], a multistage neural network was proposed to improve the accuracy of reconstruction for low-amplitude seismic data. Further in [33], Residual Deep Learning network with wavelet transform was proposed to reconstruct regular and irregular missing seismic data. The accuracy of the residual blocks in the network was improved with the use of customized loss function (SSIM + Huber). Later attention modules were introduced along with neural network architectures to enhance the accuracy for various applications in seismic data analysis such as denoising, reconstruction, earthquake detection, porosity, permeability prediction and earthquake detection [34]–[40]. In [35], an unsupervised deep learning approach, which is based on variational autoencoder (VAE) and squeeze-and-excitation (SE) networks is used for enhancing micro seismic signals, as well as suppressing noise. The SE network is used to guide the VAE to preserve the useful information from the clean signal. Similarly, in [36], the authors developed a deep learning framework based on deep image prior (DIP) and attention networks for 3-D seismic data enhancement. Further, in [38], [39] attention mechanisms are used to enhance the accuracy of earthquake detection and seismic interpretation. From literature, we observed that the attention mechanisms have shown significant impact on seismic data analysis.

However, the attenuation of noise is a significant consideration for the later stages of seismic processing in addition to reconstruction. Henceforth, simultaneous seismic data denoising and reconstruction were performed based on rank reduction methods in [14] [21], sparse transform method in [20] and dictionary learning based methods in [4], [41], [42], [43]. All of the aforementioned techniques, however, are inappropriate for complex events such as hyperbolic event, crossed event etc. that occur in seismic data. In [41], a double sparsity dictionary learning method was proposed for joint seismic data denoising and interpolation. An extended sparse K-SVD method for dictionary update was used where the atoms are updated through

© 2023 IEEE. Personal use is permitted, but republication/redistribution requires IEEE permission. See https://www.ieee.org/publications/rights/index.html for more information.
Authorized licensed use limited to: DELHI TECHNICAL UNIV. Downloaded on April 24,2023 at 06:10:10 UTC from IEEE Xplore. Restrictions apply.

This article has been accepted for publication in IEEE Transactions on Geoscience and Remote Sensing. This is the author's version which has not been fully edited and content may change prior to final publication. Citation information: DOI 10.1109/TGRS.2023.3267037

weighted low rank approximation and hence computationally complex. Further in [44], structure-oriented filtering (SOF) was used for simultaneous attenuation of spike-like noise and interpolation of missing seismic data with curved events. Further in [45], an unsupervised deep learning framework with an iterative process is proposed to denoise and reconstruct the 3D seismic data. However, in [45], the DL framework is combined with conventional method (Projection onto Convex Sets) to enhance the seismic data reconstruction. Whereas in [46], deep learning based Convolutional Auto encoder (CAE) network was used to denoise and reconstruct the seismic data simultaneously. From the above literature, we infer that deep learning methods were deployed in various scenarios of seismic data denoising and reconstruction such as regular, irregular missing data, consecutively missing data, random noise etc. However, most of the methods aimed at either only denoising or reconstruction and considered the features only in time domain seismic data, ignoring the frequency information. Moreover, the existing max or avg pooling operation may result in information loss which further affects the process of feature extraction [47], [48]. From literature, we observed that the capsule neural network (CapsNet) was proposed to avoid the information loss in various seismic data applications [49], [50]. However, the CapsNet is more computationally expensive than traditional CNNs, which can lead to longer training times and higher computational costs in practice [51]. Hence, we propose to use Discrete Wavelet Transform (DWT) as pooling operator and Inverse Wavelet Transform (IWT) as upsampling operator in the network architecture. In addition, inspired by the human nature i.e., understanding a scenario within short period of time by focusing on unique strong characteristics, we add an attention mechanism i.e., squeeze and excitation block to the U-Net architecture to increase the attention and overall performance of seismic data denoising and reconstruction. The added attention mechanism can model the global information and can handle long-range dependencies [52]. The important contributions of our work are

1) We propose an attention based wavelet U-Net, a deep learning framework by considering the multi-scale and global features in the seismic data.
2) We proposed a hybrid loss function for seismic data denoising and reconstruction, i.e. the log_cosh + Huber loss, which improves the accuracy of the seismic data denoising and reconstruction.
3) We demonstrated the proposed method on various cases of denoising and reconstruction such as consecutively missing data (large gap) and irregularly missing seismic data, random and erratic noise attenuation on synthetic data and field data, which prove the effectiveness of our method.
4) We discussed the effect of various hyper parameters of neural network and future scope in detail.

In section II, we give the signal model and methodology which describes about the network architecture followed by the results in III. Finally, the conclusion is mentioned in the section IV.

II. Methodology

A. Signal model

In this section, we describe the signal model for noisy and missed seismic data. Let $C \in \mathbb{R}^{M\times N}$ be the complete clean seismic data with N traces having M data points each, mathematically expressed as:

$$C = [d_1, d_2, \cdots d_N], \tag{1}$$

where $d_i \in \mathbb{R}^{M\times 1}$ is the noise-free ith trace. In the process of seismic data acquisition, the signal recorded by geophones is afflicted by noise and also some traces are lost. Let $G \in \mathbb{R}^{M\times N}$ be the noise and $B \in \mathbb{R}^{M\times M}$ be the sampling matrix with L non-zero diagonal entries and $M-L$ diagonal elements with zeros. Then the observed noisy and incomplete seismic data $Y \in \mathbb{R}^{M\times N}$ is expressed as:

$$Y = B(C + G) \tag{2}$$

B. Overview of Network Architectures

Deep Learning (DL) techniques are based on learning and recognizing the relationships in the data, similar to operations inside the human brain. From literature, we observe that the commonly used neural network architectures in seismic data denoising and reconstruction are either based on Fully Connected Networks (FCN) or convolutional neural networks [53]. In FC networks, each neuron in one layer is connected to every other neuron in the next layer. The advantage of FC networks is that the input does not require any particular assumptions to be made. In general, the FCN consists of an input layer, hidden layers and an output layer. During the training process, the input layer of the network is fed with training data and is linearly combined to feed to the subsequent layer. The outcome is then passed via a non-linear activation function, which aids the network's ability to learn and carry out more difficult tasks.The same procedure is followed for the total number of hidden layers and the output is obtained based on whether the problem is classification or regression. The mathematical model for the FC network is as follows. Let $W_1, W_2 ... W_n, b_1, b_2, ... b_n$ be the initial weights and biases of the layers in the network. The output of the K^{th} layer is given as

$$f^K(x) = v(w_0^{(K)} + \sum_{i=1}^{M_{K-1}} w_i^{(K)} f_i^{(K-1)}(x)) \tag{3}$$

where v is the activation function, M_{K-1} are the number of neurons in the particular layer $K-1$.

Further, the loss function is used to obtain the error between the obtained output and the true label. To obtain optimum weights, the loss function is minimized with the optimization algorithms. The obtained optimum weights and biases are used during the testing process.

CNN, on the other hand, is employed in a wide range of real-world applications [53]. CNN can recognize the patterns in the data, which is important for classification, object identification, and natural language processing. The CNN architecture is build by stacking three main layers: Convolution, Pooling and Fully-connected layer. CNNs operate by utilizing

© 2023 IEEE. Personal use is permitted, but republication/redistribution requires IEEE permission. See https://www.ieee.org/publications/rights/index.html for more information.
Authorized licensed use limited to: DELHI TECHNICAL UNIV. Downloaded on April 24,2023 at 06:10:10 UTC from IEEE Xplore. Restrictions apply.

This article has been accepted for publication in IEEE Transactions on Geoscience and Remote Sensing. This is the author's version which has not been fully edited and content may change prior to final publication. Citation information: DOI 10.1109/TGRS.2023.3267037

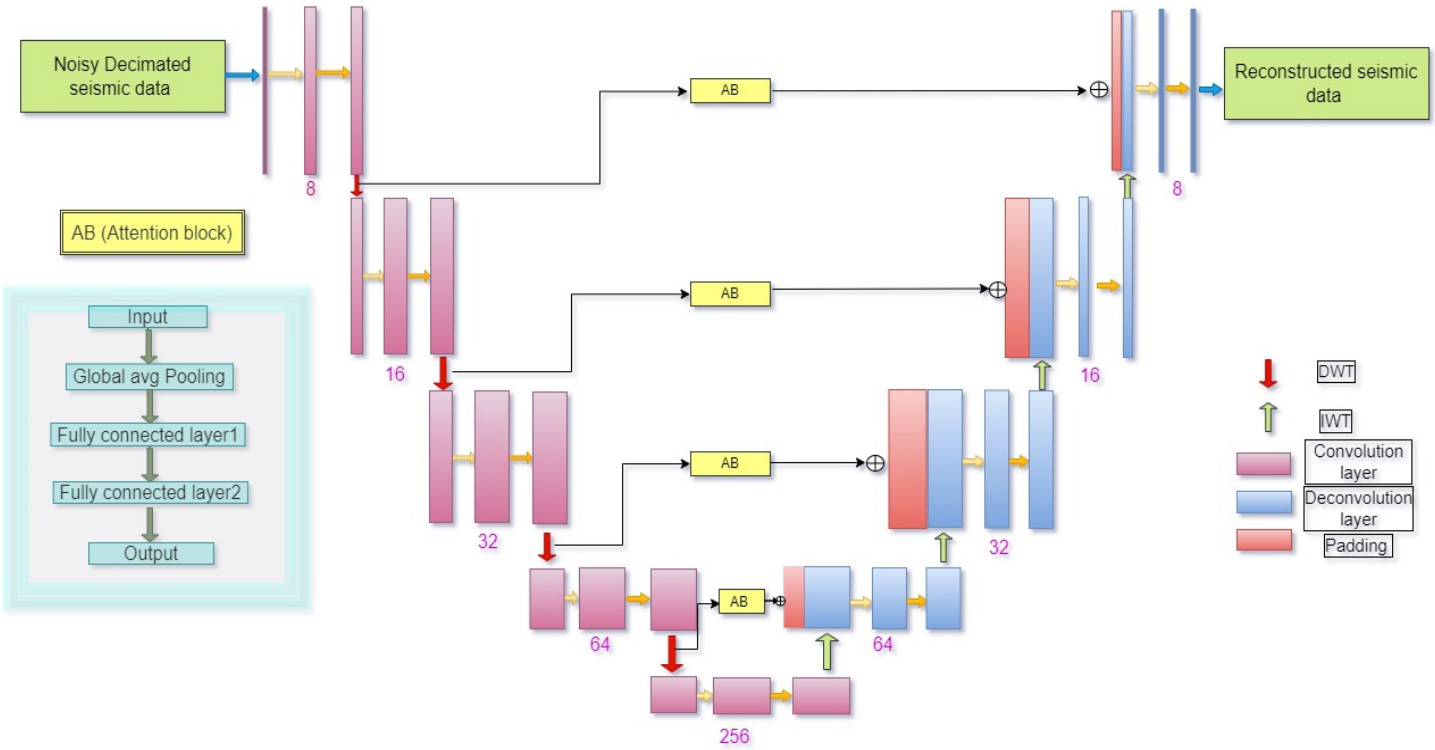


Fig. 1: Proposed AWUN architecture

layers with filters positioned along each dimension gathering particular information about the visual field. In the training process of CNN, the filter is shifted over the input volume's width and height during the forward pass to generate an activation map that contains the responses of that filter at each spatial point. The stacking of conv-pool layers is used to identify complex features from previous layers. The pooling layers are used to get downsampled data and reduce the computational complexity, while preserving the input features. The output is now flattened using fully-connected layer and back propagation is performed using chosen loss function on each training cycle for the specified number of epochs.

C. Proposed Methodology

In our work, we propose to use Wavelet Convolutional U-Net with attention mechanism. The U-Net architecture consists of two blocks; encoder (contracting) and decoder (expansive). The encoder consists of repetitive blocks of convolutional layers followed by activation and pooling layer. After every down sampling operation, the feature channels are doubled. Whereas in the decoder, the upsampling operation is performed with convolution layer which reduces the feature channels by half [54]. In our proposed network, element wise summation is used to combine the feature channels in the contracting path and expansive path. Followed by, the network has symmetric repetitive convolution layers and an activation layer. In the proposed network, we use DWT and IWT as pooling and up sampling layers respectively. Using the DWT, we obtain both frequency and spatial information from the input data. The given data Y can be decomposed into four sub-bands; $Y_{LL}, Y_{LH}, Y_{HL}, Y_{HH}$ using four convolutional filters i.e., $f_{LL}, f_{LH}, f_{HL}, f_{HH}$. Considering the example of Haar wavelet, the filters are defined as [47]:
$f_{LL} = \begin{bmatrix} 1 & 1 \\ 1 & 1 \end{bmatrix}$, $f_{HL} = \begin{bmatrix} -1 & 1 \\ -1 & 1 \end{bmatrix}$, $f_{LH} = \begin{bmatrix} -1 & -1 \\ 1 & 1 \end{bmatrix}$, $f_{HH} = \begin{bmatrix} 1 & -1 \\ -1 & 1 \end{bmatrix}$.

The filters are orthogonal to each other and have fixed parameters with a stride of 2. The DWT with these four fixed filters of stride 2, implements the downsampling function i.e., $Y_{LL} = (f_{LL} \otimes Y) \downarrow_2$, $Y_{LH} = (f_{LH} \otimes Y) \downarrow_2$, $Y_{HL} = (f_{HL} \otimes Y) \downarrow_2$, $Y_{HH} = (f_{HH} \otimes Y) \downarrow_2$. In our network, DWT is used as downsampling operator given as below:

$$\begin{cases} Y_{LL}(a,b) = Y(2a-1,2b-1) + Y(2a-1,2b) \\ \qquad +Y(2a,2b-1) + Y(2a,2b), \\ Y_{LH}(a,b) = -Y(2a-1,2b-1) - Y(2a-1,2b) \\ \qquad +Y(2a,2b-1) + Y(2a,2b), \\ Y_{HL}(a,b) = -Y(2a-1,2b-1) + Y(2a-1,2b) \\ \qquad -Y(2a,2b-1) + Y(2a,2b), \\ Y_{HH}(a,b) = Y(2a-1,2b-1) - Y(2a-1,2b) \\ \qquad -Y(2a,2b-1) + Y(2a,2b), \end{cases} \tag{4}$$

where $Y_{LL}(a,b), Y_{LH}(a,b), Y_{HL}(a,b), Y_{HH}(a,b)$ are values at the a^{th} row and b^{th} column of $Y_{LL}, Y_{LH}, Y_{HL}, Y_{HH}$ respectively. On the reconstruction end, due to the orthogonality nature of the DWT, the input data can be reconstructed without any loss in features by Inverse Wavelet Transform given as follows [47]:
$Y = IWT(Y_{LL}(a,b), Y_{LH}(a,b), Y_{HL}(a,b), Y_{HH}(a,b))$, where

© 2023 IEEE. Personal use is permitted, but republication/redistribution requires IEEE permission. See https://www.ieee.org/publications/rights/index.html for more information.
Authorized licensed use limited to: DELHI TECHNICAL UNIV. Downloaded on April 24,2023 at 06:10:10 UTC from IEEE Xplore. Restrictions apply.

This article has been accepted for publication in IEEE Transactions on Geoscience and Remote Sensing. This is the author's version which has not been fully edited and content may change prior to final publication. Citation information: DOI 10.1109/TGRS.2023.3267037

$$\begin{cases} Y(2a-1,2b-1) = Y_{LL}(a,b) - Y_{LH}(a,b) \\ \qquad\qquad -Y_{HL}(a,b) + Y_{HH}(a,b))/4, \\ Y(2a-1,2b) = Y_{LL}(a,b) - Y_{LH}(a,b) \\ \qquad\qquad +Y_{HL}(a,b) - Y_{HH}(a,b))/4, \\ Y(2a-1,2b) = Y_{LL}(a,b) + Y_{LH}(a,b) \\ \qquad\qquad -Y_{HL}(a,b) - Y_{HH}(a,b))/4, \\ Y(2a,2b) = Y_{LL}(a,b) + Y_{LH}(a,b) \\ \qquad\qquad +Y_{HL}(a,b) + Y_{HH}(a,b))/4, \end{cases} \tag{5}$$

DWT can preserve both spatial information and good frequency resolution, therefore it is used to retain detailed information, which aids in reconstruction of the seismic data. In our proposed network, the pooling layer is replaced with DWT to enhance the accuracy of the model for seismic data denoising and reconstruction. Further we use attention module to scale the features obtained from the encoder (contracting) layers. In general, the channels of the network are given equal priority while obtaining the feature maps. This mechanism is altered with the addition of attention module which weighs the channels adaptively. The input to the attention module is convolutional layer and number of channels in that particular layer. Then average pooling is used to squeeze each channel to obtain single value. To introduce non-linearity, we use two fully connected layers with an activation function. Finally, the output of attention module is obtained by multiplying the output of excitation layers with the input of the attention module which is given as input to the next convolution layer. In addition, the advantage of attention module is to avoid the vanishing gradient problem and to provide better explainability about the model.

D. Loss Function

The selection of loss function is very important to train the deep learning models. The MSE loss function is widely used to denoise and reconstruct the seismic data. While, the MSE loss can speed up the convergence, l_2 norm penalizes the small errors. To overcome this issue, we propose a hybrid loss function which is a combination of $logcosh$ and huber loss. The $logcosh$ is a logarithmic hyperbolic cosine loss which acts as l_2 norm for small values and as l_1 norm at large values of the argument and is differentiable everywhere.

$$L_{log_cosh}(Y,\hat{Y}) = log(cosh(a(Y-\hat{Y})) \tag{6}$$

where Y is the ground truth and $\hat{Y}$ is the predicted output, and a is a constant. The log_cosh function is less sensitive to small errors as it acts as MSE scaled by $0.5 \times a$ near the origin. Whereas huber loss is used in regression problems, and is also termed as smoothed mean absolute error. The huber loss function is defined as:

$$L_{Huber_loss} = \begin{cases} \frac{1}{2}(Y-\hat{Y})^2 & \text{for } |\hat{Y}-Y| \le \delta \\ \delta(|\hat{Y}-Y| - \frac{1}{2}\delta^2) & \text{otherwise,} \end{cases} \tag{7}$$

where Y is the ground truth and $\hat{Y}$ is the predicted output, δ is a threshold to be selected before training the model. When δ is near to zero, the huber loss gives the MAE loss; whereas when δ tends to $\inf$, the huber loss outputs MSE loss. The advantage of huber loss is that it is less sensitive to outliers and helps to preserve the local features of the data. Taking the advantage of log_cosh and huber loss, we propose hybrid loss function, a combination of these two loss functions.

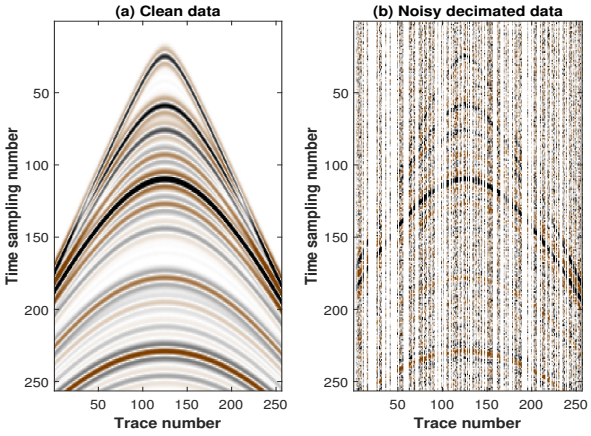


Fig. 2: (a) Clean data (b) Noisy decimated data

$$Total\ \ loss(L) = L_{log_cosh} + L_{huber_loss} \tag{8}$$

Further, the selection of activation function also has an impact in obtaining the accurate model. We used Parametric Rectified Linear Unit (PReLU) as an activation function to train the network. The benefit of PReLU is that it features a learning parameter function that adjusts the activation function in accordance with its rate of learning. Hence, we used PReLU as an activation function to train the network.

III. Numerical Results

In this section, we demonstrate the various numerical results obtained using proposed AWUN method and hybrid loss function on both synthetic and field data. We tested the model on regularly and irregularly missing noisy seismic data. In case of irregularly missing seismic data, various levels of decimation is made at random positions in the data. Further, we varied the noise levels and tested the performance of the proposed method. The model is built using Tensorflow deep learning library using python 3.8 on server with configuration Intel® Xeon® Silver 4216 CPU @2.10 GHz (2 processors) with 256 GB RAM, 64-bit operating system. For fair comparison, in case of all DL models, the batch size is chosen as 128 and number of epochs as 10. The ADAM optimization algorithm is used with a learning rate of 0.01. We used PReLU as an activation function. We adopted the U-Net [54] architecture, and trained the network with proposed configurations: (a) with and without wavelet transform as pooling operation, (b) hybrid loss function and only MSE loss function (c) Presence and absence of PReLU activation function and attention module. Furthermore, we compared the denoising and reconstruction results with the dense layered neural network [36].

© 2023 IEEE. Personal use is permitted, but republication/redistribution requires IEEE permission. See https://www.ieee.org/publications/rights/index.html for more information.
Authorized licensed use limited to: DELHI TECHNICAL UNIV. Downloaded on April 24,2023 at 06:10:10 UTC from IEEE Xplore. Restrictions apply.

This article has been accepted for publication in IEEE Transactions on Geoscience and Remote Sensing. This is the author's version which has not been fully edited and content may change prior to final publication. Citation information: DOI 10.1109/TGRS.2023.3267037

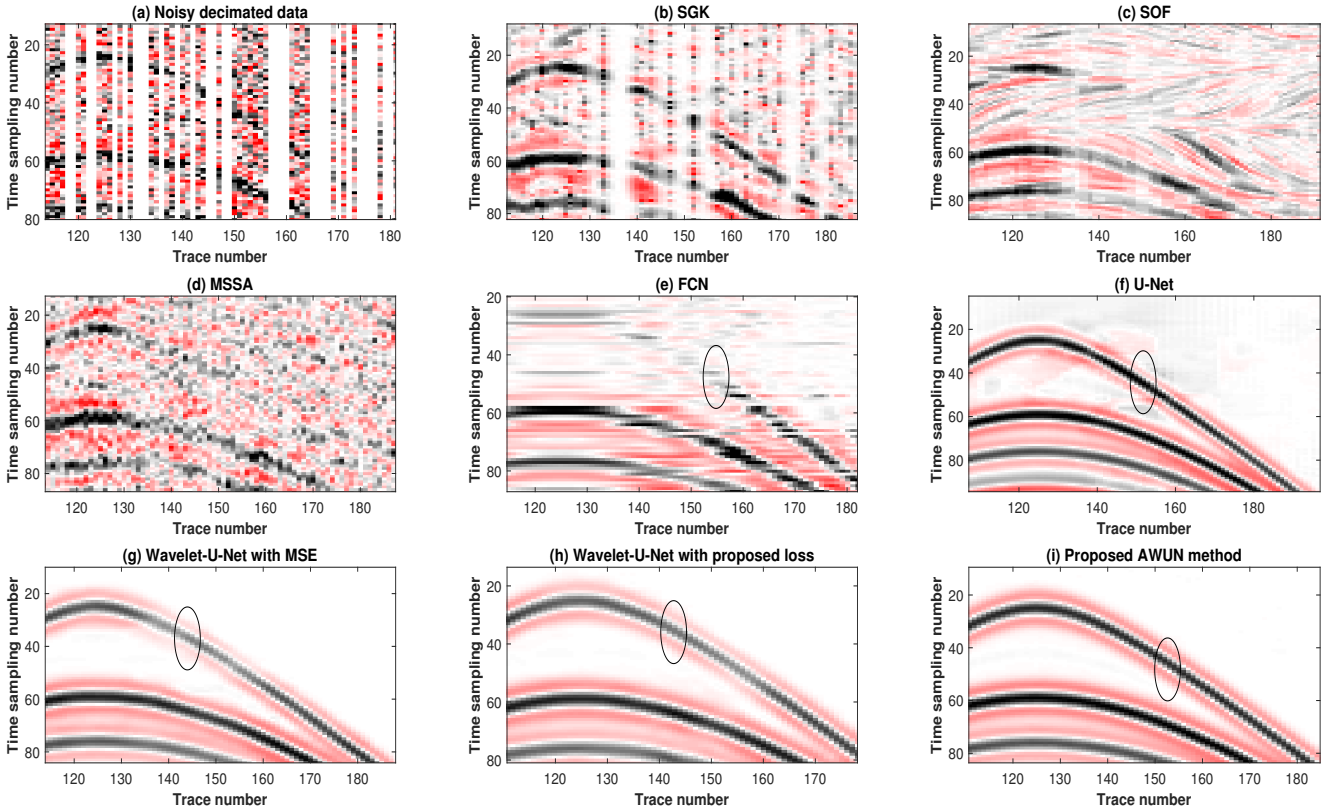


Fig. 3: Zoomed sections (a) Noisy decimated data (b) Reconstructed seismic data for SGK (c) SOF (d) MSSA (e) FCN (f) Basic U-Net (g) Wavelet U-Net with MSE (h) Wavelet U-Net with proposed loss (i) Proposed AWUN method respectively.

A. *Performance metrics*

The proposed method is evaluated using MSE, SNR and local similarity maps as performance metrics which are described as follows.

Mean Squared Error

$$MSE = \frac{1}{N}\sum_{i=1}^{N}(\hat{y}_i - d_i)^2, \tag{9}$$

where $\hat{y}_i, d_i$ denote the predicted and clean (true) i^{th} seismic trace respectively, N represents the number of traces. The ideal value of MSE is 0, when the predicted data is same as the clean seismic data. A lower value of MSE indicates better performance of the model.

Signal-to-Noise-Ratio

$$SNR = 10\ \log_{10}\ \Big(\frac{\sum_{i=1}^{N} d_i^2}{\sum_{i=1}^{N}(\hat{y}_i - d_i)^2}\Big), \tag{10}$$

The higher the SNR value, the better the denoising and reconstruction efficiency of the method.

Local Similarity

The local similarity metric was described by Fomel et.al. in [55]. In general, the local similarity (γ) between the predicted data $\hat{Y}$ and clean data C is given by:

$$\gamma \quad = \quad \sqrt{(\hat{Y}^T\hat{Y})^{-1}(\hat{Y}^T C)(C^T C)^{-1}(C^T\hat{Y})} \tag{11}$$

We calculate mean energy of the obtained local similarity maps and compare the values with the existing methods [56]. In general, if two seismic data are identical, mean energy value is 1.

B. *Training data*

We generated synthetic dataset with hyperbolic events similar to [57] for training and testing the proposed AWUN method. The sampling rate of the seismic data is 4 ms. The clean seismic data is shown in Fig. 2(a). An additive white Gaussian noise is generated and is added to the clean synthetic data to obtain the noisy seismic data. Then we perform 50% decimation on noisy seismic data at random positions from the seismic data as shown in Fig. 2(b). We generate 100 such synthetic noisy and decimated seismic data sets with 50% decimation (missing data at random positions). Similarly, the noisy field data from [57] was decimated and is used to train

© 2023 IEEE. Personal use is permitted, but republication/redistribution requires IEEE permission. See https://www.ieee.org/publications/rights/index.html for more information.
Authorized licensed use limited to: DELHI TECHNICAL UNIV. Downloaded on April 24,2023 at 06:10:10 UTC from IEEE Xplore. Restrictions apply.

This article has been accepted for publication in IEEE Transactions on Geoscience and Remote Sensing. This is the author's version which has not been fully edited and content may change prior to final publication. Citation information: DOI 10.1109/TGRS.2023.3267037

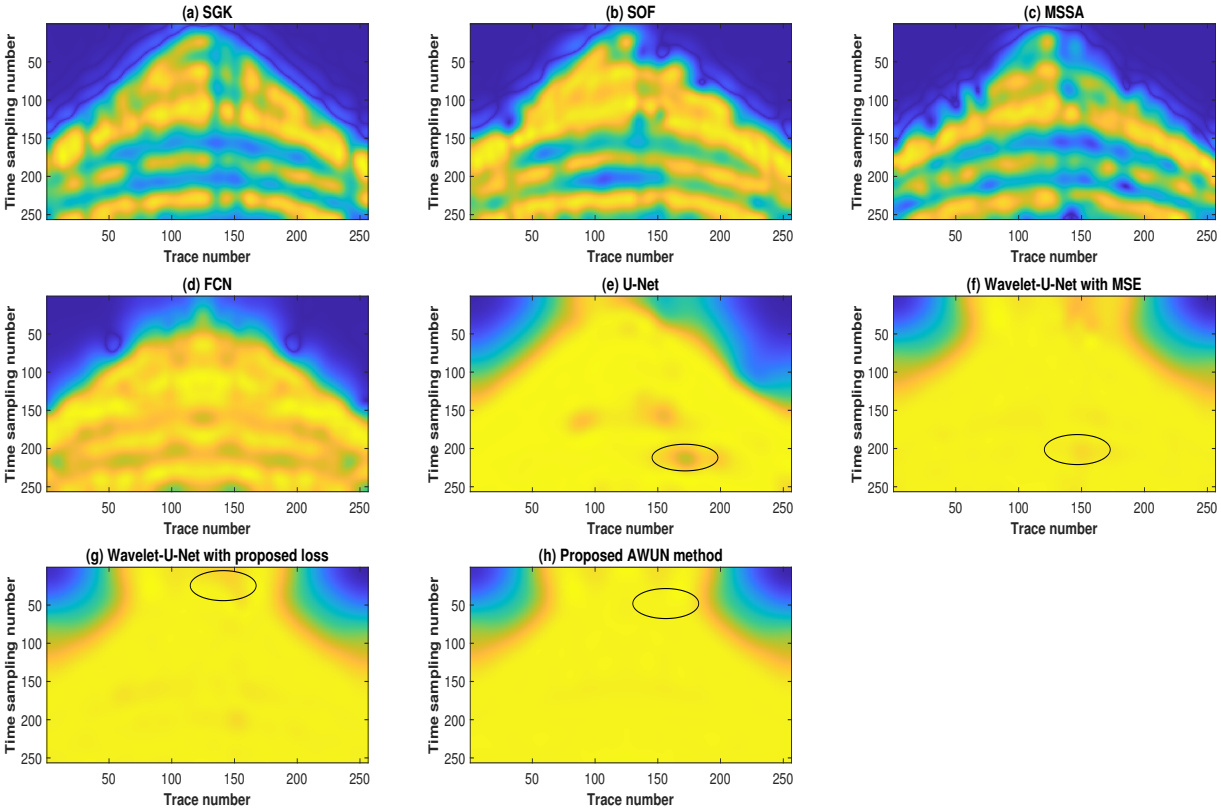


Fig. 4: Local similarity map between clean seismic data and reconstructed seismic data for (a) SGK (b) SOF (c) MSSA (d) FCN (e) Basic U-Net (f) Wavelet U-Net with MSE (g) Wavelet U-Net with proposed loss (h) Proposed AWUN method respectively.

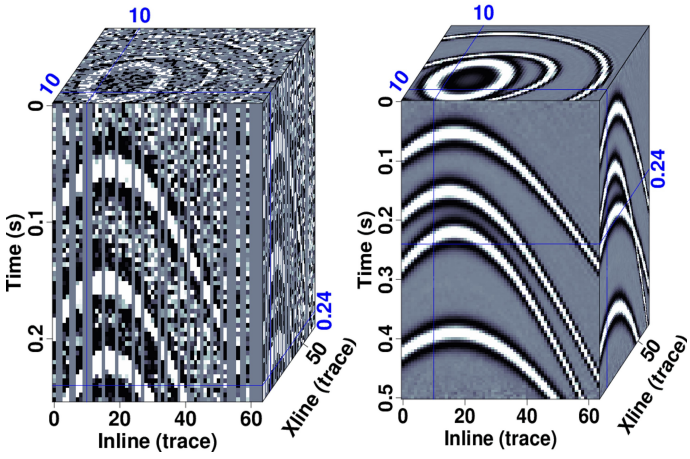


Fig. 5: (a) Noisy decimated data (b) reconstructed data (proposed method)

the network with the pre trained parameters obtained from the synthetic data. From these seismic datasets, the train-test data was split to 70-30 percent respectively. The synthetic and field data consists of 256 traces and 256 time sampling points.

Synthetic Data Example

In this study, we analyzed the performance of proposed method with existing methods such as filtering (SOF), rank-reduction (MSSA), dictionary learning (SGK) and deep learning methods on synthetically generated seismic data with more number of hyperbolic events. We applied both proposed AWUN and existing methods (Structure Oriented Filtering (SOF) [58], Sequential Generalized K-means (SGK) [59] and rank reduction method based on MSSA [21]) on the noisy decimated data. The quantitative performance metrics such as SNR and MSE are tabulated in TABLE I.

In addition, we plotted the local similarity maps and corresponding local similarity energy values are tabulated in TABLE I. We fine tuned the parameters of each method to obtain the improved results in terms of SNR. From TABLE-I, we can observe that the SGK, SOF, MSSA methods improved the SNR to 3.71 dB, 2.96 dB, 6.54 dB respectively.

We performed the ablation study for the proposed method i.e., with Fully Connected Network (FCN), basic U-Net, Wavelet U-Net with MSE loss function, Wavelet U-Net with proposed loss and PReLU activation function and proposed AWUN method. The SNR values obtained are 7.2427, 18.08, 24.03, 26.11, 29.94 dB respectively. In addition, we infer that the MSE values calculated are less while compared to the existing methods. The reconstructed plots of existing methods (zoomed version) are shown in Fig. 3(b) to 3(e), where noise can be seen in the reconstructed data and missing traces

© 2023 IEEE. Personal use is permitted, but republication/redistribution requires IEEE permission. See https://www.ieee.org/publications/rights/index.html for more information.
Authorized licensed use limited to: DELHI TECHNICAL UNIV. Downloaded on April 24,2023 at 06:10:10 UTC from IEEE Xplore. Restrictions apply.

This article has been accepted for publication in IEEE Transactions on Geoscience and Remote Sensing. This is the author's version which has not been fully edited and content may change prior to final publication. Citation information: DOI 10.1109/TGRS.2023.3267037

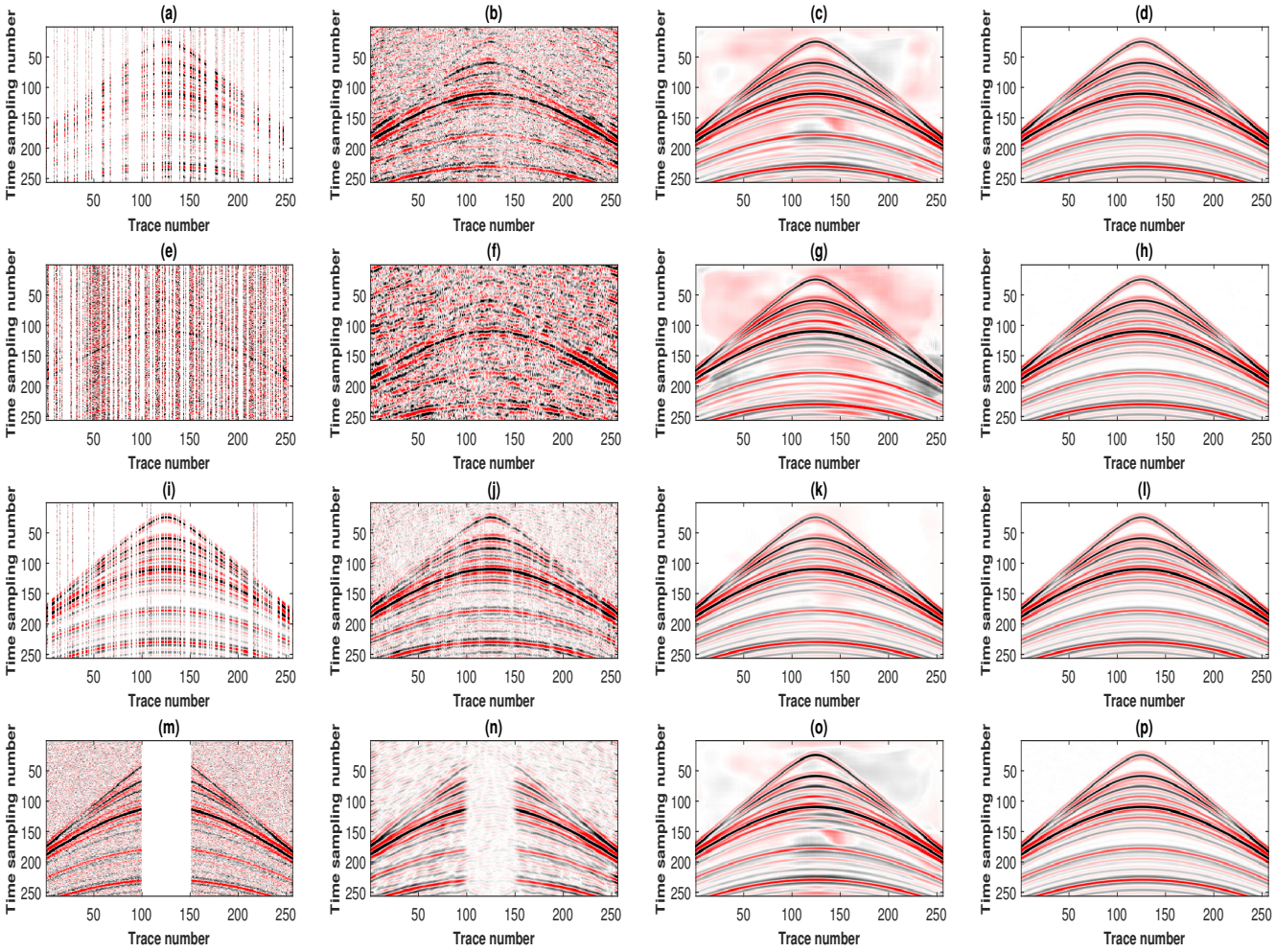


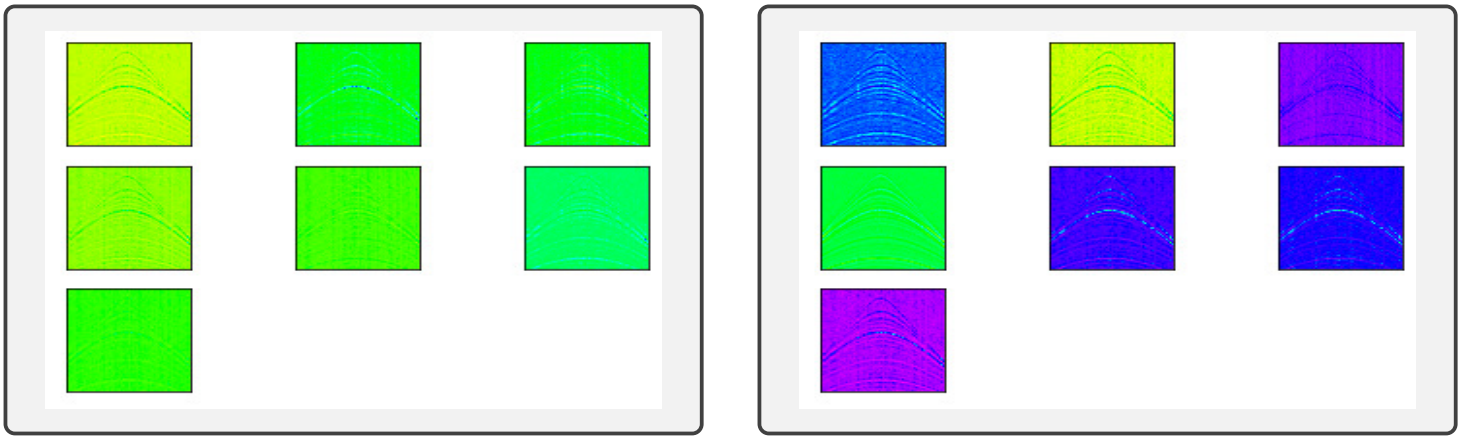
Fig. 6: (a) Noisy decimated seismic data (80%) (b) Reconstructed result for MSSA (c) Basic U-Net (d)Proposed method respectively (e) noisy decimated data with SNR=-2.06 dB (f) Reconstructed seismic data for MSSA (g) Basic U-Net (h) Proposed method respectively (i) Erratic decimated data (50%) (j) Reconstructed seismic data for MSSA (k) Basic U-Net (l) Proposed method respectively (m) noisy decimated data with consecutively missing data (50%) (n) Reconstructed seismic data for MSSA (o) Basic U-Net (p) Proposed method respectively.

are reconstructed partially. In Fig. 3(b), we infer that SGK performs partial reconstruction but some residual noise is present. Whereas in Fig. 3(c), SOF performs the reconstruction better than SGK but the amount of residual noise is high. The output from MSSA is shown in Fig. 3(d), where we can observe moderate reconstruction but more amount of residual noise is present when compared to SGK and SOF. In Fig. 3(d), (e), (f) events are reconstructed but noise still remains. Whereas in Fig. 3(i), the plot of reconstructed seismic data corresponding to the proposed AWUN method is presented. It can be observed that the proposed method has better performance for denoising and reconstruction of hyperbolic events compared to existing methods.

In addition, we analyzed the performance of the proposed method on seismic data in different cases: (a) Various decimations (30% and 80%) and noise levels (0.1283 dB, -2.0611 dB) (b) erratic noise with 50% decimation and (c) regularly missing data (Consecutively 50% decimation). The noisy and decimated data with SNR values are 0.30 dB, -2.06 dB, 2.86 and 4.16 dB respectively shown in Fig. 6 (a), (e), (i) and (m). The corresponding reconstruction results of the proposed method are shown in Fig. 6(d), (h), (l) and (p) respectively. The SNR and MSE of the reconstructed data with existing state-of-the-art methods and the proposed method are tabulated in TABLE II. From TABLE II, it is observed that the proposed method has an improved performance over a wide range of noise levels with different decimations on regularly and irregularly sampled seismic data. In addition, we tested the proposed method on 3D dataset and the obtained results are as shown in Fig. 5. The SNR of the 3D data prior to

© 2023 IEEE. Personal use is permitted, but republication/redistribution requires IEEE permission. See https://www.ieee.org/publications/rights/index.html for more information.
Authorized licensed use limited to: DELHI TECHNICAL UNIV. Downloaded on April 24,2023 at 06:10:10 UTC from IEEE Xplore. Restrictions apply.

This article has been accepted for publication in IEEE Transactions on Geoscience and Remote Sensing. This is the author's version which has not been fully edited and content may change prior to final publication. Citation information: DOI 10.1109/TGRS.2023.3267037



(a) Without Attention Module (b) With Attention Module

Fig. 7: Extracted feature maps from the synthetic data set (with and without attention module)

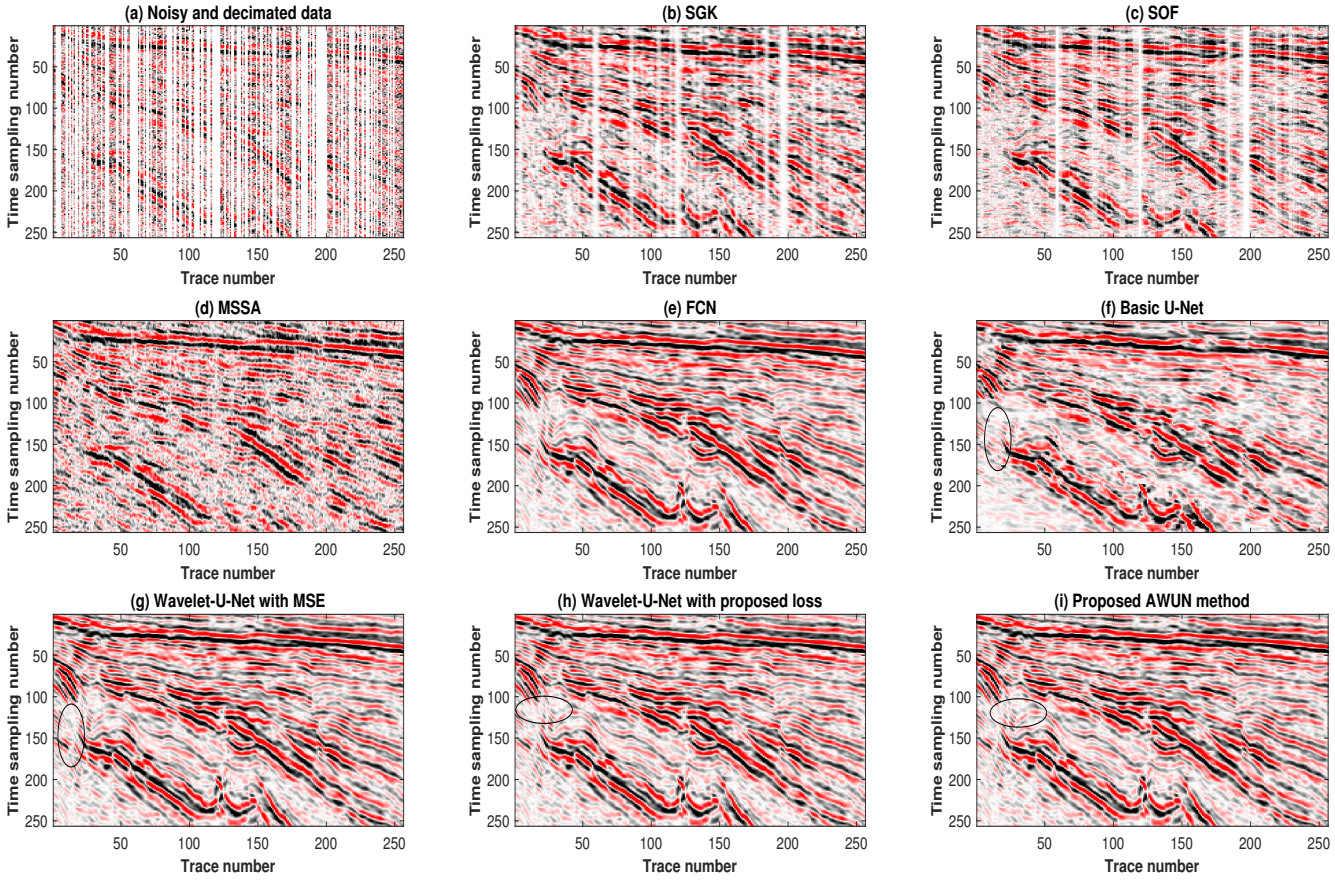


Fig. 8: (a) Noisy decimated field data (b) Reconstructed seismic data for SGK (c) SOF (d) MSSA (e) FCN (f) Basic U-Net (g) Wavelet U-Net with MSE (h) Wavelet U-Net with proposed loss (i) Proposed AWUN method respectively.

reconstruction is -1.026 dB and after applying the proposed method, we obtained the SNR is 19.06 dB.

Field Data Example

In this study, we compared the proposed method on noisy field data in [57] with filtering (SOF), rank-reduction (MSSA), dictionary learning (SGK) and deep learning methods. The noisy field data is depicted in Fig. 8(a). The noisy field data decimated by 50 percent is presented in Fig. 8(a). The output

© 2023 IEEE. Personal use is permitted, but republication/redistribution requires IEEE permission. See https://www.ieee.org/publications/rights/index.html for more information.
Authorized licensed use limited to: DELHI TECHNICAL UNIV. Downloaded on April 24,2023 at 06:10:10 UTC from IEEE Xplore. Restrictions apply.

This article has been accepted for publication in IEEE Transactions on Geoscience and Remote Sensing. This is the author's version which has not been fully edited and content may change prior to final publication. Citation information: DOI 10.1109/TGRS.2023.3267037

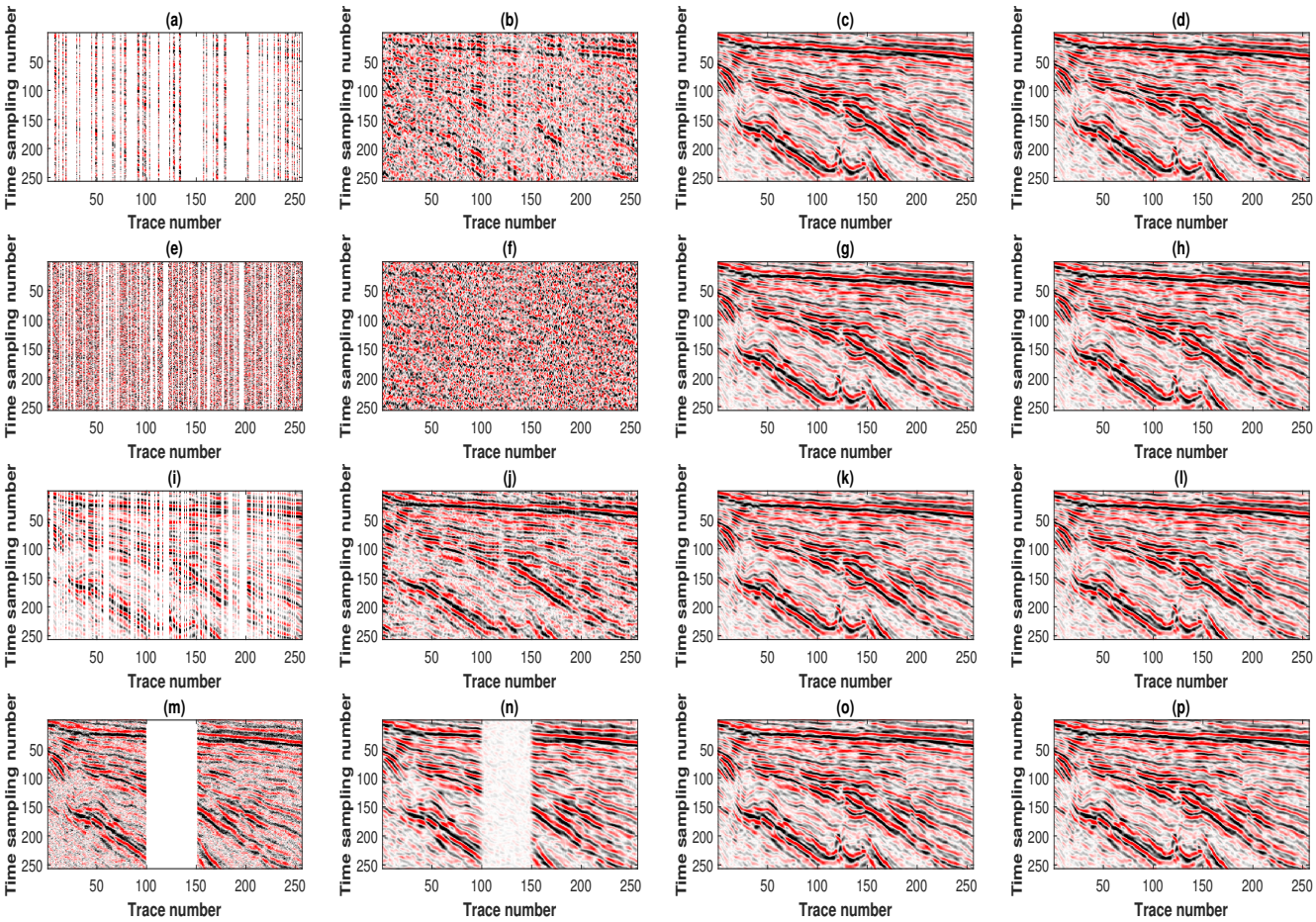


Fig. 9: (a) Noisy decimated seismic data (80%) (b) Reconstructed result for MSSA (c) Basic U-Net (d)Proposed method respectively (e) noisy decimated data with SNR=-2.06dB (f) Reconstructed seismic data for MSSA (g) Basic U-Net (h) Proposed method respectively (i) Erratic decimated data (50%) (j) Reconstructed seismic data for MSSA (k) Basic U-Net (l) Proposed method respectively (m) noisy decimated data with consecutively missing data (50%) (n) Reconstructed seismic data for MSSA (o) Basic U-Net (p) Proposed method respectively.

TABLE I: SNR and MSE comparison of proposed method using AWUN on hyperbolic events with existing methods.

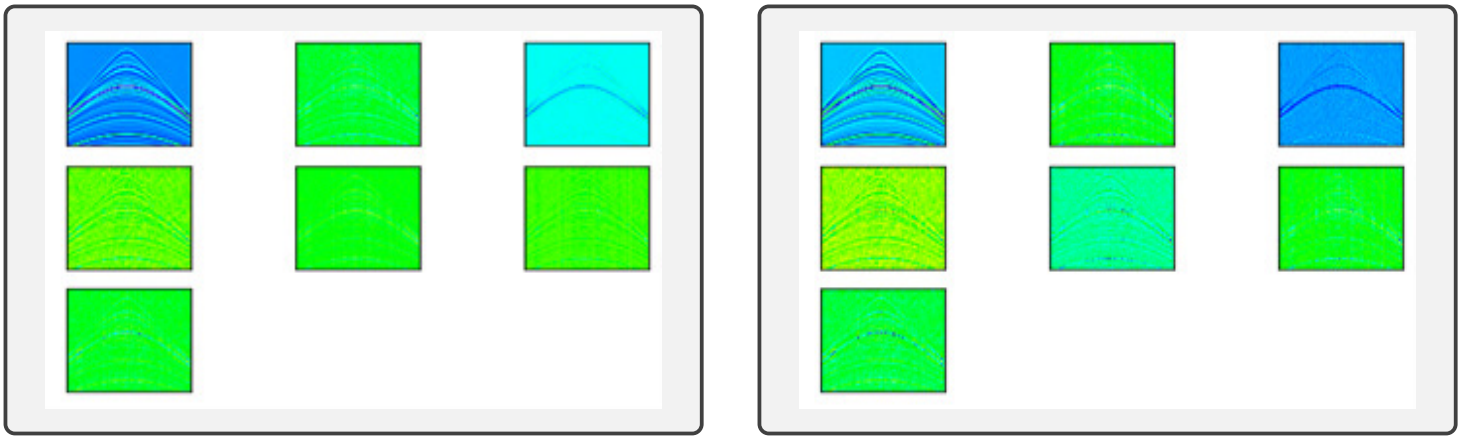
Methods	SNR(dB)	MSE	Energy
Noisy and incomplete data	0.1283	0.0203	-
SGK	3.7111	0.0089	0.4944
SOF	2.9678	0.0105	0.5426
MSSA	6.5453	0.0116	0.5413
FCN	7.2427	0.0039	0.6313
U-Net	18.0852	3.2462e-04	0.8250
Wavelet-U-Net with MSE	24.03	1.2317e-04	0.9012
Wavelet-U-Net with proposed loss + PReLU	26.1174	6.0539e-05	0.9040
Proposed AWUN	29.9479	2.0596e-05	0.9108

of existing methods SGK, SOF, MSSA, FCN, basic U-Net, Wavelet U-Net with MSE loss function, Wavelet U-Net with proposed loss and PReLU activation function and proposed AWUN method on incomplete field data are shown in Fig. 8(b), 8(c), 8(d), 8(e), 8(f), 8(g), 8(h) and 8(i) respectively.

Further, we analyzed the performance of the proposed method on seismic data with different decimation, noise level, erratic noise and regularly missing data (consecutively) with 50% decimation. The resulting noisy and decimated data shown in Fig. 9 (a), (e), (i) and (m) and their corresponding denoised and reconstructed data is shown in Fig. 9 (b-d), (f-h), (j-l), (n-p) respectively. Visually, we can observe that the proposed method has improved performance over a wide range of noise levels with different decimation, removal of erratic noise and reconstruction of regularly sampled seismic data. We also plotted feature visualizations before and after applying DWT at layer 8 after first convolutional block for synthetic data

© 2023 IEEE. Personal use is permitted, but republication/redistribution requires IEEE permission. See https://www.ieee.org/publications/rights/index.html for more information.
Authorized licensed use limited to: DELHI TECHNICAL UNIV. Downloaded on April 24,2023 at 06:10:10 UTC from IEEE Xplore. Restrictions apply.

This article has been accepted for publication in IEEE Transactions on Geoscience and Remote Sensing. This is the author's version which has not been fully edited and content may change prior to final publication. Citation information: DOI 10.1109/TGRS.2023.3267037



(a) Feature maps prior to DWT (b) Feature maps after applying DWT

Fig. 10: Extracted feature maps from the synthetic data set (Before and after DWT)

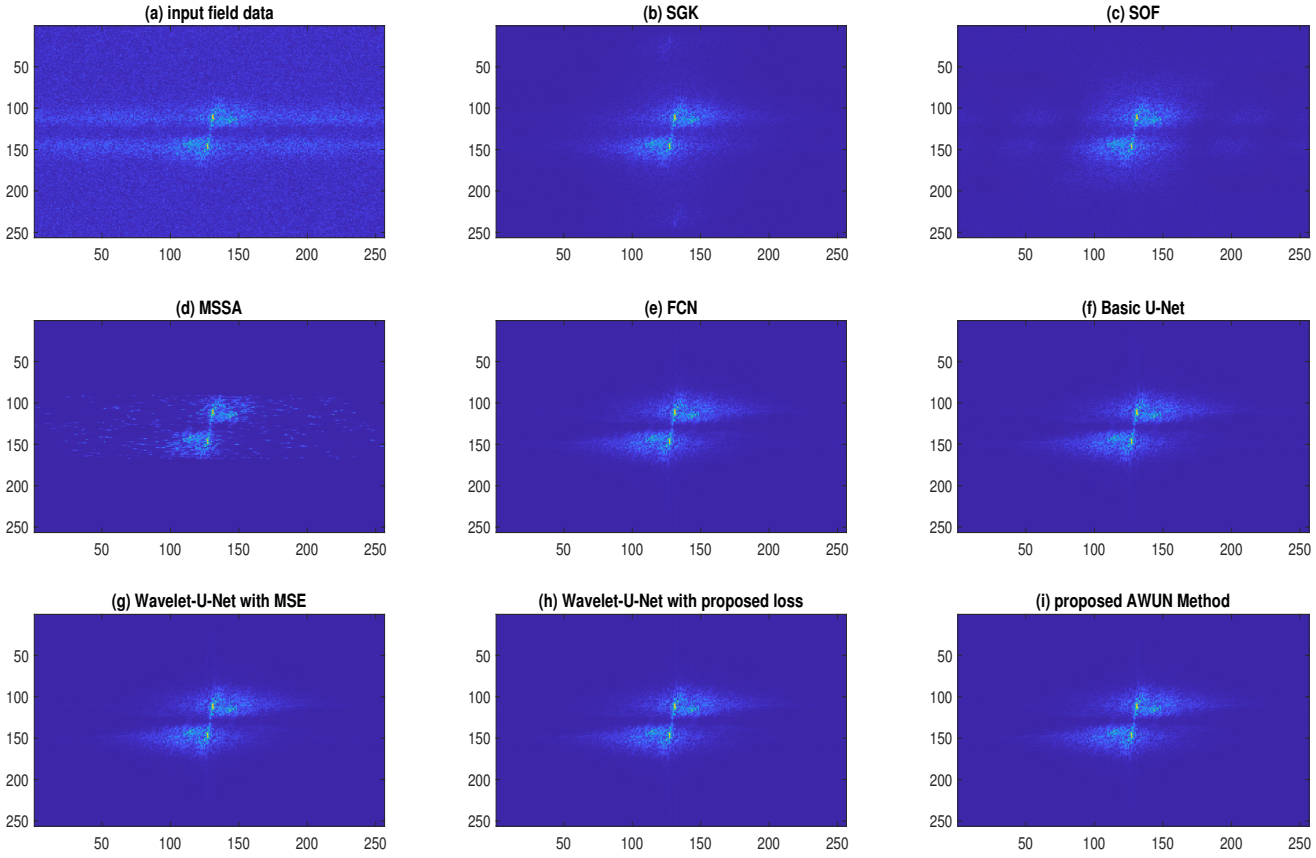


Fig. 11: Frequency spectra of reconstructed seismic data for (a) SGK (b) SOF (c) MSSA (d) FCN (e) Basic U-Net (f) Wavelet U-Net with MSE (g) Wavelet U-Net with proposed loss (h) Proposed AWUN method respectively.

which are shown in Fig. 10(a) and Fig. 10(b) respectively. Moreover, we visualized the frequency spectra of denoised and reconstructed seismic data shown in Fig. 11. From this, we can say that the reconstructed data using proposed method is preserving the features and removing the noise efficiently while compared to the existing methods.

© 2023 IEEE. Personal use is permitted, but republication/redistribution requires IEEE permission. See https://www.ieee.org/publications/rights/index.html for more information.
Authorized licensed use limited to: DELHI TECHNICAL UNIV. Downloaded on April 24,2023 at 06:10:10 UTC from IEEE Xplore. Restrictions apply.

This article has been accepted for publication in IEEE Transactions on Geoscience and Remote Sensing. This is the author's version which has not been fully edited and content may change prior to final publication. Citation information: DOI 10.1109/TGRS.2023.3267037

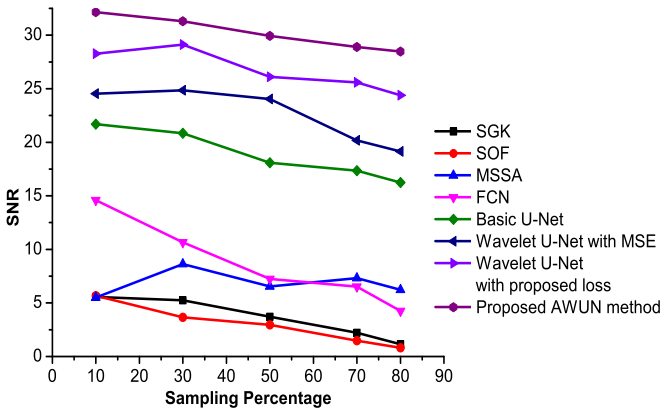


Fig. 12: SNR vs Sampling percentage

TABLE II: SNR and MSE comparison of proposed method using AWUN with existing methods for different noise level, decimation percentage, erratic noise and regularly sampled (consecutively) on hyperbolic events

Noisy and incomplete data with SNR(dB)	Method	Denoised and reconstructed data SNR(dB)	MSE
0.7560 (80% decimate)	MSSA	6.2310	0.0050
	U-Net	16.5243	4.1076e-04
	Proposed AWUN	28.4852	4.0017e-05
1.2550 (30% decimate)	MSSA	8.6256	0.0004
	U-Net	20.8526	2.0358e-04
	Proposed AWUN	31.2948	2.2497e-05
-2.0611	MSSA	1.1516	0.0160
	U-Net	34.7207	1.5609e-05
	Proposed AWUN	40.8729	3.7839e-06
0.5615 (Erratic noise)	MSSA	5.7228	0.0056
	U-Net	31.0326	3.6493e-05
	Proposed AWUN	43.2167	2.2082e-06
2.7519 (Consecutively missing)	MSSA	3.244	0.0099
	U-Net	34.3403	1.7039e-05
	Proposed AWUN	41.3428	3.3937e-06

C. Role of Attention Module

In order to observe the effect of attention module, we plot the feature maps of the convolutional layers with and without attention module in Fig. 7. The proposed network consists of 4 repetitive convolutional blocks on the encoder side. The seven feature channels after first convolutional block before applying attention module are shown in Fig. 7(a) and after applying attention module are shown in Fig. 7(b). The size of each channel is 256x256. The purpose of attention module is to adaptively recalibrate the weight of each channel and improve the representation ability [60]. From the Fig. 7(b), it is clear that features in each channel are highlighted compared to the channels in Fig. 7(a). Thus, we can infer from Fig. 7 that the attention module guides the proposed network to extract the prominent features related to the seismic signal during training. Further in Table I, the Wavelet U-Net with proposed loss + PReLU method without attention module achieves an output SNR of 26.11 dB and the proposed method with attention module achieves an output SNR of 29.94 dB.

D. Discussion and Future scope

The selection of hyper-parameters during training process is very important to obtain an optimum model. In FC networks, the hyper-parameters that can be tuned are: number of layers, number of neurons in each layer, activation function, optimizer, learning rate, batch size, and number of epochs. In addition, the model's performance depends on selection of network architecture and loss function. Whereas in case of CNN, apart from FC networks hyper-parameters, there is a need to tune the number of convolution layers, kernel size and number of filters. In our work, we used convolutional layers in the network architecture. First, we varied the number of filters used in the contracting path convolutional layers to 4, 8, 16, 32 and obtained the SNRs of 26.34, 29.94, 30.12, 28.43 dB respectively. Here, the SNRs achieved are nearly same with number of filters as 8 and 16. Hence, we chose the number of filters to be 8 in the initial convolutional block to reduce the computational cost. Second, we varied the number of convolutional repetitive blocks and achieved high SNR when the number of blocks is chosen as 4 (Contracting path). Next, we varied the size of kernel to 3x3, 5x5, 7x7 and obtained the SNRs as 29.94, 24.87, 19.46 dB respectively. Further, we observed the change in SNR vs sampling percentages: 10, 30, 50, 70, and 80 for various state of the art methods and the proposed method shown in Fig. 12. It can be observed that the proposed AWUN method has better output SNR.

We observed that with increase in kernel size, the SNR is decreasing. Hence we choose the kernel size as 3x3. Further, we tested various activation layers PReLU, ReLU, ELU, Selu, tanh, and obtained highest SNR with PReLU as it gets adapted well with the data. The selection of appropriate optimizer is essential for minimizing the loss function. We chose ADAM as the optimization algorithm as it has faster computation time and requires few parameters for tuning. Further in the optimizer, learning rate determines how fast the model can adapt to the data. After testing with various learning rates: 0.1, 0.01, 0.001, 0.0001, we achieved high SNR with learning rate of 0.01. Finally, we used all the obtained optimum parameters and varied number of epochs. We observed that with minimum number of 10 epochs, our proposed network achieved good denoising and reconstruction capability. However, in future we would like to apply various automated methods to obtain optimum hyper-parameters for the network which saves time and resources. In addition, instead of wavelet transform as pooling operation, we would like to research on combining curvelets, contourlets, shearlets etc with CNN models based on the characteristics of the data.

Moreover, apart from these hyper-parameters, the training data is very important in data-driven methods. The limitations of supervised learning is the requirement of large amounts of labeled data, and further in few cases, it may not generalize well to new or unseen features. With the use of different

© 2023 IEEE. Personal use is permitted, but republication/redistribution requires IEEE permission. See https://www.ieee.org/publications/rights/index.html for more information.
Authorized licensed use limited to: DELHI TECHNICAL UNIV. Downloaded on April 24,2023 at 06:10:10 UTC from IEEE Xplore. Restrictions apply.

This article has been accepted for publication in IEEE Transactions on Geoscience and Remote Sensing. This is the author's version which has not been fully edited and content may change prior to final publication. Citation information: DOI 10.1109/TGRS.2023.3267037

distributed and large amount of data in the training process, we can obtain the generalized model which works well on any test data but at the cost of computational resources. To overcome these limitations, future work will be carried out using un-supervised learning, and federated learning. The un-supervised learning involves training models on unlabeled data using clustering or by identifying patterns in the data. Particularly, in case of seismic data reconstruction, we can further explore on usage of conventional methods in combination with deep learning methods to obtain better results. Whereas, Federated learning (FL) is a machine learning technique that allows multiple devices or machines to collaborate on training a model without sharing their data with a central server [61]. The FL is helpful in cases where seismic data is not available and private. Hence, in future, we would research on combination of federated learning with unsupervised learning for seismic data processing.

IV. Conclusion

In this paper, we proposed a novel method for simultaneous seismic data denoising and reconstruction based on deep learning method. In our proposed method, we perform denoising and reconstruction through attention based wavelet U-Net architecture. The attention module is used to better retrieve the features and improve the denoising and reconstruction of seismic data. The wavelet transform is used as pooling layer and inverse wavelet transform is used instead of upsampling layers which aids in considering frequency features. In addition, we propose to use hybrid loss function Logcosh + Huberloss and an activation function i.e.,PReLU to accurately reconstruct and denoise the seismic data. Moreover, the affect of various hyper parameters in the training process of convolutional neural network (U-Net) is analyzed. The efficacy of the proposed deep learning method is observed using synthetically generated seismic data and field seismic data. The studies with synthetic and field data show that the proposed method has better denoising and reconstruction capability when compared to existing methods and has better SNR, MSE and local similarity.

V. Acknowledgement

Authors would like to acknowledge the financial support from Science and Engineering Research Board, Department of Science and Technology, India through Core Research Grant, Ref: CRG/2019/001234. The authors would like to thank Prof. Yangkang Chen and Omar M Saad at the University of Texas at Austin, for providing research data.

References

[1] W. Huang, D. Feng, and Y. Chen, "De-aliased and de-noise cadzow filtering for seismic data reconstruction," *Geophysical Prospecting*, vol. 68, no. 2, pp. 553–571, 2020.

[2] L. Fu, M. Zhang, Z. Liu, and H. Li, "Reconstruction of seismic data with missing traces using normalized gaussian weighted filter," *Journal of Geophysics and Engineering*, vol. 15, no. 5, pp. 2009–2020, 2018.

[3] X. Chai, H. Gu, F. Li, H. Duan, X. Hu, and K. Lin, "Deep learning for irregularly and regularly missing data reconstruction," *Scientific Reports*, vol. 10, no. 1, pp. 1–18, 2020.

[4] H. Wang, W. Chen, Q. Zhang, X. Liu, S. Zu, and Y. Chen, "Fast dictionary learning for high-dimensional seismic reconstruction," *IEEE Transactions on Geoscience and Remote Sensing*, vol. 59, no. 8, pp. 7098–7108, 2020.

[5] S. Spitz, "Seismic trace interpolation in the fx domain," *Geophysics*, vol. 56, no. 6, pp. 785–794, 1991.

[6] J. Ronen, "Wave-equation trace interpolation," *Geophysics*, vol. 52, no. 7, pp. 973–984, 1987.

[7] M. A. N. Siahsar, S. Gholtashi, V. Abolghasemi, and Y. Chen, "Simultaneous denoising and interpolation of 2d seismic data using data-driven non-negative dictionary learning," *Signal Processing*, vol. 141, pp. 309–321, 2017.

[8] M. D. Sacchi, T. J. Ulrych, and C. J. Walker, "Interpolation and extrapolation using a high-resolution discrete fourier transform," *IEEE Transactions on Signal Processing*, vol. 46, no. 1, pp. 31–38, 1998.

[9] Y. Wang, "Seismic trace interpolation in the fxy domain," *Geophysics*, vol. 67, no. 4, pp. 1232–1239, 2002.

[10] J. Claerbout and S. Fomel, "Geophysical image estimation by example: Stanford exploration project," 2014.

[11] M. Naghizadeh and M. D. Sacchi, "f-x adaptive seismic-trace interpolation," *Geophysics*, vol. 74, no. 1, pp. V9–V16, 2009.

[12] W. Huang and J. Liu, "Robust seismic image interpolation with mathematical morphological constraint," *IEEE Transactions on Image Processing*, vol. 29, pp. 819–829, 2019.

[13] J. Cheng and M. D. Sacchi, "Fast dual-domain reduced-rank algorithm for 3d deblending via randomized qr decomposition," *Geophysics*, vol. 81, no. 1, pp. V89–V101, 2016.

[14] Y. Chen, D. Zhang, Z. Jin, X. Chen, S. Zu, W. Huang, and S. Gan, "Simultaneous denoising and reconstruction of 5-d seismic data via damped rank-reduction method," *Geophysical Journal International*, vol. 206, no. 3, pp. 1695–1717, 2016.

[15] H. Tao, X. Tang, J. Liu, and J. Tian, "Superresolution remote sensing image processing algorithm based on wavelet transform and interpolation," in *Image Processing and Pattern Recognition in Remote Sensing*, vol. 4898. International Society for Optics and Photonics, 2003, pp. 259–263.

[16] G. Hennenfent, L. Fenelon, and F. J. Herrmann, "Nonequispaced curvelet transform for seismic data reconstruction: A sparsity-promoting approach," *Geophysics*, vol. 75, no. 6, pp. WB203–WB210, 2010.

[17] J. Wang, M. Ng, and M. Perz, "Seismic data interpolation by greedy local radon transform," *Geophysics*, vol. 75, no. 6, pp. WB225–WB234, 2010.

[18] L. Jicheng, C. Yongxin, and Z. Jianjiang, "Interpolating seismic data via the pocs method based on shearlet transform," *Journal of Geophysics and Engineering*, vol. 15, no. 3, pp. 852–876, 2018.

[19] S. Gan, S. Wang, Y. Chen, Y. Zhang, and Z. Jin, "Dealiased seismic data interpolation using seislet transform with low-frequency constraint," *IEEE Geoscience and remote sensing letters*, vol. 12, no. 10, pp. 2150–2154, 2015.

[20] B. Wang, R.-S. Wu, X. Chen, and J. Li, "Simultaneous seismic data interpolation and denoising with a new adaptive method based on dreamlet transform," *Geophysical Journal International*, vol. 201, no. 2, pp. 1182–1194, 2015.

[21] V. Oropeza and M. Sacchi, "Simultaneous seismic data denoising and reconstruction via multichannel singular spectrum analysis," *Geophysics*, vol. 76, no. 3, pp. V25–V32, 2011.

[22] J. Yu and B. Wu, "Attention and hybrid loss guided deep learning for consecutively missing seismic data reconstruction," *IEEE Transactions on Geoscience and Remote Sensing*, vol. 60, pp. 1–8, 2021.

[23] L. Kuruguntla, V. C. Dodda, and K. Elumalai, "Study of parameters in dictionary learning method for seismic denoising," *IEEE Transactions on Geoscience and Remote Sensing*, vol. 60, pp. 1–13, 2021.

[24] Y. Jia and J. Ma, "What can machine learning do for seismic data processing? an interpolation application," *Geophysics*, vol. 82, no. 3, pp. V163–V177, 2017.

[25] A. Siahkoohi, R. Kumar, and F. Herrmann, "Seismic data reconstruction with generative adversarial networks," in *80th EAGE conference and exhibition 2018*, vol. 2018, no. 1. European Association of Geoscientists & Engineers, 2018, pp. 1–5.

[26] H. Kaur, N. Pham, and S. Fomel, "Seismic data interpolation using cyclegan," in *SEG technical program expanded abstracts 2019*. Society of Exploration Geophysicists, 2019, pp. 2202–2206.

[27] D. Chang, W. Yang, X. Yong, G. Zhang, W. Wang, H. Li, and Y. Wang, "Seismic data interpolation using dual-domain conditional generative adversarial networks," *IEEE Geoscience and Remote Sensing Letters*, vol. 18, no. 10, pp. 1856–1860, 2020.

© 2023 IEEE. Personal use is permitted, but republication/redistribution requires IEEE permission. See https://www.ieee.org/publications/rights/index.html for more information.
Authorized licensed use limited to: DELHI TECHNICAL UNIV. Downloaded on April 24,2023 at 06:10:10 UTC from IEEE Xplore. Restrictions apply.

This article has been accepted for publication in IEEE Transactions on Geoscience and Remote Sensing. This is the author's version which has not been fully edited and content may change prior to final publication. Citation information: DOI 10.1109/TGRS.2023.3267037

[28] B. Wang, N. Zhang, W. Lu, P. Zhang, and J. Geng, "Seismic data interpolation using deep learning based residual networks," in *80th EAGE Conference and Exhibition 2018*, vol. 2018, no. 1. European Association of Geoscientists & Engineers, 2018, pp. 1–5.

[29] D. Yoon, Z. Yeeh, and J. Byun, "Seismic data reconstruction using deep bidirectional long short-term memory with skip connections," *IEEE Geoscience and Remote Sensing Letters*, vol. 18, no. 7, pp. 1298–1302, 2020.

[30] S. Pan, K. Chen, J. Chen, Z. Qin, Q. Cui, and J. Li, "A partial convolution-based deep-learning network for seismic data regularization1," *Computers & Geosciences*, vol. 145, p. 104609, 2020.

[31] H. Huang, T. Wang, J. Cheng, Y. Xiong, C. Wang, and J. Geng, "Self-supervised deep learning to reconstruct seismic data with consecutively missing traces," *IEEE Transactions on Geoscience and Remote Sensing*, vol. 60, pp. 1–14, 2022.

[32] T. He, B. Wu, and X. Zhu, "Seismic data consecutively missing trace interpolation based on multistage neural network training process," *IEEE Geoscience and Remote Sensing Letters*, vol. 19, pp. 1–5, 2021.

[33] N. Liu, L. Wu, J. Wang, H. Wu, J. Gao, and D. Wang, "Seismic data reconstruction via wavelet-based residual deep learning," *IEEE Transactions on Geoscience and Remote Sensing*, vol. 60, pp. 1–13, 2022.

[34] X. Dong, J. Lin, S. Lu, H. Wang, and Y. Li, "Multiscale spatial attention network for seismic data denoising," *IEEE Transactions on Geoscience and Remote Sensing*, vol. 60, pp. 1–17, 2022.

[35] O. M. Saad, M. Bai, and Y. Chen, "Uncovering the microseismic signals from noisy data for high-fidelity 3d source-location imaging using deep learning," *Geophysics*, vol. 86, no. 6, pp. KS161–KS173, 2021.

[36] O. M. Saad, Y. A. S. I. Oboué, M. Bai, L. Samy, L. Yang, and Y. Chen, "Self-attention deep image prior network for unsupervised 3-d seismic data enhancement," *IEEE Transactions on Geoscience and Remote Sensing*, vol. 60, pp. 1–14, 2021.

[37] L. Yang, S. Wang, X. Chen, W. Chen, O. M. Saad, and Y. Chen, "Deep-learning missing well-log prediction via long short-term memory network with attention-period mechanism," *Geophysics*, vol. 88, no. 1, pp. D31–D48, 2023.

[38] H. S. Elsayed, O. M. Saad, M. S. Soliman, Y. Chen, and H. A. Youness, "Attention-based fully convolutional densenet for earthquake detection," *IEEE Transactions on Geoscience and Remote Sensing*, vol. 60, pp. 1–10, 2022.

[39] L. Yang, S. Wang, X. Chen, W. Chen, O. Saad, X. Zhou, N. Pham, Z. Geng, S. Fomel, and Y. Chen, "Deep learning framework with period and attention mechanisms for porosity and permeability prediction," in *83rd EAGE Annual Conference & Exhibition*, vol. 2022, no. 1. EAGE Publications BV, 2022, pp. 1–5.

[40] L. Yang, S. Wang, X. Chen, W. Chen, O. M. Saad, X. Zhou, N. Pham, Z. Geng, S. Fomel, and Y. Chen, "High-fidelity permeability and porosity prediction using deep learning with the self-attention mechanism," *IEEE Transactions on Neural Networks and Learning Systems*, 2022.

[41] L. Zhu, E. Liu, and J. H. McClellan, "Joint seismic data denoising and interpolation with double-sparsity dictionary learning," *Journal of Geophysics and Engineering*, vol. 14, no. 4, pp. 802–810, 2017.

[42] S. Yu, J. Ma, X. Zhang, and M. D. Sacchi, "Interpolation and denoising of high-dimensional seismic data by learning a tight frame," *Geophysics*, vol. 80, no. 5, pp. V119–V132, 2015.

[43] J. Wu, Q. Chen, Z. Gui, and M. Bai, "Fast dictionary learning for 3d simultaneous seismic data reconstruction and denoising," *Journal of Applied Geophysics*, vol. 194, p. 104446, 2021.

[44] Y. Zhou and S. Li, "Simultaneous deblending and interpolation using structure-oriented filters," *Journal of Applied Geophysics*, vol. 150, pp. 230–243, 2018.

[45] O. M. Saad, S. Fomel, R. Abma, and Y. Chen, "Unsupervised deep learning for 3d interpolation of highly incomplete data," *Geophysics*, vol. 88, no. 1, pp. WA189–WA200, 2023.

[46] J. Jiang, H. Ren, and M. Zhang, "A convolutional autoencoder method for simultaneous seismic data reconstruction and denoising," *IEEE Geoscience and Remote Sensing Letters*, vol. 19, pp. 1–5, 2021.

[47] P. Liu, H. Zhang, W. Lian, and W. Zuo, "Multi-level wavelet convolutional neural networks," *IEEE Access*, vol. 7, pp. 74 973–74 985, 2019.

[48] O. M. Saad and Y. Chen, "Capsphase: Capsule neural network for seismic phase classification and picking," *IEEE Transactions on Geoscience and Remote Sensing*, vol. 60, pp. 1–11, 2021.

[49] O. M. Saad, M. S. Soliman, Y. Chen, A. A. Amin, and H. Abdelhafiez, "Discriminating earthquakes from quarry blasts using capsule neural network," *IEEE Geoscience and Remote Sensing Letters*, vol. 19, pp. 1–5, 2022.

[50] O. M. Saad and Y. Chen, "Earthquake detection and p-wave arrival time picking using capsule neural network," *IEEE Transactions on Geoscience and Remote Sensing*, vol. 59, no. 7, pp. 6234–6243, 2020.

[51] G. E. Hinton, S. Sabour, and N. Frosst, "Matrix capsules with em routing," in *International conference on learning representations*, 2018.

[52] A. Vaswani, N. Shazeer, N. Parmar, J. Uszkoreit, L. Jones, A. N. Gomez, Ł. Kaiser, and I. Polosukhin, "Attention is all you need," *Advances in neural information processing systems*, vol. 30, 2017.

[53] L. Alzubaidi, J. Zhang, A. J. Humaidi, A. Al-Dujaili, Y. Duan, O. Al-Shamma, J. Santamaría, M. A. Fadhel, M. Al-Amidie, and L. Farhan, "Review of deep learning: Concepts, cnn architectures, challenges, applications, future directions," *Journal of big Data*, vol. 8, no. 1, pp. 1–74, 2021.

[54] O. Ronneberger, P. Fischer, and T. Brox, "U-net: Convolutional networks for biomedical image segmentation," in *International Conference on Medical image computing and computer-assisted intervention*. Springer, 2015, pp. 234–241.

[55] S. Fomel, "Local seismic attributes," *Geophysics*, vol. 72, no. 3, pp. A29–A33, 2007.

[56] L. Kuruguntla, V. C. Dodda, A. K. Mandpura, and K. Elumalai, "Erratic noise attenuation using double sparsity dictionary learning method," *IEEE Transactions on Geoscience and Remote Sensing*, 2022.

[57] O. M. Saad and Y. Chen, "Deep denoising autoencoder for seismic random noise attenuation," *Geophysics*, vol. 85, no. 4, pp. V367–V376, 2020.

[58] H. Wang, Y. Chen, O. M. Saad, W. Chen, Y. A. S. I. Oboué, L. Yang, S. Fomel, and Y. Chen, "A matlab code package for 2d/3d local slope estimation and structural filtering," *Geophysics*, vol. 87, no. 3, pp. F1–F14, 2022.

[59] J. Wu, Q. Chen, Z. Gui, and M. Bai, "Fast dictionary learning for 3d simultaneous seismic data reconstruction and denoising," *Journal of Applied Geophysics*, vol. 194, p. 104446, 2021.

[60] M.-H. Guo, T.-X. Xu, J.-J. Liu, Z.-N. Liu, P.-T. Jiang, T.-J. Mu, S.-H. Zhang, R. R. Martin, M.-M. Cheng, and S.-M. Hu, "Attention mechanisms in computer vision: A survey," *Computational Visual Media*, pp. 1–38, 2022.

[61] Q. Yang, Y. Liu, Y. Cheng, Y. Kang, T. Chen, and H. Yu, "Federated learning," *Synthesis Lectures on Artificial Intelligence and Machine Learning*, vol. 13, no. 3, pp. 1–207, 2019.

© 2023 IEEE. Personal use is permitted, but republication/redistribution requires IEEE permission. See https://www.ieee.org/publications/rights/index.html for more information.
Authorized licensed use limited to: DELHI TECHNICAL UNIV. Downloaded on April 24,2023 at 06:10:10 UTC from IEEE Xplore. Restrictions apply.

arXiv:2304.02608v1 [math.CV] 5 Apr 2023

SOME DIFFERENTIAL SUBORDINATION RESULTS FOR A CLASS OF STARLIKE FUNCTIONS

MRIDULA MUNDALIA AND S. SIVAPRASAD KUMAR

Abstract. In this paper, first order differential subordination implication results are derived for $\mathcal{S}^*_\varrho$, a subclass of starlike functions, defined as

$$\mathcal{S}^*_\varrho = \left\{ f \in \mathcal{A} : \frac{zf'(z)}{f(z)} \prec \varrho(z) := \cosh\sqrt{z}, z \in \mathbb{D} \right\},$$

where we choose the branch of the square root function so that $\cosh\sqrt{z} = 1 + z/2! + z^2/4! + \cdots$. Further we deduce Briot-Bouquet differential subordination results along with some examples.

1. Introduction

Let $\mathcal{A}$ be the class of all analytic functions defined on the unit disc $\mathbb{D} := \{z \in \mathbb{C} : |z| < 1\}$, with the usual normalization $f(0) = 0$ and $f'(0) = 1$, i.e of the form $f(z) = z + a_2z^2 + a_3z^3 + \cdots$. Let $\mathcal{S}$ denote the class of all univalent functions in $\mathcal{A}$. If $f(z)$ and $g(z)$ are analytic functions in $\mathbb{D}$, then $f(z)$ is said to be subordinate to $g(z)$, written symbolically as $f \prec g$, if there exists a Schwarz function $w(z)$ such that $w(0) = 0$ and $f(z) = g(w(z))$. In particular, if $g(z)$ is a univalent function in $\mathbb{D}$, then $f \prec g$ if and only if $f(0) = g(0)$ and $f(\mathbb{D}) \subset g(\mathbb{D})$. In 1992, Ma and Minda [9] investigated the following special subclass of $\mathcal{S}$,

$$\mathcal{S}^*(\phi) = \left\{ f \in \mathcal{A} : \frac{zf'(z)}{f(z)} \prec \phi(z), z \in \mathbb{D} \right\},$$

where $\phi(z)$ is an analytic univalent function so that $\phi'(0) > 0$ and $\operatorname{Re}\phi(z) > 0$ $(z \in \mathbb{D})$. Also, $\phi(z)$ is symmetric about the real axis and starlike with respect to $\phi(0) = 1$. The class $\mathcal{S}^*(\phi)$ has been extensively studied by various authors for different choices of $\phi(z)$, see [3, 4, 5, 7, 8]. Below we enlist some Ma and Minda subclasses of starlike functions, obtained for different choice of $\phi(z)$.

Table 1. Ma and Minda subclasses of starlike functions

Class $\mathcal{S}^*(\phi)$	$\phi(z)$	**References**
$\mathcal{S}^*_e$	e^z	[11] Mendiratta et al.
$\mathcal{S}^*_L$	$\sqrt{1+z}$	[16] Sokół et al.
$\mathcal{S}^*_q$	$z + \sqrt{1+z^2}$	[14] Raina et al.
$\mathcal{S}^*[A, B]$	$(1 + Az)/(1 + Bz)$	[6] W. Janowski
$\mathcal{S}^*(q_\kappa)$	$\sqrt{1+\kappa z}$, $0 < \kappa \leq 1$	[2] Sokół et al.
$\mathcal{S}^*_s$	$(1 + sz)^2$, $-1/\sqrt{2} \leq s \leq 1/\sqrt{2}$	[10] Masih et al.

The classes $\mathcal{S}^*_e, \mathcal{S}^*_s$, $\mathcal{S}^*(q_\kappa)$, and $\mathcal{S}^*[A, B]$ (see Table 1) were widely studied in [2, 6, 10, 11]. Motivated by the above Ma and Minda subclasses of starlike functions, recently Mundalia and

2010 *Mathematics Subject Classification.* 30C45, 30C80.

Key words and phrases. Univalent functions, Starlike functions, Differential subordination, Briot-Bouquet differential subordination, hyperbolic cosine function.

The first author is supported by Delhi Technological University, New Delhi.

Kumar [13] introduced and studied the following subclass of starlike functions associated with a hyperbolic cosine function, given by

$$\mathcal{S}^*_\varrho = \left\{ f \in \mathcal{A} : \frac{zf'(z)}{f(z)} \prec \varrho(z) := \cosh\sqrt{z}, z \in \mathbb{D} \right\},$$

where the branch of the square root function is so chosen such that

$$\cosh\sqrt{z} = 1 + \frac{z}{2!} + \frac{z^2}{4!} + \cdots = \sum_{n=0}^{\infty} \frac{z^n}{(2n)!}.$$

Miller and Mocanu have extensively discussed the theory of differential subordination, see [12]. In the recent past, several authors have established conditions on η, so that $1+\eta zp'(z)/p^n(z) \prec \phi(z)$ $(n = 0, 1, 2)$ implies $p(z) \prec \psi(z)$, for different choices of $\phi(z)$ and $\psi(z)$ such as e^z, $\sqrt{1+z}$ and $(1 + Az)/(1 + Bz)$ $(-1 \le B < A \le 1)$, see [1, 5, 8, 11]. In the present investigation, we establish certain differential subordination implication results for the dominants $e^z, (1 + Az)/(1 + Bz), z + \sqrt{1 + z^2}$ and $(1 + sz)^2$, where $0 < s \le 1/\sqrt{2}$ (see Table 1). Furthermore results related to Briot-Bouquet type differential subordination have been discussed in context of the class $\mathcal{S}^*_\varrho$. We need the following definition and lemmas to prove our subsequent results.

Definition 1.1. Let $\mathcal{Q}$ be the set of functions q that are analytic and injective on $\overline{\mathbb{D}}\backslash E(q)$, where

$$E(q) = \left\{ \zeta \in \partial\mathbb{D} : \lim_{z\to\zeta} q(z) = \infty \right\},$$

such that $q'(\zeta) \ne 0$ for $\zeta \in \partial\mathbb{D}\backslash E(q)$.

Lemma 1.2. [12] *Let q be analytic in $\mathbb{D}$ and let φ be analytic in domain $\mathcal{D}$ containing $q(\mathbb{D})$ with $\varphi(w) \ne 0$ when $w \in q(\mathbb{D})$. Set $\mathcal{Q}(z) := zq'(z)\varphi(q(z))$ and $h(z) := \nu(q(z)) + \mathcal{Q}(z)$. Suppose (i.) either h is convex, or $\mathcal{Q}$ is starlike univalent in $\mathbb{D}$ and (ii.) $\mathrm{Re}(zh'(z)/\mathcal{Q}(z)) > 0$ for $z \in \mathbb{D}$. If p is analytic in $\mathbb{D}$, with $p(0) = q(0)$, $p(\mathbb{D}) \subset \mathcal{D}$ and*

$$\nu(p(z)) + zp'(z)\varphi(p(z)) \prec \nu(q(z)) + zq'(z)\varphi(q(z)),$$

then $p(z) \prec q(z)$, and q is the best dominant.

Lemma 1.3. [15, Lemma 1.3, p.28] *Let w be a meromorphic function in $\mathbb{D}$, $w(0) = 0$. If for some $z_0 \in \mathbb{D}$, $\max_{|z|\le|z_0|} |w(z)| = |w(z_0)|$, then it follows that $z_0w'(z_0)/w(z_0) \ge 1$.*

2. Subordination Results

In this section, we study subordination results pertaining to the class $\mathcal{S}^*_\varrho$. We begin with the following result.

Theorem 2.1. *Suppose η satisfies $|\eta| \ge 2|A - B|/(1 - |B|)\tanh 1$, where $(A, B) \in \mathbb{C} \times \mathbb{C}$, with $A \ne B$ and $|B| < 1$. Let $p(z)$ be an analytic function in $\mathbb{D}$, with $p(0) = 1$, satisfying the subordination $1 + \eta(zp'(z))/p(z) \prec (1 + Az)/(1 + Bz)$, then $p(z) \prec \cosh\sqrt{z} =: \varrho(z)$.*

Proof. Let $T(z) = z\varrho'(z)/\varrho(z) = (\sqrt{z}\tanh\sqrt{z})/2$, then clearly it is a starlike function in $\mathbb{D}$ and $\mathrm{Re}(\sqrt{z}\,\mathrm{csch}\,2\sqrt{z}) > 0$. Let $v(u) = 1$ and $\psi(u) = \eta/u$. Note that $\mathrm{Re}\, z\mathfrak{h}'(z)/T(z) - 1 = \mathrm{Re}\,\sqrt{z}\,\mathrm{csch}\,2\sqrt{z} > 0$, where $\mathfrak{h}(z) = v(\varrho(z)) + T(z)$. Assume $\Psi(z) = (1 + Az)/(1 + Bz)$. Then $\Psi^{-1}(u) = (u - 1)/(A - Bu)$. Let

$$M(z) = 1 + \frac{\eta}{2}\sqrt{z}\tanh(\sqrt{z}).$$

We show that $\Psi(z) \prec M(z)$. For this purpose, we shall prove that $|\Psi^{-1}(M(e^{it}))| \geq 1$ for each $-\pi \leq t \leq \pi$. On the boundary of $\mathbb{D}$, we have

$$|\Psi^{-1}(M(e^{it}))| \geq \frac{|\eta||\tanh(e^{it/2})|}{2|A-B|+|\eta B \tanh(e^{it/2})|}.$$

As $|\tanh(e^{it/2})|$ attains its minimum at $t = 0$, we get the required lower bound on $|\eta|$. Thus the result follows at once by applying Lemma 1.2. ∎

Upon substituting $p(z) = zf'(z)/f(z)$, we deduce the following corollary.

Corollary 2.2. *Assume A and B be as defined in Theorem 2.1 and let $f \in \mathcal{A}$ such that*

$$1 + \eta\left(1 + \frac{zf''(z)}{f'(z)} - \frac{zf'(z)}{f(z)}\right) \prec \frac{1+Az}{1+Bz}$$

then $f \in \mathcal{S}^*_\varrho$.

Theorem 2.3. *Let $p(z)$ be an analytic function in $\mathbb{D}$ such that $1 + \eta z p'(z) \prec \cosh\sqrt{z}$ with*

$$\kappa = \frac{Chi(1) + Ci(1) - 2\xi}{Chi(1) - Ci(1)},$$

where

$$Chi(1) = \xi + \int_0^1 (\cosh\sqrt{t} - 1)/t \ dt, \quad Ci(1) = \xi + \int_0^1 (\cos\sqrt{t} - 1)/t \ dt.$$

then

(i) $p(z) \prec e^z$, whenever $(e-1)\eta \geq 2e(\xi - Ci(1))$.
(ii) $p(z) \prec z + \sqrt{1+z^2}$, whenever $(\sqrt{2}-1)\eta \geq \sqrt{2}(\xi - Ci(1))$.
(iii) $p(z) \prec (1+Az)/(1+Bz)$, where $-1 < B < A \leq 1$, whenever $\eta \geq \eta_0$, where

$$\eta_0 = \begin{cases} \dfrac{2}{A-B}(1-B)(\xi - Ci(1)) & \text{if } -1 < B \leq -\kappa, \\ \dfrac{-2}{A-B}(1+B)(\xi - Chi(1)) & \text{if } -\kappa < B < 1. \end{cases} \tag{2.1}$$

(iv) $p(z) \prec (1+sz)^2$ whenever $\eta \geq \eta_0$, where

$$\eta_0 = \begin{cases} \dfrac{2}{s(s+2)}(Chi(1) - \xi) & \text{if } 0 < s \leq 2\kappa, \\ \dfrac{2}{s(s-2)}(Ci(1) - \xi) & \text{if } 2\kappa < s \leq 1/\sqrt{2}. \end{cases} \tag{2.2}$$

Proof. Let $q_\eta(z)$ be an analytic function, $q_\eta : \overline{\mathbb{D}} \to \mathbb{C}$ defined by

$$q_\eta(z) = 1 + \frac{1}{\eta}\left(2Chi\sqrt{z} - \log z - 2\xi\right).$$

Then $q_\eta(z)$ is a solution of the differential equation $1 + \eta z p'(z) = \cosh\sqrt{z}$. Let $v(u) = 1$ and $\psi(u) = \eta$. Define an analytic function $T : \overline{\mathbb{D}} \to \mathbb{C}$ by

$$T(z) = zq'_\eta(z)\psi(q_\eta(z)) = \cosh\sqrt{z} - 1.$$

Note that $T(z)$ is a starlike function in $\mathbb{D}$. Observe that $\mathfrak{h}(z) = v(q_\eta(z)) + T(z)$ satisfies

$$\mathrm{Re}\left(\frac{z\mathfrak{h}'(z)}{T(z)}\right) = \mathrm{Re}\left(\frac{1}{2}\sqrt{z}\coth\left(\frac{\sqrt{z}}{2}\right)\right) > 0.$$

Thus by Lemma 1.2, we deduce that $p(z) \prec q_\eta(z)$. In each of the above cases, we deduce conditions on η such that $p(z) \prec \mathcal{G}(z)$, for various choices of $\mathcal{G}(z)$ such as $e^z, z+\sqrt{1+z^2}, (1+Az)/(1+Bz)$ and $(1+sz)^2$. Further if $q_\eta(z) \prec \mathcal{G}(z)$, then

$$\mathcal{G}(-1) \leq q_\eta(-1) < q_\eta(1) \leq \mathcal{G}(1) \tag{2.3}$$

holds true. In the following cases, we shall obtain conditions on η so that (2.3) holds.

(i) Let $\mathcal{G}(z) = e^z$, then the inequalities (2.3) yields the following

$$e^{-1} \leq 1 + \frac{2}{\eta}(Ci(1) - \xi) < 1 + \frac{2}{\eta}(Chi(1) - \xi) \leq e, \tag{2.4}$$

Inequality (2.4) holds true, provided $\eta \geq \eta_0$, where $\eta_0 = 2e(\xi - Ci(1))/(e-1)$. Thus, for each $\eta \geq \eta_0$ the result follows.

(ii) For $\mathcal{G}(z) = z + \sqrt{1+z^2}$, the expression in (2.3), gives

$$\sqrt{2} - 1 \leq 1 + \frac{2}{\eta}(Ci(1) - \xi) < 1 + \frac{2}{\eta}(Chi(1) - \xi) \leq \sqrt{2} + 1, \tag{2.5}$$

which further gives that (2.5) holds for each $\eta \geq \eta_0$, where $\eta_0 = \sqrt{2}(\xi - Ci(1))/\big(\sqrt{2}-1\big)\big)$. Therefore for each $\eta \geq \eta_0$, $q_\eta(z) \prec \mathcal{G}(z)$. This leads us to the conclusion that $p(z) \prec \mathcal{G}(z)$.

(iii) Let $\mathcal{G}(z) = (1+Az)/(1+Bz)$. Then for (2.3) to hold true, proceeding as in the previous cases, we must have $\eta \geq \eta_0$ where η_0 is as given in (2.1).

(iv) For $\mathcal{G}(z) = (1+sz)^2$, if η in (2.3) satisfies the conditions given in (2.2), then it yields the required subordination implication.

∎

Theorem 2.4. *Let $-1 < B < A \leq 1$ and $\mu = (\cosh 1 - 1)/(1 - \cos 1)$. Suppose $p(z)$ is an analytic function in $\mathbb{D}$ such that $1 + \eta z p'(z) \prec (1+Az)/(1+Bz)$, where η satisfies the following*

$$\begin{cases} \eta B(\cosh 1 - 1) \leq (A-B)\log(1+B) \text{ if } -1 < B \leq B_0, \\ \eta B(\cos 1 - 1) \geq (A-B)\log(1-B) \text{ if } B_0 < B < 0, \\ \eta B(\cos 1 - 1) \leq (A-B)\log(1-B) \text{ if } 0 < B < 1, \end{cases} \tag{2.6}$$

where B_0 is the root of the equation $(1+B)(1-B)^\mu = 1$. Moreover, for $B = 0$, if η satisfies $2\eta \geq A \csc^2(1/2)$, then $p(z) \prec \cosh\sqrt{z}$.

Proof. Let $q_\eta(z)$ be an analytic function, $q_\eta : \overline{\mathbb{D}} \to \mathbb{C}$ defined as follows:

$$q_\eta(z) = 1 + \frac{A-B}{\eta B}\log(1+Bz),$$

be a solution of the differential equation $1 + \eta z p'(z) = (1+Az)/(1+Bz)$. Let $v(u) = 1$ and $\psi(u) = \eta$. Define an analytic function $T : \overline{\mathbb{D}} \to \mathbb{C}$ by $T(z) = z q_\eta'(z)\psi(q_\eta(z))$. Clearly for the given choice of A and B, $T(z) = (A-B)z/(1+Bz)$ is a starlike function in $\mathbb{D}$. Note that the function $\mathfrak{h}(z) = v(q_\eta(z)) + T(z)$ gives $z\mathfrak{h}'(z)/T(z) = 1/(1+Bz)$. Thus $\operatorname{Re} z\mathfrak{h}'(z)/T(z) > 0$. Further by Lemma 1.2 we deduce that $p(z) \prec q_\eta(z)$. We need to prove that $p(z) \prec \cosh\sqrt{z} =: \varrho(z)$. It can be easily seen from the graphs of $q_\eta(z)$ and $\varrho(z)$ that whenever $q_\eta(z) \prec \varrho(z)$, then we have

$$\varrho(-1) \leq q_\eta(-1) < q_\eta(1) \leq \varrho(1). \tag{2.7}$$

On taking suitable values of η, the inequalities (2.7) becomes a necessary as well as sufficient condition for $q_\eta(z) \prec \varrho(z)$. For $B \neq 0$, we have

$$\cos 1 \leq 1 + \frac{A-B}{\eta B}\log(1-B) < 1 + \frac{A-B}{\eta B}\log(1+B) \leq \cosh 1.$$

On solving the above inequalities the conditions on η given in (2.6) can be established. Further for $B = 0$, we get $m_\eta(z) = 1 + Az/\eta$ such that inequality $\cos 1 \leq m_\eta(-1) < m_\eta(1) \leq \cosh 1$ holds. This inequality holds if and only if $A \leq 2\eta \sin^2(1/2)$. Hence $p(z) \prec \cosh\sqrt{z}$. ∎

Theorem 2.5. *Suppose $(\eta, \gamma) \in \mathbb{R} \times \mathbb{R} - \{(\eta, -\eta)\}$ satisfy the following inequalities:*

$$0 \leq \gamma + \eta\cosh 1 \leq \frac{\sinh 1}{2\left(1 + \sqrt{2} - \cosh 1\right)} \text{ and } 0 \geq \gamma + \eta\cos 1 \geq -\frac{\sin 1}{2\left(1 + \sqrt{2} - \cos 1\right)}. \tag{2.8}$$

Let $p(z)$ be an analytic function, such that $p(0) = 1$ and satisfies

$$p(z) + \frac{zp'(z)}{\eta p(z) + \gamma} \prec z + \sqrt{1 + z^2} \tag{2.9}$$

then

$$p(z) \prec \cosh\sqrt{z}.$$

Proof. We define analytic functions $M(z)$ and $w(z)$, as $M : \mathbb{D} \to \mathbb{C}$ and $w : \mathbb{D} \to \mathbb{C}$ defined by

$$M(z) = p(z) + \frac{zp'(z)}{\eta p(z) + \gamma} \quad \text{and} \quad p(z) = \cosh\sqrt{w(z)} \tag{2.10}$$

where $w(z)$ is defined on the principle branch of logarithmic and square root function. Clearly $w(z)$ is analytic with $w(0) = 0$. We need to prove that $|w(z)| < 1$. Let $z_0 \in \mathbb{D}$ such that $\max_{|z|\leq|z_0|}|w(z)| = |w(z_0)| = 1$. Further using Lemma 1.3, $z_0 w'(z_0) = k w(z_0)$ where $k \geq 1$. Assume $w(z) = e^{it}$, $-\pi \leq t \leq \pi$. Consider the expression

$$\begin{aligned}
|M(z_0) - 1|^2 &= \left|\cosh\sqrt{w(z_0)} - 1 + \frac{z_0 w'(z_0)\sinh\sqrt{w(z_0)}}{2\sqrt{w(z_0)}(\eta\cosh\sqrt{w(z_0)} + \gamma)}\right|^2 \\
&= \left|\cosh e^{it/2} - 1 + \frac{k e^{it/2}\sinh e^{it/2}}{2(\eta\cosh e^{it/2} + \gamma)}\right|^2 \\
&= \frac{A_N(\tau)}{A_D(\tau)} \quad (\tau = t/2, -\pi \leq \tau \leq \pi),
\end{aligned}$$

where

$$\begin{aligned}
A_N(\tau) = {} & (4\eta^2\cos^3(\sin\tau)\cosh^3(\cos\tau) - \eta\cosh^2(\cos\tau)(k\sin\tau\sin(2\sin\tau) \\
& + 4(\eta - 2\gamma)\cos^2(\sin\tau)) + \eta\sinh^2(\cos\tau)(k\sin\tau\sin(2\sin\tau) - 4\eta\sin^2(\sin\tau)) \\
& + 2\gamma k\cos\tau\cos(\sin\tau)\sinh(\cos\tau) + \eta k\cos\tau\sinh(2\cos\tau) - 4\gamma^2 \\
& + \cosh(\cos\tau)(4\eta^2\sin^2(\sin\tau)\cos(\sin\tau)\sinh^2(\cos\tau) - 2\gamma k\sin\tau\sin(\sin\tau) \\
& + 4\gamma(\gamma - 2\eta)\cos(\sin\tau)))^2 + (3\eta^2\sin(\sin\tau)\sinh(\cos\tau)\cosh^2(\cos\tau) \\
& + 2\gamma k\sin(\sin\tau)\cos\tau\cosh(\cos\tau) + \eta\sinh(2\cos\tau)(k\sin\tau + 2\gamma\sin(2\sin\tau)) \\
& + \sinh(\cos\tau)(2\gamma k\sin\tau\cos(\sin\tau) - 2(\eta^2 - 2\gamma^2)\sin(\sin\tau) + \eta^2\sin(3\sin\tau)) \\
& + \eta k\sin(2\sin\tau)\cos\tau + \eta^2\sin(\sin\tau)\sinh^3(\cos\tau))^2
\end{aligned}$$

and

$$A_D(\tau) = 16((\gamma + \eta\cos(\sin\tau)\cosh(\cos\tau))^2 + \eta^2\sin^2(\sin\tau)\sinh^2(\cos\tau))^2$$

Define $F(\tau) = A_N(\tau) - 2A_D(\tau)$ on $[-\pi/2, \pi/2]$, then clearly $F(\tau)$ is an even function. Therefore we verify that $F(\tau)$ is non-negative for each $\tau \in [0, \pi/2]$ and minimum of $F(\tau)$ is attained at either $\tau = 0$ or $\tau = \pi/2$. Observe that

$$F(0) = (k(\eta\sinh 2 + 2\gamma\sinh 1) - 4(1 - \cosh 1)(\gamma + \eta\cosh 1)^2)^2 - 32(\gamma + \eta\cosh 1)^4$$

and

$$F\left(\frac{\pi}{2}\right) = (k(\eta\sin 2 + 2\gamma\sin 1) - 4(\cos 1 - 1)(\gamma + \eta\cos 1)^2)^2 - 32(\gamma + \eta\cos 1)^4.$$

For the sake of simplicity, we assume $\eta_0 = \sinh 1/(2\cosh 1\left(1+\sqrt{2}-\cosh 1\right)) - \gamma/\cosh 1$, $\eta_1 = -\gamma/\cosh 1$, $\eta_2 = -\sin 1/(2\cos 1\left(1+\sqrt{2}-\cos 1\right)) - \gamma/\cos 1$ and $\eta_3 = -\gamma/\cos 1$. As per the conditions in (2.8) it can be deduced that $F(0) \geq (4(\cosh 1-1)(\gamma+\eta\cosh 1)^2+(\eta\sinh 2+2\gamma\sinh 1)^2)^2 - 32(\gamma+\eta\cosh 1)^4 =: X(\eta)$. From inequalities in (2.8) we deduce that $X(\eta) \geq 0$, provided $\eta_0 \leq \eta \leq \eta_1$. Thus $F(0)$ is a non-negative quantity. Further as $\eta \leq \eta_3$, so we have $F(\pi/2) \geq ((\eta\sin 2 + 2\gamma\sin 1) - 4(\cos 1 - 1)(\gamma + \eta\cos 1^2)^2 - 32(\gamma + \eta\cos 1)^4 =: Y(\eta)$. Note that $\eta_2 \leq \eta \leq \eta_3$, leads to $(\eta\sin 2 + 2\gamma\sin 1) - 4(\cos 1 - 1)(\gamma + \eta\cos 1)^2 \geq 4\sqrt{2}\,(\gamma + \eta\cos 1)^2$. Thus $Y(\eta) \geq 0$ and eventually $F(\pi/2)$ is a non-negative quantity. Hence we conclude that $|M(z_0) - 1|^2 \geq 2$. This contradicts the assumption in (2.9). Thus $p(z) \prec \cosh\sqrt{z}$. ∎

In Corollary 2.6, we give an illustration for Theorem 2.5. It can be verified that for $\vartheta \in \mathcal{A}$ the Briot-Bouquet differential equation [12] is related to an integral operator $\mathcal{L}$ defined as follows:

$$\mathcal{L}(z) := \frac{\eta+\gamma}{z^\gamma}\int_0^z \vartheta^\eta(t)t^{\gamma-1}dt.$$

Corollary 2.6. *Let $(\eta,\gamma) \in \mathbb{R}\times\mathbb{R} - \{(\eta,-\eta)\}$ satisfy the conditions given in (2.8). If $\vartheta \in \mathcal{S}_q^*$, then $\mathcal{L} \in \mathcal{S}_\varrho^*$.*

Proof. Suppose $p(z) = z\mathcal{L}'(z)/\mathcal{L}(z)$ be analytic in $\mathbb{D}$, then through this substitution we obtain the Briot-Bouquet type differential equation of the form

$$p(z) + \frac{zp'(z)}{\eta p(z)+\gamma} = \frac{z\vartheta'(z)}{\vartheta(z)}.$$

Thus by applying Theorem 2.5 the result holds true. ∎

Theorem 2.7. *Suppose $(\eta,\gamma) \in \mathbb{R}\times\mathbb{R} - \{(\eta,-\eta)\}$ satisfy the following conditions:*

$$0 < \gamma + \eta\cosh 1 \leq \frac{\sinh 1}{2(e-\cosh 1)} \text{ and } -\frac{\sin 1}{2(e-\cos 1)} \leq \gamma + \eta\cos 1 < 0, \tag{2.11}$$

Let $p(z)$ be an analytic function, such that $p(0) = 1$ and satisfies

$$p(z) + \frac{zp'(z)}{\eta p(z)+\gamma} \prec e^z \tag{2.12}$$

then

$$p(z) \prec \cosh\sqrt{z}.$$

Proof. Suppose $w(z)$ and $M(z)$ be analytic functions defined in (2.10). Then proceeding as in Theorem 2.5 we have $z_0w'(z_0) = kw(z_0)$, where $k \geq 1$ and let $w(z) = e^{it}$, $-\pi \leq t \leq \pi$. For the purpose of proving this result we need to show that

$$|\log P(z_0)|^2 \geq 1. \tag{2.13}$$

Consider

$$\begin{aligned} A_N(\tau) = \kappa_\tau^{-1}&(\cosh(\cos\tau)(4\eta^2\sin^2(\sin\tau)\cos(\sin\tau)\sinh^2(\cos\tau) + 4\gamma^2\cos(\sin\tau)) \\ &- 2\gamma k\sin(\sin\tau)\sin\tau + \eta\cosh^2(\cos\tau)(8\gamma\cos^2(\sin\tau) - k\sin(2\sin\tau)\sin\tau) \\ &+ k(\eta\cos\tau\sinh(2\cos\tau) + \eta\sin(2\sin\tau)\sin\tau\sinh^2(\cos\tau) \\ &+ 2\gamma\cos\tau\cos(\sin\tau)\sinh(\cos\tau)) + 4\eta^2\cos^3(\sin\tau)\cosh^3(\cos\tau)) \end{aligned}$$

and

$$\begin{aligned}A_D(\tau) = \kappa_\tau^{-1}(&\eta\sinh(2\cos\tau)(k\sin\tau + 2\gamma\sin(2\sin\tau)) + \eta k\sin(2\sin\tau)\cos\tau\\ &+ 2\gamma k\sin(\sin\tau)\cos\tau\cosh(\cos\tau) + 3\eta^2\sin(\sin\tau)\sinh(\cos\tau)\cosh^2(\cos\tau)\\ &+ \eta^2\sin(\sin\tau)\sinh^3(\cos\tau) + \sinh(\cos\tau)(2\gamma k\sin\tau\cos(\sin\tau)\\ &- 2(\eta^2 - 2\gamma^2)\sin(\sin\tau) + \eta^2\sin(3\sin\tau))),\end{aligned}$$

where $\kappa_\tau := 4((\gamma + \eta\cos(\sin\tau)\cosh(\cos\tau))^2 + \eta^2\sin^2(\sin\tau)\sinh^2(\cos\tau))$ and $\tau = t/2$. In order to show (2.13) for $-\pi/2 \le \tau \le \pi/2$, we equivalently prove that

$$F(\tau) := 4|\log p(z_0)|^2 - 4 = \log^2(A_N^2(\tau) + A_D^2(\tau)) + 4\left(\tan^{-1}\frac{A_N(\tau)}{A_D(\tau)}\right)^2 - 4 \ge 0.$$

Clearly $F(\tau)$ is an even function, so we shall restrict our findings to $[0, \pi/2]$. We show that $F(\tau) \ge 0$ on $[0, \pi/2]$. Observe that

$$F(0) = \left(\log\left(\cosh 1 + \frac{k(\eta\sinh 2 + 2\gamma\sinh 1)}{4(\gamma + \eta\cosh 1)^2}\right)^2\right)^2 - 4$$

and

$$F\left(\frac{\pi}{2}\right) = \left(\log\left(\cos 1 - \frac{k(\eta\sin 2 + 2\gamma\sin 1)}{4(\gamma + \eta\cos 1)^2}\right)^2\right)^2 - 4$$

Since $\log x$ is a monotonically increasing function, so it is enough to obtain the minimum of $X(k) := \cosh 1 + k(\eta\sinh 2 + 2\gamma\sinh 1)/4(\gamma + \eta\cosh 1)^2$. Observe that $X'(k) = (2\gamma\sinh 1 + \eta\sinh 2)/4(\gamma + \eta\cosh 1)^2 > 0$, provided $\eta > -\gamma/\cosh 1$. Due to the conditions in (2.11), $X(k) \ge X(1) = \cosh 1 + (2\gamma\sinh 1 + \eta\sinh 2)/4(\gamma + \eta\cosh 1)^2 \ge e$. Therefore we deduce that $(\log(X^2(k)))^2 \ge (\log e^2)^2 = 4$. Thus we have $F(0) \ge 0$. Similarly as $-\sin 1/(2\cos 1(e - \cos 1)) \le \eta + \gamma/\cos 1 < 0$, we deduce that $Y(k) \ge Y(1) = \cos 1 - (\eta\sin 2 + 2\gamma\sin 1)/(4(\gamma + \eta\cos 1)^2) \ge e$. Thus we obtain $(\log(Y^2(k)))^2 \ge (\log e^2)^2 = 4$, that leads to $F(\pi/2) \ge 0$. Hence we get a contradiction to (2.12). Hence $p(z) \prec \cosh\sqrt{z}$. ∎

In Example 1, we illustrate a particular case of the above theorem. Best dominant for the differential subordination implication is obtained, that supports Theorem 2.7, for suitable values of η and γ.

Example 1. *Substitute $\eta = 1/2$, in Theorem 2.7 we get that $-\cos 1(1 + \sin 1/\cos 1(e - \cos 1)) \le 2\gamma \le -\cosh 1(1 - \sinh 1/\cosh 1(e - \cosh 1))$. Upon taking $n = a = 1, \eta = 1/2$ and $h(z) = e^z$ in* [12, Theorem 3.2d, p.86] *we obtain $\mathrm{Re}(\eta a + \gamma) = \mathrm{Re}(\gamma + 1/2) > 0$. Further suppose $\gamma + e^z/2 = \eta h(z) + \gamma \prec R_{\eta a+\gamma,n}(z) = R_{\gamma+1/2,1}(z)$, where $R_{\gamma+1/2,1}(z) = (\gamma + 1/2)(1 + z)/(1 - z) + 2z/(1 - z^2)$ is an open door function, that is univalent in $\mathbb{D}$. Therefore by an application of* [12, Theorem 3.2d, p.86]*, we deduce that*

$$q_\gamma(z) = \left(\frac{1}{2}\int_0^1 t^{\gamma-1}\left(e^{Chi(tz)-Chi(z)+Shi(tz)-Shi(z)}\right)^{1/2}dt\right)^{-1} - 2\gamma,$$

where $Chi(z) := \xi + \log z + \int_0^z (\cosh t - 1)/t\ dt$ and $Shi(z) = \int_0^z \sinh t/t\ dt$, is a solution of the differential equation $q(z) + (zq'(z))/(\eta q(z) + \gamma) = e^z$, then $q_\gamma(z) \prec \cosh\sqrt{z}$. Moreover, as e^z is a convex function, then due to [12, Theorem 3.2j, p.97]*, $q_\gamma(z)$ is univalent. For $n = 1$, if $p \in \mathcal{H}(1,1)$ ($\mathcal{H}(a,n) := \{p \in \mathcal{H} : p(z) = a + \sum_{k=n}^\infty a_k z^k, a \in \mathbb{C}\}$) satisfies (2.12), then $p \prec q_\gamma$ and $q_\gamma(z)$ is the best (1,1)-dominant.*

Corollary 2.8. *If $\vartheta \in \mathcal{S}_e^*$ and $(\eta,\gamma) \in \mathbb{R}\times\mathbb{R} - \{(\eta,-\eta)\}$ satisfy the conditions given in (2.11), then $\mathcal{L} \in \mathcal{S}_\varrho^*$.*

Theorem 2.9. *Suppose $0 < s \le 1/\sqrt{2}$ and $(\eta,\gamma) \in \mathbb{R}\times\mathbb{R} - \{(\eta,-\eta)\}$ satisfy the following inequalities:*

$$\eta_3 \le \eta - \eta_2 \le 0 \text{ and } \begin{cases} \eta \ge \eta_0 & \text{if } 0 < s \le -1+\sqrt{\cosh 1}, \\ 0 \le \eta - \eta_0 \le \eta_1 & \text{if } -1+\sqrt{\cosh 1} < s \le 1/\sqrt{2}, \end{cases} \tag{2.14}$$

where

$$\eta_0 = -\frac{\gamma}{\cosh 1}, \quad \eta_1 = \frac{\sinh 1}{2\cosh 1((1+s)^2-\cosh 1)},$$
$$\eta_2 = -\frac{\gamma}{\cos 1} \quad \text{and} \quad \eta_3 = -\frac{\sin 1}{2\cos 1((1+s)^2-\cos 1)}.$$

If $p(z)$ is an analytic function such that $p(0)=1$ and satisfies

$$p(z) + \frac{zp'(z)}{\eta p(z)+\gamma} \prec (1+sz)^2 \tag{2.15}$$

then

$$p(z) \prec \cosh\sqrt{z}.$$

Proof. Define two analytic functions $M(z)$ and $w(z)$ in $\mathbb{D}$, as in (2.10). Consider the expression

$$|M(z_0)-1|^2 = \left|\cosh e^{it/2} - 1 + \frac{ke^{it/2}\sinh e^{it/2}}{2(\eta\cosh e^{it/2}+\gamma)}\right|^2$$
$$= \frac{A_N(\tau)}{A_D(\tau)} \quad (-\pi/2 \le \tau = t/2 \le \pi/2),$$

where

$$\begin{aligned} A_N(\tau) = {} & (\cosh(\cos\tau)(4\eta^2\sin^2(\sin\tau)\cos(\sin\tau)\sinh^2(\cos\tau) + 4\gamma(\gamma-2\eta)\cos(\sin\tau) \\ & - 2\gamma k\sin(\sin\tau)\sin\tau - \eta k\sin(2\sin\tau)\sin\tau + \eta k\cos\tau\sinh(2\cos\tau) \\ & + 2\gamma k\cos\tau\cos(\sin\tau)\sinh(\cos\tau) + 4\eta^2\cos^3(\sin\tau)\cosh^3(\cos\tau) - 4\gamma^2 \\ & - 4\eta(\eta\sin^2(\sin\tau)\sinh^2(\cos\tau) + (\eta-2\gamma)\cos^2(\sin\tau)\cosh^2(\cos\tau)))^2 \\ & + (\sinh(\cos\tau)(2\gamma k\sin\tau\cos(\sin\tau) - 2(\eta^2-2\gamma^2)\sin(\sin\tau) + \eta^2\sin(3\sin\tau)) \\ & + \eta\sinh(2\cos\tau)(k\sin\tau + 2\gamma\sin(2\sin\tau)) + \eta k\sin(2\sin\tau)\cos\tau \\ & + 2\gamma k\sin(\sin\tau)\cos\tau\cosh(\cos\tau) + 3\eta^2\sin(\sin\tau)\sinh(\cos\tau)\cosh^2(\cos\tau) \\ & + \eta^2\sin(\sin\tau)\sinh^3(\cos\tau))^2 \end{aligned}$$

and

$$A_D(\tau) = 16((\gamma+\eta\cos(\sin\tau)\cosh(\cos\tau))^2 + \eta^2\sin^2(\sin\tau)\sinh^2(\cos\tau))^2.$$

Assume $F(\tau) = A_N(\tau) - ((s+1)^2-1)^2 A_D(\tau)$, where $0 \le \tau \le \pi/2$. Now

$$\begin{aligned} F(0) = {} & (4(\cosh 1 - 1)(\eta\cosh 1+\gamma)^2 + k(\eta\sinh 2 + 2\gamma\sinh 1))^2 \\ & - 16((s+1)^2-1)^2(\eta\cosh 1+\gamma)^4 \end{aligned} \tag{2.16}$$

and

$$\begin{aligned} F\left(\frac{\pi}{2}\right) = {} & (4(\cos 1 - 1)(\eta\cos 1+\gamma)^2 - k(\eta\sin 2 + 2\gamma\sin 1))^2 \\ & - 16((s+1)^2-1)^2(\eta\cos 1+\gamma)^4. \end{aligned}$$

Let $X(k,s) := F(0)$ and $Y(k,s) := F(\pi/2)$. For each $k \geq 1$, it can be easily verified that $X(k,s)$ is a monotonically increasing function of k, provided $\eta \geq \eta_0$, therefore $X(k,s) \geq X(1,s)$. Moreover, due to the conditions given in (2.14), $\eta \sinh 2 + 2\gamma \sinh 1 + 4(\cosh 1 - (s+1)^2)(\eta \cosh 1 + \gamma)^2 \geq 0$, holds for each $0 < s \leq \sqrt{\cosh 1} - 1$, provided $\eta \geq \eta_0$. Thus as a result of the equation in (2.16), $X(1,s) \geq 0$, for each $0 < s \leq \sqrt{\cosh 1} - 1$. Similarly for each $\sqrt{\cosh 1} - 1 < s \leq 1/\sqrt{2}$, the inequality $4((s+1)^2 - \cosh 1)(\eta \cosh 1 + \gamma)^2 \leq \eta \sinh 2 + 2\gamma \sinh 1$ is valid if $\eta_0 \leq \eta \leq \eta_0 + \eta_1$. Eventually, (2.16) gives $F(0) \geq 0$. Further $Y(k,s) \geq Y(1,s)$ provided $\eta \leq \eta_2$. The condition $\eta \geq \eta_2 + \eta_3$ leads to $Y(1,s) \geq 0$, for each $0 < s \leq 1/\sqrt{2}$. Therefore $F(\pi/2) \geq 0$. Hence $F(\tau) \geq 0$ for each $\tau \in [-\pi/2, \pi/2]$. This gives a contradiction to (2.15). Hence $p(z) \prec \cosh \sqrt{z}$. ∎

Corollary 2.10. *Let $0 < s \leq 1/\sqrt{2}$ and $(\eta, \gamma) \in \mathbb{R} \times \mathbb{R} - \{(\eta, -\eta)\}$ satisfy the conditions given in (2.14), if $\vartheta \in \mathcal{S}^*_L(s)$, then $\mathcal{L} \in \mathcal{S}^*_\varrho$.*

Example 2. *Let $\gamma = -3/5$ and $s = 1/2$, then Theorem 2.9 gives*

$$\frac{3}{5\cos 1} - \frac{2\sin 1}{\cos 1\,(9 - 4\cos 1)} \leq \eta \leq \frac{3}{5\cosh 1} + \frac{2\sinh 1}{\cosh 1\,(9 - 4\cosh 1)}.$$

Choose $a = 1 = n$ and $h(z) = (1 + (1/2)z)^2$ in [12, Theorem 3.2d, p.86]*, then $\eta h(z) + \gamma = \eta(1 + (1/2)z)^2 - 3/5$ and $\mathrm{Re}(\eta a + \gamma) = \mathrm{Re}(\eta - 3/5) > 0$. Also $\eta(1 + (1/2)z)^2 - 3/5 \prec R_{\eta - 3/5, 1}(z)$ where $R_{\eta-3/5,1}(z) = (\eta - 3/5)(1+z)/(1-z) + 2z/(1-z^2)$ is an open door function, that is univalent in $\mathbb{D}$. Then*

$$q_\eta(z) = \left(\eta \int_0^1 t^{-8/5} e^{(t-1)(z\eta(z(1+t)+8))/8} dt\right)^{-1} + \frac{3}{5\eta}$$

is a solution of the differential equation $q(z) + zq'(z)/(\eta q(z) + \gamma) = (1 + (1/2)z)^2$, then $q_\eta(z) \prec \cosh \sqrt{z}$. Furthermore as $h(z)$ is a convex function, so by [12, Theorem 3.2j, p.97] *$q_\eta(z)$ is univalent. For $n = 1$, if $p \in \mathcal{H}(1,1)$ satisfies (2.15), then $p \prec q_\eta$ and $q_\eta(z)$ is the best $(1,1)-$dominant.*

The proof of Theorem 2.11 is much akin to the previous theorems, so we omit the proof.

Theorem 2.11. *Let $-1 \leq B < A \leq 1$ and $(\eta, \gamma) \in \mathbb{R} \times \mathbb{R} - \{(\eta, -\eta)\}$ satisfy the following conditions:*

(i) $(1 - B^2)\sinh 1 + 2(\gamma + \eta \cosh 1)(\cosh 1 - 1 + B(A - B\cosh 1)) \geq 0$
(ii) $(\sinh 1 + 2(\cosh 1 - 1)(\gamma + \eta \cosh 1))^2 \geq (B \sinh 1 - 2(A - B\cosh 1)(\gamma + \eta \cosh 1))^2$
(iii) $(1 - B^2)\sin 1 + 2(\gamma + \eta \cos 1)(1 - \cos 1 - B(A - B\cos 1)) \geq 0$
(iv) $(\sin 1 + 2(\cos 1 - 1)(\gamma + \eta \cos 1))^2 \geq (B \sin 1 + 2(A - B\cos 1)(\gamma + \eta \cos 1))^2$

Let $p(z)$ be an analytic function, such that $p(0) = 1$ and satisfies

$$p(z) + \frac{zp'(z)}{\eta p(z) + \gamma} \prec \frac{1 + Az}{1 + Bz}$$

then

$$p(z) \prec \cosh \sqrt{z}.$$

Corollary 2.12. *Let $\vartheta \in \mathcal{S}^*(A,B)$ and parameters A, B and $(\eta, \gamma) \in \mathbb{R} \times \mathbb{R} - \{(\eta, -\eta)\}$ satisfy the conditions given in Theorem 2.11, then $\mathcal{L} \in \mathcal{S}^*_\varrho$.*

Corollary 2.13. *If an analytic function $p(z)$ with $p(0) = 1$, satisfies:*

$$\left| p(z) + \frac{zp'(z)}{\eta p(z)} - 1 \right| < 1,$$

where $-\tanh 1 \operatorname{sech} 1 \leq 2\eta \leq (\tan 1)/(2 - \cos 1)$ or

$$\left| p(z) + \frac{zp'(z)}{p(z) + \gamma} - \frac{4}{3} \right| < \frac{2}{3},$$

where $(2(3\cos 1-4)(\gamma+\cos 1)\leq 3\sin 1)\wedge(2(\cosh 1-2)(\gamma+\cosh 1)\geq -\sinh 1)$. *Then*

$$p(z)\prec \cosh\sqrt{z}.$$

Proof. By replacing $A=1$ and $B=0$ with $\gamma=0$ or $A=0$ and $B=-1/2$ with $\eta=1$ in Theorem 2.11 we establish the required result. ∎

References

[1] Alotaibi A., Arif M., Alghamdi, M. A., Hussain, S.: Starlikness associated with cosine hyperbolic function. Mathematics **8**(7), 1118(2020). https://doi.org/10.3390/math8071118

[2] Aouf, M. K., Dziok J., Sokół, J.: On a subclass of strongly starlike functions. Appl. Math. Lett. **24**(1), 27–32(2011)

[3] Cho, N. E., Kumar, V., Kumar, S. S., Ravichandran, V.: Radius problems for starlike functions associated with the sine function. Bull. Iranian Math. Soc. **45**(1), 213–232(2019)

[4] Ebadian, A., Bulboacă, T., Cho, N. E., Adegani, E. A.: Coefficient bounds and differential subordinations for analytic functions associated with starlike functions. Rev. R. Acad. Cienc. Exactas Fís. Nat. Ser. A Mat. RACSAM **114**(3), 1–19(2020)

[5] Goel, P., Kumar, S. S.: Certain class of starlike functions associated with modified sigmoid function. Bull. Malays. Math. Sci. Soc. **43**(1), 957–991(2020)

[6] Janowski, W.: Some extremal problems for certain families of analytic functions. I. Ann. Polon. Math. **28**(3), 297–326(1973)

[7] Kumar, S. S., Kamaljeet, G.: A cardioid domain and starlike functions. Anal. Math. Phys. **11**(2), 1-34(2021)

[8] Kumar, S., Kumar, V., Ravichandran, V., Cho, N. E.: Sufficient conditions for starlike functions associated with the lemniscate of Bernoulli. J. Inequal. Appl. **2013**, 13(2013).

[9] Ma, W. C., Minda, D.: A unified treatment of some special classes of univalent functions. In: Proceedings of the Conference on Complex Analysis (Tianjin, 1992), pp. 157–169, Conf. Proc. Lecture Notes Anal., I, Int. Press, Cambridge, MA

[10] Masih, V. S., Kanas, S.: Subclasses of starlike and convex functions associated with the Limaçon Domain. Symmetry **12**, 942(2020)

[11] Mendiratta, R., Nagpal, S., Ravichandran, V.: On a subclass of strongly starlike functions associated with exponential function. Bull. Malays. Math. Sci. Soc. **38**(1), 365–386(2015)

[12] Miller, S. S., Mocanu, P. T.: Differential subordinations, Theory and Applications, vol.225. Marcel Dekker, New York (2000)

[13] Mundalia, M., Kumar, S. S.: On a Subfamily of starlike functions related to Hyperbolic Cosine function, The Journal of Analysis, 2023 (to appear), Preprint arXiv:2201.05811

[14] Raina, R. K., Sokół, J.: Some properties related to a certain class of starlike functions. C. R. Math. Acad. Sci. Paris **353**(11), 973–978(2015)

[15] Ruscheweyh, S.: Convolutions in Geometric Function Theory. Les Presses De L'Universite De Montreal, Montreal (1982)

[16] Sokół, J., Stankiewicz, J.: Radius of convexity of some subclasses of strongly starlike functions. Zeszyty Nauk. Politech. Rzeszowskiej Mat. **19**, 101–105(1996).

Department of Applied Mathematics, Delhi Technological University, Delhi–110042, India

Email address: mridulamundalia@yahoo.co.in

Department of Applied Mathematics, Delhi Technological University, Delhi–110042, India

Email address: spkumar@dce.ac.in

Proceedings of the 7th International Conference on Computing Methodologies and Communication (ICCMC-2023)
IEEE Xplore Part Number: CFP23K25-ART; ISBN: 978-1-6654-6408-6

SupRes: Facial Image Upscaling Using Sparse Denoising Autoencoder

Manan Agrawal
Dept. of Computer Science and Engineering
Delhi Technological University
Delhi, India
manan.ag9@gmail.com

Mohd Ayaan Anwar
Dept. of Computer Science and Engineering
Delhi Technological University
Delhi, India
ayaan.anwar7@gmail.com

Nakul Saroha
Dept. of Computer Science and Engineering
Delhi Technological University
Delhi, India
nakulsaroha08@gmail.com

Anurag Goel
Dept. of Computer Science and Engineering
Delhi Technological University
Delhi, India
0000-0003-2660-7540

2023 7th International Conference on Computing Methodologies and Communication (ICCMC) | 978-1-6654-6408-6/23/$31.00 ©2023 IEEE | DOI: 10.1109/ICCMC56507.2023.10083628

***Abstract*— Even in this era of digital images, still many images and media are hazy, pixelated, and blurry. This could be due to low-quality imaging sensors, poor image stabilization, or the image itself being old. This study proposes the Sparse Denoising Autoencoders (SDAEs) for upscaling blurry images. The performance of the proposed SDAEs is then compared with the deep learning architecture, Pix2Pix Generative Adversarial Networks (GANs) by primarily focusing on the facial images. The experimental results show that the SDAEs give slightly better results than GANs. Additionally, the SDAE architecture is computationally 30% efficient when compared to the Pix2Pix GAN.**

Keywords*— *Image Upscaling, Convolutional Neural Networks, Generative Adversarial Networks, Sparse Denoising Autoencoders

I. Introduction

Predicting, or rather, generating a high-resolution image from a low-resolution image is a challenging task. This process, also known as Super-Resolution (SR), has garnered much attention from the computer vision research community.

Autoencoders are a kind of generative deep learning model. They take some input **x**, try learning the latent features of the input, and then try reconstructing this **x** as the output. Denoising autoencoders are an advanced version of autoencoders in which some noise gets added to the input **x** while keeping the target image the same as the actual image. This process allows the network to learn to "clean" images with noise in them. Sparse autoencoders are autoencoders with sparsity or regularization added to the layers to prevent overfitting.

Generative Adversarial Networks (GANs) consist of a generator and a discriminator. The job of the generator is to generate images on its own and try fooling the discriminator, whose job it is to identify which image is "real" (from the data) and which image is "fake" (generated by the generator). The Pix2Pix GAN architecture is used here as it is especially suited for Image-to-Image translation [1].

A. Motivation

- *NVIDIA's Deep Learning Super Sampling (DLSS)* technology, introduced in 2019, tried to solve a very challenging task [2]. Game rendering is extremely challenging for GPUs, especially in 4K and 8K resolutions. So why not render it at a lower resolution and upscale it to higher resolutions using deep learning? NVIDIA achieved great results due to the huge amount of game data they already had.

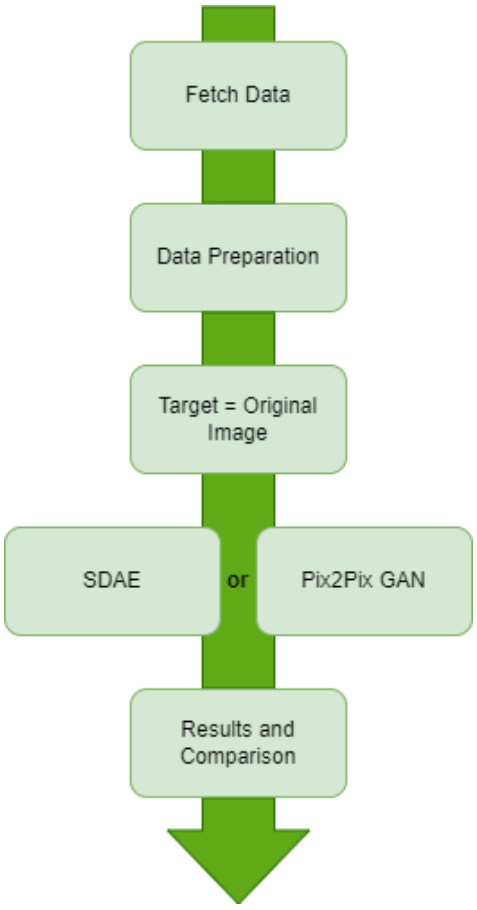


Fig. 1. Flow Diagram for Methodology

- *Autoencoder*, with added sparsity to prevent overfitting, is a powerful tool that can expand latent feature spaces [3]. This property is utilized to increase the resolution of images while still being computationally efficient. These remain underused in terms of new and emerging architectures.
- *Generative Adversarial Networks (GANs)* has cemented itself as one of the most flexible and powerful generative tools in Computer Vision and Deep Learning. Their uses include colourizing grayscale pictures, generating images from descriptions, converting day pictures to night, and many more. The proposed research work focuses on a

Authorized licensed use limited to: DELHI TECHNICAL UNIV. Downloaded on April 10,2023 at 07:28:12 UTC from IEEE Xplore. Restrictions apply.

specific GAN architecture, Pix2Pix, which performs Image-to-Image translation tasks [1].

- Facial image upscaling can be the foundation step for many important tasks such as face sentimental analysis [4], facial image manipulation [5] and detection of manipulated facial images [6].

II. Related Work

Early methods for tackling the super-resolution problem focused on interpolation techniques based on sampling theory. However, such approaches have limits regarding forecasting accurate, realistic textures. Works relying on the interpolation technique include algorithms proposed by Allebach and Wong [7] and Zhang and Wu [8].

Nasrollahi and Moeslund [9] pointed out the limitations of hardware-based solutions for the problem of increasing the resolution of lower-quality images. They also observed how interpolation-based techniques used previously failed to restore high-frequency details of low-resolution images.

Zou and Yuen [10] proposed machine learning-based methods for face recognition in low-resolution images. They utilized algorithms like PCA+KNN, PCA+SVM, Kernel LDA+KNN, and Kernel LDA+SVM to use two proposed constraints- new data and discriminative constraints for better visuality and facial recognition.

In the field of deep learning, Kim et al. were the first to propose the use of residual networks to train considerably deeper network topologies and were able to achieve superior results. They demonstrated, in particular, that skip connection and recursive convolutions reduce the load of carrying identification information in the super-resolution network [11].

In their study, Dong et al. suggested employing a deep convolutional neural network (CNN) to translate a low-resolution picture as the input to a high-resolution one for a single image super-resolution [12]. This method was a ground breaking innovation to jointly optimize all layers with a lightweight structure that achieves excellent restoration quality and quicker speed for practical online usage compared to traditional sparse-coding super-resolution methods.

Another fascinating approach that utilizes sparsity to resolve the discontinuity due to ringing and blurring artefacts that make images noisy was by Kim et al. [13]. They used differentiable Kernel ridge regression (KRR) to build a sparse basis set using gradient descent and kernel matching pursuit (KMP) [14]. Thus, training and testing for regression became less time-consuming due to this procedure. Exploiting a prior image structure eliminates the ringing artefacts problem by considering pixel values' discontinuity across edges.

Using this technique of image priors for single picture super-resolution, [15], [16], [17], and [18] also attain nearly state-of-the-art performance.

III. Methodology Used

Fig. 1 gives an overview of the methodology followed in this work.

A. Dataset

This study uses the publicly available "Labelled Faces in the Wild (LFW)" dataset rom the University of Massachusetts Amherst – Manning College of Information & Computer Sciences [19]. Since the pictures are snapshots from the wild, they represent real-world conditions. We refrain from using other popular facial image datasets like CelebA [20] as we find that the pictures in them are too "perfect"- they do not represent the actual-world photos as they tend to have perfect lighting and focus.

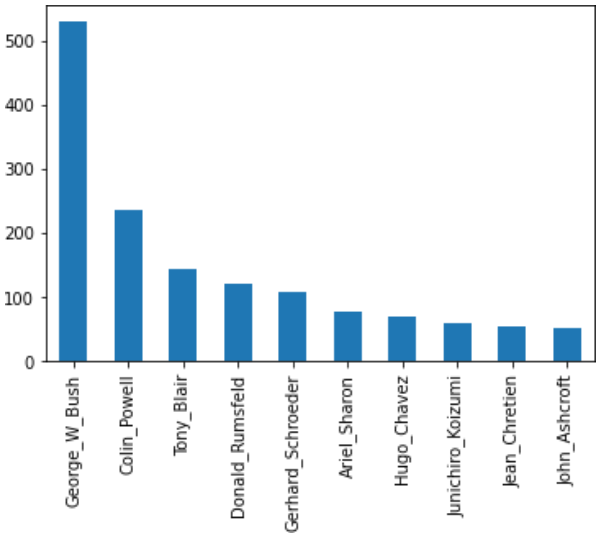


Fig. 2. Top 10 image samples per subject to highlight the significant class imbalance

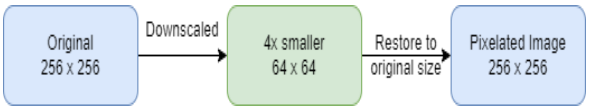


Fig. 3. Image pixelation process

Performing fundamental Exploratory Data Analysis, we find that the dataset contains 13,233 images of 5,479 unique celebrities. 3,799 of the total 5,479 celebrities have a single image sample in the dataset. Each image is of the size 250x250. The face of each subject is in the centre of the image. Also, a significant class imbalance is present, as shown in Fig. 2.

B. Pixelating the Data

We use a custom function to pixelate the images in the training set artificially. The images are downscaled four times from 256x256 to 64x64 resolution using OpenCV's *INTER_AREA* interpolation technique [21]. It uses interpolation to scale down the original images by four times from 256x256 resolution to 64x64 resolution. These downscaled images are restored to their original 256x256 resolution by stretching. These artificially pixelated images form the input for deep-learning models. Fig. 3 represents the process of artificial pixelation.

C. Technical Specifications

- This work uses the Python 3 programming language and relies on popular libraries like NumPy, Pandas, Matplotlib, Scikit-Learn, and OpenCV.
- Tensorflow v2.8.0 with the Keras API is the deep learning framework used.
- The data is processed, and Google Colab is used to train the models with the GPU runtime. However, the Pix2Pix GAN model exceeds the GPU usage limits

Authorized licensed use limited to: DELHI TECHNICAL UNIV. Downloaded on April 10,2023 at 07:28:12 UTC from IEEE Xplore. Restrictions apply.

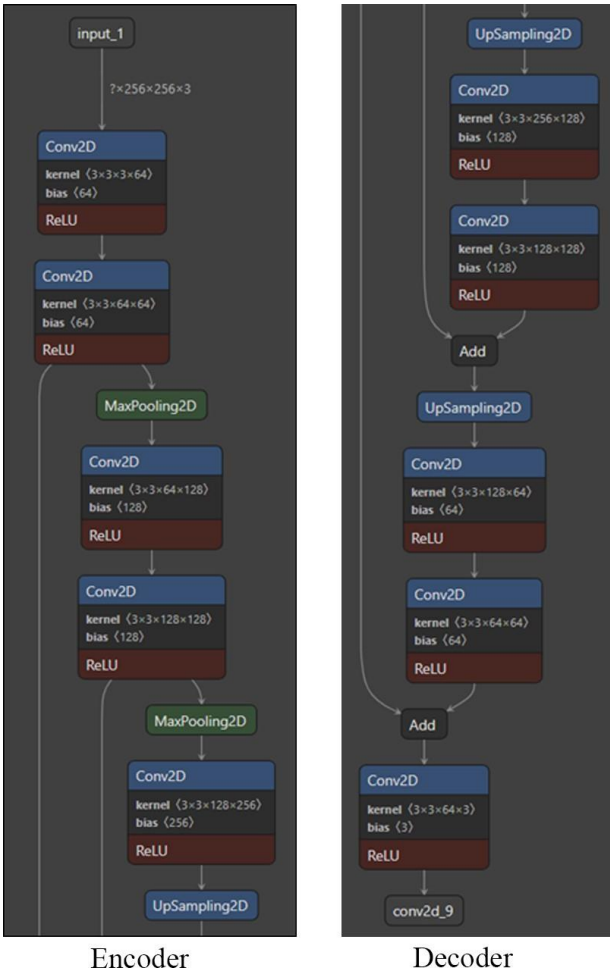


Fig. 4. SDAE Architecture

despite trying several workarounds, including iterative training and smaller batch sizes. Therefore, it is trained on the Kaggle Kernel with the NVIDIA P100 GPU.

D. Model Architecture

1) Sparse Denoising Autoencoder

The proposed Sparse Denoising Autoencoder (SDAE) consists of an encoder and a decoder. Fig. 4 represents the SDAE architecture.

a) ***Encoder***

- The encoding architecture consists of two sets of double-stacked *Conv2D* layers, both of which are followed by a *MaxPooling2D* layer.
- At the end, we have used a final *Conv2D* layer with increased neurons to expand the latent space.
- The *Rectified Linear Activation Unit ('ReLU')* activation function is used for the *Conv2D* layers.
- The *L1 regularization* with a regularization factor of *1e - 9* added to each Conv2D layer adds sparsity to the autoencoder. This method is employed to prevent overfitting the training data.

b) ***Decoder***

- The decoding architecture consists of two *UpSampling2D* layers, both of which are followed by double stacked *Conv2D* layers.

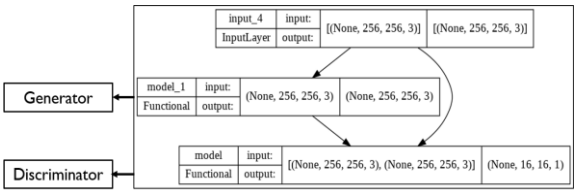


Fig. 5. Pix2Pix GAN Architecture

- *UpSampling* layers allow the model to produce sparse feature maps of higher resolution.
- The output layer is a *Conv2D* layer that produces images of the same dimensions as the Input image but with higher clarity.
- The *Rectified Linear Activation Unit ('ReLU')* activation function is used for the *Conv2D* layers.
- The *L1 regularization* with a regularization factor of *1e - 9* added to each Conv2D layer adds sparsity to the autoencoder. This method is employed to prevent overfitting the training data.

2) Pix2Pix GAN

The Pix2Pix GAN follows the traditional GAN architecture of a generator and a discriminator, as shown in Fig. 5.

a) Generator

- The generator consists of an encoder and a decoder.
- **Encoder:** C64-C128-C256-C512-C512-C512-C512-C512
- **Decoder:** CD512-CD1024-CD1024-C1024-C1024-C512-C256-C128

  Here, **Cn** denotes *Convolution-BatchNorm-ReLu* layers in succession with number of filters = n, and, **CDn** denotes *Convolution-BatchNorm-Dropout-ReLu* layers in succession with number of filters = n.
- *LeakyReLU* is the activation function for the encoder layers.
- *ReLU* is the activation function for the decoder layers.
- For the final output layer, the *tanh* activation function is used.

b) Discriminator

- Following the convention mentioned above, the architecture of the discriminator is: C64-C128-C256-C512
- *LeakyReLU* is the activation function for the hidden layers of the discriminator.
- For the final output layer, the *sigmoid* activation function is used.

Authorized licensed use limited to: DELHI TECHNICAL UNIV. Downloaded on April 10,2023 at 07:28:12 UTC from IEEE Xplore. Restrictions apply.



Fig. 6. SDAE Results on Training Set

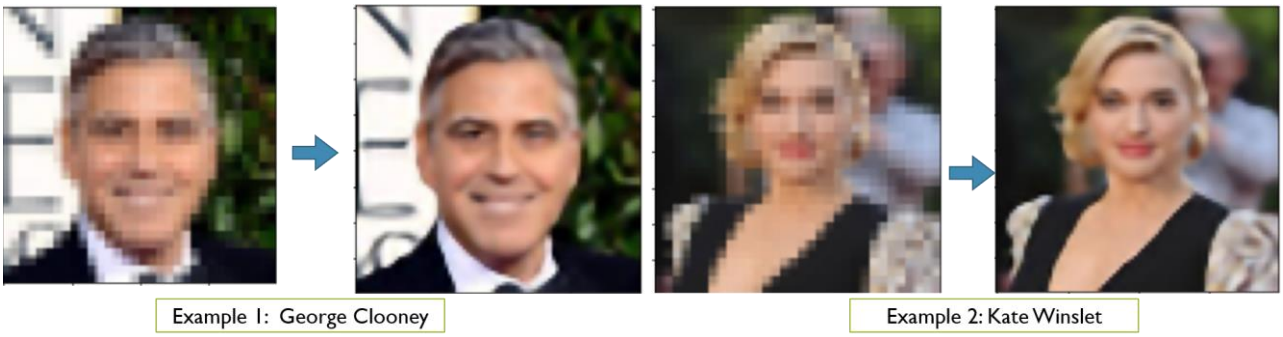


Fig. 7. SDAE Results on Test Set

E. *Evaluation Metrics*

- **Optimizer:** The *Adam* optimizer is used for both of the models. It is a stochastic optimization approach initially introduced in 2014 [22]. It is based on adaptive estimation of first and second-order moments and is the most extensively used optimizer in Deep Learning. It has gained popularity as it efficiently deals with memory and the number of computations and is well-suited for large feature spaces and datasets.
- **Loss Function(s):**

1) **SDAE:** *Mean Squared Error (MSE)*

MSE is used as the loss function in the proposed model since the performed task is more when compared to the regression problem statement, where an attempt has been made to produce a higher-resolution image from a pixelated (lower-resolution image) image. Other loss functions, such as cross-entropy loss are not used, since they are more suitable for solving classification problems.

2) **Pix2Pix GAN:** *Binary Crossentropy (BCE)*

BCE is the most common loss function used in GANs to measure the delta between the predicted distribution (discriminator) and the true distribution of the data.

IV. Results Analysis

Fig. 6 depicts the results of Sparse Denoising Autoencoders (SDAEs) results on a few training set images. Analyzing the results, we observe that SDAEs generate high-resolution images with a good amount of clarity from very low-resolution inputs. SDAEs also give good results on images from the test set, as shown in Fig. 7.

For the training set images, Pix2Pix Generative Adversarial Network (GAN) performs well and generates high-resolution images with good clarity from very low-resolution inputs, as shown in Fig. 8. However, Pix2Pix GAN fails to generate good quality high-resolution output for testing images, as shown in Fig. 9.

TABLE I. SDAE AND Pix2Pix GAN Results on Test Set

Model	Inference Time	MSE	MAE
SDAE	1664 ms	8.96×10^{-4}	1.55×10^{-2}
Pix2Pix GAN	2284 ms	2.44×10^{-3}	2.50×10^{-2}

SDAEs and Pix2Pix GAN models follow a similar loss curve and converge smoothly without any significant spikes. To better compare the results of SDAEs and Pix2Pix GAN, a test set containing 200 unseen images is used to test both models. The testing environment conditions are kept the same for both models, which are as follows:

- Google Colab Python 3 Runtime

Authorized licensed use limited to: DELHI TECHNICAL UNIV. Downloaded on April 10,2023 at 07:28:12 UTC from IEEE Xplore. Restrictions apply.

- Test set size: 200 images
- GPU: Tesla T4 (16 GB VRAM)

We compute the Mean Squared Error (1) and Mean Absolute Error (2) for both the models, namely SDAEs and Pix2Pix GAN.

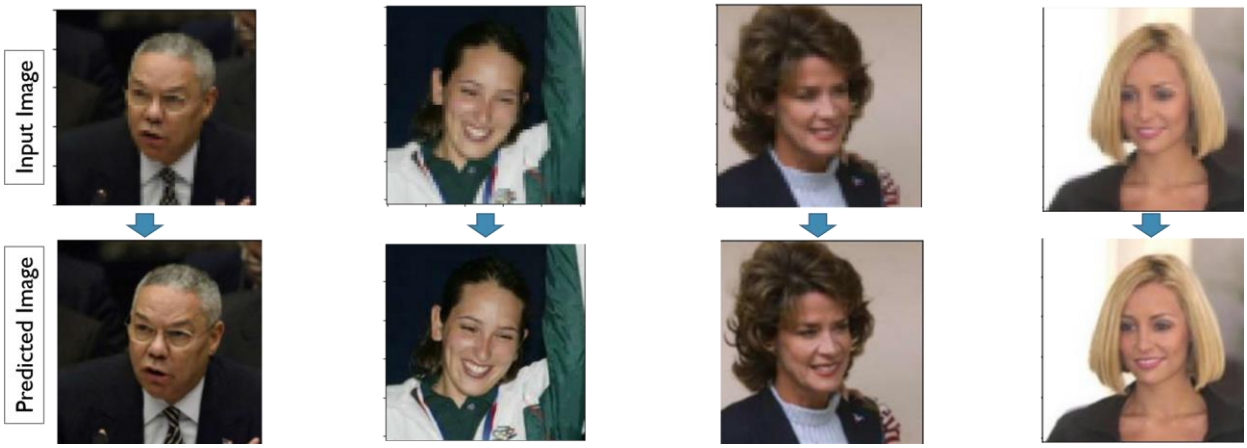


Fig. 8. Pix2Pix GAN Results on Training Set

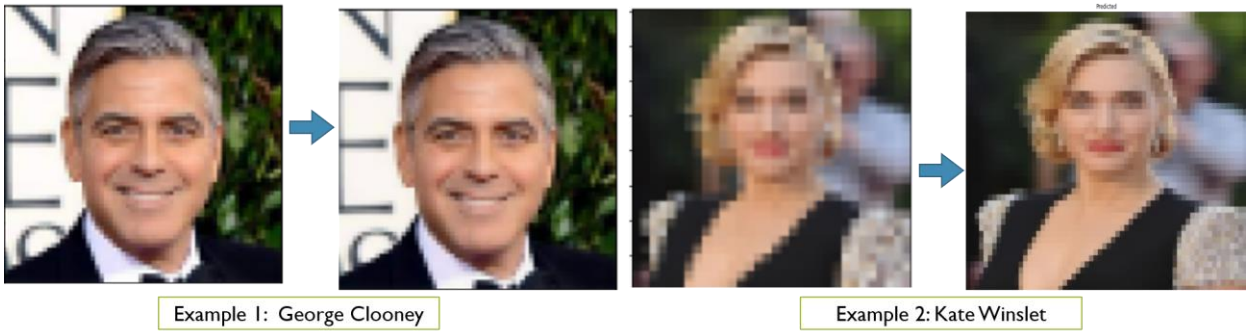


Fig. 9. Pix2Pix GAN Results on Test Set

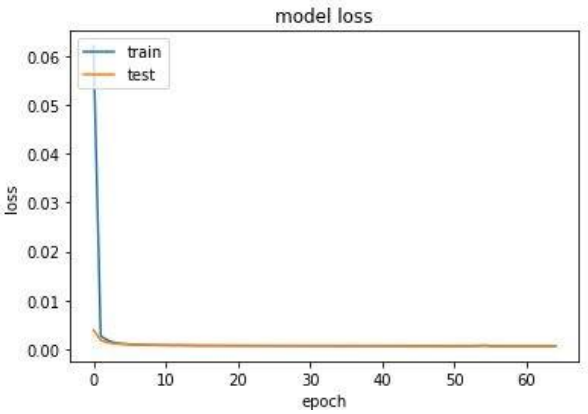


Fig. 10. SDAE Loss Curve

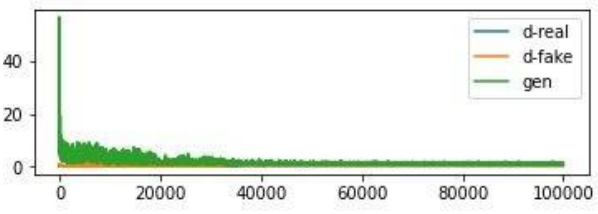


Fig. 11. GAN Loss Curve

$$MSE = \sum_{i=1}^{n=200} \left(Y_{predicted} - Y_{original}\right)^2 \quad (1)$$

$$MAE = \sum_{i=1}^{n=200} \left|Y_{predicted} - Y_{original}\right| \quad (2)$$

where $Y_{predicted}$ is the image generated from the model and $Y_{original}$ is the original image from the test set.

We measure the inference time for both the models. We repeat this test for three distinct test sets, and the average value is presented in Table I. The proposed SDAE is about 30% faster than Pix2Pix GAN when generating high-resolution

facial images. The MSE and MAE are also considerably lower for SDAEs as compared to Pix2Pix GAN.

A. Limitations

The Pix2Pix GAN fails at generalizing for unseen data as it requires a much larger dataset for training. Consequently, Pix2Pix requires a lot more computational power to achieve better results. Another reason behind the bottleneck of Pix2Pix GAN could be the high resemblance between the input and output images; as a result, the discriminator is fooled at a very early stage, and the basic principle of GANs avoids the generation of more complex images.

One limitation in the SDAEs outputs is in the case of those images where there is an unclear face with a blurred background. For such images, the model tends to generate superficial features. Fig. 12 shows an example of this

Authorized licensed use limited to: DELHI TECHNICAL UNIV. Downloaded on April 10,2023 at 07:28:12 UTC from IEEE Xplore. Restrictions apply.

limitation. Here, SDAE adds extra "wrinkles" on the cheeks of the given subject.



Fig. 12. Limitations Example

B. Result Summary

The SDAE and the Pix2Pix GAN models perform equally well on the training data. They can learn the specific facial features and generate images similar to the original high-resolution image. However, if we compare the images predicted from the test set, we observe that the SDAE model manages to preserve more desirable facial features than the Pix2Pix GAN. The output of the Pix2Pix GAN is blocky, while the SDAE model outputs a relatively smoothed image.

The Pix2Pix GAN model is slower by about 30% during inference, while the SDAE model is relatively faster. As the previous sub-section highlights, it also tends to generate superficial features on the output images.

V. CONCLUSION AND FUTURE WORK

In this work, we propose a Sparse Denoising Autoencoder (SDAE) model for facial image upscaling, which excels over the popular Pix2Pix GAN. Moreover, the inference computation employing the SDAE takes significantly less time than the Pix2Pix GAN. Another powerful insight that this paper brings forth is that GANs, in particular, require extensive and exhaustive training data. Due to this, the Pix2Pix GAN could not generalize and reconstruct the distorted unseen images in the test set as efficiently as the SDAE model.

The SDAE can achieve superior performance with a lightweight structure than the Pix2Pix GAN. We conjecture that performance can be diversely observed using different training strategies. Apart from pixelations, quick shots from video sequences and images taken from a shaky camera setup can provide a feasible exploration in the future.

REFERENCES

[1] P. Isola, J.-Y. Zhu, T. Zhou, and A. A. Efros, "Image-to-image translation with conditional adversarial networks," 2016. [Online]. Available: https://arxiv.org/abs/1611.07004

[2] N. Corp., "Nvidia dlss 2.0: A big leap in ai rendering," 2020. [Online]. Available: https://www.nvidia.com/en-gb/geforce/news/nvidia-dlss-2-0-a-big-leap-in-ai-rendering/

[3] Shikha, M. Agrawal, M. A. Anwar, and D. Sethia, "Stacked sparse autoencoder and machine learning based anxiety classification using eeg signals," in *The First International Conference on AI-ML-Systems*, ser. AIMLSystems 2021. New York, NY, USA: Association for Computing Machinery, 2021. [Online]. Available: https://doi.org/10.1145/3486001.3486227

[4] M. Sushith, "Semantic feature extraction and deep convolutional neural network-based face sentimental analysis," *Journal of Innovative Image Processing*, vol. 4, no. 3, pp. 157–164, 2022.

[5] C.-H. Lee, Z. Liu, L. Wu, and P. Luo, "Maskgan: Towards diverse and interactive facial image manipulation," in *Proceedings of the IEEE/CVF Conference on Computer Vision and Pattern Recognition (CVPR)*, June 2020.

[6] A. Rossler, D. Cozzolino, L. Verdoliva, C. Riess, J. Thies, and M. Niessner, "Faceforensics++: Learning to detect manipulated facial images," in *Proceedings of the IEEE/CVF International Conference on Computer Vision (ICCV)*, October 2019.

[7] J. Allebach and P. W. Wong, "Edge-directed interpolation," in *Proceedings of 3rd IEEE International Conference on Image Processing*, vol. 3, 1996, pp. 707–710 vol.3.

[8] L. Zhang and X. Wu, "An edge-guided image interpolation algorithm via directional filtering and data fusion," *IEEE Transactions on Image Processing*, vol. 15, no. 8, pp. 2226–2238, 2006.

[9] K. Nasrollahi and T. B. Moeslund, "Super-resolution: a comprehensive survey," *Machine vision and applications*, vol. 25, no. 6, pp. 1423–1468, 2014.

[10] W. W. Zou and P. C. Yuen, "Very low resolution face recognition problem," *IEEE Transactions on image processing*, vol. 21, no. 1, pp. 327–340, 2011.

[11] J. Kim, J. K. Lee, and K. M. Lee, "Deeply-recursive convolutional network for image super-resolution," in *Proceedings of the IEEE conference on computer vision and pattern recognition*, 2016, pp. 1637–1645.

[12] C. Dong, C. C. Loy, K. He, and X. Tang, "Image super-resolution using deep convolutional networks," *IEEE Transactions on Pattern Analysis and Machine Intelligence*, vol. 38, no. 2, pp. 295–307, 2016.

[13] K. I. Kim and Y. Kwon, "Single-image super-resolution using sparse regression and natural image prior," *IEEE Transactions on Pattern Analysis and Machine Intelligence*, vol. 32, no. 6, pp. 1127–1133, 2010.

[14] P. Vincent and Y. Bengio, "Kernel matching pursuit," *Machine learning*, vol. 48, no. 1, pp. 165–187, 2002.

[15] D. Glasner, S. Bagon, and M. Irani, "Super-resolution from a single image," in *2009 IEEE 12th international conference on computer vision*. IEEE, 2009, pp. 349–356.

[16] R. Timofte, V. De Smet, and L. Van Gool, "Anchored neighborhood regression for fast example-based super-resolution," in *Proceedings of the IEEE international conference on computer vision*, 2013, pp. 1920–1927.

[17] C.-Y. Yang, C. Ma, and M.-H. Yang, "Single-image super-resolution: A benchmark," in *European conference on computer vision*. Springer, 2014, pp. 372–386.

[18] J. Yang, Z. Lin, and S. Cohen, "Fast image super-resolution based on in-place example regression," in *Proceedings of the IEEE conference on computer vision and pattern recognition*, 2013, pp. 1059–1066.

[19] G. B. Huang, M. Ramesh, T. Berg, and E. Learned-Miller, "Labeled faces in the wild: A database for studying face recognition in unconstrained environments," University of Massachusetts, Amherst, Tech. Rep. 07-49, October 2007.

[20] Z. Liu, P. Luo, X. Wang, and X. Tang, "Deep learning face attributes in the wild," in *Proceedings of International Conference on Computer Vision (ICCV)*, December 2015.

[21] G. Bradski, "The OpenCV Library," *Dr. Dobb's Journal of Software Tools*, 2000.

[22] D. P. Kingma and J. Ba, "Adam: A method for stochastic optimization," 2014. [Online]. Available: https://arxiv.org/abs/1412.6980

Authorized licensed use limited to: DELHI TECHNICAL UNIV. Downloaded on April 10,2023 at 07:28:12 UTC from IEEE Xplore. Restrictions apply.

This article has been accepted for publication in IEEE Journal of Emerging and Selected Topics in Industrial Electronics. This is the author's version which has not been fully edited and content may change prior to final publication. Citation information: DOI 10.1109/JESTIE.2023.3262451

Switched Capacitor Based High Gain Boost Converter for Renewable Energy Application

Manikant Kumar, Vinod Kumar Yadav and Arun Kumar Verma, *Senior Member, IEEE*

***Abstract*—This article presents an improved non-isolated high voltage gain boost converter (NI-HGBC) with a switched capacitor and reduced voltage stress across the switches for low voltage applications. In the proposed topology, a coupled inductor (CI) and a switched capacitor (SC) are incorporated to get a high voltage gain. The output of the coupled inductor has low voltage ripples, which reduces the size of the output filter capacitor. Further, switched capacitor and coupled inductor form a resonating circuit that helps to achieve zero voltage switching (ZVS) and zero current switching (ZCS) at full load. Additionally, stress across the switches is reduced, leading to low-rated switches utilization, which makes it cost-effective. The bridge diode, coupled with a switched capacitor and mutual inductor, inherently works as a snubber circuit for switch protection. A converter with an input voltage of 48 V and an output voltage of 380 V is developed in this article to meet the requirements of a grid-connected inverter for household applications. Finally, an experimental 500W high-gain boost converter prototype is developed, tested, and the simulink results is verified with hardware results. It has been found that the converter is 96.20% efficient at full load and achieves low stress across the switches.**

***Index Terms*—Coupled inductor, switched capacitor, high gain boost converter (HGBC), renewable energy sources (RES), zero current switching (ZCS), zero voltage switching (ZVS).**

I. Introduction

Modern power conversion technology faces new challenges due to the increase in demand for renewable energy sources (RES) such as fuel cells, and PV cells, which provide electrical energy at low voltages. Solar photovoltaic (SPV) panels are interconnected in series and parallel to meet the voltage and power requirements of the 48V DC system. Integrating these low-voltage resources into high-voltage applications requires a power electronics interface. As illustrated in Fig. 1, the 12–48V output from SPV is stepped up to 360-400V to produce an RMS voltage of 127-240V, which requires a high gain boost converter (HGBC). The HGBC can be categorized into an isolated and non-isolated converter. Non-isolated high gain boost converters provide many advantages over isolated converters, including lower switching stress, smaller size, higher efficiency, and higher frequency operating [1], [2]. Generally, HGBC is implemented in SPV [3]–[5], fuel cell-powered systems [6], server rooms [7], and continuous power supply [8] requirements.

Conventional boost converters such as half-bridge [9], and full-bridge converters have been used for industrial applications as high gain boost converters by operating it at a high duty cycles; which are now replaced by HGBC because of the demerits of size and low efficiency of conventional boost converters [10], [11]. Also, as the duty ratio increases, the conduction losses increases, and makes the system inefficient [12]. CI-based HGBC offers a high gain at a lower turn ratio

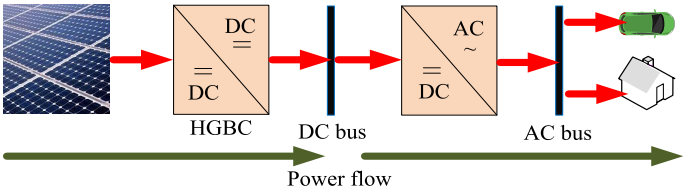


Fig. 1. A schematic of a grid-connected system with a high gain boost converter (HGBC).

that makes the converter less sensitive to EMI issues. To reduce EMI and voltage stress across the switches, leakage inductance is introduced in quadratic boost converter [13] and hybrid boost converter [14]. A cascaded version of the typical boost converter is presented in [15], where all the inductors are coupled in parallel to provide a high voltage gain. However, the CI development for a particular leakage inductance is challenging task, also the high stress at output diodes causes inappropriate working. Multiple levels of high gain boost converters have been presented in [16], but their complicated control strategies and high ripple current at input lead to switching spikes at turn-on and turn-off instant. The article in [17] presents an enhanced ripple-free input current-based high gain boost converter, where CI is replaced by an inductor and built-in transformer to achieve high voltage gain. However, it fails to discuss the ripple in output voltage also, a built-in transformer, and an extra inductor increases the overall size and makes the converter bulky. A non-isolated high-step DC-DC converter with CI and SC is developed in [18], where the converter claimed a low duty cycle operation with a high gain, but a ripple in output voltage is high which requires a large sized capacitor. A soft switched high gain boost converter for low power applications is developed in [19], in which has high voltage gain and low switched stress are addressed. A transformer-less high step-up DC-DC converter with active SC and switched inductor (SI) is presented, having high voltage gain [20] which addresses the problem of high input ripple current but requires a high value of capacitor at the input side. To attain a high gain, a three-state switching cell-based DC-DC boost converter is proposed. The whole evolution of the TSSC is seen in article [21], [22], where a coupled inductor and voltage multiplier cell increase the voltage level. Although it shows excessive switching losses and poor efficiency. A soft-switched-based converter that reduces the switching losses with an auxiliary circuit is implemented as a clamping circuit in [23] to address switch voltage stress but due to more number of semiconductor switches, the converter has low efficiency. Switching losses are due to.

1) Reverse recovery of stored charge frequently results

© 2023 IEEE. Personal use is permitted, but republication/redistribution requires IEEE permission. See https://www.ieee.org/publications/rights/index.html for more information.
Authorized licensed use limited to: DELHI TECHNICAL UNIV. Downloaded on April 03,2023 at 05:18:49 UTC from IEEE Xplore. Restrictions apply.

This article has been accepted for publication in IEEE Journal of Emerging and Selected Topics in Industrial Electronics. This is the author's version which has not been fully edited and content may change prior to final publication. Citation information: DOI 10.1109/JESTIE.2023.3262451

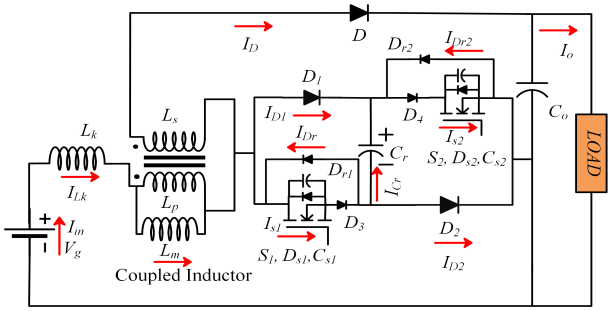


Fig. 2. Proposed HGBC topology

in considerable conduction and reverse recovery losses during the turn-ON/OFF transition.

2) Due to considerable time in recombination/removable of charges from the surface of diodes.
3) The loss of energy due to the internal capacitance C_{ds} of the MOSFET.
4) The loss caused by the MOSFET's body diode, which is used in the reverse recovery process.

To address these issues, this article proposes an efficient soft-switched high-gain boost converter with reduced voltage stress across all semiconductor devices. Coupled inductor with switched capacitor in conjunction switches help to mitigate the false triggering of MOSFETs. Moreover, the proposed converter achieves high voltage gain with reduced voltage stress across the switches and diodes. Since the voltage stress across the MOSFETs is low, it helps to select low-rating power switches whose R_{ds} is low. This aids in lowering conduction loss. In addition to this, the leakage inductance helps reduce the reverse recovery losses of the diode. In the proposed converter, the leakage energy of the CI is not only used to get high voltage at the output but also to achieve ZVS for the MOSFETs at full load. This aids in achieving low switching losses and helps to improve the efficiency of the converter. High frequency reduces the size of passive components, which enhances the power density of the converter by reducing the size of the coupled inductor.

This paper is put together like this: Section II talks about the proposed converter's circuit description and mode of operation. Section III presents the mathematical analysis. Section IV talks about experimental results and comparison of the proposed converter, and Section V concludes the paper.

II. Analysis and Mode of Operation of the Proposed Converter

The circuit diagram of the proposed high-gain boost converter is shown in Fig. 2, where L_m is the equivalent magnetising inductance for the primary side, and L_k is the leakage inductance, C_o is the output load capacitor, S_1, S_2 are the switches, D_1, D_2, D_3, D_4 and D are the diodes, and C_r is the switched capacitor. An auxiliary circuit made up of diodes D_{s1}, D_{s2}, C_{s1}, C_{s2}, and C_r is responsible for soft switching on the switches. Fig. 3 presents the steady state theoretical waveforms of the proposed high gain boost converter, and its working mode is illustrated in Fig. 4.

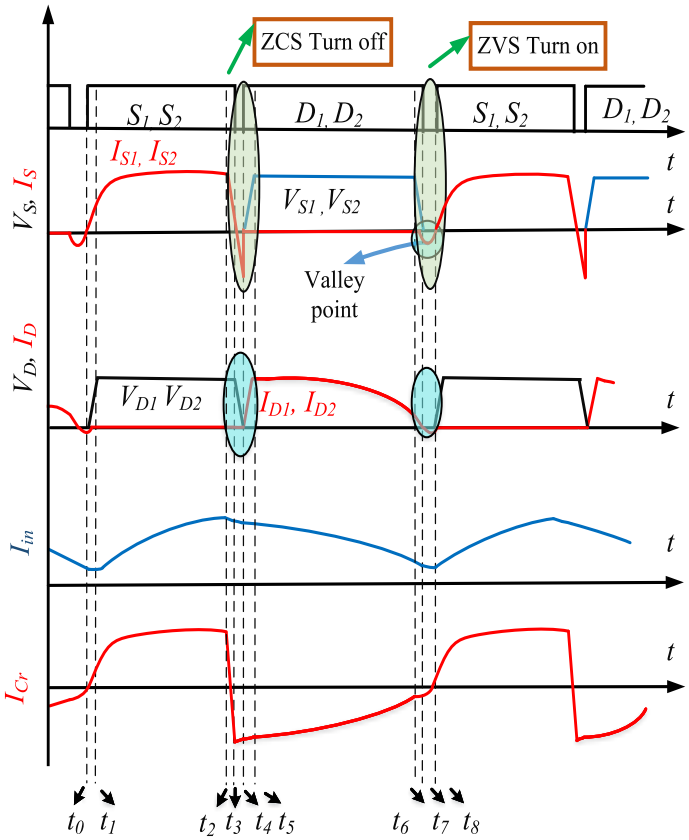


Fig. 3. Steady state theoretical waveform of proposed converter

The following assumptions are made to understand the mathematical analysis and describe how the proposed converter works.

1) The converter operates in the steady state and continuous conduction mode.
2) The components of the converter, including the voltage sources as well as the active and passive components, are ideal.
3) Filter capacitor is large enough to maintain a constant voltage at the output.
4) The coupled inductor is assumed to be linear with the turns ratio (n) as $n = \frac{N_S}{N_P}$.

The complete working of the proposed converter is divided into eight modes, as shown in Fig. 4 and is as follows:

Mode 1 (t_0 - t_1):- This mode begins with switches S_1 and S_2 being turned ON in the ZVS condition. Due to the initial polarity of capacitor C_r the diodes D, D_1, and D_2, are reverse biased. The input current going through the magnetising winding L_m charges the capacitor C_r. The output capacitor supplies power to the load maintaining a constant voltage.

Mode 2 (t_1 - t_2):- In this mode, both switches are ON, and diodes D_1, and D_2 are in a reverse biased state with diode D turning ON. The input current I_{in} increases linearly and completes its path via two loops $(V_g - L_k - D - C_o)$ and $(V_g - L_k - S_1 - S_2 - C_o)$. In this mode, the capacitor discharging and current flowing through the capacitor slows down. In this mode, the voltage across the V_{Cr} appears across

© 2023 IEEE. Personal use is permitted, but republication/redistribution requires IEEE permission. See https://www.ieee.org/publications/rights/index.html for more information.
Authorized licensed use limited to: DELHI TECHNICAL UNIV. Downloaded on April 03,2023 at 05:18:49 UTC from IEEE Xplore. Restrictions apply.

This article has been accepted for publication in IEEE Journal of Emerging and Selected Topics in Industrial Electronics. This is the author's version which has not been fully edited and content may change prior to final publication. Citation information: DOI 10.1109/JESTIE.2023.3262451

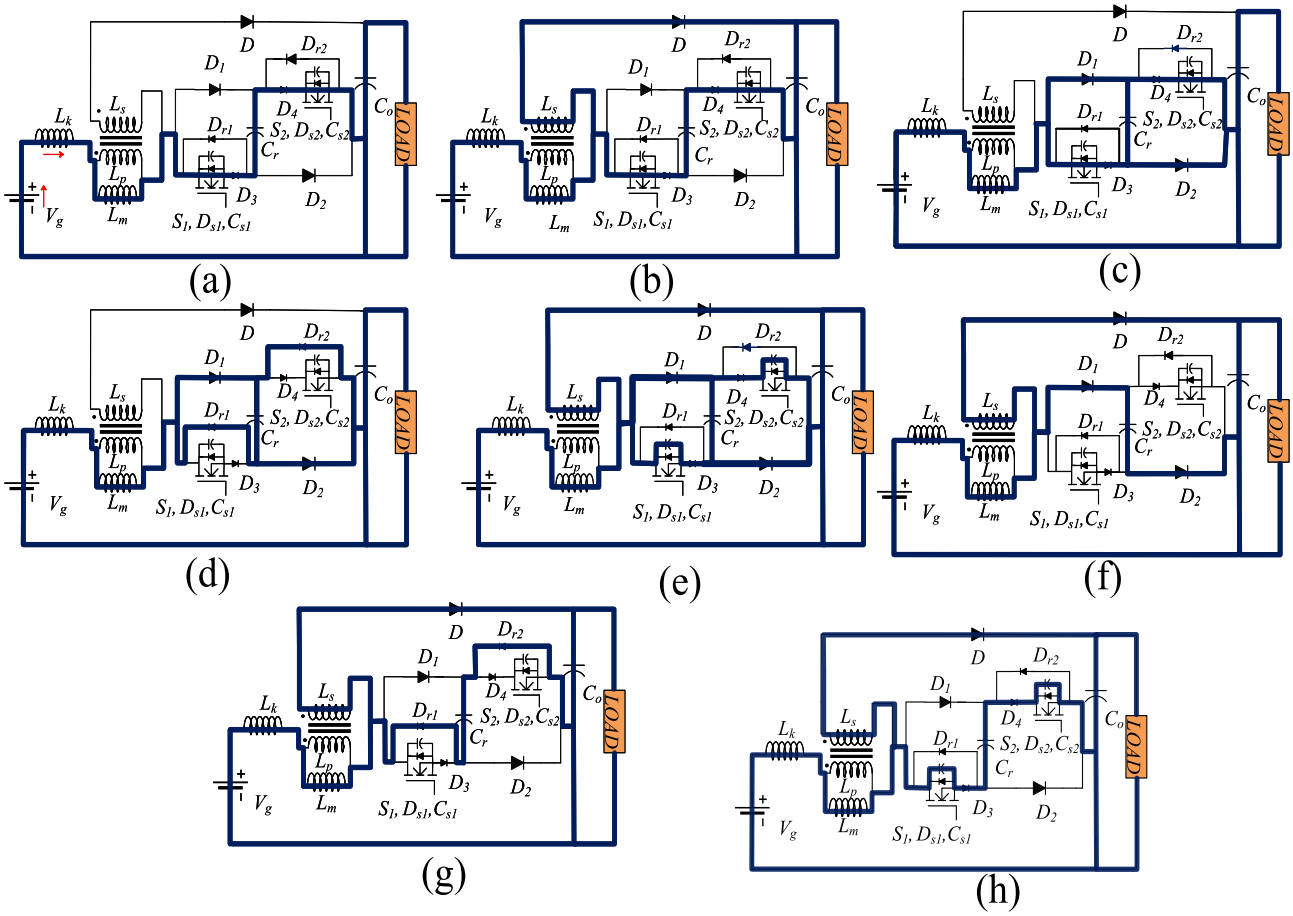


Fig. 4. The proposed converter's equivalent circuit with all modes of operation, (a) Mode 1, (b) Mode 2, (c) Mode 3, (d) Mode 4, (e) Mode 5, (f) Mode 6, (g) Mode 7, (h) Mode 8.

the diode D_1, since the C_r discharges, its voltage reaches zero, which implies voltage across D_1 is also zero. At this instant, the transition between mode 2 and mode 3 takes place.

Mode 3 (t_2 - t_3):- This mode starts with the transition of mode 2. As the current in switch S_1 decreases, the current flowing through D_1 increases. In this mode, all the switches are ON, and the current flowing through S_1 reaches zero. As the current becomes zero at the end of this mode, it is perfect timing to achieve ZCS across the switches S_1 and S_2.

Mode 4 (t_3 - t_4):- At the end of mode 3, the transaction current flowing through the diode D_1 increased. Now the current I_{Cr} starts charging the switched capacitor C_r. In this mode , as the D_{r1} and D_{r2} is also forward biased the current also flows through D_{r1} and D_{r2} as shown in Fig. 4(d).

Mode 5 ($t_4 - t_5$):- The diodes D_1 and D_2 are forward biased at the end of mode 4 (refer to Fig. 4(e)) due to sufficient voltage across C_r. In this mode, the current passing through D_{s1} and D_{s2} starts charging the parasitic capacitor as shown in Fig. 4(e).

Mode 6 (t_5 - t_6):- Current flows through C_r, D_1, and D_2 during this mode of operation (refer to Fig. 4(f)). D_{r1} and D_{r2} is reverse biased and load current is sustained by the output capacitor C_o. In this mode, diode current I_{D1} and I_{D2} decreases as shown in Fig. 3.

Mode 7 (t_6 - t_7):- Mode 7 starts with the transition of current from D_1 and D_2 to D_{r1} and D_{r2}. The current will not change its direction and flows through the D as shown in Fig . 4g. In this mode, the voltage across the switches becomes zero.

Mode 8 (t_7 - t_8):- In this mode, the parasitic capacitor of both the switches is charged, and the voltage across MOSFETs will not change abruptly, causing a delay in the MOSFET's turn-on process. This is the perfect time to give the pulses to S_1 and S_2 to turn on the switches at ZVS turn-ON mode.

III. Steady State Analysis of Proposed Converter

The following assumptions are made to analyze the steady-state operation of the proposed converter.

- During the switching period, it is assumed that all capacitors are fully charged. In addition, it is assumed that all of the converter's passive elements have already attained a steady state during the previous switching cycle.
- All the passive and solid state semiconductors devices are considered as ideal.
- CCM is assumed for the analysis of proposed converter, and Mode II and Mode VI, is considered for all mathematical analysis.
- The value of leakage inductance is considered negligible, as compared to L_m. Therefore ($L_k \ll L_m$) is taken for mathematical analysis.

© 2023 IEEE. Personal use is permitted, but republication/redistribution requires IEEE permission. See https://www.ieee.org/publications/rights/index.html for more information.
Authorized licensed use limited to: DELHI TECHNICAL UNIV. Downloaded on April 03,2023 at 05:18:49 UTC from IEEE Xplore. Restrictions apply.

This article has been accepted for publication in IEEE Journal of Emerging and Selected Topics in Industrial Electronics. This is the author's version which has not been fully edited and content may change prior to final publication. Citation information: DOI 10.1109/JESTIE.2023.3262451

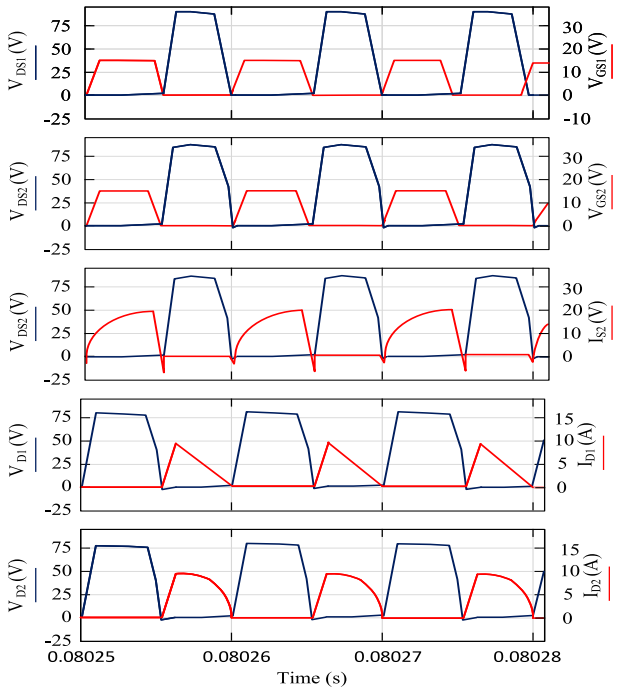


Fig. 5. Simulation waveforms for the switches and diodes

A. Voltage Conversion Ratio

Voltage conversion ratio of the proposed converter can be found by applying vol-sec balance method. When the main switch S_1 and S_2 are ON, the magnetizing inductance and capacitor is charged by input voltage V_g. Applying the volt-ses balance on the inductor L_m, we get,

$$V_{Lm}^{on} DT_s + V_{Lm}^{off}(1-D)T_s = 0 \tag{1}$$

$$(V_g - V_{Cr})DT_s + (V_g - V_{Cr})(1-D)T_s = 0 \tag{2}$$

$$V_{c_r} = \frac{V_g}{(1-2D)} \tag{3}$$

We know that

$$\frac{V_{L_p}}{V_{L_s}} = \frac{N_p}{N_s} = N \tag{4}$$

substituting $V_{L_m}^{on} = NV_{L_s}$

$$V_{L_s}^{on} = \frac{V_o - V_g}{(1-N)} \tag{5}$$

applying volt-sec balance at inductor L_s,

$$\left(V_{L_s}^{on}\right) DT_s + \left(V_{L_s}^{off}\right)(1-D)\,T_s = 0 \tag{6}$$

$$\frac{(V_o - V_g)}{(1-N)} DT_s + (V_o + V_{C_r})\ \ (1-D)\,T_s = 0 \tag{7}$$

substituting (3) in (7), (8) is obtained

$$\frac{(V_o - V_g)}{(1-N)} DT_s + \left(V_o + \frac{V_g}{(1-2D)}\right)(1-D)\,T_s = 0 \tag{8}$$

By solving (8), the voltage gain of the proposed converter can be derived and given in (9)

$$M = \frac{V_o}{V_g} = \frac{1 - N(1-D) - 2D^2}{(1-2D)(1-N+ND)} \tag{9}$$

Turns ratio of the coupled inductor is defined as $n = \frac{1}{N}$ Hence, voltage gain in terms of turns ratio is given by (10)

$$M = \frac{V_o}{V_g} = \frac{n - (1-D) - 2D^2 n}{(1-2D)(n-1+D)} \tag{10}$$

Substituting $D = 0.4$ and $n = \frac{20}{48}$ = 0.42 in (10), voltage gain $M = 8$ is achieved which is required for the single phase grid connected inverter for houses-hold application. For input voltage of $48V$, output will be $48 \times 8 = 384V$. The RMS value of the current passing through S_1 is given in (11)

$$I_{s1(rms)} \approx \frac{I_o(1 - N(1-D) - 2D^2)}{(1-2D)(1-N+ND)} \times \sqrt{D\Big(1 + \frac{1}{3}\Big(\frac{4N(1-D)}{D(1+2N-ND)}\Big)^2\Big)} \tag{11}$$

B. Voltage stress

During turn-OFF, a reverse voltage is applied across S_1 and S_2, and it is lower than the output voltage and higher than the input voltage. The voltage stress is given as:

$$V_{sw} = \frac{V_g D}{(1-2D)} = 96\text{V} \tag{12}$$

Therefore, the switch must be selected having a reverse voltage greater than 10% of maximum voltage calculated in (12).

C. Selection of output capacitor

Since, 0.2% voltage ripple is assumed at output voltage, the filter capacitor is given by (13).

$$C_o \geq \frac{I_o D}{\Delta V_o f_s}$$
$$C_o \geq \frac{1.3 \times 0.4}{0.76 \times 100 \times 1000} = 6.84\mu\text{F} \tag{13}$$

where f_s switching frequency and ΔV_o is ripple in output voltage. The output capacitance is provided by a parallel combination of two electrolytic capacitors, rated at 5 μF. When it comes to electrolytic capacitors, the equivalent series resistance value (ESR) drops as the capacitance level increases. So, a relatively high value is chosen and connected in parallel to reduce the effect of the ESR further and reduce the ripple and power loss in the capacitance.

D. Soft switching condition for the proposed converter

Soft switching occurs because of energy stored in series inductance and the energy stored in switches. Broadly, it is given as follows,

- The stored energy of the magnetising inductance must be sufficient to charge and discharge the switched capacitor and the capacitance of the switches, which is C_{s1} and C_{s2}.
- There must be enough dead time to charge and discharge the magnetising current and capacitors C_{s1} and C_{s2}. This may be accomplished if the magentizing current reaches the negative valley point, as illustrated in Fig. 3.

© 2023 IEEE. Personal use is permitted, but republication/redistribution requires IEEE permission. See https://www.ieee.org/publications/rights/index.html for more information.
Authorized licensed use limited to: DELHI TECHNICAL UNIV. Downloaded on April 03,2023 at 05:18:49 UTC from IEEE Xplore. Restrictions apply.

This article has been accepted for publication in IEEE Journal of Emerging and Selected Topics in Industrial Electronics. This is the author's version which has not been fully edited and content may change prior to final publication. Citation information: DOI 10.1109/JESTIE.2023.3262451

TABLE I
BRIEF COMPARISON OF VARIOUS STATE-OF-THE-ART HGBC [4], [5], [9], [11], [17], [20], [23]–[25] TOPOLOGIES WITH THE PROPOSED TOPOLOGY

Ref.	No. of components					Voltage gain	Normalized V across switches	Iso.	Eff.(%)	power	Freq.	Switching	P.D. mW/mm^3
	CI, L	S	D	C	Total								
[4]	3,0	4	6	5	18	$\frac{3n}{(1-d)}$	$\frac{d(1-d)}{3n(1-2d)}$	Yes	92	0.2	100	ZVS - ON	-
[5]	0,2	2	8	6	18	$\frac{4}{(1-d)}$	$\frac{d(1-d)}{4(1-2d)}$	No	94	1	50	ZVS - ON	6.18
[9]	1,2	4	4	3	14	$\frac{n}{(1-d)}$	$\frac{d(1-d)}{n(1-2d)}$	Yes	-	0.4	50	ZVS - ON	-
[11]	1,1	2	2	4	10	$\frac{n}{(1-d)}$	$\frac{d(1-d)}{n(1-2d)}$	Yes	95.8	0.34	100	ZVS - ON	-
[17]	1,1	2	3	5	12	$\frac{d(n-1)+n+2}{(1-d)}$	$\frac{d(1-d)}{(1-2d)(2+n+(n-1)d)}$	No	95.8	0.25	70	ZVS - ON	11.66
[20]	1,2	2	2	3	10	$\frac{(1+3d)}{(1-n)}$	$\frac{d(1-n)}{(1+3d)(1-2d)}$	No	94.27	0.2	50	-	3.92
[23]	2,2	4	4	5	17	$\frac{n(2-d)+(1-d)^2}{(1-d)^2}$	$\frac{d(1-d)^2}{(n(2-d)+(1-d)^2)(1-2d)}$	No	94.81	1	100	Full ZVS	6.74
[24]	1,1	2	2	4	10	$\frac{(n+2)}{(1-d)}$	$\frac{d(1-d)}{(2+n)(1-2d)}$	No	93.9	0.12	78	ZCS- OFF	17.53
[25]	1,1	4	4	3	13	$\frac{n}{2(1-d)}$	$\frac{2d(1-d)}{n(1-2d)}$	Yes	-	-	50	ZVS - ON	-
[26]	1	2	8	5	16	$\frac{n(2-d)}{(1-d)^2}$	$\frac{d(1-d)^2}{n(2-d)(1-2d)}$	Yes	90.5	0.5	50	Hard switching	3.11
[Prop.]	1,0	2	5	3	11	$M = \frac{n-(1-d)-2d^2n}{(1-2d)(n-1+d)}$	$\frac{d}{M(1-2d)}$	No	96.2	0.5	100	Full ZVS	7.36

Note: CI = Coupled Inductor, L= Inductor, S= MOSFET, D= Diode, C= Capacitor, d= duty ratio, P.D. Power Density. power = in kW and Freq. = in kHz

TABLE II
BRIEF COMPARISON OF VARIOUS DEVICES USED IN [11], [17], [20], [23], [24] WITH THE PROPOSED HGBC TOPOLOGY

Reference	Converter input/output (Volt)	Switches specification/ R_{ds}	Diodes specification/V_F	Switching frequency (kHz)	L_m, L_k
[9]	48 to 280	IRF840/850mΩ	MUR460	100	(95 μH, 3μH)
[11]	48 to 400	IPP200N15N3/20mΩ	C3D06060F	100	(180 μH, 5μH)
[17]	(16 - 20) to 400	IPP023N08N5AKSA1 / 2.3mΩ	MUR1540 / 1.25V	70	(67 μH, 1μH)
[20]	20 to 260	IRFB4321PbF/ 15mΩ	SDT10S60/ 1.7 V @ 10 A	50	(223μH , -)
[23]	50 to 470	IRFP4668PBF/8mΩ, IRFP460/270mΩ	STPR860DF	100	(200 μH; 33μH)
[24]	(20 - 30) to 200	IRFR3607PBF / 7.34mΩ	MUR820G / 0.9V	78	(24.8 μH; 1.9 μH)
Proposed	48 - 400	IRFP4227PBF/ 21mΩ	C1707	100	(80 μH, 3μH)

1) ZVS condition: To achieve a perfect ZVS condition, the switch voltage must be kept at zero when the gate pulse is supplied to the switch, as illustrated in Fig. 3. A snubber capacitor is connected in parallel to the switches to get a successful ZVS turn-ON. The snubber capacitors are utilized to increase the rising time of the MOSFETs by reducing their rising speed. Here snubber capacitors C_{s1} and C_{s2} are taken into consideration for ZVS, whose practical value will be greater than the theoretical value, and it can be calculated by (14) and (15)

$$C_{s1} \geq \frac{t_{d1(ON)}}{V_{C(s1)}}[i_{LM1}]|_{out-max} \tag{14}$$

$$C_{s2} \geq \frac{t_{d2(ON)}}{V_{C(s2)}}[i_{LM2}]|_{out-max} \tag{15}$$

where $t_{d1(ON)}$ and $t_{d2(ON)}$ are the switching turn-ON time from the datasheet of MOSFETs IRF4227PDF.

2) Design of coupled inductor: Minimum value of magnetizing inductance is required for the successful CCM mode of operation. This value can be calculated at boundary condition mode (BCM) where minimum current reaches to zero and starts charging again. At BCM, maximum value of the magnetizing current is given by (16) and (17)

$$I_{Lm(Peak)} = \frac{(V_g + V_{Cr})DT_s}{L_m} = \Delta i_{Lm} \tag{16}$$

$$I_{Lm(Peak)} = \frac{2V_g(1-D)DT_s}{(1-2D)L_m} = \Delta i_{Lm} \tag{17}$$

At BCM, average value of I_{Lm} is given by (18)

$$I_{Lm} = \frac{\Delta i_{Lm}}{2} = (N-1)\frac{I_o}{(1-2D)} \tag{18}$$

Therefore, the calculated value of the magnetizing inductance at boundary condition Lm_B, is given by (19)

$$Lm_B = \frac{RD(1-D)(1-2D)^2(1-N+ND)}{(1-N(1-D)-2D^2)f_s} \tag{19}$$

where f_s is the switching frequency, R_o is load at boundary condition and Lm_B is mutual inductance at boundary condition. Considering 20% of the full load (1500Ω) for successful continuous conduction mode, the minimum inductance required is given by

$$Lm_B = \frac{1500 \times 0.4 \times 0.6 \times 0.2^2(1-2.2+0.88))}{(1-2.2\times 0.6-2\times 0.4^2)\times 100\times 10^3} = 72\mu\text{H} \tag{20}$$

Hence, for the boundary condition under CCM, requires Lm_B approximately 72μH. Here, for CCM operation L_m must be greater than Lm_B, thus, a coupled inductor of 80μH is selected. $I_{Lm(Peak)}$ is calculated from (17) and the value is 14.4A. I_{Lm} is calculated using (18) and the value is 7.2A. Sendust core (MS-184090-2) core from ARNOLD Micrometals is selected for the designing of coupled inductor because of thermal stability and presence of the distributed air gap over the ferrite core. A_L value of the core is 202nH/Turns^2. Number of turns calculated is 20, because of DC bias and A_L

© 2023 IEEE. Personal use is permitted, but republication/redistribution requires IEEE permission. See https://www.ieee.org/publications/rights/index.html for more information.
Authorized licensed use limited to: DELHI TECHNICAL UNIV. Downloaded on April 03,2023 at 05:18:49 UTC from IEEE Xplore. Restrictions apply.

This article has been accepted for publication in IEEE Journal of Emerging and Selected Topics in Industrial Electronics. This is the author's version which has not been fully edited and content may change prior to final publication. Citation information: DOI 10.1109/JESTIE.2023.3262451

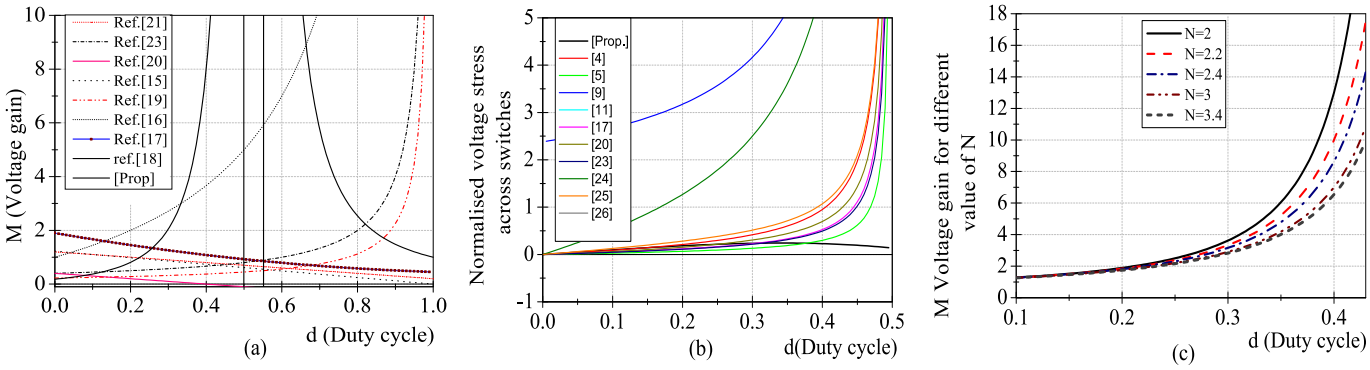


Fig. 6. (a) Voltage gain vs duty cycle, (b) Normalised voltage stress across the switch vs duty cycle, (c) Voltage gain for different values of N vs duty cycle.

TABLE III
LOSS ESTIMATION FOR THE PROPOSED CONVERTER

Components	Type of loss	Symbol	Loss calculation
Diode	Conduction loss	$P_{\text{D,con}}$	$P_{D,Loss} = P_{\text{D,con}} + P_{\text{D,rev}}$
	Reverse recovery losses	$P_{\text{D,rev}}$	$P_{D,Loss} = V_F.I_{D,avg} + R_D \cdot I^2_{D,rms}$
			$P_{\text{D,Loss}} = 3.69 + 3.69{+}2.1{+}2.1{+}0.95 \approx 12.59$
Switch loss	Conduction loss	$P_{s(1,2),on}$	$P_{s,Loss} = P_{\text{s1,on}} + P_{\text{s2,on}} + P_{\text{s1,off}} + P_{\text{s2,off}}$
			$= R_{\text{ds(s(1,2)on)}}.I^2_{\text{D(1,2)rms}} + 0.5[V_{\text{ds}}.I_{D(1,2)off}.(t_{ri} + t_{fv})]$
	Switching loss	$P_{s(1,2),off}$	$P_{s(1,2),Loss} = P_{s(1,2),on} + P_{s(1,2),off}$
			$P_{s(1,2),Loss} = 0.70 + 0.70{+}\ 0.38{+}0.38 \approx 2.16$W
Coupled inductor	Core loss	$P_{L,core}$	$P_{L,Loss} = P_{L,core} + P_{L,copper}$
			$P_{L,core} = 0.126 \times 9.365 \approx 1.18$W
			$P_{L,copper} = I^2_{L,rms}.R_{ds}$
	Conduction loss	$P_{L,copper}$	$P_{L,copper} = 1.51 + 0.54 \approx 2.05$W
			$P_{L,Loss} = 1.18 + 2.05 \approx 3{,}23$
Specifications			
Diode	$V_F = 0.76$V, $I_{\text{D1,avg}} = I_{\text{D2,avg}} = 4.86$A, $I_{\text{D3,avg}} = I_{\text{D4,avg}} = .8$A, $I_{\text{D}} = 1.3$A		
MOSFET	$R_{ds} = 21\text{m}\Omega$, $I_{D,rms} = 5.8$A, $V_{\text{DS}} = 95$V, $I_{Doff} = 10.50$A, $t_{\text{ri}} = 2$-ns, $t_{\text{fv}} = 31$ns		
Coupled Inductor	$P_c(f(\Delta B)) = 0.136\text{Wcm}^3$, $V_L = 9.365\text{cm}^3$, $I_{\text{Lpri,rms}} = 8.54$A, $I_{\text{Lsec,rms}} = 0.75$A, $R_{\text{dc}} = 21\text{m}\Omega$		

values, the required turns is taken as 48. Total switching and conduction losses of the proposed converter can be categorised into three parts i.e diode loss, switch loss and coupled inductor loss. Table III gives the detailed calculation of the losses taken into the consideration during CCM operation.

$$P_{sw} = 12.59 + 2.16 + 3.23 = 17.98\text{W} \tag{21}$$

miscellaneous losses are taken 1.02W. Hence 96.30% efficiency is calculated for the proposed HGBC.

3) Design of switched capacitor: Selection of switched capacitor depends upon two factor. 1) Ripple in capacitor voltage 2) Output power level. 0.2% ripple in coupled capacitor is assumed for best performance. It is calculated using charge-time balance and it is given by

$$\begin{aligned} C_r &\geq \frac{I_o(1-2D)}{f_s \Delta V_{Cr}} \\ &\geq \frac{1.3 \times (1-0.8)}{100 \times 10^3 \times 0.76} = 3.42\mu\text{F} \end{aligned} \tag{22}$$

E. Loss auditing

The current passing through S_1 can be calculated by (11). Total input power of the converter must be equal to summation of output power, power losses in operating switches and miscellaneous. The input power is calculated by

$$P_{in} = I_{in} \times V_{in} = 10.68 \times 48 = 513\text{W} \tag{23}$$

and output is given by

$$P_{out} = I_{out} \times V_{out} = 1.3 \times 380 = 494\text{W} \tag{24}$$

There are two types of losses in MOSFETs: conduction and switching losses. In contrast, conduction and reverse recovery losses occur in diodes, while conduction and core losses occur in the coupled inductor. Table III depicts the numerical methods to calculate the losses in the proposed topology. Fig. 8 shows the loss distribution for the proposed topology, where diodes share the maximum loss contribution..

F. Comparison of projected converter performance

The performance comparison of the proposed converter with other existing HGBC [4], [5], [9], [11], [17], [20], [23]–[25] is shown in Table I. The voltage gain of the proposed converter is compared with other existing topologies. A voltage gain vs. duty ratio plot is shown in Fig. 6(a). It is evident that the proposed converter can achieve a voltage gain like others at

© 2023 IEEE. Personal use is permitted, but republication/redistribution requires IEEE permission. See https://www.ieee.org/publications/rights/index.html for more information.
Authorized licensed use limited to: DELHI TECHNICAL UNIV. Downloaded on April 03,2023 at 05:18:49 UTC from IEEE Xplore. Restrictions apply.

This article has been accepted for publication in IEEE Journal of Emerging and Selected Topics in Industrial Electronics. This is the author's version which has not been fully edited and content may change prior to final publication. Citation information: DOI 10.1109/JESTIE.2023.3262451

TABLE IV
COMPONENTS SPECIFICATIONS

Component	Specification
Power	P_o = 500W
Output voltage	380V
Input voltage	48V
Turn's ratio	1:2.2
Switching frequency	100kHz
Output capacitors C_o	10 μF, 450 V
Magnetizing Inductance	80μH
Leakage Inductance	3μH

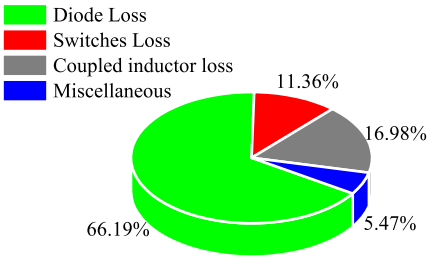


Fig. 8. Loss distribution of the porposed converter: Diode losses are contributing 66.19% due to conduction losses. Switching losses participate in 11.26% of total load due to conduction losses, switching losses of MOSFETs are sigificantly zero due to soft switching.

a lower duty cycle. The designed converter has two degrees of freedom to achieve high voltage gain. Changing the turn ratio can further enhance the voltage gain by lowering the duty ratio. The conventional boost converter achieves the same gain at 80% duty ratio. A comparison of normalised voltage stress (V_{DS}) is shown in Fig. 6(b). The MOSFETs of the proposed converter have lower voltage stress. Thus, the MOSFET of lower R_{ds} can be selected to reduce the conduction loss. The voltage stress of the converter can be further reduced by increasing the turn ratio. The stress across the diode is also lower, i.e., 106V, and can be further reduced by increasing the turn ratio. The leakage inductance plays a vital role in reducing reverse recovery losses of the diodes. In addition, when the diode is turned OFF, the SC starts charging through the MOSFET, and the leakage energy is utilized in charging the SC. Since the parasitic capacitance is much smaller than the switched capacitor and connected in series with mutual inductance, some of the charges flow through the switched capacitor, and resonant current flows. So the resonance between mutual inductance and SC is eliminated by the inherent snubber made by the diode and SC. Compared to [17] and [23], the proposed topology showcases improved voltage stress and a lower number of components required. It also showcases a lower component count than [4], [5], [9], [17], [23], [25], hence it is cost-effective. The full load efficiency of [20] is 95.8% which is lower than the proposed topology.

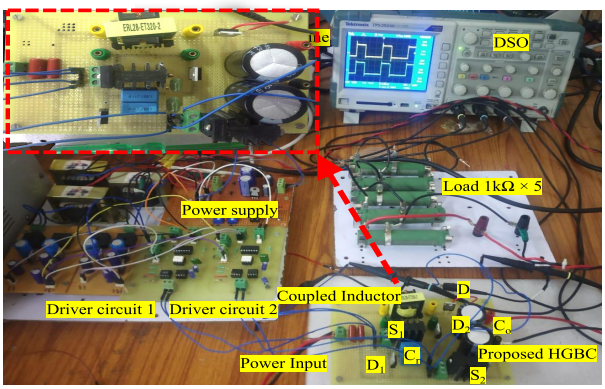


Fig. 7. Experimental set-up for the proposed converter

IV. EXPERIMENTAL RESULTS AND VERIFICATION

To verify the performance of the proposed converter, a laboratory prototype of 500W is developed as shown in Fig. 7. The prototype is tested at an input voltage of i.e. V_g= 48V, an output voltage, V_o= 380V and output power, P_o= 500W. The converter's performance is tested at full load, i.e., at R_o = 300 Ω and a duty cycle of 40%, and the obtained waveform is shown in Fig. 9. The proposed high-gain boost converter for low voltage renewable energy applications is developed and verified using MATLAB/Simulink, and waveforms of switches and diodes stress, ZVS turn-ON, and ZCS turn-OFF operations are shown in Fig. 5. The key parameters used to develop the proposed topology is shown in Table IV. A single coupled inductor of sendust core (MS-184090-2 of ARNOLD Micrometals) with the primary and secondary winding 22:48; N = 2.2 is used to implement the converter. The primary winding of the coupled inductor is wound by Litz wire of 0.1×400 strands, while 175 × 40 AWG is used for the secondary side. Measured magnetizing inductance referred to the primary side is 80μH, while the calculated value is 72μH. Measured leakage inductance at the primary side is 3μH. Fig. 2 depicts the schematic diagram of the hardware developed for the proposed converter. A power supply (100V/15A) and a load (500Ω × 5) are connected in series in an experimental setup. Also, one SG3424 IC is used to generate pulses of 100kHz and two driver circuits have been developed to operate the MOSFETs separately. Operation at high frequency leads to the use of low-rating passive components applied to the converters. Fig. 9(a) shows the gate pulse and current waveform of S_1 at duty cycle of 40%. The current passing through S_1 and gate pulse V_{GS1} shows the turn-ON and turn-OFF at ZVS and ZCS conditions. Channel 2 and channel 4 shows voltage and current waveforms of diode (D_1) as depicted in Fig. 9(a). Fig. 9(b) shows the gate voltage and voltage across S_1 at 0.4 duty ratio. Here the main switch withstand a voltage stress of 96V. The slow rise of V_{GS} can be easily seen in Fig. 9(b). The capacitors, C_{S1} and C_{S2} increases the rise time of MOSFETs, and gives sufficient time to turn-ON the switch at ZVS condition. Stress across the diode D_2 and the current flowing through the switched capacitor is shown in Fig. 9(c). Fig. 9(d) depicts the output voltage, i.e 380V (approx.) and output current, i.e. 1.3A (approx.). Fig. 9(e) shows the output and input current, which are 1.3A and 11.3A, respectively. The dynamic performance of the proposed converter is shown in

© 2023 IEEE. Personal use is permitted, but republication/redistribution requires IEEE permission. See https://www.ieee.org/publications/rights/index.html for more information.
Authorized licensed use limited to: DELHI TECHNICAL UNIV. Downloaded on April 03,2023 at 05:18:49 UTC from IEEE Xplore. Restrictions apply.

This article has been accepted for publication in IEEE Journal of Emerging and Selected Topics in Industrial Electronics. This is the author's version which has not been fully edited and content may change prior to final publication. Citation information: DOI 10.1109/JESTIE.2023.3262451

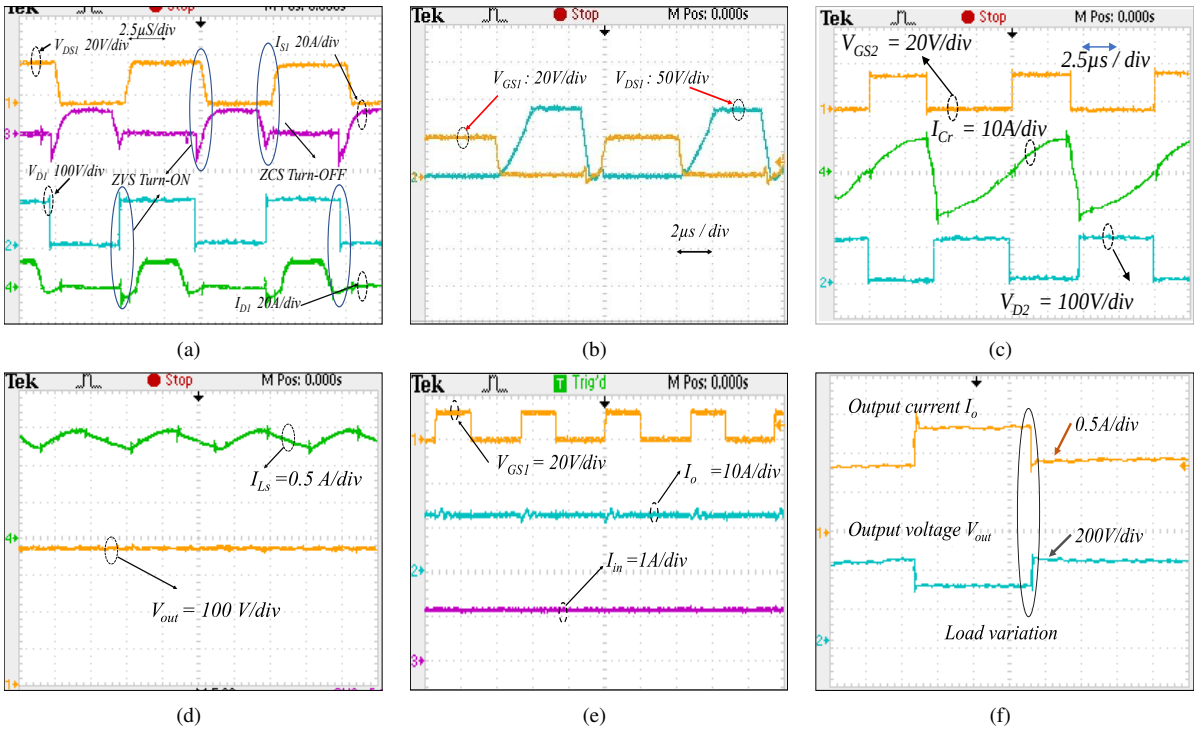


Fig. 9. Experimental result of the proposed topology. (a) Ch.1 and ch.3 shows V_{DS1} and I_{DS1} respectively. soft-switching is achieved successfully, (b) ch. 1 shows V_{GS1} and ch.2 shows V_{DS1} , (c) ch.1, ch. 2 and ch. 4 shows V_{GS2}, diode stresses D_2 and switched capacitor current, (d) output voltage = 380V and I_{Ls} is shown in ch. 1 and ch. 4, (e) ch. 1, ch. 2 and ch. 3 shows V_{GS1}, output current and input current I_{in} , I_o respectively,(f) Dynamic response for 50% load adjustment.

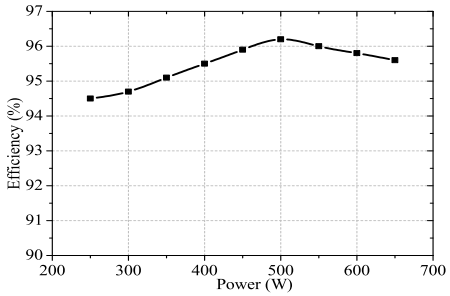


Fig. 10. Efficiency vs power curve, Max. η= 96.2% at 500W

Fig. 9(f) When the proposed converter is run at a 50% load increment, the current rises while the output voltage decreases. The efficiency of the proposed converter is evaluated under various load conditions as shown in Fig. 10. The proposed converter is found to be 96.20% efficient at full load, and its efficiency increases as load increases and reaches its maximum at 500W. Also, it is observed that the converter efficiency is 94.5% at half load.

V. Conclusion

This article presents a laboratory prototype of a 500 W, soft-switched, high-gain non-isolated boost converter for single-phase grid-connected low-voltage PV applications. With an input voltage of 48 volts and an output voltage of 380 volts, the proposed converter is suitable for single-phase inverter integration. Due to soft switching operation, the converter achieves maximum efficiency 96.20% at full load. Due to the low switch stress, a low-rated MOSFETs are employed, which helps to reduce the conduction losses. Additionally, the quantitative analysis of the converter has made it possible to obtain optimised design parameters. With this, an experimental laboratory prototype of 500 W is developed, tested, and the results obtained are satisfactorily verified for low-voltage renewable energy applications.

References

[1] M. Das and V. Agarwal, "Design and analysis of a high-efficiency dc–dc converter with soft switching capability for renewable energy applications requiring high voltage gain," *IEEE Transactions on Industrial Electronics*, vol. 63, no. 5, pp. 2936–2944, 2016.

[2] S. Sathyan, H. Suryawanshi, M. Ballal, and A. Shitole, "Low switching stress dc-dc converter with capability of high voltage gain for low voltage energy sources," *EPE Journal*, vol. 27, no. 2, pp. 74–84, 2017.

[3] S. V. Araújo, P. Zacharias, and R. Mallwitz, "Highly efficient single-phase transformerless inverters for grid-connected photovoltaic systems," *IEEE Transactions on Industrial Electronics*, vol. 57, no. 9, pp. 3118–3128, 2009.

[4] M. Delshad and H. Eghbali, "A new soft switching current-fed converter with high voltage gain," in *2011 International Conference on Electronic Devices, Systems and Applications (ICEDSA)*. IEEE, 2011, pp. 142–146.

[5] B. Zhu, Q. Zeng, Y. Chen, Y. Zhao, and S. Liu, "A dual-input high step-up dc/dc converter with zvt auxiliary circuit," *IEEE Transactions on Energy Conversion*, vol. 34, no. 1, pp. 161–169, 2018.

[6] S. V. Araújo, R. P. Torrico-Bascopé, and G. V. Torrico-Bascopé, "Highly efficient high step-up converter for fuel-cell power processing based on three-state commutation cell," *IEEE Transactions on Industrial Electronics*, vol. 57, no. 6, pp. 1987–1997, 2009.

[7] E. Candan, P. S. Shenoy, and R. C. Pilawa-Podgurski, "A series-stacked power delivery architecture with isolated differential power conversion for data centers," *IEEE Transactions on Power Electronics*, vol. 31, no. 5, pp. 3690–3703, 2015.

© 2023 IEEE. Personal use is permitted, but republication/redistribution requires IEEE permission. See https://www.ieee.org/publications/rights/index.html for more information.
Authorized licensed use limited to: DELHI TECHNICAL UNIV. Downloaded on April 03,2023 at 05:18:49 UTC from IEEE Xplore. Restrictions apply.

This article has been accepted for publication in IEEE Journal of Emerging and Selected Topics in Industrial Electronics. This is the author's version which has not been fully edited and content may change prior to final publication. Citation information: DOI 10.1109/JESTIE.2023.3262451

[8] E. K. Sato, M. Kinoshita, Y. Yamamoto, and T. Amboh, "Redundant high-density high-efficiency double-conversion uninterruptible power system," *IEEE Transactions on Industry Applications*, vol. 46, no. 4, pp. 1525–1533, 2010.
[9] M. Delshad, "A new soft switching coupled inductor half bridge current fed converter," in *2011 International Conference on Applied Electronics*. IEEE, 2011, pp. 1–4.
[10] A. B. Shitole, S. Sathyan, H. Suryawanshi, G. G. Talapur, and P. Chaturvedi, "Soft-switched high voltage gain boost-integrated flyback converter interfaced single-phase grid-tied inverter for spv integration," *IEEE Transactions on Industry Applications*, vol. 54, no. 1, pp. 482–493, 2017.
[11] A. Kumar and P. Sensarma, "Ripple-free input current high voltage gain dc–dc converters with coupled inductors," *IEEE Transactions on Power Electronics*, vol. 34, no. 4, pp. 3418–3428, 2018.
[12] G. Spiazzi, P. Mattavelli, and A. Costabeber, "High step-up ratio flyback converter with active clamp and voltage multiplier," *IEEE Transactions on Power Electronics*, vol. 26, no. 11, pp. 3205–3214, 2011.
[13] Y.-m. Ye and K. W. E. Cheng, "Quadratic boost converter with low buffer capacitor stress," *IET Power Electronics*, vol. 7, no. 5, pp. 1162–1170, 2014.
[14] S.-M. Chen, T.-J. Liang, L.-S. Yang, J.-F. Chen, and K.-C. Juang, "A quadratic high step-up dc-dc converter with voltage multiplier," in *2011 IEEE International Electric Machines & Drives Conference (IEMDC)*. IEEE, 2011, pp. 1025–1029.
[15] Y.-m. Ye and K. W. E. Cheng, "Quadratic boost converter with low buffer capacitor stress," *IET Power Electronics*, vol. 7, no. 5, pp. 1162–1170, 2014.
[16] A. Zavala, B. Vidales, D. Torres, and M. Madrigal, "Study, analysis and optimization of multilevel inverters based in a high stepping dc/dc converter for renewable energies," in *2017 IEEE International Conference on Environment and Electrical Engineering and 2017 IEEE Industrial and Commercial Power Systems Europe (EEEIC/I&CPS Europe)*. IEEE, 2017, pp. 1–4.
[17] K. Zaoskoufis and E. C. Tatakis, "An improved boost-based dc/dc converter with high-voltage step-up ratio for dc microgrids," *IEEE Journal of Emerging and Selected Topics in Power Electronics*, vol. 9, no. 2, pp. 1837–1853, 2020.
[18] S.-W. Seo, J.-H. Ryu, Y. Kim, and H. H. Choi, "Non-isolated high step-up dc/dc converter with coupled inductor and switched capacitor," *IEEE Access*, vol. 8, pp. 217 108–217 122, 2020.
[19] M. Kumar, K. Mathuriya, V. K. Yadav, and A. K. Verma, "Soft switched high gain boost converter for low voltage applications," in *2021 IEEE Energy Conversion Congress and Exposition (ECCE)*. IEEE, 2021, pp. 245–252.
[20] M. A. Salvador, T. B. Lazzarin, and R. F. Coelho, "High step-up dc–dc converter with active switched-inductor and passive switched-capacitor networks," *IEEE Transactions on Industrial Electronics*, vol. 65, no. 7, pp. 5644–5654, 2017.
[21] A. Shenkman, Y. Berkovich, and B. Axelrod, "Novel ac-dc and dc-dc converters with a diode-capacitor multiplier," *IEEE Transactions on Aerospace and Electronic Systems*, vol. 40, no. 4, pp. 1286–1293, 2004.
[22] G. A. Henn, R. Silva, P. P. Praca, L. H. Barreto, and D. S. Oliveira, "Interleaved-boost converter with high voltage gain," *IEEE Transactions on Power Electronics*, vol. 25, no. 11, pp. 2753–2761, 2010.
[23] P. Mohseni, S. H. Hosseini, and M. Maalandish, "A new soft switching dc–dc converter with high voltage gain capability," *IEEE Transactions on Industrial Electronics*, vol. 67, no. 9, pp. 7386–7398, 2019.
[24] L. C. Mazza, D. S. Oliveira, F. L. Antunes, D. B. Alves, L. H. Barreto, and J. J. Souza, "A soft switching bidirectional dc-dc converter based on three-state switching cell," in *2015 IEEE Energy Conversion Congress and Exposition (ECCE)*. IEEE, 2015, pp. 4656–4663.
[25] G. Chen, Y. Deng, X. He, Y. Hu, and L. Jiang, "Analysis of high voltage gain dc-dc converter with active-clamping current-fed push-pull cells for hvdc-connected offshore wind power," in *IECON 2016-42nd Annual Conference of the IEEE Industrial Electronics Society*. IEEE, 2016, pp. 1288–1293.
[26] G. A. Henn, R. Silva, P. P. Praca, L. H. Barreto, and D. S. Oliveira, "Interleaved-boost converter with high voltage gain," *IEEE transactions on power electronics*, vol. 25, no. 11, pp. 2753–2761, 2010.



Manikant Kumar was born in West Champaran, India. He received a B.Tech. degree in Electrical Engineering from the West Bengal University of Technology, West Bengal, India, in 2013 and completed his M.Tech. degree in Power Electronics and Drives from the National Institute of Technology Rourkela, Orissa, India, in 2017. He also worked as a research scholar at IIT Delhi in 2018. He worked as an assistant professor at the University College of Engineering and Technology, Bikaner, Rajasthan, during 2018-2023. He is currently working toward his PhD degree in the Department of Electrical Engineering at Malaviya National Institute of Technology Jaipur, Jaipur, India. His research interests are high-gain boost converters for low-power applications, battery management systems, soft switching, grid-connected system and AC-DC systems.



Vinod Kumar Yadav was born in Allahabad, India. He received the B.E. degree in Electrical Engineering from the Jabalpur Engineering College, Jabalpur, India, in 2015, the M.Tech. degree in Power Electronics and Drives from the National Institute of Technology Rourkela, Orissa, India, in 2017. He is currently working toward the Ph.D. degree in the Department of Electrical Engineering, Malaviya National Institute of Technology Jaipur, Jaipur, India. He worked as an assistant professor in the Department of Electrical Engineering at Government Engineering College Bikaner, Rajasthan India. He also worked as a Research Associate at Delhi Technological University, Delhi, India and Motilal Nehru National Institute of Technology, Allahabad, India. His research interests include AC-DC PFC converters, LED driver circuits, high-gain boost converters, and soft switching.



Arun Kumar Verma (Senior Member, IEEE) received the master's degree in energy studies and the Ph.D. degree in power electronics from the Indian Institute of Technology Delhi, New Delhi, India, in 2010 and 2015, respectively. He was a Visiting Graduate Researcher with the Smart Grid Energy Research Centre, University of California, Los Angeles, CA, USA, during 2014 – 2015. He was a Postdoctoral Research Fellow with the Energy Research Institute, Nanyang Technological University, Singapore, during 2015–2016. He is currently working as an Associate Professor with the Department of Electrical Engineering, Indian Institute Of Technology-Jammu, India. His research interests include power electronics, power conversion techniques, power quality, smart grid and smart building, electric vehicle, and bidirectional power flow. Dr. Verma was the recipient of the prestigious BASE Fellowship for advance solar energy research, in 2014, and the prestigious POSOCO Power System Research Award 2016.

© 2023 IEEE. Personal use is permitted, but republication/redistribution requires IEEE permission. See https://www.ieee.org/publications/rights/index.html for more information.
Authorized licensed use limited to: DELHI TECHNICAL UNIV. Downloaded on April 03,2023 at 05:18:49 UTC from IEEE Xplore. Restrictions apply.

SYNTHESIS AND EFFECT OPTIMIZATION OF M R FLUID COMPOSITION FOR REDUCTION IN INDUCED RESIDUAL STRESS

Anil Kumar[1*], Neeraj Kumar[2], M.S. Niranjan[3]

ArticleHistory: **Received:** 12.12.2022 **Revised:** 29.01.2023 **Accepted:** 15.03.2023

Abstract

Stresses are produced during manufacturing of Mechanical parts. Sometimes these stresses are useful and sometimes detrimental for the parts depending upon the application of these parts. The stress generated during the manufacturing processes of parts affects the life of these parts and are responsible most of the time for premature failure of parts. Therefore, the detailed analysis of induced stresses in machined parts is essential to the performance of a machined component. There are many methods available for stress analysis of mechanically manufactured parts. The first type of method which is Non-Destructive techniques i.e., x-ray diffraction, Neutron diffraction, etc. The second type of method is the destructive technique i.e., Contour method and sectioning method. The third type of method which is Semi Destructive techniques i.e., hole drilling, deep hole drilling, etc. The Induced residual stress in a component machined with traditional manufacturing processes i.e., Grinding, Milling, Turning, etc. can be reduced by using the Novel finishing process of BEMRF (Ball End Magnetorheological finishing). This finishing process can produce a very good surface finish with comparatively low induced residual stress in finished components. In this paper, we will explain the residual stress analysis of machined hard metal work-piece before and after Ball End Magneto-rheological finishing. Experimental method employing a Bi-dispersible composition of M R Fluid will be investigated. Further optimization of Bi-dispersible M R Fluid results will be done by use of optimization techniques to find out the best operating parameters to achieve a maximum % reduction in residual stress. M R fluid composition with Bi-dispersible CIP used in this experiment has not been investigated so far by using BEMRF.

Keywords: Residual Stress, Non-destructive method, X-ray diffraction, Neutron diffraction, Bi-dispersible MRF, BEMRF, Magnetic tool, Tool rotational speed, Working gap, etc.

[1*]Mechanical Engineering Department, Suresh Gyan Vihar University, Jaipur
[2]Mechanical Engineering Department, Suresh Gyan Vihar University, Jaipur
[3]Mechanical Engineering Department, DTU, New Delhi
Corresponding Author: [1*]akumar14916@gmail.com
ORCID: 0000-0002-5878-0543

DOI: 10.31838/ecb/2023.12.1.109

1. Introduction

Residual stress is the stress which residue in a part that is not exposed to external forces. Residual Stress is being caused by manufacturing operations or processing operations or the service environment. Generation of residual stresses happens during most manufacturing processes which involve deformation of the material, generation of heat, and change in physical shape or size or variation in material's mechanical properties. They can be originated from many sources during manufacturing and can exist in the mechanical components even due to in-service loading. Term surface integrity is used to indicate the properties of machined surface post manufacturing operations. Surface integrity aspects include metallurgy characteristics, topography, and residual stress. The topography is a mix of surface roughness, flaws, and waviness. The metallurgy characteristics include grain size, micro-hardness, plastic deformation, re-crystallization, phase transformation, etc. The analysis of residual stress is crucial in predicting working lifespan, investigating distortion and the reasons for failure. All the stress measurement techniques can be classified into two classes: One which measures actual strain, and the second which measures changes in strain (Mishra & Prasad, 1985). The method of measurement choice should be based on the type of information required, economic factors, and limitations of each technique. The relieving of residual stress present in a component after conventional machining method of cylindrical grinding can be done by using advance finishing techniques i.e., Magnetorheological finishing. The effect of this finishing process on residual stress present in machined components will be studied by experimental technique.

1.1. Residual Stress

Residual stresses are in equilibrium as tensile residual stresses (disadvantageous) and compressive residual stresses (advantageous). For example, if a component's surface is created in tensile stresses, it will be containing compressive residual stresses, and if the component's surface is created in compressive stresses, it will be containing tensile residual stresses (Mishra & Prasad, 1985).

1.1.1. Tensile Residual Stresses: - The generations of tensile residual stresses (TRS) generally happen due to production processes i.e., aggressive grinding which produces the growth of cracks. They can also be created with other mechanical methods i.e., Fitting, shrinking, bending, or torsion. For example, Cracks on the component surface are produced due to remaining tensions as residual stresses in components produced using the casting method. Moreover, due to the presence of tensile residual stresses, the defect of stress corrosion cracking also happens in these components (Mishra & Prasad, 1985).

1.1.2. Compressive Residual Stresses: - The fatigue strength, as well as resistance to stress corrosion cracking, is enhanced by compressive residual stresses (CRS). Compressive residual stress is intentionally generated during manufacturing processes i.e., laser peening, shot peening, auto-fretting, low plasticity burnishing, etc. During these processes strain hardening of material takes place due to cold working. The detrimental effect of residual tensile stress is counter balanced with the introduction of compressive residual stresses. Residual tensile stresses can also be reduced by using suitable heat treatment processes (Perry, Sue, & Martin, 1996).

The Sum of all the residual stresses and all the applied service stresses on a component is called the total stress of that component. The known residual stresses are of three types: -

(A) Type-1 Residual Stress: - When the stresses are developed in several grains of material, it is called Macro-residual stress. Macroscopic dimensions will change if there is any change in the Type-1 residual stress equilibrium. Residual stresses of Type-1 are produced because of methods that cause inhomogeneous strain distribution.

(B) Type-2 Residual Stress: - When development of stresses in one grain of the material happens, it is called Micro-residual stress. Type-2 residual stresses are produced during martensitic transformation where the incomplete transformation of austenite is observed during the transformation process. Due to the difference in the volume of austenite and martensite, residual stresses are produced.

(C) Type-3 Residual Stress: - When within several atomic distances of the grains, stresses are developed; it is called sub-micro residual stress. It is produced due to crystalline defects such as dislocations, vacancies, etc.

In actual conditions, all the residual stress types are present in all the components. All manufacturing Operations produce some quantity of residual stresses. Cracks can occur because of these stresses. Due to these residual stresses welded and cast components even at room temperature and without any external

loading may fail disastrously. The service lifetime of the components is directly affected due to residual stresses present in these components. Due to this, the investigation of residual stress is very essential in many industries.

1.2. Residual Stress Analysis Methods

There are many residual stress analysis (RSA) techniques. In these techniques, the residual stress effect is measured and not stresses itself. There are three types in which these techniques can be classified: Non-destructive techniques, semi-destructive techniques, and destructive techniques (Perry, Sue, & Martin, 1996)

1.2.1. Destructive Technique

The destructive residual stress measurement technique is also called MSR (Mechanical Strain Release) technique. The methods used under this technique are detailed below: -

1) Sectioning method.
2) Contour method.

1.2.2. Semi-Destructive Technique

The semi-destructive techniques use the "strain release" principle for residual stress measurement. They do not change the overall integrity of the structure of component material; by removing a small amount of material under this category following methods are included:

1) Deep hole drilling (DHD) Method.
2) Incremental hole drilling (IHD) Method.

1.2.3. Nondestructive Technique

This technique is based on a relationship between the component's physical properties and stress. The diffraction method (NDT) measures variations in properties due to lattice space variation in component material due to stress. In this technique, ultrasound waves passed through the stressed material and variations in the speed of ultrasound waves are measured to determine the residual stress in the ferromagnetic material components.

.

1) Neutron diffraction.
2) X-Ray diffraction.
3) Ultrasound method.

2. Materials and Methods

2.1. Synthesis of Magnetorheological Fluid (MRF)

Magnetorheology is a branch of material science where the impact of employed magnetic field at material deformation and movement pattern of material are studied. Jacob Rabinow invented MR fluid in 1949. The rheological properties of M R fluid help to control its actions in the application of an exterior magnetic field (Jian & Peng, 2012) (Jha & Jain, 2004). The Composition of M R fluid generally consists of three components or faces i.e., Magnetic face (20 %), Cutting Face (25 %), and Carrier face (55 %) (Singh, Jha, & Pandey, 2015). The magnetic face contains materials such as Carbonyl Iron Powder, Nickel Alloys, Cobalt Alloys, etc. The desirable property of these materials is that their physical flow and shape can be changed using a changeable magnetic effect. Cutting Face contains abrasive materials such as SiC, which is used for cutting off material from the surface of work-piece. The Carrier Face contains the materials which help for movement of the two other faces such as AP-3 Grease, heavy-duty Paraffin oil, etc. Conventionally MRFs (magnetorheological fluids) are a combination of micron-sized ferromagnetic grains mixed with micron-sized SiC grains and hydraulic oil (mono-disperse). If the particle size of materials is within the range of equal to or less than 100 nm, then these materials are called nano-materials. The surface chemistry of the micro-scale particles differs from nano-scale particles. Hence by varying the % of nano-scale particles the behavior of the mixture can be controlled. If M R fluid contains micron size and nano-sized particles it called bi-disperse fluid. The advantage of nano-sized particles is that it reduces the M R fluid settling rate as Nano-sized particles fill the pores between micron-size particles (Kumar, Kumar, & Niranjan, 2020).

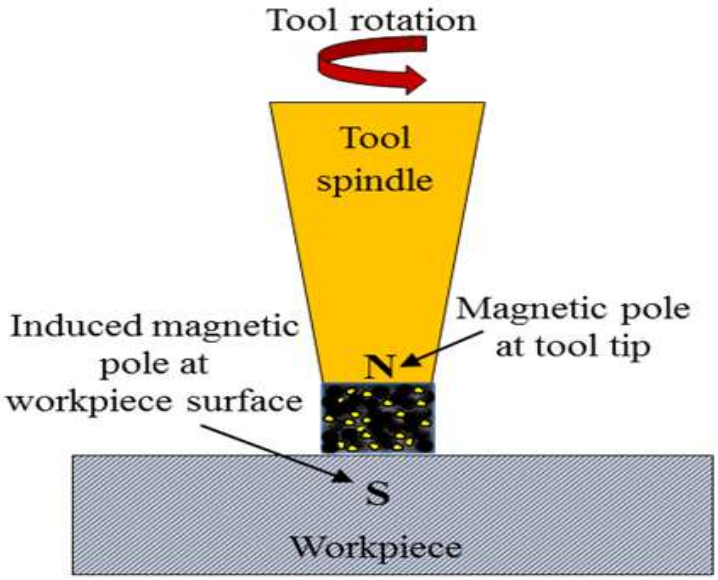


Fig.1 Mechanism of Ball End Magnetorheological finishing Tool

In preliminary experiments, different compositions of Bi-dispersible M R fluid were tested to find the best composition of M.R fluid on % reduction in Residual stress. The composition of bi-dispersible fluid which is used in this experimentation work has not been investigated earlier for its performance on finishing a hard metal work-piece. The composition which produced the highest % reduction in residual stress in components machined by conventional cylindrical grinding was 20 % Magnetic face (having 4% Nano CIP and 16% Micro CIP CS grade), 25% Cutting face (SiC of 800 mesh size) with 55% Carrier fluid (20 % AP-3 Grease and 80% Heavy duty Paraffin oil) on volume % basis (optimum M R fluid composition). Now during this experimentation work, confirmatory experiments to confirm the findings of earlier experiments and further optimize the effectiveness of M R Fluid composition by varying the process parameters of the BEMRF (Ball end magneto-rheological finishing) process to achieve better results. The schematic layout of the BEMRF process mechanism is displayed in the fig. No.1 (Peter, Andreas, Helmut , & Svea , 2017).

2.2. Experimental Set Up To Study Effect of M R Fluid Composition on Induced Residual Stress in Machined Hard Metal Work-Piece

The constituents of Magnetorheological fluid such as Carbonyl Iron Powder and SiC has been procured from BASF Corporation for using in this experimental study. BEMRF [Ball End Magneto-rheological Finishing] process is considered a new innovative finishing process and precisely used to finish simple as well as very complex three-dimensional surfaces (Singh & Singh, 2018). The residual stress and surface finish produced during the manufacturing processes of parts affect the life of these parts and are responsible most of the time for the premature failure of these parts. Therefore, the detailed analysis of induced stresses in machined parts is very important for the desired performance of a machined component (Singh, Jha, & Pandey, 2015). The goal of this experimental paper is to confirm and optimize the % reduction in residual stress of hard metal specimens by using BEMRF process. EN-31 work-pieces were used in this experimental work as specimens (Shunmugam & Kanthababu, 2020). These work-pieces were first finished using a cylindrical grinding process. Their residual stress measurements were done at four points across each specimen length of 70 mm. All the measurements were done using portable x-ray residual stress analyzer micro-μ-x360s.



[A] MR Fluid Sample [B] MR Finishing Process Set Up

Fig 2. Actual set up of the BEMRF Equipment

The EN-31 work-pieces were then finished using BEMRF set up as shown in fig.1.The BEMRF process setup (Niranjan & Jha, 2015) and its components are shown in figure no 2. During this experiment, the same optimum composition was used to carry out confirmatory experiments to confirm the findings of earlier experiments and further optimize the effect of process parameters to achieve better results. The optimum Magneto-rheological fluid has a composition of 20 % Magnetic face (having 4% Nano CIP and 16% Micro CIP CS grade), 25% Cutting face (SiC of 800 mesh size) with 55% Carrier fluid (20 % AP-3 Grease, and 80% Heavy duty Paraffin oil) on volume % basis was used during the finishing process (Kumar, Kumar, & Niranjan, 2020). DC Power supply was used to provide current supply to the magnetic tool for producing magnetization effect on the tooltip of the magnetic tool that helps in the development of the bi-dispersible MRF hard ball at the tooltip. This MRF ball acts as a cutting tool and its stiffness can be manipulated by altering the current supply in the magnetic coil of the magnetic tool. The supply current is controlled with the help of a DC power supply.

The MR fluid ball rotates at the speed of the magnetic tooltip. The current was kept at 2.5 amperes (MC) during the experiments. The tool rotational speed (TRS) was kept at 500 R.P.M. during the experiments. The working gap in the middle of the magnetic tooltip and the work-piece (WG) was kept at 1.5 mm. The total operation time for finishing each work-piece was maintained as 30 minutes. The feed rate was maintained as 50 mm/min. (Manjesh, Hari, Abhinav , & Manas, 2021). After finishing the EN-31 work-pieces with the BEMRF process, residual stress measurements were again repeated at the same points as it was done before finishing. It was noticed that induced residual stress level that was at 130 MPa before finishing the work-pieces with BEMRF was reduced to 62 MPa level after the finishing process. It proves the fact that BEMRF is one finishing process that can help to relieve the stress present in machined components. Further analysis and optimization were done by doing more experiments as per the Design of Experiments (DOE) and to study the impact of different process factors that have substantial influence on the output of the BEMRF process i.e., Magnetizing Current(MC), Tool Rotational Speed (TRS) and working Gap (WG) (Iqbal Faiz & Sunil Jha, 2019).

2.3. Experimental Setup for Residual Stress Analysis of a Hard Metal Work-piece

X-ray diffraction (Perry, Sue, & Martin, 1996) types of equipment are based on non-destructive type technique. The micro-μ-X360s residual stress analyzer is used to evaluate residual stress [RS] in components without having direct contact between the component and sensor unit. It is very secure and popular due to its various unique features (N., M. , K., & A., 2012). Important features of this device are given below: -

i. It's lightweight and portable having only 2.4kg sensor unit weight.
ii. It can measure the inner surface residual stress of the pipe down to the diameter of 170mm.
iii. Easy it is set up, having a sample position tolerance of +/-5mm.
iv. It has a CCD camera to assist with sample positioning and a built-in marker as well to highlight important points.

v. It has a fast measurement speed of 60 seconds per measurement point.
vi. It has high reliability & repeatability as measurement by the cos α method ensures reliable and repeatable data.
vii. Its 2D detector captures the complete Debye ring.
viii. It is secure and has low power X-ray emission due to the high sensitivity of the detector.

2.3.1. Construction and Working of Portable x-ray residual stress analyzer micro-µ-X360s: -

It is a non-contact type Instrument and consists of the following parts: -

(a) Sensor Unit (b) Power Supply Unit (c) Flexible Arm (d) Hand Carry Case (e) Safety Cabinet

2.3.2. Measurement of Residual Stress using Portable X-ray Residual Stress Analyser Micro-µ-X360s: -

The experimental setup is illustrated in figure no.3. This setup measures the residual stress of all the samples of EN-31 having the size of 10 * 10* 60 mm were finished using grinding operation. After that four points (A, B, C, and D) were marked on each work-piece to measure the residual stress at these four points in each sample. Now by using the procedure prescribed by the manufacturer, the residual stress value was recorded one by one on all four points in each work-piece by directing the sensor unit on these points as shown in fig. 2. The recorded values obtained during this experiment are tabulated in table no. 2 (Perry, Sue, & Martin, 1996).

.



Fig.3 Components of Portable X-Ray Residual Stress Analyser Micro-µ-360s

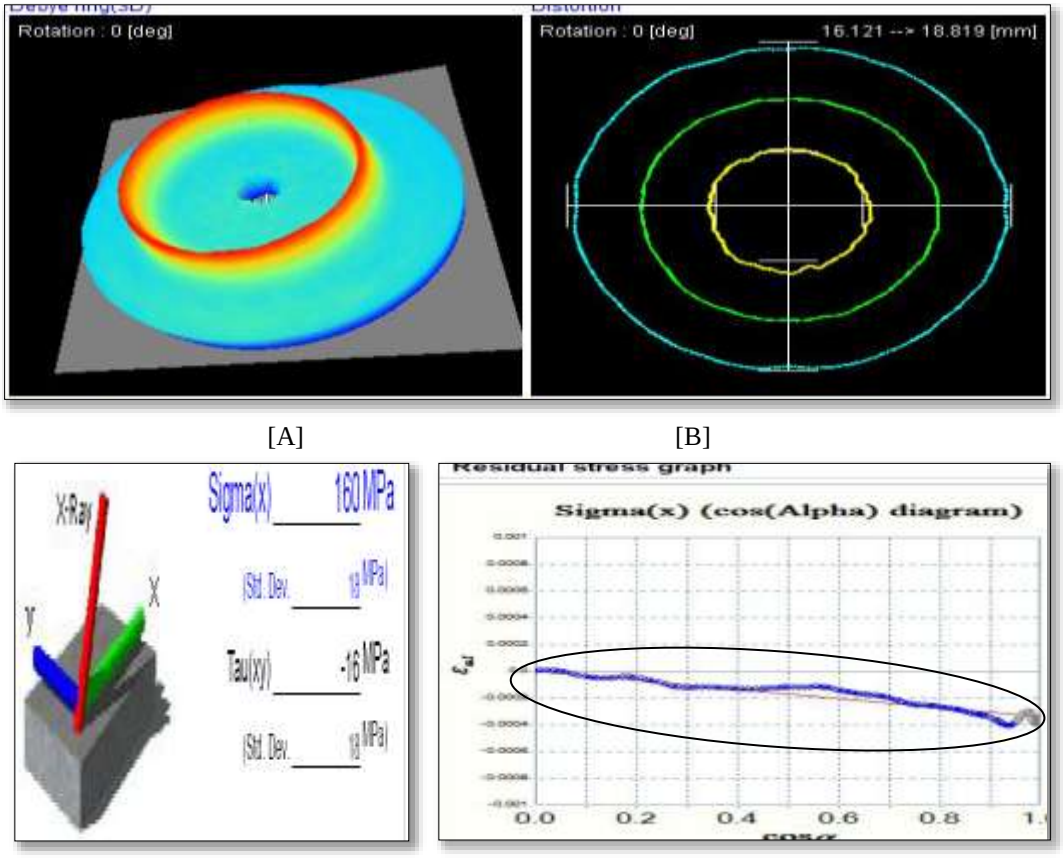
3. Results Interpretation and Evaluations

The output value of residual stress in specimens before finishing and after finishing with BEMRF using Pulse (with a duty cycle 0.16) is listed in the table 2. The % reduction in induced residual stress (%ΔRS) can be calculated using the equation given below: -

%ΔRS = (Initial Residual Stress - Final Residual Stress) X 100/ Initial Residual Stress

From the Debye ring given in fig. No. 4 (A), the grinding process finished work-piece has more irregularities and not having a very clear ring; its Distortion diagram also is also less uniform. Whereas as displayed in Fig No. 4 (B) the Debye ring for work-piece finished with BEMRF process using MR fluid has fewer irregularities and a clear ring, as seen in its distortion diagram the ring is also more uniform (Kumari, Chak, & Vani, 2020). The Residual stress Cos α Graph also shows more deviation of the center line for the grinding process finished work-piece, whereas the deviation from the center line is decreased after finishing the work-piece with the BEMRF process. During the preliminary experimentation on EN-31 steel work-pieces, it was found that after finishing these work-pieces with the BEMRF process the induced residual stress during the grinding process which was 160 MPa was reduced to 66 MPa, which is very important for the working life of a component. Surface roughness was also reduced after this process. The component with little Induced residual stress can complete their expected working life without premature sudden failure. There are main three factors which have significant impact on the output response in residual stress reduction. One factor is Magnetizing

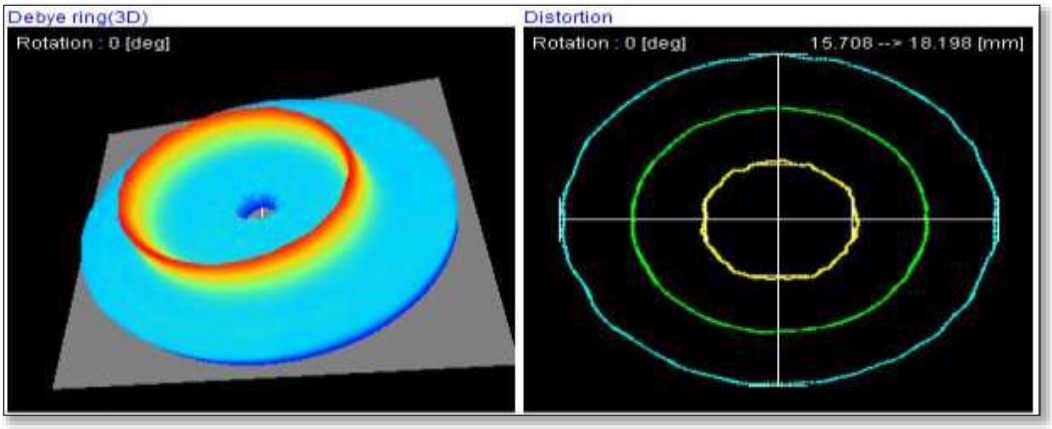
Current, Second is the Working Gap between the work-piece and Tool tip and the third factor is Tool rotational speed. The impact of these three parameters can be observed in % reduction in residual stress by varying these parameters over the range of their significance (Niranjan & Jha, 2015).



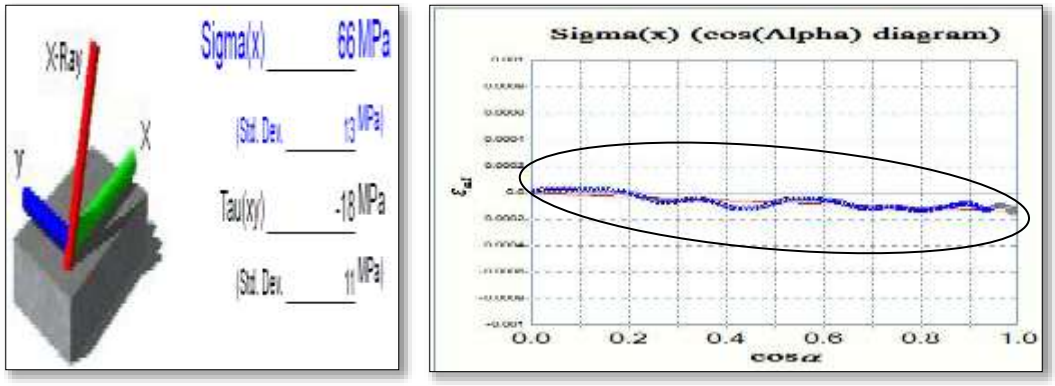
[A] [B]

.. [C] [D]

Fig.4 (a) Residual Stress Graphs [160 MPa] of point "A" of sample-1(S-1) after Grinding Process generated by Micro- µ-x360s
[A] Debye Ring [B] Distortion Ring [C] Stress Components [D] Cos α stress graph



[A] [B]



[C] [D]

Fig.4 (b) Residual Stress Graphs [66 MPa] of point "A" of Sample1(S-1) after finishing with BEMRF Process generated by Micro-μ-x360s
[A] Debye Ring [B] Distortion Ring [C] Stress Components [D] Cos α stress graph

To analyze the influence of process factors over the range of its significance, analyze and optimize output response, further experiments were done at different parameter combinations. Design Expert software was used. The RSM Method with Central Composite Design (CCD) was utilized to find order of RUNs and parameter's values for the experiments. The Output responses % reduction in Residual stress is tabulated below Given Table No1 and 2 respectively:

Table 1**:** Factors, Levels, and Range of Process Parameters for Design of Experiments using (CCD)

S No	Process Parameter	Unit	Levels				
			-2	**-1**	**0**	**1**	**2**
1	Magnetizing Current (MC)	A	1.5	2	2.5	3	3.5
2	Tool Rotational Speed (TRS)	RPM	300	400	500	600	700
3	Working Gap (WG)	MM	0.5	1	1.5	2	2.5

Based on these limits of parameter further experiments were designed and performed.

Table 2: Design of Experiments with % Residual Stress Reduction (% RSR)

Std Order	Run Order	Magnetizing Current (A)	Tool Rotation Speed (Central Core) (RPM)	Working Gap (MM)	% Residual Stress Reduction (RSR)
10	1	2.5	700	1.5	52.63
6	2	3	400	1	53.83
18	3	2.5	300	1.5	38.21
5	4	3.5	500	1.5	55.36
20	5	2	400	1	25.65

19	6	3	600	2	40.84
3	7	3	400	2	39.65
2	8	2.5	500	1.5	45.26
13	9	2	400	2	23.38
17	10	2.5	500	2.5	22.53
15	11	1.5	500	1.5	16.96
1	12	2	600	2	29.13
11	13	2.5	500	1.5	44.53
9	14	2	600	1	37.93
16	15	2.5	500	0.5	52.21
14	16	2.5	500	1.5	49.69
4	17	3	600	1	56.93
8	18	2.5	500	1.5	48.13
7	19	2.5	500	1.5	45.96
12	20	2.5	500	1.5	45.76

As per CCD Design total of 20 Experiments were done with parameter combination as indicated in table No 3, after finishing with the same composition of MRF the residual stress of all the 20 work-pieces was measured using Micro-µ-x360s, and recorded are shown in table No 2. The information generated by the analysis is tabulated in the table No.3 and 4.

Table 3: Fit Summary for Response: Residual Stress Reduction (RSR)

Source	**Sequential p-value**	**Lack of Fit p-value**	**Adjusted R^2**	**Predicted R^2**	**Remarks**
Linear	< 0.0001	0.0083	0.7929	0.7277	
2FI	0.4848	0.0067	0.7875	0.6365	
Quadratic	**0.001**	**0.105**	**0.9418**	**0.801**	**Suggested**
Cubic	0.6332	0.025	0.9332	-1.9012	**Aliased**

Quadratic Model was selected for analysis of the results given in table No.2.

Table 4: ANOVA table for % Residual Stress Reduction

Source	Sum of Squares	Df	Mean Square	F-value	p-value	Remarks
Model	602.56	9	66.95	60.27	< 0.0001	**Significant**
A-MC	354.47	1	354.47	319.09	< 0.0001	
B-TRS	25.98	1	25.98	23.39	0.0007	
C-WG	156.94	1	156.94	141.27	< 0.0001	
AB	0.183	1	0.183	0.1647	0.6934	
AC	35.07	1	35.07	31.57	0.0002	
BC	0.8515	1	0.8515	0.7665	0.4018	
A^2	14.25	1	14.25	12.83	0.005	
B^2	8.11	1	8.11	7.3	0.0223	
C^2	18.29	1	18.29	16.46	0.0023	
Residual	11.11	10	1.11			
Lack of Fit	9.16	5	1.83	4.69	0.0575	**Not Significant**
Pure Error	1.95	5	0.3901			
Cor Total	613.66	19				

The F-value 60.27 of Model in table no. 4, suggests that the model being used for further analysis is meaningful. As the Lack of Fit is therefore not substantial so that model is suitable for further analysis. The equation for an actual reduction in Residual stress on a % basis can be written as: -

%ΔResidual Stress =
+46.29+18.17*MC+6.05*TRS-11.30*WG-
4.87*MC*TRS-8.60*MC*WG-4.22*TRS*WG-
12.09*MC^2-2.36*TRS^2-12.80*WG^2

Based on a statistical analysis of data given in table No 4 by using analysis of Variance (ANOVA) the outcome of many process constraints such as Magnetizing Current (MC), Tool Rotational Speed (TRS), and Working Gap (WG) is clarified with the help of Graph plots and 3D diagrams generated for all three factors used during the experiments.

3.1. Impact of Magnetizing Current (MC) on % Residual Stress Reduction (RSR):

From figure No 5[A] given below it can be seen that due to the increase in magnetization current the Residual Stress reduction (RSR) increases. The effect of Increasing magnetization current has been found as the best useful factor for residual stress reduction as compared to other two factors as per details available in table 5 where value of F for all the three factors is given (Niranjan & Jha, 2015). The contribution of this factor (MC) is 58.24% reduction in residual stress.

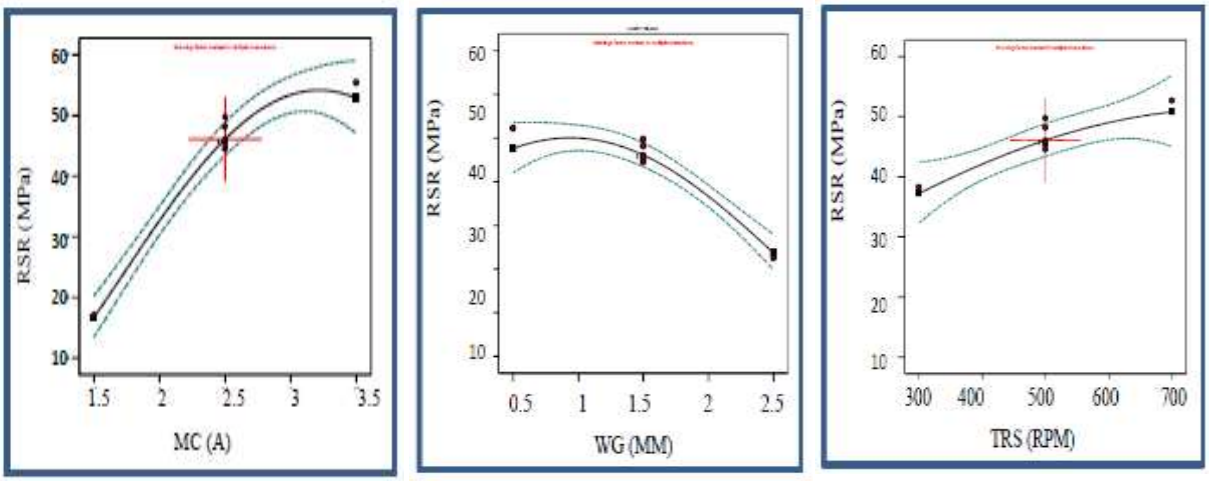


Fig 5. [A]. RSR (MPa) Vs MC (A), [B].RSR (MPa) Vs WG (MM) AND [C] RSR (MPa) Vs TRS (RPM)

3.2. Impact of Working Gap (WG) on % Residual Stress Reduction (RSR):

From figure No 5[B] given above due to the increase in working Gap the Residual Stress reduction (RSR) decreases. The effect of increasing the working gap is less effective than the effect of increasing Magnetizing current but it is more effective than the effect of increasing Tool rotational speed (TRS) as per details available in ANOVA table 5, this factor has 141.27 as F value (Niranjan & Jha Sunil, 2016).

3.3. Impact of Tool Rotational Speed (TRS) on % Residual Stress Reduction (RSR) (Niranjan & Jha Sunil, 2016)**:**

From the figure, No 5[C] given above it noticed that on increasing the tool rotational speed (TRS) the Residual Stress reduction (RSR) rate increases. The effect of increasing tool rotational speed is found least effective factor as compared to other two factors. This factor has least 23.39 as F-value.

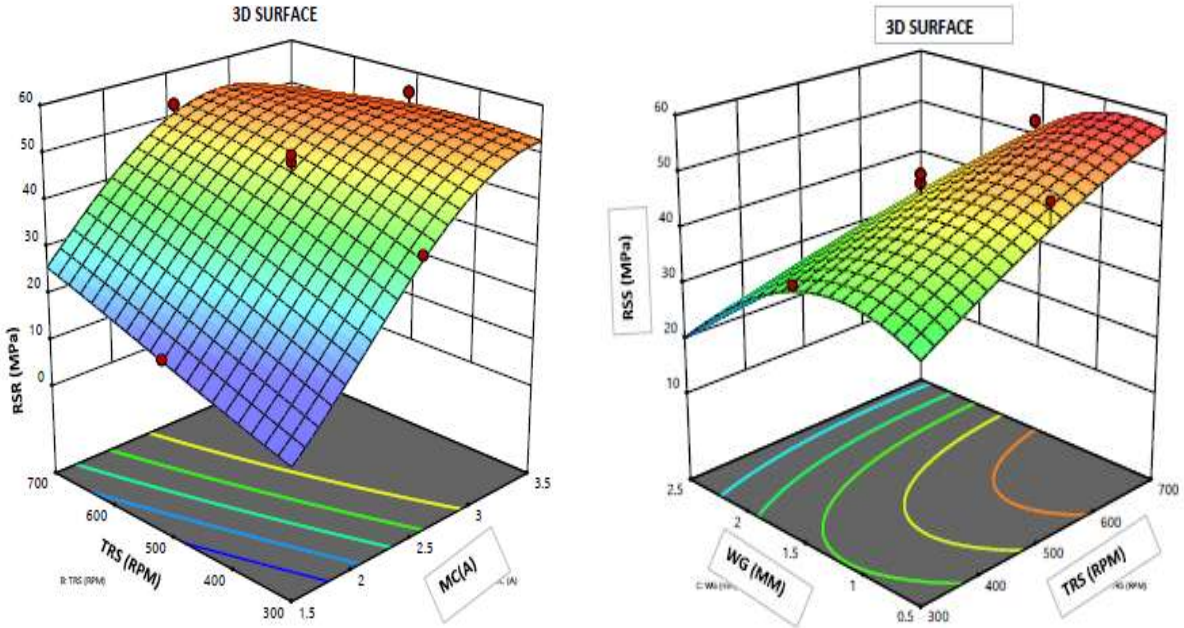


FIG. 6[A]. FIG. 6[B].

Fig. 6 [A] [B] &[C]. Percentage Reduction in Residual Stress with 3D Surface Diagrams

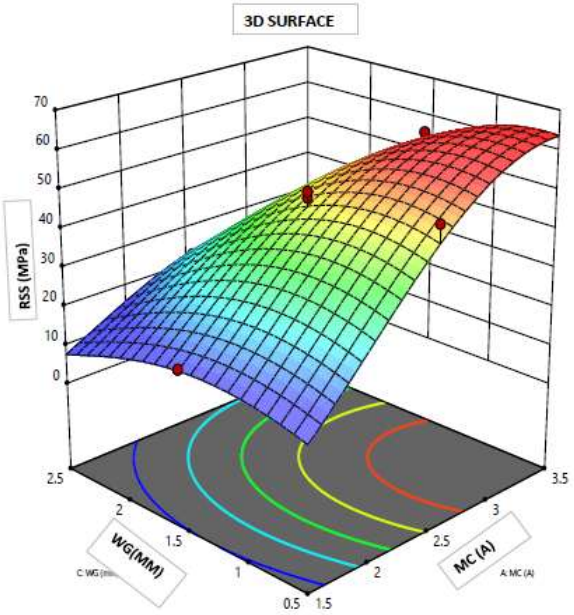


FIG.6[C].

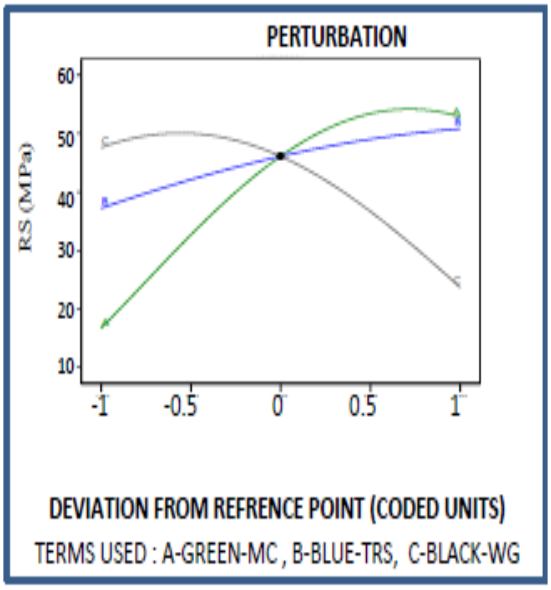


Fig.7. Perturbation Diagram for % Δ RSR

3.4. Interactive impact of different process factors at the Residual Stress Reduction (RSR)

The interactive effect of magnetization current (MC), Working Gap (WG) and Tool Rotational Speed (TRS) are shown in figure No 6.The Perturbation Graph of all three factors is also drawn as shown in fig. (7) (Kumari, Chak, & Vani, 2020).

4. Optimization of Output Responses

To optimize the output responses to obtain the best results in respect of Residual Stress reduction (RSR) Desirability Technique was used.

Table No. 5: Top Ten Predicted Solutions using the Desirability Technique

S. No.	MC (A)	TRS (RPM)	WG (MM)	%RSR	Desirability	Remarks
1	**3.20**	**660**	**0.60**	**61.23**	**1**	**Selected**
2	**3.10**	**670**	**0.90**	**60.54**	**1**	**Selected**
3	3.00	654	0.85	60.81	1	
4	3.26	531	0.77	60.07	1	
15	3.02	583	0.927	59.30	1	
6	3.06	537	0.69	58.47	1	
7	3.28	562	1.19	58.35	1	
8	3.27	459	0.86	58.23	1	
9	3.46	430	0.76	58.18	1	
10	3.43	433	0.70	58.09	1	

The top ten best solutions for residual stress reduction are shown in table no.5. The responses having a highest % Residual Stress reduction rate &having desirability value of '1' on the top of the table are selected for further confirmatory experiments. The results of confirmatory experiments are listed in table No. 6. The confirmatory experiments have confirmed that these results can be reproduced, and the solution obtained after optimization is correct.

.

Table No.6**:** Confirmatory Experiments Results

S. No.	MC (A)	TRS (RPM)	WG (MM)	% RSR		% Error	Remarks
				Predicted	Actual	% RSR	
1	**3.20**	**660**	**0.60**	**61.23**	**61.96**	**-1.19**	**Selected**
2	3.10	670	0.90	60.54	60.92	-0.62	

5. Conclusions

Residual stresses in machined parts play a very important role and it will affect the performance & expected life cycle of these parts.

I. Three main factors are affecting the performance of the BEMRF process i.e., Magnetizing Current, Tool Rotational Speed and Working Gap.

II. Magnetizing Current is the most contributing factor out of the three factors and can be utilized to manipulate the magnetic field existing near the tooltip. By increasing the current supply, the strength of the magnetic field can be controlled. An increase in magnetizing current increases the % reduction in residual stress. Its contribution towards % reduction in residual stress is 58.24 %.

III. The working gap is the second largest contributing factor and as the working gap goes on increasing the % reduction in residual stress starts decreasing.

IV. Initially the rise in tool rotational speed enhances the % reduction in residual stress rate but its contribution is minimal and after reaching a particular speed further increases in tool rotation speed do not produce any positive effect on the % reduction in residual stress.

V. It can be concluded that by using ball end magneto-rheological finishing process using Pulse DC power supply (with a duty cycle 0.16)with a magneto-rheological fluid having the composition as 20 % Magnetic face (having 4% Nano CIP and 16% Micro CIP CS grade), 45% Cutting face (SiC of 800 mesh size) with 55% Carrier fluid (20 % AP-3 Grease and 80% Heavy duty Paraffin oil) on volume % basis the residual stress in EN-31 work-piece can be reduced 61.96%.

6. Acknowledgements

I would like to show my gratitude towards my mentor and guide Dr. M.S. Niranjan, Associate Professor, Delhi Technological University for extending all the research resources, domain expertise and support to perform these experiments. I also want to thank my mentor and guide Dr. Neeraj Kumar, Professor, SGVU, Jaipur for his timely support, innovative ideas, and guidance during this experimental work

7. **Abbreviations used in Graphs and Data Tables**: WG: Working gap, TRS: Tool Rotational Speed, MC: Magnetizing Current, RSR: Residual Stress Reduction, MRF: Magneto-rheological Fluid, BEMRF: Ball End Magneto-rheological Finishing and % Δ RSR: % Reduction in Residual Stress

References

F. Iqbal and S. Jha, "Closed Loop Ball End Magnetorheological Finishing Using In-situ Roughness Metrology," Experimental Techniques, vol. 42, no. December 2018, p. 659–669, 2018.

A. Mishra and T. Prasad, "Residual Stresses Due to a Moving Heat Source," International Journal of Mechanical Sciences, vol. 27, no. 9, pp. 571-581, 1985.

A. J. Perry, J. A. Sue and P. J. Martin, "Practical measurement of the residual stress in coatings," Surface and Coatings Technology, vol. 81, pp. 17-28, 1996.

K. Jian and X. Peng, "Cylindrical Magnetorheological Fluid Variable Transmission Controlled by Shape-Memory Alloy," Science and Technology of Nuclear Installations, vol. 2012, no. Special Issue, 2012.

S. Jha and V. K. Jain, "Design and development of the magnetorheological abrasive flow finishing (MRAFF) process," International Journal of Machine Tools and Manufacture, vol. 44, no. Issue 10, pp. 1019-1029, 2004.

A. K. Singh, S. Jha and P. Pandey, "Performance analysis of ball end magne-torheological finishing process with MR polishing fluid," Materials and Manufactur-ing Processes, vol. 30, no. 12, pp. 1482-1489, 2015.

A. Kumar, N. Kumar and M. S. Niranjan, "Synthesis and Characterization of Magnetorheological Fluids," International Journal of Innovative Technology and Exploring Engineering (IJITEE), vol. 9, no. 6, pp. 272-277, 2020.

M. S. Shunmugam and M. Kanthababu, Advances in Unconventional Machining and Composites, Singapore: Springer Science and Business Media, LLC, 2020.

S. Peter, S. Andreas, C. Helmut and M. Svea , Neutrons and Synchrotron Radiation in Engineering Materials Science: From Fundamentals to Applications, 2nd Edition, Verlag : Wiley-VCH Verlag GmbH & Co. KGaA., 2017, p. 488.

M. Singh and A. K. Singh, "Parametric Optimization for Nano-Finishing of the External Cylindrical Surfaces Using Rotating Core Magnetorheological Finishing Process," in International Manufacturing Science and Engineering Conference, College Station, Texas, USA, 2018.

M. S. Niranjan and S. Jha, "Statistical analysis of magnetorheological ball end finishing parameters using response surface methodology," International Journal of Manufacturing Technology and Management, vol. 30, no. july 2016, pp. 240-252, 2016.

M. S. Niranjan and S. Jha, "Optimum selection of machining parameters in ball end magnetorheological finishing process," International Journal of Precision Technology, vol. Vol.5, pp. 217-228, 2015.

E. H. J., L. H. S., Y. K., D. J. and S. F. T., "Experimental characterization of dynamic heat exchanger behavior," International Journal of Heat and Mass Transfer, vol. 121, no. June, pp. 933-942, 2018.

K. Manjesh, N. S. Y. Hari, K. Abhinav and . D. Manas, "An overview of magnetorheological polishing fluid applied in nano-finishing of components," Journal of Micromanufacturing, vol. April 2021, no. April, 2021. .

H. Li, I. Jönkkäri, E. Sarlin and F. Chen, "Experimental Comparison of Constitutive Models for Magnetorheological Fluids Under Different Conditions," Brazilian Journal of Physics, no. September, 2021.

S. M. T, "Effect of friction stir processing on electrical conductivity and corrosion resistance of AA6063-T6 Al alloy," Proceedings of the Institution of Mechanical Engineers Part C Journal of Mechanical Engineering Science, vol. 222, no. 7, pp. 1117-1123, 2008.

L. Wei, F. Meriem , H. Fan, H. Xuanhong, Z. Jun and H. Hua, "Mixed hemimicelle solid-phase extraction based on magnetic halloysite nanotubes and ionic liquids for the determination and extraction of azo dyes in environmental water samples," Journal of Chromatography A, vol. 5551, no. May, pp. 10-20, 2018.

S. R. N., D. M. , Y. B. K. and G. O. A., "Methods of measuring residual stresses in components," Materials & Design, vol. 35, no. March, pp. 572-588, 2012.

C. Kumari, C. K. Chak and V. V. Vani, "Experimental investigations and optimization of machining parameters for Magneto-rheological Abrasive Honing process," Materials and Manufacturing

Processes, vol. June 2020, no. Online, pp. 1622-1630, 2020.

P. M. Pandey, P. Kumar and V. Sharma, Advances in Production and Industrial Engineering, Heidelberg NY 5: Springer Science and Business Media LLC, 2021.

H. M. Aldawsari, N. R. Naveen, N. A. Alhakamya and ors, "Compression-coated pulsatile chronomodulated therapeutic system: QbD assisted optimization," Drug Delivery, vol. 29, no. 1, pp. 2258-2268, 2022.

A. K. Singh and K. P. Singh, "Response surface optimization of nitrite removal from aqueous solution by Fe3O4 stabilized zero-valent iron nanoparticles using a three-factor, three-level Box-Behnken design," Research on Chemical Intermediates, vol. 42, no. 3, p. 2247–2265, 2015.

F. Iqbal and S. Jha, "Experimental investigations into transient roughness reduction in ball-end magneto-rheological finishing process," Materials and Manufacturing Processes, vol. 32, no. 2, pp. 224-231, 2019.

N. Khatri, J. X. Manoj, V. Mishra, H. Garg and V. Karar, "Experimental and simulation study of nanometric surface roughness generated during Magnetorheological finishing of Silicon," Materials Today: Proceedings, vol. Volume 5, no. 2 Part-1, pp. 6391-6400, 2018.

Z. Alam, D. A. Khan and S. Jha, "A study on the effect of polishing fluid volume in ball end magnetorheological finishing process," Materials and Manufacturing Processes, vol. 33, no. 11, pp. 1197-1204, 2017.

Int. j. inf. tecnol.
https://doi.org/10.1007/s41870-023-01242-6

ORIGINAL RESEARCH

Technology enabled communication during COVID 19: analysis of tweets from top ten Indian IT companies using NVIVO

Swati Chawla[1] · Puja Sareen[1] · Sangeeta Gupta[2] · Meha Joshi[3] · Ritu Bajaj[4]

Received: 12 January 2023 / Accepted: 21 March 2023
© The Author(s), under exclusive licence to Bharati Vidyapeeth's Institute of Computer Applications and Management 2023

Abstract The corona virus (COVID-19) pandemic has impacted industries across the globe. Lockdown was imposed to curb the spread of the deadly virus. This resulted in closure of the factories and manufacturing units. Few sectors switched to work from home (WFH) for the first time. The present study aims to understand and analyze the way in which Information Technology (IT) sector communicated on Twitter during the pandemic. The top ten IT companies in India were selected on the basis of net sales. Qualitative data analysis was employed to extract tweets, understand and analyze them. Tweets were extracted from the official Twitter handles of these top ten IT companies using N-Capture extension tool of NVivo 12 software from April 1, 2020 to April 30, 2021. To get insights out of collected data, Word Cloud, TreeMap and Sentiment Analysis of tweets were carried out using NVivo 12 software. The research found that IT companies focussed on digital transformation, business development, customer satisfaction and enriching customer experience, new product development for healthcare and insurance and organizational resilience. They also focussed on effective communication through Twitter in times of crisis. Most of the companies tweeted moderately positive. Very small numbers of tweets were found to be very negative.

Keywords COVID-19 · Organization resilience · Twitter · Word cloud · Tree map · Sentiment analysis · Content analysis · NVIVO

1 Introduction

India has passed through several waves of coronavirus, a disease caused by severe acute respiratory syndrome coronavirus 2 (SAR CoV-2), also known as novel coronavirus (COVID-19). Covid 19 affected people across the globe in different ways. The outbreak of corona virus (COVID-19) was declared as a pandemic by World Health Organization (WHO) in 2020 [1]. This announcement changed people's lives economically, socially, and psychologically. COVID-19 caused an extensive damage to businesses in India. The COVID-19 induced lockdown forced people to stay away from work place. COVID-19 in India initially was characterised by fewer cases and lesser fatalities in comparison to many other developed countries, due to an early lockdown. Subsequently, the economic constraints forced government to ease COVID-19 restrictions. Hence there was surge in COVID-19 cases and India became the third-worst affected country worldwide. The second wave was more fatal as compared to the first wave. There was chaos, shortage of medical supplies, high mortality rate and spread of virus at an

✉ Swati Chawla
swati.phdamity@gmail.com

Puja Sareen
psareen@amity.edu

Sangeeta Gupta
sangeet_gju@yahoo.co.in

Meha Joshi
mehajoshi@dtu.ac.in

Ritu Bajaj
drritu76@gmail.com

[1] Amity Business School, Amity University, Noida, Uttar Pradesh, India

[2] Management Education and Research Institute, New Delhi, India

[3] Delhi School of Management, Delhi Technological University, New Delhi, India

[4] Indira Gandhi University, Meerpur, Haryana, India

Published online: 10 April 2023

alarming rate. The industries in India responded to it with various efforts and policies such as work from home (WFH), physical distancing, COVID leave, provision of mass insurance, COVID allowances etc. IT sector was fast to respond towards resilience. These companies responded with twin aim. The first aim was to slow down and reduce the spread of the virus. The second aim was to provide sense of security and care during the pandemic. These companies realised the fact that people need money to survive, stress and boredom. Organizations found that global COVID-19 outbreak was the new reality. It had completely changed the way people worked or lived. Hence, it was necessary for organizations to acclimatise with the change [2]. Therefore, to manage brand communications during pandemic, using online communication technology became imperative. It has been observed organizations extensively used social media platforms to promote their products and services before pandemic [3]. During the crisis, physical events such as business conferences, meetings, consortiums were cancelled and there was a sudden increase of people staying indoors. Perhaps, people shifted to spending more time online than before. Hence, organizations used online communication technology such as email, social media platforms, etc. to professionally interact with each other [4].

Throughout the pandemic, twitter served as leading public platform for sharing, receiving and engaging content among different groups of people. It emerged out as a powerful tool to communicate with customers, employees and society at a large [5]. Twitter was also quick in response to the pandemic. Twitter enforced strict content-vetting policies to protect netizens from rampant misinformation. The purpose of the same was to protect users from harmful content and benefit them with healthier feed.

1.1 Background

The Information Technology (IT) industry of India benefited hugely from the liberalization of the Indian economy. It is primarily a knowledge-based industry dependent upon skilled manpower. Availability of skilled personnel has resultedin the growth of IT sector in India. The Indian IT sector can be classified into four broad categories namely IT services, IT enabled services, software products, and hardware.

The information technology (IT) industry in India is highly accomplished and dynamic and thus globally recognised. The ‘dotcom bubble’ or ‘millennium bug’ was the turning point in the IT sector phenomenal and historic rise. The sector provided unmatched solution to sort out the issue of turn of millennium. This solution established the technological supremacy of the Indian IT sector. India is not only enjoying supremacy in software space, but also leader in the rapidly evolving global IT-Business Process Outsourcing (BPO) or Business Process Management (BPM) market.

India is a leading sourcing destination as it accounts for roughly 55% market share of the US$ 200–250 billion global services sourcing business in 2019-20 (IBEF Report). The sector has increased its contribution to India’s GDP from 1.2% to 1998 to 8% in 2020. The increase in export could be attributed to rapid digitization and timely transition to remote working environments by the IT companies amid coronavirus pandemic.The IT industry maintained the growth momentum in hiring and recruitment too. The IT industry registered 138,000 fresh recruitments in FY20. The IT & BPM industry provides employment opportunity to more than 4.5 million employees in India in FY21. There is increasing trend witnessed in IT & BPM industry’s revenue too. The IT & BPM industry revenue is expected to increase by of 2.3% than the previous financial year. The domestic revenue and export revenue is estimated at US$ 45 billion and US$ 150 billion respectively in FY21. There is 7.3% growth in the IT spending in FY21 India from the previous year (Gartner Estimates). It is valued at US$ 93 billion in 2021. The spending is further estimated to be at US$ 98.5 billion in 2022.

Indian software product industry is also riding the growth path andforecasted to reach US$ 100 billion by 2025. The Indian IT companies are focussing on increasing their global footprint by investing internationally and overseas. This will enable them to enhance and expand the global service delivery centres. Tata Consultancy Services (TCS) has already taken step in this direction. In February 2021, it has announced to recruit about 1500 technology employees for United Kingdom team over the next year. This will further consolidate the capabilities of TCS to serve and deliver the clients in efficient manner. United States of America (USA) is the largest contributor to the data annotation market in India. USA commanded 60% share of the US$ 250 million data annotation market in India in FY20. The data annotation market is expected to grow exponentially by 2030 around US$ 7 billion. Therefore, the Indian tech giants like Infosys, TCS and Tech Mahindra are continuously diversifying and innovating in block chain and artificial intelligence to create differentiated offerings.

By now, India has become the most preferred off shoring destination for IT companies across the world. Many countries have shown greater confidence in Indian IT companies. India’s IT sector is forecasted to reach US$ 100 billion by 2025. India is already a leader in the global sourcing market and now it is all set to tap the growing opportunities in the emerging technologies such as digital transformation, artificial intelligence, voice command and robotics.

1.2 Contribution of the research

IT sector of India has always been known for its cutting-edge innovation. During crisis, there was a need for IT sector to support their employees. Hence, the aim of the study is to understand how rapidly the IT industry transitioned to WFH model keeping the health and safety of employees as its foremost priority. Since, majority of IT companies were working remotely, there was a need to develop robust communication strategies to deal with different phases of pandemic communication. As a part of research in this article, it is reviewed how IT companies responded/tweeted to COVID-19 to deal with crisis in India. Furthermore, the research explores the programme and policies adopted by IT companies to ease out vulnerabilities caused by COVID-19. This research contributes to the growing body of knowledge in direction of measures taken by IT companies towards the safety and well-being of its employees and their dependents during COVID-19.

The novelty of the study lies in its approach to understand the resilience and proactivity of IT companies during coronavirus crisis; to understand the key focus areas of concerns of the companies towards the leaders of the IT sector in India during the period and to understand the sentiments.

Due care was taken to ensure that the limitations do not plague the study and the analysis is done with objectivity [34–36]. To the knowledge of the researchers, this is the first study of its kind to provide a comprehensive overview of the sentiments of the tweets of top IT companies of India during COVID 19.

2 Literature review

2.1 Online communication technology

The need of integration of business strategy and IT strategy has been previously recognized by [6, 7]. As the global community faces COVID-19 pandemic together, the significance of strategic alignment of business and IT has gone to next level. In response to global pandemic it is essential for organizations to prepare for the new normal. The COVID-19 pandemic has accelerated the need for digital transformation. With maximum number of employees working remotely, the use of digital tools for communication has accelerated. During pandemic, people extensively used twitter to talk about recent issues and interests. State leaders, politicians and organizations used twitter to communicate about emergencies, health bulletins, advisory, policies and measures during pandemic.

Twitter witnessed 20% user growth during COVID-19 due to surge in pandemic posts and ongoing product improvement [8]. Since March 2020, COVID-19 related posts dominated on twitter. Twitter enabled real time communication with public during crisis [9]. In 2021, twitter audience has counted approximately 322.4 million monthly active users in comparison to 290.5 million monthly active users in 2019 and is projected to reach more than 340 million monthly active users [10].

2.2 Organizational resilience

Resilience can be termed as capabilities that enable individuals, firms or ecosystems to combat deep crisis [11]. It is robustness of any firm to withstand difficult situations or crisis. The concept of resilience can be understood from different perspectives—from personal to organizational and from sectoral to societal [12]. The researchers of ecology opined the concept of resilience with an objective to study the impact of external disturbances on ecosystems [13]. Further, resilience has also been applied in various other fields like engineering, psychology, economics, management and political science [13–17].

Resilience is a broader term and is an aggregation of preparedness, response and adaption [18]. resilience can occur at three levels—firstly at the microeconomic level, the resilience of an individual firm, another at the macroeconomic level, resilience of a sector, market or an industry and lastly at the macroeconomic level, collective resilience of all individual firms and markets [19]. However, management studies look resilience from two perspectives, one at the individual level [20] and another at the organizational level [21]. The present study focuses on resilience at the organizational level.

Due to pandemic, organizational resilience has gained momentum and it can be understood as an organization's ability to survive and thrive amid adversity by engaging in transformative activities [15]. Hence, organizational resilience can be described through four key skills—responding, monitoring, anticipating and learning [22]. The global uncertainties and unprecedented situations have prompted organizations to build resilience [23]. The outbreak of coronavirus has undoubtedly disrupted business operation. Companies have embraced the change and endured to the new environment by navigating to new business models. The increasing threat of recent coronavirus has encouraged organizations to mount for a quick holistic response to ensure well-being of employees.

Resilience is a process-oriented approach with three interrelated stages—anticipation, coping and adaption [22]. Another study points out the dynamic nature of resilience as an interaction between organization and the environment [13]. Hence, organizations are required to effectively respond during and after adverse events such as pandemic. Therefore, it is espoused that resilient organizations not only respond to past events but also to current events and

anticipate future to continuously innovate and evolve during crisis [22]. In response to corona virus, firms are required to chalk out strategies and communicate their COVID 19 preparedness, response and control plans to employees to build trust. These plans should incorporate several workplace factors such as maintaining social distancing, hygiene and cleanliness at workplace to reduce the risk of exposure at work. The organizations should also identify all areas and job tasks with potential exposures to coronavirus and outline the preventive measures. Employers should carry out risk assessment work related exposures to protect their employees. Employer's COVID 19 preparedness should also include relief packages such as care leave, vaccination drives and medical support for employees and dependents. It is necessary for organizations to develop policies and infrastructure that supports employees and their families to cope with the pandemic.

3 Research methodology

The research methodology section describes the methods and techniques used to conduct the Twitter analysis for the paper. It discusses the aspects related to framework within which the research was conducted. The framework employed for conducting the analysis included identification of the IT companies for research and the selection criteria of tweets; extraction of tweets using N-Capture extension tool of NVivo 12 software; data sets used and time frame for the study; followed by data analysis strategy discussion. It also discusses the nuances associated with each of the aforementioned steps in detail and presents the skeleton of the research. Section 3.1 through Sect. 3.4 presents the algorithmic view of the research methods employed for the study.

3.1 Identification of companies and selection criteria

Due the high potential of the IT companies in terms of huge turnover and growth, this sector was deemed appropriate for the study. The list of top 10 companies considered for analysis were obtained from Statistica report for the year 2021 (Table 1).

Table 1 The top ten IT companies in India on the basis of net sales for the year 2021

Sr. no	IT companies	Net sales
1	Tata Consultancy Services (TCS)	1359.63
2	Infosys	859.23
3	Wipro	502.99
4	HCL Technologies	356.73
5	Tech Mahindra	296.41
6	Larsen and Tubro Infotech (L&TI)	115.63
7	Mindtree	79.68
8	Mphasis	55.61
9	Oracle Financial Services Software (OFS)	36.45
10	Persistent Systems	24.8

Source: Statistica Research Department, 2021

Table 2 Official Twitter handles of Top 10 IT companies in India

Sr. no	Company	Twitter handle
1	TCS	@TCS
2	Infosys	@Infosys
3	Wipro	@Wipro
4	HCL Technologies	@hcltech
5	Tech Mahindra	@tech_mahindra
6	L&TI	@LTI_Global
7	Mindtree	@Mindtree_Ltd
8	Mphasis	@Mphasis
9	OFS	@OracleFS
10	Persistent Systems	@Persistentsys

Source: Generated by authors from Twitter

3.2 Data extraction strategy

Twitter is one the world's biggest social media platform and is widely used by companies to reach out to their stakeholders [5]. It hosts abundant user generated data which closely reflects public's response/reaction/sentiment towards any issue [24]. In this research, the tweets of the top ten IT Companies were extracted from their official twitter handles using NVivo 12 (Trial Version) with Licence Key NVD20-KZ000-SH020-5RE82. These IT companies are Infosys, Tata Consultancy Services (TCS), Wipro, Larsen and Toubro Infotech (LTI), HCL Technology, Tech Mahindra, Mindtree, Mphasis, Oracle Financial Services (OFS), and Persistent Technology. The tweets were extracted using the N-Capture tool for Google Chrome. The tweets were also checked manually by visiting the twitter account of the top ten IT companies and reading tweets [25].

The twitter handles of these companies are presented in Table 2.

3.3 Data sets used and time frame used for the study

Tweets from the twitter handles of the respective companies were extracted from April 1, 2020 to August 31, 2021. The rationale for the selecting this time frame is to capture the communication of these companies during first and second wave of Covid 19 pandemic in India. India witnessed the voluntary one-day lockdown in the month of April, 2020. Thereafter, complete lockdown was imposed from May, 2020 owing to the spread of the disease. India witnessed

much stronger second wave of the pandemic during April–May 2021. The tweets from April, 2020 were chosen to describe how these companies communicated on Twitter during first wave of the pandemic. It also included their preparedness towards tackling the pandemic. Tweets from April, 2021 captured the organization resilience, vaccination and recovering from the aftershock of pandemic.

3.4 Data analysis strategy

In the first stage, the tweets were segregated into two categories (2020 and 2021) for all the IT companies. Thereafter, tweets were filtered using the key words Covid, Covid 19 and pandemic. This process was repeated for rest of the companies. This exercise resulted into providing tweets related to Covid, Covid 19 and pandemic for 2020 and 2021. Table 3 present the total number of tweets and Covid related tweets for these companies for the year 2020 and 2021.

The data collected was then coded using NVivo 12 software and analysed with the help of qualitative analysis techniques. The study excluded re-tweets, photos and video messages. Qualitative research methods provide in-depth description and insightful interpretations of socio, contextual and environmental factors [26, 27]. It gives the provision of analyzing existing documents. There are two categories of documents for qualitative analysis, viz. Public Records and Personal documents/archives [28].

The data that was grouped was then analyzed using the quantitative content analysis technique in NVIVO 12 software. Different from qualitative content analysis, quantitative content analysis is more directed towards quantitative descriptions of the visible communication content [29, 30]. Content analysis was chosen because it can describe the communication content of a person or media [31]. Content analysis is suitable because it can see the relationship between the content and communication goals, describe the meaning, and focus on quantitative description, meaning the frequency of appearance of the characteristics of existing content [32].

Further word cloud analysis, tree map analysis and sentiment analysis were done to examine the way in which IT companies communicated with their stakeholders on Twitter. The algorithmic view of the research methods employed for the study is presented in Fig. 1.

Table 3 Total tweets and Covid related tweets by top ten IT companies in India (2020 and 2021)

Companies	2020		2021	
	Tweets	Covid related tweets	Tweets	Covid related tweets
TCS	628	39	489	48
Infosys	1484	120	1501	120
Wipro	1537	67	600	28
HCL Technologies	1133	188	870	63
Tech Mahindra	1751	263	872	47
L&TI	587	41	486	18
Mindtree	973	146	349	22
Mphasis	645	51	418	38
OFS	305	7	119	7
Persistent Systems	872	89	481	15
Total tweets	9915	1011	6185	382

Source: Generated by the authors from the twitter handles of respective companies

4 Analysis and findings

The extracted data was analyzed using qualitative software tool NVIVO. This section presents the analysis of the data. Tweets were analysed using word cloud analysis, tree map analysis and sentiment analysis. Section 4.1 presents the critical Analysis through Word cloud and tree map for tweets by Top 10 IT companies selected for the study. Section 4.2 presents the sentiment analysis for the tweets done in context of the study.

4.1 Critical analysis

Word Cloud and Tree map offer better visualization of results [33]. Word cloud is generated on the basis of frequency and percentage of words in the data set. The word cloud is generated on the basis of keywords being represented as per the frequency in the data sets in the study [34].

In order to show large amounts of data in hierarchical order, NVivo provides a treemap diagram as an output. Treemap is a data visualization technique in a hierarchical order. The space in the visualization is split up into a series of nested rectangles of different dimensions, sizes and shapes with a number of coding references. A node with a large number of coding references displays the largest rectangle. The sizes of other rectangles are considered in relation to each other.

Following Figs. 2, 3, 4, 5, 6, 7, 8, 9, 10, 11, 12, 13, 14, 15, 16, 17, 18, 19, 20 and 21 represents the word clouds and tree maps for the top ten IT Companies in India.

Figure 2 represents the word cloud and Fig. 3 represents the tree map for the IT company TCS. The twitter handle of TCS is at the centre represented by its web address. It is then surrounded by business, digital services, customer experiences, innovation, growth, digital transformation, pandemic, and healthcare. TCS primarily focussed on business, organization resilience, and successful pandemic management.

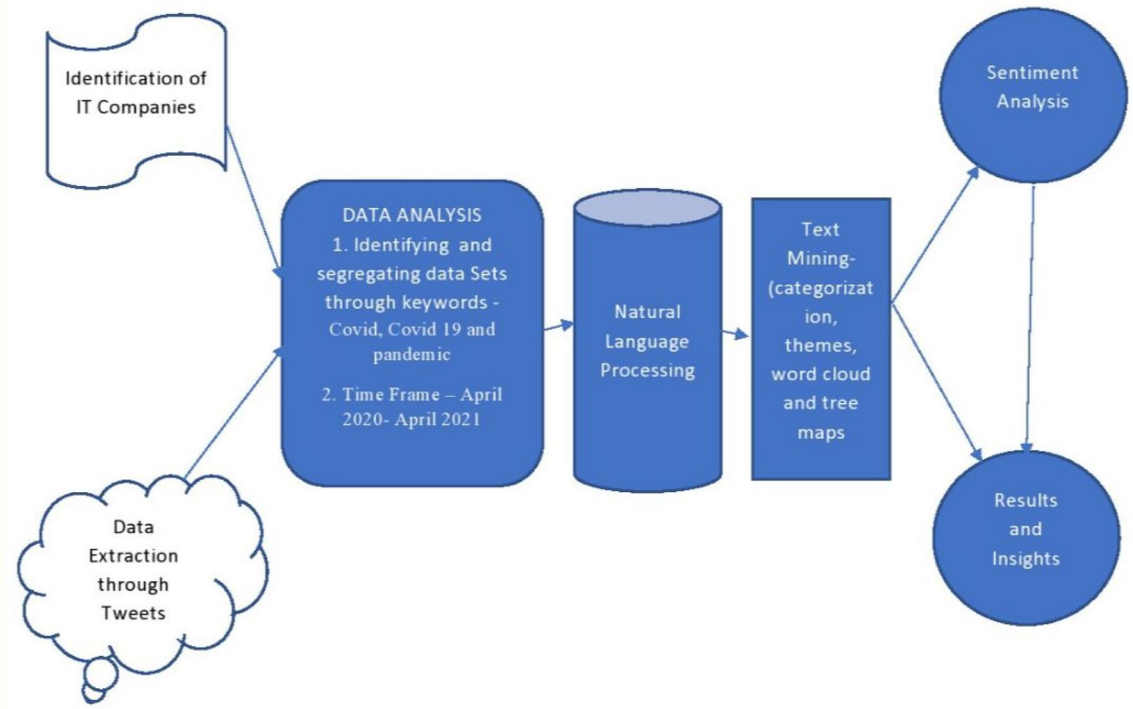


Fig. 1 A framework used to conduct analysis of tweets of top 10 IT companies during COVID-19

Fig. 2 Word cloud for TCS



Fig. 3 Tree map for tweets by TCS

Figure 4 represents the word cloud and Fig. 5 represents the tree map by the IT company Infosys. Https Infosys is at the center surrounded by themes like solutions, experience, industry work, growth, business, clients, digital technology, services, cyber security, customers and help customers during the pandemic, digital transformation, and being resilient.

Figure 6 represents the Word cloud and Fig. 7 represents the treemap for Wipro. Wipro is at the center surrounded by transformation, learn and know business, innovations, customers, industry, Wipro virtual, services, technologies, organizations etc.

Figure 8 represents the word cloud and Fig. 9 represents the treemap for HCL Technologies. Learn, digital technology, customer, enterprise, global, services, women, pandemic, Covid, employees, innovation, cloud were the key highlights of the word cloud by HCL.

Figure 10 represents the word cloud and Fig. 11 represents the treemap for Tech Mahindra. It focussed on unlock the next, technology, business, 5G, read and know, digital transformation, technology, services, customer experiences, Covid, solution, enterprise, etc.


https
infosys
#infosys
#navigateyournext
#digitaltransformation
#rolandgarroswithinfosys
#ausopenwithinfosys
#forwardwithinfosys
#fortifyyourenterprise
#infytq
#cloud
#ai
#data
#5g
#iot
#cybersecurity
#infinitethinking
#infinitethinkingwithinfosys
#infosysnowledge
#infosyscobalt
#infosysvillage
#infosysinstitute
#infosysbpm
#infosysconsulting
#infosysfoundation
#infosysprize
#infosysscholarship
#infosysleadership
#infosysinternship
#infosysfellowship
#infosysmentor
#infosysinnovationnetwork
#infosysinnovationhub
#infosysinnovationlabs
#infosysinnovationpartner
#infosysinnovationcenter
#infosysinnovationchallenge
#infosysinnovationprize
#infosysinnovationaward
#infosysinnovationgrant
#infosysinnovationfellowship
#infosysinnovation



Fig. 10 Word cloud for tweets by Tech Mahindra

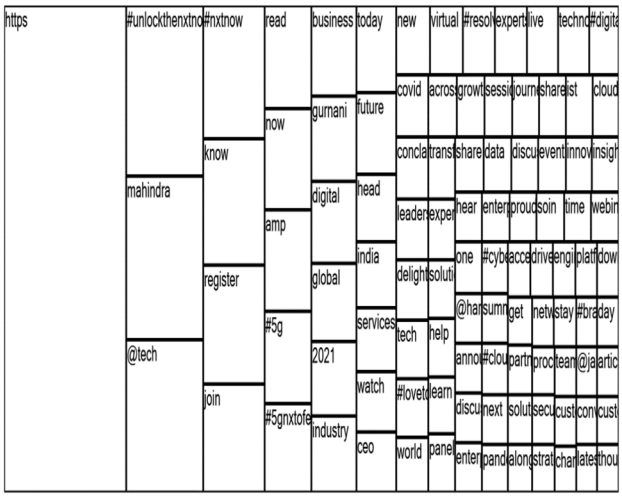


Fig. 11 Tree map for tweets by Tech Mahindra



Fig. 12 Word cloud for tweets by LTI

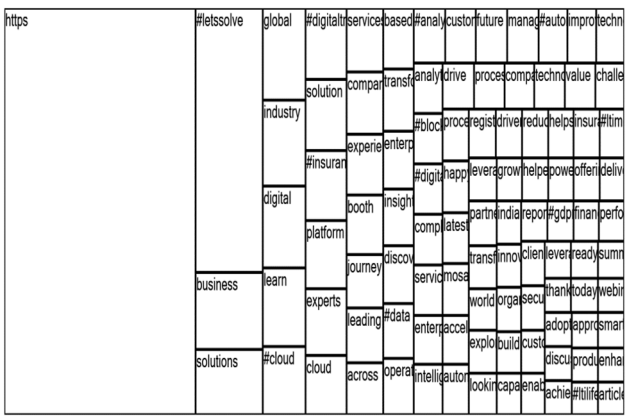


Fig. 13 Tree map for tweets by LTI

Figure 12 represents the word cloud and Fig. 13 represents the treemap of LTI. It talked about business, solution, digital transformation, lead, global, cloud, digital insurance, people, process, industry, Block chain, innovation, help, performance, organizations etc.

Figure 14 represents the word cloud and Fig. 15 represents the treemap for Mindtree. Mindtree is at the center surrounded by digital technology, digital transformation, business, industry, customers, cloud, learn digital, services, challenges, virtual, insurtech, reimagine new normal, global, organization, transformation, experts, agile, operating, leadership, strategy and many more.

Figure 16 represents the word cloud and Fig. 17 represents the treemap of Mphasis. Mphasis is at the center of the word cloud being surrounded by learn, solution, customers, digital, articles, services, clients, industry, stay ahead, security, infrastructure, innovation, transformation, pandemic and many more.

Figure 18 represents word cloud and Fig. 19 represents tree map of OFS. It focussed on banks, banking services, Oracle fs, digital, better banking, digital banking, technology, management, transformation, healthcare, customers, cloud, Covid, billing, health insurance and many more.

Figure 20 represents the word cloud and Fig. 21 represents the tree map of Persistent Systems. The key focus points of Persistent Systems are digital, business, solution, digital transformation, solution, customer, healthcare, innovation, cloud, platform, enterprise, data, working, banking, experience, sales force and more.



Fig. 14 Wordcloud for tweets by Mindtree

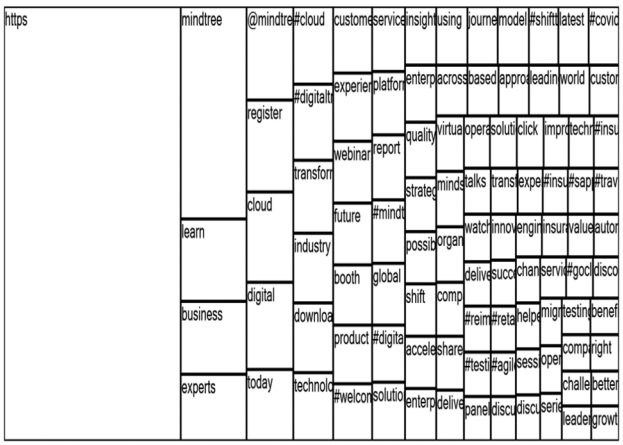


Fig. 15 TreeMap for tweets by Mindtree

4.2 Sentiment analysis

Twitter sentiment analysis is a specialized area within sentiment analysis for computer assisted qualitative study tool. NVivo performs sentiment analysis by identifying and evaluating opinions expressed in text/tweets using automated methods. It is useful in predicting feelings behind words, sentences, or a whole document [35]. Sentiment Analysis has gained importance in the recent years [36, 37]. There



Fig. 16 Word cloud for tweets by Mphasis

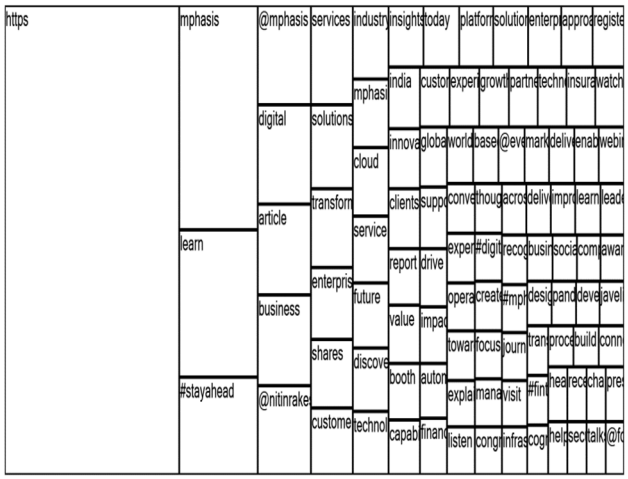


Fig. 17 Tree map for tweets by Mphasis

is an ample amount of literature available on Sentiment Analysis of Tweets on Twitter [38, 39]. Sentiment Analysis is an automated way to extract the sentiment of people from opinion, reviews or tweets on the twitter platform [40]. Sentiment Analysis helps to categorize large number of opinions on online communication channels like Twitter [41, 42]. The companies can use sentiment analysis to know about customer, employees and various stakeholders' sentiments about its policies, programmes and welfare activities. This very usefulness of Sentiment Analysis has spread the use of this technique to management and social science discipline



Fig. 18 Word cloud for tweets by OFS

Fig. 20 Word cloud for tweets by Persistent Systems

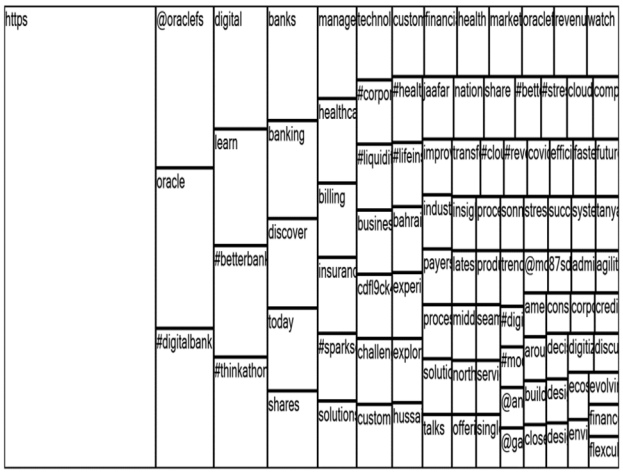


Fig. 19 Tree map for tweets by OFS

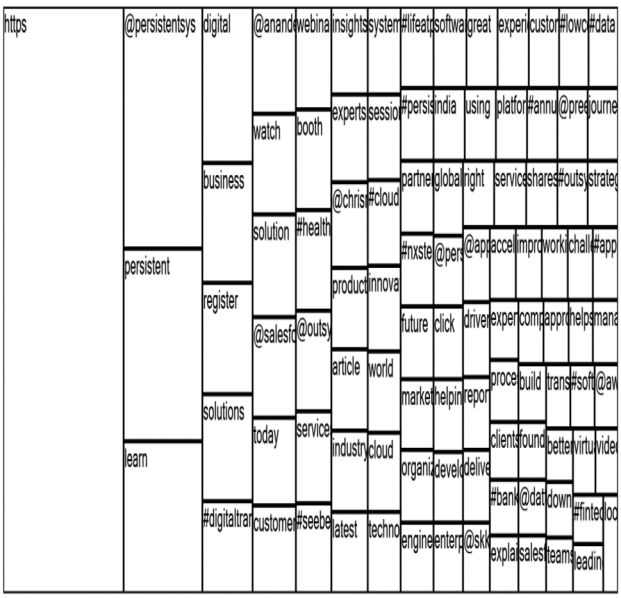


Fig. 21 Tree map for tweets by Persistent Systems

apart from computer science [43]. Initial sentiment analysis included binary classifications (positive and negative) of tweets. NVivo allows extracting four sentiments based on the opinion of people on twitter [44, 45] The four sentiments extracted automatically are; very negative, moderately negative, moderately positive and very positive. The sentiment analysis of tweets by Top 10 IT companies on Twitter is presented in Table 4.

Table 4 contains the sentiment analysis of tweets by the IT companies on Twitter. Most of the stakeholders of the IT companies perceived tweets as moderately positive except for OFS. There is equal number of moderately positive and moderately negative sentiments for tweets by OFS. Persistent Systems has the highest number of moderately positive and very positive sentiments in total 1841 followed by Wipro and MindTree with a total of 1369 and 1090 respectively. The sentiment analysis of the tweets by the IT companies suggests that most of the stakeholders found these tweets to be positive. It is clearly visible that only a few tweets were very negative for all the top ten IT companies under study in this paper. Overall, it is evident that the IT industry tweeted and responded positively during Covid crisis.

Table 4 Sentiment analysis of Tweets by the top ten IT companies

Sr. no	Company	Very negative	Moderately negative	Moderately positive	Very positive
1	TCS	73	158	558	290
2	Infosys	101	344	769	194
3	Wipro	132	420	1028	341
4	HCL Technologies	101	344	769	194
5	Tech Mahindra	37	75	296	139
6	L&T I	101	344	769	194
7	Mindtree	71	238	820	270
8	Mphasis	88	271	700	277
9	OFS	6	20	20	5
10	Persistent Systems	182	218	836	1005

Source: Analysis by the authors

5 Conclusion and directions of future research

The COVID-19 crisis affected organizations across the globe. India witnessed the disruptive impact of COVID-19 in terms of economic activity as well as loss of lives. Several organizations in India struggled to cope up with the crisis. However, IT companies embraced the pandemic by being more resilient and quickly switched to a remote-working model and gave highest importance to employee's health and safety. For example top Indian IT companies TCS and Infosys decided to discard the 20-year-old work model and switched to new mode of work.

The text sets and data sets revealed the following themes under the #COVID19 keyword for all the top 10 IT companies—digital transformation, the future of technology, adopting global practices, healthcare, transformative leadership, and being agile. TCS through #TCSEmpowers contributed $200 million to COVID 19 relief and response efforts. From setting up isolation centers, to distributing medical supplies like PPE kits, respiratory systems and meals to health workers to bridging education gaps through Edu Virtual Assist and providing access to emergency ambulance services/food/health materials to more than 200,000 households. TCS extended its support to more than 1,80,000 people across India during pandemic.

In the wake of COVID-19, IT companies realized that robust IT infrastructure was needed to support business and other functions during and post-COVID-19. Therefore, several technological advancements in the fields of generative Artificial Intelligence tools like Chat Generative Pretrained Transformer, Machine Learning, Robotics, Data Analytics, insurtech and Cybersecurity accelerated during the pandemic. The IT sector was also very swift in responding to the COVID-19 crisis by adopting various customer-friendly approaches, employee welfare activities and stakeholder concerns. The COVID-19 crisis accelerated digitization of customer interactions in India as customers preferably communicated through several digital channels and IT companies responded in turn. IT sector focussed on business development by incorporating customer-centric approaches. Customer satisfaction and customer experience were given much importance in their tweets. The National Association of Software and Service Companies (NASSCOM) reported that the Indian IT sector's revenue increased by 15.5% to $227 billion in FY22, adding 3.33 lakh jobs annually, bringing the sector's total employment to 5.84 million. TCS generated the highest revenue of 1,67,311 Crores in FY22 followed by Infosys which stood at the second place with total revenue of 1.02 Crores followed by HCL Technologies which generated total revenue of approximately 80,000 crores [46].

Further, every study is constrained by certain research limitations. The limitations of this study are the direction for future research. Future researchers may look at thematic analysis of the tweets by the IT companies. Another study can be conducted to compare the analysis of tweets from the IT and non-IT sectors. The third direction for future research could be to take up a quantitative study and present an algorithmic model for the same.

Acknowledgements I am grateful to Dr. Meha Joshi and Dr. Ritu Bajaj for their substantial contribution to present the research methodology algorithmically.

Funding This research did not receive any specific grant from funding agencies in the public, commercial, or non-profit sectors. No animals were harmed during the research work.

Declarations

Conflict of interest We declare no conflicts of interest with respect to the authorship and/or publication of this article.

References

1. World Health Organization (WHO) (2020) Rolling updates on coronavirus disease (COVID-19) [Online]. http://www.euro.who.int/en/health-topics/health-emergencies/coronavirus-covid-19/news/news/2020/3/who-announces-covid-19-outbreak-a-pandemic2. Accessed 26 Sept 2021
2. Bardesi H, Al-Mashaikhi A, Basahel A, Yamin M (2021) COVID-19 compliant and cost effective teaching model for King Abdulaziz University. Int J Inf Technol 13(4):1343–1356. https://doi.org/10.1007/s41870-021-00684-0
3. Hope L (2021) Protecting pandemic conversations: tracing Twitter's evolving content policies during COVID-19. J Bus Tech Commun 35(1):88–93. https://doi.org/10.1177/1050651920958393
4. Wong A, Ho S, Olusanya O, Antonini MV, Lyness D (2021) The use of social media and online communications in times of pandemic COVID-19. J Intens Care Soc 22(3):255–260. https://doi.org/10.1177/1751143720966280
5. Zhang S, Gosselt JF, De Jong MDT (2020) How large Information Technology companies use Twitter: arrangement of corporate accounts and characteristics of tweets. J Bus Tech Commun 34(4):364–392. https://doi.org/10.1177/1050651920932191
6. Ciborra CU (1997) De profundis? Deconstructing the concept of strategic alignment. Scand J Inf Syst 9(1):2. https://aisel.aisnet.org/sjis/vol9/iss1/22
7. Kearns GS, Lederer AL (2000) The effect of strategic alignmenton the use of IS-based resources for competitive advantage. J Strateg Inf Syst 9(4):265–293
8. Business Standard (2021) At 199 million, Twitter logs 20% user growth as pandemic posts surge . https://www.business-standard.com/article/technology/at-199-million-twitter-logs-20-user-growth-as-pandemic-posts-surge-121043000235_1.html. Accessed 27 Feb 2022
9. Haman M (2020) The use of Twitter by state leaders and its impact on the public during the COVID-19 pandemic. Heliyon 6(11):e05540. https://doi.org/10.1016/j.heliyon.2020.e05540
10. Statistica Research Report (2022) Number of Twitter users worldwide from 2019 to 2024 (in millions) . https://www.statista.com/statistics/303681/twitter-users-worldwide/#:~:text=In%202019%2C%20Twitter's%20audience%20counted,and%20a%20popular%20marketing%20channel. Accessed 27 Feb 2022
11. Juvet TM, Corbaz-Kurth S, Roos P, Benzakour L, Cereghetti S, Moullec G, Suard JC, Vieux L, Wozniak H, Pralong JA, Weissbrodt R (2021) Adapting to the unexpected: problematic work situations and resilience strategies in Healthcare Institutions during the COVID-19 pandemic's first wave. Saf Sci 139:105277. https://doi.org/10.1016/J.SSCI.2021.105277
12. Sawalha IHS (2015) Managing adversity: understanding some dimensions of organizational resilience. Manag Res Rev 38(4):346–366. https://doi.org/10.1108/MRR-01-2014-0010
13. Williams TA, Gruber DA, Sutcliffe KM, Shepherd DA, Zhao EY (2017) Organizational response to adversity: fusing crisis management and resilience research streams. Acad Manag Ann 11(2):733–769. https://doi.org/10.5465/annals.2015.0134
14. Shirali GA, Mohammadfam I, Ebrahimipour V (2013) A new method for quantitative assessment of Resilience Engineering by PCA and NT approach: a case study in a process industry. Reliab Eng Sys Saf 119:88–94. https://doi.org/10.1016/j.ress.2013.05.003
15. Barasa E, Mbau R, Gilson L (2018) What is resilience and how can it be nurtured? A systematic review of empirical literature on organizational resilience. Int J Health Policy Manag 7(6):491–503. https://doi.org/10.15171/ijhpm.2018.06
16. Boin A, van Eeten MJG (2013) The resilient organization. Public Manag Rev 15(3):429–445. https://doi.org/10.1080/14719037.2013.769856
17. Ruiz-Martin C, Lopez-Paredes A, Wainer G (2018) What we know and do not know about organizational resilience. Int J Prod Manag Eng 6(1):11. https://doi.org/10.4995/ijpme.2018.7898
18. Ponomarov S, Holcomb M (2009) Understanding the concept of supply chain resilience. Int J Logist Manag 20:124–143. https://doi.org/10.1108/09574090910954873
19. Rose A (2006) Economic resilience to disasters: toward a consistent and comprehensive formulation. In: Douglas JMD (ed) Disaster resilience: an integrated approach. Charles C Thomas Publisher Ltd, Paton, pp 226–248
20. Kossek EE, Perrigino MB (2016) Resilience: a review using a grounded integrated occupational approach. Acad Manag Ann 10(1):00–00. https://doi.org/10.5465/19416520.2016.1159878
21. Hillmann J, Guenther E (2021) Organizational resilience: a valuable construct for management research? Int J Manag Rev 23(1):7–44. https://doi.org/10.1111/ijmr.12239
22. Duchek S (2020) Organizational resilience: a capability-based conceptualization. Bus Res 13:215–246. https://doi.org/10.1007/s40685-019-0085-7
23. Paluszak GT, Wi´sniewska-Paluszak JA, Schmidt J, Lira J (2021) The organisational resilience (OR) of rural non-profits (RNPOs) under conditions of the COVID-19 pandemic global uncertainty. Agriculture 11(7):670. https://doi.org/10.3390/agriculture11070670
24. Liu B (2012) Sentiment analysis and opinion mining. Morgan & Claypool Publishers, San Rafael
25. Lewis SC, Zamith R, Hermida A (2013) Content analysis in an era of big data: a hybrid approach to computational and manual methods. J Broadcast Electron Media 57(1):34–52
26. Holloway I, Galvin K (2016) Qualitative research in nursing and Healthcare. Wiley, London
27. Smith J, Bekker H, Cheater F (2011) Theoretical versus pragmatic design in qualitative research. Nurse Res 18(2):39–51
28. O'Leary MB, Wilson JM, Metiu A (2014) Beyond being there: the symbolic role of communication and identification in perceptions of proximity to geographically dispersed colleagues. MIS Quart 38(4):1219–1244. https://www.jstor.org/stable/26627969
29. Neuendorf KA (2002) Defining content analysis. Content analysis guidebook. Sage, Thousand Oaks
30. Riff D, Lacy S, Fico F (2013) Analyzing media messages: using quantitative content analysis in research, 3rd edn. Routledge, New York
31. Wimmer RD, Dominick JR (2003) Content analysis. Mass media research:an introduction. Thomson-Wadsworth, Belmont, pp 139–165
32. Atali L, Gürer B (2015) Content analysis of official Twitter account of under-20 Football World Cup. Adv Phys Educ 5(2):103–106. https://doi.org/10.4236/ape.2015.52013
33. Kaurav RPS, Suresh KG, Narula S, Baber R (2020) New Education Policy: qualitative (contents) analysis and Twitter mining (sentiment analysis). J Content Community Commun 12(1):4–13. https://doi.org/10.31620/JCCC.12.20/02
34. Sinclair J, Cardew-Hall M (2008) The folksonomy tag cloud: when is it useful? J Inf Sci 34(1):15–29. https://doi.org/10.1177/0165551506078083
35. Kumar P, Vardhan M (2022) PWEBSA: Twitter sentiment analysis by combining Plutchik wheel of emotion and word embedding. Int J Inform Technol 14(1):69–77. https://doi.org/10.1007/s41870-021-00767-y
36. Chauhan D, Sutaria K (2019) Multidimensional sentiment analysis on twitter with semiotics. Int J Inform Technol 11(4):677–682. https://doi.org/10.1007/s41870-018-0235-8

37. Gupta M, Gupta P (2019) Research and implementation of event extraction from twitter using LDA and scoring function. Int J Inform Technol 11(2):365–371. https://doi.org/10.1007/s41870-018-0206-0
38. Yi J, Nasukawa T, Bunescu R, Niblack W (2003) IBM confidential sentiment analyzer: extracting sentiments about a given topic using Natural Language Processing Techniques. http://www.cnet.com
39. Go A, Bhayani R, Huang L (2009) Twitter sentiment classification using distant supervision. http://tinyurl.com/cvvg9a
40. Aqlan AAQ, Manjula B, Lakshman Naik R (2019) A study of sentiment analysis: concepts, techniques and challenges. https://doi.org/10.1007/978-981-13-6459-4_16
41. Paroubek P, Pak A (2010) Twitter as a corpus for sentiment analysis and opinion mining. http://tumblr.com
42. Desai M, Mehta MA (2016) Techniques for sentiment analysis of Twitter data: a comprehensive survey. In: 2016 international conference on computing, communication and automation (ICCCA), pp 149–154. https://doi.org/10.1109/CCAA.2016.7813707
43. Farhadloo M, Rolland E (2016) Fundamentals of sentiment analysis and its applications. Springer International Publishing, Switzerland. https://doi.org/10.1007/978_3_319_30319_2_1
44. Gupta S, Sharma J, Najm M, Sharma S (2020) Media exaggeration and information credibility: qualitative analysis of fear generation for Covid-19 using Nvivo. J Content Community Commun 12(6):14–20. https://doi.org/10.31620/JCCC.12.20/03
45. Kharde VA, Sonawane SS (2016) Sentiment analysis of twitter data: a survey of techniques. Int J Comput Appl. https://doi.org/10.45585/arXiv.1601.06971
46. Technology Sector in India Report (2022) Resilience to resurgence/strategic review https://community.nasscom.in/communities/bpm/technology-sector-india-2022-resilience-resurgence strategic-review. Accessed Online on 27 Feb 2022

Springer Nature or its licensor (e.g. a society or other partner) holds exclusive rights to this article under a publishing agreement with the author(s) or other rightsholder(s); author self-archiving of the accepted manuscript version of this article is solely governed by the terms of such publishing agreement and applicable law.

2023 International Conference on Intelligent Systems, Advanced Computing and Communication (ISACC) | 979-8-3503-9938-7/23/$31.00 ©2023 IEEE | DOI: 10.1109/ISACC56298.2023.10084051

The Role of Deep Learning in Diagnosis and Grading of Diabetic Retinopathy: A Review

Samarpit Minz
Computer Science & Engineering Department
Delhi Technological University
New Delhi, India
samarpitminz@gmail.com

Saarthak Seth
Computer Science & Engineering Department
Delhi Technological University
New Delhi, India
saarthakseth@gmail.com

Sarvesh Tiwari
Computer Science & Engineering Department
Delhi Technological University
New Delhi, India
sarveshtiwari.work@gmail.com

Rahul Katarya
Computer Science & Engineering Department
Delhi Technological University
New Delhi, India
rahuldtu@gmail.com

***Abstract*—In developing nations, diabetic retinopathy is a leading cause of blindness. It often has no early warning signs; however, monitoring the eyes could prevent the progression to more severe forms of sight-threatening retinopathy and maculopathy. The primary diagnostic method for diabetic retinopathy is analyzing fundoscopic images; however, manually examining such images can be time-consuming and unreliable because the ability to spot abnormalities varies with the physician's expertise. This manual effort has been lessened by computer-aided diagnosis tools that automatically detect diabetic retinopathy on retinal scans. Deep Learning techniques offer an excellent way of creating computer-aided diagnosis tools, delivering highly efficacious diabetic retinopathy detection and grading results. This review lists the current state-of-the-art Deep Learning approaches in the application of detection and grading of diabetic retinopathy, some of which include transfer learning, Convolutional Neural Networks, and object detection techniques, among others. It further identifies potential research gaps in these approaches and the future research direction to find solutions to address them.**

***Keywords*—Deep Learning, Diabetic Retinopathy, Fundoscopic Images, Healthcare, Machine Learning**

I. Introduction

Diabetes is a major chronic disease infesting the world population right now. It has made its place among the ten major causes of mortality [1]. In India alone, it affected 77 million people in 2019, which, if continued at the present trend, would reach an overwhelming 135 million by the year 2045 [2]. Out of the different harmful effects that diabetes causes on various organs of the body, one of the most prominent diseases is Diabetic Retinopathy (DR), which is caused by the damage to blood vessels in the retina because of an increase in glucose levels in the body.

Globally, DR is the most frequent cause of vision loss or blindness in the age group 20 to 74 years [3]. In 2020, the number of adults affected by DR was estimated to be 103.12 million, with Africa registering the highest prevalence of 35.90% [4]. Presently, there is no known cure for DR, but if detected at an early stage, the treatment is efficacious in preventing, delaying, or even reducing vision loss. Evidence-based treatment can significantly aid in the prevention of blindness, with clinical trials demonstrating a possible risk reduction of more than 90% [5]. DR detection is done by catching abnormalities in the retina called lesions, which are the spots that occur due to leaking blood and fluids in vessels. These are mainly of two types: red and bright lesions. Red Lesions consist of Microaneurysm (MA) and Hemorrhages (HEM), whereas bright lesions are classified as soft exudates and hard exudates [6]. These lesions are detected from retinal images taken using a clinical instrument called a fundoscope. At the early stage of the disease, it is known as non-proliferative diabetic retinopathy (NPDR), where damage to blood vessels starts to appear. As the severity of the disease increases, new abnormal blood vessels are formed, leading to a stage known as proliferative DR [7]. There are five severity stages of DR. Grades 0 to 4 are assigned to the five stages [8] (Table I).

The primary obstacle to DR diagnosis is that it is a silent disease with no early warning signs, making it challenging to diagnose it promptly. The number of diabetic patients is

Authorized licensed use limited to: DELHI TECHNICAL UNIV. Downloaded on April 17,2023 at 06:06:51 UTC from IEEE Xplore. Restrictions apply.

TABLE I
GRADING OF DIABETIC RETINOPATHY [8]

Grade	Clinical Features	Category
0	Symptoms not seen	No Diabetic Retinopathy
1	only MAs are present	Mild NPDR
2	more than MAs are present, but still less dangerous than Severe NPDR	Moderate NPDR
3	Presence of any of the following conditions: Definite venous beading in 2 or more quadrants, Intraretinal microvascular abnormalities in 1 or more quadrants, Intraretinal HEM ($\geq$ 20 in each quadrant)	Severe NDPR
4	Neovascularization, i.e., formation of new blood vessels	Proliferative DR

unabatingly increasing, and the rate is expected to escalate further. This would create a serious problem for ophthalmologists, as their number would not be commensurate with the increment in that of diabetic patients, paving the way for an overall collapse of the healthcare system. In addition, the outcome of such a diagnosis varies across different doctors and extensively depends on their experience. Moreover, some geographical areas with a high occurrence rate of DR may need to be more resourcefully equipped to combat such tremendous numbers. This creates a dire need to automate the DR detection and grading process to the greatest extent possible. Research and development of such automated systems for the detection of DR has been growing rapidly in the last decade, especially since 2015 [9].

Machine Learning (ML) as a technique is the most popular approach for the detection of DR using fundus images or symptoms among patients [9]. Research on various ML methods for DR detection has been going on for a long time now, with many conventional ML algorithms as well as their ensemble being examined along with feature selection [10]–[12]. Yunlei et al. [10] and Tsao et al. [11] have drawn a comparison between various conventional ML algorithms trained on patients' health records to diagnose DR. Ahmadrezai et al. [12] have put forth a novel feature selection method to reduce the number of predictors for DR detection using electronic medical records. Among various types of learning architectures in ML, Deep Learning (DL) has emerged as one of the most prominent and efficient techniques being contemporarily studied and applied for detecting DR. Supervised training techniques used in DL and ML enable machines to learn any task on their own through the use of experience in the form of data [13].

DL uses artificial neural networks that are inspired by the structure of biological neural networks and works great for creating end-to-end models for the automation of various tasks. Unlike conventional approaches of ML, where the process is divided into various sub-processes to get the final result, DL has the advantage of learning strategy directly from the dataset to provide a complete model without extensively engineering features such as in ML. A typical design of DL approaches in detection, grading, and segmentation is shown in Figure 1. In recent times, research approaches using DL have become increasingly popular, partly owing to their convenient use resulting from the advent of various new and advanced libraries and frameworks that provide an abstract framework to developers, relieving them from undertaking the onerous task of *de novo* development [14]. Even among DL, Convolutional Neural Networks (CNNs) have emerged as the most prominent method for image classification tasks. CNNs consist of not only fully connected layers, as in the dense neural nets, but also convolution layers consisting of the image convolutions using different kernel sizes. In recent times, several new novel architectures based on CNNs have been introduced, like Ziyuan et al. [15] introducing SEA-Net or Zhan et al. [16] introducing Coarse to Fine-DR network (CF-DRnet), among many others for DR detection or severity classification.

This review article is structured as follows: section II i.e., Literature Review summarizes the existing literature on the use of DL for the detection and grading of DR. For convenience, it has been bifurcated into Deep Learning Architectures and Fundoscopic Image Datasets. The section III, i.e., Research Gaps and Future Work, identifies potential research gaps and suggests solutions thereof. Finally, the key outcomes of the study are encapsulated in the concluding section IV.

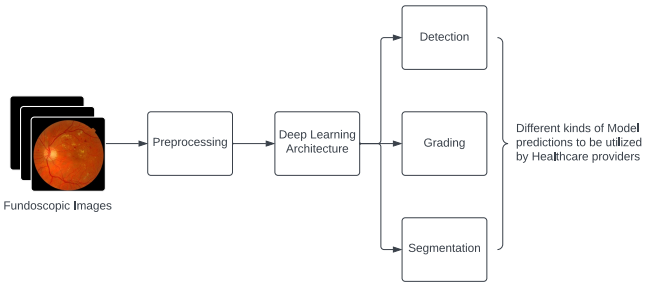


Fig. 1. A schematic representation of a typical design of deep learning approaches in detection, grading, and segmentation.

Authorized licensed use limited to: DELHI TECHNICAL UNIV. Downloaded on April 17,2023 at 06:06:51 UTC from IEEE Xplore. Restrictions apply.

II. Literature Review

The application of DL has been growing rapidly since the previous decade, with promising results in image processing, and medical image analysis, among other things. DL algorithms have also had a substantially positive impact on healthcare by advancing segmentation, prediction, and classification in this field. Given the significance of recent scientific advancements in the field of diabetic retinopathy, an analysis of DL techniques used in various studies is discussed in Table III. Area Under the receiver operating characteristic Curve (AUC), accuracy, sensitivity, specificity, and Average Class Accuracy (ACA) are some of the commonly used performance evaluation parameters that have been observed.

A. Deep Learning Architectures

Various DL methods and models with different architectures are used for DR diagnosis to perform either detection, i.e., binary classification (DR or No DR), or grading. Most of the proposed solutions made use of the transfer learning technique by pre-training their model's weights and hyper-parameters on the ImageNet dataset. CNNs, EfficientNetB0 [17], and the pre-trained convolutional part of InceptionV3 [18] are used for feature extraction. InceptionV3 model [18], [19], Deep Recurrent Neural Network (DRNN) architecture [20], Deep CNN (DCNN) [21], AlexNet and GoogleNet [22] and the pre-trained Coarse Network with attention modules [16] are used for detection. ResNet [23], YOLOv3 [17] and Faster Region-based CNN (RCNN) [24] are used for lession detection. Mask-RCNN [23] and Entropy weighted power k-means clustering [21] are used for lesion segmentation. ResNet-50 [25], the pre-trained Fine Network [16], Deep Graph Correlation Network (DGCN) [26], E-DenseNet BC-121 [27], ResNeXt ensembled with DenseNet101 [28], InceptionV3, ResNet101, DenseNet121 [29], Shepard CNN (ShCNN) [21] and various classifiers like support vector machine, k-nearest neighbors [17] and random forest [25] are used for DR grading.

Figures 2, 3, and 4 illustrate, respectively, the performance metrics of the studies that carried out the International Clinical Diabetic Retinopathy (ICDR) grading task on the IDRiD and EyePACS datasets and the binary classification task on the DIARETDB1 dataset. Further, after comparing the performance metrics of the various studies mentioned in Table III, the top three studies performing the best in terms of accuracy for the task of ICDR grading are shown in Figure 5.

B. Fundoscopic Image Datasets

This section discusses the various fundoscopic datasets available that could be used for DR Grading. A common severity scale was agreed upon out of various different methods for assessing the severity of DR, known as the International Clinical Diabetic Retinopathy scale. It consists of a grading scale of 5 points that correspond to no DR, mild NPDR, moderate NPDR, severe NPDR, and proliferative DR [8]. A summary of some common datasets which have labeled ICDR ratings is given in Table II.

TABLE II
Summary of Datasets with Labeled International Clinical Diabetic Retinopathy Scale Grading

Dataset	Labeled Images				
	No DR	**Mild NPDR**	**Moderate NPDR**	**Severe NPDR**	**Proliferative DR**
EyePACS [30]	25810	5292	2443	873	708
DDR [31]	6266	630	4477	236	913
APTOS [32]	1805	999	370	295	193
MESSIDOR-2 [33], [34]	1017	347	270	75	35
IDRiD [35]	168	25	168	93	62
FGADR [36]	101	212	595	647	287
DeepDRiD [37]	200	36	72	72	20

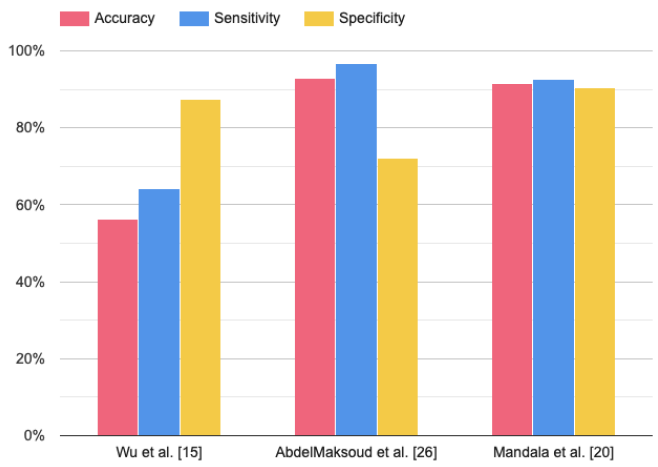


Fig. 2. Performance metrics of the studies using IDRiD dataset for International Clinical Diabetic Retinopathy grading.

III. Research Gaps and Future Work

Although DL models have shown promising results in the detection and grading of DR in retinal images, a few research gaps exist which must be addressed in order to improve these models' performance, interpretability, and clinical utility. The most significant of such gaps, along with their possible solutions are discussed in this section.

Authorized licensed use limited to: DELHI TECHNICAL UNIV. Downloaded on April 17,2023 at 06:06:51 UTC from IEEE Xplore. Restrictions apply.

TABLE III
SUMMARY OF RELATED WORK ON DIABETIC RETINOPATHY DETECTION AND GRADING

Authors	**Model(s) Used**	**Task Performed**	**Result**	**Dataset**
Mike Voets et al. [19], 2019	InceptionV3	Binary classification: moderate or worse DR (moderate, severe or proliferative grades)	0.951 AUC for EyePACS 0.853 AUC for Messidor-2	EyePACS, Messidor-2
Shri Kant et al. [18], 2019	InceptionV3	Binary classification: DR or no DR	90.9% accuracy	EyePACS
Doshna Umma Reddy et al. [38], 2020	VGG-16	5 scale grading	80% sensitivity, 65% specificity, 0.80 AUC, 74% ACA	EyePACS
Zhan Wu et al. [16], 2020	CF-DRNet	5 scale grading	53.99% sensitivity, 91.22% specificity, 83.10% accuracy for EyePACS 64.21% sensitivity, 87.39% specificity, 56.19% accuracy for IDRiD	EyePACS, IDRiD
Abdüssamed Erciyas et al. [24], 2021	Faster RCNN, CNN	5 scale grading for EyePACS 4 scale grading for Messidor	99.1% accuracy, 0.999 AUC, 99.1% sensitivity, 99.1% specificity for EyePACS 100% accuracy, 1 AUC, 100% sensitivity, 100% specificity for Messidor	EyePACS, Messidor, IDRiD, DIARETDB
Ashish Bora et al. [39], 2021	InceptionV3	Detecting onset of DR in next 2 years	0.71 AUC	EyePACS
Ling Dai et al. [23], 2021	ResNet	5 scale grading	0.944 AUC for NDSP 0.943 AUC for EyePACS	NDSP, EyePACS
Muhammad Kashif Yaqoob et al. [25], 2021	ResNet-50	5 scale grading for EyePACS Binary classification: No Referable Diabetic Macular Edema(DME) or Referable DME for Messidor-2	75.09% accuracy for EyePACS 96% accuracy for Messidor-2	EyePACS, Messidor-2
Sraddha Das et al. [40], 2021	CNN	Binary classification: DR or no DR	97.2% precision, 98.2% specificity, 99.6% sensitivity, 98.7% accuracy	DIARETDB1
Wejdan L. Alyoubi et al. [17], 2021	CNN512 and YOLOv3	5 scale grading	89% accuracy, 89% sensitivity, 97.6% specificity for DDR	DDR, APTOS
Ching-Yao Tsai et al. [29], 2022	InceptionV3, ResNet101, DenseNet121	5 scale grading	InceptionV3: 84.64% sensitivity, 82.41% precision, 84.64% accuracy; ResNet101: 83.89% sensitivity, 81.47% precision, 83.89% accuracy; DenseNet121: 84.05% sensitivity, 81.29% precision, 84.05% accuracy for EyePACS InceptionV3: 83.80% sensitivity, 85.23% precision, 83.80% accuracy; ResNet101: 82.99% sensitivity, 84.91% precision, 82.99% accuracy; DenseNet121: 84.67% sensitivity, 84.80% precision, 84.67% accuracy for TCH	EyePACS, Taipei City Hospital (TCH)
Eman AbdelMaksoud et al. [27], 2022	E-DenseNet BC-121	5 scale grading	94% sensitivity, 73% specificity, 84% accuracy for APTOS 98.3% sensitivity, 72% specificity, 96.8% accuracy for EyePACS 95% sensitivity, 58% specificity, 91.6% accuracy for Messidor 96.7% sensitivity, 72% specificity, 93% accuracy for IDRiD	APTOS, EyePACS, Messidor, IDRiD

Authorized licensed use limited to: DELHI TECHNICAL UNIV. Downloaded on April 17,2023 at 06:06:51 UTC from IEEE Xplore. Restrictions apply.

TABLE III
CONT.

Authors	Model(s) Used	Task Performed	Result	Dataset
Guanghua Zhang et al. [26], 2022	DGCN	5 scale grading	89.9% accuracy, 88.2% sensitivity, 91.3% specificity for EyePACS 91.8% accuracy, 90.2% sensitivity, 93.0% specificity for Messidor-2	EyePACS, Messidor-2
Jyothi Mandala et al. [21], 2022	DCNN, ShCNN	Binary classification: DR or no DR 5 scale grading	Binary classification: 92.54% sensitivity, 89.54% specificity, 90.87% accuracy; grading: 92.54% sensitivity, 90.54% specificity, 91.42% accuracy for DDR Binary classification: 91.42% sensitivity, 89.58% specificity, 90.25% accuracy; grading: 92.54% sensitivity, 90.54% specificity, 91.42% accuracy for IDRiD	DDR, IDRiD
R. Pitchai et al. [20], 2022	DRNN, U-Net	Detecting onset of DR in next 2 years	95.6% precision for DRIVE 0.992 AUC for EyePACS 1.964 AUC for Messidor-2	DRIVE, EyePACS, Messidor-2
Suresh Batha et al. [22], 2022	AlexNet and GoogleNet	Binary classification: DR or no DR	99.5% sensitivity, 99% specificity, 94% accuracy for DIARETDB0 93.2% sensitivity, 92% specificity, 94.83% accuracy for DIARETDB1	DIARETDB0, DIARETDB1
Zhaomin Yao et al. [41], 2022	Swin Transformer	Binary classification: DR or no DR 4 scale grading	93.76% sensitivity, 81.71% specificity, 90.62% accuracy for binary classification 81.54% sensitivity, 94.13% specificity, 84.12% accuracy for grading	Messidor
Sambit S. Mondal et al. [28], 2023	Ensembled DenseNet101 and ResNeXt	5 scale grading for APTOS Binary classification: DR or no DR for DIARETDB1	82% sensitivity, 76% precision, 86.08% accuracy for APTOS 97% sensitivity, 97% precision, 96.88% accuracy for DIARETDB1	APTOS, DIARETDB1

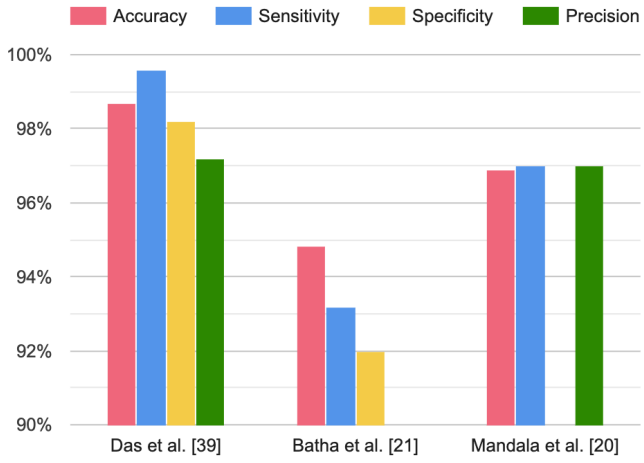


Fig. 3. Performance metrics of the studies using DIARETDB1 dataset for binary classification.

A. Need for larger and more diverse datasets

One of the major challenges in using DL for DR detection and classification is the need for larger and more diverse datasets for training and evaluating DL models. Many current datasets for DR may not adequately represent the variability seen in clinical retinal images. This may limit the models' generalizability and performance on real-world data. It is critical to consider the dataset's size, diversity, and quality when assessing its suitability for training and evaluating the models. To capture the full range of variability in retinal images and to support the training of more complex models, larger datasets may be required. The dataset's diversity can help increase the robustness of the model to handle different imaging conditions and patient characteristics. The image quality is also important, as poor image quality can have an impact on the model's performance.

Authorized licensed use limited to: DELHI TECHNICAL UNIV. Downloaded on April 17,2023 at 06:06:51 UTC from IEEE Xplore. Restrictions apply.

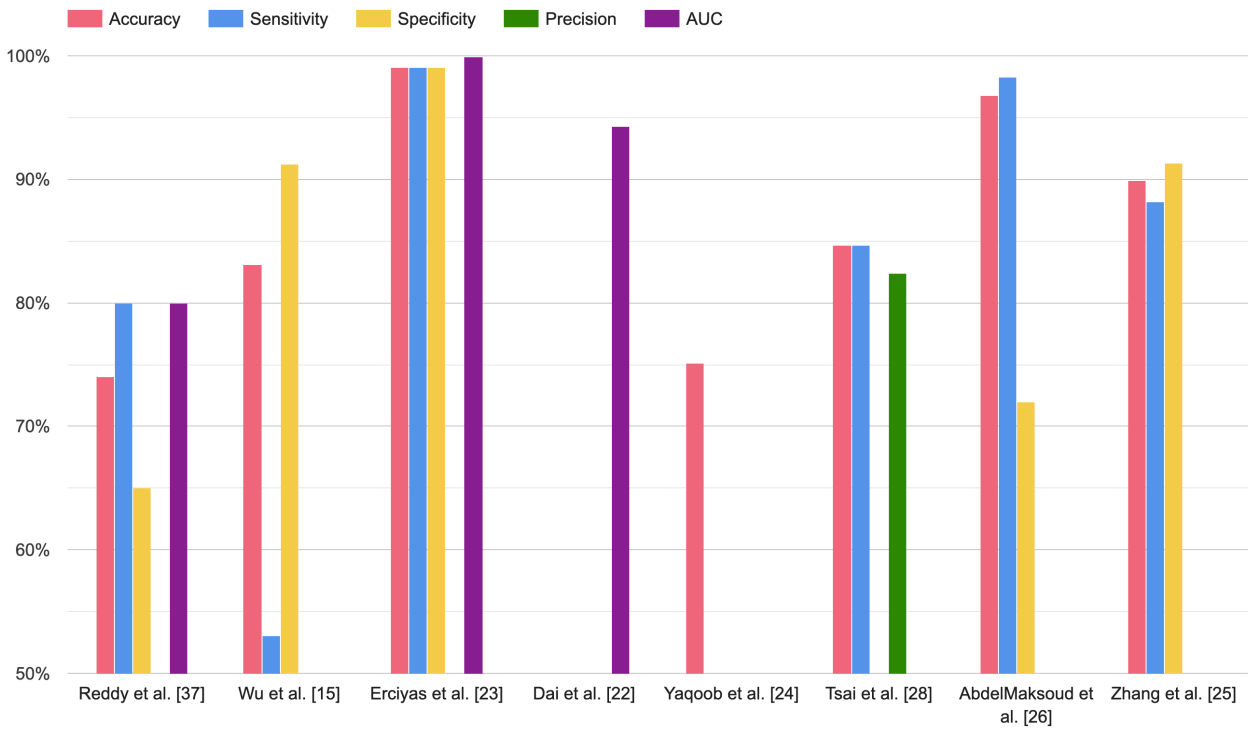


Fig. 4. Performance metrics of the studies using EyePACS dataset for International Clinical Diabetic Retinopathy grading.

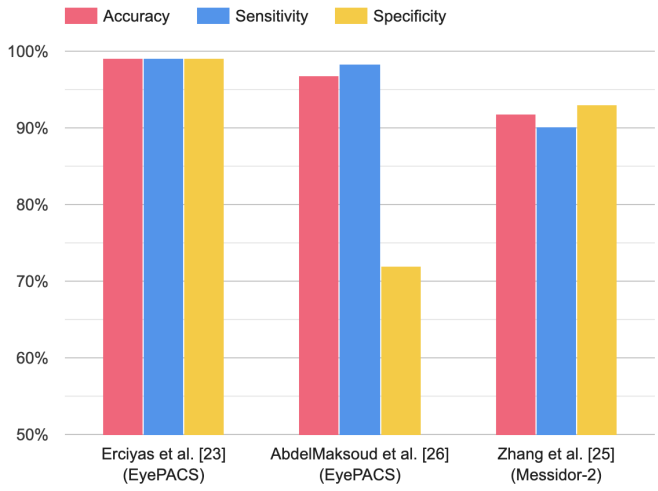


Fig. 5. Performance metrics of the top three studies performing International Clinical Diabetic Retinopathy grading.

B. Availability of custom datasets that are not openly accessible

The availability of custom datasets that are not publicly accessible presents another difficulty in the use of DL for the detection and classification of DR. Custom datasets that are not publicly accessible have been used in some research studies, which makes it challenging to compare the research results and replicate the study.

It is critical to encourage the use of openly accessible datasets in research to address this issue. This facilitates the comparison of results and the replication of studies, and helps to ensure that the research is transparent and reproducible. Furthermore, openly accessible datasets allow more researchers to contribute to the field and advance the current state of the art.

C. Variability in image capture conditions

Images in the datasets may be captured under different lighting conditions, magnifications, and other factors, which impacts the performance of DL models. It is important to consider the variability in image capture conditions when designing DL models for DR. This may involve the use of

Authorized licensed use limited to: DELHI TECHNICAL UNIV. Downloaded on April 17,2023 at 06:06:51 UTC from IEEE Xplore. Restrictions apply.

datasets with a wide range of imaging conditions and the development of models that are resilient to these variations.

This is an important area of future work, research on techniques to normalize or standardize the images, or apply image augmentations while preprocessing needs to be done such that the performance of the model increases.

D. Class imbalances in the dataset

Another challenge in the use of DL for the detection and classification of DR is the presence of class imbalances in the dataset. If the dataset has a skewed distribution of normal and abnormal images, it affects the performance of the DL model. This may occur if the dataset contains more examples of one class (*e.g.*, normal images) than the other (*e.g.*, abnormal images).

When training and evaluating the models, it is imperative to consider the balance of normal and abnormal images in the dataset. This may involve techniques to oversample or undersample the minority class or to weigh the loss function differently for each class. Additionally, research on techniques to address class imbalances in DL models would be useful in improving their performance in this task.

E. Lack of interpretability and explainability

DL models are often considered "black boxes" because it is difficult to understand how they make their predictions [42]. This lack of interpretability can be a barrier to their adoption in clinical settings, where it is important to understand the basis for the model's decisions and to be able to justify and communicate them to stakeholders.

There is a need for more research on methods to improve the interpretability and explainability of such models in general, as well as for DR specifically. This may involve the development of techniques to visualize and understand the internal workings of the model, as well as the use of more transparent and interpretable models that are easier to understand and explain. Improving the interpretability of the models for DR would facilitate their clinical adoption and enable more informed decision-making based on their predictions.

F. Lack of standardization in evaluation

The lack of standardization in the evaluation of these models is another impediment to the use of DL for the detection and classification of DR. Different studies may use different datasets, performance metrics, and evaluation protocols, making it difficult to compare results and determine which approaches are most effective.

Because of such lack of standardization, determining the relative strengths and weaknesses of different approaches and identifying areas for future research and improvement is difficult. Standardization in the evaluation of these models for DR is important to ensure that the results of different studies can be meaningfully compared.

G. Lack of standardization in preprocessing and augmentation

Preprocessing and augmentation impacts the performance and generalizability of the models. It is important to consider the impact of preprocessing and augmentation on the performance and generalizability of DL models for DR while comparing different models.

Future work may focus on the standardization of preprocessing and augmentation of the dataset. There is a huge potential for research on developing standardized pipelines for preprocessing and image augmentations, which would aid in ensuring that the results of different studies can be meaningfully compared and that the models are robust to variations in the dataset.

IV. Conclusion

Manual detection of diabetic retinopathy is time-consuming, labor-intensive, costly, and can overburden healthcare systems. The application of Deep Learning has undoubtedly displayed promising results in the clinical diagnosis and grading of diabetic retinopathy. It is highly successful in diabetic retinopathy detection and grading; and requires minimal human effort, apart from being time-efficient and cost-effective.

Notwithstanding this, there remain some challenges that must be overcome in order to improve its efficacy. These include the need for larger and more diverse datasets, the difficulty of comparing results across studies that use custom datasets, the impact of variations in image capture conditions, and the presence of class imbalances in the dataset, among others. These can be duly addressed by considering the dataset's size, diversity, and quality, developing techniques to normalize or standardize the images, or applying image augmentations while preprocessing. It is also essential to evolve techniques to address class imbalances in deep learning models. Ethical and legal compliances are also obligations that are fundamental to consider while carrying out such studies.

Therefore, with these research gaps resolved, deep learning would equip both the health care providers as well as the seekers across the globe to make better-informed decisions with regard to the treatment of diabetic retinopathy.

References

[1] "The top 10 causes of death." https://www.who.int/en/news-room/fact-sheets/detail/the-top-10-causes-of-death.

Authorized licensed use limited to: DELHI TECHNICAL UNIV. Downloaded on April 17,2023 at 06:06:51 UTC from IEEE Xplore. Restrictions apply.

[2] R. Pradeepa and V. Mohan, "Epidemiology of type 2 diabetes in india.," *Indian journal of ophthalmology*, vol. 69, pp. 2932–2938, 12 2021.

[3] S. Vujosevic, S. J. Aldington, P. Silva, C. Hernández, P. Scanlon, T. Peto, and R. Simó, "Screening for diabetic retinopathy: new perspectives and challenges," *The Lancet Diabetes & Endocrinology*, vol. 8, pp. 337–347, 12 2020.

[4] Z. L. Teo, Y.-C. Tham, M. Yu, M. L. Chee, T. H. Rim, N. Cheung, M. M. Bikbov, Y. X. Wang, Y. Tang, Y. Lu, I. Y. Wong, D. S. W. Ting, G. S. W. Tan, J. B. Jonas, C. Sabanayagam, T. Y. Wong, and C.-Y. Cheng, "Global prevalence of diabetic retinopathy and projection of burden through 2045," *Ophthalmology*, vol. 128, pp. 1580–1591, 11 2021.

[5] J. R. Willis, Q. V. Doan, M. Gleeson, Z. Haskova, P. Ramulu, L. Morse, and R. A. Cantrell, "Vision-related functional burden of diabetic retinopathy across severity levels in the united states.," *JAMA ophthalmology*, vol. 135, pp. 926–932, 9 2017.

[6] R. N. Frank, "Diabetic retinopathy," *Progress in Retinal and Eye Research*, vol. 14, pp. 361–392, 12 1995.

[7] "Diabetic retinopathy: Causes, symptoms, treatment." https://www.aao.org/eye-health/diseases/what-is-diabetic-retinopathy.

[8] C. P. Wilkinson, F. L. Ferris, R. E. Klein, P. P. Lee, C. D. Agardh, M. Davis, D. Dills, A. Kampik, R. Pararajasegaram, and J. T. Verdaguer, "Proposed international clinical diabetic retinopathy and diabetic macular edema disease severity scales," *Ophthalmology*, vol. 110, pp. 1677–1682, 12 2003.

[9] G. Selvachandran, S. G. Quek, R. Paramesran, W. Ding, and L. H. Son, "Developments in the detection of diabetic retinopathy: a state-of-the-art review of computer-aided diagnosis and machine learning methods," *Artificial Intelligence Review*, 12 2022.

[10] Y. Sun and D. Zhang, "Diagnosis and analysis of diabetic retinopathy based on electronic health records," *IEEE Access*, vol. 7, pp. 86115–86120, 2019.

[11] H.-Y. Tsao, P.-Y. Chan, and E. C.-Y. Su, "Predicting diabetic retinopathy and identifying interpretable biomedical features using machine learning algorithms," *BMC Bioinformatics*, vol. 19, p. 283, 8 2018.

[12] A. Homayouni, T. Liu, and T. Thieu, "Diabetic retinopathy prediction using progressive ablation feature selection: A comprehensive classifier evaluation," *Smart Health*, vol. 26, p. 100343, 12 2022.

[13] Y. LeCun, Y. Bengio, and G. Hinton, "Deep learning," *Nature*, vol. 521, pp. 436–444, 12 2015.

[14] L. Alzubaidi, J. Zhang, A. J. Humaidi, A. Al-Dujaili, Y. Duan, O. Al-Shamma, J. Santamaría, M. A. Fadhel, M. Al-Amidie, and L. Farhan, "Review of deep learning: concepts, cnn architectures, challenges, applications, future directions," *Journal of Big Data*, vol. 8, p. 53, 12 2021.

[15] Z. Zhao, K. Chopra, Z. Zeng, and X. Li, "Sea-net: Squeeze-and-excitation attention net for diabetic retinopathy grading," 10 2020.

[16] Z. Wu, G. Shi, Y. Chen, F. Shi, X. Chen, G. Coatrieux, J. Yang, L. Luo, and S. Li, "Coarse-to-fine classification for diabetic retinopathy grading using convolutional neural network," *Artificial Intelligence in Medicine*, vol. 108, p. 101936, 8 2020.

[17] W. L. Alyoubi, M. F. Abulkhair, and W. M. Shalash, "Diabetic retinopathy fundus image classification and lesions localization system using deep learning," *Sensors*, vol. 21, p. 3704, 12 2021.

[18] M. T. Hagos and S. Kant, "Transfer learning based detection of diabetic retinopathy from small dataset," 5 2019.

[19] M. Voets, K. Møllersen, and L. A. Bongo, "Reproduction study using public data of: Development and validation of a deep learning algorithm for detection of diabetic retinopathy in retinal fundus photographs," *PLOS ONE*, vol. 14, p. e0217541, 6 2019.

[20] K. Gunasekaran, R. Pitchai, G. K. Chaitanya, D. Selvaraj, S. A. Sheryl, H. S. Almoallim, S. A. Alharbi, S. S. Raghavan, and B. G. Tesemma, "A deep learning framework for earlier prediction of diabetic retinopathy from fundus photographs," *BioMed Research International*, vol. 2022, pp. 1–15, 12 2022.

[21] J. G. R. Elwin, J. Mandala, B. Maram, and R. R. Kumar, "Ar-hgso: Autoregressive-henry gas sailfish optimization enabled deep learning model for diabetic retinopathy detection and severity level classification," *Biomedical Signal Processing and Control*, vol. 77, p. 103712, 8 2022.

[22] B. Venkaiahppalaswamy, P. V. P. Reddy, and S. Batha, "Hybrid deep learning approaches for the detection of diabetic retinopathy using optimized wavelet based model," *Biomedical Signal Processing and Control*, vol. 79, p. 104146, 1 2023.

[23] L. Dai, L. Wu, H. Li, C. Cai, Q. Wu, H. Kong, R. Liu, X. Wang, X. Hou, Y. Liu, X. Long, Y. Wen, L. Lu, Y. Shen, Y. Chen, D. Shen, X. Yang, H. Zou, B. Sheng, and W. Jia, "A deep learning system for detecting diabetic retinopathy across the disease spectrum," *Nature Communications*, vol. 12, p. 3242, 5 2021.

[24] A. Erciyas and N. Barışçı, "An effective method for detecting and classifying diabetic retinopathy lesions based on deep learning," *Computational and Mathematical Methods in Medicine*, vol. 2021, pp. 1–13, 12 2021.

[25] M. K. Yaqoob, S. F. Ali, M. Bilal, M. S. Hanif, and U. M. Al-Saggaf, "Resnet based deep features and random forest classifier for diabetic retinopathy detection," *Sensors*, vol. 21, p. 3883, 6 2021.

[26] G. Zhang, B. Sun, Z. Chen, Y. Gao, Z. Zhang, K. Li, and W. Yang, "Diabetic retinopathy grading by deep graph correlation network on retinal images without manual annotations," *Frontiers in Medicine*, vol. 9, 12 2022.

[27] E. AbdelMaksoud, S. Barakat, and M. Elmogy, "A computer-aided diagnosis system for detecting various diabetic retinopathy grades based on a hybrid deep learning technique," 7 2022.

[28] S. S. Mondal, N. Mandal, K. K. Singh, A. Singh, and I. Izonin, "Edldr: An ensemble deep learning technique for detection and classification of diabetic retinopathy," *Diagnostics*, vol. 13, 1 2023.

[29] C.-Y. Tsai, C.-T. Chen, G.-A. Chen, C.-F. Yeh, C.-T. Kuo, Y.-C. Hsiao, H.-Y. Hu, I.-L. Tsai, C.-H. Wang, J.-R. Chen, S.-C. Huang, T.-C. Lu, and L.-C. Woung, "Necessity of local modification for deep learning algorithms to predict diabetic retinopathy," *International Journal of Environmental Research and Public Health*, vol. 19, p. 1204, 1 2022.

[30] "Kaggle eyepacs dataset." https://www.kaggle.com/c/diabetic-retinopathy-detection/data.

[31] T. Li, Y. Gao, K. Wang, S. Guo, H. Liu, and H. Kang, "Diagnostic assessment of deep learning algorithms for diabetic retinopathy screening," *Information Sciences*, vol. 501, pp. 511 – 522, 2019.

[32] "Kaggle aptos 2019 blindness detection." https://www.kaggle.com/c/aptos2019-blindness-detection.

[33] E. Decencière, X. Zhang, G. Cazuguel, B. Lay, B. Cochener, C. Trone, P. Gain, R. Ordonez, P. Massin, A. Erginay, B. Charton, and J.-C. Klein, "Feedback on a publicly distributed image database: The messidor database," *Image Analysis & Stereology*, vol. 33, p. 231, 8 2014.

[34] J. Krause, V. Gulshan, E. Rahimy, P. Karth, K. Widner, G. S. Corrado, L. Peng, and D. R. Webster, "Grader variability and the importance of reference standards for evaluating machine learning models for diabetic retinopathy," *Ophthalmology*, vol. 125, pp. 1264–1272, 8 2018.

[35] P. Porwal, S. Pachade, R. Kamble, M. Kokare, G. Deshmukh, V. Sahasrabuddhe, and F. Meriaudeau, "Indian diabetic retinopathy image dataset (idrid): A database for diabetic retinopathy screening research," *Data*, vol. 3, p. 25, 12 2018.

[36] Y. Zhou, B. Wang, L. Huang, S. Cui, and L. Shao, "A benchmark for studying diabetic retinopathy: Segmentation, grading, and transferability," 8 2020.

[37] R. Liu, X. Wang, Q. Wu, L. Dai, X. Fang, T. Yan, J. Son, S. Tang, J. Li, Z. Gao, A. Galdran, J. Poorneshwaran, H. Liu, J. Wang, Y. Chen, P. Porwal, G. S. Wei Tan, X. Yang, C. Dai, H. Song, M. Chen, H. Li, W. Jia, D. Shen, B. Sheng, and P. Zhang, "Deepdrid: Diabetic retinopathy—grading and image quality estimation challenge," *Patterns*, p. 100512, 2022.

Authorized licensed use limited to: DELHI TECHNICAL UNIV. Downloaded on April 17,2023 at 06:06:51 UTC from IEEE Xplore. Restrictions apply.

[38] N. B. Thota and D. U. Reddy, "Improving the accuracy of diabetic retinopathy severity classification with transfer learning," pp. 1003–1006, IEEE, 8 2020.

[39] A. Bora, S. Balasubramanian, B. Babenko, S. Virmani, S. Venugopalan, A. Mitani, G. de Oliveira Marinho, J. Cuadros, P. Ruamviboonsuk, G. S. Corrado, L. Peng, D. R. Webster, A. V. Varadarajan, N. Hammel, Y. Liu, and P. Bavishi, "Predicting the risk of developing diabetic retinopathy using deep learning," *The Lancet Digital Health*, vol. 3, pp. e10–e19, 12 2021.

[40] S. Das, K. Kharbanda, S. M, R. Raman, and E. D. D, "Deep learning architecture based on segmented fundus image features for classification of diabetic retinopathy," *Biomedical Signal Processing and Control*, vol. 68, p. 102600, 12 2021.

[41] Z. Yao, Y. Yuan, Z. Shi, W. Mao, G. Zhu, G. Zhang, and Z. Wang, "Funswin: A deep learning method to analysis diabetic retinopathy grade and macular edema risk based on fundus images," *Frontiers in Physiology*, vol. 13, 7 2022.

[42] M. W. Nadeem, H. G. Goh, M. Hussain, S.-Y. Liew, I. Andonovic, and M. A. Khan, "Deep learning for diabetic retinopathy analysis: A review, research challenges, and future directions," *Sensors*, vol. 22, p. 6780, 9 2022.

Authorized licensed use limited to: DELHI TECHNICAL UNIV. Downloaded on April 17,2023 at 06:06:51 UTC from IEEE Xplore. Restrictions apply.

Eur. Phys. J. Plus (2023) 138:321
https://doi.org/10.1140/epjp/s13360-023-03917-2

THE EUROPEAN PHYSICAL JOURNAL PLUS

Regular Article

Theoretical modeling and numerical simulation of enhanced graphene growth under the influence of oxidizers in RF-PECVD plasma using finite element method

Sagar Khanna, Suresh C. Sharma[a]

Plasma and Nano Simulation Research Laboratory, Department of Applied Physics, Delhi Technological University, Shahbad Daulatpur, Bawana Road, New Delhi 110042, India

Received: 17 November 2022 / Accepted: 20 March 2023
© The Author(s), under exclusive licence to Società Italiana di Fisica and Springer-Verlag GmbH Germany, part of Springer Nature 2023

Abstract This study aims to devise a computational model to understand and investigate the growth enhancement of graphene-nanosheet under various plasma environments. We methodically introduced an oxygenated environment to the conventional argon-acetylene plasma model. An oxygenated environment stimulates necessary etching phenomena to remove amorphous carbon over the catalyst during the growth process, which enhances the overall growth process. We used COMSOL simulation software to model a radio frequency-powered inductively coupled plasma enhanced chemical vapour deposition chamber operating at 30 mTorr pressure. The plasma parameters, such as electron and ion densities, along with growth parameters, such as accumulated graphene growth height and growth rates, were obtained and compared with that of the conventional argon-acetylene plasma model. The main findings of the paper are testing of the upper crest in (a) the horizontal graphene growth rates upto 1.7×10^{-5} m/s and (b) the accumulated growth height of horizontal graphene up to 58 nm (almost 1.5 times increase) over the catalyst surface, which has been shown via localized graphs. In addition, the spatial distribution of various plasma species formed in the region above the surface of the substrate and within the plasma chamber was obtained graphically and compared. The simulation results depict that by introducing minor changes in the growth environments, much better nanostructure yields can be obtained, even with the existing infrastructure. The variations in accumulated graphene growth and growth rates to change in plasma environments from the simulation hold a good constructive agreement with the existing experimental observations.

1 Introduction

In the past few decades, carbon nanostructures have increasingly gained attention in the field of science and technology due to their astounding properties and having numerous applications such as in ultrafast transistors [1], field emission devices [2], micro-electro-mechanical systems [3], etc., for the enhancement of prevailing device performance. On downscaling the materials from bulk to nanoscale, various changes in the physical properties like surface morphology, conductivity, etc. as well as the chemical properties such as reactivity, adsorption, etc. occur [4]. The nanostructures formed with carbon as base material includes graphene, carbon nanotubes, nanofibers, buckyballs, quantum dots, etc. There are numerous properties of the wonder material graphene that makes it lucrative for application in fields like gas separation, catalysis and energy storage [5–9].

For the synthesis of graphene, there are two prominent and widely used methods i.e. Chemical Vapor Deposition (CVD) and Plasma Enhanced Chemical Vapor Deposition (PECVD) [10]. Among these two, PECVD synthesis can take place at near room temperature [11] which is much lower than that needed in CVD [12]. PECVD offers a lot of advantages in general, such as higher growth selectivity and ease of realizing large growth areas of films [11]. The technique used in the present work is inductively coupled plasma-enhanced CVD, where the gas present inside the chamber is ionized to form plasma using power that is induced from coils to chamber through dielectric [13–15]. The plasma environment so formed helps in the growth process of nanostructures over the catalyst surface by providing amorphous carbon, which dissociates over the catalyst and thus the formation begins [16]. However, it is noticed that the amorphous carbon slowly inhibits further growth and thus is required to be etched out effectively. The etching gas helps in providing an active catalyst site to retain the growth process of carbon nanostructure [17, 18]. This improves the nanostructure yield without needing much change in existing industrial infrastructure. Hydrogen and nitrogen are considered to be prominent etching gases. But it has been observed in chemical vapor deposition (catalytic methods) that a small amount of water and/or oxygen can perform etching action and thus can aid in the growth rates to a large extent. Water vapors help in increasing the lifetime of active catalyst sites [19, 20]. There are a few experimental studies that show the enhancement in the length of CNT, under the presence of oxidizers in PECVD [21–26]. In addition to this, it has been observed that under a slight change in the plasma

[a] e-mail: suresh321sharma@gmail.com (corresponding author)

Published online: 07 April 2023

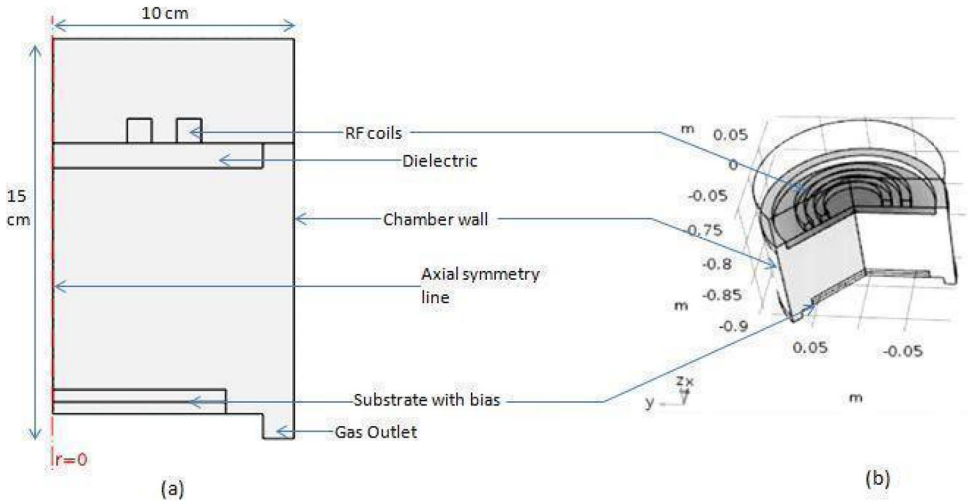


Fig. 1 Schematic of the geometry of PECVD reactor to carry out various reactions, **a** 2D axis-symmetric geometry, **b** the 3D geometry

environment, the growth rate increases [25]. In the presence of an oxygen environment, energy barriers are slightly reduced as compared to without-oxygen [27], which further increases the attachment of atomic carbon on graphene edges [28]. The presence of hydrogen radicals in high concentration (up to 10% of gas composition) attracts the carbon atoms and consequently, a lesser number of carbon atoms are available to precipitate over the catalyst surface to form graphene sheet. If oxygen is present, it garners the hydrogen radicals as well as removes amorphous carbon (formed over catalyst), leaving more carbon species to support the nanostructure growth mechanism in PECVD [25].

Based on the above literature, we are trying to establish a fluid model that describes both the physical as well as the chemical aspects of oxygenated plasma based graphene sheet. This can lead to the better understanding of the distribution and variation of the plasma parameters with respect to change in plasma environment and the improvement in the growth parameters of the graphene nanosheet. This knowledge about the chemical composition of oxidative plasmas and the quantitative growth results of graphene can be very helpful for carrying out experimental research in future such as in plasma based nanofabrication processes.

The paper is divided into various sections. After Introduction in Sects. 1 and 2 elaborates the model in which the geometry, physics and the chemical reactions used in the simulation process are described. Section 3 comprises the results section in which various graphs and diagrams of the obtained outcomes have been documented. Section 4 finally gives the conclusive remarks.

2 Methods

This section shows a simulation model in which the graphene nanosheet has been grown in three different types of plasma environments using COMSOL simulation software. The text refers to $Ar/C_2H_2/H_2$ as conventional argon plasma. $Ar/C_2H_2/H_2$ with water and $Ar/C_2H_2/H_2$ with oxygen are the two plasma environments used and compared with the conventional argon plasma model. Figure 1 shows the geometry used by us to carry out the simulation process. For a more straightforward analysis, we have used a 2D axis-symmetric geometry. We have used a substrate coated with a thin nickel catalyst layer of about 200 nm, over which graphene grows. The bias voltage has been set at $-$ 50 V using a copper coil kept beneath the substrate. For the ions and neutrals, it has been assumed that they follow the Maxwellian distribution. Furthermore, we followed the literature from Refs. [29] and [30] to understand plasma dynamics.

In order to establish the desired conditions using the software, we defined a few modules along with the geometry. The plasma interface consists of the electron impact reactions inside the chamber caused by the ionization of Argon using inductively coupled radio frequency (RF) coils due to the transformer action (explained in Sect. 2.1). The heavy species transport module defines the hydrocarbon-based reactions in the plasma to generate ionic species inside the chamber volume. We kept the initial density of gases at 10^{13} m^{-3}, pressure at 30 mTorr, and temperature at 350 K, respectively. The radius of the cylindrical chamber is 10 cm, and the height is 15 cm. Length of the substrate that acts as a platform is kept equal to 7 cm. Two current-carrying coils represented by small squares in an axis-symmetric diagram provide RF power at 13.56 MHz. The RF coils' conductivity and substrate bias were 6×10^7 S m^{-3} and 4×10^3 S m^{-3}, respectively. The permeability of dielectric was 4.2 μ_0 (where μ_0 is the permeability of free space), relative permittivity as unity and conductivity as zero [15–17]. The substrate bias draws the positive ions toward the substrate inside the plasma sheath region. The choice of the neutral and positive ionic species depends upon the reaction types inside the bulk plasma and over the surface region, which are discussed in detail in Sect. 2.2. We have not accounted for anions in our study as the hydrocarbon-based plasma does not have electronegative features, like in the case of CH_4 and H_2 plasma [31, 32]. Also, we assumed that the substrate temperature equals the catalyst temperature.

2.1 Physics involved

The electron transport is the most vital process in the ion formation for the various species in the chamber, which is governed by the equation $\mu_e = \mu_{red}/N_n$ with number density N_n and reduced electron mobility μ_{red}. Source coefficients are defined using Maxwellian electron energy distribution function (Maxwellian-EEDF) $f(\varepsilon) = \phi^{-3/2}\beta_1 \exp(-(\varepsilon\beta_2/\phi))$. Here, $\beta_1 = \Gamma(5/2)^{3/2}\Gamma(3/2)^{-5/2}$, $\beta_2 = \Gamma(5/2)\,\Gamma(3/2)^{-1}$, ε is the electron energy (in eV), ϕ is mean electron energy (in eV) and the incomplete gamma function is denoted by Γ.

$$\frac{\partial n_e}{\partial t} + \nabla.\Gamma_e = R_e, \tag{1}$$

$$\frac{\partial n_\varepsilon}{\partial t} + \nabla.\Gamma_\varepsilon + E.\Gamma_e = R_\varepsilon, \tag{2}$$

$$\Gamma_e = -n_e\mu_e E - D_e\nabla n_e, \tag{3}$$

$$\Gamma_\varepsilon = -n_\varepsilon\mu_\varepsilon E - D_\varepsilon\nabla n_\varepsilon, \tag{4}$$

$$R_e = \sum_{j=1}^{M} x_j k_j N_n n_e, \tag{5}$$

$$R_\varepsilon = \sum_{j=1}^{P} x_j k_j N_n n_e \Delta\varepsilon_j, \tag{6}$$

$$k_j = \gamma \int_0^\infty \varepsilon\sigma_j(\varepsilon) f(\varepsilon) d\varepsilon, \tag{7}$$

$$\gamma = (2q/m)^{1/2}, \tag{8}$$

$$\rho = q\left(\sum_{k=1}^{M} Z_k n_k - n_e\right), \tag{9}$$

$$K_{f,i} = \left(\frac{\gamma_i}{1-\gamma_i/2}\right)\left(\frac{1}{(\Gamma_{tot})^m}\right)\left(\frac{1}{4}\right)\sqrt{\frac{8RT_e}{\pi M_n}}, \tag{10}$$

COMSOL solves a drift–diffusion equation pair in order to compute electron density using Eqs. 1, 3, 5 and electron energy density using Eqs. 2, 4, 6. Electrons diffuse by Fick's law of diffusion. Flux corresponding to this diffusion is Γ_e. D_e is the diffusion constant. For any reaction j, rate coefficient is given by k_j, energy loss by $\Delta\varepsilon_j$, collision cross section σ_j and mole fraction x_j. Plasma potential $-\nabla.\varepsilon_o\varepsilon_r\nabla V = \rho$, where ρ is space charge density. Its computation is defined from the number densities of charged species and electrons, as given in Eq. 9. Equation 10 shown above is used to determine surface rate constant of sticking coefficient. Sticking coefficient in the last equation above (Eq. 10) denoted by γ_i is equivalent to the term:-$\gamma_i = a_1 T_e{}^{b1} \exp(e_i/RT_e)$, where R is gas constant, M_n is mean molecular weight, T_e is electron temperature and constants are a_1 and b_1. The interface on which the diffusion of carbon species (generated through various reactions) occur is the substrate interface. The velocity of this substrate interface is represented by variable vy and the expression $v_y = \frac{\overrightarrow{j}_m.\widehat{n}_y}{\rho_{carbon}}$. Here, the mass flux in the y-direction is represented by $\overrightarrow{j}\, m \cdot \widehat{n}y$ and the carbon density by $\rho_{carbon}(= 2.267\ \mathrm{g/cm^3})$. Therefore, the equation $d = vy * t$ calculates the thickness (d) of the segregated carbon material (planar graphene films) in time 't'.

When the driving coil (the primary) receives current, the plasma also experiences current (the secondary). The coil's resistance then rises as a result of the plasma's induction of an opposing current. The current supplied to the coil, and the reaction kinetics determine the current flowing in the plasma. The overall plasma current can range from zero (no sustained plasma) to the same current as the primary, corresponding to a perfect coupling between the coil and the plasma. Due to this action, the gas mixture inside the chamber gets ionized because the creation of high-power radio frequency waves with the aid of coils to start the ionization of gases to produce the plasma by inductive effect depends heavily on the magnetic field that is induced through the dielectric. Further, this ionization leads to electron impact reactions because of the generation of electrons [33, 34].

2.2 Species and the chemical reactions involved

This subsection specifies the various chemical species and reactions inside the plasma chamber. Table 1 below lists the species involved in the various chemical reactions in the non-equilibrium plasma bulk and on the substrate surface inside the PECVD chamber. By plasma particles, we mean electrons, ions and neutrals present inside the chamber volume [35, 36]. The ionization of nascent gas Argon forms the plasma. So the impact reactions for Argon are listed in Table 2. These reactions are common in all three cases. Table 3 lists the reactions taking place in the plasma bulk region and on the surface. While modeling, we were more concerned about the ionic and neutral species that dominate in generating the required carbon nanostructure in the plasma. Denysenko et al. [35] presented various types of species and processes responsible for the growth of self-assembled vertically

Table 1 Species involved

Plasma case	Ions involved	Neutral species involved
Argon/acetylene/hydrogen	$C_2H_2^+$, $C_2H_3^+$, C_2H^+, CH^+, H_2^+, H^+	Acetylene, hydrogen
Argon/acetylene/hydrogen/water	$C_2H_2^+$, $C_2H_3^+$, OH^+, O^+, C_2H^+, CH^+, H_2^+, H^+, H_2O^+,	Acetylene, hydrogen, water
Argon/acetylene/hydrogen/oxygen	$C_2H_2^+$, $C_2H_3^+$, C_2H^+, CH^+, H_2^+, HCO^+, H^+, OH^+, O^+, O_2^+	Acetylene, hydrogen, oxygen

Table 2 Reactions involved

Electron impact reactions

S. no	Reaction	Type	Threshold [eV]	References
1	e + Ar => e + Ar	Elastic	0	[46, 47]
2	e + Ar => e + Ars	Excitation	11.5	[46, 47]
3	e + Ars => e + Ar	Super elastic	− 11.5	[46, 47]
4	e + Ar => 2e + Ar^+	Ionization	15.8	[46, 47]
5	e + Ars => 2e + Ar^+	Ionization	4.24	[46, 47]
6	Ars + Ars => e + Ar + Ar^+	Penning ionization	–	[46, 47]
7	Ars + Ar => Ar + Ar	Metastable quenching	–	[46, 47]

Plasma chamber Wall Surface reaction

S. no	Reaction	Sticking coefficient	Ref
8	Ars => Ar	1	47
9	Ars^+ => Ar	1	47

aligned carbon nanostructures (CNs) in the PECVD system. Deschenaux et al. [36] showed the presence of abundant species via FTIR in various plasmas. Contributions of various ions and radicals in CNT growth were shown by Marvi et al. [37]. Benndorf et al. [38] demonstrated the dominant species with the help of optical emission spectra. Contributions from Denysenko et al. [39–41], Marvi et al. [37], Mehdipour et al. [29], and Mantzaris et al. [42] were helpful for processes taking place on the surface. As per the ternary phase diagram published by Benndorf et al. [38], the plasma chemistry for a defined C/H/O ratio leads to identical radicals and gas phase species independent of different gaseous sources. Based on the above literature, we categorize our model into two significant parts: the gas discharge model and the surface deposition model. The latter consists of different surface-level reactions and processes. So it is required to have their threshold energies, which may be obtained from calculations at an atomic level and/or obtained calculations from experimental data [42–44]. The characteristics of ion and neutral species, obtained from the gas discharge model, act as input parameters for the surface deposition model in the form of sticking coefficients, as presented in the literature [38, 45].

3 Results and discussion

This section describes the outcomes of numerous simulations carried out using COMSOL software. Figure 2 below shows the spatial distribution of the electron density (m^{-3}) inside the PECVD chamber along with a comparative graph with respect to the changing plasma environments. We considered the sheath kinetics from the Ref. [29, 30] to investigate the dynamics of electrons and ionic species. We observed a decreasing trend in electron densities as we moved towards a more oxidizing plasma environment. This is because of the increase of oxygen content in the plasma environment. Compared to $Ar/C_2H_2/H_2$ plasma, the case of $Ar/C_2H_2/H_2/H_2O$ plasma has more oxygen content due to the presence of water, and it is the maximum in the oxygen plasma case, among all the plasma environments investigated in the paper. With the increase in oxygen content, more electrons will be adsorbed by the oxygen atoms (formed after ionization) to form negative ions. This decreases the available electron density in the plasma and hence, we observe a decreasing trend (cf. Fig. 2b). Electron density was found to decrease in the experimental observation of Wang et al. [49], where they used Langmuir single probe method in RF inductively coupled discharge.

Apart from studying electron density, we tried to investigate few more plasma parameters such as collisional power losses, electron energy densities and ion number densities of a few carbon based positive ions. Figure 3 shows the collisional power loss inside the PECVD chamber for various plasma environments. It is basically the power loss taking place due to the collisions among the electrons and gas constituents present inside the chamber volume [50]. The collisional loss is maximum in the $Ar/C_2H_2/H_2$ plasma whereas it is minimum for with-oxygen plasma. This is due to the fact that the electron and ion densities are minimum for the oxygen plasma case due to which lesser collisions take place as compared to $Ar/C_2H_2/H_2$ plasma case, resulting in lower

Table 3 Plasma chamber reactions involving carbon species

S. No	Reaction	Rate coefficient (m^3/s.mol)	References
10	$Ar^+ + C_2H_2 => C_2H_2^+ + Ar$	25.29×10^8	[48]
11	$Ar^+ + H_2 => Ar + H_2^+$	0.448×10^8	[48]
12	$C_2H_2^+ + H_2 => C_2H_3^+ + H$	0.1656×10^6	[48]
13	$H_2^+ + H => H^+ + H_2$	1.062×10^7	[48]
14	$C_2H_2 + H^+ => C_2H^+ + H_2$	0.713×10^8	[48]
15	$C_2H_3^+ + H => C_2H_2^+ + H_2$	1.126×10^6	[48]
16	$C_2H^+ + H_2 => C_2H_2^+ + H$	0.182×10^8	[48]
17	$C_2H_2^+ + H^+ => C_2H_2^+ + H_2$	0.713×10^8	[48]
S. no	Reactions with etchant	Rate coefficient (m^3/s.mol)	References
18	$Ar^+ + H_2O => H_2O^+ + Ar$	3.3×10^8	[48]
19	$H^+ + H_2O => H_2O^+ + H$	2.9×10^6	[48]
20	$H_2^+ + H_2O => H_2O^+ + H_2$	0.513×10^7	[48]
21	$OH^+ + OH => H_2O^+ + O$	2.86×10^7	[48]
22	$Ar^+ + O_2 => O^+ + O + Ar$	1.81×10^7	[48]
23	$C_2H_2 + O_2^+ => HCO^+ + H + CO$	1.75×10^7	[48]
24	$H_2^+ + O => OH^+ + H$	1.3×10^7	[48]
25	$H_2 + O^+ => OH^+ + H$	0.117×10^8	[48]
26	$O^+ + O_2 => O_2^+ + O$	1.05×10^9	[48]

Surface reactions

S. no	Reaction	Type	Sticking coefficient	References
27	$C_2H^+ => 2C(b) + H_2$	Dissociation of hydrocarbon	1	[29, 37, 39–41]
28	$C_2H^+ => C_2H$	Stabilization of ions	0.8	[29, 37, 39–41]
29	$C_2H_2 => C_2H_2(ads)$	Hydrocarbon adsorption on the nickel coated silicon substrate	0.5	[29, 37, 39–41]
30	$C_2H => C_2H(ads)$		0.8	[29, 37, 39–41]
31	$H => H(ads)$	Hydrogen specie adsorption on the nickel coated silicon substrate	0.01	[29, 37, 39–41]
32	$H_2 => H_2(ads)$		0.02	[29, 37, 39–41]
33	$C_2H^+ + C_2H(ads) => 2C(b) + H(b) + C_2H^+$	Ion-induced dissociation of hydrocarbons and hydrogen generation	0.9	[29, 37, 39–41]
34	$C_2H(ads) + C_2H_2^+ => H(b) + C_2H_2^+ + 2C(b)$		0.9	[29, 37, 39–41]
35	$C_2H_2(ads) + C_2H_2^+ => H_2 + C_2H_2^+ + 2C(b)$		0.9	[29, 37, 39–41]
36	$C_2H_2(ads) => 2C(b) + 2H$	Hydrocarbon thermal decomposition	1	[29, 37, 39–41]
37	$C_2H(ads) => 2C(b) + H$		1	[29, 37, 39–41]
38	$C_2H_2^+ + C_2H_2(ads) = > C_2H_2^+ + H + 2C(b)$	Ion-induced hydrocarbon dissociation	0.9	[29, 37, 39–41]
39	$C_2H^+ + C_2H_2(ads) => H + 2C(b) + C_2H^+$		0.9	[29, 37, 39–41]
40	$H + C_2H_2(ads) => C_2H_3$	Interaction of hydrocarbons with atomic hydrogen	0.3	[29, 37, 39–41]
41	$C_2H(ads) + H => C_2H_2$		0.5	[29, 37, 39–41]
42	$C_2H(ads) => C_2H$		0.8	[29, 37, 39–41]

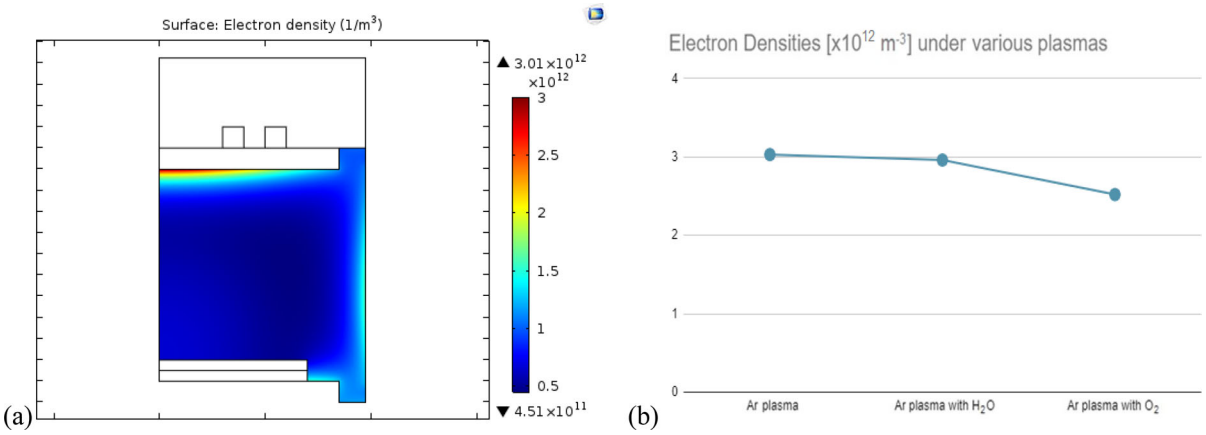


Fig. 2 **a** 2D axis-symmetric spatial distribution of the electron density inside the plasma chamber with peak value of 3.01×10^{12} m^{-3} for $Ar/C_2H_2/H_2$ plasma. **b** Line chart showing the comparison of the electron densities for the three plasma environments, where the first one is the $Ar/C_2H_2/H_2$ plasma, second being $Ar/C_2H_2/H_2/H_2O$ plasma and third one is for $Ar/C_2H_2/H_2/O_2$ plasma

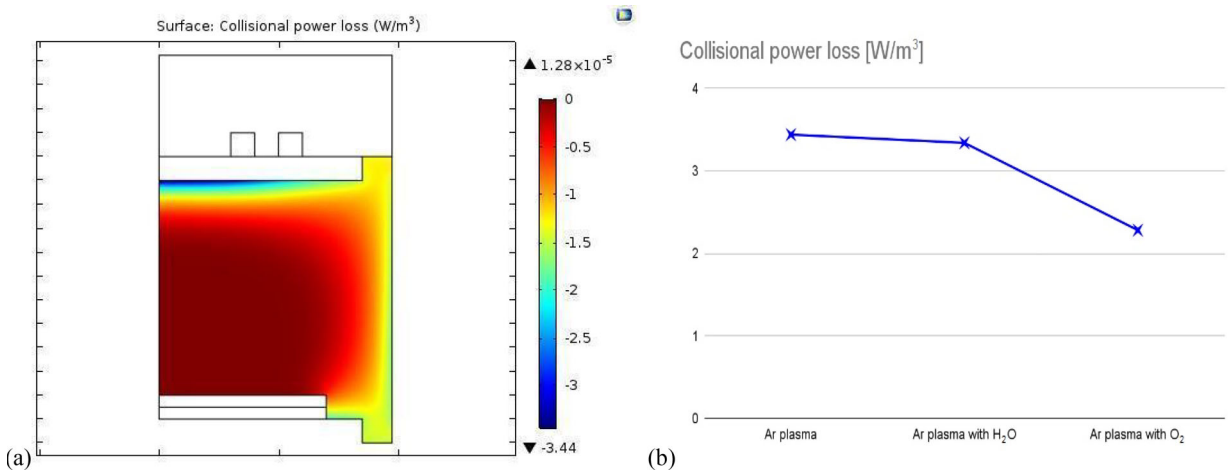


Fig. 3 **a** 2D axis-symmetric spatial distribution of the collisional power loss inside the plasma chamber with maximum loss value as 3.44 W/m^3 for $Ar/C_2H_2/H_2$ plasma. **b** Line chart showing the comparison of the collisional power loss for the three plasma environments, where the first one is the $Ar/C_2H_2/H_2$ plasma, second being $Ar/C_2H_2/H_2/H_2O$ plasma and third one is for $Ar/C_2H_2/H_2/O_2$ plasma

power loss in collisions. Figure 4 shows the electron energy density inside the plasma chamber. Peak values were found to be 1.86×10^{13} kg/(m s^3 A) for $Ar/C_2H_2/H_2$ plasma, 1.83×10^{13} kg/(m s^3 A) for $Ar/C_2H_2/H_2/H_2O$ plasma and 1.47×10^{13} kg/(m s^3 A) for $Ar/C_2H_2/H_2/O_2$ plasma, respectively. As there has been a decline in the peak electron density (cf. Fig. 2), the kinetic energy of the electrons in the system also tends to decrease and thus the electron energy density values show a downfall as we change the plasma environment to oxygen plasma case (cf. Fig. 4).

Figure 5 shows the ion density over the surface region of some of the ions inside the plasma chamber modeled using the software. The average ion density of C_2H^+ is approximately 15.1×10^{19} m^{-3} for $Ar/C_2H_2/H_2$ plasma, 10.2×10^{19} m^{-3} for water plasma and 8.08×10^{19} m^{-3} for oxygen plasma case. They have been shown in Fig. 5a. The two turn coils are placed at about 0.1 m distance above the substrate surface. Similarly, the average ion density of $C_2H_2^+$ (m^{-3}) over the substrate surface was found to be approximately 16.9×10^{20} in $Ar/C_2H_2/H_2$ plasma, 10.7×10^{20} in water plasma and 8.43×10^{20} in oxygen plasma, respectively, as shown in Fig. 5b. As per the graphs in Fig. 5, both C_2H^+ and $C_2H_2^+$ ion density values shows a decreasing trend w.r.t. changing plasma environment from $Ar/C_2H_2/H_2$ to water plasma and finally oxygen plasma. This is because of the decreasing trend in the values of the fundamental plasma parameter viz., electron density. As there are lesser number of electrons to interact with the available neutral species, lesser neutral species get ionized to their respective ions and hence, a reduction in the ion density of the ionic species is observed.

Figure 6 shows the growth rate of the graphene sheet. We found the average growth rate over the surface for graphene to be approximately equal to 4.4×10^{-6} m/s in $Ar/C_2H_2/H_2$ plasma, whereas 1.2×10^{-5} m/s in plasma with water and 1.7×10^{-5} m/s in oxygen plasma, respectively. Also, a spike in the form of vertically oriented graphene (towards the substrate edge) is observed. This is so because the plasma sheath exerts alignment force and this force combined with the internal stress results in vertical bending

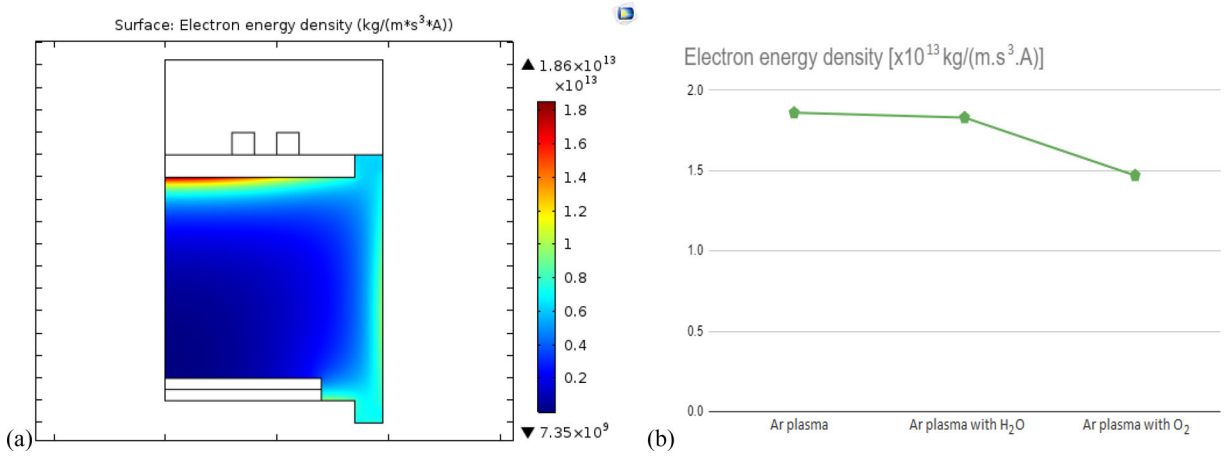


Fig. 4 **a** 2D axis-symmetric spatial distribution of the electron energy density inside the plasma chamber with peak value of 1.86×10^{13} kg/(m s^3 A) for $Ar/C_2H_2/H_2$ plasma. **b** Line chart showing the comparison of the electron energy density for the three plasma environments, where the first one is the $Ar/C_2H_2/H_2$ plasma, second being $Ar/C_2H_2/H_2/H_2O$ plasma and third one is for $Ar/C_2H_2/H_2/O_2$ plasma

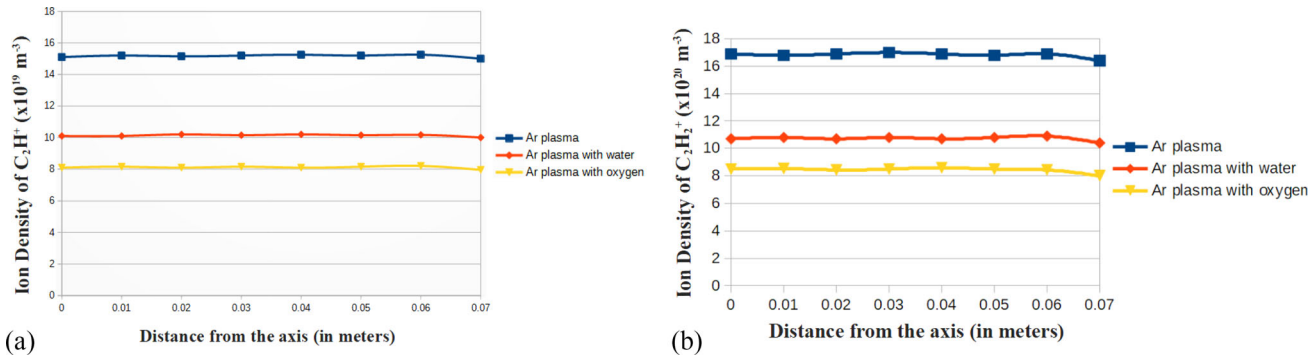


Fig. 5 **a** Ion density of C_2H^+ inside the plasma chamber for **i** $Ar/C_2H_2/H_2$ plasma with average density over the surface of about 15.1×10^{19} m^{-3}, **ii** $Ar/C_2H_2/H_2/H_2O$ plasma with 10.2×10^{19} m^{-3} and **iii** $Ar/C_2H_2/H_2/O_2$ plasma with 8.08×10^{19} m^{-3}. **b** Ion density of $C_2H_2^+$ inside the plasma chamber for **i** $Ar/C_2H_2/H_2$ plasma with average density over the surface of about 16.9×10^{20} m^{-3}, **ii** $Ar/C_2H_2/H_2/H_2O$ plasma with 10.7×10^{20} m^{-3} and **iii** $Ar/C_2H_2/H_2/O_2$ plasma with 8.43×10^{20} m^{-3}

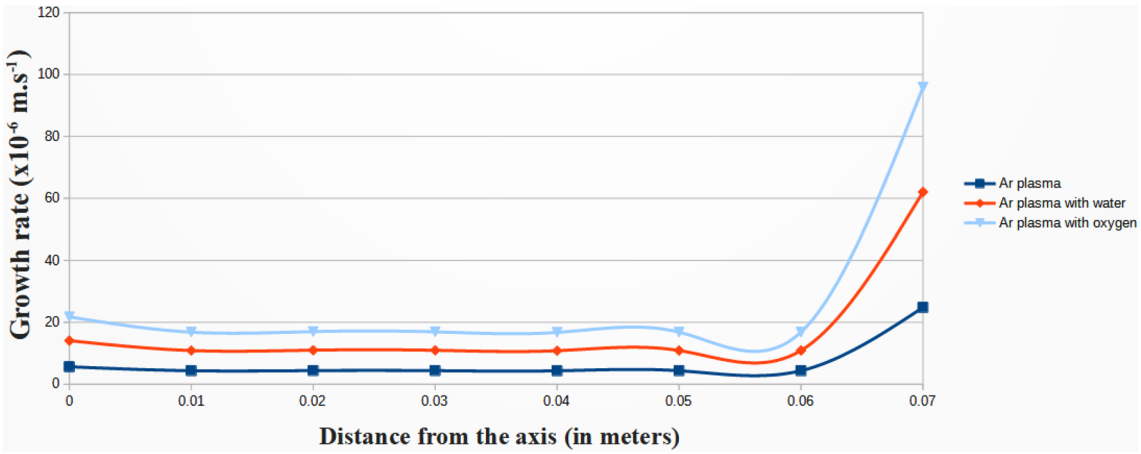


Fig. 6 Growth rate of graphene inside the chamber over the substrate surface for three different plasmas viz. **i** $Ar/C_2H_2/H_2$ plasma with average growth rate of approximately 4.4×10^{-6} m/s, **ii** $Ar/C_2H_2/H_2/H_2O$ plasma with 12×10^{-6} m/s, and **iii** $Ar/C_2H_2/H_2/O_2$ plasma with 17×10^{-6} m/s. Growth rates for the aforementioned cases at the edges are 25×10^{-6} ms^{-1}, 62×10^{-6} ms^{-1} and 97×10^{-6} ms^{-1} respectively

[51]. So by comparing these values, we observed that the growth rate in oxygen plasma is the maximum, followed by with-water and conventional argon plasma, respectively.

Hydrocarbons in the plasma reach the catalyst and dissociate on its surface. For the continuous growth of carbon-based nanostructure, it is crucial to etch out amorphous carbon from the catalyst surface, which is done by atomic hydrogen. However, due to the continuous formation of carbon nanostructure, hydrogen blocks the etching process, which further inhibits the hydrocarbon dissociation from plasma over the catalyst surface. This slowly leads to saturation in the growth process, and we obtain graphene of a certain thickness. Nevertheless, consider the case of plasma with water. Here, the water molecules help conserve the catalyst activity during the growth process. The carbon atoms that could have blocked the catalyst layer for further dissociation are etched away by water molecules [52]. Therefore, the growth rate observed is more in this plasma case than in the previous one. Considering the dynamics of electron and ionic species, the electron density plots in Fig. 2 and ionic densities in Fig. 5 show a decreasing trend on changing plasma environments towards a more oxidizing one. Lesser densities of electron and ionic species correspond to lower ionization. This results in development of relatively lower surface potential of the graphene surface. Due to this effect, more ions now stick onto the surface, which increase the graphene growth [53, 54]. Regions of activity of reactive species however remain the same, therefore the nature of plots signifying morphology of growth remains similar in all the three plasma environments. Wei et al. [55] observed experimentally that the kinetic barrier is reduced by adding water, which significantly increases the graphene growth rate, as seen in Fig. 6. Yoshihara et al. [56] and Hussain et al. [57] have also observed that the growth rate increased in plasma environments containing H_2O compared to $Ar/C_2H_2/H_2$ plasma. It was recently observed by Hata et al. and Yamada et al. [21, 58] that the addition of small amounts of water drastically improved the catalytic activity in a CVD system with ethylene as a source gas, which resulted in improved SWNT growth. Water constrains the catalyst's ripening because it helps produce large amounts of OH groups on carbon. It keeps the catalyst active so that continuous growth can take place, and thus the amorphous carbon is kept at bay from the catalyst surface [21, 59].

The growth rate is found to be maximum in the last case, viz. $Ar/C_2H_2/H_2/O_2$ plasma because the oxygen molecules perform two functions. Firstly, they form CO with the carbon molecules present on the catalyst surface via various reactions [25, 38], thus preventing catalyst poisoning. Secondly, they remove the hydrogen radicals that are very reactive by forming OH + O when combined with hydrogen radicals, leaving even more carbon species to get dissociated on the catalyst [25, 38]. Zhang et al. [25] experimentally showed that the growth rate of the carbon nanostructure increased upon adding oxygen to $Ar/C_2H_2/H_2$ plasma. Xu et al. [28] experimentally showed that strategically placing the metal foil above the oxide substrate aids in a continuous supply of oxygen, which helps in a tremendous increase in the growth rate of graphene under the influence of oxygen. They also reported that oxygen helps reduce relative energy barriers because it promotes the attachment of atomic carbon on graphene edges. It was shown experimentally (dr/dt at a particular temperature T, cf. Fig. 3g, Hao et al. [27]) that the growth rate was more for the with-oxygen case in comparison to without oxygen case due to reduction in relative energy barriers. DFT calculations have also reported that hydrocarbon adsorption is improved in the oxygen environment [60]. The meek oxidative effects of H_2O help in the etching process of amorphous carbon [55]. Therefore, the growth rate and the accumulated growth are found to increase in both the water and the oxygen plasmas. The nucleation is decreased by introducing water as it passivates the active sites of the surface of the substrate [61].

The accumulated growth of horizontal graphene was the maximum for the case of oxygen plasma compared to the other two, as shown in Fig. 7. Respective heights were 38.6 nm in conventional argon plasma, 43 nm in plasma with water, and 58 nm in oxygen plasma (the maximum among the three). The plots shown in Figs. 6 and 7 are 1D representations of the growth rates and accumulated growth height of the graphene nanosheet film over the entire substrate surface. These are not straight lines, signifying surface imperfections due to defects and impurities over the surface, as shown experimentally by Nie et al. and Han et al. [62, 63]. As the amorphous carbon formation on the catalyst increases, the oxygen in the plasma decreases.

In Fig. 8, we have shown the variation of growth rate w.r.t. increasing values of initial concentration of (a) H_2O in H_2O plasma and (b) of O_2 in oxygen plasma. All the reactions from Tables 2 and 3 except the reactions numbered 22–26 were considered for defining $Ar/C_2H_2/H_2/H_2O$ plasma with the help of contributions from Ref. [38, 39, 42, 48]. Initial concentrations of the water based reactant species in reactions 18–21 were altered and growth rates were obtained. These findings were plotted graphically in Fig. 8a. The growth rate was found to first increase up to a certain level and then decrease, resulting in formation of a peak, signifying optimal efficiency conditions. This clear signal shows that a significant factor for the enhanced growth so observed is the water acetylene ratio and thus, a balance between the relationships of these two entities needs to be maintained [64]. This relation further shows that the amount of acetylene and water molecules consumed by the catalysts before they degrade is determined by the water/acetylene ratio. Water maintains the catalyst activity only till a certain percentage, beyond which the hydrogen species get to increase near the catalyst. A similar peak was observed experimentally by Futaba et al. [64]. The carbon diffusion process is interrupted by those hydrogen species, so the growth retards. A similar simulatory phenomenon was observed with oxygen plasma as well when we altered the oxygen based reactants in Eqs. 22–26, just in a similar fashion as done for water plasma. As a result, a similar type of plot was obtained (cf. Fig. 8b). It starts oxidizing surface carbon species and sinks the carbon. We look forward to refining the growth model and emphasizing that any future model may add up to explain this observation. Wang et al. [65] showed that with an increase in growth time, the rate of growth started to decrease.

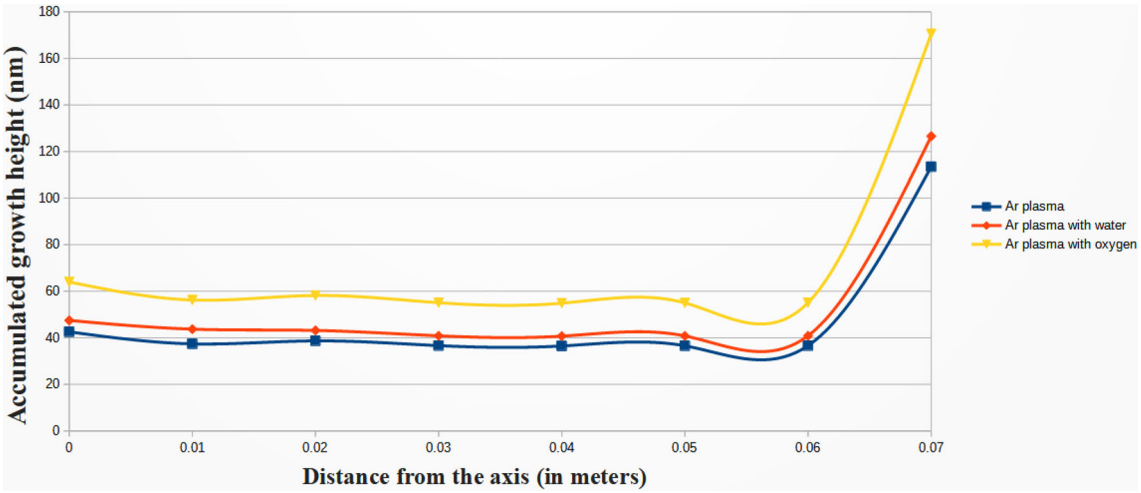


Fig. 7 Growth height of graphene inside the chamber over the entire substrate surface for three different plasmas, where the average growth height in the region near central axis in (**i**) $Ar/C_2H_2/H_2$ plasma is about 38.6 nm, (**ii**) in $Ar/C_2H_2/H_2/H_2O$ plasma is about 43 nm, and (**iii**) in $Ar/C_2H_2/H_2/O_2$ plasma is about 58 nm in the substrate region near the centre. Growth height of vertical graphene at the edge is 117 nm, 126 nm and 171 nm respectively

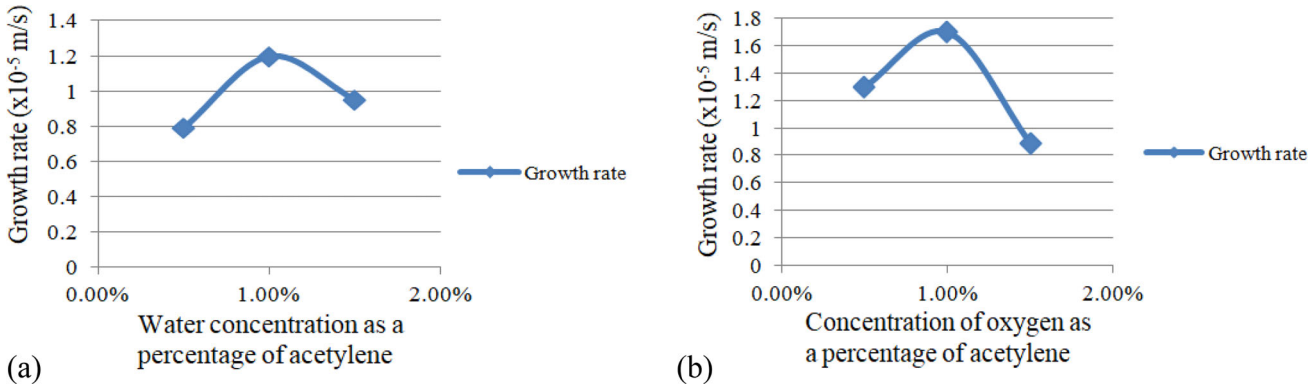


Fig. 8 Growth rate of graphene inside the plasma chamber for slight initial concentration variations of: **a** water in $Ar/C_2H_2/H_2/H_2O$ plasma, which resulted in peak of about 1.2×10^{-5} m/s and **b** oxygen in $Ar/C_2H_2/H_2/O_2$ plasma, where the growth rate peak was found to be about 1.7×10^{-5} m/s

4 Conclusion

With the advent of the PECVD method, the growth process of carbon nanostructures on temperature-sensitive substrates has been made possible, which was otherwise very difficult using chemical vapor deposition and other methods. It is because of the reason that the plasma can be produced at comparatively lower temperatures. This advantage is beneficial in various technology industries like the semiconductor industry, where the materials used in the fabrication may not withstand high temperatures. In this paper, we conducted a comparative study by designing a plasma chamber in COMSOL simulation software using the finite element method. Densities of various species, such as ions and neutrals, were obtained by carrying out the simulations under the three different types of plasma environments: conventional argon plasma, argon plasma with water & argon plasma with oxygen. We found that the growth rate improved if we changed the plasma composition by introducing oxidizers as etchants. This slight variation in the plasma chemistry provided high gains in growth rate and accumulated growth without needing to change the existing chamber mechanics. With the help of growth rate graphs, as shown in Fig. 6, it can be seen that oxygen plasma proves to provide the best environment among the three for the growth of carbon nanostructure. It is because the oxygen molecules play two crucial roles during the growth process. It removes carbon (amorphous) from the surface of the catalyst by the etching process and combines with hydrogen radicals that otherwise would have combined with carbon to prevent growth.

Moreover, by slightly varying the water concentrations, we found that the growth rate first increased and then decreased, signifying that one cannot endlessly increase the water concentration, as shown in Fig. 8a. Similarly, the optimum concentration was also found for oxygen, as shown in Fig. 8b. It is because excessive use of water or oxygen leads to more carbon precipitation near the catalyst, leading to occlusion for further growth. Our simulation-based results are significant for carrying out future experimental research more effectively and can pave new avenues in understanding the growth of graphene and other carbon based nanostructure, specifically in oxygenated plasma environments.

Acknowledgements Author Sagar Khanna acknowledges Delhi Technological University, Delhi for providing the resources for carrying out the research.

Data Availability Statement This manuscript has associated data in a data repository. [Authors' comment: The authors confirm that the data supporting the findings of this study are available within the article itself, and are available from the corresponding author [Prof. S. C. Sharma] upon reasonable request].

Declarations

Conflict of interest The authors have no competing interests to disclose.

References

1. S.J. Tans, A.R.M. Verschueren, C. Dekker, Nature **393**, 49–52 (1998)
2. W.B. Choi, J.H. Kang, H.Y. Kim, Appl. Phys. Lett. **75**, 3129 (1999)
3. M.B. Nardelli, J. Bernholc, Phys. Rev. B **60**, 7828 (1999)
4. A.A. Salman, Application of nanomaterials in environmental improvement, in *Nanotechnology and the Environment*. (IntechOpen, 2020)
5. Y.Z. Bin, Q.Y. Chen, Y. Nakamura, K.T. Matsuo, Carbon **45**, 1330–1339 (2007)
6. D. Yang, L. Xia, H. Zhao, X. Hu, Y. Liu, J. Li, X. Wan, Chem. Commun. **47**, 5873–5875 (2011)
7. H.C. Foley, Microporous Mater. **4**, 407–433 (2005)
8. K.Y. Sheem, E.H. Song, Y.H. Lee, Electrochim. Acta **78**, 223–228 (2012)
9. S.C. Tsang, V. Caps, I. Paraskevas, D. Chadwick, D. Thompsett, Angew. Chem. Int. Engl. **43**, 5645–5649 (2005)
10. M. Meyyappan, L. Delzeit, A. Cassell, D. Hash, Plasma Sources Sci. Technol. **12**, 205 (2003)
11. S. Chen, Q. Jiang, Y. Chen, L. Feng, D. Wu, Nanomaterials **9**, 628 (2019)
12. U. Narula, C.M. Tan, Front. Mater. **5**, 43 (2018)
13. T. Okumura, Phys. Res. Int. **2010**, 164249 (2010)
14. M. Kumar, S. Khanna, N. Gupta, R. Gupta, S.C. Sharma, IEEE TNANO **18**, 401–411 (2019)
15. T. Okumura, I. Nakayama, Rev. Sci. Instrum. **66**(11), 5262–5265 (1995)
16. N. Abid, A.M. Khan, S. Shujait, Adv. Coll. Interface Sci. **300**, 102597 (2022)
17. C.S. Cojocaru, A. Senger, F.L. Normand, J. Nanosci. Nanotechnol. **6**, 1331 (2006)
18. N.M. Rodriguez, J. Mater. Res. **8**, 3233 (1993)
19. D.H. Seo, S. Kumar, A.E. Rider, Z. Han, K. Ostrikov, Opt. Mat. Express **2**, 700 (2012)
20. L. Valentini, J.M. Kenny, L. Lozzi, S. Santucci, J. Appl. Phys. **92**, 6188 (2002)
21. K. Hata, D.N. Futaba, K. Mizuno, T. Namai, M. Yumura, S. Iijima, Science **306**(5700), 1362 (2004)
22. L. Song, G. Toth, R. Vajtai, M. Endo, P.M. Ajayan, Carbon **50**, 5521 (2012)
23. L. Kurzepa, A.L. Raus, J. Patmore, K. Koziol, Adv. Funct. Mater. **24**, 619 (2014)
24. C. Zhang, Y. Fu, Q. Chen, Y. Zhang, Front. Mater. Sci. China **2**(1), 37 (2008)
25. G. Zhang, D. Mann, L. Zhang, A. Javey, Y. Li, E. Yenilmez, Q. Wang, J.P. McVittie, J. Gibbons, H. Dai, Proc. Natl. Acad. Sci. U.S.A. **102**(45), 16141 (2005)
26. Y. Kim, W. Song, S.Y. Lee, S. Shrestha, C. Jeon, W.C. Choi, M. Kim, C.Y. Park, Jpn. J. Appl. Phys. Part 1 **49**, 085101 (2010)
27. Y. Hao, M.S. Bharathi, L. Wang, Science **342**, 720 (2013)
28. X. Xu, Z. Zhang, L. Qiu, Nat. Nanotechnol. **11**, 930–935 (2016)
29. H. Mehdipour, K. Ostrikov, A.E. Rider, Nanotechnology **21**(45), 455605 (2010)
30. M.A. Lieberman, A.J. Lichtenberg, *Principles of Plasma discharges and Material Processing* (Wiley Interscience, New York, 1994)
31. E. Gogolides, D. Mary, A. Rhallabi, G. Turban, Jpn. J. Appl. Phys. Part **1**(34), 261 (1995)
32. J. Geddes, R.W. McCullough, A. Donnelly, H.B. Gilbody, Plasma Sources Sci. Technol. **2**, 93 (1993)
33. A.O. Brezmes, C. Breitkopf, Vacuum **116**, 65–72 (2015)
34. A.V. Vasenkov, J. Kushner, Phys. Rev. E **66**, 066411 (2002)
35. I.B. Denysenko, S. Xu, J.D. Long, P.P. Rutkevych, N.A. Azarenkov, K. Ostrikov, J. Appl. Phys. **95**, 2713 (2004)
36. Ch. Deschenaux, A. Affolter, D. Magni, Ch. Hollenstein, P. Fayet, J. Phys. D: Appl. Phys. **32**, 1876 (1999)
37. Z. Marvi, S. Xu, G. Foroutan, K. Ostrikov, Phys. Plasmas **22**, 013504 (2015)
38. C. Benndorf, P. Joeris, R. Kroger, Pure Appl. Chem. **66**, 1195 (1994)
39. I. Denysenko, N.A. Azarenkov, J. Phys. D Appl. Phys. **44**(17), 31 (2011)
40. I. Denysenko, K. Ostrikov, J. Phys. D Appl. Phys. **42**, 015208 (2009)
41. I. Denysenko, K. Ostrikov, Appl. Phys. Lett. **90**, 251501 (2007)
42. N.V. Mantzaris, E. Gogolides, A.G. Boudouvis, A. Rhallabi, G. Turban, J. Appl. Phys. **79**, 3718 (1996)
43. A. Von Keudell, W. Moller, J. Appl. Phys. **75**, 7718 (1994)
44. S. Hofmann, G. Czanyi, A.C. Ferrari, M.C. Payne, J. Robertson, Phys. Rev. Lett. **95**, 036101 (2005)
45. M. Meyyappan, J. Phys. D Appl. Phys. **42**, 213001 (2009)
46. T.G. Beuthe, J.S. Chang, Jpn. J. Appl. Phys. **38**, 4576 (1991)
47. A. Bogaerts, K. de Bleecker, V. Georgieva, I. Kolev, M. Madani, E. Neyts, Plasma Process. Polym. **3**, 110–119 (2016)
48. Y. H. Le Teuff, T. J. Millar, A. J. Marckwick, UMIST database for astrochemistry, http://www.rate99.co.uk (2001)
49. Y. Wang, J. Chen, Y. Wang, W. Xiong, Vacuum **149**, 291–296 (2018)
50. M. Gryzinski, J. Physique Colloques **40**, 171–177 (1979)
51. J.W.G. Wildoer, L.C. Venema, A.G. Rinzler, R.E. Smalley, C. Dekker, Nature **391**, 59–62 (1998)
52. T.M. Minea, S. Point, A. Granier, M. Touzeau, Appl. Phys. Lett. **85**, 1244 (2004)
53. S.F. Lee, Y.-P. Chang, L.-Y. Lee, J. Mater. Sci. Mater. Electron **20**, 851 (2009)
54. S.K. Srivastava, A.K. Shukla, V.D. Vankar, V. Kumar, Thin Solid Films **515**, 1851 (2006)
55. S. Wei, L.P. Ma, M.L. Chen, Z. Liu, W. Ma, D.M. Sun, H.M. Cheng, W. Ren, Carbon **148**, 242–243 (2019)

56. N. Yoshihara, H. Ago, M. Tsuji, J. Phys. Chem. C **111**, 11577 (2007)
57. S. Hussain, R. Amade, E. Bertran, Mater. Chem. Phys. **148**, 914 (2014)
58. T. Yamada, T. Namai, K. Hata, D.N. Futaba, K. Mizuno, J. Fan, M. Yudasaka, M. Yumura, S. Iijima, Nat. Nanotechnol. **1**, 131 (2006)
59. K. Xie, M. Muhler, W. Xie, Ind. Eng. Chem. Res. **52**, 14081 (2013)
60. H. Choi, M.S. Thesis. University of Massachusetts Lowell, Lowell, MA, (2008), UMI no. 1458539
61. J. Chen, Y. Wen, Y. Guo, J. Am. Chem. Soc. **133**, 44 (2011)
62. S. Nie, J.M. Wofford, N.C. Bartelt, O.D. Dubon, K.F. McCarty, Phys. Rev. B **84**, 155425 (2011)
63. G.H. Han, F. Gunes, J.J. Bae, Nano Lett. **11**, 4144–4148 (2011)
64. D.N. Futaba, K. Hata, T. Yamada, K. Mizuno, M. Yumura, S. Iijima, Phys. Rev. Lett. **95**, 056104 (2005)
65. X. Wang, Y. Feng, H.E. Unalan, G. Zhong, P. Li, H. Yu, A.I. Akinwande, W.I. Milne, Carbon **49**, 214 (2011)

Springer Nature or its licensor (e.g. a society or other partner) holds exclusive rights to this article under a publishing agreement with the author(s) or other rightsholder(s); author self-archiving of the accepted manuscript version of this article is solely governed by the terms of such publishing agreement and applicable law.

Journal Pre-proof

Zinc Oxide incorporated Molybdenum Diselenide Nanosheets for Chemiresistive Detection of Ethanol Gas

Nikita Jain, Nitin K. Puri



PII: S0925-8388(23)01481-0

DOI: https://doi.org/10.1016/j.jallcom.2023.170178

Reference: JALCOM170178

To appear in: *Journal of Alloys and Compounds*

Received date: 13 January 2023
Revised date: 13 April 2023
Accepted date: 16 April 2023

Please cite this article as: Nikita Jain and Nitin K. Puri, Zinc Oxide incorporated Molybdenum Diselenide Nanosheets for Chemiresistive Detection of Ethanol Gas, *Journal of Alloys and Compounds,* (2023) doi:https://doi.org/10.1016/j.jallcom.2023.170178

This is a PDF file of an article that has undergone enhancements after acceptance, such as the addition of a cover page and metadata, and formatting for readability, but it is not yet the definitive version of record. This version will undergo additional copyediting, typesetting and review before it is published in its final form, but we are providing this version to give early visibility of the article. Please note that, during the production process, errors may be discovered which could affect the content, and all legal disclaimers that apply to the journal pertain.

© 2023 Published by Elsevier.

Zinc Oxide incorporated Molybdenum Diselenide Nanosheets for Chemiresistive Detection of Ethanol Gas

Nikita Jain[1] and Nitin K. Puri[1*]

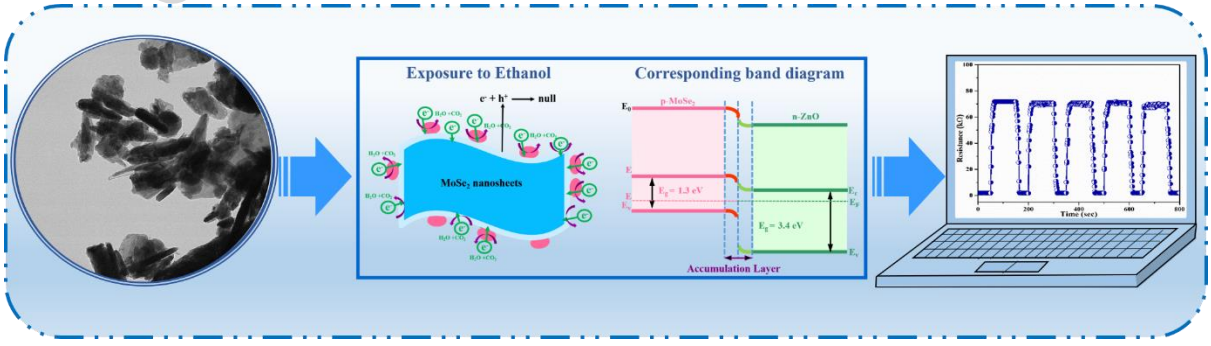
[1]Nanomaterials Research Laboratory (NRL), Department of Applied Physics, Delhi Technological University, Delhi 110042, India

[*]email: nitinkumarpuri@dtu.ac.in, ORCID: 0000-0003-2563-3747

Highlights

- Facile hydrothermal synthesis of ZnO incorporated-$MoSe_2$ nanosheets based nanocomposite.
- A highly selective ethanol gas sensor is fabricated based on $MoSe_2$/ZnO nanocomposite.
- The sensor exhibits high gas sensing response (R_g/R_a) of 37.8 at room-temperature to 500 ppm of ethanol gas.
- The sensor performs far better when operated in dry N_2 than in dry air.
- The synergistic effects due to ZnO incorporated-$MoSe_2$ nanosheets boosted the sensing performance.

Graphical Abstract



Journal Pre-proof

Abstract

Herein, a room-temperature chemiresistive ethanol gas sensor based on hydrothermally synthesized zinc oxide (ZnO) incorporated-molybdenum diselenide ($MoSe_2$) nanosheets was demonstrated. The sensing properties of the $MoSe_2$/ZnO nanocomposite sensor were investigated systematically by exposing the sensor to various ethanol gas concentrations (10-500 ppm) in dry N_2 and dry air. The synergistic effect due to the incorporation of ZnO nanorods in $MoSe_2$ nanosheets was found to enhance the sensor response to ethanol gas (when operated in dry N_2) with improved response and recovery time of 8.4 and 14.7 seconds respectively, high selectivity, stability, and reproducibility. The nanocomposite-based sensor showed high gas sensing response (R_g/R_a) of 37.8 to 500 ppm of ethanol gas. While the response of the nanocomposite-based sensor decreased to 15.3 to 500 ppm of ethanol gas in dry air which suggests that the sensor performs better when operated in dry N_2 than in dry air. On the basis of experimental results, a plausible mechanism has been proposed based on the formation of p-n heterojunction and potential barrier modulation at the interface of the $MoSe_2$/ZnO nanocomposite sensor. The results demonstrated that $MoSe_2$/ZnO-based nanocomposite may pave the way for the fabrication of ethanol gas sensors for real-time electronics applications.

Keywords: $MoSe_2$/ZnO nanocomposite, Electrophoretic Deposition, Chemiresistive, Ethanol Sensing, Heterojunction.

1. Introduction

Rapid industrialization and socio-economic development have resulted in the release of volatile organic compounds (VOCs) in the environment [1, 2]. Exposure to most VOCs, not only causes environmental pollution but is also detrimental to human health. One of the typical VOCs “ethanol gas”, is extensively used as a valuable ingredient in alcoholic

beverages, paints, medicines, cosmetics, etc [3, 4]. Despite its numerous applications in a variety of fields, its long-term exposure causes various ailments such as eye and skin irritation, headaches, nausea, vomiting, kidney failure, and even damage the central nervous system [5, 6]. Therefore, it is the need of the hour to timely monitor and detects ethanol gas, especially at room-temperature (RT) as a part of the safety system. Among various types of sensors developed by scientists for the effective detection of VOCs, chemiresistive sensors have generated huge interest due to their low-cost, simple monitoring techniques, easy design, and high chemical and thermal stability [7, 8].

Recently molybdenum diselenide ($MoSe_2$), a two-dimensional (2D) transition metal dichalcogenides (TMDs) has attracted considerable attention for multifunctional applications due to its significant physical and chemical properties [9, 10]. Its outstanding gas sensing properties have been explored owing to the large surface-to-volume ratio which provides elevated sites for the adsorption and desorption of target gasses [11]. In addition to this, it also exhibits higher adsorption energy with chemical molecules [12]. Some pioneering studies based on the gas sensing properties of $MoSe_2$ have been investigated (targeting several analytes like H_2S, NH_3, NO_2 C_2H_5OH, etc.) which led a path to explore this material in-depth [13-16]. Jha et al. studied the gas sensing properties of $MoSe_2$ for the detection of H_2S gas down to the ppb level. But pristine $MoSe_2$ showed a recovery time of 5 min at 90 ºC [13]. Late et al. used a single-layer $MoSe_2$-based NH_3 gas sensor at RT. The sensor displayed a bit large response (2.5 min) and recovery (9 min) time [14]. In another report, Singh et al. made use of liquid-exfoliated $MoSe_2$ nanosheets for RT ammonia sensing. The corresponding response and recovery times were 15 s and 135 s respectively [15]. In another study, Zhang et al. reported the sensing potential of $MoSe_2$ toward ethanol gas at 90 ºC. It was observed that the nanosheets took a long time to restore its original state at RT. Although the temperature was raised higher, still the recovery time was 5 min [16]. Therefore, these studies

demonstrate that pristine $MoSe_2$-based gas sensors exhibit sluggish response and recovery time which challenges the use of intrinsic $MoSe_2$-based gas sensors. In this regard, various strategies have been employed to improve the sensor performance of $MoSe_2$ gas sensors such as synthesizing composites, combining with noble metals (gold (Au), silver (Ag), platinum (Pt), etc.), surface functionalization, and many more. For instance, Jha et al. demonstrated the use of reduced graphene oxide/molybdenum diselenide nanocomposite for the detection of ammonia at RT. The sensor showed the limit of detection down to 300 ppb, with an operating voltage of 2 mV [17]. Li et al. prepared pristine $MoSe_2$ and Ag-modified $MoSe_2$-based ethanol gas sensors at RT. The sensor exhibited a low detection limit, good response properties, and excellent repeatability [10]. Abun et al. fabricated a hydrogen gas sensor based on p-n heterostructures comprising exfoliated $MoSe_2$ nanosheets doped on the surface of n-type ZnO nanorods. The hybrid p-n heterostructure showed better sensor response in comparison to pristine ZnO and $MoSe_2$ [18]. Hence it is clear from the above studies that modification of $MoSe_2$ with other elements provides alternate strategies for the development of practical gas sensors. This encourages us to explore $MoSe_2$/ZnO nanocomposite for ethanol sensing application which can effectively improve the response/recovery time of the existing 2D nanomaterials-based ethanol sensors.

To the best of our knowledge, there are no reports available focussing on hydrothermal synthesis of ZnO incorporated- $MoSe_2$ nanosheets-based nanocomposite towards their utilization for the chemiresistive detection of ethanol gas at RT. The sensor was recovered in two different environments i.e., in dry N_2 and dry air. Various characterization techniques are employed to confirm the successful synthesis of the as-synthesized nanocomposite. For fabricating the ethanol sensor, $MoSe_2$/ZnO nanocomposite powder so-obtained is deposited on indium tin oxide (ITO) coated corning glass substrate using a facile electrophoretic deposition (EPD) technique. The as-fabricated sensor is exposed to various ethanol gas

concentrations (10-500 ppm) and its response is systematically investigated at RT. The synergistic effect due to the incorporation of ZnO in $MoSe_2$ is explained in detail and a sensing mechanism is proposed based on this.

2. Experimental

2.1 Chemical Profile

The chemicals used in the synthesis were Sodium Molybdate Dihydrate ($Na_2MoO_4.2H_2O$), Selenium (Se) powder, Hydrazine Hydrate-86% ($N_2H_4.H_2O$), Zinc Acetate ($Zn(CH_3COO)_2{\cdot}2H_2O$), Sodium Hydroxide (NaOH) pellets, and Ethanol (C_2H_5OH). All the chemicals were purchased from Sigma Aldrich and were employed without further purification.

2.2 Synthesis Procedure

A facile hydrothermal method was used to synthesize ZnO incorporated- $MoSe_2$ nanosheet-based nanocomposite. Fig. 1 displays the schematic of the fabrication process. Firstly, $MoSe_2$ nanosheets were synthesized. Typically, 2 mmol of sodium molybdate dihydrate was dissolved in deionized (DI) water and ethanol (volume 1:1) with stirring for 45 min to obtain a clear solution. Meanwhile, a solution containing selenium powder (4 mmol) was prepared separately in 10 mL hydrazine hydrate-86% with stirring. It was followed by the addition of selenium solution in sodium molybdate dehydrate solution dropwise under continuous stirring for 45 min. Then, the above mixture was transferred into a 50 mL hydrothermal autoclave and was kept at 220 °C for 24 h. After several washings with DI and ethanol, the black color powder was obtained which was then dried overnight at 100 °C.

Then, ZnO nanorods were prepared by dropping 5 mol of sodium hydroxide solution in 0.5 mol of zinc acetate dihydrate solution under continuous stirring for 45 min. Then, the above solution was kept in an oven at 120 °C in a 100 mL hydrothermal autoclave for 24 h. After

washing it with DI water and ethanol, the white color powder so obtained was left for drying at 80 °C.

For preparing $MoSe_2$/ZnO nanocomposite, a quantitative amount of $MoSe_2$ and ZnO synthesized by the above procedure were dispersed in ethanol and sonicated for 2 h. The dispersed solution was transferred to a 100 mL hydrothermal autoclave and heated at 120 °C for 24 h. The final product was washed with DI and ethanol to yield grey color powder which was then dried overnight in a vacuum.

2.3 Sensor fabrication for ethanol gas sensing

For fabricating the ethanol sensor, $MoSe_2$/ZnO nanocomposite powder so-obtained was deposited on pre-hydrolyzed indium tin oxide (ITO) coated corning glass substrate using electrophoretic deposition (EPD) technique. $MoSe_2$/ZnO nanocomposite powder was dispersed in a suitable solvent with a concentration of 1 mg/mL. This dispersion was ultrasonicated for 2 h. The dispersed solution was then poured into a 2-electrode glass cell comprising copper as a connector to attach the working electrode (WE) and platinum as the counter electrode (CE). The ITO was attached to WE and an optimized constant potential was applied for 60 s. The film so formed of $MoSe_2$/ZnO nanocomposite was left for drying. Finally, silver (Ag) contacts were made on the prepared films with the help of the thermal evaporation technique. A similar process was devised to obtain pristine-$MoSe_2$ and pristine-ZnO films. These films were used for performing sensing measurements.

Journal Pre-proof

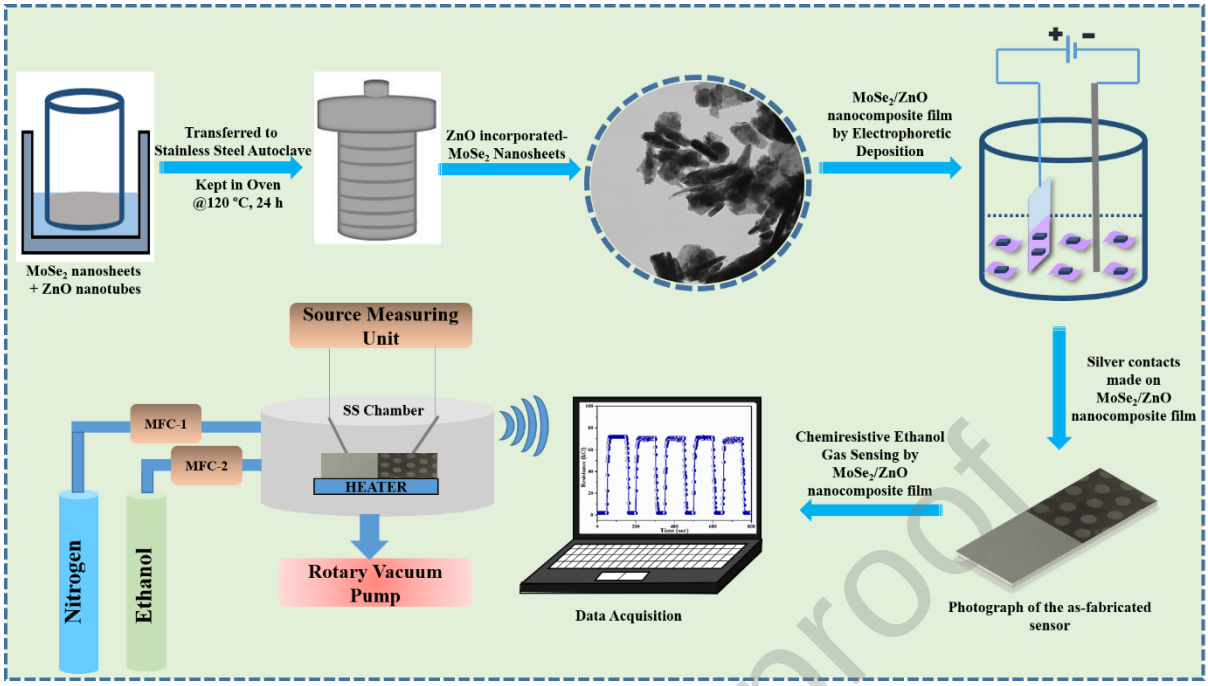


Fig. 1: Step-by-step preparation of $MoSe_2$/ZnO nanocomposite sensor for the detection of ethanol gas.

2.4 Gas Sensing Experimental Set-up

The gas sensing behavior of the $MoSe_2$/ZnO nanocomposite-based chemiresistive gas sensor was investigated in a customized stainless steel (SS) chamber by the use of 1% ethanol balanced with nitrogen (N_2) gas. The chamber was attached to two gas mass flow controllers (MFC). The MFC was used to maintain the flow of the target gas analyte and dry N_2/ dry air (standard composition: N_2 = 79% and O_2 = 21% by volume) inside the chamber. A source measuring unit was employed to provide a constant current supply to the as-fabricated ethanol gas sensor. A rotary pump was connected to the SS chamber to create rough vacuum pressure. A digital hygrometer was employed to measure the relative humidity (RH) in the SS chamber. Ethanol gas sensing was performed by introducing the dry N_2/ dry air first to sustain standard ambient conditions for 50 s. Thereafter, ethanol (1 %) / nitrogen (99 %) mixture was introduced inside the SS chamber for 100 s at different concentrations like 10,

100, 200, 300, 400, and 500 ppm at RT. The formula given below (eqn. 1) was used to calculate the concentration of ethanol gas in the SS chamber:

$$C = \frac{22.4 \times \Psi \times \rho \times V_1}{M \times V_2} \times 1000 \quad \text{(eqn. 1)}$$

In the above formula (eqn. 1), C is the concentration of ethanol gas (ppm), Ψ is the required gas volume fraction, ρ is the density of ethanol ($kg.m^{-3}$), V_1 is the volume of ethanol gas, M is the molecular weight of ethanol ($kg.mol^{-1}$), and V_2 is the volume of the SS chamber (m^3) [19, 20]. The change in resistance of sensing films was recorded using a Lab-View data acquisition software connected to the source measuring unit. The gas sensing measurements of the sensing films were carried out at room-temperature (27 °C) and relative humidity (29 %). The selectivity performance of as-fabricated ethanol gas sensors was investigated with other VOC gases like acetone, benzene, and formaldehyde.

3. Results and Discussions

3.1 Structural analysis using XRD

The crystallographic structure of the as-synthesized pristine-$MoSe_2$, pristine-ZnO, and $MoSe_2$/ZnO nanocomposite is investigated using XRD (Fig. 2). The diffraction peaks of as-synthesized pristine-$MoSe_2$ (Fig. 2a) are attributed to the (002), (100), (103) and (110) planes of the hexagonal phase of $MoSe_2$ (JCPDS 029-0914) [21]. XRD pattern of ZnO (Fig. 2b) shows all the diffraction peaks which are congruous with the standard data available for the wurtzite structure of ZnO (JCPDS 36-1451) [22]. The diffractogram of the $MoSe_2$/ZnO nanocomposite (Fig. 2c) consists of all the peaks corresponding to ZnO nanorods and some major planes of (002), (100), and (110) corresponding to $MoSe_2$ which indicates the successful interaction between $MoSe_2$ nanosheets and ZnO nanorods. The reason for the invisibility of two other planes of $MoSe_2$ i.e. (004) and (103) can be ascribed to the much higher intensity of ZnO diffraction peaks [23]. In addition to this, there is a decrease in the

intensity of diffraction peaks of $MoSe_2$ and ZnO in $MoSe_2$/ZnO nanocomposite which further confirms the formation of nanocomposite [24].

It is also observed that there is a shift in the diffraction peaks of the nanocomposite with respect to the pristine materials in Fig. 2a and 2b. To confirm the shifting of diffraction peaks in the nanocomposite, zoomed highest intensity diffraction peaks of pristine-$MoSe_2$ (100) and ZnO (101) were considered (Fig. 2(d) and Fig. 2(e)) for comparison. As can be seen in Fig. 2(d), the (100) diffraction peak of $MoSe_2$/ZnO nanocomposite is slightly shifted to a higher diffraction angle (31.76°) compared to the (100) diffraction peak of pristine-$MoSe_2$ (31.67°). Similarly, in Fig. 2(e), the (101) diffraction peak of the nanocomposite is slightly shifted to a lower diffraction angle (36.24°) compared to the (101) diffraction peak of pristine-ZnO (36.27°). This shift can correspond to the lattice mismatch between the pristine materials or strain generated in the nanocomposite after interaction during the synthesis [25].

Journal Pre-proof

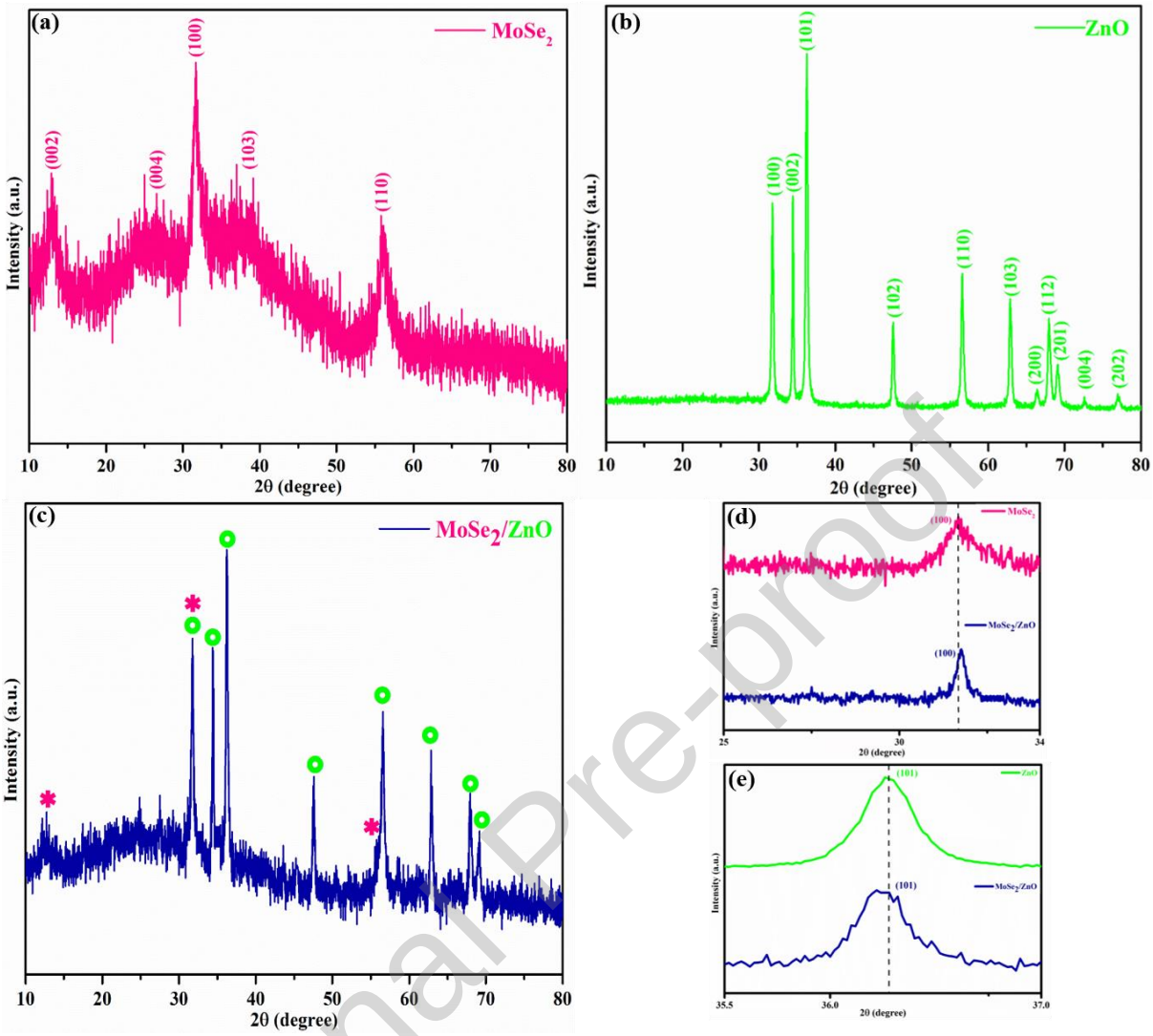
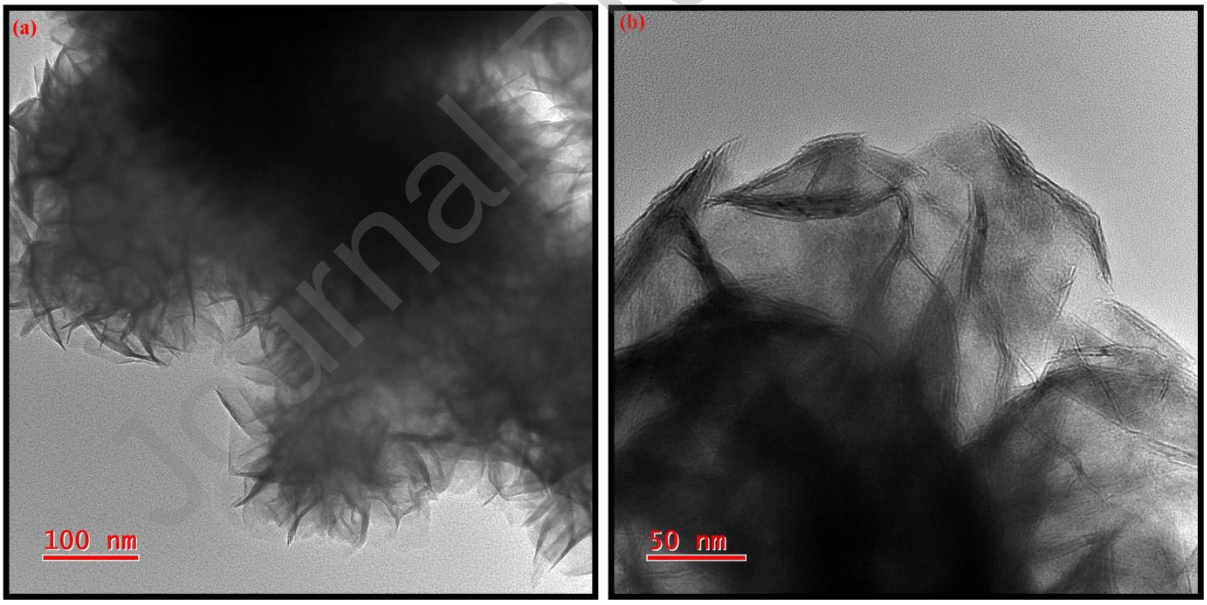


Fig. 2: XRD pattern of the as-synthesized (a) pristine-$MoSe_2$, (b) pristine-ZnO, (c) $MoSe_2$/ZnO nanocomposite, (d) zoomed (100) diffraction peak of pristine-$MoSe_2$ and $MoSe_2$/ZnO nanocomposite, and (e) zoomed (101) diffraction peak of pristine-ZnO and $MoSe_2$/ZnO nanocomposite.

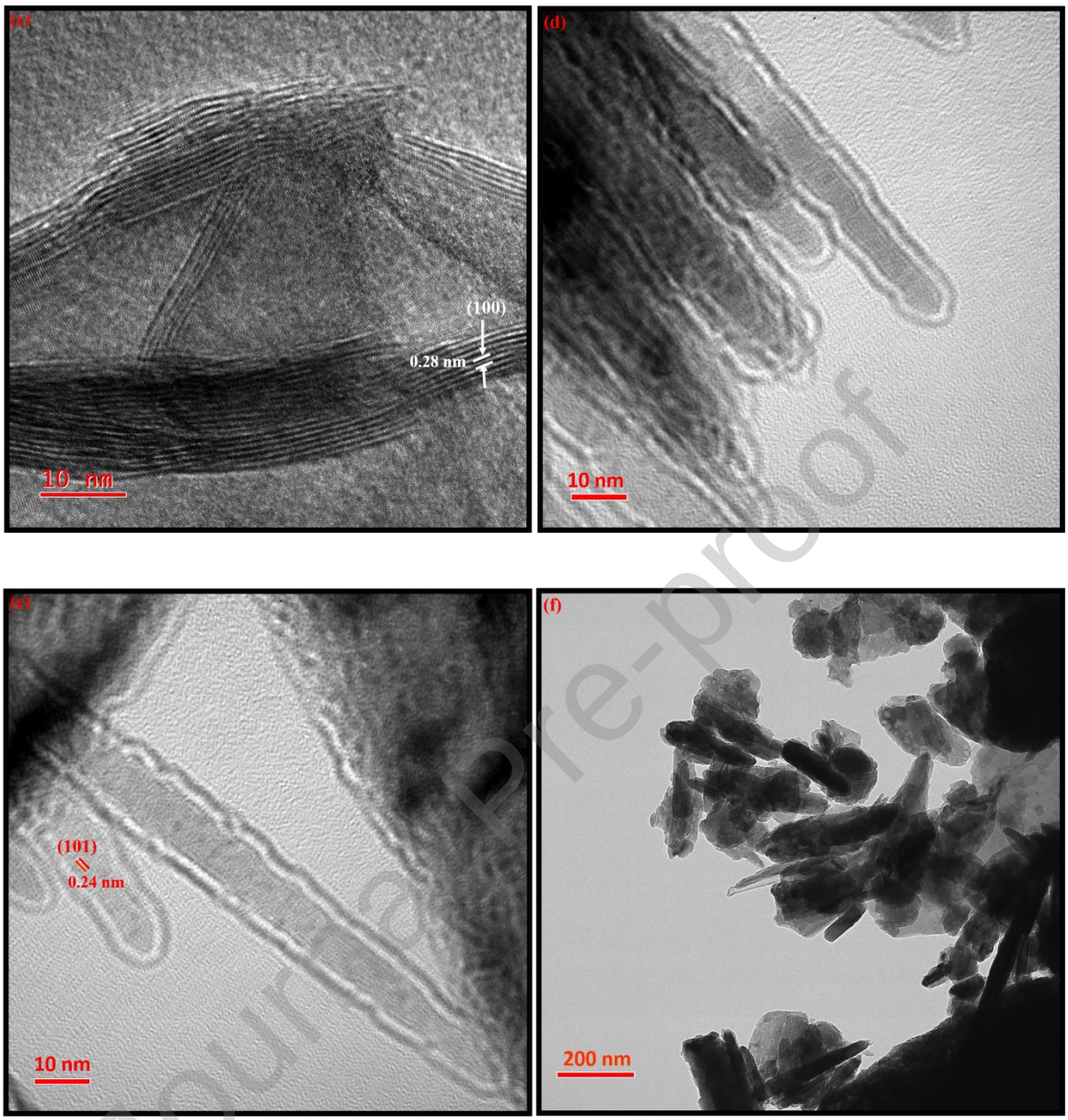
3.2 Microstructure analysis using HRTEM

The high-resolution transmission electron microscopy HR-TEM images of pristine-$MoSe_2$, pristine-ZnO, and $MoSe_2$/ZnO nanocomposite are shown in Fig. 3. Fig. 3a and 3b display a large area of $MoSe_2$ nanosheets stacked over one another, which are wrinkled and curled at the edges. The fine lattice fringes of $MoSe_2$ nanosheets can be seen in Fig.

3c with the interplanar spacing of 0.28 nm which is related to the (100) lattice plane of $MoSe_2$. Fig. 3d shows an HRTEM image of ZnO nanorods and Fig. 3e shows the measured interplanar spacing of 0.24 nm which corresponds to the (101) lattice plane of ZnO nanorods. Evidence for modification of the $MoSe_2$ nanosheets by ZnO nanorods is given in Fig. 3f and 3g, which shows the successful incorporation of ZnO nanorods in $MoSe_2$ nanosheets. A clear heterogeneous interface between $MoSe_2$ nanosheets and ZnO nanorods can be seen in $MoSe_2$/ZnO nanocomposite at a 200 nm and 100 nm scale bar. The corresponding selected area electron diffraction (SAED) pattern of the $MoSe_2$/ZnO nanocomposite is shown in Fig. 3h. Hence from the HRTEM analysis, the successful incorporation of ZnO nanorods in $MoSe_2$ nanosheets is evident, which is consistent with the XRD analysis as well.



Journal Pre-proof



Journal Pre-proof

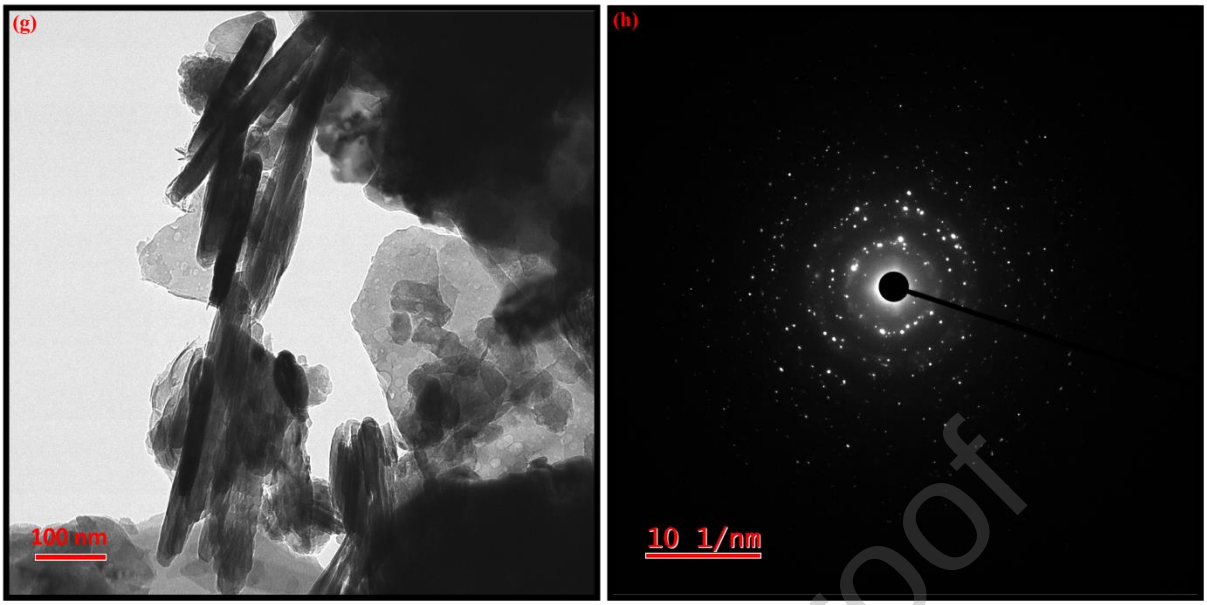


Fig. 3: HRTEM images of as-synthesized (a) and (b) pristine-$MoSe_2$ nanosheets (c) Lattice fringes of $MoSe_2$ nanosheets with measured interplanar spacing, (d) pristine-ZnO nanorods, (e) Measured Interplanar spacing of pristine-ZnO nanorods (f, g) $MoSe_2$/ZnO nanocomposite, and (h) corresponding SAED pattern of $MoSe_2$/ZnO nanocomposite.

3.3 Study of vibrational modes using Raman spectroscopy

The Raman spectrum of pristine-$MoSe_2$, pristine-ZnO, and $MoSe_2$/ZnO nanocomposite acquired using an excitation wavelength of 532 nm is shown in Fig. 4. Raman spectroscopy measurements of $MoSe_2$ shows a strong out-of-plane mode A_{1g} mode at 238 cm^{-1} which is the characteristic peak of $MoSe_2$ [26]. The other two in-plane modes E_{1g} and E^1_{2g} of $MoSe_2$ are observed at 167 cm^{-1} and 283 cm^{-1} which are in good agreement with the earlier reports [15]. Fig. 4 shows an intense Raman peak of ZnO at 437 cm^{-1} (E_2^{high}) which is the characteristic peak of the hexagonal wurtzite phase of ZnO [27].

The corresponding spectrum of $MoSe_2$/ZnO nanocomposite in Fig. 4 displays the presence of modes belonging to both $MoSe_2$ and ZnO. In addition to this, it is noted that the modes in $MoSe_2$/ZnO nanocomposite are shifted from their respective position in their individual

spectrum in Fig. 4a and 4b. In the $MoSe_2$/ZnO nanocomposite, there is a red shift in the A_{1g} mode (233.7 cm^{-1}) corresponding to $MoSe_2$ as well as in the E_2^{high} (431.3 cm^{-1}) mode corresponding to ZnO. This is attributed to the defects produced due to electronic interactions between $MoSe_2$ and ZnO during the hydrothermal synthesis process [28]. Hence, the Raman spectrum of $MoSe_2$/ZnO nanocomposites confirms that the nanocomposite is successfully synthesized, as confirmed by XRD and HRTEM analysis.

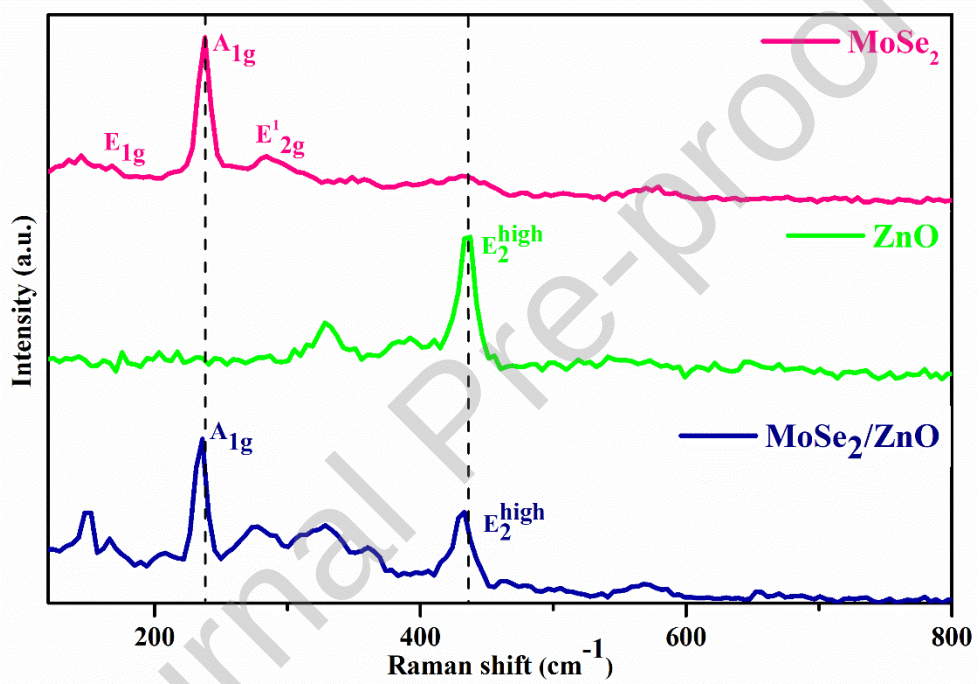


Fig. 4: Raman spectrum of the as-synthesized pristine-$MoSe_2$, pristine-ZnO, and $MoSe_2$/ZnO nanocomposite.

3.4 Identification of functional groups using Fourier Transform Infrared Spectroscopy (FTIR)

FTIR Spectroscopy is performed to investigate and elucidate the presence of functional groups in the prepared samples of pristine-$MoSe_2$, pristine-ZnO, and $MoSe_2$/ZnO nanocomposite in the range of 400 – 4000 cm^{-1}. Peaks in the FTIR spectrum of $MoSe_2$ nanosheets are observed corresponding to O-H (3420 cm^{-1}), C-H (2910 cm^{-1}), COO^{-1} (1620

cm^{-1}), Mo-O (1000-750 cm^{-1}), and Se-O-Se (420 cm^{-1}) as shown in Fig. 5 [29, 30]. The FTIR spectrum of ZnO nanorods (Fig. 5) consists of peaks corresponding to O-H (3438 cm^{-1}), COOH (1620 and 1480 cm^{-1}), Zn-OH (920 cm^{-1}), and Zn-O (577 and 427 cm^{-1}) [27]. The corresponding spectrum of $MoSe_2$/ZnO nanocomposite in Fig. 5 displays the peaks corresponding to both $MoSe_2$ and ZnO. Furthermore, the peaks in the as-synthesized nanocomposite are shifted as compared to pristine-$MoSe_2$ and ZnO indicating the electronic interaction between the pristine materials. Hence, from the FTIR spectrum of $MoSe_2$/ZnO nanocomposite, the co-existence of both $MoSe_2$ and ZnO is confirmed which is in good accordance with the XRD analysis, Raman spectroscopy, and HRTEM observations.

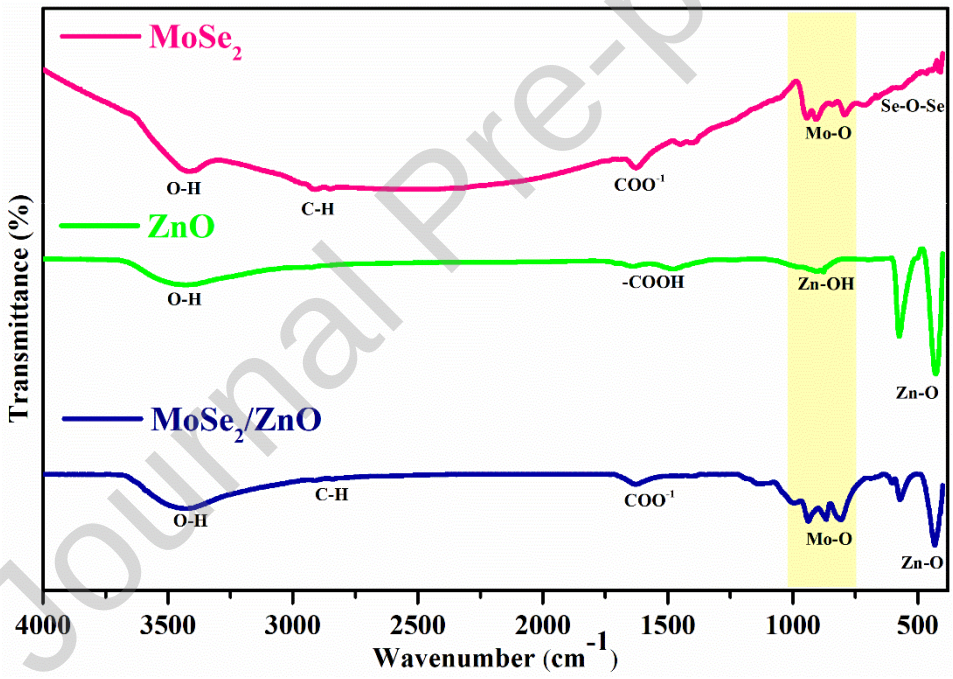


Fig. 5: FTIR spectrum of the as-synthesized pristine-$MoSe_2$, pristine-ZnO, and $MoSe_2$/ZnO nanocomposite.

3.5 Gas sensing performance

The gas sensor response characteristics of pristine-$MoSe_2$, and $MoSe_2$/ZnO nanocomposite are investigated towards different ethanol concentrations ranging from 10-500 ppm at RT in dry N_2 as illustrated in Fig. 5a. Fig. S1 (Supporting Information) shows the response

characteristics of pristine-ZnO towards different ethanol concentrations at RT in dry N_2. It can be observed in Fig. 5a that the sensing response (resistance versus time graph) of pristine-$MoSe_2$ is low and the resistance changes slightly under exposure to different concentrations of ethanol gas. However, the $MoSe_2$/ZnO nanocomposite sensor exhibited a much higher response towards the same concentration of ethanol gas. The response value (R_g/R_a) of the as-fabricated nanocomposite sensor is 37.8 to 500 ppm ethanol gas where R_g and R_a represent the value of the sensor's resistance in presence of ethanol gas mixture and dry N_2 respectively. But, the response from the same pristine-$MoSe_2$ and $MoSe_2$/ZnO nanocomposite sensor decreased significantly when recovered in dry air. Specifically, the response of 4.5 and 15.3 is obtained to 500 ppm ethanol gas for pristine-$MoSe_2$ and $MoSe_2$/ZnO nanocomposite sensor as shown in Fig. S2 (Supporting Information).

Therefore, the improved response of the nanocomposite sensor when operated in dry N_2 than dry air encouraged us to measure sensor performance in this environment. Fig. 5b defines three parameters that describe the properties of the sensor which are: the sensing response (R_g/R_a), the response time (t_{resp}), and the recovery time (t_{rec}). Firstly, we note that the resistance of the $MoSe_2$/ZnO nanocomposite sensor increased from base resistance R_a = 1.9 kΩ in dry N_2 to R_g = 71.9 kΩ when the sensor is exposed to 500 ppm of ethanol. The sensing response of the nanocomposite sensor is calculated using R_g and R_a values obtained and is found to be 37.8 at 500 ppm ethanol. This also suggests that the response of the nanocomposite sensor is p-type towards ethanol gas [10, 16]. Furthermore, full recovery to the same base resistance is observed for both pristine and nanocomposite sensor. This reveals the reversible interaction between the as-fabricated nanocomposite sensor and ethanol gas due to the physisorption process. It is also evident from Fig. 5a and 5b. that the base resistance of the $MoSe_2$/ZnO nanocomposite sensor is higher as compared to the pristine-$MoSe_2$ sensor. The other two parameters are t_{resp} and t_{rec} which are calculated to be 11 s and

18 s for the pristine-$MoSe_2$ sensor respectively. An improvement in t_{resp} and t_{rec} is observed for $MoSe_2$/ZnO nanocomposite sensor and are found to be 8.4 s and 14.7 s respectively. A comparison of performance parameters such as sensing response, response, and recovery time of pristine- $MoSe_2$, pristine-ZnO, and ZnO/$MoSe_2$ nanocomposite sensor in dry N_2 is shown in Table S1 (Supporting Information). Therefore, the ZnO/$MoSe_2$ nanocomposite sensor exhibits a faster response than the pristine-$MoSe_2$.

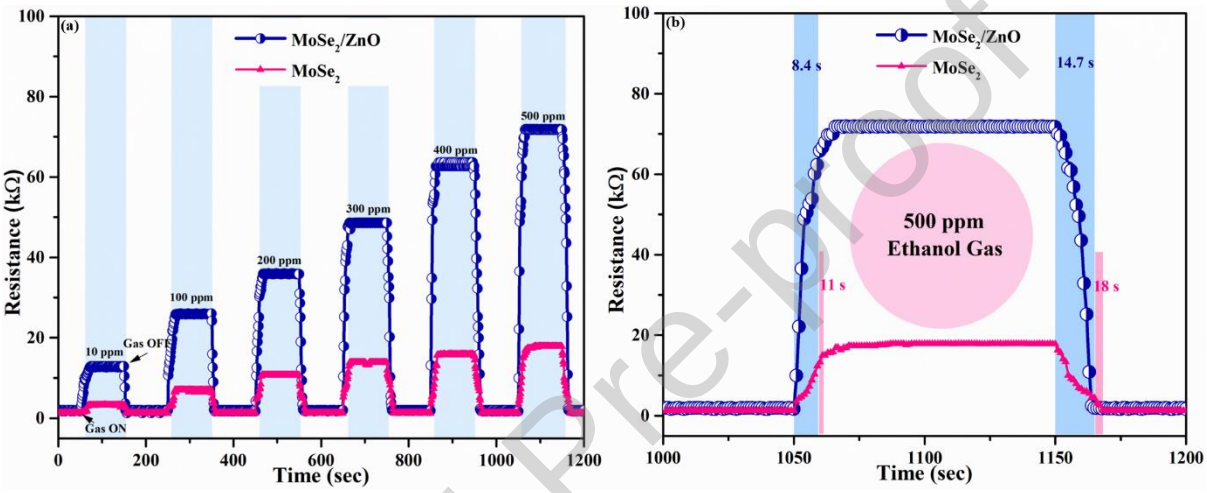


Fig. 5: (a) Resistance variation of pristine-$MoSe_2$ and $MoSe_2$/ZnO nanocomposite sensor wrt. to various ethanol concentrations at RT in dry N_2 and (b) The t_{resp} and t_{rec} characteristics of $MoSe_2$ and $MoSe_2$/ZnO nanocomposite sensor exposed to 500 ppm ethanol at RT in dry N_2.

Similarly, t_{resp} and t_{rec} of the $MoSe_2$/ZnO nanocomposite sensor are calculated for different ethanol gas concentrations and shown in Fig. 6a. It is observed that the t_{resp} decreases and the t_{rec} increases as the ethanol gas concentration increases from 10 to 500 ppm. The reason for a decrease in t_{resp} may be attributed to the availability of large sites on the sensor's surface for gas adsorption. On the other hand, the increase in t_{rec} may be due to the chemisorption of ethanol molecules and their reaction products which took time to desorb from the surface of the sensor [26].

Journal Pre-proof

Fig. 6b and 6c demonstrate the repeatability of the $MoSe_2$/ZnO nanocomposite sensor exposed to 10 ppm and 500 ppm ethanol gas at RT for five consecutive cycles respectively. The results suggest that the sensor exhibited almost the same response during each cycle.

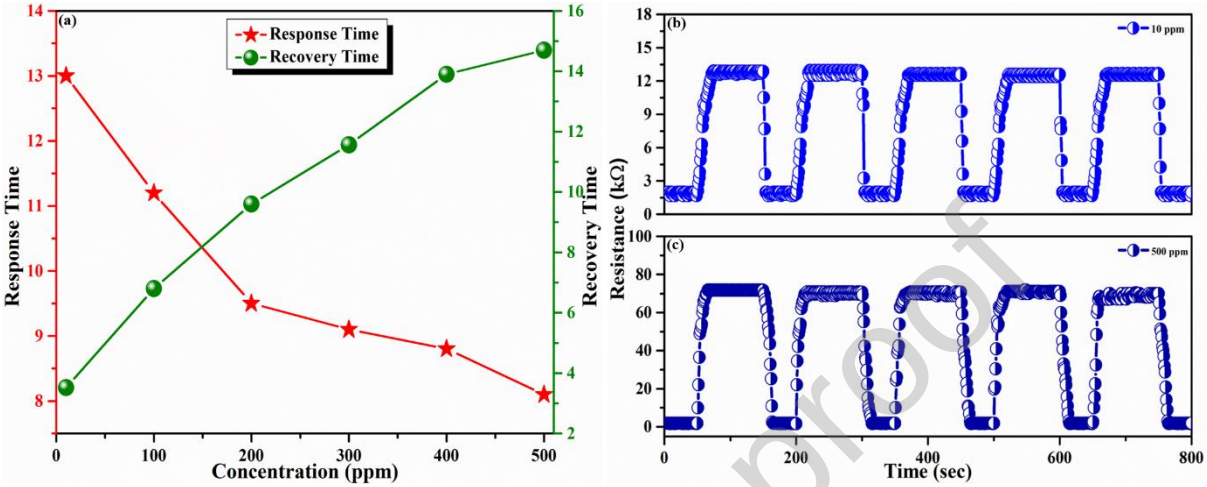


Fig. 6: (a) Response and recovery time versus concentration curves of ethanol for the $MoSe_2$/ZnO nanocomposite sensor at RT in dry N_2, (b) and (c) Five consecutive sensing cycles of the $MoSe_2$/ZnO nanocomposite sensor exposed to 10 and 500 ppm ethanol at RT in dry N_2.

For real-life applications, the gas sensor should have good stability. As shown in Fig. 7a the long-term stability of the $MoSe_2$/ZnO nanocomposite sensor is also conducted to evaluate its stability. The sensor is tested under 10 and 500 ppm of ethanol gas at RT at an interval of 7 days. The response values of the sensor showed no distinct changes in a month (30 days) which confirmed the excellent stability of the $MoSe_2$/ZnO nanocomposite sensor.

Selectivity is also a very important parameter for evaluating the sensor's performance. Fig. 7b shows the response of pristine-$MoSe_2$ and $MoSe_2$/ZnO nanocomposite sensors toward a few VOCs with a concentration of 500 ppm at RT, which involves ethanol, acetone, benzene, and formaldehyde. The corresponding bar chart depicts that $MoSe_2$/ZnO nanocomposite sensor is highly selective towards ethanol.

Journal Pre-proof

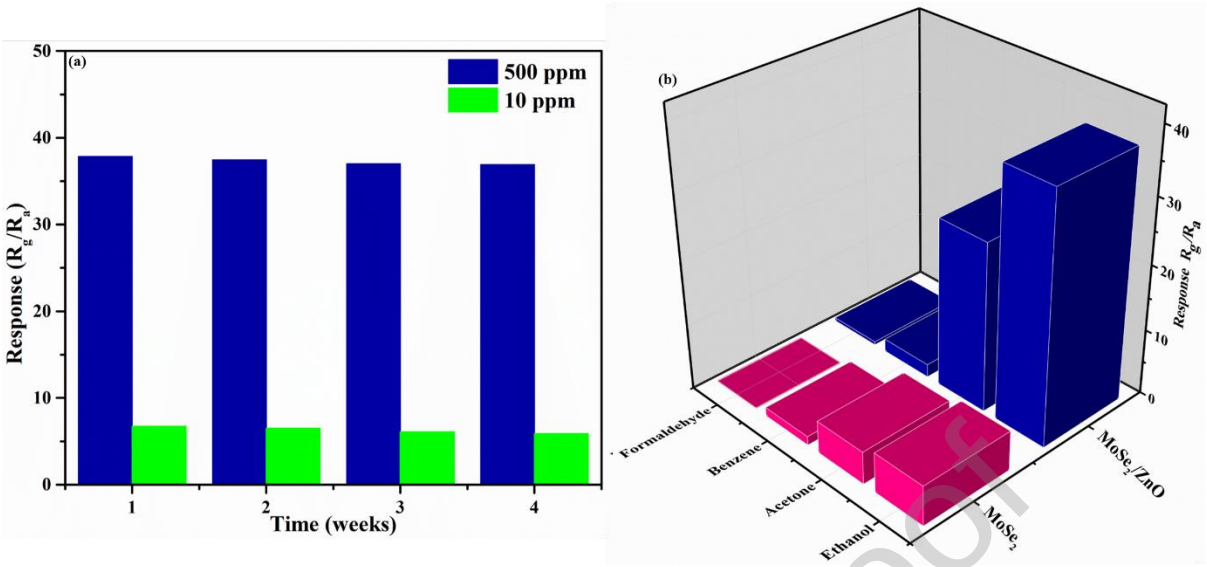


Fig. 7: (a) Long-term stability (30 days) under 500 ppm and 10 ppm ethanol at RT for the $MoSe_2$/ZnO nanocomposite sensor in dry N_2, and (b) Corresponding response bar chart showing the selectivity of the $MoSe_2$/ZnO nanocomposite sensor towards a few VOCs with a concentration of 500 ppm at RT in dry N_2.

Table 1 compares the ethanol sensing properties of previous research work in terms of working temperature, response, and recovery time with our work. The comparative results demonstrate that $MoSe_2$/ZnO nanocomposite sensor have better response and recovery time, and operate at room-temperature. Therefore, $MoSe_2$/ZnO nanocomposite sensor has better sensing characteristics than others indicating that it can become a great potential candidate for ethanol gas sensing.

Table 1: A comparison of performance parameters of this work with previous work for ethanol gas sensing.

Senor Materials	Concentration (ppm)	Sensor Respons e	Operating Temperature (°C)	Response/Recov ery Time (sec)	Refs.
MoS_2/TiO_2	500	100 %	300	70 ± 10 s / 90 ± 20 s	[3]
ZnO	500	32	160	14 / 13	[31]
Pd decorated ZnO	500	81%	260	6 / 95	[32]

WO_3/g-C_3N_4	500	62.5%	RT	30 / 25	[33]
$MoSe_2$/ZnO	500	37.8	RT	8.4 / 14.7	This work

Ethanol sensing mechanism

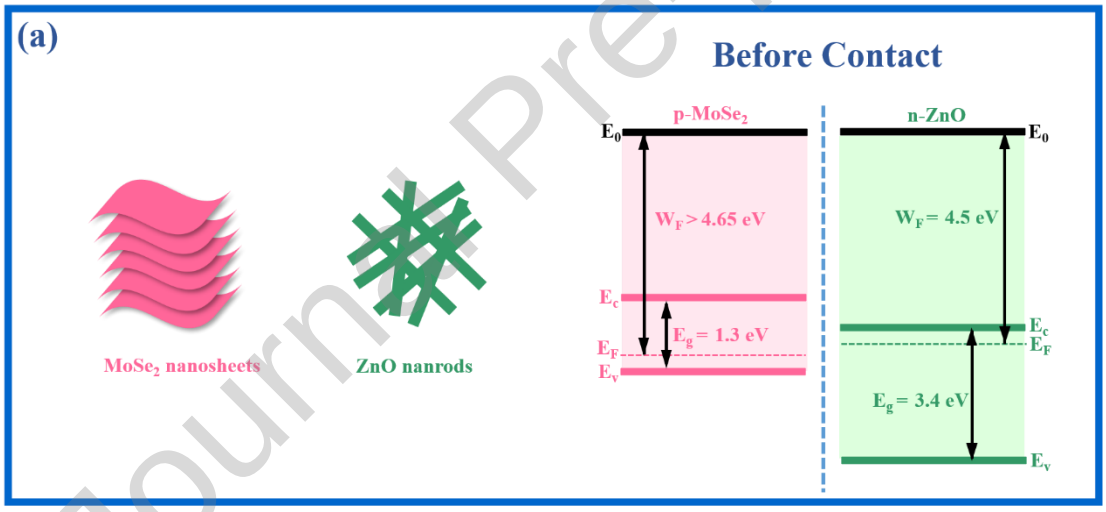
The gas sensing mechanism is attributed to the change in resistance with respect to baseline due to the interaction of ethanol molecules with the surface of the sensing material. From the response curves (Fig. 5a and 5b), the pristine-$MoSe_2$ nanosheets exhibit a p-type character, pristine-ZnO exhibits an n-type character and $MoSe_2$/ZnO nanocomposite sensor exhibits a p-type character. Based on these data, the sensing mechanism of pristine sensors as well as nanocomposite sensor is explained as follows:

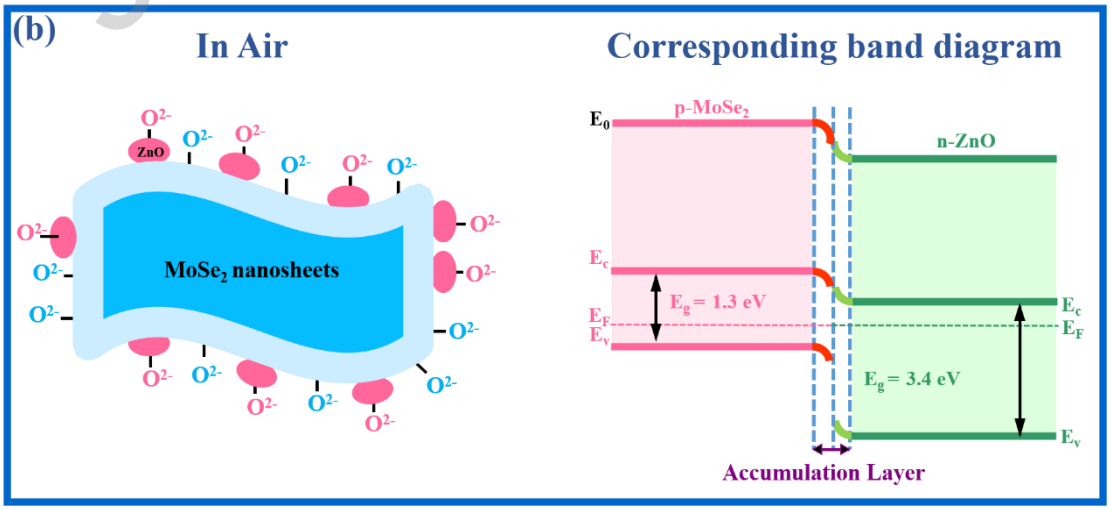
The sensing behavior of $MoSe_2$ nanosheets showed a p-type characteristic response during ethanol gas exposure (Fig. 5a). It has been proved in the literature that, although semiconducting TMD nanosheets are intrinsically n-type, adsorption of oxygen molecules from the air atmosphere can introduce p-type doping [17, 34]. During the synthesis, a number of defects are created in the $MoSe_2$ nanosheets. These defects act as an active point for the adsorption of oxygen molecules from the air atmosphere during the fabrication of process of the sensor [35]. The adsorbed oxygen molecules tend to trap electrons from the $MoSe_2$ nanosheets which creates a large number of oxygen ion species. These oxygen ion species induce the formation of a thick accumulation layer near the surface of $MoSe_2$ nanosheets. When the $MoSe_2$ nanosheets are exposed to ethanol gas, the electrons are donated by the ethanol to the $MoSe_2$ nanosheets as ethanol is a reducing agent. This results in decreasing the majority charge carrier concentration in $MoSe_2$ nanosheets and hence an increase in sensor resistance [13, 36]. The gas sensing mechanism of pristine-ZnO is explained in Section-S.1. (Supporting Information).

Journal Pre-proof

A plausible mechanism for enhanced ethanol gas sensing of the $MoSe_2$/ZnO nanocomposite sensor compared to the pristine-$MoSe_2$ and pristine-ZnO sensor can be explained by considering the p-n heterojunction generated at the interface of p-$MoSe_2$ and n-type ZnO [37]. Fig. 8a shows the schematic representation and energy band diagram of p-$MoSe_2$ nanosheets and n-type ZnO nanorods in air. The band gap of $MoSe_2$ and ZnO is 1.3 eV and 3.4 eV respectively [12, 38, 39]. The discrepancy of the bandgap in the nanocomposite is attributed to the formation of heterojunction between $MoSe_2$ and ZnO. The current-voltage characteristic curve of the $MoSe_2$/ZnO nanocomposite sensor is also obtained at RT using Keithley 2450 SMU to confirm the existence of p-n heterojunction in the nanocomposite sensor (Supporting Information: Fig. S3). Under the scanning voltage of -2 V to 2 V, it can be seen that the reverse current of the nanocomposite sensor is smaller than the forward current which indicates the existence of p-n heterojunction at the interface of $MoSe_2$ nanosheets and ZnO nanorods [20, 40]. The work function of n-type ZnO is 4.5 eV [39]. According to the literature, the work function of pure $MoSe_2$ is 4.65 eV, and the withdrawal of electrons from the nanosheets would increase the work function of $MoSe_2$ [41]. Therefore, the work function of ZnO is lower than that of $MoSe_2$. The distinction in the work function of $MoSe_2$ and n-type ZnO results in the diffusion of electrons from ZnO to $MoSe_2$ and the holes will diffuse from $MoSe_2$ to ZnO until an equilibrium of Fermi level is achieved. The energy band bends at the interface of $MoSe_2$ and ZnO as shown in Fig. 8b. An accumulation layer is formed at the interface of $MoSe_2$ to ZnO, where the electrons accumulate at the side of $MoSe_2$ and the holes accumulate at the side of ZnO. A potential barrier is formed due to carrier trapping at the interface of the $MoSe_2$/ZnO nanocomposite which increased the resistance of the nanocomposite films in the air. As mentioned above, the R_a value of the $MoSe_2$/ZnO nanocomposite sensor is higher as compared to the pristine-$MoSe_2$ sensor owing to the presence of an enhanced potential barrier (Fig. 5a). When the nanocomposite sensor is

exposed to ethanol molecules (Fig. 8c), this results in thinning of the charge carrier accumulation layer near the surface of $MoSe_2$ nanosheets. The free electrons so released during this process neutralize the majority of charge carriers in the $MoSe_2$ nanosheets. Similarly, the released electrons on the surface of ZnO lead to more electron-hole recombination on the interface of $MoSe_2$ nanosheets and ZnO. Finally, the electron transfer from the ZnO to the $MoSe_2$ is impeded which overall results in an increased change in resistance and enhanced sensitivity [42]. The p-type behavior of the $MoSe_2$/ZnO nanocomposite sensor is similar to the pristine-$MoSe_2$ sensor, which suggests a synergistic effect between $MoSe_2$ nanosheets and ZnO nanorods in which p-type $MoSe_2$ nanosheets act as majority charge carriers [39, 43].





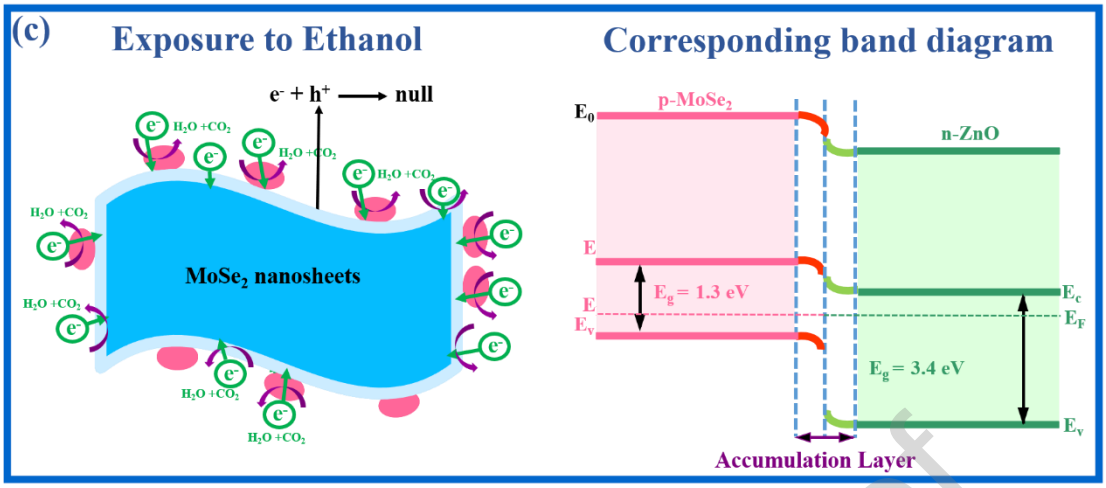


Fig. 8: Schematic representation and energy band diagram of ethanol gas sensing mechanism of $MoSe_2$/ZnO nanocomposite sensor in (a) before contact, (b) air condition, and (c) ethanol atmosphere.

The reason for a better response of pristine-$MoSe_2$ and $MoSe_2$/ZnO nanocomposite sensor to ethanol gas in dry N_2 than dry air can be explained as: It is evident from the literature that adsorption of oxygen on the surface of the $MoSe_2$ trap electrons from the $MoSe_2$ nanosheets by occupying the reactive sites on the surface of the sensing layer [35, 44, 45]. An increase in the baseline resistance of the sensor in the presence of dry air compared to dry N_2 (Supporting Information: Fig. S2) indicates that more reactive sites are occupied by oxygen thereby reducing the sensing response of the pristine-$MoSe_2$ sensor. As mentioned above, the p-type response of the nanocomposite sensor indicates that $MoSe_2$ nanosheets act as majority charge carriers. Hence, the response from the $MoSe_2$/ZnO nanocomposite sensor also decreased significantly when recovered in dry air.

From the above ethanol gas sensing results, we surmise that the superior gas sensing properties of $MoSe_2$/ZnO nanocomposite sensor in the presence of dry N_2 can contribute to the development of ethanol gas sensors with high sensitivity, good selectivity, stable repeatability, and fast adsorption/desorption at RT, which are suitable for practical applications.

Conclusions

A highly selective, stable, and reproducible chemiresistive ethanol gas sensor based on $MoSe_2$/ZnO nanocomposite was developed. Specifically, the response value of the as-fabricated nanocomposite sensor was 37.8 to 500 ppm ethanol gas when operated in dry N_2 and 15.3 to 500 ppm ethanol gas when operated in dry air. This suggests that the sensor performs better when operated in dry N_2 than in dry air. The sensor demonstrated a p-type characteristic response. Importantly, the sensor operates at room-temperature and can detect ethanol down to 10 ppm. The sensor also exhibited improved response (8.4 s) and recovery (14.7 s) time to 500 ppm ethanol gas compared to previously reported values. The enhancement in performance of the sensor was due to the formation of a p-n heterojunction at the interface of the $MoSe_2$ nanosheets and ZnO nanorods in $MoSe_2$/ZnO nanocomposite sensor. Furthermore, potential barrier modulation at the interface provided a positive effect on sensitivity performance. The results demonstrated that this work may open new avenues to engineer 2D nanomaterials/metal-oxide-based nanocomposites for the fabrication of ethanol gas sensors for real-time electronics applications.

Acknowledgments

The authors are grateful to the Hon'ble Vice-Chancellor, Delhi Technological University, Delhi, India for providing support and facilities for conducting quality research work. The authors are grateful to Dr. Saurabh Srivastava, Dr. Senthil Kumar Kandasamy, Dr. Kamal Arora, Dr. Archit Dhingra, Dr. Rishibrind K. Upadhyay, Ritika Khatri, Saroj Kumar Jha, Hemant K. Arora, Sunil Kumar, Anmol Aggarwal, and Ashi Mittal for their valuable review of the manuscript.

Conflict of Interest: The authors declare that there is no conflict of interest.

References

Journal Pre-proof

[1] V. Shah, J. Bhaliya, G. M. Patel, and P. J. T. i. C. Joshi, "Recent Advancement in Pd-Decorated Nanostructures for Its Catalytic and Chemiresistive Gas Sensing Applications: A Review," *Topics in Catalysis*, pp. 1-41, 2022.

[2] A. Mirzaei, S. Leonardi, and G. J. C. i. Neri, "Detection of hazardous volatile organic compounds (VOCs) by metal oxide nanostructures-based gas sensors: A review," *Ceramics International*, vol. 42, no. 14, pp. 15119-15141, 2016.

[3] S. Singh, S. J. S. Sharma, and A. B. Chemical, "Temperature dependent selective detection of ethanol and methanol using MoS2/TiO2 composite," *Sensors and Actuators B: Chemical*, vol. 350, p. 130798, 2022.

[4] M. J. Ahemad, T. D. Le, D.-S. Kim, Y.-T. J. S. Yu, and A. B. Chemical, "Bimetallic AgAualloy@ ZnO core-shell nanoparticles for ultra-high detection of ethanol: Potential impact of alloy composition on sensing performance," *Sensors and Actuators, B: Chemical* vol. 359, p. 131595, 2022.

[5] S. S. Scindia, R. B. Kamble, and J. A. J. I. S. J. Kher, "Organic surfactant assisted polypyrrole materials as effective chemiresistive gas sensors for VOCs and toxic gas detection," *IEEE Sensors Journal*, vol. 20, no. 23, pp. 14072-14080, 2020.

[6] D. Zhang, Y. Cao, J. Wu, and X. J. A. S. S. Zhang, "Tungsten trioxide nanoparticles decorated tungsten disulfide nanoheterojunction for highly sensitive ethanol gas sensing application," *Applied Surface Science*, vol. 503, p. 144063, 2020.

[7] T. T. N. Phan *et al.*, "Hierarchically structured LaFeO3 with hollow core and porous shell as efficient sensing material for ethanol detection," *Sensors and Actuators B: Chemical*, vol. 354, p. 131195, 2022.

[8] N. Roy *et al.*, "Paper based enzymatic chemiresistor for POC detection of ethanol in human breath," *IEEE Sensors Journal* vol. 20, no. 5, pp. 2278-2286, 2019.

Journal Pre-proof

[9] G. Jeevanandham, K. Vediappan, Z. A. ALOthman, T. Altalhi, and A. K. J. S. r. Sundramoorthy, "Fabrication of 2D-MoSe2 incorporated NiO Nanorods modified electrode for selective detection of glucose in serum samples," *Scientific Reports,* vol. 11, no. 1, pp. 1-13, 2021.

[10] T. Li, S. Yu, Q. Li, M. Chi, and P. J. N. J. o. C. Li, "Room temperature ethanol gas-sensing properties based on Ag-doped MoSe 2 nanoflowers: experimental and DFT investigation," *New Journal of Chemistry,* vol. 45, no. 45, pp. 21423-21428, 2021.

[11] S. Zhang, T. H. Nguyen, W. Zhang, Y. Park, and W. J. A. P. L. Yang, "Correlation between lateral size and gas sensing performance of MoSe2 nanosheets," *Applied Physics Letters,* vol. 111, no. 16, p. 161603, 2017.

[12] Z. Yang, D. Zhang, D. J. S. Wang, and A. B. Chemical, "Carbon monoxide gas sensing properties of metal-organic frameworks-derived tin dioxide nanoparticles/molybdenum diselenide nanoflowers," *Sensors and Actuators B: Chemical,* vol. 304, p. 127369, 2020.

[13] R. K. Jha, J. V. D'Costa, N. Sakhuja, N. J. S. Bhat, and A. B. Chemical, "MoSe2 nanoflakes based chemiresistive sensors for ppb-level hydrogen sulfide gas detection," *Sensors and Actuators B: Chemical,* vol. 297, p. 126687, 2019.

[14] D. J. Late, T. Doneux, and M. J. A. p. l. Bougouma, "Single-layer MoSe2 based NH3 gas sensor," *Applied Physics Letters,* vol. 105, no. 23, p. 233103, 2014.

[15] S. Singh, J. Deb, U. Sarkar, and S. J. A. A. N. M. Sharma, "MoSe2 crystalline nanosheets for room-temperature ammonia sensing," *ACS Applied Nano Materials,* vol. 3, no. 9, pp. 9375-9384, 2020.

[16] S. Zhang, W. Zhang, T. H. Nguyen, J. Jian, W. J. M. C. Yang, and Physics, "Synthesis of molybdenum diselenide nanosheets and its ethanol-sensing mechanism," *Materials Chemistry and Physics,* vol. 222, pp. 139-146, 2019.

Journal Pre-proof

[17] R. Jha, A. Nanda, and N. J. I. S. J. Bhat, "Ammonia Sensing Performance of rGO-Based Chemiresistive Gas Sensor Decorated With Exfoliated MoSe 2 Nanosheets," *IEEE Sensors Journal*, vol. 21, no. 9, pp. 10211-10218, 2021.

[18] A. Abun, B.-R. Huang, A. Saravanan, D. Kathiravan, and P.-D. J. A. A. N. M. Hong, "Exfoliated MoSe2 Nanosheets Doped on the Surface of ZnO Nanorods for Hydrogen Sensing Applications," *ACS Applied Nano Materials*, vol. 3, no. 12, pp. 12139-12147, 2020.

[19] Q. Chen *et al.*, "Optimization ethanol detection performance manifested by gas sensor based on In2O3/ZnS rough microspheres," *Sensors and Actuators B: Chemical*, vol. 264, pp. 263-278, 2018.

[20] J. Zhang, T. Li, J. Guo, Y. Hu, and D. J. A. S. S. Zhang, "Two-step hydrothermal fabrication of CeO2-loaded MoS2 nanoflowers for ethanol gas sensing application," *Applied Surface Science*, vol. 568, p. 150942, 2021.

[21] H. R. Inta, S. Ghosh, A. Mondal, G. Tudu, H. V. Koppisetti, and V. J. A. A. E. M. Mahalingam, "Ni0. 85Se/MoSe2 interfacial structure: an efficient electrocatalyst for alkaline hydrogen evolution reaction," *ACS Applied Energy Materials*, vol. 4, no. 3, pp. 2828-2837, 2021.

[22] Y. Navale, S. Navale, M. Chougule, N. Ramgir, and V. J. J. o. M. S. M. i. E. Patil, "NO2 gas sensing properties of heterostructural CuO nanoparticles/ZnO nanorods," *Journal of Materials Science: Materials in Electronics*, vol. 32, no. 13, pp. 18178-18191, 2021.

[23] Y. Huang, Y.-E. Miao, J. Fu, S. Mo, C. Wei, and T. J. J. o. M. C. A. Liu, "Perpendicularly oriented few-layer MoSe 2 on SnO 2 nanotubes for efficient hydrogen evolution reaction," *Journal of Materials Chemistry A*, vol. 3, no. 31, pp. 16263-16271, 2015.

[24] N. Elavarasan *et al.*, "Integrating gC3N4 nanosheet with MoS2 and ZnO-Ag: Remarkably enhanced photocatalytic performance under visible-light irradiation," *Colloid and Interface Science Communications*, vol. 44, p. 100474, 2021.

[25] N. Roy, R. Sinha, H. B. Nemade, T. K. J. J. o. A. Mandal, and Compounds, "Synthesis of MoS2-CuO nanocomposite for room temperature acetone sensing application," *Journal of Alloys and Compounds*, vol. 910, p. 164891, 2022.

[26] X. T. Tran, S. Poorahong, and M. J. R. a. Siaj, "One-pot hydrothermal synthesis and selective etching method of a porous MoSe 2 sand rose-like structure for electrocatalytic hydrogen evolution reaction," *RSC advances*, vol. 7, no. 82, pp. 52345-52351, 2017.

[27] N. Jain, S. Sharma, and N. K. J. J. o. M. S. M. i. E. Puri, "Investigation of charge transport mechanism in hydrothermally synthesized reduced graphene oxide (rGO) incorporated zinc oxide (ZnO) nanocomposite films," *Journal of Materials Science: Materials in Electronics*, vol. 33, no. 3, pp. 1307-1323, 2022.

[28] U. Krishnan *et al.*, "MoS2/ZnO nanocomposites for efficient photocatalytic degradation of industrial pollutants," *Materials Research Bulletin*, vol. 111, pp. 212-221, 2019.

[29] M. S. Vidhya, R. Yuvakkumar, P. S. Kumar, G. Ravi, and D. J. T. i. C. Velauthapillai, "Hydrothermal Synthesis of Flower Like MnSe2@ MoSe2 Electrode for Supercapacitor Applications," *topics in Catalysis*, vol. 65, no. 5, pp. 615-622, 2022.

[30] A. Mishra, J. Narang, C. S. Pundir, R. Pilloton, and M. J. A. o. Khanuja, "Morphology-preferable MoSe2 nanobrooms as a sensing platform for highly selective apta-capturing of salmonella bacteria," *ACS Omega*, vol. 3, no. 10, pp. 13020-13027, 2018.

Journal Pre-proof

[31] G. Ren *et al.*, "ZnO@ ZIF-8 core-shell microspheres for improved ethanol gas sensing," *Sensors and Actuators B: Chemical*, vol. 284, pp. 421-427, 2019.

[32] P. Cao *et al.*, "Ethanol sensing behavior of Pd-nanoparticles decorated ZnO-nanorod based chemiresistive gas sensors," *Sensors and Actuators B: Chemical*, vol. 298, p. 126850, 2019.

[33] S. Vijayakumar, S. J. O. Vadivel, and L. Technology, "Fiber optic ethanol gas sensor based WO3 and WO3/gC3N4 nanocomposites by a novel microwave technique," *Optics & Laser Technology*, vol. 118, pp. 44-51, 2019.

[34] H. Nan *et al.*, "Strong photoluminescence enhancement of MoS2 through defect engineering and oxygen bonding," *ACS Nano*, vol. 8, no. 6, pp. 5738-5745, 2014.

[35] H. Qiu, L. Pan, Z. Yao, J. Li, Y. Shi, and X. J. A. P. L. Wang, "Electrical characterization of back-gated bi-layer MoS2 field-effect transistors and the effect of ambient on their performances," vol. 100, no. 12, p. 123104, 2012.

[36] J. Jaiswal, A. Das, V. Chetry, S. Kumar, R. J. S. Chandra, and A. B. Chemical, "NO2 sensors based on crystalline MoSe2 porous nanowall thin films with vertically aligned molecular layers prepared by sputtering," *Sensors and Actuators B: Chemical*, vol. 359, p. 131552, 2022.

[37] P. Zhao *et al.*, "One-dimensional MoS2-decorated TiO2 nanotube gas sensors for efficient alcohol sensing," vol. 674, pp. 252-258, 2016.

[38] S. Li *et al.*, "Heterojunction engineering of MoSe2/MoS2 with electronic modulation towards synergetic hydrogen evolution reaction and supercapacitance performance," *Chemical Engineering Journal*, vol. 359, pp. 1419-1426, 2019.

[39] Y. Han *et al.*, "Design of hetero-nanostructures on MoS2 nanosheets to boost NO2 room-temperature sensing," *ACS Applied Materials & Interfaces*, vol. 10, no. 26, pp. 22640-22649, 2018.

Journal Pre-proof

[40] Y. Zhou, G. Liu, X. Zhu, Y. J. S. Guo, and A. B. Chemical, "Ultrasensitive NO2 gas sensing based on rGO/MoS2 nanocomposite film at low temperature," *Sensors and Actuators B: Chemical*, vol. 251, pp. 280-290, 2017.

[41] P. Panigrahi, T. Hussain, A. Karton, and R. J. A. s. Ahuja, "Elemental substitution of two-dimensional transition metal dichalcogenides (MoSe2 and MoTe2): implications for enhanced gas sensing," *ACS Sensors*, vol. 4, no. 10, pp. 2646-2653, 2019.

[42] A. V. Raghu, K. K. Karuppanan, J. Nampoothiri, and B. J. A. A. N. M. Pullithadathil, "Wearable, flexible ethanol gas sensor based on TiO2 nanoparticles-grafted 2D-titanium carbide nanosheets," *ACS Applied Nano Materials*, vol. 2, no. 3, pp. 1152-1163, 2019.

[43] M. Ikram, H. Lv, Z. Liu, K. Shi, and Y. J. J. o. M. C. A. Gao, "Hydrothermally derived p–n MoS 2–ZnO from p–p MoS 2-ZIF-8 for an efficient detection of NO 2 at room temperature," *Journal of Materials Chemistry A*, vol. 9, no. 26, pp. 14722-14730, 2021.

[44] R. Kumar *et al.*, "Growth of MoS2–MoO3 hybrid microflowers via controlled vapor transport process for efficient gas sensing at room temperature," *Advanced Materials Interfaces*, vol. 5, no. 10, p. 1800071, 2018.

[45] W. Park *et al.*, "Oxygen environmental and passivation effects on molybdenum disulfide field effect transistors," *Nanotechnology*, vol. 24, no. 9, p. 095202, 2013.

Credit Authorship Contribution Statement

Ms. Nikita Jain: Conceptualization, Methodology, Investigation, Data curation, Writing - original draft, **Prof. Nitin K. Puri:** Conceptualization, Methodology, Writing - review & editing at different stages, Supervision.

Declaration of interests

☒The authors declare that they have no known competing financial interests or personal relationships that could have appeared to influence the work reported in this paper.

☐The authors declare the following financial interests/personal relationships which may be considered as potential competing interests:

Highlights

- Facile hydrothermal synthesis of ZnO incorporated-$MoSe_2$ nanosheets based nanocomposite.
- A highly selective ethanol gas sensor is fabricated based on $MoSe_2$/ZnO nanocomposite.
- The sensor exhibits high gas sensing response (R_g/R_a) of 37.8 at room-temperature to 500 ppm of ethanol gas.
- The sensor performs far better when operated in dry N_2 than in dry air.
- The synergistic effects due to ZnO incorporated-$MoSe_2$ nanosheets boosted the sensing performance.

Journal Pre-proof